





SELECTED PAPERS OF THE 4<sup>TH</sup> INTERNATIONAL CONFERENCE ON CIVIL, ARCHITECTURAL  
AND HYDRAULIC ENGINEERING (ICCAHE 2015), GUANGZHOU, CHINA, 20–21 JUNE, 2015

# Progress in Civil, Architectural and Hydraulic Engineering IV

*Editor*

**Yun-Hae Kim**

*Korea Maritime and Ocean University, Yeongdo-gu, Busan, South Korea*



**CRC Press**

Taylor & Francis Group

Boca Raton London New York Leiden

---

CRC Press is an imprint of the  
Taylor & Francis Group, an **informa** business

A BALKEMA BOOK

*CRC Press/Balkema is an imprint of the Taylor & Francis Group, an informa business*

© 2016 Taylor & Francis Group, London, UK

Typeset by V Publishing Solutions Pvt Ltd., Chennai, India

All rights reserved. No part of this publication or the information contained herein may be reproduced, stored in a retrieval system, or transmitted in any form or by any means, electronic, mechanical, by photocopying, recording or otherwise, without written prior permission from the publisher.

Although all care is taken to ensure integrity and the quality of this publication and the information herein, no responsibility is assumed by the publishers nor the author for any damage to the property or persons as a result of operation or use of this publication and/or the information contained herein.

Published by: CRC Press/Balkema

P.O. Box 11320, 2301 EH Leiden, The Netherlands

e-mail: [Pub.NL@taylorandfrancis.com](mailto:Pub.NL@taylorandfrancis.com)

[www.crcpress.com](http://www.crcpress.com) – [www.taylorandfrancis.com](http://www.taylorandfrancis.com)

ISBN: 978-1-138-02916-3 (Hbk)

ISBN: 978-1-315-63856-0 (eBook PDF)

## Table of contents

Preface	xix
Conference organization	xxi
<i>Structural engineering</i>	
Self-vibration characteristics and influence factors analysis on the monopile foundation support structure of offshore wind turbine <i>X. Wang, Z. Y. Li &amp; C. Chen</i>	3
Cyclic loading test and single plastic hinge analytical analyses of Precast Segmental Bridge Columns with a circular section <i>J. Guo, Z.-Y. Bu &amp; W.-Y. Wu</i>	9
Establishment and seismic performance analysis of AFRP-reinforced concrete frame structure finite element model <i>G. Zhao &amp; X.S. Xu</i>	15
Micro damage in the structural deformation verification under expected rare earthquake <i>X.M. Chen, J. Duan, H. Qi &amp; Y.G. Li</i>	21
Experimental study on the axial bearing capacity and ductility of concrete column confined with double stirrups <i>Y. Y. Li, Y. Y. Zhang, L. Z. Sun &amp; L. Sun</i>	27
The model design of fatigue test of steel-concrete composite segment of railway hybrid girder cable-stayed bridge <i>Y. Zhou, Q. Pu, Z. Shi &amp; Z. Liu</i>	31
Mechanical properties of RC pile strengthened by effective CFRP composites <i>N. Zhuang, Y.J. Zhou, H.D. Sun &amp; S. Ge</i>	35
Applied research of acoustic transmission method on the detection of pile foundation <i>J. Zhang, B. Wang, M. Jing, Z. Sun &amp; Y. Lin</i>	41
A brief discussion on the causes and treatment measures of bridge pile foundation defects <i>J. Li, W. Ren, J. Wang, Z. Zhang, X. He &amp; B. Wang</i>	45
Analysis on load-carrying capacity of a ribbed stiffener shallow spherical shell roof <i>D. Y. Jia, T. Wang &amp; J. Yang</i>	47
Analysis on wind-induced effects of simply supported beam roof structure with metal roof panels <i>L. Huang, W. Wang &amp; H. Deng</i>	51
Shaking table test study on a retrofit method of bottom-business multi-story building <i>Y. Liang, X. Guo, Y. Zhou, J. Jiang &amp; Y. Li</i>	59
Force analysis on continuously pouring outer wrapped concrete based on a SRC arch bridge <i>G. Wei &amp; Z. Gu</i>	63
The analysis of the influence of material strength on the shear capacity of steel tube-reinforced concrete composite column <i>B. Wang, X. Liu &amp; T. Xu</i>	69

Research on the strength of structural Steel Tubes and Coupler Scaffolds <i>Z. Lu, Y. Wen, L. Zhao, T. Liu, C. Li, C. Guo &amp; W. Wang</i>	73
Theoretical analysis on the bearing capacity of structural Steel Tube and Coupler Scaffolds <i>Z. Lu, Y. Wen, L. Zhao, C. Huang, S. Cao, C. Guo &amp; W. Wang</i>	79
Vibrations and buckling analysis of Mindlin plates with stepped variable thickness <i>S.F. Yang, H. Chen &amp; J.P. Wei</i>	85
Analysis of a new Tensairity bridge section <i>D.C. Yuan &amp; M.S. Jiang</i>	93
Experimental research on the stability bearing capacity of Q420 high-strength steel tubular members <i>B. Li, P. Cao, D. Zhang &amp; T. Xu</i>	97
Analysis of the slope pre-stressed anchoring effect on Xiaowan Hydropower Station <i>Y.H. Jiang, G.L. Long, Z. Fan &amp; Z.C. Lu</i>	103
Study on mode II fracture initiation using the strain energy density criterion <i>W. Gao, S.N. Wang &amp; Y. Su</i>	109
Discussion on methods of strengthening concrete structures <i>L. Dou &amp; T. Chen</i>	117
Freeze-thaw damage model for polypropylene fiber concrete <i>S.-p. Chen &amp; F. Ten</i>	121
Design and application of real-time deformation monitoring system for factory building <i>X.D. Pan, Z.B. Yao &amp; L. Zhao</i>	127
Analysis for seismic performance of sheer wall-steel truss structure system <i>W. Sun, X. Niu &amp; H. Chen</i>	131
Seismic performance and retrofit for a historic concrete building in Shanghai <i>H.N. Wang &amp; H.B. Liu</i>	137
Strength model of FRP confined concrete cylinders <i>J.-S. Wang &amp; D.-S. Gu</i>	141
Joints transferring forces outside box columns with different beams' height and columns' deviation of verticality—finite element method simulation <i>Z.G. Xu, R. Yang, Z.B. Zhang &amp; C.G. Deng</i>	145
Reliability of non-resonant quasi-integrable Hamiltonian systems under wide-band random excitations <i>J. Lan, H. Y. Wang &amp; Y.J. Wu</i>	149
Research progress on diaphragm-through joint of Concrete-Filled Square Steel Tube and steel beam <i>M. Li, M. Zhao, Y. Wang, W. Tao, S. Li &amp; R. Shan</i>	155
Analysis of influencing factors on stiffness degradation of Parallel Double Coupling Beams with different width <i>M. Li, C. Wang, Y. Wang, W. Tao, B. Wan &amp; R. Shan</i>	159
Study on parameter optimization of static performance for long-span elliptic suspended dome structure <i>K.R. Shi &amp; Z.R. Jiang</i>	165
A review of analyzing influences of excavation of foundation pits on the surrounding environment <i>S.M. Zhang &amp; F.W. Jing</i>	173
A detailed analysis of the steel strand corrosion effect on serviceability state of PC continuous rigid frame bridges <i>P. Wang, F. Wang, L. Zhang &amp; Z. Zhang</i>	177

Research of the composite wallboard mould connection with multiple assembly mould pouring <i>C. Xu, Y. Zhao, F. Chen &amp; C. Xu</i>	183
Effects of height and span of structures on the vibration period of steel moment resistant frames <i>M. Shadab Far, N. Hassani &amp; A. Dalvand</i>	187
Installation study of transverse brace of stacked tied arch bridges for safety of out-plane buckling <i>Y. Niu &amp; P. Lin</i>	195
Experimental study on mechanical properties of stabilized clay soils used in hydraulic engineering <i>J. Chen, J. Leng, Y. Mao, Y. Yang &amp; Y. Pan</i>	199
Experimental study on the interior joints of the unsymmetrical hybrid connection <i>P.X. Liang, H. Zhang &amp; M.G. Sun</i>	203
Application and numerical simulation of polyurethane insulation board in concrete lining canal <i>Y. Yin &amp; D. Zhang</i>	207
<i>Geotechnical engineering</i>	
Test on the mechanical properties of cement treatment soil under triaxial compression <i>T.W. Zhang, Y.Y. Zhao, X.L. Zhang &amp; X.C. Zhang</i>	213
Influence factors analysis of settlement characteristic of CFG pile-net composite foundation during embankment construction <i>H. Zhang, J.-j. Wu, X.-m. Huang, L.-p. Zhang &amp; X.-m. Yang</i>	219
Construction analysis of cellular sheet piles in thick clay condition <i>Y.Z. Bai</i>	223
The soil dynamic structural parameters based on the view of equivalent elastomer <i>X. Chen, H. Guo &amp; Y.X. Yan</i>	227
Comparison of the mechanical properties of clay rock in Tamusu region and abroad <i>H. Liang, Y. Liu, Q. Lu, S. Chen &amp; W. Bian</i>	233
Study on the simulation test for Osterberg cell test of large pile foundation <i>L. Xu</i>	237
Numerical analysis of settlement of the soft clay foundation <i>X. Jiang &amp; Y. Li</i>	243
Numerical analysis of bearing capacity of single pile under axial loading <i>X. Zhang &amp; Y. Li</i>	247
Analysis of dynamic responses of loess slope by compaction loads <i>Z. Sun, J. Zhao &amp; L. Dong</i>	251
Consolidation analysis of concrete-cored sand-gravel columns improved composite foundation <i>G.B. Ye, Q.W. Zhang &amp; Z. Zhang</i>	255
Application of the correlation method on the analysis of the influence factor of heading blast vibration <i>L. Yan</i>	263
Study on the dynamic deformation characteristics of loess landslide <i>X.M. Cui &amp; X.H. Sun</i>	269
The deformation characteristics of Xi'an aquifer sand under high-stress condition <i>X.H. Sun &amp; X.M. Cui</i>	275

Experiment research on the creep model of aquifer sand in Xi'an <i>X.H. Sun &amp; X.M. Cui</i>	281
Fractal study of debris flow provenance granularity in Qinling temple valley <i>X.C. Xue, D. Han, L. Y. Zhang, P.B. Yang, L.J. Shi, S. Y. Huang &amp; Y.C. Zhang</i>	287
Research on the effect of bank slope on rising and drawdown of water level <i>C. Wang, Y. He &amp; M. Zhang</i>	291
Efficient simulation for subsidence induced by dewatering of pit <i>J.H. Wang, L.J. Tao, X. Han &amp; H.L. Zhou</i>	295
Statistical study on bond strength of rock anchor <i>M. Tang, H. Hu &amp; C. Zhang</i>	301
Particle breakage characteristics of calcareous sand under P-wave <i>X.-Y. Xu, X.-F. Chen, G.-H. Chen, S.-J. Di &amp; W.-Q. Cheng</i>	305
Parameter sensitivity analysis of marine steel pipe pile in sandy soil foundation based on <i>p-y</i> curve method <i>S.-j. Di, X.-y. Xu, X.-f. Chen, X. Wang &amp; L.-f. Bu</i>	309
Kinematic analysis of slope failure modes based on stereographic projection <i>S. Xiao, Y.T. Gao, S.C. Wu, B. Liu &amp; Q.M. Tian</i>	313
Numerical analysis of continuous loading oedometer test <i>Y.-S. Zhang, Y.-T. Gao, Z. Wang &amp; T. Zhang</i>	319
A calculating model for acid load settlement based on mass transfer process of AMD corrosion <i>L. C. Jiang, W.W. Li &amp; J.J. Zeng</i>	325
Investigations into creeping characteristics and constitutive models of soft-rock in deep cretaceous strata <i>H. Li &amp; L.-s. Cui</i>	331
Analysis of characteristics of saline soil in Yanqing new town <i>H.D. Wang, Y.H. Sun, X. Huang, Q.X. Lu &amp; J. He</i>	339
The influences of soil characteristics on the Negative Skin Friction on a single pile <i>T. Huang &amp; S. Y. Fu</i>	343
Numerical analysis of pile uplift bearing capacity with enlarged head <i>F.F. Li, H.F. Qian, H.R. Qin &amp; T.Q. Zhou</i>	347
The load deformation behaviour and the bulging patterns of reinforced gabion retaining walls <i>Y. Jiang, H. Shen, J. Xia &amp; B. Chen</i>	351
The influence of geometric parameters on the deformation behaviour of reinforced gabion retaining walls <i>Y. Jiang, H. Shen &amp; J. Xia</i>	355
Study on crack-generated characteristics of expansive soil <i>L. Cao, M.M. Xin, Z.X. Zhai, Q. Zhou &amp; Z. Y. Ye</i>	359
Finite element analysis of reinforced soil retaining wall <i>Q. Wang, F.F. Li, H.F. Qian, H.R. Qin &amp; T.Q. Zhou</i>	365
The research progress of water-salt mechanism and migration model <i>G.-l. Zhu, L. Zhu &amp; C. Yu</i>	369
Application of strain softening model to numerical analysis of deep tunnel <i>X.H. Diao, S.X. Yang &amp; K. Wang</i>	373
Study on the relation between rock size effect and uniaxial compressive strength <i>Q. Zhang, M. Huang &amp; H. Chen</i>	379
Displacement response of buildings under debris flow impact load <i>J.X. Cao, F.L. Zhang &amp; M.H. Zhou</i>	383



### *Tunnel, subway and underground facilities*

- Displacement analytic solution of a deep elliptical tunnel in a transversely isotropic rock mass considering the shear stress effect 393  
*Z. Zhang & X. Li*
- The effect analysis of subway tunnel construction accidents on adjacent buildings 397  
*X.W. Peng & D.C. Yuan*
- Experimental study on properties of zeolite powder concrete under the hot and humid environment 403  
*Z.T. Chen*
- Study on influence of foundation pit excavation on existing tunnels 407  
*Y. Cui, S.M. Zhang, T. Feng, X.Q. Wang & M.M. Sun*
- Study on numerical simulation of influence of excavation on existing tunnels 411  
*S.M. Zhang, Y. Cui, Y.S. Huang & M.M. Sun*
- Study on deformation control of the existing tunnels under foundation pit excavation 415  
*H.F. Xu, W.G. Liu, G.M. Zhao, Y. Cui & S.M. Zhang*
- The study on safety evaluation method of metro construction based on SHEL—BP neural network 419  
*J.X. Zhao, K. Fan, J.H. Sun & M. Liu*
- Influence of box culvert construction on running metro shield tunnel 425  
*T. Liu, G. An & H. Liang*
- Seismic engineering*
- Quasi-static cyclic loading test and simulation of precast segmental bridge columns with a circular section 433  
*Z.-Y. Bu, W.-Y. Wu & J. Guo*
- A hysteretic model for Precast Segmental Bridge Columns with unbonded posttensioned tendons 437  
*Z.-Y. Bu, W.-Y. Wu & J. Guo*
- The effect of convex friction distribution on the seismic performance of friction systems 441  
*B. Wei, T.H. Yang, X.D. Yu, P. Wang & L.Z. Jiang*
- Seismic performance of the convex-friction and damper systems 447  
*B. Wei, T.H. Yang, X.D. Yu, P. Wang & L.Z. Jiang*
- Quasi-static finite element analysis of a precast concrete frame shear wall structure 453  
*Y.g. Zhang, Q. Zhong, L.g. Jia & W.j. Zhao*
- Discussion on the relation between  $V_{S30}$  and  $V_{SZ}$  461  
*Z.R. Tao, B.H. Zhu & X.X. Tao*
- Structural dynamic anti-seismic performance analysis on the main machine hall in conventional island of Tianwan nuclear power station unit 5, 6 465  
*Y.-h. Jin, J. Zhao & G.-x. Wang*
- Behavior of steel double-channel built-up chords of special staggered truss steel frames structure under reversed cyclic bending 471  
*H.D. Ran & W.L. Liang*
- Seismic influences on high-speed elevators in Super-High-Rise buildings 477  
*I. Torguet & W. Lu*
- Comparison of deep soil deposit seismic response with three basement models 489  
*X.B. Peng & W.L. Yang*

### *Coastal engineering*

- An electrochemical impedance spectroscopy method for identifying the Threshold Chloride Level for rebar in simulated concrete pore solutions 495  
*J.Z. Hu, X.Q. Cheng, X.G. Li, P.C. Deng & G. Wang*
- The corrosion of the pipeline steel in thermocline of the tropical oceans 501  
*P.C. Deng, G. Wang, J.Z. Hu, X.G. Li & X.Q. Cheng*
- Numerical study of typhoon waves with the typhoon hindcasted model 505  
*J. Dong, J.-F. Zhai, Z.-X. Zhu & P.-H. Dong*
- Model study on the sediment dynamics in the Bohai Sea 511  
*H. Liu, H.X. Kang, B.S. Yin & D.Z. Yang*
- Three-dimensional numerical simulation of the tidal flat and channel during flood tide 515  
*Z. Jiao, X. Zhang, X. Dou, Y. Pan & L. Ding*
- Numerical modeling of regional hydrodynamic and seabed morphological effects from the construction of artificial islands in Danzhou, Hainan 519  
*S.H. Zuo, B. Li & Z. Zhang*
- 3D numerical simulation of local scour around regulating structures in tidal reaches 525  
*X. Zhang, X. Dou & Z. Jiao*
- Numerical simulation study of sedimentation downstream tide gates influenced by the length of the irrigation channel 531  
*X. Zhang, Z. Jiao & J. Zhang*
- Application of ecological revetment in Lianshen waterway regulation project 535  
*J. Chen, J. Zhang, Y.-p. Zhou & L.-Y. Xu*
- ### *Road and bridge engineering*
- Numerical simulation analysis of the pressure-dispersed anchor cantilever retaining wall's effect mechanism 541  
*C. Wang, C. Li, X.G. Song, H.B. Zhang & Q.Y. Meng*
- Simulations of transit priority under multi-flow conditions 547  
*J. Ding, Y.Y. Ma, M. Yang & W. Wang*
- Diseases of long span steel bridge pavement and their solutions 551  
*S. Ji, Y. Yang & G. Gong*
- The research on the internal force effect of different vertical curves on a curved box girder bridge 555  
*Y.-x. Liao & J.-h. Gao*
- A study on the stretch tensor of the beam end in a curved girder bridge caused by environmental temperature change 559  
*J.-s. Liu & J.-h. Gao*
- Shear-lag effect in a prestressed continuous rigid frame bridge 565  
*X. Wu, H. Li & X. Yuan*
- Analysis of influencing factors on central load and temperature coupling effect of tram monolithic roadbed 569  
*C. Huang, Y. Xie, Y. Wei & K. Wang*
- Shear failure mechanism of highway subgrade in seasonal frozen area during spring-thawing period 577  
*L. Zhou, E. Su, Y. Wei, C. Huang & Y. Xie*
- The study progress of performance reliability of rolling bearings for urban rail 583  
*X.T. Xia, S.J. Dong, W.H. Zhu & Y.Y. Meng*
- Aircraft taxiing trajectories partly update approach for A-SMGCS 587  
*X. Zhu, Z. Tang & Z. Xia*

Performance analysis of prestressed concrete T-beam structure after fire <i>Q.-f. Wang</i>	593
Cross tensioned and Reinforced Concrete composite pavements application in heavy traffic <i>C. Guo, M.-j. Zhang &amp; Z.-r. Lu</i>	597
Study on reinforcement effect of modified epoxy resins by repeated loading <i>L. Zhao &amp; D. Wei</i>	601
Safety evaluation of long and steep slope based on BP neural network <i>J. Zhang, J. Chen &amp; X. Li</i>	605
Safety audit of continuous downhill in Ma-Chao expressway <i>S.H. Chen, J.H. Liao &amp; X. Wang</i>	609
Reynolds-number effects on static force coefficients of $\Pi$ -shape bridge deck section with wind fairing <i>Q. Zhan, Z. Zhou &amp; Y. Ge</i>	613
Study on performance of cold recycling mixture with emulsified asphalt or foamed asphalt <i>M. Hao</i>	619
Analysis of safety criterion on track irregularities of heavy haul railway under 30t axle load <i>H.F. Zhang &amp; S.L. Lian</i>	623
Analysis of rail thermal effect due to wheel-rail rolling contact in heavy-haul railway <i>S.J. Gu, X.W. Yang &amp; S.L. Lian</i>	627
Research of computation methods on self-anchored cable-stayed suspension bridge <i>J.-l. Chai &amp; J. Shi</i>	633
<i>Hydraulic engineering</i>	
Analysis of the influence of Poyang Lake on convective systems and lightning transited <i>Y.H. Cao, X.F. Ye &amp; X.M. Liu</i>	639
Simulation and cause analysis of the piezometer tube abnormality in a dam <i>D. Li, T. Sheng &amp; D. Zhang</i>	643
Restoration of karst water system in Jinan, China <i>J. Zhou, L. Xing, S. Wang, H. Zhuang, T. Dou &amp; Z. Yang</i>	647
Stability analysis of the cracks of the concrete gravity dam due to the explosion damage <i>C.D. Liu, Z.J. Wang &amp; Y. Xiang</i>	653
Optimization of irrigation mode with brackish water for winter wheat in shallow groundwater areas based on the FEFLOW model <i>G.B. Pang, Z.H. Xu &amp; S. Zhang</i>	659
Seepage analysis of human earth-rock dam during a flood <i>C.D. Liu, J.Z. He &amp; Z.J. Wang</i>	665
Review and prospect of urban storm water simulation technology <i>Z.P. Chen, Y.F. Chen, S.H. Chen &amp; M.J. Chen</i>	671
Analysis on the right abutment stability of Gomal Zam Dam against sliding <i>X.E. Xu &amp; H. Y. Fang</i>	675
Study on optimum band combination of multi spectral vegetation information extraction in Taihu Basin <i>T.T. Cui, Y.Q. Long, Y.T. Wang, Q.F. Hu &amp; Y. Liu</i>	681
Agricultural water-saving zoning and suitable water-saving measures in the Yellow River Delta <i>G.B. Pang &amp; S. Zhang</i>	685
Study on the influence of the miter gate thrust on the lock head structure <i>W.C. Xu, Q.C. Ning, C. Li &amp; Y.Q. Shi</i>	691

Study on the prediction of flood disaster in Nanning City based on the gray neural network <i>R. Y. Ma, M. Lu &amp; S. Y. Wang</i>	697
Study on the hydraulic model test of diversion-type hydropower station <i>C. Qiu &amp; C. Liu</i>	701
Discussion on the development of remediation technology in Chinese metropolitan large mountainous river bank protection <i>W. Guo, J. Dai, Y. Zhou &amp; Y. Zeng</i>	707
In-situ measurement study on stress of frozen inclined shaft lining crossing water-rich sand stratum <i>J. Ren &amp; J. Sun</i>	713
Numerical study on effect of opening ratio for flow field of artificial reefs based on VOF model <i>R.J. Zhang, M. Tao, J.M. Zhou, X.Z. Huang &amp; P. Lian</i>	717
Quantities calculation of truncated cone-shaped metal structural steel funnel <i>N.-m. Mo &amp; L.-y. Wang</i>	721
Numerical research on the effect of the water level on the urban drainage network in Huinan, Pudong district <i>J. Huang, S.Z. Wang, S.Z. Deng &amp; X.B. Yang</i>	727
On inverse problems for a beam with added spring <i>X. Tian &amp; C.-x. Li</i>	731
Hydraulic characteristics of nature-friendly groynes in NanSi river <i>B. Qin, L.Q. Yang &amp; J. Ma</i>	735
Research on flood model of Nansi Lake <i>L.Q. Yang, B. Qin &amp; J. Ma</i>	739
Study on the comprehensive response to drought in China <i>B.S. Weng, D.H. Yan &amp; S.J. Bao</i>	743
Distributed hydrological and silty model in Chabagou basin of Yellow River based on DEM <i>H.J. Zhao, Y.D. Jin &amp; F.X. Chai</i>	747
Numerical simulation on the impact of oil spills on a fishing port <i>R.J. Zhang, J.M. Zhou &amp; X.Z. Huang</i>	753
Status review and prospect of the research into physical model of the impact force of ice on Yellow River-related buildings <i>G. Y. Wu, Y.F. Li &amp; C.P. Wu</i>	757
Characterization of urban rainwater quality for the reuse purpose <i>Z. Li, W. Chen, J. Li &amp; S. Yue</i>	761
Converse intruding by density current, case study in the Xiao Lang Di Reservoir <i>T. Li, J. Zhang, H. Ma &amp; Z. Ren</i>	765
Study on the drainage system of the tailing pond by numeric simulation and model test <i>Q.L. Qi, Q. Li, S.X. Zhang &amp; Z.L. Wang</i>	771
Analysis on optimizing preloading water head of water distribution ring pipe in hydropower station <i>B. Liu &amp; J.T. Lai</i>	777
Based on the grey GM (1,1) model to predict the total water consumption of Liaoning Province <i>J. Chen</i>	781
Analysis of research status of the effect of pollutant adsorption on the motion characteristics of sediment <i>Y. Ren, C. Zhu &amp; L. Zhao</i>	785
Discussion of the quality and safeguard measures of secondary water delivery <i>W. Zhang, Y. Deng &amp; A. Wang</i>	791
Model and application of pressure-dependent leakage detection in water distribution network <i>J.J. Wang, Z.Z. Tang, Y.W. Gui, W.Y. Wu &amp; M. Zhao</i>	795

Analysis on the status and measures of development and utilization of water resources in Lanling <i>X. Zhang, J.W. Huang, H.W. Chen, B. Li &amp; Z.H. Zhang</i>	803
Stochastic optimal operation and improved multi-objective particle swarm algorithm for water supply and environment <i>J. He, S.P. Gu &amp; W.X. Tan</i>	809
Influence of moisture gradient to concrete strength based on Weibull statistical model <i>D. Zheng, Q. Chen &amp; S.W. Chen</i>	813
<i>Disaster prevention and mitigation</i>	
The positioning performance comparison of BeiDou-2 second stage and GPS in some typical regions at home and abroad <i>H.-p. Li, H.-p. Cheng &amp; G.-l. Feng</i>	821
Analysis of roof water inrush risk and forecast of the outflow rate of 3229 working face in Tianzhu Coal Mine <i>H. Wang</i>	825
Prediction research on the hazardous extent of volcano secondary debris flow in Changbai Mountains based on simulation of FLOW3D <i>X. Tong, P. Xu, G. Li, M. Zhang, P. Li &amp; Z. Chen</i>	833
Research trend on the prediction of coal and gas outburst <i>X. Wu</i>	837
The research significance of the steel reinforced recycled aggregate concrete's fire resistance <i>B. Wang, X. Liu &amp; L. Gao</i>	841
Constitutive model derivation and numerical simulation of iron based Shape Memory Alloy pipe joint <i>W. Wang, B. Wang, J.Y. Liu &amp; H. Hai</i>	845
Evaluation on thermal stress distribution of a cable-stayed footbridge under temperature loading <i>X.F. Fan, B. Chen, Y.J. Jiang &amp; Y.Q. Xu</i>	849
Investigation on dynamic properties of a steel-concrete composite cable-stayed footbridge <i>X. Fei</i>	855
Wind-induced dynamic responses of a transmission tower with legs at different height <i>Y.J. Wu, B. Chen, X.X. Song &amp; X.F. Gong</i>	861
The interference effect on aerostatic coefficients of beam in parallel bridge <i>J. Wang &amp; J.X. Liu</i>	867
<i>Computer simulation and CAD/CAE</i>	
Study on the effect of batch piling of coal on silo wall <i>T.J. Tao, M.S. Zhao &amp; Q. Kang</i>	875
An algorithm for random cave geometry generation in Karst landform <i>X.-j. Cui &amp; C. Shi</i>	879
Research on the wind-induced vibration response of adhesive integral-lift scaffold <i>W. Pan, N. Kong, X. Ye &amp; G. Li</i>	887
Finite element analysis for a composite rib floor slab of steel fiber foam concrete <i>Y. Wang, G. Dou, C. Xi, L. Qian &amp; H. Liu</i>	893
Finite element analysis of steel reinforced recycled aggregate concrete axial compression short column <i>B. Wang, X. Liu &amp; L. Gao</i>	899
Research and development of visual monitoring system for prestressed steel structure <i>Z. Li</i>	903

Ballast particle model and initial packing numerical simulation <i>W.J. Shao &amp; S.L. Lian</i>	907
The comparison of integration methods in cellular material model <i>L. Hou &amp; Y.Q. Feng</i>	911
<i>Computational mechanics and construction technology</i>	
Radial temperature field simulation of overhead conductor <i>K. Xiao, P.Y. Li, L. Y. Mo, Z.W. Chen &amp; Q. Gu</i>	917
Analysis and optimization of the slab transition story support system <i>S. Y. Xu, S.H. Deng &amp; S.R. Zhu</i>	923
Research of roof waterproof technology of steel structure factory building <i>H. Chen, C.H. Wei &amp; H.L. Li</i>	927
Investigation of the effectiveness of vertical load on bending responses for a pile subjected to combined lateral and vertical loads <i>F. Mei &amp; G. Li</i>	931
Study of integral lifting spots of steel structure for steel truss structures <i>M. Chen &amp; Y.D. Chen</i>	937
Free vibration analysis on paraboloidal shells of revolution using the Wittrick-Williams algorithm with the consideration of shear deformation and rotary inertia <i>X.D. Chen</i>	943
R-Function Theory method for free vibration of slip clamped trapezoidal shallow spherical shell <i>S. Li &amp; H. Yuan</i>	947
Reducing blasting vibration technique of the hole-bottom air space charging <i>M.S. Zhao, Q. Kang &amp; T.J. Tao</i>	951
Application of module construction in Beijing elevated subway <i>X.F. Xu &amp; J.F. Xu</i>	955
<i>Advanced construction materials</i>	
Effect of metakaolin quantity on the mechanical properties of high-performance concrete <i>H.B. Liu, K.L. Xiao, W.Q. Tang, W.Z. Ma, Z.Q. Shi &amp; X.G. Li</i>	961
Study on mechanical behavior and thermal properties of recycled brick concrete mixed with cinder insulation <i>C. Chen, Y. Wu, Y. Lei &amp; F. Li</i>	965
Calculation of Poisson's ratio of laminate composite <i>Y.R. Li, H.B. Jiang &amp; W.S. Chen</i>	971
The effects of nanophase SiO <sub>2</sub> for the performance of epoxy resin <i>Y.J. Jin &amp; SH.J. Wang</i>	977
The study of alkaline-activated magnesium slag cementitious material <i>Y.J. Jin, SH.J. Wang &amp; L.G. Xiao</i>	981
Effect of lithium on the microstructure and properties of Al-Mg-Si-Li alloys with different Si contents <i>Z.K. Zhao, Q. Gao, Y. Yao, B.Z. Liu, D. Zhang &amp; G.Q. Wang</i>	985
Laboratory study on performance of semi-flexible mixture <i>L. Zhang, H. Wang &amp; R. Li</i>	989
Preparation of C <sub>3</sub> S by the sol-gel method <i>C.L. Zhang, P. Song &amp; Q. Wang</i>	995
Study of durability of concrete mixed with cement reducing agent <i>S.Z. Yue &amp; Y.F. Zuo</i>	1001

Residual stress influence on stability of thin-walled box section column of high-strength steel <i>L. Gao, K. Jiang, X. He &amp; L. Bai</i>	1005
Laboratory research of hard asphalt applied on bus lane renewal <i>L. Zhang &amp; Z. Liu</i>	1011
Self-Compacting Concrete prepared with solid waste <i>G.X. Han, X.H. An, F. Jin, C.J. Chen &amp; H. Zhou</i>	1017
Experimental study on mechanical properties of fiber reinforced lightweight aggregate concrete after freeze-thaw cycle <i>J. Huang, J. Wang &amp; A. Liu</i>	1023
Influence of aggregates on coefficient of thermal expansion of concrete <i>M. Gao, G. Yuan, L. Wang &amp; G. Gao</i>	1029
Analysis of environmental hazard and leaching characteristics of heavy metals in solid waste <i>S.H. Zhou, H.Q. Yang, J.J. Yan &amp; J. Su</i>	1035
Frost resistance of city sludge sintered shale brick <i>B. Zhang, B.-Z. Huang &amp; J. Lai</i>	1039
The influence of the lithium content on performance to $\text{Li}_x\text{FePO}_4$ <i>R. He, Z. Liu, L. Zhang, M. Yan &amp; Y. Zhang</i>	1045
Research on recycling waste concrete <i>H.Z. Zhang, W.R. Cao, L.Z. Yu, X.H. Zhang &amp; L. Shang</i>	1049
Discussion on the cause of concrete floor crack <i>Z.N. Tong</i>	1055
Manufactured sand make pumping of high-level concrete mix design and optimization <i>X. Chen, X. Liang &amp; Z. Li</i>	1059
Experimental research on compounding high-performance pavement concrete by utilizing high titanium heavy slag <i>J. Sun, J. Guo &amp; H.F. Duan</i>	1065
Experimental study on axial compression behavior of recycled aggregate concrete <i>J.X. Deng, X.G. Zhang, X.J. Qi &amp; X.H. Huang</i>	1069
Study on mixture ratio design and performance of cement stabilized gravels based on vibratory compaction method <i>H.Y. Pan, L.M. Qin, X.J. Qi, L.L. Xie &amp; M.Q. Jin</i>	1075
Contrast on axial compressive strength between FRP and steel reinforced confined concrete <i>T.W. Bi, D. Gu &amp; X. Zhang</i>	1079
Research on the fracture toughness of PC/ABS blend <i>M.-H. Ho, J.-P. Yeh &amp; P.-N. Wang</i>	1083
Research on anti-aging performance of high modulus asphalt <i>H. Wei, W. Cao, W. Li &amp; X. Guo</i>	1089
Experimental study on low-intensity self-compacting concrete with non-continuous gradation recycled coarse aggregates <i>J. Ma, C.Y. Wu &amp; Z.H. Pan</i>	1093
<i>Engineering management</i>	
Study on the pre-evaluation of the bench blasting effect based on the uncertainty measurement theory <i>T.J. Tao, M.S. Zhao &amp; Q. Kang</i>	1101
Dynamic analysis on the ballast track application in urban railway tunnels <i>Y. Wang, X. Zhang &amp; J. Chen</i>	1105
Influence of mixture proportion on bleeding of concrete <i>J. Yang, R. Bai, J. Cai, J. Wu &amp; W. Liu</i>	1111

The impact of curved track irregularities on dynamical response of rising speed trains <i>J. Fang, X. Y. Lei, S. L. Lian &amp; L. Y. Liu</i>	1115
Risk analysis of green building project at the decision-making stage <i>W. Xu &amp; S. Liu</i>	1121
Research on collaborative design application based on BIM <i>W. Xu &amp; Y. Liu</i>	1125
Experimental study on smoke propagation in titled underground tunnel fires <i>J. M. Li, Z. H. Huang, C. Chen, J. Chuang &amp; Y. Li</i>	1129
Joint operation of water quantity and water quality based on dualistic water cycle <i>J. He, S. P. Gu &amp; L. S. Suo</i>	1133
Design of long-span double-layer steel bracket for the roof of squat silo <i>J. H. Shao, X. F. Ye, Z. H. Wang &amp; X. B. Huang</i>	1139
An empirical study on the task assignment model building of indemnification for housing construction project—take a case of Guangzhou <i>L. Chen, J. Tan, J.-h. Tan, Z.-p. Zhang &amp; T. Tao</i>	1145
<i>Architecture, landscape planning and design</i>	
Research on spatial morphology characteristics of traditional “bottom-up” settlements—a case study of Licha Village and Xiangang Village in Gaoyao, Guangdong Province <i>Y. Lin &amp; J.-g. Wang</i>	1153
Bamboo tower—the design exploration of landscape tower in Zunyi Normal College <i>Z. Song, X. Liu &amp; X. Fang</i>	1163
Analysis of building materials transparency effects on building space <i>H. H. Hu &amp; X. H. Ding</i>	1169
SWMM-based evaluation and improvement of drainage infrastructure: A case in Beijing, China <i>Y. Sun, Q. Chang, F. Han, H. J. Li &amp; L. J. Zhang</i>	1173
Analysis on the river channel landscape design of Lianjiang River New Town <i>Y. Du</i>	1179
The principles of the spatial layout for the traditional villages in the Northwest Plateau of Sichuan based on the ecological concept <i>J. W. Hou, Y. Cao, W. Zhu &amp; P. F. Qiu</i>	1183
Study on index system and method of evaluating land suitability for construction in gentle-slope hilly areas at county level in Yunnan Province <i>S.-q. Zhang, Z.-s. Yang, Y. Yang, S.-l. Ma, Y.-m. He &amp; M.-j. Xu</i>	1187
A brief discussion about design research on traditional residence renovation as a resort hotel <i>Y. Shi &amp; Z. Zhuo</i>	1191
Finite element analysis of confined precast concrete shear wall <i>L. J. Dou &amp; M. L. Gao</i>	1195
Research on the unification of architecture and art, technology and art in architecture—Take I. M. Pei’s Architectural Design Works for Example <i>L. Guo</i>	1199
Research on brickwork dwelling optimization design in Nu-Jiang River drainage basin <i>F. Wang, J. Chen, Q. Zhang &amp; J. Liu</i>	1203
Landscape pattern dynamic variation for 30 years in Chuanjiang River Basin <i>Z. L. Yu, T. L. Qin, S. Y. Zhang, C. L. Hao, M. J. Yang &amp; M. He</i>	1209
Effect of motor vehicle emissions on air quality of green urban community <i>S. M. Zhao, Q. Q. Li &amp; X. Y. You</i>	1215
The old town of Wubu the forgotten stone castle <i>X. Liang</i>	1219



Inspiration of evaluation criteria of international historic site to China heritage protection system <i>X. Y. Zhao &amp; J. Gao</i>	1223
The application of modular building in post-disaster reconstruction of the countryside <i>X. S. Wang &amp; Q. Zhao</i>	1229
Analysis of development trend of country parks in China <i>L. N. Li &amp; J. Gao</i>	1235
The analysis of urban underground space based on environmental comfort <i>Y. P. Gong</i>	1241
Post occupancy evaluation of urban public space environment: Take Yingze Park in Taiyuan as an example <i>X. R. Zhao &amp; Q. F. Shi</i>	1245
Influence of the Chinese traditional Feng-shui theory on the layout of contemporary residential space <i>B. Wang &amp; T. Li</i>	1249
Research on strategy of ecological security assessment in Beijing urban space <i>X. Y. Ma, L. Feng &amp; W. L. Zhang</i>	1253
Study on types of rural landscape <i>Y. Liu</i>	1259
Study on the numerical model and design optimization of a green office building in Wuhan, China <i>W. Liu, J. Yang &amp; W. Hu</i>	1263
Research on rural greenway suitable for Beijing <i>L. Feng &amp; X. Y. Ma</i>	1269
Numerical evaluation for climates adaptive capability of traditional alkaline soil dwelling <i>T. Zhang, J. Liu &amp; Q. Zhang</i>	1273
Qualitative study of climate adaptability of traditional alkaline dwelling <i>T. Zhang, J. Liu &amp; Q. Zhang</i>	1279
Plant configuration discussion of urban riparian park in the loess plateau region: Setting Taiyuan Fenhe Park as an example <i>J. Y. He &amp; J. Gao</i>	1283
Analysis of traditional architectural heritage protection strategy: Taking Jiajiazhuang historical and cultural district in Xiaoyi as an example <i>D. Zhang &amp; Y. Liu</i>	1287
 <i>Sustainable development of building energy, traffic and environment</i>	
Study on the application of iron tailings for the improvement of saline-sodic soil <i>A. L. Shao</i>	1293
The general solution of the Sturm–Liouville equation in heat conduction problems <i>F. B. Lu, Y. Z. Fu &amp; S. Y. Su</i>	1297
Solar Decathlon—entries of Tongji University <i>L. Yang &amp; F. Qian</i>	1301
The ecological restoration of building landfill and garbage landfill <i>J. N. Yang, H. Y. Li &amp; L. Y. Lv</i>	1305
The key technologies of ecological restoration of sanitary landfill <i>J. N. Yang, H. Y. Li &amp; L. Y. Lv</i>	1309
Experimental verification and pair-group analysis study of passive space design strategies <i>J. Li, Y. Song &amp; Q. Wang</i>	1313

Research into the measurement detection and line optimization of the carbon capture ability of Italian poplars <i>Z. Wang &amp; Q. Liu</i>	1319
Analysis of current situation after restoration in the Tianjin Lingang ecological wetland park <i>N. Zhao, H. Y. Li, J. Hu, J.W. Hou &amp; T. Wen</i>	1323
The analysis of Lingang Wetland Park's eco-efficiency <i>Y. Y. Wan, H. Y. Li, J. Hu, J.W. Hou &amp; T. Wen</i>	1327
A study on the influence of space expansion in the urban fringe area in megalopolis on urban land used for carbon source and sink: A case of Shanghai <i>M.L. Qin, J. Zhao, H. Li, J. Ya &amp; Y. Tang</i>	1331
The study on the characteristics of the spatial structure of carbon source and carbon sink in megalopolis: Shanghai as a case <i>M.L. Qin, H. Li, J. Zhao &amp; J. Ya</i>	1339
The environmental factor evaluations on the recycling models of WHA reverse logistics <i>Y. Liu, T. Hu &amp; F. Xie</i>	1345
Practice of interprovincial public transport in Beijing–Tianjin–Hebei region <i>Y. Y. Mai &amp; X.N. Sun</i>	1351
Research on adsorption of methyl orange by magnetic activated carbon prepared by Eucalyptuses <i>J. Liu, H. Zhang, L. Luo, H. Huang &amp; W. Chen</i>	1357
Dynamic distribution and balance technique of energy-saving ventilation system <i>K. Zhang &amp; J.L. Wang</i>	1363
Application of energy-saving technology of outer wall <i>Z.N. Tong</i>	1367
Advanced treatment of rainwater by H <sub>2</sub> O <sub>2</sub> /UV process <i>Z. Li, W. Chen, J. Li &amp; S. Yue</i>	1371
Effects of ozone and drought on fluorescence physiology of three seedling types in China <i>X. Hou &amp; X. Li</i>	1377
Study on Shenyang region PM 2.5 concentration variation characteristic based on GIS <i>H. Ding, L. Sun &amp; X. Wang</i>	1383
Studies on the thallium emission standard of industrial wastewater <i>H. Yi, D.-g. Luo, Y.-h. Chen &amp; Q.-h. Wu</i>	1387
Limit of abandoning wind and sunshine rate research based on wind-photovoltaic-thermal coordinated dispatch model <i>R. Li, L. Dang &amp; Z. Dong</i>	1393
A research on intelligent management strategies for municipal solid waste disposal in Wuhan, China <i>W. Liu, J. Yang &amp; W. Hu</i>	1399
Experimental study of infiltration characteristics of outdoor particulate matter into the indoor <i>Z. Li, F. Zhang &amp; Q. Shi</i>	1403
The prediction research of underground road pollutant distribution <i>Z. Li, Q. Shi, H. Zhang &amp; C. Chen</i>	1407
Design and calculation of fluid equilibrium flow in parallel plate-exchangers <i>W. Pang, G. Li, M. Liu &amp; J. Wang</i>	1411
Health risk assessment of heavy metals in PM <sub>2.5</sub> of major and typical cities in China <i>L. Lv, H. Li &amp; J. Yang</i>	1417
Author index	1423

## Preface

This proceeding contains the accepted papers from The 2015 4th International Conference on Civil, Architectural and Hydraulic Engineering (ICCAHE2015). The first of this conference was held in Zhangjiajie, China on 10–12 August 2012, the second conference was held in Zhuhai, China on 27–28 July, 2013, and the third conference was held in Hangzhou, China on 30–31 July, 2014. Following the success of the previous conferences, The fourth of this conference series (ICCAHE 2015) was held in Guangzhou, China, on June 20–21 2015. This conference series is a forum for enhancing mutual understanding between scientists, engineers, policymakers and experts in the civil, architectural and hydraulic engineering field. This proceeding is enriched by contributions from many experts representing many industry and academic establishments worldwide. Authors from more than 20 different countries have pooled their rich multi-disciplinary up-to-date knowledge, in order to share their invaluable experience with the community. All papers published in this volume have been peer reviewed through processes administered by the proceedings editors. Reviews were conducted by expert referees to the professional and scientific standards.

We would like to express our deep gratitude to all the keynote speakers, authors, referees, exhibitors, technical co-sponsoring organizations, committee members, and many others on whom the success of this prestigious event depends.

The Organizing Committee of ICCAHE2015



## Conference organization

### CHAIRMEN

Prof. Yun-Hae Kim, *Korea Maritime and Ocean University, Korea*  
Prof. Xun Wu, *Tongji University, China*  
Prof. Weizhen CHEN, *Tongji University, China*

### INTERNATIONAL SCIENTIFIC COMMITTEE

Prof. Huaizhi Su, *Hohai University, China*  
Dr. Ahmed Sarhan, *Malaya University, Malaysia*  
Dr. Gui Wang, *The University of Queensland, Australia*  
Dr. Scott T. SMITH, *Hong Kong University, Hong Kong*  
Dr. Sreenivasan M, *SR Technical University, IN*  
Dr. Tianjian Ji, *The University of Manchester, UK*  
Prof. Abdul Amir H. Kadhum, *Malaysia*  
Prof. A. Kaveh, *Iran University of Science and Technology, Iran*  
Prof. Aftab Mufti, *University of Manitoba, Canada*  
Prof. Antoine E. Naaman, *University of Michigan, USA*  
Prof. Ayman Mosallam, *Univ of California Irvine, USA*  
Prof. B.H.V. Topping, *Heriot-Watt University, Edinburgh, UK*  
Prof. Chao Hsun Haung, *National Taipei University of Technology, Taiwan*  
Prof. Chiew Sing-Ping, *Nanyang Technological University, Singapore*  
Prof. Carlos Aquino, *Ritsumeikan University, Japan*  
Prof. David Hui, *University of New Orleans, USA*  
Prof. Hamid Ronagh, *The University of Queensland, Australia*  
Prof. Han-Bin Ge, *Meiju University, Japan*  
Prof. I.E. Harik, *University of Kentucky, USA*  
Prof. J.H. Bungey, *University of Liverpool, Liverpool, UK*  
Prof. Jian-Fei Chen, *The University of Edinburgh, UK*  
Prof. Jongwook Park, *Sungkyunkwan University, Korea*  
Prof. Katsuyuki Kida, *Kyushu University, JP*  
Prof. Ken-ichi Manabe, *Tokyo Metropolitan University, Japan*  
Prof. Kum-Gil Sung, *Inha University, Korea*  
Prof. Kyung-Man Moon, *Korea Maritime University, Korea*  
Prof. K.J. Bathe, *Massachusetts Institute of Technology, USA*  
Prof. Kang Seok Lee, *Chonnam National University, South Korea*  
Prof. Lau Hieng Ho, *Curtin University of Technology, Malaysia*  
Prof. Luciano Feo, *University of Salerno, Italy*  
Prof. Lawrence C. Bank, *University of Wisconsin-Madison, USA*  
Prof. Marcus M.K. Lee, *The University of Southampton, UK*  
Prof. Mark G Stewart, *The University of Newcastle, Australia*  
Prof. M.N. Soutsos, *University of Liverpool, Liverpool, UK*  
Prof. Nangkula Utberta, *The National University of Malaysia, Malaysia*  
Prof. Ramiro Sofronie, *University of Bucharest, Romania*  
Prof. R. Sri Ravindra rajah, *University of Technology, Australia*  
Prof. Tim Ibell, *University of Bath, UK*

Prof. Tamon UEDA, *Hokkaido University, Japan*  
 Prof. TAN Kang-Hai, *Nanyang Technological University, Singapore*  
 Prof. Tan Kiang Hwee, *National University of Singapore, Singapore*  
 Prof. Wen-Hsiang Hsieh, *National Formosa University, Australia*  
 Prof. Zhi-Shen Wu, *Ibaraki University, Japan*  
 Prof. Zong Woo Geem, *Gachon University, South Korea*  
 Prof. Hansong Tang, *The City University of New York, USA*  
 Prof. Shixiong Hu, *East Stroudsburg University of Pennsylvania, USA*  
 Dr. Dar Hao Chen, *Texas Department of Transportation, USA*  
 Prof. Zhouhui Yang, *University of Alaska Anchorage, USA*  
 Prof. Chunsheng Cai, *Louisiana State University, USA*  
 Prof. Qiusheng Li, *City University of Hong Kong*  
 Prof. Jianguo Liang, *Changsha University of Science and Technology, China*  
 Prof. Weiliang Jin, *Zhejiang University, China*  
 Prof. Xianglin Gu, *Tongji University, China*  
 Prof. Chunyu Wei, *Hunan University, China*  
 Prof. Feng Liu, *Guangdong University of Technology, China*  
 Prof. Shilang Xu, *Zhejiang University, China*  
 Prof. Shanhua Xu, *Xi'an Univ. of Architecture and Technology, China*  
 Prof. Lieping Ye, *Tsinghua University, China*  
 Prof. Jianguo Nie, *Tsinghua University, China*  
 Prof. Tiejun Zhao, *Qingdao Technological University, China*  
 Prof. Xingang Zhou, *Yantai University, China*  
 Prof. Jiru Zhang, *Wuhan University of Technology, China*  
 Prof. Chuangbin Zhou, *Wuhan University, China*  
 Prof. Xuejun Zhou, *Shandong Jianzhu University, China*  
 Prof. Guoqiang Zhang, *Hunan University, China*  
 Prof. Yibin He, *Hunan University, China*  
 Prof. Ditao Niu, *Xi'an Univ. of Architecture and Technology, China*  
 Prof. Zhiwu Yu, *Central South University, China*  
 Prof. Baihao Li, *Dongnan University, China*  
 Prof. Shuguo Liang, *Wuhan University, China*  
 Prof. Shicheng Ma, *Xiangtan University, China*  
 Prof. Bowang Chen, *Hunan City University, China*  
 Prof. Xijun Liu, *Hunan University of Science and Technology, China*  
 Prof. Shuibo Xie, *Nanhua University, China*  
 Prof. Wanlin Cao, *Beijing University of Technology, China*  
 Prof. Chaohe Chen, *South China University of Technology, China*  
 Prof. Changyu Cui, *Harbin Institute of Technology, China*  
 Prof. Yaojun Ge, *Tongji University, China*  
 Prof. Linhai Hang, *Tsinghua University, China*  
 Prof. Yong Huang, *Guizhou University, China*  
 Prof. Guoqiang Li, *Tongji University, China*  
 Prof. Lijuan Li, *Guangdong University of Technology, China*  
 Prof. Aiqun Li, *Southeast University, China*  
 Prof. Guangfan Li, *Hainan University, China*  
 Prof. Weijun Yang, *Changsha University of Science and Technology, China*

*Structural engineering*

# Self-vibration characteristics and influence factors analysis on the monopile foundation support structure of offshore wind turbine

X. Wang, Z.Y. Li & C. Chen

*State Key Laboratory of Hydrology-Water Resources and Hydraulic Engineering, Nanjing Hydraulic Research Institute, Nanjing, China*

**ABSTRACT:** Self-vibration characteristic and influence factors analysis on the monopile foundation support structure of offshore wind turbine was conducted for the structural dynamic design. The results indicated that the fundamental frequency of the towering support structure was 0.437 Hz. The fluid-solid coupling effect was very weak; that is, the self-vibration frequency decreased within 5% when the flow action was considered. The fundamental frequency was affected obviously with the turbine unit mass and the elastic modulus of the soil foundation, and it could be raised through reducing the unit mass. The actual elastic modulus should be employed for vibration analysis. A nonlinear positive relation was shown between the thickness of the support structure wall and the vibration fundamental frequency. The fundamental frequency increased quickly when the surface wall was relatively thin, whereas the increase speed became slow when the wall became thick. It was reasonable that the wall thickness was designed by 1% of the diameter of the monopile.

**Keywords:** offshore wind turbine; monopile; self-vibration characteristics; influence factor

## 1 INTRODUCTION

Due to environment pollution and energy crisis, the wind power as a kind of clean energy has developed swiftly in recent years. Wind energy on the sea was abundant and stable; therefore, offshore wind power has become the investment focus at home and abroad. Europe is leading in the world, and China is still in its beginning stage. The “12th Five-year Plan” of China shows that the offshore wind power capacity would be up to 5 million kilowatt, which indicated that the offshore wind power in China is going to a rapid development period. At present, the planning and development of wind power at sea in China is mainly centered around offshore. The typical monopile foundation widely used at abroad is suitable for the offshore wind power of China, which has adopted in the offshore wind power design, for example the Xiangshui intertidal area wind farm in Jiangsu Province and the Wailuo offshore wind farm in Guangdong Province. The monopile foundation would become a popular type in the offshore wind power in China.

However, the towering structure formed by wind turbine, pylon and foundation pile suffered the impact of the wave and tide flow that did not exist for onshore wind. Meanwhile, there was a complicated coupling effect between the

wave flow and the supporting structure. With the increase in the single unit capacity and weight, the vibration safety of the supporting system has become more outstanding. It is known from the structure dynamic mechanics that the dynamic emphasize coefficient would be up to the maximum value when the self-vibration frequency of the structure is close to the main frequency of the load. So, the self-vibration frequency should be kept away from the main frequency of the load and the deviation should be more than 20%. As the inner reason of vibration, the structure self-vibration characteristics determined the vibration response, and still provided reference for resonance check and structural dynamic design optimization. Therefore, self-vibration characteristics and influence factors analysis such as fluid-solid coupling, unit weight, soil foundation elastic modulus, and structure dimension on the monopile foundation support structure of offshore wind turbine were conducted.

## 2 STUDY METHOD

When the hydraulic structure vibrates, the adjacent fluid inertial force, damping force and elastic force corresponding with the vibration acceleration, velocity and displacement would apply on



the structure, which would change the mass, damping and stiffness of the vibration system and then the vibration characteristic of the structure would be changed. It is shown that the self-vibration frequency of the hydraulic structure would usually decrease by about 20%~30% when the fluid-structure coupling effect is considered. For the steel gate with thin walls, the basic frequency would decrease up to 50%. Therefore, the influence of the fluid on the structure's self-vibration characteristics could not be neglected.

At present, the additional mass method was used to describe the interaction between the fluid and the solid. The most common additional mass method was based on the Laplace equation that is met by the dynamic water pressure. The additional mass matrix was derived for the dynamic equation of the finite element method. That is, the form of the dynamic equation did not vary but added an additional mass matrix based on the mass matrix. Then, the FEM dynamic equation considering the additional mass would become as follows:

$$[K]\{\delta\} + [C]\{\dot{\delta}\} + ([M] + [M_p])\{\ddot{\delta}\} = \{R_0\} \quad (1)$$

where  $[M_p]$  is the additional mass matrix and  $\{R_0\}$  is the load vector. Damping had a little effect on the self-vibration frequency and vibration modes. As a result, the damping of the structure was ignored in the analysis.

### 3 FEM MODEL

Monopile support structure used for offshore wind power was taken for example. A three-dimensional FEM model was built, which consisted of the monopile, the foundation and the flow. The monopile was dispersed by the Shell element with six degrees of freedom and four nodes, the foundation and water were dispersed by the Hexahedral element. The whole model was divided into 17164 nodes and 14460 elements, as shown in [Figure 1](#).

Materials included the support structure, foundation and water, in which the structure and the foundation were regarded as the linear elastic material, and the water was considered as the potential flow to calculate the additional mass. These material parameters are listed in [Table 1](#).

In order to avoid the effect on the modes from the limited range foundation, the stiffness of the foundation without mass was only considered. The wind turbine was not built in the whole model and the unit mass would add to the top of the tower tube. To study the effect factor on the modes of the support structure, some conditions are listed in [Table 2](#), among which, the first was the basic condition.

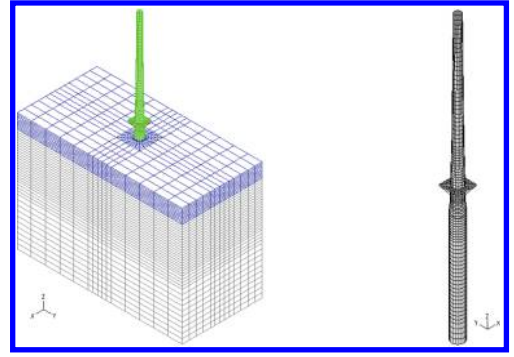


Figure 1. The FEM grid.

Table 1. Material parameters.

Material	Density ( $\text{kg} \cdot \text{m}^{-3}$ )	Elastic modulus (Pa)	Poisson ratio
Support structure	7850	2.00E+11	0.3
Foundation	0	2.00E+08	0.2
Water	1000	2.56E+09	

Table 2. Calculation conditions.

Condition number	Foundation	Water	Unit mass	Support structure
1	√	√	√	√
2	√		√	√
3	√			√
4	Different elastic modulus		√	√
5	√		√	Different wall thickness

### 4 SELF-VIBRATION CHARACTERISTICS

The first five phases of self-vibration characteristics parameters of the support structure under the basic condition are listed in [Table 3](#), and the first three phases of vibration types are shown in [Figure 2](#). It could be found that the fundamental frequency of the foundation-water-support structure system was 0.437 Hz, which is relatively low due to its towering characteristics. The mode indicated the first phase bend vibration. The second-phase frequency was 2.243 Hz and showed the second-phase bend vibration. The third-phase frequency was 5.482 Hz and showed the third bend vibration. The high-phase modes expressed the local weak component

Table 3. Self-vibration characteristics of the parameters.

Phase number	Frequency/Hz	Mode participation parameters		
		X	Y	Z
1	0.437	-5.89E-03	-6.43E+02	2.91E-11
2	2.243	8.50E-05	4.97E+02	5.21E-10
3	5.482	1.91E-04	3.84E+02	7.53E-09
4	8.911	-4.55E-08	1.46E-07	9.65E+02
5	9.050	1.43E-08	1.92E-08	4.80E-02

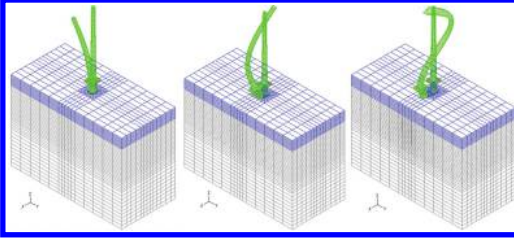


Figure 2. The first three-phase vibration modes.

vibration, which would provide little contribution to the support structure vibration.

## 5 INFLUENCE FACTORS ANALYSIS

### 5.1 FSI influence

For the second condition, the water elements were removed from the whole model; that is, the water additional mass was not considered. Table 4 presents the comparison of the self-vibration frequency of the two conditions. It could be found that the self-vibration frequency altered little, and the first five modes were consistent whether the water additional mass was considered. The self-vibration frequency decreased only about 5%, considering the FSI influence. This was mainly because the water force range was relatively little compared with the whole towering support structure, and the force position was still near the bottom of the monopile.

### 5.2 Unit mass influence

With the increase in the unit power of the offshore wind turbine, the blade dimension and the unit mass greatly increased. For the towering, long and thin support structures, the huge mass on the top would affect the self-vibration characteristics and dynamic responses.

The unit was simplified as a concentrate mass on the top of the tower. The first five self-vibration

Table 4. Self-vibration frequency comparison whether the water was considered.

Phase number	Frequency/Hz		Decrease/%
	Without water	With water	
1	0.441	0.437	0.90
2	2.295	2.243	2.24
3	5.754	5.482	4.73
4	9.231	8.911	3.47
5	9.280	9.050	2.48

Table 5. Self-vibration frequency comparison whether the unit mass was considered.

Phase number	Frequency/Hz		Decrease/%
	Without unit mass	With unit mass	
1	0.666	0.441	33.8
2	2.859	2.295	19.7
3	6.804	5.754	15.4
4	10.689	9.231	13.6
5	11.020	9.280	15.8

frequencies of the support structure whether the unit mass was considered are listed in Table 5. It could be found that the fundamental frequency decreased by 33.8% when the unit mass was taken into account, but the first five modes were still consistent. Therefore, the unit mass should not be neglected in the dynamic characteristic analysis. It still indicated that the fundamental frequency could be raised by reducing the unit mass pursue to the technology progress.

### 5.3 Foundation elastic modulus influence

As the monopile connected with the soil foundation, the foundation elastic modulus would influence the whole stiffness of the support structure and then affect the structure's self-vibration characteristics. In order to study the influence of the foundation elastic modulus, several different foundation elastic moduli were adopted to analyze the self-vibration frequency of the support structure. Figure 3 shows the nonlinear relation between the fundamental frequency and the elastic modulus. It could be found that the frequency decreased with the decreasing elastic modulus. When the foundation elastic modulus was low, the self-vibration frequency altered obviously, while with the increase in the modulus, the self-vibration frequency increase became slow. For example, the fundamental

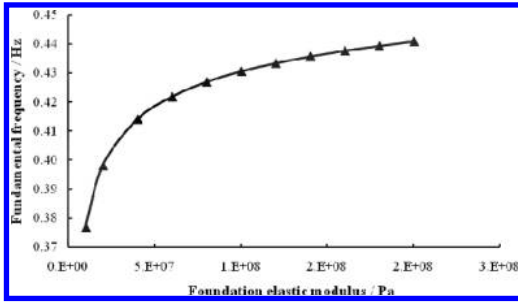


Figure 3. The influence of the foundation elastic modulus.

frequency increased by 14.3% when the elastic modulus increased from  $1e7$  Pa to  $1e8$  Pa, while that increased by 2.4% when the elastic modulus increased from  $1e8$  Pa to  $2e8$  Pa. Therefore, due to the low fundamental frequency of the support structure and the great influence of the foundation elastic modulus, the actual foundation parameter obtained from geological data should be adopted to calculate the self-vibration characteristics of the support structure to ensure the dependability of the result.

#### 5.4 Influence of the monopile wall thickness

The towering structure with a thin wall was mainly comprised of monopile and tower tube, and the wall thickness was designed by about 1% of the monopile diameter at present. With the increase in the unit capacity and mass, blade dimension and mass, the monopile diameter also increased. The support structure was simple and the wall thickness maybe was one of the important influencing factors when the shape dimension was determined. In this paper, the actual project Wailuo offshore wind farm in China was taken as an example. The outer diameter of the monopile was 5.5 m, and the wall thickness was 0.064 m. Several other wall thicknesses were selected to study the influence on the self-vibration frequency and the first three mode frequencies are listed in Table 6. It could be found that the frequency increased with the increase in the wall thickness, but the whole change was very little. Figure 4 shows the nonlinear relationship between the fundamental frequency and the wall thickness. The fundamental frequency increased slowly when the wall thickness increased, simply because the mass of the structure was still increasing. Therefore, for the support structural dynamic design, some structure optimization, such as changing the wall thickness or strength of the wall surface, could change the structure's self-vibration characteristics to avoid resonance.

Table 6. Relationship between the wall thickness and the self-vibration frequency.

Wall thickness/m	Frequency/Hz		
	First phase	Second phase	Third phase
0.03	0.346	2.185	4.574
0.04	0.382	2.208	5.341
0.05	0.408	2.225	5.432
0.064	0.437	2.243	5.482
0.10	0.482	2.274	5.533
0.15	0.514	2.295	5.554

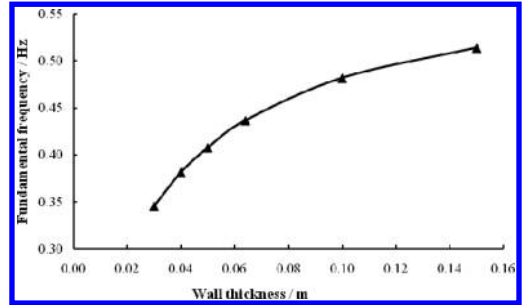


Figure 4. Wall thickness influence on the fundamental frequency.

From the relationship curve, it was reasonable that the wall thickness of the monopile was designed by about 1% of the pile diameter.

## 6 CONCLUSIONS

Self-vibration characteristics and influencing factors of the monopile support structure of offshore wind power were studied to guide the structural dynamic design. Based on the above results, some conclusions were obtained:

1. The fundamental frequency of the towering support structure of the wind turbine was 0.437 Hz. The FSI influence was weak and the self-vibration frequency decreased below 5% when the water additional mass was considered.
2. The frequency was affected obviously by the unit mass and the foundation elastic modulus. The fundamental frequency could be raised by reducing the unit mass, and the actual foundation parameter should be adopted for analysis to ensure the dependability of the result.
3. With the increase in the monopile wall thickness, the fundamental frequency was increased

with a nonlinear relationship. It was reasonable that the wall thickness of the monopile was designed by about 1% of the pile diameter.

#### ACKNOWLEDGMENTS

We are grateful for the financial support provided by the National Natural Science Foundation of China (No. 51109143, 51479124, 51209144, 51309159).

#### REFERENCES

Pan S.J., Wang X. 2011. Experimental study and numerical computation on flow-induced vibration of large plate gate. *Water resource and power*, 29(8): 148–151.

Wang X., Pan S.J. 2007. Effects of fluid-solid coupling and foundation radiation damping on seismic response in Wudongde rrrh dam. *Water resource and power*, 25(2): 42–45.

Zaaijer M.B. 2006. Foundation modelling to assess dynamic behaviour of offshore wind turbines[J]. *Applied Ocean Research*, 28(1): 45–57.

Zhang L.C., Wang X., Luo S.Z. 2012. Structural dynamic response of offshore wind turbine support system. *Proceedings 2012 international conference on materials for renewable energy and environment*. Beijing, China. 597–600.

# Cyclic loading test and single plastic hinge analytical analyses of Precast Segmental Bridge Columns with a circular section

Jian Guo

*School of Architecture and Civil Engineering, Zhejiang University Technology, Hangzhou, China*  
*Ningbo Institute of Technology, Zhejiang University, Ningbo, China*  
*Zhoushan Bridge Construction and Administrative Bureau, Zhoushan, Zhejiang, China*

Zhan-Yu Bu & Wei-Ye Wu

*Faculty of Architectural, Civil Engineering and Environment, Ningbo University, Ningbo, China*

**ABSTRACT:** Cyclic loading tests of two precast segmental columns and one monolithic bridge column with a circular section were conducted. Then, a single plastic hinge analytical pushover method for precast segmental bridge columns was presented based on the moment-curvature analyses of critical joints. Energy Dissipation (ED) bar unbonded length and elongation of unbonded prestressing tendon were considered in the method. The P-delta effect was included through iteration after the moment-curvature analyses. The analytical pushover method was validated through comparison with static cyclic loading test results. Parametric analyses were conducted afterwards. The influence of the variation of aspect ratio, axial load of gravity and prestressing, and ED bar ratio on the responses of lateral force-drift, joint opening and tendon stress was investigated.

**Keywords:** segmental column; energy dissipation; pushover analyses; parametric analyses; joint opening

## 1 INTRODUCTION

The Cast-in-Place (CIP) construction of bridge engineering is matured technology nowadays. However, the construction usually causes severe destruction of the natural environment due to the massive labors and equipment needed (Ou et al. 2010). CIP construction also leads to traffic jam and detour to local transportation systems. Accelerated Bridge Construction (ABC) is a strategy plan to address these issues by segmented bridge superstructure and substructure construction technologies developed in recent years (ABC-AC 2008). Among these technologies, the precast columns design was given more attention for its important roles in the seismic-resistant design of bridges.

Previous researchers have conducted analytical pushover analyses with the assumption that the column has a certain plastic hinge length at critical joints (Hewes & Priestley 2002, Chou & Chen 2006, Palermo et al. 2007). This method was also called the beam analogy method. Ou et al. based on this method raised a joint bar-slip rotation method to consider the concentration of inelastic rotation effects (Ou et al. 2010). However, in this method, the axial load was assumed to be constant, which has a conflict with the actual condition.

Bu and Ou suggested a revised analytical pushover method based on the beam analogy method (Bu & Ou 2013).

In this paper, first, the method of literature (Bu & Ou 2013) was introduced and used to analyze the cyclic reversal static test of two Precast Segmental Bridge Columns (PSBC) with a circular section to validate the method. Then, parametric analyses were carried out to study the performance of PSBC with various design parameters of aspect ratio, axial load (tendon ratio and dead load ratio), and Energy Dissipation (ED) bar ratio.

## 2 SINGLE PLASTIC HINGE ANALYTICAL ANALYSES

Through the observations of cyclic loading test results, if the reinforcements are the same for all segment joints, normally one plastic hinge will be formed at the column base. Moment-curvature analyses were conducted first to derive the relation between the exerted lateral force and deformation at the critical section. As the tendons are unbonded with sectional concrete, the consistency conditions between the reinforcement and the concrete no longer exist. An iteration procedure was

required to get a force-balanced state. Then, the lateral force-displacement relation was deduced considering the P-delta effects.

### 2.1 Material models

Concrete was modeled with the Kent-Scott-Park model (Scott et al. 1982), which was composed of the parabolic ascending part, the linear descending part and the horizontal part. ED bars were modeled with an ideal elastic-plastic model with both the post-yielding plateau part and the ascending part. Prestressing tendons were modeled with an ideal elastic-plastic model with the post-yielding ascending part only.

### 2.2 Moment curvature analyses

The moment curvature analyses procedure at critical joints can be summarized in six steps:

1. Increase the curvature from zero to a large value with appropriate intervals.  $\phi_t = \phi_e + \phi_p$ , where  $\phi_t$  is the total curvature;  $\phi_e$  is the elastic curvature; and  $\phi_p$  is the inelastic curvature.
2. Assume the compressive depth  $c$  and calculate the concrete compressive strain at an extreme fiber  $\epsilon_c = \phi_p \cdot c$ .
3. Calculate the joint inelastic rotation  $\theta_p = l_p \cdot \phi_p$ , where  $l_p$  is the plastic hinge length.
4. Calculate the elongation or shortening of the ED bar and tendon, and then calculate the corresponding strain (stress) and the force of the ED bar and tendon.
5. Calculate the resultant force of compressive concrete with the strip method and the integration of stress, check the sectional force equilibrium, if not fulfill then to go to step (2), and change the compressive depth  $c$ .
6. Calculate the sectional moment resistant capacity.

### 2.3 Lateral force-displacement response

The moment in preceding section step (6) equals the sum of the lateral force multiplying the column height and the axial force multiplying the lateral displacement. In stage one, the joint is not decompressed. The column has only elastic deformation. In stage two, joint opens, and the column has both elastic deformation and inelastic deformation. Elastic deformation (curvature and lateral displacement) is in proportion to the applied lateral force. The inelastic deformation can be calculated by multiplying the inelastic curvature by the plastic hinge length  $l_p$  and the column height  $H$ . The lateral force can be updated with the axial force and the lateral displacement to account for the P-delta effect.

### 2.4 Failure criteria

The column is considered to be damaged if the concrete crushes, or the ED bar and/or tendon fractures, or the lateral strength capacity decreases to 80% of the peak value.

## 3 VALIDATION OF THE TEST RESULTS

Three specimens were designed and tested under cyclic reversal static loading. The first specimen MRC was the monolithic column. This specimen was designed as the reference CIP column.

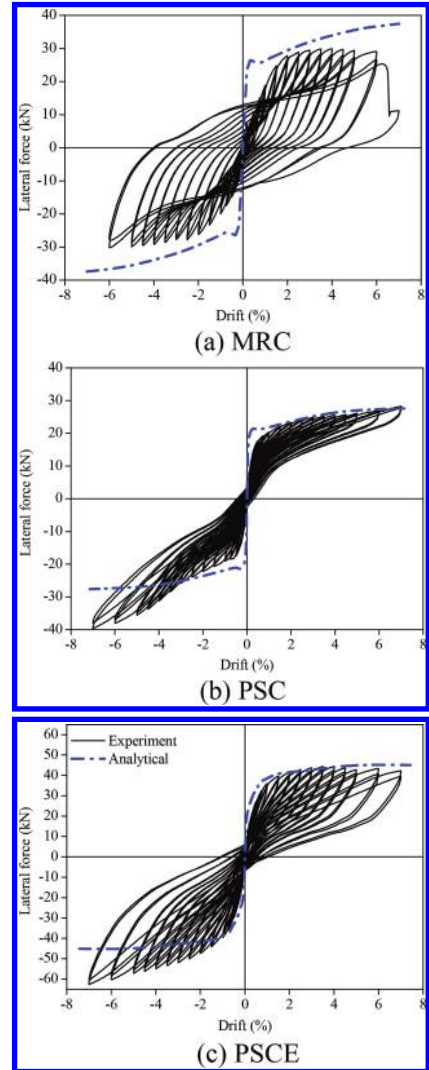


Figure 1. Comparison of lateral force-displacement responses of the specimens.

The second specimen PSC and the third specimen PSCE were segmental columns with four 400 mm-depth segments. The column height measured from the column base to the center of the loading block was 1850 mm for all the three specimens. The section of all the specimens had a diameter of 350 mm. The longitudinal reinforcement of MRC was 10 D12 mm mild steel bars. The longitudinal reinforcement of PSC was 3 D12.7 mm tendon. The specimen PSCE used 3 D12.7 mm tendons plus 6 D12 mild steel bars as ED bars. The latter two specimens had an effective tendon stress of 780 MPa.

Figure 1 shows the lateral force-displacement responses of specimen test results and analytical pushover results. The test results were not symmetric in positive and negative loading directions because of the tendon eccentric at top of the column relative to the base section center.

The analytical result was in good accordance with the tested data. So, the analytical model can be used to study the response of PSBC under the lateral force loading.

#### 4 PARAMETRIC ANALYSES

Three main parameter variations were considered in parametric analyses, i.e. the ED bar ratio, the aspect ratio, and the axial force ratio. The axial force was composed of the superstructure dead load and the tendon force. The ED bar ratio had five cases, with a diameter of 0 mm, 8 mm, 12 mm, 16 mm, and 20 mm, thus taking the value of 0.00%, 0.31%, 0.70%, 1.25%, and 1.96%, respectively. The column height took the value of 875 mm, 1850 mm, and 2625 mm, and the corresponding aspect ratio (A) was  $A = 2.5$ ,  $A = 5.29$ , and  $A = 7.5$ , respectively.

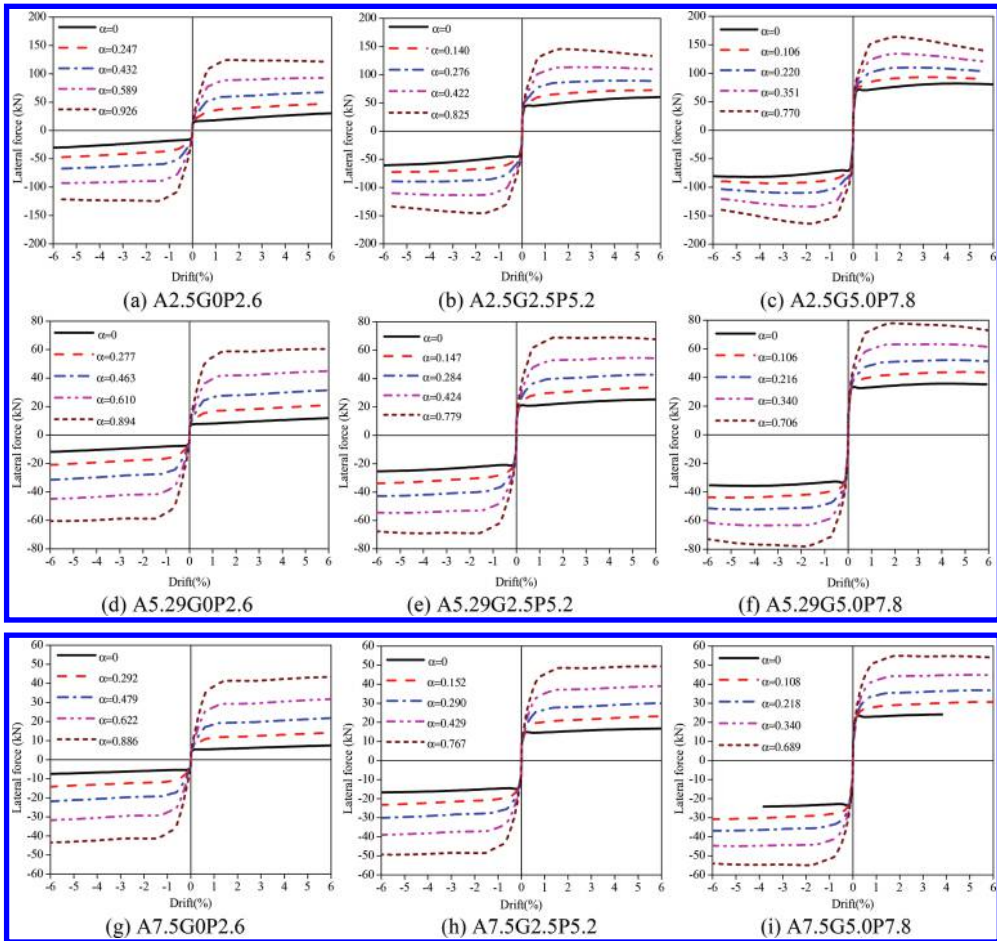


Figure 2. Pushover analyses of 45 column cases.

The axial load had three cases: 77 kN (tendon force only,  $G = 0$ ,  $P = 2.6$ ), 228.1 kN (74.1 kN dead load and 154.0 kN tendon force,  $G = 2.5$ ,  $P = 5.2$ ), and 379.3 kN (148.3 kN dead load and 231.0 kN tendon force,  $G = 5.0$ ,  $P = 7.8$ ), where  $G$  is the ratio of gravity axial load to sectional concrete compressive capacity and  $P$  is the ratio of prestressing axial load to sectional concrete compressive capacity. A total of forty-five cases of columns were calculated in parametric analyses. A parameter represents the ED bar moment contribution defines as  $\alpha = M_s/M_t$ , where  $M_s$  is the moment contribution of the ED bar in tension to the center of the compressive ED bar, and  $M_t$  is the total moment to the center of the compressive ED bar.

Figure 2 shows the parametric analysis results of lateral force-drift responses. The moment contributions of the ED bar corresponding to the ED bar ratios of 0.00%, 0.31%, 0.70%, 1.25%, and 1.96% are also shown in Figure 2. The following points can be derived from the parametric analyses: (1) with the increasing ED bar ratio, the column lateral strength increases; (2) with the increasing axial load, the column lateral strength increases;

(3) with the increasing aspect ratio, the column lateral strength decreases; (4) with the increasing aspect ratio, the moment contribution of the ED bar normally increases, except the G5.0P7.8 cases and the ED bar ratio 1.96% of the G2.5P5.2 cases; and (5) with the increasing axial load, the moment contribution of the ED bar decreases.

Figure 3 shows the base joint opening at a 3% drift in the 45 cases considered in the parametric analyses: (1) with the increasing ED bar ratio, the joint opening decreases; (2) with the increasing axial load, the joint opening decreases; and (3) with the increasing aspect ratio, the joint opening increases.

Figure 4 shows the tendon stress variation with drift for different design parameters of the column: (1) with the increasing ED bar ratio, the tendon stress decreases; (2) with the increasing aspect ratio, the tendon stress decreases and (3) with the increasing axial load, the tendon stress decreases.

## 5 CONCLUSIONS

A simplified pushover analytical method for precast segmental bridge columns was introduced. The analytical model was based on the moment-curvature analysis of the critical joint. The unbonded length and unbonded tendon stress variations of the ED bar were included in the procedure. The method was first validated through comparison with three tested column results. Then, the proposed method was used for parametric analyses. In the parametric analyses, the variation of the aspect ratio, axial load (superstructure gravity load and prestressing tendon force), and ED bar ratio was considered. The following conclusions can be reached on the basis of the investigations undertaken in this paper:

1. The proposed analytical pushover method was capable of predicting the PSBC lateral force-drift response with an acceptable precision.

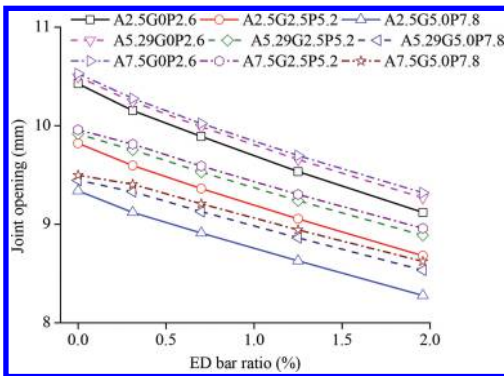


Figure 3. Base joint opening at the 3% drift.

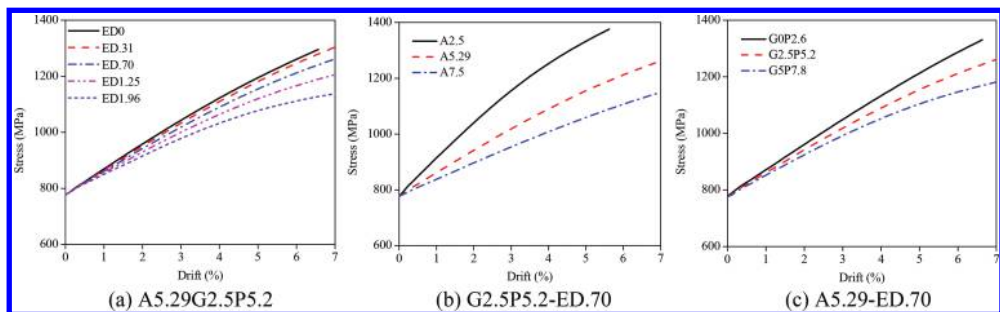


Figure 4. Tendon stress.



2. The column lateral strength increases with the increasing ED bar ratio and/or axial load, and the column lateral strength decreases with the increasing aspect ratio. The moment contribution of the ED bar decreases with the increasing axial load.
3. The joint opening decreases with the increasing ED bar ratio and/or axial load, and increases with the increasing aspect ratio.
4. The tendon stress decreases with the increasing ED bar ratio, the increasing aspect ratio, and/or the increasing axial load.

#### ACKNOWLEDGMENTS

This work was financially supported by the National Natural Science Foundation of China under Project Grant No. 51208268, the National Natural Science Foundation of China under Project Grant No. 51178429, the Transportation Science and Technology Project of Ningbo City under Grant No. 201507, and the Discipline Research Fund Project of Ningbo University under Project No. XKL14D2070. This work was also sponsored by K.C. Wong Magna Fund at Ningbo University. The authors gratefully acknowledge their support.

#### REFERENCES

ABC-Advisory Council 2008. Caltrans ABC strategic plan-development of practice and policy for future bridge projects. <http://mceer.buffalo.edu/meetings/6nsc/review/Cal-transABCStrategicPlan.pdf>.

- Bu, Z.Y. & Ou, Y.C. 2013. Simplified analytical pushover method for precast segmental concrete bridge columns. *Advances in Structural Engineering* 16(5): 805–822.
- Chou, C.C. & Chen, Y.C. 2006. Cyclic tests of posttensioned precast CFT segmental bridge columns with unbonded strands. *Earthquake Engineering and Structural Dynamics* 35(2): 159–175.
- Hewes, J.T. & Priestley, M.J.N. 2002. Seismic design and performance of precast concrete segmental bridge columns. *Technical Report No. SSRP-2001/25, University of California*. San Diego, California, USA.
- Ou, Y.C., Tsai, M.S., Chang, K.C., & Lee, G.C. 2010. Cyclic behavior of precast segmental concrete bridge columns with high performance or conventional steel reinforcing bars as energy dissipation bars. *Earthquake Engineering and Structural Dynamics* 39(11): 1181–1198.
- Palermo, A., Pampanin, S., & Marriott, D. 2007. Design, modeling, and experimental response of seismic resistant bridge piers with posttensioned dissipating connections. *Journal of Structural Engineering* 133(11): 1648–1661.
- Scott, B.D., Park, R., & Priestley, M.J.N. 1982. Stress-strain behavior of concrete confined by overlapping hoops at low and high strain rates. *ACI Journal* 79(1): 13–27.

# Establishment and seismic performance analysis of AFRP-reinforced concrete frame structure finite element model

G. Zhao & X.S. Xu

*University of Jinan, Jinan, Shandong, China*

**ABSTRACT:** On the basis of the structure test model, AFRP-reinforced concrete frame structural nonlinear finite element model was established. Under repeated load of AFRP-reinforced concrete frame, the simulation analysis of mechanical performance has been carried out, which compared with the test skeleton curve showed that the fitting effect is good; the stress distribution of the AFRP bar is consistent with the experiment. On the basis of these results, and the analysis of hysteretic curve and skeleton curve, ductility, rigidity degeneration, and energy dissipation capacity performance such as seismic performance characteristics of the model, a comprehensive understanding on the seismic performance of the AFRP-reinforced concrete frame is built, providing reference for the design of a FRP-reinforced concrete structure.

**Keywords:** AFRP-reinforced concrete frame; finite element analysis; ABAQUS; seismic performance

## 1 INTRODUCTION

FRP bar is a brittle material, with no yielding phenomenon. Before reaching ultimate strength, the stress-strain relationship is a linear relationship, and tensile strength is significantly higher than ordinary steel, but the compressive strength and modulus of elasticity is relatively small. These characteristics of the FRP bar determine the FRP-reinforced concrete structure in elastic-plastic deformation characteristics, which are also much different compared with the ordinary reinforced concrete structure, which does not conform to the modern seismic design based on the requirement of ductility performance; thus, we should strengthen the test and theoretical research of this aspect.

In recent years, although the research on the FRP bar concrete structure at home and abroad has been the focus in engineering practice, the United States, Japan, Canada and other developed countries successively formulated a series of design standards, construction procedures and application guidelines, but research results are mainly concentrated on bearing performance, durability, and fire prevention performance, such as the basic performance of FRP-reinforced concrete member. The study of the overall seismic performance of FRP-reinforced concrete structure is poor, restricting the development of the FRP-reinforced concrete structure. Therefore, according to the characteristics of FRP bar learning performance, on the basis of bearing performance of FRP-reinforced con-

crete member, we perform further research on the seismic performance of framework, with an overview of the elastic-plastic deformation characteristics of framework, for the FRP-reinforced concrete structure in the promotion and application in the field of civil engineering in China, which has an important scientific significance.

In this paper, with reference to Fukuyama and other researchers who designed a three-layer AFRP-reinforced concrete frame structure specimen (Fukuyama, 1995), using the finite element software ABAQUS, a nonlinear finite element model of AFRP-reinforced concrete frame is established, under repeated load of AFRP-reinforced concrete frame of the simulation analysis of mechanical performance, through the comparative analysis with the test results, verifying the effectiveness of the model. Then, through the analysis of hysteretic curve and skeleton curve, ductility, rigidity degeneration, energy dissipation capacity performance such as seismic performance indicators of the model, a comprehensive understanding of the seismic performance of the AFRP-reinforced concrete frame is built.

## 2 AFRP-REINFORCED CONCRETE FRAME FINITE ELEMENT MODEL

### 2.1 *Source of the model*

Bond performance of the FRP bar and concrete is similar to that of concrete and steel, which is good

and the material performance is certain, and the ordinary design method can be used for designing. In this paper, the analysis model is derived from the AFRP-reinforced concrete frame structure test model of Fukuyama et al. The test model is a three layer of pure frame structure buildings. The building height is 3.6 m. There are two spans across the X axis, with the span of 7 m, and the Y axis direction has three spans, with the span of 5.5 m. AFRP bar is used to bear steel bar and stirrup in beam, plate, column, such as the concrete members, for the C30 strength grade concrete design. The finite element model is a reference to try to design buildings of one framework for the model design of the X direction.

## 2.2 Constitutive relation of the material

### 2.2.1 Constitutive relation model of the AFRP bar

Reference to FRP bar mechanics performance test was made by previous researchers (Xu, 2008). From the beginning loading to the fracture failure of the entire process, the FRP bar is linear elastic, almost producing no plastic deformation, and no obvious yield point and yield stage, so the AFRP bar stress-strain relationship is given in Equation (1):

$$\sigma_f = E_f \varepsilon_f \quad (0 \leq \varepsilon_f \leq \varepsilon_u) \quad (1)$$

where  $\sigma_f$ ,  $\varepsilon_f$ ,  $E_f$  and  $\varepsilon_u$  represent the stress, strain, elastic modulus and ultimate tensile strain of AFRP, respectively.

FRP bar has no yield point and yield stage such as reinforced concrete (Jin, 2006), bonding strength and ductility. FRP bar in the name of the yield point is as follows:

$$\sigma_{f\lambda} = \lambda_f \sigma_{fu} \quad (2)$$

where  $\sigma_{f\lambda}$  is the yield stress in the name of FRP bar;  $\lambda_f$  is the strength reduction factor of the FRP bar, which generally takes the value of 0.75; and  $\sigma_{fu}$  is the ultimate tensile strength of the FRP bar.

### 2.2.2 Constitutive relation model of concrete

In order to easily simulate the mechanical properties of concrete material, ABAQUS comes with diffuse crack, damage in the plastic and brittle fracture of three different concrete constitutive relation models (Nie, 2013; Zhang, 2011). In this paper, the concrete damage in the plastic model is used to simulate the mechanical performance of concrete.

## 2.3 The choice of the finite element model

For the analysis of reinforced concrete structure with finite element analysis software, usually three

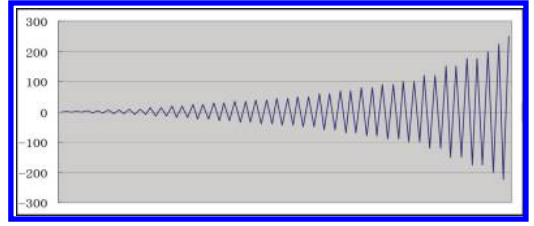


Figure 1. Loading system.

kinds of model are used: separate, modular, and integrated (Jiang, 1994). The numerical simulation is used to study, respectively, the stress state in the FRP bar and concrete materials, so the simulation should adopt a separate modeling method to establish the model.

## 2.4 The boundary conditions and load

### 2.4.1 The boundary conditions

FRP-reinforced concrete frame specimen and base were poured integrally; therefore, a layer of the bottom of the column location can be considered as consolidation, and so need to be fixed constraints imposed on the bottom section of the column, with all displacements of the column root cross-section being limited.

### 2.4.2 The load

To better simulate the force bearing status of FRP-reinforced concrete frame under low reversed cyclic loading, we get more complete hysteresis curves, on the basis of the original test loading system, and increase the load series and cycles. A new loading system is shown in Figure 1.

## 3 THE RESULTS OF NUMERICAL SIMULATION

### 3.1 Load-displacement hysteretic curve

According to the simulation results of statistics, we draw the simulated load-displacement curves of specimens, as shown in Figure 2a. When comparing the curves with the hysteretic curve of the test of AFRP-reinforced concrete frame structure, the simulation results show a knead gathering effect, which is not obvious, and plastic deformation is larger. The main reason is that the FRP bar is embedded into concrete when establishing the finite element model. Therefore, the software could not take bond slip into consideration between them while calculating, which led to the part deformation that cannot be recovered.

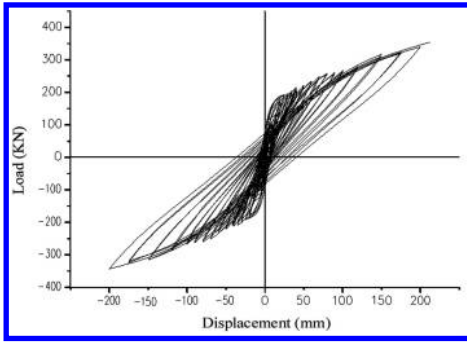


Figure 2a. Results of the simulation.

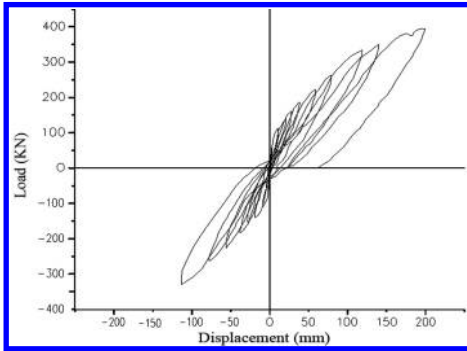


Figure 2b. Results of the test.

### 3.2 Skeleton curve

According to the numerical simulation of the load-displacement hysteretic curve, we draw a skeleton load-displacement curve and compare with the load-displacement skeleton curves gained by the analysis of the test results, as shown in Figure 3.

Figure 4 shows that two skeleton curves fit better and have the same tendency. Ultimate bearing capacity of the specimen reaches up to 340.4 KN when the FRP bar is cracked, and the load value of the model is 373.97 KN when the FRP bar approaches the ultimate stress, with a difference of 9.8%. As a whole, for each load peak, the simulated load value is greater than the test load value, with the difference being within 20%. The main reason for the simulation results being greater than the test results is that the numerical simulation belongs to the ideal load, so the model does not have the initial defects, and in software simulation, the concrete is assumed to be an isotropic homogeneous material while it is not the case in the actual situation.

### 3.3 The stress

Figure 4 shows the stress distribution of the FRP bar under a certain load and displacement. From

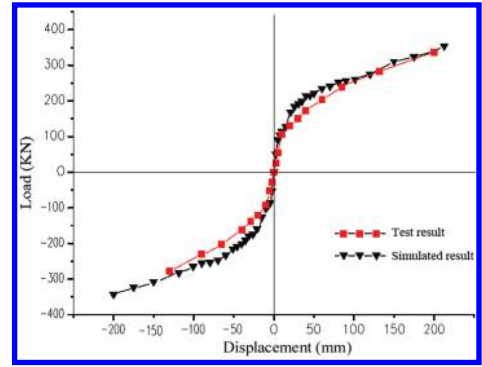


Figure 3. Comparison chart of the skeleton curve.

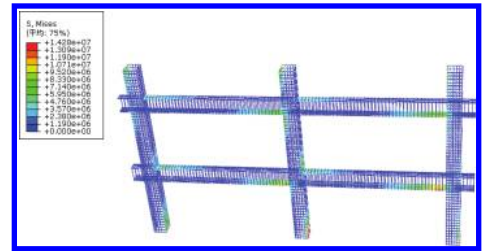


Figure 4. Stress diagram of the FRP bar.

the figure, we can see that the stress of the FRP bar has a linear distribution along the direction of the beam body, which is consistent with the results obtained in the experiment. In addition, because of the low compressive strength of the FRP bar, when modeling, the compression of the FRP bar is not considered. So, the stress of the compression the FRP bar is free.

## 4 SEISMIC PERFORMANCE ANALYSIS OF AFRP-REINFORCED CONCRETE FRAME STRUCTURE

### 4.1 Skeleton curve analysis

Through the analysis of the skeleton curve, the elastic-plastic dynamic characteristics of the structure can be studied. The load-displacement skeleton curve of the AFRP-reinforced concrete frame structure does not have a standard antisymmetric shape, as shown in Figure 4, where the reverse loading point load value is greater than the positive load point load values. In addition, the limit displacement of the skeleton curve of the model is larger. Because the lateral displacement size has a great influence on the normal use of the structure, in the design of the FRP-reinforced concrete frame structure, controlling

the structure's lateral displacement or displacement between layers appear to be more important.

#### 4.2 Ductility performance analysis

Ductility is used to measure the deformation of structure, which is an important parameter. In seismic fortification for structural design, some necessary calculation method and design principles are usually considered, to guarantee the ductility of the structure and the component, and the structure design to be more economic and reasonable.

Usually, the ductility of the frame structure can be evaluated by the ductility coefficient: the greater the ductility coefficient, the more better the structure ductility; conversely, structural ductility is worse. Ductility coefficient basically has the displacement ductility coefficient and the curvature ductility coefficient. This paper uses the displacement ductility coefficient  $\mu$  to evaluate the ductility performance of the FRP-reinforced concrete frame structure model, where  $\mu$  can be calculated by using Equation (3):

$$\mu = \frac{\Delta_u}{\Delta_y} \quad (3)$$

where  $\Delta_u$  is the limit displacement and  $\Delta_y$  is the yield displacement.

According to Formula (3), the ductility coefficient of the AFRP-reinforced concrete frame structural model is 5.03, which is relatively small and indicates the poor ductility of the structure.

#### 4.3 Stiffness degradation analysis

Stiffness refers to the structure's ability to resist deformation. Stiffness degradation refers to the structure under the repeated load. The phenomenon of stiffness gradually reduces due to concrete crack and crack development. Stiffness degradation is a major factor of structure seismic performance degradation, so study stiffness degradation situation of the structural analyzes the stiffness degradation rule, which is very necessary.

The stiffness degradation curves of the AFRP-reinforced concrete frame model, as shown in Figure 5, indicate that the load of the displacement is small, the stiffness is larger, stiffness degradation with the increase in load, and the early stage of the stiffness degradation is rapid, and the latter due to the concrete damage tends to be stable and stiffness degradation of the model is slow.

#### 4.4 Energy dissipation analysis

The stand or fall of dissipating energy performance is an important basis of the seismic performance

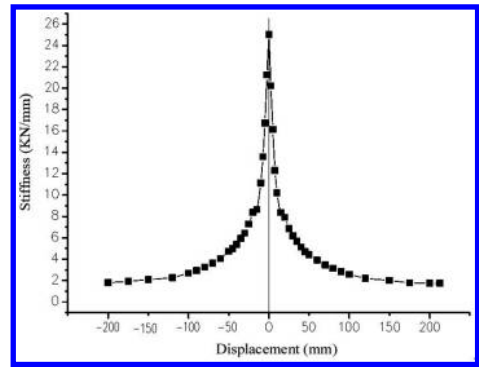


Figure 5. Stiffness degradation curve of the AFRP-reinforcement concrete frame model.

evaluation of the structure. Viscous damping coefficient can be used to estimate the energy dissipation capacity of the structure, with the equivalent viscous damping coefficient of the AFRP reinforced concrete frame model being 0.369, which explains that the energy dissipation capacity of the AFRP-reinforced concrete frame structure is poor.

## 5 CONCLUSIONS

Through the above analysis, the skeleton curve simulated by the software and test curve fitting effect is shown to be good, and the FRP bar stress distribution is consistent with the experimental measurement results. So, in this paper, we can assume that the mathematical model of the AFRP-reinforced concrete frame is effective and feasible, and the finite element model can be used for seismic performance analysis. By analyzing the hysteretic curve and skeleton curve, ductility, rigidity degeneration, energy dissipation capacity performance such as seismic performance characteristics of the model, we find that the seismic performance of the AFRP-reinforced concrete frame structure has a large difference compared with the reinforced concrete frame structure, so measures must be taken to improve the ductility performance of the AFRP-reinforced concrete frame structure, to enhance AFRP-reinforced concrete structure seismic performance, to expand the FRP-reinforced concrete structure in practical engineering application.

## ACKNOWLEDGMENT

The work was supported by the Natural Science Foundation of Shandong Province of china under

Grant No. ZR2014EEM036 and the Project of Science and Technology Plan of Jinan under Grant No. 201305029.

## REFERENCES

- Fukuyama, H. & Masuda, Y. 1995. Structural Performances of Concrete Frame with FRP Reinforced. *Non-metallic (FRP) Reinforced for Concrete Structures*: 275–286.
- Jiang, J.J., 1994. Nonlinear Finite Element Analysis of Reinforced Concrete Structures. Xi an: Science and Technology Press.
- Jin, W.C., Jian, F.L., Zhang, X.F., 2006. Research of Totally Non-metallic Materials Reinforced Concrete Structure: 169–173.
- Nie, J.G., Wang, Y.H., 2013. Constitutive Model of Concrete Structure in ABAQUS is used to simulate the Static Behavior of Comparative Study. *Engineering Mechanics* 30(4) :59–67.
- Xu, X.S., Ji, T., Gu, Y., 2008. Study of the Mechanics Performance Index and Test Method. *Building Structure* 38(11): 114–116.
- Zhang, Z.T., Liu, Y.F., 2011. Plastic Damage Model of Concrete in ABAQUS. *Building Structure* 41(Supplement):129–131.

## Micro damage in the structural deformation verification under expected rare earthquake

X.M. Chen, J. Duan, H. Qi & Y.G. Li

*China State Construction Technical Center, Beijing, China*

**ABSTRACT:** In the structural deformation verification under expected rare earthquake, the macro results such as displacement angle and base shear force usually are taken as the criterion for collapse, but sometimes, these horizontal responses cannot embody the probability of vertical collapse exactly. The relative reasons have been researched by numerical method in this paper including the improper constitutive model of material and discrete model of element. For these reasons, the micro damage of member sections must be used together with the macro results as displacement angle to verify the structural property under expected rare earthquake.

**Keywords:** displacement angle; damage; elastic-plastic; time-history analysis

### 1 INTRODUCTION

The design for high buildings may contain two main steps, the first step is the section design for small earthquake or fortification intensity, and the second step is the deformation verification for expected rare earthquake. For the first step, elastic methods such as spectrum analysis are widely used for the structural maximum response, and then probabilistic limit state design method will be used for the section verification and reinforcement. For the second step, usually only the deformation verification has to be done to ensure the structural performance under the expected rare earthquake through the performance point formulated via static PUSH or the envelope of displacement angle via nonlinear dynamic time-history analysis. Compared with the static analysis PUSH, the dynamic time-history method can be used widely for more complex structures without the limitation of first-order mode being dominant.

To ensure the structures without crash under expected rare earthquakes, the limitations of displacement angle are regulated by many national codes, for example, in the ‘Chinese Code for Seismic Design of Buildings’ (2010a), the maximum displacement angle is 1/100 for both shear wall structures and frame-core-tube structures, and the maximum displacement angle is 1/50 for frameworks. Except the displacement angle, several other results are usually taken as the auxiliary tools for assessment or optimization of the structural scheme but not being taken as the main basis for structural crash, such as shear forces at the base,

shear force ratios and turn-over moment ratios carried by frames and shear walls respectively of each floor, damage of those most important members, and so on. This principle doesn’t mean that the structural crash has no direct relationship with the damage of members, in fact, serious damage of some crucial members may lead to instantaneous unloading, and then induce an impact load on the other members which may make the whole structure collapse.

Although the national code (2010b) has concerned the analysis of progressive collapse, but different with the deformation verification of expected rare earthquake by nonlinear time-history method, the analysis of progressive collapse induced by earthquake or other occasionally loads usually is regarded as a different mechanical problem. That is because much more complex nonlinear problem should be considered in the progressive collapse analysis, such as impact and contact. Therefore, this classification is based on the complexity, and there are no essential mechanical differences between them. Actually, in the analysis of deformation verification, the collapse possibility induced by the serious damage of some members mustn’t be neglected, even though the displacement angle may within the limitation.

In this paper, the section damage of frameworks is researched by numerical examples through ABAQUS for deformation verification under expected rare earthquake. The relationship of material damage and envelope of displacement angle is analyzed for the principle of no collapsing with strong earthquakes. Based on these numerical

results, the rationality of the constitute model and elemental discrete mode of frameworks, which is used widely, is also discussed.

The results show that the concrete in the RC columns may be damaged seriously even though the displacement angles are within the limitation, this kind of damage will then reduce the compression area of sections and make the stirrups unworkable and the longitudinal bars buckling, and at last, unreliable displacement angle will be solved out because the degradation of bearing capacity hasn't been estimated accurately.

## 2 MODEL OF MATERIALS AND ELEMENTS

In the analysis of nonlinear time-history under expected rare earthquake, elastic-plastic model with kinematic hardening is used for steel, plastic damage model is used for concrete proposed by Chinese code (2010c), and as the affection of stirrups to concrete is very important as proved

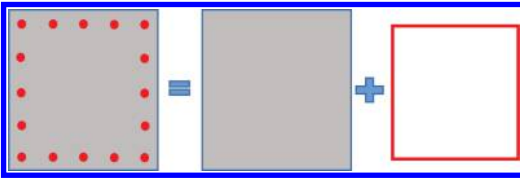


Figure 1. Discrete of RC column.

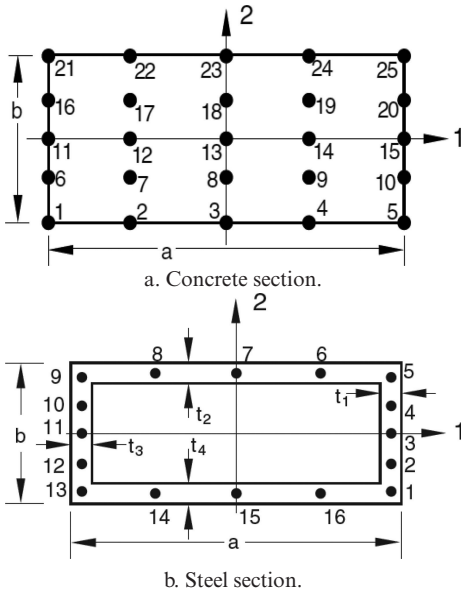
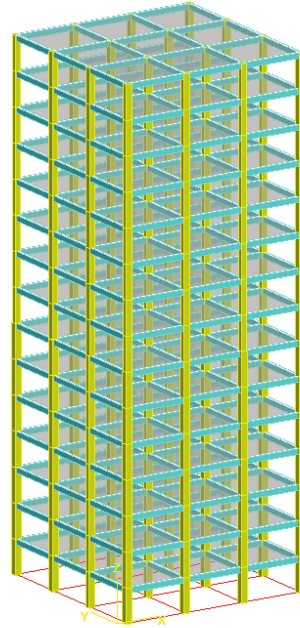


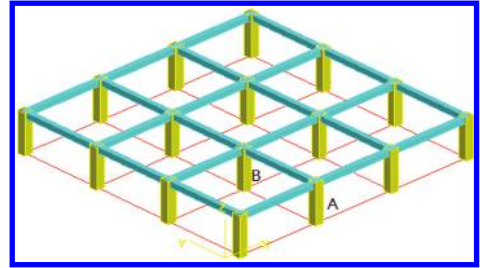
Figure 2. Integral points of sections.

by J.B. Mander [1988a,b], it is also researched by H. Qi (2011).

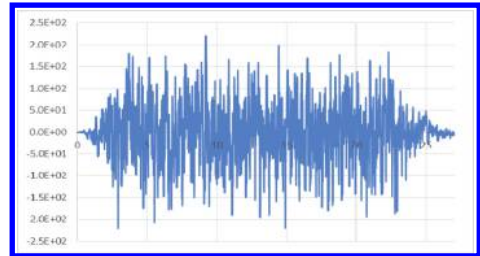
For the elements in ABAQUS (2006), rebar can be embedded in the shell element for walls and plates, but the same function is not available for beam elements in explicit method, so equivalent discrete models are usually used, in which the concrete section



a. Structural model.



b. Standard floor.



c. Seismic wave.

Figure 3. Structural model and seismic wave.



and the longitudinal bars would be formulated with fiber beam element respectively (Fig. 1). The integral points of each section are shown in Figure 2.

### 3 NUMERICAL EXAMPLE

The frame work, its first floor and the seismic wave are all shown in Figure 3.

According to Chinese codes, the structure would be regarded as no collapse if the displacement angle is less than 1/50 under the maximum acceleration 310 gal. For comparison, the results of the wave with peak acceleration equal to 220 gal is also presented.

The envelopes of displacement angle are shown in Figure 4. It can be seen that the maximum displacement angle is 3/200, and it is less than the limitation of 1/50. If taking the displacement angle as the unique criterion, this structure will not collapse under both two levels of acceleration.

Displacement angle is the direct reflection of structural lateral stiffness. The degradation of lateral stiffness can be induced by the degradation of shear stiffness, but in most situations, it is

induced by the degradation of bending stiffness which is the result of vertical stiffness reduction. Although the degradation of vertical stiffness may lead to collapse directly, but the horizontal stiffness of plates is so enormous that this factor may be underestimated in the calculation of displacement angle. Thus for accurate result about collapse, the vertical stiffness degradation of those most important members should be analyzed in detail.

For both columns A and B noted in Figure 3, the damages of 25 integral points in the concrete section are shown in Figure 5 with the peak acceleration equal to 220 gal, and equivalent strain of the longitudinal bars are shown in Figure 6. It can be seen that both concrete and steel are damaged slightly, and there are only slight fluctuation in the time-history of axial forces in Figure 7.

Amplify the peak acceleration from 220 gal to 310 gal, the concrete is damaged seriously for both columns as shown in Figure 8. For column A, both the left and right sides of concrete section are damaged seriously, and for column B, the whole

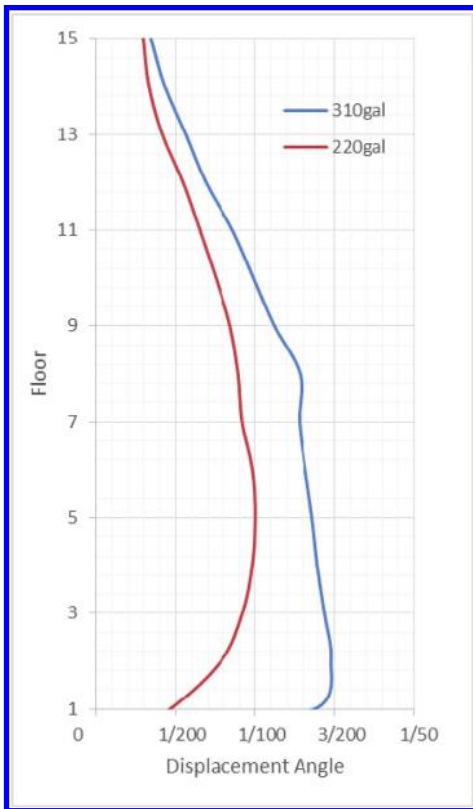


Figure 4. Envelope of displacement angle.

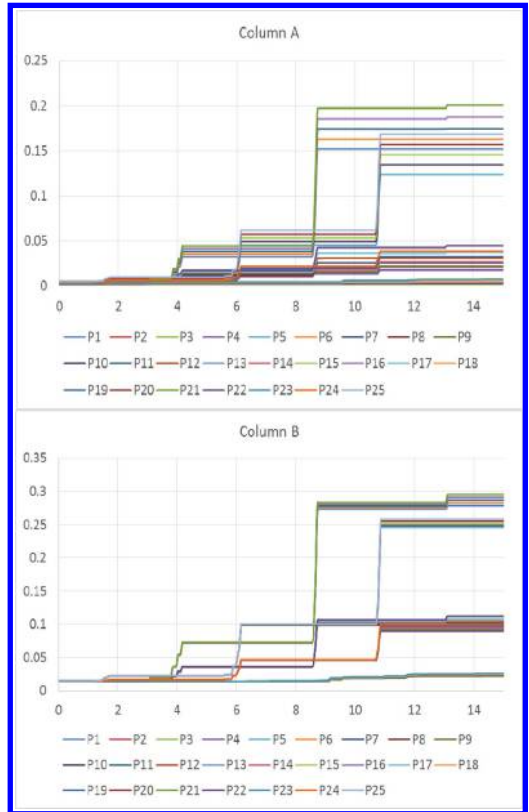


Figure 5. Compression damage of concrete section in column A and B under 220 gal.

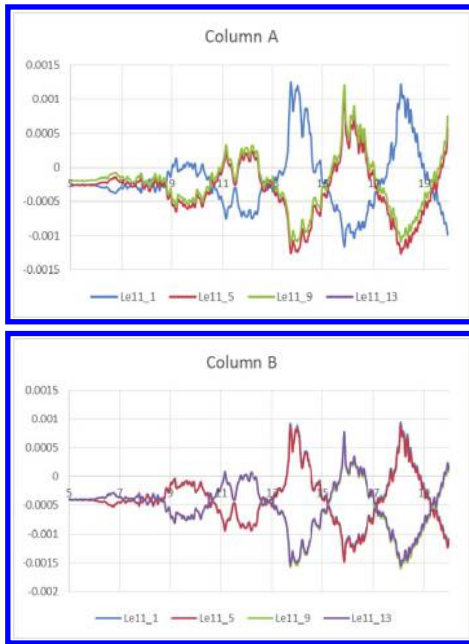


Figure 6. Equivalent strain Le11 of steel in column A and B under 220 gal.

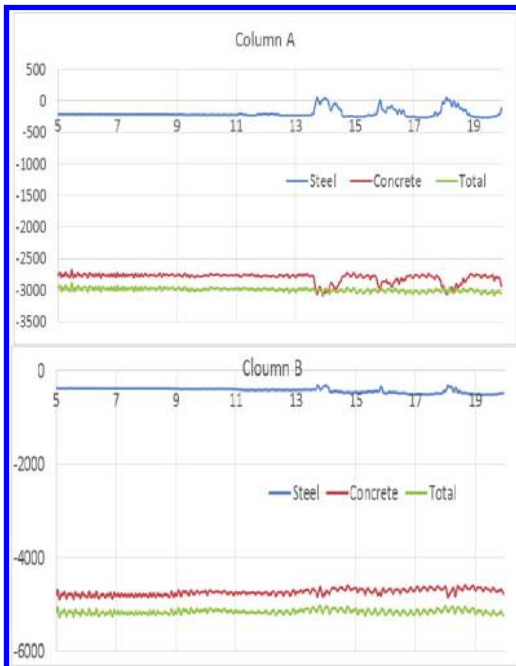


Figure 7. Time histories of SF1 in column A and B under 220 gal.

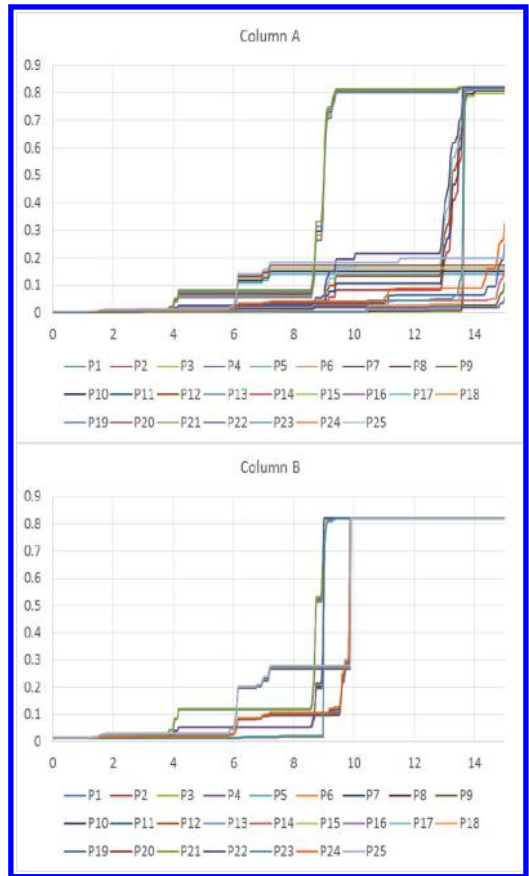


Figure 8. Compression damage of concrete section in column A and B under 310 gal.

concrete section is damaged seriously. Besides this, tremendous plastic deformation occurred in the steel sections (Fig. 9).

For both columns, the axial forces fluctuated significantly because of the compression damage of concrete. As shown in Figure 10, the axial force of column A increased about 1000 KN, but the axial force of concrete section in column B decreased even to zero with the axial force of steel section increased from 500 KN to 3500 KN. It is obvious that this phenomenon is not reasonable. By the result of concrete compression damage, the column B is crushed and the column A only keep a concrete core, both with the stirrups disabled and the longitudinal bars buckled.

Thus it can be seen, the first floor of this structure has lost at least eight columns, and the structure will collapse though the displacement angle is less than the limitation.

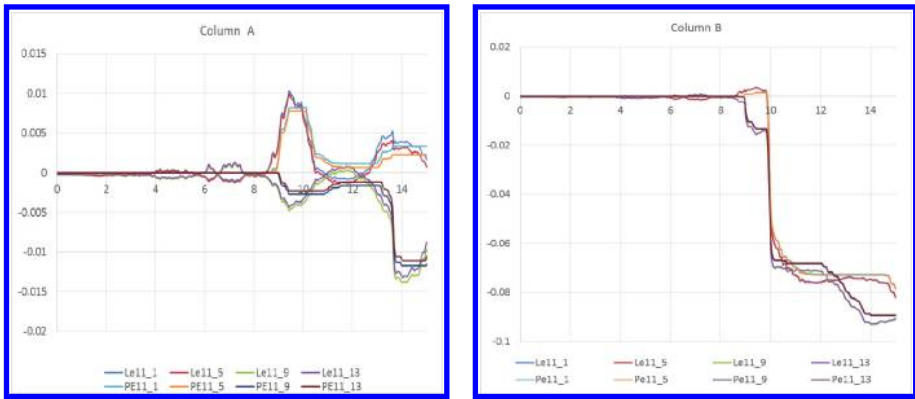


Figure 9. Equivalent strain Le11 and plastic strain PE11 of steel in column A and B under 310 gal.

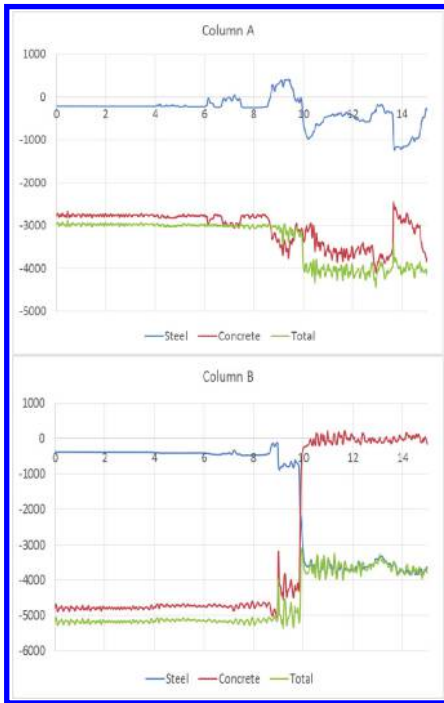


Figure 10. Time histories of SF1 in column A and B under 310 gal.

#### 4 CONCLUSION

Under the action of seismic waves, the envelope of displacement angle is usually taken as the main criterion for collapse. Limited by the material constitutive model and elemental discrete model,

the concrete compression damage in those key members would not be reflected accurately in the displacement angle, and this may lead to unreliable results. Therefore, the displacement angle cannot embody the vertical bearing capacity sufficiently, the degradation of vertical bearing capacity of those key members can lead to collapse with allowable displacement angle. Thus in the deformation verification under expected rare earthquake, the damage of members is as important as the displacement angle.

#### REFERENCES

- ABAQUS Inc (2006). ABAQUS User Manual, V6. 5. 5.
- China architecture & building press (2010a). Code for Seismic Design of Buildings. Beijing, China. (In Chinese).
- China architecture & building press (2010b). Technical specification for concrete structures of tall building. Beijing, China. (In Chinese).
- China architecture & building press (2010c). Code for design of concrete structures. Beijing, China. (In Chinese).
- Mander, J.B., M.J.N. Priestly & R. Park (1988a). Theoretical Stress—Strain Model for Confined Concrete. Journal of Structural Division, ASCE, Vol. 114, p.1804.
- Mander, J.B., M.J.N. Priestley & R. Park (1988b). Observed stress-strain behavior of confined concrete. Journal of Structural Engineering, Vol. 14, p.1827.
- Qi, H., Y.G. Li & X.L. Lv (2011). Study of uniaxial mechanical behavior of concrete confined with hoops. Building Structure, Vol. 41, p.79.

# Experimental study on the axial bearing capacity and ductility of concrete column confined with double stirrups

Y.Y. Li & Y.Y. Zhang

*Hebei University, Baoding, China*

L.Z. Sun & L. Sun

*Wenzhou University, Wenzhou, China*

**ABSTRACT:** In order to reduce the cross-section size of the reinforced concrete columns in the premise of improving its bearing capacity and ductility, 5 columns confined with double stirrups were designed as the study object. Concentric compression tests were conducted with the columns by using an electro-hydraulic servo loading machine using the displacement controlled loading scheme. The load-deformation behavior of the columns was analyzed. The test results show that the displacement ductility ratio varies between 4.04 and 6.17. By comparing the effects of different factors, it can be found that a better ductility was achieved for columns with a small stirrup spacing and a large stirrup diameter.

**Keywords:** double stirrups; confined concrete; displacement ductility ratio

## 1 INTRODUCTION

In recent years, the most disastrous earthquake has occurred many times in China and abroad, such as the Wenchuan earthquake, Yushu earthquake, Haiti, and Chile earthquake. Many buildings collapsed or destroyed badly in the earthquake, which caused a large number of casualties and huge economic losses. Column is an important bearing component of the structure, its insufficient function or degradation will have a great influence on the whole building, even leading to the collapse of the whole building. An important reason causing the damage of the reinforced concrete column is the lack of ductility. The essays point out that the axial compression ratio and stirrup characteristic value are the two main factors influencing the ductility of concrete columns.

According to Guan Ping and others, the stirrup characteristic value is much more important than other factors in influencing the column ductility. Guo Zhenhai and others in Tsinghua University, who have studied the stirrups concrete stress-strain curve under the action of repeated loading, suggested that enlarging the stirrup ratio can increase the peak strain of the concrete apparently, especially during the drop period, which can change the ductility of concrete substantially. After studying the axial bearing capacity of a single-layer high-strength stirrup and compound high-strength stirrup restraint concrete separately, Yang Kun and others put forward that a high-strength stirrup can

greatly improve the concrete ductility and provide a certain amount of axial bearing capacity. The restriction for core concrete of compound stirrups is stronger than single-layer stirrups and evenly distributed.

At present, lots of research have been done on ordinary strength stirrup concrete and FRP confined concrete by researchers at home and abroad, but the study of double stirrup concrete is much more less. Kent and Park put forward that in the rectangular stirrup-confined concrete, stirrups do not work before the pressure reaches the concrete compressive strength; while gradually achieving the compressive strength, stirrups begin to have a force and deform, which will develop a constraint force in the concrete specimen. Stirrup-confined concrete belongs to active constraint, and its constraint force changes with different stages of the test.

This experiment tries to decrease the size of the column section and improve the ductility of the column through configuring double stirrup, which may increase the stirrup reinforcement ratio.

## 2 TEST GENERAL SITUATION

### 2.1 *Template specimen preparation*

According to the proportion of test, the admixture, water, sand, gravel, cement, fly ash and silica fume are placed in the blender after weighing. There are two steps for pouring. First, casting the column base, after the concrete strength is increased to

70% for the chiseling process, and then casting the scape. Because the spacing of double hoop stirrup reinforced concrete column is small, this test adopts the hierarchical pouring. In order to avoid the phenomenon of honeycomb and empty, the vibrator is used to vibrate the concrete close-grained after casting 300 mm. Natural curing lasts for 60 days after the completion of the casting, ensuring that concrete strength meets the design standards. The specimen size is 25 \* 25 \* 140 cm, a total of five pillars, as shown in Figure 1. Reinforcement parameters are listed in Table 1.

### 2.2 The test procedure

In order to prevent the end effect, a 20 cm FRP carbon fiber cloth is packed at the top of pillars to reinforce the end of pillars before the test. This experiment is conducted on a WAW-10000F type electro-hydraulic servo multi-function experimental machine. First, the component is placed under the pressure plate, and the central axis is drawn around the pillar. Then, the position of the column is calibrated with the laser level. In the compression process, to ensure the specimen under uniform compression, high-strength gypsum is daubed on the top of pillars and pressed flat. A rod displacement meter is installed, whose

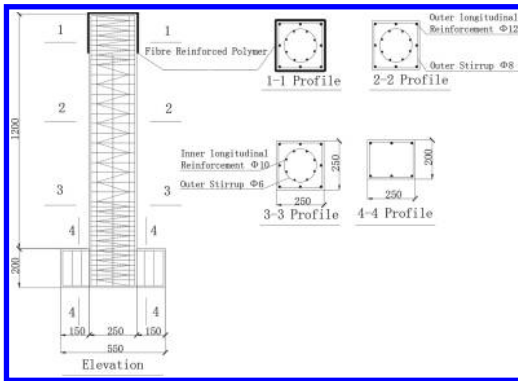


Figure 1. Specimen details.

Table 1. The parameters of the specimen.

Serial number	Concrete strength/MPa	Longitudinal reinforcement strength	Longitudinal reinforcement diameter	Stirrup strength/MPa	Stirrup spacing and diameter	Barrel diameter of stirrups/mm
SC-1	43.15	HRB335	8 $\phi$ 10/8 $\phi$ 12	1209.5/1209.5	$\phi$ 6@35/ $\phi$ 6@35	180/230
SC-2	43.15	HRB335	8 $\phi$ 10/8 $\phi$ 12	1321.9/1321.9	$\phi$ 8@75/ $\phi$ 8@75	180/230
SC-3	43.15	HRB335	8 $\phi$ 10/8 $\phi$ 12	1209.5/1209.5	$\phi$ 6@55/ $\phi$ 6@55	180/230
SC-4	43.15	HRB335	8 $\phi$ 10/8 $\phi$ 12	1209.5/1321.9	$\phi$ 6@75/ $\phi$ 8@75	180/230
SC-5	43.15	HRB335	8 $\phi$ 10/8 $\phi$ 12	1321.9/1321.9	$\phi$ 8@35/ $\phi$ 8@35	180/230

specification is ZS1100-DT100 on both sides of the pillar. Acquisition instrument is used to collect data. Preloading is carried out on the specimen prior to the commencement of the experiment. The purpose is to eliminate the adverse impact of the internal defects. After completion of preloading, two devices begin to collect at the same time and record the starting time. Loading regimes of the experimental machine are taken as 240 kN/min load to 2000 kN, and then are changed to 0.5 mm/min until the specimen is broken. The test set-up is shown in Figure 2.

## 3 TEST RESULTS

### 3.1 The experimental phenomena

With the gradual increase of the vertical axial force, destructive forms of columns are virtually the same. In the stage of force control, the test specimen has no obvious cracks, and then turns to the stage of displacement control. When the axial force of the concrete column reaches 80% of the ultimate bearing capacity, some small vertical cracks appear on the surface of the test specimen with small noise. When the bearing capacity gets the peak load, a number of cracks explode and develop swiftly. Finally, these cracks become oblique failure surface, which penetrate the concrete column. In this process, there is no obvious sound. When continuing loading on the concrete column, it shows that the bearing capacity of double stirrups concrete column declines slowly, protective layer gradually cracks and then falls off.

After observing the destruction, the longitudinal reinforcement in the test specimens is forced to bend outward. All inner and outer stirrups in the test specimen are not broken, as shown in Figure 3. Because of the form of double stirrups, which have high strength, the stirrup characteristic value improves much. With the load increasing, longitudinal cracks develop rapidly in the inner concrete column, while transverse cracks are effectively blocked. Cracks develop

in the weak layer that is the weld between longitudinal reinforcement and stirrups. The angles between the plane of rupture and the horizontal plane are roughly 60°–80°, which show that the specimens are compression and shear failure.



Figure 2. Test set-up.

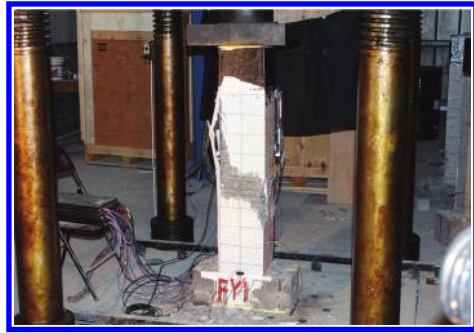


Figure 3. Typical failure mode.

Damage characteristics of different concrete columns are given in Table 2.

### 3.2 Analysis of test results

1. The area representing the test specimen with double high-strength stirrups (round inside but square outside) constrained concrete is shown in Figure 4. The four corners of the square stirrups confined core concrete from the figure and sanction decreased slowly from angle to the middle part. The spiral stirrups, which are in the confined area of the outer stirrups work with outer stirrups together and can effectively control transversal strain of concrete, improve the capability of stirrups constraints. The displacement ductility ratios of SC-1~SC-5 are more than 4.04, as given in Table 2. This shows that double stirrups play an important role in the lateral restraint of concrete and can improve effectively the disadvantage that brittle failure in concrete column.
2. As shown in Table 2, displacement ductility ratios of pillars are around 4~6, which show that this test specimen has a good ductility. Specimens SC-1 SC-3 have the same concrete strength and diameter of the stirrup, but SC-3 has a greater inner and outer layer spacing of stirrup than SC-1. Compared with SC-5, SC-1 has the same concrete strength, spacing of stirrup and smaller diameter of the stirrup. Figure 5 indicates that the ductility of SC-5 is better than SC-1 and the ductility of SC-3 is the worst. Because the larger stirrup spacing ( $s$ ) and the smaller diameter ( $d$ ), the test specimens have a lower stirrup parameter so that there is not enough sanction to prevent lateral deformation of specimen, which lead to a bad ductility. These results are consistent with the those reported by Qian, J.R.

Table 2. Failure characteristics of specimens.

Serial number	Inner stirrup characteristic value	Outer stirrup characteristic value	Displacement ductility ratio $\mu_{\Delta} = \Delta_u / \Delta_y$	Failure characteristics	Longitudinal reinforcement yielding conditions	Ultimate load/kN
SC-1	0.552	0.430	5.21	Compression and shear failure	Yield	3578
SC-2	0.562	0.445	4.04	Compression and shear failure	Yield	3342.5
SC-3	0.399	0.311	4.66	Compression and shear failure	Yield	3277
SC-4	0.285	0.431	4.9	Compression and shear failure	Yield	3278.5
SC-5	1.181	0.929	6.17	Compression and shear failure	Yield	3594

\*( $\Delta_u$  represents the ultimate displacement of specimens. The displacement occurs when the bearing capacity is decreased to 50% ultimate load capacity.  $\Delta_y$  is the yield displacement, which is the average value of displacement, when inner and outer longitudinal reinforcement are tensile and subdued).

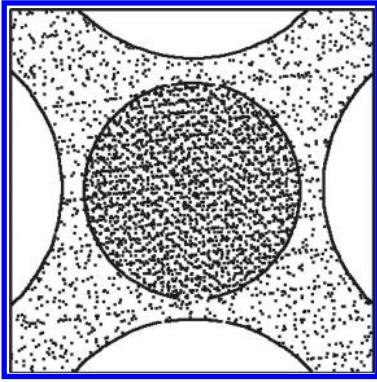


Figure 4. Effective confinement area for double-stirrup column.

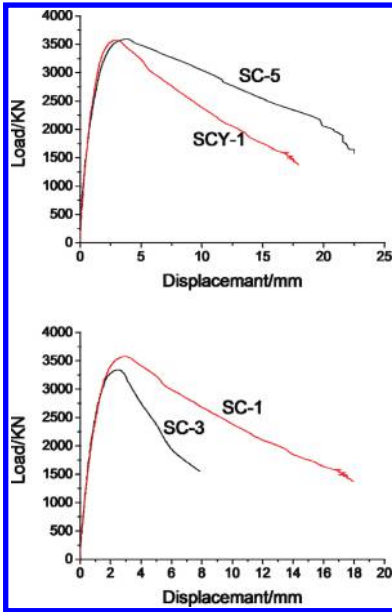


Figure 5. Comparison of load-displacement curves.

#### 4 CONCLUSIONS

1. According to the test results in the present study, using double stirrup can improve the stirrup characteristic value of RC columns and the bearing capacity of high strength concrete columns, as well as prevent the brittle failure effectively. The displacement ductility ratio of the columns tested in this study varies between 4.04 and 6.17.
2. All specimens show good ductility during the process of gradual failure. The axial bearing capacity of the designed specimens was enhanced to a great extent while guaranteeing the ductility. The design can reduce the section

- size of the column, and as a result the cost will reduce, which has a very high economic benefit.
3. Under the same strength grade of concrete, reinforcement characteristic value has a great influence on the ductility of the concrete columns. In addition, the inner and the outer stirrup characteristic values have a disproportionate level of influence on the ductility of the double stirrup reinforcement concrete column. However, the specific influence coefficient needs further study.

#### ACKNOWLEDGMENTS

The authors are grateful for the financial support provided by the Natural Science Foundation of China (Project No. 51178356, 51378398).

#### REFERENCES

- Chen, T., Xiao, C.Z., Tian, C.Y., et al. 2011. Experimental study of the compression-bending behavior of composite shear walls of high axial compression ratios [J]. *China Civil Engineering Journal*, 44(6):1–7. (in Chinese).
- GB50011-2010 A seismic Design Code for Buildings [S]. *Beijing China Architecture & Building Press 2010*. (in Chinese).
- Guan, P., Wang, Q.X., Zhao, G.F. 1998. Experimental study on the ductility of concrete columns with high strength C80 [J]. *Journal of Dalian University of Technology*, 38(3):93–99. (in Chinese).
- Guo, Z.H., Zhang, X.Q., Zhang, D.C., et al. 1982. Experimental study on complete stress-strain curves of concrete [J]. *Journal of Building Structures* 3(1):1–12. (in Chinese).
- Murat, S. & Salim, R.R. 2002. Displacement based design of reinforced concrete columns for confinement [J]. *ACI Structural Journal*, 99(1):3–31.
- Qian, J.R., Cheng, L.R., Zhou, D.L. 2002. Behavior of axially loaded concrete columns confined with ordinary hoops [J]. *Journal of Tsinghua University (Science and Technology)*, 42(10):1369–1373. (in Chinese).
- Wu, G. & Lu, Z.T. 2004. Study on the stress strain relationship of FRP-concrete rectangular columns [J]. *Journal of Building Structures*, 25(3):99–106. (in Chinese).
- Xu, Y.D., Wang, Q.W., Chen, Y.X. 2012. Research on limiting value of axial compression ration and ductility behavior of RC square column [J]. *Journal of Building Structures*, 33(6):103–109. (in Chinese).
- Yang, K., Shi, Q.X., Wang, Q.W., et al. 2009. Analyse on behavior of concrete confined by high-strength stirrups under concentric loading [J]. *Journal of Xi'an University of Architecture & Technology (Natural Science Edition)* 41(2):160–172. (in Chinese).
- Zeng, J.F., Zhu, R.F., Sun, L.Z., et al. 2013. Research on the mechanical characteristics of square stub columns with double stirrup [J]. *Journal of Jiangxi University of Science and Technology* 34(3):23–31. (in Chinese).
- Zhao, Y.J., Chen, Y.X., Yu, S.Q. 2004. A research on limited value of axial compression ratio of arbitrarily shaped RC columns [J]. *Journal of Tianjin University* 37(7):600–604. (in Chinese).

# The model design of fatigue test of steel-concrete composite segment of railway hybrid girder cable-stayed bridge

Yang Zhou, Qianhui Pu & Zhou Shi

*School of Civil Engineering, Southwest Jiaotong University, Chengdu, Sichuan, China*

Zhenbiao Liu

*China Railway Siyuan Survey and Design Group Co. Ltd., Wuhan, China*

**ABSTRACT:** The fatigue properties of the steel-concrete composite segment were investigated based on the Yong-Jiang Bridge, the first railway hybrid girder cable-stayed bridge in China. In this paper, the design process of the fatigue model test for steel-concrete composite segment of Yong-Jiang Hybrid Girder Bridge was introduced. In order to investigate the stress condition of the structure, a finite element model of the whole bridge was established by the software MIDAS/CIVIL. Then, the stress state of steel-concrete composite segment was calculated under various working conditions. The stress amplitude plays an important role in fatigue performance of the structure. The steel cells of composite segment located on the bottom plate, which suffered the largest stress amplitude, were selected as the test object. Lastly, considering the effects of the initial defects and laboratory equipment, a full-scale partial model with one steel cell was proposed based on the equivalent stress principle.

**Keywords:** hybrid girder cable-stayed bridge; steel-concrete composite segment; model design; fatigue test

## 1 INTRODUCTION

The first hybrid girder cable-stayed bridge, which combined the advantage of the steel and concrete, was built in Germany in 1972. Later on, this kind of bridge was introduced to China in 1990s and developed very fast in long-span bridges, especially in the field of highway bridges. In recent years, a series of hybrid girder cable-stayed bridges have appeared in China, such as Xupu Bridge, Shantou Queshi Bridge, Wuhan Baishazhou Bridge and Erqi Yangtze River Bridge. Because of the large span development of railway bridges, the hybrid girder cable-stayed bridge was applied to railway engineering. Yong-Jiang Bridge is the first railway hybrid girder cable-stayed bridge in China.

As a critical component of the hybrid girder bridge, the steel-concrete composite segment plays a crucial role in transferring force and transformation of bridge. According to statistics of existing hybrid girder cable-stayed bridges, steel-concrete composite segments can be subdivided into 4 types, in terms of bearing-plate and steel cells. These include a rear bearing-plate without cells, a rear bearing-plate with steel cells, a front bearing-plate with steel cells and both front and rear bearing-plates with steel cells. Meanwhile, shear connectors installed in bearing plate and steel cell are responsible for

connecting the steel and concrete girders and transferring shear force. In China, a majority of hybrid girder cable-stayed bridges adopted a rear bearing-plate with steel cells. In the existing literature, a majority of investigations have been focused on the static mechanical properties of the composite segment. Few researchers have paid attention to the fatigue characteristics of the steel-concrete composite segment because of the huge costs and long time consumption of the fatigue test.

In this paper, the process of designing the test specimen of the steel-concrete composite segment was introduced based on the stress equivalent principle. First, to obtain the internal force and the stress state of the composite segment, a FEM of the Yong-Jiang Bridge was proposed by the software MIDAS/CIVIL. Then, a partial full-scale model was designed by the maximum stress amplitude and test equipment. Lastly, loading force of the test specimen was determined by the stress equivalent principle of several key sections of the composite segment.

## 2 FEM OF THE YONG-JIANG BRIDGE

In this study, the applied load of the test specimen is based on the stress state of the original bridge.



So, a FEM of Yong-Jiang Bridge is established by the software MIDAS/CIVIL, as illustrated in Figure 1. Unlike static structure design, fatigue design is always based on the frequently loading instead of CR-live loading for railway bridges.

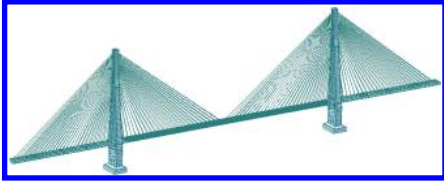


Figure 1. Three-dimensional view of the Yong-Jiang Bridge.

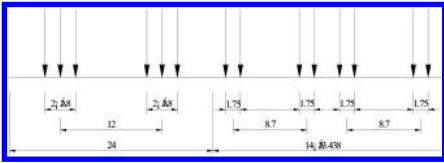


Figure 2. Wheelbase of the vehicle.

Table 1(a). Internal force of key sections under the dead loads.

Section	Axial force/kN	Shear force/kN	Bending moment/kN·m
Section 1/right	-244134	2130	40132.84
Section 2/right	-243987	6526	36687
Section 3/right	-241433	-3788	38571
Section 4/right	-225853	4659	40213
Section 1/left	-244134	2130	40132.84
Section 2 left	-242632	254	37920
Section 3/left	-226955	-2858	43200
Section 4/left	-73457	4327	73439

Table 2(a). Maximum/minimum internal force of steel-concrete section under the live load.

Section	Maximum internal force			Minimum internal force		
	Axial force/kN	Shear force/kN	Bending moment/kN·m	Axial force/kN	Shear force/kN	Bending moment/kN·m
Section 1/right	-287.49	-1451.70	2680.72	-17268.34	-1804.63	-76017.20
Section 2/right	-317.90	-1071.66	5143.15	-17302.80	-1437.25	-73336.82
Section 3/right	-295.35	-1174.72	6990.98	-17282.89	-1558.82	-70763.01
Section 4/right	-294.59	-427.52	9421.41	-17282.88	-1558.91	-65279.82
Section 1/left	-318.26	-1445.26	2673.15	-17302.77	-1437.50	-76428.31
Section 2 left	-295.40	-1174.71	5159.07	-17282.95	-1558.11	-73235.97
Section 3/left	-294.97	-801.12	6976.15	-17282.89	-1558.77	-71632.81
Section 4/left	-294.60	-427.52	9409.09	-17282.89	-1558.88	-66002.28

A trip of (1DF4 + 14C64) vehicle, whose axle load is ( $6 \times 230 \text{ kN} + 14 \times 4 \times 230 \text{ kN}$ ), has been adopted in this research. The wheelbase is shown in Figure 2. Table 1 (a, b) and Table 2 (a, b) present the internal force and the stress state of the key sections under the dead load and live load, respectively.

### 3 TEST SPECIMEN

#### 3.1 Location selection of steel cells

The fatigue performance of the composite segment is associated with fatigue stress amplitude. The structure would be more prone to fatigue problem if suffering great stress amplitude. The stress state at the top and bottom steel cells are listed in Table 3 and Table 4, respectively. From Table 3 and Table 4, it can be noted that the bottom steel cells are suffering the greater stress amplitude than the top cells. The bottom cells are chosen to be the object of the study.

Table 1(b). Stress state of key sections under the dead load/MPa.

Section	$\sigma_{st-u}$	$\sigma_{st-l}$	$\sigma_{b-u}$
Section 1/right			-4.404
Section 2/right	-12.984	-11.594	-2.330
Section 3/right	-12.715	-11.134	-2.265
Section 4/right	-17.794	-16.605	-3.093
Section 1/left	-17.273	-17.235	-3.240
Section 2 left	-13.437	-11.903	-2.417
Section 3/left	-14.660	-12.832	-2.548
Section 4/left	-7.231	-1.394	

\* $\sigma_{st-u}$ ,  $\sigma_{st-l}$ ,  $\sigma_{b-u}$  and  $\sigma_{b-l}$  represent the stress value of the upper or lower edge of the steel and concrete beam in the joint of steel and concrete.

Table 2(b). Maximum/minimum stress state of steel-concrete section under the live load.

Section	Maximum internal force				Minimum internal force			
	$\sigma_{st-u}$	$\sigma_{st-l}$	$\sigma_{b-u}$	$\sigma_{b-l}$	$\sigma_{st-u}$	$\sigma_{st-l}$	$\sigma_{b-u}$	$\sigma_{b-l}$
Section 1/right			0.036	0.060			-1.557	-2.231
Section 2/right	0.230	0.425	0.030	0.073	-4.601	-7.378	-0.653	-1.271
Section 3/right	0.296	0.583	0.042	0.100	-4.214	-7.113	-0.632	-1.226
Section 4/right	0.628	0.907	0.109	0.156	-6.114	-8.043	-1.063	-1.387
Section 1/left	0.230	0.233	0.024	0.040	-8.861	-8.934	-1.087	-1.540
Section 2/left	0.247	0.456	0.032	0.078	-4.876	-7.838	-0.691	-1.351
Section 3/left	0.313	0.608	0.054	0.105	-4.711	-7.742	-0.819	-1.335
Section 4/left	1.722	2.470			-17.704	-22.951		

\* $\sigma_{st-u}$ ,  $\sigma_{st-l}$ ,  $\sigma_{b-u}$  and  $\sigma_{b-l}$  represent the stress value of the upper or lower edge of the steel and concrete beam in the joint of steel and concrete.

Table 3. Stress state of top steel cell/MPa.

Section	Maximum internal force		Minimum internal force		Stress amplitude	
	$\sigma_{st-u}$	$\sigma_{b-u}$	$\sigma_{st-u}$	$\sigma_{b-u}$	$\Delta\sigma_{st-u}$	$\Delta\sigma_{b-u}$
Section 1/right		-0.056		1.075		1.131
Section 2/right	-0.366	-0.063	3.902	0.667	4.269	0.730
Section 3/right	-0.487	-0.084	3.715	0.635	4.201	0.719
Section 4/right	-0.714	-0.123	3.185	0.543	3.899	0.665
Section 1/left	-0.227	-0.039	4.213	0.719	4.440	0.759
Section 2/left	-0.391	-0.067	4.195	0.717	4.586	0.785
Section 3/left	-0.494	-0.085	3.577	0.611	4.071	0.696
Section 4/left	-1.883		7.583		9.466	

Table 4. Stress state of bottom steel cell/MPa.

Section	Maximum internal force		Minimum internal force		Stress amplitude	
	$\sigma_{st-l}$	$\sigma_{b-l}$	$\sigma_{b-u}$	$\sigma_{b-l}$	$\Delta\sigma_{st-l}$	$\Delta\sigma_{b-l}$
Section 1/right		0.060		-2.231		2.291
Section 2/right	0.425	0.073	-7.378	-1.271	7.803	1.345
Section 3/right	0.583	0.100	-7.113	-1.226	7.696	1.326
Section 4/right	0.907	0.156	-8.043	-1.387	8.950	1.543
Section 1/left	0.233	0.040	-8.934	-1.540	9.167	1.580
Section 2/left	0.456	0.078	-7.838	-1.351	8.294	1.429
Section 3/left	0.608	0.105	-7.742	-1.335	8.350	1.439
Section 4/left	2.470		-22.951		25.421	

\* $\sigma_{st-u}$ ,  $\sigma_{st-l}$ ,  $\sigma_{b-u}$  and  $\sigma_{b-l}$  represent the stress value of the upper or lower edge of the steel and concrete beam in the joint of steel and concrete.

### 3.2 Selection of bottom steel cells

The test specimen is designed by the stress equivalent principle. The stress of the composite segment is given in Table 1(b) and Table 2(b). Based on the equivalent calculation, the applied loads of the specimen of two steel cells and one steel cell are

given in Table 5 and Table 6. These two kinds specimen are shown in Figure 3 and Figure 4. The maximum applied stress load of the specimen with two steel cells is -3756.16 kN. The test equipment MTS with the maximum loading tonnage of  $\pm 2500$  kN is considered, which does not achieve the applied

Table 5. Applied load of the specimen of two steel cells.

Section	Applied maximum loads		Applied maximum loads	
	Bending moment/kN·m	Axial force/kN	Bending moment/kN·m	Axial force/kN
Section 1/right	3.31	78.98	-93.81	-3097.45
Section 2/right	19.86	151.68	-283.16	-2877.82
Section 3/right	30.55	235.59	-309.22	-3101.20
Section 4/right	10.61	280.22	-73.54	-2581.13
Section 1/left	2.25	42.88	-64.41	-1776.69
Section 2/left	21.28	163.06	-302.03	-3052.15
Section 3/left	22.36	235.98	-229.58	-3195.49
Section 4/left	19.40	387.98	-136.07	-3756.16

Table 6. Applied load of the specimen of one steel cell.

Section	Applied maximum loads		Applied maximum loads	
	Bending moment/kN·m	Axial force/kN	Bending moment/kN·m	Axial force/kN
Section 1/right	1.65	39.49	-46.90	-1548.72
Section 2/right	7.16	72.77	-102.15	-1361.31
Section 3/right	10.85	102.55	-109.80	-1350.88
Section 4/right	5.30	140.11	-36.75	-1290.56
Section 1/left	1.50	28.59	-42.94	-1184.46
Section 2/left	7.68	78.22	-108.95	-1444.13
Section 3/left	11.18	117.99	-114.78	-1597.76
Section 4/left	9.52	193.16	-66.75	-1870.04

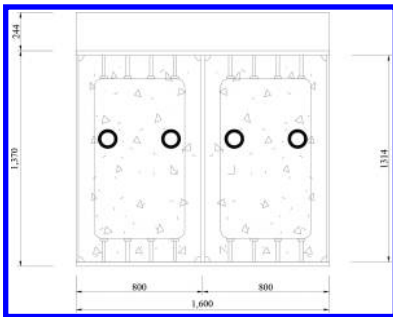


Figure 3. Cross section of two steel cells.

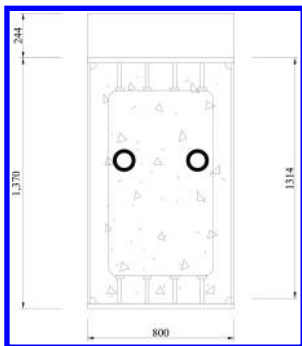


Figure 4. Cross section of one steel cell.

load of two steel cells model. So, the specimen with one steel cell is chosen as the final test model.

#### 4 CONCLUSION

In this paper, the design process of the fatigue model test for steel-concrete composite segment of the Yong-Jiang Hybrid Girder Bridge was introduced.

1. First, a finite element model of the whole bridge was established by the software MIDAS/CIVIL to investigate the stress condition of the structure. Then, the stress state of steel-concrete composite segment was calculated under various working conditions.
2. The range of stress amplitude was the main factors influencing the structure fatigue characteristics. The steel cells of composite segment located on the bottom plate, which suffered the largest stress amplitude, were chosen as the test object.
3. Lastly, considering the effects of the initial defects and laboratory equipment, a full-scale partial model with one steel cell was proposed based on the equivalent stress principle.

# Mechanical properties of RC pile strengthened by effective CFRP composites

N. Zhuang, Y.J. Zhou, H.D. Sun & S. Ge

*College of Harbor, Coastal and Offshore Engineering, Hohai University, Nanjing, China*

**ABSTRACT:** Carbon Fiber-reinforced Polymer Fabric (CFRP) as a kind of high quality and efficient new composite material was widely used in various kinds of reinforcement of structure components. CFRP sheet bonding in the concrete face would offer effective lateral confinement and make core concrete under three-dimensional compression, which improved the compressive strength and deformation capacity of column. In this paper, the load features of six Reinforced Concrete (RC) piles, which were strengthened by different widths and strip spacings, were numerically simulated by finite element software. The load was added along the axial direction of the column to research the failure process. By comparing the bearing capacity and displacement of piles, the effect of spacing and width on mechanical property was investigated. The results indicated that the strength of piles was all increased after repair, and the extent of property improving depending on different repairing schemes.

**Keywords:** Carbon Fiber Reinforced Polymer Fabric (CFRP); pile foundation; mechanical properties; numerical simulation; bearing capacity

## 1 INTRODUCTION

### 1.1 Piles of wharf strengthened by composites

Strengthening reinforced concrete members, such as beams, walls, columns, and slabs (Sang-Wook Bae and Abdeldjelil Belarbi, 2009; Issa et al. 2009; Eid et al. 2009; Ilki et al. 2008; Soudki, K.S. 2007; Wang et al. 2006; Adhikary and Mutsuyoshi 2005; Imran A. 2013), with external bonding CFRP is a new strengthening technique with advantages of easy application, lower cost, and high strength to weight ratio. High-piled wharf is normally composed of pile foundation, reinforced concrete beams and slabs. The pile foundation is the most important load-bearing structure that transfers the upper load from the beam and slab to the bottom soil. The pile directly contacts the sea water that causes it under a poor marine environment. So the pile suffers the most severe corrosion among the structure members of high piled wharf. The harsh marine environment makes the pile inevitably to produce corrosion damage in less than a decade. The structure strengthened by CFRP could resist the corrosion caused by acid alkali for CFRP's good corrosion resistance, which is most suitable for the strengthening of the pile in the marine environment.

In this paper, the model of piles strengthened by different widths and spacings of external bonding CFRP strips was built. Then, the mechanical character of the pile before and after reinforcement was investigated.

## 2 NUMERICAL SIMULATION OF PILE STRENGTHENED BY CFRP SHEET

### 2.1 Numerical model of piles

Ordinarily micro cracks usually increased gradually from the pile's surface to its inside as the pile was applied top load. When these micro cracks extended and connected each other into larger cracks, the pile would be divided into some smaller columns and lose the bearing capacity.

The mechanism of CFRP strengthening technique used in pile was that CFRP strips would form an effective circumambient restraint around the pile, and thus, the pile's concrete core was in a three-dimensional state, which resulted in a significant improvement of bearing capacity, ductility, and anti-seismic property of the pile.

In this paper, a three-dimensional finite element model of piles would be simulated and analyzed by finite element software of ANSYS, as shown in [Figure 1](#). The concrete was simulated by the unit of solid 65; the steel bar was simulated by the unit of link 8; and carbon fiber sheet was simulated by the unit of shell 41. The numerical model has 1136 units and 2819 nodes. The numerical pile model took the vertical direction as the Z-axis and the horizontal radial direction of wharf structure as the X-axis; the Y-axis was then determined by the right hand rule. The physical and mechanical parameters of the beam are given in [Table 1](#).

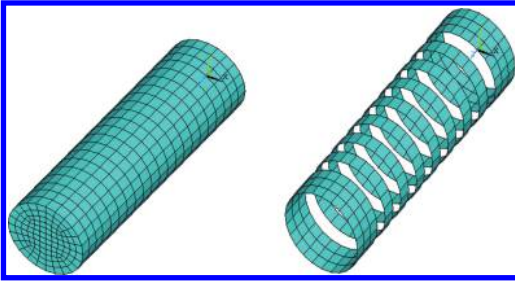


Figure 1. Numerical model of the pile and CFRP.

Table 1. Physical and mechanical parameters of the beam.

Parameter	Concrete	Steel bar	CFRP
Poisson's ratio	0.2	0.3	0.2
Elastic modulus/MPa	$3 \times 104$	$2.0 \times 105$	$2.42 \times 105$
Density/ $\text{kgm}^{-3}$	30	7850	
Yield strength/MPa		300	
Compressive strength/MPa	30		
Tensile strength/MPa			4223
Mass per unit area/ $\text{gm}^{-3}$			200
Thickness/mm			0.167

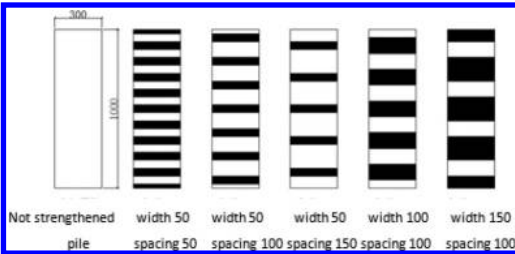


Figure 2. Different reinforcing methods of CFRP strips.

### 2.2 Simulation of piles strengthened by CFRP

In order to avoid local premature failure caused by stress concentration, the bottom and top sides of the pile were bonded by two layers of CFRP strips. The undersurface displacement of the model was fixed, and the horizontal displacement of the upper surface was free. Axial load was added to piles by the equal-added load method. In the numerical experimentation, the bearing capacity and deformation of each pile reinforced by different CFRP strip widths and spacings was studied, as shown in Figure 2. The column DBZ0 was not strengthened

by CFRP sheet as the control column. Column JGZ6 had zero sheet space and was fully wrapped by CFRP sheet. Columns JGZ2, JGZ4 and JGZ5 that had the same sheet space were applied to study the influence of sheet width. And columns JGZ1-JGZ13 having the same sheet width were used to investigate the influence of sheet space.

## 3 NUMERICAL EXPERIMENTAL RESULTS

### 3.1 Analysis of pile bearing capacity

When concrete subjected to axial load the concrete would generate lateral deformation due to Poisson's effect. When the load was small, the lateral deformation was in proportion to the longitudinal deformation. At critical stress, the lateral deformation grew rapidly, which caused internal cracks in concrete because lateral strain grew faster than the longitudinal strain, as shown in Figure 3. These internal cracks would become big cracks and parallel to the load direction, which caused the failure of concrete at last. The RC pile was reinforced by CFRP reinforcing concrete by restraining concrete lateral deformation through high tension strength of CFRP. And the stress of CFRP increased with concrete deformation. When the lateral deformation was larger, the tension strength would be brought into full play. Then, the bearing capacity would be improved.

The amount and area of CFRP strips were different because the width  $B$  and spacing  $S$  of CFRP were different, which caused different bearing capacities of piles. The maximum bearing capacity of each pile is listed in Table 2. The pile bearing capacity was increased after being repaired, but the

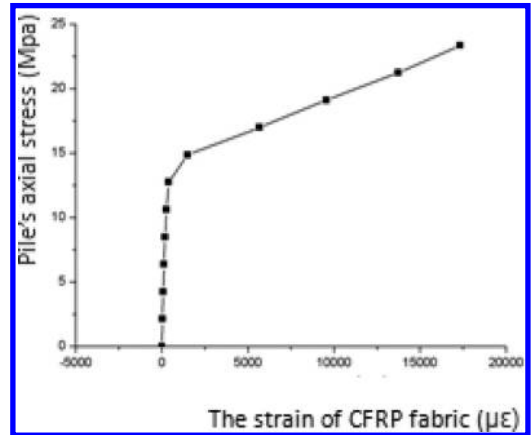


Figure 3. Axial stress to CFRP strain for pile fully wrapped by CFRP.

Table 2. Numerical simulation of column specimens.

Specimens	Sheet width (B/mm)	Space of sheet (S/mm)	Relative sheet width (H)	Ultimate capacity (/kN)	Capacity increasing (%)
DBZ0	0	0	0	1008	0
JGZ1	50	50	0.50	1200	19
JGZ2	50	100	0.33	1090	8
JGZ3	50	150	0.25	1065	6
JGZ4	100	100	0.50	1186	18
JGZ5	150	100	0.60	1160	15
JGZ6	1000	0	1	1650	64

Note:  $H = B/(B + S)$  represented the relative sheet width; the magnitude of the bearing capacity increase was calculated by comparing with the control column of DBZ0.

growth extent was different. Column JGZ6 fully wrapped by CFRP sheet had the biggest increasing level because the full wrap could constrain deformation to the greatest extent and avoid stress concentration in concrete.

It could be concluded that the bearing capacity would increase with relative width H of CFRP strip, as shown in Figure 4. When the relative sheet width was 0.25, 0.33, 0.50, 0.60 and 1, the ultimate bearing capacity of columns increased by 6%, 8%, 18%, 15% and 64% compared with the control pile. Columns JGZ1 and JGZ4 had the same relative sheet width of 0.5, while their width and space of CFRP sheet was 50 mm and 100 mm, respectively. So their increasing degree of ultimate bearing capacity was different, the strengthening effect of JGZ1 was higher than that of JGZ4.

The different spacings of CFRP strip changing with the ultimate bearing capacity are shown in Figure 5. When the width of CFRP strip was constant, the ultimate bearing capacity would decrease with the spacing the CFRP strip increasing. And when the CFRP width was smaller, the growth extent of ultimate bearing capacity would increase obviously.

The effects of different stripe widths on ultimate bearing capacity of the pile are shown in Figure 6 when the spacing of CFRP was constant. The ultimate bearing capacity of pile increased with the CFRP strip width increasing. When the width reached a certain value, the ultimate bearing capacity would not increase because the ends of the pile were not constrained well and result in premature destruction due to a very large increase in the width in the middle of the pile.

The relationship between the axial stress and the height of the pile that was not reinforced by CFRP, as shown in Figure 7. The value of “0” on the horizontal axis represented the bottom elevation of the pile; and the value of “1000” represented the top elevation of the pile.

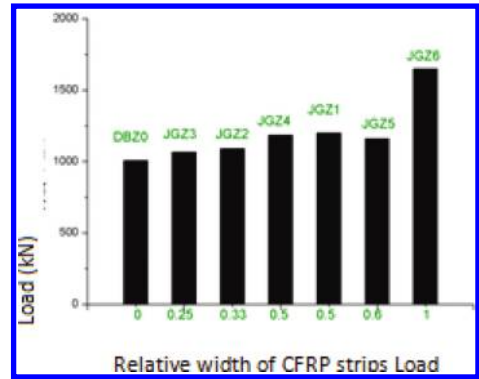


Figure 4. Relation between ultimate bearing capacity and relative width of CFRP strips.

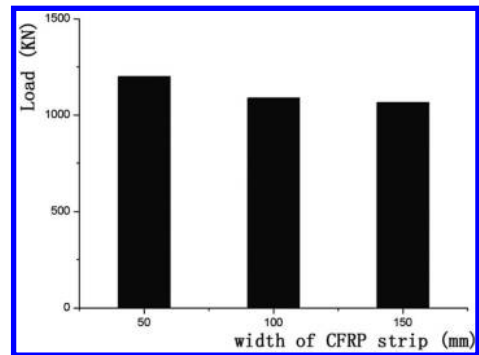


Figure 5. Various spacings of CFRP strips to ultimate bearing capacity.

And the stress in the middle of pile was relatively uniform and smaller than that of at two ends. As the pile was fully wrapped by CFRP strip, the stress in the concrete was uniform, which could avoid stress concentration and prevent premature failure.

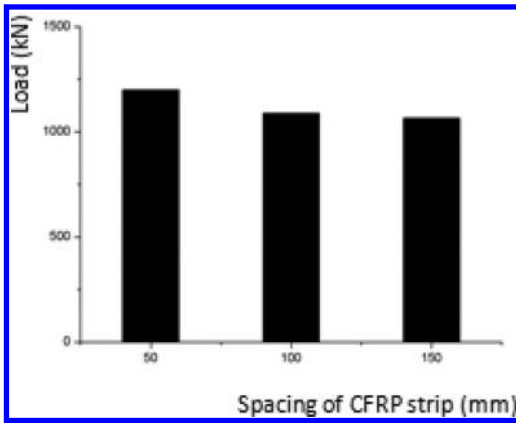


Figure 6. Various widths of CFRP strips to ultimate bearing capacity.

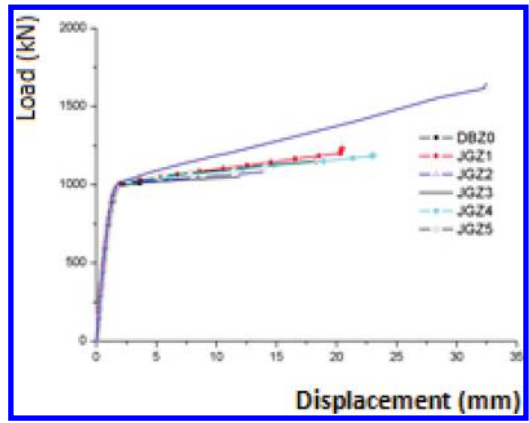


Figure 8. Load-displacement of piles.

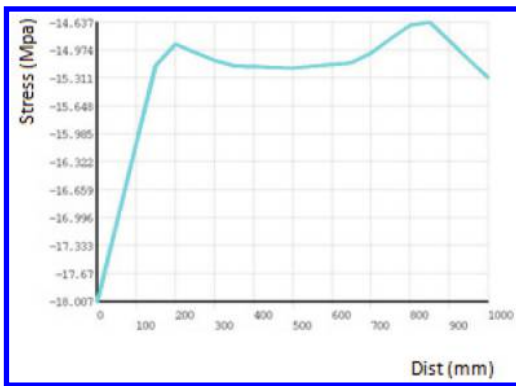


Figure 7. Curve of stress-height in control pile named DBZ0.

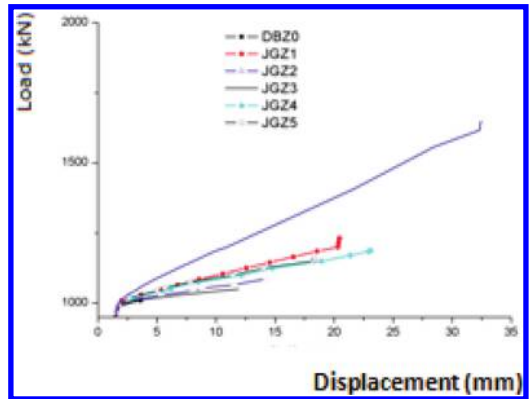


Figure 9. The second stage of the load-displacement curve.

### 3.2 Analysis of pile load-displacement

The change in load to deformation for pile before and after reinforcement is shown in Figure 8 and Figure 9. The bearing capacity and deformation were both improved when the pile was reinforced by CFRP strips. The load-deformation could be divided into two stages. In the first stage, the restriction of CFRP to the pile was small; and two curves before and after reinforcing were similar. In the second stage, as the pile was subjected to axial stress, the RC pile generated lateral expansion, which caused circumferential deformation of CFRP strips and generated lateral restriction for the concrete of the pile. So after strengthening the bearing capacity, the ductility of the pile was improved obviously. Under the same load, the pile deformation would decrease with the relative CFRP width increasing because the CFRP strips generated more lateral confinement.

## 4 NUMERICAL EXPERIMENTAL RESULTS

This paper presented the results of a numerical experimental program investigating the mechanical properties of CFRP-strengthened reinforced concrete pile. Based on the numerical test results, the following conclusion can be drawn:

Bonding CFRP strips on the surface of RC pile could significantly enhance the performance of RC pile. The ultimate bearing capacity of RC pile reduced along with the increasing spacing of CFRP strips when the CFRP strip was constant.

When the relative width of CFRP strip was over 0.5, the increase extent of bearing capacity would become smaller compared with the relative width of CFRP strip below 0.5. Stress concentration occurred at the both ends of the RC pile, which caused premature local failure when the relative

width of CFRP strips was over 0.5. So, the effect of CFRP reinforcing was not obvious when the relative width of CFRP strip was over 0.5.

The pile fully wrapped by CFRP strips had the highest increasing level because full wrap could constrain deformation to the greatest extent and avoid stress concentration in concrete, which improved the mechanical property and increased the ultimate bearing capacity of the pile.

## ACKNOWLEDGMENTS

This research was financially supported by the National Natural Science Foundation of China (51379073) and the Natural Science Foundation of Jiangsu Province (BK20131317).

## REFERENCES

- Adhikary, B.B. 2004. Mutsuyoshi, H. Behavior of concrete beams strengthened in shear with carbon-fiber sheets. *J. Compos. Constr.* 8(3):258–264.
- Eid, R., Roy, N., and Paultre, P. 2009. Normal and high strength concrete circular elements wrapped with FRP composites. *J. Compos. Constr.* 13(2):113–124.
- Ilki, A., Peker, O., Karamuk, E., Demir, C., and Kumbasar, N. 2008. FRP retrofit of low and medium strength circular and rectangular reinforced concrete columns. *J. Mater. Civ. Eng.* 20(2):169–188.
- Imran A., Bukhari., Robert Vollum., Saeed Ahmad. 2013. Shear Strengthening of Short Span Reinforced Concrete Beams with CFRP Sheets. *Arab J Sci Eng.* 38:523–536.
- Issa, M.A., Alrousan, R.Z., and Issa, M.A. 2009. Experimental and parametric study of circular short columns confined with CFRP composites. *J. Compos. Constr.*, 13(2):135–147.
- Sang-Wook Bae and Abdeldjelil Belarbi. 2009. Effects of Corrosion of Steel Reinforcement on RC Columns Wrapped with FRP Sheets. *Journal of Performance of Constructed Facilities*, 23(1):20–31.
- Soudki, K.S., El-Salakawy, E., and Craig, B. 2007. Behavior of CFRP strengthened reinforced concrete beams in corrosive environment. *ASCE J. Compos. Constr.* 11(3):291–298.
- Wang, W.W., and Li, G. 2006. Experimental study and analysis of RC beams strengthened with CFRP laminates under sustaining load. *Int. J. Solids Struct.* 43(6):1372–1387.



# Applied research of acoustic transmission method on the detection of pile foundation

Jianning Zhang, Baohui Wang, Mingcheng Jing, Zhaoyu Sun & Yansheng Lin  
Gansu ZhiTong Technology Engineering Detection Consulting Co. Ltd., Lanzhou, China

**ABSTRACT:** The principle, test method and test procedure of the ultrasonic transmission method are elaborated, and the ways to analyze test datum and judge the integrity of pile body are analyzed in detail through practical engineering cases, which is instructive for practical engineering application.

**Keywords:** ultrasonic transmission method; detection of pile foundation; integrity

## 1 INTRODUCTION

In recent years, along with the increasing investment of infrastructure construction project from the country, pile foundation has been widely used as the important component and main foundation form of various engineering structures [1]. According to relevant documents, the amount of the concrete cast in-place piles used in the country exceeds 1 million every year, including the ones of overlength and large diameter, and the cost of pile foundation often accounts for more than a quarter of the whole of the engineering project [2].

The concrete cast in-place piles belong to concealment engineering, and generally the quality of piles cannot judge from the exterior. Because of the influence of factors like construction site environment or construction management and so on, multiple harmful defects like necking, mud-clamping and holes may exist in the shaped pile bodies [4].

## 2 THE PRINCIPLE AND METHOD OF ULTRASONIC DETECTION

### 2.1 The principle of ultrasonic detection

The ultrasonic is a type of mechanical wave, so mechanical vibration and fluctuation are the physics basis of ultrasonic detection. It is also one of the elastic wave test method, with the theoretical basis of the propagation theory of elastic wave in solid medium. The data-processing system realize the judgment of the property, size and position of various defects inside the pile foundation and provide the assessment criteria of concrete overall homogeneity and strength grade according to the synthetical judgment and analysis of various parameters of signals received by the software.

### 2.2 The burying of sonic-testing tubes and testing preparation

#### 2.2.1 The burying of sonic-testing tubes

When the pile diameter is less than 1500 mm, 3 pipes are buried; when the pile diameter is greater than 1500 mm, 4 pipes are buried (see Fig. 1).

The sonic-testing tubes are metal, and the connections of pipes use screw joint, which makes the pipes water-tight. The reliability of the detection results and the success of the detection tests are directly influenced by the burying quality of sonic-testing tubes.

#### 2.2.2 Preparations before detecting

1. The concrete age of the detected piles should be greater than 14 d.
2. The sonic-testing tubes should be filled with water and keep free.
3. Investigate and collect relevant technical documentations and construction records of the projects to be detected.
4. Check the clear condition of sonic-testing tubes before placing the transducers.

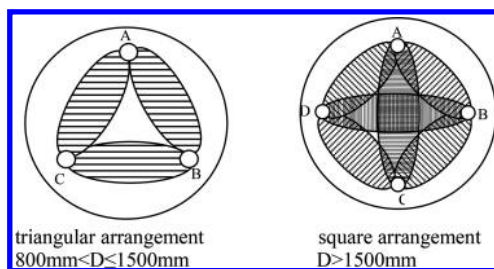


Figure 1. The arrangement diagram of testing tubes. (Note: the shaded area in the figure is the effective detecting range of sonic wave).

- Measure the clearance distance between the outside walls of each sonic-testing tube at pile top surface with steel tape, and check the distance measurement between each measured point of the profile section.

### 3 ENGINEERING PROJECTS

#### 3.1 Engineering project 1

The punched grouting pile foundation is used in a project, the design pile diameter of which is  $\phi 1500$  mm and the concrete design strength grade is C25; the construction length of the defective pile is 39.40 m.

Test result (see Fig. 2): within 0.00–2.00 m of the pile body concrete of the tested pile, both of the acoustic velocity and the amplitude are lower than the critical value; the PSD curve is distorted; the departure of wave speed and amplitude between the measured and the average reach around 200 m/s and 10 dB respectively. The phase of the defective position is opposite to that of the normal concrete, inferred that the thickness of concrete cover in that position is low and tendons leak partially.

#### 3.2 Engineering Project 2

The punched grouting pile foundation is used in a project, the design pile diameter of which is  $\phi 1300$  mm and the concrete design strength grade is C25; the construction length of the defective pile is 18.00 m.

Test result (see Fig. 4): the concrete of the tested pile body lies 1.6 m from the pile top, both of the acoustic velocity and the amplitude are lower than the critical value; the PSD curve is seriously distorted; the wave speed of the defective position is 3000 m/s, 1500 m/s deviated from the average value

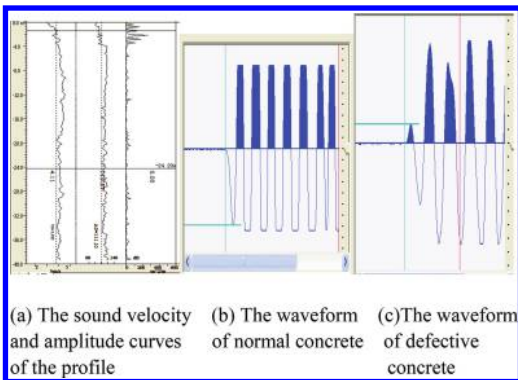


Figure 2. Test results of project 1.



Figure 3. Leakage tendon of the defective position.

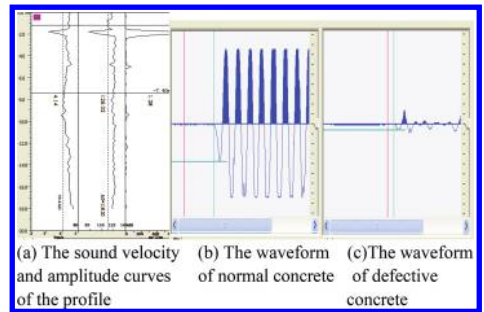


Figure 4. Test results of project 2.



Figure 5. Mud-clamping of defective position.

(the wave speed of norm concrete in nearby area is 4500 m/s), and the departure of the amplitude between the measured and the average is around 30 dB, inferring that the concrete is clamped with mud in this position.

## 4 CONCLUSIONS

Combining the acoustic crosshole transmission method used in the pile foundation detection in the engineering practice, it can be found that: (1) the acoustic crosshole transmission method is an effective way to test the quality of inner concrete, and it can find out the variation conditions of the quality of pile body inner concrete in detail with higher accuracy and resolution and obvious detection effect; (2) the acoustic crosshole transmission method can detect the quality of any section along the length of pile body especially for the piles with large diameter and super length, which is more micromesh and accurate than dynamic measurement method. (3) the application of concrete quality ultrasonic detection provides reliable basis for the quality treatment of concrete.

## REFERENCES

- [1] Cai Yuen. The Application of Ultrasonic Transmission Method to the Test of Bored Concrete Pile [J]. Geophysical And Geochemical Exploration, 2005, 29(3):276–278.
- [2] Zhang Weidi. Pile foundation detection and the development and application of new techniques [J] Hei Longjiang scientific and technologica information. 2011,(18):290.
- [3] Shen Zhongwu. Treating Methods for the Displacement of Reinforcing Cage and Pile Breaking in Bored and Cast-in-place Pile Work [J]. Journal of Railway Engineering Society, 2009,(5):12–15.
- [4] Zhang Cunliang et al. Application of ultrasonic transmission method to detecting integrity of bored cast-in-place piles [J]. Concrete, 2011,(7):148–150.
- [5] Zhao Baidong. To Determine and Investigate a Single Pile loading Capability [J]. Journal of Liaoning Technical University (Natural Science), 2002, 1(2):171–173.
- [6] Zhou Mingxing, Cheng Baohui. State-of-the-Art and Prospecting of Inspection Techniques for Vertical Bearing Capacity of Bridge Foundation Piles [J]. Bridge Construction, 2009,(z2):1–6.
- [7] Ng S.C et al. Ultrasonic NDE for internal defect detection in multi-layered composite materials by multi-resolution signal decomposition [J]. Journal of Applied Sciences, 2013,13(1):87–94.
- [8] Ito. Yu et al. Cepstrum analysis applied to ultrasonic reflection wave detection wave method to investigate the depth and the damage of the pile [C]. SICE-ICASE International Joint Conference, 2006:1561–1564.
- [9] Guangde Song et al. An intelligent instrument for ultrasonic nondestructive examination flaw inspection of rails [C]. Fifth World Congress on Intelligent Control and Automation, 2004:3632–3635.
- [10] Popovics J.S, Rose J.L. A survey of developments in ultrasonic NDE of concrete [J]. IEEE Transactions on Ultrasonics, Ferroelectrics and Frequency Control, 1994,41(1):140–143.
- [11] Zhang Bing et al. Dynamic parameters identification of waveguides using reflection and transmission coefficients [J]. Journal of Vibration and Shock, 2011,30(3):228–233.
- [12] Wu Qingpu. Acoustic and Dynamic Detection Techniques of Pile Foundation [M]. Beijing: China Electric Power Press, 2009:15–28.

# A brief discussion on the causes and treatment measures of bridge pile foundation defects

Juan Li, Wenhong Ren, Jihong Wang, Zhao Zhang, Xiaohui He & Baohui Wang  
*Gansu ZhiTong Technology Engineering Detection Consulting Co. Ltd., Lanzhou, China*

**ABSTRACT:** In this paper, several defects and causes of bridge pile foundation commonly observed under construction are analyzed based on the survey of current pile foundation construction status of multiple bridges, and corresponding treatment measures are proposed.

**Keywords:** bridge; pile foundation; defect

## 1 INTRODUCTION

During the construction of bridge pile foundation, some small faults often lead to quality defects of pile foundation, which generally can be prevented. However, it could cause greater economic loss and delay construction schedule if the chosen methods dealing with the defects are inappropriate. In this paper, combining with the analysis of pile foundation construction status, the causes and precautions of bridge pile foundation defects are summarized, and several simple and economical treatment measures are proposed.

## 2 ANALYSIS OF DEFECT CAUSES

### 2.1 *Manually excavated pile*

The construction difficulty is small for the excavated piles, but it has more defects than the bored pile, because it is easily neglected under construction for its small construction difficulty and the causes leading to defects are minor faults mostly, which hardly attracts attention. At present, the schedules of most projects are compressed, and in order to catch the time limit, the majority of excavated piles are altered designed from the bored piles while the groundwater level is high and the capacity of water inrush is large, leading to severe segregation of pile bottom concrete during the construction process.

1. The quality of protective wall is low, and hole collapse occurs when pouring concrete;
2. Concrete disintegrates, segregation layer occurs on the pile body;
3. Pile bottom dreg is too thick.

### 2.2 *bored pile*

The main quality defects of bored pile are pile silted and excessively thick pile bottom sediment layers, and the reasons for the above factors are as follows:

1. Pile silted.
2. Pile bottom sediment layer is too thick.
3. Hole-wall collapses.

## 3 SEVERAL COMMON TREATMENT MEASURES OF DEFECTS

### 3.1 *Rebuild*

Those defects that are discovered in time and detected by ultrasonic during construction can be completely handled by rebuilding a new pile at the origin place after thorough cleaning. This method has a good effect but great difficulty, long operation period and high cost. It can be adopted based on the factors such as importance of project, geological conditions, and number of defects.

### 3.2 *Pile extension*

First, we determine the location of concrete by acoustic detecting on the pile; second, we determine the well-points dewatering based on the geological data offered by the design and excavate the plain concrete to encase the wall.

### 3.3 *Pile core well-shaft method*

This method is easier to be said than done, that is to use a pneumatic pick to chisel a well with a diameter of 80 cm at the center of the defective pile while dewatering at the same time, and the depth

should surpass the defective position at least, and then clean sediments in a sealed manner, place reinforcement cage and cast expansive concrete using the excavating-hole concrete construction method. The daily advance of this method is 0.6 m, but it will involve much more difficulties if individual piles cannot dewater well, leading to massive loss on project quality, schedule and money.

#### 4 TREATMENT MEASURES OF DEFECTIVE PILES

##### 4.1 *For piles of diameter-shrinking and mud-clamping*

This technique attempts to adopt the mudjacking reinforcement method that is commonly used in reinforcing. The conclusion is that the mudjacking reinforcement method is unsuitable for mud-clamping piles.

##### 4.2 *High pressure jet grouting and compaction grouting method*

Strengthening schemes as high pressure water rotary jet grouting cut, eliminating dregs with air, high pressure jet grouting and compaction grouting can be adopted and used on defective piles to achieve the strengthening goal.

##### 4.3 *Static pressure grouting construction*

In order to reduce the possible settlement shrinkage when the jet grouting body consolidates, the size is made to fully penetrate into the bottom of the pile and pile-side gap, and then increase the strength of grouting consolidation body and the friction resistance of pile bottom and hole side effectively, orifice static pressure grouting is proceeded before the final set of cement grout after the processes above are finished, and eliminate the retraction of grout until the orifice is full of grout.

##### 4.4 *Preventive measures of pile breaking*

The key to preventing pile breaking accident is precaution. Each operation aspect and post should be checked and effective preventive measures made seriously before perfusing. The operating instruction should be strictly followed during perfusing, ensuring the continuity, compactness and orderliness of perfusing operation; observe the surface of concrete repeatedly and carefully and calculate the height of concrete surface by theoretical method,

and take the lower one as the standard of disassembling the conductor pipe after comparing; raise the pipe constantly, smoothly and slowly; control the perfusing time in a suitable range. The proper functioning of the facilities should be guaranteed and standby ones prepared; inform the power distribution sector before perfusing to ensure the supply of electricity during perfusing; pay attention to the weather forecast and arrange the perfusing time rationally.

#### 5 CONCLUSIONS

The quality control of pile foundation should be taken seriously in bridge construction, reducing the formation of pile foundation defects as far as possible through studying and knowing various causes of the defects. The existing defects should be treated by the most efficient, economical and quick method, combining the factors as types of defect, severity degree, position and design parameters of pile foundation and synthetically considering the costs, construction schedule and governance effect. Nowadays, the study of defect treatment measures of pile foundation is still inadequate domestically, and there are no proven technical measures to rely on the treatment of defective piles, merely depending on experience and often failing of achieving the best effectiveness in the treatment. It is expected that the relevant administrative and quality supervision departments develop the integral technical measures and reinspection code for the field of treatment measures of pile foundation, and increase the quality control power of the retreatment of defective pile foundation, guaranteeing the quality of bridge pile foundation.

#### REFERENCES

- [1] Chen Qiunan, Wang Xiangqiu. Analysis And Solution Of Bored Piling Failure In A Bridge Foundation Works [J]. Architecture Technology, 2002(4):281–287.
- [2] Yi Jinming. Defect Treatment Examples of Cast-in-place Concrete Piles [J]. Technology of Highway and Transport. 2002(2):76–77.
- [3] JTJ041-2000, Technical Specification for Construction of Highway Bridge and Culvert [s].
- [4] Sun Bin. Quality Control and Defect Retreatment of Bridge Pile Foundation [z]. Administration of High-grade Highway of JiangXiProvince.
- [5] JuJianxun, Chen Hailong. The Retreatment Techniques of A Broken Bridge Pile [J]. Geotechnical Engineering World, 2008.11(6).

# Analysis on load-carrying capacity of a ribbed stiffener shallow spherical shell roof

D.Y. Jia, T. Wang & J. Yang

School of Civil Engineering and Architecture, Anhui University of Technology, Maanshan, China

**ABSTRACT:** According to the construction data of the roof structure for a 100,000 m<sup>3</sup> gas tank, the FEM model of the ribbed stiffener shallow spherical shell is established. The static analysis is taken to check the strength. The eigenvalue buckling analysis is taken to get the first order buckling mode. Then the arc length method is used on the nonlinear stability analysis, and the critical buckling load and allowable overall stability capacity of the roof structure is obtained. By analyzing the checking results of the strength and the stability, the instability is the decisive factor that causes the roof structure to lose the load carrying capacity.

**Keywords:** roof structure; ribbed stiffener shallow spherical shell; load-carrying capacity; overall stability

## 1 INTRODUCTION

In recent years, according to the reasonable utilization of iron and steel plant by-product energy, reduce air pollution, energy saving and environmental protection requirements, the large capacity storage tanks emerge. However, in practical application, be lacking of theoretical research and design code, structural instability occurs in large scale storage tanks which have been built [1]-[5]. Ribbed stiffener shallow spherical shell is a form of spatial structure which is used for the roof of storage tanks. The load carrying capacity of the roof structure is the important design content.

The roof structure of a 100,000 m<sup>3</sup> gas tank in east China consists of center ring beam, edge ring beam, longitudinal ribs, circumferential ribs, longitudinal secondary ribs and cover plate. The section of ribs is channel C18a, the section of secondary ribs is angle L75x6, the thickness of cover plate is 4 mm. The configuration of the roof structure is shown in Figure 1.

FEM analysis model is established by ABAQUS. For steel materials, density is 7850 kg/m<sup>3</sup>, elastic modulus is 206 GPa, Poisson's ratio is 0.3, yield strength is 235 N/m<sup>2</sup>. The element type for all components is S4R. Tie constraints are set between the components, as well as between the component and the cover plate. Since the edge ring beam is stiffer than ribs and cover plate, the boundary condition is assumed as fixed connection.

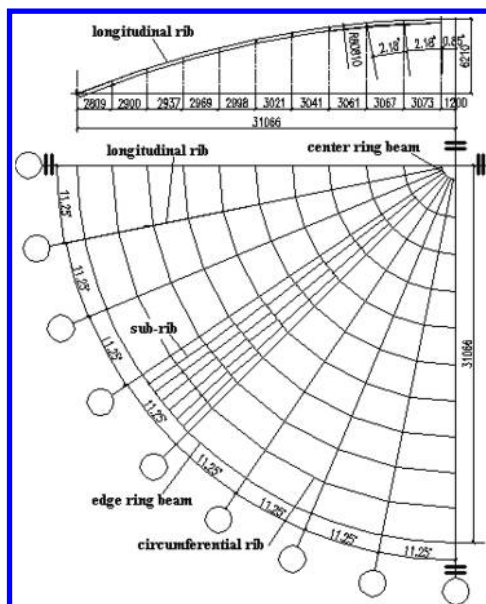


Figure 1. Configuration of the roof structure.

## 2 STRENGTH CHECKING

### 2.1 The displacement and stress of cover plate

According to the actual situation of roof structure, the characteristic value of uniform loads are taken as: dead load 0.6 kN/m<sup>2</sup>, live load 0.5 kN/m<sup>2</sup>, dust

load  $0.75 \text{ kN/m}^2$ , snow load  $0.75 \text{ kN/m}^2$ . Because the live load and snow load is not considered at the same time, the combined characteristic load value is taken as:  $0.6 + 0.75 + 0.75 = 2.1 \text{ kN/m}^2$ . The uniform surface load is applied on the FEM model, the static elastic analysis is taken to get the Mises stress and displacement results. Figures 2 and 3 show the distribution of displacement and Mises stress on the cover plate. The maximum displacement value is  $6.003 \text{ mm}$ , appears at central cover plate between secondary ribs in the fourth band; the maximum Mises stress is  $26.43 \text{ N/mm}^2$ , appears at the joint of cover plate and the ring beam in third band.

### 2.2 The displacement and stress of longitudinal rib

The displacement and Mises stress along the longitudinal rib are shown in Figures 4 and 5. The maximum displacement value is  $5.094 \text{ mm}$ , appears at the middle of rib in the sixth band; the maximum Mises stress is  $57.38 \text{ N/mm}^2$ , appears at the joint of longitudinal rib and the edge beam in the first band.

### 2.3 The displacement and stress of circumferential rib

Figures 6 and 7 show the displacement and Mises stress along the circumferential rib at the

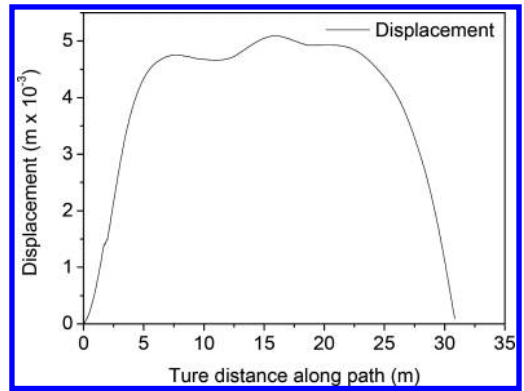


Figure 4. Displacement of longitudinal rib.

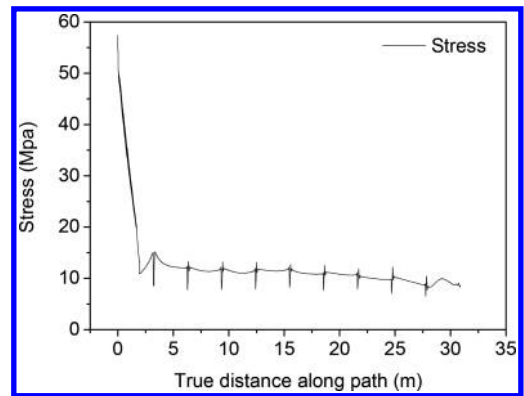


Figure 5. Mises stress of longitudinal rib.

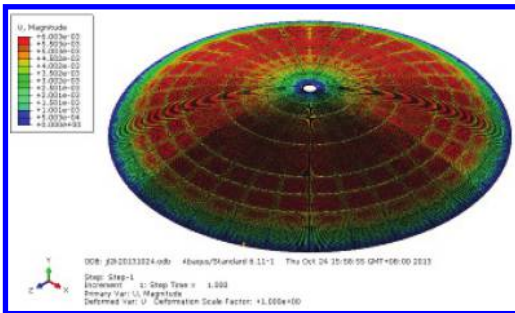


Figure 2. Displacement of cover plate.

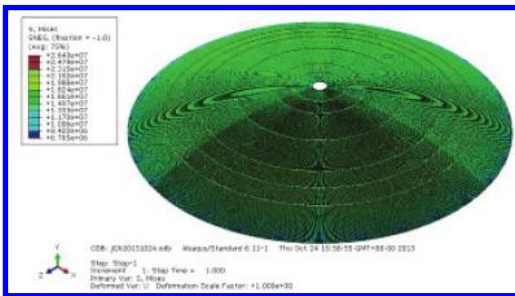


Figure 3. Mises stress of cover plate.

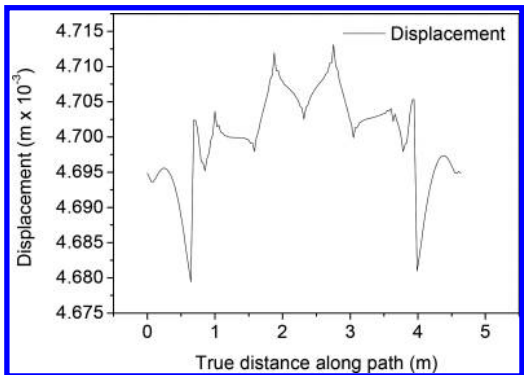


Figure 6. Displacement of circumferential rib.

third band. The maximum displacement value is  $4.712 \text{ mm}$ , appears at the middle of rib; the maximum Mises stress is  $40.52 \text{ N/mm}^2$ , appears at the joint of longitudinal secondary rib and the circumferential rib.

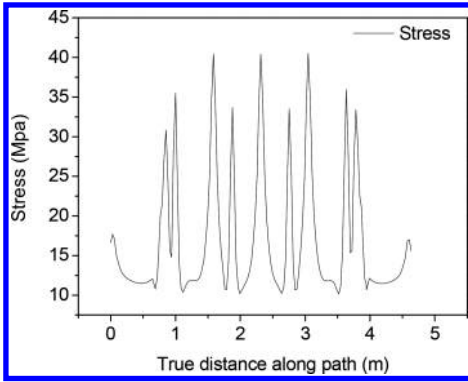


Figure 7. Mises stress of circumferential rib.

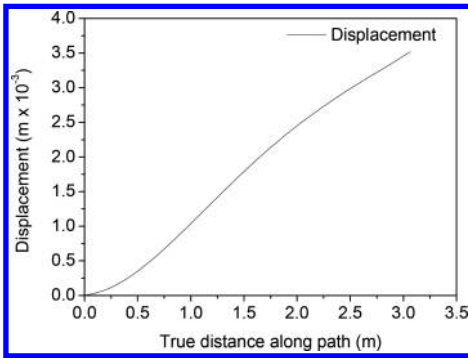


Figure 8. Displacement of longitudinal secondary rib.

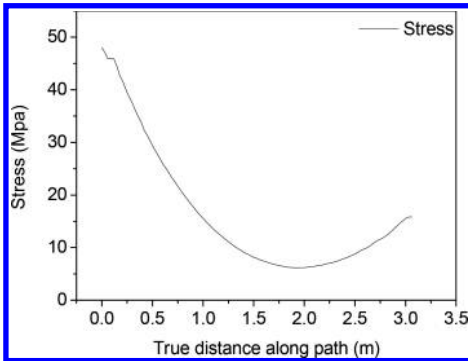


Figure 9. Mises stress of longitudinal secondary rib.

#### 2.4 The displacement and stress of longitudinal secondary rib

Figures 8 and 9 show the displacement and Mises stress along the longitudinal secondary rib at the first band. The maximum displacement value is 3.518 mm, appears at the middle of rib; the maximum Mises stress is 48.04 N/mm<sup>2</sup>, appears at the

joint of longitudinal secondary rib and the circumferential rib.

### 3 STABILITY CHECKING

#### 3.1 Eigenvalue buckling

Considering the material as ideal elastic type, the first order buckling mode is obtained by the eigenvalue buckling analysis. It can be seen from the Figure 10, the maximum buckling deformation occurs at the middle of cover plate in the fifth and sixth bands.

#### 3.2 Overall instability

Taking the first order buckling mode as the initial structure, the initial imperfection value is taken as 200 mm, which is the value of 1/300 span referring to the rules in “Technical Specification for Space Frame Structures”<sup>[6]</sup>. Considering the material as ideal elastoplastic type, the initial defects of structure as the consistent imperfection modal method<sup>[7]</sup>, the arc length method for nonlinear buckling analysis is taken to obtain the overall instability deformation which is shown in Figure 11. In the figure, a wide range collapse occurs in the sixth and seventh bands.

The node at which the maximum vertical displacement occurs on longitudinal ribs is selected. The load-displacement diagram of the node is shown in Figure 8, which express the whole process of tracking analysis of the instability of the structure. Upon loading, the roof structure initially exhibits a linear relationship between the load and the displacement. The structure displacement is very small, that means the structure is in the elastic state with the larger stiffness; Upon continuing the loading, before the maximum load (the critical buckling load) point is reached, the increment ratio of displacement is larger than the load increment, which shows that the structure is in the elastic-plastic state with the stiffness degradation, but still in a stable equilibrium state. At the first upper extreme point,

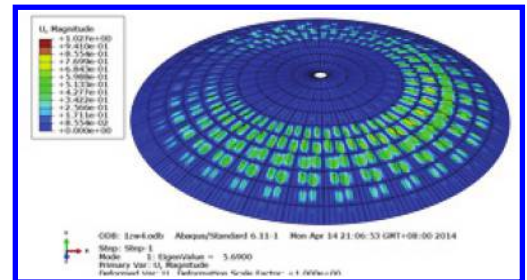


Figure 10. Eigenvalue buckling deformation of roof structure.



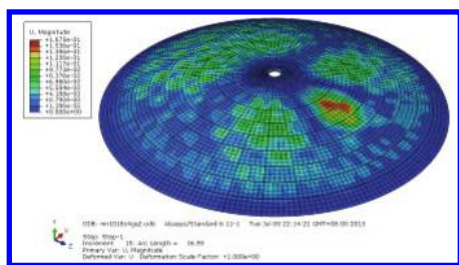


Figure 11. Overall instability of roof structure.

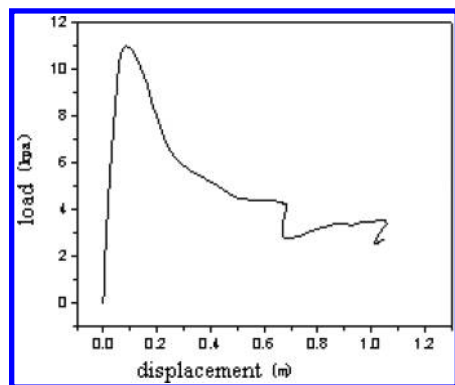


Figure 12. Load-displacement diagram.

the displacement is 0.087 m, the corresponding load value is 10.97 kN/m<sup>2</sup>. After that, the curve is very steep decline, structure deformation speed up, when the load is reduced to 4 kN/m<sup>2</sup>, the displacement is about 0.64 m. Then the first lower extreme point of the curve is reached, that means the structure achieves the reverse balance position. After that, the curve slowly rises, when the load upon to 3.5 kN/m<sup>2</sup>, the displacement is about 1.05 m, the second upper extreme point is reached, and then the second lower extreme point.

Based on Figure 11 and 12, the whole process of instability of tracking analysis of the roof structure can be obtained. Upon loading, the local buckling occurs at the cover plate with initial imperfections near the sixth band, and then the range of buckling deformation increases as well as the values, the work of structure turns into the elastic-plastic state. After the load reaches the first upper extreme point on the curve, the sharp declination shows that the stiffness degradation and brittle failure characteristics of roof structure. As the deformation continues to increase, although the curve rises slightly at the first lower extreme point, the structural deformation has exceeded the allowable value; the structure is in an unstable equilibrium state. Finally, a larger range of collapse occurs, the roof structure is in the state of overall instability.

According to the work performance of roof structure, the first upper extreme load value, which corresponds to the critical buckling load of the structure, can be regarded as the ultimate overall stability capacity of the structure. Referring “Technical specification for latticed shells” provisions, the stability safety factor of the FEM calculation result is 5<sup>[6]</sup>. The critical buckling load value is 10.97 kN/m<sup>2</sup>, that is, the allowable overall stability capacity of the roof structure is 2.19 kN/m<sup>2</sup>.

#### 4 CONCLUSION

According to an actual gas tank construction, the roof structure is a ribbed stiffener shallow spherical shell. The finite element model is established. Based on the FEM analysis results of strength checking and stability checking, the following conclusions can be obtained:

1. In normal operating conditions, under the characteristic combination of external uniform load 2.10 kN/m<sup>2</sup>, the maximum Mises stress is 57.38 N/mm<sup>2</sup>, which is less than the yield strength; the maximum displacement is 6.003 mm, which are far less than the allowable value (1/300 of span).
2. The external load 2.10 kN/m<sup>2</sup> is slightly less than the allowable overall stability capacity 2.19 kN/m<sup>2</sup>. Therefore, as for the roof structure in the form of ribbed stiffener shallow spherical shell, the instability is one of the decisive factors which leads to the failure of structure.
3. The simplified formula for checking the load-carrying capacity of the ribbed stiffener shallow spherical shell shall be deducted.

#### REFERENCES

- [1] Jingbo, Li. 2007. The supergage size of ribbed vault storages design. *Shandong Chemical Industry* 36(6): 23–24.
- [2] GB50341-2003. *Code for design of vertical cylindrical welded steel oil tanks*. Beijing: China Planning Press.
- [3] Wenxia, Huang. 2008. Analysis on vault losing stability of oil tank and discussion of the rectification. *Petro-Chemical Equipment Technology* 29(1):25–28.
- [4] Xuefeng, Zheng. 2001. Analysis on heavy oil tank empowerments concave and countermeasures. *Petro-Chemical Equipment Technology* 30(supplement):117–119.
- [5] Yongjie, Meng. 2013. Single-layer reticulated shell in the application of large span structure. *Low Temperature Architecture Technology* 6(1):83–85.
- [6] JGJ61-2003, *Technical specification for space frame structures*. Beijing: China architecture & building Press.
- [7] Xin, Chen & Shizhao, Shen. 1990. Geometrically nonlinear analysis of reticulated shells. *China civil engineering journal* 23(3):47–57.

# Analysis on wind-induced effects of simply supported beam roof structure with metal roof panels

Li Huang

*Department of Real Estate and Engineering Management, Zhejiang University of Finance and Economics, Hangzhou, China*

Wei Wang & Hua Deng

*Space Structures Research Center, Zhejiang University, Hangzhou, China*

**ABSTRACT:** A simply supported beam roof structure is employed as an example. The mid-span moment time history of the main beam is investigated to study the finite stiffness of the roof panel and the damping properties of the sandwich core effect on simply supported beam wind-induced vibration effects. The numerical results reveal that the finite stiffness of the roof panel and the damping properties of the sandwich core can reduce the amplifying magnitude of the moment and affect the high-frequency segment response mainly, and the extent is limited. For this flexible simply supported beam roof structure, the finite stiffness of the roof panel effect on the wind-induced vibration response of roof structure is prominent.

**Keywords:** metallic roof panel; simply supported beam; roof structure; fluctuating wind; wind-induced vibration

## 1 INTRODUCTION

The impact of the roof panel is usually ignored in the wind-resistant design and analysis of the large span roof structure, during which the wind load is directly applied as a kind of nodal load on the nodes of the main structure generally. Nowadays, the roof panel used in the large span roof structure is the metal composite roof panel, which is made into a kind of sandwich plate in some process. Its top and bottom surfaces are made from thin pressed metal plates, while the middle layer is filed with the damping materials such as polyurethane foaming plastic, the mineral wool or the fiberglass cotton. The sandwich plate is of finite stiffness, so it is not realistic to assume the sandwich plate as the rigid plate in the process of wind load transformation. The roof panel is taken as a thin single plate to consider the effect of its self-vibration, with which the wind vibration coefficient of the large span structure becomes bigger<sup>[1]</sup>. For the polyurethane metal roof panel, a study has shown that its finite stiffness and the damping of its sandwich layer can affect the pulse property of the wind load<sup>[2]</sup>. Beside the effect of the roof panel self-vibration on the amplitude and frequency of the fluctuating wind pressure, the roof panel will work together with the main structure, which affects the stiffness and damping as well as the wind vibration of the whole structure further,

while it is seldom studied in the field of the wind vibration of a large span roof structure.

Research in this paper is focused on the polyurethane metal roof panel. The simply supported beam roof is taken as the numerical example based on the former established composite sandwich shell element for the polyurethane metal roof panel<sup>[3]</sup>, during which the polyurethane metal roof panel is incorporated into the FEM analysis of the roof structure wind vibration. By the analysis of the roof structure wind vibration response incorporating with the influence of the metal roof panel, a preliminary discussion on how much influence the polyurethane metal roof panel will make on the roof structure wind vibration response is presented in this article.

## 2 CALCULATION MODEL

### 2.1 Structure mode

The simply supported beam model is composed of 3 simply supported beams that span 24 m. The distance between the primary beam spacing is 2.4 m, and these beams are connected by the secondary beams (purlins) of 2.4 m spacing. The connections between the primary beams and the secondary beams are rigid, as shown in [Figure 1](#). Section applied for the primary and secondary

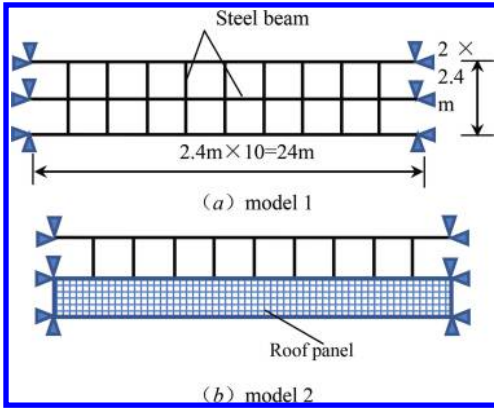


Figure 1. Model of a simply supported beam roof structure.

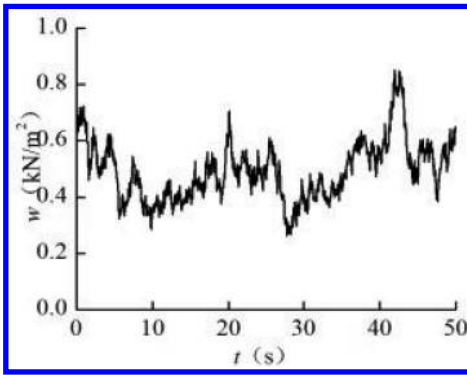


Figure 2. Time history of artificial wind load.

beams is H350 × 175 × 6 × 10 Q235 steel section. The top and bottom surfaces of the roof panel are set by steel with a density of 7850 kg/m<sup>3</sup>, Young's modulus of 206 GPa and Poisson's ratio of 0.3. The density of the hard polyurethane foam sandwich layer is set by 42.87 kg/m<sup>3</sup>, as well as the basic mechanical parameters are set as those described in reference<sup>[4]</sup>. Regardless of the mass of the roof panel, the fundamental frequency of the structure is  $f = 0.95$  Hz, which is almost equal to the fundamental frequency of the large span roof structure with a big span. It shows that the stiffness of the structure is flexible.

Modeling and analysis are processed in the ANSYS software. In order to analyze the influence of the roof panel on the response of the structure wind vibration, comparative analysis is taken by these two kinds of models.

Model 1: beam 4 element is applied as the beams, while the wind load is directly applied on the structure nodes as nodal load, as shown in Figure 1(a).

Model 2: roof panels fully laid on the steel beams are simulated by eight-node sandwich shell elements. The roof panel and the beam connect on the 4 corresponding nodes, which couples 6 freedoms. Wind load is vertically applied on the roof panels as the surface load. This model is shown in Figure 1(b).

## 2.2 Wind load history

Wind pressure is taken as 0.5 kN/m<sup>2</sup>, irrespective of the spatial correlation between the nodes. Wind pressure history on the roof surface is artificially simulated by the AR method, as shown in Figure 2.

## 3 MODEL ANALYSIS

By examining the mid-span moment response of the beam in the middle frame, analysis of the effects of the roof panel stiffness and sandwich damping on the roof structure wind vibration response is carried out.

### 3.1 The influence of the roof panel stiffness

Different material and thickness selection for the top and bottom roof panel surfaces will lead to largely different roof panel stiffnesses. It is so complicated to adjust the parameters described above that in this paper, roof panel stiffness is changed by adjusting the thickness of the sandwich layer, namely, variation of the roof panel stiffness caused by kinds of parameters is unified by adjusting the thickness of the sandwich layer. The sandwich layer thickness is set to 0 mm, 60 mm, 80 mm and 100 mm, which is referred to as model 2-1, model 2-2, model 2-3 and model 2-4, respectively. The structure's damping ratio is set to 0.02 according to the steel structure.

Mid-span moment history curves of these models are shown in Figure 3. As we can see, the structure response amplitude with consideration of roof panels decreases. In Figure 3(f), amplitudes in model 2-2 and model 2-3 are small, while those in model 2-1 and model 2-4 are big, which indicates that from model 2-1 to model 2-3, as the stiffness (thickness) of the roof panel increases, the structure response amplitude decreases, and as the stiffness (thickness) of the roof panel increases further, the structure response amplitude increases again.

The beam mid-span moment Power Spectral Density (PSD) distribution is shown in Figure 4. As we can see, the low-frequency stage in the PSD is very close, but the high-frequency stage diverges significantly. By comparison, the high-frequency PSD amplitude of model 2-4 is the smallest, and the high-frequency PSD amplitude of model 2-1

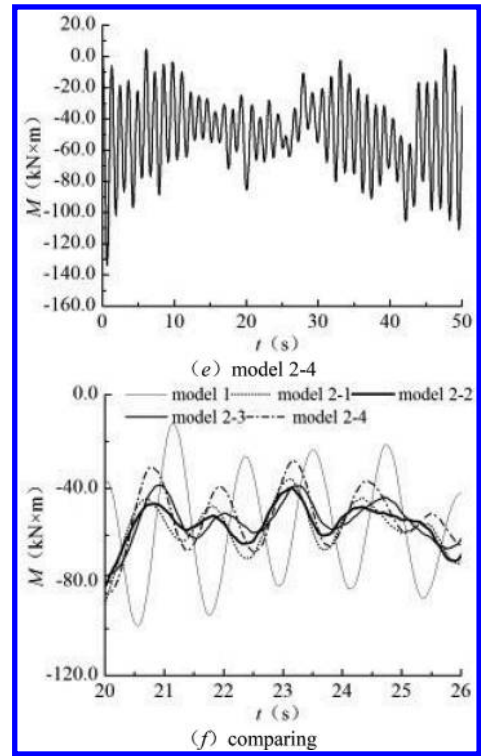
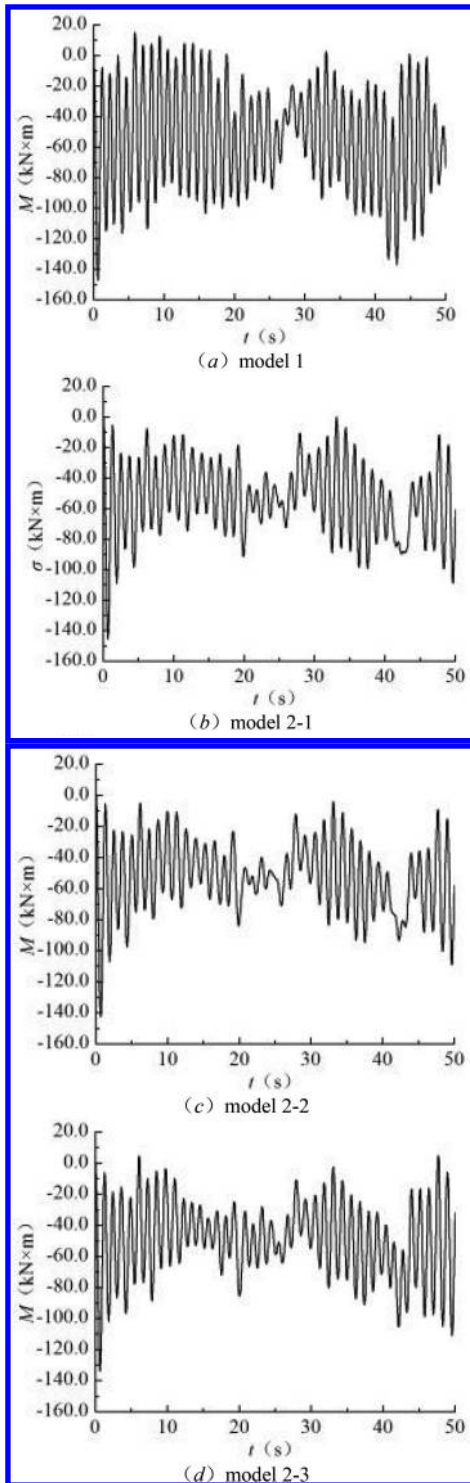


Figure 3. The time history of mid-span bending moment of the main beam.

is the largest, while the corresponding amplitudes of model 2-2 and model 2-3 are between the two values. The law presented here is that the more rigid the roof panel stiffness is, the smaller the amplitude of the high-frequency moment response PSD will get.

### 3.2 The influence of the sandwich layer damping

Modal strain energy method<sup>[6,7]</sup> is applied to calculate the structure's damping ratio of each order. For model 2, 3 cases are taken to make comparative analysis, which are as follows:

1. Damping ratio is set to 0.02 for all orders, namely, the structure is taken as a regular steel structure, which is called model 2-i-a;
2. The material loss factor of the roof panel sandwich layer is set according to the test in literature<sup>[1]</sup>, and the material loss factor of the steel is taken to be 10<sup>-4</sup>, which is called model 2-i-b;
3. The material loss factor of the roof panel sandwich layer is taken to be 0.5, regardless of its variation with frequency<sup>[8]</sup>, which is called model 2-i-c, where i is the model number in 2.1.

Figure 3. (Continued)

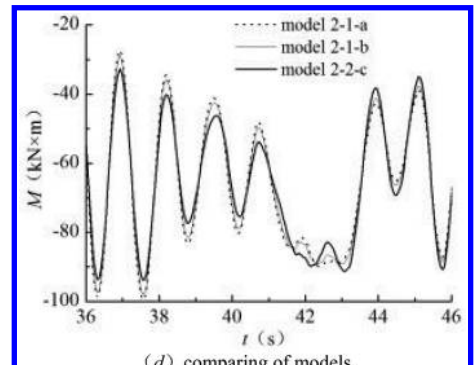
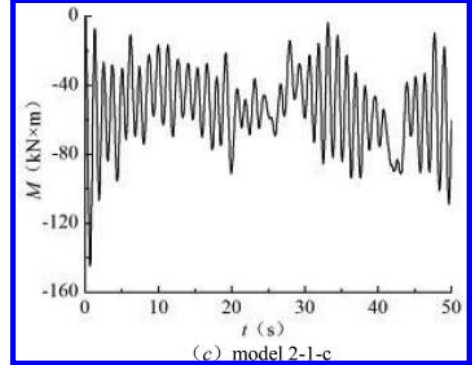
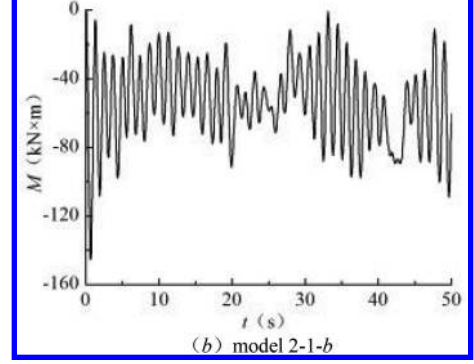
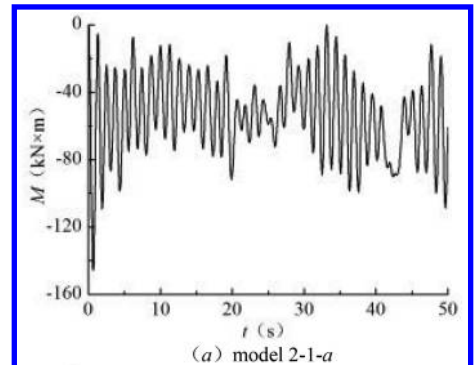
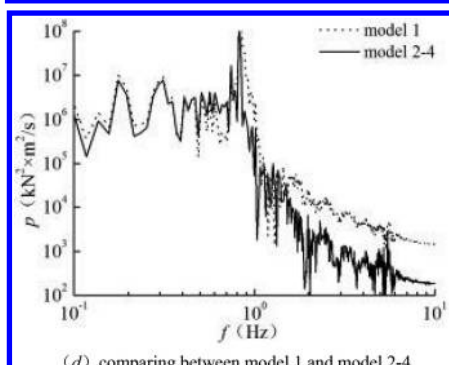
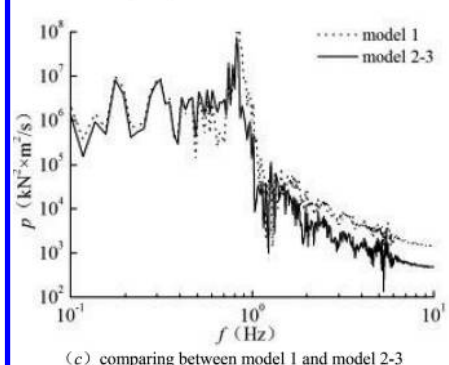
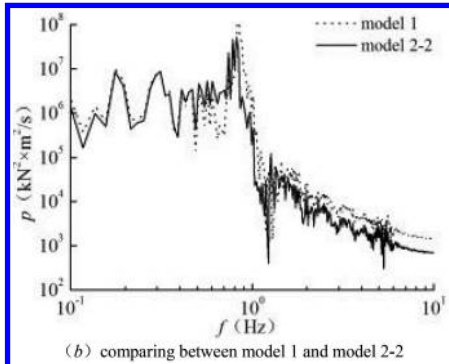
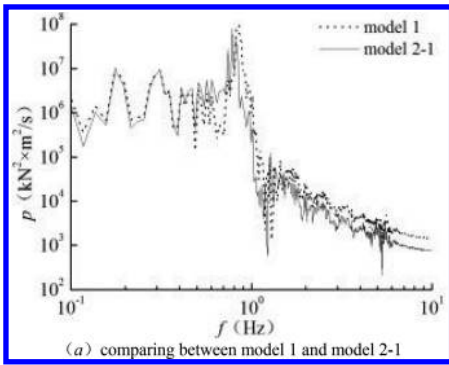


Figure 4. Power spectrum of bending moment time history.

Figure 5. Mid-span bending moment time history of main beam in model 2-1.

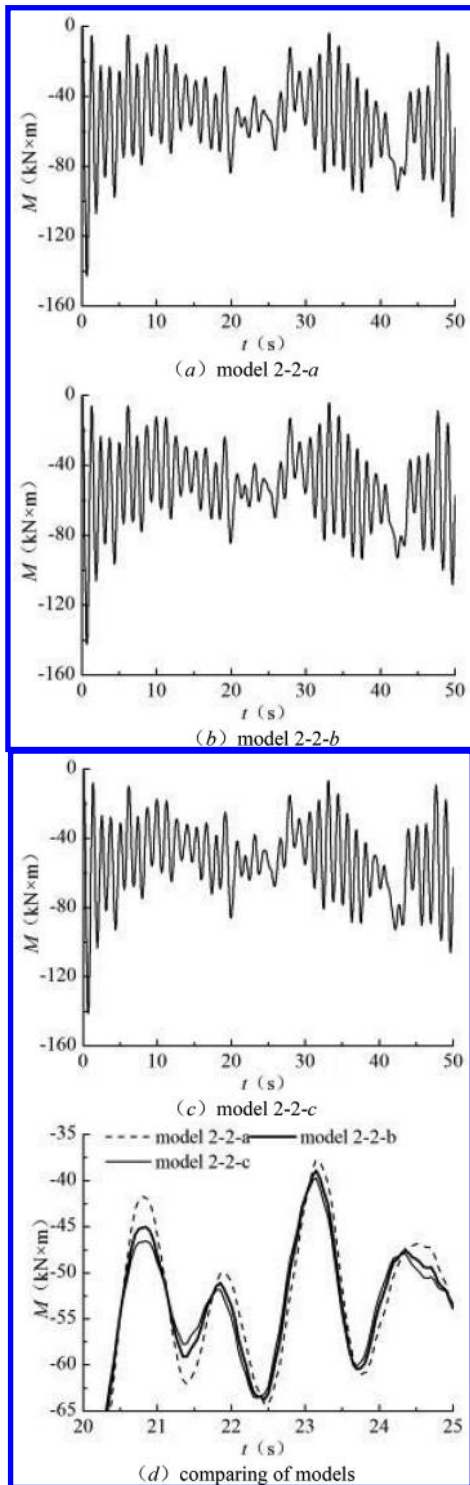


Figure 6. Mid-span bending moment time history of main beam in model 2-2.

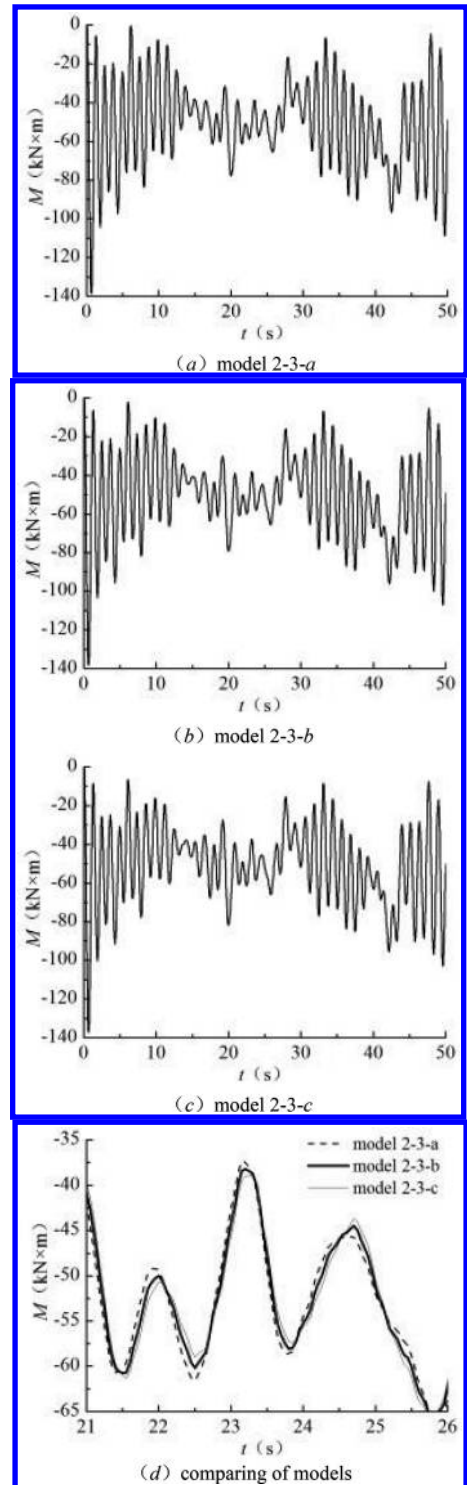


Figure 7. Mid-span bending moment time history of main beam in model 2-3.

### 3.2.1 Model 2-1

The mid-span moment time history curve of the model 2-1 is shown in Figure 5. Curves appear to be similar, while in Figure 5(d) we can see that the amplitudes of the curves show little difference. The amplitude of the model 2-1-c is the smallest, the amplitude of the model 2-1-a is the largest and the amplitude of the model 2-1-b is between the two values. The PSD distributions of the 3 models are similar. Above all, improving the damping ratio of the sandwich layer makes little difference for the whole structure.

### 3.2.2 Model 2-2

The mid-span moment history of model 2-2 is shown in Figure 6, which has the same rule of model 2-1.

### 3.2.3 Model 2-3

The mid-span moment history of model 2-3 is shown in Figure 7, in which it shows the same law as those shown for model 2-1 and model 2-2. Three curves take similar shapes as well as different strain amplitudes.

The moment PSD analysis (Fig. 8) indicates that, during the high-frequency stage, the PSD

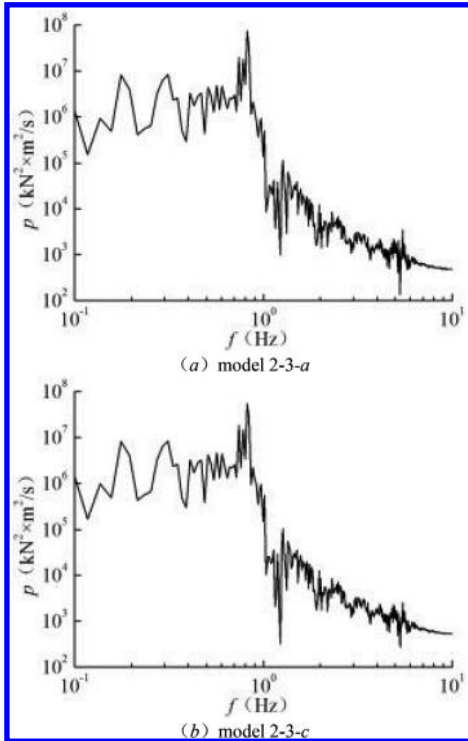


Figure 8. Mid-span bending moment time history of main beam in model 2-3.

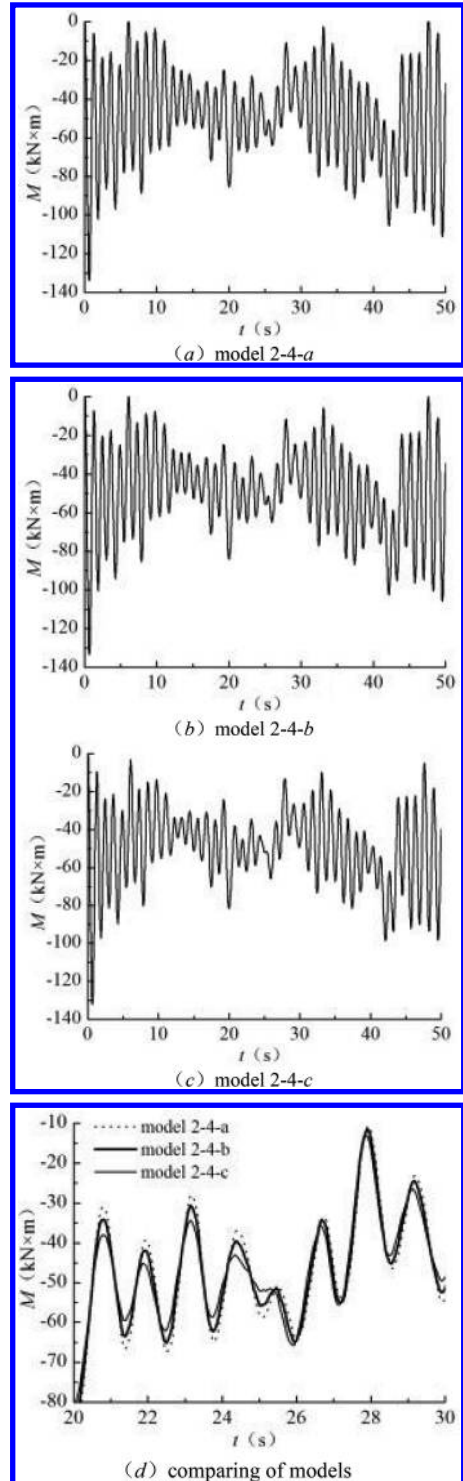


Figure 9. Mid-span bending moment time history of main beam in model 2-3.

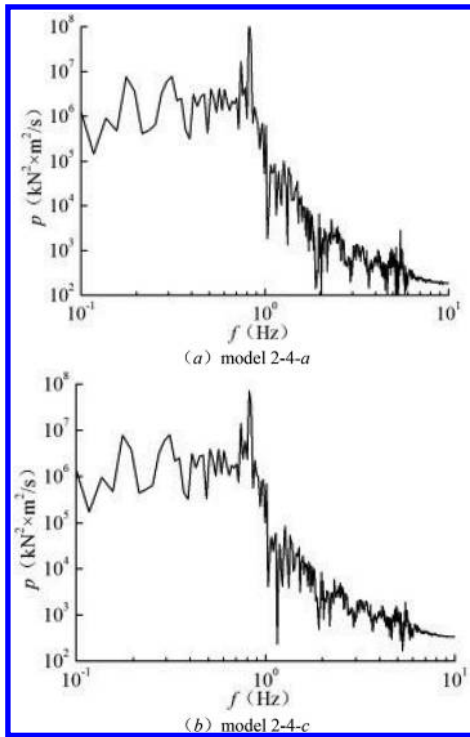


Figure 10. Mid-span bending moment time history of main beam in model 2-4.

amplitude of model 2-3-c is bigger than that of model 2-1-a, which shows the same regular pattern as the one indicated in reference<sup>[1]</sup>, in which the dynamic properties of the roof panel are studied alone. The damping ratio of the sandwich layer changes the spectral character of the structure's dynamic response.

### 3.2.4 Model 2-4

The mid-span moment history curve and moment response PSD attribution are shown in Figure 9 and Figure 10, respectively. Taken together, the results of model 2-4 show the same rule as those for the above 3 models, but the dynamic response amplitude differs more significantly, and the spectral characteristics of the dynamic response change more obviously.

## 4 CONCLUSIONS

1. For the simply supported beam roof structure with relatively soft stiffness, the mid-span

moment response amplitude decreases obviously when the roof panel is taken into account. But the reduced amplitude does not change linearly with the variation of the roof panel stiffness. In general, the roof panel affects the response amplitude of the high-frequency stage;

2. After consideration of the material damping of the roof panel, moment response amplitude becomes lower, though it is of limitation generally and mainly affects the response amplitude of the high-frequency stage;
3. The numerical results show that the stiffness of the roof panel affects the wind-vibration response of the simply supported beam roof structure more significantly.

## REFERENCES

- [1] Ding Yang, Qi Lin, Zhao Yicheng, etc. Wind vibration coefficient of long-span spatial structures with self-oscillating of roof and fluid-structure coupling effect [J]. Journal of Building Structures, 2008, 29(5): 101–105.
- [2] Deng Hua, Huang Li, Wang Chen. Analysis on wind-induced dynamic behaviors of polyurethane sandwich roof panels [J]. Journal of Zhejiang University (Engineering Science). 2013, 47(12): 2125–2131+2175.
- [3] Huang Li, Deng Hua. Hoff theory-based sandwich shell element for metal composite roof panel [J]. Journal of Zhejiang University (Engineering Science), to be published.
- [4] Huang Li, Deng Hua, Wang Chen. Study on Mechanical Properties of Rigid Polyurethane Foam Core Used in Metal Composite Roof Panels [J]. Journal of building materials, 2014, 17(4): 320–325+348.
- [5] Shu Xin-ling, Zhou Dai. AR model of wind speed time series and its rapid implementation [J]. Spatial Structures. 2003, 9(4): 27–32.
- [6] Dai De-pei. The technology of damping vibration and noise reduction [M]. Xi'an Jiaotong University Press. 1986: Xi'an.
- [7] M.H. Tsai, K.C. Chang. A study on modal strain energy method for viscoelastically damped structures [J]. Journal of the Chinese Institute of Engineers. 2001, 24(3): 311–320.
- [8] Chen Ye, Liu Yunhang, Tian Guohua, etc. Studies on polyurethane/benzoxazine resin interpenetrating polymer networks damping properties [J]. Journal of shanghai jiaotong university, 2002, 36(10): 1506–1508.
- [9] Luo Zhong, Zhu Xi, Mei Zhi-yuan, et al. Studies on the damping property of sandwich structures with composite material core [J]. Journal of vibration and shock. 2008(11): 134–136.
- [10] Wang Xinmin. Ansys numerical analysis of engineering structure [M]. China Communications Press. 2010.



# Shaking table test study on a retrofit method of bottom-business multi-story building

Yongduo Liang

Earthquake Administration of Liaoning Province, Liaoning, Shenyang, China

Xun Guo & Yang Zhou

Institute of Disaster Prevention, Hebei, Sanhe, China

Jinzheng Jiang & Ying Li

Earthquake Administration of Liaoning Province, Liaoning, Shenyang, China

**ABSTRACT:** Through a comparative experiment between the earthquake simulation shaking table test of three double-deck models, the differences in the aspects of structure frequency, acceleration, displacement and strain state between the common bottom-business multi-story masonry structure, and the bottom-business multi-story masonry structure reinforced through rectangular steel pipe and steel channel are analyzed. Based on the test results, the destroy mode of each longitudinal wall and the invalidate order are obtained, and the feasibility and practicality of the retrofit method through rectangle steel pipe is proved. Finally, the retrofit method of balancing stiffness and increasing ductility is put forward, which may provide reference for retrofitting design of the existing houses.

**Keywords:** bottom-business multi-story masonry structure; earthquake simulation shaking table test; retrofit; seismic resistant capacity; story stiffness

## 1 INTRODUCTION

In Wenchuan earthquake, 80% of the bottom-business multi-story masonry buildings were ruined, while this kind of structure is very popular in the small and middle towns in the south of China and do not disappear in short time. So, it is urgent to study the earthquake-resistant mechanism of this building form and the methods to retrofit the existing buildings in order to reduce the damages caused by earthquakes.

## 2 SHAKING TABLE TESTS

### 2.1 Test preparation

According to the test aim and content, two double-deck models were designed, with the first floor plan of models, as shown in Figure 1, and the front view of model 2, as shown as Figure 2.

There are 16 acceleration sensors, 4 displacement sensors and 26 strain gauges (model 1), 21 strain gauges (model 2) were set at a proper position. During the tests, Wolong wave was used and the tests were carried out in 5 steps (model 1) and 4 steps (model 2).

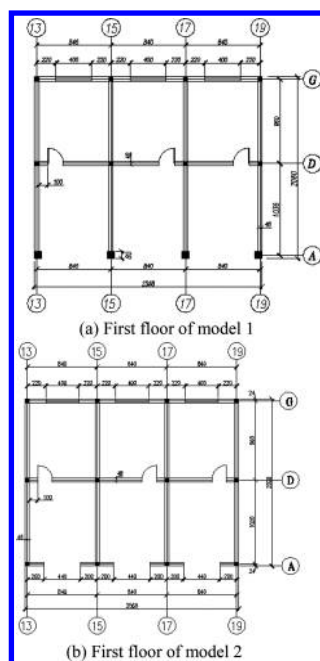


Figure 1. The first floor plan of the models.

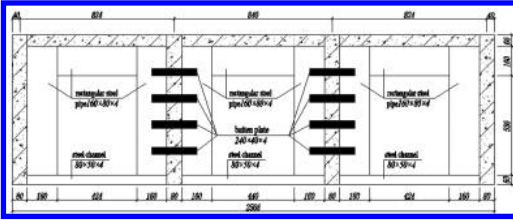


Figure 2. The front view of model 2.

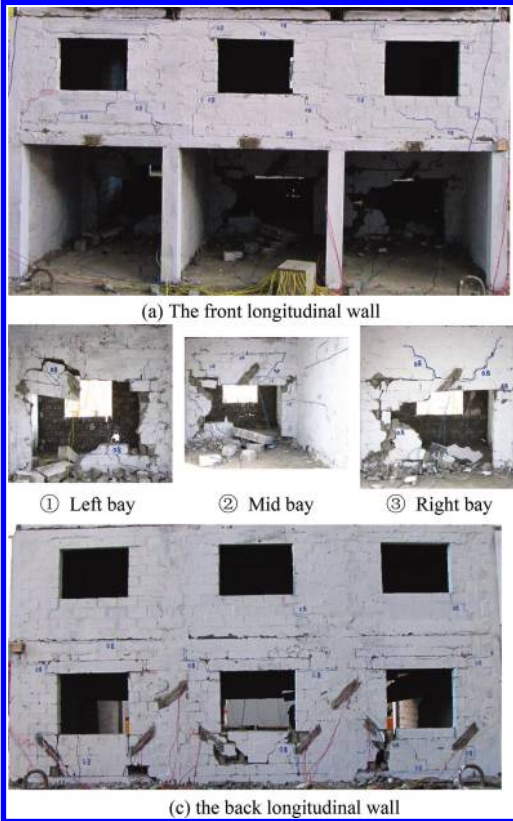


Figure 3. The cracks distribution of model 1 after PGA = 0.82 g.

## 2.2 Test phenomenon

As model 1, after PGA = 0.10 g and 0.35 g, there were no appearance of cracks. From PGA = 0.45 g, near windows of the second floor, there were some fine cracks occurring. With the growing of PGA, the quantity and width of cracks were increasing. After 0.82 g, the damage state could be observed, as shown in Figure 3.

From Figure 3, it could also indicate that the damage order and degree is mid longitudinal wall, back longitudinal wall and front longitudinal wall.

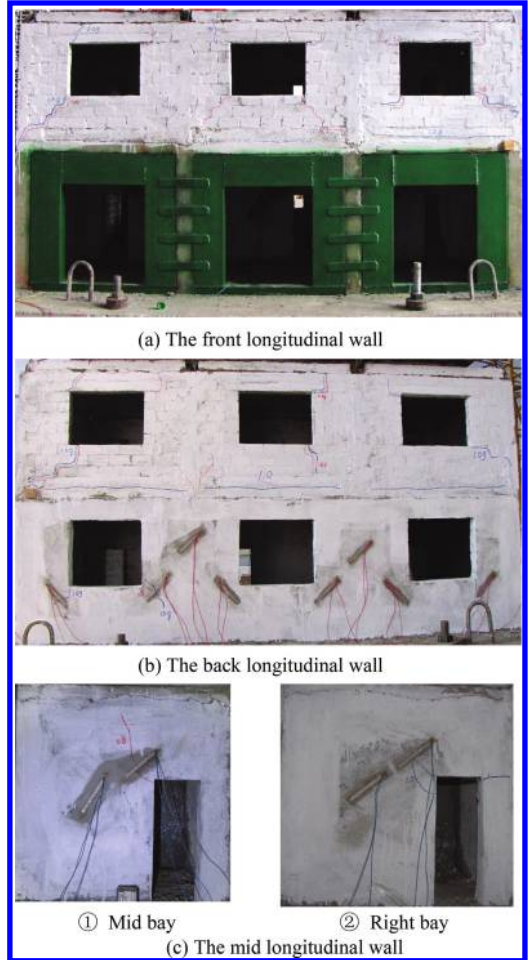


Figure 4. The cracks distribution of model 2 after GA = 0.88 g.

As model 2, the time of cracks appearing is later than model 1, the first fine crack occurs at PGA = 0.84. The details of the damage are shown in Figure 4.

## 3 COMPARISON OF REINFORCEMENT

### 3.1 Modal comparative analysis

The pulsation method is used in testing the modal of the two models before and after loading.

The results include the natural frequency and the torsional frequency, and the details as given in Table 1 and Table 2.

From the two tables, with the increasing load, the frequency of models decreasing trend occurs. The first-order frequency of model 1 reduces by 36%,

Table 1. The modal results of model 1.

Modal	Before load	After PGA = 0.35 g	After PGA = 0.45 g	After PGA = 0.82 g
First-order frequency/Hz	15.0	9.6	9.0	5.6
Second-order frequency/Hz	26.0	13.4	13.4	12.9
Torsional frequency/Hz	24.8	19.6	N/A	19.2

Table 2. The modal results of model 2.

Modal	Before load	After PGA = 0.84 g	After PGA = 0.88 g
First-order frequency/Hz	14.4	5.6	5.4
Second-order frequency/Hz	22.4	13.5	14.1
Torsional frequency/Hz	20.3	15.9	11.3

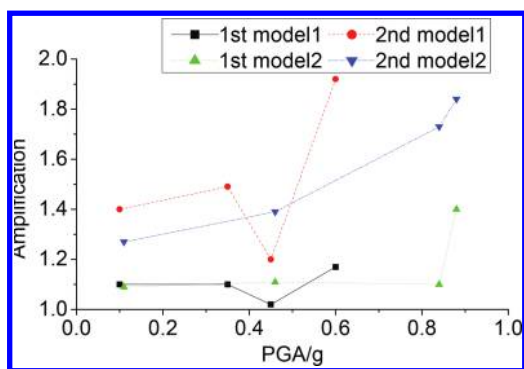


Figure 5. Acceleration amplification.

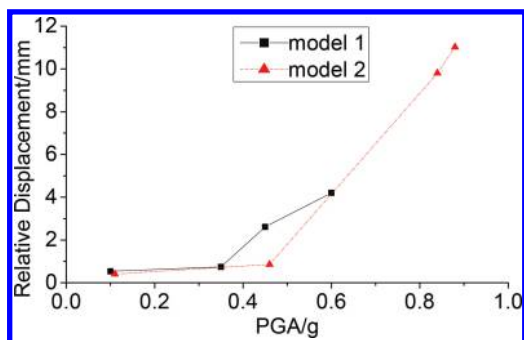


Figure 6. Relative displacement.

40% and 63% after PGA = 0.35 g, 0.45 g and 0.82 g, respectively, and the second-order frequency is 36%, 40% and 63%. And torsional frequency reduces by 21% and 23% after PGA = 0.35 g and 0.82 g, respectively. The same law appeared in model 2.

Because of the positive correlation between the frequency and failure degree, it can be proved that the failure degree of model 2 is lighter than that of model 1 at the same level of earthquake.

### 3.2 Acceleration response comparative analysis

The dynamic amplification effect can be attained through the acceleration earthquake response of the model during the earthquake simulation shaking table test. The data curve of the acceleration amplification contrast of the two models is shown in Figure 5.

From the curve, it can be seen that the data of model 1 is larger than that of model 2 at the second floor except at a special point. This indicated that the failure degree of model 1 is more serious than that of model 2 at the same level of earthquake.

### 3.3 Relative displacement comparative analysis

The curve of relative displacement is shown in Figure 6. From the curve, it can be seen that the data are less than 1 mm at the first and second loads, indicating that the structures are in the elastic state. The data of model 2 is larger than that of model 1 obviously, and from the test phenomenon, it is known that the failure level of model 1 is more serious than that of model 2. Thus, the seismic performance of the retrofit model is significantly improved.

### 3.4 Strain comparative analysis

The strain values of the representative corresponding position of the three longitudinal walls of the two models are shown in Figure 7.

From Figure 7, it can be seen that all values are compressive strain and increasing as the

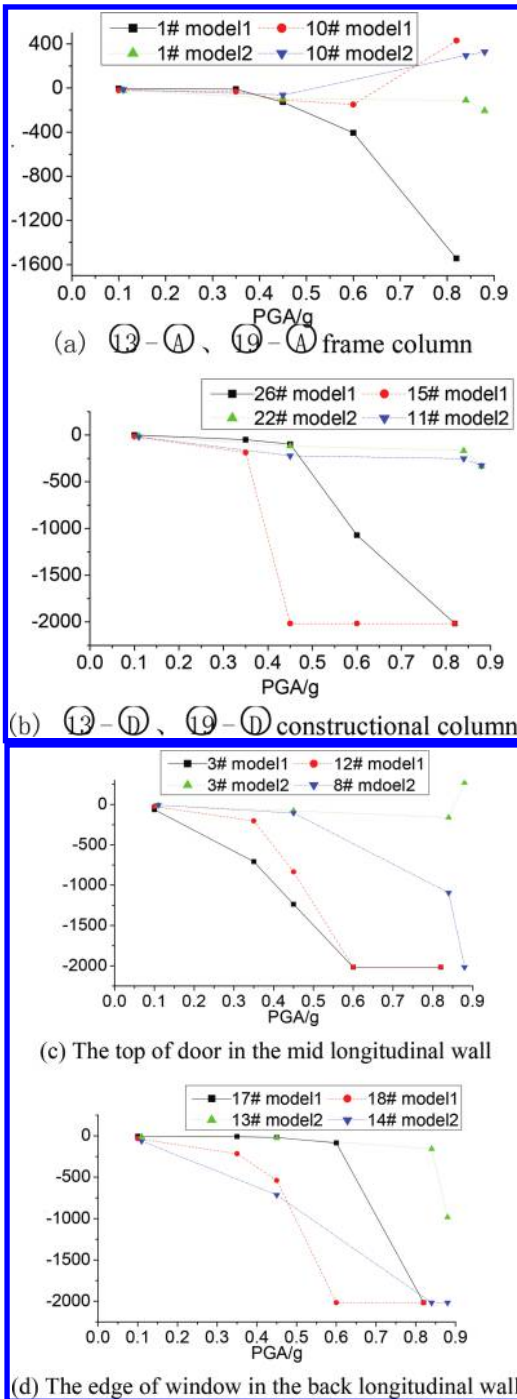


Figure 7. Strain contrast of the corresponding position of the two models.

acceleration of ground motion increases. Collectively, the values of the two models show a consistent rule, that is, the value of mid longitudinal wall is the largest, then the back longitudinal wall and the mid constructional column of transverse wall, the smallest is the front longitudinal wall (frame column and constructional column); and most of the values show the value of model 1 to be larger than that of model 2.

#### 4 SUMMARY

1. The damage degree of model 2 (retrofit) is obviously lighter than that of model 1 (ordinary).
2. The failure sequence of the three longitudinal elements is the mid longitudinal wall, the back longitudinal wall and the front wall (or frame columns).
3. The stiffness of the front longitudinal wall may be strengthened because of rectangle steel pipes and steel channels were added on both sides of the frame columns, and this can balance the distribution of earthquake inertial forces among walls. It is proved that this method may be an effective measure for retrofitting existing normal bottom-business multi-story masonry buildings. The idea may be concluded as “balancing stiffness and increasing ductility”.

#### ACKNOWLEDGMENTS

This work was financially supported by the Doctoral Fund of Liaoning Earthquake Administration (LNDZBSJJ002).

#### REFERENCES

- [1] “Seismic Code for Buildings (GB 50011-2010)”, China Architecture Press, Beijing, 2010.
- [2] Li Xiaojun, Yu Aiqin, Gan Pengxi, etc. Survey and Analysis of the Disaster and Engineering Damage of Beichuan County Seat in Ms8.0 Wenchuan Earthquake [J], Technology For Earthquake Disaster Prevention, 2008,3(4):352–362.

# Force analysis on continuously pouring outer wrapped concrete based on a SRC arch bridge

G. Wei & Z. Gu

Guangxi University, Nanning, Guangxi, China

**ABSTRACT:** This paper takes a long-span concrete-filled steel tubular arch bridge as the research object. The model of the main arch rib plate unit, which includes the beam element and the space finite element, is established by Midas Civil 2012. This paper conducts the computational analysis of the construction process of the main arch ring when it adopts inclined cable-stayed buckle to pour outer wrapped concrete continuously. Besides, it also explores the effect of the main arch ring stress and deformation under the control of non-cable-inclined and four inclined cables. The results show that, under the control of four inclined cables, the nominal pressure and tensile stress of the structure are admissible, the structure shows less deformation repetition, and the arch ring has no upper vault deflection. Thus, the results indicate that the control of the cable-inclined method can achieve a good effect.

**Keywords:** Steel Reinforced Concrete arch bridge (SRC); cable-inclined; continuously concreting; outer wrapped concrete; computational analysis

## 1 INTRODUCTION

The concrete-filled steel tubular arch bridge is mainly used in the long-span concrete arch bridge. After more than 20 years development, the construction technology of the SRC has developed rapidly. In recent years, it has gradually become a main type of bridges of the large span bridges, because it has a great spanning capacity, strong bearing, good stability, and convenience of construction. The outer wrapped concrete of the long-span concrete-filled steel tubular is heavy and massive, and the largest stress and deformation emerge in this construction stage, so it is necessary to conduct force analysis in the stage of casting outer wrapped concrete.

## 2 THE THEORY OF THE CABLE-INCLINED CONTINUOUSLY CONCRETING

The stiffness and strength of rigid skeleton gradually form during the outer wrapped concrete construction progress. As this bridge type possesses complicated structural system transformation and much construction difficulties, the construction method of outer wrapped concrete on the main arch ring is crucially significant. The outer wrapped concrete continual pouring refers to dividing rings firstly, concreting the first ring continuously and

symmetrically from the arch foot to the vault, concreting the next ring after the strength formation, until all the concrete is finished. This construction method is convenient, rapid and has good concrete quality. But, if measures are not taken, the stress and deformation will be out of range. Setting several stayed-buckle cables to regulate the nearby peak of the bending moment influences lines of the controlling section, and applying a changing tension above the oblique arch axis can effectively control the vault deflection and the foot arch hogging moment during the continuous concreting of outer wrapped concrete. Thus, the stress and deformation of steel reinforced concrete arch bridge can be kept within the designed range.

## 3 THE GENERAL SITUATION OF ENGINEERING

### 3.1 Engineering background

The bridge is 852 meters in length, and the single span of main bridge reaches 416 m, which is deck concrete-filled steel tubular railway arch bridge. The rise of arch is 99 m, the rise of the span ratio is 1/4.2, the arch axis shape is catenary, and the arch-axis coefficient is 1.8.

The section of the main arch ring is a single box, including three rooms, whose width is changed but height is invariable. The height of the arch rib is 8.5 meters. In the range of 65 m

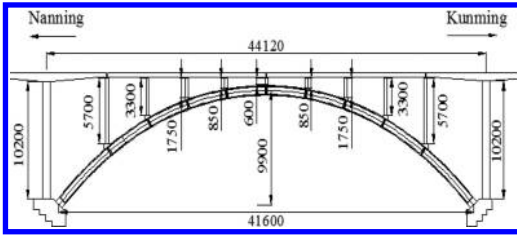


Figure 1. The elevation of main bridge (unit: cm).

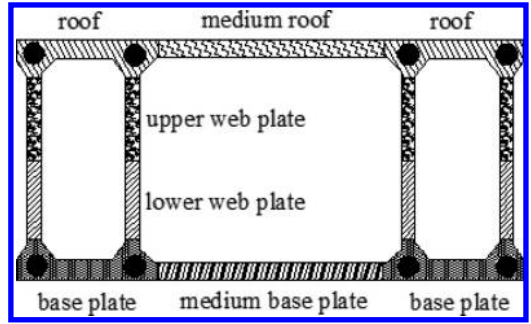


Figure 5. The outer wrapped concrete dividing ring of the arch rib.

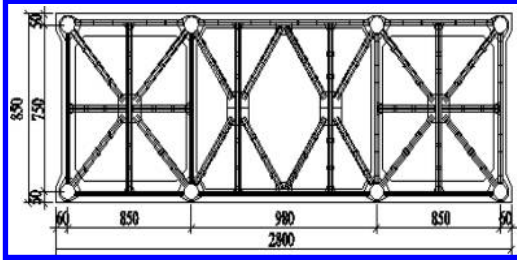


Figure 2. The vault section of arch rib (unit: cm).

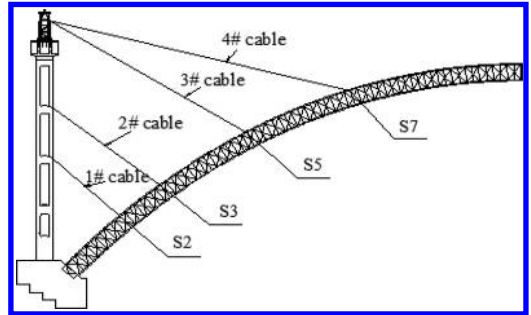


Figure 6. Layout of 4 inclined tensioned cables.

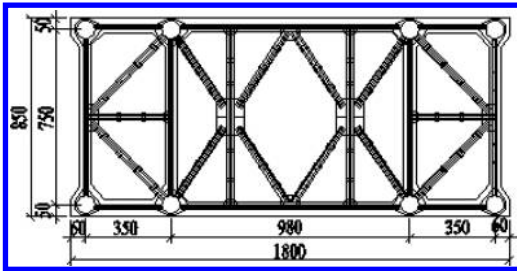


Figure 3. The foot section of arch rib (unit: cm).

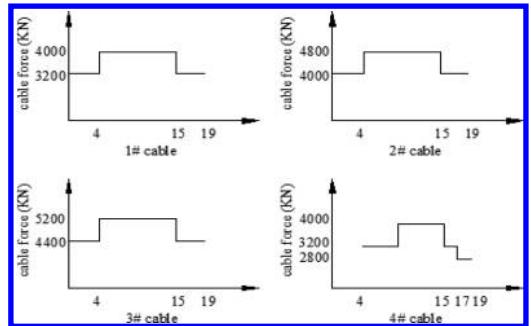


Figure 7. Cable force variation in different stages of construction.

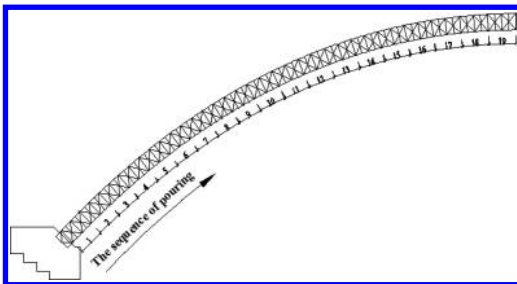


Figure 4. Arch rib segment division.

from the arch foot to the vault, the width of the arch rib changes from 28 m to 18 m linearly. In the range of 286 m in horizontal length, the length is 18 m and the middle room is 9.8 m in width. The stiff skeleton is mainly composed of steel and

steel tube concrete, the upper and lower chords adopt the steel tube of  $\Phi 750 \times 22$  mm. The chord is connected by angle steel, and transverse cross brace is set in the right position to strengthen the horizontal connection, which forms a steel and concrete-filled steel tubular truss frame. There are 38 lateral braces to connect the arch rib, and the link of each chord is welded. Concrete is poured after the arch rib is finished, the concrete

Table 1. Scheme stage of construction.

Conditions	Description	Conditions	Description
1	Concrete-filled steel tube	89	Remove the fourth template
2	Install the first template	90	Install the fifth template
3–21	Pour the part 1 to 19 of the first ring	91–109	Pour the part 1 to 19 of the fifth ring
22	The first ring is finished	110	The fifth ring is finished
23	Remove the first template	111	Remove the fifth template
24	Install the second and third template	112	Pour the part 1, 4 of median septum
25–43	Pour the part 1 to 19 of the second ring	113	The part 1, 4 of median septum is finished
44	The second ring is finished	114	Pour the part 2, 5 of median septum
45–63	Pour the part 1 to 19 of the third ring	115	The part 2, 5 of median septum is finished
64	The third ring is finished	116	Pour the part 3, 6 of median septum
65	Remove the second and the third template	117	The part 3, 6 of median septum is finished
66	Pour the edge septum	118	Install the sixth template
67	The edge septum is finished	119–137	Pour the part 1 to 19 of the sixth ring
68	Install the fourth template	138	The sixth ring is finished
69–87	Pour the part 1 to 19 of the fourth ring	139	Remove the sixth template
88	The fourth ring is finished	140	Ten years of shrinkage and creep

adopts C80 weakly expansive concrete, and the outer wrapped concrete is C60 high-strength concrete.

### 3.2 The scheme stage of construction

For rational utilization of the original cable, the position of cable-inclined is the same as the lift of steel skeleton. After construction of the steel skeleton, and reaching the designed strength, parts of inclined cables are removed, except 2#, 3#, 5#, and 7# cables. The way of pouring arch ridge concrete is split-ring continuous pouring. The half span arch ridge is divided into 19 parts longitudinally and 6 rings vertically. The Concrete is poured continuously and symmetrically from the arch foot to the vault, the order of concreting is the first side room, then the middle room; first base plate, then the web plate, and finally the roof. The scheme stage of construction is given in Table 1.

## 4 FINITE ELEMENT MODEL

The model includes 3001 nodes and 10852 elements, including 8324 concrete-filled steel tube beam elements and 2528 outer wrapped concrete plate elements. The beam element and the plate element adopt co-node to realize the combination of two structures together into a whole load. The arch-springing is all fixed. The model keeps the longitudinal direction as the X-axis, the transverse direction as the Y-axis, and the vertical as the Z-axis.

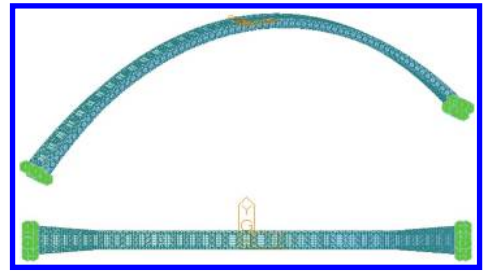


Figure 8. The MIDAS/Civil model of the main arch.

A few notes about the model:

1. Regard the concrete-filled steel tube rigid skeleton as the initial state, do not consider the effect of the pre-camber and the steel tube primary stress.
2. The stiffness and strength of the concrete-filled steel tubular member will be reduced if the steel tube and the concrete are void, this article adopts C80 weakly expansive concrete and introduces the lift-up method to place concrete uninterruptedly, so it does not consider the effect of the void.
3. Adopt the material conversion method to calculate the material and geometric characteristics.
4. Do not take into account the effect of the strength of former concrete when pouring on one ring, but regard the weight of concrete as the concentrated force to act on the right element.
5. Consider the combined action of the concrete-filled steel tubular rigid skeleton and the outer wrapped concrete after the strength form.

## 5 THE RESULTS OF FORCE ANALYSIS

This paper takes the bottom concrete, for example, to calculate by using the stress superposition method, the vault deflection, the steel stress, the concrete-filled steel tube stress and the outer wrapped concrete stress as control targets, chooses the foot arch, the L/8, L/4, 3 L/8, the vault and the abrupt change in section as control sections. The finite element analysis on non-cable-inclined and four inclined cables continuous of outer wrapped concrete is carried out to study the stress and deformation of the structure.

According to The Code for Design on Steel Structure of Railway Bridge (TB10002.2-2005), the maximum allowable stress is as follows:

The maximum allowable stress of the Q370 steel is 263 MPa;

The C80 steel tube concrete:

$$f_{cd} = 34.6 \text{ MPa}, f_{td} = 2.14 \text{ MPa} \quad (1)$$

The C60 outer wrapped concrete:

$$[\sigma_b] = 20.0 \text{ MPa}, [\sigma_{tp-1}] = 3.15 \text{ MPa} \quad (2)$$

### 5.1 The vault deflection

Taking the concrete-filled steel tube rigid skeleton for reference, the added displacement of the vault deflection can be taken from the MIDAS model. Thus, the difference between the added displacement of the initial state and each construction step is the current deflection.

Figure 9 shows that the repeated deformation is great and the largest vault deflection reaches 31 cm when continuously concreting the first ring. The reason is attributed to the fact that the stiffness of rigid skeleton is lesser and the deformation is greater when it stands all the weight of concrete. Under the control of four inclined cables, although the arch ring has repeated deformation,

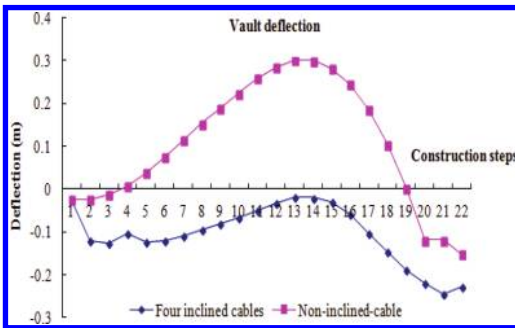


Figure 9. Comparison of vault deflection.

the amplitude is smaller. Besides, the arch ring has no upper vault deflection, whose changing curve is smooth. And the maximum lower vault deflection is 21.0 cm after the first ring is formed, and it meets the requirement of regulation which is  $L/800 = 52.0$  cm, and the effect of regulating the main arch ring deformation by four inclined cables is good.

### 5.2 The stress of the upper and lower chords

Figures 10 and 11 show that the largest pressure stress is 422 MPa of the foot arch, which is exceeded greatly, and the stress of the others control sections is nearly 225 MPa with a lower safety which need to regulate and control. The reason is that the rigid skeleton stands all the concrete weight without stayed-buckle cable before the strength of former concrete formed, which leads to the higher stress of the steel tube.

Figures 12 and 13 show that the largest pressure stress of the upper chord is 194 MPa in the vault section, and the largest pressure stress of the lower chord is 210 MPa in the foot arch. Besides, the range of stress of others chords is 100 MPa to 150 MPa. This means the stress is low and the structure has

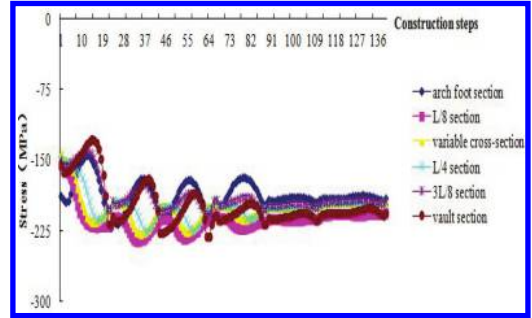


Figure 10. Correlation line of pipe stress in control sections of the lateral upper chord member.

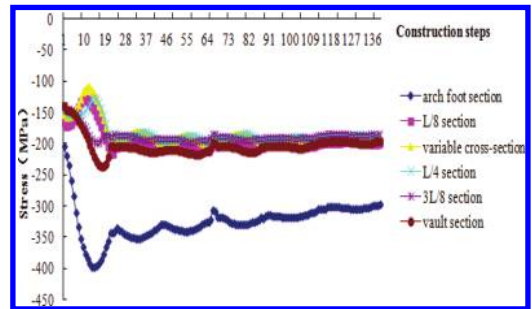


Figure 11. Correlation line of pipe stress in control sections of the lateral lower chord member.



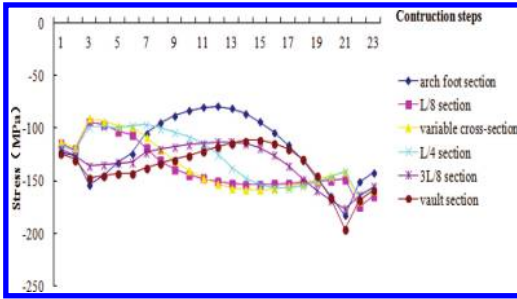


Figure 12. Correlation line of pipe stress in control sections of the lateral upper chord member.

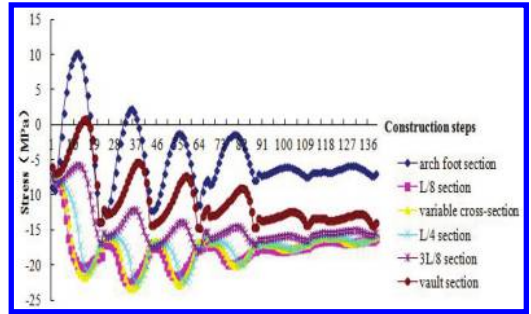


Figure 14. Correlation line of concrete stress in control sections of the upper chord member.

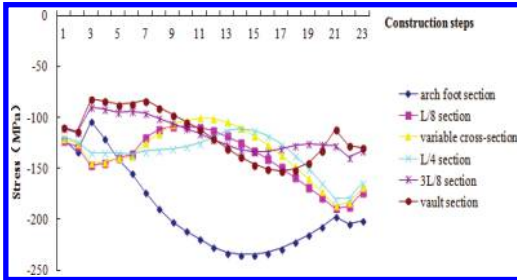


Figure 13. Correlation line of pipe stress in control sections of the lateral lower chord member.

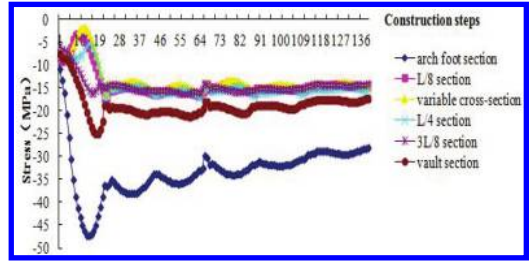


Figure 15. Correlation line of concrete stress in control sections of the lower chord member.

a high safety space. Taking the allowable stress of the Q370 steel to check, compared with the non-inclined cable, the steel stress of the control sections is within a permissible range, which means a higher safety. The stress level of the steel tube has improved obviously, and the problem of the over proof lower stress of the foot arch is solved.

### 5.3 The stress of concrete in the steel tube

Figures 14 and 15 show that the maximum nominal tensile stress of concrete in the tube reaches 11.2 MPa in the upper chord of the foot arch, and the maximum pressure stress reaches 47.0 MPa in the lower chord of the foot arch. The nominal and pressure stress of concrete in the steel tube far exceeds its permissible range, which needs to adjust and control. Comparison between the stress of the steel tube and concrete in the steel tube can be made, and it is easy to draw a conclusion that under the corresponding construction step and at the corresponding place, there is a nominal tensile stress in the concrete in the steel tube, but the stress of the steel tube is always under the dimensional compression, because it has original steel stress to counteract partly a smaller nominal stress.

Figures 16 and 17 show that the stress of concrete of the upper and lower chord is pressure in

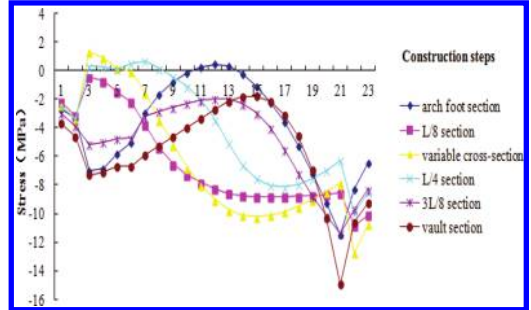


Figure 16. Correlation line of pipe stress in control sections of the upper chord member.

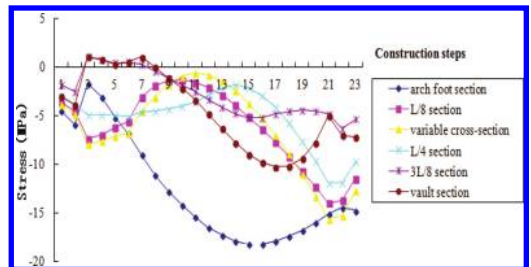


Figure 17. Correlation line of pipe stress in control sections of the lower chord member.

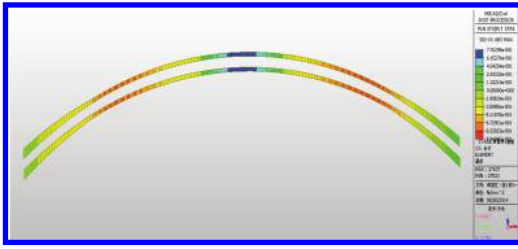


Figure 18. Outer wrapped concrete stress of ring 1 after construction.

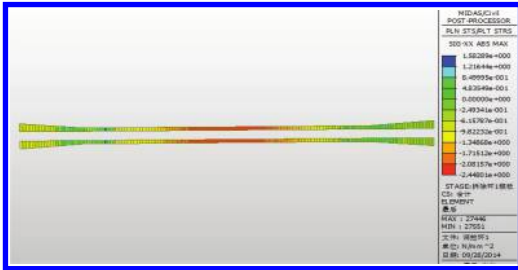


Figure 19. Outer wrapped concrete stress of ring 1 after construction.

the mass, the maximum pressure stress of concrete in the tube reaches 18.2 MPa in the lower chord of the arch foot; parts of the construction steps have a smaller tensile stress and the maximum reaches to 1.04 MPa in the variable section, and the nominal pressure and tensile stress of the control section are within the permissible range.

#### 5.4 The stress of outer wrapped concrete

Figures 18 and 19 show that the outer wrapped concrete stress of the first ring after construction is pressure in the mass, and the maximum pressure and tensile stress reaches to 11.5 MPa and 0.77 MPa. Under the control of four inclined cables, the maximum pressure and tensile stress reaches to 2.45 MPa, nearly 3 L/8 section, and to 1.58 MPa, nearly L/4 section, which are within the permissible range.

On the whole, the stress and deformation of the main arch ring has a great improvement under the control of four inclined cables, which shows that the construction method is feasible.

## 6 CONCLUSION

The computational analysis on the continuous concreting of outer wrapped concrete of a

long-span concrete-filled steel tubular arch bridge is conducted, and comparison between the regulating effects of non-inclined-cable and four inclined cables is made, on the basis of which the following conclusions are drawn:

1. Without cable-inclined concreting, the arch ring produces a greater deformation and has an upper vault deflection. Besides, the stress of the structure far exceeds its permissible range. So, it is necessary to take measure to control.
2. The inclined cables can effectively regulate the stress and deformation of the main arch ring, and keep the vault deflection, the nominal pressure and tensile stress of the structure within the permissible range. The method achieved the continuous concreting of floor outer wrapped concrete successfully, which theoretically proved that the method of cable-stayed buckle to continuous concreting of the main arch ring outer wrapped concrete is feasible.

## REFERENCES

- [1] Bao-chun, Chen. 2007. Concrete Filled Steel Tubular Arch Bridge. *The People's Communication Publishing Company*.
- [2] Jie-lian, Zheng. 2011. Discussion on Placing Concrete Uninterruptedly on Closure Arch Rigid Skeleton. *Journal of Chongqing Jiaotong University* 11(12):1099–1105.
- [3] Shan-shan, Cao & Chuan-xi, Li. 2010. The Force Analysis and The Stability in The Main Arch Ring Construction Stage of Long-Span SRC Arch Bridge. *High & Automotive Applications* 10(142):121–123.
- [4] Fu-gui, Zhang & Yong-shui, Zhang. 2012. Outsourcing Concrete Pouring Scheme of Long Span Stiff Skeleton Arch Bridge. *Journal of Chongqing Jiaotong University* 12(4):210–213.
- [5] Chun-jiao, Lin. 2004. A Comprehensive Review of Study of The Separation of The CFST. *Journal of China & Foreign Highway* 04(4):54–58.
- [6] Ying, Gu. 2011. Stability Analysis of Long-Span Concrete Arch Bridge with Stiff Skeleton. *Southwest Jiaotong University*.
- [7] Jian-min, Zhang. 2001. Bearing Capacity and Construction Control Research of Long-Span Concrete Filled Steel Tubular Arch Bridges. *South China University of Technology*.
- [8] Xiao-ming, Liu. 2007. Study on Construction Course of Long-span Concrete-filled Steel Tubular Stiffening Framework Arch Bridge. *Chang'an University*.
- [9] Code for Design on Steel Structure of Railway Bridge. (TB10002.2–2005). 2005. *Industry standard of the People's Republic of China*.
- [10] Xiao-bo Chen. 2015. The Analysis on The Stress and Stability of Long-Span Concrete-filled Steel Tube Stiff Skeleton Arch Rib Construction Stage. *Journal of China & Foreign Highway* 15(2):134–138.

# The analysis of the influence of material strength on the shear capacity of steel tube-reinforced concrete composite column

Bing Wang, Xiao Liu & Tiancheng Xu

School of Architectural and Civil Engineering, Shenyang University, Shenyang, China

**ABSTRACT:** In this paper, the reasonable selection of component parameters and the property of shear components of the steel tube-reinforced concrete under the effect of lateral horizontal displacement are analyzed using the ABAQUS finite element model. Weak and strong axis loading, concrete strength, and steel yield strength factors are selected as the parameter variation of components. It is concluded that the major axis is higher than the shear bearing capacity of the weak axis, increase of concrete strength against the influence of shear bearing capacity is not obvious, and improving the steel yield strength can effectively improve the bearing capacity of the component.

**Keywords:** steel tube-reinforced concrete; material strength; shear capacity

## 1 INTRODUCTION

In order to overcome the weakness of heavy concrete structure, the poor bending performance and the poor steel fire resistance, concrete and steel are combined, which can play their respective advantageous roles. Besides, a layer of steel tube is wrapped on the component. The structure is in a state of very unsafe because of the sharp decrease in the bearing capacity of the external steel tube under the fire. Inserting i-steel inside the component can continue to play a strong load-bearing role after the outside steel pipe losing bearing capacity. The existence of core concrete delays the internal steel bone expiry time, which gives people plenty of time to escape the rescue, thereby reducing property and life loss [1–4].

Researchers have focused on concrete column, mainly studying the performance of the concrete column under different stress states. Three of which are bending shear, tense bending shear, and tense bending shear twist, which relate to the shear performance of stress. Curved scissors refers to the concrete member only under the effect of transverse shear. Bending shear is influenced by transverse shear force and axial pressure or eccentric. Bending torsional shear refers to the concrete column under transverse shear, axial pressure and torque under the action of stress. Bending shear and bending shear is the basis of the study compound stress; therefore, studying the basic shear performance has an important significance. In this article, the material strength is studied by using finite element analysis software ABAQUS, and the analysis of the strength parameters is carried out to determine their effects on the bearing capacity.

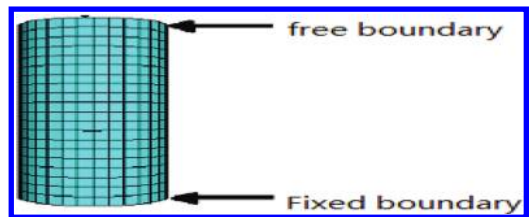


Figure 1. The applied shear load.

## 2 SHEAR LOADING OF THE FINITE ELEMENT MODEL

This article adopts the steel tube concrete column filled with steel bone, which is fixed on the one end and loaded the horizontal transverse load on the other end, as shown in Figure 1.

## 3 PARAMETER SETTING AND ANALYSIS OF STEEL TUBE-REINFORCED CONCRETE COMPOSITE COLUMN

Steel pipe-reinforced concrete composite column is made up of steel pipes, beams and a combination of core concrete composite component. The intensity of each part has different effects on shear bearing capacity. Different force states also lead to different shear bearing capacities. Loading direction will affect the shear bearing capacity as well. This article selects three parameters namely concrete strength, loading direction, and steel strength. We, respectively, study their effect on the

Table 1. Shear component parameters of steel tube filled with steel tube-reinforced concrete composite column.

Serial number	Component size (D × t × l)/mm	Displacement direction	$f_{ck}$ /MPa	$f_{sk}$ /MPa	$f_{tk}$ /MPa	$\theta$	$\lambda$	$n$
B-1	160 × 5 × 500	Strong axis	C70	235	235	0.28	3.125	0
B-2	160 × 5 × 500	Weak axis	C70	235	235	0.28	3.125	0
D-1	160 × 5 × 500	Strong axis	C50	235	235	0.28	3.125	0
D-2	160 × 5 × 500	Strong axis	C90	235	235	0.28	3.125	0
E-1	160 × 5 × 500	Strong axis	C70	345	235	0.28	3.125	0
E-2	160 × 5 × 500	Strong axis	C70	390	235	0.28	3.125	0

Note:  $\theta$  is the effect of the restraint coefficient;  $\lambda$  is the shear span ratio; and  $n$  is the axial compression ratio.

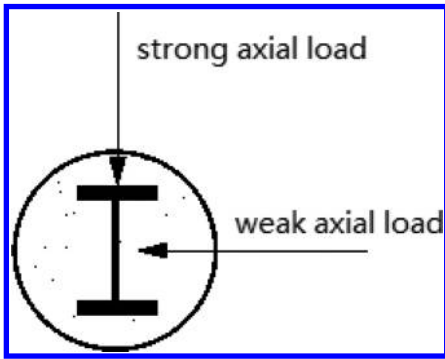


Figure 2. Strong and weak axial loading diagram.

shear bearing capacity of the steel tube concrete column-filled steel bone.

### 3.1 Component parameter

Component parameter selection is the key step of calculation and analysis. Reasonable parameter selection will take to get twice the result with half the effort effect. On the basis of many times simulation, we select the parameters, as listed in Table 1.

### 3.2 Parameter analysis

#### 3.2.1 The strong and weak axis displacement influences

Due to the geometric characteristics of i-steel, steel pipe-reinforced composite column is not an axisymmetric graphic. There is a difference between the strong axial load and the weak axis load, as shown in Figure 2, and the shear bearing capacity is also different.

This article, respectively, forces the strength and weak axis load to three sets of specimen, namely A-1, A-2, B-1, B-2, C-1, C-2. Using the ABAQUS finite element simulation, the shear capacity curves are shown in Figure 3.

We can find out the following factors from the above chart:

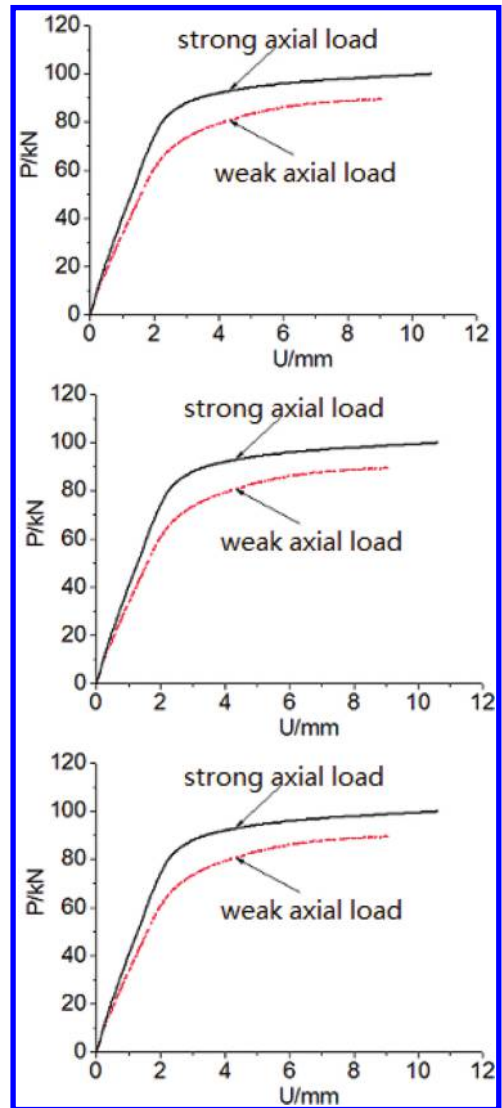


Figure 3. Shear bearing capacity of strength and weak axial loading direction.

1. The elastic stage: elastic modulus of the strong axis load is bigger than the weak axis load. This is because that the built-in i-steel flange is far away from the centroid, and the action of shear function of the flange area is larger in the horizontal strong axis load. The weak axis loading function of the flange area is lesser.
2. The ultimate bearing capacity: strong axial shear ability is superior to the weak axis, because of the strong axial load. The bone involved in the area of tensile steel is bigger than the weak axis load.

### 3.2.2 Concrete strength

The strength of the concrete commonly used ranges from C10 to C90. In order to better use the compressive strength of concrete, in the compression state of steel-reinforced concrete filled steel tube column, high strength concrete is adopted. This paper continues to use high-strength concrete. Using three grades of high-strength concrete, namely C50, C70, C90, in components B-1, D-1, D-2 for simulation analysis, the result is shown in Figure 4.

We can find out the following factors from the P-U curve:

1. With the increase of concrete strength, the shear capacity of steel-reinforced concrete filled steel tube column increases gradually, but the increase is not obvious.
2. The slope of the elastic stage with the increase of concrete strength also has no obvious change, this is because with the strength of the concrete improving, the elastic modulus of concrete also gradually improves. Compared with the steel elastic modulus, concrete elastic modulus nearly equals to 10 percent, which makes little contribution on the whole for the components of the elastic modulus.
3. Regardless of the kind of concrete strength, after the yield point, the shear bearing capacity

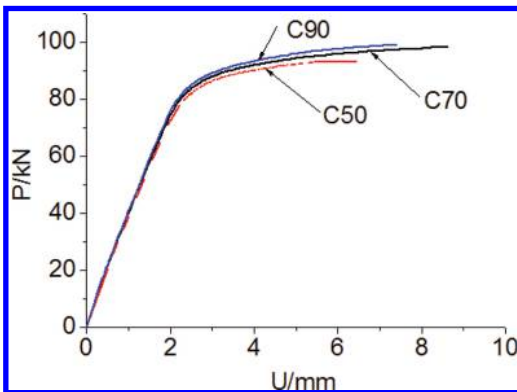


Figure 4. P-U curve.

of steel-reinforced concrete filled steel tube did not immediately decrease. On the contrary, there will be a little rising trend, which illustrates that the steel-reinforced concrete filled steel tube column has a very good ductility.

### 3.2.3 Steel strength

There are four kinds of commonly used steel. Their yield strength is Q235, Q345, Q390, and Q420. This article uses only three kinds of steel components, namely Q235, Q345, and Q390, in components B-1, E-1, E-2 and B-1, F-1, F-2 for simulation analysis. The P-U curve are shown in Figures 5 and 6.

We can find out the following factors from the above chart:

1. Shear bearing capacity of whatever strength of steel bone or steel tube, in the elastic stage, the overall elastic modulus is constant, that is because, while it improves the strength of the steel, the elastic modulus of steel has not changed, thus the whole component of the elastic modulus has not changed.

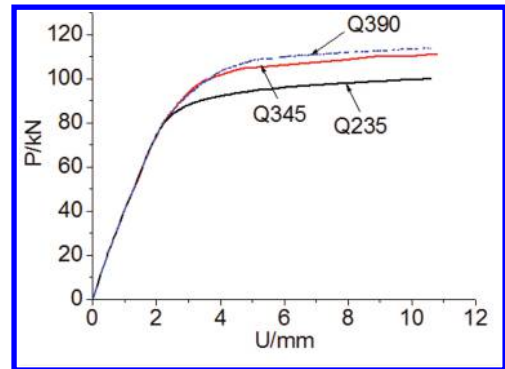


Figure 5. The P-U curve different steel-reinforced intensity.

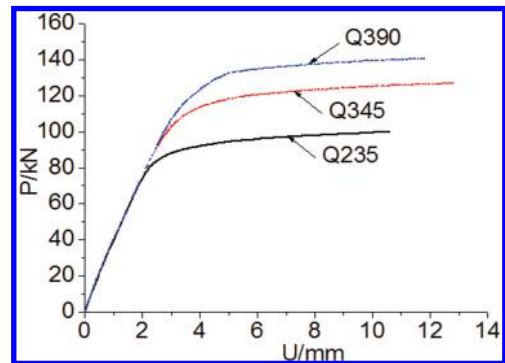


Figure 6. The P-U curve different steel tube intensity.

2. To be loaded into yield strength of the components, the strength of the steel bone and steel tube is gradually shown. With the improvement of strength of steel pipe and steel bone, yield strength of the components also increased dramatically. While steel yield strength improves to Q390, improving the capacity effect of the components is not obvious. But increasing the yield strength of steel tube to Q390, the promotion effect of component bearing capacity is more apparent.
3. To improve the strength of the steel tube has a more obvious effect on the shear bearing capacity of components than the steel bone.

As can be seen from the above analysis, the loading direction, concrete strength, steel strength, the three parameters selected in this paper has a certain influence on the shear capacity of steel tube-reinforced concrete composite column. In engineering practice, we should strictly control these three factors.

#### 4 CONCLUSION

The ABAQUS finite element model established, the reasonable structure parameters selected in this paper, shear components under the effect of lateral horizontal displacement in the steel tube-reinforced concrete composite column is calculated and analyzed the shear capability. Using the P-U curve of the computational analysis, we analyze the three main parameters, namely loading direction, concrete strength, steel strength, which have the effects on the P-U curve of steel tube-reinforced concrete composite column shear component. We draw the conclusion that the bearing capacity of the strong axis is higher than that of the weak axis, the effect of the increase of concrete strength

against the influence of shear bearing capacity is not obvious, and improving the steel yield strength can effectively improve the bearing capacity of the component.

#### ACKNOWLEDGMENT

This work was supported by the National Science Foundation (51308347), the Shenyang Science Plan project (F13-171-9-00, F14-028-2-00, F14-210-6-00), and the Liaoning Science Public Research Funds (2014004025).

#### REFERENCES

- [1] Lianguang Wang. The theory and calculation of steel concrete composite structure [M]. Beijing: Science Press, 2005.
- [2] Guoliang Bai, Fuhua Qin. The design and principle of steel reinforced concrete [M]. Shanghai: Shanghai Science And Technology Press, 2000.
- [3] Fam A., Qie F.S., Rizkalla S. Concrete-Filled Steel Tubes Subjected to Axial Compression and Lateral Cyclic Loads [J]. Journal of Structural Engineering, 2004, 130(4):631–640.
- [4] Linhai Han, Youfu Yang. Modern technology of steel tube concrete structure [M]. Beijing: China Architecture Industry Press, 2004.
- [5] Genping Zeng. The mechanical property study on the bending and shear complex stress state of Circular hollow interlayer steel tube concrete components. [D]. Transportation University Of Eastern China, 2014.
- [6] Guohuang Yao. The mechanism research on concrete filled steel tube under complex stress state [D]: [Ph.D. Thesis]. Fuzhou: Fuzhou University, 2006.
- [7] Lin-Hai Han, Guo-Huang Yao, Zhong Tao. Behaviors of Concrete-Filled Steel Tubular Members Subjected to Combined Loading. Thin-Walled Structures, 2007, 45(6):600–619.

# Research on the strength of structural Steel Tubes and Coupler Scaffolds

Zhengran Lu, Yongqin Wen, Liang Zhao, Tong Liu & Chongyang Li

Department of Civil Engineering, Jilin Jianzhu University, Changchun, China

School of Management, Shenyang Jianzhu University, Shenyang, China

Chao Guo & Wei Wang

School of Civil Engineering, Shenyang Jianzhu University, Shenyang, China

**ABSTRACT:** How to calculate the bearing capacity of structural steel tubes and coupler scaffolds (henceforth referred to as STCS) was currently an urgent problem to be solved. Based on the previous experimental studies, advanced non-linear FEM of thirteen STCS specimens were established considering the semi-rigid character of the couplers to evaluate the critical loads and failure modes under idealized conditions in ANSYS and to compare with the experimental results. Furthermore, new simplified three-column calculation model and corresponding calculation formulas were established for the STCS under uniform load, which were verified by the experimental and analytical results and turned out to be of valuable reference in predicting the strength.

**Keywords:** structural steel tubes and coupler scaffolds; strength; semi-rigid; full-scale specimen test; three-column model for sway frame

## 1 INTRODUCTION

For many years, structural steel tubes and coupler scaffolds (hereinafter referred to as STCS) were commonly used as a temporary structure to support workers, materials and structural members during construction due to the ease of fabrication, installation and dissemination. However, structural failure of these scaffolds often occurred from time to time due to poor installation, inadequate design and knowledge of relationship between construction factor and bearing capacity.

Currently, most researchers have focused on the door-type modular steel scaffolds, high clearance scaffolds, as well as single-wall and two-wall steel tubular scaffold, but very few have focused on the STCS.

## 2 ANALYTICAL INVESTIGATION AND DISCUSSION

Full-scale static tests were conducted on thirteen STCS specimens in order to obtain the bearing capacity and failure modes of STCS and the corresponding details of all components were described in [1] and [2]. Based on the above experimental studies, advanced non-linear finite element models of thirteen STCS test specimens were established to evaluate the critical loads and failure modes under

idealized conditions in ANSYS. The geometric properties of the specimens, the test results  $P_{\text{test}}$  and the critical buckling load  $P_{\text{FEA}}$  obtained from the eigenvalue buckling analysis are listed in Table 1.

In Table 1,  $L_h$  is the lift height;  $S_1$  and  $S_2$  are the horizontal spacing of posts in transverse and longitudinal direction, respectively;  $H_1$  is the whole height of the tested STCS;  $Br$  is the sweeping staff height;  $Cl_u$  is the U-head height. The loading area was expressed by the arithmetic product of the number of spans in the transverse direction and the number of spans in the longitudinal direction.  $B_{ri}$  is the bridgings setting;  $V$  is the vertical bridgings; and  $H$  is the horizontal bridgings.

From Table 1, it can be revealed that the strength  $P_{\text{FEA}}$  was generally consistent with the full-scale test results, and the effect tendency of all geometric parameters on bearing capacity of STCS was consistent:

1. The bearing capacity of a STCS would increase to some extent if the U-head height reduced, proven by test specimen 11 ( $P_{\text{test}} = 16.64$  kN;  $P_{\text{FEA}} = 15.30$  kN) versus specimen 12 ( $P_{\text{test}} = 19.14$  kN;  $P_{\text{FEA}} = 17.86$  kN).
2. The bearing capacity of a STCS would increase to some extent if the storey height reduced, proven by test specimen 1 ( $P_{\text{test}} = 23.57$  kN;  $P_{\text{FEA}} = 19.54$  kN) versus specimen 13 ( $P_{\text{test}} = 33.90$  kN;  $P_{\text{FEA}} = 33.93$  kN);

Table 1. Comparison of FEM analysis with full-scale test results.

NO.	Lh (m)	S <sub>1</sub> ×S <sub>2</sub> (m×m)	H <sub>1</sub> (m)	Bri	Br (m)	Chu (m)	Loading area	P <sub>test</sub> (kN)	P <sub>FEA</sub> (kN)
1	1.5	0.9×0.9	8.15	N	0.2	0.50	5×5	23.57	19.54
2	1.5	0.9×0.9	8.15	V	0.2	0.50	5×5	28.38	30.53
3	1.5	0.9×0.9	8.15	V+H	0.2	0.50	5×5	36.26	38.55
4	1.2	0.9×0.9	8.15	N	0.2	0.50	5×5	23.76	20.39
5	1.2	0.9×0.6	8.15	N	0.2	0.50	5×5	25.31	25.27
6	0.9	0.9×0.6	8.15	N	0.2	0.50	5×5	23.76	23.12
7	0.9	0.6×0.6	8.15	N	0.4	0.50	5×5	21.74	21.13
8	0.9	0.6×0.6	8.15	V	0.4	0.50	5×5	34.76	34.74
9	0.6	0.4×0.4	8.15	N	0.2	0.50	5×5	21.87	21.58
10	1.5	1.2×1.2	8.15	N	0.2	0.00	4×4	16.75	15.70
11	1.5	1.2×1.2	5.50	N	0.2	0.80	4×4	16.64	15.30
12	1.5	1.2×1.2	5.20	N	0.2	0.50	4×4	19.14	17.86
13	1.5	0.9×0.9	5.20	N	0.2	0.50	5×5	33.90	33.93

- The bearing capacity of a STCS would increase to some extent if the lift height and post spacing reduced together, proven by test specimen 7 ( $P_{test} = 21.74$  kN;  $P_{FEA} = 21.13$  kN) versus specimen 9 ( $P_{test} = 21.87$  kN;  $P_{FEA} = 21.58$  kN).
- The bearing capacity of a STCS would increase to some extent (increase 20%–40% approximately) if setting vertical bridgings, proven by test specimen 1 ( $P_{test} = 23.57$  kN;  $P_{FEA} = 19.54$  kN) versus specimen 2 ( $P_{test} = 28.38$  kN;  $P_{FEA} = 30.53$  kN), and that would increase to a higher extent if setting vertical and horizontal bridgings together, proven by test specimen 1 ( $P_{test} = 23.57$  kN;  $P_{FEA} = 19.54$  kN) versus specimen 3 ( $P_{test} = 36.26$  kN;  $P_{FEA} = 38.55$  kN). The degree of improvement not only changed with the geometric parameters but also the bridgings setting. This conclusion provided a useful reference for the adjustment of the calculation result of STCS without bridgings.

### 3 SIMPLIFIED ANALYSIS MODEL FOR STCS

#### 3.1 Formulation

Based on the previous research<sup>[3,4]</sup>, considering the semi-rigid characteristics of the right angle coupler, the STCS system without bridgings could be simplified into a three-dimensional multi-storey semi-rigid frame, and furthermore be simplified into a two-dimensional multi-storey frame model, with semi-rigid rotational restraints at each storey provided by the horizontal tubes and couplers. Considering that the typical failure mode of STCS without bridgings was global buckling about the weak axis, and the three-column model developed by [5], shown in Figure 1, was used to calculate the bearing capacity of STCS here. Thus, the above two-dimensional multi-storey semi-rigid

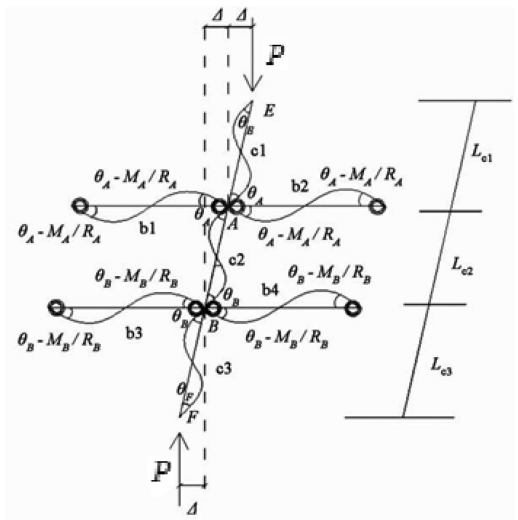


Figure 1. Three-column model for sway frame.

frame may be further simplified into a single post model.

The strength of the STCS system under a uniform load can then be calculated as a summation of the strength of each single post, which is defined by Equation (1) as follows:

$$P_{cr} = \frac{\pi^2 EI}{(\mu L_c)^2} \quad (1)$$

where  $P_{cr}$  is the strength of each single post;  $EI$  is the flexural resistance;  $\mu$  is the effective length factor of single post;  $L_c$  is the length of single post, which is equal to Lh (lift height). On this basis, considering the effect of bridgings as a safety margin received from test and FEA results, the strength of the STCS system with bridgings could thus be obtained.



### 3.2 Horizontal tube element

The horizontal tube element with semi-rigid restraints at each end is shown in Figure 2. In Figure 2,  $L_b$  is the length of the horizontal tube  $\theta_1$ ,  $\theta_2$  are the end nodal rotations at nodes 1 and 2, and  $R_{k1}$ ,  $R_{k2}$  are the rotational stiffness of springs at nodes 1 and 2, respectively. The relationship between the nodal rotations at nodes 1 and 2 under end moments  $M_1$ ,  $M_2$  are given by Equation (2) as follows:

$$\begin{aligned} M_1 &= \frac{i_b}{R^*} \left[ \left( 4 + \frac{12i_b}{R_{k2}} \right) \theta_1 + 2\theta_2 \right], \\ M_2 &= \frac{i_b}{R^*} \left[ 2\theta_1 + \left( 4 + \frac{12i_b}{R_{k1}} \right) \theta_2 \right] \end{aligned} \quad (2)$$

where

$$R^* = \left( 1 + \frac{4i_b}{R_{k1}} \right) \left( 1 + \frac{4i_b}{R_{k2}} \right) - \frac{4i_b^2}{R_{k1}R_{k2}} \quad (3)$$

$i_b = EI_b / L_b$  is the linear stiffness of the horizontal tube.

In the sway frame, assuming that the horizontal tube was bent in a double curvature, the end nodal rotations  $\theta_1$  and  $\theta_2$  were assumed to be equal at buckling. In addition, the rotational stiffness of springs at nodes 1 and 2 was a constant ( $R_{k1} = R_{k2}$ ); thus, the relationship between the nodal rotations at nodes 1 and 2 under end moments  $M_1$ ,  $M_2$  is given by Equation (4) as follows:

$$M_1 = M_2 = 6i_b \alpha_u \theta_1 \quad (4)$$

where  $\alpha_u = \left( 1 + \frac{2i_b}{R_{k1}} \right) / R^*$ .

### 3.3 Vertical post element

The vertical post element with semi-rigid restraints at each end is shown in Figure 3. The relationship between the nodal rotations at nodes A and B under end moments  $M_A$ ,  $M_B$  is given by Equation (5) as follows:

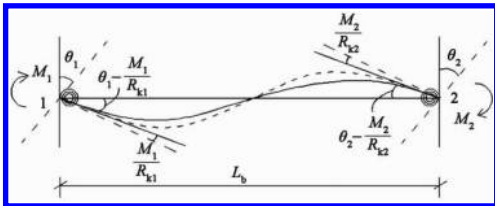


Figure 2. Horizontal tube element restrained by semi-rigid connections.

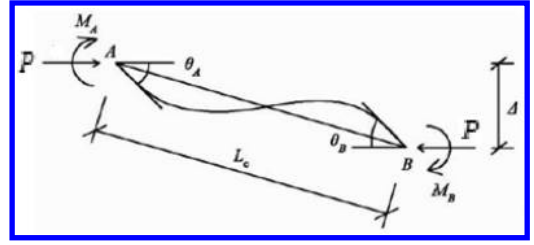


Figure 3. Vertical post element.

$$\begin{aligned} M_A &= \frac{EI_c}{L_c} \left[ S_{ii}\theta_A + S_{ij}\theta_B - (S_{ii} + S_{ij}) \frac{\Delta}{L_c} \right], \\ M_B &= \frac{EI_c}{L_c} \left[ S_{ji}\theta_A + S_{jj}\theta_B - (S_{ji} + S_{jj}) \frac{\Delta}{L_c} \right] \end{aligned} \quad (5)$$

where  $\Delta$  is the relative lateral displacement of nodes A and B;  $L_c$  is the length of the vertical post;  $\theta_A$  and  $\theta_B$  are nodal rotations at nodes. The stability function  $S_{ii} = S_{jj}$ ,  $S_{ij} = S_{ji}$  could be expressed as follows:

$$S_{ii} = S_{jj} = \frac{\frac{\pi}{\mu} \sin \frac{\pi}{\mu} - \left( \frac{\pi}{\mu} \right)^2 \cos \frac{\pi}{\mu}}{2 - 2 \cos \frac{\pi}{\mu} - \frac{\pi}{\mu} \sin \frac{\pi}{\mu}} \quad (6)$$

$$S_{ij} = S_{ji} = \frac{\left( \frac{\pi}{\mu} \right)^2 - \frac{\pi}{\mu} \sin \frac{\pi}{\mu}}{2 - 2 \cos \frac{\pi}{\mu} - \frac{\pi}{\mu} \sin \frac{\pi}{\mu}}$$

where  $\mu = \frac{\pi}{kL_c}$  and  $k = \sqrt{\frac{P}{EI_c}}$ .

### 3.4 Effective length factor $\mu$

For the three-column model shown in Figure 1, considering the boundary conditions at the distal end of vertical posts c1, c3 as the roller condition, the moments in vertical posts c1, c2, c3 at nodes A and B are given by Equations (7)–(10) as follows:

$$(M_A)_{c1} = \frac{EI_{c1}}{L_{c1}} \left( S_{ii} - \frac{S_{ij}^2}{S_{ii}} \right) \left( \theta_A - \frac{\Delta}{L_{c1}} \right) \quad (7)$$

$$(M_A)_{c2} = \frac{EI_{c2}}{L_{c2}} \left[ S_{ii}\theta_A + S_{ij}\theta_B - (S_{ii} + S_{ij}) \frac{\Delta}{L_{c2}} \right] \quad (8)$$

$$(M_B)_{c2} = \frac{EI_{c2}}{L_{c2}} \left[ S_{ji}\theta_A + S_{ii}\theta_B - (S_{ii} + S_{ij}) \frac{\Delta}{L_{c2}} \right] \quad (9)$$

$$(M_B)_{c3} = \frac{EI_{c3}}{L_{c3}} \left( S_{ii} - \frac{S_{ij}^2}{S_{ii}} \right) \left( \theta_B - \frac{\Delta}{L_{c3}} \right) \quad (10)$$

The moments in horizontal tubes b1, b2, b3, b4 at nodes A and B are given by Equation (11) as follows:

$$\begin{aligned} (M_A)_{b1} &= 6i_{b1}\alpha_u\theta_A, (M_A)_{b2} = 6i_{b2}\alpha_u\theta_A \\ (M_B)_{b3} &= 6i_{b3}\alpha_u\theta_B, (M_B)_{b4} = 6i_{b4}\alpha_u\theta_B \end{aligned} \quad (11)$$

Considering the equilibrium of vertical post c1, the equilibrium conditions at nodes A and B, and the same flexural resistance of all tubes in STCS, the following calculation equation of effective length factor  $\mu$  can be obtained:

$$\begin{aligned} &\pi \left[ (6\mu^2 - 36\mu^2K - 2\pi^2) \cos^2 \left( \frac{\pi}{\mu} \right) + (\pi^2 - 12\mu^2 \right. \\ &\quad \left. + 24\mu^2K) \cos \left( \frac{\pi}{\mu} \right) + (6\mu^2 + \pi^2 + 12\mu^2K) \right] \sin \left( \frac{\pi}{\mu} \right) \\ &\quad + \mu \left[ (12\pi^2K - 24\mu^2K - 7\pi^2) \cos^2 \left( \frac{\pi}{\mu} \right) + (9\pi^2 \right. \\ &\quad \left. + 24\mu^2K) \cos \left( \frac{\pi}{\mu} \right) + (24\mu^2K + 32\pi^2 \right. \\ &\quad \left. - 12\pi^2K) \right] \cos \left( \frac{\pi}{\mu} \right) - \mu(5\pi^2 + 24\mu^2M) = 0 \end{aligned} \quad (12)$$

where  $K = \frac{\sum_A \alpha_u EI_b / L_b}{\sum_A EI_c / h} = \frac{\sum_B \alpha_u EI_b / L_b}{\sum_B EI_c / h}$  is the end restraint coefficient of the vertical post in the sway frame model, and the length of the vertical post  $L_c$  was equal to the lift height  $h$ . The effective length factor  $\mu$  could be solved numerically. Furthermore, the strength of STCS could be received through substituting  $\mu$  into Equation (1).

#### 4 COMPARISON OF RESULTS FROM TEST, FEA AND ANALYSIS MODEL

The strength of models with various geometric parameters without bridgings  $P_{sim}$  based on the analysis model above is given in Table 2.

In Table 2, Error 1 =  $\frac{P_{sim} - P_{FEA}}{P_{FEA}} \times 100$ . From Table 2, it could be found that the effect of geometric parameters on STCS strength obtained from the analysis model is generally consistent with that obtained from FEA. The bearing capacity of a STCS increased to some extent if the lift

Table 2. Comparison between the results obtained from FEA and the simplified model.

No.	Lh (m)	$S_1 \times S_2$ (m × m)	$P_{FEA}$ (kN)	$P_{sim}$ (kN)	Error 1 (%)
1	1.5	0.9 × 0.9	19.54	11.59	-40.69
2	1.2	0.9 × 0.9	20.39	13.65	-33.06
3	0.9	0.6 × 0.6	21.13	16.47	-22.05
4	0.6	0.4 × 0.4	21.58	20.36	-5.65

height and post spacing reduced, which proved the feasibility and validity of using the three-column model to calculate the STCS strength. It could also be found that the strength  $P_{sim}$  of specimen 3 and 4 were generally consistent with the FEA results, with a maximum difference of -22.05%. Reasons attributing to the discrepancies might include the variance in the rotational stiffness of couplers, the variance in the mechanical properties of steel tubes, and initial imperfections of the steel tubes. The strength  $P_{sim}$  of specimens 1 and 2 was not consistent with the FEA results. The reasons attributing to these discrepancies not only include the above factors, but also include that the effect of additional spans was considered in these two specimens in the FEA but not considered in the simplified model, and the presence of additional spans could increase the system's strength significantly.

#### 5 CONCLUSIONS

1. From the full-scale tests and FEM analyses, it was clear that the bearing capacity of STCS was affected by a series of erection parameters such as lift height, spacing of vertical post, erection height, bridgings setting, and U-head height, and the existence of bridgings and additional spans could increase the strength of STCS significantly.
2. A simplified three-column model was developed for the STCS post, and design formulas were established for calculating the strength of a single post. Both the simplified model and the formulas were verified by the full-scale test and analytical results. In practical projects, the effect of bridgings could be seemed as a safety margin based on these findings.

#### ACKNOWLEDGMENTS

This research project was supported by the National Natural Science Foundation of China (No. 51308255, No. 51308357), the Colleges and

Universities of Liaoning Province Outstanding Young Scholars Growth Plan (No. LJQ2014059), and the Youth Fund of Shenyang Jianzhu University (No. 2014003).

## REFERENCES

- [1] Lu Zhengran, Chen Zhihua, Wang Xiaodun, Guo Chao, Liu Qun. Study of the bearing capacity of fastener steel tube full hall formwork support using the theory of stability of pressed pole with three-point rotation restraint, *China Civil Engineering Journal*, 2012, 45(5), 104–113 [In Chinese].
- [2] Lu Zhengran, Chen Zhihua, Wang Xiaodun, Liu Qun, Liu Hongbo. Experimental and theoretical study of the bearing capacity of fastener steel tube full-hall formwork support system, 2012, 45(1), 49–60 [In Chinese].
- [3] Chen Zhihua, Lu Zhengran, Wang Xiaodun. Numerical analysis and experimental study of the stiffness of right angle couplers in tubular steel scaffolds, *China Civil Engineering Journal*, 2010, 43(9), 100–108 [In Chinese].
- [4] Chen Zhihua, Lu Zhengran, Wang Xiaodun, Liuqun. Research on the bearing capacity of steel tubular formwork support with coupler without X-bracing based on the partially-sway single post stability theory, *Engineering Mechanics*, 2010, 27(11), 99–105 [In Chinese].
- [5] Wang Jing-feng, Li Guo-qiang. Stability analysis of columns in sway and semi-rigid composite frames, *Journal of harbin institute of technology*, 2009, 41(4), 126–130 [In Chinese].

# Theoretical analysis on the bearing capacity of structural Steel Tube and Coupler Scaffolds

Zhengran Lu, Yongqin Wen, Liang Zhao, Changtie Huang & Shuo Cao

*Department of Civil Engineering, Jilin Jianzhu University, Changchun, China*  
*School of Management, Shenyang Jianzhu University, Shenyang, China*

Chao Guo & Wei Wang

*School of Civil Engineering, Shenyang Jianzhu University, Shenyang, China*

**ABSTRACT:** Structural Steel Tube and Coupler Scaffolds (STCS) have collapsed quite often at many sites, with a considerable number of reported casualties. However, their behavior has not been studied to the same extent as that of many other permanent structures. Using advanced nonlinear finite element analysis on different STCS models, the strength and failure modes of the STCS's were evaluated in this paper. Furthermore, a simplified model using the theory of single multi-story post with four semi-rigid restraints and corresponding calculation formulae were established for the bearing capacity of STCS. The above presented simplified structural model and formulas are verified by the analytical results, and it has been turned out to be accurate enough for predicting the strength of STCS's.

**Keywords:** structural Steel Tube and Coupler Scaffold; bearing capacity; semi-rigid; finite element analysis; simple formula

## 1 INTRODUCTION

Structural Steel Tube and Coupler Scaffolds (STCS) have been widely used as temporary structures in concrete casting construction, which involves the handling of large loads, in countries such as China and the United Kingdom because of their ease of fabrication, installation, and dissemination. However, STCS failures often occur on construction sites, which cause not only project delays but also serious injuries and casualties among construction workers.

To enhance the safety of scaffolds during construction, experimental and analytical studies had been conducted in the past on the structural behavior of high-clearance scaffolds [1,2], multi-story door-type modular steel scaffolds, single-pole and double-pole steel tubular scaffolds [3]. However, almost no research had been conducted on STCS, which are widely used in China and the UK in the construction of large-span spatial structures such as gymnasiums, train stations, and bridges. So, it is extremely important to understand the structural behavior of STCS's through both experimental and analytical studies and propose rational design recommendations.

On the basis of right angle coupler torsion stiffness tests and thirteen prototype tests on STCS that described in [4] and [5] respectively, the critical

loads and failure modes of many STCS with and without bridging were evaluated using non-linear FEM in ANSYS, and the effect of a series of erection parameters on bearing capacity of STCS was studied quantitatively. Furthermore, a simplified model and formula were put forward for the strength of STCS which consider the semi-rigid character of right-angle couplers and the effect of adjacent horizontal tubes.

## 2 ANALYTICAL INVESTIGATION

Commercial Finite Element Analysis (FEA) software ANSYS was used to study the behavior of STCS models that are commonly used in actual projects. To simulate the semi-rigid behavior of the couplers, a spring-damper element (COMBIN14) was added to simulate the in-plane rotational restraints provided by the couplers. The spring constant was set to 19.0 kN·m/rad, which was the mean initial rotational stiffness obtained from previous coupler tests. The geometric properties of the models and the FEM analysis results are summarized in Table 1. In Table 1,  $\text{Diff} = (P_{b\text{FEA}} - P_{\text{FEA}}) / P_{\text{FEA}} \times 100$ .

From Table 1, it could be concluded that the STCS strength increased to some extent because of

Table 1. Strength of STCS models for different geometric parameters.

h (m)	S <sub>1</sub> × S <sub>2</sub> (m × m)	STCS without	STCS with	Diff (%)
		bridging	bridging	
		P <sub>FEA</sub> (kN)	P <sub>bFEA</sub> (kN)	
1.8	1.2 × 1.2	17.25	22.27	29.1
	1.0 × 1.0	18.01	24.03	33.4
	0.9 × 0.9	19.64	24.46	24.5
	0.9 × 0.6	20.59	26.92	30.7
	0.6 × 0.6	18.52	26.55	43.4
1.2	1.2 × 1.2	21.51	28.08	30.5
	1.0 × 1.0	22.35	28.69	28.4
	0.9 × 0.9	24.47	29.18	19.2
	0.9 × 0.6	25.27	32.53	28.7
	0.6 × 0.6	20.08	30.71	52.9
0.9	1.2 × 1.2	21.46	28.82	34.3
	1.0 × 1.0	22.08	31.14	41.0
	0.9 × 0.9	24.67	31.26	26.7
	0.9 × 0.6	26.49	34.81	31.4
	0.6 × 0.6	21.13	34.74	60.6
0.6	1.2 × 1.2	22.65	30.79	35.9
	1.0 × 1.0	23.18	33.09	42.6
	0.9 × 0.9	25.32	34.62	36.7
	0.9 × 0.6	28.98	36.99	27.6
	0.6 × 0.6	23.29	34.64	48.7

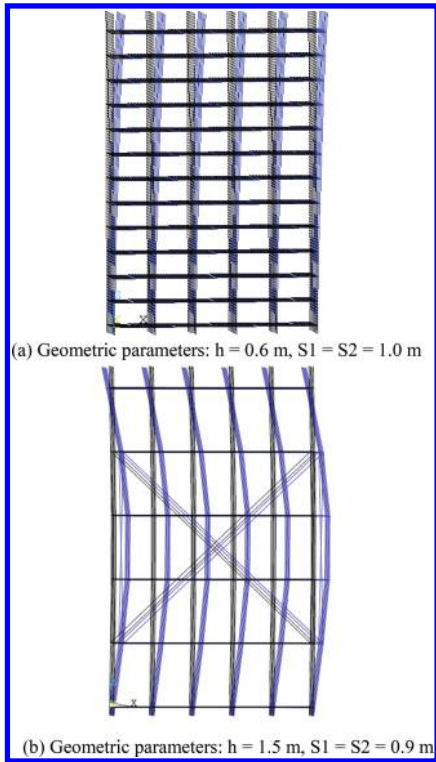


Figure 1. Failure modes identified from nonlinear FEA.

the existence of bridging, but the degree of improvement changed with the geometric parameters and bridging setting. All the above nonlinear analysis results indicated that the typical failure mode of STCS's without bridging was global lateral buckling about the longitudinal weak axis. However, the typical failure mode of STCS's with bridging was local buckling with a large wavelength ranging from two to four times the lift height, which depended on the bridging setting pattern. Typical failure modes identified from the FEA are shown in Figure 1.

### 3 SIMPLIFIED MODEL FOR STCS'S

Considering the semi-rigid characteristics of the right-angle coupler, the STCS system without bridging could be simplified into a three-dimensional multi-story semi-rigid frame. Based on previous research, the STCS system could be simplified into a two-dimensional model and further simplified into a one-dimensional multi-story post, with semi-rigid rotational restraints provided by the horizontal tubes and couplers at each story. The rotational restraint at each story could be expressed by a rotational spring with a rotational stiffness  $C$ . The rotational stiffness  $C$  could be deduced using the slope-deflection method.

Furthermore, the strength of the STCS without bridging under a uniform load could then be calculated as a summation of the strength of each multi-story post, which is defined as

$$P = \frac{\pi^2 EI}{(\mu h)^2} \quad (1)$$

where  $P$  is the strength of a single multi-story post,  $EI$  is the flexural resistance of the steel tube,  $\mu$  is the effective length factor for a single multi-story post with semi-rigid restraints at each story, and  $h$  is the lift height.

From the above FEA results, it was clear that the strength of an STCS increased significantly when the bridging was present; therefore, the bridging is generally required in actual engineering projects. The effective length factor  $\mu$  for a single multi-story post with semi-rigid restraints at each story could be calculated by analyzing the limit state during buckling of the STCS at different bridging settings, and furthermore, the strength of the STCS system without bridging could be determined while considering the effect of bridging as a safety margin. Thus, the strength of the STCS system with bridging could be determined. A simplified model with a buckling wavelength of approximately 3 times the lift height is shown in Figure 2.

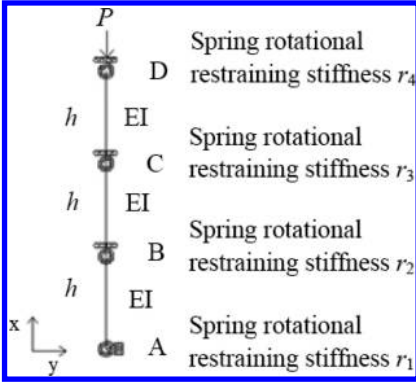


Figure 2. Model for a single multi-story post with four semi-rigid restraints at each story.

In this model, the rotational restraining stiffnesses of the four springs were assumed to be  $r_1$ ,  $r_2$ ,  $r_3$ , and  $r_4$ , considering the variance in the rotational stiffness of couplers and the mechanical properties of steel tubes. The rotational angles of springs at points A, B, C, and D were  $\theta_1$ ,  $\theta_2$ ,  $\theta_3$ , and  $\theta_4$ , respectively, and the vertical post AD underwent buckling. In Figure 2,  $x$  represents the coordinate along the span and  $y$  represents the transverse nodal displacement. The equilibrium of the post under the critical buckling condition is described by the following differential equations.

For  $0 < x < h$ , the equilibrium equation is:

$$-EIy_1'' + r_1\theta_1 = Py_1 \quad (2)$$

Assuming  $k^2 = P/EI$ , the following formula is obtained:

$$y_1'' + k^2y_1 - \frac{r_1\theta_1}{EI} = 0 \quad (3)$$

The general solution of differential equation (3) is given by

$$y_1(x) = \sin(kx) \times C_1 + \cos(kx) \times C_2 + \frac{r_1\theta_1}{k^2EI} \quad (4)$$

The boundary conditions are as follows:

1. At  $x = 0$ , the horizontal displacement is 0:

$$y_1(0) = 0 \quad (5)$$

2. At  $x = 0$ , the shear force is 0:

$$-(EIy_1'''(0) + Py_1'(0)) = 0 \quad (6)$$

Substituting Eqs. (5) and (6) into Eq. (4), the following equation is obtained:

$$y_1 = \frac{\sin(kx)\theta_1}{k} - \frac{\cos(kx)r_1\theta_1}{k^2EI} + \frac{r_1\theta_1}{k^2EI} \quad (7)$$

For  $h < x < 2h$ , the equilibrium equation is

$$-EIy_2''' + r_1\theta_1 + r_2\theta_2 = Py_2 \quad (8)$$

The general solution of differential equation (8) is

$$y_2(x) = \sin(kx) \times C_3 + \cos(kx) \times C_4 + \frac{r_1\theta_1 + r_2\theta_2}{k^2EI} \quad (9)$$

The boundary conditions are as follows:

1. At  $x = h$ , the shear force is 0:

$$-(EIy_2'''(h) + P\theta_2) = 0 \quad (10)$$

2. At  $x = 2h$ , the shear force is 0:

$$-(EIy_2'''(2h) + P\theta_3) = 0 \quad (11)$$

Substituting Eqs. (10) and (11) into Eq. (9), the following equation is obtained:

$$y_2 = -\frac{1}{\sin(kh)k^2EI} \times (-kEI\theta_3\cos(kx - kh) + kEI\theta_2\cos(kx - 2kh) + \sin(kh)r_1\theta_1 + \sin(kh)r_2\theta_2) \quad (12)$$

For  $2h < x < 3h$ , the equilibrium equation is

$$-EIy_3''' + r_1\theta_1 + r_2\theta_2 + r_3\theta_3 = Py_3 \quad (13)$$

The general solution of differential equation (13) is

$$y_3(x) = \sin(kx) \times C_5 + \cos(kx) \times C_6 + \frac{r_1\theta_1 + r_2\theta_2 + r_3\theta_3}{k^2EI} \quad (14)$$

The boundary conditions are as follows:

1. At  $x = 3h$ , the shear force is 0:

$$-(EIy_3'''(3h) + P\theta_4) = 0 \quad (15)$$

2. At  $x = 2h$ , the shear force is 0:

$$-(EIy_3'''(2h) + P\theta_3) = 0 \quad (16)$$

Substituting Eqs. (15) and (16) into Eq. (14), the following equation is obtained:

$$y_3(x) = \frac{1}{k^2 \sin(kh)EI} \times (-kEI \theta_4 \cos(kx - 2kh) + kEI \theta_3 \cos(kx - 3kh) + \sin(kh)r_1 \theta_1 + \sin(kh)r_2 \theta_2 + \sin(kh)r_3 \theta_3) \quad (17)$$

The compatibility conditions among the three tubes are as follows:

1. At  $x = 2h$ , the tubes had the same displacement:

$$y_2(2h) = y_3(2h) \quad (18)$$

2. At  $x = h$ , the tubes had the same displacement:

$$y_1(h) = y_2(h) \quad (19)$$

3. At  $x = h$ , the tubes had the same rotation angle:

$$y_1'(h) = y_2'(h) \quad (20)$$

The following formula is obtained based on the boundary condition at  $x = 3h$ :

$$M_{(3h)} = r_4 \theta_4 \quad (21)$$

If all the four spring rotational restraining stiffnesses were the same, it could be assumed that  $r_1 = r_2 = r_3 = r_4 = C$ . The linear rigidity of the vertical post was assumed to be  $C_c = EI/3h$ ,  $kh = \pi/\mu$ , and the final governing equation for determining the effective length factor  $\mu$  is obtained by simplifying the above simultaneous equations Eqs. (18) to (21):

$$\begin{aligned} & \left[ (324\pi^3 \mu C C_c^3 - 18\pi \mu^3 C^3 C_c) \cos^3\left(\frac{\pi}{\mu}\right) + (18\pi \mu^3 C^3 C_c \right. \\ & \left. - 216\pi^3 \mu C C_c^3) \cos\left(\frac{\pi}{\mu}\right) \right] \sin\left(\frac{\pi}{\mu}\right) + (324\pi^4 C_c^4 + \mu^4 C^4 \\ & - 117\pi^2 \mu^2 C^2 C_c^2) \cos^4\left(\frac{\pi}{\mu}\right) + (-2\mu^4 C^4 - 405\pi^4 C_c^4 \\ & + 144\pi^2 \mu^2 C^2 C_c^2) \cos^2\left(\frac{\pi}{\mu}\right) \\ & + (\mu^4 C^4 - 27\pi^2 \mu^2 C^2 C_c^2 + 81\pi^4 C_c^4) = 0 \end{aligned} \quad (22)$$

#### 4 COMPARISON BETWEEN THE SIMPLIFIED MODEL CALCULATION RESULTS AND FEA RESULTS

The strengths of the models with various geometric parameters without bridging  $P_{sim}$  were calculated

Table 2. Comparison between strengths determined from FEA and the simplified model.

No.	h (m)	$S_1 \times S_2$ (m $\times$ m)	$P_{FEA}$ (kN)	$P_{sim}$ (kN)	Error (%)
1	1.5	0.9 $\times$ 0.9	22.43	20.73	-7.58
2	0.9	1.2 $\times$ 1.2	21.46	22.32	4.01
3	0.9	1.0 $\times$ 1.0	22.08	22.77	3.13
4	0.9	0.9 $\times$ 0.9	24.67	23.01	-6.73

using Eq. (22), as listed in Table 2. In the table, the error represents the difference between  $P_{sim}$  and  $P_{FEA}$ . Accordingly,  $P_{sim}$  could be modified by considering the effect of the safety margin of bridging according to different bridging settings, and the degree of improvement could reference the results that listed in the fifth column in Table 1 approximately. in Table 2  $P_{sim}$  = strength determined from a simplified model calculation. Error =  $(P_{sim} - P_{FEA})/P_{FEA} \times 100$ .

#### 5 CONCLUSIONS

1. From the FEM analyses, it was clear that the main failure mode of the STCS without bridging was global flexural buckling about the longitudinal weak axis and that of the STCS with bridging was local buckling.
2. From FEM analysis results list in Table 1, it was clear that the strength of the STCS was affected by a number of erection parameters such as the lift height, spacing between vertical posts, erection height, U-head height, and it could increase significantly because of the existence of bridging.
3. A simplified model was developed for the STCS post and design formulae were established for calculating the strength of a multi-story post with semi-rigid rotational restraints at each story. The strength of the STCS system without bridging under a uniform load was then calculated as the summation of the strength of each single multi-story post. Accordingly, considering the effect of the bridging setting as a safety margin, the strength of the STCS system with bridging was determined by adjusting the result of the STCS system without bridging.

#### ACKNOWLEDGEMENTS

This research project was supported by the National Natural Science Foundation of China (No. 51308255), the Science and Technology Planning Project of ministry of housing and urban-rural

development (2013-K2-38), the Colleges and Universities of Liaoning Province Outstanding Young Scholars Growth Plan (No. LJQ2014059) and the Youth Fund of Shenyang Jianzhu University (No. 2014003).

## REFERENCES

- [1] J.L. Peng, A.D. Pan, D.V. Rosowsky et al. High clearance scaffold systems during construction-I Structural modeling and modes of failure, *Engineering Structures*, 1996, 18(3), 247–257.
- [2] J.L. Peng, A.D. Pan, D.V. Rosowsky et al. High clearance scaffold systems during construction-II Structural modeling and modes of failure, *Engineering Structures*, 1996, 18(3), 258–267.
- [3] Jui-Lin Peng. Stability Analyses and Design Recommendations for Practical Shoring Systems during Construction, *Journal of construction engineering and management*, 2002, 128:536–544.
- [4] Chen Zhihua, Lu Zhengran, Wang Xiaodun. Numerical analysis and experimental study of the stiffness of right angle couplers in tubular steel scaffolds, *China Civil Engineering Journal*, 2010, 43(9), 100–108 [In Chinese].
- [5] Chen Zhihua, Lu Zhengran, Wang Xiaodun, Liuqun. Research on the bearing capacity of steel tubular formwork support with coupler without X-bracing based on the partially-sway single post stability theory, *Engineering Mechanics*, 2010, 27(11), 99–105 [In Chinese].



## Vibrations and buckling analysis of Mindlin plates with stepped variable thickness

S.F. Yang, H. Chen & J.P. Wei

*Chongqing Creation Vocational College, Chongqing, China*

**ABSTRACT:** A new semi-analytical solution has been developed based on the domain superposition method and the differential cubature method as well as the Levy's general solution, for buckling and free vibration analysis of moderately thick plates having stepped thickness. Through Fourier series expansion, the governing equations and boundary conditions of the plate are transformed to one-dimensional differential equations. Then these equations are discretized into several linear algebraic equations by the general differential cubature element method. The basic idea of the differential cubature element method is to divide the entire variable domain into several sub-domains (elements) and to apply the differential cubature method for each element. Compatibility conditions are developed for the conjunction nodes on the interface points of elements in order to connect the elements. When the plate boundary conditions are introduced, a set of algebraic homogeneous equations about the displacements of grid points can be derived. This is a standard eigenvalue problem, from which the buckling parameters and natural frequencies of the plate can be calculated numerically. The convergent characteristics and comparison studies are carried out carefully in order to verify the present method. Also, some new results are tabulated for engineers and investigators to use as benchmarks in future studies.

**Keywords:** stepped thick plates; buckling; free vibration; differential cubature method; domain superposition

### 1 INTRODUCTION

Plates with stepped variable thickness have very wide applications in modern structural engineering. As it can save materials, reduce weight, increase stiffness and improve fundamental frequency, its excellent performance arouses people's interest to research stability and free vibration of this structure, etc. in recent decades. For such problems, many scholars proposed various theories and adopted a variety of methods for extensive study. Chopra<sup>[2]</sup> divided stepped plate into several homogeneous regions, assumed continuous and boundary conditions at the mutation thickness and obtained eigenvalue equation of the problem. However, it has error in dealing with bending moment and shearing force consecutive conditions at the section, as what Yuan and Dickinson<sup>[19]</sup> pointed out. Cortinez and Laura<sup>[6]</sup> adopted Kantorovich continuation method to analyze natural vibration frequency of stepped plate. The formula contains an index optimization parameter. Bambill, etc.<sup>[1]</sup> combined Rayleigh-Ritz solution and Fourier series expansion technique, obtained base and of simply supported rectangular stepped plate. However, continuous assumption of displacement function at the cross-section

is the flaw. Harik, etc.<sup>[9]</sup> made modification when dealing with continuity conditions, used the modified analytical spline to satisfy mutation condition in one direction. Yuan and Dickinson<sup>[19]</sup> used method proposed by Chopra<sup>[2]</sup>, modified continuous condition of bending moment and shearing force, and obtained the exact vibration frequency of stepped plate under simply supported boundary condition. Recently, Cheung introduced a set of interpolation functions that meet C1 continuous condition to solve buckling issue<sup>[5]</sup> of stepped variable section plate. These interpolation functions are composed of beam modal function and piecewise cubic polynomial. The author pointed out: These displacement functions are with advantages of fast convergence, appropriate continuous order and high accuracy of harmonic function. Yingshi Zhang and Chiping Jiang used singular function to establish continuous differential equation of stepped thin plate and provided analytical solution<sup>[22]</sup> of free vibration and forced vibration of stepped plate under various boundary conditions with operator operation.

It is worth noting that, there are two important directions in stepped research: one is committed to seeking the plate analytical solution to

verify calculation accuracy of various numerical solution; the other focuses on establishment of theoretical models of various plates to adapt to a variety of different applications. In this paper, on the basis of Mindlin plate model, semi-analytical method to solve stepped plate with two opposite edges simply supported will be given. First, it uses Levy's solving technique, assumes that displacement function is harmonic function that meets boundary condition in the direction of simply supported edge, substitutes it into governing equation to transform the problem into a one-dimensional one, then uses differential quadrature numerical method for solution.

Differential quadrature method first proposed by Civan<sup>[3-4]</sup> aims to simply and efficiently solve multi-dimensional high-order differential equation, a numerical method for direct holistic dissociation of governing differential equation based on polynomial. Its biggest features are simple formula, easiness to prepare computer program, and overall good convergence. Recently, Liew and Liu, mechanical workers, introduced the method into engineering applications to solve the bending problem<sup>[13-15]</sup> of thin plate and thick plate of arbitrary shape, and achieved very good numerical results. On this basis, Lanhe Wu applied this method to project eigen value problem for the first time to solve free vibration<sup>[20]</sup> of rounded rectangular plate, and also received good results. However, this method can only be used to solve the problem of uniform continuous geometry, unable to be directly applied to solve problems such as stepped plate. To this end, Lanhe Wu combined regional superposition method and differential volumetric method, proposed differential cubature element method<sup>[21]</sup>, and solved vibration problem of plate with mutation geometry characteristic. However, although this method can solve two-dimensional problem in principle, in fact, it is simpler and more effective for one-dimensional problem. Based on the previous study, the paper first uses Fourier series expansion, transforms two-dimensional problem into one-dimensional one, and then reuses one-way differential cubature method to disperse, which gives full play to the advantages of analytical method and differential cubature method and thus is a good method.

## 2 BASIC FORMULA

Considering the rectangular plate shown in Figure 1, we can assume that the plate is only stepped in the direction of  $x$ . Based on the actual thickness mutation, it can be divided into several units in the direction of  $x$ . Each unit has a uniform thickness, uniform boundary condition and

continuous geometry, wherein thickness, rotational inertia of unit  $l$  are  $h_l, J_l$  respectively, elastic modulus, shear modulus, Poisson's ratio and density of the material are  $E, G, \nu, \rho$  respectively. According to Mindlin plate theory, the governing differential equation is

$$\begin{aligned} \frac{D_l}{2} \left[ (1-\nu) \nabla^2 \psi_x + (1+\nu) \frac{\partial \phi}{\partial x} \right] - kGh_l \left( \psi_x + \frac{\partial w}{\partial x} \right) + \rho J_l \omega^2 \psi_x &= 0 \\ \frac{D_l}{2} \left[ (1-\nu) \nabla^2 \psi_y + (1+\nu) \frac{\partial \phi}{\partial y} \right] - kGh_l \left( \psi_y + \frac{\partial w}{\partial y} \right) + \rho J_l \omega^2 \psi_y &= 0 \\ kGh_l (\nabla^2 w + \phi) + \rho h_l \omega^2 w - N \left( \beta \frac{\partial^2 w}{\partial x^2} + \gamma \frac{\partial^2 w}{\partial y^2} \right) &= 0 \end{aligned} \quad (1)$$

where in

$$\phi = \frac{\partial \psi_x}{\partial x} + \frac{\partial \psi_y}{\partial y} \quad (2)$$

In the formula,  $w$  is lateral deflection of plate;  $\psi_x$  and  $\psi_y$  are average angles of the middle surface normal around  $x$  and  $y$  axis respectively;  $k$  is shear correction factor, taken as  $5/6$ ;  $J_l = h_l^3/12$  is rotational inertia of plate;  $D_l = Eh_l^3/[12(1-\nu^2)]$  is bending stiffness of plate;  $\omega$  is system angular frequency;  $N$  is load factor;  $\beta$  and  $\gamma$  are load combination factors;  $\nabla^2$  is two-dimensional Laplace operator.

According to the relationship between internal force and displacement, plate bending moment,

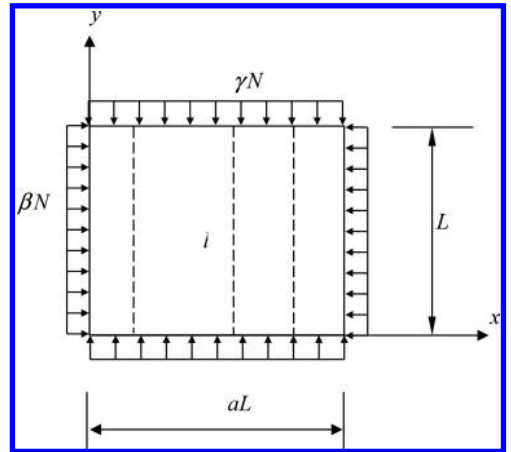


Figure 1. Geometry graph and coordinate of stepped rectangular plate.

torque and shearing force can be expressed with plate deflection and rotation as

$$\begin{aligned} M_x &= D_l \left( \frac{\partial \psi_x}{\partial x} + \nu \frac{\partial \psi_y}{\partial y} \right), \\ M_y &= D_l \left( \nu \frac{\partial \psi_x}{\partial x} + \frac{\partial \psi_y}{\partial y} \right), \\ M_{xy} &= \frac{1-\nu}{2} D_l \left( \frac{\partial \psi_x}{\partial y} + \frac{\partial \psi_y}{\partial x} \right) \\ Q_x &= kGh_l \left( \psi_x + \frac{\partial w}{\partial x} \right), \quad Q_y = kGh_l \left( \psi_y + \frac{\partial w}{\partial y} \right) \end{aligned} \quad (3)$$

If the plate is simply supported at both sides ( $y=0, L$ ) parallel to the  $x$  axis, then the corresponding boundary condition is

$$w = 0; \quad M_y = 0; \quad \psi_x = 0 \quad (4)$$

Assume

$$\psi_x = \Psi_x \sin \frac{n\pi y}{L}, \quad \psi_y = \Psi_y \cos \frac{n\pi y}{L}, \quad w = W \sin \frac{n\pi y}{L} \quad (5)$$

Apparently, it meet simply supported boundary condition in formula (4). Substitute (5) into (1) and obtain

$$\begin{aligned} D_l \left[ \frac{\partial^2}{\partial x^2} - \frac{1-\nu}{2} \left( \frac{n\pi}{L} \right)^2 - kGh_l \right] \Psi_x \\ - \frac{1+\nu}{2} D_l \left( \frac{n\pi}{L} \right) \frac{\partial \Psi_y}{\partial x} - kGh_l \frac{\partial W}{\partial x} + \rho J_l \omega^2 \Psi_x = 0 \\ \frac{1+\nu}{2} D_l \left( \frac{n\pi}{L} \right) \frac{\partial \Psi_x}{\partial x} + D_l \left[ \frac{1-\nu}{2} \frac{\partial^2}{\partial x^2} - \left( \frac{n\pi}{L} \right)^2 - kGh_l \right] \Psi_y \\ - kGh_l \left( \frac{n\pi}{L} \right) W + \rho J_l \omega^2 \Psi_y = 0 \\ kGh_l \frac{\partial \Psi_x}{\partial x} - kGh_l \left( \frac{n\pi}{L} \right) \Psi_y + kGh_l \left[ \frac{\partial^2}{\partial x^2} - \left( \frac{n\pi}{L} \right)^2 \right] W \\ - N \left[ \beta \frac{\partial^2}{\partial x^2} - \gamma \left( \frac{n\pi}{L} \right)^2 \right] W + \rho h_l \omega^2 W = 0 \end{aligned} \quad (6)$$

So the two-dimensional problem is transformed into a one-dimensional one. Now, use differential cubature method to disperse equation (6). As shown in Figure 2. In the entire structure, arbitrarily set  $e$  collocation points along the direction of  $x$ . Assume the starting end collocation point mark

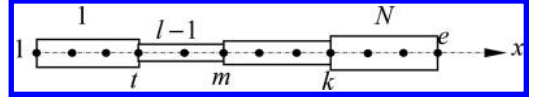


Figure 2. Structure collocation point setting along the direction of  $x$ .

of unit  $l$  is  $m$ , tail end collocation point mark is  $k$ , coordinate of each collocation point is  $x_i (i = m, m+1, \dots, k)$ . To disperse the equation, first define linear differential operator as follows

$$\hat{\lambda}_1 = \frac{d}{dx}, \quad \hat{\lambda}_2 = \frac{d^2}{dx^2} \quad (7)$$

With step of differential cubature method, governing equation (6) in collocation point  $i$  in unit  $l$  can be dispersed into [3-4]

$$\begin{aligned} D_l \left[ \sum_{j=m}^k C_{ij}^{(2)} \Psi_{xj} - \frac{1-\nu^2}{2} \left( \frac{n\pi}{L} \right)^2 \Psi_{xi} - kGh_l \Psi_{xi} \right] \\ - \frac{1+\nu}{2} \left( \frac{n\pi}{L} \right) D_l \sum_{j=m}^k C_{ij}^{(1)} \Psi_{yj} - kGh_l \sum_{j=m}^k C_{ij}^{(1)} W_j \\ + \rho J_l \omega^2 \Psi_{xi} = 0 \\ \frac{1+\nu}{2} \left( \frac{n\pi}{L} \right) D_l \sum_{j=m}^k C_{ij}^{(1)} \Psi_{xj} \\ + D_l \left[ \frac{1-\nu}{2} \sum_{j=m}^k C_{ij}^{(2)} \Psi_{yj} - \left( \frac{n\pi}{L} \right)^2 \Psi_{yi} - kGh_l \Psi_{yi} \right] \\ - kGh_l \left( \frac{n\pi}{L} \right) W_i + \rho J_l \omega^2 \Psi_{yi} = 0 \\ kGh_l \sum_{j=m}^k C_{ij}^{(1)} \Psi_{xj} - kGh_l \left( \frac{n\pi}{L} \right) \Psi_{yi} \\ + kGh_l \left[ \sum_{j=m}^k C_{ij}^{(2)} w_j - \left( \frac{n\pi}{L} \right)^2 w_i \right] \\ - N \left[ \beta \sum_{j=m}^k C_{ij}^{(2)} w_j - \gamma \left( \frac{n\pi}{L} \right)^2 w_i \right] + \rho h_l \omega^2 w_i = 0 \\ (i = m, m+1, \dots, k) \end{aligned} \quad (8)$$

$C_{ij}^{(a)}$  in all the above formula corresponds to quadrature coefficient of differential cubature method of operator  $\hat{\lambda}_a (a=1,2)$ , which can be solved by means of a set of linearly independent monomials, i.e.

$$\begin{aligned} \sum_{j=m}^k C_{ij}^{(\alpha)} (x_j^p) = \hat{\lambda}_\alpha (x_i^p); \quad i = m, 2 \dots, k; \\ p = 0, 1, 2, \dots, k-m \end{aligned} \quad (9)$$

At this point, governing equation has been dispersed into a system of linear algebraic equations concerning collocation point displacement within the unit  $l$ . The connection point of unit  $l-1$  and unit  $l$  should meet the following continuity condition and equilibrium condition

$$\begin{aligned} \Psi_{xm}^{(l-1)} &= \Psi_{xm}^{(l)}; \Psi_{ym}^{(l-1)} = \Psi_{ym}^{(l)}; W_m^{(l-1)} = W_m^{(l)}; \\ M_{xm}^{(l-1)} &= M_{xm}^{(l)}; M_{xym}^{(l-1)} = M_{xym}^{(l)}; \\ Q_{xm}^{(l-1)} - \beta N \frac{\partial W^{(l-1)}}{\partial x} \Big|_{x=x_m} &= Q_{xm}^{(l)} - \beta N \frac{\partial W^{(l)}}{\partial x} \Big|_{x=x_m} \end{aligned} \quad (10)$$

If nodes in various units are consecutively numbered in unification, displacement continuity condition in connection conditions will certainly be met, and then there is only need to consider the later three equations in formula (10). With differential cubature method, values of plate internal force at various points can be represented as weighted combination of all collocation point displacement within the unit

$$\begin{aligned} M_{xi}^{(l)} &= D_l \left[ \sum_{j=m}^k c_{ij}^{(l)} \Psi_{xj} - \nu \left( \frac{n\pi}{L} \right) \Psi_{yi} \right] \sin \frac{n\pi y}{L} \\ M_{xyi}^{(l)} &= \frac{1-\nu}{2} D_l \left[ \sum_{j=m}^k c_{ij}^{(l)} \Psi_{yj} + \left( \frac{n\pi}{L} \right) \Psi_{xi} \right] \cos \frac{n\pi y}{L} \\ Q_{xi}^{(l)} &= kGh_l \left( \sum_{j=m}^k c_{ij}^{(l)} W_j + \Psi_{xi} \right) \sin \frac{n\pi y}{L} \end{aligned} \quad (11)$$

Equilibrium condition of plate at connection point  $m$  can be expressed as

$$\begin{aligned} D_{l-1} \left[ \sum_{j=1}^m c_{ij}^{(l)} \Psi_{xj} - \nu \left( \frac{n\pi}{L} \right) \Psi_{ym} \right] &= D_l \left[ \sum_{j=m}^k c_{ij}^{(l)} \Psi_{xj} - \nu \left( \frac{n\pi}{L} \right) \Psi_{ym} \right] \\ D_{l-1} \left[ \sum_{j=1}^m c_{ij}^{(l)} \Psi_{yj} + \left( \frac{n\pi}{L} \right) \Psi_{xm} \right] &= D_l \left[ \sum_{j=m}^k c_{ij}^{(l)} \Psi_{yj} + \left( \frac{n\pi}{L} \right) \Psi_{xm} \right] \\ kGh_{l-1} \left( \sum_{j=1}^m c_{ij}^{(l)} W_j + \Psi_{xm} \right) - \beta N \sum_{j=1}^m c_{ij}^{(l)} W_j &= kGh_l \left( \sum_{j=m}^k c_{ij}^{(l)} W_j + \Psi_{xm} \right) - \beta N \sum_{j=m}^k c_{ij}^{(l)} W_j \end{aligned} \quad (12)$$

Apply boundary condition at both left and right ends ( $x = x_1, x_e$ ) of plate

$$\text{Simply supported edge (S): } W = 0; M_x = 0; \Psi_y = 0 \quad (13)$$

$$\text{Fixed edge (C): } W = 0; \Psi_x = 0; \Psi_y = 0 \quad (14)$$

$$\text{Free edge (F): } Q_x = \beta N \frac{\partial W}{\partial x}; M_x = 0; M_{xy} = 0 \quad (15)$$

These equations can also be dispersed with differential cubature method. Now, with point 1 as example, write the boundary condition after dissociation

Simply supported edge (S):

$$D_1 \left[ \sum_{j=1}^t c_{ij}^{(l)} \Psi_{xj} - \nu \left( \frac{n\pi}{L} \right) \Psi_{y1} \right] = 0; \Psi_{y1} = 0; W_1 = 0 \quad (16)$$

$$\text{Fixed edge (C): } W_1 = 0; \Psi_{x1} = 0; \Psi_{y1} = 0 \quad (17)$$

Free edge (F):

$$\begin{aligned} D_1 \left[ \sum_{j=1}^t c_{ij}^{(l)} \Psi_{xj} - \nu \left( \frac{n\pi}{L} \right) \Psi_{y1} \right] &= 0; \\ \frac{1-\nu}{2} D_1 \left[ \left( \frac{n\pi}{L} \right) \Psi_{x1} + \sum_{j=1}^t c_{ij}^{(l)} \Psi_{yj} \right] &= 0; \\ kGh_l \Psi_{x1} + kGh_l \sum_{j=1}^t c_{ij}^{(l)} W_j &= \beta N \sum_{j=1}^t c_{ij}^{(l)} W_j \end{aligned} \quad (18)$$

To solve the critical load and inherent frequency of the entire plate, frequency equation of the entire system needs to be established. To this end, all collocation points within the plate zone need to be numbered in unification (overall coding). Then collect the governing equation sets at various nodes together and write in matrix form as follows

$$([K] - \omega^2 [M] - N[\bar{K}])\{d\} = 0 \quad (19)$$

In the formula,  $K$ ,  $M$  and  $\bar{K}$  are structural stiffness matrix, mass matrix and geometric stiffness matrix;  $\{d\}$  is displacement array of the entire structure at various collocation points.

It should be noted that, at connection points of adjacent units, equilibrium condition of connection points between the various units should be used to substitute their respective equations, while applying corresponding boundary condition at both end points.

### 3 CALCULATION EXAMPLES AND DISCUSSION

To facilitate expression, define dimensionless critical load factor and frequency factor as follows

$$\lambda = N_{cr}L^2/(\pi^2 D_1), \quad \Omega = (\omega L^2/\pi^2)\sqrt{\rho h_1/D_1} \quad (20)$$

wherein,  $h_1$  and  $D_1$  are thickness and bending stiffness of first-order plate.

First, with second-order plate of equal length as example, study convergence of the research method. Assume  $h_2/h_1 = 1.1$ ,  $h_1/L = 0.1$ . Apparently, in calculation, the plate should be divided into two units in the direction of  $x$ . Convergence situation of buckling load factor  $\lambda$  of the plate in one-way compression ( $\beta = 1$ ,  $\gamma = 0$ ) corresponding to the collocation point number  $e$  in each unit is shown in Figure 3, in which the letters C, F, S respectively denote the fixed, free and simply supported boundary conditions. As can be seen from the figure, regardless of what kind of boundary condition, load factor  $\lambda$  can quickly converge. We can also see that when the plate has free edge, the convergence is alternating and turbulence-like, and when the plate boundary doesn't have free edge, convergence shows monotone decreasing. Figure 4-6 depicts convergence of the first sixth-order frequency factor of the plate with different boundary conditions. Also, it can be seen that this method has very good convergence. In particular, the first second-order frequency converges very quickly. In general, setting 11 collocation points within a unit can render sufficient accuracy. In the following calculations, set 11 collocation points within each unit. It can be seen from the figure that, when plate has free edge, convergence is poor, remaining turbulence-like.

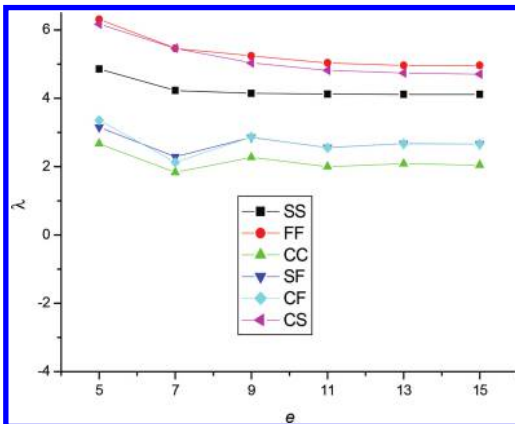


Figure 3. Convergence situation of critical load factor  $\lambda$  under one-way second-order plate compression.

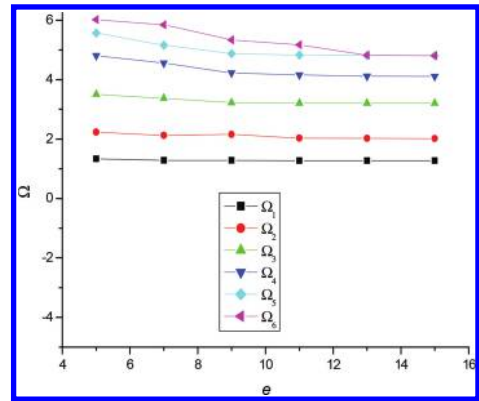


Figure 4. Convergence situation of inherent frequency factor  $\Omega$  of second-order plate with two opposite edges simply supported.

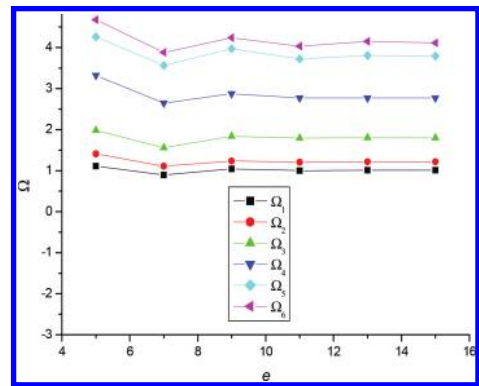


Figure 5. Convergence situation of inherent frequency factor  $\Omega$  of second-order plate with two opposite free edges.

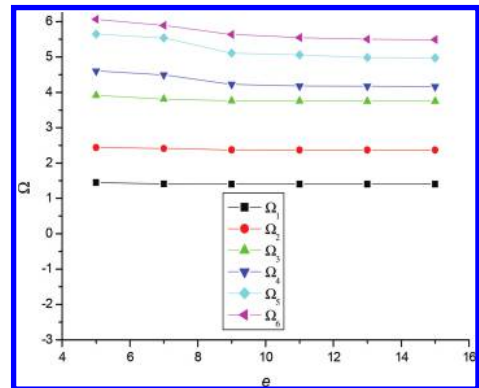


Figure 6. Convergence situation of inherent frequency factor  $\Omega$  of second-order plate with two opposite fixed edges.

For verification of calculation accuracy, compare critical load factor and vibration frequency factor of second-order thin plate with two opposite edges simply supported, with different relative thicknesses and geometry sizes under one-way compression to the relevant results, as shown in Figure 7. Table 1 and Table 2 are calculation and

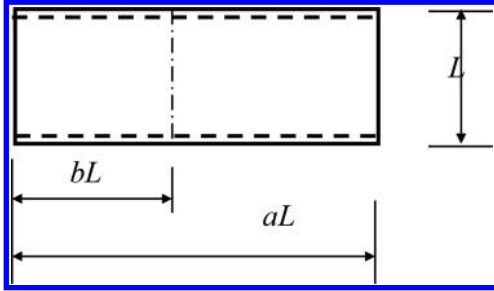


Figure 7. Geometry graph of second-order stepped plate.

Table 1. Comparison of critical load factor  $\lambda$  of second-order simply supported rectangular plate.

$h_2/h$	$\lambda$			
	This paper	Eisenberger and Alexandrov[7]	Xiang and Wei[18]	Xiang and Wang[17]
0.4	0.3085	0.8619	0.30826	0.3083
0.6	1.0245	1.0245	1.02444	1.0246
0.8	2.3445	2.3442	2.34385	2.3442
1.0	4.0011	4.0000	3.99947	4.0000
1.2	4.5342	4.5324	4.53154	4.5325
1.4	4.6678	4.6663	4.66512	4.6663
1.6	4.7330	4.7292	4.72798	4.7292
1.8	4.7669	4.7652	4.76394	4.7652
2.0	4.7888	4.7877	4.78646	4.7877
2.2	4.8028	4.8026	4.80137	4.8027

Table 2. Comparison of inherent frequency factor  $\Omega$  of second-order simply supported rectangular plate.

$b$	$h_2/h$	Source	Modal number					
			1	2	3	4	5	6
0.5	0.25	This paper	1.29348	2.87255	2.89988	4.92335	5.41566	5.68214
		Xiang[18]	1.29237	2.87075	2.89858	4.91918	5.41389	5.67875
		Yuan[19]	1.29333	2.87183	2.89981	4.92249	4.41555	5.67965
0.8	0.25	This paper	1.70406	4.18733	4.19696	6.76881	8.25147	8.48308
		Xiang[18]	1.70367	4.18625	4.19615	6.76425	8.24811	8.47926
		Yuan[19]	1.70392	4.18715	4.19685	6.76611	8.25094	8.48212
0.5	0.5	This paper	1.63038	4.04919	4.34444	6.87192	8.57733	8.71464
		Xiang[18]	1.62893	4.04723	4.34043	6.86416	8.57067	8.70775
		Yuan[19]	1.62903	4.04892	4.34142	6.86923	8.57562	8.71333
0.75	0.5	Chopra[2]	1.744	3.902	4.149	6.3875		
		This paper	1.88945	4.68996	4.78453	7.56130	9.41236	9.62887
		Xiang[18]	1.88915	4.68884	4.78228	7.55768	9.39662	9.62323
		Yuan[19]	1.88936	4.68981	4.78334	7.56023	9.40069	9.62732

comparison results. In calculation of critical load factor, Table 1 shows the critical load factors of thin plates with different relative thicknesses. As can be seen from Table 1, the results coincide with those in other literatures, with good accuracy. In addition, the maximum relative errors between the result in this paper and paper [7], [17], [18] are respectively. Obviously, the values given by Eisenberger and Alexandrov differ from the results of this paper and other literatures. In fact, what they give is third-order buckling load, not the minimum critical load. The result of this paper is correct. Table 2 shows a comparison of inherent frequency, with  $h_1/L = 0.005$ ,  $a = 1$  in calculation of inherent frequency. The table shows inherent frequency factors of plates of different sizes and different relative thickness. As can be seen, the result of this paper is slightly larger than those given by Xiang<sup>[18]</sup> and Yuan<sup>[19]</sup>. Despite the maximum relative errors of, respectively between this result and them, it still has a relatively good calculation accuracy.

Based on the above comparative study of convergence and numerical accuracy, this paper calculates buckling load and inherent frequency of multi-order plates with variable thickness, as listed in Table 3 and Table 4. In calculation,  $h_1/L = 0.1$  is taken. Different combinations of S, F, C in the table represent different boundary conditions. As can be seen from Table 3, along with the enhancement of boundary constraint, critical load factor increases; critical load factor varies little with the order number of plate, as the plate buckling factor is mainly determined by first-order thin plate. We also find that right end boundary condition of plate exerts relatively large influence on critical load factor, but the influence from left end boundary condition is small. This is because flexural rigidity of plate mainly concentrates on the right end. Naturally, the

Table 3. Critical load factor  $\lambda$  of second, third, fourth-order plate with equal length.



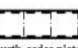
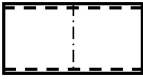
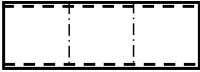

Plate Shape	$\beta, \gamma$	SS	FF	CC	SF	CF	CS
 Second-order plate with variable thickness ( $h_2/h_1 = 1.1, a = 2$ )	(1,0)	4.1145	2.0437	4.9622	2.6687	2.6689	4.7126
	(0,1)	1.7247	1.0533	2.8630	1.3133	1.3563	1.9148
	(1,1)	1.3685	0.9665	1.6061	1.2073	1.2387	1.5081
 Third-order plate with variable thickness ( $h_2/h_1 = 1.1, h_3/h_2 = 1.2, a = 3$ )	(1,0)	4.1440	2.0516	4.8488	3.4069	3.4085	4.8387
	(0,1)	1.5233	1.0839	1.6435	1.4491	1.4998	1.6152
	(1,1)	1.3262	0.9689	1.4348	1.3194	1.4066	1.4257
 Fourth-order plate with variable thickness ( $h_2/h_1 = 1.1, h_3/h_2 = 1.2, h_4/h_3 = 1.3, a = 4$ )	(1,0)	4.1489	2.0533	4.8425	4.1438	4.2568	4.8435
	(0,1)	1.4981	1.0868	1.5769	1.4923	1.5601	1.5750
	(1,1)	1.3243	0.9692	1.4198	1.3235	1.4193	1.4199

Table 4. Inherent frequency factor  $\Omega$  of second, third, fourth-order plate with equal length.

Plate shape	Modal number	<i>SS</i>	<i>FF</i>	<i>CC</i>	<i>SF</i>	<i>CF</i>	<i>CS</i>
 Second-order plate with variable thickness ( $h_2/h_1 = 1.1$ )	1	1.2793	1.0081	1.4069	1.0978	1.1129	1.3428
	2	2.0208	1.2134	2.3682	1.5232	1.6164	2.1879
	3	3.2074	1.7967	3.7498	2.3883	2.5835	3.4751
	4	4.1085	2.7672	4.1634	2.6648	3.9487	4.1468
	5	4.8014	3.7910	4.9755	4.0089	4.0241	4.8944
	6	4.8148	4.1165	5.4884	4.3447	4.3930	5.1437
 Third-order plate with variable thickness ( $h_2/h_1 = 1.1, h_3/h_2 = 1.2$ )	1	1.1845	1.0258	1.2259	1.1338	1.1444	1.2122
	2	1.5402	1.1874	1.6675	1.3159	1.3537	1.6064
	3	2.1058	1.4583	2.3340	1.7382	1.8197	2.2218
	4	2.8784	1.9427	3.1997	2.3596	2.4886	3.0399
	5	3.8413	2.6139	4.1068	3.1764	3.3481	4.0436
	6	4.0756	3.4699	4.2385	4.0745	4.1030	4.1065
 Fourth-order plate with variable thickness ( $h_2/h_1 = 1.1, h_3/h_2 = 1.2, h_4/h_3 = 1.3$ )	1	1.1667	1.0279	1.1896	1.1584	1.1746	1.1868
	2	1.3968	1.2192	1.4543	1.2883	1.3053	1.4323
	3	1.7302	1.3615	1.8436	1.5198	1.5669	1.7935
	4	2.1885	1.6488	2.3598	1.8967	1.9661	2.2794
	5	2.7699	2.0584	2.9967	2.3871	2.4858	2.8886
	6	3.4624	2.5789	3.7350	2.9943	3.1203	3.6069

boundary condition on the end has relatively large influence on buckling factor. Table 4 shows the inherent frequencies of the first six orders of plate. Different from critical load factor, we see that, for the most part, with the increasing order number of plate, inherent frequency factor will decrease, especially high order frequency.

#### 4 CONCLUSION

This paper adopts a new numerical method—Differential Cubature Element method (DCE) and combines Levy solving technique to solve the problem of buckling free vibration of stepped plate with boundary condition of two opposite simply supported edges. By assuming displacement function of order form, it transforms two-dimensional problem into one-dimensional one, and then begins unit division in one-dimensional domain, sets collocation points in each unit, disperses governing equation and boundary conditions into a set of homogeneous linear algebraic equations with differential cubature method and obtains classic eigenvalue problem. Convergence analysis and numerical accuracy study confirms feasibility and effectiveness of the proposed method.

With the characteristics of good convergence, high accuracy of differential cubature method and strong feasibility of finite element method, the method proposed by the paper is good.

#### REFERENCES

- [1] Bambill D.V., Laura P.A.A., Bergmann A., Carnicer R. Fundamental frequency of transverse vibration of symmetrically stepped simply supported rectangular plates. *Journal of Sound and Vibration*, 1991, 150(1):167–169.
- [2] Chopra I. Vibration of stepped thickness plates. *International Journal of Mechanical Science*, 1974, 16:337–344.
- [3] Civan F. Differential cubature for multi dimensional problems [C]. Proc. Of the 20th Annual Pittsburgh Conf, Univ of Pittsburgh, published by Instrument Society of AM, N Carolina 20, Pt.5, 1843–1847.
- [4] Civan F. Solving multivariable mathematical models by the quadrature and cubature methods [J]. *Numerical Methods for Partial Differential Equations*, 1994, 10(4):545–567.
- [5] Cheung Y.K., Au F.T.K., Zheng D.Y. Finite strip method for the free vibration and buckling analysis of plates with abrupt changes in thickness and complex support conditions. *Thin-Walled Structures*, 2000, 36:89–110.
- [6] Cortinez V.H., Laura P.A.A. Analysis of vibrating rectangular plates of discontinuously varying thickness by means of the Kantorovich extended method. *Journal of Sound and Vibration*, 1990, 137(3):457–461.
- [7] Eisenberger M., Alexandrov A. Stability analysis of stepped thickness plates. In: Papadrakakis M, Samartin A, Onate E(Eds.). *Computational methods for shell and spatial structures*, IASS-IACM 2000, ISASR-NTUA, Athens, Greece.
- [8] Guo S.J., Keane A.J., Moshrefi-Torbati M. Vibration analysis of stepped thickness plates. *Journal of Sound and Vibration*, 1997, 204:645–657.

- [9] Harik I.E., Liu X., Balakrishnan N. An analytical solution to free vibration of rectangular plates. *Journal of Sound and Vibration*, 1992, 153(1):51–62.
- [10] Hwang S.S. Stability of plates with piecewise varying thickness. *Journal of Applied Mechanics*, 1973, 40:1127–1129.
- [11] Ju F., Lee H.P., Lee K.H. Free vibration of plates with stepped variations in thickness on non-homogeneous elastic foundations. *Journal of Sound and Vibration*, 1995, 183:533–545.
- [12] Levy R. Rayleigh-Ritz optimal design of orthotropic plates for buckling. *Structural Engineering and Mechanics*, 1996, 4:541–552.
- [13] Liew K.M., Liu F.L. Differential cubature method: a solution technique for Kirchhoff plates of arbitrary shape[J]. *Computer Methods in Applied Mechanics and Engineering*, 1997, 145 (1):1–10.
- [14] Liew K.M., Ng T.Y., Kitipornchai S. A semi-analytical solution for vibration of rectangular plates with abrupt thickness variation [J]. *International Journal of Solids and Structures*, 2001, 38:4937–4954.
- [15] Liu F.L., Liew K.M. Differential cubature method for static solutions of arbitrary shaped thick plates [J]. *International Journal of Solids and Structures*, 1998, 35(28–29):3655–3674.
- [16] Navaneethakrishnan P.V. Buckling of non-uniform plates: spline method. *Journal of Engineering Mechanics*, ASCE 1988, 114:893–898.
- [17] Xiang Y., Wang C.M. Exact buckling and vibration solutions for stepped rectangular plates. *Journal of Sound and Vibration*, 2002, 250:503–517.
- [18] Xiang Y., Wei G.W. Exact buckling and vibration solutions for stepped rectangular Mindlin plates. *Intl. Journal of Solids and Structures*, 2002, 250:503–517.
- [19] Yuan J., Dickinson S.M. The flexural vibration of rectangular plate systems approached by using artificial springs in the Rayleigh-Ritz method. *Journal of Sound and Vibration*, 1992, 159:39–55.
- [20] Lanhe Wu, Jin Liu, Yanqiang Li. Free Vibration of Hyperelliptic Plate of Moderate Thickness [J]. *Engineering Mechanics*, 2002, 19 (6):120–125.
- [21] Lanhe Wu. Differential Cubature Method to Solve Free Vibration of Discontinuous Plate of Moderate Thickness [J] *Journal of Computational Mechanics*, 2004, 21 (1):121–128.
- [22] Yingshi Zhang, Chiping Jiang. Vibration of Stepped Rectangular Plate [J]. *Journal of Applied Mechanics*, 1998, 15 (4):109–115.



## Analysis of a new Tensairity bridge section

D.C. Yuan

College of Military Officer's Primary Education, National University of Defence Technology, Changsha, China

M.S. Jiang

Logistics Department of National University of Defence Technology, Changsha, China

**ABSTRACT:** To feature river-crossing and bridging equipment with characteristics such as light weight, fast set up, small storage volume, high load bearing capacity and low construction costs, the Tensairity structure was introduced into the design of bridge section in this paper. By using the Patran/Nastran software, a finite element model of the Tensairity bridge section was established in numerical simulation analysis, the distortion and stress of the structure under the effect of typical wheel load was studied, and the limit of load bearing capacity of the structure was obtained. Studies in this paper provide technical support for the research on new river-crossing and bridging equipment.

**Keywords:** airbag; beam string structure; Tensairity bridge section; numerical simulation

### 1 INTRODUCTION

Traditional river-crossing and bridging equipments have drawbacks such as heavy weight, large volume, slow erection, low load bearing capacity and bulk support personnel and vehicles, which adversely affect its maneuvering characteristics. To meet the requirements of future high-tech warfare and non-military rescue, it is significant to develop new river-crossing and bridging equipment with characteristics like light weight, fast set up, high load bearing capacity and high maneuver. Tensairity structure is a new structure system consisting of airbeams with low internal pressure, flexible cables and rigidity compression elements and is featuring light weight, small size, fast set up and high load bearing capacity, as shown in Figure 1. Tensairity, a blending word coming from the three words “tension”, “air” and “integrity”, was proposed by Dr. Mauro Pedretti, the chief engineer of the Swiss Airlight Co. Ltd. in 2002, whose research has the leadership in the field of structural engineering. Researches on Tensairity structure at home and abroad focus on the structure of one dimension

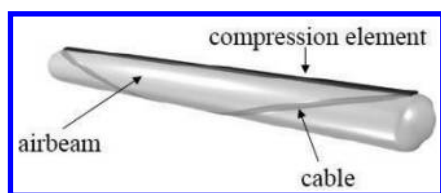


Figure 1. The basic element of a Tensairity beam.

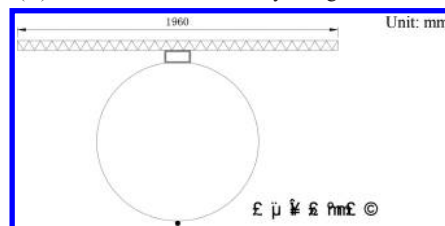
beam and column. To meet the requirements of the development of river-crossing and bridging equipment, Tensairity structure was brought in section design, and by employing the method of numerical simulation the mechanical properties of the new Tensairity bridge section was analyzed, which provided technical support for the research on new river-crossing and bridging equipment.

### 2 DESIGN OF THE TENSAIRITY BRIDGE SECTION

Against temporary bridges for flood-fighting and emergency rescues and river-crossing and bridging



(A) Front view of a tensairity bridge section



(B) Sectional view of 1/2 segment of a tensairity bridge section

Figure 2. Geometric drawing of a tensairity bridge section.

Table 1. Parameters of elements of a Tensairity bridge section.

Item	Section (mm)	Material	Elasticity modules (MPa)	Yield strength (MPa)
Bridge deck slab	t = 3	Aluminum alloy	$7.0 \times 10^4$	283.55
Upper compression chord	210 × 100 × 10	Steel	$2.1 \times 10^5$	235
Lower cable	R = 6	Stress relieving steel wire	$1.95 \times 10^5$	1570
Airbeam	t = 1.5	PVC	500	100

equipment, based on the theoretical research of Tensairity structure, the present study conducts a primary design of the Tensairity bridge section, whose span and bridge deck width are designed to be 8 meters and 4 meters, respectively. Aluminum alloy sandwich panel is applied to act as bridge deck slab to bear upper vehicle load, and the design of bridge deck slab is based on aluminum alloy pontoon deck panel. Tensairity beam uses rectangular steel tube as upper compression chord, and asymmetric fusiform airbeam, whose radius of center section is 0.5 meter and material is PVC coating and internal pressure is 40 KPa, is applied in this study. Steel strand is used as tension member for lower chord. The design is shown in Figure 2, and parameters of structural elements are listed in Table 1, where t is thickness.

Material constitutive models employed in the numerical simulation are as follows: the ideal elastic-plastic model is applied to PVC and steel wire, the elastic hardening constitutive model is applied to aluminum alloy.

### 3 COMPUTING OF THE TENSIRITY BRIDGE SECTION

The present study selects the representative diaxon wheel-type load LT-20 as the subject of numerical simulation research. Due to the symmetry of the Tensairity bridge section, half of the model is analyzed and the connections between elements in modeling are not considered.

Since the landing area (length × width) of the front wheel of LT-20 vehicles is 0.3 m × 0.2 m, and the back wheel is 0.6 m × 0.2 m, the exact computing model is shown as Figure 3.

#### 3.1 Displacement of Tensairity bridge section under the wheel type load

The Tensairity bridge section forms its stiffness and reached self-balance under the internal pressure and therefore possesses the capacity to stand up to external load. The structural displacement response of the Tensairity bridge section under the typical wheel type load (LT-20) is shown in Figure 4.

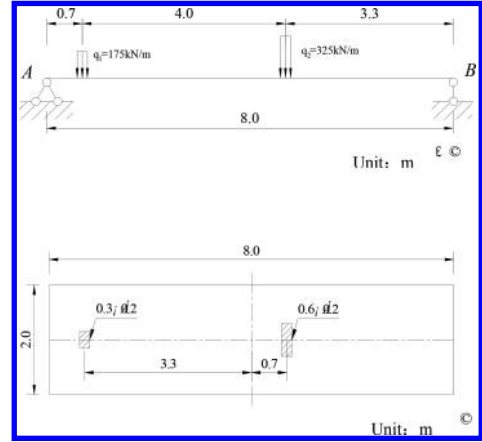


Figure 3. Loading pattern of wheel type load (LT-20).

The pictures of displacement of the Tensairity bridge section under the wheel type load, as shown in Figure 4, illustrate that the maximum displacement value lies in 4.4 meters along the direction of bridge span, which means that the maximum vertical distortion occurs on the point that is 20 centimeters length from the back wheel's edge and the maximum displacement is 1.98 centimeters. The top of airbeam is linked to the upper compression chord and has the same displacement, resulting in the expansion outside of both sides of the airbeam with the maximum displacement. The lower cable distorts downward subject to the load and the cable near to the top distorts outward subject to the internal pressure of the airbeam, which lead to the inclination of upward displacement in the middle part of the cable. The displacement of the bridge deck slab and upper compression chord are far more greater than that of the lower cable, which can be attributed to following reasons: first, the internal shearing force of the structure delivers through inflatable airbeams when subjected to external load and therefore the displacement of the lower cable lags behind that of upper compression elements; second, the lower cable stays in the state of compression and bellies out due to the pressure of the top of the airbeam, resulting in the upward inclination of the cable.

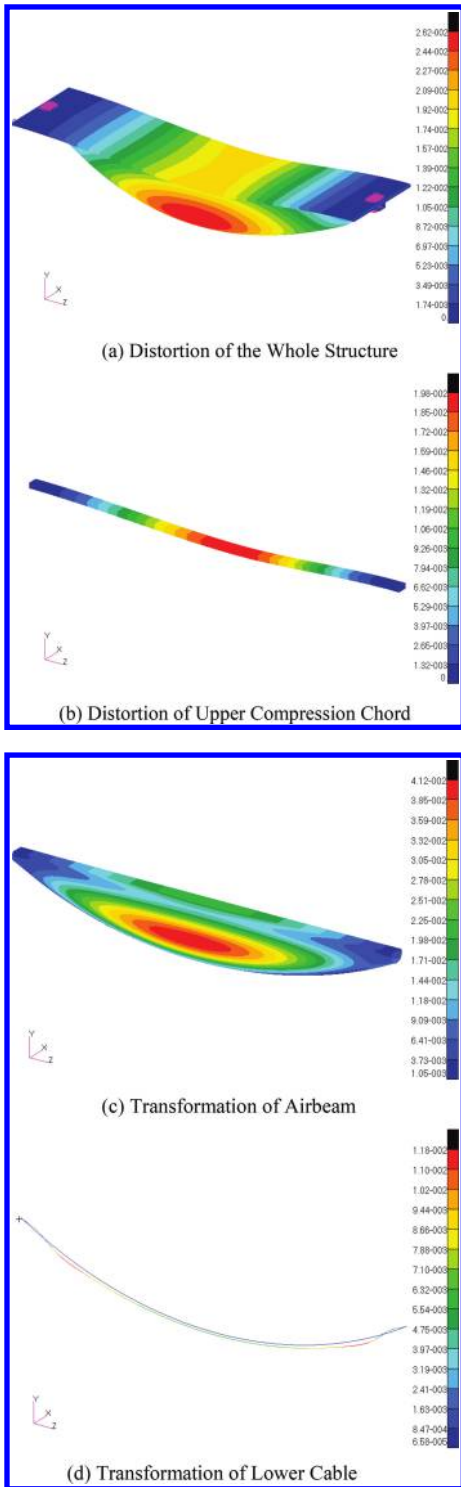


Figure 4. Displacement of a Tensairity bridge section under the wheel type load.

### 3.2 Stress of the Tensairity bridge section under the wheel type load

As to the internal force of the elements of the Tensairity bridge section under the wheel type load, the present study focuses on the stresses of upper bridge deck slab, upper compression chords, airbeams and lower cables. The stresses of the elements of the bridge section are shown in Figure 5.

As shown in Figure 5, under the wheel type load, as for the Tensairity bridge section, stress concentration of the bridge deck slab lies in the landing area of the back wheel and the joint to the top of the cable, the stress is symmetrically distributed. Besides stress concentration of the bridge support, the maximum stress lies in the 4.65 meters along the bridge span of the bottom flange of the upper compression chord, with a stress of 124 MPa. More than being the stiff compression element of the airbeam, the upper compression chord also acts as stiffening ribs of the upper bridge deck slab, therefore, the stress of the upper compression chord increases in spots like the back wheel and joint to the cable. The stress of the bottom flange of the chord is larger than that of the top, which shows that the upper chord bears bending moment. The stress of the airbeam gradually decreases from the middle part to the two sides, and that of the joint of upper compression chord is large.

### 3.3 The limits of load bearing capacity of the Tensairity bridge section under the wheel type load

The load bearing capacity of the bridge structure is one important measurement indicator of the bridge performance. To explore the limits of load bearing capacity of the Tensairity bridge section subject to the wheel type load, the present study assumes that the structure is damaged when any spots of the structure or of the cross section fail to meet the material failure criteria and the corresponding load is defined as the limit of load bearing capacity. If the stiffness requirement of the structure is not met when structure is damaged, the limit of load bearing capacity is the one meeting the stiffness requirement. As for the numerical simulation, considering the nonlinearity of the material and the structure, Mises yield criterion is applied to the aluminum alloy sandwich panel. A heavy load is exerted to the active area of the load of the bridge deck slab and the Newton-Raphson Iteration is employed for calculating. When the calculating terminates, the percentage of convergence ratio multiplying the overall load is the limit of load bearing capacity.

It is shown by the calculating results of numerical simulation that when the value of the load reaches 127.6 KN, the airbeam and the upper compression chord are damaged because the stress

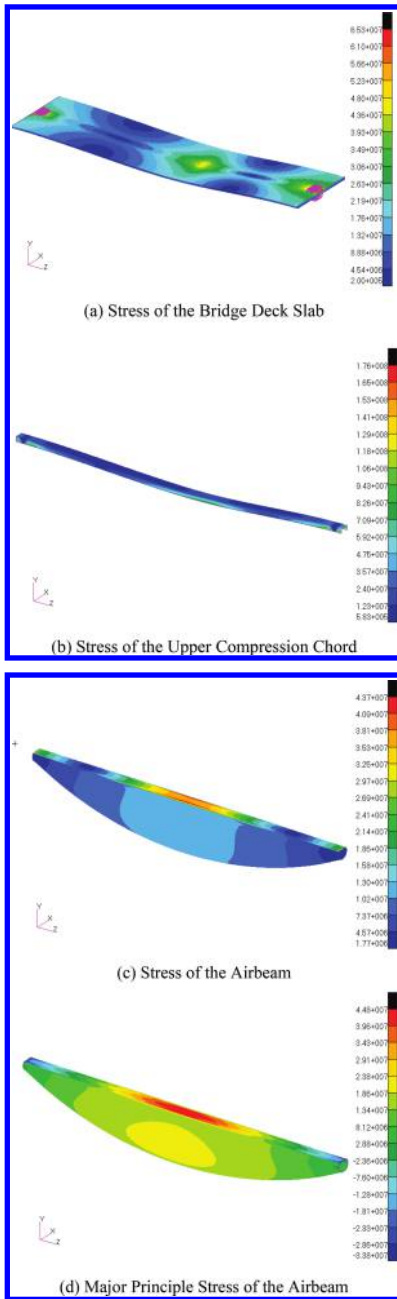


Figure 5. Stress of the Tensairity bridge section under the wheel type load.

of their contact area reaches the yield point. The maximum stress of the midspan of the bridge deck slab is 67 Mpa and the maximum stress of the upper compression chord is 158 Mpa, at the same time, the maximum displacement of the

structure is 3.3 centimeters and the other elements of the structure meet the material requirements and overall stiffness requirements. Therefore, the limit of load bearing capacity is mostly determined by the membrane materials of the airbeam and the limit can be promoted by improving the performance of the membrane materials.

#### 4 CONCLUSION

The Tensairity structure is an innovative expanded structure of the pneumatic membrane, which greatly increases the load bearing capacity of the pneumatic structure by adding lower cable and upper compression chord and at the same time effectively reduces the internal pressure, and therefore, overcomes the contradictions among the inner gas pressure, material strength and load bearing capacity of the pneumatic structure and provides a new means of applying the pneumatic structure. In this paper, we designed the Tensairity bridge section based on the principle of the Tensairity structure, and by employing the method of numerical simulation, analyzed the distortion and stress of the Tensairity bridge section subject to the typical wheel type load, and obtained the limits of load bearing capacity of the structure subject to the load, shown as follows:

1. Under the wheel type load, the maximum displacement of the Tensairity bridge section lies in the 4.4 meters of the direction of bridge span and the maximum stress lies in the 4.65 meters of the direction of bridge span.
2. The limits of load bearing capacity of the 1/2 Tensairity bridge section subject to the wheel type load is 127.6 KN, and the limit is mostly determined by the performance of the membrane materials.

#### REFERENCES

Cao Z.G., et al. Basic mechanical behavior of spindle Tensairity structures [J]. *China Civil Engineering Journal*, 2011, 44(1):11–18.

Cao Z.G., et al. Static experimental research and finite element analysis of Tensairity [J]. *Journal of building structures*, 2012, 33(5):31–37.

Luchsinger R.H., Crettol R. Experimental and Numerical Study of Spindle Shaped Tensairity Girders [J]. *International Journal of Space Structures*, 2006, 21(3):119–130.

Luchsinger R.H., et al. Light weight structures with Tensairity, in: Motro, R., ed., *Shell and Spatial Structures from Models to Realization*, Editions de l'Espèrou, Montpellier, 2004.

Luchsinger R.H., Sydow A., Crettol R. Structural behavior of asymmetric spindle-shaped Tensairity girders under bending loads [J]. *Thin-Walled Struct.* 2011, 49(9):1045–1053.

# Experimental research on the stability bearing capacity of Q420 high-strength steel tubular members

Buhui Li & Pingzhou Cao

*College of Civil and Transportation Engineering, Hohai University, Nanjing, China*

Dachang Zhang

*College of Civil Engineering, Nanjing University of Technology, Nanjing, China*

Tao Xu

*Jiangsu Electric Power Design Institute, Nanjing, China*

**ABSTRACT:** This paper presents a series of compression tests on steel tubular members fabricated from Q420 high-strength steel plates, to study the compression stability behavior and failure mechanism. The tests were performed over a range of member lengths. The overall geometric imperfections and the material properties were measured prior to the tests. The test specimens were placed between pinned ends and tested in a horizontal way. The Finite Element Analyses (FEA) were conducted to simulate their experimental behavior by using ANSYS, and the Shell elements were used to create the circular hollow sections. Moreover, the test stability coefficients were compared with the design coefficients predicted using different provisions, and the design guidance was also proposed for later use.

**Keywords:** Q420 high-strength steel; circular hollow section; stability bearing capacity; FEA; design guidance

## 1 INTRODUCTION

The steel circular hollow section, with closed cross section, has good integral rigidity, high bearing capacity, and relatively small drag coefficient. It can be designed without framing eccentricities, and is applied widely in engineering structures, such as grid structures, pipe trusses, steel towers and offshore platforms. Due to the development of the power grid and the promotion of loading criterion, increasing amounts of high-capacity, high-voltage and multi-loop transmission lines have been constructed. These impose higher loads on steel towers, both dead loads and wind loads. Q420 high-strength steel tubes have been applied in a large amount of transmission lines, including 500 kV,  $\pm 800$  kV and 1000 kV lines<sup>[1-2]</sup>.

Yang Mei et al.<sup>[3]</sup> adopted a modified CDC method to derive the overall stability coefficients of Q420 and Q460 high-strength steel tubes. Han J.ke et al.<sup>[4]</sup> raised the recommended diameter-to-thickness value of leg members of steel tubular tower, based on the research results of a typical 1000 kV double-circuit transmission tower. Yang Longyu et al.<sup>[5]</sup> performed compression tests on high-strength steel tubular members between pin

ends, with different steel materials and geometric dimensions. He also proposed the reduction methods of local stability strength and slenderness application scope of steel tubes. Gu Q. et al.<sup>[6]</sup> employed the elastoplastic beam-column theory and numerical integration to calculate the load-deflection curves of round and square steel tubes. Chen W.F. et al.<sup>[7]</sup> raised a simplified residual stress mode of circular steel tube, not considering the change of residual stress along the wall thickness. Pan et al.<sup>[8]</sup> used the hole drilling method to measure the residual stress distribution of a welded circular hollow steel section. Demao Yang et al.<sup>[9]</sup> carried out compression tests on high-strength box-shaped columns, and proposed improved column design of high-strength slender sections. Ben Yong et al.<sup>[10]</sup> conducted compression tests of stainless-steel tubular members, and compared test strengths with the design strengths using different codes. Rasmussen and Hancock<sup>[11]</sup> presented a test program comprising high-strength box and I-section specimens, including fix-ended stub columns and pin-ended long columns.

This paper describes a series of compression tests on Q420 steel tubular members. The test stability coefficients are compared with the design coefficients predicted by American, European, and

Chinese standards. Finally, the design recommendations are proposed on the basis of the theoretical research results.

## 2 EXPERIMENTAL INVESTIGATIONS

### 2.1 Test specimens

Due to the field investigation results of steel tubular towers and limited experimental conditions, the steel tubes with a specification of  $\Phi 377 \times 8$  were selected as test specimens. The steel was classified as Q420 to the Chinese standards GB50017<sup>[12]</sup>. The specimens are cold-formed from flat steel sheets and seam-welded with a longitudinal full penetration weld. In order to investigate the influence of the slenderness ratio on compression stability behavior, the slenderness of 30, 40, 50, 60, 80, 100 was chosen for specimens, with three specimens in each group, i.e. 18 specimens in total. Besides, the tensile coupon tests were performed with standard specimens extracted from steel plates used in specimen fabrication and steel tubes used for the test, respectively. The material properties are listed in Table 1. Initial overall geometric imperfections of the specimens were measured, as well as the geometric imperfections along the longitudinal welds. The maximum overall flexural imperfection at mid-length of steel tubes was  $l/1400$ , where  $l$  is the length of the specimen.

### 2.2 Test set-up and procedure

As depicted in Figure 1, the concentric compression was applied horizontally as the effect of self-weight was negligible. Two 6000 kN spherical hinges, with the outer diameter of 450 mm and the total height of 120 mm, were placed at both ends. The square end plates were 500 mm wide to confirm full contact with the hinges and enough local rigidity. A 5000 kN hydraulic jack was employed to apply monotonic

Table 1. Actual material properties of Q420 steel.

Plate shape	Yield stress (MPa)	Ultimate stress (MPa)	Elastic modulus (MPa)
Flat	439.4	500.2	$2.1 \times 10^5$
Rolled	432.6	505.6	$2.1 \times 10^5$

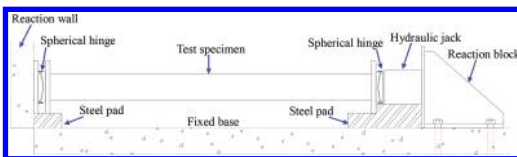


Figure 1. Compression test set-up.

central loading in one side, with the reaction blocks connecting fixed base using anchor bolts, and the other side was set to contact with the reaction wall.

The compression tests were conducted by applying multi-stage loading, and each load step was held for 1–2 minutes. Prior to the tests, a theodolite was used to ensure that the tubular member was loaded in the center, and electrical strain gauges and displacement transducers were arranged at the typical positions of the test specimens. The strain gauge dimension was  $10.0 \text{ mm} \times 4.0 \text{ mm}$ , with a maximum ultimate strain of 2%–3%.

As illustrated in Figure 2, the strain gauges were mounted on three cross-sections of test members, i.e. mid-section and other two sections with one-eighth lengths from the mid-section. Four displacement meters, with a measuring range of  $\pm 100 \text{ mm}$ , were placed at four corners of the end plate to measure the axial shortening and rotation of the bearing plate during the loading process. At the regular interval, a data acquisition system, named DH3816, was adopted to record the readings of strains and displacements.

### 2.3 Test results

In the early stage of loading, the test members remained elastic, and no obvious deformation was observed. The strain and displacement developed approximately linearly. With the increasing compression, the strains at typical positions bifurcated gradually. When reaching the ultimate bearing capacity, the strains descended immediately, and the axial shortening increased rapidly. Meanwhile, the overall flexural deformation and local buckling developed rapidly.

The failure modes of the test specimens with series slenderness ratios are shown in Figure 3. The experimental failure modes were generally in agreement with the ideal ones. The failure mode of test tubular members was a mixture of overall flexural buckling and local stability. In general, for the test specimen with a slenderness ratio of 30 and 40, the local buckling was more obvious, as shown in Figure 3. For the test specimen with a slenderness more than 50, the overall flexural deformation was

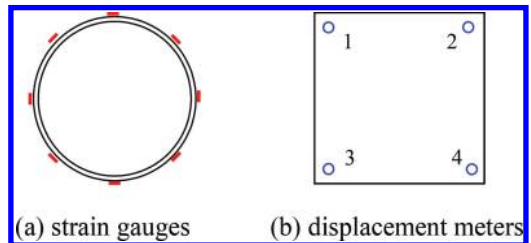


Figure 2. Arrangement of measuring points.

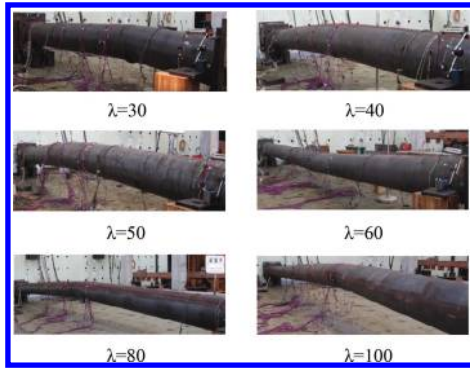


Figure 3. Overall flexural buckling of the specimens.

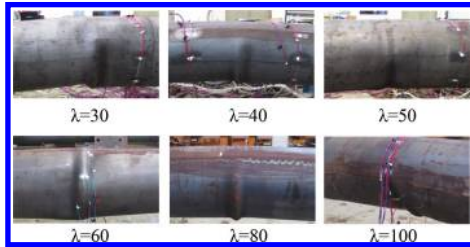


Figure 4. Local buckling of the specimens.

more obvious, as depicted in Figure 4. As the steel circular hollow section has numerous symmetric axes, the specimens bent freely, just as predicted beforehand. Relative rotation of the end plate was also observed in the test process.

### 3 FINITE ELEMENT ANALYSES

Following the completion of the experimental tests, a nonlinear finite element model was developed using ANSYS, and a four-node Shell181 element was selected to simulate the steel tubes. The Young's modulus was  $2.1 \times 10^5$  MPa, and the Poisson ratio was taken as 0.3. The steel material was modeled by an ideal elastoplastic tri-linear model with actual properties, and the tangent modulus was taken as  $0.1 E$  in the post yield range to ultimate strength, as shown in Figure 5. The end plates were created with Solid45 elements, and their MOE were set as  $2 \times 10^8$  MPa to increase the local stiffness and reduce the local stress concentration in the bearings.

For eigen buckling analyses, the corresponding mode shape was obtained by adopting the Block Lanczos eigenvalue extraction method. Then, the imperfect model was created by adding  $l/1400$  overall flexural deformation, and the residual stress was also taken account. Uniaxial compression forces were

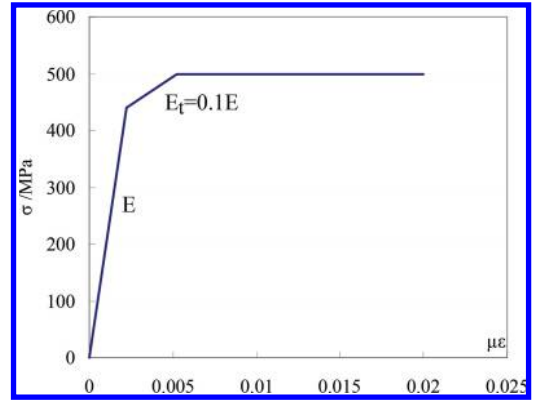


Figure 5. Tri-linear model of Q420 high-strength steel.

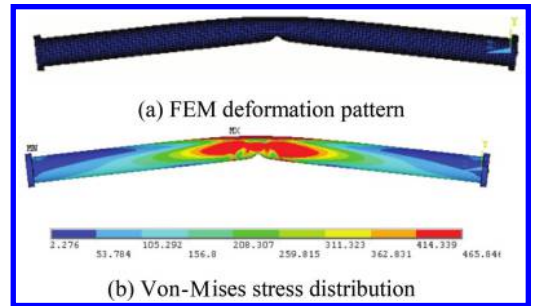


Figure 6. Failure pattern and stress distribution.

Table 2. Limited values of  $d/t$  of steel tubular members.

Design standard	Limited values of $d/t$	
AISC 360-05	$0.11E/f_y$	55.0
BS 5950	$94(235/f_y)$	52.6
ASCE 48-11	$26220/f_y$	62.4
GB 50017	$100(235/f_y)$	55.9
Eurocode 3	$90(235/f_y)$	50.4

applied on the analytical models and a large deformation option was activated. The arc-length method in conjunction with the modified Newton Raphson method is used to accelerate the numerical solution convergence. The model deformation and von Mises stress distribution are depicted in Figure 6.

### 4 THEORETICAL ANALYSES

#### 4.1 Local stability

For compression members, local buckling can not occur before overall stability, i.e. the critical stress of local stability shall be more than that of overall

Table 3. Comparisons of overall stability coefficients.

$d$	$t$	$\lambda$	$\varphi_{\text{exp}}$	$\varphi_{\text{FEA}}$	$\varphi_{\text{exp}}/\varphi_{\text{FEA}}$	GB50017		AISC 360-05 <sup>[13]</sup>	BS EN 1993-1 <sup>[14]</sup>	ASCE 48-11 <sup>[15]</sup>
						$\varphi_a$	$\varphi_b$	$\varphi_{\text{AISC}}$	$\varphi_{\text{BS}}$	$\varphi_{\text{ASCE}}$
377	8	30	0.908	0.924	0.983	0.939	0.895	0.921	0.874	0.951
		40	0.844	0.858	0.984	0.9	0.833	0.864	0.791	0.913
		50	0.795	0.809	0.983	0.849	0.763	0.796	0.701	0.864
		60	0.76	0.738	1.030	0.77	0.675	0.72	0.609	0.804
		80	0.641	0.686	0.934	0.57	0.499	0.558	0.443	0.651
		100	0.501	0.484	1.035	0.397	0.357	0.402	0.322	0.459

stability. In order to meet this stipulation, a limited value of the diameter-to-thickness ratio ( $d/t$ ) is provided in different codes. Table 2 summarizes the limited values of  $d/t$  according to the design standards, with the nominal yield stress, where  $f_y$  is 420 N/mm<sup>2</sup>. The  $d/t$  value of the test specimens was 47.1, which was less than the limited values given in the table.

#### 4.2 Overall stability

Under the axial compression  $P$ , the equilibrium equation of an ideal member with both ends pin supported could be established, based on the small flexural deformation theory. The value of  $y'$  can be taken as 0 due to the small deformation condition, and expression (1) can be obtained. The deformed member presents a half sinusoidal curve shape, and the curvilinear equation can be defined as  $y = A \sin \pi x / l$ . Then, the critical force can be expressed as  $P_{cr} = \pi^2 EI / l^2$ , where  $E$  is the modulus of elasticity and  $l$  is the length of the tubular member:

$$EIy'' + Py = 0 \quad (1)$$

However, various defects exist in the actual compression member inevitably, and member presents flexural deflection even under a small load. The concept of the overall stability coefficient  $\varphi$  was put forward in current design codes, and  $\varphi$  is the ratio of overall critical stress  $\sigma_{cr}$  to design stress  $f$ .

#### 4.3 Comparative analyses

As to the welded tubular member, the residual stress usually generates in the fabrication procedures, such as cold-forming and welding. For the steel tubes with the same geometric dimension, the distributions of residual stresses are similar. On this basis, one can suggest that the effect of residual stresses is less detrimental to the strength of the high-strength steel column than that of the ordinary steel column. For the welded circular steel section investigated here, GB 50017 terms it as the

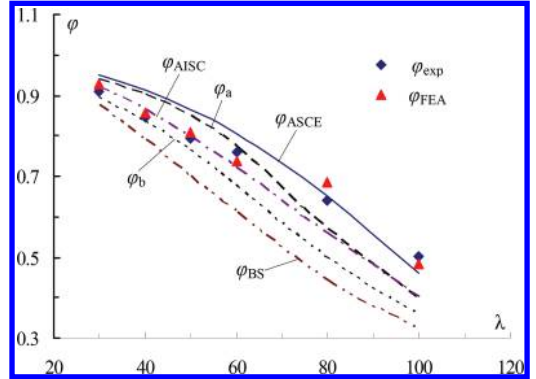


Figure 7. Comparisons of overall stability coefficients.

b-type section, while other standards do not provide the detail classifications.

The calculated overall stability coefficients calculated from test strengths, simulated strengths and predicted strengths using different design standards are summarized together in Table 3. Meanwhile, the calculated stability coefficients were plotted against the slenderness ratio ( $\lambda$ ), as illustrated in Figure 7. It is obvious that the ASCE standard provides the maximum stability coefficient, while BS offers the minimum values, with the error more than 8%. The test strengths agree well with that obtained from the FEA results, with the ratios ranging from 0.983 to 1.035. For the test specimen with the slenderness ratio more than 60, the stability bearing capacity can be calculated according to AISC 360-05 and GB 50017 (class a section). For the test specimen with the slenderness less than 50, the stability strength can be computed as per GB 50017 (class b section) and BS EN 1993-1.

## 5 CONCLUSIONS

A series of compression tests are performed on Q420 high-strength steel tubular members with



both ends pin supported. Meanwhile, the finite element program, ANSYS, is used to simulate the experimental behavior. Finally, the test stability coefficients are compared with that predicted by different standards. It can be concluded as follows:

1. The failure modes of the test specimens mainly exhibit an extremum behavior, together with obvious local buckling, which shows a similar trend with the analytical results. The failure mode of test tubular members was a mixture of overall flexural buckling and local stability.
2. The test strengths agree well with that obtained from the analytical results, with the ratios ranging from 0.983 to 1.035. Therefore, ANSYS can be used widely to simulate the tubular members with different sizes, which the tests do not cover.
3. Among the design standards, BS code gives the conservative predictions, and ASCE is proved to be not conservative, with the error more than 8%.
4. For Q420 high-strength steel tubular members with the slenderness ratios more than 60, the stability strengths can be calculated according to AISC or GB 50017 (class a section). For the test specimen with the slenderness less than 50, the strengths can be computed as per GB 50017 (class b section) or BS EN 1993-1.

## REFERENCES

- [1] He C.H. 2004. Feasibility discussion on application of high-strength cold-formed section steel in transmission tower. *Steel Structure* 19(74): 35–37.
- [2] Guo Y., Shen J.G., Ying J.G. 2012. Stability analysis on the multiple angle members of transmission towers. *Steel Structure* 27(155): 11–16.
- [3] Yang M., Li Z.L., Liu H.J. 2011. Test research on ultimate bearing capacity of high strength steel tubes. *Sichuan Architecture* 31(6): 144–147.
- [4] Han J.K., Yang J.B., Yang F.L., Li F. 2009. Value selection of slenderness ratio and diameter-thickness ratio of steel tube for 1000 kV transmission steel tubular tower legs. *Power System Technology* 33(19): 17–20.
- [5] Yang L.Y., Li Z.L., Wei L., Kang D.C. et al. 2010. An investigation of high strength steel tube's ultimate load capacity under axial compression. *J. Xi' Univ. of Arch. & Tech. (Natural Science Edition)* 42(2): 201–204.
- [6] Gu Qiang, Jiang H.Y., Gao X.Y. 2005. Brittle buckling of cold-formed welded steel tube struts under axial load. *Journal of Building Structures* 26(4): 76–80.
- [7] Chen W.F., Ross David A. 1977. Test of fabricated tubular columns. *Journal of the Structural Division* 103(3): 619–634.
- [8] Pan Hanming, Liang S., Pei S.X., Liang W.S., Wang L.W. 2006. Stability analysis of large-size thin-walled tubes members subjected to axial force. *Steel Construction* 21(87): 5–8.
- [9] Demao Yang, Gregory J. Hancock; Kim J.R. Rasmussen. 2004. Compression tests of cold-reduced high strength steel sections. II: Long Columns. *Journal of structural engineering* 130: 1782–1789.
- [10] Ben Young, Wibisono Hartono, M. ASCE. 2002. Compression tests of stainless steel tubular members. *Journal of structural engineering* 128: 754–761.
- [11] K.J.R. Rasmussen, G.J. Hancock. 1995. Tests of high strength steel columns. *J. Construct. Steel Research* 34: 27–52.
- [12] GB 50017-2003. Code for design of steel structures. Beijing, 2003.
- [13] ANSI/AISC 360-05. An American National Standard Specification for Structural Steel Buildings. Chicago, 2005.
- [14] BS EN 1993-1-1. Euro-Code 3: Design of Steel Structures. British standard, 2005.
- [15] ASCE/SEI 48-11. Design of steel transmission pole structures. ASCE standard, 2011.

# Analysis of the slope pre-stressed anchoring effect on Xiaowan Hydropower Station

Y.H. Jiang

*China Institute of Water Resources and Hydropower Research, Beijing, China*

*State Key Laboratory of Simulation and Regulation of Water Cycle in River Basin, Beijing, China*

G.L. Long

*HydroChina Kunming Engineering Corporation, Kunming, China*

Z. Fan & Z.C. Lu

*China Institute of Water Resources and Hydropower Research, Beijing, China*

*State Key Laboratory of Simulation and Regulation of Water Cycle in River Basin, Beijing, China*

**ABSTRACT:** The slope of the Xiaowan Hydropower Station slope is huge, complex, high, and steep, with a maximum excavation height of nearly 700 m. The structural plane of rock mass along the river is developed and unloads strongly, but the deposit slope has a wide distribution and is unstable. A large number of pre-stressed anchors, anchor bolts, and other measures have been adopted in the slope reinforcement design to improve the safety factor and the slope stability. The pre-stressed anchoring effect is analyzed by studying the monitoring results of slope pre-stressed anchoring. The analysis result provides a scientific basis for slope reinforcement design, construction, and stability evaluation.

**Keywords:** pre-stressed; anchoring effect; anchor load cell

## 1 BRIEF INTRODUCTION TO THE XIAOWAN HYDROPOWER STATION SLOPE ANCHORING PROJECT

Xiaowan Hydropower Station is located in a high-intensity earthquake area with narrow terrain, steep slope, and closely packed buildings. The main projects have mass open excavation and are focused within the range of approximately 3 km<sup>2</sup>. Open excavation forms a 700 m-high slope. The stability of such a high slope is one key technological issue in project construction.

A natural slope in the main slope zone is about 42°. Based on its lithological characteristics, the slope consists of biotite granitic gneiss and amphibole plagioclase gneiss. The rock shows a monoclinic structure, transverse distribution, and steep upstream slope that stretches along the river direction and cuts off crack growth along the slope angle. The Yinshuigou accumulation and the Dachunshu ditch accumulation distributed before the dam on each side of the river. They have a significant impact on engineering owing to their deep-seated coverage and complicated composition natures. The diverse of this rock slope failure have typical slope type reservoir features, and the complicated slope excavation body makes construction more difficult.

Given the complicated geological conditions of excavation slopes, the engineering design adopts a multitude of pre-stressed anchor and supporting measures—about more than 10,000—to meet the stability requirements of slope excavation during construction and operation.

## 2 TEST OF SLOPE ANCHORING PRODUCTION

Slope anchorage of the Xiaowan Hydropower Station is a key construction project with a limited construction period, heavy construction work, and difficult hole-forming. Two test areas were selected from the left and right river banks for anchoring site production testing prior to the start of the project to determine the anchoring materials and construction techniques that meet the project requirement, optimize the design parameters, investigate the construction approach, monitor the accelerating construction progress, and accumulate experience for the large-scale construction. The process included 1) testing the match of the grout in the anchoring segment with the concrete in the outer anchor head, the cement-proof ring, and the material's mechanical properties; 2) measuring pre-stressed

anchoring load and load loss law; 3) testing the stress distribution law of pre-stressed strand in the anchoring and free segments; 4) analyzing the effect of the anchor group by testing the rock deformation law and the influencing range of anchoring tension; and 5) testing the real stretching range of the pre-stressed strand during the tension of each anchoring strand in the right bank after the project started in order to solve rock weathering and the accumulation of anchoring devices, the hole-making method, and the blocking and grouting technique.

### 3 ANALYSIS OF SLOPE ANCHORING STABILITY

#### 3.1 Main monitoring result of slope pre-stressed anchoring

Xiaowan Hydropower Station mainly uses common tension-type anchors as reinforcement

for 1000, 1800, and 3000 KN designed loads. According to monitoring technical requirements, about 3% of pre-stressed anchors are selected based on load level to arrange load cells in vary locations, observe pre-stressed anchoring load and its changes, as well as realize pre-stressed anchoring effect on slope rock and long-term work requirement for safety forecast during construction. The load cell is BGK4900 produced by Geokon Instruments (Beijing) Co., Ltd. Table 1 shows the main technical index of the anchoring load cell.

Excavation of the Xiaowan Hydropower Station slope started in February 2002. By December 2004, slope excavation of more than elevation 1000 m was basically completed. About 10,000 pre-stressed anchors were used on the slope. By the end of December the following year, 285 anchor load cells were installed. Table 2 shows the statistics of pre-stressed anchor monitoring of all the location.

Table 1. Main technical index of the BGK4900 anchor load cell.

	Range (KN)	Over range tension (% FS)	Resolution (% FS)	Accuracy (% FS)
Technical Index	1000 ~10,000	150	±0.025	±0.25 ~±0.5

Table 2. Statistics of pre-stressed anchor monitoring result.

Locations	Tensile load/design load	Locked load/design load	Observation value/design load	Mean locked loss (%)	Mean later loss (%)	Loss range (%)
Slope at the right bank above 1,365 m	1.07	0.97	0.94	9.72	3.22	-9.5~9.2
Slope at the right bank between 1245 m to 1365 m	1.09	1.00	0.95	8.02	4.76	-8.4~12.3
Intake slope at the right bank	1.08	1.003	1.048	7.15	-3.74	-18.3~7.1
Slope at the upstream of the right bank abutment slot	1.09	0.997	0.965	9.03	2.03	-3.3~4.6
Slope at the downstream of the right bank abutment slot	1.12	1.039	0.99	7.27	5.03	2.7~7.4
Slope at the right bank of plunge pool	1.13	1.019	0.969	8.83	4.89	3.6~6.3
Slope at the right bank of tailwater tunnel	1.12	1.027	0.965	8.23	6.11	-0.1~9.0
Slope at the No.4 ridge above 1,380 m	1.18	1.09	1.039	7.73	5.73	2.4~6.0
Slope at the No.4 ridge between 1245 m to 1380 m	1.06	0.995	0.952	6.39	4.87	1.9~16.2
Slope at the left bank of plunge pool	1.11	1.022	0.984	7.53	3.75	0.8~7.8
Slope at the upstream of the left bank abutment slot	1.14	1.06	1.018	6.85	4.25	2.3~7.2
Intake slope of spillway tunnel at the left bank	1.12	1.045	1.004	6.59	3.96	1.6~7.0
High telpher base at the left bank	1.16	1.082	1.051	6.62	2.92	0.3~6.0
Low telpher base at the left bank	1.14	1.057	1.038	7.35	1.75	1.4~2.1
High telpher base at the right bank	1.05	0.967	0.928	7.43	3.97	0~12.4
Low telpher base at the right bank	1.05	0.972	0.94	6.95	3.27	1.3~4.9
Dachushu ditch accumulation slope	1.01	0.942	0.896	6.28	4.30	-19.6~11.9
Yinshuigou accumulation slope	0.995	0.933	0.898	6.34	-1.19	-115.7~24.8

### 3.2 Analysis and evaluation of slope pre-stressed anchoring effect

#### 3.2.1 Prestress loss

For anchoring prestress of the rock slope, the average locked later loss, average loss, and total loss were 6.31%, 3.55%, and 11.16%, respectively. For anchoring prestress of the homogenous slope, figures for such losses were 7.61%, 1.56%, and 9.17%, respectively.

#### 3.2.2 Anchoring load

The ratio of average anchoring load of the rock slope and that of the designed load was 0.986, which was 1.4% lower than the designed load. The ratio of average anchoring load of the homogeneous slope and that of the designed load was 0.897, 10.3% lower than the designed load.

#### 3.2.3 Dynamic change laws of anchoring load

The dynamic change laws of the anchoring load can be summarized as follows:

1. Anchoring load declines slowly and tends toward stability, showing that the pre-stressed anchor is normal and that the slope where the anchor is located deforms slightly.
2. Anchoring load increases due to the occurrence in slopes of certain deformations, such as Yinshuigou accumulation slope and intake slope of the power station. Slope deformation causes anchoring load increasing, which reflects the inhibition of pre-stressed anchor on slope deformation.
3. Anchoring load fluctuates in anchors positioned around those with larger environmental changes, thereby reflecting the impact of environment on slope deformation.
4. Anchoring load suddenly reduces in anchors that are placed in Yinshuigou accumulation slopes. After the anchoring load is locked and unloaded, the load does not increase, but instead continues to decrease because of slope deformation. This finding indicates that rocks in the anchoring section are very complicated.

## 4 ROLE OF PRE-STRESSED ANCHORING MONITORING RESULT IN WARNING AND FORECASTING SLOPE STABILITY

After the pre-stressed anchoring tension is locked, the changes in its load can intuitively reflect the work status of pre-stressed anchor as well as the practical conditions and work features of the slope. In the slope anchoring construction of Xiaowan Hydropower Station, monitoring results of the pre-stressed anchor was fully used for warning and forecasting.

### 4.1 Intake slope forecast

In the intake slope of the station, the height of slope excavation was 106 m below EL. 1245 m, whereas vertical excavation was conducted below EL. 1220 m in the front slope. Vertical slope was 81 m in height. Given the complicated geological conditions, the excavation started from EL. 1245 m in September 2003. The load in the anchor load cell of the intake front slope continued to increase in different degrees on October 15, 2004; by October 26, a crack had appeared between the front slope and the abutment slot slope. The No. 1 intake and the rock pillar were blasted on February 4, 2004. The No.1 to No. 4 slots were dug at EL. 1150 m on December 10. In December 14–19, 2004. The No. 1 to No. 4 slots in the intake front slope were dug up to 1150 m to 1145 m. Load unloading for the slope excavation and maintaining the rock pillar failed, loads of partial anchor load cells in the front slope showed an accelerated increase in different degrees, such that fine cracks occurred in the slope above EL. 1220 m. On December 11, the load rate of the C2B-3IV-PR-32 anchor was up to 26.5 KN/d; on December 12, the supporting

Table 3. Typical load rate statistics of the anchor load cell of the intake slope.

Point no.	Dec. 6– Dec. 13	Dec. 19– Dec. 26	Dec. 26– Jan. 3	Jan. 3– Dec. 31 (next year)
C2B-3IV- PR-03	2.84	2.50	1.80	0.11
C2B-3IV- PR-08	8.42	3.48	3.53	0.10
C2B-3IV- PR-11	9.49	3.92	4.2	0.18
C2B-3IV- PR-32	19.29	5.01	5.19	0.18

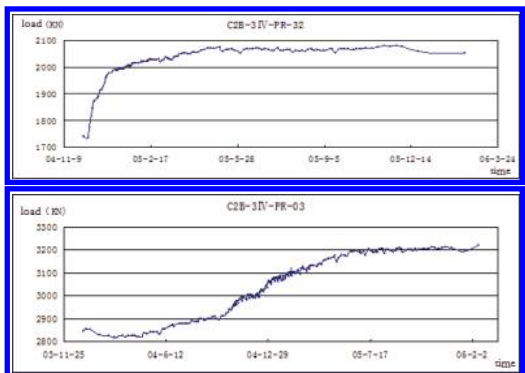


Figure 1. Typical load–time curve of the anchor load cell.

Table 4. Load rate statistics of the C2A-III-PR-04 dynamometer (Unit: KN/d).

	Nov. 25– Dec. 2	Dec. 2– Dec. 16	Dec. 16– Dec. 9	Jan. 9– Jan. 29	Jan. 29– Feb. 29	Feb. 29– Mar. 15	Mar. 15– Apr. 5
Load rate	-1.18	0.71	2.04	5.49	3.47	2.62	0.74

construction above EL. 1162 m in the intake front slope had been completed. The deformation rate of most monitoring points above EL. 1180 m had slowed, but the rates of monitoring points below 1180 m elevation were still high. The load rate of the C2B-3IV-PR-32 anchor (1171 m in elevation) was up to 5.19 KN/d. Anchoring load was high at 1.10 times the designed load, and deformation rate at this location was also higher. With the completion of the intake slope support and the gradual pouring of the intake tower, intake slope deformation gradually stabilized starting in 2005. Table 3 shows the slope of this location, and Figure 1 shows the typical load–time curve of the anchor load cell.

#### 4.2 Forecast of the Yinshuigou accumulation slope

The Yinshuigou accumulation slope was excavated in the early part of the year 2002. When slope excavation reached the elevation 1276 m on December 14, 2003, displacements at many monitoring points suddenly improved. Moreover, loads in the C2 A-III-PR-04 anchor load cell arranged on the high road at elevation 1389 m increased. A rechecking was followed by explanations to the related parties on December 17. Intensive observations made afterwards for the slope of this location showed that the changes in anchoring load increased after the rain on January 9, 2004, and that the changes showed accelerated development until January 29. Slope stability forecasting was raised again by combining the apparent phenomenon and the inner monitoring result. Real-time monitoring conducted mainly for the changes in anchoring load found that the monitoring load was 1350.0 KN at 1630 h of April 5, within the designed load limitation. Anchoring load was reduced to 1321.8 KN at 2130 h after which the anchor was observed continuously. The anchoring load then reduced to 1122.3 KN and tended to stabilize at 0730 h of April 6. At 2200 h of April 10, the anchoring load was 1120.2 KN, but suddenly changed to 363.4 KN at 0830 h of April 12 and became 363.7 KN at 0400 h. The anchor head was pulled out on April 14 because the anchor was a complete failure. Table 4 shows the load rate statistics of the C2 A-III-PR-04 anchor load cell. Figure 2 refers to the load–time process curve.

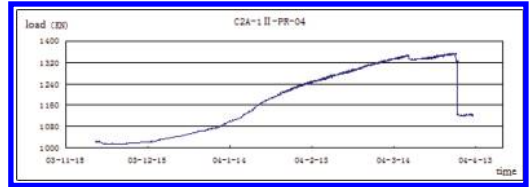


Figure 2. Typical load–time curve of the anchor load cell.

## 5 CONCLUSION

1. The greatest excavation height at Xiaowan Hydropower Station is close to 700 m. Numerous pre-stressed anchors were used to reinforce the support for engineering design. Monitoring the slope pre-stressed anchoring plays a very important role in realizing the anchoring effect of pre-stressed anchor on slope rock and its long-term working status, adjusting and optimizing reinforcement parameters, organizing constructions, and accelerating the construction process to ensure engineering safety during the construction period.
2. The monitoring results of pre-stressed anchor in the slope show that the average locked loss of prestress is 6.31%, the average later loss is 3.55%, and the total loss is 11.16%. Anchoring load basically reaches the design requirements.
3. The changes in pre-stressed anchoring load and other monitoring data show that the changes in slope pre-stressed anchoring load meet the practical conditions of all slopes and the specific working features. Slopes are generally stable except for a certain deformation in local slopes.
4. After the pre-stressed anchoring tension is locked, the changes in its load show the work status of pre-stressed anchor as well as the real conditions and work feature of the slope in this location. The Xiaowan Hydropower Station anchoring project made a creative exploration in warning and forecasting slope stability by means of pre-stressed anchor monitoring results. It also provided valuable experience for analysis and evaluation of slope stability of similar engineering projects.

## ACKNOWLEDGMENTS

This study was financially supported by the National Basic Research Program of China (973 Program 2013CB036406, 2013CB032904, 2013CB035903, 2013CB035904), the Twelfth-five Science and Technology Support Project (2013BAB06B02, SQ2013BAJY4138B02), China Institute of Water Resources and Hydropower Research (1361, 1353), and the Basin Water Cycle Simulation and Regulation of the State Key Laboratory Special Research Foundation.

## REFERENCES

- [1] Liu Wei, Wang Ya-bin, Xue Zhong. Experimental Study on Stress Distribution in Bond Body of Pre-stressed Anchor Rope of Xiaowan Hydropower Station[J]. Construction Technology. 2006(11), Vol 35 No 11, p12–p29.
- [2] Ma yong-jun, Cun Jin-peng. Introduction of pre-stress anchor grouting test in No 6 ridge of Xiaowan Hydropower station[J]. Yunnan Water Power, 2010(5), Vol 26, No 5, p30–p31.
- [3] Zhang De-sheng, Pan Yong, Lin Ge. Xiaowan Hydropower Station Slope pre-stressed anchor Construction[J]. Railway Engineering. 2009(2), p71–p73.
- [4] Zhu Chun-liang, Wei Jun-shan. The Pre-stressed anchoring cable application in reinforcing high slope[J]. ShanXi Architecture. 2009(6), Vol 35, No 16, p119–p120.
- [5] Xue Zhong, Guo Wan-li. Discussions on the construction of pre-stressed anchorage cable for Xiaowan Hydropower Station under unfavorable geological conditions[J]. Water Power. 2004(10), Vol 30, No 10, p50–p60.

## Study on mode II fracture initiation using the strain energy density criterion

W. Gao, S.N. Wang & Y. Su

*School of Aeronautics, Northwestern Polytechnical University, Xi'an, China*

**ABSTRACT:** The Brazilian disc specimen and the semi-circular bend specimen have been used by many researchers to study mode I, mode II and mixed mode I–II brittle fracture in different materials. However, the mode II fracture toughness obtained experimentally in the past from these two specimens show large inconsistencies compared with the theoretical predictions. In this paper, a modified strain energy density criterion is used to study the effect of  $T$ -stress on the fracture initiation angle and the fracture toughness ratio  $K_{IIc}/K_{Ic}$ , then the theoretical predictions are compared with the relevant published experimental results obtained from fracture tests on the Brazilian disc specimen and the semi-circular bend specimen. A very good agreement is shown between the predicted results and the experimental results.

**Keywords:** brittle fracture; strain energy density criterion; mode II fracture;  $T$ -stress

### 1 INTRODUCTION

Brittle fracture is a major mode of failure in components and structures containing cracks. According to the classic fracture model, for mode II loading condition, the crack propagates if the mode II stress intensity factor  $K_{II}$  reaches its critical value (or mode II fracture toughness,  $K_{IIc}$ ). Therefore, it is important to develop appropriate theoretical and experimental methods for determining mode II fracture toughness  $K_{IIc}$  in brittle materials.

In the past years, many different test specimens have been designed for determining  $K_{IIc}$  for various engineering materials (Erdogan & Sih 1963, Ueda et al. 1983, Awaji & Sato 1978, Chong & Kurrupu 1984). Among those testing specimens the Brazilian Disc (BD) specimen and the semi-circular specimen under three-point bending (SCB) are two of the most favorite specimens for fracture tests in brittle material. Mode I, Mode II and mixed mode I/II could be provided easily for each of these two specimens by setting the crack line in an appropriate angle relative to the loading direction and the test procedures in both the BD specimen and SCB specimen are easy and cost effective.

In addition to the experimental techniques mentioned above for obtaining the fracture toughness of engineering materials, there are several theoretical criteria for predicting mixed mode I/II in cracked bodies. The Maximum Tangential Stress (MTS) criterion (Erdogan & Sih 1963), the Maximum Energy Release Rate (MERR) (Hussain et al. 1963) and the minimum Strain Energy Density criterion (SED) (Sih 1974) are three most

important criteria for brittle fracture under mixed mode loading condition. Among these criteria, the minimum strain energy density criteria has been found to be a powerful tool to predict the fracture and fatigue behavior of cracked and notched components (Sih & Ho 1991, Nobile et al. 2004, Sih & Tang 2005, Berto & Lazzarin 2009). Theoretical predictions based on this criterion suggest that the ratio of mode II fracture toughness  $K_{IIc}$  over mode I fracture toughness  $K_{Ic}$  is a fixed value just depends on the Poisson's ratio  $\nu$ . For example, for  $\nu = 0.3$ , the value of  $K_{IIc}/K_{Ic}$  predicted by the SED criterion is 0.96 and for  $\nu = 0.2$ , the value is 1.07. However, there are many experimental investigations reporting a ratio of  $K_{IIc}/K_{Ic}$  significantly higher or lower than the fixed value. A review of the related papers shows that depending on the tested material and the specimen geometry, the value of  $K_{IIc}/K_{Ic}$  varies typically from 0.42 to 2.2 (Lim et al. 1994a, b, Khan & Al-Shayea 2000, Ayatollahi et al. 2006, Awaji & Sato 1987). Such inconsistencies between the theoretical and experimental results restrict the validity of fracture criteria like the conventional SED criteria to limited geometry and loading conditions. There have been some attempts to justify such large inconsistencies. Liu et al. (1998) suggested that possible formation of shear banding in front of the crack tip prior to the initiation of fracture can be the reason of  $K_{IIc}$  in the epoxy resin being much higher than  $K_{Ic}$ . However, they could provide only a qualitative interpretation of test results.

In this paper, a modified SED criterion is used for predicting brittle fracture in mode II loading.

The modified SED criterion takes into account the effect of non-singular stress term ( $T$ -stress) in addition to the singular stress term. Then, the theoretical predictions calculated from the modified SED criterion are verified by using some experimental results obtained from mode II fracture tests on the BD specimen and SCB specimen in the past.

## 2 MODIFIED MINIMUM STRAIN ENERGY DENSITY CRITERION

Elastic stress field around the crack tip in linear elastic homogeneous and isotropic material for I/II mixed loading can be written as (Williams 1957):

$$\sigma_{xx} = \frac{1}{\sqrt{2\pi r}} \left( K_I \left( \frac{3}{4} \cos \frac{\theta}{2} + \frac{1}{4} \cos \frac{5\theta}{2} \right) - K_{II} \left( \frac{7}{4} \sin \frac{\theta}{2} + \frac{1}{4} \sin \frac{5\theta}{2} \right) \right) + T + O(r^{1/2}) \quad (1.a)$$

$$\sigma_{yy} = \frac{1}{\sqrt{2\pi r}} \left( K_I \left( \frac{5}{4} \cos \frac{\theta}{2} - \frac{1}{4} \cos \frac{5\theta}{2} \right) + K_{II} \left( -\frac{1}{4} \sin \frac{\theta}{2} + \frac{1}{4} \sin \frac{5\theta}{2} \right) \right) + O(r^{1/2}) \quad (1.b)$$

$$\tau_{xy} = \frac{1}{\sqrt{2\pi r}} \left( K_I \left( -\frac{1}{4} \sin \frac{\theta}{2} + \frac{1}{4} \sin \frac{5\theta}{2} \right) + K_{II} \left( \frac{3}{4} \cos \frac{\theta}{2} + \frac{1}{4} \cos \frac{5\theta}{2} \right) \right) + O(r^{1/2}) \quad (1.c)$$

$$\sigma_{zz} = \begin{cases} 0 & \text{for plane stress} \\ \nu(\sigma_{xx} + \sigma_{yy}) & \text{for plane strain} \end{cases} \quad (1.d)$$

where  $r$  and  $\theta$  are the polar coordinates with the origin located at the crack tip,  $K_I$  and  $K_{II}$  are the mode I and mode II intensity factors respectively,  $\nu$  is the Poisson's ratio,  $\sigma_{xx}$ ,  $\sigma_{yy}$ , and  $\sigma_{zz}$ , are the stress in the Cartesian coordinates. The first term in each stress component is singular and the second term  $T$ , is constant and independent of the distance  $r$  from the crack tip. The higher order terms  $O(r^{1/2})$  are often negligible at location very close to the crack tip.

The SED criterion, formulated by Sih (1974), states that the onset of brittle fracture takes place when the strain energy density factor  $S$  at a constant distance  $r_c$  around the crack tip reaches a critical value  $S_c$  and the direction of crack initiation angle  $\theta_0$  coincides with the direction of minimum strain energy density. In mathematical form, the SED criterion can be written as:

$$\left. \frac{\partial S}{\partial \theta} \right|_{\theta=\theta_0} = 0, \quad \frac{\partial^2 S}{\partial \theta^2} > 0 \quad (2)$$

where  $S$  is the strain density factor, defined as:

$$S = r_c \frac{dW}{dV} \quad (3)$$

$$\begin{aligned} \frac{dW}{dV} &= \frac{1}{2E} (\sigma_{xx}^2 + \sigma_{yy}^2 + \sigma_{zz}^2) \\ &\quad - \frac{\nu}{E} (\sigma_{xx}\sigma_{yy} + \sigma_{xx}\sigma_{zz} + \sigma_{yy}\sigma_{zz}) \\ &\quad + \frac{1+\nu}{E} (\tau_{xy}^2 + \tau_{xz}^2 + \tau_{yz}^2) \end{aligned} \quad (4)$$

where  $dW/dV$  is the strain energy density function per unit volume,  $E$  is the modulus of elasticity. Both  $r_c$  and  $S_c$  are assumed to be constant material properties.

The SED criterion in general can be used for pure mode I, pure mode II and mixed mode I/II and the conventional SED criterion only takes into account the singular term in Eq. (1). Here in this paper, the SED criterion is modified by using the stress field (Eq. (1)) considering both the singular term and the  $T$ -stress term. The strain energy density function can be written as:

$$\begin{aligned} S &= \frac{1}{16G\pi} (a_{11}K_I^2 + a_{12}K_I K_{II} + a_{22}K_{II}^2 \\ &\quad + a_{1T}K_I T + a_{2T}K_{II} T + a_T T^2) \end{aligned} \quad (5)$$

where the factors  $a_{ij}$  are functions of the angle  $\theta$ , and defined as:

$$a_{11}(\theta) = (1 + \cos \theta)(\kappa - \cos \theta),$$

$$a_{12}(\theta) = 2 \sin \theta (2 \cos \theta - (\kappa - 1)),$$

$$a_{22}(\theta) = ((\kappa + 1)(1 - \cos \theta) + (\cos \theta + 1)(3 \cos \theta - 1)),$$

$$a_{1T}(\theta) = 2\sqrt{2\pi r_c} \cos \frac{\theta}{2} ((\kappa - 2) - \cos \theta + 2 \cos^2 \theta),$$

$$a_{2T}(\theta) = -2\sqrt{2\pi r_c} \sin \frac{\theta}{2} (\kappa + \cos \theta + 2 \cos^2 \theta),$$

$$a_T(\theta) = (1 + \kappa)\pi r_c.$$

where  $G$  is the modulus of rigidity, for plane strain,  $\kappa = 3 - 4\nu$ , for plane stress,  $\kappa = (3 - \nu)/(1 + \nu)$ .

For pure mode II under plain strain condition,  $K_I = 0$ ,  $\kappa = 3 - 4\nu$ , Eq. (5) can be written as:

$$\begin{aligned} S &= \frac{(1 + \nu)K_{II}^2}{8\pi E} \left( \left( \left( \frac{9}{2} - 4\nu \right) + (4\nu - 2)\cos \theta + \frac{3}{2}\cos 2\theta \right) \right. \\ &\quad \left. - B\alpha \left( (7 - 8\nu)\sin \frac{\theta}{2} + \frac{1}{2}\sin \frac{5\theta}{2} \right) + 2(1 - \nu)(B\alpha)^2 \right) \end{aligned} \quad (6)$$



where  $B$  is the biaxiality ratio (Leevers & Radon 1976) and the definition is:

$$B = \frac{T\sqrt{\pi a}}{K_{II}} \quad (7)$$

and  $\alpha$  in Eq. (7) is defined as:

$$\alpha = \sqrt{\frac{2r_c}{a}} \quad (8)$$

where  $a$  is the crack length for edge cracks and the semi-crack length for center crack,  $r_c$  is the constant distance. The terms involving  $B\alpha$  in Eq. (6) represent the contribution of  $T$ -stress in the near crack-tip strain energy density.

By substituting Eq. (6) into Eq. (2), the fracture initiation angle  $\theta_0$  is determined by solving:

$$2\left((2-4\nu)\sin\theta_0 - 3\sin 2\theta_0\right) - B\alpha\left((7-8\nu)\cos\frac{1}{2}\theta_0 + 5\cos\frac{5}{2}\theta_0\right) = 0 \quad (9)$$

For any given value of  $B\alpha$ , the angle  $\theta_0$  can be calculated from Eq. (9). Figure 1 shows the variation of fracture initiation angle  $-\theta_0$  versus  $B\alpha$  for  $\nu = 0.2, 0.3,$  and  $0.4$ . According to Figure 1, the initiation angle  $-\theta_0$  increases by rising the  $B\alpha$  (or  $T$ -Stress), it's clear from this figure that  $T$ -stress has a significant effect on the initiation angle of mode II fracture.

Then the initiation angle  $\theta_0$  is replaced into Eq. (6) and the conditions related to the onset of crack propagation can be found  $S = S_c$ . Eq. (5) can be written as:

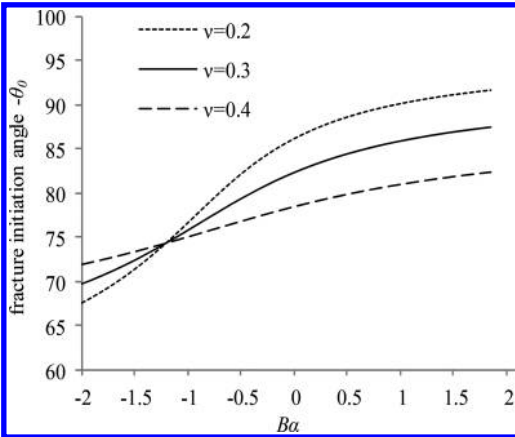


Figure 1. The effect of  $T$ -stress on the fracture initiation angle for different Poisson ratio.

$$S_c = \frac{(1+\nu)K_{IIc}^2}{8\pi E} \left( \left( \frac{9}{2} - 4\nu \right) + (4\nu - 2)\cos\theta_0 + \frac{3}{2}\cos 2\theta_0 \right) - B\alpha \left( (7-8\nu)\sin\frac{\theta_0}{2} + \frac{1}{2}\sin\frac{5\theta_0}{2} \right) + 2(1-\nu)(B\alpha)^2 \quad (10)$$

where  $S_c$  is the critical strain energy density factor and  $K_{IIc}$  is the critical value of mode II stress intensity factor corresponding to the fracture load for plane strain conditions.

Under pure mode I loading the fracture initiation angle is zero, therefore, for  $\theta_0 = 0$  and  $T = 0$ , the critical strain energy density factor  $S_c$  is determined from Eq. (5) as:

$$S_c = \frac{(1+\nu)(1-2\nu)K_{Ic}^2}{2\pi E} \quad (11)$$

Thus, the plane strain mode I fracture toughness can be defined as:

$$K_{Ic} = \sqrt{\frac{2\pi E S_c}{(1+\nu)(1-2\nu)}} \quad (12)$$

If  $S_c$  is considered to be a constant material property, Eq. (10) suggests that  $K_{IIc}$  is not constant but depends on  $B$  or the  $T$ -stress. Using Eq. (10) and Eq. (12), the critical intensity factor of material for different geometry and loading condition is written in terms of  $K_{Ic}$  as:

$$\frac{K_{IIc}}{K_{Ic}} = \left( \frac{(4.5-4\nu) + (4\nu-2)\cos\theta_0 + 1.5\cos 2\theta_0}{4(1-2\nu)} - \frac{B\alpha}{4(1-2\nu)} \left( (7-8\nu)\sin\frac{\theta_0}{2} + \frac{1}{2}\sin\frac{5\theta_0}{2} \right) + \frac{1-\nu}{2(1-2\nu)}(B\alpha)^2 \right)^{-1/2} \quad (13)$$

Figure 2 shows the variation of  $K_{IIc}/K_{Ic}$  versus  $B\alpha$  for plane strain condition. The results are based on different values of Poisson's ratio. It is shown that according to the modified SED criterion, the  $T$ -stress has a considerable influence on the critical mode II intensity factor. As illustrated in Figure 2, when the  $T$ -stress is negative, the critical stress intensity factor first increases by rising the  $T$ -stress ( $B\alpha$ ) till it reaches its maximum value which is dependent on the Poisson's ratio. From this point, a sharp decrease in the critical stress intensity factor of the material can be observed. On the other hand, an increase in the positive  $T$ -stress generally leads

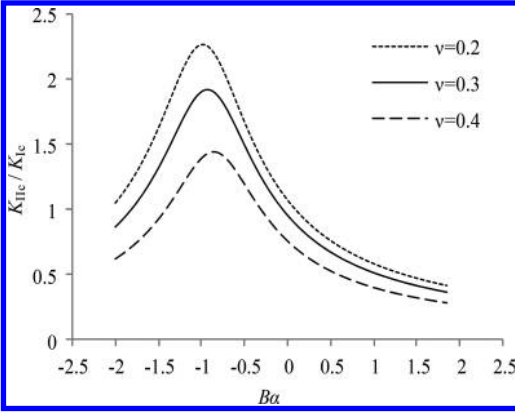


Figure 2. The effect of  $T$ -stress on the critical stress intensity factor for mode II.

to a considerable decrease in the mode II critical intensity factor. The modified SED criterion suggests that the  $T$ -stress plays an important role in calculating the mode II fracture toughness of materials.

### 3 FRACTURE PARAMETERS

As shown in Figure 3, the Brazilian Disc (BD) is a circular disc of radius  $R$  and thickness  $t$  containing a central crack of length  $2a$  and subjected to a diametral compressive load  $P$ . The Semi-Circular Bend (SCB) specimen is a semi-circular disc of radius  $R$  and thickness  $t$  having an edge crack of length  $a$  and subjected to three point bending with a span of  $2S$  for the bottom support distance. For both specimens, the crack makes an angle  $\alpha$  with respect to the loading direction. When the inclined angle  $\alpha$  is zero, both specimens are loaded in pure mode I. By increasing  $\alpha$ , the crack is subjected to a combination of mode I and mode II deformation. Pure mode II are provided in specific angles depending on the crack length ratio  $a/R$  and the loading support ratio  $S/R$ . The crack inclination angle corresponding to pure mode II loading condition typically varies between  $20^\circ$  and  $30^\circ$  for the BD specimen and  $35^\circ$  and  $60^\circ$  for the SCB specimen (Ayatollahi & Aliha 2007).

The stress intensity factors ( $K_I$  and  $K_{II}$ ) and the  $T$ -stress in these specimens are often written as:

$$K_I = \begin{cases} Y_I \frac{P}{Rt} \sqrt{\frac{a}{\pi}} & \text{for BD specimen} \\ Y_I \frac{P\sqrt{\pi a}}{2Rt} & \text{for SCB specimen} \end{cases} \quad (14)$$

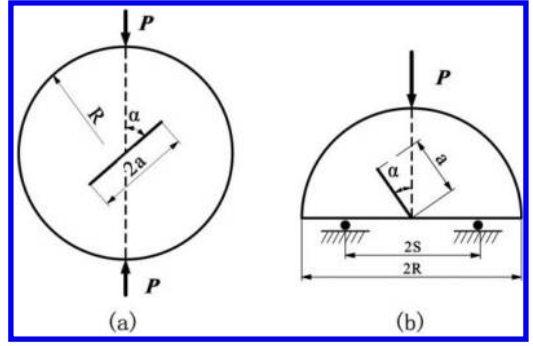


Figure 3. (a) Centrally cracked Brazilian disk specimen and (b) semi-circular specimen under three point bending.

$$K_{II} = \begin{cases} Y_{II} \frac{P}{Rt} \sqrt{\frac{a}{\pi}} & \text{for BD specimen} \\ Y_{II} \frac{P\sqrt{\pi a}}{2Rt} & \text{for SCB specimen} \end{cases} \quad (15)$$

$$T = \begin{cases} \frac{T^*P}{\pi Rt(R-a)} & \text{for BD specimen} \\ \frac{T^*P}{2Rt} & \text{for SCB specimen} \end{cases} \quad (16)$$

where  $Y_I$  and  $Y_{II}$  and  $T^*$  are the normalized forms of  $K_I$ ,  $K_{II}$  and  $T$  respectively. These parameters are functions of the crack length, the crack angle and the loading support distance. Different analytical and numerical techniques have been used by researchers calculating the factors  $Y_I$  and  $Y_{II}$  and  $T^*$  for the BD specimen (Awaji & Sato 1987, Atkinson et al. 1982, Ayatollahi & Aliha 2007) and SCB specimen (Ayatollahi & Aliha 2004, 2007, Kuruppu & Chong 1986, Lim et al 1993). Atkinson et al. (1982) have calculated the related mode II angle  $\alpha_{II}$  for the BD specimen with different ratio of  $a/R$ . Fett (2001) calculated the  $T$ -stress for the cracked Brazilian disc specimen by using the boundary collocation method. Theoretical investigations show that the  $T$ -stress in the BD specimen is always negative and in the SCB specimen is always positive when the specimens are subjected to pure mode II (Ayatollahi & Aliha 2004, 2007).

### 4 RESULTS AND DISCUSSION

There have been considerable amount of experimental results reported in the papers for mode I and mode II fracture toughness data obtained from fracture tests on the BD specimen and SBC specimen. A review of the experimental results shows that the fracture ratio,  $K_{IIc}/K_{Ic}$  determined from the

BD specimen is always significant higher than the value predicted by the conventional SED criterion, meanwhile, the value of  $K_{IIc}/K_{Ic}$  determined from the SBC specimen, is always lower than the theoretical predictions.

The reported experimental values for  $K_{IIc}/K_{Ic}$  typically commence from 1.09 for graphite SM-124 (Awaji & Sato 1987) and increase to a figure as high as 2.165 for Saudi Arabian limestone (Khan & Al-Shayea 2000) using the BD specimen. For example, the mode I fracture toughness  $K_{Ic}$  and mode II toughness  $K_{IIc}$  obtained through experiment using the BD specimen for limestone material are  $13.28 \text{ MPa} \cdot \sqrt{\text{mm}}$  and  $29.25 \text{ MPa} \cdot \sqrt{\text{mm}}$  and the value of  $K_{IIc}/K_{Ic}$  is 2.165. The mode I and mode II fracture toughness obtained for grain marble are reported to be  $35.42 \text{ MPa} \cdot \sqrt{\text{mm}}$  and  $71.15 \text{ MPa} \cdot \sqrt{\text{mm}}$  respectively and the ratio of  $K_{IIc}/K_{Ic}$  is 2.009 (Aliha et al. 2006). However, the values of  $K_{IIc}/K_{Ic}$  for limestone and grain marble predicted by the conventional SED criterion are 1.074 and 0.957 which are much lower than the experimental results. Lim et al. (1994a, b) conducted a series of fracture tests on a water-saturated synthetic mudstone called Johnstone using the SCB test configuration. The pure mode II was obtained in their tests at the angle of crack inclination of  $\alpha = 54^\circ$  and by considering  $S/R = 0.5$ ,  $a \approx 16.5 \text{ mm}$ ,  $R \approx 8 \text{ mm}$  and  $w \approx 17.7\%$  (where  $w$  is the percent of saturated water content). The average value of  $K_{IIc}$  obtained from the results of the tests was approximately  $0.935 \text{ MPa} \cdot \sqrt{\text{mm}}$ , and the value of  $K_{Ic}$  obtained from the experiment is  $2.2 \text{ MPa} \cdot \sqrt{\text{mm}}$ . Thus, the ratio of  $K_{IIc}/K_{Ic}$  for Johnstone is about 0.425. The fracture ratio  $K_{IIc}/K_{Ic}$  for PMMA is obtained using the SBC specimen with the values of  $a/R$  and  $S/R$  are 0.3 and 0.43 respectively and the pure mode II could be provided at the crack angle  $\alpha = 50^\circ$ , the reported experimental value of  $K_{IIc}/K_{Ic}$  for PMMA is 0.526 (Ayatollahi et al. 2006). However, the value of  $K_{IIc}/K_{Ic}$  predicted by the conventional SED criterion is 0.811 for PMMA, and for Johnstone, the prediction result is 1.074. The experimental results presented in Lim et al. (1994a, b) and Ayatollahi (2004) show that the values of  $K_{IIc}/K_{Ic}$  obtained from fracture tests on the SBC specimen are significant lower than the results predicted by the

conventional SED criterion. It is pointed that the mode I fracture toughness value used here was taken from a fracture tests in which the loading direction was perpendicular to the bedding planes.

Eq. (9) and Eq. (13) indicate that the value of  $T$ -stress,  $K_{II}$  and  $r_c$  are required for calculating the ratio of  $K_{IIc}/K_{Ic}$ . For the BD specimen and SBC specimen, when the specimen geometry is available, the values of  $T$ -stress and  $K_{II}$  can be extracted from Ayatollahi & Aliha (2004, 2007) or directly calculated by finite element analysis software such as ABAQUS. For some brittle materials, the critical distance  $r_c$  is often approximated by the radius of fracture process zone. Schmidt (1980) proposed a maximum normal stress criterion to predict the size of fracture process zone as:

$$r_c = \frac{1}{2\pi} \left( \frac{K_{IIc}}{\sigma_t} \right)^2 \quad (17)$$

where  $\sigma_t$  is the tensile strength. By replacing  $K_{Ic} = 2.2 \text{ MPa} \cdot \sqrt{\text{mm}}$  and  $\sigma_t = 0.435 \text{ MPa}$  (for  $w \approx 17.7\%$ ) in Eq. (17), the value of  $r_c$  is estimated for Johnstone to be 4 mm. Based on the results of earlier fracture tests reported by Smith et al (2006) the critical radius  $r_c$  for PMMA is about 0.1 mm. The value of  $r_c$  calculated by using the same method is 9 mm and 14 mm for limestone and coarse grain marble respectively.

Table 1 shows the comparison between the experimental results and the theoretical predictions. It can be seen that the modified SED criterion described in this paper can provide very good predictions for mode II fracture test results. For Johnstone, the theoretical predictions based on the modified SED criterion suggests that the value of  $K_{IIc}/K_{Ic}$  is 0.385 that is consistent well with the average of the experimental results  $K_{IIc}/K_{Ic} = 0.425$  as described above. For PMMA, the prediction value of  $K_{IIc}/K_{Ic}$  is 0.538 that also is consistent well with the average of the experimental results 0.542. And for limestone and grain marble, the ratios of  $K_{IIc}/K_{Ic}$  predicted by the modified SED criterion are 2.238 and 1.943 respectively, the average of experimental results are 2.20 and 2.009. Again it is seen that a good agreement exists between the experimental

Table 1. Fracture toughness ratio  $K_{IIc}/K_{Ic}$  predicted from the modified SED criterion.

Specimen	Material	$r_c$ (mm)	$B\alpha$	$K_{IIc}/K_{Ic}$ (predicted by SED criterion)	$K_{IIc}/K_{Ic}$ (predicted by modified SED criterion)	$K_{IIc}/K_{Ic}$ (average of test results)
SBC	Johnstone	4.0	2.100	1.074	0.385	0.425
	PMMA	0.1	0.585	0.811	0.538	0.526
BD	Limestone	9	-1.068	1.074	2.238	2.165
	Marble	14	-0.892	0.957	1.943	2.009

results and the theoretical predictions when the modified SED criterion is used.

The modified SED criterion can be used for predicting the mode II fracture toughness of brittle materials from other mode II crack specimens as well and it provides an appropriate method for calculating the mode II fracture toughness from the mode I fracture toughness, this prevents the expensive and time-consuming procedure required for the design, preparation and conduction of mode II fracture tests. The modified SED criterion suggests that the mode II fracture toughness is significantly dependent on the geometry and loading conditions. The SBC specimen always underestimates the value of mode II fracture toughness in engineering materials. This is because a large positive  $T$ -stress is present in the SBC specimen when the specimen is subjected to mode II. And for the BD specimen, a negative  $T$ -stress is present when the specimen is under mode II loading condition and the absolute value of the  $T$ -stress in a mode II BD specimen is small, the mode II fracture toughness is often overestimated in a mode II BD specimen. Therefore, despite several advantages of the BD specimen and SBC specimen for measuring fracture toughness, in brittle materials, it is important to keep in mind that the mode II fracture toughness determined from these two specimens often overestimates or underestimates the fracture resistance of mode II cracks in engineering components and structures.

## 5 CONCLUSIONS

1. The minimum strain energy density criterion was modified to include the effect of  $T$ -stress in predictions of critical mode II fracture toughness. The modified SED criterion suggests that the  $T$ -stress has a considerable influence on the critical stress intensity factor and the fracture initiation angle of brittle and quasi-brittle materials.
2. The theoretical analysis shows that when the  $T$ -stress is negative the critical stress intensity factor first increases as the magnitude of  $B\alpha$  rises, then it declines after a specific value of  $B\alpha$ . Meanwhile, when the  $T$ -stress is positive, increasing  $B\alpha$  generally leads to decreased values of critical stress intensity factor.
3. The  $T$ -stress in the BD specimen is always negative and in the SCB specimen is always positive when the specimens are subjected to pure mode II. The SBC specimen used to measure the mode II fracture toughness can significantly overestimate the value of  $K_{IIc}$  while the BD specimen, underestimate the value of  $K_{IIc}$  in real structure and components.
4. The modified SED criterion was used to predict the fracture toughness ratio  $K_{IIc}/K_{Ic}$  and the predictions show a good agreement with the experimental results.

## REFERENCES

- Aliha, M.R.M., Ashtari R., Ayatollahi M.R. 2006. Mode I and Mode II fracture toughness testing for a coarse grain marble. In: *Applied Mechanics and Material* 5-6:181-188. Trans tech publication, Switzerland.
- Atkinson, C., Smelser, R.E. & Sanchez, J. 1982. Combined mode fracture via the cracked Brazilian disc test. *International Journal of Fracture* 18(4):279-291.
- Awaji H. & Sato S. 1987. Combined mode fracture toughness measurement by the disc test. *Journal of Engineering Material and Technology* 100(2):175-82.
- Ayatollahi, M.R. & Aliha, M.R.M. 2004. Fracture parameters for cracked semi-circular specimen. *International Journal of Rock Mechanics and Mining Science* 41(1):20-25.
- Ayatollahi, M.R., Aliha, M.R.M., Hassani M.M. 2006. Mixed mode brittle fracture in PMMA—an experimental study using SCB specimens. *Materials Science and Engineering: A* 417:348-356.
- Ayatollahi, M.R. & Aliha, M.R.M. 2007. Wide range data for crack tip parameters in two disc-type specimens under mixed mode loading. *Computational Materials Science* 38:660-670.
- Berto, F. & Lazzarin, P. 2009. A review of the volume-based strain energy density approach applied to V-notches and welded structures. *Theoretical and Applied Fracture Mechanics* 52(3):183-194.
- Erdogan, F. & Sih, G.C. 1963. On the crack extension in plates under plane loading and transverse shear. *Journal of Basic Engineering* 85: 525-52.
- Fett, Theo 2001. Stress intensity factors and  $T$ -stress for internally cracked circular disks under various boundary conditions. *Engineering Fracture Mechanics* 68(9):1119-1136.
- Hussain, M.C., Pu, S.L., Underwood J. (1973). Strain Energy Release Rate for a Crack Under Combined Mode I and Mode II. In *Fracture Analysis* 560:2-28, Proceedings of the 1973 National Symposium on Fracture Mechanics, Part II, ASTM Special Technical Publication.
- Khan, K. & Al-Shayea, N.A. 2000. Effect of specimen geometry and testing method on mixed I-II fracture toughness of a limestone rock from Saudi Arabia. *Rock Mechanics and Rock Engineering* 33(3):179-206.
- Kuruppu, M.D. & Chong, K.P. 1986. New specimens for mode I and II fracture investigations of geometries. In: *Proceedings of the Society of Experimental Mechanics, Spring Conference on Experimental Mechanics*, New Orleans, USA 31-38.
- Lam, Y.C. 1989. Mixed mode fatigue crack growth and the strain energy density factor. *Theoretical and Applied Fracture Mechanics* 12(1):67-72.
- Leevers, P.S., Radon, J.C., Culver, L.E. 1976. Fracture trajectories in a biaxially stressed plate. *Journal of the Mechanics and Physics of Solids* 24(6):381-395.

- Lim, I.L., Johnston, I.W., Choi, S.K. 1993. Stress intensity factors for semi-circular specimen under three-point bending. *Engineering Fracture Mechanics* 44(3), 363–382.
- Lim, I.L., Johnston, I.W., Choi, S.K., Boland, J.N. 1994a. Fracture testing of a soft rock with semi-circular specimens under three-point bending. Part 1—mode I [J]. *International Journal of Rock Mechanics and Mining Science Geomechanics Abstract* 31(3): 185–197.
- Lim, I.L., Johnston, I.W., Choi, S.K., Boland, J.N. 1994b. Fracture testing of a soft rock with semi-circular specimens under three-point bending. Part 2—mixed mode. *International Journal of Rock Mechanics and Mining Science & Geomechanics Abstracts* 31(3):199–212.
- Liu, C., Huang, Y., Stout M.G. 1998. Enhanced mode II fracture toughness of an epoxy resin due to shear banding. *Acta Materialia* 46(16): 5647–5661.
- Maccagno, T.M. & Knott J.F. 1989. The fracture behavior of PMMA in mixed modes I and II. *Engineering Fracture Mechanics* 34(1):65–86.
- Nobile, L., Carloni C., Nobile M. 2004. Strain energy density prediction of crack initiation and direction in cracked T-beams and pipes. *Theoretical and Applied Fracture Mechanics* 41(1–3):137–145.
- Schmidt, R.A. 1980. Micro-crack model and its significance to hydraulic fracturing and fracture toughness testing. In: *Proceedings of 21st US symposium rock mechanics* 581–590.
- Sih, G.C. 1974. Strain energy density factor applied to mixed mode crack problems. *International Journal of Fracture* 10(3): 305–321.
- Sih, G.C. & Ho J.W. 1991. Sharp notch fracture strength characterized by critical energy density. *Theoretical Applied Fracture Mechanics* 16(3):179–214.
- Sih, G.C. & Tang, X.S. 2005. Scaling of volume energy density function reflecting damage by singularities at macro-, meso- and microscopic level. *Theoretical and Applied Fracture Mechanics* 43(2):211–231.
- Smith, D.J., Ayatollahi, M.R., Pavier M.J. On the consequences of *T*-stress in elastic brittle fracture. *Proceedings of the Royal Society A* 462:2415–2437.
- Ueda, Y., Ikeda, K., Yao, T., Aoki M. 1983. Characteristics of brittle fracture under general combined modes including those under bi-axial tensile loads. *Engineering Fracture Mechanics* 18(6):1131–1158.
- Williams, M.L. 1957. On the stress distribution function of wide applicability. *Journal of Applied mechanics* 24:109–144.

## Discussion on methods of strengthening concrete structures

Lijun Dou & Tianyu Chen

*Structure Engineering, Changchun Institute of Technology, Changchun, China*

**ABSTRACT:** Due to various factors, the problem of inadequate carrying capacity may appear in the process of construction or use of concrete structures. In this case, some appropriate strengthening methods must be taken in order to keep the safety of the buildings. An account of the commonly used strengthening methods will be given by the author, and the scope, the advantages, and disadvantages of each method will be discussed to provide reference for practical engineering application.

**Keywords:** concrete structure; strengthening methods; safety

### 1 INTRODUCTION

For years, concrete has been the engineering material which is most widely used in the world. However, due to the influence of the disasters, such as earthquake, hurricane, and fire, or exceeding its service life, the carrying capacity of the construction members of existing buildings will be reduced. In this case, in order to ensure the safety and avoid the resources loss of reconstruction, strengthening ought to be chosen prior and it has valuable practical engineering significance.

Since the 1980s, the amount of building strengthening has risen continuously in the United States, the Great Britain, Sweden, and some other developed countries. A large number of buildings have been strengthened properly. In this century, the proportion of the strengthened buildings has already been more than the new construction. In China, according to statistics, more than 40% of the existing buildings need to be strengthened, of which most are of the concrete structures. Especially after the Wen Chuan earthquake and other serious natural disasters, the state launched a new version of the code for seismic design and other relevant regulations, though some buildings cannot meet the requirements for the new code, seismic strengthening is essential, such as the nationwide seismic strengthening project of primary and secondary school building. Thus, the structural strengthening in China is still a long way, and it brings excellent opportunities for development of structural strengthening industry.

### 2 GENERAL PRINCIPLES OF STRENGTHENING CONCRETE STRUCTURE

There has already been force and deformation before the strengthening work begins. The strengthening process will force the structure second. Thus, it must be very cautious and follow certain principles during the strengthening process in order to ensure that the old and the new structures can work together. There are three general principles of strengthening concrete structure.

First, the destruction of the original structure members should be avoided. The engineering quantities and the negative impact should be minimized as much as possible. It must make sure that the old and the new structure can bear some of the loads at the same time, and mainly by the original structure members.

Second, the function of the building should not be affected. While developing a strengthening program, it must be in conjunction with the identification and the use requirement so that the program is scientific and reasonable. Then, some ill-considered factors and errors can be avoided. The function of the building will keep regular.

Third, the integrity of the structure must be ensured. Due to the force generated by the secondary and hysteresis effect when strengthening, the reasonable structure and the reliable connection must be guaranteed during the process of strengthening, to avoid new weak parts from appearing in the structure, thus resulting in the poor integrity.

Strengthening work is different from the construction of new structure, which needs to be

higher and stricter. The strengthening work staff must be on a high professional level to detect the problems and deal with the actual situation. In China, the strengthening of concrete structure must follow the “Code for design of strengthening concrete structure” (GB50367-2013).

### 3 INTRODUCTION TO THE COMMONLY USED STRENGTHENING METHODS

The strengthening methods of concrete structure are divided into direct strengthening and indirect strengthening. The appropriate method is selected according to the actual conditions and use requirements.

#### 3.1 *Direct strengthening methods*

##### 3.1.1 *Increasing section area*

Structure strengthening with increasing section area is a method, which has a wide scope of application and the obvious strengthening effect. It is mainly used for strengthening the bending and the compression members of concrete structure. The method is to increase section area by adding a layer of concrete on the outside surface of the member. For a beam member, the concrete is added in the compression zone and the rebars are added in the tension zone. For a column member, the rebars are added in its marginal area. Like this, the bearing capacity of cross section and the inflexibility of concrete members get improved.

Now, the technology of this strengthening method is mature and costs low. The bearing capacity of the members improves obviously. The durability and the stability are also superior. However, the method belongs to wet work. It takes a period of time to conserve. So it affects production and life. Besides, as the section area is increasing, the appearance of the building may be affected. The headroom decreases. The weight of structure increases.

##### 3.1.2 *Externally wrapped steel section*

Structure strengthening with externally wrapped steel section is divided into two types: dry work and wet work. It is mainly used for strengthening concrete beam and column. Dry work refers to the section steel and batten plates are directly placed around the member. There is no cementation between steel and concrete member. The reliability of this type is poor, so it is rarely utilized. Wet work refers to stick steel to concrete members tightly with adhesive material. At present, modified epoxy cement is widely utilized which is poured between steel and concrete member. The cement layer can pass stress so that the externally wrapped steel section and the member work together.

The steel section area is increased by a large margin in this strengthening method. At the same time, the bearing capacity and inflexibility are also improved. The technology is simple, the amount of work is small. But the consumption of steel is great, there are some requirements of adhesive material. Thus, the expense is higher.

##### 3.1.3 *Bonded steel plate*

Structure strengthening with bonded steel plate is mainly used for strengthening the bending, the tension and the large eccentric compression members of concrete structure. The specific method is to stick the thin steel plate to the surface of concrete member with adhesive material. Then the steel plate and the original member combine into a combinational member. Like the externally wrapped steel section, the cement layer can pass stress. The steel plate and concrete member can work together well so it has high bearing capacity. The code allows that the strength level of the original member is not less than C15, and the tensile bond strength is not less than 1.5 MPa.

The technology of this method is simple and fast. There is an excellent integrity of the combination. The construction has little impact on normal production and life. There is no obvious impact on the appearance of original structure and the headroom. However, its durability is poor. It costs a lot because the consumption of steel is large. Additionally, it does not apply to the members, which bear dynamic load.

##### 3.1.4 *Concrete displacement*

Structure strengthening with concrete displacement is suitable for strengthening the load-bearing member, for which the strength of compression zone is low or serious defect appears. The specific method is to remove the concrete of the member, which is in poor condition and pour the new concrete. Whether the old and the new combine well or not is the key to the effect of concrete displacement. During the construction, reliable measures must be taken on the concrete joint surface.

According to the rules of the code, there must be effective top support to the original member when strengthening horizon members such as beam and slab. It must make sure that there is no tensile stress on joint surface through checking calculation, observation, and control. The strength level of the concrete which is utilized to displace is one level higher than the original, and not less than C25.

The method is widely suitable. Almost all concrete members can be strengthened by it. The effect is good and the member can keep its original appearance. However, the amount of wet work is large, and it may cause some damages to concrete members.

### 3.1.5 *Bonded carbon fiber material*

Structure strengthening with bonded carbon fiber material is suitable for strengthening the bending, the axial compression, large eccentric compression and the tension concrete member. The method is to use a carbon fiber impregnated with resin adhesive to laminate the concrete structure in the bearing parts. Make the two into one so as to improve the bearing capacity, reduce deformation and control cracks of the member.

This method makes concrete member to have better durability, corrosion resistance, and anti-fatigue performance. Carbon fiber material has little impact on the weight of structure and the maintenance cost is low. However, the fire and high temperature resistance of carbon fiber material are poor. When there is a great temperature difference, concrete may crack as a result of the cohesive force between carbon fiber and concrete is destroyed. Carbon fiber may fissure due to lack of ductility when there is a large deformation.

## 3.2 *Indirect strengthening methods*

### 3.2.1 *Externally prestressed*

Structure strengthening that was externally prestressed is the method which utilizes prestressed steel rod and section steel bar to strengthen the structure. The distribution of internal force changes and stress level decreases through prestressing the steel. Strengthening by this method can effectively avoid the hysteresis of stress and strain in general strengthened structures. It is suitable for strengthening the beam, the slab, the column, and the truss, which has small section, needs to increase load, needs to improve performance or is in a high state of stress and strain.

The prestressed rebar and section steel utilized in this method can enhance the bearing capacity of cross section and oblique section. The strengthened structure can work effectively. The prestress is able to offset some stress, this is beneficial to control the deflection and crack of members. There are also some disadvantages, such as the complex construction process, demanding highly on environment. Stress concentration of prestress rebar is produced in the bolted part or the corner. It may lead to rebar's fissure and flab.

### 3.2.2 *Adding fulcrums*

Structure strengthening with adding fulcrums is suitable for strengthening beams, slabs, and trusses. The method is to diminish the structure's span by adding fulcrums in order to decrease the internal force and enhance the bearing capacity of the structure. The method can be divided into two types according to the different mechanical per-

formances of the support structure: rigid fulcrum strengthening and elastic fulcrum strengthening. Rigid fulcrum strengthening is to exert the load on the fulcrum and pass it to the column and the foundation. Its stress is definite and the bearing capacity is enhanced well. Elastic fulcrum strengthening is to pass the load to support structure indirectly by bending of structure or truss' effect. It cannot enhance the bearing capacity obviously, but there is less impact on inner space than rigid fulcrum. There are some regulations about the connection between original members and new numbers. The wet hoop connection is selected when the support structure is reinforced concrete. The dry hoop connection is selected when the support structure is section steel.

The method is simple, reliable, and effective. However, it is easy to influence the building's appearance and function. Therefore, the method should be selected under certain permission conditions.

In addition to the above strengthening methods, structure strengthening with wire wrapped, adding shear wall, and some other methods are also used in some practical engineering. In the process of strengthening concrete structure, there are some related techniques, such as crack repair, embedded rebars, anchor, antitrust and supporting beams, and demolishing columns. The methods and the techniques are introduced in "Code for design of strengthening concrete structure" (GB50367-2013) and "Configuration diagram for strengthening concrete structure" (13SG311-1).

## 3.3 *Precautions of the method selection*

The selection of strengthening method is the prerequisite of strengthening design. It directly influences the quality and cost of the strengthening work. Therefore, a variety of factors should be considered and analyzed comprehensively when selecting an appropriate method. The following points need to be focused on:

1. Select the method, which is economical, simple, and less-impacted on production and life in the premise of ensuring safety.
2. Figure out the advantages, disadvantages, applicable conditions, and special requirements of each method.
3. Consider the feasibility of the method fully, ensure that it can implement smoothly and meet the requirement of strengthening.
4. Strengthening is a comprehensive technology, which may apply several different methods. The superiority of every method should be taken to achieve the good effect.



#### 4 THE DEVELOPMENT TREND OF STRENGTHENING CONCRETE STRUCTURE

As far as the current development situation, strengthening building structure especially strengthening concrete structure has drawn a widespread attention. As hot field-related academic groups all over the world have carried out a lot of technical exchanges and cooperation. Therefore, its application and development has a very bright future.

In recent years, the application of composite materials leads the strengthening technology a significant progress, such as utilizing the inorganic composite mortar pasting steel mesh to strengthen the members of concrete structure. This new strengthening method has the features of anti-aging, fire resistance and superior durability, and the performance of the composite mortar is better than that of the organic cementing material. Fiber composite material strengthening is also a new method, which has been utilized in some countries. It has superior mechanical properties, durability, corrosion resistance, and wide range of applications. The strengthening work is of high quality and efficiency with it. From now on, the study on fiber composite material will be carried out thoroughly to get over the shortcomings of fiber material and obtain a more perfect strengthening method.

In addition, more and more new strengthening methods will be brought out as the development of new material and technology in civil engineering.

#### 5 CONCLUSION

With the increasing size and the total amount of construction in China, as the development of modern technology and construction industry, strengthening concrete structure has become one of the most promising and dynamic technical branches of modern building technology. In the coming period, the practical engineering experience will constantly promote the progress of its

basic theory and technology. In turn, with the level of study and application improves, some more scientific, safer and more economical strengthening methods will be put forward to service the practical engineering.

#### REFERENCES

- 13SG311-1 (2013). *Configuration diagram for strengthening concrete structure*. Beijing: China Planning Press.
- Chang, X.W. (2013). Methods of strengthening concrete structure. *China Construction*, 07, 128–129.
- Feng, Q. (2013). Problems and solutions of strengthening concrete structure technology. *Shanxi Architecture*, 32, 36–37.
- Fu, X.M. (2013). Preliminary analysis on strengthening concrete structure. *Urbanism and Architecture*, 12, 55–60.
- GB50367-2013 (2013). *Code for design of strengthening concrete structure*. Beijing: China Architecture & Building Press.
- Hu, J.Q. (2013). Design plans and construction methods of strengthening concrete structure. *The World of Building Materials*, 2, 25–27.
- Liu, C.H., & He, H.R. (2014). Discuss on technology of strengthening concrete structure. *Sichuan Building Materials*, 01, 70–72.
- Wang, L.L. (2013). Construction methods of strengthening concrete structure. *Privately Operated Science and Technology*, 4, 315.
- Xu, C.H. (2013). Study on technology of strengthening concrete structure. *Technology Innovation and Application*, 33, 238.
- Zhang, C.L., & Xu, H. (2014). Methods of strengthening concrete structure. *Shanxi Architecture*, 12, 26–27.
- Zhang, X.Z., & Han, P.F. (2014). Discuss on the methods and applications of strengthening concrete structure. *Journal of Henan Science and Technology*, 3, 87.
- Zhang, Y. (2014). Discuss on technology and development trend of strengthening building structure. *Doors & Windows*, 9, 154–156.
- Zheng, H.Y. (2014). Analysis on construction plan of strengthening concrete structure. *Doors & Windows*, 1, 150.
- Zhou, R.L. (2014). Main point analysis on design of strengthening concrete structure buildings. *Science & Technology Vision*, 6, 95–110.

# Freeze-thaw damage model for polypropylene fiber concrete

Sheng-ping Chen & Fei Ten

*School of Civil Engineering and Architecture, Hubei University of Technology, Wuhan, China*

**ABSTRACT:** The mechanical performance of polypropylene fiber concrete under cyclic freezing and thawing actions was experimentally conducted in this paper. 100 mm × 100 mm × 100 mm cubic specimens and 100 mm × 100 mm × 400 mm beam specimens were made with two different volume ratio of polypropylene fiber. The compressive strength, bending behavior and dynamic elastic modulus of polypropylene fiber concrete were tested after different freeze-thaw cycles. The experimental results demonstrate that, with the increase of freeze-thaw cycles, the frost damage of polypropylene fiber concrete was cumulated, and the relative dynamic modulus, the compressive strength and flexural strength were reduced. By adding polypropylene fiber to concrete, the loss of dynamic modulus was improved, and the flexural strength was increased obviously, but the compressive strength had no significant variance. Furthermore, a freeze-thaw damage model of polypropylene fiber concrete was established.

**Keywords:** polypropylene fiber concrete; freezing and thawing cycle; damage model; strength; dynamic elastic modulus

## 1 INTRODUCTION

Concrete structure is often damaged by cyclic freeze-thaw actions in cold areas, and the freeze-thaw resistance is regarded as the most important index of concrete durability<sup>[1]</sup>. The freeze-thaw damage can be understood as the internal damage of concrete structure. From the point of view of damage mechanics, the definition of damage variable and the establishment of fiber concrete freeze-thaw damage model under cyclic loading are of important reference value to the prediction of the life of concrete structures in cold area and the evaluation of the durability of concrete structure.

Polypropylene fiber can inhibit crack propagation, prevent crack diffusion, improve the long-term performance of the concrete structure and improve structure durability. The frost resistance of polypropylene fiber reinforced concrete has been obtained a lot of attention. The study on freeze-thaw damage of fiber concrete has obtained certain results in experimental data and damage model<sup>[2-5]</sup>. The damage behavior of polypropylene fiber concrete in freeze-thaw is studied by conducting an experiments of freeze-thaw on the polypropylene fiber concrete specimens. From the macroscopic physical properties, the frost damage is reflected as the loss of dynamic elastic modulus, the reduced mechanical properties, such as the compressive strength, the flexural strength. In this paper, a freeze-thaw damage model is established, which is based on the two parameter Weibull

distribution, and on the basis of the test data from the polypropylene fiber concrete under cyclic freezing and thawing actions.

## 2 FREEZE-THAW TEST

### 2.1 *Experiment materials*

The design strength of polypropylene fiber concrete is C45. The ordinary Portland cement, coarse river sand with a maximum particle size of 20 mm, and polypropylene fiber with a length of 19 mm were used.

### 2.2 *Freeze-thaw test*

The specimens are divided into two series of specimens. The first series are 100 mm × 100 mm × 100 mm cubic specimens, which are used to determine its compressive strength. The second series are 100 mm × 100 mm × 400 mm beam specimens, which are used to measure the relative dynamic elastic modulus, mass loss and flexural strength. Three different volume ratios of fiber contents were made. Fast freezing and thawing test method was adopted according to the Chinese national standard GB/T50082-2009. Freeze-thaw equipment come from Shanghai Sanhao refrigeration equipment factory. Before the experiment, specimen should be soak in the water of 20–25 °C for 4 days to make the specimen come to water saturation state. Every freeze-thaw cycle is about

4 hours, the frozen and melt state transition time is about 10 minutes. The temperature in the center of the specimen under completely frozen is  $-17\text{ }^{\circ}\text{C}$ , and the highest temperature is about  $8\text{ }^{\circ}\text{C}$ .

### 3 EXPERIMENTAL RESULTS AND ANALYSIS

#### 3.1 Experiment phenomena

When the freeze-thaw cycles are 50 times, the three groups of specimens emerge no obvious change, only have a small amount of thin skin loss. The polypropylene fiber concrete was not significantly exposed, and the mass loss of block is small, and even there were some slightly increasing trend. This shows that, after freeze-thaw action, the surface of concrete appear tiny cracks, cause the block absorbs water. The damage in the three groups of specimens are in a lesser degree. When cycle time of freeze-thaw reached 100 times, protective layer on the surface of the block is flaking off, peeling powder particles increased obviously. Due to the effect of polypropylene fiber, surface of fiber concrete cohere residual fragments which is not peeling off completely. When freeze-thaw cycles reached 150 times, protective layer of block surface peels off in great quantities. A majority of internal aggregate has been exposed. Surface damage degree of fiber concrete with 0.75% fiber content is significantly better than that of plain concrete. The polypropylene fiber can alleviate the effect of concrete internal stress because of temperature variance, prevent the expansion of the micro cracks. With the increase of fiber content, the phenomenon is more obvious, and the quality loss rate is smaller. When freeze-thaw cycles reached 200 times, block

surface layer has been exfoliated completely, internal aggregate naked completely. With the increase of fiber content, the damage degree of block surface have no obvious difference.

#### 3.2 The mass loss rate and relative dynamic modulus

Specimen's mass is measured after every 25 times freeze-thaw cycles. The relative dynamic elastic modulus for concrete is expressed:

$$P_n = \frac{f_n^2}{f_0^2} \times 100\% \quad (1)$$

where  $P_n$  represents specimen's relative dynamic elastic modulus after n times freeze-thaw cycles (%);  $f_n$  represents specimen's transverse resonance frequency after n times freeze-thaw cycles (Hz);  $f_0$  represents specimen's transverse resonance frequency before freeze-thaw test (Hz).

Mass loss rate of concrete is expressed:

$$W_n = \frac{G_0 - G_n}{G_0} \times 100\% \quad (2)$$

where  $G_0$  represents specimen's initial mass,  $G_n$  represents specimen's mass after n times freeze-thaw cycles. The test data were shown in [Table 1](#) and [Table 2](#).

The relationship between freeze-thaw cycles and relative dynamic elastic modulus, mass loss rate are shown in [Figure 1](#) and [Figure 2](#), respectively. [Figure 1](#) and [2](#) indicate that, for P1 and P2 group with polypropylene fibers, the loss of dynamic modulus and mass loss of concrete is less than that

Table 1. The mass loss rate.

No.	The mass loss rate							
	25 times	50 times	75 times	100 times	125 times	150 times	175 times	200 times
P1	-0.31	0.56	0.94	1.67	2.32	2.84	3.44	4.15
P2	-0.16	0.43	0.91	1.52	2.20	2.41	2.79	3.39
P3	-0.09	0.28	0.72	1.21	1.67	2.16	2.45	2.84

Table 2. The relative dynamic elastic modulus.

No.	The relative dynamic elastic modulus							
	25 times	50 times	75 times	100 times	125 times	150 times	175 times	200 times
P1	98.21	95.78	91.66	86.40	81.57	75.28	69.49	62.60
P2	98.74	96.86	92.85	88.59	84.13	78.36	73.17	67.77
P3	98.24	98.24	94.90	90.95	87.82	83.65	78.24	76.87

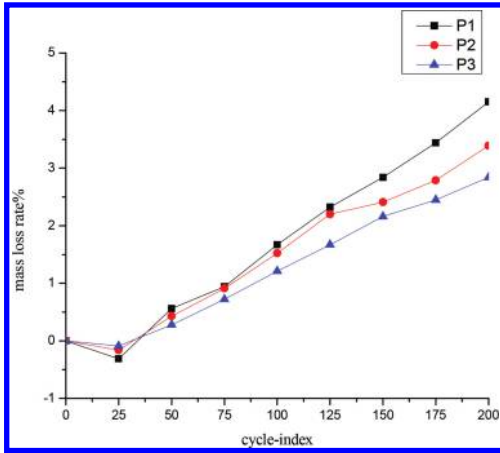


Figure 1. Mass loss for polypropylene fiber concrete.

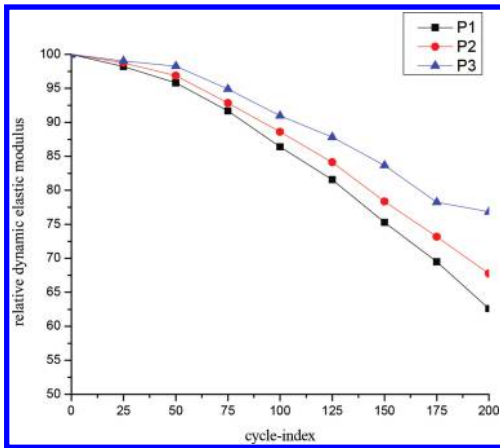


Figure 2. Relative dynamic elastic modulus for polypropylene fiber concrete.

of plain concrete in each stage of freeze-thaw. And the reinforcing effect of high fiber content is better than that of low fiber content. This shows that polypropylene fiber can improve the frost resistance of concrete materials effectively.

### 3.3 Concrete freeze-thaw strength

With the increase of freeze-thaw cycles, internal damage is accumulated, and concrete compressive strength and flexural strength is decreased, the strength tendency of concrete with different polypropylene fiber volume fractions was reflected in Figure 3 and Figure 4. For the compressive strength, the initial strength of concrete with 0.75% fiber content is enhanced, but with the number of freeze-thaw accumulate, strength decline quickly. Strength is

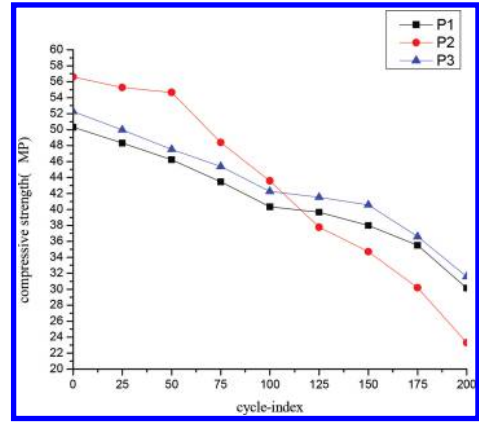


Figure 3. Compressive strength of polypropylene fiber concrete.

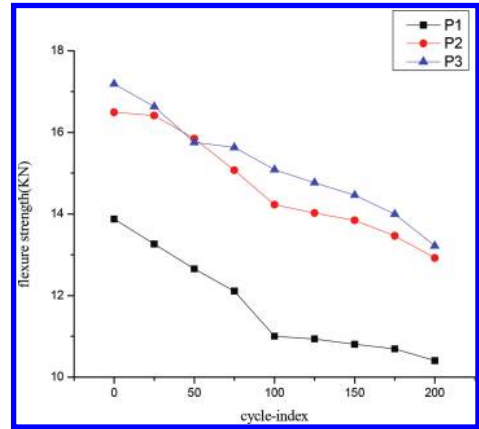


Figure 4. Flexure strength of polypropylene fiber concrete.

least after 200 times freeze-thaw. For the specimens with 1.5% fiber content, strength is higher than plain concrete's under different freeze-thaw cycles. Moreover, 1.5% fiber content is better than 0.75% fiber content. Adding fiber content has a more significant effect for flexural strength. Fiber can significantly increase the content's flexural capacity, and two kinds of concrete of different fiber content have no significant difference for the flexural strength.

## 4 FREEZE-THAW DAMAGE MODEL

### 4.1 Definition of damage variable

The damage variable is defined as:

$$D = 1 - \frac{E_u}{E_0} \quad (3)$$

When  $D$  is the damage variable,  $E_n$  is the dynamic elastic modulus of concrete after  $n$  times freeze-thaw cycles,  $E_0$  is the initial dynamic elastic modulus.

#### 4.2 Freeze-thaw damage model

The Weibull distribution model can be regarded as the life of the material distribution model. According to the two-parameter Weibull probability model, the probability distribution function is:

$$F(N) = 1 - \exp\left[-\left(\frac{N}{\eta}\right)^\beta\right] \quad (4)$$

where  $\eta$  is the characteristic parameter,  $\beta$  is shape parameter.

After  $n$  times of freeze-thaw cycles, the failure probability of concrete is:

$$P_f(n) = 1 - \exp\left[-\left(\frac{n}{\eta}\right)^\beta\right] \quad (5)$$

After  $n$  times freeze-thaw cycle, the damage of concrete is defined as  $D(n)$ . When the freeze-thaw cycles of concrete achieves  $n$ ,  $D(n) = 1$ , it means the failure of concrete material, failure rate  $P_f(N) = 1$ . To concrete material, after  $n$  times freeze-thaw cycles, failure rate of this material is  $P_f(n)$ , while the failure damage of concrete is  $D(n)$ , at this time we can regard failure rate of this material as the amount of damage, thus there be:

$$P_f(n) = D(n) \quad (6)$$

And that also is

$$D(n) = 1 - \exp\left[-\left(\frac{n}{\eta}\right)^\beta\right] \quad (7)$$

From the formula (7):

$$\ln\left(\ln\frac{1}{1-D}\right) = \beta\ln\frac{1}{\eta} + \beta\ln(n) \quad (8)$$

Instruct  $Y = \ln(\ln(1/(1-D)))$ ,  $X = \ln(n)$ , formula (8) can be written as a first order linear function:

$$Y = a + bX \quad (9)$$

Based on the definition of variable damage, the experiment data of the dynamic elastic modulus  $E_n$  can be used as the calculated value of freeze-thaw damage regulation  $D = 1 - E_n/E_0$ .

Table 3. Parameter of linear regression.

No.	a	b ( $\beta$ )	$\eta$	$R^2$
P1	-9.252	1.592	334.153	0.99596
P2	-9.969	1.708	342.630	0.99409
P3	-10.385	1.726	410.264	0.97970

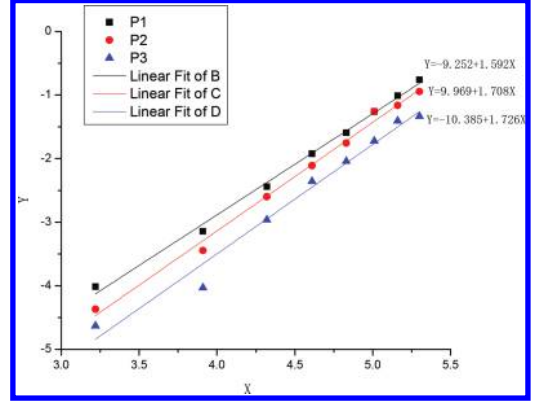


Figure 5. Linear fitting of Weibull distribution.

In order to make the scatter  $(X_i, Y_i)$  reach the best state of linear, we can use maximum likelihood to estimation parameters a, b. Parameter estimation data as shown in Table 3.

Data points fall on a straight line basically as shown in Figure 5. All of the correlation coefficient more than 0.97. This shows that choosing the two-parameter Weibull distribution probability model to establish fiber concrete freeze-thaw damage constitutive model is rational.

Therefore, the freeze-thaw damage equation of different fiber content concrete is established as

$$D(n) = 1 - \exp\left[-\left(\frac{n}{334.153}\right)^{1.592}\right] \quad (10)$$

$$D(n) = 1 - \exp\left[-\left(\frac{n}{342.630}\right)^{1.708}\right] \quad (11)$$

$$D(n) = 1 - \exp\left[-\left(\frac{n}{410.264}\right)^{1.726}\right] \quad (12)$$

## 5 CONCLUSION

1. Polypropylene fibers on the structure hinders the permeate of concrete internal water, the frost resistance of concrete was enhanced from

the internal structure. With the increase of fiber volume, mass loss rate and the concrete of the dynamic modulus loss rate accumulated slowly with freezing thawing cycles. The polypropylene fiber can improve the frost resistance of concrete test piece.

2. Establishing concrete freeze-thaw model by using the Weibull probability distribution equation is feasible. The model can meet the experimental data well and reflect the real environment. So the model can be used as evaluation reference of the fiber concrete life under the action of freeze-thaw.
3. Concrete strength is improved under the action of freeze-thaw by mixing fiber, but with the cumulative number of freeze-thaw, the effect of polypropylene fiber hinder decline of concrete compressive strength is not very obvious, but fibers can improve the flexural strength significantly obviously. Finally, the damage model of polypropylene fiber concrete is established, and the experimental data fitting accuracy is higher. But the damage model still need a lot of test data to verify.

## REFERENCES

- [1] Kang Jingfu, Feng Naiqian. The durability of the hydraulic structure and high performance hydraulic structure concrete [J]. China Concrete Cement Products, 1997, 04:4–10. (In Chinese).
- [2] Niu Ditao, Xiao Qianhui. Analysis on damage characteristic of concrete under freezing-thawing action and evaluation of life [J]. Journal of Xi'an University of Architecture & Technology (Natural Science Edition), 2010, 03:319–322+328. (in Chinese).
- [3] Ji Xiaodong, Song Yupu, Liu Jian. Research on freeze-thawing damage model of concrete [J]. Chinese Journal of Computational Mechanics, 2011, 03:461–467. (in Chinese).
- [4] Luo Xin, Wei Jun. Research on damage variable and strength correlation of concrete under action of freeze-thaw cycle [J]. Journal of Huazhong University of Science and Technology (Natural Science Edition), 2006, 01:98–100.
- [5] Cheng Hongqiang, Gao Danying. Experimental study of freeze-thawing damage of Polypropylene fiber concrete [J]. Journal of Southeast University (Natural Science Edition), 2010, S2:197–200.
- [6] Long Yuan, Wan Wenqian, Ji Chong, Zhou Xiang, Tang Xiansu. Study on Damage Evolvement of Steel Fiber Concrete Material by WEIBULL Probability Distribution [J]. Journal of Materials Science and Engineering, 2007, 06:830–832. (in Chinese).
- [7] Bryan Dodson. The Weibull Analysis Handbook [D]. Milwaukee, Wisconsin, ASQ Quality Press, 2006: second edition.
- [8] Yan Jiachuan, Zou Chaoying. Life assessment method of concrete under the action of freeze-thaw cycle [J]. Journal of Harbin Institute of Technology, 2011, 06:11–15.

# Design and application of real-time deformation monitoring system for factory building

XiaoDong Pan, ZhiBin Yao & Lei Zhao

College of Civil Engineering, Zhejiang University of Technology, Hangzhou, China

**ABSTRACT:** It is hard to detect the settlement and incline of the structure timely and accurately by the traditional methods of measurement, which use level and total station. This program will establish a set of system for real-time deformation monitoring and safety warning. The whole system consists of sensor module, signal transmission module, signal processing module, and feedback module. The deformation of factory structure can be precisely and continuously monitored in the coming years. If the deformation exceeds warning level, the system will be automatically alarmed. This paper will analyze the components of system and the principle of monitoring. The foundation settlement and inclination of a machine repair workshop is monitored and the feasibility of the system is verified.

**Keywords:** real-time monitoring; sensor; monitoring system; safety warning

## 1 INTRODUCTION

In recent years, we routinely use the total station and other conventional measuring instruments to measure structural settlement and deformation. But the conventional methods have some disadvantages. It will take a long and slow process for them to obtain the deformation. It is difficult to reflect the health and safety of structure in time because the measuring frequency is not enough.

The deformation monitoring is a series of long-term and repetitive measuring work. The key of monitoring is setting monitoring point in the important position of the structure and observing periodically to obtain the information of deformation. Then we need to check and process the deformation data and ensure the safety of the construction. Therefore, it has important significance to establish a structural health monitoring system, which can immediately make the monitoring deformation of structure be done and diagnose its safety.

For that reason, we need to establish a high degree of automation system which can timely measure out the deformation and transmit to the computer. Then through the software system of data processing, the monitoring system will achieve automatic identification and let users have a clear understanding of the deformation condition in a graphical form. The system will automatically be alarmed if the deformation exceeds the alarm value.

## 2 THE MONITORING PRINCIPLE AND SYSTEM COMPOSITION

### 2.1 The monitoring principle

Single-layer factory building is composed of vertical and horizontal framed bents. We generally calculate

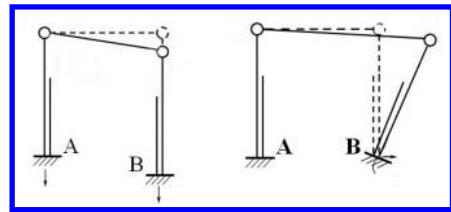


Figure 1. Settlement and incline influence to structure.

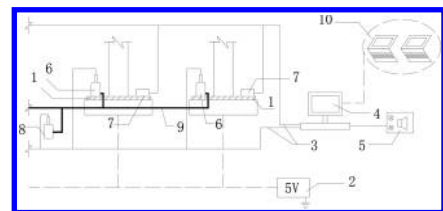


Figure 2. Design of system structure.

1—monitoring fixed mount, 2—supply for electrical, 3—signal bus, 4—processing system, 5—warning indicating device, 6—static force level, 7—biaxial inclinometer, 8—Benchmark static force level, 9—connecting wire, and 10—remote feedback device.

Table 1. The structure deformation monitoring content.

Monitoring content	Monitoring technology	Monitoring instrument	Monitoring period	Monitoring type
Settlement	Physics sensors	Static force level	Dynamic	Real-time automatic
Inclination	Physics sensors	Biaxial inclinometer	Dynamic	Real-time automatic

the transverse frame bent for structure analysis. So we can choose a representative framework in the whole structure as a calculated element. Uneven settlement and inclination will induce the structural change due to its internal force and cause deformation. The schematic diagram is shown in Figure 1.

At the bottom of each frame column, sensors will be installed and the signal from the sensors will be output to the processing system by transmission module. Then, the results of the settlement and inclination will be displayed on a computer screen in the form of a graph. Finally, the system will output signal to the warning device.

## 2.2 System composition

According to the single-layer factory structure model, a system that can do real-time measurements, settlement, and inclination is designed. The whole system can be divided into four modules: sensor module, signal transmission module, signal processing module, and feedback module. The design of system construction has been shown in Figure 2.

Sensor module: we regard a frame column as a monitoring element, and then install sensors at the bottom of each frame column to get the data of settlement and inclination of every moment. We will get the settlement date from static force level and  $t$  the inclination from biaxial inclinometer. The monitoring content is shown in Table 1.

Signal transmission module: This module is composed of a serial port communication, connecting wire, signal bus, and so on. It can realize the data transmission.

Signal processing module and feedback module: The main function of this module is to manage and collect dates, analyze structure safety, and give signal back to the remote feedback device. We choose Microsoft Visual Studio 2008, which can display monitoring data in the form of dynamic graphic to design the program code of safety warning system. According to the different security level, the system will give the device a corresponding signal. Once the monitoring data have achieved a warning value, the device will be warned.

## 3 FIELD TEST

### 3.1 Engineering background

Due to age, the factory building has been degraded in the process of using and has a hidden trouble

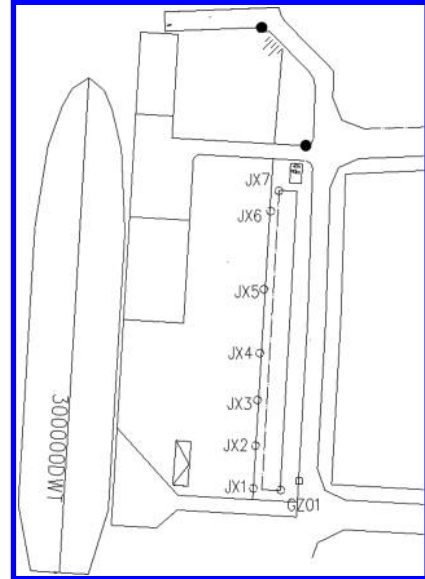


Figure 3. Monitoring point of factory building.

in security issue. The main deformation monitoring work is measuring the settlement and inclination of the factory building. The work has begun in October 2013 and has been finished in March 2014, lasting half-a-year.

### 3.2 Arrangement of measuring points

When we arrange sensor placement for factory building, we should fully consider the influence of the wires on daily work. On this basis, we optimize economic efficiency by the way of choosing sensor wire path which has the shortest and the least interference to the factory daily operation. According to the factory building layout and engineering characteristics, we decorate seven monitoring points and a datum mark. Monitoring points (JX1, JX2, JX3, JX4, JX5, JX6, JX7 and GZ01) are shown in Figure 3.

## 4 MONITORING DATA ANALYSIS

### 4.1 Monitoring data statistics

The factory building has been real-time monitored for more than six months. Monitoring frequency



is twice a day and no less than 50 times a month. According to the surrounding environmental situation, we appropriately increase or decrease monitoring frequency. Based on the monitoring data, we draw the settlement curve in Figure 4 and the biaxial angle statistics in Table 2.

#### 4.2 The summary and rating of monitoring

The settlement points JX1, JX2, JX5, and JX7 are larger than others. The biggest was JX5 whose

accumulated maximum settlement is 11.1 mm and maximum subsidence rate (the ratio of cumulative settlement monitoring and monitoring time) is 0.0845 mm/d. Generally speaking, the settlement point which is close to the road side is bigger than others. The inclination point of JX2 and JX5 are larger; their maximum angle is 0.045 degrees.

According to the current national standard “industrial building reliability appraisal standard” GB 50144-50144, we assess the safety of factory building which is on A level.

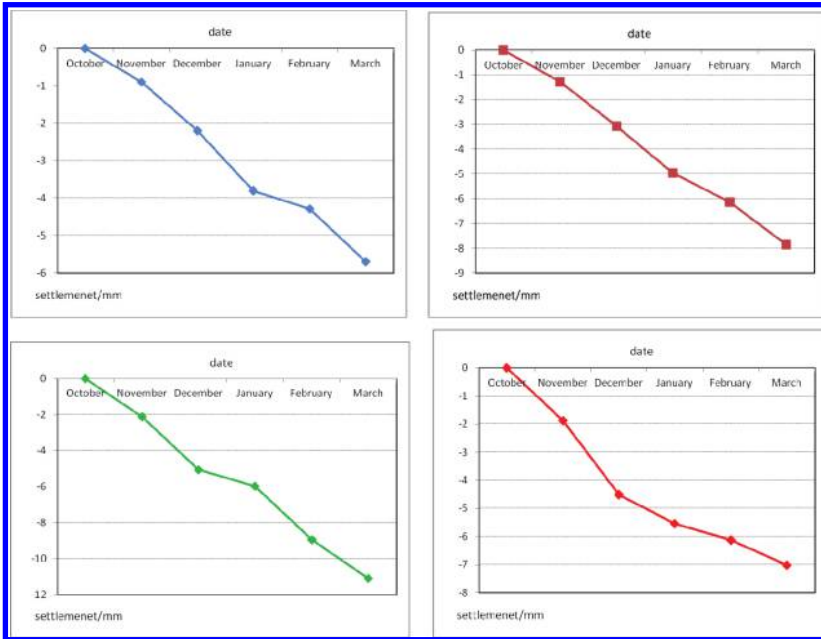


Figure 4. The accumulated settlement curve of four monitoring points (JX1, JX2, JX5, and JX7).

Table 2. The biaxial angle statistics of factory building.

	Direction	October–November	November–December	December–January	January–February	February–March	Max inclination
JX1	x	0.02	0.02	0.01	0.01	0.01	0.028
	y	-0.02	-0.01	-0.02	-0.02	-0.02	
JX2	x	0.01	0.01	0.02	0.02	0.01	0.045
	y	0.03	0.03	0.04	0.03	0.02	
JX3	x	0.01	0.00	-0.01	-0.01	0.01	0.032
	y	-0.02	-0.03	-0.03	-0.03	-0.02	
JX4	x	-0.01	-0.01	0.00	0.01	-0.01	0.032
	y	0.02	0.03	0.03	0.03	0.02	
JX5	x	-0.02	-0.02	-0.02	-0.02	-0.01	0.036
	y	-0.03	-0.02	-0.01	-0.01	-0.02	
JX6	x	-0.01	-0.02	-0.03	-0.04	-0.01	0.045
	y	0.01	0.01	0.01	0.02	0.01	
JX7	x	-0.01	-0.01	0.00	0.00	-0.01	0.032
	y	-0.03	-0.03	-0.03	-0.03	-0.02	

## 5 CONCLUSION

Real-time deformation monitoring system for factory building overcomes the defects of the traditional monitoring which cannot finish timely, long-term monitoring. The interface is simple and users can see the deformation of structure on the remote PC and mobile phones. Monitoring data and warning signs can be displayed in the form of dynamic graphic in time. The feasibility of the system is verified by the application of real-time deformation monitoring system. Monitoring results show that the system is able to coordinate the operation and realize the expected function design. What is more, the system provides a useful data for the structure safety assessment method and accumulates engineering experience for similar deformation monitoring system.

## ACKNOWLEDGMENTS

The authors wish to acknowledge the supports of the Zhejiang Science and Technology Program (2012C23039).

## REFERENCES

- [1] Jiao JianHui. Building deformation measurement and its method [J]. Chinese and Overseas Architecture. 2001 (02): 45–46.
- [2] Farrar C.R., Worden K. An introduction to structural health monitoring [J]. Philosophical Transactions of the Royal Society A: Mathematical, Physical and Engineering Sciences. 2007, 365(1851): 303–315.
- [3] Xiong Huixia, Li Huiqiang. Single-layer factory building reliability evaluation study [J]. Academic Forum of Nandu (natural science edition), 2001, 21(3): 53–54.
- [4] Farrar C.R., Sohn H.Y. Condition/damage monitoring methodologies. [R]. Los Alamos National Laboratory, 2001.
- [5] Kim H. Sensors and systems for structural health monitoring [P]. U.S. Patent No. 7,117,742. 2006.
- [6] Hao Jian, li Ming, Zhou Taoyu. Civil engineering structural health monitoring research progress [J]. Transportation Science & Technology, 2008 (6): 26–29.

## Analysis for seismic performance of shear wall-steel truss structure system

Weidong Sun, Xinyu Niu & Hongbin Chen

Jilin Key Laboratory of Disaster Prevention and Reduction, Faculty of Civil Engineering, Changchun Institute of Technology, Changchun, China

**ABSTRACT:** In order to reduce the seismic response of concrete shear wall structure and prevent it from brittle failure, concrete shear wall and steel truss are combined to form the shear wall-steel truss structure system, and the steel truss system is equipped with buckling-restrained brace to strengthen the energy consumption capacity of the structure and decrease the seismic response. A framed-tube structure model is used as example in this paper. The tube has ordinary concrete tube structure and shear wall-steel truss structure. Dynamic elastic-plastic time-history analysis method is used to analyze the seismic response of different cases under the rarely met earthquake. The calculation result showed that, seismic response of the shear wall-steel truss structure system's storey shift, speed, acceleration and total shearing force of substrate has been effectively controlled, thus reducing the seismic response of the overall structure.

**Keywords:** shear wall-steel truss structure; seismic response; time history analysis; seismic damping effect

### 1 INTRODUCTION

Concrete shear wall structure is featured by big rigidity and strong anti-lateral force, which is extensively applied in high-rise buildings; the shear wall, however, has big rigidity resulting in stronger seismic response, and easily causes brittle failure. Its main problems are to ensure the shear wall structure to have enough anti-lateral force rigidity under normal operation, and reduce seismic response in case of rarely met earthquake to prevent against brittle failure. Therefore, domestic and foreign scholars have studied many approaches [1, 2]. Current approaches mainly start with the shear wall itself and take measures, leading to more difficult construction and higher cost. The author has proposed, based on the structure system, combining concrete shear wall and steel truss to form shear wall-steel truss structure system, and installing some buckling-restrained brace dampers in the truss system to increase the energy consumption capacity of the structure, and lessen its seismic response [3]. The schematic diagram of shear wall-steel truss structure system is as shown in Figure 1. The buckling-restrained brace has advantages of low cost, good energy consumption, very stable hysteresis property, excellent low cycle fatigue property, strong adaptability to environment and temperature, and long-term stable performance [4]. In normal operation stage, the buckling-restrained brace can be used as ordinary rod; in case of rarely met earthquake, it can be yielded first to play its role in energy consumption. Such structure owns

anti-lateral force rigidity of the shear wall, and the steel truss has excellent ductility and energy consumption capacity, which only needs simple construction, convenient for repair and replacement after earthquake. When a hole opening is required

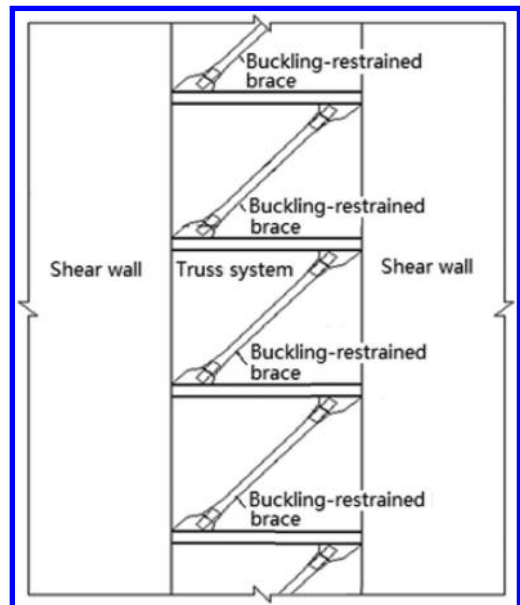


Figure 1. Schematic diagram of shear wall-steel truss structure system.

for construction, a reasonable support form can be placed for making the hole opening. If the hole is not unnecessary, thermal insulation materials can be filled.

In order to analyze the seismic resistance of shear wall-steel truss structure system, in this paper, a framed-tube structure model is taken as an example. The tube has ordinary concrete tube structure and shear wall-steel truss structure. Dynamic elastic-plastic time-history analysis method is used to analyze the seismic response of different cases under the rarely met earthquake to compare the seismic damping effect of steel truss-shear wall structure.

## 2 CALCULATION MODEL AND CALCULATION CASE

### 2.1 Calculation model

The layout of frame-core tube structure is as shown in Figure 2. The structure has 27 storeys, substrate storey is 4.2 m high, and 2–27 storeys are 3.6 m high. Specific dimensions of columns, beams and wall components are as shown in Table 1. The floor thickness is 0.12 m. The floor's constant standard load is 4 kN/m<sup>2</sup>, standard live load 2.5 kN/m<sup>2</sup>, roof's constant standard load, and standard active load 2 kN/m<sup>2</sup>. The standard linear load of frame beams surrounding the storey is 8.0 kN/m, and the standard linear load of frame beams surrounding the roof is 3.0 kN/m.

### 2.2 Calculation case

3 structural cases are adopted in this paper: CASE1: the tube has ordinary concrete tube structure, and

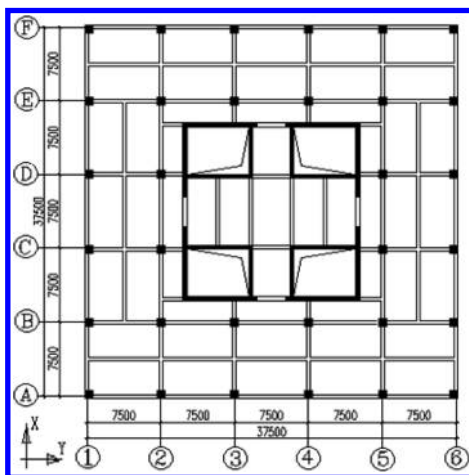


Figure 2. Structural layout of frame-core tube.

Table 1. Dimension table of calculation model construction members.

Member	Dimension (mm)	Concrete grade	Storey
Column	1000 × 1000	C50	1–5 storeys
	900 × 900		6–10 storeys
	800 × 800		11–15 storeys
	700 × 700		16–20 storeys
	600 × 600		21–27 storeys
Secondary beam	300 × 600	C40	1–27 storeys
Main beam	350 × 750	C40	1–9 storeys
	350 × 700		10–19 storeys
	300 × 700		20–27 storeys
	400	C50	1–9 storeys
	300		10–19 storeys
	200		20–27 storeys

hole openings are made at X and Y directions of the core tube (see Fig. 2), with width 3 m, height of first storey 2.7 m, and height of other storeys 2.4 m. The place with the opening width is installed with ordinary reinforced concrete coupling beams; CASE2: the tube has shear wall-braced frame, and the truss can meet the construction requirements and is arranged for the purpose of reasonable stress and convenient construction. The steel truss is placed at X direction of the tube is as shown in Figure 1. The diagonal web member is equipped with buckling-restrained brace. Y direction of the tube can accomplish the construction functions. The hole width span is broadened, that is, the horizontal span of truss in the middle of the tube is increased. The diagonal web member is arranged as reverse V shape for setting up openings. The schematic diagram of truss is as shown in Figure 3. The diagonal web member also adopts buckling-restrained brace; CASE3: the structural layout same as CASE2 is used. The only difference is that, buckling-restrained brace is only used in truss diagonal web members at 8–12 storeys with big calculation shift in CASE1, and the remaining storeys of truss diagonal web members are ordinary steel rods.

When designing truss rods in CASE2 and CASE3, we will enable two cases inter-storey angle shift under the effect of frequent earthquake to be basically in conformity with CASE1, ensure the deformation capacity of two cases during normal application, and make two cases realize early yield of buckling-restrained brace when the big earthquake happens. Rod types and dimensions of CASE2 and CASE3 got from repeated calculations are as shown in Figure 3 and Figure 4.

Main aim of this paper is to compare the seismic response of three cases in the effect of rarely

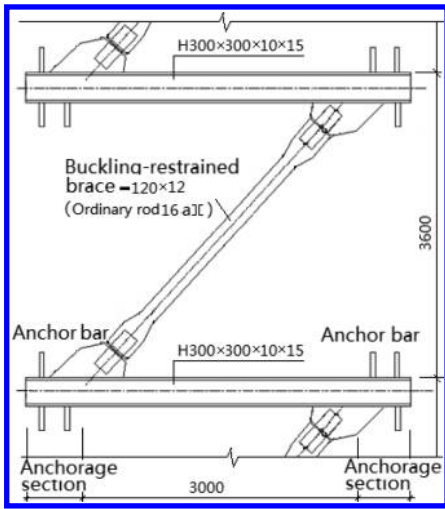


Figure 3. Single inclined layout of diagonal web member.

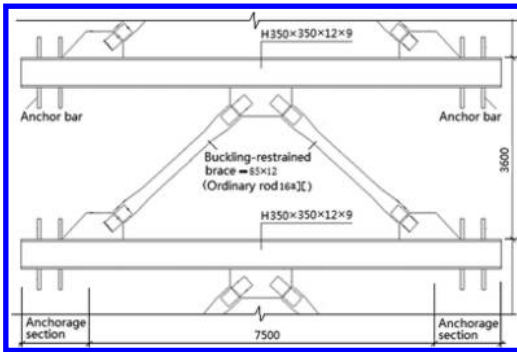


Figure 4. Schematic diagram of reverse V shape layout of diagonal web member.

met earthquake. The buckling-restrained brace and some structural members will enter elastic-plastic stage in the effect of rarely met earthquake, so dynamic elastic-plastic time history analysis method is used for analysis. This case uses components of EL Centro seismic waves in 1940 at south and north directions for dynamic elastic-plastic time history analysis. Maximum acceleration of the seismic wave is  $3.417 \text{ m/s}^2$ . Ground acceleration time history is as shown in Figure 5.

Midas/Gen analysis software is used for dynamic elastic-plastic time history analysis, buckling-restrained brace is simulated with nonlinear linkage unit—hysteresis system in Midas/Gen, and the hysteresis system is consisted of 6 springs with unidirectional plasticity at the degree of freedom. In this project, only  $D_x$  (axial direction) has characteristic

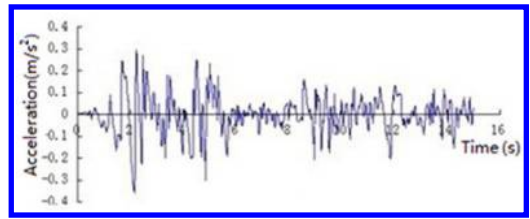


Figure 5. Schematic diagram of components acceleration of EL centro seismic waves at south and north directions.

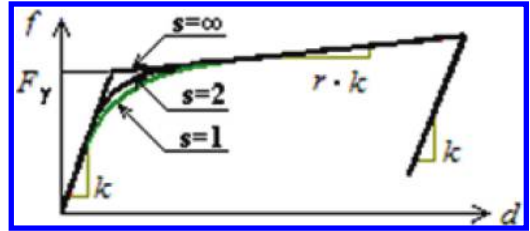


Figure 6. Model of buckling-restrained brace hysteresis system.

value of spring plasticity. The model of hysteresis system is as shown in Figure 6. According to the early-stage buckling-restrained brace test result, set up elastic rigidity  $k$  of buckling-restrained brace as  $1.24 \times 10^6 \text{ kN/m}$ , yield strength  $F_y$  2632 kN, specific value  $r$  between rigidity and elastic rigidity after yielding of buckling-restrained brace 0.1, and yield index  $s$  of buckling-restrained brace 2. The relational expression of strength  $f$  and deformation  $d$  is:

$$f = r \cdot k \cdot d + (1 - r) F_y \cdot z. \quad (1)$$

### 3 CALCULATION RESULT ANALYSIS

#### 3.1 Comparative analysis of shift, speed and acceleration

The dynamic elastic-plastic time history analysis result of shift, speed and acceleration at top storey and the ninth storey in 3 cases is as shown in Table 2. The curve of shift, speed and acceleration time history curve at the ninth storey is as shown in Figure 7, Figure 8 and Figure 9. According to the analysis result, the seismic response of shear wall-steel truss structure system regarding storey shift, speed and acceleration is smaller than that of ordinary concrete tube structure. Compared with CASE1, average control rate of three indexes in CASE2 and CASE3 is 10%–20%; based on the contrast between CASE3 and CASE2, the average control rate at each storey is similar, indicating that installing buckling-restrained brace at the

Table 2. Analysis result table of shift, speed and acceleration.

Seismic response	CASE1	CASE2	
	Seismic response peak value	Seismic response peak value	Control rate compared with CASE1
Top storey shift (m)	0.169	0.135	18.45%
	-0.143	-0.119	
Top storey speed (m/s)	0.912	0.754	11.65%
	-1.005	-0.945	
Top storey acceleration (m/s <sup>2</sup> )	5.586	4.789	16.49%
	-7.576	-6.158	
9th storey shift (m)	0.033	0.031	13.64%
	-0.033	-0.026	
9th storey speed (m/s)	0.227	0.180	21.03%
	-0.206	-0.162	
9th storey acceleration (m/s <sup>2</sup> )	2.364	1.770	21.34%
	-2.877	-2.372	

Seismic response	CASE3		
	Seismic response peak value	Control rate compared with CASE1	Control rate compared with CASE2
Top storey shift (m)	0.145	16.19%	-2.86%
	-0.117		
Top storey speed (m/s)	0.736	14.97%	-2.86%
	-0.898		
Top storey acceleration (m/s <sup>2</sup> )	4.773	17.41%	3.68%
	-6.041		
9th storey shift (m)	0.027	21.21%	1.12%
	-0.025		
9th storey speed (m/s)	0.162	26.94%	8.34%
	-0.154		
9th storey acceleration (m/s <sup>2</sup> )	1.718	25.22%	4.84%
	-2.212		

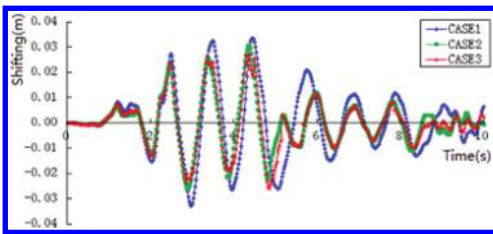


Figure 7. Curve graph of 9th storey shift time history.

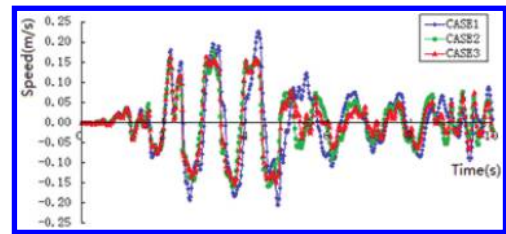


Figure 8. Curve graph of 9th storey speed time history.

storey with big lateral sway can get good effect. The buckling-restrained brace placed at the storeys with small inter-storey shift is always elastic, stopping the ordinary steel rod from exerting the role of energy consumption and seismic damping. The comparative diagram of inter-storey shift angles of CASE1 and CASE3 is as shown in Figure 10. The correlation curve can show that, under the effect of rarely met earthquake, the inter-storey

shift angle of shear wall-steel truss structure has become smaller than that of ordinary concrete tube structure.

### 3.2 Comparative analysis for total shearing force at the structure substrate

The analysis result of total shearing force at the structure substrate is as shown in Table 3.

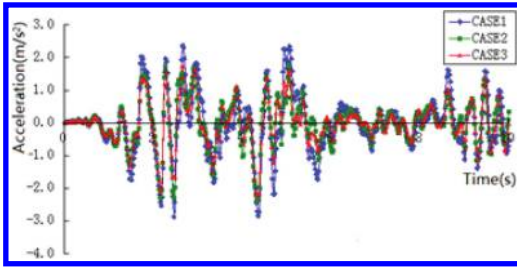


Figure 9. Curve graph of 9th storey acceleration time history.

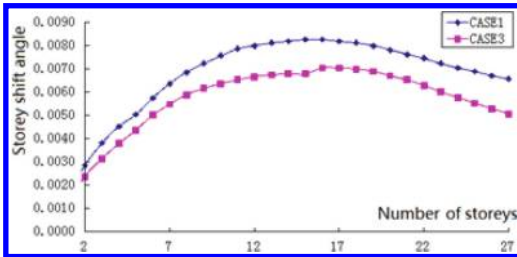


Figure 10. Comparative graph of inter-storey shift angles of CASE1 and CASE3.

Table 3. Table of analysis result of total shearing force at the structure substrate.

CASE	CASE1	CASE2	
Content	Seismic response peak value	Seismic response peak value	Control rate compared with CASE1
Total substrate shearing force (kN) and control rate	50118 -48231	46635 -39678	12.34%
CASE	CASE3		
Content	Seismic response peak value	Control rate compared with CASE1	Control rate compared with CASE2
Total substrate shearing force (kN) and control rate	45531 -36763	16.46%	4.86%

According to the time history analysis result, the total substrate shearing force peak value of shear wall-braced-frame system fell by 12.34% and 16.46% compared with the ordinary concrete tube structure, so the difference between CASE2 and CASE3 is not obvious.

#### 4 SUMMARY

Based on the analysis for dynamic elastic-plastic time history in the effect of rarely met earthquake of three cases, the following conclusion is given below:

- Compared with ordinary reinforced concrete tube structure case, seismic response of the shear wall-steel truss structure system's storey shift, speed, acceleration and total shearing force of substrate has been effectively controlled.
- In the shear wall-steel truss structure system, all storeys are arranged with buckling-restrained brace. Compared with the case that only sets up buckling-restrained brace at the storeys with big inter-storey shift, the difference between their seismic damping effect is not big, indicating that, installing buckling-restrained brace at the storeys with big inter-storey shift can exert stronger seismic damping function. The buckling-restrained brace placed at the storeys with small inter-storey shift is always in elastic stage, so it can only play a role of the normal steel rod, and its energy consumption and seismic damping functions cannot be fully exerted.

#### ACKNOWLEDGEMENTS

This project was financially supported by the Education Department of Jilin Province, Wang Yu from Midas company and professor Xiangyang Zou from Changchun Institute of Technology. This project was financially supported by the Education Department of Jilin Province, Wang Yu from Midas company and professor Xiangyang Zou from Changchun Institute of Technology.

#### REFERENCES

- [1] Hongying Dong, Feng Jiang, Wanlin Cao. Development and Research in Seismic Performance of Steel-Concrete Composite Sheer Wall. *Journal of Earthquake Engineering and Engineering Vibration*, Vol. 32(1)(2012), p. 54.
- [2] Yanlin Guo, Ming Zhou, Quanli Dong. Experimental Study on Three Types of Steel Plate Sheer Walls *Journal of Building Structures*, Vol. 32(1)(2011), p.17.
- [3] Weidong Sun, Jiuyang Li. Chinese patent CN201220386739.7.(2013).
- [4] Baolin Hu, Guoqiang Li, Feifei Sun. The Current Research and Domestic and Foreign Application of Buckling-Restrained Braced Frames. *Building Science Research of Sichuan*. Vol. 33 (4)(2007), p. 9.

# Seismic performance and retrofit for a historic concrete building in Shanghai

H.N. Wang

*College of Civil Engineering, Shanghai Normal University, Shanghai, China*

H.B. Liu

*Shanghai Research Institute of Building Sciences, Shanghai, China*

*Shanghai Key Laboratory of New Technology Research on Engineering Structure, Shanghai, China*

**ABSTRACT:** Seismic retrofitting of the cultural heritage, especially of the historic buildings, requires compliance with the severe restrictions of Code related to the preservation of the original artistic and structural features. In order to meet the rebuilding needs, safety inspection, seismic evaluation and strengthening design for a historic building are carried out. This building, completed in 1930s, was designed without considering the effect of possible earthquakes which cannot meet the current seismic criteria. Safety and seismic behavior are analyzed. According to the evaluation, the design idea and strengthening methods are put forward.

**Keywords:** historic building; seismic evaluation; retrofit; design criteria

## 1 INTRODUCTION

There are many historic buildings in Shanghai. In order to reuse the available existing buildings, structures must be adapted for the new use and upgraded to current building code requirements. However, few historic buildings meet current code seismic requirements for life safety, and most have architecturally significant elements that are threatened by future earthquakes.

The need for evaluating the seismic adequacy of those existing buildings has come into focus following the damage of numerous concrete structures during earthquakes. In particular, the seismic rehabilitation of older concrete buildings, which were designed prior to the advent of modern seismic design codes, is a matter of growing concern.

We know almost everything about earthquakes (in reality every earthquake teaches us something more) and how to mitigate their risks but the major problem are all the buildings erected before the Standards were issued. Seismic retrofitting means improving the resistance of a structure so that it will be in accordance with the seismic standards. Hence, it is necessary to evaluate these building's seismic performance and to retrofit them using appropriate methods.

## 2 APPLICATION EXAMPLE

A typical historic concrete building is selected as an application example to evaluate the seismic

performance of existing historic buildings in Shanghai (see Fig. 1). As many rehabilitation projects, the existing as-built documentation of the structural system was sparse. This structure was designed without considering the effect of possible earthquakes. The seismic design forces are significantly lower than what is now required by the current standard.

A 9-story historic building is located in Shanghai, China, and was designed and constructed in early 1930s per the applicable building codes at the time of construction. It is a reinforced concrete frame building with brick infill walls, and elevator shafts, flues and part of stair well walls are solid reinforced concrete walls. Therefore, the lateral system for the building consists of a non-ductile reinforced concrete frame system. The building is U-shaped in plan, as shown in Figure 1, with two,

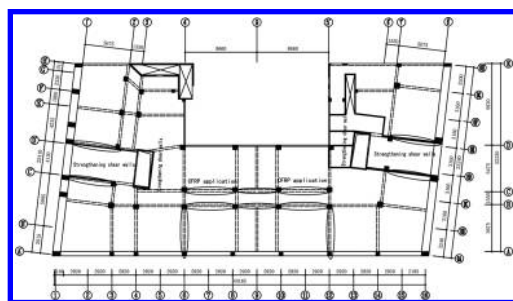


Figure 1. Plan view of case study building.



9-story wings almost equally expanded 9.3 m. The 28.88 m tall building is 44.2 m long and 22.2 m wide. The first story height is 3.97 m and the others are 3.05 m. There are four elevators. The building is supported on a pile foundation system.

### 3 EVALUATION OF EXISTING BUILDING

In any retrofit project the foremost problem the structural engineer is faced with is the evaluation of the existing structural strength and deformation capacity. For nonhistoric structures, these issues are not very important since the primary intent of retrofit there is to provide life safety. For historically significant structures, where the performance objective extends beyond those of life safety and includes protection of architectural features, a reliable estimate of the existing structural capacity and of the dynamic characteristics of the structure is important.

#### 3.1 Comprehensive material testing

Coring samples and laboratorial testing for concrete and reinforcing steel was conducted by a licensed testing laboratory.

According to standard requirements, a minimum of three samples of concrete cores and reinforcing steel were extracted from the various structural components and tested. The final testing result shows that the concrete strength ( $f_c$ ) varies from 16.8 MPa to 25 MPa, and the average is 21.6 MPa. The yield strength ( $f_y$ ) of reinforcing steel varies from 500 MPa to 512 MPa. In addition to destructive tests, several site visits and condition assessments investigations were conducted. Concrete members appeared intact with minimal cracking or evidence of reinforcement corrosions. The in-situ dimensions, member sizes, reinforcement sizes, and concrete cover are all measured.

#### 3.2 Modal analysis

Structural analysis was performed to assess the seismic performance of the building and identify deficiencies (see Fig. 2). The analytical model of the building incorporated the dimensions of structural members measured on site. The beam-column joints located around the perimeter of the building are taken as rigid joints. The interior beams of frame are taken as hinged joints due to fewer bars. Except the shear walls of two elevator shafts, others can't link with the ground. Structural walls and floor slabs were modeled using shell elements, whereas line elements were used for the beams and columns. Walls and columns were assumed to be restrained at the foundation level with full fixity.

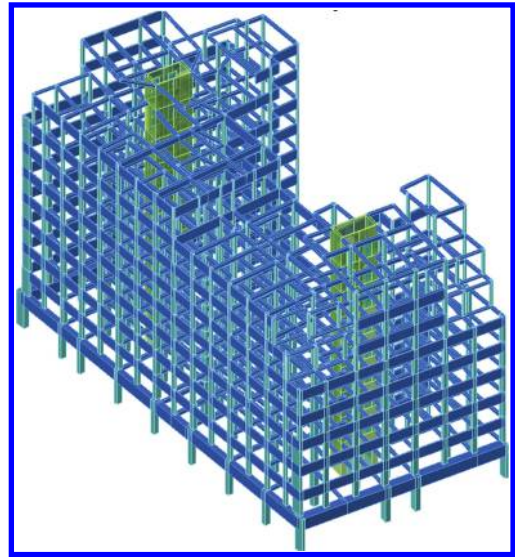


Figure 2. Model of structure.

#### 3.3 Structural analysis

Seismic fortification intensity is 7 degree. According to the result, the building periods in the x- and y-directions are similar. The first mode is 1.20 s in the X direction. The second one is 1.19 s, which represents the vibration in the Y direction. The third mode is 0.86 s, which represents the torsional vibration of the structures. The maximum story drifts is 1/547 in the X direction and 1/486 in the Y direction. This analysis clearly indicated that the building has lowly torsional response and excessive story drift.

A preliminary evaluation of the building revealed several seismic deficiencies, including the following.

(1) non-ductile detailing, such as lack of beam confinement reinforcement, (2) flexible lateral system with excessive building deflections, and (3) inadequate strength of the shear walls at the stairwells. In addition, the foundation pressure under columns mainly meets the requirements of bearing capacity of foundation soil.

#### 3.4 Structural shortcomings in details

A preliminary investigation of this historic structure was performed to determine the building's ability to adequately respond to future seismic events. The results of analytical investigations showed that the building in its current configuration possessed major seismic deficiencies. The main structural deficiencies are the following:

- Structural system: irregularities in the column grid; the lack of beams at the corridor is an irregularity; discontinuity in vertical lateral

components due to many transfer components. All of these can lead to important damage in this part of the building during an earthquake.

- Reinforcement details: the lack of bars at the end of beams; the lack of hooping in the core area of beam-and-column joint; no bars at the top of slabs.
- Size of member section: part of the columns section is too small; the thickness of elevator shafts walls, which act as shear walls, is small.
- Other details: Inadequate anchorage bars of column reinforcement into the filler walls.

In conclusion, seismic deficiencies that should be evaluated include shear walls that are not properly reinforced; irregular features like concrete walls or columns; components weakened due to less reinforcement and sections; insufficient lateral capacity of the building. The methods described below are commonly used for concrete buildings based on these deficiencies.

## 4 RETROFIT DESIGN

### 4.1 Design criteria

Since the renovation constitutes major structural changes, the structure in the new configuration must comply with the current seismic provisions of 2010 *Code for Seismic Design of Buildings* and 2009 *Technical Specification for seismic strengthening of Buildings* (Ministry of Construction of the People’s Republic of China), which provide guidance for evaluating the seismic performance of existing structures and determining the necessary retrofitting methods to achieve the performance objectives. In addition, since it’s a historical building, it must comply with the more stringent requirements of 2004 *Protective Technology Criterion for Remarkable Historic Architecture in Shanghai*. Furthermore, Shanghai Cultural Relics Protection Law stipulates owners of the protected buildings cannot change the facade, structure or inner decoration of the buildings.

### 4.2 Retrofit objective

The main objective of retrofit is to be cost-effective, applicable and functional solution that upgrades the seismic safety of the building to meet the desired performance criteria. An effective retrofit application should avoid the possibility of non-ductile failure modes by proper precautions.

### 4.3 Strengthening shear walls

To mitigate the above-mentioned seismic deficiencies, a comprehensive retrofit methodology

was investigated. The components of the seismic retrofit are briefly discussed here.

Strengthening shear walls with RC layers is a conventional method of strengthening in China. In this method a mesh of reinforcing bars is first placed in one or both sides of the wall and then it is covered with a thin concrete layer (Fig. 3). The concrete layer and reinforcing bars should be anchored to the wall to ensure that the wall and RC layers work together.

Considering the service requirement of elevator shafts, a 60 mm thick shotcrete cover would be applied to the exterior faces of the perimeter walls. The shotcrete will be reinforced with a horizontal and a vertical mat of closely spaced No. 8 reinforcement. Sufficient dowels will be provided to attach the shotcrete to the existing walls to ensure that the completed unit works in unison. As a result, the effective reinforcement ratio and spacing of reinforcement would then meet the current Code requirements. By extending the shotcrete vertical reinforcement mat through the slab, these bars would be used to provide sufficient anchorage of the slab.

### 4.4 Strengthening beams using Carbon Fiber Reinforced Polymer (CFRP)

The substandard beams would also be retrofitted by externally bonded CFRP. CFRP can be used for increasing beams strength. It is observed that CFRP retrofits increase the flexural and shear strength of beams. In addition to the high strength-to-weight ratio and excellent corrosion resistance of CFRP composites, the bonded CFRP strengthening technique has many advantages, such as its simplicity of construction and minimal impact on the dimensions and service conditions of existing structures. Due to the flexibility of CFRP fabrics, they are also easy to install and can have an advantage when the retrofit is applied at hard-to-reach locations.

One or two horizontal CFRP sheet and fibers oriented in longitudinal direction was first installed

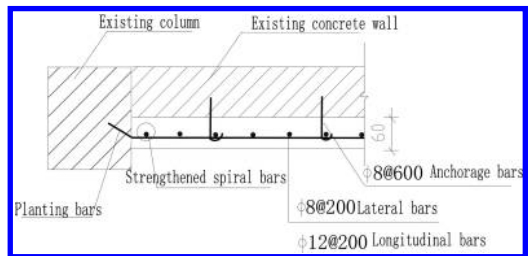


Figure 3. Typical detail of concrete wall strengthening with reinforced concrete layer.

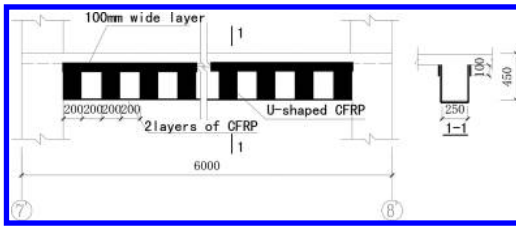


Figure 4. Layout of CFRP strengthening beam.

at each side of the beam web (Fig. 4). Two layers of CFRP bonded at the bottom of the whole beam. The vertical U-shaped CFRP sheets were then applied followed by the installation of a mechanical end anchorage. The U-shaped CFRP sheets had a width of 200 mm and a center-to-center spacing of 400 mm. The web corners were chamfered to a radius of approximately 10 mm prior to CFRP application.

## 5 SUMMARY AND CONCLUSIONS

The traditional historical buildings are generally more affected during earthquakes. For historic buildings, the selection of retrofit should be based on the existing constraints, desired superstructure performance, and the overall economics. There are number of seismic retrofit techniques available for concrete structures, depending on the type and

condition of the deficiencies. It is important to obtain accurate as-built information and analytical data to perform a seismic evaluation of the existing structure and to select the appropriate retrofitting strategy. The selection of retrofit is based on the results of seismic performance evaluation. Furthermore, appropriate seismic retrofit can effectively achieve life safety criteria and minimize damage to the typical architectural features of historic buildings.

## REFERENCES

- Binici, B., Ozcebe, G., and Ozcelik, R. 2007. Analysis and design of FRP composites for seismic retrofit of infill walls in reinforced concrete frames. *Composites, Part B*, 38(5–6), 575–583.
- Bousselham, A., and Chaallal, O. 2006. Behavior of RC T-beams strengthened in shear with CFRP: An experimental study. *ACI Struct. J.*, ICE, Melbourne, Australia 103(3): 339–347.
- GB50011 2010. Code for seismic design of buildings, Ministry of Housing and Urban-Rural Development of People's Republic of China.
- JGJ116 2009. Technical specification for seismic strengthening of buildings, Ministry of Housing and Urban-Rural Development of People's Republic of China.
- Miyamoto, H.K. and Scholl, 2002. Seismic rehabilitation of an historic non-ductile soft-story concrete structure using fluid viscous dampers, *Proceedings of the 11th, World Conference on Earthquake Engineering*, 2002.

## Strength model of FRP confined concrete cylinders

Ji-Shuai Wang & Dong-Sheng Gu

College of Environmental and Civil Engineering, Jiangnan University, China

**ABSTRACT:** Fiber Reinforced Polymer or plastics (FRP) has been widely used as a new material for strengthening existing civil infrastructures, due to their advantages in the high tensile strength, light weight, ease for construction, no addition to dimensions of members etc. There have been a number of studies on the uses of this technique. But theoretic researches of those still drops behind in its applications in construction and the need being further perfected. In order to confirm the calculating method of FRP confined concrete circular columns in engineering practice and based on relevant results of studies, authors have analyzed the representational FRP confined concrete strength models and compared the value of these models with the data of relevant experiments. Analyzed the precision from strength constraint factor and concrete strength, and fitted the collected data for two different forms and then proposed an improved simplified model for calculating axial compressive strength of FRP confined columns. The value of this model could tally with the experimental results. The proposed model may be a reference for practical engineering.

**Keywords:** FRP circular concrete columns; the axial compressive strength; strength calculating model

### 1 INTRODUCTION

FRP confined concrete is of passive constraints. When FRP confined concrete columns under axial pressure and lateral expansion of concrete column results in FRP materials' hoop tension, tension of FRP with hoop strength also, in turn, limits the lateral of the concrete column, which make the restraining affection of concrete column. What's more, making concrete column in the three-way compression state, and the bearing capacity of reinforced concrete columns and ductility can be increased at the same time. Starting from the initial loading stage, the difference of ring expansion deformation between FRP material and concrete was produced because of the difference of stiffness and Poisson's ratio. The deformation of concrete is greater than FRP outsourcing material, and then a squeeze between the two is made, generating constraint stress. Early constraint stress to a certain extent delayed the initial cracks to appear. With the increase of axial load, longitudinal cracks began to appear, and the lateral strain growth is increasing quickly, and this intensifies the squeezing effect between FRP outsourcing material and the core concrete, and due to the increasing of restraint stress, the further development of longitudinal cracks in the concrete gets restricted, and also the compressive strength of the concrete is improved. When load increases to maximum axial load, FRP material is destroyed and the longitudinal stress of the core concrete is also at a peak, eventually it

leads to the destruction of the components. The core concrete in three-way compression state in the whole loading process, and the FRP material in a vertical pressure—ring pull bidirectional stress state in the late stress and FRP materials mainly subject to ring tensile stress. The stress of the FRP material mechanics model is as shown in Figure 1. The thickness of FRP, ultimate tensile strength and the diameter of the core concrete have an effect on the size of the core concrete binding. Through calculations we can get the formula of  $f_i = 2f_j t/D$ ,  $f_j$  on behalf of the FRP binding of circular concrete columns;  $f_j$  and  $t$ , respectively, representing the ultimate tensile strength of FRP materials and thickness;  $D$  representing the diameter of the core concrete.

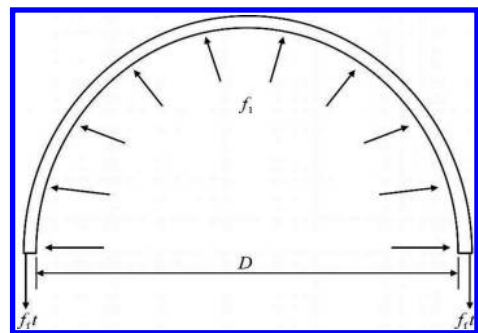


Figure 1. The stress of the FRP material mechanics model.

## 2 DATA COLLECTION

Since the 1980s, various countries' scholars have done a lot of experimental studies on FRP confined concrete. The author collected 182 groups of experimental data of past scholars. Having established  $f_l/f_{co}$  and  $f_{cc}/f_{co}$  as the X axis and Y axis of rectangular coordinate system as shown in the Figure 2,  $f'_{cc}$  and  $f_{cc}$ , respectively, represent the calculation axial compressive strength and experimental axial compressive strength of FRP confined concrete specimens,  $f_{co}$  represent the axial compressive strength of concrete specimens of no lateral stress constraints.

## 3 THE EXISTING CALCULATION MODELS

1. At present, scholars home and abroad have proposed many strength model. Listed some of them which have representation as follows:

$$\frac{f'_{cc}}{f_{co}} = 1 + 3.4 \left( \frac{f_l}{f_{co}} \right) \quad (1)$$

$$\frac{f'_{cc}}{f_{co}} = 1 + 2.25 \left( \frac{f_l}{f_{co}} \right)^{\frac{5}{4}} \quad (2)$$

$$\frac{f'_{cc}}{f_{co}} = 1 + 2.0 \left( \frac{f_l}{f_{co}} \right) \quad (3)$$

2. To see the difference of calculated value and experimental value, the corresponding charts are listed in the Figure 3. From the chart we can see the calculated value of Wang and Wu's model is larger and the precision of Youssef's

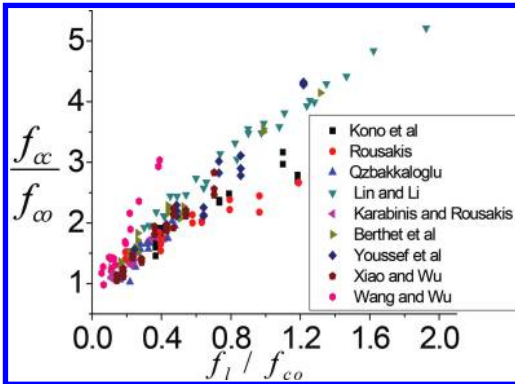


Figure 2. Scholars and their data.

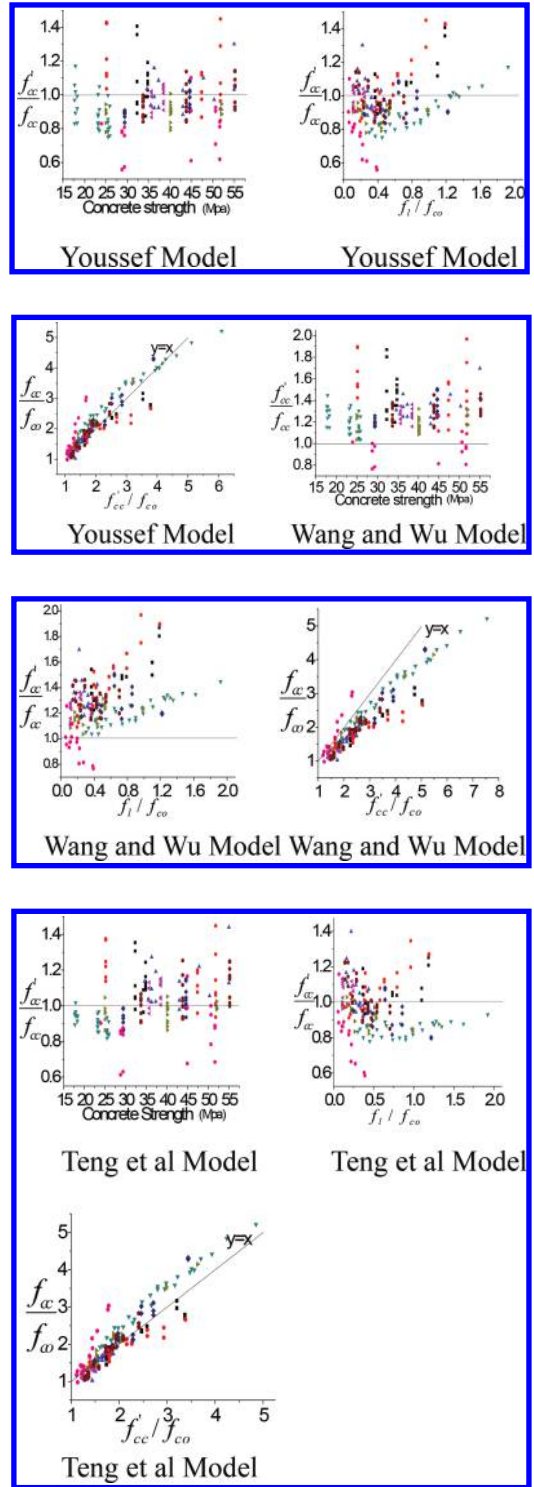


Figure 3. Performance of existing models for circular columns.

and Teng's model is higher than Wang and Wu's model in this data. But the strength calculation value of Youssef's and Teng's model is respectively bigger and smaller than the experimental value. So it is necessary to put forward the precise calculating model which has more extensively applicable scope.

#### 4 FITTING CALCULATION MODEL

In this paper, by fitting the collected data, we get two different forms of strength calculating models listed in the Figure 4 and 5. The accuracy from the aspects of constraint intensity coefficient and strength of concrete are compared. It can be easily obtained by chart, the precision of the two fitting models are similar, and they basically can make all the data scatter evenly distributed on both sides of bisector.

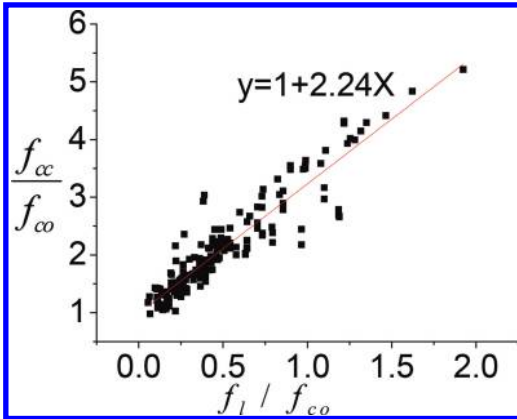


Figure 4. Linear fitting model.

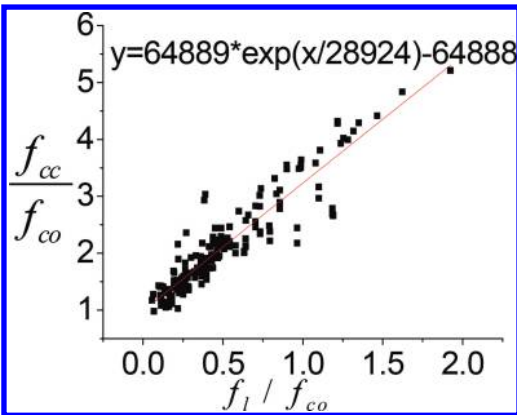


Figure 5. Exponential fitting model.

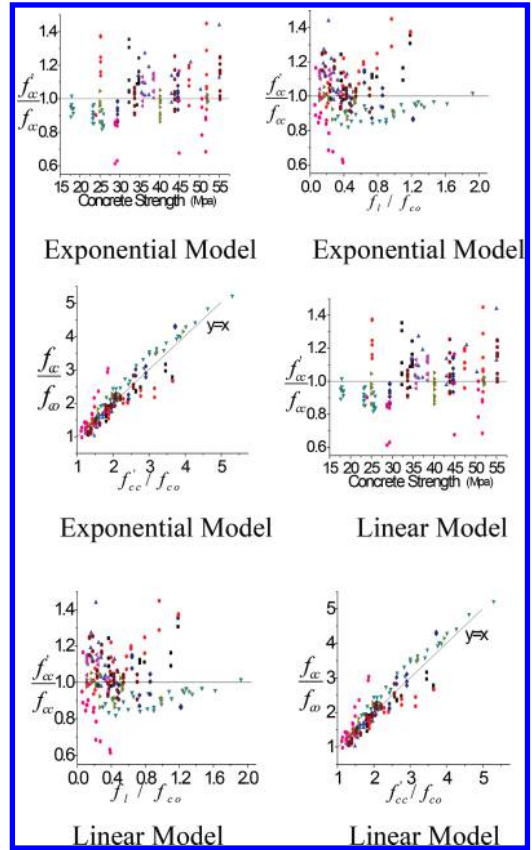


Figure 6. Performance of fitting models for circular columns.

#### 5 MODEL ANALYSIS AND COMPARISON

In order to select the optimum FRP strength calculation model, the average of  $f'_{cc}/f_{co}$ , discrete coefficient (Cv) and  $\Sigma Q$  are listed as follows. We all know that the closer the average is to 1.00, the smaller the discrete coefficient and the smaller the value  $\Sigma Q$ , the degree of discrete is higher. The discrete degree of Wang and Wu's model and Youssef's model is big and the discrete degree of Teng's model and two fitting models is small, the average is closer to 1, therefore, in this paper, the accuracy is significantly better than the first two models, has a better agreement with experimental data.

$$\Sigma Q = \Sigma \left[ \left( \frac{f_{cc}}{f_{co}} \right) - \left( \frac{f'_{cc}}{f_{co}} \right) \right]^2$$

$$\text{Exponential Fit: } \frac{f'_{cc}}{f_{co}} = 64889e^{\frac{\left(\frac{f_l}{f_{co}}\right)}{28924}} - 64888$$

$$\Sigma Q = 17.32 \quad \mu = 1.02 \quad C_v = 0.14 \quad (4)$$

Linear Fit:  $\frac{f'_{cc}}{f_{co}} = 1 + 2.24 \left( \frac{f_l}{f_{co}} \right)$

$$\Sigma Q = 17.32 \quad \mu = 1.02 \quad C_v = 0.14 \quad (5)$$

Wang and Wu model:  $\frac{f'_{cc}}{f_{co}} = 1 + 3.4 \left( \frac{f_l}{f_{co}} \right)$

$$\Sigma Q = 108.74 \quad \mu = 1.27 \quad C_v = 1.24 \quad (6)$$

Youssef et al model:  $\frac{f'_{cc}}{f_{co}} = 1 + 2.25 \left( \frac{f_l}{f_{co}} \right)^{\frac{5}{4}}$

$$\Sigma Q = 22.26 \quad \mu = 0.95 \quad C_v = 0.87 \quad (7)$$

Teng et al model:  $\frac{f'_{cc}}{f_{co}} = 1 + 2.0 \left( \frac{f_l}{f_{co}} \right)$

$$\Sigma Q = 20.81 \quad \mu = 0.97 \quad C_v = 0.13 \quad (8)$$

## 6 CONCLUSIONS

In this paper, the method for calculating the strength of FRP confined concrete model is analyzed, and the collected data was in the form of linear and exponential fitting. Then analyzing and comparing the experimental value and calculating value from two aspects of constraint intensity coefficient and the strength of concrete. The discrete degree of linear fitting model, exponential

fitting model and Teng's model is small and the differences are not big, but the form of exponential fitting model is too complex and Teng's model slant a bit bigger, it is no doubt that the linear fitting model is one of the best in them. With a large number of test results is good and the form of the model is simple, it may be applied to practical engineering.

## ACKNOWLEDGMENT

The authors would like to acknowledge financial support from the Natural Science Foundation of Jiangsu province (No. BK20131105).

## REFERENCES

- [1] Wu, Y.F., and Wang, L.M., Journal of Structural Engineering, A.S. (2009). Unified strength Model for Square and Circular Concrete Columns Confined by External Jacket. 253–261.
- [2] Li, G.Q., Engineering Structure, (2006). Experimental study of FRP confined concrete cylinders [J]. 28: 1001–1008.
- [3] Xiao, Y., and Wu, H. (2003). "Compressive behavior of concrete confined by various types of FRP composite jackets." J. Rein. plast. Compos., 22(13), 1187–1201.
- [4] Youssef, M.N., Feng, Q., and Mosallam, A.S. (2007). "Stress-strain model for concrete confined by FRP composites." Composites, Part B, 38, 614–628.

# Joints transferring forces outside box columns with different beams' height and columns' deviation of verticality—finite element method simulation

Z.G. Xu, R. Yang & Z.B. Zhang

Faculty of Civil Engineering, Guangzhou University, Guangzhou, China

C.G. Deng

Department of Structural Engineering, Tongji University, Shanghai, China

**ABSTRACT:** Design of beams' height in steel frame structure should be based on loads and deformation of structure. It can lead to beams with different heights in the central joints of steel frame. A performance of joint with different beams' height is different from the normal joint. This paper presents a joint transferring force outside box columns with different beams' height. Three groups of specimens were designed to compare with traditional joints by finite element method program ANSYS, considering steel columns' deviation of verticality up to code limits and four times of code limits. By adding force-transforming elements, the results show that joints carrying capacity have greatly increased and the influence of deviation has reduced.

**Keywords:** joints, verticality, force-transforming elements

## 1 INTRODUCTION

In structural design, the height of the beam of a steel frame should be based on loads and deformation of structure<sup>[1]</sup>. As to the central joints of steel frame, the connection between steel beams may be unproportioned to the height of the beams, which will lead to the performance of joint with different beam heights different with that of normal joint. Therefore, it is necessary to carry out stress analysis for joints with different beam heights in steel frame. This paper presents a joint transferring force outside box columns with different beam heights. They are analyzed and compared with the traditional joints by finite element method program ANSYS. In addition, a practical steel structure inevitably has residual stresses, initial deflection, initial deviation of column's location axis, and other defects<sup>[2,3]</sup>. It is also analyzed with steel column verticality deviation by the code limits and four times the limit. We found that adding the force-transforming elements can improve the initial deflection of joints.

## 2 CREATION OF FINITE ELEMENT MODELS

### 2.1 Model design

This paper mainly focuses on research of joints transferring beam forces outside box columns with

different beam heights. Details of the joint are shown in Figures 1 and 2 of lower adding element. The box column with a deviation of verticality is shown in Figure 3. The material of steel specimens is Q345B, with Modulus of elasticity  $E = 2.00 \times 10^5$

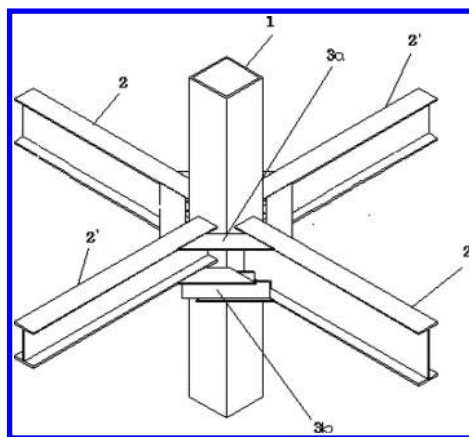


Figure 1. Joint transferring beams' forces outside box columns with different beams' height.

Note: 1—Rectangular section steel column; 2—"H" section steel beam; 2'—"H" section steel low beam; 3a—Upper transferring forces plate; 3b—adding element; 3b-1—Upper cover plate; 3b-2—Lower cover plate; 3b-3—Web plate.



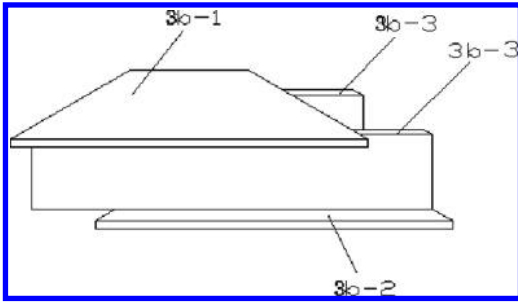


Figure 2. Detail of lower adding element.

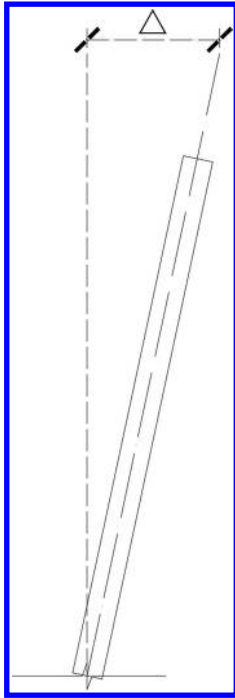


Figure 3. The box columns with a deviation of verticality  $\Delta$ .

MPa and Poisson's ratio  $\nu = 0.3$ . Three groups of specimens were designed according to the conference<sup>[4]</sup>. The column length is 2 m. The length of the beam is 1.5 m. The other parameters are shown in Table 1. In this ANSYS analysis, material

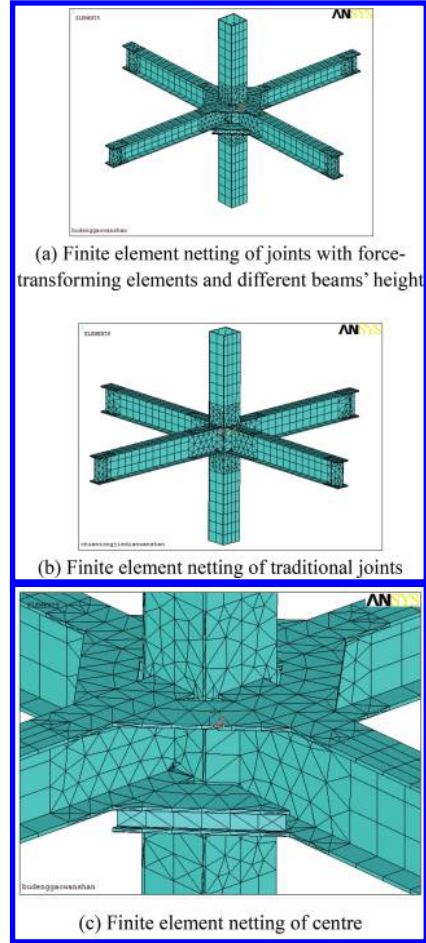


Figure 4. Finite element discretization of the joints.

Table 1. The parameters of test specimens.

Specimens	Upper cover plate (mm)			Lower cover plate (mm)			Web plate (mm)			Vertical deviation (mm)
	Length	Width	Thickness	Length	Width	Thickness	Height	Thickness	Length	
SJ-1a	374.07	125	9	374.07	125	9	50	6	374.07	None
SJ-1b	None			None			None			None
SJ-2a	374.07	125	9	374.07	125	9	50	6	374.07	2
SJ-2b	None			None			None			2
SJ-3a	374.07	125	9	374.07	125	9	50	6	374.07	10
SJ-3b	None			None			None			10

nonlinearity and geometric nonlinearity are considered, and the model of Multilinear Isotropic is selected. SOLID45 with 8 nodes is chosen as the beam-column elements which are far away from the panel zone. The high-precision SOLID95 with 20 nodes is chosen as the beam-column elements and the inner plates, and Von-Mises criterion is chosen as the yielding criterion.

## 2.2 Model discretization

In this paper, we focus on the performance of joint zone, so we create smaller elements of the centre part and bigger elements far away from the panel zone, as shown in Figure 4.

## 2.3 Constraints and loading

To fit for the actual situation in engineering, the constraints along three directions x, y, and z are set at the bottom of the column. Constraints of two directions x and y are set at the top of the column. Vertical load is applied at the top of the column, while concentrated loads are applied onto the top flange of all four steel beams. Slowly loading of the 60 sub-steps is used in this simulation.

## 3 RESULTS OF FINITE ELEMENT ANALYSIS

According to “Code for acceptance of construction quality of steel structures” (GB50205-2001)<sup>[5]</sup>, the deviation of verticality  $\Delta$  of a single column should have an allowable deviation of verticality  $\Delta$  no greater than  $h/100$  (the column length is  $h$ ) and also should not be greater than 10.0 mm. The column length is 2 m in this paper, so the deviation of verticality allowable deviation should not be greater than 2 mm.

### 3.1 The joints transferring beams’ forces outside box columns with different beams’ height and the deviation of verticality is 2 mm—finite element method simulation

Take SJ-2a and SJ-2b columns’ deviation of verticality  $\Delta = 2$  mm on the premise of recent code, and compare the results with those of specimen SJ-1a and SJ-1b, which are perfect traditional joints. Take short beam as the reference points on the flange of the central axis, we got load–displacement curves are shown in Figure 5.

In Figure 5, SJ-1a is a specimen transferring beams’ forces outside box column with different beam height. Comparing with traditional specimen, we find that yielding stresses, stiffness, and ultimate carrying capacity have greatly increased.

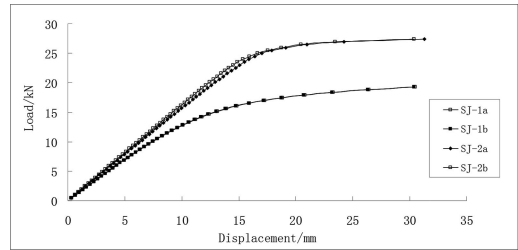


Figure 5. Load–displacement curves of SJ-1a, SJ-1b, SJ-2a, SJ-2b.

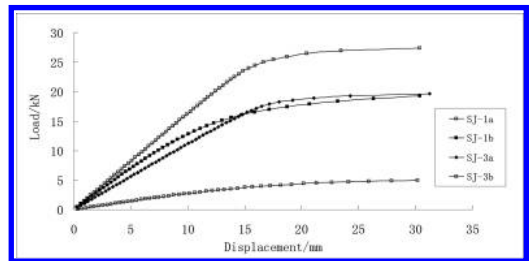


Figure 6. Load–displacement curves of SJ-1a, SJ-1b, SJ-3a, SJ-3b.

The yielding capacity increases 56.2%, and ultimate carrying capacity increases 40%. It means that adding force-transforming elements can greatly increase performance of joint with different beam heights.

If verticality deviation of steel column is 2 mm, the carrying capacities of the joint transferring beams forces’ outside box columns and the traditional joint which stiffness are decreased, less than 5%, so they can satisfy the need of engineering. It means that the deviation limits of verticality in the code can ensure the sufficient carrying capacity of the joints.

### 3.2 The joints transferring beams’ forces outside box column with different beams’ height and the deviation of verticality is 10 mm—finite element method simulation

In order to get more clear effect of steel columns’ deviation of verticality on its capacity, the deviation of verticality have to be increased to 10 mm and compared its result with that of perfect joint. Take short beam as reference points on the flange of the central axis, we got load–displacement curves are shown in Figure 6.

In Figure 6, if steel column verticality deviation is 10 mm, performance of specimen SJ-3a, which is a joint transferring beams’ forces outside box columns, and traditional joint specimen SJ-3b are

decreased obviously. Comparing with specimen SJ-3a and specimens with perfect joints transferring beams' forces outside box columns, the yielding capacity of SJ-3a decreases by 38.4%, and ultimate the carrying capacity of SJ-3a decreases 28.6%. Comparing SJ-3b and perfect traditional specimen, the yielding capacity of SJ-3b decreases by 73.3%, and the ultimate carrying capacity of SJ-3b decreases by 75%. By adding force-transforming elements, the influence of deviation can be reduced.

#### 4 CONCLUSION

A joint transferring force outside box columns with different beam heights is present. Three groups of specimens were designed to compare with traditional joints by finite element method program ANSYS. Considering columns' deviation of verticality, the conclusions are as follows:

1. Without initial defects, the stiffness, yielding stresses, and ultimate carrying capacity of joints have greatly increased by adding force-transforming elements. Its yielding capacity increases 56.2%, and ultimate carrying capacity increases 40%.
2. If column verticality deviation is 2 mm, stiffness and carrying capacity of the joints transferring beam forces outside box columns and traditional joints are decreased, less than 5%. It means that the deviation within code limits can ensure sufficient carrying capacity of the joint.
3. If column verticality deviation is 10 mm, performance of the joints transferring forces outside box columns and traditional joints will decrease obviously. By adding force-transforming elements, the influence of deviation can be reduced.

#### ACKNOWLEDGEMENTS

This research is sponsored by the National Natural Science Foundation of China (Grant No. 51478330).

#### REFERENCES

- [1] GB50017-2003, "Code for design of steel structures". Beijing: China Architecture & Building Press. 2003 (in Chinese).
- [2] Frank, K.H., Barsom, J.M., Hamburger, R.O. State of the Art Report on Base Metals and Fracture [R]. Federal Emergency Management Agency, Washington, 2000.
- [3] Guang Xian Liang, Zhong Gen Xu, Wei Ming Chen, Chang Gen Deng. Rigid joints transferring forces outside box columns with deviation of column's verticality-finite element method simulation [J]. *Advanced Materials Research*: 2014, 945: 1201–1206.
- [4] Ding Rong Cheng. Experiment and analysis of connection of steel frames rectangular tube column without inner plates [D]. Guangzhou University, 2012 (in Chinese).
- [5] GB50205-2001, "Code for acceptance of construction quality of steel structures". Beijing: China Planning Press. 2001 (in Chinese).

# Reliability of non-resonant quasi-integrable Hamiltonian systems under wide-band random excitations

J. Lan, H.Y. Wang & Y.J. Wu

*Department of Engineering Mechanics, Shanghai Jiao Tong University, Shanghai, P.R. China*

**ABSTRACT:** In this paper, the reliability problem based on the first-passage model of non-resonant quasi-integrable Hamiltonian system under wide-band random excitations is studied analytically. By using stochastic averaging method, the equations of motion of the original Hamiltonian system are reduced to a set of averaged Itô stochastic differential equations. The backward Kolmogorov equation governing the conditional reliability function and the Pontryagin equation governing the mean first-passage time are established under appropriate boundary and (or) initial conditions. An example is given to show the accuracy of the analytical method. All results are verified by Monte Carlo simulation.

**Keywords:** stochastic averaging method; reliability function; mean first-passage time; Monte Carlo simulation

## 1 INTRODUCTION

It is widely been recognized that the random excitations are ubiquitous in engineering, such as turbulent wind, seismic ground motion, etc. When investigating the dynamical behavior of a randomly excited structure, a key issue is to determine the probability that the structure works safely and reliably. In general, this problem of dynamical reliability can be converted into the problem that the response of the system stays within a safety domain probabilistically. Failure occurs when the state of the responses leaves the safety domain for the first time. This is the so-called first-passage (excursion, or exit) problem (Goller et al. 2013).

To solve the first-passage problem, a straightforward way is direct simulation, such as Monte Carlo Simulation (MCS). A major defect of MCS is that the computational cost is expensive. The other method is theoretical analysis based on appropriate mathematical model (Ghazizadeh et al. 2012). So far, a well developed theoretically analytical method for solving first-passage problem is built on the theory of diffusive Markovian process. This method requires that the random excitation is modeled as Gaussian White Noise (GWN). However, when the random excitation is not GWN, such as wide-band random noise, bounded noise, or Poisson white noise, the response of the randomly excited system is not diffusive Markovian process. In this case, one can not directly establish the PDEs governing the conditional reliability function and the moment of mean first-passage time. Previous studies have demonstrated that stochastic

averaging method is a powerful tool to overcome this difficult (Wu et al. 2013, Zhu 2006).

Hamiltonian system plays an important role in dynamics analysis. In this work, the reliability problem based on the first-passage model of Many-Degrees-of-Freedom (MDOF) non-resonant quasi-integrable Hamiltonian system under wide-band random excitations is studied analytically. The equations of motion of the original Hamiltonian system are reduced to a set of averaged Itô stochastic differential equations after stochastic averaging. The Backward Kolmogorov (BK) equation governing the conditional reliability function and the Pontryagin equation governing the mean first-passage time are established under appropriate boundary and (or) initial conditions. An example is given to show the accuracy of the analytical method. The reliability function and mean first-passage time are obtained. Monte Carlo simulation is performed to verify the analytical results.

## 2 AVERAGED ITÔ STOCHASTIC DIFFERENTIAL EQUATIONS

Consider the following n-DOF quasi-Hamiltonian system

$$\begin{aligned} \dot{Q}_i &= \frac{\partial H}{\partial P_i}, \\ \dot{P}_i &= -\frac{\partial H}{\partial Q_i} - \varepsilon c_{ij}(\mathbf{Q}, \mathbf{P}) \frac{\partial H}{\partial P_j} + \varepsilon^{1/2} h_{ik}(\mathbf{Q}, \mathbf{P}) \xi_k(t), \\ i, j &= 1, 2, \dots, n; \quad k = 1, 2, \dots, m. \end{aligned} \quad (1)$$

where  $Q_i$  and  $P_i$  are generalized displacements and momenta, respectively;  $H = H(\mathbf{Q}, \mathbf{P})$  is Hamiltonian;  $c_{ij}(\mathbf{Q}, \mathbf{P})$  denote quasi linear damping coefficients;  $h_{ik}(\mathbf{Q}, \mathbf{P})$  denote amplitudes of stochastic excitations;  $\varepsilon$  is a small positive parameter;  $\xi_k(t)$  are stationary wide-band random excitations with correlation functions  $R_{kk}(\tau) = E[\xi_k(t)\xi_k(t + \tau)]$  or spectral density  $S_{kk}(\omega)$ . The repeated subscript denotes summation.

Assume  $H$  is separable and each  $H_i$  can be expressed as

$$H_i(Q_i, P_i) = P_i^2/2 + U_i(Q_i). \quad (2)$$

Hence, system (1) is a quasi-integrable Hamiltonian system.

If the specified conditions in the paper (Cheung & Xu 1995) are satisfied, the solution of Equation (1) can be expressed as the following form of generalized harmonic function

$$\begin{aligned} Q_i(t) &= A_i \cos \Phi_i(t) + B_i, \\ P_i(t) &= -A_i v_i(A_i, \Phi_i) \sin \Phi_i(t), \end{aligned} \quad (3)$$

where

$$\begin{aligned} \Phi_i(t) &= \eta_i(t) + \Theta_i(t), \\ v_i(A_i, \Phi_i) &= \frac{d\eta_i}{dt} \\ &= \sqrt{\frac{2[U_i(A_i + B_i) - U_i(A_i \cos \Phi_i + B_i)]}{A_i^2 \sin^2 \Phi_i}}, \\ U_i(A_i + B_i) &= U_i(-A_i + B_i) = H_i. \end{aligned} \quad (4)$$

$A_i$ ,  $\eta_i$ ,  $v_i$  and  $\Theta_i$  are all stochastic processes.  $A_i$  and  $v_i$  are the amplitude and instantaneous frequency of the  $i$ th sub-system of the system (1), respectively.

If the system is not resonant, according to Stratonovich-Khasminskii limit theory (Khasminskii 1996, Stratonovitch 1963) and performing averaging with respect to the rapidly varying variables  $\Phi$ , one can obtain the following averaged Itô equations about  $\mathbf{A}$

$$\begin{aligned} dA_i &= \varepsilon \bar{m}_i(\mathbf{A})dt + \varepsilon^{1/2} \bar{\sigma}_{ie}(\mathbf{A})dB_e(t), \\ i &= 1, 2, \dots, n; \quad e = 1, 2, \dots, l. \end{aligned} \quad (5)$$

### 3 CONDITIONAL RELIABILITY FUNCTION AND MEAN FIRST-PASSAGE TIME

$\mathbf{A}$  are amplitudes of the original system (1). It is reasonable to assume that first-passage occurs once  $A_i(t)$  exceeds a certain critical value  $A_{ic}$  for the first time. The conditional reliability function,

denoted by  $R(t | \mathbf{A}_0)$ , is defined as the probability of  $\mathbf{A}(t)$  being in the safety domain  $\Omega_s$  within interval  $(0, t]$  given initial state being in  $\Omega_s$ .  $R(t | \mathbf{A}_0)$  is determined by the following BK equation:

$$\frac{\partial R}{\partial t} = \varepsilon \bar{m}_{i0} \frac{\partial R}{\partial A_{i0}} + \frac{1}{2} \varepsilon \bar{b}_{ij0} \frac{\partial^2 R}{\partial A_{i0} \partial A_{j0}}, \quad (6)$$

where

$$\bar{m}_{i0} = \bar{m}_i |_{\mathbf{A}=\mathbf{A}_0}, \quad \bar{b}_{ij0} = \bar{\sigma}_{ie} \bar{\sigma}_{je} |_{\mathbf{A}=\mathbf{A}_0}. \quad (7)$$

The initial and boundary conditions of Equation (6) are

$$\begin{aligned} R(0 | \mathbf{A}_0) &= 1, \quad A_{i0} \in [0, A_{ic}), \\ R(t | \mathbf{A}_0) &= 0, \quad A_{i0} = A_{ic}, \\ R(t | \mathbf{0}) &= \text{finite}. \end{aligned} \quad (8)$$

The conditional Mean First-Passage Time (MFPT)  $T(\mathbf{A}_0)$  is also a function of the initial state  $\mathbf{A}_0$ .  $T$  is determined by the following Pontryagin equation:

$$-1 = \varepsilon \bar{m}_{i0} \frac{\partial T}{\partial A_{i0}} + \frac{1}{2} \varepsilon \bar{b}_{ij0} \frac{\partial^2 T}{\partial A_{i0} \partial A_{j0}}, \quad (9)$$

The boundary conditions of Equation (9) are

$$\begin{aligned} T(\mathbf{A}_0) &= 0, \quad A_{i0} = A_{ic}, \\ T(\mathbf{0}) &= \text{finite}. \end{aligned} \quad (10)$$

Solving the partial differential equations (6) and (9) by finite difference method, one can obtain the approximate reliability function and mean first-passage time of the original system (1).

## 4 NUMERICAL EXAMPLE

Consider the following 5-DOF coupled Duffing-van der Pol system.

$$\begin{aligned} \dot{Q}_i &= P_i, \\ \dot{P}_i &= -(\beta_{i0} + \beta_{ij} Q_j^2) P_i + \omega_{i0}^2 Q_i + \alpha_i Q_i^3 \\ &= \xi_{i1}(t) + Q_i \xi_{i2}(t), \quad (i, j = 1, \dots, 5). \end{aligned} \quad (11)$$

Herein,  $\xi_{ik}(t)$  are independent wide-band random excitations with the following spectral density function:

$$S_{ik}(\omega) = \frac{D_{ik}}{\pi} \frac{1}{\omega^2 + \omega_{ik}^2}, \quad i = 1, \dots, 5; \quad k = 1, 2. \quad (12)$$

The parameters are chosen as:  $A_{ic} = 0.5$ ,  $\beta_{i0} = -0.01$ ,  $\beta_{ij} = 0.01$ ,  $\omega_{01}=1.0$ ,  $\omega_{02} = \sqrt{3}$ ,  $\omega_{03} = \sqrt{5}$ ,  $\omega_{04} = \sqrt{7}$ ,  $\omega_{05} = \sqrt{10}$ ,  $\omega_{ik} = 50$ ,  $D_{ik} = 12$  ( $i, j = 1, \dots, 5$ ;  $k = 1, 2$ ). There is no resonance in system (11). The averaged Itô stochastic differential equations are:

$$dA_i = \bar{m}_i(A)dt + \bar{\sigma}_{ik}dB_k(t), \quad (k = 1, 2). \quad (13)$$

The drift coefficients are

$$\begin{aligned} \bar{m}_i &= \bar{s}_i + \bar{m}_{i1} + \bar{m}_{i2} + \bar{m}_{i3} + \bar{m}_{i4}, \\ \bar{s}_i &= -A_i \left[ \left( 2\beta_{i0} + \sum_{j=1, j \neq i}^5 A_j^2 \beta_{ij} \right) (8\omega_{0i}^2 + 5A_i^2 \alpha_i) \right. \\ &\quad \left. + A_i^2 \beta_{ii} (3A_i^2 \alpha_i + 4\omega_{0i}^2) \right] / \left[ 32(A_i^2 \alpha_i + \omega_{0i}^2) \right], \\ \bar{m}_{i1} &= m_{i11} S_{i1}(\omega_i(A_i)) + m_{i13} S_{i1}(3\omega_i(A_i)) \\ &\quad + m_{i15} S_{i1}(5\omega_i(A_i)) + m_{i17} S_{i1}(7\omega_i(A_i)), \\ \bar{m}_{i3} &= m_{i31} S_{i1}(\omega_i(A_i)) + m_{i33} S_{i1}(3\omega_i(A_i)) \\ &\quad + m_{i35} S_{i1}(5\omega_i(A_i)) + m_{i37} S_{i1}(7\omega_i(A_i)), \\ \bar{m}_{i2} &= m_{i22} S_{i2}(2\omega_i(A_i)) + m_{i24} S_{i2}(4\omega_i(A_i)) \\ &\quad + m_{i26} S_{i2}(6\omega_i(A_i)) + m_{i28} S_{i2}(8\omega_i(A_i)), \\ \bar{m}_{i4} &= m_{i42} S_{i2}(2\omega_i(A_i)) + m_{i44} S_{i2}(4\omega_i(A_i)) \\ &\quad + m_{i46} S_{i2}(6\omega_i(A_i)) + m_{i48} S_{i2}(8\omega_i(A_i)), \\ m_{i11} &= \pi [2b_{i0}(A_i) - b_{i2}(A_i)] \\ &\quad \times \frac{d}{dA_i} \left[ \frac{2b_{i0}(A_i) - b_{i2}(A_i)}{A_i^2 \alpha_i + \omega_{0i}^2} \right] / \left[ 8(A_i^2 \alpha_i + \omega_{0i}^2) \right], \\ m_{i13} &= \pi [b_{i2}(A_i) - b_{i4}(A_i)] \\ &\quad \times \frac{d}{dA_i} \left[ \frac{b_{i2}(A_i) - b_{i4}(A_i)}{A_i^2 \alpha_i + \omega_{0i}^2} \right] / \left[ 8(A_i^2 \alpha_i + \omega_{0i}^2) \right], \\ m_{i15} &= \pi [b_{i4}(A_i) - b_{i6}(A_i)] \\ &\quad \times \frac{d}{dA_i} \left[ \frac{b_{i4}(A_i) - b_{i6}(A_i)}{A_i^2 \alpha_i + \omega_{0i}^2} \right] / \left[ 8(A_i^2 \alpha_i + \omega_{0i}^2) \right], \\ m_{i17} &= \pi b_{i6}(A_i) \frac{d}{dA_i} \left[ \frac{b_{i6}(A_i)}{A_i^2 \alpha_i + \omega_{0i}^2} \right] / \left[ 8(A_i^2 \alpha_i + \omega_{0i}^2) \right], \\ m_{i22} &= \pi A_i [2b_{i0}(A_i) - b_{i4}(A_i)] \\ &\quad \times \frac{d}{dA_i} \left\{ \frac{[2b_{i0}(A_i) - b_{i4}(A_i)] A_i}{A_i^2 \alpha_i + \omega_{0i}^2} \right\} / \left[ 32(A_i^2 \alpha_i + \omega_{0i}^2) \right], \\ m_{i24} &= \pi A_i [b_{i2}(A_i) - b_{i6}(A_i)] \\ &\quad \times \frac{d}{dA_i} \left\{ \frac{[b_{i2}(A_i) - b_{i6}(A_i)] A_i}{A_i^2 \alpha_i + \omega_{0i}^2} \right\} / \left[ 32(A_i^2 \alpha_i + \omega_{0i}^2) \right], \end{aligned}$$

$$\begin{aligned} m_{i26} &= \pi A_i b_{i4}(A_i) \frac{d}{dA_i} \left[ \frac{b_{i4}(A_i) A_i}{A_i^2 \alpha_i + \omega_{0i}^2} \right] / \left[ 32(A_i^2 \alpha_i + \omega_{0i}^2) \right], \\ m_{i28} &= \pi A_i b_{i6}(A_i) \frac{d}{dA_i} \left[ \frac{b_{i6}(A_i) A_i}{A_i^2 \alpha_i + \omega_{0i}^2} \right] / \left[ 32(A_i^2 \alpha_i + \omega_{0i}^2) \right], \\ m_{i31} &= \pi [4b_{i0}^2(A_i) - b_{i2}^2(A_i)] / \left[ 8A_i (A_i^2 \alpha_i + \omega_{0i}^2) \right], \\ m_{i33} &= 3\pi [b_{i2}^2(A_i) - b_{i4}^2(A_i)] / \left[ 8A_i (A_i^2 \alpha_i + \omega_{0i}^2) \right], \\ m_{i35} &= 5\pi [b_{i4}^2(A_i) - b_{i6}^2(A_i)] / \left[ 8A_i (A_i^2 \alpha_i + \omega_{0i}^2) \right], \\ m_{i37} &= 7\pi b_{i6}^2(A_i) / \left[ 8A_i (A_i^2 \alpha_i + \omega_{0i}^2) \right], \\ m_{i42} &= \pi A_i [2b_{i0}(A_i) - b_{i4}(A_i)] \\ &\quad \times [2b_{i0}(A_i) + 2b_{i2}(A_i) + b_{i4}(A_i)] / \left[ 16(A_i^2 \alpha_i + \omega_{0i}^2) \right], \\ m_{i44} &= \pi A_i [b_{i2}(A_i) - b_{i6}(A_i)] \\ &\quad \times [b_{i2}(A_i) + 2b_{i4}(A_i) + b_{i6}(A_i)] / \left[ 8(A_i^2 \alpha_i + \omega_{0i}^2) \right], \\ m_{i46} &= 3\pi A_i b_{i4}(A_i) \\ &\quad \times [b_{i4}(A_i) + 2b_{i6}(A_i)] / \left[ 16(A_i^2 \alpha_i + \omega_{0i}^2) \right], \\ m_{i48} &= \pi A_i b_{i6}^2(A_i) / \left[ 4(A_i^2 \alpha_i + \omega_{0i}^2) \right]. \end{aligned} \quad (14)$$

The diffusion coefficients are

$$\begin{aligned} \bar{b}_{ii} &= \bar{\sigma}_{i1}(A_i) \bar{\sigma}_{i1}(A_i) + \bar{\sigma}_{i2}(A_i) \bar{\sigma}_{i2}(A_i) = \bar{b}_{i11} + \bar{b}_{i22}, \\ \bar{b}_{i11} &= b_{i11} S_{i1}(\omega_i(A_i)) + b_{i13} S_{i1}(3\omega_i(A_i)) \\ &\quad + b_{i15} S_{i1}(5\omega_i(A_i)) + b_{i17} S_{i1}(7\omega_i(A_i)), \\ \bar{b}_{i22} &= b_{i22} S_{i2}(2\omega_i(A_i)) + b_{i24} S_{i2}(4\omega_i(A_i)) \\ &\quad + b_{i26} S_{i2}(6\omega_i(A_i)) + b_{i28} S_{i2}(8\omega_i(A_i)), \\ \bar{b}_{i11} &= \pi [b_{i2}(A_i) - 2b_{i0}(A_i)]^2 / \left[ 4(\alpha_i A_i^2 + \omega_{0i}^2) \right], \\ \bar{b}_{i13} &= \pi [b_{i2}(A_i) - b_{i4}(A_i)]^2 / \left[ 4(\alpha_i A_i^2 + \omega_{0i}^2) \right], \\ \bar{b}_{i15} &= \pi [b_{i4}(A_i) - b_{i6}(A_i)]^2 / \left[ 4(\alpha_i A_i^2 + \omega_{0i}^2) \right], \\ \bar{b}_{i17} &= \pi b_{i6}^2(A_i) / \left[ 4(\alpha_i A_i^2 + \omega_{0i}^2) \right], \\ \bar{b}_{i22} &= \pi A_i^2 [b_{i4}(A_i) - 2b_{i0}(A_i)]^2 / \left[ 16(\alpha_i A_i^2 + \omega_{0i}^2) \right], \\ \bar{b}_{i24} &= \pi A_i^2 [b_{i2}(A_i) - b_{i6}(A_i)]^2 / \left[ 16(\alpha_i A_i^2 + \omega_{0i}^2) \right], \\ \bar{b}_{i26} &= \pi A_i^2 b_{i4}^2(A_i) / \left[ 16(\alpha_i A_i^2 + \omega_{0i}^2) \right], \\ \bar{b}_{i28} &= \pi A_i^2 b_{i6}^2(A_i) / \left[ 16(\alpha_i A_i^2 + \omega_{0i}^2) \right], \end{aligned}$$

$$\begin{aligned}
b_{i0}(A_i) &= (\omega_{0i}^2 + 3\alpha_i A_i^2/4)^{1/2} (1 - \lambda_i^2/16), \\
b_{i2}(A_i) &= (\omega_{0i}^2 + 3\alpha_i A_i^2/4)^{1/2} (\lambda_i/2 + \lambda_i^3/64), \\
b_{i4}(A_i) &= (\omega_{0i}^2 + 3\alpha_i A_i^2/4)^{1/2} (-\lambda_i^2/16), \\
b_{i6}(A_i) &= (\omega_{0i}^2 + 3\alpha_i A_i^2/4)^{1/2} (\lambda_i^3/64), \\
\lambda_i &= \alpha_i A_i^2/4 (\omega_{0i}^2 + 3\alpha_i A_i^2/4).
\end{aligned} \tag{15}$$

The BK equation associated with the averaged system (13) is

$$\frac{\partial R}{\partial t} = \bar{m}_{i0} \frac{\partial R}{\partial A_{i0}} + \frac{1}{2} \bar{b}_{i0} \frac{\partial^2 R}{\partial A_{i0}^2}, \quad (i = 1, 2, 3, 4, 5). \tag{16}$$

The initial and boundary conditions of Equation (16) are

$$\begin{aligned}
R(0 | \mathbf{A}_0) &= 1, \quad A_{i0} \in [0, A_{ic}), \\
R(t | \mathbf{A}_0) &= 0, \quad A_{i0} = A_{ic}, \\
\frac{\partial R}{\partial A_{i0}} &= 0, \quad A_{i0} = 0.
\end{aligned} \tag{17}$$

The Pontryagin equation associated with the averaged system (13) is

$$-1 = \bar{m}_{i0} \frac{\partial T}{\partial A_{i0}} + \frac{1}{2} \bar{b}_{i0} \frac{\partial^2 T}{\partial A_{i0}^2}, \quad (i = 1, 2, 3, 4, 5). \tag{18}$$

The boundary conditions of Equation (18) are

$$\begin{aligned}
T(\mathbf{A}_0) &= 0, \quad A_{i0} = A_{ic}, \\
\frac{\partial T}{\partial A_{i0}} &= 0, \quad A_{i0} = 0.
\end{aligned} \tag{19}$$

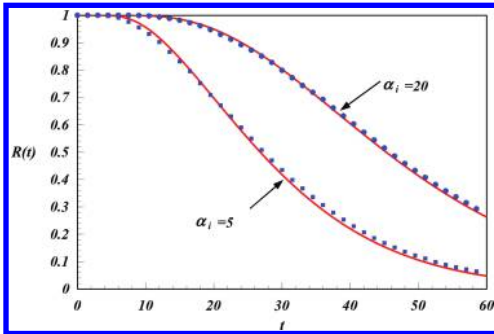


Figure 1. Conditional reliability functions of the system (11) ( $A_0 = 0$ ).

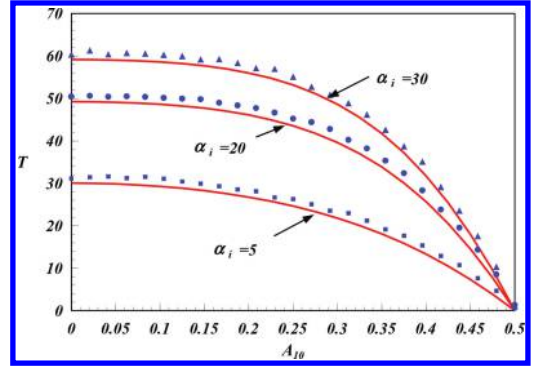


Figure 2. MFPT of the system (10).  $A_{i0}$  is a variable.

Solving the 5+1-dimensional BK Equation (16) and 5-dimensional Pontryagin equation (18), we obtain the conditional reliability function and mean first-passage time of the system (11), respectively. Figure 1 shows results of conditional reliability function. The solid lines are analytical results while the discrete symbols are results from Monte Carlo simulation. Obviously, the agreement is very good. Figure 2 shows that the mean first-passage time is a decreasing function of the initial state. This is physically meaningful because first-passage happens more easily when the initial state is closer to the threshold.

## 5 CONCLUSIONS

In the present paper, the reliability problem of MDOF strongly nonlinear quasi-integrable Hamiltonian systems is studied. The BK equation and the Pontryagin equation are established to determine the conditional reliability function and the conditional mean first-passage time, respectively. A 5-DOF coupled Duffing-van der Pol system is given to illustrate the application of the analytical method. The 5+1-dimensional BK equation and 5-dimensional Pontryagin equation are solved under suitable initial and boundary conditions. It is seen that the agreement between the analytical method and MCS is very good.

## ACKNOWLEDGEMENTS

This work was financially supported by the National Natural Science Foundation of China (Grant Nos. 11272201, 11372271, 11132007).

## REFERENCES

- Cheung, Y.K. & Xu, Z. 1995. Internal resonance of strongly non-linear autonomous vibrating systems with many degrees of freedom. *Journal of Sound and Vibration* 180(2): 229–238.
- Ghazizadeh, S. et al. 2012. New analytical solution of the first-passage reliability problem for linear oscillators. *ASCE Journal of Engineering Mechanics* 138: 695–706.
- Goller, B. et al. 2013. Reliability assessment in structural dynamics. *Journal of Sound and Vibration* 332: 2488–2499.
- Khasminskii, R.Z. 1966. A limit theorem for the solutions of differential equations with random right-hand sides. *Theory of Probability and Its Applications* 11(3): 390–406.
- Stratonovitch, R.L. 1963. *Topics in the Theory of Random Noise*. New York: Gordon and Breach.
- Wu, Y.J. et al. 2013. First-passage problem of strongly nonlinear stochastic oscillators with external and internal resonances. *European Journal of Mechanics A/Solids* 39: 60–68.
- Zhu, W.Q. 2006. Nonlinear stochastic dynamics and control in Hamiltonian formulation. *Applied Mechanics Reviews* 59: 230–248.



# Research progress on diaphragm-through joint of Concrete-Filled Square Steel Tube and steel beam

Ming Li

*Civil Engineering College, Shenyang Jianzhu University, Shenyang, China*  
*Jangho Group Co. Ltd., Beijing, China*

Ming Zhao

*Civil Engineering College, Shenyang Jianzhu University, Shenyang, China*

Yuanqing Wang

*Civil Engineering College, Tsinghua University Beijing, China*

Wei Tao & Shoukun Li

*Jangho Group Co. Ltd., Beijing, China*

Renliang Shan

*Civil Engineering and Mechanics, China University of Mining and Technology, Beijing, China*

**ABSTRACT:** Diaphragm-through joint of Concrete-Filled Square Steel Tube and steel beam is a form of rigid joints. It has the characteristics of good seismic behavior, high bearing capacity, and good ductility. The research progress in China of this kind of joint is reviewed from both experimental study and theoretical analysis, including the forms of direct welding type, side plate strengthen type, circular fillet type, fillet slope type, circular slope combination type, and Steel beam end clap and board bolted type. The form of this kind of joint adopted in Chinese specification is also introduced. Finally, the problems existing in the current research and those that needed to be further studied are pointed out.

**Keywords:** concrete filled steel tubular; diaphragm-through; joint; experimental study; theoretical analysis

## 1 INTRODUCTION

Concrete Filled Steel Tube (CFST) gives full play to the advantages of them, and has high bearing capacity, good plasticity and high toughness etc. It can meet the needs of large span, tall, heavy-duty and other structures, so it has been widely used in engineering (Shantong Z., 2003). According to the different cross-section forms, CFST can be divided into round, square and polygon section concrete filled steel tube, etc. Among them, the round and square ones are widely applied. In the CFST structure, beam-column joint plays a role of passing moment and shear force between beam and column, which is the key part of design and is also difficult in construction. To meet the project needs, different scholars have put forward many kinds of joints for connecting CFST and beam, including inner diaphragm joints, strengthening ring plate joints, vertical stiffener joints and diaphragm-through joints. Among them, the diaphragm-through joint is one

of the forms of joint recommended by Chinese specification (Xilin et al, 2004). In the following, the forms of Diaphragm-Through Joint (DJ) of Concrete Filled Square Steel Tube (CFSST) and Steel Beam (SB) and the research progress of it in China will be reviewed, which will provide reference for designing this kind of joint.

## 2 FORMS OF DJ OF CFSST-SB

DJ of CFSST and SB is made by the following steps: the steel tube and SB are connected by two diaphragms, in which part of the two diaphragms pass through and are welded in the tube; the flanges ends of SB are welded or bolted on the diaphragms; the web of SB are welded or bolted on one ends of a steel plates; the other end of the plates is welded on the steel tube. It has the forms of direct welding type, side plate strengthen type, circular fillet type, fillet slope type and circular

slope combination type, Steel beam end clap and board bolted type, as shown in Figures 1–6. These developments and changes in the forms of joints solve the problems of large welding residual stress between the beam end and diaphragm, and meet the requirements of engineering function.

Direct welding type, as shown in Figure 1, means that the beam flange and diaphragm are welded directly without any transition method, which is the structure form recommended by Chinese rectangle steel tube concrete specification. It is convenient for construction and the amount of steel used for connection is small, but the stress concentration between the beam flanges and the diaphragm is large. It needs high requirements for welding quality. Side plate strengthen type, as shown in Figure 2, means that side panels are welded on both sides of the flanges at the beam

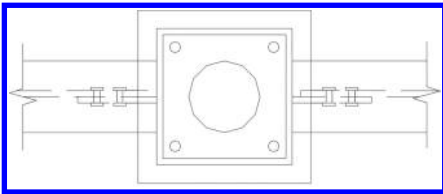


Figure 1. Direct welding type.

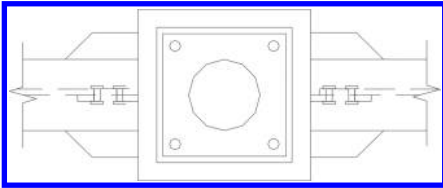


Figure 2. Side plate strengthen type.

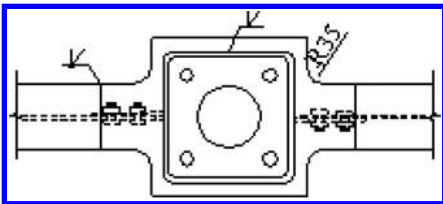


Figure 3. Circular fillet type.

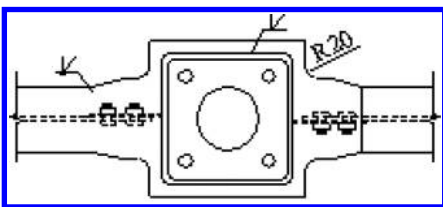


Figure 4. Fillet slope type.

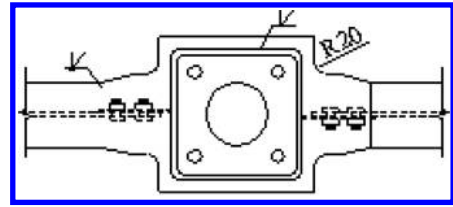


Figure 5. Circular slope combination type.

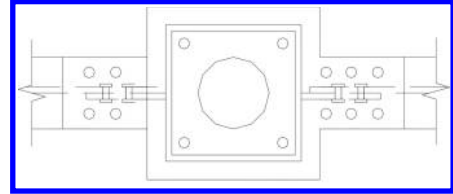


Figure 6. Full-bolt type.

end additionally, of which the lateral plate and the beam flange are located on the same plane or close to the inner beam flange, so as to reduce the stress concentration of the weld place, and prevent the occurrence of brittle failure. But it has large amount of welding and is difficult for machining and site weld, and the beam flange edge are easy to be torn in the lateral plate ends. So there are a lot of project risks. Circular fillet type, as shown in Figure 3, is a kind of structure setting an arc transition at the connections of steel beam flange and diaphragm. Circular fillet can effectively reduce stress concentration at the end of beam flange edge, and it is beneficial to improve the ductility and seismic energy dissipation of joints. Fillet slope type, as shown in Figure 4, makes diaphragm from two sides turn into slope angle less than 1:4, and sets an arc transition at variable cross-section. This kind of structure cannot only effectively reduce the stress concentration of connections for the slope angle is small, but also have no problems in wallboard installation. Circular slope combination type, as shown in Figure 5, means that it adopts a processing mode of fillet slope at up diaphragm plane and adopts a processing mode of circular fillet at down diaphragm plane of joint. The diaphragm and beam flanges are connected with groove welding, and the beam web and the steel pipe column wall are connected by high-strength bolt. Increasing diaphragm size will not affect the beauty of architecture structure; instead, it provides a certain condition for concealment of the upper structure and join processing. Thus it is convenient to install bolt and connection plate (Liang W., 2009). Steel beam end clap and board bolted type, as shown in Figure 6, means that steel beam is inserted among the up and down diaphragms, then the steel beam flange

and diaphragm are connected by bolts. Compared with the above joints, there is no problem of stress concentration at the beam end due to welding, but as a result of diaphragm extruding beam flange, this causes some difficulties in installation.

### 3 RESEARCH ON DJ OF CFSST-SB

#### 3.1 Experimental study

Experimental study about DJ of CFSST-SB is mainly carried out after 2005 in China, including static tensile test, low-reversed cyclic loading test. The static tensile test aims to test the tension force on the beam flange in the diaphragm, diaphragm and cylindrical wall weld, transfer and destruction of the weld, and the influencing factors. The low-reversed cyclic loading test aims to test the joint's seismic performance, failure mode, and influence factors. The experimental study is carried out mainly as follows. Hong F. & Lihua X. & Guofeng D. (2007) have done experimental study about nine side plate strengthen diaphragm-through joints specimens under low-reversed cyclic load and static tensile test in 2007 and 2008. The results show the hysteresis curves attained in the experiment are full and the connections have a good energy dissipation capacity. The width to thickness ratio of the column has little influence on the bearing capacity of the connection, but it has a little influence on the stains of the gusset plate. The stress distributing can be ameliorated and the ductility of the connections can also be improved through welding the additional plates to both sides of the flanges. Jikui M. & Bin R. & Xinliang J. & Zhihua C. (2008, 2009, 2012) have investigated thirty specimens subjected to low-reversed cyclic load and static tensile test. It was found that tensile load from steel beam flange was mainly shared by square steel tube and diaphragm and there were 3 kinds of failure modes: steel beam flange fracture, weld fracture, and joint broken. For steel square tube, plastic zone appeared around intersections between steel square tube and diaphragm. However, for diaphragm, plastic zone appeared along the cross-section lines enclosed by steel square tube. Joints of circular fillet type and fillet slope type have high load-bearing capacity and good ductility. Details of the steel beam flange with the diaphragm have obvious effect on the ductility, energy dissipation and rigidity degeneration, and the seismic performance of joint of circular fillet type and fillet slope type are better than those reinforced by taper plate welded to the beam flanges and diaphragm. Since all the specimens fail in the beam, diaphragm thickness, diameter of concrete cast hole and width to thickness ratio of the tube have less influence on joint seismic behavior, however, the concrete filled in the tube can greatly reduce bearing deformation of joint panel zone, improve the joint stiffness and the

seismic performance of it. Zilin L. et al (2014) have done experiment of six full-scale specimens under low-reversed cyclic load. The result of the experiment shows that the joint is characterized by good seismic behavior, high bearing capacity, and full hysteresis curve. The eccentric specimens failed due to the cracking of corner bolt hole on the diaphragm, and the specimens without eccentricity failed due to the cracking of diaphragm. Welded diaphragm had no effect on the bearing capacity. The end of the beam, and stress focus phenomena were easily seen at the connection of the partition and the beam.

#### 3.2 Theoretical analysis

Theoretical analysis about DJ of CFSST-SB is mainly carried out after 2005 in China, mainly using the software of ANSYS and ABAQUS. In addition to the problem considered in the above experiment, study should also include further finite element simulation results for establishing simplified calculation method for designing. The theoretical analysis carried out mainly as follows.

Lei Z. (2006) has done theoretical analysis and finite element calculation, the result shows that the seismic design method used in current structural design specification is suitable for the joints discussed in the paper. And its strength formula and thickness requirement are proposed. It is also analyzed the influence of diaphragm thickness, extend length, and axial compression ratio on joint behavior. Jikui M. (2008) analyzed the joint under low-reversed cyclic load and static tensile load by finite element method. The yield mechanism is studied, formula for calculating tensile capacity is proposed, which take account of the force that transferred to the diaphragm plate and tube. Stress distribution in the joint panel zone and the damage mechanism is simulated. Some suggestions for improving joint design are presented. Qin L. (2010) simulated the seismic performance of the side plate strengthen of the joint under low-reversed cyclic load by the finite element simulation method. The results showed the joints have good strength, stiffness, ductility, and the hysteresis curves attained are full. Jingjing B. (2012) researched the seismic performance of the joints with fillet and slope at the connecting zone. The results demonstrated that stress concentration

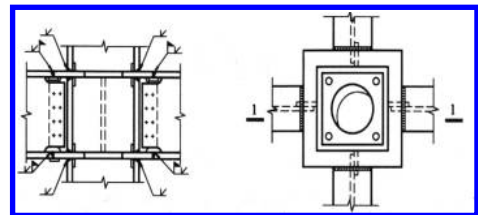


Figure 7. Overhanging inner diaphragm connection.

occurred at the areas like the diaphragm edge spot, the soldering hole, the welded area between diaphragm and beam. More attention should be paid to the soldering hole design and processing.

#### 4 RECOMMENDED FORM IN CHINESE SPECIFICATION

The forms of the joint of CFST and SB recommended in Chinese code CECS 159: 2004 (Xilin et al, 2004) include sinner diaphragm connection, overhanging inner diaphragm connection, outer diaphragm connection, and inner diaphragm connection with short beam. In which, the overhanging inner diaphragm connection is the form of DJ of CFSST and SB, as shown in Figure 7.

It is required in the specification that in the principle of design, the form of joints should be with simple structure, good integrity, clear force transmission path, safe, reliability, saving material, and convenient for construction. In joint design, it should make the joint accomplish reasonable structure and have the necessary ductility, which can guarantee welding quality and avoid the stress concentration and large constraint stress. When calculating the rigid welded joint between CFSST with internal diaphragms and SB, in addition to check the strength of the weld seam and high strength bolt, it should check the bending and shear bearing capacity of the joint.

It can be seen from the above specification, the form of DJ of CFSST-SB is single, and it's only considered the influence of the material strength in the method for checking the bending and shear bearing capacity of the joint, while such factors as the steel ratio, axial compression ratio, etc., are not considered.

#### 5 CONCLUSIONS

From the above reviewing, it can be seen:

1. For DJ of CFSST and SB, in the design, the main problems needed to be considered include how to solve much stress between the beam end and diaphragm, reduce the number of welding and meet the requirements of architectural appearance.
2. DJ of CFSST and SB has direct welding type, side plate strengthen diaphragm-through joint type, circular fillet type, fillet slope type, and circular slope combination type, which solves the larger welding residual stress between the beam end and diaphragm and meets the requirements of architectural function.
3. It has been made much research achievements for DJ of CFSST and SB in China, but in Chinese specification, the recommended form of DJ of CFSST and SB is single, and in the

process of checking, such factors as the steel ratio, axial compression ratio, etc., are not considered. These problems need to be further studied in the future.

#### ACKNOWLEDGMENT

This work is financially supported by the Science and Technology Plan Projects of MOHURD (2014-K2-017), the China Postdoctoral Science Foundation funded project (2014M560938), and the Beijing Postdoctoral Research Foundation.

#### REFERENCES

- Bin R., Zhihua C., Nan Y. & Jikui M. 2012: Static tensile loading experiment and finite element analysis of diaphragm-through joint of concrete-filled square steel tubular column.
- Hong F., Lihua X. & Guofeng D. 2007: Experimental Studies on Static Behavior of Concrete-Filled Square Tubular Column—Steel Beam Connection.
- Jikui M., Xinliang J., Zhihua C. 2009: Static Tensile Test on Diaphragm-Through Joints of Concrete-Filled Square Steel Tubular Column.
- Jikui M. 2008: Behavior of diaphragm-through connection between concrete-filled square tubular column and steel beam.
- Jikui M., Zhihua C. & Xinliang J. 2008: Experimental study on load-bearing capability of connection between concrete-filled square steel tubular column and steel beam.
- Jingjing B. 2012: Seismic behavior of through—diaphragm connection between rectangular concrete filled tube column and H-shaped steel beam.
- Lei Z. 2006: Study on the seismic performance of H-beam 4to square tubular column connections with trough diaphragms.
- Liang W. 2009: Behavior and construction of diaphragm-through connection between concrete-filled square tubular column and H-steel beam.
- Lihua X., Hong F., Shengbing L. & Dan X. 2008: Experimental studies on aseismic behavior of connection between concrete-filled steel square tubular column and steel beam.
- Qin L. 2010: Nonlinear finite element analysis of concrete-filled squared tubular column connected to steel beam.
- Shantong Z. 2003: Concrete-filled steel tubular structure.
- Xilin L. et al. 2004: Technical specification for structures with concrete—filled rectangular steel tube members.
- Xinliang J., Jikui M. & Zhihua C. 2009: Experiment on seismic performance of diaphragm-through joint between concrete-filled square steel tubular column and steel beam.
- Zilin L., Cong Z., Jiang X. & Xiaojie Z. 2014: Experimental studies on all-bolts and diaphragm-through joint's aseismic behavior of concrete-filled steel tubular structure.
- Zilin L., Hongyi D. & Jiang X. 2014: Experimental study on seismic performance of all—bolt connected and diaphragm—through joint between concrete—filled square steel tubular column and steel beam.

# Analysis of influencing factors on stiffness degradation of Parallel Double Coupling Beams with different width

Ming Li

*Civil Engineering College, Shenyang Jianzhu University, Shenyang, China*  
*Jangho Group Co. Ltd., Beijing, China*

Chunyan Wang

*Civil Engineering College, Shenyang Jianzhu University, Shenyang, China*

Yuanqing Wang

*Civil Engineering College, Tsinghua University Beijing, China*

Wei Tao & Bin Wan

*Jangho Group Co. Ltd., Beijing, China*

Renliang Shan

*Civil Engineering and Mechanics, China University of Mining and Technology, Beijing, China*

**ABSTRACT:** In reinforced concrete Frame-shear Wall Structure (FWS), Coupling Beam (CB) of shear wall and the corresponding frame beam up to it, i.e., Frame Coupling Beam (FCB), has a stage of cooperative working under horizontal load. It will be helpful for knowing the whole working mechanism of FWS if the working mechanism of that stage is deeply analyzed. So, the parallel double coupling beams with different widths composed of CB and FCB, briefly called Double Beams (DBs), is taken as a research object. The load-bearing process of 11 DBs under low-cycle repeated loads are simulated with finite element simulation method. How the stiffness degradation of DBs are influenced by different influencing factors are analyzed. The results show that the span-depth ratio of FCB and the span-depth ratio of SCB have the largest and second largest influence on the stiffness degradation of DBs separately, yet the width of FCB, the strength of concrete, and the reinforced area ratio of DBs has no less effect on the stiffness degradation of DBs.

**Keywords:** double coupling beams; frame coupling beam; shear coupling beam; stiffness degradation

## 1 INTRODUCTION

In reinforced concrete Frame-shear Wall Structure (FWS), there are Parallel Double Coupling Beams (PDCB) of different size, which are composed of part of Frame Coupling Beam (FCB) and Coupling Beam (CB) of shear wall in FWS. In shear wall structure, there are also PDCB, which is composed of two coupling beams with the same width. But these two kinds of PDCB are different not only because of the width of the beams, but also because of their reinforcement requirements (Cui J.J., 2012). Many different kinds of coupling beam are promoted by different researchers through changing reinforcement arrangement, taking new structure measurement or changing material etc, and much research work is also done on them accordingly (Cao W.L. et al. 2010, Shuai J., 2011, Zhou J.H. et al. 2012, Jia L.G. et al. 2013 &

Paulay T. et al. 1999). But little study is done on the PDCB in FWS. Therefore, it becomes one of the focuses of civil engineers on how the force behavior of parallel double coupling beams with different widths is (Li M. et al. 2013). So, in this paper, the factors influenced the stiffness degradation of it will be analyzed.

## 2 DESIGNED SPECIMENS

The factors that influence the stiffness degradation of PDCB mainly includes the Span Length (SL) of the CB and the FCB, the Section Height (SH), the Section Thickness (ST), the Span-Depth Ratio (SDR) of the beams, the Concrete Strength (CS), and the Reinforced Area Ratio (RAR) which is the area ratio of longitudinal reinforcement in the CB and the FB. In order to analyze how these factors

Table 1. List of the specimens.

No	FCB				CB				CS	RAR
	SL (mm)	SH (mm)	ST (mm)	SDR	SL (mm)	SH (mm)	ST (mm)	SDR		
1	1200	800	300	1.5	1200	400	200	3	14.3	2
2	1200	480	300	2.5	1200	400	200	3	14.3	2
3	1200	600	300	2	1200	400	200	3	14.3	2
4	1200	600	300	2	1200	800	200	1.5	14.3	2
5	1200	600	300	2	1200	550	200	2.2	14.3	2
6	1200	600	400	2	1200	400	200	3	14.3	2
7	1200	600	250	2	1200	400	200	3	14.3	2
8	1200	480	300	2.5	1200	400	200	3	C25	2
9	1200	480	300	2.5	1200	400	200	3	C35	2
10	1200	480	300	2.5	1200	400	200	3	C30	2.5
11	1200	480	300	2.5	1200	400	200	3	14.3	1.5

influence the stiffness degradation, 11 specimens are designed shown in Table 1. The longitudinal bars of the CB and the FCB are all HRB335 and the stirrups of them are all HPB300.

### 3 FINITE ELEMENT SIMULATION

In order to simulate the load-bearing process of PDCB, blocks are set at both of the beam ends to make it easy to apply low cyclic load, shown in Figure 1. The loading process of the PDCB is simulated by finite element software. In simulation: the stress-strain curve of the concrete is plastic damage model; eight-node reduced integration of the three-dimensional solid elements (C3D8R) are used to simulate the concrete and upper and lower blocks. TRUSS elements are used to simulate steel. The “embedded” is used to simulate the contact between steel and concrete (Zhu Z.F., 2013, Zhang B.B., 2005, Dai F.T., 2006 & Jia Y.G. et al, 2005). The lower block is consolidated by limiting displacement of all-directions. The vertical displacement and internal and external plane rotation of the upper block is limited, which makes it can solid along the horizontal direction. Anti-symmetric low cyclic loading is applied on both ends of the upper block. Newton-Raphson iteration method is adopted to solve the problem. The finite element model is shown in Figure 2.

### 4 STIFFNESS DEGRADATION OF DBS INFLUENCING FACTORS

Under cyclic loads, the stiffness degradation is characteristic that stiffness of the structure lower with the load displacement amplitude and the number of cycles increases. In this paper, stiffness degradation characteristics of structure under low

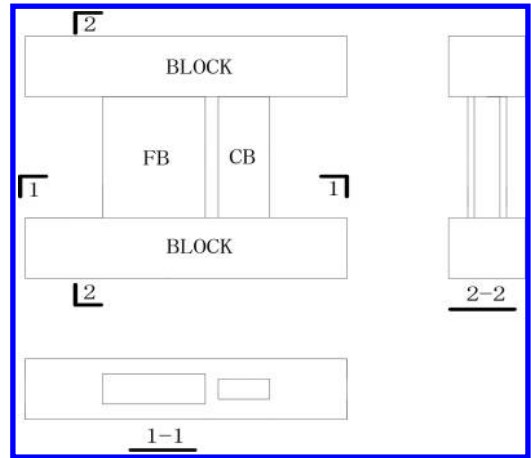


Figure 1. Designed PDCB.

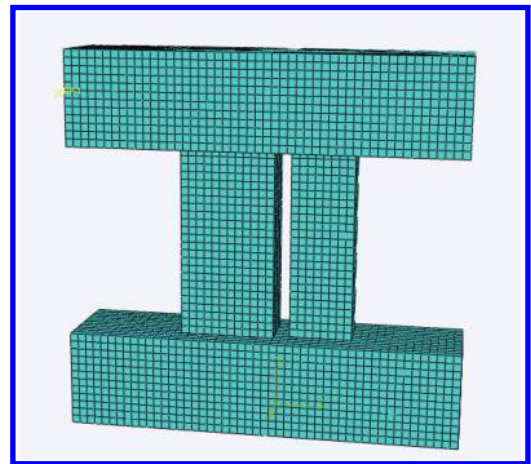


Figure 2. Finite element model of PDCB.

cycle reciprocating load denoted loop stiffness of the first cycle of the corresponding under the same level displacement loading. The diagram of specimen stiffness calculation method is shown in Figure 3.  $K_i$  is the stiffness degradation coefficient,  $P_A, P_B$  is load values of peak point,  $\Delta_A$  and  $\Delta_B$  is displacement values of peak point. Calculated stiffness changes of specimens under different loading cycles are shown in Figure 4 to Figure 8.

#### 4.1 Influence of the span-depth ratio $\alpha$

The stiffness degradation curve of double beams numbered 1, 2 and 3 under low cycle reciprocating load are shown in Figure 4, of which other parameters are unchanged, but the span-depth ratio of FB is changed. It's 1.5, 2, and 2.5 respectively. It can be seen from Figure 3 that span-depth ratio of FB influences the initial ring stiffness of DB greatly, with the increase of span-depth ratio of FBs, the corresponding stiffness of DB is decreases obviously. When the span-depth ratio changes from 1.5 to 2.5, the initial ring corresponding stiffness

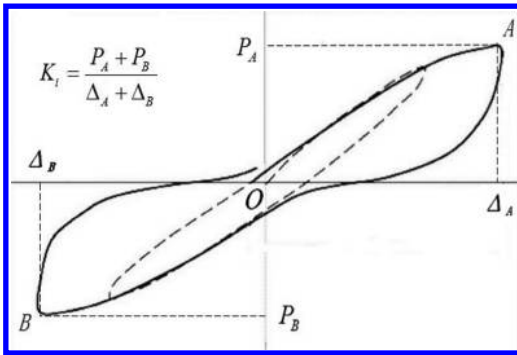


Figure 3. Schematic of how to calculate stiffness.

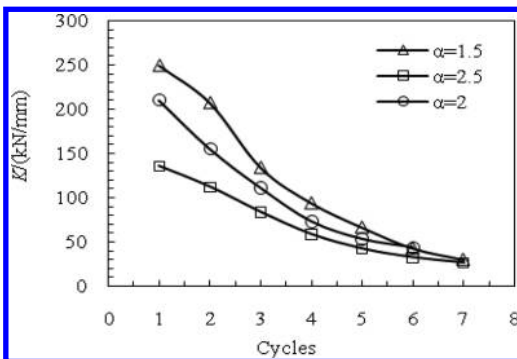


Figure 4. Influence of  $\alpha$  to the stiffness degradation of DB.

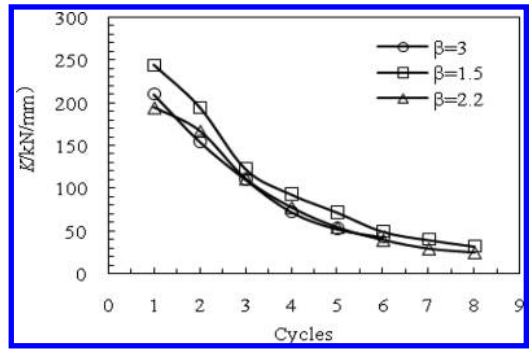


Figure 5. The influence of  $\beta$  to stiffness degradation of DB.

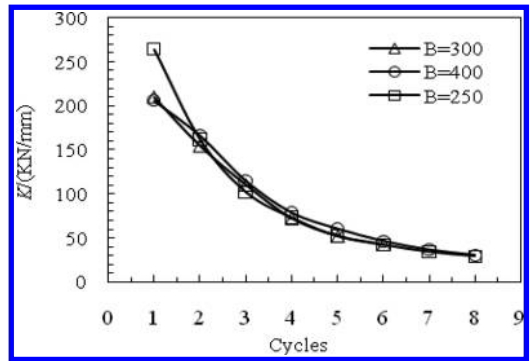


Figure 6. The influence of  $B$  to stiffness degradation of DB.

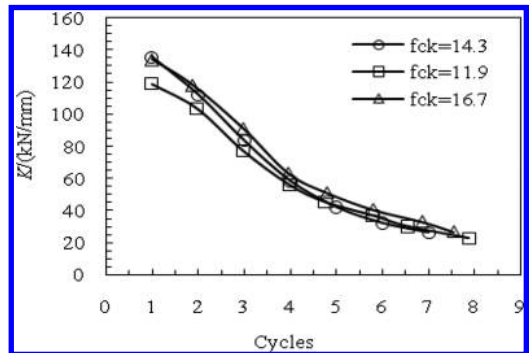


Figure 7. Influence of  $f_{ck}$  to the stiffness degradation of DB.

decreases by about 50%. With the increase of cycle number, the influence of span-depth ratio of FB decreases, when the loop reaches the 7 ring, the corresponding DB stiffness of every SDR is almost the same. Accordingly, the span-depth ratio of FB

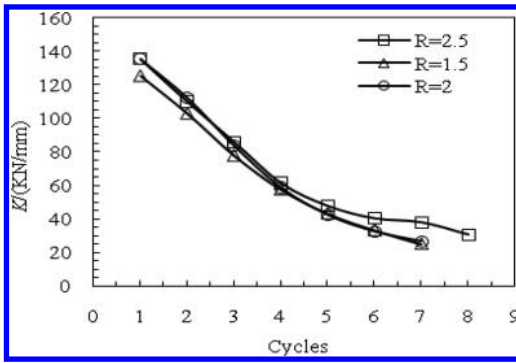


Figure 8. The influence of  $R$  to the stiffness degradation of DB.

is an important parameter which influences stiffness degradation of DB.

#### 4.2 Influence of span-depth ratio $\beta$

The stiffness degradation curve numbered 3, 4 and 5 under low cycle reciprocating load are shown in Figure 5, of which other parameters are unchanged and the span-depth ratio of CB is changed, it is 3, 2.2, and 1.5, respectively. It can be seen from the Figure 4, the stiffness of DB influenced by the span-depth ratio of SWB, but it isn't obvious compared with FB, when the SDR changes from 1.5 to 3, the first ring corresponding stiffness decreases by about 20%, and the span-depth ratio of SWB changes from 2.2 to 3, very close to stiffness degradation curve of DB, however, when the cycle number increases to the 8 ring, the stiffness of DB that different span-depth ratio of SWB is almost the same. From this we can conclude that the span-depth ratio of SWB influences stiffness degradation of DB but it isn't obvious compared with FB.

#### 4.3 Influence of the section width $B$

The stiffness degradation curve of frame beams numbered 6, 3 and 7 under low cycle reciprocating load are shown in Figure 6, of which other parameters are unchanged and the Section Width (SW) of FB is changed, it is 400 mm, 300 mm, and 250 mm, respectively. It can be seen from the figures, the first lap of the DB with 250 mm section width of FB has the largest stiffness, about 1.3 times of FB with 400 mm and 300 mm section width, the 2 ring later, stiffness degradation curve of DB that width of FB is 250 mm, 300 mm and 400 mm is almost the same. And stiffness degradation curve of DB that width of FB is 300 mm and 400 mm always close to each other. Therefore, only when the frame beam width is small and close to

the shear wall width, the section width of FB have influences in the first ring stiffness of DB, beyond this scope, the width of frame beam almost had no effect on stiffness degradation of DB.

#### 4.4 Influence of concrete strength $f_{ck}$

The stiffness degradation curve of frame beams numbered 8, 10 and 9 under low cycle reciprocating load are shown in Figure 7, of which other parameters are unchanged and the CS is changed, it is 11.9 Mpa (C25), 14.3 Mpa (C30), and 16.9 Mpa (C35) respectively. It can be seen from the figures, generally, the higher the CS, the greater the stiffness of the double beam, but the change is not big, the first ring corresponding stiffness of DB that concrete strength is 16.9 Mpa is 1.13 times of CS with 11.9 Mpa, and the first ring corresponding stiffness of DB that concrete strength is 16.9 Mpa is almost the same with the CS is 14.3 Mpa. It shows that concrete strength has a little effect on DB stiffness degradation.

#### 4.5 Influence of reinforced area ratio $R$

The stiffness degradation curve of frame beams numbered 11, 2, and 10 under low cycle reciprocating loads are shown in Figure 8, of which other parameters are unchanged and the reinforced area ratio is changed. It is 1.5, 2, and 2.5, respectively. It can be seen from the figures, the larger the reinforced area ratio, the greater the double beam stiffness. The first ring corresponding stiffness of DB that RAR is 2.5 is 1.1 times of RAR with 1.5, but when the RAR increases to a certain extent, it only has a little influence in the stiffness of DB. It shows that with the increase of the reinforced area ratio, the stiffness of DB has increased, but it isn't obvious.

## 5 SUMMARY

Based on the above analysis, the following conclusions can be drawn:

1. The largest factor that influence the stiffness degradation of DB is the SDR of FB, and the span-depth ratio of CB is the secondary. With the increase of span-depth ratio of FB and CB, the stiffness of DB decreases, therefore, the degree of the decrease is reducer with the increase of the number of cycles. When the number of cycle increases to a certain extent, the span-depth ratio of the FB and the CB has almost no effect on stiffness of DB.
2. The stiffness degradation is influenced by the section width of FB, concrete strength and RAR. With the increase of the section width of FB, concrete strength and increase of RAR, the stiffness of DB increases, but the increase is a little.



## ACKNOWLEDGMENT

This work was financially supported by China Postdoctoral Science Foundation funded project (2014M560938) and Beijing Postdoctoral Research Foundation funded project.

## REFERENCES

- Cao W.L., Zhang J., Yin H.P. & Chen J.L. 2010. Experimental study on the seismic behavior of recycle concrete frame-shear-wall structure.
- Cui J.J. 2012. Seismic performance analysis of frame-shear wall structure.
- Dai F.T. 2006. On the calculation of reinforced concrete beam and pile cracking moment and yield moment.
- Jia L.G., Iang Y., Liu X., Chen Y. & Zhang Z.N. 2013. Experimental Study on Joints of Built-in Steel Plate Reinforced Concrete Coupling Beam and Shear Wall.
- Jia Y.G., Tu X.Q. 2005. A non-linear analysis method of moment modulating of continuous RC beams.
- Li M., Chen J.G. & Zhao W.J. 2013. Research Progress on Coupling Beam.
- Liu J.B., Chen Y.G., Guo Z.X. & Zhang J.X. 2013. Test on seismic performance of precast concrete shear wall with U-shaped closed reinforcements connected in horizontal joints.
- Ming H. 2012. Experimental research on seismic behavior of small-span-to-depth-ratio dual coupling beams with HRB500 bar.
- Paulay T. & Priestley M.J.N. 1999. Seismic design of reinforced concrete and masonry buildings.
- Shuai J. 2011. Experimental study on the seismic behavior of the frame-shear-wall structure of steel tube concrete.
- Zhang B.B., Bai S.L., Fu J.P. & Deng L.L. 2005. Experimental research of reasonable reinforcement of short coupling beams of shear walls.
- Zhou J.H., Wang Z.Z., Meng X.H. & Yang Y.S. 2012. Influence of Aspects Ratios on Seismic Behavior of Recycled Concrete Lattice Walls.
- Zhu Z.F. & Guo Z.X. 2013. Test on fabricated short shear wall under low cyclic loading.

# Study on parameter optimization of static performance for long-span elliptic suspended dome structure

K.R. Shi & Z.R. Jiang

State Key Laboratory of Subtropical Building Science, South China University of Technology, Guangzhou, China

**ABSTRACT:** Taking the new type hybrid structure of elliptic suspended dome as the analytical object, the parameter optimization of static performance is studied in detail. By the method of nonlinear static analysis, the effects of different parameters on the static performance are systematically analyzed i.e. rise-span ratio, plane shape factor, prestress and strut's length. The results show that rise-span ratio and strut's length have greater effects on the structural static performance than plane shape factor and prestress. The smaller rise-span ratio and the larger plane shape factor are good for improving static performance. Prestress should be rational as over-high prestress or over-low prestress would cause disadvantageous problems. The longer strut can improve static performance, but over-long strut affects stability and reduces head room of the building.

**Keywords:** elliptic suspended dome; static performance; nonlinear analysis; prestress; parameter optimal analysis

## 1 INTRODUCTION

Analysis of structural static performance provides basic theoretical foundation for structure design, which offers necessary reference for other kinds of analysis such as dynamics performance analysis, stability analysis and so on [1]. There are some studies on static performance of circle suspended dome [2–8], however, only few studies are about elliptic suspended dome [9–10]. Elliptic suspended dome is a new structure form, and its structural performance becomes more complex with the increase of structural span. To meet the requirements of engineering practice, this paper is going to research on parameters optimization of static performance for large-span elliptic suspended dome by utilizing a typical calculation example, which aims at achieving regular conclusions and giving rational suggestions.

## 2 CALCULATION MODEL AND PLAN OF PARAMETRIC ANALYSIS

### 2.1 Calculation model

The calculation model should be representative and able to reflect general character of homogeneous structures. So the following typical model is chosen, namely, a long-span elliptic suspended dome (Fig. 1). The span of long axis of the model is  $2a = 80$  m, and the span of short axis

is  $2b = 64$  m. The relevant plane shape factor is  $\delta = 0.8$ . Its surface shape is an elliptic paraboloid with the arch rise of  $f = 6.667$  m. The upper chord layer is a single-layer latticed shell, whose members are made of the steel pipes of 203 mm in diameter and 10 mm in thickness. The characteristic value of yield strength of the steel pipe members is 345 MPa, which connected by rigid joint. The lower cable-strut system consists of three-ring hoop cables, radial cables and struts, whose hoop cables are set at a ring interval and struts at a joint interval. The twisted-type parallel steel-wire cables are used, whose ultimate tensile strength is 1670 MPa, and the diameter of each steel-wire is 5 mm. The section types of the hoop cables are respectively PES C5-61, PES C5-91, PES C5-121 from the inner ring to the outer ring, and the section type of all the radial cables is PES C5-55. The struts are used the steel pipes of 168 mm in diameter and 8 mm in thickness with the characteristic value of yield strength of 345 MPa. The lengths of the struts are respectively 4.889 m, 5.723 m, 6.556 m from the inner ring to the outer ring. The anchor joints of the cable-strut system are fixed.

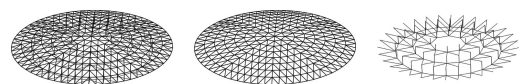


Figure 1. Calculation model of elliptic suspended dome ( $\delta = 0.8$ ).

The Young's modulus of the steel pipes and cables are  $2.06 \times 10^5$  MPa and  $1.95 \times 10^5$  MPa, respectively. The initial prestress of the hoop cables are respectively 315.6 kN, 472.8 kN and 731.9 kN from the inner ring to the outer ring. The radial sliding supports are used in the suspended dome model. For conveniently description, the suspended dome model is called 'basic model'.

### 2.2 Load condition

Take common roof load conditions: characteristic values of permanent load  $g = 1.0$  kN/m<sup>2</sup> (including structure self-weight) and characteristic values of live load  $p = 0.5$  kN/m<sup>2</sup>. According to the structural characteristics of elliptic suspended dome, loading state analyses by 3 kinds of load combination are conducted.

### 2.3 Parameter selection

Compared comprehensively, influences of four main parameters on the structural stability are taken into account, i.e. rise-span ratio, plane shape factor, prestress and strut's length. Among these parameters, the plane shape factor is the ratio of short-axis's length and long-axis's length in horizontal projection of the elliptic suspended dome, that is:

$$\delta = \frac{b}{a} \quad (1)$$

where,  $a$  is half length of elliptic long-axis and  $b$  is half length of elliptic short-axis.

## 3 PARAMETER INFLUENCE ANALYSIS OF STRUCTURAL STATIC PERFORMANCE

### 3.1 Influence of rise-span ratio

In order to get different rise-span ratio, only the arch rise is changed while other parameters keep unchanged (Table 2). In the Table 2, the rise-span ratio of long-axis of the 'basic model' is 1/12, and the corresponding rise-span ratio of long-axis is 1/9.6.

Figures 2-6 shows influences of different rise-span ratio on vertical deformation, horizontal radial displacement of support, axial force of member in the upper shell and internal force of cable-strut system.

1. According to Figure 2, rise-span ratio makes a great difference on the vertical deformation of suspended dome, the maximum vertical displacement of node decreases as the rise-span ratio increases. However, the influence is gradually weaken as rise-span ratio becomes larger. The maximum vertical displacement of node all appears in load Comb-III, which shows half span live load distribution (on short-axis) controls vertical deformation of the structure. Also, differences of the maximum vertical displacement of node among the three load combinations decrease with the increase of rise-span ratio. Horizontal radial displacement of support also obeys the similar rules (Fig. 3).
2. According to Figure 4, the change of rise-span ratio makes a great difference on axial force of the upper member, and the effects from different load combinations on the maximum tensile force

Table 1. Load combination.

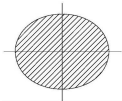
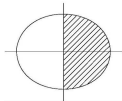
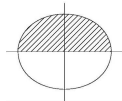
Code	Comb-I	Comb-II	Comb-III
Combination	All span permanent load + all span live load	All span permanent load + half span live load (on long-axis)	All span permanent load + half span live load (on short-axis)
Live load distribution chart			

Table 2. Different values of rise-span ratio.

Arch rise	4 m	6.667 m	8 m	10 m	16 m
Rise-span ratio of long-axis	1/20	1/12	1/10	1/8	1/5
Rise-span ratio of short-axis	1/16	1/9.6	1/8	1/6.4	1/4

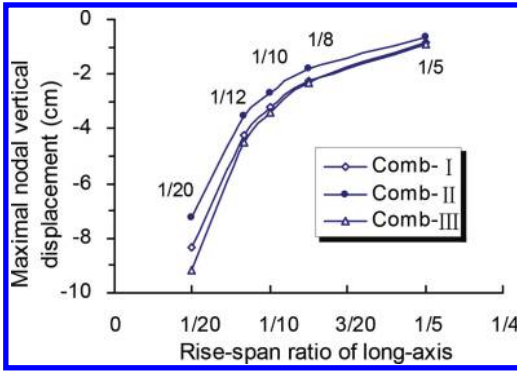


Figure 2. Influence of rise-span ratio on vertical deformation.

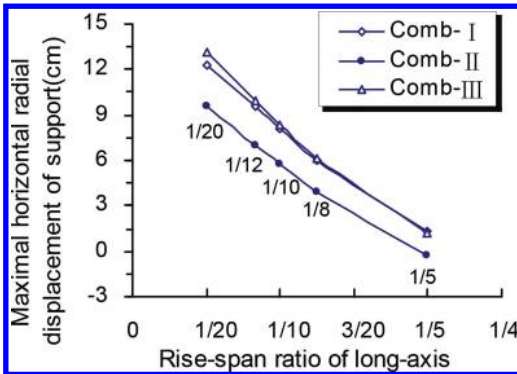


Figure 3. Influence of rise-span ratio on support displacement.

and compressive force differ. If rise-span ratio is relatively small, unsymmetrical distribution of live load is not critical to the maximum tensile force of the upper member. When rise-span ratio increases to a certain degree (for the proposed example, when its rise-span ratio of long-axis is more than 1/8), the maximum tensile force occurs in Comb-III (half span live load distribution along the short-axis), and the maximum compressive force of the upper member occurs in Comb-III regardless of the value of rise-span ratio.

- Similarly, the internal force of cable-strut system decreases with the increase of rise-span ratio, and the smaller rise-span ratio makes a greater difference (Figs. 5-6). Cable force and axial compressive force of strut are larger when the suspended dome has smaller rise-span ratio, which makes full use of the high-strength materials and advantages of elastic support of the strut. However, the maximum internal force of cable-strut system occurs in Comb-I.

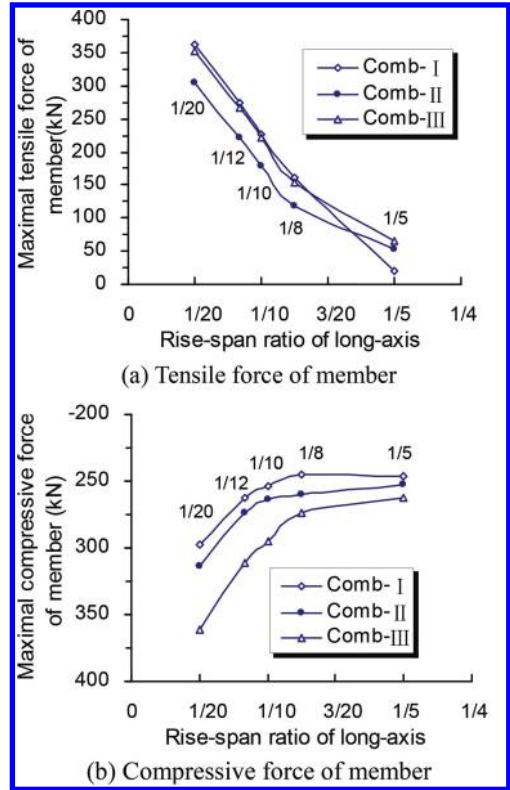


Figure 4. Influence of rise-span ratio on axial force of member.

- As shown in Figures 2-6, Comb-II (half span live load distribution on the long-axis) controls neither structural deformation nor internal force of member.

In summary, rise-span ratio has obvious influence on static performance of suspended dome, and suspended dome with smaller rise-span ratio takes more advantages of this structural system.

### 3.2 Influence of ratio plane shape factor

Base on the 'basic model' ( $\delta = 0.8$ ), as shown in Table 3, the values of plane shape factor change from 0.6 to 1.0 while the span of long-axis (80 m), the arch rise (6.667 m) and other parameters keep unchanged.

Figures 7-11 shows influences of different plane shape factors on vertical deformation, horizontal radial displacement of support, axial force of member in the upper shell and internal force of cable-strut system.

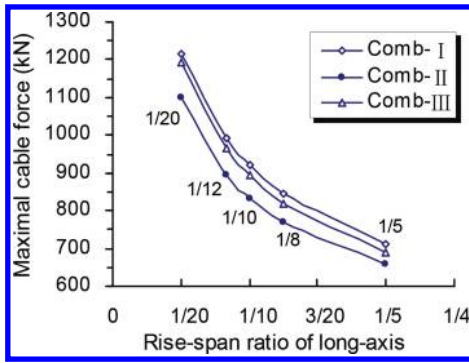


Figure 5. Influence of rise-span ratio on cable force.

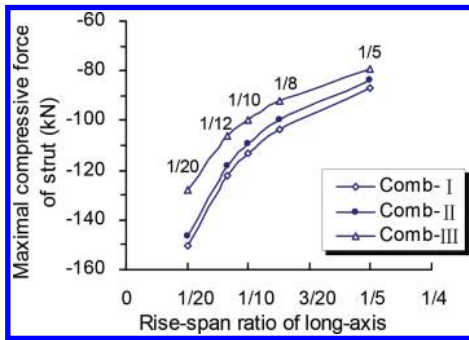


Figure 6. Influence of rise-span ratio on internal force of strut.

Table 3. Different values of plane shape factor.

Plane shape factor $\delta$	0.6	0.7	0.8	0.9	1.0
Span of long-axis (m)	80	80	80	80	80
Span of short-axis (m)	48	56	64	72	80

1. According to Figure 7, plane shape factor makes a great difference on the vertical deformation of suspended dome, the vertical displacement of node increases with the increase of plane shape factors. Increase speed of the maximum vertical displacement of node differs in each load combination, Comb-I and Comb-III are basically same, Comb-II is the fastest. When  $\delta$  increases to 1.0, horizontal projection of suspended dome changes into a circle and calculation results of Comb-II and Comb-III are the same.

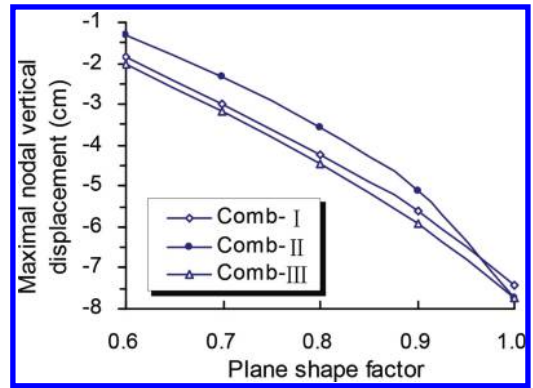


Figure 7. Influence of plane shape factor on vertical deformation.

2. According to Figure 8, the maximum horizontal radial displacement of support all increases with the increase of  $\delta$  under each load combination. Among the three load combinations, displacement keeps linear growth in Comb-I and Comb-III, while in Comb-II, the displacement increases faster and faster with the increase of  $\delta$  and it is equal to the displacement of Comb-III when  $\delta$  reaches 1.
3. Similarly, plane shape factor has an obvious effect on axis force of the upper member and internal force of the lower cable-strut system (Fig. 9–11).
4. It is the same with the parameter analysis results of rise-span ratio that load combination II (half span live load on the long-axis) controls neither transformation nor stress.

In summary, plane shape factor makes a great difference on static performance of suspended dome, and the increase of plane shape factor is helpful for improving structural performance.

### 3.3 Influence of prestress

Base on the ‘basic model’ ( $\delta = 0.8$ ), the influences of different prestress values on vertical deformation, horizontal radial displacement of support, axial force of member in the upper shell and internal force of cable-strut system are studied.

Figures 12–16 shows the calculation results of different prestress values, among which the prestress value of the ‘basic model’ is set to Unit 1.

1. According to Figure 12, prestress makes a great difference on the vertical deformation of suspended dome. The maximum vertical displacement of node decreases with the increase of prestress and it keeps linear growth under different load combinations. It is showed that prestress can adjust structural deformation effectively

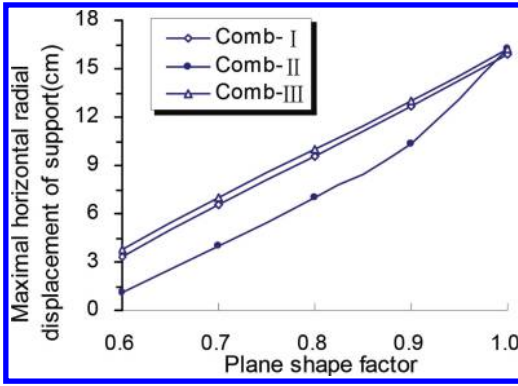


Figure 8. Influence of plane shape factor on support displacement.

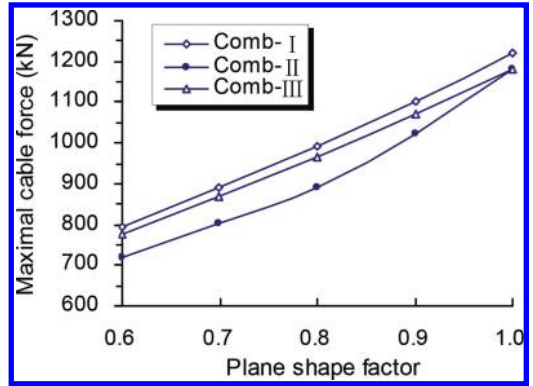


Figure 10. Influence of plane shape factor on cable force.

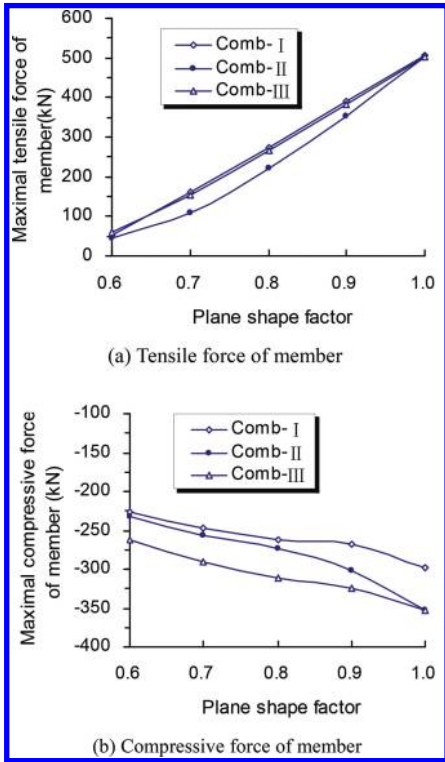


Figure 9. Influence of plane shape factor on axis force of member.

and nonlinear characteristic of formed structure is inconspicuous.

- According to Figure 13, the influence of prestress on support displacement is obvious. The maximum horizontal radial displacement of support decreases linearly with the increase of prestress.

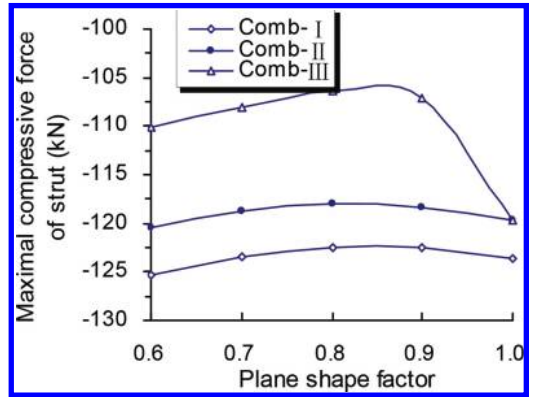


Figure 11. Influence of plane shape factor on internal force of strut.

- According to Figure 14, increase of prestress reduces the maximum tensile force of member in the upper shell obviously and makes the maximum compressive force of member increase. However, over-high prestress not only can't improve structural static performance, but also increases the burden of the structure itself. However, over-low prestress can't take full advantage of suspended dome system.
- Change of prestress has effect on the internal force of cable-strut system naturally, as shown in Figure 15 and Figure 16. The maximum cable force and the maximum axial compressive force of strut keep linear growth with the increase of prestress.

In summary, prestress has obvious influence on static performance of the suspended dome. Furthermore, only reasonable prestress can improve structural performance.

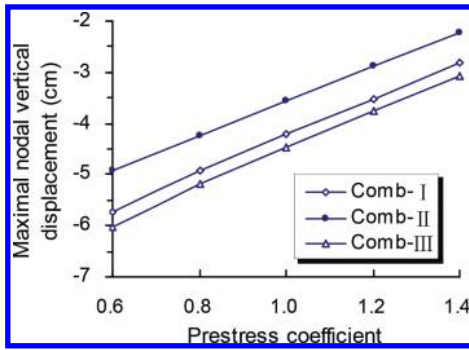


Figure 12. Influence of prestress on vertical deformation.

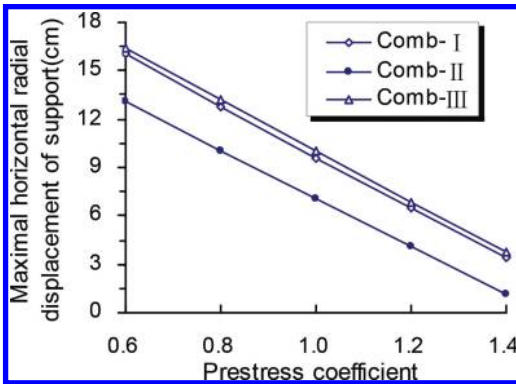


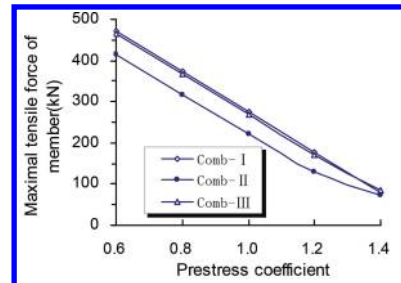
Figure 13. Influence of prestress on support displacement.

### 3.4 Influence of strut's length

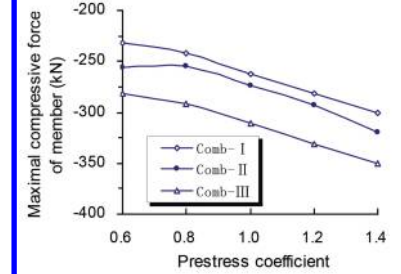
As shown in Table 4, strut's length is changed by adjusting the angle between radial cable and horizontal plane in long-axis direction, among which the angle of the 'basic model' is 20 degree.

Figures 17~21 shows influences of different strut's length on vertical deformation, horizontal radial displacement of support, axial force of member in the upper shell and internal force of cable-strut system.

1. According to Figure 17 and Figure 18, strut's length makes a great difference on the vertical deformation of suspended dome and support displacement, the maximum vertical displacement of node and horizontal displacement on support decreases continuously with the increase of strut's length. It is concluded that increase of strut's length largens strut's vertical component of forces with the same prestress (Fig. 21). Sequentially, it reduces vertical deformation and horizontal displacement effectively, which is no longer obvious as strut's length



(a) Tensile force of member



(b) Compressive force of member

Figure 14. Influence of prestress on axial force of member.

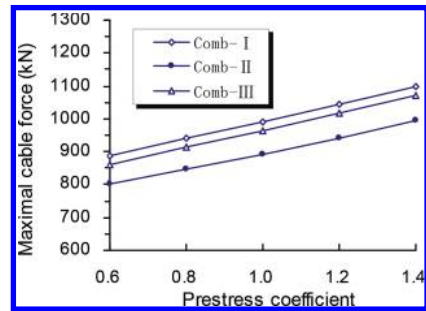


Figure 15. Influence of prestress on cable force.

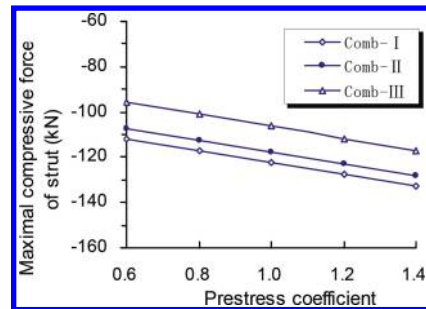


Figure 16. Influence of prestress on internal force of strut.

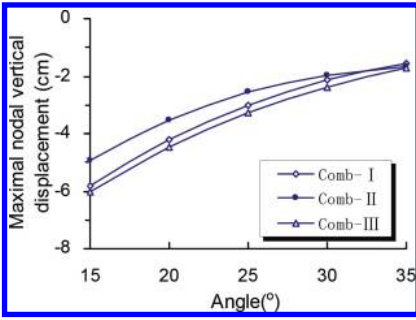


Figure 17. Influence of strut's length on vertical deformation.

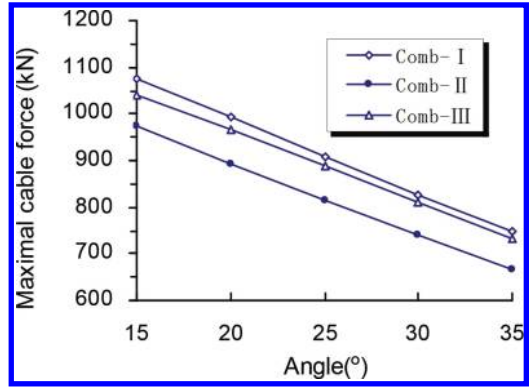


Figure 20. Influence of strut's length on cable force.

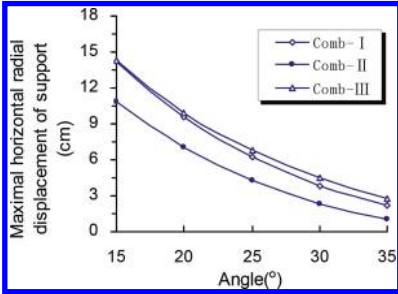


Figure 18. Influence of strut's length on support displacement.

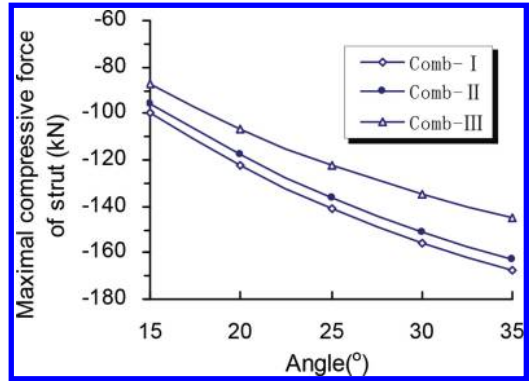


Figure 21. Influence of strut's length on internal force of strut.

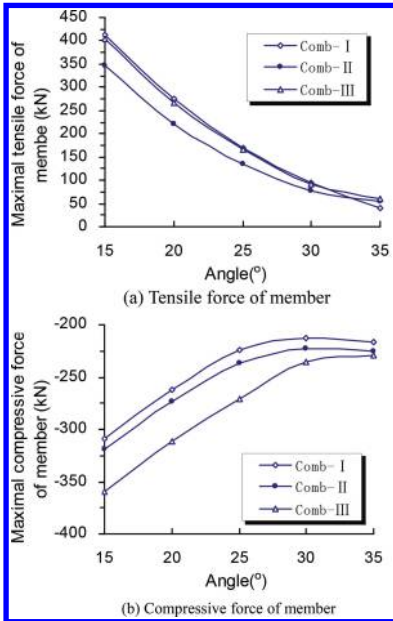


Figure 19. Influence of strut's length on axial force of member.

reaches to a certain degree. Therefore, strut's length should be chosen rationally just like the prestress. What's more, stability of over-long strut must be noticed.

2. According to Figures 19-21, increase of strut's length reduced peak of internal force of structural member. Similarly, effect on reducing inner-force peak is no longer obvious as strut's length increases to a certain degree.

In summary, strut's length has an obvious influence on static performance of suspended dome. The longer strut improved structural static performance effectively, but over-long strut is bad for strut's stability and reduces head room of the building.

#### 4 CONCLUSIONS

1. Rise-span ratio has a significant influence on static performance of suspended dome, and smaller rise-span ratio takes more advantages of this structural system.



2. Plane shape factor has a notable influence on static performance of elliptic suspended dome, and increase of plane shape factor is helpful for improving structural performance.
3. Prestress has obvious influence on static performance of suspended dome. Furthermore, only reasonable prestress can improve structural performance.
4. Strut's length makes a great difference on static performance of suspended dome. The longer strut improved structural static performance effectively, but over-long strut is bad for strut's stability and reduces head room of the building.

#### ACKNOWLEDGEMENTS

The writers want to express their gratitude for the financial support of the Opening Project of State Key Laboratory of Subtropical Building Science, South China University of Technology, China (Grant No. 2012KB31); the Fundamental Research Funds for the Central Universities, South China University of Technology, China (Grant No. 2014ZZ0025).

#### REFERENCES

[1] Zhang, Z.H. 2003. *Theoretical research on large-span tensile spatial structures composed of cables, bars and beams*. Hangzhou: Zhejiang University. (in Chinese).

[2] Mamoru K., Masaru A., Ikuo T. 1999. Design, tests and realization of "suspension-dome" system. *Journal of the IASS* 40(3): 179–192.

[3] Li Y.M. 2004. *Theoretical and experimental research on new cable-supported lattice shell structure system*. Beijing: Beijing Transportation University (in Chinese).

[4] Zhang M.S. 2004. *Theoretical research on suspended dome*. Hangzhou: Zhejiang University. (in Chinese).

[5] Chen Z.H., Li Y., Kang W.J. 2005. Analysis of lamella suspended dome systems. *China Civil Engineering Journal*, 38(5): 34–40 (in Chinese).

[6] Kang W.J., Chen Z.H., Lam H.F., Zuo C.R. 2003. Analysis and design of the general and outmost-ring stiffened suspension-dome structures. *Engineering Structure*, 25(13): 1685–1695.

[7] Kitipornchai S., Kang W.J., Lam H.F., Albermani F. 2005. Factors affecting the design and construction of Lamella suspension-dome systems. *Journal of Constructional Steel Research*, 61(6): 764–785.

[8] Chen Z.H. 2004. Analysis of suspended dome and its structural characteristics. *Building Structure*, 34(5): 38–41 (in Chinese).

[9] Wang Z.Q., Qin J., Li G.L., Zhang R., Wu J.X. Study on Static Capability of Ellipse Plane Suspended dome, *Building Structure*, 38(2): 39–42 (in Chinese).

[10] Wang Z.Q., Qin J., Li G.L., Xu R.L., Zhang R., Chen X.L., Treatment of hoop cable and support condition and experimental study on the annular ellipse suspension-dome. *Spatial Structures*, 12(3): 12–17 (in Chinese).

# A review of analyzing influences of excavation of foundation pits on the surrounding environment

Shi Min Zhang

*School of Civil Engineering and Architecture, Anhui University of Science and Technology, Huainan, China*  
*The Department of Civil Engineering, Zhejiang University City College, Hangzhou, China*

Feng Wei Jing

*School of Civil Engineering and Architecture, Anhui University of Science and Technology, Huainan, China*

**ABSTRACT:** From the aspects of mechanics effect, foundation pit excavation is a kind of unloading of excavation on the surrounding environment. This will cause displacement of the surrounding soils and change the internal structure of the corresponding, using different tools and methods for studying the influence of the foundation pit excavation has become a hot topic in academia. Combined with the analysis of the influence of excavation on the surrounding environment, the paper uses the DCFEM method and two-stage analysis method to study this influence.

**Keywords:** foundation pit excavation; two-stage method for analyzing; soil settlement; impact analysis

## 1 INTRODUCTION

The utilization rate of the city land resources continuous improvement, the continuous development of underground space, and the development of foundation pit engineering gradually to the ultra deep is being done on a large scale with the continuous expansion of the city.

Foundation pit engineering is a traditional topic in the construction of foundation and underground engineering. At the same time, it also has strong comprehensive geotechnical engineering problems. It is not only related to the typical strength problems of soil mechanics and deformation problems, but also involves the interaction of soil and support structure of support. The soil around the foundation pit is affected by different disturbances in the process of excavation of foundation pit; this is called environmental effect. If this situation is handled properly, it will not only cause a waste of resources, but also casualties and significant economic losses. There have been many engineering accidents that have caused destruction of the surrounding buildings, underground pipelines, and facilities by the excavation of foundation pit. It is visible, there is a great risk in the process of foundation pit excavation, It is an urgent need for this topic for more in-depth research about the impact on the surrounding environment of foundation pit excavation. In this paper, through the research of the research status on the foundation pit of domestic and foreign, According to the problems

about the failure of surrounding environment in the process of foundation pit, to study using the method of finite element method and data analysis to solve different kinds of problems.

## 2 CHINA AND ABROAD RESEARCH STATUS

Terzaghi and Peck et al have begun to study geotechnical engineering problems in Foundation Pit Engineering and put forward the total stress method that can estimate the stability degree of excavation and support load size. The principle of this theory has been used until now after constant improvement and revision.

Bjeruum and Eide presented a method of analysis of deep foundation pit in uplift set in the 1950's. They began monitoring deep foundation pit engineering in soft clay in Oslo and the city of Mexico in 1960's, which play a role in promoting to improve the accuracy of prediction.

Lambe believes that there are 8 factors on the deformation of soil around the pit through the research in 1970's: the length of excavation, the width and depth of excavation, soil conditions of pit, groundwater level, the exposure time of pit, support system, the order of the excavation and support, the adjacent structures, and facilities and construction load.

Leung analysis of a set of uniform distribution that reflects the maximum horizontal displacement

and the maximum settlement of the surface and the relationship between the stiffness of a bracing system and those, comparing the research results of Peck, Mana, Clough, and Long.

The ground loss method that was put forward by Professor Hou Xueyuan can be used to estimate the settlement of the soil around deep foundation and calculate subsidence displacement of ground based on the related principle of ground movement area of wall displacement and ground settlement.

Gong Xiaonan et al deduct a calculation method that calculation of ultimate resistance before and after excavation based on the classical resistance formula of clayey soil pile. He also analyzes the change rule of coefficient of resistance is reduced under the condition of different excavation depth, excavation length, length width ratio and pile length, through comparing the results of theory with the measured data, the results of finite element analysis and other methods.

Obviously, the research about the foundation pit supporting has been relatively mature, but there are few researches on the effect of pit excavation on the surrounding environment. The theoretical research on the topic has aroused the attention of many scholars at home and abroad. Increasing the research in this area will increase the safety of excavation engineering, and promote the development of the theory of foundation pit engineering.

### 3 THEORETICAL ANALYSIS METHODS

Over the past ten years, the foundation pit engineering has been rapidly developing in our country, with the basic construction of our country and a large area of old city transformation like a raging fire. The problems in excavation engineering are increasing more and more, and even more and more complex. Foundation pit engineering is excavating deeper foundation pits, larger excavation areas, surrounding environment is more complex. The unknown risks in excavation also increased, especially to the surrounding structures and surrounding buildings, underground pipelines etc. in the process of excavation. The following will introduce and analyze the changes of the surrounding environment caused by excavation.

#### 3.1 *The uneven settlement of soil around the foundation due to pit excavation*

In the process of construction of deep foundation pit engineering, the surrounding soil will be disturbed by different degree, this will affect the normal use of the surrounding buildings, structures and underground pipeline, even cause engineering accident. The uneven subsidence of the surrounding surface is one of the important influence which caused by excavation. Factors of

ground settlement: the state of stress and strain of the soil around changes, the displacement of surrounding soil, strata consolidation caused by well point precipitation, sand loss, sand flow, piping loss caused by pumping.

#### 3.2 *Analysis of the surrounding soil stress-strain state change*

The main way of impact that the excavation to adjacent underground structure is that the surrounding soil will be disturbed, and that will lead the stress and strain state of the surrounding soil to change, eventually leading to stress and strain state of neighboring structures to change. The reason for the change of soil strain state is that plastic deformation of the soil caused by stress perturbations and the strain caused by soil creep. However, the strain of soil is mainly remolded. Soil turns to reconsolidation soil. With the depth of excavation increasing, the internal forces of the soil around the pit increasing, the soil around the foundation pit will produce a large plastic zone, the lateral soil of the foundation pit will cause a destructive sliding toward the foundation pit. Eventually, the foundation pit becomes unstable and a lot of subsidence is generated around the foundation pit. These subsidence can cause a large margin of formation loss. This is also an important factor arises engineering accident.

#### 3.3 *Analysis of displacement of soil around foundation pit*

The stability of the soil is weakened when the excavation plane push down, the shear force of the soil will be increased. When the strain of the soil is greater than the shear strain, the structure of soil is damaged, the surrounding soil is moved, so, the unstable state region is appeared in the surrounding soil. In particular, when the stress change region between two underground engineering is in a whole, this area will have a large loose range of soil. The soil between the two underground engineering will be unstable, at the same time, the retaining structure will change. This change will vary according to the width of the separation zone between the adjacent underground engineering. The results show that the width of separation zone is set to two times excavation depth, the mutual influence of deep foundation pit construction can be reduced effectively. This kind of interaction has some relationships with the excavation sequence of adjacent foundation pit and effect of variable position of supporting structure and so on.

#### 3.4 *Analysis of settlement caused by foundation pit precipitation*

During foundation pit excavation, when the water level of the groundwater level is reduced too low

or the structure of the retaining structure is too large, it can reduce subsidence of ground around the foundation pit. If the uneven settlement is too large, There may also cause buildings tilt, crack of wall, road and underground pipeline cracking, and other serious problems.

The amount of moisture content in the soil directly affects the mechanical properties of the soil structure. When the moisture changes in the soil body, the soil will generate a reshaping. Experiment shows, for the same kind of soil, the mechanical properties of undisturbed soil samples are very different with remodeling soil samples. During the excavation of foundation pit, the constant drainage causes the groundwater level fall. The moisture content of soil around the foundation pit is changed, and the stress state of the soil also changes. This will cause the remodeling of the structure of soil around the foundation pit, the mechanical properties of soil are changed. This remodelled soil will produce uneven settlement under the same load, especially in soft soil region, this performance is more obvious, the great harm, because the soil moisture content is high, the soil loses the moisture, the soil produces the consolidation.

#### 4 RESEARCH ON SOME OUTSTANDING ISSUES

##### 4.1 Analysis of the influence of foundation pit excavation on the foundation of near buildings

Research on the influence of foundation pit excavation near pile foundation has been studied by domestic and foreign scholars with different methods. Leung et al. has discussed the influence of foundation pit excavation on the foundation of adjacent piles under no support conditions through centrifugal model test, and has analyzed the influence to single pile and group piles with different piles. Pan et al. and Miao et al. has discussed deformation and mechanical properties of passive single piles and extracted P-y curve of single pile uniform soil under horizontal displacement condition.

The influence of foundation pit excavation on the foundation of adjacent buildings is a passive pile problem. Zhu Xiaoyu et al. has discussed the influence of the foundation pit excavation to the single pile and the group pile at the different distance with DCFEM (finite element method control the displacement, the simplified method has been applied to the analysis of environmental impact of underground excavation). Then, they also compared the test results of influence of foundation pit excavation on adjacent piles with results of centrifugal model test.

Figure 1 (a) and (b) are the comparison of results between DCFEM and centrifuge tests, The displacement of the piles obtained by DCFEM

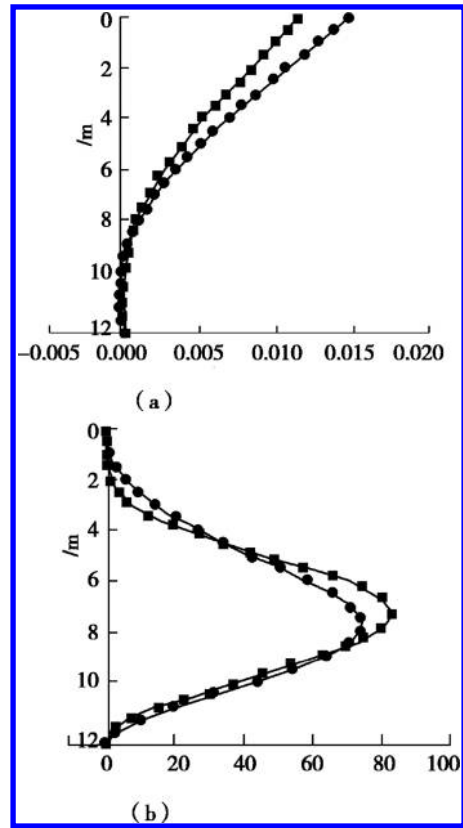


Figure 1. Comparison of results between DCFEM and centrifuge tests.

method is more than that of the centrifugal model. The calculated moment is smaller than the centrifugal test result. But the displacement curves and bending moment curves of the two methods are similar, the displacement values are all at the top of the pile, and the maximum bending moment is located in middle of the pile body.

##### 4.2 Analysis of the influence of excavation on near metro tunnel

People's living standards improved with the rapid development of economy. City traffic is becoming increasingly congested. The trend is that the Metro has become construction of urban transport. But in this times of land-scarcity, It is inevitable that excavation pit near the subway will be used to construct high-rise buildings. The subway track has strict requirement for the soil mass below the orbit. This gives the study of the excavation of the subway tunnel important significance. The research on the influence of the excavation to the subway tunnel is not a new problem. Domestic scholars have carried out a thorough study on the subject.

Zhang Zhiguo et al. have adopted a two-stage analysis method which can consider unloading effects at the bottom and around the pit wall soil due to excavation. This method is based on the Winkler foundation model to establish the basic differential equation of the longitudinal deformation of the subway tunnel. According to the Galerkin method, the equation is converted to a one-dimensional finite element equation for calculation. At the same time, they have studied the factors of the longitudinal deformation of tunnel: different tunnel depth, distance from the excavation site, different foundation soil and different tunnel diameter, and so on. The results of this method are compared with the field measurement data. The results were in good consistency.

## 5 THE DIRECTION OF THE FUTURE RESEARCH ON THE ENVIRONMENT INFLUENCED BY THE EXCAVATION OF FOUNDATION PIT

Foundation pit is as temporary structure, strength safety reserve is also lower relative to the main body structure, at the same time, the external environment factors of foundation pit is so many, for example, geological conditions and different sites of different regions, even though the same sites are not the same in different regions, many factors make it a comprehensive system engineering. Whether the surrounding environment is influenced by foundation pit excavation is also a comprehensive study, the engineering situation around the foundation pit will be more and more complex in future studies. With the continuous progress of Technology, we can apply professional software to study the interaction between foundation pit and buildings, select the appropriate constitutive model of soil, and combine with the surrounding engineering situation to simulate construction and forecast construction risk. This can ensure the safety of the construction, at the same time, it can also speed up the construction progress to make up for foundation pit temporary problem. The data fed back through the construction process can verify the correctness of the simulation. The combination of theory, software and construction site is the ultimate design through the continuous improvement. Eventually, we will design a more safe and efficient construction scheme.

## 6 CONCLUSION

In the era of vigorous economic development, The foundation pit engineering continuously develop to deeper and larger area, which is also the opportunity and challenge for geotechnical workers.

Many geotechnical workers have made remarkable achievements in the foundation pit after years of unremitting efforts and development, but in recent years, some technical problems of foundation pit engineering are still waiting to be resolved. Applying the theory of foundation pit to guide practice, we will verify the correctness of theory from practice, it also helps to achieve a greater breakthrough in theory at the other way round. There are some another problems and valuable research results of foundation pit engineering are not reflected in this paper due to the limited level and space, I hope that scholars give me some criticisms.

## REFERENCES

Clough G.W, Reed, M.W. Measured Behavior of braced wall in very soft clay [J], *Journal of the Geotechnical Engineering Division*, 1984, 11 (1): 1–19.

Gong Xiaonan, Gao Youchao. The manual of Deep foundation pit engineering design and Construction [M], Beijing: Chinese Architectural Press, 1999, 18–23.

Leung, E.H. Y, Ng, C.W.W., Wall and ground movement associated with deep excavations supposed by cast in situ wall in mixed ground conditions [J], *Journal of Geotechnical and Geoenvironmental Engineering*, 2007, 133 (2): 129–143.

Shen Jian. Analyses and countermeasures on interaction among large-scale group excavation projects [J] *Chinese Journal of Geotechnical Engineering Suppl.*, 2012, 34 (11): 272–276.

Shen Weida. The research on the influence between adjacent deep foundation pit and tunnel construction [D], Changsha University of Science and Technology: 2012, 05.

Teng Fei, Ma Kesheng. Two dimensional finite element analysis of the interaction of adjacent foundation pit [J]. *Shanxi Architecture*, 2012, 21 (7): 87–88.

Xu Yihe. The analysis of the technology status of foundation pit engineering [J]. *Sichuan Building Science*, 2005, 6 (12): 113–117.

Zhang Zhiguo, Zhang Mengxi, Wang Weidong. Two-stage method for analyzing effects on adjacent metro tunnels due to foundation pit excavation [J]. *Rock and Soil Mechanics*, 2011, 32 (7): 2085–2092.

Zhang Chenrong, Yu Jian, Huang Maosong. Deformation controlling criterion of effect on underground pipelines due to foundation pit excavation [J]. *Rock and Soil Mechanics*, 2012, 33 (7): 2027–2034.

Zhang Aijun, Mo Haihong, Li Aiguo, et al. Two-stage analysis method for behavior of adjacent piles due to foundation pit excavation [J]. *Chinese Journal of Rock Mechanics and Engineering*, 2013, 32 (1): 2746–2750.

Zhu Li. Influence of High-rise Building Foundation Excavation to Adjacent Building Foundations [J]. *Construction Technology*, 2008, 37 (6): 106–108.

Zhu Xiaoyu, Huang Maosong, Zhang Chenrong. Displacement-controlled FEM for analyzing influences of excavation of foundation pits on adjacent pile foundations [J]. *Chinese Journal of Geotechnical Engineering Suppl.* 1, 2010, 32 (7): 181–185.

# A detailed analysis of the steel strand corrosion effect on serviceability state of PC continuous rigid frame bridges

Peng Wang, Fumin Wang, Li Zhang & Zanpeng Zhang

China Merchants Chongqing Communications Technology Research and Design Institute Co. Ltd.,  
Chongqing, China

**ABSTRACT:** Based on the degradation model for sectional area and mechanical properties of corroded steel strands, a detailed analysis is done to find the effect of steel strand corrosion on serviceability state of PC continuous rigid frame bridge by finite element method. The result shows that corrosion of steel strands have very serious effects on the prestress reserves, especially the upper steel tendons in the top slab and the steel tendons in the bottom slab of the box girder. It is an important cause for long-term deflection and cracks of this kind of bridge.

**Keywords:** Prestressed Concrete; continuous rigid frame bridge; steel strands; corrosion; crack; deflection

## 1 INTRODUCTION

PC (Prestressed Concrete) continuous rigid frame bridges have advantages such as high stiffness, seismic resistance, and less expansion joints. So they are widely used. There are two kinds of common diseases in the girder of the bridge, which should be paid attention to: one is concrete cracking and the other is excessive deflection under long-term load effect. Both often go together and enhance mutually.

There are long-term deflection data of 15 bridges listed in Figure 1 a). It can be seen that the deflection-to-span ratios are between 1/393 and 1/4242, most of them are more than the expected value. The average annual increment of deflection under long-term load effect of some bridges are shown in Figure 1 b), most of them are between 1 cm/a and 5 cm/a. They have no clear relationship with the length of the bridge span.

The causes for cracks and long-term deflections are complex, and thus a debatable problem. The corrosion of steel tendons may be one reason for it to cause reduction of the cross-sectional area, strength, elastic modulus, and elongation of steel tendon, it also leads to reduction of the prestress reserve and bearing capacity of the girder, but the degree of the effect still needs further research.

## 2 MECHANICAL PROPERTIES OF CORROSION STEEL STRANDS [1]

**Corrosion rate.** The corrosion rate of a piece of steel strand can be determined by weight or average cross-sectional area after corrosion.

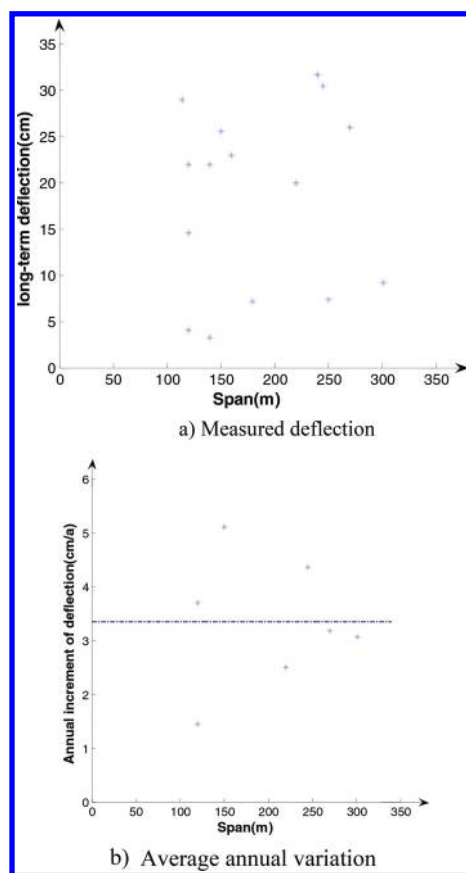


Figure 1. Statistics of long-term deflection of PC continuous rigid frame bridges.

$$\rho_w = \frac{g_0 - g_t}{g_0} = \frac{A_p - A_{pt}}{A_p} \quad (1)$$

where:  $g_0$ ,  $g_t$  is the weight of steel strand before and after corrosion respectively,  $A_p$ ,  $A_{pt}$  is the average cross-sectional area of steel strand before and after corrosion respectively.

**Nominal ultimate strength.** A model for the nominal ultimate strength of corroded steel strands is as formula (2).

$$f_{ul} = (1 - 8.422\rho_w^{1.351})f_u \quad (2)$$

where,  $0 < \rho_w < 10.4\%$ ,  $f_{ul}$  is the nominal ultimate strength of corroded steel strands;  $f_u$  is the ultimate strength of un-corroded steel strands.

**Nominal elastic modulus.** A model for the nominal elastic modulus of corroded steel strands is as formula (3).

$$E_{p1} = (1 - 40.4633\rho_w^{2.366})E_p \quad (3)$$

where,  $E_{p1}$  is the nominal elastic modulus of corroded strands;  $E_p$  is the elastic modulus of un-corroded strands.

### 3 EFFECT OF STRAND CORROSION ON PC CONTINUOUS RIGID FRAME BRIDGE

**Project case.** A PC continuous rigid frame bridge is adopted for analysis, detailed dimensions of the bridge are shown in Figure 2. The girder is built with concrete C55 according to Chinese Code. It has a three-dimension prestressing system, in which the longitudinal prestressing tendons are the most important part, they consist of top slab tendons, web tendons, bottom slab tendons as shown in Figure 3.

According to Figure 3, the upper tendons in the top slab are prone to corrode for they are closer to external environment and traffic loading; the lower tendons in the top slab are protected by thicker concrete cover, so they are affected by external environment more weakly than the upper tendons. The corrosion order of the steel tendons in the girder may be the upper tendons in the top slab firstly, the lower tendons in the top slab secondly, and the last are the

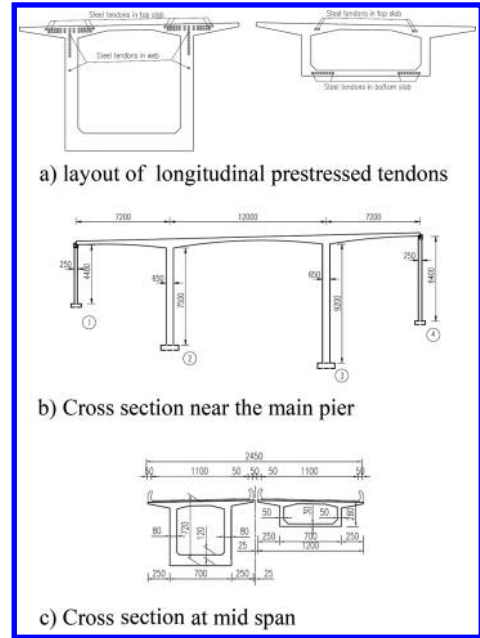


Figure 3. Layout of longitudinal prestressing tendons.

Table 1. Section area and mechanical properties of corroded tendons.

Corrosion rate	$E_p$ [MPa]	$F_{pk}$ [MPa]	$A_p$ [mm <sup>2</sup> ]		
			15-16	15-13	15-19
0.00	195000.0	1860.0	2224.0	1807.0	2641.0
0.02	194246.1	1780.6	2179.5	1770.9	2588.2
0.04	191113.4	1657.6	2135.0	1734.7	2535.4
0.06	184856.2	1509.9	2090.6	1698.6	2482.5
0.08	174964.2	1343.6	2046.1	1662.4	2429.7
0.10	161030.0	1161.9	2001.6	1626.3	2376.9
0.12	142707.6	966.9	1957.1	1590.2	2324.1

bottom slab tendons. But because the bottom slab cracks sometimes in the early age of the girder, tendons in the bottom slab may corrode firstly. All the cases above are considered in this paper.

According to formula (1) to (3), mechanical properties of corroded tendons can be obtained under various corrosion rates, which are listed in Table 1.

Because the PC continuous rigid frame bridge is a hyperstatic structure, the internal force will redistribute if steel tendons corrode, it is a complex problem, so the corrosion effect analysis is carried out by finite element method. The FE model is shown in Figure 4.

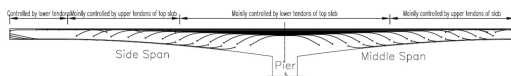


Figure 2. Layout of PC continuous rigid frame bridge.

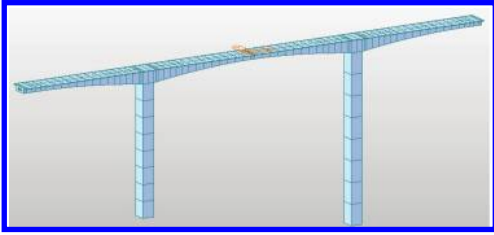


Figure 4. FE model.

**Corrosion effect of the upper tendons in the top slab.** Analyses are carried out to calculate the deflection of the middle span, the principal tensile stress of the webs, normal stress of the bottom slab, and effective prestress of the corroded steel tendons.

As shown in Figure 5, the deflection under long-term load effect increases along with the increasing of the corrosion rate of the upper tendons, and the increase tends to accelerate. When the corrosion rate is 10%, the deflection reaches  $-19.16$  mm, which is  $1/6263$  of the main span. When the corrosion rate is 12%, the deflection reaches to a  $-25.35$  mm, which is  $1/4734$  of the main span. Herein brittle fracture may happen when corrosion rate is more than 10%, so 12% is only for reference.

When the corrosion rate is 10%, the nominal ultimate strength decreases to 1161.9 MPa, approximately to effective prestress of normal steel tendons; when the corrosion rate is 12%, the strength decreases to 966.9 MPa, lower than the effective prestress. When the corrosion rate is between 10% and 12%, tendon fracture is likely to happen, so prestress reserved and bearing capacity of the girder will decrease rapidly, and long-term deflection will become worse.

As shown in Figure 6a), principal tensile stress under short-term load effect is in proportion to the corrosion rate of the upper tendons in the top slab. When the corrosion rate is 10%, the tensile stress reaches 0.95 MPa, when the corrosion rate is 12%, the tensile stress reaches 0.98 MPa, getting close to the limit value of the tensile stress of 1.096 MPa. As shown in Figure 6b), normal stress at the bottom of the mid span increases along with the increasing of the corrosion rate.

As shown in Figure 7, the effective prestress of tendons decreases along with the increasing of the corrosion rate of the upper tendons. When the corrosion rate is 10%, the effective prestress drops from 1172.1 MPa to 1110.8 MPa, and the prestress loss rate is 14% considering section area loss of the tendons. When the corrosion rate is 12%, the loss rate reaches 18%.

**Corrosion effect of the lower tendons in the top slab.** Assuming that the upper prestressing tendons have been corroded, the corrosion rate is 10%. The

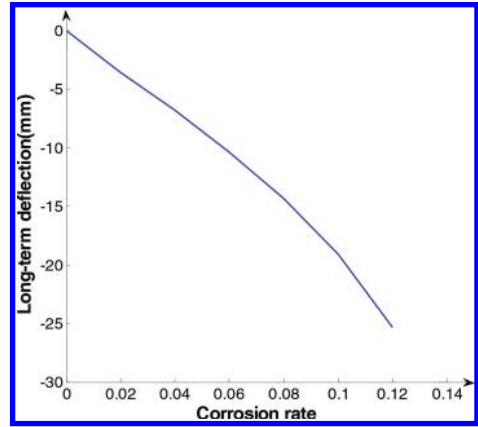


Figure 5. Corrosion effect of the upper tendons on deflection.

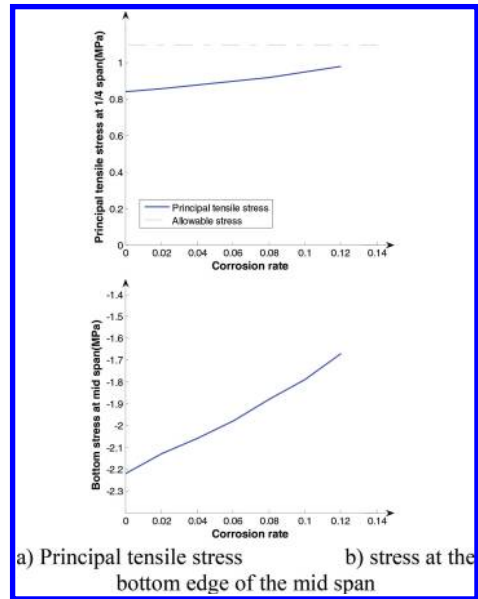


Figure 6. Corrosion effect of the upper tendons on the stress.

corrosion rate of the lower tendons grows from 0 to 10%, and then the deflection drops from  $-19.16$  mm to  $-22.78$  mm, reduced by 3.61 mm in total. Stress at the bottom of mid span rises from  $-1.79$  MPa to  $-1.67$  MPa, increased by 0.12 MPa in total under short-term load effect, and the principal stress of the web at the 1/4 span drops from 0.95 MPa to 0.93 MPa, decreased by 0.02 MPa in total.

**Corrosion effect of the web tendons.** Assuming all the prestressed tendons of the top slab have been corroded, the corrosion rate is 10%. The



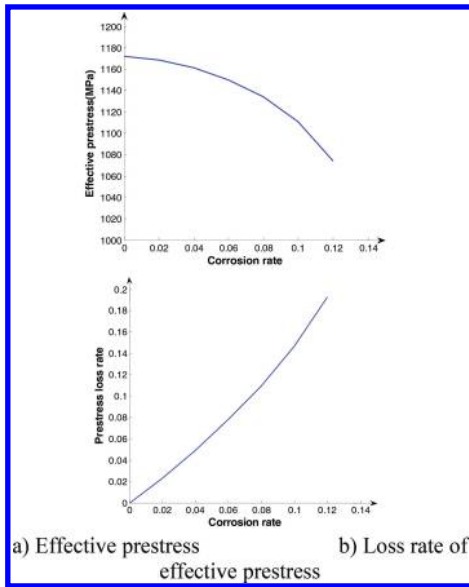


Figure 7. Corrosion effect of the upper tendons on the effective prestress.

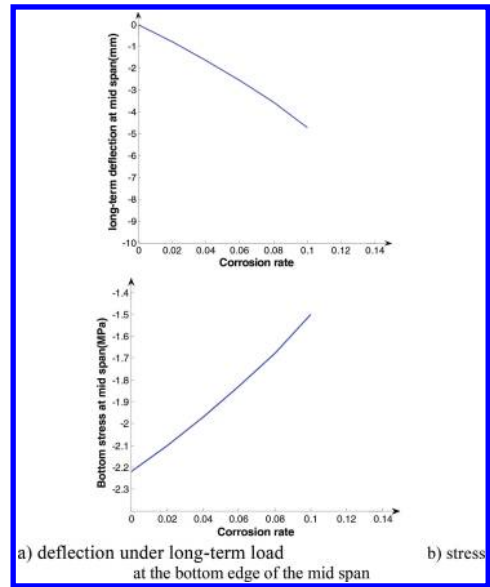


Figure 8. Corrosion effect of the bottom slab tendons.

corrosion rates of tendons in the web grows from 0 to 10%, then the deflection drops from  $-22.78$  mm to  $-24.74$  mm, reduced by  $1.96$  mm. Stress at the bottom of mid span rises from  $-1.67$  MPa to  $-1.61$  MPa, increased by  $0.05$  MPa under short-term load effect, the principal stress of the web at the  $1/4$  span rises from  $0.93$  MPa to  $0.95$  MPa, increased by  $0.02$  MPa.

**Corrosion effect of the bottom slab tendons.**

When tendons in the bottom slab corrodes individually, the corrosion rate of the tendons in the bottom slab grows from 0 to 10%, the deflection rises from 0 to  $-4.72$  mm, as shown in Figure 8, and normal stress at the bottom of mid span rises from  $-2.22$  MPa to  $-1.5$  MPa, increased by  $0.72$  MPa under the short-term load effect. In addition, the principal stress of the web at the  $1/4$  span drops from  $0.87$  MPa to  $0.86$  MPa, reduced by  $0.01$  MPa.

If the top slab tendons have been corroded, and the bottom slab begins to corrode, insignificant rebound of deflection might occur due to redistribution of the internal force.

**Some tendons are corroded and fractured.** As mentioned above, when the corrosion rate is more than 10%, steel strand might be fractured. For example, when the upper tendons of the top slab corrode alone, in which 3 pieces of strand of each tendon ( $16\phi^{15.2}$ ) get fractured, while the corrosion rate of other strands is 10%, the girder deflection drops from  $-19.16$  mm to  $-37.24$  mm, the principal

tensile stress of the web at  $1/4$  span reaches  $1.08$  MPa under short-term load effect, close to the limited value. When there are 6 fractured strands, the girder deflection rises to  $-58.98$  mm, the principal tensile stress of the web at  $1/4$  span will reach  $1.26$  MPa, exceeding limited value, while the stress at the bottom slab of mid span reaches  $0.6$  MPa, the webs and the bottom slab crack, resulting in the decrease of the girder stiffness and accelerated growth of the long-term deflection.

**4 SUMMARY**

In this paper, research is carried out to analyze the effect of steel tendon corrosion on a PC continuous rigid frame bridge. It is concluded that:

1. The corrosion effect of the upper tendons on the long-term deflection and principal tensile stress of the web is most significant, but the effect on the normal stress of the bottom slab is slightly lower than that of the bottom slab tendons. The corrosion effect of the lower tendons and the web tendons is insignificant. The corrosion of the tendons in the bottom slab exerts the most significant effect on the stress of the bottom slab.
2. PC continuous rigid frame bridge is a hyperstatic structure with complicated prestressed system. When the tendons in the top slab have

been corroded and the tendons of bottom slab begins to corrode, insignificant re-bounce of deflection might occur due to redistribution of the internal force.

3. When part of the tendons especially the upper tendons of the top slab corrode and fracture, the prestress reserved decreases rapidly, diagonal cracks will appear on the web, and lateral cracks might appear at the bottom of mid span, resulting in accelerated growth of the deflection.

All in all, steel tendons corrosion is one of the important reasons for a long-term deflection and crack of PC continuous rigid frame bridge.

#### ACKNOWLEDGMENTS

This work was financially supported by the China Ministry of transportation, that is a Science and

technology project of Western Transportation Construction (2010 318 740 008).

#### REFERENCE

- [1] Peng Wang, Li Zhang, Fumin Wang, Zanpeng Zhang, Yun He. The Time-dependent Effect of Steel Strands Corrosion on Prestressed Concrete Beam Bridges. Progress in Industrial and Civil Engineering III, Part 2. Trans Tech Publications. (2014), p. 1038–1044.

# Research of the composite wallboard mould connection with multiple assembly mould pouring

Chunyi Xu, Yipeng Zhao & Fengchuang Chen

*School of Civil Engineering, Shenyang Jianzhu University, Shenyang, China*

Chunlei Xu

*Tieling Municipal Commission of Housing and Urban-Rural Development, Tieling, China*

**ABSTRACT:** The nature of affordable housing industrialized building system is to realize its large-scale and industrial production in the field of urban construction. Its core is changing the housing construction projects from the traditional field construction to factory manufacturing. To achieve these objectives we need to standardize, modularize, and serialize its key assemble parts, design, and produce the matching mould, and assemble the mode parts. Mould plays a connecting role in these aspects, its applicability and advanced nature, directly affect the degree of the factory automation and efficiency of field installation and parts quality, mould design optimization problem should be taken seriously enough. On the foundation of the detailed investigation and study, the composite wallboard mould was analyzed, concluded, and summarized, which requires multiple groups of pouring in the northern area.

**Keywords:** composite wallboard; mould; group technology

## 1 INTRODUCTION

Industrialization of buildings is an inevitable trend in the construction industry [1]. The prefabricated building structures has to achieve the most efficient industrial production structure. Precast concrete is the main way of concrete construction, comparing with cast-in-place concrete, its features include factory construction, construction convenient, low impact on the surrounding environment, the surface roughness, the exact appearance of size, short construction period and fast return on investment [2–3]. With the continuous development of the technology of prefabricate concrete, the demand of mould is increasing, so mould design optimization problem should be taken seriously enough.

## 2 THE PROBLEMS OF PREFABRICATED MOULD AT PRESENT

The formwork Engineering is an important part of the reinforced concrete structural engineering [4]. With the continuous development of the technology of prefabricate concrete, the demand of mould is increasing. But there are several questions of the traditional mould of precast wall:

1. Severe deformation during the life of the interior wall mould.
2. The mould is difficult to disassemble.

3. A mold can only produce a wall, this mode of production wastes material.

## 3 CONNECTION OF COMPOSITE WALLBOARD MOULD

Composite wallboard in fixed mould is composed of the following parts, they are bottom mold steel base, the bottom bracket and the bottom mold steel mold, mold wall outer leaves, inner leaf mold wall, and window mode. These parts are assembled into a unified whole composite wallboard production process.

Dies use reasonable connection, the quality of the connection design affects productivity of compound wall and quality of the mold. Currently there are connections of mold including weld connections and bolted connections [5]. With fixed steel pedestal base mold, according to the actual support cases, desirable on both sides of the support or the support sides to be calculated.

## 4 CONNECTION DESIGN OF MOULD

In order to facilitate, this mold will make a list of standard components involved in schematic (see [Table 1](#)) text, part of the direct use of its number.

Table 1. Steel component list.

Number	Section size	Steel grade	Remarks
GL1	20b	Q235	
GL2	L100 × 10	Q235B	
GL3	L50 × 4	Q235B	
GL4	14b	Q235B	
GL5	16a	Q235B	
GL6	16a	Q235B	
GL7	L50 × 4	Q235B	

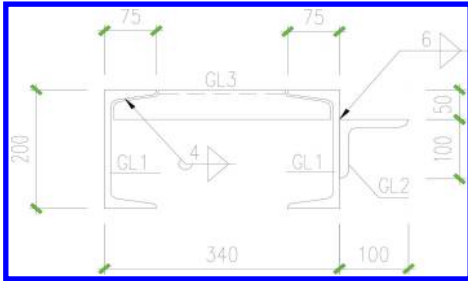


Figure 1. Base component connection diagram.

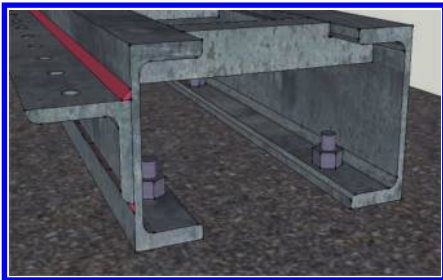


Figure 2. Three-dimension of base component conjunction.

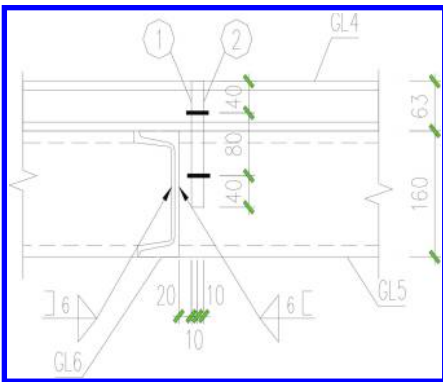


Figure 3. Conjunction diagram of GL5 and GL6.

1. Steel dock connector of bottom mold

The connection of base and the concrete floor through bolt, the diameter of bolt is 20 mm, spacing is 300–500 mm embedded in concrete within a length of 30 d. Part of the base steel welded: GL2 and GL1 welding, GL1 and GL3 use double-sided fillet welds (see Figs. 1 and 2).

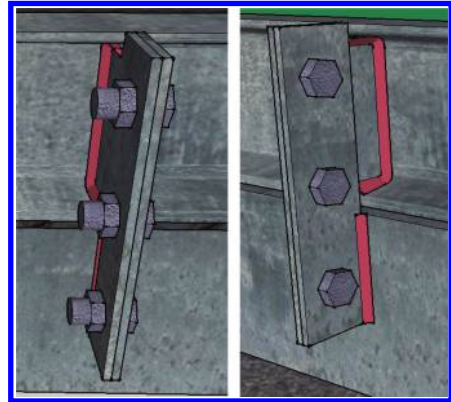


Figure 4. Conjunction three-dimension of GL4 GL5 and GL6.

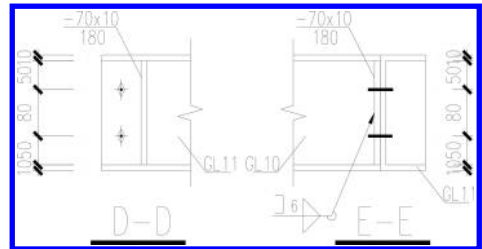


Figure 5. Conjunction node diagrams of GL10 and GL11.

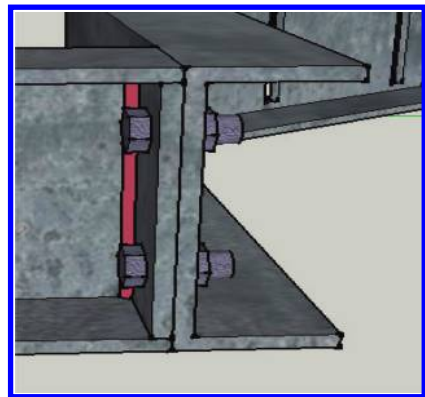


Figure 6. Conjunction node of GL10 and GL11.

- The connection of the bottom mold steel frame and outer leaves die side  
Wall GL6 main beam and secondary beams GL7 using double-sided “L” shaped fillet, angle-cut case of channel flanges using limbs, connections shown in Figure 2.20. Bottom mold

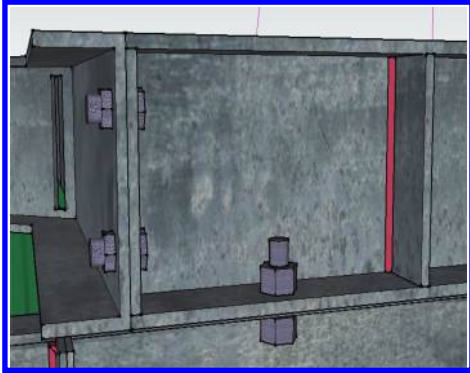


Figure 7. Bolt conjunction of inner wall lobe and lateral wall.



Figure 9. Conjunction node three-dimension of the window mold.

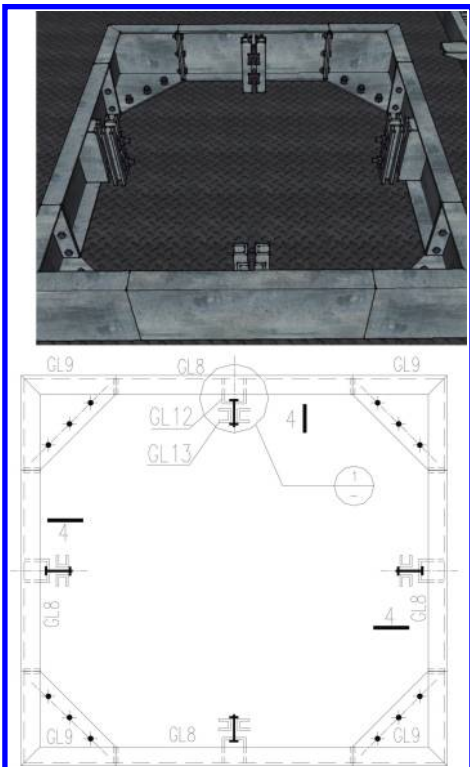


Figure 8. Three-dimension and plan drawing of the window mold conjunction.

bracket GL5 and GL6 connected to the outer side wall leaf mold GL4 using gusset plate welded then use bolt connection, gusset plate number ① (shaped) and the outer wall leaf mold GL4 Trilateral Wai-sided fillet weld connection, ② number gusset plate (rectangle) and GL5 limb back with double-sided fillet welds, bolts connecting the outer leaf node board wall mold and the bottom mold assembly, the specific connection node in Figures 3 and 4.

- The connection of inner lobe mould and lateral lobe mould

Inner lobe mould leaf mould GL11 and GL10 connected by webs plus tip set bolted ways, shown in Figures 5 and 6; inner leaf mould side wall and the side wall of the outer leaves die down side position coincides with bolts, another side using overhung steel outer leaves from the side wall of the mold to support and fixate the leaf mold wall, in order to solve the problem, is fixed between the lower mould sandwich panel, shown in Figure 7.

- The connection of window mould and bottom mould

Floorplan of window mould and bottom mould is Figures 8 and 9.

## 5 CONCLUSIONS

This paper describes the design principle of the mold connected, and the technical characteristics

of composite wall in northern China, and the original mold problems were analyzed and summarized. On the foundation of the detailed investigation and study, the composite wallboard mould was analyzed, concluded and summarized, which requires multiple groups of pouring in the northern area. Its design theory and calculation method were elaborated. The author optimized the mould design in the area of the original mould composition and connection structure using three-dimensional design software SKETCHUP and AUTOCAD plane drawing combination design method that provide the basis for other similar structure design.

#### ACKNOWLEDGMENT

Natural Science Foundation Project (grant number: 51408373) and Liaoning Province Education Department Project (grant number: L2013231).

#### REFERENCES

- [1] Cheng Zhi-gang, Cao Ping. The Present Situation, Problems and Countermeasures in the Implementation of Housing Policies for Low-income Groups of Our Country [J]. *Journal of Xiangtan University (Philosophy and Social Sciences)*, 2011,35(6):36-40.
- [2] Zhihong Gong. Design Method and Application of Precast Concrete Units in Housing Industrialization [D]. South China University of Technology, 2010:11-12.
- [3] David Ardit, Uluc Ergin, Suat Gunhan, Factors affecting the use of precast concrete systems[J]*Journal of architectural engineering*, 2000,6(3):79-86.
- [4] Li xianjing. Study and Application of New Type Architecture Mode [J]. Zhejiang University [D], 2003:1-9.
- [5] Liaoning Province local standards. Technical specification for manufacture and acceptance of precast concrete components (DB21/T1872-2011). Harbin Institute of Technology Press, 2012.

# Effects of height and span of structures on the vibration period of steel moment resistant frames

M. Shadab Far

*College of Civil and Transportation Engineering Department, Hohai University, Nanjing, China*

N. Hassani

*Water and Environmental Engineering Department, Shahid Beheshti University, Tehran, Iran*

A. Dalvand

*Geotechnical Engineering Department, Shahid Chamran University, Ahvaz, Iran*

**ABSTRACT:** The dominant vibration period is one of the most important behavioral parameters of the structures that are widely used in most of the seismic design codes of structures. The proposed methods by the Codes and Standards for calculation of the dominant vibration period are only dependent to Structure's height, and are obtained based on the first vibration mode. Thus, in cases with a small ratio of height to span of the structure, could not give sufficient accurate results. In this paper, we have studied the effects of height and the span of structures on the vibration periods and the mass participation ratios in higher vibration modes after performing the modal analysis for several steel moment resistant frames. Then, we have developed a simplified formula, based on the results. The relations presented in this article, besides considering the effect of the height and span of structure in estimating the first and second vibration modes, have no certain complexity and could present a good alternative for the formulae incorporated in the codes.

**Keywords:** modal analysis; vibration period; mass participation ratio; first and second vibration modes; codes formulae

## 1 INTRODUCTION

Many structures should be designed against the seismic loads due to their special functionality. The full dynamic analysis of structures could not be utilized inclusively because of its time-consuming solution process and computational complexity (Goel & Chopra 1997). Therefore, the seismic design codes of structures have tended towards the "quasi-static method". This method is based on the substitution of seismic loads by the base shear force at the base level and its distribution over the height of the building (Salama 2014), and it has been introduced by most of the structural design codes such as the International Building Code (IBC) or Euro code (IBC 2000, Eurocode 2004).

Calculating the base shear coefficient is based on the several proposed factors, including behavior factor (R), response factor (B), importance factor (I) and design base acceleration ratio (A) (Chopra 2011).

B, the response factor, which is obtained from the standard design response spectrum, shows that what

percentage of seismic acceleration at the building floor level, enters the structure and affects the mass of different floor levels. For calculating this factor, the dominant structural vibration period should be calculated first, and then, using the standard design response spectrum, the response factor could be read (Chopra & Goel 2000).

To calculate the dominant vibration period, the Codes have provided several empirical relationships for conventional structures, but each of them has its own deficiencies (Carrillo & Alcocer 2013). For example, these relationships are just a function of structure height. In other words, the only factor in determining the dominant vibration period of a structure is the height of the structure, while other factors such as span of the structure and architectural configuration of the structure can also be effective. On the other hand, in calculating the dominant vibration period, only, the first vibration mode of structure is considered, and the effects of higher vibration modes are neglected. While by increasing the height of structure (H), or the height-to-span ratio of structure (H/L), the

effects of higher vibration modes will be significant, and the seismic behavior of structure is highly affected by them. For instance, a structure, which is considered as “mid-rise building”, may have a large height-to-span ratio because of the smallness of the span, and therefore, in this case, the effect of higher vibration periods on the seismic behavior of the structure is impressive. That is why the proposed Codes formulae do not provide an accurate estimate of the structural vibration period.

In this paper, twelve steel structures with moment resistant frames at different heights and spans have been examined, and then, using modal analysis, the first and second vibration modes of these structures have been extracted. Next, the effects of height—to- span ratio on the vibration period and mass participation factor have been studied, and finally, considering the height and span of structures, some simplified equations have been developed to estimate the dominant vibration period of structures for the first and second vibration modes. In addition to the proposed simplified formulae, the relative accuracy of the formulae included in the Code has also been studied and compared for different kinds of structures.

## 2 REVIEW OF TECHNICAL LITERATURE

The existing deficiencies in the seismic design of structures codes, including not covering all types of the structures in engineering constructions, neglecting the effects of higher vibration modes and ignoring the geometric characteristics of structures in estimating the dominant period have led many researches to estimate the vibration periods for the seismic behavior of structures during earthquakes.

In this regard, Skinner et al. (1993) studied the use of the seismic isolation systems to improve the seismic behavior of structures. They stated that using seismic isolation systems, increases the dominant period and damping of the structures, and as a result, reduces the input seismic demand of the structure. They evaluated the period of structures, before and after using seismic isolators and studied the reduction of higher modes' effects after rehabilitation of the structures with seismic isolation systems.

Chun et al. (2000) assessed the accuracy of Korean Building Code of 1988 in calculating the dominant period of the reinforced concrete buildings with shear wall systems. For this purpose, they conducted some full-scale measurements for 50 different buildings and compared the results of the measurements with the dynamic modeled ones, and also formulae proposed by Codes. The results of this study showed that the stiffness of the tested buildings is different from the results obtained

from the formulae in Codes. At the end of the study, to have a better estimation of the stiffness, they proposed an expression to calculate the shear wall period of the reinforced concrete buildings.

Balkaya & Kalkan (2013), using three-dimensional finite element dynamic analysis, studied the behavior of tunnel form concrete buildings with shear walls, and then, using the obtained results, tried to investigate the effects of architectural configuration, roof weight and arrangement of shear walls on the dominant period of analytical models.

Balkaya & Kalkan (2004) studied the behavior factor ( $R$ ) and dominant period of tunnel form structures with concrete shear walls. They discussed the flow of transferring load from shear walls to foundation and studied the effects of Structures' vibration modes on the plastic behavior.

Bratosin et al. (2009), using the Kelvin-Voigt nonlinear model, proposed a method for modeling the resonance peaks in the nonlinear analysis of site materials. He, in addition to studying the dynamic behavior of rock and soil media and magnification of seismic waves, tried to provide a better estimate of the Environment's dominant period and its effect on the site-structure resonance.

This research, after modeling and designing of several steel structures with moment resistant frames at different heights and spans, used modal analysis to examine the shape modes of structures in higher vibration modes. It evaluated the effects of height and span of structures on the mass participation factor and dominant period in different vibration modes. Finally, some simplified equations were provided to estimate the dominant period of structures in the first and second vibration modes and evaluate the accuracy of Code formulae in estimating the dominant period of steel structures.

## 3 PROBLEM SOLVING METHODOLOGY

The governing dynamic motion equation in a multi-degree of freedom system with viscous damping is (Chopra 2011),

$$M\ddot{U} + D\dot{U} + KU = F \quad (1)$$

where  $U$ ,  $\dot{U}$  and  $\ddot{U}$  are displacement, velocity and acceleration vectors, respectively, and  $F$  is the external load vector in the system.  $M$ ,  $D$  and  $K$  represent the mass, damping and stiffness matrixes of the system, respectively. The free vibration equation of the system without damping could be written as follows,

$$M\ddot{U} + KU = 0 \quad (2)$$



Assuming a cosine harmonic response as  $U = \varphi \cos(\omega t - \theta)$  for this differential equation, the solution will be,

$$[-M\omega^2 + K]\varphi = 0 \quad (3)$$

Eq. (3) is a linear system of “n-equations, n-unknown parameters” which has answer only if the determinant of the coefficient matrix is zero (Eq. 4).

$$\Delta = |-M\omega^2 + K| = 0 \quad (4)$$

Eq. (4) that is called characteristic equation of the system, is a linear function of  $\omega^2 = \lambda$  (Eq. 5).

$$\begin{aligned} \Delta = 0 &= a_0 + a_1\omega^2 + a_2\omega^4 + \dots + a_{2n}\omega^{2n} \\ &= a_0 + \sum_{i=1}^n (a_i\lambda^i) \end{aligned} \quad (5)$$

This linear equation has n roots as  $\{\lambda_k\}_{k=1,2,\dots,n}$  or  $\{\pm\omega_k\}_{k=1,2,\dots,n}$ , where  $\lambda$  is the Eigen value of coefficient matrix and  $\omega$  ( $\omega = \pm\lambda^{1/2}$ ) is the natural frequency of the system. Thus, by calculating n values for  $\omega$ , n values for natural period are calculated in accordance with Eq. (6).

$$T = \frac{2\pi}{\omega} \quad (6)$$

As it is shown in Eq. (7), corresponding to any values of natural frequencies (or Eigen values), there is a natural mode vector (or Eigen vector),

$$[-M\lambda_i + K]\varphi_i = 0, \quad i = 1, 2, \dots, n \quad (7)$$

The ratio between the components of eigenvectors obtained from the above equation forms the mode shape matrix which reflects the system vibration.

$$\Phi = \begin{bmatrix} \varphi_{11} & \varphi_{12} & \dots & \varphi_{1n} \\ \varphi_{21} & \varphi_{22} & \dots & \varphi_{2n} \\ \vdots & \vdots & \vdots & \vdots \\ \varphi_{n1} & \varphi_{n2} & \dots & \varphi_{nn} \end{bmatrix} \quad (8)$$

The following equation shows the percentage of mass participation, which represents the percentage of structure mass involved in the structure's vibration mode.

$$[-M\lambda_i + K]\varphi_i = 0, \quad i = 1, 2, \dots, n \quad (9)$$

#### 4 MODELING AND ANALYSIS

Twelve steel moment resistant frames, including four five-story structures, four twelve-story structures, and four twenty-story structures were analyzed by SAP2000 software to examine the vibration period changes against structure geometry. In this regard, seismic loading and designing of these structures were considered in accordance with the Iranian Code of practice for seismic resistant design of building (Code 2800, 2005). The results of this design are shown in Tables 1 to 3.

In the next step, the structures were analyzed by the modal analysis method and the dominant period and mass participation factor of the first and second vibration modes were calculated.

To compare the results from modeling by software, and the results from Code prescribed equations (Eq. 10), apart from the modal analysis results, the dominant vibration period was calculated for all the structures with proposed equations, prescribed in Code 2800 (Code 2800, 2005). The results, then, were presented in Table 4 with respect to the structures' geometry (number of stories and spans), structures' height (H), structures' span length (L), periods calculated by Code 2800 ( $T_{2800}$ ), periods of the first vibration mode calculated by the modal analysis ( $T_{\text{mode1}}$ ), periods of second vibration mode calculated by the modal analysis ( $T_{\text{mode2}}$ ), mass participation factors of the first vibration mode ( $L_1$ ), mass participation factors of the second vibration mode ( $L_2$ ) and total mass participation factors of the first and second vibration modes ( $L_1 + L_2$ ).

$$T = 0.08H^{\frac{3}{4}} \quad (10)$$

Table 1. The results of designing 5-story building in four different spans.

Story:		1	2	3	4	5
beam	1 span frame		IPE200			IPE180
	2 span frame		IPE200			IPE180
	3 span frame		IPE200			IPE180
	4 span frame		IPE200			IPE180
column	1 span frame		IPB200			IPB180
	2 span frame		IPB200			IPB180
	3 span frame		IPB200			IPB180
	4 span frame		IPB200			IPB180

Table 2. The results of designing 12-storey building in four different spans.

Story:		1	2	3	4	5	6	7	8	9	10	11	12
beam	1 span frame	IPE200				IPE200				IPE180			
	2 span frame	IPE200				IPE200				IPE180			
	3 span frame	IPE200				IPE200				IPE180			
	4 span frame	IPE200				IPE200				IPE180			
column	1 span frame	IPB220				IPB200				IPB180			
	2 span frame	IPB220				IPB200				IPB180			
	3 span frame	IPB220				IPB200				IPB180			
	4 span frame	IPB220				IPB200				IPB180			

Table 3. The results of designing 20-storey building in four different spans.

Story:		1	2	3	4	5	6	7	8	9	10	11	12	13	14	15	16	17	18	19	20
beam	1 span frame	IPE220				IPE200				IPE200				IPE180							
	2 span frame	IPE220				IPE200				IPE200				IPE180							
	3 span frame	IPE220				IPE200				IPE200				IPE180							
	4 span frame	IPE220				IPE200				IPE200				IPE180							
column	1 span frame	IPB280				IPB260				IPB220				IPB180							
	2 span frame	IPB280				IPB260				IPB220				IPB180							
	3 span frame	IPB280				IPB260				IPB220				IPB180							
	4 span frame	IPB280				IPB260				IPB220				IPB180							

Table 4. Results of the modal analysis in comparison with Code's formula.

Frame type*	H (m)	L (m)	H/L	T <sub>2800</sub> (s)	T <sub>mode1</sub> (s)	T <sub>mode2</sub> (s)	L <sub>1</sub>	L <sub>2</sub>	L <sub>1</sub> + L <sub>2</sub>
5-1	15	4	3.75	0.6097593	0.926047	0.302715	0.79	0.12	0.91
5-2	15	8	1.875	0.6097593	0.972155	0.324641	0.8	0.12	0.92
5-3	15	12	1.25	0.6097593	0.983985	0.331299	0.8	0.12	0.92
5-4	15	16	0.9375	0.6097593	1.034984	0.343114	0.79	0.13	0.92
12-1	36	4	9	1.17575508	2.371253	0.818634	0.76	0.12	0.88
12-2	36	8	4.5	1.17575508	2.396337	0.8416	0.77	0.11	0.88
12-3	36	12	3	1.17575508	2.48707	0.863269	0.76	0.12	0.88
12-4	36	16	2.25	1.17575508	2.492906	0.867886	0.77	0.12	0.89
20-1	60	4	15	1.72465974	3.470907	1.128263	0.75	0.12	0.87
20-2	60	8	7.5	1.72465974	3.565241	1.198341	0.75	0.12	0.87
20-3	60	12	5	1.72465974	3.625631	1.248011	0.75	0.11	0.86
20-4	60	16	3.75	1.72465974	3.584841	1.234965	0.75	0.11	0.86

\* First number is the story number, and the second one is the span number.

The diagram of Figure 1 compares the periods obtained by the modal analyses in the first and second vibration modes and the values obtained by Code 2800 (Code 2800, 2005). It can be seen that in all structures, the period estimated by Code 2800 is between the periods of first and second vibration modes obtained from the modal analysis. It can also be seen that with higher structures, the difference between the periods of the first and second vibration modes is greater.

We arrange values in Table 4 in terms of structure's height-to-span ratio (H/L), to examine changes in the vibration period of the structure, compared with geometric characteristics of the structure (Table 5).

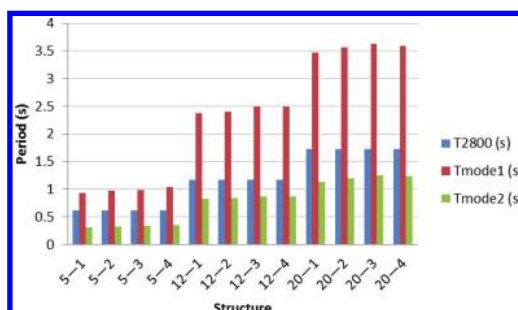


Figure 1. Comparing the results of modal analysis and Code 2800 formula.

Table 5. Sorted results of the modal analysis.

H/L	$T_{2800}$ (s)	$T_{mode1}$ (s)	$T_{mode2}$ (s)	$L_1$	$L_2$	$L_1 + L_2$
0.94	0.60976	1.03498	0.34312	0.79	0.13	0.92
1.25	0.60976	0.98399	0.33130	0.80	0.12	0.92
1.88	0.60976	0.97216	0.32464	0.80	0.12	0.92
2.25	1.17576	2.49291	0.86789	0.77	0.12	0.89
3	1.17576	2.48707	0.86327	0.76	0.12	0.88
3.75	1.72466	3.58484	1.23497	0.75	0.11	0.86
4.5	1.17576	2.39634	0.84160	0.77	0.11	0.88
5	1.72466	3.62563	1.24801	0.75	0.11	0.86
7.5	1.72466	3.56524	1.19834	0.75	0.12	0.87
9	1.17576	2.37125	0.81863	0.76	0.12	0.88
15	1.72466	3.47091	1.12826	0.75	0.12	0.87

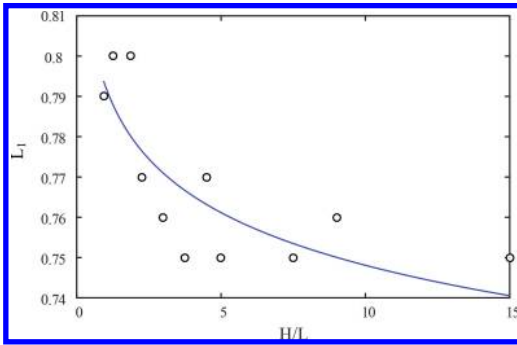


Figure 2. Changes in mass participation factor of first mode to H/L.

Figure 2 shows the change of mass participation factor in the first vibration mode against height-to-span ratio of the structure (H/L). As it could be seen, by increasing the height-to-span ratio (H/L), the mass participation factor will decrease sharply. When the height increases, higher modes will have a greater effect on the structural response, therefore, actual behavior of structure could not be modeled just by considering the first vibration mode.

In Figure 3, the sum of mass participation factor in the first and second vibration modes (i.e.  $L_1 + L_2$ ) is plotted against the height-to-span ratio of the structure (H/L). As it is seen from this diagram, the total mass participation of the two first modes has a downward trend. In other words, there are some cases in which more than one vibration mode is effective on the structural response. Therefore, to estimate the dynamic structural behavior, higher vibration modes of the structure might also need to be considered.

As previously mentioned, Code formulae are just a function of structure height and only calculate the period of first vibration mode. To solve

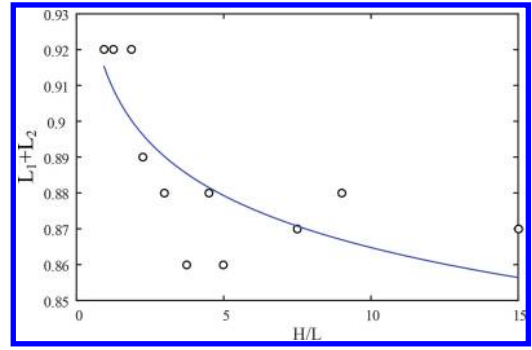


Figure 3. Changes in mass participation factor of two first modes against H/L.

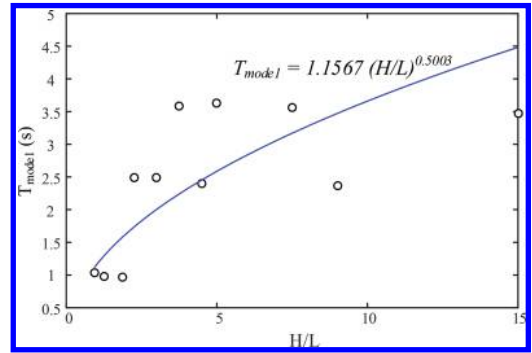


Figure 4. The relationship between height to span ratio and period of first vibration mode.

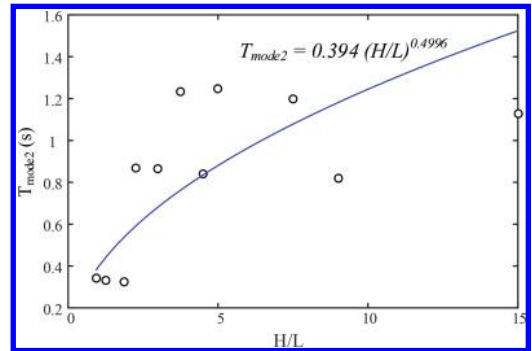


Figure 5. The relationship between height to span ratio and period of second vibration mode.

this problem, according to Figures 4 and 5, by fitting a curve to the results from the modeling software, two simplified equations are developed. These equations could be used to determine the first and second vibration periods considering the height-to-span ratio of the structures.

Table 6. Relative error percent in Code use (Error%).

H (m)	L (m)			
	4	8	12	16
3	0–10%	0–10%	0–10%	0–10%
6	0–10%	0–10%	0–10%	0–10%
9	0–10%	0–10%	0–10%	0–10%
12	0–10%	0–10%	0–10%	0–10%
15	10–30%	0–10%	0–10%	0–10%
18	10–30%	0–10%	0–10%	0–10%
21	10–30%	0–10%	0–10%	0–10%
24	10–30%	0–10%	0–10%	0–10%
27	30–100%	10–30%	0–10%	0–10%
30	30–100%	10–30%	0–10%	0–10%
33	30–100%	10–30%	0–10%	0–10%
36	30–100%	10–30%	10–30%	0–10%
39	30–100%	10–30%	10–30%	0–10%
42	30–100%	10–30%	10–30%	0–10%
45	30–100%	10–30%	10–30%	0–10%
48	30–100%	10–30%	10–30%	0–10%
51	30–100%	30–100%	10–30%	10–30%
54	30–100%	30–100%	10–30%	10–30%
57	30–100%	30–100%	10–30%	10–30%
60	30–100%	30–100%	10–30%	10–30%

We can use the provided equations instead of Code formulae in order to calculate the vibration period of steel structures with moment resistant frames (Eqs. 11 and 12). These equations could be used to calculate the vibration periods of the first and second modes as a function of height-to-span ratio of the structure.

$$T_{model1} = 1.1567 \left( \frac{H}{L} \right)^{0.5008} \quad (11)$$

$$T_{model2} = 0.394 \left( \frac{H}{L} \right)^{0.4996} \quad (12)$$

The Table 6 is provided in order to investigate the relative error of equations proposed by Code compared to equations proposed by this paper. In this Table, there are three error ranges of 0 and 10%, 10 to 30% and over 30%.

## 5 CONCLUSION

Codes formulae provided for calculation of the period are only a function of structure's height. In other words, the only factor, affecting the variation of the period of a structure, is its height, while adding a span to the structure can change its stiffness extremely, and therefore, the period of the structure changes, without any change in its height. Apart

from this issue, by increasing the height-to-span ratio of the structure, the effect of higher vibration modes in structural behavior are consequently increased, and we cannot calculate the period, by just relying on the first vibration mode. Hence, in this paper, using the modal analysis of steel structures with moment resistant frames, we have studied the effect of structure height-to-span ratio on period and mass participation factor of the first and second vibration modes and developed two simplified equations for this purpose. Comparing the results of Code relationships and equations proposed in this paper, relative error percentage is presented in Table 7 in terms of the height and the span length of different structures. According to this table, the error percentage at lower heights is less than 10% while this amount is over 30% for higher heights.

Regarding the assumptions used in this article, and to continue working on this paper, some points and suggestions are offered as follows:

- This paper discussed the steel moment resistant frames with different spans and heights. Other types of structures including concrete or steel structures such as bracing steel frame and double steel frames can be studied in the same way.
- In this study, steel frames are modeled and analyzed in two-dimensional form. To examine issues such as irregularity in plan and height, this study should be done using a three-dimensional modeling tool.
- In seismic rehabilitation of the structures, utilizing passive controllers such as dampers or seismic isolators, estimating the vibration period of the structure before and after the rehabilitation is necessary. Therefore, the current study can be developed for seismic rehabilitation of structures as a new research project.

## REFERENCES

- Balkaya, C., and Kalkan, E. (2003). "Estimation of Fundamental Periods of Shear-wall Dominant Building Structures." *Earthquake Engineering and Structural Dynamics*, vol. 32, pp. 985–999, DOI: 10.1002/eqe.258.
- Balkaya, C., and Kalkan, E. (2004). "Relevance of R-factor and Fundamental Period for Seismic Design of Tunnel Form Buildings." Proc., 13th World Conference on Earthquake Engineering (13 WCEE), Vancouver, Canada.
- Bratosin, D., Balan, F.Ş. and Cioflan, C.O. (2009). "Soils Nonlinearity Effects on Dominant Site Period Evaluation." *Proceedings of the Romanian Academy*, vol. 10, no. 3/2009, pp. 261–268.
- Carrillo, J., and Alcocer, S.M. (2013). "Simplified Equation for Estimating Periods of Vibration of Concrete Wall Housing." *Engineering Structures*, vol. 52, pp. 446–455, DOI: 10.1016/j.engstruct.2013.03.011.

- Chopra, A.K. (2011). *Dynamics of Structures: Theory and Applications to Earthquake Engineering*, Prentice Hall, United States.
- Chopra, A.K., and Goel, R.K. (2000). "Building period formulas for estimating seismic displacements." *Earthquake Spectra*, vol. 16, no. 2, pp. 533–536, DOI: <http://dx.doi.org/10.1193/1.1586125>.
- Chun, Y.S., Yang, J.S., Chang, K.K., and Lee, L.H. (2000). "Approximate Estimations of Natural Periods for Apartment Buildings with Shear-wall Dominant System." Proc., 12th World Conference on Earthquake Engineering (12 WCEE 2000), Auckland, New Zealand.
- Code No. 2800–05 (2005). *Iranian Code of Practice for Seismic Resistant Design of Building*, Iranian Building and Housing Research Centre.
- Eurocodes (2004). *Design of Structures for Earthquake Resistance*, European Committee for Standardization (CEN).
- Goel, R.K., and Chopra, A.K. (1997). "Period Formulas for Moment-Resisting Frame Buildings." *Journal of Structural Engineering*, vol. 123, no. 11, pp. 1454–1461, DOI: 10.1061/(ASCE)0733-9445(1997)123:11(1454).
- IBC (2000). *International Building Code (IBC)*, International Code Council (ICC).
- Salama, M.I. (2014). "Estimation of Period of Vibration for Concrete Moment-resisting Frame Buildings." *HBRC Journal*, pp. 1–6, DOI: 10.1016/j.hbrej.2014.01.006.
- Skinner, R.I., Robinson, W.H., and McVerry, G.H. (1993). *An Introduction to Seismic Isolation*, John Wiley & Sons Ltd., Chichester, England.

# Installation study of transverse brace of stacked tied arch bridges for safety of out-plane buckling

Youjun Niu

Gansu First Installation Engineering Co. Ltd., Lanzhou, China

Pengzhen Lin

School of Civil Engineering, Lanzhou Jiaotong University, Lanzhou, China

**ABSTRACT:** Stacked arch bridge is a new bridge system, based on four different styles of installation of transverse brace of a stacked tied arch bridge. Out-of-plane buckling is analyzed according to different position and different form of installation of transverse brace; the safety factor of stability and buckling model of each analysis models are get, the more important influence factors to out-of-plane buckling are analyzed, the results have reference value to same bridge application.

**Keywords:** bridges; stacked arch bridges; tie arch bridges; transverse brace; out-of-plane buckling; safety factor

## 1 INTRODUCTION

Stacked arch bridge is a new bridge system. It means its upper and lower arch ribs of main arch rib are separated and the skewbacks (support points) are set up on the different piers, which is shown in Figure 1. In Japan, the similar system of the bridge existed. The main arch ribs of stacked arch bridge is composed of upper and lower arch ribs, separation sections, dumbbell sections, and web members. Suspender is anchored in arch rib. In order to balance their horizontal thrust, tie bar is anchored in skewback of the upper and lower arch rib by batch. This system bears vertical loads, which is transferred by suspender. The dumbbell section and web member can coordinate the stress distribution of arch rib. The main arch rib separates into some parts in-plane, which makes the style of bridge unique, increases grandeur of the bridge and gives a person with strong space aesthetic feeling.

To the stacked tied arch bridge, a single arch rib can be considered to be composed of upper and lower two arch ribs. The setting location of lateral connection systems in the upper and lower two arch ribs and the structure of installation of transverse brace all can influence the whole out-plane buckling. Comparing with the most four intuitive styles of the transverse brace of a stacked tied arch bridge, the safety factor of stability and buckling model are analyzed with different setting positions and forms of the transverse brace under three kinds of load condition at the finished bridge state. The more obvious form of the transverse brace can be

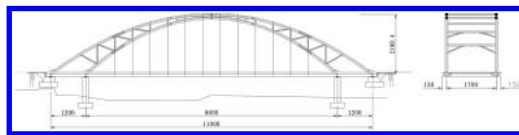


Figure 1. Stacked tied arch bridges system (unit: cm).

obtained, which influences out-of-plane stability. The results have reference value to same bridge application.

## 2 ANALYSIS OF THE MODEL

### 2.1 Basic information

A bridge's preliminary scheme is that the stacked arch bridge structure system uses concrete filled steel tubular. The bridge is bi-directional four-lane design. Its main span is 12 m + 86 m + 12 m and deck width is 20 m. According to comprehensive analysis of mechanics and styles of the arch rib, choosing upper arch rib's rise-span ratio is 1/5 and lower rise-span ratio is 1/4.15. Both upper and lower arch ribs use concrete filled circular steel tubular and the thickness of steel pipe wall is  $t = 10$  mm, diameter  $\Phi = 900$  mm. The cross-section of main arch's dome roof is dumbbell-shaped (Fig. 2). Away from the vault at 12.3 m, upper and lower ribs are separated by dumbbell-shaped and intermediate connecting rods and vertical diagonals which are made up of steel pipe, with thickness of 10 mm, diameter 500 mm.

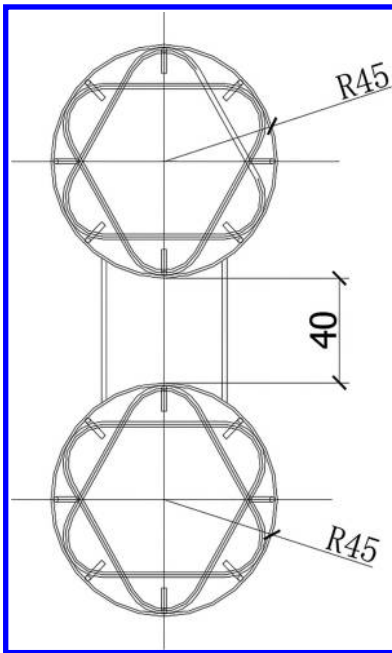


Figure 2. Section of the main arch vault (unit: cm).

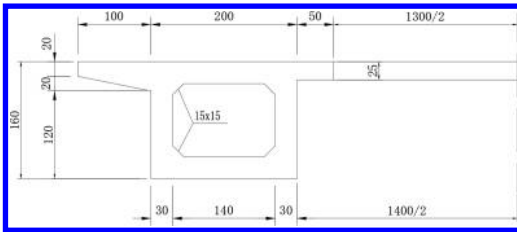


Figure 3. Section of prestressed concrete beam (unit: cm).

Tie bar is rigid and longitudinal beam is prestressed concrete box girder (Fig. 3). Middle cross beam uses prestressed concrete T-shape beam. To facilitate anchoring steel strands of suspender and cross-beam, middle cross beam needs to be thickened to 50 cm at the intersection of the middle cross beam and longitudinal beam. The spaces of middle cross beam and suspender are 6 m. Close to the lower arch foot, the distance between middle cross beam and the arch foot end beam is 10 m. Installation of transverse brace uses steel pipe is 10 mm thick with a diameter of 600 mm.

## 2.2 Finite element model

ANSYS8.1 is used to analyze the model. Arch rib uses BEAM4. Composite sectional characteristic is used for calculating sectional characteristic, and

conversion elastic modulus is put to use. Longitudinal beam and crossbeam employ BEAM4. The prestressed of longitudinal beam should be taken into account when it shares nodes with LINK10. Suspender uses LINK10 and initial tension should be taken into consideration. Tie bar and installation of transverse brace use BEAM4 as well. Supporting way is a continuous beam support method. Upper arch foot is a movable support, and one side of lower arch foot is a fixed support, the other side is movable support. Simulation of dumbbell-shaped section is realized through coupling the corresponding node-freedom degree of the upper and lower arch rib at the dumbbell section.

## 2.3 Loading conditions

According to lane loading calculation, the live load and dead load must be considered at the finished bridge state. Considering that the lower arch rib needs to bear large axial force and the lower rise-span ratio is larger, the axial force influence-line loading calculation was carried out on arch rib and arch foot. The lane load is highways-I-level. Uniform load is 10.5 KN/m and concentrated force is 432 KN (taken shear force calculation value).

Loading condition can be classified into 3 kinds:

1. Only taken the dead load into account (concluding structure weight, the prestressed of tie beam, suspender initial tension).
2. The dead load, crowd load, wind force, and transverse live load, which loads by influence-line of four-lane (considering transverse reduction). Loads are combined by ultimate limit states.
3. The dead load, crowd load, wind force, and transverse live load, which loads by influence-line of two-lane (considering transverse reduction). Loads are combined by ultimate limit states.

## 2.4 Analysis patterns

Comparative analysis is carried out through the following four modes for different settings of installation of transverse brace.

- a. Both upper and lower arch ribs set 5 transverse braces, which are located on the lower arch rib. The corresponding setting positions are 1/6, 1/3, 1/2, 2/3, 5/6 span of the lower arch rib. Installation of transverse braces at mid-span are “\*” shapes, set on the webs of the dumbbell section. Other transverse braces are “K” shapes (Fig. 4).
- b. On the basis of “a” model, the transverse brace located in the lower arch rib is removed, and the transverse brace of upper arch ribs and mid-span is unchanged.
- c. On the basis of “a” model, the transverse brace located in the lower arch rib is removed, and the



Figure 4. Finite element model for stability analysis.

transverse brace of lower arch ribs and mid-span is unchanged.

- d. Change the “\*” shape to the “I” shape on the basis of “c” model.

In 4 kinds of cases: “a” reflects that setting transverse braces of upper and lower arch ribs have an impact on the overall out-plane buckling; “b” and “c”, respectively, reflect that setting transverse braces of upper and lower arch ribs have an influence on the overall out-plane instability; “d” reflects that the forms of transverse braces at mid-span influence the overall out-plane instability.

### 3 BUCKLING ANALYSIS

#### 3.1 Linear buckling analysis theory

According to the theory of linear buckling, the structure buckling load can come down to solve equation (1)’s eigenvalue under the action of the external load  $F$ :

$$(K + \lambda S)\delta = 0 \quad (1)$$

In which:  $K$  is the structural stiffness matrix;  $S$  is the initial stress stiffness matrix;  $\lambda$  is characteristic values;  $\delta$  is buckling mode.

If the equation (1) is  $n^{\text{th}}$ -order linear differential equation, Then theoretically exist  $n$  eigenvalues— $\lambda_1, \lambda_2 \dots \lambda_r$ . But for the engineering issues discussed, only the smallest eigenvalue is also the minimum safety factor has actual significance.

Assuming the critical eigenvalues is  $\lambda_{cr}$  and critical load is  $\lambda_{cr}$ . If the equation (1) is the spatial model, then the eigenvalues and modes include the in-plane and out-plane buckling.

#### 3.2 Buckling analysis

Critical eigenvalues of the analysis modes and the corresponding instability modes are shown in Table 1 and Figure 5.

Table 1. Stability analysis of mode  $\lambda_{cr}$ .

Mode	Load pattern		
	I	II	III
a	12.50	8.86	9.23
b	9.62	7.09	7.35
c	11.66	8.25	8.60
d	7.84	5.63	5.88

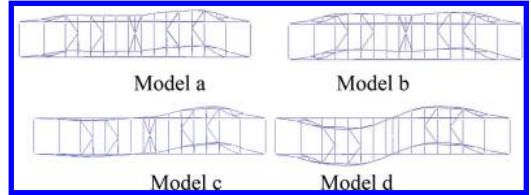


Figure 5. The main each sidewise buckling mode.

As can be seen in Table 1 and Figure 5, the first-order of structural instability is due to plane instability under the load of conditions and calculation modes, and also of the first-order sidewise instability safety factors and modals can be obtained from different transverse braces. But at the same installation of transverse brace setting mode, loading case only affects the safety factor and has nothing to do with the first-order instability mode. All in all, dead load cases the largest buckling safety factor, followed by a two-lane loading conditions, and the four-lane is minimum. So in this paper a four-lane loading is the most unfavorable way at the operating conditions. Operating conditions can meet standard buckling safety factor, which is greater than the safety factor of 4 to 6, except the d mode.

When the transverse braces of upper and lower rib are set, the overall lateral stiffness of structure is larger and the sidewise buckling safety factor is largest—dead load is 12.5, four-lane 8.86, two-lane 9.23. As the number of transverse braces decreased, the buckling safety factor of the second mode decreases compared to the first mode at the 3 kinds of loading condition. The first condition is reduced by 23%, and the second and the third cases are decreased by 20%. But the instability mode and the first mode are basically the same.

For another reduction of transverse braces, when only the lower arch ribs set transverse braces (third mode), the sidewise instability safety factor is larger than the transverse braces that are set on the upper arch ribs (second mode) under each loading condition. The first condition is reduced by 21.2%. The second condition is decreased by 16%, and the



third case is decreased by 20%. Under this mode, the structural instability mode is anti-symmetric.

In the fourth mode, when the “\*” shape transverse brace is changed into “I” shape, the sidewise instability safety factors are reduced. The first condition is reduced by 33%, and the second and the third cases are decreased by 32%. But the instability mode is the same as the “\*” shape.

In view of the above analysis, the overall stability of structure is most outstanding that is influenced by the lateral stability of lower arch rib. Meanwhile, the power transverse connection system is also important to sidewise instability at the mid-span. Therefore, they should be strengthening in design.

#### 4 CONCLUSIONS

Compared to the different transverse braces of stacked tied arch bridge in this paper, we can obtain the following conclusions.

1. Different forms of transverse brace have a certain gap to the out-plane sidewise safety factor, also to the sidewise buckling mode. Setting a number of transverse braces on the upper and lower arch ribs can get the maximum safety factor, and four-lane loading is the most unfavorable instability condition.
2. Under the circumstances of setting transverse braces on the upper or lower arch ribs, the sidewise buckling safety factor is more larger when the transverse brace is only set on the lower arch rib. In this paper, when the transverse brace is set on the lower arch rib, the safety factor can be increased by 1.2 times as compared with setting on the upper arch rib.
3. Setting a number of rigid transverse braces at the mid-span have a prominent influence on sidewise safety factor, and the safety factor is increased by about 1.5 time when the “\*” shape is set at the mid-span compared to the “I” shape.
4. Setting location of transverse brace has an impact on first-order lateral instability mode. When setting transverse braces on upper arch ribs, the out-plane first-order structural instability mode is symmetric, but on the lower arch ribs is anti-symmetric.

Setting transverse braces on upper and lower arch ribs can get the maximum safety factor, but third form is the best. Not only can we obtain the safety factor which is closer to the first condition, but also it is the most economical one.

#### REFERENCES

CECS 28:90. 1992. Specification for Design and Construction of Concrete Filled Steel Tubular Structures.

Chen. B.C. 2000. Design and Construction of Concrete-filled Steel Tube Arch Bridge, China Communications Press, China.

JTG D60-2004. General Specification for Design of Highway Bridges and Culverts.

Li. G.H. 1992. Stability and Vibration of Bridge Structure. China railway Publishing House, China.

Ning, G.X, & Tian, Q. 2004. The Design and Construction of the Japanese Dream Dance Bridge, World Bridge, (2):1-4.

Xiang, H.F. & Liu, G.D. 1991. Stability and Vibration of Arch Structure, People's Communications Press China.

Zhong, S.T. 2003. Concrete-filled Steel Tubular Structures, (third edition). Tsinghua University Press, China.

# Experimental study on mechanical properties of stabilized clay soils used in hydraulic engineering

Jie Chen, Jie Leng, Yongjing Mao, Yubao Yang & Yuepeng Pan

College of Harbor, Coastal and Offshore Engineering, Hohai University, Nanjing, China

**ABSTRACT:** In order to produce stabilized clay soils, which can be applied into harbor and coastal engineering locally as a substitute for concrete, inorganic cementitious materials including cement, Ground Granulated Blastfurnace Slag (GGBS), gypsum, and lime were mixed by semi-dry finished form with same dosage of clay soil. Experimental results shows that the best mixing ratio for materials used in clay stabilization is 65% clay soil, 18% cement, 12% GGBS, 2.5% gypsum, and 2.5% lime. The compressive, tensile, and softening strength of this stabilized clay soil at 28 day is 25.6 MPa, 2.4 MPa, and 7 MPa, respectively, meeting the demand of hydraulic engineering and can be used in harbor and coastal engineering.

## 1 INTRODUCTION

Soil stabilization is a measure that solidifies the detrital soil grain into solid matter with certain strength level and the soil stabilized called stabilized soil<sup>[1]</sup>. For their relative stable physical and chemical property, cementitious materials such as cement, gypsum, lime, and GGBS is a kind of stabilizer. Tomohisa<sup>[2]</sup> has ever proposed that concrete powder, GGBS and volcanic ash can be used to strengthen soil with high water and organic contend; Zalihe<sup>[3]</sup> proved that gypsum and GGBS can effectively stabilized the organic swelling clay; Shirazl<sup>[4]</sup> pointed that the mixture of gypsum and GGBS is able to eliminate warping and cracking caused by concrete shrinkage; Wenzhong Song<sup>[5]</sup> proved that the mixture of cement, gypsum, and lime can excite the activity of GGBS and improve its initial setting time and strength; Shanghua Jia<sup>[6]</sup> researched the effect of the lime on the physical filling, hydration, coagulation, and ion exchange of cement, which increases the unconfined compressive strength of soil; Some other inorganic and organic materials are also taken into consideration concerning soil stabilization. Renjian Shao<sup>[7]</sup> has made some relevant research in this area and a good result is obtained. In conclusion, the most of the research productions mentioned has been applied into road engineering, and little of which is applied into harbor and waterway engineering.

In this paper, the stabilized clay soils used in hydraulic engineering to substitutes concrete of grade C20 was studied. The lowest cement content under this premise was determined first. Then substitutes cement with the mixture of gypsum, lime, and GGBS to research on the best optimal composition of the stabilizer.

## 2 EXPERIMENTAL MATERIALS AND METHODS

### 2.1 Experimental raw materials

The water content of clay soil sample used in this experiment is 25.2% and its PH value is 7.6. The physical and chemical properties of the soil are shown in Table 1.

As is shown in Table 1, SiO<sub>2</sub> is the main substance in soil sample, the percentage of which is 55.37%, followed by Al<sub>2</sub>O<sub>3</sub> (19.13%) and the proportion of other substances are all less than 10%. During these chemical substances, SiO<sub>2</sub>, Al<sub>2</sub>O<sub>3</sub>, CaO and Fe<sub>2</sub>O<sub>3</sub> play a decisive role in the physical and chemical properties of the soil.

Raw materials include Portland cement produced by Conch Corporation, GGBS with S95 standard produced by Meibao construction materials co, ordinary lime in bulk with 98% purity and gypsum with 98% purity.

Table 1. Chemical composition of clay soil sample.

Ingredients	Average value (%)
SiO <sub>2</sub>	55.37
Al <sub>2</sub> O <sub>3</sub>	19.13
Fe <sub>2</sub> O <sub>3</sub>	7.47
CaO	8.03
MgO	3.92
K <sub>2</sub> O	3.28
Na <sub>2</sub> O	0.81
TiO <sub>2</sub>	1.07
SO <sub>3</sub>	0.41

## 2.2 Experimental methods

Before experiment, the clay soil is grinded into powder after air drying and then be filtrated by sieve pit (1.8 mm). Then all materials are weighed precisely according to mix proportion, then, they are put into JJ-5 cement mortar mixer and mixed well. Third, the materials are pouring into 70.7 mm × 70.7 mm × 110 mm steel mold and made into specimens by vibration compression.

The concrete proposal is as follows: in first step, the mold is filled with materials and the pressure on the mold increased to 2 MPa with velocity of 400 NV/s, then the remainder is poured into mold and pressed again. At this step, the pressure rise to 10 MPa with velocity of 400 N/s and maintain in this level for 2 minutes, after that, the pressure keeps rising to 20 MPa with the same velocity and maintained in peak for two minutes. Two minutes later, the pressure is removed and the specimens are taken out with approximately 70 mm × 70 mm × 110 mm size.

After being cured for 28 days in standard conditions, specimens are put in universal testing machine to be test for the compressive strength, tensile strength and water stability followed by corresponding standard. The water stability is tested by detecting its softening strength.

## 3 OPTIMUM MIXTURE RATIO

### 3.1 The determination of optimum dosage of cementitious materials

Cement first acts as the only cementitious material to be mixed with clay soil sample and then the lowest dosage of cement is determined while the compressive strength and tensile strength of clay stabilized material is more than 20 MPa, and the softening strength is above 2.4 MPa. The result is shown in Table 2.

As is shown in Table 2, when the dosage of cement is larger than 35%, the strength of clay

Table 2. Influence of cement content on strength of clay soil stabilized after 28 days.

Number	1	2	3	4	5	6
Clay soil (%)	95	85	75	70	60	65
Cement (%)	5	15	25	30	35	40
Water (%)	15.5	15.5	15.5	15.5	15.5	15.5
Compressive strength (MPa)	/	8.1	14.3	18.7	23.3	26.7
Tensile strength (MPa)	/	1.1	1.52	1.87	2.36	2.5
Softening strength (MPa)	/	5.7	11.9	16.3	21.0	23.8

stabilized can be up to the standard. Every factor taken into consideration, the optimum proportion is 35% cementitious material and 65% clay soil.

### 3.2 The determination of optimum dosage of other materials

#### 3.2.1 The influence of cement and GGBS's mixing ratio on stabilized clay soil

In this group of experiment, content of lime and gypsum is unchanged (3% and 4% respectively). Changing the content of cement and GGBS, a curve of compressive strength, tensile strength and softening strength with different mixing ratio can be plotted, which is shown in Figure 1.

As is shown in Figure 1, with the increase of content of cement and the decrease of content of GGBS, the curve of strength rise first and decline later. When the content of cement is under 20%, the compressive strength fluctuates little and maintain in the level over 20 MPa. If too much cement is mixed with clay soil, the water-cement ratio will decline, which results in lower strength.

GGBS has pozzolanic effect and more active silica, alumina and higher ash activity than clay soil used in experiment. In alkaline environment, GGBS can generate C-S-H gel structure, which has strong cementing power. P.V. Sivapullaiah<sup>[8]</sup> pointed that adding some materials with pozzolanic effect can effectively enhance the unconfined compressive strength of stabilized soil. GGBS can also mediate the compressive and tensile strength to some degree.

However, too much or less GGBS can undermine the strength and GGBS with content of 8%~16% has the best effect on compressive and tensile strength. The softening strength showed in Figure 1 gradually grows over compressive strength, which means that the water stability of clay stabilized rises with the increase of GGBS's dosage.

Every factor taken into consideration, the optimum mixing ratio of cement and GGBS is 16:12.

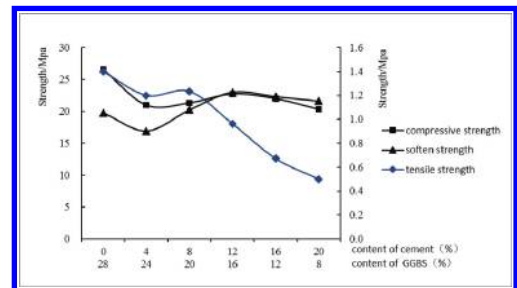


Figure 1. The influence of cement and GGBS's mixing ratio on strength of stabilized soil.

### 3.2.2 The influence of gypsum and GGBS's mixing ratio on clay soil stabilized

In this experiment, content of cement and lime is unchanged (18% and 4% respectively). Changing the content of GGBS and gypsum, the change of compressive strength, tensile strength, and softening strength with different mixing ratio of gypsum and lime is showed in Figure 2.

Hydration structure of test sample is not compact and it has much interspace, as well as many unhydrated mineral powder particles. At the same time, because of the mixture of flue gas desulfurization gypsum which excites the activity of cement and GGBS, Aft is turned into AFm and the hydraulic degree deepens<sup>[9]</sup>.

With the existence of GGBS, Hydrated calcium aluminate can react with plaster and generate hydrated calcium aluminate. The main property of ettringite is expansibility and the existence of interspace allows the ettringite to expand after cement hydration, which enhance the strength.

As is shown in Figure 2, with the increase of gypsum's dosage and the decrease of GGBS, the compressive strength rises at first and declines later. If the quantity of gypsum is too small, calcium sulfoaluminate hydrates will be generated, on the contrary, if the quantity of which is too large, gypsum cannot be consumed and the strength can be undermined as well. As for the hydra stability, gypsum is not the main influence. Every factor taken into consideration, the optimum mixing ratio of gypsum and GGBS is 11:2.

### 3.2.3 The influence of gypsum and GGBS's mixing ratio on clay stabilized

In this experiment, content of cement and GGBS is unchanged (18% and 12% respectively). Changing the content of gypsum and lime, the change of compressive strength, tensile strength, and softening strength with different mixing ratio can be plotted, which is shown in Figure 3.

As it is mentioned before, SiO<sub>2</sub> is the main ingredient which takes percentage of 55.37%,

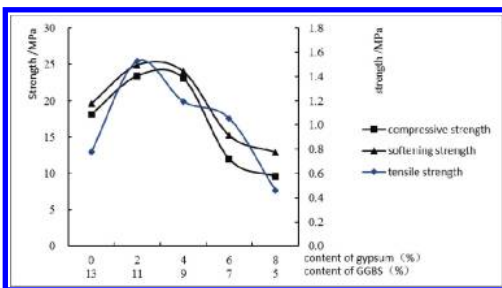


Figure 2. The influence of GGBS and gypsum mixing ratio on strength of stabilized soil.

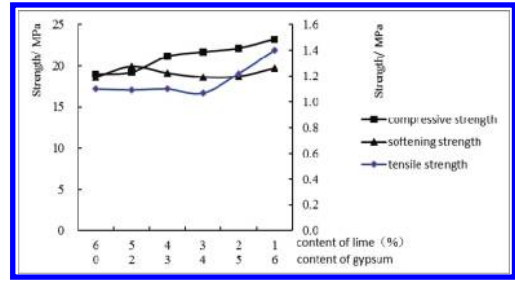


Figure 3. The influence of gypsum and lime mixing ratio on strength of stabilized soil.

followed by Al<sub>2</sub>O<sub>3</sub> (19.13%). SiO<sub>2</sub> and Al<sub>2</sub>O<sub>3</sub> are likely to react with alkaline substance and can generate Ca(OH)<sub>2</sub> after the addition of lime, which can hydrolysis and released Ca<sup>2+</sup> that will later exchange with K<sup>+</sup>, Na<sup>+</sup> and H<sup>+</sup> and thin the capillary film. This phenomenon can contribute to the decrease of soil's dispersibility and viscoplasticity. Because of this, the strength and stability of soil particle can be enhanced. Also Ca(OH)<sub>2</sub> can react with active silica and alumina, which can generate hydrated calcium silicate gel and hydrated calcium aluminate gel. The two products reduce the interspace among particles and the water permeability, as well as improving the compactness and increase the velocity and degree of reaction of ash.

As is shown in Figure 3, with the increase of content of lime, the strength of clay stabilized decreased and reasons can be divided into two main aspects. First, with more lime is added into clay soil, the more carbonization reaction mainly occurs on the surface of specimens, the compact carbon film generated prevents CO<sub>2</sub> and O<sub>2</sub> from entering inside and the harden process slows; Second, the lime slaking consumes huge quantity of water, which contributes interspace after the evaporation of water and the strength is undermined. Though more lime is harmful to strength, when the percentage of lime and gypsum is 3% and 4% respectively, the strength of clay stabilized can still go up to 20 MPa. In construction, appropriate amount of lime can improve the post-strength of concrete and can operate under more stress. As is shown in Figure 3, the dosage of lime is beneficial to clay soil's hydra stability. Every factor taken into consideration, the optimum cementitious materials mixing ratio is 3% lime, 4% gypsum.

As a conclusion, the optimum proportion of cement and GGBS is 16:12, which of GGBS and gypsum is 11:2. Optimal content of gypsum and lime is 4:3. Overall, the proportion of four ingredients (cement, GGBS, gypsum and lime) is 52%, 34%, 6.9%, and 1%, respectively. Considering economy, the proportion can be adjusted into 52%,

Table 3. Law of development of various properties of clay stabilized.

Curing days	7 d	28 d	90 d
Compression strength (MPa)	10.1	25.6	28.1
Tensile strength (MPa)	1.0	2.4	2.7
Softening strength (MPa)	9.5	7	3.2
Dry-shrinkage ratio (%)	0.01	0.008	0.002
Volume density (%)	2.15	2.14	2.13
Water absorption (%)	9.1	7	3.2

34%, 7%, and 7%, respectively. Since the percentage of clay soil is 65%, the optimum mixing ratio of cementitious materials is cement (18%), GGBS (12%), gypsum (2.5%), and lime (2.5%).

#### 4 PERFORMANCE TEST FOR CLAY STABILIZER IN OPTIMUM CEMENTITIOUS MATERIALS MIXING RATIO

The physical and mechanical properties of the stabilized material with the optimal proportion obtained from above experiment were tested in this section. Produced follow the optimum mixing ratio and cured 7, 28 and 56 days, respectively, the properties of specimens such as compressed, tensile, and softening strength, dry-shrinkage ratio, volume density and water absorption were tested at 7, 28, and 56 days, respectively. The result is shown in [Table 3](#).

As is shown in [Table 3](#), compressive, tensile strength of clay stabilized can achieve standard of 20 MPa at 28 days. The strength of the material is qualified, as well as the growth of later strength. Also the later softening strength of clay stabilized is good, which means high hydra stability and adaptation to the construction of hydraulic engineering. [Table 3](#) also demonstrates that the dry-shrinkage ratio and water absorption of clay stabilized declines gradually, while the volume density is almost unchanged, which contributes to the stability of property.

#### 5 CONCLUSION

1. It is feasible to use waste clay to produce specimens by stabilization. The production made in this way has enough compressive, tensile, and softening strength, as well as good

water stability. It can substitute concrete to be applied to hydraulic engineering.

2. Among cementitious materials used in clay stabilization, with the increase of cement's content, the strength of stabilized clay grows while the utilization of clay soil declines and the optimum dosage of cement is 18%. Right amount of gypsum is helpful to generate ettringite to enhance the strength and the best dosage of gypsum is 2%. Lime is involved in the chemical reaction of generating high-early-strength calcium aluminate, which is beneficial to strength and the optimum dosage of lime is 6%. The dosage of GGBS can reduce the content of cement and the best dosage of GGBS is 12%.
3. When the content of waste clay soil is 60% and the dosage of cement, GGBS, gypsum, and lime is 18%, 12%, 4%, and 6%, respectively, the softening strength after 28 days of stabilized clay soil is over 22 MPa and the tensile strength of which is 2.4 MPa, meeting the standard of materials used in hydraulic engineering.

#### REFERENCES

- [1] Yongxiang Zhou. Technology and its development of soil-reinforced [J], *Journal of Railway Science and Engineering*, 2006, 3(4):35-40.
- [2] Tomohisa S., Sawa K., Naitoh N. Hedoro hardening treatment by industrial wastes [J]. *Zairyo/Journal of the Society of Materials Science Japan*, 1995, 44(503):1023-1026.
- [3] Zalihe N., Emin G., Improvement of calcarous expansive soils in semi-arid environments [J]. *Journal of Arid Environments*, 2001, 47(4):453-463.
- [4] Hadi Shirazl. Field and laboratory evaluation of the use of lime fly ash to replace soil cement as a base course [J]. *Transportation research record*, 1999, 1652: 270-275.
- [5] Wenzhong song. Study on applied technology of inorganic solidified fly ash [J]. *Coal Science and Technology*, 2004, 09:64-67.
- [6] Shanghua Jia. Reinforcement mechanism and Mechanical Properties of lime-cement soil [D]. Inner Mongolia Agricultural University, 2011.
- [7] Renjian shao. Application of the soil solidification reagent in the channel anti-seepage project [J]. *Jiangxi Hydraulic Science & Technology*, 2002, 02:81-85.
- [8] P.V. Sivapullaiah, J.P. Prashanth, A. Sridharan, B.V. Narayana. Technical note reactive silica and strength of fly ashes [J]. *Geotechnical and geological engineering*, 1998, (16):239-250.
- [9] Qing zhang. Study on the engineering and expensive properties of solidified dredged sludge-phosphogypsum blends [D]. Kunming University of Science & Technology, 2013.

# Experimental study on the interior joints of the unsymmetrical hybrid connection

P.X. Liang

Nanjing Institute of Technology, Nanjing, China

H. Zhang & M.G. Sun

JinKen College of Technology, Nanjing, China

**ABSTRACT:** Unsymmetrical hybrid connection consists of precast members, unbonded post-tensioned tendons, and mild steel bars that are only placed on the upside of the beam section. The mild steel bars are set partly unbonded near the interface to prevent from the bars. The experiment for three interior joints under low reversed cyclic loading is introduced. Results of experiment show that the unsymmetrical hybrid connection has good performance of seismic resisting.

**Keywords:** unsymmetrical hybrid connection; energy-dissipation component; interior joints; performance of seismic resisting

## 1 INTRODUCTION

Unsymmetrical hybrid frame (Fig. 1) evolves from the hybrid frame (Stanton, 1997) which consists of precast members, post-tensioned prestressed tendon, and bonded mild steel bars. For simplifying the construction and increasing the speed of assembly in place, there are no mild steel bars as energy-dissipation component on the bottom of the beam in unsymmetrical hybrid connection. According to the suggestion of PRESS (Jubum, 2005), prestressed tendon should be designed to be unbonded near the interface. There are two mechanisms in unsymmetrical hybrid connection. First, the post-tensioned prestressed tendons keep elastic all along and restore the frame to its original configuration and maintain continuity between beam and column after the earthquake. In other words, the post-tensioned tendon is used to clamp the beam against

the column, providing the shear resistance through friction developed at the beam–column interface. Second, mild steel bars dissipate energy by yielding in tension and compression. Because the function of the mild steel bars is to dissipate energy, the energy-dissipation capability of unsymmetrical hybrid connection is weaker than the hybrid connection.

## 2 EXPERIMENT DESIGN

### 2.1 Design of experiment members

Three full size interior joints (Fig. 2) are fabricated for the experiment. Several design parameters list in Table 1. The intensity of concrete's is  $f_{cu} = 43.9$  MPa, and the high strength grout is  $f_{cu} = 37.7$  MPa (in 7 d). The low looseness steel strand with the intensity of 1860 MPa is used as prestressed tendon. The mild steel bars are grouted in holes. After the high strength grout is daubed on the surface of the interface of the members, the beam, and column are integrated by prestressing the sand. Then the mild steel bars are put on the top of the beam and grouted. High strength grout is also used to fill up the beam and maintained to the designed intensity. The mild steel bars are set partly unbonded, near the interface by daubing butter and wrapping with plastic paper.

### 2.2 Experiment loading

The axial load of the column is applied to the value ( $\mu = 0.25$ ), then the jacks are used to apply positive

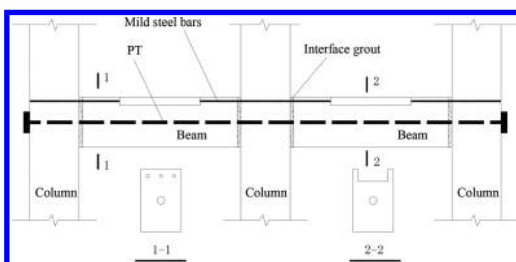


Figure 1. Unsymmetrical hybrid frame.

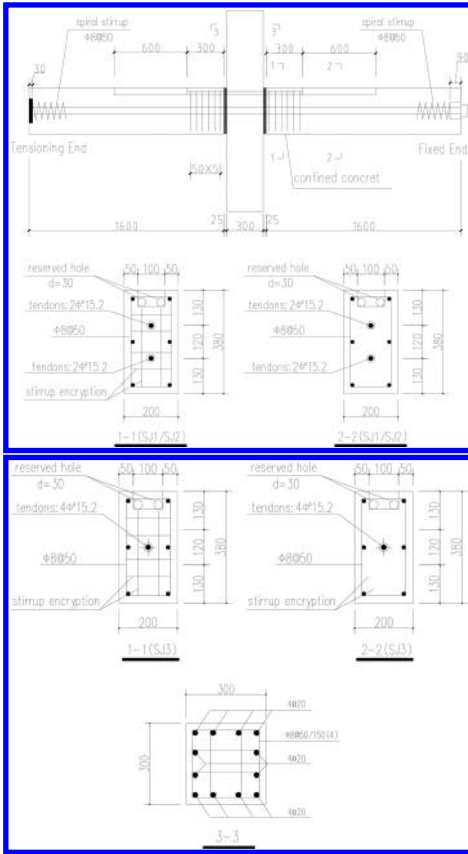


Figure 2. Design of experiment members.

Table 1. Main design parameters of experiment members.

Joint number	Beam stress (MPa)	Mild steel bars	Unbonded length of mild steel (mm)
SJ-1	2.88	2C20	200
SJ-2	2.98	2C20	250
SJ-3	2.98	2C20	200

and negative loads at the end of the beam. The displacement control method of reverse cyclic loading is applied in the experiment. The load-controlling method is applied before the beam section of the interface yield, and after the section yielding the displacement-controlling method is applied. The data collection system that can measure and auto-record consists of a sensor, a data-collection apparatus, and a computer. The positive loading refers to loading down and the negative loading refers to loading upon.

### 3 RESULTS AND ANALYSIS OF EXPERIMENT

#### 3.1 Joint behavior of damage

Under the reverse cyclic loading, the whole process of the experiment can divide into four stages: elastic, cracking, yielding, and damage. The damage modes of the joints all belong to beam plastic-hinge mode, and damage concentrates near the beam-column interface; however, beam and column remain elastic with few cracks (Fig. 3). Crossing inclined cracks

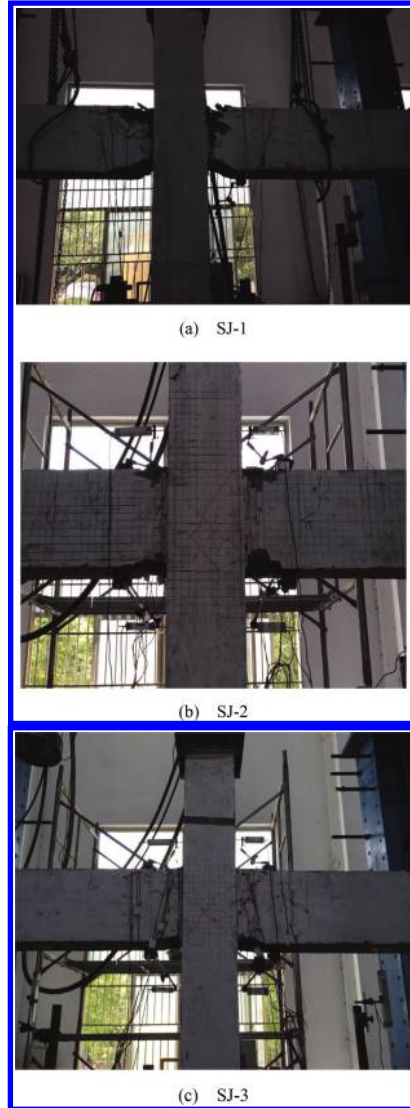


Figure 3. The load-displacement cycling curves of the experiment joints.

Table 2. Main experiment data.

Joints number	Cracking load $P_c$ (kN)	Yielding load $P_y$ (kN)	Yielding displacement $\Delta_y$ (mm)	Peak load $P_u$ (kN)	Ultimate displacement $\Delta_u$ (mm)
SJ-1	-22.4/29.97	-22.05/29.3	10.0/-10.0	-32.2/77.59	60/-60
SJ-2	-31.39/42.38	-71/59	16.0/-16.0	-92.91/61.41	78/-78
SJ-3	-32.77/39.12	41.4/-52.9	14.0/-14.0	-71.72/49.68	60/-60

occur at the end of the loading and close when unloading in the joint core of SJ-1, SJ-2, and SJ-3. The cover concrete shells off, and the length  $h$  is 180 mm ~ 200 mm, which is about 1/2 of the beam height. A gap opens at the bottom or top of the interface under loading and closes when interface under loading and closes when unloading, and the residual deformation is small. The main experiment data list is given in Table 2 (“+” and “-” refers to positive loading and negative loading, respectively).

### 3.2 Cycling curves

Figure 4 is the load-displacement ( $P-\Delta$ ) cycling curves. There are several common features: All the curves show the “s” shape and the prestressing effect is very clear. The curves are unsymmetrical and show plumper under positive loading. Before the crack occurs, the area of cycling loop is small its shape is near straight line, and the residual deformation is small. From the crack occurring to the connection yielding, the shape of cycling loop begins to show curvilinear, the area of cycling loop gradually increases. The shape of the cycling curves shows from “S” to arched under positive loading, and displays some features of the joint cast-in-place. When unloading, the curves look sharp, and the joints have strong ability of restoring to its original configuration, and show distinctly the features of prestressed concrete joint.

The difference of the cycling curves can be concluded as: (1) After the SJ-1 yielding, the strength of the main cycling loop kept increasing, while the displacement of the beam increasing. When the displacement arrived at 60 mm of the second cycle, the strength dropped to 85% of the peak load value and the joint damaged. (2) SJ-2’s storey drift arrived at 0.034. When the displacement arrived at 78 mm of the second cycle, the strength dropped to 85% of the peak load value and SJ-2 damaged. (3) SJ-3’s storey drift arrived at 0.0144, its deformation ability is weaker than SJ-2’s. Its skeleton curve shows clearly declining shape. After SJ-3 yielding, the area of cycling loop gradually increased, however, because of the different ways of tension in the SJ-3, the area cycling loop of SJ-3 is less than the area of SJ-1 or SJ-2.

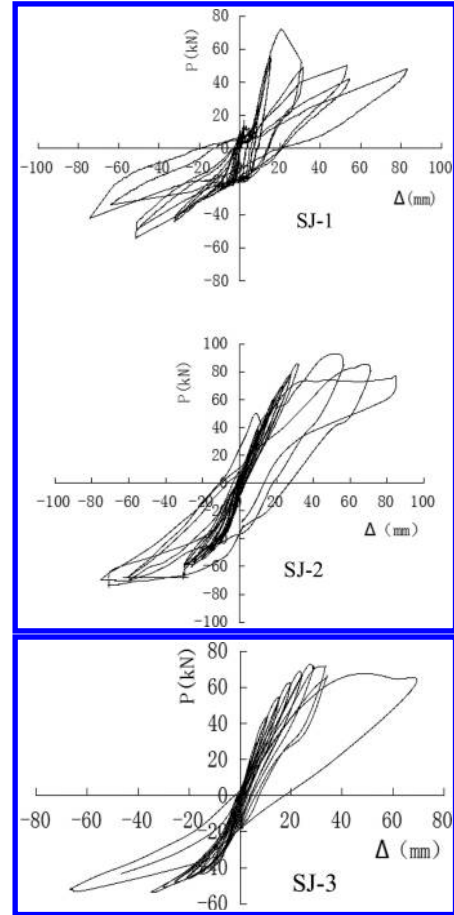


Figure 4. The load-displacement cycling curves of the experiment joints.

### 3.3 Displacement ductility

Table 3 is the displacement ductility coefficient of SJ-1 ~ SJ-3. The displacement ductility coefficients of the joints are between 4.29 ~ 6.0, which is near the coefficient of reinforced concrete structure. Axial forces in the beam reduce the ductility of the joint. The relation of displacement ductility



Table 3. Ductility coefficient of displacement.

Joints number	Yielding displacement $\Delta_y$ (mm)	Ultimate displacement $\Delta_u$ (mm)	Displacement ductility coefficient $\mu_\Delta$
SJ-1	10.0	60.0	6.0
SJ-2	16.0	78.0	4.88
SJ-3	14.0	60.0	4.29

Table 4. Equivalent viscous damping.

Joints number	SJ-1	SJ-2	SJ-3
$h_e$	6%	5.8%	7.6%

is:  $SJ-1 > SJ-2$ . So, the longer the unbonded length is the lower displacement ductility the joint has.

### 3.4 Energy-dissipation ability

Equivalent viscous damping (Zhenzheng Fang, 2005) ( $h_e$ ) is used to express the energy dissipation ability of the joint. Table 4 shows the equivalent viscous damping of the joints in different stage. Table 4 shows that: (1) As equivalent viscous damping gradually increased, and the energy dissipation of the connection also increased. The equivalent viscous damping of SJ1 and SJ2 is approximate. (2) The equivalent viscous damping of SJ-3 is largest, which shows SJ-3 has the strongest energy dissipation ability. The prestressing degree of SJ-1 is higher than that of SJ-2, so the SJ-2's ductility is weaker.

## 4 SUMMARY

Through the experiment for three unbonded post-tensioned unsymmetrical hybrid joints under

reverse cyclic loading, some features of the connection are acquired. The main contents are as follows:

1. The damage modes of the joints belong to beam plastic-hinge mode. Damage concentrates near the beam-column interface, however, beam and column remain elastic with few cracks; There is no slip between the interfaces, which proved that the shearing forces of the beam being carried by the friction is available.
2. The unbonded length of mild steel affects the connection, the shorter the unbonded length of mild steel is, the lower ductility the joint has.
3. The cycling curves are unsymmetrical and show plumper under positive loading because of the unsymmetrical mild steel bars. The energy dissipation ability under positive loading is stronger than under negative loading.
4. As the displacement increased, equivalent viscous damping gradually increased, and the energy dissipation of the connection also increased. The equivalent viscous damping of unsymmetrical connection is about 6% ~ 8%.

This work was supported by the General Project of Natural Science Foundation research of College and University in Jiangsu Province of China (Found Number: 12KJB560001), also by the Cyanine Project in Jiangsu Province of China in 2014.

## REFERENCES

- [1] Stanton, J.F., Stone, W., and Cheok, G. A hybrid reinforced precast frame for seismic regions [J]. PCI Journal, 1997, 42(2): 20–32.
- [2] Jubum Kim. Behavior of hybrid frames under seismic loading [D]. University of Washington, 2005: 18–21.
- [3] Zhenzheng Fang. Theory and Application of Prestressed Structure [M]. China Building Industry Press, 2005. 12: 211–212. (in Chinese).

# Application and numerical simulation of polyurethane insulation board in concrete lining canal

Yingzi Yin & Dong Zhang

The School of Architecture and Civil Engineering, Inner Mongolia University of Science and Technology, Baotou, China

**ABSTRACT:** At present, polyurethane board has been widely used as insulation material in lining canal. Yet, it is hard to scientifically define the thickness of polyurethane board in different positions of a canal. Based on the site test research of polyurethane board in the south main canal in Linhe Area of Inner Mongolia, we utilize the ANSYS to analyze the influence of various insulation board thicknesses on canal's temperature and displacement field, and obtain frost heaving values at different positions of the canal. The calculated value is consistent with measured data, which provides technical support for the thickness of polyurethane board in the lining canal construction.

**Keywords:** polyurethane; canal; application; numerical simulation

## 1 INTRODUCTION

The north canals located in the seasonal frozen soil area are very easy to frost heave due to the long frozen period every winter. The temperature rises and thaws the soil out after the freeze. The concrete channel rigid lining is very easy to damage under these kinds of repeated freeze-thaw cycles. In recent years, the integrity of the concrete lining canal is improved through adopting some antifreeze bilge and heat preservation measures. With the development of the geotechnical material science, there has been a lot of heat preservation materials used in channel lining. The thermal insulation material proposed in this paper is being heavily promoted in the current canals-polyurethane insulation board. This material has a small coefficient of thermal conductivity, light weight, ageing resistance, convenient transportation, and construction. Due to different areas such as climate and soil conditions, the reasonable thickness of these kinds of polyurethane insulation board is still not calculated. Now just to do a field test, and then according to the monitoring results determine the reasonable thickness of the insulation board in the regional channels.

### 1.1 Project overview

The South Main Canal is located in Shuanghe town, Linhe district of Inner Mongolia. It is east-west and has a high underground water level. The channel soil with strong frost heave belongs to seasonal frozen soil. The cross section of the South Main Canal in Linhe is trapezoidal. A thickness of

6 cm precast concrete panel lining is used to prevent water seepage. The channel cross section and the frost heaven measured data are respectively shown in Figure 1 and Table 1.

According to the demand for lining channel insulation board of national standard *the Canal Seepage Control Engineering Technical Specifications (SL 18-2006)*, the test using polyurethane insulation board density is about 45 Kg/m<sup>3</sup>.

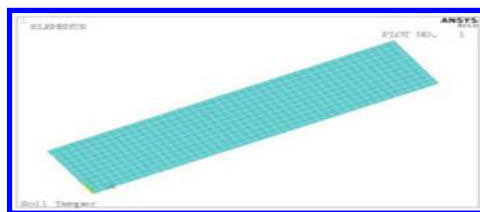


Figure 1. The cross section of the South Main Canal.

Table 1. The canal frost heaving measured data.

Part	Maximum frozen depth (h/cm)		The largest amount of frost heaving ( $\Delta_f$ /cm)		Frost heaving ratio ( $\eta$ /%)	
	Upper	Below	Upper	Below	Upper	Below
Shady slope	92	76.6	8.8	14	9.6	18.3
Sunny slope	16.7	20.6	2.3	4.7	13.8	22.8

Table 2. The mechanical properties of polyurethane insulation board.

Item	Density (Kg/m <sup>3</sup> )	Water absorption (%)	Compressive strength (KPa)	Bending strength (KPa)	Dimensional stability -40°C~+70°C (%)	Thermal conductivity [W/(m·K)]
Standard indicators	≥15	≤6	≥60	≥180	≤4	≤0.041
Testing values	45.48	1.98	323	196	±1.5	0.029

The mechanical properties of polyurethane insulation board are shown in Table 2.

## 2 FINITE ELEMENT ANALYSIS

### 2.1 Finite element model

Through the comprehensive analysis of the south main canal soil, climate and the trapezoidal channel mechanism of frost heave in the Inner Mongolia Linhe district, canal bed is heavy silty loam soil. Finite element model is shown in Figure 2. Take 1.0 m along the vertical direction of the slope, take 4.6 m along the length direction of the slope, and establish a two-dimensional plane model.

In the calculation of temperature field, the temperature boundary conditions imposed by the data in Table 3, left and right boundary are thermal insulation.

In the calculation of stress field, the constraint conditions for both sides of the model vertical section are x constraints, the horizontal section of model bottom is y constraints, top boundary is free, the rest are x and y constraints.

### 2.2 Parameter selection

The calculation of temperature field only related to the coefficient of thermal conductivity, regard the linear expansion coefficient of the frozen soil as a negative value at the thermal coupling calculation. Freezing temperature is close to 0°C and 0°C which is adopted as a benchmark. Due to the limited measured parameters, regardless of the difference of the vertical and horizontal directions, take the  $\eta/T$  for the unified frost heaving coefficient, the  $\eta$  is the frost heave rate, refer to Table 1, T is temperature. Foundation soil modulus of elasticity and poisson's ratio are determined according to the reference [5]. Material mechanics parameters are shown in Tables 4 and 5.

## 3 THE COMPUTER SIMULATION RESULTS AND ANALYSIS

### 3.1 Temperature field analysis

It is can be seen in Figure 3, the zero temperature lines in temperature field rise significantly after

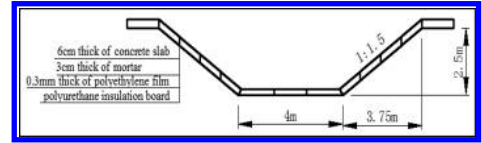


Figure 2. Finite element model.

Table 3. The temperature boundary conditions (unit: °C).

Boundary	Shady slope upper	Shady slope below	Sunny slope upper	Sunny slope below
Upper boundary	-12	-12	-7	-7
Lower boundary	1	1	3	3

Table 4. Frozen soil elastic modulus.

Temperature (°C)	0	-1	-2	-3	-5
Elastic modulus (Pa)	11e6	19e6	26e6	33e6	46e6

laying the different thicknesses of polyurethane insulation board on the slopes. The thicker the plate is, the higher the zero line temperature rises. The polyurethane insulation board has heat preservation effect, abates the transmission of ground temperature, and raises the ground temperature obviously.

### 3.2 Displacement field analysis

It is can be seen in Figure 4, the maximal displacement of model 1 is 14.5 cm on the shady slope. The upper maximal displacements of model 2 and model 3 are respectively 2.9 cm and 3.7 cm, and the below maximal displacements of model 2 and model 3 are respectively 1.7 cm and 2.8 cm on the shady slope. The maximal displacement of model 1 is 6.7 cm on the sunny slope. The upper maximal displacements of model 2 and model 3 are respectively 1.7 cm and 2.9 cm, and the below maximal displacements of model 2 and model 3 are respectively 0.5 cm and 0.2 cm on the sunny slope. In theory, the thicker the insulation board is, the smaller the frost heaving

Table 5. Material mechanics parameters.

Item	Thermal conductivity (w/(m°C))	Elastic modulus (Pa)	Poisson's ratio	Thermal expansion Coefficient (1/°C)
Polyurethane	0.029	$2.1 \times 10^9$	0.4	$1.4 \times 10^{-4}$
Mortar	1.54	$2.0 \times 10^{10}$	0.2	$1.1 \times 10^{-5}$
Concrete	1.58	$2.4 \times 10^{10}$	0.167	$1.1 \times 10^{-5}$
Frozen soil	1.987		0.330	$\eta/T$
Unfrozen soil	1.320	$1.5 \times 10^7$	0.375	0

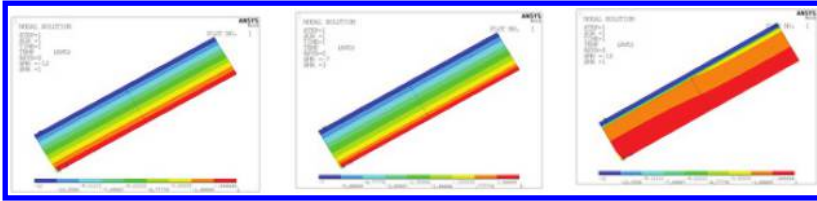


Figure 3. The temperature field distribution of various measures (unit: °C).

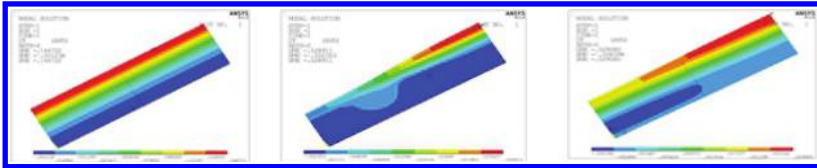


Figure 4. The normal displacement field distribution of various models (unit: °C).

amount is. But the frost heave is affected by the underground water level in practical channels. The below frost heaving amount on both slopes is greater than the upper because of the high underground water level and the rich soil water content. And the software simulation results only consider a single temperature, and don't take the moisture content into account. So the result of simulation is that the thicker the insulation board is, the smaller the frost heaving amount is. The numerical simulation results accord with basic monitoring data. The different thicknesses of the insulation board cut the different frost heaving amounts.

#### 4 CONCLUSIONS

1. The canal frost heave is influenced by adjacent foundation soil temperature field; therefore, we suggest laying polyurethane insulation board in certain ranges of canal top and bottom, so that the canal concrete rigid lining is protected perfectly.
2. At present the software simulation results only consider a single temperature field, and don't take the moisture content and soil property into account. Though the numerical simulation results accord with basically monitoring data, it

can be only approximately referenced for actual construction. The several factors are considered in the future frost heaving simulation.

3. Many simulation parameters can be selected only according to references due to the limited test condition. Sometimes those parameters do not reflect the real value of the region, so establishing a perfect material parameters database is proposed.
4. Many monitoring data is manual measuring due to the limited site conditions, this may lead to inaccurate measurements. So the test conditions should be improved and reducing artificial operation makes results more accurate.

#### REFERENCES

- [1] Ying Zi, Yin, Ying Hao, Wang, & Yun Chi, Song. Study and computer simulation of hydraulic structure heat preservation measures [J]. Journal of Inner Mongolia University of Science and Technology, 2007, 26(2):183–186.
- [2] Li Xia, Guo, Zheng Zhong, Wang, & Jia lin, Li. Finite element analysis of trapezoidal or quasi trapezoidal channel frost heave [J]. Water Saving Irrigating, 2007, (4), 44–47.
- [3] Jie Ming, Ke. Numerical simulation analysis of artificial freezing soil frost heave [D]. Nan Jing: Nan Jing Forestry University, 2004:35–36.

*Geotechnical engineering*

## Test on the mechanical properties of cement treatment soil under triaxial compression

T.W. Zhang

*School of Architectural Engineering, Jiamusi University, Jiamusi, Heilongjiang, China*

Y.Y. Zhao

*School of Architectural Engineering, Jiamusi University, Jiamusi, Heilongjiang, China*

*School of Civil Engineering, Harbin Institute of Technology, Harbin, Heilongjiang, China*

X.L. Zhang

*Department of Architecture, Shanghai Institute of Architectural Design and Research Co. Ltd., Shanghai, China*

X.C. Zhang

*School of Civil Engineering, Harbin Institute of Technology, Harbin, Heilongjiang, China*

**ABSTRACT:** The influences of cement content (ratio of cement weight to dry weight of soils) and confining pressure on the mechanical properties of cement-treated sandy soil are investigated by consolidated-undrained triaxial compression tests. Cement contents adopted in the tests are 0%, 2.5%, 5%, 7.5% and 10%. Confining pressures applied around specimens are as follows: unconfined, 30, 100 and 200 kPa. The test results show that the addition of cement or a high confining pressure can significantly improve the compression strength of the soil. It is observed from stress-strain behaviors that a transition of failure type from ductility to brittleness occurs with the increasing cement content, and the soil at higher confining pressure presents better ductility than at lower confining pressure with the same cement content. Furthermore, cement content and confining pressure both present perfect linear relationships with the compression strength of the soil. A linear expression of such linear relationship is obtained through the multiple regression analysis. The axial stiffness of the soil increases with increasing cement content and confining pressure, whereas the yield strain of the soil decreases with increasing confining pressure only for the cemented soil.

**Keywords:** sandy soil; compressive strength; cement content; confining pressure; triaxial compression test

### 1 INTRODUCTION

To achieve the purpose of saving the construction cost, instead of completely replacing the original local soils with high-quality materials, soil stabilization techniques have been adopted in practice to improve the mechanical properties of bad soils. Several kinds of additives such as cement, lime, fly ash, polymers and fibers have attracted much concern under various geology conditions. Comparing with other stabilization techniques, cement treatment has many beneficial effects on engineering behavior for a wide range of soils (Uddin et al. 1997, Lo & Wardani 2002, Lorenzo & Bergado 2004), such as rapid stabilization, constructing convenience and cost saving. So, the cement treatment technique based on the laboratory test

has attracted much attention in the last decades. Sariosseiri et al. (2009, 2011) investigated the influence of cement content addition on the soil in the State of Washington by using consolidated-undrained triaxial compression tests. The results showed a significant improvement in drying rates, workability, unconfined compressive strength and shear strength of the soil, and pointed out that the brittle type of failure may appear in high-cement content cases. Ajorloo et al. (2012) and Schnaid et al. (2001, 2003) quantified the effects of cementation on the stress-strain behavior, stiffness and shear strength of sand by using triaxial tests, and indicated that higher confining pressure or higher cement content, or both can apparently improve the stiffness and strength of the sand. The brittle behavior of the cemented sand appeared

at lower confining pressure and higher cement content. da Fonseca et al. (2009) studied the stabilization effects of cement content on Osorio sand and Botucatu residual sandstone. The results are in close agreement with the aforementioned conclusions. Moreover, a general formulation that was used to evaluate unconfined compression strength as a function of absolute volume of voids divided by absolute volume of cement was presented. Pantazopoulos et al. (2012) presented the influences of cement type and gradation on the stress-strain-strength behavior of sands. It concluded that microfine cement can improve the strength higher than ordinary cement.

Although the aforementioned research results show similar conclusions, for one soil type, targeted test investigation also have to be performed to quantify the influence of factors on its mechanical properties. The present study focuses on the mechanical properties of subgrade soil of the Beijing-Harbin railway. The influences of cement content and confining pressure on the stress-strain behavior and compression strength of the soil are investigated and quantified in this study.

## 2 MATERIALS AND TEST PROCEDURES

### 2.1 Materials

The soil used in this study was sampled from the roadbed of the Beijing-Harbin railway, in northern China. It was dried and screened using a sieve with a diameter of 2 mm, in accordance with the “Test Methods of Soils for Highway Engineering”. The grain size distribution curve of the soil is shown in Figure 1. According to the “Standard of Engineering Classification of Soil”, the soil is classified as poorly graded sandy soil. The physical properties of the soil are listed in Table 1. Portland cement type II-Tehran determined by ASTM C150-07, as

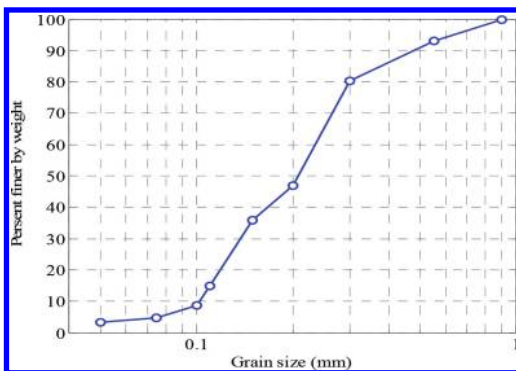


Figure 1. Grain size distribution curve of the sandy soil.

Table 1. Physical properties of the soil used in this study.

Property	Value
Specific gravity (G)	2.54
Constrained grain size (D60) (mm)	0.23
Effective grain size (D10) (mm)	0.085
Uniformity coefficient (Cu)	10.4
Curvature coefficient (Cc)	7.62
Maximum void ratio (emax)	0.65
Minimum void ratio (emin)	0.51
Optimum water content (%)	8.7

Table 2. Composition of the cement type II-Tehran (%).

CaO	SiO <sub>2</sub>	Al <sub>2</sub> O <sub>3</sub>	MgO	Fe <sub>2</sub> O <sub>3</sub>	SO <sub>3</sub>	K <sub>2</sub> O
62.24	20.65	4.26	3.72	3.14	1.6	0.93

the additive, is adopted in this study, and the composition is listed in Table 2.

### 2.2 Test procedures

The specimens were prepared by remodeling the sample soils in cylindrical molds of diameter 50 mm and height 100 mm. The dry density of the specimens is 1.69 g/cm<sup>3</sup>, and the optimum water content is 9.5% on the basis of the average values obtained from standard Proctor compaction tests carried out on uncemented soils. The specimens were then stored in a curing chamber for 28 days before testing.

An automatic data acquisition triaxial compression test apparatus model GSZ302 was used to measure the stress-strain behavior data of the specimens. The uncemented specimens were consolidated for 2 hours at the corresponding confining pressure. Then, consolidated-undrained tests were undertaken to measure the stress-strain behavior of the specimens. The tests were performed in the strain control mode and the axial movement control at a velocity of 0.002 mm/min. Four cement content scenarios (0%, 2.5%, 5%, 7.5% and 10%) and five confining pressure scenarios (unconfined, 30, 100 and 200 kPa) were adopted, and the corresponding 20 specimens were prepared herein.

## 3 RESULTS AND DISCUSSION

### 3.1 Stress-strain behavior

Figure 2 shows the curves between the shear stress and shear strain of the specimens with different

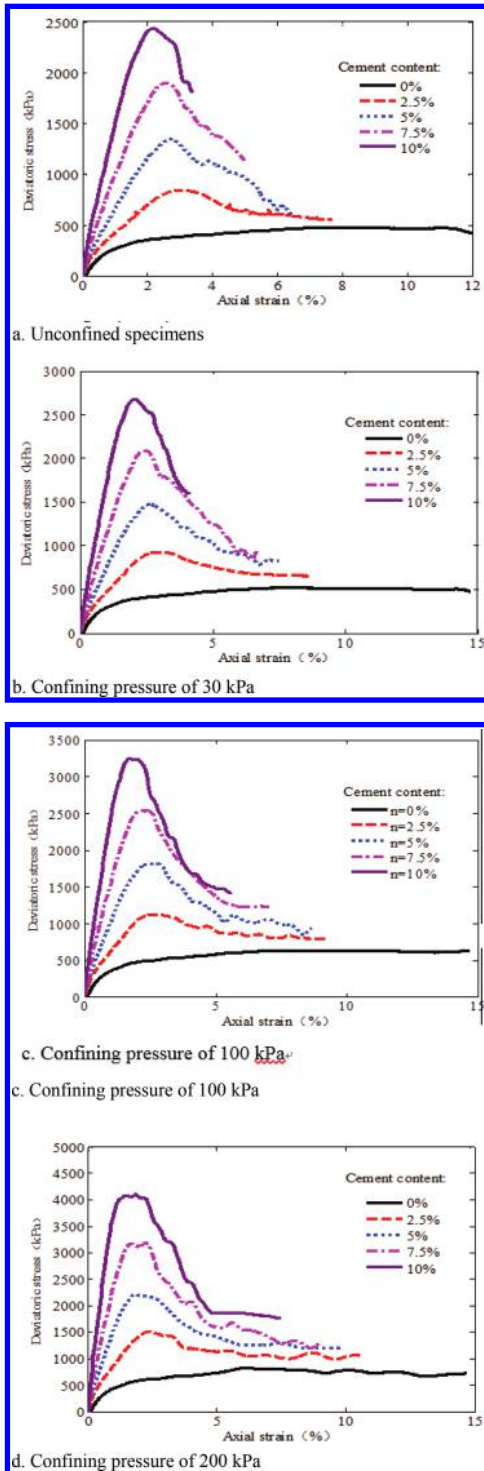


Figure 2. Deviatoric stress-axial strain behavior of uncemented and cemented sandy soils at confining pressures of 30, 100 and 200 kPa, after 28 days curing.

cement contents at the corresponding confining pressure after 28 days curing. It can be observed that the enhancement effect of cement addition is strongly dependent on cement content in this study. The stress-strain behaviors of all the cemented soils, compared with uncemented soils, are linear up to the peak point stress and then enter the plastic states until failure. Furthermore, the slopes of the stress-strain curves at a low strain area (below 0.025) increase with increasing cement content. As cement content increases, the deviatoric stress increases at the same strain. The peak point stresses do not achieve at the same strain; instead, the strain rates of the peak point stresses decreases with increasing cement content. On the other hand, comparing the peak stresses of specimens in Figure 2, as confining pressure increases, the peak stress of the specimen increases with the same cement content.

The failure types of specimens varied apparently with different cement contents. The specimens of uncemented, 2.5% and 10% cement content presented ductile, planar, and brittle type of failure, respectively, for unconfined scenarios (Figure 2a), whereas at a confining pressure of 200 kPa (Figure 2d), the specimens of uncemented and cement content of 2.5% exhibited the ductile type of failure and those of 10% cement content displayed the tendency to planar type of failure. This illustrates the transition of failure type from ductile to brittle that occurs with increasing cement content from uncemented to 10%, whereas with increasing confining pressure, the transition of failure type from brittleness to ductility occurs.

It should be noted that the compression strength of the specimen at a constant confining pressure increases with increasing cement content. A well-defined linear relationship between shear strength and cement content is obtained in the tests. Also, the relationships between compression strength and confining pressure of the specimens illustrate that compression strength appears to be linear to confining pressure. In order to quantify the influences of cement content and confining pressure on the compression strength of the soil, multiple regression analysis of compression strength as a linear function of cement content and confining pressure is performed, and the regression equation is obtained as follows:

$$S_{eq,p} = 2.52C_c + 4.86\sigma_3 + 125 \quad (1)$$

Where  $S_{eq,p}$  is the equivalent compression strength;  $C_c$  is the cement content and  $\sigma_3$  is the confining pressure.

The influence of cement content and confining pressure on the compressive strength and the corresponding regression plan is shown in Figure 3.



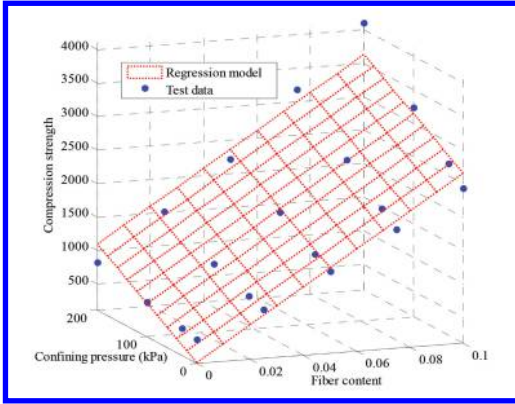


Figure 3. Variation of compressive strength of sandy soil with cement content and confining pressure.

It should be noted that the correlation coefficient of the regression is equal to 0.982, which illustrates that the relationship between compression strength and the two test parameters is highly linear dependent.

### 3.2 Secant modulus

Secant modulus is generally adopted to evaluate the stiffness of the soil through processing of the test data. In order to investigate the dependence of stiffness on cement content and confining pressure, secant moduli versus axial strain in logarithmic scale curves are plotted in Figure 4. It can be found that for all the scenarios, as the axial strain increases, the secant moduli almost keep at a constant value at a small strain area followed by gradual attenuations. It is easy to understand that the horizontal lines of the curves indicate the linear elastic stage of the soils, and the break points of curves define the yield secant moduli of the soils. It should be noted that the curves of cemented specimens (Fig. 4b) present a longer linear stage (below 1%) than those (below 0.1%) of uncemented specimens (Fig. 4a), which means that the addition of cement can significantly improve the linear elastic performance of the soil. On the other hand, as confining pressure increases, the secant modulus of either the uncemented or the cemented soil increases, which illustrates that under a higher confining pressure, the stiffness of the soils can be improved effectively. During the variation of confining pressure from 30 to 200 kPa, the secant modulus of uncemented specimens (Fig. 4a) at a linear elastic stage is enhanced by a ratio of 0.2–0.7, and the secant modulus of cemented specimens (Fig. 4b) with a cement content of 7.5% at a linear elastic stage is enhanced by a ratio of 0.25–1.8. It should be noted that the break points

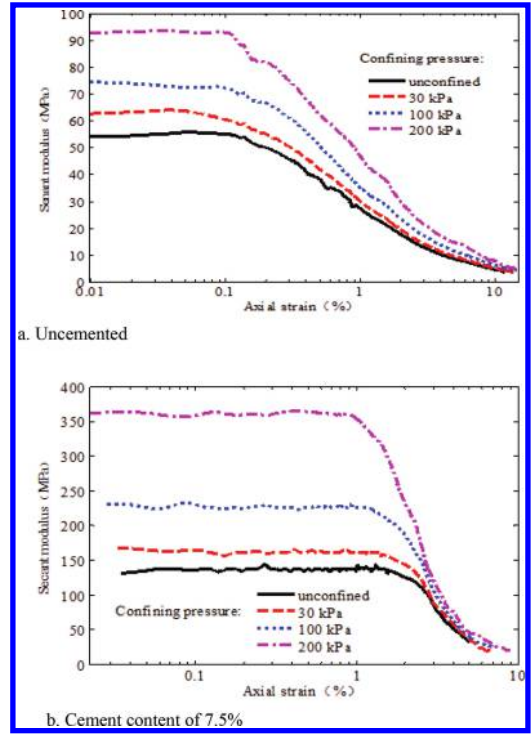


Figure 4. Secant modulus versus axial strain on the logarithmic scale for uncemented and cemented soils with a cement content of 7.5%.

in the curves of uncemented specimens at different confining pressures almost keep at a constant value of axial strain (0.1%), whereas for cemented specimens with a cement content of 7.5%, the axial strain at the break point decreases with increasing confining pressure. It means that the yield strain of the soil is not expected to improve dramatically with increasing confining pressure under the uncemented condition.

## 4 CONCLUSIONS

The present study aims at investigating the influences of cement content and confining pressure on the mechanical properties of cemented soils in the roadbed of the Beijing-Harbin railway. On the basis of the present results, the following conclusions can be drawn.

Addition of cement as the additive can significantly improve the strength of sandy soils. The compression strength increases with increasing cement content, whereas the failure type of soil varied from ductility to brittleness with increasing cement content from uncemented to 10%.

As confining pressure increases, the compression strength of the soil increases and a positive effect occurs on failure type: brittleness reduction or ductility improvement.

A linear relationship between compression strength and cement content, as well as the confining pressure, is observed and a linear equation of such linear relationship is obtained through the multiple regression analysis, by which the compressive strength of the soil can be easily evaluated.

Axial stiffness of the sandy soil increases with increasing cement content and confining pressure. The yield strain of the soil decreases with increasing confining pressure for the cemented soil, but not for the uncemented one.

#### ACKNOWLEDGMENT

This work was supported by the Undergraduate Training Programs for Innovation and Entrepreneurship of Heilongjiang (No. 20140222038). The authors are grateful for the support.

#### REFERENCES

- Ajorloo, A., Mroueh, H. & Lancelot, L. 2012. Experimental investigation of cement treated sand behavior under triaxial test. *Geotechnical and Geological Engineering* 30(1): 129–143.
- Carlson, K., Sariosseiri, F. & Muhunthan, B. 2011. Engineering properties of cement kiln dust-modified soils in Western Washington State. *Geotechnical and Geological Engineering* 29(5): 837–844.
- da Fonseca, A.V., Cruz, R.C. & Consoli, N.C. 2009. Strength properties of sandy soil–cement admixtures. *Geotechnical and geological engineering* 27(6): 681–686.
- Lo, S.R. & Wardani, S.P.R. 2002. Strength and dilatancy of a stabilized by a cement and fly ash mixture. *Canadian Geotechnical Journal* 39(1): 77–89.
- Lorenzo, A.L. & Bergado, D.T. 2004. Fundamental parameters of cement-admixed clay–new approach. *Journal of Geotechnical and Geoenvironmental Engineering, ASCE* 130(10): 1042–1050.
- Pantazopoulos, I.A., Markou, I.N. & Atmatzidis, D.K., et al. 2012. Triaxial compression testing of microfine cement grouted sands. *Grouting and Deep Mixing, ASCE* 2012: 1721–1730.
- Sariosseiri, F. & Muhunthan, B. 2009. Effect of cement treatment on geotechnical properties of some Washington State soils. *Engineering Geology* 104(1): 119–125.
- Schnaid, F. & Mantaras, F.M. 2003. Cavity expansion in cemented materials: structure degradation effects. *Geotechnique* 53(9): 797–807.
- Schnaid, F., Prietto, P.D.M. & Consoli, N.C. 2001. Characterization of cemented sand in triaxial compression. *Journal of Geotechnical and Geoenvironmental Engineering* 127(10): 857–868.
- Uddin, K., Balasubramaniam, A.S. & Bergardo, D.T. 1997. Engineering behaviors of cement-treated Bangkok soft clay. *Geotechnical Engineering Journal* 28(1), 89–119.

# Influence factors analysis of settlement characteristic of CFG pile-net composite foundation during embankment construction

Hong Zhang, Jian-jia Wu & Xian-ming Huang

*Department of Civil Engineering and Architecture, Nanchang Institute of Technology, Nanchang, China*

Li-ping Zhang & Xiao-ming Yang

*Jiangxi Highway Development Corporation, Nanchang, China*

**ABSTRACT:** This paper took a deep soft foundation section in the project of CFG pile-net composite structure treatment of a highway in Jiangxi province as the research object. The influence of design parameters on the settlement of pile-net composite foundation during embankment construction was analyzed by using the finite difference software FLAC3D, including pile length, pile spacing, cushioning layer thickness and geogrid layers. The calculation results are as follows: the influence of pile spacing on settlement of soft foundation is very significant, the settlement of subgrade surface increases by 71.86% with pile spacing varying from 3 d to 8 d; pile length affects obviously the settlement of soft foundation, the settlement of subgrade surface decreases by 38.30% with pile length varying from 15 m to 21 m; the influence degree of cushioning layer thickness and geogrid layers on the settlement of soft foundation is relatively smaller.

**Keywords:** expressway; pile-net composite foundation; embankment construction; settlement; numerical analysis

## 1 INTRODUCTION

Due to the advantages of small settlements, high stability, short duration and convenient construction, the pile-net composite foundation is widely used in construction, highway, railway and other engineering fields, and good economic benefits were obtained (Dai et al. 2010, Sun et al. 2013). While the working mechanism of pile-net composite foundation is very complicated, theoretical research is far behind the engineering practice, and there is no mature design calculation method today. As a result, a large number of scholars at home and abroad studied the pile-net composite foundation on engineering test, theory study, numerical simulation and other aspects, and obtained some achievements (Cao et al. 2006, Chen et al. 2004, Cai et al. 2010, Huang et al. 2013). Hewlett (1998) put forward the calculation formula of pile-soil load share ratio through the indoor model test. Rao et al. (2001) considered the specific situation of pile-net composite foundation, and then deduced the three point method to calculate the amount of post-construction settlement. Xue et al. (2014) carried on the finite element analysis of pile-net composite foundation in highway widening engineering, and the results indicated that pile-net composite foundation treatment technology solved

the problems of differential settlements caused by new and old subgrade. This paper took a deep soft soil foundation test section in the project of CFG pile-net composite structure treatment of the Jiu-jiang ring expressway A1 block in the city of Jiu-jiang in Jiangxi province as the research object. The finite difference software FLAC3D was carried to analyze the influence of pile length, pile spacing, cushioning layer thickness and geogrid layers on the deformation of pile-net composite foundation, and the design parameters were to be optimized.

## 2 ENGINEERING SITUATION

Jiu-jiang ring expressway whose route crosses the soft soil district of Poyang Lake is located in the city of Jiu-jiang, Jiangxi province. The depth of soft soil foundation is from 12 m to 20 m in the A1 block of the ring expressway. The reinforcement design scheme of the soft soil foundation test section makes use of the cement flyash gravel pile (CFG pile) and geogrid net to deal with it. The CFG pile average length is 20 m, pile diameter is 0.5 m and pile spacing is 2 m, strength grade of concrete is C15; cushioning layer takes gravel whose thickness is 0.5 m, and geogrid net laying on the cushioning layer is 1 layer.

### 3 CALCULATION MODEL AND PARAMETER SELECTION

This paper assumed that each soil layer distributed uniformly along the depth direction in the calculation model, the effect of mechanical load during construction period was not considered when the model was analyzed. The Mohr-Coulomb constitutive model was adopted by assuming that the soft soil foundation and gravel cushion were elastic-plastic material. The calculation depth of foundation adopted 40 m, it is divided into three layers, the first layer is plastic silty clay whose thickness is 4 m, the middle layer is soft plastic silty clay whose thickness is 16 m, the last layer is hard plastic silty clay whose thickness is 20 m. Horizontal calculation width of foundation model adopted 100 m, and the longitudinal length adopted 10 m. With the symmetry on the geometric model of soft road embankment, the 1/2 model was adopted to calculate and analyze. Geogrid and CFG pile adopted geogrid unit and pile unit which were from inside of FLAC3D. Calculation model is shown in Figure 1. Model calculation parameters of soft soil, embankment and gravel cushioning are shown in Table 1.

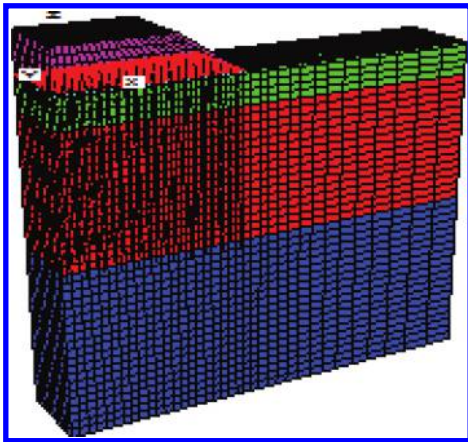


Figure 1. Calculation model of soft foundation.

Table 1. Physical-mechanical properties of foundation filling of every layer.

	Thickness/m	Bulk modulus (K/MPa)	Shear modulus (G/MPa)	Density ( $\rho$ /KN/m <sup>3</sup> )	Cohesion (c/KPa)	Angle of internal friction/ $^{\circ}$
Embankment	5.0	11.36	5.86	22.0	40.8	25.2
Gravel cushion	0.4	43.86	19.08	22.0	0.0	37.0
Plasticity silty clay	4.0	6.20	2.07	20.1	40.3	19.5
Silty clay	16.0	5.67	1.21	17.9	20.1	17.8
Hard plastic silty clay	20.0	9.63	3.45	20.1	75.6	27.3

### 4 CALCULATION RESULTS ANALYSIS

#### 4.1 The influence of different pile length on the subgrade deformation

In order to study the influence degree of different pile length on the subgrade deformation, this paper took the CFG pile-net composite foundation as the basic model (cushioning thickness is 0.5 m, geogrid layer is one layer, pile diameter is 0.5 m and pile spacing is 2.00 m). Three different CFG pile length were selected to carry on the numerical simulation: (1) the pile length is 21 m (2) the pile length is 15 m (3) the pile length is mixed 15 m with 20 m (the pile length adopt 15 m except shoulder of the road). After the construction load the calculation results are shown in Figure 2.

The Figure 2 shows that the settlement of subgrade surface decreases with the increase of pile length. The maximum settlement value of subgrade surface are respectively 20.60 cm, 12.71 cm and 12.96 cm under the situation of pile length are respectively 15 m, 21 m and 15 m mixed with 20 m. The maximum settlement value of subgrade surface reduces by 38.30% when the pile length varies from 15 m to 20 m, which indicates that the increase of pile length has a better control effect on subgrade settlement. Compared with the situation that pile length is 21 m, the settlement of subgrade surface is slightly larger under the condition of pile length mixing 15 m with 21 m, but mixed pile can greatly reduce the project cost.

#### 4.2 The influence of different pile spacing on the subgrade deformation

In order to study the influence degree of different pile spacing on the subgrade deformation, this paper took the CFG pile-net composite foundation as the basic model. Four different CFG pile spacing were selected to carry on the numerical simulation: (1) the pile spacing is 3d (2) the pile spacing is 4d (3) the pile spacing is 6d (4) the pile spacing is 8d (d is the pile diameter). After the construction load the calculation results are shown in Figure 3.

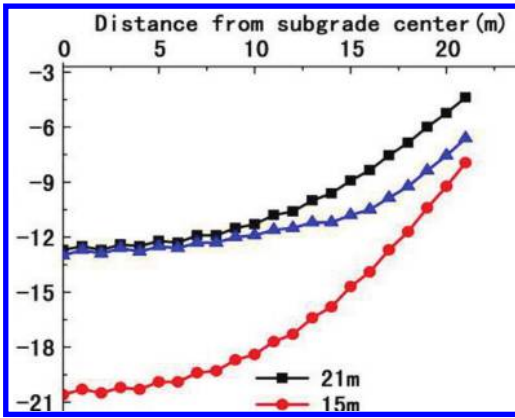


Figure 2. Accumulative settlement distribute curve of subgrade surface with different pile length.

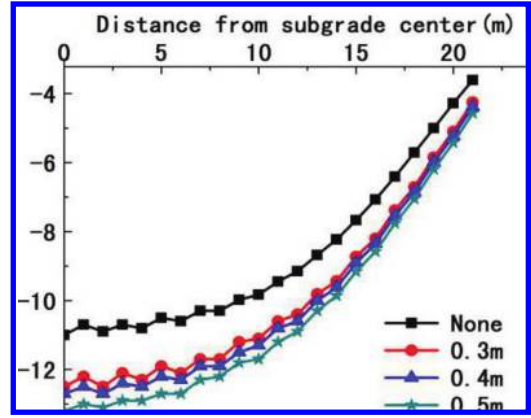


Figure 4. Accumulative settlement distribute curve of subgrade surface with different cushioning layer thickness.

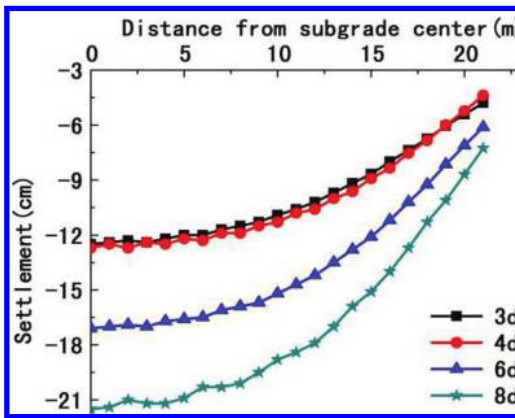


Figure 3. Accumulative settlement distribute curve of subgrade surface with different pile spacing.

The Figure 3 shows that the settlement of subgrade surface increases with the increase of pile spacing. The maximum settlement value of subgrade surface are respectively 12.51 cm, 12.71 cm, 17.13 cm and 21.50 cm under the situation of pile spacing are respectively 3d, 4d, 6d and 8d. The maximum settlement value of subgrade surface increases by 71.86% when the pile spacing varies from 3d to 8d, which indicates that the increase of pile spacing has a significant control effect on subgrade settlement.

#### 4.3 The influence of different cushioning layer thickness on subgrade deformation

In order to study the influence degree of different cushioning layer thickness on the subgrade deformation, this paper took the CFG pile-net

composite foundation as the basic model (geogrid layer is one layer, pile length is 21 m and pile spacing is 4d). Four different cushioning layer thickness were selected to carry on the numerical simulation: (1) no cushioning layer (2) cushioning layer thickness is 0.3 m (3) cushioning layer thickness is 0.4 m (4) cushioning layer thickness is 0.5 m. After the construction load the calculation results are shown in Figure 4.

The Figure 4 shows that the settlement of subgrade surface increases with the increase of cushioning layer thickness under the situation of different cushioning layer thickness. The maximum settlement value of subgrade surface are respectively 10.96 cm, 12.52 cm, 12.71 cm and 13.15 cm under the situation of cushioning layer thickness are respectively 0, 0.3 m, 0.4 m and 0.5 m. The maximum settlement value of subgrade surface increases by 19.98% when the cushioning layer thickness varies from 0 to 0.5 m, which indicates that the increase of cushioning layer thickness has a certain degree effect on subgrade settlement.

#### 4.4 The influence of different geogrid layers on subgrade deformation

In order to study the influence degree of different geogrid layers on the subgrade deformation, this paper took the CFG pile-net composite foundation as the basic model. Four different geogrid layers were selected to carry on the numerical simulation: (1) no geogrid (2) one layer geogrid (3) two layers geogrid (4) three layers geogrid. After the construction load the calculation results are shown in Figure 5.

The Figure 5 shows that the settlement distribution curves of subgrade surface are basically

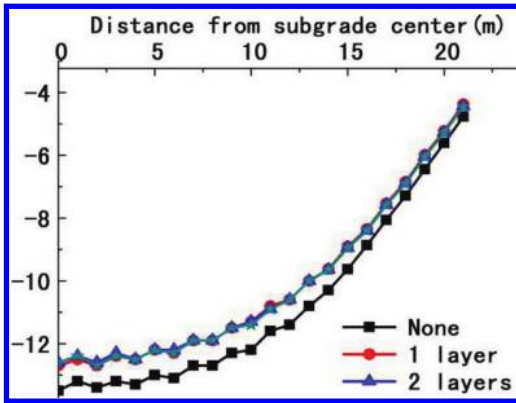


Figure 5. Accumulative settlement distribute curve of subgrade surface with different geogrid layers.

same under the situation of different geogrid layers; Under the situation of no geogrid, the settlement of subgrade surface is slightly larger than the other situations. The maximum settlement value of subgrade surface are respectively 13.48 cm, 12.71 cm, 12.64 cm and 12.65 cm under the situation of geogrid layers are respectively 0, one, two and three, which indicates that influence degree of geogrid layers on the settlement of pile-net composite foundation is relatively smaller.

## 5 CONCLUSION

Based on the analysis on the settlement of soft foundation test section of the Jiu-jiang ring expressway reinforced by CFG pile-net composite structure, design parameters of the CFG pile-net composite foundation are optimized with considering the cost factors of construction. We can adopt the reinforcement program that the pile length is mixed 15 m with 21 m, pile spacing is 2.00 m, cushioning layer thickness is 0.4 m and geogrid layer is one layer.

## ACKNOWLEDGEMENTS

This research was supported by the key Program of Jiangxi Province Department of Communication and Transportation (Project No.: 2013C006, 2013C0009, 2013C0010, 2013C0013) and Jiangxi Province Department of Education plan projects (Project No.: GJJ13754) and 2014 National (Jiangxi Province) College Students' Innovation and Entrepreneurship Training Funded Project.

## REFERENCES

- Cao, X.W., Qing, S.H. & Zhou, L.X. 2006. Experimental study on reinforcement effect of geogrid on composite foundation with dry jet mixing piles. *Chinese Journal of Rock Mechanics and Engineering*, 25(S1): 3162–3267.
- Cai, D.G. & Ye, Y.S. 2010. Numerical analysis on the mechanical properties of geosynthetic reinforced and pile supported embankment. *China Railway Science*, 31(3):1–8.
- Chen, Y.M., Jia, N. & Chen, R.P. 2004. Soil arch analysis of pile-supported embankments. *China Journal of Highway and Transport*, 17(4):1–6.
- Dai, H.J., Liu, X.L. & Ren, Z.J. 2010. Prototype testing study of pile-net composite foundation of circular coal yard. *Rock and Soil Mechanics*, 32(2):487–494.
- Hewlett, W.J. & Randolph, M.F. 1998. Analysis of piled embankments. *Ground Engineering*, (3):12–18.
- Huang, G.H. Wang, D.J. & Chen, Z.A. 2013. Numerical simulation of the settlement deformation of pile-network structure subgrade in high-speed railway. *Safety and Environmental Engineering*, 20(2):156–161.
- Rao, W.G., Jiang, H.H. & Rou, C.L. 2001. Three-point calculation method of settlement post construction of pile-net composite foundation. *Geotechnical Engineering World*, 4(8):55–57.
- Sun, Q., Zhang, X.D. & Yang, Y. 2013. Research on settlement of pile-net composite foundation of high-speed railway in soft soil area. *Journal of Guangxi University*, 28(1):157–165.
- Xue, J.R. & Yang, C.J. 2014. Theory analysis and numerical simulation of pile-net composite technology in highway subgrade widening. *Journal of Chongqing Jiaotong University (Nature Science)*, 33(3):58–62.

# Construction analysis of cellular sheet piles in thick clay condition

Y.Z. Bai

China Harbor Engineering Company Ltd., Beijing, China

**ABSTRACT:** Cellular structures constructed of interlocking steel sheet piles are used in marine environments as cofferdams, bulkheads, mooring dolphins, and lock guide walls. During the construction process, great difficulty is occasionally met because interlock forces between sheet piles surge when sheet piles penetrate specific geological layer such as hard clay. This paper presents a new method to evaluate the impact of geological condition on cellular sheet pile construction. A new parameter based on CPT tests is applied to determine the difficulty of penetrating process of sheet piles. Total 26 cellular sheet piles are evaluated in according with this method. The results show that this method supplies a new idea for evaluation of cellular structure construction.

**Keywords:** cellular sheet pile; construction analysis; clay

## 1 INTRODUCTION

A sheet-pile cellular structure is constructed by arranging straight web sheet piles in a cylindrical shape. The structure may be used singly as a mooring structure in a harbor, or several may be interconnected to form a retaining structure or cofferdam. With the growing requirement for environment protection and construction efficiency, this new technology is more and more often applied in many Chinese projects as different as Guangzhou Xinscha Harbor, Sutong Bridge pile support. Based on its wide application, Great achievements have been made both in design and construction areas. On the design side, many researchers applied finite element analyses and instrumentation measurements to study cellular structure's safety against sliding, bearing failure, overturning, and tilting, as well as sheet pile interlock rupture<sup>[1][2]</sup>. On the construction side, powerful vibrating hammers have been invented and incorporated into the penetrating process of sheet pile to dense sand layer. But for penetrating hard clay, there is still great difficulty met in the vibrating process because of the sharp increase of interlock forces between sheet piles. How to evaluate the impact of geological condition on cellular sheet pile construction is a key task in front of researchers and engineers.

## 2 GEOLOGICAL CONDITION

Water depth in construction site is between 4 m to 12 m and 11~28 m marine deposit is underneath sea bed with levels on a range from -2.5 mPD

to -10 mPD. Under the marine deposit, alluvium is followed. Specific physical and strength parameters of soil layers are shown in Table 1.

Due to environmentally friendly requirement, non-dredging measures such as cellular sheet piles and stone column are taken to form the seawall and improve ground. With the driving of vibrating hammer, cellular sheet piles pass through 15~25 m marine deposit and penetrates into 10~18 m alluvium. Its low stiffness makes it difficult to combine each sheet pile into a cellular structure.

Table 1. Physical and strength parameters of soils.

Parameters	Soil types	Recommended values
Bulk density	Marine deposits	1.50 Mg/m <sup>3</sup>
	Alluvium	1.90 Mg/m <sup>3</sup>
	Decomposed rock	1.90 Mg/m <sup>3</sup>
Drained shear strength	Marine deposits	$C' = 4 \text{ kPa}, \Phi' = 24^\circ$
	Alluvium (Clay)	$C' = 7 \text{ kPa}, \Phi' = 26^\circ$
	Alluvium (Silt)	$C' = 3 \text{ kPa}, \Phi' = 30^\circ$
	Alluvium (Sand)	$C' = 0 \text{ kPa}, \Phi' = 35^\circ$
Undrained shear strength, $C_u$	Marine clay	$C_u = 1+1.1z$ , for depth $z$
	Alluvium clay	$C_u = 2+1.3z$ , for depth $z$
Soil stiffness	Alluvium	$E = 0.9z-1$ (MPa), reduced level $z$
Coefficient of consolidation, $C_v$	Marine deposits	0.67 m <sup>2</sup> /year
	Alluvium clay/alluvium silt	1.50 m <sup>2</sup> /year

Every disturbance of vibrating operation and geotechnical change will cause large deformation, thus resulting in great difficulty of driving cellular sheet pile.

### 3 THE IMPACT OF GEOLOGICAL CONDITION ON CELLULAR SHEET PILE CONSTRUCTION

The Site composed mainly of marine deposit, alluvial sand alluvial clay layers. In view of its relatively low strength, the Contractor encounters no difficulty so far when driving the sheet piles through the marine deposit layer. The Contractor however concerns the difficulty encountered during the process of driving sheet piles into the alluvial sand and alluvial clay layers. Table 2 compares the construction mechanism of driving sheet piles into alluvial sand and alluvial clay layers.

In view of the explanation provided in Table 2 and because of the fundamental difference in geological structure, the alluvial sand can be liquefied when the sheet piles are being driven down causing the frictional resistance between the sheet piles and the surrounding liquefied sand to be reduced, which in turn facilitates further penetration of the sheet piles. The occurrence of liquefaction in alluvial sand layers is the main reason as to why it is relatively easier for cellular structures, where the

subsoil has high proportion of sand, to achieve the toe levels as determined by the Engineer.

Unlike alluvial sand, there is in general no occurrence of liquefaction in alluvial clay layers. Hence, both the strong cohesion amongst the clay particles as well as the friction between the sheet piles and the surrounding clay particles resist the downward force exerted by the vibratory hammer and the self-weight of the sheet piles. During the vibrating and penetrating process of sheet pile, its deformation occurs and is transferred and accumulated by the interlock among sheet piles. This will cause immense difficulty to the installation of main cell which is composed of a series of sheet piles.

### 4 RESISTANCE TO DRIVING OF SHEET PILES IN ALLUVIAL CLAY

The resistance to driving of sheet piles in alluvial clay mainly comes from the friction between the sheet piles and the clay. According to de Ruiter and Beringen<sup>[3]</sup>, the unit frictional resistance can be determined by the following equation:

$$f_s = \alpha \times S_u \quad (1)$$

where,

$\alpha = 1$  (normally consolidated clay)

Table 2. Mechanism of driving sheet piles into alluvial sand and alluvial clay.

Geological stratum	Alluvial sand	Alluvial clay
Net cone resistance (qnet)	1~20 MPa	0.5~2.5 MPa
Characteristics	There is no cohesion between the soil particle sand the strength mainly comes from the interlocking and the frictional resistance developed between the soil particles in contact with each other. The denser the soil, the higher the net cone resistance.	There is strong cohesion between the soil particles and the strength mainly comes from this cohesive force. The stiffer the soil, the higher the net cone resistance.
Source of downward force	The force exerted by the vibrating hammer at the top of the sheet piles and the self-weight of the sheet piles.	
Resistance to downward force	Friction between the sheet piles and sand particles.	Friction between the sheet piles and clay particles.
Any liquefaction occurred during sheet pile driving?	The high frequency vibration during sheet pile driving causes the surrounding sand layers to liquefy. The liquefied sand particles suspend in the water, and thus, greatly reduce the coefficient of friction between the sand layers and the surface of the sheet piles.	The high-frequency vibration during sheet pile driving cannot cause the surrounding clay layers to liquefy, and thus, cannot reduce the coefficient of friction between the clay layers and the surface of the sheet piles.
Change of frictional resistance	Due to liquefaction, significant reduction in frictional resistance to the driving of sheet piles.	Because of no liquefaction, minimal reduction in frictional resistance to the driving of sheet piles.
Comparison of frictional resistance	After liquefaction, the frictional resistance of the alluvial sand layer to the driving of sheet piles is smaller than that before liquefaction, and is also much smaller than that of the alluvial clay layer to the driving of sheet piles.	



$\alpha = 0.5$  (over-consolidated clay)  
 $S_u =$  undrained shear strength.

Senneset (1982)<sup>[4]</sup> established the following equation to estimate the undrained shear strength of clay based on the net cone resistance obtained for cone penetration test:-

$$S_u = \frac{q_e}{N_{ke}} \quad (2)$$

where,  
 $N_{ke}$  is a constant in the range of  $9 \pm 3$ .  
 Here,  $N_{ke}$  can be adopted as 12.

Combining (1) and (2), the unit frictional resistance can be determined by the following equation:

$$f_s = \alpha \times \frac{q_e}{N_{ke}} \quad (3)$$

Hence, the total frictional resistance experienced by the sheet pile in alluvial clay can be determined by the following equation:-

$$F = f_s A = \alpha \times \frac{q_e}{N_{ke}} \times B \times H \quad (4)$$

where,  
 $B =$  width of the sheet pile,  
 $H =$  length of penetration of sheet pile into the alluvial clay layer.

As the width of the sheet pile is constant, the total frictional resistance experienced by the sheet pile is therefore determined by  $q_e \times H$ , or the product of the average net cone resistance of the alluvial clay and the length of penetration of the sheet pile.

Based on the average values summarized in Table 3, the product of the average net cone resistance of the alluvial clay and the length of penetration of the sheet pile for the as-installed cellular structures are graphically presented in Figure 1.

As demonstrated in Figure 1, when the product of the average net cone resistance of alluvial clay and the length of penetration of sheet pile reaches certain level, the process of downward force overcoming the total frictional resistance between the sheet pile and the alluvial clay will cause large deformation thus increasing the interlock force between sheet piles. Cellular structures cannot be driven any further down to achieve designed toe levels. The specific information is shown in Table 4 based on the experience gained so far from the as-installed cellular structures.

Table 3. Average thickness and strength of the layered alluvial sand and alluvial clay.

Cellular structure no.	Top level of alluvium (mPD)			Average top level of alluvium (mPD)	Toe level determined by the engineer (mPD)	Average embedment into alluvium (m)	Alluvial sand			Alluvial clay		
	CPT-A	CPT-B	CPT-C				Thickness (m)	Net cone resistance $q_{net}$ (MPa)	Thickness (m)	Net cone resistance $q_{net}$ (MPa)	Thickness (m)	Net cone resistance $q_{net}$ (MPa)
	K28	-15.9	-18.2				-16.8	-17.0	-28	11.0	4.3	13.90
K31	-18.8	-20.3	-21.2	-20.1	-30	9.9	2.4	12.90	7.5	1.23		
K34	-17.0	-16.5	-17.7	-17.1	-23	5.9	1.3	11.76	4.6	1.22		
K38	-15.1	-15.4	-16.0	-15.5	-26	10.5	3.2	2.64	7.3	1.39		
K39	-15.5	-14.4	-14.8	-14.9	-27.5	12.6	1.0	5.98	11.6	1.64		
K41	-16.3	-17.0	-16.5	-16.6	-28	11.4	0.9	6.81	10.5	1.74		
K45	-18.5	-19.4	-17.0	-18.3	-26	7.7	1.3	4.37	6.4	0.96		
K46	-19.7	-22.8	-26.3	-22.9	-30	7.1	1.4	7.15	5.7	1.38		
K49	-19.0	-23.7	-22.5	-21.7	-30	8.3	1.3	12.59	7.0	1.06		
K55	-20.5	-19.0	-19.5	-19.7	-28	8.3	0.3	4.96	8.0	1.45		
K56	-23.8	-23.3	-21.0	-22.7	-30	7.3	1.5	2.69	5.8	1.64		

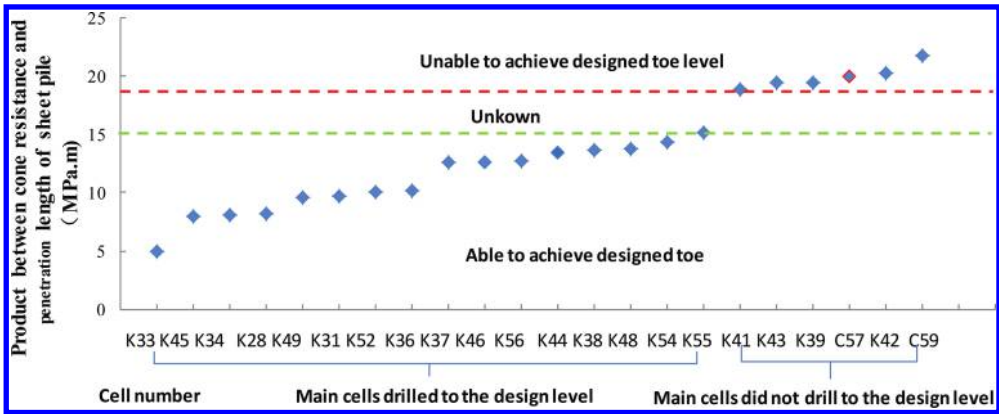


Figure 1. Product of the average net cone resistance of alluvial clay and the length of penetration of sheet pile.

Table 4. Drilling result prediction of cell structures by geological information.

$q_{ex}$ H (MPa · m)	Remark
>18.3	Unlikely to achieve
12.4–18.3	May be able to achieve
≤ 12.4	Likely to achieve

- [2] Charles T. Jahren, Reliability comparison for sheet-pile cellular structures, *Journal of Performance of Constructed Facilities*, 4(4), 216–235, 1990.
- [3] De Puitet, J. and Beringen, F.L, Pile foundation for large North Sea structures, *Marine Geotechnology*, 3(3), 267–314, 1979.
- [4] Senneset, K., Jabu, N. and Svano, G., Strength and deformation Parameters from cone penetration tests, *Proceedings of the 2nd European symposium on Penetration Testing, ESOPT-II, Amsterdam*, 2, 863–70, Balkema Pub., Rotterdam, 1982.

REFERENCES

- [1] Wissmann, K., Filz, G., Mosher, R., and Martin, Sheet pile tensions in cellular structures, *Journal of Geotechnical and Geoenvironmental Engineering*, 129(3), 224–233, 2003.

# The soil dynamic structural parameters based on the view of equivalent elastomer

X. Chen & H. Guo

*School of Civil Engineering and Architecture, Shaanxi University of Technology, Hanzhong, Shaanxi, China*

Y.X. Yan

*School of Foreign Studies, Shaanxi University of Technology, Hanzhong, Shaanxi, China*

**ABSTRACT:** Soil structural properties are the intrinsic factors which determine the dynamic characteristic of the soil. Firstly, on the basis of previous studies, this paper analyzes the substance of conventional soil dynamic structural parameters, namely, the dynamic structural property of soil in any state is the dynamic shear secant modulus of it. It is discovered that the description of the dynamic structure of soil by using dynamic shear secant modulus is quite different from the fact. Secondly, the paper suggests using the dynamic structural parameters based on the view of equivalent elastomer that is dynamic tangent modulus. Thirdly, the paper defines the soil dynamic structural residual degrees to reflect the three external effects on soil structure: disturbance, loading and humidification. Lastly, the paper gives the expression of dynamic structural residual degrees based on Hardin-Drnevich hyperbola model when external condition varies.

**Keywords:** dynamic structure; dynamic tangent modulus; dynamic structural residual degrees

## 1 INTRODUCTION

To study the dynamic characteristics of soil is one of the soil dynamics research tasks. From the structural point of view, the soil structural properties which show the physical condition of soil (Xie and Qi, 1999) are the intrinsic factors determining the mechanical properties of soil (Qi, 1999). The soil dynamic characteristics are the outward manifestation of the change or destruction of soil structural characteristics under the coupled action of dynamic load and other external forces. Therefore, it is necessary to research soil structural characteristics under the coupled action of dynamic load and other external forces (hereinafter referred to as soil dynamic structure) in order to further reveal the change laws of soil dynamic characteristics.

At present, there are three basic ways to study structural properties of soil (Xie and Qi, 1999): Firstly, the microstructure morphology methods; Secondly, solid mechanics methods; thirdly, soil mechanics methods. Among them, soil mechanics methods demonstrate great potentialities and developmental prospect. Since Xie ding-yi and Qi ji-lin mooted to determine soil structural quantitative parameters based on releasing soil structure potential the correlative research is in the ascendant. Structural research scholars firstly obtain a wealth of achievements under static conditions about soil

structural characteristics (Luo et al., 2004; Shao et al., 2004; Xia, 2005; Chen et al., 2007; Chen and Gao, 2006; Chen et al., 2006). Meanwhile, Luo Ya-sheng, et al. (Luo, 2003; Wang et al., 2010) extend this method to the field of soil dynamics and establish the soil dynamic structural parameters based on dynamic shear stress method. The structural parameters obtained from static mechanics through simple and clear experiment method and mechanism can reflect some effects on soil structure.

However, the determination of these parameters are dependent on one or more of the three external function—disturbance, loading and humidification. Therefore, to some certain questions, these parameters cannot well provide direct answers. Here are three questions: First, what are the change rules in the soil structure when the soil is immersed? Second, what are the change rules in the soil structure when the soil is only disturbed? Third, what are the change rules in the soil structure when the soil is both disturbed and immersed? Because the soil dynamic structural parameters are derived from static structure parameters, the above problems still exist in the soil dynamic structural parameter research.

In light of this, through analyzing the soil dynamic structural parameters based on the same dynamic shear stress method, the paper proposes soil dynamic structural parameters based

on equivalent elastomer views, and defines the dynamic structural residual degrees. The paper also gives the expression of dynamic structural residual degrees based on Hardin-Drnevich hyperbola model according to different external conditions.

## 2 THE SOIL DYNAMIC STRUCTURAL PARAMETERS BASED ON THE VIEW OF EQUIVALENT ELASTOMER

### 2.1 The essence of the traditional soil dynamic structure parameters

At present, many soil dynamic structural parameters under the dynamic loading conditions proposed by Xie Dingyi and Qi Jilin are gained from the generalizing of soil structural parameters under the static load conditions. The idea is to seek structural quantitative indicator by releasing structure potential. Soil dynamic structural parameters based on the same dynamic shear stress method are firstly proposed in Luo Ya-sehng's doctoral thesis titled *structural constitutive relation of unsaturated loess under static and dynamic complex stress conditions*. Its expression is:

$$m_{\gamma d} = \tau_{do}^2 / (\tau_{ds} \tau_{dr}) \quad (1)$$

where  $m_{\gamma d}$  is the soil dynamic structural quantitative parameter based on the dynamic shear stress;  $\tau_{do}$  is undisturbed soil dynamic shear stress at dynamic shear strain  $\gamma_d$ ;  $\tau_{ds}$  is undisturbed saturated soil dynamic shear stress at dynamic shear strain  $\gamma_d$ ;  $\tau_{dr}$  is disturbed soil dynamic shear stress at dynamic shear strain  $\gamma_d$ .

Considering that  $\tau_{do}$ ,  $\tau_{ds}$  and  $\tau_{dr}$  are soil dynamic shear stress at the same dynamic shear strain  $\gamma_d$ , the Formula 1 can be further simplified as:

$$m_{\gamma d} = \frac{\tau_{do}^2}{\tau_{ds} \tau_{dr}} = \frac{G_{do}^2 \gamma_d^2}{G_{dr} \gamma_d G_{ds} \gamma_d} = \frac{G_{do}^2}{G_{dr} G_{ds}} \quad (2)$$

where  $G_{do}$  is undisturbed soil dynamic shear secant modulus at dynamic shear strain  $\gamma_d$ ;  $G_{ds}$  is undisturbed saturated soil dynamic shear secant modulus at dynamic shear strain  $\gamma_d$ ;  $G_{dr}$  is disturbed soil dynamic shear secant modulus at dynamic shear strain  $\gamma_d$ .

The simplification of soil structural quantitative parameters based on the same dynamic shear strain method can get the same result:

$$m_{\tau d} = \frac{\gamma_r \gamma_s}{\gamma_o^2} = \frac{\tau_d \tau_d}{G_{dr} G_{ds}} = \frac{G_{do}^2}{\left(\frac{\tau_d}{G_{do}}\right)^2 G_{dr} G_{ds}} \quad (3)$$

where:  $\gamma_o$  is undisturbed soil dynamic shear strain at dynamic shear stress  $\tau_d$ ;  $\gamma_s$  is undisturbed saturated soil dynamic shear strain at dynamic shear stress  $\tau_d$ ;  $\gamma_r$  is disturbed soil dynamic shear strain at dynamic shear stress  $\tau_d$ ;  $G_{do}$  is undisturbed soil dynamic shear secant modulus at dynamic shear stress  $\tau_d$ ;  $G_{ds}$  is undisturbed saturated soil dynamic shear secant modulus at dynamic shear stress  $\tau_d$ ;  $G_{dr}$  is disturbed soil dynamic shear secant modulus at dynamic shear stress  $\tau_d$ .

According to the definition of soil dynamic structural parameters  $m_{\gamma d}$ :

$$m_{\gamma d} = m_1 / m_2 \quad (4)$$

Among them,  $m_1 = \tau_d / \tau_s$  shows the size of the structural variability, which is the release of soil inherent dilatant-consolidatory potentials by immersion;  $m_2 = \tau_r / \tau_o$  shows the size of the structural stability, which is the release of soil coupling effect by disturbing.  $m_1$  and  $m_2$  can be further simplified as:

$$m_1 = G_{do} / G_{ds} \quad (5)$$

$$m_2 = G_{dr} / G_{do} \quad (6)$$

Through the above analysis, the essence of soil dynamic structural parameters based on the same dynamic shear stress method and the same dynamic shear strain method can be found is the soil dynamic structural changes, which can be reflected by loading, disturbance and water immersion.

The dynamic structural property of soil in any state is the soil dynamic shear secant modulus  $G_d$ , which corresponds to the state. Then type 5 means that under the same dynamic shear strain, the reciprocal of the ratio between the residual structural property after water immersion and the structural property before water immersion can be used to reflect the extent to which the water immersion influences on the soil dynamic structural property. Water immersion causes the chemicals weakening, dissolving and suction connection losing. The wedging action of water film can release soil inherent shear-shrinkage potential, namely, water immersion influences structural variability. Thus, type 5 can be used to measure the size of structural variability. Type 6 means that under the same dynamic shear strain, the ratio between the residual structural property after disturbance and the structural property before water immersion can be used to reflect the extent to which the disturbance influences on the soil dynamic structural property. By damaging the soil coupling effect, disturbance reduces the coupling strength between the soil particles, influencing the structural stability. Therefore, type 6 can be used to measure the size of structural stability.

## 2.2 The proposal of the soil dynamic structural parameters on the view of equivalent elastomer

Soil is the elastic-plastic body. Supposing that soil elastic part and plastic part were independent of each other, then the dynamic shear secant modulus  $G_d$  can only represent the elastic property of soil. Obviously, there is a huge difference between the soil dynamic structural property described by dynamic shear secant modulus  $G_d$  and the real soil structural property. Therefore, using dynamic shear tangent modulus to describe soil dynamic structural is recommended.

Dynamic shear tangent modulus  $G_t$  is the first-order derivative of dynamic shear stress to dynamic shear strain at any point of the dynamic shear stress—dynamic shear strain curve. Compared with dynamic shear secant modulus  $G_d$  which is the ratio between dynamic shear stress and dynamic shear strain, dynamic shear tangent modulus  $G_t$  is more inclusive to soil elastic part and plastic part of soil. Soil dynamic shear tangent modulus describing soil structural properties can be understood as follows: if soil dynamic structural properties which own the dynamic shear tangent modulus  $G_t$  can be equivalently described by the dynamic shear tangent modulus  $G_{t1}$  ( $G_{t1} = G_t$ ) of elastomer, then, the soil structural property of any state has a correspondently equivalent structural property of elastomer. It is called the equivalent elastic elastomer view. Based on this view, soil dynamic structural parameters can be described by the dynamic shear tangent modulus.

## 3 SOIL DYNAMIC STRUCTURAL RESIDUAL DEGREE

The soil mechanics research through ages has revealed that the fundamental way to change or destroy soil structural properties is disturbance, loading and water immersion. Disturbance can damage the soil coupling effect, reducing the coupling strength between the soil particles; loading can change arrangement mode as well as coupling characteristics of soil particles; water immersion can make the chemicals in the soil weakened, dissolved and the suction connection lost. Water film wedging action can release the soil inherent shear shrinkage potential. In order to quantitatively describe these three external effects to soil dynamic structural properties, the paper defines a new coefficient—soil dynamic structural residual degree  $n_m$ .

For one or more external effects, the soil dynamic structural has (or not) residue in the soil after the initial soil dynamic structural changes (or destruction). The residual degree of soil dynamic

structural in the external effect is the ratio of between dynamic structural parameters (dynamic shear tangent modulus)  $G_t$  and initial soil dynamic structural parameters (initial dynamic shear tangent modulus)  $G_{t0}$ , that is:

$$n_m = G_t/G_{t0} \quad (7)$$

By formula (7) it can be seen that the value of  $n_m$  is 1-centered, changing away from 1 in two directions. Without any external effect,  $n_m = 1$ , namely, the original soil dynamic structural property is invariant; when  $n_m > 1$ , the soil dynamic structural property is strengthened under external effect, such as dehumidification; when  $n_m < 1$ , the soil dynamic structural property is weakened under external effect, such as immersion.

If the initial state of the soil is unloaded, the moisture content is  $w_0$ , and the initial dynamic structural parameter (initial dynamic shear tangent modulus) of undisturbed soil is  $G_{t0}$ , then the residual degree under different external effects is:

1. The soil dynamic structural residual degree under load

$$n_m = G_{td}/G_{t0} \quad (8)$$

where  $G_{td}$  is the dynamic structural parameter of undisturbed soil (dynamic shear tangent modulus) for moisture content  $w_0$  when the dynamic shear stress is  $\tau_d$ .

2. The soil dynamic structural residual degree in immersion (the answer of the first question in the introduction)

$$n_m = G_{tw}/G_{t0} \quad (9)$$

where  $G_{tw}$  is the dynamic structural parameter of undisturbed soil (dynamic shear tangent modulus) for water immersion to  $w$ .

3. The soil dynamic structural residual degree of disturbance (the answer of the second question in the introduction)

$$n_m = G_{td}/G_{t0} \quad (10)$$

where  $G_{td}$  is the dynamic structural parameter of soil (dynamic shear tangent modulus) for moisture content  $w_0$  after disturbance.

4. The soil dynamic structural residual degree under the coupling effect of loading and immersion

$$n_m = G_{tdw}/G_{t0} \quad (11)$$

where  $G_{tdw}$  is the dynamic structural parameter of soil (dynamic shear tangent modulus) for water immersion to  $w$  after disturbance when dynamic shear stress is  $\tau_d$ .

5. The soil dynamic structural residual degree under the coupling effect of loading and disturbance

$$n_m = G_{irzd}/G_{io} \quad (12)$$

where  $G_{irzd}$  is the dynamic structural parameter of soil (dynamic shear tangent modulus) for water immersion to  $w_0$  after disturbance when dynamic shear stress is  $\tau_d$ .

6. The soil dynamic structural residual degree under the coupling effect of water immersion and disturbance (the answer of the third question in the introduction)

$$n_m = G_{irw}/G_{io} \quad (13)$$

where  $G_{irw}$  is soil dynamic structural parameters (dynamic shear tangent modulus) for water immersion to  $w$  after disturbance.

7. The soil dynamic structural residual degree under the coupling effect of loading, water immersion and disturbance

$$n_m = G_{irzdw}/G_{io} \quad (14)$$

where  $G_{irzdw}$  is the dynamic structural parameter of soil (dynamic shear tangent modulus) for water immersion to  $w$  after disturbance when dynamic shear stress is  $\tau_d$ .

#### 4 THE EXPRESSION OF DYNAMIC STRUCTURAL RESIDUAL DEGREES BASED ON HARDIN-DRNEVICH HYPERBOLA MODEL

The curve showing the relationship between dynamic shear stress amplitude and dynamic shear strain amplitude is named backbone curve. A large number of experiments show that backbone curve under loading is hyperbolic, displaying non-linear characteristics, which can be described by Hardin-Drnevich hyperbola model (Xie, 2007), as is shown in formula 15:

$$\tau_d = \gamma_d / (a + b\gamma_d) \quad (15)$$

where  $a, b$  are test constants.

Its dynamic shear tangent modulus equation is:

$$G_t = a / (a + b\gamma_d)^2 \quad (16)$$

The initial dynamic shear tangent modulus (structural parameters for the initial state) is:

$$G_{io} = 1/a \quad (17)$$

According to equations from (8) to (14) and from (16) to (17), can obtain the expressions of soil dynamic structural residual degrees under different external effects in Table 1.

Table 1. Under different external conditions, soil dynamic structural residual degrees list.

External effect	Dynamic structural residual degrees	Expression	Note
Loading	$\frac{G_{irzd}}{G_{io}}$	$\frac{a^2}{(a + b\gamma_d)^2}$	$a, b$ are test constants of undisturbed soil based on Hardin-Drnevich hyperbola model experiment at moisture content $w_0$ .
Immersion	$\frac{G_{irw}}{G_{io}}$	$\frac{a}{a_1}$	$a_1$ is test constant of undisturbed soil based on Hardin-Drnevich hyperbola model experiment for water immersion to moisture content $w$ .
Disturbance	$\frac{G_{ir}}{G_{io}}$	$\frac{a}{a_2}$	$a_2$ is test constant of soil based on Hardin-Drnevich hyperbola model experiment for disturbance to moisture content $w_0$ .
Loading and immersion	$\frac{G_{irzd,w}}{G_{io}}$	$\frac{a_1 a}{(a_1 + b_1 \gamma_d)^2}$	$a_1, b_1$ are test constants of undisturbed soil based on Hardin-Drnevich hyperbola model experiment for loading and immersion to moisture content $w$ .
Loading and disturbance	$\frac{G_{irzd}}{G_{io}}$	$\frac{a_2 a}{(a_2 + b_2 \gamma_d)^2}$	$a_2, b_2$ are test constants of soil based on Hardin-Drnevich hyperbola model experiment for loading and disturbance to moisture content $w_0$ .
Disturbance and immersion	$\frac{G_{irw}}{G_{io}}$	$\frac{a}{a_3}$	$a_3$ is test constant of soil based on Hardin-Drnevich hyperbola model experiment for disturbance and immersion to moisture content $w$ .
Loading, disturbance and immersion	$\frac{G_{irzdw}}{G_{io}}$	$\frac{a_3 a}{(a_3 + b_3 \gamma_d)^2}$	$a_3, b_3$ are test constants of soil based on Hardin-Drnevich hyperbola model experiment for loading, disturbance and immersion to moisture content $w$ .

## 5 CONCLUSIONS

This paper analyzes substance of soil dynamic structural parameters on the basis of previous research about soil structural properties. It is deemed that soil dynamic structural changes can be reflected in loading, disturbing and water immersing. In addition, the soil dynamic structural property is its dynamic shear secant modulus in any state. It is discovered that the description of soil dynamic structural properties by using dynamic shear secant modulus is quite different from its real structural properties. The paper suggests using the dynamic structural parameters based on the view of equivalent elastomer (dynamic tangent modulus), which defines the soil dynamic structural residual degrees that reflect impact of the disturbance, load and humidification on soil structural properties. This paper also gives the expression of dynamic structural residual degrees based on Hardin—Drnevich hyperbola model in different external conditions.

## REFERENCES

- Chen, C.L., and Gao, P. (2006). "Structural and deformation characteristics of undisturbed loess." *Rock and Soil Mechanics*, china, Vol. 27, No. 11, pp. 1891–1896, DOI: 10.3969/j.issn.1000-7598.2006.11.006.
- Chen, C.L. Gao, P., and Hu, Z.Q. (2006). "Moistening deformation characteristics and its structural relationship of the loess." *Rock Mechanics and Engineering*, china, Vol. 25, No. 7, pp. 1352–1360, DOI: 10.3321/j.issn:1000-6915.2006.07.009.
- Chen, C.L. Hu, Z.Q., and Gao, P. (2006). "Structural and deformation characteristics of undisturbed loess." *Rock and Soil Mechanics*, china, Vol. 27, No.11, pp. 1891–1896, DOI: 10.3969/J. ISSN.1000-7598.2006.11.006.
- Luo, Y.S. (2003). "Variation characteristics of structural characteristics and constitutive relation of Unsaturated loess under static and dynamic conditions." Xi'an University of Technology Doctoral Dissertation, china, DOI: 10.7666/d.d013340.
- Luo, Y.S., Xie, D.Y., and Shao, S.J. (2004). "Soil structural parameters under complex stress conditions." *Rock Mechanics and Engineering*, China, Vol. 23, No. 24, pp. 4248–4251, DOI: 10.3321/j.issn: 1000-6915.2004.24.027.
- Qi, J.L. (1999). "Soil structure characteristics and study of its quantitative parameter." Xi'an University of Technology Doctoral Dissertation, China, pp. 15–20.
- Shao, S.J., Zhou, F.F., and Long, J.Y. (2004). "Study of the structural and quantitative parameters of undisturbed loess." *Chinese Journal of Geotechnical Engineering*, china, Vol. 26, No. 4, pp. 531–536., DOI: 10.3321/j.issn:1000-4548.2004.04.021.
- Wang, Z.J., Luo, Y.S. and Yang, Y.J. (2010). "Study of dynamic structural characteristics of unsaturated loess in different regions." *Rock and Soil Mechanics*, china, Vol. 31, No. 8, pp. 2461–2464, DOI: 10.3969/j.issn.1000-7598.2010.08.018.
- Xia, W.M. (2005). "Loess elasto-plastic damage constitutive model and engineering application." Xi'an University of Technology Doctoral Dissertation, China, DOI: 10.7666/d.d012984.
- Xie, D.Y., and Qi, J.L. (1999). "Soil structure characteristics and new approach in research on its quantitative parameter." *Chinese Journal of Geotechnical Engineering*, China, Vol. 21, No. 6, pp. 651–656.
- Xie, D.Y., Yao, Y.P. and Dang, N.F. (2007). "Advanced soil mechanics." Higher Education Press, Beijing, China.

# Comparison of the mechanical properties of clay rock in Tamusu region and abroad

Haian Liang

*State Key Laboratory Breeding Base of Nuclear Resources and Environment, East China Institute of Technology, Nanchang, China*  
*School of Civil Engineering, Guangzhou University, Guangzhou, China*

Yunqing Liu, Qingrui Lu, Shijun Chen & Weiwei Bian

*Architectural College, East China Institute of Technology, Nanchang, China*

**ABSTRACT:** A comparative study on the mechanical properties of clay rock in Tamusu region and abroad was carried out, by collecting relevant data and by conducting point-loading test, uniaxial tension test and rock triaxial tests. The research indicates that the mechanical strength of clay rock in Tamusu region is superior to that of clay rock from abroad. The clay rock in Tamusu region takes on the brittle deformation as a whole, and takes on plastic deformation only when subject to high temperature and large pressure. In addition, the tensile strength of clay rock in Tamusu region is similar to that of Callovo-Oxfordian rock in France, and decreases with the increasing depth. The research is intended for providing certain technical support for the site selection of high-level radioactive waste repository in China.

**Keywords:** high-level radioactive waste; deep geological repository; clay rock; mechanical properties

## 1 INTRODUCTION

High-level radioactive waste deep geological repository is considered as a type of the most complex deep underground projects being studied by the nuclear-armed countries, while the subjects on deep rock mechanical properties are becoming the research hotspots during site selection, design, construction and operation of underground laboratories and deep geological repositories of high-level waste<sup>[1]</sup>. The research at home and abroad shows that both the granite and clay rocks are suitable for the deep disposal of high-level radioactive wastes<sup>[2]</sup>. For example, Amann et al. conducted the research on the brittle behavior of deep Opalinus clay rocks in Switzerland<sup>[3-4]</sup>, and Brapi et al. investigated the fracture mechanics of the Opalinus clay rock<sup>[5]</sup>. In China, Liu Y et al. studied the basic physical mechanics and time-temperature effect of granite in Beishan area, Gansu province<sup>[6]</sup>. However, few researches on the mechanical behavior of clay rock for the site selection of deep disposal repositories have been performed in China. In view of this, a series of tests on the mechanical properties of deep clay rock in Tamusu region of Inner Mongolia Gobi have been carried out, together with comparing its mechanical behavior with that of foreign clay rock, with the aim of

providing valuable data for the research on the construction conditions of geological repositories for high-level radioactive waste.

## 2 COMPARISON ON THE BASIC BACKGROUND

The adopted clay rock in this paper was taken from the southern part of Tamusu region, Bayingobi basin of Inner Mongolia. It was formed in the Middle stage of Early Cretaceous with warm and humid climate, and the environment can be regarded as typical lakeshore delta facies. The gray clay rock that we selected was formed by the sedimentary of grey continental debris of the Lower Cretaceous Bayingobi Group, with a buried depth ranging from 550 to 650 m. The rock can be characterized mainly by horizontal bedding, and the petrographic composition is comparatively uniform, with asphalt in some local area. The formation age can be considered as 120 Ma, which is earlier than the Boom Clay of Belgium (Oligocene, 30 Ma<sup>[1,6]</sup>), as shown in [Table 1](#), and later than the Callovo-Oxfordian Clay of France (Middle Jurassic—late Jurassic, 145 Ma) and the Opalinus Clay of Switzerland (Middle Jurassic, 180 Ma). Both its formation age and buried depth



Table 1. Main characteristics of the different geological media for high-level waste from abroad<sup>[11–15]</sup>.

	Opalinus clay	Callovo-Oxfordian clay	Boom clay
Thickness (m)	80–120	135	100
Buried depth (m)	500–1000	300–600	1800
Density (g/cm <sup>3</sup> )	2.5–2.6	2.32–2.61 (2.42)	2.67
Uniaxial compression strength (MPa)	4–8	12–49 (26)	2.0–2.2
Tensile strength (MPa)	1–2	0.9–5.4 (2.6)	–
Young's modulus (MPa)	2000–3000	4000–5600 (4900)	200–400 (300)
Poisson's ratio	–	0.3	0.125
Internal friction angle (°)	23–25(24)	–	18
Formation age	Aalenian (Dogger) 180 Ma	Middle Callovian to lower Oxfordian 145 Ma	Rupelian 30 Ma

are close to that of the Callovo-Oxfordian Clay of France.

### 3 COMPARISON OF BASIC MECHANICAL PROPERTIES

The fundamental parameters of mechanical properties of clay rock such as point-loading strength, elastic modulus, Poisson's ratio, tensile strength, triaxial compression strength, internal friction angle and cohesion were determined by a series of tests. The rock samples were prepared according to the provisions of Rock Physical and Mechanical Properties Test (GB/T9966-2001) and Suggested Methods of Rock Mechanics Laboratory Tests by the International Society for Rock Mechanics.

#### 3.1 Tensile strength

Tensile strength was determined using point-loading test estimation and Brazilian tests. With the rock samples taken at the buried depth of 650 m and 555 m, respectively, the point loading strength of vertical bedding was obtained at the range of 3.52–5.49 MPa, while that of horizontal bedding ranged from 2.61 to 3.21 MPa.

It can be inferred from the point loading strength that the tensile strength of vertical bedding is about 3.3–5.3 MPa, and for horizontal bedding is about 2.1–3.1 MPa, which show little discrepancy in the two directions, and therefore the anisotropy is not clear. Meanwhile, the estimated tensile strength is distinctly smaller than the estimated compressive strength, and the discrepancy almost reaches 25 times. The estimated compressive strength is about 80–140 MPa, much larger than that of Opalinus Clay (4–8 MPa), Callovo-Oxfordian Clay (12–49 MPa) and Boom Clay (2–2.2 MPa).

Brazilian test can be used indirectly to determine the tensile strength of rock. According to their

buried depth, the rock samples were divided into 2 groups. For the sample at the depth of 641 m, the tensile strength ranges from 1.77 to 2.14 MPa, and for the sample of 627 m, the tensile strength reaches 2.05–2.62 MPa, which is shown in Table 2.

The comparison shows that the result obtained from Brazilian test is relatively smaller than the estimated value of the point loading tests; however, the tensile strength for vertical bedding of clay rock in Tamusu region is in the range of 2–3 MPa, which falls into the range of that of the Callovo-Oxfordian clay rock, and 1 time higher than that of the Opalinus clay rock (1–2 MPa). Moreover, the tensile strength gradually decreases with the increasing depth, and the varying characteristic with depth should be further studied.

#### 3.2 Triaxial compression strength

Using the microprocessor control Electro-hydraulic servo rock triaxial testing machine TAW-2000 of East China Institute of Technology, we performed a series of tests for which the radial deformation was controlled, and the testing data were recorded automatically by the computer. Due to that the nuclear waste generally releases heat during the operation of high-level geological repositories, the triaxial tests were conducted under a high temperature and high pressure. With the temperature controlled at 60°C, the confining pressures at 10 MPa, 20 MPa and 30 MPa were, respectively, fixed, and the corresponding mechanical parameters can therefore be determined as shown in Table 3. Poisson's ratio falls within the range of 0.023–0.038, which is much lower than that of the foreign clay rock, and therefore little anisotropy can be proved by the point loading tests. The elastic modulus ranges from 2800 to 3100 MPa, similar to that of Opalinus Clay, lower than that of Callovo-Oxfordian Clay, and 8–10 times higher than that of Boom Clay.

Table 2. Results of Brazilian test.

Dimension of samples						Tensile strength		
Rock type	Sample numbering	Depth/m	Forced direction	Diameter D/mm	Height H/mm	Ultimate load/kN	Single value/Mpa	Average value/Mpa
Rock clay	16-16-L1	641	Radial	49.50	25.48	3.5	1.77	2.00
	16-16-L2			49.50	25.48	4.26	2.14	
	16-16-L3			49.58	25.00	4.04	2.08	
Rock clay	8-14-L1	627	Radial	49.60	25.00	3.99	2.05	2.26
	8-14-L2			49.58	25.54	5.21	2.62	
	0-16-L1	630.5		49.58	25.62	4.19	2.10	

Table 3. Results of triaxial compression test.

Temperature	Samples numbering	Mass of samples M/g	Volume	Density	Pressure $\sigma^3$	Axial ultimate load P	Ultimate axial stress $\sigma_1$	Elastic modulus MPa	Poisson's ratio	Internal friction angle $\varphi^\circ$
60°C	32-19	178.00	449.15	2.51	10	83.75	45.69	—	—	54.72
	32-19-1	177.29	452.8	2.55	20	372.30	202.10	3100	0.038	
	36-32	178.24	435.89	2.45	30	478.05	265.06	2800	0.028	

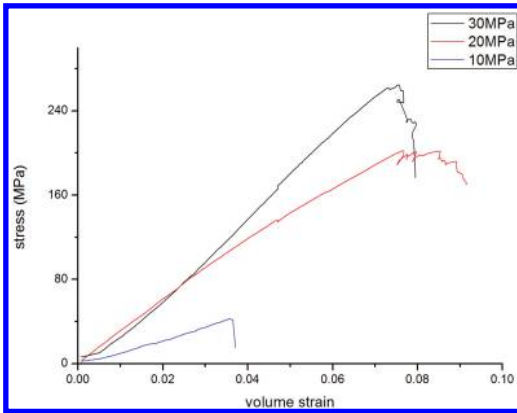


Figure 1. Stress-strain curves under different confining pressures at 60°C.

Figure 1 shows stress-strain curves under different confining pressures at 60°C. It can be inferred that the rock samples manifest distinct brittleness. Especially under the confining pressure of 10 MPa, an obvious brittle failure can be noticed. With the increasing confining pressure, the samples show brittleness at the beginning, and plastic deformation occurs in the later stage. The strain and compressive strength increases sharply when the samples break. The compressive strength of clay rock in Tamusu region,

no matter estimated from point loading test or determined by triaxial tests, is higher than that of foreign clay rock. As a result, from the mechanical point of view, the clay rock in Tamusu region can be used as the geological medium for high-level waste.

#### 4 CONCLUSIONS

By comparing the conducted tests and the foreign data, we can draw the following conclusions about the clay rock in Tamusu region: 1) the mechanical strength is superior to that of foreign clay rock as a whole; however, it shows distinct brittleness. Little discrepancy exists between horizontal and vertical beddings, and the anisotropy is not obvious; 2) the estimated compressive strength is 25 times of tensile strength, and much higher than that of foreign clay rock; 3) tensile strength is obtained as about 2 MPa, similar to that of the Callovo-Oxfordian clay from France. Tensile strength decreases with the depth, of which the varying tendency needs to be further studied; 4) the triaxial data show that the strength increases sharply with the increasing confining pressure, and plastic failure occurs in the later stage. However, because the discreteness is notable, the varying pattern of elastic modulus and Poisson's ratio with confining pressure needs to be further investigated.

## ACKNOWLEDGMENTS

This work was financially supported by the Special Scientific Found (DHBK2013103), the Scientific Found (20151BBG70004) and grants from the State Key Laboratory Breeding Base of Nuclear Resources and Environment (NRE1325).

## REFERENCES

- [1] Wang Ju, Xu Guoqing, Jin Yuanxin. On the host rock for the geological repositories of high level radioactive waste [J]. *World Nuclear Geoscience*, 2006 (04): 222–231.
- [2] Jing Lanru, Feng Xiating. Main rock mechanics issues in geological disposal of radioactive wastes [J]. *Chinese Journal of Rock Mechanics and Engineering*, 2006 (04): 833–841.
- [3] Savage D. *The Scientific and Regulatory Basis for the Geological Disposal of Radioactive Waste* [M]. Chichester: John Wiley and Sons, 1995.
- [4] Wang Ju Chen Weiming Su Rui, et al. Geological disposal of high-level radioactive waste and its key scientific issues [J]. *Chinese Journal of Rock Mechanics and Engineering*, 2006 (04): 801–812.
- [5] Zheng Hualing, Fu Bingjun, Fan Xianhua, et al. Focusing on clay formation as host media of hlv geological disposal in china [J]. *Radiation Protection*, 2007 (02): 92–98.
- [6] Wang Changxuan, Liu Xiaodong, Liu Pinghui. The general situation of clay site for high-level waste geological disposal repository [J]. *Radiation Protection*, 2008 (05): 310–316.
- [7] Li Xiangling, Bernier Frédéric, Bel Johan. The Belgian HLW Repository Design and Associated R&D on the THM [J]. *Chinese Journal of Rock Mechanics and Engineering*, 2006 (04): 681–692.
- [8] Su Kun, Lebon P. ANDRA's feasibility study on deep geological disposal of high-level long-lived radioactive waste [J]. *Chinese Journal of Rock Mechanics and Engineering*, 2006 (04): 813–824.
- [9] Jean-Louis G. French URL project context, schedule and contents [EB/OL]. WM'02 Conference, Tucson [2013-01-15]. <http://www.wmsym.org/archives/2002/Proceed-ings/59/579.pdf>.
- [10] Verstricht J, Blümling P, Merceron. Repository concepts for nuclear waste disposal in clay formations[C]//Field Measurements in Geomechanics. OSLO, Norway, 2003: 15–18.
- [11] Thury M. The characteristics of the Opalinus Clay investigated in the Mont Terri underground rock laboratory in Switzerland [J]. *Comptes Rendus Physique*, 2002, 3(78): 923–933.
- [12] Dehandschutter B, Vandycke S, Sin Tubin M, et al. Brittle fractures' and ductile shear bands in argillaceous sediments: inferences from Oligocene Boom Clay (Belgium) [J]. *Journal of Structural Geology*, 2005, 27(6): 1095–1112.
- [13] Yu Hongdan. Study on Long Term Hydro-mechanical Coupled Behavior of Belgium Boom Clay [D]. Institute of Rock and Soil Mechanics, Chinese Academy of Science, 2010.
- [14] Andra-Cea A. Dossier 2005 Argile—Tome Phenomenological evolution of a geological repository, C RPADS 04 0025 B[R], 2005.
- [15] Delage P. Clays in radioactive waste disposal [J]. *Journal of Rock Mechanics and Geotechnical Engine*, 2010 (02): 111–123.

# Study on the simulation test for Osterberg cell test of large pile foundation

Lina Xu

Jilin Jianzhu University, Changchun, China

**ABSTRACT:** This paper makes a comparative study on the methods to determine the bearing capacity of all kinds of pile foundations. Based on the study, it analyses the advantages of Osterberg cell test. Based on the field test data obtained on the Lanqi Songhua River Bridge of Jilin province, this paper applies the simulated test to simulate the Osterberg cell test, and the results show that the simulation and field measurements are highly consistent. Meanwhile, the load characteristics, including the load bearing features of pile foundation and the distribution features of displacement field of rock-soil mass around the pile, could be studied through the simulation. It can make up for a lack of field tests and laboratory tests. This illustrates that the method has certain feasibility and is of certain reference value for the future study on the bearing capacity of pile foundation.

**Keywords:** pile foundation; bearing capacity; Osterberg cell test; simulation

## 1 INTRODUCTION

At present, a large amount of pile foundations are used in key projects in China such as railway, bridge, high-rise buildings and others. Determining the bearing capacity of pile foundation in a correct and reasonable manner can enhance the economic performance on the basis of achieving a quality construction.

As the development of science and technology, the methods used to determine the bearing capacity of pile foundation are continuously improved as well. In particular, the rapid development of computer technology also drives the study on the pile foundation in simulated aspects. I. Said et al. (2009), Chen Lun et al. (2002), Wang Lijuan (2003), and Li Jin et al. (2004) conducted a study on the load transfer mechanism targeted at different types of piles by applying different numerical simulation software programs, respectively. Ottaviani (1975), Emilioms M. Comdromos et al. (2003), Panich Voottipiyex et al. (2011) carried out the study on bearing features of grouped piles. Wang Youqing et al. (2002), and Zhou Gang et al. (2010) conducted the numerical simulation study on the mechanism of action between the pile and soil.

This paper has first carried out a comparative study on the methods used to determine the bearing loads of pile foundation and analyzed the

advantages and disadvantages of these methods. Based on the field test data obtained on the Lanqi Songhua River Bridge of Jilin province, this paper applies the simulated test to simulate the Osterberg cell test, and the results show that the results of simulation and field measurements are highly consistent. Meanwhile, the load characteristics, including the load bearing features of pile foundation and the distribution features of displacement field of rock-soil mass around the pile, could be studied through the simulation. This illustrates that the method has certain feasibility and is of certain reference value for the future study on the bearing capacity of pile foundation.

## 2 STUDY ON THE METHODS TO MEASURE THE BEARING LOADS OF LARGE PILE FOUNDATION

At present, the methods used to measure the bearing loads of pile foundation mainly include single pile static load test, Osterberg cell test, dynamic test method (low strain detection method and high strain detection method), static-dynamic method, sound wave transmission method, model test method, simulation test and others. All these methods have displayed their own advantages and limitations during long term uses, as shown in [Table 1](#).

Table 1. Comparison of different methods to measure the bearing loads of all the pile foundations.

	Static load test	Osterberg cell test	Model test method	Simulation test
Advantages	The most reliable, accurate and direct method recognized internationally to determine the bearing capacity of single pile	Has avoided the problem of stacking in static load. Can directly measure the resistance of tip and side of pile; 3. Has a relatively lower requirement for the site	Being more targeted and purpose oriented during the research on the interaction of pile-soil, and conducting comparative study through changing the design parameters	Being able to simulate the complex mechanics and transformation features during the interaction of pile and soil. And the interaction process between pile and soil visually can be capable of observing through computer software
Limitations	Hard to set up the counter force device and require an open and flat site. The test piles can no longer be used as the engineering piles	Not able to carry out the random sample detection. And it is difficult to determine the correct position of loading box	It is hard to simultaneously achieve the similarity in size, physics and environment of the model	Results are affected by the selection of parameters and simulation model
			Dynamic test method	
	Static-dynamic method	Sound wave transmission method	Low strain detection method	High strain detection method
Advantages	Being low in cost, short in duration and convenient and flexible	It serves as an efficient method to inspect the internal defects of the concrete cast-in-place pile and assess its integrity, and it is not limited by the site and possesses high test accuracy	It is used to detect the integrity of pile body structure. It can be used to calculate the location of defect, distinguish the hole shrinkage from the hole enlargement, and discover the shallow defects or tiny horizontal fracture	It can have a relatively clear reflection on the deeper pile body. It can be used to detect the integrity of pile body, test the vertical compressive capacity of single pile and monitor the piling process
Limitations	Static-dynamic method is still a dynamic test method; the dynamic phenomenon still exists and a certain hypothesis is required to adjust the data; meanwhile, it also has the limitations existing in dynamic test methods	It only applies to the cast-in-place pile with the diameter of pile being 0.6–0.8 m and the sounding pipe is required to be embedded and the sampling is bad in randomness	This method is not suitable for piles such as deformed pile, pile with branches and plates, root pile, and the pile in which the resistance of pile body differs little from that of soil around the pile	It is inadvisable to be used alone in the acceptance check of engineering pile alone, and can only be used in the test pile for verification, not in test pile for design

### 3 COMPUTER SIMULATION ANALYSIS

The application of computer-based simulation technology can better simulate the features of strain and displacement changes in the process of pile-soil interaction.

#### 3.1 Overview of the Lanqi Songhua River Bridge

Jilin Lanqi Songhua River Grand Bridge is located in the Lanqi–Jiangmifeng section of Jilin ring expressway and also in the connection section of national road Chang-Hui highway and the national road Hei-Da highway; the bridge starts from Lanqi village located in the west line of Ji-Feng highway and ends at Yongqing village located in the east line of Ji-Feng highway with an overall length of 625 m, spanning the second Songhua River; the cast-in-situ bored piles are adopted for all the design foundation of the main bridge. Three piles are selected, and a self-balancing test method is adopted for static load test.

#### 3.2 Numerical calculation model

In this paper, FLAC3D is adopted to establish the numerical calculation model, and the size of the model is 30 m × 60 m × 80 m, with 9587 panel points and 8020 units in total. As the test pile belongs to an overlong and large diameter pile owing to its length of 50 m and diameter of 2 m, both the pile and rock-soil mass adopt the physical model. Besides, the rock-soil mass adopts the Mohr-Coulomb Model and the pile body adopts the Elastic Model. Laboratory test can be used to obtain the material parameters of all the soil layers, as shown in Figure 1.

#### 3.3 Load application

During the loading of Osterberg cell test on site, the estimated load value is 2 × 33000 kN and the load value of each grade is 1/11 of the limit value. In order to reflect the results of Osterberg cell test on site in the real manner, the loading procedure used in Osterberg cell test shall be adopted during simulation, and the load values of each grade are given in Table 2.

#### 3.4 Analysis of simulation results

##### 3.4.1 Comparison of numerical simulation and Osterberg cell test

Figure 2 shows the relations between loads and the displacement.

As shown in Figure 2, the results obtained from the numerical simulation are rather identical with that measured actually on site, and the change

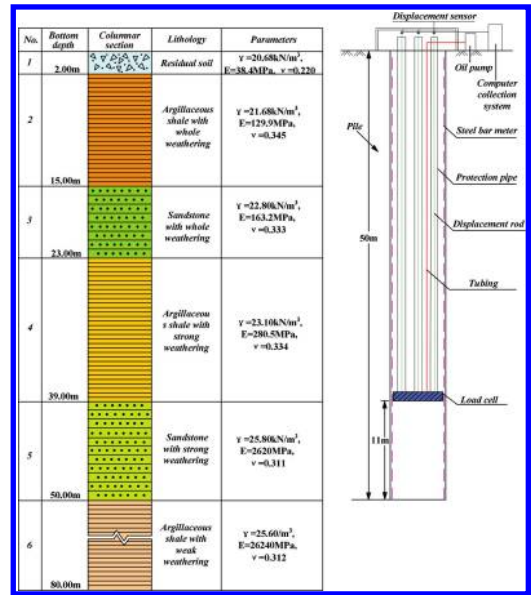


Figure 1. Engineering geologic columnar profile and pile foundation self-balancing loading system.

Table 2. Grading of estimated load value.

Series of loading	Load value (kN)
1	6000
2	9000
3	12000
4	15000
5	18000
6	21000
7	24000
8	27000
9	30000
10	33000

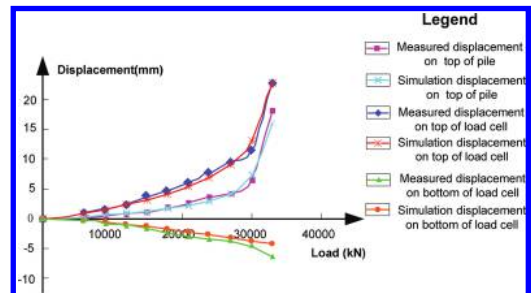


Figure 2. Curve graph showing the relations between loads and displacement.

rules are consistent. As the loads are exerted, all displacements increase accordingly. The displacement of the upper segment of the pile is larger than that of the lower segment of the pile, which shows that the side friction on the upper section of the pile body plays a better role than that on the lower section. When the load reaches 33000 kN, the upward displacement of the upper segment of the pile increases dramatically, which shows that the side friction on the upper segment of the pile plays to its limit. In the process of numerical simulation, when the load of the last grade is exerted, the displacement of the upper segment of the pile increases continuously and the calculation is hard to be converged, and this can be explained by the fact that the ultimate bearing capacity is approached at this moment. The displacement of the lower segment of the pile is relatively smaller due to the combined action of the side friction of the pile and the resistance on the tip of the pile and always shows a linear variation.

### 3.4.2 Study on transmission rules of loads

#### 1. Distribution features of the axial force of the pile body

Figure 3 shows the distribution rules of axial forces of the pile body at different elevations under the effect of loads of all levels. From the figure, it can be seen that the results obtained from the numerical simulation has the same

variation trend as that measured in the Osterberg cell test. When being exerted by the same load, the maximum axial force of the pile body is generated at the load cell, and if the upper segment of the pile is affected by the side friction, the axial force decreases gradually and the axial force on top of the pile reaches the minimum. As for the upper segment of the pile, the axial force of the pile body decreases more rapidly along with the increase of loads. This is because the side resistance of the pile will increase as well along with the increase of loads.

#### 2. Distribution features of displacement field of geotechnical body around the pile

As the loads are exerted, the displacement of the upper segment of the pile and that of the lower segment of the pile increase continuously and the geotechnical body around the pile also brings about the displacement accordingly. Figure 4 shows the contour maps showing the displacement fields of geotechnical body around the pile when the loads 6000 kN and 15000 kN are exerted, respectively. It can be seen from it that the geotechnical body around the upper segment of the pile brings about the upward displacement, which decreases gradually from the top of the load cell to the ground surface and the side friction also plays its role gradually from the loading box to the top of

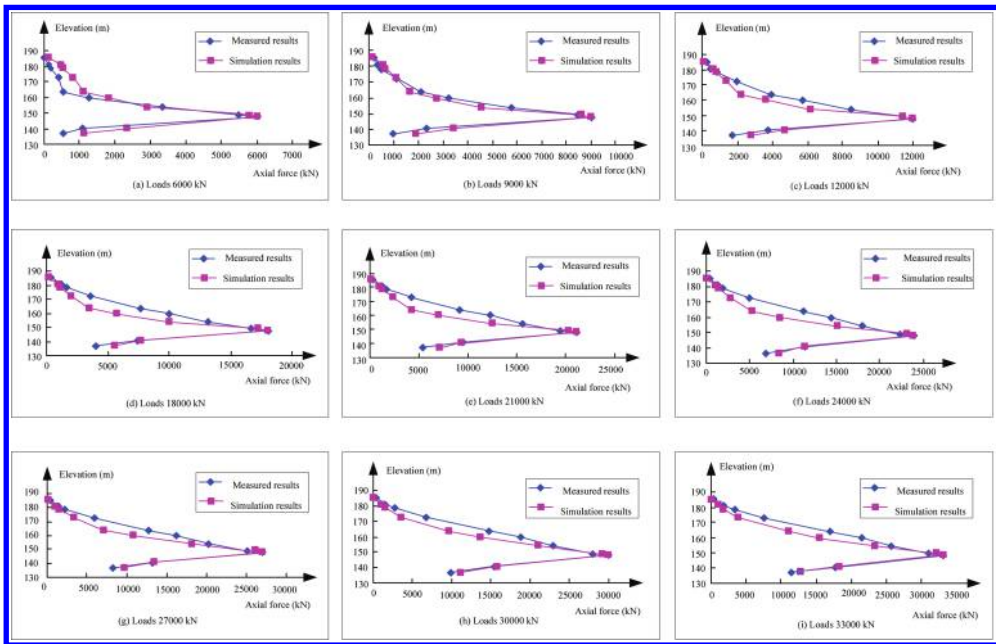


Figure 3. Distribution rules of axial forces of pile body.

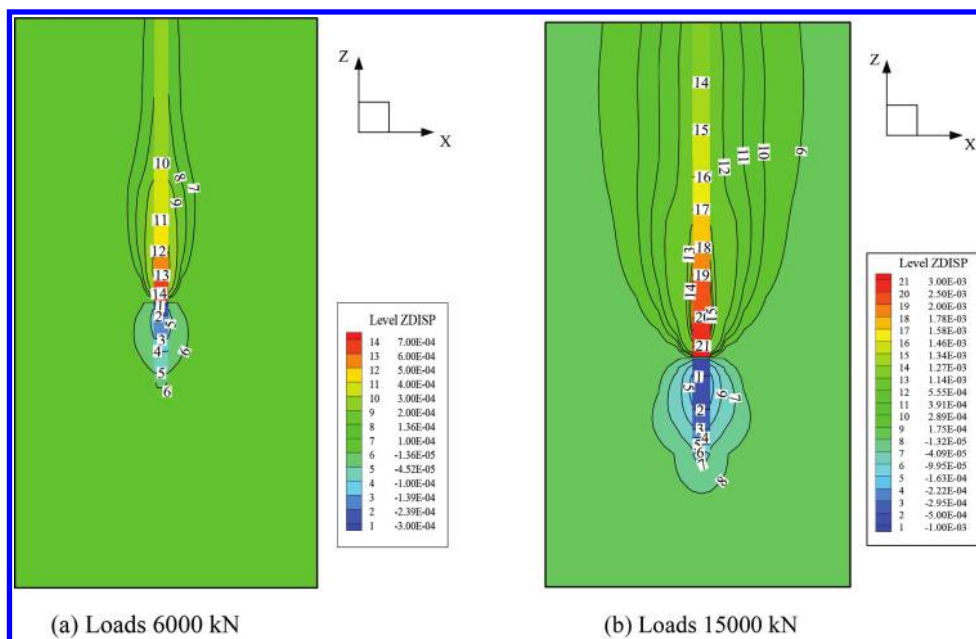


Figure 4. Contour map showing the distribution of displacement field of rock-soil mass around the pile under the action of different loads (Unit: m).

the pile. As the loads exerted increase, the displacement of the geotechnical body around the pile will be brought about in larger areas. This is because as the side friction of the pile plays its role gradually, the friction exerted on the geotechnical body that is on the lateral side of the pile increases gradually as well. In this way, the upward displacement of the soil increases, which affects even larger areas as well. The geotechnical body around the lower segment of the pile brings about the upward displacement which decreases gradually from the bottom of the load cell to the bottom of the pile. The numerical simulation analysis can be used to observe variation rules and distribution features of displacement of rock-soil mass around the pile. It is extremely necessary to understand the distribution features of the displacement field of geotechnical body mass around the pile in the intensive study of interactions between the load transmission mechanism and pile-soil in the Osterberg cell test method.

#### 4 CONCLUSIONS

This paper has carried out a study on the bearing features of pile foundation through numerical simulation and the following conclusions can be drawn:

1. Through the comparative study on all kinds of test methods used to determine the bearing capacity of pile foundation, the advantages and shortcomings of the various test methods have been summarized and the back analysis based simulation test method used to determine the bearing capacity of pile foundation has been put forward.
2. Through the numerical simulation test, the bearing features of pile foundation can be better simulated, including the relations between displacement and loads, the distribution features of axial force of pile body and others. Besides, the test can help to visually observe the distribution features of displacement field of rock-soil mass around the pile, which cannot be achieved by using the field test and the laboratory test.

#### REFERENCES

Emilios M. Comodromos, Christos T. Anagnostopoulos, Michael K. Georgiadis. Numerical assessment of axial pile group response based on load test. *Computers and Geotechnics*, 2003, 30:505–515.

Gang Zhou, San-zhen Liu, Huai-ren Pu, Xiao-jun NING. Analysis on internal force of pile foundation with finite-boundary element method considering the interaction of pile and soil[J]. *Journal of Kunming University of School and Technology (Science and Technology)*, 2010, 5:113–116.



- Jin Li, Zhong-ju Feng, Yong-li XIE. Numerical simulation of large diameter hollow pile bearing performance[J]. *Journal of Chang'an University (Natural Science Edition)*, 2004, 24(4):37–39.
- Li-juan Wang. 3-D FEA of effect of pushing against soil of driven piles[D]. School of Civil Engineering, Tianjin University, 2003.
- Lun Chen, Dong-dong Chang, Guang-xin Li. Finite element analysis of bearing capacity of a single DX pile[J]. *Engineering Mechanics*, 2002, 19(6):67–72.
- Ottaviani, M. Three dimensional finite element analysis of vertically loaded pile groups, *Geotechnique*, 1975, 25(2):159–174.
- Panich Voottipruex, Taweephong Suksawat, D.T. Bergado, Pitthaya Jamsawang. Numerical simulations and parametric study of SDCM and DCM piles under full scale axial and lateral loads. *Computers and Geotechnics*, 2011, 38:318–329.
- Said I., V. De Gennaro, R. Frank. Axisymmetric finite element analysis of pile loading tests. *Computers and Geotechnics*, 2009, 36:6–19.
- You-qing Wang, Ke-xu Zhang. Behavior of single pile foundation under vertical load[J]. *Journal of Harbin Institute of Technology*, 2002, 34 (5):667–669.

# Numerical analysis of settlement of the soft clay foundation

Xiaocheng Jiang

Henan Electric Power Survey and Design Institute, Zhengzhou, China

Yongquan Li

College of Civil Engineering and Architecture, Henan University of Technology, Zhengzhou, China

**ABSTRACT:** The Modified Cam-clay Model and the Drucker-Prager Creep Model are deduced and dealt with in detail. The two model are applied to the finite element calculation of soft foundation treatment of a dam. It shows that the results calculated are similar and close to the monitoring data with those two models. By comparison, it can be got that the displacement calculated by the Drucker-Prager Creep Model is closer to monitoring data than that calculated by the Modified Cam-clay Model. It demonstrates the reasonableness and efficiency of the viscoelasto-plastic model.

**Keywords:** soft clay; Modified Cam-clay model; Drucker-Prager creep model; finite element

## 1 INTRODUCTION

Soil has various properties, including elastoplasticity, dilatation, shear contraction, stickiness and so on<sup>[1-2]</sup>. At present, a lot of constitutive models have been developed, but they have their own merits, defects and application limits. Rheology is one obvious and important mechanical property of soft soil, so it must be taken into account when it comes to engineering in soft soil.

Based on Drucker-Prager creep model, this paper deals with the improvement of it in consideration of Rheology<sup>[3-4]</sup>, by which the displacement of soft soil is calculated and compared to that calculated by general modified Cam-Clay model. In addition, the method of transferring to equivalent sand wall is introduced when soft soil is treated by plastic drainage plate.

## 2 MODIFIED CAM-CLAY MODEL

The Cam-clay model proposed by ROSCOE et al is the first critical-state model for describe clay soil. ROSCOE and BURLAND amend the shape of the yield curve and obtained the modified Cam-clay model. The Modified Cam-clay model is based on few parameters which can be obtained from conventional laboratory tests. Since then the Modified Cam-clay model is widely referenced and has now been widely used in solving boundary value problems in geotechnical engineering practice.

The yield function formula of the Cam-clay model can be expressed:

$$f(\sigma) = p \left( 1 + \frac{\eta^2}{M^2} \right) - p_0 = 0 \quad (1)$$

In above formula,  $\eta = q/p$ ,  $p$ ,  $q$  are respectively the average stress and the shear stress which can be expressed below.

$$p = \frac{1}{3}(\sigma_z + 2\sigma_x) \quad (2)$$

$$q = \sqrt{(\sigma_x - \sigma_z)^2 + 3\tau_{xz}^2} \quad (3)$$

$M$  is the stress ratio which equals  $\eta$  when soil failure happens.  $M$  can be calculated by below expression.

$$M = \frac{6 \sin \phi'}{3 - \sin \phi'} \quad (4)$$

When only volume is considered, the total volumetric strain increment includes two parts.

$$\Delta \varepsilon_v = \Delta \varepsilon_v^e + \Delta \varepsilon_v^p \quad (5)$$

Plastic volumetric strain increment can be described:

$$\Delta \varepsilon_v^p = A \frac{\partial f}{\partial p} \Delta p_0 \quad (6)$$

$A$  is plastic parameter. Plastic volumetric strain increment can be got from  $\varepsilon_v - \ln p$  curve:

$$\Delta \varepsilon_v^p = (\lambda - \kappa) \ln \frac{p_0}{p_i} \quad (7)$$

where  $p_i$  is the initial stress. The plastic parameter  $A$  can be concluded:

$$A = \frac{\lambda - \kappa}{p_0 \frac{\partial f}{\partial p}} \quad (8)$$

where  $\lambda$  and  $\kappa$  are respectively Volume compression index and Volume rebound index.

$$\varepsilon_v^e = \kappa \ln \frac{p_0}{p_i} \quad (9)$$

Volume rebound modulus  $M_v$  can be expressed by:

$$M_v = \frac{3\Delta p_0}{\Delta \varepsilon_v^e} = \frac{3p_0}{\kappa} \quad (10)$$

Through associated flow rule, elastic-plastic matrix can be got by:

$$[D]_{ep} = [D] - \frac{[D] \left\{ \frac{\partial f}{\partial \sigma} \right\} \left\{ \frac{\partial f}{\partial \sigma} \right\}^T [D]}{\frac{1}{A} + \left\{ \frac{\partial f}{\partial \sigma} \right\}^T [D] \left\{ \frac{\partial f}{\partial \sigma} \right\}} \quad (11)$$

where

$$\left\{ \frac{\partial f}{\partial \sigma} \right\} = \begin{Bmatrix} \frac{\partial f}{\partial \sigma_x} \\ \frac{\partial f}{\partial \sigma_z} \\ \frac{\partial f}{\partial \tau_{xz}} \end{Bmatrix} = \begin{Bmatrix} \frac{2}{3} \left[ 1 + \frac{6p(\sigma_x - \sigma_z) - q^2}{M^2 p^2} \right] \\ \frac{1}{3} \left[ 1 + \frac{6p(\sigma_z - \sigma_x) - q^2}{M^2 p^2} \right] \\ \frac{6\tau_{xz}}{M^2 p} \end{Bmatrix} \quad (12)$$

$1/A$  can be calculated by:

$$\frac{1}{A} = \frac{1}{\lambda - \kappa} \left[ p \left( 1 + \frac{\eta^2}{M^2} \right) \left( 1 + \frac{2p(\sigma_x - \sigma_z) - q^2}{M^2 p^2} \right) \right] \quad (13)$$

### 3 DRUCKER-PRAGER CREEP MODEL

Drucker-Prager creep model implies that the Drucker-Prager plasticity model uses isotropic

linear elasticity, a hyperbolic plastic flow potential, and the linear Drucker-Prager yield surface with a circular yield surface in the deviatoric plane ( $K = 1$ ). The creep laws for the Drucker-Prager creep models are written in terms of an equivalent creep stress, which is a measure of the creep "intensity" of the state of stress at a material point. The definition of depends upon the type of hardening (compression, tension, or shear) used with the linear Drucker-Prager plasticity model, but in all cases  $\bar{\sigma}^{cr} = \bar{\sigma}^{cr}(q, p, \beta)$ :

$$\bar{\sigma}^{cr} = \frac{(q - p \tan \beta)}{(1 - (1/3) \tan \beta)} \quad (\text{compression}) \quad (14)$$

$$= \frac{(q - p \tan \beta)}{(1 + (1/3) \tan \beta)} \quad (\text{tension}) \quad (15)$$

$$= (q - p \tan \beta) \quad (\text{shear}) \quad (16)$$

There is a cone in the meridional plane in which no creep deformation will occur. The default creep laws provided are simple and are intended to model these condary creep of the material. Use this creep law when the stress in the material remains essentially constant:

$$\dot{\bar{\varepsilon}}^{cr} = A (\bar{\sigma}^{cr})^n t^m \quad (17)$$

Use this creep law when the stress in the material varies during the analysis:

$$\dot{\bar{\varepsilon}}^{cr} = \left( A (\bar{\sigma}^{cr})^n \left[ (m+1) \bar{\varepsilon}^{cr} \right]^m \right)^{\frac{1}{m+1}} \quad (18)$$

Use this creep law when an exponential relationship between stress and creep strain rate is needed:

$$\dot{\bar{\varepsilon}}^{cr} = A e^{(\alpha \bar{\sigma}^{cr})} (t/t)^m \quad (19)$$

The Drucker-Prager creep model uses a hyperbolic creep flow potential that ensures the creep (deformation) flow direction is always defined uniquely:

$$G^{cr} = \sqrt{(\varepsilon \bar{\sigma}|_0 \tan \Psi)^2 + q^2} - p \tan \Psi \quad (20)$$

### 4 ENGINEERING APPLICATION

A soil dam is built above a recently sedimentary silt of a lake base, with a depth of 8–10 m, underlying by a 8 m depth of clayey loam and base rock.

The physical and mechanical properties of the foundation soil are shown in Table 1 and Table 2. The width of the dam base is 44 m, the ratio of the slope is 1:2, the thickness of filling soil is 10 m, and the period of operation is 180 d. The plastic drainage plate method is applied to consolidate

Table 1. Parameters of Cam-clay model.

Material	Filling (silty clay)	Soft clay
$\gamma_d$ (KN/m <sup>3</sup> )	18.5	17.5
$v$ (°)	0.29	0.29
$\kappa$	0.007	0.012
$\lambda$	0.06	0.05
$M$	1.3	1.32
$e$	0.8	0.9
$k_z$ (m/s)	$5.8 \times 10^{-9}$	$3.4 \times 10^{-9}$
$k_r$ (m/s)	$6.7 \times 10^{-9}$	$4.9 \times 10^{-9}$

Table 2. Parameters of Drucker-Prager creep model.

Material	Filling (silty clay)	Soft clay
$\varphi$ (°)	28.6	8.5
$m$	7.8	7.5
$n$	10.5	3.5
$k_z$ (m/s)	$5.8 \times 10^{-9}$	$3.4 \times 10^{-9}$
$k_r$ (m/s)	$6.7 \times 10^{-9}$	$4.9 \times 10^{-9}$

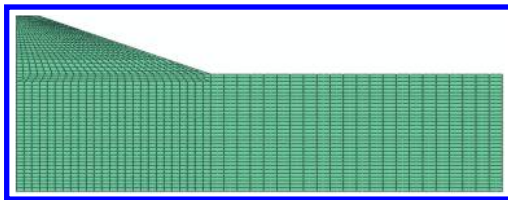


Figure 1. Finite element mesh for the dam.

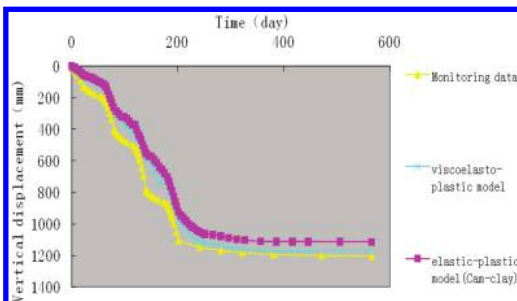


Figure 2. Relationship between vertical displacement and time at the centre of the dam.

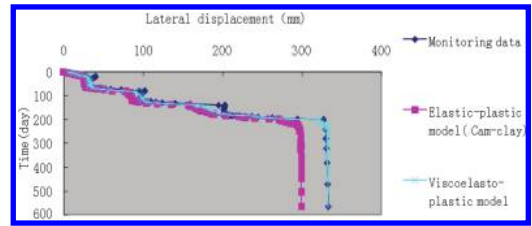


Figure 3. Relationship between horizontal displacement and time at the toe of the dam.

the foundation. First, a cofferdam was constructed and fluidized silt discharged by mud pump. Then a layer of 1 m silt clay was laid to enhance the strength of the ground to enable the movement of the plastic plate plugging machine. A cushion layer of 50 cm medium to coarse sand was laid over the silt clay as the path of horizontal drainage. The distribution of the plastic drainage plate is club, with an interval of 1.5 m. The plate is placed about 0.5 m in the mild clay.

## 5 CONCLUSIONS

The Modified Cam-clay model and the Drucker-Prager creep model are applied in the 2 dimension finite element calculation respectively. FE mesh of the dam is showed in Figure 1. Then the results of surface settlement at the center of the soil dam and displacement of slop toe are compared with field monitoring data, shown in Figure 2 and Figure 3. The conclusion can be drawn that the results calculated are similar and close to the monitoring data with those two models. Thus those two models are also suited to soft soil. In addition, the results also show that the results calculated with the Drucker-Prager creep model are closer to the monitoring data.

## REFERENCES

- [1] Zongze Yin. One double yield surface constitutive model of soil [J]. Chinese Journal of Geotechnical Engineering, 1988, 10(1): 64–71, in Chinese.
- [2] Xiaoping Chen, Shiwei Bai. Research on creep-consolidation characteristics and calculating model of soft soil [J]. Chinese Journal of Rock Mechanics and Engineering, 2003, 22(5): 728–734, in Chinese.
- [3] Zhiwan Yu, Weibing Zhao, Ji Gu. 3-D FEM Analysis of Soft Viscoelastic/Viscoplastic Foundation with Drainage Preloading [J]. Journal of Hohai University, 1995, 23(5): 1–7, in Chinese.
- [4] Indraratna B, etc. Performance of embankment stabilized with vertical drains on soft clay [J]. JGE, ASCE, 1994, (2): 257–273.

# Numerical analysis of bearing capacity of single pile under axial loading

Xianfeng Zhang

Henan Electric Power Survey and Design Institute, Zhengzhou, China

Yongquan Li

College of Civil Engineering and Architecture, Henan University of Technology, Zhengzhou, China

**ABSTRACT:** A finite element model has been developed to simulate single pile under axial loading via Drucker-Prager model. Pile-soil interaction is analyzed by Mohr-Coulomb formula. Based on the results of the analysis, the bearing capacity of single pile and the scope of plastic zone can be got. Those results gained by numerical method may provide reference to pile engineering practice.

**Keywords:** soil-pile interaction; axial loading; Drucker-Prager; finite element

## 1 INTRODUCTION

Soil-pile interaction is an important topic in the development of a performance based design procedure. With the rapid advances of computing technology, finite element analysis is assuming more important role in engineering practice. The advantage of finite element analysis lies in its ability to accommodate complex soil stratigraphy and its potential for solving three-dimensional soil-structure interaction problems. However, to be successfully used in practical design, the soil model should be simple and can be easily calibrated by conventional field or lab testing. On the other hand, the model should be able to realistically capture the most important aspects of soil-structure nonlinearities. Since it was first introduced, Drucker-Prager type model has been successfully adopted in analysis of geomaterials due to its relative simplicity<sup>[1-2]</sup>. For example, a comprehensive nonlinear finite element analysis of vertically loaded pile was carried out using ABAQUS TM. In this study, the surrounding soil was modeled using extended Drucker-Prager plasticity while the piles were modeled as linearly elastic material. Yang and Jeremi used non-associative Drucker-Prager for cohesionless soil and von Mises criterion for cohesive soil, and developed p-y curves for laterally loaded piles in multi-layered soil profiles<sup>[3-4]</sup>. Although these previous analyses dealt with pile-soil interaction with various degrees of success, detailed information on model assumptions and uncertainties associated with model selection are not available. In the following sections, we describe a parametric study of the various factors associated with simple model simulation.

## 2 MODEL FORMULATION

Pressure-sensitive failure mechanism of soil is represented by a cone-shape yield surface:

$$F = \alpha I_1 + \sqrt{J_2} - Y = 0 \quad (1)$$

where  $I_1$  is the first invariant of stress tensor and  $J_2 = (1/2)S_{ij}S_{ij}$  is the second invariant of deviatoric stress tensor  $S_{ij} = \sigma_{ij} - (1/3)I_1\delta_{ij}$ .  $\alpha$  and  $Y$  are material parameters related to the soil friction angle and the cohesion.

For small strain formulation, strain rate is usually additively decomposed into elastic and plastic components,

$$\dot{\epsilon}_{ij} = \dot{\epsilon}_{ij}^e + \dot{\epsilon}_{ij}^p \quad (2)$$

such that rate form of stress-strain relation can be written as

$$\dot{\sigma}_{ij} = C_{ijkl}(\dot{\epsilon}_{kl}^e - \dot{\epsilon}_{kl}^p) \quad (3)$$

To better describe volumetric behavior of soil, non-associative flow rule is usually adopted. The plastic flow is defined through potential surface  $Q$  with parameter  $\beta$  controlling soil dilatancy,

$$Q = \beta I_1 + \sqrt{J_2} - Y \quad (4)$$

Plastic strain rate is defined normal to the potential surface via

$$\dot{\epsilon}_{ij}^p = \lambda \frac{\partial Q}{\partial \sigma_{ij}} = \lambda \left( \frac{s_{ij}}{2\sqrt{J_2}} + \frac{1}{3}\beta\delta_{ij} \right) \quad (5)$$

where  $\lambda$  is plastic multiplier and can be determined by consistency condition.

### 3 PILE-SOIL INTERACTION

An extended version of the classical isotropic Coulomb friction model is provided in Abaqus for use with all contact analysis. The extensions include an additional limit on the allowable shear stress, anisotropy, and the definition of a “secant” friction coefficient. A special case of friction in Abaqus/Standard is so-called rough friction, where it is assumed that there is no bound on the shear stress; that is, no relative motion can occur as long as the surfaces are in contact. Rough friction is implemented with the Lagrange multiplier method.

In Abaqus/Explicit the relative motion in the absence of slip is always equal to zero if the kinematic contact algorithm is used with hard tangential surface behavior; at the end of each increment the positions of the nodes on the contact surfaces are adjusted so that the relative motion is zero. With the penalty contact algorithm in Abaqus/Explicit the relative motion in the absence of slip is equal to the friction force divided by the penalty stiffness.

Pile-Soil interaction is stimulated by Mohr-Coulomb formula.

$$\tau_{lim} = \mu \cdot P + b, \quad |\tau| \leq \tau_{lim} \quad (6)$$

where:  $\tau_{lim}$ —critical sliding shear stress;  
 $\tau$ —equivalent shear stress;  
 $\mu$ —friction coefficient;  
 $P$ —contact normal stress;  
 $b$ —contact cohesion.

### 4 ENGINEERING APPLICATION

To demonstrate the capacity of Drucker-Prager model prediction, consider a 0.75 meter circular concrete pier installed to 20 meter of depth in sand. The pile is vertically loaded on its top under drained condition. A finite element model was developed to simulate the pile behavior. Due to axisymmetry of this problem, only one quarter of the cross section is meshed using axisymmetric bilinear element. The mesh, shown in Figure 1. The base of the mesh is fixed and only vertical movement is allowed along right hand side of the mesh and the axis of symmetry (the left hand side of the mesh). The pile is modeled with linearly elastic elements with a Young’s modulus  $E_p = 20\ 106\ \text{kPa}$  and Poisson’s ratio  $\nu_p = 0.1$ . Elastic parameter and density are defined and for soil by elastic, density and Mohr coulomb. Where  $c = 45\ \text{kPa}$  and friction and dilation angle are equal to zero. After assigning sections and meshing each

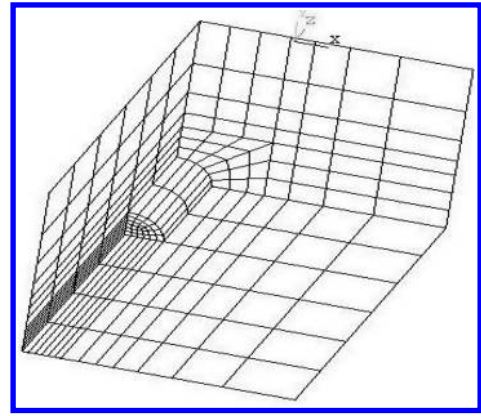


Figure 1. Finite element mesh.

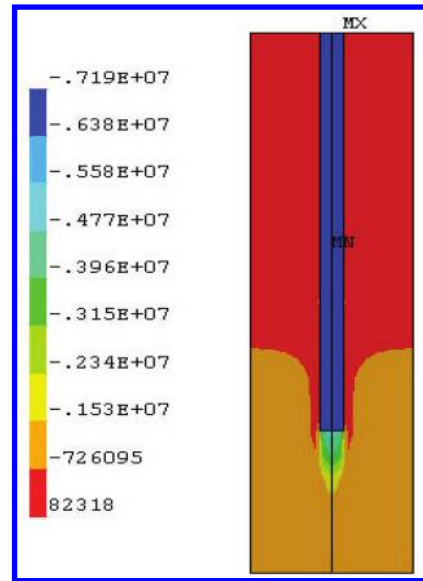


Figure 2. Diagram of the vertical stress ( $S_2$ ).

part, two parts are assembled together and an interface is created between pipe and soil. Tangential and normal behavior is used for interface. And friction coefficient is 0.6. There is an initial step where the boundary conditions are defined and then a geostatic step where the gravity load is applied to whole model. the pile is constrained in the three direction ( $U1 = U2 = U3 = 0$ ) at the Geostatic step and then release it in the next step. Analysis is separated in three different steps. Step 1: Geostatic. In this step, we consider only the soil element and deactivated the pipe element as mentioned above. Step 2: Static, General. In this step you can activate the interface between pipe and soil by released the pipe. Step 3: Static, General. In this step, you

can perform loading, displacement. etc. dam shell is 21.7 cm. When the slaking deformation is considered, the uplift move diminishes manifestly, and the maximal value is only 13.4 m, which obviously contains the weakening impact caused by the slaking deformation.

When single pile is loaded by 1400 KN, from Figure 2, the stress of piles and soils decreases gradually with the increase of depth, which is in accordance with the general Soil-pile interaction law. From Figure 3, Figure 4, and Figure 5, it can be seen that the pile end soil is effected in vertical 6D depth and in radial 2D depth. Besides, Plastic zone  $r_p = 1.44$  can be seen. For the soil is not damaged, the bearing capacity of single pile is approximately 1400 KN.

In general, pile end resistance give full play which need large displacement. Pile end cone angle

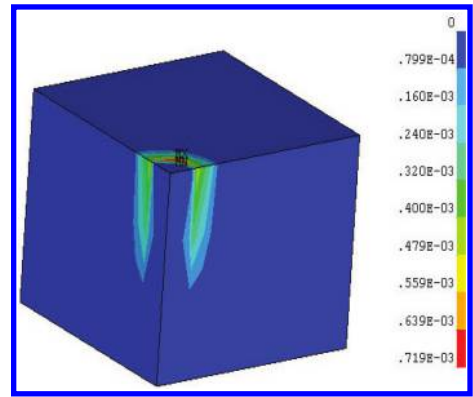


Figure 5. Diagram of plastic zone for pile end.

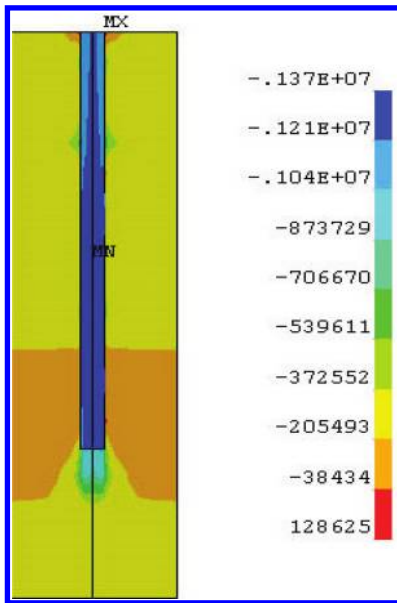


Figure 3. Diagram of the radial stress ( $S_x$ ).

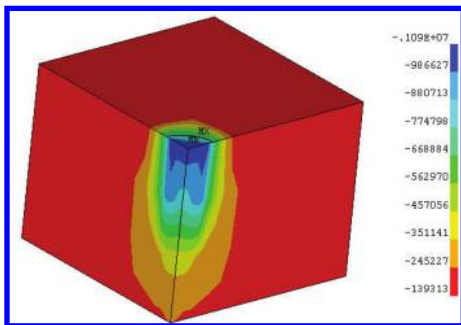


Figure 4. The vertical displacement contour after completing the dam construction (m).

is smaller, pile end resistance need greater displacement value to give play. This shows that the pile end cone angle is smaller, the pile tip penetration is more conducive, the radial displacement of pile end soil is smaller, namely the region of influence is smaller on pile end bearing layer; The load transmission process can be divided into the following four stages of of pile under step loading process: ① Pile side friction playing ② Pile side friction and end resistance of the pile sharing ③ pile end resistance bearing ④ Pile bearing stratum plastic state is reached or the pile structure damage.

## 5 CONCLUSIONS

Drucker-Prager type plastic model has been developed to simulate vertically loaded pile response in cohesionless soil. Pile-soil interaction is analyzed by Mohr-Coulomb formula. Based on the results of the analysis, the bearing capacity of single pile and the scope of plastic zone can be got. Those results gained by numerical method may provide reference to pile engineering practice.

## REFERENCES

- [1] Trochanis, A.M., Bielak, J., and Christiano, P. (1991). "Three-dimensional Nonlinear Study of Piles", *ASCE Journal of Geotechnical Engineering*, 117(3), 429-447.
- [2] Simo, J.C. and Hughes, T.J.R. (1997). *Computational Inelasticity. Interdisciplinary Applied Mathematics Vol. 7*, Springer.
- [3] Yang, Z and Jeremi, B. (2002). "Numerical analysis of pile behavior under lateral loads in layered elastic-plastic soils", *Int. J. Num. Anal. Geomech.*, 26(14), 1385-1406.
- [4] Pereira J.H.F., Fredlund D.G. Volume change behavior of collapsible compacted gneiss soil [J]. *Journal of Geotechnical and Geoenvironmental Engineering*, 2000, 126(10): 907-916.

# Analysis of dynamic responses of loess slope by compaction loads

Zhijie Sun, Jianbin Zhao & Lishan Dong

*Key Laboratory of Highway Construction and Maintenance Technology in Loess Region,  
Ministry of Transport, P.R. China*

*Shanxi Key Laboratory of Highway Construction and Maintenance Technology in Loess Region,  
Shanxi Transportation Research Institute, Taiyuan, China*

**ABSTRACT:** Through the project example, the finite element software GTS was used to simulate change rules of dynamic properties and dynamic response of expressway loess slopes on compaction loads. The results showed that the amplitude of the dynamic response for loess slopes in dynamic compaction fades out rapidly with the impact loading effect, and the amplitude of the horizontal dynamic response and the amplitude vertical dynamic response take place at the same time. The slope has an amplification effect on the horizontal dynamic response, and the amplification effect increases with the increase in the height of slope. The amplification phenomenon of amplitude vibration in the upper and central parts of the slope surface is obvious compared with the internal part of the slope. In conclusion, the dynamic response amplitude fades out with the depth increasing, the horizontal dynamic response amplitude decays faster than the vertical dynamic response amplitude, the decay rate decreases with the increase in the height of slope.

**Keywords:** compaction; soil slope; dynamic performance; acceleration; displacement

## 1 INTRODUCTION

The construction of dynamic compaction will produce a larger vibration shock wave, which will bring certain harm on the construction site and nearby buildings. The commonly used “Blasting Safety Regulations” [6] evaluate the dynamic environment caused by dynamic compaction, and then determine the safe construction distance. It will draw different conclusions according to the energy of dynamic compaction, shape of hammer, site conditions and the shape of adjacent structures, which different engineering projects need to be determined individually according to the corresponding conditions. In recent years, scholars at home and abroad conducted a series of research work for the compaction of the adjacent building by dynamic compaction, and proposed the safety distance of vibration and formula of vibration attenuation [7–12].

But the study on the construction of loess engineering on the condition of dynamic compaction, especially the dynamic response problem of the adjacent slope, is scarce.

Therefore, the numerical simulation was used to simulate the dynamic response on the condition of the dynamic compaction in this paper, and the rules of dynamic parameters such as acceleration, velocity and displacement were studied, so as to provide instructive reference for

the engineering design and construction in loess regions.

## 2 PROJECT OVERVIEW

Taking the natural loess slopes in the Xiangnnng area as the investigation object, focusing on the survey and statistics of loess slope height around 20 M, as shown in [Figure 1](#), with its lithology being loess  $Q_3$ , the slope can be approximated as linear, undisturbed loess of different parts in slope, which were considered to perform an indoor physical mechanics parameter test.



Figure 1. Loess slope.



### 3 COMPUTATIONAL MODEL

The dynamic model of the slope focuses on the simulations of boundary conditions. Under the condition of static analysis, boundary conditions of the infinite soil model can be established to some extent; however, for dynamic analysis, the general boundary conditions, which are the same as the static boundary conditions, can cause large errors due to the wave of reflection. So, in order to resolve this issue, we used the viscous boundary condition proposed in 1972 by Lysmer and Wass (Viscous Boundary). The finite element model is shown in Figure 2.

The material used in the model was the loess soil of the Xiangning section in the Jixian-Hejin expressway. The loess soil is mainly Q3 loess, and the mechanical properties are according to indoor physical tests. The physical and mechanical indices of the average value are listed in Table 1.

In the single-point tamping energy 600 kN·m model, the tamping load is simulated to the node dynamic load, and the compaction process is simulated to the dynamic load function by time history.

For the dynamic response law analysis of the slope in different parts and at different soil depths, the profile is set, as shown in Figure 4, and the feature points on the slope are used to research on the dynamic characteristics under compaction



Figure 2. Dynamic finite element model.

Table 1. Basic model calculation parameters.

Type	Elastic modulus/MPa	Poisson's ratio	Cohesion/kPa	Friction angle/°
Soil	150	0.3	91.81	35.24

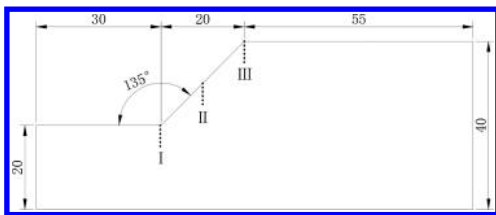


Figure 3. Slope size and test section (unit: m).

load disturbances. The slope geometry and monitoring sections are shown in Figure 3.

### 4 DYNAMIC ANALYSIS RESULTS

In order to study the dynamic response of loess slope caused by compaction vibration, and to investigate on the dynamic responses of the surface of the slope and different positions inside the slope and slope into different positions, the analysis of the loess slope stability on the dynamic compaction effect is carried out. The analysis focuses on acceleration, velocity and displacement, monitoring sites, mainly including the top, middle and toe of the slope, surface and below about 10 m depth of the slope.

#### 4.1 Typical waveforms

To reveal the effect of the tamping load on the slope, we select the monitoring section II with H/2 height of the slope. Extraction of the acceleration, velocity and displacement time history curves in horizontal and vertical directions is performed. The curves are shown in Figure 4.

In Figure 4, the vibration variation of monitoring point in the middle of the slope is that the acceleration, velocity and displacement of both horizontal and vertical directions occurs with compaction load and rapid decay with the disappearance of compaction load. In a period ( $T = 0.1$  s) of compaction load, the horizontal dynamic response and vertical dynamic response occur in the same time.

Due to the impact load applied to the vertical direction, the vertical dynamic amplitude is larger than the horizontal dynamic amplitude. The vertical acceleration amplitude of the monitoring point is  $0.4 \text{ m/s}^2$ , and the horizontal acceleration amplitude of the monitoring point is  $0.26 \text{ m/s}^2$ . The vertical velocity amplitude of the monitoring point is  $0.75 \text{ mm/s}$ , and the horizontal velocity amplitude of the monitoring point is  $0.34 \text{ mm/s}$ . The vertical displacement amplitude of the monitoring point is  $0.17 \text{ mm}$ , and the horizontal displacement amplitude of the monitoring point is  $0.085 \text{ mm}$ .

#### 4.2 Variation of acceleration along the surface of the slope

The acceleration amplitude curves in horizontal and vertical directions with the height of the slope are shown in Figure 5. Hmax represents the horizontal acceleration amplitude, and Vmax the vertical acceleration amplitude.

The vertical acceleration amplitude decreases gradually from the toe of the slope to the shoulder of the slope, whose maximum vertical acceleration amplitude is  $0.61 \text{ m/s}^2$  in the toe of the slope. The attenuation amplitude is maximum in the range of 5 m of slope height. The horizontal acceleration

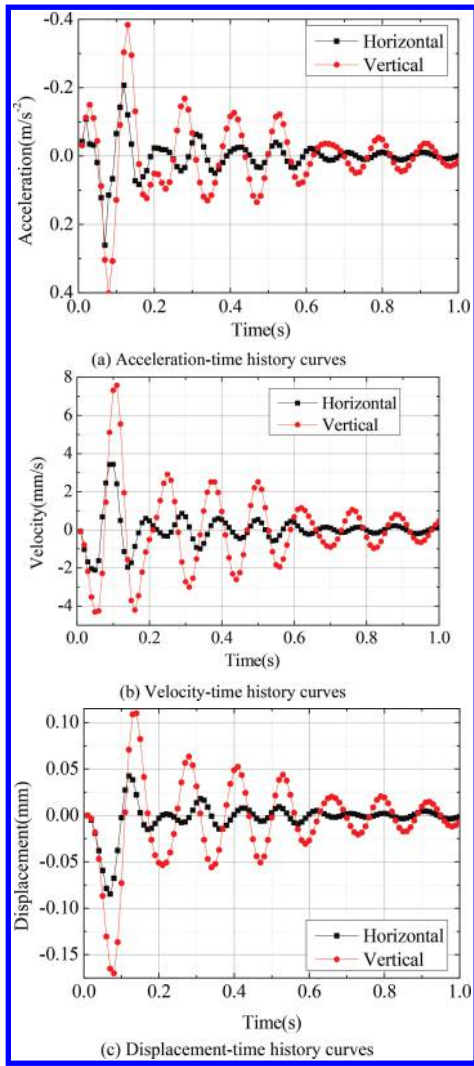


Figure 4. Dynamic response time curves in section II.

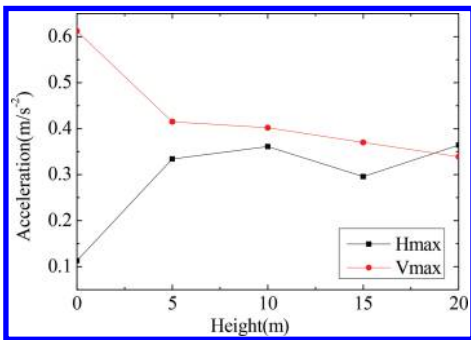


Figure 5. The acceleration amplitude curves along the slope surface.

amplitude increases from the toe of the slope to the shoulder of the slope, whose maximum horizontal acceleration amplitude is  $0.37 \text{ m/s}^2$  in the slope shoulder. The slope has an amplification effect on the horizontal acceleration.

#### 4.3 Variation of acceleration along inside of the slope

The variation curves of acceleration amplitude along the depth in the toe of the slope are shown in Figure 6.

As shown in Figure 6, the horizontal acceleration amplitude and vertical acceleration amplitude were gradually increased with the depth increasing in the range below 7 m depth of the slope surface. When the depth is more than 7 m, the vertical acceleration attenuates and the horizontal acceleration continues to increase.

The horizontal acceleration amplitude increases from the toe of the slope to the shoulder of the slope, whose maximum horizontal acceleration amplitude is  $0.17 \text{ m/s}^2$  in the slope shoulder. The soil depth has an amplification effect on the toe of the horizontal acceleration.

From the surface to the inside of 10 m depth of the slope, the vertical acceleration amplitude ranges from  $0.55 \text{ m/s}^2$  to  $0.68 \text{ m/s}^2$ , and the horizontal acceleration amplitude ranges from  $0.11 \text{ m/s}^2$  to  $0.17 \text{ m/s}^2$ .

The variation curves of the acceleration amplitude along the depth in the middle of the slope are shown in Figure 7.

As shown in Figure 7, from the surface to the inside of 6 m depth of the slope, the horizontal acceleration amplitude and vertical acceleration amplitude were gradually decreased with the depth increasing. When the depth is more than 6 m, the horizontal acceleration attenuation continues to decrease, while the vertical acceleration increases slowly.

From the surface to the inside of 10 m depth of the slope, the vertical acceleration amplitude ranges from  $0.36 \text{ m/s}^2$  to  $0.40 \text{ m/s}^2$ , and the horizontal acceleration amplitude ranges from  $0.084 \text{ m/s}^2$  to  $0.26 \text{ m/s}^2$ .

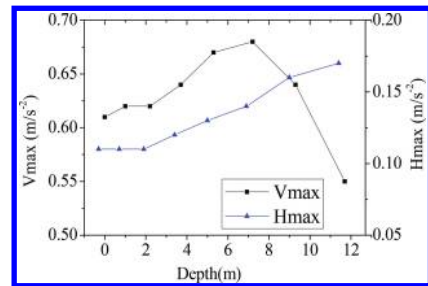


Figure 6. The acceleration curves of the toe of the slope.

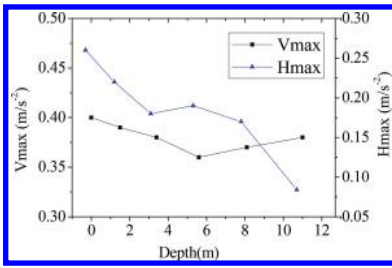


Figure 7. The acceleration curves of the middle of the slope.

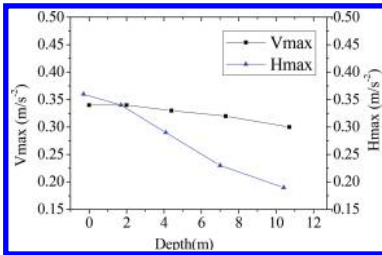


Figure 8. The acceleration curves of the shoulder of the slope.

The variation curves of the acceleration amplitude along the depth in the shoulder of the slope are shown in Figure 8.

As shown in Figure 8, the acceleration law of the slope shoulder is different from that of the toe and middle of the slope, with both horizontal and vertical acceleration decreasing with the increasing depth.

From the surface to the inside of 10 m depth of the slope, the vertical acceleration amplitude ranges from 0.30 m/s<sup>2</sup> to 0.34 m/s<sup>2</sup>, and the horizontal acceleration amplitude ranges from 0.19 m/s<sup>2</sup> to 0.36 m/s<sup>2</sup>.

## 5 CONCLUSION

Through the study on the change rules of dynamic properties and dynamic response of expressway loess slopes on compaction loads, the research results show that:

1. The amplitude of dynamic response for loess slope in dynamic compaction fades out rapidly with the impact loading effect, and the amplitude of horizontal dynamic response and the amplitude vertical dynamic response take place in the same time.
2. The slope has an amplification effect on the horizontal dynamic response, and the amplification effect increases with the increase in the height of the slope.

3. The amplification phenomenon of amplitude vibration in the upper and central parts of the slope surface is obvious compared with the internal part of the slope. The dynamic response amplitude fades out with the depth increasing, the horizontal dynamic response amplitude decays faster than the vertical dynamic response amplitude, and the decay rate decreases with the increase in the height of the slope.

The simulation results are helpful to reveal the dynamic response rules of loess slope under the condition of dynamic compaction, which provide instructive reference for the engineering design and construction in loess regions.

## ACKNOWLEDGMENTS

This work was financially supported by the Shanxi Province Transportation Construction Project “Study on the loess roadbed monitoring and early warning technology for intelligent control” (2014-2-03).

## REFERENCES

- [1] China Association of Engineering Blasting. Safety regulations for blasting GB6722-2003 [S]. China Standard Press, 2003.
- [2] Luo Xing-wen, Chen Jing-xi, Wang Ji-li. Experimental study on foundation improvement by dynamic consolidation on loess region[J]. Rock and Soil Mechanics, 2004, 25(4), pp: 654–656.
- [3] Tamrakar S.B., Toyosawa Y., Itoh K., et al. Failure mechanism of slopes in the centrifuge using in-flight excavator[C]//Proceeding of International Symposium on Landslide Hazard in Orogenic Zone from the Himalaya to Island Arc in Asia. Kathmandu: [s. n.], 2005: 255–264.
- [4] Shen C.K., Kim Y.S., Bang S., et al. Centrifuge modeling of lateral earth support[J]. Journal of Geotechnical Engineering, ASCE, 1982, 108(9): 1150–1164.
- [5] Tamrakar S.B., Mitachi T., Toyosawa Y., et al. Measurement of slope movement during the slope excavation of small size full scale model[C]//Proceeding of International Symposium on Landslide Hazard in Orogenic Zone from the Himalaya to Island Arc in Asia, Kathmandu: [s. n.], 2005: 265–274.
- [6] Zhang Meng-xi, Wang Yu-ling, Feng Jian-long. Engineering properties of loess disturbed and geo-environmental damage due to dynamic consolidation[J]. Rock and Soil Mechanics, 2004, 25(12), pp: 1903–1909.
- [7] Xu Guang-xing, Yao Ling-kan, Gao Zhao-ning, et al. Large-scale shaking table model test study on dynamic characteristics and dynamic responses of slope[J]. Chinese Journal of Rock Mechanics and Engineering, 2009, 27(3), pp: 624–632.
- [8] Gong Cheng-ming, Cheng Qian-gong, Liu Zheng-ping. Model test study of dynamic responses of loess slope by dynamic compaction[J]. Rock and Soil Mechanics, 2011, 32(7), pp: 2001–2006.

## Consolidation analysis of concrete-cored sand-gravel columns improved composite foundation

G.B. Ye, Q.W. Zhang & Z. Zhang

*Key Laboratory of Geotechnical and Underground Engineering of Ministry of Education, Tongji University, Shanghai, China*

*Department of Geotechnical Engineering, Tongji University, Shanghai, China*

*Collaborative Innovation Center of Geohazard Prevention (CICGP), Chengdu, Sichuan, China*

**ABSTRACT:** A new type of composite column called concrete-cored sand-gravel column has been proposed, which consists of a prefabricated inner pile and surrounding sand-gravel materials. The engineering practices have demonstrated that the concrete-cored sand-gravel columns can be used to improve bearing capacity and accelerate consolidation of soft soil effectively. To theoretically analyze the characteristics of consolidation of the composite foundation, the equal strain assumption is modified and the differential equations for consolidation of the composite foundation under time-dependent loading were established considering both horizontal and vertical flows. The general analytical solutions for consolidation equations were derived, and the solutions under multi-staged linear loading were developed. To verify the validity of the proposed solutions, a case history of embankment supported by concrete-cored sand-gravel columns was analyzed. The predicted ground settlements at the centerline of embankment base agreed well with the field data.

**Keywords:** concrete-cored sand-gravel column; composite foundation; time-dependent loading; consolidation; analytical solution

### 1 INTRODUCTION

Due to the rapid development of soft soil improvement technique, some new ground improvement methods have been proposed, such as soil-cement columns combining with PVDs (Ye et al. 2012, 2013), stiffened deep cement mixing piles (Ye & Cai 2012) and concrete-cored sand-gravel columns (Chen et al. 2007, Tang et al. 2010). The concrete-cored sand-gravel column is composed of a prefabricated inner concrete pile and surrounding sand-gravel materials. The prefabricated inner piles can be used to improve bearing capacity of the composite foundation, and the sand-gravel annulus can shorten drainage paths and accelerate consolidation of subsoil.

The concrete-cored sand-gravel columns have been used in practical projects successfully. Chen et al. (2007) and Tang et al. (2010) presented a series of field test results in Zhen-Li highway, China, including pile-soil stress ratio, ground settlement and differential settlement between pile and soil, lateral displacement, excess pore water pressure, etc. Cheng et al. (2007) studied the embankment strengthening effects by the concrete-cored sand-gravel columns in Shenzhen River estuary, China.

Limited theoretical researches of consolidation of concrete-cored sand-gravel columns improved

composite foundation have been conducted so far. Yu et al. (2012) proposed analytical solutions for low-grade concrete-cored sand-gravel column composite foundation. Shi et al. (2013) derived the theoretical solutions for the concrete-cored sand-gravel column composite foundation, considering both radial and vertical flows within the sand-gravel annulus.

For composite foundation improved by granular columns (Han & Ye 2001, 2002) or flexible columns (Ye et al. 2012), the upward penetration into cushion and downward penetration into substratum of columns are inconsiderable due to small modulus difference between columns and subsoil, so the application of equal strain assumption between columns and subsoil is reasonable. However, the equal strain assumption is unsuitable for the rigid pile composite foundation because of considerable penetration of rigid piles caused by great modulus difference between rigid piles and subsoil. The prefabricated inner pile belongs to rigid pile. Thus, the analytical solutions of concrete-cored sand-gravel columns improved composite foundation derived by Yu et al. (2012) and Shi et al. (2013) based on equal strain assumption are inappropriate.

The equal strain assumption is modified for the concrete-cored sand-gravel column composite

foundation in this study. The analytical solutions of concrete-cored sand-gravel columns improved composite foundation under time-dependent loading are derived based on the modified equal strain assumption. A history case is analyzed to verify the validity of the proposed analytical solutions, and the predicted ground settlements agree well with the field measurements.

## 2 CONSOLIDATION OF THE COMPOSITE FOUNDATION

### 2.1 Consolidation problem

The schematic diagram of the concrete-cored sand-gravel column composite foundation is shown in Figure 1. The consolidation model of the composite foundation is axisymmetric and cylindrical coordinates are adopted, in which  $P(t)$  = time-dependent loading;  $H$  = improvement depth of concrete-cored sand-gravel column;  $r_e$ ,  $r_s$ ,  $r_w$  and  $r_c$  = radius of influential zone, smear zone, sand-gravel annulus and inner pile, respectively;  $E_c$ ,  $E_s$ ,  $E_w$  and  $E_p$  = modulus of cushion, subsoil, sand-gravel annulus and inner pile, respectively;  $k_h$  and  $k_s$  = horizontal conductivity of undisturbed zone and smear zone, respectively;  $k_w$  and  $k_v$  = vertical conductivity of sand-gravel annulus and subsoil, respectively.

The main assumptions made in the analysis are summarized below:

1. Modified equal strain assumption and only vertical strain are considered;
2. The soil is fully saturated, and the water flows obey the Darcy's law;

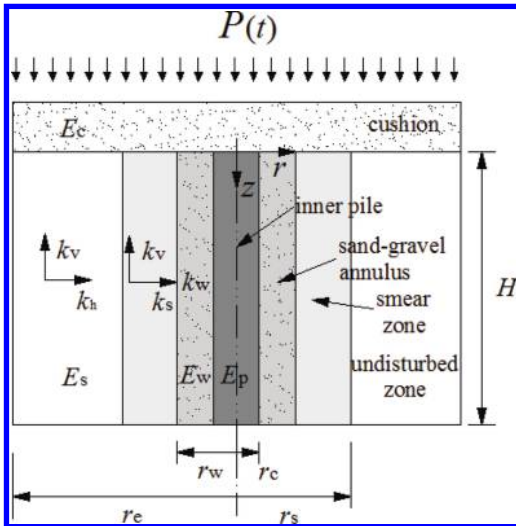


Figure 1. Schematic diagram of calculation model.

3. The permeability and modulus of subsoil are assumed to be constant during consolidation.

### 2.2 Modified equal strain assumption

Li et al. (2014) developed a theoretical solution of consolidation of rigid pile composite foundation, which took the modulus of cushion, pile and subsoil into consideration. Based on the research results of Li et al. (2014), the equal strain assumption for the concrete-cored sand-gravel column composite foundation is modified.

In this study, the concrete-cored sand-gravel columns are sat on hard substratum, and the penetration of column tip into substratum is not considered. According to deformation compatibility, the compression of subsoil in improvement depth equals to upward penetration into cushion and compression of inner pile, i.e.

$$S_S = S_P + S_T \quad (1)$$

where  $S_S$  = compression of subsoil in improvement depth;  $S_P$  = compression of inner pile shaft;  $S_T$  = upward penetration into cushion.

The upward penetration of inner pile into cushion can be calculated using vertical surface displacement of rigid circle footing on semi-infinite mass by Poulos & Davis (1974):

$$S_T = \frac{\pi}{2} (1 - \nu_c^2) \frac{P_a r_p}{E_c} \quad (2)$$

where  $E_c$ ,  $\nu_c$  = compression modulus and Poisson's ratio of cushion, respectively;  $p_a$  = vertical pressure on inner pile head;  $r_p$  = radius of inner pile.

The compression of inner pile shaft can be computed by

$$S_P = \int_0^H \frac{p(z)}{E_p} dz \quad (3)$$

where  $p(z)$  = vertical stress along pile shaft; and  $E_p$  = elastic modulus of inner pile.

When side friction of pile is not taken into consideration,  $p(z)$  is a constant value along pile shaft, i.e.

$$p(z) = p_a \quad (4)$$

Assuming that only positive side friction  $\tau$  is considered, and  $\tau$  is constant along pile shaft,

$$p(z) = p_a - \frac{\tau \cdot 2z}{r_p} \quad (5)$$

Since the distribution of side friction of pile is very complicated, Equation 6 is adopted in this

study to simplify the calculation of compression of inner pile.

$$S_p = \psi \frac{P_a}{E_p} H \quad (6)$$

where  $\psi$  is an empirical coefficient relating to overloading, length and modulus of pile, and site conditions, etc.

Combining Equations 1–2, 6 yields

$$\varepsilon_v = \frac{S_s}{H} = \frac{S_p + S_T}{H} = \psi \frac{P_a}{E_p} + \frac{\pi}{2} (1 - \nu_c^2) \frac{P_a r_p}{H E_c} \quad (7)$$

where  $\varepsilon_v$  = volumetric strain of subsoil.

As a consequence, the equivalent modulus of inner pile can be defined as

$$E_p^{eq} = \frac{P_a}{\varepsilon_v} = \left[ \frac{\psi}{E_p} + \frac{\pi}{2} (1 - \nu_c^2) \frac{r_p}{H E_c} \right]^{-1} \quad (8)$$

Due to high strength of inner concrete pile, the compression of pile is insignificant compared to upward penetration, and the influence of  $\psi$  on equivalent modulus of inner pile is unimportant. As a result, the value of  $\psi$  can be taken as unity for simplicity. The detailed discussions about  $\psi$  can be seen later.

Thus, the equal strain assumption for the concrete-cored sand-gravel column composite foundation can be expressed as

$$\frac{\bar{\sigma}_s - \bar{u}_s}{E_s} = \frac{\bar{\sigma}_w - u_w}{E_w} = \frac{\bar{\sigma}_p}{E_p^{eq}} = \varepsilon_v \quad (9)$$

In the above equation  $\bar{\sigma}_s, \bar{\sigma}_w, \bar{\sigma}_p$  = average total additional stress at any depth within subsoil, sand-gravel annulus and inner pile, respectively;  $\bar{u}_s$  = average excess pore water pressure in subsoil at any depth;  $u_w$  = excess pore water pressure within sand-gravel annulus at any depth.

### 2.3 Deduction of differential equations

At any time, the subsoil, the sand-gravel annulus and the inner pile carry the applied loads, i.e.

$$\pi(r_c^2 - r_w^2) \bar{\sigma}_s + \pi(r_w^2 - r_p^2) \bar{\sigma}_w + \pi r_p^2 \bar{\sigma}_p = \pi r_c^2 P(t) \quad (10)$$

The partial differential equations in subsoil can be expressed as

$$-\frac{k_s}{\gamma_w} \left( \frac{1}{r} \frac{\partial u_m}{\partial r} + \frac{\partial^2 u_m}{\partial r^2} \right) - \frac{k_v}{\gamma_w} \frac{\partial^2 \bar{u}_s}{\partial z^2} = \frac{\partial \varepsilon_v}{\partial t} \quad r_w \leq r \leq r_s \quad (11a)$$

$$-\frac{k_h}{\gamma_w} \left( \frac{1}{r} \frac{\partial u_n}{\partial r} + \frac{\partial^2 u_n}{\partial r^2} \right) - \frac{k_v}{\gamma_w} \frac{\partial^2 \bar{u}_s}{\partial z^2} = \frac{\partial \varepsilon_v}{\partial t} \quad r_s \leq r \leq r_c \quad (11b)$$

where  $u_m, u_n$  = excess pore water pressure at any point in smear zone and undisturbed zone, respectively;  $\gamma_w$  = unit weight of water.

The average excess pore water pressures of the subsoil and the composite foundation, respectively, can be defined as follows:

$$\bar{u}_s = \frac{1}{\pi(r_c^2 - r_w^2)} \left[ \int_{r_w}^{r_s} 2\pi r u_m dr + \int_{r_s}^{r_c} 2\pi r u_n dr \right] \quad (12)$$

$$\begin{aligned} \bar{u} &= \frac{1}{\pi(r_c^2 - r_p^2)} \left[ \int_{r_p}^{r_w} 2\pi r u_w dr + \int_{r_w}^{r_s} 2\pi r u_m dr \right] \\ &= \frac{1}{(n^2 - m^2)} \left[ (1 - m^2) u_w + (n^2 - 1) \bar{u}_s \right] \end{aligned} \quad (13)$$

where  $n = r_c/r_w$ ;  $m = r_p/r_w$ .

Xie et al. (2009) pointed out that the quantity of water flowing into the column through the disturbed zone is not equal to that flowing out from the column and the difference between them is equal to the volume change of the column. Thus, for the concrete-cored sand-gravel composite foundation,

$$-\frac{2}{(1 - m^2)} \frac{1}{r_w} \left( \frac{k_s}{\gamma_w} \frac{\partial u_m}{\partial r} \right) \Big|_{r=r_w} - \frac{k_w}{\gamma_w} \frac{\partial^2 u_w}{\partial z^2} = \frac{\partial \varepsilon_v}{\partial t} \quad (14)$$

The boundary conditions and initial conditions of Equations 11a, b are described as follows:

$$\text{As } r = r_c, \quad \frac{\partial u_n}{\partial r} = 0; \quad (15a)$$

$$\text{As } r = r_s, \quad u_m = u_n, \quad \frac{k_s}{\gamma_w} \frac{\partial u_m}{\partial r} = \frac{k_h}{\gamma_w} \frac{\partial u_n}{\partial r}; \quad (15b)$$

$$\text{As } r = r_w, \quad u_m = u_w; \quad (15c)$$

$$\text{As } z = 0, \quad \bar{u} = 0; \quad (15d)$$

$$\text{As } z = H, \quad \frac{\partial \bar{u}}{\partial z} = 0; \quad (15e)$$

$$\text{As } t = 0, \quad \bar{u} = \sigma_0(z); \quad (15f)$$

where  $\sigma_0(z)$  = initial excess pore water pressure at depth  $z$ .

Let  $Y_1 = E_p^{eq}/E_s$  and  $Y_2 = E_w/E_s$ , combining Equations 9–10, substituting Equation 13 and getting derivative with respect to time  $t$  yields

$$\frac{\partial \mathcal{E}_v}{\partial t} = \frac{n^2 \frac{dP(t)}{dt} - (n^2 - m^2) \frac{\partial \bar{u}}{\partial t}}{\left[ m^2 Y_1 + (1 - m^2) Y_2 + (n^2 - 1) \right] E_s} \quad (16)$$

Integrating Equations 11a, b and using the boundary conditions 15a, b and c, the following equations can be derived

$$\frac{\partial u_m}{\partial r} = \frac{\gamma_w}{2k_s} \left( \frac{\partial \mathcal{E}_v}{\partial t} + \frac{k_v}{\gamma_w} \frac{\partial^2 \bar{u}_s}{\partial z^2} \right) \left( \frac{r_e^2}{r} - r \right) \quad (17)$$

$$u_m = \frac{\gamma_w}{2k_s} \left( \frac{\partial \mathcal{E}_v}{\partial t} + \frac{k_v}{\gamma_w} \frac{\partial^2 \bar{u}_s}{\partial z^2} \right) \left( r_e^2 \ln \frac{r}{r_w} - \frac{r^2 - r_w^2}{2} \right) + u_w \quad (18a)$$

$$u_n = \left[ \frac{\gamma_w}{2k_h} \left( r_e^2 \ln \frac{r}{r_s} - \frac{r^2 - r_s^2}{2} \right) + \frac{\gamma_w}{2k_s} \left( r_e^2 \ln \frac{r_s}{r_w} - \frac{r_s^2 - r_w^2}{2} \right) \right] \left( \frac{\partial \mathcal{E}_v}{\partial t} + \frac{k_v}{\gamma_w} \frac{\partial^2 \bar{u}_s}{\partial z^2} \right) + u_w \quad (18b)$$

Substituting Equations 18a, b into Equation 12 yields

$$\bar{u}_s = \frac{\gamma_w r_e^2 F_a}{2k_h} \left( \frac{\partial \mathcal{E}_v}{\partial t} + \frac{k_v}{\gamma_w} \frac{\partial^2 \bar{u}_s}{\partial z^2} \right) + u_w \quad (19)$$

In the above equation

$$F_a = \left( \ln \frac{n}{s} + \frac{k_h}{k_s} \ln s - \frac{3}{4} \right) \frac{n^2}{n^2 - 1} + \frac{s^2}{n^2 - 1} \left( 1 - \frac{k_h}{k_s} \right) \left( 1 - \frac{s^2}{4n^2} \right) + \frac{k_h}{k_s} \frac{1}{n^2 - 1} \left( 1 - \frac{1}{4n^2} \right) \quad (20)$$

where  $s = r_s/r_w$ .

By substituting Equation 17 into Equation 14, the following equation can be obtained

$$-\frac{n^2 - 1}{n^2 - m^2} \frac{k_v}{\gamma_w} \frac{\partial^2 \bar{u}_s}{\partial z^2} - \frac{1 - m^2}{n^2 - m^2} \frac{k_w}{\gamma_w} \frac{\partial^2 u_w}{\partial z^2} = \frac{\partial \mathcal{E}_v}{\partial t} \quad (21)$$

Substituting Equation 13 into Equation 19 and Equation 21, respectively, the following equations can be derived

$$\frac{\partial \mathcal{E}_v}{\partial t} = \frac{n^2 - m^2}{n^2 - 1} \frac{2k_h}{\gamma_w r_e^2 F_a} (\bar{u} - u_w) - \frac{n^2 - m^2}{n^2 - 1} \frac{k_v}{\gamma_w} \frac{\partial^2 \bar{u}}{\partial z^2} + \frac{1 - m^2}{n^2 - 1} \frac{k_v}{\gamma_w} \frac{\partial^2 u_w}{\partial z^2} \quad (22)$$

$$\frac{\partial \mathcal{E}_v}{\partial t} = -\frac{k_v}{\gamma_w} \frac{\partial^2 \bar{u}}{\partial z^2} - \frac{1 - m^2}{n^2 - m^2} \frac{k_w - k_v}{\gamma_w} \frac{\partial^2 u_w}{\partial z^2} \quad (23)$$

Combining Equations 22–23, and then substituting the result into Equation 16, Equation 16 can be solved as

$$u_w = \bar{u} - A \frac{\partial^2 \bar{u}}{\partial z^2} + B \frac{\partial \bar{u}}{\partial t} - C \frac{dP(t)}{dt} \quad (24)$$

In the above equation

$$A = \frac{\gamma_w r_e^2 F_a}{2k_h} \frac{k_w}{k_w - k_v} \frac{k_v}{\gamma_w} \quad (25)$$

$$B = \frac{r_e^2 F_a}{2C_h} \left( \frac{n^2 - 1}{n^2 - m^2} + \frac{k_v}{k_w - k_v} \right) \times \frac{n^2 - m^2}{m^2 Y_1 + (1 - m^2) Y_2 + (n^2 - 1)} \quad (26)$$

$$C = \frac{r_e^2 F_a}{2C_h} \left( \frac{n^2 - 1}{n^2 - m^2} + \frac{k_v}{k_w - k_v} \right) \times \frac{n^2}{m^2 Y_1 + (1 - m^2) Y_2 + (n^2 - 1)} \quad (27)$$

where  $C_h = k_h E_s / \gamma_w$  is coefficient of consolidation of subsoil in the horizontal direction.

Substituting Equations 16, 24 into Equation 23 yields

$$D \frac{\partial^4 \bar{u}}{\partial z^4} - E \frac{\partial^3 \bar{u}}{\partial z^2 \partial t} - F \frac{\partial^2 \bar{u}}{\partial z^2} + G \frac{\partial \bar{u}}{\partial t} = \frac{dP(t)}{dt} \quad (28)$$

In the above equation

$$D = \frac{k_w k_v E_s r_e^2 F_a}{2\gamma_w k_h} \frac{1 - m^2}{n^2 - m^2} \frac{m^2 Y_1 + (1 - m^2) Y_2 + (n^2 - 1)}{n^2} \quad (29)$$

$$E = \frac{r_e^2 F_a}{2} \frac{k_v}{k_h} \left[ \frac{n^2 - 1}{n^2 - m^2} \left( \frac{k_w}{k_v} - 1 \right) + 1 \right] \frac{1 - m^2}{n^2} \quad (30)$$

$$F = \left[ 1 + \frac{1 - m^2}{n^2 - m^2} \left( \frac{k_w}{k_v} - 1 \right) \right] \times \frac{m^2 Y_1 + (1 - m^2) Y_2 + (n^2 - 1)}{n^2} C_v \quad (31)$$

$$G = \frac{n^2 - m^2}{n^2} \quad (32)$$

where  $C_v = k_v E_s / \gamma_w$  is coefficient of consolidation of subsoil in the vertical direction.

#### 2.4 Analytical solutions

According to the intrinsic function method of non-homogeneous equations, the intrinsic function corresponding to Equation 28 is  $\sin(Mz/H)$  where

$$M = (2k + 1)\pi/2, k = 0, 1, 2 \dots$$

In Equation 28,  $dP(t)/dt$  can be developed as the Fourier series at  $[0, H]$  on the basis of the intrinsic function

$$\frac{dP(t)}{dt} = \sum_{k=0}^{\infty} f_k(t) \sin\left(\frac{M}{H}z\right) \quad (33)$$

In the equation

$$f_k(t) = \frac{\int_0^H P'(t) \sin\left(\frac{M}{H}z\right) dz}{\int_0^H \sin^2\left(\frac{M}{H}z\right) dz} = \frac{2}{M} P'(t). \quad (34)$$

Using the intrinsic function method of non-homogeneous equations, the solution to Equation 28 can be assumed to have the following form, which satisfies boundary conditions 15d, e.

$$\bar{u} = \sum_{k=0}^{\infty} V_k(t) \sin\left(\frac{M}{H}z\right) \quad (35)$$

Substituting Equations 33, 35 into Equation 28,  $V_k(t)$  can be derived as

$$V_k(t) = \left\{ \frac{2}{M} \int_0^t P'(\tau) e^{\beta_m \tau} d\tau + C_1 \right\} e^{-\beta_m t} \quad (36)$$

where  $\beta_m = [D(M/H)^4 + F(M/H)^2]/[E(M/H)^2 + G]$ ;  $C_1 =$  arbitrary constant.

Thus, the solution to Equation 28 can be obtained as

$$\bar{u} = \sum_{k=0}^{\infty} \left\{ \frac{2}{M} \int_0^t P'(\tau) e^{\beta_m \tau} d\tau + C_1 \right\} \sin\left(\frac{M}{H}z\right) e^{-\beta_m t} \quad (37)$$

Using initial condition 15f, and the orthogonality of the Fourier series, the average excess pore water pressure  $\bar{u}$  can be expressed as

$$\bar{u} = \sum_{k=0}^{\infty} \sin\left(\frac{M}{H}z\right) e^{-\beta_m t} \left\{ \frac{2}{H} \int_0^H \sigma_0(l) \sin\left(\frac{M}{H}l\right) dl + \frac{2}{M} \left[ \int_0^t P'(\tau) e^{\beta_m \tau} d\tau - \int_0^t P'(\tau) e^{\beta_m \tau} d\tau \Big|_{t=0} \right] \right\} \quad (38)$$

The overall average degree of consolidation in terms of stress is defined as the ratio of average effective stress at time  $t$  to time  $t = \infty$  in a composite foundation.

$$\bar{U}(t) = \frac{\int_0^H (P_u + \sigma_0(z) - \bar{u}_s - P_0) dz}{\int_0^H (P_u + \sigma_0(z) - P_0) dz} \quad (39)$$

where  $P_0 =$  initial loading;  $P_u =$  ultimate loading.

### 3 SOLUTIONS FOR SPECIAL CASE

The external loading is assumed to vary linearly with time as shown in Figure 2, and can be expressed as

$$P(t) = \begin{cases} R_1 t & 0 \leq t < t_1 \\ \sum_{i=1}^j R_i (t_i - t_{i-1}) + R_{j+1} (t - t_j) & t_j \leq t < t_{j+1} \\ \sum_{i=1}^n \Delta P & t_n \leq t \end{cases} \quad (40)$$

where  $i, j =$  loading stage;  $t_{i-1}, t_i =$  initial time and terminal time of loading stage  $i$ ;  $R_i =$  loading rate at loading stage  $i$ ;  $\sum \Delta P =$  accumulated value of loading at all stages;  $n =$  the last loading stage. The initial excess pore water pressure  $\sigma_0(z)$  is zero.

By substituting Function 40 into Equations 38 and 39, the solutions of average excess pore water

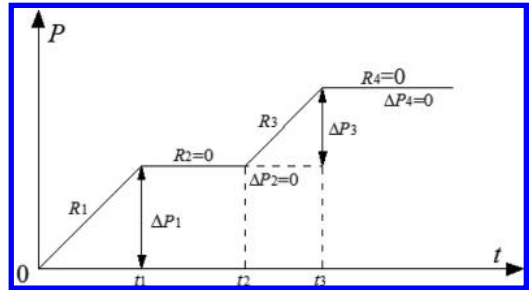


Figure 2. Multi-staged linear loading.



pressure and average degree of consolidation under multi-staged linear loading can be obtained.

As  $0 \leq t < t_1$ ,

$$\bar{u} = \sum_{k=0}^{\infty} \frac{2}{M} \sin\left(\frac{M}{H} z\right) \frac{R_1}{\beta_m} (1 - e^{-\beta_m t}) \quad (41)$$

$$\bar{U}(t) = \frac{1}{\sum \Delta P} \left[ R_1 t - \sum_{k=0}^{\infty} \frac{2}{M^2} \frac{R_1}{\beta_m} (1 - e^{-\beta_m t}) \right] \quad (42)$$

As  $t_j \leq t < t_{j+1}$ ,

$$\bar{u} = \sum_{k=0}^{\infty} \frac{2}{M} \frac{1}{\beta_m} \sin\left(\frac{M}{H} z\right) e^{-\beta_m t} \cdot \left[ \sum_{i=1}^j R_i (e^{\beta_m t_i} - e^{\beta_m t_{i-1}}) + R_{j+1} (e^{\beta_m t} - e^{\beta_m t_j}) \right] \quad (43)$$

$$\bar{U}(t) = \frac{1}{\sum \Delta P} \left\{ \left[ \sum_{i=1}^j R_i (t_i - t_{i-1}) + R_{j+1} (t - t_j) \right] - \sum_{k=0}^{\infty} \frac{2}{M^2} \frac{1}{\beta_m} e^{-\beta_m t} \right\} \cdot \left[ \sum_{i=1}^j R_i (e^{\beta_m t_i} - e^{\beta_m t_{i-1}}) + R_{j+1} (e^{\beta_m t} - e^{\beta_m t_j}) \right] \quad (44)$$

As  $t \geq t_n$ ,

$$\bar{u} = \sum_{k=0}^{\infty} \frac{2}{M} \frac{1}{\beta_m} \sin\left(\frac{M}{H} z\right) e^{-\beta_m t} \sum_{i=1}^n R_i (e^{\beta_m t_i} - e^{\beta_m t_{i-1}}) \quad (45)$$

$$\bar{U}(t) = 1 - \frac{\sum_{k=0}^{\infty} \frac{2}{M^2} \frac{1}{\beta_m} e^{-\beta_m t} \sum_{i=1}^n R_i (e^{\beta_m t_i} - e^{\beta_m t_{i-1}})}{\sum \Delta P} \quad (46)$$

## 4 CASE APPLICATION

The field experiment described by Chen et al. (2007) and Tang et al. (2010) was conducted at stations K63 + 046 – K63 + 066 on the Zhen-Li expressway in Jiangsu Province, China. The soft soil was improved by the concrete-cored sand-gravel columns, which were installed a triangular pattern at a spacing of 2.1 m and a depth of 20 m. The C20 concrete was used to prefabricate the square inner piles with cross-sectional dimensions of 200 mm × 200 mm. The outer diameter of the sand-gravel annulus was 0.5 m. The gravel cushion was 0.5 m thick including a layer of geo-grid. The physical and mechanical properties of soils at the site are listed in Table 1. Section K63 + 056 was taken as the monitoring cross section. The loading process and instrumentation were introduced by Chen et al. (2007) and Tang et al. (2010).

Figure 3 shows the steel bar stresses monitored at the center of K63 + 056 cross section. Table 3 lists the compression of inner pile calculated using axial stresses along pile shaft and soil pressures at pile head, respectively. The axial stresses along pile shaft are calculated from steel bar stresses monitored as shown in Figure 3. The value of  $\psi$  is back-calculated by comparing the compression results computed from equations  $S_p = \int_0^H p(z) E_p dz$  and  $S_p = p_a / E_p H$ .

At 112 days when embankment filling is completed, the upward penetration of inner pile into cushion is 78 mm as shown in Table 2, while the compression of inner pile is 5.39 mm; at 269 days, the upward penetration of inner pile into cushion is 112 mm, while the compression of inner pile is only 7.16 mm. It can be seen that the compression of inner pile is far less than the upward penetration into cushion due to high strength of rigid inner pile, thus the effects of compression of inner pile on calculation of composite modulus are insignificant. The value of  $\psi$  converges quickly with time and verges on

Table 1. Physical and mechanical properties of soils.

Material	Depth (m)	Unit weight $\gamma$ (kN/m <sup>3</sup> )	Compression modulus $E_s$ (MPa)	Direct shear test	
				Cohesion $c$ (kPa)	Friction angle $\phi$ (°)
Fill	2.0~3.7	–	–	–	–
Silty clay	1.6~2.6	18.4	7.28	2.0	17.1
Mucky-silty clay	6.6~10.9	17.9	4.47	7.0	24.5
Silty clay	0.6~2.5	18.3	5.37	18.0	16.5
Silt	0.7~2.9	18.5	5.68	10.0	25.5
Silty clay	0~4.4	19.3	3.94	25.0	13.7
Silty clay	9.6~10.1	18.7	5.29	13.0	12.2
Breccia	–	–	–	–	–

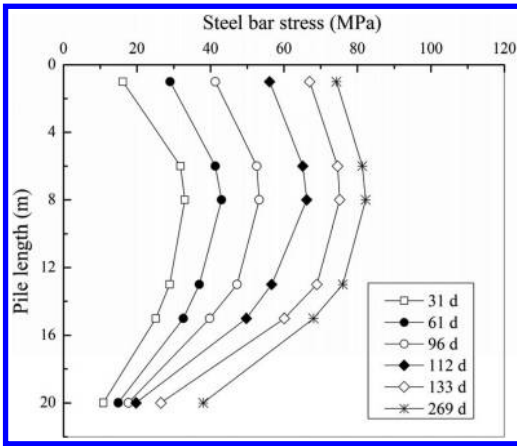


Figure 3. Variation of steel bar stress with time.

Table 2. Differential settlement between pile head and surrounding soil.

Time/d	29	87	112	210	269
Differential settlement/mm	13	63	78	109	112

Table 3. Compression of inner pile.

Time/d	31	61	96	112	133	269
$S_p = \int_0^H \frac{p(z)}{E_p} dz$	2.50	3.39	4.32	5.39	6.38	7.16
$S_p = \frac{p_a}{E_p} H$	0.50	1.56	2.27	3.67	4.74	5.41
$\psi$	5	2.17	1.90	1.47	1.35	1.33

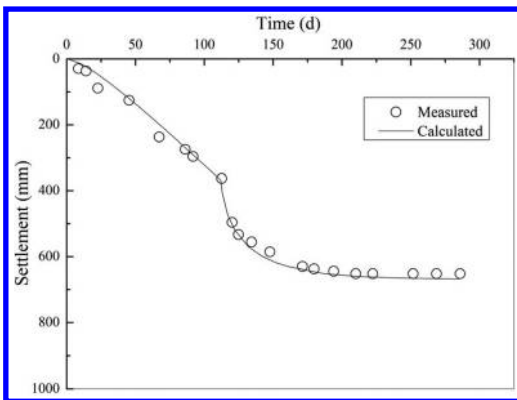


Figure 4. Variation of settlement with time.

unity. Due to the insignificant effects of compression of inner pile and variation trend of  $\psi$ , the value of  $\psi$  can be taken as unity for simplicity when predicting the degree of consolidation of the concrete-cored sand-gravel column composite foundation.

Figure 4 shows a comparison of the calculated results and the measured ground settlements at the center of K63 + 056 cross section. It can be seen that the predicted settlements agree well with the monitored field results, which verifies the validity of the proposed solutions for concrete-cored sand-gravel columns improved composite foundation.

## 5 CONCLUSIONS

The analytical solutions of the concrete-cored sand-gravel column composite foundation under time-dependent loading are derived considering the modified equal strain assumption. The value of  $\psi$  can be taken as unity for simplicity in practical application. The analytical solutions have been used for predicting ground settlements of a history case successfully, which verifies the feasibility and reasonability of the proposed analytical solutions. Only upward penetration of pile into cushion is considered in this study. Both upward penetration into cushion and downward penetration into substratum of pile are expected to be taken into account in the further study.

## REFERENCES

- Chen J.S., Tang T.Z., Zhao W.B et al. 2007. Field tests on composite foundation with concrete-cored sand-gravel piles. *Chinese Journal of Geotechnical Engineering* 29(7):957–962.
- Cheng W.Z., Yue M.H., Wang F.Y. et al. 2007. Field tests study of concrete-cored sand-gravel piles applied to strength embankment engineering. *Journal of Hydraulic Engineering* 38(Suppl.1):675–681.
- Han J. & Ye S.L. 2001. Simplified method for consolidation rate of stone column reinforced foundations. *Journal of Geotechnical and Geoenvironmental Engineering* 127(7):597–603.
- Han J. & Ye S.L. 2002. A theoretical solution for consolidation rates of stone column-reinforced foundations accounting for smear and well resistance effects. *The International Journal Geomechanics* 2(2):135–151.
- Li Y.K., Ji J., Zhang W.J. et al. 2014. Analysis of seepage and consolidation properties of rigid-pile composite foundation. *Journal of Building Structures* 35(3):208–214.
- Poulos, H.G. & Davis E.H. 1974. *Elastic solutions for soil and rock mechanics*: 166. New York: John Wiley & Sons, INC.
- Shi B.X., Yang Y.W., Xie R.X. et al. 2013. Analytical solution for consolidation of composite foundation with concrete-cored sand-gravel pile. *Rock and Soil Mechanics* 34(10):2835–2840.

- Tang T.Z., Zhao W.B., Chen J.S. et al. 2010. Experimental study on deformation and bearing capacity of composite foundation with concrete-cored sand-gravel piles under high embankment load. *Chinese Journal of Geotechnical Engineering* 32(12):1829–1836.
- Xie, K.H. & Lu M.M. 2009. Equal strain consolidation for stone columns reinforced foundation. *International Journal for Numerical and Analytical Methods in Geomechanics* 33(15):1721–1735.
- Ye G.B. & Cai Y.S. 2012. Bearing capacity and settlement calculation of stiffened deep cement mixing (SDCM) pile. *Theories and technologies for high-speed transportation infrastructure*: 320–328. *International Symposium on Geotechnical Engineering for High-Speed Transportation Infrastructure, Hangzhou, 26–28 October 2012*.
- Ye G.B., Zhang Z., Han J. et al. 2013. Performance evaluation of an embankment on soft soil improved by deep mixed columns and prefabricated vertical drains. *Journal of Performance of Constructed Facilities* 27:614–623.
- Ye G.B., Zhang Z., Xing H.F. et al. 2012. Consolidation of a composite foundation with soil-cement columns and prefabricated vertical drains. *Bulletin of Engineering Geology and the Environment* 71(1):87–98.
- Yu J., Qi Z.B, Cai Y.Y. et al. 2012. Study on consolidation calculation of low-grade concrete-cored sand-gravel pile composite foundation. *Engineering Mechanics* 29(6):218–240.

## Application of the correlation method on the analysis of the influence factor of heading blast vibration

Li Yan

*School of Architecture and Civil Engineering, Chengdu University, Chengdu, Sichuan, China*

**ABSTRACT:** In order to reduce the size of the heading blast vibration strength and control vibration hazard, blasting vibration influence factors on the basis of the Gray Relation Analysis (GRA) are analyzed. At first, vibration velocity is determined, and the main vibration frequency and vibration duration are regarded as the systematic characteristic variables. The total explosive charge, maximum explosive, medicine chamber length, principal piece sewn dosage, segments, blasting pitch, and minimum delay interval time are taken as related factor variables. In combination with heading blast monitoring data of dam foundation in Longbeiwang hydropower station, gray correlation calculation is done. Finally, the results of the systematic characteristic variable correlation degree are sorted and its advantages are analyzed. The order of blasting vibration effect factors is obtained as follows: total dosage and the main segment sewed dosage are the first influence factors, and the second ones are medicine chamber length and the most explosive. In conclusion, the theoretical basis can be provided to control blasting vibration effectively by using the method of GRA to determine the main influencing factors of blasting vibration.

**Keywords:** heading blast; blast vibration revision; Gray Correlation Analysis (GRA); characteristics variables; related factor variable

### 1 INTRODUCTION

The method of chamber blasting is attended by more people with the development of the Engineering construction and energy resources in China. However, the adverse effects are resulted from the influence of blasting vibration on the surrounding environment and structure when blasting is done. The main influential factors of blasting vibration are analyzed to reduce the hazard of blasting vibration effectively. Both the blasting resources and route of transmission are included in these factors. The common action of both factors influences the strength of blasting vibration (Huo 2003, Zhang 2007, Zhang 2005). The total dose, the maximum dose of single segment, the direction of resistance line, segment number of the blasting, the interval time of the segment, hole parameters, and the number of free surface are included in the factor of blasting resources. The distance, altitude difference, and geological condition are included in the route of transmission. Influential level of different factors are analyzed and compared for each factor. The main influential factors are determined, and thus it is prerequisite to control the blasting vibration effectively.

Influential degree of the factors of blasting has been investigated by many researchers at home and abroad. According to the actual data in engineering,

the influence of the total dose and distance from the blasting center on the blasting vibration is analyzed using both linear and nonlinear regression in MATLAB by Zhang Guang Zhou, etc (Zhang 2005). The hierarchical structure of different factors is analyzed using the hierarchical analytical method by Yuan Mei (Yuan & Wang 2010). The main factors of influence on the blasting vibration velocity are selected to build a BP neural network model, and the blasting vibration velocity peak of particles is predicted by Tang Ha (Tang 2004, Cai 1997, Xu 1998, Wang 2003). The method of numerical simulation is used to analyze the blasting vibration, and concluded that the distance from the blasting center has a great influence on the blasting vibration velocity. The distance is the main factor to affect blasting vibration, and concluded on the basis of Brazil yatfai greenstone quarry blasting data in combination with the method of probability and statistics. The influential factor analysis of blasting vibration is done using the method of field experiment in combination with the numerical simulation in a open pit mining field in India by Venkatesh H.S (Venkatesh H.S 2005). It was concluded that the total dose is irrelevant to the blasting vibration when the distance from the blasting center is between 100 and 3000 meters.

However, the above methods have still some shortcomings: first, a large amount of data are

needed because using few data is difficult to find out the statistical law; second, a certain distribution of typical probability is required to obey for the sample; third, amount of calculation is large, and quantitative results are inconsistent with qualitative analysis. From the perspective of system engineering, the effect of the blasting vibration is actually the gray system including a part of known information and part unknown information, so the method by using gray correlation is more reasonable to analyze the degree of the influence factors of blasting vibration. Gray Relational Analysis (GRA Gray) was first proposed in 1984 by Professor Deng Julong. The advantages of this method can make up for the lack of mathematical statistical analytical methods. Only a small amount of the sample is supplied, and a typical distribution (Deng 2002, 2005; Liu, 2010) is not needed. The relationship between the primary and secondary influence factors of blasting vibration can be determined accurately. So, blasting parameters are optimized, and the hazard of the blasting vibration is reduced.

## 2 THE PRINCIPLE AND STEPS OF GRAY CORRELATION METHOD

The relationship between the data can be found out, and the major and minor relation and magnitude of influence degree in a system containing a variety of factors are analyzed. The close degree is judged according to the similar degree of sequential curve geometry. Its basic characteristics are as follows: the curve is close to the corresponding sequence; the correlation between the corresponding sequences is larger; and it can reflect the proximate degree of the discrete space.

### 2.1 The choice of the variable between characteristic factors and related factors

$Y_j(k)$ ,  $X_i(k)$  represent the  $j$ th systematic feature vector and the  $i$ th relevant factor variable, respectively in  $k$ th tests. The main influential factors of the systematic feature vector are determined by using the tests' data. Then, the corresponding data in the test form the sequence of relevant factors and systematic feature variable sequence, namely:

$$X_i = [X_i(1), X_i(2), \dots, X_i(n)] \quad (1)$$

$$Y_j = [Y_j(1), Y_j(2), \dots, Y_j(n)] \quad (2)$$

### 2.2 The original data standardization

Because of different dimensions and magnitude of various factors, the data is not comparable,

Dimensionless data sequence is demanded to assure the accuracy of the relevant degree. So, these factors must be transformed numerically.

The usually dimensionless methods include the following: initialization method, equalization method and interval value method. Equalization method is adopted in the text.  $X$  and  $Y$  are intervalled by using the interval operators  $D_i$  and  $D'_i$ , and the interval value is as follows:

$$X'_i = X_i D_i = [x'_i(1), x'_i(2), \dots, x'_i(k), \dots, x'_i(n)] \quad (3)$$

$$Y'_j = Y_j D'_j = [y'_j(1), y'_j(2), \dots, y'_j(k), \dots, y'_j(n)] \quad (4)$$

where

$$x'_i(k) = \frac{x_i(k)}{\bar{x}_i}, \quad \bar{x}_i = \frac{1}{n} \sum_{k=1}^n x_i(k), \quad (5)$$

$$y'_j(k) = \frac{y_j(k)}{\bar{y}_j}, \quad \bar{y}_j = \frac{1}{n} \sum_{k=1}^n y_j(k)$$

### 2.3 Gray correlation calculation

After the data is dimensionless, characteristic variables data sequence and related factors data sequence are  $x'_i(k)$  and  $y'_j(k)$ , respectively. According to the definition,

$$\gamma(x'_i(k), y'_j(k)) = \frac{\Delta_{\min} + \zeta \cdot \Delta_{\max}}{\Delta_{ij}(k) + \zeta \cdot \Delta_{\max}} \quad (6)$$

where  $x'_i(k), y'_j(k)$  are gray correlation coefficient, respectively.

$\Delta_{ij}(k) = |x'_i(k) - y'_j(k)|$  is the absolute difference,  $\Delta_{\min} = \min_i \min_k \Delta_{ij}(k)$  is the smallest difference, and  $\Delta_{\max} = \max_i \max_k \Delta_{ij}(k)$  is the biggest difference.  $\zeta$  is the distinguish coefficient, with general  $\text{agv}$  is  $[0,1]$ , In the practical application,  $\zeta = 0.5$ : the smaller the value of  $\zeta$ , the greater the resolution ratio. It actually proves that its value of change will only change the size of the relative value, but will not affect the ranking of the gray correlation degree.

### 2.4 Solving the correlation

The formula can be obtained as follows:

$$\gamma(y_j(k), x_i(k)) = \frac{1}{n} \sum_{k=1}^n \gamma_{ij}(k) \quad (7)$$

where  $i = 1, 2, \dots, s; j = 1, 2, \dots, m$ .

### 2.5 Analysis of the correlation matrix results

Gray correlation matrix is given by

$$\Gamma = (\gamma_{ij}) = \begin{bmatrix} \gamma_{11} & \gamma_{12} & \cdots & \gamma_{1m} \\ \gamma_{21} & \gamma_{22} & \cdots & \gamma_{2m} \\ \cdots & \cdots & \cdots & \cdots \\ \gamma_{s1} & \gamma_{s2} & \cdots & \gamma_{sm} \end{bmatrix} \quad (8)$$

The effect of related and characteristic factors is judged based on the size of gray correlation of rows and columns in Equation (8). The main and secondary factors are analyzed, and the main influence factors are called advantage factors among them.

If there is  $a, b \in \{1, 2, \dots, j\}$ , it meet  $\gamma_{ia} \geq \gamma_{ib}$ ,  $i = 1, 2, \dots, s$ . The factor  $X_a$  is better than  $X_b$ ; if it meet  $\sum_{i=1}^s \gamma_{ia} \geq \sum_{i=1}^s \gamma_{ib}$ ,  $i = 1, 2, \dots, s$ . The factor  $X_a$  is quasi superior to  $X_b$ .

If there is  $j \in \{1, 2, \dots, m\}, j = 1, 2, \dots, m, j \neq h, X_h$  is superior to  $X_j$ , then the factor  $X_h$  is the optimal factor; if  $i \in \{1, 2, \dots, n\}, i \neq h, X_h$  is quasi superior to  $X_i$ , then the factor  $X_h$  is a quasi-optimal factor.

### 3 CAVERN BLASTING ENGINEERING EXAMPLE

#### 3.1 Determining the system feature variables and related factors

As blasting seismic wave parameters, vibration peak parameters are used only to judge the size of the vibration, and not the duration of

the vibration. Vibration frequency also plays an important role on vibration intensity, so three factors are taken as systematic feature factors. In combination with the Longbeiwang hydropower station cavern blasting test site, in the design of blasting parameters, the relevant factors including the total amount, the number of segments, maximum explosive, blasting distance and elevation difference are selected, and the chamber length and the main line charge should also be considered due to the cavern blasting.

Therefore, the total amount and maximum explosive, chamber length, main line charge and the number of segments, blasting distance and the minimum delay time interval elevation difference were regarded as related variables, and recorded for  $X_i$  ( $i = 1, 2, 3, \dots, 8$ ), respectively. The monitoring data of a cavern blasting vibration in Hubei is established in this paper. Part of the monitoring data is presented in Table 1.

#### 3.2 Calculated gray correlation

##### 3.2.1 The original data, the cavern blasting vibration velocity, the main vibration frequency and the duration of blasting vibration testing data

It can be seen from Table 2, the system characteristics variable sequence is  $Y1 = [10.24 \ 5.184 \ 5.158 \ 10.98 \ 6.507 \ 4.064]$ ,  $Y2 = [8.673 \ 9.363 \ 11.17 \ 11.01 \ 11.35 \ 4.792]$  and  $Y3 = [0.7466 \ 0.6843 \ 1.057 \ 0.870$

Table 1. Monitoring data samples of blasting vibration.

X1	X2	X3	X4	X5	X6	X7	X8
Total amount	Maximum explosive	Chamber length	Main line charge	Segments	Blasting distance	Elevation difference	Delay time interval
kg	kg	m	kg/m		m	m	ms
14700	4412	18.36	240	2	356.22	72	50
15330	4600	22.30	216	2	494.12	66	100
12570	3772	18.30	240	4	447.85	42	150
11280	3384	18.18	192	6	259.11	40	200
10830	3248	12.74	144	8	545.91	28	250
14850	4456	28.91	264	10	325.34	77	250

Table 2. Monitoring data samples of blasting vibration.

System characteristics variable	Y <sub>1</sub>	Vibrate velocity /cm/s	10.24	5.18	5.16	10.98	6.50	4.06
	Y <sub>2</sub>	Main frequency /Hz	8.67	9.36	11.17	11.01	11.35	4.79
	Y <sub>3</sub>	The duration /s	0.75	0.68	1.06	0.87	0.59	0.74

0.5966 0.7434]. The associated factors variable matrix is shown as follows:

$$X' = \begin{bmatrix} 1.12 & 1.16 & 0.95 & 0.85 & 0.82 & 1.12 \\ 1.11 & 1.15 & 0.96 & 0.84 & 0.83 & 1.10 \\ 0.93 & 1.13 & 0.92 & 0.92 & 0.64 & 1.46 \\ 1.11 & 1.00 & 1.11 & 0.89 & 0.67 & 1.22 \\ 0.38 & 0.38 & 0.75 & 1.13 & 1.50 & 1.88 \\ 0.88 & 1.22 & 1.10 & 0.64 & 1.35 & 0.80 \\ 1.33 & 1.22 & 0.78 & 0.74 & 0.52 & 1.42 \\ 0.30 & 0.60 & 0.90 & 1.20 & 1.50 & 1.50 \end{bmatrix} \quad (9)$$

### 3.2.2 Using the average method to dimensionless data

Average method is used to dimensionless Equations (4) and (5), and the matrix  $X'$  of the new matrix  $X$  can be obtained as Equation (10):

$$X = \begin{bmatrix} 14700 & 15330 & 12570 & 11280 & 10830 & 14850 \\ 4412 & 4600 & 3772 & 3384 & 3248 & 4456 \\ 18.36 & 22.30 & 18.30 & 18.18 & 12.74 & 28.91 \\ 240.0 & 216.0 & 240.0 & 192.0 & 144.0 & 264.0 \\ 2.000 & 2.000 & 4.000 & 6.000 & 8.000 & 10.00 \\ 356.2 & 494.1 & 447.9 & 259.1 & 545.9 & 325.3 \\ 72.00 & 66.00 & 42.00 & 40.00 & 28.00 & 77.00 \\ 50.00 & 100.0 & 150.0 & 200.0 & 250.0 & 250.0 \end{bmatrix} \quad (10)$$

### 3.2.3 Calculating the correlation

Excel is used and combined with Equations (6) and (7) to calculate the correlation degree of the characteristic vector sequence  $Y$  and influencing factors of the variable  $X$ , as given in Table 3.

### 3.3 The result analysis

1. The order of the influence of various factors on blasting vibration velocity is as follows: total amount, maximum explosive, elevation difference, main line charge, delay time interval, number of segments, chamber length, and blast-

ing distance. The major role is played in cavern blasting vibration strength.

- The order of the influence of various factors on blasting vibration frequency is as follows: blasting distance, main line charge, chamber length and maximum explosive, total amount, delay time interval, number of segments, elevation difference among them, effect of blasting distance is the largest, maximum explosive takes the second place, and influence of the elevation difference is relatively small.
- The order of the influence of various factors on duration of blasting vibration is as follows: main line charge, chamber length, total amount, maximum explosive, blasting distance, number of segments, delay time interval, elevation difference, associated value of the main line charge and chamber length is much bigger than other factors in the main influence factors on the duration.
- As three parameters were chosen to be systematical characteristics variables of blasting vibration, the sum value of correlation degree of vibration velocity and vibration frequency and duration of vibration are adopted to evaluate the impact degree of various factors on blasting vibration, and the result is relatively reasonable. The major influence factors of the cavern blasting vibration intensity are the total amount and the main line charge, that is to say, in the cavern blasting, their influence of blasting vibration should be considered first.
- Based on past experience in blasting engineering, it was found that the total amount and the maximum explosive have great influences on blasting vibration. It can be seen from the gray correlation calculation results that the total amount and the maximum explosive play an important role in the influence of blasting vibration. This result is consistent with related projects basically. Therefore, the blasting vibration on slope rock mass can be reduced and slope rock mass stability is protected by controlling

Table 3. Correlation results (non-dimensional).

	Total amount	Maximum explosive	Chamber length	Main line charge	Segment	Blasting distance	Elevation difference	Delay time interval
Vibration velocity	0.730	0.728	0.619	0.656	0.622	0.597	0.710	0.625
Vibration frequency	0.612	0.612	0.645	0.709	0.519	0.757	0.478	0.583
Duarte time	0.784	0.784	0.834	0.835	0.551	0.715	0.586	0.587
Summation	2.126	2.124	2.098	2.2	1.692	2.069	1.774	1.795

the total amount and the maximum explosive in the future.

#### 4 CONCLUSIONS

Through the above application, the gray relational analysis method can be used to analyze the influencing factors of blasting vibration in a cavern, and the following conclusions can be obtained:

1. Gray relational analysis method can be used for fewer samples to identify the primary and secondary relations of a variety of factors that affect the blasting vibration under a certain blasting condition. It provides scientific evidence for the reasonable control of blasting vibration. Moreover, it is a simple and effective method.
2. When the influence factors of blasting vibration were analyzed, it is found to be more reliable and multiple feature variables were chosen to analyze. When multiple blasting characteristics variables were used, different situations of different blasting characteristic variables of the optimal factor often appeared, and then the size of the blasting characteristics and values of correlation between variables were considered to determine the factors that influence the blasting. Thus, more reasonable results can be obtained.
3. The above results of the gray correlation and analysis advantages were sorted and can be seen from the correlation. Cavern blasting is different from other blasting. The main period of feeds and the medicine chamber length effect on the size of the vibration strength is more important. So, in the cavern blasting, the effect of the two factors on the influence of blasting vibration should be considered.

#### 5 DISCUSSION

1. In order to control the blasting vibration, the domestic and foreign scholars are basically focused on the design of blasting parameters. However, the influence of the topography and geomorphology, geological conditions on blasting vibration is ignored. Although there are some scholars who began to pay attention to this problem, the results are mainly amplified with the lash effect and site effect. However, the influence of and the form and geological conditions on blasting vibration will be the trend of the blasting vibration research.
2. At present, a lot of methods are used to study the influence factors of blasting vibration, but commons area involve analyzing the influence degree of various factors, single affect peak speed, duration of vibration, and the main vibration frequency, respectively. The coupling effect between the influence factors cannot be considered, and the research on the coupling action is very effective on controlling the blasting vibration.

#### REFERENCES

- Desuo, Hu Cai. & Tiesong, Zhang. 1997. Forecast research on effect of vibration and damage in rock mass blasting. *Chinese Journal of Geotechnical Engineering*, 19(1):43-49.
- De La Corte Bacci, & Denise, et al. 2002. Statistical methods applied to the analysis of blasting vibrations in a diabase quarry in the city of Campinas, (SP)-Brazil *Proceedings of the Annual Conference on Explosives and Blasting Technique*, vI, p 265-279,.
- Guangzhou Zhang. & Desheng Wang. et al. 2005. The regression analysis of blast vibration based on MATLAB. *Shanxi Architecture*, (16): 102-103.



- Hai, Shi Tang. & Yongqiang, Li. et al. 2007. Action of peak velocity of blasting vibration based on neural network. *Chinese Journal of Rock Mechanics and Engineering*, (7): p 3534–3539.
- Huaqi Zhang. & Songxin Zhang, et al. 2007. Influence of blasting vibration on nearby buildings. *Blasting*, 24(2):98–101.
- Jinxue Wang. & Yong Guo. et al. 2003. Preliminary analysis of predicting the velocity of the blasting vibration by neural network. *Non-ferrous Mining and Metallurgy*, 19(1):13–16.
- Julong Deng. 2002. Grey System Theory. *Wuhan: Huazhong University of Science and Technology Press*.
- Julong Deng. 2005. Basic Method of Grey System. *Wuhan: Huazhong University of Science and Technology Press*.
- Mei Yuan, & Zuoqiang Wang. et al. 2010. Evaluation and Study on the effect of deep-hole lasting in open-pit mine based on fuzzy mathematics and analytic hierarchy process. *Mining Research and Development*, (5):1–3.
- Mingbiao Xu. & Dehong Peng, et al. 2004. Application of AHP in optimization choice of blasting program. *West-China Exploration Engineering*, (4):118–120.
- Quanjun Xu. & Qingming Zhang. et al. 1998. Neural network model for forecasting peak acceleration of blasting vibration. *Journal of Beijing Institute of Technology*, 18(4):472–475.
- Resende R, & Gomes J P. 2010. Simulation of vibration generated by underwater blasting using statistical analysis and numerical modeling, *Rock Mechanics in Civil and Environmental Engineering-Proceedings of the European Rock Mechanics Symposium*, Eurock, p 313–316.
- Sifeng Liu. & Yaoguo Dang, et al. 2010. Grey System Theory and Its Application. *Beijing: Science Press*.
- Venkatesh, H S. 2005. Influence of total charge in a blast on the intensity of ground vibrations-Field experiment and computer simulation. *Frag blast*, v 9, n 3, p 127–138.
- Yongji Huo. 2003. Blasting vibration effects on structures and safety analysis. *Blasting*. 20(1):1–6.
- Yiping Zhang. & Xibing LI. et al. 2005. Analysis of chamber blasting vibration based on HHT method. *Chinese Journal of Rock Mechanics and Engineering*, 24 (Supp.1): 4784–4787.

# Study on the dynamic deformation characteristics of loess landslide

X.M. Cui & X.H. Sun

*School of Geology Engineering and Surveying, Chang'an University, Xi'an, Shaanxi, China*

**ABSTRACT:** Dangjiacha landslide was triggered by Haiyuan earthquake. Based on the site investigation, representative soils on the sliding surface were collected for soil tests. By using the advanced dynamic torsional shear triaxial apparatus, a series of shear tests were carried out to study the loess's dynamic characteristics of Dangjiacha landslide. The dynamic torsional shear test results show that the dynamic shear stress-strain curves can be described with hyperbola under complex stress conditions. Consolidation confining pressure influences the dynamic shear stress-strain relationship curve obviously, but the influence of vibration frequency is not obvious. The relationship between the dynamic shear modulus and dynamic shear strain is little influenced by consolidation confining pressure and vibration frequency. The dynamic shear modulus attenuates quickly when the dynamic shear strain is in the range of 0–1. However, when the dynamic shear strain is larger than 3, the dynamic shear modulus attenuates very slowly.

**Keywords:** Haiyuan earthquake; Dangjiacha landslide; dynamic torsional shear triaxial apparatus; consolidation stress; vibration frequency

## 1 INTRODUCTION

Loess is covered with more than 9.3 percent of the world's land mass, with a total area of about 13 million. The most typical loess is located in China. In China, the area of loess region is about 640,000 km<sup>2</sup>. It is one of the main areas of seismic activity. Previous strong earthquakes have caused a lot of landslides, subsidence due to earthquake, cracks and other disasters, which is a threat to human life and property seriously (Wan 2003). Thus, the study of the loess structural characteristics under seismic forces is significant for earthquake disaster reduction, economic and social development in the loess area.

In view of this, loess dynamic characteristics under the earthquake have been studied by many scholars. Some have studied using the seismic wave and random wave exerted on a standard specimen to study the dynamic strength and deformation characteristics of loess (Duan, Zhang, and Li 1990; Wang and Zhang 1991; Wang, Zhang, and Wang 1994). Others have studied by considering the simplified earthquake wave as an equivalent sine wave, and then exerted the equivalent sine wave on the soil samples. The test result has been carried out on similar dynamic strength—dynamic strain rules (Wu and Xie 1987, 1994; Xie 2001). Dynamic stress-strain relationship, the dynamic elastic modulus, dynamic strength and damping ratio of loess in different regions under different consolidation stresses and different moisture contents have also been studied by other scholars (Chen, He, and Gao 2006;

Luo 2000; Luo and Tian 2005; Luo, Xie, and Li 2000; Tian, Zhang, and Zhang 2004). However, the study on the dynamic characteristics of loess under complex stress conditions is still not sufficient.

This paper aims to disclose the dynamic characteristics of loess earthquake landslide. Dangjiacha landslide triggered by Haiyuan earthquake was selected as the research object. Representative loess on the sliding surface was collected for soil tests. By using the advanced dynamic torsional shear triaxial apparatus, a series of shear tests were carried out.

## 2 DANGJIACHA LANDSLIDE BACKGROUND

Dangjiacha landslide was one of the typical high-speed remote loess landslides triggered by Haiyuan earthquake in 1920. It is located in Dangjiacha



Figure 1. Dangjiacha landslide (Sun et al. 2009).

Table 1. Physical property indices of intact loess.

Density g/cm <sup>3</sup>	Specific gravity	Liquid limit %	Plastic limit %	Plastic index %	Particle composition		
					Sand %	Silt %	Clay %
1.3	2.71	31.1	21.4	9.7	13.0	71.9	15.1

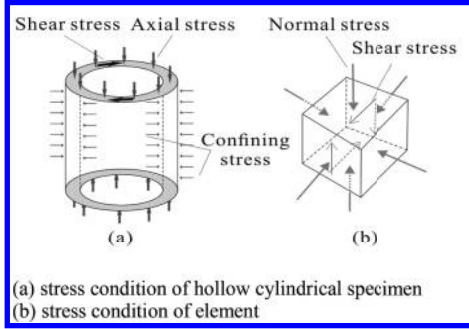


Figure 2. Stress state of the sample.

village, Xiji County, Ningxia Autonomous Region (Fig. 1). The landslide is mainly composed of Late Pleistocene Malan loess (Q3), and the sliding surface shape looks like a chair. The sliding direction is 295°, and the average slope angle is about 25 m. When the earthquake occurred, the landslide moved down to the Nilan River, and formed a lake (Sun et al. 2009).

### 3 TEST DESIGN

#### 3.1 Soil sample preparation

Representative loess on the sliding surface was collected for soil tests. Its indices of physical properties are listed in Table 1. Using specialized tools, the soil was collected into hollow cylindrical specimens of height 100 mm, outer diameter 70 mm, and inner diameter 30 mm. The hollow cylindrical specimens were sealed with plastic wrap to prevent evaporation.

The stress state of the specimen is shown in Figure 2. The hollow cylindrical sample bears internal and external confining pressure, the axial load and vibration torque on the cross section. These forces can simulate the radial stress, circumferential stress, axial normal stress and torsional shear stress. Using the to and fro movement, the dynamic test can be implemented.

#### 3.2 Test apparatus and design

The dynamic torsional shear triaxial apparatus developed by Japan HiTi Ltd was used in this

experiment. This apparatus composed of the host, pressure control system, power control system and measurement system. The measurement system automatically collected the data every 0.03 s. During the test, data on static pressure, dynamic pore water pressure, axial deformation, dynamic torque and dynamic angle were recorded.

In this test, the consolidation ratio was 1.5, and confining pressures were 100 kPa, 200 kPa, 300 kPa. Under each confining pressure, five vibration frequencies were selected in this test (Cui 2011).

## 4 ANALYSIS OF THE TEST RESULTS

### 4.1 Relationship of dynamic shear stress and shear strain of intact loess

Dynamic torsional shear tests of intact loess under different consolidation stresses and vibrational frequencies were carried out. Through the analysis of the test results, a series of dynamic shear stress ( $\tau_d$ ), dynamic shear strain ( $\gamma_d$ ) relation curves, dynamic shear modulus ( $G_d$ ), and dynamic shear strain ( $\gamma_d$ ) relation curves were obtained (Figs. 3 and 4).

It can be seen from Figure 3 that consolidation confining pressure influences the  $\tau_d$ - $\gamma_d$  relation curves obviously, but the influence of vibration frequency is not obvious. With the decrease in the consolidation confining pressure, the relationship curve has a downward trend. This means that dynamic stress decreases with the decrease in the consolidation confining pressure under the same dynamic strain. The relation curves exhibit no cross phenomenon under different confining pressures. During the vibration frequency at 0.5 Hz, 1 Hz, 2 Hz, the  $\tau_d$ - $\gamma_d$  relationship curves concentrated in a very narrow stripe. During the vibration frequency at 5 Hz, 10 Hz, the  $\tau_d$ - $\gamma_d$  relationship curves moved up.

This is because the loess has a loose structure, and the soil density increases with the increasing consolidation pressure. So, to produce the same dynamic shear strain, they need a bigger dynamic shear stress. Moreover, the smaller the vibration frequency, the greater the corresponding amplitude, and the soil structure can be easily damaged.

Figure 4 shows the  $1/G_d$ - $\gamma_d$  relation curves of intact loess under different test conditions. It can be seen that  $1/G_d$ - $\gamma_d$  relation curves conform to the linear relationship. Its expression is given as follows:

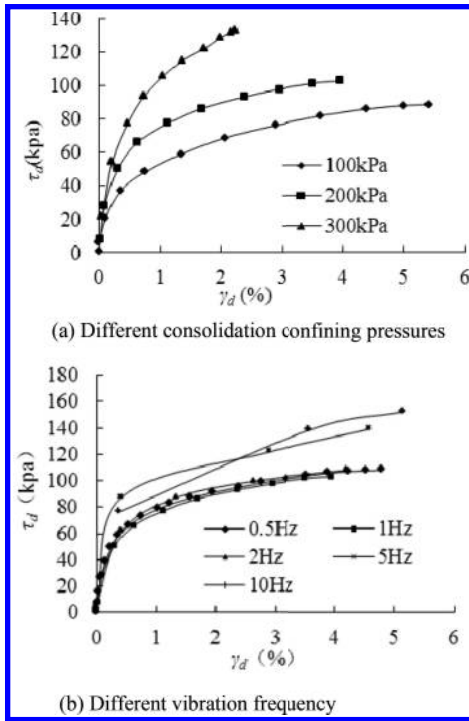


Figure 3.  $\tau_d-\gamma_d$  relationship curves.

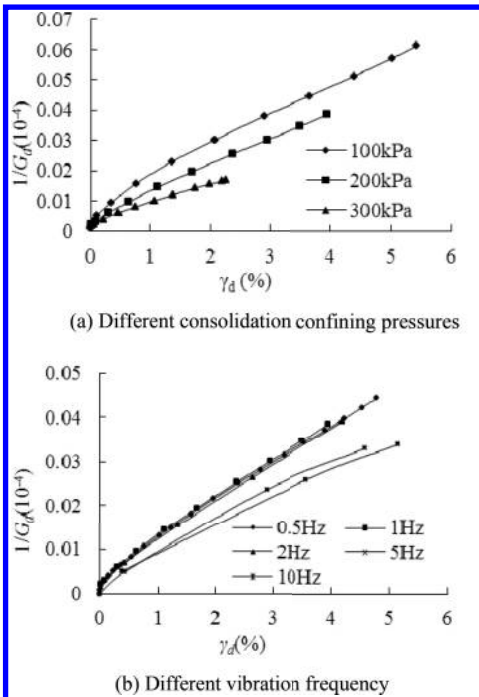


Figure 4.  $1/G_d-\gamma_d$  relationship curves.

$$\frac{1}{G_d} = a + b\gamma_d \quad (1)$$

where

$G_d$  is the dynamic shear modulus;  
 $\gamma_d$  is the dynamic shear strains;  
 $a = 1/G_0$  is the  $1/G_d-\gamma_d$  curve in the y intercept;  
 $b = 1/\tau_{dmax}$  is the  $1/G_d-\gamma_d$  relation curves' slope;  
 $G_0$  is the maximum dynamic shear modulus or the initial dynamic shear modulus; and  $\tau_{dmax}$  is the maximum dynamic shear stress.

Moreover, substituting  $1/G_d = \gamma_d/\tau_d$  into (1) equation, it becomes

$$\tau_d = \frac{\gamma_d}{\frac{1}{G_0} + \frac{\gamma_d}{\tau_{dmax}}} = \frac{\gamma_d}{a + b\gamma_d} \quad (2)$$

Thus,  $\tau_d-\gamma_d$  relation curves conform to the hyperbolic model.

#### 4.2 Dynamic shear modulus

The dynamic shear modulus of the soil is the dynamic shear stress required to produce units of dynamic shear strain. It can be expressed by the ratio of dynamic shear stress and shear strain. It is the ability of the soil to resistant dynamic shear deformation. It is an important index to evaluate soil seismic performance.

Figure 5 shows  $G_d-\gamma_d$  relation curves. It shows that the dynamic shear modulus ( $G_d$ ) decreases with the increase in the dynamic shear strain. The attenuation of  $G_d$  within the range of 0–1 of the dynamic shear strain is rapid. When the dynamic shear strain is  $\geq 3$ , the attenuation of  $G_d$  almost close to zero. The value of  $G_d$  is distributed within a very narrow strip under different consolidation confining pressures and different vibration frequencies. Therefore, the consolidation confining pressure and the vibration frequency have little influence on the  $G_d-\gamma_d$  relation curves.

#### 4.3 The initial dynamic shear modulus and the maximum dynamic shear stress

From the above findings, we can see that the initial dynamic shear modulus ( $G_0$ ) is the reciprocal of  $1/G_d-\gamma_d$  relation curve on the vertical intercept, and the reciprocal of the slope of  $1/G_d-\gamma_d$  relation curve is the maximum dynamic shear stress ( $\tau_{dmax}$ ). The initial dynamic shear modulus and the maximum dynamic shear stress can be obtained from the test. The results are summarized in Table 2 and Table 3.

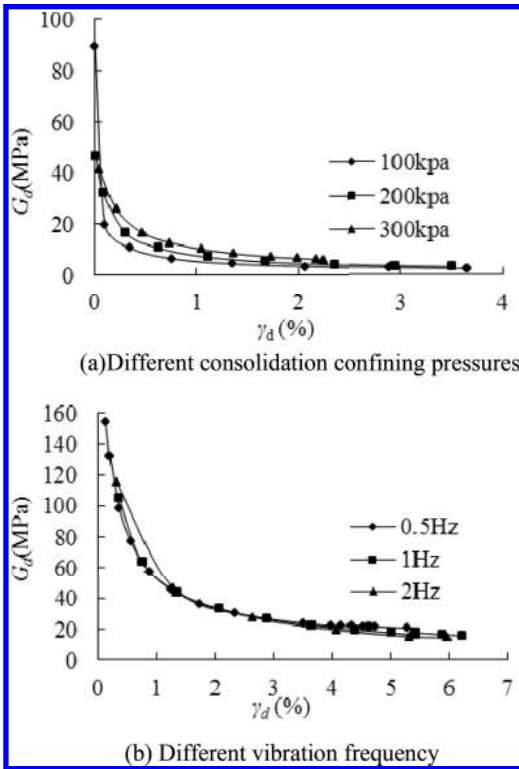


Figure 5.  $G_d-\gamma_d$  relationship curves.

Table 2. The initial dynamic shear modulus of intact loess.

Vibration frequency	Initial dynamic shear modulus $G_0$		
	$\sigma_3 = 100$ kPa	$\sigma_3 = 200$ kPa	$\sigma_3 = 300$ kPa
0.5 Hz	161	370	384
1 Hz	142	312	357
2 Hz	192	384	500
5 Hz	163	370	400
10 Hz	238	333	625

Table 3. The maximum dynamic shear stress of intact loess.

Vibration frequency	Maximum dynamic shear stress $\tau_{dmax}$		
	$\sigma_3 = 100$ kPa	$\sigma_3 = 200$ kPa	$\sigma_3 = 300$ kPa
0.5 Hz	100	111.11	135.14
1 Hz	98.04	109.89	156.25
2 Hz	92.59	113.64	188.68
5 Hz	105.26	156.25	188.63
10 Hz	84.75	163.93	125

It can be seen from Tables 2 and 3, under the same vibration frequency, the greater the consolidation stress, the larger the initial dynamic shear modulus and the maximum dynamic shear stress. This is because the loess is a kind of unsaturated and under consolidated soil, and has macro pores and vertical fissures. Therefore, loess is consolidated under a certain consolidation confining pressure: the larger the pressure is, the better the loess consolidation will be, and the greater the loess dynamic strength will become. Under a certain consolidation confining pressure, applying different vibration frequencies on soil specimens, the value of the initial dynamic shear modulus and the maximum dynamic shear stress becomes more dispersed and has no obvious regularity.

## 5 CONCLUSION

In this paper, we take the loess under different consolidation confining pressures and different vibration frequencies as the research subject, and using the dynamic torsional shear triaxial apparatus, we studied the dynamic characteristics of the intact loess of Dangjiacha landslide. The main result can be summarized as follows:

1. The dynamic shear stress and dynamic shear strain relation curves conform to a hyperbolic model under different consolidation confining pressures and vibration frequencies. Consolidation confining pressure influences the  $\tau_d-\gamma_d$  relationship curve obviously, but the influence of vibration frequency is not obvious. The influence can be described by the changing rules of the initial dynamic shear modulus and the maximum dynamic shear stress under complex stress conditions. These characteristics of landslide soil are consistent with the previous research results of loess.
2. Dynamic shear modulus and dynamic shear strain have little influence on the relationship between the dynamic shear modulus and dynamic shear strain. The dynamic shear modulus attenuates quickly when the dynamic shear strain is in the range of 0–1; however, when the dynamic shear strain is much larger than 3, the dynamic shear modulus attenuates very slowly.
3. The initial dynamic shear modulus and the maximum dynamic shear stress increase with the increase in consolidation confining pressures. Under a certain consolidation confining pressure, applying different vibration frequencies on soil specimens, the value of the initial dynamic shear modulus and the maximum dynamic shear stress becomes more dispersed and has no obvious regularity.

## REFERENCES

- Chen, Cunli, Junfang He, and Peng Gao. 2006. 'Dynamic Deformation Characteristics of Intact Loess under Different Water Content', *Journal of Xi'an University of Technology*, Vol. 22 No. 4.
- Cui, Xiangmei. 2011. 'The dynamic characteristics and structure of loess under dynamic torsional shear', Chang'an University.
- Duan, Ruwen, Zhenzhong Zhang, and Lan Li. 1990. 'Further research on dynamic characteristics of loess', *Northwestern Seismological Journal*, Vol. 12, No. 3.
- Luo, Yasheng. 2000. 'Experimental study of dynamic properties and parameters of typical loess in China', Xi'an University of Technology.
- Luo, Yasheng, and Kanliang Tian. 2005. 'Dynamic shear modulus and damping ratio of unsaturated loess', *Journal of hydraulic engineering*, 36(7).
- Luo, Yasheng, Dingyi Xie, and Yonghong Li. 2000. "Experimental study and exploration of dynamic triaxial test of intact loess." In *Collapsible loess study and engineering*, 830–34. Beijing: China Building Industry Press.
- Sun, Ping, Yueping Yin, shuren Wu, Fawu Wang, and Liwei Chen. 2009. 'An experimental study on the initiation mechanism of rapid and long run-out loess landslide caused by 1920 Haiyuan earthquake', *Journal of Engineering Geology*, 17(4).
- Tian, Kanliang, Huili Zhang, and Boping Zhang. 2004. 'An experimental study on dynamic properties of unsaturated loess under dynamic torsional shear', *Chinese journal of rock mechanics and engineering*, 23(24).
- Wan, Lanmin. 2003. *Loess Dynamics* (Seismological Press: Beijing).
- Wang, Lanmin, and Zhenzhong Zhang. 1991. 'Test method of dynamic strength of loess under random seismic load', *Northwestern Seismological Journal*, 13(3).
- Wang, Lanmin, Zhenzhong Zhang, and Jun Wang. 1994. "Dynamic behavior of loess under irregular seismic loading." In *Proceedings of the second international conference on earthquake resistant on construction and design*.
- Wu, Zhihui, and Dingyi Xie. 1987. "Dynamic Characteristics of Intact Loess." In *ASCE*. New Jersey: Geotechnical Special Publication.
- Wu, Zhihui, and Dingyi Xie. 1994. 'Study of Luochuan loess on dynamic deformation and shear strength', *Journal of Hydraulic Engineering*, (12).
- Xie, Dingyi. 2001. 'Exploration of some new tendencies in research of loess soil mechanics', *Chinese Journal of Geotechnical Engineering*, 23(1).

# The deformation characteristics of Xi'an aquifer sand under high-stress condition

X.H. Sun & X.M. Cui

*School of Geology Engineering and Surveying, Chang'an University, Xi'an, China*

**ABSTRACT:** By using self-designed high-pressure consolidation system, one dimensional consolidation test on aquifer sand under high-stress state is conducted. The test simulates the process of compaction and expansion of aquifer caused by fluctuation of water table in confined aquifer. The relationship between the deformations of aquifer sand sample and pore water pressure was analyzed. Test results show that: aquifer sands present complex deformation characteristics under different stress state. When pore pressure drops, the aquifer sand is compacted. Most of the deformation is plastic and creep characteristic is obvious. When pore pressure arises, the aquifer sand expands very little and the deformation is mainly elastic. There are significant differences between the particle size distribution curves before and after the test. The rupture and crush of sand particle can be seen in The SEM images directly. The sand deformation is related to the rupture and sand particles as well.

**Keywords:** aquifer compaction; high-stress state; sand deformation; land subsidence; water table decline

## 1 INTRODUCTION

Excessive withdrawal of groundwater has caused severe land subsidence in Xi'an, China (Lee, et al., 1996). In the process of land subsidence both the aquifer and the aquitard have been compacted (Galloway, et al., 1999). In the early stage of land subsidence, many researchers have put great emphasis on the deformation of aquitard (Holzer, 1995, Shearer, 1998). Some researchers take the view that majority of permanent deformation is caused by the compression of aquitard which is composed of fine-grain sediment (Ortega-Guerrero, et al., 1999). The compaction of coarse-grain sediment (such as sand) during the process of subsidence is very small and recoverable (Tolman and Poland, 1940). With the accumulation of extensometer and laboratory data, it was found that deformation of aquifer can take up more than 50% of the total subsidence and become the main compaction layer (Zhang, et al., 2006). Thus, the deformation of aquifer sand gradually aroused research's attention and the study of sand deformation increase gradually (Hoffmann, et al., 2003).

In the initial stage of groundwater exploitation, the pumpage is relative small and depths of wells are shallow, the compacted layers mainly located in shallow strata. Aquifer sand is under low-stress state and its deformation characteristic is clarity known by researchers. As the increase of groundwater demand, aquifer system loses

balance between recharge and discharge. Long-term ground-water withdrawal caused significant drop of water table in confined aquifers. The aquifer sand is gradually influenced by pumping and produces deformation. In Xi'an, a long history of ground-water withdrawal have created severe land subsidence hazard. According to the monitor data of extensometer group which located in the southern suburb of Xi'an, all of the hydrostratigraphic units within 300 m depth were compressed obviously (Peng, 2012). In this context, understanding the deformation characteristics of each stratum has become a necessary condition for calculating land subsidence (Sun, 2014). Under different stress state, the deformation characteristics of the aquifer sand vary greatly. How to simulate the in-situ stress state of aquifer which buried deep under the ground become the key difficulties to test (Xue, 2003). For the stress conditions is strict and difficult to meet, there are a few related research have been conducted (Huang, 2007, Li, et al., 2007, Ma, et al., 2008, Shi, et al., 2007). The degree of the research is still not enough.

The medium-fine sand in Xi'an aquifer is selected as sample in this test. Self-designed high-pressure consolidation system is used to accurately simulate the in-situ stress condition of aquifer and fluctuation of water table caused by groundwater withdrawal. Deformation characteristics of aquifer sand are detail analyzed after the test.

## 2 HIGH-PRESSURE CONSOLIDATION TEST

### 2.1 Testing devices

The test is performed on self-designed high-pressure consolidation system (Fig. 1). The total stress (axial stress) in the test is applied by the axial stress loading parts (part 2). The pore water pressure is applied by pore pressure loading parts (part 3). The confining chamber is a hollow drum shape cylinder and soil sample is placed in it. Its inner diameter is 125 mm and the internal height is 440 mm. The confining chamber is made of stain steel and it can withstand 10 MPa pressure during the test. During the test the specimen is always under the water to maintain saturation. There are four pore transducer installed on wall of confining chamber to measure pore pressure.

### 2.2 Test sample

The main lithology of Xi'an aquifers is medium-fine sand. The sample chosen for this test is sampling from a 5 m-deep pit which located in the western suburbs of Xi'an. The basic characteristics of sand

sample are as follows: specific gravity  $G_s = 2.675$ , effective size  $d_{10} = 0.223$  mm and average size  $d_{50} = 0.614$  mm.

### 2.3 Stress levels and loading methods

Based on the monitor data of extensometer group, the stratum which buried from 0 to -300 m are main compaction layers and their compression accounted for 89% of the total land subsidence.

Therefore, this test is mainly to consider the deformation of aquifer which buried shallower than -300 m. The depth of Xi'an confined aquifer mainly located in the depth from -100 to -300 m. The total stress of aquifer sand is proportional to the depth they was buried. When the bulk density is assumed equal to 20 kN/m, the total stress is from 2 MPa to 6 MPa. Total stress is applied by means of axial stress in the test. The pore water pressure is proportional to water table of aquifer. The water table is assumed equal to -50 m before ground water has been heavily pumped. And gradually decline to depth they are buried and then recovery to the initial depth. Thus the pore pressure applied in the test related to the aquifer depth and range from 0.5 MPa to 2 MPa (Table 1).

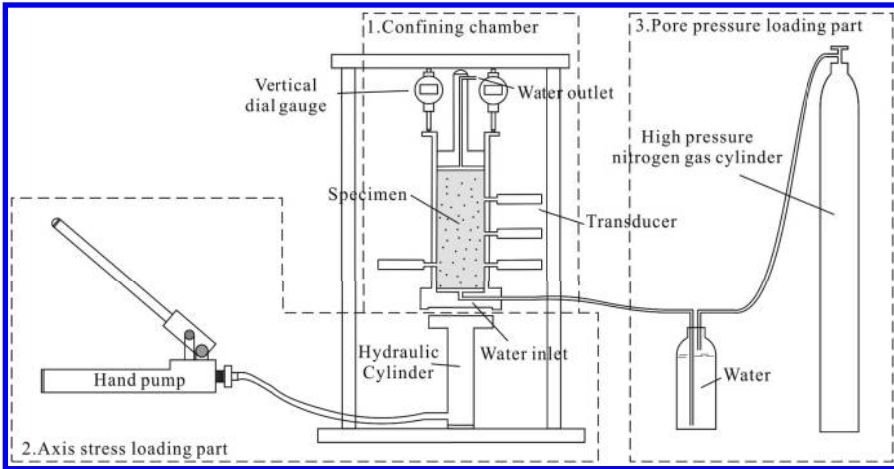


Figure 1. High-pressure consolidation system.

Table 1. Stress applied in the test.

Stage	Axial stress (MPa)	Simulated depth (m)	Pore pressure (MPa)	Simulated water table(m)
1	2	-100	0.5→0→0.5	-50→-100→-50
2	3	-150	1→0→1	-50→-150→-50
3	4	-200	1.5→0→1.5	-50→-200→-50
4	5	-250	2→0→2	-50→-250→-50
5	6	-300	2.5→0→2.5	-50→-300→-50



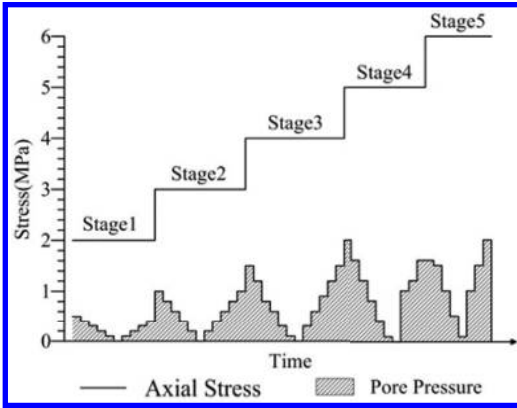


Figure 2. Stress levels and sequence in the test.

The staged loading method is adopted in this test. To simulate the total stress and water pressure in reality, the axial stress and pore pressure are independent applied by part 2 and part 3 of the high-pressure consolidation system respectively. Keeping the axial stress unchanged, change the pore water pressure step by step after the deformation of sand sample become stable. When the pore pressure restores to the original value in this stage, increase the axial stress to the next stage level. According to the difference in axial stress, the test can be divided into five loading stages. From stage 1 to stage 5, the magnitude of axis stress were 2, 3, 4 and 5 MPa respective (Fig. 2).

### 3 RESULTS OF HIGH-PRESSURE CONSOLIDATION TEST

Through applying a series of stress on the sand sample strain-time and strain-stress characteristics of sample can be determined.

#### 3.1 Strain-time curves

The stage 3 in Figure 2 was selected as typical case for analysis in this stage. The test results can be drawing into form of strain-time curve. The axial stress keeping unchanged at 4 MPa, and pore pressure dropped progressively from 1.5 Mpa to 1.2, 0.9, 0.6, 0.3 and 0 Mpa, then gradual return to 1.5 MPa (Fig. 3). During the process of pore pressure fluctuation, the aquifer sand shows complex deformation characteristics. (1) During the whole process of pore pressure fluctuation, the majority of deformation of sand sample is unrecoverable. it means the deformation of sand is plastic rather than elastic. The plastic deformation of the vertical strain is about 0.7%. (2) The deformation of sand is not finished instantaneous. When the pore

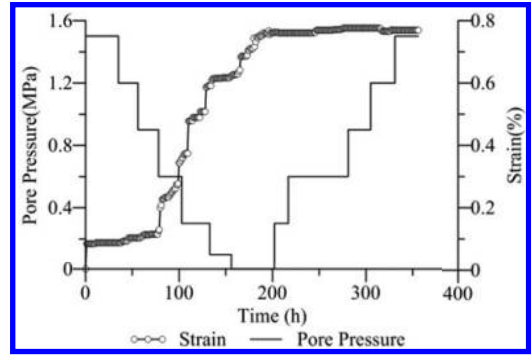


Figure 3. Stress applied in Stage 3.

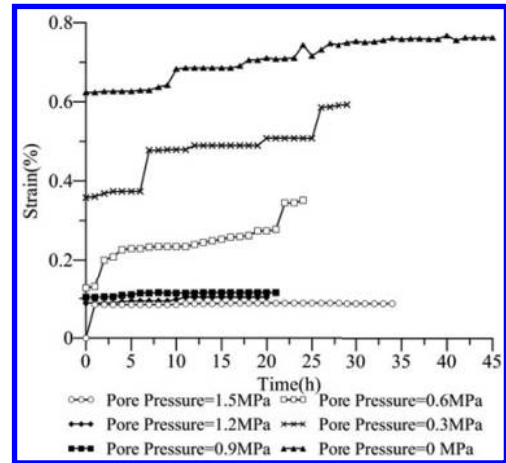


Figure 4. Strain-time curves in Stage 3 (axial stress = 4 Mpa).

pressure drops from 0.9 MPa to 0.6 MPa and from 0.6 MPa to 0.3 MPa, the delay compaction caused by consolidation can be ignored due to high permeability coefficient of sand. Deformations of sand sample stabilize in more than 20 hours after pore pressure changed is caused by creep (Fig. 4). (3) When the pore pressure was arising the sand expands so small.

#### 3.2 Strain-stress curve

After the test is finished, the plot of the effective stress (calculated from axial stress and pore pressure) versus the corresponding compaction strain of each stress state can be drawn (Fig. 5).

The Figure 5 shows, deformation of the sand is not only related to the effective stress, but also related to the stress history of sand. When pore pressure drops but higher than any previous value (preconsolidation stress), the change of pore pressure creates

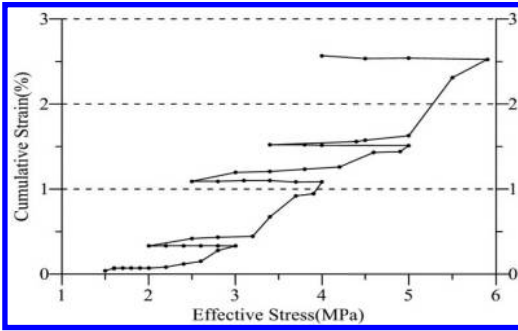


Figure 5. Strain-stress relations curve.

only a small deformation. When the pore pressure drops and lower than previous value, the sand may undergo significant, permanent compaction. The compaction includes elastic, plastic and viscose components. When pore pressure arises, along with the effective stress reducing, the sand sample has a small amount of expansion. It is inconsistent with the traditional view on sand deformation.

#### 4 MICROSCOPIC ANALYSIS OF THE TEST

##### 4.1 Laser particle size analysis

In order to explore the deformation mechanism of Xi'an aquifer sand, laser particle analyses were conducted (Fig. 6).

Through the comparisons of particle size distribution curve before and after the test, it can be seen that the sand particle size distribution curves have changed markedly. The percentage of coarse particles with diameter larger than 0.36 mm was reduced after the test. The percentage of sand with diameter smaller than 0.36 mm was rising meanwhile. This phenomenon shows that sand has various deformation mechanisms under high-stress state. Besides mutual slip between the particles, the sand grains may crack during the compression. This phenomenon is more common for large size of the sand particles.

##### 4.2 Images of SEM

High-precision Scanning Electron Microscope (SEM) was used to observe the microstructure of sample after the test. It can easily found and directly observed cracks and scratches in the surface of sand grain in SEM images (Fig. 7).

##### 4.3 Mechanism of sand deformation under high-stress state

Prior to the deformation of sand, arrangement of sand grains are loose and the soil skeleton is

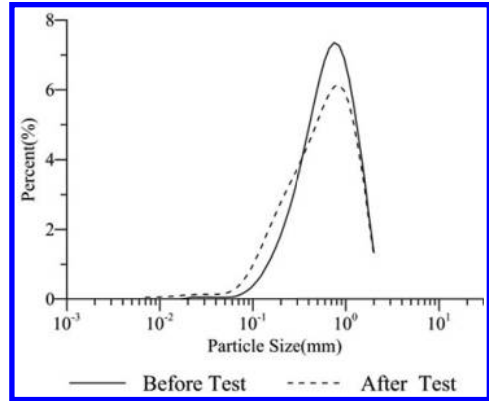


Figure 6. Particle size distribution curve in the test.

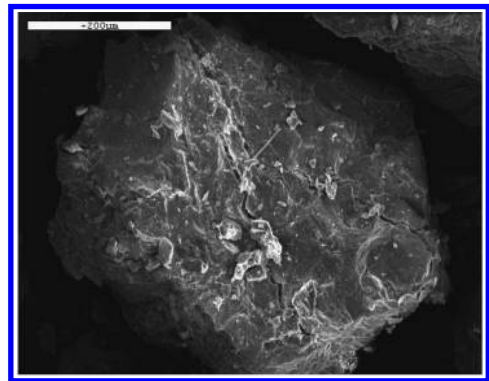


Figure 7a. Sand after test (magnify = 200).

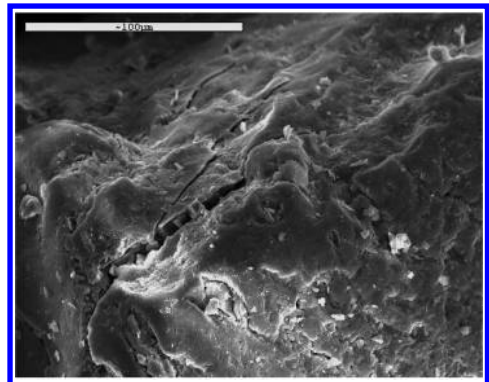


Figure 7b. Sand after test (magnify = 600).

not stable. There are a lot of pores with different size spread over the soil body. After effective stress is applied, soil skeleton start to deform, and sand particles start to move. In the process of grain moving, some small sand particles filled into the

big pores lead to quickly decrease in sand porosity and high-rate deformation. With the increasing number of big pores are filled gradually, space for sand particles moving is limited. As the resistance increases gradually, the moving speed of particles slow down. In macroscopic, the rate of sand deformation changes from fast to slow as time goes on. With the increase of effective stress, the acting force between soil particles increases accordingly. Usually, the interfaces between sand particles are not Surface-to-surface contact, but face-angular contact or angular-angular contact.

So there is a large stress concentration in contact position. When effective stress is large enough, the sand particles with shape of flake, columnar, angular, and larger particle are prone to rupture, crushing or grinding. A big particle may crush into some smaller particles. The smaller particles filled into the spaces between larger particles and soil begins to further deformation. For both the sand particles moving and crushing are need some time to finished, thus the sand exhibit creep characteristics. In unloading process (pore pressure arise), the small particles that have been crushed before cannot be re-cemented and returned to its original position (McDowell, 2003). So the sand has large irrecoverable plastic compaction.

## 5 CONCLUSION

In this paper, the deformations of aquifer sand under high-stress state are the main research subject. By using high-pressure consolidation system, characteristics of sand sample are analyzed and the mechanism of sand deformation is discussed. The main result summarized as follows:

1. The deformation characteristics of sand under high stress are complex. The compaction includes not only elastic and plastic deformation, but the viscous deformation as well.
2. Deformation characteristics of sand are related to changing patterns of pore pressure. When pore water pressure drops. Sand creeps and most of the deformation are irreversible. When pore pressure arises, sand compression stops or takes very slight expansion.
3. Sand deformation not only related to the slip between the particles but also to the crushed or fractured of some particles as well.

## REFERENCES

- Galloway D., Jones D.R., Ingebritsen S.E. 1999. Land subsidence in the United States *US Geological Survey Reston, VA*.
- Hoffmann J., Leake S.A., Galloway D.L, Wilson A.M. 2003. MODFLOW-2000 Ground-Water Model—User Guide to the Subsidence and Aquifer-System Compaction (SUB) Package USGS.
- Holzer T.L. 1995. The history of the aquitard-drainage model pp. 7–12.
- Huang W. 2007. Testing study on particle breakage mechanism of quartz sand under high pressure stress. Master, Wuhan University of ethnology.
- Lee C., Zhang J., Zhang Y. 1996. Evolution and origin of the ground fissures in Xian, China. *Engineering geology* 43: 45–55.
- Li W., Yin Z., Li G., Chi H. 2007. Sandy one-dimension circulating compression test and application to groundwater reservoir (in Chinese). *Rock and Soil Mechanics* 28: 2145–2148.
- Ma J., Cui G., Qin Y., Zhou G. 2008. Experimental on unloading compression test and application to high pressure (in Chinese). *Journal of China Coal Society* 33: 1239–1242.
- McDowell G.R. 2003. Micromechanics of creep of granular materials. *Géotechnique* 53: 915–916.
- Ortega-Guerrero A., Rudolph D.L., Cherry J.A. 1999. Analysis of long-term land subsidence near Mexico City: Field investigations and predictive modeling. *Water Resources Research* 35: 3327–3341.
- Peng J. 2012. Geo-hazards of Xi'an earth fissures science Press.
- Shearer T.R. 1998. A numerical model to calculate land subsidence, applied at Hangu in China (in Chinese). *Engineering Geology* 49: 85–93.
- Shi X., Xue Y., Wu J., Zhang y., Ye s., Yu J. 2007. Uniaxial compression test for creep model of saturated sand in Changzhou (in Chinese). *Journal of Engineering Geology* 15: 212–216.
- Sun G. 2014. Test study on deformation characteristics of soils in Xi'an Under condition of groundwater fluctuation (in Chinese). Chang'an University.
- Tolman C.F., Poland J.F. 1940. Ground-water infiltration, and ground-surface recession in Santa Clara Valley, Santa Clara County, California. *Transactions American Geophysical Union* 21: 23–34.
- Xue Y. 2003. Present status of modeling land subsidence in China and problems to be solved (in Chinese). *Hydrogeology & Engineering geology* 30: 1–5.
- Zhang Y., Xue Y., Wu J., Li Q. 2006. Characteristics and parameters of sand strata deformation due to groundwater pumping in Shanghai (in Chinese). *Shui Li Xue Bao* 37: 560–566.

# Experiment research on the creep model of aquifer sand in Xi'an

X.H. Sun & X.M. Cui

School of Geology Engineering and Surveying, Chang'an University, Xi'an, China

**ABSTRACT:** The long history of ground-water pumping has caused a severe land subsidence hazard in Xi'an, China. During the process of ground-water pumping, deformation of confined aquifer has an influence on the total subsidence. In order to ascertain the deformation characteristics of aquifer, which is mainly composed of sand, a series of tests were conducted. By using a self-designed high-pressure consolidation system, the *in situ* stress states of aquifers were simulated in the test. The test results show that the sand of aquifer expresses a complex deformation characteristic under high-stress states. The aquifer sand shows a remarkable creep characteristic when the water table drops. When the water table arises, the creep of sand is not obvious. When the water table drops, the stress-strain and strain-time relation curves of sand can be described by the Generalized Kelvin Model with five components. Five rheological parameters in the Generalized Kelvin Model are not constant but varied, which are related to effective stress.

**Keywords:** aquifer sand; creep model; land subsidence; high-pressure consolidation system; Xi'an

## 1 INTRODUCTION

Xi'an is located in the northwestern of China where the amount of annual rainfall is often less than 400 mm (Lee et al., 1996). The industrial and municipal use of water depends almost entirely on groundwater. The amount of explored ground water began to increase substantially after 1960s (Peng, 2012). The long history of groundwater pumpage has caused a severe land subsidence hazard. In the early stage of land subsidence research, many researchers have put great effort on the deformation of aquitard. It was usually thought that the land subsidence was caused by the compaction of aquitard, which composed of fine-grained sediments primarily. Almost all of the subsidence is caused by compaction of clay layers (Holzer, 1995; Ortega-Guerrero et al., 1999; Shearer, 1998). Comparatively, the compaction of sand or coarser-grained sediments is elastic and small that can be negligible (Tolman and Poland, 1940).

With the accumulation of monitoring data, researchers have gradually realized that the aquifer can also be compacted substantially. The coarser-grained sediments (e.g. sand) and fine-grained sediments (e.g. clay and silty clay) have differences in compressibility. However, when the accumulative thickness of sand layers was large enough, the total compression of sand layers may be remarkable (Liu et al., 1994). Thus, the deformation of aquifer should be calculated in the land subsidence model (Hoffmann et al., 2003).

In reality, the aquifer system is buried deep under the ground. The total stress of the aquifer is

equal to the weight of the overlying stratum. The pore water pressure is related to the change in the water table. Long-term ground-water withdrawal from confined aquifers reduces fluid pressures and causes the sand layer to compact. Since the change in the water table is very slow and cyclical, both the changing patterns of effective stress and deformation characteristics of the sand layer are different from that under the low-stress state in the conventional consolidation test (Zhang et al., 2012). Under the high-stress state, the aquifer sand has complex deformation characteristics (Sun, 2014). It not only depends on the magnitude of the effective stress and impose orders, but also is related to time. Compared with the low-stress state, the aquifer deforms plastically and deformation lags behind the change in pore water pressure in them. It shows the characteristics of creep. Concisely, it describes the deformation characteristics of aquifer sand during compaction, and the expansion process is the key factor in land subsidence modeling.

Recent years, many researchers have taken these complex deformation characteristics of the aquifer sand into consideration, and have finished some field and laboratory tests. However, there are no creep models to describe such deformation characteristics of aquifer sand under *in situ* stress conditions for Xi'an yet. Therefore, a self-designed high-pressure consolidation system was used to accurately simulate the *in situ* stress condition of aquifer and fluctuation of water table caused by groundwater withdrawal. By simulating the stress changes, the deformation was measured. Furthermore, the deformation characteristics of

aquifer sand were analyzed and a new creep model was constructed.

## 2 ONE-DIMENSIONAL CREEP TEST

### 2.1 Testing device

Creep test is conducted on a self-designed high-pressure consolidation system. This system mainly composed of axis stress applying parts, pore pressure applying parts and confining chamber. The confining chamber is the key components of the high-pressure consolidation system. Soil sample is placed inside the stain steel cylinder. Axial stress is applied to the specimen through a rigid piston and porous stone located on the top of the soil specimen (Fig. 1). The advantage of the test system is that it can control the magnitude of axial stress and pore pressure independently, and thus it can be used to simulate the overlaying load and pore water pressure, respectively.

### 2.2 Test sample

The main lithology of Xi'an aquifers is a medium-fine sand. The sample sand chosen for this experiment is sampled from a 5 m-deep pit, which is located in the western suburbs of Xi'an. The basic characteristics of the sand sample are as follows: specific gravity  $G_s = 2.675$ , effective size  $d_{10} = 0.223$  mm and average size  $d_{50} = 0.614$  mm. During the test, the temperature is set as  $15 \pm 5^\circ\text{C}$ .

### 2.3 Stress levels and loading methods

The test used the staged loading method. There were four loading stages in the test. From stage 1 to stage 4, the magnitude of axis stress was 1.72, 2.99, 4.25 and 4.88 MPa, respectively. For each stage, the

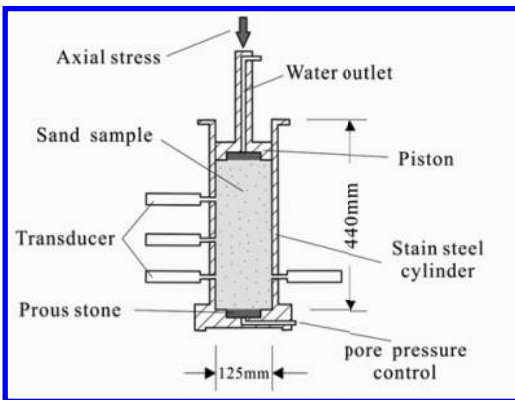


Figure 1. Confining chamber.

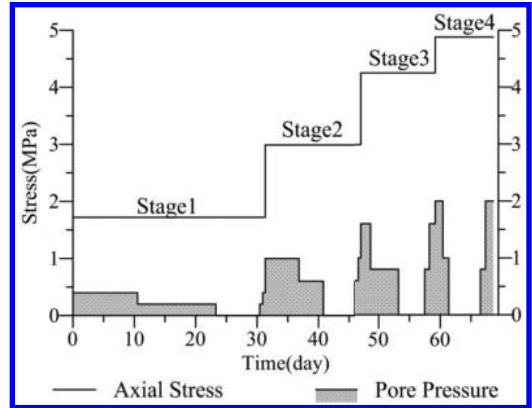


Figure 2. Axial stress and pore pressure in the test.

pore pressure was applied from an initial value that was gradually reduced to 0, and then progressively restored to its original value (Fig. 2). It then took stage 2 as example. The axial stress was 2.99 MPa, and approximately equal to the total stress of the aquifer, which was buried 150 m under the ground. Pore pressure had an initial value of 1 MPa, and then stepped down to 0 MPa and gradually returned to 1 MPa. The fluctuation of pore pressure simulated the process of the water table in Xi'an confined aquifer, which dropped from  $-50$  m to  $-150$  m depth and then returned to  $-50$  m. In the test, changing either the axial stress or the pore pressure of the aquifer sand sample reached a stable state. The criterion for the sand sample to reach a stable state is the rate of deformation less than  $0.001$  mm/h.

The axis stress, pore pressure, the sand sample's compression or expansion and time were all documented during the whole test.

## 3 RESULTS OF THE CREEP TEST

The result of the test is expressed by the plots of strain versus time in minutes, as shown in Figure 3.

From the strain-time curves under the multi-level stress state, some features different from the low-stress state can be found.

When changing the pore pressure each time, the compression of the sand sample increased with time rapidly, but the rate of compression decreased gradually. The deformation process of the aquifer sand can be divided into two phases.

In the first phase, the change in the pore pressure caused the same magnitude change in effective stress. Sand began to consolidate and made large deformation. Due to high permeability, the

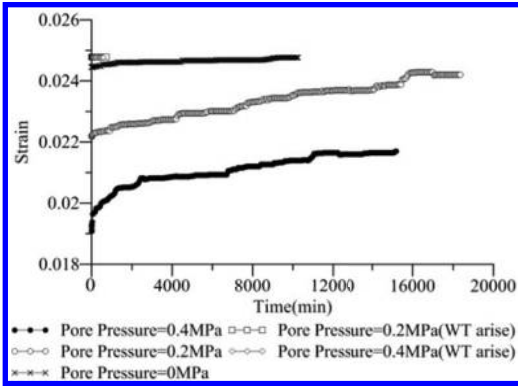


Figure 3a. Creep curve in stage 1, axis stress = 1.72 Mpa.

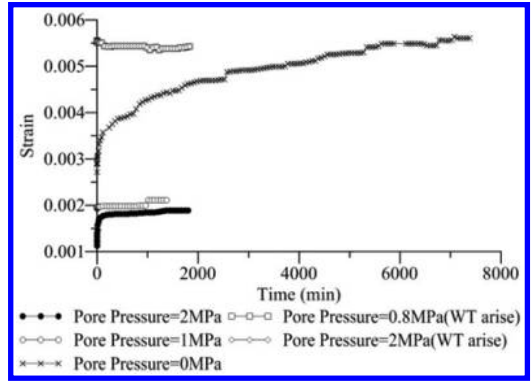


Figure 3d. Creep curve in stage 4, axis stress = 4.88 Mpa.

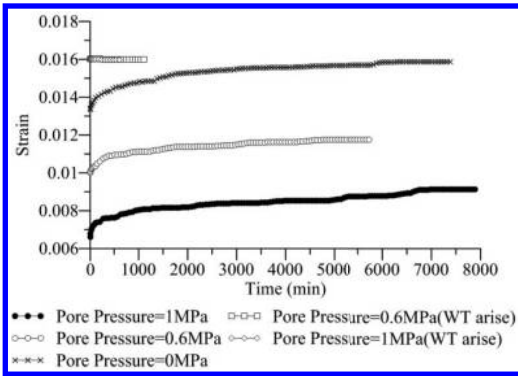


Figure 3b. Creep curve in stage 2, axis stress = 2.99 Mpa.

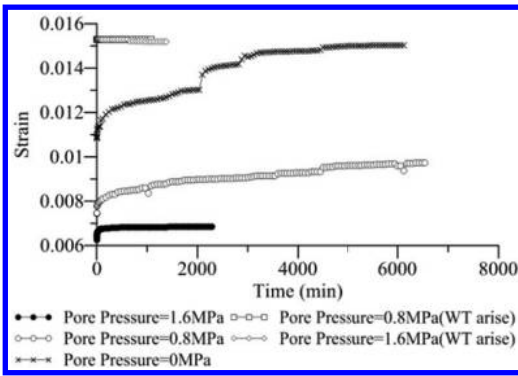


Figure 3c. Creep curve in stage 3, axis stress = 4.25 Mpa.

excessive pore water pressure in the sand sample dissipated immediately after the pore pressure changed. So, the first phase lasted for a very short time and instantaneous compaction was caused by consolidation.

In the second phase, the aquifer sand sample was under constant effective stress, but its deformation continued to grow as time increased. Aquifer sand began to creep obviously.

When the pore pressure was increasing, the sand expanded so small that the strain curve was almost horizontal. In other words, Xi'an aquifer sand had a creep feature only when loading or the water table dropped.

#### 4 RESULTS OF THE CREEP TEST

Based on the test results, it is found that the deformation of Xi'an aquifer sand has the characteristics of elastic, plastic and viscosity. In order to apply these features to land subsidence calculation model, a creep model should be constructed for the deformation of Xi'an aquifer sands. Based on the rheological model theory, the aquifer sand can be seen as a homogeneous continuum with elastic, plastic and viscosity. Some basic rheological components are combined to fit the complex characteristic of aquifer sand in the test. These basic rheological components include the Hook model, the Newton model, and the St Venant model (Fig. 4a-c).

##### 4.1 Selection of the creep model

The deformation of aquifer sand has some instantaneous compaction. It should have the Hook model in the creep model, and the hook model should be connected in series with other components. The rate of sand compression decreases gradually. And creep deformation tends to a limit value. It should have components that have a decaying creep feature, such as Kelvin model (Fig. 4d). Merchant model can fit the above requirements. Due to steep parts of creep curves, the Merchant model cannot quite

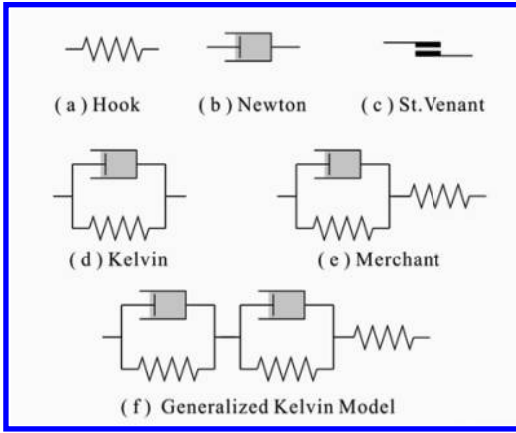


Figure 4. Creep model for the deformation of aquifer sand.

fit the first phase of sand deformation (Fig. 4e). Multiple Kelvin model connected in series can avoid the above shortcomings. The more the Kelvin body in series, the steeper the initial stage of the creep curve is. Land subsidence is a regional geological hazard. Many parameters of the rheological model may be hard to obtain in reality. Thus, the components used in the constructed creep model should be as little as possible. A generalized Kelvin model with five components is used to describe the characteristics of aquifer sand deformation (Fig. 4f).

#### 4.2 Model parameter fitting

The generalized Kelvin model, which is used in this article, is composed of two Kelvin bodies and a Hook body in series, so the relation between strain and stress can be expressed as follows:

$$\sigma_1 = \sigma_2 = \sigma_3 = \sigma \quad (1)$$

$$\sigma_1 = \sigma = E_H \varepsilon_1 \quad (2)$$

$$\sigma_2 = \sigma = E_{K1} \varepsilon_2 + \eta_{K1} \dot{\varepsilon}_2 \quad (3)$$

$$\sigma_3 = \sigma = E_{K2} \varepsilon_3 + \eta_{K2} \dot{\varepsilon}_3 \quad (4)$$

where  $E_H$ ,  $E_{K1}$ ,  $E_{K2}$  are the modulus of elasticity, and  $\eta_{K1}$ ,  $\eta_{K2}$  are the coefficient of viscosity.

From Equation (2), we obtain

$$\varepsilon_1 = \frac{\sigma}{E_H} \quad (5)$$

And from Equation (3), we obtain

$$\varepsilon_2 = e^{-\int \frac{E_{K1}}{\eta_{K1}} dt} \left( c + \int \frac{E_{K1}}{\eta_{K1}} \frac{\sigma}{E_{K1}} dt \right) \quad (6)$$

When  $t = 0$ ,  $\varepsilon_2 = 0$ , we thus obtain

$$c = -\frac{\sigma}{E_{K1}} \quad (7)$$

Equation (6) becomes

$$\varepsilon_2 = \frac{\sigma}{E_{K1}} \left( 1 - e^{-\frac{E_{K1}t}{\eta_{K1}}} \right) \quad (8)$$

Similarly,

$$\varepsilon_3 = \frac{\sigma}{E_{K2}} \left( 1 - e^{-\frac{E_{K2}t}{\eta_{K2}}} \right) \quad (9)$$

So, the strain of the generalized Kelvin model can be expressed as follows:

$$\varepsilon = \frac{\sigma}{E_H} + \frac{\sigma}{E_{K1}} \left( 1 - e^{-\frac{E_{K1}t}{\eta_{K1}}} \right) + \frac{\sigma}{E_{K2}} \left( 1 - e^{-\frac{E_{K2}t}{\eta_{K2}}} \right) \quad (10)$$

Table 1. Parameters of the generalized Kelvin model.

Axis stress/MPa	2.99		
Pore pressure/MPa	0	0.6	1
$E_H$ /MPa	227.3	238.1	312.5
$E_{K1}$ /MPa	1639.3	2941.2	1470.6
$E_{K2}$ /MPa	3636.4	2040.8	434.8
$\eta_{K1}$ /MPa · d	2180.3	382.7	102.6
$\eta_{K2}$ /MPa · d	203.5	4617.5	6680.4
Correlation coefficient	0.9934	0.995	0.9774

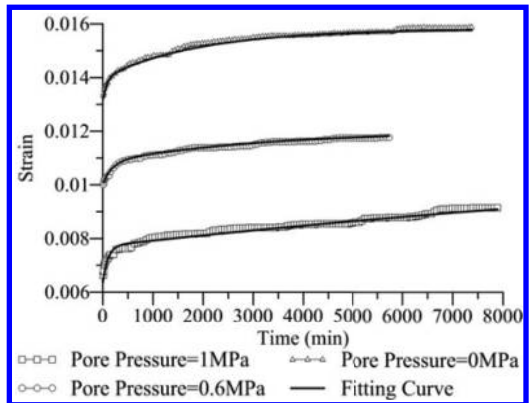


Figure 5. Fitting curves of stage 2 by using the generalized Kelvin model.

Table 2. The correlated coefficient of the generalized Kelvin model under different stress states.

Axial stress (MPa)	Pore pressure (MPa)	Correlation coefficient
1.72	0.4	0.9523
	0.2	0.9384
	0	0.9635
4.25	1.6	0.9702
	0.8	0.9798
	0	0.9237

Deformation can be calculated by using Equation (10). We choose the creep curve in stage 2 as representation. According to the test data, the parameters in the generalized Kelvin model were determined. Each value is given in Table 1, and the fitting curves are shown in Figure 5.

It can be seen from Table 1 that the five parameters of the generalized Kelvin model under different effective stress conditions vary. So, the parameters of the generalized Kelvin model are not constant, but vary with the change in effective stress.

Table 2 lists the correlation coefficient of the generalized Kelvin model in fitting each stress state curve in the test. The generalized Kelvin model can thus describe the deformation feature under *in situ* stress states.

## 5 CONCLUSION

In this paper, the deformations of aquifer sand under high stress states are the main research subject. By using a high-pressure consolidation system, the characteristics of the sand sample are analyzed and a creep model is constructed. The main result can be summarized as follows:

1. Xi'an aquifer sand showed a significant creep characteristic when the water level dropped. And no creep occurred when the water table arose.

2. Generalized Kelvin model was composed of five components. It could describe the complex compaction characteristic of Xi'an aquifer sand.
3. The parameters of the creep model of Xi'an aquifer sand were not constant but varied. By using the variable parameter model, it could improve the model precision.

## REFERENCES

- Hoffmann, J., Leake, S.A., Galloway, D.L., Wilson, A.M., 2003. MODFLOW-2000 Ground-Water Model—User Guide to the Subsidence and Aquifer-System Compaction (SUB) Package. *USGS Report*
- Holzer, T.L., 1995. The history of the aquitard-drainage model pp. 7–12.
- Lee, C., Zhang, J., Zhang, Y., 1996. Evolution and origin of the ground fissures in Xian, China. *Engineering geology* 43, 45–55.
- Liu, Y., Chen, Z., Ni, W., 1994. Discussion for Xi'an ground fissures and land subsidence disaster mechanism and countermeasures (in Chinese). *The Chinese Journal of Geological and Hazards and Control*.
- Ortega-Guerrero, A., Rudolph, D.L., Cherry, J.A., 1999. Analysis of long-term land subsidence near Mexico City: Field investigations and predictive modeling. *Water Resources Research* 35, 3327–3341.
- Peng, J., 2012. Geo-hazards of Xi'an ground fissures. *Science Press*, Beijing.
- Shearer, T.R., 1998. A numerical model to calculate land subsidence, applied at Hangu in China. *Engineering Geology* 49, 85–93.
- Sun G, 2014. Test study on deformation characteristics of soils in Xi'an Under condition of groundwater fluctuation. Thesis for doctor's degree. Chang'an University.
- Tolman, C.F., Poland, J.F., 1940. Ground-water infiltration and ground-surface recession in Santa Clara Valley, Santa Clara County, California. *Transactions American Geophysical Union* 21, 23–34.
- Zhang, Y., Xue, Y., Wu, J., Wang, H., He, J., 2012. Mechanical modeling of aquifer sands under long-term groundwater withdrawal. *Engineering Geology* 125, 74–80.



# Fractal study of debris flow provenance granularity in Qinling temple valley

X.C. Xue, D. Han, L.Y. Zhang, P.B. Yang, L.J. Shi, S.Y. Huang & Y.C. Zhang  
*College of Geology and Environment, Xi'an University of Science and Technology, Xi'an, China*

**ABSTRACT:** The research of debris flow provenance and deposit granularity is one of the debris flow researches in the field of basic content and the characteristics of fractal theory solution of complex problems are widely used. The fractal dimension of provenance granularity of mine debris flow is one of the important structure indexes of potential landslide, which reflects the formation mechanism and dynamics, kinematics characteristics of debris flow. This paper based on fractal theory studies the debris flow provenance of Qinling mountain temple valley mine, and based on the obtained debris flow provenance granularity fractal dimension value in the study area offers the date to support the prevention of debris flow disasters in the study area.

**Keywords:** Qinling; temple valley; mine debris flow; provenance granularity; the fractal

## 1 INTRODUCTION

Debris flow is one of the common geological disasters in mountain. It has the characteristics of sudden, ferocious, briefly, scouring and silting in large scale, devastating, and often caused great damage to people's life and property<sup>[1]</sup>. In the mineral resources area, there has been massive artificial loose solid material, increased in the natural ground slope, which has made the non-debris flow gully turn into debris flow gully, from fewer area into high incidence and formed the mine debris flow disaster due to large-scale mining beneficiation activities, solid waste emissions and burden, such as solid waste emissions and burden.

Affected by multiphase tectonic movement and weathering denudation of joint action for a long time, the mine debris flow gully topography in the study area is various, and the grain composition of wasted slag is complex. In order to explore the nonlinear characteristic of the main controlling factors of the mine debris flow in the study area, we made a fractal study of wasted slag based on on-site measurement, photographs, measurements, graphics, statistics, and sampling tests.

## 2 INTRODUCTION OF FRACTAL DIMENSION

Fractal dimension is a value that is used to measure a set of irregular and broken degree of geometrical or natural object and usually expressed in scores or

decimal number. Fractal theory is put forward by American B.B.M andelbrot at first in the 1970s<sup>[2]</sup>. It can be used to research no characteristic length but has self-similarity of graphics and phenomena in the nature. Fractal dimension can be given a quantitative description to complex configuration that the traditional mathematics is difficult to answer in the nature<sup>[3]</sup>.

## 3 GRANULARITY FRACTAL DIMENSION CALCULATION

Granularity fractal dimension generally has the following several kinds of calculation methods: calculating the fractal dimension by changing the size of observation, analyzing the granularity of provenance, calculating the fractal dimension according to the measure dimension and according to the correlation function and dimension, etc<sup>[4]</sup>. This paper selects changing the size of observation and analyzes the granularity of provenance to realize the Debris flow provenance granularity fractal calculation.

### 3.1 Changing the size of observation

Changing the size of observation is also called Box counting method<sup>[5]</sup>. It is the use of different lengths of a square grid to cover the object under the test. When a square grid length changes, the number  $N(r)$  of grid covered with the object has inevitable changes. When the lengths of a square grid are  $r_1$ ,

$r_2, r_3, \dots$ , fairly  $r_k$ , the number of square grid is covered with measured object corresponding to  $N(r_1), N(r_2), N(r_3), \dots N(\text{fairly } r_k)$ , we can calculate the granularity fractal dimension by formula (1):

$$\lg N(r) = -D \lg r + A \quad (1)$$

Type: A is undetermined constants and D is the dimensions of the measured object; its value is equal to the absolute value of the type slope value.

### 3.2 Analysis of the granularity provenance

The formation process of debris flow is a very complicated nonlinear process and the composition particle of debris flow is a no characteristic length structure graph. The fractal of debris flow is a self-similar particle size distribution based on a statistical sense. The fractal dimension of particle is calculated by using formula (2):

$$D = b - 3 \quad (2)$$

According to the analysis results of granularity of debris flow, we can find a straight line from the particle size of log-log graph of cumulative percentage of the particle and particle size, then search for a straight line segment of slope, and get the Granularity fractal dimension of wasted slag sources<sup>[6]</sup>.

## 4 THE RESEARCH OF PROVENANCE GRANULARITY FRACTAL

### 4.1 The fractal features of coarse particle

We adopted “changing the size of observation” to calculate the fractal dimension of coarse particles whose diameter is larger than 1 cm of debris flow source. The specific methods: choosing coarse particle with diameter greater than a certain grain size as the research object, and determining the measurement scale by blockiness size. Generally, we called the particles whose diameter is larger than 20 cm as rubble, and called the diameter between 1 cm and 20 cm as crushed stone. Particle dimension is 1 cm that can be used as a lower bound of the scale of the field fractal measurement.

Since the statistical work progress is slow, in order to get more accurate data, we took massive photos of debris flow source using a high-resolution digital camera (Fig. 1). Then, we measured the maximum diameter of each stone using the AutoCAD software, and calculated the actual diameter through certain proportion relationship with the tools of Excel. Finally, we acquired grain-size statistical results in the study area (Table 1).

We took the logarithm of measure as abscissa and the logarithm of the count of aggregate that



Figure 1. The statistical photo of source.

Table 1. The statistical table of wasted slag granularity.

r (cm)	>50	>25	>12.5	>6.25
N (1-2)	0	0	21	105
N (1-3)	0	0	14	122
N (1-4)	0	0	30	98
N (1-5)	0	1	24	95
N (2-1)	0	0	8	83
N (3-1)	0	1	6	58
N (3-2)	0	1	17	80
N (3-3)	0	0	9	70
N (4-1)	0	2	37	101
N (4-4)	0	0	8	85

Note: r—particle size, cm; N—the accumulative frequency of the rubble whose diameter is greater than r; 1-2, 1-3 point number of photos or sample.

corresponds to scale as ordinate. Then, we can obtain a set of data and put all data in the rectangular plane coordinate system. According to the definition of fractal, if the object of study in accordance with fractal rule, the point will land on a straight line; if the object of study in a certain interval in accordance with the law of fractal, and in other interval does not conform to the fractal rule, then the point in the range of fractal will fall on a straight line. According to “Change the size of observation” and Table (1), the absolute value of straight slope is the fractal dimension of the particle size in the study area.

According to the above principles, finished the fractal calculation of 10 samples, we can obtain fractal dimension of samples in the study area (Table 2).

### 4.2 The fractal features of granule

The diameter of grain between 0.0625 mm ~ 1 cm of the debris flow provenance, we used the sieving to get grain composition and then we calculated

Table 2. The fractal dimension of coarse particle of wasted slag in Temple ditch mine.

Sample	1-2	1-3	1-4	1-5
Fractal dimension	1.504	1.964	1.096	1.149
Related coefficient	0.911	0.896	0.906	0.850

Table 3. The granularity cumulative percentage distribution table of granule.

Sample	r	The percentage of grain $\eta$ (%)		
		<0.066	<0.090	<0.100
1	m (g)	0.50	59.50	77.30
	$\eta$ (%)	0.03	3.90	5.06
2	m (g)	0.10	3.90	37.70
	$\eta$ (%)	0.01	0.13	1.27
3	m (g)	0.80	41.10	31.00
	$\eta$ (%)	0.04	2.10	1.58
4	m (g)	0.30	26.90	35.90
	$\eta$ (%)	0.02	1.55	2.07

Note: r—particle size, mm;m—the cumulative of particles of the wasted slag, g;  $\eta$ —the cumulative percentage,%

Table 4. The fractal dimension of granule of wasted slag in Temple ditch mine.

Sample	1	2	3	Average
Fractal dimension	2.6033	2.5277	2.4310	2.4439
Related coefficient	0.9687	0.9941	0.9948	0.9870

the fractal dimension by “analysis the granularity of provenance”. Through sieving, we let diameter of slag to be 3.2, 2, 1, 0.5, 0.4, 0.25, 0.2, 0.1, 0.09, and 0.066 mm standard sample sieve, and obtained grain size distribution data of various samples (Table 3).

According to sieving result of sample, we can get the slope of the straight line and obtained the granularity of the fractal dimension according to formula (2) (Table 4).

#### 4.3 The fractal features of particle

To the diameter of the grain less than 0.0625 mm of debris flow provenance, we gained grain composition by using a laser diffract instrument. The particle size of wasted slag ranged from 20 to 80 microns. Then, we calculated the fractal dimension by “principle of granularity analysis”. According to the formula (2), it is not difficult to draw fractal dimension of wasted slag (Table 5).

Table 5. The fractal dimension of the particle of wasted slag in Temple ditch mine.

Sample	1	2	3	Average
Fractal dimension	2.2361	2.3220	2.4152	2.3078
Related coefficient	0.9976	0.9978	0.9922	0.9964

## 5 CONCLUSION

Through the fractal research of debris flow provenance granularity multi-scale, we can draw the following conclusions:

1. Mine debris flow provenance whether large particles, medium particles, or micro particles, can be characterized by fractal dimension; a variety of particle scales have good fractal characteristics.
2. From the point of fractal dimension, the fractal dimension of coarse particles tend to be scattered (1.012~2.929), and the mean value is 1.926; the fractal dimension of granule is relatively concentrated, and the mean value is 2.511. The fractal dimension of particle is concentrated, and the mean value is 2.309. These values indicate that the larger particle has the smaller fractal dimension. From the correlation coefficient, the fractal dimensions of the average correlation coefficient of the three particles are 0.909, 0.974, and 0.996. That indicated the particle of debris flow source has more obvious fractal characteristics.
3. The fractal dimension of provenance granularity of mine debris flow is one of the important structure indexes of potential landslide, which reflects the formation mechanism and dynamics, kinematics characteristics of debris flow. The greater the provenance granularity fractal dimension the more the particles in clay composition has, which the probability of viscous debris flow is greater, the higher the risk of the mine debris flow at the same time, the stability is worse.

## REFERENCES

- [1] Pan Mao tie-feng li. Disaster geology [M]. Cambridge university press. 2006.
- [2] Mandelbrot B.B. The Fractal Geometry of Nature [M]. New York: W.H. Freeman and Co: 1982.
- [3] Sun Boling. Fractal dimension and its measuring method [J]. Journal of northeast forestry university, 2004, 32 (3): 116-119.
- [4] Xiao-hua Zhu, wang jian. The relationship between fractal dimension and scale of geological phenomenon [J]. Earth information science, 2003, 3 (1): 67-71.
- [5] Grassberger P. On efficient box counting algorithms. International Journal of Modern Physics C, 1983, 4 (3): 515-523.
- [6] Docile subjects. The fractal structure characteristics of the debris flow deposits [J]. Journal of natural disasters, 1994, 3 (2): 91-96.

# Research on the effect of bank slope on rising and drawdown of water level

Chunmei Wang & Yuelei He

*Urban Railway Transportation College, Shanghai University of Engineering Science, Shanghai, China*

Minglu Zhang

*State Key Laboratory of Mining Disaster Prevention and Control, Co-founded by Shandong Province and the Ministry of Science and Technology, Shandong University of Science and Technology, Qingdao, China*

**ABSTRACT:** For this study, a soil–rock mixture slope was taken, for example, the coupled stress and seepage field and stability characteristic during rising and drawdown of reservoir water level were studied based on finite element model. Proper calculation parameters were selected in the landslide simulation according to the engineering condition. The results indicated that groundwater levels in different lithological mediums varied at different speeds; variation of groundwater level was lagged behind the variation of reservoir level when the reservoir is filling fast. But it was not so different from that of the reservoir level during the drainage process. In addition, the sudden rise of the reservoir water level did affect the stability of the slope greatly, and the decreasing value of the safety factor will increase with the amplitude of the increase of the water level. The stability of the landslide fell down during the rising of the level, and fell down at first and then rise during the falling of the level.

**Keywords:** stress field; seepage field; geostudio; landslide; stability

## 1 INTRODUCTION

Landslide on the reservoir bank caused by water–rock interaction (Louis C. 1974) is a kind of geological hazard, which is a long-time difficult problem. As is accepted, the change of water-level is the main reason of landslide. In recent years, more and more researches have been focused on landslide, and have made some desirable results (Morgerns Stern N. 1963; Berilgen M.M. 2007; Liao Hong-jian et al. 2005). Failure of slope contains many factors such as stress field, chemical field, temperature field, seepage field, etc. Coupling typically exists between different factors (Wang Xue-wu et al. 2006). Seepage field will be primarily affected when the water-level changes, then the stress field variation may lead to instability and failure of the slope (Xu W.J. et al. 2009). In recent years, with the application and popularization of finite element method and computer technologies, another effective way was found to calculate and analyze problems of landslide (Guo Ming-wei et al. 2012; Yang Jin et al. 2012; Huang Man et al. 2013; Pan Guo-lin et al. 2015).

In order to ensure the safe operation of the reservoir, it is necessary to check the stability of the dam. Seepage low and WRI were researched first

in this article and, based on this, the effect to the slope stability in rising and drawdown of water level was researched, some preliminary conclusions were drawn and those may provide helpful reference for related research.

## 2 GEOLOGICAL CHARACTERISTICS

### 2.1 Landform of the reservoir

The reservoir bank consists of oblique layered rocks, the top-down view is like an asymmetric pear, 260 meters as trailing edge height of the landslide mass, 190 meters as width, 770 meters as the leading edge width, 12–57 meters as thickness, 0.37 square kilometres as area,  $824 \times 104$  cubic meters as volume, and  $70^\circ$  as main sliding direction. The terrain in the middle to low part of the landslide mass slopes gently and there is no negative volcanic form.

### 2.2 Physical character of the rock

The landslide mass consists of soil with macadam, gravelly soil, and pebbly silty clay from front to back in turn. The whole structure has an initial medium dense and weathering weakens from the

surface to the centre. Gray pebbly silty clay is the major component of the slip band whose thickness varies from 0.7 to 1.5 meters; 30% of the pebbly is sandstone and marlstone which have a diameter of 20–100 mm and water content of the silty clay is 10.8%–18.3%, the compression ratio is 0.602. Through many shear strength tests show that cohesion can take a value from 14 to 16 kilo Pascal and internal friction angle usually varies from 18 to 25.5. In addition, inclination of the landslide bed varies from 30 to 80.

### 3 ANALYSIS OF SEEPAGE CHARACTERISTICS

#### 3.1 Calculation model

Select a section of the reservoir dam to build model, as shown in Figure 1.

The landslide mass is mainly composed of gravelly soil and the landslide bed consists of mudstone and marlstone.

#### 3.2 Parameter selection

Hydraulic conductivity and water content were indispensable for dam seepage simulation; changing curves of conductivity and water content with pressure are shown in Figure 2. Confining boundary is adopted for slip plane while variable water head boundary was applied to the model.

#### 3.3 Calculation results and analysis

##### 3.3.1 Storage process

Groundwater level will elevate as a result of reservoir storage, so this process was simulated using the transient method. According to actual condition, the water level rises from 145 to 175 meters within a month, then the water rise speed should be 1 meter per day. Calculation result using SEEP/W module was shown in Figure 3.

All Seepage lines of the dam curve left, which illustrates that “backflow” appears inside the

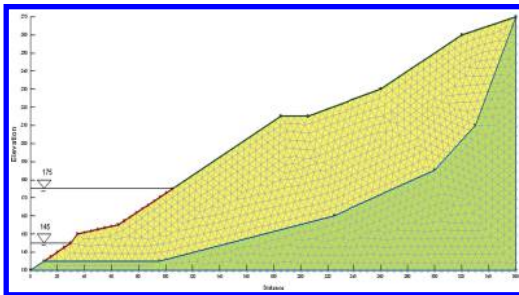


Figure 1. Calculation model of seepage.

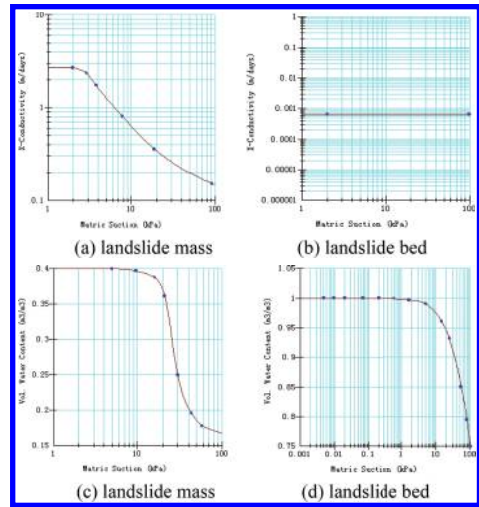


Figure 2. Conductivity and water content curves.

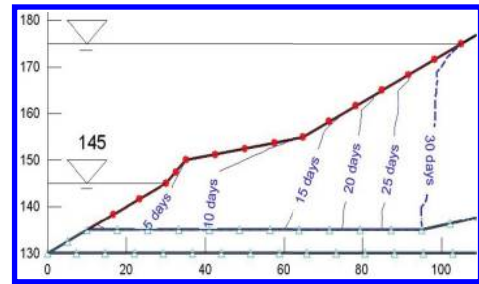


Figure 3(a). Seepage lines during storage process.

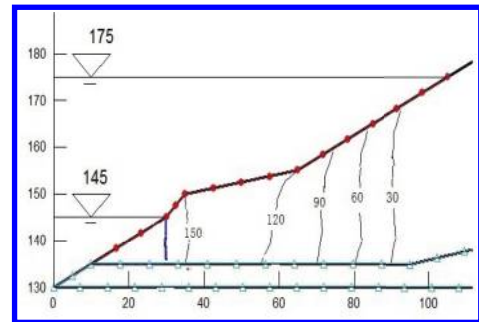


Figure 3(b). Seepage lines during drainage process.

landslide mass. Groundwater level rises quickly in the initial impoundment period and changes to be steady on later stage. Although the landslide mass has good conductivity, the variation of groundwater level was generally delayed relating to that of the reservoir level when the reservoir is filling fast.

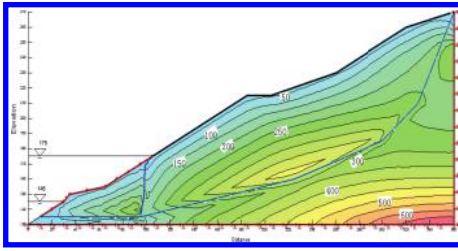


Figure 4. Distribution of the minor principal stress during drainage process.

### 3.3.2 Drainage process

It took 180 days for the reservoir level to decrease from 175 to 135 meters, and hence the velocity of water level drawdown should be 5 meter per month. Adopt the same module as in the previous section and the result was shown in Figure 4.

As the landslide mass has good conductivity, and the reservoir level dropped very slowly, so the variation of groundwater level was not so different from that of the reservoir level.

## 4 SLOPE STABILITY ANALYSIS

### 4.1 WRI analysis

Characteristic of water–rock interaction was researched based on coupled stress and seepage field. Variation of seepage causes the variation of water load, and then lead to the change of stress field.

The same calculation model as previous section was applied in this section, and expected preferences are shown in Table 1.

The calculation showed that the maximum principal stress was characterized by compressive stress, which increased with the rise in reservoir water level and was nearly parallel to the bank slope. The minor principal stress varied along the bank slope. Also, minor principal stress above the sliding surface was greater than that below the sliding surface that may lead to some destruction (see Fig. 4). The maximum shear stress decreased with the falling of water level and reached the maximum at the bottom rear of the dam, so pull apart plane may form easily at this point.

### 4.2 Calculation result during storage process

Traditional limit equilibrium method is adopted by SLOPE/W program, and slope stability in this article was calculated using the following methods: the Janbu method, Bishop method, and Morgenstern–Price method. The result of storage process was shown in Figure 5.

The exported safe factors of the most dangerous slip surface were shown in Table 2. The Bishop

Table 1. Coupling analysis parameters.

Parameters	Landslide mass	landslide bed
Unit weight (KN/m <sup>3</sup> )	18	26
Deformation modulus (Mpa)	0.03	0.85
Internal friction angle	20°	34°

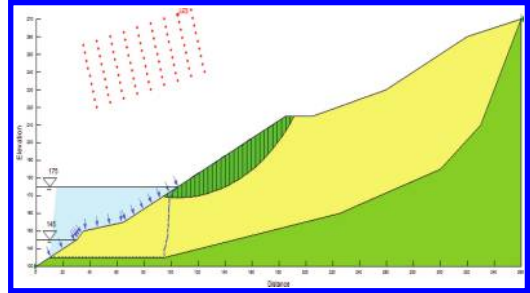


Figure 5. Calculation result of landslide stability (30 d).

Table 2. Safe factors with different methods.

Time/d	M-price	Janbu	Bishop
0	1.275	1.179	1.338
5	1.231	1.143	1.294
10	1.206	1.112	1.261
15	1.187	1.095	1.237
20	1.178	1.083	1.22
25	1.175	1.08	1.218
30	1.175	1.08	1.218

method gave the largest safe factor and Janbu method gave the smallest ones, but the variation trends of those three methods were similar.

Line graph could describe the variation more intuitively (see Fig. 5).

Figure 6 shows that the safe factor decreased slowly during storage process, so the stability of the landslide will fall down during the rising of the level.

### 4.3 Calculation result during drainage process

Similarly, the result of drainage process was shown in Figure 7 and the variation of safe factors in Figure 8.

Figure 8 shows that the stability decreased in the first 30 days and then rebound slowly in the following 150 days. The cause of the above phenomenon was that the gravity and sliding force of the slope was aggravated by hydrodynamic pressure. As the landslide mass has good conductivity, and the reservoir level dropped very slowly, the hydrodynamic pressure was decreased fast.

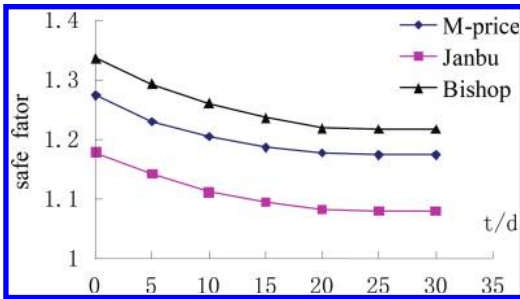


Figure 6. Variation of safe factors.

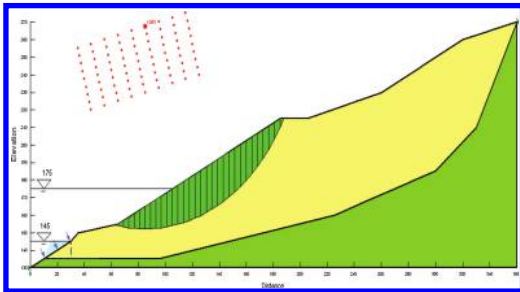


Figure 7. Calculation result of landslide stability (180 d).

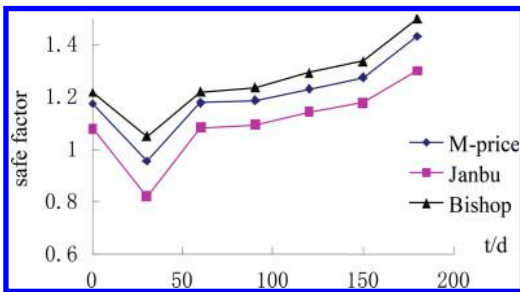


Figure 8. Variation of safe factors.

## 5 CONCLUSION

Seepage low and WRI were researched first in this article and then discussed the distortion-destruction mechanism of slope, finally studied the effect to bank slope in rising and drawdown of water level. Major results can be concluded as follows:

1. Groundwater levels in different lithological mediums varied in different speed. Mainly composed of sandstone, the landslide mass has better permeability than that of the landslide bed which consists mainly of marlstone.

2. The variation of groundwater level was generally delayed relating to that of the reservoir level when the reservoir is filling fast. While, the variation of groundwater level was not so different from that of the reservoir level during the drainage process.
3. Due to the sudden rise and slow fall of the water level, rising water level gave a more obvious effect on the bank slope than those in decreasing of the water level.
4. The stability of the landslide fell down during the rising of the level, and fell down at first and then rise during the falling of the level of style is very important. Note the spacing, punctuation and caps in all the examples below.

## ACKNOWLEDGEMENTS

This project is sponsored by Shanghai University of Engineering Science Innovation Fund for Graduate Students (14KY1005); Shanghai Graduate Education Innovation Project in Layout and Construction Project (13sc002).

## REFERENCES

- Berilgen M.M. 2007. Investigation of stability of slopes under drawdown conditions. *Computers and Geotechnics* 34(2): 81–91.
- Guo Ming-wei et al. 2012. Three-dimensional slope stability analysis based on finite element stress. *Chinese Journal of Rock Mechanics and Engineering* 31(12): 2494–2500.
- Huang Man et al. 2013. Study of inverse controlling technology for series scales similar surface model making of rock structural plane. *Rock and Soil Mechanics* 34(4): 1211–1216.
- Liao Hong-jian et al. 2005. Influence of drawdown of reservoir water level on landslide stability. *Chinese Journal of Rock Mechanics and Engineering* 24(19): 3454–3458.
- Louis C. 1974. *Rock hydraulics in rock mechanics*. New York: Verlay Wien.
- Morgernsster N. 1963. Stability charts for earth slopes during rapid drawdown. *Geotechnique* 13(2): 121–131.
- Pan Guo-lin et al. 2015. Deformation Analysis of Debris Landslides Based on Finite Element Numerical Simulation. *Safety and Environmental Engineering* 22(2): 19–24.
- Wang Xue-wu et al. 2006. Study on the Effect to the bank landslide in rising and drawdown of water level of the Three Gorges Reservoir. *Research of Soil and Water Conservation* 13(5): 232–234, 237.
- Xu W.J. et al. 2009. Genesis and stability of the Zhoujiawan landslide, Three Gorges, China. *Bulletin of Engineering Geology and the Environment* 68(1): 47–54.
- Yang Jin et al. 2012. Dynamic variation rule of phreatic line in Huangtupo landslide in Three Gorges reservoir area. *Rock and Soil Mechanics* 33(3): 853–857.

## Efficient simulation for subsidence induced by dewatering of pit

J.H. Wang

*Beijing University of Technology, Beijing, China*  
*BGI Engineering Consultants Ltd., Beijing, China*

L.J. Tao

*Beijing University of Technology, Beijing, China*

X. Han & H.L. Zhou

*BGI Engineering Consultants Ltd., Beijing, China*

**ABSTRACT:** To meet the needs of scientific calculation of subsidence caused by dewatering of pit, on the basis of the previous work and fully integrated with numerical simulation technology, the scientificity of Area Sink Method (ASM) in calculating subsidence is studied theoretically, and numerically realized by PM software, which is especially focused on. Then, by a set of numerical examples, the subsidence caused by dewatering is calculated by ASM, and by comparing with sophisticated Point Well Method (PWM), the accuracy and efficiency of ASM are analyzed. Finally, the applicability and practicability of ASM in calculating subsidence caused by dewatering is summarized systematically.

**Keywords:** dewatering of pit; subsidence; PWM; ASM

### 1 INTRODUCTION

Calculation of subsidence induced by dewatering of pit is a classical problem in geotechnical engineering. In some guides or standards, it is required, and the most popularized method is called Layer-Wise Summation Method (LSM), but LSM is too idealized to analyze more complex problems, such as dewatering through multilayered aquifers or dewatering under cut-off walls, or some unsteady problems, etc. In order to solve the problems beyond LSM, numerical method becomes more and more necessary.

With the development of numerical method, especially in the field of regional subsidence induced by widespread exploitation of groundwater for water resource, many complex problems can be accurately modeled by softwares, the most popularized one of which is Processing Modflow (PM) which has two unique modules: WELL (Point Well Method, abbrev PWM) and IBS (inter-bedded system). In the recent 10 years, PM has tried to model subsidence induced by dewatering in pits, but only the simple problem can be accurately modeled, such as dewatering in single aquifer without cut-offs. With the development of deep pits, PM is faced 2 major difficulties in modeling subsidence induced by dewatering with the module Well as follows: 1) Multiscale problems in pretreatments

and calculations. On one hand, the extent of models is always very large, which are dependent on the radius of influence, sometimes 1000 meters or even more. On the other hand, the spacing of wells is very small, which is usually between 6–8m. So, in order to accurately characterize the dewatering condition, the model should be divided into many meshes, which will increase numerical calculations, or even make convergence difficulties. 2) Drainage of aquifer. As it is known, the WELL module in PM cannot model drainage of aquifers with the water table declining near to the bottom of the aquifer, WELL module will stop working, and numerical calculation of the drawdown will be wrong, thus making numerical errors in modeling the subsidence with IBS according to the principle of effective stress.

The two problems in the WELL module above greatly retarded further popularized PM in modeling subsidence. So some simplification of wells in pretreatment is very important, which will improve the efficiency of numerical calculation as highly as possible, under the premise that the accuracy is enough for engineering evaluation.

Recently upon previous work, with systematical numerical tests, Wang Junhui (2015) has introduced an equivalent method called Area Sink Method (ASM) to approximate wells for calculating discharge rate of put-upon which a series of



valuable conclusion has been made. Can wells also be treated by ASM approximately in modeling subsidence induced by dewatering? (Some mathematical derivation and systematical numerical tests has been done from which the efficiency of simulation for subsidence with ASM is proved and tested.

## 2 MATHEMATICAL THEORY

### 2.1 Mathematical deduction

As it is shown in the **Figure 1**, the dewatering domain is  $\Omega_1$ , whose boundary is  $\Gamma_1$  (slightly larger than the pit), inside which dewatering is carried out, and the required drawdown is  $s_d(x, y)$ , which is also called designed drawdown.  $\Omega_2$  indicates the model domain, whose boundary is  $\Gamma_2$ .

On curve  $\Gamma_1$ , a group of wells are assigned, the flow rate of the well  $i$  ( $i = 1, 2, 3 \dots n$ ) is  $Q_i$  correspondingly.

With PWM, a drawdown distribution approximately designed to drawdown can be derived, thus

$$s^P(x, y) = s_d(x, y) \quad x, y \in \Omega_1 \quad (1)$$

where  $s^P(x, y)$  indicates distribution of drawdown by PWM;  $s_d(x, y)$  indicates distribution of designed drawdown for dewatering.

And with AWM, whose flow rate is  $q(x, y)$  (shown as the dashed area in **Fig. 1**), another drawdown distribution approximated to the designed drawdown can also be derived, thus

$$s^A(x, y) = s_d(x, y) \quad x, y \in \Omega_1 \quad (2)$$

where  $s^A(x, y)$  indicates the distribution of drawdown by ASM.

By using formulas (1) and (2), we can derive that,

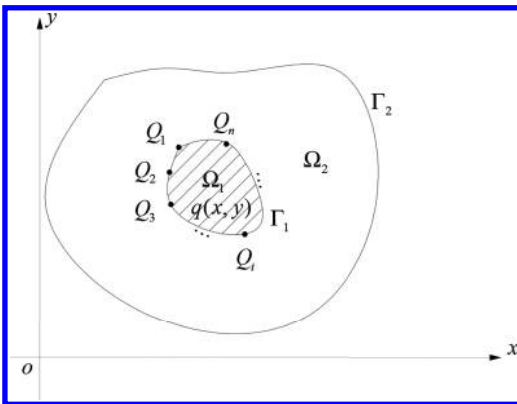


Figure 1. Sketch map of ASM and PWM.

$$s^A(x, y) = s^P(x, y) \quad x, y \in \Omega_1 \quad (3)$$

For convenience, a new function on  $\Omega_2$  is just introduced as follows:

$$F(x, y) = s^P(x, y) - s^A(x, y) \quad x, y \in \Omega_2 \quad (4)$$

With (3) and (4), the following can be concluded:

$$F(x, y) = 0 \quad x, y \in \Omega_1 \quad (5)$$

As it is known, the contribution of any well  $Q_1$  to an arbitrary point  $(x, y)$  in  $\Omega_2$  has the same mechanism, so the mathematical formula of  $s^P(x, y)$  is identical throughout  $\Omega_2$ . According to the principle of superposition,  $s^A(x, y)$  by ASM can be regarded as the results of superposition by innumerable imaginary point wells, from which it can be concluded that the formulation of  $s^A(x, y)$  is also identical on  $\Omega_2$ . Upon above deduction, it can be derived that the formulation of function  $F(x, y)$  is identical throughout  $\Omega_2$ .

Upon above discussion and according to (5),  $F(x, y)$  is a constant function equal to zero, thus

$$F(x, y) \equiv 0 \quad x, y \in \Omega_2 \quad (6)$$

With (4) and (6), it can be derived as

$$s^A(x, y) = s^P(x, y) \quad x, y \in \Omega_2 \quad (7)$$

According to principle of effective stress and (7), it can be concluded that the subsidence calculated by PWM and ASM is identical theoretically, thus

$$sub^A(x, y) = sub^P(x, y) \quad x, y \in \Omega_2 \quad (8)$$

where  $sub^P(x, y)$  indicates distribution of subsidence by PWM;  $sub^A(x, y)$  indicates distribution of subsidence by ASM.

### 2.2 Numerical solutions by PM

In the software PM,<sup>[12]</sup> there are some modules that can be used as ASM indirectly by setting appropriate parameters, such as Drain and Evaporation.

#### 1. With module Drain

In the module Drain, in order to make the designed water level after dewatering, approaching the Elevation of drainage, the calculation of the distribution of Drain hydraulic conductance can be made, from which subsidence can be easily calculated.

#### 2. With module Evaporation

By setting Elevation of the ET surface as the bottom of aquifer, ET Extinction Depth at 0.5–1.0m below the bottom of pit, adjusting

the value of the maximum ET rate the calculated water level approaches the designed water level.

### 3 NUMERICAL TEST

#### 3.1 Project overview

There is a square pit with the scale of  $50\text{m} \times 50\text{m}$ , and the depth of its bottom is 30m.

The elevation of site is 25m, there exists a confined aquifer between the depth of 15–40m, whose lithology is fine sand, hydraulic conductivity is 50m/d, specific storage is 0.0001/m, specific yield

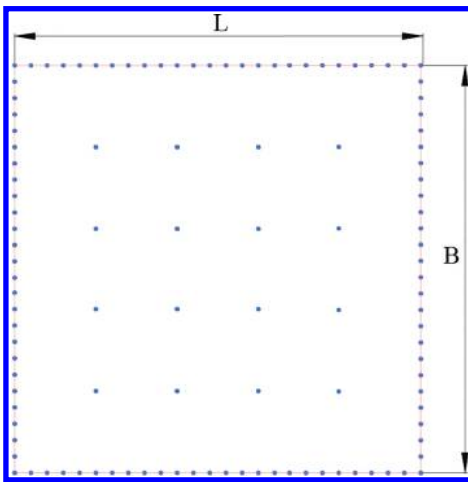


Figure 2. Sketch map of relationship between wells distribution and the pit.

is 0.12, radius of influence is 400m, and the depth of water level is 5m.

In the dewatering schedule, 112 tube wells are arranged, the spacing of wells on the edges and inside of the pit is 8m and 40m respectively, and the elevation of designed water level is 6m.

In order to evaluate the subsidence induced by dewatering, PWM and ASM are applied, respectively.

#### 3.2 Pretreatment and efficiency of PWM against ASM

PWM and ASM are implemented by the module Well and the module Drain, respectively. According to radius of influence and the scale of the pit, the model domain is defined as a square of  $1000\text{m} \times 1000\text{m}$ . In order to ensure the accuracy and efficiency of calculation, the density of grids should be high near the pit and low far away from the pit.

As it is known, the tube well should be located accurately in PWM, so the spacing of tube well should be as small as possible near the pit, the smallest of which is within 2m, the total number of grids in PWM is  $158 \times 158$  as is shown in Figure 3(a). While the geometrical characteristic in ASM is much more simple than PWM, the spacing of tube wells can be enlarged properly, the spacing of grids near the pit is 10m, the total number of grids is  $62 \times 62$ , which is only 15% of PWM, as is shown in Figure 4(b).

Since the number of grids in ASM is much lesser than that of PWM, so, in theory, the efficiency of calculation by ASM is much higher than by PWM. From the unsteady dewatering numerical tests with 200 steps, it is found that, the calculation time

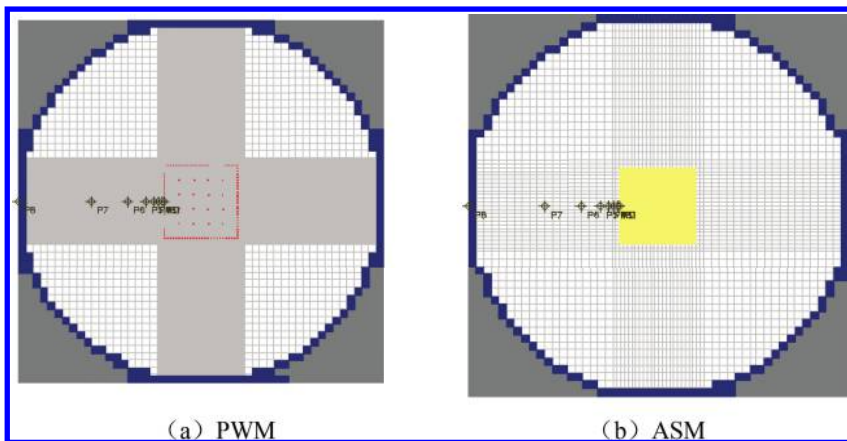


Figure 3. Preprocessing of PWM and ASM (P1 to P8 indicates the reference points from the borderline of pit to outward).

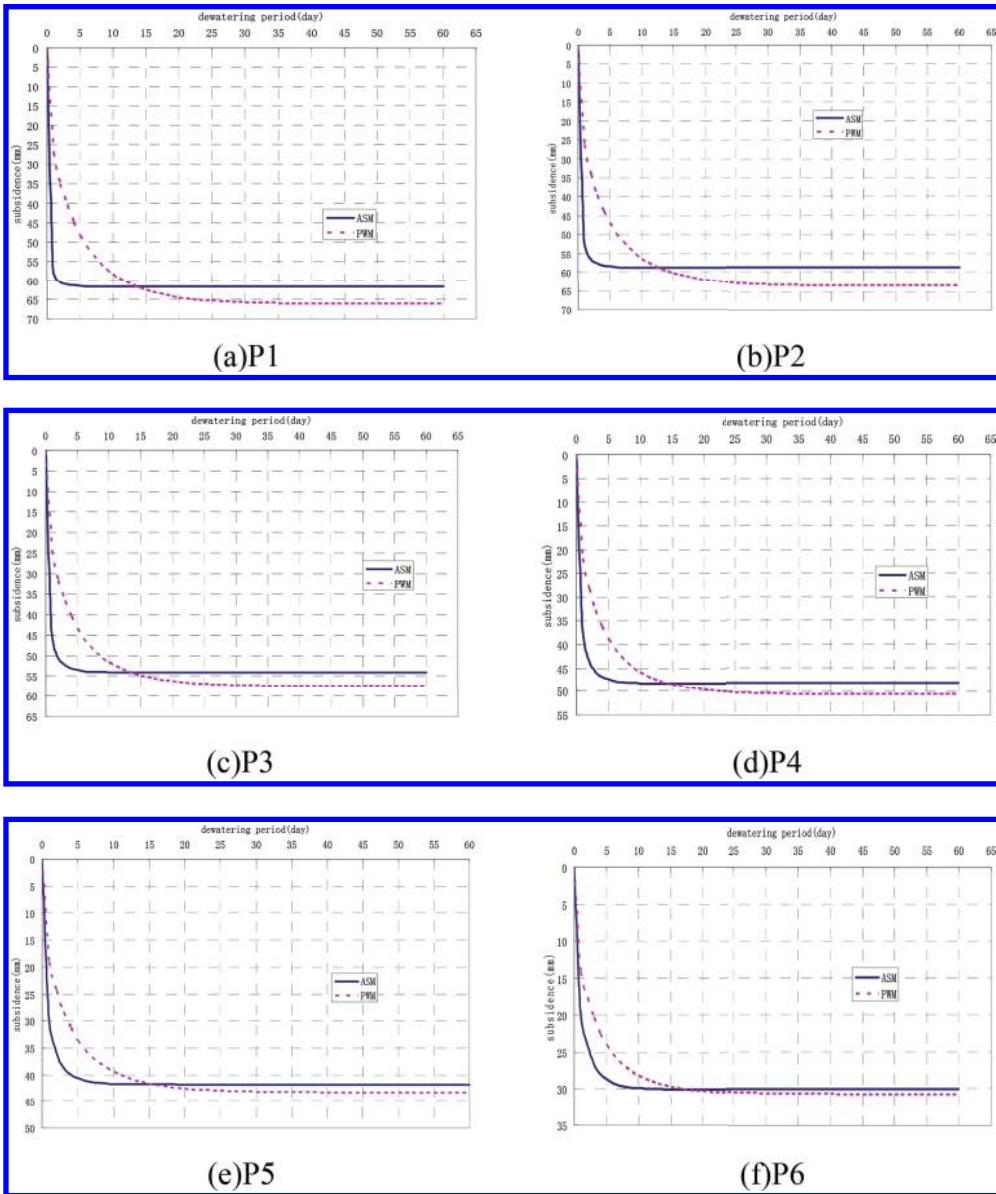


Figure 4. Dynamic curve of subsidence calculated by PWM versus ASM.

consumed by PWM is 75 seconds, while the calculation time consumed by ASM is only 6 seconds, from which it can be also concluded that the efficiency of calculation by ASM is much higher than by PWM.

### 3.3 Errors between PSM and ASM

Figure 4 shows the subsidence calculated by ASM and PWM, at different distance from the pit edge.

From Figure 4, you can see that nearer to the pit more errors between PWM and ASM are found. With the distance from pit increasing, the calculation results by ASM approached to that by PWM. (P5 and P6).

In fact, the final subsidence is more significant for engineering, while the maximum relative error of final subsidence is calculated by ASM to PWM within 10% (Fig. 4), so the accuracy of ASM is sufficient for engineering.

## 4 CONCLUSION

By the deduction and numerical tests, ASM is more efficient in calculating subsidence induced by dewatering of pit than PWM, under the premise of sufficient accuracy for engineering.

## REFERENCES

- [1] Zhang Zaiming. Groundwater and building foundation engineering [M]. Beijing: China Building Industry Press, 1999.
- [2] Zhang Zaiming, Du Xiuli and Luo Furong etc. Influence of groundwater on metro planning and construction and engineering measures in Beijing City [R], Internal data of Beijing investigation design and Research Institute Co., Ltd. 2009.
- [3] CIGS(China). Profession Standard Of The People's Republic Of China, Technical specification for retaining and protection of building foundation pit (JGJ120-2012) [S]. Beijing: China Building Industry Press, 2012.
- [4] CIGS(China). Technical specification of architectural and municipal dewatering engineering [S]. Beijing: China Building Industry Press, 1999.
- [5] Yao Tianqiang, Shi Zhenhua. Handbook of foundation pit dewatering [M]. Beijing: China Building Industry Press, 2006.
- [6] P.M. Cashman and M. Preene. Groundwater Lowering in Construction [M]. London and New York: Spon Press, 2001.
- [7] Fu Yanling Guo Zhengfa. Application of Processing Modflow in groundwater seepage and Ground Settlement [J]. Site investigation science and technology, 2006, (4): 19~23.
- [8] Kan Jinghan, Luo Lihong. Application of Processing Modflow Model in Prediction of Ground Subsidence [J]. Journal of Railway Engineering, 2010, (2): 27~31.
- [9] Su Cheng, Cui Yali, Shao Jingli. Advances in numerical models of land subsidence based on comprehensive theories [J]. Hydrogeology and Engineering Geology, 2014, 41 (6): 147~152.
- [10] Chen Chongxi, Lin Min. Groundwater dynamics [M]. Wu Han: China University of Geosciences press, 1999.
- [11] Wang Junhui, Tao Lianjin. Area Sink Method for pit flow rate [J] (to be published in 2015).
- [12] Wen-Hsing Chiang. 3D-Groundwater Modeling with PMWIN, Second Edition [M]. Berlin Heidelberg NewYork, HongKong London and Milan Paris Tokyo: Springer, 2005.

## Statistical study on bond strength of rock anchor

Mengxiong Tang, Hesong Hu & Chenglin Zhang

Guangzhou Institute of Building Science Co. Ltd., Guangzhou, China

**ABSTRACT:** Comparisons between the hyperbolic model and exponential model prediction effect have been made and the exponential model is selected to analyze P-S curve of rock anchor test data. Ultimate bearing capacity of anchor is predicted by exponential model firstly then the bond strength of rock anchor is calculated and these results are classified according to the hardness degree of rock. It is shown that bond strength of rock anchor recommended in the code is larger than 20% the statistic on the soft rock condition and both are in agreement on the hard rock condition.

**Keywords:** exponential model; rock anchor; bond strength; statistic

### 1 INTRODUCTION

Rock anchor is widely used in excavation pit supporting, slope reinforcement, underground anti-floating structures, and other projects.

It is required to determine the ultimate bearing capacity according to anchor rod pull-out test for building foundation design level in grade A and according to specification recommended value of the bond strength between the mortar and rock for other grades. The core issue of the engineering design reasonably determines the bond strength between the mortar and rock. Existing specifications recommended by the characteristic value of bond strength between mortar and rock recommended are relatively general, and brought the security risks to engineering application. It is necessary to get a more reasonable and reliable value of experience by statistically analyzing the bonding strength between mortar and rock through a lot of experimental data in different geological conditions.

It costs a lot of time and money to get the rock anchor ultimate bearing capacity by destructive test.

As an alternative, reasonable theoretical model can be chosen to fit the rock anchor inspection  $p$ - $s$  curve and forecasting the ultimate bearing capacity of rock anchor in practical application and theoretical analysis, due to the rock bolt destructive testing data is scarcer than acceptance test data. Then the bond strength between mortar and rock in different geological conditions can be calculated inversely. The results of inversion calculated can be used in improving the exiting standards.

### 2 COMPARISON FOR MATHEMATICAL MODEL

$p$ - $s$  curve of rock anchor and pile to be similar and include the fallow stages: elastic stage, elastic-plastic deformation, damage evolution. It is usually to fit the  $p$ - $s$  curve of pile by hyperbolic model and exponential model. Hyperbolic model and exponential model is used to describe the  $p$ - $s$  curve of rock bolt in this paper and according to the basic experimental data of an engineering project to the discussion of the applicability of the two models.

#### 2.1 Hyperbolic model

Assume that  $p$ - $s$  curve accords with hyperbolic equation.

$$p = \frac{s}{as + b} \quad (1)$$

$p$  is the load ( $kN$ ),  $s$  is the anchor displacement ( $mm$ ), and  $a$  and  $b$  are the fitting parameters. Ultimate bearing capacity is as follows:

$$P_u = \lim_{s \rightarrow \infty} \frac{S}{aS + b} = \frac{1}{a} \quad (2)$$

Assuming that  $y = s/p$ ,  $x = s$ , after transformation to get the linear equation:

$$y = ax + b \quad (3)$$

Using the least squares fitting, can calculate parameters  $a$ ,  $b$ .

## 2.2 Exponential model

Assume that  $p$ - $s$  curve accords with exponential equation.

$$P = P_{max} (1 - e^{-as}) \quad (4)$$

$P_{max}$  is the solvable load of rock anchor ( $kN$ );  $a$  is the subsidence attenuation factor ( $mm^{-1}$ ); unknown parameters  $P_{max}$  and  $a$  can be determined by computer analyzing the pull-out test data, *matlab* *n l in fit* function was used to write the corresponding program.

After confirming the  $P_{max}$  and  $a$  can be plugged into our index equation and get the fitting  $p$ - $s$  curve equations. The ultimate bearing capacity  $P_u$  of the pile can be to write as follow according to  $(\Delta S_{i+1}/\Delta P_{i+1}) \geq 0.1 mm/kN$ .

$$P_u = P_{max} - 10/a \quad (5)$$

## 2.3 Comparison of the model results and measured data

Reinforced pull-out rock bolt was set in a 2-layer bottom central in the anti-floating design on the Guangzhou Pearl river new town core area of

municipal traffic projects. Medium and weakly weathered rocks anchor the body. The anchor hole diameter is 150 mm, anchor length is 6 ~ 15 m, All the rod material is 428 steel. The engineering rock anti-floating anchor test measured data was used to fit the hyperbolic model and exponential model respectively to predict the ultimate bearing capacity and test the applicability of the two models. Comparison results are shown in Table 1 and Figures 1–5.

The ultimate bearing capacity is determined by assuming that the values of the displacement are at infinity for the hyperbolic model, so do not tally with the actual project and affect the fitting precision of the hyperbolic model. The result of predicting the ultimate bearing capacity of the rock bolt is not ideal by using the hyperbolic model, error in the range of 20% ~ 30%. Exponential model fitting precision of rock bolt bearing capacity is accurate; the error is very small, in the range of 3% ~ 13%.

## 3 STATISTICAL ANALYSIS OF ROCK BOLT PULLING TEST DATA

The upliftment bearing capacity's characteristic value can be calculated according to the bond

Table 1. Comparison between two models prediction effect.

Bolt	Measured/ $kN$	Exponential/ $kN$	Error/%	Hyperbolic/ $kN$	Error/%
1#	771.6	808.2	4.7	955.5	23.8
3#	900.2	1013.0	12.5	1166.3	29.6
4#	771.6	863.1	11.9	973.9	26.2
5#	900.2	928.1	3.1	1097.0	21.9
6#	771.6	867.2	12.4	970.2	25.7

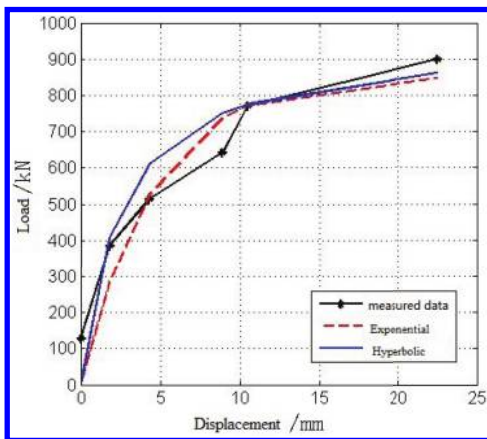


Figure 1. Assessing fit of 1# anchor.

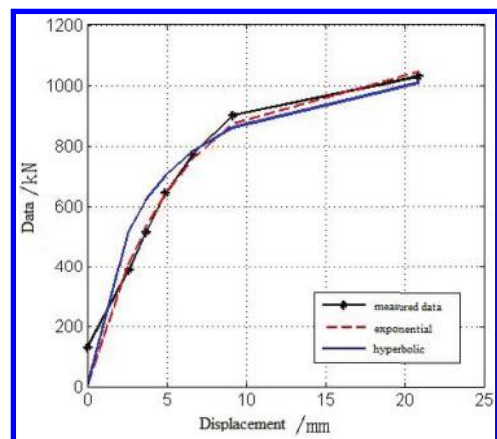


Figure 2. Assessing fit of 3# anchor.

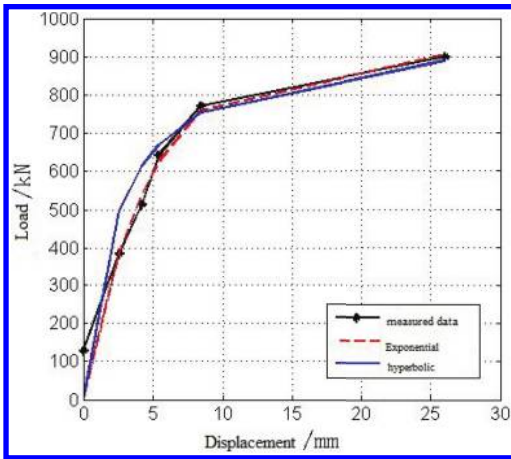


Figure 3. Assessing fit of 4# anchor.

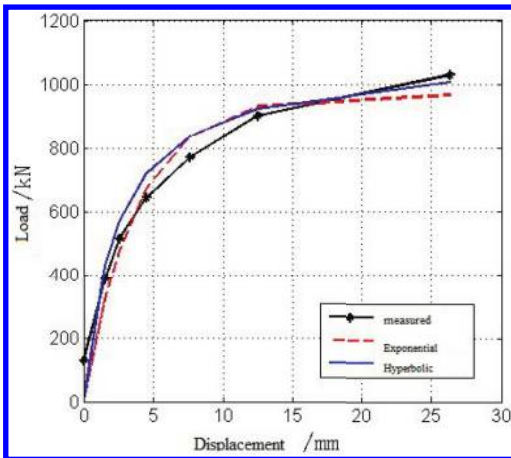


Figure 4. Assessing fit of 5# anchor.

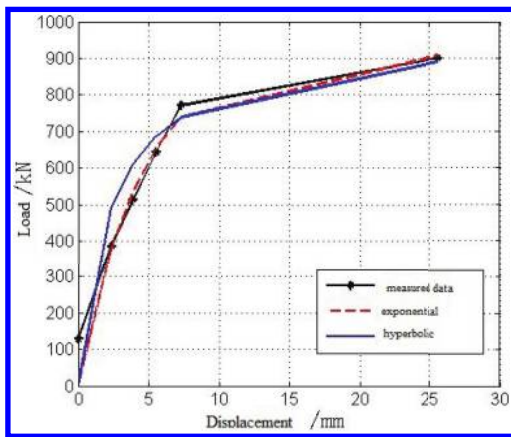


Figure 5. Assessing fit of 6# anchor.

strength between the cement mortar or concrete and rock anchor, its formula is:

$$R_t = 0.8\pi d_1 \sum l_i f_i \quad (6)$$

$f_i$  is the bond strength characteristic value between the cement mortar and concrete rock layers  $i$  ( $kPa$ ).  $d_1$  is the anchor diameter (mm).  $l_i$  is the length of anchoring section.

The exponential mathematical model was used to fit the rock anchor rod pull-out test  $p$ - $s$  data according to the previous conclusions and predict the ultimate bearing capacity of the rock bolt, thus get  $f_i$  values according to the calculated by formula (6). 380 bolts testing data in 38 projects were selected to analyze, including 160 anchors in soft rock geology, 93 anchors in less soft rock geology and 127 anchors in hard rock geological.

Numerous experimental data were statistically analyzed by writing a batch program in *Matlab* and get the distribution of bond strength characteristic value between the cement mortar or concrete and rock. As shown in Figures 6–8. The bond strength of rock anchor can be gained by getting in the corresponding 90% cumulative frequency.

As can be seen from the Figure 6, for soft rock geology, rock bolt bond strength of mortar or concrete are mainly distributed in less than 210  $kN$  area, which accounts for 90.63% of the total. It is suggested that bond strength of rock bolt mortar can be assigned a value in 110 ~ 160  $kPa$  for the middle weathered soft rock and assigned a value in 110 ~ 160  $kPa$  for the lightly weathered soft rock.

As can be seen from the Figure 7, for less soft rock geology, rock bolt bond strength of mortar or concrete are mainly distributed in less than 330  $kN$  area, accounting for 89.25% of the total. It is suggested that bond strength of rock bolt mortar can be assigned a value in 180 ~ 230  $kPa$  for the middle weathered soft rock and assigned a value in 230 ~ 330  $kPa$  for the lightly weathered soft rock.

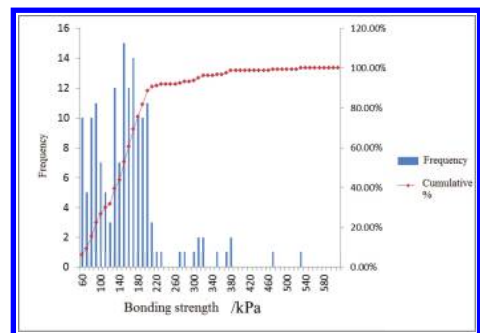


Figure 6. Histograms of bond strength of rock anchor on soft rock condition (160 anchors).

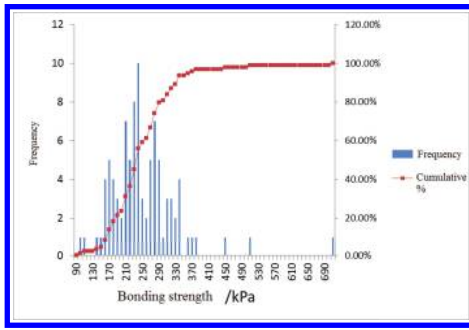


Figure 7. Histograms of bond strength of rock anchor on less soft rock condition (93 anchors).

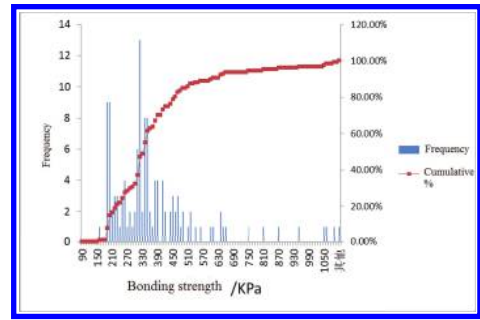


Figure 8. Histograms of bond strength of rock anchor on hard rock condition (127 anchors).

Table 2. Comparison between bond strength of rock anchor recommended in the code and statistic.

Stiffness	Representative	Weathered	Code value (kPa)	Statistics (kPa)
Soft rock	Mudstone	Middle weathered	150~200	110~160
		Lightly weathered	200~250	160~210
Less soft rock	Tufa	Middle weathered	200~250	180~230
		Lightly weathered	250~400	230~330
Hard rock	Granite	Middle ~ lightly weathered	400~600	400~600

As can be seen from the Figure 8, for hard rock geology, rock bolt bond strength of mortar or concrete are mainly distributed in less than 600 kN area, accounting for 89.75% of the total. It is suggested that bond strength of rock bolt mortar can be assigned a value in 400 ~ 600 kPa for the hard rock.

#### 4 CONCLUSION

The appropriate mathematical model was selected in this paper to statistically analyze the rock bolt acceptance test data and get the following conclusion:

1. Described by the exponential model of rock bolt  $p$ - $s$  curve to predict the ultimate bearing capacity is feasible, small error and good stability, meeting the precision requirement in engineering and providing the convenient for researching the bond strength of the rock anchor.
2. The bond strength of mortar or concrete and rock can be back calculated by the exponential model to predict the ultimate bearing capacity of anchor. The statistical results show that in the soft rock and less soft rock geological conditions, specification recommends value is 20% larger than the statistics, the specification values match the statistics suggested in hard rock geological conditions.

Results in this paper have been submitted to the standard specifications for design of building foundation of Guangdong province DBJ (15-31-2003) revised group for reference.

#### REFERENCES

- [1] Construction department of Guangdong province. DBJ 15-31-2003. Building foundation design specification [s]. Beijing: China building industry press. 2003.
- [2] Chen Tang-yin, Wang Xian-neng. Linear elastic analysis of stress-strain state of anti-float anchor Rock and Soil Mechanics. 2006, 27(11): 2034–2036, 2049.
- [3] Deng Zhi-yong. Lu Pei-yi. Comparison and analysis of several predicting models of ultimate bearing capacity of single pile [J]. Rock and Soil Mechanics, 2002, 23(4): 428–431, 464.
- [4] Wu Yong-hong, Liu Shu-lin, Zhang Jing-heng, et al. P-S curve and bearing capacity of precast RC pile [J]. Geotechnical Investigation & Surveying, 2000, (3): 44–46.
- [5] Li-Seng, Tang Meng-xiong. Contrast analysis on prediction models for load-displacement curve of up lift pile. Chinese Journal of Underground Space and Engineering, 2009, 5(4).
- [6] Xu Hong-fa, Qian Qi-hu, Jing Feng-nian. Power function model to describe load-displacement curve of tension pile [J]. Chinese Journal of Geotechnical Engineering, 2000, 22(5).
- [7] Ying Zhi-min, Zhang Jie, Shang Yue-quan. Exponential model for simulating load-displacement curve of anchor rod [J]. Rock and Soil Mechanics, 2000, 21(2).



# Particle breakage characteristics of calcareous sand under P-wave

Xue-Yong Xu, Xiao-Fen Chen, Guo-Hai Chen, Sheng-Jie Di & Wan-Qiang Cheng  
*Power China Huadong Engineering Corporation Limited, Hangzhou, China*

**ABSTRACT:** Calcareous sand is a special marine geotechnical medium that exhibits interesting physical and mechanical properties resulting from its composition and structure. Calcareous sand particles are fragile and irregular and thus, may break under common stress such as the overpressure from an explosion in a nearby field. In the current paper, the particle breakage characteristics of calcareous sand under explosion were studied through mini-explosion experiments and the measurement method of Hardin was adopted to estimate the degree of particle breakage. The results show that calcareous sand exhibits strong absorption and attenuation effects on the P-wave because of its particle breakage characteristics. The relative degrees of particle breakage of the calcareous sand are 0.532, 0.217 and 0.06, at the distance from blasting source center position 5 cm, 10 cm and 15 cm. Many particles were broken near the blasting zone. The broken, compress, and damage zones are formed, which consume most of the energy and result in an increase in the attenuation effect. Through theoretical calculations, the energy for the formation of the broken, compress, and damage zones is found to consume 25% of the total energy.

**Keywords:** marine geotechnical medium; calcareous sand; P-wave; particle breakage; relative degree

## 1 INTRODUCTION

Calcareous sand is a special marine geotechnical medium composed primarily of calcium carbonate. The special sedimentary environment of calcareous sand, particularly its deposition process which does not involve long-distance transport, resulted in the preservation of the small pores in the original skeleton<sup>[1-2]</sup>. Studies have shown that the irregular shape and particle breakage characteristics of calcareous sand account for its engineering properties, which are significantly different from those of other terrestrial sand<sup>[3-5]</sup>.

At present, docks, airport runways, collecting tanks, and other kinds of civil and military infrastructures are constructed on coral reefs because of necessity, as well as for protection and the development of marine resources. These infrastructures potentially cause accidental and man-made explosions. Thus, studies on explosion safety and protection for these buildings are becoming increasingly significant.

Calcareous sand is the most common material medium on coral reefs, and its mechanical properties significantly affect the propagation and attenuation of the explosion wave. In recent decades, extensive studies on the dynamic characteristics of terrestrial sand or soil have been conducted. For example, Gohl W.B. et al. (2000)<sup>[6]</sup>, Dontsov V.E. et al. (2001)<sup>[7]</sup>, WANG Ming-yang et al. (2002)<sup>[8]</sup>, Qu Jun-tong et al. (2006)<sup>[9]</sup>, MU

Chao-min et al. (2010)<sup>[10]</sup>. These studies can be classified into two categories, namely, the experimental method and numerical simulations. The experimental method obtains the relationship between the material medium parameter and the explosion load. For example, different densities, grain compositions, and sand saturation exhibit different characteristics in response to explosions. On the other hand, numerical simulations are mostly performed by establishing physical models based on experimental test results and then using the ANSYS/LS-DYNA software to imitate the explosive process<sup>[12]</sup>. Studies on the dynamic response characteristics of calcareous sand under explosion are rare. Hence, the conduct of research on this field is necessary. Understanding the explosion compression wave propagation and attenuation can provide basic information for engineering constructions. In the current paper, the explosion compression wave propagation of calcareous sand would be examined through indoor explosion experiments. In addition, the particle breakage characteristics would be analyzed.

## 2 EXPERIMENT MATERIAL

The calcareous sand used in this experiment was sampled from China Nansha Islands. The physical parameters were determined and a granulometric

Table 1. Physical properties of calcareous sand.

$D_{60}$ (mm)	$D_{30}$ (mm)	$D_{10}$ (mm)	$e_{max}$	$e_{min}$	$d_s$
0.876	0.579	0.112	1.405	0.766	2.76

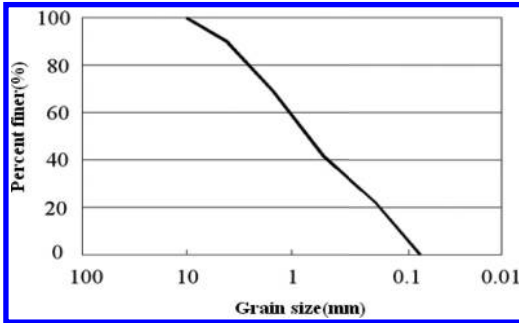


Figure 1. Granulometric analysis of calcareous sand.

analysis experiment was conducted prior to the indoor explosion experiment. The results show that 50% of the particles have sizes larger than 0.5 mm, and the non-uniform coefficient is 7.83, indicating that the samples could be classified as coarse sand. Table 1 and Figure 1 show the detailed physical properties of the calcareous sand and the results of the granulometric analysis experiment, respectively.

### 3 MEASUREMENT OF PARTICLE BREAKAGE

A previous study has shown that soil particles are incompressible, and that soil deformation results from the reduction of gas and water in the soil pores and the recombination of soil particles. The study also showed that the intensity theory is based on the friction and slippage between soil particles.

However, experiments showed that soil particles may partially or wholly break when they are subjected to stress from an external force greater than their own strength. Calcareous sand particles are fragile and irregular and thus, may break under common stress such as the overpressure from an explosion in a nearby field, which can exceed up to several hundred MPa. As such, the strong impact can cause a large number of calcareous sand particles to break.

After the explosion experiments, the samples were obtained from the area 5 cm to 20 cm from the blast center. Granulometric analysis was then conducted, and a granulometric analysis curve before and after the explosion was drawn. The calcareous sand particle breakage characteristics were

also described, and the measurement method of Hardin (1985) was adopted to estimate the degree of particle breakage of calcareous sand under an explosion. Finally, the value of the explosion energy loss in forming the crush, compression, and damage zones of calcareous sand were calculated.

### 4 TEST RESULTS

After the explosion experiments, the samples obtained at 5 cm, 10 cm, and 15 cm from the center of the explosion were subjected to granulometric analysis, and the granulometric analysis curve before and after the explosion was drawn. The results are shown in Figure 2.

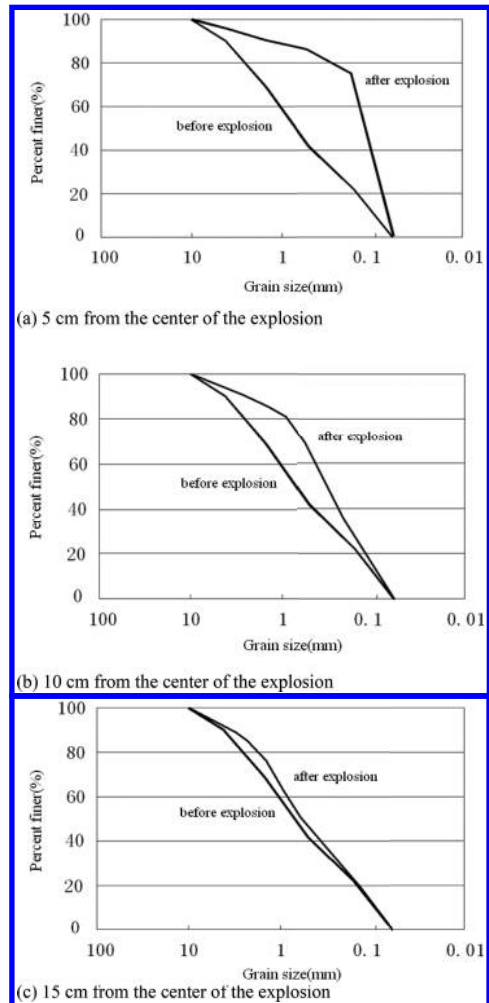


Figure 2. Granulometric analysis results of the samples at different distances.

In the examination of the particle breakage characteristics, many different methods of measuring the degree of particle breakage were proposed based on the study objectives. These methods are mostly empirical. In the current paper, the measurement method of Hardin (1985) was used to estimate the degree of calcareous sand particle breakage under explosion. This model proposed the concept of breakage potential by assuming that 0.074 mm is the minimum particle breakage size and is greater than the size of all particles, which have varying degrees of potential for breakage.

$$b_p = \log_{10} \left[ \frac{D \text{ mm}}{0.074 \text{ mm}} \right] \quad (1)$$

where  $D$  is the particle size, and when  $D < 0.074$  mm,  $b_p = 0$ .

For the samples, the potential for breakage ( $B_p$ ) is defined as follows:

$$B_p = \int_0^1 b_p df \quad (2)$$

For the tests before and after the break, the overall potential for fragmentation or the overall potential for breakage is defined as  $B_t$ , as shown in Eq. (3).

$$B_t = \int_0^1 (b_{p0} - b_{pt}) df \quad (3)$$

where  $b_{p0}$  and  $b_{pt}$  are the potential for breakage before and after the explosion, respectively. Meanwhile,  $B_r$  is defined as the relative degree of particle breakage, as expressed in Eq. (4).

$$B_r = \frac{B_t}{B_{p0}} \quad (4)$$

The relative degrees of particle breakage of the calcareous sand at different distances from the center of the explosion can be obtained from the results and are presented in Table 2.

A large number of calcareous sand particle breakage occur within a certain range, especially near the explosion site, which result in the formation of the crush, compression, and damage zones. An immense energy blast is consumed during the formation of these regions, and the explosive stress wave propagation is also affected.

Table 2.  $B_r$  at different distances from the center.

Distance (cm)	5	10	15
$B_r$	0.532	0.217	0.06

## 5 CALCULATION OF THE ENERGY LOSS

The total chemical energy of the blasting agent for the experiment can be expressed as follows:

$$E_0 = mQ \quad (5)$$

where  $E_0$  is the total energy released by the blasting agent,  $m$  is the quality of the blasting agent, and  $Q$  is the detonation heat of the unit plastic blasting agent, which is the constant (3.545 kJ/g) for the current experiment.

Some assumptions are made to simplify the calculation process, such as the spherical shape of the broken, compress, and damage zones. Therefore, the relationship of the energy conservation for a one-dimensional blasting wave can be expressed as

$$e + \frac{p}{\rho} + \frac{1}{2}(D-u)^2 = e_0 + \frac{p_0}{\rho_0} + \frac{1}{2}(D-u_0)^2 \quad (6)$$

where  $e_0$ ,  $p_0$ ,  $\rho_0$ , and  $u_0$  and  $e$ ,  $p$ ,  $\rho$ , and  $u$  are the internal energy, pressure, density, and velocity of the mass point before and after the action of the blasting wave, respectively.  $D$  is the propagation velocity of the shock wave front, and  $v = 1/\rho$ . The energy relationship between the energy and the unit volume change can then be derived as

$$\Delta e = \frac{1}{2}(p + p_0)(v + v_0) \approx \frac{3(1+2\gamma)p^2}{2\rho_0 E} \quad (7)$$

where  $\gamma$  and  $E$  are Poisson's ratio and the elastic modulus, respectively, where as  $p$  is the stress wave attenuation formula in calcareous sand. Eq. (7) can then be rearranged as follows:

$$\Delta e = 32.5 \left( \sqrt[3]{Q/R} \right)^{2.95} \quad (8)$$

Therefore, the energy consumed by the compression zone can be expressed as

$$e = \frac{1}{2} \Delta e \frac{4}{3} \pi R_d^3 \rho \quad (9)$$

where  $R_d$  is the radius of the compression zone.

The calculated total energy of the blasting agent and the consumed energy from the broken, compress, and damage zones are shown in Table 3.

A previous study has shown that the consumed energies for the broken, compress, and damage zones are 8~15% of the total energy for rock and cement material, but the value is approximately 25% for calcareous sand. These results indicate that particle breakage consumes a large amount of

Table 3. Reference table for all kinds of energy.

Q/g	$E_0$ /kJ	$e$ /kJ	$e/E_0$
1.5	5.318	1.432	0.269
3.0	10.636	2.675	0.252

blasting energy that can lead to the formation of these zones and the increased attenuation of the compression wave.

## 6 CONCLUSIONS AND DISCUSSIONS

The particle breakage characteristic was analyzed through indoor explosion experiments, main conclusions are summarized as follows:

1. Calcareous sand is a special marine geotechnical medium. Exploring saturated calcareous soil explosion compacting mechanism and effect through the experimental study have great theoretical and practical significance to engineering construction in calcareous soil area.
2. A large number of calcareous sand particle breakage occur within a certain range, especially near the explosion site, which result in the formation of the crush, compression, and damage zones. An immense energy blast was consumed during the formation of these regions, and the explosive stress wave propagation was also affected. The results show that relative degrees of particle breakage of the calcareous sand are 0.532, 0.217 and 0.06, at the distance from blasting source center position 5 cm, 10 cm and 15 cm.
3. Under the effect of a blasting load, many particles were broken near the blasting zone. The broken, compress, and damage zones are formed, which consume most of the energy and result in an increase in the attenuation effect. Through theoretical calculations, the energy for the formation of the broken, compress, and damage zones is found to consume 25% of the total energy.

## ACKNOWLEDGEMENTS

This work was supported by the Natural Science Foundation of China (41101519) and Zhejiang Provincial Natural Science Foundation of China (LY14D020001).

## REFERENCES

- [1] Liu Chongquan, Yang Zhiqiang, Wang Ren. The present condition and development in studies of mechanical properties of calcareous soils [J], *Rock and Soil Mechanics*, 1995, 16(4):75–83.
- [2] Wang Ren, Song Chaojing, Zhao Huanting. Engineering Geological Properties of Coral Reefs on Nansha Islands [M]. *Beijing: Science Press*, 1997.
- [3] Xu Xue-yong, Wang Ren, Wang Xin-zhi, et al. Experimental study on dynamic behavior of saturated calcareous soil due to explosion [J]. *Rock and Soil Mechanics*, 2012, 33(10):2953–2959.
- [4] Wang Xinzhi, Wang Ren, Meng Qinshan, et al. Study of plate load test of calcareous sand [J]. *Rock and Soil Mechanics*, 2009, 30(1): 147–156.
- [5] Chen Qingyun, Sun Jizhu, Wang Ren. Triaxial experiment study of acoustic emission laws of calcareous sand. *Rock and Soil Mechanics*, 2009, 30(7):2027–2036.
- [6] Van Impe W.F., Meyus I. Soil Compaction by Blasting in the Zeebrugge Area [C]. 1st Iranian Int. Sem. On Smfe, Tehran, Iran. 1989.
- [7] Gohl W.B., Jeferies M.G., Howie J.A. Explosive Compaction: Design, Implementation and Effectiveness [J]. *Geotechnique*, 2000, 50 (6):657–665.
- [8] Dontsov V.E., Nakoryakov V.E. Enhancement of shock waves in a porous medium saturated with a liquid containing gas bubbles [J]. *International Journal of Multiphase Flow*, 2001, (27):2033–2041.
- [9] Wang Ming-yang, Zhao Yue-tang, Qian Qi-hu. Study on dynamic behaviour and numerical method for saturated sand [J]. *Chinese Journal of Geotechnical Engineering*, 2002, 24(6):723–729.
- [10] Qu Jun-tong, Zhou Jian, Wu Xiao-feng. Explosive Compaction of Sand Ground Foundation [J]. *Engineering Blasting*, 2006, 12(3):14–17.
- [11] Mu Chao-min, Ren Huiqi, Li Yongchi, et al. Propagation laws of blast wave in saturated soils with high saturation degree [J]. *Rock and Soil Mechanics*, 2010, 31(3):875–880.
- [12] Guo Sheng-bing, Gao Peizheng, Pan Yuefeng, et al. Explosive wave propagation in quasi-saturated sandy soil [J]. *Rock and Soil Mechanics*, 2004, 25(12):1897–1899.
- [13] Xu Xue-yong, Di Sheng-jie, Cheng Wan-qiang. P-wave attenuation mechanism of calcareous sand under explosion [J]. *Appl. Mech. Mater.* Vols. 580–583(2014) pp 268–272.
- [14] Shi Jiaowang, Tong Jinyue, Xiong Changhan, et al. An Experimental Research on Compaction of Saturated Sand Soil by Explosion [J]. *Journal of Yangtze River Scientific Research Institute*, 1992, 9(4):25–32.
- [15] Xu Xue-yong, Wang Ren, Hu Ming-jian, et al. Experimental study on dynamic characteristics of saturated calcareous soil explosion compaction [J]. *Rock and Soil Mechanics*, 2012, 33(2):402–406.
- [16] Hardin B.O. Crushing of Soil Particles [J]. *Journal of Geotechnical Engineering*, 1985, 111(10): 1177–1192.

# Parameter sensitivity analysis of marine steel pipe pile in sandy soil foundation based on $p$ - $y$ curve method

Sheng-jie Di, Xue-yong Xu & Xiao-fen Chen

Power China Huadong Engineering Corporation Limited, Hangzhou, China

Xiang Wang & Ling-fang Bu

Power China Zhejiang Huadong Construction Engineering Corporation Limited, Hangzhou, China

**ABSTRACT:** Each parameter of pile and soil in marine sandy soil foundation is analyzed based on  $p$ - $y$  curve method, including qualitative analysis and quantitative analysis. With engineering design index such as the displacement and deflection slope of pile top, max moment and max shear of pile shaft, max soil pressure to judge standard, we distinguish the sensitivity factors and the non-sensitivity factors. Research conclusions are as follows: the internal friction angle  $\phi$  and the bending stiffness  $EI$  of pile are sensitivity factor, the effective unit weight  $\gamma$  is moderate sensitivity factor, and the effective unit weight  $\gamma$  is relative insensitive factor. Research results can provide beneficial reference for engineering surveyors and designers.

**Keywords:** sandy soil foundation; pile and soil interaction;  $p$ - $y$  curve method; parameter sensitivity

## 1 INTRODUCTION

Coastal and offshore engineering including harbor and wharf engineering, breakwater engineering, offshore drilling platform engineering, offshore wind farm engineering, anti-collision pier engineering and so on, these structures are supported by pile foundation subjected to horizontal load performance. The horizontal load performance is the control factor to design those pile foundations. The pile foundations can bear part of the action of horizontal loading, and the soil around the pile can also bear the rest action of loading. The combinations of pile-soil interaction mechanical properties have the ability to resist the whole horizontal deformation of the pile body [1, 2].

The internationally recognized effective analysis method of pile foundation with large deformation is the  $p$ - $y$  curve method; this method has been used widely by the American Petroleum Institute (API) and Det Norske Veritas (DNV) [3, 4].  $p$ - $y$  curve analysis method is also used by the Chinese standard code for Specifications for offshore Platform Engineering Geology investigation (GB/T 17503-2009) and the industry standard for Code for Pile Foundation of Harbor Engineering (JTS 167-4-2012) [5, 6]. The method can better simulate the response of piles and soil elastic-plastic development process.

At the offshore engineering site in the southeast of the yellow sea in China, shallow strata have a wide range of sand distribution; state of structure

from loose to close-grained is complex. Their mechanical property is the key to influence the survey and design of pile foundation engineering. Statistical analysis and reading values of the shear strength parameters are more important. The parameters of  $p$ - $y$  curve method also are crucial. However, the discussion of the content and research are few reported so far. All these are matters worthy of attention.

Only after the sensitivity of the pile foundation design index have been confirmed and obtained will the engineers of in-situ test and indoor experiments be granted access to hold the key of the problem. No matter from sampling, sample preparation, transport, in situ test, indoor test and parameter statistics, all should be strictly implement the relevant regulations, and striving for accuracy.

## 2 CALCULATION METHOD

In the conventional engineering design, the mechanical responses of pile foundation under the load combination are commonly used as the design indexes, such as the deflection at pile top or at the mudline, deflection slope of pile, maximum bending moment, maximum shear force, and the maximum soil pressure. The  $p$ - $y$  curve method and its principle with sandy soil foundations are shown in the reference [3]. Based on the  $p$ - $y$  curve method, assume that the soil reaction  $p$  is the function of

the pile depth  $z$  and the pile deflection  $y$ , the function is shown as  $p = p(z, y)$ . At the same time, the both side of pile at the unit  $dz$  are respectively distributed load  $q(z)$  and soil counterforce  $p(z, y)$ , and the shear force in the cross section of pile is  $S$ , bending moment is  $M$ . For the balance of the unit  $dz$ , the sum of the horizontal force should be zero. Therefore, the following equations can be derived:

$$(S + dS) - S - p(z, y)dz + q(z)dz = 0 \quad (1)$$

$$\frac{dS}{dz} = p(z, y) - q(z) \quad (2)$$

$$S = \frac{dM}{dz} \quad (3)$$

$$\frac{dS}{dz} = \frac{d^2M}{dz^2} = p(z, y) - q(z) \quad (4)$$

According to the mechanics of materials, the symbols of second order differential  $d^2y/dz^2$  and bending moment  $M$  are opposite, so it can be concluded that the bending moment differential equations as follows:

$$EI \frac{d^2y}{dz^2} = -M \quad (5)$$

where  $E$  is elasticity modulus,  $I$  is geometrical moment of inertia, and  $EI$  is the bending stiffness of pile.

$$EI \frac{d^4y}{dz^4} = -p(z, y) + q(z) \quad (6)$$

The [equation \(6\)](#) is the deflection differential equation of pile in the soil foundation. For general structure foundation under the horizontal load effect, the interface between soil and pile has the trend of separating, at the same time, the cohesion force between pile and soil is smaller than the effect force in the direction of attack, so it can be generally assumed to  $q(z) = 0$ , so the [equation \(6\)](#) can be expressed as:

$$EI \frac{d^4y}{dz^4} + p(z, y) = 0 \quad (7)$$

Regardless of the soil foundation is elastic or inelastic, the deflection differential [equation \(7\)](#) is always founded.

According to each division point deflection  $y$  of pile body, the rest indexes including the bending moment  $M$ , the shear force  $S$ , deflection slope  $St$  and the soil pressure  $R$  can be obtained from deflection at any unit of pile, which can be expressed as follows:

$$EI \left( \frac{d^2y}{dz^2} \right) = M \quad (8)$$

where  $z$  is depth of calculation point, and  $y$  is deflection of pile at the depth  $z$ .

$$EI \left( \frac{d^3y}{dz^3} \right) = S \quad (9)$$

$$\frac{dy}{dz} = St \quad (10)$$

$$EI \left( \frac{d^4y}{dz^4} \right) = R \quad (11)$$

It can be programmed through the above relations to obtain the design indexes.

### 3 ANALYSIS SCHEME

Take a large diameter steel pipe pile in offshore sandy soil ground for an example. The pile diameter  $D = 1.2$  m, pipe thickness  $t$  is 19 mm, the height of the pile above the mud line  $H$  is 7.9 m, the depth of pile under the mud line  $L$  is 45 m, the bending stiffness of pile  $EI = 2.46 \times 10^6$  kN/m<sup>2</sup>, soil effective unit weight  $\gamma = 9$  kN/m<sup>3</sup>, and internal friction angle of soil  $\phi = 35^\circ$ . Under the horizontal load  $F = 400$  kN at the top of pile, the deflection of pile top is 13 mm, and the maximum bending moment of pile is 3700 kNm. Based on the  $p$ - $y$  curve method, through calculation and analysis, the pile top deflection  $y = 14.7$  mm, the maximum bending moment  $M = 3880$  kNm. These design indexes of pile under different horizontal loads are shown in [Figure 1](#). In addition, the calculation result is basically corresponding to the measured value. Therefore, the computational results show that the method and the program we developed are correct and available.

In order to make the sensitivity analysis on some parameters under different horizontal loads, we develop the analysis scheme. The load changes at the range of 50 kN to 400 kN under different internal friction angles  $\phi$  of sandy soil. The reference value of  $\phi$  is set to be  $35^\circ$ , the corresponding design indexes can be obtained respectively according to the increment of 50%, -50% and -70% (corresponding to the internal friction angles  $\phi = 52.5^\circ$ ,  $17.5^\circ$  and  $10.5^\circ$  respectively).

For the sandy soil parameters  $\phi$ ,  $\gamma$  and pile structure parameter  $EI$ , we use the reference values mentioned above to fluctuate 20% and 5% interval as calculating parameters. Therefore, the sensitivity analysis of a certain parameter is made when the rest parameters are constant, so it can be to determine the quantitative influence of each single parameter.

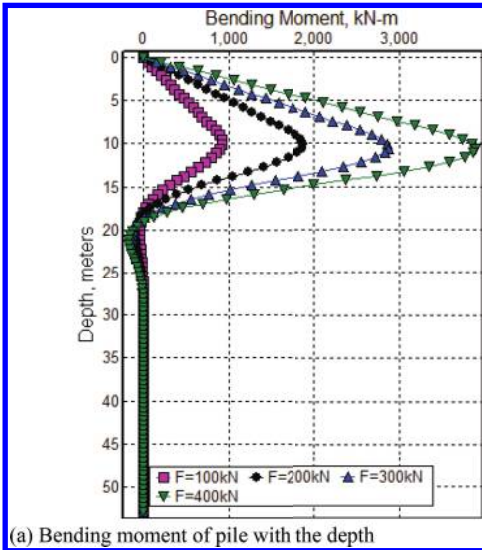
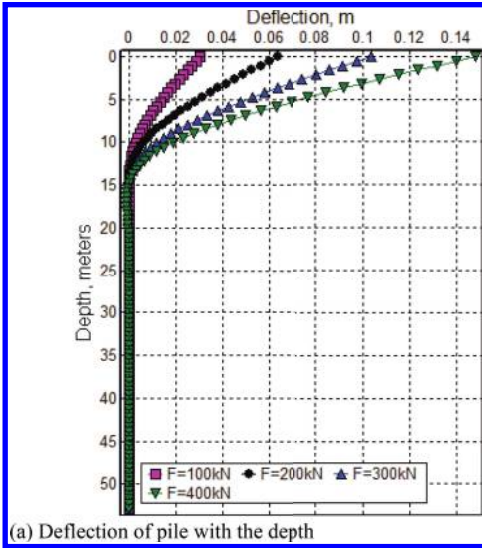


Figure 1. Design indexes of pile under different horizontal loads.

#### 4 ANALYSIS RESULTS

The curves of pile design indexes under different internal friction angles and different horizontal loads are shown in Figure 2. From the curves, we can easily and clearly to obtain the rules. Under the same increase and decrease amplitude, the shapes of curves are significantly different. The sensitivity of internal friction angle to the deflection is greater than the maximum bending moment of pile.

Parameter sensitivity analysis curves of sandy soil and pile structure are shown in Figure 3

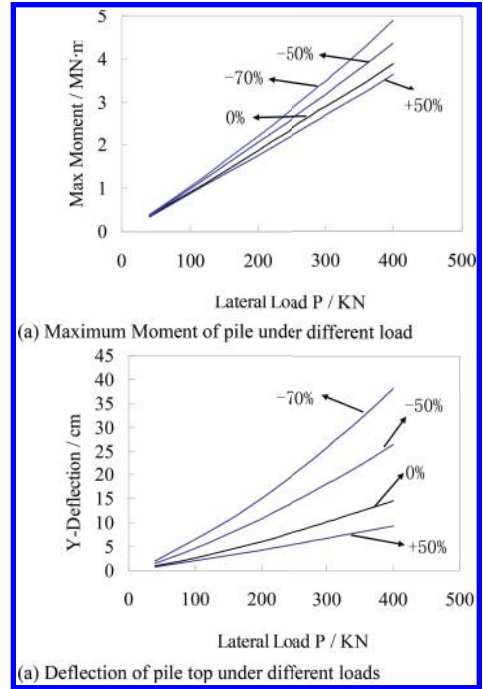


Figure 2. Design indexes of pile with different internal friction angles of sandy soil and horizontal loads.

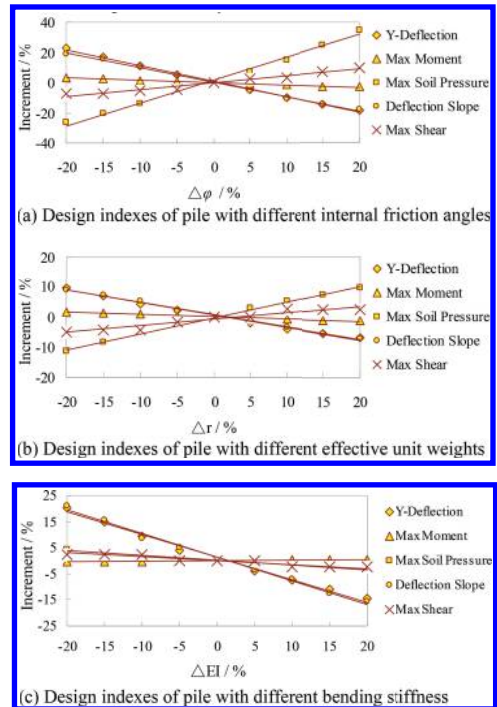


Figure 3. Parameter sensitivity analysis curves.

Table 1. Parameter sensitivity analysis based on  $p$ - $y$  curve method under different friction angles.

Friction angle $\varphi$ (°)	Y deflection (cm)	Increment $\Delta$ (%)	Max moment (KNm)	Increment $\Delta$ (%)	Max shear (KN)	Increment $\Delta$ (%)	Max soil pressure (KPa)	Increment $\Delta$ (%)	Deflection slope (rad)	Increment $\Delta$ (%)
28.00	18.1	23.13	4010	3.35	698.1	-7.50	40.00	-26.16	-0.01259	19.22
29.75	17.2	17.01	3970	2.32	698.1	-7.50	43.13	-20.38	-0.01222	15.72
31.50	16.3	10.88	3940	1.55	717.0	-4.99	46.67	-13.85	-0.01167	10.51
33.25	15.5	5.44	3910	0.77	722.2	-4.31	50.12	-7.48	-0.01111	5.21
35.00	14.7	0	3880	0	754.7	0	54.17	0	-0.01056	0
36.75	14.0	-4.76	3850	-0.77	773.6	2.50	58.12	7.29	-0.01	-5.30
38.50	13.3	-9.52	3820	-1.55	777.8	3.06	62.50	15.38	-0.00944	-10.61
40.25	12.6	-14.29	3790	-2.32	811.3	7.50	67.71	24.99	-0.00907	-14.11
42.00	12.0	-18.37	3770	-2.84	830.2	10.0	73.13	35.00	-0.0087	-17.61

and Table 1. Within  $\pm 20\%$  of internal friction angle, the maximum horizontal deflection at pile top is in  $-18.37\%$ ~ $23.00\%$ . In the meantime, the changing of the slope at pile top are similar to the deflection, it is about  $-17.61\%$ ~ $19.22\%$ .

The biggest impact of indexes is the maximum soil pressure, and its maximum amplitude value can reach  $35.00\%$ . In terms of internal friction angle, the influence of effective unit weight is reduced. Therefore, for the sandy soil, we can determine that the internal friction angle is sensitive factor, and the unit weight is relative less sensitive factor.

In addition, for the deflection and slope at pile top, the bending stiffness  $EI$  is sensitive factor, the change range is  $12.60\%$ ~ $17.70\%$ . However, for the design indexes shear force and bending moment,  $EI$  is the relative less sensitive factor, the change amplitude is less than  $5\%$ .

## 5 CONCLUSIONS AND DISCUSSIONS

Through the parameter sensitivity analysis of marine sandy soil and pile, main conclusions are summarized as follows:

1. Through the design indexes of pile foundation as the judgment standard, the parameter sensitivity analysis results are more clearly, the conclusions can provide a reference for engineering survey and design engineer directly.
2. The sensitivity factors and less sensitivity factors studied are distinguished. Among them, internal friction angle  $\varphi$  of sandy soil is the most critical parameter, and pile bending stiffness  $EI$  is basically as important as  $\varphi$ . At the same time, effective unit weight  $\gamma$  of sandy soil is relatively less critical, but it also has major impact.
3. Because the influence of the pile bending stiffness is greater, so under the premise of

unimproved foundation soil, we can improve the pile bending stiffness to control the deflection and deflection slope of pile under the horizontal load, such as expansion of pile diameter or grouting in the pile pipe.

## ACKNOWLEDGEMENTS

This work was supported by Zhejiang Provincial Natural Science Foundation of China (LY14D020001), Major Science and technology project of PowerChina Corporation and HydroChina Corporation (GW-KJ-2011-18, GW-KJ-2013-17, SD2013-10).

## REFERENCES

- [1] Reese L.C., Van Impe W.F. Single Pile and Pile Group under Lateral Loading [M]. *Rotterdam: Balkema A A*, 2001.
- [2] Hald T., Mørch C., Jensen L., et al. Revisiting Monopile Design Using P-Y Curves—Results from Full Scale Measurements on Horns Rev [J]. *Proceedings of European Offshore Wind*. 2009, Vol. 3: 93–99.
- [3] American Petroleum Institute. Recommended Practice for Planning, Designing and Constructing Fixed Offshore Platforms—Working Stress Design [M]. *API RP2A-WSD*, 2007: 128–137.
- [4] Det Norske Veritas (DNV). Structure Design of Offshore Units (WSD Method) [M]. *Offshore Standard DNV-OS-C201*. 2005.
- [5] The PRC Standard. GB/T 17503-2009: Specifications for Offshore Platform Engineering Geology Investigation [S]. Beijing: Standards Press of China, 2010.
- [6] The Ministry of Communications of PRC. JTS167-4-2012: Code for Pile Foundation of Harbor Engineering [S]. Beijing: China Communication Press, 2012.



# Kinematic analysis of slope failure modes based on stereographic projection

S. Xiao, Y.T. Gao, S.C. Wu, B. Liu & Q.M. Tian

*Key Laboratory of Ministry of Education for Efficient Mining and Safety of Metal Mine, University of Science and Technology Beijing, Beijing, China*

**ABSTRACT:** On the basis of surveying and mapping data of joints and structural planes in Muliashi Open Pit, the kinematic analysis of slope failure modes was carried out on the tenth survey area (Area 10) of this open pit, using stereographic projection. The key points in graphic analysis process, criterion of potential failure modes and corresponding probabilities of the four kinds of slope failure modes, including planar sliding, wedge sliding, flexural toppling and direct toppling, were analyzed in detail. The results obtained in Area 10 were compared with the actual situation of instability slope on site. Comparison results show that this method could effectively identify potential slope failure mode. Furthermore, all slopes within the survey areas of the open pit were statistical analyzed, and results showed that wedge sliding failure in the open pit was most likely slope failure mode, successively followed by the toppling failure in northern slopes and the planar sliding failure in southern slopes. This method could identify potential slope instability mode effectively, and has important guiding significance for slope stability analysis and instability slope treatment.

**Keywords:** stereographic projection; kinematic analysis, failure mode; open pit slope

## 1 INTRODUCTION

Stereographic projection, widely used in structural geology and rock geotechnical engineering, is a method of reflecting objects' three-dimensional geometric elements (etc. line, polygon) onto the projection plane for further research (He 1965; Sun et al. 1980). It has been extensively documented that stereographic projection can be applied well in slope stability analysis by reflecting the spatial relationships between slope plane and joint planes (Hoek 1977; Goodman 1980; Hudson et al. 1997).

Kinematic analysis refers to analyzing the movement of object only from its spatial relationship and geometry and meanwhile ignoring the mass and external force. Kinematic analysis has been used to analyze the instabilities of discontinuity-controlled rock slopes (Aksoy et al. 2007), as well as the probability of block toppling failure and planar sliding. This method also can be applied for finding stable blocks within the Fraser's Hill granite slopes (Wangsa et al. 2008).

Combined use of stereographic projection and kinematic analysis has been recently proposed to analyze the potential failure modes and corresponding probabilities based on the spatial relationship between the slope surface and the joint planes. Specifically, by using the methods of

stereographic projection and kinematic analysis, Wang et al. (2011) analyzed the maximum safe excavation slope angle of double free face slopes, Smith et al. (2015) studied the instability of structural slopes under local stress trajectories, and moreover Admassu et al. (2013) analyzed the potential failure probability under different failure modes. All these researches promote the combined application of the stereographic projection and kinematic analysis.

In the present study, stereographic projection was used to map survey data of joints and structural planes from Muliashi Open Pit onto equatorial plane. Furthermore, four kinds of slope failure modes—planar sliding, wedge sliding, flexural toppling and direct toppling, were discussed in details using kinematic analysis focus on three aspects, including graphic analysis process, criterion of potential failure and corresponding probabilities. Research works have important guiding significance for slope stability analysis and instability treatment.

## 2 PROJECT OVERVIEW

Muliashi Open Pit (Fig. 1) located in Luanshya, Zambia, which is a deep open pit with a design



Figure 1. Muliashi open pit (partial).

mining depth of 175 m. The border elevation is 1280 m, and has mined to platform of 1190 m. The bench height is 15 m, which will be 30 m after benches combination. The instability phenomena such as small and medium scale collapse occurred to the southern slope during upper mining.

The rock mass of the open pit has developmental joints and structural planes. Site investigation found that the main cause of failure was ill-structure planes, especially the existence of multiple sets of structural planes cutting the rock mass, or the tendency of structural planes which were consistent with the tendency of slope, which would greatly reduce the slope stability.

In order to study the influence of rock joints on slope stability, mapping of joints and structural planes of slope rock mass has been made, which could effectively expose the distributing features of joints and structural planes in mine rock slope. In addition, it was conducive to know the distribution of lithology, characteristics of geological engineering, the rock group division, the engineering geological zoning, and etc. All these could provide guidance for the treatment of instability slope.

### 3 FIELD SURVEYING OF JOINTS AND STRUCTURAL PLANES

According to Code for Investigation of Geotechnical Engineering in China (GB50021-2001), weak intercalations and the distribution, composition, degree of consolidation and the features of the structure should be investigated in the engineering survey. The occurrence, crack width and persistence of joints should be measured by different parts of rock.

Fifty scan lines were layout in the outcrops in Muliashi Open Pit to get statistical materials of geological and geometric features of joints, which divided the open pit into 12 areas according to

different area conditions and lithology of rock mass. Projection diagram of joints occurrence poles and the favorite joint sets were illustrated. And then, the slope failure modes could be analyzed. The preliminary results are shown in Figure 2.

## 4 STEREOGRAPHIC PROJECTION KINEMATIC ANALYSIS

Given the relationship between the rock joints occurrence and slope plane, the stereographic projection kinematics analysis method was used to analyze the potential failure modes and the corresponding probabilities. The Area 10 in Figure 2 was cohosted to take analysis in detail.

### 4.1 Failure modes analysis of Area 10

The Area 10 with development joints and structural planes is located in southern slope, which belongs to the orebody footwall. The region slope angle is 65 degrees, and the average dip direction is 30 degrees. According to the regional joint survey data, four failure modes, including planar sliding, wedge sliding, flexural toppling and direct toppling, were applied to analyze the potential instability probability.

#### 4.1.1 Planar sliding

If planar sliding occurred, the dip direction of joint plane and the slope plane must have a same tendency. Also, the structural plane angle must be greater than the friction angle of rock mass, but be smaller than the slope angle.

The analysis graph of planar sliding mode is shown in Figure 3. The friction angle of rock mass in the slope is the friction angle cone in Figure 3 which set to 23 degree from the project materials. Based on empirical observations, a typically value of 20 to 30 degrees was assigned to the lateral limits. According to the stereographic projection kinematic analysis theory, the red zone is the critical pole vector zone for planar sliding. Joint poles in this area would easily cause planar sliding. The statistical analysis showed that the critical poles in red zone are 66, which accounted for 10.38% in the all joints. The analysis results are shown in Table 1.

#### 4.1.2 Wedge sliding

Wedge sliding includes double (along the line of intersection) and single sliding plane (if one plane has a more favorable orientation for sliding than the line of intersection). Wedge sliding is based on the analysis of joint plants intersections.

When two joint planes intersect together, they will form a three dimensional intersecting line which will form a intersection point with the polar

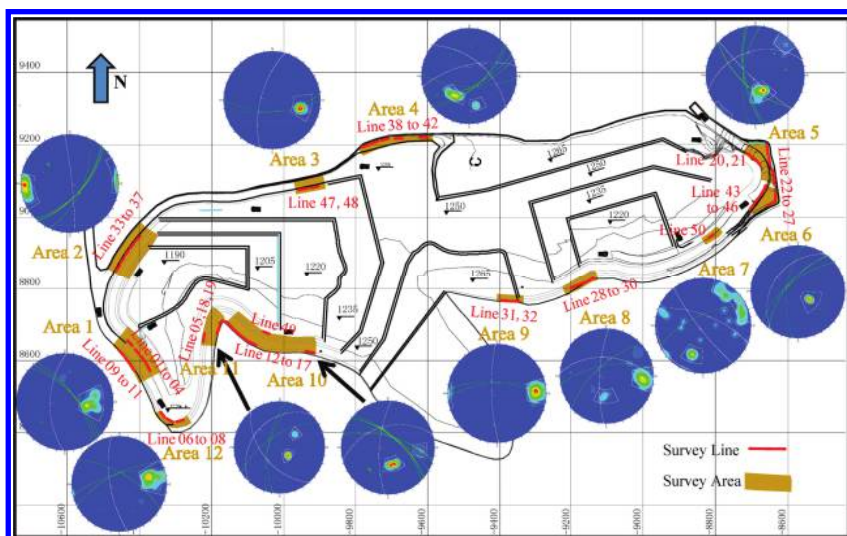


Figure 2. Field joint survey results.

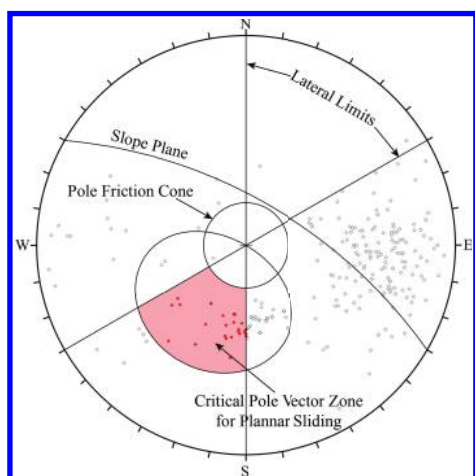


Figure 3. Graphic analysis of planar sliding mode.

Table 1. Analysis results of planar sliding mode.

Type	Critical poles	All poles	Percentage of critical poles/%
Planar sliding	66	636	10.38

projection ball. If the intersection point falls in the red area in Figure 5, the intersection of two joint planes could cause a wedge sliding.

There are totally 188932 intersections formed by the entire joint planes, the number of which fall into the red zone is 139992, accounting for

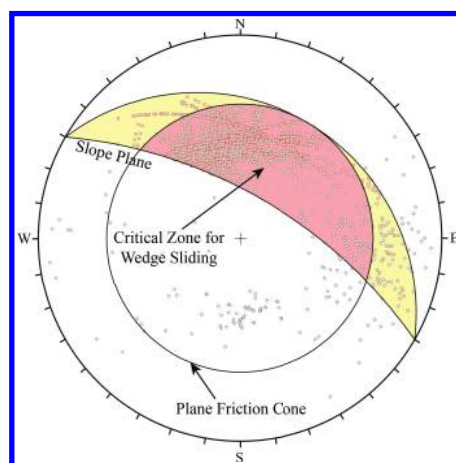


Figure 4. Graphic analysis of wedge sliding mode.

74.10% (Table 2). The results show that the collapse of slope is likely caused by wedge sliding.

#### 4.1.3 Flexural toppling

The slip limit plane is defined in the flexural toppling failure according to Goodman's (1980). If slip occurs, the bedding normal must be inclined less steeply than a line inclined at an angle equivalent to the friction angle above the slope. The dip direction of the slip limit plane is equal to the slope, and the dip angle is equal to the results of slope angle minus the rock mass friction angle.

The red zone in Figure 6 represented the critical pole vector zone of flexural toppling mode. There is

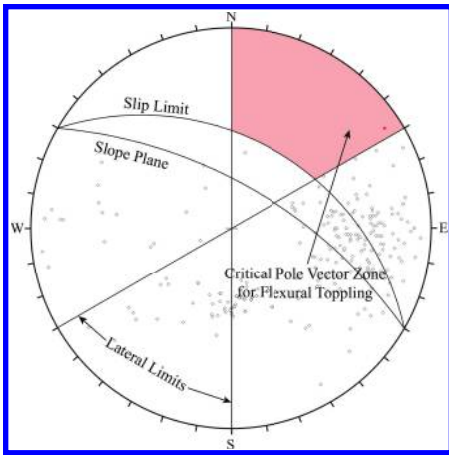


Figure 5. Graphic analysis of flexural toppling mode.

Table 2. Analysis results of wedge sliding mode.

Type	Critical intersections	All intersections	Percentage of critical intersections/%
Wedge sliding	139992	188932	74.10

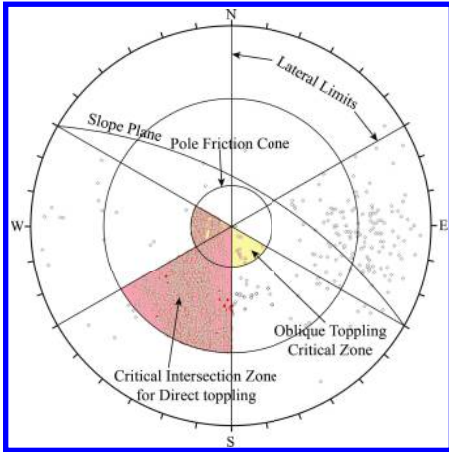


Figure 6. Graphic analysis of direct toppling mode.

only one joint pole in this zone, accounting for 0.16% in the entire poles (Table 3). The results proved the low possibility of flexural toppling damage.

#### 4.1.4 Direct toppling

The analysis of direct toppling is based on two conditions. Firstly, two joint sets intersect so that the intersection lines dip into the slope and form

Table 3. Analysis results of flexural toppling mode.

Type	Critical poles	All poles	Percentage of critical poles/%
Flexural toppling	1	636	0.16



Figure 7. Failure slope on site.

Table 4. Analysis results of direct toppling mode.

Type	Critical intersections	All intersections	Percentage of critical intersections/%
Forward	3654	188932	1.93
Oblique	903	188932	0.48%

discrete toppling blocks. Then, a third joint set exists, which act as release or sliding planes, allowing the blocks to topple. The damage mode can be further subdivided into forward toppling and oblique toppling by the relationship between sliding block and slope dip direction.

The red and yellow zones in Figure 7 are likely to generate positive toppling and oblique toppling, respectively. The statistical analysis showed that the proportion of forward toppling and oblique toppling were 1.93% and 0.48% (Table 4), respectively.

#### 4.1.5 Results discussion of Area 10

According to the stereographic projection kinematic analysis of slope within the Area 10, the probabilities of planar sliding, wedge sliding, flexural toppling, forward toppling and oblique toppling were 10.38%, 74.10%, 0.16%, 1.93% and 0.48%, respectively. The probability of wedge sliding in Area 10 is the greatest, followed by planar sliding.

The failure slope on site of Area 10 is showed in Figure 7. The sliding rock mass was controlled by the two intersecting joint planes, and caused a wedge sliding failure. The analysis result is consistent with the fundamental instability of site conditions, proving the effectiveness of this analysis method.

Table 5. Potential failure probability under different modes.

Area	Type			Direct toppling		Main critical modes
	Planar sliding	Wedge sliding	Flexural toppling	Forward	Oblique	
1	0.00%	6.25%	16.25%	26.73%	0.92%	Forward toppling, flexural toppling
2	0.92%	18.62%	0.00%	0.37%	15.39%	Wedge sliding, oblique toppling
3	6.96%	28.88%	1.74%	16.62%	1.04%	Wedge sliding, forward toppling
4	0.83%	5.67%	14.64%	32.66%	0.49%	Forward toppling, flexural toppling
5	1.27%	35.83%	0.64%	1.53%	0.89%	Wedge sliding
6	78.62%	54.47%	1.41%	0.26%	0.23%	Planar sliding, wedge sliding
7	0.00%	29.71%	0.00%	15.22%	7.97%	Wedge sliding, forward toppling
8	9.09%	43.12%	0.00%	2.75%	2.61%	Wedge sliding, planar sliding
9	0.00%	19.06%	3.64%	27.88%	9.90%	Wedge sliding, forward toppling
10	10.38%	74.10%	0.16%	1.93%	0.48%	Wedge sliding, planar sliding
11	64.24%	74.34%	0.61%	0.55%	0.00%	Wedge sliding, planar sliding
12	0.00%	22.27%	0.00%	13.24%	1.94%	Wedge sliding, forward toppling

#### 4.2 Analysis results of the open pit

The method of stereographic projection kinematic analysis was used to analyze the 12 areas of open pit slope from the four failure modes. Results are shown in Table 5.

The Area from 2 to 4 belonging to the northern slope (ore body hanging wall) have a maximum possibility of wedge sliding, followed by toppling failure. The Area from 6 to 11 belonging to the southern slope (Ore body footwall slope) have a maximum possibility of wedge sliding, followed by planar sliding.

The analysis results could be a preliminary identification of potential instability of slope, which has important guiding significance for slope stability analysis and slope engineering management treatment.

## 5 CONCLUSION

By stereographic projection kinematic analysis of Muliashi Open Pit, we've got basic conclusions as follows:

1. The probability of wedge sliding is the greatest in Area 10, followed by planar sliding. The analysis result is consistent with the fundamental instability of site conditions, proving the effectiveness of this analysis method.
2. The northern slope has a maximum possibility of wedge sliding, followed by toppling failure. The southern slope has a maximum possibility of wedge sliding, followed by planar sliding.
3. The analysis results could be a preliminary identification of potential instability of slope, which

has important guiding significance for slope stability analysis and slope engineering management treatment.

## REFERENCES

- Admassu, Y. & Shakoor, A. 2013. DIPANALYST: A computer program for quantitative kinematic analysis of rock slope failures. *Computers & Geosciences* 54: 196–202.
- Aksoy, H. & Ercanoglu, M. 2007. Fuzzified kinematic analysis of discontinuity-controlled rock slope instabilities. *Engineering Geology* 89(3–4): 206–219.
- Goodman, R.E. 1980. *Introduction to Rock Mechanics (Chapter 8)*. Toronto: John Wiley.
- Hammett, R.D. & Hoek, E. 1981. *Design of large underground caverns for hydroelectric projects with particular reference to structurally controlled failure mechanisms*. New York: ASCE.
- He, Z.L. 1965. *Application of stereographic projection in geological sciences*. Beijing: Science Press.
- Hoek, E. 1977. *Structurally controlled instability in underground excavations*. Keystone, Colorado.
- Hudson, J.A. & Harrison, J.P. 2007. *Engineering Rock Mechanics—An Introduction to the Principles*. Pergamon Press.
- Smith, J.V. 2015. A new approach to kinematic analysis of stress-induced structural slope instability. *Engineering Geology* 187: 56–59.
- Sun, Y.K. & Gu X. 1980. *Application of stereographic projection in rock engineering and geology mechanics*. Beijing: Science Press.
- Wang, L.Q. and et al. 2011. Kinematic analyses of sliding and toppling failure of double free face rock mass slopes. *Rock and Soil Mechanics* 32(S1): 72–77.
- Wangsa, A.H & Rafek, A. 2008. Kinematic and block theory applications to rock slope stability analysis at Fraser's Hill Pahang Malaysia. *Electronic Journal of Geotechnical Engineering* 13.

# Numerical analysis of continuous loading oedometer test

Yuan-Sheng Zhang & Yong-Tao Gao

*School of Civil and Environment Engineering, University of Science and Technology Beijing, Beijing, China*

Zhe Wang

*Dalian Academy of Reconnaissance and Mapping Co. Ltd., Dalian, China*

Taibao Zhang

*The Supervision and Administration of Production Safety Erguna City, Erguna, China*

**ABSTRACT:** Based on Terzaghi's one-dimensional consolidation theory, this study was carried out on oedometer test, with further analysis in comparing the numerical simulations of the finite difference method using a numerical simulation program written in C++. The results show that the proposed numerical simulation procedure could simulate the oedometer test well, which have a certain theoretical value and practical significance for revealing the deformation of soft soil consolidation.

**Keywords:** soft clay; oedometer test; numerical simulation; finite difference method

## 1 INTRODUCTION

In consolidation of soft clay, many areas of modern construction were involved. It occupies a very important position in civil engineering. The consolidation test of soil was established according to the classic Terzaghi consolidation theory. At present, the incremental hierarchical loading method is the standard method commonly used at home and abroad. The essence of this method is when the last level of loading reaches stability, then it is applied to the next level of loading [1]. Because of the time reaching to the needed level is long, usually it is completed in several days or 10 more days, it is difficult to accurately determine the value of pre-consolidation pressure with less and discontinuous test data. Therefore, this paper applies a numerical analysis to the continuous loading compression test. In addition, in the incremental hierarchical loading experiment, there is an uneven distribution of effective stress on the horizontal planes, which along the height of the specimen, will lead to a very uneven compression. In this case, the specimen's structures are susceptible to damage and the test cycle is long.

In order to overcome the above disadvantages, foreign scholars have conducted intense researches on the consolidation test from the end of the 60s and developed the continuous loading consolidation test. According to different control conditions in the tests, the successive loading consolidation test can be divided into equivalent lumped

parameter method (Smith & Wahls [2], 1969), control the pore pressure gradient consolidation (Lowe [3], 1969), loading rate such as consolidation test (Aboshi [4], 1970; Von Fay [5], 1986), control the degree of consolidation test (Janbu [6]), control of hydraulic gradient strain consolidation test (Attasit Korchaiya-pruk [7], 2007).

Meanwhile, experimental results have a lot of discreteness due to the man-made factors on the consolidation test [8]. In this paper, we use Terzaghi as a one-dimensional consolidation theory [9], combining the constant strain consolidation test and the control of hydraulic gradient constant strain consolidation test, to analyze the control hydraulic gradient of constant strain consolidation test (GCRS), and to compile numerical simulation program of the indoor consolidation test using C++ programming language, the correctness of the simulation program according to the pre-existing experimental results was verified.

## 2 THE THEORY AND PROGRAM OF MERICAL SIMULATION

### 2.1 Basic idea

In GCRS consolidation test, the pore pressure of the specimen is the sum of the pore pressure of consolidation deformation and generated by the additional hydraulic gradient. The flow direction of pore water is determined by strain rate and additional hydraulic gradient of the base.

In order to simulate GCRS consolidation test, the specimen is divided into two parts, the upper part and the lower part, and the interface of the two parts is in the middle plane. Then two parts are further divided into several sub layers respectively (generally 20 or more).

## 2.2 Basic theory

At the beginning of GCRS consolidation simulation test, assuming that the middle plane occupies the center of the sample, namely

$$(NA \text{ Location})_{initial} = \frac{H_0}{2} \quad (1)$$

$$H_{Ti} = H_{Bi} = \frac{H_0}{2} \quad (2)$$

where,  $H_{Ti}$  and  $H_{Bi}$  is the height of upper and lower part of the specimen. Every part of the specimen is divided into  $n$  layers, the thickness of each layer is

$$H_{TLi} = H_{TBi} = \frac{H_{Ti}}{n} = \frac{H_{Bi}}{n} \quad (3)$$

where,  $H_{TLi}$ ,  $H_{TBi}$  is the thickness of upper and lower sublayer;  $n$  is the number of sublayers in each part. At the beginning of the simulation test, a void ratio was assumed after a period of consolidation settlement according to the initial void ratio of specimen. In the process of simulation, the mathematical convergence method was applied, thereby, to ensure that the specimen deformation simulated values are equal to the calculated values. The height of each sublayer after the consolidation can be calculated according to the assumed void ratio:

$$H_s = \frac{H_T}{(1+e_0) \cdot n} = \frac{H_{TLi}}{(1+e_0)} \quad (4)$$

$$H_{Lf} = H_{Li} - \left[ \frac{(H_{Li} - H_s)}{H_s} - e_{fa} \right] \cdot H_s \quad (5)$$

where,  $H_{Lf}$  is sublayers high after  $\Delta t$  consolidation;  $e_{fa}$  is sample's void ratio after  $\Delta t$  consolidation;  $H_s$ ,  $e_0$  is high of sample solid phase and initial void ratio; All the sub-layers have the same initial void ratio and height at the beginning of the simulation test.

Sub-layer's permeability coefficient can be obtained by:

$$C_k = \frac{\Delta e}{\Delta \log(k)} = \frac{e_{fa} - e_i}{[\log(k_L) - \log(k_0)]} \quad (6)$$

$$C_k [\log(k_L) - \log(k_0)] = e_{fa} - e_i \quad (7)$$

$$\log(k_L) = \frac{[e_{fa} - e_i + C_k \cdot \log(k_0)]}{C_k} \quad (8)$$

$$k_L = 10^{\left[ \frac{e_{fa} - e_i + C_k \cdot \log(k_0)}{C_k} \right]} \quad (9)$$

where,  $C_k$  is  $e \sim \log k$  curve's slope;  $k_L$  is Sub-layer's permeability coefficient;  $k_0$  is initial permeability coefficient.

Based on the deformation of soil layer, we can get the calculating formula of seepage velocity:

$$V_d = \frac{q}{A} \quad (10)$$

$$V_d = \frac{\Delta Volume}{\Delta t \cdot A} = \frac{\Delta H \cdot A}{\Delta t \cdot A} = \frac{\Delta H}{\Delta t} \quad (11)$$

where  $V_d$  is the seepage velocity caused by the soil deformation,  $q$  is the seepage flow, and  $\Delta t$  is the time increment.

In addition, another part of the seepage is due to the additional hydraulic gradient at the bottom of the specimen, which can be calculated by

$$i = \frac{\Delta u_b}{H} \cdot \frac{1}{\gamma_w} \quad (12)$$

$$V_i = k \cdot i \quad (13)$$

$$V_i = k_L \cdot \left( \frac{\Delta u_b}{H} \cdot \frac{1}{\gamma_w} \right) \quad (14)$$

where  $\Delta u_b$  is the excess pore water pressure at the bottom of the sample and  $\gamma_w$  is the severe of water.

Therefore, the total seepage flow velocity of sample is the sum of two parts, namely

$$V = V_d + V_i \quad (15)$$

The average excess pore water pressure will be achieved based on the calculation formula of hydraulic gradient and flow velocity, for

$$V = k \cdot i \quad (16)$$

$$V = k_L \cdot \left( \frac{\Delta u_L}{H_L} \right) \cdot \frac{1}{\gamma_w} \quad (17)$$

$$\Delta u_L = \frac{V \cdot H_L \cdot \gamma_w}{k_L} \quad (18)$$

where  $\Delta u_L$  is excess pore water pressure of each soil layer.

By (18), we can calculate the mean effective stress with the normal orientation of each layer:

$$\sigma'_{vL(avg)} = \sigma_v - \Delta u_L = \sigma_v - \frac{V \cdot H_L \cdot \gamma_w}{k_L} \quad (19)$$

where  $\sigma'_{vL(avg)}$  is the mean effective stress with the normal orientation of soil layer, and  $\sigma_v$  is the total stress. Therefore, we can calculate the new void ratio,

$$C_c = \frac{\Delta e}{\Delta \log(\sigma'_v)} \quad (20)$$

$$C_c \cdot [\log(\sigma'_{vL(avg)}) - \log(\sigma'_{v0(avg)})] = e_n - e_i \quad (21)$$

$$e_n = e_i + C_c \cdot [\log(\sigma'_{vL(avg)}) - \log(\sigma'_{v0(avg)})] \quad (22)$$

where  $C_c$  is the compression index,  $\sigma'_{v0(avg)}$  is effective stress for the average initial method, and  $e_n$  is the new calculated void ratio.

Using the new void ratio, the deformation of soil layer can be calculated. Each soil layer (from top layer to middle plane) has the same calculation process.

The simulation process of the lower part of the specimen is the same to that of the upper part except that the calculation of soil layer is from the base to middle plane, step by step. Therefore, after  $\Delta t$  consolidation, the height of the sample becomes

$$H_f = H_{Tf} + H_{Bf} \quad (23)$$

Comparing the calculated sample height with the theoretical value (calculated by strain rate and time increment). If their difference is beyond the setting error range showing that hypothesis void ratio is not correspondent with practice and needs to be corrected. Therefore, we should modify the void ratio constantly in the process of simulation using iteration method until the calculated height is equal to the theoretical value. The void ratio is modified by the convergence algorithm,

$$e_{update} = \frac{e_a}{\left[ \frac{H_f(\text{predicted})}{H_f(\text{expected})} \right]} \quad (24)$$

Not only the deformation conditions should be satisfied, but the boundary conditions, including the excess pore water pressure at the top of the sample  $\Delta u_t$ , the excess pore water pressure at the bottom of sample  $\Delta u_b$ , the excess pore water pressure of the boundaries of the sample  $\Delta u_{NA(t)}$ ,  $\Delta u_{NA(b)}$ . If the value of  $\Delta u_{NA(t)}$  is not equal to  $\Delta u_{NA(b)}$ , it shows the middle plane, which divided the specimen into the upper and the lower parts disagrees with the practical and we need to modify it. If the value of  $\Delta u_{NA(t)}$  is greater than  $\Delta u_{NA(b)}$ , it shows that the middle plane is lower, and should be up-regulated;

Table 1. Summary of the input parameters for CGC simulation.

Parameter	Physical meaning
$H_0$	Initial drainage height
$\dot{\epsilon}$	Strain rate
$e_0$	Initial void ratio
$k_0$	Initial permeability coefficient
$C_k$	Slope of $e \sim \log(k)$
$C_c$	Compression index
$\Delta u_b$	Pore pressure
$\Delta t$	Time increment

if the value of  $\Delta u_{NA(t)}$  is less than  $\Delta u_{NA(b)}$ , it shows that the middle plane is higher, and should be down-regulate. The correction calculation formula of middle plane position is as follows:

$$\Delta(NA) = NA_i \pm \frac{H_i}{m} \quad (25)$$

where  $\Delta(NA)$  is the correction value of middle plane position,  $NA_i$  is the initial set of middle plane position,  $H_i$  is total height of the sample, and  $m$  is correction coefficient of the middle plane position.

The value of  $m$  controls the middle plane's extent of variation. In order to get the appropriate correction value, the set value of  $m$  should be larger (100 or more). After the new middle plane is determined, dividing the upper and lower part of the sample into  $n$  layers separately, and conducting the simulation experiment until boundary conditions of the deformation condition and the excess pore water pressure are met, then the simulation experiment of  $\Delta t$  is finished.

### 2.3 The numerical simulation parameters

Based on the simulation theory above, the main simulation parameters includes: the drainage height of specimen, the strain rate, the initial void ratio, the permeability coefficient, the curve's slope, the compression index of pore pressure, etc. Table 1 shows the simulation parameters and physical meaning of them.

## 3 ANALYSIS OF EXPERIMENT RESULT

In the range of experimental error, the deformation index measured by the GCRS test is equivalent to the one which is measured by the routine consolidation test. Judging from the comprehensive technical and economical comparison, we can expect that GCRS test is superior to routine consolidation test.



### 3.1 Compression curve drawing

In the continuous load test, take semi-continuous observation into normal stress, sedimentation, and pore water pressure. Calculating the void ratio basis on the current load, and then a compression curve using the effective stress, the void ratio can then be obtained.

### 3.2 To solve the $c_v$ , $m_v$ , $k_v$

The coefficient of consolidation could be obtained by the theory

$$c_v = \frac{\Delta\sigma}{\Delta t} \cdot \frac{H^2}{2\Delta u_b} \quad (26)$$

Therefore, as long as we know the normal pressure increment  $\Delta\sigma$  within a tiny period,  $\Delta t$  we can calculate the coefficient of consolidation  $c_v$  directly by formula (26), and have no more need of mapping. At the same, we can calculate the average void ratio  $c_v$  at any time.

In addition, the volume compressibility coefficient and the permeability coefficient can be calculated directly by the following formula:

$$m_v = \frac{1}{H} \cdot \frac{\Delta\delta/\Delta t}{\Delta\sigma/\Delta t} \quad (27)$$

$$k = \frac{\gamma_w H}{2u_b} \cdot \frac{\Delta\delta}{\Delta t} \quad (28)$$

where  $\Delta\delta$  is the normal increment of deformation and  $\gamma_w$  is the volume weight of water.

## 4 THE RESULT OF NUMERICAL ANALYSIS

Conduct the above simulation program on sample of consolidated soil. The simulation parameters of soil sample are shown in Table 2:

Table 2. Input parameter values for oedometer simulation.

Parameter	Value
$H_0$	2.54 cm
$\dot{\epsilon}$	0.002
$e_0$	1.0
$k_0$	$6 \times 10^{-5}$ cm/s
$C_k$	0.4478
$C_c$	-0.4478
$\Delta u_b$	20 kPa
$\Delta t$	120 s

### 1. Compression Curve

We can get the relation curve of the void ratio changes along with axial stress by the simulation results, namely the compression curve. As shown in Figure 1 and Figure 2, they are the relation curve of  $e \sim p$  and  $e \sim \log p$ , respectively.

The same as the conventional consolidation test, we can calculate the consolidation parameters such as modulus of compressibility  $E$ , coefficient of volume compressibility  $m_v$ , and compression index  $C_c$  and so on by relation curve of  $e \sim p$  and  $e \sim \log p$ . However, due to the graphic solution will produce some error; here we adopt to point the coordinate to solve the problem directly.

### 2. Consolidation Parameters

After the simulation test was conducted  $\Delta t = 120$  s, increment of normal pressure  $\Delta\sigma = 30.5981 - 30.0 = 0.5981$  kPa, the applied pore water pressure is 20 kPa, coefficient of consolidation can be calculated by the formula (26). And by the simulation results, we can get

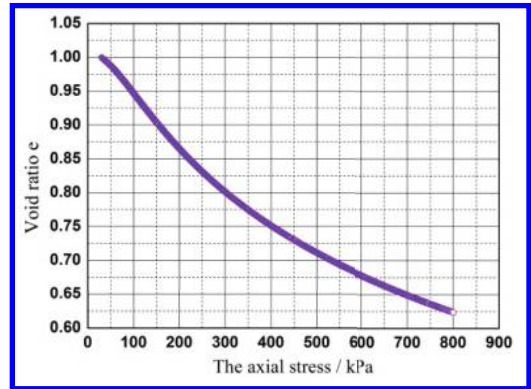


Figure 1. Relation curve of  $e \sim p$ .



Figure 2. Relation curve of  $e \sim \log p$ .

Table 3. Engineering characteristics of saturated loess.

The category of the soil	Dry density	The content of water	The initial void ratio	The proportion of soil particles	Saturation
The saturated loess	1.353 g/cm <sup>3</sup>	34%	0.996	2.7	92.2%

Table 4. Comparison of experimental data and simulation data.

The axial stress (kPa)	50	100	200	400	800
The test results of void ratio	0.8967	0.8388	0.7695	0.6977	0.6265
The simulated results of void ratio	0.9131	0.8538	0.7804	0.6986	0.6121

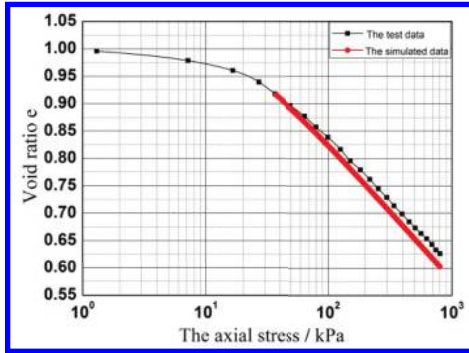


Figure 3. Comparison of experiment and simulation  $e \sim p$  curve.

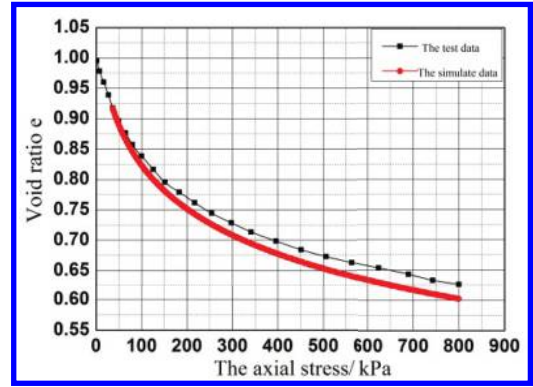


Figure 4. Comparison of experiment and simulation  $e \sim \log p$  curve.

the normal deformation  $\Delta\delta = 4.8 \times 10^{-3} \text{ cm}$ . Then, coefficient of volume compressibility  $m_v$  and coefficient of permeability  $k$  will be calculated separately by formulas (27) and (28).

$$c_v = \frac{\Delta\sigma}{\Delta t} \cdot \frac{H^2}{2\Delta u_b} = \frac{0.5981}{120} \times \frac{4.0^2}{2 \times 20} = 0.00199 \text{ cm}^2/\text{s}$$

$$m_v = \frac{1}{H} \cdot \frac{\Delta\delta/\Delta t}{\Delta\sigma/\Delta t} = \frac{1}{4.0} \times \frac{4.8 \times 10^{-3}/120}{0.5981/120} = 0.2006 \text{ MPa}$$

$$k_v = \frac{\gamma_w H}{2u_b} \cdot \frac{\Delta\delta}{\Delta t} = 3.924 \times 10^{-5} \text{ cmls}$$

## 5 EXAMPLE OF VERIFICATION

This paper refers to Beibei-Yao's [10] parameters of saturated remodeling loess consolidation test under continuous load, as shown in Table 3, using the proposed GCRS numerical simulation program to test the engineering properties of saturated loess.

According to simulation results, take the void ratio where the axial stress is 25 kPa, 50 kPa, 100 kPa, 200 kPa, 400 kPa, and 800 kPa to compare with the test results, and the comparison results which are shown in the Table 4. Then drawing the simulated curve by simulated results, and taking the simulated curve and test curve into comparison, as shown in Figure 3 and Figure 4.

By the two comparisons of the data and curve changes, the axial strain test values are close to simulated values when the per level load is stable, moreover, the curve's coincidence is very high. This shows the correctness of the simulation program, which was put forward in this paper, can be used for indoor consolidation simulation test of saturated soil, as well as be able to use the results of simulation to calculate consolidation parameters.

## 6 CONCLUSIONS

This paper, based on Terzaghi's one-dimensional consolidation theory, conducted the finite difference method for numerical simulation on the

consolidation test control hydraulic gradient, discussed the strain rate, sample size, permeability coefficient, pore pressure and other parameters that effect the consolidation test results. Research results show as follows:

1. The numerical simulation program presented in this paper can be applied to control hydraulic gradient consolidation simulation test with different sizes of the sample.
2. The results of the control hydraulic gradient consolidation simulation test shows that the void ratio change value obtained by numerical simulation is very close to the test data, and it has verified the rationality and correctness of approach which was proposed by this paper.

## REFERENCES

- [1] National standard of china. Standard for soil test method [S].Beijing: China plans to press, 1999.
- [2] Smith R.E. and Wahls H.E. Consolidation under constant rate of strain [J]. Journal of the Soil Mechanics and Foundations Division, 1969, 95(SM2): 519–539.
- [3] Lowe J.I, Jonas E and Obrician V. Controlled gradient consolidation test [J]. ASCE Journal of the Soil Mechanics and Foundations Division, 1969, 95(SM1), 77–97.
- [4] Aboshi H, Yoshikumi H and Maruyama S. Constant loading rate consolidation test [J]. Soils and Foundations, 1970, 10(1), 43–56.
- [5] Von Fay K.F and Cotton C.E. Constant-Rate-of-Loading (CRL) Consolidation test. Consolidation of Soil [J]; Testing and Evaluation. Fort Lauderdale, FL.USA, 1986: 236–256.
- [6] Janbu, N., Tokheim, O., Senneset, K. Consolidation tests with continuous loading [A]. Proc. 10th Int. Conf. Soil Mech Fdn. Engng. Stockholm 1, 1981: 645–654.
- [7] Attasit Korchaiya-pruk. Experimental and numerical study of primary consolidation of soft clay. Massachusetts Institute of Technology, 2007.
- [8] Lin Zheng, Chen Renpeng, Chen Yunmin etc. A method for in-situ testing of coefficients of consolidation and permeability of soils [J]. Journal of Geotechnical Engineering, 2004, 26(4): 505–510.
- [9] Huang Wenxi. Engineering properties of the soil [M]. Beijing: China Water Power Press, 1983.
- [10] Yao Beibei. The continuous loading consolidation test method research on the soil [D]. Chang. An University, 2010.

# A calculating model for acid load settlement based on mass transfer process of AMD corrosion

L.C. Jiang

*School of Civil Engineering and Transportation, South China University of Technology, Guangzhou, China*

W.W. Li & J.J. Zeng

*School of Mechanical and Automotive Engineering, South China University of Technology, Guangzhou, China*

**ABSTRACT:** Analyze mass transfer process of AMD corrosion and put forward the calculating model for acid load on the base of the experiment on AMD corrosion and the mechanism of sulfide oxidation. The model could be used to get AMD corrosion load while measuring instant concentration of corrosion solution. The corrosion load settlement of a slope is analyzed applying this model. The analysis results shows that: (1) in the puddle, water storage, fracture and other mineral water gathering areas, the acid load settlement is very serious, reaching more than 500 mg/L, significantly higher than other regions; (2) on the position of slope surface, due to AMD corrosion effect in a relative short time, the acid load is between 166–300 mg/L, relatively low; (3) away from the mines, such as streams, the acid load is below 20 mg/L, the lowest.

**Keywords:** AMD corrosion; AMD corrosion experiment; mass transfer process; calculating model for acid load settlement

## 1 INTRODUCTION

In the chemical, metal and coal mines that exploit sulfide ore, AMD (Acid Mine Drainage) action is the remarkable effects of slope failure. Sulfide and its residue oxidize with air and water, and then produce AMD solution that contains heavy metal ions (Wang, J. et al. 2007).

AMD solution is with strong corrosion capability. Long-term corrosion reaction and stress corrosion eventually lead to the structure destruction of the rock mass.

The water-rock chemical interaction is a hot spot research area in the civil engineering in recent years (Xiang, R.J. et al. 2012, Feng, X.T. et al. 2002). Related researches mainly focus on the damage to the environment by acid liquor, the influence on the mechanical parameters of rock or soil mass, and the influence on slope stability, etc. AMD corrosion is obviously different from the chemical interaction with common acid liquor, so as the mechanism (Tang, L.S. et al. 2000). Corrosion action makes the instability mechanism of side slope complicated at the sulfide mine (Jiang, L.C. et al. 2013), main stability analysis belongs to the qualitative analysis. In order to quantify AMD corrosion influence on sulfide mine, mass transfer process of AMD corrosion reaction needs to be analyzed and then investigate acid load of

AMD corrosion, which the current research hasn't involved in yet.

With a large-scale domestic pyrite mine slope as the study object, on the basis of the related experiments, starting with the research of the oxidation mechanism of the sulfide minerals, this paper has analyzed AMD chemical mass transfer behavior and carried out the researches on the settlement calculation for acid load in the process of AMD corrosion.

## 2 AMD CORROSION EXPERIMENT

The engineering study object of this paper is the slope located in a large-scale domestic open-pit pyrite mine. The slope rock mass mainly contains quartz sandstone, diorite, dioritic porphyrite and a small amount of limestone in some area.

The standard specimen is processed (Fig. 1) according to the Specifications for Rock Tests in Water Conservancy and Hydroelectric Engineering (SL264-2001), and the AMD solution collected at the bottom of mining pit (Fig. 2).

Specimens are soaked for 25 days and the interval time for sampling collection is 5 days. The indoor temperature is kept stable during the test process. Table 1 shows the concentration of major ions of AMD solution before vs. after the test.



Figure 1. Rock samples.



Figure 2. AMD solution of mine.

Table 1. Composition variation of AMD solution before vs. after the corrosion reaction.

AMD solution		The concentration of major ions (mg/L)					
		SO <sub>4</sub> <sup>2-</sup>	Fe <sup>2+</sup>	Ca <sup>2+</sup>	Mg <sup>2+</sup>	K <sup>+</sup>	Na <sup>+</sup>
pH=1.25	before corrosion	3.7×10 <sup>3</sup>	43.7	137.1	45.4	1.1	4.7
	after corrosion	5.3×10 <sup>3</sup>	60.8	458.1	71.3	3.0	8.2
pH=3.38	before corrosion	2.7×10 <sup>3</sup>	39.9	124.0	42.8	0.8	4.4
	after corrosion	4.1×10 <sup>3</sup>	54.3	352.6	55.6	2.2	6.3

The results show that the concentration of the ion varies obviously in the solution after corrosion, and the concentration of Ca<sup>2+</sup>, Fe<sup>2+</sup> and SO<sub>4</sub><sup>2-</sup> is significantly increased.

After SEM scanning, a large number of pores and cavity appears in the specimen, which shows

the soluble calcium salt (CaCO<sub>3</sub>), mudstone and sulfide minerals (FeS<sub>2</sub>) are dissolved between the joints of the specimen. AMD corrosion is the process of chemical mass transfer of mineral.

### 3 MASS TRANSFER PROCESS ANALYSIS OF AMD CORROSION

AMD solution consists of multiple acid liquors and its pH value is generally between 2 and 5 with high conductivity, and the high conductivity of AMD solution increased the rhythm of ion replacement which will increase the corrosion rate. The essence of the slope damage process by AMD corrosion is the process of ion exchange; the ion exchange rate directly affects the corrosion rate.

According to microcosmic chemical mass transfer principle, the dissolved minerals flux caused by ion exchange can be expressed by fluid velocity of pore rocks (Jiang, L.C. 2012) and AMD solution concentration as

$$J_{adv} = v^*(nc) = vc \quad (1)$$

where  $J_{adv}$  is the solute flux, namely the damage quantity of slope rock mass;  $v$  is the fluid velocity of corrosion liquid;  $c$  is local concentration of ion in AMD solution;  $n$  is the porosity which shows the influence of the integrity of rock mass on corrosion;  $v^*$  is the fluid velocity of liquid in the pore.

The diffusion (or dispersion) flux of the solute can be represented as

$$J_s = D_s \frac{\partial C}{\partial n} \quad (2)$$

where  $J_s$  is diffusion flux;  $C$  is the overall concentration of the solution;  $D_s$  is the diffusion coefficient;  $\bar{n}$  is the normal vector.

When minerals of rock mass are dissolved or new attachments are generated on rock surface, the dissolution rate can be expressed as

$$\text{Rate}_i = r_i \frac{A_0}{V} \left( \frac{m_i}{m_{i0}} \right)^n \quad (3)$$

There into,

$$r_i = k_i \left[ 1 - \left( \frac{IAP}{K_k} \right)^\sigma \right] \quad (4)$$

where  $r_i$  is the specific speed of medium;  $A_0$  is the initial surface area of rock mass;  $V$  is the volume of the solution;  $m_{i0}$  is the initial molar coefficient

of minerals;  $m_i$  is the molar coefficient of minerals at  $t$  moment;  $IAP$  is ion product;  $K_k$  is chemical equilibrium constant;  $\sigma$  is non-dimensional coefficient.

During the process of AMD corrosion, the expression for the porosity of rock mass is

$$\left. \begin{aligned} \frac{dn_i}{dt} &= \gamma V_i Rate_i \\ n &= n_0 + \sum_{i=1}^{M_i} Rate_i \end{aligned} \right\} \quad (5)$$

Thus, mathematical expressions of mineral dissolution quantity of AMD corrosion are

$$\left. \begin{aligned} \frac{\partial(nC_i)}{\partial t} &= D \frac{\partial^2(nC_i)}{\partial n^2} - v \frac{\partial(nC_i)}{\partial t} + \sum_{i=1}^{M_i} Rate_i \\ Rate_i &= r_i \frac{A_0}{V} \left( \frac{m_i}{m_{i0}} \right)^n \\ C_i(x, y, z)_{t=0} &= 0 \\ C_i(t) &= C_0 - \gamma Rate_i \end{aligned} \right\} \quad (6)$$

where  $C_i(x, y, z)$  is the boundary conditions of corrosion concentration at  $t$  moment.

The mathematical model includes the main exchange process between corrosion solution and the rock mass, dynamic change of the solution characterization represents the AMD corrosion process.

Analyzing the solution acid load can effectively evaluate the degree of AMD corrosion.

#### 4 SETTLEMENT CALCULATION FOR ACID LOAD OF AMD CORROSION

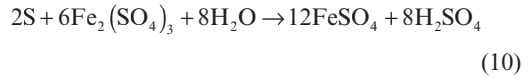
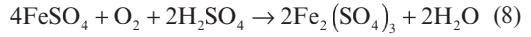
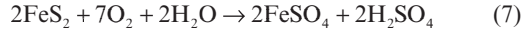
The field investigation results show that, in the process of sulfide mineral mining, along with the change of the ore bodies exposed area, depth, slope runoff and the external rainfall, AMD acidity will also continue to change. But within a certain time period  $t$ , the acid settlement quantity in the mine pit area is relatively stable. On the basis of chemical mass transfer process, the researches on the acid load for slope rock mass by the AMD corrosion have been carried out.

##### 4.1 The chemical process of acid generation

The main mining product is sulfide minerals ( $FeS_2$ ), and under the strong acid environment, acid production action of hydration of Fe element in pyrite will be restrained (Feng, X.T. 2010). Meanwhile, during the acid settlement processing, hydrolytic acidification of basic group positive ion and hydrolytic acidification action of carbonate are difficult

to proceed. Based on the analysis, acid generation of AMD corrosion mainly comes from the oxidation process of S element.

The main oxidation reaction of pyrite in water environment is as follows



According to the Equation (6) which is the mass transfer of AMD corrosion, the velocity of  $H_2SO_4$  by AMD corrosion is calculated.

Supposed that the reaction rates of Equation (7) to (10) respectively correspond to  $R_1$ ,  $R_2$ ,  $R_3$  and  $R_4$ ; the solute concentration at  $t$  moment is  $C_{it}$  and the mass is  $m_{it}$ . Based on the chemical dynamics theory, the reaction constant of the four equations can be obtained as Equation (11):

$$\left. \begin{aligned} R_1 &= \gamma_1 (C_{FeSO_4 0} - C_{FeSO_4 t}) (C_{H_2SO_4 0} - C_{H_2SO_4 t}) \\ R_2 &= \gamma_2 (C_{Fe_2(SO_4)_3 0} - C_{Fe_2(SO_4)_3 t}) \\ R_3 &= \gamma_3 (C_{FeSO_4 0} - C_{FeSO_4 t}) (m_{s0} - m_{st}) \\ R_4 &= \gamma_4 (C_{H_2SO_4 0} - C_{H_2SO_4 t}) (m_{s0} - m_{st}) \end{aligned} \right\} \quad (11)$$

where  $\gamma_1$ ,  $\gamma_2$ ,  $\gamma_3$  and  $\gamma_4$  are reaction coefficients that can be acquired according to reaction temperature (Jiang, L.C. 2007).

Thus, in the process of analyzing the load settlement of AMD corrosion, for simplifying the calculation, the influence of AMD corrosion on the slope body is evaluated by corrosion settlement rate by means of the measurement of PH variation.

##### 4.2 Dimensionless method of parameter

When calculating the generation amount of  $H_2SO_4$  by AMD corrosion, Equation (6) can be transferred to the response numerical model characterized by porosity.

Assumed the initial porosity is  $\phi_0$  and the dimensionless of the porosity is

$$\phi = \frac{\phi_t}{\phi_0} \quad (12)$$

The dimensionless of the flow velocity is

$$v = \frac{1 - \phi_t}{1 - \phi_0} \quad (13)$$

Similarly, related concentration parameters of AMD corrosion solution can be processed with dimensionless method.

## 5 CALCULATION OF AMD ACID LOAD

Because of the Equation (9) shows no acid production or consumption, it should not be taken into consideration during calculation. Other components such as oxygen, moisture and Fe<sub>2</sub>S are regarded as sufficient, and their dimensionless parameters are set to 1.

Based on the previous analysis, the influence of the initial medium parameters mainly divides into two aspects including temperature and concentration. The influence value of temperature and concentration can be represented by the Damkoler number of  $\zeta_1$ ,  $\zeta_2$ ,  $\zeta_3$  and  $\zeta_4$  whose range is [0,1]. The calculation process can refer to Wang, N. et al. (2012) and Michaela, S. (2011). Substitute each dimensionless parameter into Equation (6), the formula of the acid production of AMD corrosion can be obtained as

$$\begin{aligned} \frac{\partial C_{H_2SO_4}}{\partial t} = & -\frac{1-\phi_t}{1-\phi_0} \left[ \gamma_3 \zeta_3 (m_{S_0} - m_{S_t}) (1 - C_{FeSO_4}) \right] \\ & + \gamma_1 \zeta_1 (1 - C_{FeSO_4}) (1 - C_{H_2SO_4}) \\ & + \gamma_4 \zeta_4 (m_{S_0} - m_{S_t}) (1 - C_{H_2SO_4}) \end{aligned} \quad (14)$$

where the 1st item is the consumption amount of sulfuric acid for Equation (8), and this process mainly takes place near the pore which is mostly influenced by pore fluid velocity parameters; the 2nd item is the amount of acid production by Equation (7); the 3rd item corresponds with the amount of acid production for Equation (10).

During the reaction process, the products and reactants of sulfide minerals interact as basis, then the constrained relation can be established with Damkoler number from Equation (7) to (10):

$$\zeta_1 + \zeta_2 + \zeta_3 + \zeta_4 = 1 \quad (15)$$

In the Equation (14), the generation rate of Fe<sub>2</sub>(SO<sub>4</sub>)<sub>3</sub> and FeSO<sub>4</sub> are

$$\begin{aligned} \frac{\partial C_{FeSO_4}}{\partial t} = & -\frac{1-\phi_t}{1-\phi_0} \left[ \gamma_2 \zeta_2 (1 - C_{Fe_2(SO_4)_3}) \right] \\ & + \gamma_1 \zeta_1 (1 - C_{FeSO_4}) (1 - C_{H_2SO_4}) \\ & + \gamma_4 \zeta_4 (m_{S_0} - m_{S_t}) C_{H_2SO_4} \end{aligned} \quad (16)$$

$$\begin{aligned} \frac{\partial C_{Fe_2(SO_4)_3}}{\partial t} = & -\frac{1-\phi_t}{1-\phi_0} \left[ \gamma_3 \zeta_3 (m_{S_0} - m_{S_t}) (1 - C_{FeSO_4}) \right] \\ & + \gamma_4 \zeta_4 (m_{S_0} - m_{S_t}) C_{H_2SO_4} \\ & + \gamma_2 \zeta_2 (1 - C_{Fe_2(SO_4)_3}) \end{aligned} \quad (17)$$

The Equation (14) to (17) constitute the model of calculation for acid load.

On this basis, with the calculation program compiled by the CAD and measurement of real time concentration of the corrosion solution, the load value of AMD corrosion, namely the concentration of H<sub>2</sub>SO<sub>4</sub>, is then obtained.

## 6 ENGINEERING APPLICATION

In a large domestic pyrite mine slope, the sulfide ore bodies is adhere to the location between Huanglong group and Chuanshan group limestone, whose baseboard consists of the arenaceous shales of Gaolishan group and quartz sand, and roof with diorite, Qixia limestone and Chuanshan limestone. The ore body mainly consists of the pyrite (FeS<sub>2</sub>). In the process of mining, the acid corrosion is serious.

In order to evaluate the corrosion status of slope rock mass at the mine, the water areas near line11 to line 19 are selected as study object, including seepage water of slope surface, water in mining pit, acid water sump, the nearby stream and so on (Guo, J.C. et al. 2005). Part of the sample composition is shown in Table 2 (test temperature is 25 °C). Locations include: ①Seepage water of slope surface on +23 m; ②Seepage water of slope surface on -24 m; ③Water in the middle mining pit on -48 m; ④Water warehouse in mining pit on -48 m; ⑤East No.1 dewatering well; ⑥Seepage water of slope surface on +24 m; ⑦Gutterway outside the stope; ⑧Upstream of the Xinxi River.

Table 2. Slope water composition (unit: mg/L).

Locations	pH	SO <sub>4</sub> <sup>2-</sup>	TFe	Cu
①	4.81	171	0.03	0.35
②	4.31	199	0.03	0.35
③	1.03	284	86	24.90
④	2.27	374	105	20.90
⑤	4.20	523	0.04	13.70
⑥*	4.60	500	1.27	1.36
⑦	6.00	261	0.022	0.13
⑧	6.80	118	0.20	0.04

\*+24 m slope surface is on the main crack F<sub>13</sub> of the slope

Based on the concentration of the reactants and the environment temperature, the undetermined parameter value in the corrosion load formula can be acquired by table look-up. Time nodes are subject to pore 0.1 (Jiang, L.C. et al. 2011) to 0.25 (Du, Y.J. et al. 2014). The  $H_2SO_4$  settlement of slope corrosion solution and the content of  $Fe_2(SO_4)_3$  and  $FeSO_4$  can be obtained by calculation, as shown in Table 3.

Data in the table shows that there is a significant difference of AMD corrosion load at the different sections of the slope: the most powerful acid settlement appears at East No. 1 dewatering well and +24 m slope surface, which are up to 500 mg/L or more; acid settlement at the upstream of Xinxi River is minimum, which is less than 20 mg/L. The amount of acid production near the slope region is between 166~300 mg/L.

Based on the analysis of the phenomenon above, AMD corrosion solution is converged at the locations such as sump and well, which cumulative settlement of AMD acid load. Thus the acid load at those locations, where the most severe location of corrosion of rock happens, is higher than other locations. +24 m step is on the main crack  $F_{13}$  of the slope. Since the water has been contacted with the sulfide ore body for a long period, acid generation amount has reached 505 mg/L with significant destruction of corrosion. At the remaining regions of the slope, infiltration of main surface water and ground water has formed AMD corrosion solution. With short duration of reaction and the lower acid generation, there is weak corrosion interaction. Streams far away from the mines have not been affected by acid oxidation of sulfide minerals and the acidification load is extremely low.

Data in Table 3 can be converted into a histogram as shown in Figure 3 which intuitively represents the settlement of  $H_2SO_4$ ,  $Fe_2(SO_4)_3$  and  $FeSO_4$  under the corrosion at different locations.

As the analysis, the concentration of  $Fe_2(SO_4)_3$  and the  $FeSO_4$  in the sump or dipole is more obvious while not in the remaining positions of

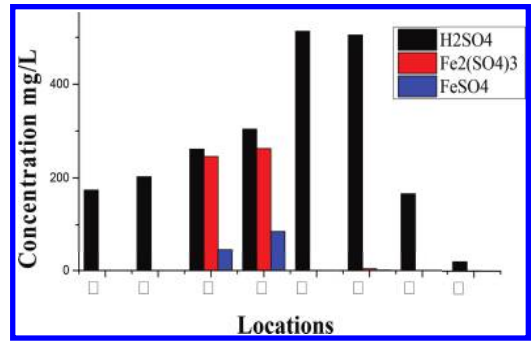


Figure 3. Basic material relationship of the corrosion solution.

the measurement, which matches well with the mine actual situation. The main reason is that the remaining areas of the measuring position are all small catchment areas and they are limited to the production  $Fe_2(SO_4)_3$  and  $FeSO_4$ . Since the confluence time of AMD in the catchment is longer, the amounts of the three corrosion products by AMD are a bit higher than those in the dipole. Therefore, the conclusion is the model calculation results is consist with mine actual situation.

## 7 CONCLUSIONS

According to the oxidation mechanism of sulfide minerals, the chemical mass transfer of AMD corrosion has been researched. By introducing the concept of acid load settlement, the acidification model of AMD corrosion is established and has applied into some large-scale sulfide mining slope. This research reaches conclusions as follows:

1. Based on the conservation of S content element, the chemical mass transfer behavior of AMD has been analyzed. The dynamic acidification model of AMD corrosion was established by studying the calculation formula of dynamic changes of concentration of  $H_2SO_4$ ,  $Fe_2(SO_4)_3$  and  $FeSO_4$  solutions.
2. The analysis of slope acid corrosion shows that the sumps, wells and structural surfaces of slope are the weak areas of land slide. It provides evidence for putting forward the relevant effective control strategies.
3. The settlement analysis of acid load for corrosion indicates that the settlement in slope catchment area is the most obvious area where corrosion settlement is above 500 mg/L, and acid production this area around the slope ranges from 166 to 300 mg/L.

Table 3.  $H_2SO_4$  settlement of slope corrosion solution (unit: mg/L).

Locations	$H_2SO_4$	$Fe_2(SO_4)_3$	$FeSO_4$
①	173.95	0.073	0.03
②	202.53	0.083	0.02
③	261.28	245.714	46.69
④	304.06	262.500	85.50
⑤	512.64	0.108	0.04
⑥	504.98	3.629	0.69
⑦	166.18	0.055	0.02
⑧	19.87	0.500	0.16



## ACKNOWLEDGEMENT

The authors are grateful to the National Natural Science Foundation of China (51174093, 51374035) and the National “Twelfth Five-Year” Plan for Science and Technology Support Program (2012BAB08B02).

## REFERENCES

- Ata, A. & Soner, K. 2006. Acid Mine Drainage (AMD): causes, treatment and case studies. *Journal of Cleaner Production* (14): 1139–1145.
- Du, Y.J. & Wei, M.L. 2014. Effect of acid rain pH on leaching behavior of cement stabilized lead-contaminated soil. *Journal of Hazardous Materials* 2(271): 131–140.
- Feng, X.T. & Ding, W.X. 2010. *Coupled chemical-stress on rock fracturing process*. Beijing: Science Press.
- Feng, X.T. & Wang, C.Y. 2002. Testing study and real-time observation of rock meso-cracking process under chemical erosion. *Chinese Journal of Rock Mechanics and Engineering* 21(7): 935–939.
- Guo, J.C. & Chen, C.G. 2005. Research and application of sandstone matrix acidizing model. *Journal of Oil and Gas Technology* 27(4):485–488.
- Jiang, L.C. & Wen, Y. 2011. Damage constitutive model of sandstone during corrosion by AMD. *Journal of Central South University (Science and Technology)* 42(11): 3502–3506.
- Jiang, L.C. & Yin, S.H. 2013. Slope Instability in high sulfur open mine by Acid Mine Drainage Erosion. *The 2nd SREE Conference on Hydraulic Engineering (CHE 2013)*: 55–61.
- Jiang, L.C. & Wen, Y. 2012. Mesoscopic mechanical effect on sandstone corroded by acid mine drainage. *Journal of the China Coal Society* 37(6):931–935.
- Jiang, L.C. & Chen, J.S. 2007. Erosion characteristic of slope sandstone soaking in acid mine drainage. *Journal of Central South University of Technology (English Edition)* 14(2): 236–242.
- Michaela, S. 2011. Sulfide oxidation and acid mine drainage formation within two active tailings impoundments in the Golden Quadrangle of the Apuseni Mountains, Romania. *Journal of Hazardous Materials* (189): 624–639.
- Tang, L.S. & Zhang, P.C. 2000. Influence of Chemical Damage of Water on Elastic Modulus of Rocks. *Acta Scientiarum Naturalium Universitatis Sunyatseni* 39(5): 126–128.
- Wang, J. & Yin, F.C. 2007. Study of AMD from the discarded rocks in the Xinqiao pyrite, Tongling. *Journal of Hefei University of Technology (Natural Science)* 30(3): 367–370.
- Wang, N. & Yi, X.Y. 2012. Investigation on Mechanism of Pyrite Oxidation in Acidic Solutions. *Environmental Science* 33(11): 3916–3921.
- Xiang, R.J. & Chai, L.Y. 2012. Ions distributional characteristics of wet precipitation in typical acid rain of China. *Journal of Central South University (Science and Technology)* 43(1): 38–45.

## Investigations into creeping characteristics and constitutive models of soft-rock in deep cretaceous strata

Hui Li

*College of Civil Engineering and Architecture, Anhui University of Science and Technology, Huainan, China*  
*The Urban Management Enforcement Bureau of Huainan City, Huainan, China*

Long-sen Cui

*Hua Kang of Huainan City Road Enginee, China*

**ABSTRACT:** The stress alteration in the course of tunneling through soft rocks is simulated when under predetermined pressure from the strata and by fixing first and radical unloading second, a tri-axial creeping experiment is conducted. The tri-axial unloading shearing experiment indicates that with the shearing stress decreasing, the creeping rate will apparently go down. When the shearing stress reaches a value (It turns out to be 0.5 MPa in the present experiment) below the critical point, the axial creeping almost approaches zero. When the shearing stress exceeds a critical value (It turns out to be 3.5 MPa in the present experiment), the creep of the cretaceous strata will experience the different damages composed of such three stages as those of decelerating, being constant and accelerating. In accordance with the experiments results, a constitutive model is constructed for the visco-elasto-plastic cretaceous soft rock stratum creeping. Then the secondary development is conducted of the finite element procedure and then the constitutive model we have developed is embedded in the large non-linear finite element program ADINA8.3. Upon the completion of the above-mentioned work, a numerical simulation experiment is conducted with the supporting process while tunneling in the soft rock strata in a coal mine in Inner Mongolia. The experiment indicates that the constitutive model for the elasto-visco-plastic creeping can tell the deformation characteristics of soft rock strata rather precisely. And the experiment results are well comparable with those of the numerical simulation, showing that our experiment results can be employed as a reference for the design of roadways in cretaceous soft rock strata and the corresponding tunneling performance.

*Keywords:* experiment with creeping deformation affected by unloading; cretaceous formation; soft-rock roadway; secondary development of finite element

### 1 INTRODUCTION

Most of the coal mines in the Western regions of China traverse the Cretaceous and Jurassic Formations of the Mesozoic Strata, characterized by argillaceous cementation, low strength and apparent creeping. In deep underground roadway supporting, no one can afford to neglect such important phenomenon as soft rock deformation. Therefore, investigations into the phenomenon are increasingly conducted with rich and satisfactory results obtained. By turning to experiments, component model theories and finite element methods, scholars abroad have founded constitutive models for soft rock creeping and developed soft rock engineering calculation procedures. However, most of the models cannot be used to describe the stages of the creeping<sup>[1-3]</sup>. Taking this

into account, scientific researchers at home and abroad are devoting themselves to the study of the phenomenon by turning to soft rock experiments and theoretic deduction, aiming to find a satisfactory solution.

For example, Liu Yeke, Deng Zhibin, Cao Ping, et al<sup>[4]</sup> from Central South University have carried out experiments with sticky clay in the lab, aiming to reveal the tri-axial creeping characteristics by turning to cascade loading method and obtained rich experiment data and curves. By improving on the Burgers soft rock creeping model, which has taken into consideration the impacts exercised by soft rock parameter deterioration, Yang Wendong, Zhang Qiangyong, Zhang Jianguo, et al<sup>[5]</sup> have perfected the FLAC-3D finite element model database. By deriving from the constitutive formulae for the Kelvin creeping model and

combining the soft rock constitutive model with the non-linear mechanics theory, Jiang Binsong, Cai Meifeng, et al<sup>[6]</sup> have proved that the deep underground soft rock creeping is characterized by chaotic behaviors and described the conditions for the chaotic behavior to occur. She Chengxue, et al<sup>[7-9]</sup> have clarified the characteristics for mudstone creeping by gradual loading. Based on their soft rock creeping experiment results, Wang Yongyan, et al<sup>[10-12]</sup> have established a constitutive model for creeping under high pressure in deep underground mines. Xian Xuefu, Jiang Yongdong, et al<sup>[13-15]</sup> have founded a constitutive model for sandstone creeping, providing references for rock engineering design and supporting. By conducting experiments with mudstone creeping under different conditions, Yang Chunhe, et al<sup>[16-18]</sup> have analyzed the laws governing the impacts moisture content exercise on mudstone creeping characteristics. By experimental investigation into tri-axial rheological mechanic characteristics under the impact of breccia penetration, Wang Rubin, Xu Weiya, et al<sup>[19]</sup> have discovered that when the stress is greater or less or approaching the stress for rocks to break, apparent creeping can be witnessed. Wang Deng ke, Yin Guangzhi, et al<sup>[20]</sup> have founded a constitutive model for creeping under different loads, different stratum pressures and different gas pressures. Tang Mingming, Wang Zhiyin, et al<sup>[21]</sup> have conducted experiments with three kinds of core samples from rock salt, pure salt rock and pure mudstone to investigate the tri-axial shearing creeping under different stratum pressures and discovered the laws governing the creeping with corresponding creeping formulae established. Through experiments, Zhao Yangsheng, et al<sup>[22]</sup> have come to know how creeping rate is closely related to the composition and structure, to find that the rate for stable creeping of bedded rock salt can be described by turning to power function.

In recent years, scholars at home and abroad have conducted numerous investigations into constitutive relations for soft rocks with rich results obtained. However, reports have not been published with regard to the rheological properties of soft rocks in the Cretaceous formation under stress induced by engineering construction, nor has any report been published with regard to researches conducted by turning to finite numerical simulation. By carrying out main in a deep underground mine in the Western region of China investigations into soft rock behaviors under unloading impacts induced by roadway tunneling, we have founded a constitutive mechanic model for elastic, sticky and plastic soft rock. And the model is applied on a large non-linear finite element procedure ADINA8.3.

## 2 EXPERIMENTS WITH THE TRI-AXIAL CREEPING OF MUDSTONE IN THE CRETACEOUS FORMATION IN THE STRESS APPLICATION DIRECTION

The experiments with the tri-axial creeping of mudstones in the Cretaceous Formation along stress are carried out by turning to the tri-axial shearing creeping experiment system developed by ourselves. To be specific, the device is developed jointly by The State Engineering Laboratory for Deep Underground Coal Mine Construction Technology and Xi'an Lichuang Facilities. And it can be employed to simulate tri-axial creeping deformation behaviors when the axial and radical loads are applied to the pre-consolidated sample. For the tri-axial creeping experiment system, the maximal axial load is 1200 kN, the stratum pressure is 60 MPa and the fluctuation range is confined to  $\pm 10$  kPa. The experiment system is composed of a loading system, a computer-aided automatic sampling system and a controlling system.

### 2.1 Preparation of experiment samples

The samples used in the tri-axial creeping laboratory experiment are obtained from the mudstone strata in the Cretaceous Formation in a coal mine in Inner Mongolia. The raw sample is then turned into a cylindrical sample of  $\phi 50$  mm  $\times$  100 mm. The sample processing craft and precision are compatible to *Methods and Standards for Engineering Rock Mechanics Experiment* (GB/50266-99). The processed specimen for the experiment has a side flatness confined within 0.02 mm, with the surface error confined within  $\pm 0.05$  mm. The specimen contains as much moisture as it did when it lay in the mine. Then the specimens are weighed and numbered. The physical parameters such as moisture content, density and the like are listed in [Table 1](#).

### 2.2 The experiment procedure

To simulate the process for coal mine roadway tunneling and supporting in soft rocks, the following tri-axial shearing creeping experiment procedure is designed:

Table 1. Basic physical parameters of the muddy soft rock specimen.

Burial depth (m)	Moisture content (%)	Saturated uniaxial strength (MPa)	Plastic limit index	Liquid limit index	Saturation degree (%)
550	24.5	4.65	16.2	-0.21	95.6

1. In the process of the creeping experiment, three values for the pre-consolidated stratum are selected and of the three, the value in the middle position is obtained by calculating the weight of the soil. The three values for the consolidated stratum pressure are  $(p-1)$  MPa,  $(p)$  MPa and  $(p+1)$  MPa respectively.
2. Consolidation is carried out in the condition that the predetermined stratum pressure  $\sigma_2 = \sigma_3$ . And it is required by the experiment that when the deformation is not greater than 0.005 mm/h, the experiment should stop.
3. To obtain creeping parameters, series of creeping curve families should be established. And for the success of the experiment, different stress coefficients  $k_i$  should be determined.
4. To carry out the tri-axial shearing creeping experiment under the impact of radial unloading while the axial pressure is kept constant, the value for the load should be determined according to  $k_i \sigma_s$ , where  $\sigma_s$  is the strength for the tri-axial shearing of the soft rock, to be obtained through tri-axial shearing strength experiment.
5. When the specimen deformation is stabilized for more than 24h (when  $d\epsilon/dt \leq 0.0005h^{-1}$  and it is the first degree stabilized creeping) or when the specimen is damaged (and it is the second degree accelerating creeping), the experiment should come to an end.
6. With stratum pressure and axial pressure gradually unloaded, take out the specimen and describe its damage, and measure the moisture content and density of the frozen soil specimen after the experiment.
7. Repeat the experiments specified by the 1–6 steps of the procedure.

The experiments with the tri-axial shearing creeping under the impact of unloading the stratum pressure after consolidation shed much light on the dynamic stress variation process under the impact of roadway tunneling in Cretaceous soft rocks. Through the derivation with time as a function of the tri-axial shearing creeping stress, time as a function of creeping rate can be obtained as shown in Figure 3.

The tri-axial shearing creeping experiment by turning to consolidating and radical unloading in sequence, the laws governing Cretaceous soft rock deformation are obtained as follows:

1. The curves (as shown in Fig. 2) for time as a function of Cretaceous soft rock creeping under the impact of radical unloading shows that when the shearing stress is smaller than a critical value (or 0.5 MPa as obtained by our experiment), the axial creeping rate approaches 0. When the shearing stress is greater than a critical value (or 3.5 MPa as obtained by our experiment), the Cretaceous soft rock creeping process is marked by

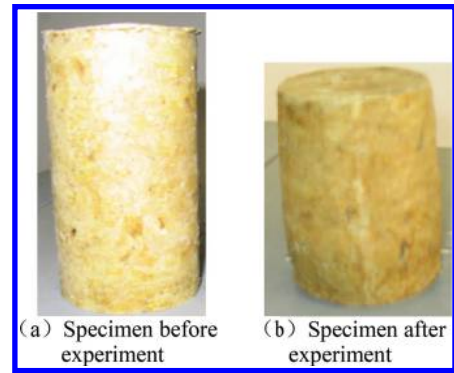


Figure 1. The samples model.

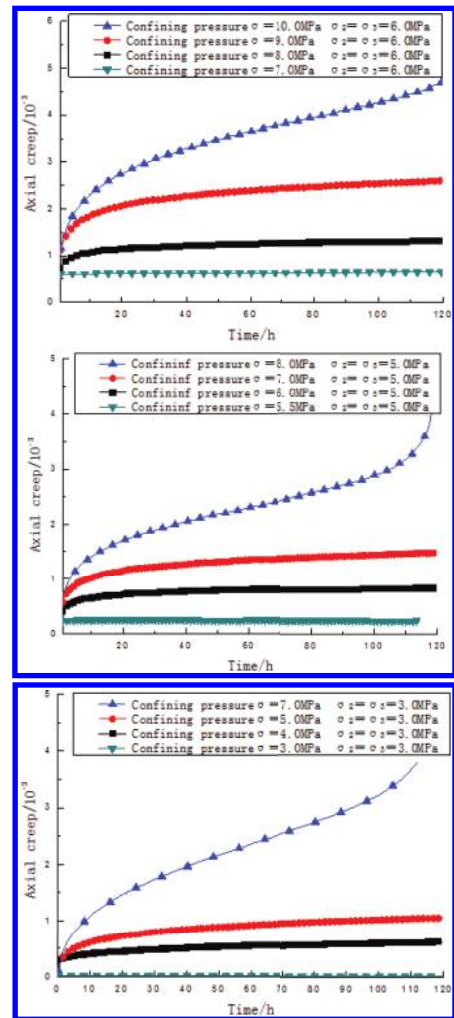


Figure 2. Curves for Cretaceous mudstone creeping under the impact of radial unloading.

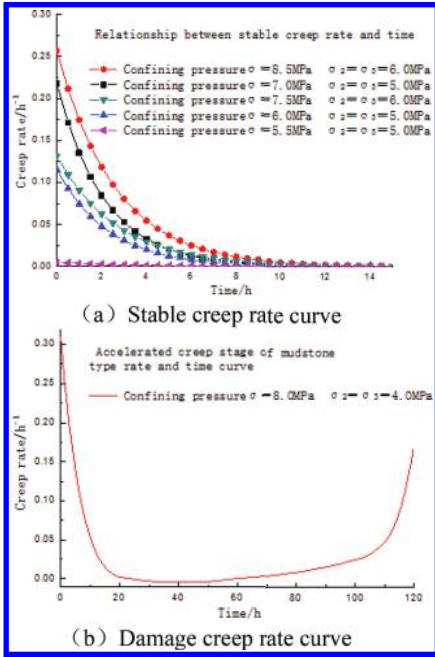


Figure 3. Relation between axial creep rate and creep time.

such three stages as accelerating, being constant and decelerating. This shows that there should be a threshold for the Cretaceous soft rock creeping stress at the beginning of the creeping and a critical stress for creeping to do damage.

- As shown in Figure 3(b), when the creeping stress is smaller than  $\sigma_1 = \sigma_3 < 3.5 \text{ MPa}$ , no apparent creeping is witnessed in the Cretaceous formation; when it reaches  $3.5 \text{ MPa} > \sigma_1 - \sigma_3 \geq 0.5 \text{ MPa}$ , the deformation in the Cretaceous soft rock stratum is marked by decelerating creeping; when it reaches  $\sigma_1 = \sigma_3 \geq 3.5 \text{ MPa}$ , the deformation in the Cretaceous soft rock stratum is marked by accelerating creeping, pointing to the conclusion that the creeping has experienced the decelerating, being constant and accelerating stages.

### 3 THE CONSTITUTIVE MODEL FOR CRETACEOUS SOFT ROCKS AND THE DEVELOPMENT OF FINITE ELEMENT PROCEDURE

#### 3.1 The mathematics for the Cretaceous soft rock creeping model

By sorting out the tri-axial shearing creeping data for Cretaceous soft rocks, we have obtained isochronous stress-strain curves as shown in

Figure 4 and the enveloping line for the creeping strength as shown in Figure 5.

- As shown in Figure 4, the isochronous stress-strain curves for Cretaceous soft rocks indicate that when the deviatoric stress is not strong, the stress-strain curves become straight lines. But when the deviatoric stress is rather strong, they become parabolas. Therefore, isochronous stress-strain deformation behaviors of soft rock can be described by turning to the laws governing visco-elasto-plastic deformation.
- As shown in Figure 5, the enveloping lines for Cretaceous soft rock creeping strengths indicate that the Drucker-Prager criterion function can be used to describe the yielding of the soft rock creeping strength. In the application of the criterion function, the initial critical stress function can be selected by turning to Mohr-Coulomb strength function by taking the experiment results into consideration.

As shown in Figure 6, the results obtained from the experiments with tri-axial creeping point to the

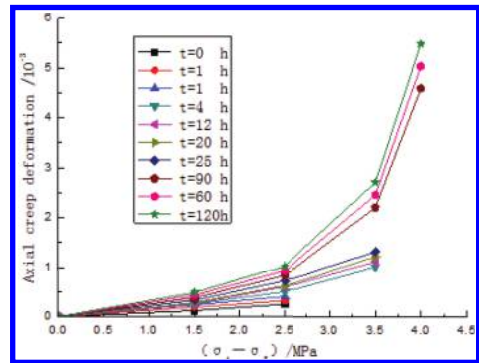


Figure 4. The isochronous stress-strain curves for Cretaceous muddy soft rocks.

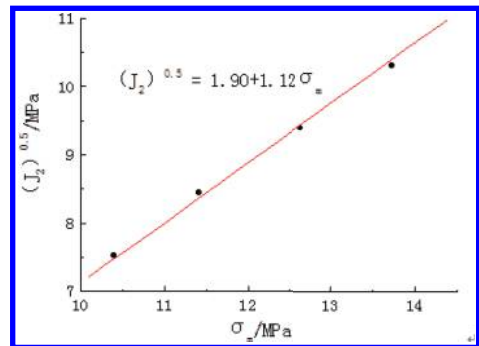


Figure 5. The creeping strength enveloping line for Cretaceous muddy soft rocks.

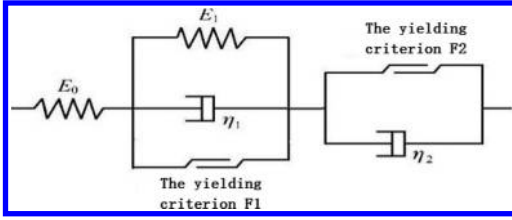


Figure 6. The elasto-visco-plastic constitutive model for mudstone.

possibility that by using the basic component combinations, the laws governing Cretaceous soft rock tri-axial creeping deformation under the impact of unloading can be well simulated.

From the constitutive model as shown in Figure 6, the mathematic expression for the constitutive model of the Cretaceous soft rock creeping under the impact of radical unloading can be derived as follows:

$$\begin{aligned} \{\varepsilon\} = & \frac{1}{E_0}\{\sigma\} + \frac{1}{E_1}(1 - e^{-E_1 t/\eta_1}) < \frac{F_1}{F_0} > \{\sigma\} \\ & + < \frac{F_2}{F_0} > \frac{t}{\eta_2} \{\sigma\} \end{aligned} \quad (1)$$

where  $E_0$  stands for the elastic modulus (MPa) for Cretaceous soft rocks;  $E_1$  stands for the damping deformation modulus (MPa) for Cretaceous soft rocks;  $\eta_1, \eta_2$  stand for visco-elastic and visco-plastic coefficients for Cretaceous soft rocks (MPa.min) and  $t$  stands for the external loading time (min).

$$F_1 = \frac{\sin \phi}{3} \times I_1 + \sqrt{J_2} \left( \cos \theta - \frac{\sqrt{3}}{3} \sin \theta \sin \phi \right) - c \cos \phi \quad (2)$$

$$F_2 = \frac{6 \sin \phi}{(3 - \sin \phi)} \sigma_m + \sqrt{3} J_2 - \frac{6c \cos \phi}{(3 - \sin \phi)} \quad (3)$$

### 3.2 The compliance matrix for the finite element calculation

From soft rock rheological mechanics, we know that the total stress  $\{\varepsilon\}$  is the sum total of instantaneous elastic strain  $\{\varepsilon\}^e$ , the visco-elastic strain  $\{\varepsilon\}_t^e$  and the visco-plastic strain  $\{\varepsilon\}_t^p$ :

$$\{\varepsilon\} = \{\varepsilon\}^e + \{\varepsilon\}_t^e + \{\varepsilon\}_t^p \quad (4)$$

From Formulae (1) and (4), the compliance matrix for instantaneous elasticity  $[C]^e$ , that for visco-elasticity  $[C]_t^e$  and that for visco-plasticity  $[C]_t^p$  can be derived.

1. When  $F_1 \leq 0$ , only instantaneous elastic deformation of Cretaceous soft rocks can be witnessed. From elastic mechanics and the finite element theory, the elastic compliance matrix  $[C]^e$  can be derived as follows:

$$[C]^e = \frac{1}{E_0} [R] \quad (5)$$

$$[R] = \begin{bmatrix} 1 & -\mu & -\mu & 0 & 0 & 0 \\ -\mu & 1 & -\mu & 0 & 0 & 0 \\ -\mu & -\mu & 1 & 0 & 0 & 0 \\ 0 & 0 & 0 & 2(1+\mu) & 0 & 0 \\ 0 & 0 & 0 & 0 & 2(1+\mu) & 0 \\ 0 & 0 & 0 & 0 & 0 & 2(1+\mu) \end{bmatrix} \quad (6)$$

where  $\mu$  stands for the Poisson's ratio, determined by uniaxial compression experiments.

2. When  $F_1 > 0$  and  $F_2 \leq 0$ , visco-elastic deformation of the soft rock can be witnessed. From elastic mechanics and the mechanic principle for creeping, the following can be derived:

$$\{\varepsilon_{ij}\}_t^e = [C]_t^e \{\sigma_{ij}\} \quad (7)$$

where  $[C]_t^e$  stands for visco-elastic compliance matrix, determined by the formula below:

$$[C]_t^e = \frac{1}{E_1} (1 - e^{-E_1 t/\eta_1}) [R] \quad (8)$$

3. When  $F_2 > 0$ , visco-plastic deformation of the soft rock is witnessed. By turning to the finite element for calculation, generally, implicit integration is used to determine the relations between the visco-plastic strain and stress as components. At time  $t^n$  the displacement for each node  $\{\delta^n\}$  and the stresses for all the nodes  $\{\sigma^n\}$  are derived. Within the time step  $\Delta t = t^{n+1} - t^n$ , the creeping strain increment in the soft rock can be calculated by turning to Formula (9):

$$\{\Delta \varepsilon_{vp}\}_t = \{\varepsilon_{vp}'\}_t \Delta t + [C]_t^p \{\Delta \sigma\}_t \quad (9)$$

where,  $\{\Delta \sigma\}$  stands for the strain increment within time  $\Delta t$ ,  $[C]_t^p$  stands for the visco-plastic compliance matrix. Then from rheological mechanics and the calculation methods it contains, the visco-plastic compliance matrix can be derived as follows:

$$[C]_t^p = \left\{ \frac{\partial \dot{\varepsilon}^p}{\partial \sigma} \right\} = \frac{1}{\eta_2} \left\{ \left( \frac{\partial F_2}{\partial \sigma} \right) \left( \frac{\partial F_2}{\partial \sigma} \right)^T + F_2 \frac{\partial^2 F_2}{\partial \sigma^2} \right\} \quad (10)$$

where:

$$\frac{\partial F}{\partial \{\sigma\}} = \left\{ \alpha \frac{[P]}{9\sigma_m} + \frac{[Q]}{2\sqrt{J_2}} \right\} \{\sigma\} \quad (11)$$

$$\left( \frac{\partial F}{\partial \sigma} \right) \left( \frac{\partial F}{\partial \sigma} \right)^T = \left\{ \alpha \frac{[P]}{27\sigma_m^2} + \frac{1}{4J_2} [S] \right\} \{\sigma\} \quad (12)$$

$$\frac{\partial^2 F}{\partial \{\sigma\}^2} = - \left\{ \frac{\alpha}{3} \frac{[P]}{(\sigma_m)^2} + \frac{[S]}{4J_2\sqrt{J_2}} \right\} \{\sigma\} \quad (13)$$

where  $[P]$ ,  $[R]$  and  $[S]$  stand for coefficient.

$$[P] = \begin{bmatrix} 1 & 1 & 1 & 0 & 0 & 0 \\ 1 & 1 & 1 & 0 & 0 & 0 \\ 1 & 1 & 1 & 0 & 0 & 0 \\ 0 & 0 & 0 & 0 & 0 & 0 \\ 0 & 0 & 0 & 0 & 0 & 0 \\ 0 & 0 & 0 & 0 & 0 & 0 \end{bmatrix} \quad (14)$$

$$[Q] = \frac{1}{3} \begin{bmatrix} 2 & -1 & -1 & 0 & 0 & 0 \\ -1 & 2 & -1 & 0 & 0 & 0 \\ -1 & -1 & 2 & 0 & 0 & 0 \\ 0 & 0 & 0 & 6 & 0 & 0 \\ 0 & 0 & 0 & 0 & 6 & 0 \\ 0 & 0 & 0 & 0 & 0 & 6 \end{bmatrix} \quad (15)$$

$$[S] = \frac{1}{3} \begin{bmatrix} 2 & -1 & -1 & 0 & 0 & 0 \\ -1 & 2 & -1 & 0 & 0 & 0 \\ -1 & -1 & 2 & 0 & 0 & 0 \\ 0 & 0 & 0 & 12 & 0 & 0 \\ 0 & 0 & 0 & 0 & 12 & 0 \\ 0 & 0 & 0 & 0 & 0 & 12 \end{bmatrix} \quad (16)$$

Therefore, Formulae (5), (8) and (10) perfect visco-plastic compliance matrixes for soft rock and different matrixes can be selected to perform finite element calculation operations in accordance with different states for stress.

### 3.3 The flow chart for ADINA constitutive procedure development

ADINA provides the users with a rich possibility for the secondary development, allowing them to define in the time of need various functions such as constructing material constitutive models, developing contact elements, judging material breakage, calculating crack expansion, determining users' boundary conditions and ranges of load, etc.

By turning to Fortran, the constitutive model is compiled in accordance with the flowing process as shown in Figure 7. And the environment for ADINA development is Compaq Visual Fortran6.6 A. In the development, by turning to Makefile provided by ADINA, various \*.f files will be automatically linked to generate a dynamically linking file library.

The process for the secondary development of the soft rock constitutive model is as follows:

1. By turning to the flow chart shown in Figure 7, compile the soft rock visco-elsasto-plastic constitutive model by using Fortran;
2. Compile Makefile by modifying its parameters  
`MAT2D_OBJ = ovl30u_user.obj`  
`MAT2D_OBJ = ovl40u_user.obj`  
 Where user stands for the file name selected or defined by the user;
3. Compile the. dll file by following the procedure below:  
`cd D:\program files\df98\bin`  
`cd c:\program files\ADINA\user.dll`
4. bstitute the. dll file in the linking library to be compiled by the user for the user in nmake/f Makefile.user;
5. Add the. dll file generated by the user to the content of bin.

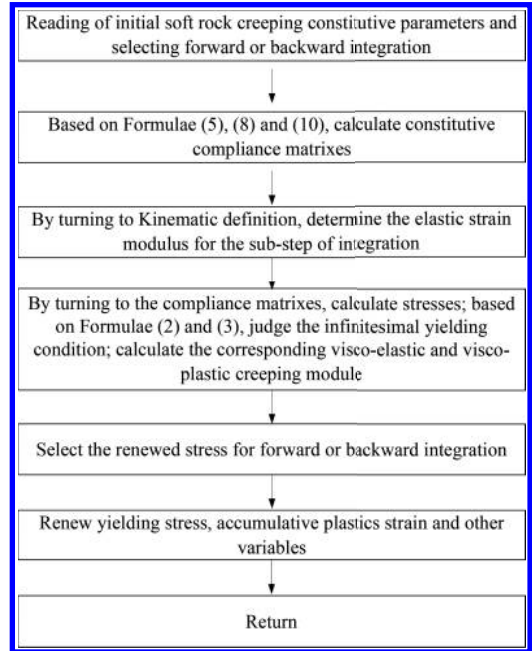


Figure 7. The flow chart for the development of the soft rock visco-elasto-plastic constitutive finite element procedure.

#### 4 ENGINEERING NUMERICAL SIMULATION AND CONCLUSION

The cross-section of the roadway in the mine of Inner Mongolia is a vertical wall semicircular in shape, whose tunneling area  $S_{\text{dig}} = 11.6 \text{ m}^2$  and net area  $S_{\text{net}} = 10.6 \text{ m}^2$ . The roadway is supported by the combination of anchoring rods and cables with concrete sprayed. The layout is shown in Figure 8, where mm is used as the measuring unit. And the roadway is located in the muddy soft rock strata.

As shown in Table 2, by turning to the experiment method presented in the present paper, the parameters for the soft rock constitutive model can be obtained.

By turning to ADINA numerical simulation, the law governing the distribution of anchoring rods and cables in the soft rock roadway can be obtained (as shown in Fig. 9a) and so can the distribution for the vertical displacement of the roadway (as shown in Fig. 9b).

As shown in Table 3, the results obtained from numerical simulation and on-spot measuring for the roadway anchoring rod and cable convergence displacement are compared. And the results obtained by numerical simulation and laws governing on-spot measuring with regard to the road side convergence displacement are shown in Figure 10.

By turning to numerous experiments with soft rock creeping and corresponding numerical simulation, the following conclusions are drawn:

- ① With Mohr-Coulomb and Drucker-Prager strength functions introduced into the element model and through analysis of the experiments with the soft rock creeping under the impact of tri-axial unloading and the rheological model

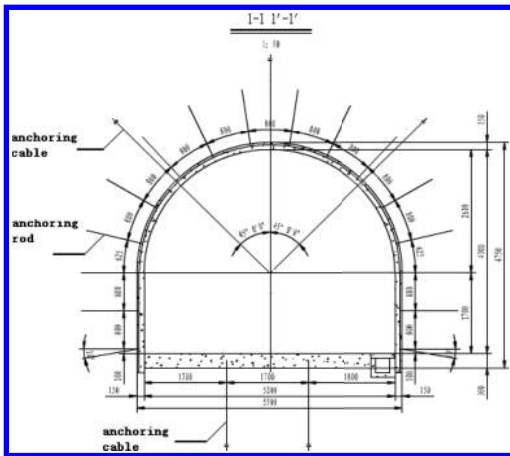


Figure 8. The illustrated cross-section of a roadway in soft rock strata.

Table 2. The calculation parameters for the soft rock constitutive model.

$E_1/$ MPa	$E_2/$ MPa	$\eta_1/$ MPa · min	$\eta_2/$ MPa · min	$c/$ MPa	$\phi/$
180	265	4 035	6 150	3.15	26

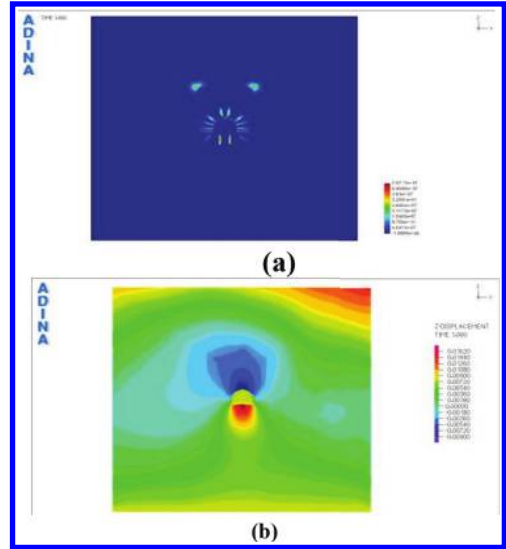


Figure 9. Results of the numeral simulation.

Table 3. The comparison of the results obtained by numerical simulation and on-spot measuring.

Items for comparison	Numerical simulation	On-spot measuring
The maximal pulling force for the anchoring rod/kN	6.95	6.80
The maximal pulling force for the anchoring cable/kN	51.8	46.20
Convergence value/cm	25.4	22.6

- for the element, a constitutive model is founded for Cretaceous soft rock non-linear creeping.
- ② Numerical simulations are conducted of the internal force of the anchoring rod, the stress for the anchoring cable, the roadway displacement distribution and the roadway stress distribution. The results point to the fact that the laws revealed by numerical simulation and those by on-spot measuring are in perfect agreement. And for this reason, the foundation of a soft rock constitutive model is justified.
- ③ By turning to the secondary development of the finite element procedure, the soft rock constitutive



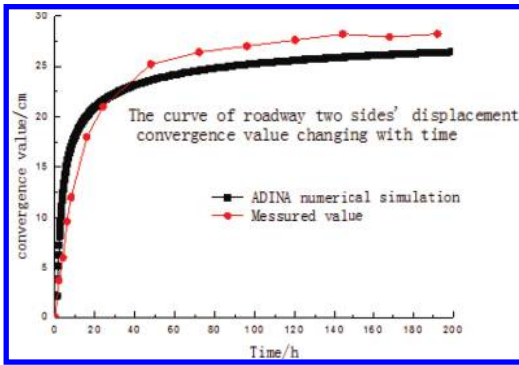


Figure 10. Comparison of the convergences for the two sides of the roadway obtained by numerical simulation and by on-spot measuring.

model is embedded into ADINA finite element procedure. Consequently, the database for the ADINA is enlarged, making it possible to carry out numerical simulation of the soft rock roadway, to monitor and predict the roadway stress field and displacement. All these can provide a guarantee for the scientific tunneling.

## REFERENCES

- [1] Li Dongwei, Wang Ren-he, Lin Bin. Viscoelastic Plastic Model of Frozen Soil and Numerical Calculation Soft Matrix Applied [J]. *Journal of Glaciology and Geocryology*, 2007, 29(2):321–326.
- [2] Zhu Hehua, Ye Bin. Experimental study on mechanical properties of rock creep in saturation [J]. *Chinese Journal of Rock Mechanics and Engineering*, 2002, 21(12):1791–1796.
- [3] Fan Qingzhong, Gao Yanfa. Study on creep properties and nonlinear creep model of soft rock [J]. *Chinese Journal of Rock Mechanics and Engineering*, 2007, 26(2):391–396.
- [4] Liu Ye-ke, Deng Zhi-bin, Cao Ping, Huang Yongheng, Lin Hang. Triaxial creep test and modified Singh-Mitchell creep model of soft clay [J]. *Journal of Central South University (Science and Technology)*, 2012, 29(4):1440–1446.
- [5] Yang Wen-dong, Zhang Qiang-yong, Zhang Jianguo, HE. Second development of improved Burgers creep damage constitutive model of rock based on FLAC3D [J]. *Rock and Soil Mechanics*, 2010, 31(6):1956–1964.
- [6] Jiang Binsong, Cai Meifeng, He Yongnian, Han Lijin. Chaotic behavior of nonlinear kelvin creep of rock mass in deep ground [J]. *Chinese Journal of Rock Mechanics and Engineering*, 2009, 28(6):1462–1467.
- [7] She Chengxue, Cui Xuan. Influence of high pore water pressure on creep properties of rock [J]. *Chinese Journal of Rock Mechanics and Engineering*, 2010, 29(8):1603–1609.
- [8] She Chengxue. Research on nonlinear viscoelastoplastic creep model of rock [J]. *Chinese Journal of Rock Mechanics and Engineering*, 2009, 28(10):2006–2011.
- [9] She Chengxue, Cui Xuan. Research on nonlinear creep model of rock [J]. *Engineering Journal of Wuhan University*, 2009, 42(1):25–28.
- [10] Wang Yong-yan, Lv Yi-mei, Xiao Zhi-juan,. Research on sandstone creep models under chemical corrosion [J]. *Journal of China Coal Society*, 2010, 35(7):1095–1098.
- [11] Wang Yong-yan, Wei Jia, Qi Jun,. Study on prediction for nonlinear creep deformation of deep rocks [J]. *Journal of China Coal Society*, 2005, 30(4):409–413.
- [12] Wang Yong-yan, Qi Jun, Yang Cai-hong. A study of Nonlinear Creep law in Deep Rocks [J]. *Rock and Soil Mechanics*, 2005, 26(1):117–121.
- [13] Guo Chenye, Xian Xuefu, Jiang Yongdong. Experimental research on creep of fractured sandstone [J]. *Chinese Journal of Rock Mechanics and Engineering*, 2010, 29(5):990–995.
- [14] Jiang Yong-dong, Xian Xue-fu, Yang Chun-he. Forecasting of instability zones induced by creep fracture of tunnel rockmass [J]. *Chinese Journal of Geotechnical Engineering*, 2008, 30(6):906–910.
- [15] Jiang Yong-dong, Xian Xue-fu, Xiong De-guo. Study on creep behaviour of sandstone and its mechanical models [J]. *Chinese Journal of Geotechnical Engineering*, 2005, 27(12):1478–1481.
- [16] Wan Lin, Peng Xiang-he, YANG Chun-he. An investigation to the creep of claystone [J]. *Rock and Soil Mechanics*, 2005, 26(6):924–928.
- [17] Ren Song, Jiang De-yi, Yang Chun-he, Teng Hongwei. Creep tests on shale of cracking position in Gonghe tunnel and simulating it by DEM [J]. *Rock and Soil Mechanics*, 2010, 31(2):416–426.
- [18] Huang Xiaolan, Yang Chunhe, Liu Jianjun. Experimental study on mudstone's creep behavior under different water contents and its effect on casing damage [J]. *Chinese Journal of Rock Mechanics and Engineering*, 2008, 27(S2):3477–3482.
- [19] Wang Rubin, Xu Weiya, Wang Wei. Experimental investigation on creep behaviors of hard rock in dam foundation and its seepage laws during complete process of rock creep [J]. *Chinese Journal of Rock Mechanics and Engineering*, 2010, 29(5):960–969.
- [20] Wang Dengke, Liu Jian, Yin Guangzhi,. Test study of creep properties of gas-bearing coal specimens under triaxial compression [J]. *Chinese Journal of Rock Mechanics and Engineering*, 2010, 29(2):349–356.
- [21] Tang Ming-ming, Wang Zhi-yin, Ding Guo-sheng. Creep property experiment and constitutive relation of salt-mudstone interlayer [J]. *Journal of China Coal Society*, 2010, 35(1):42–45.
- [22] Zhang Ning, Zhao Yang-sheng, Wan Zhi-jun. Creep constitutive relationship of lu gray granite under high temperature and three-dimensional stress [J]. *Chinese Journal of Geotechnical Engineering*, 2009, 31(11):1757–1762.

## Analysis of characteristics of saline soil in Yanqing new town

H.D. Wang & Y.H. Sun

*School of Mechanical Engineering, Beijing Institute of Petrochemical Technology, China*

X. Huang

*Beijing Institute of Geological and Prospecting Engineering, China*

Q.X. Lu & J. He

*School of Engineering and Technology, China University of Geosciences, Beijing, China*

**ABSTRACT:** Saline soil disaster is one of the environmental geological problems in the construction of Yanqing new town. In this paper, the saline soil distribution area, chemical composition, and causes of Saline soil in new town area were described, the types of saline soil were divided, and the salt expansion and corrosion were evaluated, which provides the basis for the planning and construction of Yanqing new town and the prevention of disasters.

**Keywords:** saline soil; causes; salinization degree; evaluation of salt expansion and corrosion

### 1 INTRODUCTION

Yanqing new town is located near the Guanting Reservoir and the southeast bank of Caijia River, where saline soil distributes relatively wide about 7.33 km<sup>2</sup> on area. The saline soil disaster is one of the environmental and geological problems in the construction of the new town. Soil salinization has seriously restricted the development of local agriculture. In the past, the land on banks of Guanting Reservoir and Caijia River could have produced 150~200 kg of corn or wheat per acre every year, but now the production has reduced and there were only about 50 kg per acre every year, also no production due to consecutive years of drought. In addition, in the soil salinization area, due to the effect of salt expansion, the foundation bearing capacity reduced, which caused cracks in some houses. In this paper, based on the field survey, the distribution, chemical composition and causes of saline soil in Yanqing new town area were analyzed, the salt expansion and corrosion of saline soil were evaluated, which provides for the basis for the planning and construction of Yanqing new town and the prevention of disasters.

### 2 DISTRIBUTION AND CHARACTERISTICS OF SALINE SOIL

The saline soil in Yanqing new town is mainly distributed in the low-lying area near the Guanting

Reservoir and Caijia River. Through the investigation, the terrain is a flat low-lying area around Guanting Reservoir and on both sides of Caijia River, and due to the water storage of Guanting Reservoir, the groundwater dammed up in the surrounding area, where the depth groundwater is relatively shallow (about 1.3 to 3.0 meters), the hydraulic gradient decreased and the underground runoff slowed even at a standstill. The chemical type of the groundwater under the bank of reservoir and river is sodium chloride-sulfuric water, whose degree of mineralization is 1.0 to 2.5 g/L. The soil above the saline soil is mainly silt, sticky silt and silty-fine sand about 0.5 to 1.0 m thick. Formed by long-term evaporation salt accumulation, the saline soil belongs to secondary-primary saline soil [1].

Through investigation, the soil samples were made at different depths (0 to 0.05 m, 0.5 to 0.55 m, and 1.0 to 1.05 m) in 24 typical districts in the saline soil distribution area to carry out soluble salt tests. Among them, Y1, Y2, Y3, Y4, Y6, and Y7 are sampling points along Caijia River, Y5, Y8, and Y9 are sampling points near Guanting Reservoir. The results of chemical composition tests of the soil (Fig. 1) show that: in the majority of the surface area within 0 to 0.05 m depth, the chemical composition of the soil is mainly chloride-carbonic acid-sulfuric acid type; within 0.5 to 0.55 m depth, the chemical composition of the soil is sulfuric acid-carbonated. According to the classification standard in “Code for Investigation of Geotechnical

Engineering” [2], the saline soil in this area belongs to sulfite or sulfate saline soil (Table 1).

In the new town area, the degree of soil salinization decreases with depth (Fig. 2). The salinity is relatively higher in the 0 to 0.05 m depth, generally in 0.3% to 0.54%, where the degree of salinization is relatively high, of which the highest can reach to 1.17%; within 0.5 to 0.55 m, the salinity is 0.06% to 0.08%, where the highest is 0.19%; within 1.0 to

1.05, the salinity is less than 0.06%. It can be seen that the soil salinization in this area mainly occurs within 0 to 0.5 m under surface, and below 0.5 m the degree of salinization is relatively low. According to the standard in “Code for Investigation of Geotechnical Engineering” sixth chapter, soil within 0 to 0.5 m under the surface of new town area is mainly moderate saline soil, and the lower soil within 0.5 to 1.0 m depth is weak saline soil. The distribution area of moderate salinity in shallow surface is 6.98 km<sup>2</sup>, where the weak salinity is 0.35 km<sup>2</sup>.

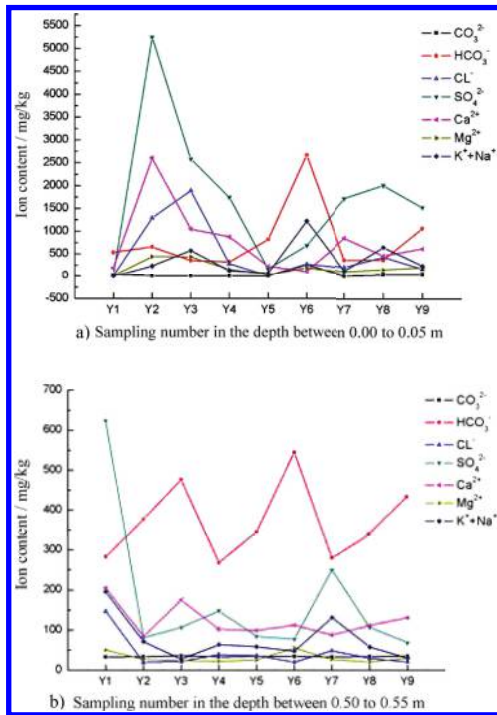


Figure 1. The chemical composition of soil in different places in Yanqing new town area.

### 3 ANALYSIS ON THE CAUSES OF SALINE SOIL

The formation conditions of saline soil are: firstly, high salinity of groundwater, which can provide adequate salt; secondly, high water table, which can reach or be close to the surface by capillary action and to be affected by evaporation; thirdly, relatively dry climate, generally where annual evaporation is greater than rainfall, which is easy to form saline soil. Saline soil is the product of combined effects of multiple factors like climate, geology, geomorphology, and hydrogeological conditions and so on.

#### 3.1 Climatic factors

Climatic conditions on the formation of saline soil are mainly drought, large evaporation. Yanqing area is in the transition zone in semiarid and sub-humid climate zone. Over the years of drought, evaporation is about 10 times of precipitation. In the summer hot environment, with evaporation the salt in the shallow groundwater near the Guanting Reservoir and Caijia River banks, it migrates endlessly to the surface and aggregates to form surface salt accumulation; while in cold winter, the lowest temperature below zero, because the salt solubility in aqueous

Table 1. Chemical composition and classification of saline soil in the main sampling points in the new town area.

Sampling depth 0–0.05 m					Sampling depth 0.5–0.55 m				
Serial number	Cl <sup>-</sup> mg/kg	SO <sub>4</sub> <sup>2-</sup> mg/kg	$\frac{c(Cl^-)}{2c(SO_4^{2-})}$	Saline soil type	Serial number	Cl <sup>-</sup> mg/kg	SO <sub>4</sub> <sup>2-</sup> mg/kg	$\frac{c(Cl^-)}{2c(SO_4^{2-})}$	Saline soil type
Y1	18.2	41.9	1.17	Sulfurous acid type	Y1	146.8	623.0	0.118	Sulfuric acid type
Y2	1286.7	5246.9	0.66		Y2	19.9	80.8	0.123	
Y3	1888.4	2580.7	1.98		Y3	21.3	106.8	0.100	
Y4	283.4	1745.9	0.44		Y4	39.0	147.9	0.132	
Y5	18.3	168.5	0.29	Sulfuric acid type	Y5	36.1	84.3	0.214	
Y6	274.9	681.8	1.09	Sulfurous acid type	Y6	20.3	76.9	0.132	
Y7	183.8	1699.8	0.29	Sulfuric acid type	Y7	48.5	249.6	0.097	
Y8	410.8	1987.7	0.56	Sulfurous acid type	Y8	29.6	106.8	0.138	
Y9	145.7	1501.0	0.26	Sulfuric acid type	Y9	21.0	68.2	0.154	

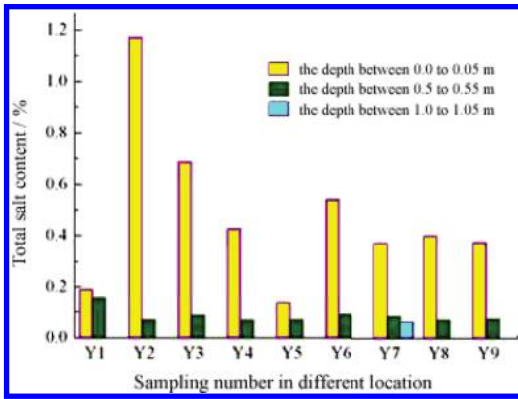


Figure 2. The salinity of saline soil change with depth.

decreases with decreasing temperature, the salt can be saturated and separated by crystallization.

### 3.2 Soil properties

The height and speed of the capillary action are determined by soil properties which also control the groundwater flow conditions, thus affecting the accumulation and transport of salts in the soil and groundwater. When the level and quality of water are roughly the same, the capillary action of silty-fine sand and sticky silt is relatively strong, and the salinization degree is relatively high. The soil in the survey area near the Guanting Reservoir and Caijia River is in the Quaternary system, Holocene series. Alluvial soil is mainly composed of silt and sticky silt whose capillary action is strong, which is conducive to the formation of saline soil.

### 3.3 Hydrogeological conditions

Hydrogeological conditions which include groundwater depth, runoff conditions, and salinity are the decisive factors in the formation and development of the saline soil. Shallow groundwater and strong evaporation are favorable conditions for the formation of saline soil. Under normal circumstances, when the phreatic level is within 2.5 to 3 m depth, the surface salinization is relatively weak; when within 3 to 5 m depth, the surface salinization is extremely weak; when deeper than 5 m, the soil is non-saline soil; when within 2 to 2.5 m depth, different degrees of salinization occur in the soil; and when within 1 to 2 m depth, the soil salinity content increases sharply and the soil can form sulfuric acid-chloride type and chloride-sulfuric acid type of saline soil and solonchak soil. While highly mineralized water is the main material source of the formation of saline soil, and under the condition of same water depth, the salinization degree is heavier in the high mineralized groundwater distribution area. In addition,

runoff conditions also influence the degree of soil salinization, and when the runoff is slow, the salt in the groundwater is easy to accumulate. In the planning area near the banks of Guanting Reservoir and Caijia River, the surface water is closely related to the groundwater hydraulic. Especially after the construction and water storage of reservoir, the groundwater got supplies, which raises the level of groundwater near the reservoir bank and river bank, and as the groundwater depth reduces, groundwater overflows to the surface in low-lying places, which can form wetlands. Because the terrain is relatively flat, the underground runoff slows down and the groundwater salinity increases, coupled with the regional climate drought for years, different degrees of salinization occurs to the soil.

It is worth noting that the trend of soil salinization is closely related to the environmental conditions. If the climate in this area is drought with little rainfall in the future, the evaporation of groundwater will increase, and the soil salinization will show an increasing trend; when the drought climate weakens and the rainfall intensity increases, infiltration dripping effect of the rain is enhanced, and the salinity of groundwater decreases, which is not conducive to the accumulation of soil salinity and weakening the salinization.

## 4 EVALUATION ON SALT EXPANSION AND CORROSION OF SALINE SOIL

The saline soil in this area which is harmful to the construction of new town area is mainly due to salt expansion and corrosion.

### 4.1 Evaluation on salt expansion

Salt expansion mainly occurs in the saline soil containing sulfate which absorbs water forming crystals and increases its volume when the temperature decreases, causing the soil expansion. When the temperature rises, the sulfate loses water and becomes smaller, resulting in loose soil, which causes thaw collapse. The harm to the saline soil salt expansion and thaw collapse to the construction of planning area is mainly caused by expansion of building foundation, causing building deformation damage and difficulties in construction and transportation.

According to the result of a lot of investigation, the soil that occurred in volume expansion is always within 1 m under the surface. When the foundation depth is more than 1 m, generally the salt expansion hazards do not occur. The test results show that when the base pressure is above 50 kPa, the expansion is not obvious. So for salt expansion of foundation soil it is enough to consider only the soil about 2 m below the surface. The thickness of saline soil in this area is small, within 0 to 1 m depth, the salinization degree is

Table 2. Risk evaluation results of saline soil hazards in the new town planning area.

Location	Saline soil type	Total salt content/%	Saline soil designations	Degree of harm	Risk
<i>Guanting reservoir bank</i>					
Y5	Sulfuric acid type	0.10	Weak saline soil	Slight	Low
Y9		0.23	Weak saline soil	Slight	Low
Y8		0.22	Weak saline soil	Slight	Low
<i>Near Caijia river</i>					
Y1	Sulfurous acid type	0.12	Weak saline soil	Slight	Low
Y2		0.62	Moderate saline soil	Moderate	Middle
Y3		0.39	Moderate saline soil	Moderate	Middle
Y4		0.25	Weak saline soil	Slight	Low
Y6		0.32	Moderate saline soil	Moderate	Middle
Y7	Sulfuric acid type	0.17	Weak saline soil	Slight	Low

\*The total salt content is the average within 0 to 1 m depth.

Table 3. Evaluation results of groundwater corrosion to concrete and steel in the new town saline soil area.

Location	Water depth/m	PH	Cl <sup>-</sup> /mg/L	SO <sub>4</sub> <sup>2-</sup> /mg/L	Cl <sup>-</sup> + SO <sub>4</sub> <sup>2-</sup> /mg/L	Corrosion degree to concrete	Corrosion degree to steel
Guanting reservoir bank	3.8–5.0	7.76	55.8	18.6	70.5	Weak	Weak
<i>Near Caijia river</i>							
Tiansongyin	3.6	7.65	19.5	27.9	47.4	Weak	Weak
Upstream	4.5	7.54	12.1	12.0	24.1	Weak	Weak
Midstream	4.1 m	7.66	697.7	341.0	1038.7	Weak	Moderate
Downstream	5.2	7.84	53.2	16.3	69.5	Weak	Weak

weak to moderate (Table 2), and the depth of building foundation is generally greater than 1.0 m, so the harm of saline soil to the new town construction is slight, and the risk for hazards is low.

#### 4.2 Evaluation on corrosion

Corrosion is mainly caused by the high mineralized water and the soluble salts in saline soil, which can cause corrosion to the concrete structures and the steel structures. Based on “Code for Investigation of Geotechnical Engineering”, the corrosivity of saline soil was evaluated, of which the results are shown (Table 3). The groundwater in the location of saline soil in the new town area can cause weak crystallinity corrosion to the concrete structure, and mostly weak corrosion to the steel structure, moderate degree of corrosion only in the middle reaches of Caijia River. On the whole, the harm degree is slight to moderate.

## 5 CONCLUSION

In Yanqing new town area, the saline soil distributed within 0 to 1.2 m depth belonging to sulfate or sulfite saline soil, where the degree of salinization is mainly from slight to partly moderate, and has partly

influence on constructions and crops. So it is recommended to take the following control measures.

In the engineering construction, due to the shallow depth of saline soil, the saline soil can be directly excavated and replaced by easy compacted coarse-grained soil (such as sand), which can cut off the rise of harmful capillary water; more than 30 cm thick of compacted orthod should be laid on the top to isolate the infiltration of surface water, which can remove the salt expansion and corrosion harm of saline soil.

For the saline soil of farmland, according to the actual situation, crop species can be adjusted, farming methods can be changed, and appropriate measures of irrigation and drainage could be taken. For moderate saline soil, freshwater washing salt method and biological improvement method are combined to control harm.

## REFERENCES

- [1] Wang Yihong etc: Preliminary Engineering Geological Investigation Report in Yanqing New Town Area (Beijing Institute of Geological & Prospecting Engineering, 2010).
- [2] Wu Wei, Gu Baohe etc: GB50021-2001 Code for Investigation of Geotechnical Engineering (China Architecture & Building Press, Beijing 2009).

# The influences of soil characteristics on the Negative Skin Friction on a single pile

T. Huang

*College of Harbour, Coastal and Offshore Engineering, Hohai University, Nanjing, P.R. China*  
*Key Laboratory of Hydraulic and Waterway Engineering of the Ministry of Education, Chongqing Jiaotong University, Chongqing, P.R. China*

S.Y. Fu

*Jiangsu East China Engineering Design Co. Ltd., Nanjing, P.R. China*

**ABSTRACT:** Pile foundation is used widely because of good applicability for foundation soil. However, there are still some problems in the appliance of pile foundation, such as Negative Skin Friction (NSF). A series of model tests which aimed at the NSF on the pile under different soil conditions were carried out. Pile stress, displacement of pile head and layered settlement of soil were tested under different surcharge load. The influences of soil characteristics on the NSF on single pile were analyzed mainly, and the relationship between the depth of neutral plane and surcharge load was also research. The results of test can provide references for the related experiment research.

**Keywords:** pile; negative skin friction; model test; soil characteristic; settlement

## 1 INTRODUCTION

Negative Skin Friction (NSF) may occurred by downward vertical soil stress near the pile transferred to the pile shaft when the soil next to a pile settles more than the pile under surface load or groundwater lowering conditions. Because of the development of additional compressive force in a pile and excessive pile settlement, NSF could cause serious problem in pile integrity and maintenance of the structure supported (Fellenius 1998, Acar et al. 1994, Davisson, M.T. 1993).

Some researchers have conducted field tests to study the behavior of pile subject to NSF (Endo et al. 1969, Walker & Darvall 1970, Briaud 1997, Fellenius 2006), which were aimed mostly at NSF on single pile with different kinds of the soil surround the pile. In recent years, some model tests have been carried out to research the NSF on piles (Huang et al. 2013, Leung et al. 2004, Kong et al. 2009). Ng et al. (2008) reported the results of four centrifuge model tests which investigated the response of a single pile subjected to NSF with different pile tip location with respect to the end-bearing stratum layer.

As discussed above, these studies are very helpful for understanding the behavior of pile subjected to NSF. However, the mechanism is still not well understood and existing design methods

are mainly empirical in nature. The literatures on such studies on the influences of soil characteristics (type of the soil around pile, rigidity of end-bearing stratum) on NSF are relatively less. Based on model tests, this paper research the influences of soil characteristics on the NSF on single pile.

## 2 EXPERIMENTAL PROGRAM

### 2.1 Test description

In order to study the difference of NSF on pile in sand and in clay and the influence of pile end-bearing stratum rigidity, two test groups were designed in this work as summarized in Table 1. All the tests were performed in a steel tank (2000 mm × 2000 mm × 1400 mm) with 10 mm in thickness, which was large enough to reduce of the effect of the edges. Reinforcing bands was welded on tank side to reduce the tank deformation caused by applying surcharge load on soil. There were 4 drain valves on the bottom of the tank side, which pore size was 20 mm for drained consolidation.

The model piles were embedded in 1 m thick homogeneous saturated sand bed. The parameters of saturated sand for test are listed in Table 2. In order to ensure the consistency of sand bed in each test, the sand was filled into the tank with the compactness controlled at 45% by weighing

Table 1. Summary of tests.

Test No	Soil type	End-bearing stratum simulation	End-bearing stratum thickness/mm	Surcharge Load/kPa	Pile head load/kN
1	Sand	Gravelly sand	50	120	0.25
2	Sand	Rubber gasket	40	120	3.35

Table 2. Summary of tests.

Internal friction angle/°	Wet density/ $g \cdot cm^{-3}$	Minimum dry density/ $g \cdot cm^{-3}$	Maximum dry density/ $g \cdot cm^{-3}$	Permeability coefficient/ $10^{-6} cm/s$
34.52	1.649	1.249	1.682	934.57

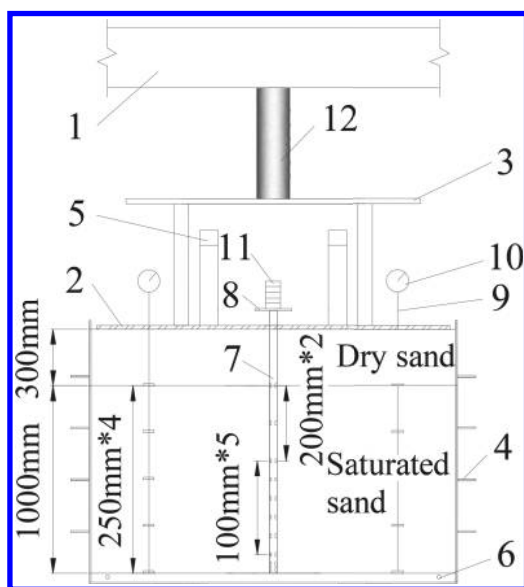


Figure 1. Experiment set-up and pile arrangement: 1-counterforce frame; 2-lower loading plate; 3-upper loading plate; 4-reinforcing band; 5-balance beam; 6-drain valve; 7-model pile; 8-steel plate; 9-settlement standard; 10-dial gauge; 11-dead load; 12-hydraulic jack.

and compaction. To simulate different rigidities of the end-bearing stratum, gravel sand stratum layers with thickness 50 mm and rubber gaskets with thickness 40 mm were installed below the pile tip as end-bearing stratum. The Young's modulus of rubber gasket is about 22.59 MPa.

Model piles were prepared from thin-wall steel pipes of 1.4 m length, 40 mm outer diameter, and 1.18 mm thickness with strain gauges on the inner wall of the pipe piles. The length of embedment of pile (L) in sand bed was 1 m. The modulus of pile was  $2.1 \times 10^5$  MPa. Strain gauges and wires were

arranged on the inner wall of the pipe that can protect the test element not be damaged and can avoid the surrounding soil influenced by test element.

## 2.2 Test procedure

First, the drain valves were closed and gravel sand was put into the tank. Secondly, model piles were arranged on designed position, and then the saturated sand or saturated clay was pushed into the tank. Thirdly, the drain valves were opened and the process of saturated sand consolidation was finished by self-weight after the burying process and standing for 12 h. Fourthly, the drain valves were closed again and 0.3 m thickness dry sand was put into tank as the surcharge load. Finally, the down and up loading plate were successively put on soil surface, and pile cap and bearing plate were successively set on the pile.

The model pile was step-loaded every 15 min by using weight (Test 1) or hydraulic jack (Test 2). After pile head loaded, the surcharge load on soil surface was applied. For the test in sand, the next surcharge load grade was applied when the soil settlement rate was less than 0.01 mm/10 min. However, the next surcharge load was loaded to 80 kPa directly for the test in clay.

## 3 RESULTS AND DISCUSSION

Pile stress, pile head displacement, and the layered settlement of the soil were tested under different surcharge loads.

The test result of single pile in sand is shown in Figure 2 which S means soil settlement and P means p settlement. Figure 2(a) shows the layered settlement of soil increases with the increase of surcharge load, but the increment decreases. The neutral plane is the intersection point between layered soil settlement curve and pile settlement curve

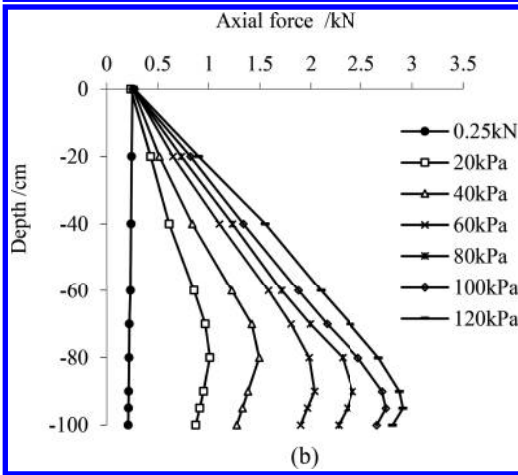
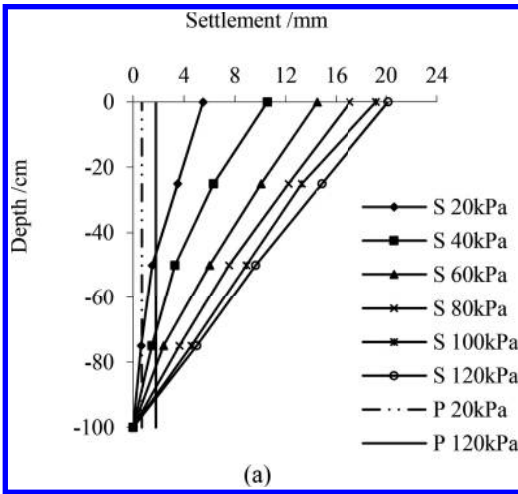


Figure 2. The test result of the pile with gravelly sand layer: (a) The layered settlement of soil and the single pile settlement; (b) The relationship between axial force of pile and surcharge load.

(pile head settlement equals pile bottom settlement because of the less compression of steel model pile), which depth increases with the increase of surcharge load. The axial force of pile indicates that the neutral point varies from 0.8 L to 0.95 L and dragload (subtract the pile head load from the max. axial force) varies from 0.77 kN to 2.64 kN as shown in Figure 2(b). Because the increment of soil is larger than that of pile when the surcharge load increases, the neutral plane shifts down.

For the single pile with rubber gasket stratum layer, the settlement of the pile head under pile head load is shown in Figure 3(a), and the pile head settlement under different surcharge loads is shown in Figure 3(b). Because the rigidity of gravel sand stratum layer is much larger than that

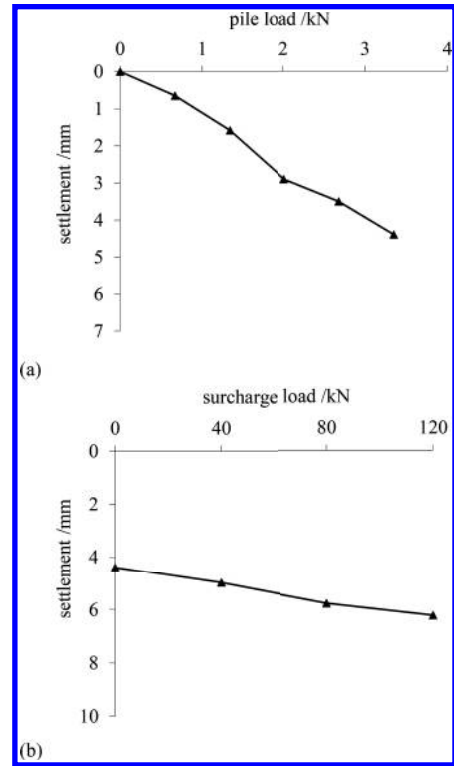


Figure 3. The settlement of pile: (a) Curves of pile head load vs. pile head settlement; (b) Curves of surcharge load vs. pile head settlement.

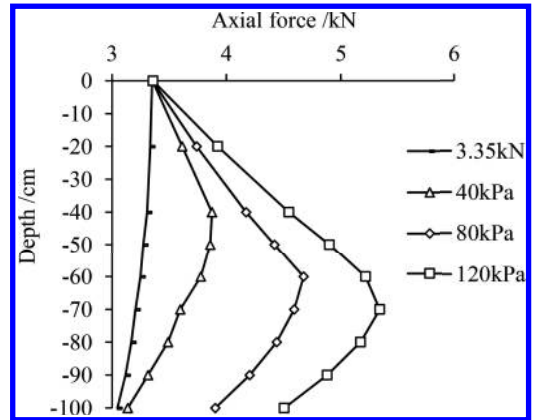


Figure 4. Curves of axial force vs. pile depth.

of rubber gasket, the pile head settlement was much larger than that of pile with gravel sand stratum.

Figure 4 shows the distribution of axial force in the pile shaft with pile depth. The axial force in the



pile shaft of Test 2 reached to the maximum values of 5.34 kN, respectively, when the surcharge load was 120 kPa. When the surcharge load was zero, the decreasing rate of the axial force in the pile shaft was low because of the low effective stress in the soil. As the surcharge load increased, the axial force decreased more obviously with increasing depth because of the high effective stress. Based on test result, the neutral plane depth changed from 0.4 to 0.6 L. When the surcharge load remained constant, the depth of the neutral plane increased with the decrease in  $K_r$ . Furthermore, the depth of the neutral plane decreased with increasing surcharge load for constant  $K_r$ .

Based on the above experimental results, it can be found that the influences of the end-bearing stratum rigidity on neutral plane depth and dragload are significant. Therefore, it is important for engineering designers to carefully consider pile settlement controls and NSF action when choosing the end-bearing stratum during pile foundation design.

#### 4 CONCLUSIONS

Based on the results of model tests, some useful conclusions can be obtained.

1. The layered settlement of soil increases with the increase of surcharge load, but the increment decreases.
2. The neutral plane depth increases with surcharge load, and the axial force varies more obviously with increasing depth as the surcharge load increased.
3. Neutral plane depth increases with increasing end-bearing stratum rigidity under the same test load conditions. The influences of the end-bearing stratum rigidity on neutral plane depth and dragload are significant.

#### ACKNOWLEDGMENTS

This paper was financially supported by the Fundamental Research Funds for the Central Universities (No. 2013B03214), the Natural Science Foundation

of Jiangsu province (No. BK20130843), the Jiangsu Planned Projects for Postdoctoral Research Funds (No. 1302048B), the Key Laboratory of Hydraulic and Waterway Engineering of the Ministry of Education (No. SLK2013B01), China Postdoctoral Science Foundation funded project (No. 2014M561564), and National Natural Science Foundation of China (No. 51408185).

#### REFERENCES

- Acar, Y.B. Avenit, R. & Taha, M.R. 1994. Downdrag on friction piles: A case history. *Proc., Settlement 94: vertical and horizontal deformations of foundations and embankment, 16–18 June 1994*, Texas: College Station.
- Briaud, J.L. 1997. Bitumen selection for reduction of downdrag on piles. *Journal of Geotechnical and Geoenvironmental Engineering* (123)12:1127–1134.
- Davissou, M.T. 1993. Negative skin friction in piles and design decisions. *Proc. of the 3rd International Conference Case Histories Geotechnical Engineering, 1–6 June 1993*, Missouri: St. Louis.
- Endo, M. Minou, K. & Shibata, T. 1969. Negative friction acting on steel pipe piles in clay. *Proc. of the 7th International Conference on Soil Mechanics and Foundation Engineering*, Mexico City.
- Fellenius, B.H. 1998. Recent advances in the design of piles for axial loads, dragloads, downdrag, and settlement. *Proceedings of a Seminar by American Society of Civil Engineers*. New York.
- Fellenius, B.H. 2006. Results from long-term measurement in piles of drag load and downdrag. *Canadian Geotechnical Journal* 43:409–430.
- Huang, T. Gong W.M. Dai G.L. et al. 2013. Experimental study of the time effect of negative skin friction on pile. *Rock and Soil Mechanics* 34(10):2841–2846.
- Kong, G.Q., Yang, Q., Zheng, P.Y. & Luan, M.T. 2009. Evaluation of group effect of pile groups under dragload embedded in clay. *Journal of Central South University of Technology* 16(3):503–512.
- Leung, C.F. Liao, B.K. Chow, Y.K. et al. 2004. Behavior of pile subject to negative skin friction and axial load. *Soils and Foundations* 44(6):17–26.
- Ng, C.W.W. Poulos, H.G. Chan, V.S.H. et al 2008. Effects of tip location and shielding on piles in consolidating ground. *Journal of Geotechnical and Geoenvironmental Engineering* 134(9):1245–1260.
- Walker, L.K. & Darvall, P.L. 1970. Some aspects of drag-down on piles. *Proc., 2th South-East Asian conference on Soil Eng., 11–15 June 1970*, Singapore.

# Numerical analysis of pile uplift bearing capacity with enlarged head

F.F. Li, H.F. Qian, H.R. Qin & T.Q. Zhou

College of Environmental and Civil Engineering, Jiangnan University, Wuxi, China

**ABSTRACT:** Determination of the ultimate uplift capacity for tension piles is an important part in engineering design. Adopting the contact modeling for the pile-soil interface, the elasto-plastic finite element method is proposed to analyze the uplift pile with enlarged head. The simulated results are in good accordance with the field test data. The plastic region is like the semielliptical curve starting from the enlarged pile tip to the pile shaft. The friction resistance in the enlarged pile tip greatly improves the limit uplift bearing capacity.

**Keywords:** uplift bearing capacity; pile; enlarged head; finite element analysis

## 1 INTRODUCTION

The enlarged piles are widely used in underground structural engineering for uplift resistance design. Compared with the common piles, the enlarged pile has the characteristic of higher uplift bearing capacity with fewer materials. In most situations the ability of a foundation to resist uplift loading is the critical design criterion considerably. Both experimental and numerical analysis is performed to investigate the mechanism of uplift bearing capacity. Based on the uplift centrifugal test of enlarged piles, Dickin[1] used the limit equilibrium method to develop the enlarged pile uplift bearing capacity calculation method. Wu Jiangbin[2] and Huang Maosong[3] used the asymmetrical finite element model to analyze the enlarged pile uplift bearing characteristic.

In the paper, the finite element model for the enlarged pile is developed using ABAQUS. The contact option is used to model the interaction between the pile and the soil. The nonlinear geometric analysis is used to analyze the problem. The relation between the uplift force and the displacement is analyzed. Also the plastic zone of the soil is investigated to model the bearing capacity mechanism.

## 2 FINITE ELEMENT MODELLING USING ABAQUS

With consideration of symmetry of structural, soil and loading condition, half finite element model of the pile-soil is modeled, as shown in Figure 1. The two dimensional reduced integration solid element C2D4R is used to model the soil. The bottom

boundary condition is restrained in x, y directions. The side boundary is restrained in x direction. The Mohr-Coulomb yield criterion is used to model the soil behavior. The elastic model is used to model the pile. The calculation region is taken as 20 times of pile radius in radial direction and 15 times of pile length in depth direction.

### 2.1 Contact

In ABAQUS, the contact pair calculation method is used to model the interaction. In the model, the master-slave surface method is used to model the interaction between the pile and the soil. In the computation, the contact state is determined

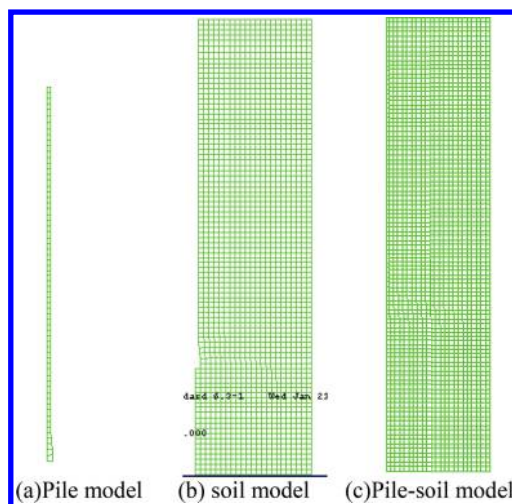


Figure 1. Finite element model.

Table 1. Physical and mechanical parameters of soils and piles.

Stratum	Density/ KN/m <sup>3</sup>	Cohesion/ KPa	Depth/m	Friction angle/°	Elastic modulus/MPa	Possion (μ)
①	18.0	0	1.6	22	10.0	0.40
②	17.4	2	1.4	22	8.0	0.40
③	16.6	12	7.0	18	15.0	0.40
④	16.8	16	2.5	12	21.0	0.35
⑤	19.6	15	7.4	20	32.0	0.32
⑥	19.3	36	5.1	33	40.0	0.30
⑦	19.4	5	5.0	43	100.0	0.25
Pile	25.0				28000.0	0.16

using the normal stress between the pile and soil. When the normal stress is tensile stress, the separation occurs between the pile and the soil. When the normal stress is compressive stress, the contact is maintained between the pile and soil. The interface frictional force is determined using Coulomb friction model, determined as:  $f_{crit} = \mu p$ .

When the tangential stress is less than critical value of  $f_{crit}$ , the relative slip occurs in the contact interface. When the contact interface changes from the stick state to the slip state, the discontinuity occur, which causes the finite element analysis failure. In order to solve the problem, the penalty stiffness method is used in ABAQUS. The elastic slip penalty stiffness factor is introduced to allow for the elastic relative slip occurring in the stick state contact interface.

### 2.2 Selection of loading type

In analogous to the model experiment, the force control method or the displacement control method is used in the finite element calculation and analysis. Compared with the force control method, the more accurate force-displacement curve could be obtained using the displacement control method. Another advantage of displacement control method is that when the force amounts to the limit uplift bearing capacity, the accurate limit bearing capacity could be obtained using the displacement control method. When using the force control method, the force loading is not effective when the external force exceeds the limit bearing capacity, which causes the calculation failure. In the paper, the displacement control method is used to apply the loading to obtain limit uplift bearing capacity.

## 3 FINITE ELEMENT ANALYSIS

The uplift bearing capacity of engineering pile full scale experiment in Shanghai is used as the

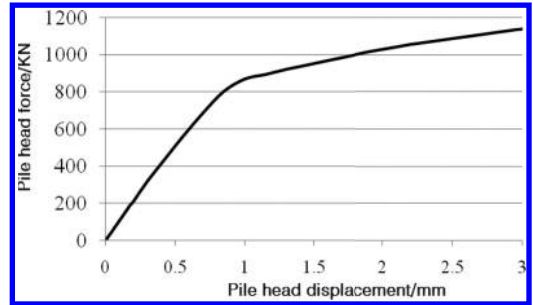


Figure 2. FEM simulation results of Q-S curve.

numerical analysis with pile length of 27 m and pile diameter 450 mm. The enlarged pile diameter is 0.45 m. The friction coefficient between the pile and soil is taken as 0.2. The displacement control method is used to apply the loading. The soil geological information and the soil mechanical parameter is shown in Table 1.

The computed Q-S curve is shown in Figure 2. As shown in Figure 2, the computed uplift bearing capacity is about 1180 KN, which is close to the experimental value of 1100 KN.

The computed soil displacement and soil vertical stress is shown in Figure 3 and Figure 4 respectively.

The soil yield zone and the plastic distribution is shown in Figure 5 and Figure 6 respectively.

As shown in Figure 5 and Figure 6, the plastic region is like the semielliptical curve starting from the enlarged pile tip to the pile shaft. The enlarged pile tip has the effect of compressing the surrounding soil locally, which causes the local shear failure of soil.

The computed friction resistance distribution along depth of piles during uplift is shown in Figure 7. It can be seen from Figure 7 that the friction resistance in the enlarged pile tip increases greatly, which contributes a lot to the limit uplift bearing capacity.

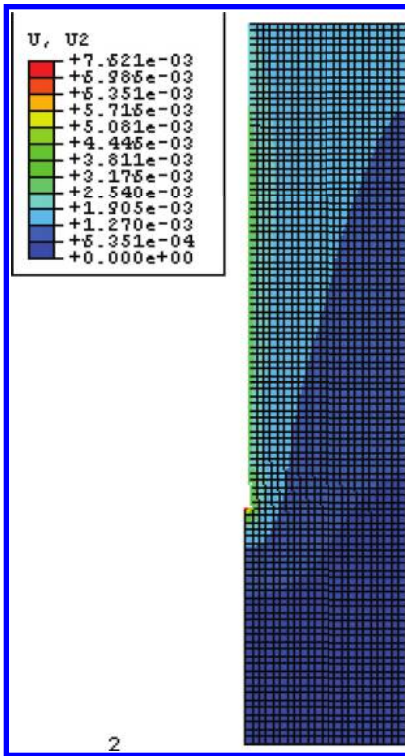


Figure 3. Soil displacement.

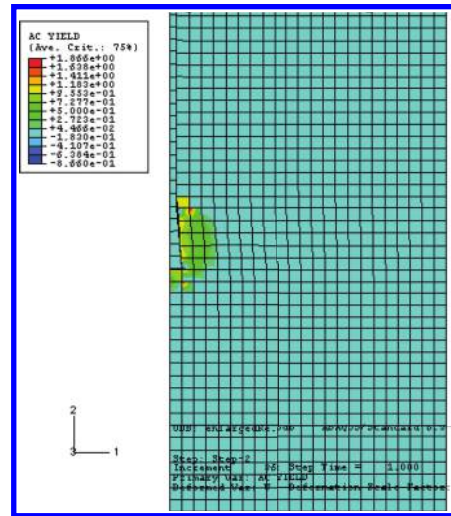


Figure 5. Soil yield zone.

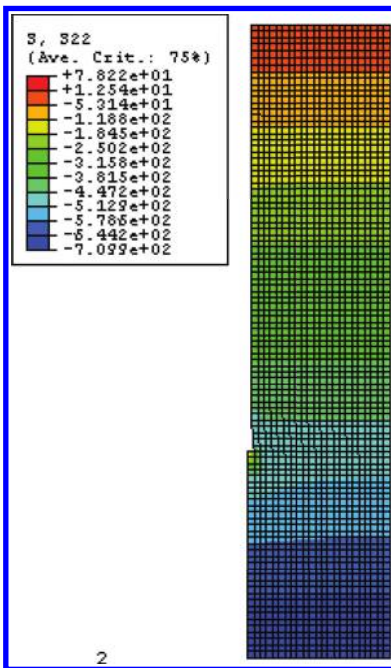


Figure 4. Soil vertical stress/KPa.

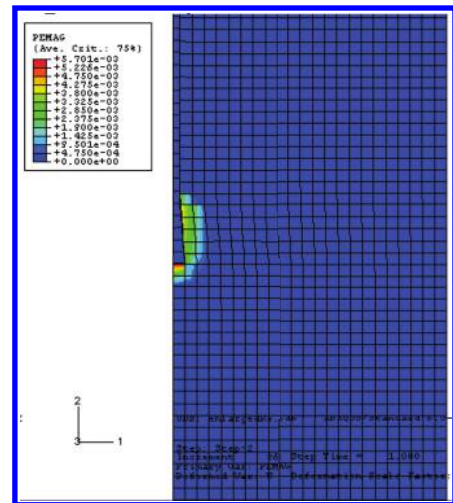


Figure 6. Plasticity distribution.

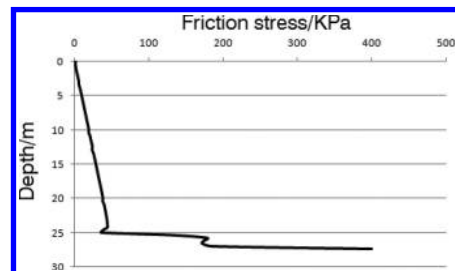


Figure 7. Distribution of friction resistance along depth of piles during uplift.

#### 4 CONCLUSIONS

The numerical analysis is performed to investigate the uplift behavior of enlarged pile. The plastic region is like the semielliptical curve starting from the enlarged pile tip to the pile shaft. The enlarged pile tip has the effect of compressing the surrounding soil locally, which causes the local shear failure of soil. The friction resistance in the enlarged pile tip greatly improves the limit uplift bearing capacity.

#### ACKNOWLEDGEMENT

Funding support to the research by National University Students Innovation Training Plan

(No. 201410295052) of Jiangnan University is greatly acknowledged.

#### REFERENCES

- [1] Dick in E.A., Leung C.F. 1990. Performance of piles with enlarged base subject to uplift forces. *Canadian Geotechnical Journal* 27(5): 546–556.
- [2] Wu J.B., Wang W.D., Huang M.S., et al. 2008. Uplift mechanism enlarged base of pedestal piles by numerical analysis. *Rock and Soil Mechanics* 29(8): 2115–2120.
- [3] Huang Mao-song, Ren Qing, Wang Wei-dong, Chen Zheng. 2007. Analysis for ultimate uplift capacity of tension piles under deep excavation. *Chinese Journal of Geotechnical Engineering* 29(11): 1689–1695.

# The load deformation behaviour and the bulging patterns of reinforced gabion retaining walls

Yang Jiang

*Faculty of Architecture and Civil Engineering, Huaiyin Institute of Technology, Huaian, China*  
*School of Highway, Chang'an University, Xi'an, China*

Huarong Shen, Jiangtao Xia & Baohai Chen

*Faculty of Architecture and Civil Engineering, Huaiyin Institute of Technology, Huaian, China*

**ABSTRACT:** Gabion retaining walls are commonly built as gravity type walls for low wall heights and as reinforced soil type for medium and high walls. Reinforced gabion retaining walls can generally accommodate large lateral and vertical movements without excessive structural distress, thus they offer technical and economical advantage over the conventional concrete gravity retaining walls. Experiments were conducted on small scale models of reinforced gabion retaining walls. Conclusions are drawn: The quarry dust filled gabion walls show more lateral deformation than that of the coarse aggregate filled gabion walls. As the percentage of quarry dust increased, top lateral deformation and bulging also increased. An inference can be made that the walls with lesser quantity of quarry dust behave in a stiffer manner than the other walls with higher quantities of quarry dust.

**Keywords:** gabion; reinforced earth retaining wall; the load deformation behaviour; the bulging patterns

## 1 INTRODUCTION

Reinforced gabion retaining walls are essentially semi rigid structures that can generally accommodate large lateral and vertical movements without excessive structural distress. Because of this inherent feature, they offer technical and economical advantage over the conventional concrete gravity retaining walls. Although they can be constructed either as gravity type or reinforced soil type, this work mainly deals with reinforced gabion retaining walls as they are more suitable to larger heights.

Experiments were conducted on small scale models of reinforced gabion retaining walls. While doing so, an attempt was made to explore the possibility of reducing the cost of construction by using quarry dust as a gabion fill material. The most attractive feature of the gabion walls is their cost effectiveness. Gabion walls can achieve around 30–60% savings when compared to Reinforced cement concrete walls constructed in similar situations. Even though the structure is a cost effective one, it can be seen that the stone filling used inside gabion boxes increases the cost of construction. In this work, an attempt is made to examine the effects of replacement of the stone filling in the gabion boxes with a mixture of stone and rock waste. The use of rock waste would relieve some of the problems associated with its

disposal and it may turn into an inexpensive and advantageous construction product. It can also be noted that there is an added advantage in the use of rock waste from the quarries in the sense that the otherwise colossal cost of the conventional retaining structures is reduced to a very low value. Different experiments were carried out for determining the load deformation behaviour of the walls using gabions with different combinations of fill materials [1].

## 2 MODEL STUDIES

In gabion walls, gravity force (self weight) is the predominant stabilizing force, which depends on the unit weight of the material ( $\gamma_m$ ) used for construction, which in turn is dependent on the specific gravity ( $G$ ) of the material by the relation,  $\gamma_m = G \cdot \gamma_w$ , where  $\gamma_w$  is the unit weight of water. The specific gravity of rock waste is nearly equal to that of stone. Therefore, gravity force is not affected by the replacement of stone with rock waste. Considering all these points, rock waste was selected as a substitute for stone filling in this work. To represent the rock waste in the model studies, quarry dust, which is one of the easily and cheaply available waste materials, was used. Similarly stone filling was represented by 20 mm coarse aggregate filling inside

the gabion boxes. Instead of the actual gabion wall with stone filling, the one with a combination of stone filling and quarry dust was considered for the studies. Five different combinations were tried by varying the quantities of quarry dust and stone filling. Load tests were conducted on model gabion retaining walls to study the deformation characteristics of gabion faced retaining walls. The purpose of this study was to find out an optimum combination of quarry dust and stone filling, to replace the stone filling in gabion boxes and thus, further reduce the cost of construction of gabion wall. For this, five different combinations of quarry dust and coarse aggregate were used in the gabion fill supporting the model retaining wall. The combinations were varied by percentage weight of the filling materials in gabion boxes [2].

### 3 FIELD MODEL STUDIES

#### 3.1 Construction of model gabion wall

For the reinforcement purpose the base of the gabion boxes are provided with an extension. Generally 0.6 to 0.8 times the height of the wall is taken as the reinforcement extension including the base of the box. The extension and boxes act monolithically. Boxes are provided with a top cover and internal partitions called as diaphragms to prevent bulging of the box. The model gabion wall was constructed over a length of 2 m. The height of the wall was fixed as 1 m. The wall was constructed at a distance of 2.5 m from the natural slope and the space was filled with sand, which acted as a backfill to the wall. Brick bays were constructed on either side to limit the length of the wall. Sixteen numbers of gabion boxes each of size  $0.5 \text{ m} \times 0.25 \text{ m} \times 0.25 \text{ m}$  were used to retain the backfill. Boxes were provided with an extension of 0.55 m at the base. Top cover was also provided. Because of the small size of the box, diaphragm walls were avoided.

For the load tests, using coarse aggregate as filling material, the above described model gabion boxes were used as such. But for the quarry dust and other combinations of quarry dust and coarse aggregate as filling material, the inner sides of the gabion boxes were stitched with geotextile Terram 1000. Nylon wires were used for stitching. The geotextile prevents the escape of quarry dust through the mesh openings.

The ground was levelled and 5 cm thick layer of sea sand was spread over it. The first layer of four boxes was placed on the levelled ground surface where the wall had to be constructed. The boxes were connected together with steel wires so that they behave as a single unit. The extensions of the boxes were spread over the sand layer. Boxes were

filled with filling material corresponding to the cases considered. In the case of combination filling, the quarry dust and coarse aggregate were filled in the boxes after mixing them properly in the required proportions. Filling was done with proper compaction to achieve the required unit weight of  $15 \text{ kN/m}^3$ . After filling the boxes, the top cover was closed and tightly connected to the sides of the boxes using steel wires. Behind the boxes, geotextile was placed in order to avoid the entry of granular backfill into the boxes. Then backfilling of sand was done up to the height of the boxes. The backfill sand was compacted in each layer to get an average unit weight of  $17.6 \text{ kN/m}^3$ . Each layer of the fill was compacted to get the same density by controlling the weight of soil and thickness of layer. After levelling the backfill, the next layer of gabion boxes was placed above the first layer and the two layers were stitched with steel wires and the procedure was continued up to the required level. Since the height of the wall was fixed as 1 m, four layers of boxes each of height 0.25 m were placed to complete the construction. Markings were made on the front of each box of the facing unit for taking measurement due to surcharge loading [3].

#### 3.2 Loading set up

After the construction of wall using gabion boxes loading was done with sand bags. Before placing the sand bags a concrete slab was placed over the retaining wall to enable the surcharge loads to give a uniform pressure as well as to act as a loading platform. Sand bags were placed in layers. Each layer constituted of 25 bags filled with sand. Each layer provides a surcharge pressure of 2 kPa. The load for the first layer of sand bag (2 kPa) and load from the concrete slab (1 kPa) was taken as the seating load and the initial deformations were noted. An aluminium rod was placed above gabion wall, supported by the brick walls of the bay. This was used as a reference mark to measure the deformations.

In order to measure the lateral deflection the outer edge of the aluminium rod was used as the datum point. A plumb bob was hung down vertical from the outer edge of aluminium bar. Using a metre scale the initial position of wall and the changed position after loading, were measured. The difference between these values gave the lateral deformation at each point. In total, six layers of sand bags were placed one over the other, above the retaining wall. Thus at the end of loading a total pressure of 13 kPa was acting on the wall. After placing each layer of sand bag the loading was kept undisturbed till the deformations stabilized. Before placing the next layer of sand bags, lateral deformations were measured. The walls were not loaded to failure due to the practical difficulty of increasing the height of dead load.

## 4 LABORATORY MODEL STUDIES

### 4.1 Experimental set up

The experiments consisted of studies on model gabion retaining wall constructed in a steel tank of size  $1\text{ m} \times 1\text{ m} \times 1\text{ m}$  in the Geotechnical Engineering laboratory. The height of the wall was fixed as  $0.6\text{ m}$  and the dimensions of the boxes and basal extension were designed using the physical properties of backfill soil and steel mesh which were obtained from laboratory experiments. Sixteen numbers of gabion boxes each  $0.25\text{ m}$  long,  $0.15\text{ m}$  wide and  $0.15\text{ m}$  high and with basal reinforcement of  $0.35\text{ m}$  were used to retain the sand backfill inside the tank. The boxes were fabricated by stitching steel mesh panels to get the required shape.

Four such boxes were stitched one beside the other to form a layer such that they behave as a single unit. Four layers were placed one above the other to form the wall. The horizontal deformations at the front face of the wall were measured using dial gauges.

For the load tests using coarse aggregate alone as the filling material, the above described model gabion boxes were used as such. But for the cases where quarry dust is also used as filling material, the inner sides of the gabion boxes were stitched with geotextile Terram 1000. Nylon wires were used for stitching. The geotextile prevents the escape of quarry dust through the mesh openings. The filling material in the boxes was filled at an average unit weight of  $15\text{ kN/m}^3$ . In this laboratory experiment, the combination filling was done in layers. The required proportion of quarry dust was placed as the bottom layer and the coarse aggregate as the top layer, the separation between the two being made using the geotextile material. The backfill sand was compacted in each layer to get an average unit weight of  $16\text{ kN/m}^3$ . Each layer of the fill was compacted to get the same density by controlling the weight of soil and thickness of layer. After leveling the backfill, the next layer of gabion boxes was placed above the first layer and they were stitched with nylon wires and the procedure was continued up to the required level. Four layers of boxes each of height  $0.15\text{ m}$  were placed one above the other to complete the construction. The layers were also interconnected using steel wires such that the entire wall behaves as a single block. Markings with small metal strips were made on the front face of the circled boxes at the centre for taking deformation measurements with dial gauges.

### 4.2 Loading set up

After the construction of the wall using gabion boxes, loading is done using hydraulic jack and lever arrangement. The loading pattern used is of

two-point loading acting on a  $25\text{ mm}$  thick and  $0.2\text{ m}$  wide strip placed over the sand backfill parallel to the gabion wall. Load was applied using a hydraulic jack, in increments of  $3\text{ kN}$  till failure. After applying each increment, the load was kept constant till the deformations stabilized. Prior to next increment lateral deformations were measured using dial gauges.

## 5 LOAD DEFORMATION CHARACTERISTICS

An account of the results obtained from the experimental studies is presented in this paper.

The field model experiment was loaded up to  $13\text{ kPa}$  which included a seating load of  $3\text{ kPa}$  and initial deformations were measured only after stabilization of the deformations due to the seating load. For the laboratory model experiment, the wall was kept undisturbed for a day for the stabilization of post construction deformations and loading was done on the succeeding day in increments. The load—deformation measurements were noted till failure.

The effective replacement of stone filling in gabion boxes by a cheaper material is the focus of the study and is done by comparing the load deformation behaviour of the five different walls. Figure 1 shows the load deformation characteristics for field model experiment in which the deformation is expressed in terms of a dimensionless quantity, top sway factor,  $\delta_1$  which is defined as  $U_1/H$  where  $H$  is the wall height and  $U_1$  is the top lateral deformation of the wall at the midsection. Although  $U_1$  is referred as top lateral deformation, it is measured as the average of the lateral deformations at the centre of gabion boxes. From the figures, it can be seen that as the load increases, the lateral deformation also increases, as expected.

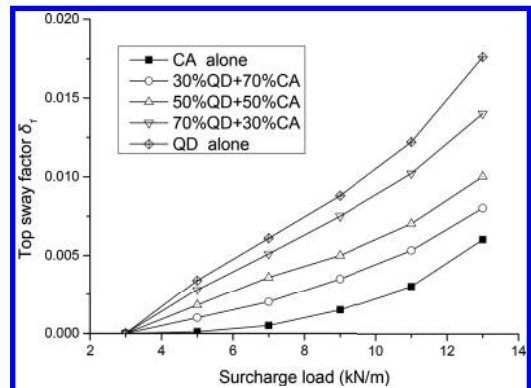


Figure 1. Load deformation behaviour after seat load (Field model experiment).



The quarry dust filled gabion walls show more lateral deformation than that of the coarse aggregate filled gabion walls. The combinations showed intermediate deformations. This may be due to the low stiffness characteristics of quarry dust filled gabions. As a result, as the percentage of quarry dust increased, top lateral deformation also increased. The 50–50 combination shows a top lateral deformation less than that of quarry dust alone and 70% quarry dust and 30% coarse aggregate combination [4].

## 6 BULGING PATTERNS

The variation of lateral deformation along the height of the wall which is termed as “bulging pattern”, also show the behaviour of retaining walls. The lateral deformations at the mid length of the wall ( $U_2$ ) in all the four layers at a specific load value were measured in the experiments to understand the behaviour of the fill materials in the wall facings. The bulging patterns are plotted with the sway factor,  $\delta_s = U_2/H$  along the x-axis and the wall elevation along the y-axis. The bulging patterns are studied for a uniform surcharge load of  $13 \text{ kN/m}^3$ .

Figure 2 shows the bulging patterns of the model gabion walls for different combinations of fill. As the percentage of quarry dust increased bulging was observed to increase. It is seen that, the top layer experienced more bulging than the lower layer for the first three walls with lesser quantity of quarry dust. The other two walls with larger quantity of quarry dust showed an intermediate bulging in the third layer. An inference can be made at this point that the walls with lesser quantity of quarry dust behave in a stiffer manner than the other walls with higher quantities of quarry dust [5].

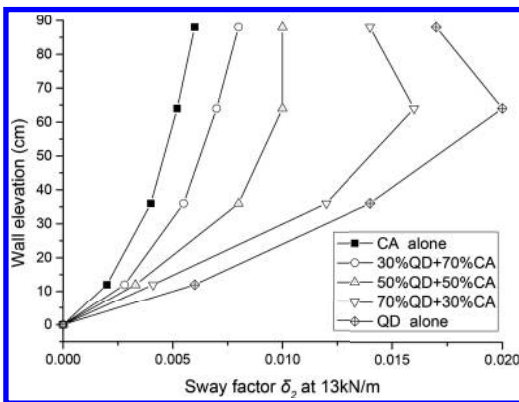


Figure 2. Bulging of front face of walls (Field model experiment).

The difference between the two sets of experiments lies in the loading difference and the mode of filling the boxes. Even with these differences, the results are found to be comparable near to the failure points. From this, it can be inferred that the mode of filling has no effect on the load deformation behaviour of the system.

On quantifying the increase in top lateral deformation of the quarry dust filled walls with respect to coarse aggregate filled wall, it is seen from the experiment that filling 30% quarry dust increases the top lateral deformation approximately by 35%. When quarry dust is increased to 50%, almost 70% hike is seen in the deformation value. In general, as the quantity of quarry dust increased, the deformation also increased.

## 7 CONCLUSIONS

Experiments were conducted on small scale model walls in the field and in the laboratory to investigate the effects of replacement of the stone filling in the gabion boxes used as facing in gabion walls, with a mixture of stone and rock waste. To find an optimum mixture of stone and rock waste to be filled in the gabion boxes, walls were constructed with different combinations of stone and rock waste and were loaded to study the variation in the deformation behaviour of the system.

As the load increases, the lateral deformation of reinforced earth retaining wall also increases. The quarry dust filled gabion walls show more lateral deformation than that of the coarse aggregate filled gabion walls. As the percentage of quarry dust increased, top lateral deformation also increased. As the percentage of quarry dust increased, bulging was observed to increase. An inference can be made that the walls with lesser quantity of quarry dust behave in a stiffer manner than the other walls with higher quantities of quarry dust.

## REFERENCES

- [1] M. Isabel, M. Pinto and T.W. Cousins: Geotextiles and Geomembranes Vol. 14(1996), P. 449.
- [2] B. Villemus, J.C. Morel and C. Soutin: Engineering Structures Vol. 29(2007), P. 2124.
- [3] M. Nimmegern: Application, Design and Construction (1996), P. 171.
- [4] C.X. Lu, Z.Q. Li and Z.M. Yang: Express Water Resources and Hydropower Information Vol. 25 (2004), P. 26 (In Chinese).
- [5] J.G. Bentler and J.F. Labuz: Journal of Geotechnical and Geoenvironmental Engineering Division Vol. 132 (2006), P. 1062.

# The influence of geometric parameters on the deformation behaviour of reinforced gabion retaining walls

Yang Jiang

*Faculty of Architecture and Civil Engineering, Huaiyin Institute of Technology, Huaian, China*  
*School of Highway, Chang'an University, Xi'an, China*

Huarong Shen & Jiangtao Xia

*Faculty of Architecture and Civil Engineering, Huaiyin Institute of Technology, Huaian, China*

**ABSTRACT:** Conventional design procedures of retaining walls in general, do not take into account wall deformation which is usually considered as a minor criterion in design. But in the present trend, a deformation study for retaining walls is important. Finite element analyses were carried out for different reinforcement spacings, reinforcement lengths and facing widths on low, medium, and high walls. The relation between those geometric parameters and the effect of the earth pressure acting on the wall and the facing deformation are discussed in detail in this paper. Moreover, the optimum values have been suggested as follows: the ideal spacing of reinforcement may be fixed as  $0.1 H$ – $0.2 H$ ; the ideal reinforcement length may be fixed as  $0.4 H$ – $0.6 H$ ; the facing width may be fixed as  $0.1 H$ – $0.15 H$ ; the most ideal position for placing the strip loading is at least  $1.5 L$  away from the back face of the wall.

**Keywords:** gabion; reinforced earth retaining wall; deformation behaviour; geometric parameters; finite element method

## 1 INTRODUCTION

Reinforced gabion retaining walls are essentially semi rigid structures that can generally accommodate large lateral and vertical movements without excessive structural distress. Because of this inherent feature, they offer technical and economical advantage over the conventional concrete gravity retaining walls.

Conventional wall design procedures are primarily stress based and do not consider deformations separately. Reason for the same being, deformations are relatively insignificant for the typical conditions of wall geometry and loading for which the design procedures were developed. But in circumstances where walls with non—standard geometry or loading cannot be avoided, deformation criteria should be carefully considered. For example, the use of shortened reinforcement layers due to topographic or economic constraints will cause increased deformations which would otherwise become critical, if avoided. Walls with large external loading or sloping backfills, walls where performance criteria requires very small deformations etc., are some other examples where deformations have more or less equal importance to stresses. Hence this work concentrates on deformation studies [1, 2].

This paper explains the analyses conducted on gabion faced reinforced soil walls of three different wall heights—3 m, 6 m and 9 m representing the low, medium and high walls respectively. Finite element studies were performed by varying the spacing as well as the length of reinforcement and the width of gabion facing. The effect of the position of strip loading on the behavior of walls was also investigated.

## 2 FE MODEL FOR THE PARAMETRIC STUDIES

The reinforcement extending into the soil was assumed to be of same length through out the height of the wall and was taken as equal to  $H$  (the height of Reinforced gabion retaining walls) in the basic system chosen for the parametric study. The wall facing at the bottom was assumed to have an embedment of  $0.15 H$  into the soft clay. Horizontal translation was restricted for the nodes on the left and right end boundaries and all the bottom nodes were completely restrained. The geometry of the model was kept the same for all the parametric studies and only the parameter to be studied was varied accordingly. The FE mesh was fixed such

that the same mesh could be used for all the parametric studies performed.

The basal reinforcing mesh of the gabion boxes extending into the soil were modelled using 288 two noded truss elements with axial stiffness only, assuming linear stress strain relationship. The properties of the gabion mesh were determined in the laboratory by conducting tension tests on a sample specimen of the gabion mesh. The gabion wall facing was modelled as a composite material assigning properties obtained from literature. The soil material was modelled using 2066 four noded isoparametric quadrilateral elements. The non linear stress—strain behaviour of soil was simulated using Duncan and Chang hyperbolic model following Mohr—Coulomb failure criterion. The backfill was assumed to be beach sand and the foundation was assumed to be clayey silt. In reinforced soil structures, the main criterion adopted in the design is that the desirable failure mode is pullout failure rather than the breaking of reinforcement. This is because the failure due to rupture can reduce the shear strength of the structure to a very low value which may cause catastrophic effects to the structure. Hence the failure of reinforcement was not modelled here and it was assumed that the system does not fail by the rupture of reinforcement. The pullout failure of the reinforcement was modelled using four noded zero thickness interface elements at the top and bottom of the reinforcement. The interface elements were also used behind the vertical face of the gabion wall in contact with the back fill, at the base and in the front face (foundation) in contact with the foundation soil. The interface elements were modelled such that the shear stiffness is governed by a hyperbolic rule similar to that of the soil model and related the interface shear stress and displacement [3].

### 3 EFFECT OF REINFORCEMENT SPACING

It is a common practice in the construction of gabion faced walls to provide the reinforcement at uniform spacing. Considering the economic aspects, varied spacing can be more advantageous than uniform spacing. Hence an attempt is made here to study the influence of spacing of reinforcement on the behaviour of gabion faced reinforced soil walls and to arrive at an optimum value of spacing.

For this, different configurations of reinforcement have been chosen, studies were conducted varying reinforcement spacing ( $h$ ) as  $0.08 H$ ,  $0.17 H$ ,  $0.25 H$ ,  $0.33 H$  and  $0.50 H$ . The horizontal deformations of the facing for all the configurations were noted and plotted as shown in figure,

which shows the variation of lateral deformation of gabion wall facing for the different models discussed above for  $H = 6$  m. The lateral deformation increases as the spacing of the basal reinforcement increases, in all the cases, there is not much variation of lateral deformation in the embedded portion of the wall since the outward deformation is restricted by the foundation soil. The shape of the facing deformation changes from a linear form to a bow shaped form as the spacing of basal reinforcement of the reinforced gabion walls decreases and the maximum deformation is as low as  $0.0036 H$ . It is also seen that for medium to large spacings, namely  $h/H = 0.25$  to  $0.5$ , the deformation increases almost linearly with height from bottom to top and the maximum deformation at top is nearly  $0.012 H$  for  $h/H = 0.25$  and  $0.04 H$  for  $h/H = 0.5$ .

The reduction in deformation of reinforced gabion faced walls are plotted against the normalized spacing for the case  $L/H = 1.00$ , where  $L$  is the reinforcement length. Here, the percentage reduction in deformation is defined as,

$$\Delta u = (u_0 - u_1) / u_0 \times 100\% \quad (1)$$

where  $u_0$  is the maximum lateral deformation in the unreinforced case;  $u_1$  is the maximum lateral deformation in the different reinforced cases. As expected, as the spacing becomes smaller the percentage reduction in deformation increases (Fig. 1).

The percentage reduction in deformation is seen to be smaller for low height walls and it increases as the height increases. The variation in percentage reduction in deformation between walls of 3 m height and 6 m (or 9 m) height, is larger for smaller spacings and decreases gradually as spacing increases. The values become almost constant for walls of all heights at large spacings. From the

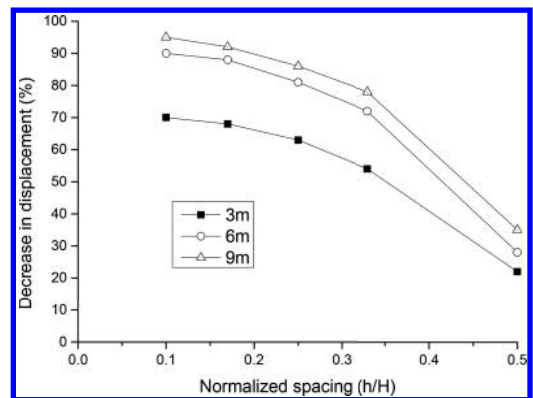


Figure 1. Effect of reinforcement spacing.

above discussions, it may be concluded that for any wall height, the ideal spacing of reinforcement may be fixed as,  $h = 0.1 H$  to  $0.2 H$ , as observed from Figure 1.

#### 4 EFFECT OF REINFORCEMENT LENGTH

To explore the reasonable reinforcement length in gabion faced reinforced soil walls, studies were conducted varying the lengths of reinforcement as  $0.125 H$ ,  $0.25 H$ ,  $0.5 H$ ,  $0.75 H$  and  $1.00 H$ .

As the length of reinforcement increases, percentage increase in lateral force with respect to the unreinforced case increases. In other words, as the quantity of reinforcement increases, the earth pressure exerted on the back face of the wall increases, indicating the transformation of the state of earth pressure from below active condition to near to at-rest condition, the system changes from an unstable to a stable state which is clearly indicated by the reduction in deflection values with the increase in the quantity of reinforcement [4, 5].

The variation in length was plotted against the change in deformations with respect to the unreinforced case (Fig. 2). Here also, as expected, as the length of reinforcement increases, the reduction in displacement increases.

As the wall height increases, the percentage increase in lateral force increases, but the variation is very small. The percentage reduction in deformation is lower for low height walls and it increases gradually for walls of larger heights and the variation is nominal for medium and high walls. Moreover, observing from Figure 2, the ideal reinforcement length for gabion faced reinforced soil walls may be fixed as  $0.4 H$ – $0.6 H$ , beyond which the deformation variations are seen to be constant.

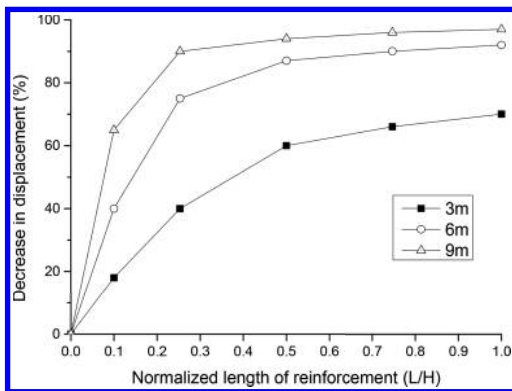


Figure 2. Effect of reinforcement length.

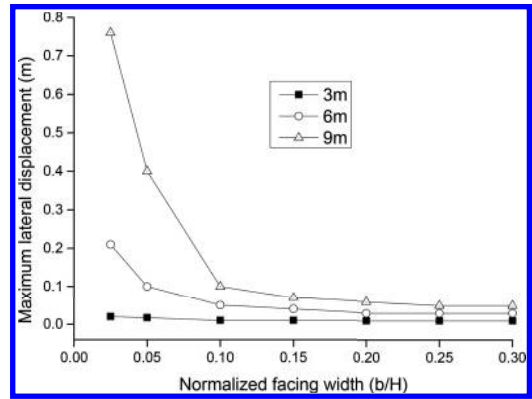


Figure 3. Effect of facing width.

#### 5 EFFECT OF FACING WIDTH

In order to investigate the effect of the width of gabion facing on the behaviour of gabion faced reinforced soil walls, the same was varied keeping all the other parameters constant. Studies were conducted varying the widths of gabion facing as  $0.025 H$ ,  $0.05 H$ ,  $0.10 H$ ,  $0.15 H$ ,  $0.20 H$ ,  $0.25 H$  and  $0.30 H$ .

Results show that as the facing width increases, there is not much variation in the lateral force exerted at the back face of the wall. This means that the facing rigidity has not much effect on the lateral force developed in the backfill. The variation in facing width has also been plotted against the maximum lateral deflection with respect to the unreinforced case (Fig. 3). Here it is seen that the increase in facing width decreases the maximum lateral displacement. For very thin facings, the displacements are seen to be maximum. For  $b/H \geq 0.1$ , the displacement values are almost constant giving a linear horizontal shape to the latter part of the plot.

As the wall height increases, the lateral force and the displacement values also increase (Fig. 3). The variation in lateral force is nominal for medium and high walls. In the case of displacements, for thin facings, the variation in displacements with increase in wall height is seen to be large. For thicker facings, the corresponding variations are small. To summarise the study, the facing width may be fixed as  $0.1 H$ – $0.15 H$ , beyond which the effect of deformations are seen to be marginal.

#### 6 EFFECT OF POSITION OF STRIP LOADING

Strip loads like pipelines, edges of bridge seating, cranes, compactors etc., are commonly seen at a retaining wall project site. These are permanent loadings and before the placement of these loads

over the structure in the case of a gabion faced reinforced soil wall, the behaviour of the walls should be studied under the action of these loads.

For this, FE studies were conducted by applying strip load of same intensity (35 kN/m which is the usual load taken for the design of bridges etc.), but of varying widths at various positions and maximum lateral deformation is noted. Strip width is denoted as  $B$  and the position is denoted as  $D_e$ .  $D_e$  denotes the distance of the start of strip load from back face of wall.

Strip was varied in position at different values of  $D_e/L = 0.25, 0.50, 0.75, 1.00, 1.25, 1.50, 1.75$  and  $2.00$ . The strip width was varied at values of  $B/L = 0.10, 0.20, 0.30, 0.50, 0.75$  and  $1.00$  for the parametric studies. The deformation is expressed in terms of percentage increase in deformation with respect to the case with no strip loading.

The variation of top lateral deformation of the facing with change of strip position from back face of wall for different width of strip loading was achieved. As expected, the deformation increases with increase in width of strip loads. Regarding the strip position, the ratio  $D_e/L = 0$ , represents that the start of the strip loading is at the back face of the wall. Results show that it is the most critical loading position as the percentage increase in deformation with respect to the unloaded case is maximum here. One more critical plane can be identified from the result where all the curves show a peak. This is at  $D_e/L = 1$ , where the percentage increase in deformation is found to be more compared to other positions. The best position of strip loading can also be identified which is  $D_e/L > 1.5$ . Another suitable position range may also be located from as  $D_e/L = 0.5$  to  $0.75$ . It is at these two positions where the percentage increase in deformation is lesser compared to other positions.

Thus the critical planes where the strip loading should not be placed are the beginning and end of the reinforcement lengths. The most ideal position for placing the strip loading is at least  $1.5 L$  away from the back face of the wall, where  $L$  is the length of the reinforcement. Strip should be placed away from the reinforced region. If in any case, the strip has to be placed inside the reinforced area, the best position is that the start of the strip loading should be within the range  $0.5 L - 0.75 L$  from the back face of the wall. The results of the FE studies performed here were replotted to develop a design chart from which the position of strip loading may be fixed by considering the deformation criteria.

With the aid of this chart, knowing the limiting deformation and strip width, the ideal position of strip loading can be selected.

## 7 CONCLUSIONS

FE analyses of gabion faced reinforced soil retaining walls were carried out for different reinforcement spacings, reinforcement lengths and facing widths on low (3 m), medium (6 m) and high (9 m) walls. The relation between those geometric parameters and the effect of the earth pressure acting on the wall and the facing deformation are discussed in detail in this paper.

Moreover, the optimum values have been suggested in each case. Suggestions are as follows:

For any wall height, the ideal spacing of reinforcement may be fixed as  $0.1 H - 0.2 H$ . The ideal reinforcement length for gabion faced reinforced soil walls may be fixed as  $0.4 H - 0.6 H$ , beyond which the deformation variations are seen to be constant. The facing width may be fixed as  $0.1 H - 0.15 H$ , beyond which the effect of deformations are seen to be marginal.

The strip loading should not be placed at the beginning and end of the reinforcement lengths. The most ideal position for placing the strip loading is at least  $1.5 L$  away from the back face of the wall, where  $L$  is the length of the reinforcement. If the strip has to be placed inside the reinforced area, the best position is that the start of the strip loading should be within the range  $0.5 L - 0.75 L$  from the back face of the wall.

## REFERENCES

- [1] G.V. Rao, J.M. Kate and A. Saxena: First Indian Geotextile Conference on Reinforced Soil and Geotextiles (1988), P.A. 35.
- [2] W.L. Xie, J.D. Wang and L.H. Zhang: Chinese Journal of Rock Mechanics and Engineering Vol. 24(2005), P. 430 (In Chinese).
- [3] B. Villemus, J.C. Morel and C. Soutin: Engineering Structures Vol. 29(2007), P. 2124.
- [4] C.X. Lu, Z.Q. Li and Z.M. Yang: Express Water Resources and Hydropower Information Vol. 25 (2004), P. 26 (In Chinese).
- [5] J.G. Bentler and J.F. Labuz: Journal of Geotechnical and Geoenvironmental Engineering Division Vol. 132 (2006), P. 1062.

# Study on crack-generated characteristics of expansive soil

L. Cao

*Department of Civil Engineering, Shanghai Jiaotong University, Shanghai, China  
School of Civil and Architecture Engineering, China Three Gorges University, Yichang, China*

M.M. Xin, Z.X. Zhai, Q. Zhou & Z.Y. Ye

*School of Civil and Architecture Engineering, China Three Gorges University, Yichang, China*

**ABSTRACT:** To simulate the process of expansive soil fissure cracking correctly under the action of the rainfall evaporation, we changed the moisture content of expansive soil in the laboratory. To observe and analyze fracture characteristics of the key factors, we used Matlab software to get the binary cracks image to calculate and analyze the fracture rate under different moisture content of different cycle times, such as the area of the fracture rate, width, quantity, and so on. In addition, this experiment also uses the method of pouring wax to get fracture model. Combined with two-dimensional and three-dimensional analyses, this research makes the results more reliable. The research results show that in the process of a dry-wet circulation, cracks generated quickly, and then slow over time, eventually achieving stability. In five dry-wet circulation processes, the number of fractures appear increasingly at end of each cycle. Gradually, fractures ultimately achieve stability after five dry-wet circulations.

**Keywords:** expansive soil; dry-wet circulation; fracture patterns; binarization; fracture model

## 1 INTRODUCTION

Expansive soil has the characteristics of fractures, over consolidation, and expansion; these three properties are closely related with water content of expansive soil. The soil fissures destroy the integrity of actual engineering, which is one of the most difficult problems in engineering. Previous study of expansive soil fissure was mostly on the qualitative analysis. Quantitative analysis was gradually being taken seriously in recent years. This paper takes the highway-ring around Nanjing weak expansive soil roadbed as the research object. We study cracks in the expansive soil generated under the influence of the climate and those generated in the expansive soil in the laboratory simulation process of natural rainfall dry-wet circulation. We compare the qualitative and quantitative observation statistics to determine key factors of fracture characteristics. Through the representative area of expansive soil in the laboratory on small dry-wet circulation, we observe the expansive soil fracture process and geometric feature of the network. With a larger workload and a small representative area, observation of scene fracture statistics and measurement with a certain randomness is not easy. Crack observation statistics to determine geometrical characteristics of the fracture network is one of the key factors that can greatly reduce the field work of all the

crack observation and statistics and human error, and provide convenience for the follow-up study of expansive soil.

## 2 EXPANSIVE SOIL CRACKS GENERATED TEST

### 2.1 Test tool

Expansive soil for test: the Nanjing highway-ring roadbed weak expansive soil; two same specification (30 mm × 40 mm) of the iron plate (A is used for test photos, B is used for weighing the soil quality change); the camera; the computer; watering can; platform scale.

### 2.2 Test procedure

The basic data:

Plate weight: 2250 g, soil weight 5151 g, water Weight 1199 g, total quality 7401 g, initial moisture content: 23.28%, the dry density: 1.47 g/cm<sup>3</sup>.

To determine the initial moisture content of 23%, calculated with the content of expansive soil and water, and then mixed the original expansive soil with water, so that conforms to the moisture content in soil moisture content, and iron soil compacted. After a period of time with the surface of the expansive soil both A and B generating

cracks, A plate is used to take photos with camera at definite time, B plate is used to record the soil and the iron plate quality on time. To take off the soil surface crack at an appropriate time when the crack no longer change, with watering the surface simulate nature rainfall until the fracture healing, record water supply volume before the next cracks generated. Then do five dry-wet cycles test like this. After five loops by the test results before fracture is basically stable, so this test selects five times of the dry-wet circulation.

### 2.3 Test phenomenon

As shown in Figure 1, in a dehumidifying process experiment, no any cracks are generated in expansive soil surface, except when the soil gradually becomes dry at the beginning after a period of time. As time goes by, expansive soil surface begins to produce small cracks. Then the cracks gradually become wider. Big cracks connect with each other and bestrew the surface of the earth. The whole expansive soil surface will divide into several pieces in different kinds of size and shape and tends to be stable in the end.

In the process of five dry-wet circulations as shown in Figure 2, along with the increase in number of dry-wet circulation, the fracture number on the surface of expansive soil increasing constantly, the block number is also gradually becoming more, and fissure between connected more thoroughly. However, the average width of fissure is reducing, the change of amplitude decreases with the increase of cycling time, finally reached a steady.

When simulated nature rainfall make fissure healing, expansive soil surface become moist and soft gradually. Along with the increase in quantity of water added, accompanied with the collapse of the surface soil particle and the water flow into the crack and crack healing slowly. The healing speed increases as water added quickly before they are



Figure 1. A dehumidifying process of fracture development.



Figure 2. The final fracture after five times dry-wet circulation.



Figure 3. Fissure healing process.

gradually slow down. It was not until after the expansive soil saturated water stop adding water, soil surface eventually become a bit uneven, no longer like initial moisture level.

Expansive soil dry hard before sprinkler, soil surface is relatively smooth, fissure is clearly visible, mutual penetrated. During the preliminary stage of watering the fracture did not heal, but the process of expansive soil surface get Moist and soften gradually, gave a name to this process: the first stage of crack healing when expansive soil get Moist and soften stage. A period of time after watering, the surface of the expansive soil gets more humid, part of the cracks begin to be filled by the expansive soil fine particles which are softening in water. During this period, the speed of crack healing is fastest, gave a name to this process: the second stage of crack healing, the stage of fracture healing. Water after crack healing will have little impact on the crack. A period of time after watering when Fracture surface is almost flush with the soil horizontal plane which can think fissure expansive soils water saturated, gave a name to this process: the third stage of crack healing, the fissure water saturation stage. A period of time after Complete with water, the expansive soil surface will remain some white minerals which are mainly concentrated in on both sides of the original crack. Where there are more cracks, there are more white minerals.

## 3 TEST RESULT ANALYSIS

### 3.1 The relationship between the moisture content and fractures during a cycle process

The chart that the test record of the data analysis to obtain one circulation process with the change of moisture content.

Select two representative point analysis:  $(t_0, w_0)$  and  $(t_1, w_1)$ . Among them: the initial moisture content  $w_0 = 23\%$ , the critical moisture content  $w_1 = 21\%$ ; Moment  $t_0$ : 22:40 when to start to take off the wet, moment  $t_1$ : 1:00 just produce crack. Obtained from experiments:

- $t \in \langle t_0, t_1 \rangle$ , the fitting function:  $y = 0.0028t + 0.3261$ , the moisture content between  $(w_0, w_1)$ , Water content ( $w$ ) decreases and is proportional to the time ( $t$ ).
- $t \in \langle t_1, t_2 \rangle$ , the fitting function:  $y = 0.079 \ln x + 0.079$ , the moisture content

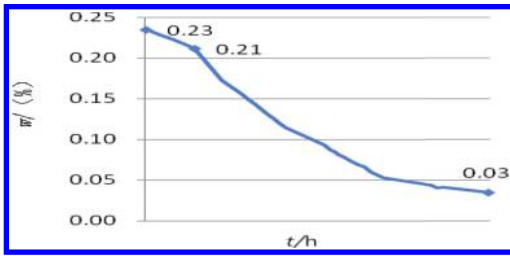


Figure 4. The change of moisture content within a cyclic process.

between  $(w_1, w_2)$ , which is a fissure development period, the speed of moisture content ( $w$ ) reduce speed up before slow down.

Under the invariable conditions of outside air velocity and temperature, the generation of crack is associated with the factors such as development of soil, soil moisture evaporation rate, the stress state, and expansive soil shrinkage characteristics [1]. The shrinkage characteristics associated with the composition of expansive soil and the soil moisture evaporation rate and the stress state are related to the moisture content of soil. When outside conditions are unchanged and expansive soil moisture content is large enough (greater than 21%), the evaporation rate of water is smooth and steady, the soil stress state is hardly changed, and there will be no cracks. When the moisture content of expansive soil is less than the crack generating critical moisture content (21%), the smaller the moisture content, the better the permeability of soil mass becomes, the faster evaporation, soil mass stress state changes, and the easier the soil fissure development. However, when the moisture content is below a certain value (3%), soil moisture content change is not obvious; there is almost no soil mass stress state change and fractures are largely discontinued.

When a crack starts generating, the whole airport surface area increases. This increases the evaporation surface greatly, thus accelerating the speed of internal moisture content reduction. In addition, in the local scope around the fissure, water evaporation rate is faster than the place without cracks, which led to increase the speed of the moisture content reduction of expansive soil in the local scope and new secondary fractures will develop around the main crack.

At the moment of taking off the wet, expansive soil began to produce crack moment, which is puberty before the crack. Water content ( $w$ ) decreases and is almost proportional to the time ( $t$ ). The expansive soil does not produce during fracture. When the moisture content decreased to critical moisture content, ( $w_1$ ) begins to

produce crack. Just produce crack to the ground to a halt is fissure development period, the speed of moisture content ( $w$ ) reduce, the length and speed of the growth rate of Crack change over time quickly before they are slow. When the moisture content down to smaller critical moisture content ( $w_2$ ) the fracture morphology become stable and Fracture largely discontinued, which is a period of fracture stability.

### 3.2 A dehumidifying process fracture characteristics

In the process of one cycle, Matlab software is used to analyze the crack image to get the area change rate and the total length of line chart as shown: (note: crack length in the soil use pixel as units).

In the process of a dry-wet circulation, with the growth of the dehumidifying time, the crack area ratio and the total length does not appear from the moment of  $t = 0$ . That is to say there is no crack generation in the early stages of the dehumidifying process. When cracks began to appear, the crack area ratio and the total length is not starting growth from 0 because the soil surface crack begins to generate at the same time in several locations. The total crack length and area ratio gradually accelerate after a period of time, increase its speed, and finally stabilize.

### 3.3 Analysis of fissure characteristics under the dry-wet circulation

Cutting Test pictures that five dry-wet cycles after each crack completely stability into the same size in the same area, then using Matlab software to get the binary fissure images (morphology theory).

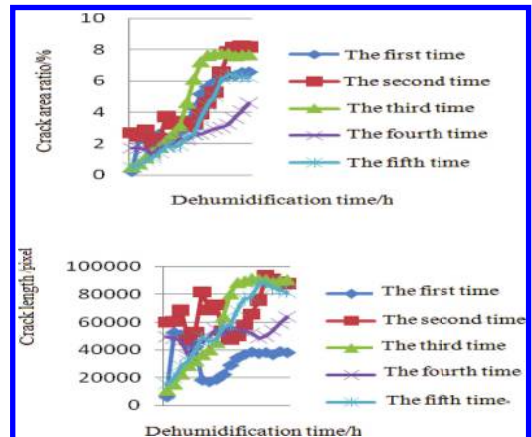


Figure 5. The relationship between crack area ratio and the total length over time.



Programming analysis to calculate the area of the crack rate and the length of the crack will get the data into a line chart, as shown in Figure 6.

After the first time adding water, internal stress of expansive soil changes obviously, degree of expansive soil shrinkage increases sharply. After the second time adding water, degree of expansive soil shrinkage increases lesser, and shrinkage degree reaches the maximum. After the third time adding water, soil structure has changed and become relatively loose, lead to reduce the shrinkage space inside of the soil. After the fourth time adding water, internal structure of the soil changes more which reduces potential energy reserves of the expansive soil and the soil become fluffier.

With the increase of dry-wet cycles, crack area ratio and the total length is increased in the beginning and then decreases, this is due to dry-wet circulations make the internal structure of soil shrinkage stress space and irreversible changes have taken place. Expansive soil to dehydrate contraction, make its internal close-grained, result in fracture. Making the soil samples that complete dehumidified to water saturation again, cracks will be healed, but the soil is not back to the original state before the test, the crack healing doesn't make the place of tensile strength of soil restoration, the original cracks in the structure stress and tensile properties of soil have been destroyed. Under the influence of dry-wet circulation over and over again, the destruction of soil structure gradually accumulated, and internal tectonic stress of soil changes greatly, making the soil loose, plastic

deformation and plastic deformation accumulated with the dry-wet circulation of soil gradually [3], the internal structure, stress and dehumidifying space of soil become more complicated. Therefore, when soil samples to take off the wet process again, the expansive soil generates new crack more easily. Due to the soil dry shrinkage deformation space is limited, and the new crack share some space which cause the crack width on average decreases. The area of the crack rate has maximum, the maximum is associated with the function of internal force and contraction space of soil.

In the process of one cycle, the width of crack has showed a trend of increase with the decrease of the moisture content. And in the process of multiple cycles, the average width of the eventually stabilized crack showed a trend of decrease with the increase of cycling times. And the more cycles, the less number of fractures which width more than 5 mm, what's more, the average width of fracture for the first time cycle is the largest. It is obvious that crack width has close relationship with the area and the length of the crack.

#### 4 FISSURE PARAFFIN WAX MODEL

So far, there are several crack observation methods such as photographic technique, sketch method, conductivity method, CT method and ultrasonic method. Photographic technique and sketch method called direct observations of fracture, the operation is simple but greatly influenced by artificial factors and can only be observed in a crack in the two-dimensional plane [2]. This experiment solid paraffin wax with sand bath, and then pouring liquid paraffin to the expansive soil after dry-wet circulations (as shown in Fig. 7).

Separating the expansive soil and paraffin wax crack model after waiting for a certain period of time that paraffin wax fully solidified, than we can

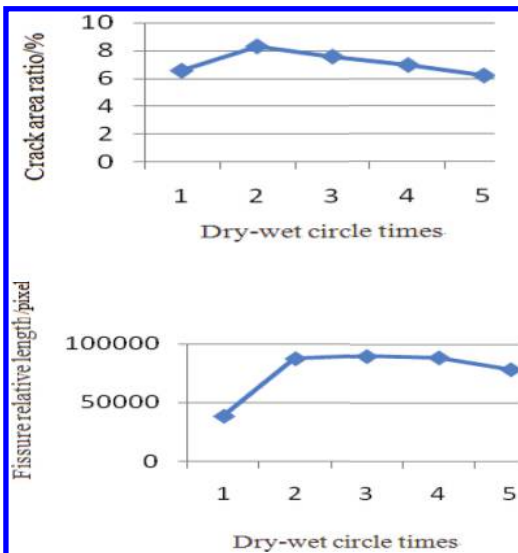


Figure 6. The eventually crack area ratio and length after five times dry-wet circulation.



Figure 7. Original fracture of expansive soil.

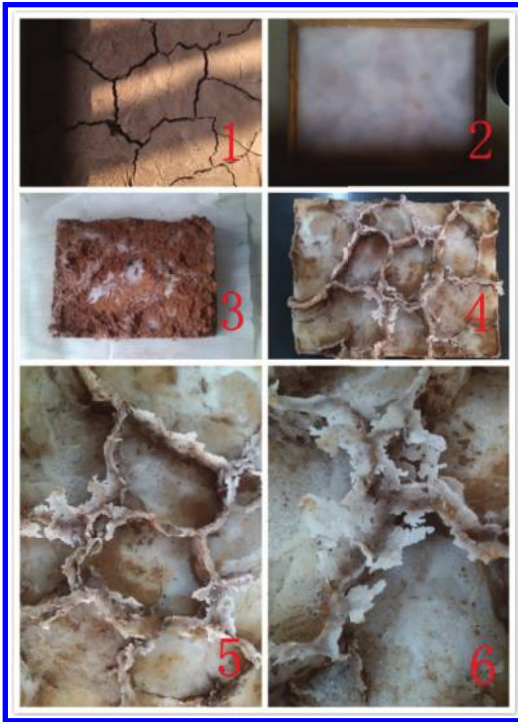


Figure 8. The process of irrigation wax test.

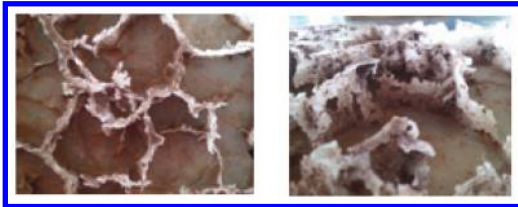


Figure 9. The details of fissure paraffin wax model.

get the three-dimensional expansive soil fracture paraffin model.

Crack model appears grid and spread around, divided the whole model into several blocks in different size. Most fractures are arrived at the bottom of the test plate except a few cracks still not. The fractures that arrived at the bottom are coarser and longer. Most of these are connected together and belong to the main crack. The fractures that have not arrived at the bottom are finer and shorter, and most of the fine fissures are not connected to the main crack on both ends of the crack, which belong to secondary fractures. Crack is not always distributed vertically; there are some that bend from top to bottom, and the fissure walls are uneven. Some fractures have bifurcation phenomenon at the bottom, formatting two or more

fine fissures. Fracture thickness has a tendency of becoming narrower from top to the bottom, looking like a “V” glyph.

Comparing four dry-wet circulation models, the crack block number of the second test article is significantly more than the first, which illustrates that the more cycles, the more fractures. The main fracture number accounts for the vast majority of the total number of fractures. (There is a greater difference between the data of model 1 and model 2; the main reason is not stirring well when making model of expansive soil). The average width of twelve randomly selected typical cracks at the bottom of the model was measured.

Small crack width is less than 1.5 mm, the average width of the main fracture usually between 1.5~5.0 mm. It is obvious that the average width of main fractures is bigger than secondary fractures (small crack). We can saw cracks in the three-dimensional space form more intuitively, and the fracture internal structural is clearer through fissure paraffin model. Crack width decreases from the soil surface to the bottom (looks like “V” glyph). Crack is not always perpendicular to the surface of soil; some cracks even grow sideways; some fractures surface appear on a curved surface and generate new fractures in the fracture surface, which illustrates the internal structure, stress state, non-uniform shrinkage properties of expansive soil. The generation of crack also has certain order which indirectly illustrates the in homogeneity of internal moisture content of soil that proved the correctness of the test results.

## 5 CONCLUSION AND PROSPECT

In the process of one dry-wet circulation, the production and development of expansive soil crack is roughly divided into three stages: crack not puberty, crack development, and crack stop development.

Fractures' influence on expansive soil depends mainly on the strength of expansive soil. Cracks damaged the integrity of the soil and changed the stress state of the soil internal structures. Dry-wet circulation even exacerbated the impacts that form a vicious circle. These bad properties of expansive soil caused much trouble in practical engineering, which is also a headache. Therefore, the importance of studying the crack of expansive soil, the necessity, and urgency is self-evident. Research in the future on expansive soil should be divided into two directions: one is to study from the angle of the micro analysis of the internal structure of expansive soil or its physical and chemical biology and the other is from the macroscopic angle to improve bad properties of expansive soil itself to meet the

needs of the project. This experiment was carried out on expansive soil using dry-wet circulation by simulation to research and analyze expansive soil fissures' "generate—development—healing" characteristics of the cycle for the further research of expansive soil foundation.

#### ACKNOWLEDGMENT

It is a project supported by "The Crack Properties of Expansive Soil during the Rainfall—Evaporation Process (A14-302-a10)" and "The influence of crack development on the slope stability during the Rainfall—Evaporation Process (D20151201)".

M.M. Xin is the corresponding author of this paper.

#### REFERENCES

- [1] Tang, Chaosheng Shi, Bin & Liu, Chun. Expansive soil shrinkage cracking characteristics research [J], TU44 *Journal of engineering geology* No. 05.2012.
- [2] Wu, Tanghua, Yuan, Junping & Zhao, Shiwen. Fracture properties of the expansive soil research review and outlook [J]. 78 *Jiangsu building*. No. 01.2012.
- [3] Zhang, Jiajun, Gong, Biwei, Hu, Bo etc. The experimental study of dry-wet circulation under the action of expansive soil crack evolution [J], TU443 *Rock and soil mechanics*. No. 09.2011.

# Finite element analysis of reinforced soil retaining wall

Q. Wang, F.F. Li, H.F. Qian, H.R. Qin & T.Q. Zhou

College of Environmental and Civil Engineering, Jiangnan University, Wuxi, China

**ABSTRACT:** The deformation and bearing capacity mechanism is important for the engineering design of reinforced soil retaining wall. Adopting embed modeling for the interaction between the reinforced bar and the soil, the elasto-plastic finite element method is proposed to analyze the behavior of reinforced soil retaining wall. The simulated results are in good accordance with the experimental test data. The plastic region in the retaining wall coincides with the Rankin assumption. The reinforced bar resistance in the retaining wall greatly improves the limit bearing capacity.

**Keywords:** bearing capacity; reinforced soil retaining wall; finite element analysis

## 1 INTRODUCTION

The application of reinforced earth retaining wall has gained great popularity in hydraulic engineering, civil engineering, and transportation construction engineering. The finite element method is a versatile tool to analyze the complex structural mechanical characteristics. The finite element analysis has been performed to examine the behavior of reinforced earth retaining wall since 1970's. Most of the research results were based on nonlinear elastic or simple elasto-plastic model. Liu Huabei [1] used an elasto-plastic model with bounding surface to investigate the geogrid reinforced soil retaining wall. Based on the wedge failure mode of the reinforced soil retaining wall, Lv Wenliang, Yanshuwang and Liu Run [2] used the Mohr-Coulomb material to model the soil and used the ideal plastic spring to model the reinforced bar. The numerical analysis proved that the method was effective and accurate to understand the behavior of the retaining wall.

In the paper, the finite element model for the reinforced soil retaining wall is developed using ABAQUS. The embed option is used to model the interaction between the reinforced bar and the soil. Nonlinear geometric analysis is used to analyze the problem. The plastic zone of the soil is investigated to model the bearing capacity mechanism. Also, the deformation behavior of the retaining wall facing is examined.

## 2 FINITE ELEMENT MODELLING USING ABAQUS

### 2.1 Finite element model

Considering the symmetry of structure, soil, and loading condition, the plain strain finite element

model of the reinforced soil retaining wall is modeled, as shown in Figure 1. The two-dimensional reduced integration solid element C2D4R is used to model the soil. The bottom boundary condition is restrained in x, y directions. The side boundary is restrained in x direction. The Mohr-Coulomb yield criterion is used to model the soil behavior. The elastic model is used to model the pile. The calculation region is taken as 20 times the pile radius in the longitudinal direction. The reinforced rib is assumed to be contact with soil. The embedded option is used to model full contact between reinforced rib and sand.

### 2.2 Boundary and loading

The side view of the reinforced rib distribution is shown in Figure 2. As it can be seen from the figure, the length of the reinforced rib varies in depth. The longer reinforced rib is used in the upper region while the shorter reinforced rib is used in the lower region.

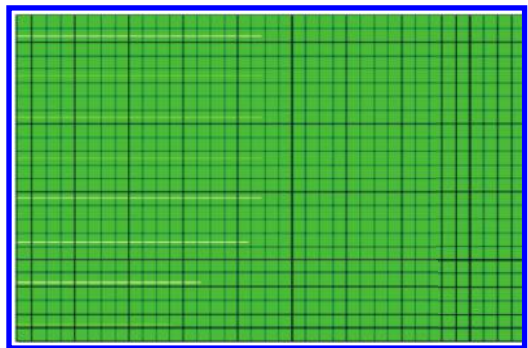


Figure 1. Finite element model.

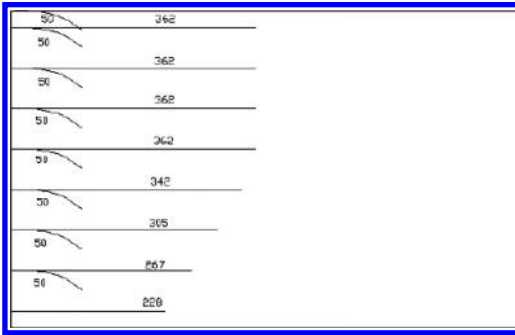


Figure 2. Side view of the reinforced rib (unit: mm).

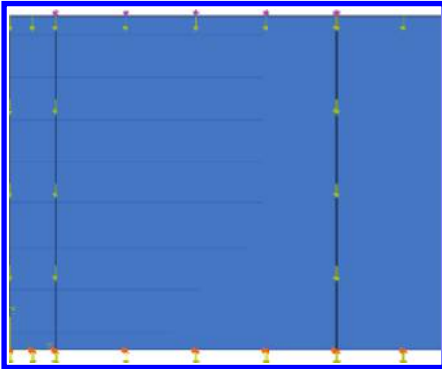


Figure 3. Boundary condition.

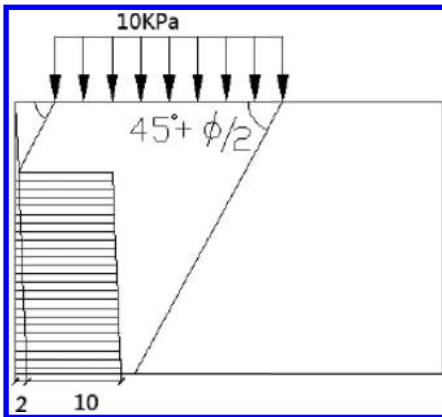


Figure 4. The applied loading.

The boundary condition for the finite element analysis is shown in Figure 3. The bottom of the retaining wall is restrained in x and y directions. The right side of the retaining wall is restrained in y direction.

In geotechnical analysis, the geostatic analysis is performed firstly to establish the initial stress condition corresponding to the establishment of the reinforced soil retaining wall construction. In the geostatic analysis, gravity loading is applied to the soil region while the initial stress is defined in equilibrium with gravity. Then the loading on the top of the retaining wall is applied in the loading step, as shown in Figure 4.

### 3 FINITE ELEMENT ANALYSIS

The Mohr-Coulomb model is used to model the sand with cohesion  $c = 0$  KPa and friction angle  $35^\circ$ .

The computed Q-s curve is shown in Figure 2. As shown in Figure 2, the computed uplift bearing capacity is about 1180 KN, which is close to the experimental value of 1100 KN.

The computed soil displacement and soil vertical stress is shown in Figure 5 and Figure 6, respectively.

The soil yield zone and the plastic distribution is shown in Figure 7 and Figure 8, respectively.

As shown in Figure 7 and Figure 8, the plastic region limit is like the log-spiral curve starting from the top of the retaining wall to the bottom of the reinforced rib. When the plastic limit forms, the global failure will occur.

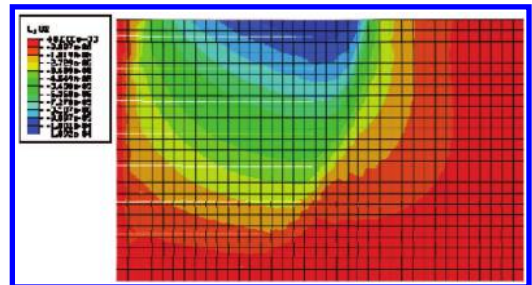


Figure 5. Vertical displacement distribution.

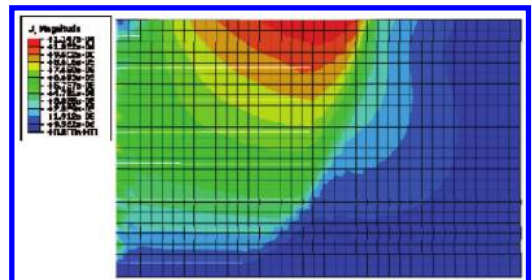


Figure 6. Total displacement distribution.

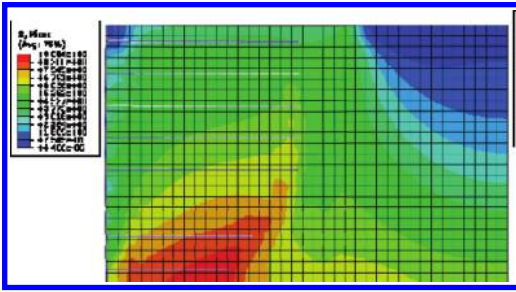


Figure 7. Mises stress distribution.

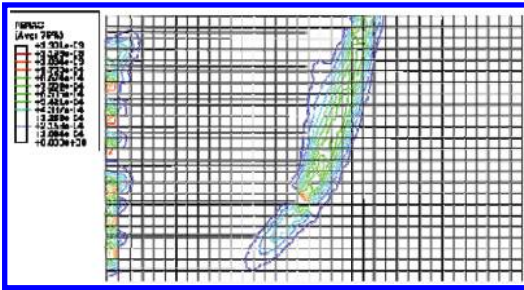


Figure 8. Plasticity distribution.

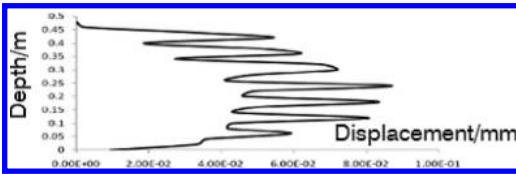


Figure 9. Distribution of face displacement along retaining wall depth.

The computed face horizontal displacement distribution along retaining wall depth is shown in Figure 9. It can be seen from Figure 9 that the plastic region in the retaining wall coincides with the Rankin assumption. The reinforced bar resistance in the retaining wall greatly improves the limit bearing capacity.

#### 4 CONCLUSIONS

The numerical analysis is performed to investigate the deformation behavior of reinforced soil retaining wall. The plastic region limit is like the log-spiral curve starting from the top of the retaining wall to the bottom reinforced rib. The plastic region in the retaining wall coincides with the Rankin assumption. The reinforced bar resistance in the retaining wall greatly improves the limit bearing capacity.

#### ACKNOWLEDGMENT

Funding support to the research by National University Students Innovation Training Plan (No. 201410295052) of Jiangnan University and Jiangnan University Students Innovation Training Plan (No. 2014267) is greatly acknowledged.

#### REFERENCES

- [1] H.B. Liu, H.I. Ling. 2004. Elasto-plastic finite element study for parameters of geogrid-reinforced soil retaining wall. *Chinese Journal of Geotechnical Engineering* 26(5):668–673.
- [2] Lv Wenliang, Yan Shuwang et al. 2008. Application of Finite Element Method in Reinforced Soil Retaining Wall. *Journal of Tianjin University* 35(5):596–600.

# The research progress of water-salt mechanism and migration model

Guang-li Zhu, Long Zhu & Chao Yu

*Transportation Design Co. Ltd., Wuhai Shi-da Inner Mongolia, P.R. China*

**ABSTRACT:** Soil salinization is one hot issue of numerous interdisciplinary research which involved soil science, environmental science, and geotechnical engineering. Scientific understanding of water-salt migration model and mechanism in soil has great significance for solving soil salinity in agricultural engineering and preventing subgrade salinization in subgrade engineering. Widely accepted at home and abroad; agricultural engineering water migration model (capillarity force hypothesis, film water migration hypothesis, crystallization force hypothesis and adsorption-film capillarity); migration mode of ion in saline soil (seepage flow migration, diffusive migration and seepage-diffusive migration); and water-heat, water-salt, water-heat-salt migration model, and mechanism in soil are introduced. And also the research progress in the area of road engineering is introduced. Principle, similarities and differences, advantages and disadvantages, and applicability and application status of correlation model are analyzed and evaluated.

**Keywords:** soil; salinization; migration mechanism; model

## 1 INTRODUCTION

Yield in arid and semiarid area are affected by soil salinization, especially with the increase of the population in the world, there is an unprecedented pressure for maintaining grain yield. For our country (China), farmland salinization makes great population and less arable land contradiction fierce. In addition, in arid and semiarid area, secondary salinization of subgrade soil leads to pavement disease and reduces performance of pavement. Therefore, research on water-salt migration model and salt accumulation mechanism in soil and subgrade have great significance for solving soil salinity in agricultural engineering and preventing subgrade salinization in subgrade engineering.

## 2 WATER-SALT MIGRATION MODEL

Water-salt migration is a complicated process. From classic literature data motive power hypothesis, which is suitable for water migration in saline soil include following types: (1) capillarity force hypothesis: water transfers to the cold end along the fractures and void in soil with the capillarity force. This theory is suitable for the soil with larger water content. (2) Film water migration hypothesis: Coupling effect of temperature field and water field as cooling progress is the reason for water

migration and redistribution that is water migration with the effect of temperature gradient. Water migration changes the original water distribution in soil and produces uneven distribution of spatial position of soil framework-water-crystal. Physical and mechanical properties of soil are changed. The theory is suitable for fine saline soil. (3) Crystallization force hypothesis: In the cooling progress of soil, solubility of the cold end is lower and more crystal precipitated. Due to the precipitation absorbs 10 crystal water moleculars, water content of the end with more precipitation decreases which causes hydraulic gradient and water transfers from the end with higher water content to the lower. (4) Adsorption-film capillarity: water molecules and salt molecules transfer from point more active and with thicker hydration film to the point more stable and with thinner hydration film. Under natural conditions, the migration of water depends on comprehensive effect of mechanics, physics, and physical chemistry. Each hypothesis mentioned above can represent water migration motive power only at certain conditions.

The migration of ions in saline soil at present research is considered as mainly three types: (1) Seepage flow migration: salt transfers as water in seepage flow. (2) Diffusive migration: salt transfers with the effect of gravity and temperature gradient. (3) Seepage-diffusive migration: At cooling process, salt transfers with the mixing effect of seepage flow and diffusive.

### 3 THE MECHANISM OF SOIL WATER AND SALT MOVEMENT IN AGRICULTURE ENGINEERING

#### 3.1 *The mechanism of soil water and salt movement*

The theory of Soil Water and Salt Movement originated from Darcy's law, and the equation of the advent of solid heat conduction provides the basis for soil solute transport. Since Buckingham (1907) introduced the concept of energy into soil water, Richards (1931)<sup>[1]</sup> described the operation of the unsaturated soil water by using partial differential equation, established the basic equation for water flow in porous media, then the quantitative research of the soil moisture began. Because of the salt movement and the soil moisture migration occurred at the same time, as a result, the soil solute migration equation is developed by soil moisture equation. The common of these equations is that they all analyze the soil water and salt movement with dynamics views, material, and energy balance principle.

The initial research took isothermal conditions as assumptions, and mostly only considered gravity potential and matric potential in water, salt convection and dispersion interaction, and rarely involved other interactions between water and salt, such as the effects of salt concentration gradient on moisture migration, in fact, the salt concentration has an important role on soil water movement. In unsaturated soil, especially the heavy clay, the osmotic potential of the soil is an important driver of soil water movement. Many experiments and simulation results show that the water-holding capacity of the soil is greatly influenced by soil temperature; the water temperature effect of the surface tension is one of the main reasons for this impact. In the mathematical simulation of soil water movement, if the temperature effects of the soil hydraulic properties are ignored, it will produce large prediction error. Therefore, since the 1950s, the soil water movement equation in non-isothermal conditions to be taken seriously and developed, in which it mainly started from the temperature effect of soil hydraulic properties.

In the Middle and Late 1970s, the mechanism studies of water and salt movement began to pay attention to the actual situation in the complex field, for example, for the way of soil water and salt movement with good structure, it not only considered the convection and diffusion, also considered the movable and immobile water, macropore flow, preferential flow and pipe flow, etc. and set up a two-area model of the soil water and salt migration. In two-region model, Van Genuchten considered the solute in the pore between movable

water and immobile water can transport between two region, and considered the effect of moving and immobile water and influenced each other, which is more practical. It can be used to describe the migration of salts in the soil column, and the solute migration under the adsorption condition.

Melsen (1985) introduced the theory of soil spatial variability, put forward theories and method about how to determine the average of soil parameters, the variance and correlation scale. Afterwards, many scholars had set up random logarithmic convection model which includes random convection diffusion model, obtained the probability distribution function of solute transport speed, and the average concentration distribution. This model is suitable for the research of unsaturated soil solute migration in the wild field, which has better results, but it lacks of the measured data validation, still needs further improvement.

The domestic and foreign researchers have done a lot of work about Movement Law of Water and Salt under the condition of evaporation. Recent research demonstrates that plastic film mulching has the role of increasing temperature, keep moisture, water saving, and salt restraint. Through the study of farmland soil water and salt migration under the condition of mulching, aimed at to provide theoretical basis and technical guidance for observing in the field, developing and improving in saline-alkali land and film hole irrigation technology.

#### 3.2 *Soil moisture, heat and salt coupling transport model*

Soil moisture, heat and salt coupling transport models built up on the basis of moisture isothermal model. LA Richards (1931) applied continuity theorem to Darcy flow equation and used a continuous flow equation instead of the instantaneous flow equation to study unsaturated flow in soil, which is known as the basic equation of soil water movement—*isotherm equation*. Klute (1952) changed L.A. Richards' isothermal equation into non-isothermal diffusion flow equation and then a lot of researchers used the equation to determine the diffusion rate of the liquid under the action of the temperature difference. Two types of coupling numerical model, the model based on mass-energy balance and linear equations on the basis of irreversible thermodynamics, are developed.

Philip & De Vries<sup>[2]</sup> (1957), De Vries (1958) proposed the migration of water vapor thermal coupling theory on the basis of the establishment of the mass and energy balance and built soil liquid and gas two-phase flow of water sports model under the influence of precipitation and elevation gradient. Their hydrothermal coupled equation is



a function in which water content and temperature is unknown. Due to the change in temperature can cause a phase change of soil water, such as under freeze-thaw conditions, the liquid and solid state water make mutual conversion and in the evaporation, liquid water change into gaseous water, etc. It is more realistic to use soil water potential and temperature as an unknown function of the equation to indicate the soil moisture and heat conservation process. Milly<sup>[3]</sup> etc. (1982, 1984) improved the mode of Philip (1957). Milly<sup>[4]</sup> used the matric potential gradient instead of moisture gradient to make the modified model applicable to heterogeneity soil. They thought that model can well in line with the actual situation in the complex soil environment and parameters of equations can be obtained from theoretical or empirical equations. Based on Philip (1957) model, Nassar<sup>[5]</sup> etc. (1989, 1992) used moisture, heat and salt transport equations (that is Darcy, Fourier, Fick's law) and continuity equation to establish moisture, heat and solute three coupling shift model and studied moisture, heat and solute simultaneous transport in closed soil column affected by the temperature gradient.

Thermodynamic model was first proposed in 1985. It created expressions and equations about corresponding free energy and dissipated energy of multi-phase medium on the basis of mass conservation, energy conservation and entropy inequality about three-phase medium including soil, ice, water in frozen soil micro unit. Suction of void was caused by a soil frost heave, moisture and heat transfer and water freeze in the thermodynamic model and it is not required to determine the relationship between the water content and negative temperature. Clausius-Clapeyron equation was introduced to seek soil water potential in the process of model derivation. Generally, this type of model is only applicable to a limited freezing temperatures range in the soil. For the low negative temperature, the applicability of this model has not yet been verified.

Flerchinger & Saxton (1989) set up SHAV model to simulate the transmission among water content, heat and the flux of the solute during the process of soil freezing and thawing. Flerchinger & Hanson (1989) used SHAW model to simulate frozen depth of soil, snow layer, and soil temperature in the ranch under three different climatic conditions in America. Nassar & Horton etc. (2000) used SHAW model to study the transmission among water, heat, and the solute in saline and non-saline soil of closed soil columns and analyze the temperature distribution of two soils. Besides, both observed value and predicted value of the water distribution of the non-solute soil showed that water aggregate to 40 cm in soil and frozen

depth in this type of soil is about 45–65 cm. There is no obvious migration of solute in saline soil and slight water decrease at 20 cm. Compared with non-saline soil, solute concentration decreased the freezing temperature.

#### 4 PROSPECT

In summary, there are more research on the unilateral combination of water and salt or water and heat in the study of soil water, heat, salt migration, especially, more achievements in the agricultural engineering, while the research on relationships and interactions between soil moisture, heat, and salt migration are a little. For the salinization of subgrade soil in road engineering, it is some different from agricultural engineering because of the effect of road coverage. Therefore, on the basis of referring to migration law on natural soil water, heat, and salt. We urgently need to research the law of water and salt movement deeply and systematically under the conditions of the road surface coverage to reveal salt accumulation mechanism in highway engineering.

#### REFERENCES

- [1] Richards, L.A. Capillary conduction of liquids in porous mediums [J]. *Physic*, 1931, 1, 318–333.
- [2] Philip J.R., Vries D.A. Moisture movement in porous materials under temperature gradients [J]. *Trans. Am. Geophy. Union*, 1957, 38:222–231.
- [3] Milly C.P.D. Moisture and heat transport in hysteretic, inhomogeneous porous media: A matric head-based formulation and a numerical model [J]. *Water Resources Res.*, 1982, 18(3):489–498.
- [4] Milly C.P.D. A simulation analysis of thermal effects on evaporation from soil [J]. *Water Resources Res.*, 1984, 20(8):1087–1098.
- [5] Nassar I.N., Robert Horton. Water Transport in unsaturated noniso-thermal salty soil: I. Experimental results [J]. *SoilSci. Soc. Am. J.*, 1989, 53, 1323–1329.
- [6] Chen Xiaobo, QiuGuoqing, Wang Yaqing, et al. Physical, chemical and mechanical properties with the effect of temperature change on solonchak soil [J]. *Science in China, Ser. A*, 1988, (2):245–254.
- [7] Chen Xiaobo, QiuGuoqing, Wang Yaqing, et al. Salt redistribution and heave of saline soil during cooling [J]. *Journal of Glaciology and Geocryology*, 1989, 11(3):232–238.
- [8] XuXuezu, Wang Jiacheng, Zhang Lixin. *physics of frozen soil* [M]. Beijing: Science Press. 2001.
- [9] Shi Jianxun, Liu Xinrong, Yang Baocun. A study on influence of water table and salinity movement on frost heaving metamorphosis of roadbed [J]. *Journal of Shandong university*, 2009, 39 (S2):22–25.
- [10] Cao Fugui. Laboratory and field research on coupled hydro thermo saline mechanical behavior of subgrade in vitriol saline soil areas and field numerical simulation [D]. Master's thesis of Changan university, 2009.

- [11] NiuXirong. The study and numerical simulation on moisture-heat-salt stress coupled mechanism in the sulphate saline soil subgrade [D]. Master's thesis of Changan university, 2006.
- [12] Yang Han. Research on indoor and field Slots test and numerical simulation of coupling effect of water, heat, salt and force [D]. Master's thesis of Changan university, 2007.
- [13] Chang Liang. Laboratory study on subgrade and pavement salt expansion characteristic of sulfuric saline soil area by using large- scale experimental tank [D]. Master's thesis of Changan university, 2010.
- [14] Weng Tong. Research of capillary water and compaction characteristics of saline soil [D]. Master's thesis of Changan university, 2006.
- [15] Wu Ai'hong, GuKangqiang, Li Wan. Research of capillary water migration of airport saline soil [J]. Subgrade Engineering, 2008, (6):137-138.

# Application of strain softening model to numerical analysis of deep tunnel

X.H. Diao, S.X. Yang & K. Wang

*School of Civil Engineering and Architecture, East China Jiaotong University, Nanchang, Jiangxi, China*

**ABSTRACT:** According to the incremental theory, the expression of plastic parameter of strain-softening model was deduced in this paper. Based on the In line fish language of FLAC3D, the program which is used to compute the safety factor of surrounding rock was compiled. At the same time, two experiments about uniaxial numerical were designed to compare and analyze Mohr-Coulomb elastic-plastic model and strain softening model, finding the differences of the stress-strain law of the rock under different constitutive conditions. Numerical simulation of a deep buried roadway in an iron mine is carried out as the engineering background. The law of displacement, plastic area distribution of surrounding rock under different constitutive were analyzed, and the surrounding rock stability under different constitutive model were evaluated.

**Keywords:** deep tunnel; surrounding rock softening; numerical analysis; safety factor

## 1 INTRODUCTION

With the rapid development of underground engineering in our country, more and more underground engineering safety problems occur and need to be solved. The problem of deep engineering rock mechanics is one of research directions to be studied, intensively. During the process of excavating the tunnel, due to the deep engineering is in high stress conditions the stress in rock will be distributed again. And it will cause concentration phenomenon by the surrounding roadway, as well as surrounding rock deformation. However, the deformation is often non-linear, and it when reaches a certain degree, it will cause the failure of surrounding rock.

Research shows that during the excavation of deep buried rock, due to the continuous expansion of micro crack in the rock, strength parameters in the nonlinear phase will obviously decrease, which is called rock softening phenomenon [1–4]. When the rock stress reached peak strength, as the deformation continues to increase, the material degradation phenomenon becomes more obvious. Many scholars work at numerical simulation and strain softening theory in order to establish the constitutive relationship, which can reflect the rock nonlinear mechanical response [5–8]. The rock strain softening problem has been paid much attention for the engineering field. However, in Mohr-Coulomb elastic-plastic model, when the parameters of the material are presented as constant value, they often can not reflect the softening effect of deep buried

rock, which is caused by the change of the parameters of surrounding rock [9–11].

To solve this problem, this paper carried out a comparative study by using the strain softening model and Mohr-Coulomb elastic-plastic model which are carried by FLAC3D, analyzed the surrounding rock in two different constitutions under the mechanical response and displacement of different state, and evaluated the stability of surrounding rock under different constitutive relations. The findings of the study have some significant guiding for engineering practice.

## 2 STUDY ON STRAIN SOFTENING MODEL

In FLAC3D, the stage of elastic strain of softening model and Mohr-Coulomb elastic-plastic model are exactly identical [12]. The difference between the two models is that after the plastic yield, in the strain softening model with the increasing of plastic strain, material cohesion, internal friction angle, dilatancy angle, tensile strength will decay. In the process of application, the user can customize these material parameters as a function of plastic strain, the tri-linear softening law is used more common (Fig. 1). Strain softening model in each time step increases the hardening parameter to calculate the total plastic shear strain and tensile strain, thus making consistent the material properties and the material function which the users define. The strain softening model of yield

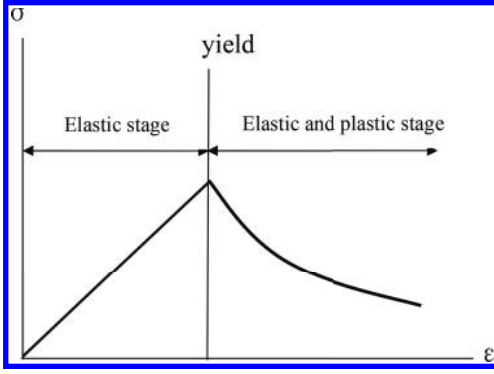


Figure 1. Stress-strain relation of strain-soft model.

function, flow rule, stress correction are compatible with Mohr-Coulomb model.

From Figure 1, before reaching the yield point, only the elastic strain exists, there is:

$$\varepsilon = \varepsilon^e \quad (1)$$

After reaching the yield point, the strain is equivalent to the sum of elastic strain and plastic strain, where:

$$\varepsilon = \varepsilon^e + \varepsilon^p \quad (2)$$

The plastic strain is divided into plastic shear strain and the plastic tensile strain, where:

$$\varepsilon^p = \varepsilon^{ps} + \varepsilon^{pt} \quad (3)$$

Then formula (2) can be transformed to:

$$\varepsilon = \varepsilon^e + \varepsilon^{ps} + \varepsilon^{pt} \quad (4)$$

### 2.1 Elastic law

The expression of Hooke's law and the main form of stress strain form are expressed as following.

$$\begin{cases} \Delta\sigma_1 = \alpha_1\Delta\varepsilon_1^e + \alpha_2(\Delta\varepsilon_2^e + \Delta\varepsilon_3^e) \\ \Delta\sigma_2 = \alpha_1\Delta\varepsilon_2^e + \alpha_2(\Delta\varepsilon_1^e + \Delta\varepsilon_3^e) \\ \Delta\sigma_3 = \alpha_1\Delta\varepsilon_3^e + \alpha_2(\Delta\varepsilon_1^e + \Delta\varepsilon_2^e) \end{cases} \quad (5)$$

### 2.2 The yield function and potential function

In FLAC3D, the function of shear strain softening model, there is,

$$F^s = \sigma_1 - \sigma_3 N_\varphi + 2c\sqrt{N_\varphi} \quad (6)$$

In the formula  $N_\varphi = \frac{1+\sin\varphi}{1-\sin\varphi}$ , where  $c$  = cohesion force,  $\varphi$  = angle of internal friction,  $\sigma_1$  = the first principal stress,  $\sigma_3$  = the third principal stress.

The tensile yield function as following description.

$$F^t = \sigma_t - \sigma_3 \quad (7)$$

Shear plastic potential function is based on the non-associated flow rule, while the tensile plastic potential function is based on the associated flow rule.

The shear plastic potential function, there is,

$$g^s = \sigma_1 - \sigma_3 N_\varphi \quad (8)$$

The tensile plastic potential function, where:

$$g^t = -\sigma_3 \quad (9)$$

### 2.3 Plastic correction

When the shear failure, there exists orthogonal flow rule:

$$\Delta\varepsilon_i^p = \lambda^s \frac{\partial g^s}{\partial \sigma_i} \quad (10)$$

The tensile failure flow rule:

$$\Delta\varepsilon_i^p = \lambda^t \frac{\partial g^t}{\partial \sigma_i} \quad (11)$$

$\lambda^s, \lambda^t$  are plastic parameters.

To expand formula (10) and (11), there exists:

$$\begin{cases} \Delta e_1^{ps} = \lambda^s \\ \Delta e_2^{ps} = 0 \\ \Delta e_3^{ps} = -\lambda^s N_\varphi \end{cases} \quad (12)$$

$$\begin{cases} \Delta e_1^{pt} = 0 \\ \Delta e_2^{pt} = 0 \\ \Delta e_3^{pt} = -\lambda^t \end{cases} \quad (13)$$

Putting the formula (12) into the incremental elastic law (5) can be obtained as below.

Shear failure stress correction are:

$$\begin{cases} \sigma_1^N = \sigma_1^I - \lambda^s(\alpha_1 - \alpha_2 N_\varphi) \\ \sigma_2^N = \sigma_2^I - \alpha_2 \lambda^s(1 - N_\varphi) \\ \sigma_3^N = \sigma_3^I - \lambda^s(\alpha_2 - \alpha_1 N_\varphi) \end{cases} \quad (14)$$

Among  $N_\psi = \frac{1+\sin\psi}{1-\sin\psi}$ ,  $\psi$  = dilatancy angle. The superscript N, I are represented the unit of new and old state of stress.

Combining formula (14) with (6) by method of substitution:

$$[\sigma_1^I - \lambda^s(\alpha_1 - \alpha_2 N_\psi)] - [\sigma_3^I - \lambda^s(\alpha_2 - \alpha_1 N_\psi)] N_\phi + 2c\sqrt{N_\phi} = 0 \quad (15)$$

Then the solution is:

$$\lambda^s = \frac{f^{sI}}{(\alpha_1 - \alpha_2 N_\psi) - (\alpha_2 - \alpha_1 N_\psi) N_\phi} \quad (16)$$

Similarly, putting the type (13) into the incremental elastic law (5) leads to tensile failure stress correction:

$$\begin{cases} \sigma_1^N = \sigma_1^I + \lambda^I \alpha_2 \\ \sigma_2^N = \sigma_2^I + \lambda^I \alpha_2 \\ \sigma_3^N = \sigma_3^I + \lambda^I \alpha_1 \end{cases} \quad (17)$$

Substitute equation (17) into equation, there is

$$\sigma^I - \sigma_3^I - \lambda^I \alpha_1 = 0 \quad (18)$$

The solution is:

$$\lambda^I = \frac{f^{tI}}{\alpha_1} \quad (19)$$

### 3 ENGINEERING APPLICATION

#### 3.1 Project overview

Xiaoguangzhuang Iron Mine is one of the three iron mine beds which spread in half round in the plunging end of mine arc anticline in Laiwu Graben Basin, belonging to high temperature hydrothermal contact Metasomatic skarn Magnetite deposit generated by the invasion of Diorite magma into Ordovician limestone. The strike of the orebody is NE17°, and the dip of the orebody is NW73°. The buried depth of orebody ranges from 420 to 100 m, the length along the strike is 2150 m, and the thickness of the orebody is 25 to 50 m, up to 80 meters in some parts. The average grade stands at 46.42%. The ore is moderately stable, with the roof of orebody made of tertiary-conglomerates and clayey sandstone and the floor mainly made of altered diorite which is extremely unstable. There are relatively more interlayers which are mainly made

of diorite-porphyrite and serpentinized marble, while conglomerate, clayey sandstone and hornstone constitute the easy-collapse wall rocks near the orebody which have poor stability, loose structure and well-developed cleavage fracture.

#### 3.2 The related parameters and the calculation model

A deep buried scraper tunnel was selected for the numerical analysis. The net cross section of the main roadway is 2.0 m wide, 2.5 meters high and the top is a circular arc shape, arc radius is 1.8 m. The size of the roadway both vertical and horizontal are about 10 m, the longitudinal is 2 m and the buried depth is 1000 meters. The roadway cross-section is shown in Figure 2. Mohr-Coulomb elastic-plastic model and strain softening model are adopted, respectively, in the following paper to analyze and evaluate the displacement, plastic zone distribution and safety factor of surrounding rock.

##### 1. The parameters of the rock

The analysis adopts a kind of rock material. The numerical model of the surrounding rock parameters is shown in Table 1.

##### 2. Calculation model

The calculation model and mesh size as shown in Figure 2 and Figure 3.

Calculating model of node is divided into 5327, and 4344 units.

##### 3. Geostress stress conditions

The model is applied gravity stress in vertical direction, while the horizontal stress field is applied with lateral pressure coefficient. According to the results of geostress measurement, the horizontal stress is greater than the vertical stress, horizontal and vertical stress ratio is about 2.

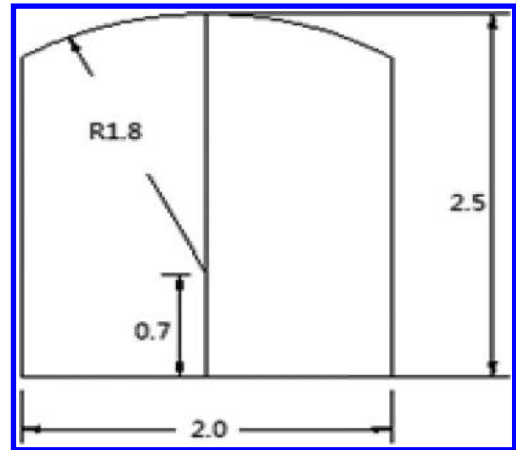


Figure 2. Cross section of tunnel (unit:m).

Table 1. Mechanical parameter of surrounding rock numerical model.

Modulus of elasticity/ GPa	Poisson's ratio	Cohesion/ MPa	Internal friction angle/(°)	Density/ (Kg/m <sup>3</sup> )	Tensile strength/ MPa
1.2	0.22	2.0	42	2500	0.5

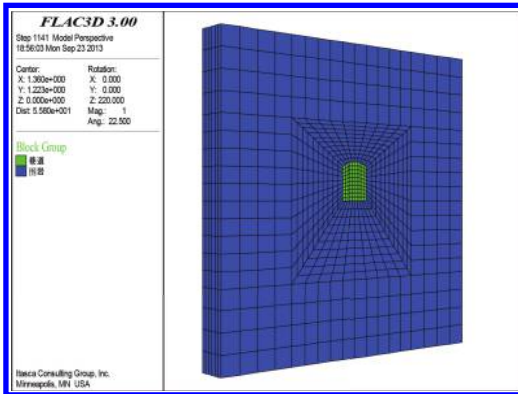


Figure 3. Computation model of tunnel.

### 3.3 Analysis of displacement of surrounding rock

Horizontal displacement to the right is positive, negative to the left. Vertical displacement to the upward is positive, downward is negative. Vertical displacement of surrounding rock calculation results, as shown in Figures 4(a) and (b).

From analysis of Figure 4, in strain softening model the calculation of the maximum vertical displacement is 45 mm, while in Mohr-Coulomb elastic-plastic model the maximum vertical displacement of calculation is about 5 mm. The calculation results of vertical displacement in strain softening model is obviously greater than Mohr-Coulomb elastic-plastic.

The calculation results of horizontal displacement of surrounding rock are shown in Figures 5 (a), (b).

From the analysis of Figure 5, in strain softening model the calculation of maximum horizontal displacement is about 20 mm, while the maximum value of horizontal displacement calculated by Mohr-Coulomb elastic-plastic model is about 10 mm. Two models of roadway under the horizontal deformation are basically symmetrical, the results of horizontal displacement in strain softening model was significantly larger than the Mohr-Coulomb elastic-plastic model.

Analyzing Figures 4 and 5 comprehensive, the overall trend of the calculated displacement of surrounding rock of two models is identity, but the calculated results of displacement in strain

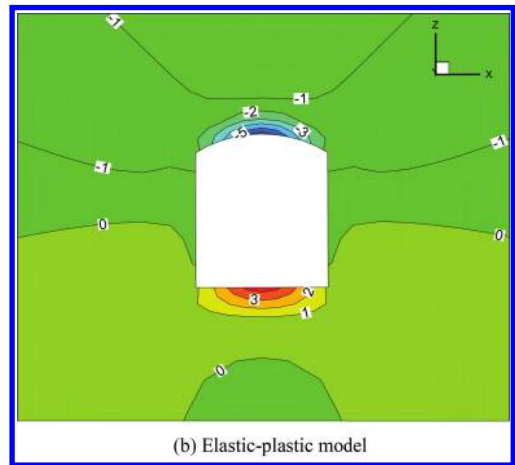
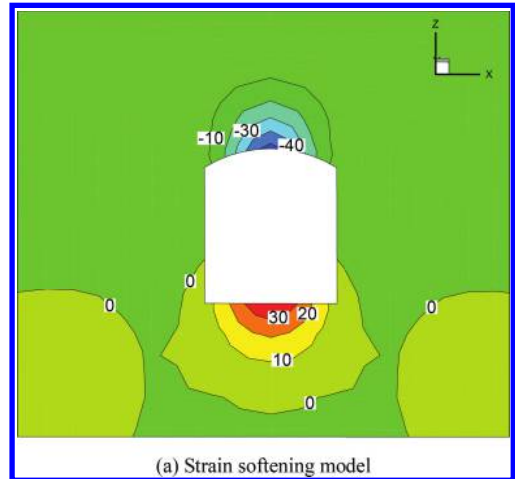


Figure 4. Horizontal displacement of surrounding rock (unit:mm).

softening model is obviously greater than the Mohr-Coulomb elastic-plastic model. In the strain softening model, the deformation of rock softening was reflected obviously.

### 3.4 Analysis of surrounding rock plastic zone

The distribution of plastic zone of surrounding rock is shown in Figure 6 (a), (b).

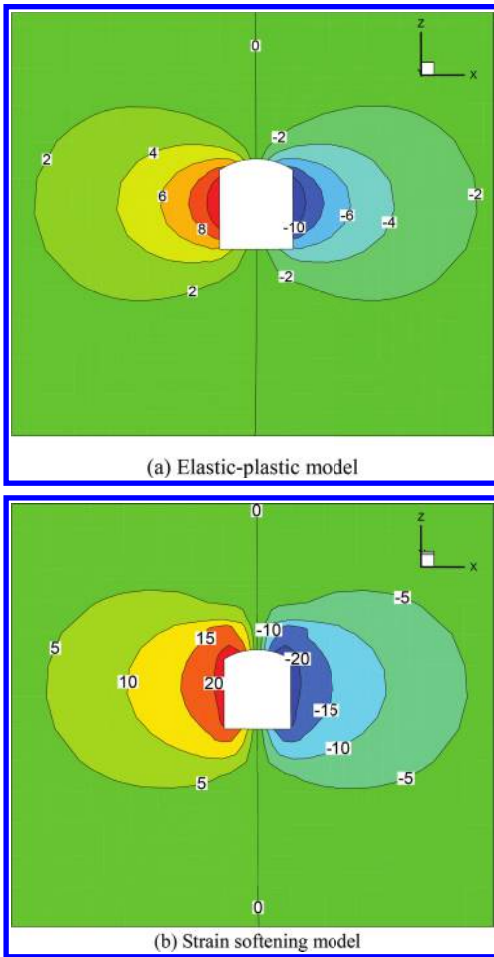


Figure 5. Vertical displacement of surrounding rock mass sample (unit: mm).

From Figures 6 (a), (b) can be seen, in the calculation of elastic-plastic model the plastic zone is mainly distributed in the vault and spandrel, the thickness of plastic zone is 0.5 ~ 1 m. While in strain softening model the plastic zone is mainly distributed in the vault, spandrel and the bottom of arch, the plastic zone extended to the entire area of the side wall on both sides. The distribution range of plastic zone is wider than the elastic-plastic model, and the distribution depth is deeper than the elastic-plastic model. The thickness of plastic zone is about 1.5 ~ 2.5 m.

### 3.5 Stability analysis of surrounding rock

According to the calculation results of stress, Mohr-Coulomb yield criterion is applied to calculate the safety factor of surrounding rock [13–14].

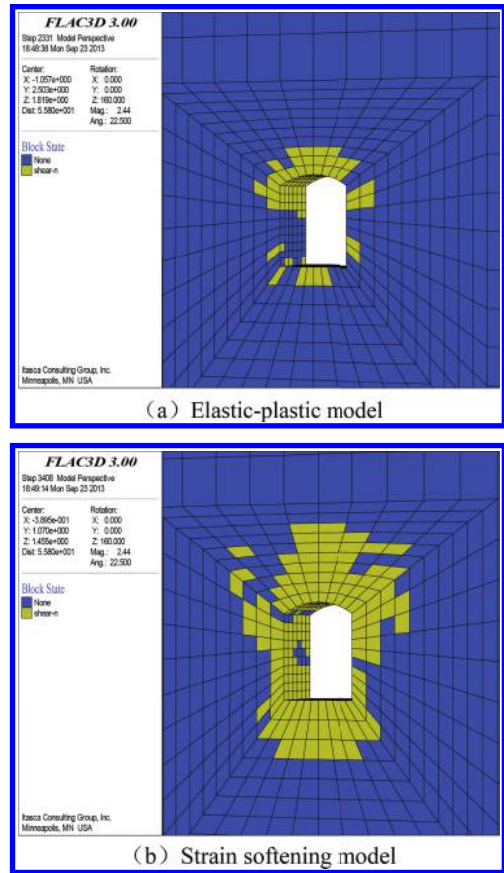


Figure 6. Plastic zone distribution of surrounding rock.

Based on the In line fish language of FLAC3D, the point safety factor of calculating program is compiled. The calculated safety factor of different constitutive models, as shown in Figure 7 (a) and (b).

Two conclusions can be drew From Figures 7 (a) and (b):

1. The point safety factor is calculated by strain softening model is smaller than that of elastic-plastic model.
2. The unstable region of the surrounding rock, which is calculated by Strain softening model is larger than Mohr-Coulomb elastic-plastic model. For deep engineering, comparing and analyzing strain softening model and ideal elastic-plastic constitutive model, the results show that, when ignoring the strength softening characteristic it will partial to unsafe for engineering. When the strain softening model is adopted the stress and deformation of surrounding rock can be reflected more reasonable.

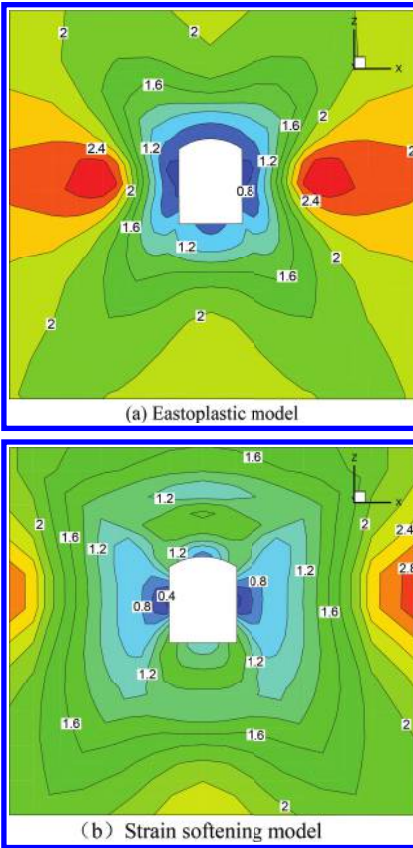


Figure 7. Safety factor of surrounding rock.

#### 4 CONCLUSIONS

1. In the process of deep buried tunnel excavation, the strength parameters of surrounding rock will be decreased continuously, which is caused by stress concentration and redistribution in rock micro crack expansion. In the numerical calculation process of deep buried tunnel, if the classic Mohr-Coulomb model was adopted, the mechanical characteristics of surrounding rock will not be able to response the change.
2. The results of the total deformation of surrounding rock that calculated by using the strain softening model is larger than adopting the elastic-plastic model, and have the greater scope of excavation disturbance. The central tendency of plastic zone of surrounding rock which is calculated by strain softening model and Mohr-Coulomb model are basically same, but its distribution range and thickness would be wider and deeper.
3. When the elastic-plastic model is adopted to calculate the excavation of deep buried tunnel stability

problem, the results are conservative. However, it cannot reflect the true state of rock mechanics and displacement. The strain softening model is recommended to the simulation analysis of deep engineering, in order to evaluate the deformation and support strength of rock mass accurately.

#### REFERENCES

- [1] Zhou Xiaoping, Qian Qihui Yang Haiqing. 2008. Strength criteria of deep rock mass [J]. *Journal of Rock mechanics and engineering* 27(1):117–123.
- [2] Wang S., Zheng H., Li C., Ge X. 2011. A finite element implementation of strain-softening rock mass [J]. *Journal Rock Mechanics and Mining Sciences* 48(1):67–76.
- [3] Zhou Jiawen, Xu Weiya, Li Mingwei et al. 2009. Application of rock strain softening model to numerical analysis of deep tunnel [J]. *Journal of Rock Mechanics and Engineering* 28(6):1116–1127.
- [4] Zhao Qilin, Niu Haiqing, Zhuo Jiatao. 2001. Basic problems of strain-softening material [J]. *Hydro-science and engineering* (3):73–77.
- [5] Lee Y.K. Pietruszczak S. 2008. A new numerical procedure for elastic-plastic analysis of a circular opening excavated in a strain-softening rock mass [J]. *Tunneling Underground Space Technology* 23:588–599.
- [6] He Manchao, Xie Heping, Peng Suping, et al. 2005. Study on rock mechanics in deep mining engineering [J]. *Journal of Rock mechanics and engineering* 24(16):2803–2813.
- [7] Alonso E., Alejano L.R., Varas F., et al. 2003. Ground response curves for rock masses exhibiting strain-softening behavior [J]. *International Journal for Numerical and Analytical Methods in Geomechanics* 27:1153–85.
- [8] Zhang Qiang, Wang Shuilin, Ge Xiurun. 2010. Elasto-Plastic Analysis of Circular Openings in Strain-Softening Rock Masses [J]. *Journal of Rock mechanics and engineering* 29(5):1031–1035.
- [9] Pan yue, Wang Zhiqiang. 2005. Elasto-plastic analysis on surrounding rock of circular chamber based on strain nonlinear softening [J]. *Journal of Rock mechanics and engineering* 24(6):915–920.
- [10] Park K.H., Tontavanich B., Lee J.G. 2008. A simple procedure for ground response curve of circular tunnel in elastic-strain softening rock masses [J]. *Tunnelling and Underground Space Technology* 23(2):151–159.
- [11] Lu yinlong, Wang lianguo, Yang feng et al. 2010. Post—Peak strain softening mechanical properties of weak rock [J]. *Journal of Rock mechanics and engineering* 29(3):640–648.
- [12] Itasca Consulting Group. 2002. *Theory and Background* [R]. Minnesota: Itasca Consulting Group.
- [13] Li Shuzhen, Li shucaï, Xu bangshu. 2007. Minimum safety factor method for stability analysis of surrounding rock mass of tunnel [J]. *Rock and Soil Mechanics* 28(3):549–554.
- [14] Jiang Qingqing. 2009. Stability of point safety factor of slope based on Hoek-Brown criterion [J]. *Journal of Central South University* 40(3):786–7.



# Study on the relation between rock size effect and uniaxial compressive strength

Qiumei Zhang

*Chang'an University, Shanxi, Xi'an, China*

*Yunnan Broadvision Engineering Consultants, Yunnan, Kunming, China*

Mulin Huang

*Yunnan Broadvision Engineering Consultants, Yunnan, Kunming, China*

Huabin Chen

*Chang'an University, Shanxi, Xi'an, China*

**ABSTRACT:** Rock samples of different sizes have different uniaxial compressive strengths. In this study, based on actual project, we process samples of different sizes and measure their uniaxial compressive strength. Contrastive analysis shows that uniaxial compressive strength decreases with the increase of sample size. Through fitting, we get the relation formula between uniaxial compressive strength and size effect. When side length of sample is 30 mm, the uniaxial compressive strength is close to the standard strength defined in the code. In actual project, if sample size can not meet the required finish size of the code due to limitation of project conditions, we can process 30 mm samples, measure its uniaxial compressive strength, and then calculate the compressive strength of standard samples using the formula.

**Keywords:** size effect; cube sample; uniaxial compressive strength

## 1 INTRODUCTION

Rocks are the product of earth formation and crustal activity. With wide existence in the nature, rocks are often used as building foundation, building materials or surrounding rock. In geotechnical engineering investigation design, the carrying capacity of bedrock, stability of rock slope, stress distribution, stabilization, and deformation of surrounding rocks in underground chamber (tunnel, etc) excavation are all closely related to physical and mechanical property of rocks. Rock uniaxial compressive strength test mainly focuses on the ultimate load per unit area borne by regular-shaped rock samples (e.g. cylindrical sample of building foundation, cubic sample of bridge engineering, or samples of both shapes in pavement engineering), when compression failure is caused by axial compressive force without lateral confinement. That is to say, the ratio between ultimate load and the section area perpendicular to loading direction under sample failure is an important parameter to reflect the physical and mechanical property of rocks.

Factors influencing rock compressive strength can be classified into two aspects: (1) rock conditions, such as diagenesis model, weathering degree,

mineral composition, stratification, fracture direction, etc; (2) test conditions, such as sample processing method, shape, size, load rate, etc.

Sample state includes shape, size, and height-diameter ratio. The influences of the three factors on test result are called size effect. The application of standard samples can eliminate influence of samples with different states, and thus facilitate the comparison of test results. In actual project, influenced by various factors, samples are of different sizes, so some samples can not be processed into standard sized samples. To get rock compressive strength, we need to modify samples with non-standard sizes. In this way, we can get the compressive strength of their corresponding standard samples.

## 2 ENGINEERING BACKGROUND

In this study, we process samples of various sizes for compressive strength test. By analyzing test results, we explore the law of rock compressive strength at different rock sizes, and provide evidence for the relation between compressive strength and rock size.

### 2.1 Petrological characteristics

The samples, gray, are collected from moderately weathered limestone in the exploration field of an expressway in Yunnan Province. The main component is calcite, with other components less than 5%. Dense and hard in texture, the rocks have developed fractures, and most of the fractures are closed. Rock cores are mostly long-column in shape, and knot length is generally 15 ~ 30 cm. The rocks distribute extensively in the field, and constitute the major rock of the field.

### 2.2 Processing of samples

Test Methods of Rock for Highway Engineering (JTGE41-2005) (TMRHE) and Standard for Test Methods of Engineering Rock Mass (GB/T50266-1999) (STMERM) defines that: Stones and rocks used in pavement engineering should adopt cylinder or cube samples. The diameter/side length and height should be  $50\text{ mm} \pm 2\text{ mm}$ .

For this test, we adopt cube samples, with 6 samples as a group. As our purpose is to study the influence of rock size effect, so we process samples of other sizes except for samples with conventional sizes. All the samples are cubic, with sizes of  $30\text{ mm} \pm 2\text{ mm}$ ,  $70\text{ mm} \pm 2\text{ mm}$  and

$100\text{ mm} \pm 2\text{ mm}$ . As limestone particles are fine and small, the sample sizes meet the requirement of “diameter of compressive strength test samples should be 10 times larger than the maximum particle diameter of the rock” defined in TMRHE and STMERM. To avoid influence of chemical blasting on rock property, samples are excavated with manpower from the pit, and then moved indoor for processing. Samples of the same size ( $n = 12$ ) are divided into 2 groups: air-dried group and water-saturated group. Electronic drying cabinet is used for air drying, with the temperature controlled between  $100^\circ\text{C} \pm 5^\circ\text{C}$  and drying time of 8 h. Free water absorption is used for water-saturation, with absorption time of 48 h.

### 2.3 Test method

The samples are put on 200 t–500 t press machine and exerted with longitudinal load (axial direction) under no lateral confinement. To be specific, put the samples at the center of bearing plate of the press machine. Adjust the bearing plate to make sure the samples receive even stress. Exert load at a rate of 0.5–1 MPa/s until the samples are damaged.

Table 1. Strengths of rocks with different side length.

Diameter (mm)	Moisture state	The compressive strength value (Mpa)						Average strength (Mpa)
30±2	Air dry	75.3	78.9	78.6	77.2	76.0	74.8	76.8
	Saturated water	62.6	60.8	59.4	58.7	63.3	60.5	60.9
50±2	Air dry	79.2	81.1	81.6	78.3	80.7	80.0	80.5
	Saturated water	66.0	68.3	62.5	61.6	64.6	67.9	65.2
70±2	Air dry	68.7	62.1	69.6	61.5	60.9	60.6	63.9
	Saturated water	46.4	43.8	45.9	44.0	42.6	43.5	44.4
100±2	Air dry	58.8	60.6	59.7	53.5	52.4	60.9	57.7
	Saturated water	39.4	32.5	38.3	39.6	40.5	27.8	36.3

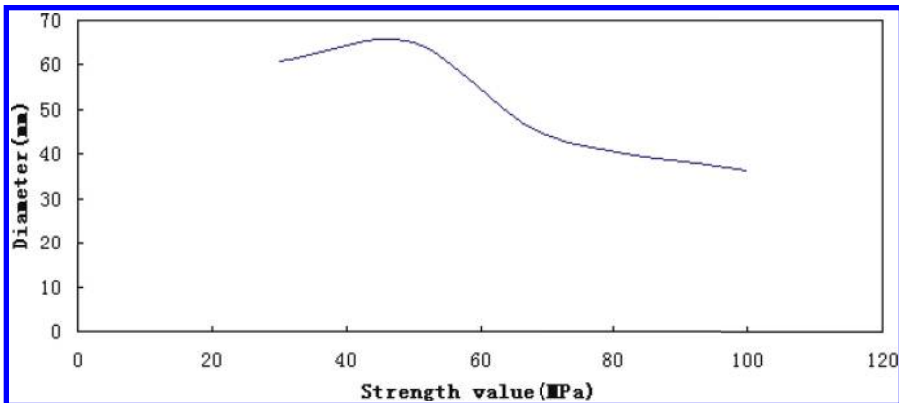


Figure 1. Relation between side length and strength of cube limestone rock.

Table 2. Point load test value of weathered rocks.

Measuring points number	Moisture state	Load orientation	Failure load(KN)	Load spacingD (mm)	Width of failure surface Wf (mm)		Average width (mm)	Equivalent circle square diameter(mm <sup>2</sup> )	Point load strength (MPa)	Size amend coefficient	Convert compressive strength(MPa)
1	Air dry	Radial	18.6	55.60	73.76	76.41	75.1	5318.1	3.50	1.19	69.1
2	Air dry	Radial	17.7	47.64	81.75	83.24	82.5	5006.4	3.54	1.17	
3	Air dry	Radial	16.0	34.09	75.31	73.92	74.6	3240.3	4.94	1.06	
4	Air dry	Radial	15.2	24.85	75.98	76.82	76.4	2418.5	6.28	0.99	
5	Air dry	Radial	13.9	45.21	85.11	84.55	84.8	4885.6	2.85	1.16	
6	Air dry	Radial	14.8	47.25	67.91	69.08	68.5	4122.8	3.59	1.12	

Table 3. Point load test value of water-saturated rocks.

Measuring points number	Moisture state	Load orientation	Failure load(KN)	Load spacingD (mm)	Width of failure surface Wf (mm)		Average width (mm)	Equivalent circle square diameter(mm <sup>2</sup> )	Point load strength (MPa)	Size amend coefficient	Convert compressive strength(MPa)
1	Saturated water	Radial	12.7	55.60	73.76	76.41	75.1	5318.1	2.39	1.19	55.9
2	Saturated water	Radial	13.8	47.64	81.75	83.24	82.5	5006.4	2.76	1.17	
3	Saturated water	Radial	13.2	34.09	75.31	73.92	74.6	3240.3	4.07	1.06	
4	Saturated water	Radial	12.0	24.85	75.98	76.82	76.4	2418.5	4.96	0.99	
5	Saturated water	Radial	11.9	45.21	85.11	84.55	84.8	4885.6	2.44	1.16	
6	Saturated water	Radial	10.5	47.25	67.91	69.08	68.5	4122.8	2.55	1.12	

2.4 Test result analysis

For the 4 rock groups of different side lengths, the average saturated water absorption is 0.44%. Longitudinal wave velocity is 4.8 ~ 5.6 km/s, and the average value is 5.3 km/s. The dynamic poisson ratio is 0.22. The Table 1 and Figure 1 present the result of uniaxial compressive strength test.

From the Table 1 and Figure 1 shows above, we can lean with side length at 30 mm, the softening coefficients of rocks in the same group are of remarkable difference; With side length at 100 mm, due to rock sample’s own limitation, uniformity is worse. For cube limestone rock samples, the strength of rocks with 30 mm side length is closest to that of rocks with standard 50 mm side length. Compressive strength takes on a descending trend with the increase of side length.

To better measure the true-value of compressive strength of rocks in the sampling location, we also collect relatively intact rocks for point load test. The Tables 2 and 3 set forth the test result.

From the Tables 2 and 3, we can lean that the strength value calculated from the point load test result is basically identical with the strength value of standard samples. This shows that sample processing and test result are safe and reliable.

3 CONCLUSION

We conduct contrastive analysis to various-sized samples and fit out the relation between rock uniaxial compressive strength and size effect, and derive a new non linear formula:

$$Y = e^{(49.8-6.4/x-7/\ln x)}$$

The samples for the formula above are collected from limestone. Considering differences of regions and rock properties please modify the formula through experiment or relevant experience when you use it.

REFERENCES

[1] Yan Feng, Jiang Fu-xing. Experiment on rock damage under blasting load [J]. Explosion and Shock Waves, 2009, 29(3): 275–279.  
 [2] Zhu He-hua, Zhou Zhi-guo, Deng Tao. Acoustic parameters of low-porosity rock under dry and saturated conditions [J]. Chinese Journal of Rock Mechanics and Engineering, 2006, 24(3): 823–828.  
 [3] Wang Jin-xing, Wang Ling-min, Yang Xiao-lin. Tensile test methods for rock materials [J]. Journal of Jiaozuo Institute of Technology (Natural Science), 2004, 23(3): 205–208.

# Displacement response of buildings under debris flow impact load

J.X. Cao, F.L. Zhang & M.H. Zhou

Research Institute of Structural Engineering and Disaster Reduction, Tongji University, China

**ABSTRACT:** This paper presents the work on investigating the damage buildings including burying and collapse under debris flow, on the basis of investigation in Sanyan Valley. The impact load of debris flow is simplified into triangular impulse load, rectangular impulse load and spike impulse load, through theoretical derivation, the results show that: when the ratio of impulse duration to natural vibration period of building  $\beta$  is less than 0.15, for spike impulse load, the displacement response ratio  $R_{max}$  is much larger than 2, especially when the  $\beta$  is less than 0.02. While  $\beta$  is more than 0.15, for all of three impulse load,  $R_{max}$  is less than or equal to 2, the maximum displacement amplitude  $v_{max}$  only depends on the magnitude of impulse load, thus it is recommended to set the displacement response ratio  $R_{max} = 2$  to estimate the maximum impact load, which could provide reference for future engineering design.

**Keywords:** debris flow; building in town; impulse load; displacement response ratio

## 1 INTRODUCTION

Debris flow is a complex multiphase fluid with huge energy when it happens, which may cause severe damage to nearby buildings, especially in some mountainous areas. Due to natural conditions and economy, structural styles of buildings in mountainous areas are simple, which are unable to effectively resist the impact of debris flow. In August 2010, a severe debris flow ruined more than 5500 houses in Zhouqu, Gansu Province, China and the Yueyuan Village was almost completely buried (Yu et al. 2010). In July 2013, a debris flow destroyed more than 90% houses in Qipangou gully, Sichuan Province, China (Yang et al. 2014). It has drawn much attention in the past few decades due to the large number of disasters.

In China, some research on the impact load of debris flow have been carried out: ① Investigation: Hu et al. (2012) surveyed the Zhouqu severe debris flow, and summarized buildings damage characteristics and suggested some measures to reduce damage. Zeng et al. (2014) derived some static calculation formula, on the basis of 98 building samples in Qipan gully. ② Numerical simulation: Liu (2013) simulated the damage of masonry structure under the debris flow by LS-DYNA software and proposed some measures from the perspective of failure mechanism and energy. Di (2012) simulated the displacement of a second-floor frame structure under the impact of debris flow and contrasted different conditions. Due to the complexity of debris flow component, and the randomness of its impact loading, numerical simulation is certainly

different from the actual situation. ③ Model experiment: Zhang et al. (2006) tested the wall of brick-concrete structure. The experiment could simulate the actual situation, but there is only a piece of walls which neglect the integrity of structure, so they can not completely reflect the real damage under debris flow.

This paper is organized as follow: Section 2 analyzes the damage characteristics of buildings in debris flow prone areas on the basis of investigation in Sanyan Valley. In Section 3, taking triangular impulse load, rectangular impulse load and spike impulse load as debris flow impact load, the dynamic response of buildings is derived. And the maximum impact load of buildings is estimated by a numerical example. The paper will be concluded in Section 4.

## 2 DAMAGE CHARACTERISTICS OF BUILDINGS

Sanyan Valley is situated on the left of Bailongjiang River, north of Zhouqu County. The whole valley looks like “funnel”, which consists of Dayan ditch and Xiaoyan ditch. In August 7, 2010, Sanyan valley basin suffered from heavy rainfall, causing large debris flow disaster. This debris flow is reported to be viscous mud-flow (Hu et al. 2010).

The buildings in Sanyan Valley show two kinds of failure modes: ① Burying. Burying (Fig. 1) refers to the debris flow going into the building interior, and the building is basically intact but lose its function. In nature, the buildings damage caused



a)



b)

Figure 1. Burying of frame structure.



Figure 2. Global overturning of masonry structure.

by debris flow is the process of energy conversion. When the impact energy of debris flow is higher than deformation energy of building, building will show impact damage. Oppositely, the buildings will not damage but its function may lose. © Collapse.



Figure 3. Partial collapse of masonry structure.

Collapse includes overturning collapse and vertical collapse according to the final collapse mode. Overturning collapse (Fig. 2) is due to the weakness of the lateral stiffness, leading to large deformation with the gravity of the two order effect. Vertical collapse (Fig. 3) is defined as the damage of main load-bearing components and unable to resist the weight of building. Actually, both two models appear in many collapse buildings.

### 3 THE DYNAMIC RESPONSE OF BUILDING UNDER DEBRIS FLOW IMPACT LOAD

#### 3.1 Introduction

Impact load is not only the main factor of building damage, but also the important parameter of dynamic response and the debris flow control project design. Wu (1990) generally summarizes the impact load into three types: zigzag impulse (Fig. 4), rectangular impulse (Fig. 5) and spike impulse (Fig. 6). In order to obtain the dynamic response of buildings under impact load, the hypothesis is established: 1) The buildings in town are always one floor, so it can be simplified to be a single degree of freedom. 2) As the duration of impulse load is short, and the damping effect on the structural response is small, so this effect can be neglected.

Based on the above assumptions, the displacement response of building under impact load is derived from Duhamel integral:

$$x(t) = \frac{1}{m\omega} \int_0^t P(\tau) \sin \omega(t - \tau) d\tau \quad (1)$$

where  $x(t)$  is the displacement response of building;  $m$  is the mass of building;  $\omega$  is natural vibration

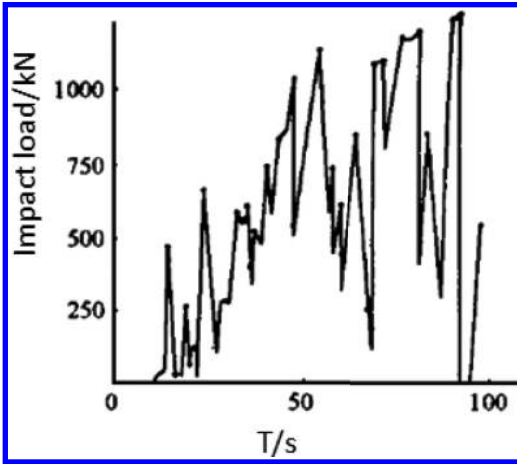


Figure 4. Zigzag impulse.

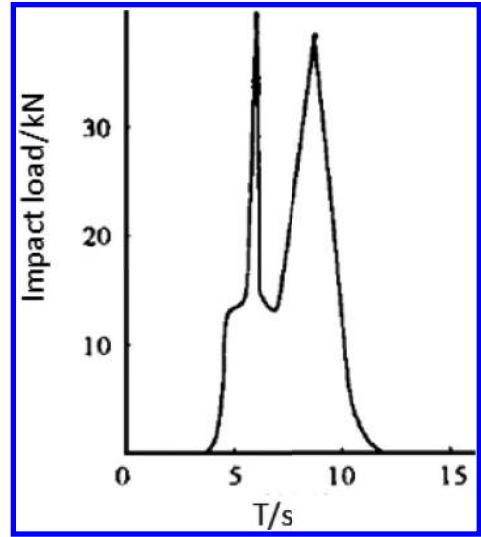


Figure 6. Spike impulse.

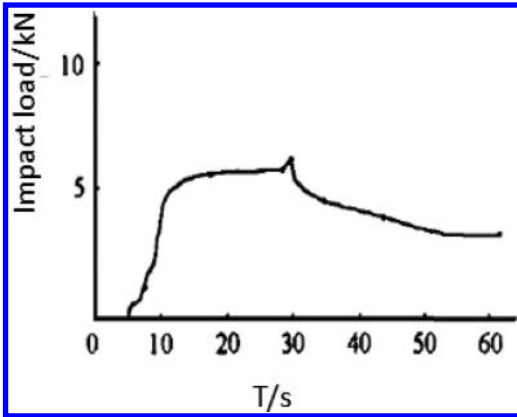


Figure 5. Rectangular impulse.

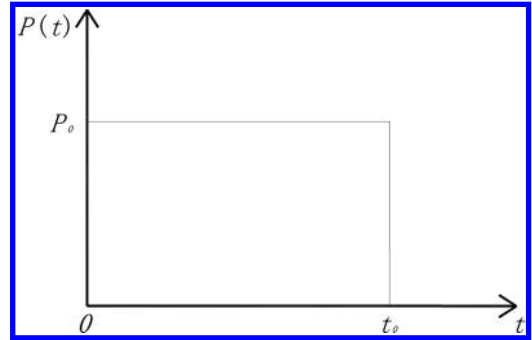


Figure 7. Rectangular impulse load.

frequency of building;  $t$  is the time of impulse load;  $P(\tau)$  is impulse load.

### 3.2 Dynamic response of buildings under rectangular impulse loads

The mathematical expression of rectangular impulse load is given by:

$$P(t) = \begin{cases} P_0, & t \leq t_0 \\ 0, & t > t_0 \end{cases} \quad (2)$$

where  $P_0$  is impulse load,  $t_0$  is duration of impulse load. As shown in Figure 7.

when  $0 \leq t \leq t_0$ ,

$$x(t) = \frac{1}{m\omega} \int_0^t P_0 \sin \omega(t - \tau) d\tau \quad (3)$$

Integration by fraction, the displacement of building can be calculated as follow:

$$x(t) = \frac{P_0}{m\omega^2} (1 - \cos(\omega t)) \quad (4)$$

when  $t > t_0$ ,

$$x(t) = \frac{1}{m\omega} \int_0^{t_0} P_0 \sin \omega(t - \tau) d\tau \quad (5)$$

Integration by fraction, the displacement of building can be calculated as follow:

$$x(t) = \frac{P_0}{m\omega^2} \sin(\omega t) \sin(\omega t_0) + \frac{P_0}{m\omega^2} \cos(\omega t) (\cos(\omega t_0) - 1) \quad (6)$$

The ratio of response (Clough, 1981) is defined as the ratio of dynamic displacement to displacement causing by static load, as shown in Eq. (7), which is a measurement of dynamic load:

$$R(t) \equiv \frac{x(t)}{x_{st}} = \frac{x(t)}{P_0/k} \quad (7)$$

where  $x_{st}$  is the displacement of structure under static load,  $k$  is stiffness of structure.

Set  $\alpha = (t/t_0)$ ,  $\beta = (t_0/T)$ , where  $T$  is natural vibration period of building. The ratio of response is

$$R(t) = \begin{cases} 1 - \cos(2\pi\alpha\beta), & \alpha \leq 1 \\ \sin(2\pi\alpha\beta)\sin(2\pi\beta) + \cos(2\pi\alpha\beta)\cos(2\pi\beta) \\ - \cos(2\pi\alpha\beta), & \alpha > 1 \end{cases} \quad (8)$$

Taking  $\beta$  and  $R(t)$  as horizontal coordinate and longitudinal coordinate, respectively, and  $\alpha$  is ranged from 0.1 to 1.9 with 0.2 as increasing step, Figure 8 can be obtained. From this figure, it shows that: under rectangular impulse load, when  $\beta < 0.17$ ,  $R_{max} < 1$ ; while for any value of  $\alpha$  and  $\beta$ ,  $R_{max} \leq 2$ .

### 3.3 Dynamic response of buildings under triangle impulse loads

The mathematical expression of triangle impulse load is given by:

$$P(t) = \begin{cases} P_0(1 - t/t_0), & t \leq t_0 \\ 0, & t > t_0 \end{cases} \quad (9)$$

as shown in Figure 9.

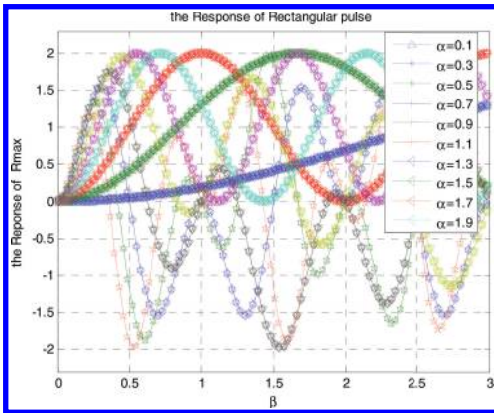


Figure 8. Displacement response of building under rectangular impulse load.

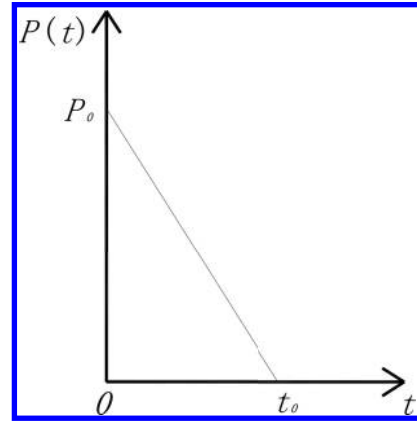


Figure 9. Triangle impulse load.

when  $0 \leq t \leq t_0$ ,

$$x(t) = \frac{1}{m\omega} \int_0^t P_0 \left(1 - \frac{\tau}{t_0}\right) \sin \omega(t - \tau) d\tau \quad (10)$$

Similarly, integration by fraction, the displacement of buildings can be calculated as follow:

$$x(t) = \frac{P_0}{m\omega^2} \left(1 - \frac{t}{t_0} + \frac{1}{\omega t_0} \sin(\omega t) - \cos(\omega t)\right) \quad (11)$$

when  $t > t_0$ ,

$$x(t) = \frac{1}{m\omega} \int_0^{t_0} P_0 \left(1 - \frac{\tau}{t_0}\right) \sin \omega(t - \tau) d\tau \quad (12)$$

Integration by fraction, the displacement of buildings can be calculated as follow:

$$x(t) = \frac{P_0}{m\omega^2} \sin(\omega t) \frac{1}{\omega t_0} (1 - \cos(\omega t_0)) + \frac{P_0}{m\omega^2} \cos(\omega t) \left( \frac{1}{\omega t_0} \sin(\omega t_0) - 1 \right) \quad (13)$$

Set  $\alpha = (t/t_0)$ ,  $\beta = (t_0/T)$ , the ratio of response is

$$R(t) = \begin{cases} 1 - \alpha + \frac{1}{2\pi\beta} \sin(2\pi\alpha\beta) - \cos(2\pi\alpha\beta), & \alpha \geq 1 \\ \frac{1}{2\pi\beta} (1 - \cos(2\pi\alpha\beta)) \sin(2\pi\beta) \\ + \frac{1}{2\pi\beta} \sin(2\pi\beta) \cos(2\pi\alpha\beta) \\ - \cos(2\pi\alpha\beta), & \alpha > 1 \end{cases} \quad (14)$$

Taking  $\beta$  and  $R(t)$  as horizontal coordinate and longitudinal coordinate, respectively, and

$\alpha$  is ranged from 0.1 to 1.9 with 0.2 as increasing step, Figure 10 can be obtained. From this figure, it shows that: under triangle impulse load, when  $\beta < 0.37$ ,  $R_{\max} < 1$ ; while for any value of  $\alpha$  and  $\beta$ ,  $R_{\max} \leq 1.704$ .

### 3.4 Dynamic response of buildings under spike impulse load

The mathematical expression of spike impulse load is given by:

$$P(t) = \begin{cases} P_0 \cdot t/t_0, & t \leq t_0 \\ (2 - t/t_0), & t_0 \leq t \leq 2t_0 \\ 0, & t > 2t_0 \end{cases} \quad (15)$$

as shown in Figure 11.

when  $0 \leq t \leq t_0$ ,

$$x(t) = \frac{1}{m\omega} \int_0^t P_0 \frac{\tau}{t_0} \sin \omega(t - \tau) d\tau \quad (16)$$

Similarly, integration by fraction, the displacement of building can be calculated as follow:

$$x(t) = \frac{P_0}{m\omega^2} \left( \frac{t}{t_0} - \frac{1}{\omega t_0} \sin(\omega t) \right) \quad (17)$$

when  $t_0 < t < 2t_0$ ,

$$x(t) = \frac{1}{m\omega} \int_0^{t_0} P_0 \frac{\tau}{t_0} \sin \omega(t - \tau) d\tau + \frac{1}{m\omega} \int_{t_0}^t P_0 \left( 2 - \frac{\tau}{t_0} \right) \sin \omega(t - \tau) d\tau \quad (18)$$

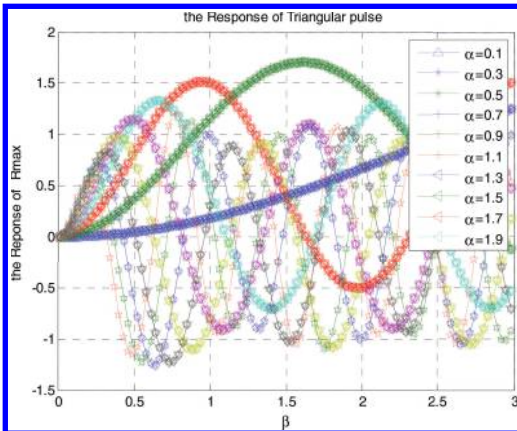


Figure 10. Displacement response of building under triangle impulse load.

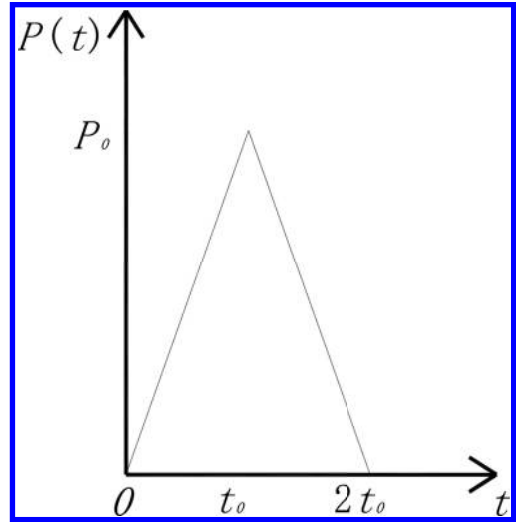


Figure 11. Spike impulse load.

Integration by fraction, the displacement of building can be calculated as follow:

$$x(t) = \frac{P_0}{m\omega^2} \left( \frac{2}{\omega t_0} \sin(\omega t) \cos(\omega t_0) - \frac{2}{\omega t_0} \cos(\omega t) \sin(\omega t_0) + 2 - \frac{t}{t_0} - \frac{1}{\omega t_0} \sin(\omega t) \right) \quad (19)$$

when  $t > 2t_0$ ,

$$x(t) = \frac{1}{m\omega} \int_0^{t_0} P_0 \frac{\tau}{t_0} \sin \omega(t - \tau) d\tau + \frac{1}{m\omega} \int_{t_0}^{2t_0} P_0 \left( 2 - \frac{\tau}{t_0} \right) \sin \omega(t - \tau) d\tau \quad (20)$$

Integration by fraction, the displacement of building can be calculated as follow:

$$x(t) = \frac{P}{m\omega^3 t_0} (\sin(2\omega t_0) \cos(\omega t) - \cos(2\omega t_0) \sin(\omega t) - 2 \sin(\omega t_0) \cos(\omega t) - \sin(\omega t)) \quad (21)$$

Set  $\alpha = (t/t_0)$ ,  $\beta = (t_0/T)$ , the ratio of response is. when  $\alpha < 1$ ,

$$R(t) = \alpha - \frac{1}{2\pi\beta} \sin(2\pi\alpha) \quad (22)$$

when  $1 < \alpha < 2$ ,



$$R(t) = \frac{1}{\pi\beta}(\sin(2\pi\alpha\beta)\cos(2\pi\beta) - \cos(2\pi\alpha\beta)\sin(2\pi\beta)) + 2 - \alpha - \frac{1}{2\pi\beta}\sin(2\pi\alpha\beta) \quad (23)$$

when  $\alpha > 2$ ,

$$R(t) = \frac{1}{2\pi\beta}((\sin(4\pi\beta) - 2\sin(2\pi\beta))\cos(2\pi\alpha\beta) - \frac{1}{2\pi\beta}(\cos(4\pi\beta) + 1)\sin(2\pi\alpha\beta)) \quad (24)$$

Taking  $\beta$  and  $R(t)$  as horizontal coordinate and longitudinal coordinate, respectively,  $\beta$  is ranged from 0.01 to 0.15 with 0.01 as increasing step and  $\alpha$  is ranged from 0.1 to 3.9 with 0.2 as increasing step, Figure 12 can be obtained. From this figure, it shows that: under spike impulse load, when  $\beta < 0.15$ ,  $R_{\max} > 2$ ; Furthermore, with decreasing of  $\beta$ ,  $R_{\max}$  is larger, especially  $\beta < 0.02$ ,  $R_{\max} > 5$ .

Meanwhile, taking  $\beta$  and  $R(t)$  as horizontal coordinate and longitudinal coordinate, respectively,  $\beta$  is ranged from 0.15 to 3 with 0.2 and  $\alpha$  is ranged from 0.1 to 3.9 with 0.2 as increasing step, Figure 13 can be obtained. From this figure, it shows that: under spike impulse load, when  $\beta > 0.15$ ,  $R_{\max} < 2$ , Furthermore, when  $\beta > 1$ ,  $R_{\max} < 1$ .

Based on the above observation, it is found that for rectangular impulse load, triangular impulse load and spike impulse load, displacement response of structure is related to  $\alpha$ ,  $\beta$ . When  $\beta < 0.15$ , for rectangular impulse load and triangular impulse load, the ratio of response  $R_{\max} \leq 2$ , for spike impulse load, the ratio of response  $R_{\max}$  becomes very large. While  $\beta > 0.15$ , for all of the three impulse load, the ratio of response  $R_{\max} \leq 2$ .

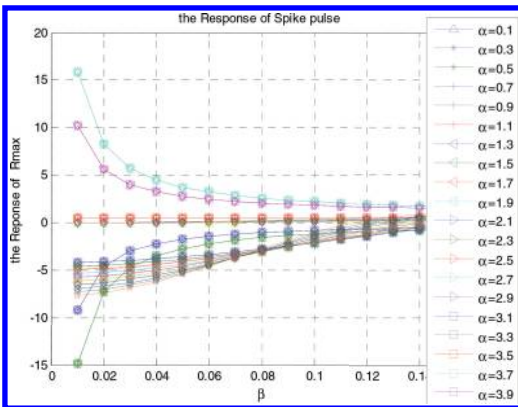


Figure 12. Displacement response of building under spike impulse load.

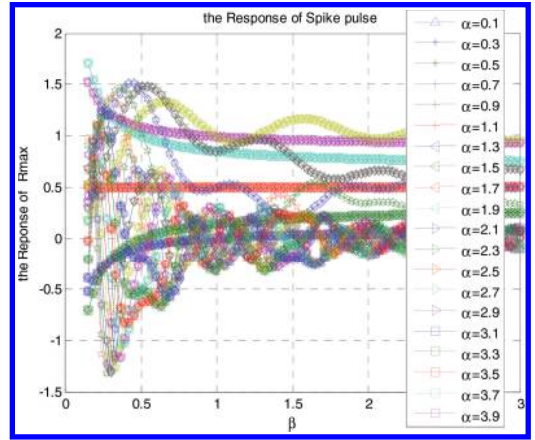


Figure 13. Displacement response of building under spike impulse load.

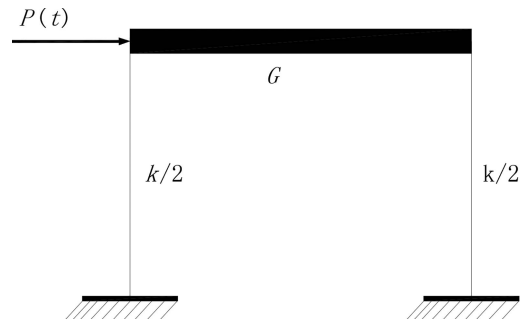


Figure 14. A sketch of building.

Thus the maximum impact load on buildings can be predicted.

### 3.5 Illustrative example

A building located in debris flow prone area is simulated as shown in Figure 11. The total weight of building is all focused on the beam, i.e.,  $G = 2 \times 10^6 \text{ N}$  while the total stiffness of building  $k = 2 \times 10^8 \text{ N/m}$ . Assume the displacement is limited to 5 mm. Based on the above discussion the maximum impact load on building can be calculated when, (1)  $t_0 = 0.03 \text{ s}$ , (2)  $t_0 = 0.3 \text{ s}$ .

The natural frequency of building can be given by

$$\omega = \sqrt{\frac{k}{M}} = 31.6 \text{ rad/s}$$

with the period of  $T = 2\pi/\omega = 0.2 \text{ s}$ .

The ratio of response  $R_{\max}$  can be obtained as

1.  $\beta = t_0/T = 0.15$   
 When triangle impulse load is applied on building,  $R_{\max} = 0.46$   
 When rectangular impulse load is applied on building,  $R_{\max} = 0.91$   
 When spike impulse load is applied on building,  $R_{\max} = 1.71$
2.  $\beta = t_0/T = 1.5$   
 When triangle impulse load is applied on building,  $R_{\max} = 1.69$   
 When rectangular pulse load is applied on building,  $R_{\max} = 2$   
 When spike impulse load is applied on building,  $R_{\max} = 1.1575$
- c. Calculate the maximum impact load on building according to:  

$$v_{\max} = R_{\max} \cdot P_0/k$$

Thus

1. when  $\beta = 0.15$ ,  $R_{\max} = 1.71$   

$$P_0 = v_{\max} \cdot k/R_{\max} = 584 \text{ kN}$$
2. when  $\beta = 1.5$ ,  $R_{\max} = 2$   

$$P_0 = v_{\max} \cdot k/R_{\max} = 500 \text{ kN}$$

From the result of illustrative example, it shows that: when  $\beta > 0.15$ , the ratio of response  $R_{\max} \leq 2$ , the maximum displacement amplitude  $v_{\max}$  depends on the magnitude of the pulse load. For engineering design, it is suggested to select  $R_{\max} = 2$  to estimate the maximum impact load.

#### 4 CONCLUSIONS

Based on field investigation, this paper analyzes the damage characteristics of buildings under debris flow, and displacement response of buildings under impact load is also discussed. The following conclusions are obtained:

1. Displacement response of structure is only related to  $\alpha, \beta$  under impact load. When the impact load is simplified into a triangular impulse load or rectangular impulse load, the ratio of response  $R_{\max}$  is less than or equal to 2, when it is simplified into a spike impulse load, the ratio of response  $R_{\max}$  is very large if  $\beta$  is less than 0.15. Thus it is very important to select a suitable impulse load, which may affect the result.

2. For the impact load of debris flow, when  $\beta$  is large than 0.15, the ratio of response  $R_{\max}$  is less than or equal to 2, the maximum displacement amplitude  $v_{\max}$  only depends on the magnitude of impulse load. For engineering design, it is suggested to select  $R_{\max} = 2$  to estimate the maximum impact load, which buildings can resist.
3. For spike impulse load, when  $\beta$  is less than 0.15, the ratio of response  $R_{\max}$  especially large. Thus it is recommended to control the natural vibration period of structure, which can reduce the ratio of response.

#### REFERENCES

- Clough, R.W. & Peng, J.J. 1981. Structure dynamics. Beijing: Science Press.
- Di, S.K., Li, J.Z., De, Q. 2012. Damage mechanism of frame structures impacted by debris flow. Journal of Mountain Science 30(2):201–206.
- Grove, A.T. 1980. Geomorphic evolution of the Sahara and the Nile. In M.A.J. Williams & H. Faure (eds), The Sahara and the Nile: 21–35. Rotterdam: Balkema.
- Hu, K.H., Cui, P., Ge, Y.G. 2012. Building destruction patterns by August 8, 2010 debris flow in Zhouqu Western China. Journal of Mountain Science 30(4):484–490.
- Liu, C. 2013. The failure mechanism and anti-collapse analysis of masonry structures under the action of debris flow. Lanzhou: Lanzhou University of Technology.
- Wu, J.S., Kang, Z.C., Tian, L.Q. 1990. Observation and study of debris flow in Jiangjiang gully in Yunnan Debris Flows. Beijing: Science Press.
- Yang, X.Y., Cai, L.L. & Tian, Y.T. 2014. The present situation and the risk assessment of Qipangou, Sichuan Province. Yangtze River 45(sup):60–63.
- Yu, B., Yang, Y.H., Su, Y.C. et al. 2010. Research on the giant debris flow hazards in Zhouqu county, Gansu province on August 7. Journal of engineering Geology 18(4):437–444.
- Zeng, C., Cui, P., Ge, Y.G., et al. 2014. Characteristics and mechanism of buildings damaged by debris flows on 11 July, 2013 in Qipangou of Wenchuan, Sichuan. Journal of Earth Sciences and Environment 36:81–91.
- Zhang, Y., Wei, F.Q., Jia, S.W. et al. 2006. Experimental research of unreinforced masonry wall under dynamic impact of debris flow [J]. Journal of Mountain Science 24(3):340–345.

*Tunnel, subway and underground facilities*

# Displacement analytic solution of a deep elliptical tunnel in a transversely isotropic rock mass considering the shear stress effect

Zhizeng Zhang & Xiaochang Li

School of Civil Engineering and Architecture, Zhongyuan University of Technology, Zhengzhou, China

**ABSTRACT:** Sedimentary rocks with a layered structure account for two-thirds of the global land area, and this proportion is 77.3% in China. Many metamorphic rocks also have significant features of layered structure, so there are a large number of stability problems about layered rock mass in mining engineering. Layered rock mass is generally considered to be transversely isotropic solid in mechanics. Based on the complex variable expression of displacement components of transverse isotropy, the displacement analytical solution of a deep elliptical tunnel in a transversely isotropic rock mass considering the shear stress effect is derived by the conformal mapping method.

**Keywords:** shear stress; transversely isotropic; elliptical tunnel; displacement; analytical solution

## 1 INTRODUCTION

The displacement about deep tunnels is often of interest to the geotechnical engineers and to be studied. There exist many elliptical tunnels in mining and rock engineering. In order to analyze the stability of elliptical tunnels and research the maintenance measures, it is significant to get the accurate stress and displacement solutions.

Muskhelishvili (1953) gave the stress and displacement distribution of an elliptic tunnel on an infinite plane under tensile, compressive and shear stress conditions, respectively. Cai (2008) obtained the stress and displacement analytic formulae by using the conformal mapping method.

In the above literature, the surrounding rock was regarded as isotropic. Due to the complexity of rock anisotropy, there were only a few papers on the displacement analytic solution of a tunnel in anisotropic rock mass. Lekhnitskii (1981) gave the displacement analytic solution of a circular silo in a transversely isotropic rock mass under the axisymmetric ground stress condition. Zhang (2010, 2012) derived the displacement analytic solutions for tunnels with an arbitrary and elliptical cross-section in two unequal normal stresses, and also gave the complex variable expression of displacement components of transverse isotropy, which helps to obtain the displacement analytic solution of complex tunnels. However, the displacement solution may become more complex when the shear stress effect is considered in a transversely isotropic rock mass.

Based on the above research, this paper attempts to derive the displacement analytic solution of a

deep elliptical tunnel in a transversely isotropic rock mass considering the shear stress effect.

## 2 PROBLEM DESCRIPTION

The following assumptions are made for the model used in this paper:

(1) the surrounding rock is continuous, homogeneous, linear elastic and transversely isotropic, and the displacement and strain are small; (2) the cross-section of the tunnel is elliptical and parallel to the isotropic plane, the length of the long and short axis is, respectively,  $2a$  and  $2b$ ; (3) the length of the tunnel is much larger than the size of the cross-section, so the plane strain condition is

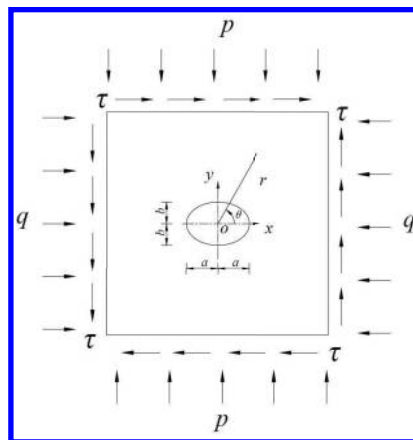


Figure 1. Model of a deep elliptical tunnel.

used; (4) the tunnel is deep; (5) the initial stress in the ground is idealized as a normal stress  $p$ , which acts in the vertical direction, and a normal stress  $q$ , which acts in the horizontal direction, and a shear stress  $\tau$ , (6) compared with the initial stress, the rock weight is small and is ignored in the deduction. Figure 1 shows an ideal model of a deep elliptical tunnel in a transversely isotropic rock mass.

### 3 PHYSICS EQUATIONS OF TRANSVERSE ISOTROPY

A model of a transversely isotropic solid is shown in Figure 2, in which the  $xoy$ -plane and  $oz$  is regarded, respectively, as the isotropic plane and symmetry axis. The generalized Hooke's law equations for transverse isotropy are as follows (Ding, 2006):

$$\begin{Bmatrix} \varepsilon_x \\ \varepsilon_y \\ \varepsilon_z \\ \gamma_{yz} \\ \gamma_{xz} \\ \gamma_{xy} \end{Bmatrix} = \begin{bmatrix} S_{11} & S_{12} & S_{13} \\ S_{12} & S_{11} & S_{13} \\ S_{13} & S_{13} & S_{33} \\ & & & S_{44} \\ & & & & S_{44} \\ & & & & & S_{66} \end{bmatrix} \begin{Bmatrix} \sigma_x \\ \sigma_y \\ \sigma_z \\ \tau_{yz} \\ \tau_{xz} \\ \tau_{xy} \end{Bmatrix} \quad (1)$$

where the parameter  $S_{ij}$  is related to the elastic constants as follows:

$$\begin{aligned} S_{11} &= \frac{1}{E}, \quad S_{12} = -\frac{\mu}{E}, \quad S_{13} = -\frac{\mu'}{E'}, \quad S_{33} = \frac{1}{E'}, \\ S_{44} &= \frac{1}{G}, \quad S_{66} = \frac{1}{G} \end{aligned} \quad (2)$$

where  $E$ ,  $\mu$  and  $G$  are, respectively, the elastic modulus, the Poisson ratio and the shear modulus in the isotropic plane, and  $E'$ ,  $\mu'$  and  $G'$  are those in the direction normal to the isotropic plane.

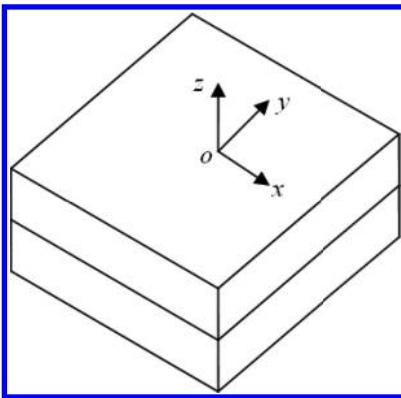


Figure 2. Model of a transversely isotropic solid.

### 4 THE COMPLEX VARIABLE EXPRESSION OF DISPLACEMENT COMPONENTS OF TRANSVERSE ISOTROPY

Zhang (2010) proved that when the stress boundary condition is only applied, the complex variable expression of stress function and stress components of transverse isotropy is the same as that of isotropy. However, the complex variable expression of displacement components is unequal because of the difference in physics equations. Furthermore, he also obtained the complex variable expression of displacement components of transverse isotropy under plane strain condition as follows:

$$u + iv = \left( \frac{3 - \mu}{E} - \frac{4\mu'^2}{E'} \right) \varphi_1(z) - \frac{1 + \mu}{E} [z \overline{\varphi_1'(z)} + \overline{\psi_1(z)}] \quad (3)$$

where  $\varphi_1(z)$  and  $\psi_1(z)$  are both analytic functions.

### 5 DISPLACEMENT ANALYTIC SOLUTION OF A DEEP ELLIPTICAL TUNNEL IN A TRANSVERSELY ISOTROPIC ROCK MASS

The conformal mapping method should be used in the solving process. Assuming that the mapping function that transforms the region exterior of a tunnel in the  $z$ -plane onto the exterior of a unit circle in the  $\zeta$ -plane is  $z = \omega(\zeta)$  (Fig. 3), all formulae with the independent variable  $z$  should be transformed into that with the independent variable  $\zeta$ . In order to establish the appropriate transformation relations, the following symbols should be adopted (Lv, 2007):

$$\left. \begin{aligned} \varphi(\zeta) &= \varphi_1(z) = \varphi_1[\omega(\zeta)] \\ \psi(\zeta) &= \psi_1(z) = \psi_1[\omega(\zeta)] \\ \Phi(\zeta) &= \varphi_1'(z) = \frac{\varphi'(\zeta)}{\omega'(\zeta)} \\ \Psi(\zeta) &= \psi_1'(z) = \frac{\psi'(\zeta)}{\omega'(\zeta)} \end{aligned} \right\} \quad (4)$$

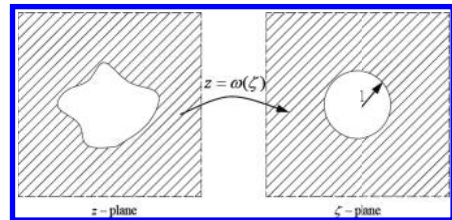


Figure 3. Conformal mapping of a region exterior to a tunnel onto the exterior of a unit circle.

Based on Equation (3) and Equation (4), the displacement components in the  $\zeta$ -plane becomes

$$u + iv = \left( \frac{3 - \mu}{E} - \frac{4\mu'^2}{E'} \right) \varphi(\zeta) - \frac{1 + \mu}{E} \left[ \frac{\omega(\zeta)}{\omega'(\zeta)} \overline{\varphi'(\zeta)} + \overline{\psi(\zeta)} \right] \quad (5)$$

For the stress boundary condition shown in Figure 1,  $\varphi(\zeta)$  and  $\psi(\zeta)$  can be written as follows (Zhang, 2001):

$$\left. \begin{aligned} \varphi(\zeta) &= \frac{p+q}{4} \omega(\zeta) + \varphi_0(\zeta) \\ \psi(\zeta) &= \left( \frac{p-q}{2} - i\tau \right) \omega(\zeta) + \psi_0(\zeta) \end{aligned} \right\} \quad (6)$$

where  $\varphi_0(\zeta)$  and  $\psi_0(\zeta)$  are analytic in the exterior of the unit circle.

The displacement field consists of two parts (Cai, 2002). One is represented by the  $p + q/4 \omega(\zeta)$  and  $((p - q/2) - i\tau)\omega(\zeta)$ , which is caused by the initial stress field and takes place before tunnel excavation; the other is represented by  $\varphi_0(\zeta)$  and  $\psi_0(\zeta)$ , which is caused by tunnel excavation. The latter one is measurable and should be obtained. Eliminating  $p + q/4 \omega(\zeta)$  and  $((p - q/2) - i\tau)\omega(\zeta)$ , the displacement components caused by tunnel excavation can be written as follows:

$$u + iv = \left( \frac{3 - \mu}{E} - \frac{4\mu'^2}{E'} \right) \varphi_0(\zeta) - \frac{1 + \mu}{E} \left[ \frac{\omega(\zeta)}{\omega'(\zeta)} \overline{\varphi_0'(\zeta)} + \overline{\psi_0(\zeta)} \right] \quad (7)$$

The mapping function that transforms the region exterior of an elliptical tunnel in the  $z$ -plane onto the exterior of a unit circle in the  $\zeta$ -plane is as follows:

$$z = \omega(\zeta) = c \left( \zeta + \frac{m}{\zeta} \right) \quad (8)$$

$$\text{where } c = \frac{a+b}{2}, \quad m = \frac{a-b}{a+b}.$$

Based on Equation (8),  $\varphi_0(\zeta)$  and  $\psi_0(\zeta)$  can be expressed as follows:

$$\left. \begin{aligned} \varphi_0(\zeta) &= -\frac{c}{2\zeta} [m(p+q) + (p-q) + i \cdot 2\tau] \\ \psi_0(\zeta) &= -\frac{c}{2\zeta(\zeta^2 - m)} [(p+q)\zeta^2(m^2 + 1) + (p-q)(1 - m^2 + 2m\zeta^2) + i \cdot 2\tau(1 + m^2)] \end{aligned} \right\} \quad (9)$$

Substituting Equation (9) into Equation (7) yields

$$u + iv = \left( \frac{3 - \mu}{E} - \frac{4\mu'^2}{E'} \right) \left[ \frac{p+q}{2} f_1(\zeta) + \frac{p-q}{2} f_2(\zeta) - \tau f_3(\zeta) \right] + \frac{1 + \mu}{E} \left[ \frac{p+q}{2} f_4(\zeta) + \frac{p-q}{2} f_5(\zeta) - \tau f_6(\zeta) \right] \quad (10)$$

where

$$\left. \begin{aligned} f_1(\zeta) &= -\frac{mc}{\zeta}; \quad f_2(\zeta) = -\frac{c}{\zeta}; \quad f_3(\zeta) = \frac{ic}{\zeta} \\ f_4(\zeta) &= \frac{c\bar{\zeta}(1+m^2) - mc \left( \zeta + \frac{m}{\zeta} \right)}{\bar{\zeta}^2 - m} \\ f_5(\zeta) &= \frac{c(1-m^2 + 2m\bar{\zeta}^2)}{\bar{\zeta}(\bar{\zeta}^2 - m)} - \frac{c \left( \zeta + \frac{m}{\zeta} \right)}{\bar{\zeta}^2 - m} \\ f_6(\zeta) &= \frac{ic(1+m^2)}{\bar{\zeta}(\bar{\zeta}^2 - m)} - \frac{ic \left( \zeta + \frac{m}{\zeta} \right)}{\bar{\zeta}^2 - m} \end{aligned} \right\} \quad (11)$$

There are no physical parameters (e.g.  $E, \mu, E'$  and  $\mu'$ ) in  $f_k(\zeta)$ , but only the function of coordinates. It is assumed that the inverse function of  $f_k(\zeta)$  is  $F_k(Z)$ , which is also only the function of coordinates. The  $u$  and  $v$  in Equation (10) are displacement components in rectangular coordinates, but the radial displacement component  $u_r$  is easy to measure in practice, which can be expressed by  $u$  and  $v$  as follows:

$$u_r = u \cos \theta + v \sin \theta \quad (12)$$

Substituting  $u$  and  $v$  of Equation (10) into Equation (12), and replacing  $f_k(\zeta)$  with  $F_k(z)$ , yields the radial displacement component as follows:

$$\begin{aligned} u_r &= \left( \frac{3 - \mu}{E} - \frac{4\mu'^2}{E'} \right) \left[ \frac{p+q}{2} R_e[F_1(z)] + \frac{p-q}{2} R_e[F_2(z)] \right. \\ &\quad \left. - \tau R_e[F_3(z)] \right] \cos \theta + \frac{1 + \mu}{E} \left[ \frac{p+q}{2} R_e[F_4(z)] \right. \\ &\quad \left. + \frac{p-q}{2} R_e[F_5(z)] - \tau R_e[F_6(z)] \right] \cos \theta \\ &\quad + \left( \frac{3 - \mu}{E} - \frac{4\mu'^2}{E'} \right) \left[ \frac{p+q}{2} I_m[F_1(z)] + \frac{p-q}{2} I_m[F_2(z)] \right. \\ &\quad \left. - \tau I_m[F_3(z)] \right] \sin \theta + \frac{1 + \mu}{E} \left[ \frac{p+q}{2} I_m[F_4(z)] \right. \\ &\quad \left. + \frac{p-q}{2} I_m[F_5(z)] - \tau I_m[F_6(z)] \right] \sin \theta \end{aligned} \quad (13)$$

Equation (13) is the displacement analytic solution of a deep elliptical tunnel in a transversely isotropic rock mass considering the shear stress effect. When shear stress is not considered, namely  $\tau = 0$ , Equation (13) reduces to the displacement analytic solution with two unequal normal stresses (Zhang, 2012). In case of  $E' = E$  and  $\mu' = \mu$ , Equation (13) reduces to the displacement analytic solution in a transversely isotropic rock mass (Zhang, 2001). They verify the truth of the derivation.

Particularly, for a circle tunnel, in which  $a = b = r$  (where  $r$  is the radius),  $f_1(\zeta) \sim f_6(\zeta)$  can be expressed as follows:

$$\begin{aligned} f_1(\zeta) &= 0; f_2(\zeta) = -\frac{r}{\zeta}; f_3(\zeta) = \frac{ir}{\zeta}; f_4(\zeta) = \frac{r}{\zeta} \\ f_5(\zeta) &= \frac{r}{\zeta^3} - \frac{r\zeta'}{\zeta^2}; f_6(\zeta) = \frac{ir}{\zeta^3} - \frac{ir\zeta'}{\zeta^2} \end{aligned} \quad (14)$$

Accordingly,  $F_1(z) \sim F_6(z)$  should be expressed as follows:

$$\begin{aligned} F_1(z) &= 0; F_2(z) = -\frac{a^2}{z}; F_3(z) = \frac{ia^2}{z}; F_4(z) = \frac{a^2}{z} \\ F_5(z) &= -\frac{a^2z}{z^2} + \frac{a^4}{z^3}; F_6(z) = -\frac{ia^2z}{z^2} + \frac{ia^4}{z^3} \end{aligned} \quad (15)$$

Substituting Equation (15) into Equation (13) and noting that  $z = re^{i\theta}$ , we get the displacement analytic solution for a deep circle tunnel as follows:

$$\begin{aligned} u_r &= \frac{p+q}{2} \frac{a^2}{r} \frac{1+\mu}{E} + \frac{p-q}{2} \left[ \frac{a^4}{r^3} \frac{1+\mu}{E} \right. \\ &\quad \left. - \frac{4a^2}{r} \left( \frac{1}{E} - \frac{\mu'^2}{E'} \right) \right] \cos 2\theta + \tau \left[ \frac{a^4}{r^3} \frac{1+\mu}{E} \right. \\ &\quad \left. - \frac{4a^2}{r} \left( \frac{1}{E} - \frac{\mu'^2}{E'} \right) \right] \sin 2\theta \end{aligned} \quad (16)$$

## 6 CONCLUSIONS

1. In this paper, the radial displacement analytic solution for a deep elliptical tunnel in a

transversely isotropic rock mass considering the shear stress effect is obtained based on the complex variable expression of displacement components for transverse isotropy by using the conformal mapping method.

2. Although the cross-section is assumed to be parallel to the isotropic plane in the deduction, the displacement analytic solution indicates that the radial displacement of the surrounding rock is related not only to the elastic modulus and the Poisson ratio in the isotropic plane, but also to that in the direction normal to the isotropic plane.
3. The cross-section is assumed to be parallel to the isotropic plane in the deduction in this paper. Further research can be carried out on the problems that the cross-section intersects the isotropic plane.

## REFERENCES

- Cai Meifeng, He Manchao & Liu Dongyan. 2002. *Rock mechanics and engineering*. Beijing: Science Press.
- Cai Xiaohong, Cai Yongbin, Cai Yongping, Gan Xiaorong & Sun Fuxue. 2008. Computation of elliptic tunnel under the combined action of two-dimensional unequal adjoining rock pressure and internal pressure. *Chinese Journal of Underground Space and Engineering* 4(3): 453–458.
- Ding Haojiang, Chen Weiqiu & Zhang Ling. 2006. *Elasticity of Transversely Isotropic Materials*. Dordrecht: Springer-Verlag.
- Lekhniskii S.G. 1981. *Theory of elasticity of an anisotropic body*. Moscow: Mir Publisher.
- Lv Aizhong & Zhang Luqing. 2007. *Complex variable function method for underground engineering*. Beijing: Science Press.
- Muskhelishvili, N.I. 1953. *Some basic problems of the mathematical theory of elasticity*. Groningen: Noordhoff.
- Zhang Zhizeng, Li Zhongkui & Xu Mengguo. 2010. Displacement analytic solution of a deep tunnel with arbitrary cross section in transversely isotropic rock mass. *Mining Research and Development* 30(3): 24–19.
- Zhang Zhizeng, Zhang Jinhu, Hou Dongqi & Chen Xiaopeng. 2012. Displacement analytic solution of a deep elliptical tunnel in transversely isotropic rock mass. *Advanced Materials Research* 402: 593–597.
- Zhang Luqing & Jia Zhengxue. 2001. Inversion uniqueness of elastic displacement back-analysis for ground stress, elastic modulus and Poisson's ratio. *Chinese Journal of Geotechnical Engineering* 23: 172–177.

# The effect analysis of subway tunnel construction accidents on adjacent buildings

X.W. Peng & D.C. Yuan

College of Basic Education, National University of Defense Technology, Changsha, Hunan, P.R. China

**ABSTRACT:** In order to obtain the effect rules of subway tunnel construction accidents on adjacent buildings, the material point method was employed to build a simplified model of subway tunnel construction accidents. The deformation and failure patterns of surrounding soils were studied. Furthermore, the mechanical properties and deformation characteristics of the adjacent masonry building under different locations, different embedded depths of tunnel and different degrees of damaged tunnel segment were discussed. As a result, the scope and intensity of the affected area are proposed.

**Keywords:** subway tunnel; material point method; masonry building; construction accidents; numerical simulation

## 1 INTRODUCTION

With the rapid process of urbanization, subway construction scale is expanding in China. During the construction process, subway projects (subway tunnel, foundation pit and connected aisle) in the high water-level soft soil area are exposed to high risks. Both in China and abroad, there are plenty of construction accidents, such as the tunnel collapsed accident of Guangzhou Metro Line 3, the foundation pit collapsed accident of Hangzhou, and the connected aisle collapsed accident of Germany subway tunnel. Accordingly, all of these accidents have a certain effect on adjacent buildings.

Due to the large deformation of soils occurring in the subway tunnel construction accidents, if the finite element method was applied to build the model, the mesh distortion would ultimately lead to the termination of the calculation. To overcome this problem, the material point method was employed in an innovative way, as it can avoid mesh distortion problems and suitably analyze large deformation of the subway tunnel.

In this study, a simplified model of subway tunnel construction accidents is built based on the material point method. Through controlling variables of location of adjacent building, the embedded depth of the tunnel and the damage degree of the segment, the effect rules of subway tunnel construction accidents on adjacent buildings are proposed.

## 2 NUMERICAL ANALYSIS OF SUBWAY TUNNEL DESTRUCTION

### 2.1 Computing model

In order to achieve the precise analysis of the deformation of adjacent buildings, a fine model of the building is shown in [Figure 1\(a\)](#). The building is a typical masonry structure, such as historical buildings. To simplify the calculation, the length in the y direction is 1 m, and the width and height of the building are 12 m and 8 m, respectively. The lengths of each layer and each truss are both 4 m, and the opening sizes of doors and windows are both 2.0 m × 2.0 m. In the model, the inside diameter of the shield tunnel is 2.7 m, and its outside diameter is 3 m. The lining structure of the shield tunnel is composed of three A-type segments, namely two B-type segments and one K-type segment, of which A, B, K are the standard block, adjacent block and capped block, respectively. As shown in [Figure 1\(b\)](#), the central angle of the capped block is 20°, and the central angle of the adjacent block and the standard block are both 68°.

For simplicity, the soil layer is assumed to be a single homogeneous soft clay in the model. Meanwhile, the segment, masonry building and soil are simulated based on the Drucker-Prager model. All of the parameters are listed in [Table 1](#).

The model simulated the practical construction process and then dynamically analyzed the effect



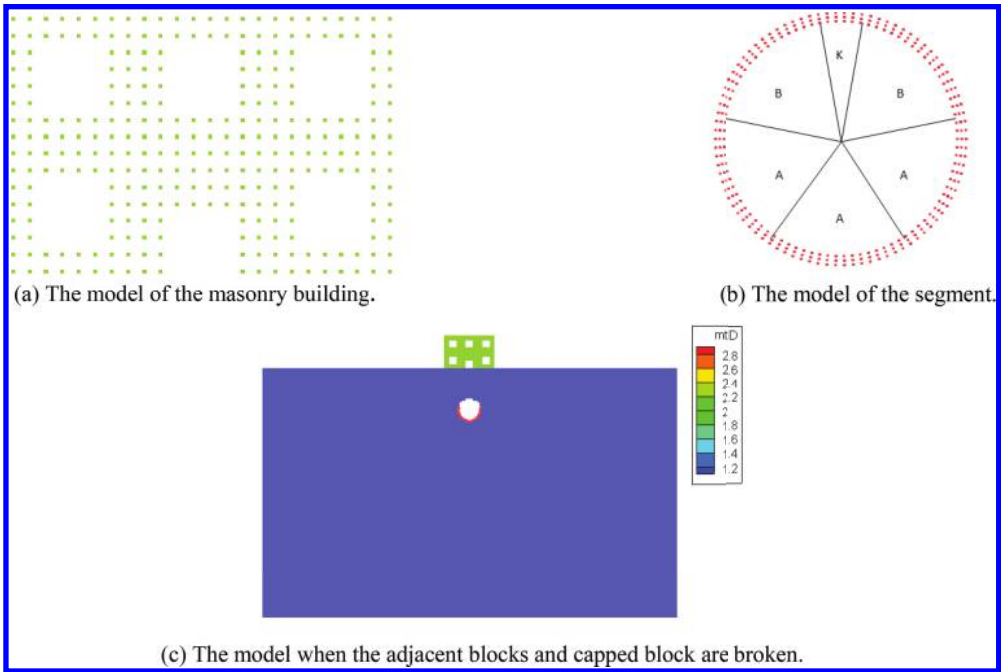


Figure 1. Network diagram of the model.

Table 1. Physical and mechanical parameters of materials.

Material type	Elastic modulus $E$ /(MPa)	Poisson's ratio $\mu$	Density (kg/m <sup>3</sup> )	Angle of internal friction $\Phi$ (°)	Cohesive force $C$ /(kPa)	Dilation angle (°)
Soft clay	7.5	0.49	1600	0	15	0
Tunnel segment	$3.55 \times 10^4$	0.2	2600	60	550	0
Masonry building	220	0.2	2000	30	100	0

of tunnel excavation on adjacent buildings, which are as follows:

- The number of material points and material types are counted.
- Background grid is divided, where the mesh size is  $x$  (0,100),  $y$  (0,1),  $z$  (0,100), and the unit is m.
- Boundary conditions are constrained.
- Physical mechanical parameters are assigned to segment, soil, and the building.
- Geometric models of the tunnel and adjacent building are built, and the parameters of the building location, embedded depth of tunnel, and degree of damaged tunnel segment are controlled to simulate different types of tunnel construction accidents. For example, the adjacent blocks and capped block are broken (segment partially broken), and the model is shown in Figure 1(c).
- Initial stress is balanced.

## 2.2 Failure patterns under different distances that the adjacent masonry building from the tunnel

In the model, equivalent plastic strain is calculated based on the distortion energy theory (the fourth strength theory). This theory considers that when the distortional energy density stored in unit body (vd) is approximated to the uniaxial tensile yield distortion energy density (vds), the material enters the plastic yield. As shown in Figure 2, when the segment is whole broken, the masonry building that is right above the tunnel will produce a plastic deformation zone toward the bottom along two sides of the corner. The plastic deformation region that is in two corners of the building and in the tunnel is integrated into a whole, forming a huge symmetric shear failure area. With the masonry building away from the

tunnel, the building inclines towards the side that is away from the tunnel, and the tilt increases and then decreases gradually.

### 2.3 Failure patterns under different embedded depths of the tunnel

Figure 3 shows the impact of tunnel destruction on surrounding soils that may be related to embedded depths of the tunnel, and the affected region is a semicircular area with a radius that is equal to the embedded depth of the tunnel. As shown in Figure 4, after the destruction of the tunnel, there is a plastic deformation zone around it. Influenced by the stress field, as the embedded depth of the tunnel decreases, the plastic deformation zone extends to the ground.

### 2.4 Failure patterns under different degrees of damaged tunnel segment

Subway tunnel accidents include failure of the un-supported section, failure of the tunnel heading, and failure of the both. To simplify the calculations, the simulation analysis is only for the case of un-supported section failure. As shown in Figure 5, the affected area of lateral displacement is small for segment whole broken, while it is large for the segment partially broken. It may be due to the soil right above the tunnel that partially collapses when the segment is partially broken, causing both sides of soil to be swarmed into the tunnel. In contrast, when the segment is whole broken, the soil beneath the tunnel rebounds, which reduces soil deformation on both sides.

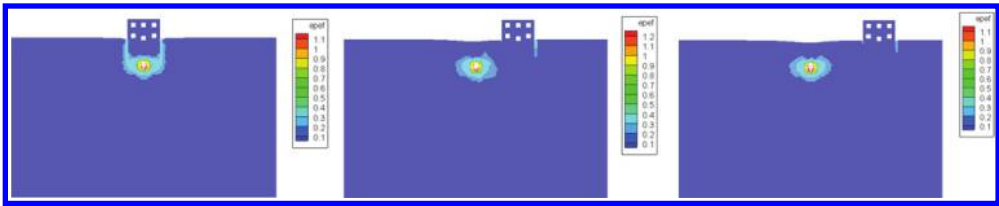


Figure 2. Equivalent plastic strain cloud diagram under different distances from the tunnel.

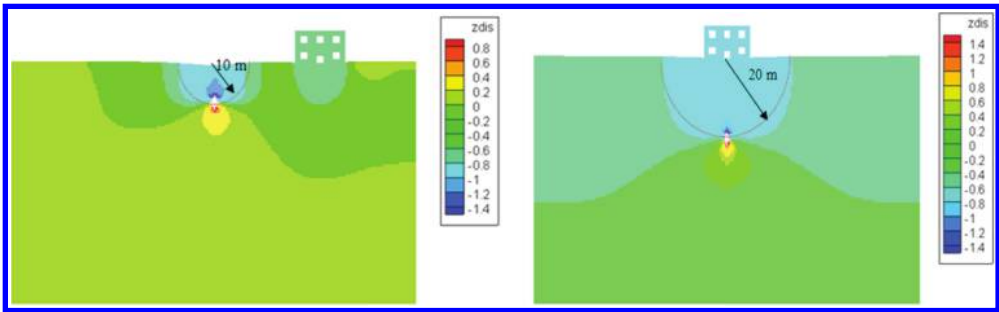


Figure 3. Vertical settlement cloud diagram under different embedded depths of the tunnel.

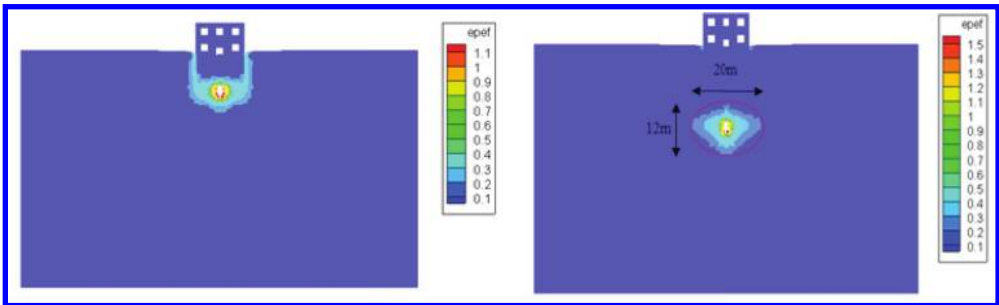


Figure 4. Equivalent plastic strain cloud diagram under different embedded depths of the tunnel.

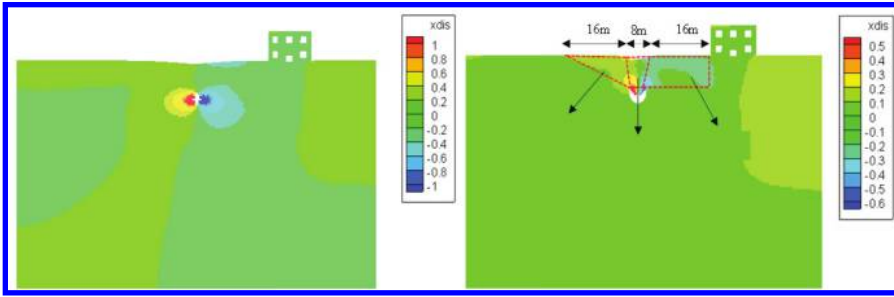


Figure 5. Lateral displacement cloud diagram under different degrees of damaged tunnel segment (left: segment whole broken; right: segment partially broken).

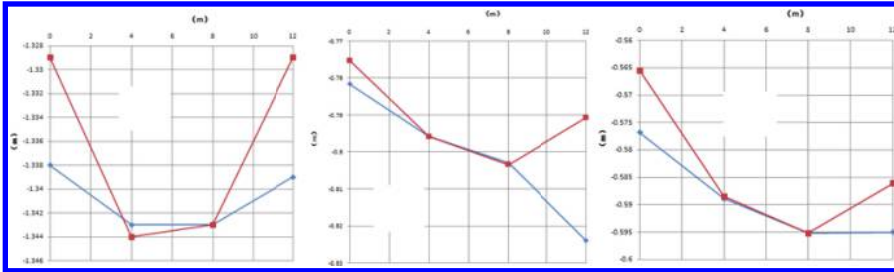


Figure 6. Vertical settlement scatter diagram under different distances from the tunnel (from the left to the right, the distance is 0 m, 10 m, 20 m, respectively).

### 3 ANALYSIS OF DEFORMATION OF THE ADJACENT MASONRY BUILDING

#### 3.1 Deformation of the adjacent masonry building at different distances from the tunnel

Assumed that the embedded depth of tunnel is 10 m and the segment is whole broken, the vertical settlement of the adjacent masonry building is obtained by recording the key points on the roof and floor ( $x = 0$  m, 4 m, 8 m, 12 m). As could be seen from Figure 6, when  $D = 0$  m ( $D$  represents the distance between the left side of the building and the point right above the tunnel), tension strain appears on the central of the building, while compression deformation exists on the both sides of it. With the  $D$  increasing, the whole settlement of the building decreases, indicating that the extent of damage to the building reduces. As the  $D$  increases from 0 to 20, an uneven sedimentation of the building emerges immediately and then decreases gradually.

#### 3.2 Deformation of the adjacent masonry building with different embedded depths of the tunnel

As could be seen from Figure 7, with the embedded depth of the damaged subway tunnel increasing, the

transverse compression value of the adjacent building within the affected area decreases, indicating that the degree of damage to the building reduces. The whole settlement of the building also reduces from 1.3 m to 0.7 m, which is in agreement with the expansion of the plastic deformation zone produced by the damaged tunnel shown in Figure 4.

#### 3.3 Deformation of the adjacent masonry building with different degrees of the damaged tunnel segment

By recording the key points on the left side and right sides of the wall ( $z = 0$  m, 4 m, 8 m), the lateral displacement ( $xdis$ ) of adjacent masonry building was investigated. As shown in Figure 8, when the segment is partially broken, a tensile failure appears on the first floor of the masonry building, while almost no lateral displacement appears on the second floor. When the segment is whole broken, monolithic translation to the right side (the side away from the tunnel) and tiny transverse compression appear on the first floor, while almost no lateral displacement appears on the second floor. In contrast, the segment partially broken evidently leads to a greater lateral displacement of the adjacent masonry building.

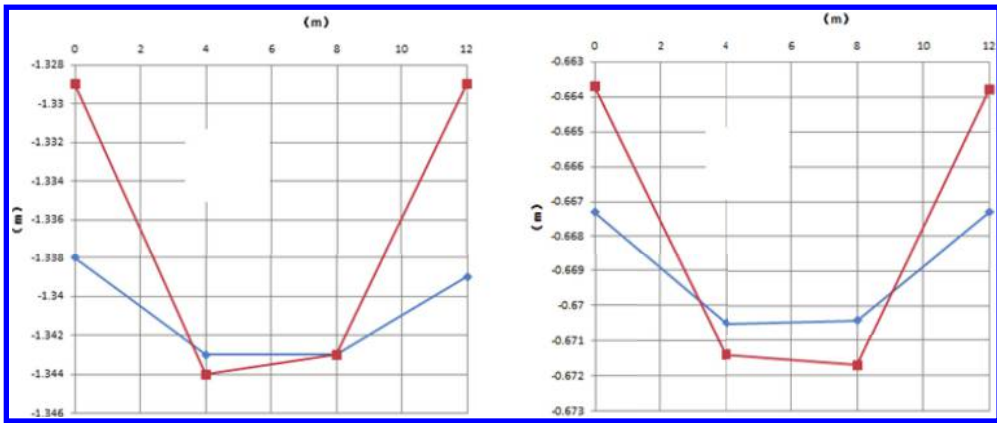


Figure 7. Vertical settlement scatter diagram under different embedded depths of the tunnel (left: 10 m; right: 20 m).

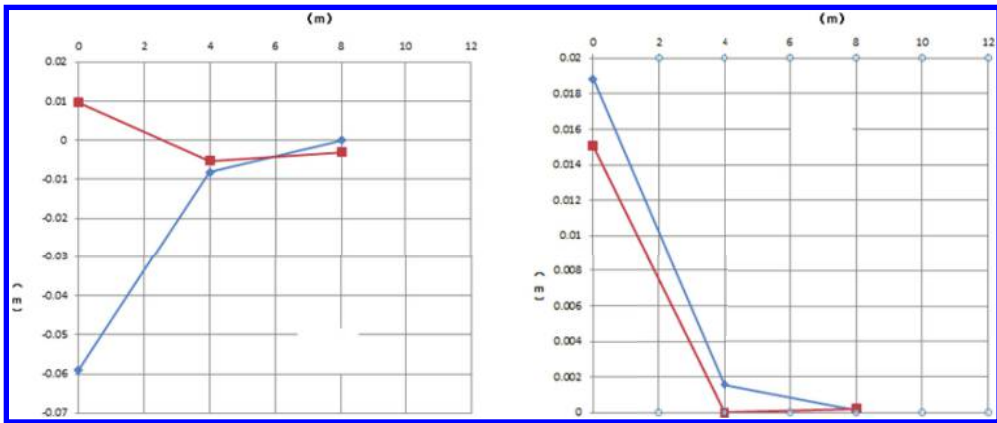


Figure 8. Lateral displacement scatter diagram under different degrees of damaged tunnel segment (left: segment partially broken; right: segment whole broken).

#### 4 CONCLUSIONS

In conclusion, as buildings get closer to the tunnel, the deformation caused by the damaged tunnel is larger. Correspondingly, the damage of buildings is greater. The obviously affected area may be a semicircular area with the radius of the embedded depth above the damaged tunnel, and with the embedded depth decreasing, the deformation of the building within the affected area increases. The segment partially broken leads to the partial collapse of the soil above the tunnel, which will enlarge the affected area of the lateral displacement. Whereas the segment whole broken mainly causes vertical settlement to the surrounding soils and buildings, and the affected area of the lateral displacement is smaller.

#### REFERENCES

Atkinson, J.H., Potts, D.M., and Schofield, A.N., 1977, "Centrifugal model tests on shallow tunnels in sand." *Tunnel and Tunneling*: 59–64.

Deng, F.H., 2009, "The shield tunnel segment displacement response analysis in the subway operation period." *Science Technology and Engineering*, 07:3684–3688.

Lian, Y.P., Zhang, F., Liu, Y., 2013, "Theory and application of the material point method." *Advances in Mechanics*, 02:237–264.

Zheng, G., Li, Z.W., 2012, "Comparison analysis of the effects of foundation pit excavation on adjacent buildings." *Chinese Journal of Geotechnical Engineering*, 969–977.

Zheng, Y.R., Qiu, C.Y., 2008, "The exploration of soil tunnel surrounding rock stability analysis method." *Chinese Journal of Rock Mechanics and Engineering*: 27(10).

# Experimental study on properties of zeolite powder concrete under the hot and humid environment

ZhongTian Chen

*Southwest Jiaotong University, Chengdu, Sichuan, China*

**ABSTRACT:** With the tunnel construction gradually growing deep in direction, problems caused by high geothermal heat damage becomes increasingly prominent. High geothermal occurred mainly in two forms: dry heat and the hot and humid. Under these 2 conditions, the strength of concrete can be affected. Using zeolite powder as admixture is a viable way to improve the mechanical properties. But it remains unknown whether it performs better in hot and humid condition or dry heat. So we set 5 groups of experiments to determine the mechanical properties of zeolite powder concrete. Throughout the date we find that dry heat condition can cause a significant loss of zeolite powder concrete. But in hot and humid conditions, cement and zeolite powder can be fully hydrated, and calcium hydroxide active silica and zeolite powder contained in an alumina produced with cement hydration reaction to form secondary hydration, increasing the content of gelled material, thereby increasing the strength of the concrete. So that similar to the zeolite powder concrete and fly ash concrete, dry heat intensity decreases, and significantly increased strength under hot and humid conditions, it is more suitable for steam curing.

**Keywords:** zeolite powder concrete; hot and damp condition; mechanical properties; secondary hydration

## 1 INTRODUCTION

### 1.1 Background

The project comes from the topics of National Natural Science Foundation: <thermal properties of concrete harm Tunnels> (51008253).

When the tunnel construction gradually grows deeper in direction, problems caused by high geothermal heat damage becomes increasingly prominent. High geothermal occurred mainly in two forms: dry heat and the hot and humid.

Dry heat is the heat inside the geological strata in geological formations where there will be better spread through the rock tunnel surface. The hot and humid occurs in a high degree of development of rock crushing fracture zone, the underground water is easier to enrichment, which form hot springs. Injection concrete's performance differs in construction process parameters and physical mechanical properties contrast with normal temperature condition. High-temperature and high-temperature could lead sprayed concrete action to increased strength retraction system volume stability deteriorates and adhesion rock heavy losses and other issues. When the tunnel faced with thermal damage, it also faced erosion of sulfate and chloride. Coupling factors that could cause the ejection durability of concrete faced with great challenges,

whether it relates to the normal functioning of shotcrete tunnel lining role. [1]

The trial will focus on the mechanical properties of concrete zeolite powder at a relatively humid and dry heat harm environment.

Zeolite is a natural zeolite rock as raw material, crushing, grinding into powder materials. Zeolite powder contains large amounts of  $\text{SiO}_2$  and  $\text{Al}_2\text{O}_3$ , silica fume after its pozzolanic activity. Its activity is better than fly ash and slag after volcanic ash silica fume. In addition to the active effect, Zeolite powder also has a special porous structure, pore zeolite adsorption of water can also be in the conservation of hydration to further promote the growth of strength. [2]

Therefore, this project tests these problems by simulating the thermal effects of different design than the preservation of the environment, mechanical testing, and other means of concrete mix, the mechanical properties of concrete with different contents of zeolite powder, thermal properties of concrete in hot condition to provide some guidance to improve the properties of concrete.

### 1.2 Zeolite powder

Zeolite is a natural zeolite rock from the ground. Zeolite rock is volcanic ash after an aluminosilicate mineral natural calcine, will have a certain amount

of active silica and alumina. The color is white (Fig. 1) Zeolite powder having a large internal surface area and an open structure, the fineness of 0.08 mm sieve <5%, an average particle diameter of 5.0 ~ 6.5 μm.

The chemical composition is shown in Table 1. [3]

It contains most of all the major elements and trace elements the aquatic animal growth needs, all these elements exist in ionic form easily used by aquatic animals. Therefore, aquaculture is the most commonly used zeolite powder. [4] Zeolite rock series has more than 30 varieties and ash zeolite and mordenite are commonly used as admixture of concrete. The micro structure is shown in Figure 2. [4]



Figure 1. Zeolite powder.

Table 1. Chemical composition of zeolite powder.

SiO <sub>2</sub>	Al <sub>2</sub> O <sub>3</sub>	Fe <sub>2</sub> O <sub>3</sub>	TiO <sub>2</sub>	CaO	MgO	K <sub>2</sub> O	Ignition loss
62.87	13.46	1.35	0.11	2.71	2.38	2.78	12.80

## 2 THE EXPERIMENT DESIGN

### 2.1 Dividing groups

In order to distinguish the performance of fly ash concrete and the zeolite powder concrete, we set 5 groups of experiments. Concrete blocks from each group will be cared in three different conditions: Hot water, dryer, and normal maintenance, and will be put into two kinds of mechanical test.

Every block is made into one unified size of 100 mm\*100 mm\*100 mm and will be cared for four weeks. The strength level of concrete is C30. [5]

To distinguish the blocks from three different conditions, we name the blocks cared in hot water with a word S in the end of its name. So as the ones from dryer with G, and normal condition with BZ.

After naming the groups, we determined the percentage of cement and other materials of each group. The detail is shown as follows.

### 2.2 The experimental group

- 2.2.1 Group 1 (100% cement) {1,2}
- 2.2.2 Group 2 (70% cement + 30% zeolite) {3,4}
- 2.2.3 Group 3 (70% cement + 30% fly ash) {5,6}
- 2.2.4 Group 4 (60% cement + 20% zeolite + 10% silicon ash) {7,8}
- 2.2.5 Group 5 (65% cement + 20% zeolite + 5% silicon ash) {9,10}

The number in these groups means whether the block will be tested in which way, the tensile splitting experiment or compressive experiment. Those with uneven number will be tested in compressive experiments, and others will be tested in tensile splitting experiment.

Each group has 3 blocks for the compressive experiment, and another 3 blocks for splitting the

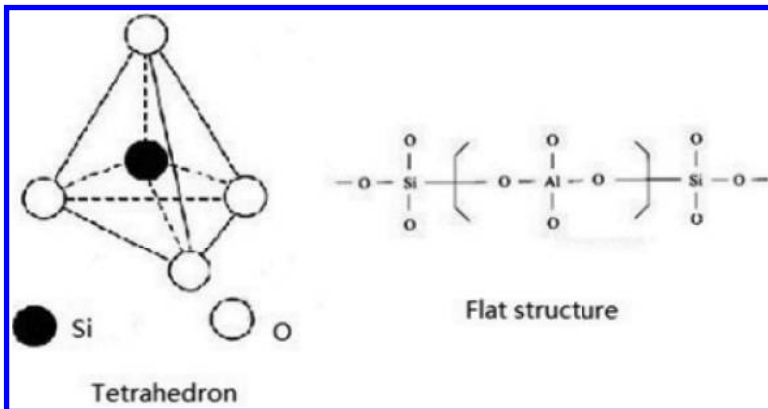


Figure 2. Micro structure.

compressive experiments. The actual data after the test are shown in Table 2.

The blocks just made and names are shown in Figure 3.

### 2.3 The experiment data (MPa)

Table 2. Experiment data.

	1	2	3	AVA
1BZ	37.993	37.888	38.478	38.11966667
1G	34.338	34.652	36.187	35.059
1S	29.875	32.842	28.982	30.56633333
2BZ	5.95	4.35	5.19	5.163333333
2G	4.96	4.96	4.56	4.826666667
2S	5.02	5.39	5.39	5.266666667
3BZ	27.858	28.166	29.042	28.35533333
3G	22.434	22.132	22.249	22.27166667
3S	32.645	31.802	30.109	31.51866667
4BZ	3.066	2.516	2.385	2.655666667
4G	1.267	2.063	2.785	2.038333333
4S	2.657	2.977	3.012	2.882
5BZ	34.561	34.617	32.865	34.01433333
5G	13.152	19.763	20.378	17.76433333
5S	40.159	37.783	35.167	37.703
6BZ	2.573	2.662	2.875	2.703333333
6G	2.151	2.537	2.666	2.451333333
6S	4.016	4.117	4.303	4.145333333
7BZ	23.286	22.137	23.546	22.98966667
7G	17.446	16.896	17.233	17.19166667
7S	37.62	33.75	37.281	36.217
8BZ	2.883	2.874	2.799	2.852
8G	0.988	0.83	0.9	0.906
8S	3.957	3.84	3.906	3.901
9BZ	28.217	29.096	29.437	28.91666667
9G	11.988	16.025	15.845	14.61933333
9S	29.245	29.006	29.437	29.22933333
10BZ	2.882	2.945	2.706	2.844333333
10G	1.794	1.682	1.915	1.797
10S	4.461	4.358	4.236	4.351666667



Figure 3. Name the blocks.

## 3 ANALYZE AND CONCLUSION

As we can see in Table 2, both the compressive properties and tensile splitting properties of concrete mixed with zeolite or fly ash cured in water tank is clearly higher than those cured under normal condition. But it comes to the same. Similarly, the zeolite powder concrete in hot and humid conditions exhibits mechanical properties of fly ash concrete, namely a significant reduction of breaking strength in dry heat conditions, and fracture strength under hot and humid conditions increase, which indicates that the dry and hot conditions on the zeolite powder concrete strength development is detrimental to the development and humid strip of concrete strength advantageous zeolite powder.

So we get the conclusion: Although the zeolite powder has a porous absorbent structure, but in the development of concrete strength under dry and hot conditions, the moisture in the concrete cement and zeolite powder is insufficient to support the completion of their hydration, that is, under these conditions, a portion of the water in the concrete cement hydration role, but zeolite powder lacks water and hydration cannot completely occur, resulting in incomplete gray concrete hydration which causes less gelled substance. In this case, early strength of concrete developed rapidly, due to lack of water, affects the development of late strength of concrete.

But in hot and humid conditions, water is abundant, cement and zeolite powder can be fully hydrated, and calcium hydroxide active silica and zeolite powder contained in an alumina produced with cement hydration reaction to form secondary hydration, increasing the content of gelled material, thereby increasing the strength of the concrete. So that, similar to the zeolite powder concrete and fly ash concrete, dry heat intensity decreases, and significantly its strength increases under hot and humid conditions; it is more suitable for steam curing.

## REFERENCES

- [1] Zeolite Powder and Its Use in High Strength Concrete (In Chinese)-Shujin Li, Keru Wu, -TU528.31-1003-1324(2004)01-0040-04.
- [2] Information on <http://www.wikipedia.org>.
- [3] Information on <http://baike.baidu.com>.
- [4] Produce and Usage of Zeolite Powder in Pumping Concrete (In Chinese)-Xiaoli Zhong, Zemin Zhu, 1002-3550(2005)07-0084-02 *Typography for references*.
- [5] Use of Natural Zeolite in aquaculture (In Chinese)-Hongmei Gao, Mingxue Wang, 1003-1278(2005)01-0001-03.

# Study on influence of foundation pit excavation on existing tunnels

Y. Cui

*School of Civil Engineering and Architecture, Anhui University of Science and Technology, Huainan, China*

S.M. Zhang

*School of Civil Engineering and Architecture, Anhui University of Science and Technology, Huainan, China*  
*Department of Civil Engineering, Zhejiang University City College, Hangzhou, China*

T. Feng

*School of Civil Engineering and Architecture, Anhui University of Science and Technology, Huainan, China*

X.Q. Wang & M.M. Sun

*Department of Civil Engineering, Zhejiang University City College, Hangzhou, China*

**ABSTRACT:** Soil unloading caused by excavation will inevitably lead to the change of displacement and stress field, and this threatens the security of the subway at the bottom or side. Researches focus on vertical rebound deformation rules of existing tunnels under excavation and the reinforcement methods, and quantitative displacement calculation is also needed. Considering the soil plastic flow and groundwater buoyancy, the causes of foundation pit uplift are summarized. In addition, the study method of foundation pit excavation influence on existing tunnels can be summed up using theoretical calculation method, field measurement analysis method, numerical simulation, empirical formula method, and the centrifugal test. Finally, some problems which need to be further probed are presented.

**Keywords:** excavation of foundation pit; the existing tunnel; foundation pit uplift; study methods; deformation rules

## 1 INTRODUCTION

With the vigorous development of infrastructure, while the urban construction is growing on the ground, the underground construction is gradually expanding. The excavation of foundation pit will have an adverse impact on existing tunnels situated at the bottom or side, so this is related to the safe operation of subway tunnel. For the foundation pit located in the city center, the protection of surrounding pipelines and structures is becoming a controlling factor in the design and construction, so the impact of excavation on the tunnel should be controlled within the permissible range.

## 2 CAUSES OF FOUNDATION PIT UPLIFT

Foundation pit uplift is generally considered to be primarily caused by several factors: (1) rebound deformation produced by soil excavation; (2) due to soil pressure, the deformation of retaining wall below the basement is toward the center of the pit, and that shoves the soil in pit to uplift;

(3) irreversible soil deformation formed by plastic flow because of the existing weak layer in pit bottom; (4) uplift of soil caused by groundwater buoyancy and seepage flow; and (5) deformation due to the secondary release of cumulative stress from surrounding buildings during excavation. Moreover, the degree of resilience is also relevant to geological conditions, unloading volume, size of the pit, exposure time, sequence of excavation and equipment conditions, and so on. By analyzing these factors, the deformation mechanism of foundation pit uplift will be further understood.

## 3 RESEARCH STATUS

Issues related to this research focus on the following aspects domestically and abroad: (1) the variation of both the deformation and force of the existing tunnels during the construction of foundation works; (2) the influence factors and range of the tunnel deformation, and the prediction methods of the maximum tunnel uplift value; (3) the effect degree of different construction conditions on the



tunnel, and then to get the best design and construction scheme; and (4) the impact of foundation pit dewatering.

## 4 RESEARCH METHODS

Surrounding the influence of excavation on existing tunnels, many scholars have done a lot of works using a variety of methods, including theoretical calculation method, field measurement analysis method, numerical simulation, empirical formula method, and the centrifugal test.

### 4.1 Theoretical calculation method

Zhang Zhiguo proposed the two-stage method for analyzing effects on adjacent metro tunnels due to foundation pit excavation. Firstly, the additional stress due to adjacent foundation pit excavation is calculated. Secondly, the governing differential equation is built based on Winkler model. Then the differential equation is deduced to the finite element equation by the Galerkin method. Furthermore, the parametric analysis of existing tunnels is carried out, including the different depths and distance from the excavation site, the different geologic conditions, and the different outer diameters of the tunnel.

A simple two-stage method for estimating the longitudinal deformation of existing tunnels caused by adjacent excavation in soft soils is presented. In the first stage, the Loganathan and Poulos analytical solution is used to estimate the free-soil settlement induced by adjacent tunneling. The additional stress due to adjacent foundation pits excavation is calculated based on the Mindlin solutions. In the second stage, existing tunnels are considered as beams with infinite length based on the Winkler foundation model. The free-soil settlement or additional stress is then imposed on the existing tunnels. Displacements and internal forces of the existing tunnels are obtained.

Assuming that the tunnel deformation agrees with the soil displacement, the theory of residual stress and stress path method are used to build a predictive calculation model of tunnel deformation considered excavation, and it was applied to Shanghai square excavation under which the two existing tunnels lie. Meanwhile, using Boussinesq equation, soil resilience value  $s$  due to excavation can be calculated:

$$s = \frac{1 - \mu^2}{E} \omega b p_0$$

$b$  is the width of rectangular load or the diameter of circular load;  $\omega$  is the rebound influence coefficient of center point;  $E$  is the elastic modulus of

soil and usually replaced by deformation modulus;  $p_0$  is uniform load on foundation surface; and  $\mu$  is Poisson's ratio of soil.

Considering the equivalent stiffness of tunnel, excavation unloading and foundation reinforcement, deformation mechanisms are conducted on tunnel uplift due to mixing-piles driving above. Based on data from the East Road Underpass Project, a method to calculate the vertical displacement of tunnels using the Winkler model was derived, and the calculation is carried out. The result was compared with the measured data. It is indicated that effects of above foundation pit reinforcement on the vertical displacement of tunnels are considerable.

### 4.2 Field measurement analysis method

Through the arrangement of the measuring point, field monitoring is widely used in the study. The information of construction process can be acquired in time, and monitoring results can also be used to evaluate the security situation of the tunnel.

Combined with the field monitoring date from East Road Underpass Project in Shanghai, the influence of foundation pit excavation on adjacent tunnels is analyzed, and it shows that: with soil rebound the subway tunnel uplifts like a normal distribution curve, and the maximum point approaches the center of excavation; in quite a long period of time after the excavation, the soil in pit continues the trend of rebound, but rebound deformation is limited because of the upper load; some factors are remarkable to the displacement of the tunnel including the exposure time of excavation and the distance between tunnel axis and foundation pit, and the tunnel uplift presents a nonlinear increase with the increase of exposure time and excavation volume.

The horizontal and vertical displacement of the tunnel and the chordwise deformation of tunnel lining were measured in Shanghai Square excavation adjacent to tunnel. The results show the tunnel produces lateral displacement to foundation pit direction when deep excavation adjacent to tunnel, and the section of tunnel produces a lateral ellipse shaped deformation; the construction of concrete cushion timely can effectively control the further development of lateral tunnel displacement, and only after the completion of the foundation slab the displacement of the tunnel achieves stability; and grouting rectification in the outside of the tunnel can promptly correct the lateral displacement of subway tunnel, but the comprehensive effect is not very satisfactory.

Field measurement analysis can monitor the tunnel deformation in real time, and the data is reliable

and can provide guidance for the construction. However, most monitoring is for the vertical and horizontal displacement of the tunnel at present. Due to a limited number of measuring points there are less monitoring dates from convergence deformation of tunnel, soil pressure and pore water pressure.

#### 4.3 Numerical simulation

Compared with the field measurement analysis method, numerical simulation has the following advantages: (1) it can simulate the variation of tunnel deformation and stress state with pit reinforcement and excavation process; (2) through simulation to compare different effects of pit reinforcement measures on existing tunnel, and then to get the optimization scheme; and (3) by changing the parameters to study the influence extent of tunnel uplift by different factors. But some certain deviations are presented leading to the difference between calculated value and measured results, including parameter selection, mesh generation and unreasonable assumptions, and simplification.

#### 4.4 Empirical formula method

Based on measured dates from the Dongfang Road Underpass Project, the analysis shows that the maximum vertical uplift value of tunnel  $S$  increases with an increase in excavation width  $B$ , and their relation is a hyperbolic curve. The formula is:

$$S = A_1 \times e^{A_2/B}$$

$$A_1 = 12.614e^{-7.1246/t}$$

$$A_2 = 8.9151/t - 6.5242$$

$A_1$  is the extreme coefficient.  $A_2$  is the spatial sensitivity coefficient.  $t$  is the exposure time of excavation. The formula can simply estimate the maximum uplift value at any time of excavation and in any excavation width. The disadvantage is the formula is obtained only by the one project, so its reliability is difficult to guarantee, meanwhile the value of the exposure time of excavation is difficult to acquire.

#### 4.5 The centrifugal test

With a case of the excavation of Century Metropolis in Shanghai, centrifugal model tests are used to study the deformation of the retaining walls and tunnel structures. The studies show that test results conform to the actual project and can relatively reflect the practical situation. Excavating large

part of the pit firstly is more reasonable to control the deformation of the retaining walls and tunnel structures.

## 5 CONCLUSIONS

The protection of the underground environment is becoming the controlling factor in urban areas, and the design of foundation pit engineering has gradually changed from the stability control to deformation control. According to the research status, there are several shortage as follows: (1) There is only the qualitative explanation to the impact of the stiffness and insertion depth of retaining structure on foundation pit deformation, and shortage of a complete theoretical formula to quantitatively calculate; (2) During the construction the size of excavation area and the excavation depth of each step are ordinarily based on experience, so measures should be taken to optimize the parameters of foundation pit excavation; and (3) Studies on the influence of tunnel mainly concentrate on the period of excavation construction, however the long-term tracking studies are few, so subsequent related studies should be strengthened.

In general, the current study on this aspect isn't mature completely. Most researches are based on single project and lack of systems analysis; therefore, monitoring and analysis should be strengthened during foundation pit reinforcement and excavation to accumulate practical experiences for further theoretical analysis.

## ACKNOWLEDGMENT

The work is supported by Science Technology Department of Zhejiang Province (2013C31041), Zhejiang Provincial Department of Housing and Urban-Rural Development (2014Z099), Teacher Fund of Zhejiang University City College (J-15017), and Student Research Program of Zhejiang University City College (XZ2015524070).

## REFERENCES

- Chen, Y. & Zhang, D.M. 2004. Analysis of monitoring data on tunnel heaving due to unloading of foundation pit excavation. *Chinese Journal of Underground Space and Engineering* 24(5): 748–751.
- Ding, T.H., Ding, H.G., He, G.J. & Wang, H.J. 2008. Construction technology for building deep foundation pit adjacent to subway tunnel on both sides. *Building Construction* 30(7): 511–514.
- Hou, X.Y., Liu G.B. & Huang, Y.X. 2000. Several views on the development of urban foundation work. *Construction Technology* 29(1): 5–7.

- Ji, M.J. & Liu, G.B. 2001. Prediction method of displacement due to excavation. *Journal of Tongji University* 29(5): 531–535.
- Jia, J. & Xie, X.L. 2008. Deformation and control measures of deep and large foundation pits in Shanghai soft clay area. *Chinese Journal of Geotechnical Engineering* 30(Supp.): 376–380.
- Kuang, L.C. 2000. Influence of construction of deep foundation pit on tunnels of metro. *Chinese Journal of Geotechnical Engineering* 22(3): 284–288.
- Li, P., Yang, T., Wang, Y. & Chen, Y.M. Summary of heave deformation of foundation pit engineering. *Journal of Hohai University: Natural Sciences* 38(2): 196–201.
- Li, Z.G., Liu, H., Liu, G.B. & Bi, H.M. 2005. Influence analysis of deep-dip excavation on down tunnel based on the measured displacement. *Chinese Journal of Underground Space and Engineering* 1(4): 619–623.
- Liang, F.Y., Chu, F., Song, Z. & Li, Y.S. Centrifugal model test research on deformation behaviors of deep foundation pit adjacent to metro stations. *Rock and Soil Mechanics* 33(3): 0657–0664.
- Liu, G.B., Huang, Y.X. & Hou, X.Y. 2001. The prediction and control of rebound deformation of the existed tunnels right under excavation. *Chinese Journal of Rock Mechanics and Engineering* 20(2): 202–207.
- Liu, T., Liu, G.B. & Shi, S.Y. 2009. Displacement of subway tunnels induced by above foundation pit reinforcement. *Journal of Harbin Institute of Technology* 41(2): 141–144.
- Loganathan, N. & Poulos, H.G. 1998. Analytical prediction for tunneling-induced ground movements in clays. *Journal of Geotechnical and Geoenvironmental Engineering* 124(9): 846–856.
- Wang, W.D., Shen, J., Weng, Q.P. & Wu, J.B. 2006. Analysis and countermeasures of influence of excavation on adjacent tunnels. *Chinese Journal of Geotechnical Engineering* 28(Supp.): 1340–1345.
- Wu, S.Y., Yang, X.P. & Liu, T.J. 2012. Analysis of influence on deformation of adjacent subway tunnel due to bilateral deep excavations. *Chinese Journal of Rock Mechanics and Engineering* 5(S1): 3452–3458.
- Yao, Y.M., Zhou, S.H., Sun, W. & Chen, X.L. 2004. Calculation and an analysis of influence of bottom strengthening on deformation of foundation pit for parallel transition station. *Underground Space* 24(1): 7–10.
- Yao, W.H., Liao, X.G., Ma, H.L. & Wei, G. 2013. Review of the impact of foundation pit excavation passing below existing shield tunnel. *Municipal Engineering Technology* 31(2): 105–110.
- Zhang, Z.G., Zhang, M.Q. & Wang, W.D. 2011. Two-stage method for analyzing effect of adjacent metro tunnels due to foundation pit excavation. *Rock and Soil Mechanics* 32(7): 2085–2092.
- Zhang, Z.G., Huang, M.S. & Wang, W.D. 2009. Response of existing tunnels induced by adjacent excavation in soft soils. *Rock and Soil Mechanics* 30(5): 1373–1380.
- Zheng, G., Liu, Q.C., Deng, X. & Zhang, L.M. 2012. Field measurement and analysis of effect of excavation on existing tunnel boxes of underlying metro tunnel in operating. *Rock and Soil Mechanics* 33(4): 1109–1116.

# Study on numerical simulation of influence of excavation on existing tunnels

S.M. Zhang

*Department of Civil Engineering, Zhejiang University City College, Hangzhou, China*

*School of Civil Engineering and Architecture, Anhui University of Science and Technology, Huainan, China*

Y. Cui

*School of Civil Engineering and Architecture, Anhui University of Science and Technology, Huainan, China*

Y.S. Huang & M.M. Sun

*Department of Civil Engineering, Zhejiang University City College, Hangzhou, China*

**ABSTRACT:** For the issue of foundation pit excavation on adjacent tunnels, numerical simulation software is applied to dynamically simulate the excavation and reinforcement process. The interaction of foundation pit and existing tunnels in four different relative positions is analyzed, including the tunnel under the foundation pit, the tunnel beside the foundation pit, the tunnel between the foundation pits and the foundation pit between the tunnels. Based on the simulation results, the effectiveness of soil reinforcement in passive zone, heap loading, and anti-floating pile is presented by comparative evaluation and the optimized excavation sequences are probed. Moreover, the superiorities and the deficiencies of numerical methods are introduced emphatically.

**Keywords:** numerical simulation; foundation pit excavation; existing tunnels; excavation sequences; deformation control

## 1 INTRODUCTION

In recent years, with the construction of the subway, the area along with the subway has been the flourishing region, and more and more construction projects are located on the subway tunnel or the side. Excavation will have an impact on the stability of the existing subway. The essential reason is the soil stress redistribution caused by surrounding excavation, which leads to a series of mechanical change. Therefore, it is essential to control the impact of the excavation pit on the subway tunnel within the allowable range.

Surrounding the influence of excavation on existing tunnels, many scholars have done a lot of works using numerical simulation methods. As a kind of mechanical state analysis tool, numerical simulation is a more effective means to solve the problem of geotechnical engineering and has been accepted by academia and engineering field widely. It is more and more applied in the stability analysis of rock and soil mass, geotechnical engineering design, and optimization of the construction process.

Numerical simulation method has the following advantages: (1) It can simulate the variation of

tunnel deformation and stress state with pit reinforcement and excavation process; (2) Through simulation to compare different effects of pit reinforcement measures on existing tunnel, and then to get the optimization scheme; (3) By changing the parameters to study the extent of different factors on tunnel uplift; and (4) The simulation is low-cost and can be repeatable.

## 2 NUMERICAL SIMULATION OF THE RELATIVE POSITIONS

### 2.1 *The tunnel under the foundation pit*

Based on the Xiqing Road Tunnel crossing over the existing tunnel boxes of the Tianjin Metro Line, the simulation models of the actual construction process and four other calculation conditions are built by using ABAQUS, as shown in [Table 1](#).

The effectiveness of the soil reinforcement alongside the existing tunnel is prominent by comparison especially to reduce the different deformations between the two adjacent boxes of deformation joint. The increase of the different reinforcement parameters can reduce the uplift of the track in the tunnel and the different deformations between the

Table 1. The calculation condition.

Calculation condition name	Soil reinforcement on both side of existing tunnel box	“Protection hoop” of anti-floating piles and foundation slab	Heap loading on the foundation slab
Model 1	N	N	N
Model 2	Y	N	N
Model 3	N	Y	N
Model 4	N	Y	Y
Actual construction	Y	Y	Y

two adjacent boxes of deformation joint, but the reinforcement effect decreases with increase of the parameters, and it exists within a reasonable scope of the reinforcement.

To investigate the influence of the construction of the underground passage on the East Yan'an Road Tunnel in Shanghai and to evaluate the effectiveness of two protective measures, the numerical analysis of four different conditions is performed using the finite element code PLAXIS-GID, as shown in Table 2.

The results indicate that when excavating the bottom, the underlying tunnel uplifts in a range of about six times of the width of the pit. Each section of the tunnel produces a vertical egg-shaped plane deformation. The maximum of tunnel's curvature appears where the tunnel uplifts most. Unlike the above conclusion from the excavation of the Xiqing Road Tunnel in Tianjin, the result presents here that surcharge by heap loading is more effective to reduce the tunnel's curvature.

### 2.2 The tunnel beside the foundation pit

Based on the dates from the excavation of Daning Commercial Center in Shanghai, 3D FEM method is used to analyze the environmental effect due to excavation, and the modified Cambridge model was used to simulate soils. The results show that horizontal and vertical displacement of the tunnel gradually increases with the excavation of the basin edge in the side of subway, and then it reaches its maximum at the end of the excavation. The interval excavation in tunnel side can limit the deformation of retaining structures.

The numerical models of six different conditions are built to analyze the reinforcement effect of different widths and depths in foundation pit for the background of the excavation of the Pacific Plaza in Shanghai. The simulation results show that with the increase of the width and depth of the reinforced region, horizontal and vertical displacement of the tunnel decreases slightly, but some areas of which are flat or slightly uplifted. Passive zone reinforcement can slow down the tunnel settlement deformation, but simultaneously it shows that its

effect on horizontal displacement is greater than the vertical.

Pipeline protections are analyzed by numerical simulation to simulate three kinds of conditions, including passive zone reinforcement in pit, and reinforcement under and beside the pipelines. It turns out that the most effective method of controlling the displacement of underground pipelines is passive zone reinforcement. The closer the distance of the pit and the lateral reinforced structure is, generally the better the effect is. Grouting reinforcement under the pipelines can effectively control the vertical displacement of underground pipelines, but it has a lesser impact on the control of horizontal displacement. The bottom grouting reinforcement was not applied to prevent the deformation of the subway tunnel, and it needs further study to see if grouting reinforcement itself can cause the tunnel uplift.

### 2.3 The tunnel between the foundation pits

According to the practice of deep excavation adjacent to subway tunnel in Guangzhou, Midas/GTS is used to establish a 3D numerical model to analyze the interactive impact on the crossing tunnel caused by three kinds of different excavation sequences of the adjacent deep excavations on both sides of the tunnel. The calculation condition and the plane position are shown in Table 3 and Figure 1.

The result shows that the excavation and the support construction should be synchronous and symmetrical to control the horizontal displacement of the tunnel when excavating on both sides of the tunnel, but it is not suitable for controlling the vertical displacement of the tunnel. Partitioned excavation should be adopted to control the single unloading volume along the tunnel.

With a case in Lujiazui Financial District of Shanghai, a numerical simulation is conducted to analyze the influence of various factors, including the excavation sequence, installation of resistance piles, and relationship between tunnel and retaining wall of excavation. Plane position is as shown in Figure 2.

Table 2. The calculation condition.

Calculation condition name	Model 1	Model 2	Model 3	Model 4
Protective measures	Nothing	Soil reinforcement	Heap loading	Soil reinforcement and heap loading

Table 3. The calculation condition table.

Calculation condition name	Model 1	Model 2	Model 3
Excavation sequences	Symmetrical excavation of A1 pit and A2 pit	First excavation of A1 pit and then A2 pit	First excavation of A2 pit and then A1 pit

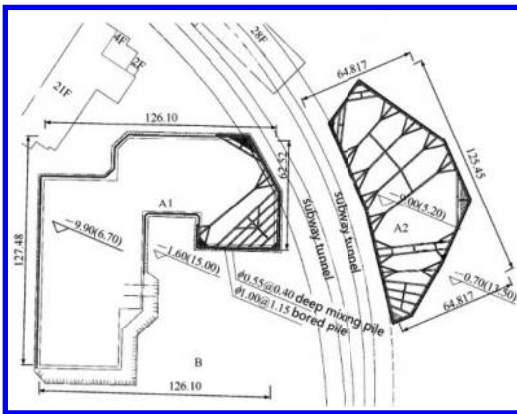


Figure 1. Plane position diagram.

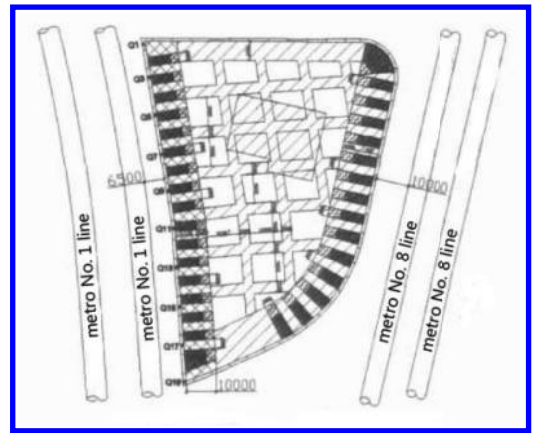


Figure 3. Plane position diagram.

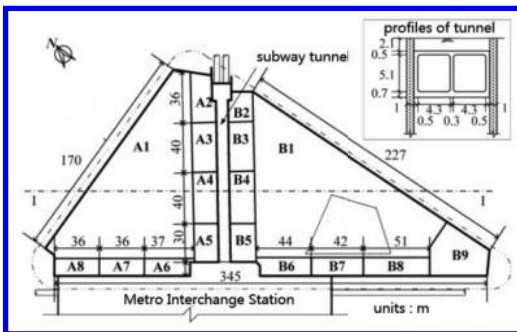


Figure 2. Plane position diagram.

It proves that when the excavation of foundation pit is divided into the small parts near the tunnel and the large parts in the distance, the method can isolate the impact on tunnels due to the excavation of the large parts. The displacement of tunnel

is mainly caused by the small excavation near the tunnel, and this method also can reduce tunnels uplift. The asymmetric excavation reduces the single unloading volume, but it can cause the lateral displacement of tunnels. Resistance piles connected with underground continuous wall of the tunnel in rigid connection can effectively control the vertical displacement of the tunnel.

#### 2.4 The foundation pit between the tunnels

Based on the excavation of Yajule International Plaza in Shanghai, the analysis of the deep foundation pit adjacent to tunnel on both sides is conducted. Plane position is as shown in Figure 3. With the support of multifarious construction technology including underground continuous wall, soil reinforcement with high-pressure rotary jet grouting pile in pit, well point dewatering, symmetrical excavation, and limited interval concrete

pouring, each step of construction completes successfully, so it is proved that the scheme is safe and economical.

### 3 CONCLUSIONS

For numerical simulation analysis: (1) Parameter selection and mesh generation have a great effect on calculation results; (2) Assumptions and simplification must be done for complex project, so it can not truly simulate completely; (3) The impact of construction technique on tunnel cannot reasonably simulate, such as trench construction of underground continuous wall and dynamic real-time tracing of grouting reinforcement. Therefore, some certain deviations are presented leading to the difference between calculated value and measured results.

Due to the complexity of the practical problems in geotechnical engineering, separately using a numerical method for the analysis of the engineering problems is not enough, therefore, the numerical analysis method of fluid-solid coupling analysis can be utilized fully in order to achieve the most effective analysis results. But in the meantime, geotechnical engineering materials is a complicated geological material with the feature of heterogeneity, anisotropy, and discontinuity, which presents the mechanical properties of nonlinear and inelastic. Therefore, the idea and method of numerical simulation should be improved to provide a high use value for practical engineering.

### ACKNOWLEDGMENTS

The work is supported by Science Technology Department of Zhejiang Province (2013C31041), Zhejiang Provincial Department of Housing and Urban-Rural Development (2014Z099), Teacher Fund of Zhejiang University City College (J-15017) and Student Research Program of Zhejiang University City College (XZ2015524070).

### REFERENCES

Chen, J.J., Wang, J.H., Du, Y., Wen, S.L. & Xiang, G.W. 2011. Movement of the shallow operating tunnel due to adjacent deep excavation on both sides. *Chinese Journal of Underground Space and Engineering* 7(6): 1163–1167.

Ding, T.H., Ding, H.G., He, G.J. & Wang, H.J. 2008. Construction technology for building deep foundation pit adjacent to subway tunnel on both sides. *Building Construction* 30(7): 511–514.

Hou, X.Y., Liu, G.B. & Huang, Y.X. 2000. Several views on the development of urban foundation work. *Construction Technology* 29(1): 5–7.

Huang, H.W., Huang, X., Schweiger, F.H. 2012. Numerical analysis of the influence of deep excavation on underneath existing road tunnel. *China Civil Engineering Journal* 45(3): 182–189.

Ji, M.J. & Liu, G.B. 2001. Prediction method of displacement due to excavation. *Journal of Tongji University* 29(5): 531–535.

Jia, J. & Xie, X.L. 2008. Deformation and control measures of deep and large foundation pits in Shanghai soft clay area. *Chinese Journal of Geotechnical Engineering* 30(Supp.): 376–380.

Li, D.Y., Gong, X.N. & Zhang, T.Q. 2001. Numerical simulation of the buried pipelines protection adjacent to deep excavation. *Chinese Journal of Geotechnical Engineering* 23(6): 736–740.

Wang, Q. 2011. Field and numerical analysis of a deep foundation in sensitive environment. *China Civil Engineering Journal* 44(Supp.): 98–101.

Wang, W.D., Shen, J., Weng, Q.P. & Wu, J.B. 2006. Analysis and countermeasures of influence of excavation on adjacent tunnels. *Chinese Journal of Geotechnical Engineering* 28(Supp.): 1340–1345.

Wang, W.D., Wu, J.B. & Weng, Q.P. 2004. Numerical modeling of affection of foundation pit excavation on metro tunnel. *Rock and Soil Mechanics* 25(Supp.): 251–255.

Wu, S.Y., Yang, X.P. & Liu, T.J. 2012. Analysis of influence on deformation of adjacent subway tunnel due to bilateral deep excavations. *Chinese Journal of Rock Mechanics and Engineering* 5(S1): 3452–3458.

Yao, W.H., Liao, X.G., Ma, H.L. & Wei, G. 2013. Review of the impact of foundation pit excavation passing below existing shield tunnel. *Municipal Engineering Technology* 31(2): 105–110.

Yao, Y.M., Zhou, S.H., Sun, W. & Chen, X.L. 2004. Calculation and an analysis of influence of bottom strengthening on deformation of foundation pit for parallel transition station. *Underground Space* 24(1): 7–10.

Zhang, Z.G., Zhang, X.D. & Wang, W.D. 2007. Numerical modeling analysis on deformation effect of metro Tunnels due to adjacent excavation of foundation pit. *Journal of Wuhan University of Technology* 29(11): 93–97.

Zheng, G., Liu, Q.C., Deng, X. & Zhang, L.M. 2012. Field measurement and analysis of effect of excavation on existing tunnel boxes of underlying metro tunnel in operating. *Rock and Soil Mechanics* 33(4): 1109–1116.

# Study on deformation control of the existing tunnels under foundation pit excavation

H.F. Xu, W.G. Liu & G.M. Zhao

*Zhejiang Xinsheng Group Co. Ltd., Hangzhou, China*

Y. Cui & S.M. Zhang

*Department of Civil Engineering, Zhejiang University City College, Hangzhou, China*

*School of Civil Engineering and Architecture, Anhui University of Science and Technology, Huainan, China*

**ABSTRACT:** In order to limit the impact of the excavation on tunnels within the allowable range, the construction must be controlled strictly. The deformation rules of tunnels are summarized during the foundation pit reinforcement and excavation. In addition, the application of time–space effect, piling sequence, foundation pit dewatering, and passive zone reinforcement of foundation pit are analyzed in detail and also the combined application of temporary diaphragm wall and divisional excavation is introduced emphatically. Finally, the practice proved that all these measures can be successful to control the further deformation and have a reference value for the similar design and construction.

**Keywords:** foundation pit uplift; deformation control; time–space effect; passive zone reinforcement; temporary diaphragm wall

## 1 INTRODUCTION

Because of the importance of the subway tunnels, a strict requirement is needed for the deformation of their own and adjacent foundation pits. For Shanghai subway, the horizontal displacement of retaining wall of level-one foundation pit is required to be less than 0.14%H (H is the excavation depth). Moreover, it has the explicit requirements for construction projects in the protected areas of metro: The value of absolute settlement and horizontal displacement is not more than 20 mm; the radius of curvature of the tunnel deformation is more than 15000 m; relative bending is not more than 1/2500; vibration peak velocity caused by piling and explosion is not more than 2.5 cm/s.

## 2 DEFORMATION CONTROL MEASURES

### 2.1 Reducing exposure time of excavation

The pit bottom bounce capacity is affected by time factor. After excavation without support, the uplift value of the pit increases with an increase in exposure time, so it promotes the uplift deformation of tunnel under the foundation pit. Therefore, during excavation, the adverse effects of exposure time should be considered, and some measures should be taken including overbreak control, installation

of support, and pouring concrete bottom plate in time.

### 2.2 Reasonable excavation method

At present, there are a variety of excavation methods such as excavation in strips and section, excavation in layers, basin excavation, island excavation, and so on. The excavation of Shanghai Daning Commercial Center is divided into ten districts, where the each excavation performed step by step. First, slope excavating to the base and pouring the foundation slab, after the foundation slab reaches the design intensity, the next earthwork construction can conduct. The district in the range of 50 m around the tunnel is left for excavation finally, and set plain stage of slope with a certain width. The final excavation of surrounding slope in tunnel side is conducted in strips and the length of the strip limits within 20 m to control the deformation of retaining structure.

### 2.3 Concrete pouring timely and heap loading

Fully considering the space-time effect, for reducing the exposure time of soil in pit, concrete pouring of the underground structure timely and adding early strength agent to the concrete is effective. Using the prepared sand bag for heap loading on the foundation slab which has reached a certain intensity can



offset the lifting deformation, and the heap capacity should be dynamically adjusted to guarantee the structure safety based on the monitoring data.

#### 2.4 Increasing stiffness and insertion depth of retaining structure

The insertion depth of retaining structure and the load around foundation pit are the determinant for the stability coefficient of resisting upheaval, which affects the upheaval value of foundation pit. With the decrease of insertion depth of retaining structure and the increase of the load around foundation pit, the upheaval value of foundation pit becomes large, and it presents a non-linear relationship.

Soil mixing wall is adopted as the retaining structure of the foundation pit of new Jingqiao Square in Shanghai. It is  $\Phi 850 \text{ mm} @ 600 \text{ mm}$  soil-cement mixed piles by triaxial stirring machine and also the I-beam of  $H700 \times 300$  inserts the mixing piles. It forms the compound retaining structure and sealing structure. Moreover, the insertions of I-beam are more intensive in the critical parts to improve the fender piles lateral stiffness and reduce horizontal deformation of retaining structures.

Based on the construction technology of the two-time reinforcement outside the deep excavation adopted in the station of Shanghai metro line 7 Jing'an temple, underground obstacle as the barrier against the displacement transfer induced by deep excavation is presented for the first time. Before the construction of diaphragm wall, the reinforcement with SMW should be finished in outside row of the foundation pit for the first time, and when it reaches the intensity the construction of diaphragm wall can be conducted. After that, jet grouting pile is adopted to reinforce the soil between the diaphragm wall and the reinforcement of SMW for the second time, as shown in Figure 1.

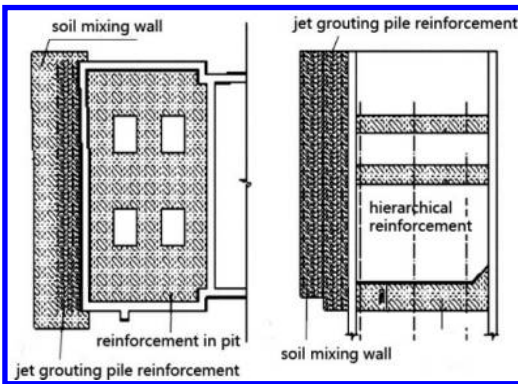


Figure 1. The reinforcement scheme.

The practice has proved that compared with the surrounding natural soil, the underground reinforcement structure as the large-stiffness barrier has the effect of obstructing displacement.

#### 2.5 Foundation pit dewatering

Foundation pit dewatering is an effective and economical measure in foundation reinforcement. Based on the CheKung Temple interchange project of Shenzhen Metro, two-dimension finite element software Plaxis is used to establish the model of plane strain to analyze the impact of dewatering on tunnel uplift deformation. Analysis shows that the step of the greatest influence on existing tunnel deformation is foundation pit dewatering in the strong water permeability strata like Shenzhen region. Foundation pit dewatering can control the upheaval of underneath tunnel, but it is an adverse factor for controlling the horizontal deformation. Therefore, the displacement values of the underneath tunnel in different orientations should be considered to take the reasonable dewatering measures.

#### 2.6 Passive zone reinforcement

Mixing piles commonly are used to reduce the tunnel deformation within the scope of excavation. First of all, foundation reinforcement can increase internal friction angle  $\phi$ , cohesive force  $c$  and elastic modulus of soil, and as a consequence the coefficient of subgrade reaction increases. Second, reinforcement body forms a space plate system with great integrality, and under the soil compaction effect of piles the constraint on tunnels increases. The arrangement form of passive zone reinforcement in pit can take many forms, including grid type reinforcement and full pit reinforcement.

##### 2.6.1 Grid type reinforcement

High-pressure rotary jet grouting pile and deep mixing pile are employed in passive zone reinforcement of Shanghai Square as shown in Figure 2. Reinforcement thickness is 5 m, and the grille width is 1.2 m at 5.8 m intervals; the two gratings on both sides of the tunnel are 2.2 m in width and 11.5 m in thickness. In addition, to reduce the disturbance above the reinforced plane, high-pressure rotary jet grouting pile and deep mixing pile are continued grouting above the reinforced plane with the drill pipe lifting.

##### 2.6.2 Full pit reinforcement and anti-floating pile

Full pit reinforcement with cement-soil mixing piles are used in the project of Xiqing Road Tunnel crossing over the existing tunnel boxes of the Tianjin Metro Line 1, as shown in Figure 3.

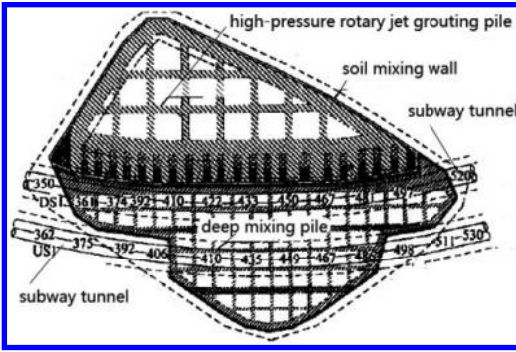


Figure 2. The foundation pit soil reinforcement scheme.

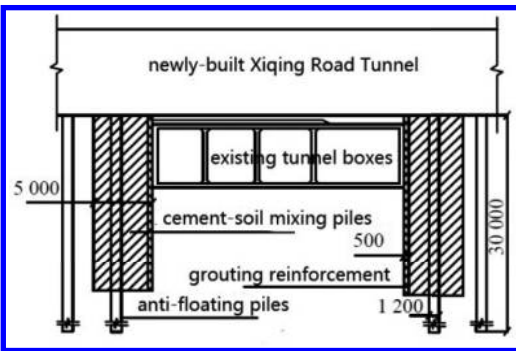


Figure 3. Reinforcement along both sides of tunnel boxes.

Because the distance of the newly-built tunnel floor from the existing tunnel boxes is only 0.3 m, the pit reinforcement is only carried out on both side of the existing tunnel boxes with cement-soil mixing piles, meanwhile, anti-floating piles are also set on both sides. When the effective connection of anti-floating piles and the newly built tunnel floor is finished, a “protection hoop” is built around the existing tunnel boxes to limit the deformation.

### 2.7 Optimizing piling sequence

After the partial dissipation of pore water pressure, controlling the number of continuous piling is the effective method to control the tunnel uplift. For using barrier effect of pile driving itself, reasonable arrangement of piling sequence is a economical and practical method. Due to piling to one direction, the front soil will continue to accumulate the outward and upward displacement, piling sequence largely determines the direction of compaction. When piling away from or paralleled to the tunnel, the tunnel displacement is small, and it turns out just the opposite when piling towards the tunnel.

Based on the practice of the East Road Underpass Project in Shanghai, optimal piling sequence is firstly using cement–soil mixing piles to reinforce the soil above the tunnel, and then reinforce the soil near the tunnel as a barrier structure. After reaching the basic intensity, piling can gradually continue away from the tunnel for the dissipation of pore water pressure.

### 2.8 Reinforcement and rectification with two-shot grouting

Two-shot grouting reinforcement can be used to adjust the curvature and horizontal displacement of the tunnel if necessary. In the aforementioned project of Xiqing Road Tunnel in Tianjin, due to the small distance of the newly built tunnel floor from the existing tunnel boxes, the mixing pile reinforcement on the boxes is infeasible. Therefore, the two-shot grouting reinforcement is adopted to combine the existing tunnel boxes with the surrounding reinforced structure in the range of 0.5 m surrounding the tunnel, as shown in Figure 3.

Analogously, in the project of the East Road Underpass in Shanghai, before the construction of anti-floating pile on both sides of the tunnel, the two-shot grouting is used to reinforce the soil on upper half circle of the tunnel, and grouting thickness is 1 m, as shown in Figure 4.

### 2.9 Temporary diaphragm wall inside foundation pit

According to the practice of deep excavation of Shanghai Wheelock Square adjacent to Shanghai Metro Line 2, the simulation of the excavation method is conducted. A temporary diaphragm wall is located 7.5–12.5 m to the northern diaphragm wall, so the large foundation pit is divided into the north and south foundation pit, as cross-section of retaining structure is shown in Figure 5. First, the excavation of the south pit (the large foundation pit far from the subway) is executed and heaping

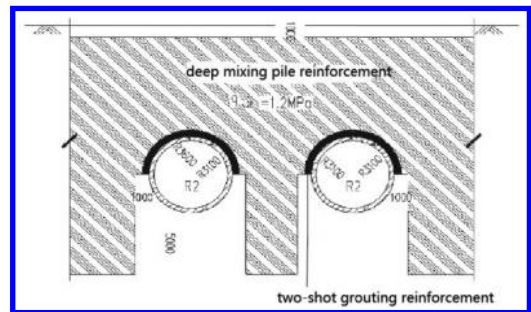


Figure 4. Cross-section of foundation reinforcement.

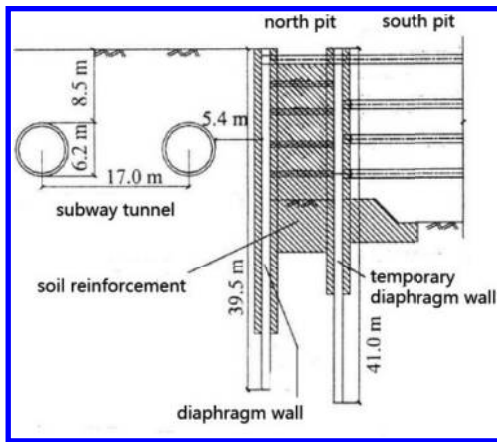


Figure 5. Cross-section of retaining structure.

loading on the foundation slab stabilizes the settlement deformation of tunnels, and then the north pit is excavated. Divisional construction can narrow the exposure range of excavation near the side of subway tunnel, and reduce the adverse effect of the whole excavation on subway tunnel.

### 2.10 Construction monitoring

The foundation pit excavation surrounding tunnels is a high-risk project, so the monitoring is very important for the operating metro tunnel and the surrounding environment. During excavation and reinforcement, based on the monitoring data the next deformation can be forecasted by using theoretical and numerical analysis tools. It is convenient to grasp the tunnel deformation, estimate the cause of the tunnel deformation and guide the construction.

## 3 CONCLUDING REMARKS

The protection of the underground environment is becoming the controlling factor in urban area, and the design of foundation pit engineering has also gradually changed from the stability control to deformation control. In summary, with the development of city construction in our country, the effects of foundation pit excavation and the related measures of controlling deformation will be paid much attention, and more effective and economic construction plan will be used to ensure the safety of the project.

## ACKNOWLEDGMENT

The work is supported by the Science Technology Department of Zhejiang Province (2013C31041),

Zhejiang Provincial Department of Housing and Urban-Rural Development (2014Z099), Teacher Fund of Zhejiang University City College (J-15017), and Student Research Program of Zhejiang University City College (XZ2015524070).

## REFERENCES

- Fu, Y.B., Liao, S.M. & Zhu, H.H. 2009. Soil squeezing effect of DCM pile and its application to subway tunnel. *Rock and Soil Mechanics* 30(7): 2005–2010.
- Gao, G.Y., Gao, M., Yang, C.B. & Yu, Z.S. 2010. Influence of deep excavation on deformation of operating metro tunnels and countermeasures. *Journal of Geotechnical Engineering* 32(3): 453–460.
- Li, J.J. & Wang, W.D. 2011. Design and construction of deep excavation engineering adjacent to the subway tunnel. *Journal of Railway Engineering Society* 2011(11): 104–110.
- Li, P., Yang, T., Wang, Y. & Chen, Y.M. 2010. Summary of heave deformation of foundation pit engineering. *Journal of Hohai University: Natural Sciences* 38(2): 196–201.
- Li, Z.G., Liu, G.B., Zeng, Y. & Wu, X.J. 2006. Control measures of tunnel displacement by over-excavation unloading. *Chinese Journal of Underground Space and Engineering* 2(3): 430–432.
- Liu, G.B., Huang, Y.X. & Hou, X.Y. 2001. The prediction and control of rebound deformation of the existed tunnels right under excavation. *Chinese Journal of Rock Mechanics and Engineering* 20(2): 202–207.
- Liu, J.Q., Ou, X.F., Zhang, X.M., Liang, Q.H., Yang, J.S. & Liu, X.Q. 2014. Study on effects of group foundation pits excavation on heaving/settlement of adjacent metro tunnel in operation. *Modern Tunneling Technology* 51(4): 81–87.
- Luo, Z. & Li, F.M. 1998. Analysis of the effect of ambient environment caused by deep mixing piles construction. *Soil Engineering and Foundation* 12(3): 1–5.
- Wang, W.D., Wu, J.B. & Weng, Q.P. 2004. Numerical modeling of affection of foundation pit excavation on metro tunnel. *Rock and Soil Mechanics* 25(Supp.): 251–255.
- Wang, X.B. & Jia, J. 2009. The influence of deep foundation pit excavation on nearby metro tunnel. *Urban Mass Transit* 12(5): 52–57.
- Wei, G. 2013. Measurement and analysis of impact of foundation pit excavation on below existed shield tunnels. *Rock and Soil Mechanics* 35(5): 1421–1428.
- Zhang, Z.G., Zhang, X.D. & Wang, W.D. 2007. Numerical modeling analysis on deformation effect of metro Tunnels due to adjacent excavation of foundation pit. *Journal of Wuhan University of Technology* 29(11): 93–97.
- Zheng, G., Liu, Q.C., Deng, X. & Zhang, L.M. 2012. Field measurement and analysis of effect of excavation on existing tunnel boxes of underlying metro tunnel in operating. *Rock and Soil Mechanics* 33(4): 1109–1116.

# The study on safety evaluation method of metro construction based on SHEL—BP neural network

J.X. Zhao, K. Fan, J.H. Sun & M. Liu  
*Qingdao Technological University, Qingdao, China*

**ABSTRACT:** From the perspective of improving the safety construction control level, we are applying the SHEL model to evaluate safety of the subway construction project in order to establish evaluation index system. We are using the BP neural network to establish the subway construction safety evaluation model due to the nonlinear relationship between the elements in the system. By performing research on multiple projects, using MATLAB software to training and testing the model, the empirical study shows that the evaluation model of the safety of subway construction project can give a more accurate rating. This model provides a scientific and effective evaluation method for the safety subway construction.

**Keywords:** metro construction; safety evaluation; SHEL; BP neural network

## 1 INTRODUCTION

At present, the metro construction has entered a stage of rapid development, in view of the characteristics like large scale construction, complex technology and catastrophic accidents of the project, early intervention and evaluation of construction safety has become increasingly important. According to W.H. Heinrich survey found that the cause of the accidents 88% were due to people's unsafe behaviors, 10% attributed to the unsafe state of object, 2% due to force majeure factors. The focus of prevention should be put on the control of people's unsafe behavior in the engineering (Qian, 2012). To reduce the metro construction safety risk, we need to start from people that is the most active factor in the engineering evaluate safety control.

For the metro construction safety evaluation, many scholars both at home and abroad adopt the method that figure out reasons from the results to put forward safety control index evaluation system. But Elwyn Edwards (Wang, 2010) established a people-centered elements of security model that make the index system of metro construction safety be sorted out from the origin of risk. In view of the above reasons, this paper based on the SHEL model, according to system decomposition and data analysis of metro construction process and the nonlinear relationship of each factor in the metro project, introduced BP neural network to evaluate the metro construction safety risk. In hope to provide a reference for the safety evaluation of metro construction projects.

## 2 SAFETY RISK INDEX SYSTEM

Elwyn Edwards in 1972 first proposed the SHEL model (Zhou et al., 2014), in which, the “Liveware” in the security work is at the specific system interface. This interface including Liveware—Software, Liveware—Hardware, Liveware—Environment, and Liveware—Liveware four links. In this coupling model, the “Liveware” is in the key position, the connection of the zigzag reflects the fragile relationship between the four nodes. The model has a good simulation of the key link in the construction environment, and has a general guidance for the safety construction, the details are shown in [Figure 1](#).

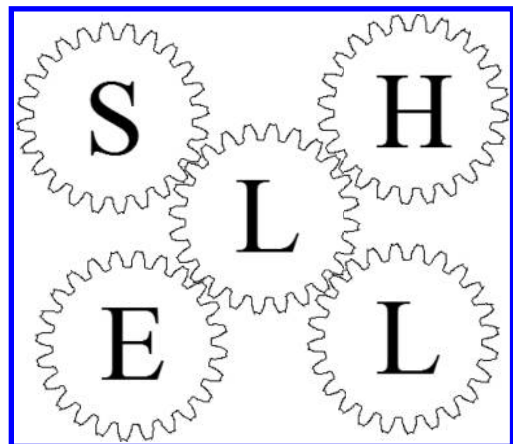


Figure 1. The SHEL model.

In the metro engineering construction:

1. L: It refers to all the factors that affect the construction safety in metro projects and have a direct contact with engineering personnel. As an organism who has subjective consciousness, people's behavior are limited by their own abilities and the objective project environment. Liveware generally includes the metro construction crew, material engineer, inspector, measurement engineer, technician, safety officer, mechanical operation team, design engineer, project manager and other related personnel in the system.
2. L-S: It refers to the degree of compliance with the work system, method in technical specifications and operation process for metro construction workers. If people free from the software interface or the interface is not scientific, it will increase the risk of accidents, and safety ratings downgrade.
3. L-H: It refers to the adaptive relationship between the metro construction personnel and physical factors. It would be a security risk during subsequent construction if operator can't correctly use system, material and advanced large equipment in the project.
4. L-E: It refers to the impact of the external environment on staff, including the construction environment, the meteorological environment, the company culture etc.
5. L-L: It refers to the collaborative relationship between underground engineering staff, is also the link that is most prone to errors in the system, reflecting in communication, technology level, cultural quality, etc.

The establishment of the metro construction safety evaluation index system based on the safety management's principles of integrity, unity and operability, considering the whole production safety activities process (Tian et al., 2011), combining with the literature (Ding et al., 2011) and the investigation of construction site workers and experts. The details are shown in Figure 2.

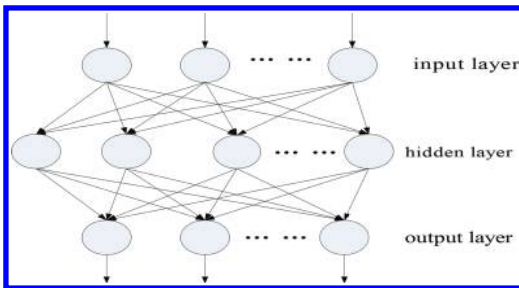


Figure 2. A typical structure of neural network.

### 3 METRO CONSTRUCTION SAFETY EVALUATION MODEL

#### 3.1 The BP neural network theory

BP neural network is an intelligent algorithm to mimic the human brain, it has a strong ability of imitation and association, due to a number of artificial neuron similar to natural nerve cells. Compared with the widely researched methods of fuzzy theory analysis, the BP neural network has a strong superiority between various factors about nonlinear causality in the evaluation of metro construction. It usually consists of three layers of neurons and its topology structure as shown in Figure 3.

#### 3.2 Establish the evaluation model

##### 1. index processing

In order to meet the requirements of the implementation of the BP neural network, we need

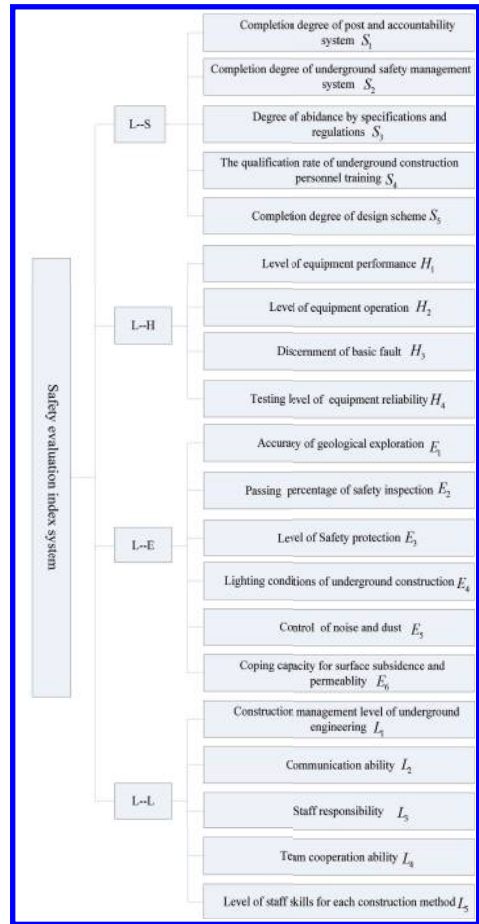


Figure 3. The evaluation index system.

to normalize index of different metrics datum, and convert it into a dimensionless index on [0, 1]. For qualitative indicators, we adopt expert scoring method and divide the indexes into five levels, that can be made of very poor, poor, general, good, excellent level. Specific definitions are shown in Table 1 (Li et al., 2014). We process the positive quantitative indicators with the formula (1) and process the negative quantitative indicators with the formula (2).

$$y = \frac{x - x_{\min}}{x_{\max} - x_{\min}} \quad (1)$$

$$y = \frac{x_{\max} - x}{x_{\max} - x_{\min}} \quad (2)$$

where  $y$  = processing after the index value and  $x$  = practical index value.

2. determine the output layer

The number of output layer neurons should be determined according to the system needs, the results of the model evaluation are the

safety of metro construction. Therefore, it can be described by a real number of continuous changes in [0, 1]. The output data can be converted into five qualitative index with very poor (0.1), poor (0.3), general (0.5), good (0.7) and excellent (0.9) level.

3. determine the hidden layer

There is not a definite theory to guide the hidden layer number, its selection is more flexible. If the node number is too little, network approximation effect is poor and it is not easy to convergence. Increasing the number of nodes can improve the approximation effect of existing discrete point sets, but the increased number of nodes inevitably leads to slow down the speed of training and make the calculated curve too flat (Chen et al., 2012). Generally, to best minimize the hidden layer number should follow that the output results should close to the simulation sample and meet the accuracy requirement. Therefore, many scholars use empirical formula (3) to determine the number of hidden layer.

$$n_y = \sqrt{n + m} + a \quad (3)$$

where  $n_y$  = the number of hidden layer neurons;  $n$  = the number of input layer neurons;  $m$  = the number of output layer neurons; and  $a$  is constant between 1 to 10.

Through experiment comparison, when the number of hidden layer neurons is 14, the speed

Table 1. Qualitative indicators rating.

Grades	Very poor	Poor	General	Good	Excellent
Index value	[0,0.3]	(0.3,0.5]	(0.5,0.7]	(0.7,0.9]	(0.9,1]

Table 2. Training and testing sample data.

Index	S <sub>1</sub>	S <sub>2</sub>	S <sub>3</sub>	S <sub>4</sub>	S <sub>5</sub>	H <sub>1</sub>	H <sub>2</sub>	H <sub>3</sub>	H <sub>4</sub>	E <sub>1</sub>	E <sub>2</sub>	E <sub>3</sub>	E <sub>4</sub>	E <sub>5</sub>	E <sub>6</sub>	L <sub>1</sub>	L <sub>2</sub>	L <sub>3</sub>	L <sub>4</sub>	L <sub>5</sub>
1	0.6	0.5	0.6	0.65	0.7	0.7	0.7	0.6	0.5	0.6	0.4	0.7	0.8	0.7	0.5	0.6	0.4	0.6	0.5	0.5
2	0.8	0.9	0.8	0.85	0.9	0.8	0.8	0.8	0.7	0.9	0.87	0.8	0.7	0.7	0.8	0.7	0.9	0.8	0.8	0.8
3	0.6	0.6	0.5	0.7	0.9	0.7	0.6	0.7	0.8	0.7	0.8	0.6	0.6	0.5	0.4	0.5	0.6	0.8	0.5	0.4
4	0.7	0.4	0.6	0.8	0.7	0.7	0.8	0.6	0.6	0.65	0.78	0.6	0.4	0.6	0.5	0.7	0.7	0.4	0.6	0.8
5	0.7	0.4	0.7	0.55	0.5	0.8	0.4	0.5	0.4	0.55	0.55	0.7	0.4	0.7	0.8	0.8	0.6	0.5	0.8	0.6
6	0.8	0.5	0.8	0.55	0.7	0.6	0.6	0.6	0.6	0.8	0.9	0.8	0.5	0.8	0.7	0.6	0.5	0.6	0.7	0.8
7	0.7	0.6	0.6	0.6	0.8	0.8	0.5	0.4	0.8	0.7	0.5	0.6	0.6	0.8	0.8	0.5	0.6	0.5	0.8	0.6
8	0.6	0.8	0.5	0.5	0.9	0.8	0.5	0.8	0.5	0.8	0.65	0.6	0.9	0.7	0.6	0.8	0.4	0.8	0.6	0.7
9	0.5	0.7	0.7	0.7	0.6	0.7	0.7	0.6	0.6	0.65	0.45	0.7	0.7	0.6	0.7	0.6	0.6	0.7	0.7	0.5
10	0.8	0.8	0.5	0.6	0.7	0.7	0.5	0.5	0.8	0.6	0.6	0.5	0.8	0.5	0.8	0.8	0.5	0.6	0.5	0.6
11	0.8	0.8	0.7	0.9	0.9	0.8	0.7	0.8	0.7	0.9	0.9	0.6	0.8	0.7	0.7	0.7	0.6	0.7	0.8	0.8
12	0.4	0.9	0.4	0.6	0.8	0.6	0.4	0.6	0.8	0.88	0.8	0.4	0.9	0.4	0.6	0.6	0.5	0.7	0.8	0.8
13	0.5	0.4	0.6	0.75	0.7	0.8	0.8	0.8	0.6	0.7	0.85	0.6	0.5	0.6	0.4	0.5	0.8	0.5	0.7	0.7
14	0.5	0.5	0.4	0.54	0.5	0.5	0.6	0.5	0.5	0.6	0.45	0.4	0.5	0.8	0.7	0.6	0.8	0.5	0.5	0.5
15	0.5	0.6	0.5	0.8	0.7	0.8	0.5	0.7	0.6	0.7	0.75	0.5	0.6	0.7	0.8	0.6	0.6	0.6	0.6	0.8
16	0.6	0.8	0.8	0.5	0.7	0.9	0.4	0.8	0.6	0.85	0.65	0.8	0.8	0.4	0.7	0.4	0.4	0.8	0.5	0.7
17	0.5	0.8	0.9	0.8	0.9	0.8	0.8	0.8	0.6	0.9	0.5	0.9	0.8	0.8	0.8	0.8	0.8	0.6	0.8	0.6
18	0.5	0.7	0.7	0.6	0.6	0.6	0.6	0.9	0.8	0.5	0.5	0.7	0.7	0.6	0.7	0.8	0.7	0.8	0.7	0.6
19	0.8	0.8	0.8	0.92	0.9	0.8	0.7	0.9	0.8	0.9	0.86	0.7	0.8	0.7	0.6	0.6	0.5	0.8	0.6	0.8
20	0.7	0.9	0.7	0.88	0.7	0.9	0.5	0.5	0.7	0.7	0.7	0.7	0.7	0.8	0.8	0.7	0.6	0.7	0.8	0.7

of training is fast, the fitting degree of the test sample is good, and the error is smaller.

#### 4. build neural network

NEWFF function is adopted to establish the feed forward network, the two layers of transfer function select the TANSIG that is a nonlinear hyperbolic tangent sigmoid function, training function selects the TRAINGD that the weights and threshold drop along the negative gradient direction of network performance function, the maximum number of training is 50000 epochs, learning step size is 0.1, the minimum mean square error is 0.00001, the layers of neural network is 3 and the rest of the parameters select system default values of the kit, in this paper.

### 4 EXAMPLE ANALYSIS

#### 4.1 Select Sample and network training

Chosen samples should follow the principle of typicality, authenticity and objectivity, we received 20 representative sets of data, and make surveys through Shanghai, Qingdao, Guangzhou and other metro construction projects, such as in Table 2. Through comprehensive assessments from multiple experts and third parties to obtain the expected output data, among which the previous 15 sets are used as training samples, the later 5 sets as the simulation test samples. The neural network whose mean squared error is not more than 0.00001 meet the requirements after 30274 times training. As shown in Figure 4.

#### 4.2 The simulation test

The simulation test tests trained neural network through the later 5 sets (16–20) datum as test sample. The error between the actual output and the expected output is small by comparison, among

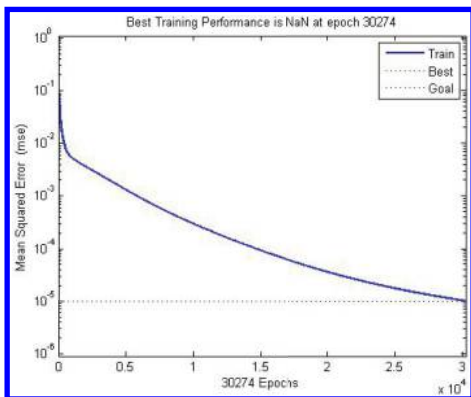


Figure 4. The mean squared error curve.

Table 3. Contrast of expected and actual value.

	Actual output value	Expected output value	Error
16	0.7238	0.7 (good)	0.0238
17	0.5002	0.5 (general)	0.0002
18	0.3407	0.3 (poor)	0.0407
19	0.9125	0.9 (excellent)	0.0125
20	0.6771	0.7 (good)	0.0229

which the biggest error is 0.0407, the minimum error is 0.0002, all details are shown in Table 3. The above datum show that the results of the metro construction project safety evaluation conform to the practicality, and it is effect and feasibility, thus the model can be promoted for using.

### 5 CONCLUSIONS

1. This paper teases out the important factors from factors that affecting the safety of metro construction by using the idea of people-centered in SHEL model and build the index system of metro construction safety, quantitative processing method is given.
2. With the relationship of complex nonlinearity between the various influencing factors and final results taken into account, the paper establishes the metro construction safety evaluation model based on BP neural network. We found the model output can achieve the desired standard and the test results are in consistent with the actual situation by the training and simulation of samples. The process of evaluation is simple, feasible and the results are accurate after the model training.
3. The evaluation model need to collect a large number of datum as the training and testing samples during the initial period, after the completion of network training the corresponding security rating can be easily realized by input the relevant parameter values. Further, evaluation method has certain reference significance to relevant enterprises and institutions in metro construction safety control, with its simple process and strong feasibility. By further improvement it can be extended to other areas in safety control and evaluation.

### REFERENCES

- Chen. F & Xie. H.T. 2012. Metro construction safety early warning research based on factor analysis and BP network, *China Safety Science Journal* 08: 85–91.

- Ding, L.Y & Wu, X.G. 2011. Research on standard for construction safety assessment of metro engineering, *China Civil Engineering Journal* 11:121–127.
- Li, L & Zhao, J.X. 2014. Evaluation of metro project management effect based on entropy value method and gray theory *Journal of Qingdao Technological University* 35(3):50–55, 60.
- Qian, Q.H. 2012. Challenges faced by underground projects construction safety and countermeasures, *Chinese Journal of Rock Mechanics and Engineering* (10):1945–1956.
- Tian, Y.Q & Yang, Z.H. 2011. On a risk early—warning model for the workplace based on BP neural network, *Journal of Safety and Environment* 11(6):255–259.
- Wang, Q.Q. 2010. Neural network safety assessment method for aviation enterprises based on SHEL model, *China Safety Science Journal*. 20(2):46–53.
- Zhou, H, & Wang, Y. 2014. Human error risk assessment model for air traffic control based on GA—BP algorithm, *Research and Exploration in Laboratory* 33(10):98–102.



# Influence of box culvert construction on running metro shield tunnel

Tianjun Liu, Guanfeng An & Hao Liang

*Guangzhou Municipal Engineering Group, Guangzhou, Guangdong, China*

**ABSTRACT:** This paper is based on a culvert construction method on the highway, above metro tunnels, and the loading and geological condition that sets up a three-dimensional numerical analysis modeled to analyze the influence of the culvert excavation construction. Studies show when it was digging or backfilling, the largest horizontal and vertical displacement appeared on the metro tunnel. The total maximum displacement was 1.84 mm, which was less than the subway protection requirements of the total displacement control values (8 mm). At the same time, the maximum displacement of tunnel rail was 1.37 mm, which was less than the value of the early warning system for metro rail deformation and control values (4 mm) that it would not affect the normal operation of the subway. That is to say, the construction measures, therefore, will not endanger the bottom of the box culvert construction of metro tunnel structure safety, the engineering experience can be provided as a reference for similar projects.

**Keywords:** box culvert; shield tunnel; MIDAS/GTS; displacement; bending moment

## 1 INTRODUCTION

With the speeding up of the national economy development and the increase of the urban traffic pressure, more and more metro are being constructed, the scale of operations and mileage raise rapidly. Most subway lines locate in the center of big city that much more construction projects will excavate near metro tunnels or stations. It will inevitably affect the subway structure so the protection of the subway tunnel and station is put forward severe challenges. From the situation of the current study, however, because of the complexity of the working condition, diversity of the construction methods, there is not a comparatively accurate theoretical analytical solution [1]. Most projects, before the construction, use numerical simulation methods to estimate the displacement of subway tunnel or station. How can better simulate the excavation influence on metro tunnel, there is a lot of research published for simulating the excavation influence on metro tunnel [2–4].

Box culvert can be defined as a long and narrow type of foundation pit. The excavation will influence the stability of the existing subway below. Its most essential reason is caused by box culvert of excavation unloading of surrounding rock stress state redistribution again, resulting in a series of mechanical behavior changes. Tunnel deformation of existing subway tunnel surrounding may be caused by the load changes that grasp the existing subway tunnel in the process of box

culvert excavation deformation characteristics and the internal force distribution is very important. Therefore, reasonable selection control is below the deformation of metro tunnel design and construction process, to ensure the normal use of the subway tunnel, which must be solved [5]. Due to foundation pit excavation boundary construction, such as box culvert, being complex, it is difficult go to through the analytical method to analyze the excavation impacts of metro tunnel. The numerical method provides a powerful tool for solving this problem [6].

Based on a box culvert construction in a highway above a certain operating metro tunnel, using the method of numerical simulation to analyze the whole process, evaluated the excavation unloading effect on both the deformation of metro tunnel and rail below. The results can be reference for similar projects.

## 2 PROJECT INTRODUCTION AND CONSTRUCTION SITUATION

### 2.1 *Project introduction*

The project locates in Liwan district of Guangzhou. It is an urban arterial road, which has a design speed of 60 km/h, planning for the urban expressway. This project main content for 7 new reinforce box culverts, 3 overpasses, an across river bridge. In this paper, the No. 3 box culvert construction and operating impacting the metro tunnels would be analyzed and the conclusions and suggestions

were proposed. The relationship between box culvert and tunnel is shown in Figure 1.

This box culvert excavation length was 80.6 m, height was 3.8 m, south end of it crosses above the north of metro tunnel, end in the bi-directional tunnel. Slope excavation was 1:1, considering on the bottom of the box culvert in fill when the excavation depth of 4.9 m. At the bottom of the box culvert with tunnel, the vertical net top edge distance is 6.1 m. Due to excavation at the bottom of the box culvert in filling, the excavation bottom distance at the top of the outer edge of vertical interval was only 5.0 m.

## 2.2 Construction condition

Due to the spatial location of the box culvert is near subway shield tunnel and the mechanics characteristic of narrow excavation. It accords section excavation, timely backfill, less digging above tunnel. Based on this principle, the whole box culvert construction is in accordance with the following steps.

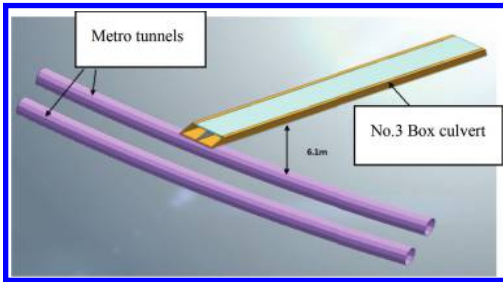


Figure 1. Location relationship between No. 3 box culvert and metro tunnels.

Table 1. Construction condition of the culvert.

Construction condition	Characteristics
1	According to the steel sheet pile supporting structure, the excavation section of box culvert, layered with steel support excavation to the pit
2	Section of box culvert and backfill, the excavation section of box culvert, layered with steel support excavation to the pit
3	Section on the box culvert and backfill, the excavation section of box culvert, layered with steel support excavation to the pit
4	Section of box culvert and backfill, the demolition of the old southern box cover board for new box cover plate

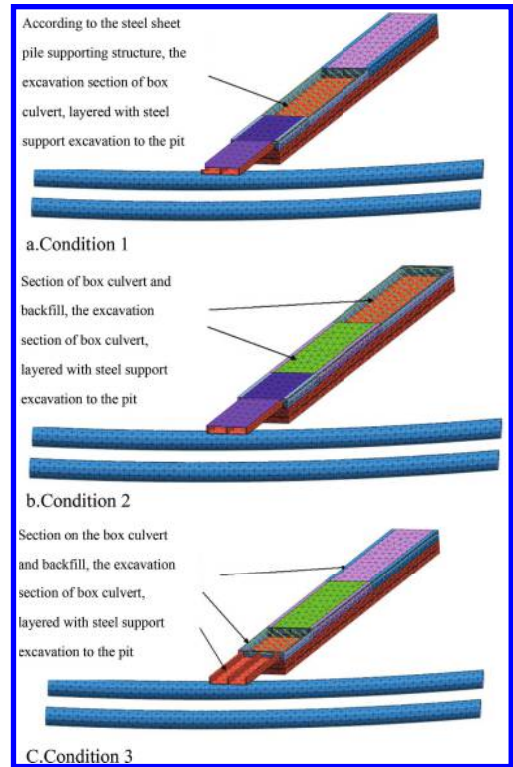


Figure 2. Construction condition.

## 3 THREE-DIMENSIONAL NUMERICAL ANALYSIS OF THE IMPACT BY NO. 3 BOX CULVERT CONSTRUCTION ON THE TUNNELS

### 3.1 Establish model

According to the geotechnical engineering investigation report, select the number 3 box culvert neighboring H3ZK1 drilling geological data as a basis for calculating model of soil. The soil parameters of the calculation model main bases on it, the missing part of the soil parameters refers to the "Foundation pit supporting technology regulations in Guangzhou area" and engineering experience. The specific parameters are shown in Table 2.

In addition, the calculation model mechanical parameters of tunnel, the culvert, and the original old box culvert structure are shown in Table 3. With considering the subway segment assembling results in the decrease of overall stiffness, combined with field investigation and related domestic subway engineering experience, the selected segment level corresponding to the elastic modulus of concrete on the basis of the original value may reduce to 80%.

Table 2. Soil mechanics parameters.

Soil layer	Weight (kN/m <sup>3</sup> )	Modulus of elasticity (MPa)	Poisson's ratio	Angle of internal friction (°)	Cohesion (kPa)
Grain filling 1-2	19	11	0.36	10	10
Muddy sand 2-3	19	18	0.35	22	5
Silty clay 3-1	20	22.5	0.34	10	20
Silty clay 4-2	19.9	30	0.32	20	20
Full-weathering silty mudstone 5-1	19.8	33.5	0.32	16	38
Moderately weathering silty mudstone 5-2s	23	1700	0.30	33	400
Intense weathering silty mudstone 5-2	23	300	0.30	32	4
Filling under the culvert	20	100	0.30	32	100

Table 3. Structural mechanics parameters.

Section	Material grade	Weight (kN/m <sup>3</sup> )	Modulus of elasticity (MPa)	Poisson's ratio	Notes
Tunnel segment	C50	25	$2.76 \times 10^4$	0.2	Reduce 80%
No. 3 new culvert	C35	25	$3.15 \times 10^4$	0.2	
Old culvert	C20	25	$2.55 \times 10^4$	0.2	
Pavement structure layer	C20	25	$2.55 \times 10^4$	0.2	

According to the spatial location relations and the construction characteristics, using numerical analysis software MIDAS GTS, to establish a three-dimensional finite element numerical calculation model is shown in Figure 3.

In terms of material model, soil model is the Moore—coulomb constitutive model and interval box culvert structure is the linear elastic model. In terms of load, it considers the weight and overloading during construction of the ground and road operation load. Z direction displacement is restrained, boundary conditions, forward and back of Y direction is restrained, left and right of X direction is restrained. Simulation for the real number three new box culvert construction and operation process of subway line below the influence of structure, calculation model fully considers the various working conditions during the construction period and operation period. Specific see Table 4.

### 3.2 Results analyze

Table 5 shows the box culvert in construction and operating period of different construction conditions and a horizontal displacement DXY, vertical displacement DZ and the maximum total displacement DXYZ. Figure 4 (1)—(4) respectively shows the box culvert in construction and operating period that the shield tunnel structure

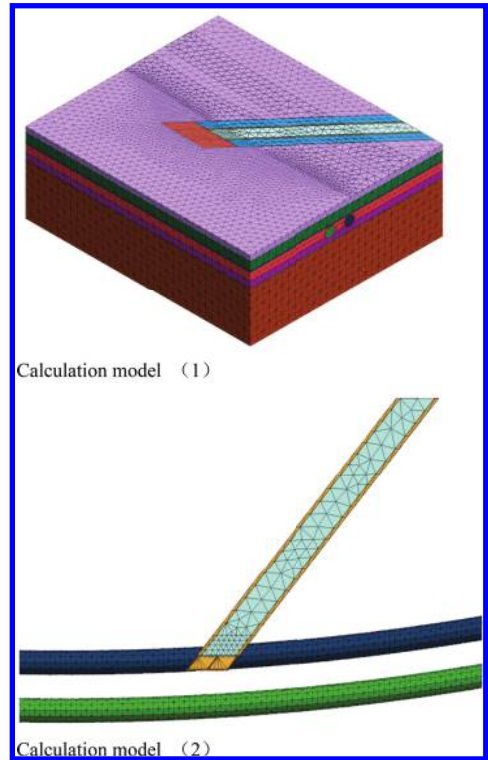


Figure 3. Calculation model.

Table 4. Construction condition of the model.

Construction condition	Characteristic
1	Establish strata, weight of in-situ stress analysis (excluding displacement)
2	According to the steel sheet pile supporting structure, the excavation section of box culvert, layered with steel support excavation to the pit
3	Section of box culvert and backfill, the excavation section of box culvert, layered with steel support excavation to the pit
4	Section on the box culvert and backfill, the excavation section of box culvert, layered with steel support excavation to the pit
5	According to the steel sheet pile supporting structure, the excavation section of box culvert, layered with steel support excavation to the pit
6	Section of box culvert and backfill, the demolition of the old southern box cover board for new box cover plate
7	The road into a permanent operation

Table 5. Maximum displacement values of different construction condition.

Construction condition	Horizontal displacement DXY (mm)	Vertical displacement DZ (mm)	Overall displacement DXYZ (mm)
1	1.03	+1.22	1.41
2	1.08	+1.04	1.44
3	1.13	+1.63	1.84
4	1.09	+1.05	1.46

Note: +/- means uplift/settlement of values DZ of vertical displacement.

in different working conditions of the overall displacement DXYZ distribution nephogram.

This section will analyze the deformation situation of the metro tunnel during the culvert construction and operating. On the new track location, set up a series of nodes to extract the deformation data of the orbit. Picture below is for the two-way operation line of the four tracks; the maximum total displacement of track and the total displacement curve when the steps in different conditions (because the first two conditions became zero, the working condition of the two data is not provided).

As the calculation results,

1. When No. 1 and 3 box culvert were during excavation construction and construction backfill,

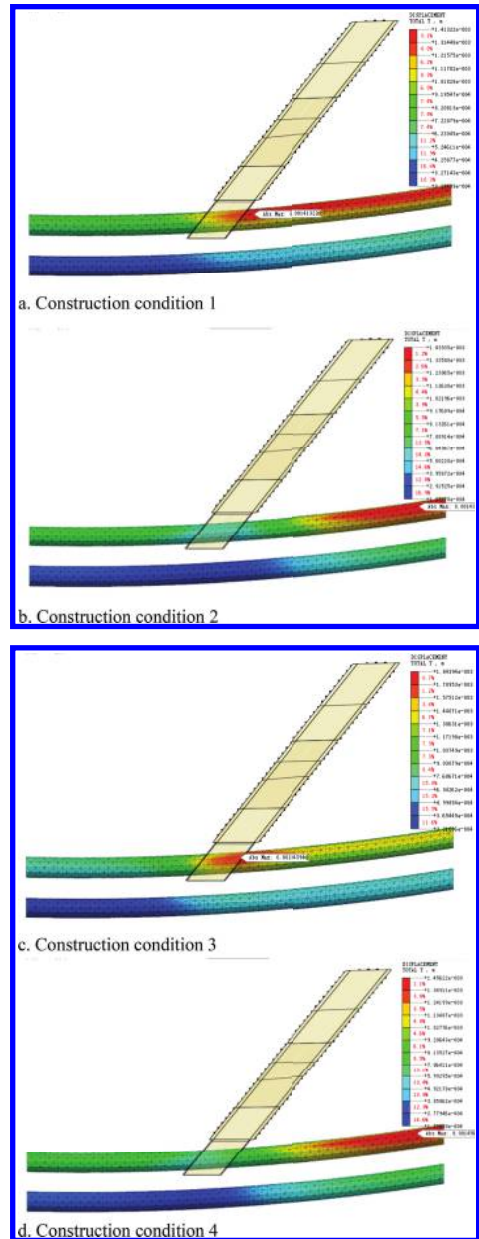


Figure 4. Total displacement DXYZ distribution of tunnels during culvert constructions.

the maximum horizontal value of a tunnel of metro line was 1.13 mm, maximum vertical displacement value was +1.63 mm (elevation), the overall displacement of a maximum was 1.84 mm, less than the total displacement control values (8 mm). That is to say the No. 3 box culvert in construction period impacted slightly

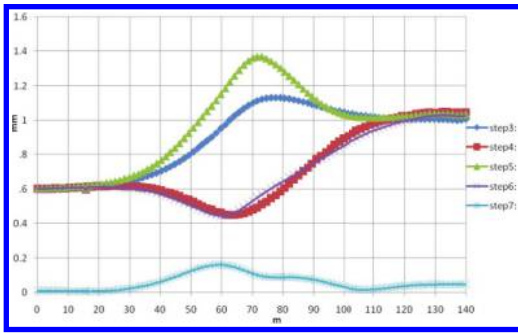


Figure 5. Tunnel displacement curve in different conditions.

on the tunnels, significantly less than the total displacement control values, less than a quarter of the control values.

2. In the condition of completing No. 3 box culvert construction and restoring the road after operation, the maximum horizontal value of tunnels was 0.26 mm, maximum vertical displacement was 0.42 mm (elevation), the overall displacement of a maximum was 0.44 mm that early stage of the box culvert construction caused by the uplift substantially reduce the settlement of become tiny. Therefore, there is also small effect.
3. When No. 3 box culvert construction and the avenue was put into operation, the maximum displacement value of the orbit was 1.37 mm, less than the value of early warning system for the deformation of metro rail and the control values that it may not affect the normal operation of the subway.

#### 4 CONCLUSION

This paper established a three-dimensional numerical analysis model of the project, specific analysis conclusion is as follows.

The influence causes by the project mainly includes: Old No. 3 box culvert would be dismantled, the steel sheet pile support or put at the bottom of the slope excavation to the bottom of the in filling culvert elevation and new on both sides of box culvert structure casting and backfilling effect on tunnel beneath the rapidness. The impact of

road on the tunnels during construction and road surface treatment.

The construction measures proposed in this paper, No. 3 box culvert construction and the construction of Guangfo metro tunnel excavation is less affected which significantly less than the total displacement control values, less than a quarter of the controlled variable; and track the maximum displacement value was 1.37 mm, less than the value of the early warning system for metro rail deformation and control values.

No. 3 box culvert construction will not endanger the Guangfo metro tunnel structure safety and normal operation of the subway.

#### ACKNOWLEDGMENT

Supported by Pearl River S & T Nova Program of Guangzhou (No. 2013J2200077).

#### REFERENCES

- Zhao Zhiqiang, Zhang Dongmei. The Impact Assessment of Excavation near Subway Tunnel [J]. Chinese Journal of Underground Space and Engineering, 2011.7(5): 1040-1046.
- Jiang Hongsheng, Hou Xueyuan. The Influence Of Deep Excavation On Adjacent Metro Tunnel In Soft Ground [J]. Industrial Construction. 2002.32(5): 53-56.
- Zhang yi, Fang ming. Study on Influence of Shield Tunnels Traversing Under Existing Tunnel by 3D Numerical Simulation [J]. Guangzhou Construction, 2012.40(6): 12-15.
- Qi Ke-jun, Wang Xu-dong, Jiang Gang, Chang Yin-sheng, Chen Ya-dong. Analysis Of Deep Pit Excavation Adjacent To Tunnel [J]. Chinese Journal of Rock Mechanics and Engineering, 2005.24(S2): 5485-5489.
- Zhang Yu-cheng, Yang Guang-hua, Yao Jie etc. Numerical simulation and analysis of effect of excavation of foundation pits on metro tunnels [J]. Chinese Journal of Geotechnical Engineering, 2010.32(S1): 109-115.
- Wang Wei-dong, Wu Jiang-bin, Weng Qi-ping. Numerical modeling of affection of foundation pit excavation on metro tunnel [J]. Rock and Soil Mechanics, 2004. 25(S1): 251-255.
- Zeng Dong-yang, He Chuan. Comparison and Analysis Research of Different Shield Tunnel Lining Internal Forces Design Methods [J]. Chinese Journal of Underground Space and Engineering, 2005.1(5): 707-712.

*Seismic engineering*

# Quasi-static cyclic loading test and simulation of precast segmental bridge columns with a circular section

Zhan-Yu Bu & Wei-Ye Wu

*Faculty of Architectural, Civil Engineering and Environment, Ningbo University, Ningbo, China*

Jian Guo

*Ningbo Institute of Technology, Zhejiang University, Ningbo, China*

**ABSTRACT:** Precast segmental bridge column is an important part in accelerated bridge construction. Two unbonded prestressing segmental bridge columns and one monolithic reference column were fabricated and tested under a quasi-static cyclic loading. The first segmental column has only an unbonded prestressing tendon through segment joints. The second segmental column has an unbonded prestressing tendon as well as bonded energy dissipation bars to connect all segments together. The test results show that both segmental columns survived the cyclic loading at the end of the 7% drift level with no longitudinal reinforcement fracture, but only minor cracks were observed at column toes. Energy dissipation bars greatly enhanced the lateral strength and energy dissipation ability of the segmental column. Unbonded prestressing tendon plus energy dissipation bars reinforcement scheme was a good choice for moderate- to high-seismicity area segmented bridge column configurations.

**Keywords:** segmental column; cyclic loading; seismic response; unbonded prestressing tendon; energy dissipation

## 1 INTRODUCTION

As an important part of Accelerated Bridge Construction (ABC), precast segmental bridge construction can improve site constructability, total project delivery time, material quality and product durability, and work-zone safety for the traveling public and contractor personnel (Culmo 2011). Starting in 2008, Caltrans initiated a practice development and implementation for ABC. The main task of this project was to develop standards, guidelines, and key policies for implementing the structure design for Accelerated Bridge Construction (ABCAC 2008).

Precast Segmental Bridge Columns (PSBC) have bonded or unbonded post-tensioned strands, and/or bonded mild steel bars through segment joints. Many researchers have conducted model tests, finite simulation and analytical modeling of seismic behavior of PSBCs. Hewes and Priestley (2002) conducted a cyclic loading test of four PSBCs with steel jackets in the plastic end. A simple analytical model was proposed to predict the pushover curve of the test. Yamashita and Sanders (2002) carried out a shake table test of unbonded tendon PSBC with a hollow section. A two-dimensional finite element model was used for pushover parametric analyses. Chou and Chen (2006) tested two

unbonded Concrete-Filled Tube (CFT) PSBCs; among which, one contained energy-dissipating devices at the base to increase the hysteretic energy. Ou et al. (2010) investigated the seismic performance of PSBC with high-performance ED bars and conventional mild steel ED bars, and found that the unbonded length in the ED bar can reduce the stress concentration and increase its fatigue life. More recently, some innovative techniques started to be employed in PSBCs, such as external replaceable dissipaters (Marriott et al. 2009), concrete-filled fiber-reinforced polymer tubes (ElGawady et al. 2010), Shape Memory Alloy (SMA) bars (Roh and Reinhorn 2010), fiber-reinforced concrete/cement composite (Trono et al. 2004), embedded elastomeric pads (Motaref et al. 2014), and shear resistant connectors (Kim et al. 2010).

In this paper, the quasi-static cyclic loading test of two PSBCs and one monolithic column results were introduced, then fiber beam-column model was used to simulate the test results, and both the results were analyzed and compared.

## 2 SPECIMEN DESIGN

Two PSBCs and one monolithic reference column were cast for the cyclic loading test. [Figure 1](#) shows

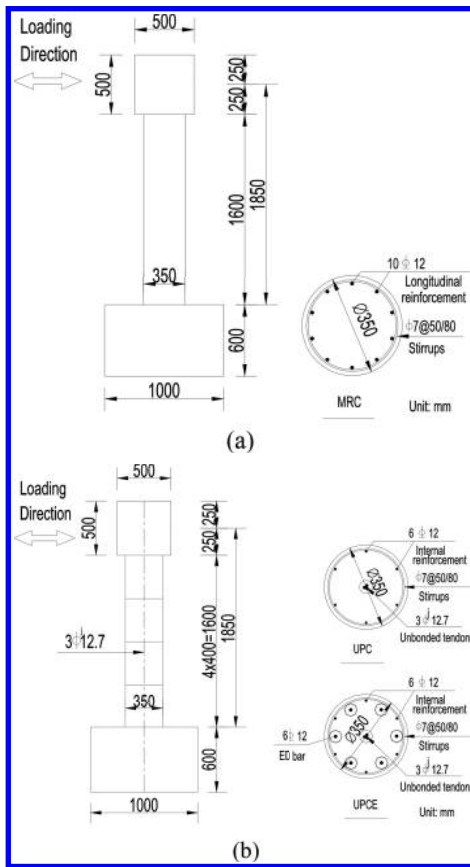


Figure 1. Test specimens (a) MRC, (b) UPC and UPCE.

the configuration of three specimens. All three specimens have the same footing and loading block dimensions. The footing dimension is 1500 mm by 1000 mm by 600 mm. The loading block is 500 mm cube. The monolithic specimen, first segmental specimen with only an unbonded tendon, and the second segmental specimen with an unbonded tendon plus Energy Dissipation (ED) bars are abbreviated as MRC, UPC and UPCE, respectively. The columns of MRC, UPC and UPCE have the same diameter of 350 mm, and the total height of 1600 mm, with a cubic compressive strength of 44 MPa. The columns of UPC and UPCE are divided into four segments, each having a height of 400 mm. The nominal column height of three specimens is 1850 mm, measured from the column base to the center of the loading block. MRC uses 10 D12-mm deformed bars as longitudinal reinforcement with a yield stress of 491 MPa. UPC uses 3 D12.7-mm unbonded strands as longitudinal reinforcement with a yield stress of 1672 MPa. UPCE uses

3 D12.7-mm unbonded strands plus 6 D12-mm bonded ED bars as longitudinal reinforcement. The ED bar yield stress is 301 MPa. Segmental columns use 6 D12-mm deformed bars as longitudinal reinforcement inside the segments with a yield stress of 491 MPa to position spirals. The spiral stirrups used in three specimens are D7 mm deformed bar with a yield stress of 575 MPa. The spiral stirrups have a layer space of 50 mm and 80 mm for the base 400 mm in depth and other places of column, respectively. MRC has no axial force exerted. The axial forces of UPC and UPCE are provided by the prestressing load of tendons, which are 252 kN for both specimens, and the corresponding axial load ratio is 0.075.

### 3 LOADING PROTOCOL

The quasi-static cyclic loading is displacement controlled. The displacement levels of loading are: 0.1%, 0.2%, 0.3%, 0.5%, 0.75%, 1.0%, 1.5%, 2.0%, 2.5%, 3.0%, 3.5%, 4.0%, 4.5%, 5.0%, 6%, and 7%. Each displacement level repeated twice to observe the damage pattern and to incorporate the fatigue effect to reinforcement.

### 4 QUASI-STATIC CYCLIC LOADING TEST

The three specimens, shown in Figure 1, were loaded under the preceding cyclic displacement protocols, respectively. Force-displacement responses were monitored with an actuator data acquisition system. Reinforcement and concrete strain were monitored by strain gauges. The test results are discussed in the subsequent section.

### 5 CYCLIC LOADING SIMULATION USING FIBER MODEL

#### 5.1 Global response

The cyclic loading tests were modeled with OpenSees (OS) software (Mazzoni et al. 2007). The concrete column was modeled with a fiber beam-column element. Bonded ED bars were modeled with fibers inside the concrete section. Unbonded prestressing tendons were modeled with the truss element. The initial stress was considered in the tendon material model. Concrete was modeled with concrete01 material in OS. ED bar and tendon were modeled with steel02 material in OS. Reinforcement steel inside the segment was not explicitly modeled. The confinement or reinforcement was considered through enhancing the compressive strength of the core concrete.



Figure 2 (a), (b) and (c) shows the lateral force versus drift test results and fiber model simulation results. MRC experienced longitudinal reinforcement fracture during the first cycle of 7% drift. UPC and UPCE had no reinforcement fracture at the end of the 7% drift. The results were compared at the end of the 6% drift. The lateral forces of MRC, UPC and UPCE were 29.39 kN, 32.46 kN, and 51.57 kN, respectively. The asymmetric of lateral force response in UPC and UPCE was caused by the eccentric of prestressing tendon at the top of the loading block to the center of the column base section (Hewes and Priestley 2002). The fiber model gave a good prediction for lateral force responses of MRC and UPCE.

However, the unloading paths of UPC by the fiber model showed big discrepancies with the test results. This reveals the characteristics of OS software, which has a good precision in modeling mild steel reinforcement concrete cyclic responses, but has a bad precision in modeling unbonded prestressing reinforcement concrete cyclic responses. In the 6% drift cycle, the residual drifts of MRC, UPC, and UPE were 3.42%, 0.18% and 0.75%, respectively.

### 5.2 Stiffness, damping and energy

Figure 3 (a) shows the effective stiffness results from the test and simulation. The suffixes “T” and “M”

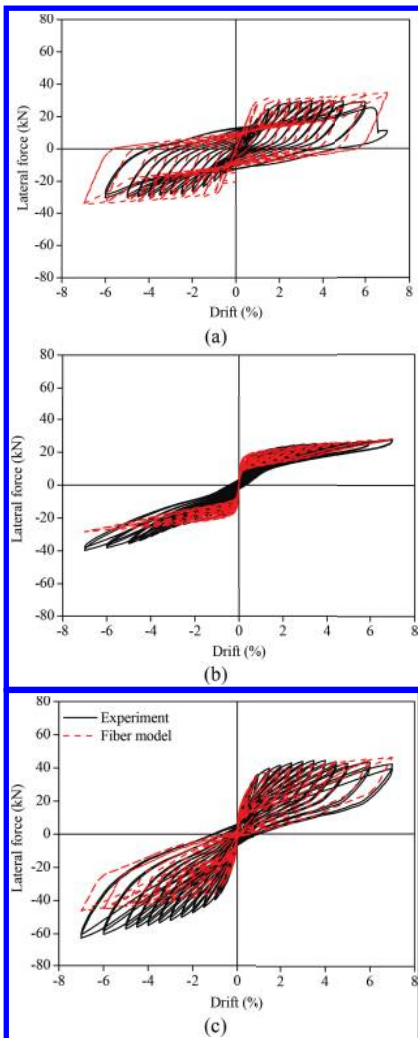


Figure 2. Lateral force-displacement comparison (a) MRC, (b) UPC, (c) UPCE.

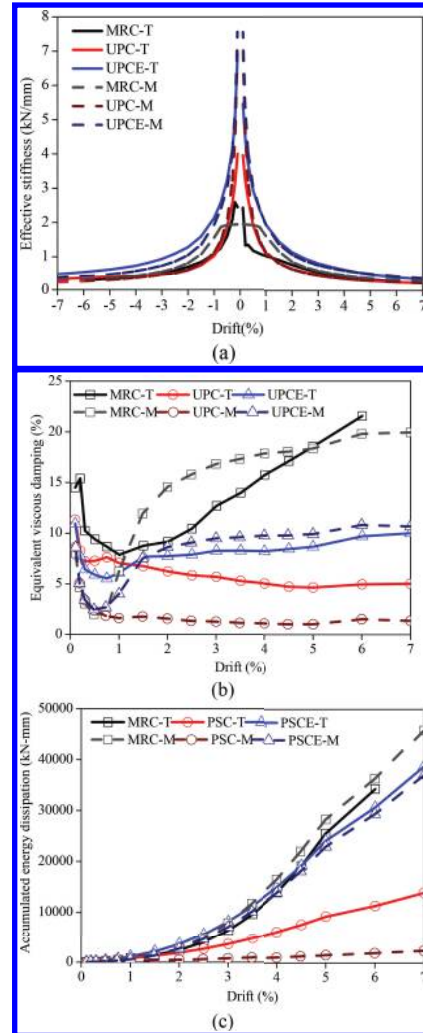


Figure 3. Stiffness, damping and energy comparison: (a) effective stiffness; (b) equivalent viscous damping; (c) accumulated energy dissipation.

mean test and model, respectively. MRC and UPC have a similar effective stiffness, while UPCE has a higher effective stiffness due to the added bonded ED bar compared with UPC. The fiber model gave a good approximation of effective stiffness for the three specimens. Figure 3 (b) shows the equivalent viscous damping of specimens as well as by fiber model simulations. MRC has a damping ratio between 10% and 20% for most of the drift levels. UPC and UPCE have damping ratios near 5% and 8%, respectively. The fiber model normally predicted the damping ratio of MRC and UPCE with a higher precision. Figure 3 (c) shows the accumulated energy dissipation of specimens. UPCE has approximately the same energy dissipation ability as MRC. UPC has the lowest energy dissipation as the column can only dissipate energy through prestressing tendon yielding and concrete minor cracking at critical joints. The fiber model gives a poor prediction for UPC for the reasons stated above.

## 6 CONCLUSIONS

Two segmental bridge columns and one monolithic column cyclic loading test and simulation are presented. The following conclusions can be derived on the basis of the results of the specimen test.

1. At the 6% drift, MRC and UPC have relatively lower lateral forces, and UPCE has the highest lateral force. The residual drifts of MRC, UPC, and UPCE are 3.42%, 0.18% and 0.75%, respectively.
2. MRC and UPC have a relatively lower effective stiffness, and UPCE has a highest effective stiffness.
3. MRC has a higher damping ratio ranging from 10% to 20%; UPCE has a moderate damping ratio of nearly 8%; UPC has a lower damping ratio about 5%.
4. MRC and UPCE have a similar energy dissipation ability; UPC has a lower energy dissipation ability.

From the test results conducted in this paper, UPCE is suggested to be used in moderate to high-seismicity areas; MRC and UPC are suggested to be used in low-seismicity areas.

## ACKNOWLEDGMENTS

This research was financially supported by the National Natural Science Foundation of China under Project grant No. 51208268 and No. 51178429, the Transportation Science and Technology Project of Ningbo City under grant No. 201507, and the Discipline Research Fund

Project of Ningbo University under Project No. XKL14D2070. This work was also sponsored by K.C. Wong Magna Fund at Ningbo University. The authors gratefully acknowledge their support.

## REFERENCES

- ABC-Advisory Council 2008. Caltrans ABC strategic plan- development of practice and policy for future bridge projects. <http://mceer.buffalo.edu/meetings/6nsc/review/Cal-transABCStrategicPlan.pdf>.
- Chou, C.C. & Chen, Y.C. 2006. Cyclic tests of posttensioned precast CFT segmental bridge columns with unbonded strands. *Earthquake Engineering and Structural Dynamics* 35 (2): 159–175.
- Culmo, M.P. 2011. Accelerated Bridge Construction— Experience in design, fabrication and erection of prefabricated bridge elements and systems. *Report No. FHWA-HIF-12-013, Federal Highway Administration*. McLean, VA.
- ElGawady, M.A., Booker, A.J., & Dawood, H.M. 2010. Seismic behavior of posttensioned concrete-filled fiber tubes. *Journal of Composites for Construction* 14(5): 616–628.
- Hewes, J.T. & Priestley, M.J.N. 2002. Seismic design and performance of precast concrete segmental bridge columns. *Technical Report No. SSRP-2001/25, University of California*. San Diego, California, USA.
- Kim, T.H., Lee, H.M., Kim, Y.J. & Shin, H.M. 2010. Performance assessment of precast concrete segmental bridge columns with a shear resistant connecting structure. *Engineering Structures* 32: 1292–1303.
- Marriott, D., Pampanin, S., & Palermo, A. 2009. Quasi-static and pseudo-dynamic testing of unbonded post-tensioned rocking bridge piers with external replaceable dissipaters. *Earthquake Engineering and Structural Dynamics* 38: 331–354.
- Mazzoni, S., McKenna, F., Scott, M.H., Fenves, G.L., et al. 2007. OpenSees Command Language Manual. *Open System for Earthquake Engineering Simulation (OpenSees)*.
- Motaref, S., Saiidi, M.S., & Sanders, D. 2014. Shake table studies of energy-dissipating segmental bridge columns. *Journal of Bridge Engineering* 19(2): 186–199.
- Ou, Y.C., Tsai, M.S., Chang, K.C., & Lee, G.C. 2010. Cyclic behavior of precast segmental concrete bridge columns with high performance or conventional steel reinforcing bars as energy dissipation bars. *Earthquake Engineering and Structural Dynamics* 39(11): 1181–1198.
- Roh, H., & Reinhorn, A.M. 2010. Hysteretic behavior of precast segmental bridge piers with superelastic shape memory alloy bars. *Engineering Structures* 32(10): 3394–3403.
- Trono, W., Jen, G., Panagiotou, M., Schoettler, M., & Ostergag, C.P. 2014. Seismic response of a damage-resistant recentering posttensioned-HYFRC bridge column. *Journal of Bridge Engineering* DOI: 10.1061/(ASCE)BE.1943-5592.0000692.
- Yamashita, R. & Sanders, D.H. 2009. Seismic performance of precast unbonded precast concrete columns. *ACI Structural Journal* 106(6): 821–830.

# A hysteretic model for Precast Segmental Bridge Columns with unbonded posttensioned tendons

Zhan-Yu Bu & Wei-Ye Wu

*Faculty of Architectural, Civil Engineering and Environment, Ningbo University, Ningbo, China*

Jian Guo

*Ningbo Institute of Technology, Zhejiang University, Ningbo, China*

**ABSTRACT:** A hysteretic model for Precast Segmental Bridge Column with unbonded posttensioned tendons was formed and validated through quasi-static cyclic specimen loading test. The model was capable of predicting the lateral force-displacement hysteretic response with high precision. The peak orienting assumption of post-yielding branches in hysteretic responses was more appropriate to the segmental columns with ED bars than those with only unbonded tendons. Earthquake history responses were also calculated using the proposed hysteretic model, and good correlation was found with quasi-static test results.

**Keywords:** hysteretic model; segmental column; unbonded tendon; cyclic test; earthquake response

## 1 INTRODUCTION

Self-centering unbonded Precast Segmental Bridge Columns (PSBC) are seismic resilient structures (Hewes & Priestley 2002), which can relieve the imparted earthquake loading through rocking of segment-segment joints, and keep the column with minor damage during the earthquake. As an important part of accelerated bridge construction scheme, PSBC provides several benefits to contractors and owners, including reduced traffic disruption, improved work zone safety, reduced environmental impact, improved constructability, increased quality and lower life cycle cost (Hieber et al. 2005). The lateral force-drift response of PSBC reveals flag-shape with essentially little residual drift at the end of earthquake excitation (Yamashita & Sanders 2009). Unlike the conventional steel reinforced concrete bridge columns, few shake table test results are available for PSBC, also simple and accurate hysteretic models are still lacking.

In previous studies by researchers, various self-centering systems have been developed, including unbonded posttensioned tendon (Yamashita & Sanders 2009, Ou et al. 2010), self-centering braces (Christopoulos et al. 2008), shape memory alloy (Roh & Reinhorn 2010) and elastomeric rubber pad (Motaref et al. 2014). Hewes (2002) used ideal flag shape hysteretic model to calculate the seismic response of unbonded posttensioned PSBCs.

Christopoulos et al. (2002) proposed a flag shape hysteretic model for posttensioned energy dissipating connections of precast frame structures. Ou et al. (2007) developed a peak oriented hysteretic model for PSBC based on experimental observation results.

In this contribution, a hysteretic model revised from literature (Ou et al. 2007) was developed and was used to model the PSBC quasi-static cyclic loading test, and history responses under ground motion excitation.

## 2 HYSTERETIC MODEL

The lateral force—displacement hysteretic model for Single Degree of Freedom System (SDOF) used in this contribution was shown in Figure 1. The first loading path was designated as path (1), which has fixed yielding point “A”. The elastic loading stiffness is  $k_e$ . The post-yielding stiffness is  $k_p$ . The unloading stiffness  $k_u$  is in relation with history peak displacement  $\Delta_m$  and yield displacement  $\Delta_y$ , as shown in Eq. (1).

$$k_u = k_e \left( \frac{\Delta_y}{\Delta_m} \right)^\gamma \quad (1)$$

where  $\gamma$  = coefficient, which is assumed to be constant for particular hysteretic model. The unloading

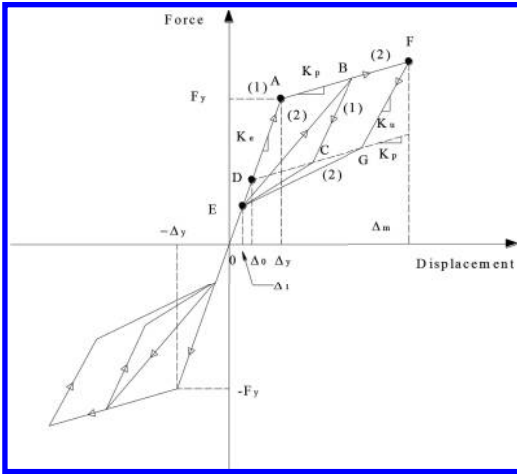


Figure 1. Hysteretic models for PSBC.

transition point is “C”, and the unloading path is ultimately directed to point “D” on elastic loading path.

The reloading path is directed to previous peak point “B” from elastic loading path point “E”. Then the loading path reloads with stiffness  $k_p$  till reaching peak point “F”. The unloading path has a transition “G” when intersects with the extending line of “D” and “C”. After that, the unloading is directed to “E”. In Figure 1, point “D” has a displacement of  $\Delta_0$  and point “E” has a displacement of  $\Delta_1$  on the elastic loading path.

The negative direction has same loading path definitions with those in positive direction, hence the critical points were not illustrated in Figure 1.

### 3 IMPLEMENTATION IN SDOF EQUATION OF MOTION

The equation of motion of damped SDOF system shown in Figure 2 can be written as,

$$m\ddot{x}(t) + c\dot{x}(t) + f(x(t), \dot{x}(t)) = -m\ddot{x}_g(t) \quad (2)$$

where  $m$  = mass;  $c$  = the damping coefficient;  $f$  = nonlinear spring force;  $x(t)$ ,  $\dot{x}(t)$ , and  $\ddot{x}(t)$  = relative displacement, relative velocity and relative acceleration of SDOF system to ground, respectively;  $\ddot{x}_g(t)$  = absolute acceleration of ground.  $f$  = loading history dependent (position and direction), so  $f$  is function of relative displacement and relative velocity. In Figure 2, wheels on the SDOF system has no friction force

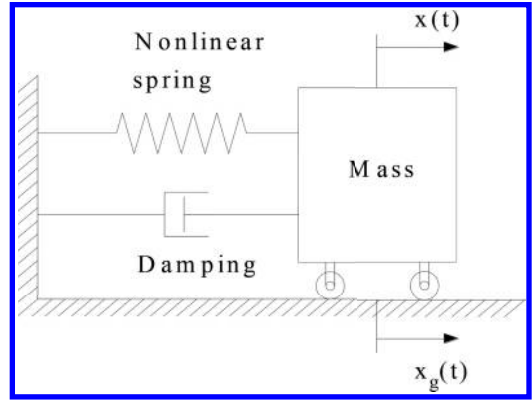


Figure 2. SDOF system.

with the boundary ground,  $x_g(t)$  is absolute displacement of ground.

Assume the damping force is small and effects can be eliminated in the reaction force, then  $f(x(t), \dot{x}(t))$  in Equation 1 can be looked as the reaction force shown in Figure 1. The relative displacement  $x(t)$  in Eq. (2) can be solved with average acceleration method with input ground motion acceleration  $\ddot{x}_g(t)$ , mass  $m$ , damping coefficient  $c$ , and nonlinear spring force  $f(x(t), \dot{x}(t))$  determined.

### 4 CYCLIC LOADING TEST MODELING

Two 1/4 scale segmental column specimens were fabricated and tested under cyclic reversal loading in laboratory. The columns had circular section with diameter of 350 mm. The column height was 1850 mm measured from column base to center of loading block. The column was composed with four 400 mm depth segments. Concrete cubic compressive strength was 44 MPa. First specimen PSC uses 3D12.7-mm unbonded strands as longitudinal reinforcement. Second specimen PSCE uses 3D12.7-mm unbonded strands plus 6 D12-mm bonded Energy Dissipation (ED) bars as longitudinal reinforcement. Prestressing strands had yield stress of 1672 MPa. ED bar had yield stress of 301 MPa. The effective prestressing force in PSC and PSCE are both 252 kN.

The parameters to define the hysteretic model in Figure 1 were identified from test lateral force-displacement curves as shown in Table 1. The comparison between the test results and hysteretic model modeling results were shown in Figure 3. The modeling had very high precision with test data, though some discrepancies existed in the post-yielding branches.

Table 1. Parameters identified from cyclic test.

Specimen	$k_c$ (kN/mm)	$k_p$ (kN/mm)	$\Delta_y$ (mm)	$\Delta_0$ (mm)	$\Delta_1$ (mm)	$\gamma$
SPC	2.22	0.063	9.45	7.37	2.90	0.235
SPCE	2.41	0.032	16.95	5.83	0.68	0.370

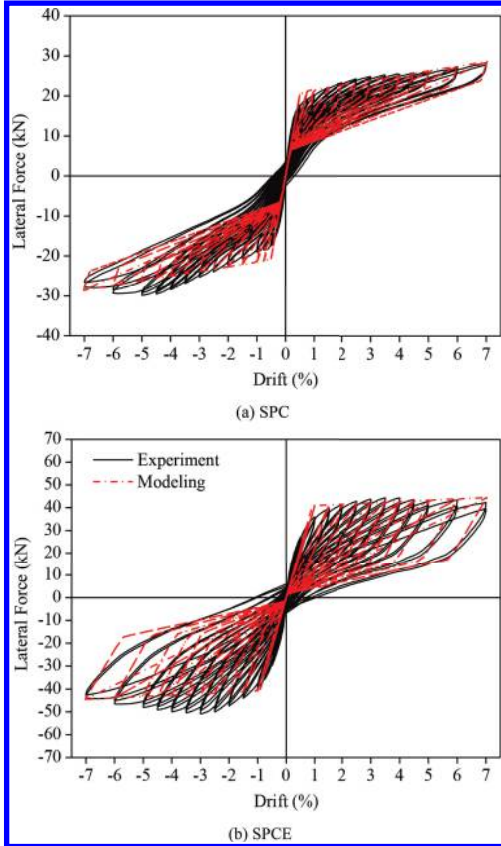


Figure 3. Quasi-static cyclic test modeling.

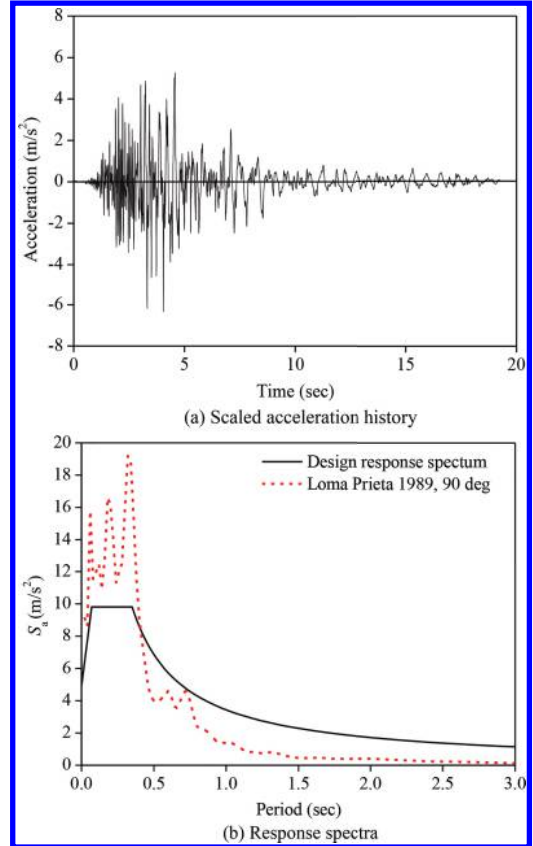


Figure 4. Selected ground motion input.

## 5 HISTORY RESPONSE MODELING

The design response spectra used for define the ground motion intensity was taken from AASHTO with a 7 percent exceedance in 75 years (1000 year return period) (AASHTO 2011). The acceleration response spectra was scaled with period scale factor of  $S_T = \sqrt{S_L} = 2.0$ , where  $S_L$  = the geometry scale factor. One typical history ground motion (Loma Prieta 1989 47125 Capitola 090 deg) was selected from PEER strong motion database. The ground motions were recorded on soil type C, and were generated

by the earthquake with a moment of magnitude of 6.9. The distance of the record stations to the nearest fault rupture was 14.5 km. Figure 4 (a) shows the scaled ground motion acceleration history. Figure 4 (b) shows the response spectra comparison between design and the scaled ground motion. Figure 5 shows the history responses of specimen SPC and SPCE under the selected ground motion excitation. The hysteretic model gave good prediction to envelope curve of specimens. The detailed hysteretic rules need more specimen tests validation under different loading protocols.

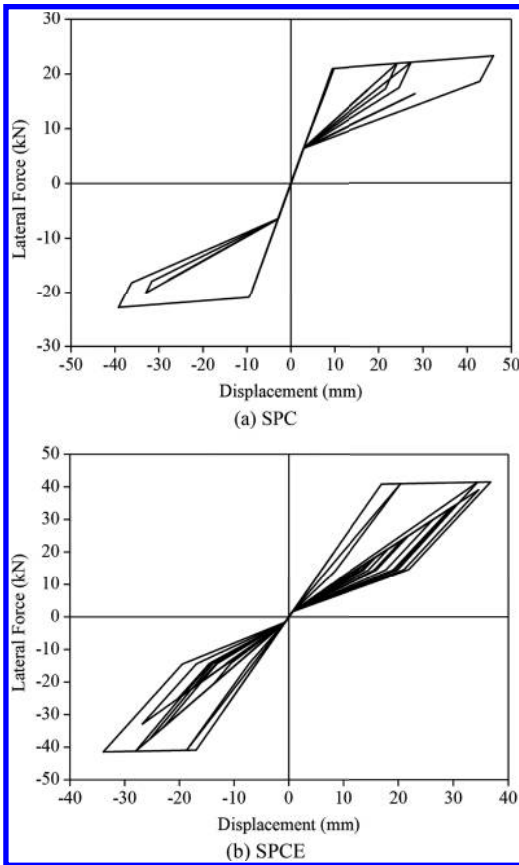


Figure 5. History response modeling.

## 6 CONCLUSIONS

A hysteretic model for unbonded posttensioned segmental columns was first validated through quasi-static cyclic loading tests, then was used for earthquake history response calculations. The following conclusions can be reached within the studies of this contribution.

1. The hysteretic model generally gave good prediction to quasi-static cyclic loading test lateral force-displacement cyclic responses. The hysteretic rules of peak orienting used in defining the model was more appropriate for segmental columns with ED bars than those only has unbonded prestressing tendons.
2. The envelope responses of specimens under ground motion were in accordance with cyclic loading test results, although the exact hysteretic rules need different loading path cyclic test validation in the future research work.

## ACKNOWLEDGEMENTS

The research work of this paper was financially supported by National Natural Science Foundation of China under Project grant No. 51208268, National Natural Science Foundation of China under Project grant No. 51178429, Transportation Science and Technology Project of Ningbo City under grant No. 201507, and Discipline Research Fund Project of Ningbo University under Project No. XKL14D2070, this work was also sponsored by K.C. Wong Magna Fund in Ningbo University. Their supports were gratefully acknowledged.

## REFERENCES

- AASHTO 2011. *AASHTO Guide Specifications for LRFD Seismic Bridge Design, 2nd Edition*. Washington, DC: AASHTO.
- Christopoulos, C., Filiatrault, A., & Folz, B. 2002. Seismic response of self-centring hysteretic SDOF systems. *Earthquake Engineering and Structural Dynamics* 31: 1131–1150.
- Christopoulos, C., Tremblay, R., Kim, H.J., & Lacerte, M. 2008. Self-centering energy dissipative bracing system for the seismic resistance of structures: development and validation. *Journal of Structural Engineering* 134(1): 96–107.
- Hewes, J.T. 2002. Seismic design and performance of precast concrete segmental bridge columns. *Ph. D. dissertation of University of California*, San Diego.
- Hewes, J.T. & Priestley, M.J.N. 2002. Seismic design and performance of precast concrete segmental bridge columns. *Technical Report No. SSRP-2001/25, University of California*. San Diego, California, USA.
- Hieber, D.G., Wacker, J.M., Eberhard, M.O. & Stanton, J.F. 2005. Precast Concrete Pier Systems for Rapid Construction of Bridges in Seismic Regions. *Technical Report No. WA-RD 611.1, University of Washington*. Seattle, Washington, USA.
- Motaref, S., Saiidi, M.S., & Sanders, D. 2014. Shake table studies of energy-dissipating segmental bridge columns. *Journal of Bridge Engineering* 19(2): 186–199.
- Ou, Y.C., Chiewanichakorn, M., Aref, A.J., & Lee, G.C. 2007. Seismic performance of segmental precast unbonded posttensioned concrete bridge columns. *Journal of Structural Engineering* 133(11): 1636–1647.
- Ou, Y.C., Tsai, M.S., Chang, K.C., & Lee, G.C. 2010. Cyclic behavior of precast segmental concrete bridge columns with high performance or conventional steel reinforcing bars as energy dissipation bars. *Earthquake Engineering and Structural Dynamics* 39(11): 1181–1198.
- Roh, H., & Reinhorn, A.M. 2010. Hysteretic behavior of precast segmental bridge piers with superelastic shape memory alloy bars. *Engineering Structures* 32(10): 3394–3403.
- Yamashita, R. & Sanders, D.H. 2009. Seismic performance of precast unbonded precast concrete columns. *ACI Structural Journal* 106(6): 821–830.

# The effect of convex friction distribution on the seismic performance of friction systems

B. Wei, T.H. Yang, X.D. Yu, P. Wang & L.Z. Jiang

*School of Civil Engineering, Central South University, Changsha, China*

*National Engineering Laboratory for High Speed Railway Construction, Changsha, China*

**ABSTRACT:** When the bearings were destroyed by the earthquake, a rough friction surface would be formed while the surrounding contact surface was smooth. The isolation condition of the damaged bearings, namely a convex friction distribution, was considered. By taking a friction-based isolation system as the study object, the effect of the convex distribution of friction coefficient on the structural isolation performance under different ground motions was analyzed by utilizing a compiled computer program. The results show that the convex distribution of friction coefficient almost always makes the structural maximum acceleration the largest and obviously increases the structural maximum relative displacement and the structural residual displacement. In general, it is unfavorable to the isolation system. Therefore, the convex distribution of friction coefficient should be avoided in the actual projects.

**Keywords:** bridge; isolation; friction; bearing; horizontal earthquake

## 1 INTRODUCTION

As to effectively isolate horizontal earthquake, several researchers have paid attention to the new isolation method based on friction. In order to avoid a five-floor RC frame structure building's earthquake damage subjected to soft soil earthquake in Mexico, Flores designed rolling ball devices. Ou et al. (2010) and Lee et al. (2010) designed a two-layer roller isolation device for use in highway bridges. Jangid (1998, 2000) first considered that elliptical rolling rods are more effective than rolling rods in reducing the seismic response of the structure, and then he considered that rolling rods with re-centering device also have an effective isolation performance. Guerreiro et al. (2007) invented a rolling-ball isolation system to protect light structures or other devices. Harvey & Gavin (2014) carried out a mathematical model and experimental validation for double rolling isolation systems, and the effects of the initial conditions, the mass of the isolated object, and the amplitude and period of the disturbance on the system's performance were assessed. As for some bridges, the bearings are often first destroyed by the earthquake. Although some designers considered that the destruction of bearings would protect other components of bridges from seismic damage, it lacks rigorous analysis. The stochastic damage of bearing will form a rough contact surface (Wei et al. 2015), i.e. a large friction coefficient exists. However, other contact surfaces are very smooth

with a less friction coefficient. Therefore, a natural isolation system with a convex distribution of friction coefficient is formed.

The objective of this paper is to investigate a friction isolation system and artificially interfere with the uneven distribution of friction coefficient to be convex, i.e. the friction coefficient in the center of the seismic isolation device is the largest one, and it gradually decreases along the surrounding path. Utilizing a numerical analysis method, we analyze the impact of the convex distribution of friction coefficient on the seismic performance under different ground motions.

## 2 CALCULATION PROCESS

### 2.1 Structure model

The study object of this paper, i.e. a friction isolation system, is shown in [Figure 1](#). In order to analyze the effect of the 'convex' distribution of friction coefficient on the seismic isolation performance in detail, this paper divides the friction coefficient and the earthquake input into several groups, and then obtains many combination cases.

As demonstrated in related studies, the isolated structure can be built as a rigid body since the stiffness of the isolation device is far less than that of the structure (Wei et al. 2014). So, in this paper, the superstructure is temporarily simplified to a rigid body. The superstructure mass is set to be 300 t.

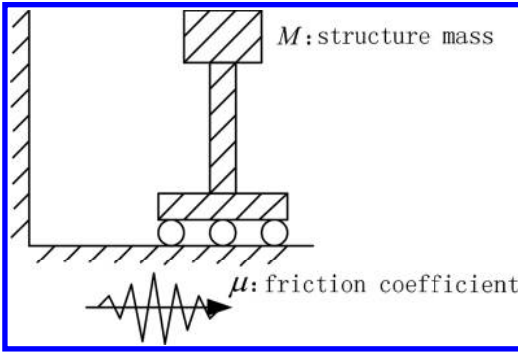


Figure 1. Structure model.

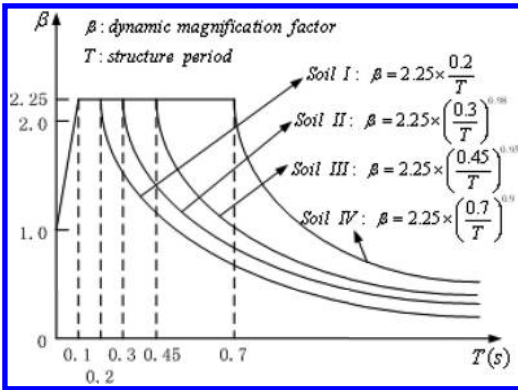


Figure 2. Four types of response spectrum.

For the convex friction distribution, the friction coefficient in the center of the isolation device is the largest one, which is assumed to be 0.03, and it gradually decreases along the surrounding path whose decrement ratios are assumed to be 0, 0.005, 0.010, 0.015, 0.020, 0.025 and 0.030, respectively.

### 2.2 Earthquake input

As shown in Figure 2, for each elastic response spectrum for the soil profiles I, II, III, and IV in Chinese criteria (JTJ 004-89), one accelerogram is generated by the Simqke procedure as the ground motion input of the structural model.

### 2.3 Calculation cases

For each case of the 6 friction distributions, each accelerogram in Section 2.2 is input as the ground motion, whose Peak Ground Accelerations (PGA) are adjusted to be 0.2, 0.4, 0.6 and 0.8 g, respectively. Hence, 112 cases are generated for further calculation utilizing a computer program (Wei et al. 2013).

In the following sections, only classical and common results are discussed in a detailed manner due to space limitations, while other results are considered but not listed.

## 3 STRUCTURAL ACCELERATION

Structural acceleration is considered for the isolated structure, as it directly indicates whether the earthquake will destroy the structure or not. Therefore, this section analyzes on the structural maximum acceleration.

Figure 3 shows the influence of the variability slopes of friction coefficient on the structural maximum acceleration for all cases in Section 2.3. As the slopes of friction coefficient variability increase, the maximum acceleration applied to the structure remains constant.

As for the isolation system based on friction, the acceleration that the ground motion transmits to the superstructure is  $\mu g$ . For the case of the “convex” friction distribution, although  $\mu$  varies regularly along with the position of friction surface, the maximum  $\mu$  appears at the original location of the structure. Thus, as soon as the structure starts moving under the earthquake, the acceleration reaches the peak point and gradually reduces as the structure moves away from the original location.

Therefore, for the case of the convex friction distribution, the maximum acceleration value depends on the friction coefficient value of the structural original location, and has no relation with the decrement ratio of the convex friction distribution or the earthquake situation.

The analysis results show that as the soil profiles and PGA of earthquake increase, the structural maximum acceleration remains constant, and the corresponding figures are omitted herein.

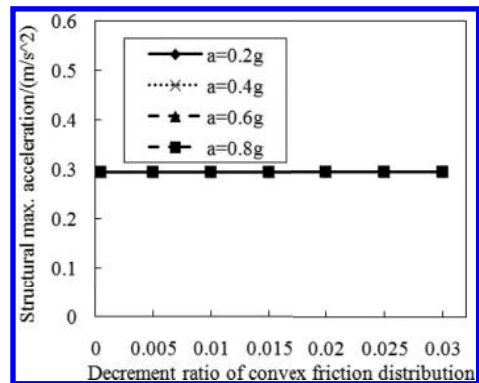


Figure 3. Effect of the decrement ratio of the convex friction distribution on the structural maximum acceleration.



## 4 STRUCTURAL RELATIVE DISPLACEMENT

### 4.1 The influence of the friction coefficient

For the isolation system, the structural relative displacement indicates whether the structure would leave away from its foundation, and whether the structure would collide with other things. This section and the following sections analyze the maximum relative displacement.

Figure 4 shows the influence of the decrement ratio of the convex friction distribution on the structural maximum relative displacement in the cases with soil profile III. On the whole, as the decrement ratio of the convex friction distribution increases, the structural maximum relative displacement increases gradually. The increasing trend is more significant when the PGA is larger.

In Figure 1, as for the cases of the convex friction distribution, when the ground velocity  $v_e$  is larger than the structural velocity  $v_s$ , the structural acceleration  $\mu g$  makes the structure have the tendency of moving forward, and there are two possibilities:

1. If the moving structure is on the left of its origin position, it means that the friction coefficient  $\mu g$  on the contact surface is decreasing, and the reduction of the structural acceleration  $\mu g$  is conducive to increasing the structural relative displacement.
2. If the moving structure is on the right of its origin position, it means that the friction coefficient  $\mu g$  on the contact surface is increasing, and the increment of the structural acceleration  $\mu g$  is conducive to increasing the structural relative displacement.

When the ground velocity  $v_e$  is smaller than the structural velocity  $v_s$ , the similar rules can be drawn.

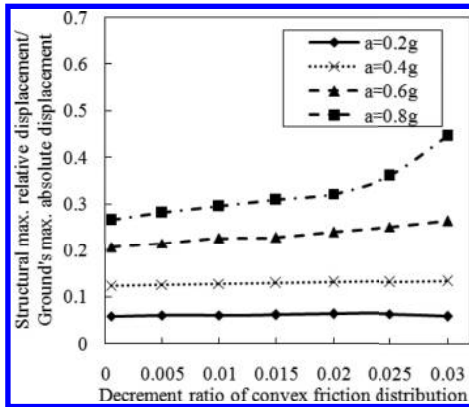


Figure 4. Effect of the decrement ratio of the convex friction distribution on the structural maximum relative displacement with soil profile III.

In a word, the convex friction distribution is conducive to increasing the structural relative displacement.

### 4.2 The influence of earthquake

Figures 5 and 6 show the influence of the site type of soil profile and PGA on the structural maximum relative displacement in the cases with the decrement ratio 0.01 of the convex friction distribution.

In Figure 5, when the earthquake soil profile number increases, the structural maximum relative replacement also increases gradually. As for the larger PGA, this incremental trend is more evident.

In Figure 6, the structural maximum relative displacement increases with the PGA.

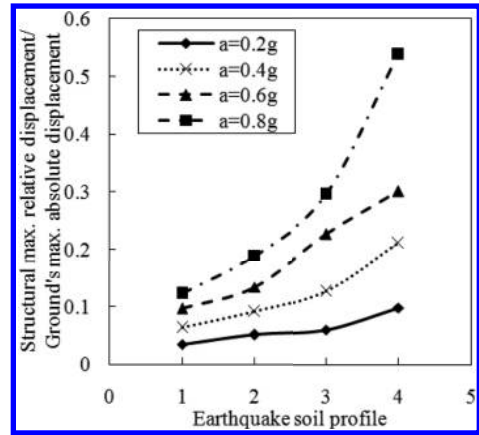


Figure 5. Effect of the site type of soil profile on the structural maximum relative displacement with the decrement ratio 0.01 of the convex friction distribution.

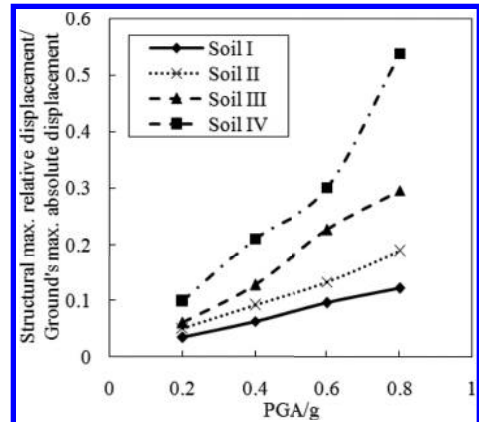


Figure 6. Effect of the PGA on the structural maximum relative displacement with the decrement ratio 0.01 of the convex friction distribution.

This incremental trend is more evident when the soil profile number increases.

A larger site type of soil profile or PGA means a larger absolute displacement of the ground motion, while the structural acceleration  $\mu g$  generated by the friction force  $\mu mg$  is a limited value. Thus, a larger site type of soil profile or PGA means a larger structural maximum relative displacement.

## 5 STRUCTURAL RESIDUAL DISPLACEMENT

### 5.1 The influence of the friction coefficient

The structural residual displacement should also be considered for the isolated structure, as it relates to the repair after the earthquake. Therefore, this section and the following sections analyze on the structural residual displacement.

Figure 7 shows the influence of the decrement ratio of the convex friction distribution on the structural residual displacement in the cases with soil profile III. The figure shows that the structural residual displacement is large.

As for the cases of the convex friction distribution in Figure 1, the structural motion direction after the ground motion just stops moving will influence the structural residual displacement:

1. If the structure moves away from the origin position, it indicates that the friction coefficient  $\mu$  on the contact surface decreases, which benefits on increasing the structural residual displacement.
2. Otherwise, it indicates that the friction coefficient  $\mu$  on the contact surface increases, which also benefits on increasing the structural residual displacement.

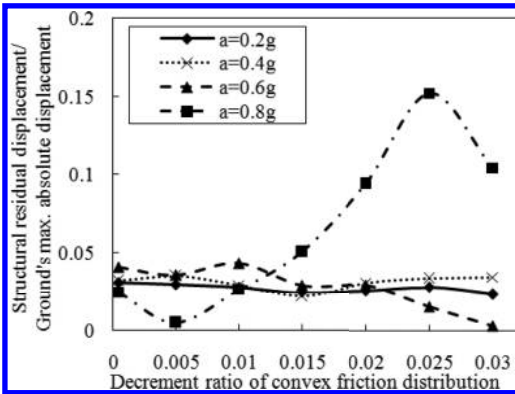


Figure 7. Effect of the decrement ratio of the convex friction distribution on the structural residual displacement with soil profile III.

Hence, the convex friction distribution outwardly increases the structural residual displacement.

However, as the structural residual displacement is just a special relative displacement when the structure stops moving, its value is naturally affected by that of the structural relative displacement. From the analysis in Sections 4.1 and 4.2, the influence factors on the structural relative displacement are so complicated that they have a sophisticated impact on the structural residual displacement.

Moreover, no matter in which direction the structure relatively moves to the original position, the existence of friction prevents the structure from moving. At this moment, the value of the friction coefficient is closely related to that of the structural relative displacement just as the ground stops moving. It may lead to the cases as follows:

1. If the structure moves away from the original position, and when the relative displacement is relatively large, the friction coefficient will be so small that it just faintly prevents the structure from moving away from the original position. However, as the relative displacement is relatively small, the friction coefficient will be large enough to effectively prevent the structure from moving away from the original position.
2. If the structure moves towards the original position, and when the relative displacement is relatively large, the friction coefficient will be large enough to effectively prevent the structure from moving towards the original position. However, as the relative displacement is relatively small, the friction coefficient will be so small that it just faintly prevents the structure from moving towards the original position.

Based on the comprehensive effect of the above-mentioned influence factors, the convex friction distribution may increase or decrease the structural residual displacement.

### 5.2 The influence of earthquake

Figures 8 and 9 show the influence of the site type of soil profile and PGA on the structural residual displacement in the cases with the decrement ratio 0.01 of the convex friction distribution.

In Figure 8, as the site type of soil profile becomes larger, the structural residual displacement first remains constant, and then increases.

In Figure 9, as the PGA increases, there is no obvious change rule. However, the structural residual displacement is large.

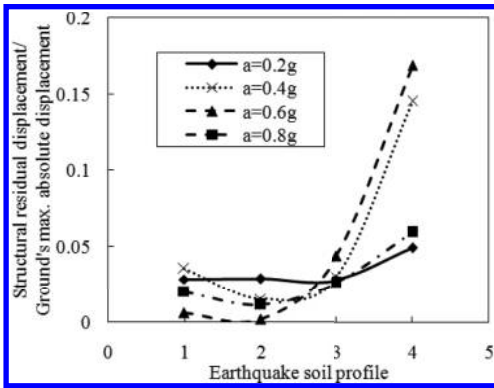


Figure 8. Effect of the site type of soil profile on the structural maximum relative displacement with the decrement ratio 0.01 of the convex friction distribution.

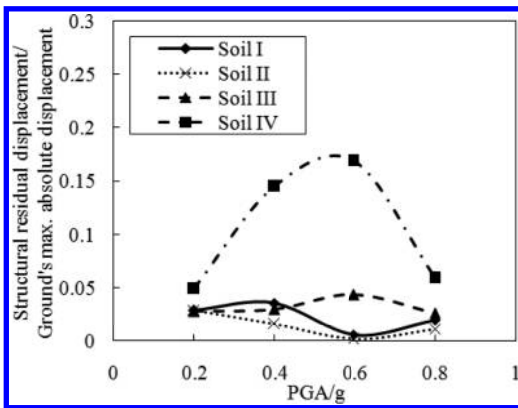


Figure 9. Effect of the PGA on the structural maximum relative displacement with the decrement ratio 0.01 of the convex friction distribution.

## 6 CONCLUSIONS

The convex distribution of friction coefficient almost always makes the structural maximum acceleration the largest and obviously increases the structural maximum relative displacement and the structural residual displacement. In general, it is unfavorable to the isolation system. Therefore, the convex distribution of friction coefficient should be avoided in the actual projects.

## ACKNOWLEDGMENTS

This research was jointly supported by the National Natural Science Foundations of China under Grant No. 51308549 and 51378504, the Natural Science Foundations of Hunan Province under Grant No. 2015JJ3159, the Program for Changjiang Scholars and Innovative Research Team in University (PCSIRT) (Grant No. IRT1296), and the Scientific Research and Development Program of China Railway Corporation under Grant No. 2013G002-A. The authors greatly appreciate their support.

## REFERENCES

- Guerreiro, L., Azevedo, J. & Muhr, A.H. 2007. Seismic tests and numerical modeling of a rolling-ball isolation system. *Journal of Earthquake Engineering* 11: 49–66.
- Harvey, P.S. & Gavin, H.P. 2014. Double rolling isolation systems: a mathematical model and experimental validation. *International Journal of Non-Linear Mechanics* 61(1): 80–92.
- Jangid, R.S. & Londhe, Y.B. 1998. Effectiveness of elliptical rolling rods for base isolation. *Journal of Structural Engineering* 124(4): 469–472.
- Jangid, R.S. 2000. Stochastic seismic response of structures isolated by rolling rods. *Engineering Structures* 22: 937–946.
- Lee, G.C., Ou, Y.C., Niu, T.C., et al. 2010. Characterization of a roller seismic isolation bearing with supplemental energy dissipation for highway bridges. *Journal of Structural Engineering* 136(5): 502–510.
- Ou, Y.C., Song J.W. & Lee, G.C. 2010. A parametric study of seismic behavior of roller seismic isolation bearings for highway bridges. *Earthquake Engineering and Structure Dynamics* 39: 541–559.
- Wei, B., Cui, R.B. & Dai, G.L. 2013. Seismic performance of a rolling-damper isolation system. *Journal of Vibroengineering* 15(3): 1504–1512.
- Wei, B., Yang, T.H. & Jiang, L.Z. 2015. Influence of friction variability on isolation performance of a rolling-damper isolation system. *Journal of Vibroengineering* 17(2): 792–801.
- Wei, B., Dai, G.L., Wen, Y., et al. 2014. Seismic performance of an isolation system of rolling friction with spring. *Journal of Central South University* 21(4): 1518–1525.

## Seismic performance of the convex-friction and damper systems

B. Wei, T.H. Yang, X.D. Yu, P. Wang & L.Z. Jiang

*School of Civil Engineering, Central South University, Changsha, China*

*National Engineering Laboratory for High Speed Railway Construction, Changsha, China*

**ABSTRACT:** As for a bridge with damper, a friction and damper isolation system was formed after the fixed bearings were sheared off during an earthquake. And the spatial distribution of friction coefficient was convex due to the smooth surface around the roughly damaged bearings. By taking a friction and damper isolation system as the study object, this paper analyzes the impact of the convex distribution of friction coefficient on the structural isolation performance under different ground motions through a compiled computer program. The results show that the convex distribution of friction coefficient increases the structural maximum relative displacement and residual displacement. Although those responses can be weakened by the damper, the convex distribution of friction coefficient should be avoided in the actual projects.

*Keywords:* bridge; bearing; damper; friction; horizontal earthquake

### 1 INTRODUCTION

In 2014, many researchers have investigated the new friction-based isolation methods with the aim to get optimum seismic isolation performance. Harvey & Gavin (2014) carried out a mathematical model and experimental validation for double rolling isolation systems, and the effects of the initial conditions, the mass of the isolated object, and the amplitude and period of the disturbance on the system's performance were assessed. As for Harvey et al (2014), a simplified model presented in their paper was applicable to RISs with any potential energy function, was amenable to both lightly- and heavily-damped RISs, and was validated through the successful prediction of peak responses for a wide range of disturbance frequencies and intensities. Ismail & Casas (2014) investigated the Near-Fault (NF) seismic performance of a novel isolation system, referred to as the Roll-N-Cage (RNC) isolator, considering the cable-stayed Bill Emerson Memorial Bridge in Missouri, which showed that the RNC isolator was a convenient isolation system in protecting cable-stayed bridges against NF earthquakes. Wang et al (2014) studied the sloped multi-roller isolation devices for seismic protection of equipment and facilities and obtained an excellent in-plane seismic isolation performance.

And before 2014, these similar friction-based isolation devices were also paid attention by several famous researchers. In Japan, Kurita et al (2011) developed a new device for seismic response

reduction, and the peak acceleration amplitude was decreased by about 50–90%. Nanda et al (2012) in India considered that the base isolation in the form of Pure Friction (P-F), among all other isolation methods developed so far, was the simplest one, which could be easily applied to low cost brick masonry buildings. Furthermore, the P-F isolation is one of the best alternatives for reducing earthquake energy transmission to superstructure during strong earthquake.

Although the friction isolation device avoids seismic damages caused in structure, the induced displacement may be very large and difficult to control. Therefore, restoring devices, such as springs and dampers, are usually used to avoid excessive relative displacement and reduce the structural residual displacement. As for some bridges, the springs, such as the fixed bearings, are often firstly destroyed by the earthquake. Although some designers considered that the destruction of bearings would protect other components of bridges from seismic damage, it is lack of rigorous analysis. The stochastic damage of bearing will form a rough contact surface (Wei et al. 2015), namely a large friction coefficient exists. However, other contact surfaces are very smooth with a less friction coefficient. Therefore, a natural isolation system with a convex distribution of friction coefficient is formed. Combined with the damper, a convex-friction and damper system is obtained.

The objective of this paper is to investigate a friction and damper system and artificially interfere the uneven distribution of friction coefficient to

be convex, i.e. the friction coefficient in the center of the seismic isolation device is the largest one, and it gradually decreases along the around path. Utilizing a numerical analysis method analyzes the impact of the convex distribution of friction coefficient on the seismic performance under different ground motions.

## 2 CALCULATION PROCESS

### 2.1 Structure model

In order to analyze the effect of the ‘convex’ distribution of friction coefficient on the seismic isolation performance in detail, this paper divides the friction coefficient, the damping constant and the earthquake input into several groups, and then obtains many combination cases.

As demonstrated in the related studies, for the isolation structure, the structure is built as a rigid body since the stiffness of the isolation device is far less than that of the structure (Wei et al. 2014). So in the computer program, the superstructure is temporarily simplified to a rigid body. The superstructure mass is set to be 300t and the damping constants adopt 100, 200, 300, 400 and 500 kN·s/m, respectively.

For the ‘convex’ distribution of friction coefficient, the friction coefficient in the center of the seismic isolation device is the largest one which is assumed to be 0.030, and it decreases gradually along the around path whose decrement ratios are assumed to be 0, 0.005, 0.010, 0.015, 0.020, 0.025 and 0.030, respectively. They are the main analysis objects in this paper.

### 2.2 Earthquake input

As shown in Figure 2, for each elastic response spectrum for the soil profile I, II, III, and IV in Chinese criteria (JTJ 004-89), one accelerogram is generated by Simqke procedure to be the ground motion input of the structural model.

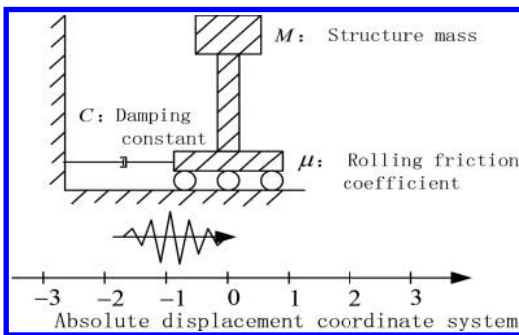


Figure 1. Structure model.

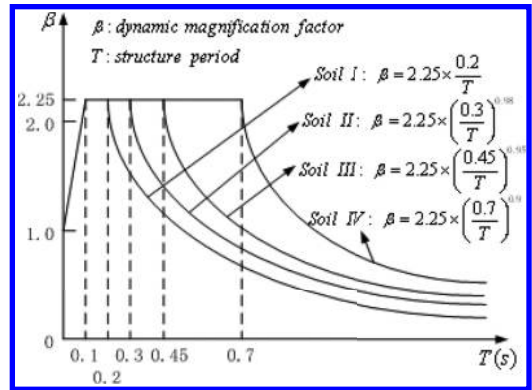


Figure 2. Four types of response spectrum.

### 2.3 Calculation cases

35 cases are obtained by combining 5 damping constants and 7 friction coefficients.

As for each case, each accelerogram in Section 2.2 is input as the ground motion, whose Peak Ground Accelerations (PGA) are adjusted to be 0.2, 0.4, 0.6 and 0.8 g, respectively. Thus, 560 cases are generated for the further calculation.

Then each case is calculated by the computer program (Wei et al. 2013).

## 3 STRUCTURAL ACCELERATION

### 3.1 The influence of friction coefficient

The structural acceleration is concerned for the isolated structure, as it directly indicates whether the earthquake will destroy the structure or not. Therefore, this section analyzes on the structural maximum acceleration.

Figure 3 shows the effect of the decrement ratio of convex friction distribution on the structural maximum acceleration. On the whole, as the decrement ratio of convex friction distribution increases, the structural maximum acceleration gradually decreases with some fluctuations. When the PGA is larger, the decreasing trend is more significant.

### 3.2 The influence of damping constant

Figure 4 shows the effect of the damping constant on the structural maximum acceleration. As the damping constant increases, the structural maximum acceleration gradually increases. When the PGA is larger, the increasing trend is more significant.

As demonstrated in the related researches, with regard to the general isolation structures, e.g. lead rubber bearing, as the structural period is close

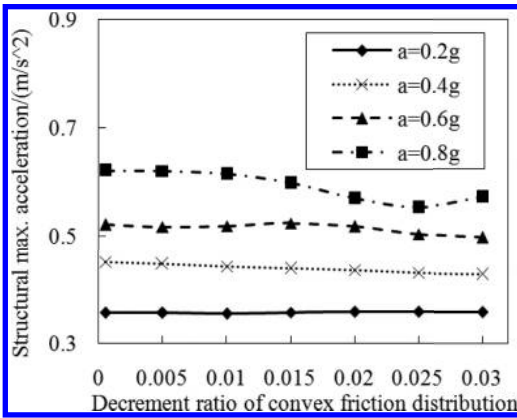


Figure 3. Effect of the decrement ratio of convex friction distribution on the structural maximum acceleration with soil profile IV and damping constant 100 kN·s/m.

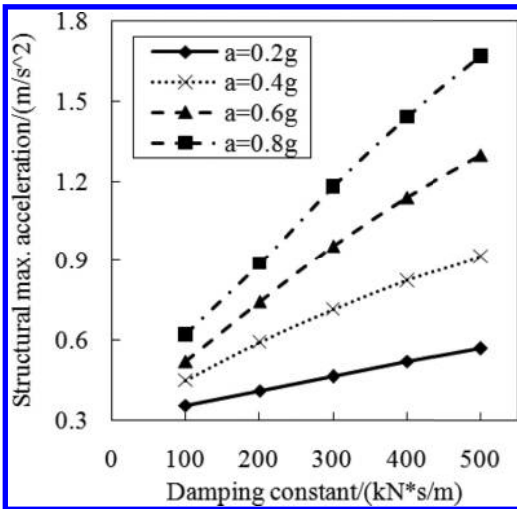


Figure 4. Effect of the damping constant on the structural maximum acceleration with soil profile IV and decrement ratio 0.03 of convex friction distribution.

to the seismic predominant period, increasing the damping constant of the isolation layer reduces the structural acceleration. As the structural period is much larger than the seismic predominant period, increasing the damping constant of isolation layer promotes a larger structural acceleration. The friction and damper isolation system doesn't have a fixed structural period, so it is approximately considered that the structural period is much larger than the seismic predominant period. And logically, just as illustrated in Figure 4, increasing the damping constant of the

isolation layer eventually increases the structural acceleration.

### 3.3 The influence of earthquake

Figures 5 and 6 show the effect of the site type of soil profile and the PGA on the structural maximum acceleration. As the site type of soil profile or the PGA is larger, the structural maximum acceleration gradually increases.

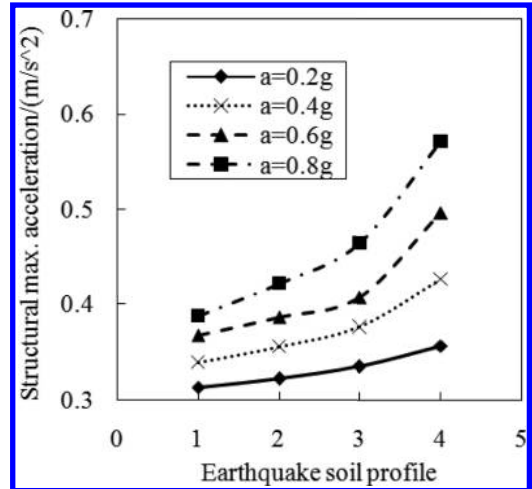


Figure 5. Effect of the soil profile on the structural maximum acceleration with damping constant 100 kN·s/m and decrement ratio 0.03 of convex friction distribution.

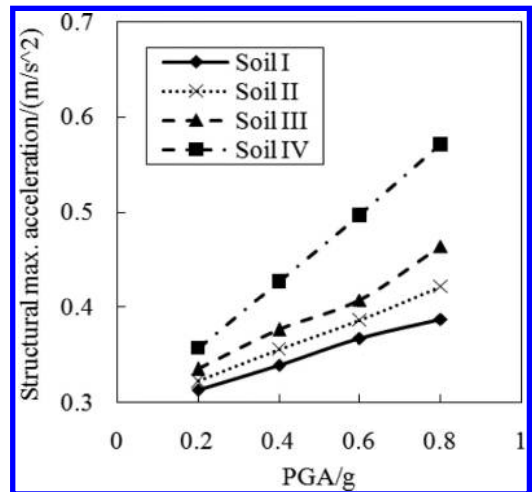


Figure 6. Effect of the PGA on the structural maximum acceleration with damping constant 100 kN·s/m and decrement ratio 0.03 of convex friction distribution.

## 4 STRUCTURAL RELATIVE DISPLACEMENT

### 4.1 The influence of friction coefficient

The structural relative displacement should be also concerned for the isolated structure, as it indicates if the superstructure will leave away from its foundation, and if the structure will collide with other things. Therefore, this section analyzes on the structural maximum relative displacement.

Figure 7 shows the effect of the decrement ratio of convex friction distribution on the structural maximum relative displacement. In general, as the decrement ratio of convex friction distribution increases, the structural maximum relative displacement gradually increases. When the PGA is larger, the increasing trend is more significant.

The convex friction distribution is conducive to increasing the structural relative displacement. Furthermore, as analyzed above, when the decrement ratio of convex friction distribution is larger, the structural maximum relative displacement increases as well.

### 4.2 The influence of damping constant

Figure 8 shows the effect of the damping constant on the structural maximum relative displacement. In general, as the damping constant increases, the structural maximum relative displacement gradually decreases. When the PGA is larger, the decreasing trend is more significant.

As the damper limits the structural relative velocity, it reduces the structural relative displacement. And as the damping constant is larger, this effect will be more significant.

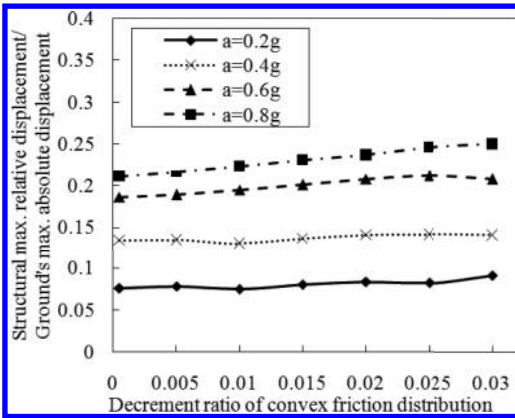


Figure 7. Effect of the decrement ratio of convex friction distribution on the structural maximum relative displacement with soil profile IV and damping constant 100 kN·s/m.

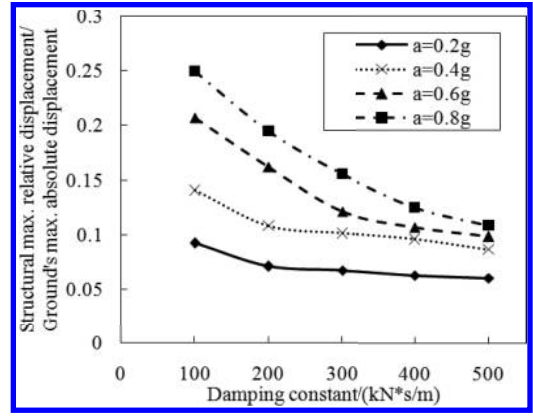


Figure 8. Effect of the damping constant on the structural maximum relative displacement with soil profile IV and decrement ratio 0.03 of convex friction distribution.

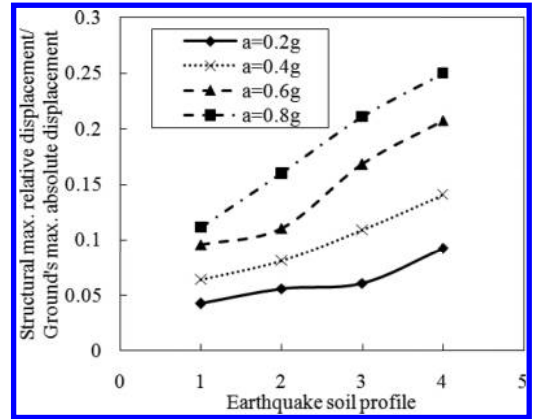


Figure 9. Effect of the soil profile on the structural maximum relative displacement with damping constant 100 kN·s/m and decrement ratio 0.03 of convex friction distribution.

### 4.3 The influence of earthquake

Figures 9 and 10 show the effect of the site type of soil profile and the PGA on the structural maximum relative displacement. In general, as the site type of soil profile or the PGA is larger, the structural maximum relative displacement increases gradually.

A larger site type of soil profile or PGA means a larger absolute displacement of the ground motion while the structural acceleration  $\mu g$  generated by the friction force  $\mu mg$  is a limited value. Therefore, a larger site type of soil profile or PGA means a larger structural maximum relative displacement. As the damper is conducive to

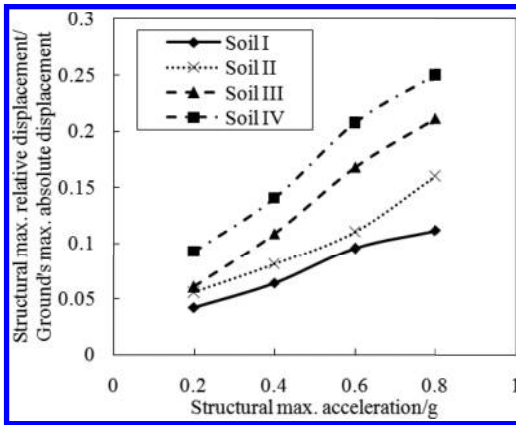


Figure 10. Effect of the PGA on the structural maximum relative displacement with damping constant 100 kN·s/m and decrement ratio 0.03 of convex friction distribution.

reducing the structural relative displacement, the increment of the site type of soil profile or PGA will not significantly increase the structural relative displacement.

## 5 STRUCTURAL RESIDUAL DISPLACEMENT

The structural residual displacement is noted for the isolated structure, as it relates to the repair after earthquake. Therefore, this section analyzes on the structural residual displacement.

The results show that the convex friction distribution increases the structural residual displacement sometimes. The other three parameters, including the damping constant, the site type of soil profile and the PGA, have no obvious influence on the structural residual displacement. And the corresponding figures are not presented herein.

## 6 CONCLUSIONS

The convex distribution of friction coefficient increases the structural maximum relative displacement and residual displacement. Although those responses can be weakened by the damper, the convex distribution of friction coefficient should be avoided in the actual projects.

## ACKNOWLEDGEMENTS

This research is jointly supported by the National Natural Science Foundations of China under grant No. 51308549 and 51378504, the Natural Science Foundations of Hunan Province under grant No. 2015 JJ3159, the Program for Changjiang Scholars and Innovative Research Team in University (PCSIRT) (Grant No. IRT1296), and the Scientific Research and Development Program of China Railway Corporation under grant No. 2013G002-A. The above support is greatly appreciated.

## REFERENCES

- Harvey, P.S. & Gavin, H.P. 2014. Double rolling isolation systems: a mathematical model and experimental validation. *International Journal of Non-Linear Mechanics* 61(1): 80–92.
- Harvey, P.S., Zehil, G.P. & Gavin, H.P. 2014. Experimental validation of a simplified model for rolling isolation systems. *Earthquake Engineering & Structural Dynamics* 43(7): 1067–1088.
- Ismail, M. & Casas, J.R. 2014. Novel isolation device for protection of cable-stayed bridges against near-fault earthquakes. *Journal of Bridge Engineering* 19(8): 50–65.
- Kurita K., Aoki S., Nakanishi Y., et al 2011. Fundamental characteristics of reduction system for seismic response using friction force. *Journal of Civil Engineering and Architecture* 5(11): 1042–1047.
- Nanda R.P., Agarwal P. & Shrikhande M. 2012. Base isolation system suitable for masonry buildings. *Asian Journal of Civil Engineering (Building and Housing)* 13(2): 195–202.
- Wang, S.J., Hwang, J.S., Chang, K.C., et al 2014. Sloped multi-roller isolation devices for seismic protection of equipment and facilities. *Earthquake Engineering & Structural Dynamics* 43(10): 1443–1461.
- Wei, B., Cui, R.B. & Dai, G. L. 2013. Seismic performance of a rolling-damper isolation system. *Journal of Vibroengineering* 15(3): 1504–1512.
- Wei, B., Yang, T.H. & Jiang, L.Z. 2015. Influence of friction variability on isolation performance of a rolling-damper isolation system. *Journal of Vibroengineering* 17(2): 792–801.
- Wei, B., Dai, G.L., Wen, Y., et al 2014. Seismic performance of an isolation system of rolling friction with spring. *Journal of Central South University* 21(4): 1518–1525.



## Quasi-static finite element analysis of a precast concrete frame shear wall structure

Yue guo Zhang, Quan Zhong, Lian guang Jia & Wei jian Zhao  
Shenyang Jianzhu University, Shenyang, China

**ABSTRACT:** In order to research the overall seismic performance of a precast concrete frame shear wall structure, a three-floor three-span concrete frame shear wall is built as the calculation model. This paper, respectively, calculates the precast structure and cast-in-place structure under low cyclic loading using general finite element software ABAQUS, and makes comparison between the two structure models in hysteresis curves, deformation and energy dissipation performance. The analysis results show that the bearing capacity of the cast-in-place structure is more than that of the precast structure. In the stiffness degradation process, the lateral stiffness of the cast-in-place structure is greater than that of the precast structure. Compared with the cast-in-place structure, energy consumption of the precast structure is lower in late loading, while the ductility of the precast structure is better in the loading. Failure modes of the precast structure are different from the cast-in-place structure, some structural measures should be taken to guarantee safety in design.

**Keywords:** precast structure; frame shear wall; quasi static

### 1 INTRODUCTION

With the introduction of green, environmental-friendly, energy-saving building, the state vigorously promotes the “building industrialization, housing industry”. The study and application of prefabricated concrete structure has become a hot issue.

There have been numerous studies carried out abroad on the fabricated structure<sup>[1-3]</sup>. Research and practice of precast concrete structures at home mainly concentrated on the prefabricated shear wall structure<sup>[4,5]</sup>, mainly for residential construction. Prefabricated frame structure research<sup>[6-8]</sup> is aimed at the multi-layer structure. By using ABAQUS finite element software, this paper, respectively, analyzes the precast structure and the cast-in-place structure of a three-floor three-span concrete frame shear wall under low cyclic loading, and draws a difference between bearing capacity, stiffness, ductility and energy dissipation. So, we can give reference conclusions for further studies.

### 2 MODEL VALIDATION

ABAQUS is a powerful finite element software, which can analyze complex solid and structural mechanics problems, simulate a very large and complex numerical model, and deal with a highly

nonlinear problem<sup>[9]</sup>. However, it is necessary to choose the parameters for verification to establish the precast model and to ensure the accuracy and applicability of the parameters used.

The validation of the model proposed in this article is shown in [Figure 1](#). Model structure size, reinforcement conditions, boundary conditions and loading of the SW1 specimen have been reported in the literature<sup>[10]</sup>.

Concrete constitutive model for the selection of ABAQUS finite element software comes with the plastic damage model of concrete, concrete uniaxial compression, tensile stress-strain curve values, reported in appendix C in Design of Concrete

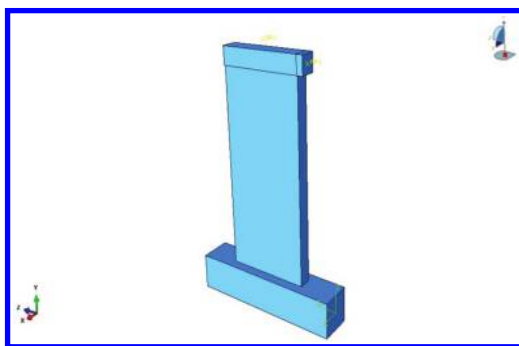


Figure 1. Validation of the finite element model.

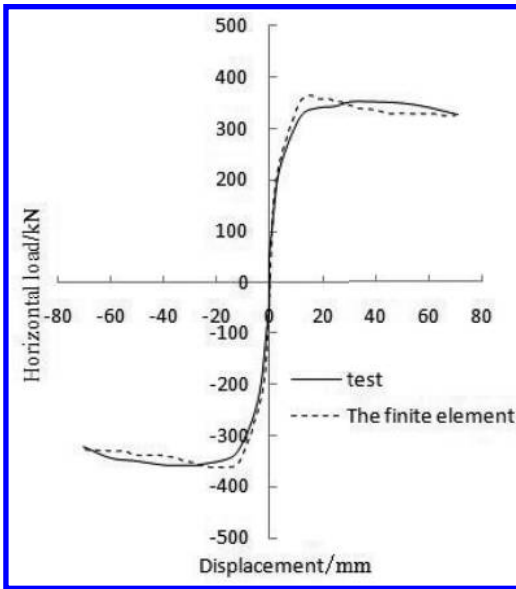


Figure 2. Comparison between the curve of the finite element calculation and the curve of the experiment skeleton.

Structures (GB50010-2010). At the same time, we introduce damage factors and stiffness coefficient of restitution, which has been referred to in the papers of Nie Jianguo<sup>[11]</sup> and Zhang Jin<sup>[12]</sup>. Reinforcement constitutive selects the bilinear kinematic hardening model, considering the influence of the Bauschinger effect, and the strengthening modulus takes the value of  $0.01E_s$ .

The horizontal force-displacement skeleton curve of the finite element model under low cycle reciprocating loading and SW1 horizontal force-displacement skeleton curve were compared, as shown in Figure 2. The maximum error is less than 10%, indicating that the parameters of numerical simulation are selected accurately and can be applied to the analysis of the frame shear wall model in this paper.

### 3 OVERVIEW OF THE FRAME SHEAR WALL MODEL

#### 3.1 Specimen size and reinforcement

One structure is a three-floor three-span cast-in-place concrete frame shear wall structure (henceforth referred to as the cast-in-place structure), and the other is a three-floor three-span precast frame shear wall structure (henceforth referred to as the precast structure). Shear walls are decorated in the side span whose span is 2.1 m, and another two span is 3.3 m, each storey is 2.4 m high. Section dimensions of the column are  $400\text{ mm} \times 400\text{ mm}$ ,

while the beam is  $200\text{ mm} \times 400\text{ mm}$ , and the thickness of the shear wall is 200 mm. C30 concrete is used, steel bar of beams, columns, and walls adopt HRB400, stirrups using HPB300. Reinforcement of shear walls is the double two-way  $C10@200$ . Model structure layout and beams, columns sectional reinforcement are shown in Figure 3 and Figure 4.

#### 3.2 Split form of the precast model

Split form of the actual structure model is shown in Figure 5. Beams, columns and walls are precast, while the concrete of the joint core is cast. There is a latter pouring belt between walls and columns. In order to simplify the model, the contact surface is established between the precast components and cast nodes, so are shear walls and the beams on its upper part. The finite element analysis model is shown in Figure 6, where the dark solid line section is the position that defines the contact surface.

#### 3.3 The selection of the material constitutive relation

Cast-in-place structure and precast structure select the material constitutive relation whose validation has been verified in this paper, and which can be used in the finite element simulation analysis.

#### 3.4 Establishment of the finite element model

Both the analysis model of concrete and steel bar select measured values, reference [10], [13], [14]. Concrete unit adopts the C3D8R reduced integral unit and reinforced unit adopts the T3D2 truss unit, using the embedded relationship between the steel and concrete<sup>[15]</sup>. We consider mutual friction

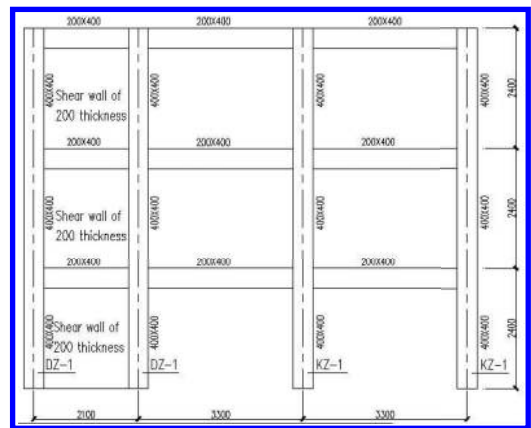


Figure 3. Arrangement of the model structure.

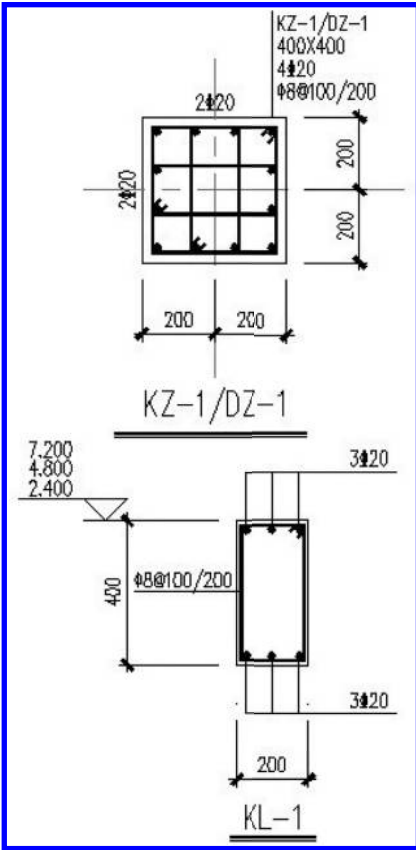


Figure 4. Reinforcement of beams and columns.

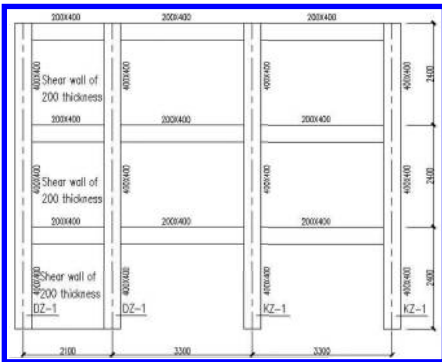


Figure 5. Disassembling of the actual structure.

at the contact surface between the splices, obtaining a normal and tangential effect.

The axial compression ratio of the column is 0.4. Using the displacement load, the horizontal load applied displacement on three layers at the same time, and the loading points are located in

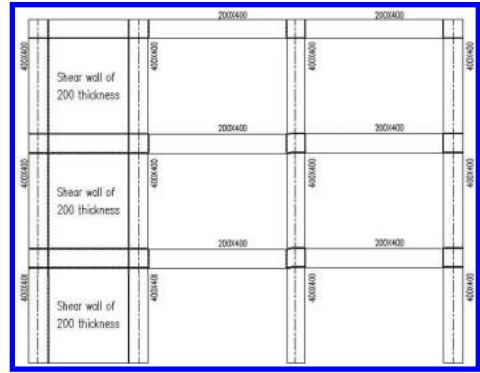


Figure 6. Disassembling of finite element analysis.

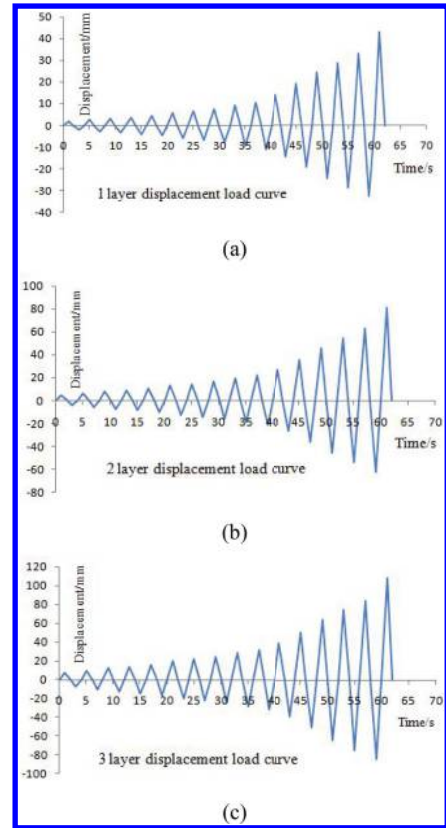


Figure 7. Curves of displacement loading.

the joints of the beams, columns on each shear wall side. Loading from the shear wall side to the side of the frame column is defined as the positive load, and vice versa for the negative load. Curves of displacement loading are shown in Figure 7.

## 4 FINITE ELEMENT ANALYSIS

### 4.1 ABAQUS stress analysis

For the precast structure, its yield first appeared in the longitudinal reinforcement in the shear wall, which assembled with beams together, and then the horizontal reinforcement of the shear wall yield. This is followed by the longitudinal reinforcement of the edge component of the shear wall yield, and the longitudinal reinforcement of each layer of the beam end yield. The last one is the longitudinal reinforcement of roots of the framework of the column yielding, stirrups yielding. There are differences between the precast structure and the cast-in-place structure observed from the failure mode. Necessary measures should be taken to ensure the safety for the failure mode of the precast structure in design.

von Mises stress at yield of concrete, and steel bar of the cast-in-place structure and the precast structure are shown in Figure 8 and Figure 9, respectively.

### 4.2 Hysteresis curve

The top load-displacement curves of the cast-in-place structure and the precast structure are shown in Figures 10 and 11. There are differences observed between the precast structure and the cast-in-place structure. The difference is that the surrounded area in the hysteretic curve of the precast structure is less than that of the cast structure, indicating that each hysteresis loop energy consumption of the precast structure is slightly lower than that of the cast structure. However, two hysteresis curves are relatively full, and there is no obvious “pinch shrinkage” phenomenon. This is because this article uses a separate modeling of ABAQUS, taking the embedded relationship between steel and concrete into account. The degree of freedom of embedded and embedding regions is fully constrained<sup>[6]</sup>, namely the bond and slip between steel and concrete are not consider completely. So, there is no obvious pinch effect, which is different from the actual structure hysteretic loading curve.

### 4.3 Analysis of capacity, ductility and deformation capacity

Displacement ductility coefficient, top limit displacement, yield displacement and corresponding yield and limit load of the precast structure and the cast-in-place structure of finite element analysis are listed in Table 1.

Displacement ductility coefficient of the specimens is the ratio of ultimate displacement to yield

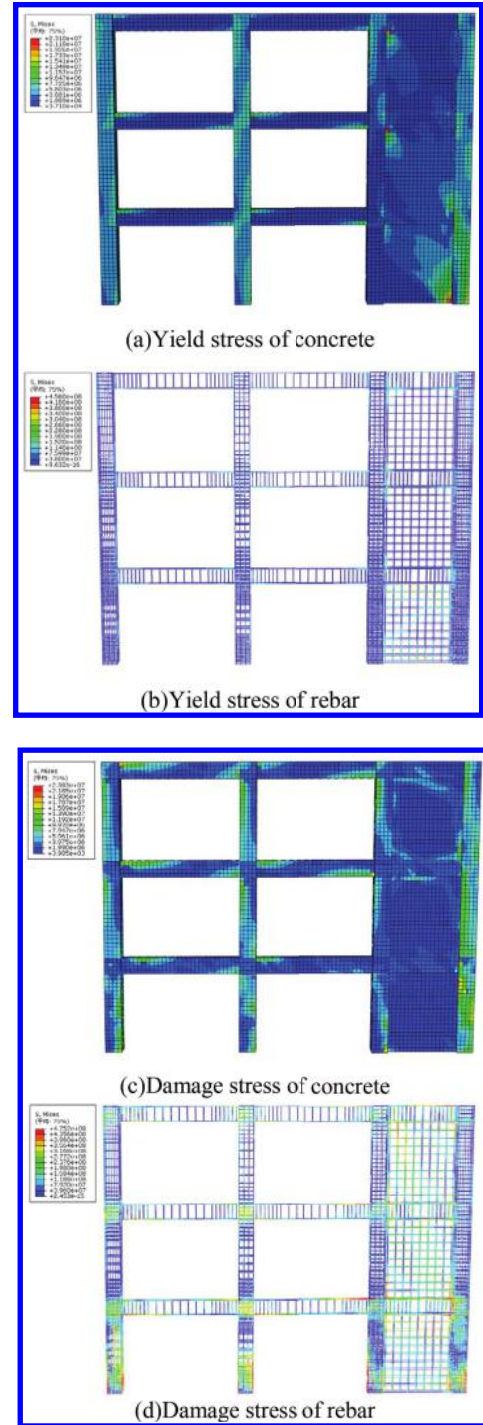


Figure 8. von Mises stress of concrete and rebar in the precast structure.

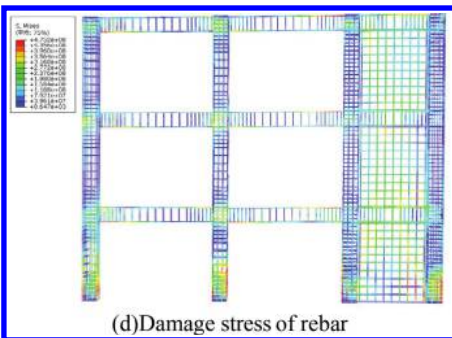
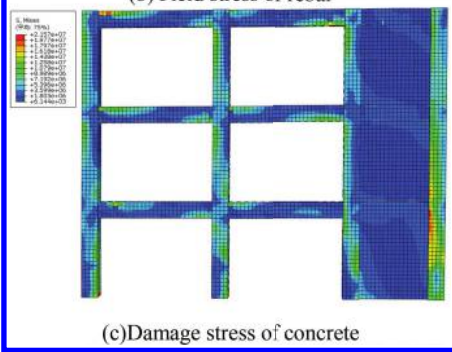
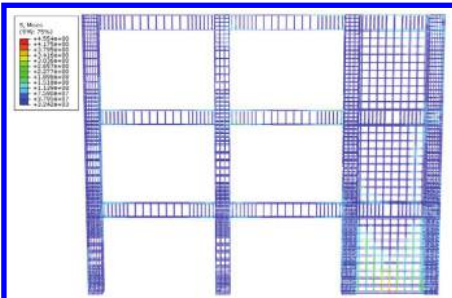
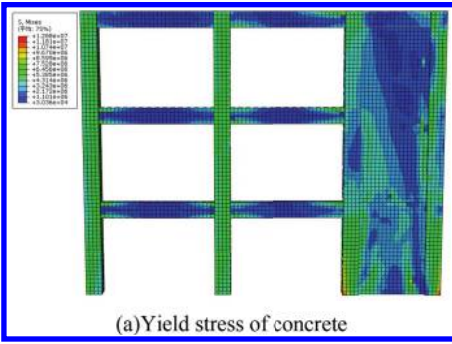


Figure 9. von Mises stress of concrete and rebar in the cast-in-place structure.

displacement, i.e.  $\mu = \Delta_u / \Delta_y$ . As can be seen from the table, the displacement ductility of the precast structure is superior to that of the cast structure. Yield load, peak load and ultimate load of the cast-in-place structure are higher than those of the precast structure.

#### 4.4 The stiffness degradation curve

To describe that the trends stiffness varies with displacement, the overall stiffness parameter is introduced. The overall stiffness of the specimen is the ratio of horizontal force to top displacement. Overall stiffness curves of the cast-in-place structure and the precast structure are shown in Figure 12.

By comparing the curve of overall stiffness degradation, we can see that the initial stiffness of the cast-in-place structure is greater than that of the precast structure, and in the process of loading, the stiffness

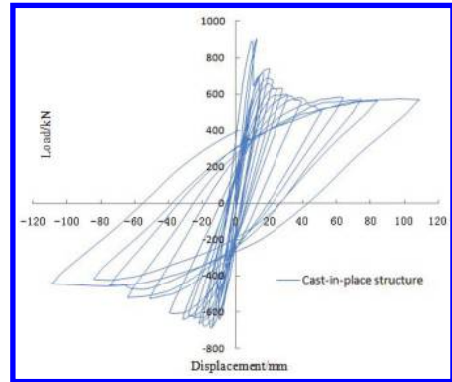


Figure 10. Top load-displacement curve of the cast-in-place structure.

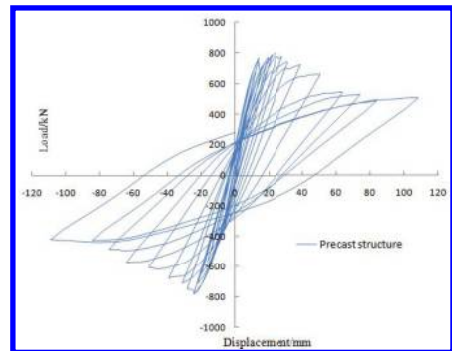


Figure 11. Top load-displacement curve of the precast structure.

Table 1. Load and displacement of feature points and displacement ductility factor.

Structure	Direction of load	Yield load (kN)	$\Delta_y$ (mm)	Peak load (kN)	$\Delta_m$ (mm)	Ultimate load (kN)	$\Delta_u$ (mm)	$\mu$
Cast-in-place structure	Positive	954.074	14.134	1283.58	39.260	1091.043	79.384	5.62
	Negative	837.959	10.061	1199.07	39.588	1161.400	72.156	7.17
Precast structure	Positive	817.269	12.308	1134.87	50.923	964.640	77.030	6.26
	Negative	636.788	10.063	1086.54	51.064	1015.960	74.810	7.43

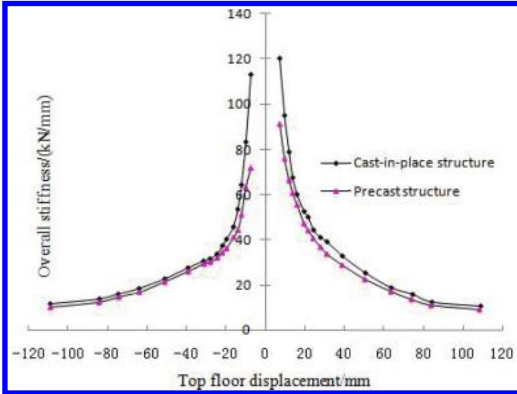


Figure 12. The overall stiffness contrast.

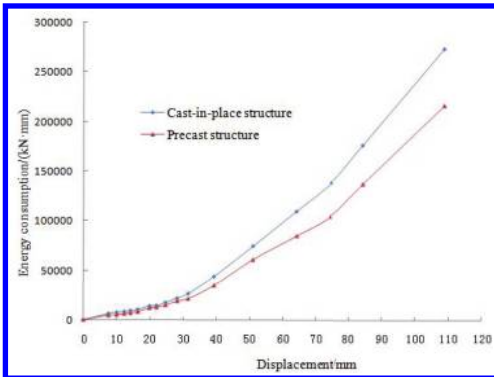


Figure 13. Comparison of energy consumption.

of the cast-in-place structure is always greater than that of the precast structure, which is caused by the characteristics of the precast structure. Whether it is the cast-in-place or the precast structure, the stiffness of the cast-in-place and the precast structure is reduced with loading, is close in late loading.

#### 4.5 Capacity of energy dissipation

In order to calculate energy consumption of the structure, we calculate the area of the hysteresis

loop with origin software. Energy consumption of the cast-in-place and the precast structure is shown in Figure 13.

We can see that in late loading, each loading cycle's energy consumption of the precast structure is lower than that of the cast-in-place structure. The reason is that the precast structure uses frictional contact at the junction, and there is mutual slip. Without considering the slip of steel in the process of simulation, the actual energy consumption is smaller, as shown in Figure 13.

## 5 CONCLUSION

1. Only considering the impact of the contact face, failure mode of the precast structure is different with the cast-in-place structure. Steel yielding of the precast structure first appeared in the longitudinal reinforcement of the shear wall, and then the horizontal reinforcement of the shear wall yield. This is followed by the longitudinal reinforcement of the edge component of the shear wall yield, and longitudinal reinforcement of each layer of the beam end yield. The last is the longitudinal reinforcement of roots of the framework of the column yielding, stirrups yielding.
2. The bearing capacity of the precast structure is lower than that of the cast-in-place structure. However, displacement ductility of the precast structure is better than that of the cast structure.
3. Lateral stiffness of the precast structure is smaller than that of the cast-in-place structure in early loading. Stiffness of the cast-in-place and precast structure is reduced with loading, but the stiffness of the cast-in-place structure is always greater than that of the precast structure.

## REFERENCES

[1] Pampanin S. Emerging solutions for high seismic performance of precast/prestressed concrete buildings [J]. Journal of Advanced Concrete Technology, 2005, 3(2): 207–223.

[2] Ertas, Onur, Sevket Ozden, et al. Ductile Connections in Precast Concrete Moment Resisting Frames [J]. PCI Journal, 2006, 51(3): 66–76.

- [3] Blandon, John J., Mario E. Rodriguez. Behavior of Connections and Floor diaphragms in Seismic-Resisting Precast concrete Buildings [J]. PCI Journal, 2005, (02): 56–75.
- [4] Jiang Hongbin, Chen Zaixian, Zhang Jiaqi, et al. Pseudo-static experimental research on precast reinforced concrete shear wall structure [J]. Journal of building structures, 2011, 32 (6): 34–40.
- [5] Zhu Zhang feng, Guo Zhengxing. Experimental study on seismic behavior of node of prefabricated shear wall structure [J] Civil Engineering Journal, 2012, 45 (1): 69–76.
- [6] Wang Honglin. Analysis of seismic performance of two floor double-span pre-stressed fabricated concrete frame [D]. Hefei University of Technology, 2010.
- [7] Pan Qijian. Experimental study on seismic capacity of precast prestressed concrete frame structures [D]. Southeast University, 2006.
- [8] He Lili. Analysis of pseudo-static experiment of pre-stressed fabricated concrete frame [D]. Hefei University of Technology, 2012.)
- [9] Shi Yiping, Zhou Yurong. Practical examples detailed explanation of ABAQUS finite element analysis [M]. Machine Press, 2007.
- [10] Peng Yuanyuan. Experimental study on seismic behavior of pre-cast reinforced concrete shear walls [D]. Tsinghua University, 2010.
- [11] Nie Jianguo, Wang Yunhang. Comparison study of constitutive model of concrete in ABAQUS for static analysis of structures [J] Engineering Mechanics, 2013, 30 (4): 59–67.
- [12] Zhang Jin, Wang Qingyang, Hu Shouying, et al. Parameters verification of concrete damaged plastic model of ABAQUS [J] building structure, 2009, 38 (8): 127–130.
- [13] Zhang Zhen. Seismic performance research of precast concrete columns in high-rise buildings [D]. Harbin Institute of Technology, 2013.
- [14] Song Yupu, Wang Jun, et al. Experimental study of mechanical properties of prefabricated frame structure beam-column joint [J] Dalian University of Technology, 2014, 54 (4): 438–444.
- [15] Wang Yuzhuo, Fu Chuanguo. Structural engineering analysis and detailed examples of ABAQUS [M]. Chinese Building Industry Press, 2010.
- [16] Zhu Lei, Huang Yuxing, Wang Yuanqing, Liu Ming. Quasi-static comparative analysis of a side corridor frame with ABAQUS [J] Shenyang Jianzhu University, 2014, 30 (3): 464–469.

## Discussion on the relation between $V_{S30}$ and $V_{SZ}$

Z.R. Tao & B.H. Zhu

Key Laboratory of Earthquake Engineering and Engineering Vibration, Institute of Engineering Mechanics, China Earthquake Administration, Harbin, China

X.X. Tao

Harbin Institute of Technology, Harbin, China

**ABSTRACT:** The time-averaged shear-wave velocity to a certain depth is an important parameter, which is used in seismic building codes and the Ground Motion Prediction Equation (GMPE). However, the main distinction is the different calculating depths. The relations between the shear-wave velocity to the depth less than 30 m  $V_{SZ}$  and that to the depth 30 m  $V_{S30}$ , developed by profiles in California and Japan, are verified by the data in China. The shear-wave velocity structures to shallow depths (<10 m) are found to be similar between California and Japan, through comparing the shear-wave velocity structure and the variation gradient of velocity. The velocity profiles obtained from the borehole measurements in California, Japan and China are adopted. The implication is that the sites in Japan are stiffer than the ones in California. The variation of the shear-wave velocity structure and the gradient variation of velocity are greater in the database of China. Surface sediments, soil physical properties and other factors are significantly different in these three regions. Therefore, it is not appropriate to estimate  $V_{S30}$  from  $V_{SZ}$  in China by the regression models from the databases of California and Japan.

**Keywords:**  $V_{S30}$ ;  $V_{SZ}$ ; relation

### 1 INTRODUCTION

The time-averaged shear-wave velocity  $V_S$  is a crucial factor in classifying sites in seismic codes (e.g., Dbry et al., 2000; BSSC, 2001; Eurocode 8, 2004 et al.). There are various calculating depths of  $V_S$  in different seismic codes of different countries, caused by construction cost, engineering technology, built environment and other factors. The average shear-wave velocity to a depth of 30 m,  $V_{S30}$ , is used in the National Earthquake Hazards Reduction Program (NEHRP 2009). Seismic ground motion parameter zonation map of Japan (2009) states that the calculating depths of the average shear-wave velocity are to the soil layer with a shear wave velocity more than 400 m/s. In the code for seismic design of building of China (2010), a smaller value between the overlaying depth (the surface to the soil layer with the shear-wave velocity greater than 500 m/s) and 20 m is used. The calculating depth is usually less than 30 m. Even in the USA, the calculating depth does not extend to 30 m, restricted by site conditions in some cases. The average shear-wave velocity to

a depth  $Z < 30$  m  $V_{SZ}$  can be calculated by using Equation (1):

$$V_{SZ} = \frac{Z}{\sum_{i=1}^n \frac{Z_i}{V_{Si}}} \quad (1)$$

where  $Z_i$  is the thickness of the  $i$ th soil layer in the calculating depth  $Z$  (m);  $V_{Si}$  is the shear-wave velocity of the  $i$ th soil layer (m/s); and  $n$  is the number of soil layers.

The time-averaged shear-wave velocity to 30 m ( $V_{S30}$ ) has a number of applications in the field of engineering seismology. Some researchers have attempted to establish the relationship between  $V_{S30}$  and the average shear-wave velocity  $V_{SZ}$  to the depth  $Z$  ( $Z = 5$  m–29 m), especially in California and Japan with rich borehole data. Boore (2004b) established the log-linear model between  $V_{S30}$  and  $V_{SZ}$  using shear-wave velocities to the depths not less than 30 m, based on 135 California borehole data. Kanno et al. (2006) obtained a  $V_{S20}$ - $V_{S30}$  relation by KiK-net borehole data to the depth, and it can be used to extend  $V_{S20}$  in the K-NET stations



to  $V_{S30}$ . Cadet & Duval (2009) proposed the linear regressions of the logarithmic values of  $V_{SS}$ ,  $V_{S10}$  and  $V_{S20}$  with  $V_{S30}$ , which agree with those proposed by Boore (2004b), and applied to some European borehole data, whose standard deviation is smaller. Thus, Cadet & Duval (2009) concluded that the relations from the KiK-net database were adaptable to those from the non-Japanese data available for their study. Boore (2011) considered that the correlation for  $Z < 30$  m that was proposed by Boore (2004b) is unfit to Japanese data by comparing the shear-wave structure and the variation gradient of velocity from Japan, California, Turkey and Europe, and proposed the logarithmic quadratic polynomial model of  $V_{SZ}$  with  $V_{S30}$  by KiK-net data.

The 134 borehole data in California, 606 borehole data from KiK-net stations, used in this paper, are similar to those proposed by Cadet & Duval (2009) and Boore (2011). The 577 borehole data in China to a depth more than 30 m are used to discuss the suitability of empirical relations, developed by data from California and KiK-net stations.

## 2 THE COMPARISON OF THE REGIONAL DATABASE

The 134 borehole data in California, 606 borehole data from KiK-net stations and 577 borehole data in China to a depth more than 30 m are used and divided into 12 groups by the interval of 100 m/s, to compare the structures of these databases. The histogram of the proportion of each group is shown in Figure 1 to depths of 5 m, 10 m, 20 m and 30 m.

As shown in Figure 1, to a shallow depth (< 10 m), the shear-wave velocity structures of California and Japan are similar; to a deep depth (> 10 m), the shear-wave velocity structures are different. There is a great difference between the Chinese data and those from California and Japan.

The correlation coefficients of  $V_{SZ}$  with  $V_{S30}$  from 5 m to 29 m are calculated for these three sets, respectively, as listed in Table 1 and shown in Figure 2.

From Table 1 and Figure 2, we can see that the correlation coefficient increases with depth, the change in curve slopes from California is similar to that from Japan. However, the increase in the curve slope from Japan is faster than that from California, which indicates that the gradient change in the sites in Japan is greater than that in California, and that the near-surface soil layer of the former is stiffer than that of the latter. These curves are significantly different from the curve from China, which demonstrates that the statistical relations from the data of Japan and California are unfit to Chinese sites.

Cadet & Duval (2009) argued that the statistical relation from KiK-net data could be used for some non-Japanese sites. Both this model and the models

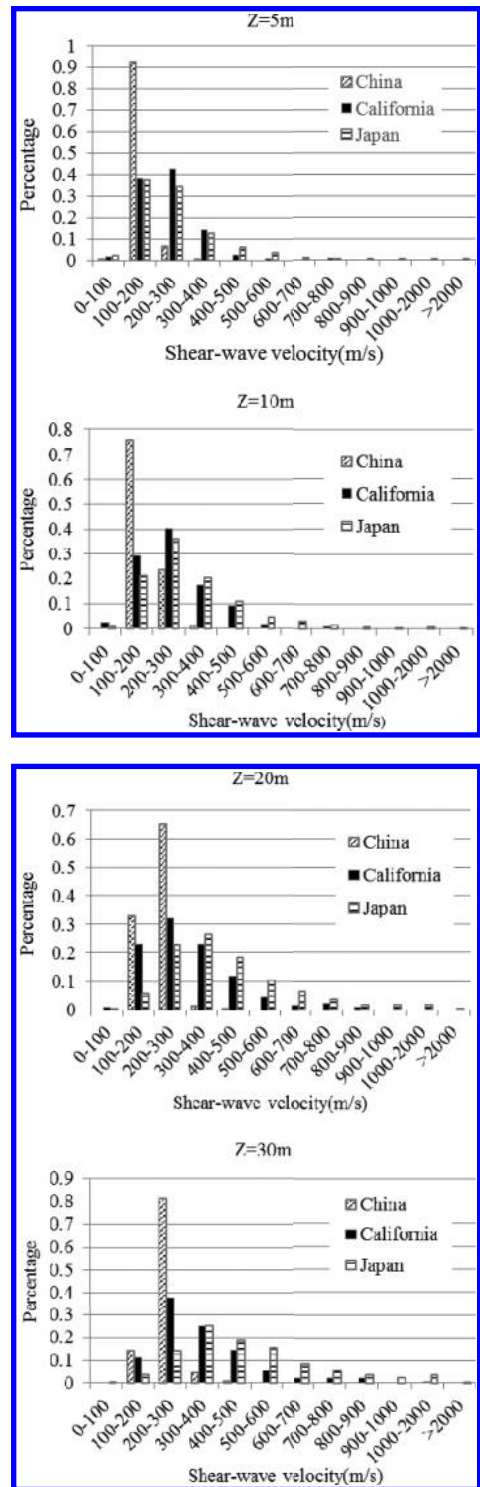


Figure 1. Proportion of 12 shear-wave velocity groups to the depths of 5 m, 10 m, 20 m and 30 m.

Table 1. Correlation coefficients of VS30 with VSZ from 5 m to 29 m.

Z (m)	China	California	Japan
5	0.820702	0.72433	0.793655
6	0.845255	0.780795	0.818373
7	0.864416	0.810846	0.843068
8	0.880919	0.839230	0.862222
9	0.895630	0.869309	0.881443
10	0.909287	0.891879	0.896636
11	0.920957	0.909929	0.911586
12	0.929920	0.923964	0.923676
13	0.936473	0.936407	0.934597
14	0.941941	0.947557	0.943742
15	0.947583	0.956571	0.952365
16	0.952804	0.964397	0.959526
17	0.957300	0.970143	0.967692
18	0.961178	0.975362	0.973761
19	0.964677	0.979756	0.979209
20	0.967408	0.983397	0.983539
21	0.969801	0.986994	0.987379
22	0.971605	0.989895	0.990468
23	0.972928	0.992512	0.993027
24	0.973919	0.994671	0.995046
25	0.974620	0.996388	0.996697
26	0.975098	0.997819	0.997942
27	0.975382	0.998851	0.998894
28	0.975546	0.999513	0.999526
29	0.975830	0.999883	0.999886

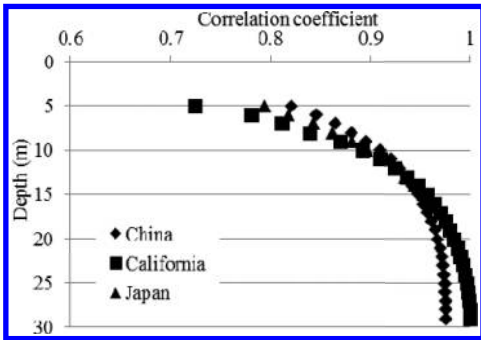


Figure 2. Correlation coefficient with depth.

of Boore (2004b) and Boore (2011) are employed to estimate  $V_{S30}$  by  $V_{SZ}$ , which are compared with the  $V_{S30}$  from borehole measurements. Mean values and standard deviations are shown in Figure 3.

From Figure 3, it can be seen that the standard deviations of Japan and California are similar, and their mean values are different obviously. The mean values and standard deviations of Chinese data are greater than those of Japan and California. The mean value from Europe is close to that from California; however, the difference in the standard deviations of Europe and California is great. It indicates

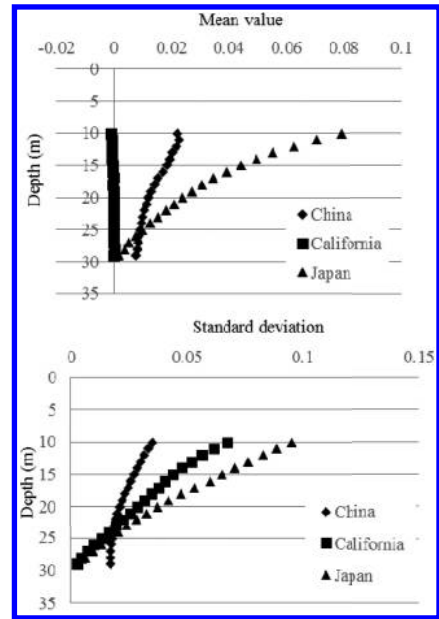


Figure 3(a). Mean values and standard deviations of the residuals between the estimated values (Boore model, 2004b) and the borehole measured values.

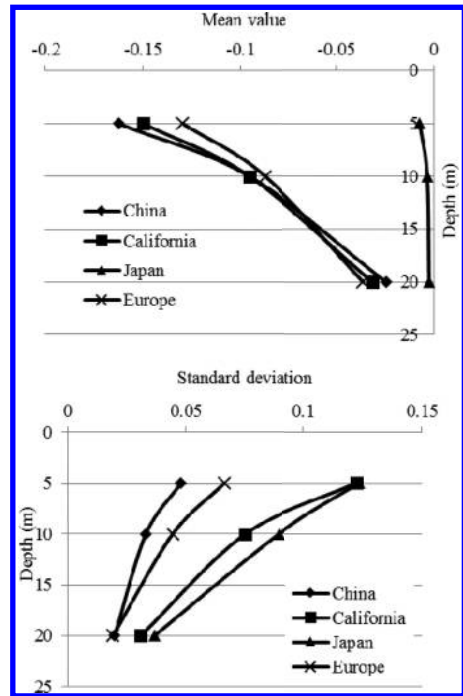


Figure 3(b). Mean values and standard deviations of the residuals between the estimated values (Cadet & Duval model, 2009) and the borehole measured values.

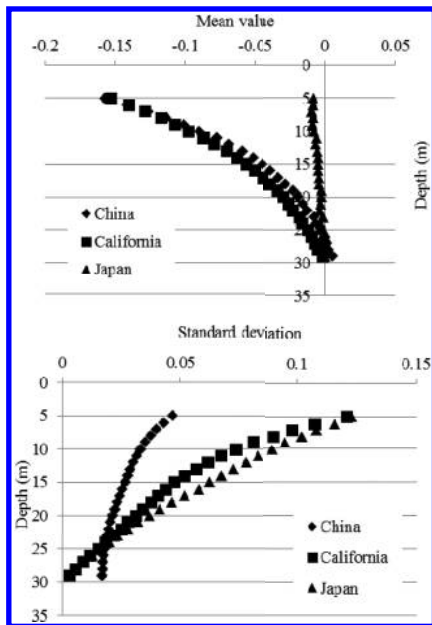


Figure 3(c). Mean values and standard deviations of the residuals between the estimated values (Boore model, 2011) and the borehole measured values.

that the statistical relation using the data of Japan and California is unfit to China, and that the statistical regression method has regional characteristics.

### 3 CONCLUSION

Three databases, including 134 borehole data in California, 606 borehole data from KiK-net stations from Cadet & Duval (2009) and Boore (2011), and 577 borehole data in China to a depth more than 30 m, are used to discuss the suitability of empirical relations, developed by data from California and KiK-net stations. The histogram of the proportion of each shear-wave velocity group to the depths of 5 m, 10 m, 20 m and 30 m and the correlation coefficients of  $V_{S30}$  with  $V_{SZ}$  ( $Z = 5\text{ m} \sim 29\text{ m}$ ) shows that the site conditions of Japan and California are similar, but the sites in Japan are stiffer than those in California, and that of China is obviously different from those of the other two countries. So, the statistical relation using the data of Japan and California is unsuitable for China.

Three statistical models are adopted to estimate  $V_{S30}$  from  $V_{SZ}$ . The mean values and standard deviations of the residuals between the estimated values and the borehole measured values show a great difference among these three databases. It can be inferred that the statistical regression results are regional, and it is not fit to the Chinese data.

### ACKNOWLEDGMENTS

The authors thank Associate Professor LIU Hongshuai for providing a part of Chinese borehole data. This work was financially supported by the National Nature Science Foundation of China (51178435 and 51478443).

### REFERENCES

- Boore, D.M. (2004b). Estimating  $V_{S30}$  (or NEHRP site-classes) from shallow velocity models (depths < 30 m), *Bull. Seismol. Soc. Am.* 94, 591–59.
- Boore, D.M., Thompson, E.M. & Cadet, H. (2011). Regional correlations of  $V_{S30}$  and velocities averaged over depths less than and greater than 30 meters. *Bull. Seismol. Soc. Am.* 101, 3046–3059.
- Building Seismic Safety Council (BSSC) (2001). *NEHRP recommended provisions for seismic regulations for new buildings and other structures, 2000 Edition, Part 1: Provisions*, prepared by the Building Seismic Safety Council for the Federal Emergency Management Agency (Report FEMA 368), Washington, D.C.
- Cadet, H. & Duval, A.M. (2009). A shear wave velocity study based on the KiK-net borehole data. *A short note, Seismol. Res. Lett.* 80, 440–445.
- Dobry, R., Borcherdt, R.D., Crouse, C.B., Idriss, I.M., Joyner, W.B., Martin, G.R., Power, M.S., Rinne, E.E. & Seed, R.B. (2000). New site coefficients and site classification system used in recent building seismic code provisions, *Earthquake Spectra* 16, 41–67.
- Eurocode 8 (2004). *Design of structures for earthquake resistance, part 1: General rules, seismic actions and rules for buildings*, EN 1998–1, European Committee for Standardization (CEN), <http://www.cen.eu/cenorm/homepage.htm>.
- Holzer, T.L., Bennett, M.J., Noce, T.E., Padovani, A.C. & Tinsley, J.C.I.I.I. (2005). Shear-wave velocity of surficial geologic sediments in northern California: statistical distributions and depth dependence. *Earthquake Spectra* 21 (1), 161–177.
- International Code Council, Inc. (ICC) (2009). *International Building Code*, Washington D.C.
- Japan Road Association (2002). *Specification for Highway Bridges, Part V: Seismic Design*. Tokyo, Japan.
- Kanno, T., Narita, A., Morikawa, N., Fujiwara, H. & Fuku shima, Y. (2006). A new attenuation relation for strong ground motion in Japan based on recorded data, *Bull. Seismol. Soc. Am.* 96, 879–89.
- Kuo, C.H., Wen, K.L., Hsieh, H.H., Lin, C.M., Chang, T.M. & Kuo, K.W. (2012). Site classification and  $V_{S30}$  estimation of free-field TSMIP stations using the logging data of EGDT. *Engineering Geology* 129–130 (2012) 68–75.
- Ministry of Construction of the People's Republic of China and General Administration of Quality Supervision, Inspection and Quarantine of the People's Republic of China (2010). *National Standard of People's Republic of China, Code for Seismic Design of Buildings*. China Architecture & Building Press, Beijing, 18–21 (in Chinese).
- Wald, D.J., & Allen, T.I. (2007). Topographic slope as a proxy for seismic site conditions and amplification, *Bull. Seismol. Soc. Am.* 97, 1379–1395.

# Structural dynamic anti-seismic performance analysis on the main machine hall in conventional island of Tianwan nuclear power station unit 5, 6

Yu-hao Jin, Jie Zhao & Gui-xuan Wang

*Dalian University R&D Center of the Civil Engineering Technology, Dalian, China*

**ABSTRACT:** Development of nuclear power has great significance to energy saving and optimizing energy structure in China and, therefore, much attention has been paid to the safety of nuclear power buildings. However, the research of the building's seismic performance is not enough at present. On the basis of the existing research, this paper used SAP2000 and ANSYS for elastic analysis and elastic-plastic deformation analysis of a severe earthquake on one main workshop in conventional island (pushover analysis), which analyzed the periods, modes and floor displacement angle among layers of main structure component, protracted capacity spectrum-demand spectrum curve and got a more complete dynamic response of structures from elasticity to elastic-plastic phase. Under a more severe earthquake, the response spectrum analysis and time—history analysis indicated that the structural seismic performance was good. Periods and vibration modes of the structure and the interlayer displacement angle of the elastic stage met the specification requirements. Under the strong seismic action, the static elastoplastic pushover analysis showed that the performance point that was obtained by the intersection of the demand spectrum curve and capacity spectrum curve appeared early, and was in the elastic range of the power spectrum, and structural seismic performance met the specification requirements. The analysis process for the anti-seismic performance analysis of main plant building in a normal island and other major construction projects has a certain reference and practical value.

**Keywords:** conventional island; anti-seismic performance; elastic analysis; elastic-plastic deformation analysis; pushover analysis

## 1 INTRODUCTION

Nuclear power has become an important energy for human use, and is an important part of the electric power industry. Its economic and social benefits are very significant. In recent years, safety accidents of nuclear power buildings have occurred many times (e.g., Chelo Bailey, Fukushima nuclear power plant), which not only caused serious economic losses, but also had a great influence on the society and the human mind. So, the safety of nuclear power building becomes the focus of attention. At present, the domestic and foreign research on the seismic performance of the conventional island nuclear power plant is not sufficient, and research still remains in the analysis of seismic performance of thermal power plant, which obtained some research results. For example, Liu zhiqing<sup>[1]</sup> studied on the seismic behavior of the frame bent hybrid structure of SRC columns—RC shear walls for the main building of thermal power plants. Shan liang<sup>[2]</sup> used the PKPM to research on the seismic performance of thermal power plant.

Wu tao<sup>[3]</sup> conducted an experimental study on the seismic behavior of RC bent structure of a large-scale power plant. These studies have to a certain degree demonstrated the seismic performance of this type of buildings and drew some conclusions, but lacked elastic-plastic deformation analysis<sup>[4]</sup>. Zhang qin<sup>[5]</sup> carried out a performance-based seismic design of nuclear plant, which is a trend for earthquake-resistant design. But this design has not been widely used because some problems still need to be studied and improved. The current specification<sup>[6][7]</sup> also lacks of relevant provisions of seismic design for the conventional island of nuclear power.

Therefore, using the structural analysis software SPA2000 and ANSYS, we carry out an analysis on the seismic performance of the conventional island of Tianwan Nuclear Power Station Unit 5, 6 to study on the deformation characteristics of the main plant system in the elastic stage and the plastic stage, and to discuss the stress of the conventional island under different earthquake scenarios. Thus, we provide the necessary basis to further

study on the seismic performance of the conventional island of nuclear power plant.

## 2 SEISMIC ANALYSIS METHODS OF STRUCTURE

Seismic analysis methods of structure include response spectrum analysis and time history analysis. The response spectrum analysis<sup>[8]</sup> is based on the modal decomposition response spectrum theory. This is only a common calculation method of structural dynamic response that is limited to the linear elastic structure under earthquake action. The first step is to use the reciprocal theorem (Betty theorem) to get the modal orthogonality so that we can break the vibration partial differential equations of multiple degrees of freedom into ordinary differential equations of the single degree of freedom system, which can achieve the displacement response of structure solution.

Time history analysis<sup>[9]</sup> is a kind of advanced analysis method in seismic analysis of structures, including linear elastic time history analysis and elastic-plastic time history analysis. The elastic-plastic time history analysis can be divided into static elastic-plastic time history analysis and elastic-plastic time history analysis. Dynamic elastic-plastic time history analysis inputs the earthquake acceleration data into the structure. According to the structural dynamic equations, we can solve the seismic response of structures by the numerical method. However, this method often needs more time and energy. The pushover method<sup>[10]</sup> is plastic static analysis under monotonic loading, which applies lateral force to the analysis model in some way of simulating seismic horizontal inertia force that gradually increases. If the structure fractures or yields, changing the stiffness parameters makes the structure reach a predetermined state. The horizontal load distribution form is as follows: bottom shear, first mode of structure, and modal decomposition of response spectrum<sup>[11]</sup>. Time history analysis is generally used only for important buildings and very complex buildings.

## 3 PROJECT OVERVIEW

In this paper, the conventional island of Tianwan Nuclear Power Station Unit 5,6 is taken as the research object. The workshop is 108 m long and the total span is 59 m. The structure of distribution is as follows. The cast-in-place reinforced concrete frame structure is composed of a steam room and an auxiliary room, the vertical axis (A,B,C) uses a frame structure;  $\pm 0.000$  m and 8.500 m platforms

of the steam room are the cast-in-place reinforced concrete structure, so the gable is less than 8 meters. The gable near the island sets the main steam pipe swinging proof structure, and the anti-rejection structure adopts the shear wall structure.

This structure is a semi-basement structure. Seismic grade is class one and the structure arrangement is very irregular. The load varies and the distribution of quality is very uneven. The effect of nuclear power equipment in the main building for structural seismic performance cannot be ignored<sup>[12]</sup>. In addition to the elastic analysis of the structure, plastic deformation analysis under the rare earthquake is also needed. According to the drawings and load data of the conventional island, SAP2000 and ANSYS are used for elastic analysis and elastic-plastic deformation analysis.

## 4 THE MAIN BUILDING MODEL

### 4.1 Input conditions

The design of load conditions of this project is as follows: (1) constant load, mainly the weight of the structure; (2) process load, including pipeline lifting, weight of equipment, maintenance of crane load; (3) crane load from four directions; (5) earthquake, considering torsional effect; (6) whipping loads of the main steam pipeline and main water supply pipeline; and (7) floor live loads and roof live load.

The seismic fortification intensity is 7 degrees and of the third earthquake group. The earthquake acceleration is 0.10 g and the site category is the second. The surface design ground motion parameters are listed in Table 1.

### 4.2 The main building model

During the establishment of the SAP2000 model, the beam-column element is imitated by the truss element. The node is rigid and the floor is the elastic shell element. Steel structure beams are all articulated and the concrete side wall around the main building is applied to the soil pressure; Eccentric setting is for all surface elements and beam elements, considering the actual elevation of the structure.

Table 1. The surface design ground motion parameters.

Earthquake level	Peak acceleration (cm/s <sup>2</sup> )	$\alpha_{max}$	T <sub>g</sub>	Damping ratio
Frequent	35	0.08	0.45	0.05
Rare	220	0.50	0.45	0.05

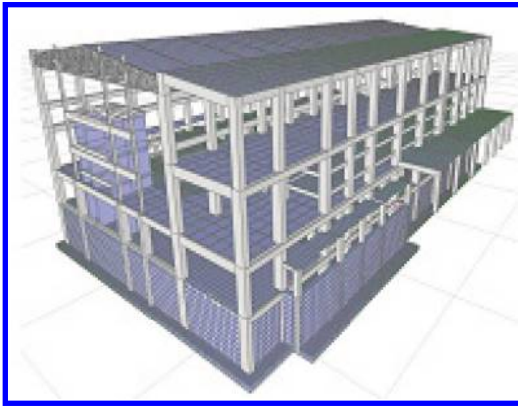


Figure 1. SPA2000 model.

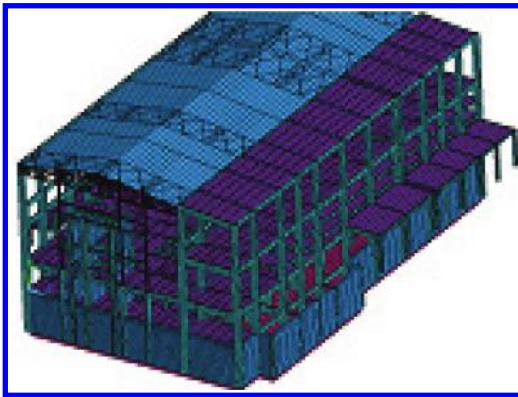


Figure 2. ANSYS model.

In the ANSYS analysis model of three-dimensional calculation, roof truss structure is simulated by link8. Beam189 is used to show the beam-column component. Shell99 is used to simulate all the surface shell elements. The three-dimensional model of the structure is shown in Figure 1 and Figure 2.

## 5 A SEISMIC ANALYSIS OF THE MAIN BUILDING STRUCTURE

### 5.1 Period and mode of vibration

In a given design ground motion, Table 2 lists the vibration period of the main plant structure. It can be seen that the first natural vibration period T1 and the second natural vibration period T2 of the structure calculated by using the SAP2000 and ANSYS models are dominated by translation. The natural vibration period T3 reverses, and

Table 2. Structure natural vibration periods of the main machine hall in the conventional island.

Item	Period	
	SAP2000	ANSYS
<i>Natural vibration period of structure</i>		
T1	1.082	1.091
T2	0.998	1.052
T3	0.891	0.905
T4	0.849	0.544
T5	0.464	0.492
T6	0.458	0.484
T7	0.419	0.458
T8	0.407	0.402
T9	0.396	0.389
T10	0.393	0.388
Torsional/translational	T3/T1 = 0.82	T3/T1 = 0.83

Table 3. Computing mode number and quality of modal participation factor.

Item	Period			
	SAP2000		ANSYS	
	Number of modes		Number of modes	
<i>Calculation of the number of modes and mode participation mass ratio</i>				
X	80	97%	80	99%
Y	80	98%	80	99%

T3/T1 is less than 0.9, meeting the “Technical specification for concrete structures of tall building” requirements.

The effect of higher modes of the seismic design of the building structure cannot be ignored. When the base shear and top displacement error is less than 5%, the cumulative mass participation ratio should be greater than 90% stipulated by the “Technical specification for concrete structures of tall building”. Table 3 gives the calculation of the number of modes and mode participation mass ratio. It can be seen from the table that up to 80 order vibration mode, the modal mass coefficient reaches 90%, meeting the requirements of the specification.

Vibration is the relative displacement of each particle when the free vibration occurs in the structure, which could be used to determine whether the structure system layout is reasonable or not. The first three modes of the structure are as follows: 1 translation, 2 translation, and 3 reverse. If the

torsional mode is premature, it is unfavorable to the seismic behavior of the building.

### 5.2 The elastic layer displacement angle under frequent earthquake

Under the influence of wind load and earthquake, the interlayer displacement angle of the main plant structure can meet the requirements of the specification (1/550). The interlayer displacement angle of the structure is given in Table 4.

### 5.3 The overall stability of structures in the elastic stage under frequent earthquake

The calculation results show that each layer frame ratio of stiffness to weight is greater than 10, which meets the standard requirements for the overall stability. When the ratio of stiffness to weight is greater than 20, it is unnecessary to consider the two-order effect. The ratio of stiffness to weight is given in Table 5.

### 5.4 The elastic-plastic deformation analysis under the rare earthquake

The seismic grade of the main building structure in this project is level 1, and the structure is irregular. The elastic-plastic deformation analysis

under the rare earthquake should be conducted after the elastic analysis. The pushover analysis in the structural model is built in SAP2000 (Pushover Analysis).

In the architecture of SAP2000, the specific reinforcement of beams and columns is made according to the reinforcement scheme to design the specific parameters of the plastic hinge. Moment rotation curve relationship of double section beams is worked out by the section size and reinforcement arrangement in the section designer, and then input the number to joint design parameters, the analysis results of which are as follows. From the spectrum-demand spectrum curve to capacity in the X axis and the spectrum-demand spectrum curve capacity in the Y axis<sup>[13]</sup>, it can be known that the performance point appears earlier and is in the elastic range capacity spectrum, which indicates that the structure has a good seismic performance of reserves and meets the standard requirements of fortification.

From the performance point of the structure, we can obtain vertex displacement corresponding to the structure according to formula (1), which can reflect the deformation structure under the rare earthquake:

$$S_d = \frac{\Delta_{top}}{\gamma_1 X_{top,1}} \quad (1)$$

According to the specification, we calculate the structure angle of floor displacement and test the structure to satisfy the deformation requirement of large earthquakes. The performance point of the interlayer displacement angle is given in Table 6.

It can be seen from Table 6 that the maximum drift angle is 1/242, which meets the specifications of the reinforced concrete frame structure elastic-plastic displacement angle limit of 1/50 requirements under the rare earthquake. At the same time, the calculated maximum displacement of the top layer is 0.112 m, which is far less than the  $1/50 \times 33 = 0.66$  m vertex lateral displacement limit, meeting the requirements of the specification.

After the determination of the structure that meets the earthquake deformation, the judgment

Table 4. Interlayer displacement angle of the structure.

Item	SAP2000	ANSYS
<i>The interlayer displacement</i>		
<b>X</b>		
Small earthquake	1/1527	1/1324
Wind	1/2629	1/2245
<b>Y</b>		
Small earthquake	1/1412	1/1207
Wind	1/5780	1/5321

Table 5. The ratio of rigidity-to-gravity computing of the structure.

Item	SAP2000	ANSYS
Total quality of structures (t)	35984.5	
<i>The overall stability of structures</i>		
<b>X</b>		
Ratio of stiffness to weight	①156 ②83.6 ③192	①142 ②78.4 ③183
<b>Y</b>		
Ratio of stiffness to weight	①232 ②104 ③128	①211 ②95 ③105

Table 6. Interlayer displacement angle of strong seismic action.

Layer number	Interlayer displacement angle in X	Interlayer displacement angle in Y
1	1/1257	1/1223
2	1/464	1/548
3	1/535	1/242

of weak structural layer can be made based on the distribution of the structural components of the plastic hinge. Observation of performance point hinge<sup>[4]</sup> is shown in Figures 3 and 4.

Figure 5 shows the hinge state graph. In the pushover analysis in X, framework beams and columns located in the performance of point are still in the A-B elastic stage, with no plastic hinge. In the pushover analysis in Y, the plastic hinge appeared in the end of the beam located in the performance of the main points, where the structure is in the elastic yielding stage, at the point B on the hinge state graph. Hinge is in beam ends that meet the seismic code “strong column and weak beam” seismic design concept in the structure. So, it satisfies the requirements of the local deformation component requirements.

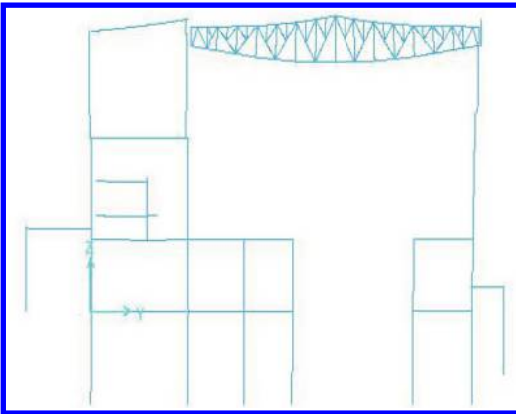


Figure 3. Hinge state in X performance points to the pushover analysis.

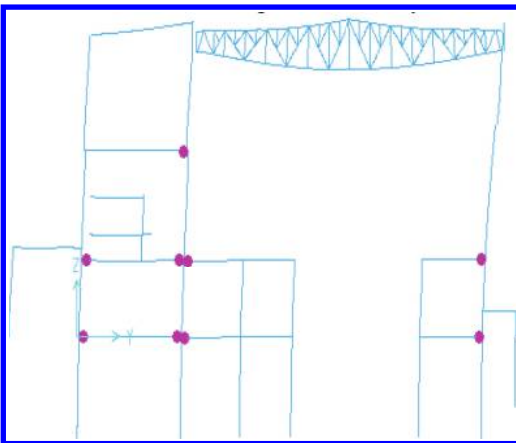


Figure 4. Hinge state in Y performance points to the pushover analysis.

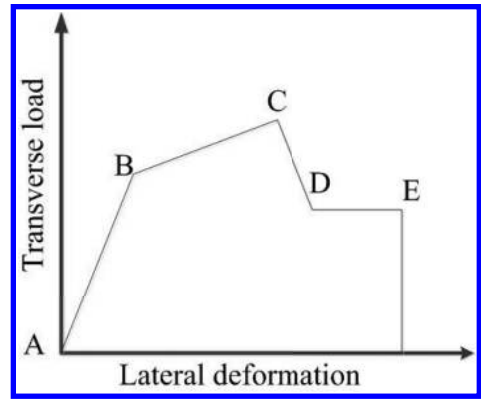


Figure 5. Hinge state curve.

## 6 CONCLUSION

Using the SAP2000 and ANSYS models, we carry out the analysis on the main building structure in Tianwan Nuclear Power Station Unit 5 and 6, obtaining the structural dynamic response under different effects of earthquake. We then compared the elastic response under frequent earthquake and time history analysis, and conducted plastic deformation analysis under severe earthquake. On this basis, the results showed that:

1. Under the frequent earthquake, response spectrum analysis and time history analysis show that the structural seismic performance is good. The cycle and vibration mode of the structure and the elastic layer displacement angle can meet the requirements of the specification.
2. The pushover analysis under the rare earthquake shows that the performance point that is from the intersection of the demand spectrum and the response spectrum appears earlier. The seismic performance of the structure can meet the requirements of the specification.
3. Hinge is in the beam ends, which meets the seismic code “strong column and weak beam” seismic design concept in the structure. So, it satisfies the requirements of the local deformation requirements.

## REFERENCES

- [1] Liu Zhi-qin, Bai Guo-liang. Study on Seismic Behavior of the Frame—Bent Hybrid Structure of SRC Columns—RC Shear Walls for the Main Building of Thermal Power Plants [J]. Building Science, 2013, 29(1):41–43. (in Chinese).
- [2] Shan Liang, Li Yue-bing. Research on seismic behavior of frame-bent structure of thermal power plant [J]. ChengShi Jianshe Lilun Yanjiu 2012, 24(1): 307–310. (in Chinese).



- [3] Wu Tao, Liu Bo-quan. Experimental study on seismic behavior of RC frame, bent structure of a large—scale power plant [J]. *Journal of Building Structures*, 2007, 28(3):46–50. (in Chinese).
- [4] Miao Zhi-wei, Ye Lie-ping. Nonlinear Static Analysis for Frame-shear-wall Structures [J]. *Earthquake Resistant Engineering and Retrofitting*, 2008, 30(6):43–46. (in Chinese).
- [5] Zhang Qin, Zhang Yang. Performance—based seismic design method of mill building for conventional Island of nuclear power plant [J]. *Journal of industrial architecture*, 2010, 40(4):51–54. (in Chinese).
- [6] GB50011-2010, Code for seismic design of buildings [S]. China Architecture & Building Press, 2010.
- [7] JGJ3-2010, Technical specification for concrete structures of tall building [S]. China Architecture & Building Press, 2010.
- [8] Lin Sheng-yi. PBSO study on seismic behavior of main machine hall in conventional island [J]. *Earthquake Engineering and Engineering Vibration*, 2011, 31(5):50–53. (in Chinese).
- [9] Zhang Jian. Research on Issues of Elastic-plastic Dynamic Time-history Analysis [J]. *Earthquake Resistant Engineering and Retrofitting*, 2011, 33(5): 75–78. (in Chinese).
- [10] Yi Hua-wei, Wang Meng-fu. Studies and improvements on structural static pushover analysis method [J]. *Engineering Mechanics*, 2003, 20(4):45–49. (in Chinese).
- [11] Miu Zhi-wei, Ma Qian-li. Study on the Accuracy and Applicability of the Pushover Analysis [J]. *Earthquake Resistant Engineering and Retrofitting*, 2008, 30(1):56–59. (in Chinese).
- [12] Wang Shao-he, Xu Zi-guo. Study on the Seismic Performance of a High Rise Building with Different Structure Schemes for Mechanical Floor [J]. *Building Science*, 2011, 27(5):6–9. (in Chinese).
- [13] Gong Jin-xin, Yu Zhong-han. Pushover-based seismic reliability analysis of structures [J]. *Journal of Harbin Engineering University*, 2013, 34(12): 1545–1547. (in Chinese).
- [14] Zhang Shu-yun, Bai Guo-liang. Research on the plastic hinge property of steel reinforced concrete members based on push—over analysis [J]. *China Civil Engineering Journal*, 2010, 28(7):55–58. (in Chinese).

# Behavior of steel double-channel built-up chords of special staggered truss steel frames structure under reversed cyclic bending

H.D. Ran & W.L. Liang

*School of Civil Engineering of Xi'an University of Architecture and Technology, Xi'an, China*

**ABSTRACT:** Finite element results from the tests of eight cantilever double-channel built-up members under reversed cyclic bending are presented. The main parameters investigated were stitch spacing, lateral bracing spacing, depth-thickness ratio of web and setting stiffeners. The moment-drift hysteretic loops, skeleton curves, the moment and drift values for different loading stages and seismic behavior index were obtained. According to these curves, the failure characteristic, ductility, and energy dissipation capacity of this type of structure were analyzed in this paper. The results indicate that the cantilever double-channel built-up members have good hysteretic behaviors. The reduction in stitch spacing can prevent lateral-torsional buckling of individual elements. A thicker web improves the bearing capacity. The stiffeners limit the buckling of web and flange, as well as improve hysteretic energy of the member.

**Keywords:** cantilever double-channel built-up members; reversed cyclic bending; hysteretic behavior; finite element

## 1 INTRODUCTION

As economic, efficient, the staggered truss frame system was a line with the development direction of Chinese steel buildings [1–2]. Because of the advantages, domestic and foreign scholars have done a lot of research. The results indicate that composite staggered truss frame steel structure under reversed cyclic bending, the developing sequence of plastic hinges was truss web members→truss chords→column [3], which was adverse to the seismic performance of structure. This paper proposed a method to promoted performance of the composite staggered truss frame, that is, chords were used as special segments to dissipate energy by yielding, and other members of structure remain elastic. This method improved the overall seismic performance of structures. With its rational use of material, high stiffness and well preventing lateral-torsional, steel built-up members were often used in earthquake-resistant structures or chord members in special truss girders. As the less study about double-channel built-up members' flexural performance, the research on double-channel built-up members under reversed cyclic bending has important practical significance in the hysteretic behavior.

## 2 MODEL OVERVIEW

A three-dimensional finite element model of the tested system has been developed via the Finite

Element Package ABAQUS to detect in detail the local and global behavior of the base connection. The finite elements used for the discretization are brick-type solids with 8 nodes (C3D8R). The channels, gussets and stitch plates were made of Q235, while modulus of elasticity  $E_s = 2.06 \times 10^5$  MPa, Poisson's ratio  $\nu = 0.3$ , and yielding strength  $\sigma_y = 235$  MPa. Material constitutive relation obeyed the ideal elastic-plastic material.

## 3 DESIGN OF SPECIMENS

The cantilever specimens would represent the chord member between the end of the special staggered truss steel frames structure (fixed end in test specimen) and midspan point of inflection of the special staggered truss steel frames structure (free end in test specimen) (Fig. 1). The load P in term of displacement acted on 200 mm below the free end. There were restraint about x, y and z direction on the ends of grade beam, as well as x direction on the loading point.

This paper consisted of testing of eight cantilever double-channel built-up members under reversed cyclic bending. Each specimen consisted of a gusset plate, and a double-channel built-up member made of either 2-C25a or 2-C25c sections. Figure 2 were the layout and geometrical sizes of specimens. There was no provisions about double-channel built-up members under bending on code for design of steel structures [4] (GB50017-2003).

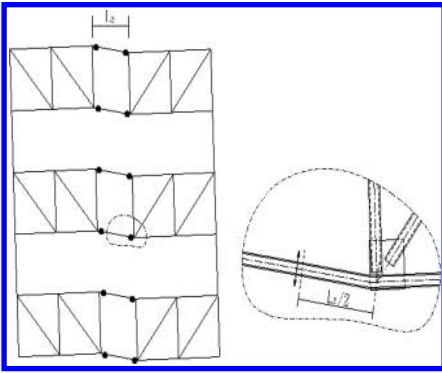


Figure 1. Location of specimens and plastic hinge.

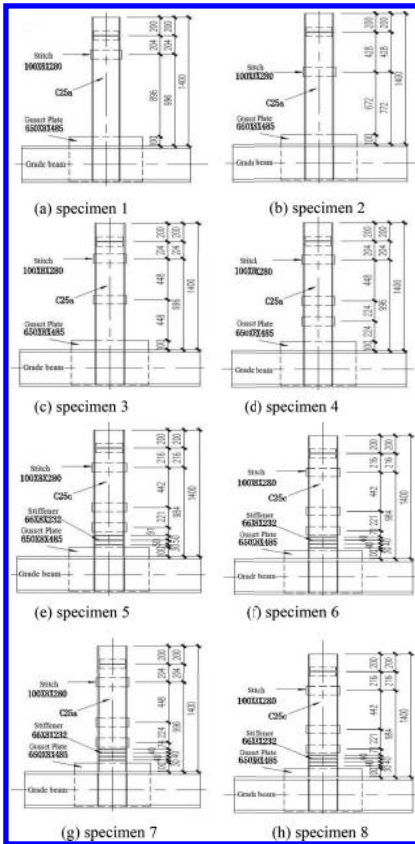


Figure 2. Layout and geometrical sizes of specimens.

Specimens 1–4 consisted of a 2-C25a built-up member, while the distance of stitch spacing was  $40i$ ,  $30i$ ,  $20i$ ,  $10i$ , respectively. Where  $i$  was the individuals' radius of gyration to weak axis. The four elements are designed such that buckling of the entire brace occurs prior to buckling of the

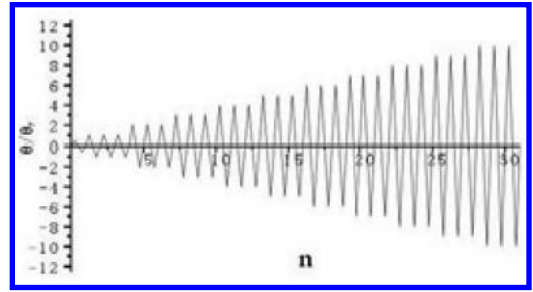


Figure 3. Displacement history.

individual members. Specimen 5 consisted of a 2-C25c built-up member, while the distance of stitch spacing was  $10i$ . It was setting stiffeners between the first stitch and 30 mm above the gusset plate. The distance of stiffeners was 50 mm. Specimen 6 was “identical” to Specimen 5, except for a reduced stiffener spacing of 40 mm, which could prevent local buckling of web and flange. Specimen 7 featured the same details as in Specimen 6, but was changed C25a. Based on specimen 6, specimen 8 set restraint about x direction on the first stitch. That could ensure the stable of members to study variations of depth-thickness ratio on member's behavior. The lateral bracing on specimen 8 met the chapter 8.5.5 on Code for seismic design of buildings [5] (GB50011-2010).

The method of cyclic displacement loading was based on specification of testing methods for earthquake resistant building [6] (JGJ 101-96) (Fig. 3).

#### 4 TEST RESULTS

The displacement was the horizontal displacement of loading direction. Conveniently, Rotation (rad) = displacement (mm)/1200 (mm).

Yielding of the channels in Specimen 1 was noticed at early stages of the test (about 4.25 mm) and spread over approximately 100 mm above the gusset plate during the later loading cycles. Lateral-torsional buckling of the individual channels was first noticed during the  $3\Delta_y$  cycles. This lateral-torsional buckling became severe during the cycles at  $10\Delta_y$  cycles, which ultimately led to the termination of the test. Specimen 2 showed a very similar response compared to Specimen 1 with a short stitch spacing of  $20i$ , but for yielding drift of 8.51 mm. Specimen 3 showed no deterioration of strength up to 8.72 mm. At  $4\Delta_y$  stage, slight local buckling in the channel web was observed, and failure due to lateral-torsional buckling of individuals occurred during the  $10\Delta_y$  (Fig. 4). A reduced center-to-center stitch spacing of 224 mm ( $10i$ ) was provided in Specimen 4. Yielding in the channels

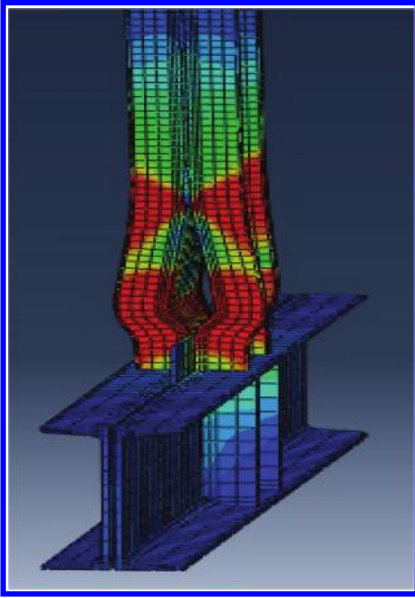


Figure 4. Lateral-torsional buckling of individuals.

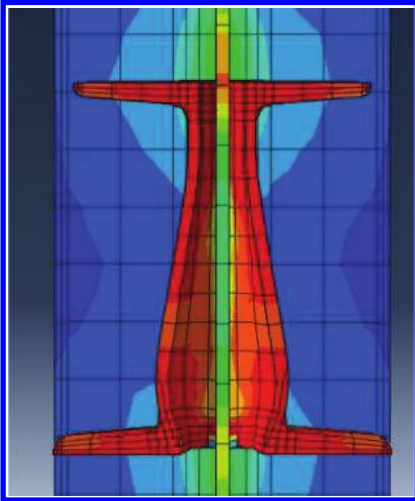


Figure 5. Local buckling of web.

of Specimen 4 was first noticed at approximately 8.75 mm and spread over 100 mm above the gusset plate during 17.5 mm cycles. It had higher bearing capacity and hysteric energy compared to Specimen 3. For the cycle to 96.25 mm ( $11\Delta_y$ ), the maximum moment of specimen 4 dropped to 86% of extreme moment. For the cycle to 100 mm, the maximum moment dropped to 85% of extreme moment, while flange and web severe buckling (Fig. 5). The reason for dropped bearing moment

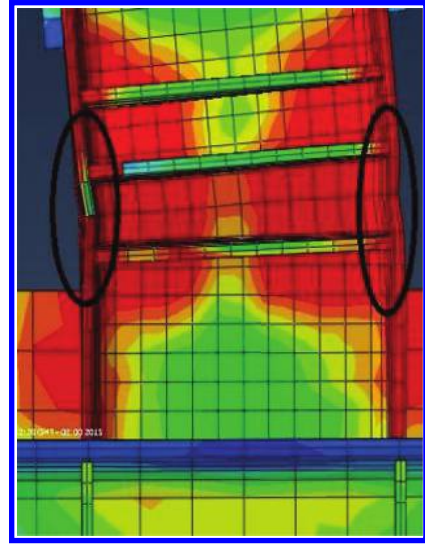


Figure 6. Local buckling of flange.

was local buckling of flange and web. FEM and analysis indicated that the individuals could act as a member to bear load for the stitch spacing of 10i.

Yielding of the channels in Specimen 5 was noticed at early stages of the test (about 9.87 mm). Slightly buckling of flange was first noticed at  $7\Delta_y$ , while severely at  $9\Delta_y$  (Fig. 6). For the cycle to 100 mm, the maximum moment dropped to 97% of extreme moment, while reached the target rotation 0.08 rad, terminated. Yielding of the channels in Specimen 5 was 10.8 mm. The maximum moment dropped to 97% of extreme moment at 100 mm. That indicated that stiffeners spacing of 40 mm could ensure local stability. Yielding of the channels in Specimen 7 and Specimen 8 was 9.76 mm, 11.1 mm, respectively.

## 5 ANALYSIS OF TEST RESULTS

### 5.1 *Moment-drift hysteric loops*

The moment-drift hysteric loops of Specimens 1–4 were shown in Figure 7a–d. In the elastic stage, overall deformation was small in the early loading, with linear relationship of moment versus drift and a small residual deformation after unloading. The hysteresis loop was not obvious in this cyclic. In the elastic-plastic stage, with the increase of horizontal load, the area of hysteresis loop was increasing and the moment reached to maximum after yielding of the channels. The hysteresis loop was larger on the later loading. For the Specimens 1–3, carrying capacity dropped and hysteresis loop had rheostriction when rotation

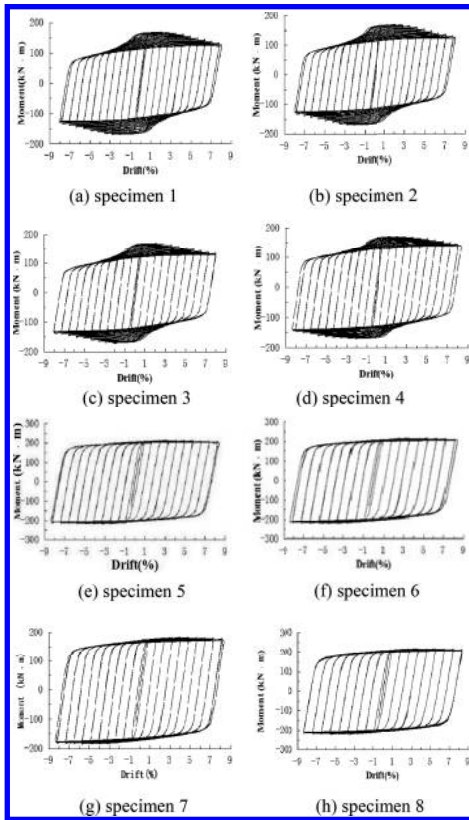


Figure 7. Moment-drift hysteretic loops.

exceeded 0.03 rad. The reason was lateral torsional buckling of individuals which resulted in losing carrying capacity, severely local buckling of flange and web. Specimen 4 enhanced the connection of individuals with the stitch spacing of 10i. Carrying capacity dropped when rotation exceeded 0.04 rad. The reason was local buckling of flange and web. Comparing to Specimen 1–3, Specimen 4 had a better plastic deformation and energy dissipation capacity and full hysteresis loop.

The moment-drift hysteretic loops of Specimens 5–8 were shown in Figure 7e–h. The hysteretic loops of four Specimens was similar in the elastic stage. The shape of hysteretic loops of four Specimens showed fusiform and was very full in later loading. When rotation exceeded 0.03 rad, the flange of Specimen 5 appeared slightly buckling. Compared to Specimen 5, the area of hysteresis loop of Specimen 6 slightly increased. Specimen 7 with fuller hysteresis loop to Specimen 4, which indicated set stiffeners prevented local buckling of flange and web. Compared to 7, the area of hysteresis loop of Specimen 8 slightly increased to 6. Until completion

of the loading, here was buckling of individuals and local buckling of web and flange.

### 5.2 Moment-drift skeleton curves, carrying capacity, ductility

The moment-drift skeleton curves of eight Specimens was shown Figure 8. From this figure, moment and drift in various loading stage can be calculated, as shown in Table 1. It was concluded the yielding point and extreme point shown ascendant trend. Compared to 3, the yielding moment of Specimen 4 improved to about 1.9% and yielding drift to 3.0%, while extreme point exhibited an almost identical. Which indicated Specimen 4 had a good ductility. The yielding and extreme moment of Specimen 7 was higher than Specimen 4. The yielding moment and drift improved to 2.8%, 11.5%, respectively. The extreme moment and drift improved to 6.9%, 178%, respectively. It was increased ductility of member by set stiffeners, which prevented local buckling of flange and web. The yielding and extreme moment of Specimen 6 was higher than Specimen 5. The yielding moment and drift improved to 1%, 9.4%, respectively. The extreme moment and drift improved to 1.4%, 9.4%, respectively. Which indicated the behavior of member slightly changed when reduced stiffeners spacing to 40 mm. The yielding and extreme moment of Specimen 8 approximately equaled to Specimen 6, but ductility increased. Specimen 8 with lateral bracing reduced effective length of out-of-plane improved behavior of member. Ductility factor also listed in the Table 1.

### 5.3 Energy-dissipating capacity

Figure 9 was the energy dissipation of eight specimens. As the big initial stiffness, specimens dissipated little energy and the loops of energy dissipation was gentle in the elastic stage.

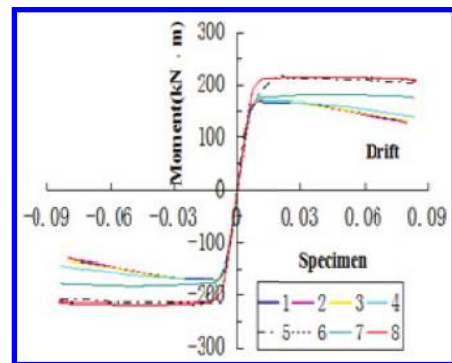


Figure 8. Moment—drift skeleton curves.

Table 1. Characteristic moment and drift.

Specimen	My (kN·m)	$\theta_y$ (rad (%))	Mu (kN·m)	$\theta_u$ (rad (%))	$\mu$
1	159.87	0.703	68.03	1.4167	2
2	160.35	0.7092	168.67	2.1275	3
3	161.98	0.7267	169.27	1.4533	2
4	164.16	0.7292	169.32	1.4583	2
5	200.21	0.8225	212.47	3.2900	4
6	202.09	0.000	215.41	3.6000	4
7	168.71	0.8133	181.00	4.0667	5
8	202.88	0.9250	215.40	4.6250	5

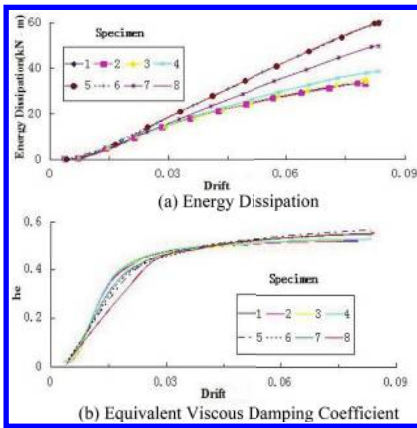


Figure 9. Energy dissipation of specimens.

After yielding drift, the area of hysteretic loop of every specimens increased by yielding to dissipate. The equivalent viscous damping coefficient ( $h_e$ ) of eight specimens grow fast which indicated energy-dissipating capacity increased with development of plastic. At late load, every specimen showed good energy-dissipating capacity, with  $h_e$  to 0.522, 0.524, 0.527, 0.530, 0.565, 0.551, 0.547, 0.559, respectively. On the whole, a thicker web improved the carrying capacity, energy-dissipating capacity and  $h_e$ . The specimen with stiffeners, which prevented local buckling of flange and web, relied on yielding to dissipate energy. As no buckling of member, lateral bracing on plastic hinge slightly increased the behavior of dissipating energy. All the results indicated specimen 8 had the best hysteretic behavior.

## 6 SUMMARY AND CONCLUSIONS

1. The hysteretic loops of cantilever double-channel built-up members was full, whose shape was fusiform, indicated strong energy-dissipating capacity. It could be used as the chords of special staggered truss steel frames structure.

2. For the double-channel built-up members under reversed cyclic bending, the stitch spacing was advised  $10i$ .  $i$  was the individuals' radius of gyration to weak axis.
3. The specimen with stiffeners prevented local buckling of flange and web and increased carrying and energy-dissipating capacity. But the limit of stiffeners spacing was still a question.
4. Lateral bracing on plastic hinge slightly increased the behavior of member.

## ACKNOWLEDGMENTS

This research project was sponsored by the National Natural Science Foundation of China (51208412), and special fund of ministry of Housing and Urban-rural development (2013-K2-019). The writers greatly appreciate them. The opinions expressed in this paper are solely those of the writers.

## REFERENCES

- Liu Hongliang & Liu Zhixiong & Lu Qinnian. 2004. Structural performance of the staggered-truss system. Journal of Harbin Institute of Technology, 2004, 35(9):1173–1176.
- Zhou Xuhong & Zhou Qishi. 2000. Calculation of internal forces and drift of staggered truss structures under lateral loads Journal of Building Structure, 2000, 21(4):49–54.
- Ran Hongdong & Su Mingzhou, et al. 2008. Experimental study on seismic behavior of composite staggered truss steel structures under cyclic load. Journal of Building Structure, 2008, 29(6):91–98.
- GB50017-2003, Code for design of Steel structures. Beijing: China Architecture & Building Press, 2010. (in Chinese).
- GB50011-2010, Code for seismic design of buildings. Beijing: China Architecture & Building Press, 2010. (in Chinese).
- Jgj 101-1996 Specification of testing methods for earthquake resistant building. Beijing: China Architecture & Building Press, 1997. (in Chinese).

# Seismic influences on high-speed elevators in Super-High-Rise buildings

I. Torguet & W. Lu

*Research Institute of Structural Engineering and Disaster Reduction of Tongji University, Shanghai, China*

**ABSTRACT:** In the last few years, we have experienced an advent of Super-High Rise Buildings all around the globe, aiming to become iconic landmarks not only in height, but also in uniqueness and complexity of their structure. Along with the SHR buildings, new requirements have to be dealt to ensure their serviceability and safety, especially, when they are more vulnerable to get damaged: during an earthquake event. In essence, this study aims at first to provide guidelines for the analysis of the dynamic behavior of such structures, taking as example the Shanghai Tower and, furthermore, seeks to implement the behavior of the elevators in the overall response of the structures, to see how they interact between them. The research introduces the concept of the elevator's velocity in conjunction with the dynamic behavior analysis, implementing several configurations to determine the responses and relationships between the structure and the non-structural element.

**Keywords:** Super-High-Rise buildings; high-speed elevators; modal analysis; dynamic behavior; envelopes of excitation; acceleration spectrum; elevator velocity

## 1 INTRODUCTION

### 1.1 *Change of paradigm in Super-High-Rise Buildings*

Even though Super-High-Rise Buildings (SHR) have historically been located mainly in the US, in the past years there has been a shift of momentum, resulting in the Asian and Middle East countries being in the frontline of this kind of structure's development (Lu, 2011a).

Starting with the Petronas Twin Towers in Kuala Lumpur in 1998 and also with Taipei 101 in Taiwan in 2004 (Fan, 2009), this shift not only represents a geographically transition, but also a change in approach of SHR building's design. Now there is no further desire on an international style building, but rather a landmark to exhibit a design that avails itself of the country historical elements. The Jin Mao Tower in Shanghai, resembling an Asian Pagoda, or the Burj Khalifa in Dubai, currently the world's tallest building, which recalls some of the Islamic Art, are clear examples of such to reflect the culture of the country where they stand.

As a direct result of this change of paradigm, the SHR are becoming more and more complex structures, with upcoming requirements that cannot be assured by regular code complying techniques, and need further investigation and development (Jiang, 2011).

### 1.2 *Super-High-Rise Buildings in China*

China has experienced, in the last few decades, a rapid economic growth that continues up to date. As a consequence, China has seen a huge increase in the needs of urbanization and renewal of facilities, mainly focused on the big cities spread across the country.

Regarding the High-Rise Building field, Mainland China's boom in such kind of construction started in the 1990s, bearing in mind the fact that in places such as Hong Kong, some Super-Tall buildings were already constructed. Owing to the wide variety of social requirement for commercial or aesthetic purposes, the limited availability of land, and the preference for centralized services, the height of tall buildings had to grow taller, and the configuration as well as structural system, in consequence, has become more and more complex in recent years.

Nowadays, China has some of the tallest buildings in the world, and is aiming to construct even taller buildings than the ones already existing.

A key issue that must be fully understood in relation with SHR Buildings in China is their seismic safety, due to the fact that most of the buildings having been completed or being under construction are located in earthquake prone areas. Furthermore, a large amount of SHR buildings are located in the east coastal area of China, where the effects on structures by wind actions are significantly important.

Regarding all the possible threats, it is mandatory to attract researchers and investigation institutes in order to develop more reliable code provisions and design methods to deal with such threats. There is a need to undergo seismic dynamic analysis, such as the one aimed in this paper, to give further insight in such important matter.

## 2 SEISMIC BEHAVIOR OF SHANGHAI TOWER

### 2.1 Overview of the structure

As third tower in the trio of SuperTall buildings at the heart of Shanghai's Lujiazui Finance and Trade Zone, the Shanghai Tower is meant to represent a new way of thinking in SHR buildings (Xia, 2010). Placed in close proximity to Jin Mao Tower and Word Financial Center, the new tower rise high above the skyline and presumably become a symbol of the economic strength of China.

The Shanghai Tower will be a multi-functional office building, with a total height of 632 m and 121 storeys, filled with a unique mix of restaurants, shops, hotels, and offices spaced throughout the building. In addition, it will provide SHR buildings a new insight in how to improve the sustainability of such kind of structures, with the concept of vertical cities, wrapping the whole building in public spaces and sky gardens.

### 2.2 Shanghai Tower's model

The Shanghai Tower is a state-of-art structure, with some of the newest constructing techniques and element's performance. As a result, numerous studies are at the moment working on reliable and precise computational models to determine the responses of this structure (Lu, 2011b). The key insight that differs most of the models and the one that we are presenting relies on the approach. In some of the other researches, Finite Element Models have been conducted to simulate the Shanghai Tower, with more or less precision (Zhou, 2013). The problem is that these FE models consist on, as a piece of example, 19973 elements, 45418 shell elements, and 14376 solid elements, resulting in extremely complicated designs, only enabled by powerful software and great deal of computational process. Due to the complexity explained above, and aiming to find a simpler version, the structure model will be reduced into a set of lumped masses, which bundle the different elements' characteristics (Lu, 2014).

As a matter of fact, we know that the Shanghai's Tower program is organized into eight vertical zones, each with 12 to 15 floors, covering a different

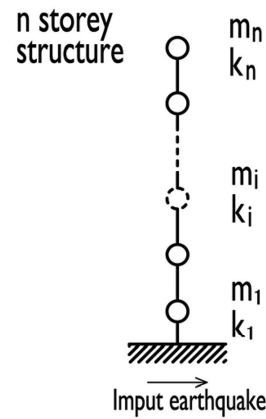


Figure 1. Shanghai Tower Model. Approach of layout.

type of facility, but having a similar layout. Taking that into consideration, we have created our model lumping the elements in each zone, solving the need of an easy tool for understanding and properly collecting the responses of structures.

Once stated the approach for our model, several assumptions in terms of stiffness, mass, and damping have to be noted. In terms of the stiffness, the elements with the most contribution to the Shanghai Tower's stiffness are the core-tube, the super-columns and the outriggers with their belt truss. In this sense, it is assumed that the overall stiffness of the lumped mass is the sum of the stiffness of each structural element for a given zone (Carpinteri, 2013). Therefore, we will have stiffness for each floor separately. What's more, the stiffness depends on the direction along the axis desired, and for the purpose of our study we will select the one's from the X direction to undergo the dynamic analysis.

Regarding the mass of the structure, we will assume the same behavior as in the stiffness, having an overall lumped mass for each zone of the Shanghai Tower. Moreover, effective masses depending on the direction along the axis desired are taken into the analysis.

Finally, the damping will remain constant through all the building and, according to the latest regulation in Design Codes, precisely in the Section 5.3.4 of the Specification for the Design of Steel-Concrete Hybrid Structures in tall buildings (CECE230:2008), will have a value of 4%. If there is a need to vary that number in order to meet the requirements, it will be done during the computational process.

The data collected to model the Shanghai Tower is to be found in Table 1.

With the information collected, a modal analysis was carried out, in order to determine the



Table 1. Overall data for the zones in Shanghai Tower Model.

Zone	Mass (kN/g)	Kx (kN/mm)	Ky (kN/mm)
8	71656.3	172.09	177.47
7	59396.9	240.82	247.67
6	68695.8	372.62	374.90
5	82736.3	536.99	543.42
4	93246.8	877.36	878.11
3	108921.4	1295.76	1325.18
2	121295.4	2494.52	2658.71
1	68652.6	16215.13	17309.65

dynamic properties of the structure, such as the natural frequencies. It is crucial to know the frequencies and, therefore the periods, because they are the ones at which the structure will naturally resonate (Meera, 2013). In an event of an earthquake, it is imperative that the building's natural period does not match the period of the seismic action, or it will resonate and experience damage due to severe oscillations. The natural periods of our model, from the first to the eighth mode, are shown in Table 2.

Besides the values for the periods, the UX, UY, and RZ show the modal participation of each mode. As a matter of fact, modes 1, 3, and 6 are primarily the ones with greatest significance along the X direction. They will be the most contributors to the response of our model in the desired direction.

Hence, the mode shapes are generated. A mode shape of an oscillating system is the pattern of motion that will experience an object when all the parts of it move sinusoidally, with the same frequency and with a fixed phase relation. Using the commercial software ETABS, the modal shapes are drawn as shown in Figures 2 and 3.

### 2.3 Earthquake wave selection

According to the Chinese code "Code for Seismic Design of Buildings," the earthquakes, in terms of Peak Ground Acceleration (PGA), are categorized as: Minor or Frequently occurred, when their PGA is 0.035g, Basic or Moderate when the PGA is 0.1g, and Strong or Rare when the earthquake has a PGA of 0.25 or above.

In our analysis, we have chosen the Basic or Moderate earthquake type to be our ground motion input. The reason is that, even though it is a quite severe excitation, buildings have to deal with the deformations and remain operational once the event is over (Tenozhi, 2013). As a matter of fact, if we were to set our standards to the

Table 2. Modes of vibration of Shanghai Tower.

Mode	Period(s)	UX	UY	RZ
1	9.49	44.18	0.00	0.00
2	9.35	0.00	43.83	0.00
3	2.20	22.73	0.00	0.00
4	2.16	0.00	22.83	0.00
5	1.44	0.00	0.00	53.30
6	0.88	10.54	0.00	0.00
7	0.86	0.00	10.64	0.00
8	0.71	0.00	0.00	20.32

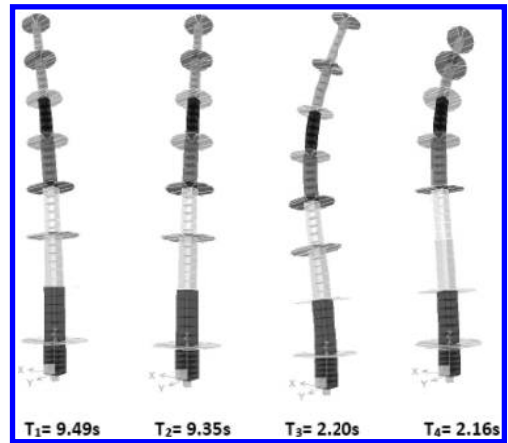


Figure 2. Mode shapes of vibration from 1-4.

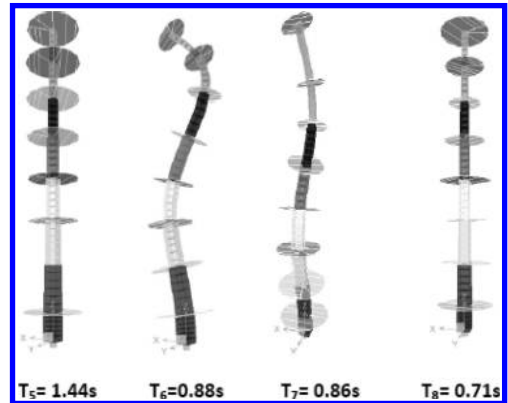


Figure 3. Mode shapes of vibration from 5-8.

Strong or Rare earthquake, we could easily fall into over dimensioning our building. The requirements in terms of dynamic behavior are tougher, and the probability of such excitation happening is unlikely.

In addition to the categorization of type of earthquake, the Code also states that if a dynamic analysis is conducted, one must use at least seven different earthquake records. In that way, the Code enables us to find an average response of the structure throughout the comparison of the different responses achieved. Furthermore, as long as our model is set in the elastic range of deformation, the results with different earthquakes but with same peak ground motion can be compared directly. If it were a non-linear approach, such assumption would not be correct (Lee, 2002).

In our study, we have chosen as earthquake records the following: Mexx, L725, S790x, SHW3, El Centro NS, L604, and USx, having all of them a PGA of 0.1g. To show how the data from the earthquake records is treated we present Figure 4, extracted from Mexx earthquake, which displays the Time History of this ground motion.

#### 2.4 Seismic behavior: Elastic response

The study undertakes a behavioral analysis of the model, using as input the excitations events above, with the goal of obtaining the time domain history of the response, in terms of displacement, velocity, and acceleration. Furthermore, we have also extracted from the results the interstory drifts of the floors due to such excitations.

The displacement of our model due to the set of earthquakes is of vital importance. In essence, what we obtain is the history of the deformation from static position of our structure. With a quick look at the data, we are not only able to determine the absolute values of displacement, but also the shapes that the structure will take when excited. Knowing the possible shapes of a structure will enable us to determine the serviceability and safety of the structure in an event of excitation.

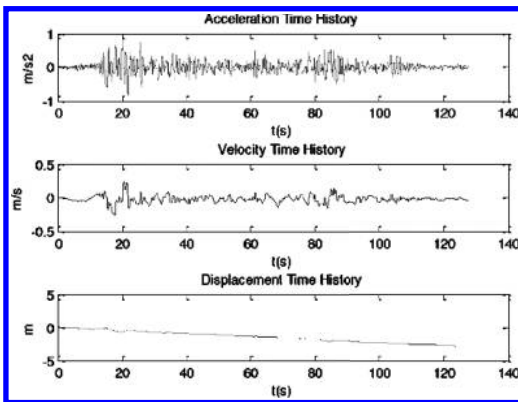


Figure 4. Mexx earthquake in time history.

Table 3. Average earthquake response. Overall maximums.

Floors	Displacement (m)	InterStory Drift (m)	Velocity (m/s)	Acceleration (m/s <sup>2</sup> )
8	0.938	0.312	0.924	2.366
7	0.658	0.255	0.573	2.386
6	0.464	0.183	0.603	2.272
5	0.324	0.136	0.474	2.010
4	0.203	0.099	0.349	1.911
3	0.109	0.069	0.257	1.909
2	0.041	0.035	0.137	1.685
1	0.007	0.007	0.028	0.764

The InterStory Drift gives us insight in the relative displacement between consecutive floors (Rofooei, 2012). In this sense, it is of great value because it helps us understand the actions and reactions that the floors have to manage due the motion of the others. In a particular way, to ensure the correct functioning of an elevator within the structure, there is a need to study the progression of the InterStory Drifts along the height of the structure. Any abrupt change in displacement between floors could damage the whole elevator machinery and represent a dramatic scenario (Yang, 2010). Therefore, we are keen on taking a closer look into the Drifts.

Acceleration is perhaps the most important factor when studying the behavioral dynamic analysis of a structure. This is due to the fact that it is closely related to the inertial effects of the structure due to the excitation, and it is an effective approach to deal with the frequencies that excite the structure (Miranda, 2005). When we examine the accelerations of a building, separately occurring in each floor, we are able to determine the frequencies that will contribute the most to the motion of that floor.

What's more, a study along the height of the structure showcases the relationships between floor's acceleration and, thus, the shape of the acceleration path. This aspect will be broadly used afterwards, in order to create the envelopes of excitation.

Once the dynamic analysis is done, the data is collected and compiled to further processing and treatment. With all the extracted data, an average response is developed. Taking into consideration that all the analysis is on the elastic range and that the values obtained are all dependent to a 0.1g of PGA earthquake, the comparison between them is feasible, computing the mean values.

As a result of that, the research obtains average maximum figures, again in terms of displacement, interstory drift, velocity, and acceleration.

That would be the expected values for a 0.1g earthquake. It is truly important for us because it gives an insight of what response would give our structure back in a random earthquake.

In this sense, we have knowledge of up to what value our structure has answer back due to the excitation. In other words, we are now capable to give a value of the threshold of response for each variable (displacement, interstory drift and so on), for any given floor.

Hence, we introduce the concept of Envelope of Excitation to our analysis. An envelope of excitation is the compilation, along the height of the structure, of the maximum values achieved in each floor. It gives us a frame, a restriction, to the response of the building, because it is composed of all the limits obtained. In a way, it is conceptual due to the fact that all maximum responses do not necessarily happen at the same time and, therefore, the response path is not likely to occur as we see it. However, it is of vital significance because, in a single graph, we can judge the possible deformation and reaction scenarios in our building.

Lastly, we are able to generate an average earthquake envelope, represented in Figure 5. The average earthquake envelope will represent the expected path and dynamic behavior for any given basic or moderate earthquake as stated in the Code for Seismic Design of Buildings.

With such envelopes, we are able to underline several important issues regarding the variables used. The displacement of the expected earthquake response follows with great similarity the first mode of vibration of the structure. In consequence, we are able to assume that the most contributors to the dynamic behavior of Shanghai Tower are the first mode of vibration, with a natural period of 9.49 s. The InterStory Drift also follows a similar path, stressing the assumption above.

The velocity of the Shanghai Tower under a 0.1g earthquake follows an approximately linear path, giving sense to an increase of the floors along the height. As we can see in the graph, at the seventh

floor there is a slight change in velocity, due to the way of motion of the structure itself.

The acceleration obtained follows a fairly straight line when deals with the upper floors, as expected. The lower floors, and specially the first floor, have a behavior that relates to the high frequencies of excitation.

Numerous studies undergone before in the Shanghai Tower (Lu, 2011) give a factor of  $k = 3$  as multiplication of the response in terms of acceleration. In our case, if we linearize our model envelope, we will get to a  $k = 2.5$ . Our results, pretty close to the ones from previous research, give strength to our analysis and ensure that our overall dynamic study is a good approach.

### 3 SEISMIC ACTIONS OF HIGH-SPEED ELEVATORS

#### 3.1 Overview. Analyzing the phenomenon

Since the invention of the safety elevator by Otis in 1852, there has been a need to ensure the serviceability and safety for the passengers in an elevator for any given circumstance. However, as long as the buildings where those elevators were implemented were not tall enough to fall into damage due to large oscillations in response, not much research was focused in that field.

In fact, the major shift in the elevator performance analysis would come after a series of damaging earthquakes in the United States. First in Alaska earthquake in 1964 and, after that, in San Fernando earthquake in 1971, the damage in the elevators was so significant that forced the competent organizations to look for better elevator seismic capacity (Anshell, 2008). From that moment on, people began to realize the seriousness of the matter and started to propose improvements and renewed techniques in order to overcome such undesired reactions in the non-structural elements.

Not with standing, research work was still scarce and much of it was mainly related to the counterweight dynamical behavior (Mirabdollah, 2012). From that time, many data was obtained by computer-based simulators that enable to see the behavior of the ropes and counterweight, but lacked accuracy. The problem was that the damage assessments, as their name indicated, were issued once the earthquake had already occurred, so it was unable to provide provisions for the maintenance and inspection, but rather to determine ways of dealing after such event.

In the experimental side, the most common practice is to work close to the elevator companies that have deployed the elevator mechanisms in the area of the earthquake event (Yao, 2007). In other

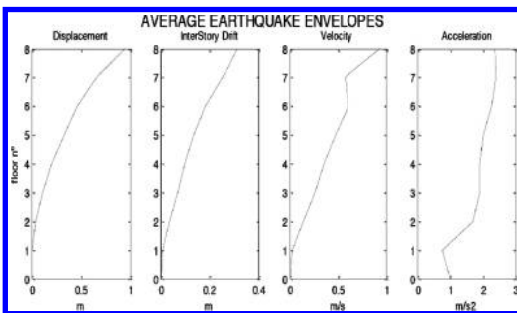


Figure 5. Average earthquake envelopes of excitation.

words, once an earthquake happens in a certain region, it is a must to convey a series of inspections to the damaged sites in order to get as much information about the performance as possible. As long as, presumably, there are more than one elevator companies in the area affected, the survey will have to be conducted by all of them at the same time. Hence, there will be a need to organize it via a government committee, who will unite the struggle of all parties affected in obtaining the response data.

In a way, there is still a long way to go in the seismic performance analysis of elevators. Nowadays, many new researchers are taking into closer examination the actions on elevators, aiming to develop techniques and computer-based models to guide the requirements these non-structural elements need to deal with in events of excitation (Arrassate, 2014).

### 3.2 Usage of the envelopes

In our previous dynamic analysis for the Shanghai Tower, we have ended up with a compilation of envelopes for an expected given earthquake of 0.1g, in terms of displacement, interstory drift, velocity and acceleration. At this stage appears the concept of envelope excitation. Used mainly in Nuclear Power Plants and other complex structures, the envelope excitation represents a quite intuitive restriction for the behavior of a structure. In its essence, its aims to show that, to model one structure to deal with a set of inputs, it needs to be able to deal with the most significant, and therefore, the most damaging of the responses due to that excitation.

As a matter of fact, the structure will experience the biggest response when subjected to an artificial sinusoidal wave with amplitude the maximum value of the variable in the response desired. But the problem now is that when we use a sinusoidal wave, we need to input amplitude and a frequency. In our case, we need as frequency the one that excites each floor, because it is the one that contributes to achieve the greatest response for a given zone. To do so, Fourier Transformations are carried out, deriving into a frequency domain analysis.

Therefore, we have undergone the envelope excitation analysis on the four variables (displacement, velocity, interstory drift and acceleration). The variables are differently treated due to the specific needs for each of them.

### 3.3 Overall Maximum Input

In this case, we have generated a single sinusoidal wave, with the information regarding the maximum response of the variable desired (in terms of

amplitude and frequency). As stated before, if our structure is able to deal with the inputs that excite its most significant response, then it is able to deal for the rest of inputs below that one. For the Overall Maximum Input, we have chosen the displacement and the velocity.

First, we proceed with the Displacement response. As we can see in the envelope in Figure 5, we experience the greatest deflection in the eighth floor, achieving a maximum value of 0.938 m. That is going to be our threshold, our envelope of excitation value. Hence, we run through all the earthquake records responses of displacement for the eighth floor. Meaning, we have chosen, for example, the Mexx earthquake, have taken the response in displacement of the eighth floor for that earthquake, and extracted the frequency. The same procedure will be carried out for each earthquake, finding in the end the frequencies that drive into that response for an expected earthquake.

The data collected is shown in Table 4.

Once we have the data, we are able to generate the sinusoidal wave. Using as amplitude the maximum displacement of the eighth floor, the outcome can be obtained by using the average frequency (as seen in Equation 1), or it can be an integral for the input, using as boundaries the maximum and minimum frequencies obtained (as in Equation 2).

$$d = 0.938\sin(2\pi \cdot 0,109t) \tag{1}$$

$$d = \int_{0,1038}^{0,1282} 0,938\sin(2\pi \cdot wt)dw \tag{2}$$

Regarding the velocity variable, we have undertaken in the same way that we have done with the displacement. In the velocity case, the maximum velocity is also located in the eighth floor, with an absolute value of 0.924 m/s.

Thus, the presentation of both the data collected and the waves generated is provided in the same format in Table 5, and Equations 3-4.

Table 4. Frequencies to excite the Top Floor Displacement.

Earthquake	Frequency for Top Floor Displacement (Hz)
ElCentroNS	0.1068
L604	0.1068
L725	0.1282
MEXX	0.1068
S790X	0.1038
SHW3	0.1068
USX	0.1038
Average	0.1090

Table 5. Frequencies to excite the InterStory Drift.

Floor	InterStory Drift (m)	Frequency for Drift (Hz)
8	0.312	0.205
7	0.255	0.109
6	0.183	0.109
5	0.136	0.109
4	0.099	0.109
3	0.069	0.205
2	0.035	0.205
1	0.007	0.205

$$v = 0.924 \sin(2\pi \cdot 0.2053t) \tag{3}$$

$$v = \int_{0.1038}^{0.4578} 0.924 \sin(2\pi \cdot wt) dw \tag{4}$$

### 3.4 Floor-by-floor Input

In this case we aimed to obtain a sinusoidal wave for each floor of the Shanghai Tower for a given variable. In this new scenario, we want to gather the frequencies for all the floors, throughout the seven earthquakes. This means that, in the end, we will have eight frequencies, one per each floor, times seven due to the earthquakes. What's more, we are able to find average values for each floor, so that we will know what frequencies make the largest responses per floor.

The InterStory Drift follows a similar path that the one from displacement. In a way, as long as the displacements go increasing along the height of the building, so it does the drift between them.

Once we have undergone the analysis for all floors and earthquakes, we are able to gather them in a single table, as presented in Table 6. The table also contains the data from the average values for each floor.

Furthermore, to present the data obtained in a prescriptive way, we have created a graph, where it is plotted together the path achieved with the average frequencies throughout the InterStory Drift values, and the tolerances for each floor drift, extracted from the maximum and minimum values in the seven earthquake records responses.

In essence, we have a tool that tells us in an easy visual way not only what are going to be the expected drifts for any given frequency, but also the boundary tolerances inherent to it due to the stochastic nature of an earthquake input.

Figure 6 is the figure explained above. In it, the thick horizontal lines represent the different floors InterStory Drift with the range of frequencies from maximum to minimum values. The thin continuous

Table 6. Frequencies to excite the Top Floor Displacement.

Earthquake	Frequency for Top Floor Velocity (Hz)
ElCentroNS	0.1068
L604	0.1068
L725	0.4486
MEXX	0.1068
S790X	0.1038
SHW3	0.1068
USX	0.4578
Average	0.2053

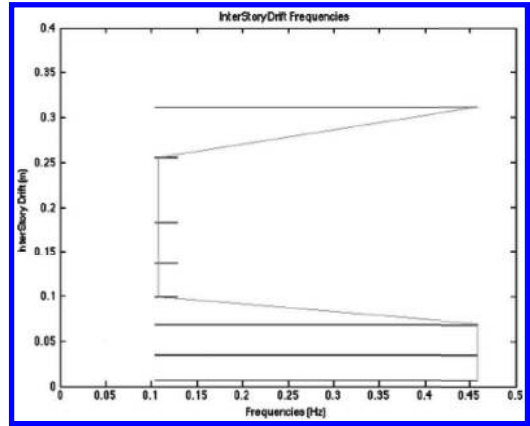


Figure 6. InterStory Drift frequency spectrum.

line represents the path of the average InterStory Drift and their inherent mean frequency.

A graph of this kind is significantly helpful for elevator manufacturing companies, because when design and mount an elevator, can benefit from this graph, as it is an easily understood tool to determine for any given floor, what is the range in input that the elevator will have to deal with. In other words, for an elevator to properly function, it will need to be able to deal with all the frequencies expressed in the graph for that floor (Villaverde, 2004).

In terms of the acceleration, the research is conducted in the same way as in the InterStory Drift, collecting the frequencies for each floor throughout the seven earthquake records. The data of the mean values, extracted from the analysis, is shown in the Table 7.

Moreover, once again we have created the plot combining both mean frequencies and tolerance frequency ranges, which is presented in Figure 7, located in the next page.

Table 7. Frequencies to excite the acceleration.

Floor	Acceleration (m/s <sup>2</sup> )	Frequency for Drift (Hz)
8	2.366	0.455
7	2.386	0.699
6	2.272	0.790
5	2.010	0.895
4	1.910	0.669
3	1.909	0.884
2	1.685	1.537
1	0.764	10.015

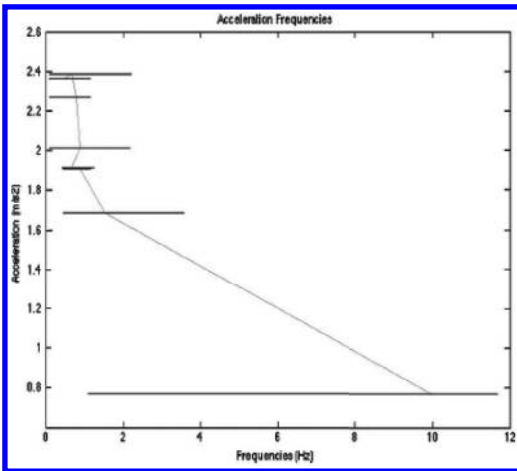


Figure 7. Acceleration frequency spectrum.

This graph has the same explanation that the one about InterStory Drift, seen previously. It gives us information about the ranges in frequency that an element will experience in each floor. With this information, we can determine the restrictions that an elevator should abide in order to properly function during an average event of excitation.

From the data extracted, we can see that there are two differentiated parts in our graph. From 0.455 Hz up to 1.537 Hz, that represents the floors ranging from 2 to 8, the slope is really steep, having not much of a change in frequency. However, if we take a closer look into the floors 1 and 2, the frequencies have a much broader range, driving from 1.537 Hz to 10.015 Hz. In consequence, it can be stated that in the Shanghai Tower there are two differentiated areas, and the threshold is the second floor (at approximately 140 m from ground level). The range of frequencies being much bigger than the above floors is due to the significance in contribution of the higher frequencies in the acceleration at the lower parts. This lower parts excitation was

already noted when dealing with the envelope of acceleration in the SHR building section, where we noted a shifting inwards in the path. Therefore, it makes total sense the shape that this graph takes and, hence, it is a great tool for setting the requirements for the elevator's behavior.

### 3.5 Seismic actions of high-speed elevators: The velocity issue

All the information regarding the elevator analysis has been undergone with a static elevator, aiming to determine the reactions of it due to the excitation event. But we want to understand what impact will have to the elevator the fact that is moving, and, at last instance, how the velocity of the elevator itself will affect the response. Beforehand, we realize that there has to be a change in the behavior due to the speed at which the elevator moves along the tower. Therefore, what we aim is to stress is the variations in frequency range, due to the speed at which the elevator travels. In a way, the research is relying on the areas enclosed between the range of frequencies for a given floor and the graph of frequencies-accelerations.

In order to see the variations, 10 m/s and 20 m/s velocities have been selected. The reason is that 10 m/s is the current top speed for most of the SHR Buildings nowadays, whereas 20 m/s has been theorized as mechanically feasible, even though it hasn't actually been mounted on a SHR Building.

Nevertheless, as stated before, in our graphs there are two separated areas: below second floor and above second floor. Therefore, the study underlines these two cases and, afterwards, drives some conclusions.

#### 3.5.1 Case 1. Cabinet under the second floor

Prior to the analysis, an artificial earthquake scenario has been created, with PGA of 0.1g, a natural frequency of 5 Hz and time duration of 7 seconds. This earthquake is the one used to determine the reactions due to the speed.

The domain of the frequency-acceleration graph for the first two floors is quite large. As a matter of fact, an elevator that starts in the bottom will first experience a frequency input equivalent to the one from the ground motion, then achieve frequencies up to 12 Hz in the first floor, and finally get to the 1.5 Hz value. As a result of such disparity, the behavior of the elevator within that height will be highly affected by the rate of change of the frequency. Let's see what happens in the event of excitation explained above, taking as starting point the ground floor.

With a 10 m/s cabinet, during the seven seconds of the earthquake, the elevator will reach the first floor. Regarding the frequencies that the elevator

will have to deal with, those are going to be ranging from the initial frequency of 5 Hz, given by the earthquake, up to approximately 10 Hz. In other words, will suffer frequencies enclosed in the interval from 5 to 10 Hz.

Nevertheless, doubling the velocity, during the seven seconds that lasts the earthquake, the cabinet will reach the second floor (the threshold of 140 m). As a result of such increase in speed, the elevator will not only need to deal with the frequencies ranging from 5 to 12 Hz, but also with the frequencies from the first floor to the second. Those are ranging from 1,5 Hz to 12 Hz approximately.

As a consequence, if we were intending to design a suitable elevator to this scenario, we will have to bear in mind that in such event of ground motion, our elevator would have to be able to meet from 5 to 10 Hz in frequency requirements to be fully operational for a 10 m/s cabinet, while we would need to improve the requirements for the 20 m/s case. The improvement would provide a wider range of frequencies in order to deal with the overall response. Therefore, we are able to state that if the cabinet is located between ground floor and second floor, it will experience much different responses according to the velocity of the elevator itself.

To illustrate the range of frequencies affected by each case scenario, Figure 8 is presented below. In the graph, the enclosed area of horizontal lines is the one for 10 m/s cabinet, whereas the vertical lines represent the 20 m/s case.

### 3.5.2 Case 2. Cabinet above the second floor

The second case is when the elevator is moving along the height compressed between the second to the eighth floor. At this point, the graph of

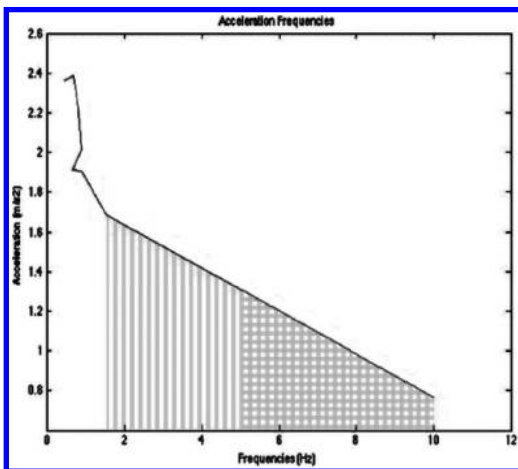


Figure 8. Acceleration frequencies depending on the velocity of the cabinet under the second floor.

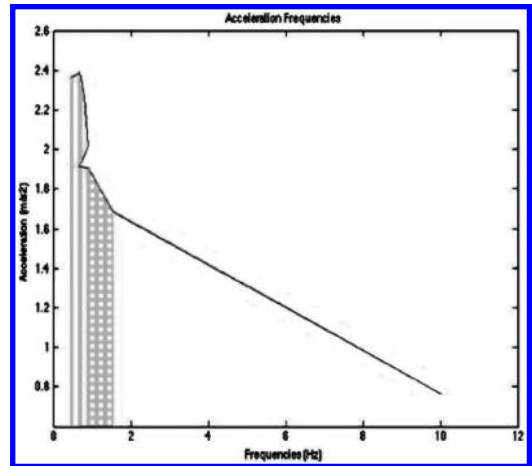


Figure 9. Acceleration frequencies depending the velocity of the cabinet above the second floor.

frequencies is much steeper, tending to a vertical shape.

As a result of that, there is not a big disparity among the frequencies, as long as they are all located in the range from 0.1038 Hz to 1.537 Hz. What's more, the new scenario contains more floors to be studied and, in consequence, we have treated it with a longer earthquake. In this case, the artificial earthquake has a PGA of 0.1g, a natural frequency of 5 Hz and time duration of 21 seconds.

With a 10 m/s cabinet, starting at the second floor, the elevator during the 21 seconds of earthquake will travel up to the fifth floor. During its journey, it will start getting as input 1,537 Hz, and by the time it gets to the top will be experiencing an average frequency of 0.895 Hz. From an engineering point of view, they behave similarly due to the fact that both of them are located in the low frequencies spectrum. As a matter of fact, even though the elevator travel during a quite long time, the change in frequency is not much significant. This will help greatly the manufacturers to design the elevators, as long as the requirements for the frequency do not vary much.

With a greater velocity, achieved by the 20 m/s cabinet, the elevator during the earthquake will travel from second floor to eighth floor. In this new scenario, the elevator will face a shift from 1.537 to 0.455 Hz, representing a similar range to the one obtained at 10 m/s. The key issue in that zone of the Shanghai Tower, the structure is mainly excited by the first three modes of vibration; the little discrepancies that might arise in the frequency range are not significant enough.

In consequence of the lack of remarkable disparity in the frequency, in this section of the building

an increase in velocity is not decisive enough for a drastic change in the requirements.

As a direct result of our analysis, we might state that the elevator company in charge of the designing of the elevator will be able to use mostly the same provisions as the ones used for the regular speed of 10 m/s after the second floor.

#### 4 CONCLUSIONS

This research, underlining the needs for this kind of study and according to the current situation in SHR Buildings, has provided the guidelines to determine not only the dynamic behavior, but also the implementation of non-structural elements to the analysis.

Using as example the iconic Shanghai Tower, the study has set the bases for a complete dynamic analysis of the structure, providing a computer-based model to compile the linear behavior of the building. We have been able to, in a simple and visual way, create a good approach to the actual response of the structure due to any given 0.1g of PGA earthquake.

One of the advantages of using our model is the simplicity inherent in it. The model is based in the mass-spring-damper system, having lumped masses that combine the different features of the structure. As a result, our model is no longer an over-complicated finite element method structure, with huge mesh and thousands of shells and elements involved, but rather an intuitive idea of the big picture that is the Shanghai Tower. Moreover, the analysis makes a step forward into the usual calculations in events of earthquake excitation, which are mainly based on post-earthquake damage control scenarios. Whereas, applying the rules from the Design Codes of China, we have obtained the average response for any given earthquake that abides certain characteristics. Therefore, it is a trustworthy data for the expected behavior to be used not only for future studies in the structure itself, but also in the construction of new structures. An average response path will further help researchers to know what are the thresholds and possible outcomes to expect in any earthquake.

In terms of the dynamic analysis, the results point out the following key issues:

1. The Displacement of the Shanghai Tower follows a similar path as the one from the first natural mode of vibration of the structure. In that sense, we are able to state that our model validates the idea that the most important contributor to Shanghai Tower's Displacement behavior is his first mode, with a 9.49s natural period.

The Acceleration of the Shanghai Tower, according to our model, is mainly affected by the second and third modes of vibration, with the frequencies of those as the most damaging to the structure. Such fact complies with most of the guidelines provided by the High-Rise building construction companies, where it is stated that such frequencies are the most significant in the dynamic behavior.

The course taken generates, thanks to the information of the dynamic behavior of the Shanghai Tower, a set of guidelines of what an elevator should be able to deal with in order to operate. So to speak, we have given the threshold of performance for elevators to cope if they want to remain in a serviceable state while an earthquake is happening.

Using the frequencies that excite our structure the most, both in the overall maximum input method and the floor-by-floor method, we have obtained an easy target for the performance of the elevator. As we have seen in the study, most of the times we are not only needing the average value obtained by the mean of the seven earthquakes, but we are rather interested in compiling all of them.

Another key issue of our study is the envelope excitation idea. In our perception, such method can be a genuinely new and plausible tool for implementing the frequencies obtained into the structural analysis of the whole structure.

Regarding the velocity issue, derived from the advent of High-Speed Elevators, we can conclude that, in terms of the Shanghai Tower behavior:

1. Elevator under the second floor. The range of frequencies that the elevator will have to deal with along the height is really wide, ranging from 1.5 Hz up to 12 Hz. As a result of that large range, the velocity becomes a crucial factor. This is because for a given earthquake with specific time duration, the velocity will determine the change in height and, therefore, the ranges will vary.
2. Elevator above the second floor. As long as the graph in this section of the structure gets more steep, the frequencies do not vary that much, staying mostly in the range of the first three modes of vibration. As a result, the velocity will not play a role as important as the one below the second floor. Despite the changes in velocity that will carry different frequency requirements, those will be minimized due to the vertical shape and, at last, will be treated almost indistinctively.

Despite the remarkable achievements carried out by this research, it faces the problem of experimental data. Real testing would definitely be



needed to validate the conclusions that arise from the theoretical treatment of the data. Without a testing part, the results lack of physical backing and can only be served as guidelines for posterior studies.

As a consequence of this, the next step in the study would be to build up a real model of an elevator installation in a Shaking Table Laboratory and put into test our theoretical model. In the laboratory, then, researchers would carry out sets of excitation events to the elevator specimen, and check out the responses. The outcomes of such testing experimentation would validate or not our model, and would definitely provide a deeper understanding of the behavior of this kind of elements.

To summarize, our study represents the first steps of a complex and lasting endeavor, which will seek to provide the direct correlation between the non-structural elements and the structures in which they are implemented. In essence, as the need of further research will become a high priority due to the current construction requirements, studies such as the one we have presented will serve as a pragmatic tool to help set the bases of them, as well as provide knowledge into many other future developments in dynamic behavior analysis.

## ACKNOWLEDGMENTS

The authors are grateful to the members of the Research Institute of Structural Engineering and Disaster Reduction of Tongji University, as well as the Civil Engineering School of Tongji University, for all the insight and support to our endeavor in carrying out this study.

## REFERENCES

- Adachi, F. 2013. Importance of interstory velocity on optimal along-height allocation of viscous oil dampers in super high-rise buildings, *Engineering Structures* 56, 489–500.
- Anshel Schiff, The Shake-out scenario. Elevators, U.S. Geological Survey Open File Report 2008-1150.
- Arrasate, X. 2014. The modelling, simulation and experimental testing of the dynamic responses of an elevator system, *Mechanical Systems and Signal Processing* 42, 258–282.
- Carpinteri, A. 2013. Structural analysis of high-rise buildings under horizontal loads: A study on the Intesa Sanpaolo Tower in Turin, *Engineering Structures* 56, 1362–1371.
- Chen, K.Y. 2014. Dynamic modelling and input-energy comparison for the elevator system, *Applied Mathematical Modelling* 38, 2037–2050.
- China Elevator Standardization Technical Committee, Safety rules for the construction and installation of hydraulic lifts, GB21240-2007.
- Fan, H. 2009. Seismic analysis of the world's tallest building, *Journal of Constructional Steel Research* 65, 1206–1215.
- Goksenli, A. 2009. Failure analysis of an elevator drive shaft, *Engineering Failure Analysis* 16, 1011–1019.
- Jiang, H. 2012. Performance-based seismic analysis and design of Code-exceeding tall buildings in Mainland China, *Structural Engineering and Mechanics*, Vol. 43, No. 4.
- Lee, D. 2002. Efficient seismic analysis of high-rise building structures with the effects of floor slabs, *Engineering Structures* 24, 613–623.
- Lu, X.L. 2011a. Research and Practice of Response Control for Tall Buildings in Mainland China, *Procedia Engineering* 14, 73–83.
- Lu, X.L. 2011b. Collapse simulation of a super-high-rise building subjected to extremely strong earthquakes, *Sci China Tech Sci*, 54(10): 2549–2560.
- Lu, X. 2014. Development of a simplified model and seismic energy dissipation in a super-tall building, *Engineering Structures* 67, 109–122.
- Meera, R. 2013. Effect of ground motion duration on earthquake-induced structural collapse, *Structural Safety* 41, 119–133.
- Ministry of Construction of the People's Republic of China, Code for seismic design of Buildings, GB50011-2001EN.
- Mirabdollah, Y. 2012. A closed-form solution for nonlinear oscillation and stability analyses of the elevator cable in a drum drive elevator system experiencing free vibration, *Community Nonlinear Scientific Numerical Simulation* 17, 4467–4484.
- Miranda, E. and S. Taghavi. 2005. Approximate floor acceleration demands in multistory buildings. I: Formulation. *Journal of structural engineering*, 131(2): 203–211.
- Pacific Earthquake Engineering Research Center (Peer), Seismic design guidelines for Tall buildings, Berkeley Report 2010/05.
- Rofooei, F.R. 2012. Inter-Story Drift Spectra for Tall Buildings under Near-Field Earthquakes Based on Non-Uniform Lumped Mass Beam Model, Department of Civil Engineering, Sharif University of Technology, Iran, 15 WCEE Lisboa 2012.
- Sailful Islam, A.B.M. 2012. Non-linear time domain analysis of base isolated multi-storey building under site specific bi-directional seismic loading, *Automation in Construction* 22, 554–566.
- Saligrama, R.V. 2002. Robust control of vertical motions in ultra-high rise elevators, *Control Engineering Practice* 10, 121–132.
- Takewaki, I. 2011. The 2011 off the Pacific coast of Tohoku earthquake and response of high-rise buildings under long-period ground motions, *Soil Dynamics and Earthquake Engineering* 31, 1511–1528.
- Tenozhi, S. 2013. Advances in modeling and vibration control of building structures, *Annual Reviews in Control* 37, 346–364.
- Villaverde, R. 2004. Seismic Analysis and Design of Nonstructural Components. *Earthquake Engineering: From Engineering Seismology to Performance-Based Engineering*. Y. Bozorgnia and V.V. Bertero, CRC.
- Xia J et al., Case study: Shanghai Tower, *CTBUH Journal Issue 2*, 2010.

- Yang, D. 2010. Interstory drift ratio of building structures subjected to near-fault ground motions based on generalized drift spectral analysis, *Soil Dynamics and Earthquake Engineering* 30, 1182–1197.
- Yao, G. 2007. Seismic Performance of Passenger Elevators in Taiwan, Department of Architecture, National Cheng Kung University, Tainan, Taiwan 701, R.O.C.
- Zhu, W.D. 2003a. Vibration of elevator cables with small bending stiffness, *Journal of Sound and Vibration* 263, 679–699.
- Zhu, W.D. 2003b. Design and analysis of a scaled model of a high-rise, high-speed elevator, *Journal of Sound and Vibration* 264, 707–731.
- Zhou, X. 2013. A macro-element based practical model for seismic analysis of steel–concrete composite high-rise buildings, *Engineering Structures* 49, 91–103.

# Comparison of deep soil deposit seismic response with three basement models

X.B. Peng & W.L. Yang

*Earthquake Administration of Jiangsu Province, Nanjing, China*

**ABSTRACT:** To the deep soil deposit, that the shear velocity is less 500 m/s while the burial depth is 100 m, the present methods in China dealing with the basement in seismic response estimation are discussed. Based on theoretical analysis and engineering case, 3 basement models (linear extrapolation, soft interlayer assumption and stiff basement) are created. The relative soil nonlinear parameters are provided by experiments and the models' dynamic response under different seismic intensity is calculated by 1D equivalent linearization routine. The PGA and response spectra in ground surface of those models are compared and the results show that the stiff basement model do not underestimate the seismic risk, while it is easy to build. The stiff model is recommended in engineering application.

**Keywords:** deep soil deposit; basement; seismic response; PGA; response spectra

## 1 INTRODUCTION

Special and systematic seismic risk evaluation is legally required for important engineering projects in China. The seismic response of engineering site is a key part in determining the final earthquake affecting coefficient, which is named design ground motion parameters. Previous researches have showed that the peak and spectrum are strongly affected by the site's soil characteristics (Hartzell, S. et al. 2004, Li, X. J. 2013). The soil characteristics are quantified by soil profiles, shear wave velocity, static and dynamic parameters, which are acquired by drilling, in situ tests and laboratory experiments. At present, the depth of drilling for seismic risk evaluation is not required to exceed 100m for most of engineering projects, according to the technical specification. However, in some areas with deep soft soil deposit, the shear wave velocity is apparently less than 500 m/s, which is the minimum requirement in the specification, in the depth range (Lu, S. D. 2005). In this situation, the basement for the site seismic response is required to special study.

Under the circumstances, there are 3 methods to determine the basement: (1) choosing the obvious velocity jumping interface, (2) using the soil comparison and empirical equation to estimate velocity, (3) linear or nonlinear extrapolating velocity (Hong, H.C. et al. 2013). The first method needs deeper drilling and testing. Although some velocity tomography technologies may reflect the inhomogeneity (Fan, X.P. et al. 2011, 2013), they do not have enough resolution and reliability to

employ in soil seismic response computation. The second method needs some typical reference data, which are not always existing or collectible. The tendency of velocity increasing along the depth is assumed to be same in third method. The assumption may be proper in some cases, but there are also some cases in which the velocity increase slowly or decrease in certain depth range.

The input basement can affect site seismic response in varying degrees for different soil velocity structures (Lou, M.L. et al. 2006, Shi, C.H. et al. 2009). In general, the soil characteristics in deep range have less significant effect to the ground surface seismic response of deep deposit site (Chen, G.X. & Chen, J.H. 2005) for the velocity is relatively high, such as greater than 400 m/s, and the nonlinearity is relatively weak. On the other hand, for the energy-dissipation of deep soil, the velocity extrapolation and small impedance ratio between the basement and the adjacent soil layer may underestimate the seismic response.

In this paper, based on a true engineering case, the seismic responses in the ground surface of a site under 3 basement model assumptions with 3 boreholes (zk1, zk2 and zk3), whose shear velocity are just about 450 m/s at 100m in depth, are studied.

## 2 DATA AND METHOD

The soil profile and in situ shear velocity of a true engineering site with 3 boreholes, whose depth is 100 m, are presented in [Figure 1](#). The figures show the

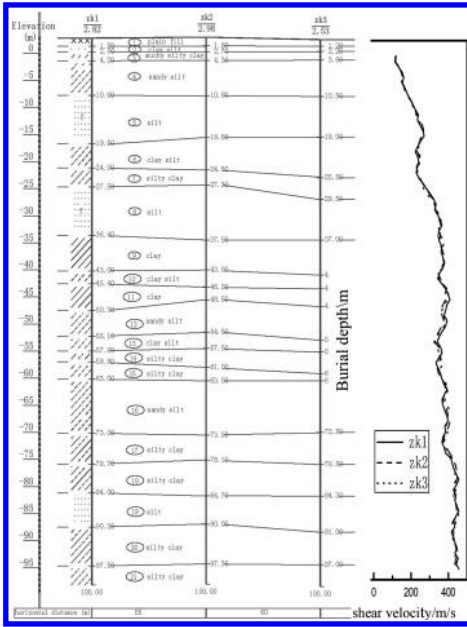


Figure 1. Profile and shear velocity of deep soil deposit.

soil is stratified and the velocity is very close at same depth of the 3 boreholes. The borehole is divided into 21 layers and each layer's depth is 10 m less. As the Figure 1 shows, it's difficult to predict what kind of soil will be in deeper zones. The characteristics of shear velocity are: (1) the tendency of the velocity along the depth is increasing, where the rate of increase is higher in 0–40m and gentler below 40 m, (2) controlled by the soil properties, there are relatively low velocity layers at different depth.

For the shear velocity of the boreholes is 500 m/s less, the choice of the basement needs to be considered when computing the seismic response. According to the geophysical prospecting and collecting information, we infer that the bed rock is about 300 m beneath the ground surface and there are not severe soft layers between 100m and 300m in depth. However, these data are not exact and complete enough to build a reliable model. So, for the sake of simplicity and engineering application, we propose 3 basement models to deal with the uncertainty of the deeper soil.

The soil seismic response is calculated by 1D equivalent linearization routine. The static and dynamic soil parameters are determined by experiments. For the degree of soil nonlinear strength reduction is different according to the earthquake intensity, we consider 3 levels of input strong motion, naming small earthquake, middle earthquake, and large earthquake, whose peak accelerations are 32.0 cm/s<sup>2</sup>, 144.0 cm/s<sup>2</sup> and 280.0 cm/s<sup>2</sup>. The response spectra

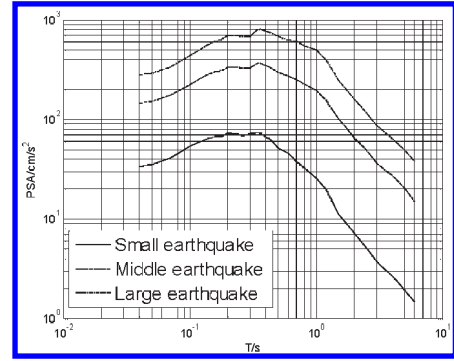


Figure 2. Response spectra of input strong motions.

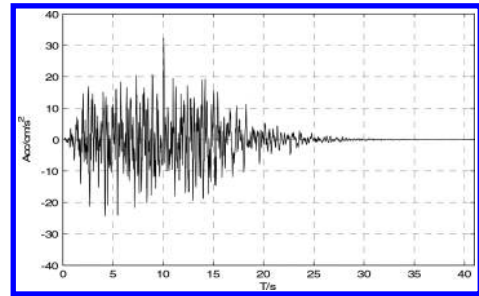


Figure 3. Example of acceleration time series.

of the input are shown in Figure 2. The acceleration time series are artificially synthesized with the spectra, and one of it is shown in Figure 3. To eliminate the effect of input, 12 acceleration time series are employed for each calculation.

### 3 BASEMENT MODELS

#### 3.1 Linear extrapolation model

According to the rising tendency of shear velocity with depth, we employ the data during the depth range of 60–100 m to linear fit the equation between the shear velocity and the burial depth. The linearly dependent coefficient is 0.868. The fitting result is shown in Figure 4 and the equation is:

$$V_s = 2.4010 D + 216.9733 \quad (1)$$

where,  $V_s$  is shear velocity and  $D$  is burial depth.

Following the equation, we extrapolate the shear velocity to 500 m/s with  $D$  being 118 m. Then the deeper zone below 118 m is treated as the basement, which is stiff. This model is named M1.

### 3.2 Soft interlayer assumption model

Based on the M1, the velocity during 100–106m is replaced by a soft interlayer with velocity being 400 m/s, while the other part remains unchanged. This model is named M2.

### 3.3 Stiff basement model

For the lack of the wdeeper soil information and shear velocity data, a stiff basement with shear velocity being 500 m/s is assumed just beneath 100 m. This model is named M3.

## 4 RESULTS ANALYSIS

To eliminate the uncertainty, the mean of PGA and response spectra in ground surface excited by the 12 input motions is used in following analysis.

### 4.1 PGA

The mean PGA under 3 levels of input strong motion is listed in Table 1. There are several points we can infer from the table:

1. Controlled by the similar soil structure and shear velocity, the PGA of the 3 boreholes with same basement is close to each other. The maximum relative error is 1.5%, 1.9% and 7.5%

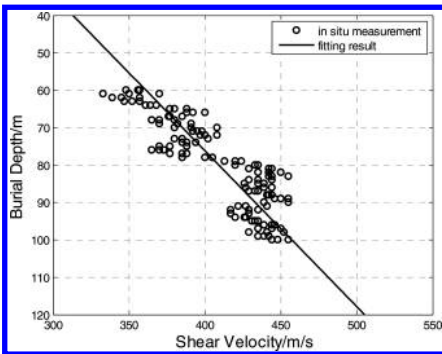


Figure 4. Linear fitting of wave velocity with burial depth.

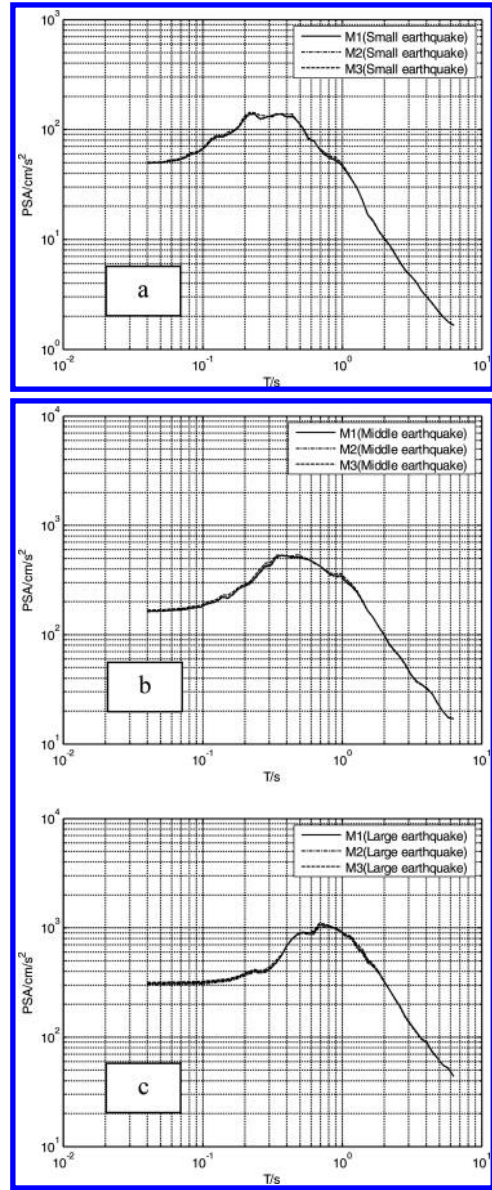


Figure 5. Comparison of 3 models' response spectra in ground surface.

Table 1. Comparison of 3 models' PGA in ground surface.

Model	Small earthquake			Middle earthquake			Large earthquake		
	zk1	zk2	zk3	zk1	zk2	zk3	zk1	zk2	zk3
M1	47.1	46.8	47.5	161.4	163.3	163.8	296.6	309.8	319.2
M2	46.8	46.8	46.8	160.2	161.6	161.7	289.1	301.7	308.7
M3	47.2	47.4	47.2	164.9	167.5	168.0	304.5	317.3	327.8

under small earthquake, middle earthquake, and large earthquake, correspondingly. The more apparent error under large earthquake implies that PGA is more sensitive to soil properties, especially nonlinear parameters under strong input motion. It is consistent with the fact that it is more difficult to predict the PGA in near-fault area, where the bedrock motion is usually stronger.

2. Generally, the sort of the PGA among the 3-basement model is  $M2 \cong M1 \cong M3$ , which means the soft interlayer assumption reduces the response while the stiff basement enhances it. However, maximum relative error for different basement model is 1.5%, 3.5%, and 5.8% under small earthquake, middle earthquake, and large earthquake, correspondingly.

#### 4.2 Response spectra

For the response spectra of the 3 boreholes is very close, the mean response spectra of the 3 basement model under 3 levels of input strong motion is displayed in Figure 5. The figures show that the results from M3 are slightly larger in short period range, while all the curves are almost overlapping after about 1s. Although as assumed soft interlayer is put into M2, it does not lead to apparent lengthening of characteristic period, which is one of the important design ground motion parameters. So, it is confirmed that the variation of velocity in deep part have no significant effect on ground surface seismic response.

## 5 CONCLUSION

1. Based on the true engineering case, the different basement assumptions have no significant effect on ground surface seismic response for deep soil deposit. In general, the stiff basement does not underestimate the seismic effect.
2. For the sake of simplicity and safety, the stiff basement can be used for the situation where

the shear velocity is less than 500m/s for deep soil deposit. The optimized choice of basement shear velocity should be studied further.

## ACKNOWLEDGMENTS

The work is supported by the National Science Foundation under grant 51208234 and Jiangsu Province Science and Technology support plan under grant BE2014731.

## REFERENCES

- Chen, G.X. & Chen, J.H. 2005. A study on the influence of seismic wave inputting interface on the earthquake response of deep soft sites. *World Earthquake Engineering*, 21(2): 36–43.
- Fan, X.P., Yang, C.J. & Li, Q.H. 2013. The effect of inhomogeneity parameters on scattering wave envelopes. *Progress in Geophys* 28(2): 0687–0694.
- Fan, X.P., Li, Q.H., Yang, C.J. & et al. 2011. Spectral structure of velocity inhomogeneity of crust medium in Changbaishan Tianchi volcano. *Chinese J. Geophys* 54(5): 1215–1221.
- Hartzell, S., Bonilla, L.F. & Williams, R.A. 2004. Prediction of Nonlinear Soil Effects. *Bulletin of the Seismological Society of America* 94(5): 1609–1629.
- Hong, H.C., Xu, H.G., Tao, X.S. & et al. 2013. Determination and effect of earthquake input interface of deep governing holes. *Technology for Earthquake Disaster Prevention* 8(1): 52–61.
- Li, X.J. 2013. Adjustment of seismic ground motion parameters considering site effects in seismic zonation map. *Chinese Journal of Geotechnical Engineering*, 35(S2): 21–29.
- Lou, M.L., Li, Y.C., Li, N.H. & et al. 2006. Some problems in seismic response analysis of soil layer with deep deposit. *Journal of Tongji University (Natural Science)* 34(4): 427–432.
- Lu, S.D. 2005. Teaching material of ‘Seismic safety assessment of engineering site (GB17741-2005)’. Beijing: China Standard Press.
- Shi, C.H., Lu, Y.J., Peng, Y.J. & et al. 2009. A study on the influence of seismic wave inputting interface on ground motion parameters. *Earthquake Research in China*, 25(3): 282–293.

*Coastal engineering*

# An electrochemical impedance spectroscopy method for identifying the Threshold Chloride Level for rebar in simulated concrete pore solutions

J.Z. Hu, X.Q. Cheng & X.G. Li

Corrosion and Protection Center, University of Science and Technology Beijing, Beijing, China  
Engineering College, Ocean University of Guangdong, Zhanjiang, China

P.C. Deng

College of Ocean and Meteorology, Ocean University of Guangdong, Zhanjiang, China

G. Wang

Engineering College, Ocean University of Guangdong, Zhanjiang, China

**ABSTRACT:** A novel approach was proposed for determining the threshold Chloride Level (CTL) of rebar (HRB400). The  $Z_{1\text{ Hz}}$ , which is the resistance value when the frequency is 1 Hz, was extracted from the Electrochemical Impedance Spectroscopy (EIS) data. In a plot of the change in  $Z_{1\text{ Hz}}$  with  $[\text{Cl}^-]$ , the  $Z_{1\text{ Hz}}$  value was observed to shift sharply when the  $[\text{Cl}^-]$  was at the CTL. The EIS method has a wide application range and is highly sensitive compared with the potential method and current method. The Simulated concrete Pore Solutions (SPSs) were composed of 0.6 mol/L KOH, 0.2 mol/L NaOH and 0.001 mol/L  $\text{Ca}(\text{OH})_2$ . The carbonation process of concrete was simulated by adjusting the pH value using  $\text{NaHCO}_3$ . The penetration of chloride was simulated by adding NaCl. The influence of the pH on the CTL of HRB400 was significant and non-linear. The temperature had a relatively high impact on the CTL of HRB400.

**Keywords:** concrete reinforcement; Threshold Chloride Level (CTL); Open Circuit Potential (OCP); Electrochemical Impedance Spectroscopy (EIS); rebar (HRB400)

## 1 INTRODUCTION

Steel-reinforced concrete, a major engineering structural material, is widely used in civil engineering applications such as roads, bridges and harbors. However, the corrosion of steel bar inevitably results in severe damage to reinforced concrete structures in two ways<sup>[1]</sup>. Firstly, it reduces the cross-sectional area of the steel bar. Secondly, it produces more corrosion products than the steel itself. Such an increase causes tensile stress in the concrete, leading to cracking and, eventually, structural failure.

It is well known that the steel reinforcement in concrete is normally in a passive state against corrosion due to a thin iron oxide layer that is formed on the steel surface and remains stable in the highly alkaline environment of the concrete<sup>[2]</sup>. However, this passive state can be inhibited by the destruction of the passive film by aggressive ions (chlorides, sulfates) or by acidification of the environment near the rebar (carbonation). Corrosion of the reinforcing steel is the natural result of chloride penetration in reinforced concrete.

Tuutti<sup>[3]</sup> suggested that, from the point of view of reinforcement corrosion, the service life of a concrete structure could be subdivided into an incubation period ( $t_1$ ) and a propagation period ( $t_2$ ) (Fig. 1).

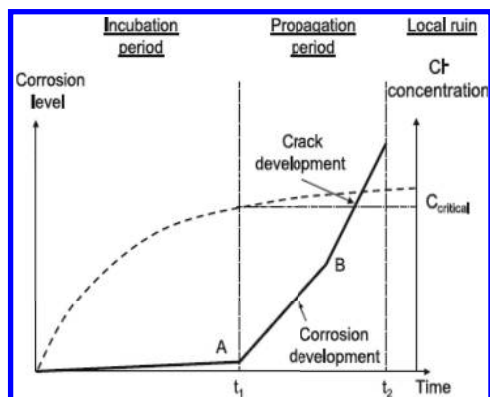


Figure 1. Schematic sketch of the steel corrosion sequence in concrete<sup>[3]</sup>.



- A. The incubation period ( $t_1$ ) corresponds to the chloride penetration within the porous materials and chloride ion accumulation in the vicinity of the rebar. The duration of this period depends on the concrete cover and the chloride concentration required to start the corrosion process.
- B. The propagation period ( $t_2$ ) corresponds to the stage when the chloride ions depassivate the reinforcing steel surface, leading to the development of corrosion and, at term, to the local ruin of the structure.

Chloride-induced corrosion of reinforced steel bar (rebar) is one of the major causes of premature degradation of reinforced concrete and consequent structure collapse<sup>[4]</sup>. The importance of chloride ions in the corrosion of steel in concrete has led to the concept of a Chloride Threshold Level (CTL). The CTL can be defined as the content of chloride at a given steel depth that is necessary to sustain local passive film breakdown and hence initiate the corrosion process<sup>[5]</sup>. Knowledge of the CTL for the corrosion of a steel reinforcement is essential for predicting the durability and service life of reinforced concrete contaminated with chloride ions. Consequently, numerous investigations<sup>[6-8]</sup> have been devoted to identifying the threshold value. Half-cell potential (Open Circuit Potential, OCP) measurements for determining rebar corrosion initiation have been standardized<sup>[9]</sup>. Another nondestructive technique, Linear Polarization Resistance (LPR), has also been used to characterize corrosion initiation and propagation according to a defined criterion value of the corrosion current density,  $i_{corr}$ , or the abrupt variation of  $i_{corr}$ <sup>[10]</sup>. Among the various electrochemical methods widely developed in the literature, Electrochemical Impedance Spectroscopy (EIS) seems to be the most reliable technique for monitoring the corrosion process in reinforced concrete<sup>[11-12]</sup>. This method, contrary to the stationary techniques (e.g., the anodic polarization method), allows the characterization, in a nondestructive way, of both the diffusion of aggressive species within the cement-based materials and the kinetics of the electrochemical reactions that occur on the steel electrode surface.

In this paper, we propose an EIS method to identify the CTL. The advantages of the EIS method

were compared with the OCP and LPR methods. The CTL, represented with  $[Cl^-]$ , for pre-rusted bars at four different pHs and three temperature SPSs was investigated using the EIS technique.

## 2 EXPERIMENT

### 2.1 Specimen preparation

Thread steel bar (HRB400) specimens were prepared for this study. The specimen types were cut into 30 mm lengths from black steel rebar of 12 mm nominal diameter. The unexposed faces were sealed with epoxy resin. Before exposure, the as-received surfaces were mechanically polished using 400, 800 and 1200 emery papers and lubricated using distilled water. The polished samples were cleaned with acetone, washed with distilled water, dried in air and stored over a desiccant. The average area of the exposed rebar surfaces was  $1.1 \pm 0.02 \text{ cm}^2$ .

### 2.2 Experimental setup

A 1 L glass container was used as a test cell in this study. Four types of Simulated concrete Pore Solutions (SPSs) were selected as pore water solutions. The chemical compositions of the SPSs are presented in Table 1<sup>[13]</sup>. The lower pH (SPS1) solution was intended to present pore water within a carbonated concrete environment. Approximately 0.8 L of SPS was used in each glass container, and the pH was monitored throughout the experiment. Because the deviation results were less than 0.1, the effects on the experimental results induced by pH fluctuations were ignored. The chloride concentrations in the SPSs were adjusted stepwise by adding reagent-grade NaCl crystals. For the chloride adjusting process, approximately 100 mL of solution was extracted with a syringe from the test cell. After the NaCl crystals completely dissolved, the extracted solution was poured back into the cell<sup>[10]</sup>. A magnetic stirring bar was placed at the bottom of each container and was set to rotate at the lowest rate to continuously and homogeneously mix the solution throughout the experiment, including

Table 1. Chemical compositions and nominal pH values of fresh simulated pore solutions.

Composition	pH	NaOH (mol/L)	KOH (mol/L)	Ca(OH) <sub>2</sub> (mol/L)	NaHCO <sub>3</sub>
SPSs1	9.6	0.6	0.2	0.001	Proper
SPSs2	10.6	0.6	0.2	0.001	Proper
SPSs3	11.6	0.6	0.2	0.001	Proper
SPSs4	12.6	0.6	0.2	0.001	Proper

the period when the electrochemical measurements (see below) were conducted. The ambient temperature was held at  $25 \pm 2$  °C,  $35 \pm 2$  °C and  $45 \pm 2$  °C. To reduce carbonation, all of the cells were covered except during the NaCl crystal addition and pH monitoring. At the beginning of the experiment, the specimens were immersed in the designated SPSs for 3 days for preconditioning. Subsequently, chloride was adjusted, and the interval for the stepwise chloride increment was approximately 2 days.

### 2.3 Electrochemical measurements

To assess the corrosion conditions of steel bars, electrochemical measurements were carried out. The rebar was used as the working electrode, a platinum net was used as the counter electrode, and a Saturated Calomel Electrode (SCE) was used as the reference electrode. During the course of the experiment, the rebar electrode was always immersed in the SPSs. For the open circuit potential measurement, the linear polarization measurement and the electrochemical impedance spectroscopy measurement, the Autolab Aut84458 Advanced Potentiostat/Galvanostat/FRA system was used. The linear polarization scan was carried out between  $-15$  mV and  $+15$  mV with respect to the rest potential ( $E_{\text{corr}}$ ). The potential was applied at a rate of  $0.0167$  mV/s. Electrochemical Impedance Spectroscopy (EIS) was measured with a sinusoidal potential excitation of  $15$  mV amplitude in the frequency range from  $100$  KHz to  $10$  mHz at the corrosion potential.

## 3 RESULTS AND DISCUSSION

### 3.1 Comparison of the methods for determining the CTL

#### 3.1.1 Determination of the CTL for the corrosion of rebar in the pH 9.6 spss at 25°C

Figure 2 shows the evolution of the OCP and corrosion potential ( $E_{\text{corr}}$ ) of HRB400 rebars with  $[\text{Cl}^-]$  increment in the pH 9.6 SPSs at 25°C. The solid shapes and the shaded area are the upper and lower boundaries of a dramatic shift in the OCP and  $E_{\text{corr}}$ , implying the initiation of corrosion of the rebar in the corresponding  $[\text{Cl}^-]$  range. To be conservative, the  $[\text{Cl}^-]$  value at the middle of the shaded area was considered the threshold value in this study. For the pH 9.6 SPSs at 25°C, prior to reaching the threshold value, the OCP and  $E_{\text{corr}}$  were more positive than  $-240$  mV vs. SCE, and the values remained in a relatively stable trend. After the  $[\text{Cl}^-]$  exceeded the threshold value, the OCP and  $E_{\text{corr}}$  shifted negatively by more than  $600$  mV.

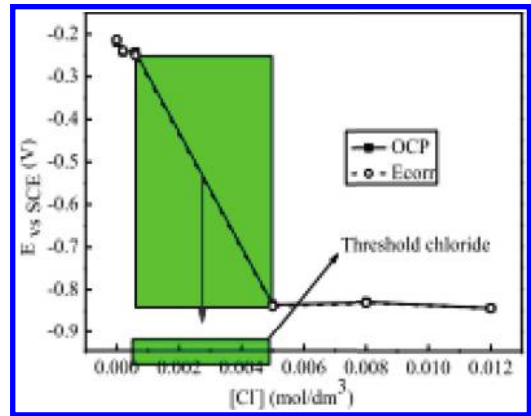


Figure 2. The influence of the  $[\text{Cl}^-]$  on the OCP and  $E_{\text{corr}}$  of HRB400 in the pH 9.6 SPSs at 25°C.

The values for the corrosion potentials and corrosion current densities ( $i_{\text{corr}}$ ) were estimated from the intersection of the anodic and cathodic Tafel lines. Figure 3 presents the  $i_{\text{corr}}$  variation of the HRB400 bar as a function of the  $[\text{Cl}^-]$  stepwise increment variation in the pH 9.6 SPSs at 25°C. For all of the SPSs and all of the stepwise  $[\text{Cl}^-]$  additions, the  $i_{\text{corr}}$  fluctuations ranged from  $1 \times 10^{-4}$  to  $3 \times 10^{-2}$  mA/cm<sup>2</sup>. After the  $[\text{Cl}^-]$  reached the threshold value, sharp  $i_{\text{corr}}$  fluctuations were apparent.

EIS is a powerful technique for obtaining detailed knowledge of the conductive anode system. EIS provides information on a number of parameters, such as the presence of surface films, interfacial reactions and mass-transfer phenomena. Figure 4 shows the EIS data for the HRB400 bars, which were immersed in the pH 9.6 SPSs with different  $[\text{Cl}^-]$  at 25°C. The plots could be divided into two parts in the  $[-1, 1]$  range of  $\log f$ , and the CTL could be distinctly determined. The  $Z_0$ , which is the resistance value when  $\log f$  equals 0 (frequency is 1 Hz), was extracted from the EIS data. A plot of the change in  $Z_{1\text{Hz}}$  with  $[\text{Cl}^-]$  was drawn, as shown in Figure 5. The value of  $Z_{1\text{Hz}}$  sharply shifted, implying damage of the passive film by chloride ions. The  $[\text{Cl}^-]$  was at the CTL when the  $Z_{1\text{Hz}}$  value sharply shifted. The CTL could be easily determined using the potential, current and resistance methods; however, the resistance method is more sensitive than the others.

#### 3.1.2 Determination of the CTL for the corrosion of rebar in the pH 10.6 spss at 25°C

Figures 6–8 show the evolution of OCP,  $E_{\text{corr}}$ ,  $i_{\text{corr}}$  and  $Z_{1\text{Hz}}$  of the HRB400 rebars with  $[\text{Cl}^-]$  increment in the pH 10.6 SPSs at 25°C. The CTL could be easily determined using the current and

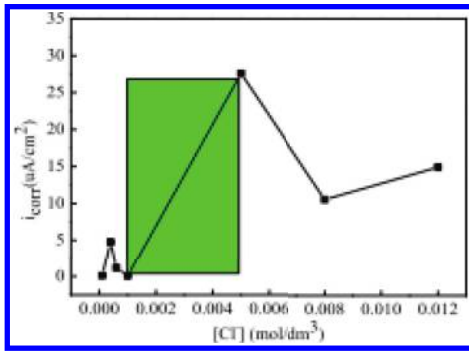


Figure 3. The influence of the  $[Cl^-]$  on the  $i_{corr}$  of HRB400 in the pH 9.6 SPSs at 25°C.

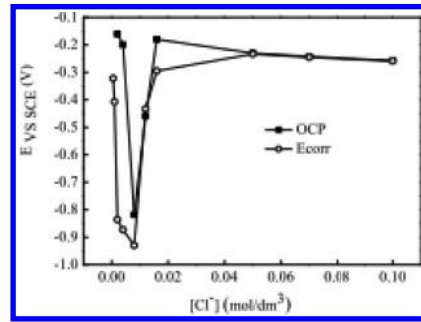


Figure 6. The influence of the  $[Cl^-]$  on the OCP and  $E_{corr}$  in the pH 10.6 SPSs at 25°C.

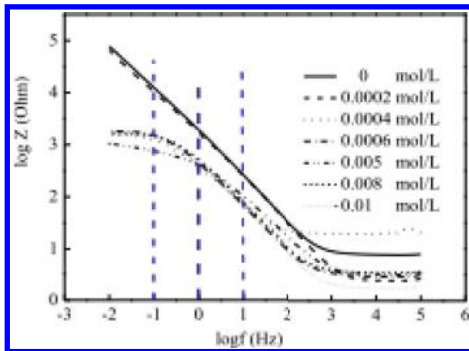


Figure 4. The EIS of HRB400 in the pH 9.6 SPSs with different  $[Cl^-]$  at 25°C.

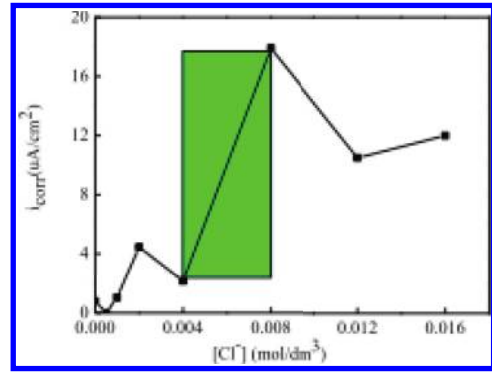


Figure 7. The influence of the  $[Cl^-]$  on the  $i_{corr}$  of HRB400 in the pH 10.6 SPSs at 25°C.

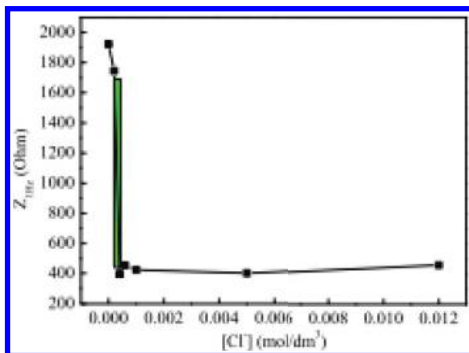


Figure 5. The influence of the  $[Cl^-]$  on the  $Z_{1 Hz}$  of HRB400 in the pH 9.6 SPSs at 25°C.

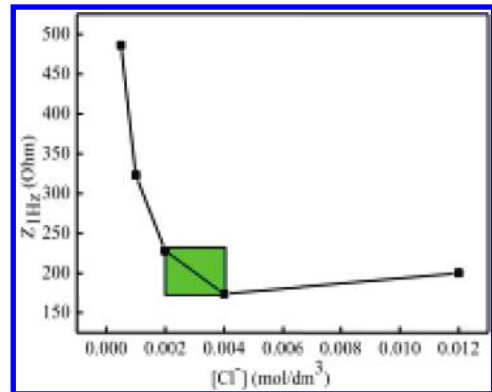


Figure 8. The influence of the  $[Cl^-]$  on the  $Z_{1 Hz}$  of HRB400 in the pH 10.6 SPSs at 25°C.

resistance methods but not the potential method. Of the available methods for determining the CTL, the new resistance method was more sensitive and had a wider application range than the others. The resistance method allows the characterization,

in a nondestructive way, of both the diffusion of aggressive species within the cement-based materials and the kinetics of the electrochemical reactions that occur on the steel electrode surface. In this paper, the CTL was determined using the new resistance method.

### 3.2 The influence of temperature and pH on the CTL of HRB400 rebar in SPSs

Figure 9 shows the CTLs of HRB400 rebar in pH 9.6, 10.6, 11.6 and 12.6 SPSs at 25°C, 35°C and 45°C. Corrosion occurred on the HRB400 rebar without adding NaCl in the pH 9.6 SPSs at 45°C; therefore, the CTL was zero. Figure 10 shows the influence of the temperature and pH on the CTLs of HRB400 rebar in SPSs. The influence of the pH on the CTL of HRB400 was significant and non-linear. The carbonation of reinforced concrete was simulated by decreasing the pH, and carbonation had a very large and complicated influence on the CTL. The ambient temperature had a relatively high impact on the CTL of HRB400.

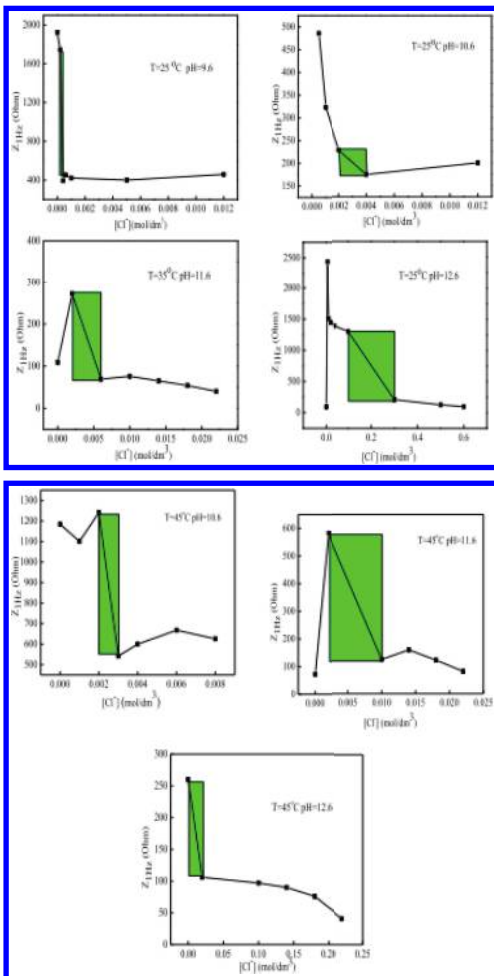


Figure 9. The CTLs of HRB400 rebars in SPSs with different temperatures and pH values.

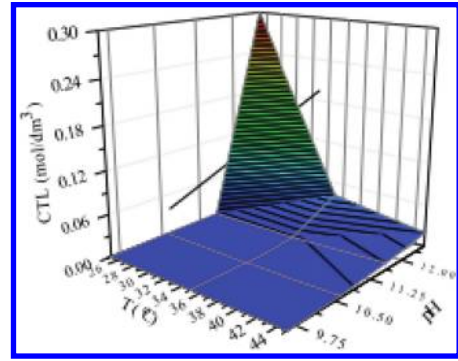


Figure 10. The influence of temperature and pH on the CTLs of HRB400 rebars in SPSs.

## 4 CONCLUSIONS

According to the experimental results and discussion presented above, the following conclusions could be drawn:

1. The EIS method was proposed to identify the CTL: The  $Z_1$ , which is the resistance value when the frequency is 1 Hz, was extracted from the EIS data. In a plot of the change in  $Z_{1\text{Hz}}$  with  $[\text{Cl}^-]$ , a sharp shift in the  $Z_{1\text{Hz}}$  value was observed when the  $[\text{Cl}^-]$  was the CTL. The resistance method is more sensitive and has a wider application range than the other methods.
2. The carbonation of reinforced concrete was simulated by decreasing the pH. The influence of the pH on the CTL of HRB400 was significant and non-linear. Therefore, carbonation had a very large and complicated influence on the CTL. In addition, the ambient temperature had a relatively high impact on the CTL of HRB400.

## ACKNOWLEDGMENTS

The authors gratefully acknowledge financial support from the National Basic Research Program of China (973 Program) (No. 2014CB643300).

## REFERENCES

- [1] Chunlei Geng, Yongmo Xu, Duan Weng, Xiaodong Wu. A time-saving method to determine the chloride threshold level for depassivation of steel in concrete [J]. *Construction and Building Materials*, 2010, 24(6):903–909.
- [2] Ghods P., Isgor O.B., McRae G.A., Gu G.P. Electrochemical investigation of chloride-induced depassivation of black steel rebar under simulated service conditions [J]. *Corrosion Science*, 2010, 52(5):1649–1659.

- [3] Tuutti K. *Corrosion of steel in concrete*, CBI Research Report no. 4.82, Swedish Cement and Concrete Research Institute, Stockholm, Sweden, 1982.
- [4] Hodhod O.A., Ahmed H.I.. Modeling the corrosion initiation time of slag concrete using the artificial neural network [J]. *Housing and Building National Research Center Journal*, 2014, 10(3): 231–234.
- [5] Yong Ann Ki, Won Song Ha. Chloride threshold level for corrosion of steel in concrete [J]. *Corrosion Science*, 2007, 49(11):4113–4133.
- [6] Ueli M. Angst, Bernhard Elsener, Claus K. Larsen, Øystein Vennesland. Chloride induced reinforcement corrosion: Electrochemical monitoring of initiation stage and chloride threshold values [J]. *Corrosion Science*, 2011, 53(4):1451–1464.
- [7] Olivier Poupard, Abdelkarim Ait-Mokhtar, Paul Dumargue. Corrosion by chlorides in reinforced concrete: Determination of chloride concentration threshold by impedance spectroscopy [J]. *Cement and Concrete Research*, 2004, 34(6):991–1000.
- [8] Xu, J.X., Jiang, L.H., Wang, W.L., Jiang, Y. Influence of CaCl<sub>2</sub> and NaCl from different sources on chloride threshold value for the corrosion of steel reinforcement in concrete [J]. *Construction and Building Materials*, 2011, 25(2):663–669.
- [9] Meira G.R., Andrade C., Vilar E.O., Nery K.D.. Analysis of chloride threshold from laboratory and field experiments in marine atmosphere zone [J]. *Construction and Building Materials*, 2014, 55:289–298.
- [10] Hui Yu, Kuang-Tsan K. Chiang, Lietai Yang. Threshold chloride level and characteristics of reinforcement corrosion initiation in simulated concrete pore solutions [J]. *Construction and Building Materials*, 2012, 26(2):723–729.
- [11] Jing Xu, Wu Yao. Electrochemical studies on the performance of conductive overlay material in cathodic protection of reinforced concrete [J]. *Construction and Building Materials* 2011, 25(5):2655–2662.
- [12] Ping Gu, S. Elliot, J.J. Beaudoin, B. Arsenaault, Corrosion resistance of stainless steel in chloride contaminated concrete [J]. *Cement and Concrete Research* 1996, 26 (8):1151–1156.
- [13] Kitowski C.J. Wheat H.G. Effect of chlorides on reinforcing steel exposed to simulated concrete solutions [J]. *Corrosion*, 1997, 53(3):216–226.

# The corrosion of the pipeline steel in thermocline of the tropical oceans

P.C. Deng

College of Ocean and Meteorology, Ocean University of Guangdong, Zhanjiang, China

G. Wang & J.Z. Hu

Engineering College, Ocean University of Guangdong, Zhanjiang, China

X.G. Li & X.Q. Cheng

Corrosion and Protection Center, University of Science and Technology Beijing, Beijing, China

**ABSTRACT:** The concentrations of dissolved oxygen, pH value and the other chemical factors, dramatically change in the thermocline of the tropical oceans. There is superior influence of the temperature and the dissolved oxygen concentration upon the corrosion of pipeline steel in the thermocline. With the decreasing of temperature and increasing of dissolved oxygen, the OCP of pipeline steel in the thermocline of tropical oceans rises. With the decreasing of temperature and dissolved oxygen, the Ecorr drops down and Icorr enlarges. If the pipeline steel is placed through the thermocline, the corrosion would occur that caused by the temperature difference and the oxygen concentration difference. The influence of the oxygen concentration on the corrosion was of significance.

**Keywords:** corrosion; thermocline; dissolved oxygen; temperature; tropical oceans

## 1 INTRODUCTION

The thermocline is a thin but distinct layer in a large body of fluid (e.g. water, such as an ocean or lake, or air, such as an atmosphere) in which temperature changes more rapidly with depth than it does in the layers above or below<sup>[1, 2]</sup>. In the ocean, the thermocline may be thought of as an invisible blanket which separates the upper mixed layer from the calm deep water below. The thermocline exists all year in the tropical oceans and subtropical oceans<sup>[3]</sup>. The concentrations

of dissolved oxygen, pH value and the other chemical factors, dramatically change in the thermocline<sup>[4]</sup>. The temperature, dissolved oxygen and pH value are important factors of metal corrosion. The corrosion behavior of metal material that subjected to a tropical marine atmosphere environment was investigated<sup>[5-7]</sup>. The corrosion behavior of metal material was studied in tropical seawater<sup>[8-10]</sup>. The effect of the sea mud on erosion-corrosion behaviors was studied<sup>[11, 12]</sup>. However, very few studies have been dedicated to the corrosion of metal material in the thermocline of ocean.

In this study, we use the sea water of the South China Sea as based electrolyte. By adjusting the temperature and dissolved oxygen, the upper and underlying water of thermocline were simulated. The corrosion of the pipeline steel was studied in the ocean thermocline. It is important for industrial and scientific research.

## 2 EXPERIMENTAL

### 2.1 Electrode and solutions

Test specimens were made of pipeline steel (X70), with a chemical composition (wt%) C 0.061%, Si 0.24%, Mn 1.53%, P 0.011%, S 0.009% and Fe balance. Specimens were cut into

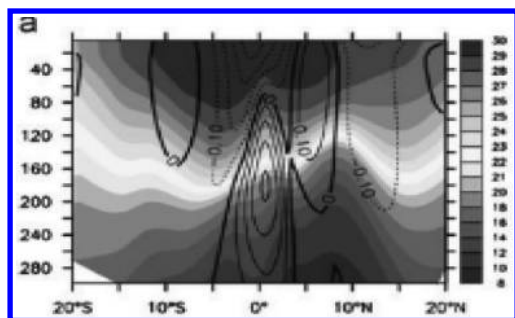


Figure 1. Annual mean vertical ocean profile from 0–300 m along 160°E in the Western Tropical Pacific. Colors represent temperature (°C)<sup>[13]</sup>.

10 mm × 10 mm × 3 mm coupons. The unexposed faces were sealed with epoxy resin with an exposed area of 1.0 cm<sup>2</sup>. Before exposure, the samples were mechanically polished using 400, 800 and 1200 emery papers and lubricated using distilled water. The polished samples were cleaned with acetone, washed using distilled water, dried in air and stored over a desiccant.

The test solution used for the investigation was seawater collected from Zhanjiang Bay, Guangdong, China. The upper water of thermocline was prepared by adjusting the temperature of the basic test solution, the underlying water of thermocline was prepared by adjusting the temperature and adding Na<sub>2</sub>SO<sub>3</sub> (0.001 mol/dm<sup>3</sup> concentration) for controlling the dissolved oxygen of the basic test solution.

## 2.2 Electrochemical measurements

Electrochemical measurements were performed on a three electrode cell through an AUTOLAB (aut84458) electrochemical measurement system. Pipeline steel was used as working electrode, a platinum net as counter electrode, and a Saturated Calomel Electrode (SCE) as reference electrode. Prior to electrochemical measurements, the electrode was immersed in the test solution for at least 1 h until a steady-state corrosion potential was reached<sup>[14]</sup>.

The Linear Polarization (LP) was performed using a potentiostat/galvanostat (AUTOLAB aut84458). The linear polarization curve was measured by potential scanning from -800 to +500 mV vs. corrosion potential at a sweep rate of 1 mV/s.

The corrosion tests of pipeline steel caused by the difference of oxygen concentration and temperature were performed using the Electrochemical Noise (ECN) method. For this work we used an AUTOLAB potentiostat and the NOVA1.10, specific software for electrochemical noise studies.

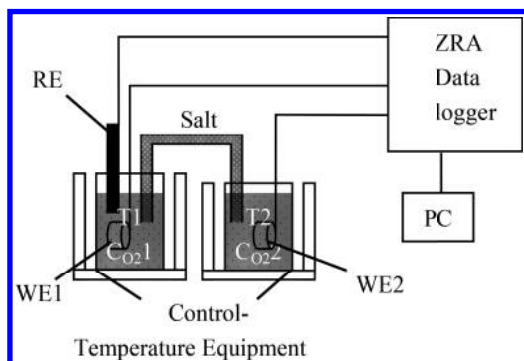


Figure 2. Standard “Salt-Bridge” arrangement for electrochemical noise measurement.

The electrode assembly consisted of two working electrodes of pipeline steel and a Saturated Calomel Reference (SCE) electrode (VSCE = 0.244 V/NH). This disposition allows the simultaneous measurement of galvanic potential and galvanic current (Fig. 2)<sup>[15]</sup>.

## 3 RESULTS AND DISCUSSION

### 3.1 Open Circuit Potential (OCP) of pipeline steel in the thermocline

The OCPs of pipeline steel were measured for 1 hour in the four kinds of electrolyte (A 303 K seawater; B 303 K seawater + SO<sub>3</sub><sup>2-</sup>; C 288 K seawater; D 288 K seawater + SO<sub>3</sub><sup>2-</sup>) (Fig. 3). The 303 K seawater corresponds to the upper water of the tropical oceans thermocline which saturated with dissolved oxygen. The 288 K seawater + SO<sub>3</sub><sup>2-</sup> correspond to the underlying water which is low concentration of dissolved oxygen. The OCP raises in the cold seawater towards more positive value, on the contrary, the OCP drops down due to the low concentration of dissolved oxygen. The difference between the maximum value and minimum value of OCP was about 200 mV, which was a strong power to the corrosion of pipeline steel if it was placed in the upper and underlying seawater of thermocline.

### 3.2 The corrosion of the pipeline steel that is placed in the different areas of thermocline

The corrosion of the pipeline steel, which is placed in the thermocline, was measured by using LP measurements in the four kinds of electrolyte. Figure 4 represents the linear polarization curves of pipeline steel in the different layer of thermocline. From the figure, it can be

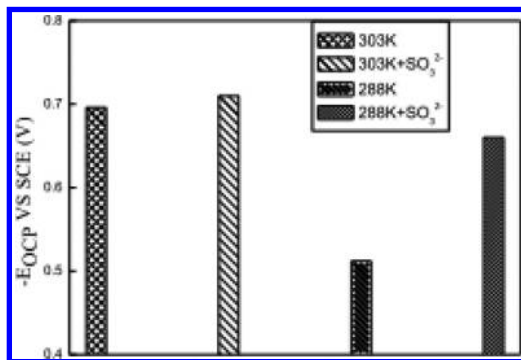


Figure 3. The OCPs were measured for pipeline steel in: (A: 303 K seawater; B: 303 K seawater+ SO<sub>3</sub><sup>2-</sup>; C: 288 K seawater; D: 288 K seawater+ SO<sub>3</sub><sup>2-</sup>).

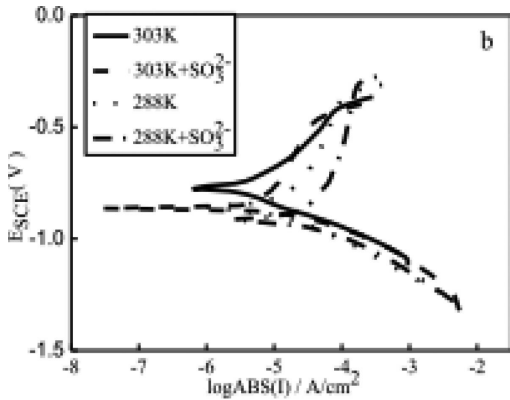


Figure 4. Potentiodynamic polarization curves for pipeline steel in the four kinds of electrolyte: (A: 303 K seawater; B: 303 K seawater +  $\text{SO}_3^{2-}$ ; C: 288 K seawater; D: 288 K seawater +  $\text{SO}_3^{2-}$ ).

seen that the corrosion potential ( $E_{\text{corr}}$ ) values in the low-temperature seawater and in the presence of reductant are shifted to negative direction, the anodic current densities obtained in the low-temperature seawater and in the presence of reductant are higher than that of in the high-temperature seawater and the absence of reductant, the cathodic current densities obtained in the high-temperature seawater are higher than that of in the low-temperature seawater, no differences of the cathodic current densities were found in the absence or presence of reductant.

The values for the corrosion potentials and corrosion current densities were estimated from the intersection of the anodic and cathodic Tafel lines<sup>[8]</sup>. The corresponding corrosion potentials ( $E_{\text{corr}}$ ), corrosion current density ( $i_{\text{corr}}$ ), anodic Tafel slopes ( $b_a$ ) and cathodic Tafel slopes ( $b_c$ ) are listed in Table 1. From results obtained, it can be concluded that:

- The values of corrosion current density ( $i_{\text{corr}}$ ) increase with the decreasing of temperature and dissolved oxygen. The values of corrosion potentials ( $E_{\text{corr}}$ ) decreased with the decreasing of temperature and dissolved oxygen.
- The rate of anodic reaction controls the rate of the corrosion process in the high-temperature seawater. The rate of cathodic reaction controls the rate of the corrosion process in the low-temperature seawater.
- The corrosion current increases obviously after sodium sulfite is added in high-temperature seawater and low-temperature seawater. It is clear that the reducing of dissolved oxygen in seawater causes the markedly increase of in the corrosion rate.

Table 1. Electrochemical parameters: corrosion potential ( $E_{\text{corr}}$ ), corrosion current density ( $i_{\text{corr}}$ ), and Tafel slopes ( $b_a$  and  $b_c$ ) of pipeline steel in seawater.

Condition	Potentiodynamic polarization			
	$E_{\text{corr}}$ (mV)	$i_{\text{corr}}$ ( $\mu\text{Acm}^{-2}$ )	$b_a$ (mVdec <sup>-1</sup> )	$b_c$ (mVdec <sup>-1</sup> )
303 K	-800	3.304	234.64	98.93
303 K+ $\text{Na}_2\text{SO}_3$	-854	7.369	537.24	90.03
288 K	-912	16.14	109.40	667.5
288 K+ $\text{Na}_2\text{SO}_3$	-948	45.09	134.15	1050

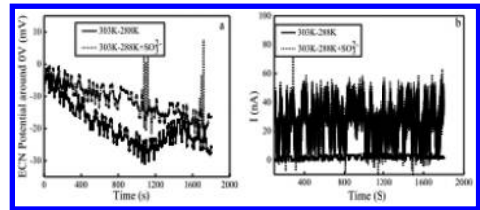


Figure 5. ECN data in the time for pipeline steel that was placed through the thermocline: a potential around 0 V, b current.

### 3.3 The corrosion of the pipeline steel that is placed through the thermocline

The corrosion of the pipeline steel, which is placed through the thermocline, was measured by using the electrochemical noise method and using the experimental devices as Figure 2. Figure 5 shows the experimental ECN data for pipeline steel. The pipeline steel was placed in the high-temperature seawater (303 K) and in the low-temperature seawater (288 K), the potential difference between them is always negative and the current ( $I_{\text{High-DO}}$ ) caused by the temperature difference varies from 0 nA to 5 nA. The potential difference is the power of the corrosion caused by the temperature difference. The pipeline steel was placed in the high-temperature seawater (303 K) and in the low-temperature seawater added reductant (288 K +  $\text{SO}_3^{2-}$ ), the potential difference between them is always negative, but the absolute values of potential difference are decreased. The current ( $I_{\text{Low-DO}}$ ) caused by the temperature difference and the oxygen concentration difference varies from 0 nA to 50 nA. The mean of  $I_{\text{Low-DO}}$  enlarges about 10 times compared with the  $I_{\text{High-DO}}$ .

## 4 CONCLUSIONS

There is superior influence of the temperature and the dissolved oxygen concentration upon



the corrosion of pipeline steel in the thermocline of tropical oceans. With the decreasing of temperature and increasing of dissolved oxygen, the OCP of pipeline steel in the thermocline of tropical oceans rises. With the decreasing of temperature and dissolved oxygen, the Ecorr drops down and Icorr enlarges. If the pipeline steel is placed through the thermocline, the corrosion would occur that caused by the temperature difference and the oxygen concentration difference. The influence of the oxygen concentration on the corrosion was of significance.

#### ACKNOWLEDGEMENT

The authors gratefully acknowledge financial support from the National Basic Research Program of China (973 Program) (No. 2014CB643300), the Science Research Project of the Education Department of Guangdong Province (No. 2012LYM-0071), the Scientific Research Program of Zhanjiang (No. 2014C01003).

#### REFERENCES

- [1] Li Ren, Stephen C. Riser. Observations of decadal time scale salinity changes in the subtropical thermocline of the North Pacific Ocean [J]. *Deep-Sea Research II*, 2010, 57(13–14):1161–1170.
- [2] Alvera-Azcarate, A., Barth, A., Weisberg, R.H., Castaneda, J.J., Vandenbulcke, L., Beckers, J.-M. Thermocline characterisation in the Cariaco basin: A modelling study of the thermocline annual variation and its relation with winds and chlorophyll-a concentration [J]. *Continental Shelf Research*, 2011, 31(1):73–84.
- [3] Xiao Zhang, Matthias Prange, Silke Steph, Martin Butzin, Uta Krebs, Daniel J. Lunt, Kerim H. Nisancioglu, Wonsun Park, Andreas Schmittner, Birgit Schneider, Michael Schulz. Changes in equatorial Pacific thermocline depth in response to Panamanian seaway closure: Insights from a multi-model study [J]. *Earth and Planetary Science Letters*, 2012, 317:76–84.
- [4] Paul Loubere, Mathieu Richaud, Susan Mireles. Variability in tropical thermocline nutrient chemistry on the glacial/interglacial timescale [J]. *Deep-Sea Research II*, 2007, 54(5–7): 747–761.
- [5] Zhongyu Cui, Xiaogang Li, Kui Xiao, Chaofang Dong. Atmospheric corrosion of field-exposed AZ31 magnesium in a tropical marine environment [J]. *Corrosion Science*, 2013, 76:243–256.
- [6] Corvo, F., Perez, T., Dzib, L.R., Martin, Y., Castaneda A., Gonzalez, E., Perez, J. Outdoor-indoor corrosion of metals in tropical coastal atmospheres [J]. *Corrosion Science*, 2008, 50(1):220–230.
- [7] Pech-Canul, M.A., Castro, P. Corrosion measurements of steel reinforcement in concrete exposed to a tropical marine atmosphere [J]. *Cement and Concrete Research*, 2002, 32(3):491–498.
- [8] Rosliza, R., Senin, H.B., Wan Nik, W.B. Electrochemical properties and corrosion inhibition of AA6061 in tropical seawater [J]. *Colloids and Surfaces A: Physicochem. Eng. Aspects*, 2008, 312(2–3):185–189.
- [9] Yusoff, N.H.N., Ghazali, M.J., Isa, M.C., Daud, A.R., Mughtar, A. Effects of powder size and metallic bonding layer on corrosion behaviour of plasma-sprayed Al<sub>2</sub>O<sub>3</sub>-13% TiO<sub>2</sub> coated mild steel in fresh tropical seawater [J]. *Ceramics International*, 2013, 39(3):2527–2533.
- [10] Charles, R. Southwell. The Corrosion rates of structural metals in sea water, fresh water and tropical atmospheres [J]. *Corrosion Science*, 1969, 9(3):179–183.
- [11] Zheng, Y.G., Yu, H., Jiang, S.L., Yao, Z.M. Effect of the sea mud on erosion–corrosion behaviors of carbon steel and low alloy steel in 2.4% NaCl solution [J]. *Wear*, 2008, 264(11–12):1051–1058.
- [12] Fengling Liu, Jie Zhang, Caixia Sun, Zhenhua Yu, Baorong Hou. The corrosion of two aluminium sacrificial anode alloys in SRB-containing sea mud [J]. *Corrosion Science*, 2014, 83:375–381.
- [13] Peter J. Leech, Jean Lynch-Stieglitz, Rong Zhang. Western Pacific thermocline structure and the Pacific marine Intertropical Convergence Zone during the Last Glacial Maximum [J]. *Earth and Planetary Science Letters*, 2013, 363:133–143.
- [14] Mahdi, E., Rauf, A., Eltai, E.O. Effect of temperature and erosion on pitting corrosion of X100 steel in aqueous silica slurries containing bicarbonate and chloride content [J]. *Corrosion Science*, 2014, 83:48–58.
- [15] Sina S. Jamali, Douglas J. Mills, John M. Sykes. Measuring electrochemical noise of a single working electrode for assessing corrosion resistance of polymer coated metals [J]. *Progress in Organic Coatings*, 2014, 77(3):733–741.

# Numerical study of typhoon waves with the typhoon hindcasted model

Jia Dong, Jian-Feng Zhai, Zhi-Xia Zhu & Pei-Hua Dong

*Jiangsu Provincial Communications Planning and Design Institute Co. Ltd., Nanjing, China*

*Jiangsu Provincial Technology Research Center for Water Transport Engineering, Nanjing, China*

**ABSTRACT:** In this paper, the typhoon hindcasted model and third-generation wave model SWAN are coupled to simulate the typhoon wave. First, the gradient wind field of “KeLuoSha” was simulated with the Fujita-Takahashi Typhoon hindcasted model. Then, ambient wind and gradient wind are used to computed the typhoon field. In addition, three stations are chosen to validate the wind velocity of the model. Finally, typhoon wave is simulated with the SWAN model, and the wave parameters of the model are validated well with buoyed parameters. The result shows that the typhoon hindcasted model coupled with the wave model can simulate the typhoon wave precisely.

**Keywords:** typhoon simulation; typhoon wave; wave simulation

## 1 INTRODUCTION

Typhoon plays an important role in ocean and coastal engineering. It causes huge losses in China every year. In order to study the typhoon, a lot of work has been done by researchers<sup>[1-6]</sup>. Currently, there are two ways to simulate the typhoon field. One is through the weather model such as the WRF and MM5 model, another way is by using the typhoon parameters model. In this paper, the Fujita-Takahashi typhoon parameter model and the wave model SWAN are coupled to simulate the typhoon field and the wave field. First, the NECP-reanalyzed wind field data are interpolated to meet the accuracy of time and space. Then, the Fujita-Takahashi parameter model is used to calculate the gradient wind field of the typhoon. Then, the typhoon field is composed and validated well with measured parameters. Finally, the third-generation wave model SWAN is used to simulate the wave field induced by the typhoon. The result shows that the typhoon parameters model coupled with the SWAN model can simulate the typhoon wave accurately.

## 2 MODEL THEORY AND PARAMETER SETTING

### 2.1 Typhoon parameters model of Fujita-Takahashi

The typhoon field can be decomposed into the gradient wind field and the ambient wind field. The Fujita-Takahashi Typhoon model are used to

simulate the gradient wind field, which is described below<sup>[5]</sup>.

As  $0 \leq r < 2R$ , the wind velocity can be computed as follows:

$$W_z = C_1 V_{dz} \exp\left(-\frac{\pi}{4} \cdot \frac{|r-R|}{R}\right) - C_2 \left\{ -\frac{f}{2} + \sqrt{\frac{f^2}{4} + \frac{2\Delta P}{\rho_a R^2} \left[1 + 2\left(\frac{r}{R}\right)^2\right]^{\frac{3}{2}}}\right\} \cdot [(x-x_0)\sin\theta + (y-y_0)\cos\theta] \quad (1)$$

$$W_y = C_1 V_{\theta j} \exp\left(-\frac{\pi}{4} \cdot \frac{|r-R|}{R}\right) - C_2 \left\{ -\frac{f}{2} + \sqrt{\frac{f^2}{4} + \frac{2\Delta P}{\rho_a R^2} \left[1 + 2\left(\frac{r}{R}\right)^2\right]^{\frac{3}{2}}}\right\} \cdot [(x-x_0)\cos\theta + (y-y_0)\sin\theta] \quad (2)$$

As  $2R \leq r < \infty$ , the typhoon velocity in the x and y direction can be described as follows:

$$W_z = C_1 V_{dz} \exp\left(-\frac{\pi}{4} \cdot \frac{|r-R|}{R}\right) - C_2 \left\{ -\frac{f}{2} + \sqrt{\frac{f^2}{4} + \frac{\Delta P}{\rho_a R r} \left[1 + \frac{r}{R}\right]^2}\right\} \cdot [(x-x_0)\sin\theta + (y-y_0)\cos\theta] \quad (3)$$

$$W_y = C_1 V_{dy} \exp\left(-\frac{\pi}{4} \cdot \frac{|r-R|}{R}\right) + C_2 \left\{ -\frac{f}{2} + \sqrt{\frac{f^2}{4} + \frac{\Delta P}{\rho_a R r} \left[1 + \frac{r}{R}\right]^{-2}} \right\} \cdot [(x-x_0)\cos\theta - (y-y_0)\sin\theta] \quad (4)$$

$$f = 2 * 7.292 * 10^{-5} * \sin\phi \quad (5)$$

where  $C_1$  and  $C_2$  are the empirical coefficient;  $r$  is the distance from the center of typhoon to the calculated point;  $f$  is the Coriolis coefficient; and  $W_x$ ,  $W_y$  are the wind velocity in the x and y direction, respectively.

## 2.2 Wave model of SWAN

The third-generation wave model SWAN is based on the balance of energy spectrum, in the coordinate of Cartesian, which can be described as follows<sup>[6]</sup>:

$$\frac{\partial}{\partial t} N + \frac{\partial}{\partial x} c_x N + \frac{\partial}{\partial y} c_y N + \frac{\partial}{\partial \sigma} c_\sigma N + \frac{\partial}{\partial \theta} c_\theta N = \frac{S_{\cos}}{\sigma} \quad (6)$$

where  $N$  is the action density;  $c_x$ ,  $c_y$  are the speed of the wave group in the x and y direction, respectively; and  $c_\sigma$ ,  $c_\theta$  are the frequency and direction of the speed, respectively.

## 2.3 Parameter setting

In the typhoon wind field gradient field of the model, the typhoon center movement speed and the typhoon center typhoon related data, such as maximum wind speed and air pressure can be obtained from the typhoon yearbook. The typhoon wind field space step length is  $0.05^\circ * 0.05^\circ$ , time step of 1 hour, the time span for September 29, 2007 to October 16, 2007. The north and south direction space spans  $14.5^\circ \text{N} - 41.5^\circ \text{N}$ , east-west  $118.5^\circ \text{E} - 138.5^\circ \text{E}$ . The typhoon field environment wind field is mainly adopted to analyze the NECP wind field. Its space and time step is longer, in order to meet the accuracy requirement of the typhoon wind field, on the linear interpolation. For obtaining the typhoon wind field, the proportion of weight, and with the longer the distance the distances from the center of the typhoon, the gradient wind place much proportion of the smaller.

In the wind and waves in the process of simulation, the calculation of the wave model range is shown in Figure 1: the northwest boundary of Yantai to Dalian, the northeast border for South Korea to Japan, and south near the boundary for the Philippines. In order to better fit the complex

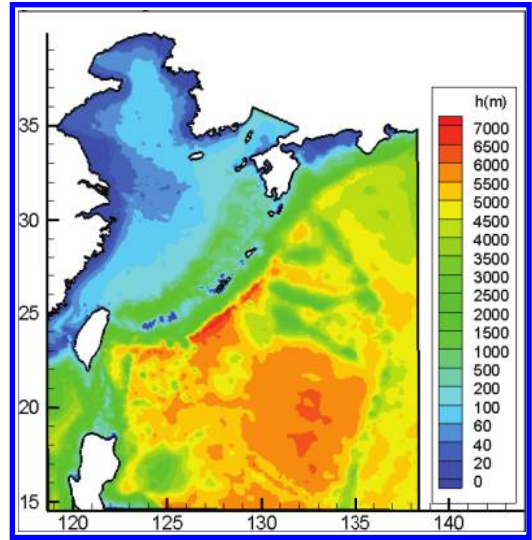


Figure 1. The depth of computational domain in the wave model.

coastline, the model adopted in an unstructured grid. Calculation, initial conditions with the method of the cold start, driving stress for the typhoon wind field, considering the nonlinear interaction between waves in the process of simulation, white hat losses, the bottom friction and physical phenomena such as wave breaking wave spectrum using Jonswap spectrum, strengthen the spectral peak factor of 3.3, spectrum for 0.05 1 Hz, which is divided into 30, the direction will be divided into the 36, computing time step for 5 min, output time step for 30 min.

## 3 MODEL VERIFICATION AND ANALYSIS

### 3.1 Verification of the typhoon wind field

Typhoon wind field can be obtained by the gradient wind farm and environmental wind farm. Currently, the parameter model of typhoon gradient wind farm is developed. This paper selects the internationally popular Fujita-Takahashi formula to calculate the typhoon gradient wind farm. Since the model belongs to the theoretical pressure model, the calculated wind field is circular. The characteristics of wind speed distribution are as follows: the speed of the typhoon wind field center is 0m/s, with the distance from the center of typhoon being much far, the wind speed shows an increased trend and then a decreased one. The wind speed reaches the maximum in the vicinity of typhoon maximum radius. Figure 2 shows the

distribution of the typhoon wind speed field at some point. The red circles represent the location of typhoon. We can see that relative to the whole computational domain, the influence of typhoon is relatively small, in five times the radius maximum wind speed, the typhoon influence is relatively large, while beyond five times, the radius of the maximum wind speed influencing the typhoon is very small.

Whether the typhoon wind speed simulation is accurate or not has an important influence on the accuracy of the simulation of the wave. In order to verify the accuracy of typhoon wind speed, this paper selects three stations near the typhoon path to validate the wind speed. These three stations are Hualian buoy (121.63°E, 24.03°N), Kueishan Island buoy (121.93°E, 25.85°N) and Suao buoy (121.88°E, 24.63°N). The simulation of the wind speed value is compared with the observation value, and the results are shown in Figure 2–Figure 5.

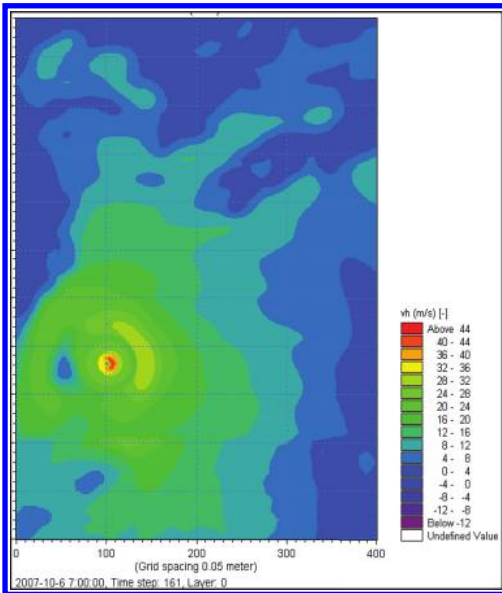


Figure 2. The distribution of wind velocity of the typhoon.

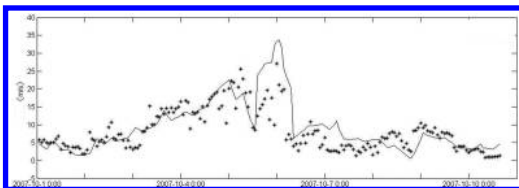


Figure 3. The comparison of wind velocity of the model measured in HuaLian.

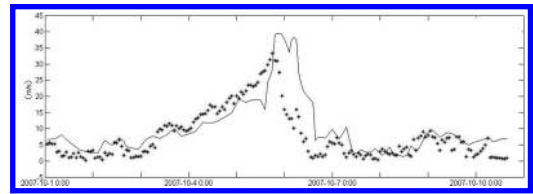


Figure 4. The comparison of wind velocity of the model measured in Guishan.

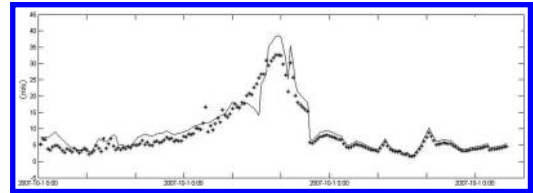


Figure 5. The comparison of wind velocity of the model measured in Suao.

We can see that the simulation value and the observation value of wind speed fit very well for these three stations. Not only the change in the trend is consistent, but also the size is similar. It shows that the typhoon parameter model can simulate the typhoon process very well, and the precision is higher, so it provides a reliable basis for the later period to simulate wave field accurately.

### 3.2 Verification and analysis of typhoon waves

Typhoon waves can cause great harm to engineering every year. Many engineering problems are directly or indirectly related to typhoon waves, such as the design wave elements problems in engineering, sudden siltion problem caused by typhoon, security issues caused by the effect of waves on building structures and the local scour problem of the bottom of buildings under the waves, so it has an important engineering significance for the accurate simulation of typhoon waves. Whether the typhoon wave simulation is accurate or not mainly depends on the accuracy of bathymetric and precision of the driving wind field. After the previous wind speed verification, we can see that the wind speed has reached a high accuracy. Typhoon is generally formed in deep sea, so water depth has a relatively small effect on it. In order to verify the reliability of the simulation results of the model, this paper compares the simulation results with the observed value of three wave floating stations, and the results of the comparison are shown in Figure 6–Figure 8. Figure 6 shows the results of the comparison of the simulated and observed values of Hualian floating station height and period.

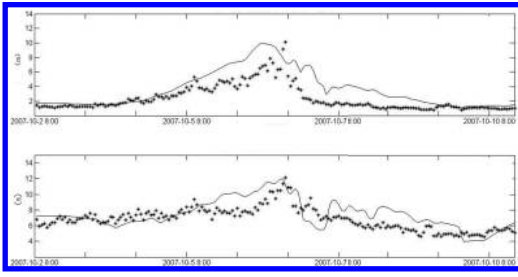


Figure 6. The comparison of wave parameters of the model measured in Hualian.

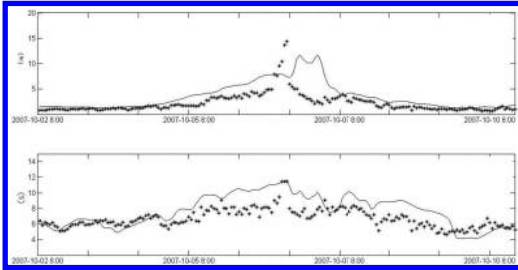


Figure 7. The comparison of wave parameters of the model measured in Guishan.

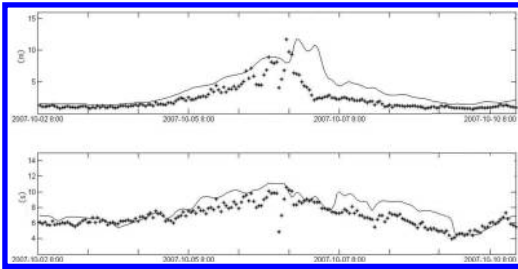


Figure 8. The comparison of wave parameters of the model measured in Suao.

During the typhoon process, the maximum wave height for Hualian station reached 11m, and the maximum average period reached 13s. The wave heights and periods have a similar change in trend, both of them first become larger and then gradually decrease. Figure 7 shows the results of the comparison of the simulated and observed values of height and period for Kameyama station, with the maximum wave height reaching 15m and the maximum average period reaching 12s. Figure 8 shows the results of the comparison of the simulated and observed values of height and period for SuAo station. As can be seen from the graph, only the wave heights and periods have a similar

change in trend but the size is similar. When the typhoon passed, the maximum wave height of this station reached 12m, the maximum average period reached 12s. On the whole, the typhoon wave model has a high precision simulation result. The simulation accuracy of the Kameyama station is lower than that of the Hualian station and SuAo station. Generally, the simulation accuracy of the wave period is higher than the wave height at these three stations. Although the wave simulation has

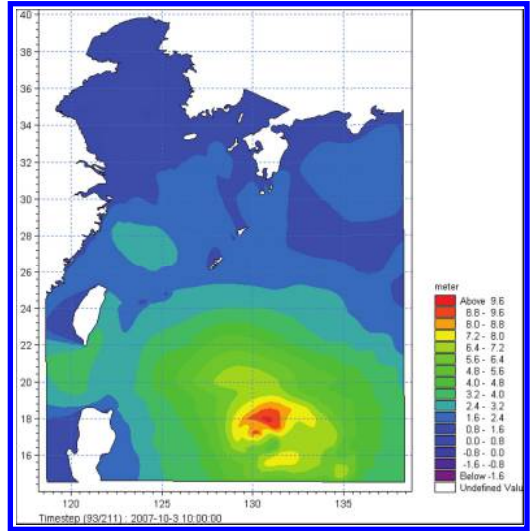


Figure 9. The distribution of wave height as typhoon develops.

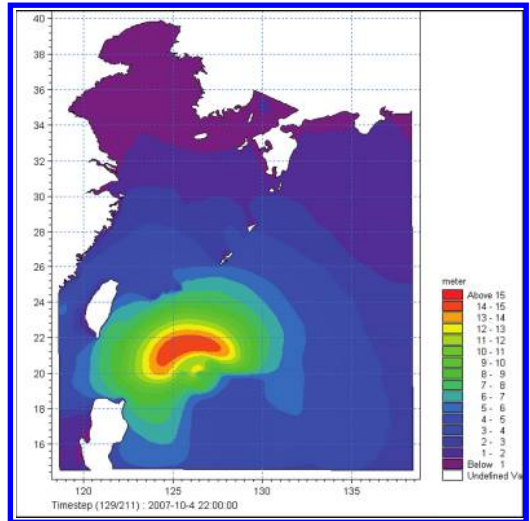


Figure 10. The distribution of wave height as typhoon grows up.

a high precision, there are also some error. This is mainly due to the accuracy of the wind field data and depth data.

In order to study the distribution of the wave field at different times, Figure 9 and Figure 10 show the distribution of typhoon waves at two different times. Figure 9 shows the distribution of the wave field in the typhoon development process, with the maximum wave height reaching about 9m. Figure 10 shows the distribution of the wave field after the typhoon has grown, with the maximum wave height reaching about 15m. From the two graphs, we can see that the overall trend of the distribution of wave height is that the wind speed is relatively large when close to the center of typhoon, and the wave height decreases when the distance from the center of the typhoon is much far.

#### 4 CONCLUSION

Through the above research, we can find that using the Fujita-Takahashi model of typhoon parameters coupled with the third-generation wave model SWAN is a good solution to solve the simulation problem. The overall trend of the distribution of typhoon waves is that the wind speed is relatively large when close to the center of typhoon, and the wave height decreases when the distance from the center of the typhoon is much far. The coupled model can simulate the typhoon waves relatively

accurately, so it has a practical significance in engineering.

#### ACKNOWLEDGMENTS

This work was financially supported by the Transportation Science and Technology Projects in Jiangsu Province (2011Y01).

#### REFERENCES

- [1] Yang Yang, Zhixia Zhu. *Harbor, Waterway and Coastal Engineering*. Shanghai: Shanghai Jiao Tong University, 2009.
- [2] Lihong Pan, Jianrong Zhu. *Assessment of Defense Capability of Sea Dikes in Shanghai for Typhoon*. Shanghai: East China Normal University, 2011.
- [3] Weiwei Song, Guoping Chen, Shichang Yan, Xiaoting chen. Wave parameters analysis of different return period in the open sea with a hindcast model of typhoon waves, *Port & Waterway Engineering*, 2013, 474(1):51–54.
- [4] Xiaocui Shi, Fei Fan, Bingcheng Liang. Study of wave climate of Shandong peninsula, *Journal of Waterway and Harbor*, 2013, 34(5):376–379.
- [5] Lisong Zheng, Xiping Yu. *Development and Application of A Numerical Model Coupling Storm Surge, Tide and Wind Wave*. Beijing: Tsinghua University, 2010.
- [6] Ris R.C., Booij N., Holthuijsen L.H. A third-generation wave model for coastal regions. *Journal of Geophysical Research*. 1999, 104(4):7667–7684.

# Model study on the sediment dynamics in the Bohai Sea

H. Liu & H.X. Kang

College of Marine Sciences, Shanghai Ocean University, Shanghai, China

B.S. Yin & D.Z. Yang

Institute of Oceanology, Chinese Academy of Sciences, Qingdao, China

**ABSTRACT:** A surface wave and 3-dimensional current interaction model is coupled to a Suspended Particulate Matter (SPM) transport model to reproduce the sediment dynamics in the Bohai Sea (BS). Both simulations and observations show that the highest SPM concentration appears in the mouth of the Yellow River. In addition, both the Laizhou and Bohai bays are characterized by the high level of riverine sediments due to the evolution of the river plume under the predominant southeasterly wind in the flood season, and the high level of SPM in the Laidong Bay can be ascribed to the joint effects of the riverine inputs from the Liaohe River and the strong tidal currents that erode the bottom sediments into the water column. The least SPM concentration appears in the central basin. Since the central basin is characterized by strong wave-induced mixing and weak tidal mixing, it can be suggested that wind waves may play a minor role in the local sediment dynamics in summer.

**Keywords:** numerical model; water mixing; SPM transport; Bohai Sea

## 1 INTRODUCTION

The transport of Suspended Particulate Matter (SPM) in coastal seas plays an important role in many oceanic processes, not only in marine geology but also in marine ecology. Therefore, this topic attracts more attention of oceanographers with different disciplines. For example, the SPM transport is tightly correlated with light intensity in the water column, and the latter is one of the dominating parameters in ecological modeling. Thus, it can be suggested that to develop a robust SPM transport model that reflects the local sediment dynamics is imperative to reproduce a better marine ecosystem.

The SPM transport in the Bohai Sea (BS) is mainly governed by the tidal currents and wind waves. In previous studies, the wave or current simulations were carried out independently, that is, wave features were reproduced using the wave models, and the currents were simulated using the ocean circulation model (Yang et al., 2005; Liu et al., 2005; Liu, 2011). More often than not, the wave-current interaction is seldom put together in a single numerical model. In this paper, a surface wave and three-dimensional current interaction model was developed to simulate the key hydrodynamics in the BS, and further coupled to a sediment transport model to examine how these physical processes govern the sediment dynamics in the BS.

## 2 MODEL DESCRIPTION

### 2.1 Equation of the sediment dynamics

The feature and application of the surface wave and three-dimensional current interaction model has been introduced elsewhere (Liu et al., 2013). Using the same model design as the hydrodynamic model, the three-dimensional equation of the sediment dynamics can be written as follows:

$$\begin{aligned} \frac{\partial C}{\partial t} + \frac{\partial UC}{\partial x} + \frac{\partial VC}{\partial y} + \frac{1}{D} \frac{\partial (w - w_s)C}{\partial \sigma} = \frac{\partial}{\partial x} \left( A_H \frac{\partial C}{\partial x} \right) \\ + \frac{\partial}{\partial y} \left( A_H \frac{\partial C}{\partial y} \right) + \frac{1}{D} \frac{\partial}{\partial \sigma} \left( \frac{K_H}{D} \frac{\partial C}{\partial \sigma} \right) + S_C \end{aligned} \quad (1)$$

where  $C$  is the SPM concentration;  $A_H$  and  $K_H$  are the horizontal and vertical diffusivities, which are calculated from the Smagorinski scheme and the MY turbulence closure model, respectively;  $S_C$  is the riverine load of SPM ( $\text{gs}^{-1}$ ).

In this study, the sediment flux via atmospheric deposition is assumed to be null. The sediment erosion and deposition are highlighted since the vertical mass exchange between the sea bed and the bottom layer of seawater is important. As a consequence, the vertical boundary conditions on the sea surface and bottom can be expressed as follows:

$$\begin{cases} \frac{K_H}{D} \frac{\partial C}{\partial \sigma} = 0 & \sigma \rightarrow 0 \\ \frac{K_H}{D} \frac{\partial C}{\partial \sigma} = F_{ero} - F_{dep} & \sigma \rightarrow -1 \end{cases} \quad (2)$$

where  $F_{ero}$  and  $F_{dep}$  represent the flux of sediment resuspension and deposition, respectively. Following Einstein and Krone (Arndt et al., 2007), these terms can be, respectively, expressed as follows:

$$\begin{cases} F_{ero} = p_{ero} \cdot e_c \cdot C_{kb} \\ F_{dep} = p_{dep} \cdot w_s \cdot C_{kbm1} \end{cases} \quad (3)$$

where  $C_{kbm1}$  is the SPM concentration in the bottom layer of seawater; and  $C_{kb} = \rho_b(1 - \phi)$  is the concentration of total solids in the sediment, in which  $\rho_b = 2650 \text{ kgm}^{-3}$  is the sediment density and the sediment porosity is assumed to be  $\phi = 0.7$ ;  $e_c = 5.5 \times 10^{-4}$  is the erosion constant; and  $w_s$  is the SPM settling velocity. In addition, according to the Stokes' law that assumes a spherical particle shape, the following formula can be used:

$$w_s = \frac{1}{18} \frac{(\rho_s - \rho)gd^2}{\rho\nu} \quad (4)$$

where  $\rho_s$  and  $\rho$  are the densities of SPM and seawaters, and their values are assumed to be 1760 and  $1025 \text{ kg m}^{-3}$ , respectively; the fluid kinetic viscosity is assumed to be  $\nu = 5.5 \times 10^{-6} \text{ m}^2 \text{ s}^{-1}$ ; and  $d$  is the averaged grain diameter.

From Figure 1, we can see that the BS sediment consists of a heterogeneous mix of the river-derived mud and the fine-to-coarse marine sand. Therefore, the simulation of the SPM transport processes must account for these heterogeneities. In the model design, Arndt's method is adopted. It means that the SPM size class  $C_i$  ( $i$  indicates clay mud, silt mud, coarse silt, fine sand, respectively) is characterized by a specific flux change due to the erosion and deposition, so a unique particle diameter

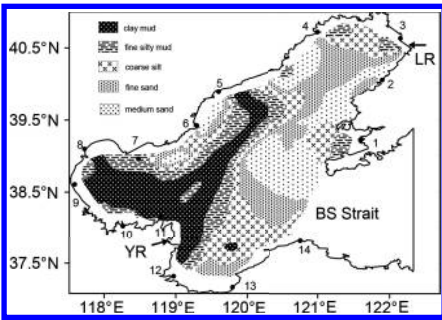


Figure 1. Sediment type distribution in the BS and two major rivers: Yellow River and Liaohe River.

and a continuous Gaussian grain size distribution are used. This distribution is totally characterized by the averaged grain diameter  $d$  and its standard deviation  $\delta d^2$ , which are given as follows:

$$\begin{cases} d = \sum_i d_i \frac{C_i}{C} \\ \delta d^2 = d^2 - \sum_i d_i^2 \frac{C_i}{C} \end{cases} \quad (5)$$

where  $d_i$  indicates the representative particle diameter in the individual size classes  $C_i$ .

Due to the erosion and deposition processes,  $d$  experiences the temporal evolution as a response to the variation in the composition of SPM. For instance, the resuspension of the coarse sediments leads to an increase in  $d$ , while the higher settling velocity of the coarser grains and their preferential deposition results in a decrease of the averaged grain size.

Equation (3) shows that the mass exchange between seawater and sea floor mainly depends on the solid concentration in the bottom layer of the water column as well as that in the bottom sediments. Therefore, by adapting the depth-mean formula of Wirtz and Eckhardt (1996) to the present three-dimensional sediment dynamic model, the time-dependent variance in the average grain diameter of suspended sediment  $d$  and bottom sediment  $d_b$  due to erosion and deposition processes can be approximated as follows:

$$\begin{cases} \frac{d}{dt}(d)|_{ero} = e_c \cdot p_{ero} \cdot \frac{C_{kb}}{C_{kbm1}}(d_b - d) \\ \frac{d}{dt}(d)|_{dep} = \delta d^2 \cdot p_{dep} \cdot \frac{(\rho_s - \rho)g}{9\mu} \cdot d \\ \frac{d}{dt}(d_b)|_{dep} = w_s \cdot p_{dep} \cdot \frac{C_{kbm1}}{C_{kb}}(d - d_b) \\ \frac{d}{dt}(d_b)|_{ero} = 0 \end{cases} \quad (6)$$

where  $p_{ero}$  and  $p_{dep}$  represent the possibilities for sediment erosion and deposition, respectively, and can be formulated as follows:

$$\begin{cases} p_{ero} = \begin{cases} \frac{\tau_b}{\tau_{crd}} - 1 & \tau_{crd} \leq \tau_b \\ 0 & \tau_{crd} > \tau_b \end{cases} \\ p_{dep} = \begin{cases} 1 - \frac{\tau_b}{\tau_{crd}} & \tau_{crd} \geq \tau_b \\ 0 & \tau_{crd} < \tau_b \end{cases} \end{cases} \quad (7)$$

where the bottom shear stress  $\tau_b = \rho u_b |u_b|$ , in which  $u_b$  is the bottom friction velocity; and  $\tau_{crd}$  is the critical shear stress for erosion and deposition, which can be given as follows:



$$\tau_{crd} = (\rho_b - \rho)g \cdot d_b \cdot \theta_{crd} \quad (8)$$

where  $\theta_{crd}$  is the critical mobility parameter, and is given by the following empirical formulations:

$$\begin{cases} \theta_{crd} = 0.24d_*^{-1} & d_* \leq 4 \\ \theta_{crd} = 0.14d_*^{-0.64} & 4 < d_* \leq 10 \\ \theta_{crd} = 0.04d_*^{-0.10} & 10 < d_* \leq 20 \\ \theta_{crd} = 0.013d_*^{-0.29} & 20 < d_* \leq 150 \\ \theta_{crd} = 0.055 & d_* > 150 \end{cases} \quad (9)$$

where  $d_*$  is a non-dimensional particle parameter, and can be written as follows:

$$d_* = \left[ \frac{(\rho_b - \rho)g}{\rho v^2} \right]^{1/3} d_b \quad (10)$$

## 2.2 External forcings and data sources

The model is driven by true forcings, considering tides, wind currents and waves, as well as the river discharges. Eight major tides, namely  $M_2$ ,  $S_2$ ,  $N_2$ ,  $K_2$ ,  $K_1$ ,  $O_1$ ,  $P_1$  and  $Q_1$ , are superimposed on the southeastern open lateral boundary to simulate tidal wave propagations. The wind field is derived from 14 coastal meteorological stations around the BS by means of interpolation and extrapolation. The monthly mean river runoff and riverine sediment load data have been provided by Zhang et al. (2004). Because the input of freshwater and river-borne sediments mainly concentrates in the flood season, we would like to focus our interests on this situation.

## 3 SIMULATIONS

### 3.1 Key physical process

The key hydrodynamics is investigated using a surface wave and three-dimensional current interaction model. It is found that the semi-diurnal tides are dominant in the BS, and the wind-induced surface currents are conducive to the offshore transport of the riverine materials. The significant wind wave height is also reproduced, which shows the large value in the central basin and the wave heights reduce towards the shallow bays. Such knowledge is crucial for better understanding the sediment dynamics in the BS. Detailed descriptions of simulated tides, wind currents and waves have been provided by Liu et al. (2013).

### 3.2 SPM transport characters

Figure 2 shows the simulated and observed depth-mean sediment distribution in the BS. Observations show that the highest level of SPM appears in the mouth of the Yellow River, and the Bohai bay is

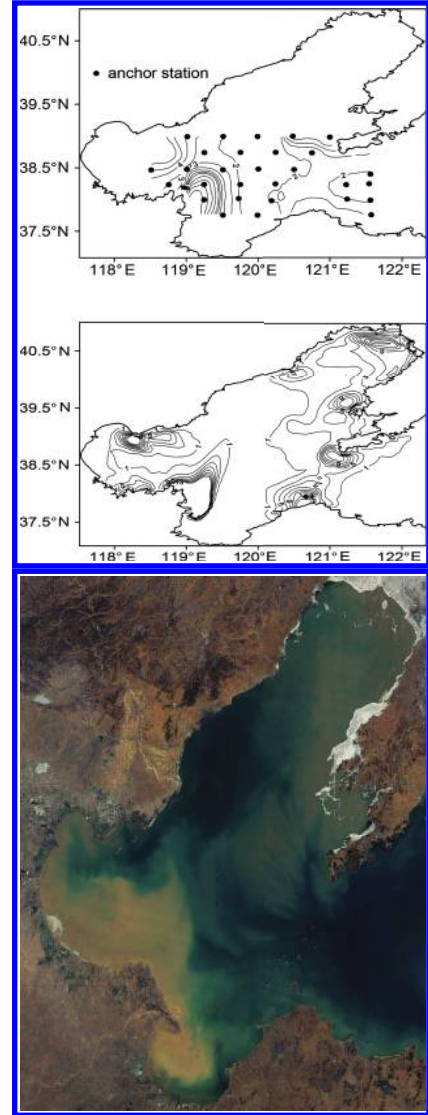


Figure 2. (a) Observed, (b) simulated SPM concentrations ( $\text{gm}^{-3}$ ), and (c) SPM distribution from the Terra-MODIS image on June 4, 2004.

also characterized by the high concentration of SPM. Comparatively, the SPM concentration in the central basin is small. Compared with the observation, the simulation also reflects the same situation. According to the model results, the highest level of SPM in the YR estuary is induced by the riverine sediments from the YR. Driven by the southeasterly winds, the river plume of the YR extends northeastwards and enters the central basin. Since the large amounts of riverine sediments have settled down around the mouth of the YR due to gravity, the concentrations of riverine SPM in the mouth of the YR

plume decrease significantly. It is one of the reasons why the central basin seems to be clearer than three bays. The alongshore currents may be responsible to carry the riverine sediments into the Bohai Bay.

Although the *in situ* investigations for the Liaodong Bay are not available for us to check the model results, a satellite image taken on June 4, 2004 can be used as an alternative. Driven by the south-easterly wind, the river plume of the Liaohe River (LR) is confined to the end of the Liaodong Bay, so the riverine sediments from the LR concentrate there and form a patch of SPM. Besides the river-induced SPM patch, the regions around the headland of Liaodong Peninsula and Changxing Isle are also characterized by the high level of SPM. These regions are relatively far from the river mouth, hence there must be different mechanisms responsible for the high sediment concentrations. In order to investigate what is the governing mechanism, two numerical experiments are carried out: in experiment one, we run the coupled model with all specified external forcings, except the mean wind field; in experiment two, we rebuild the model design but omit the tidal impact purposely. The model results show that the SPM patches far from the estuaries are more probably induced by strong tidal currents. As indicated by Lin et al. (2011), the wave-induced mixing mainly functions in the upper layer of the water column; if the wind field is not strong enough or the water is relatively deep, the wind wave-induced mixing is hard to reach the sea floor to disturb the sediments. The long-term averaged wind field in summer is generally no more than  $5 \text{ ms}^{-1}$ , so it can be suggested that wind waves may play a subordinate role in sediment dynamics in the BS. Both observations and simulations show that the central basin is characterized by strong wind-wave forces and the least SPM concentration, which also suggests the minor role that wind waves play in the local sediment dynamics. Comparing the simulations with the satellite image, it can be found that the fundamental distribution features of SPM are reproduced by the coupled model, though some discrepancies also exist in the meantime. For instance, the observation shows an evident patch of SPM with high concentration in the southern part of Laizhou, but it is not captured by our model. Since only the mean wind field is used in this study, implying that some extreme climate or intermittent northerly and westerly winds are smoothed out, the simulated clear waters in the southern part of the Laizhou Bay can be imagined. Of course, there are still other causes responsible for the differences between simulations and observations, among which the relatively coarse description of the erosion and deposition processes may be a key one, due to the fact that the involved parameters are either taken from literature or from very rough estimations. Overall, the model results

show a general structure that is similar to that visualized in the satellite image.

## 4 CONCLUSIONS

A coupled physical and sediment dynamic model is used to reproduce the SPM transport in the BS. It is found that the tidal current plays the major role, especially in eroding sediments, whereas the effect of the wind wave is relatively small due to the weak mean wind field in summer months (flood season). It should be pointed out that the SPM transport in a shelf sea is determined by a large number of complicated processes, and at present, the dynamics concerning the SPM transport are far from fully understood. In this sense, there are many efforts that should be done to improve the present research. In the near future, the key processes such as beach erosion, bio-turbulence or bio-stabilization function in the local sediment dynamics need to be investigated, and the quantification of these processes should be highlighted.

## ACKNOWLEDGMENTS

This work was financially supported by the Special Project of Marine Strategy Guide, Chinese Academy of Sciences (XDA11020305.2).

## REFERENCES

- Arndt, S., Vanderborcht, J.P., & Regnier, P. 2007. Diatom growth response to physical forcing in a macrotidal estuary: Coupling hydrodynamics, sediment transport, and biogeochemistry, *Journal of Geophysical Research* 112: doi:10.1029/2006JC003581.
- Lin, X.P., Xie, S.P., Chen, X., et al. 2006. A well-mixed warm water column in the central Bohai Sea in summer: Effects of tidal and surface wave mixing, *Journal of Geophysical Research* 111(C11017): doi:10.1029/2006JC003504.
- Liu, H. 2011. Fate of three major rivers in the Bohai Sea: a model study, *Continental Shelf Research* 31: 1490–1499.
- Liu, H., Luo, D., & Yin, B.S. 2013. Model study on the key hydrodynamics in the Bohai Sea. *Applied Mechanics and Materials* 303–306: 2727–2730.
- Liu, H., Yin, B.S., Xu, Y.Q., et al. 2005. Numerical simulation of tides and tidal currents in Liaodong Bay with POM, *Progress in Natural Science* 15(1): 47–55.
- Wirtz, K.M., Eckhardt, B. 1996. Effective variables in ecosystem models with an application to phytoplankton succession, *Ecological Modelling* 92: 33–53.
- Yang, D.Z., Yin, B.S., Xu, Y.Q., et al. 2005. Application of the SWAN wave model to Bohai Sea: Improvement of Phillips linear growth term, *Advances in Water Science* 16(5): 710–714. (in Chinese)
- Zhang, J., Yu, Z.G., Raabe, T. et al. 2004. Dynamics of inorganic nutrient species in the Bohai seawaters, *Journal of Marine System* 44: 189–212.

# Three-dimensional numerical simulation of the tidal flat and channel during flood tide

Zengxiang Jiao, Xinzhou Zhang, Xiping Dou, Yun Pan & Lei Ding

Nanjing Hydraulic Research Institute Key Laboratory of Port, Waterway and Sedimentation Engineering of the Ministry of Transport, Nanjing, China

**ABSTRACT:** In this paper, the flow pattern between the channel and tidal flat with free surface flow was simulated using a numerical model analyzed by Fluent. The cross-section is divided into the main channel, the tidal-flat adjacent channel, and the tidal flat and bank. It obtained the distribution of transverse velocity during the flood tide. The water surface profile was obtained by using the Volume Function Method (VOF) method. During the flood, the velocity of the main channel landward decreased and transverse velocity increased. The velocity of the main channel seaward increased during the ebb by the influence of runoff and tidal. The transverse velocity decreased from the area of the near wall to the zone of tidal-flat adjacent channel.

**Keywords:** numerical simulation; cross section; volume function method

## 1 INTRODUCTION

More recent work has addressed the hydrodynamic between the tidal flat and channel in an estuary<sup>[1]</sup>. During the flood, water diverges from the deep channel to the tidal flat and ebbs converge to from the tidal-flat to the channel<sup>[2]</sup>. Chanyan Li<sup>[3]</sup> identified that the lateral velocity was influenced by the following parameters: the ratio of depth about the tidal and channel; the ratio of tidal level and the average of depth; the ratio of the length wave and estuary. The VOF method has an advantage to treat the free surface. Wang Xuejun<sup>[4]</sup> analyzed the problem of wave flume by using this method. Li Zhiqin<sup>[5]</sup> obtained the distribution of flow velocity around the groyne field with this method.

## 2 NUMERICAL MODEL AND METHODS

### 2.1 Numerical model

This experiment was conducted in a flume with dimensions of 16 m wide, 10 m deep and about 20 m long. While the channel was 6 m wide and 10 m deep, the tidal flat was 5 m wide, 2 m deep at one side. In order to simulate the free surface level, there must be 3 m depth air on the free surface.

### 2.2 VOF model

To represent the sharp interface between the air and water, the VOF method was used. In this

approach, the interface is tracked by introducing the volume fraction for the  $i$  phase.

Water phase:

$$\frac{\partial \alpha_w}{\partial t} + \nabla \cdot (\mathbf{v} \cdot \alpha_w) = 0 \quad (1)$$

where  $\alpha_w$  is the volume fraction of water. Only such transport equation needs to be solved since the volume fraction of the other phase can be inferred from the constraint  $\alpha_a = 1 - \alpha_w$ , where  $\alpha_a$  is the volume fraction of air. The FVM is used to solve the above equation and relies on the flow domain being divided into a grid consisting of a large number of cells. In each cell, if it contains only water, then  $\alpha_w = 1$ , if none,  $\alpha_w = 0$  for each cell that spans the interface between the air and water, with  $0 < \alpha_w < 1$ . Thus, it can be assumed that the surface is on the volume fraction of 0.5.

### 2.3 Equations and calculation methods

Fluent computation fluid dynamic code was used for 3D numerical modeling. Numerical modeling involves the solution of the Navier-Stokes equations, which are based on the assumption of conservation of mass and momentum within a moving fluid. The conservation of mass is described by the differential equation:

$$\frac{\partial}{\partial t}(\rho) + \nabla \cdot (\rho \vec{v}) = 0 \quad (2)$$

where  $\bar{v}$  is the flow rate and  $\rho$  is the fluid density.

The momentum equation can be described as follows:

$$\frac{\partial}{\partial t}(\rho\bar{v}) + \nabla \cdot (\rho\bar{v}\bar{v}) = -\nabla p - \nabla \cdot [\mu(\nabla\bar{v} + \nabla\bar{v}^T)] + \rho\bar{g} + \bar{F} \quad (3)$$

here,  $P$  is the pressure;  $\bar{v}$  is the velocity;  $g$  is the gravity;  $\mu = \mu_0 + \mu_t$ , where  $\mu_0$  is the viscosity of the fluid and  $\mu_t$  is the turbulent viscosity; and  $\bar{F}$  is the body force.

Turbulence model can be obtained using the standard model. The  $k - \varepsilon$  model, which was proposed by Launer in 1972, is used widely as follows:

$$\mu_t = \rho C_\mu \frac{k^2}{\varepsilon} \quad (4)$$

$$\begin{aligned} & \frac{\partial(k\rho)}{\partial t} + \frac{\partial(\bar{u}_i k \rho)}{\partial x_i} \\ &= \frac{\partial}{\partial x_i} \left( \frac{\mu_t}{\sigma_k} \frac{\partial k}{\partial x_i} \right) + \mu_t \left( \frac{\partial \bar{u}_i}{\partial x_j} + \frac{\partial \bar{u}_j}{\partial x_i} \right) \frac{\partial \bar{u}_i}{\partial x_j} - \rho \varepsilon \end{aligned} \quad (5)$$

$$\begin{aligned} & \frac{\partial(\varepsilon\rho)}{\partial t} + \frac{\partial(\bar{u}_i \varepsilon \rho)}{\partial x_i} \\ &= \frac{\partial}{\partial x_i} \left( \frac{\mu_t}{\sigma_\varepsilon} \frac{\partial \varepsilon}{\partial x_i} \right) + C_{\varepsilon 1} \frac{\varepsilon}{k} \mu_t \left( \frac{\partial \bar{u}_i}{\partial x_j} + \frac{\partial \bar{u}_j}{\partial x_i} \right) \frac{\partial \bar{u}_i}{\partial x_j} - C_{\varepsilon 2} \rho \frac{\varepsilon^2}{k} \end{aligned} \quad (6)$$

where  $k$  is the turbulent kinetic energy;  $\varepsilon$  is the turbulent dissipation rate;  $C_\mu$ ,  $\sigma_k$ ,  $\sigma_\varepsilon$ ,  $C_{\varepsilon 1}$ ,  $C_{\varepsilon 2}$  are constant in this study, taking the value of 0.09, 1.00, 1.30, 1.45, and 1.92.

Boundary conditions are shown in Figure 1. The river discharge is 28 L/s upstream, and at 20 m, the wave boundary, where wavelength is 2 m, the

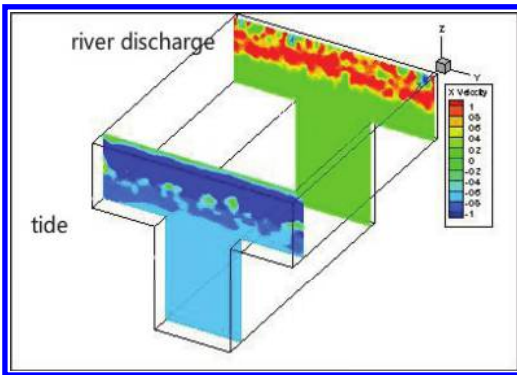


Figure 1. Initial velocity of flume.

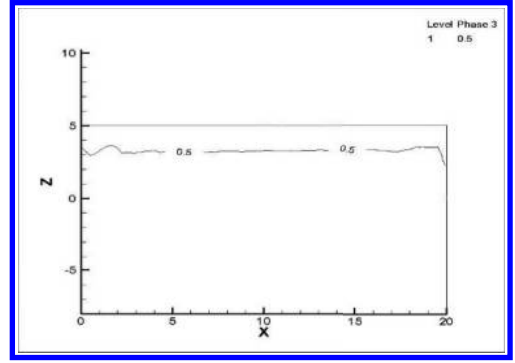


Figure 2. Initial surface level.

amplitude was 0.4 m high. To estimate the effect of the wall on the flow, the empirical wall function, known as the standard wall function, was used.

### 3 CALCULATION RESULTS

In  $X = 10$  section, we choose four lines, namely 1# ( $y = 0$ ), 2# ( $y = 3$ ), 3# ( $y = 5$ ), and 4# ( $y = 7.5$ ), to find the velocity distribution from the bottom to the surface.

Transverse circulation with the interaction of river discharge and tide will occur during the flood. Velocity along the axial direction in the channel reaches to 0.56 m/s at the depth of  $-4$  m, and the surface flow to the seawards, and the bottom flow to the landwards. The velocity along the axial direction on the tidal-flat adjacent channel varied from 0.2 to 0.2 m/s, and on the tidal and bank water flow to the landwards, and the channel velocity is greater than the tidal flat, as shown in Figure 3.

As shown in Figure 4, the channel transverse velocity is near 0 m/s during the flood. It reached 0.5 m/s on the surface at the tidal-flat adjacent channel as with the tidal flat. And it decreased from the tidal flat to the bank along the cross-section. Water flows from the channel to the tidal flat.

As shown in Figure 5, the surface water in the channel flows to the seawards, and the bottom flows to the landwards. The maximum velocity is at 10 m along the channel. The channel velocity increases compared with the tidal flat velocity during the flood, and the gradient on the tidal-flat adjacent channel is greatest. This means that momentum exchanges from the channel to the tidal flat.

Velocity along the axial direction in the channel reaches to 0.65 m/s at the depth of  $-0$  m, and the surface flows towards the landwards. The velocity along the axial direction on the tidal-flat adjacent channel decreases, and on the tidal and bank water flows to the seawards, the channel velocity

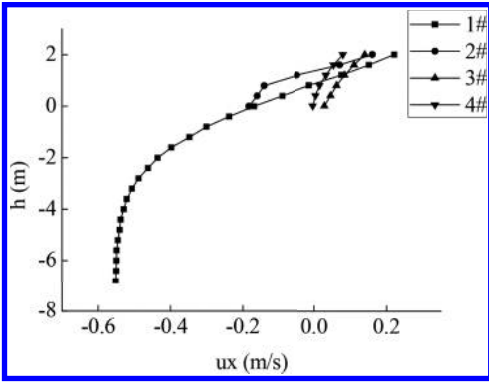


Figure 3. Velocity along the axial direction.

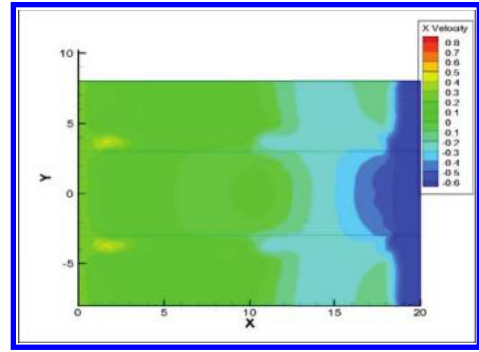


Figure 6. Distribution of velocity on the horizontal coordinate.

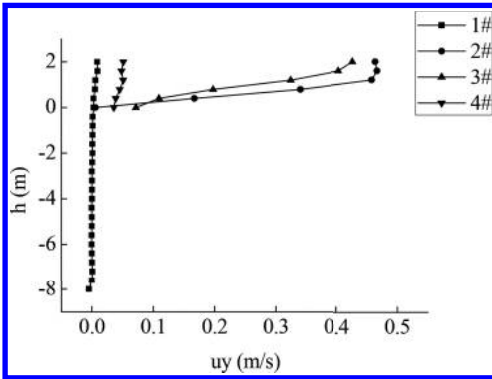


Figure 4. Transverse velocity.

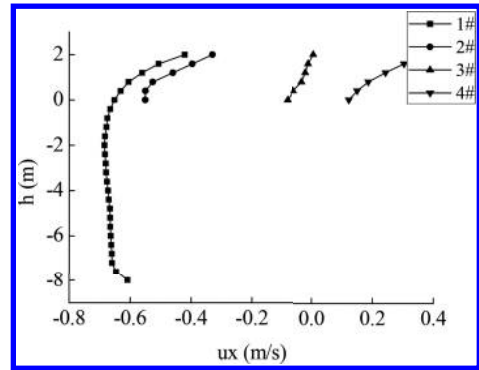


Figure 7. Velocity along the axial direction.

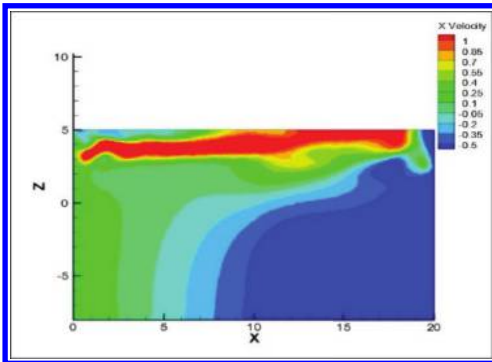


Figure 5. Distribution of velocity on the vertical coordinate.

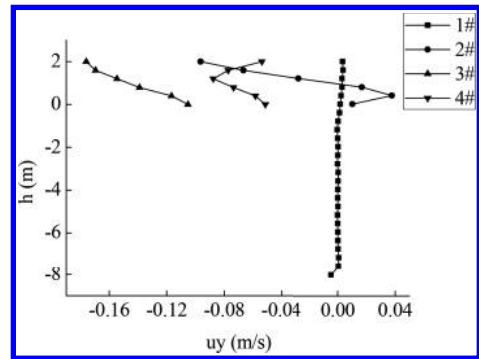


Figure 8. Transverse velocity.

is greater than the tidal-flat velocity, as shown in Figure 7.

As shown in Figure 8, the transverse velocity from the tidal to the channel decreases across the section. On the tidal flat, the surface velocity

reaches to 0.16 m/s, with 0.12 m/s at bottom. On the tidal-flat adjacent the channel, it varies from 0.08 to 0.02 m/s to the channel.

As shown in Figure 9, the surface water in channel flows to the seaward, and the bottom flows to the landward. The maximum velocity occurs at 10 m

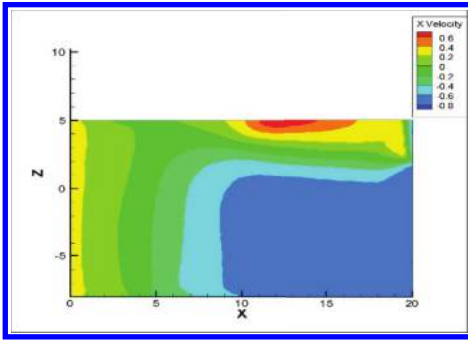


Figure 9. Velocity on the vertical coordinate.

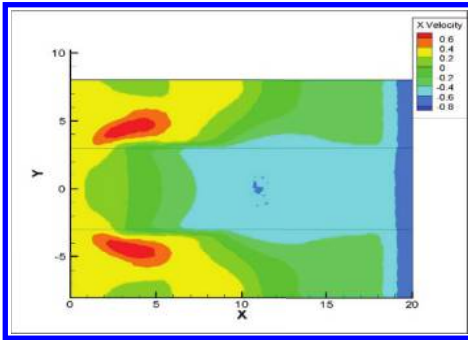


Figure 10. Velocity on the horizontal coordinate.

along the channel. The channel velocity increases compared with the tidal-flat velocity during the flood, and the gradient on the tidal-flat adjacent channel is greatest. This means that momentum exchanges from the channel to the tidal flat.

#### 4 CONCLUSIONS

In this paper, the flow pattern between the channel and tidal flat during flood was studied using a 3-D

numerical hydraulic model. The  $k - \varepsilon$  turbulence model with the VOF method was used to simulate a fully three-dimensional flow. In the channel and tidal flat during the initial flood tide, the velocity along the channel increased compared with that along the tidal flat. The transverse velocity reached the peak on the tidal-flat adjacent the channel, and decreased from the tidal-flat to the bank. At the end of the flood tide, the velocity decreased along the channel flow to the landward, the transverse velocity decreased from the tidal flat to the channel, and the flow from the tidal to the channel.

#### ACKNOWLEDGMENTS

This work was supported by the National Natural Science Foundation (No. 51479122), the Ministry of transport (No. 2012-329-A06-040), and the Nanjing Hydraulic Research Institute Foundation (No. LB21405).

#### REFERENCES

- [1] Li, C.Y., and J. O'Donnell (2005). The effect of channel length on the residual circulation in tidally dominated channels, *J. Phys. Oceanogr.*, 35(10), 1826–1840, doi:10.1175/JPO2804.1.
- [2] Lacy, J.R., M.T. Stacey, J.R. Burau, and S.G. Monismith (2003). Interaction of lateral baroclinic forcing and turbulence in an estuary, *J. Geophys. Res.*, 108(C3), 3089, doi:10.1029/2002JC001392.
- [3] Chunyan Li, James O'Donnel. Tidally driven residual circulation in shallow estuaries with lateral depth variation. *JOURNAL OF GEOPHYSICAL RESEARCH*. Vol. 10 2. No. C13, Pages 27, 915, 27, 929, Decemeber 15, 1997.
- [4] Wang Xuejun. Non-reflective wave numerical wave tank [J]. *Hydrodynamics Research and Development (A)*, 1994, 9(2):204–205.
- [5] Li Zhiqin, Li Hong, Lijia. Experimental and numerical overflow heights near the free surface [J]. *Journal of Hydraulic Engineering*, 2003(8):53–57.

# Numerical modeling of regional hydrodynamic and seabed morphological effects from the construction of artificial islands in Danzhou, Hainan

S.H. Zuo, B. Li & Z. Zhang

Key Laboratory of Engineering Sediment of Ministry of Communications, Tianjin Research Institute of Water Transport Engineering, Tianjin, China

**ABSTRACT:** Haihua Island is a large artificial island in Danzhou, Hainan. The construction of Haihua Island changes the hydrodynamic environment of Yangpu's sea area, and further affects its morphological change. A 2-D numerical model combining the effects of tides and waves was set up to study the regional hydrodynamic and seabed morphological effects from the construction of Haihua Island in the Yangpu's sea area of Hainan. Verification and validation were carried out against the measured data. Details were given about the variations of nearshore hydrodynamic characteristics of the Yangpu Bay with the construction of artificial island engineering. In addition, the influence on the seabed, with the transportation of sediment considered, was computed. The outcomes of this study lay a foundation for the feasibility analysis of Haihua Island's exploitation.

**Keywords:** Haihua Island; tidal currents; sediment; mathematical model; Yangpu Bay

## 1 INTRODUCTION

The artificial island project of Haihua Island is located in the Yangpu waters in Danzhou of Hainan Province, China (Fig. 1). The project intends to adopt the form of an offshore artificial island with planning five artificial islands, and bridges among the islands and between the island on both sides and the land. The area of artificial islands is 7.53 km<sup>2</sup> and the coastline is 39.44 km.

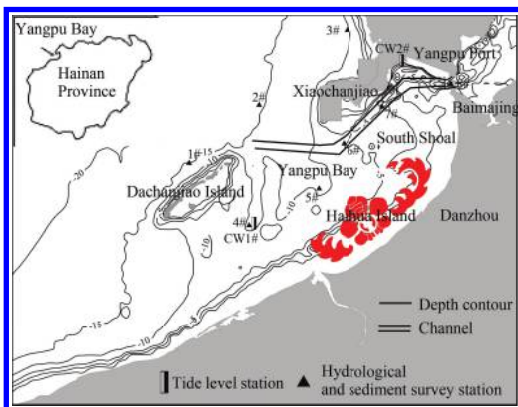


Figure 1. Location of Haihua Island in Hainan, the depth of Yangpu waters and hydrological stations.

The minimum area of the five artificial islands is about 0.146 km<sup>2</sup>, and the maximum area is about 3.811 km<sup>2</sup>, and the distance among the islands is about 48 m–196 m. Haihua Island is mainly located in Yangpu shallows (Fig. 1) with the depth less than 2 m.

Haihua Island belongs to a large-scale reclamation project, and the project implementation causes hydrodynamic environment changes in Yangpu waters and adjacent area, and further affects the seabed morphological change. With the development of theories about numerical simulation and the improvement of computational facilities, two-dimensional (2D) mathematical models have been widely used in the solution of many real-life engineering problems involving hydrodynamic and sediment transport by tidal currents and waves (Li, 2006a, 2006b; Zuo, 2009). A 2-D numerical model is used to simulate the effects of hydrodynamic and seabed morphological change caused by the project in this paper.

## 2 GENERAL SITUATION OF THE STUDY REGION

The tide is irregular diurnal with the mean tidal range 1.91 m in Yangpu waters, and the tidal flow has a reciprocating flow with a slight rotation.

The measured surface flow velocity is about 0.82 m/s, and the maximum current velocity is 0.3–0.5 m/s with reversing directions of SW-NE near the project area. The annual average wave height is 0.8 m in the Dongfang Station located near the project. The Suspended Sediment Concentration (SSC) is low with the average value of 0.02–0.03 kg/m<sup>3</sup>. The tidal passage of the Yangpu Bay is a curved deep channel with the length of 8.2 km, the width of 600 m and the depth of 10 m–20 m. The deepest depth is above 24 m, and the shallowest depth is about 5 m in the sandbar area, and the length of the depth less than 8.5 m is about 3.5 km. The seabed around the Yangpu Bay is mainly silty clay, and the sea bed nearby the Haihua Island is relatively coarse, and the median size is from 0.05 m to 0.9 mm (Wang, 2006; Zuo, 2010).

### 3 NUMERICAL MODEL

#### 3.1 2D tidal current model under the function of waves

The continuity equation is as follows:

$$\frac{\partial z}{\partial t} + \frac{\partial(hu)}{\partial x} + \frac{\partial(hv)}{\partial y} = 0 \quad (1)$$

The momentum equation is given as follows:

$$\frac{\partial u}{\partial t} + u \frac{\partial u}{\partial x} + v \frac{\partial u}{\partial y} = -g \frac{\partial z}{\partial x} + \frac{\tau_{sx}}{h\rho} + \frac{\tau_{bx}}{h\rho} + f v + R_x + \lambda \Delta u \quad (2)$$

$$\frac{\partial v}{\partial t} + u \frac{\partial v}{\partial x} + v \frac{\partial v}{\partial y} = -g \frac{\partial z}{\partial y} + \frac{\tau_{sy}}{h\rho} + \frac{\tau_{by}}{h\rho} - f u + R_y + \lambda \Delta v \quad (3)$$

where  $z$  = water level, the distance between the free surface and the base level;  $h$  = water depth, the distance between the free surface and the seabed,  $h = z + z_0$ ;  $z_0$  = seabed surface elevation, the distance between the base level and the seabed surface;  $u, v$  are the horizontal velocity components in the  $x$  and  $y$  directions, respectively;  $f$  = Coriolis parameter;  $g$  = gravity acceleration,  $g = 9.81$  m/s<sup>2</sup>;  $\rho$  = water density;  $\tau_{sx}, \tau_{sy}$  are components of wind stress  $\tau_s$  in the  $x$  and  $y$  directions, respectively;  $\tau_{bx}, \tau_{by}$  are components of bottom shear stress  $\tau_b$  with interactions of wave and tidal current in the  $x$  and  $y$  directions, respectively;  $\lambda$  = horizontal eddy viscosity coefficient;  $\Delta = \frac{\partial^2}{\partial x^2} + \frac{\partial^2}{\partial y^2}$ ;  $T_x = -\frac{1}{\rho h} \left( \frac{\partial S_{xx}}{\partial x} + \frac{\partial S_{xy}}{\partial y} \right)$ ;  $T_y = -\frac{1}{\rho h} \left( \frac{\partial S_{yx}}{\partial x} + \frac{\partial S_{yy}}{\partial y} \right)$ ;  $S = \begin{pmatrix} S_{xx} & S_{xy} \\ S_{yx} & S_{yy} \end{pmatrix}$  is radiation stress.

#### 3.2 2D model of suspended sediment transport under the function of waves and currents

##### 3.2.1 General equation

Because sediment transport produced by tidal current velocity is larger than natural diffusion of the sediment, sediment yield of suspending can be ignored, and the two-dimensional suspended sediment transport equation under the function of waves and currents can be written as follows:

$$\frac{\partial(hC)}{\partial t} + u \frac{\partial(hC)}{\partial x} + v \frac{\partial(hC)}{\partial y} = \alpha \omega_s (C - C^*) \quad (4)$$

where  $\alpha$  can be expressed in the following form:

$$\alpha = \begin{cases} \alpha_1 & (C < C^*) \\ -\alpha_2 & (C \geq C^*) \end{cases} \quad (5)$$

##### 3.2.2 Seabed deformation equations due to suspended sediment

$$\frac{\partial(hS)}{\partial t} + u \frac{\partial(hS)}{\partial x} + v \frac{\partial(hS)}{\partial y} = -\gamma_s \frac{\partial z_0}{\partial t} \quad (6)$$

where  $\gamma_s$  is the dry unit volume weight of bed bottom sediment particles; and  $z_0$  is the depth from the undisturbed sea level to the sea floor.

### 3.3 Solution conditions

#### 3.3.1 Initial conditions

Initial conditions are related to the initial distributions of surface elevation, velocity and sediment concentration. As shown in Equation (14),  $\zeta_0(x, y, t_0)$  is the tidal level when  $t = t_0$ ;  $u_0(x, y, t_0)$  and  $v_0(x, y, t_0)$  are the tidal velocity along the  $x$  and  $y$  directions, respectively, when  $t = t_0$ ; and  $S_0(x, y, t_0)$  is the sediment concentration when  $t = t_0$ :

$$\left. \begin{aligned} \zeta(x, y, t) \Big|_{t=t_0} &= \zeta_0(x, y, t_0) \\ u(x, y, t) \Big|_{t=t_0} &= u_0(x, y, t_0) \\ v(x, y, t) \Big|_{t=t_0} &= v_0(x, y, t_0) \\ S(x, y, t) \Big|_{t=t_0} &= S_0(x, y, t_0) \end{aligned} \right\} \quad (7)$$

In this paper, the initial tidal level is taken as the mean tidal level and the initial tidal velocity is taken as zero on the computational boundary. The initial sediment concentration can be obtained from interpolation of the measured values.

#### 3.3.2 Boundary conditions

There are four open sea boundaries in the model. The tidal levels control them. The sediment



concentrations at the open boundaries are obtained from the nearest survey point.

### 3.3.3 Computational area and the grids

According to the characteristic of the study area, unstructured grids are applied to fit the boundaries of the estuary and the harbor project because the grids can be used in irregular geometries and the elements may have arbitrary sizes in regions of interest. The simulated study area is about 1848 km<sup>2</sup>. The east-west length of the simulated study area is 56 km and the north-south width is 33 km. Overall, 45869 nodes are included in the model. The spatial steps are between 30 and 600 m, and the smaller grids are used in the harbor project region.

Using the project boundary and topography data of 2011, the actions of tidal currents and wind waves are simulated in the model. The movement of both tidal currents and suspended sediment is simulated. The results of calibration of velocity, direction, sediment concentration, and variation of the seabed are given.

### 3.3.4 Selection of parameters

The Manning roughness coefficient,  $n$ , is estimated to range from 0.010 to 0.025. According to the model calibration, the coefficient is adjusted to the landform change. According to the characteristics of the bed sediment, the Yangpu waterway sea area belongs to the class of a muddy coast. The dry unit volume weight of seabed sediment particles,  $\gamma_s$ , is 750 kg/m<sup>3</sup>; the specific weight of water,  $\gamma$ , is 1000 kg/m<sup>3</sup>. The settling velocity,  $\omega_s$ , is related to many factors, such as sediment particle size, sediment concentration, salinity, and temperature.

## 4 MODEL CALIBRATION

Using the data of July 2011, the computational results for the water-surface elevation, velocity, flow direction and suspended sediment concentration are found to be in good agreement with the field data. Owing to space limitations, only parts of the results are shown in this paper (Fig. 2–Fig. 4).

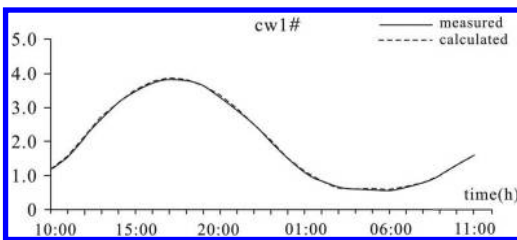


Figure 2. Calibration results for the tidal level.

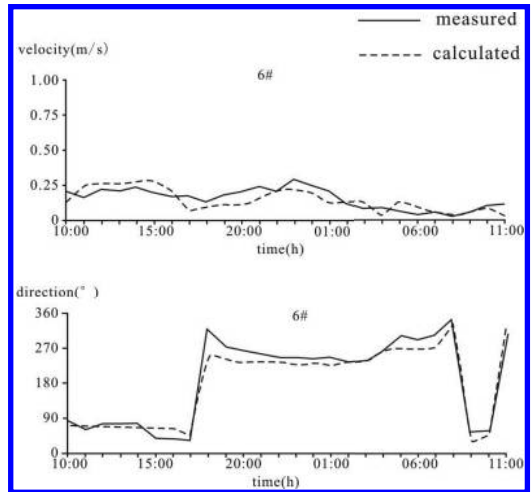


Figure 3. Calibration of current velocity and direction.

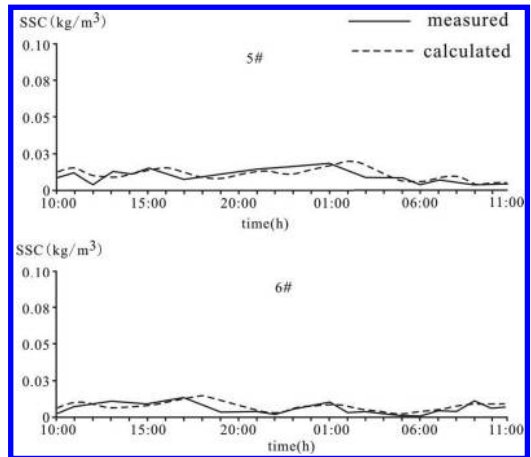


Figure 4. Calibration of suspended sediment concentration.

According to the seabed deposition and erosion in the Yangpu Bay measured from 2006 to 2007, the seabed deformation is calibrated in detail. So, the model would be combined with the simulations of flow motion, sediment transportation and bed-form reworking.

## 5 HYDRODYNAMIC AND SEABED MORPHOLOGICAL IMPACT ANALYSIS

### 5.1 Change of tidal currents after the project

After the implementation of the project, the overall trend of tidal current in the whole sea area is

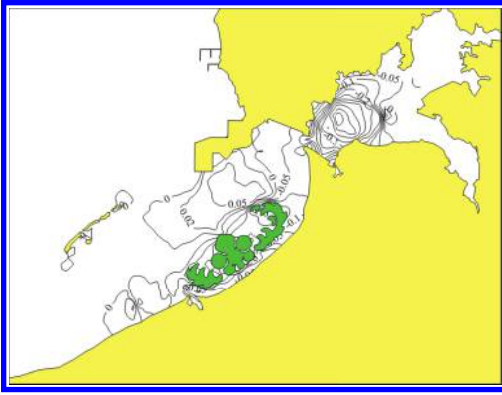


Figure 5. The change of tidal current velocity (+ increase; - decrease).

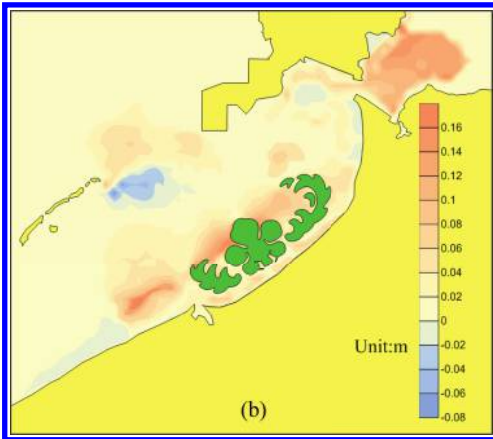
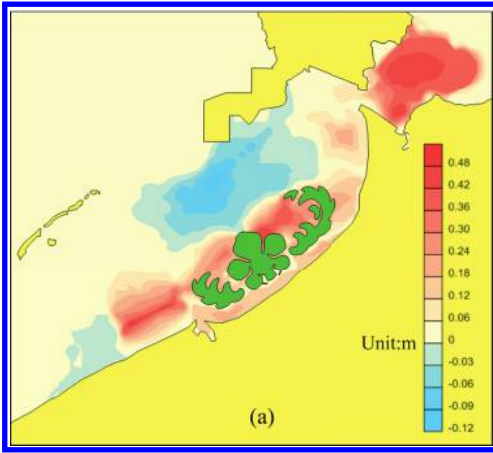


Figure 6. Seabed change during different weather conditions. (a: three years after the project in normal weather conditions; b: strong wind weather conditions).

not change, the current is still reversing current with the direction of NE-SW in the deep channel of Yangpu Bay. The local current is forced to the waterway.

Figure 5 shows the change of tidal current velocity. The artificial islands project makes the local flow velocity increase by 10% or 0.02 m/s. The maximum velocity has increased by about 0.05 m/s in the Yangpu Port Channel.

## 5.2 Seabed evolution after the project

It can be seen from Figure 6 that the seabed change is from  $-0.12$  m to  $0.48$  m during 3 years after the implementation of the project in normal weather conditions. As can be seen in Figure 5, the flow velocity increases with about  $0.02$ – $0.05$  m/s in the south of Xiaochantan. Therefore, the seabed erodes in both the south of Xiaochantan and the Haihua Island. The seabed around the Haihua Island is mainly deposited due to the reduction of the flow velocity.

According to the calculations, the seabed change is from  $-0.03$  m to  $0.15$  m for 24 hours during the strong wind weather condition.

## 6 CONCLUSIONS

Haihua Island belongs to a large-scale reclamation project. The construction of Haihua Island changes the hydrodynamic environment of Yangpu's sea area, and further affects its morphological change. A 2-D numerical model combining the effects of tides and waves was set up to study the regional hydrodynamic and seabed morphological effects from the construction of Haihua Island in the Yangpu's sea area of Hainan.

The validity of the model is verified by the observation data obtained in July 2011 including the tidal flow and suspended sediment concentration in the vicinity of the sea area. The verification of the calculation shows that the calculated values are in good agreement with the measured data. The field of tidal currents, suspended sediment concentration and the deformation of seabed can be successfully simulated. Using the numerical model, a case study was applied to research the effects from the construction of Haihua Island.

The results show that: (1) the construction of Haihua Island makes the local flow velocity increase; (2) within 3 years, the waters between Haihua Island and Xiaochanjiao are eroded with the value from  $0.03$  m to  $0.12$  m due to the velocity increase in the area; the bed level deposits with the value from  $0.06$  m to  $0.18$  m in the south area of the Yangpu channel (i.e. the South Shoal); the waterways between the islands are deposited with

the value from 0.06 m to 0.30 m; (3) the seabed are deposited in the surrounding sea area of the Haihua Island by the SW wave of 50-year return period, and the deposited rate is 0.05–0.15 m/d.

## REFERENCES

- Li, M.G. 2006a. A review on mathematical models of sediment in coastal and estuarine waters (in Chinese). *The Ocean Engineering* 24(1): 139–154.
- Li, M.G., Zhang, H.Q. & Chen, H.B., et al. 2006b. Study on multi-function mathematical model software package TK-2D and its application for coast and estuary (in Chinese). *Journal of Waterway and Harbor* 27(1): 51–56.
- Wang, B.C, Chen, S.L. & Gong, W.P., et al. 2006. *The formation and evolution of Hainan embayed coast* (in Chinese). Beijing: Ocean Press.
- Zuo, S.H., Zhang, N.C, & Li, B. et al. 2009. Numerical simulation of tidal current and erosion and sedimentation in the Yangshan deep-water harbor of Shanghai, *International Journal of Sediment Research* 24(3): 287–298.
- Zuo, S.H., Li, B. & Yang, H. 2010. GIS-based analysis on stability of the Yangpu deep trough in the Yangpu harbor sea area, Hainan Island, China (in Chinese). *Journal of Waterway and Harbor* 31(4): 242–246.

## 3D numerical simulation of local scour around regulating structures in tidal reaches

Xinzhou Zhang & Xiping Dou

*Nanjing Hydraulic Research Institute, Key Laboratory of Port, Waterway and Sedimentation Engineering, Ministry of Transport, Nanjing, China*

Zengxiang Jiao

*Nanjing Hydraulic Research Institute, Nanjing, China*

**ABSTRACT:** The flow and sediment transport, and local scour characteristics around the regulating structures in tidal reach were analyzed. Tidal reach regulating structures near the three-dimensional characteristics of water and sediment movement and local scour analyses were two-dimensional and three-dimensional turbulent sediment mathematical models developed for the next tide heights near velocity distribution role, local erosion processes, erosion and scour depth morphology that were simulated. It was pointed out that although the two-dimensional mathematical model of sediment can obtain a more accurate scour hole depth, it cannot obtain the right shape and scour erosion position.

**Keywords:** regulating structures; local scour; 3D characteristics; numerical simulation

### 1 INTRODUCTION

With the accelerated development along the coast and the river, the tidal channel and coastal estuary have been vigorously trained. In the regulations, a groin is a commonly used hydraulic structure. When the groin is used for river regulation, the best embedding depth should be first designed so as to ensure the safety of the groin. This is because a larger scour pit is always formed at the groin head, endangering its own safety and restricting the effectiveness of groin works. The flow and sediment movement near the groin are the typical three-dimensional problem. Especially at the tidal river reaches, the tidal movement is characterized as tidal unsteady reciprocating flow at estuaries, and the hydrodynamic conditions and sediment movement show periodical changes, so that this problem becomes more complex. Therefore, it is of far-reaching importance for the construction and protection of navigation channels to conduct research on the local water flow and the law of sediment movement near hydraulic structures like groins at the tidal reaches and to predict the formation of the maximum scour depth of local scour. In this paper, a three-dimensional numerical model is established to simulate the local scour of groins at the tidal reaches.

### 2 3D CHARACTERISTICS OF LOCAL SCOUR AROUND REGULATING STRUCTURES

Local scour renovation process nearby a regulating structure is a very complex three-dimensional phenomenon, including the strong three-dimensional nature of the flow movement and sediment transport. It is generally believed that after setting piers, groins and other hydraulic structures in the river, artificially increasing the flow resistance will form the upstream backwater, which will change the original velocity field and pressure field in front of structure formation pressure gradient, accompanied by the increase in the rate of water flow to generate a three-dimensional separation that occurs on the side of the boundary layer structure, resulting in a series of swirls. Horseshoe vortex formation including the scour edge flow downstream side of the vertical vortex structures generated as a result of the separation boundary velocity gradient formation, as well as the downstream movement of wake vortices. Many scholars have used the prototype observation, model test and numerical simulation, different methods and means of local scour to conduct a comprehensive study of the phenomenon, widely believed by local scour spur dike whirlpool, dive flow, increasing the flow rate per unit width of spur dike and other factors

resulting from the combined effects. In summary, the formation of the scour hole is mainly caused by changes in the local water flow and sediment conditions.

### 3 2D AND 3D NUMERICAL SIMULATION OF LOCAL SCOUR AROUND REGULATING STRUCTURES

#### 3.1 Simulation reach

The reach to simulate is generalized from the North Passage at the Yangtze River Estuary (Fig. 1). The generalized reach is about 10 km long, and its longitudinal gradient is designed with reference to 0.027% of the actual longitudinal gradient of the North Passage at the Yangtze River estuary. Two guide levees not crossing water are arranged on the southern and northern sides respectively. The reach between guide levees is about 6 km long and about 2 km wide, and the outlet is a widened section, which is 3 km at its widest point. The bottom elevation of the channel between the guide levees is  $-10$  m and the bottom width is 160 m, while the side slope of the channel is 150 km. The bottom centerline of the channel is about 1.3 km away from the north guide levee and about 0.7 km away from the south one. The bottom elevation of both sides of the channel is generalized as  $-6$  m (Fig. 2). A pair of groins is arranged in the guide levees (Fig. 3). The long groin is about 660 m long, while the short

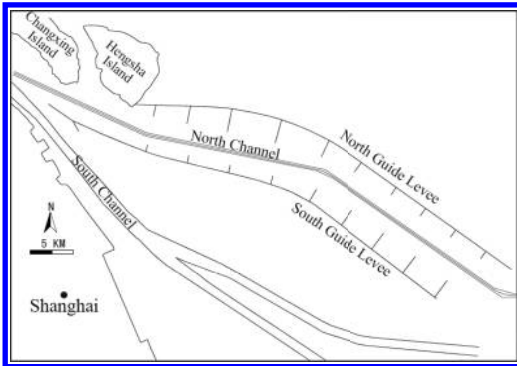


Figure 1. Arrangement diagram of guide levees and groins under the deep water channel regulation works at the Yangtze River Estuary.

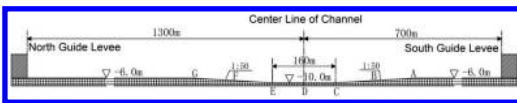


Figure 2. Cross-section drawing of the generalized reach.

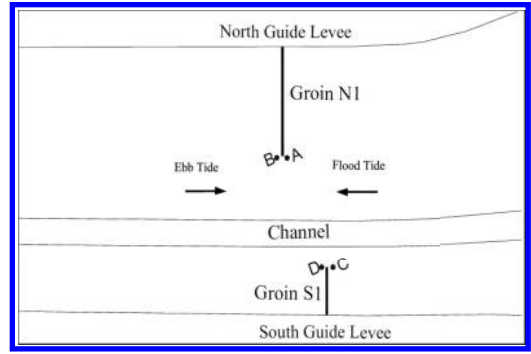


Figure 3. Arrangement of groins Deepwater Channel Regulation Project and observation points.

groin is about 270 m long. Both types of groin are non-submerged and vertical to the guide levee.

Under the action of tidal flow and unidirectional flow, the local scour processes of a pair of groins (only the south groin S1 and the north groin N1) at the generalized river reaches are separately studied through the numerical model, and four points A–D are set at the head of the groin to specifically observe the changes of scour depth at four points (Fig. 3).

#### 3.2 Model establishment

The turbulent movement of incompressible viscous fluid can generally be described by the Reynolds Equation:

$$\frac{\partial u_i}{\partial x_i} = 0 \quad (1)$$

$$\frac{\partial u_i}{\partial t} + u_j \frac{\partial u_i}{\partial x_j} = X_i - \frac{1}{\rho} \frac{\partial p}{\partial x_i} + \nu \frac{\partial^2 u_i}{\partial x_j \partial x_j} + \frac{1}{\rho} \frac{\partial(-\rho u'_i u'_j)}{\partial x_j} \quad (2)$$

where  $u_i$  is the component of time average velocity in the direction  $i$ ;  $X_i$  is the mass force;  $\nu$  is the coefficient of kinematic viscosity;  $\rho$  is the fluid density;  $-\rho u'_i u'_j$  is the Reynolds stress; and  $p$  is the pressure.

As an unclosed equation, the Reynolds equation contains the Reynolds stress. It needs to be closed by a turbulent model. Currently, the most widely used equations are  $k$  and  $\varepsilon$  equations raised by Launder and Spalding (1974):

$$\frac{\partial k}{\partial t} + u_i \frac{\partial k}{\partial x_i} = \frac{\partial}{\partial x_i} \left( C_k \frac{k^2}{\varepsilon} \frac{\partial k}{\partial x_i} + \nu \frac{\partial k}{\partial x_i} \right) - \overline{u'_i u'_j} \frac{\partial u_i}{\partial x_j} - \varepsilon \quad (3)$$

$$\frac{\partial \varepsilon}{\partial t} + u_i \frac{\partial \varepsilon}{\partial x_i} = \frac{\partial}{\partial x_i} \left( C_{\varepsilon} \frac{k^2}{\varepsilon} \frac{\partial \varepsilon}{\partial x_i} + \nu \frac{\partial \varepsilon}{\partial x_i} \right) - C_{\varepsilon 1} \frac{\varepsilon}{k} \overline{u'_i u'_j} \frac{\partial u_i}{\partial x_j} - C_{\varepsilon 2} \frac{\varepsilon^2}{k} \quad (4)$$

The three-dimensional suspended sediment transport equation can be expressed as follows:

$$\frac{\partial S}{\partial t} + u \frac{\partial S}{\partial x} + v \frac{\partial S}{\partial y} + w \frac{\partial S}{\partial z} = \frac{\partial}{\partial x} \left( \varepsilon_{sx} \frac{\partial S}{\partial x} \right) + \frac{\partial}{\partial y} \left( \varepsilon_{sy} \frac{\partial S}{\partial y} \right) + \frac{\partial}{\partial z} \left( \varepsilon_{sz} \frac{\partial S}{\partial z} \right) + \frac{\partial \omega_s S}{\partial z} \quad (5)$$

where  $S$  is the sediment concentration;  $\omega_s$  is the settling velocity of sediment grains;  $\varepsilon_s$  is the sediment diffusion coefficient; and  $\sigma_s$  is the Schmidt number with a value range of 0.5~1.0. Based on the suspended sediment transport equation, the bottom boundary condition for the suspended sediment movement is given by

$$\omega_s s + \frac{\nu_t}{\sigma_s} \frac{\partial s}{\partial z} = D_b - E_b \quad (6)$$

where  $D_b$  is the deposition flux on the riverbed interface and  $E_b$  is the uptrend flux of the sediment on this interface. According to the conservative flux, the equation for the riverbed deformation caused by the suspended sediment is as follows:

$$-\gamma'_s \frac{\partial \eta_s}{\partial t} = -D_b + E_b \quad (7)$$

where  $\gamma'_s$  is the dry density of the sediment;  $\eta_s$  is the thickness of silt or scour caused by the suspended sediment; and  $E_b - D_b$  is the net flux on the sediment interface.

The bottom sediment transport equation is as follows:

$$\frac{\partial N_b}{\partial t} + \frac{\partial u_b N_b}{\partial x} + \frac{\partial v_b N_b}{\partial y} = \beta_s w_s (N_b - N_b^*) \quad (8)$$

where  $N_b$  is the amount of the bed load sediment in a unit volume; and  $u_b$  and  $v_b$  are the flow velocity at the calculation points near the bottom grid. The riverbed deformation caused by the bed load can be expressed as follows:

$$\gamma_0 \frac{\partial \eta_b}{\partial t} = \beta_s w_b (N_b - N_b^*) \quad (9)$$

There is a great difference between local scour and general scour. Through the study of local scour,

many scholars have discovered that local scour is produced when the velocity of approach does not reach the incipient velocity of general scour. Dou Xibing (1997) gained a new formula for the critical incipient velocity of local scour by taking into consideration the action of vertical water flow during the local scour. This new equation is as follows:

$$\frac{U_{b,cr}^2}{(\rho_s/\rho-1)gd} = 3.61(\tan \phi \cos \alpha - \sin \alpha) + \left[ -B \frac{|w|^2}{(\rho_s/\rho-1)gd} \right] \quad (10)$$

where  $B$  is an undetermined coefficient. This equation takes into consideration the action of vertical flow velocity in addition to the impact of the slope and repose angle, which can be used to calculate the critical incipient velocity of the sediment at the time of the occurrence of local scour.

### 3.3 Local scour process

Figure 4 and Figure 5 show the simulation results of the local scour processes of the N1 and S1 groin heads.

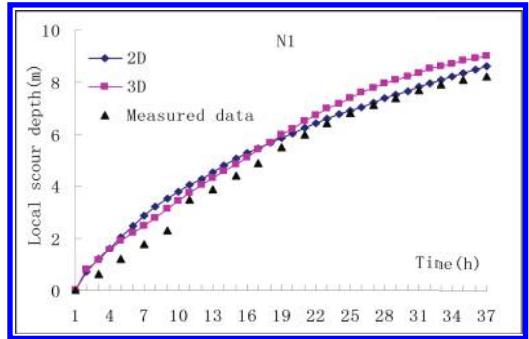


Figure 4. Local scour processes around groin N1.

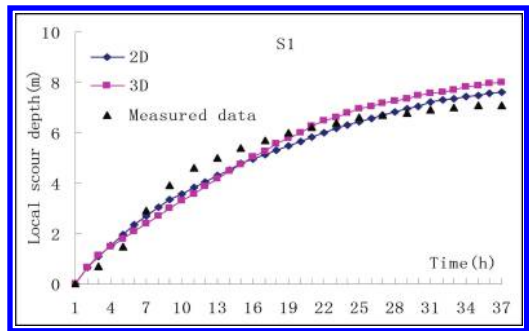


Figure 5. Local scour processes around groin S1.

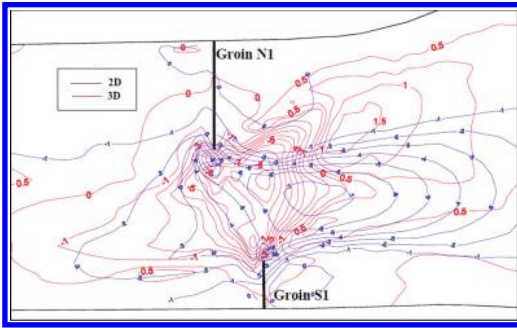


Figure 6. Local scour shape comparison of 2D and 3D.

According to the calculated results, the scour depth increasing trend of the groin heads under the action of tide is consistent with the measured results. The local scour depth of 3D is slightly deeper than that of 2D. The main reason is that the vertical velocity of flow around regulating structures takes a key role in the three-dimensional calculation for the critical starting velocity of the sediment.

### 3.4 Local scour shape

Figure 6 shows the numerical simulation results of the local scour shape of 2D and 3D. The maximum local scour positions of 2D and 3D are located at the groin head similarly, but the position of the three-dimensional calculation of the maximum scour is farther from the mainstream area and close to the main water area. The distribution of sediment erosion and deposition zone is also significantly different from the two-dimensional calculation results.

## 4 COMPARATIVE ANALYSIS OF TWO-DIMENSIONAL AND THREE-DIMENSIONAL CALCULATION RESULTS

The flow line around the groin near the bed bottom of 2D and 3D is shown in Figure 7. The flow becomes a kind of jet-flow and deviates to the transverse direction before the upstream face of the groin in 3D lowest level flow, and then bypasses the groins and joins back in the recirculation zone quickly.

Figure 8 shows the velocity distribution of the YZ plane before the upstream face of the groin calculated by the 3D model. As can be seen in the figure, the transverse velocity suddenly increases before the upstream cross-section of the groin, where the transverse velocity is much closer to the

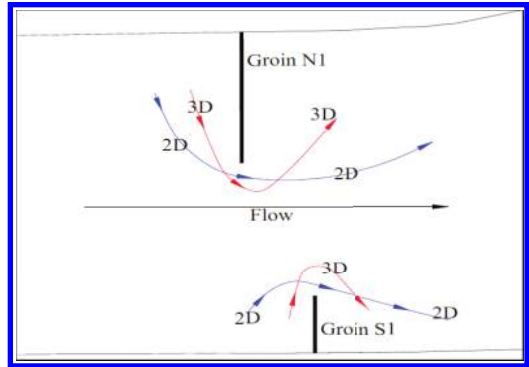


Figure 7. The flow line around the groin near the bed bottom.

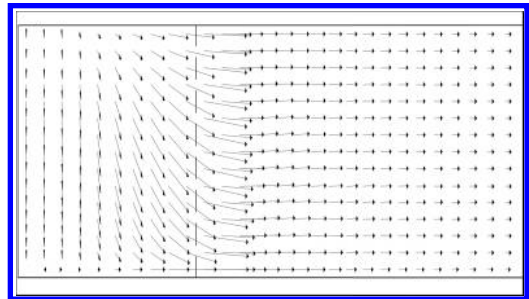


Figure 8. The velocity distribution before the upstream face of the groin calculated by the 3D model (Y-Z profile).

bottom. This is the reason that the flow deviates to the transverse direction before the upstream face of the groin in the 3D model.

## 5 CONCLUSION

1. The erosion around the groin is different because the flow structure is different from the 2D and 3D simulation results. Three-dimensional model simulates the groins area near the bottom of the velocity distribution more accurately. Although the two-dimensional mathematical model for the sediment can obtain a more accurate scour hole depth, it cannot obtain the right shape and scour erosion position.
2. The velocity distribution between the surface and bottom is different from each other. The sediment erosion and deposition are determined by the velocity and the concentration of the sediment near the bottom. Theoretically, a more realistic calculation not only results in the size of the largest scour depth with the measured data

agreeing well, but also provides a more reasonable results with respect to the form of erosion than the two-dimensional mathematical model.

3. The results illustrate that groins local scour problem is a typical three-dimensional problem, so we must adopt a three-dimensional model that can be more accurate and provide a reasonable size and scope of erosion simulation.

#### ACKNOWLEDGMENT

This research work was supported by the National Natural Science Foundation No. 51409163 and No. 51479122.

#### REFERENCES

- [1] Kamil Hmali, Karim O. Simulation of flow around piers [J]. *Journal of Hydraulic Resource*, 2002, 40(2): 161~174.
- [2] Graf W.H., Istiarto I. Flow pattern in the scour hole around a cylinder [J]. *Journal of Hydraulic Resource*, 2002, 40(1):13~20.
- [3] Terry W. Sturm. Clear-Water Scour Around Abutments In Floodplain [J]. *Journal of Hydraulic Engineering*, 1994, 120(8):956~971.
- [4] Melville, B.W. Pier and abutment scour: integrated approach [J]. *Journal of Hydraulic Engineering*, 1997, 123(2).
- [5] I-Chi Chan, Liang-Hsiung Huang and Ping-Cheng Hsieh, Analysis of Water Waves Passing Over a Submerged Rectangular Dike, *J. of Engineering Mechanics*, ASCE, Vol. 129, No. 6, 2003:613~626.
- [6] Terunori Ohmoto, Ryuichi Hirakawa and Nobukazu Koreeda, Effects of Water Surface oscillation on Turbulent Flow in an Open Channel with a Series of Spur Dikes, *Hydraulic Measurements and Experimental Methods Conference 2002*, Estes Park, Colorado, USA.
- [7] Robert Ettema and Marian Muste, Scale Effects in Flume Experiments on Flow around a Spur Dike in Flatbed Channel, *J. of Engineering Mechanics*, ASCE, Vol. 130, No. 7, 2004:635~646.



# Numerical simulation study of sedimentation downstream tide gates influenced by the length of the irrigation channel

Xinzhou Zhang & Zengxiang Jiao

*Key Laboratory of Port, Waterway and Sedimentation Engineering, Nanjing Hydraulic Research Institute, Ministry of Transport, Nanjing, China*

Jimin Zhang

*Water Resources Protection Bureau Songliao Water Resources Commission, Ministry of Water Resources, China*

**ABSTRACT:** Siltation in the rivers downstream of floodgates has become a serious problem in China, making the discharge capacity of rivers to decrease obviously and threatening the flood control in upper rivers. Tidal wave deformation is one conclusive dynamic factor leading to siltation downstream of floodgates in estuaries. The hydrodynamic characteristics of tidal wave deformation are different with different river lengths downstream of floodgates, so the fluvial processes and morphology characteristics are also different. A 2D numerical model is established to simulate the tidal wave deformation and sediment deposition with river of different lengths downstream the floodgate. The length of the river downstream of floodgates influences sediment deposition obviously. On this basis, several conclusions are obtained in this paper, which can provide some theoretical basis for the prediction and analysis of the siltation characteristics in the lower reach caused by floodgates with different lengths in estuaries.

**Keywords:** sedimentation downstream tidal gates; length of irrigation channel; physical model; numerical model

## 1 INTRODUCTION

In order to defend against tides for the development of agricultural production, lots of sluices have been built in the coastal areas of China since 1950s, with the number of about 300 at present. Siltation in the rivers downstream of floodgates is a very serious problem in China. According to statistics, among the 58 sluices with the drainage flow of over 100 m<sup>3</sup>/s in Jiangsu Province, 5 are almost silted up, 15 are in severe siltation and the other 38 are relatively less silted. Besides, in the 35 estuaries with sluice constructed in the Haihe River basin, 22 are in serious siltation, where the upper and lower reaches are universally silted, causing the river drainage capacity to reduce by 60%. Siltation in the rivers downstream of floodgates makes the discharge capacity of rivers to decrease obviously and threatens the flood control in upper rivers, and influences the agricultural production. Therefore, it is vital to perform research on siltation downstream of floodgates.

Study on siltation downstream of floodgates in China began with the research on the Sheyang estuary by G.R. Dou, showing that tidal wave deformation was the main factor leading to sedimentation

downstream sluice. Then, many scholars have studied the silting mechanism and basically agreed with the conclusion that tidal wave deformation is one conclusive dynamic factor causing siltation downstream of floodgates. Tidal wave deformation and reflection usually occur under the influence of river morphologic resistance when it comes into the estuary, which will be more evident in the estuaries where floodgates have been built. Tidal wave will be reflected fully by the floodgate, and tidal wave properties change from a progressive wave to a standing wave, with a significant phase difference between the hydrographs of flow velocity and tidal level. Besides, the high tidal level rises while the low tidal level goes down, and the duration of flood tide is shortened and the mean depth of flood tide decreases, while that of ebb tide goes opposite. Therefore, the flow velocity of flood tide increases and that of ebb tide decreases, respectively. Sediment transport capacity of flood tide is enhanced relative to that of ebb tide due to the change in hydrodynamic characteristics, so that the sediment, which is carried into the river by flood tide, cannot be taken back to the estuary by ebb tide, and then deposited in the lower reach downstream the floodgate.

## 2 NUMERICAL MODEL AND VERIFICATION

### 2.1 Simulation schemes

To study how the length of the approach channel at the downstream of the floodgate influences the sediment deposition, a 2D numerical tidal current and sediment transport model is built based on the prototype of the floodgate in the estuary of the Sheyang River. The actual morphology of the estuary of the Sheyang River is simplified and applied as the open sea condition of the model. The open boundary of the model is about 6.5 km from the estuary, near the  $-7$  m contour. In addition, the area covered by the model between its south and north boundaries is about 7.2 km wide (Fig. 1). In the model, the approach channel was simplified into a 77 km-long and 660 m-wide compound channel. The bottom of the inner passage of the approach channel is about 220 m wide, with its elevation at  $-4.0$  m. The side slope of the passage is 1:8, and the bottom elevation of the point bar is about 3.0 m.

The hydrodynamic boundary condition of the model is designed on the basis of the actual condition in the estuary of the Sheyang River. The high tidal level is at 4.05 m and the low tidal level is at 1.8 m (Fig. 2). The hydrodynamic boundary condition of the open sea remains unchanged in the study; however, we hypothesize various lock sites of the floodgates and different lengths of the approach channel so as to study how the sediment deposition at the downstream of the floodgate is influenced accordingly.

### 2.2 Numerical model establishment

The continuity equation, momentum equation of tidal current and sediment transport equation in the numerical model are discretized using FVM (Finite Volume Method) as follows:

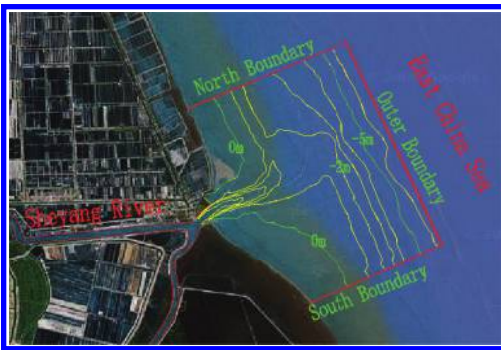


Figure 1. Domain of the model boundary.

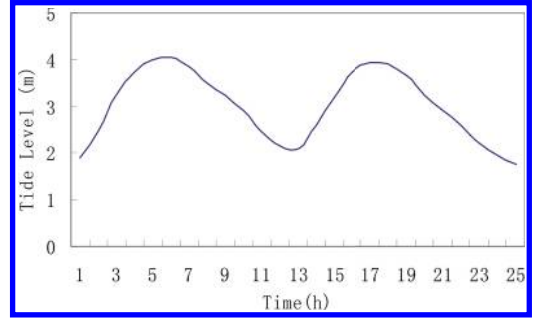


Figure 2. Design curve of the tide on the outer boundary.

$$\frac{\partial \zeta}{\partial t} + \frac{\partial Hu}{\partial x} + \frac{\partial Hv}{\partial y} = 0 \quad (1)$$

$$\begin{aligned} \frac{\partial Hu}{\partial t} + \frac{\partial Huu}{\partial x} + \frac{\partial Huv}{\partial y} = & -gH \frac{\partial \zeta}{\partial x} - \frac{\partial Hu'u'}{\partial x} - \frac{\partial Hu'v'}{\partial y} \\ & + \frac{\tau_{sx} - \tau_{bx}}{\rho} + fHv \end{aligned} \quad (2)$$

$$\begin{aligned} \frac{\partial Hv}{\partial t} + \frac{\partial Huv}{\partial x} + \frac{\partial Hvv}{\partial y} = & -gH \frac{\partial \zeta}{\partial y} - \frac{\partial Hv'u'}{\partial x} - \frac{\partial Hv'v'}{\partial y} \\ & + \frac{\tau_{sy} - \tau_{by}}{\rho} - fHu \end{aligned} \quad (3)$$

$$\begin{aligned} \frac{\partial HS}{\partial t} + \frac{\partial HuS}{\partial x} + \frac{\partial HvS}{\partial y} = & \frac{\partial}{\partial x} \left( H \varepsilon_x \frac{\partial S}{\partial x} \right) \\ & + \frac{\partial}{\partial y} \left( H \varepsilon_y \frac{\partial S}{\partial y} \right) + \alpha \omega (S_* - S) \end{aligned} \quad (4)$$

River bed evolution can be calculated by the following formula:

$$\gamma_0 \frac{\partial \eta_s}{\partial t} = \alpha \omega (S - S_*) \quad (5)$$

Incipient motion estimate formula of cohesive sediment and sediment transport capacity of tidal currents and waves are key parameters in the numerical model of tide and sediment transport. Dou (1999) analyzes the group characteristics and the movement characteristics of cohesive sediment, and deduced a calculation formula for starting velocity including the bulk density effect, according to the effect of cohesive force between fine particles, water depth and bulk density:

$$u_c = k' \left( \ln 11 \frac{h}{\Delta} \right) \times \left( \frac{\Delta}{\Delta_*} \right)^{1/6} \sqrt{3.6 \frac{\rho_s - \rho}{\rho} g d + \left( \frac{\gamma_0}{\gamma_0^*} \right)^{2.5} \frac{\varepsilon_0 + g h \delta (\delta/d)^{1/2}}{d}} \quad (6)$$

where  $k'$  is the coefficient ( $k' = 0.26$  for impending motion,  $k' = 0.32$  for little motion,  $k' = 0.41$  for general motion);  $\Delta$  is the roughness height of the bed surface ( $\Delta = 1 \text{ mm}$  for  $d \leq 0.5 \text{ mm}$ ,  $\Delta = 2d$  for  $d > 0.5 \text{ mm}$ ),  $\Delta_* = 20 \text{ mm}$ ; and  $\rho_s$  and  $\rho$  are the density of sediment particles and that of water, respectively,  $\gamma_0$  and  $\gamma_0^*$  are the dry volume weight and the stable dry volume weight of the sediment on the bed surface;  $\varepsilon_0$  is the synthetic parameter of cohesive force whose value is related to the physical and chemical properties of the particle materials, and also to the organic content and siltation environment for cohesive soil, with  $\varepsilon_0 = 1.75 \text{ cm}^3/\text{s}^2$  for natural sediment; and  $\delta$  is the parameter of water film thickness, with  $\delta = 2.31 \times 10^{-5} \text{ cm}$ .

Luo (1997) deduced a calculation formula for sediment transport and carrying capacity for different wet densities of fluid mud, with an overall verification of the calculation formula being made, and satisfactory results were obtained, showing that the calculation formula can be used as the practical formula for the study of engineering-related sediment problems:

$$S^* = 0.296 \gamma_s \left( \frac{\gamma}{\gamma_w} \right)^{12.8} \frac{V^2}{gD} \quad (7)$$

where  $\gamma_w$  is the wet density of fluid mud;  $\gamma$  is the density of water;  $\gamma_s$  is the density of sediment;  $V$  is the water velocity under the common action of tidal currents and waves; and  $D$  is the water depth.

### 2.3 Numerical model verification

The corresponding boundary conditions of the model are controlled by tidal levels. The upstream of the model is the floodgate, and it is treated as the closing boundary. In addition, the moving boundary method is used to discriminate the land area from the water area. The orthogonal curved grid is used in the model with the grid size ranging between 50 m and 200 m, and the time step is 2 seconds.

The numerical model was verified by the data of the physical model, for which the tidal level is shown in Figure 2, and the length of the irrigation channel is 12.5 km. The verification of the tidal level (Z1) and the current velocity (V1) in the estuary are shown in Figure 3 and Figure 4, respectively, and deposition depth along the

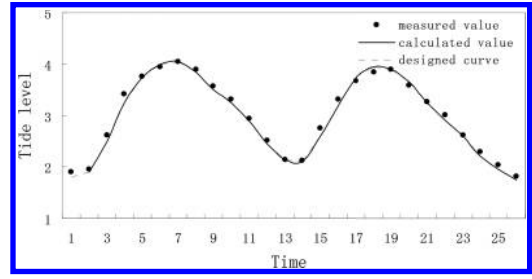


Figure 3. Verification of tidal level.

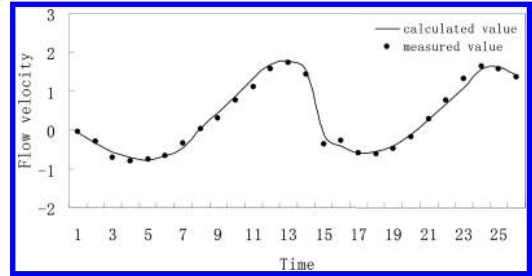


Figure 4. Verification of flow velocity.

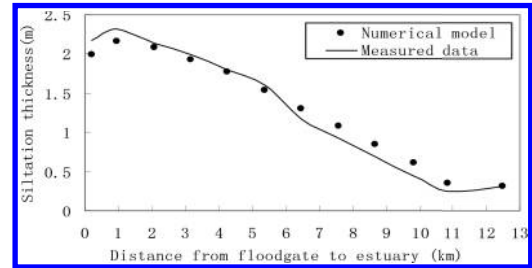


Figure 5. Deposition depth along the distance.

distance is shown in Figure 5. The results indicate that the model can simulate the process of deposition and accord with the physical model, and that the accuracy of the numerical model is satisfactory.

## 3 EFFECT OF IRRIGATION CHANNEL LENGTH ON DEPOSITION DOWNSTREAM THE TIDE GATE

The distribution of the average deposition depth downstream tide gate along the irrigation channel with different lengths under the action of spring tidal condition is shown in Figure 6, where the simulation time is about 180 days.

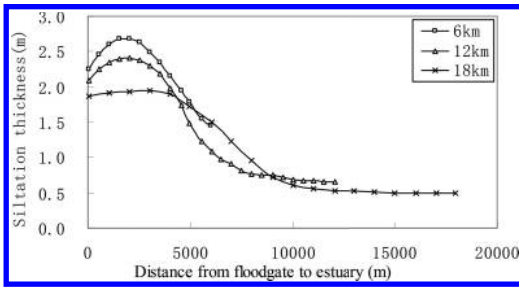


Figure 6. Deposition depth distribution along the irrigation channel with different lengths.

The result shows that the deposition is affected by length of irrigation seriously in the same hydrodynamic boundary condition. All the three conditions showed that the depth of silting decreases from the tide gate to the estuary. The velocity of the short irrigation is greater than that of the long one, so the silting increases greatly. In the long irrigation channel, the sediment transport a long time to the tide gate, the silting increases slowly. The depth profile appears triangle to the estuary.

The rate of deposition is decreased linearly with time under three irrigation channel conditions. The more the length of the irrigation, the smaller the ratio of silting, and the slower the decay of the ratio. Total river silting is the longest irrigation channel.

#### 4 CONCLUSION

This paper proposed a 2D tidal current and sediment numerical model to simulate the process of deposition downstream the tide gate, and analyzed

the different irrigation channels that affected the silting, and the results showed that:

1. The deposition was affected by the length of irrigation seriously in the same hydrodynamic boundary condition. All the three conditions showed that the depth of silting decreased from the tide gate to the estuary.
2. The velocity of the short irrigation was greater than that of the long one, so the silting increased greatly. This would shorten the irrigation channel to reduce the total river siltation and was propitious to maintain the depth of the channel.

#### ACKNOWLEDGMENT

This project was financially supported by the Ministry of Transport Major Special Science and Technology Projects of China (Grant No. 201132874640) and the National Science Foundation (No. 51409163).

#### REFERENCES

- [1] Dou Guoren, Analysis of Silting Problems under Sheyang River Floodgate. Collected Paper of Dou Guoren, Beijing: China Water Power Press (2003).
- [2] Xu Xuesong: Study on Siltation Characteristics in the Estuary with Sluices Constructed. Master Degree Dissertation, Hohai University (2012).
- [3] Luo Zhaosen: Study on Fluid Mud-Carrying Capacity, Sediment Transport and their Application, Journal of Sediment Research, Vol. 4, (1997), p. 42-46.
- [4] Dou Guoren: Incipient Motion of Sediment under Currents, China Ocean Engineering, Vol. 14, (2000), p. 391-416.

# Application of ecological revetment in Lianshen waterway regulation project

Jie Chen, Jian Zhang, Yun-peng Zhou & Li-Yuan Xu

*Jiangsu Provincial Communications Planning and Design Institute Co. Ltd., Nanjing, China*

**ABSTRACT:** As a new revetment technique, ecological revetment has become a trend of waterway regulation. On the basis of ecological revetment classification, the schemes of LianShen waterway regulation project are analyzed according to local natural conditions, and then used for ecological revetment. It may serve as a reference for other waterway regulation projects.

**Keywords:** waterway regulation; ecological revetment; application

## 1 INTRODUCTION

With the development of society and economy, people have started paying more attention to waterway ecology. Therefore the concept of ecological revetment for reinforcement was proposed. Because land limitation restricted the waterway, a reasonable structure and other measures should be adopted to reduce land acquisition. Lianshen waterway is located in the Yangtze river region, which flows through most of the developed regions and play a positive role in promoting economy of Jiangsu province.

## 2 TYPES OF ECOLOGICAL REVETMENT

According to practical situation of Jiangsu province, ecological revetment has been promoted in Grand Canal, Yanhe waterway regulation etc. and obtained better results. Summarizing the application of ecological revetment in Jiangsu province can be divided into three categories: whole-ecological revetment, half-of ecological revetment and part-ecological revetment.

There are two types of complete ecological revetment: the first is to keep original ecosystem which means repairing or reinforce only a part of slope; the second is using less hard cover and more vegetation on slope. Complete ecological revetments are mainly applied in waterways that have wide sections or more bottomland. Common types of whole-ecological revetment are vegetation revetment, reed revetment, timber pile revetment etc.

Half-ecological revetment uses part of hard cover, keeping the rest of the ecosystem on

original slope. Half-ecological revetments are mainly applied in waterways, which have narrow sections and large construction areas. The ecosystem of half-ecological revetment reflects in secondary revetment, which is above normal water level. Common types of half-ecological are ecological bag revetment, self-embedded revetment, box-type revetment etc.

## 3 ECOLOGICAL REVETMENT SCHEMES OF LIANSHEN WATERWAY

Lianshen waterway flows through two different sections between the town and village. According to using conditions and geological environment, different types of ecological revetments are used in Lianshen waterway regulation.

### 3.1 Town section

Vertical-type revetments occupy less area, which is suitable for the waterway. It does not easily expand or demolish and is also economical. Most of the towns that Lianshen waterway flows through are advanced regions. Therefore, vertical-type revetments are adopted for saving land, reducing demolition and costs. Town section schemes for ecological revetment of Lianshen waterway adopt ecological bag revetment, box-type revetment, and self-embedded revetment.

#### 1. Ecological bag revetment

Ecological bags have filter function, which not only prevent loss of filler, but also realize normal moisture communication in the soil. Ecological bag can provide plenty of moisture and let the plant grow through the bag body. The roots

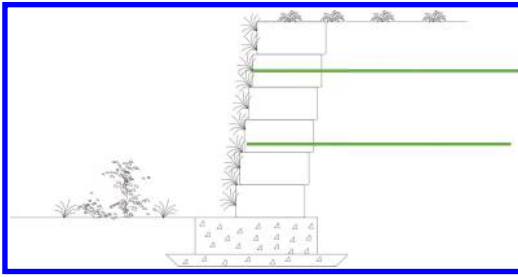


Figure 1. Ecological bag revetment.

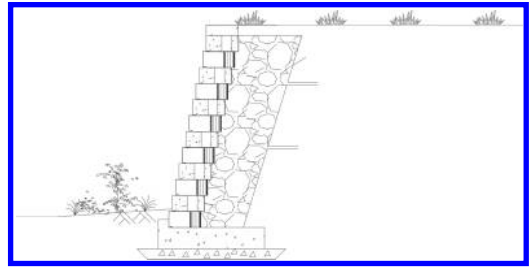


Figure 3. Self-embedded revetment.

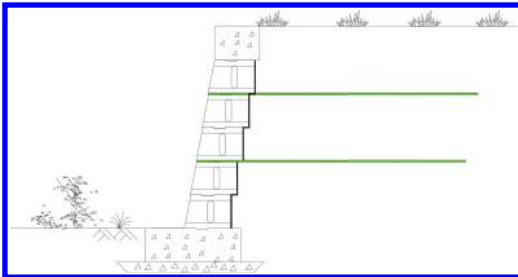


Figure 2. Box-type revetment.

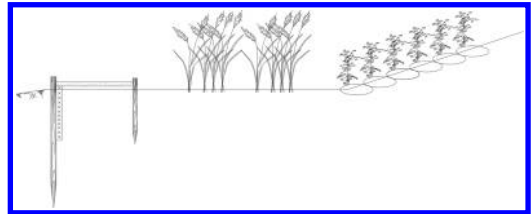


Figure 4. Vegetation revetment.

pass into soil of the engineering foundation, like countless anchors which stable bag bodies. Further, the permanent stability slope is achieved and greatly reduces the maintenance cost.

## 2. Box-type revetment

The advantage of box-type structure lies in saving loss of concrete material, and the cavity reserved along length direction could fill with non-fine concrete, stone etc. This kind of revetment has an effective to waste soil, and a low project cost. In addition, structure of box-type revetment is simple and the stress condition is good, and overturning resistance moment improves because of friction force between concrete and wall.

## 3. Self-embedded revetment

In this method, blocks between lumps of self-embedded revetment without mortar and other consolidation measures are used, which have characteristics of good stability, fast construction, low cost, adaption to soft ground etc. By optimizing self-embedded structure, self-embedded green revetment is generated. This kind of structure consists of embedded block, plastic stick, filter, and soil, where wall surface and body could be planted. When applied in water environment, underwater structure could have aquatic plants and provide survival space for fish, giving a better interpretation of ecological revetment.

## 3.2 Rural section

Relative to sloping ecological revetment, vertical ecological revetments are slight deficiency in water permeability and hydrophilic. Then sloping ecological revetments could be used in widely section or of waterway.

Vegetation revetment technology includes planting submerged plants, floating-leaved plants, emerging plant and hygrophyte from the foot to the top of slope, which shapes into multi-level ecological protection. The principles of vegetation revetment stabiling slope are vegetation water culvert and soil conservation; both take ecological function and landscape function into account.

## 4 APPLICABILITY OF ECOLOGICAL REVETMENT

Because of resistance and durability is weakness under the influence of water flow and ship wave, so vegetation revetment is mainly applied to waterway which river is wide or original condition is better. Ecological bag revetment has advantages as economic price and high plant coverage, which is applicable to land shortage and poor soil conditions. Box-type revetment has advantages as saving materials and low cost, which is applicable to land shortage and poor soil conditions. Self-embedded revetment has advantages as quick construction and high durability, which is applicable to land shortage and poor soil conditions.

## 5 CONCLUSIONS

1. Ecological revetment is the development trend of revetment construction because of scour prevention and beautifying the environment. Attention should be paid to popularizing it and applying ecology revetment if the desired engineering effects are achieved and conditions are permissible.
2. The application of ecology revetment should follow the requirement of hydrodynamic and surround environment, selection of a reasonable ecological revetment type, and paying attention to the joint using with hard revetment engineering.

## ACKNOWLEDGMENTS

The authors are grateful for the financial support from the Natural Science Foundation of Jiangsu Province (BK2012086). We would also like to thank the anonymous reviewers for their assistance.

## REFERENCES

- Chen Min-xi, Chen Fang-qing. (2007). Application of landscape ecology principle in river levee construction [J]. *China Rural Water and Hydropower*, 49(1):84–87. (in Chinese).
- He Heng, Chen De-chun, Wei Wen-bai. (2005). Ecological bank and its application in regulation of urban rivers [J]. *Water Resource Protection*, 21(6):56–58. (in Chinese).
- Hession W.C., Johnson T.E., Charles D.F., et al. (2000). Ecological benefits of riparian restoration in urban watersheds study design and preliminary results [J]. *Environmental Monitoring and Assessment*, 63:211–222.
- Kristina M. Hufford, Susan J. Mazer. (2003). Plant ecotypes: genetic differentiation in the age of ecological restoration [J]. *Trends in Ecology and Evolution*, 18(3):147–155.
- Wang Xin-jun, Luo Ji-run. (2006). A preliminary study of ecological embankment construction for urban river restoration [J]. *Journal of Fudan University (Natural Science)*, 45(1):120–127. (in Chinese).
- Xia Ji-hong, Yan Zhong-min. (2004). Advances in research of ecological riparian zones and its trend of development [J]. *Journal of Hohai University (Natural Sciences)*, 32(3):252–255. (in Chinese).
- Xie San-tao, Zhu Qing. (2009). Review on Ecological Restoration on Flinty Riparian by Urban Rivers [J]. *Environmental Science & Technology*, 5(32):83–87. (in Chinese).

*Road and bridge engineering*



# Numerical simulation analysis of the pressure-dispersed anchor cantilever retaining wall's effect mechanism

C. Wang

*School of Mechanical Engineering, USTB, Beijing, China*

C. Li, X.G. Song, H.B. Zhang & Q.Y. Meng

*School of Civil Engineering, Shandong University, Jinan, China*

**ABSTRACT:** Based on practical engineering, the pressure-dispersed anchor cantilever retaining wall's effect mechanism was calculated by the FLAC3D program. Through the simulation test, the soil stress, anchor axial force, stress and horizontal displacement of this new type of retaining wall were analyzed, and conclusions were obtained as follows. (1) The upper and lower soil of the anchor plate was in the state of shear and compression, the influence scope was about 1.5 times the anchor plate width on both sides of the plane of the anchor plate, and the shear stress of soil on both sides of the anchor plate was in the opposite direction. (2) The longer the length of the anchor cable, the smaller the horizontal displacements in the operation period and the greater the axial force. (3) When the horizontal displacement of the crown was smallest in the operating period, the horizontal displacement of the bottom slab was the largest. The displacement changed linearly along the wall height, and the horizontal displacement of the whole wall decreased after being prestressed. (4) The horizontal stress of the upper wall was comparatively less, the horizontal stress of the bottom slab was largest, and the stress concentration appeared in the position of the anchor, which became more distinct after being prestressed.

**Keywords:** pressure-dispersed; retaining wall; FLAC3D; effect mechanism

## 1 INTRODUCTION

Pressure-dispersed anchored cantilever retaining wall consists of the cantilever retaining wall, the pressure dispersed anchor rod (rope) and the anchor plate. This type of retaining wall combines the advantages of cantilever, anchor plate and anchor rod retaining wall, and the pressure-dispersion characteristic of pressure-dispersed anchor rope. It is a new type of retaining wall developed in recent years, which improves the overall stability by inflicting prestress to the anchor and has a remarkable effect on high filled embankment slope reinforcement. Currently, studies of this type of retaining wall are few. Xue (2013) analyzed the mechanical characteristic of pressure-dispersed anchor retaining wall consolidated high filled embankment during the construction process. Song (2014) studied the earth pressure distribution regularity of pressure-dispersed anchor retaining wall. Wu (2014) analyzed the earth pressure distribution regularity, mechanical characteristic during the construction period and the operation period of a pressure-dispersed anchor retaining wall, and the major controlling factors that influenced the

bearing capacity of a pressure-dispersed anchored cantilever retaining wall. Wang (2011) carried out the design and calculation of the structural theory of a pressure-dispersed anchor retaining wall, and through some methods such as field monitoring and finite element analysis, the mechanical properties of this type of retaining wall were analyzed under the situation of construction, operation and earthquake, which has deepened the understanding of this new type retaining wall.

Based on the above research and the substantial project of the pressure-dispersed anchor cantilever retaining wall on QingLin expressway, this paper established a finite difference numerical model by FLAC3D, and conducted the simulation analysis of this new type of retaining wall.

## 2 NUMERICAL CALCULATION MODEL

### 2.1 *Fundamental assumption of the model*

To truly reflect the mechanical and deformation characteristics of the retaining wall in the engineering and to study the effect mechanism of the retaining wall conveniently, the following

assumptions were made to the numerical calculation model:

1. There is no longitudinal deformation that occurs along the way of the model;
2. The surface and base materials of the road are elastic, between which the deformation is successive and no slippage or separation will occur;
3. The material of the retaining wall is elastic and there may be slippage or separation among the retaining wall, filling earth behind and foundation soil.
4. Subgrade filling construction is completed in one time, and equal prestress is inflicted to each bundle of the anchor cable.

## 2.2 Model building

In the actual project, a cluster of pressure-dispersed anchors were installed on the retaining wall longitudinally at the interval of 4 m, so the longitudinal size of the model along the road is 3 m. Because the subgrade filler soil is laminar and isotropic, and the model is a typical axisymmetric problem whose axis of symmetry is the center line of the road, half of the actual engineering were taken to analyze when modeling, setting the upper surface of the model free and the others fixedly constrained. Model groups include the subgrade, the foundation, the cantilever retaining wall, and the gravel replacement cushion rubber, and the model size is 30 m \* 4 m \* 19 m (length \* width \* height), the grid size is 0.3–0.5 m, the total number of units is 24224, and the calculation ignores the influence of groundwater. The grid division of the calculation model is shown in Figure 1.

FLAC3D contains multiple structural elements to simulate the beam, anchor cable, pile, shell, geogrid, and lining; among which, shell as the finite

element with identical thickness can be regarded as an isotropic linear elastic material without a failure limit, and cable as the linear element with a uniform section composed of 2 node yields in the tensile and compressive sides, and fails in the resistance of bending moment. According to the basic assumption and the related research of this paper, the shell element was adopted to simulate the subgrade surface, base and anchor plate, and the cable element was employed to simulate the pressure-dispersed anchor. The model structure unit (marked red) is shown in Figure 2.

The size of the anchor plate in the model is 1 m \* 0.6 m \* 0.3 m (length \* width \* height), and the length of the anchor cable is 8 m, 11 m, 14 m and 17 m, with one end of the anchor cable being connected to the anchor plate and the other end connected to the cantilever retaining wall.

In the numerical calculation, there are two main methods to inflict prestress to the anchor cable, namely the command “Sel node apply force” and the command “Sel cable pretension”. Command one is used to inflict prestress load directly to the element node, equivalent to exerting the concentrated load, which is usually used to simulate the influencing process of inflicting prestress to the cable on the working condition and reinforcement mechanism; Command two is used to inflict prestress to each anchor cable, of which each micro portion has the equal stress, before the numerical calculation. This command suits for the situation that the outside anchor head is locked after inflicting prestress to the anchor cable.

Based on the assumption of this article, this passage adopts command two to inflict prestress to the anchor cable, the stress value inflicted to each bundle of the anchor cable is 80 kN.

Because of the significant stiffness difference among the cantilever retaining wall, gravel replacement cushion rubber and soil layer, slippage and

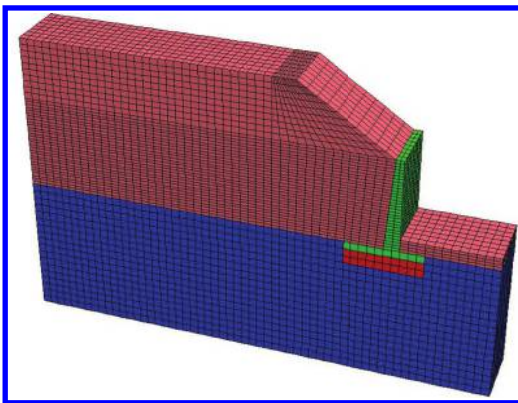


Figure 1. The grid division of the calculation model.

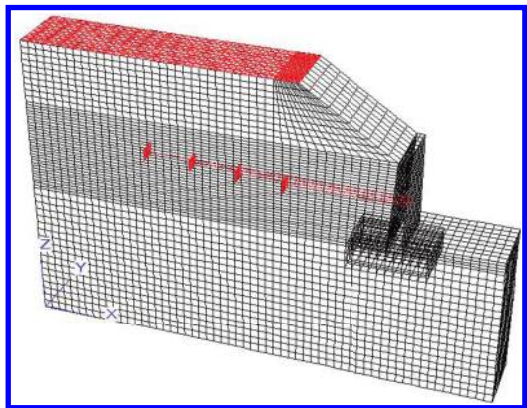


Figure 2. Model structure unit (marked in red).

Table 1. Computational mechanics parameter.

Material	Density ( $\text{kg}\cdot\text{m}^{-3}$ )	Bulk modulus (K/MPa)	Shear modulus (G/MPa)	Cohesion (c/kPa)	Angle ( $\phi/^\circ$ )
Subgrade	1950	8.46e1	3.91e1	41	37
Foundation	1800	3.33e1	1.54e1	15	13
Retaining wall	2550	2.17e4	1e4	**	**
Cushion rubber	1840	3.33e2	1.54e2	0	40
Pavement	2550	**	**	**	**
Anchor plate	2550	**	**	**	**

separation may occur on the actual contact surface. For this purpose, this paper established FLAC3D contact area, to better simulate the slippage and separation on the contact surface.

In order to compare with the influence of prestress on the pressure-dispersed anchor cantilever retaining wall, this paper additionally established the anchor cable calculation model without prestress. The only difference is the anchor cable prestress value before the unprestressed anchor cable model calculation, which can be null or not, while the rest of the parameters, boundary conditions and calculation methods are all the same.

### 2.3 Model parameters

Mohr-Coulomb is chosen as the constitutive model, while for the calculations of soil and gravel replacement cushion rubber, the constitutive model of the cantilever retaining wall is considered as the elastic model. Model parameters can be obtained according to the field survey and indoor experiment. Computational mechanics parameter summary is given in Table 1.

## 3 CALCULATION RESULTS AND ANALYSIS

Calculation process was carried out in accordance with the actual construction, namely establishing the model of the cantilever retaining wall on the weight self-balancing foundation. 80 kN prestress was inflicted to each anchor cable and subgrade filling construction should be completed in one time, and then the numerical calculation of the retaining wall during operation periods can be conducted.

### 3.1 Stress analysis of soil mass

Anchor cable is unbonded type, and anchoring force is mainly provided by the soil around the anchor plate. To analyze the stress state of soils surrounding the anchor plate, shear stress nephogram (Fig. 3) and its local amplification figure

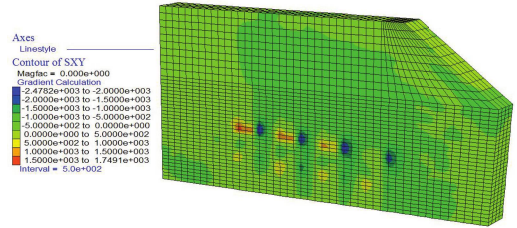


Figure 3. Sxy shear stress nephogram.

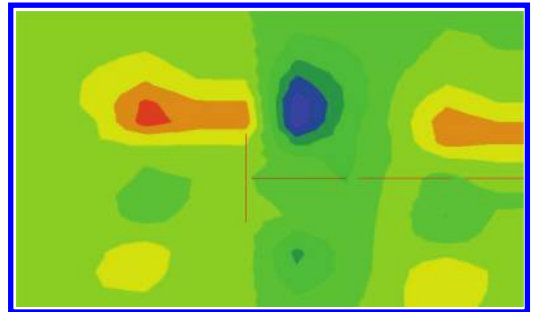


Figure 4. Sxy shear stress nephogram local amplification figure.

(Fig. 4), the principal stress nephogram of soil (Fig. 5) and its local amplification figure (Fig. 6) were extracted.

Figure 3 and Figure 4 shows that the soil around the anchor plate is affected by the shearing action, and the sheared soil is mainly distributed in the upper and lower anchor plate, and 1.5 m to both sides of the plane of the anchor plate, i.e. the main shear influence scope was about 1.5 times the anchor plate width on both sides of the plane of the anchor plate. Besides, the shear stress of the soil on both sides of the anchor plate was in the opposite direction.

Figure 5 and Figure 6 show that the soil around the anchor plate is in the state of compression, the areas of which mainly locate in the upper anchor

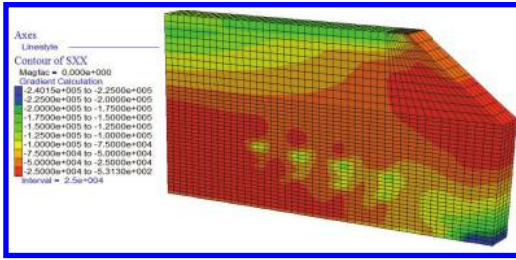


Figure 5. Sxx principal stress nephogram of the soil.

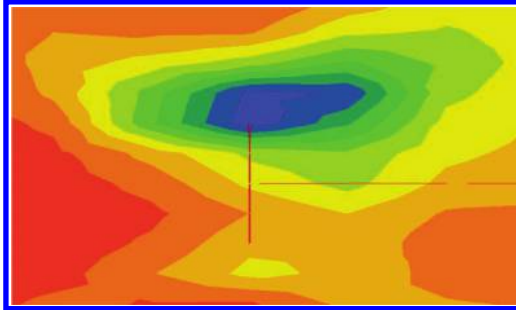


Figure 6. Sxx principal stress nephogram local amplification figure.

plate, while less in the lower soil. The soil under pressure distributes on both sides of the anchor plate, about a 1.5 m range, roughly equal to the distribution of the sheared soil.

Figure 3 and Figure 5 show that the soil around the anchor plates is influenced by shear stress and compressive stress, the values of which are approximately constant in the soil, showing that the distribution of the pressure subjected to the anchor plate is approximately identical; in other words, the pressure is dispersed evenly.

### 3.2 Axial force analysis of the anchor cable

After being inflicted prestress, the anchor cable will be affected by the tension from the cantilever retaining wall in the operation period, which is similar to the process of all-tension after each bundle of the anchor cable is tensioned. So, the axial force is bound to increase. To analyze the change rule of the anchor axial force, each computed result of the anchor axial force in the operating period was extracted, as shown in Table 2.

From Table 2, it can be seen that the shorter the anchor cable, the smaller the axial force in the operating period, which is different from the previous axial force distribution law of unit under equal stress tension<sup>[9]</sup>. Therefore, this paper extracts the displacement vector graph of each anchor plate

Table 2. Axial force of the anchor cable during the operating period.

Anchor plate	Axial force/kN			
Interval	8 m	11 m	14 m	17 m
3 m	80.44	82.03	83.54	85.05

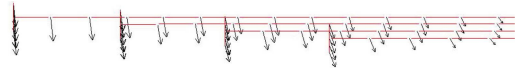


Figure 7. The displacement vector graph of structure units.

element and anchor cable element, as shown in Figure 7. As shown in Figure 7, the displacement vector of the shorter anchor is in the ramp below direction and its horizontal displacement component is bigger; nevertheless, the displacement vector of the longer anchor is approximately in the downward direction and its horizontal displacement component is smaller. Consequently, when the cantilever retaining wall is in integral tension, the elongation per unit length of the longer anchor cable is bigger and the elongation per unit length of the shorter anchor cable is smaller, which manifests that the longer the anchor cable, the larger the axial force increment of anchor cable in the operating period, accordingly the larger the axial force.

### 3.3 Horizontal displacement and stress analysis of the anchor cantilever retaining wall

Through the establishment of the unprestressed anchor cable calculation model, the influence of prestress on stress and horizontal displacement of the cantilever retaining wall was obtained in this paper, as shown in Figure 8 and Figure 9.

As shown in Figure 8, the horizontal displacement on the top of the cantilever retaining wall is the smallest and the horizontal displacement of the bottom slab is the largest, and the displacement changes linearly along the wall height and reaches the maximum on the bottom slab. Compared with the retaining wall anchor cable without prestress, the horizontal displacement of the whole wall decreases after inflicting prestress to the anchor cable, and the maximum horizontal displacement reduced from 17.78 mm to 17.1 mm. Thus, we can clearly draw the conclusion that the infliction of prestress can restrict the lateral sliding of the retaining wall to a certain extent.

As shown in Figure 9, the horizontal stress of the upper wall is smaller and the bottom slab is the largest. This explains the reason why the horizontal

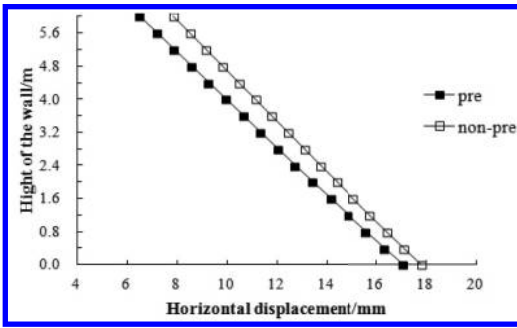


Figure 8. Horizontal displacement of the cantilever retaining wall.

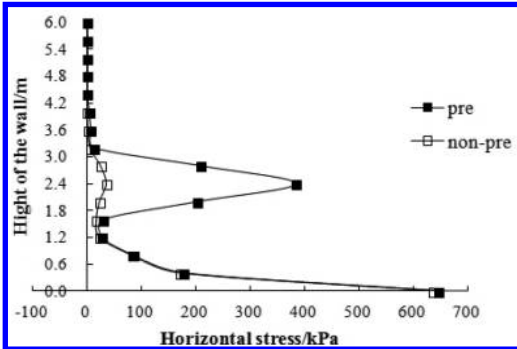


Figure 9. Horizontal stress of the cantilever retaining wall.

displacement distribution is larger at the upper part, while less at the bottom slab. These two sets of curves show the stress concentration phenomenon at the 2.4 m height, which is exactly the position of pressure-dispersed anchor cable layouts. Pressure-dispersed anchor cable make the stress concentration phenomenon emerge at this position and after inflicting prestress, the stress concentration phenomenon is more obvious, in which the peak value increases from 35.02 kPa to 383.8 kPa. While the excessive stress concentration is harmful to the wall mechanic characteristic; therefore, reinforcement treatment should be applied to this area of the retaining wall when designing and construction.

#### 4 CONCLUSIONS

1. Upper and lower soil around the anchor plate of the pressure-dispersed anchor cantilever retaining wall was in the state of shear and compression, the influential area of which is 1.5 m to both sides in the plane of the anchor plate,

i.e. the influential scope was about 1.5 times the anchor plate width on both sides of the plane of the anchor plate, and the shear stresses of the soil on both sides of the anchor plate are in the opposite direction.

2. The longer the length of the anchor cable, the smaller the horizontal displacements in the operation period, and thus the greater the axial force.
3. When the horizontal displacement of the wall crown is smallest in the operating period, the horizontal displacement of the bottom slab is the largest. The displacement increased linearly along the wall height and the horizontal displacement of the whole wall decreased after being prestressed.
4. The horizontal stress of the upper wall is comparatively less and the horizontal stress of the bottom slab is the largest. The stress concentration appears in the position of the anchor, which is more severe after being prestressed. Such excessive stress concentration is harmful to the wall mechanic characteristic. Therefore, reinforcement treatment should be applied to this area of the retaining wall during designing and construction.

#### REFERENCES

Chen S.Y. 2012. Numerical Simulation on Anchoring Mechanism of Pressure-dispersion Anchor Cable and Dynamic Response of Ground Motion. *Wuhan University of Technology*.

Song X.G. 2014. Analysis on Earth Pressure Distribution of Dispersed Pressure Retaining Wall. *Science Technology and Engineering*, 20:106–110.

Wang H.H. 2011. Support Theory and Application of Pressure-Dispersed Anchor Cantilever Retaining Wall. *ShanDong University*.

Wu J.Q. 2014. Analysis of Mechanical Properties for Dispersed Pressure Retaining Wall during Construction and Operations. *Highway*, 06:36–40.

Wu J.Q. 2014. A Model Test Study of Mechanical Behavior for the Dispersed Pressure Retaining Wall. *Industrial Construction*, 09:83–87.

Wu J.Q. 2014. Bearing Capacity Analysis on Pressure Dispersion Suspended-anchor Retaining Wall. *China Concrete and Cement Products*, 10:82–86.

Xia Y.Y. 2008. Numerical simulation analysis of pressure diffusion anchor cable's effect mechanism. *Rock and Soil Mechanics*, 11:3144–3148.

Xue Z.C. 2013. Stress Characteristics of Pressure Dispersive Retaining Wall for Supporting High-filling Embankment during Construction. *Journal of Highway and Transportation Research and Development* 04: 11–16.

Zhang Y.X. 2009. Influence of stretching technology on load non-uniform coefficient of pressure-dispersive anchor cable. *Chinese Journal of Rock Mechanics and Engineering*, S1:2954–2959.

## Simulations of transit priority under multi-flow conditions

J. Ding, Y.Y. Ma, M. Yang & W. Wang

School of Transportation, Southeast University, Sipailou, Nanjing, P.R. China

**ABSTRACT:** Transit priority is a fundamental support for improving buses' level of service. The most common way to ensure the buses to run fluently is to equip roads with bus lines. Besides, buses can get signal priority in some cases. To evaluate the effects of transit priority on the entire intersection under different traffic flows, the Shuanglong-Jiyin Intersection was taken as a case. According to the simulations results, hybrid transit priority together with bus line and signal priority can cut down 60% of intersection delay, but transit priority should be considered when the intersection is under heavy traffic pressure.

**Keywords:** transit priority; bus line; signal control; microscopic simulation; traffic flow sensitivity

### 1 INTRODUCTION

The transit priority has numerous intensions since the development of nearly six decades (Yagar, S. 1993, Ji, Y.J. et al. 2005, Arasan, V.T. & Vedagiri, P. 2010). The most direct and operable to help the transit system operate efficiently is to give more right-of-way to buses. Generally, two main parts of transit priority in the right-of-way are exclusive bus lines in the space level and the signal priority in time level (Sunkari, S.R. et al. 1995). More and more cities are establishing their bus lines, and signal priority has been applied in some cases, although it's not as popular as the former strategy. Thus, it may be interesting to explore the effects of different kinds of transit priority strategies under different conditions.

According to early researches, the exclusive bus lines can improve the safety and pollution of transit system, as well as increasing the travel speed of buses by more than 10% (Zargari, S.A. & Khan, A.M. 1998). Signal priority can promote the buses to operate more smoothly in the intersection (Li, J. et al. 2012, Shen, F. & Yang, X.G. 2009). Ma and Yang (Ma, W.J. & Yang, X.G. 2006) tried three signal strategies by simulation, consequently, the delay of buses might drop sharply and meanwhile, it could interrupt automobiles to different extents.

However, few early studies can combine the spatial and temporal transit priority together and most the simulations focused on the original traffic flow rate, therefore, the effects of transit priority can't be evaluate in a relevant wide range, and the references for building up transit priority might be unscientific owing to the lack of experiments.

To explore the performances of buses and automobiles under different priority strategies and traffic flow rates. Shuanglong-Jiyin Intersection

was simulated in the microscopic simulation tool, VISSIM. Three scenarios was designed, which are the current scenario, the bue line only scenario and the bus line with signal priority scenario. Each scenario has 10 flow rates reformed from the observed data.

### 2 DATA

The study is based on the case of the Shuanglong Road—Jiyin Road Intersection. The Shuanglong Road is an arterial road which stretches from south to north. It has all together 8 lanes, with the bus going straight through the road. The Jiyin Road is a secondary main road in Nanjing, China, and

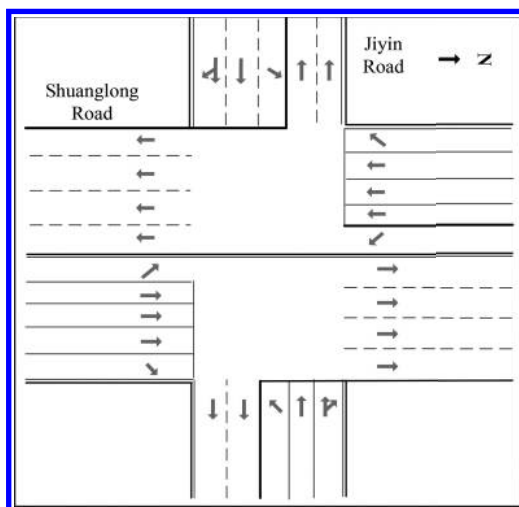


Figure 1. The canalization of Shuanglong-Jiyin Intersection.

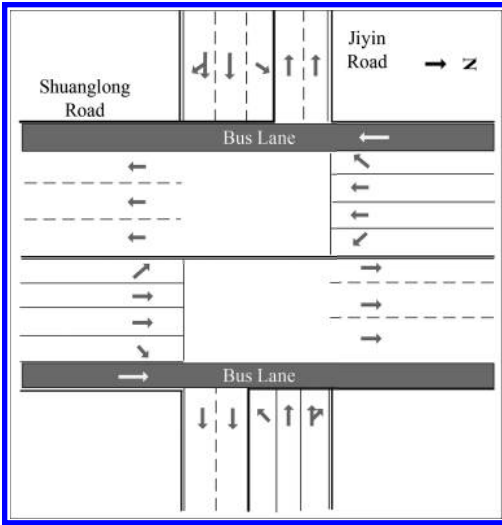


Figure 2. The canalization with bus lines.

Table 1. Traffic flows of Shuanglong-Jiyin Intersection (pcu/h).

Entrance	South	North	East	West
Left	188	178	136	135
Straight	1654	1637	812	831
Right	180	199	90	96

it crosses with the Shuanglong Road vertically. To verify the effectiveness of the priority for buses, the study puts a bus line on the outer side of the intersection. The intersection's original and reformed canalizations are showed in Figure 1 and Figure 2. The traffic volumes of the intersection are acquired through video tapes on the morning peak period in a work day. The statistics are shown in Table 1.

### 3 SIMULATIONS

#### 3.1 Building the simulation scenarios

The microscopic simulation software VISSIM is used in the study. To verify the influence on the intersection if giving the priority to buses, the study researches on three different simulation scenarios: the original one, the one with the bus line only and the one that applies the bus line and the signal priority at the same time.

**Scenario 1:** The original scenario, which is completely the same with the real conditions.

**Scenario 2:** The road with the bus lane. The bus lane is placed at the sides of Shunanglong road,

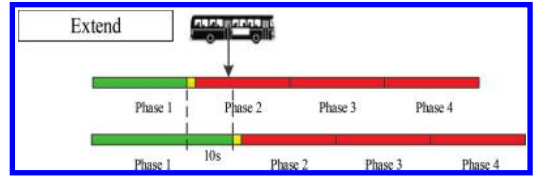


Figure 3. Extend the green time for buses.

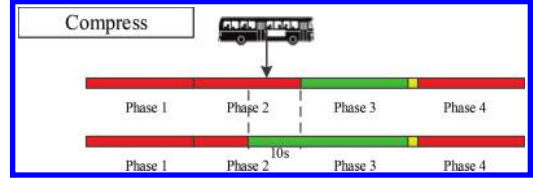


Figure 4. Compress the green time for the former phase.

as shown in Figure 2. The signal timing, however, is still in accordance with the field statistics.

**Scenario 3:** Use the bus line and the signal priority at the same time. Add a bus arrival detection which uses the “green time starting early and cutting off late” method to give buses the priority in the signal timing. The detailed method is explained as follows.

#### 3.2 Signal priority for buses

The bus arrival detection is placed about 80 meters before the stop line. Once the detector is activated, it immediately judges whether the phase for buses is green light or not. If the signal is green, then nothing has to be changed, otherwise, the time difference between the activated time to the beginning and end of the pass phase for buses should be compared. If the time difference to the phase beginning is shorter, then the pass phase for buses will start 10 seconds earlier. Contrarily, the phase end will extend for extra 10 seconds. The process is illustrated in Figures 3 and 4.

In order to find out the influence that bus priority will bring to the intersection on different scenarios, the study uses 10 different volumes for each scenario. New volumes are acquired by multiplying the original volume with 60%–105%, and the interval is 5%.

### 4 ANALYSIS AND DISCUSSIONS

Delay is often used as an index in evaluating the efficiency of travelling. The study tests on 10 different volumes through 3 scenarios. The results are shown in Figure 5.

From the figures above, we can draw the conclusion that the delay of buses is relatively stable

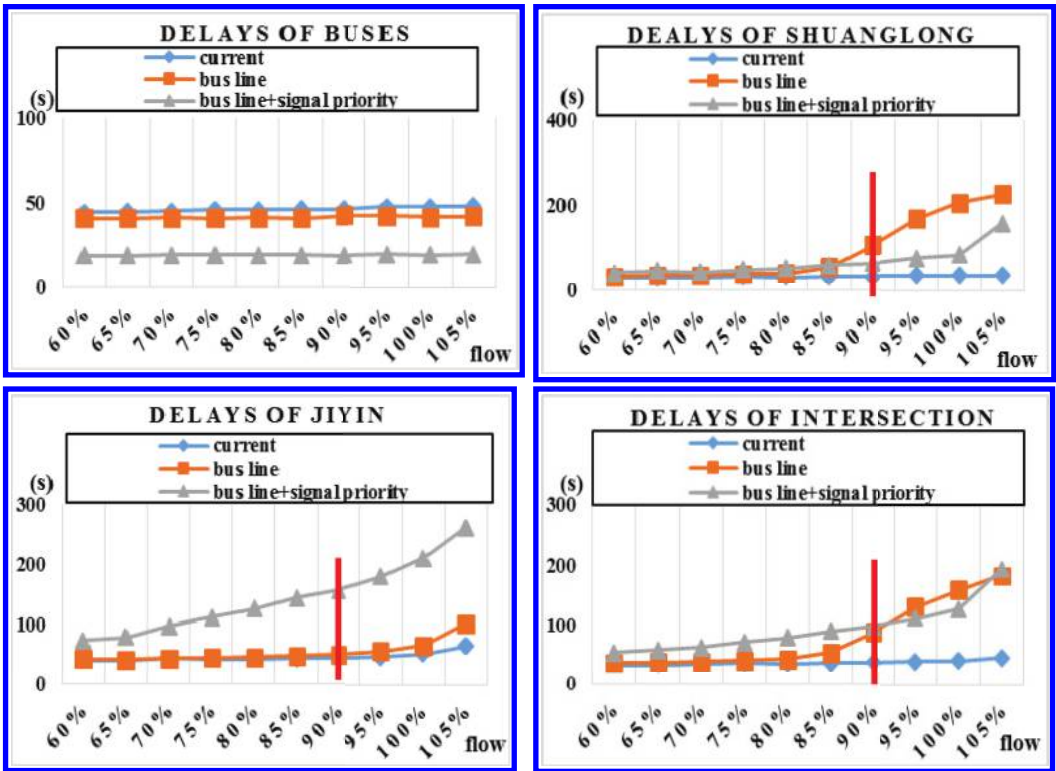


Figure 5. Delays of simulation results.

no matter what the scenario is. The bus line could decrease delay for about 10%. Together with signal priority, the delay could drop significantly for more than 50%. Thus, the priority for buses, especially the integrated one involves time and space, will bring huge augment in the efficiency of travelling of buses.

However, as an arterial road, the Shuanglong Road doesn't get benefits. The priority for buses means less road resources for social vehicles, and thus the delay of social vehicles increases, especially when the volume grows bigger than 90% of the original one. Under that circumstance, there will be severe congestions at the intersection, and thus this condition is inappropriate for the priority for buses. What's more, it's noticeable that some social vehicles which share the same phase with buses also get benefits if the buses have signal priority. That can explain why the delay of social vehicles in Scenario 3 is much smaller than that in Scenario 2.

Bus priority has some negative influences on the traffic capacity of secondary main road. Because when the signal controllers accept the priority applications of buses, more green time will be provided for the phase for buses and social

traffic sharing the same phase with them, which also results in lower probability and higher delay for vehicles travelling on the secondary road to pass the intersection. The signal priority increases its delay further. Even though the volume is 90% of the original one, bus priority will still trigger the collapse of social vehicle system. The last diagram in Figure 5 illustrates that when the volume in intersection is close to its saturation point, the bus priority affects the passage of social vehicles greatly.

## 5 CONCLUSION

The bus priority is an unavoidable trend for the development of the public transit. The hybrid temporal and spatial priority for buses can boost buses' efficiency of travelling remarkably, but its application should be considered carefully according to the real conditions, as what we want to achieve is that we can operate the whole transportation system with as few congestions as possible, the bus priority shouldn't ignore the social traffic who run on the road recently. Also, the most efficient bus priority happens under the condition that



local automobiles don't have the ability to fulfill the roads.

This passage is based on the case study of the Shuanglong Road and Jiyin Road Intersection, tested the sensitivity under different volume conditions by the microscopic simulation software on three different scenarios: the original one, the bus line only one and the bus line plus signal priority one. The study shows that, in this case, the hybrid temporal and spatial priority for buses can decrease the delay of buses for more than 60%, but it affects the efficiency of social vehicles. So when the volume of intersection is close to its saturation point, the application of bus priority should be further considered. Besides this, finding out a priority method that can handle the contradiction between buses and social vehicles, and generalizing it into all traffic webs, is definitely a key point in future studies.

#### ACKNOWLEDGEMENTS

This study is supported by the National Key Basic Research Program (NKBRP) of China (No. 2012CB725402), the National Natural Science Foundation of China (51338003 and 51378120) and the Student's Research and Technology Program (T15212015).

#### REFERENCES

- Arasan, V.T. & Vedagiri, P. 2010. Microsimulation study of the effect of exclusive bus lanes on heterogeneous traffic flow. *Journal of Urban Planning and Development*, 136(1): 50–58.
- Ji, Y.J., Deng, W., Wang, W. et al. 2005. Study on the Design of Signal Phase Based on Bus Priority Intersections. *Journal of Highway and Transportation Research and Development*, 21(12): 118–122.
- Li, J., Wang, W., Van Zuylen, H.J., et al. 2012. Predictive transit signal priority strategy at fixed-Time signalized intersections: Case study in Nanjing, China. *The Annual Meeting of Transportation Research Board*. Washionton D.C.: the United States.
- Ma, W.J. & Yang, X.G. 2006. Study on Calculation of Real-time Delay and Simulation at Signalized Intersection. *Computers and Communications*, 24(3): 1–4.
- Shen, F. & Yang, X.G. 2009. Research on Multi-objective Optimization Algorithm of Urban Road Traffic Lights. *Journal of Tongji University (Natural Science)*, 7: 898–902.
- Sunkari, S.R., Beasley, P.S., Urbanik, T. et al. 1995. Model to Evaluate the Impacts of Bus Priority on Signalized Intersections. *Transportation Research Record: Journal of the Transportation Research Board*, 1494: 117–123.
- Yagar, S. 1993. Efficient transit priority at intersections. *Transportation Research Record*, (1390).
- Zargari, S.A., Khan, A.M. 1998. A simulation model of the bus transit way. *Journal of advanced transportation*, 32(2): 152–174.

# Diseases of long span steel bridge pavement and their solutions

Shanshan Ji, Yaxun Yang & Gao Gong

*Highway Institute in Chang'an University, Xian'an, Shanxi, China*

**ABSTRACT:** This paper mainly focuses on the analysis of the stress state of long span steel orthotropic plate and highlights the influence of the structure of bridge deck on the mechanical characteristics of the bridge pavement. Also, it uses Ansys to simulate that condition. At the same time, aiming to solve the diseases, we could try to find answers from the structure of the bridge deck and materials.

**Keywords:** orthotropic plate diseases; materials; bridge pavement

## 1 INTRODUCTION

With the development of road transport, rapid development has been made in bridge construction technology. Bridges of sleek and innovative structure at medium-size continue to emerge across the country. Deck as an important component of the overall structure of the bridge, its quality and durability directly affect safety, comfort of driving, durability, and investment benefits during operation. But over the years many of China's new long-span bridges (e.g. the Jiangyin Yangtze River Bridge, the Runyang Yangtze River Bridge) in deck paving of steel bridge, they have suffered various degrees of damage, seriously affecting the driving comfort and durability of steel girder. And these long-span bridges as a transportation hub, repairing them would bring a great deal of disturbance to the community, and costing a large sum of money. So, the study of the causes of large-span bridge deck pavement damage has a great value, also guiding us to find a solution to this problem.

## 2 ANALYSIS OF CAUSES FOR DEFECTS

Bridge deck gets damaged for many reasons, including all aspects of design, construction, the environment of operations, and conservation. The design of deck pavement is unreasonable, or construction technology and construction organization are not comprehensive, over-weight vehicle traffic overload, untimely conservation, which are the main causes of such diseases. With complicated geometry and large flexibility, the stress state of orthotropic steel panel pavement is more complex

than the ordinary cement concrete pavement. Thus, under the external force, they will produce a lot of shear stress between layers, and corresponding higher interlayer adhesion requirements. From the whole of the structure, the steel box girder is an excellent main beam structure. However, due to the special quality of its structure, steel deck pavement has often some diseases occurring on it. Similarly, the destruction of the adhesive layer between the pavement and the steel greatly reduces the composite action, and even may accelerate the destruction of pavement. The reasons for the rut include heavy traffic, channelization of traffic and the nature of pavement materials. But at the same time, we should also take into account the effect of the orthotropic bridge deck structure on force of the bridge deck pavement.

## 3 SOLUTIONS

In view of the above analysis of the causes of disease, we can solve this problem from two aspects. First, orthotropic deck plate is an excellent form of bridge structure; however, it is not researched deeply at the present stage and the stress state lacks clarity, which may lead to some unforeseen problems when designing. Therefore, strengthening the research to find a reasonable form, or giving a reasonable reference range of design parameters, has a great significance in guiding the designer. At the same time, asphalt concrete has been used for a long period, and has the advantage such as comfortable driving. But it also has its own shortcomings. And asphalt concrete may be not the best combination with steel bridge, so we can try to find a new alternative material.

### 3.1 The impact of performance of the orthotropic steel bridge deck on bridge deck pavement

To investigate this question, we use a finite element software, Ansys, to simulate a long-span steel bridge deck in China. The simulation uses a simplified model. The basic model of structure is shown in Figure 3. By simplifying the structure, we can save a large amount of calculation, which is very convenient for the designer to simulate the deck of the bridge. During FEA simulation, we use shell181 element to mesh the structure and control the size of element at 10 mm. Due to stress concentration of wheel load, it is necessary to refine the grid, whose Young's modulus is equal to 210000 MPa and Poisson's ratio is equal to 0.25. Model sizes involved in the argument are listed in Table 1.

At the same time, we need to simplify the wheel load. The wheel load is distributed on double rectangles, as shown in Figure 1. There are two load rectangular areas, with the width set to 200 mm and the length converted according to the load size. When the length is translated into approximately 250 mm, the weight of the rear axle is about 14 ton. A square load is used to adapt the shape of the element. The distributed load size is 0.7 Mpa, as shown in Figure 2.

In order to find the most unfavorable load position, we need to create the FEA model, and put the load on the designated place and then get the most unfavorable position. First, we need to select some position, as shown in Figure 4.

Table 1. Parameters of the structure.

Thickness of the roof	12	U-shaped rib height	280
Diaphragm distance	3200	U-shaped rib width	300
U-shaped rib spacing	600	U-shaped rib thickness	6

Note: Unit in mm.

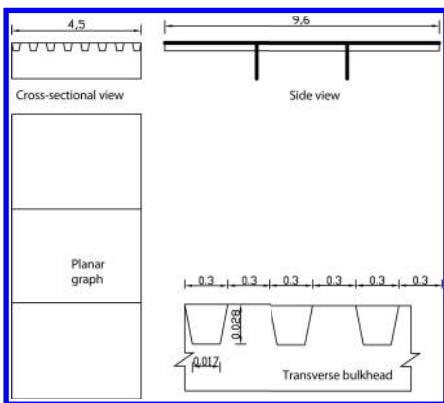


Figure 1. Diagram of the basic model structure size.

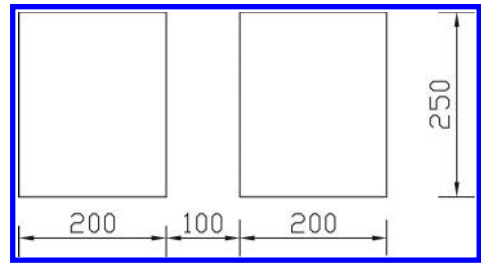


Figure 2. Wheel load diagram (Unit: mm).

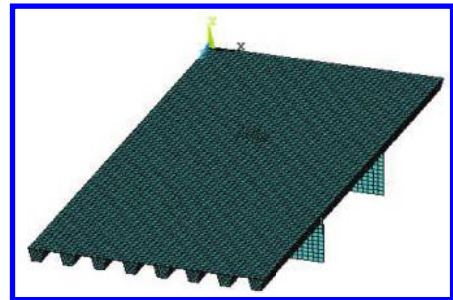


Figure 3. Simplified model of orthotropic bridge deck in Ansys.

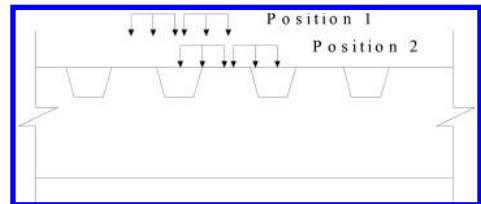


Figure 4. Lateral position of vehicle load.

We need to check the lateral loads on different locations and find the maximum value. Also, we need to arrange the position of the vehicle load in the longitudinal direction.

In the process of loading to the model, by comparing, we can find out the most unfavorable load position, observing the distribution regularity of stress and strain under the double-deck wheel load.

As can be seen from the figure, the force of orthotropic bridge deck is very complex, and under the wheel load, the maximum tensile strain occurs in combination of ribs with the bridge deck, reaching its maximum value of 549  $\mu\epsilon$ .

This can easily lead to fatigue cracking of the deck pavement under repeated loads and vehicles that cause pavement slip off due to insufficient

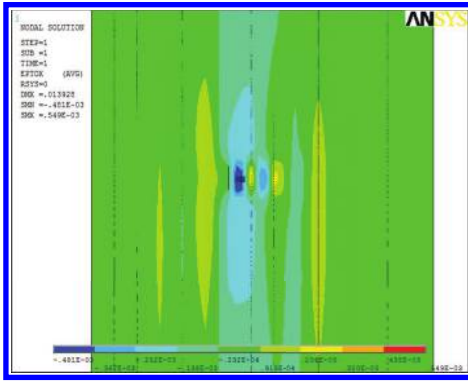


Figure 5. Transverse strain.

capacity shear of the adhesive layer. This is also the main reason for the destruction of the bridge deck early. The main reason of crack is the complex of bridge deck and severe traffic environment, which are prone to make pavement produce fatigue cracking, such as steel bridge, asphalt pavement deck supported by steel deck acted by the vehicle load will produce deformation leading to longitudinal stiffeners, transverse bulkhead or transverse stiffeners, clapboard, stiffening girder webs and other components and welded steel deck at a high-stress area. Moreover, it would produce a greater negative moment in the pavement at the position that tensile stress or tensile strain concentration area of at the surface of the pavement at these locations. Crack appeared first on the surface of the pavement, and then gradually developed to the underside. In the longitudinal stiffeners, the surface of deck pavement the main beam web will appear longitudinal cracks, transverse cracks at the surface of the deck pavement, transverse bulkhead or transverse stiffeners and at the intersection of the transverse bulkhead and stiffeners, pavement surface prone to develop into a network of cracks. With pavement cracking and slip, some steel panels will be further damaged. Since this disease is caused by the characteristics of orthotropic plate structural, we can adjust some parameters structure to control the maximum value of positive strain reasonably. With foreign scholars having used the finite element method, by 8-node isoparametric element analysis of space with a roof deck stiffener, obtaining the position of the vehicle loading on the deck pavement surface where transverse tensile stress achieved maximum, we can, from the viewpoint of tensile failure, get the suggested values, such as spacing between stiffeners, beams and thickness of steel plate. For example, the width of the U-shaped rib should be not more than 350 mm. The recommended parameters have better guidance for design.

### 3.1.1 Effect of opening width of U-shaped rib on orthotropic plate

We still use the same FEA model, just changing the opening width of U-shape and watch the change of transverse tensile strain values. As shown in Figure 6, it is the result of the situation where the width is equal to 0.5. From the picture, we can get the maximum value of transverse tensile strain (i.e. 1020  $\mu\epsilon$ ). We can build other model in the same way, and list the result on Table 2.

From the table and Figure 7, we can get the conclusion that with the increasing opening width of U-shaped ribs, the maximum value gets larger. So, when we design the size of the ribs, we should control the size during the suitable range. Last but not least, we also can research the effect of the thickness of deck and space of the diaphragm.

### 3.2 Finding a new bridge deck replacement material

Asphalt is certainly not the best material for long-span steel bridge deck. Temperature properties of bituminous materials are poor, and prone to cracking in winter, to soften in summer and higher thermal efficiency of steel structures and combined with the complex mechanical characteristics of orthotropic, so it is easy for bridge pavement made of asphalt concrete deck to catch crack. Asphalt concrete is difficult to overcome the shortcomings of its own.

Ultra High Toughness Cementitious Composite (UHTCC) is a good choice. UHTCC came out not

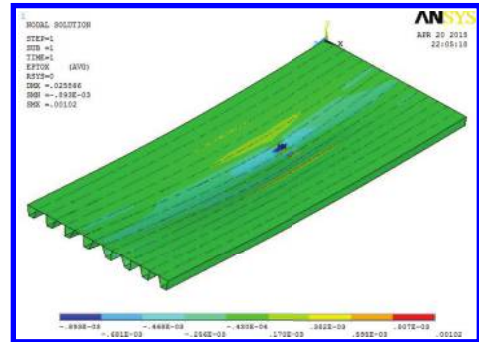


Figure 6. Maximum value of transverse tensile strain.

Table 2. Regular of changing opening width.

Opening width (mm)	Max value of transverse tensile strain ( $\mu\epsilon$ )
300	549
400	706
500	1020

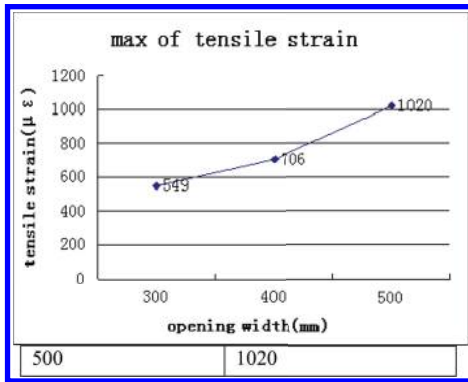


Figure 7. The effect of the opening width of the rib.

long ago, but researchers carried out many studies, and research results also show us the strengths of the material. It is sure that all the RC members inevitably crack, and cracks conventionally from concrete structures usually are above one millimeter. It can also be seen from these advantages that UHTCC is more suitable to work with orthotropic plate than asphalt concrete. First, UHTCC in direct tension and strain can best be stabilized at 3%, and sometimes as high as 6%, hundreds of times that of ordinary concrete, 10–20 times that of yield strain of the steel bar. At the same time, when it reaches the ultimate tensile strain, crack corresponds to no more than 100 μm, which are difficult to detect with the naked eye. Self-heal refers that the material has ability to repair cracks without any outside intervention. Crack self-healing can reduce the width of the fractures, so that the durability and mechanical properties of materials can be improved, which is important to the security of structure and extending the useful life of infrastructure. Meanwhile, UTCC is a new kind of material with a high-performance fiber-reinforced cementitious composites. Because it has performance of multiple cracking and excellent controllability of the crack width, it has a more excellent self-healing properties. At the same time, we can find the strength of the UHTCC by comparing the experiment with normal concrete. The result is shown in Figure 8.

It is clear that UHTCC has higher carrying capacity and better deformability than normal concrete, which is important for the material used as pavement, especially suffering largely repeated vehicle load. Obviously, if we use this material, we need not worry about cracks due to exceeding the maximum tensile strain, and even at the ultimate tensile strain, its protective effect on the bridge deck still exists. Furthermore, the temperature linear expansion coefficient of UHTCC and steel is closer, so the two can work better.

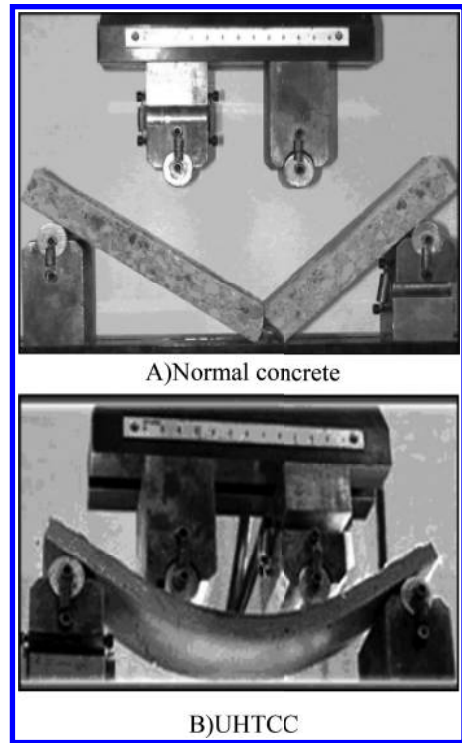


Figure 8. Bending test of high strength concrete.

### 3.3 Conclusions

From the above analysis, we can get that there are two main reasons of the damage of the bridge pavement especially for a long span bridge. First, the special structure of the orthotropic plate can produce complex stress and strain state, being prone to crack. Second, we notice the inherent weakness of the asphalt. According to these main reasons, we find different methods to overcome the diseases of the pavement. Controlling the size of the U-shaped ribs, thickness of plate and finding new alternative materials is a good way. Thus, UHTCC is a good choice.

### REFERENCES

- [1] Zhang Xiufang Xu Shilang: Improvement of the flexural and cracking behavior of RC beams using ultra-high toughness cementitious composites (I): theoretical analysis.
- [2] Xu Shi-lang, Li Qing-hua: Performance and Application of Ultra High Toughness Cementitious Composite.
- [3] Huang Wei, Liu Zhen-qing: Research on theory and method of long span steel bridges deck surfacing design.

# The research on the internal force effect of different vertical curves on a curved box girder bridge

Yu-xiao Liao & Jing-hong Gao

Department of Mechanics and Civil Engineering, Jinan University, Guangzhou, China

Key Laboratory of Disaster Forecast and Control in Engineering, Ministry of Education of China, Guangzhou, China

**ABSTRACT:** Using the stimulated structure MIDAS Civil to conduct the calculation with REM modeling, this paper analyzes the internal force of the curved girder bridge whose radius of curvature is  $R = 200$  m. Under the condition of the unaltered span and radius of curvature, this paper investigates the effect of the internal force variation of the continuous curved box girder bridge that is influenced by permanent load and moving load with different vertical curves.

**Keywords:** curved girder bridge; vertical curves; internal force variation

## 1 INTRODUCTION

With the rapid development of scientific technology and economy, nowadays, the quality of the construction of highway bridges has become critical increasingly. Compared with the traditional bridges that suffer the impact of terrain, surface features and floor space, curved bridges are widely applied to the modern highways as well as urban overpasses, with their numbers also increasing every year. The requirements for the highways and their bridges are not only to ensure the rationality and the networked characteristic, but also to enhance the line grade for accelerating the speed, improving security and comfort. In recent years, curved bridges have attracted much attention from China's national engineering, and are increasingly applied to the highways and urban overpasses.

The operating function of curved bridges mainly depends on the curvature. When vertical load works on the bridge, the bending moment and torque of the curved bridge will come into contact simultaneously and interact with each other, complicating the mechanical analysis of curved bridges. When the centrifugal force of the live load works on the curved bridge, the lateral bending moment and torque of the curved bridge will appear, complicating the stress of the curved bridge as well. Therefore, it is very useful and necessary to determine the principles of designing and the methods of calculating.

## 2 PROJECT OVERVIEW

In this section, a straight girder bridge with a span of  $36\text{ m} + 60\text{ m} + 36\text{ m}$  is considered. Many nodes

are set in the top and bottom of supports. In the bottom of each support, a general support constraint (constrain of D-all) via elastic connection (general) is simulated (which means the strength of supports). Finally, the top of the support and girder are connected in a rigid manner.

A curved of the box girder bridge is modeled with Midas. Here, its radius of curvature is 200 m, and longitudinal gradient varies from 0 degrees to 6 degrees (where the alpha is changed from 0 degrees to 6 degrees). Then, they are analyzed and contrasted between several box girder bridges with the same span but different longitudinal gradients.

## 3 FINITE ELEMENT MODEL

The main girder is modeled by 3-Dimension. A fixed boundary condition is set in the bottom of the bridge pier. Its longitudinal gradient varies from 0 degrees to 6 degrees gradually. In this model of continuous bridge piers, the whole bridge is divided into 149 nodes and 76 unites, and the main girder nodes occupy from 1 to 77 and unite to take 1 to 76 around them. The X, Y, Z axes are created

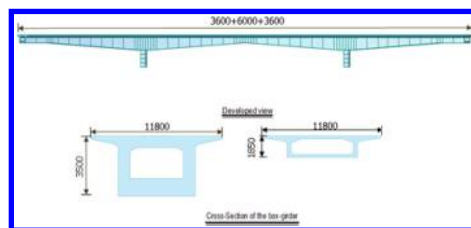


Figure 1. Curved continuous box girder bridge.

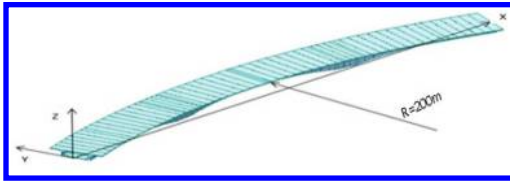


Figure 2. Finite element model.

across the centerline in one side of the girder and extended to the other side, as shown in Figure 2.

#### 4 ANALYSIS RESULT OF THE FINITE ELEMENT MODEL

For the curved girder is a symmetrical structure, the analysis result is worked out in the force of permanent loads and pre-stressing strain force. Units 2, 21, 39, 57, and 76 are considered for analysis.

##### 4.1 In the work of permanent load

At different longitudinal gradients, the axial force, torque, bending moment Y, and bending moment Z are shown in Figures 3 to 6.

In the force of self-gravity, the curved girder with 0 degrees of longitudinal gradient operates with little axial force and bending moment in the Z axis, which can be ignored. When the longitudinal gradient grows with gradient per degree, the axial force, torque, and bending moment of the Z axis of the girder increase gradually. The maximum axial force in the middle of the span is 1911 KN, which is close to the theoretical force. The torque and bending moment that developed by self-gravity are steady with the change in the longitudinal gradient. And the anti-banding moment of the girder around the support is in a large force, and the maximum anti-banding moment is 122591 KN·m, which is also is close to the theoretical result.

Comparing between axial force, torque, and bending moment created by self-gravity, it can be seen around the sheet. With the increasing longitudinal gradient, axial force increases at a rate of 32%, torque decreases at a rate of 8.7%, the bending moment in the Y axis has no change, the bending moment in the Z axis increases obviously at a rate of 370%, which has a maximum bending moment of 3133 KN·m when the longitudinal gradient is 6 degrees.

##### 4.2 In the work of moving load

At different longitudinal gradients, the axial force, torque, bending moment Y, and bending moment Z are showed in Figures 7 to 10.

Under the moving load, the radius of the 200 m curved bridge's axial force increases gradually as the

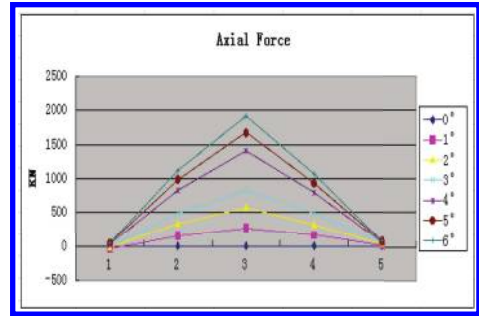


Figure 3. Permanent load-axial force.

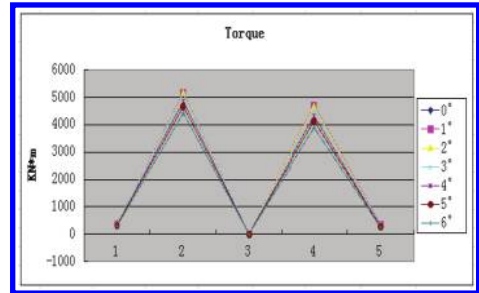


Figure 4. Permanent load-torque.

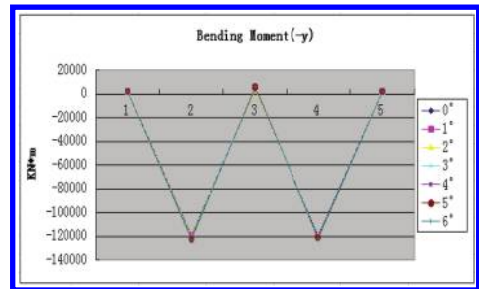


Figure 5. Permanent load-bending moment (-y).

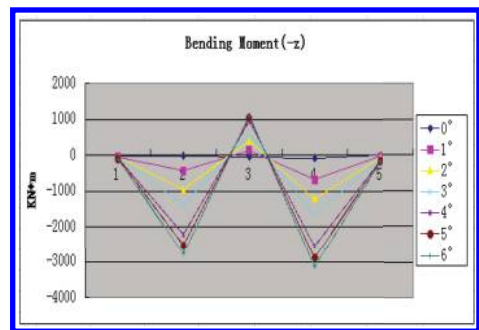


Figure 6. Permanent load-bending moment (-z).

Table 1. Permanent load.

Increase in the rate of gradient	Increase in the rate of axial force (%)	Increase in the rate of torque (%)	Increase in the rate of bending moment (-y) (%)	Increase in the rate of bending moment (-z) (%)
0°	0.00	0.0000	0.0000	0.00000
1°	0.49	-0.0077	0.0019	07.3241
2°	0.32	-0.0254	0.0047	13.9291
3°	0.31	-0.0456	0.0075	19.2497
4°	0.42	-0.1072	0.0151	30.2424
5°	0.28	-0.1465	0.0191	34.3855
6°	0.15	-0.1888	0.0231	37.3724

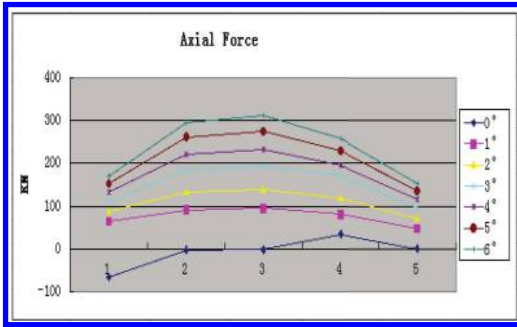


Figure 7. Moving load-axial force.

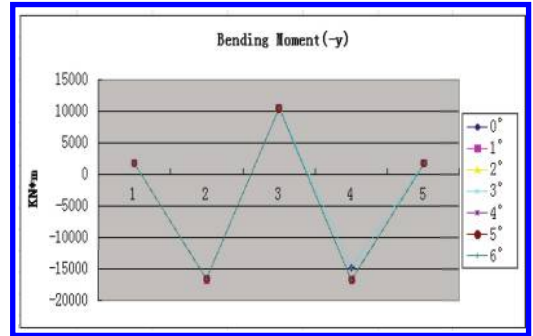


Figure 9. Moving load-bending moment (-y).

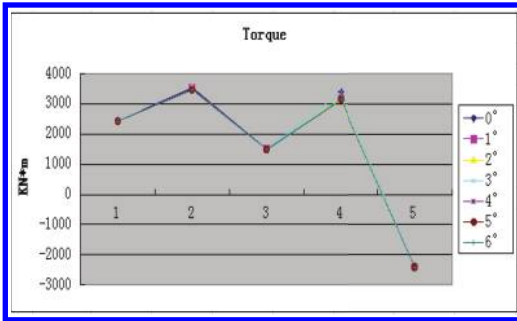


Figure 8. Moving load-torque.

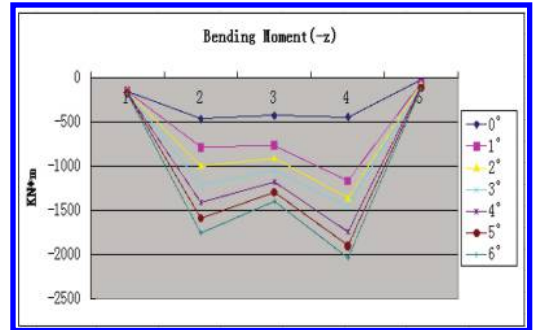


Figure 10. Moving load-bending moment (-z).

slope increases and the change is obvious, but their values are not within reasonable limits. The slope of the zero curved bridge in the z-direction bending moment is small, which can be approximated to zero. As the slope increases, the corresponding torque, axial force, and bending moment in the z direction increase gradually. The middle span axial force is maximum 2036 kN, which does not differ significantly with theoretical result. The torque and bending moment developed by self-gravity are steady with the change in the longitudinal gradient.

And the anti-bending moment of the girder around the support is in a large force, and the maximum anti-bending moment is 120752 KN·m, which is also close to the theoretical result.

Under the moving load, as the slope increases, the axial force increases by 20%. However, the torque is reduced relevantly, but its values differ little. In the Y and Z directions, bending moment increases by 10%, but it is still in the same order of magnitude, which can be ignored in actual projects.



Table 2. Moving load.

Increase in the rate of gradient	Increase in the rate of axial force (%)	Increase in the rate of torque (%)	Increase in the rate of bending moment (-y)(%)	Increase in the rate of bending moment (-z)(%)
0°	0.0000	0.0000	0.0000	0.00000
1°	0.4700	-0.0613	0.1267	0.6209
2°	0.4500	-0.0016	0.0010	0.1687
3°	0.1257	-0.0016	0.1103	0.0755
4°	0.1819	-0.0673	0.1272	0.1868
5°	0.1233	-0.0044	0.0019	0.0940
6°	0.2400	-0.0053	0.0021	0.0722

## 5 CONCLUSION

Base on the internal force data by varying the longitudinal gradient in a symmetric curved girder, conclusion can be drawn. Designing a main curved girder spanning less than 60 meters can be followed by that. In self-gravity, there is a steady bending moment in the Y axis, so the method of strengthening could be done in the same was as the normal horizontal girder. However, an obviously increasing bending moment in the Z axis must be taken care when the longitudinal gradient is changed. The torque decreases by 8.7% at the lift longitudinal gradient, which is due to the complex interaction between the bending moment and torsion, so this should not be ignored while designing.

## REFERENCES

- Dong, J. and R. Sause: *Engineering Structures*, 2010. 32(1), p. 319–327.
- Gu, X., S.-Y. Xie, and S.-M. Jia: Analysis of parameters influence on structure of continuous curved bridge. in 3rd International Conference on Civil Engineering and Transportation, ICCET 2013, December 14, 2013–December 15, 2013. 2014. Kunming (China: Trans Tech Publications Ltd).
- Waldron, P: *Engineering Structures*, 1985. 7(2): p. 93–104.
- Wang, B. and Y. Liu: Effect of radius of curvature on seismic response of curved bridge. in 2011 International Conference on Civil Engineering and Building Materials, CEBM 2011, July 29, 2011–July 31, 2011 (2011. Kunming, China: Trans Tech Publications).
- Wang, L. and T. Qu: Seismic response analysis of the long-span curved bridge. in 2nd International Conference on Transportation Engineering, ICTE 2009, July 25, 2009–July 27, 2009 (2009. Chengdu, China: American Society of Civil Engineers (ASCE)).
- Xi, J., Q. Li, and T. Wang: Calculation of state transfer of curved bridge. in 1st International Conference on Civil Engineering, Architecture and Building Materials, CEABM 2011, June 18, 2011–June 20, 2011 (2011. Haikou, China: Trans Tech Publications).
- Zakeri, J.A., M. Shadfar, and M.M. Feizi: *Latin American Journal of Solids and Structures*, 2014. 11(4), p. 598–612.

# A study on the stretch tensor of the beam end in a curved girder bridge caused by environmental temperature change

Jie-shan Liu

College of Science and Engineering, Jinan University, Guangzhou, China

Jing-hong Gao

Key Laboratory of Disaster Forecast and Control in Engineering, Ministry of Education of China, Guangzhou, China

**ABSTRACT:** With day turning to night and summer to winter, the girder in the bridge would be lengthened or shortened. This is a normal phenomenon in every object. However, the curved girder bridge has a dissymmetric structure, supported shearing force, bending moment and torsion in the same node, which would stretch in an abnormal way when the temperature is changed. In this paper, using Midas Civil app after the theoretical analysis of thermodynamics, the displacement of the beam end is simulated in this finite element analysis software with the altering radius of the road centerline. By comparing these data of displacement with central angle in the equal radius of the girder, which work at the same temperature condition, the result shows that the connection between the displacement and central angle becomes approximate when considering in a small angle at the center. In addition, it would be a useful reference when installing the expansion joint.

**Keywords:** curved girder bridge; displacement of beam end

## 1 INTRODUCTION

### 1.1 Current circumstance

With a growing pace of economic increasing, the requirements of traffic are gradually rigorous when the ground area is limited. Overpass has been the new design method in these several decades. On the one hand, bridge is built in a limited space. On the other hand, curved girder bridge is a significant element in the crossroad design. Nowadays, curved girder bridge takes an enlarged part in crossroads in order to satisfy the smooth line for an easy driving condition.

### 1.2 Research in this paper

Each bridge works in a normal environment, in which the temperature alters throughout day and night, and season cycle. Thermal expansion and contraction is easy to grasp in straight line girders, but it is uncertain in curved girder bridges. Because of the dissymmetry in the curved girder bridge, its deformation is complicated, including the impact of supported shearing force, bending moment and torsion, when the temperature changes around the girder. In this research, displacement of the beam end caused by temperature stress in the curved

girder bridge is taken into consideration. Within Midas Civil app and building several curved girder bridges, the displacement of the beam end is collected and analyzed, and then the results are discussed, which can be a reference to the installation of the expansion joint.

## 2 BASE OF THE MODEL

### 2.1 Origin of the analysis model

In this paper, a model is sampled from a city's overpass curved girder bridge, whose radius of circular curve is 400 meters. It is a continuous curved box girder bridge, whose cross span combination is 36 meters in side span and 60 meters in main span, adding up to 132 meters. The schematic diagram of this curved girder bridge is shown in [Figure 1](#).

The cross-section of this curved girder bridge is a variable cross-section with a concrete single box beam. Its cross-section of two typical sections and the longitudinal section is shown in [Figure 2](#).

The body of the prestressed box girder is made of C55 concrete in JTG D62-2004, which could support 55Mpa in axial compressive experiments. The prestressed steel strand is arranged in the same direction with a center line of the curved girder

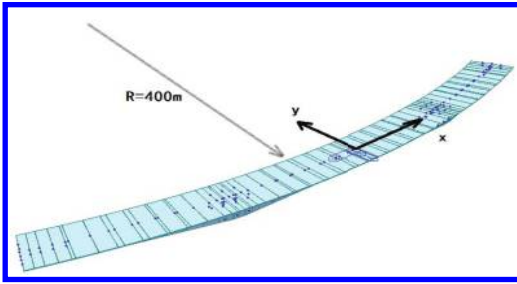


Figure 1. A schematic diagram of the origin curved girder bridge.

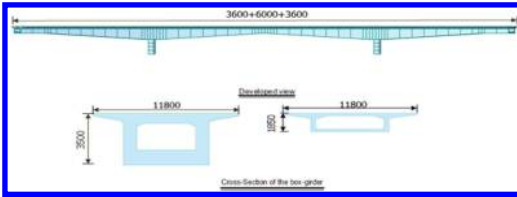


Figure 2. A longitudinal section and two typical cross-sections.

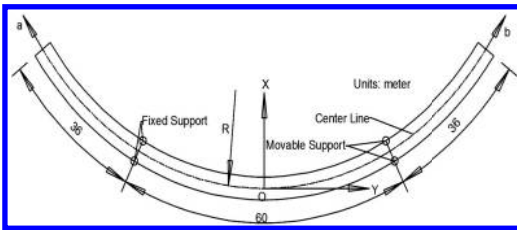


Figure 3. A planar graph about the curved girder.

bridge. It can endure 1860 Mpa in the tensile test, and is settled at a low relaxation level. A basin rubber support is installed between the curved girder and the bridge pier.

## 2.2 Model simplification

In this research, the curved girder bridge is made of C55 concrete, and linked with other beams through the expansion joint. Then, one pier connects the box girder with two fixed basin rubber supports; in the other pier, there are two movable basin rubber supports that connect with the box girder. So, it can be suggested that the whole concrete box girder bridge acts as an unconstrained body and free to deformation in the direction of the central line.

From Figure 3, it can be seen that two vectors  $\vec{a}$  and  $\vec{b}$  are the displacement of the beam end. The  $\vec{a}$

side is near to the fixed supports, and  $\vec{b}$  side is near to the movable supports.

## 3 CONCEPT OF THERMODYNAMICS

### 3.1 Linear expansion coefficient

Based on the above discussion, the factor that should be taken into consideration is deformation of the whole concrete box girder, especially the displacement of the beam ends. Also, the discussion ignores the influence of deformation of prestressed steel strand because of its ratio of reinforcement that takes a low-section occupation and can be negligible.

We then take the linear expansion coefficient into consideration. The concrete is so complicated and disordered that its exact parameters cannot be located. It is known that the linear expansion coefficient of concrete is  $\alpha_c = 1 \times 10^{-5}/^\circ\text{C}$  at the temperature between  $0^\circ\text{C}$  and  $100^\circ\text{C}$ .

This means that when the temperature of the concrete is increased or decreased per  $1^\circ\text{C}$ , the rate of the dilatation-magnification ratio is  $1 \times 10^{-5}$  square the whole length of the concrete body. The calculating formula is as follows:

$$\alpha_c = \frac{l_t - l_0}{l_0 \Delta t} \quad (1)$$

where  $l_0$  is the length of the original structure;  $l_t$  is the length of the structure after deformation; and  $\Delta t$  is the temperature difference between the original structure and after deformation.

So, the calculating formula (1) can be transposed to be other formulation as follows:

$$l_t = l_0 (1 + \alpha_c \Delta t) \quad (2)$$

### 3.2 Temperature setting

On the basis of statistical data, a typical value of temperature is set at  $40^\circ\text{C}$  at fluctuating temperature in total. It is means that an original box girder works in a normal environment in which the temperature increases or decreases less than  $20^\circ\text{C}$ .

### 3.3 Extension in the linear model

According to formulation (2), the length of expansion can be calculated. The original engineering model can be modified into a theoretical straight box girder bridge, and the cross span of the whole box girder bridge is 132 meters, which is 36 meters in two side spans and 60 meters in main span. By substituting 132 meters into  $l_0$ ,  $20^\circ\text{C}$  into  $\Delta t$  in formulation (2),  $\alpha_c$  will be equal to  $1 \times 10^{-5}/^\circ\text{C}$ .

Then, the main girder extension can be calculated as follows:

$$l_t = 132m \times (1 + 1 \times 10^{-5} \times 20^\circ C) = 132.0264m$$

The difference in length compared with the original one is 0.0264 meters, which is 26.4 millimeters in total.

## 4 MODEL ESTABLISHMENT

### 4.1 Circle curve of the girder bridge

This research analyzes the beam end displacement between different curve radii of box girders. In the real engineering practice, the radius of the circular curved girder bridge is 400 meters and cross-section is 132 meters in length.

Thus, by comparison, there are 7 different curve radii of the box girder to be established and simulated. The radii of the circle curve of each girder are 200 meters, 250 meters, 300 meters, 350 meters, 400 meters, 450 meters and 500 meters.

The main girder beam is simulated by a three-dimensional model. In the setting of the section material characteristic value, the material characteristic of the concrete is C55 in accordance with the JTG04 (RC) standard, and prestressed reinforcement is Strand1860 in accordance with the JTG04 (S) standard.

### 4.2 Support between the girder and the pier

This box girder bridge is a structure that consists of two piers with three spans. Each pier has two supports that connect with the main girder. In these finite element models, only two supports in a same pier are fixed support, another two supports in the other pier is a movable support along the central line. The schematic diagram is shown in Figure 3.

Thus, we establish nodes in the top and bottom of supports in each pier to simulate the actual box girder bridge. Under the bottom of the girder that is located above one pier is a rigid connection. And on the top of the pier and under the support is a general support with constraint.

### 4.3 Central angle of the girder bridge

The above-discussed model differs only in curve radius, which is set as 200 meters, 250 meters, 300 meters, 350 meters, 400 meters, 450 meters and 500 meters. Thus, the central angle can be calculated according to the following formula:

$$\beta = \frac{l_0}{R} \quad (3)$$

Table 1. Central angle of the girder at each radius.

Radius (meters)	200	250	300	350
Central angle (rad)	0.660	0.528	0.440	0.377
Radius (meters)	400	450	500	
Central angle (rad)	0.330	0.293	0.264	

where  $\beta$  is the central angle of the curved girder bridge (unit: rad);  $l_0$  is the total span of the curved girder bridge, with  $l_0/L$  equal to 132 meters; and  $R$  is the curve radius of the curved girder bridge.

Table 1 summarizes the calculating result for each girder bridge.

## 5 OPERATION AND DATA

After the setting of all bridges, we start to operate the analysis. Each model is operated independently. When the operation analysis is finished, we click the beam ending node, and check the displacement of the two ends of the girder. The below table presents the displacement of each beam end of each girder bridge model. According to the formula for the calculation of displacement angle,

$$\cos \gamma = \frac{\vec{a} \cdot \vec{b}}{|\vec{a}| |\vec{b}|} \quad (4)$$

where  $\vec{a}$  is the displacement of one side of the beam end that is near the fixed support; the  $\vec{b}$  is the displacement of the beam end that is far from the fixed support; and  $\gamma$  is the angle between the displacement directions of  $\vec{a}$  and  $\vec{b}$ .

According to the Midas Civil app,  $D_x$  is the displacement component in the  $X$  axis, and  $D_y$  is the displacement component in the  $Y$  axis,  $D_x D_y$  is the modules of vectors  $\vec{a}$  and  $\vec{b}$ . The angle part is the angle between the vectors, which is  $\vec{a}$  or  $\vec{b}$ , and  $Y$  axis. The relative angle is the angle between  $\vec{a}$  and  $\vec{b}$ , which, in these tables, is an acute angle. After running and analysis in the Midas Civil app, we search the result of the displacement of the side node. Then the angle between the two displacement directions of each beam end can be calculated, as given in Tables 2-8.

## 6 ANALYSIS AND CONCLUSION

### 6.1 Analysis

The whole extension length of the curved girder bridge is added up with  $\vec{a}$  and  $\vec{b}$ , which is the digital of  $D_x D_y$  in the table on the 5 sections, and the

Table 2. The displacement and angle data of the 200-meter curved girder bridge.

	$D_x$	$D_y$	$D_x D_y$	Angle	Relative angle
$\vec{b}$	18.523	6.371	19.588	0.331	0.662
$\vec{a}$	6.949	2.384	7.346	0.331	

Table 3. The displacement and angle data of the 250-meter curved girder bridge.

	$D_x$	$D_y$	$D_x D_y$	Angle	Relative angle
$\vec{b}$	19.676	2.976	19.900	0.150	0.541
$\vec{a}$	7.441	3.065	8.047	0.391	

Table 4. The displacement and angle data of the 300-meter curved girder bridge.

	$D_x$	$D_y$	$D_x D_y$	Angle	Relative angle
$\vec{b}$	19.544	2.056	19.652	0.105	0.384
$\vec{a}$	7.369	2.114	7.666	0.279	

Table 5. The displacement and angle data of the 350-meter curved girder bridge.

	$D_x$	$D_y$	$D_x D_y$	Angle	Relative angle
$\vec{b}$	19.467	1.506	19.525	0.077	0.385
$\vec{a}$	7.326	1.547	7.488	0.208	

Table 6. The displacement and angle data of the 400-meter curved girder bridge.

	$D_x$	$D_y$	$D_x D_y$	Angle	Relative angle
$\vec{b}$	19.035	1.428	19.088	0.075	0.234
$\vec{a}$	7.228	1.149	7.249	0.159	

method is added  $D_x D_y$  of  $\vec{a}$  and  $D_x D_y$  of  $\vec{b}$ , as listed in Table 9.

Mathematically, the central angle is equal to the angle between the normal directions of the two beam ends. Thus, we take the simulation results and the theoretical result of the central angle, as given in Table 10.

By comparing the result of the data, some conclusion can be drawn.

In the model of the short radius, which is a large central angle, the angle between the extension

Table 7. The displacement and angle data of the 450-meter curved girder bridge.

	$D_x$	$D_y$	$D_x D_y$	Angle	Relative angle
$\vec{b}$	19.384	0.908	19.405	0.047	0.174
$\vec{a}$	7.280	0.931	7.339	0.127	

Table 8. The displacement and angle data of the 500-meter curved girder bridge.

	$D_x$	$D_y$	$D_x D_y$	Angle	Relative angle
$\vec{b}$	19.360	0.729	19.374	0.038	0.140
$\vec{a}$	7.267	0.747	7.305	0.102	

Table 9. The comparison of total extension length.

Radius (m)	200	250	300	350
Practical result (mm)	26.934	27.947	27.318	27.013
Radius (m)	400	450	500	Theoretical result
Practical result (mm)	26.337	26.744	26.679	26.4

Table 10. The comparison between the relative angle and the central angle.

Radius (m)	200	250	300	350
Relative angle (rad)	0.662	0.541	0.384	0.385
Central angle (rad)	0.660	0.528	0.440	0.377
Radius	400	450	500	
Relative angle	0.234	0.174	0.140	
Central angle	0.330	0.293	0.264	

displacements of the two side beam ends is larger than that of the long radius. As the radius increased, and the central angle decreased, the angle between the two beam ends also decreased.

Except the two curved girder bridges with the shortest radius in this discussion, others are not approximated to its own central angle, also with a tendency that the angle increasing between the two side beam ends becomes more deviated from its own central angle.

The direction of displacement of the beam end that is near the fixed support is larger than that of the other side that is near the movable supports.

By calculating the extension of each side beam end in one curved girder bridge, the theoretical displacement can be expressed as follows:

$$|\vec{a}| = 36m \times (1 \times 10^{-5} \times 20^\circ C) = 0.0072m = 7.2mm$$

$$|\vec{b}| = (36 + 60)m \times (1 \times 10^{-5} \times 20^\circ C) \\ = 0.0192m = 19.2mm$$

By comparing with the data given in [Table 9](#), it is clear that the practical displacement is very close to the theoretical result.

Also, the data given in the table that represent the whole extension displacement of each curved girder bridge show that the result is close to the theoretical calculation.

## 6.2 Conclusion

From the analysis of the results, some conclusion can be drawn as follows:

In the curved girder bridge with a short radius, the extension displacement could be considered to be along the same line of the road line.

When installing the expansion joint, it can use a one-way expansion joint, which is more costly than the other type. And the allowance displacement of the expansion joint could be decided by the length of the whole girder bridge.

## REFERENCES

- [1] Tazawa E, Miyazawa Shingo. Influence of Cement and Admixture on Autogenous Shrinkage of Cement Paste [J]. Cement and Concrete Research, 1995, 25(7):281–287.
- [2] ACI Committee 116. Cement and Concrete Terminology (ACI 116R-00), 2005.
- [3] U.S. Bureau of Reclamation. Thermal Properties of Concrete [M]. 1940.

## Shear-lag effect in a prestressed continuous rigid frame bridge

Xun Wu, Hui Li & Xin Yuan

Department of Bridge Engineering, Tongji University, Shanghai, China

**ABSTRACT:** Continuous rigid frame bridge is one of the main forms of long-span bridges. The shear-lag effect of the box girder should be taken into consideration when designing a continuous rigid frame bridge. In this paper, a three-span prestressed concrete continuous rigid frame bridge is taken as the example. The finite element method is used to analyze the shear-lag effect of each critical section under the action of structure weight and the interaction of structure weight and prestressing action. The results show that under the action of structure weight, the shear-lag coefficient is small. The shear-lag effect varies under the interaction of structure weight and prestressing action.

**Keywords:** continuous rigid frame bridge; shear-lag effect; finite element method; prestressing action

### 1 INTRODUCTION

Since the continuous rigid frame bridge has many advantages, it has become one of the main form of long-span bridges. Existence of the shear-lag effect of the box girder makes stress obtained through theory to be smaller. Shear-lag coefficient is commonly used to estimate the value of the shear-lag effect. In this paper, a three-span continuous rigid frame bridge (65 + 110 + 65 m) is analyzed. The finite element method is used to analyze the shear-lag effect of each critical section under the action of structure weight and prestressing force, respectively. The conclusion can be applied in the design and review of other similar bridges.

Shear-lag coefficient is commonly used to estimate the value of the shear-lag effect. In this paper, the shear-lag coefficient is defined as follows:

$$\lambda = \frac{\sigma_{\max}}{\bar{\sigma}_s}$$

$\sigma_{\max}$ —the maximum normal stress;



Figure 1. Finite element model of the bridge.

$\bar{\sigma}_s$ —the average normal stress obtained by the integration of normal stress along the transverse floor of the box girder.

For a large bridge, dead load plays a main role. Therefore, the study of the shear-lag effect under dead load makes great significance. The action of structure weight and the interaction of structure weight and prestressing action are analyzed.

### 2 SHEAR-LAG EFFECT UNDER THE ACTION OF STRUCTURE WEIGHT

Shear-lag coefficient defined in this paper is applied to analyze the shear-lag effect in the top and bottom flange of the main section. The main sections are section of closure segment of side spans, 1/4 side span, consolidation

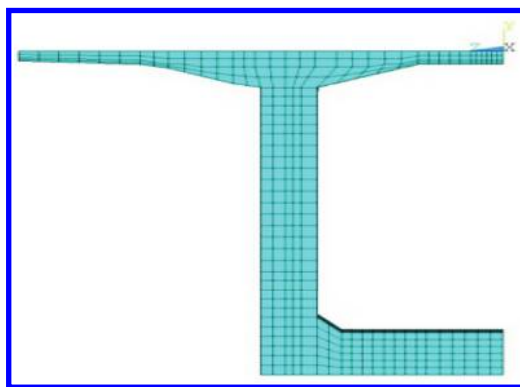


Figure 2. Finite element model of the section.

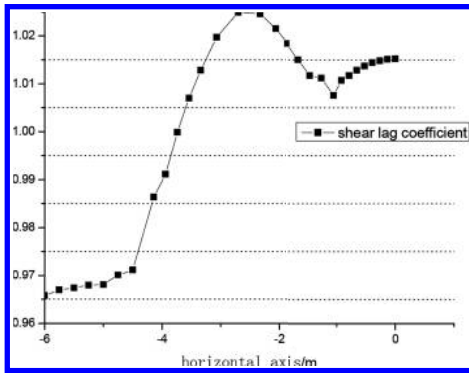


Figure 3. Shear-lag coefficient of the top slab.

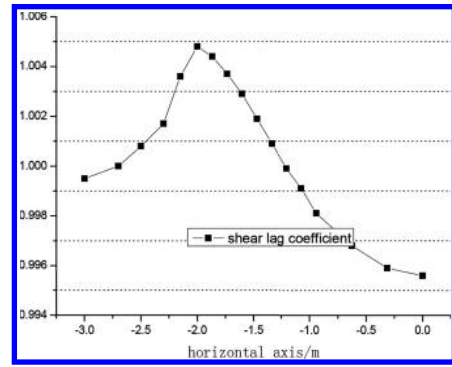


Figure 6. Shear-lag coefficient of the bottom slab.

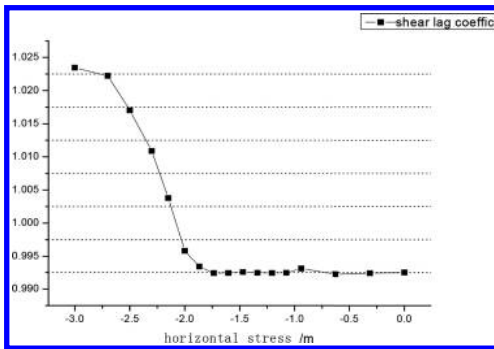


Figure 4. Shear-lag coefficient of the bottom slab.

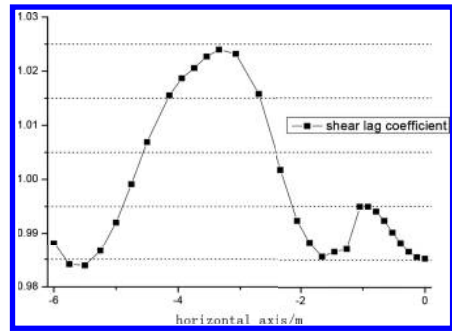


Figure 7. Shear-lag coefficient of the top slab.

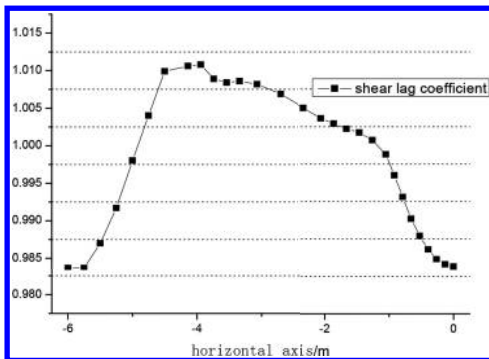


Figure 5. Shear-lag coefficient of the top slab.

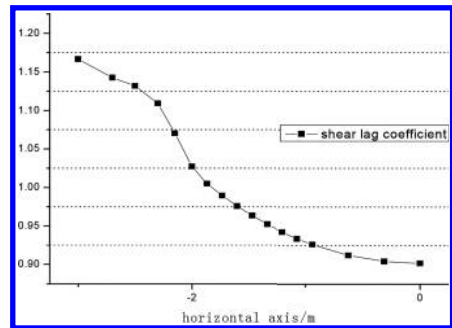


Figure 8. Shear-lag coefficient of the bottom slab.

segment of pier and beam and closure segment of middle span.

### 2.1 Shear-lag effect on the section of closure segment of side spans

For the closure segment of side spans, the shear-lag effect is not obvious. The maximum shear-lag

coefficient of the top slab is 1.025, while the minimum is 0.966. For the bottom slab, the maximum shear-lag coefficient is 1.024, and the minimum is 0.992.

### 2.2 Shear-lag effect on the section of 1/4 side span

The shear-lag effect is not obvious at 1/4 L. The maximum shear-lag coefficient of the top slab is



1.011, while the minimum is 0.984. For the bottom slab, the maximum shear-lag coefficient is 1.005 and the minimum is 0.996.

2.3 *Shear-lag effect on the section of consolidation segment of the pier and the beam*

The shear-lag effect is obvious, especially the maximum shear-lag coefficient of the bottom slab is 1.167. In actual engineering, attention should be paid to such region. The maximum shear-lag coefficient of the top slab is 1.023, while the minimum is 0.984. For the bottom slab, the maximum shear-lag coefficient is 1.167 and the minimum is 0.902. Compared with the top slab, the shear-lag effect of the bottom slab is more obvious, due to the existence of the thin-wall piers and cross beam.

2.4 *Shear-lag effect on the section of closure segment of the middle span*

The maximum shear-lag coefficient of the top slab is 1.025, while the minimum is 0.971. For the bottom slab, the maximum coefficient is 1.055 and the minimum is 0.973.

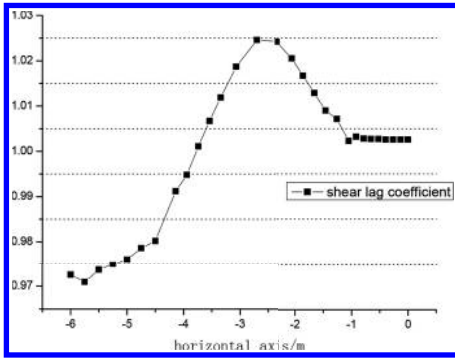


Figure 9. Shear-lag coefficient of the top slab.

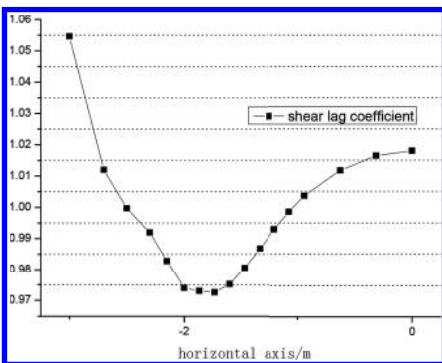


Figure 10. Shear-lag coefficient of the bottom slab.

It is concluded that for a large span continuous rigid frame bridge, under the action of structure weight, the shear-lag effect is not obvious. Due to the external force, the shear-lag effect of the region in piers is apparent. More accurate research should be done to ensure safety.

3 SHEAR-LAG EFFECT UNDER THE INTERACTION OF STRUCTURE WEIGHT AND PRESTRESSING ACTION

Considering the interaction of structure weight and prestressing action, the shear-lag coefficients are obtained, which are compared with those under the action of only structure weight.

For the top slab near the closure segment of side spans, since the internal force distribution of the structure changes due to prestressing steels, a negative shear-lag effect occurs. For the bottom slab, the shear-lag coefficient does not change very much.

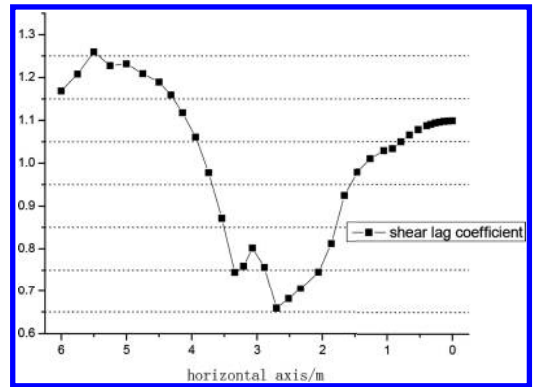


Figure 11. Shear-lag coefficient of the top slab in the closure segment of side spans.

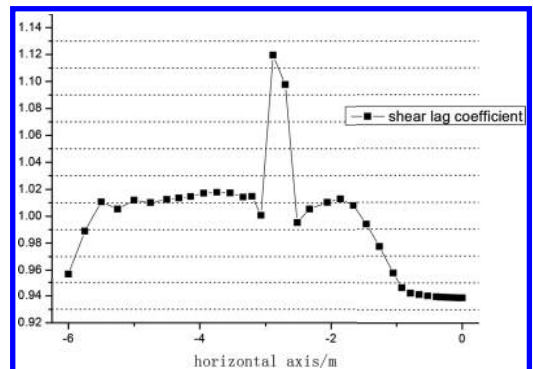


Figure 12. Shear-lag coefficient of the top slab in the 1/4 side span.

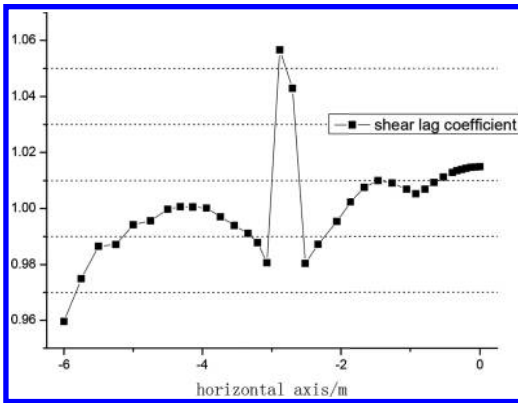


Figure 13. Shear-lag coefficient of the top slab in the pier center.

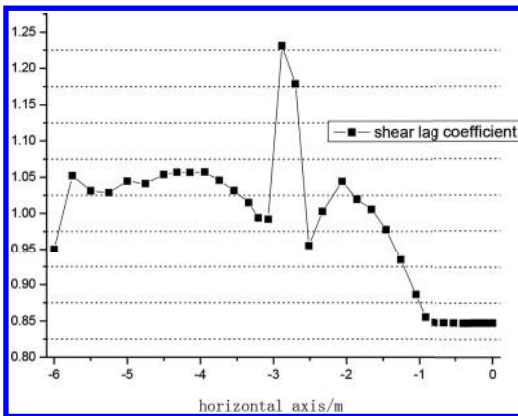


Figure 14. Shear-lag coefficient of the top slab in the closure segment of the middle span.

For the top slab of the other three sections, the shear-lag coefficient reaches its peak over the web, because the prestressing steels are mainly concentrated in the region over the web. Besides, due to the effect of prestressing, the original tensile stress

region with an obvious shear-lag effect becomes compressive, which is good for the safety of the structure.

#### 4 CONCLUSION

1. For the prestressed concrete continuous rigid frame bridge, under the action of structure weight, the shear-lag effect is not obvious. Due to the external force, the shear-lag effect of the region in piers is apparent.
2. When under the interaction of structure weight and prestressing action, the shear-lag coefficients vary to some extent, compared with those under the action of only structure weight. The effect of prestressing makes the original tensile stress region with an obvious shear-lag effect to become compressive, which can make a contribution to the safety of the structure.

#### REFERENCES

- [1] Adel Fam, Cart Turkstra, A Finite Element Scheme for box bridge analysis, computers & Structures, 1975, 5(2/3), 179~186.
- [2] Zihai Shi, Masaaki, Nakano. Three-dimensional finite element analysis on crack behaviors of RC cantilever decks. Construction and Building Materials, 13(1999): 33~47.
- [3] JinQong Guo. Research on shear lag effect of box girder. [J]. China Civil Engineering Journal, 1983, 16(1): 1~3. (in Chinese).
- [4] QiZhi Luo. beam finite element method of shear lag calculation for thin-walled box girder. [J]. Journal of hunan university 1991, 18(2), 33~38. (in Chinese).
- [5] ShiJun Zhou. Analysis of shear lag effect of box girder. [J]. Engineering Mechanics, 2008, 25(2), 204~207. (in Chinese).

# Analysis of influencing factors on central load and temperature coupling effect of tram monolithic roadbed

Chongwei Huang

Key Laboratory of Road and Traffic Engineering of the Ministry of Education, Tongji University, Shanghai, China

Yan Xie

Shanghai East China Civil Aviation Airport Construction Supervision Co. Ltd., China

Yunzhen Wei

Yangzhou Jianyuan construction Supervision Co. Ltd., Jiangsu, China

Kun Wang

Shanghai East China Civil Aviation Airport Construction Supervision Co. Ltd., China

**ABSTRACT:** Large-scale planning of tram has begun in many cities of China. While the design and construction technology lacks of profound study. In this paper, 3D finite element model was built to simulate the practice condition. Then the temperature field distribution was calculated. On this basis, the most unfavorable condition of load and temperature coupling effect, load in the center of the slab at 1.5 to 2 pm, was selected. Different values of roadbed slab thickness, support layer thickness, contact condition of roadbed slab and support layer, roadbed slab modulus, modulus of support layer and resilient modulus of subgrade were selected to calculate the stress and deflection of roadbed, which provides the design and construction with very important reference values.

**Keywords:** monolithic roadbed; coupling effect; load and temperature; 3D finite element

## 1 INTRODUCTION

Temperature has a great influence on tram monolithic roadbed. Rheda, Züblin and Bögl calculated the warping stress and buckling stability of monolithic roadbed under the action of deadweight and temperature gradient<sup>[1] [2] [3]</sup>. In Japan, many researchers analyze the hydration heat, daily and seasonal temperature difference and thermal stress using 2D finite element model<sup>[4]</sup>. And several post-graduates in South West Jiaotong University tested the effect of slab temperature stress on structure design<sup>[5] [6] [7]</sup>, then built the calculation method of bottom slab temperature stress<sup>[8] [9]</sup>.

In the field of temperature stress calculation of highway cement concrete pavement, a lot of research and tests were explored and implemented<sup>[10] [11]</sup>, from 1920s to now, until AASHO proposed the pavement design method by observation data of test road.

While, whether the monolithic roadbed or highway, the relation between temperature and load was established on the foundation of Winkler ground. And the contact condition of concrete

and steel bar, mechanic behavior under the load and temperature coupling effect and wheel-rail contact were not taken into consideration.

In this paper, monolithic roadbed slabs thickness, support layer thickness, contact condition of pavement and base, and the strength of monolithic roadbed, support layer and subgrade were analyzed in different conditions of temperature and load. 3D finite element model was used to calculate the effect of those factors on mechanic behavior of monolithic roadbed slabs.

## 2 TEMPERATURE EFFECT THEORY AND PARAMETER SETTING

### 2.1 Structure surface radiation effect parameter

Boundary conditions of tram monolithic roadbed were limited by the two methods blow:

#### 1. The third boundary condition

The relation of heat flow via the cement surface, surface temperature ( $T$ ), air temperature ( $T_a$ ) and daily radiation is:

Table 1. Materials parameters of calculation model.

Parameters	Conductivity [W/(m·°C)]	Specific heat [J/(kg·°C)]	Density [kg/m³]	Emissivity	Film coefficient [W/(m²·K)]
Monolithic roadbed	2.54	988	2500	0.94	13
Support layer	1.0	817	2000	/	/
Subgrade	1.2	879	1870	/	/
Steel	34.9	520	7800	/	/

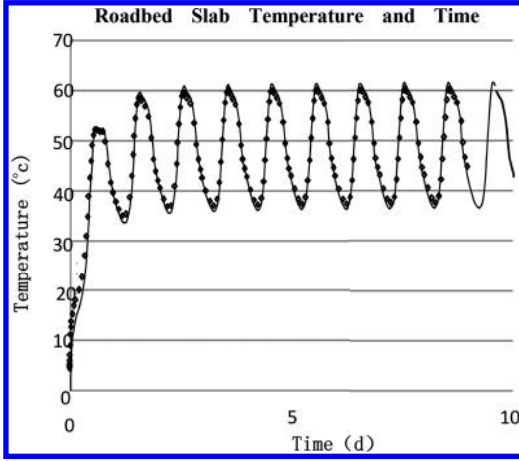


Figure 1. Temperature time history curve of roadbed slab.

$$-\lambda \frac{\partial T}{\partial n} = \beta(T - T_a) - \alpha_s S \quad (1)$$

where  $\beta$  is the total heat release coefficient of structure surface, considering heat exchange of convection and radiation;  $T_a$  is the air temperature in the place without illumination;  $\alpha_s$  is the daily radiation heat absorption coefficient of structure surface; and  $S$  is the radiation intensity.

2. The fourth boundary condition

When two kinds of solid have a good contact, the temperature and heat flow on the interface are continuous. Then the boundary condition is:

$$T_1 = T_2, \lambda_1 \frac{\partial T_1}{\partial n} = \lambda_2 \frac{\partial T_2}{\partial n} \quad (2)$$

If the contact is not good, the temperature is discontinuous. Then, the concept of thermal resistance is introduced. A hypothesis of ignorance of heat in the contact gap is built, and heat flow balance is maintained. Then, the boundary condition is:

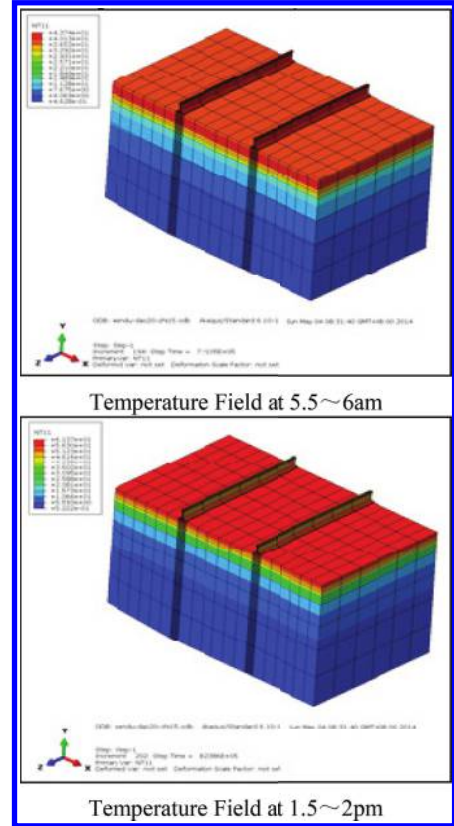


Figure 2. Calculation results of temperature field of monolithic roadbed slab.

$$\begin{cases} \lambda_1 \frac{\partial T_1}{\partial n} = \frac{1}{R_c} (T_2 - T_1) \\ \lambda_1 \frac{\partial T_1}{\partial n} = \lambda_2 \frac{\partial T_2}{\partial n} \end{cases} \quad (3)$$

where  $R_c$  is the thermal resistance caused by bad contact.

The contact of monolithic roadbed slabs is related to the fourth boundary condition.

## 2.2 Radiation intensity

Solar energy is transferred to earth in the form of electromagnetic waves. Solar constant is the energy per unit area and time from sun when the distance between the sun and earth is the average value, which can be expressed by “ $J_0$ ”. The latest observing value of  $J_0$  is  $1367 W/m^2$ . While the distance is changing every day, the daily correction coefficient ( $\xi$ ) is introduced. The equation of  $J$  can be corrected to:

$$J = \xi J_0 = \left[ 1.0 + 0.034 \cos\left(\frac{2\pi}{365} n\right) \right] J_0 \quad (4)$$

where  $n$  is the data number in a year. January 1 is the first day;  $\xi$  is the correction coefficient considering the elliptic orbit of earth revolving around the sun.

## 2.3 Material thermodynamic parameters

The material thermodynamic parameters used in the calculation of finite element model are given in Table 1.

Stefan-Boltzmann constant is  $5.775 \times 10^{-4} W \cdot m^{-2} \cdot K^4$ , absolute zero temperature is  $-273^\circ C$ .

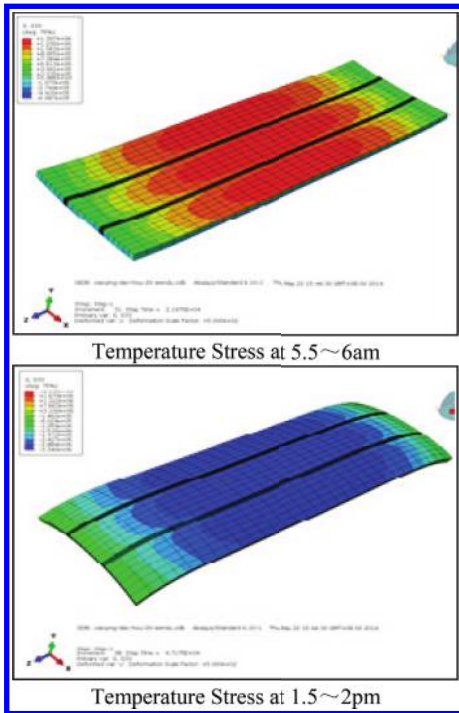


Figure 3. Calculation results of temperature stress of roadbed slab.

## 2.4 Temperature field and stress calculation

First, setting up the thermal resistance in the interlayer of roadbed slab, steel rail, support layer, and subgrade to simulate the effect of heat conduction. Then setting heat flux and heat transfer coefficient for the top of roadbed slab to calculate the transient heat conduction under the solar radiation.

As it is shown in Figure 2, the highest temperature can reach to  $62^\circ C$ , the largest difference value in temperature is  $18^\circ C$ . Importing the results to the calculation model of temperature effect to get the temperature stress relatively.

From Figure 3, we can see the highest temperature stress to be  $2.135 MPa$ . So the most unfavorable conditions of load and temperature coupling effect are load in slab end at 5.5 to 6 am and load in the middle of the slab at 1.5 to 2 pm.

## 3 CALCULATION AND ANALYSIS OF MECHANICAL BEHAVIOR OF LOAD IN THE MIDDLE WITH THE TEMPERATURE EFFECT ON ROADBED

### 3.1 Influence of structure combination

#### 3.1.1 Roadbed slab thickness

5 kinds of thickness were selected to analyze with the values of 20, 22, 24, 26, and 28 cm. Then, assuming the value of interlayer contact is 0.9. Calculating 5 times with different thickness and remaining other parameter settings the same.

The results are shown in Table 2. And variation of horizontal tensile stress on the slab bottom

Table 2. Results of mechanical response of the monolithic roadbed slabs in different slab thickness.

Slab thickness/cm	Extreme value of mechanical response			
	Cross-section			
	$\sigma_{dy}/MPa$	$D_d/mm$	$\sigma_{sz}/kPa$	$D_{ss}/mm$
20	2.174	0.929	50.363	1.524
22	1.967	0.948	49.418	1.505
24	1.746	0.964	48.328	1.484
26	1.527	0.960	47.161	1.458
28	1.313	0.941	45.901	1.435
	Vertical section			
	$\sigma_{dy}/MPa$	$D_d/mm$	$\sigma_{sz}/kPa$	$D_{ss}/mm$
20	3.422	0.414	46.788	1.490
22	3.463	0.469	45.807	1.466
24	3.475	0.548	44.449	1.440
26	3.460	0.627	43.308	1.413
28	3.422	0.704	41.019	1.391

( $\sigma_{dy}$ ), deflections on the top surface of slab ( $D_d$ ) and pressure stress ( $\sigma_{sz}$ ) and deflections on the subgrade top ( $D_{ss}$ ) with changing depths were shown in it.

As shown in these tables and figures:

1. In the cross-section, the stress distribution shapes as “M” and the concentration appear in wheelpath. The largest stress is in the bottom of wheel when thickness is 20cm with the value of 2.174MPa. It decreases to 1.313MPa with the increase in thickness. And the deflection changes a little in the same slab thickness.
2. In the cross-section, stress on the top of subgrade presents the shape of “M” with the same slab thickness. The difference in cross-section is significant, and the smallest value only accounted for 41% of the largest one, which reached 50.363kPa with the deflection of 1.524mm when thickness is 20cm.
3. In the vertical section, the stress concentration appears in the bottom of rail load. The maximum value is 3.422MPa when the thickness is 20cm, which means vertical effect is more obvious. Besides, increasing thickness leading to a larger temperature difference in vertical section makes a larger temperature deformation.
4. In axial direction of slabs, stress on the top of subgrade present the shape of “M” with the same slab thickness. The stress value decreased to 12% of former one when the thickness increases from 20cm to 28cm.

### 3.1.2 Support layer thickness

5 kinds of thickness were selected to analyze with the values of 12, 14, 16, 18 and 20cm. Then assuming the value of interlayer contact is 0.9. Calculating 5 times with different thickness and remaining other parameter settings the same.

The results were shown in Table 3.

1. In the cross-section, the stress concentration appears in wheelpath. The largest stress is in the bottom of the wheel when thickness is 12cm with the value of 1.63MPa. It decreases to 1.584MPa with the increase in thickness. And the deflection changes a little in the same slab thickness.
2. In the cross-section, stress on the top of subgrade presents the shape of “M” with the same support layer thickness. The difference in cross-section is significant, and the smallest value only accounts for 33% of the largest one. The deflection of subgrade changes a little with a shape of inverted “V”.
3. In the vertical section, the stress concentration appears in the bottom of rail load. The maximum value is 3.515MPa when the thickness is 12cm, which means vertical effect is more obvious. Besides, deflection distributed as a

Table 3. Results of mechanical response of the monolithic roadbed slabs in different support layer thickness.

Support layer thickness/cm	Extreme value of mechanical response			
	Cross-section			
	$\sigma_{dy}$ /MPa	$D_d$ /mm	$\sigma_{sz}$ /kPa	$D_{ss}$ /mm
12	1.630	0.732	46.603	1.442
14	1.645	0.783	47.642	1.466
16	1.612	0.785	46.719	1.474
18	1.606	0.787	45.796	1.482
20	1.584	0.786	44.799	1.483
Vertical section				
	$\sigma_{dy}$ /MPa	$D_d$ /mm	$\sigma_{sz}$ /kPa	$D_{ss}$ /mm
12	3.515	0.600	44.901	1.393
14	3.483	0.579	44.251	1.420
16	3.462	0.596	43.265	1.431
18	3.431	0.613	42.278	1.442
20	3.399	0.635	41.227	1.446

“W”. The maximum values in the load center is 0.258mm and that of in the end is 0.6mm. when thickness increased to 20cm, the values changed to 0.255mm and 0.635mm respectively.

4. In axial direction of slabs, stress on the top of subgrade present the shape of “M” with the same slab thickness. The stress value decreased 8% of the former one and the subgrade deflection increases 4% when the thickness increased from 12cm to 20cm.

### 3.1.3 Contact condition of roadbed slab and support layer

5 kinds of friction coefficient were selected to analyze with the values of 0.2, 0.6, 0.9, 1.2 and 1.5. Calculating 5 times with different friction coefficient and remaining other parameter settings the same. The results were shown in Table 4.

1. In the cross-section, when friction coefficient increases, tensile stress increases appreciably, while  $D_d$  and  $D_s$  decrease a little.
2. In the vertical section, when friction coefficient increases,  $\sigma_{dy}$  and  $\sigma_{sz}$  decrease a little, while  $D_d$  and  $D_s$  increase appreciably.

## 3.2 Influence of material parameters

### 3.2.1 Roadbed slab modulus

5 kinds of modulus were selected to analyze with the values of 30, 35, 40, 45 and 50GPa. Then assuming the value of interlayer contact is 0.9. Calculating 5 times with different modulus and

Table 4. Results of mechanical response of the monolithic roadbed slabs in different contact conditions.

Friction coefficient	Extreme value of mechanical response			
	Cross-section			
	$\sigma_{dy}/\text{MPa}$	$D_d/\text{mm}$	$\sigma_{sz}/\text{kPa}$	$D_{ss}/\text{mm}$
0.2	1.613	0.984	41.535	1.475
0.6	1.626	0.973	44.996	1.472
0.9	1.636	0.964	47.714	1.471
1.2	1.645	0.955	50.036	1.470
1.5	1.656	0.946	52.059	1.471
Vertical section				
	$\sigma_{dy}/\text{MPa}$	$D_d/\text{mm}$	$\sigma_{sz}/\text{kPa}$	$D_{ss}/\text{mm}$
0.2	3.502	0.565	44.942	1.427
0.6	3.483	0.578	43.840	1.426
0.9	3.471	0.588	43.796	1.426
1.2	3.461	0.596	43.949	1.426
1.5	3.453	0.604	43.891	1.427

Table 5. Results of mechanical response of the monolithic roadbed slabs in different modulus of roadbed slab.

Friction coefficient	Extreme value of mechanical response			
	Cross-section			
	$\sigma_{dy}/\text{MPa}$	$D_d/\text{mm}$	$\sigma_{sz}/\text{kPa}$	$D_{ss}/\text{mm}$
0.2	1.613	0.984	41.535	1.475
0.6	1.626	0.973	44.996	1.472
0.9	1.636	0.964	47.714	1.471
1.2	1.645	0.955	50.036	1.470
1.5	1.656	0.946	52.059	1.471
Vertical section				
	$\sigma_{dy}/\text{MPa}$	$D_d/\text{mm}$	$\sigma_{sz}/\text{kPa}$	$D_{ss}/\text{mm}$
0.2	3.502	0.565	44.942	1.427
0.6	3.483	0.578	43.840	1.426
0.9	3.471	0.588	43.796	1.426
1.2	3.461	0.596	43.949	1.426
1.5	3.453	0.604	43.891	1.427

remaining other parameter settings the same. The results were shown in Table 5.

1. In the cross-section, the stress concentration of tensile appears in wheelpath. The largest stress is in the bottom of wheel when modulus is 50GPa with the value of 2.049MPa. It decreases to 1.728MPa with the decrease in modulus. And the deflection changes a little in the same modulus.

2. In the cross-section, stress on the top of subgrade present the shape of “M” with the same modulus. The difference in cross-section was significant, and the smallest value only accounted for 40% of the largest one. The deflection of subgrade changed a little with a shape of inverted “V”.
3. In the vertical section, the stress concentration appears in the bottom of rail load. The maximum value is 4.102MPa when the modulus is 50GPa. And it decreases to 2.798MPa when modulus decreases to 30GPa. Besides, the maximum value in the load center is 0.349mm and that of it in the end is 1.457mm. When thickness increases to 50GPa, the values change to 0.18mm and 1.404mm respectively.
4. In axial direction of slabs, stress on the top of subgrade presents the shape of “M” with the same modulus. The stress value decreases 9% of former one and the subgrade deflection increases 4% when the modulus increases from 30GPa to 50GPa.

### 3.2.2 Modulus of support layer

5 kinds of modulus were selected to analyze with the values of 6, 9, 12, 15 and 18GPa. Then assuming the value of interlayer contact is 0.9. Calculating 5 times with different modulus and remaining other parameter settings the same. The results were shown in Table 6.

1. In the cross-section, the stress concentration of tensile appears in wheelpath. The largest stress is in the bottom of wheel when modulus is 6GPa

Table 6. Results of mechanical response of the monolithic roadbed slabs in different modulus of support layer.

Modulus of support layer/GPa	Extreme value of mechanical response			
	Cross-section			
	$\sigma_{dy}/\text{MPa}$	$D_d/\text{mm}$	$\sigma_{sz}/\text{kPa}$	$D_{ss}/\text{mm}$
6	1.674	0.969	47.745	1.478
9	1.654	0.966	47.720	1.476
12	1.636	0.964	47.714	1.471
15	1.619	0.961	47.695	1.467
18	1.602	0.959	47.675	1.462
Vertical section				
	$\sigma_{dy}/\text{MPa}$	$D_d/\text{mm}$	$\sigma_{sz}/\text{kPa}$	$D_{ss}/\text{mm}$
6	3.512	0.579	44.192	1.431
9	3.491	0.583	43.888	1.429
12	3.471	0.588	43.796	1.426
15	3.452	0.591	43.709	1.424
18	3.433	0.595	43.709	1.420

with the value of 1.674MPa. It decreases with the increase in modulus. And the deflection changes a little in the same support layer modulus.

2. In the cross-section, stress on the top of subgrade presents the shape of “M” with the same modulus. The difference in cross-section is significant, and the smallest value only accounts for 33% of the largest one. The deflection of subgrade changes a little with the shape of inverted “V”.
3. In the vertical section, the stress concentration appears in the bottom of rail load. The maximum value is 3.512MPa when the modulus is 6GPa. And it decreases to 3.433MPa when modulus increases to 18GPa. Besides, the maximum value in the load center is 0.268mm and that of it in the end is 1.431mm. When thickness increases to 18GPa, the values change to 0.25mm and 1.420mm respectively.
4. In axial direction of slabs, stress on top of subgrade presents the shape of “M” with the same modulus. The stress value decreased 1% of former one and the subgrade deflection decreases 1% when the modulus increases from 6GPa to 18GPa.

### 3.2.3 Resilient modulus of subgrade

5 kinds of resilient modulus of subgrade were selected to analyze with the values of 30, 45, 60, 75 and 90MPa. Then assuming the value of interlayer contact is 0.9. Calculating 5 times with different modulus and remaining other parameter settings the same. The results were shown in Table 7.

1. In the cross-section, the stress concentration of tensile appears in wheelpath. The largest stress is in the bottom of wheel when modulus is 30MPa with the value of 1.33MPa. It increases with the increase in modulus. And the deflection changes a little in the same resilient modulus of subgrade.
2. In the cross-section, stress on the top of subgrade present the shape of “M” with the same modulus. The difference in cross-section is significant, and the smallest value only accounts for 48% of the largest one. When subgrade modulus is 90MPa, the stress reaches to the maximum value of 65.747kPa and the deflection is 0.878mm.
3. In the vertical section, the stress concentration appears in the bottom of rail load. The maximum value is 3.638MPa when the modulus is 30MPa. And it decreases to 3.364MPa when modulus increases to 90MPa. Besides, the maximum value in the load center is 1.033mm and that of it in the end is 1.457mm. When thickness increased to 90MPa, the values change to 0.25mm and -0.014mm respectively.

Table 7. Results of mechanical response of the monolithic roadbed slabs in different resilient modulus of subgrade.

Resilient modulus of subgrade/ GPa	Extreme value of mechanical response			
	Cross-section			
	$\sigma_{dy}$ /MPa	$D_d$ /mm	$\sigma_{sz}$ /kPa	$D_{ss}$ /mm
30	1.330	1.884	28.448	3.112
45	1.500	1.293	38.378	2.036
60	1.636	0.964	47.714	1.471
75	1.751	0.747	56.822	1.119
90	1.849	0.591	65.747	0.878
Vertical section				
	$\sigma_{dy}$ /MPa	$D_d$ /mm	$\sigma_{sz}$ /kPa	$D_{ss}$ /mm
30	3.638	1.457	25.889	3.058
45	3.546	0.886	34.477	1.986
60	3.471	0.588	43.796	1.426
75	3.411	0.401	52.737	1.079
90	3.364	0.272	61.762	0.842

4. In axial direction of slabs, stress on the top of subgrade present the shape of “M” with the same modulus. The stress value increases 139% of former one and the subgrade deflection decreased 73% when the modulus increases from 30MPa to 90MPa.

## 4 CONCLUSION

3D finite element model was found to calculate the temperature field distribution of roadbed slab. Then different loads were imposed to slab center in the condition of largest positive temperature difference and to slab end in largest negative temperature difference. According to the calculation results, many influencing factors were analyzed contrastingly. Several conclusions are as follows:

1. The largest positive temperature difference reaches at 1.5 to 2 pm. And the largest negative temperature difference reaches at 5.5 to 6 am. The highest temperature is 62°C, and the largest temperature difference of slab is 18°C. The highest temperature stress of roadbed slab is 2.135MPa.
2. In the coupling effect of central load and temperature, slab thickness has a limited influence on the mechanical response. And the effect of support layer thickness is similar to slab. Interlayer contact condition has a great effect on stress and deflection. Subgrade modulus is important for improving the deflection of slab. The stress value increases by 139% of former



one and the subgrade deflection decreases by 73% when the modulus increases from 30MPa to 90MPa.

3. Warping stress is larger in condition of load in center than that of load in the end. When subgrade modulus is 90MPa, the stress can reach 101.216kPa. And warping stress is affected directly by joint width, which is the key of roadbed slab design.

#### ACKNOWLEDGMENT

This research was supported by the Basic research Program of Jiangsu Province (BK2012479), the National Natural Science Foundation of China (51308413), and the Shanghai Rising-Star Program (15QB1403000).

#### REFERENCES

- [1] Rail. One GnmH. Rheda 2000 Crack width calculation according to DIN 1045-1 [R], Ingolstaedter, 2005(6):45–49.
- [2] Henn W.D. System comparison: ballasted track-slab track [J]. Rail Engineering International, 1993, 22(2): 6–9.
- [3] Eisenmann J, Leykauf G. Beton-fahrbahnen. Munchen: Ernst & Sohn, [M] 2003:22–59.
- [4] Japan Railway Construction Morioka Association. Research of Subgrade Engineering Design [R]. 1999: 23–98.
- [5] Wang senrong Research of plate roadbed temperature stress [D]. chengdu: South West Jiaotong University, 2007:23–68.
- [6] Che xiaojuan. Analysis of influence of Reinforcement on Temperature Crack [D]. chengdu: South West Jiaotong University, 2007:68–79.
- [7] Zhao wei. Unit Plate Roadbed Damage and Longitudinal Stress Analysis [D]. chengdu: South West Jiaotong University, 2008:56–97.
- [8] Zhu ying. Research on Experiment and Stress Analysis of Continuous Slab Rail Structure Cross Bridge. [D]. Chengdu: South West Jiaotong University, 2007:46–57.
- [9] Deng youcun. Research on Parameters and Structure Analysis of Continuous Slab Rail Structure Cross Bridge. [D]. chengdu: South West Jiaotong University, 2007:36–50.
- [10] Tan zhiming, Yao zukang. Temperature Stress of Cement Pavement Under the Nonlinear Temperature Field. [J]. *China Journal of Highway And Transport*, 1993, 6(4):198–205.
- [11] Zhang hongbo. Temperature Stress Analysis of Pavement with Lean Concrete Base [D]. Changsha University of Science and Technology, 2005, 4: 23–45.

# Shear failure mechanism of highway subgrade in seasonal frozen area during spring-thawing period

Liang Zhou

Yangzhou Jianyuan Construction Supervision Co. Ltd., China

Erhao Su

Shanghai East China Civil Aviation Airport Construction Supervision Co. Ltd., China

Yunzhen Wei

Yangzhou Jianyuan Construction Supervision Co. Ltd., China

Chongwei Huang

Key Laboratory of Road and Traffic Engineering of the Ministry of Education, Tongji University, Shanghai, China

Yan Xie

Shanghai East China Civil Aviation Airport Construction Supervision Co. Ltd., China

**ABSTRACT:** Shear strength of some subgrade soils in seasonal frozen area was tested using the quick direct test method. To process the test data, multistage grouping variance analysis was utilized. It is shown that the significance of influence factors of subgrade shear strength is in attenuation sequence: water content, normal stress, and degree of compaction. Based on the field observation of subgrade humidity during spring-thawing period, analysis of subgrade stress and the regression relation between water content, cohesion and friction angle, the maximum value of safety for each layer was calculated. The calculation indicates that the most dangerous part of subgrade is the last-thawing layer, and overload can extend the boundary of shear failure region. The research reveals the shear failure mechanism of highway subgrade in seasonal frozen area during spring-thawing period.

**Keywords:** spring-thawing period; seasonal frozen area; highway subgrade; shear failure

## 1 INTRODUCTION

Frost heaving accompanied with frost boiling and thawing settlements are the main diseases of seasonal frozen area. Usually, frost heaving occurs in winter while the latter two diseases come out in the following spring. Since former studies<sup>[1][2][3]</sup> showed that during the circulation above, the resilient module of subgrade reaches two extreme points, including the maximum value in frost heaving and minimum value in thawing settlement, with the changing of moisture, it is chosen to be the evaluating indicator of treatment on freeze-thaw diseases.

According to field researches, it can be found that shear failure of subgrade during spring-thawing period, usually resulting in the overall lateral slippage of subgrade together with subsidence of pavement (shown in Fig. 1), is closely connected with shear strength of subgrade. Therefore, it is necessary to make deep analysis on shear strength



Figure 1. Pavement settlement and crack.

and failure mechanism on subgrade soils in seasonal frozen area in order to provide sufficient support to diseases treatment.

Considering that the subgrade in the northeast part of our country mainly consists of clayey soil and this paper focuses on the shear failure due

Table 1. Error control results of water contents.

Compactness	92%					96%				
	Target water content (%)	11.2	14.2	17.5	20.6	22.7	11.2	14.2	17.5	18.4
Tested water content (%)	11.12	14.28	17.62	20.47	22.54	11.28	14.3	17.62	18.53	20.44
Error (%)	0.71	0.56	0.69	0.63	0.70	0.71	0.70	0.69	0.71	0.69

to drainage barrier in short term during spring-thawing period, quick direct shear test is chosen.

As shear strength of subgrade is mainly affected by water content, compactness and normal stress of soil, different ways including indoor tests on shear strength of soil specimens under different working conditions, field investigations of moisture on typical roads in Jilin Province and theoretical calculations of stress level in each layer of the road structures are taken to collect enough information. Based on the results, this paper gives the detailed function of the three factors above and explains the shear failure mechanism of subgrade.

## 2 INDOOR QUICK DIRECT SHEAR TEST

### 2.1 Test material

1. Sample. According to the investigations on freeze-thaw diseases in Jilin, Road S106 (Provincial Road) is chosen to study for its bad situation. Typical soil samples are taken on the location of K108+60, right side of Changling-Changchun section. After grain size test and compaction test, these samples are defined as low liquid limit clay, with secondary freeze-thaw sensitivity, and the optimum water content ( $w_{op}$ ), saturated water content ( $w_{sat}$ ) under two compactness (92%, 96%) are 14.2%, 20.6%, and 18.4%.
2. Test Design. Considering the effect of both compactness ( $w$ , %) and normal stress ( $p$ , kPa) on shear strength, water contents are chosen as  $w_{op}-3\%$ ,  $w_{op}$ ,  $0.85w_{sat}$ ,  $w_{sat}$ ,  $1.15w_{sat}$  and compactness levels are 92% and 96% (a range of 92~98% is suggested in 《Highway engineering design and construction technology for antifreeze》 but the final value is determined for the consideration of operability). Since normal stress in actual working area of subgrade ranges from 10 kpa to 50 kpa, gradient values of 12.5 kPa, 25 kPa, 37.5 kPa, 50 kPa, 62.5 kPa are chosen.

### 2.2 Test method

After taking both the current specification on direct shear test and actual state of soils in seasonal frozen area into consideration, quick shear test is carried out with the help of test instrument (Model SDJ-II)

manufactured by Ningxi soil instrument co., LTD in Nanjing.

1. Sample Preparing. Prepare Standard specimen with size of 10 cm × 20 cm, then Cut each specimen into 5 cylinders and modify them to proper height (the upper edge of sampler) with ring sampler coated by Vaseline.
2. Data Collection. Different rules are applied to record the data according to the condition: take the reading of dial gage when the failure happen in the early stage while write down the reading at the relative displacement of 6 mm in shear container if no failure occurred at last. Figure out the shear strength of specimen according to the calculation method in the specification.

### 2.3 Error control

A total of 50 working conditions, each containing 3 parallel specimens, are simulated with different water content, compactness and normal stress. The error between target water content and tested water content is within 1% as shown in Table 1. The error between target compactness and tested compactness is also within 1%, while error of parallel specimens is within 5%.

## 3 RESULT ANALYSIS

### 3.1 Water content

Plot the results in a figure, with the horizontal and vertical coordinates representing the water content and shear strength, and fit the trend lines (Seen in Fig. 2).

From Figure 2 conclusions can be drawn as follows: (1) At the same level of normal stress and compactness, the shear strength decreases significantly with water content increasing. (2) At the compactness of 92%, these trend lines show an inverted “S” shape (shown in Fig. 2. a) with inflection points appear near  $w = 17\%$ . The declining rate of shear strength goes down with water content decreasing where  $w < 17\%$  while it rises with water content decreasing where  $w > 17\%$ , which indicates that the sensitivity of shear strength reaches a highest value at  $w < 17\%$ . (3) At the compactness of 96%, these trend lines are similar to

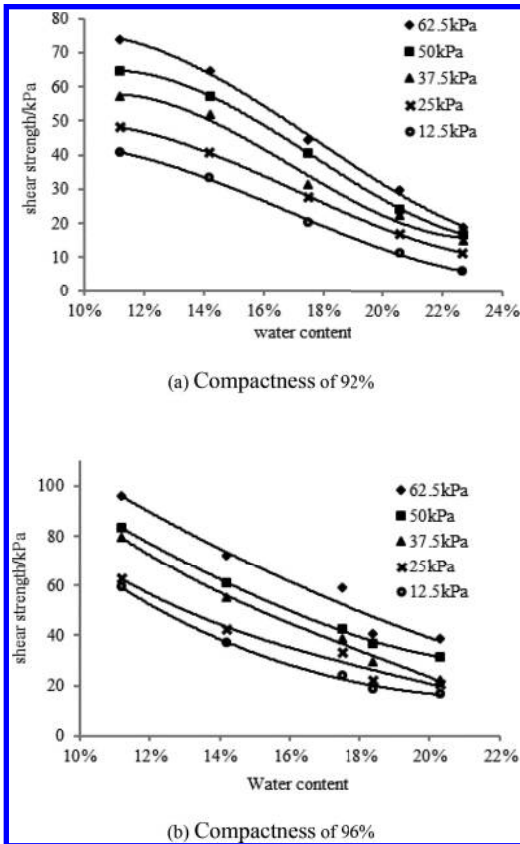


Figure 2. Shear strength vs water content at different compaction degree.

exponential function lines. The sensitivity of shear strength goes down with water content increasing and it tends to be a stable figure near  $w_{sat}$ .

### 3.2 Compactness

Compare the shear strength at different compactness while keeping the rest factors the same. The results illustrated in Figure 3 at compactness of 92% and 96%.

It can be concluded that as the shear strength rises with compactness increasing under the water content of 5. The sensitivity of shear strength towards compactness is analyzed through the way of difference comparison. The results show that: at  $w_{op}$  and  $0.85 w_{sat}$ , the shear strength is slightly affected by compactness with changes from 3~5 kPa; while at the other three water content it is obviously affected by compactness, which means the sensitivity of shear strength reach the minimum value at  $w_{op}$  and heavily increases away from  $w_{op}$ .

### 3.3 Significance analysis

Orthogonal design and variance analysis are taken in this paper to verify the significance of the following three factors: water content (A), normal stress (B) and compactness (C). The results of variance analysis are listed in Table 2.

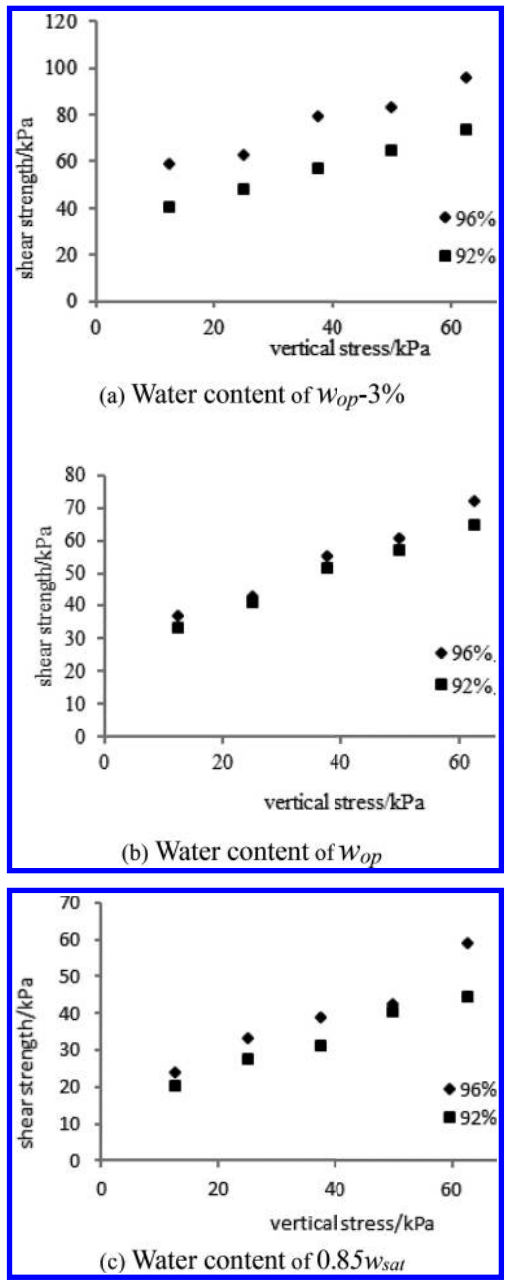


Figure 3. (Continued).

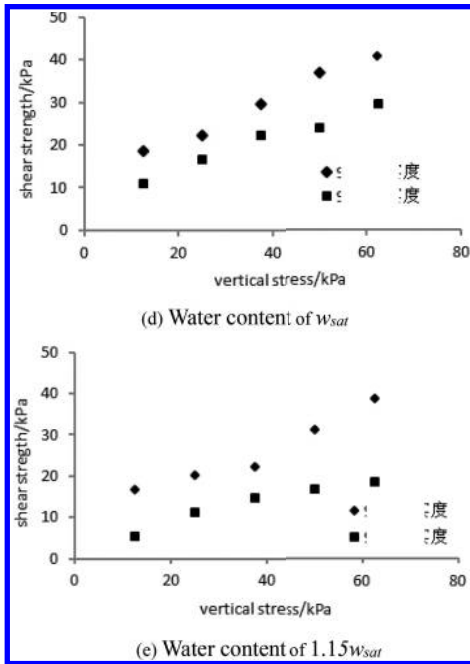


Figure 3. Shear strength vs compaction degree at different water content.

Table 2. Result of variance analysis water content see of 96%e y subgrade subgrade shear strength.

	Square	Mean			
Variance	sum	Freedom	square	F	Significance
A	1291.33	1	1291.33	672.71	**
B	410.23	1	410.23	213.71	**
A × B	20.91	1	20.91	10.89	
C	72.14	1	72.14	37.58	*
C × A	20.91	1	20.91	10.89	
Errors	3.83	2	1.92		
Sum	1830.05	7			

Seen from Table 2,  $F_{0.99}(1,2) = 98.5$ ,  $F_{0.95}(1,2) = 18.5$ . To compare with F in Table 2, when  $\alpha = 0.05$ , all of the three factor A, B, C have a significant effect on the shear strength, and the degree of influence can be ranked as below:  $A > B > C$ . However, the interaction of every two factors has no significant influence on the shear strength.

## 4 ANALYSIS ON SHEAR FAILURE

### 4.1 Humidity during spring-thawing period

The spring season frozen area of subgrade thawing period in general every year 3, April, Accord-

ing to the researches on S106 in Jilin province in April 2012, the distribution of subgrade humidity in the vertical direction is illustrated in Figure 9. Serious pavement diseases are found in positions 1 and 2.

Viewing the changes as a whole, moisture in these two points reflect the characteristics of the subgrade humidity distribution in seasonal frozen spring-thawing period: the humidity of soil is relatively high and it has even been saturated in the depth of 1.5 m~2 m due to the complex inner and outer water migration in freezing process<sup>[8]</sup>. The reasoning is also proved by the core sampling which shows that with the melt of frozen layer, water in upper and lower layers will migrate to this layer. Combining with the gravity, the subgrade humidity will remain at a high level within a period of time in the depth of 1.5 m~2 m in result to cause shear failure.

### 4.2 Stress analysis during spring-thawing period

BISAR is used to calculate the theoretical value of shear stress. Table 3 gives the parameters.

Considering about the overload in actual traffic condition and taking the standard axle load and overload (2 times the standard axle load) into account, the maximum ( $\sigma_1$ ) and minimum ( $\sigma_3$ ) principal stress can be calculated and shown in Figure 5.

Friction angle and cohesive force are obtained by direct shear test of subgrade soil under different moisture contents. Take the most unfavorable

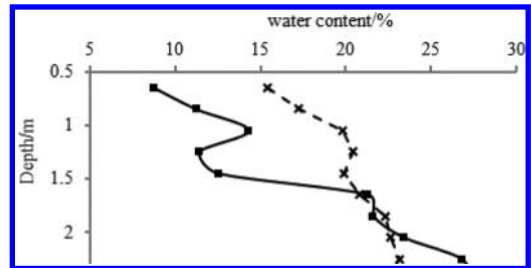


Figure 4. Subgrade humidity distribution during Spring-thawing Period.

Table 3. Parameters for pavement structure analyses of S106.

Name	Thickness/ mm	Modulus/ MPa	Poisson ratio
Pavement	18	1200	0.3
Base	32	1600	0.3
Subgrade		30	0.35

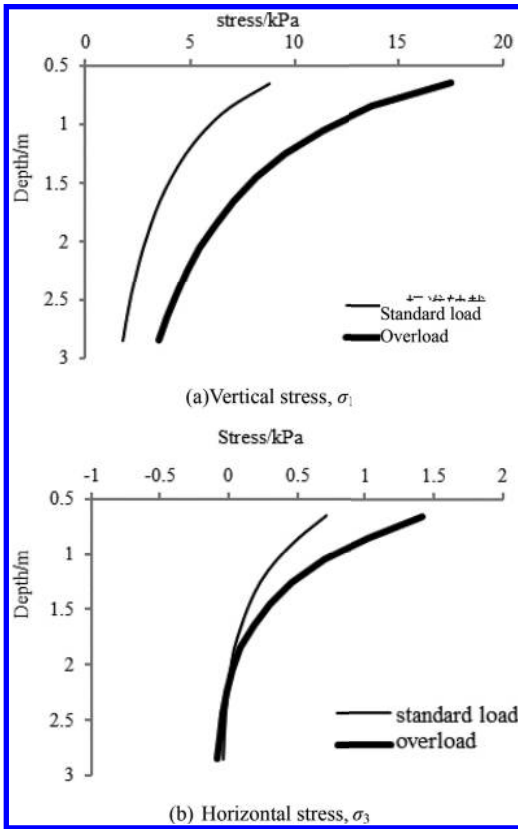


Figure 5. Calculated value of stresses in different layers of subgrade.

situation into consideration and make regression analysis at compactness at 92%, the cohesion and friction angle of the regression equation towards the water content are obtained (1) (2):

$$c = 317.91e^{-0.186W}, R^2 = 0.9622 \quad (1)$$

$$\varphi = -1.7545W + 55.405, R^2 = 0.9562 \quad (2)$$

Take measured moisture content into these two equations to obtain  $c$ ,  $\varphi$ . Calculate the minimum principal stress by using maximum principal stress under equilibrium condition:

$$\sigma_3 = \sigma_1 \tan^2(45^\circ - \varphi/2) - 2c \tan(45^\circ - \varphi/2) \quad (3)$$

According to the formula (3), compare the calculated minimum principal stress  $\sigma_3$  and theoretical value of minimum principal stress  $\sigma_1$ , shown in Figure 6.

The shear failure only happens when the calculated value of minimum principal stress is larger than the theoretical value. The potential failure in the subgrade can then be figured out by the

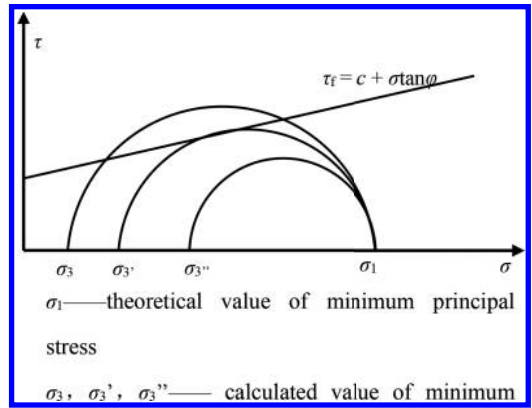


Figure 6. Checking of the limit equilibrium method.

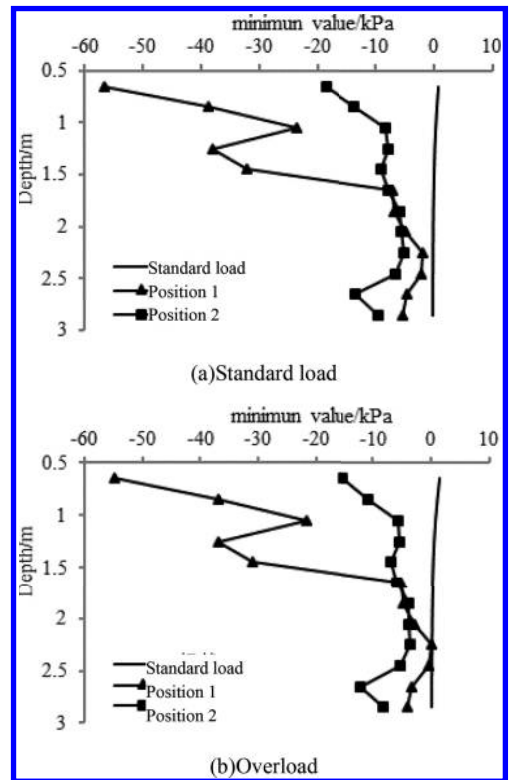


Figure 7. Calculation of subgrade stress in different traffic loads.

checking calculation for each layer, shown in Figure 7.

From Figure 7 it can be known that: (1) under the condition of standard axle loads, the minimum principal stress value of these two points are both less than the theoretical value, which means shear

failure will not occur in all of the layer in subgrade. However, there is still a potential shear failure in the depth of 2 m–2.5 m with the melt of frozen layer. (2) under the condition of overloads, the minimum principal stress value at point 1 is larger than the theoretical value and will lead to shear failure. Besides, with the melt of frozen layer in the depth of 1.5 m–2 m, the value of  $c$  and  $\phi$  may continue to decrease with the increasing water content and broken layer will move toward the final melting layers.

## 5 CONCLUSION

1. The three main factors affecting the shear strength of subgrade are water content, compactness and normal stress of soil. Besides, the water content has a maximum influence while compactness has a minimum one.
2. Based on the analysis of shear stress in the subgrade, the most unfavorable layer for shear failure is near the melted layer and has a close connection with frozen depth during frost heaving period. The checking calculations also show that there is a possible shear failure in a large range under overload situation.

## ACKNOWLEDGMENT

This research was supported by the Basic research Program of Jiangsu Province (BK2012479), the National Natural Science Foundation of China (51308413), and the Shanghai Rising-Star Program (15QB1403000).

## REFERENCES

- [1] Kubo, Hiroshi; Sakaue, Takayuki. Control of frost penetration in road shoulders with insulation boards [C]. Transportation Research Record, p 132–137, 1986.
- [2] Wallace, Mark. How to prevent frost heave [J]. Construction-world of Concrete, v 32, n 4, p 369, 371–372, Apr 1987.
- [3] Jones, R.H. Developments in the British approach to prevention of frost heave in pavements [C]. Transportation Research Record, 1987, Vol 1146, pp: 33–40.
- [4] Liang Bo, Zhang Gui-sheng, Liu De-ren. Experimental Study on Thawing Subsidence Characters of Permafrost Under Frost Heaving And Thawing Circulation [J]. Chinese Journal of Geotechnical Engineering, 2006, 28(10): 1213–1217.
- [5] Mao Xuesong, Hou Zhongjie, Wang Weina. Experimental Research on Resilient Modulus Of Remolded Soil Based On Water Content And Freeze-Thaw Cycles [J]. Chinese Journal of Rock Mechanics and Engineering, 2009, 28 (Supp. 2):3585–3590.
- [6] Liu Wei-ping, Sun Guo-jun. Renovation technology of subgrade diseases during spring-thawing period [J]. Railway Engineering, 2005(12):50–51.
- [7] The Professional Standards Compilation Group of People's Republic of China. JTGE40-2007 Test methods of soils for highway engineering [S]. Beijing: China Communications Press, 2007.
- [8] Shoop, S.A, Bigl, S.R. Moisture migration during freeze and thaw of unsaturated soils: modeling and large scale experiments [J]. Cold Regions Science And Technology, 25(1), 33–45, 1997.
- [9] Mao Xue-song, Hu Chang-shun, Dou Ming-jian. Dynamic Observation and Analysis Of Moisture And Temperature Field Coupling Process In Freezing Soil [J]. Journal of Glaciology and Geocryology, 2003, 25(1):55.

# The study progress of performance reliability of rolling bearings for urban rail

X.T. Xia, S.J. Dong, W.H. Zhu & Y.Y. Meng

*Henan University of Science and Technology, Luoyang, P.R. China*

**ABSTRACT:** With the rapid development of urban rail and traffic engineering, growing attention has been paid to the study of the performance and reliability of rolling bearings to ensure safe and reliable operation of urban rail. In most cases, the reliability distribution functions are usually a puzzle or the parameters in a known distribution function are unknown. Therefore, the performance reliability prediction and evaluation have become a key problem urgently to be solved for urban vehicles. For this end, the grey bootstrap forecasting method for the reliability of zero-failure data with poor information, the bootstrap chaotic forecasting method for the lifetime and reliability, the bootstrap weighted-norm method and dynamic bayesian significant test method of rolling bearings are summarized in this paper.

*Keywords:* subway vehicles; rolling bearing; poor information; reliability

## 1 INTRODUCTION

In order to predict different kinds of rolling bearing faults of subway vehicles, methods of fault prediction methodology based on poor information are put forward. The fault prediction method has high application value in the subway operation process. As the key component of high speed subway vehicles, the performance and reliability of rolling bearing is well worth studying for the regular running and safety [1–2]. Therefore, it is very significant for urban rail and traffic engineering to study on the performance reliability of rolling bearings.

Poor information means incomplete information, such as in system analysis, a known probability distribution with a small sample, an unknown probability distribution with only a few data, trends without any priori information, etc. The introduction of information-poor system theory to the assessment of performance and reliability of modern bearings will greatly prompt the development of the design theory of rolling bearings and relevant subjects [3–5].

So far, researches on the prediction and evaluation of the performance and reliability of rolling bearings along with poor information have made some progress. This paper mainly reviewed the prediction of the reliability of zero-failure data and that of the reliability variation process along with performance data, and the reliability evaluation with failure data under a given distribution.

## 2 RESEARCHES ON PERFORMANCE RELIABILITY OF ROLLING BEARING BASED ON POOR INFORMATION

### 2.1 *Forecasting methods for lifetime and reliability of rolling bearings along with the performance data*

A forecasting method for lifetime and reliability of bearing products along with the performance data, viz. bootstrap chaotic forecasting method is proposed by Xia [6], which fuses the principle of bootstrap method and five chaotic predicting methods. And the five chaotic methods are the adding-weight zero-rank local-region method, the adding-weight one-rank local-region method, the one-rank local-region method, the improved adding-weight one-rank local-region method and the maximum Lyapunov exponent method. It only depends on current operational information of the obtained product performances, without any prior information of performance variation over time and any prior information of the performance life probability distribution function.

The predicting procedures of the method are summarized as follows:

1. Set an evaluating indicator of the rolling bearing performance during the bearing running or testing.
2. Obtain a time series of the product performance through a measurement system, thus the time series of the current operation information are formed.



3. Apply phase space reconstruction to the time series of the current operation information, then many space points are acquired.
4. Five time series of the future operation information of the rolling bearing are predicted by the five chaotic forecasting methods.
5. Work out the five runtime data which reach the evaluating indicators by use of the five time series of the future operation information.
6. Obtain a large amount of generated data by an equiprobable resampling with replacement from the five runtime data.
7. Deduce the runtime probability density function, and then establish the estimated runtime reliability function with the performance data, finally finish the prediction of the reliability of the rolling bearing performance variation process with poor information.

### 2.2 Reliability evaluation of zero-failure data with poor information

Fusing the advantages of the bootstrap method [7] and the grey prediction GM(1,1) [8], along with an empirical failure probability function, Xia has proposed the grey bootstrap forecasting method for the reliability of zero-failure data, which is not only suitable for rolling bearings but also applicable to the reliability analysis of other products.

The specific steps of the method are described as follows: During the lifetime experiment or the service period of a product, detect the zero-failure time of individuals and the number of these data, thus obtaining the zero-failure data of product individuals; Obtain a large amount of generated data by an equiprobable resampling with replacement from the zero-failure data collected; Predict a mass of zero-failure data of the population with the generated data, thus obtaining the distribution function of the zero-failure data of the population; Construct the failure probability function of the population via the number of the zero-failure data of individuals and the distribution function of the zero-failure data of the population; Get the reliability function of the population with the population failure probability function, thus completing the evaluation of the product lifetime and reliability with zero-failure data.

A new calculation model of reliability with zero-failure data is proposed by Xia. Let the reliability coefficient be  $c$ , and then construct  $P$ , the failure probability function of the population, in the light of  $m$ , the number of the zero-failure data of product individuals, and  $F$ , the distribution function of the zero-failure data of the population.

$$P = P(x) = \frac{c}{m(1-F) + 1} \quad (1)$$

$R$ , the reliability function of the population is obtained by the failure probability function of the population as follows:

$$R = R(x) = 1 - p \quad (2)$$

In this method, it is worth noticing that the selections of parameters  $m$  and  $c$  in Eq. (1) are vital to the calculated result of reliability  $R$  in Eq. (2). The grey prediction GM(1,1) in the grey system theory and the bootstrap method require the minimum value of  $m$  to be 4, which can help to improve the reliability of the prediction.  $c$  is an empirical reliability coefficient, which has an impact on the calculated results of  $R$ . An example is taken to illustrate the effect of  $c$ , and the results are as shown in Figure 1. It can be seen that reliability  $R$  decreases as coefficient  $c$  increases. Therefore, we have to select the values of  $m$  and  $c$  reasonably according to the engineering practices.

### 2.3 The reliability calculation of given distribution

The bootstrap weighted-norm method is proposed by Xia [9], which Fusing the principle of the bootstrap method and the norm criterions, to evaluate of the optimal confidential interval of the reliability with three-parameter Weibull distribution.

The specific steps of the method are described as follows:

1. Based on the difference between empirical value and theoretical value of reliability, and six norm criterions, the optimal parameters information vector of Weibull distribution are constructed.
2. The generated parameters information vector is obtained by the bootstrap resampling from the optimal parameters information vector.
3. The probability density function of parameters is simulated by the generated parameters information vector.

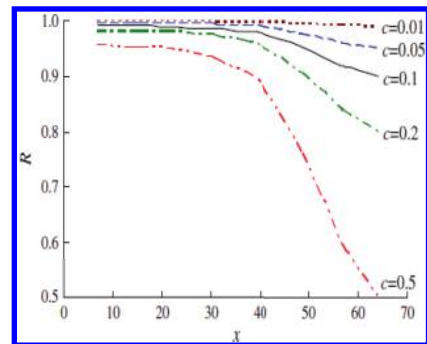


Figure 1. Relation of reliability  $R$  with empirical reliability coefficient  $c$ .

- Under the given confidence level, the estimated true value of parameters and their confidence intervals are figured out, and thus the estimated true value function of reliability and its optimal confidence interval function are established.

In the method the reason why six different norm criterions (minimum 1-norm criterion, minimum 2-norm criterion, the minimum—norm criterion, minimum weighted 1-norm criterion, minimum weighted 2-norm criterion and minimum weighted—norm criterion) are employed to estimate the parameters is that the useful information of different sides can be revealed by different criterions. Different side information can reflect different properties of parameters, therefore, the more the criterions are, the more comprehensive the parameters properties gained can be, which is conducive to the establishment of the parameter probability density function and the accurate estimation of reliability parameters, and finally to achieving the accurate evaluation of reliability.

### 3 STUDIES ON HYPOTHESIS TESTING AND IDENTIFICATION METHOD OF POOR INFORMATION PROCESS OF ROLLING BEARING PERFORMANCE

#### 3.1 *Dynamic bayesian significant test method for performance variation information of rolling bearing*

Based on maximum entropy principle and self-help method, dynamic bayesian significance test method is put forward, which can be used to solve the problem of performance variation information of rolling bearing under the condition of unknown priori information of probability distribution and trend priori knowledge. Period of time series of rolling bearing performances is obtained by regular sampling. The time origin moments can be obtained by bootstrap method and the time probability density function can be established through principle of maximum entropy. Based on the reference time series, the posteriori probability density function is established and coincidence degree is defined. Under a given significance level, the dynamic Bayesian significance test of the performance variation information of rolling bearing is carried out with the aid of coincidence degree. The experimental results show that the dynamic Bayesian significance test method can effectively test the performance variation information of rolling bearing under unknown probability distribution and trend of prior information.

#### 3.2 *Case study and discussions*

Taking vibration variation of rolling bearing caused by wear as an example. The experimental data of

vibration acceleration (unit:  $m/s^2$ ) are studied to test the wear process of bearing. Every five days for one times to get the data and a total of 10 days of data is obtained. The daily first 4000 data are selected as the research object, so each bearing has 40000 original vibration data during the whole experiment process (a total of 10 time units, each time unit has 4000 data). As shown in [Figure 2](#) and [Figure 3](#).

From [Figure 2](#) and [Figure 3](#), it can be seen that in the dynamic measurement of rolling bearing vibration, some fluctuation and variation is very complex and the probability distribution and trend are unascertained.

Bootstrap method is used for 10 data segment in the first time unit, that is to say each segment of 400 data and 500000 times bootstrap samplings are conducted respectively. Then in combination with bayesian statistics, the posterior probability density function of the prior sample is constructed and mathematical expectation and variance can be calculated, which decides to choose in which period of prior information as the prior sample. The results as shown in [Table 1](#).

From [Table 1](#), the fourth segment data in the first time unit is selected as reference time series, because of its minimal variance. 500000 times bootstrap samplings proceed by using bootstrap method on other 9 time units (a total of 90 data segment). Through bayesian statistics, the posterior probability density function is constructed and mathematical expectation, variance ratio and coincidence degree can be calculated. As shown in [Figure 4–6](#).

It can be seen the wear process and vibration performance variation process as follows. The initial

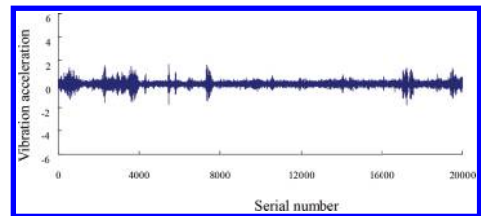


Figure 2. Vibration experimental data of rolling bearing (the first 5 days).

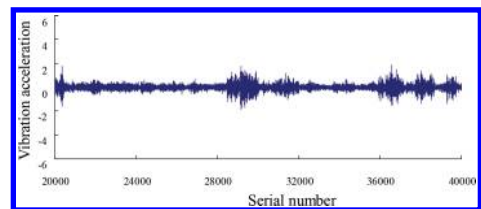


Figure 3. Vibration experimental data of rolling bearing (the last 5 days).

wear increases gradually and the vibration performance variation is progressively significant; vibration performance variation of the transition from initial wear to normal wear is not significant; vibration performance variation is not significant from the normal wear. The above analysis shows that the proposed method can accurately test the significance in the process of rolling bearing performance variation.

Table 1. Selection of reference time series.

Prior sample	Current sample	Mathematical expectation	Variance $\times 10^{-5}$
First	First	-0.003	5.8993
Second	Second	-0.0045	16.294
Third	Third	-0.0056	3.7922
Fourth	Fourth	-0.0054	1.4836
Fifth	Fifth	-0.0048	2.4824
Sixth	Sixth	-0.0012	8.7588
Seventh	Seventh	-0.0070	9.4744
Eighth	Eighth	-0.0024	43.029
Ninth	Ninth	5.2393e-004	31.533
Tenth	Tenth	-0.0035	22.149

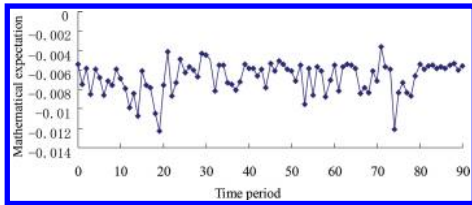


Figure 4. Mathematical expectation of the time sequence.

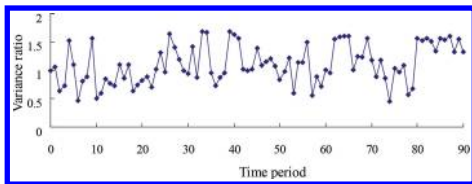


Figure 5. Variance ratio of the time sequence.

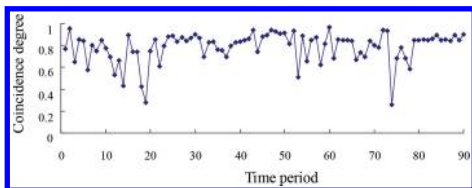


Figure 6. Coincidence degree of the time sequence.

## 4 CONCLUSIONS

The bootstrap chaotic forecasting method for the reliability along with performance data, the grey bootstrap forecasting method for the reliability of zero-failure data and the bootstrap weighted-norm method for the reliability of rolling bearing performance lifetime with failure data summarized in this paper are able to well forecast and evaluate the performance reliability of rolling bearings with poor information. Bayesian significant test method will help us detect early the hidden danger of degradation and failure of the product performance. During the rolling bearing performance experiment or its operating period, these methods can help to achieve the real-time prediction and evaluation for information of lifetime and reliability of rolling bearing performances, and detect the performance degradation and failure risks in time, thus avoiding the occurrences of serious accidents for urban vehicles.

## ACKNOWLEDGEMENTS

This project is supported by National Natural Science Foundation of China (Grant Nos. 51475144 and 51075123).

## REFERENCES

- An, Q. Qin, Y. & Chen, D.C. 2014. Research on fault diagnosis method for bearings of the urban rail transit vehicles. *Chinese Railways* (11): 96–101.
- Noriyuki, I. 2011. Technological trends of railway rolling strock bearings. *Motion and Control* (3): 2–6.
- Xia, X.T. Chen, X.Y. Zhang, Y.Z. & Yang, R.P. 2007. Experimental Analysis and Evaluation of Rolling Bearing with Poor Information. Beijing: Science Press (in Chinese).
- Oguma, N. 2011. Reliability design in rolling bearings. *Journal of Japanese Society of Tribologists* 56(11): 673–679.
- Xia, X.T. 2012. Reliability Analysis of Zero-Failure Data with Poor Information. *Quality and Reliability Engineering International* 28: 981–990.
- Xia, X.T. 2012. Forecasting Method for Product Reliability Along with Performance Data. *Journal of Failure Analysis and Prevention* 12: 532–540.
- Yatraco, Y. 2002. Assessing the Quality of Bootstrap Samples and of the Bootstrap Estimates Obtained With Finite Resampling. *Statistics and Probability Letters* 59: 281–292.
- Peng, F. Peng, L.L. & Huang, X.Y. 2013. GM(1, 1) Modeling Principle Analysis. *Journal of Grey System* 24(1): 87–95.
- Xia, X.T. Xu, Y.Z. Jin, Y.P. Shang, Y.T. & Chen, L. 2013. Assessment for Optimum Confidence Interval of Reliability with Three-Parameter Weibull Distribution Using Bootstrap Weighted-Norm Method. *Journal of Aerospace Power* (1): 481–488 (in Chinese).

## Aircraft taxiing trajectories partly update approach for A-SMGCS

Xinping Zhu, Zhixing Tang & Zhenghong Xia

College of Air Traffic Management, Civil Aviation Flight University of China, Guanghan, China

**ABSTRACT:** For airport surface operation under the control of A-SMGCS (Advanced Surface Movement Guidance and Control System), an approach on aircraft taxiing trajectories update is proposed to tackle the efficiency and safety degrades caused by surface uncertain events. Firstly, partly taxiing trajectories update strategy is adopted and Time Window Constrained Petri Net (TWCPN) is used to model local surface operation process affected by uncertain events. Secondly, time window computation rules for TWCPN model are provided to get the simplified local sub-model, also aircrafts taxi conflict conditions are derived from the sub-model. Thirdly, aircrafts taxiing trajectories update is fulfilled with the purpose of minimizing taxi cost. Finally, the proposed taxi trajectories update approach is validated through case study.

**Keywords:** air traffic control; airport; taxiing trajectories; A-SMGCS

### 1 INTRODUCTION

Advanced Surface Movement Guidance and Control System (A-SMGCS) is the most advanced airport surface control system in the world<sup>[1]</sup>. 4-Dimensional aircraft trajectory based operation is one of basic concepts in A-SMGCS, which incorporates algorithms to generate aircraft taxiing trajectories, including a series of well-spaced target points and the required time of arrival. However, surface uncertain events could bring disturbance for aircraft taxiing and lead to conformance error<sup>[2]</sup>.

Traditionally, taxi conformance and trajectories update mainly depends on air traffic controller's eye inspection and VHF talk, which can not handle large traffic volume. Past research provide taxiing trajectories at every designed period of time<sup>[3-6]</sup>. It is possible for updating taxiing trajectories in real time with information from A-SMGCS surveillance module<sup>[7-10]</sup>. Wang proposed taxiing trajectories update for airport surface operation, however, the conformance monitor and taxiing trajectories update are not integrated in a proper mechanism. TANG provided a three-stage aircraft taxiing trajectories scheduling strategy, including initial taxiing trajectories planning, taxiing trajectories assignment and update<sup>[11]</sup>. In stage of initial taxiing trajectories planning, trajectories are provided for arrival and departure flight once flight plans are transmitted to A-SMGCS. In stage of taxiing trajectories assignment, trajectories are provided before aircrafts taxi. In stage of taxiing trajectories update, trajectories are provided once conformance errors are detected. Past research is mainly

focus on the first two stages<sup>[12]</sup>. In this paper, we mainly report our research on the third stage about taxiing trajectories update.

### 2 PROBLEM DESCRIPTION

The transportation system of airport surface is divided into typical operation units, such as taxiway intersection units and line segment units. According to 4-Dimensional aircraft trajectory based operation concept, aircraft occupy units in a specified time window deriving from taxiing trajectories. However, the disturbance introducing by

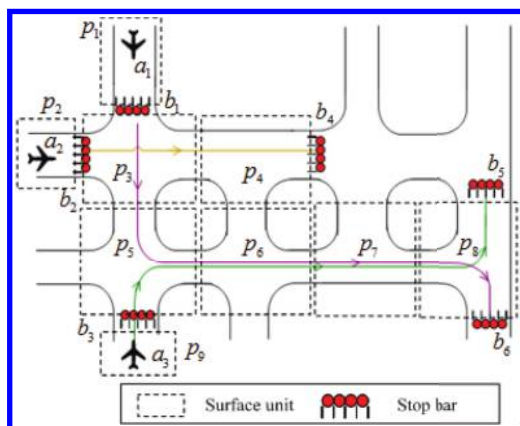


Figure 1. Aircraft taxiing process on part of airport surface.

surface uncertain events from pilots manipulation or taxiway condition could lead to conformance error or even surface conflict.

For surface demonstrated in Figure 1, assume aircraft  $a_1, a_2, a_3$  taxi through unit  $(p_3, p_5, p_6, p_7, p_8), (p_3, p_4), (p_5, p_6, p_7, p_8)$ , respectively. For taxiing process of  $a_1$  on taxiing trajectories segment, which include  $p_3, p_5, p_6, p_7$  and  $p_8$ , can not be stopped by stop bar lights (the segment is called continuous taxiing segment in this paper). Thus, when  $a_1$  has to be postponed to occupy unit  $p_1$  caused by some reasons, it will lead to conflict among flights occupy the same unit in future, such as  $a_1$  and  $a_2$  in  $p_1$ , or  $a_1$  and  $a_3$  in one of the unit  $p_5, p_6, p_7$ , and  $p_8$ . Considering surface operation safety and efficiency, aircraft taxiing process needs to be monitored and taxiing trajectories update need to be conducted in real time. Usually, A-SMGCS is implemented in large and busy airport, it is impossible to fulfill aircraft taxiing trajectories update without precise mathematical mode and algorithm. We provide approach for it.

### 3 AIRCRAFT TAXIING TRAJECTORIES UPDATE MECHANISM DESIGN

In past, aircraft taxiing trajectories update is investigated through Operational Research (OR) model of airport surface in an up-down methodology. However, this kind of model can not be resolved in real time for its complexity. We propose taxiing trajectories update mechanism, in which the optimization and feed-back are integrated. And also, the monitored surface uncertain events are the main driver of aircrafts taxiing trajectories update.

Basically, two kinds of events will bring to the update of aircraft taxiing trajectories. One is the ending of aircraft occupy taxiway unit. The other is the disturbance occurring as a result of uncertain events. The update process caused by the

former is called routine taxiing trajectories update and the latter is called non-routine taxiing trajectories update. A-SMGCS taxiing trajectories update mechanism is provided as described in Figure 2, which include aircraft taxiing process module needed to be guided and controlled by pilots and navigation aids on surface, affected by outer conditions and aircraft performance; aircraft taxiing state monitor module and the local surface operation modeling module which depict the surface operation process in a mathematical method; algorithms for the routine and non-routine taxiing trajectories update. The new taxiing trajectories are transmitted to aircrafts on surface, until the next update event occurring.

### 4 LOCAL SURFACE OPERATION PROCESS MODELLING

Definition 1 Time window constrained Petri net (TWCPN) model for surface operation is a structure

$$TWCPN = \{P, T, I, O, M_0, \delta\}$$

$P = \{p_1, p_2, \dots, p_n\}$  is finite set of place;

$T = T_1 \cup T_2$  is finite set of transition;  $T_1$  represents block transitions “|” which describe aircraft movements that can be stopped by stop bar;  $T_2$  represents line transitions “|” which describe aircraft movements that can not be stopped by stop bar;

$I(O)$  is the input (output) function of TWCPN;

$M_0$  is the initial discrete marking of TWCPN;

$\delta: P \rightarrow W$  specifies the time window associated to places, which is derived from aircraft taxiing trajectories, representing aircraft taxiing plan on surface.

For taxiing process of aircraft  $a$ , current continuous taxiing segment is denoted by  $r_a$ , the remaining taxiing segment of aircraft  $a$  is denoted by  $l_a$ , and the next continuous taxiing segment is denoted by  $r_a^*$ .

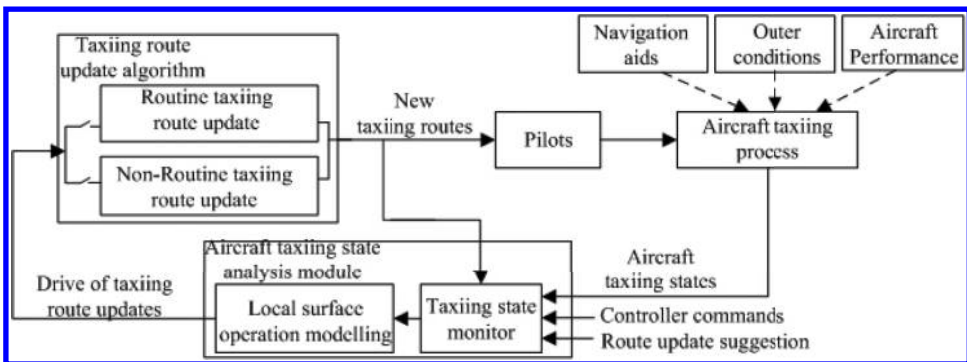


Figure 2. Aircraft taxiing trajectories update mechanism for A-SMGCS.

If there exist same unit in continuous taxiing segment of different aircrafts, the segment is called correlated segment. The generation rules of a local surface sub-model from TWCPN are as follows:

Rule 1:

$$P' = P'_a \cup P''_a \cup P'''_a,$$

$$P'_a = P(l_a) \cup P(r_a^*); P''_a = P(l_j),$$

$$l_j \in F(l_a) \cup F(r_a^*);$$

$$P'''_a = P(l_i), l_i \in F^*(l_j);$$

$$\forall p \in P', M'(p) = M(p);$$

Rule 2:

$$T' = \{t \mid t \in p^{(l)} \cap T, p \in P'_a\},$$

$$T = T_1 \cup T_2;$$

Rule 3:  $I'(p,t) = I(p,t)$ ,  $O'(p,t) = O(p,t)$

Rule 4:  $\Psi'(p) = \Psi(p)$

According to Rule 1, places of the remaining taxiing segment, of the next taxiing segment, of the correlated segment, ones in the last taxiing segment are constituted into places in local surface sub-model, and the markings of sub-model are the same as TWCPN; According to Rule 2, the output transitions of places determined by Rule 1 are constituted into transitions in local sub-model; According to Rule 3, the input and output function of local sub-model is the same as the origin function of TWCPN; According to Rule 4, current taxiing trajectories of aircraft remaining as before in TWCPN.

Example 1: The operation scenario for part of taxiway system is demonstrated in Figure 1. Assume taxiing trajectories of aircraft  $a_1$  is  $r_1(1,6) = t_1^1 t_2^1 t_3^1 t_4^1 t_5^1 t_6^1 \dots$ , and it is postponed to occupy current unit, thus the local sub-model of aircraft  $a_1$  can be established by rules proposed above.

Firstly, for current taxiing segment ( $r_1$ ) of aircraft  $a_1$ , unit represented by Place  $p_1$  is one of the units in its remaining taxiing segment  $l_1$  in  $r_1$ ; Place  $p_3, p_5, p_6, p_7, p_8$  are units of the next continuous taxiing segment  $l_1^*$  of aircraft  $a_1$ ; According to Rule 1, we get  $P'_1 = P(l_1) \cup P(l_1^*) = \{p_1, p_3, p_5, p_6, p_7, p_8\}$ . Secondly, for  $l_1$  and correlated segments of  $l_1^*$  which is denoted by  $F(l_1^*) = \{l_2, l_3\}$ , units represented by Place  $p_3$  and  $p_5$  are of the units in segment of  $l_2$ , units represented by Place  $p_5, p_6, p_7, p_8$  are of the units in segment of  $l_3$ . Thus, we get  $P''_1 = P(l_2) \cup P(l_3) = \{p_3, p_4, p_5, p_6, p_7, p_8\}$ . Thirdly, Place  $p_2$  (or  $p_5$ ) is one of units for previous continuous taxiing segment of aircraft  $a_2$  (or  $a_3$ ). Finally, transitions, time window for place can be determined by Rule 2~4. The local sub-model for aircraft  $a_1$  is demonstrated in Figure 3.

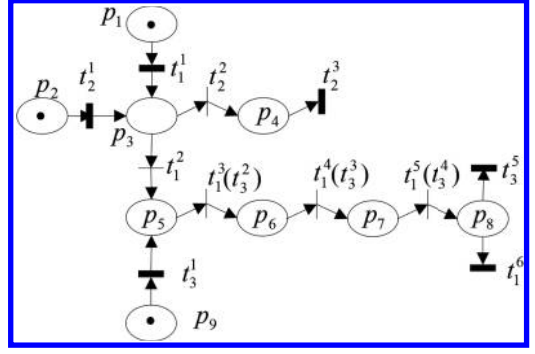


Figure 3. Sub-model of aircraft  $a_1$  in Figure 1.

## 5 AIRCRAFT TAXI CONFLICT PREDICTION ON LOCAL PART OF SURFACE

Definition 2 Currently Correlated Areas ( $CCA$ ) is segment which is related to the current continuous taxiing segment of one aircraft, and places in the corresponding local sub-model are denoted by

$$CCA = \{p \mid p \in P(l_a) \cup P(l_i), l_i \in F(l_a)\};$$

Next Correlated Area ( $NCA$ ) is segment which is related to the next continuous taxiing segment, and places in the corresponding sub-model can be denoted by

$$NCA = \{p \mid p \in P(r_a^*) \cup P(l_j), l_j \in F(r_a^*)\}.$$

Definition 3 Transition  $t \in T_1$  which meets condition  $t^{(p)} \subseteq CCA$  (or  $t^{(p)} \subseteq NCA$ ) is defined as the input transition of current correlated area (or the next correlated area).

Definition 4 Time window for aircraft occupying taxiing unit is represented as  $w_a^p = \{p, [t_a^i, t_a^o]\}$ . Of which,  $t_a^i$  is the time for aircraft  $a$  entering unit  $p$  (taxiway intersection or line segment);  $t_a^o$  is the time for aircraft  $a$  leaving unit  $p$ .

If units corresponding to place  $p_i, p_j \in CCA$  (or  $p_i, p_j \in NCA$ ) will be occupied by aircrafts at the same time, there exists taxi conflict among aircrafts. In order to analyze the conflict, we propose computation rule denoted by ad.

For time window  $w_1 = \{p_1, [\tau_1, \tau_2]\}$ ,  $w_2 = \{p_2, [\tau_3, \tau_4]\}$ , the ad computation can be fulfilled in following rules:

Rule 1:  $ad(w_1, w_2) = \{H, [\tau_1, \tau_4]\}$ , of which,  $H = \{p_1, p_2\}$ ,  $\tau_1 \leq \tau_3 \leq \tau_2$ ;

Rule 2:  $ad(w_1, w_2) = \{H, [\tau_1, \tau_2] \cup [\tau_3, \tau_4]\}$ , of which,  $H = \{p_1, p_2\}$ ,  $\tau_2 < \tau_3$ .

## 6 AIRCRAFT TAXIING TRAJECTORIES UPDATE

The local sub-model for aircraft  $a$  can be simplified using above rules, and the derived simplified model is demonstrated in Figure 4.

For continuous taxiing segments of aircraft  $a$  in local sub-model, Place sets in the resulted simplified model in Figure 4 is denoted by  $H_a$  and  $H'_a$ . For clearly, we call it model  $a$ . Similarly, for aircrafts  $a_1, a_2, \dots, a_m$  ( $a_n, \dots, a_k$ ), their continuous taxiing segments in local sub-model can be simplified, and we call them model  $a_1, a_2, \dots, a_m$  ( $a_n, \dots, a_k$ ), respectively.

Surface units corresponding to Place sets  $H_a, H_i$  ( $i=1,2,\dots,m$ ) are formed into current correlated area. Surface units corresponding to Place sets  $H'_a, H_j$  ( $j=n, n+1, \dots, k$ ), are formed into next correlated area. If aircraft  $a$  entering the taxiing segment is delayed  $\Delta\tau$  by some reasons, the conflict judgment conditions for local part of surface operation are as following:

Condition 1: condition for conflict in CCA

If aircraft  $a$  entering taxi segment corresponding to model  $H_a$  at  $\tau_0$ , aircraft  $a_1, a_2, \dots, a_m$  entering taxi segment corresponding to  $H_i$  at  $\tau_i$ , there exists conflict in CCA between aircraft  $a$  and  $a_i$  using following conditions:

- ①  $H_i \cap H_a \neq \Phi$ ;
- ②  $[\tau_0, \tau_0 + |w_a| + \Delta\tau] \cap [\tau_i, \tau_i + |w_i|] \neq \Phi$ , of which,  $|w_i|$  represents duration of time window  $w_i, i=1, 2, \dots, m$ .

Condition 2: condition for conflict in NCA

If aircraft  $a$  entering taxi segment corresponding to model  $H'_a$  at  $\tau'_0 = \tau_0 + |w_a| + \Delta\tau$ , aircraft  $a_n, \dots, a_k$  entering segment corresponding to  $H_j$  at  $\tau_j$ , there exists conflict in local correlated area for aircraft  $a$  and  $a_i$  using following conditions:

- ①  $H_j \cap H'_a \neq \Phi$ ;
- ②  $[\tau'_0, \tau'_0 + |w'_a|] \cap [\tau_j, \tau_j + |w_j|] \neq \Phi$ , of which,  $|w_j|$  represents the duration of time window  $w_j, j=n, n+1, \dots, k$ .

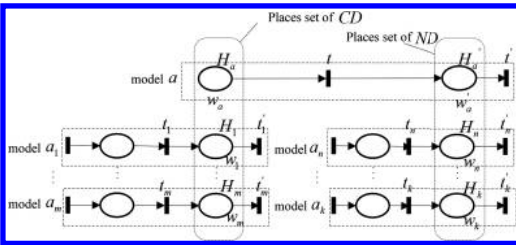


Figure 4. Simplified model for local sub-model of aircraft  $a$ .

In local sub-model corresponding to part of surface, the taxiing trajectories set is denoted by  $W_o$ . For correlated areas where exists taxi conflict, the input transition of its sub-model can be used to generate sequence  $\varepsilon$  and formed into set  $X$ .

The generation rules of sequence  $\varepsilon$  are as follows: ① transition enabled by token represented VIP flight shall be arranged in priority; ② transition enabled by token represented arrival flight shall be arranged in priority.

The taxiing cost for flights which will occupy the correlated are is set as optimization target:

$$\min_{\varepsilon \in X} f(\varepsilon, \Delta\tau, W_o)$$

The computation method is as follows:

Firstly, for transition sequence  $\varepsilon = t_1 t_2 \dots t_n$ , the firing time  $\beta_i$  ( $i=1, 2, \dots, n$ ) can be determined according to taxiing trajectories  $W_o$  in this local area; If the flight denoted by token which enabling the transition  $t_1$  meet some uncertain events, the firing time  $\beta_1$  can be adjusted by adding  $\Delta\tau$ .

And then, time for aircrafts occupy correlated areas can be computed by following steps:

- ① Time for aircraft leave the correlated area can be determined by  $\tau_i = \beta_i + \mu_i$ , of which,  $\beta_i$  is the time for transition firing,  $\mu_i$  is the duration aircraft occupying the area.
- ② For transition  $t_i$  ( $i=2, 3, \dots, n$ ) in sequence  $\varepsilon$ , we can determine its firing time by  $\beta'_i = \max\{\tau_{i-1}, \beta_i\}$  and duration  $\mu_i$  for aircraft occupy this correlated area. And also, time of aircraft leaving this correlated area can be determined by  $\tau_i = \beta'_i + \mu_i$

Finally, the taxiing cost for aircrafts can be determined by

$$f(\varepsilon, \Delta\tau, W_o) = f_1 + f_2$$

In which, taxiing cost of aircraft taxiing through the correlated area is

$$f_1 = \sum_i \mu_i \times c_i$$

$c_i$  is aircraft taxi cost in unit time.

Taxiing delayed cost of aircraft before entering this correlated area

$$f_2 = \sum_i p_d \times \max\{\tau_i - \beta_{i+1}, 0\}$$

$p_d$  is aircraft taxi delay cost in unit time.

## 7 CASE STUDY

Aircraft taxiing trajectories update in Figure 1 is analyzed, considering one of aircrafts is delayed. The assigned taxiing trajectories for aircraft  $a_1, a_2, a_3$  are listed in Table 1, and the taxiing priority of  $a_1$  is higher than  $a_2$  and  $a_3$ .

Take the operation data of A320 as an example, the taxi cost of unit time  $c_t = 84$  Yuan/min, and delayed cost of unit time  $p_d = 178$  Yuan/min. If aircraft  $a_1$  is postponed to occupy unit  $p_1$  by 50 seconds detected from surveillance module in A-SMGCS, the time occupying next segment will also be delayed 50 seconds. The local surface area affected by delay of aircraft  $a_1$  is analyzed and taxiing trajectories of aircraft through this area can be updated in the following steps:

Firstly, the local surface operation sub-model when aircraft  $a_1$  is delayed can be represented in Figure 3.

Then, the sub-model can be fatherly simplified by analyzing aircrafts in this local surface, and the resulted model is demonstrated in Figure 5.

$$w'_{a1} = \{H'_{a1}, [\tau'_1, \tau''_1]\},$$

$$H'_{a1} = \{p_3, p_5, p_6, p_7, p_8\},$$

$$\tau'_1 = 9:37:50, \tau''_1 = 9:38:50;$$

$$w_{a2} = \{H_{a2}, [\tau'_2, \tau''_2]\},$$

$$H_{a2} = \{p_3, p_4\}, \tau'_2 = 9:38:12,$$

$$\tau''_2 = 9:38:32;$$

$$w_{a3} = \{H_{a3}, [\tau'_3, \tau''_3]\},$$

$$H_{a3} = \{p_5, p_6, p_7, p_8\},$$

$$\tau'_3 = 9:38:40, \tau''_3 = 9:39:30.$$

Operation units corresponding to Place sets  $H'_{a1}, H_{a2}, H_{a3}$  are formed into the next correlated area. According to conflict judgment conditions  $H'_{a1} \cap H_{a2} \neq \Phi$  and  $[\tau'_1, \tau''_1] \cap [\tau'_2, \tau''_2] \neq \Phi$ , there exists conflict in this area between aircraft  $a_1$  and  $a_2$ . Similarly, there exists conflict between aircraft  $a_1$  and  $a_3$  in this area.

Finally, taxiing trajectories can be updated for aircrafts in this area using method proposed in

Table 1. Time window for aircrafts taxiing trajectories in Figure 1.

Aircraft	Time window for each unit of taxiing route
$a_1$	$\rightarrow \{p1, [9:36:50,9:37:00]\} \rightarrow \{p3, [9:37:00,9:37:10]\} \rightarrow \{p5, [9:37:10,9:37:25]\} \rightarrow$ $\{p6, [9:37:25,9:37:35]\} \rightarrow \{p7, [9:37:35,9:37:45]\} \rightarrow \{p8, [9:37:45,9:38:00]\} \rightarrow$
$a_2$	$\rightarrow \{p2, [9:38:02,9:38:12]\} \rightarrow \{p3, [9:38:12,9:38:22]\} \rightarrow \{p4, [9:38:22,9:38:32]\} \rightarrow$
$a_3$	$\rightarrow \{p9, [9:38:30,9:38:40]\} \rightarrow \{p5, [9:38:40,9:38:55]\} \rightarrow \{p6, [9:38:55,9:39:05]\} \rightarrow$ $\{p7, [9:39:05,9:39:15]\} \rightarrow \{p8, [9:39:15,9:39:30]\} \rightarrow$

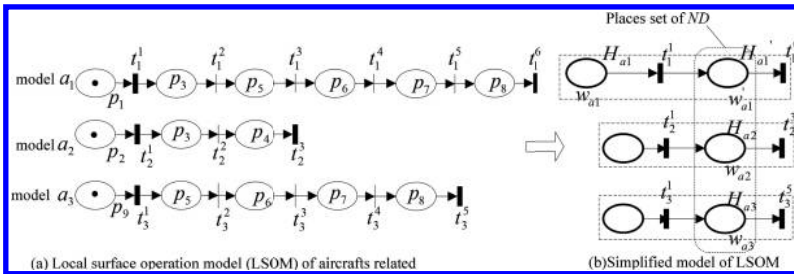


Figure 5. Taxiing model for aircrafts in Figure 3 and its simplified model.

Table 2. Updated time window of taxiing trajectories for aircrafts.

Aircraft	Updated time window for each unit of taxiing route
$a_1$	$\rightarrow \{p1, [9:37:40,9:37:50]\} \rightarrow \{p3, [9:37:50,9:38:00]\} \rightarrow \{p5, [9:38:00,9:38:15]\} \rightarrow$ $\{p6, [9:38:15,9:38:25]\} \rightarrow \{p7, [9:38:25,9:38:35]\} \rightarrow \{p8, [9:38:35,9:38:50]\} \rightarrow$
$a_2$	$\rightarrow \{p2, [9:38:02,9:38:50]\} \rightarrow \{p3, [9:38:50,9:39:00]\} \rightarrow \{p4, [9:39:00,9:39:10]\} \rightarrow$
$a_3$	$\rightarrow \{p9, [9:38:30,9:39:10]\} \rightarrow \{p5, [9:39:10,9:39:25]\} \rightarrow \{p6, [9:39:25,9:39:35]\} \rightarrow$ $\{p7, [9:39:35,9:39:45]\} \rightarrow \{p8, [9:39:45,9:40:00]\} \rightarrow$



this paper. The firing sequence for input transition of next correlated area can be determined as  $X = \{< t_1^1, t_2^1, t_3^1 >, < t_1^1, t_3^1, t_2^1 >\}$  according to taxiing priority relation among aircrafts. For transition sequence  $< t_1^1, t_2^1, t_3^1 >$ , when aircraft taxi through the correlated area, the following results can be reached: taxiing time for aircraft  $a_1$  is 60 s ( $u_1 = 60$  s), and the delayed time is 0 second; taxiing time for aircraft  $a_2$  is 20 s ( $u_2 = 20$  s), and the delayed time is 38 s; taxiing time for aircraft  $a_3$  is 50 s ( $u_3 = 50$  s), and the delayed time is 30 s; Taxiing cost for aircrafts through this local surface  $f_1 = 182$  yuan, while taxiing delay cost for aircrafts through this local surface  $f_2 = 201$  yuan; and the overall taxiing cost is 383 yuan.

Similarly, for sequence  $< t_1^1, t_3^1, t_2^1 >$ , the overall taxiing cost is 472 yuan.

Thus, by comparison, aircraft  $a_1, a_2, a_3$  should taxiing through the area according to the arrangement corresponding to sequence  $< t_1^1, t_2^1, t_3^1 >$ , updated taxiing trajectories are demonstrated in Table 2.

## 8 CONCLUSION

Aircraft taxiing trajectories update approach is proposed for surface operation under the control of A-SMGCS. The trajectories update is driven by real time information from surveillance module of A-SMGCS, combining optimization and feedback mechanism; Rules generating local sub-model from TWCPN model are provided, and conflict judgment conditions are proposed for aircrafts on surface corresponding to the sub-model. Taxiing trajectories update is fulfilled with the minimization of overall taxiing cost of aircrafts on the corresponding local surface.

For 4D trajectory based surface operation under the control of A-SMGCS, the taxiing conformance monitor and taxiing trajectories update method for aircrafts on entire surface need to be investigated in future.

## ACKNOWLEDGMENTS

The authors would like to thank the anonymous reviewers whose comments have helped us to improve the presentation of the paper. This research is supported in part by National Science Foundation of China U1433126 and General Program Foundation of CAFUC J2013-60.

## REFERENCES

[1] International Civil Aviation Organization (ICAO). 2004. Doc.9830-AN/452, Advanced surface movement guidance and control systems (A-SMGCS) Manual. Montreal.

[2] Atkins S., Brinton C., Yoon J. 2008. Implication of Variability in Airport Surface Operations on 4-D Trajectory Planning. *Proc. Of 26th Congress of International Council of the Aeronautical Science*, 2008. Alaska.

[3] Smeltink W., Soomer J., Wall R. 2004. An Optimization Model for Airport Taxi Scheduling. *Proc. of the INFORMS Annual Meeting*, 2004. Denver.

[4] Garcia A., Berlanga A., Molina J.M. 2005. Methods for operations planning in airport decision support systems. *Applied Intelligence* 22(3): 183–206.

[5] Marín Á.G. 2006. Airport management: taxi planning. *Annals of Operations Research* 143: 191–202.

[6] Pestic B., Durand N. 2001. Aircraft ground traffic optimization using a genetic algorithm. *Proc. of the Genetic and Evolutionary Computation Conference*, 2001. San Francisco.

[7] Brinton C., Atkins S. 2007. Analysis of Taxi Conformance Monitoring Algorithms and Performance. *Proc. Of the Integrated Communications, Navigation and Surveillance Conference*, 2007. Herndon.

[8] Zheng Q., Zhao Y., Capozzi B. 2010. Time-of-Arrival Based Taxi Conformance Monitoring for Surface Operation. *Proc. of AIAA Guidance, Navigation, and Control Conference* 2010. Toronto.

[9] Zheng Q., Zhao Y., Capozzi B. 2011. Taxi trajectories conformance monitoring for surface operations. *Proc. of the 2011 Integrated Communication, Navigation and Surveillance Conference* 2011. Herndon.

[10] Mann G., Hwang I. 2011. 4D Aircraft Taxiway Conformance Monitoring with Stochastic Linear Hybrid Systems. *Proc. Of AIAA Guidance, Navigation, and Control Conference* 2011. Oregon.

[11] Wang Y.J., Hu M.H., Su W. 2009. Dynamic Taxiway Routing Algorithm Based on Conflict Avoidance, *Journal of Southwest Jiao Tong University* 44(6): 933–939.

[12] Tang X.M., Wang Y.T., Han S.C. 2010. Aircraft Dynamic Taxiway Trajectories Planning for A-SMGCS based on DEDS. *Systems Engineering and Electronics* 32(12): 2669–2675.

[13] Zhu X.P., Tang X.M., Han S.C. 2013. Aircraft initial taxiing trajectories planning based on Petri net and genetic algorithm. *Journal of Southwest Jiaotong University* 48(3): 565–573.

[14] Xiong J., Zhang C. 2010. Airport Gate Assignment with Airplane Taxiing Cost Analysis. *Journal of Transportation Systems Engineering and Information Technology* 10(3): 165–170.

[15] Xu X.H., Li X. 2006. Cost Analysis of Flight Delays and Simulation in Ground-Holding Model. *Journal of Nanjing University of Aeronautics and Astronautics* 38(1): 115–120.

# Performance analysis of prestressed concrete T-beam structure after fire

Qi-feng Wang

Research Institute of Highway Ministry of Transport, Haidian District, Beijing, China

**ABSTRACT:** Combined with an engineering example of prestressed concrete T-beam, and based on the parameters investigated, such as appearance characteristics of the T-beam, compressive strength of concrete and fire temperature, structure section loss, reduction parameters of concrete and reinforcement mechanics performance are presumed. Moreover, through current state structural analysis, the structural performance of this prestressed concrete T-beam bridge is evaluated. Then some maintenance suggestions and construction methods are presented, which could provide important reference for rapid evaluation of mechanical behavior and maintenance and strengthening of the same type of bridges after fire.

**Keywords:** after fire; prestressed concrete; T-beam; mechanical performance

## 1 INTRODUCTION

In recent years, the bridges damaged due to the fire happened frequently in China. The mechanical properties of the structure were damaged under different degrees; at the same time, it caused huge economic loss. Usually, the mechanical properties of prestressed concrete structure material will change due to the physical and chemical changes in concrete and reinforcement caused by fire. As a result, significant change will happen in the mechanical behavior of structure [1]. After the fire, fire sprinklers are often used. However, the high temperature of concrete and reinforcement suffer from fire cooled sharply by the water which will result in large areas of concrete stripping, spalling, and bare bar phenomenon [2]. There may even be cracks distributed along the reinforcement. According to the relevant research results, the methods used in evaluation of the performance of prestressed concrete structure after fire can be load test [3], theoretical calculation analysis [4], or calculation, and an analysis can be adopted based on detection and load test [5]. Combined with an engineering example of prestressed concrete T-beam, an effective way of rapid evaluation through calculation and analysis is provided in this paper, which is based on the investigation of section loss, the test of compressive strength test, the presumption of fire temperature, and the calculation of reduction parameters.

## 2 PROJECT OVERVIEW

A combination of bridge span is 27.3 m + 10 × 33.0 m + 33.0 m, total length is 390.4 m, full width

is 16.8 m, the upper structure is prestressed concrete T-beam, and the clearance is about 4 m. The T-beam suffered from fire for about 2 hours due to the flammable construction (wood) materials piled under side span; therefore, the end of T-beam was badly damaged. In order to evaluate the effect of fire on the structure mechanics performance and determine maintenance method rapidly and accurately, the investigation of section loss, the test of concrete compressive strength, and presumption of fire temperature were carried out, and the analysis of structure performance was provided based on the reduction parameters.

## 3 FIRE SITUATION INTRODUCTION

The fire lasted about 110 minutes due to the wooden building materials temporarily stacked under the bridge. To get the fire under control, fire hoses sprayed water on the surface of T-beam. The strip and flake of concrete appeared immediately after spraying water on the surface area of T-beam.

## 4 INVESTIGATIONS OF APPEARANCE CHARACTERISTICS

The fire covered 22 pieces of T-beam, including 17 pieces of which local area color changed obviously and the rest were all blackened, moreover, 15 pieces of which web and flange plate local area concrete presented serious phenomenon of stripping and bare bar. The typical damage situation of T-beam suffered from is shown in the [Figure 1](#).

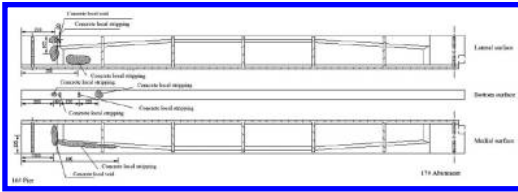


Figure 1. The typical damage situation of T-beam.

Table 1. The compressive strength.

Core sample	Compressive strength /MPa		Design strength
	1#	2#	
1	18.6	39.4	45
2	24.2	31.1	45
3	40.1	37.9	45
4	34.7	22.0	45
5	18.0	25.0	45
6	43.7	43.6	45
7	17.0	18.6	45

## 5 CONCRETE COMPRESSIVE STRENGTH

The compressive strength of the regions in T-beam which were damaged obviously was tested, and the specimens were obtained by core drilling method. The measured concrete compressive strength of T-beam are between 17.0 and 40.1 MPa, the compressive strength of concrete in the surface of T-beam decreased significantly, the compressive strength test results are shown in Table 1.

## 6 FIRE TEMPERATURE AND THE PRESUMPTION OF SECTION LOSS

According to requirements of Assessment standard of existing build structures after fire (CECS 252:2009) [6], combined with appearance investigation, color change, concrete stripping condition and hand hammer knock test: the surface temperature of the region that color changes obviously was 700°C~ 800°C, the depth that was influenced by the high temperature is about 4 cm in the side of the web, and 6 cm at the bottom of the web. Despite of surface layer, the internal temperature of concrete did not exceed 300°C. The surface burning temperature at bottom of T-beam flange plate was greater than 500°C, the temperature of other parts of flange plate was below 200°C.

## 7 STRUCTURE CALCULATION AND ANALYSIS

### 7.1 Calculation model

1. According to the original design data and presumption results of section loss, the reduction

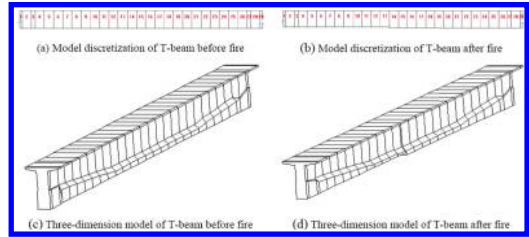


Figure 2. T-beam calculation models for different stages.

of geometric cross section is carried out for the calculation model, therefore, considering 6 cm of the concrete at the bottom of T-beam and 4 cm of web are failure. Calculation models are shown in Figure 2.

2. The compressive strength, elastic modulus, prestressed reinforced concrete bond strength are selected according to the concrete compressive strength test results and Assessment standard of existing build structures after fire (CECS 252:2009). And the reduction factors are determined based on that the concrete internal fire temperature is 300°C, so the reduction factor of concrete elastic modulus is 0.75, bond strength between prestressed reinforcement and concrete is 0.90, concrete compressive strength is 0.70. The key calculation parameter values are shown in Table 2.
3. The reduction range of the cross section and calculating parameters mentioned above is 0~12 m from the end of the beam, and cross section and calculation parameters of other beam segments used are in accordance with the original design values.

### 7.2 Strength checking of normal section

The calculation analysis results show that normal section strength of 12~13 units of T-beam after fire cannot meet the application requirements, while the rest of the section satisfy the requirements, the calculation results of the key section before and after fire are shown in Table 3.

### 7.3 Strength checking of oblique section

The calculation analysis results show that the section size of 0.7~6.7 m of T-beam after fire cannot meet the shear strength requirements, while others all satisfy the requirements. The strength calculation results of key oblique section before fire under typical load combination are shown in Table 4; moreover, the strength calculation results of key oblique section before fire under typical load combination are shown in Table 5.

Table 2. The key calculation parameter values.

Items	The original values	Reduction factors	Values after reduction
Elastic modulus(MPa)	34200	0.75	25650
Shear elastic modulus(MPa)	14706	0.75	11029.5
Linear expansion coefficient (/°C)	1.00E-05	1.00	1.00E-05
Poisson ratio	0.1666	1.00	0.1666
Volume weight (kN/m <sup>3</sup> )	25.0	1.00	25.0
Concrete mark	45.0	0.70	31.5
Axial compressive strength standard value (MPa)	32.2	0.70	22.54
Axial tensile strength standard value (MPa)	2.84	0.70	1.99
Axial compressive strength design value (MPa)	26.3	0.70	18.41
Axial tensile strength design value (MPa)	2.33	0.70	1.63

Table 3. The calculation results of the key section before and after fire.

Location and items		Before fire/MPa				After fire/MPa			
Section	Load combination	Mj	R	R-Mj	Estimation	Mj	R	R-Mj	Estimation
12#unit: left section	I	4613	8092	3479	satisfied	4538	3958	-580	unsatisfied
	II	4650	8092	3442	satisfied	4549	3958	-591	unsatisfied
	III	4435	8092	3657	satisfied	4376	3958	-418	unsatisfied
12#unit: right section	I	4753	8238	3485	satisfied	4538	3958	-580	unsatisfied
	II	4768	8238	3470	satisfied	4556	3958	-598	unsatisfied
	III	4585	8238	3653	satisfied	4376	3958	-418	unsatisfied
13#unit: left section	I	4753	8238	3485	satisfied	4622	4051	-571	unsatisfied
	II	4795	8238	3443	satisfied	4636	4051	-585	unsatisfied
	III	4585	8238	3653	satisfied	4481	4051	-430	unsatisfied

Table 4. The strength calculation results of key oblique section before fire.

X/m	Internal force	Stirrup/kN	Prestress/kN	Total resistance force VR/kN	Design shear force Vd/kN	VR/Vd	Satisfied	size
1.7	maximum shear force	560.2	280.6	840.8	615.4	1.366	√	√
2.7	maximum shear force	672.5	217.0	889.5	505.1	1.761	√	√
3.7	maximum shear force	651.9	217.0	868.9	456.5	1.903	√	√
4.7	maximum shear force	668.9	217.0	886.0	399.3	2.219	√	√
5.7	maximum shear force	679.5	217.0	896.5	349.6	2.565	√	√
6.7	maximum shear force	707.3	217.0	924.3	298.6	3.096	√	√

Table 5. The strength calculation results of key oblique section after fire.

X/m	Internal force	Stirrup/kN	Prestress/kN	Total resistance force VR/kN	Design shear force Vd/kN	VR/Vd	Satisfied	size
1.7	maximum shear force	358.0	280.6	638.6	587.9	1.086	√	=
2.7	maximum shear force	466.8	217.0	683.8	499.3	1.379	√	=
3.7	maximum shear force	446.9	217.0	664.0	455.9	1.456	√	=
4.7	maximum shear force	469.0	217.0	686.0	402.0	1.707	√	=
5.7	maximum shear force	483.5	217.0	700.5	353.8	1.989	√	=
6.7	maximum shear force	497.5	217.0	714.5	308.9	2.313	√	=

#### 7.4 Analysis of normal service condition

The stress state calculation and analysis results of T-beam which is constructed without live load (closed traffic) show that due to the section damage reduction, the compressive stress at the edge of T-beam 8–13 units can meet the requirements

Table 6. The accumulated stress state of normal section without live load (closed traffic).

Units	Left upper flange/MPa	Left lower flange/MPa	Right upper flange/MPa	Right lower flange/MPa	Axial compressive strength design value/MPa	Ultimate strength after fire/MPa	Strength of construction stage/MPa	Estimation
8	4.780	12.600	4.720	13.500	25.75	18.025	13.068	unsatisfied
9	4.720	13.500	4.820	14.000	25.75	18.025	13.068	unsatisfied
10	4.820	14.000	4.780	15.600	25.75	18.025	13.068	unsatisfied
11	4.780	15.600	4.740	15.400	25.75	18.025	13.068	unsatisfied
12	4.740	15.400	4.650	14.800	25.75	18.025	13.068	unsatisfied
13	4.650	14.800	4.420	16.600	25.75	18.025	13.068	unsatisfied

without live load, but cannot satisfy the requirements of the construction stage. It indicates that the structure is safe under the closed traffic condition; however, it will be unsafe in the later maintenance construction, the calculation results of key cross section are shown in Table 6.

## 8 CONCLUSIONS

By analyzing the structure performance, the following comments about mechanics properties of the T-beam can be made:

1. The normal section strength, oblique section strength, and the stress of normal service condition of the T-beam before fire all satisfy the design requirements.
2. When the T-beam after fire is under the live load, the normal section strength of prestressed concrete T-beam around mid-span cannot meet the application requirements, and the oblique section shear capacity from the end of the beam to L/4 cannot meet the application requirements.
3. When the T-beam after fire is without the effect of live load, the cross section stress state from the end of the beam to L/2 cannot satisfy the requirements of construction stage.

The following proposals for repairs and maintenance are provided according to the analysis of structure mechanics performance:

1. The normal section bending resistance and oblique section shear capability can be restored by means of enhancing the section, however, the stress state cannot be restored, and the compressive stress of effective section of T-beam after fire will always remain larger.
2. There might be some security risks to do the construction maintenance work on the bridge, while it is safer when using under bridge construction methods.
3. The mechanical properties of concrete and reinforced will be significantly reduced after fire, therefore, the regular observation of key position of the T-beam after the maintenance should be strengthened.

## ACKNOWLEDGEMENTS

This work was financially supported by the National Natural Science Foundation of China (51478210).

## REFERENCES

- [1] Tan Li-wu, Wang Liang-bo. The structure damage investigation of Lianxing overpass structures after fire [J]. Guangdong Architecture Civil Engineering, 2007(10):59–61. (in Chinese).
- [2] Zeng Wei-zhan. The test and reinforcement of the pre-stressed reinforced concrete hollow slab bridge after the occurrence of fire [J]. Guangdong Highway Communications, 2011(3):21–24. (in Chinese).
- [3] Liu Yong, Liu Liang, Wu Chao. The management of fire damage and load test of the traffic bridge under NiErJi dam [J]. Water Resources & Hydropower of Northeast China, 2009, 27(10):9–10. (in Chinese).
- [4] Zhang Gang, Wang Ya-kun, Wang Cuijuan. Evaluation method and durability damage assessment model for concrete bridge suffered from fire [J]. Journal of Highway and Transportation Research and Development, 2010, 27(9):99–92. (in Chinese).
- [5] Zhang Hong, Shao Yong-jun. Fire damage assessment method and application for concrete bridge [J]. Sichuan Building Science, 2011, 37(3):95–99. (in Chinese).
- [6] China construction engineering association. Assessment standard of existing build structures after fire (Cecs 252:2009) [M]. Beijing:China planning press, 2009. (in Chinese).

# Cross tensioned and Reinforced Concrete composite pavements application in heavy traffic

Chao Guo

School of Civil Engineering, Shenyang Jianzhu University, Shenyang, China

Min-jiang Zhang

School of Traffic Engineering, Shenyang Jianzhu University, Shenyang, China

Zheng-ran Lu

School of Management, Shenyang Jianzhu University, Shenyang, China

**ABSTRACT:** The composite pavements associated with up Cross Tensioned Concrete (CTC) slabs and lower Reinforced Concrete (RC) slabs, isolated by Asphaltic Sand Mixture (ASM) layer, were proposed to suit the heavy traffic, based on Xiu-Shui line traffic surveys. The up CTC slabs could bear part axle load and total temperature stress, and ensure the pavements continuous. The lower RC slabs only could bear part over axle load and no temperature gradient stress. The up CTC slabs stress elements fatigue strength is higher than the plain concrete as without lateral compression, or the RC with passive lateral compression, for the up CTC slab elements in triaxial compression state by the cross tension. The axle load is beard by lower RC slabs and up CTC slabs according to their section bending stiffness ratio.

**Keywords:** heavy traffic; cross tensioned pre-stress concrete pavements; concrete fatigue; temperature gradient stress

## 1 INTRODUCTION

Cross Tensioned Concrete Pavements (CTCP) could eliminate joints and cracks, by applying an external force with the Retard-Bonded Tendons (RBPT) (ACI325.7R-88). CTCP had better drive quality too, for the absence of transverse joints (Mustaque Hossain, et al. 2003), it was developed in china, during the past five years (Dong-sheng Zhang and Na Li, 2011). Cross Tensioned and Reinforced Concrete Pavements (CTRCP) also increased the load capacity of the pavements as shown in Figure 1. This double-slabs design technique can bear more traffic loading stress, but less temperature gradient stress than equivalent thick PCCP, CRCP and CTCP. The RBPT is applied through an un-bonded strand to a bearing plate attached to the end of the strand at first, then changed to bonded as the epoxy adhesives solidified. This paper discusses only RBPT procedures (I. Tsiafis et al. 2012).

## 2 FUNDAMENTAL DESIGN CONCEPTS

CTCP design uses the flexural-tensile strength of concrete as the strength parameter of concrete

and does not directly take advantage of the high compressive strength of concrete. The RBPT increases the flexural-tensile strength by introducing cross tension in the concrete slabs. The fundamental formula for the design of CTCP is:

$$\sigma_t + \sigma_p \geq \sigma_{\Delta t} + \sigma_F + \sigma_L \quad (1)$$

where  $\sigma_t$  = concrete allowable flexural-tensile stress;  $\sigma_p$  = RBPT compressive stress in concrete;  $\sigma_{\Delta t}$  = temperature gradient curling stress;  $\sigma_F$  = ASM friction stress; and  $\sigma_L$  = traffic loading stress in the CTC slabs. As the ASM isolated layer, there is only part axle loading fatigue stress, no temperature gradient stress in lower RC slabs.

$$\gamma_r \cdot \sigma_{bpr} \leq f_r \quad (2)$$

$$\gamma_r \cdot \sigma_{bp,m} \leq f_r \quad (3)$$

where  $\gamma_r$  = reliability coefficient;  $\sigma_{bpr}$  = axle loading fatigue stress of lower RC slabs;  $f_r$  = concrete flexural strength standard values;  $\sigma_{bp,m}$  = max axle loading stress of lower RC slabs.

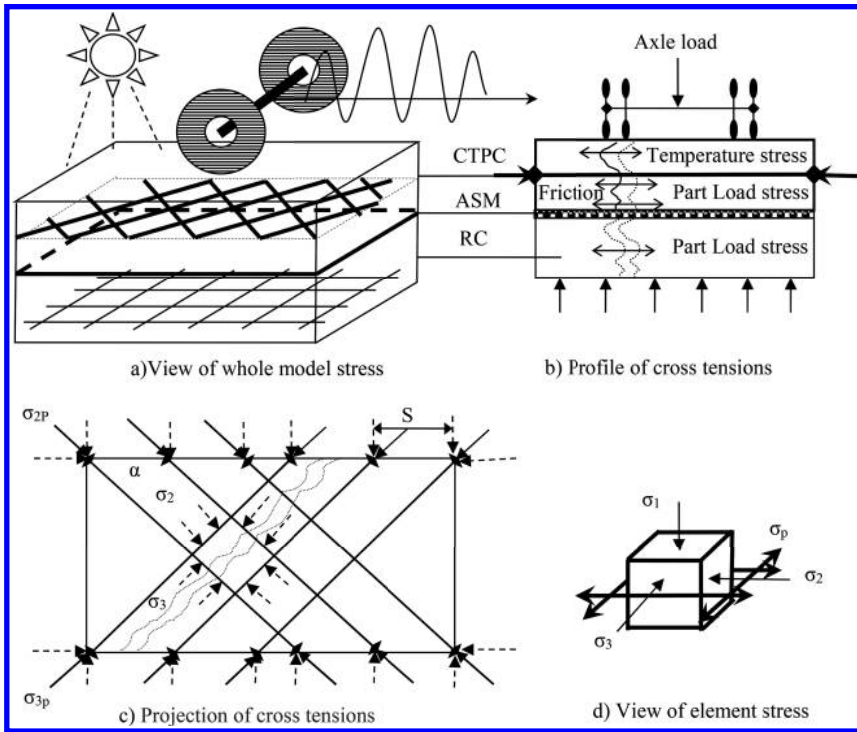


Figure 1. CTRCP structures and stresses.

### 3 AXLE LOADING STRESS ANALYSIS

Axle loading stresses of CTRCP slabs were calculated by double-elastic-deck theory (JTG D40-2011):

$$\sigma_{pr} = k_r k_f k_c \sigma_{ps} \quad (4)$$

where  $\sigma_{pr}$  = axle loading fatigue stress at the most adverse position of up CTC slabs;  $k_r$  = stress reduction factor of considering joint load transfer;  $k_f$  = fatigue stress coefficient considering cumulative fatigue load stress in design reference period;  $k_c$  = composite coefficient considering difference between theory of computation and engineering practice as well as dynamic load;  $\sigma_{ps}$  = max loading stress on up CTC slabs at the most adverse position, by standard axle load.

$$\sigma_{bpr} = k_f k_c \sigma_{bps} \quad (5)$$

where  $\sigma_{bpr}$  = axle loading fatigue stress at the most adverse position of lower RC slabs;  $\sigma_{bps}$  = max loading stress on lower RC slabs at the most adverse position.

The up CTC and lower RC slabs nearly each share half heavy traffic load stress; this is the CTRCP key advantage in over axle loading traffic.

### 4 TEMPERATURE STRESS OF UP CTC SLABS

Temperature gradient stress of up CTC slabs were calculated by gradient stress theory (JTG D40-2011):

$$\sigma_{\Delta t} = k_t \cdot \sigma_{\Delta t, m} \quad (6)$$

where  $\sigma_{\Delta t}$  = temperature gradient fatigue stress of up CTC slabs;  $\sigma_{\Delta t, m}$  = max temperature gradient stress along the longitude of up CTC slabs.  $k_t$  = temperature fatigue coefficient of up CTC slabs.

### 5 FRICTION OF UP CTC SLABS WITH ASM

The up CTC slabs would move on the ASM isolation layers for the principle of expand on heating

and contract on cooling. There were frictions between the slabs and ASM layers, the maximum at the middle of up CTC slabs.

$$\sigma_F = \frac{\mu\gamma L}{2} \quad (7)$$

where  $\mu$  = friction coefficient of up CTC slabs with ASM layers;  $\gamma$  = density of concrete.

## 6 PRESTRESS OF UP CTC SLABS

Assume that the compress by the tension in the up CTC slabs was uniform distribution; the compress of concrete stress element could be calculated from:

$$\sigma_{2p} = \frac{(\sigma_{con} - \sigma_{loss})A_p}{h_c \cdot s \cdot \sin \alpha} \quad (8)$$

$$\sigma_{3p} = \frac{(\sigma_{con} - \sigma_{loss})A_p}{h_c \cdot s \cdot \cos \alpha} \quad (9)$$

where  $\sigma_{2p}$ ,  $\sigma_{3p}$  = pre-compressive stress on the CTC elements by the cross tension along the 2 and 3 directions;  $\sigma_{con}$  = control tension stress value of tendon;  $\sigma_{loss}$  = loss of prestress during construction stage;  $A_p$  = section area of prestress;  $\alpha$  = intersection angle of tendon and road longitudinal direction;  $s$  = tendon spacing along road longitudinal direction.

Table 1. Pavement structure.

$L$ (m)	$b$ (m)	$h_c$ (m)	$h_a$ (m)	$h_b$ (m)	$h_1$ (m)	$h_2$ (m)	$h_3$ (m)	$s$ (m)	$\alpha$ (°)
100	6	0.18	0.01	0.18	0.2	0.2	0.2	0.4	45

Table 2. Materials parameter.

$f_r$ (MPa)	$E_{c,b}$ (GPa)	$v_{b,c}$ (/)	$\alpha_c$ (°C)	$\mu$	$\Phi$ (mm)	$\sigma_{con}$ (MPa)	$E_1$ (GPa)	$E_2$ (GPa)	$E_3$ (GPa)	$E_0$ (GPa)	$K_n$ (GPa/m)
5	27.6	0.15	$1.0 \times 10^{-5}$	0.15	15.2	1860	2.4	2.2	0.5	0.08	3

Table 3. Stress.

Lower RC (MPa)			Up CTCP (MPa)									
$\sigma_{ps}$	$\sigma_{p,m}$	$\sigma_{pr}$	$\sigma_{bps}$	$\sigma_{bp,m}$	$\sigma_{bpr}$	$\sigma_{2p}$	$\sigma_{3p}$	$\sigma_{tr}$	$\sigma_{\Delta,m}$	$\sigma_F$	$P$	$P_m$
-0.94	-3.05	-2.67	-0.89	-2.89	-2.9	1.64	1.64	-0.73	-1.63	-0.625	2	4.47

## 7 GROUND CONTACT PRESS

Ground contact presses were the vertical main stress of up CTC slabs element; it could be calculated from (Meng 2007):

$$A = 200p_s + 15200 \pm 7000 \quad (10)$$

$$p = \frac{P_s}{2A} \quad (11)$$

where  $A$  = ground contract area;  $\pm 7000$  = deviation range for 95% guarantee rate, “-” was recommended considering overload in Chinese;  $p$  = ground contact press.

## 8 CASE

The pavements structures, materials parameters, and stress calculated results of Xiu-Shui heavy traffic line were list in Table 1, 2 and 3. The concrete triaxial compression experimental investigation (Cao 2005) concluded as:

$$S_{max} = 2.305 - 0.1056 \log N \quad (R = 0.10) \quad (12)$$

While:  $N = 20$  Million  $S_{max} = 1.53$ . It could be concluded that the concrete fatigue strength was increased to 1.05 times max static strength by the  $0.07 f_c$  lateral pressures, which equal to 1.6 times plain concrete as without lateral compression, under the same fatigue life.



## 9 CONCLUSIONS

On the theory of concrete fatigue strength significantly enhanced by cross tension and laboratory fatigue test data, the CTRCP were introduced into the heavy traffic. By the double-elastic-deck theory, the temperature gradient stress, part axle loading stress, friction, ground contract press, lateral prestress of up CTC slabs element, and part axle loading stress of lower RC slabs were deeply analyzed.

On the up analysis, the CTRCP could bear 20 million times standard axle load (100 KN), and over axle load (350 KN) combine with max temperature stress of 50 years recurrence interval simultaneously. The most advantage of this CTRCP could keep 100 m continuous without transverse joints.

The up CTC slabs stress elements fatigue strength is higher than the plain concrete as without lateral compression, or the RC with passive lateral compression, for the up CTC slabs elements in triaxial compression state by the distribute cross tension. The over axle load is beard by lower RC slabs and up CTPC slabs according to their section bending stiffness ratio.

## ACKNOWLEDGEMENTS

This research project was supported by the National Natural Science Foundation of China (No. 51308255), the Science and Technology Planning Project of ministry of housing and urban-rural development (2013-K2-38), the Colleges and Universities of Liaoning Province Outstanding

Young Scholars Growth Plan (No. LJQ2014059) and the Youth Fund of Shenyang Jianzhu University (No. 2014003).

## REFERENCES

- [1] Aci325.7 R-88, Recommendations for Designing Prestressed Concrete Pavements [S].
- [2] Mustaque Hossain, Jeffrey Hancock, Zhong Wu. Cross Tensioned Concrete Pavement [J]. *Journal of Transportation Engineering*, 2003, 129(4):427–433.
- [3] Tsiafis, K.-D. Bouzakis, A. Tsouknidas, et al. Effects of Partial Bonding and Adhesive Thickness on the Load-Carrying Capacity of Tension Specimens Bonded with Epoxy Adhesive Investigated by Microindentation, Tensile Testing, and Fem Simulation [J]. *Journal of Aerospace Engineering*, 2012, 25(1):103–107.
- [4] Li Na, Zhang Dong-sheng, Xu Xijuan, et al. Numerical Simulation on Cross-tensioned Prestressed Concrete Pavement [C]. *Ice*. 2013:1549–1553.
- [5] Wang Xuan-cang, Yu wei, Feng Zhi-an, et al. Calculation Methods for Ultimate Axle Load on Cement Concrete Pavement under Heavy Load [J]. *China Journal of Highway and Transport*, 2013, 26(5):21–27 (in Chinese).
- [6] Cao Wei, Song Yu-pu. Research on Fatigue Properties of Concrete under Triaxial Compressive Constant—amplitude Cyclic Loading [J]. *Journal of Harbin Institute of Technology*, 2005, 37(10):1355–1359 (in Chinese).
- [7] Jtg D40-2011, Specifications for Design of Highway Cement Concrete Pavements [s] (in Chinese).
- [8] Meng Yan, Guo Lin-quan, Tan Zhi-ming. Loading Characteristics for Trucks Operating on Highway [J]. *Journal of Highway and Transportation Research and Development*, 2007, 24(4):1–6 (in Chinese).

# Study on reinforcement effect of modified epoxy resins by repeated loading

Li Zhao

Highway Administration of Lanzhou, China

Dingbang Wei

Highway Maintenance Technology Research Institute of Gansu, China

**ABSTRACT:** Hollow bridge hinge joint is one of the main damage forms of Gansu, China. Modified epoxy resin was used to reinforce hinge joints under traffic. A pulse load on reinforced composite trabecular was adopted and the stress and strain characteristics were analyzed. It was found that the composite trabecular after reinforcement has a good overall performance, and the performance was more excellent when reinforcement by high-strength mortar.

**Keywords:** bridge hinge joints; modified epoxy resin; reinforced under traffic; repeated loading

## 1 INTRODUCTION

### 1.1 Bridge disease

Concrete hollow plank has been widely used in highway bridge engineering because of light weight, good structural performance and can be prefabricated. Since 1970s, many hollow plank bridges were constructed. However, a large proportion of these bridges' hinge joint were damaged due to environmental factors, increased road traffic or unreasonable design and construction, which leads to weakening of the overall carrying capacity of bridges and culverts, and in extreme cases, hollow plate may also rupture and causing safety problems, as shown in [Figure 1](#).



Figure 1. Hollow hinge joint of one bridge in China.

### 1.2 How to repair

The conventional reinforcement method of hollow hinge joint required to clear the entire bridge deck. Although it is a good solution to solve the damage, but because of the bridge clearance process requires up to one month or even more, so a great deal of traffic pressure was faced. Therefore, a new reinforcement method without disrupting traffic was needed.

Grouting at the bottom of the hinge joint, and spraying polymer modified mortar the reinforcement can be achieved without traffic break off. A modified epoxy resin, which has a fast-curing characteristics, was used to bond a composite trabecular, simulating the vehicle load by using of pulse load. Stress and strain data was collected to evaluate the effect of the technique.

## 2 EXPERIMENT

### 2.1 Material

1. Modified epoxy resin  
Prepared in laboratory and the performance parameters were shown in [Table 1](#).
2. Polymer modified mortar  
Prepared in laboratory and the performance parameters were shown in [Table 2](#).

### 2.2 Sample preparation

To be reinforced mortar specimens with dimensions of  $20 \times 25 \times 280$  mm, which cured in room

Table 1. Performance of modified epoxy resin.

Test	Condition	Standard	Result
Application time (min)	25°C		70
Initial viscosity (mPa·s)	25°C		142
Unconstrained linear shrinkage (%)	23 ± 2°C (7 days)		0.14
Flexural strength (MPa)	23 ± 2°C (7 days)		72
Compressive strength (MPa)	23 ± 2°C (7 days)		61
Steel-concrete tensile bonding strength (MPa)	23 ± 2°C (7 days)		5.5

Table 2. Performance of polymer modified mortar.

Test	Standard	Result
Setting time/min	Initial	40
	Final	50
Flow (%)	0 mins	0
	30 mins	0
Compressive strength (MPa)	2 hour	23.3
	24 hour	45.8
	3 day	55.8
	28 day	81.6
Flexural strength (MPa)	2 hour	6.8
	24 hour	10.6
	3 day	11.7
	28 day	13.6
Bond strength/MPa	24 hour	2.5
	28 day	3.5
Expansion/%	28 day	-0.05

regimen for seven days, get a compressive strength of 52 MPa. 1 mm gap was surrounded by two mortar blocks, in which modified epoxy resin was poured. Then the prepared samples were cured in laboratory and to be tested.

### 2.3 Repeated loading test

1. The shear rheometer controlled by strain was adopted to study on the curing process of modified epoxy resin, the control strain levels were 1%, 5%, 7.5%, 10%, 20%.
2. The repeated load test was carried out by IPC Company UTM-100 universal testing machine to evaluate the reinforcement effect. 20 KPa stress was used, loading 0.1 s, unloading 0.9 s, 10,000 times. Test apparatus shown in Figure 2.

Modified epoxy resin curing rapidly with time, during the curing process, certain frequency load on the composite trabecular to simulated the traffic.

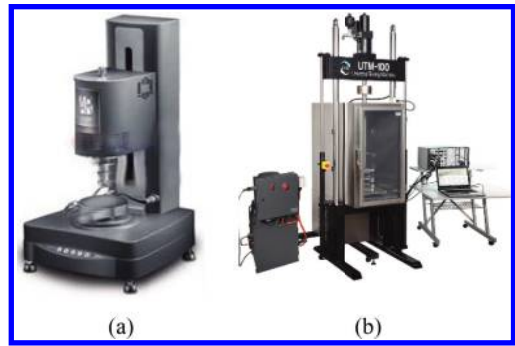


Figure 2. Experiment instruments: (a) shear rheometer; (b) universal testing machine.

## 3 RESULT AND ANALYSIS

### 3.1 Effects of different loads on modified epoxy curing effect

The modified epoxy resin used to reinforcement under traffic should have a good workability and rapid curing characteristics. Viscosity of the resin was tested during the curing process by Brookfield rotational viscometer using a Brookfield rotational viscometer as shown in Figure 3.

Figure 3 shows that, the viscosity of epoxy A and B are almost no change within 90 minutes. However, after 120 minutes, the viscosity rise quickly and generate heat significantly, indicating that fast curing occurs during this time. Compared to the sample A, B shows a more obvious mutation point.

Different strain (1%, 5%, 7.5%, 10%, 20%) was loaded to test the curing process of modified epoxy resin, for exploring the effect of load.

The complex viscosity of the modified epoxy resin, rise up with curing time. From the characteristic of these five curves, we can see that the curing process was affected by continuous strain. When the loaded strain rise from 1% to 5%, the final complex viscosity decrease from  $1 \times 10^6$  Pa·s to  $0.2 \times 10^6$  Pa·s; when the loaded strain rise from 5% to 20%, the final complex viscosity decrease from  $0.2 \times 10^6$  Pa·s to  $0.2 \times 10^5$  Pa·s.

### 3.2 Resin reinforced experimental results

Using single trabecular simulate undamaged bridge, unbonded double trabeculars simulate damaged bridge which is reinforced by modified epoxy resin A or B. Flexural strength and deformation were measured as shown in Figure 5.

From Figure 5 it can be seen that, the flexure strength of single trabecular is 7.8 MPa compared to 3.0 MPa of unbonded double trabeculars,

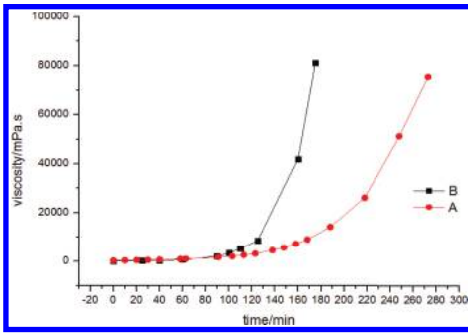


Figure 3. Viscosity of two types of epoxy during the curing process.

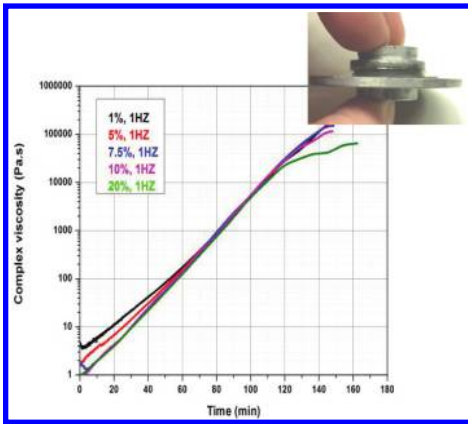


Figure 4. Complex viscosity with time of modified epoxy resin under different level strain.

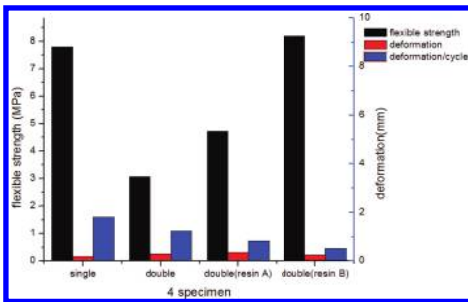


Figure 5. Test results of 4 kinds of samples.

whereas flexure elasticity modulus 10GPa to 2GPa.

Modified epoxy resin A and B was used to reinforce the double trabecular, it was found that the mechanical properties of the specimen got a improved largely after 24 hours. Resin B had a better performance than A.

Compared to “damaged” bridge, the flexure strength of specimen reinforced by resin A increased from 3.0 MPa to 4.7 MPa, resin B increased from 3.0 MPa to 8.0 MPa; The deformation/cycle of specimen reinforced by resin A decreased from 1.1 mm to 0.7 mm, resin B decreased from 1.1 mm to 0.45 mm; The flexure elasticity modulus of specimen reinforced by resin A increased from 2.0GPa to 2.5GPa, resin B increased from 2.0GPa to 6.5GPa; since it is safe to say that modified epoxy resin B have a good reinforcement effect.

### 3.3 The impact of interference on the effect of resin reinforcing process

To simulate the effect on the reinforcement under continuous load, a 20 KPa, 1 Hz stress applied on the specimen for 1 hour and 2.5 hours, another comparative specimen was set up without load. Flexible strength and deformation of all the specimens were collected after 24 hours. The results were shown in Figure 6.

As seen in Figure 6, the flexible strength of the three specimen under 1 hour loading, 2.5 hour loading and without loading were 4.42 MPa, 4.15 MPa and 4.75 MPa respectively, with a decrease of 6% and 12% after loading. Meanwhile, the deformation increase 9% and 15.6%, deformation/cycle increase 1% and 6.8% respectively.

### 3.4 Micro-analysis of bonding interface

Specimens after fracture were observed and it was found that the fracture surface of specimen reinforced by resin B is relatively smooth as shown in Figure 7.

The fracture surface of specimen reinforced by resin B was observed by SEM, and the picture was shown in Figure 8. It was found that there was a good bond of modified epoxy resin and mortar,

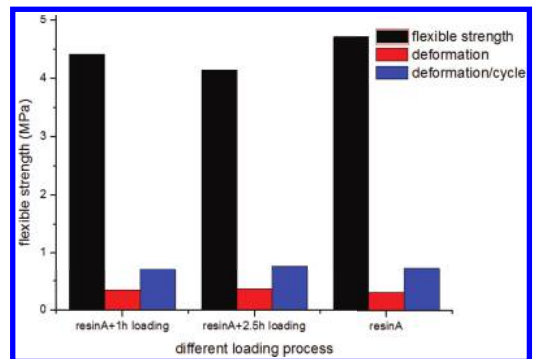


Figure 6. Impact on reinforcement under different loading time.

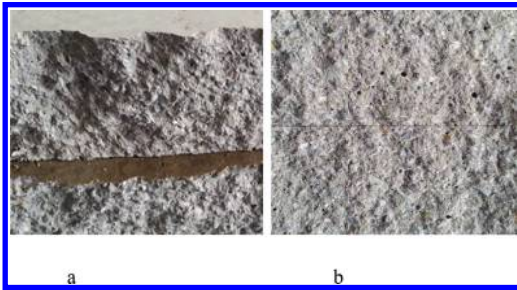


Figure 7. Fracture surface of the specimen (a): specimen reinforced by resin A; (b): specimen reinforced by resin B.

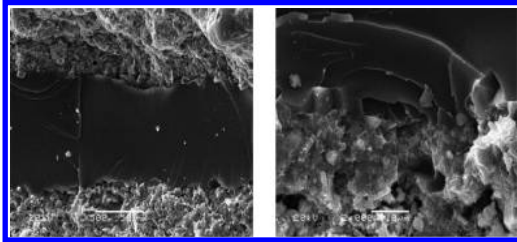


Figure 8. SEM picture of the fracture surface.

without obvious gap; because of better permeability, the resin penetrate deeper in mortar, and form a good mechanical interlocking and chemical bonds, improving bond strength.

#### 4 CONCLUSION

1. Viscosity test result by Brookfield viscometer indicates that there is a mutation point in the

curing process of the modified epoxy resin. And the dynamic shear rheometer test result shows that there is some effect on the curing process with the load strain over 5%.

2. Resin B has a better mechanical performance on trabecular reinforcement.
3. The continuous load during the curing process makes the strength of the trabecular specimen decrease 6~12%, deformation increase 9~15.6%, compared to the specimen without load; the result was acceptable.
4. A good bond was found by SEM between modified epoxy resin and mortar.

#### REFERENCES

- [1] Wei Yang, epoxy plate girder bridge hinge reinforcement applied research [J] Special Structures, 2006.12.
- [2] Ji Qiu into the hollow plate Fissure Mechanism and Control Measures damage, [M] Chang'an University master's thesis, 2010.
- [3] Liu Peilin, prefabricated reinforced concrete plate girder bridge Fissure Research on Behaviors, [M] Tsinghua University master's thesis, 2010.

# Safety evaluation of long and steep slope based on BP neural network

Juan Zhang, Jun Chen & Xiaowei Li

*Xi'an University of Architecture and Technology, Xi'an, China*

**ABSTRACT:** Evaluating the safety of long and steep slope is essential in identifying the potential road safety hazard, which could result in casualties and property losses. In this paper, a BP neural network was built by using neural network toolkit in “Matlab,” 11 long and steep slopes are used in calibrating and validating the network. The high level of predictability provided that the application of BP neural network model to road safety evaluation of long and steep slope is feasible, and evaluation results coincide with the actual situation.

**Keywords:** long and steep slope; safety evaluation; BP neural network

## 1 INTRODUCTION

Compared to other slope, long and steep slope has the characteristics of long slope, steep gradient, and bad horizontal alignment. Traffic accident statistics show that long and steep slopes appear a series of segments where accidents are facile to happen; even a lot of accidents are serious accident, causing serious casualties and economic losses. The safety of long and steep slope becomes the focus of the whole society, many university and scientific research units begin to study the safety of long and steep slope. Road safety evaluation of a specific road traffic system is the use of qualitative or quantitative way to objectively describe system's security features<sup>[1]</sup>. The core is to obtain an objective description about existing road safety status and conclude factors that may affect traffic safety, evaluate how much the factors constraint, and provide opinions for the improvement of road safety. In this paper, BP neural network was used to evaluate the safety of long and steep slope with alignment Parameters as input layer and accident data as output layer.

## 2 BP NEURAL NETWORK

### 2.1 Features of BP neural network

Back-Propagation Network (BP network) is a nonlinear differentiable function weight training multi-layer network. Its strong nonlinear mapping ability automate the correlation of known data and, hence, obtain the underlying logic in a supervised learning neural network; attributes of input samples and the desired output value were first input into the network for interaction. The outputting connection weights of neurons are knowledge,

experienced and this evaluation experience then become the criterion for solving future problems with similar situations. Further, analysis would only require input of corresponding attribute values. System will automatically assign weights of the evaluation index according to the sample training using the validated model, and adjust weight automatically within the network's iteration, which can ensure an objectives' evaluation<sup>[2]</sup>. Thus, the data of the road that selected as learning sample is reliable; the BP neural network is a good and feasible method of road safety evaluation.

### 2.2 BP algorithm

The principle of BP algorithm's is that suppose the number of learning sample is  $n$ , the sample input is  $X_1, X_2, \dots, X_n$ , the corresponding output is  $T_1, T_2, \dots, T_n$ ; The training algorithm will adjust the connection value and the threshold value according to the error between network outputs  $Y_1, Y_2, \dots, Y_n$  and the  $T_1, T_2, \dots, T_n$ , until the error between  $Y_i$  and  $T_i$  achieves the stipulated precision.

There are twice runs in the learning process. One is forward pass calculation where information of samples is passed into input-layer, through hidden-layer, output-layer, the error between the ideal output  $T_i$  and the algorithm output signal  $Y_i$  were then calculated; the other is the reverse pass calculation, information is passed from the output-layer to input-layer, modify the value iteratively according to the error between  $T_i$  and  $Y_i$ . Figure 1 shows the neural network construction. Neural network toolbox of “Matlab” has a practical package based on the algorithm; the calculation for road safety evaluation in this paper is carried out based on the package<sup>[2]</sup>.

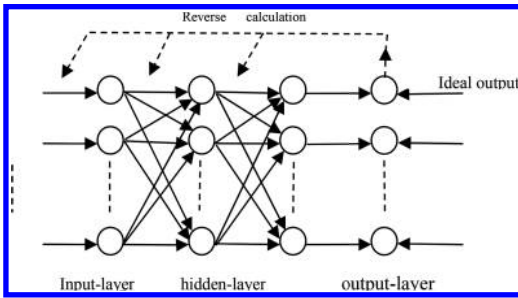


Figure 1. BP neural network construction.

### 2.3 Evaluation steps

Matlab based on neural network toolkit of “Matlab” for assessment includes the following steps:

- I. Determine evaluation objects
- II. Establish evaluation index system  
The status of the evaluation objects can be indicated by a series of evaluation index, each index reflects the status of the evaluation object from different side, which determines the nodes of input-layer, hidden-layer, and output-layer, and formed the BP neural network.
- III. Select learning samples with the evaluation index, provide them for BP neural network to train and learn, in order to get a well-trained BP neural network model.
- IV. Determine the validity of the BP neural network evaluation model using another set of actual data.
- V. Use the model to evaluate objects.

## 3 BP TRAINING MODEL FOR ROAD SAFETY EVALUATION

### 3.1 Selection of evaluation indexes

Long and steep slope, mostly in mountain area, has the characteristics of long slope, steep gradient and bad horizontal alignment, based on the above characteristics and the research results of relevant research literature<sup>[3]</sup>, this paper choose curve radius, easement curve length, curve length, difference in gradients, slope length, vertical curve radius, and vertical curve length as evaluation indexes.

### 3.2 Training model

The performance of the neural network is closely related to the selected samples; a good training sample set should not only pay attention to the sample size, but also pay attention to the quality of the sample. That means the sample should be representative. The training results can response to

its inherent law better with larger sample size. But when the sample size reaches a certain degree, with the increase of sample size, the precision of the network becomes very hard to improve, and the information capacity of network will surge. In this paper, on the basis of collecting data of road alignment and accident data, the number of input and output layer neurons, the training samples is determined for 11. The 11 training samples should be representative as for as possible, so that the training results can better response the relationship of geometric parameters, accident number and the accident consequences. Table 1 is the geometric parameters of the samples, namely, the input layer for safety evaluation indexes; Table 2 is the corresponding accident indicators of the samples, namely the output layer for target value.

### 3.3 Sample data normalization processing

To improve the learning speed of the network normalized processing of input signal, can make the means of all the samples' input signal close to 0 or relative to their mean square error is small. In addition, the incentive function of BP neural network is sigmoid function, the values the function of are between 0 and 1, the last node output of the network is also between 0 and 1, for this reason the output of the sample also need normalized. Usually, normalized processing adopt premmnx statements; its specific syntax format is: [Pn, minp maxp, Tn, mint, maxt] = premmnx (P, T); P is the original input and T is the output data; Minp is the minimum value of P and maxp is the maximum value of P; mint is the minimum value of T and maxt is the maximum value of P.

Normalized processing the geometric parameters and accident data of samples, the code is as follows:

```

P = [650 600 135 128 117 106 98.9 95.2 80.6 73.3
62.3;
0 0 104.54 99.586 46.5 84.724 79.77 77.293
67.385 62.431 55;
194 130 32.5 39.5 92.155 60.5 67.6 71.1 85.1 92.1
103;
2.2 0.3 3.412 3 1.8 2.709 3.1 2.8 0.7 0 3.5;
640 500 340 180 230 460 300 330 230 650 230;
929.22 912.72 855.94 850.54 817.68 815.48
781.12 770.1 735.96 0 632.86;
140 150 154 206 226 186 178 202 200 0 150]
T = [0 1 0 1 0 0 1 1 0 1 3 0;
1 4 1 4 15 8 6 7 8 9 5;
2 5 7 16 15 15 16 3 7 5 10;
1 0 0 1 0 1 0 0 3 2 1]
for i = 1:7;
P(i,:) = (0.8*p(i,:)-min(p(i,:)))/(max(p(i,:))-
min(p(i,:))+0.1);

```

Table 1. Geometric parameters of the samples.

Sample no.	1	2	3	4	5	6	7	8	9	10	11
Curve radius (m)	650	600	135	128	117	106	98.9	95.2	80.6	73.3	62.3
Easement curve length (m)	0	0	104.45	99.586	46.5	84.724	79.77	77.293	67.385	62.431	55
Curve length (m)	194	130	32.5	39.5	92.155	60.5	67.6	71.1	85.1	92.1	103
Difference in gradients (%)	2.2	0.3	3.412	3	1.8	2.709	3.1	2.8	0.7	0	3.5
Slope length (m)	640	500	340	180	230	460	300	330	230	650	230
Vertical curve radius (m)	929.22	912.72	855.94	850.94	827.68	815.48	781.12	770.1	735.96	0	632.86
Vertical curve length (m)	140	150	154	206	226	186	178	202	200	0	150

Table 2. Accident indicators of the samples.

	Extra serious accident	Major accident	Ordinary accident	Minor accident
1	0	1	2	1
2	1	4	5	0
3	0	1	7	0
4	1	4	16	1
5	0	15	15	0
6	1	8	15	1
7	1	6	16	0
8	0	7	3	0
9	1	8	7	3
10	3	9	5	2
11	0	5	10	1

```

end;
for i = 1:4;
T(i,:) = (0.8*t(i,:)-min(t(i,:)))/(max(t(i,:))-min(t(i,:))+0.1);
end;

```

After the normalization processing, sample data can be normalized to the interval between [0.1, 0.9].

### 3.4 Determine the number of hidden layer neurons

The neurons number of hidden-layer has a direct relationship, the neurons number of input-layer and output-layer. In this training model, input-layer has 7 neurons, Output-layer with 4 neurons, the neurons number of hidden-layer can be determined step by step based on the number of neurons of input-layer and output-layer. There is few neurons number of hidden-layer, the error will be relatively large; contrary, over conservative number of neurons selected will result in long learning time while the error is not necessarily the best. It might cause tolerance, and the sample, which not happened previously, can not be recognized.

The following formula is the reference formula which is used to determine the optimal neurons number of hidden layer.

$$n_1 = \sqrt{n+m} + a$$

where,  $n_1$  is neurons number of hidden-layer,  $n$  is neurons number of input-layer,  $m$  is neurons number of output-layer,  $a$  is constant  $\in [1, 10]$ .

From the above formula, the approximate neurons number of hidden-layer is about 14. Hence the neurons number of hidden-layer is set to be between 10 and 20, in order to determine when the network is more efficient and the output error is relatively small. Comparison of the training error and results, a reasonable neurons number of hidden-layer will be determined.

### 3.5 BP network of the MATLAB program

BP network in MATLAB software mainly call the corresponding function. The main algorithm procedure of training samples is as follows:

```

P = [650 600 135 128 117 106 98.9 95.2 80.6 73.3 62.3;
0 0 104.54 99.586 46.5 84.724 79.77 77.293 67.385 62.431 55;
194 130 32.5 39.5 92.155 60.5 67.6 71.1 85.1 92.1 103;
2.2 0.3 3.412 3 1.8 2.709 3.1 2.8 0.7 0 3.5;
640 500 340 180 230 460 300 330 230 650 230;
929.22 912.72 855.94 850.94 817.68 815.48 781.12 770.1 735.96 0 632.86;
140 150 154 206 226 186 178 202 200 0 150]
T = [0 1 0 1 0 0 1 1 0 1 3 0;
1 4 1 4 15 8 6 7 8 9 5;
2 5 7 16 15 15 16 3 7 5 10;
1 0 0 1 0 1 0 0 3 2 1]
for i = 1:7;
P(i,:) = (0.8*p(i,:)-min(p(i,:)))/(max(p(i,:))-min(p(i,:))+0.1);
end
for i = 1:4;
T(i,:) = (0.8*t(i,:)-min(t(i,:)))/(max(t(i,:))-min(t(i,:))+0.1);
end
res = 1:11

```



Table 3. Number of hidden layer neurons and training error.

Neuronal number	11	12	13	14	15
Training error	0.366	0.346	0.354	0.341	0.048
Neuronal number	16	17	18	19	20
Training error	0.364	0.371	0.378	0.386	0.392

```

S1 = 10:20
for i = 1:11
net = newff([S1(i) 2], {'tansig','logsig'}, 'traingdx');
net.trainParam.epochs = 1000;
net.trainParam.goal = 0.001;
net = train(net,P,T);
y = sim(net, P);
error = y-T;
res(i) = norm(error);
end

```

Table 3 is the training error with the number of hidden layer neurons for 11–20.

Table 3 shows that function approximation effect is best with the hidden layer neurons for 15; its training error is minimum. So, the number of hidden layer neurons was set to 15. Thus, the neural network was determined, and the training result with training error of 0.048 is quite good.

#### 4 MODEL VALIDATION

In order to determine the effectiveness of the proposed neural network model, a section of a long and steep slope was selected as a validated sample. Table 4 is the geometric parameters of the section.

The code for normalized processing of the geometric parameters, are as follows:

```

P = [340 100 336 0.3 505.6 912.72 150]
for i = 1:7;
P(i,:) = (0.8*p(i,:)-min(p(i,:)))/(max(p(i,:))-min(p(i,:))+0.1);
end

```

The trained BP neural network was used to evaluate the validated sample. The evaluation result was anti-normalized and rounded to the nearest integer, the following data was the evaluation accident number of the validated sample.

$$Y = [0 \ 0 \ 2 \ 1]$$

The above result show that the number of accidents of validated sample by model evaluation is: 0

Table 4. Parameters of validated sample.

Curve radius (m)	340
Easement curve length (m)	100
Curve length (m)	336
Difference in gradients (%)	0.3
Slope length (m)	505.9
Vertical curve radius (m)	912.72
Vertical curve length (m)	150

extra serious accident, 0 major accidents, 2 general accidents, and 1 minor accident. The result is fully consistent with the actual accident numbers. The evaluation accident number and the actual accident numbers also show that the validated sample should belong to safer roads.

#### 5 CONCLUSION

Using the established BP neural network model for safety evaluation of long and steep slope is feasible with curve radius, easement curve length, curve length, difference in gradients, slope length, vertical curve radius, and vertical curve length as evaluation indexes. Evaluation results have a good coincide with the actual data. The evaluation provides valuable insight on potential road's safety condition in the planning stage of an infrastructure project. Necessary counter measures can be incorporated into actual roadway construction to ensure high level of safety.

#### ACKNOWLEDGMENT

This work was financially supported by the National Science Foundation of China (51308449), and Scientific Research Plan of Educational Department of Shaanxi Provincial Government (2013JK095).

#### REFERENCES

- [1] Zhang Wei. Road safety evaluation based on BP neural network [D]. Chang'an University (in Chinese). 2006.
- [2] Wei Hai-kun. The theory and methods of structural design about neural network. National Defense Industry Press (in Chinese). 2005.
- [3] Zhang Juan. Continuous long slope road alignment research based on driver's factors [D]. Xi'an: Chang'an University, 2012.

# Safety audit of continuous downhill in Ma-Chao expressway

S.H. Chen

*Yunnan Highway Research Institute of Science and Technology, Yunnan, China*

J.H. Liao & X. Wang

*Research Institute of Highway Ministry of Transport, Beijing, China*

**ABSTRACT:** Based on Ma Chao highway, safety audit methods of Continuous downhill are summarized in this paper. Continuous long downhill of Ma Chao highway are analyzed and evaluated comprehensively from the aspects including the truck brake temperature, linear combination of horizontal and vertical design, and structure angle settings. Security countermeasures and recommendations are proposed to improve the traffic engineering designing and guarantee the operational safety.

**Keywords:** highway; traffic safety; continuous downhill; safety audit

## 1 INTRODUCTION

Restricted by topography conditions, geological conditions and other investment factors, highways in mountain area usually use continuous downhill to overcome dispersion which leads to a higher risk of operational safety, especially for heavy-duty trucks under the condition of overloading. Domestic road industry applications show that traffic safety audit is important to eliminate security risks and improve highway safety level. “Highway Engineering Technical Standards” (JTG B01-2014), which was implemented at January 1, 2015 has the requirements that highway and class I road should use reasonable average longitudinal gradient with a demonstration. Domestic scholars have researched more about continuous downhill safety audit. For example Truck Escape Ramp (TER) position research based on brake temperature analysis by Dong Ou (2014), mountain highway safety audit criteria research based on the average longitudinal by Huang Lin (2014), safety audit indicators and assessment System research by Weiyuan Peng (2013), Xin Guo (2014) establishes a Truck Escape Ramp (TER) evaluation Index System of continuous downhill considering braking bed length, aggregate depth, line of sight conditions, the brake bed slope, aggregate type, tip protection, angle and other factors. This paper summarizes research findings of continuous downhill, proposes safety methods, evaluates safety of continuous downhill on Ma Zhao highway and tells security countermeasures and recommendations.

## 2 SAFETY AUDIT METHODS OF CONTINUOUS DOWNHILL

### 2.1 *Safety audit methods based on brake temperature of heavy-duty trucks*

The truck has potential energy when it starts going downhill, and in the process of going down some part of potential energy is absorbed by the engine, while some part is dissipated by resistance acting, or converts into kinetic energy. Because of performance degradation, the brake system can not absorb all of the energy which is converted by potential energy. The excess will convert to kinetic energy increment, and truck running speed will continue to increase. In this case, the brake system component temperature will continue to rise which lead that speed can not be controlled. The above is basic theory of truck brake temperature prediction model (Wu 2008, Liao 2007).

Considering that a unified and recognized truck brake temperature model does not exist in the country, this paper use GSRS model to evaluate continuous downhill safety which is established based on theoretical analysis and experiments in the United States at 1980s. Safety audit techniques are based on truck brake temperature, which are further used as the key technical indicators. Research shows that: under normal circumstances, when the brake temperature does not exceed 200°C, the braking force of the vehicle will not attenuate significantly; When the brake temperature reaches 400–600°C, the braking force decreases, which can only reach 25% of normal temperature (100°C or less); When the

brake reaches 600°C, the braking force may drop to zero approximately. Generally, when the brake pads temperature rises to 200°C, the truck braking performance begin to be affected; when the temperature exceeds 260°C, the truck may have a brake failure. Therefore, 260°C is defined as critical temperature of the brake pads performance. Truck Escape Ramp (TER) is considered to set when the brake pads temperature exceeds to 260°C.

### 2.2 Truck safety audit technology based on downhill risk index

SETRA (research institute in French) determines risk deciding conditions of longitudinal sections by two methods: performance analysis of heavy vehicles on the longitudinal section; vehicle accidents Statistical Analysis occurred on longitudinal sections.

SETRA counted representative sections on 22 highways. The results [7] show that it is very suitable to use the average longitudinal gradient and slope length as a variable for researching the risk of driving the vehicle. When  $d \cdot p < 130$  ( $d$ : the total longitudinal gradient length;  $m$ : average slope, %), excessive risk will not occur; When  $d \cdot p \geq 130$  and  $p \geq 3\%$ , the accident rate on longitudinal gradient sections will begin to increase with  $d \cdot p$  increasing. When  $p < 3\%$ , there is no risk.

According to the research results, the risk of the truck on the downhill section can be evaluated. The risk index model has two parameters including the average longitudinal gradient and slope length. First, calculate the average longitudinal gradient, if the average longitudinal gradient is less than 3%, without next calculation. If more than 3%, calculated risk index. Second, determine the risk index values, if more than 130, it is necessary to focus on security facility design of continuous downhill section.

Considering the different performance and other aspects of domestic and foreign vehicles, the evaluation results is as a reference but not risk decision basis of the truck on the downhill section.

### 2.3 Safety audit technology based on operating speed

According to the observation results of the operating speed on the typical continuous downhill section, considering the factors such as the average longitudinal gradient, cumulative slope length, radius of curvature, operating speed prediction model (Liao 2012) of the continuous downhill section is as follows:

$$V_{truck} = EXP \left( \begin{array}{l} 4.1491 + 0.1880 \ln(\text{grade}) \\ + 0.0366 \ln(\text{grade})^2 \\ + 0.1241 \ln(\text{len}) - 0.1129 \ln(\text{len}) \\ \cdot \ln(\text{grade}) \end{array} \right) \quad (1)$$

Table 1. Safety audit standard based on operating speed on continuous downhill section.

Safety level	Index	Description
Well	$ \Delta v_{85}  < 10 \text{ km/h}$	Operating speed coordination is well.
Medium	$ \Delta v_{85}  \in [10, 20]$	Operating speed coordination is acceptable. The technical indicators should be adjusted if conditions permit, which makes
Poor	$ \Delta v_{85}  > 20 \text{ km/h}$	Operating speed coordination is bad. Adjust the level and the vertical design.

$$V_{car} = EXP \left( \begin{array}{l} 4.4897 + 0.0911 \ln(\text{len}) \\ + 0.1830 \ln(\text{grade}) \\ + 0.0477 (\ln(\text{grade}))^2 \\ - 0.03 \text{grade} \cdot \text{len} - 0.0052 \text{len} \cdot \text{radi} \end{array} \right) \quad (2)$$

where  $V_{car}$ —operating speed of cars (V85%, km/h);  $V_{truck}$ —operating speed of trucks (V85%, km/h);  $\text{grade}$ —average longitudinal gradient to the top of the hill (%), with the absolute value of longitudinal gradient);  $\text{len}$ —cumulative slope length to the top of the hill (km);  $\text{radi}$ —Reciprocal of curvature radius (1/km), the value of the straight line is 0.

The safety audit method of continuous downhill section based on operating speed is mainly referring to “Guidelines for Safety Audit of Highway”. Evaluating operating speed coordination is based on calculating the difference between the predicted operating speeds on adjacent section. Evaluating the coordination of design speed and operating speed is based on calculating the difference between them on the same section of the road. The evaluation standard is shown in Table 1.

## 3 CONTINUOUS DOWNHILL SAFETY AUDIT OF MA CHAO HIGHWAY AND COUNTERMEASURE

According to the design files, Ma Chao highway continuous long downhill information is as shown in Table 2.

### 3.1 Downhill risk assessment

According to downhill risk assessment method proposed by SETRA, all average longitudinal gradient of continuous downhill on Ma Chao highway are no more than -3%. So the operating risk of the 4 continuous downhill sections is low. The average

Table 2. Ma Chao expressway continuous long downhill information.

Section	Gradient (%)	Slope length (m)	Relative altitude (m)
ZK68 + 260~ZK57 + 470	-1.95	10790	210.09
ZK55 + 760~ZK51 + 300	-1.75	4460	78.17
ZK47 + 860~ZK23 + 600	-2.57	24260	623.045
ZK22 + 270~ZK0 + 200	-2.6	22470	584.825

longitudinal gradient of ZK47 + 860~ZK23 + 600 and ZK22 + 270~ZK0 + 200 exceed  $-2.5\%$ , and the cumulative slope length exceed 20 km, so it is necessary to analyze the brake temperature and geometric design further.

### 3.2 Truck brake temperature evaluation

The evaluated vehicle is a 55 tons truck, and the default of speed on downhill is 60 km/h. Brake failure temperature is  $290^{\circ}\text{C}$ . The result of the brake temperature analysis is as shown in Figure 1.

The truck has a brake temperature close to  $290^{\circ}\text{C}$  when running on the downhill. It is reasonable that Truck Escape Ramp (TER) is arranged at K22+40 in the design files.

### 3.3 Combination of horizontal and vertical design evaluation g

Through the analysis of horizontal and vertical alignment, the alignment of ZK47 + 860~ZK23 + 600 is not well. For example the S curves of composed of horizontal curves with radius as 820 m, 851.6 m, and 804 m, and the longitudinal gradients are  $-2.7\%$ ,  $-3.9\%$ ,  $-2.0\%$ , and  $-2.8\%$ . From this, we can see that the radiuses are low, and the longitudinal gradients are high, which causes that driving safety risk is relatively high.

So we suggest: 1, enhancing sight guidance of S curve; 2, ensuring roadside and central horizon; 3, setting the speed-down markings and proposed speed sign; 4, setting speed capture facility, etc.

### 3.4 Structure setting evaluation

The structures of ZK47 + 860~ZK23 + 600 continuous downhill are intensive, and there are less roadbed, more bridges and tunnels. Such as K30 + 531~K24 + 067, are "bridge + tunnel + bridge", and the longitudinal gradients are mostly above  $2.5\%$ , even the maximum longitudinal gradient is  $-3.9\%$ . This slope section is located close to the bottom of S curve, which is not conducive to driving safety.

Bridge and tunnel sections do not have conditions to set Truck Escape Ramp (TER), so

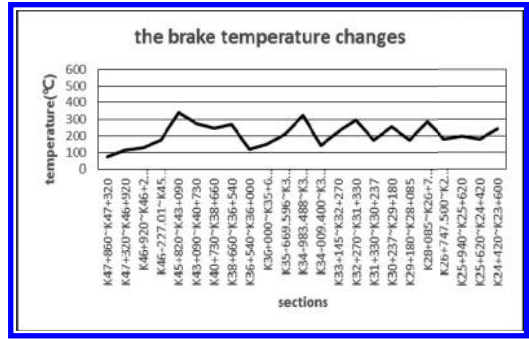


Figure 1. The result of the brake temperature analysis.

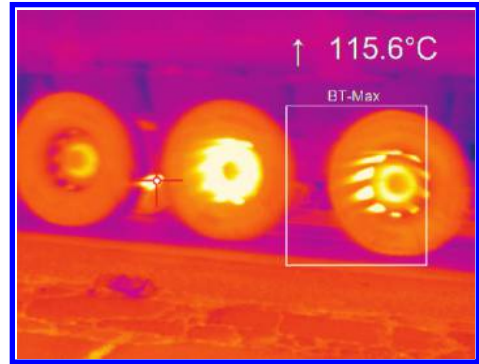


Figure 2. Infrared temperature measurement of truck wheels.

we suggest: 1, taking compulsory deceleration measures; 2, enhancing sight guidance of bridge and tunnel sections; 3, ensuring a smooth transition of light between inside and outside the tunnel entrance; 4, improving traffic signs; 5, improving the anti collision degree of bridge barrier, etc.

### 3.5 Other suggestions

According to the analysis results of typical accident case on continuous downhill, the reasons of the accidents are mainly human factors. Some truck drivers are illegal, speeding, overloading, or fatigue driving for economic benefits. Therefore, in addition to take passive protection measures, it is more important to strengthen traffic control and raise the level of law enforcement after opening and operation, especially, overloading.

We suggest: 1, prohibiting vehicles with a total weight of more than 55 tons going into a continuous downhill; 2, strengthening the control of dangerous goods transport vehicles; 3, improving the drivers' safety awareness; 4, playing the role of safety facilities; 5, checking the truck to ensure

the brake performance before continuous downhill section; 6, forbidding the vehicle to exceed the speed limit and monitoring speed by detection system; 7, installing weather monitoring station and early warning ice, and other bad weather; 8, installing brake safety warning system for trucks, such as infrared imaging sensor, as shown in [Figure 2](#).

#### 4 CONCLUSIONS

On the basis of Ma Chao highway, the safety audit methods for the continuous downhill section are summarized, and the continuous downhill section of the Ma Chao highway is evaluated. For the characteristics of the project, the safety improvement suggestions are proposed to improve the traffic engineering design, and ensure the safety level of continuous downhill section after operation. Meanwhile, it also provides a reference for the safety improvement and safety audit of the continuous downhill section of the highway.

#### REFERENCES

Dong, O. 2014. Safety assessment technology based on temperature lift model of truck brake Science & Technology information, (03): 68–53.

Guo, X. 2014. Research on safety assessment of truck escape ramps on continuous long steep downgrades. China Safety Science Journal, (04): 152–158.

Huang, L. Dan, L. 2014. Safety Audit of the continuous downhill section based on the idea of the average longitudinal gradient [J]. Science & Wealth, (4): 500–501.

Liao, J.H. & Shaom C.F. et al. 2012. Speed prediction model of trucks on continuous downhill. Journal of Beijing Institute of Technology, 32(suppl.1): 118–121.

Liao, J.H. & Wu, H.B. 2007. Research on safety assessment and Countermeasures of continuous longitudinal slope in mountainous area. Western Transportation Construction Technology Project.

Peng, W.Y. & Qi, Y.B. 2013. Continuous downhill Safety Audit of highway [J]. Modern Property Management, (08): 64–66.

Wang, Z. & Sun, Z.N & Zhang, J.H. 2008. The design technology of the longitudinal slope of the European highway. Highway, (09): 58–61.

Wu, J.M. & He, Y. et al. 2008. Continuous downhill road safety disposal technology. China Communication Press: Beijing, 2008.

# Reynolds-number effects on static force coefficients of $\Pi$ -shape bridge deck section with wind fairing

Qingliang Zhan, Zhiyong Zhou & Yaojun Ge

Bridge Engineering Department, Tongji University, Shanghai, China

**ABSTRACT:** To study the Reynolds-number effects on static force coefficients of a typical  $\Pi$ -Shape bridge section with wind fairing, both wind tunnel tests and computational fluid dynamics method are performed. Three different types of deck sections are studied to evaluate the influence of handrails and wind curtain on Reynolds-number effects. 2D CFD simulations are carried out respectively to visualize the flow pattern around deck sections and reveal the mechanism on static coefficient Reynolds-number effects. The conclusions are: (i) Drag coefficient and lift coefficient of  $\Pi$ -Shape bridge with fairing and moderate height handrails are sensitive to Re number (ii) The results of  $\Pi$ -Shape bridge with tall wind curtain are not affected by Re number significantly (iii) Drag and lift coefficient obtained from low Re is conservative.

**Keywords:**  $\Pi$ -Shape deck section, wind fairing, wind curtain, bluff body, lift coefficients, drag coefficients, moment coefficients

## 1 INTRODUCTION

A common assumption in wind engineering is that flow around bluff body with sharp corners is independent of Reynolds number, so that drag coefficients, lift coefficients and moment coefficients conducted in wind tunnel tests can be directly applied to prototype structure calculation. This is applicable for some truly bluff bodies in some specific Reynolds-number ranges. In general, flow around bluff bodies is independent of Reynolds-number, but for streamlined structures, flow pattern is quite sensitive with Reynolds-number. In this paper, we provide the results of research on Reynolds-number effects on steady force coefficients of typical  $\Pi$ -shape bridge section with wind fairings.  $\Pi$ -Shape bridge section can be viewed as bluff body but for long span bridges, this kind of shape section usually suffers from serious aerodynamic problems such as flutter and vortex induced vibration. Therefore, it is likely to add wind fairing on both side of  $\Pi$ -Shape section to improve aerodynamic stability. This kind of section can not be viewed as streamlined body any longer, and it is different from  $\Pi$ -Shape section.

Many research projects into Reynolds number effects and aerodynamic stability have been carried out recently, but they mostly involved streamlined sections with no handrails or wind curtain. Schewe [1] conducted wind tunnel testing of Great Belt East Bridge in a pressurized wind tunnel. Strouhal number at high and low Re for bridge

girder cross section is different. Flow visualization is used to analyze different flow field at different Re region. Schewe [2] also reviewed several experiments results in different Re numbers, the author concluded that 2-D sections that behaved as a bluff or streamlined body depended on Re number and slender bodies with sharp-edged cross-sections may also suffer from pronounced Reynolds-number effects. Matsuda [3] measured steady and unsteady aerodynamic force coefficients in Reynolds number region from  $1.1 \times 10^4$  to  $1.5 \times 10^6$  of central-slotted bridge deck. The author concluded that conventional wind tunnel test results in the low Reynolds number region are conservative for wind resistant-design of bridge decks. Liu [4] and Li [5] studied streamlined and bluff bridge deck Reynolds-number effects using wind tunnel test, but with out handrails and air-curtain. Li [6] studied Re number effects of two different bridge decks, however, the numerical results did not agree with experimental results.

In the present research, to study the Reynolds-number effects on static force coefficients of a typical  $\Pi$ -Shape bridge section with wind fairing, both wind tunnel tests and computational fluid dynamics method are performed. Three different types of cross sections are studied to evaluate the influence of handrails and wind curtain on Reynolds-number effects. 2D CFD simulations are carried out respectively to visualize the flow pattern around deck section and reveal the mechanism on static force coefficient Reynolds-number effects.

## 2 STUDY METHODS AND MODALS

### 2.1 Description of deck sections

$\Pi$ -Shape bridge section is widely used in bridge engineering recently especially for long span bridge. Compared with closed deck section, this kind of opening section is economic and reasonable for sustainable force. Three kinds of  $\Pi$ -Shape bridge sections are studied in this paper as shown in Figure 1. All the three sections include wind fairing as a countermeasure in order to reduce VIV and flutter problems.

### 2.2 Section model test in wind tunnel

A scaled sectional model bridge was built and tested in TJ-1 boundary layer wind tunnel of Tongji University. The rigid model, 1.47 m long, 0.58 m wide, and 0.058 m deep, is made of two steel cores, providing the stiffness, and a plywood skin to reproduce girder's aerodynamic shapes.

The model is mounted fixedly in the tunnel floor (see Fig. 2), with a force balance installed in the bottom of model. The output from the balance can be used to measure the lift and drag forces acting on the model when incoming air flows past it.

An air velocity range is set from 2.3 m/s to 8.6 m/s, to obtain a series of Reynolds number. By measuring the lift and drag forces under each air velocity, we can check the Reynolds number effects on the aerodynamic characteristics of the model.

### 2.3 CFD calculation setup

The 2D computational domain is a circle with the bridge girder placed in the center (see Fig. 3). The size of sectional model in the wind tunnel is applied in the size of bridge girder in the numerical simulation. A coarse mesh is adopted to deal with the area far field from the central wall, with a fine mesh to deal with the near-wall district (see Fig. 4). The overall grids can be added up to 420,000.

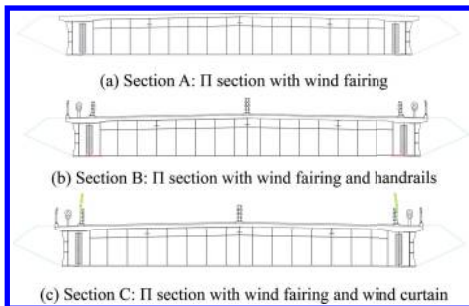


Figure 1. Three deck sections.



Figure 2. Experimental setup in the wind tunnel.

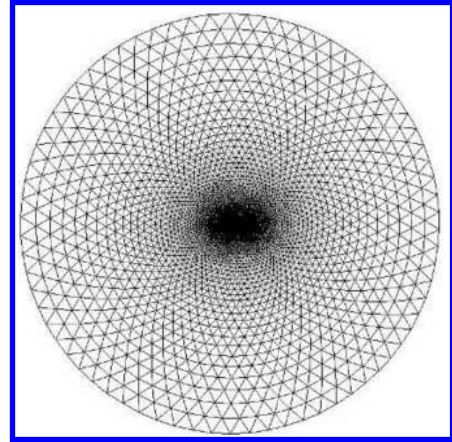


Figure 3. Overall mesh of computational domain.

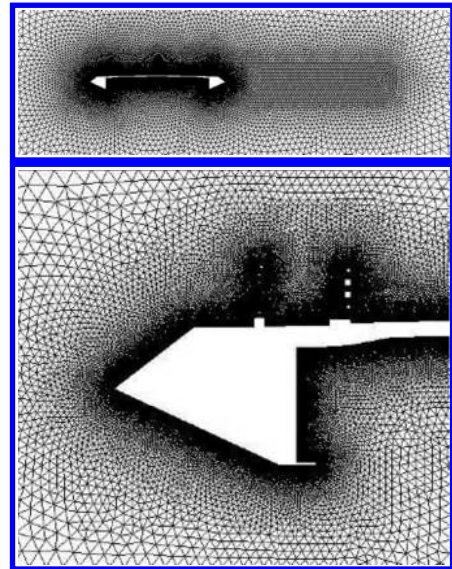


Figure 4. Near-wall mesh.

The left side of the outer boundary is set as velocity inlet, and the right side is set as pressure outlet. The velocity magnitude of inlet is set the same with experimental values, from 2 to 8 m/s. Thus the Reynolds number varies from  $0.9 \times 10^4 \sim 3.5 \times 10^4$

RANS approach is undertaken to provide steady-state solutions of the flow field and SST k- $\omega$  modal is used to consider the turbulence model.

### 3 RESULTS

#### 3.1 Drag coefficients of wind tunnel test

The definitions of the steady aerodynamic force coefficients in this research are listed as follows:

$$\begin{aligned} C_D &= \frac{F_D}{(1/2)\rho U^2 H} \\ C_L &= \frac{F_L}{(1/2)\rho U^2 B} \\ C_M &= \frac{M}{(1/2)\rho U^2 B^2} \end{aligned} \quad (1)$$

where  $C_D$ ,  $C_L$ ,  $C_M$  are the drag, lift and pitching moment coefficients, respectively.  $\rho$  is the air density,  $U$  is the wind speed,  $B$  is the deck width,  $H$  is the deck height.

Figure 5 shows the results of drag coefficients in case of different Reynolds number for three deck sections. The results of Section B are greatly affected by the Reynolds number. As Reynolds number increases, drag coefficient of Section B decreases from 2.2 to 1.15, and stay constant when Re number is greater than  $3E4$ . On the contrast,

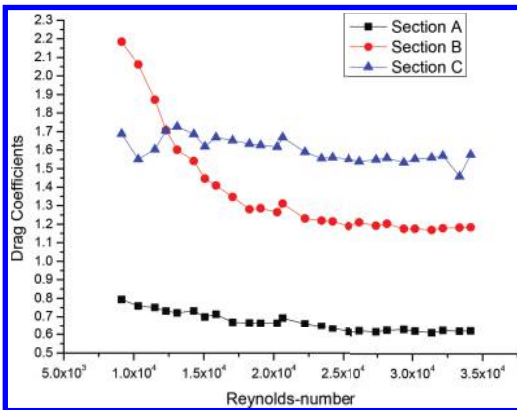


Figure 5. Drag coefficients as a function of Re number.

drag coefficients of Section A and Section C are independent of Re number.

#### 3.2 Flow characteristic of CFD calculation

In Figure 6, X-velocity contour is presented of three sections at the  $Re = 9 \times 10^3$ . Flow separation occurs at the downside opening part of Section A (Fig. 6a). And on the upside surface, there exists a thin boundary layer due to lack of handrails. So in this situation, flow always separates at some constant regions and Re number effects are not that significant for the flow pattern. For section C (Fig. 6c), wind curtain disturbed upside flow and the turbulent boundary layer of upper deck is quite thick, therefore this kind of section behave like a quasi-bluff body. For Section B (Fig. 6b), compared with Figure 6d which shows the same section under  $Re = 3.5 \times 10^4$ , it shows that in the near wake region, velocity of higher Re number is smaller than that of lower Re number, thus the pressure of wake is bigger, leading to smaller drag coefficient.

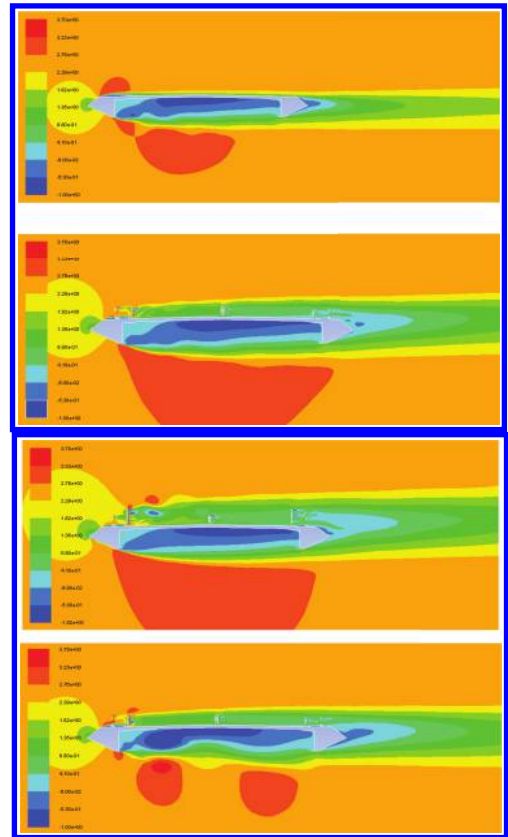


Figure 6. X-velocity counter map.



### 3.3 Lift and moment coefficient characteristic

Figure 7 shows lift coefficients as a function of Re number for three deck sections. It can be concluded that with barriers placed on the upside surface, the lift coefficient decreases. The reason is that the existence of barriers on the upside surface makes air velocity lower, so the local pressure is relatively bigger on the upside, thus the total vertical force is stronger downward.

Again, lift coefficients of Section B are greatly affected by Re number, due to the same reason as drag coefficient.

Because the downside surface of three deck sections tend to be almost the same, difference between upside surfaces cause different results of Re number effects. Figure 8 shows the detailed flow velocity contour behind upwind handrails. Boundary layer thickness of lower Re flow field is thicker and flow is much smoother under the higher Re number. It shows that, the existence of

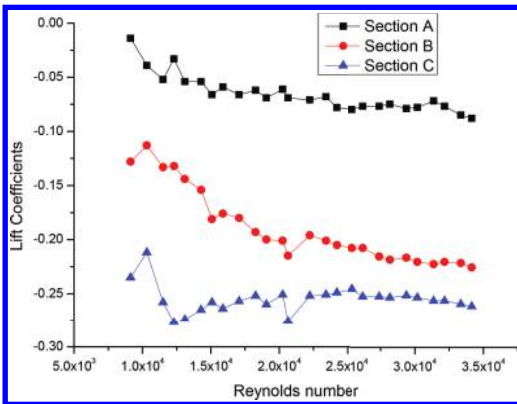


Figure 7. Lift coefficients as a function of Re number.

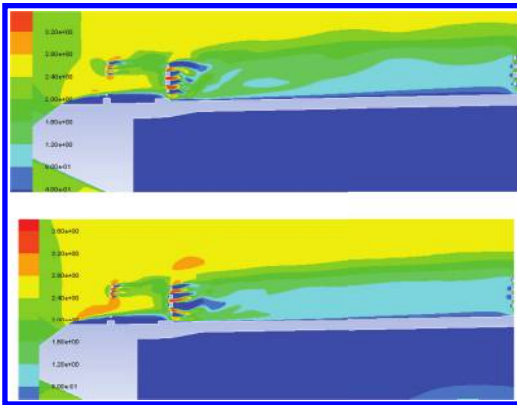


Figure 8. Local X-velocity counter map.

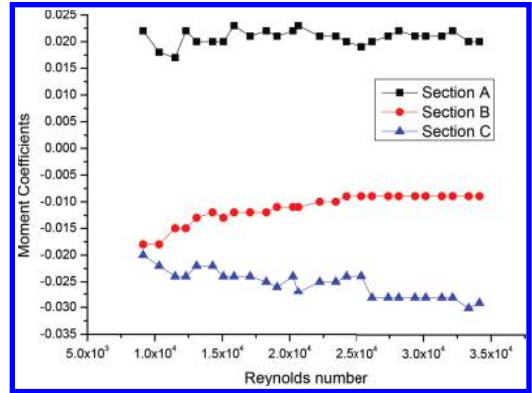


Figure 9. Moment coefficients as a function of Re number.

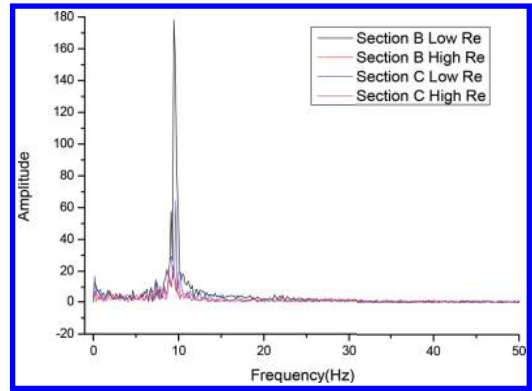


Figure 10. Frequency analysis of lift time-history.

handrails causes the Re number effects, because it causes flow disturbance on the upside surface.

From Figure 9, it can be concluded that moment coefficients of all three sections are not sensitive to Re number.

Frequency analysis of lift time-history for Section B and C is also done. And it shows that the main frequency of flow movement is independent of Re number.

## 4 CONCLUSIONS

- i. Drag coefficient and lift coefficient of  $\Pi$ -Shape bridge with faring and moderate height handrails are sensitive to Re number.
- ii. The results of  $\Pi$ -shape bridge with tall wind curtain are not affected by Re number significantly.
- iii. Drag and lift coefficients obtained from low Re is conservative.

The authors gratefully acknowledge the support of National Key Basic Research Program of China (2013CB036300) and the National Natural Science Foundation of China (91215302).

## REFERENCES

- [1] Schewe, G., Reynolds-number effects in flow around more-or-less bluff bodies. *Journal of Wind Engineering and Industrial Aerodynamics*, 2001. 89(14): p. 1267–1289.
- [2] Schewe, G. and A. Larsen, Reynolds number effects in the flow around a bluff bridge deck cross section. *Journal of Wind Engineering and Industrial Aerodynamics*, 1998. 74: p. 829–838.
- [3] Matsuda, K., et al., An investigation of Reynolds number effects on the steady and unsteady aerodynamic forces on a 1: 10 scale bridge deck section model. *Journal of Wind Engineering and Industrial Aerodynamics*, 2001. 89(7): p. 619–632.
- [4] Liu J.X., Cui X., Li J.W., Reynolds number effects of surface pressure distribution and Strouhal number of a typical bridge deck section. *Journal of Vibration and Shock*, 2010. 29(4): p. 146–149.
- [5] Li J.W., Lin Z.X., Xiang H.F. Reynolds number effects of bridge deck section. *ACTA Areodynimca SINCA*, 2005. 23(1): p. 123–128.
- [6] Li W., Hu Z.T., Li J.W., Reynolds number effects of three component coefficients in bridge deck using Computational Fluid Dynamics (CFD). *Journal of Chang'an University (Natural Science Edition)*, 2010. 30(6): p. 44–49.

# Study on performance of cold recycling mixture with emulsified asphalt or foamed asphalt

Menghui Hao

School of Highway, Chang'an University, Xi'an, China  
Henan Transport Investment Group Co. Ltd., Zhengzhou, China

**ABSTRACT:** The technology of asphalt pavement cold recycling, which can reuse the old asphalt mixture, raise resource utilization ratio and protect ecological environment, accords with the strategic policy of developing recycle economy and realizing sustainable development in our country. This paper investigates two typical cold recycling mixtures and contrastive studies pavement performance by high temperature stability, water stability, low temperature anti-cracking and water permeability performance between emulsified asphalt and foamed asphalt. The research shows that two types of cold recycling mixtures all satisfy the standard of hot-mix asphalt mixture except low temperature anti-cracking ability. And the cold recycling mixture can be used in the road engineering as the asphalt under layer.

**Keywords:** cold recycling mixture; emulsified asphalt; foamed asphalt; pavement performance

## 1 INTRODUCTION

The asphalt pavement constructed in the 1980s in our country early is entering into rehabilitation period, which produces a large amount of reclaimed asphalt mixture. The technology of asphalt pavement rehabilitation, which can reuse the old asphalt mixture, raise resource utilization ratio and protect ecological environment, accords with the strategic policy of developing recycle economy and realizing sustainable development in our country. So the study of the cold recycling technology has important practical significance.

Studies of cold recycling mixture mainly focus on the material mixture design and conventional strength currently. Less comparative study is conducted between emulsified asphalt and foam asphalt of cold-recycling mixture. The only comparative study is conducted in the 1980s, whose emulsified asphalt and foam asphalt material had a big difference from today's material, which has little applicability.

Through a lot of laboratory experiments, the paper aims to systematically study high temperature stability, water stability, and low temperature anti-cracking of the cold recycling mixture with emulsified asphalt and also compared with foamed asphalt.

## 2 RAW MATERIAL AND GRADUATION

### 2.1 Raw material

As needed, the raw material in this article includes aggregate, RAP, cement, asphalt

(for foamed asphalt) and emulsified asphalt. The test results of the raw material as follows.

#### 1. RAP

Conduct water content and sieve test on the Recycle Asphalt Pavement (RAP) material, conduct tests on the former asphalt material extracted from RAP. The test results of the raw material in Table 1.

#### 2. Asphalt

The foamed asphalt in the project adopts 70# A-class asphalt. The test results of the raw material in Table 2.

The basic process of foaming asphalt is as follows. When cold water (environment temperature) contacts with high temperature asphalt (above 140°C), it will set off a chain reaction here. The heated asphalt and water drop exchanges their energy. The water drop is heated to 100°C. The asphalt cools down at the

Table 1. Test results of RAP.

Material	Subject	Unit	Results
RAP	Water content	%	1.2
	Asphalt content	%	4.8
Asphalt in RAP	Penetration (25°C, 5 s, 100 g)	0.1 mm	48
	Ductility (15°C)	cm	14.8
	Softening point (ring and ball method)	°C	51.8

same time. The transferred heat exceeds the steam latent heat, which leads to volume expansion and steam generation. When the steam in expansion chamber pushes in asphalt continuous phase, a large number of vesical steams shoot up from the nozzle. The compressed steam expands which makes the cooled-off asphalt forms thin film. It relies on the thin film's surface tension wraps the bubble entirely. During expansion process, the asphalt film generates surface tension to resist steam pressure until reaching an equilibrium state. Because of the low thermal conductivity of asphalt and water, the equilibrium state can last only a few numbers of seconds. A large number of bubbles from the foaming process exist at certain metas Table levels, which is easily fall through.

Test the matrix asphalt through foaming experiment, the test results of the raw material in Table 3.

Table 2. Test results of asphalt.

Subject	Unit	Results	Specifications
Penetration (25°C, 5 s, 100 g)	0.1 mm	77	60~80
Ductility (15°C)	cm	>150	>100
Softening point (ring and ball method)	°C	55	>46

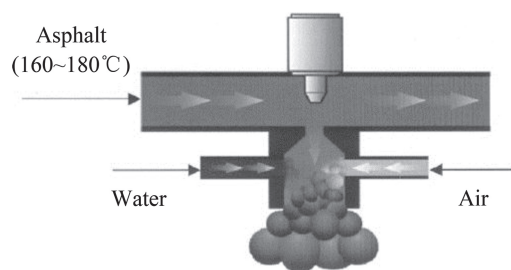


Figure 1. Asphalt foaming principle.

Table 3. Test results of asphalt foaming performance.

Foaming temperature	Subject	Mixing moisture content		
		1.0%	1.5%	2.0%
150°C	Expansion (multiple)	12	16	18
	Half-life (s)	9.4	8.2	7.6
160°C	Expansion (multiple)	18	22	24
	Half-life (s)	12	10	8
170°C	Expansion (multiple)	17	20	24
	Half-life (s)	9	8.6	7.4

From the foaming experiment, the foaming temperature is 160°C, and 1% of the foaming water consumption is satisfied.

### 3. Emulsified asphalt

The project adopts slowly splitting emulsified asphalt with smaller needle penetration. The test results of the raw material in Table 4.

### 4. Cement

Join a small number of cement in the cold-recycling to enhance its early strength. Adopt Portland cement in the cement. The test results of the raw material in Table 5.

## 2.2 Gradation design

Design the granular composition to satisfy the scope of emulsified asphalt's and foamed asphalt's granular composition. The test results of the raw material in Table 6.

## 2.3 Mix proportion design

According to the normal method, conduct a moisture-density test with compound mineral aggregate, to ensure the best moisture content. Though the Marshall's test to make sure the optimal asphalt content of mixture. The test results of the raw material in Table 7.

Table 4. Test results of emulsified asphalt.

Subject	Unit	Emulsified asphalt	Specifications
<i>Residue after evaporation</i>			
Residue content	%	63.50	≥62
Penetration (25°C, 5 s, 100 g)	0.1 mm	65.4	50~300
Ductility (15°C)	cm	78	40
<i>Storage stability</i>			
1 day	%	0.6	≤1
5 days	%	3.4	≤5

Table 5. Test results of Portland cement.

Subject	Unit	Portland cement	Specifications
<i>Setting time</i>			
Initial setting time	min	135	≥45
Final setting time	min	210	≤600
Stability	mm	1.0	≤5.0
<i>Strength</i>			
Breaking strength after 3 days	MPa	2.9	≥2.5
Compressive strength after 3 days	MPa	15.2	≥10.0

Table 6. Aggregate passing percentage and gradation design.

Mesh size (mm)	Passing percentage of each mesh (%)			
	Emulsified asphalt		Foamed asphalt	
	Gradation design	Gradation range	Gradation design	Gradation range
26.5	100	100	100.0	100
19	92.5	90~100	95.0	90~100
9.5	71.7	60~80	80.1	60~85
4.75	37.7	35~65	46.2	35~65
2.36	24.2	20~50	31.8	30~55
0.3	8.6	3~21	13.6	10~20
0.075	5.6	2~8	8.4	6~20

Table 7. Results of cold recycling mixture Marshall test in optimal asphalt content.

Mixture type	Emulsified asphalt	Foamed asphalt	Specifications
Mixing moisture content (%)	4.3	7.2	/
Optimal asphalt content (%)	2.2	2.5	/
Specific gravity	2.242	2.213	/
Volume of air voids (%)	9.2	11.6	9~14
Indirect tensile strength (MPa)	0.74	0.69	≥0.5
Water immersion indirect tensile strength (MPa)	0.66	0.59	≥0.5
TSR (%)	89.2	85.5	≥75

### 3 PAVEMENT PERFORMANCE ANALYSES

#### 3.1 High temperature stability performance

The high temperature stability performance of asphalt pavement mainly reflects by rutting resistance. Because of the heavy traffic, heavy loading, and track disease are more and more serious, it is very important to study the high temperature stability performance of cold recycling mixture. The test results are in Table 8.

According to the test results.

Two types of cold recycling mixtures all satisfy the standard of hot-mix asphalt mixture greater than 1000 dynamic stability.

The high-temperature stability of emulsified asphalt mixture is stronger than foamed asphalt. Dynamic stability of emulsified asphalt mixture is 1.09 times of those with foamed asphalt.

Looking from the data analysis of track deepness, the deformation rate of emulsified asphalt mixture is much lower than foamed asphalt.

Table 8. Results of cold recycling mixture high temperature performance test.

Mixture type	Emulsified asphalt	Foamed asphalt
<i>The depth of wheel rut after 60 mins (mm)</i>		
1	3.257	4.504
2	3.164	3.754
3	3.354	4.324
Average	3.258	4.194
<i>Dynamic stability, DS (time/mm)</i>		
1	1527	1201
2	1341	1546
3	2012	1728
Average	1627	1492

Track deepness of emulsified mixture is 0.94 mm less than those with foamed asphalt.

#### 3.2 Water stability performance

In order to examine the water stability performance of cold recycling mixture, using Marshall's vestigial stability and cycle of freezing and thawing separation experiment to test water stability performance of the mixture.

According to the test results.

Two types of cold recycling mixtures all satisfy the standard of hot-mix asphalt mixture greater than 80% immersion residual stability and 75% TSR.

The immersion residual stability of two types of cold recycling mixtures has little difference with each other.

The freeze thawing and splitting strength ratio of emulsified asphalt mixture is stronger than foamed asphalt.

#### 3.3 Low temperature anti-cracking ability

Conducting an experiment of flexural strength and breaking strain to check out the low temperature anti-cracking ability of cold recycling mixture. The test temperature is -10°C and loading rate is 50 mm/min.

According to the test results.

Two types of cold recycling mixtures all unsatisfied the standard of hot-mix asphalt mixture greater than 2000 failure strain.

The low temperature failure strain of two types of mixtures has little difference with each other.

The reason is, compared with hot-mix asphalt mixture, the freeze thawing's mechanical property is lower and asphalt content is lesser. The cohesiveness of aggregate cannot reach the hot stirring's result, which speeds the producing of low temperature crack and minify the destructed deflection. All this has an influence on bituminous mixture's breaking strain.

Table 9. Results of cold recycling mixture water stability performance test.

Mixture type	Emulsified asphalt	Foamed asphalt
Marshall stability, MS (KN)	9.48	8.69
Immerses the 48 h stability, MS1 (KN)	7.81	7.03
Immersion residual stability, MS0 (%)	82.4	80.9
Has not carried on the thaw-freeze cycle, RT1 (MPa)	0.538	0.503
Carried on the thaw-freeze cycle, RT2 (MPa)	0.435	0.381
TSR (%)	80.9	75.7

Table 10. Results of cold recycling mixture low temperature performance test.

Mixture type	Emulsified asphalt	Foamed asphalt
Maximum load (N)	1025	868
Cross amount of deflection (mm)	0.289	0.307
Intensity of anti-pulls curved (MPa)	4.4	3.7
Breaking strain ( $\mu\epsilon$ )	1778	1890
Bending stiffness modulus (MPa)	2475	1958

Table 11. Results of cold recycling mixture water permeability coefficient test.

Mixture type	Emulsified asphalt	Foamed asphalt
Water permeability coefficient (mL/min)	26	35

### 3.4 Water permeability

Conduct the water permeability coefficient experiment to check out cold recycling mixture.

According to the test results.

Two types of cold recycling mixtures all satisfy the standard of hot-mix asphalt mixture water permeability coefficient less than 120 mL/min.

## 4 CONCLUSIONS

Emulsified asphalt and foamed asphalt cold recycling mixture have well high temperature stability, which meets the standard of hot-mix asphalt. The high temperature stability of emulsified asphalt is better than foamed asphalt. Its dynamic stability is 1.60 times of foamed asphalt.

Emulsified asphalt and foamed asphalt cold recycling mixture have well water stability, which meets the standard of hot-mix asphalt mixture. The reducing range of the mixture's splitting strength becomes lesser after cycle of freezing and thawing.

The low temperature anti-cracking ability of emulsified asphalt and foamed asphalt is worse than hot-mix asphalt mixture. From the low temperature trabecula bending test, there is a little difference of two types of mixture's failure strain, which doesn't meet the standard of hot-mix asphalt mixture.

Emulsified asphalt and foamed asphalt cold recycling mixture have well closely knit. From water penetration test, the water-seepage of two kinds of recycle mixture meets the standard of hot-mix asphalt.

Emulsified asphalt and foamed asphalt cold recycling mixture meets the design base requirements of the asphalt pavement. At the same time, it satisfied the performance requirement of the asphalt under layer, which applies to the construction of highway.

## REFERENCES

- [1] Xu Jian, Huang Songchang, Qin Yongchun, Li Feng, Shi Xiaopei. 2010. Performance of Cold Recycled Mixtures with Emulsified Asphalt or Foam Asphalt [J]. Journal of Highway and Transportation Research and Development. 27(6), p:20–24. (in Chinese).
- [2] Wei Lianyu, Liu Zhaowei, Zhang Hairong, Wang Jing. 2008. Experimental Analyse of Foamed Asphalt Stabilization Cold-recycled Mixture in Old Asphalt Pavement [J]. Journal of Hebei University of Technology. 37(5), p:100–104. (in Chinese).
- [3] Hao Menghui, Hao Peiwen, Yang Qian, Yang Kai. 2011. Analysis on Pavement Performance of the Short-cut Basalt Fiber Modified Asphalt Mixture [J]. Journal of Guangxi University (Natural Science Edition). 36(1), p:101–106. (in Chinese).
- [4] Jenkins K. 2000. Mixture Design Considerations for Cold and Half-Warm Bituminous Mixes with Emphasis on Foamed Bitumen [D]. Stellenbosch, SA: University of Stellenbosch.
- [5] Epps J.A. 1990. Cold-Recycled Bituminous Concrete Using Bituminous Materials [R]. Washington, D.C.: Transportation Research Board. National Cooperative Highway Research Program, Synthesis of Highway Practice 160.
- [6] Xu Jinzhi. 2007. Mixture Technical Performance of Foamed Asphalt and Foamed Asphalt Cold Recycled Mix [D]. Xi'an, China: Chang'an University. (in Chinese).
- [7] Xing Aoxue. 2011. Study on Performance of Cold Recycling Mixture With Emulsified (foamed) Asphalt [D]. Xi'an, China: Chang'an University. (in Chinese).
- [8] P.R. China. Ministry of Communications. 2008. JTG F41-2008 Technical Specifications for Highway Asphalt Pavement Recycling [S]. Beijing: China Communications Press. (in Chinese).
- [9] P.R. China. Ministry of Communications. 2010. JTJ 052-2000 Standard Test Methods of Bitumen and Bituminous Mixtures for Highway Engineering [S]. Beijing: China Communications Press. (in Chinese).

# Analysis of safety criterion on track irregularities of heavy haul railway under 30t axle load

H.F. Zhang & S.L. Lian

Key Laboratory of Road and Traffic Engineering of the Ministry of Education, Tongji University, Shanghai, China

**ABSTRACT:** Track geometry irregularity is an important excitation source for the train vibration and dynamic response between wheel and rail, which is directly related to the train safety and stability. When the axle load is up to 30t, track irregularity has a significant effect on the train safety and dynamic force between wheel and rail. The paper establishes the 30t axle load vehicle-track coupling model with Simpack multi-body dynamic simulation software to analyze the dynamic response of the vehicle and dynamic response between wheel and rail. The simulation sample of track irregularity in a time domain is achieved through track irregularity spectrum, and taking the coexistence of detrimental wavelengths into account. The estimated safety limits of vertical, alignment, longitudinal, and gauge track irregularity are compared with the limits calculated under the excitation of single harmonic wave. The results show that the estimated method in this paper can take into account the irregularity containing a wide range of wavelength compared with the single harmonic waves as an input, and the estimated limits value are higher than the limits calculated by single harmonic waves.

**Keywords:** heavy haul railway; track irregularity; dynamic response; safety limits

## 1 INTRODUCTION

Track geometry irregularity is an important excitation source for the train vibration and dynamic response between wheel and rail, and also directly related to the train safety and stability. Since the 21st, in order to improve the single transport volume, the axle load of haul railway has improved to 30t. And the track regularity is deterioration with the increased axle load. To ensure the train safety and stability, it is necessary to limit the irregularity within a certain range. Countries like America, Japan, Germany, etc., have safe limit standard of track irregularity. Chinese academy of railway sciences obtain the track irregularity safety criterion of existing railway by field text, setting the 10 m wavelength single harmonic wave in the test line. Cai Chengbiao et al. (1995) estimated the limits based on the theory of vehicle-track coupling dynamics and simulate various types of track irregularity.

All above research regard detrimental wavelengths as an ideal single sine or cosine function, which calculating the corresponding system dynamic response by controlling its amplitude, and then estimate the limits of irregularity. But the actual railway contains many kinds of wavelength irregularity, which have different influences on vehicle-track system, only consider a single

wavelength is not comprehensive. So, when calculating the limits of irregularity, it needs to consider the influence of various wavelengths. This paper regards the time domain waveform calculated by track irregularity spectrum as excitation to simulate the relation between system dynamic response and amplitude of detrimental wavelengths, and then estimate the safety limits of track irregularity.

## 2 TRACK IRREGULARITY ESTIMATED METHOD

### 2.1 Track irregularity simulation

The simulation sample of track irregularity in time domain is achieved through track irregularity Power Spectrum Density (PSD), based on the Blackman-Turkey period gram method. According to the theory, the equation of PSD and frequency spectrum is shown in Eq. (1).

$$\begin{aligned} X(k) &= \xi_k |X(k)| = N_r \xi_k \sqrt{S_k(k)} \\ &= N_r \xi_k \sqrt{S_x(f = k\Delta f)\Delta f} \end{aligned} \quad (1)$$

where  $N_r$  is the sampling number,  $\xi_k$  is a sequence with independent phase,  $X(k)$  is the frequency

spectrum of track irregularity,  $S_k(k)$  is the track irregularity Power Spectrum Density (PSD), and  $\Delta f$  is the sampling interval in frequency domain.

The track irregularity sample in time domain is described in Eq. (2), which is achieved by the inverse Fourier transform of  $X(k)$ .

$$x(n) = \frac{1}{N} \sum_{k=1}^N X(k) \exp\left(\frac{2j\pi kn}{N}\right) \quad (2)$$

To control the amplitude of detrimental wavelengths, introduce a variable  $x(t)$  as shown in Eq. (3) which is a sine function with stochastic primary phase. The  $x(t)$  is the track irregularity with the wavelength of  $\lambda_0$ .

$$x(t) = A \sin\left(2\pi \frac{v}{\lambda_0} t + \phi\right) \quad (3)$$

where  $A$  is the half maximum and  $\phi$  is the random variables uniformly distributed on  $[0, 2\pi]$ .

Since  $x(t)$  is a second-order stationary process, its power spectral density estimation can use the Blackman-Turkey period gram method. The  $x(t)$ 's power spectral density function is shown in Eq. (4).

$$\begin{aligned} S_x(\omega) &= \int_{-\infty}^{+\infty} \frac{A^2}{2} \cos(\omega_0 \tau) \cos(\omega \tau) d\tau \\ &= \frac{A^2}{2} \pi \left\{ \delta(\omega - \omega_0) + \delta(\omega + \omega_0) \right\} \end{aligned} \quad (4)$$

As the fact that, the track irregularity spectrum is one side, so convert Eq. (4) to the one-side form as shown in Eq. (5).

$$S_x(\omega) = A^2 \pi \delta(\omega - \omega_0) \quad (5)$$

where  $\omega = 2\pi v/\lambda$ ,  $\omega_0 = 2\pi v/\lambda_0$ ,  $S_x(\omega)$  is the Power Spectral Density (PSD).

The PSD of detrimental wavelengths is described in Eq. (5). With Eq. (5), the track irregularity spectrum can be described by a piecewise function. When the  $\omega = \omega_0 = 2\pi v/\lambda$ , the spectrum use Eq. (5) and the other frequency is still calculated by the track irregularity spectrum as shown in Eq. (6). By the  $A$  in the piecewise function, the amplitude can be controlled to simulating the dynamic response excited by the detrimental wavelengths, so the safety limits can be obtained.

$$S_x(\omega) = \begin{cases} A^2 \pi \delta(\omega - \omega_0) \\ \frac{k A_v \omega_c^2}{(\omega^2 + \omega_c^2) \omega^2} \end{cases} \quad (6)$$

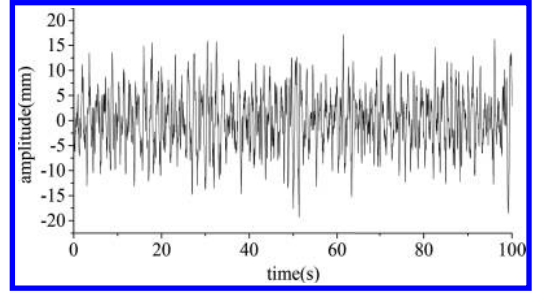


Figure 1. Track irregularity in time-domain.

As a result in the vehicle-rail coupling dynamic (Zhai Wanming 2007), 10 m wavelength is the detrimental wavelengths of the freight car and the heavy haul railway maintenance departments also use the 10 m wavelength method of chord measuring for track irregularity maintenance. So 10 m wavelength vertical, alignment, longitudinal, and gauge track irregularity are used to estimating the safety limits. In case of Chinese heavy haul railways track irregularity and field test taken by Xu Lei et al. (2013), the amplitude is not more than 20 mm, so choosing the US 5-grade spectrum for track irregularity time-domain simulation. Figure 1 shows the simulation results by the method above, which detrimental wavelengths is 10 m and amplitude is 10 mm.

## 2.2 Vehicle-rail model and calculation parameters

Based on the theory and parameters of freight car, the analysis model is established by Simpack multi-body dynamic simulation software. Rail material is U75 in China's railway, and the simulation speeds are 80,100,120 km/h.

## 2.3 Assessment criteria

To assess the safety and stability, six criteria indexes can be used: derailment coefficient ( $Q/P$ ), wheel unloading rate ( $\Delta P/\bar{P}$ ), vertical ( $P$ ) and lateral wheel-rail force ( $Q$ ), vertical ( $a_z$ ) and lateral ( $a_y$ ) vehicle acceleration, and the value of them are shown as followed defined by GB/T 5599-1985 Railway Vehicle-Specification for Evaluation of the Dynamic Performance and Accreditation Test.

$Q/P \leq 0.8$ ,  $\Delta P/\bar{P} \leq 0.65$ ,  $P \leq 250$ ,  $Q \leq 0.4P_w$  ( $P_w$  Static wheel load),  $a_z \leq 0.7 g$ ,  $a_y \leq 0.5 g$ .

## 3 RESULTS AND DISCUSSIONS

Figures 2–4 show the dynamic responses excited by the track irregularity. Since the irregularity has an effect on different types of vehicle-rail dynamic response, the figures only show the main response



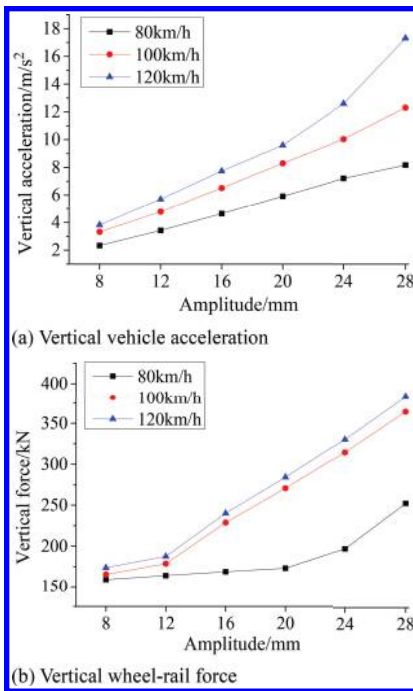


Figure 2. Dynamic responses excited by vertical irregularity.

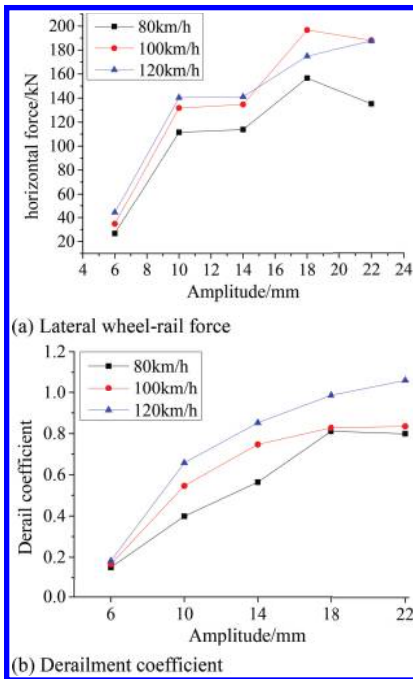


Figure 3. Dynamic responses excited by alignment irregularity.

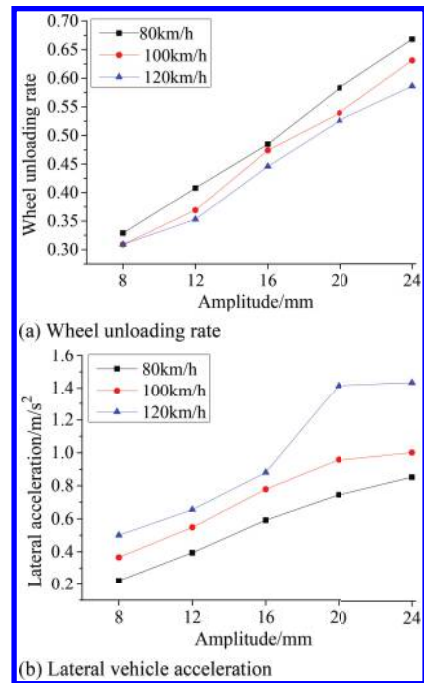


Figure 4. Dynamic responses excited by longitudinal irregularity.

Table 1. Track irregularity limit.

Irregularity	Assessment criteria	Amplitude/mm
Vertical	Vehicle acceleration	22
Alignment	Derailment coefficient and Lateral wheel-rail force	7
Longitudinal	Wheel unloading rate	20
Gauge	Geometrical dimensions	+24/-12

controlling the vehicle running safety and stability. And according to Luo Lin (1990), since gauge irregularity has a smaller influence on dynamic response, the limit of gauge irregularity is controlled by geometrical dimensions. The dynamic response results are less than the assessment criteria by the maximum and minimum gauge irregularity +24 mm/-12 mm as an input.

It can be seen from Figure 2. to Figure 4. that dynamic responses increase linearly as the amplitude of track irregularity increase. It has a higher requirement as the vehicle speed increase from 80 to 120 km/h. According to practical speed of the heavy haul railway, choose the dynamic responses under 80 km/h to estimate the safety criterion. Track irregularity limit under 80 km/h are shown in the Table 1.

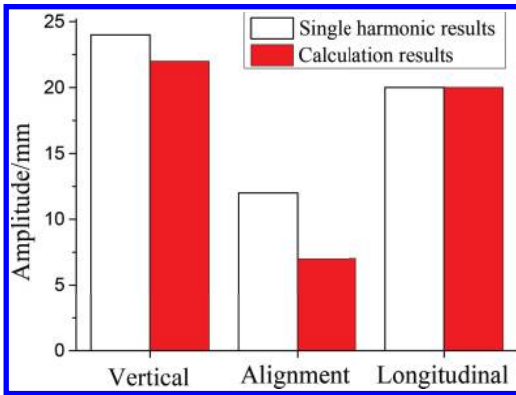


Figure 5. Track irregularity limit (single harmonic results and calculation by the method of this paper).

Figure 5 shows that the limits results calculated by the method of this paper and under the excitation of single harmonic waves. It can be seen that the limit by this paper are more than the single harmonic waves method. The effect is caused by failing to consider other wavelengths of track irregularity, when use the single harmonic waves for estimation. The method of this paper controls the amplitude of the detrimental wavelengths during the simulation of the track irregularity PSD, which contain a wide range of wavelengths.

#### 4 CONCLUSION

Track geometry irregularity has an effect on the dynamic response of vehicles and rail and also directly related to the train safety and stability. This paper based on the vehicle-rail coupling dynamics, estimate safety limits of vertical, alignment, longitudinal, and gauge track irregularity and taking the coexistence of detrimental wavelengths into account. Compared with the limits calculated by single harmonic waves, the estimated

track irregularity limits are generally more than them. This method provides a new approach for the acquisition of the theoretical track irregularity limits through dynamic simulation. But this paper is aimed at 30 t axle load vehicles, the vehicle type is unitary, the speed also to have certain restriction, and for different vehicle types, its irregularity safety limits still need according to the actual situation.

#### ACKNOWLEDGMENTS

This research was supported by the National Natural Science Foundation of China (No. 51378395).

#### REFERENCES

Cai C.B. & Zhai W.M. & Wang Q.C. 1995. Study on allowable safety criterion of track geometric irregularities. *Journal of the China Railway Society*, 17(4):82–87.

Chen D.S. & Tian X.Y. & Li W. et al. 2009. Research on Standards for Wuhuan-Guangzhou high-speed railway track irregularities. Beijing:China Academy of Railway Science.

Chen G. & Zhai W.M. 1990. Numerical simulation of the stochastic process of railway track irregularities. *Journal of Southwest Jiaotong University*, 02:13–17.

Luo L. & Luo W.C & Zhu K.M. & Li Y.X. 1990. Research on Standards for emergency repair of track irregularities for trunk main lines. *China Academy of Railway Sciences*, 02:1–24.

The Ministry of Railways of the People’s Republic of China. 1985. GB/T 5599-1985. Railway Vehicle-Specification for Evaluation the Dynamic Performance and Accreditation Test. Beijing: China Standard Press.

Xu L. & Chen X.M. & Li X.J. & Meng X.H. 2013. Track irregularity spectrum analysis of Shench-Huanghua Heavy Haul Railway. *Journal of Central South University (Science and Technology)*, 12:5147–5153.

Yang C.L. 2013. Research on matching relationship between axle load & running speed. Southwest Jiaotong University.

Zhai W.M. 2007. *Vehicle-Track Coupling Dynamics*. Beijing: Science Press, 312–314.

## Analysis of rail thermal effect due to wheel-rail rolling contact in heavy-haul railway

S.J. Gu, X.W. Yang & S.L. Lian

*Key Laboratory of Road and Traffic Engineering of the Ministry of Education, Tongji University, Shanghai, China*

**ABSTRACT:** Thermal damage caused by wheel-rail contact is one of the main failure modes of wheel-rail system in heavy-haul railway. When a heavy haul train is running, the adhesion and slip of wheel-rail contact will lead to wheel-rail temperature rise which can reduce the adhesion between the wheel-rail and also can lead to the cracks, scratches, and stripping damage on the surface of the wheel-rail. First, a wheel set axial slice projection method is used to calculate wheel-rail rigid contact point; then, a virtual penetration method and Kalker's FASTSIM Program are used to calculate wheel/rail contact stress, which can better reflect the real wheel-rail contact status; and then, a moving heat source is used to simulate the movement of the wheel on the rail; finally, the rail thermal effect is calculated. A wheel-rail contact thermal effects analysis program is compiled using Matlab software. The temperature field was analyzed on the basis of wheel-set lateral displacement, wheel speed, and the creepage of wheel-rail. The results show that the temperature of rail surface is high on the condition of wheel-rail rolling contact, and the material parameters changes along with the temperature changes should be considered when calculating wheel-rail thermal contact coupling.

**Keywords:** heavy haul railway; wheel-rail contact; thermal effect; temperature rise

### 1 INTRODUCTION

In railway transport industry, there are many problems urgently needed to be solved, such as, thermal damage caused by wheel-rail contact is one of the main failure mode of wheel-rail system in heavy-haul railway. When a heavy haul train is running, the adhesion and slip of wheel-rail contact will lead to wheel-rail temperature rise which can reduce the adhesion between the wheel-rail (Pei Youfu et al. 1996), and also can lead to the cracks, scratches, and stripping damage on the surface of the wheel-rail contact.

Many scholars have done lots of research on the wheel-rail friction temperature rise and thermal stress. Blok (1937) and Jaeger (1942) have made initiative research on sliding body heat conduction. Researching on the wheel-rail friction temperature rise, many scholars have done much mainly based on Laplace transform method and Green function method (K. Knothe & S. Liebelt 1995, F.D. Fiseher et al. 2003, Gu Shaojie et al. 2015). In those research, moving heat source method to simulate the slip and the distribution of contact pressure between the wheel-rail is Hertz contact ellipse and the heat source is transient static heat source. Generally, the wheel-rail contact is not elliptical contact. With the development of computer,

finite element method has been used to solve the wheel-rail temperature rise to increase the credibility of the engineering (Johan Ahistrom & Birger Karlsson 2002, Ji Huai-zhong et al. 2005, T.C. Kennedy et al. 2006, Qi Wanming et al. 2010, Li Wei et al. 2010, Wang Wei et al. 2012, Xiao Qian et al. 2013).

For the wheel-rail contact thermal problems caused by rolling contact, the current study is rare. In this paper, a wheelset axial slice projection method (Yan Juanmao 1983) is used to calculate wheel-rail rigid contact point; and then, a virtual penetration method (Piotrowski, J. & Kik, W. 2008) and Kalker's FASTSIM Program (Kalker, J.J. 1982) is used to calculate wheel/rail contact stress and distribution of adhesion and slip zone; finally, the rail thermal effect is calculated.

### 2 THERMAL ANALYSIS

#### 2.1 *Wheel-rail relative slip velocity*

According to virtual penetration method and Kalker's FASTSIM Program, the contact normal and creep stress can be calculated. When the creep force less than the limit, consider this element is in adhesion zone, otherwise in slip zone, and all the

process need to be modified by Cullen theorem. Based on the above, the distribution of adhesion and slip zone can be calculated, as shown in Figure 1.

The relative velocity (slip velocity) for steady-state rolling and linear elasticity is defined according to Eq. (1) (Kalker, J.J. 1990)

$$\vec{v}_{slip} = \begin{bmatrix} v_x \\ v_y \end{bmatrix} = V_{vehicle} \left[ \begin{bmatrix} \xi_1 - \xi_3 y \\ \xi_2 + \xi_3 x \end{bmatrix} - \frac{\partial \bar{u}(x, y)}{\partial x} \right] \quad (1)$$

where  $V_{vehicle}$  is the vehicle speed (m/s),  $\xi_1$  the longitudinal creepage,  $\xi_2$  the lateral creepage,  $\xi_3$  the spin creepage,  $u$  the elastic displacement, and  $x, y$  the cartesian coordinates of the contact ellipse.

However, the “elastic slip” term in Eq. (1) is not possible to calculate with FASTSIM and is thus neglected in this simulation. Since the rigid slip term is usually much larger, it is not a severe limitation to neglect the elastic part.

### 2.2 Thermal conduction analysis

When the relative slip between the wheel/rail, the surface of wheel/rail will generate a lot of friction heat, the expressions of heat flow density is as follows:

$$q(x, y) = \mu p(x, y) |\vec{v}_{slip}| \quad (2)$$

where  $q(x, y)$  is heat flow density  $q(J/m^2 \cdot s)$ ,  $\mu$  the coefficient of friction,  $p(x, y)$  contact stress and  $v_{slip}$  the slip velocity.

The classic thermal conduction equation is as follow (Caralaw, H.S & Jaeger, J.C. 1980)

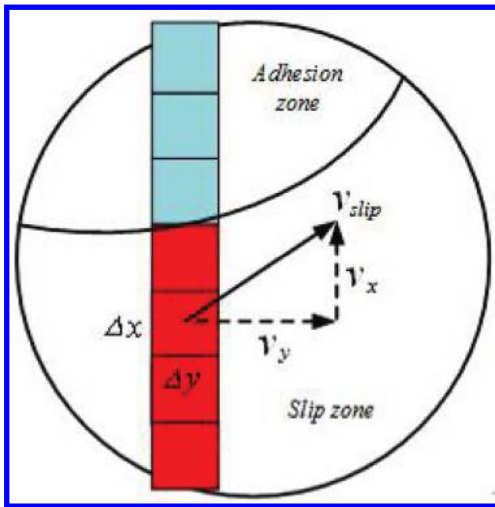


Figure 1. The distribution of adhesion and slip zone.

$$\frac{\partial^2 \theta}{\partial x^2} + \frac{\partial^2 \theta}{\partial y^2} + \frac{\partial^2 \theta}{\partial z^2} = \frac{1}{\kappa} \frac{\partial \theta}{\partial t} \quad (3)$$

where  $\theta$  is temperature rise ( $^{\circ}C$ ) and  $\kappa$  thermal diffusivity ( $m^2/s$ ).

$$\kappa = \frac{k}{\rho c_p} \quad (4)$$

where  $k$  thermal conductivity [ $W/(m \cdot K)$ ],  $\rho$  density and  $c_p$  thermal capacities [ $J/(g \cdot K)$ ].

### 3 TEXT CASE

In the present analysis, the CHN 75 kg/m rails and LM-type wheel-set profiles of China freight car (as shown in Fig. 2) are selected to calculate wheel-rail contact stress under different wheel-set lateral displacement ( $Y_w$ ), and applied to the elastic half-space model, to calculate rail surface thermal effect on the basis of wheel speed ( $V_{vehicle}$ ) and the creepage of wheel-rail ( $\xi$ ). The wheel velocity respectively take 1 km/h, 2 km/h, 5 km/h, 10 km/h, 20 km/h, 30 km/h, 40 km/h, 50 km/h, 60 km/h, 80 km/h, 100 km/h, and 120 km/h; and the creepage respectively take 0.001, 0.002, 0.003, 0.004, and 0.005 (the lateral, longitudinal and spin creepage are the same). The material parameters of rail are in Table 1.

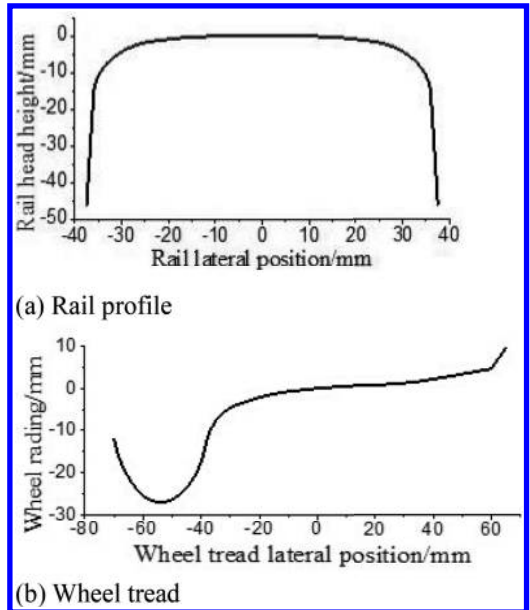


Figure 2. The profiles of wheel and rail.

Table 1. Material parameters.

Parameters	Value
Specific heat capacity $c/(J \cdot kg^{-1} \cdot K^{-1})$	470
Thermal conductivity $k/(W \cdot m^{-1} \cdot K^{-1})$	41
Density $\rho/(kg \cdot m^{-3})$	7790
Poisson's ratio $\nu$	0.3
Young's modulus $E/(N \cdot m^{-2})$	$2.07 \times 10^{11}$
Environmental temperature $T_d/^\circ C$	20

#### 4 RESULTS

Figure 3 shows that, under the condition of  $\xi$  is 0.005, the rail surface temperature change rule with the change of  $V_{vehicle}$  and  $Y_w$ . In the Figure, for the accumulation of heat at a low  $V_{vehicle}$ , the rail temperature is increased. With the increased of wheel-set lateral displacement, the rail surface temperature has a process of first decreasing and then increasing. When  $Y_w$  is 3 mm, the rail surface temperature is relatively small, for the wheel-rail is matched, so the contact stress and heat flow density is small. And when  $Y_w$  is 9.18 mm, the wheel-rail occur two-points contact, the contact stress and heat flow density is large, so the rail surface temperature is relatively large.

Figure 4a, 4b respectively show that, under the condition of  $Y_w$  is 0 mm and 9.18 mm, the rail surface temperature change rule with the change of  $V_{vehicle}$  and  $\xi$ . We can see from the figure, with the increased of  $\xi$ , the rail surface temperature is increased, this is due to the area of slip zone and relative slip velocity is increased with the increased of  $\xi$ , in this case, the heat flow density is increased, so the rail surface temperature correspondingly increased.

Figure 5 shows that the distribution of adhesion and slip status, heat flow density and rail surface temperature rise, on the conditions of  $Y_w = 0$  mm  $\xi = 0.003$ ,  $V_{vehicle} = 5$  km/h. Figure 5a shows the contact patch adhesion and slip status, the red zone represent the slip zone, the blue is adhesion zone which don't produce heat flow. Figure 5b shows the contact patch heat flow density, we can get from this figure is that all the heat come from slip zone. Figure 5c shows the rail surface temperature rise, the maximum temperature rise is  $51^\circ C$ .

Figure 6 shows that the distribution of adhesion and slip status, heat flow density and rail surface temperature rise, on the conditions of  $Y_w = 9.18$  mm  $\xi = 0.003$ ,  $V_{vehicle} = 5$  km/h. The value of this condition is larger than the condition of above (as shown in Fig. 5.), due to the condition occur two-point contact, the contact stress and relative slip velocity is more large, so the rail surface temperature is large, the maximum temperature rise is  $211^\circ C$ .

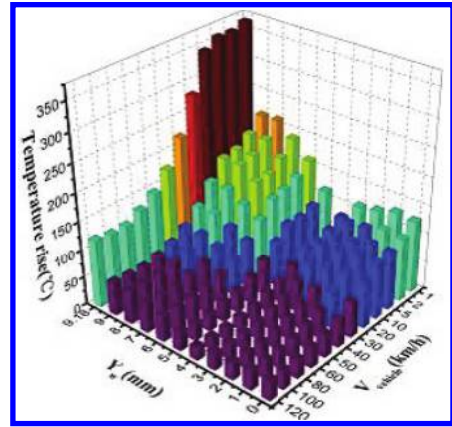
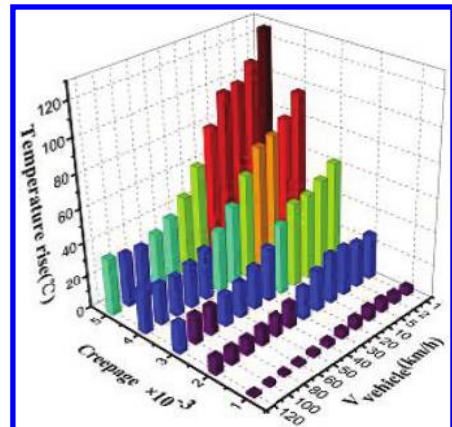
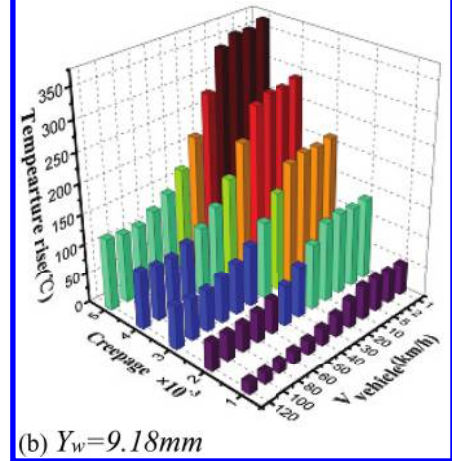


Figure 3. The rail surface temperature change rule with the change of  $V_{vehicle}$  and  $Y_w$ .

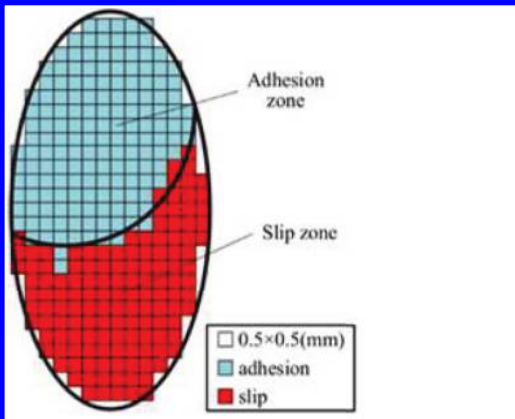


(a)  $Y_w = 0$  mm

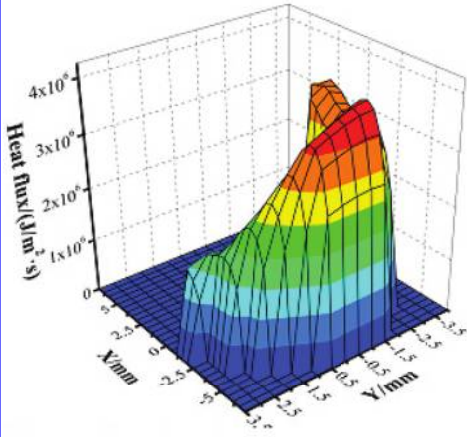


(b)  $Y_w = 9.18$  mm

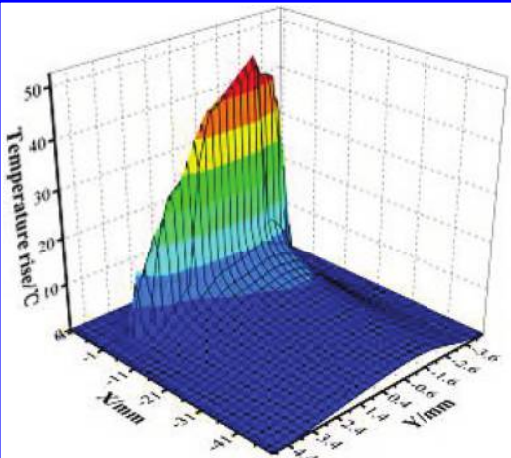
Figure 4. The rail surface temperature change rule with the change of  $V_{vehicle}$  and  $\xi$ .



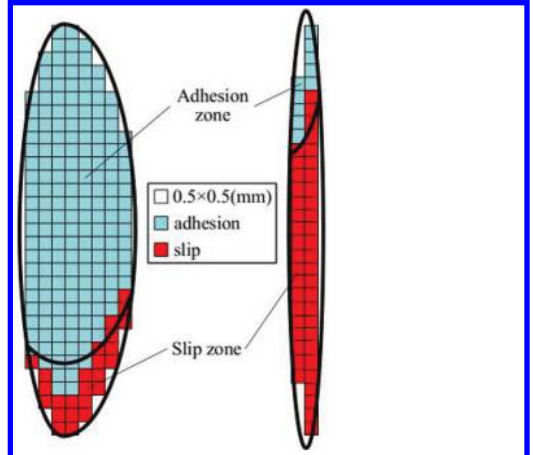
(a) The distribution of adhesion and slip status



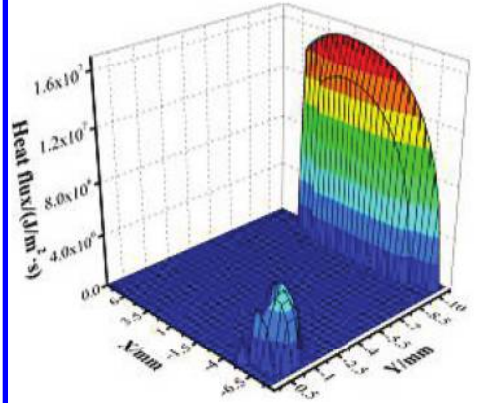
(b) Heat flow density



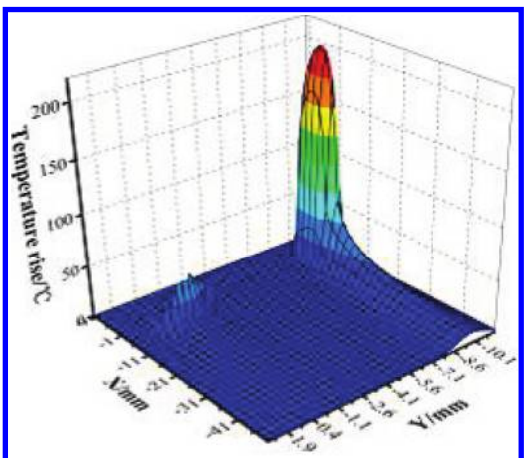
(c) The rail surface temperature rise



(a) The distribution of adhesion and slip status



(b) Heat flow density



(c) The rail surface temperature rise

Figure 5. The wheel-rail contact thermal status.

Figure 6. The wheel-rail contact thermal status.

## 5 CONCLUSION

The temperature of rail surface is high on the condition of wheel-rail rolling contact, and the material parameters changed along with the temperature changes should be considered when calculated wheel-rail thermal contact coupling. The influence of  $V_{vehicle}$  and  $\xi$  on rail surface temperature rise is obvious. With the increased of  $\xi$  and the decreased of  $V_{vehicle}$ , the rail surface temperature is increased. When wheel-rail occur two-point contact, the rail surface temperature rise is larger than one-point contact. The results can provide a support for the further research on cracks, scratches, and stripping damage on the surface of the wheel-rail.

## ACKNOWLEDGMENTS

This research was supported by the National Natural Science Foundation of China (No. 51378395).

## REFERENCES

- Blok, H. 1937. Theoretical study of temperature rise at surfaces of actual contact under oiliness conditions, *Proc. Inst. Mech. Eng. Gen. Discuss. Lubric.* 2:222–235.
- Caralaw, H. S & Jaeger, J.C. 1980. *Conduction of Heat in Solids* (Second edition). U.K: Oxford, Univ. Press.
- Fiseher F.D. et al. 2003. On the temperature in the wheel-rail rolling contact. *Fatigue Fraet Engng Mater Struet*, 26:999–1006.
- Gu Shaojie et al. 2015. Analysis of the wheel-rail friction heating during wheel based on non-Hertz rolling contact theory. *Journal of Inner Mongolia University of Science and Technology*, (34)1:67–71.
- Ji Huai-zhong et al. 2005. Friction Heat Induced Phase Transformation and Spalling Mechanism of Train Wheel Steel. *Journal of Iron and Steel Research*, 17(4):55–59.
- Jaeger, J.C. 1942. Moving sources of heat and the temperature of sliding contacts. *Proc. R. Soc. N.S.W.* 76:203–224.
- Johan Ahistrom & Birger Karlsson. 2002. Modeling of heat conduction and Phase transformations during sliding of railway wheels. *Wear*, 253:291–300.
- Kalker, J.J. 1982. A fast algorithm for the simplified theory of rolling contact. *Vehicle System Dynamics*, 11, 1–13.
- Kalker, J.J. 1990. *Three-Dimensional Elastic Bodies in Rolling Contact*. Dordrecht: Kluwer Academic Publishers.
- Kennedy T.C. et al. 2006. Transient heat Partition factor for a sliding railcar wheel. *wear*, 261:932–936.
- Knothe K. & S. Liebelt. 1995. Determination of temperatures for sliding contact with applications for wheel-rail systems. *Wear*, 189:91–99.
- Li Wei et al. 2010. Thermal-elasto-plastic Finite Element Analysis of Rail during Wheel Sliding. *Journal of Mechanical Engineering*, 46(10):95–101.
- Pei Youfu et al. 1996. An FEM Analysis of Wheel/Rail Contact Heat. *China Academy of Railway Sciences*, 04:48–58.
- Piotrowski, J. & Kik, W. 2008. A simplified model of wheel/rail contact mechanics for non-Hertzian problems and its application in rail vehicle dynamic simulations. *Vehicle System Dynamics*, 46, 27–48.
- Qi Wanming et al. 2010. Finite element analysis on wheel-rail thermal contact coupling of wheel-sliding. *Computer Aided Engineering*, 19(1):40–43.
- Wang Wei et al. 2012. Analysis of the Frictional Heating of Wheel-Rail in Rolling-Sliding Case. *Machinery Design & Manufacture*, (6):135–137.
- Xiao Qian et al. 2013. Thermal Mechanical Coupling Analysis of Wheel Rail Rolling and Sliding Contacts under Functional Friction Coefficient. *China Academy of Railway Sciences*, 34(4):60–65.
- Yan Juanmao. 1983. A Study on Wheel/Rail Spatial Geometric Constraints for Arbitrary Wheel and Rail Profiles. *Journal of Southwest Jiaotong University*, 18(3):40–48.

# Research of computation methods on self-anchored cable-stayed suspension bridge

Jin-ling Chai & Jun Shi

*Henan Vocational and Technical College of Communications, Zhengzhou, China*

**ABSTRACT:** In order to find out a reasonable finished bridge state of triple pylon self-anchored cable-stayed suspension bridge, a neoteric bridge style, the method to determine the finished bridge state of composed system bridge with unsymmetrical spans was studied, and the iteration method of geometric shapes and internal forces of spatial cables, hangers and stayed-cable was presented. The geometric nonlinear finite element model was set up. The unstrained lengths and stiffness matrix were revised continually until the nodes. Displacements met the precision requirement in the processing of nonlinear iteration calculation. Then the finished bridge state of the whole bridge was determined. With this method, the finished bridge state that meets the design requirement of self-anchored suspension bridge and the geometric shapes and internal forces of cables, hangers, and stayed-cable. An example proves that the method is valid and feasible for engineering requirement and determining the finished bridge state of spatial cable-stayed self-anchored suspension continuous composed system bridge.

**Keywords:** bridge engineering; cable-stayed self-anchored suspension continuous composed system bridge; main cable shape; segmental catenary method

## 1 INTRODUCTION

Suspension bridge and cable-stayed bridge is the first choice for large-span bridge form. Most of the suspension bridge is given priority to with anchor block, which needs to be huge and expensive anchorage to resist the powerful tension of main cable. Self-anchored suspension bridge main cable anchorage on the stiffening girder avoid building anchorage, and can also provide stiffening girder with pretested [1]. For cable-stayed bridges, suspension bridges show their shortcomings and the insufficiency, which already cannot completely meet their requirements. So self-anchored cable-stayed suspension bridge rises at the historic moment [2]. It embodies the advantages of both, and is made up for the inadequacy. In the process of the design of the bridge, the tower and form of beam section size is determined, its load is made up of main girder, a bridge tower, and the share of the stay cables, reasonably determine the ratio of each component to share is very important. So the design of the bridge cable system is to determine the reasonable first into the bridge state, namely the reasonable state of linear and internal force, and suspension—suspension cooperative system bridge is a kind of new bridge, its bridge state research is less. This paper is conducted through calculation of the segmental catenary theory stress free cable

long, through the influence matrix method, and the theory of geometric nonlinear iteration, which determine it into a state of the bridge. Using the method of a suspension—suspension cooperative system bridge is calculated, linear and completed in accordance with the actual requirements.

## 2 THE BRIDGE DESIGN CONDITION

### 2.1 *Self-anchored suspension bridge completion state*

The method of linear suspension bridge main cable into a bridge mainly adopts parabolic method, based on the catenary clues yuan of recursive method, virtual beam method, etc. Parabolic method is simple, but the precision is not high, suitable for preliminary design of suspension bridge, the Catenary method with high precision. Back cable force calculation of main basis of stiffening girder section of gravity and the second phase of constant load, Point by vice tower back the moment balance between the centroid can conclude main cable tower of the vice of horizontal force  $H$  and vertical force  $V$ . Set up the structure of the whole bridge along horizontal uniform weight and the sum total of live load for  $q$ :

The side span of main cable horizontal component  $H$  is:



$$H = \frac{qL^2}{8f} = \frac{qL}{8\lambda} \quad (1)$$

Among them:  $\lambda = \frac{f}{L}$ —rise-span ratio of the side span;  $L$ —Side span;  $f$ —Side span rise.

Rise-span ratio  $\lambda$  is calculated by type (1). Considering the actual situation, into the bridge main cable by load for main cable arc length uniformly distributed along the main cable gravity and delivering the sling concentration (unit weight of stiffening girder and the second phase of dead load). So the suspension bridge main cable force schema can be simplified as along the arc length under uniformly distributed load with concentrated force of the flexible cable, The lifting point between the main cable shape of acceptor line weight of catenary [3–5]. The main cable can be seen as more paragraphs that differentiate by the lifting point the combination of catenary, as shown in Figure 1.

For any period  $i$  of suspension cable, the equation for:

$$c = -\frac{q}{H},$$

$$a_i = sh^{-1} \frac{h_i c}{2sh\left(\frac{cl_i}{2}\right)} - \frac{cl_i}{2}, \quad (2)$$

$$b_i = -\frac{1}{c} cha_i$$

$$y_i = \frac{1}{c} [ch(cx + a_i)] + b_i \quad (3)$$

Main cable overall balance equation:

$$\begin{cases} H_1 = H_2 \\ V_1 = q \sum_{i=1}^n s_i + \sum_{i=1}^n P_i + H_2 \tan \theta_2 - H_1 \tan \theta_1 \end{cases} \quad (4)$$

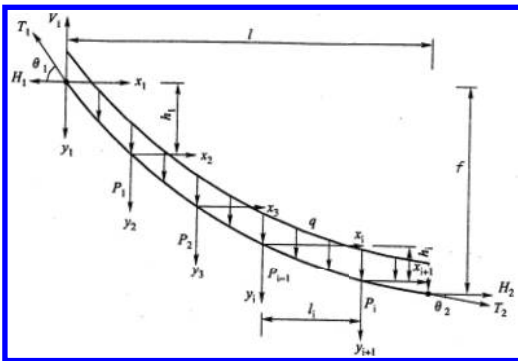


Figure 1. Main cable force analysis.

And satisfy the compatibility conditions:  $\sum_{i=1}^n h_i = f$ .

Type:  $s_i$ —The  $i$  section of long,  $s_i = \int_0^{l_i} ds = \int_0^{l_i} \sqrt{1 + (y')^2} dx$ .

And in the concentrated load point between paragraphs satisfy the force equilibrium condition:

$$\begin{cases} Hy' \big|_{x_i=l_i} - Hy' \big|_{x_i=0} = P_i, \\ H[sh(cl_i + a_i) - sha_{i+1}] = P_i, \end{cases} \quad (5)$$

Among them,  $P_i$  as the focus;  $L$  and  $h$ , respectively, as the main line at the ends of the horizontal distance and elevation difference, Computing needs to give certain initial value, iteration to get precise linear.

## 2.2 Cable-stayed bridge finished bridge state

Bridges at home and abroad experts put forward a lot of dead load cable force of cable-stayed bridge calculation method, which has rigid support continuous beam method, zero displacement method, the method of internal force balance, specify stress method, and other methods [6]. The cable force optimization method has limitations, it is difficult to obtain satisfactory results; this paper presents a method of comprehensive:

1. Deciding initial dead state using minimum bending energy method  
The cable and the axial stiffness of beam and column is increased to large enough, so to get in the main girder and the tower bending moment are relatively small, the target is basically uniform state into a bridge. This state into a bridge, one of the few to cable force may be very unreasonable, main girder and the tower bending moment small also is not reasonable. Therefore, this state is not the ultimate goal as a bridge, but is adjusted into a state of bridge foundation.
2. By adjusting cable force influence matrix method was obtained by minimum bending energy method and tower into the state of the bridge girder bending moment and rationalization [8–9]

$$[A]\{\Delta T\} = \{\Delta R\} \quad (6)$$

Type:  $[A]$ —Influence matrix;  $\{\Delta T\}$ —Cable force adjustment quantity;  $\{\Delta R\}$ —The amount of control target to adjust.

Using least squares solution [7], work out, you can get the adjusted control target:

$$\{R\} = \{R_0\} + [A]\{\Delta T\} \quad (7)$$

Type:  $\{R\}$ —After the adjustment control target;  
 $\{R_0\}$ —Before the adjustment of control target;  $\{A\}$ ,  
 $\{\Delta T\}$ —Same as above.

### 3 ACCURATE EQUILIBRIUM ANALYSIS

Cable-stayed suspension bridge width 555 m, its a composite system of tower bridge. Including the main tower system segment and the anchor cable suspension system. Combination of main span is:  $25\text{ m} + 90\text{ m} + 2 \times 25\text{ m} = 162.5\text{ m} + 90\text{ m} + 90\text{ m}$ . Based on the special finite element program MIDAS/Civil to tower suspension—since the anchor cable cooperation system bridge for 3 d modeling.

Due to the bridge tower of vice about asymmetric structure, main cable tension and back sola force will produce unbalanced moment to Kentucky vice tower under the action of dead load. So, its must control the bending moment in a certain range to ensure the safety of the tower of vice. According to this principle, to determine main cable tension stiffening girder and derrick undertake weight ratio. Nonlinear finite element equilibrium iteration calculation, determine the reasonable state into a bridge. stiffening girder maximum bending moment for  $-159137\text{ KN.M}$ , the maximum axial force  $-115519\text{ KN}$ , stiffening girder maximum bending moment for  $-159137\text{ KN.M}$ , and the maximum axial force  $-323872\text{ KN}$ . In the bridge condition, the stiffening girder internal force as shown in Figures 2–3, inclined boom internal forces are shown in Table 1.

Back into the bridge condition cable force are shown in Table 2.

From Table 2 shows, back into the bridge condition basic cable force between 6200 KN and 6600 KN, cable force was homogeneous. Into a state of suspension bridge cable force are shown in Table 3.

From Table 3, into a state of suspension bridge cable force is divided into two parts, the unit

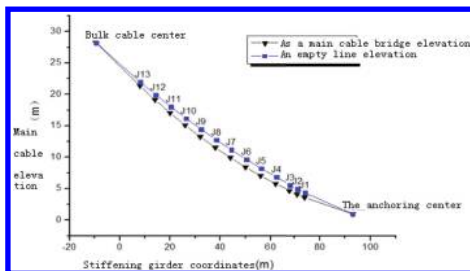


Figure 2. Main cable into the bridge and empty cable shape.

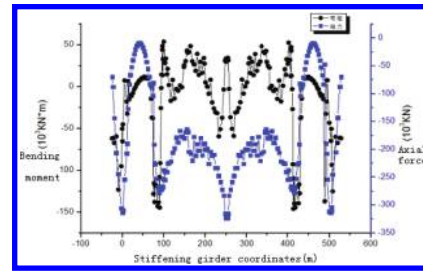


Figure 3. Stiffening beam axial force and bending moment diagram.

Table 1. Inclined boom internal force (kN).

Serial number	Beam end	Cable end
2000	1093.83	1092.20
2001	580.30	578.34
2002	250.50	248.18
2003	704.93	703.99
2004	492.08	491.16
2005	401.92	400.72
2006	404.30	403.12
2007	348.49	347.01
2008	479.43	477.96
2009	340.81	339.02
2010	429.10	427.33
2011	357.00	354.87
2012	425.41	423.30
2013	355.23	352.75
2014	454.78	452.31
2015	377.70	374.83
2016	405.77	402.92
2017	456.66	453.38
2018	540.39	537.12
2019	426.29	422.56
2020	283.90	280.00
2021	409.64	405.25
2022	474.82	470.28
/	/	/

Table 2. Back cable internal force (KN).

Serial number	Beam end	Cable end
4000	6200.92	6174.71
4001	6427.63	6399.69
4002	6577.23	6547.15
4003	6495.44	6463.64
4004	6602.32	6568.27
/	/	/

3000–3007 of suspension cable force between 6000–7800 KN, 3008–3010 of suspension cable force between 3500–3800 KN, conform to the requirements of the design of long-span cable-stayed bridge.

Table 3. The internal cable (kN).

Serial number	Beam end	Cable end
3000	7834.37	7777.24
3001	7796.13	7740.92
3002	7831.15	7777.88
3003	7575.63	7524.31
3004	7624.95	7575.58
3005	7423.14	7375.74
3006	6071.87	6030.68
3007	5944.91	5905.25
3008	3781.60	3759.34
3009	3679.48	3658.20
3010	3564.63	3544.50

#### 4 CONCLUSION

1. This paper uses the three towers self-anchored cable-stayed suspension bridge cooperation system bridge stress analysis. First segmental catenary method is used to iterative calculation, its reasonable linear, recycling limited displacement theory of derrick and stiffening girder internal force calculation, a further iteration, the geometric main cable stress free cable long, finally, got into a reasonable bridge state.
2. The research proposed for vice towers on both sides of the asymmetric into the bridge linear and internal force of the iterative calculation method, by this method can quickly find the bridge balance. Into the state of the bridge finite element model is established for the nonlinear iterative calculation to determine the whole bridge structure into a state of the bridge.

#### REFERENCES

- [1] Diana G., Cheli F., Zasso A., Collina A., Brownjohn J. Suspension bridge parameter identification in full scale test. *Journal of Wind Engineering and Industrial Aerodynamics*. 1992.
- [2] Zhang Zhe, Zhu Weizhi. Based on the geometric non-linearity self-anchored suspension bridge final cable force [J] *Journal of Shenyang Jianzhu University (Natural Science)*, 2009, 25(5), 822–828.
- [3] Kim H.K., Lee M.J., Chang S.P., Non-linear shape-finding analysis of a self-anchored suspension bridge. *Engineering Structures*. 2002.
- [4] Zhang Zhe, DuGao-ming. Model Test for Large-span Self-anchored Cable-stayed Suspension Bridge [J] *Journal of Highway and Transportation Research and Development*, 2007, 06(5), 75–91.
- [5] Xiao Ru cheng, Xiang Hai fan. Mechanics characteristics and economic performances study for cable-stayed-suspension bridges [J] *china journal of highway and transport*, 1999, 07(5), 43–48.
- [6] Luo Jian-Hui, Chen Zheng-Qing, Liu Guang-Dong. Research on instability mechanism of long-span cable-stayed bridges due to nonlinear aerostatic torsion. *Gongcheng Lixue/Engineering Mechanics*. 2007.
- [7] Kasug A. Optimum cable force adjustments in concrete cable stayed bridge [J]. *Journal of Structure Engineering ASCE*, 1995, 121(4):685–694.
- [8] Song Weon-Keun, Kim Seung-Eock, Ma Sang Soo. Nonlinear analysis of steel cable-stayed bridges. *Computer Aided Civil and Infrastructure Engineering*. 2007.
- [9] A. Ruangrassamee, K. Kawashima. Control of Non-linear Bridge Response with Pounding Effect by Variable Dampers. *Engineering Structures*. 2003.

*Hydraulic engineering*

# Analysis of the influence of Poyang Lake on convective systems and lightning transited

Y.H. Cao

*School of Science, East China Jiaotong University, Nanchang, China*  
*Mathematics and Physics College, Jinggangshan University, Ji'an, China*

X.F. Ye

*Pingxiang Meteorological Bureau, Pingxiang, China*

X.M. Liu

*Jiangxi Provincial Meteorological Research Institute, Nanchang, China*

**ABSTRACT:** In this paper, mesoscale convective systems and lightning phenomenon surrounding the Poyang Lake region were analyzed with mesoscale convective systems and lightning monitoring data in 2006–2008, to reveal the law of the influence of the Poyang Lake on the mesoscale convective system and its concomitant phenomena of lightning. The results showed (1) the characteristics of the temporal distribution of lightning activities in the Poyang Lake region: lightning activities were mainly in the late spring to early autumn, mostly in summer, while the frequency of lightning activities was mainly at 12:00–22:00, in particular, focusing at 13:00–19:00. Lightning incidence trend around the Poyang Lake area was in accordance with that in Jiangxi Province. The difference was that the Jiangxi lightning frequency changed greatly in the afternoon, and the lightning frequency around the Poyang Lake area distributed symmetrically, with obvious change. The reasons may be attributed to the difference in the underlying surface, as a result of which the land surface-underlying surface was very different (such as forests, mountains or hills), while the water surface-underlying surface was relatively homogeneous. (2) The spatial distribution characteristics of lightning activities around the Poyang Lake region: within 12:00–14:00, lightning occurred mainly in the West Bank region of the lake, followed by the central area of the Eastern bank region, within 14:00–20:00, occurred mainly in the southern area of the Lake. Such distribution patterns may be related to the topography distribution of the Poyang Lake and the local circulation of lake-land wind. In addition, they may be closely related to the moving path of mesoscale convective weather systems. (3) When the mesoscale convective system moved to the Poyang Lake, the moving speed slowed down. This was due to the surface heating by solar radiation during the day, with terrestrial heating up being much faster than that of the lake surface. Compared with land, the Poyang Lake was a cold source. Because of heat expansion, the land-based air group went up and converged, under the action of the horizontal pressure gradient force, the air flew over the lake from the sky over land, then sank to the lake, and finally, flew over the land from the lake surface, forming a local thermal circulation. (4) There was a good positive correlation between lightning frequency in the Poyang Lake area and the lake monthly evaporation. The vigorous times during which the latent heat of the lake releases was also the frequent times of convective clouds and their adjoint lightning activities. This was due to the release of the lake latent heat, which affected the energy balance of convective clouds transited and water vapor balance, by the exchange between energy and water vapor, to promote the development of strong convective clouds, the intensity and frequency of lightning activities exacerbated indirectly. (5) The vertical perturbation of the Poyang Lake area on the mesoscale convective weather systems transited led to instability of its energy and produced severe weather, such as thunder and strong convection.

**Keywords:** transiting convective systems; lightning; Poyang Lake; influence analysis

## 1 INTRODUCTION

### 1.1 Study area

The studied area in this paper was the Poyang Lake (28°22′~29°45′N, 115°47′~116°45′E). Poyang Lake

is located in the northern part of Jiangxi Province (the southern bank of the Yangtze River). The terrain is shown in [Figure 1](#), where the north region is the entrance of the Yangtze Rive, which is narrow. The south region is the lake's main body, which is



Figure 1. Geography location of the Poyang Lake by satellite remote sensing.

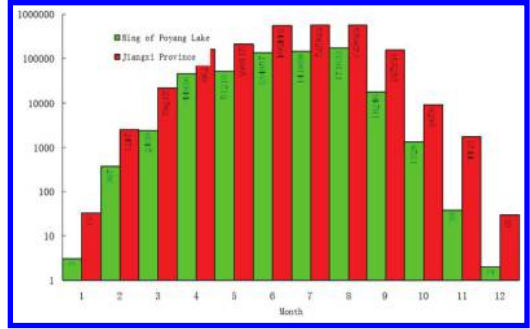


Figure 2. Monthly distribution of the lightning frequency in 2006–2008.

broad. According to the satellite remote sensing measurement, the largest area of the lake in a large water period was 5100 km<sup>2</sup>.

### 1.2 Data source

The data used in this paper were provided by the Jiangxi Provincial Institute of Meteorological Science from 2006 to 2008 on lightning location system data and image data from the observation data of Poyang Lake meteorological satellite Fengyun Fy2-c. The heat flux data used were calculated by Min Qian (2006) through the water surface evaporation climatology model of experimental data.

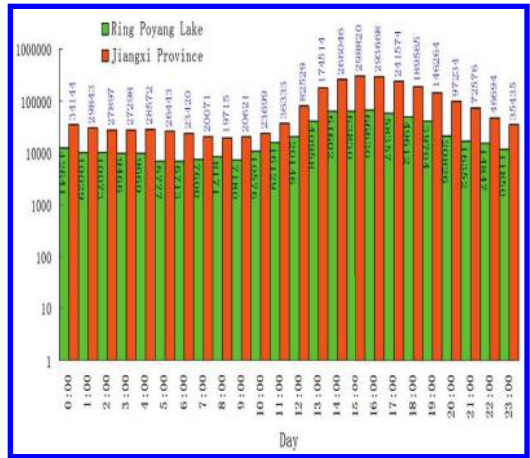


Figure 3. Daily variation of the lightning frequency in 2006–2008.

## 2 SEASONAL AND TIME OF ANNULUS POYANG LAKE CONVECTIVE CLOUDS AND LIGHTNING OCCURRENCE

The monthly distribution of Jiangxi ground lightning (Fig. 2 Y-label used the logarithmic coordinate) showed that the Jiangxi Province was a thunderstorm area. Thunderstorms occurred mainly from July to August. The second was from April to May and September. In January and December, lightning appeared rarely. The thunderstorm activity frequently occurring time (Fig. 3 Y-label used the logarithmic coordinate) was mainly concentrated from 12:00 to 22:00, especially from 13:00 to 19:00, there appeared more thunderstorms. Ring thunder occurred in the Poyang Lake region, which was in line with the trend of Jiangxi. The difference was that Jiangxi lightning frequency changed greatly in the afternoon, and the lightning frequency around the Poyang Lake area distributed symmetrically, with no obvious change. The reason for this can be attributed to the difference in the underlying surface, as a result of which the land surface-underlying surface was very different (e.g. forests, mountains or

hills), while the water surface-underlying surface is relatively homogeneous.

## 3 SPATIAL DISTRIBUTION OF THE RING POYANG LAKE

Through analyzing the data on the average number of lightning (2006–2008), it showed that around the Poyang Lake during the afternoon (12:00–14:00) lightning mainly occurred in the west coast region of the lake (Figs. 4a and 4b shading). The second occurred in the central region of the area. While during 14:00–20:00, it occurred mainly in the south region (Figs. 5a, 5b, 6a and 6b shading).

Such distribution patterns may be related to the topography distribution of the Poyang Lake and the local circulation of lake-land wind. In addition, they may be closely related to the moving path of mesoscale convective weather systems. For example,

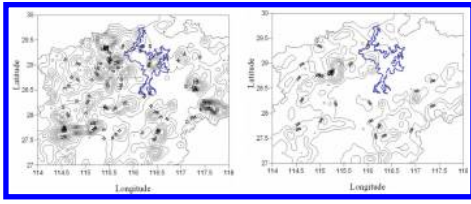


Figure 4a. Lightning distribution at 12:00–13:00.  
Figure 4b. Lightning distribution at 13:00–14:00.

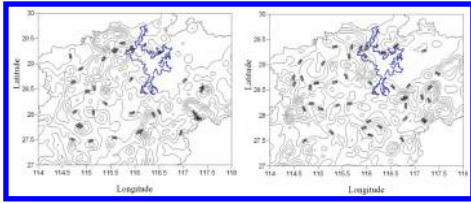


Figure 5a. Lightning distribution at 14:00–15:00.  
Figure 5b. Lightning distribution at 15:00–16:00.

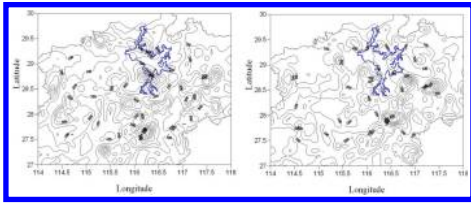


Figure 6a. Lightning distribution at 16:00–17:00.  
Figure 6b. Lightning distribution at 17:00–18:00.

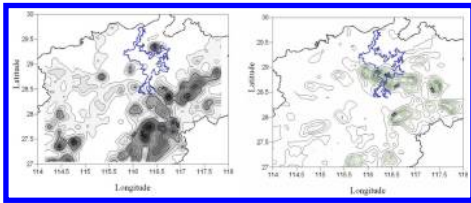


Figure 7a. Lightning distribution in June 24–27, 2006.  
Figure 7b. Lightning distribution in June 24, 2007.

in June 24–27, 2006 and in June 24–25, 2007, the strong convective weather occurred with a strong thunder process (Fig. 7a and Fig. 7b shaded part).

#### 4 THE LATENT HEAT RELEASE OF THE POYANG LAKE INFLUENCE NEAR CONVECTIVE CLOUD AND LIGHTNING

The method used herein was that of Qian Min (2006): through the water evaporation, the climatology model can be calculated as follows:



Figure 8. Mean monthly evaporation at the Poyang Lake in 1955–2004.

$$E = 2.33 B \times (1 - f \times r) \exp(0.06782T) \quad (1)$$

where  $E$  is the monthly average water evaporation (MM);  $B$  is the number of days per month (28, 29, 30, 31);  $R$  is the monthly average relative humidity; and  $T$  is the monthly average temperature ( $^{\circ}\text{C}$ ).

Based on the calculation, the result is shown in Figure 8 (the unit in the Y-label is mm). Compared with Figure 3, we can see that there is a positive correlation between the average monthly number of lightning ring at the Poyang Lake and the monthly average evaporation. From July to September, it was the most large evaporation, especially in August. Correspondingly, it was also the most frequent lightning activity period. In other words, the latent heat release active period of the lake was also the activity period of lightning and the convective cloud. This was because the release of latent heat for the lake water body affected the transit energy balance of the convective cloud and moisture. Through the exchange of energy and water vapor, it prompted strong convective cloud development. This indirectly contributed to the intensity and frequency of lightning activity.

#### 5 CONCLUSIONS

From the above discussion, the following conclusions can be made:

(1) The characteristics of the temporal distribution of lightning activities in the Poyang Lake region: lightning activities were mainly in the late spring to early autumn, mostly in summer, while the frequency of lightning activities was mainly at 12:00–22:00, in particular, focusing at 13:00–19:00. Lightning incidence trend around the Poyang Lake area was in accordance with that in Jiangxi Province. The difference was that the Jiangxi lightning

frequency changed greatly in the afternoon, and the lightning frequency around the Poyang Lake area distributed symmetrically, with no obvious change. The reason for this can be attributed to the difference in the underlying surface, as a result of which the land surface-underlying surface was very different (e.g. forests, mountains or hills), while the water surface-underlying surface was relatively homogeneous. (2) The spatial distribution characteristics of lightning activities around the Poyang Lake region: within 12:00–14:00, lightning occurred mainly in the West Bank region of the lake, followed by the central area of the Eastern bank region, within 14:00–20:00, occurred mainly in the southern area of the lake. Such distribution patterns may be related to the topography distribution of the Poyang Lake and the local circulation of lake-land wind. In addition, they may be closely related to the moving path of mesoscale convective weather systems. (3) When mesoscale convective system moved to the Poyang Lake, the moving speed slowed down. This was due to the surface heating by solar radiation during the day, with terrestrial heating up being much faster than that of the lake surface. Compared with land, the Poyang Lake was a cold source. Because of heat expansion, the land-based air group went up and converged, under the action of the horizontal pressure gradient force, the air flew over the lake from the sky over land, then sank to the lake, and finally it flew over the land from the lake surface, forming a local thermal circulation. (4) There was a good positive correlation between lightning frequency in the Poyang Lake area and the lake monthly evaporation. The vigorous times during which the latent heat of the lake releases were also the frequent times of convective clouds and their adjoint lightning activities. This was due to the release of the lake latent heat, which affected the energy balance of convective clouds transited and water vapor

balance, by the exchange between energy and water vapor, to promote the development of strong convective clouds, the intensity and frequency of lightning activities exacerbated indirectly. (5) The vertical perturbation of the Poyang Lake area on the mesoscale convective weather systems transited led to instability of its energy and produced severe weather such as thunder and strong convection.

## ACKNOWLEDGMENTS

This work was jointly supported by the Natural Science Foundation (No. 11461026) and the Natural Science Foundation of Jiangxi Province (No. 20132BAB201014).

## REFERENCES

- [1] Ill Insworth A.J, 1985. Charge separation in thunderstorms: Small scale processes [J]. *J Geophys Res*, 90 (4):6026–6032.
- [2] K.D. Hondl & M.D. Eilts, 1994. Doppler radar signatures of developing thunderstorms and their potential to indicate the onset of cloud-to-ground lightning. *Mon Wea Rev.*, 122:1818–1836.
- [3] M. Maribel, 2002. The relationships between radar reflectivity and lightning activity at initial stages of convective storms. American Meteorological Society, First Annual student Conference, Orlando.
- [4] R.V. Brandon, D.C. Lawrence & S. Douglas et al, 2003. Using WSR-88D reflectivity for the prediction of cloud-to-ground lightning: A central north Carolina study. *National Weather Digest*, 27:35–44.
- [5] Moore, P.K., & R.E. Orville, 1990. Lightning characteristics in lake-effect thunderstorms. *Mon. Wea. Rev.*, 118:1767–1782.
- [6] F.L. Neil & A.R. David, 2002. Variations of Sensible and Latent Heat Fluxes from a Great Lakes Buoy and Associated Synoptic Weather Patterns *American Meteorological Society*, 2(3):3–12.



# Simulation and cause analysis of the piezometer tube abnormality in a dam

Dandan Li

Nanjing Hydraulic Research Institute, Nanjing, China

Taozhen Sheng

Hohai University, Nanjing, China

Dawei Zhang

Nanjing Hydraulic Research Institute, Nanjing, China

**ABSTRACT:** In this paper, we made an analog computational analysis of the piezometer tube in the sections 0 + 225 of a dam. The results demonstrate that the cause of the abnormality lies in the seepage failure of the core wall, during which time the fluctuation of the water level in the tube reflects the development of seepage failure. Therefore, this research achievement may be used for reference in other projects.

**Keywords:** piezometer tube; abnormality; simulation; cause analysis

## 1 INTRODUCTION

The height of the earth-rock dam with clay core is 324.50 m. The concrete wave wall of the dam is 1.2 m high, 406 m long and 8 m wide, setting up the dam crest. The maximum height of the dam is 49.9 m. In 2013, the piezometer tube in the sections 0 + 225 of a dam raised the water levels abnormally. In this paper, through value simulated computation and abnormality analysis, we provide a theoretical basis for reference in other projects [1–3].

## 2 THE ABNORMAL PROCESS OF THE PIEZOMETER TUBE

On September 25, 2013, the water level of the tube PT2-1 in sections 0 + 225, which was 295.21 m recorded by the auto-measurement, increased to 7.88 m compared with the height of 287.33 m measured artificially on September 5. At this time, the reservoir level basically remained unchanged. After that, the water level of the tube fluctuated around 295.00 m. On October 6, the water level rose to 312.25 m suddenly, i.e., 17.04 m higher than the level on September 25. On October 8, it rose to 313.71 m and then gradually fluctuated in a down-trend. On October 30, it dropped from 306.21 m to 293.70 m suddenly, decreasing by 12.51 m. After October 31, it continued to rise slowly, and it had increased to 303.95 m with fluctuations until January 25, 2014.

Figure 1 shows the stage hydrograph of the tube from September 5, 2013 to January 25, 2014. As shown in the figure, the change in the water level in the tube PT2-1 was extremely abnormal.

Table 1 presents the change in the potential energy of the tube PT2-1's position in some



Figure 1. The stage hydrograph of the tube, from September 5, 2013 to January 25, 2014.

Table 1. Potential energy changes in the position of the tube PT2-1 in some important periods of time.

Date	Upper level (m)	Water level in the tube PT2-1 (m)
September 5, 2013	317.64	287.33
October 9, 2013	317.99	313.31
October 30, 2013	317.90	293.95
December 12, 2013	317.13	300.07
January 24, 2014	316.53	303.79
February 24, 2014	313.60	304.21

important periods of time from September 5, 2013 to February 24, 2014.

From Table 1, it can be seen that the potential energy of the tube's position accounted for only 10.1% in September 2013, which means that the core wall accounted for 89.1% of the head due to the great anti-seepage capability of the core wall. However, early in October, the potential energy of the tube's position at this point rose from 10.1% to 86.3%, indicating that the heart wall accounted for merely 13.7% of the head. In other words, the anti-seepage capability of the core wall upstream was almost lost. In late October, the anti-seepage capability of the core wall was recovered abruptly, undertaking 70.5% of the head, and then gradually declined. In late January 2014, the core wall accounted for 39.1% of the head only. In general, these data suggest that the anti-seepage capability of the core wall becomes increasingly weak with the development of seepage failure as well as the formation of the seepage flow channel.

### 3 ANALOG COMPUTATION OF THE ABNORMAL PIEZOMETER TUBE

Because of the limitation of the calculation theory and method, it is difficult to simulate holes, penetrating cracks upstream and downstream. Considering only the constant destruction of the core wall and the increasing permeability coefficient, back analysis can be carried out based on the coefficient of permeability in every zoned part, which can be compared with geological prospecting achievement for further analysis. Owing to the local failure of the core wall, we should adjust the permeability coefficient of the core wall to ensure that both the first piezometer tube of the dam and the foundation reach the observed value.

In the two cases mentioned above, water head dissipation of the core wall is limited in the upstream side of the piezometer tube, and the head is mainly bore by the core wall behind, the tube together with the inverted filter. If the width of the core wall behind the tube is 4.5 m, the average hydraulic slope would be 6.67 and 4.44. The permissible hydraulic slope for soil destruction of the core wall is 1.28. When the filter protection is taken into account, the permissible hydraulic slope can be increased 2 to 3 times. However, due to the poorly graded soil in the downstream dam shell, the filter material in the second layer or the transition layer cannot be protected. Worse still, once the downstream dam shell cannot protect the fine particles in the second reversed filter, the fine particles will be lost, resulting in weakened protection or even the situation when the second layer cannot protect the first layer of the filter material

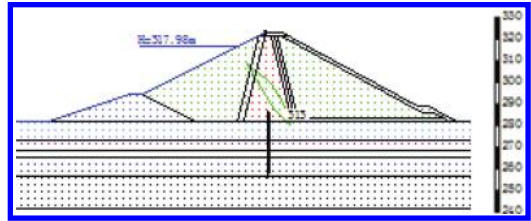


Figure 2. The water head of the piezometer tube around the sections 0 + 225 1 (after seepage failure).

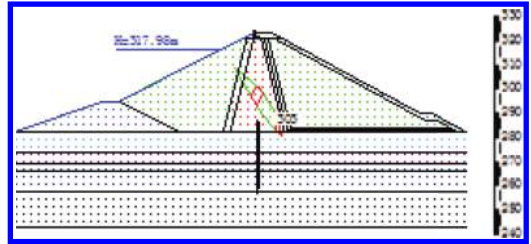


Figure 3. The water head of the piezometer tube around the sections 0 + 225 2 (after seepage failure).

effectively. Moreover, it led to the decrease or loss of protection to fine particles in the core wall by the first reversed filter. The fine particles, which should be in the core wall, will pass through the first and second reversed filters to the dam shell. Finally, the function of the filter fails and seepage failure takes place in the core wall [4].

### 4 ANALYSIS OF THE ABNORMAL PIEZOMETER TUBE

Level swelling of the tube in the sections 0 + 225 shows that the anti-seepage function of the core wall had weakened largely in the upstream side of the tube from early September to early October. The sudden drop in the water level in late October may be caused by the situation when the seepage-proofing function of the core wall was partially restored owing to the original seepage channels that were clogged by the collapsing soil. Afterwards, the water level in the tube increased slowly, which demonstrates that the seepage-proofing function of the core wall was impaired gradually. During this time, the fluctuation of the water level shows the process of seepage failure development [5].

According to a comprehensive analysis of the construction and geological exploration material, the existing construction quality of the core wall is too inferior to meet the design requirements; the water filling test in the field proved that the

permeability of the core wall did not fulfill the design requirements; the core material was poorly graded, which lacked intermediate particle size and it was easy to make seepage failure with low construction quality. Since congenital defects of the core wall led to its seepage failure easily, it is crucial to protect the filter in the downstream dam crest. The material of the first and second reversed filters satisfied the requirements of the design as well as the standards, but the sand gravel in the dam shell downstream was poorly graded, which could not prevent the washing away of fine particles from the second reversed filter material (transition layer). Furthermore, it led to the loss of fine particles in the first layer, which resulted in the inefficiency of the filter downstream. Also, under the construction of a local dam shell, size segregation may occur, which will cause the disability of protecting the second reversed filter due to the block concentrating and even the first filter. Finite element simulation analysis also confirmed that seepage failure did take place in the core wall.

## 5 CONCLUSION

In brief, this paper provides an analog computational analysis of the piezometer tube in the sections 0 + 225 of a dam, the results of which show that the occurrence of the permeability channel in the core wall upstream is the cause of the sudden rise in the tube. The reason for a sudden drop in the water level may be attributed to the clogging of the original seepage channels by the collapsing soil, and to the partial restoration of the seepage-proofing function of the core wall.

After that, the water level in the tube rose slowly, indicating that the seepage-proofing function of the core wall decreased gradually. In this process, the fluctuation of the water level shows the development process of seepage failure. Therefore, this achievement may play a referential role in other projects.

## ACKNOWLEDGMENTS

This work was financially supported by the Fundamental Research Funds of Nanjing Hydraulic Research Institute (Y714005 and Y715003).

## REFERENCES

- [1] Kang Junhong. Reason of abnormal measured value of piezometer tube in new auxiliary dam of Gangnan Reservoir in *Water Sciences and Engineering Technology*, 2013, 1: 83–85.
- [2] Wang Ping. Reason and processing of abnormal measured value of piezometer tube in Haohanbo Reservoir in *Heilongjiang Science and Technology of Water*, 2013, 5: 153–154.
- [3] Liu Zede. Reason of abnormal measured value of piezometer tube in Niansi Reservoir in *Shanxi Water Resources*. 2014, 5: 24–25.
- [4] Liu Jie. Disagreement on analysis results about cause of seepage failure of mud mountain and portage mountain embankment dams in *Hydropower Design*, vol. 25(2009):1–6.
- [5] Zeng Zeng, Dang Faning, Huang Rongwei. The analysis of failure mechanism about earth-rock dam of TETON Reservoir in Yellow River, vol. 32(2010):215–219.

## Restoration of karst water system in Jinan, China

Juan Zhou & Liting Xing

*School of Resources and Environment, University of Jinan, Jinan, China*

Song Wang & Huibo Zhuang

*Hydrographic Office of Shandong Province, Jinan, China*

Tongwen Dou & Zengyuan Yang

*Hydrographic Office of Jinan City, Jinan, China*

**ABSTRACT:** Due to the influence of overexploitation of groundwater, from 1972 to 2003, Baotu spring was dried up. The reason for the failure to successfully protect the spring for about 40 years is that the function of karst water system was not clearly grasped. The evolution trend of the Jinan spring zone resource amount is calculated by the equilibrium method, revealing the inferior degeneration of the function of the karst water system. Recharge locations are determined according to formation, structure, permeability, and water quality. A proper recharge amount (290,000 m<sup>3</sup>/d) is attained by regression analysis. Based on the analysis, a three-dimensional groundwater flow numerical model of the Jinan spring area is established. Optimizing the layout of exploitation wells and the exploitation amount of the Jinan spring area are inverted through the model, including the exploitation of Jixi (in the west of the Jinan spring area) increasing by 110,000 m<sup>3</sup>/d, that of Xijiao (the western suburbs) by 30,000 m<sup>3</sup>/d and that of Dongjiao (the eastern suburbs) by 20,000 m<sup>3</sup>/d. Conjunctive regulation of surface water and groundwater is adopted to restore the function of the groundwater system, being able to achieve flowing constantly of Jinan spring all over the year.

**Keywords:** recharge; optimizing exploitation; numerical simulation; function of resources; karst water; protecting spring

### 1 INTRODUCTION

Groundwater is the main water source of agriculture, industry and urban living, which has an important influence on economical development. The software of numerical simulation (e.g. Visual modflow, GMS, Feflow) plays a significant role in groundwater management. As for research on groundwater numerical simulation, a lot of work such as water flow transport model and solute transport model has been done worldwide, attaining great achievements (Qu, W.J., 2014; Liu, Y.P., 2014; Careghini, A., 2015; Zhao, C.Y., 2005; Xing, L.T., 2007). Research and tests on the study field of groundwater management show that artificial recharge of groundwater is an effective engineering measure to adjust and utilize groundwater resources (Wang, X.J., 2005). Artificial recharge of groundwater can not only lift the groundwater level and reduce land subsidence caused by over-exploitation, but also lift storage water resources to achieve optimized use of groundwater (Zhang, Y., 2014). However, there still exist some disadvantages such as recharge amount and determination of recharge locations.

Groundwater exploitation in Jinan City from 1958 to 2014 experienced three stages, namely the stage of low exploitation (1958–1969), the stage of over-exploitation (1970–2002) and the stage of restrictive exploitation (2003–2014) (Wang, M.M., 2008). During the stage of over exploitation, the spring water level rapidly decreased while spring flux decayed, resulting in the stoppage of Baotu spring flow. In order to realize spring perennial gushing, negative measures of restrictive exploitation of groundwater are taken. The negative measures are that groundwater only accounts for 30% of urban citizen water supply, and the inferior Yellow River water accounts for 70% of urban water supply, while a lot of superior groundwater is not utilized rationally. In order to ensure that the spring flows normally and citizens are able to use superior groundwater, it is very necessary to study optimizing the exploitation of groundwater in Jinan City.

Jinan karst water system not only functions as a resource supply, but also involves in maintaining the ecological environment. Spring cutoff means destruction of the function of keeping the ecological environment, while artificial recharge combining

increasing exploitation is to restore the function of resource supply of the groundwater system.

Therefore, this article attempts to carry out developed and utilized research of superior groundwater based on artificial recharge. Applying the numerical model of visual modflow, the groundwater system of the Jinan spring area is simulated to optimize the layout of exploitation wells and recharge sites.

## 2 GEOLOGICAL BACKGROUND

Jinan City is located in the northern edge of the central Shandong mountainous region. The terrain of south is higher than that of north (Xu, J.X., 2012). From south to north, the main exposed formations are Archean Taishan Group (Art), Cambrian system of Palaeozoic era, Ordovician, Carboniferous and Quaternary strata in the Jinan spring area. The south that the limestone exposes is the main rainfall recharge zone of the spring area. The groundwater flowing to the north is blocked by the northern rock of Yanshanian, forming the karst large spring (Fig. 1) (Xu, J.X., 2012).

## 3 ESTIMATION OF THE NUMERICAL MODEL

### 3.1 Conceptualization of the aquifer

Boundary delineation of the model is based on hydrogeological conditions and structure, as shown in Figure 1. The boundary of the west is the Mashan fracture, and that of the east is the Dongwu fracture. The boundaries of the north are Jinan rock and formation of Carboniferous-Permian system, the south is the surface dividing line of Zhangxia and Xuzhuang group of middle Cambrian.

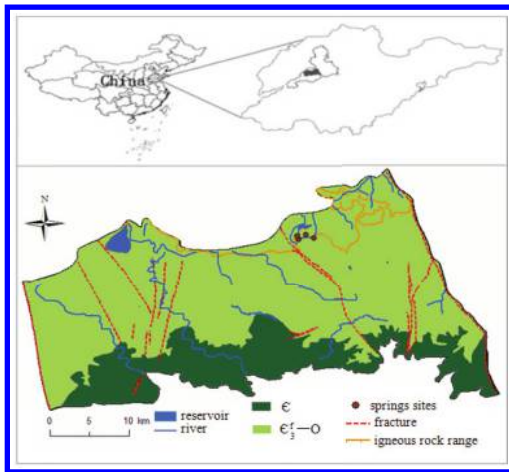


Figure 1. Geological scheme of the Jinan spring area.

Simulation area is conceptualized for three layers. The first layer that is unconfined water aquifer is mainly the formation of Holocene series and the upper Pleistocene series of the Quaternary system. Lithology of the aquifer is the formation containing medium-coarse sand and sand gravel rock. The second layer that is leaky formation is the clay layer beneath the bottom floor of the unconfined water aquifer. The third layer that is confined aquifer is the formation of the Zhangxia and Fengshan group of Cambrian and Quaternary strata. According to drill data, limestone is buried deeply. The depth of the model is about 600 m according to developed and utilized depth of karst water as well as development depth of karst.

According to the hydrogeological prospecting data of Jinan spring area, limestone layer mainly develops eroding fissure of network. Thus, fissure-karst aquifer medium is conceptualized for an anisotropic heterogeneous unsteady flow. In a word, fissure-karst aquifer system can be conceptualized for a confined three-dimensional unsteady flow of inhomogeneity and anisotropy.

### 3.2 Mathematical model building and discretization

The groundwater flow system is described by partial differential equations as follows on the condition that the elastic yield of aquitard is not considered (Xing, L.T., 2007).

$$\begin{cases} S \frac{\partial h}{\partial t} = \frac{\partial}{\partial x} \left( K_x \frac{\partial h}{\partial x} \right) + \frac{\partial}{\partial y} \left( K_y \frac{\partial h}{\partial y} \right) \\ \quad + \frac{\partial}{\partial z} \left( K_z \frac{\partial h}{\partial z} \right) + \varepsilon & x, y, z \in \Omega, t \geq 0 \quad (1) \\ h(x, y, z, t)|_{t=0} = h_0 & x, y, z \in \Omega, t \geq 0 \quad (2) \\ K_n \frac{\partial h}{\partial n} \Big|_{\Gamma_1} = q(x, y, t) & x, y, z \in \Gamma_1, t \geq 0 \quad (3) \\ K_n \frac{\partial h}{\partial n} - \frac{h - h_s}{\sigma} \Big|_{\Gamma_2} = 0 & x, y, z \in \Gamma_2, t \geq 0 \quad (4) \end{cases}$$

In the formula, the symbol is omitted.

Jinan spring area is subdivided into 6,800 cells, with each cell being square of 500 m × 500 m. Moreover, the number of cells of the simulation area is 3382, with the total area being 845.5 km<sup>2</sup> (Fig. 2).

### 3.3 Identification and calibration of the model

Identification period of model designation is from October 1, 2010 to September 30, 2011. The model



Figure 2. The graph of the grid subdivision.

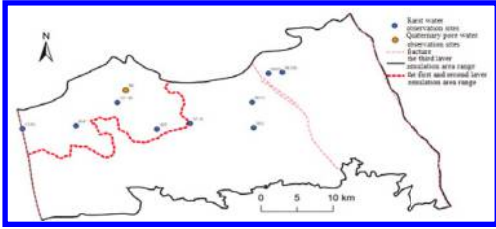


Figure 3. The distribution of observation points.

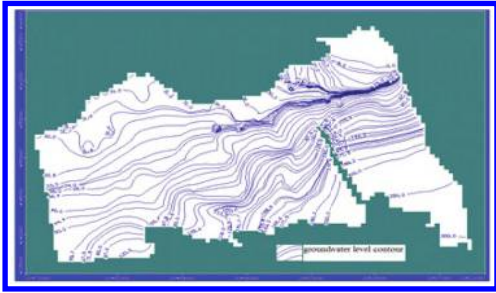


Figure 4. The simulating flow field of the identification period.

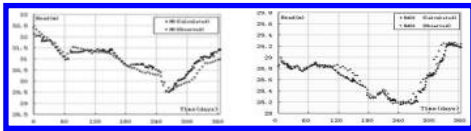


Figure 5. Simulating curves of the water level of the identification period.

conditions of flow field at the end of the simulating identification period. The total flow directions of the simulating flow field and the actual flow field are equivalent. The calculation of the hydraulic gradient is close to the real hydraulic gradient, and the simulating effect is great.

The matching flow yield (Fig. 6) and the duration curve (Fig. 7) of the calibration period are shown as follows.

The simulating flow field and the actual flow field are basically fit, with the total flow direction being equivalent (Fig. 6). The simulating model is fundamentally up to the precision requirement, meeting hydrogeological conditions, and basically reflects the hydraulic features of groundwater.

### 3.4 Reliability analysis of the model

#### 1. Analysis of matching error

Node error statistical table during the stage of model calibration is attained by comparing relative error of the actual and simulating water levels (Table 1).

Actual flow field and calculated flow field during the stage of identification and calibration are rather similar, with error being within the allowable range.



Figure 6. Matching flow field of the calibration period.

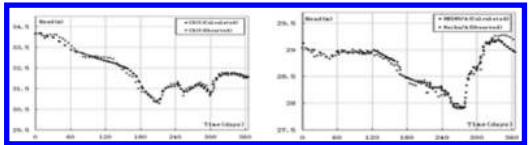


Figure 7. Matching curves of the water level of the calibration period.

calibration period is from October 1, 2011 to September 30, 2014. Figure 3 shows the locations of simulating observation holes.

The simulating flow yield (Fig. 4) and the duration curve (Fig. 5) of the identification period are shown as follows.

Simulating flow field basically reflects the trend and regulation of groundwater flowing from

Table 1. Statistical table of node error during the testing stage.

Error range	<2.0 m	2.0~5.0 m	>5.0 m
Node number	79	28	13
Ratio	65.83%	23.33%	10.83%

Furthermore, the trend of simulation water level and measured water table is relatively close. Therefore, it is regarded that the identification model and the actual hydrogeological model are basically fit.

## 2. Parameter evaluation

The model parameter value of the total calculation area is basically fit for data of single well pumping test. According to regional hydrogeological conditions and water abundance of aquifer, the simulation area is subdivided and the parameter is inverted by the calculation of the model. The inverted result is close to the result of the pumping test, the difference being about an order of magnitude. The hydrogeological parameter and subarea gained by the model inversion meet the actual hydrogeological conditions. The estimated model that the reliability is great can be used for prediction.

## 4 FEASIBILITY ANALYSIS OF RECHARGE

### 4.1 Necessity of recharge

The area of building region in Jinan City increased constantly from 1978 to 2012. The utilization of land makes roads harden, directly resulting in the decrease of the rainfall seepage recharge amount, the sedimentation of river, the recession of permeability of the riverbed as well as the reduction of the seepage amount of the river. Expansion of the city and hardness of the land surface is one of the factors that cause the decrease in the spring recharge amount.

According to the comparison and analysis of the calculation result (Table 2), the recharge resource amount decreased by 250,000 m<sup>3</sup>/d from 1960s to current year.

### 4.2 Groundwater transport conditions

According to the tracer test (Fig. 8), groundwater flow field and drilling data, it is concluded that groundwater hydrodynamic field characteristics of the Jinan karst water system mainly have four points. (1) The apparent groundwater velocity is different because fractured karst development is heterogeneity, the degree of karst development differs from different lithologies and different tectonic positions. (2) Groundwater storage space is very large because the location of high karst

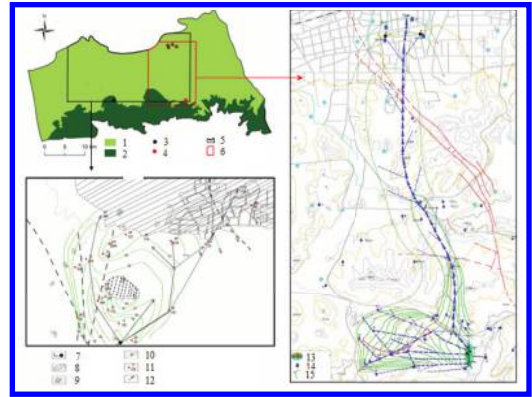


Figure 8. Time contour of the tracer spread to the peak and tracer migration path 1. C; 2. C<sub>3</sub>-O; 3&7. tracer release site (Cuima); 4&13. tracer release site (Quanlu); 5. tracer test range of Cuima; 6. tracer test range of Quanlu; 8. igneous rock range; 9. stagnant water area; 11&14. observation wells; 10&15. time contour of tracer spread to the peak; 12. the main direction of groundwater transport.

development is mainly the confluence discharge area, and karst development shape is given priority to honeycomb, reticular and holes. (3) Along the tectonic fracture zone and influence zone of fracture fissure, a good migration pathway of groundwater is formed, in which the apparent groundwater velocity is fast and the structural belt is the ideal source location. (4) Tectonic fracture zone is with good hydraulic conductivity, resulting in a good hydraulic connection between the Zhangxia group and Ordovician limestone, and recharging groundwater in Zhangxia limestone has an effect on spring protection.

### 4.3 Determination of recharge amount

The monthly variation of the water level was selected to be studied from 2008 to 2012. Monthly rainfall ( $x$ ) is represented as the horizontal coordinate and monthly variation of water level ( $y$ ) as the vertical coordinate. A scatter diagram is shown in Figure 9. It is not difficult to find a linear relation between them. The trend line is matched to show their relations. The corresponding equation is given as follows:

$$y = 0.0038x - 0.1411 \quad (5)$$

The multiple correlation coefficient ( $R^2$ ) is 0.6865.

Linear relation shows that a certain amount of rainfall can cause a certain amount of increase in the groundwater level. There is a rainfall threshold value causing the rise in the groundwater level.

Table 2. Chart of the recharge resource amount unit: 10,000 m<sup>3</sup>/d.

Stage	1960s	1970s	1980s	Current year
Resource amount	69.49	66.77	55.88	44.24

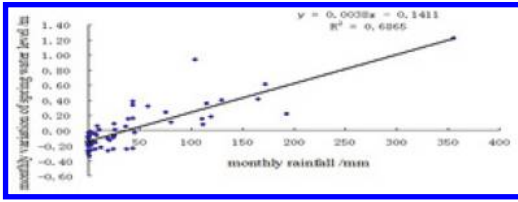


Figure 9. The correlation between variation of spring water level and rainfall in the monthly scale.

The intersection point of the linear equation and the x axis is 37.13 mm, which is the rainfall threshold value under the monthly scale. If monthly rainfall in the dry season is less than 37.13 mm, recharge needs to be done to keep the spring water steady. The 37.13 mm rainfall is converted into the recharge amount of groundwater, which is 290,000 m<sup>3</sup>/d. In other words, it is necessary to carry out groundwater recharge in order to keep the spring water table steady, and the recharge amount is 290,000 m<sup>3</sup>/d.

The 37.13 mm rainfall, which is a threshold value under the monthly scale, is different from the threshold value of the water level increase caused by single rainfall.

There are Yellow River water, Yangtze River water and local storm water in Jinan. The available water sources of recharge are relatively abundant.

#### 4.4 Determination of recharge location

Integration of strata, structure, permeability and recharge sources, main recharge locations are shown in Figure 11. Making full use of natural conditions, groundwater can be recharged by infiltration ditch and seepage of river.

### 5 RESTORATION OF THE KARST WATER SYSTEM

According to the case concerning groundwater being restrictively exploited in the spring region, adopting the condition of present artificial recharge (100,000 m<sup>3</sup>/d), acting measured rainfall as natural recharge, the predicting result shows that the water level in the annual low water season is less than the yellow warning water level of Baotu spring, which is 28.15 m. Furthermore, the water level in the dry season will be less than the orange warning water table, which is 27.6 m in the dry year when the frequency of rainfall is rather low (Fig. 10).

The principle reason is attributed to the decrease in the recharge area of rainfall infiltration, resulting in the reduction of rainfall recharge of groundwater. Thus, it is tough for the spring water level to be recovered at the historical level. If groundwater

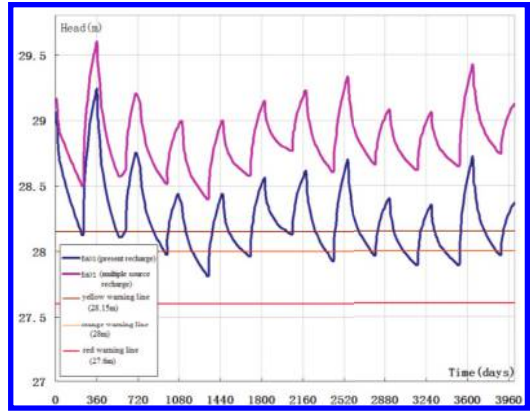


Figure 10. The forecasting curve of Baotu spring water level.

Table 3. The designation value of the recharge amount (10<sup>4</sup> m<sup>3</sup>/d).

Location	Recharge amount
①Beisha River	8
②Yufu River	14
③Fuxing cun-Xiaobaizhung	1.4
④Liyang Lake	1
⑤Xinglong	2
⑥Quanlu	0.3
⑦Jiangshuiquan	0.8
⑧Zhongjing	0.8
⑨Mengjia	1

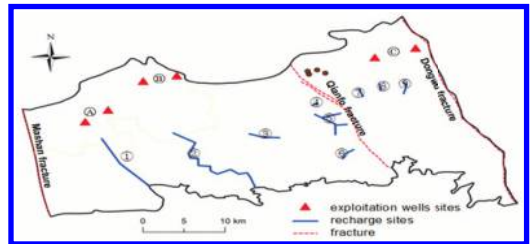


Figure 11. The graph of location of multiple recharge and exploitation.

exploitation is increased, it is inevitable for the spring to stop flowing in the dry season.

Given that the recharge amount is 290,000 m<sup>3</sup>/d that is attained by combining the above research, the permeability of recharge location, the recharge amount of designation (Table 3) and recharge locations (Fig. 11) are added to the model. Besides, the exploitation is increased in the spring area through the model to adjust, and the yellow warning water



Table 4. The optimizing exploitation amount ( $10^4$  m<sup>3</sup>/d).

Location	ⒶJixi	ⓔXijiao	ⓒDongjiao
Exploitation amount	12	3	2

level that is 28.15 m of urban spring serves as the controlling variable (warning water level is set by the department of protecting spring based on the elevation of spring vent by 26.9 m). Through repeated adjustment, the forecasting graph (Fig. 10) of the spring water level is gained finally, being able to ensure that the spring flows throughout the year, and the optimized schemes of exploitation is obtained, as shown in Figure 11 and Table 4.

## 6 SUMMARY

1. The fundamental reason for the stoppage of Jinan spring flow is the degradation of resource supply function of the karst water system under the anthropogenic influence. It is necessary to carry out artificial recharge in order to recover the spring's water level.
2. Spring water dynamic is the real-time appearance of profit and loss of the karst water system in the Jinan spring region. Regression analysis shows that keeping spring flowing under current conditions needs to increase the recharge amount to 290,000 m<sup>3</sup>/d.
3. Optimizing the calculation of the numerical simulation implies that by carrying out scientific artificial recharge, the exploitation amount in the spring area can be increased by 170,000 m<sup>3</sup>/d, which can protect the spring and water supply, and recover the natural functions of the karst water system.

## ACKNOWLEDGMENTS

This research was funded by the National Science Foundation of China (4117222, 41472216),

the Science and Technology Development of Jinan (201303082) and the Undergraduate Innovation Foundation of University of Jinan (YCXZ13004).

## REFERENCES

- Careghini, A. & Saponaro, S. & Sezenna, E. 2015. Lab-scale test and numerical simulations for in situ treatment of polluted groundwater. *Journal of Hazardous Materials* 287:162–170.
- Liu, Y.P. & Yamanaka, T. & Zhou, X. 2014. Combined use of tracer approach and numerical simulation to estimate groundwater recharge in an alluvial aquifer system: A case study of Nasunogahara area, central Japan. *Journal of Hydrology* 519:833–847.
- Qu, W.J. & Li, H.L. & Wan, L. 2014. Numerical simulations of steady-state salinity distribution and submarine groundwater discharges in homogeneous anisotropic coastal aquifers. *Advances in Water Resources* 74:318–328.
- Wang, M.M. & Shu, L.C. & Ji, Y.F. & et al. 2008. Causes of spring's of flux attenuation and simulation of spring's regime-A case in Jinan karst spring area. *Carsologica Sinica* 27(1):19–23.
- Wang, X.J. & Xie, Z.H. & Zhou, X. & et al. 2005. Simulation of artificial injection with large diameter wells in the western outskirts of Beijing. *Hydrogeology and Engineering Geology* (1):70–72.
- Xing, L.T. 2007. Study on exploitation layout of the Jinan karstic groundwater. *Yellow River* 29(2): 46–47.
- Xu, J.X. & Xing, L.T. & Wei, L.F. & et al. 2012. *Study on the karst water system in Jinan*. Beijing: Metallurgical Industry Press.
- Zhang, Y. & Jiao, J.N. & Li, F.C. & et al. 2014. Impact of groundwater recharge in underground reservoirs on groundwater production capacity. *South-to-North water transfers and water science & technology* 12(6):127–153.
- Zhao, C.Y. & Wang, Y.C. & Chen, X. & et al. 2005. Simulation of the effects of groundwater level on vegetation change by combining FEFLOW software. *Ecological Modelling* 187(3):341–351.

# Stability analysis of the cracks of the concrete gravity dam due to the explosion damage

C.D. Liu

*Nanjing Hydraulic Research Institute, Nanjing, China*

Z.J. Wang

*Changjiang Institute of Survey, Planning, Design, and Research, Wuhan, China*

Y. Xiang

*Nanjing Hydraulic Research Institute, Nanjing, China*

**ABSTRACT:** Many cracks appeared on the upstream face of Huangwo concrete gravity dam built in 1939 due to bomb explosion during the War in 1945. The cracks are not only harmful to the suitability and durability of the dam body, but also cause damage to the dam because of the unstable extension of the cracks. To determine the stability of the cracks on the upstream face of the dam, the theory of liner elastic fracture mechanics is applied to analyze the cracks. The result shows that the stress intensity factors of the crack tips are smaller than the fracture toughness of the concrete, indicating that the cracks remain stable. However, the monitoring of the cracks should be strengthened, and the treatment should be taken if the propagation of cracks is observed.

**Keywords:** concrete gravity dam; crack; explosion; stability; analysis

## 1 INTRODUCTION

Huangwo Reservoir was designed and constructed in China in 1939. This reservoir project consists of main dam, auxiliary dam, spillway and water duct. The main dam of the reservoir is gravel concrete

gravity dam. Dam upstream face is vertical above the elevation of 198.70 m, and it has a slope of 1:0.06 below that elevation. The downstream main dam slope is designed as step type with a slope of 1:0.7, and the main dam crest width is 5.0 m. The auxiliary dam is also designed as gravel concrete

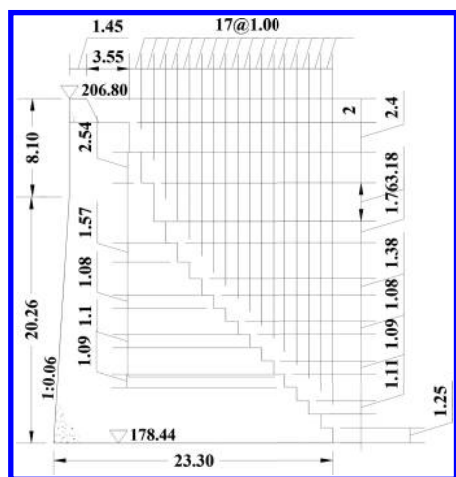


Figure 1. Typical cross-sectional view of the main dam.

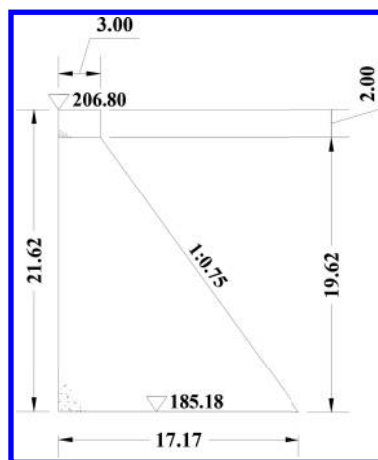


Figure 2. Typical cross-sectional view of the auxiliary dam.

gravity dam with a vertical upstream face and a slope of 1:0.75 for downstream face. The capacity of the reservoir is  $33.6 \times 10^4 \text{ m}^3$  and the dam crest elevation is 206.80 m. The maximum reservoir dam height is 28.21 m, and the cross-sectional views of the main dam and the auxiliary dam are shown in Figure 1 and Figure 2.

## 2 ONSITE OBSERVATION OF DAM CRACKS

The onsite checking was conducted on April 20, 2013, and it was found that cracks appeared on the upstream face of the dam. The cracks were mainly generated between concrete blocks and on the surface of concrete. In addition, the pitch part in the dam joints was aging. The locations of the cracks are presented in Table 1, and their distribution is shown in Figure 3. According to the introduction of administration staff of the reservoir, the dam cracks on the right bank was caused by the bomb blast in the reservoir area in 1945. The existing cracks not only are harmful to the safety, applicability and durability of the structure, but also induce structure destruction due to the unstable propagation of cracks. The computation and analysis are applied to the dam cracks based on the linear elastic fracture mechanics theory in this study, in order to understand the stability of cracks on the upstream face of the dam.

Table 1. Locations of the cracks on the upstream face of the dam.

Locations	Characteristics of cracks
Joint between the main dam and the auxiliary dam	1 crack at dam crest, with a length of about 1 m and a width of 2–5 mm 1 crack from dam crest downwards 2.2 m, inclined, with a length of 4 m and a width of 2–10 mm
Right of main dam	2 cracks on dam body, vertical, 2.3 m and 6.4 m away from the right of the main dam, with a width of 2–3 mm
Auxiliary dam	1 crack on dam body, vertical, 11 m away from the left of the auxiliary dam, with a width of 2–3 mm

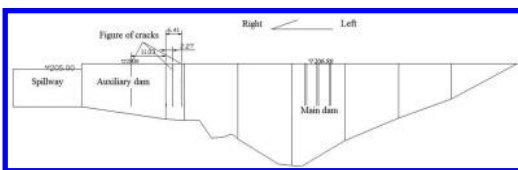


Figure 3. Distribution of cracks on the upstream face of the dam.

## 3 THEORY OF COMPUTATION

The purpose of control and determination of crack stability of the structure is to attain the Stress Intensity Factor (SIF) at crack tip under different external factors or influences. The fracture finite element method (Jiang, J.J. & Lu, X.Z. 2005; Jiang, H.D. 1992) adopted in this study is an efficient numerical method to solve the crack stability problem (Motsonelidze, A. et al. 2010; Jin, C. 2005; Das, R. & Cleary, P.W. 2013; Chen, Z.H., et al. 2006; Secchi, S. & Schrefler, B.A. 2012; Chahrour, A.H. & Ohtsu, M. 1994). The computation has two parts: one is to construct the singular element model that reflects the singularity, and to compute the SIF, i.e. stress intensity factor. The other part is to determine the fracture criterion based on the material fracture property, and to determine the stability and develop the pattern of cracks based on the criterion.

Three different basic combinations of fracture mode can be classified: Type I is the opening, Type II is the shearing and Type III is the tearing. The stress and displacement at crack tip can be expressed as follows:

$$\sigma_{ij} = \frac{K}{\sqrt{r}} f_{ij}(\theta), \quad u_i = K \sqrt{r} f_i(\theta) \quad (1)$$

where  $(r, \theta)$  is the polar coordinates with the crack vertex as the origin and  $f_{ij}(\theta)$  and  $f_i(\theta)$  are the decided functions for every type of crack.

The cracks on the upstream face of the reservoir dam can be decided as Type I, the opening crack, based on the onsite observation, and this type of crack is also the most common and dangerous crack.

The accuracy of displacement is usually higher than the stress in the finite element computation. Thus, the analysis was conducted using the stress intensity factor, which was computed from the displacement component in the fracture mechanics theory (Das, R. & Cleary, P.W. 2013). The equations of three-dimensional stress intensity factor derived from Williams' displacement expansion (Jiang, J.J. & Lu, X.Z. 2005) can be expressed as follows:

$$\left. \begin{aligned} K_I &= \lim_{r \rightarrow 0} \left[ \frac{\sqrt{2\pi E}}{4(1-\mu^2)} \cdot \frac{U'_i}{\sqrt{r_i}} \right] \\ K_{II} &= \lim_{r \rightarrow 0} \left[ \frac{\sqrt{2\pi E}}{4(1-\mu^2)} \cdot \frac{V'_i}{\sqrt{r_i}} \right] \\ K_{III} &= \lim_{r \rightarrow 0} \left[ \frac{\sqrt{2\pi E}}{4(1-\mu)} \cdot \frac{W'_i}{\sqrt{r_i}} \right] \end{aligned} \right\} \quad (2)$$

where  $E$  is the modulus of elasticity of the material;  $\mu$  is Poisson's ratio; and  $U'_i, V'_i, W'_i$  are displacements at node  $i$  perpendicular to the crack extended direction,

along the crack shearing direction and along the crack tearing direction respectively.  $r_i$  is defined as the distance between the node  $i$  and the crack tip.

Normally, the above displacements  $\{U', V', W'\}_i^T$  at node  $i$  on crack sides are not the displacements  $\{U, V, W\}_i^T$  in the global coordinates. The local coordinates  $x', y', z'$  at the crack tip can be built up to derive their relationships. The transforming relationships between global coordinates and local coordinates are shown in Figure 4.

$$\begin{Bmatrix} x' \\ y' \\ z' \end{Bmatrix} = \begin{bmatrix} l_1 & m_1 & n_1 \\ l_2 & m_2 & n_2 \\ l_3 & m_3 & n_3 \end{bmatrix} \begin{Bmatrix} x \\ y \\ z \end{Bmatrix} \quad (3)$$

$$\begin{Bmatrix} U' \\ V' \\ W' \end{Bmatrix} = \begin{bmatrix} l_1 & m_1 & n_1 \\ l_2 & m_2 & n_2 \\ l_3 & m_3 & n_3 \end{bmatrix} \begin{Bmatrix} U \\ V \\ W \end{Bmatrix} \quad (4)$$

where  $l_j, m_j, n_j$  ( $j = 1, 2, 3$ ) are the angle cosine between  $x, y, z$  and  $x', y', z'$ , respectively.

The extrapolation method (Jiang, H.D. 1992) is adopted to calculate the stress intensity factor based on the complexity of the project. The values at tips  $K_I, K_{II}, K_{III}$  are determined by extrapolating stress intensity at  $n$  nodes, which are not singularity elements on crack sides, and the equations are given in detail as follows:

$$K_I = \frac{\sqrt{2\pi E}}{4n(1-\mu^2)} \left[ \begin{aligned} & \sum_{j=1}^n \frac{U'_j - U'_0}{\sqrt{r_j}} \\ & - \frac{n \sum_{j=1}^n (U'_j - U'_0) \sqrt{r_j} - \sum_{j=1}^n r_j \cdot \sum_{j=1}^n \frac{(U'_j - U'_0)}{\sqrt{r_j}}}{n \sum_{j=1}^n r_j^2 - \left( \sum_{j=1}^n r_j \right)^2} \cdot \sum_{j=1}^n r_j \end{aligned} \right] \quad (5)$$

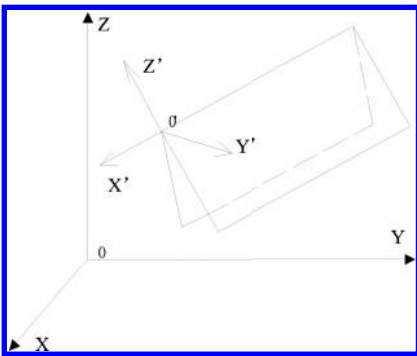


Figure 4. Transforming relationships between global coordinates and local coordinates.

$$K_{II} = \frac{\sqrt{2\pi E}}{4n(1-\mu^2)} \left[ \begin{aligned} & \sum_{j=1}^n \frac{(V'_j - V'_0)}{\sqrt{r_j}} \\ & - \frac{n \sum_{j=1}^n (V'_j - V'_0) \sqrt{r_j} - \sum_{j=1}^n r_j \cdot \sum_{j=1}^n \frac{(V'_j - V'_0)}{\sqrt{r_j}}}{n \sum_{j=1}^n r_j^2 - \left( \sum_{j=1}^n r_j \right)^2} \cdot \sum_{j=1}^n r_j \end{aligned} \right] \quad (6)$$

$$K_{III} = \frac{\sqrt{2\pi E}}{4n(1+\mu)} \left[ \begin{aligned} & \sum_{j=1}^n \frac{W'_j - W'_0}{\sqrt{r_j}} \\ & - \frac{n \sum_{j=1}^n (W'_j - W'_0) \sqrt{r_j} - \sum_{j=1}^n r_j \cdot \sum_{j=1}^n \frac{(W'_j - W'_0)}{\sqrt{r_j}}}{n \sum_{j=1}^n r_j^2 - \left( \sum_{j=1}^n r_j \right)^2} \cdot \sum_{j=1}^n r_j \end{aligned} \right] \quad (7)$$

where  $U'_0, V'_0, W'_0$  are the displacement components at crack tip in local coordinates, and  $n$  is the chosen extrapolated points.

## 4 STABILITY ANALYSIS OF CRACKS

### 4.1 Finite element model

In order to better understand the causation and stability of crack, the Finite Element Method (FEM) model was established based on the properties and cracks distribution of the reservoir dam. The model satisfies the accuracy requirement of the project. Figure 5 shows the finite element

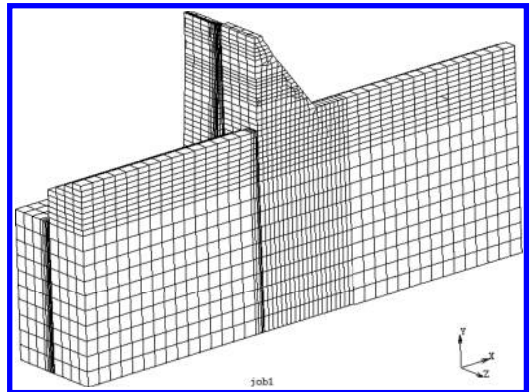


Figure 5. The FEM model for the joint part of the main dam and the auxiliary dam.

model and Figure 6 shows the local refined finite element model.

The three-dimensional finite element model was constructed for the joint part of the reservoir main dam and auxiliary dam, where many cracks appeared. The computation domain extended to a distance 1.5 times of the dam height from the dam body to both upstream and downstream, and 1 time of dam height towards the dam base. The meshes are generated using isoparametric elements with hexahedral eight nodes, and a serious crack on the joint part of the reservoir main dam and auxiliary dam and a typical crack on the main dam itself were considered in the mesh generation. There are 13,957 elements and 16,616 nodes in total in the finite element model. The nodes in crack were set with 1/4 of crack side interval in order to compute the stress intensity factor at crack tip, and then to determine the crack stability.

#### 4.2 Parameters

The model parameters are listed in Table 2.

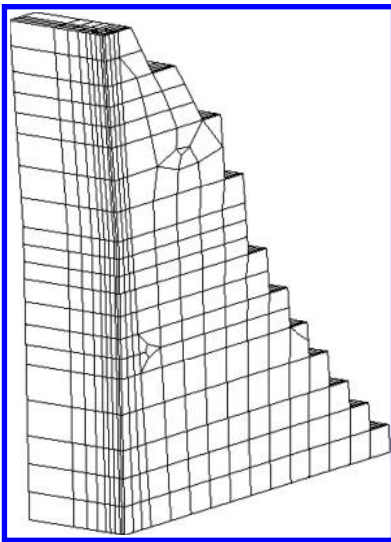


Figure 6. Local FEM model.

Table 2. The model parameters.

Material	Specific gravity, $\gamma/\text{kN/m}^3$	Modulus of elasticity, $E/\times 10^{10} \text{ Pa}$	Poisson's ratio, $\nu$
Mass concrete of the dam	24.00	2.00	0.167
Rocks of foundation	22.00	1.00	0.220

#### 4.3 Loadings of operating condition

The normal water level in the reservoir is adopted as the operating condition for computation, which includes the loadings of self-weight of the dam body, the reservoir water pressure and the uplift pressure.

#### 4.4 Crack stability criterion

The stress intensity factor of type  $K_I$  is analyzed because the cracks on the upstream face of the reservoir dam are the opening type cracks. According to the relationships between  $K_I$  and fracture toughness  $K_{IC}$ , the stability criterion of crack can be determined as follows:

$$\begin{aligned} K_I < K_{IC} & \quad \text{No propagating crack} \\ K_I = K_{IC} & \quad \text{Critical crack} \\ K_I > K_{IC} & \quad \text{Propagating crack} \end{aligned} \quad (8)$$

where  $K_{IC}$  is the fracture toughness of crack type I.

$K_{IC}$  is determined through the experiment. However, the equation from the literature (Jiang, H.D. 1992) is adopted in this study due to the lack of fracture experimental data of this dam. The equation is expressed as follows:

$$K_c = 0.28 k f_c \quad (9)$$

where  $f_c$  is the strength of the concrete cube; 0.28 is the coefficient; and  $k$  is adopted as 1.9 for mass concrete based on the influence of concrete dimension.

The fracture toughness  $K_c = 1.33 \text{ MPa} \cdot \text{m}^{1/2}$  can be obtained using Equation (9) for those typical cracks on the main dam and the upstream face of the joint part of the reservoir main dam and auxiliary dam.

#### 4.5 Results and discussion

The normal water level in the reservoir is chosen as the operating condition and the depth of crack is used by the estimated value. Since the cracks on the upstream face of the reservoir dam are opening type, the stress intensity factors of two typical cracks (one at the joint part of the main dam and the auxiliary dam and the other one on the main dam) were calculated under the operating condition. The stress intensity factor of crack at the joint part of the main dam and the auxiliary dam is  $0.467 \text{ MPa} \cdot \text{m}^{1/2}$  and a value of  $0.762 \text{ MPa} \cdot \text{m}^{1/2}$  is for the crack stress intensity factor on the main dam.

Therefore, the stress intensity factors of the two typical crack tips chosen are both smaller than the fracture toughness of mass concrete, with large values of safety coefficient. The cracks on the dam are at a stable state.

## 5 CONCLUSIONS

Cracks on the upstream face of the reservoir concrete gravity dam were caused by the bomb blast when Japanese troops retreated. The cracks were generated due to damage caused by humans, and their unstable propagation would affect the integrated dam safety system. The computation results based on the linear elastic fracture mechanics theory in this study show that the stress intensity factors at typical crack tips are smaller than the concrete fracture toughness with large values of safety coefficient, which indicates that those cracks on the dam are at a stable state. However, monitoring for the cracks is still suggested and the treatment must be done quickly if there is an observed propagation of cracks.

## ACKNOWLEDGMENT

This paper was supported by the National Natural Science Foundation of China (Grant Nos. 51209145, 51179108, 51209144) and the Fundamental Research Funds of Nanjing Hydraulic Research Institute (Grant Nos. Y715011, Y715005).

## REFERENCES

- Chahrouh, A.H. & Ohtsu, M. 1994. Crack growth prediction in scaled down model of concrete gravity dam. *Theoretical and Applied Fracture Mechanics* 21(1): 29–40.
- Chen, Z.H., Feng, J.J. Li, L. & Xie, H.P. 2006. Fracture analysis on the interface crack of concrete gravity dam. *Key Engineering Materials* 324–325: 267–270.
- Das, R. & Cleary, P.W. 2013. A mesh-free approach for fracture modelling of gravity dams under earthquake. *International Journal of Fracture* 179: 9–33.
- Jiang, H.D. 1992. Advanced numerical method and program in hydraulic structure engineering and geotechnical engineering. Nanjing: Hohai University Press.
- Jiang, J.J. & Lu, X.Z. 2005. Finite element analysis of concrete structures, Beijing: Tsinghua University Press.
- Jin, C., Soltani, M. & An, X. 2005. Experimental and numerical study of cracking behavior of openings in concrete dams. *Computers & Structures* 83(08): 525–535.
- Motsonelidze, A., Raoof, M. & Abuladze V. 2010. Prediction of concrete dam's reserve strength based on it's past loading history. Romeo Garcia et al (ed.), *Dam Maintenance and Rehabilitation II—Proceedings of the 2nd International Congress on Dam Maintenance and Rehabilitation*.
- Secchi, S. & Schrefler, B.A. 2012. A method for 3-D hydraulic fracturing simulation. *International Journal of Fracture* 178: 245–258.

# Optimization of irrigation mode with brackish water for winter wheat in shallow groundwater areas based on the FEFLOW model

G.B. Pang & Z.H. Xu

*School of Resources and Environment, University of Jinan, China*

S. Zhang

*Handun Irrigation Management Bureau of Binzhou City, China*

**ABSTRACT:** The rational development of shallow underground brackish water for agricultural irrigation can not only solve the problem of water shortage, but also descend the underground water level to reduce the soil secondary salinization hazards. In this paper, we select the Yellow River Delta as the study area, where freshwater is in short supply, groundwater is shallow, and the soil water and salt movement are active. In order to investigate the most applicable irrigation schedule with saline water (2–5g/L) for winter wheat in the area, a validated Finite Element Subsurface FLOW System (FEFLOW) model was used to evaluate the effect of various brackish water irrigation modes on soil moisture, salt balance, crop growth and groundwater table. The simulated results indicated that the optimal irrigation schedule of winter wheat was that: 1) the key time of irrigation was needed with enough saline water; 2) two times of irrigation were needed with saline water mixed with freshwater; 3) three or four times of irrigation were needed with alternate of saline water and freshwater. This paper can provide a scientific basis for reasonable exploitation and sustainable utilization for agricultural water and soil resources in the Yellow River Delta.

**Keywords:** FEFLOW; brackish water; irrigation system; soil salinity; Yellow River Delta

## 1 INTRODUCTION

The development of poor quality water (brackish water and alkaline water) for irrigation has become an important method to solve the shortage of agricultural water resources. In the Yellow River Delta, which belongs to the warm temperate semi-humid continental monsoon climate zone, the Yellow River water is the main water resources in the area, accounting for more than 90%, and the agriculture mainly depends on irrigation from the Yellow River. In recent years, the Yellow River water has decreased, and the agricultural irrigation water is facing severe challenges. According to statistics, the brackish groundwater resources are rich in the area, and the groundwater is shallow, and also easily exploited<sup>[1]</sup>. Therefore, the development of poor quality water for irrigation has become an important method to solve the shortage of agricultural water resources in this area.

In the late 1970s, the FEFLOW (Finite element subsurface FLOW system) software based on the finite element method was exploited by WASY water resources planning and Research Institute in Germany. The software can be used to simulate in a porous medium saturated and unsaturated

groundwater flow and contaminant transport, which is also widely used in groundwater environment numerical simulation, groundwater evaluation and management<sup>[2–6]</sup>. However, the FEFLOW model was used to simulate the dynamics of the groundwater table and soil salinity migration under different irrigation modes, and the simulation of irrigation management was less. In this paper, we select the Yellow River Delta as the study area, where freshwater is in short supply, groundwater is shallow, and the soil water and salt movement are active. Based on the FEFLOW software, the simulation model of water flow and solute transport numerical of Wuqi irrigation district was established. Moreover, the model was applied to simulate the brackish water irrigation scheme of winter wheat, which is helpful to establish the appropriate brackish water irrigation mode for winter wheat in the Yellow River Delta.

## 2 MATERIALS AND METHODS

### 2.1 Overview of the study area

The Wuqi irrigation district is located in the north-east of Kenli, Dongying city, Shandong province, east longitude 118°38'–118°57', north latitude

37°40′~37°43′, the Yellow River as the boundary in west, north, south, and the east to the moisture-proof dam. Climate change of the seasons is obvious, and rainfall mainly concentrated in July and August, accounting for 70% of the year. The average annual evaporation precipitation ratio is as high as 3.22. The coastal saline fluvo aquic soil is the main type of soil type in this area. The groundwater is shallow, mostly between 1.4 and 2.4m, and the average salinity is up to 32.4 g/L, thus the seasonal change in the groundwater depth and salinity is significant.

## 2.2 Field sample collection and analysis

The continuous block of a relatively flat terrain (about 4.1km long, 1.1 to 1.6 km width, about 520 hm<sup>2</sup>) was selected as the study area, and we selected three samples from the center of the study area, and each point was stratified sampling of 0~20 cm, 20~40 cm, and 40~60 cm, 60~80 cm. The time is mid-July, late October in 2011, and mid-January, mid-May, late September in 2013, when the soil moisture and salt movement are active, also the variation of the groundwater table is obvious.

Soil samples were sieved through a 2mm sieve after air-drying, and mixed with water at a 1:5 ratio, followed by sucking filtration and leaching extraction of soil solution. The measurement of the soil samples including the cation Ca<sup>2+</sup>, Mg<sup>2+</sup>, Na<sup>+</sup>, K<sup>+</sup>, the anion HCO<sub>3</sub><sup>-</sup>, CO<sub>3</sub><sup>2-</sup>, SO<sub>4</sub><sup>2-</sup>, Cl<sup>-</sup>, total salt content, conductivity and pH was made. Among them, the pH value was measured by PHSJ-5, conductivity by the conductivity meter DDS-307, CO<sub>3</sub><sup>2-</sup> and HCO<sub>3</sub><sup>-</sup> by double indicator titration, Cl<sup>-</sup> by AgNO<sub>3</sub> titrimetry, SO<sub>4</sub><sup>2-</sup> by EDTA Indirect Titration, Ca<sup>2+</sup> and Mg<sup>2+</sup> by EDTA complexometric titration, and K<sup>+</sup> and Na<sup>+</sup> by the subtraction method.

## 3 ESTABLISHMENT AND VERIFICATION OF THE MODEL

### 3.1 Model establishment

According to the hydrological geological conditions of Wuqi irrigation district, non-confined aquifer can be divided into two layers: one layer of soil for planting; the other layer is saline aquifer. Saline aquifer is set to weak aquifer, and the bottom is waterproof floor. The free water surface of phreatic aquifer was set as the upper boundary, which can accept infiltration recharge, river supplement, and evaporation discharge. Meanwhile, the interception of 5m depth was set as the lower boundary, which is an impermeable boundary. The study area can be generalized as the groundwater flow system of non-steady homogeneous, isotropic horizontal direction. Therefore, FEFLOW

software was applied to the Wuqi irrigation district to conduct the unsaturated and saturated flow numerical simulation in the paper.

### 1. Area partition

The study area was divided into 107052 grids by the automatic triangulation principle of FEFLOW software, also into 73564 grid nodes (Fig. 1). Owing to the study area and land use types being single, besides the observation hole on the network nodes, there were no local features encrypted.

### 2. Stress period

The simulation period of the numerical model from January to December in 2010, a full calendar year, was divided into 12 stress periods, with each stress period corresponding to a month. At each stress period, the balance items, including recharge and discharge input conditions, do not change, with January as the initial flow field of the model, and December as the terminal flow field.

### 3. The model parameters and input items

① Rainfall infiltration replenishment, calculated by the infiltration replenishment coefficient method.

$$R_p = \alpha P_e; P_e = \beta P \quad (1)$$

where  $R_p$  is the quantity of rainfall infiltration replenishment, mm;  $P_e$  is the effective rainfall, mm;  $\alpha$  is the coefficient of rainfall infiltration replenishment, taken as 0.2;  $\beta$  is the effective utilization coefficient, when the rainfall is less than 5mm,  $\beta$  is 0, when the rainfall is larger than 5mm,  $\beta$  is 0.8; and  $P$  is the rainfall.

② The irrigation infiltration replenishment. Irrigation mainly depends on the Yellow River, and flooding irrigation is the traditional irrigation method. The irrigation time is from March to April when winter wheat is at the reviving stage and jointing stage. Furthermore, autumn irrigation is carried out

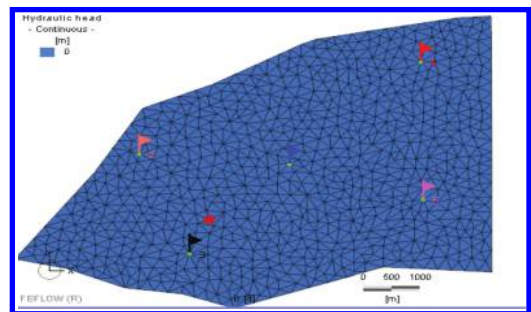


Figure 1. Grid partition graph of Wuqi irrigation district.



during harvest to freezing for salt leaching and moisture conservation of soil, usually in mid to late November. Referring to previous research results, the irrigation replenishment coefficient is 0.5.

- ③ Groundwater evapotranspiration is calculated by the groundwater evapotranspiration coefficient method as follows:

$$E = CE_0 \quad (2)$$

where  $E$  is the groundwater evapotranspiration of the quaternary pore aquifer;  $C$  is the groundwater evapotranspiration coefficient and  $E_0$  is the water surface evaporation.

The soil layer of the area is single, so we take the average of various depths as the groundwater evapotranspiration coefficient. It is ignored when the groundwater depth is more than 2.5m. Calculation of the groundwater evapotranspiration coefficient with different groundwater depths and crops cover conditions are presented in Table 1.

- ④ Solute transport parameters

Selecting the total salinity as a typical pollution ion, all inflow boundaries are given concentration values. At the same time, due to low salinity of surface water and groundwater for irrigation, we deal with the net recharge solute concentration in the model. Solute transport parameters include the retardation factor  $R_p$ , the decay coefficient  $\lambda$  and the hydrodynamic dispersion coefficient  $D$ . The simulation object is salt, which is composed of chemical group that can easily migrate and has no porous medium solid phase adsorption, so  $R_p$  is 1 in the model, and there is no attenuation in the salt migration process, so

$\lambda$  is 0, and the mechanical dispersion is much smaller than the mechanical dispersion, so  $D$  can be ignored.

- ⑤ Aquifer characteristic parameters

In the model, the aquifer characteristic parameters include the permeability coefficient and the specific yield, which referred to the existed pumping test parameters in the Yellow River irrigation district.

### 3.2 Model verification

- 1. The simulation of groundwater table

In order to identify the hydrogeological conditions, adjustment is made for the hydrogeological parameters, supply and drainage items, and fitting the groundwater dynamic process. The supplements of the model are rainfall and irrigation infiltration replenishment, while groundwater evapotranspiration and drainage are the major discharge parameters. We select the groundwater table dynamic process from January to December 2010 as the simulation object for the validation of the model (Fig. 2). According to the significance testing of the groundwater table between the simulated value and the observed value, the model has a significant correlation at the level of  $P = 0.05$ ; therefore, the simulation model can fit the hydrogeological conditions of the study area.

Table 1. The statistics of the groundwater evapotranspiration coefficient.

Month	Depth/m					Average
	0.5	1	1.5	2	2.5	
September	0.75	0.59	0.56	0.38	0.21	0.5
October	1.1	0.77	0.53	0.17	0.06	0.53
November	0.66	0.56	0.53	0.42	0.29	0.49
December	0.78	0.59	0.42	0.25	0.2	0.45
January	0.78	0.59	0.42	0.25	0.2	0.45
February	0.78	0.59	0.42	0.25	0.2	0.45
March	0.52	0.42	0.31	0.16	0.11	0.3
April	1.74	1.6	1.07	0.51	0.43	1.07
May	1.86	1.98	1.71	1.1	1.08	1.55
June	0.45	0.45	0.44	0.24	0.3	0.38
July	1.28	1.04	1.02	1.09	0.35	0.96
August	1.28	1.04	1.02	1.09	0.35	0.96

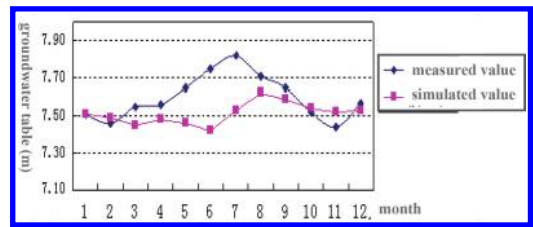


Figure 2. Simulation of the groundwater table dynamic process.

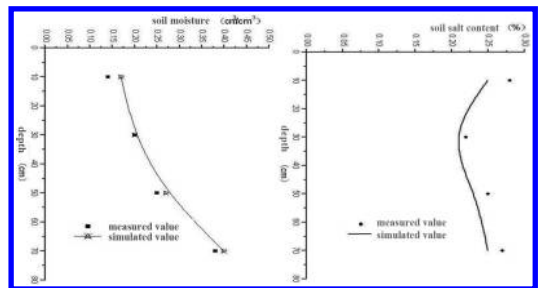


Figure 3. Simulation of soil moisture and soil salt content.

Table 2. Proposed irrigation scheme for winter wheat.

Irrigation scheme	Seeding to wintering	Reviving stage	Jointing to booting	Heading to filling
Scheme 1	Freshwater		Brackish water	
Scheme 2.1	Freshwater		Freshwater	Brackish water
Scheme 2.2	Freshwater		Brackish water	Brackish water
Scheme 3.1	Freshwater	Brackish water	Freshwater	Brackish water
Scheme 3.2	Freshwater	Freshwater	Brackish water	Brackish water

## 2. The simulation of solute transport

In the solute model, dynamic terms included irrigation infiltration, rainfall infiltration, salt exclusion, and groundwater evapotranspiration. Owing to the different concentrations of dynamic terms in each period in the area, we took the initial leaching concentration of soil moisture and salt content of 0–80cm measured in July 15, 2011 as the initial term, and the simulation and identification of the solute model in October 30, 2011 (Fig. 3). From the overall perspective, the soil moisture and salt content values of the simulation are consistent with the measured value, and the significance testing shows that the simulated and measured values are significantly correlated at the  $P = 0.01$  level, which suggest that the model is reliable and the parameters are reasonable. So, the model can be used to simulate the water and salt dynamic of long sequence.

## 4 SIMULATION OF BRACKISH WATER IRRIGATION MODE FOR WINTER WHEAT

### 4.1 Proposed irrigation scheme

Generally, there are five technical indices in the formulation of the brackish water irrigation system, respectively: ① the irrigation water salinity is less than 5g/L; ② perfect field drainage engineering; ③ each net irrigation is more than 750m<sup>3</sup>/hm<sup>2</sup>; ④ irrigation frequency is 2 to 3 times; ⑤ irrigation for wheat after the jointing stage. The investigation showed that the existing irrigation mode in Wuqi irrigation district can meet the five technical indices.

According to the existing irrigation system for winter wheat, combined with the freshwater from the Yellow River (salinity is less than 1g/L) and local brackish groundwater (salinity is 2 to 5g/L), three kinds of irrigation scheme were designed (Table 2). Scheme 1 includes seeding to overwintering irrigation water from the Yellow River, turning green to jointing irrigation of local brackish water; scheme 2 includes “two freshwater and one saline water” (seeding to wintering, jointing to heading

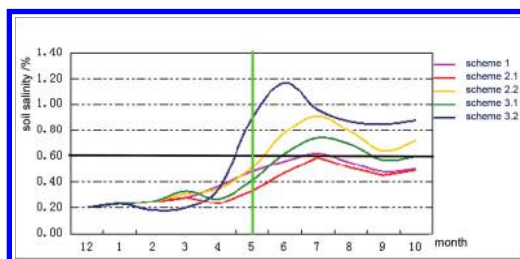


Figure 4. Soil salinity simulation under saline water irrigation.

stage irrigation water from the Yellow River, reviving to jointing stage irrigation of local brackish water), “one freshwater and two saline water” (only in seeding to wintering irrigation water of the Yellow River); scheme 3 include “alternative irrigation of freshwater and saline water” and “irrigation of freshwater and saline water, respectively”. In addition to scheme 1, jointing stage irrigation quota is 1200m<sup>3</sup>/hm<sup>2</sup>; the other irrigation quota is 750 m<sup>3</sup>/hm<sup>2</sup>. The solute transport model can simulate and forecast the soil salinity of the brackish water irrigation system, which can help to determine the optimal brackish water irrigation mode in the research area.

### 4.2 Analysis of the simulation results

We took the suitable soil salt content (seedling stage was 0.2%, from the jointing to filling stage was 0.6%) as the reference standard, and the average soil salt content of 0–80cm layer was simulated under different brackish water irrigation modes. As shown in Figure 4, the green line (late May) is the mature period of winter wheat, and the black line (salt content 0.6%) represented the limited soil salt content in the winter wheat growth period. As can be seen, the soil salt content can maintain a suitable growth level in the growth period under the irrigation mode of Scheme 1, Scheme 2.1 and Scheme 3.1. However, in the brackish water irrigation from the wheat jointing to heading stage, as carried out in Scheme 2.2 and Scheme 3.2, the soil salt content exceeded the crop salt tolerance,

which will lead to winter wheat reduction or death. Therefore, it is determined by the winter wheat soil salt tolerance that the three irrigation modes are conducive to winter wheat growth, including one-time irrigation filled with brackish water in the key stage, irrigation of brackish water mixed with freshwater, and alternative irrigation of brackish water and freshwater.

## 5 DISCUSSION AND CONCLUSION

1. Based on the FEFLOW software, the model of water flow and solute transport numerical of Wuqi irrigation district was established, and the model parameters were calibrated and verified by the experimental data of winter wheat in this area. The significance testing showed that the simulated and measured values are significantly correlated, which suggest that the model is reliable and the parameters are reasonable; therefore, the model can be used to simulate the water and salt dynamic of long sequence in the Yellow River Delta.
2. We applied the model to simulate the groundwater table and soil salt content under different brackish water irrigation modes. Three irrigation modes are conducive to winter wheat growth in this area, including one-time irrigation filled with brackish water in key time, irrigation of brackish water mixed with freshwater, and alternative irrigation of brackish water and freshwater.
3. Freshwater can be saved when brackish water is used; however, the soil cannot receive sufficient leaching, and the salt will accumulate in the root layer after several years, which will cause irreversible soil secondary salinization. Therefore, in order to maintain soil fertility, when the brackish water irrigation mode is used after 3 to

5 years, it is necessary to flush the soil by freshwater from the Yellow River.

## ACKNOWLEDGMENTS

This work was financially supported by the Shandong Natural Science Foundation (No. ZR2014EEQ020) and the Shandong Water Conservancy Science and Technology Practice Project (No. SDSLKY201306, SDSLKY201502).

## REFERENCES

- [1] Pang G.B. Zhang B.X. & Zhang S. 2014. Analysis of agricultural water utilization level in the Yellow River Delta. *Journal of University of Jinan* 28 (6): 416–420. (in Chinese).
- [2] Zhao C.Y. Wang Y.C. & Li B.G. 2003. Coupling relationship between vegetation evolution and groundwater flow in internal continent basin. *Journal of Hydraulic Engineering* 34 (12): 59–65. (in Chinese).
- [3] Huo Z.L. Feng S.Y. Kang S.Z. & Jiang J. 2009. Application of ANN and FEFLOW model to simulate groundwater level variation in arid inland area. *Journal of Hydraulic Engineering* 40(6): 724–728. (in Chinese).
- [4] Zhang J.H. Yu F.R. & Li Z.P. 2011. Application of FEFLOW in numerical simulation of groundwater in Huanglong Industrial Park. *Yellow River* 33(6): 22–23. (in Chinese).
- [5] Scibek J. Allen D.M. Cannon A.J. & Whitfield P.H. 2007. Groundwater–surface water interaction under scenarios of climate change using a high-resolution transient groundwater model. *Journal of Hydrology* (333): 165–181.
- [6] Ma L. Wei X.M. & Bao A.M. 2012. Simulation of groundwater table dynamics based on Feflow in the Minqin Basin, China. *Journal of Arid Land* 4(2): 123–131.

# Seepage analysis of human earth-rock dam during a flood

C.D. Liu & J.Z. He

Nanjing Hydraulic Research Institute, Nanjing, China

Z.J. Wang

Changjiang Institute of Survey, Planning, Design, and Research, Wuhan, China

**ABSTRACT:** Human Reservoir encountered the design flood of 100 years return period after operating five years on the basis of the dam reinforcement. As a result, the dam operates safely. The seepage field evolution of the dam core wall is investigated through analyzing the observational data of seepage behavior for the earth-rock dam during the flood. The anti-seepage effect of the core wall encountering the flood is evaluated according to the water level of several typical cross sections of the dam. And the seepage behavior for the dam under different loads is analyzed by using finite element numerical computation. The results indicate the seepage behavior of the dam is safe. However, several weak links in the seepage safety control of the dam are pointed out. The research provides guidance for the safety operation and management of such type of reservoir dams during a flood.

**Keywords:** earth-rock dam; flood; seepage; observational data; finite element analysis

## 1 INTRODUCTION

Human Reservoir (Xiang, Y. & Liu, C.D. 2012) locates in the east of Wenling City, China, which is a medium reservoir with multiple utilizations: mainly for water supply, but also for irrigation, hydropower and aquaculture. The design flood of the reservoir is a hundred year return period and the check flood is a thousand year return period. The total reservoir capacity is  $3.453 \times 10^7 \text{ m}^3$ . The reservoir project is consisting of the dam, spillway, drainage culvert, tunnel and power plant. The dam is a loess core dam with a dam crest length of 206.0 m and the maximum height of 20.60 m. The clay core wall crest has an elevation of 23.50 m and the width of 3 m. The width is 5 m at the elevation of 17.50 m and below that elevation, the upstream face of core wall has a slope of 1:2 and the downstream face has a slope of 1:1.5. The rest outside the core wall of the dam is sandy loam.

## 2 THE FLOOD

The reservoir dam after the reinforcement in 2005 has served for many years and met a flood in July, 2010. The water level in reservoir on 15 May, 2010 was 20.66 m and the rain started in reservoir area from 21 July, 2010. The water level reached 19.97 m on 24 July, 2010 while the normal water level was 20.47 m. Heavy rainfall happened on 26 July, 2010

with a precipitation of 255.3 mm on that day. The water level of the reservoir increased dramatically. The water level was 20.90 m at 14:30 on 26 July, 2010 and was 21.30 m at 00:30 on 27 July, 2010. Then the water level was only 0.67 m away from the design flood level (21.97 m). At 02:30 on 27 July, 2010, the water level of the reservoir reached the maximum value 21.41 m and later returned to the normal. At 05:10 on 27 July, 2010 the water level was 21.37 m and then came back to 20.26 m on 28 July, 2010.

## 3 THE OBSERVATIONAL DATA OF SEEPAGE

### 3.1 Dam seepage behavior before the flood

The time series of seepage pressure information before the flood can be seen in [Figure 1](#) and [Figure 2](#).

1. The reservoir water level is the main factor to influence the dam seepage pressure. The seepage pressure increases with a higher reservoir water level and vice versa.
2. From the arrangement of the piezometers, those piezometers set up before the core wall have better correlation with reservoir water level, and they almost change synchronously. For instance, the measured piezometer values in U1-1A, U1-2A and U1-3A, which set at elevation 15.00 m with a spacing of 9.5 m, have high correlation

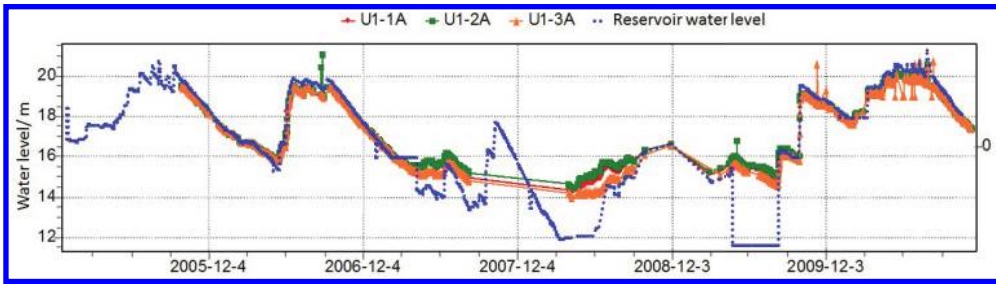


Figure 1. Time-series of measured pressure at U1-1A, U1-2A and U1-3A in front of diaphragm wall.

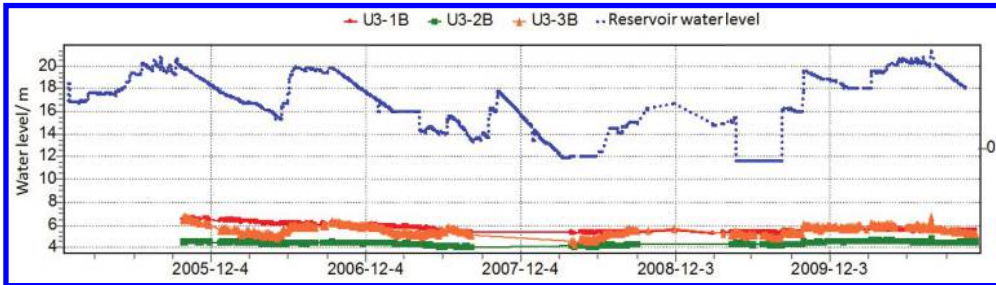


Figure 2. Time-series of measured pressure at U3-1B, U3-2B and U3-3B behind diaphragm wall.

Table 1. Variation of reservoir water level during the flood in July 2010.

Item	Time and date	Reservoir water level (m)	Comment
1	14:30, 26 July, 2010	20.90 m	Normal water level: 20.47 m.
2	00:30, 27 July, 2010	21.30 m (0.67 m below the design flood level)	Design flood level with a hundred year return period: 21.97 m.
3	02:30, 27 July, 2010	21.41 m (0.56 m below the design flood level)	Check flood level with a thousand year return period: 22.67 m.
4	05:10, 27 July, 2010	21.37 m (0.60 m below the design flood level)	
5	08:10, 28 July, 2010	20.26 m	

coefficients about 0.90 with the reservoir water level (measurements of pressure in three points can be seen in Fig. 1). However, the values have little variation of those piezometers which set close to the dam downstream, indicates a low correlation with the water level in reservoir. For instance, the measure point U3 has a rough constant value of 8.00 m and U4 has a unchanged value of 5.00 m, they are not related to the reservoir water level, which shows the anti-seepage system works well for the entire dam.

### 3.2 Dam seepage behavior during the flood

The precipitation was 255.3 mm on 26 July 2010, and at 2:30 on 27 July 2010, the reservoir water level reached 21.41 m, which was the highest water level in the history. This changing of water level can be seen in Table 1.

#### 3.2.1 Reservoir water level

#### 3.2.2 Cross section of 0+070.00 m

The variation of measured piezometer values at dam cross section of 0+070.00 m can be read in Table 2.

#### 3.2.3 Cross section of 0+110.00 m

The variation of measured seepage behavior at the cross section of 0+110.00 m can be seen from Table 3.

#### 3.2.4 Cross section of 0+150.00 m

The variation of measured seepage behavior at 0+150.00 m cross section is shown in Table 4.

As can be seen from the variations of seepage behavior inside the core wall (Table 2–Table 4), the reservoir water level increased 0.51 m within two days (26 July 2010 to 27 July 2010) and reached the maximum water level of 21.41 m, which

Table 2. Measured piezometer values at 0+070.00 m dam cross section during the flood (units: m).

Item	Time and date	Dam body				Dam foundation	
		Before core wall	Inside core wall	Behind core wall	Dam heel	Before key wall	Behind key wall
		U1-1A	U2-1A	U3-1A	U4-1A	U1-1C	U3-1B
1	8:30, 26 July 2010	19.74	14.92	8.67	3.66	11.12	5.54
2	20:20, 26 July 2010	20.23	15.06	8.76	3.87	11.33	5.64
3	0:30, 27 July 2010	20.42	15.22	8.77	3.93	11.43	5.66
4	2:35, 27 July 2010	20.52	15.58	8.78	3.95	11.46	5.65
5	9:10, 27 July 2010	<b>20.62</b>	15.59	8.78	3.99	11.46	5.63
6	15:50, 27 July 2010	20.48	15.59	8.78	3.98	11.44	5.6
7	16:15, 28 July 2010	19.86	15.33	8.74	3.8	11.23	5.54

Table 3. Measured piezometer values at 0+110.00 m dam cross section during the flood (units: m).

Item	Time and date	Dam body				Dam foundation	
		Before core wall	Inside core wall	Before core wall	Inside core wall	Before core wall	Inside core wall
		U1-2A	U2-2A	U3-2A	U4-2A	U1-2C	U2-2B
1	8:30, 26 July 2010	19.78	14.08	7.95	4.88	15.78	5.12
2	20:20, 26 July 2010	20.30	13.96	8.14	5.21	16.19	5.16
3	0:30, 27 July 2010	20.47	13.95	8.25	5.32	16.37	5.25
4	2:35, 27 July 2010	<b>20.58</b>	13.96	8.27	5.36	16.40	5.37
5	9:10, 27 July 2010	20.51	14.00	8.13	5.46	16.00	5.28
6	15:50, 27 July 2010	20.53	13.95	8.06	5.49	16.18	5.30
7	16:15, 28 July 2010	19.89	13.95	7.94	5.21	15.88	5.34

Table 4. Measured piezometer values at 0+150.00 m dam cross section during the flood (units: m).

Item	Time and date	Dam body				Dam foundation	
		Before core wall	Inside core wall	Before core wall	Inside core wall	Before core wall	Inside core wall
		U1-3A	U2-3A	U3-3A	U4-3A	U1-3C	U3-3B
1	8:30, 26 July 2010	19.73	15.71	7.94	4.19	18.98	5.91
2	20:20, 26 July 2010	20.12	15.73	8.15	4.43	19.48	6.19
3	0:30, 27 July 2010	20.26	15.73	8.24	4.49	19.67	6.33
4	2:35, 27 July 2010	20.35	15.72	8.25	4.49	19.76	6.37
5	9:10, 27 July 2010	<b>20.51</b>	15.72	8.16	4.54	19.66	6.42
6	15:50, 27 July 2010	20.44	15.72	8.25	4.54	19.46	6.69
7	16:15, 28 July 2010	19.93	15.71	8.03	4.43	19.01	6.10

was only 0.41 m below the design flood level (21.97 m). The water levels inside the core walls of 0+070.00 m, 0+110.00 m and 0+150.00 m cross sections increased by 0.61 m, 0.04 m and 0.01 m respectively. There was little variation of water level behind the core wall, with a difference smaller

than 0.10 m usually. Under the influence of diaphragm wall in dam (Fig. 3 to Fig. 5), the three piezometer values at U1-1A, U1-2A and U1-3A, which in front of the diaphragm wall, have high values and the values are close to reservoir water level. However, the piezometer readings reduce



Figure 3. The 0+070.00 m cross sectional saturation line during the flood on 27 July, 2010.

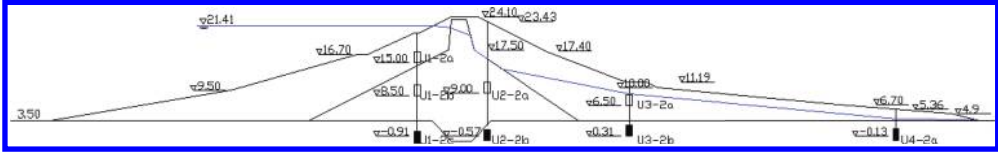


Figure 4. The 0+110.00 m cross sectional saturation line during the flood on 27 July, 2010.

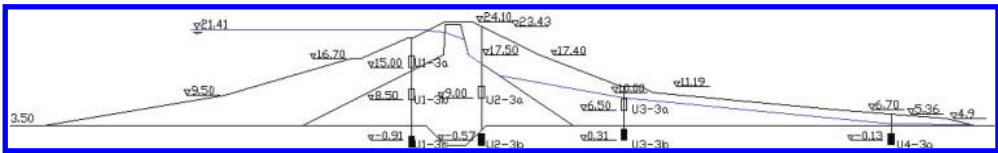


Figure 5. The 0+150.00 m cross sectional saturation line during the flood on 27 July, 2010.

a lot after the diaphragm wall. For instance, the remain water heads after diaphragm wall are about 27.49%, 17.46% and 21.45% at dam cross sections of 0+070.00 m, 0+110.00 m and 0+150.00 m. The anti-seepage effect from the diaphragm wall is significant and it works even better in 0+110.00 m cross section than any other cross sections.

#### 4 STABILITY ANALYSIS ON SEEPAGE

##### 4.1 Computation domain and permeability coefficients

The computation domain is chosen at dam cross section 0+110.00 m. The assignments of materials and finite element mesh for the computational domain can be seen in Figure 6.

The inversion algorithm (Xu, H. et al. 2013; Zhang, H.H. 2014;) is used to calculate parameters based on the observed seepage information of Human Reservoir dam. The high values of piezometers at cross section of 0+136.00 m on 27 July 2010 are selected for computation, with the corresponding reservoir water level is 21.41 m. The observed data of osmometers from 0+110.00 m cross section on that day is used as a reference. The measured values of dam piezometers and osmometers are listed in Table 5. The initial permeability coefficients for the dam computational domain are obtained from the geological survey information

and the values of coefficient are listed in Table 6. The computational results and field measurements are compared in Table 5 and the permeability coefficients after the adjustment using inverse calculation are shown in Table 6.

##### 4.2 Numerical simulation for seepage behavior during the flood

The simulated operating condition for the dam seepage behavior during flood is shown as follow. The steady seepage under the design flood level 21.97 m with the corresponding downstream water level.

The finite element model is adopted and shown in Figure 6 and the permeability coefficients obtained using the inverse calculation (shown in Table 6) are applied to the model. Some calculated dam seepage parameters during a flood are listed in Table 7.

As can be seen from the calculated results in Figure 6 and Table 7, the maximum seepage gradients in the different sections of reservoir dam during a flood are all smaller than their allowed values in gradient. The dam will remain safety running without any seepage damage. However, due to the limitation of width in dam core wall with a minimum value of 3.0 m, the anti-seepage effect is limited in high water level and the core wall will not be able to reduce the

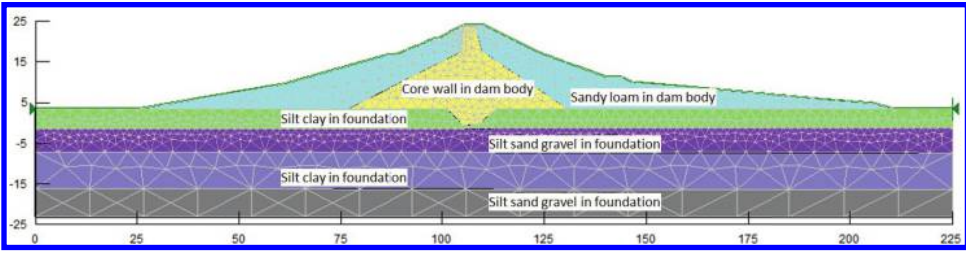


Figure 6. Finite element meshes in the computational domain.

Table 5. The measured piezometer values and inverse calculated results in the computational domain (units: m).

Item	Piezometer/osmometer readings										
	U1-2A	III-1	III-3	U2-3A	III-4	III-5	III-6	U3-2A	III-7	III-8	U4-2A
Measure point	U1-2A	III-1	III-3	U2-3A	III-4	III-5	III-6	U3-2A	III-7	III-8	U4-2A
Distance away from dam axis	-9.5	-7.0	3.0	4.5	8.0	12.0	27.0	33.0	42.0	52.0	86.6
Measured values	20.58	21.45	19.21	15.73	17.39	13.12	10.78	8.27	8.00	6.39	5.49
Calculated values	/	/	/	15.69	/	13.29	10.39	8.84	7.74	6.59	5.71

\* Note: The U2-3A piezometer is chosen with higher reading for U2.

Table 6. The inverse calculated permeability coefficients for each materials in the computational domain (units: cm/s).

Item	Material zone	Initial permeability coefficients		Inverse calculated permeability coefficients	
		$k_x$	$k_y$	$k_x$	$k_y$
1	① Sandy loam in dam body	$1.55 \times 10^{-4}$	$1.55 \times 10^{-4}$	$5.72 \times 10^{-4}$	$8.43 \times 10^{-4}$
2	② Core wall in dam body	$7.62 \times 10^{-5}$	$6.34 \times 10^{-5}$	$6.72 \times 10^{-5}$	$4.43 \times 10^{-5}$
3	③ Silt clay in foundation	$2.58 \times 10^{-6}$	$6.39 \times 10^{-7}$	$2.61 \times 10^{-6}$	$1.37 \times 10^{-6}$
4	④ Silt sand gravel in foundation	$5.00 \times 10^{-4}$	$5.00 \times 10^{-4}$	$5.00 \times 10^{-4}$	$5.00 \times 10^{-4}$
5	⑤ Silt clay in foundation	$8.55 \times 10^{-7}$	$1.28 \times 10^{-7}$	$8.55 \times 10^{-7}$	$1.28 \times 10^{-7}$
6	⑥ Silt sand gravel in foundation	$4.50 \times 10^{-4}$	$4.50 \times 10^{-4}$	$4.50 \times 10^{-4}$	$4.50 \times 10^{-4}$

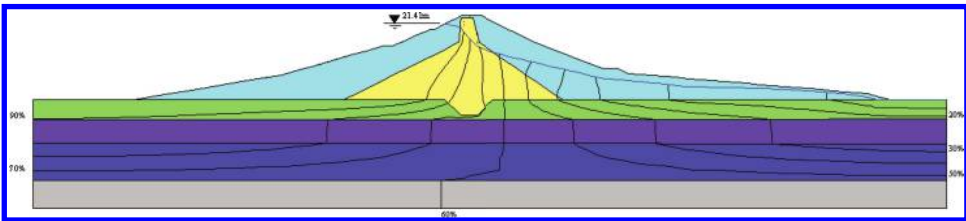


Figure 7. The dam seepage equipotential lines from numerical simulation during the flood.

seepage pressure significantly. Furthermore, the permeability coefficient is small in the dam downstream sandy loam, which is not good for draining the seepage water and thus leads to a high value of saturation line in the downstream slope of dam. Last but not least, the bottom

elevation of wave wall constructed using mortar rubbles is higher than the crest elevation of core wall in dam, which means the wave wall have no close contact with the dam anti-seepage system, and this introduces one more potential risk in seepage control.



Table 7. Seepage parameters in the different sections of dam during the flood.

Simulated situation	Seepage gradient	Sections	Allowed seepage gradient	Seepage discharge (m <sup>3</sup> /m·d)
Flood level 21.41 m	0.822	Core wall	0.894	0.551
	0.467	Downstream dam shell	0.849	
	0.390	<i>Horizontal</i> Foundation	0.894	
	0.755	<i>Vertical</i>		

## 5 CONCLUSIONS

The seepage field evolution of Human reservoir dam is investigated through analyzing the observational data of seepage behavior for the earth-rock dam during a flood. And the anti-seepage effect of the core wall encountering the flood is evaluated according to the water level of several typical cross sections of the dam by using finite element numerical computation. The results indicate the seepage behavior of the dam is safe. However, several weak links in the seepage safety control of the dam are pointed out.

## ACKNOWLEDGMENT

The paper was supported by the National Natural Science Foundation of China (Grant Nos.

51209145, 51179108, 51209144) and the Fundamental Research Funds of Nanjing Hydraulic Research Institute (Grant Nos. Y715011, Y715005).

## REFERENCES

- Xiang, Y. & Liu, C.D. 2012. Safety assessment of Human reservoir during the flood. Research Rep, Nanjing Hydraulic Research Institute, Nanjing, China.
- Xu, H., Huang, B., Rao, X.B. 2013. Research on New Dam Structure for High Earth Core Rockfill Dam on Thick Overburden. IACGE 2013: 316–323.
- Zhang, H.H., Wang, C.Y., Gong, A.M. 2014. Seepage Analysis of Plane Finite Element on Clay Core Dam of Laojunshan. Advanced Materials Research 838: 1637–1640.

# Review and prospect of urban storm water simulation technology

Z.P. Chen

*Zhejiang Jinhua Hydrology Stage, Jinhua, China*

Y.F. Chen & S.H. Chen

*Zhejiang Institute of Hydraulic and Estuary, Hangzhou, China*

M.J. Chen

*Zhejiang University, Hangzhou, China*

**ABSTRACT:** Urban flood disaster in China is becoming a serious problem caused by the rapid urbanization and global climate change. It has aroused widespread attention from all sectors of society. Urban storm water simulation is an important technical support for urban storm water management. In this paper, features, applicability and limitations of calculation methods for runoff generation and flow concentration, and main urban storm water simulation models are introduced and reviewed. Finally, the shortcomings and future challenges in urban storm water simulation research in China are pointed out.

**Keywords:** urban flood disaster; storm water simulation; GIS

## 1 INTRODUCTION

Urbanization is an important sign of development of human society. With the change of global climate and the rapid development of urbanization, a series of significant changes happened in the natural environment, ecosystems and hydrological characteristics of the city area and the nearby area. Thus, there are a series of urban hydrological problems, which are different from natural river basin. These problems can be mainly expressed as follows.

1. The increase of impervious area reduced the regional storage capacity and the precipitation loss resulted by infiltration. All of above let runoff generation happen ahead of time, reduce flow concentration detention storage time, increased the total amount of runoff and heightened the peak flow runoff. Runoff generation was uneven and behaved scary ups and downs along with time. Meanwhile, the speed of flow increased so that the content of suspended matter and pollutant increased.
2. Urban landscape features are complex, all kinds of buildings, streets and squares spread all over the place. The constant changes of urban landscape made the runoff generation and flow concentration mechanism extremely complex. Therefore, the calculation of runoff generation and flow concentration in urban area is more difficult than that in natural river basin.

Urban storm water simulation is an important technical support for urban storm water management. Its stability, accuracy, and efficiency is directly related to the effectiveness of urban flood control and disaster mitigation. In allusion to urban storm flood simulation technology, the paper reviewed the research achievement in recent years and commented on it. The paper set forth the main features, applicability and limitations of various simulation technology and different simulation models. Finally, the paper pointed out the difficulties and challenges China faced in the urban storm water simulation research and looked forward to the development direction of urban storm water simulation.

## 2 CALCULATION OF RUNOFF GENERATION AND FLOW CONCENTRATION

According to long-term observation and research, scholars at home and abroad usually conclude urban runoff generation and flow concentration in three aspects, which include urban storm water runoff generation calculation, land surface flow concentration calculation and drainage system flow concentration calculation. [Table 1](#) shows different aspects of urban storm water calculation.

It is relatively simple to calculate the runoff generation in impervious area. It is about equal to the precipitation minus the preliminary loss of depressions fill hollow, interception by plants

Table 1. Urban storm water runoff generation and concentration calculation methods.

Calculation Methods		Main Characteristics	
Runoff generation calculation	Runoff coefficient method	Calculate runoff generation according to different ground rainfall runoff coefficients.	
	Infiltration formula method	Confirm runoff generation according to infiltration amount calculated by infiltration formula.	
	SCS method	Calculate rainfall-runoff relationship by the coefficient CN which reflect comprehensive feature of basin. Applicable when lack of data.	
	Conceptual rainfall-runoff model	Using conceptual rainfall-runoff relationship to calculate land storm runoff generation and the calculation is complex.	
Surface flow concentration calculation	Rational formula method	Presuming rainfall runoff area increases linearly, runoff coefficient remains constant, only concerns peak flow but not flow duration curve.	
	Area-time method	Calculate regional flow concentration area according to same flow concentration time. Difficult when divide land flow concentration calculation.	
	Hydrological method	Instantaneous unit-line method	Complex calculation which relies on information and has normal result.
		Linear reservoir method	Simple calculation which has low accuracy and can't simulate non-linear process.
		Non-linear reservoir method	Relatively simple method which can simulate non-linear process and has high accuracy.
	Hydrodynamic method	Simulate land flow concentration based on kinematic wave equations. Physical process is clear but calculation is time-consuming.	
Drainage system flow calculation	Hydrological method	Muskingum method	Simple calculation which is applicable when the slope of pipelines and canals is steep or the downstream backwater effect is small.
		Instantaneous unit-line method	Simple calculation but has low accuracy.
		Reservoir adjustment algorithm	Simple calculation and has normal accuracy.
	Hydrodynamic method	Kinematic wave method	Ignore inertia and diffusion item of momentum equation. It is applicable when the slope of pipelines and canals is steep or the downstream backwater effect is small.
		Diffusion wave method	Ignore inertia item of momentum equation.
		Dynamic wave method	High accuracy with large applicable range.

and surface evaporation. Depending on different starting points, there are a lot of methods to calculate runoff generation in flooded area, such as runoff coefficient method, infiltration formula method, SCS method, etc.

Land runoff confluence calculation includes two aspects, hydrological models and hydrodynamic models. Hydrological method is easy to calculate, but the physical mechanism is not clear yet, so that it has great limitation. For instance, the traditional reasoning only concerns on peak flow which can't reflect the process of storm water flow; area-time method is more difficult when we divide the land runoff confluence calculation; unit line method teaches a large dependence of the measured data and is not easy to calculate flow duration curve; linear reservoir method does not consider non-linear characteristics and the result is not reliability;

nonlinear reservoir method has relatively high computational accuracy. Compared with hydrological method, hydrodynamic method can provide more detailed urban storm water surface unsteady flow process. However, hydrodynamics models need more accurate boundary, parameters (roughness, slope, etc.), initial conditions and boundary conditions. Therefore, hydrodynamic method has greater difficulty in practical applications.

Drainage system Runoff convergence calculation includes hydrological method and hydrodynamic method. Hydrological method has many types, such as Muskingum method, unit-line method, reservoir adjustment algorithm, etc. But these methods are simplified methods so that the applicable ranges are limited. Hydrodynamic method includes complete dynamic wave method, diffusion wave method and kinematic wave method. Among these methods,

diffusion wave method and kinematic wave method are simplifications of the Saint-Venant equations on the basis of certain assumptions. We can use corresponding methods according to the specific circumstances in a practical application. For example, we can use kinematic wave method when the slope of pipelines and canals is steep or the downstream backwater effect is small. When it is required to consider a variety of flow patterns coexist, pressure flow, backflow and so on, complete dynamic wave equation can be used.

### 3 URBAN STORM WATER SIMULATION

Study on urban storm water models started earlier overseas. American and European developed

countries began to develop urban storm water model since the sixties of the last century. The purpose is to meet the requirement of urban flood control and drainage, environmental governance and storm water management. There are hundreds of urban storm water models so far. Table 2 shows some wide-used and typical models.

These models are mainly concentrated in urban areas, including both simple conceptual models and complex physical models. They also include statistical analysis models and deterministic models. With the expansion of urban area and significant changes in global climate, urban hydrologic study should not be limited to urban areas. We should consider the interaction and interconnection between urban area and natural area. Therefore, there is still great limitations in the range of the application.

Table 2. Main urban storm water models.

Model	Developer	Calculation method			Main characteristics
		runoff generation	Surface flow concentration	Drainage system flow calculation	
TRRL	TRRL	Rainfall buckle loss method	Area-time method, linear reservoir method	Kinematic wave method	Only concern runoff generation in impervious and the result is lower than normal.
ILLUDAS	Illinois	Rainfall buckle loss method	Area-time method	Kinematic wave method	Modified version of TRRL which is able to concern land runoff in flooded area.
STORM	USACE	Rainfall buckle loss method, SCS	Unit-line method	Hydrological method	Using the aggregative indicator CN relied on some information which is relatively easy to determine to calculate rainfall process.
Wallingford	Wallingford hydraulic Institute	Correct reasoning formula method	Nonlinear reservoir method	Muskingum method, Hydrodynamic method	Divide each hydrological cell into roof, paving and pervious area.
Info Works CS	Wallingford software Ltd	Constant proportion runoff model, Infiltration formula method, SCS	Linear and nonlinear reservoir method, SWMM runoff module calculation	Hydrodynamic method	Various modules and complete functions.
SWMM	EPA	Infiltration formula method, SCS	Nonlinear reservoir method	Hydrodynamic method	Generalize each hydrological cell into flooded area, stagnant impervious area and fluent impervious area.
MIKE-SWMM	DHI	Infiltration formula method, SCS	Nonlinear reservoir method	Hydrodynamic method	Using MIKE 11 to replace EXTRAN in SWMM

#### 4 CONCLUSION AND OUTLOOK

In recent years, it has made considerable progress in the theory and practice of urban storm water models and built a relatively complete model framework and technical solutions. Compared with foreign mature technology, Chinese urban storm water simulation still faces many challenges and difficulties and needs to strengthen the research work in the following areas.

1. Strengthen the research on urban runoff generation and flow concentration mechanism. Through experiments and model simulation, analyzing the rule of urban runoff generation and flow concentration and responding mechanism, especially analyze the influence impervious surface distribution made on runoff generation and flow concentration.
2. Strengthen the research on urban hydrology and hydrodynamic coupling model. Consider the ease and speed of hydrological method with the accuracy of hydrologic method. Through theoretical research, experimental analysis and numerical simulation, establishing a fully functional urban storm water mode to achieve a whole process simulation of two-dimensional coupling, surface groundwater coupling and quantity and quality coupling.

3. Build a distributed database of time and space for storm water information. Establish and perfect urban storm flood monitoring system to achieve all-round, multi-angle monitor.
4. Carry out research on multi-source information coupling technology, approaching quantitative precipitation forecast and data assimilation techniques. Get the integration of GIS spatial analysis and visualization function. Gradually build urban rain flood real-time simulation and forecasting warning scientific decision support system.

#### REFERENCES

- Choe, J.S. & Bang, K.W. & Lee, J.H. 2002. Characterization of surface runoff in urban areas. *Water science and technology: a journal of the International Association on Water Pollution Research*. 45(9): 49–54.
- Akan, A.O. & Houghtalen, R.J. 2003. *Urban hydrology, hydraulics and storm water quality*. In Hoboken, NJ.
- Hu, W.X. & He, W.H. & Huang, G.R. 2010. Review of urban storm water simulation techniques. *Advances in water science*. 21(1): 137–144.
- Chen, Y.F. 2013. *Study on city-region storm water simulation and data assimilation*. In Zhejiang University, Hangzhou.

# Analysis on the right abutment stability of Gomal Zam Dam against sliding

X.E. Xu & H.Y. Fang

*China Water Resources Beifang Investigation, Design and Research Co. Ltd., Tianjin, China*

**ABSTRACT:** The stability of the right abutment against sliding is one of the critical issues for the Gomal Zam Dam Project due to the existence of Faults F2 and F3. A FEM-LEM approach, which combines the Finite Element Method (FEM) and the traditional Limit Equilibrium Method (LEM), is adopted to assess the abutment stability. First, the deformations and stresses of the dam and its foundation/abutments are calculated using 3-D FE models. Then, the overall stability of the right abutment is assessed using the LEM based on the results of FEM stress computations. Since the FE model may or may not include the concrete replacement works for the faults, the effects of the proposed treatment measures are evaluated.

**Keywords:** curved gravity dam; stability against sliding; FEM-LEM approach; Gomal Zam Dam Project

## 1 INTRODUCTION

The Limit Equilibrium Method (LEM) is still one of the main methods for assessing the sliding stability of dam abutments, and has gained wide popularity in practice. Much experience has been accumulated, and applicable safety assessment criteria have been established. Although LEM is simple, it provides no direct information regarding deformations of the abutments, and the effects of other contributing factors and interaction of the dam and the foundation/abutments could hardly be realistically considered, which can be adequately considered and modeled in FE. Thus, the FEM-LEM approach can make the analysis more applicable to the reality, and the result can be easily understood and adopted.

In the present study, the basic steps for assessing the sliding stability of the right abutment by using the FEM-LEM approach are as follows. ① Define a sliding block/wedge based on the geological conditions in the right abutment. ② Compute stresses in the dam and its abutments by using the FE program ANSYS. It may also include or not include the concrete replacement works in the right abutment depending on the purpose of the analysis. ③ Calculate the factor of safety for sliding of an assumed sliding wedge. ④ Compare the calculated value of the factor of safety for sliding with the required values specified in the relevant code to assess the stability of the assumed sliding wedge and the right abutment.

## 2 GENERAL GEOLOGY

The Gomal Zam Dam was designed to be a curved RCC gravity dam, having a maximum dam height of 133 m. The dam site is located at the west-wing of the short-sleeved fold, where it is carbonatite, sandy and clayey shale of the Jurassic System, showing a monoclinical structure with localized small folds. The general striking of the rock stratum is NW320~350°, and dips southwesterly at an angle of 30~70°. The main geological structures include faults, joints/fissures, beddings and bedding shear zones, among which Faults F2, F3 and F13 on the right bank are of significance to the project.

As shown in [Figure 1](#), Fault F2 generally trends NE55°~70° dipping northwesterly at an angle of 87°, 0.01~1.1 m wide, being filled with mylonite, breccia and clastic rock, brown colored, argillaceous cemented. Fault F3 strikes NE45° dipping northwesterly at an angle of 80°, 0.01~0.6 m wide, being filled with breccia and clastic rock, with horizontal slickenside. Fault F13 generally trends NW320°~345° dipping northeasterly at an angle of 68°, 0.60 m wide, being filled with mylonite, breccia, and clayey material, clayey calcium cemented, with slickenside.

As shown in [Figure 2](#), joints/fissures are well developed in the right abutment, mostly in the pattern of 5 joint sets: ① NW313°/NE∠54°; ② NW285°/NE∠76°; ③ NE42°/SE∠82°; ④ NE40°/NW∠75°; and ⑤ NE66°/SE∠81°. The openness of joints is typically less than 3 mm, mostly filled with rock fragments and calcite coating, some with

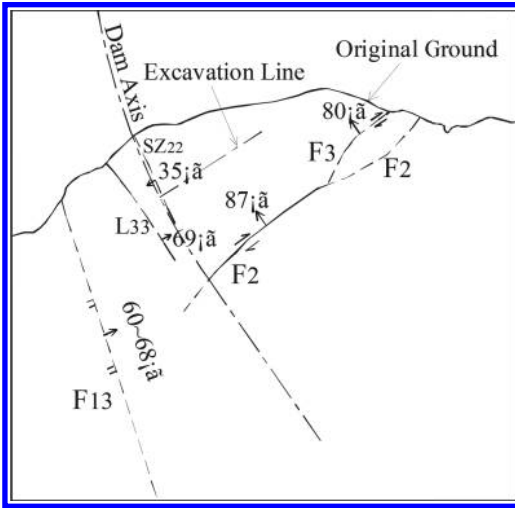


Figure 1. Horizontal section at El.690 m.

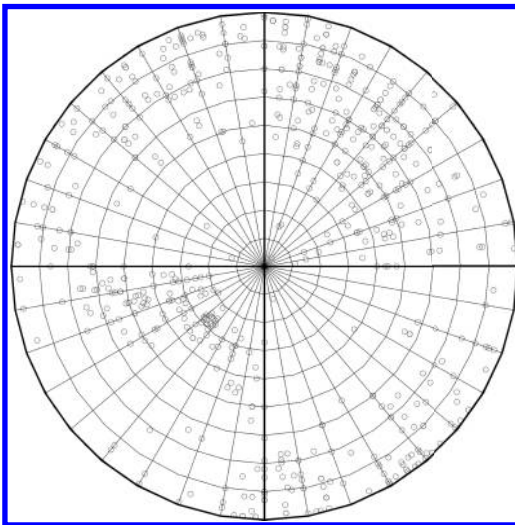


Figure 2. Pole diagram of joints.

argillaceous film. A certain number of the joints/fissures dip at an angle of 10–30°, but generally occur in random form and stretch over a short distance as observed in adits and excavation pit.

### 3 FEM MODEL

The Gomal Zam Dam is a curved gravity dam, with a downstream slope of 1:0.6 and a base thickness of 78 m. The dam along the thickness direction is divided into 8 layers of element.

The volume of the foundation included in the FE model to account for the flexibility effects of the foundation rock was selected based on the experience, the geological conditions at the dam site, and the purpose of the analysis. As shown in Figure 3, the foundation range included in the FE model is 195 m wide for the left bank, about 1.5 times of the dam height, and 271 m wide for the right bank, about 2.0 times of dam height. As the sliding stability of the right abutment in the upstream-downstream direction is to be checked, and Fault F13 is located near the dam heel and therefore weakens the restraint of upstream rocks to the right abutment, the model extends for 183 m upstream and 300 m downstream. In the vertical direction, 133 m, 1 time of the dam height, thickness of the rock beneath the dam foundation is included in the FE model.

In the FE model for the computation (Figs. 3 and 4), the geometry of the dam and its foundation/abutments, major zoning of rocks, major faults in the right abutment, such as F2, F3 and F13, and treatment works for the faults are taken into consideration. The origin of the FE grid is located at the bottom center of the central cantilever, its X axis is parallel to the dam axis with the positive direction pointed from the right bank to the left bank, its Y axis is perpendicular to the dam axis with the positive direction pointed from the downstream to the upstream, and its Z axis is vertical with the positive direction pointed upwards. The model is composed of 476828-node solid elements for the dam body and the rocks, 58324-node surface to surface contact elements for the major faults, slip surfaces and the joints between the arch and the concrete thrust blocks.

The bottom face of the model, as shown in Figure 3, is considered to be fixed in the x, y,

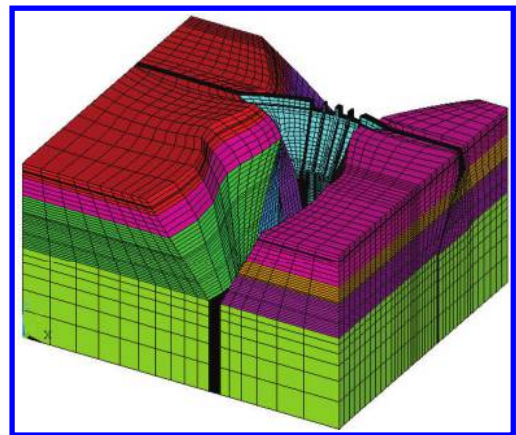


Figure 3. FE grid for dam and foundation.

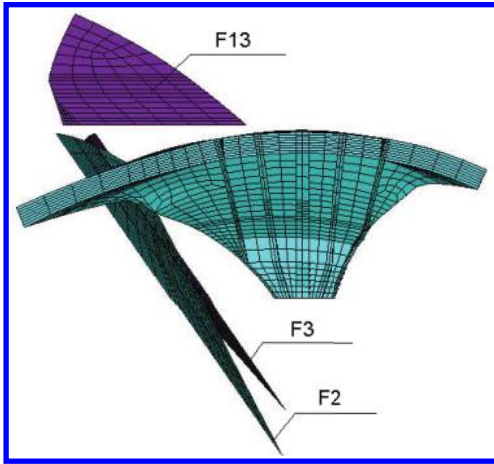


Figure 4. View of the dam and main faults.

and z directions. And all other ends (left/right ends and upstream/downstream ends) are considered to be pinned.

#### 4 SELECTION OF FAILURE WEDGE

##### 4.1 Bottom slip surfaces

As disclosed by geological mapping, the major joint sets and shear zones at the right abutment are of steep angles, and the gentle joints/fissures (dipping at an angle of not larger than 30°) only occur in random form and stretch over a short distance. They are less likely to form potential bottom slip surfaces. Meanwhile, based on the results of the FEM stress computations, the results of the point safety factor method show that the minimum values of the safety factor against sliding at El.690 m and 660 m are less than the specified value. Thus, the horizontal plane cut at El.690 m and 660 m is, respectively, assumed as the bottom slip surface, along which the shear strength is that of the rock mass.

##### 4.2 Lateral slip surfaces

It is found that two steep faults (labeled F2 and F3) and three steep joint sets run sub-parallel to the river flow in the right abutment. As the statistics show, the continuity rate of joints is only about 20%, while the extension of Faults F2 and F3 can intersect downstream river banks to form the exposed or free face. Given the compositions and thickness of faulted zones, indicating that the shear strength of the jointed rock mass is much higher than that of the faults, the potential sliding failure can only occur along the weaker Faults F2 and F3.

#### 5 PHYSICAL AND MECHANICAL PARAMETERS

Physical and mechanical parameters of the concrete, rock masses and faults are listed in Table 1 and Table 2.

#### 6 STABILITY ANALYSIS OF THE RIGHT ABUTMENT

The basic loads are mainly composed of thermal load, dead weight, upstream water pressure, downstream water pressure, wave pressure, sediment pressure, uplift pressure as well as seismic effect. The detailed load combinations are presented in Table 3.

The dam structure is simulated as the elastic structure, while the foundation rock is simulated as the elastic-plastic structure. The ideal elastic-plastic *in situ* structural property is applied for the analysis of the foundation rock. The augmented Lagrangian method is applied as the criteria for the nonlinear stress yield analysis of the major faults in the abutments and joints in the dam.

The finite element program ANSYS is used to compute the deformations and stresses in the dam and its foundation/abutments, and analyze the stability of the right abutment. Based on the results of the FEM stress computations, the Factors of Safety (FS) against sliding for potential failure wedges at natural conditions (i.e. without any replacement works, and the shear strength of the lateral slip surface is selected to be equal to that of the fault) are calculated using the following equation:

$$K = R/S = \frac{\sum N_i f_i + \sum C_i A_i}{\sum T_i} \quad (1)$$

where  $K$  is the factor of safety for sliding of the assumed sliding wedge;  $R$  is the total resistance force acting on the assumed sliding wedge;  $S$  is the total shear force acting on the assumed sliding wedge;  $N_i$  is the force acting normal to a sliding failure surface of a sliding wedge;  $f_i$  is the coefficient of internal friction of the material on a sliding failure surface;  $C_i$  is the cohesive strength of the material on a sliding failure surface;  $A_i$  is the area of a sliding failure surface;  $T_i$  is the shear force acting parallel to the assumed sliding direction.

For the calculation of  $N_i$  and  $T_i$  on a slip surface of an assumed sliding wedge, the computation results at the last step are used.

The results are summarized in Table 4.

It can be seen that in the static usual load cases (Case 1 and Case 2), the factors of safety against sliding for failure wedge with El.690 slip surface



Table 1. Physical and mechanical parameters for concrete and rock mass.

Material	Unit weight (kN/m <sup>3</sup> )	Elastic modulus (GPa)	Deformation modulus (GPa)	Poisson's ratio
Concrete	24.1	30.0		0.18
Rock	26.0	14.0	7.0	0.30
F2, F13			1.0	
F3			1.5	

Table 2. Physical and mechanical parameters for concrete and rock mass.

Material	Friction	Cohesion (MPa)	Specific heat (kJ/kg·°C)	Heat conductivity factor (kJ/m·h·°C)
Concrete	1.96	2.67	0.840	6.64
Rock	0.67	0.40	0.840	14.30
F2, F13	0.45	0.08		
F3	0.55	0.12		
Joints	0.65	0.20		

Table 3. Loading combinations.

Load cases	Usual		Unusual		Extreme		
	1	2	3	4	5	6	7
Dead weight	✓	✓	✓	✓	✓	✓	✓
Water pressure	✓	✓	✓	✓	✓	✓	✓
Uplift	✓	✓	✓	✓	✓	✓	✓
Silt pressure	✓	✓	✓	✓	✓	✓	✓
Temperature drop	✓		✓			✓	
Temperature rise		✓		✓			✓
0.1 g (OBE)			✓	✓	✓		
0.25 g (MCE)						✓	✓

Table 4. Factor of safety against sliding at natural conditions.

Bottom slip surface	El.660	El.690
Case 1	4.41	1.72
Case 2	4.52	1.69
Case 3	3.10	1.44
Case 4	3.19	1.52
Case 5	5.13	2.64
Case 6	3.39	1.73
Case 7	5.19	3.11

are less than 2.0 (criteria value in EM1110-2-2201), which indicates that the stability of the right abutment at its natural conditions, namely no treatment measures for F2 and F3 (situation S-2), would not meet the code requirement.

## 7 TREATMENT OF FAULTS F2 AND F3

To strengthen the rock mass integrity at the right bank abutment and to enhance the overall stability of the right abutment, the concrete replacement method is applied for treatment of Faults F2 and F3.

Treatment works consist of replacement adit 1 for Fault F3 and replacement adit 2 for Fault F3 at EL660 m, replacement adit 3 for F2 at EL690 m, and replacement adit 4 for F2 at EL720 m, replacement shafts 3 and 4 connecting replacement adits 3 and 4, and force-transfer adits along Fault F2 at EL660 m, EL690 m and EL720. The lengths of the replacement adits at EL660 m, EL690 m, and EL720 m are about 84 m, 50 m and 35 m, respectively, and the length of each of the two replacement shafts is about 30 m. The cross-sections of the replacement adits and shafts are dimensioned in the range of 3 m–5 m, which is about the same as the size of the elements for their surrounding rocks.

In the FE model for the computation, 2442-node beam elements are included for concrete replacement adits, replacement shafts and force-transfer adits. An area-weighted equivalent method is used to reflect the effect of fault treatment works on the increase of shear strength of the faults.

In addition to the concrete replacement works, consolidation grouting with a depth of 5 m was proposed to be conducted around the replacement adits. Deep hole consolidation grouting along Fault F2 was also proposed to be performed from replacement adits at EL660 m and EL690 m in order to enhance the shear strength and deformation modulus of the fault fractured zone.

Table 5. Factor of safety against sliding with fault-strengthening works.

Bottom slip surface	El.660
Case 1	2.60
Case 2	2.68
Case 3	2.57
Case 4	2.67
Case 5	4.42
Case 6	3.01
Case 7	2.20

The maximum grouting pressure was selected at 3.0 MPa. Contact grouting was proposed for all concrete replacement works to ensure the bond and hence increase the shear strength between the concrete and the surrounding rock.

The FS calculation follows the same [Equation \(1\)](#), and the results are summarized in [Table 5](#), which

suggest that the stability against sliding of the right abutment with the current fault-strengthening works can meet the code requirement, indicating the treatment measures are effective and feasible.

## 8 SUMMARY

Steep Faults F2 and F3 run sub-parallel to the river flow in the right abutment of the Gomal Zam Dam in such a way that it may form a lateral slip surface. A FEM-LEM approach is used to assess the right abutment stability against sliding, in which the result shows that the safety factor against sliding of the wedge combining the bottom slip surface at El.690 m and lateral slip surface of Fault F2 cannot meet the code requirement at natural conditions and can meet the code requirement with the current fault-strengthening works, indicating that the effects of concrete replacement works for Faults F2 and F3 are desired.

# Study on optimum band combination of multi spectral vegetation information extraction in Taihu Basin

T.T. Cui, Y.Q. Long, Y.T. Wang, Q.F. Hu & Y. Liu

*State Key Laboratory of Water Resources and Hydraulic Engineering and Science, Nanjing Hydraulic Research Institute, Nanjing, China*

**ABSTRACT:** Based on the Landsat ETM+/TM remote sensing data, ENVI software is employed to calculate statistical characteristics of remote sensing image. The Taihu basin is taken as the typical case. The statistical characteristics of each band, the band correlation and OIF index are analyzed. According to the data analysis and image comparison, the band combination of TM2, TM4 and TM7 is the optimum band combination for extracting vegetation information, and respectively given a red band, the green band and blue band. This band combination has achieved good results in the Taihu Basin vegetation information extraction.

**Keywords:** landsat ETM+/TM data; vegetation information extraction; optimal band combination; OIF index

## 1 INTRODUCTION

The urbanization could greatly change the vegetation which is one of the most important environmental components and one of the best marks of eco-environment. Analysis of the vegetation information could be used in urbanization management, flood protection, environment protection. Efficiency and accuracy of the extracting the vegetation information from the Remote Sensing (RS) data is the key and hot point in the field of image processing and RS image interpretation (Mei et al. 2001, Guo & Liu 2012). Artificial Visual Interpretation (AVI) is one of the major methods for vegetation information extraction. The efficacy of the AVI is depended on the image quality which is affected by the image data redundancy caused by the admixture of different bands of the multi-spectrum image (Ma et al. 2010). So extracting the clear image with plenty useful information from the RS image is the hard and important point for AVI. In this paper, the Taihu Basin in China is taken as the typical case for applying AVI in a fast urbanization area. By evaluating the different combination of bands of the multi-spectrum image, the best combination of bands of vegetation information is extracted. The method could enhance the separability of terrain and reduce image data redundancy.

## 2 BACKGROUND OF THE TAIHU BASIN

The Taihu Basin locates in the south of the Yangzi delta. The north of the Taihu Basin is the Yangzi

River, the south is the Qiantang River, the east is the East China Sea, and the west is the Tianmu Mountain. The Taihu Basin belongs to subtropics monsoon climate region with plenty rainfall and frequently typhoon. Because of the moderate climate and pleasant geographical condition, the Taihu Basin contains most of the wealthy metropolis in the north China. The rapid urbanization in the Taihu Basin greatly changes the vegetation which is one of the decisive factors of runoff, precipitation infiltration, flood and transpiration. Finding the best combination of bands for extracting vegetation information could be useful for urbanization management, flood control, groundwater protection and water resource management.

## 3 DATA

Five Landsat ETM+/TM RS scenes are spliced together to generating the whole RS image of the Taihu Basin. These Landsat ETM+/TM RS scenes are obtained from <http://www.gscloud.cn>. Their WRS path and starting row numbers are 118/038, 118/039, 119/038, 119/039 and 120/038, the acquisition dates are 2009/9/19, 2009/7/17, 2010/5/24, 2010/5/24 and 2009/5/4. All the images are acquired in sunny day without cloud, and have been applied geometric correction. So these images could be used to interpretation directly. The 6th band of these images is infrared band which is sensitive to the thermal object. The 8th band of these images is panchromatic band, and it cannot show the color

of the terrain. In this paper, we don't use the 6th and 8th bands to identify the best combination of bands for extracting vegetation information.

## 4 METHOD

The RS image spectrum characteristic analysis and the Optimum Index Factor (OIF) are used to identify the optimum band combination for extracting the vegetation information in the Taihu Basin.

There are many bands in the multi-spectrum RS image, and each band could contain information of different types of vegetation. So a good band combination is the basis to extract the vegetation information. Usually, three rules should be followed to choose proper band combination (Jiang et al. 2002, Wu & Liu 2007). Firstly, band should contain more information. Then the relativity between different bands should be as small as possible. Finally, the objective terrain should be identified easily in the band combination.

Optimum Index Factor method (OIF) proposed by Chavez et al. (1982) uses standard deviation of three band and coefficient between different band to calculate the optimum index factor. The OIF could be calculated as the followed equation.

$$OIF = \frac{\sum_{i=1}^3 S_i}{\sum_{i=1}^3 |R_{ij}|} \quad (1)$$

where the  $S_i$  is the Standard Deviation (SD) of the  $i$ th band. The  $R_{ij}$  is the Correlation Coefficient (CC) between band  $i$  and band  $j$ . The standard deviation is bigger, the more information the band has. The coefficient between two bands is smaller, the more independent these bands are, and the less data redundancy is. If an image contains many bands, the correlation matrix should be calculated and then each of the OIF combinations of three bands should be calculated. The OIF is bigger, the more information the band combination could have.

## 5 ANALYSIS OF BAND COMBINATION

### 5.1 Information of band

The statistical characteristics could be used to evaluate the plenty of band information. We calculate the statistical characteristics of the RS images of the Taihu Basin by ENVI. The statistical characteristics of the six bands are shown in Table 1.

The standard deviations of band TM4, TM7, and TM5 are bigger than the standard deviations of other bands. So the band TM4, TM7, and TM5 have more information than other band.

Table 1. Statistical characteristic of bands.

Band	Min	Max	Mean	SD
TM1	0.071	0.341	0.119	0.018
TM2	0.010	0.767	0.111	0.020
TM3	0.001	0.742	0.093	0.026
TM4	0.025	1.265	0.225	0.060
TM5	0.000	0.548	0.141	0.045
TM7	0.000	0.801	0.094	0.048

Table 2. Correlation matrix of different bands.

Coefficient	TM1	TM2	TM3	TM4	TM5	TM7
TM1	1.000	0.943	0.921	-0.201	0.249	0.553
TM2		1.000	0.970	-0.155	0.215	0.475
TM3			1.000	-0.180	0.272	0.539
TM4				1.000	0.666	0.304
TM5					1.000	0.870
TM7						1.000

Table 3. The combinations of chosen bands.

Type I	Type II	Type III	Band combination
TM1		TM5	TM1+TM4+TM5, TM1+TM4+TM7
TM2	TM4		TM2+TM4+TM5, TM2+TM4+TM7
TM3		TM7	TM3+TM4+TM5, TM3+TM4+TM7

### 5.2 Band correlation

We calculate the correlation matrix of TM1, TM2, TM3, TM4, TM5, TM6 and TM7 by ENVI.

The correlation coefficients of TM1, TM2 and TM3 are bigger than 0.92. That means the three bands have great data redundancy, and cannot be used as a combination. We take the three bands as type I. The correlation coefficients of band TM4 and other bands are smaller than 0.67. That means the TM4 is independent of the other bands, and it can assemble a combination with any band. The TM4 is taken as type II. The correlation coefficients of TM5 and TM7 is bigger than 0.87, so the two bands cannot assemble a combination. TM5 and TM7 are taken as type III. We choose a band from each type; the chosen bands can assemble six combinations (Table 3).

### 5.3 Optimum index factor

The OIF of each band combination are shown in Table 4.

### 5.4 The optimum band combination

Table 4 shows that the first three band combinations have the biggest OIF than other combinations. So the optimum band combination could be one of the three combinations. The statistical characteristics of band combination show that the first band combination in Table 4 has the smallest correlation and standard deviation. Though the data analysis show the first band combination could be the optimum combination, we still need use the AVI to confirm the judgment. Comparing the colorful images generated from the first three band combinations, we find the image corresponding to the first combination can clearly exhibit the terrain, vegetation, and the urban area. The second combination could exhibit large vegetation area, but cannot exhibit the tiny vegetation and differentiation between terrain objectives clearly. The image corresponding to the third combination is darker than the first two images. It is difficult for people to interpret information from a dark image. Finally, the first band combination is chosen as the

Table 4. The OIF of different band combination.

No.	Band combination	Sum of SD	Sum of CC	OIF
1	TM2+TM4+TM7	0.129	0.934	0.138
2	TM3+TM4+TM7	0.135	1.023	0.132
3	TM2+TM4+TM5	0.125	1.036	0.121
4	TM1+TM4+TM7	0.126	1.058	0.119
5	TM3+TM4+TM5	0.131	1.118	0.117
6	TM1+TM4+TM5	0.123	1.115	0.110

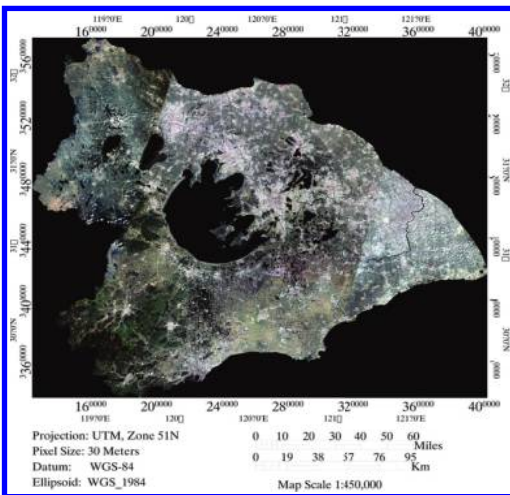


Figure 1. TM3 TM2 TM1 combined imaging.

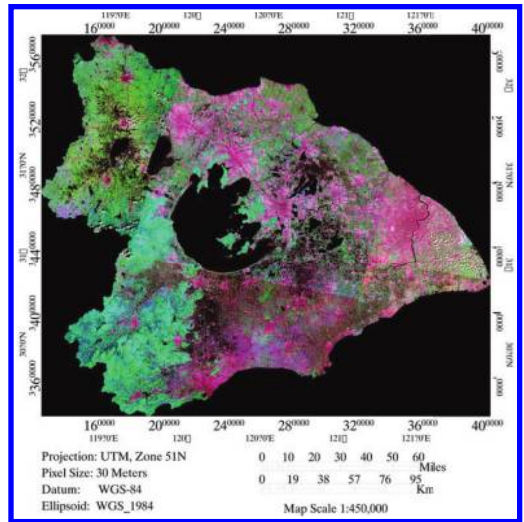


Figure 2. TM1 TM4 TM5 combined imaging.

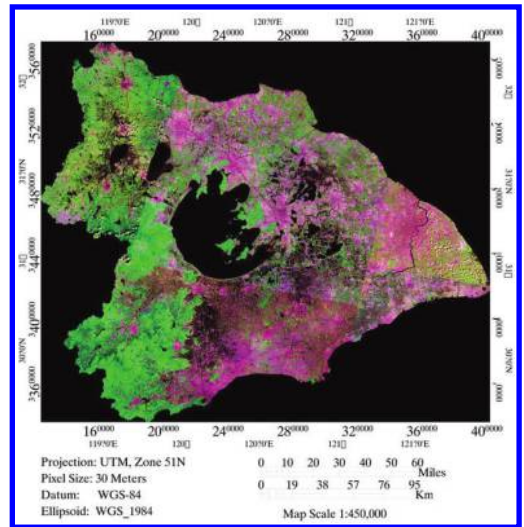


Figure 3. TM2 TM4 TM7 combined imaging.

optimum combination to interpret the vegetation information of the Taihu Basin.

## 6 CONCLUSION

The optimum band combination is very important for RS image interpretation. A reliable optimum band combination is the basis of correct and accurate artificial visual interpretation. We take the Taihu Basin as the typical case. Considering the information plenty and data redundancy, we use

the standard deviation, correlation coefficient, and OIF to identify that the optimum band combination is TM2+TM4+TM7. The combination can clearly exhibit the terrain, vegetation, and the urban area. The method in this paper could be very useful for interpreting multi-spectrum image, but further study is needed to find out whether the method is useful for interpreting high spectrum image.

#### ACKNOWLEDGEMENT

This study is supported by the Commonwealth Science Research Project of Ministry of water resources, China (Grant No. 201301075, 201501014); Program of Science and Technology Promotion, Ministry of Water Resources, P.R.C (Grant No. TG1528); The Central Public Research Institutes basic service charge (Grant No. Y515005); the National Natural Science Foundation of China (Grant No. 51409161, 51479118), and the Jiangsu Province basic research program (Natural Science Foundation funded project, Grant No. BK20140080).

Introduction of the author: Cui Tingting (1985–), Female, Master. Major: Hydrology and Water Resources.

#### REFERENCES

- Chavez P.S., Berlin G.L., Sowers L.B. 1982. Statistical method for Selecting Landsat MSS Ratios. *Journal of Applied Photographic Engineering* 8(1): 23–30. (in Chinese).
- Guo Na & Liu Jianqiu 2012. Optimal Bands Selection of Collecting Vegetation Information in TM Remote Sensing Image—Taking the Expressway from Song xi to Jian'ou in Fujian Province as an Example. *Journal of Fujian Normal University (Natural Science Edition)* 28(1): 103–107. (in Chinese).
- Jiang Xiaoguang, Tang Lingli, Wang Changyao, Wang Cheng 2002. Spectral Characteristics and Feature Selection of Hyperspectral Remote Sensing Data—Taking Shunyi Region of Beijing As a Study Area. *Remote Sensing Technology and Application* 17(2): 59–65. (in Chinese).
- Ma Nahu, Yun Feng, Zhuang Dafang, Wang Xinsheng 2010. Determination on the Optimum Band Combination of HJ-1 A Hyperspectral Data in the Case Region of Dongguan Based on Optimum Index Factor and J-M Distance. *Remote Sensing Technology and Application* 25(3): 358–365. (in Chinese).
- Mei Anxin, Peng Wang, Qing Qiming 2001. *An introduction to remote sensing*. Beijing: Higher Education Press. (in Chinese).
- Wu Wenbo & Liu Zhenggang 2007. A method of the best band combination selection based on spectral characteristics of surface features. *Engineering of Surveying and Mapping* 16(6): 22–24. (in Chinese).

# Agricultural water-saving zoning and suitable water-saving measures in the Yellow River Delta

G.B. Pang

*School of Resources and Environment, University of Jinan, China*

S. Zhang

*Handun Irrigation Management Bureau of Binzhou City, China*

**ABSTRACT:** Agricultural water-saving zoning is not only the foundation work of water-saving agricultural development, but also an important basis for the planning and implementation of regional agricultural water-saving program. Dongying city located in the hinterland of the Yellow River Delta was studied, and index systems about agricultural water-saving zoning were built in this paper, including administrative division, soil types, groundwater mineralization and distribution of river systems. In addition, the method of Geographical Information System (GIS) spatial analysis combined with geostatistics was applied to the water-saving zoning. Dongying city was divided into 5 major types; meanwhile, reasonable agricultural water-saving measures of different regions were proposed to direct the agricultural irrigation and production. This can provide a guideline for high efficiency use of water resources and healthy development of regional economy.

**Keywords:** Yellow River Delta; water-saving agriculture; zoning indicators; GIS

## 1 INTRODUCTION

In recent years, the economic development of the Yellow River Delta has increased rapidly. Due to the scheduling of the Yellow River Basin, the Yellow River water level has decreased. On the one hand, the contradiction between agricultural water and industrial water has become more acute. On the other hand, the agricultural irrigation water efficiency is only 0.45<sup>[1]</sup>. Thus, the development of water-saving agriculture and water-saving technology is critical, while the agricultural water-saving zoning as a foundation work for water-saving agriculture is to be carried out urgently<sup>[2]</sup>. Therefore, the study on the agricultural water-saving irrigation of the Yellow River Delta zoning, proposing agricultural water-saving measures and development direction, can provide a guideline for agricultural water-saving irrigation planning and implementation.

## 2 DIVISION PRINCIPLE

The formulation of agricultural water-saving zoning can reveal the diversity and consistency in the area around the range of agricultural development, and provide evidence for agricultural water conservation planning. The total principle<sup>[3]</sup> is based

on the following aspects: “generalizing similarity, distinguishing difference, considering administrative boundaries”, and following four principles in detail<sup>[4]</sup>. The first is the consistency of natural elements. It means that climate, topography, geomorphology, soil and other natural geographical conditions have a certain similarity, and water resources conditions are similar. Second, the targets of water-saving irrigation are consistent. It means that the main irrigated crops and water-saving irrigation measures should be uniform in the same area. The third one is the integrity of the administrative division. It means that the agricultural water-saving zoning should consider the existed administrative boundary. The fourth is the relative independence. It means that the division results should reflect the characteristics of water-saving irrigation districts. As part of agricultural water conservancy zoning, water-saving irrigation zoning has significantly different characteristics to other water conservancy measures, which is helpful for guiding the development of water-saving irrigation to maintain its relative independence.

## 3 ZONING INDICATOR

The indicators of agricultural water-saving zoning should meet the requirements such as

comprehensiveness, generality and obtaining easily<sup>[5]</sup>. Generally speaking, zoning indicators include 4 to 6 indicators, which are selected from landform, climate, soil, agricultural structure, type of irrigation district and degree of water shortage.

The climate of the Yellow River Delta is similar. It is a typical warm temperate zone monsoon climate area. The irrigation district are mainly the Yellow River irrigation district, where the exploitation of groundwater is rare. It belongs to the northwest plain area of Shandong, and is mainly microtopography in the region. Therefore, climate characteristics, the types of irrigation district and landform are not considered, while the soil structure and water resources distribution have an obvious influence on agricultural water-saving measures. As a result, the administrative divisions, soil type, groundwater salinity, and distribution of river system are selected as agricultural water-saving zoning indicators of Dongying city. They can exactly reflect the agricultural water-saving types and characteristics on this basis of agricultural water-saving zoning.

### 3.1 Administrative division

There are 5 counties and districts, 40 townships and streets in Dongying city. As summarized in Table 1, the Hekou district and Kenli county area are larger, accounting for 27% and 27.82% of Dongying city, while the largest agricultural land is Guangrao county, which is located in the south coast of the Yellow River, accounting for 69.05% of the county. From the overview of the city, agricultural land area accounts for only 39.78% of

Dongying city, which is mainly due to soil salinization, irrigation water shortage, and aging hydraulic project in the area.

### 3.2 Soil type

There are five soil types in Dongying city (Table 2). Cinnamon soil, accounting for about 4%, is mainly distributed in the south of the Xiaoqinghe River, where is the grain, cotton and vegetable high yield area of the city. Lime concretion black soil is mainly distributed in the low-lying place of south brown soil area of the Xiaoqinghe River, accounting for 0.6%, which is suitable for wheat, maize, sorghum and shallow root crops, where is a potential soil type of agriculture. Alluvial soil accounts for 59%, and it is suitable for wheat, maize, and cotton improved by using the tillage method. Saline soil is distributed in the zonal coast, accounting for 36%. There are natural vegetations including reeds, thatch, and wormwood, which mainly rely on aquatic and pasture products. Paddy soil is distributed in Lijin, Kenli county, and accounts for only 0.2%, which has the characteristics of paddy soil in infancy after more than 20 years of water tillage aging.

### 3.3 Groundwater mineralization

Dongying city is formed in the saline basement, in addition to sections of the south of the Xiaoqinghe River, groundwater mineralization is lower than 2 g/L, and nearly 70% of the groundwater depth is 1 to 3 meter and mineralization is 5 to 30 g/L. Moreover, nearly 20% of the

Table 1. The administrative division and agricultural land of Dongying city.

Region	Total area/km <sup>2</sup>	Proportion/%	Agricultural land/km <sup>2</sup>	Proportion/%
Dongying	1155.62	14.59	538.58	46.60
Hekou	2138.97	27.00	569.93	26.65
Kenli	2204.07	27.82	663.29	30.09
Lijin	1286.91	16.24	594.26	46.18
Guangrao	1137.87	14.36	785.75	69.05
Sum	7923.26	100.00	3151.81	39.78

Table 2. The soil types of Dongying city.

Soil types	Area/km <sup>2</sup>	Proportion/%	Distributed district
Cinnamon soil	316.92	4	South of Xiaoqinghe River
Lime concretion black soil	47.54	0.6	Low-lying place of brown soil area
Alluvial soil	4674.57	59	Middle and west of Dongying city
Saline soil	2852.28	36	Zonal coast
Paddy soil	15.85	0.2	Old paddy land of Lijin, Kenli county



groundwater mineralization is more than 30 g/L, with some areas being as high as 100 g/L. As summarized in Table 3, the mineralization of 2 to 10 g/L of groundwater accounts for 56.71%, the mineralization of 10 to 50 g/L accounts for 30.15%, and less than 2 g/L of groundwater only accounts for less than 6%. Brackish water resources should have further development and utilization.

### 3.4 River system

According to the river basin, the current river systems of Dongying city are divided into Huaihe River Basin and Haihe River Basin (Table 4). The south of the Yellow River belongs to the Huaihe River Basin, mostly from east to west, including Xiaoqinghe, Zhimaihe, Guanglihe, Yongfenghe, and its tributaries amount to 20 rivers. The north of the Yellow River belongs to the Haihe River Basin, mostly from south to north, including Chaohe and its tributaries Chuguanhe, Taipinghe, Maxinhe, Zhanlihe, Tiaohe, Shenxiangou and its tributary Xinweidonghe amount to 10 rivers.

Table 3. The groundwater mineralization of Dongying city.

Degree of mineralization/g·L <sup>-1</sup>	Area/km <sup>2</sup>	Proportion/%
<1	284.32	4.18
1~2	118.28	1.74
2~10	3859.29	56.71
10~50	2051.76	30.15
>50	491.92	7.23

## 4 DIVISION METHOD

There are many division methods, for example, empirical method, index method, type method, overlapping method, cluster method, and fuzzy cluster method<sup>[6]</sup>. The method of GIS spatial analysis combined with geostatistics has a strong spatial analysis function, and a good quantitative and spatial interpolation. It has not only the basis of significant but also characteristics of quantification, and it is superior to the traditional mapping methods, which can provide a more accurate method for regional agricultural water-saving zoning.

As shown in Figure 1, first, ArcGIS10.2 was applied to implement geometric correction, vectorization of division element base map and construct division element database. Second, the spatial analysis function of GIS was applied to draw the river system distribution density map based on the administrative divisions; at the same time, the space distribution features of groundwater mineralization, soil texture, river system distribution density were analyzed. Third, a multi-factor comprehensive analysis based on the correlation analysis of each factor and agricultural water saving was carried out; thus, the space analysis function of GIS was applied to complete the space layout of agricultural water-saving zoning. Finally, fuzzy evaluation based on the results of the multi-index spatial overlay analysis, and the thematic mapping function of GIS were used to draw the mapping of agricultural water-saving zoning.

## 5 DIVISION RESULT

As shown in Figure 2, agricultural water-saving zoning of Dongying city can be divided into

Table 4. The river system of Dongying city.

River basin	Channel	Area/km <sup>2</sup>		Length/km	
		Total	Dongying	Total	Dongying
Huaihe river basin	Xiaoqinghe	10337	585	237	34
	Zhimaihe	3382	1508	135	68.2
	Guanglihe	510	510	47.3	47.3
	Yongfeng	200	200	33.8	33.8
	Zhangzhen	140	140	28	28
	Xiaodaohe	120.8	120.8	27.5	27.5
Haihe river basin	Chaohe	1408	427.7	73.5	24
	Maxinhe	275	204	55.6	35.6
	Zhanlihe	343	343	60.7	60.7
	Caoqiao	472	472	46	46
	Tiaohe	504	504	32.6	32.6
	Shenxian	350	350	30	30

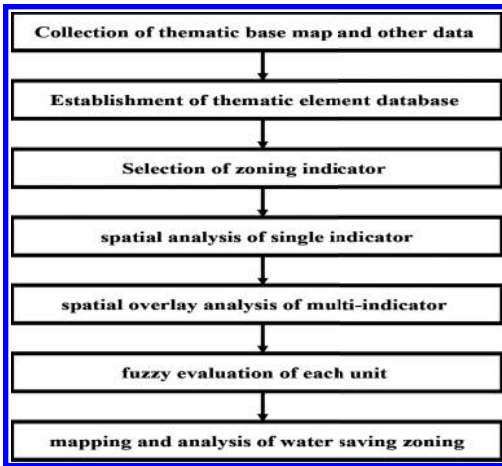


Figure 1. The flow chart of division.

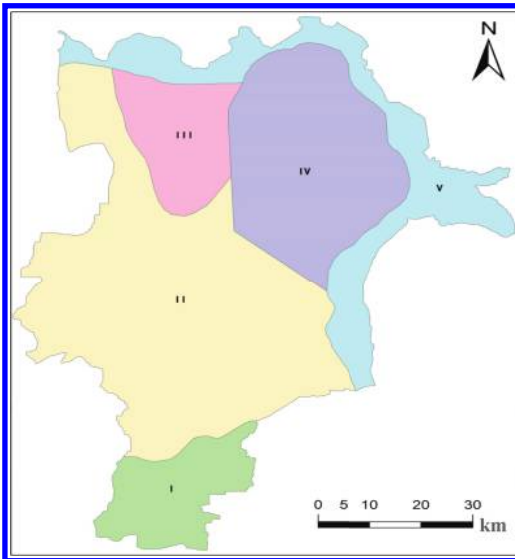


Figure 2. The agricultural water-saving zoning of Dongying city.

five types. The location, area, and proportion of each division are listed in Table 5. The suitable agricultural water-saving measures and development direction are established according to the characteristics of each division, especially water resources condition, agricultural planting structure and soil type.

I. area is 669.49 km<sup>2</sup>, it accounts for 8.45% of Dongying city, located in the south of Xiaoqing River, Guangrao county. The average annual rainfall is 602 mm, the soil and water

conditions are better, which contains high-yield grain, cotton, vegetable production areas of Dongying city. In this area, grain crops (wheat, corn) are suitable for surface irrigation and pipeline irrigation, and economic crops (cotton, vegetables) are suitable for sprinkler irrigation and drip irrigation. The strategy is priority exploitation of surface water and moderate exploitation of groundwater, maintaining the existed grain area, improving the yield, and establishing grain and vegetable production base of the city.

II. area is 3567.73 km<sup>2</sup>, which accounts for 45.03% of Dongying city, located in the middle and west of the city and distribution along the Yellow River. It is the biggest division, and the average annual rainfall is 560 mm. There is little amount of fresh groundwater in Lijin and Kenli county along the Yellow River, and the rest of the groundwater salinity is 2 to 10 g/L, which is not suitable for irrigation, so it relies mainly on Yellow River water and surface water. Major soil type is alluvial soil, and it is mainly cultivated soil of the city, which is suitable for wheat, corn, rice and other food crops after cultivation improvement. In this area, food crops (wheat, corn, rice) are suitable for surface irrigation, pipeline irrigation and controlled irrigation, and crops' brackish water irrigation technology (2–5 g/L) should be explored. The strategy is priority exploitation of surface water and Yellow River water, speeding up the engineering construction, lining the channels, expanding the existed grain area, improving the yield, and establishing the food production base of the city.

III. area is 684.55 km<sup>2</sup>, and it accounts for 8.64% of Dongying city, located in the west of the Tiaohe River, and in the east of the Zhanli River. The average annual rainfall is 530 mm, and the groundwater salinity is more than 10 g/L, so it relies mainly on the Yellow River water, and the soil types are moderate and severe salinization alluvial soil, which is suitable for wheat, cotton, and fruit trees after cultivation improvement. In this area, food crops (wheat) are suitable for surface irrigation and pipeline irrigation, and economic crops (cotton, fruit trees) are suitable for sprinkler irrigation and drip irrigation, and the area of high soil salinization can develop an agriculture-fishery mode. It mainly adopts irrigation way by plain reservoir and conveyance channel, building a new plain reservoir, speeding up the engineering construction, lining the channels, maintaining the existed grain areas, exploring the agriculture-fishery development mode actively, and establishing

Table 5. The agricultural water-saving zoning of Dongying city.

Division	Denomination	Area/km <sup>2</sup>	Proportion/%
I	South piedmont alluvial plain region	669.49	8.45
II	Middle and west Yellow River flood plain region	3567.73	45.03
III	North coastal plain region	684.55	8.64
IV	Modern Yellow River Delta region	1731.18	21.85
V	Coastal beach region	1267.68	16

an efficient planting and raising the ecological agriculture mode.

IV. area is 1731.18 km<sup>2</sup>, and it accounts for 21.85% of Dongying city, located in the east of Kenli county along the Yellow River, which includes mostly east of the Hekou district and Kenli county. The average annual rainfall is 550 mm, and the groundwater salinity is more than 2 to 10 g/L, which is not suitable for irrigation, so it relies mainly on the Yellow River water, and the soil type are moderate and severe salinization alluvial soil in the area, which is suitable for wheat, cotton, fruit trees, vegetables and other crops after cultivation improvement. In this area, food crops (wheat) are suitable for surface irrigation and pipeline irrigation, and economic crops (cotton, fruit trees) are suitable for sprinkler irrigation and drip irrigation, and crops' brackish water irrigation technology (2–5 g/L) should be explored. It mainly adopts irrigation way by plain reservoir and conveyance channel, building a new plain reservoir, speeding up the engineering construction, laying pipes, and developing facility agriculture, tourism agriculture and other modern ecological agriculture mode.

V. area is 1267.68 km<sup>2</sup>, and it accounts for 16% of Dongying city, located in the zonal coastal beach. The average annual rainfall is 560 mm, and the groundwater salinity is more than 10 to 50 g/L, and the surface water is also saline water and the fresh water relies mainly on the Yellow River. In this area, salt-tolerant economic forest is planted by using saline-alkali land afforestation technology, developing animal husbandry by rich forage grass resources, exploiting the mariculture, improving the ability of fishing, and building modern fishery production base gradually.

## 6 CONCLUSION

Index systems about agricultural water-saving zoning were established, including administrative

division, soil types, groundwater mineralization and distribution of river systems. In addition, the method of GIS spatial analysis combined with geostatistics was applied to the agricultural water-saving zoning. Dongying city was divided into 5 major types. At the same time, reasonable agricultural water-saving measures were proposed to direct the agricultural irrigation and production, which can provide a guideline for regional agricultural water-saving irrigation planning and implementation.

## ACKNOWLEDGMENTS

This work was financially supported by the Shandong Natural Science Foundation (No. ZR2014EEQ020) and the Shandong Water Conservancy Science and Technology Practice Project (No. SDSLKY201306, SDSLKY201502).

## REFERENCES

- [1] Pang G.B. Zhang B.X. & Zhang S. 2014. Analysis of agricultural water utilization level in the Yellow River Delta. *Journal of University of Jinan* 28(6): 416–420. (in Chinese).
- [2] Liu K. Li C.H. & Yang X.L. 2012. Water resources supply-consumption (demand) balance Analyses in the Yellow River Basin in 2009. *Procedia Environmental Sciences* 22(13): 1956–1965.
- [3] Lv C.B. & Zhao H.Y. 2005. Irrigation zoning and rationality analysis of Heilongjiang province. *China water resources* (1): 54–55. (in Chinese).
- [4] Li Y.N. Huang X.Q. & Wu J.S. 1998. Evaluation of soil and water resources and water-saving irrigation planning. Beijing: water conservancy and hydropower press. (in Chinese).
- [5] Bai Q.J. Zhang Q.H. Yan Y.L. Liu L. & Zhao Z.X. 2009. Indicators of Water Utilization Characteristics for the Agricultural Irrigation Dividing Area in Shandong Province. *Journal of irrigation and drainage* 28(5): 13–15. (in Chinese).
- [6] Han D. Zhou S.F. Shi Q. & Wu D.F. 2004. Water saving irrigation division methods. *Water Saving Irrigation* 23(6): 42–44. (in Chinese).

# Study on the influence of the miter gate thrust on the lock head structure

W.C. Xu

College of Harbor, Coastal and Offshore Engineering, Hohai University, Nanjing, China

Q.C. Ning

CCCC Water Transportation Planning and Design Institute Co. Ltd., Nanjing Branch, Nanjing, China

C. Li & Y.Q. Shi

College of Harbor, Coastal and Offshore Engineering, Hohai University, Nanjing, China

**ABSTRACT:** This paper uses two kinds of conventional methods to calculate the internal force of the lock head side pier and the lock head floor. The first calculation method is recommended in the *Code for design of hydraulic structures of ship locks*, calculating the internal force of the lock head structure when considering the supporting wall as an independent structure to bear the gate thrust individually. Another analytical method is to distribute the miter gate thrust to the front and rear sections of the gate before calculating the internal force of the lock head. Moreover, ANSYS software is also used to analyze the lock head structure in this article. The comparative analysis of the results shows that defects exist in the code of the first conventional method. However, the results of the second conventional method are consistent with those of the calculation of ANSYS software.

**Keywords:** miter gate thrust; lock head structure; internal force; finite element method

## 1 INTRODUCTION

The ship lock is a hydraulic structure, which ensures that the ship can sail across the channel where there is concentrated water drop. The ship lock is composed of the upper lock head, lower lock head, gate lock, water retaining structure and water conveyance system, which can ensure the rise and fall of the water level<sup>[1]</sup>.

Lock head structure can be divided into front door segment, niche segment and supporting segment in the longitudinal direction. The supporting segment of the gate refers to the section that can bear the gate thrust, and should meet the requirements of structural strength and stability. In the engineering design, the length of the supporting segment could be determined by checking the supporting segment's strength and stability under the independent working condition. Therefore, the supporting segment needs to have enough length.

## 2 ENGINEERING EXAMPLE

The lower head of a ship lock from Anhui Province is a monolithic, concrete and symmetric structure.

The lower head is composed of the miter gate, flat bottom floor, side pier with an empty container and a water transmission way. The width of the lock head is 42 m. The length of the lock head is 24 m. The length of the emergency gate is 2.4 m. The lock head structure details are shown in Figure 1.

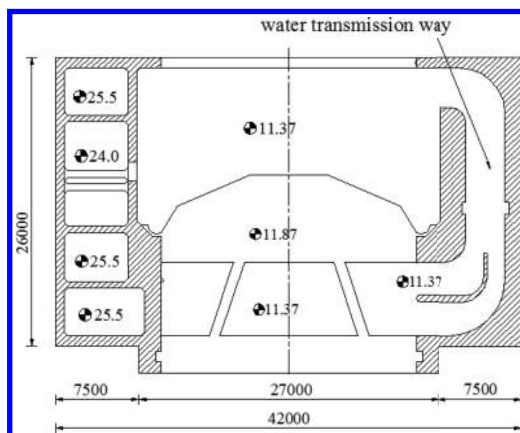


Figure 1. Planar graph of the lock head.

### 3 THE INTERNAL FORCE CALCULATION OF THE LOCK HEAD STRUCTURE

#### 3.1 The selection of the calculation conditions

The completion period is selected for the calculation conditions. During the completion period, the side pier is completed, no water in the lock head and backfill soil is backfilled temporarily to the top of the floor. So, the side pier only bears self-gravity and the earth's pressure. Then, by using the conventional methods and the finite element method, the internal force of the side pier of the lock head and that of the lock head floor can be obtained.

Because this paper is mainly focused on the influence of the miter gate thrust on the side pier and the floor, the maximum water level difference period is selected. The miter gate thrust reaches the maximum and the side pier reaches the most disadvantageous state in this period.

According to the literature data and reasonable analysis<sup>[2]</sup>, the overhaul period is often the control load for the maximum negative moment of the lock floor, because the lock head is under a high uplift pressure because there is no water in the lock head and there is a high underground water level behind the lock head wall. So, the overhaul period should be selected.

As shown in Figure 1, the lock head structure can be divided into three sections: the first section is the niche segment; the second section is the supporting segment; the third section is the front door segment. This paper focuses on the effect of the influence of the miter gate thrust on the lock head structure, so the first segment and the second segment are selected and analyzed, which are affected by the miter gate thrust.

#### 3.2 The conventional calculation methods

##### 3.2.1 The calculation method of the supporting wall

Bidirectional bending compression formula is used to calculate the strength of the supporting wall. The stress of the four corner points (A, B, C, D) is calculated by the following formula:

$$\sigma_{min}^{max} = \frac{\Sigma V}{F} \pm \frac{\Sigma M_x}{W_x} \pm \frac{\Sigma M_y}{W_y} \quad (1)$$

where  $\sigma_{max}$  = maximum stress of the bottom of the supporting wall;  $\sigma_{max} < [\sigma]$ ,  $[\sigma]$  = allowable compressive strength;  $\sigma_{min}$  = minimum stress of the bottom of the supporting wall,  $\sigma_{min} > 0$ ;  $F$  = area of the bottom of the supporting wall;  $W_x$  and  $W_y$  are the section modulus of the bottom of the supporting wall in the X and Y axis;  $M_x$  = the sum of the X axis's moment that is dependent on the

longitudinal horizontal force; and  $M_y$  = sum of the Y axis's moment that is dependent on the transverse horizontal force and vertical force.

##### 3.2.2 The calculation method of the lock head floor

When the miter gate thrust acts on the supporting segment, the cross component of the miter gate thrust can be assigned along the lock head's axial direction, which is according to the following methods: the cross component of the miter gate thrust, which is transferred along the side pier's height, can be divided into several concentrated forces ( $S_{yi}$ ). Each concentrated force is diffused into a certain range according to the diffusion angle of 45 degrees along the side pier from top to bottom (see Fig. 2). The lateral force ( $T$ ), which is transmitted to the unit length of the floor, and the moment ( $M$ ) are given in the following formulas:

$$\left. \begin{aligned} T &= \sum_{i=1}^n \frac{S_{yi}}{l_i} \\ M &= \sum_{i=1}^n \frac{S_{yi}h_i}{l_i} \end{aligned} \right\} \quad (2)$$

where  $h_i$  = distance from  $S_{yi}$  to the central axis of the floor and  $l_i$  = the distribution length of  $S_{yi}$  transferring to the lock head floor.

##### 3.2.3 The calculation methods

The conventional methods can be calculated by using the following two methods.

Method 1: using the method recommended by the Code for design of hydraulic structures of ship locks<sup>[2]</sup>. The lateral component of miter gate thrust is average supported by the supporting segment.

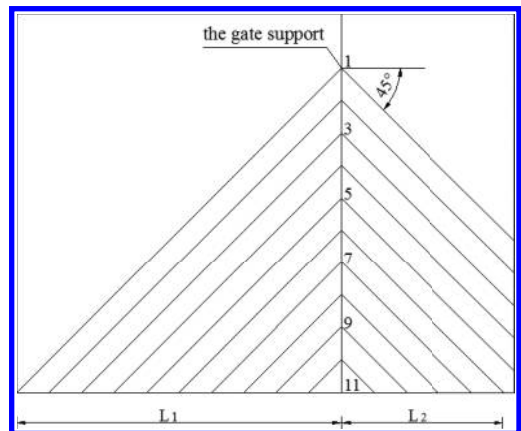


Figure 2. The lateral thrust distribution along height of the miter gate.

Then, the four corners stress can be calculated by formula (1). The internal force of the floor can be calculated by Guoshi Charts and can be adjusted by the weighted average method.

Method 2: using the method recommended by the *Canalization project*<sup>[3]</sup>. First, the cross component of the miter gate thrust is assigned to the two segments, which are calculated according to formula (2). Second, the four corners stress can be calculated by formula (1). Third, the internal force of the floor can be calculated by Guoshi Charts and need not be adjusted.

### 3.3 Comparative analysis and calculation of ANSYS

First, the internal force of the structure is analyzed by using ANSYS. Then, SOLD45 is selected, which is the three-dimensional 8-node isoparametric unit, to form the head lock. Because the lock head structure is symmetrical, it can be set up only half of the model for calculation and analysis<sup>[4-5]</sup>. Figure 3 shows the finite element model of the lower lock head. Figure 4 shows the finite element model of the lock head floor.

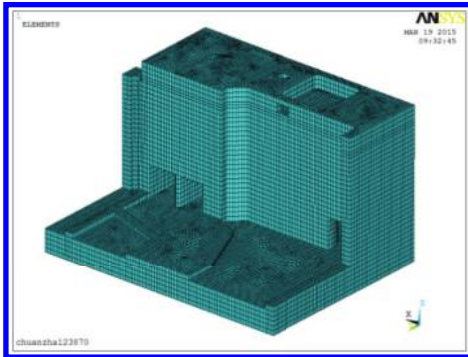


Figure 3. Finite element model of the lower lock head.

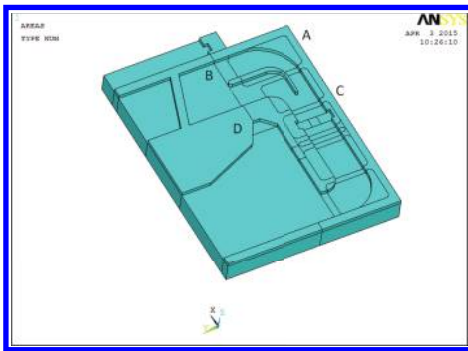


Figure 4. Finite element model of the lock head floor.

## 4 COMPARISON BETWEEN THE CALCULATION RESULTS USING THE CONVENTIONAL METHOD AND THE CALCULATION RESULTS USING THE ANSYS METHOD

Three represented conditions are selected to calculate the lock head. The four corners of the supporting wall and the lock head floor can be calculated by using the two kinds of methods.

### 4.1 The analysis of calculated results in the completion period

#### 4.1.1 The analysis of stress of the supporting wall in the completion period

The stress pattern of the Z direction, which is on the bottom of the supporting wall in the completion period, is abstracted from the ANSYS model. The stress pattern is shown in Figure 5.

As shown in Figure 5, the maximum tensile stress is 3.22 Mpa and the maximum compressive stress is 1.04 Mpa. Due to the uneven settlement of the lock head structure, the tensile stress zone appears on the bottom of the supporting wall. The area of the tensile stress zone is 2.34 m<sup>2</sup>.

The stress, which is on the bottom of the supporting wall in the completion period, is abstracted from Figure 5, which is given in Table 1.

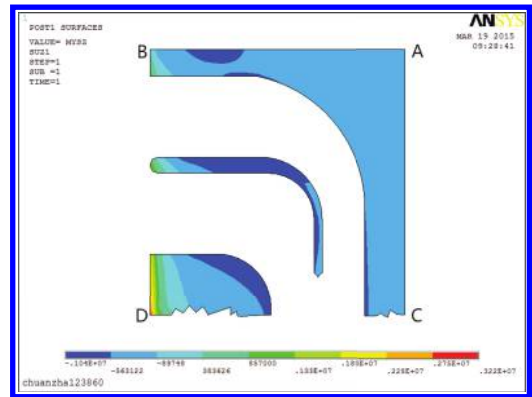


Figure 5. The stress pattern of the Z direction on the bottom of the supporting wall in the completion period.

Table 1. The stress of the bottom of the supporting wall in the completion period (kPa).

Location	A	B	C	D
ANSYS	296.8	341.4	336.2	221.4
Method 1	339.3	339.3	339.3	339.3
Method 2	339.3	339.3	339.3	339.3

Because there is no miter gate thrust in the completion period, it results in the same results according to method 1 and method 2. Through comparing the results of two conventional methods with those of one ANSYS method, the conventional method and ANSYS method calculation results are approximately the same. However, the two kinds of methods have a large difference in the results of location D. This is because ANSYS considers the overall working characteristics of the side pier. The settlement of the lock head under self-weight is not uneven, which leads to the local tensile stress zone on the bottom of the supporting wall.

#### 4.1.2 The analysis of stress of the lock head floor in the completion period

The first and the second moment values, which are on the bottom of the supporting wall in the completion period, are abstracted from the ANSYS model. The moment pattern figures are shown in Figure 6 and Figure 7.

It can be seen from Figure 6 and Figure 7 that in the absence of the miter gate thrust, the conventional methods and the ANSYS method lead to approximately the same results for the floor moment of the first section and the second section. However, the moment distribution curves of

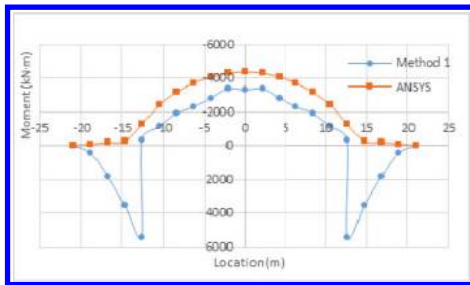


Figure 6. The first section of the moment of the lock head floor in the completion period.

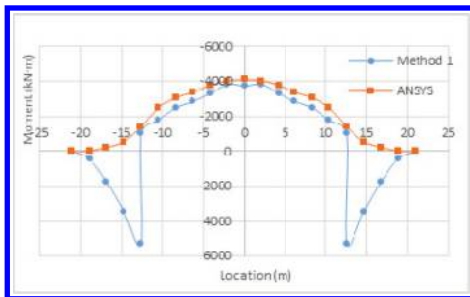


Figure 7. The second section of the moment of the lock head floor in the completion period.

the lock head floor of ANSYS calculation results are smoother than the results of the conventional method calculation.

#### 4.2 The analysis of calculated results in the maximum water level difference period

##### 4.2.1 The analysis of stress of the supporting wall in the maximum water level difference period

The stress pattern of the Z direction, which is on the bottom of the supporting wall in the maximum water level difference period, is abstracted from the ANSYS model. The stress pattern is shown in Figure 8.

As shown in Figure 8, the force of the supporting wall is in the most unfavorable circumstance under the miter gate thrust. The maximum tensile stress reaches up to 5.27 Mpa. The maximum compressive stress is 1.38 Mpa. On the bottom of the supporting wall, the distribution range of the tensile stress increases. The area of the tensile stress zone increases to 2.62 m<sup>2</sup>.

The stress, which is on the bottom of the supporting wall in the maximum water level difference period, is abstracted from Figure 8, as presented in Table 2.

Compared with the results of ANSYS, the results of method 1 in both the maximum stress

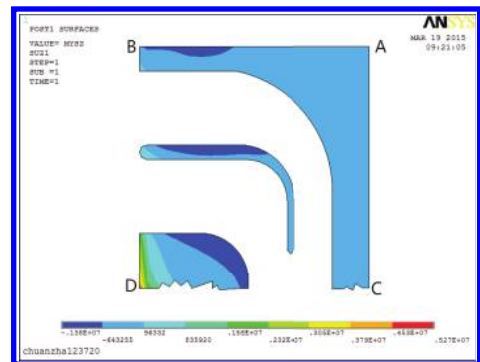


Figure 8. The stress pattern of the Z direction on the bottom of the supporting wall in the maximum water level difference period.

Table 2. The stress of the bottom of the supporting wall in the maximum water level difference period (kPa).

Location	A	B	C	D
ANSYS	320.6	497.9	280.1	160.6
Method 1	634.4	457.5	180.0	3.2
Method 2	314.9	478.9	158.6	322.7

and minimum stress are over-conservative, as it can be seen from Table 2. The results of method 2 are approximately in agreement with those of the ANSYS model. The central zone of tensile stress (Fig. 8) calculated from the ANASYS model leads to the stress result of location D, and is less than that of model 2. Therefore, a sufficient cognition about the tensile stress zone should be taken into consideration in the engineering design.

#### 4.2.2 The analysis of stress of the lock head floor in the maximum water level difference period

The values of the first and the second moment, which are on the bottom of the supporting wall in the maximum water level difference period, are abstracted from the ANSYS model. The moment pattern figures are shown in Figure 9 and Figure 10.

Figure 9 and Figure 10 reflect the moment results of the lock head floor according to the different calculation methods. As shown in the figures, the floor moment values are relatively small by using method 1, especially the gap between the results of the floor in the first section by using method 1 and the results by using the ANSYS model is very large. The reason for the gap is that

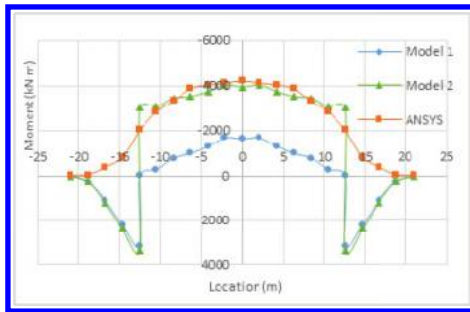


Figure 9. The first section of the moment of the lock head floor in the maximum water level difference period.

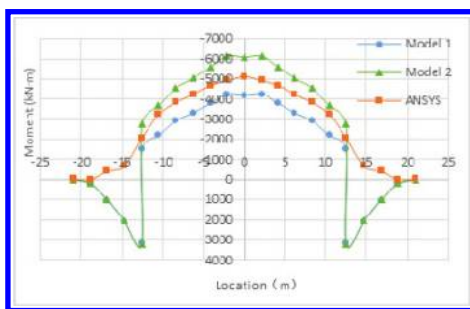


Figure 10. The second section of the moment of the lock head floor in the maximum water level difference period.

the cross component of the miter gate thrust is averagely borne by the supporting wall. Compared with method 1, the results of method 2 agree well with those of the ANSYS model and can reflect the actual working state of the floor better. The reason is that the miter gate thrust that acts on the floor is distributed by formula (2) and the middle section of the floor bears the maximum external force.

#### 4.3 The analysis of calculated results in the overhaul period

##### 4.3.1 The analysis of stress of the supporting wall in the overhaul period

The stress pattern of the Z direction, which is on the bottom of the supporting wall in the overhaul period, is abstracted from the ANSYS model. The stress pattern is shown in Figure 11.

As shown in Figure 11, the maximum tensile stress is 1.79 Mpa and the maximum compressive stress is 0.93 Mpa. There is no miter gate thrust during the overhaul period. The effect of the earth's pressure behind the wall leads to the decrease in tensile stress zone on the bottom of the supporting wall. The area of the tensile stress zone decreases to 1.1 m<sup>2</sup>.

The stress, which is on the bottom of the supporting wall in the overhaul period, is abstracted from Figure 11, which is given in Table 3.

It can be analyzed from Table 3 that the calculation results of the conventional methods agree well

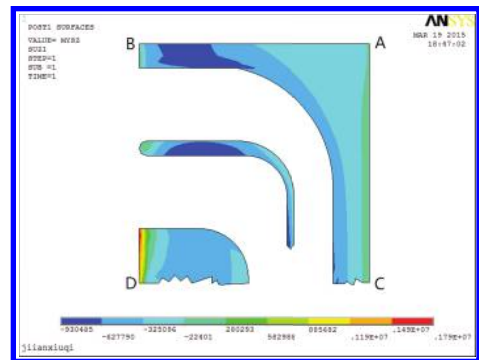


Figure 11. The stress pattern of the Z direction on the bottom of the supporting wall in the overhaul period.

Table 3. The stress of the bottom of the supporting wall in the overhaul period (kPa).

Location	A	B	C	D
ANSYS	122.9	501.2	267.2	257.4
Method 1	112.3	491.5	272.4	651.6
Method 2	112.3	491.5	272.4	651.6



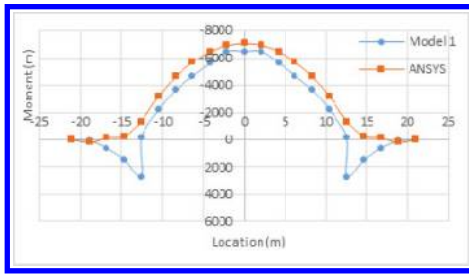


Figure 12. The first section of the moment of the lock head floor in the overhaul period.

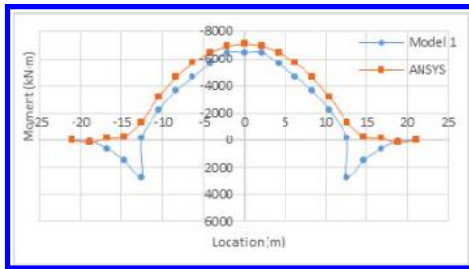


Figure 13. The second section of the moment of the lock head floor in the overhaul period.

with those of the finite element method, because there is no miter gate thrust and the supporting wall just bears water pressure and earth's pressure behind the wall.

#### 4.3.2 The analysis of stress of the lock head floor in the overhaul period

The first and the second moment values, which are on the bottom of the supporting wall in the overhaul period, are abstracted from the ANSYS model. The moment pattern figures are shown in Figure 12 and Figure 13.

It can be analyzed from Figure 12 and Figure 13 that in the absence of the miter gate thrust, the conventional methods and the ANSYS method lead to almost the same floor moment values.

## 5 CONCLUSIONS

In this paper, a lock head of a ship lock project is analyzed by using the three-dimensional nonlinear finite element method and two conventional methods. By comparing the ANSYS method with the

two conventional methods, the main conclusions can be drawn as follows:

1. In the absence of the miter gate thrust, the stress on the bottom of the supporting wall and the moment of the lock head floor, calculated by conventional methods, can reflect the lock head's overall working condition well. The results of conventional methods are approximately in agreement with the calculation results of ANSYS.
2. When the side pier of the lock head bears the miter gate thrust, the view that the supporting wall is a unique structure is too conservative when compared with the results of ANSYS. The supporting wall stress is reasonable by assigning the cross component of the miter gate thrust. There exist defects in the two conventional methods when the miter gate thrust exists. This is because the two methods cannot consider the tensile stress zone on the bottom of the supporting wall.
3. When there is no miter gate thrust that acts on the side pier, the conventional methods agree well with the ANSYS method with respect to the results of the lock head floor. But when the miter gate thrust exists, the moment results of the floor by using method 1 are relatively small, in which case, the results by using method 2 agree well with those by using ANSYS.

Therefore, in order to ensure the rationality of the engineering structure design, the two conventional methods should be calculated, respectively, and the more disadvantageous values by using the two conventional methods should be used as the design basis.

## REFERENCES

- [1] Bin, Yang. & Xu, Zhu. 2010. Calculation on lock head of ship lock by 3-D nonlinear finite element. *Journal of Waterway and Harbor* 31(5):537-542.
- [2] JTJ307-2001, Specifications for load design of hydraulic structures.
- [3] Xiaoping, Liu (ed.). & Guinan, Tao (ed.). 2009. *Canalization Project*. Beijing: Communications Press.
- [4] Zhouhong, Cao, Fengjun, Hu, Baohu, Sun, Xiaoping Liu. 2011. On reduction factors of floor's deadweight in castle shiplock design. *Port & Waterway Engineering* (4):158-161.
- [5] Liangde, He. & Gang, Li. 1997. Discussion on the calculation method of the lock head floor. *Port & Waterway Engineering* (12):30-34.

# Study on the prediction of flood disaster in Nanning City based on the gray neural network

R.Y. Ma, M. Lu & S.Y. Wang  
Guangxi University, Nanning, China

**ABSTRACT:** First, the feasibility of forecasting flood is studied, which is based on the combination model of neural network and the gray system theory. Then, taking the flood disaster of the Yu River in Guangxi Nanning City as the research object, the disastrous flood level is defined as 73 m and 75 m sequences of 2 cases for forecasting research by comparing according to the annual flood disaster data of Nanning City. By establishing the gray GM (1, 1) model of two series, respectively, and the 2 cases of the above flood series in the most recent disastrous flood year are forecasted based on the gray neural network. The results show that the predictive accuracy of the gray neural network model is very high and has high reliability. Finally, the 2 flood sequences are extrapolated to forecast, respectively, by using the trained network weights and threshold. The results show that the next disastrous flood in Nanning City will occur in 2018, which can be used as a reference for decision-making of disaster prevention and mitigation in Nanning City.

**Keywords:** combination model; gray neural network; flood disaster; flood forecasting

## 1 INTRODUCTION

Flood disaster is a common kind of disaster, which is one of the natural disasters that brings most serious losses to human life and property, and almost 40% of the loss that natural disaster brings to the modern society is caused by it. Therefore, disastrous flood forecasting is vital for preventing a city from being attacked by flood. There are different models for disastrous flood forecasting. However, due to the complication of the causes and influence factors on the formation of flood disaster, the study conducted in the field for forecasting flood disaster still needs constant exploration and improvement at home and abroad. In recent years, with the continuous progress of science and technology, new mathematical models have emerged endlessly, which provides a lot of new ways for flood forecasting, such as gray system theory method, artificial neural network method and combination model method.

The theory of combination model was proposed in the 1960s. In 1969, J.M. Bates and C.W.J. Granger explained the forecasting method of combination model systematically, and their study has been widely recognized by other experts and scholars in this relevant field. Since 1980, the combination model has been paid more attention. More scholars have put their effort into studying it, and more relevant essays have been published. In recent years, scholars in China have also made great

achievements in the study of combination model. Geng Yuemin proposed a forecasting method of combination model based on optimal weighting, which is used to solve the existing problems of various single traditional forecasting methods. The Tianhe hydrological station in Pearl River Delta was taken as an example. Under the forecasting requirements of water level, a combination model was constructed, which is composed of the multiple linear regression, GM (1, 1) and BP neural network, by using the optimal weighting method. The results show that the predictive accuracy of the combination model has a larger increase than the single model.

This paper establishes a gray neural network combination model of flood forecasting of the Yu River in Nanning City, and then extrapolates the occurrence time of the next disastrous flood in Nanning City.

## 2 GRAY NEURAL NETWORK MODEL

### 2.1 Principle theory of combination model

In practical engineering, we usually choose various different kinds of prediction model to forecast a set of time sequence variables. In the prediction process, due to the different structures and characteristics of the model, different prediction models can provide different available information. If a class of prediction errors of a model is simply

rejected, a lot of available information will be lost as well.

The comprehensive utilization of different forecasting models can reduce the randomness and make effective use of information, to avoid losing important information of a single model. Forecasting model of multiple characteristics is combined together with suitable ideas and forms through scientific analysis, and then establishes the corresponding combination model to forecast. It is the development direction for future forecasting in this field.

### 2.2 *The feasibility of the gray neural network model*

In the prediction process, how to establish a suitable prediction model is of great importance. When modeling the gray system theory, it does not fully adhere to the original data. It not only respects the rationality of the original data, but also allows for scientific treatment, adjustment and amendment to the original data of the forecasting object, which makes the gray system model combine more properly than other models, and can be used as an appropriate model to do combination forecasting with other models.

The GM model has many great advantages. For example, it weakens the randomness of the original data, needs a small amount of calculation and sample data, and has a relatively high predictive accuracy in a short period of time. But there are also some specific limitations, such as lack of self-organized adaptability and feedback corrected ability. And it is difficult to adjust by the error's feedback. However, artificial neural network has a good nonlinear learning ability and adaptive ability, and it can control the predicted error. It also has advantages such as good robustness, fault tolerance and generalization ability, which can make up the inherent limitations of the gray system models to a certain extent.

Under the condition of giving full play to the advantages of the gray system model, with the help of the advantage of the artificial neural network to modify the poor prediction residual sequence, satisfactory results can be obtained. Therefore, the establishment of the gray system combined with the neural network forecasting model will greatly improve the predictive accuracy of the models.

### 2.3 *The forecasting model structure of the gray neural network*

The basic structure of the gray neural network prediction model is essentially a kind of combination forecasting model with residual error correction. First, the original data is normalized and one-time cumulated to establish the gray neural network model.

1. Forecast with the original data sequence  $x^{(0)}(i)$ , according to the principle of the least square method and GM (1, 1). The simulated data  $\hat{x}^{(0)}(i)$  is the prediction sequence, and the residual sequence of GM (1, 1) is obtained after fitting.
2. Establish the BP neural network model, and calculate the residual sequence  $e^{(0)}(i) = x^{(0)}(i) - \hat{x}^{(0)}(i)$ ,  $i = 1, 2, \dots, n$ . If the predictive order is S, then some sequences such as  $e^{(0)}(i - 1)$ ,  $e^{(0)}(i - 2)$ , ...  $e^{(0)}(i - S)$  form. The input vectors are  $e^{(0)}(i - 1)$ ,  $e^{(0)}(i - 2)$ , ...  $e^{(0)}(i - S)$ , and the output vector is  $e^{(0)}(i)$ . The network is trained through the residual sequence based on the BP neural network algorithm, and different input vectors will get corresponding output vectors. The parameters such as weights and threshold are the trained values, which are obtained through the neural network's self-adaptive learning. After achieving the satisfactory accuracy of error, the trained BP neural network can be used as the effective means of residual sequence prediction to get better results.
3. Data combination. sequence  $e^{(0)}(i)$  is fitted and forecasted using the trained network, and then the residual sequence  $\hat{e}^{(0)}(i)$  is obtained after correction. The final model is  $\hat{X}^{(0)}(i) = \hat{x}^{(0)}(i) + \hat{e}^{(0)}(i)$ .

## 3 THE PREDICTION MODEL OF DISASTROUS FLOOD OF THE YU RIVER IN NANNING CITY BASED ON THE GRAY NEURAL NETWORK

### 3.1 *Determination of the disastrous flood level of the Yu river in Nanning City*

The warning level of flood control of the Yu River in Nanning City is 73 m. When the flood level exceeds it, Nanning will suffer different degrees of floods. A total of 131 years of historical data, from 1881 to 2012, in Nanning hydrological station II demonstrate that there are a total of 32 flood levels that exceed the warning level, as shown in [Table 1](#).

### 3.2 *The establishment and inspection of the prediction model of disastrous flood of the Yu River in Nanning City*

**3.2.1 *The establishment of the prediction model***  
 Before forecasting, the forecasting accuracy of the gray neural network should be analyzed. First, we select the first 31 sequences above 73 m and the first 31 sequences above 75 m as learning samples to forecast, while the occurrence time of the 32nd flood and the 14th flood are used as the testing dataset to know the accuracy of the gray neural network forecasting model.

Table 1. Above the warning level of the Yu River in Nanning hydrological station II.

Year	Level (m)	Flow (m <sup>3</sup> /s)
1881	79.89	19486
1908	76.13	13360
1913	79.1	18167
1914	75.15	12021
1915	77.4	15348
1936	76.37	13730
1937	77.58	15640
1947	74.06	10673
1950	73.3	9844
1954	73.03	9552
1955	74.48	11186
1958	73.73	10308
1958	74.71	11446
1960	73.07	9596
1968	75.16	12034
1968	76.39	13761
1971	75.37	12316
1973	73.64	10211
1978	73.37	9920
1978	73.12	9860
1980	73.55	10114
1985	75.42	12383
1985	73.64	10211
1986	73.44	9995
1986	75.74	12812
1992	74.18	10820
1994	75.42	12383
1994	74.36	11039
2001	77.18	14912
2008	75.18	11300
2008	74.34	11010
2012	73.06	9620

Generating matrices of the original sequence, respectively, we obtain

$$x^{(0)}(i) = (x^{(0)}(1), x^{(0)}(2), \dots, x^{(0)}(31));$$

$$y^{(0)}(i) = (y^{(0)}(1), y^{(0)}(2), \dots, y^{(0)}(13)).$$

We then normalize the model. Before establishing the model, all the original data are divided by 1000 and minus 0.881 to make the initial value as 1.

According to the gray system theory, the original data are one-time cumulated in order to improve the regularity of the original data. Establishing the corresponding albinism differential equation of GM (1, 1) model, we obtain

$$dx^{(1)}/dt + ax^{(1)} = u.$$

where  $a, u$  are parameters.

$$\text{Suppose } \hat{a} = \begin{pmatrix} a \\ u \end{pmatrix}.$$

Table 2. Parameters  $a$  and  $u$ .

Parameters	Sequence $x^{(0)}(i)$	Sequence $y^{(0)}(i)$
$a$	-0.0029	-0.0089
$u$	1.0352	1.0058

The values of the parameters can be estimated by the least-squares error method.

The solution of the differential equation is the fitting calculation value  $\hat{x}^{(1)}(i)$  of the time response function  $\hat{x}^{(1)}(k+1) = \left[ x^{(0)}(1) - \frac{u}{a} \right] e^{-ak} + \frac{u}{a}, (k=1, 2, \dots, n-1)$ . Using IAGO on the original data sequence, the predicted value can be estimated as follows:

$$\begin{aligned} \hat{x}^{(0)}(k+1) &= \hat{x}^{(1)}(k+1) - \hat{x}^{(1)}(k) \\ &= (1 - e^a) \left[ x^{(0)}(1) - \frac{u}{a} \right] e^{-ak} \end{aligned}$$

According to the formulas and the above data, values of  $a$  and  $u$  in 2 different sequences are solved by using MATLAB. The results are presented in Table 2.

Suppose that  $x^{(1)}(1) = x^{(0)}(1) = y^{(1)}(1) = y^{(0)}(1) = 1$ , then

$$\begin{aligned} \hat{x}^{(1)}(k+1) &= \left[ x^{(0)}(1) - \frac{u}{a} \right] e^{-ak} + \frac{u}{a} \\ &= 356.9655e^{0.0029k} - 355.9655 \end{aligned}$$

$$\hat{y}^{(1)}(k+1) = \left[ y^{(0)}(1) - \frac{u}{a} \right] e^{-ak} + \frac{u}{a} = 114e^{0.0089k} - 113$$

Substituting  $k = 1, 2, \dots, n - 1$  into the above formulas, we can get the simulation data and predicted value of the GM (1, 1) model.

Among these, the predicted value of sequence  $x^{(0)}(i)$  is 1.1335, and that of  $y^{(0)}(i)$  is 1.1345. It can be suggested that the next disastrous flood will occur in 2014.5 according to the sequence  $x^{(0)}(i)$ . This has a difference of 2.5 year by comparison of actual time. In addition, it has a difference of 7.5 year by comparison of actual time according to the  $y^{(0)}(i)$  sequence. The results show that the predictive one is similar to the actual one.

### 3.2.2 The inspection of the forecasting model

From the reduction of the original value and reducing value, the residuals sequence  $e^{(0)}$  of each model can be obtained. Subsequently, we test the precision of the model. The calculation process of the testing parameters is omitted, and the results are summarized in Table 3.

It can be seen from Table 3 that the testing precision of 2 gray GM (1, 1) models is satisfactory, and it demonstrates that the extrapolating predictive

Table 3. Testing parameters of the GM (1,1) model of disastrous flood of the Yu River in Nanning City.

	S1	S2	C	P	$\xi$
$x^{(0)}(i)$	0.0317	0.006575	0.2074	1	0.645775
$y^{(0)}(i)$	0.0395	0.006849	0.1734	1	0.612898

Table 4. Forecasting results of disastrous flood of the Yu River in Nanning City based on the gray neural network.

Model	$x^{(0)}(i)'$	$y^{(0)}(i)$
Forecasting values of residual error	0.000623	-0.00472
Inverse normalized value (year)	0.62325	-4.72
Occurrence time (year)	2018.12325	2018.48

results of the GM (1,1) model have certain credibility. So we can use the BP neural network to train and correct the next step.

### 3.3 The training and amendment of the predicted residual sequence made by the BP neural network

We take the sequence  $y^{(0)}(i)$  as an example. The residual errors between the simulation and historical actual value from  $e^{(0)}(1)$  to  $e^{(0)}(13)$  were trained by the BP neural network, and forecast the value of  $\hat{e}^{(0)}(14)$  again, and thus the value of  $\hat{Y}^{(0)}(14)$  can be obtained by using the following formula:  $\hat{Y}^{(0)}(i) = \hat{y}^{(0)}(i) + \hat{e}^{(0)}(i)$ .

First, the residual errors between the simulation value and the historical actual value are used as the basic data. The first 13 residual data are used as the training samples and the 14th data are used as the test samples. Each of the 3 data recurs as a cycle. That is to say, the first 3 data are the input vectors, and the latter data is the output vector.

After setting the parameters, we can initialize the neural network, and train and fit forecast based on the neural network. After 3 steps of iterative training, the BP neural network can meet the requirements of former setting accuracy, so that the predictive value -0.00755 will be obtained. After using the inverse normalization, the 14th residual predictive value is -7.55 based on the BP neural network. Therefore, we can get the predictive value of 2007.95, which coincides with the actual value of 2008.

Similarly, the residual errors of sequence  $x^{(0)}(i)$  of the flood level above 73 m are trained and fitted forecast based on the BP neural network. The predictive value is 2011.966, which coincides with the actual situation of above 73 m of disastrous flood in 2012 in Nanning City. The predictive results show that the BP neural network for the residual error of the GM (1,1) model is of great effect, and

it improves the forecasting accuracy greatly even for small samples.

## 4 THE PREDICTION OF DISASTROUS FLOOD OF THE YU RIVER IN NANNING CITY

By fitting and testing the above forecasting accuracy, the satisfactory results of the gray neural network model can be obtained, which shows that it has certain reliability. Therefore, we can use the gray neural network model to forecast the flood disaster occurring the next time in Nanning City.

All the data of Table 1 are used as learning data. Substituting the flood data in 2012 into the sequence  $x^{(0)}(i)$ , the new sequences  $x^{(0)}(i)' = (x^{(0)}(1)', x^{(0)}(2)', \dots, x^{(0)}(32)')$  can be obtained.

Similarly, substituting the flood data in 2008 into the sequence  $y^{(0)}(i)$ , the new sequences  $y^{(0)}(i)' = (y^{(0)}(1)', y^{(0)}(2)', \dots, y^{(0)}(14)')$  can be obtained.

With the above steps of prediction and methods, the forecasting results are summarized in Table 4. The extrapolating results show that there will be a disastrous flood of the Yu River in Nanning City that exceeds 75 m in 2018 or 2019. The forecasting results can be used for reference in Nanning City for flood control and disaster mitigation decision.

## 5 CONCLUSION

1. The forecasting model of the gray neural network is substantially a combined predictive model used to modify the residual error. The predicted data are derived from time series prediction through the GM (1, 1) model. By subtracting the primary data and the predicted data, a residual sequence forms. The autonomous learning ability of the BP neural network can be used to revise the residual sequence. Thus, the final predictions of the gray neural network model can be obtained though adding up the predicted data and revised residual sequence.
2. Based on the practical situations of disastrous flood of the Yu River in Nanning City, the stability of the forecasting model can be tested by comparing the two sequences of disastrous flood (above 73 m and above 75 m).
3. Since the neural network training and study has the characteristics of randomness and volatility to some extent, the data and information of the most recent disastrous flood should be used as the test sample to make predictions for examining the precision of the gray neural network model through previous data. The predictive accuracy can be greatly improved through the extrapolated forecasting of the trained gray neural network model, which is based on a good precision.

## Study on the hydraulic model test of diversion-type hydropower station

Chun Qiu & Chenglan Liu

Sichuan College of Architecture Technology, Deyang, China

**ABSTRACT:** Diversion-type hydropower station is widely used in west China. Sediment deposition often appears near the water intake for the larger angle between diversion pipe and flow direction. The discharge capacity, sediment control and other hydraulic problems are studied. Shape optimization is conducted on water intake and other hydraulic facilities. Flow velocity, water surface and scour depth are measured. Some suggestions are mentioned to ensure the safety of the project. The results obtained in this paper can provide reference to the similar hydraulic engineering.

**Keywords:** hydraulic model test; discharge capacity; sand trap; water intake; sediment control

### 1 INTRODUCTION

The hydropower project, with the total installed capacity of 96 MW and the normal water level of 3004 m, is located on the Bachu River in Cichuan Province, China. The project including three release sluices, namely 6 m wide and 3 m high, one scouring sluice, 3 m wide and 3 m high, is mainly for power generation and flood control. There are more studies on similar projects [1–5]. Under the opening conditions of 2994.58 m

(checking flood level) and 2991.6 m (designing water level), the corresponding discharge is 521 m<sup>3</sup>/s, 330 m<sup>3</sup>/s, respectively. The details of the two operating conditions are provided in Table 1.

Model experiment with a scale of 1:40, based on the gravity similarity, is conducted to study the hydraulic performance of the project. The length of the prototype simulated in the experiment is 1100 m. The panorama of the model experiment is shown in Figure 1.

Table 1. Details of the two conditions.

Operating condition	Flood frequency	Return period (year)	Flow rate (m <sup>3</sup> /s)	Water level before gate (m)	Operating mode
1	0.2	500	521	2994.58	No power generation + full opening
2	2	50	330	2991.60	No power generation + full opening

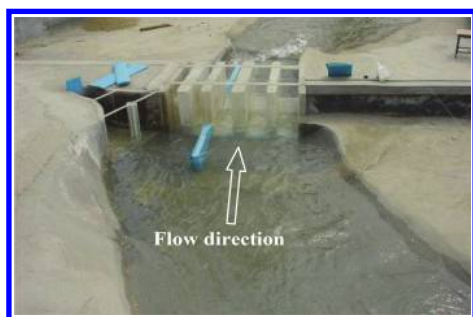


Figure 1. The panorama of the model experiment.



Figure 2. Deposit of the sediment after 12-hour scours at the check discharge.

## 2 ANALYSIS OF PRELIMINARY RESULTS

Figure 2 shows the deposit of the sediment of reservoir after a 12-hour open discharge. Though the floor elevation of water intake is 2990 m, 3 meters higher than that of the river bed, some sediment is still involved in the water intake. To ensure the safety of the hydropower station, the form of water intake must be optimized.

It can be seen from Figure 3 (a) that preventing water is apparent at the anterior part of the gate piers, which influences the flood discharge. Water-wing after gate piers is shown in Figure 3 (b), which shows the pier should be optimized to eliminate the water-wing.

The main optimization work is as follows. An arc-shaped weir is placed before the water intake with the elevation 2992 m. The height of the breast wall increases 1.5 m in order to enhance the conveyance capacity. The head parts of gate piers are replaced by ellipse one for reducing the preventing water and improving the flow rate. The straight upper reach guide wall is changed into arc one. A new device is placed to the tail of the gate piers to alleviate the water-wing.



Figure 3. Flow pattern at the check discharge.

## 3 HYDRAULIC PERFORMANCE ANALYSIS AFTER OPTIMIZATION

It can be seen from Figure 4 that the water surface keeps calm at the normal water level and dead water level, without the formation of vertical-axis vortex, which meets the requirement of the water intake. Figure 5 shows the flow property before the gate piers, while the flow discharge is  $521 \text{ m}^3/\text{s}$  and  $330 \text{ m}^3/\text{s}$ . The flow pattern is stable for the constraint of the arc-shaped guide wall.

Figure 6 shows the sediment deposition of reservoir after the 12-hour open discharge at the

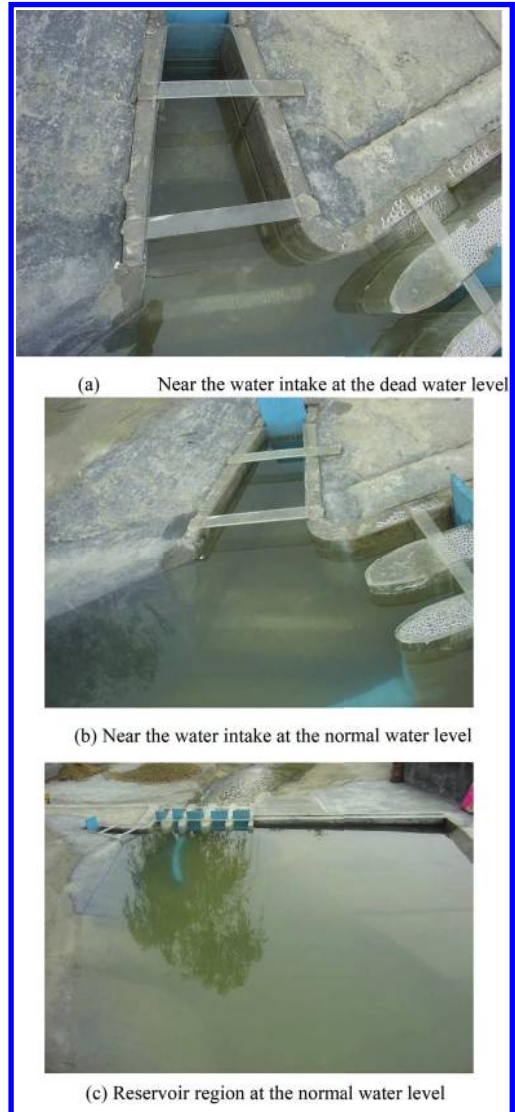


Figure 4. Water surface of the reservoir.

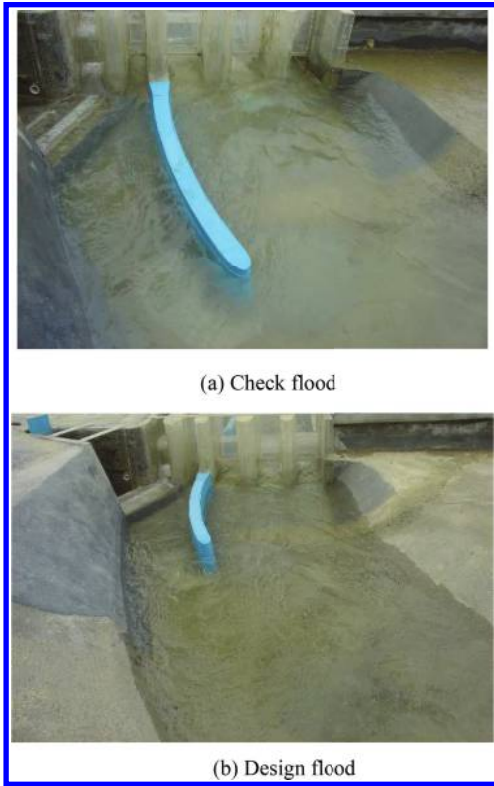


Figure 5. Flow pattern of the reservoir.



Figure 6. Deposit graph after 12-hour scour at the check flood.

discharge of  $521 \text{ m}^3/\text{s}$  during the full opening conditions of scouring sluice and release sluice. Most of the sediment near the foundation of the arch-shaped guide wall is scoured to downstream and not into the water intake, which meets the need of power generation.

Figure 7 shows the relationship between the discharge  $Q$  and the water head  $H$  before the middle-pier of the hydropower project. The water level has a little decrease by comparison with the original case. And the flow becomes free flow under every operating condition.

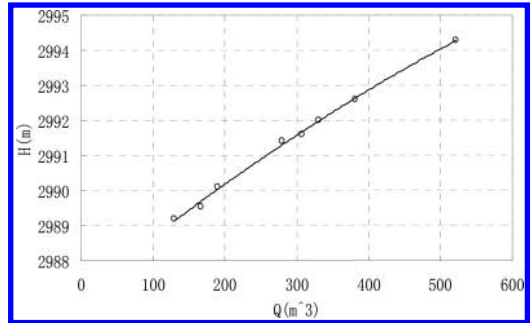


Figure 7. Variation of  $Q$  with  $H$  before the middle-pier.

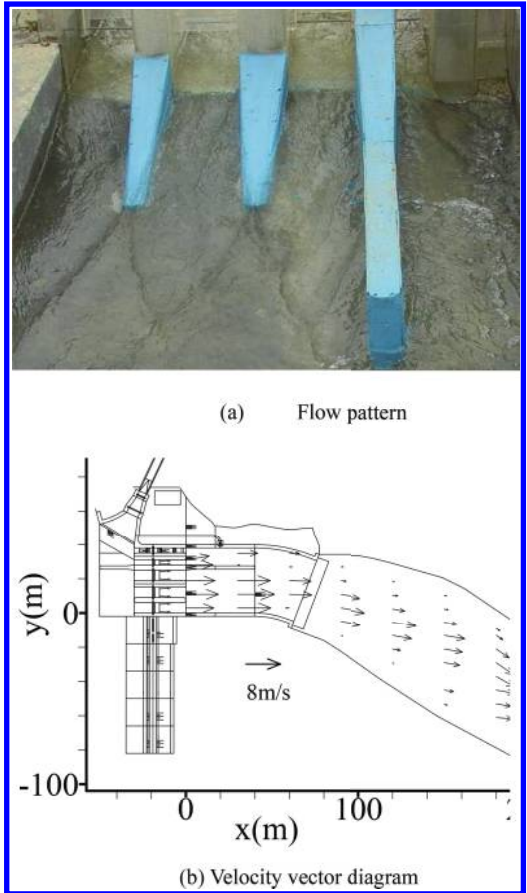


Figure 8. Flow condition at the design flood.



It can be seen from Figure 8 that the water wing after the gate piers is reduced greatly, which expressed that the device to eliminate the water wing is effective. The attention should be given while opening the gate at the normal water level of 3004 m; the flow velocity downstream reaches to 15.8 m/s near the middle release gate for the large drop height of the upper and down water levels. From Figure 8 and Figure 9, we can see that the average flow velocity on the apron is about 12.7–14.9 m/s, while the flow discharge is 521 m<sup>3</sup>/s and 330 m<sup>3</sup>/s, which is the situation that needs to be considered.

It is concluded from the model experiment that the scour depth is about 3–7 m, and the deepest point is located near the anti-scour trench. For security reasons, the corresponding foundation should be excavated to 2977 m; lead cage and riprap protection should also be added to ensure the safety. Figure 10 shows the distribution of scour and silting at design flood when all gates are opened. The similar distribution at the check flood

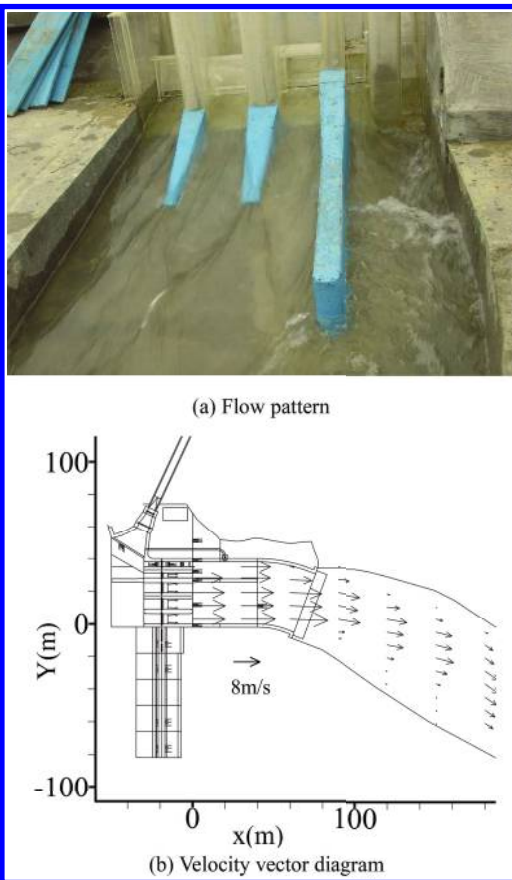


Figure 9. Flow condition at the check flood.

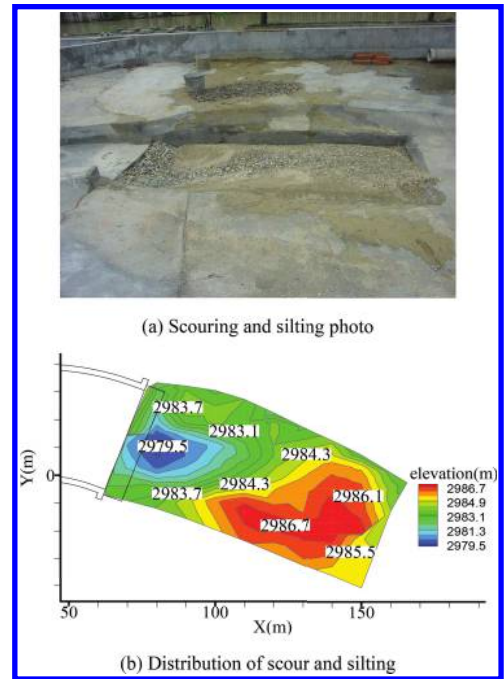


Figure 10. Scour and silting condition at the design flood.

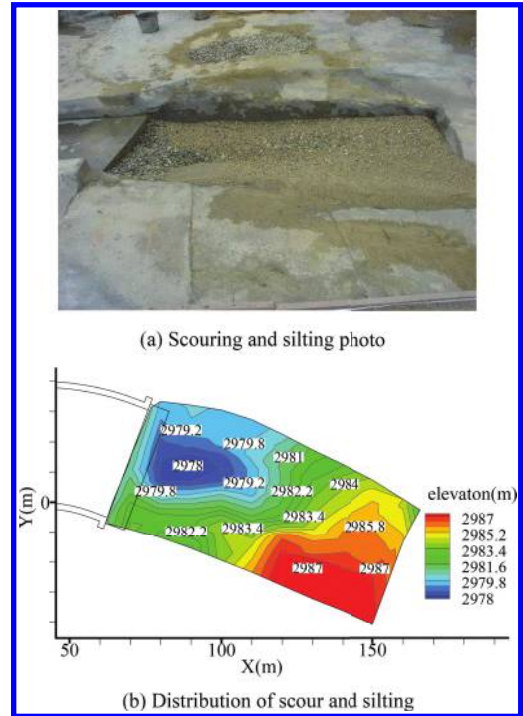


Figure 11. Scour and silting condition at the check flood.

is shown in Figure 11, where the maximal depth of the scour pool is about 7 m near the anti-scour trench.

#### 4 CONCLUSION

There are no vertical vortex and other disadvantages near the water intake after shape optimization. The sediment will not enter the water intake under different working conditions, which shows that the shape modification is effective. The magnitude of the scouring sluice and release sluices can satisfy the requirement of the draining flood. The arc-shaped guide wall makes the flow pattern smoother. The scouring sluice operating together with the release sluice will achieve better results for the sediment transport capacity. Protective measures should be made to ensure the safety of the downstream bed. The results obtained in this paper are also suitable for the similar project, which can provide an important reference for the hydraulic engineering.

#### REFERENCES

- [1] Lin Jinsong, Zhang Kuandi and Lu Hongxing. Hydraulic Modeling of Estuarial Hydroelectric Power Plant Closure of the Yellow River [J]. Yellow River, 2011, 33(2):109–112.
- [2] Yan Xueli, Yang Shengfa and Sun Lianchao. Hydraulic Model Test of Liujiagou Hydropower Plant [J]. Journal of Chongqingjiaotong University (Nature Science), 2011, 30(4):839–842.
- [3] Su Dongxi, Zhang Weiwei and Duanmu Liangzi. Protection Project Design for Paman Intake on Tarim River [J]. Yellow River, 2015, 37(1):54–56.
- [4] Yang Fan, Diao Mingjun and Xu Hongcheng. Numerical Simulation Study of the Shape Design at Horizontal Intakes [J]. Journal of Southwest University for Nationalities. Natural Science Edition, 2014, 40(3):409–414.
- [5] V.S. Neary, F. Sotiropoulos, A.J. Odgaard. Three-dimensional numerical model of Lateral-intake inflows [J]. Journal Of Hydraulic Engineering, 1999(125):126–140.

# Discussion on the development of remediation technology in Chinese metropolitan large mountainous river bank protection

Wei Guo, Juan Dai, Yinjun Zhou & Yue Zeng  
*Changjiang River Scientific Research Institute, Wuhan, China*

**ABSTRACT:** Taking the developing process of flood prevention and bank protection projects of the Yangtze River and Jialing River in Chongqing City for example, this paper conducts a summary and evaluation on the flood prevention comprehensive treatment technology of city stream segment part of Chinese large-scale mountainous river. A conclusion could be made that the concept of building a harmonious relationship between humans and water as well as the ecological bank protection treatment technology have become an inevitable tendency of present dike project technology development. The treatment concept oriented to the flood prevention treatment of city stream segment part of Chinese large-scale mountainous river has gradually changed from a single flood prevention project into a multi-objective one. Moreover, the treatment technology has also changed from the traditional project technology to ecological and natural bank protection technologies. However, the pure natural bank protection is usually applied to the recent middle and small river treatment at present, and for large rivers, the engineering natural bank protection technology is often adopted.

**Keywords:** mountainous river; flood prevention and bank protection; the harmonious relationship between human and water; natural ecology

## 1 INTRODUCTION

Just as its name implies, metropolitan large-scale mountainous river has three characteristics, namely, mountainous river has a high water level difference, the flood rises and drops very rapidly, the water contains a large number of sand and could have a big impact on the river band, so it has a high disaster-causing capacity, so the river has a high requirement on the reliability of flood control project. Second, it refers to the large-scale river: large rivers usually play a strategic role in the national flood prevention system, as its flood control is closely related to national economy and social influences, so it has a higher flood control standard. Third, these rivers belong to metropolitan rivers, so they play important roles in water supply, green land maintenance, environmental protection, resource protection, entertainment, transportation and cultural education. Moreover, its comprehensive function is also needed for the flood control project.

It can be seen that the metropolitan large-scale mountainous river revetment shall taken strong reliability, high flood control standard and comprehensive functions into consideration. Especially for some ecological problems about the rivers, advanced countries, such as Switzerland and

Germany, have subsequently proposed some ecological technologies in slope protection. In the late 1980s, a “natural bank protection” technology<sup>[1]</sup> was proposed. In the early 1990s, Japan proposed a vegetation-growing eco-concrete technology<sup>[2]</sup>; the watercourses nearby the cities along the Rhine River adopted movable embankment, which increased the hydrophilia of people<sup>[3]</sup>. For a long time, the metropolitan large-scale mountainous river bank protection project has been mainly developed based on the above-mentioned multiple objective mission. Now, taking Chongqing City as an example, we analyzed this issue from two aspects, namely, design idea and flood control technology.

## 2 CHANGES OF MANAGEMENT IDEA

The central downtown river in Chongqing locates in the junction of the Yangtze River and Jialing River, which is a mountainous river on the upstream of the Yangtze River. The gradient between the riverbed and the river is large, the river runs fasts, and under the influences of flooding water on both rivers, the flood control project has become very necessary in recent years. The management idea has gone through four stages, which are as follows:

1. Negative treatment: because of the special topographic condition and geographical conditions in the central downtown of Chongqing, and the limitation of economic conditions at that time, the central downtown of Chongqing has been lacking dike for a long time after the foundation of China. It keeps a negative attitude towards the flood control, that is, "retreat while the flooding comes, and moves forward while the flooding shrinks." But with the economic development and urban expansion increasing, the number of buildings and industries are set up along the river, so the damage and losses that flood disaster has on the nearby areas increases. For example, the worst flood in 50 years that occurred in July 1981 flooded wide areas, cities and villages along the Yangtze River and Jialing River, 130,000 people were affected by the disaster; as a result, houses collapsed, traffic stopped, water supply and power supply was interrupted, which brought a huge loss to the life and property of China and its citizens.
2. Basically meeting the demands for flood control and support transportation: in 1988, Yuzhong, Chongqing carried out the project that combined waterfront protection with the embankment project (Changbing road; full length 5.1 km), which symbolizes that the embankment project in the central downtown areas starts, but the flood control standard is still unclear. The construction of the project aimed to connect the transportation and control flood disaster. Afterwards, the flood control project from the right bank of Jialing River in Yuzhong District to Qiansimen Reach (full length 4.5 km) was started; in Nanan District, it was from the Shibampo bridge on the right bank of the Yangtze River to Shuibingying (the full length is 7.5 km) and the project from the Yudong Yangtze River bridge on Banan district to the estuary of the Jiantan River (full length 5.0 km). In 1997, Chongqing government released a report about the urban flood control project, and in 1998, Regulations on Flood Control of Rivers in Chongqing were passed, which offered basic references for the planning, implementation and management of the urban flood control project.
3. The specific flood control standard, transportation and urban environment are considered in the project construction. With the rapid development of urban construction, the effect of water conservancy project that was constructed on the upstream of the Yangtze River and that of the three gorges project on the central zone on the flood level of central downtown were considered. In 2007, Chongqing water conservancy bureau adapted the urban flood control plan, which was approved by Chongqing government. This program confirmed the flood control standard and designed the flood control level in a specific manner. However, at that time, Chongqing was in a rapid development period, so it had high requirement on land and transportation. As the flood prevention and bank protection reached the flood control standard, it occupied a large area of watercourse and capacity of reservoir, for instance, the fifth phase of the project on the Nanbing Road of Nanan District (3.96 km, occupying 1.234 million m<sup>3</sup> capacity of reservoir) and the comprehensive regulation project (5.3 km, occupying 1.13 million m<sup>3</sup>) from the Huanghuayuan Bridge to the Dafosi Bridge. It is worth pointing out that according to the confirmed flood control standard and designed flood level after confirmation, there is a 12 km substandard engineering section in the constructed embankment, including 7 km of the first phase project in Nanan District and the section from the Caiyuan Dam, Changbin Road to 5 K of the Yangtze River Bridge.
4. Comprehensive improvement on bank-protection projects for multiple objectives: with the development of urban cities, relevant departments have come up with new requirements on the bank protection project<sup>[4]</sup>, which not only has to meet the demand for flood control and transportation, but also needs to reflect the project functions as landscape greening and its hydrophilic nature. Meanwhile, the reservoir management of the three gorges project shall be strengthened, so as to avoid the occurrence of occupying the reservoir capacity. Therefore, in the project design, factors such as flood control, transportation, bank protection, urban construction, riverside greening and hydrophilic nature are considered. Moreover, the flow pattern of stored water in the three gorges reservoir, the reduction of excavation and filling in project have also been taken into consideration, so as to make the construction easier. Levee alignment has been combined with the water regime of the Yangtze River in the project and the demand of municipal construction, so the project stresses on the flood discharge and the smooth of flow line. For instance, the 3.12 km distance between Foeryan on Banan District and Yudongche Wharf and the 10.2 km comprehensive improvement project for flood prevention of Nanping Dike, Maliuzui Town of Banan district; all these projects have not occupied the reservoir capacity of the three gorges reservoir, and have created a leisure area with a strong hydrophilic nature.

### 3 ADVANCEMENT IN THE FLOOD CONTROL TECHNOLOGY

#### 3.1 Traditional river bank regulation

China has a long history in river regulation. According to the historical records, in early 28 BC, baskets weaved by willow branch and baboons were used to reinforce the river bank and channels with stones in it. To sum up, the traditional bank protection technology can be divided into slope revetment and wall revetment, where slope revetment can be further classified into loose-stone revetment, cement rubble revetment, precast concrete plank bank revetment and cast-in-situ concrete protection. Generally, these are paved on the bank slope and levee foot and formed subsequent overlay protection, which have a little effect on the riverbed boundary condition and near-shore currents and have good adaptability to the soil foundation. There are three types of retaining walls in wall revetment, namely, gravity retaining wall, anchored retaining wall and thin-wall retaining wall. These retaining walls are usually set up in important river reaches with narrow water area and no bunds. They have the advantages of little section and small land occupation. The traditional river bank regulation technologies have achieved certain outcomes until now, and also are important forms in the large-scale river flood control projects in Chongqing, but the traditional river regulation projects have cut off the interactive channels between water and soil, broken the connection between water and soil, and brought many negative effects on the ecological environment. Therefore, to develop a new river protection project with new theories, materials and technologies have become the main tasks for hydraulic engineers.

#### 3.2 New methods for revetment projects

Ecological riverbank is the latest river bank protection method. It can be divided into three types, namely, nature bank protection, natural bank protection and engineering natural bank protection<sup>[5]</sup>.



Figure 1. Nature bank protection.

The former one uses building materials and soil vegetation in bank protection. The natural bank protection usually applies building materials to river bottom protection and uses soil vegetation for slope protection. Engineering natural protection uses soil vegetation for both river bottom

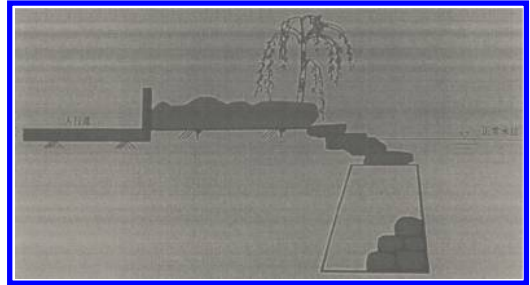


Figure 2. Natural bank protection.

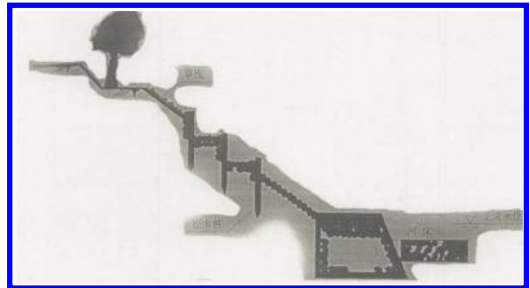


Figure 3. Engineering natural bank protection.

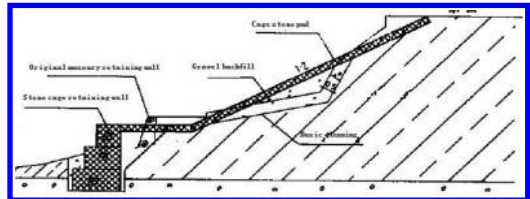


Figure 4. Cylinder mold bank protection.

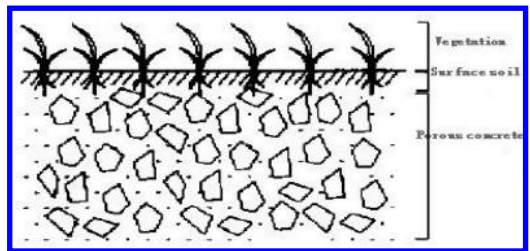


Figure 5. Conceptual graphs for ecological concrete.

protection and slope protection, and it prevents the flood shock with the soil fixation of certain plants. Obviously, the ecological management of three ecological riverbanks is being strengthened in sequence, while the structural intensity is basically becoming weaker in sequence. Therefore, pure natural bank protection is used for middle and small rivers in the plain terrain, and natural bank protection is used for large rivers in the plain terrain, while the new type of bank protection applied for large mountainous rivers is usually the engineering natural bank protection.

The studies and practices of bank protection projects of large rivers shall be started from two aspects: first, fix the stone or rubble with reseau or mesh cage to strengthen the bank and resist the flood impact, which has good air and moisture permeability and does not affect the water exchange and its ecological function. Second, new materials such as ecological concrete or cement planting material are used. These new materials have not only the intensity of traditional building materials, but also a similar ecological function of natural soil. Here, the former one refers to gabion box, gabion mesh, reno mattress, sack gabion and geotechnical net, which have integrality and flexibility, and natural vegetation can be planted on it, and the ecological environment and landscape can be improved. At present, these types of cylinder mold heel block have been put into standardized commercial production, and currently they have been widely used in all places of China, including western provinces such as Chongqing and Sichuan<sup>[6]</sup>; the latter one mainly includes cement ecological planting material, vegetation type eco-concrete<sup>[7]</sup> and soil stabilizer<sup>[8]</sup>. Most of them are introduced from foreign countries, which has strong intensity, and could meet the requirement for ecological bank protection. At present, this method has been used in many typical embankment segments and urban rivers.

Besides, there are three new technologies in bank protection, namely, concrete permeable frame of

tetrahedron with six sides, planting grass seed with waterpower and net mold water draining engineering for bank protection. The technology of concrete permeable frame of tetrahedron with six sides was developed and improved by Northwest A&F University and Hehai University, because of its good performance and impact resistance, so it has been widely applied to the regulation of large rivers. As for planting grass seed with waterpower technology, grass seed, pulp, adhesive, fertilizer and water are added into the grass spraying water tank, and then they are spread on the slope segment for grass protection. Under proper conditions, those grass seeds will sprout and result in greening and prevention of water and soil loss<sup>[9]</sup>. It is mainly used to improve the appearance of water conservancy project, so it has been used in the reconstruction and beautification of traditional water conservancy project, including the early embankment and dam project. Geotextile and grait has been used in the net mold water draining engineering for bank protection, and this technology is one of the geotextile mattresses, which belongs to the eco-type bank protection and can be used in the slope protection of river regulation. It has been applied to the river regulation of the Jinjiang River that has large river-bed deformation, and has been selected into the advanced practical technologies.

#### 4 RIVER REGULATION IDEA AND TENDENCY OF ITS TECHNOLOGICAL DEVELOPMENT

The urban river reaches of large urban rivers not only have their natural functions, but also undertake some social functions, such as urban flood control, municipal transportation, landscape, water culture and water recreation<sup>[10]</sup>, so the idea of river regulation gradually presented its comprehensiveness, and the river regulation has multiple objectives, the river regulation project must meet the demands of

Table 1. Idea development of large river improvement in Chongqing.

Idea	Requirements	Finished time	Typical projects
Negative coping	—	Before 1988	—
Flood control-centered and also involved with transportation factors	Certain flood control function and structural strength	1988–1997	Changbin Road, Yuzhong District
Meet the standard of flood control, protect the transportation and urban environment	Meet flood control and hydrophilia requirements	1997–2007	The fifth phase project of Nanbing Road, Nanan District
Comprehensive improvement for multiple objectives	Flood control, transportation, urban environment, hydrophilia, nature, meet the management requirement in the Three Gorges Reservoir Region	Recent years	Foeryan, Banan District to Yudongchedu Wharf

Table 2. Basic types of bank protection technologies.

Types	Traditional bank protections	New kind of bank protections
Types	Slope protection	Engineering natural bank protection
Typical types	Loose-stone, grouted rubble, precast concrete plank	Cylinder mold structure and new materials such as heel block and eco-concrete
	Wall revetment	Natural bank protection
	Gravity type, anchored type, Thin-walled type	Common building materials in river bottom protection + soil vegetation in slope protection
Analysis of characteristics and adaptability	No special requirement to foundation, and have strong adaptability; large space occupation; interrupted the soil and land connection between the river and the bank slope	Retain the soil and water connection along the riverbank; strong flexibility and anti-resistance; can be applied to large river regulation
	Have high requirement to foundation; small space occupation, adaptable to narrow river; interrupted the soil and water connection between the river and the bank slope, and poor hydrophilicity	Retain the soil and water connection along the riverbank; the anti-impact mainly depends on the soil reinforcement of plants; applied to small and middle river regulation
		Nature river bank, adaptable to the river regulation in the plain terrain

multiple departments of national economy and try to realize the eco-regulation, remain or optimize the natural function of river itself. Meanwhile, the flood control project of big urban rivers usually requires larger investment, so its construction also requires achieving certain economic benefits, to bring forward the rapid development of surrounding economy by reaching the flood control standard, stabilizing bank slope, improving transportation function, greening and beautifying the areas along the river, so as to solve the flood control problem with less national investment, change the environment of the construction area, improve the image of urban cities, and create considerable economic benefits, which is an important index for the feasibility assessment on a large embankment project.

At present, there are some basic problems that exist. In most large mountainous rivers, the road-embankment integrated method has been used in the construction of flood control and bank protection project. Based on the current standards, it shall be designed with a high flood control standard, while the natural development of urban cities exists nearby water, so embankment shall be constructed along the outside waterside area, so these are the protective objectives. In these places, embankments and roads are obviously higher than the land elevation in the rear area, so waterlogging occurs very frequently in the rainy season. Meanwhile, most embankment projects in the metropolis have been constructed for many years, so the standard and construction technology are different; as a result, the early embankment is a substandard, and a wooden barrel effect occurs in the entire flood control project.

For the idea of man-water harmony, eco-bank protection technology is an inevitable tendency for the development of embankment engineering project, and new materials and technologies will be more widely used in the regulation of middle and small rivers, but are not used in large river regulations, so the application and promotion of new technologies and materials shall be quickened, but problems related to cost and reliability shall be considered. In terms of the flood control and bank protection projects in the Yangtze River and Jialing River in Chongqing, engineering natural bank protection technology has been used very frequently, but pure natural bank protection is hardly adopted, so it is necessary to introduce both ideas and technologies to realize river regulations naturally with multiple objectives.

## 5 CONCLUSIONS

Development situations: for the flood control project of large-scale mountainous river nearby cities, the flood control concept gradually developed

from a singular flood control project into a multi-objective project, including transportation, landscape, ecology and cultural construction. The flood control technology already changed from the traditional engineering technology to ecotype and natural-type bank protection technologies.

Existing deficiencies and differences: there are conflicts between multi-objective projects and economic benefits. The multiple-objective task usually requires higher costs, so its implementation usually is restricted by the evaluation of economic benefits; and the nature-type bank protection is mainly used in the management of medium or small rivers, while large rivers have higher requirements to ensure the reliability of projects, but nature-type bank protection technology has been widely applied in the river regulation in China.

Development tendency: human-water harmony theory and ecotype revetment regulation technologies are the inevitable tendency for the development of embankment engineering, so a human-water harmonious relationship is a must tendency in river regulation in the future. As the ecotype revetment technology becomes more mature, the cost will reduce, while its reliability and adaptability may increase. The flood control project of large mountainous rivers in urban areas will be applied more widely.

## REFERENCES

- [1] Coppin N.J., Richarids I.G. Use of vegetation in civil engineering [M]. CIRIA: Butterworths, 1990.
- [2] Nordin A.R. Bioengineering to ecoengineering. Part one: the many rib/Ties [J]. International Group of Bioengineers Newsletter, 1993(3): 125–128.
- [3] Morgan R.R.C., Rickson R.J. Slope stabilization and erosion control: A bioengineering approach [M]. London: E&E N Spon, 1995.
- [4] Xia Jihong, Yan Zhongmin, Current Status and Developmental Tendency of Research on Urban Watercourse Ecological Revetment in China and Foreign Countries [J] Science of Soil and Water Conservation, 2004.3: 20–21.
- [5] Tang Wanjin, Huang Zhiqiang, Li Changjie, “Discussion on Mountainous River Bank Protection Project and Geological Survey Method [J] Yangtze River, 2013.6(44): 47–49.
- [6] Hu Haihong, Ecological Revetment and Its Application Prospects [J] Guangxi Water Conservancy and Hydropower, 1999, (4): 57–59.
- [7] XuGuobin, RenXiaofeng, Analysis of Several New Bank Protection Technologies [J], Yellow River, 2004, 26(8): 3–7.
- [8] JiYongxing, Liu Shuiqin, Zhang Yong, Discussion on Ecotype Bank Protection Structure in Urban River Regulation [J] Research of Soil and Water Conservation, 2001, 8(4): 30–34.
- [9] Zou Zhanguo, Application of Planting Grass Technology in the Control of Soil and Water Loss [J] Bulletin of Soil and Water Conservation, 1993, 13(4):51–55.
- [10] Yan Shuiyu, Wang Xiangrong, Significance of Urban Rivers in Ecological Construction in Urban Areas and its Application Methods [J], Urban Environment and Urban Ecology, 1999,12(6): 36–38.



## In-situ measurement study on stress of frozen inclined shaft lining crossing water-rich sand stratum

Jianxi Ren & Jielong Sun

*Xi'an University of Science and Technology, Xi'an, China*

**ABSTRACT:** There is no nature theory or method to design and construct the frozen inclined shaft lining in water-rich sand stratum. In order to solve this problem, the paper used in-situ measurement to study the stress of frozen inclined shaft lining crossing water-rich sand stratum. The results show that the force of frozen inclined shaft lining can be divided into three stages of change: Slow increase stage, rapid increase stage, and stable stage, the vertical steel bars of inner shaft lining mainly bearing tensile stress and the maximum tensile stress is 13.8 MPa, the circular steel bars bearing tensile stress fist and then turn to compression and the maximum compressive stress is 35.06 MPa, which is far less than the limit of eastern alluvium, the frozen inclined shaft lining is too thick which can increase the construction cost; therefore, the design and construction of frozen inclined shaft lining crossing water-rich sand stratum needs to be optimized.

**Keywords:** water-rich sand stratum; frozen inclined shaft; shaft lining stress; temperature; in-situ measurement

### 1 INTRODUCTION

The study on frozen shaft has already achieved significant achievement in eastern alluvium (e.g., Yang et al, 2010, review and prospects of research on freezing design theory of coal mine shaft; Wang et al, 2007, in-situ measurement on the stress of reinforcing steel bar of outer freezing shaft wall in deep alluvium; Xi et al, 2014, in-situ measurement study on stress and temperature of frozen outer Shaft lining in western cretaceous strata). But there are few studies in western water-rich sand stratum especially for the frozen inclined shaft. The theory and method for frozen inclined shaft lining is not mature and most design and construction were based on the experience of frozen shaft. And the different regions and shaft arrangement will lead to a thick shaft, high temperature stress, and so on (Fan et al, 2013, construction technology of freeze sinking method in inclined shaft soil layer; Liu et al, 2012, study on temperature field distribution law of freezing wall for inclined shaft). The paper will use in-situ measurement to study the stress mechanism of frozen inclined shaft, analysis of the stress of vertical and circular steel bars of inner shaft lining and provide the basis for frozen inclined shaft in western.

### 2 ENGINEERING SITUATION FAVOR

The coal mine is located at 20 km of Yulin City, Shaanxi Province. The design production of coal mine is 8 million tons a year. The length of main

inclined shaft is 1303.3 m, the inclination is  $14^\circ$ , the section area is  $16.3 \text{ m}^2$ , the width is 5.0 m, the vertical wall is 1.25 m, and the arch is 2.5 m. The horizontal distance from frozen position to the wellhead is 80.215 m, the inclined length of frozen shaft is 377 m, the horizontal length of frozen shaft is 365.8 m, and the vertical depth is range from 20 m to 111.208 m.

The pumping test results show that the inflow of water is  $1250 \text{ m}^3/\text{h}$ . Use multi-row freeze-tubes method to sinking shaft. The number of freeze-tubes is five and the distance is 2.35 m. The design thickness of shafts roof is 6.0 m, the roadway is 3.0, and the floor is 5.0 m. Figure 1 is the profile of freezing hole.

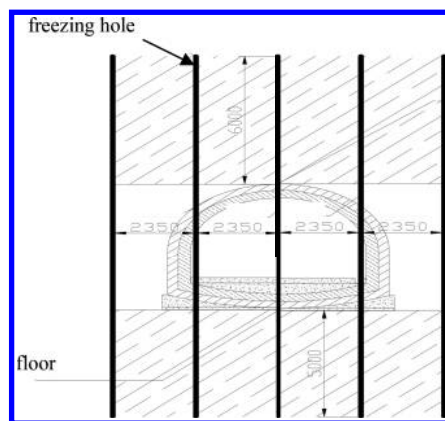


Figure 1. Profile of freezing hole.

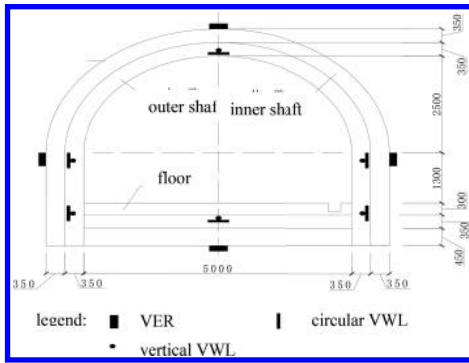


Figure 2. Schematic diagram of test point arrangement.

### 3 MEASURE SCHEME OF SHAFT LINING FORCE

The monitoring contents are freezing pressure, the stress of vertical and circular steel bars of inner shaft lining, and the temperature of shaft. The VWL Load-meter is used to monitor the freezing pressure, which can monitor the temperature of frozen shaft. The VWR Stress-meter is used to monitor the stress of steel bars. Fixed the load meter and stress meter when the shaft tunneling to the monitoring section.

The distance from monitoring section to well-head is 259 m and the vertical depth is 62.7 m. Install one load meter at shaft roof, arching, and floor. Install one stress meter at the inner steel bars of shaft roof and the outer steel bars of arching and shaft floor. Figure 2 is the schematic diagram of test point arrangement.

### 4 CHARACTERISTICS OF SHAFT LINING FORCE

#### 4.1 Analysis of freezing pressure

Figure 3 is the measured curve of freezing pressure, from the curve we can see that the range of freezing pressure is 30.69–696.87 KPa.

The Figure 3 shows that the frozen inclined shaft lining can be divided into three stages of change: Slow increase stage, rapid increase stage, and stable stage. Slow increase stage: in this stage the freeze wall can be regarded as  $t$ , which can bear the water and earth pressures with shaft. The increased shaft is caused by the frozen wall refrozen. Rapid stage: the frozen wall begin melt after monitoring 52 days, which lead to the force acting on the shaft rapid increase. At this time, the force of the frozen wall beard is reduced. Stable stage: when the monitoring carried out to 200 days, the frozen wall melted completely and the force acting on the shaft became stable.

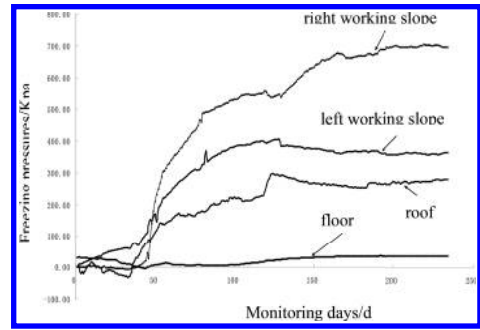


Figure 3. Measured curve of freezing pressure.

In addition, the force acting on the right shaft is lower than the left and roof before thawing, but the force acting on the right shaft rapid increases after thawing and transcendence the left and roof, which is due to the rock and soil anisotropic, freezing temperatures and frozen brine pipe deflection, and so on.

#### 4.2 Force analysis of the vertical steel bars

Figure 4 is the measured curve of the vertical steel bars and the maximum tensile stress is 13.8 MPa, which is far less than the limit of eastern alluvium 300 MPa, and the results shows the shaft is safe.

The Figure 4 shows that the mainly bearing tensile stress and the tensile experienced four stages. First, rapid increase stage: because concrete hydration heat the temperature of inner shaft increased rapidly, the compressive stress of vertical steel bars of inner shaft lining is  $-0.8$ – $3.4$  MPa and turn to tensile stress in 1–8 days then increased rapidly. Second, slow reduce stage: force acting on the shaft is reduced but the force acting on the frozen wall is increased, which has been caused by the refreezing of frozen wall. Third, stable stage: in this stage the refreezing of the frozen wall is complete; the pressure acting on the wall remains stable (the stress of a certain range). Last, slow increase stage: in conjunction with Figure 3 we can see that the frozen wall begins to melt; the force acting on the shaft increases gradually, which leads to the vertical steel bars stress increase.

#### 4.3 Force analysis of the circular steel bars

Figure 5 is the measured curve of the circular steel bars and the maximum tensile stress is 35.06 MPa, which is also less than the limit of eastern alluvium.

The Figure 5 shows that the circular steel bars bear tensile stress at the beginning of monitoring, which is caused by the concrete hydration heat and with the gradual reduction of temperature turn to compressive stress. The changes above all are

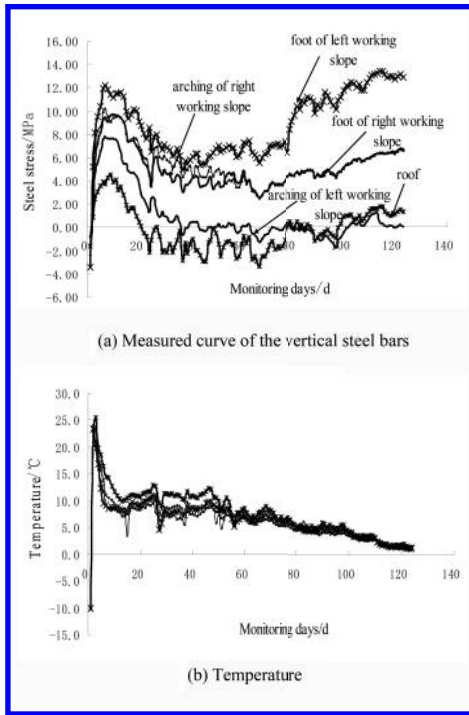


Figure 4. Measured curve of the vertical steel bars.

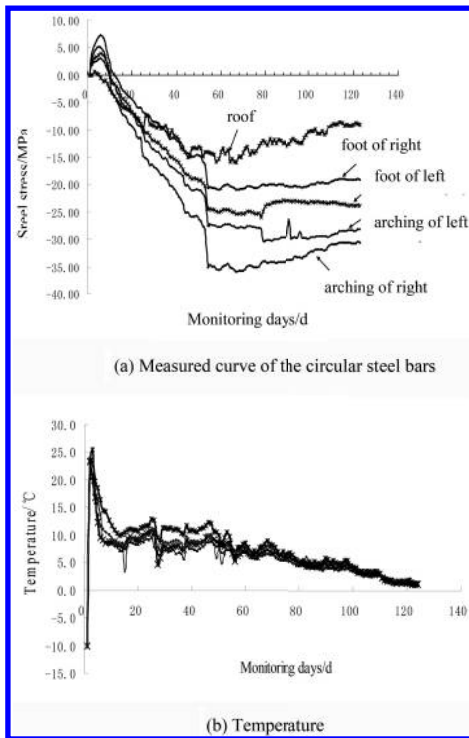


Figure 5. Measured curve of the circular steel bars.

caused by the force acting on the shaft and frozen wall refrozen. When the monitoring carried out to 52 days, the stress suddenly increases. In conjunction with Figure 3, the frozen wall began melting while it was being monitored to 52 days, which lead to the force increase that acting at shaft, also cause the mutations of circular stress. With the melt of frozen wall, the force acting on the shaft and the stress of circular steel became stable.

## 5 CONCLUSIONS

1. The maximum pressure of frozen inclined shaft lining is 696.87 KPa, which is far less than the limit of eastern alluvium; the force frozen inclined shaft lining can be divided into three stages of change: Slow increase stage, rapid increase stage, and stable stage; the pressure acting on the shaft lining is closely related to the melting of the frozen wall; the greater rate of the frozen wall, the greater rate of the pressure increase; when the frozen wall melt completely the pressure tends to be stable.
2. The vertical steel bars of inner shaft lining mainly bearing tensile stress and the maximum tensile stress is 13.8 MPa; the tensile stress can be divided into four stages of change: rapid increase stage, slow reduce stage, stable stage, and slow increase stage. The circular steel bars tensile stress first and then turn to compression and the maximum compressive stress is 35.06 MPa, which is far less than the limit of eastern alluvium.
3. The stress of steel bars and frozen pressure are less, the frozen inclined shaft lining is too thick which can increase the construction cost; therefore, the design and construction of frozen inclined shaft lining crossing water-rich sand stratum needs to be optimized.

## REFERENCES

- Fan Jiulin, et al. 2013. Construction Technology of Freeze Sinking Method in Inclined Shaft Soil Layer. 41(9):143–150.
- Liu Bo, et al. 2012. Study on Temperature Field Distribution Law of Freezing Wall for Inclined Shaft. Coal Science and Technology, 40(12):4–7.
- Wang Yansen, et al. 2007. In-Situ Measurement on the Stress of Reinforcing Steel Bar of Outer Freezing Shaft Wall in Deep Alluvium. Journal of China University of Mining & Technology, 36(3):287–291.
- Xi Jiami, Qu Yonglong, et al. 2014. In-situ Measurement Study on Stress and Temperature of Frozen Outer Shaft Lining in Western Cretaceous Strata. Safety in Coal Mines, 45(08):68–71.
- Yang Gengshe, 2010. Review and Prospects of Research on Freezing Design Theory of Coal Mine Shaft. Chinese Journal of Underground Space and Engineering, 6(3):627–635.

# Numerical study on effect of opening ratio for flow field of artificial reefs based on VOF model

RuiJin Zhang, Man Tao, JinMei Zhou, XueZhi Huang & Peng Lian

College of Marine Technology and Environment, Dalian Ocean University, Dalian, China

**ABSTRACT:** Six artificial reefs in which opening ratio differs from 0 to 0.5 have been numerically simulated to study the effect of the opening ratio for flow field of artificial reefs through the establishment of VOF model. Results show that the maximum velocity of the upwelling current decreases with the increasing opening ratio, and the reefs with larger opening ratio (0.5) produce two vortexes and reefs back at the bottom of the eddy current level (span increases with openings than a declining trend).

**Keywords:** VOF; opening ratio; flow field effect of artificial reefs

## 1 INTRODUCTION

Artificial reefs mainly aim to prolife rate fishery resources through its surrounding ecological flow field effect. Therefore, the study of flow field effect of artificial reefs is of great significance. Flume experiments and numerical simulation are the main research methods that people study the flow field effect of artificial reefs. Comparing with physical model experiments, numerical simulation study of complex single-phase or multiphase flow is more convenient. It also saves the experimental consumption expenditure. It is the major development trend of the future.

Jun et al. (2010)<sup>[1]</sup> applied numerical simulation to flow field of m-shaped artificial reefs and compared with the result of the flume experiment. Yanxuan et al. (2014)<sup>[2]</sup> used three stacking kinds of artificial reefs pipe to do flume experiments and the simulation results were compared. Hyunkyounq et al. (2003)<sup>[3]</sup> contrasted the model results and numerical simulation results in three different sizes of reefs surrounding the flow field. In the process of numerical simulation, both the upper boundary and lateral boundary adopted the symmetrical boundary condition. At present, there is no related literature of establishing a VOF model for numerical simulation of artificial reefs flow field effect. We have to make numerical simulation experiment situation more real. This paper used the VOF model to define water flow field boundary of free surface, numerically simulated the flow field surrounding different opening size cube of artificial reefs and discussed the effects of opening ratio. It also considered the effect of tank wall friction at the same time, making the numerical simulation closer to the actual working condition.

## 2 NUMERICAL SIMULATION

### 2.1 Governing equations<sup>[4]</sup>

The governing equations include the continuous equation and the momentum equations in which the fluid is assumed to be incompressible:

1. continuous equation:

$$\frac{\partial u}{\partial x} + \frac{\partial v}{\partial y} + \frac{\partial w}{\partial z} = 0 \quad (1)$$

2. momentum conservation equation:

$$\begin{aligned} \frac{\partial(\rho u)}{\partial t} + \text{div}(\rho u \vec{u}) &= \text{div}(\mu \text{grad} u) - \frac{\partial p}{\partial x} + S_u \\ \frac{\partial(\rho v)}{\partial t} + \text{div}(\rho v \vec{u}) &= \text{div}(\mu \text{grad} v) - \frac{\partial p}{\partial y} + S_v \\ \frac{\partial(\rho w)}{\partial t} + \text{div}(\rho w \vec{u}) &= \text{div}(\mu \text{grad} w) - \frac{\partial p}{\partial z} + S_w \end{aligned} \quad (2)$$

In the equations,  $u$ ,  $v$  and  $w$  are the velocity in the  $X$ ,  $Y$ , and  $Z$  direction, respectively. Also,  $t$  is the time,  $\rho$  is the density of fluid,  $\vec{u}$  is the vector of velocity,  $\mu$  is the dynamic viscosity,  $p$  is the pressure,  $S_u$ ,  $S_v$  and  $S_w$  are the generalized source terms of the equation to the momentum conservation.

### 2.2 The calculation region

Numerical calculation has been performed by simulating the actual experiment flume. The size of calculation area was set according to the circumstance of flume experiment. A tank with 160 cm long, 60 cm and 45 cm wide was simulated with 40 cm water depth. Cubes of artificial reefs with different

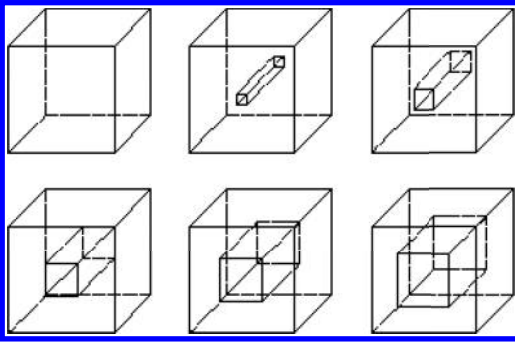


Figure 1. Model of six artificial reefs.

openings which size is  $10\text{ cm} \times 10\text{ cm} \times 10\text{ cm}$  were put in the bank. And the inlet of velocity is  $18\text{ cm/s}$ .

In order to study the influence of opening of the artificial reefs, a parameter: opening ratio ( $r$ ) is set to be the ratio of opening size and reefs' length. Six cubes whose opening ratio differs from 0 to 0.5 have been numerically simulated. If  $r$  is 0, the reef turns to be a cube.

### 2.3 The VOF model

Choose the steady-state solver in this experiment, set up two-phase flow model of air and water, and open the channel flow. Select RING  $k$ -epsilon turbulence model, call up the physical parameters of water, and set the air for the primary-phase, water for the second phase. Reference point of pressure set in the area of the air and gravity is along the  $z$ -axis direction. Water inlet boundary is defined as the velocity-inlet, with water velocity of  $18\text{ cm/s}$ , air inlet is defined as pressure-inlet, water's volume fraction in the multiphase is 0 from the air-inlet, water's volume fraction in the multiphase is 1 from the water-inlet. The out of the water and air are all pressure-outlet, need to set the out-of-water condition, open the channel from the multiphase of the water-out, and calibrate the level of the free surface. Suppose the reefs body model and the bottom and side of sink as wall. The friction coefficient is 0.5. Set flow field boundary to free surface and suppose above the sink as pressure outlet boundary conditions.

## 3 ANALYSIS AND DISCUSSION OF THE RESULTS OF NUMERICAL SIMULATION

The main flow field effects caused by artificial reefs are the upwelling current in front of the reefs and the reverse vortex flow backward. The upwelling

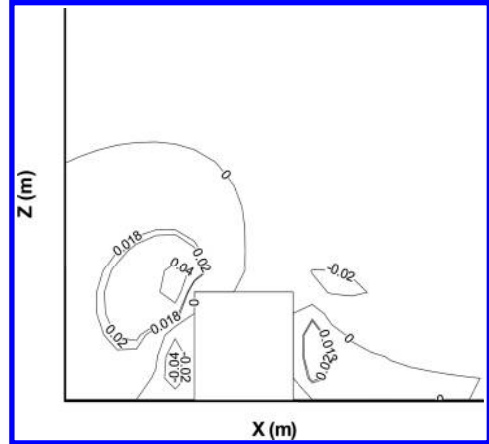


Figure 2(a). Contour map of upward velocity ( $r = 0$ ).

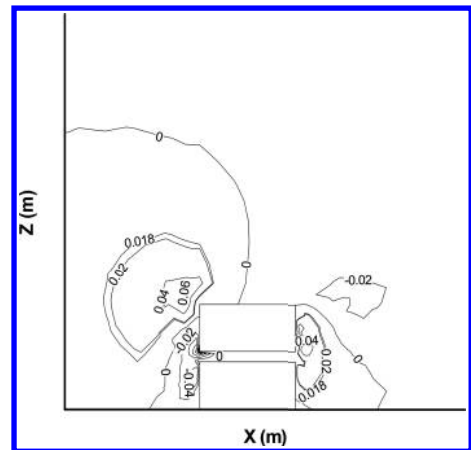


Figure 2(b). Contour map of upward velocity ( $r = 0.1$ ).

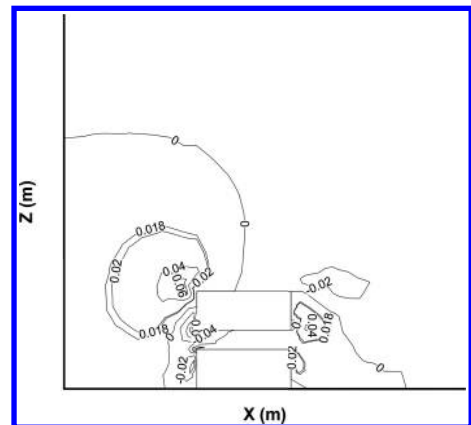


Figure 2(c). Contour map of upward velocity ( $r = 0.2$ ).

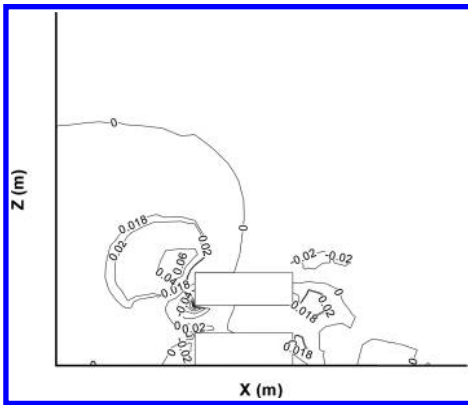


Figure 2(d). Contour map of upward velocity ( $r = 0.3$ ).

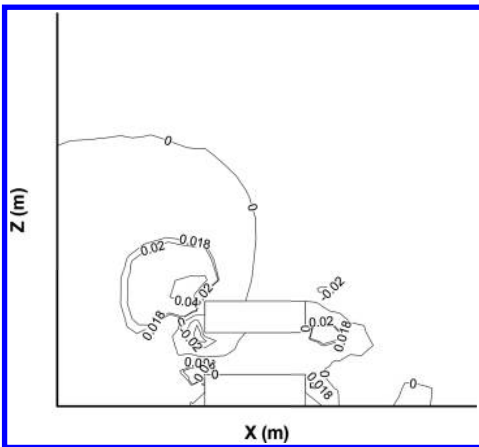


Figure 2(e). Contour map of upward velocity ( $r = 0.4$ ).

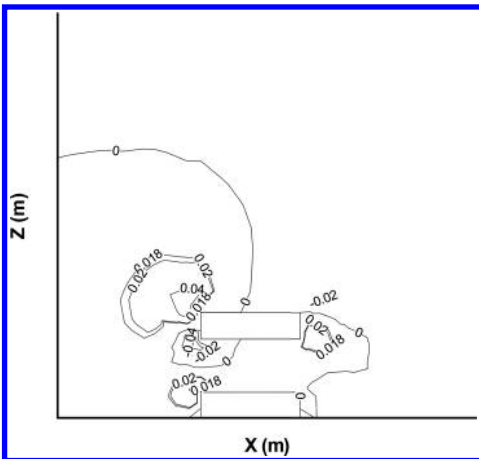


Figure 2(f). Contour map of upward velocity ( $r = 0.5$ ).

current could promote the nutrients to flow from the up and low and the reverse vortex could create a lower speed area for fish to inhabit. Opening of the artificial reefs would change the flow around the artificial reefs, resulting in changing the region of the upward and reverse vortex around the artificial reefs. Therefore, the opening ratio is an important impact factor for the flow of the artificial reefs. Here, the upward flow is defined when the Z direction velocity component ahead and above the reefs is greater than 10% of flow velocity<sup>[5]</sup>.

The distribution of upwelling current differs with the changes in opening ratios. When the opening ratio reaches a certain degree, two obvious vortexes appear in the back of the artificial reef. The upwelling current horizontally increases with the increase in opening ratios, but the reverse vortex flow gradually disappears. The distribution of upwelling current and reverse vortex are shown in Figure 2.

The paper mainly focuses on the changing trend of the maximum velocity of the upwelling current in the front part of the reefs and the width of reverse vortex current with the changing of the opening ratios. The maximum velocity of the upwelling current turns to be the maximum speed among the vertical direction in the area. There appear two vortexes right behind the reefs body while the reefs are open. And fish are more likely to gather in the lower part of vortexes, which explains the value of reverse vortex current to be the level of the largest span of the back of reefs in this paper. Figure 3 shows the maximum velocity of the upwelling current for different opening ratios. The maximum velocity of the upwelling current reduces with the increasing opening ratios.

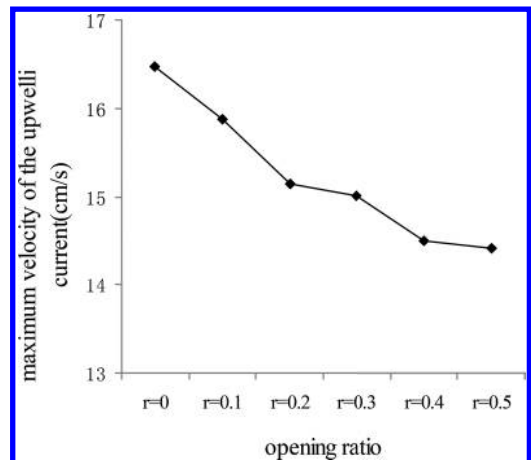


Figure 3. Change of maximum velocity of the upwelling current for different opening ratios.

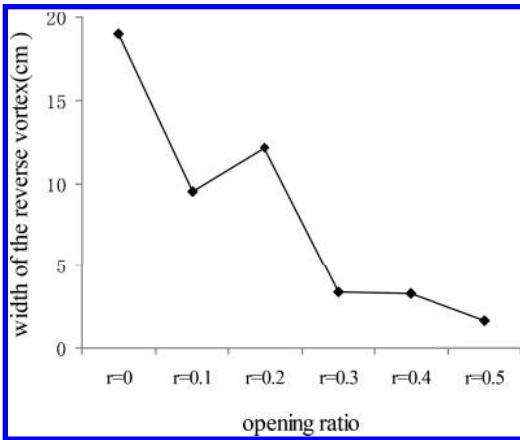


Figure 4. Change of width of the reverse vortex for different opening ratios.

When  $r$  is 0, the maximum upwelling current is the biggest, i.e. 16.47 cm/s, which is 91.5% of the inlet velocity. Figure 4 shows the width of the reverse vortex for different opening ratios. When  $r$  is 0, vortices are obvious behind the reefs, the level of the largest span of the reverse vortex current takes 18.96 cm. The width of the reverse vortex current reduces with the increasing opening ratios, but a turning point occurred when  $r$  is 0.2. The results of the experiment are consistent with the results of Dongwei et al. (2012)<sup>[6]</sup>, which turns out to be that the upwelling maximum speed and the width of reverse vortex current reduce with the increasing opening ratios.

#### 4 CONCLUSION

Six artificial reefs whose opening ratio differs from 0 to 0.5 have been numerically simulated to study the effect of the opening ratio for flow field of artificial reefs through the establishment of VOF model. It could be concluded that: (1) When the opening ratio increases from 0 to 0.5, the maximum velocity of the upwelling current decreases. When the opening ratio is 0, the maximum velocity of the upwelling current can be 91.5% of the inlet velocity. (2) When the reefs are opening, there will be two vortices right behind the reefs' body.

Through the increasing process of the opening size, the width of the reverse vortex current tends to decrease, but there is a small turning point when  $r$  is 0.2. When the opening ratio is 0, the upwelling current and reverse vortex are better than the others, but it has less area for fish to inhabit. The maximum velocity of the upwelling current and the width of the reverse vortex are not the only two factors to be concerned in designing artificial reefs; therefore, in the further work, more factors should be considered to looking for a best opening ratio of the artificial reefs.

#### ACKNOWLEDGMENT

Thanks for the support of the National Natural Science Foundation of China (No. 31302232).

#### REFERENCES

- [1] Jun Li & Shouyu Zhang. 2010. The Comparison Between Numerical Simulation And Water Channel Experiment On An Mi Zi Artificial reef. *Journal of Fisheries of China* 2010(10): 1587–1594. (In Chinese).
- [2] Yanxuan Zheng & Zhenlin Liang & Changtao Guan & Xiefa Song & Jiao Li & Yong Cui & Qiang Li & Xiaoluan Shan & Wenwen Xu. 2014. Numerical Simulation And Experimental Study On Flow Field Of Artificial Reefs In Three Tube-stacking Layouts. *Oecologia Et Limnologia Sinica* 2014(1): 11–19. (In Chinese).
- [3] Hyunkyoung Shin. 2003. Flow characteristics of artificial steel reefs. *Proceedings of the International Conference on Offshore Mechanics and Arctic Engineering—OMAE 2003(1)*: 385–389.
- [4] Fujun Wang. 2004. *Computational Fluid Dynamics analysis-Principle and application of CFD Software*. Beijing: Tsinghua University Publication. (In Chinese).
- [5] Changtao Guan & Yan Liu & Yunpeng Zhao & Yong Cui & Jiao Li. 2010. Experimental Study On Two-dimensional Flow Field Of The Compound M Artificial Reefs With Particle Image Velocimetry (PIV). *Fishery Modernization* 2010(1): 15–19. (In Chinese).
- [6] Dongwei Fu & Shuguang Luan & Ruijin Zhang & Yong Chen. 2012. Two-way Analysis of variance Of Effects Of Cut-opening Ratio And Surface Facing Flowing In Artificial Fish-reefs On The Flowing Field. *Journal Of Dalian Ocean University* 2012(27): 274–278. (In Chinese).

# Quantities calculation of truncated cone-shaped metal structural steel funnel

Nan-ming Mo

Infrastructure Construction Department of Kunming University, Kunming, Yunnan, China

Li-ya Wang

Yunnan Provincial Water Conservancy and Hydropower School, Kunming, Yunnan, China

**ABSTRACT:** Regarding it as rectangular, according to the quantities calculation principle of truncated cone-shaped steel structural steel funnel, it derives the universal theoretical calculation formula for steel plate quantities with different central angles with mathematical theory. In this way, it is not only convenient for cost members to calculate steel plate quantities and complement for theoretical knowledge about construction cost, but also provides theoretical basis for metalers to calculate the steel (copper) plate area of transition joint fittings with different sizes like air duct, exhaust hood and chimneys; and creates conditions for construction cost digitalization and quantities calculation with informational software.

## 1 INTRODUCTION

Truncated cone-shaped metal structural steel funnel is widely used in industrial and agricultural production and mankind's daily life, for example, in the joints of steel plate steel funnel, exhaust hood, cylindrical pipeline (water supply, gas supply, drainage pipeline, etc.), metal silo, metal water (oil) tank as well as other equipments and appliances, funnels have forms like circular truncated cone and quadrangular frustum pyramid. In practical construction cost, there is no research literature of quantities calculation formula for the steel plate area of steel funnel for people's full and complete use.

## 2 CALCULATION RULES FOR STEEL FUNNEL QUANTITIES

### 2.1 *The calculation principle for steel funnel quantities as the construction engineering cost valuation basis<sup>[1]</sup> for a province*

First, the quantities calculation principle of "steel structural engineering": the quantities of steel structure manufacturing shall be calculated in tons according to the steel geometry size in the design drawing (including steel plate, profile steel, excluding bolts), the weight of eyelets, cut limbs, and side cuts. The steel plate area shall be calculated as a rectangle, when calculating the area of an irregular or polygonal steel plate, it shall be calculated as the

smallest circumscribed rectangle as shown in the figure.

Second, the steel funnel manufacturing quantities shall be calculated as composed dimensions shown in the figure without deducting the areas of manhole, access hole, and cleaning hole. The profile steel attached to the funnel shall be calculated together with the funnel.

Third, the quantities calculation principle of "component transportation and installation engineering": the steel member shall be calculated in tons according to component figure. The welding structure shall be calculated as quantities plus 1.5% welding line weight, the riveted structure shall be calculated as quantities plus 2% rivet weight.

### 2.2 *The calculation principle of steel funnel quantities for Code of Valuation with Bill Quantity of Construction Works<sup>[2]</sup>*

First, the calculation principle for bill of quantities of "A.6 steel structural engineering" steel funnel (No. 010606010): calculate according to design figure in weight, including the weight of eyelets, side cuts and cut limbs but excluding the weight of welding rods, rivets and bolts, the irregular or polygonal steel plates shall be calculated as external rectangle area  $\times$  thickness  $\times$  theoretical unit mass, the funnel attached to shape steel shall be calculated together with the funnel quantities.

Second, metal faced paint (No. 020505001): shall be calculated by mass according to the dimensions in the design figure.



### 3 CALCULATION OF STEEL PLATE QUANTITIES

It can be known from the above national specification and the price foundation of construction cost of some province that the divisional work item including production, installation, transportation, and paint of metal construction need to use the area or mass of metal face as the measurement unit and quantity of quantities.

The calculation of steel plate area of pyramid-shaped funnel has been researched and described in cost member series textbook of Yunnan construction work including *Constructional Engineering Metering And Ration Application*<sup>[3]</sup>. For quantities calculation of the truncated cone-shaped funnel, there is no discussion or research in textbooks. Even if some materials may include a bit of research, it is only to calculate the volume of truncated cone-shaped funnel from aspect of math or from view of superficial area.

To calculate the metal funnel quantities is to calculate the area or mass of steel plate. Even if it is to calculate the mass, it is that the steel plate area multiplies by the steel plate mass per square meter. And the steel plate mass per square meter is a given datum (which may be got from relevant data) or calculated with the theoretical formula. Therefore, the key to quantities calculation of steel plate funnel is to calculate the steel plate area.

And the area for calculation of the steel funnel quantities is the area of external rectangle rather than the superficial area of metal construction. Therefore, the formula that is to be derived again is to calculate the truncated cone-shaped funnel of different shape, size and height. Different unfolded plane shapes can cause different calculation formulas of rectangle area. These situations have not been researched and described in the present literatures.

The basic condition of truncated area is as follows: truncated cone-shaped funnel is shown in Figure 1, and its unfolded shape is a sector shape shown in Figure 2. The central angle is  $\beta$ .

#### 3.1 Calculation of area of steel plate quantities in case of central angle $\beta$ within $180^\circ$

The central angle of wafer is  $\beta$ , and the bisected angle of wafer is  $\theta$ . In case of  $\beta < 180^\circ$  or  $\theta < 90^\circ$ , the steel funnel of metal structure is as shown in Figure 3. The radius of upper and lower bases is given or calculated according to the given outer arc length and inner arc length.

The upper base radius  $R = \text{outer arc length} / 2\pi$ , lower base radius  $r = \text{inner arc length} / 2\pi$

$$\tan \alpha = \frac{R-r}{H} \text{ is } \alpha = \arctan\left(\frac{R-r}{H}\right)$$

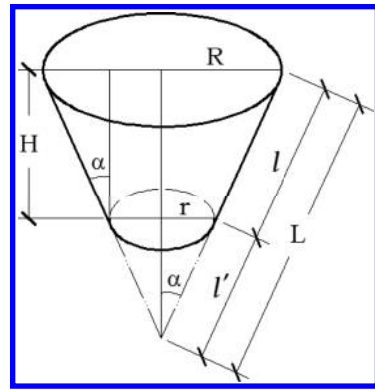


Figure 1.

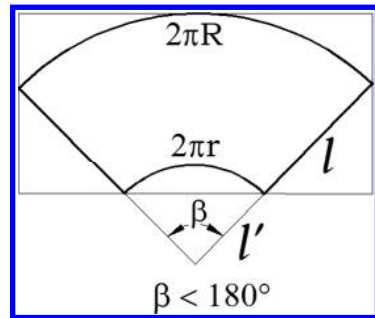


Figure 2.

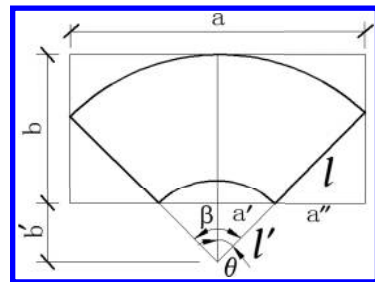


Figure 3.

$$l = \sqrt{(R-r)^2 + H^2}$$

$$l' = \frac{r}{\sin \alpha}$$

$$\text{Or } l' = r \times \csc \alpha = \frac{r}{R-r} l$$

$$L = l + l' = \sqrt{(R-r)^2 + H^2} + \frac{r}{\sin \alpha}$$

$$\text{Or } L = \frac{R}{R-r} \sqrt{(R-r)^2 + H^2} = \frac{R}{R-r} l$$

$$\beta = \frac{2\pi R}{L} \times \frac{180^\circ}{\pi} = \frac{360^\circ \times R}{L}$$

$$\text{or } \beta = \frac{360^\circ \times r}{l'} = 360^\circ \sin \alpha$$

$$a = 2(a' + a'') = 2 \left( l \sin \frac{\beta}{2} + l' \sin \frac{\beta}{2} \right) = 2L \sin \frac{\beta}{2}$$

$$b = l + l' - l' \cos \frac{\beta}{2} = L - l' \cos \frac{\beta}{2}$$

The area of steel plate quantities =  $a \times b$

$$= 2L \left( L - l' \cos \frac{\beta}{2} \right) \times \sin \frac{\beta}{2}$$

Example 1: The steel funnel designed by some project is as shown in Figure 4. In case of  $R = 64/2 = 32$  mm,  $r = 30/2 = 15$  mm and  $H = 46$  mm,

$$l = \sqrt{(R-r)^2 + H^2} = \sqrt{(32-15)^2 + 46^2} = 49.0408 \approx 49 \text{ mm}$$

$$l' = \frac{r}{R-r} l = \frac{15}{32-15} \times 49.0408 = 43.2713 \approx 43 \text{ mm}$$

$$L = \frac{R}{R-r} \sqrt{(R-r)^2 + H^2} = \frac{32}{32-15} \sqrt{(32-15)^2 + 46^2} = 92.3121 \approx 92 \text{ mm}$$

$$\begin{aligned} \beta &= \frac{360^\circ \times R}{L} = \frac{360^\circ \times R}{\frac{R}{R-r} \sqrt{(R-r)^2 + H^2}} \\ &= \frac{360^\circ \times (R-r)}{\sqrt{(R-r)^2 + H^2}} = \frac{360^\circ \times (32-15)}{\sqrt{(32-15)^2 + 46^2}} \\ &\approx 124^\circ 47' 39'' \end{aligned}$$

The area of steel plate quantities =

$$\begin{aligned} &2L \left( L - l' \cos \frac{\beta}{2} \right) \sin \frac{\beta}{2} \\ &= 2 \times 0.092 \times \left( 0.092 - 0.043 \times \cos \frac{124^\circ 47' 39''}{2} \right) \\ &\quad \times \sin \frac{124^\circ 47' 39''}{2} \approx 0.0118 \text{ m}^2. \end{aligned}$$

### 3.2 Calculation of area of steel plate quantities in case of central angle $\beta$ beyond $180^\circ$

These are steel funnel of metal structure in case of central angle  $\beta$  of wafer between  $180^\circ \leq \beta < 360^\circ$ .  $180^\circ \leq \beta < 270^\circ$  is shown in Figure 5,  $\beta = 270^\circ$  is

shown in Figure 6, and  $270^\circ \leq \beta < 360^\circ$  is shown in Figure 7. The derived formula is as follows:

$$l' = \frac{r}{\sin \alpha}, \quad l = \sqrt{(R-r)^2 + H^2}$$

By means of the principle of similar triangles, you can get  $H = \frac{l}{l'} \sqrt{l'^2 - r^2}$

$$\theta = \frac{\beta}{2} = \frac{180^\circ}{L} \times R \text{ or } \theta = \frac{\beta}{2} = \frac{180^\circ}{l'} \times r$$

Therefore, length =  $2 \times L$

Width =  $L - L \cos \theta$

The area of steel plate quantities = length  $\times$  width =  $2L^2(1 - \cos \theta)$ .

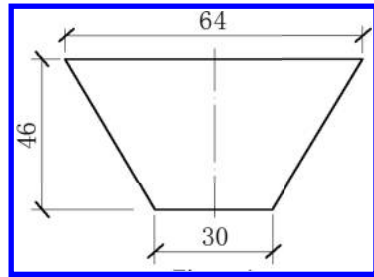


Figure 4.

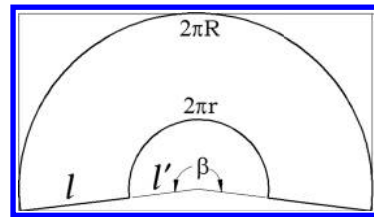


Figure 5.

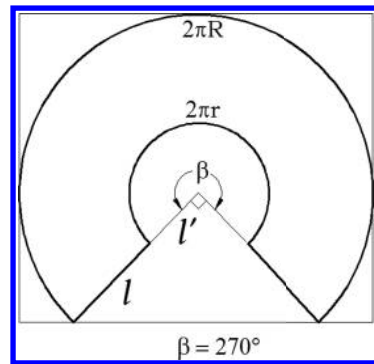


Figure 6.

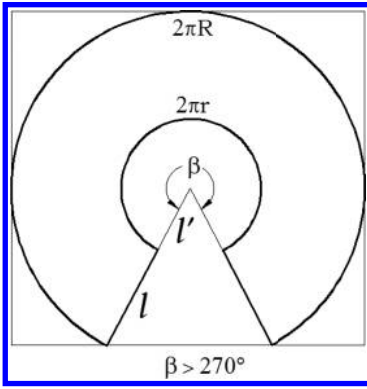


Figure 7.

Example 2: There is a steel funnel:  $l = 50$  mm,  $l' = 40$  mm,  $r = 25$  mm, and  $R = 63$  mm. Please calculate the area of steel plate quantities.

Answer:

$$\theta = \frac{180^\circ}{L} \times R = \frac{180^\circ}{90} \times 63 = 126^\circ$$

$$H = \frac{l}{l'} \sqrt{l'^2 - r^2} = \frac{50}{40} \sqrt{40^2 - 25^2} \\ = 39.03124 \approx 39 \text{ mm}$$

$$\text{Length} = 2 \times L = 2 \times (l + l') = 180 \text{ mm}$$

$$\text{Width} = L - L \cos \theta = 90 - 90 \cos 126^\circ = 142.90067 \approx 143 \text{ mm}$$

$$\text{The area of steel plate quantities} = 0.180 \times 0.143 = 0.0257 \text{ m}^2.$$

### 3.3 Calculate the area of steel plate quantities according to the diameters of upper and lower bases of steel funnel

If the diameters of upper and lower bases of steel funnel are given, the calculation method of area of steel plate quantities are as follows:

$$\tan \alpha = \left( \frac{D-d}{2} \right) / H$$

$$\alpha = \arctan \frac{D-d}{2H}$$

$$\frac{\beta \times 2\pi L}{360^\circ} = \pi D$$

$$\frac{\beta \times 2\pi l'}{360^\circ} = \pi d$$

$$(1)-(2): \frac{\beta \times 2\pi(L-l')}{360^\circ} = \pi(D-d)$$

$$\text{Namely } \beta = \frac{180^\circ \times (D-d)}{L-l'}$$

$$\text{And } L-l' = \sqrt{\left( \frac{D-d}{2} \right)^2 + H^2}$$

$$\text{Therefore, } \beta = \frac{180^\circ \times (D-d) \times 2}{\sqrt{(D-d)^2 + 4H^2}} \\ = \frac{D-d}{\sqrt{(D-d)^2 + 4H^2}} \times 360^\circ$$

According to this  $\beta$  value, the calculation types of steel plate quantities can be determined in case of  $\beta < 180^\circ$  and  $\beta > 180^\circ$ , as described above.

Then it is calculated from Formula (1) that  $L = \frac{180^\circ D}{\beta}$

Then it is calculated from Formula (2) that  $l' = \frac{180^\circ d}{\beta}$

Therefore, the length, width and area of steel plate quantities shall be calculated from  $\beta$ ,  $L$  and  $l'$ , which is not described here.

## 4 CONCLUSION

The following conclusions can be resulted from the analysis and discussion on quantities area calculation of the truncated cone-shaped funnel:

Conclusion 1: For the truncated cone-shaped funnel, a kind of method shall be chosen to calculate the quantities area of steel plate, namely the steel plate quantities, if the physical dimensions of shape are given.

Conclusion 2: In case of wafer central angle  $\beta < 180^\circ$ , the rectangle length of steel plate quantities =  $2L \sin \frac{\beta}{2}$ , width =  $L - l' \cos \frac{\beta}{2}$ , area =  $2L^2 \sin \frac{\beta}{2} - L \cdot l' \sin \beta$ ;

$$\text{or the area} = L^2 \left( 2 \sin \frac{\beta}{2} - \frac{d}{D} \sin \beta \right)$$

Conclusion 3: In case of wafer central angle  $\beta \geq 180^\circ$ , the rectangle length of steel plate quantities =  $2L$ , width =  $L - L \cos \frac{\beta}{2}$ , area =

$$(1) = 2L^2 - 2L^2 \cos \frac{\beta}{2}$$

$$(2) = 2L^2 \left( 1 - \cos \frac{\beta}{2} \right);$$

$$\text{or the area} = 2L^2 \sin \frac{\beta}{2} \times \left( 1 - \frac{d}{D} \cos \frac{\beta}{2} \right)$$

Conclusion 4: A mathematical model formula is derived for the quantities calculation in the costing area and for the digitization and information of construction cost.

## REFERENCES

- [1] Yunnan Construction Department. Price Basis for Construction Cost of Yunnan Province 2003 [M]. Kunming: Yunnan Science & Technology Press, 2003 (1).
- [2] Ministry of Housing and Urban-Rural Development of People's Republic of china (MOHURD). *Price Specification of Construction Work Qualities List* GB 50500-2008[S]. Beijing: China Planning Press, 2008 (1).
- [3] Li Chongren, Li Honglin. Metering and ration application of construction work [M]. Kunming: Yunnan Science & Technology Press, 2006.

# Numerical research on the effect of the water level on the urban drainage network in Huinan, Pudong district

J. Huang, S.Z. Wang, S.Z. Deng & X.B. Yang

Shanghai Pudong New Area Hydrology and Water Resources Administration, Shanghai, China

**ABSTRACT:** A numerical model by MIKE FLOOD software has been set up to simulate the storm waterlogging in Huinan, Pudong District. The validated urban waterlogging model with the reports in Huinan on October 8, 2013 was adopted to simulate the local storm waterlogging. Based on that, the significant effect of the water level on the urban drainage network in the local region was studied with 8.8% larger total flooded area and 50% deeper overland flow water depth, so it cost 3 more hours for the overland flood water to subside.

**Keywords:** storm waterlogging; numerical simulation; coupled; water level; urban drainage network

## 1 INTRODUCTION

The torrential rain has the characteristic of the high intensity and large amount of rainfall for the higher water level. When the rainfall exceeds the capacity of the urban drainage system, it is easy for the local ground to be waterlogged due to all the rainwater which is not drained quickly and efficiently, and then the urban flooding will occur with the low-lying houses that got drowned, the local traffic is crippled, which strongly affects the people's life and work.

The urban waterlogging is the disaster that has attracted many researchers' attentions, and a few mathematical models have been established to simulate the urban flooding (Werner, 2001); (Mark, et al. 2004); (Schmitt, et al. 2004), e.g. InfoWorks CS (Tan, 2007); Storm Water Management Model (SWMM) (Barco, et al. 2008); GIS-based urban flood inundation model (Chen, et al. 2009); 2D hydrodynamic model capable of simulating flash floods (Xia, et al. 2011); MOUSE model (Huang, et al. 2014).

Huinan, located in the south to central of Pudong District in Shanghai, has a tropical East Asian monsoon, and the oceanic climate with plenty of rains. Pudong canal, Zhonggang river, Yaogou river, and Sanzaolu river flow around it (Fig. 1), with the normal water level of 2.50 ~ 2.80 m. At present, Huinan has the drainage system depending on the gravity flow of rainfall itself, and during the heavy rain falls, the waterlogging disaster often occurs with many houses, factories and croplands suffering, especially, the region east to Yaogou river, south to Zhonggang river, west to Pudong canal, and north to Sanzaolu river (Fig. 1).

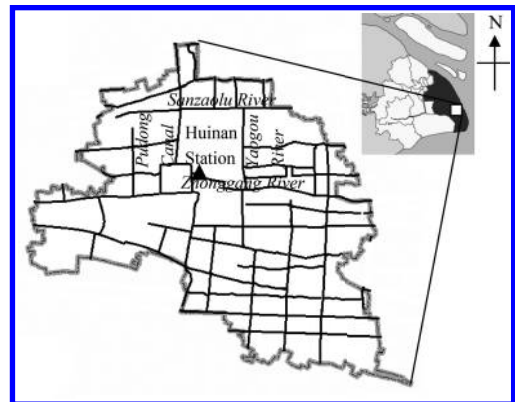


Figure 1. Diagram of the river network in Huinan, Pudong District.

To solve the urban waterlogging disaster in Huinan, Pudong District, the urban waterlogging model coupled with the rainfall runoff sub-model by MIKE URBAN, the underground network sub-model by MIKE URBAN, the river sub-model by MIKE 11 and the overland flow sub-model by MIKE 21 are established in MIKE FLOOD platform to simulate the storm waterlogging in this research, and the effect of the water level to the urban drainage network in the local region is studied.

## 2 MODEL SET-UP

### 2.1 Control equations

The runoff in the rain inlet can be calculated by Huang, et al. (2014)

$$Q = q\psi F \quad (1)$$

where  $Q$  represents the runoff in the rain inlet and  $q$  is the designed rainfall intensity; the formula of  $q = 5544 (P^{0.3} - 0.42)/(t + 10 + 7lgP)^{0.82+0.07lgP}$  is available to Shanghai (Sun, et al., 2013), where  $P$  is the designed reoccurrence period,  $t$  is the rainfall duration,  $\psi$  is the coefficient of the rainfall runoff,  $F$  is the catchment area.

The surface runoff can be calculated by Huang, et al. (2014)

$$\begin{aligned} W &= W_1 + W_2 + W_3 = HS_1 + HS_2 - Q_x + HS_3 - Q_i \\ &= qtS_1 + qtS_2 - \sum_{i=1}^m Q_i + qtS_2 - 60fS_3t \end{aligned} \quad (2)$$

where  $W$  is the surface runoff,  $W_1$  is the runoff of the impervious zone without the depression storage,  $W_2$  is the runoff of the impervious zone with the depression storage,  $W_3$  is the runoff of the pervious zone,  $S_1$  is the area of the impervious zone without the depression storage,  $S_2$  is the area of the impervious zone with the depression storage,  $S_3$  is the area of the pervious zone,  $H$  is the total rainfall,  $Q_x$  is the infiltration of the impervious zone with the depression storage,  $Q_i$  is the depression storage capacity of the  $i$ th hollow,  $Q_t$  is the infiltration of the pervious zone, and  $f$  is the infiltration rate.

The discharge of the ///pipeline can be calculated by (Huang, et al. 2014)

$$\begin{cases} \frac{\partial A}{\partial t} + \frac{\partial Q}{\partial x} = 0 \\ \frac{\partial Q}{\partial t} + \frac{\partial}{\partial x} \left( \frac{Q^2}{A} \right) + gA \frac{\partial H}{\partial x} + gAS_f + gAh_L = 0 \end{cases} \quad (3)$$

where  $A$  is the cross-sectional area of the pipeline,  $Q$  is the discharge of the pipeline,  $H$  is the water head, and  $S_f$  is the frictional resistance of the slope.

When the hollow has the storage function, its discharge can be calculated by (Huang, et al. 2014)

$$\frac{\partial h}{\partial t} = \frac{\sum Q_i}{S_i} \quad (4)$$

where  $h$  is the water head of the hollow,  $Q_i$  is the discharge of the hollow, and  $S_i$  is the water area of the hollow. But when the hollow has the only connect function, its discharge is calculated by  $\sum Q_i = 0$ .

Saint-Tenant Equation is adopted for 1D hydrodynamic model, which is

$$\begin{cases} \frac{\partial A}{\partial t} + \frac{\partial Q}{\partial x} = q \\ \frac{\partial Q}{\partial t} + \frac{\partial}{\partial x} \left( \frac{Q^2}{A} \right) + gA \frac{\partial h}{\partial x} + g \frac{Q|Q|}{C^2 AR} = 0 \end{cases} \quad (5)$$

where  $A$  is the area of the river cross-section,  $Q$  is the discharge,  $h$  is the water level,  $q$  is the lateral inflow,  $n$  is the bed roughness coefficient,  $R$  is the hydraulic radius, and  $g$  is the gravity acceleration.

## 2.2 Computational grids

The drainage system in the local region depends on the gravity flow by itself with 642 hollows, 619 pipe lines, and 22 outlets. The 23.4 km total pipe lengths, has to be divided to be  $579 \times 656$  square grids with the uniform interval of 4 m (Fig. 2). The 614 catchments in the study area has been generated with Thiessen method with one water collection hollow in each catchment to make the rainfall runoff flow into the drainage pipes.

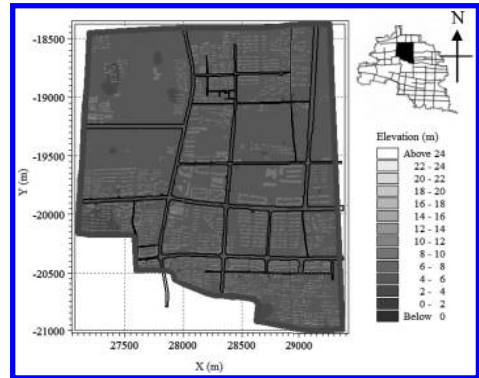


Figure 2. Layout of the computational grids of the research region with the terrain elevation in 2013.

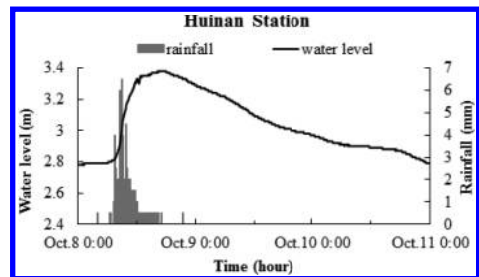


Figure 3. Graph of the observed rainfalls and water levels at Huinan Station from October 8 to October 11 in 2013.

### 2.3 Boundary conditions

In this study, the river open boundaries are setup with the field observed time-series and water levels at Huinan Station (Fig. 1). So is the rainfall condition. Considering the subsiding of overland flood, the observed time-series water levels and rainfalls at Huinan Station from 0:00 Oct 8th to 0:00 Oct 11th in 2013 have been adopted to set up the open boundary condition and rainfall condition respectively with the time interval of 5 minutes (Fig. 3). It was raining during 3:45 and 21:20 on Oct 8th in 2013, the maximum rainfall reached 40.0 mm from 8:10 to 9:10 in that day and the total rainfall in 24 hours was 127.0 mm (Fig. 3).

The simulated region is mainly composed of buildings, roads, green fields, and water. The different impervious rates have been used, e.g. 90% for buildings, 85% for roads, 25% for green fields, zero for water, 50% for the rest.

### 3 MODEL VALIDATION

The simulated results have been compared with the report of the storm waterlogging happened in Huinan on October 8 in 2013 to validate this model. After the validation, it shows that the

Table 1. Comparisons of the simulated results with the observed situation in Huinan, Pudong District.

Location	Actual situation	Simulated results
Gongji Road	≈ 0.10 m	About 0.10 m on average, and the maximum water depth of 0.25 m in the intersection of Gongji Road and Jinhai Road, and Gongji Road and Meihua Road
East Renmin Road (Nanzhu Road ~ Jinhai Road)	≈ 0.15 m	About 0.15 m on average, and the maximum water depth of 0.25 m
Jinhai Road (Gongbei Road ~ East Renmin Road)	≈ 0.20 m	≈ 0.20 m
Jinhai Road (north of Gongle Road)	≈ 0.10 m	≈ 0.10 m
Dongchenghuayuan II Neighborhood	≈ 0.05 m	About 0.05 m, and the maximum water depth of 0.20 m
Jindicheng Neighborhood	≈ 0.10 m	About 0.10 m, and the maximum depth of 0.20 m

modeled distribution range and depth of the waterlogging agree with the actual situation (Table 1). So this model could be adopted to simulate the storm waterlogging in Huinan, Pudong District.

### 4 SIMULATION RESULTS

Huinan has been suffered by the urban waterlogging disasters for years. In this research, the validated rainstorm waterlogging model has been adopted to study the effect of the water level to the urban drainage network in Huinan, Pudong District on October in 2013.

Under the condition of the pipe outlets beneath the water level, the maximum drowned area is about 0.62 km<sup>2</sup> at 10:00 on October 8 in 2013 and then it reduces until 1:25 on October 9 in 2013 with the total ponding area of 0.25 km<sup>2</sup>, while it will decrease to 0.57 km<sup>2</sup> at 9:10 on October 8 in 2013 without the interaction between the surrounding river and the pipes, under which condition the total ponding area will be stable by 0.22 km<sup>2</sup> after 22:30 on October 8 in 2013 (Fig. 4).

In fact, the river often impedes the pipe output flow and the impact depends on the water level. When the river water level exceeds the elevation of the outlets, the overland flood water depths in the roads are in the range of 0.10 ~ 0.20 m, and the waterlogged depths in the residential areas are below 0.10 m. However, if the outlets are above the water, the water depth of the overland flood will reduce to 0.05 m (Fig. 5).

In this research, the local drainage system depends on the gravity flow by itself. With the interaction effect of the river on the pipes, it is often easier to generate the surface runoff when the rainfall exceeds the full capacity of the drain lines or the rain arrives more quickly than the local pipe networks that can absorb it (Fig. 6). But if there is not the interaction, it will be hard for the overland flow (Fig. 6).

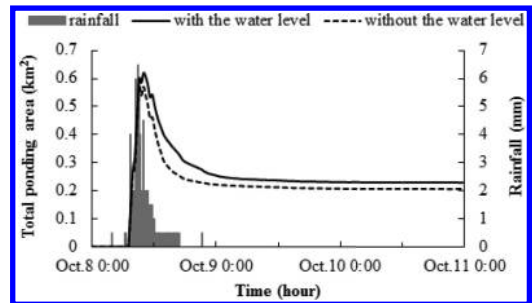


Figure 4. Changes of the total ponding areas whether the water level is considered or not.

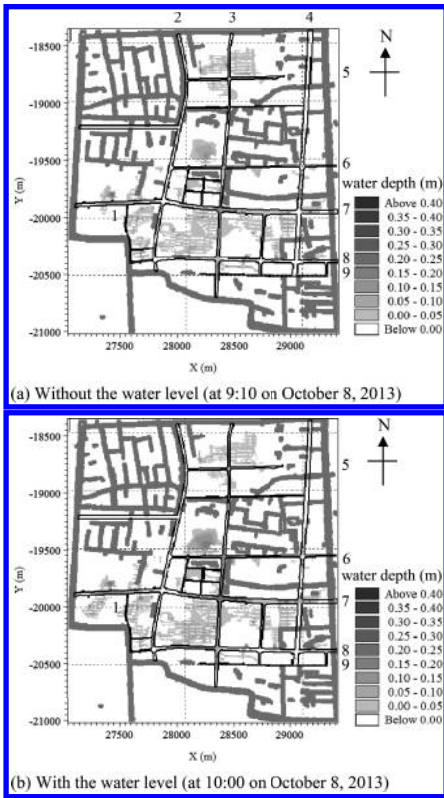


Figure 5. Comparisons of the simulated over flood depths whether the water level is considered or not (Numbers “1” ~ “9” show Meihua Road, Nanzhu Road, Jinhai Road, Chuannanfeng Road, Tanghong Road, Gongbei Road, Gongji Road, East Renmin Road and Huayuan Road).

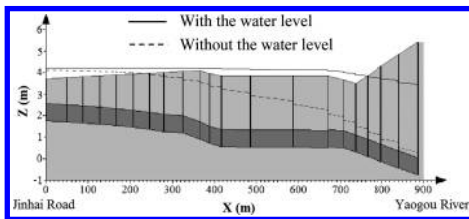


Figure 6. Profiles of the pipes at Gongji Road (Jinghai Road ~ Yaogou River) whether the water level is considered or not (the water flow is filled in dark grey).

## 5 CONCLUSIONS

In this research, a numerical model by MIKE FLOOD software has been set up with rainfall runoff coupled with the sub-model and underground network sub-model by MIKE URBAN, the river sub-model by MIKE 11 and the overland flow

model by MIKE 21 to simulate the storm waterlogging in Huinan, Pudong District. After the validation of the report of the storm waterlogging happened in Huinan on October 8, in 2013 and the simulated results, it was shown that the range and depth of the waterlogging and the time to subside water were agreed with the actual situation so that this model could be adopted to simulate the storm waterlogging in Huinan.

Based on that, the effect of the water level to the urban drainage network in Huinan has been simulated. When the river water level exceeds the elevation of the outlets, it is often easier to generate the surface runoff when the rainfall exceeds the full capacity of the drain lines or the rain arrives more quickly than the local pipe networks can absorb it, so that the total flooded area and overland flow water depth will increase by 8.8% and 50%, meanwhile, it should cost more 3 hours for the overland flood water to finish subsiding. It is indicated that the river water level has the significant effect on the urban drainage network in Huinan, Pudong District. So the measures to control the sluices for the lower water level should be taken to alleviate the storm waterlogging in Huinan, Pudong District.

## REFERENCES

- Barco, J., Wong, K.M., & Stenstorm, M.K. 2008. Automatic calibration of the U.S. EPA SWMM Model for a large urban catchment. *Journal of Hydraulic Engineering*, 134: 466–474.
- Chen, J., Hill, A.A., Urbano, D.L. 2009. A GIS-based model for urban flood inundation. *Journal of Hydrology*, 373: 184–192.
- Huang, J., Wang, S.Z., Deng, S.Z., et al. 2014. Numerical study on the impact of Gongji Road Rain Pump on the waterlogging in Huinan, Pudong District. *Journal of Geoscience and Environment Protection*, 2, 52–58.
- Mark, O., Weesakul, S., Apirumanekul, C., et al. 2004. Potential and limitations of 1D modeling of urban flooding. *Journal of Hydrology*, 35, 159–172.
- Schmitt, T.G., Thomas, M., Ettrich, N., 2004. Analysis and modeling of flooding in urban drainage systems. *Journal of Hydrology*, 299, 300–311.
- Tan, Q. 2007. Application of drainage model for urban storm water quantity management. *Doctor Dissertation of Tongji University*. (in Chinese)
- Werner, M.G.F. 2001. Impact of grid size in GIS based flood extent mapping using a 1D flow model. *Physics and Chemistry of the Earth, Part B: Hydrology, Oceans and Atmosphere*, 26 (7–8): 517–522.
- Xia, J.Q., Falconere, R.A., Lin, B.L., et al. 2011. Numerical assessment of flood hazard risk to people and vehicles in flash floods. *Environmental Modeling & Software*, 1–12.



## On inverse problems for a beam with added spring

Xia Tian

College of Science, Qilu University of Technology, Jinan, China

Chuan-xiao Li

Institute 53 of China Weapon Industry Group, Jinan, China

**ABSTRACT:** The effects of adding spring to a beam on its frequencies are investigated for cantilever beam. Consider two systems: cantilever beam and the same cantilever beam added additional spring. By using two natural frequencies of each system, we identify the structural parameter of the original system. The method is nondestructive. The stiffness of the additional springs is known. Given the natural frequencies of each system, the stiffness of the additional springs and the total mass of the beam, the bending rigidity and density of cantilever beam are reconstructed. The solution of the problem is given and the conditions for the construction of the beam are derived. It is not iterative and therefore demands a modest computational effort.

**Keywords:** inverse problem; eigen value; cantilever beam

### 1 INTRODUCTION

Consider a transversely vibrating uniform Bernoulli–Euler beam as shown in Figure 1. Physical properties of beam are modulus of elasticity  $E$ , density  $\rho$ , cross sectional area  $A$ , and moment of inertia  $I$ . The equation of motion for a transversely vibrating uniform beam is given by

$$\frac{\partial^2}{\partial x^2} \left( EI \frac{\partial^2 y}{\partial x^2} \right) + \rho A \frac{\partial^2 y}{\partial t^2} = 0 \quad (1)$$

Assuming the solution to be a following harmonic motion of the form

$$y(x, t) = Y(x) \sin(\omega t + \phi) \quad (2)$$

Substituting (2) to (1), the following eigen value problem of beam can be derived:

$$Y^4(x) - \frac{\omega^2 m}{EI} Y(x) = 0 \quad (3)$$

where  $m = \rho A$ ,  $\beta^4 = \omega^2 m / EI$ . The boundary conditions of cantilever beam are

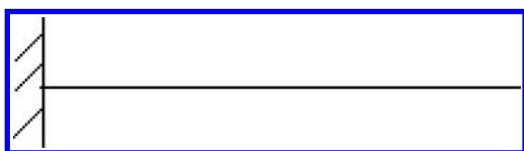


Figure 1. Uniform cantilever beam.

$$Y(0) = 0, Y'(0) = 0, Y''(l) = 0, Y'''(l) = 0 \quad (4)$$

The solution of (3) can be written as

$$Y(x) = A \sin \beta x + B \cos \beta x + C \sinh \beta x + D \cosh \beta x \quad (5)$$

where  $\beta$  must satisfy the transcendental equation  $\cos \beta l \cosh \beta l = -1$ . Now consider the cantilever beam with spring as shown in Figure 2.

In the following section, the inverse problem of beam with added spring will be discussed.

**Problem:** Suppose that the following data are given natural frequency of cantilever beam  $\omega$ , frequency of modified beam  $\mu$ , the total mass of beam  $l$ , the position of spring  $l_1$ , stiffness of translational spring  $k$ , stiffness of rotational spring  $k_\theta$ , reconstruct the physical parameters of cantilever beam  $EI, m$ .

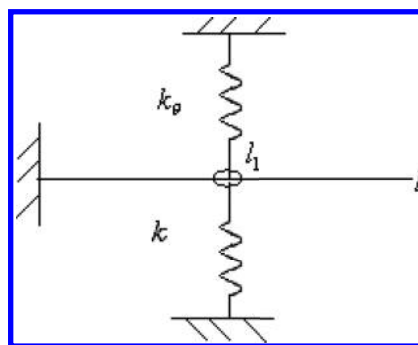


Figure 2. Modified beam (cantilever beam with translational spring and rotational spring).

## 2 SOLUTION OF PROBLEM

Consider uniform cantilever beam as shown in the [Figure 1](#). By using  $\omega_n = \frac{\chi_n \pi^2}{l^2} \sqrt{\frac{EI}{m}}$ , the following relationships can be obtained

$$m/EI = \chi_n^2 \pi^4 / \omega_n^2 l^4, \quad (6)$$

where  $\chi_n = (n - 1/2)$ .

Let  $\beta_1^4 = \mu^2 m/EI$ . The mode shape of modified beam is

$$Y_1(x) = A_1 \sin \beta_1 x + B_1 \cos \beta_1 x + C_1 sh \beta_1 x + D_1 ch \beta_1 x, \quad (7)$$

When  $0 \leq x \leq l_1$ . The mode shape of modified beam is

$$Y_2(x) = A_2 \sin \beta_1 x + B_2 \cos \beta_1 x + C_2 sh \beta_1 x + D_2 ch \beta_1 x \quad (8)$$

When  $l_1 \leq x \leq l$  is hold. The boundary conditions corresponding modified beam are written as following:

$$Y_1(0) = 0, Y_1'(0) = 0, Y_2''(l) = 0, Y_2'''(l) = 0 \quad (9)$$

$$Y_1(x) \Big|_{x=l_1} - Y_2(x) \Big|_{x=l_1} = 0, Y_1'(x) \Big|_{x=l_1} - Y_2'(x) \Big|_{x=l_1} = 0 \quad (10)$$

$$\left( (EIY_1'(x))' - (EIY_2''(x))' \right) \Big|_{x=l_1} + kY_1(x) \Big|_{x=l_1} = 0 \quad (11)$$

$$(EIY_1''(x) - EIY_2''(x)) \Big|_{x=l_1} - k_\theta Y_1'(x) \Big|_{x=l_1} = 0 \quad (12)$$

Letsin  $\beta_1 l_1 = s_1$ ,  $\cos \beta_1 l_1 = c_1$ ,  $sh \beta_1 l_1 = sh_1$ ,  $ch \beta_1 l_1 = ch_1$ ,  $\sin \beta_1 l = s$ ,  $\cos \beta_1 l = c$ ,  $sh \beta_1 l = sh$ ,  $ch \beta_1 l = ch$ . Applying the boundary conditions(9) to [equation \(7\)](#), we have

$$A_1 + C_1 = 0, B_1 + D_1 = 0, C_1 = -A_1, D_1 = -B_1$$

Similarly, applying other boundary conditions (9–11) to [equation \(7\) \(8\)](#) and expressing them to the matrix, we have  $Ax = 0$ , where,  $x = (A_1, B_1, A_2, B_2, C_2, D_2)^T$ ,

In order to obtain the non-trivial solution of equation  $Ax = 0$ , that is  $|A| = 0$ , the following equation must hold

$$\beta_1^6 a (EI)^2 + (k_\theta \beta_1^4 b + k \beta_1^2 d) EI + k k_\theta \beta_1 e = 0, \quad (13)$$

where

$$a = \begin{bmatrix} 0 & 0 & -s & -c & sh & ch \\ 0 & 0 & -c & s & ch & sh \\ s_1 - sh_1 & c_1 - ch_1 & -s_1 & -c_1 & -sh_1 & -ch_1 \\ c_1 - ch_1 & -s_1 - sh_1 & -c_1 & s_1 & -ch_1 & -sh_1 \\ -s_1 - sh_1 & -c_1 - ch_1 & s_1 & c_1 & -sh_1 & -ch_1 \\ -c_1 - ch_1 & s_1 - sh_1 & c_1 & -s_1 & -ch_1 & -sh_1 \end{bmatrix},$$

$$b = \begin{bmatrix} 0 & 0 & -s & -c & sh & ch \\ 0 & 0 & -c & s & ch & sh \\ s_1 - sh_1 & c_1 - ch_1 & -s_1 & -c_1 & -sh_1 & -ch_1 \\ c_1 - ch_1 & -s_1 - sh_1 & -c_1 & s_1 & -ch_1 & -sh_1 \\ -c_1 + ch_1 & s_1 + sh_1 & 0 & 0 & 0 & 0 \\ -c_1 - ch_1 & s_1 - sh_1 & c_1 & s_1 & ch_1 & sh_1 \end{bmatrix},$$

$$d = \begin{bmatrix} 0 & 0 & -s & -c & sh & ch \\ 0 & 0 & -c & s & ch & sh \\ s_1 - sh_1 & c_1 - ch_1 & -s_1 & -c_1 & -sh_1 & -ch_1 \\ c_1 - ch_1 & -s_1 - sh_1 & -c_1 & s_1 & -ch_1 & -sh_1 \\ -s_1 - sh_1 & -c_1 - ch_1 & s_1 & c_1 & -sh_1 & -ch_1 \\ s_1 - sh_1 & s_1 - sh_1 & 0 & 0 & 0 & 0 \end{bmatrix},$$

$$e = \begin{bmatrix} 0 & 0 & -s & -c & sh & ch \\ 0 & 0 & -c & s & ch & sh \\ s_1 - sh_1 & c_1 - ch_1 & -s_1 & -c_1 & -sh_1 & -ch_1 \\ c_1 - ch_1 & -s_1 - sh_1 & -c_1 & s_1 & -ch_1 & -sh_1 \\ -c_1 + ch_1 & s_1 + sh_1 & 0 & 0 & 0 & 0 \\ s_1 - sh_1 & c_1 - ch_1 & 0 & 0 & 0 & 0 \end{bmatrix},$$

If  $\Delta = (k_\theta \beta_1^2 b + kd)^2 - 4k k_\theta \beta_1^2 ea \geq 0$ , then  $EI = \frac{-(k_\theta \beta_1^2 b + kd) \pm \sqrt{\Delta}}{2\beta_1^3 a}$ . We can determine  $m = \chi_n^2 \pi^4 EI / \omega_n^2 l^4$  from (6).

$$A = \begin{bmatrix} 0 & 0 & -s & -c & sh & ch \\ 0 & 0 & -c & s & ch & sh \\ s_1 - sh_1 & c_1 - ch_1 & -s_1 & -c_1 & -sh_1 & -ch_1 \\ c_1 - ch_1 & -s_1 - sh_1 & -c_1 & s_1 & -ch_1 & -sh_1 \\ EI \beta_1^2 (-s_1 - sh_1) - k_\theta \beta_1 (c_1 - ch_1) & EI \beta_1^2 (-c_1 - ch_1) + k_\theta \beta_1 (s_1 + sh_1) & EI \beta_1^2 s_1 & EI \beta_1^2 c_1 & -EI \beta_1^2 sh_1 & -EI \beta_1^2 ch_1 \\ EI \beta_1^3 (-c_1 - ch_1) + k (s_1 - sh_1) & EI \beta_1^3 (s_1 - sh_1) + k (c_1 - ch_1) & EI \beta_1^3 c_1 & -EI \beta_1^3 s_1 & -EI \beta_1^3 ch_1 & -EI \beta_1^3 sh_1 \end{bmatrix}$$

### 3 NUMERICAL METHOD AND EXAMPLES

From the above discussion, give the numerical algorithm for solving problem 1.

**Example** Consider an cantilever beam with  $l = 1m$ . The spring is placed at  $l_1 = 0.5m$ , suppose that lowest natural frequencies of cantilever beam and modified cantilever beam are  $\omega_1 = \pi^2/8$  and  $\mu = 1/2$  respectively. The stiffness of translational spring and rotational spring are  $k = 0.5$  and  $k_\theta = 0.5$ .

We obtain the following data from the given data

$$\chi_1 = 1/4, m/EI = \chi_1^2 \pi^4 \omega_1^2 l^4 = 4,$$

$$\beta_1^4 = \mu^2 m/EI = 1, s_1 = 0.4794, c_1 = 0.8776,$$

$$sh_1 = 0.5211$$

$$ch_1 = 1.1276, s = 0.8415, c = 0.5403, sh = 1.1752,$$

$$ch = 1.5431,$$

Therefore, we have  $a = -14.6698, b = 8.4827, d = 0.6595, e = 0.4717, \Delta = 26.9783 \geq 0$ . Substitute these to [equation \(3\)](#), the following equation is obtained

$$-29.3397(EI)^2 + 4.5711EI + 0.1037 = 0$$

The solution of the above equation is

$$EI_1 = 0.3328, EI_2 = -0.0212 \text{ (we delete it because } EI > 0, m > 0), m = 1.3312.$$

### REFERENCES

- [1] Gladwell G.M.L. Inverse problems in vibration (Second Edition) [M]. Kluwer Academic Publishers, (2004).
- [2] V. Barcion. On the multiplicity of solutions of the inverse problem for a vibrating beam [J], SIAM J Appl Math. vol 37(1979), p. 605–613.
- [3] M. Skrinar and A. Umek, Identification of Beams by the Method Added Mass [J], Computational Methods and Experimental Measurements VI, Computational Mechanics Publications, Southampton, London, 1993, 365–377.
- [4] M. Skrinar, On elastic beams parameter identification using eigenfrequencies changes and the method of added mass [J], computational Materials science. vol. 25 ( 2002), p. 207–217.
- [5] Kumar vikram singh, The transcendental eigenvalue problem and its application in system identification [D]. B.E., Birla institute of technology. Mesra, India, A dissertation of Doctor, 2003.
- [6] Farhad Mir Hosseini, on inverse problems for a beam with attachments [D], University of Ottawa, Ottawa, Canada, A dissertation of Master, 2013.

# Hydraulic characteristics of nature-friendly groynes in NanSi river

B. Qin

*Shandong Survey and Design Institute of Water Conservancy, Jinan, Shandong Province, China*

L.Q. Yang

*School of Civil Engineer and Architecture, University of Jinan, Jinan, Shandong Province, China*

J. Ma

*School of Automation and Electrical Engineering, University of Jinan, Jinan, Shandong Province, China*

**ABSTRACT:** Groynes are the hydraulic structures that have functions of protecting bank erosion and maintaining water level by deflecting flow direction. In this paper, the research for reappraising groynes as a nature-friendly river training structure and for making full use of groynes to improve ecosystem have been introduced. By projection and experiment study, flow pattern and formation of source and sink have been studied. The form and size of eddy according to conditions of groynes are main factors causing in particularly wake vortexes in a front edge of groyne. The impermeable groyne was remarkably larger than the permeable one and the permeable groyne showed little change against varying permeability, showing overall decrease whereas permeability increased. The scour area was found to be the biggest in the impermeable groyne.

**Keywords:** hydraulic structures; groynes; flow pattern

## 1 INTRODUCTION

Groynes are the hydraulic structures that have functions of protecting bank erosion and maintaining water level by deflecting flow direction. In Europe, Japan, USA, and others, the groynes have long been used as a measure of water training. Although the usage of groynes is reduced as the development of direct methods for bank erosion protection like as concrete revetment, the groynes are continuously installed to control the flow for navigation and improve the channel alignment. Recently, groynes attract attention again because the natural bank form made by groynes is very beneficial to river ecosystem. The case of China is similar to that. In developing ages the social needs for river environment is insufficient. And groynes did not attract the attention because of the convenience of concrete revetment. However, the value of groynes as a bank protection technique with the consideration of river environment have been reevaluating recently. And various types of groynes have been installed as a pilot project. In this paper, we will introduce the research for reappraising groynes as a nature-friendly river training structure and for making full use of groynes to improve of ecosystem.

## 2 PROJECTION STUDY

In China, usually groyne is applied to the river regulation, and groynes considering river environment are established in NanSi River in Shandong Province. Si River is one of the main rivers managed by Shandong province. NanSi River originating from Mount. It has about 1,700 m<sup>2</sup> basin and it is close-to-nature comparatively. In the course of nature, concave and convex bankline was created by establishing the series of groynes at almost



Figure 1. Sand bar in downstream of NanSi River.

straightened channel and created bar in groynes downstream created habitats for protected birds, where are restored nature-friendly conditions, as in Figure 1. Previous model experiments were not practiced, but a groyne was established as an experiment in field. Design engineers were not sure because it was very venturous to construct, but at this moment the stability and effect of a groyne are verified from three-time floods in the past.

### 3 EXPERIMENT STUDY

Both thalweg and recirculation zone are important factors for the installation of groynes (Fig. 2). According to the installation of groynes thalweg would change and the velocity of main flow increases more than before the installation groynes. This increased scale of velocity is a very important variable of design relating bed erosion. Also, the recirculation zone, decreasing the velocity scale compare to the main flow, is a main factor of design to create a refuge for life in rivers. As a groyne is designed to create habitats, input conditions are the velocity scale during a flood in relevant river and ecological characteristics of life required protection (in case of fishes, the limit velocity for swimming in which relevant fish can stand). Design engineers should consider the velocity scale, which relevant life need during a flood, to construct groynes.

According to interval of groynes the change of thalweg and recirculation zone are shown in Figure 4 and 5. The position of thalweg from the installed side (TCL/B) decreases until an interval of groynes in about 3l, but it goes up as an interval is 6l. And the width of recirculation zone (Sh/B) decrease until an interval is 4l, and then it increases gradually. In the case of 1–3l, the second groyne obstructs flowing backward that occurred in recirculation zone. But in the case of more 4l, the flowing backward is fully developed. This results verifies that the scale of thalweg and recirculation zone are caused by not only a deflecting flow in a front edge of upstream groynes, but also the obstructing effect of second groyne within recirculation zone made by the first groyne.

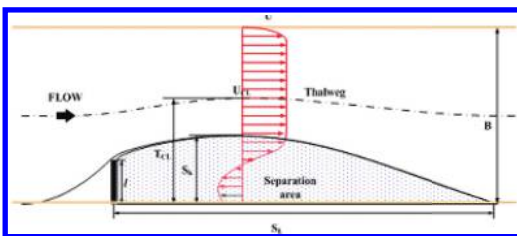


Figure 2. Outline and definition.

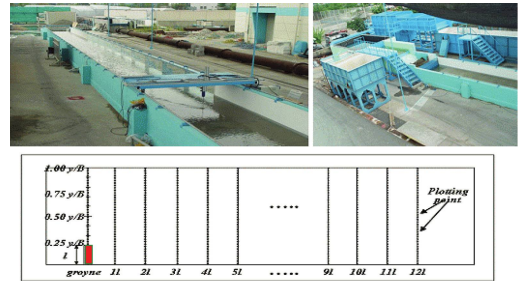


Figure 3. Equipment for experiment and measurement point.

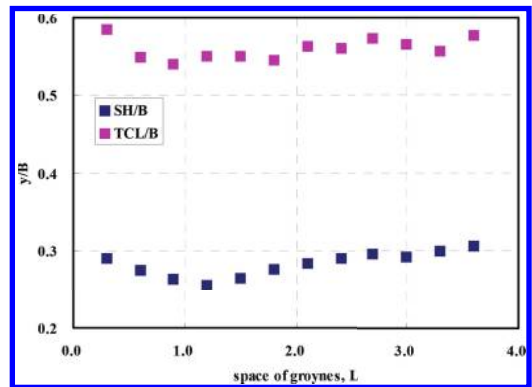


Figure 4. Variation of Sh/B and TCL/B.

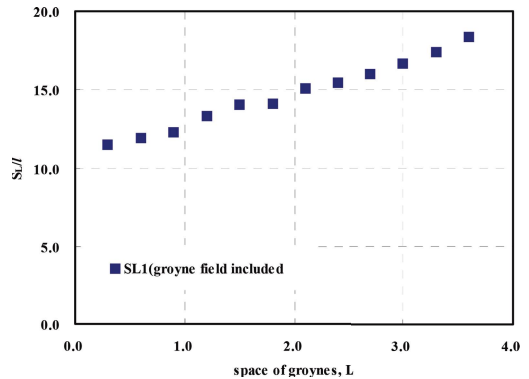


Figure 5. Variation of SL/l.

The length of recirculation zone shown in Figure 5 is measured that it increases linearly as intervals of groynes increase. In experiment conditions, the length of recirculation zone is 18l as the maximum interval of groynes is 12l. This result shows that a deflection flow in downstream groynes is smaller than in upstream groynes as considering

the recirculation of single groyne is about twelve times. According to these results, it is identified that the recirculation zone scale of groynes has close relations with a deflecting flow caused by upstream groynes and a flow of recirculation zone transformed by downstream.

The change of velocity in thalweg shown in Figure 6 is corresponding to the interval change of groynes. The velocity of thalweg has the same tendency with the velocity change in an origin spot of the maximum width of recirculation zone. The velocity change has the same tendency with the analysis of the width of thalweg and recirculation zone, and it has the minimum value as an interval of groynes is 3, 4l. It is discovered the more an interval increases, the more the velocity increases. The velocity of thalweg has the maximum value at 1.5 times compare to the approach velocity as an interval is 12. Figures 7–9 show the velocity of groyne area considering intervals. The maximum velocity of groyne area following intervals of groynes is about 1.7–1.8 times to the approach velocity without any connection with intervals. The maximum velocity of groyne area does not occur in a point in where thalweg has the maximum width, and it occurs in a downstream point to identify the difference of origin spots relating to intervals of groynes.

In designs for general structures occurrence of scour is a defensive, and it is required to identify the scale of scour for the stability of structures. However, holes created by scours can function as ecological habitats. An experiment was performed in Clear Water Scour conditions to identify scour affects caused by groynes only. Figure 10 show results of experiments according to permeability. And Figure 11 shows scour sections by groynes.

In measuring the scale of the scour area, the impermeable groyne was remarkably larger than the permeable one and the permeable groyne showed

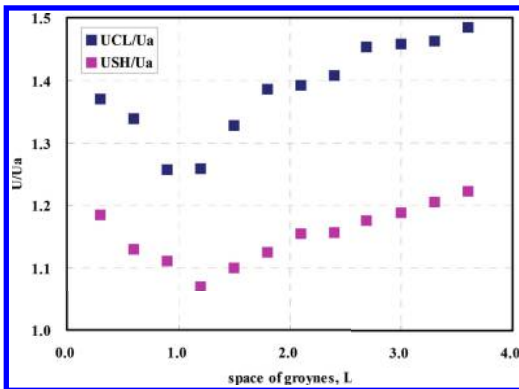


Figure 6. Variation of  $UCL/U_a$  and  $USH/U_a$ .

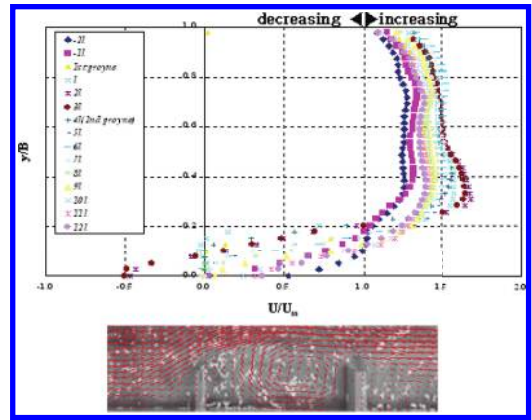


Figure 7. Distribution of velocity  $S = 41$ .

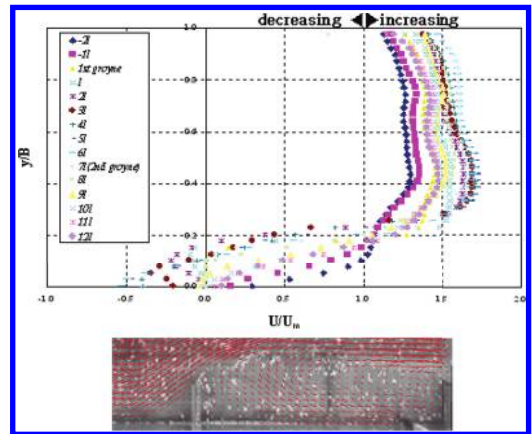


Figure 8. Distribution of velocity  $S = 81$ .

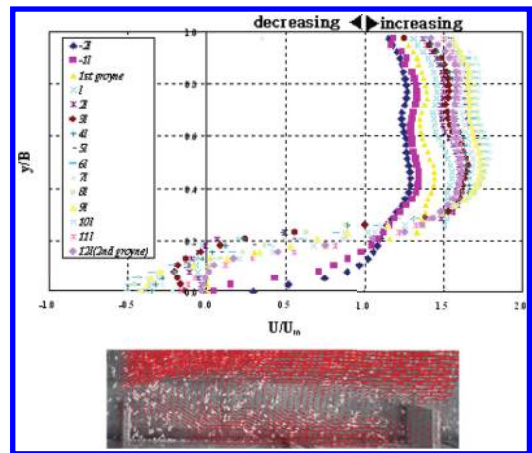


Figure 9. Distribution of velocity  $S = 121$ .

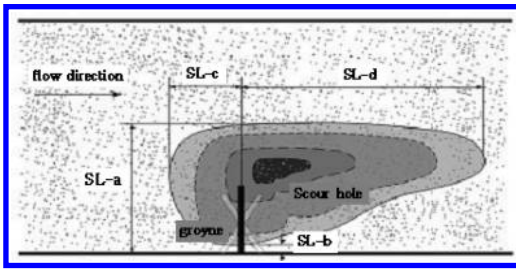


Figure 10. Outline of scour by groyne.

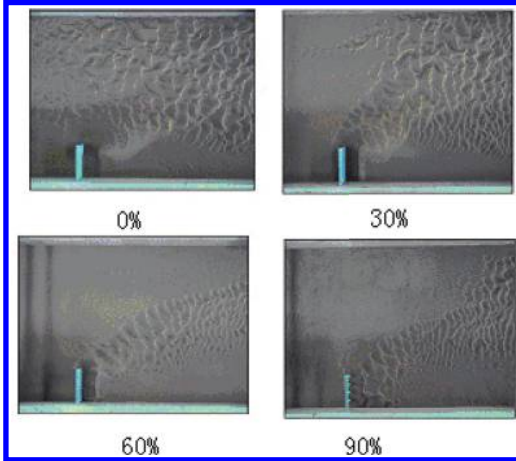


Figure 11. Scour according to permeability.

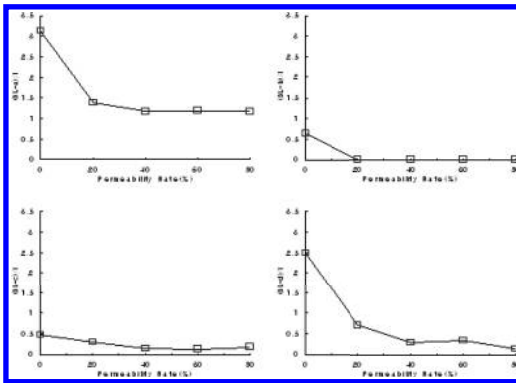


Figure 12. Comparison of scour area according to permeability.

little change against varying permeability, showing overall decrease whereas permeability increased. The scour area was found to be the biggest in the impermeable groyne. Figure 12 compares the scour area by varying permeability.

The form and size of eddy according to conditions of groynes are main factors causing in particularly wake vortexes in a front edge of groyne. The area of groyne is a main variable to generate wake vortexes, and they are different as permeability. The maximum size of eddy is occurred at the impermeable groyne having the maximum area of obstructing flow.

The location where the maximum scour depth occurs is the front edge of groyne, which is the same in case of both impermeable and permeable groynes. However, in case of impermeable groynes local scours are concentrated in front edges of groyne and the other side in cases of permeable groynes local scours with similar values are occurred around groynes.

#### 4 CONCLUSION

In China, because recently the issue considering such as “How to make a river nature-friendly?” and “How to restore river ecosystem?” is rising, groynes which provide various ecological environment and improve scenery around a riverbank including water use and flood control get lots of attention.

Few verified design guideline of groynes causes to hesitate about the application of groynes for a channel plan. Moreover, groynes depend on river conditions particularly considering structure characteristics of groynes. The result of the experience will give practical and reasonable guideline for fundamental designs of groynes.

#### ACKNOWLEDGMENTS

This work was financially supported by the Shandong Water Conservancy Science and Technology Plan (No: sdslyk201301).

#### REFERENCES

Acheson, A.R. (1968). *River Control and Drainage in New Zealand*, Ministry of Work, New Zealand.  
 Copeland, R.R. (1983). *Bank Protection Techniques Using Spur Dikes*. Miscellaneous paper HL83-1, U.S. Army Engineer Waterways Experiment Station.  
 Ettema, R. and Muste, M. (2004). “Scale effects in flume experiments on flow around a spur dike in flatbed channel.” *Journal of Hydraulic Engineering*, ASCE, Vol. 130, No. 7, pp. 635–646.  
 Thompson, D.M., 2002. “Channel-bed scour with high versus low deflectors,” *J. Hydraulic. Eng.*, 128(6), 640–643.

## Research on flood model of Nansi Lake

L.Q. Yang

*School of Civil Engineer and Architecture, University of Jinan, Jinan, Shandong Province, China*

B. Qin

*Shandong Survey and Design Institute of Water Conservancy, Jinan, Shandong Province China*

J. Ma

*School of Automation and Electrical Engineering, University of Jinan, Jinan, Shandong Province, China*

**ABSTRACT:** Nansi Lake is a famous shallow lake in China. It is very important to know the water level and runoff of different sections at different times for engineer. A new calculating method has been proposed, which is called three lakes and two rivers model. Because Nansi Lake is divided into three parts, western part, lake surface, and eastern part. There are two narrow rivers to connect the three parts. In the model, water balance equations are used to instead of continuity equations. The auxiliary curve is used to instead of momentum equation to reflect the river channel storage volume and the approximate relationship between outflow and inflow. Iteration formula is provided in the paper. The numerical calculation methods were used to verify that two rivers and three lakes model is of high precision and the calculation is simple and practical.

**Keywords:** in order to; MS word

### 1 INTRODUCTION

The research approach can be divided into hydrology method and hydraulic method. The hydrology method is based on the water balance and storage-discharge equation and the hydraulic method is based on Saint-Venant Equations. The hydrology methods mainly include the Muskingum method, reservoir flood routing method, etc. The hydrology method considers the main influence factors and their interactions, which can simplify the calculation and guarantee calculation precision; the structure is simple and the hydrology method can well simulate the flood movement in the river and gives the main characteristic of flood in a river section. But the hydrology method is not strict to basic information. The hydrology method is difficult to analyze the complex flow in river channel and main characteristics. And it is difficult to provide the spatial and time distribution of water. Hydraulics methods include characteristic line method, finite difference method, finite element method, finite analysis method and finite volume method. The hydraulic method can build the spatial distribution structure in details, so it can reflect the interaction among various factors comprehensively. The hydraulic method can be suitable for various initial boundary conditions. But the disadvantages of

hydraulic method are the cost of building model, which is high. The hydraulic method has high demands for water regime information in practical application and it is difficult in operation.

### 2 PROJECTION

Nansi Lake is located in the southwest of Shandong province; it is China's famous shallow lake. Located in east longitude  $116^{\circ}34' - 117^{\circ}21'$ , north latitude  $34^{\circ}27' - 35^{\circ}20'$ , Nansi Lake is general name for it including four tandem lakes (Nanyang Lake, Dushan Lake, Zhaoyang Lake, and Weishan Lake). Nansi lake basin precipitation is mainly influenced by monsoon circulation, changing with the seasons. The precipitation increases significantly in summer from July to September. The maximum precipitation is 1191 mm (in 1964), the minimum precipitation is 356 mm (in 1988). The variations of rainfall in a year are big. And rainfall of flood season 6–9 month accounts for 72% of the annual rainfall.

Nansi lake, which is lower in the south than in the north, and belongs to the Huaihe River basin in Yishu water river. There are 53 rivers into Nansi Lake. Nansi Lake is divided into upper and lower two parts by a dam which built in 1960, the part of



north is called upper lake whose catchment area is 27500 km<sup>2</sup>, accounting for 87% of the total drainage area and the part of south is called lower lake.

There are two ways for flood calculation, that is water balance method and flow synthesis method.

### 2.1 Water balance method

Water balance formula is as follows:

$$Q_{idea} = Q_{inflow} + \sum W_{impoundment} / \Delta t - \sum Q_{outflow} \quad (1)$$

$Q_{idea}$ : ideal flow into the lake (m<sup>3</sup>/s);  
 $Q_{inflow}$ : measured flow out of the lake (m<sup>3</sup>/s);  
 $W_{impoundment}$ : the sum of storage volume including Nansi Lake, (m<sup>3</sup>); and  
 $Q_{outflow}$ : irrigation recession water from Yellow River (m<sup>3</sup>/s).

### 2.2 Flow synthesis method

Nansi Lake is divided into three parts, western part, lake surface and eastern part to calculate the flood process respectively, the sum of the three parts as Nansi Lake natural flood process. The main flow channels in eastern lake area have the all flow observation data, but the stations fail to control the entire area of the corresponding rivers, by the survey station ideal flow process and through modifying the area and rainfall ratio to calculate the flow into the lake. The western part is divided into the Liang-Ji Canal, Mo-zhao-xin River, Wan-fu River, Dongyu River, Fuxing River, and Fengpei area, using rainfall data, calculating flood volume by rainfall-runoff relationship. The lake surface adopt rainfall and deduction evaporation to calculate flood volume, negative value as zero.

Using 24 years of measured flood volume (1951–1974) and 1703, 1730, 1921, 1926, 1931, and 1937 a total of 6 years historical max floods, which focus to consider the flood data after 1921, and using P-III curve empirical fitting to analyze different frequency flood on 7 days, 15 days, and

Table 1. Nansi Lake flood calculation results.

Return period	7 D	15 D	30 D
20a	44.3	71.2	80.7
50a	56.7	90.6	103.2
100a	66.3	106.1	120.6
200a	75.6	121.3	138.1
500a	88.2	141.2	161.1
1000a	128.8	206.8	235.1
Average	17.1	27.4	31.1
Cv	0.8	0.8	0.8
Cs/Cv	2.5	2.5	2.5

30 days. The calculation results of Nansi Lake flood volume frequency is shown in Table 1.

## 3 MATHEMATICAL MODEL OF FLOOD

### 3.1 “Three lakes and two rivers” Model

Nansi Lake is long and narrow, different from other deep water areas and mostly shallow water area. Considering the natural geographic features, Nansi Lake is divided into Nanyang Lake (A), Dushan Lake and Zhaoyang Lake (B), and Weishan Lake (C), three tandem lakes in which Nanyang Lake is from 12 K mile stone to 34 K mile stone. The narrow and shallow section is from 42 K mile stone to 94 K mile stone, which connects A lake and B lake. Wang Yan station is on behalf of the average water level of Nanyang lake, Shikou station is on behalf of the Duzhao Lake average level, the Weishan station is on behalf of the average level of Weishan Lake. The water exchange among the three lakes through steady flow calculation, regardless of river channel storage function, gets relationship simulation of  $H_{up} \sim H_{down}$ , but the volume is incorporated into the calculation of adjacent lakes. Using the flood travel time reflects the river channel storage volume, assuming the flood travel time from Nanyang Lake to Du Zhao Lake for 1 days and the flood travel time from Zhao lake to Weishan Lake for 2 days. According to the flood dispatching method of Nansi Lake, during the flood regulation once every 50 years, only Hanzhuang canal participates in operation. Nansi Lake outlet, Hanzhuang sluice gate and Yijia River sluice, are not affected by the downstream water, which have a fixed relation curve of water level and discharge.

The Saint-Venant equations are simplified and only continuity equations as a mathematical model of unsteady open-channel flows, which right there gets the water balance differential equation.

$$Q - q = \frac{dS}{dt} \quad (2)$$

$Q$  is flow into the river reach;  
 $q$  is flow out the river reach; and  
 $S$  is water storage volume in the river reach.

The finite difference form of water balance equation is:

$$\frac{Q_1 + Q_2}{2} \Delta t - \frac{q_1 + q_2}{2} \Delta t = S_2 - S_1 \quad (3)$$

$Q_1, q_1$ : inflow, outflow at the begin of the time period (m<sup>3</sup>/s);  
 $Q_2, q_2$ : inflow, outflow at the end of the time period (m<sup>3</sup>/s); and

$S_1, S_2$ : reservoir water storage at the begin and end of the time period.

Water balance equation shows the difference between the inflow and outflow as reservoir water storage changes on the time period.

According to the characteristics of the Nansi Lake, flood formula of Nansi Lake, which is as 3 tandem lakes, is as follows:

$$\frac{Q_{a_1} + Q_{a_2}}{2} \times t - \frac{q_{a_1} + q_{a_2}}{2} \times t = S_{a_2} - S_{a_1} \quad (4)$$

$$\frac{Q_{b_1} + Q_{b_2}}{2} \times t + \frac{q_{a_1} + q_{a_2}}{2} \times t - \frac{q_{b_1} + q_{b_2}}{2} \times t = S_{b_2} - S_{b_1} \quad (5)$$

$$\frac{Q_{c_1} + Q_{c_2}}{2} \times t + \frac{q_{b_1} + q_{b_2}}{2} \times t - \frac{q_{c_1} + q_{c_2}}{2} \times t = S_{c_2} - S_{c_1} \quad (6)$$

Moving the known items to the right end, then the formula becomes:

$$\frac{2S_{a_2}}{t} + q_{a_2} = Q_{a_1} + Q_{a_2} + \left( \frac{2S_{a_1}}{t} + q_{a_1} \right) - 2q_{a_1} \quad (7)$$

$$\frac{2S_{b_2}}{t} + q_{b_2} = q_{a_1} + q_{a_2} + Q_{b_1} + Q_{b_2} + \left( \frac{2S_{b_1}}{t} + q_{b_1} \right) - 2q_{b_1} \quad (8)$$

$$\frac{2S_{c_2}}{t} + q_{c_2} = q_{b_1} + q_{b_2} + Q_{c_1} + Q_{c_2} + \left( \frac{2S_{c_1}}{t} + q_{c_1} \right) - 2q_{c_1} \quad (9)$$

The water balance equations are used to instead of continuity equations. The continuity equation can be for flood regulating calculation of three tandem lakes, but the two river ways are connected the lakes. So it need to use the auxiliary curve instead of momentum equation to reflect the river channel storage volume and the approximate relationship between outflow and inflow and then flood routing from the upper lake to the lower lake, the final completion of flood routing work of the “three lakes two rivers”.

### 3.2 Numerical model

The flood travels in the river (or reservoir, lake), along the water level, flow, flow velocity with the time change. The flow regime belongs to unsteady open-channel flows and the law of motion can be described by the Saint—Venot equations:

$$B_T \frac{\partial Z}{\partial t} + \frac{\partial Q}{\partial x} = q \quad (10)$$

$$\frac{\partial Q}{\partial t} + \frac{\partial}{\partial t} \left( \frac{Q^2}{A} \right) + gA \frac{\partial Z}{\partial x} + gA \frac{|Q|Q}{K^2} = 0 \quad (11)$$

where  $q$  is the flank inflow of the channel ( $m^3/s$ );  $B_r$  is the equivalent river width (m);  $A$  is water-crossing section area ( $m^2$ );  $Z$  is section water lever (m);  $Q$  is cross section flow ( $m^3/s$ );  $K$  is the flow modulus ( $m^3/s$ );  $t$  is the time (s);  $X$  is the distance along the direction of flow (m); and  $G$  is the gravitational acceleration. Numerical model grid is as shown in Figure 1.

## 4 CALCULATION RESULTS

The two methods above were used to calculate water level process of Nansi Lake, respectively.

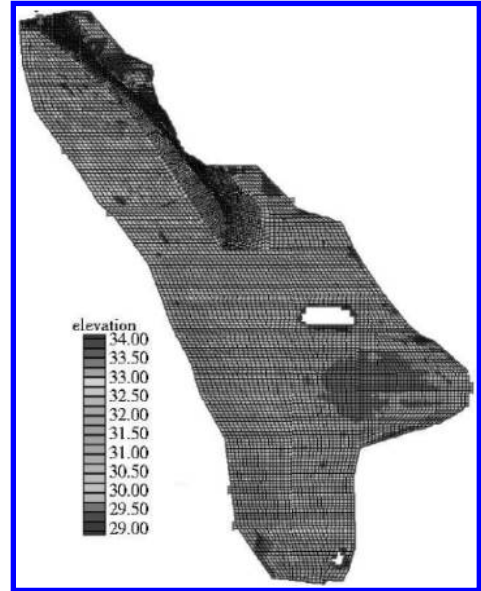


Figure 1. Numerical model.

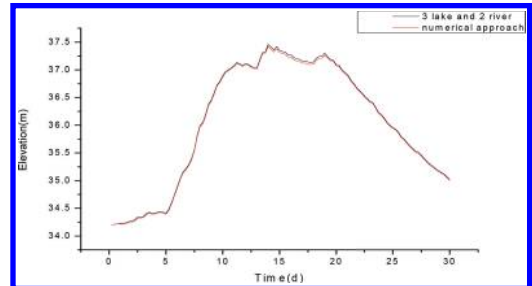


Figure 2. Two model result comparison of Nanyang Lake.

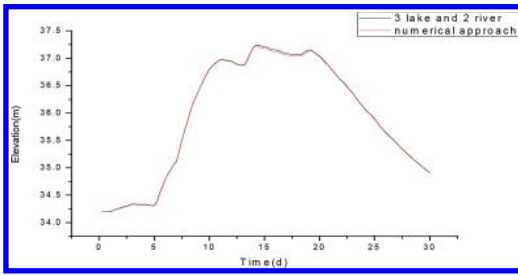


Figure 3. Two model result comparison of Duzhao.

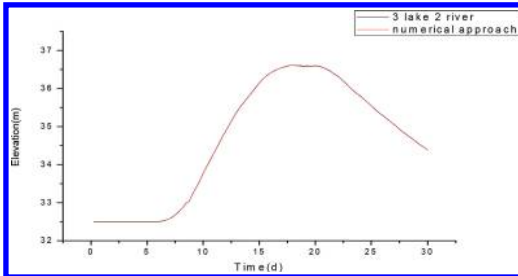


Figure 4. Two model result comparison of weishan.

The results of calculation is shown in Figures 2–4. It can be seen from the figures that the two methods are basically the same and the water level of the ‘three lakes two rivers’ model is higher than the water level of the numerical model only in the peak part.

## 5 CONCLUSION

According to the characteristics of the Nansi Lake, two rivers and three lakes model has

been proposed. In the model, water balance equations are used to instead of continuity equations. The auxiliary curve is used to instead of momentum equation to reflect the river channel storage volume and the approximate relationship between outflow and inflow. It is simple for engineer to calculate by hand. The numerical calculation methods were used to verify that two rivers and three lakes model is high precision and the calculation is simple and practical.

## ACKNOWLEDGMENTS

This work was financially supported by the Shandong Water Conservancy Science and Technology Plan (No: sdsly201301).

## REFERENCES

- Lee Zhijia, research on one-dimensional river networks unsteady flow common soft. *Journal of Hydraulic Engineering*, 1998 (08): 14–18.
- Tan Weiyuan, Hu fouryi, The new direction of computational shallow water dynamics. *Advances in Water Science*, 1992 (12): 300–318.
- Wei Zhilin, Cui Zhanfeng, A preliminary study on one-dimensional river networks unsteady flow calculation procedure. *Yangtze River*, 2001 (12): 30–32.
- Wu Zuoping, Yang Guolu, Gan Minghui, The lake flood-regulating function on river network calculation effect. *Advances in Water Science*, 2004 (9): 603–607.

## Study on the comprehensive response to drought in China

B.S. Weng, D.H. Yan & S.J. Bao

*State Key Laboratory of Simulation and Regulation of Water Cycle in River Basin, China Institute of Water Resources and Hydropower Research, Beijing, China*

**ABSTRACT:** Against the backdrop of global change with a higher and higher frequency of drought, the aim of this study is to analyze the trend and character of the drought, and to set up a series of the integrated coping technologies to cope with droughts in China. China is in urgent need of making three major shifts in terms of its drought relief patterns. First, emergency-based management pattern should be shifted to a combination of risk-based management and normal management. Second, instead of only focusing on short-term emergency-based management, the pattern should also pay due attention to mid-term and long-term management results. Third, finite objective-oriented management should be shifted to a combination of whole process-oriented management and integrated management. Proceedings from several pertinent links associated with a comprehensive drought response plan which includes drought relief planning, monitoring, evaluation, early warning/forecasting, dispatch and management, and impact assessment. We should aim at improving drought relief planning technologies of risk-based management patterns, drought monitoring technologies based on hydrological cycle process and all-dimensional pattern, drought evaluation technologies based on water resources supply and demand situations, drought early-warning and forecasting technologies based on remote sensing and land-atmosphere coupling model, comprehensive multi-water source emergency operation and management technologies geared to drought relief and integrated real-time assessment technologies on drought impact catering to coordinated regional development with the ultimate goal of developing three kinds of capabilities on risk-based drought management, monitoring and evaluation as well as early warning and forecasting, and emergency dispatch and management.

**Keywords:** drought; comprehensive response; drought assessment; drought risk management

### 1 INTRODUCTION

With the increasing impact of climate change and human activities, drought occurs in areas with higher frequency. Since 1990, drought disasters have caused more than 11 million deaths, and affected more than 2 billion people globally (United Nations International Strategy for Disaster Reduction Secretariat, 2009). The losses of drought disaster accounted for 55% of the losses of meteorological disaster which accounted for 61% of all losses from natural disasters in the last 50 years in China (Li et al., 2003). The annual average affected areas (the areas that crop yields decreased by over 10% than normal annual yields) and damaged areas (the areas that crop yields decreased by over 30% than normal annual yields) of drought disasters were nearly 21 million square km and 10 million square km from 1950 to 2010, which were 2.19 times and 1.77 times than the impacts of flood disasters, respectively (State Flood Control and Drought Relief Headquarters, 2010). Since 1990, the average annual direct economic losses above 1% of GDP over the same period in China

were caused by drought, and over 2% in case of severe drought (State Flood Control and Drought Relief Headquarters, 2010), taking the drought that happened in Southwest China in 2009 for example. Since the autumn of 2009, an unprecedented drought spell had wrought havoc in Southwest China and had extended rapidly to North China, exerting a grievous influence on regional economic and social development and threatening its ecological and environmental security. In addition to inadequate regional water projects and emergency-based drought response management pattern, both a long period of low rainfall and a record of high temperatures and the flood season, which ended much earlier last year, were mainly responsible for this disastrous drought.

Drought impacts not only on industrial and agricultural production, but also on water safety in urban and rural residents. Serious cases will bring great harm to ecosystem and impact on social and economic sustainable development. Drought response is the major question in achieving sound and fast economic and social development in China.

## 2 NEW FEATURES OF DROUGHT IN CHINA

China lies in the Asian monsoon climate zone and combines with three ladder-like pattern of the landscape, which fundamentally determines the background of the frequency of drought in China (Yu, 2003). Space does not match the soil and water resources, which is difficult to eliminate fundamentally the drought. Global warming speeds up the rate of hydrological cycle. It reduces the stability of the hydrological cycle system and improves the frequency of severe weather such as drought. Drought occurs not only in northern China with shortage of water resources, but also in southern China with relatively abundant water resources frequently, such as Xingjian River Basin, PoYang Lake Plain, Sichuan Basin, and Yunnan-Guizhou Plateau.

In the past, it was noted that drought occurs in the arid and semi-arid regions. However, the characteristics of drought have changed with a new trend of group occurrence, extensiveness and continuity. According to the analysis in temporal order, drought occurred mainly in spring and autumn in the past. But now, it takes place throughout the year and usually happens all over the country.

Climate and landscape character determine the background of the frequency of drought, while climate change and human activities exacerbate the occurrence of drought. Therefore, to adapt to the regional climate, eliminate the irrational human activities, and mitigate the losses due to drought, is an overall goal of comprehensive drought response in China.

## 3 GENERAL IDEA OF THE COMPREHENSIVE RESPONSE TO DROUGHT IN CHINA

Against the backdrop of global change with a higher and higher frequency of droughts, China is in an urgent need of making three major shifts in terms of its drought relief patterns. First, emergency-based management pattern should be shifted to a combination of risk-based management and normal management, incorporating drought response to daily IWRM routines and formulating risk-based management patterns so as to prevent drought-induced risks (ISDR, 2007; Knutson et al., 1998). Second, instead of only focusing on short-term emergency-based management, the pattern should also pay due attention to mid-term and long-term management results. On the basis of water resources carrying capacity, drought-related elements should also be taken into consideration for overall regional planning and integrated water resources planning

by means of defining drought risk areas, and accordingly the industrial layout and water conservancy project distribution will be optimized and contingency plan developed. Third, finite objective-oriented management should be shifted to a combination of whole process-oriented management and integrated management. An all-dimensional integrated monitoring and assessment system should be established to integrate drought early warning and forecasting, real-time drought relief decision making and drought impact evaluation.

Proceeding from several pertinent links associated with a comprehensive drought response plan which include drought relief planning, monitoring, evaluation, early warning/forecasting, dispatch and management, impact assessment, we should aim at improving drought relief planning technologies of risk-based management pattern, drought monitoring technologies based on hydrological cycle process and all-dimensional pattern, drought evaluation technologies based on water resources supply and demand situations, drought early-warning and forecasting technologies based on remote sensing and land-atmosphere coupling model, comprehensive multi-water source emergency operation and management technologies geared to drought relief and integrated real-time assessment technologies on drought impact catering to coordinated regional development with the ultimate goal of developing three kinds of capabilities on risk-based drought management, monitoring and evaluation as well as early warning and forecasting, and emergency dispatch and management.

## 4 OVERALL TECHNICAL FRAMEWORK OF THE COMPREHENSIVE RESPONSE TO DROUGHT IN CHINA

The overall technical framework of the comprehensive response to drought in China consists of six parts (Fig. 1). There are planning techniques, monitoring techniques, evaluation technologies, forecasting and early-warning technologies, jointing emergency dispatching and management techniques, as well as timely and comprehensive assessment techniques.

Planning techniques on drought would be based on risk management mode. Rational allocation of water resources for drought is a new approach to shift emergency management level into water resources allocation planning and carrying out water supply and demand analysis under situation of possible extreme drought in future (Wang et al., 2004). Comparing with the traditional water allocation that is just accounting for normal water resources, the new approach takes full account of the hydrological extreme events, and that of climate change (Wilhite, 2005). It could apply to

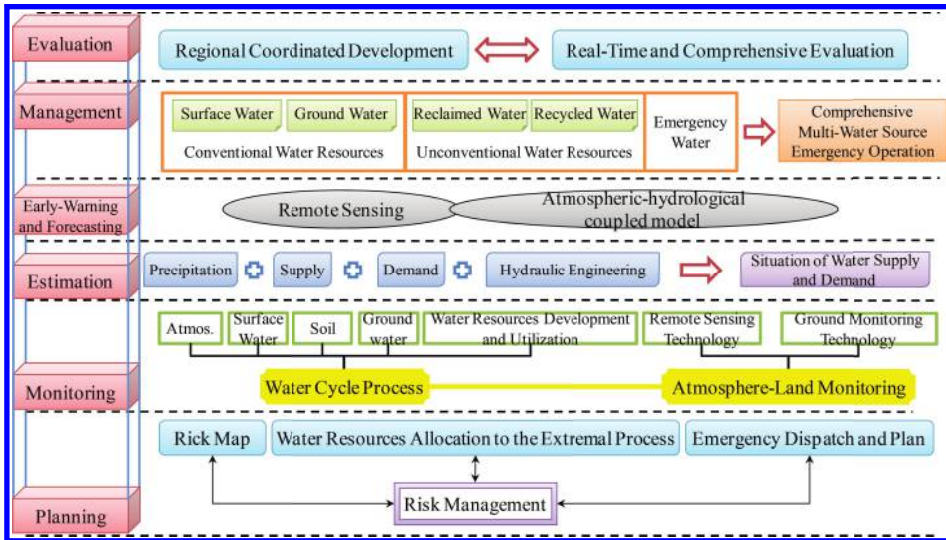


Figure 1. The overall technical framework of the comprehensive response to drought in China.

the region's water resources carrying capacity under extreme drought situation, optimize the layout of regional industry structure, and enrich the connotation of water resources management.

Monitoring techniques on drought would be based on sky–earth integration mode and water cycle process. In order to monitor the water cycle of the atmosphere, surface, soil, and groundwater and improve the utilization of water resources, a comprehensive monitoring technique system for drought should be constructed, which combines remote sensing technique (satellite remote sensing, air sounding etc.) and the ground detection technique (Dente et al., 2008).

Drought evaluation technologies would be based on supply and demand situation of water resources. According to the impacts of the evolution of elements and processes of water cycle, droughts are classified into meteorological drought, hydrological drought, agricultural drought, socio-economic drought, ecological drought, and so on (American Meteorological Society, 1997). Drought indices, such as Palmer Drought Severity Index (Palmer, 1965; Garen, 1991), Standardized Precipitation Index (McKee et al., 1993), Surface Water Supply Index (Shafer & Dezman, 1982), etc., were proposed. Dynamic evaluation of drought is required to be combined with regional precipitation, water demand, water supply, and the features of the hydro-project.

Forecasting and early-warning technologies of drought would be based on remote sensing and land–atmosphere coupling model. In combination with the unified physical model, techniques such as RS, atmospheric prediction, hydrological

prediction, ecological simulation, and crop mode are integrated into drought warning and forecasting, with the purpose of improving the accuracy of prediction. Besides, dynamic amendment and aggregation techniques should also be utilized during the whole process.

Jointing emergency dispatching and management techniques of multi-source water to drought combines the warning and forecasting of drought and its effects. It includes information gathering, assessment, prediction, strategic decision, implementation, and post-evaluation. The integrated reallocation of conventional water resources (surface water, groundwater, etc.), unconventional water resources (reclaimed water, etc.), and emergency water resources has been proposed. At the same time, comprehensive security measures are also pointed out (Weng & Yan, 2010).

Timely and comprehensive assessment techniques of drought impacts to regional development would be researched. To provide the basis for the dynamic amendment of drought prevention strategies, real time evaluation of the effects that results from drought should be implemented. At the same time, to provide the basis for post-construction planning and management, overall evaluation should be also carried out for the impacts of drought. Real-time integrated evaluation techniques are composed of three parts. The first part is the forecasting technology before the occurrence of drought. To establishing overall response scheme, activating contingency plans would be required. The second one is the evaluation technology when the drought occurs, which needs to amend the response scheme

dynamically. The last one is the impact assessment technology after the drought. To reconstruct after the drought disaster and amend the emergency plan would be required.

## 5 CONCLUSION

Drought is the extreme event in water cycle. The occurrences of drought events usually contain dual characteristics: determinacy and randomness. With the increasing impact of climate change and human activities, drought happens in more area with a higher frequency, and now it endangers the water and ecological security in the river basin. Drought has changed from its event, which is shortage of water resources to disaster. Therefore, China is in urgent need of making three major shifts in terms of its drought relief patterns. By analyzing the data of drought and flood, the general features of drought in the changing environment of China were summarized. This paper put forward and experienced a new method based on basic hydrological process for researching extreme weather issues. Finally, the integrated coping strategies have been discussed in this study, such as RS and land-atmospheric coupling mode, integrated contingency reallocation and management techniques, Real time integrated evaluation techniques. However, there are also some shortages and challenges in resist drought, such as the ability to resist drought is not balance. And the accuracy of drought monitoring and prediction should be improved so that the integrated coping strategies would be coped with drought effectively.

## ACKNOWLEDGMENTS

This work was supported by the National Science and Technology Support Program Project (2013BAC10B01) and the General Program of the National Natural Science Foundation of China (51279207, 51409266).

## REFERENCES

[1] American Meteorological Society (AMS), 1997. Meteorological drought-policy statement, Bull American Meteorological Society, 78: 847-849.

[2] Dente, L., Satelino, G., et al. 2008. Assimilation of leaf area index derived from ASAR and MERIS data into CERES-Wheat model to map wheat yield. *Remote Sensing of Environment*, 112(4): 1395-1407.

[3] Garen, D.C. 1991. Revised Surface-Water Supply Index for the western United States. *Journal Water Re-sources Plan. Manage.*, 119: 437-454.

[4] ISDR, 2007. Drought risk reduction framework and practices. United Nations.

[5] Knutson, C., Hayes, M and Phillips, T. 1998. How to reduce drought risk. Western Drought Coordination Council, National Drought Mitigation Center, Nebraska, USA.

[6] Li, W.J., Zhao, Z.G., Li, X., et al. 2003. The drought characteristics analysis in North China and its causes of formation. *Arid Meteorology*, 21(4): 2-5. (in Chinese)

[7] McKee, T.B., Doesken, N.J., Kleist, J. 1993. The relationship of drought frequency and duration to time scales. Preprints, Eighth Conf. on Applied Climatology, Anaheim, CA, Amer. Meteor. Soc., 179-184.

[8] Palmer, W.C. 1965. Meteorological drought. *Weather Bureau Research Paper*, 45: 58.

[9] Shafer, B.A., Dezman, L.E. 1982. Development of a Surface Water Supply Index (SWSI) to assess the se-verity of drought conditions in snowpack runoff areas [C]//Proceedings of the (50th) 1982 Annual Western Snow Conference, Fort Collins, CO: Colorado State University, 164-75.

[10] State Flood Control and Drought Relief Headquarters, 2010. Bulletin of flood and drought disasters in China, China Ministry of Water Resources, Beijing, China. (in Chinese)

[11] United Nations International Strategy for Disaster Reduction Secretariat (UNISDR), 2009. Global assessment report on disaster risk reduction. Risk and poverty in a changing climate. Invest today for a safer tomorrow, New York, UNISDR.

[12] Wang, H., Wang, J.H., and Qin, D.Y. 2004. Research advances and direction on the theory and practice of reasonable water resources allocation. *Advances in Water Science*, 15(1): 123-128.

[13] Weng, B.S., Yan, D.H. 2010. Reflections on integrated coping strategies for drought in China in changing environment. *China Water Resources*, 7: 4-8.

[14] Wilhite, D.A. 2005. *Drought and Water Crises: Science, Technology, and Management Issues*. Taylor and Francis, USA.

[15] Yu Q.X. 2003. Think of drought and drought disaster in China. *China Water Resources*, 4: 67-69.

# Distributed hydrological and silty model in Chabagou basin of Yellow River based on DEM

H.J. Zhao & Y.D. Jin

Beijing Engineering Corporation Limited, Beijing, China

F.X. Chai

China Institute of Water Resources and Hydropower Research, Beijing, China

**ABSTRACT:** The digital stream network and spatial information were extracted from raster-based DEM data. The grid-based distributed hydrological and silty model was developed on the basis of excess infiltration mechanism in the areas with high and coarse sediment yield, considering the impact of structural measures for soil conservation on runoff routing. The model was implemented in the Chabagou basin of the Wuding River that is a tributary of the Yellow River from the year 1970 to 1989. The results show that the developed distributed model is suitable for the small watershed in the loess area.

**Keywords:** distributed model; hydrological and silty; digital elevation model; Chabagou basin

## 1 INTRODUCTION

Soil erosion in the Yellow River basin especially the areas with high and coarse sediment yield is very serious, so the study on distributed hydrological & silty model and its application in the areas is not only helpful to understand the hydrological and sediment processes in the semi-arid regions but also in favor of quantitative analysis of soil erosion and Quantitative assessment of soil erosion control measures, which can provide scientific basis for the water and soil conservation planning and treatment in the small watershed (Zhonggen Wang, Hongxing Zheng & Changming Liu, *et al.* 2004).

## 2 MODEL PRINCIPLE AND STRUCTURE

### 2.1 Spatial analysis of watershed characteristics

The grid flow is set by D8 method and the fill algorithm to determine the direction of depression. The flow velocity and soil erosion rate of constant current were calculated by the flow path length and gradient of the grid, and the flow velocity is approximate as the confluence velocity to carry out grid convergence of water and sediment routing.

### 2.2 Runoff generation model of grid unit

Considering the underlying surface condition, precipitation characteristics and short time step

factors of the study area, the infiltration excess runoff pattern of grid unit runoff production model was used to calculate the runoff yield. Philip formula (Maidment David R., Jianyun Zhang & Jisheng Li 2002) was adopted to calculate runoff depth of each grid in different periods, followed by computing their inflow into the river network.

$$f = B^2 \left( 1 + \sqrt{1 + A\theta/B^2} \right) / \theta + A \quad (1)$$

where  $f$  is infiltration rate, mm/h; both  $A$  and  $B$  are the undetermined coefficients, which are related to soil characteristics;  $\theta$  is cumulative infiltration quantity, mm.

### 2.3 Confluence model of grid unit

1. Calculation of collection time. The confluence time is the flow translation time from the central point of the runoff grid to the river outlet, and the formula is as follows (Li Li 2003).

$$t_c = \frac{L}{V} = \frac{L}{K_v S^{1/2}} \quad (2)$$

where  $L$  is length of flow path of channel segment, m;  $S$  is slope of reach;  $V$  is flow velocity, m/s;  $K_v$  is velocity constant, containing influence of roughness, hydraulic radius and other factors to water flow.



2. Storage calculation of the pond. The pond storage coefficient  $\zeta$  was used to simulate, and the formula is as follows.

$$R' = R \cdot \zeta \quad (3)$$

where  $R$  is runoff depth of the mesh before storage, mm;  $R'$  is runoff depth of the mesh after storage, mm;  $\zeta$  is the pond storage coefficient (values 0–1).

#### 2.4 Sediment yield model of grid unit

1. Splash erosion. The magnitude of the splash erosion rate depends on the erosion force of raindrops, while the erosion force is related to the impact force of the raindrops running into the soil particles (Wenyi Yao & Liqun Tang 2001).

The splash erosion rate of a rainfall can be expressed as follows.

$$d_R = K_d \rho d_{50}^2 V_{m50}^2 \cos^2 \alpha f(y) \quad (4)$$

where  $K_d$  is the coefficient related to soil characteristics;  $d_{50}$  is median particle size of raindrop, mm;  $V_{m50}$  is raindrop terminal velocity, m/s;  $\theta$  is the slope gradient,  $f(y)$  is the function related to slope runoff depth. When there is no runoff on slope surface,  $f(y)$  is the maximum (1.0), with the increase of slope runoff depth,  $f(y)$  reduces gradually, while runoff depth is more than three times of raindrop diameter. Raindrop erosion effect becomes very small and  $f(y)$  is calculated by the formula below.

$$f(y) = \begin{cases} 1 & y = 0 \\ \frac{d_{50}^2}{y^2} e^{-\frac{3d_{50}}{8y^2}} & 0 < y < 3d_{50} \\ 0 & y \geq 3d_{50} \end{cases} \quad (5)$$

The median particle size of raindrops was calculated by the following formula.

$$d_{50} = \begin{cases} 2.77I^{0.27} & TT > 60 \text{ min} \\ 3.32I^{0.25} & TT \leq 60 \text{ min} \end{cases} \quad (6)$$

where  $I$  is rainfall intensity and  $TT$  is the duration. Terminal speed. The rain drop was calculated by the followed formula.

$$V_{m50} = \begin{cases} \sqrt{\left(\frac{38.9\nu}{d_{50}}\right)^2 + 2400gd_{50}} - \frac{38.9\nu}{d_{50}} & d_{50} \leq 3 \text{ mm} \\ \frac{d_{50}}{0.113 + 0.0845d_{50}} & 3 \text{ mm} < d_{50} \leq 6 \text{ mm} \end{cases} \quad (7)$$

where  $g$  is gravity acceleration, m/s<sup>2</sup>;  $\nu$  is air movement viscosity coefficient, m<sup>2</sup>/s.

2. Runoff erosion. According to its slopes, the grids were divided into three kinds of slope surfaces: hill slope, gully slope, and trench. Using the runoff and sediment dynamics model in small watershed, the sediment yields of three slopes were carried out separately (Wenyi Yao & Liqun Tang 2001).

Soil erosion rate calculation formulas of three kinds of grids: hilly slope, gully slope, and trench are shown as formula (8) ~ formula (10).

$$E_r = e_r \cdot b_r \quad (8)$$

$$E_g = e_g \cdot b_g \quad (9)$$

$$E_c = B_c \frac{\sqrt{\gamma_m g}}{\gamma_s - \gamma_m} \tau_0^{3/2} V \quad (10)$$

Among them:

$$E_r = A_r \frac{\gamma_m}{\gamma_s - \gamma_m} (\tau_0 - \tau_c') V \quad (11)$$

$$E_g = A_g \frac{\gamma_m}{\gamma_s - \gamma_m} (\tau_0 - \tau_c') V \quad (12)$$

$$\tau_0 - \tau_c' = \gamma_m R J + (\gamma_s - \gamma_m) d \sin \alpha - \mu (\gamma_s - \gamma_m) d \cos \alpha \quad (13)$$

$$\tau_0 = \gamma_m R J \quad (14)$$

where  $e_r$  and  $e_g$  are single width soil erosion rates of hill slope and gully slope respectively;  $b_r$  and  $b_g$  are hill slope width and gully slope width respectively. Here is grid width, m;  $\gamma_s$  and  $\gamma_m$  is sediment compacting dry density and bulk density of muddy water, respectively. N/m<sup>3</sup>;  $\tau_0$ ,  $\tau_c'$  and  $(\tau_0 - \tau_c')$  is flow shear stress, starting shear stress of sediment on the slope and effective shear stress of sediment particles on the slope, respectively. N/m<sup>2</sup>;  $V$  is flow velocity, m/s;  $h$  is runoff depth, m;  $J$  is gradient;  $d$  is sediment particle size, mm;  $\alpha$  is grid slope;  $f$  is the friction coefficient;  $A_r$ ,  $A_g$  and  $B_c$  are dimensionless synthetic coefficients, set by the measured data.

3. The overland flow sediment carrying capacity. The followed formula fitted the overland flow sediment carrying capacity better.

$$T_c = \frac{1}{22284} \left( \frac{\tau_0 - \tau_c'}{d^{0.33}} \right)^{2.457} \quad (15)$$

4. Calculation of sediment amount intercepted by the projects. The typical calculation formula of

sediment amount intercepted by the silt storage dam is as follows.

$$\Delta W_{sg} = M_s k (1 - \alpha_1) (1 - \alpha_2) \quad (16)$$

where  $\Delta W_{sg}$  is mud quantity intercepted by the silt storage dam in the watershed,  $m^3$ ;  $M_s$  is intercepted mud amount per square meter,  $m^3/m^2$ ;  $k$  is area of the dam within the grid,  $m^2$ ;  $\alpha_1$  is the scale coefficient artificial filling dam area in total dam area;  $\alpha_2$  is the proportion coefficient of bed load quantity in sediment amount intercepted by the dam.

### 2.5 Sediment converge model of grid unit

Slope and gully erosion material must be transported to the exit section to become a watershed sediment yield while the transport of erosion materials is restricted by such factors as hydraulic condition, sediment conditions and channel boundary conditions. Research in the reference (Jinren Ni, Xiaoyong Liu & Tianhong Li, *et al.* 2004) considers that most parts of the Loess Plateau Gully or river course have exposed bedrocks, that although have no bedrock, the deposits belonging to them have gravels or sands that are thicker and the sediment transport ratio is close to 1.0. So sediment yields of the watershed outlet section can be calculated by superposing soil erosion of each unit in staggered several propagation period.

## 3 SURVEY AND DATA OF THE RESEARCH AREA

### 3.1 Survey of the research area

Chabagou watershed located in the first sub region of the Loess hilly region, the northern Zizhou County of Shaanxi province, belongs to semi-arid and semi-humid area. The watershed area is  $205 \text{ km}^2$ , of which the control area of the Cao Ping hydrological station is  $187 \text{ km}^2$ . Chabagou is a branch of Dali River. Its shape is basically symmetrical, the average width is  $7.8 \text{ km}$ , the channel length is  $26.3 \text{ km}$ , and the channel density is  $1.07 \text{ km/km}^2$  (Fig. 1). The average erosion modulus of the watershed is  $22,200 \text{ t}/(\text{km}^2 \cdot \text{year})$ , the largest is  $71,100 \text{ t}/(\text{km}^2 \cdot \text{year})$ , still the smallest is  $2110 \text{ t}/(\text{km}^2 \cdot \text{year})$ .

### 3.2 Date and processing

Hydrological data include 11 sessions precipitation data extract in total and corresponding flood discharge and sediment concentration data extract of Cao Ping Station during the same period.

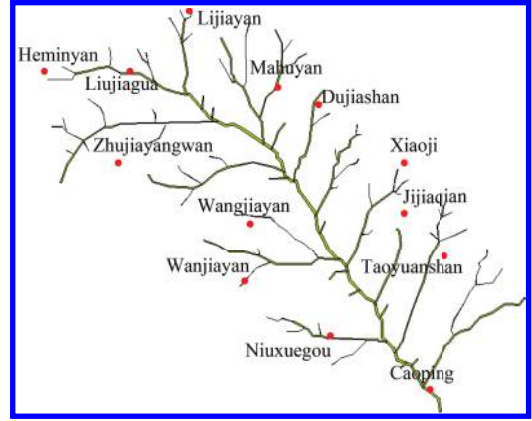


Figure 1. Drainage map of Chabagou watershed.

Because there is no evaporation data of the study area, the evaporation data of the latest Suide station on Dali River, Wuding River system was used. The topographic data was obtained from the 1:10,000 contour line map drawn by Shaanxi Province Bureau of Surveying and Mapping Bureau, resulting in the formation of  $50 \text{ m} \times 50 \text{ m}$  grid DEM, which divided the basin into 446 rows and 633 columns, i.e. a total of 282,318 grids. The extracts of the flow and precipitation process were interpolated into the time series of equal interval (30 min), while the inverse distance squared method is used to spatial interpolation of the hydrological data.

## 4 CALCULATION RESULTS AND ANALYSIS

### 4.1 Model setting

1. Floods selection. In the principles of large or middle water and unimodal or bimodal flood, 7 floods were selected from the 11 floods data of 700,718, 700,731, 710,705, 720,719, 740,731, 780,807, 790,723, 800,718, 830,726, 880,715, and 890,716 floods.
2. The determination of the initial value of the model state variables. Initial soil moisture  $W_r$ , initial linear reservoir surface water  $SS0$ , and underground water storage capacity  $SG0$  were determined by the calculation results of the daily model (here is no longer detailed); while the initial value of the pond storage coefficient  $\zeta$  was confirmed in GIS based on such composite factors as the size and shape of the ponds.
3. Parameter setting. The artificial trial calculation method was adopted to determine the parameters. It was found after debugging that the values of such parameters as  $n$ ,  $A$ ,  $B$  and

$W_i$  influenced the flood peak, flood volume and peak time greatly.  $n$  affected the peak time and peak shape mainly: the smaller the value of  $n$ , the earlier the time of the flood peak, also the peak shape was impacted;  $A$  and  $B$  mainly affected flood volume changes: the smaller the  $A$  and  $B$ , the larger flood volume; the influence of  $A_r$ ,  $A_g$ , and  $B_c$  on sediment amount is large: the greater the  $A_r$ ,  $A_g$ , and  $B_c$ , the more sediment amount.

The debugging steps were as follows: first to adjust the flow production parameters  $A$  and  $B$  to make the simulated flood volume be close to the actual process; then to adjust roughness coefficient  $n$  according to the underlying surface information to regulate the peak shape of the simulation results to improve the deterministic coefficient of flow process simulation. Adjusting 3 parameters  $A_r$ ,  $A_g$ , and  $B_c$  were adjusted to make the simulate sediment amount proves to be close to the actual sand content; the staggered transporting time was

changed to improve the deterministic coefficient of sediment amount process simulation. The average value of the seven water and sediment parameters after adjustment was adopted by the model. Table 1 shows the calculation results of the hydrological and silty model of the calibration and verification floods in Chabagou watershed.

#### 4.2 Model verification

The other 4 floods were selected, and the hydrological and silty model was tested. From the results of calculation, it can be seen that the computed quantity of flow and sediment is in line with the measured process line of discharge and sediment quantity, what verified the model is reasonable and feasible. Figure 2 and Figure 3 show the discharge and sediment transport rate comparison of the actual and the simulated, respectively. Each grid precipitation obtained from the measured rainfall data interpolation of the rainfall stations within the study area, so the discrepancy of calculated spatial

Table 1. Results of modeling calculation.

Modeling no.	Flood no.	Runoff depth relative error (%)	Peak relative error (%)	Peak time difference (h)	Certainty factor	Sediment transport rate relative error (%)
Calibration no.	700702	5.8	-4.2	0.5	0.71	-7.0
	700731	2.1	0.6	0.5	0.81	-5.7
	710705	15.5	4.2	0	0.80	13.3
	720719	3.2	1.6	0	0.79	-2.3
	740731	-14.0	-15.6	0	0.73	-2.4
	780807	-17.0	1.6	0	0.82	-8.7
	790723	-2.8	4.8	0	0.74	-4.3
Verification no.	800718	7.4	8.6	0	0.70	0.20
	830726	4.6	-5.6	0	0.72	-0.60
	880715	2.2	-7.7	0	0.61	9.8
	890716	-5.7	-5.0	0.5	0.79	3.4

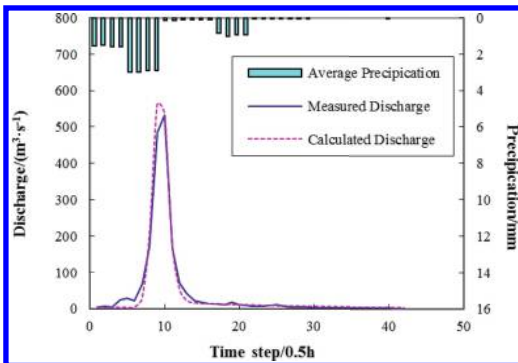


Figure 2. Flow hydrographs of observation and simulation data of No. 700702 flood.

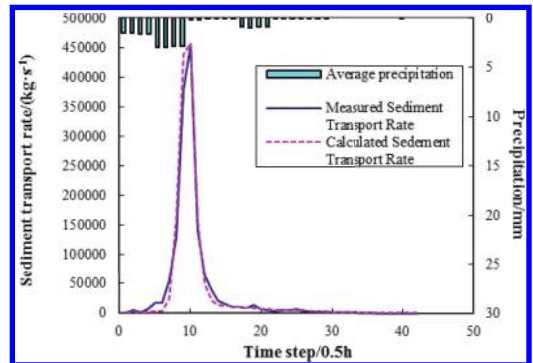


Figure 3. Silty hydrographs of observation and simulation data of No. 700702 flood.

and temporal rainfall distribution and the actual was caused, which gave rise to the error of the runoff and sediment yield calculation. In addition, due to the time step being valued by half an hour, original records of rainfall, discharge and sediment concentration data had a certain degree of homogenization, and the peak value of the rainfall, runoff and sediment concentration may be missed.

## 5 CONCLUSIONS

Based on the extraction of spatial information of watershed based on DEM data, the distributed hydrological and silty model of Chabagou watershed in the Loess Hilly Region was constructed according to the geographical and climatic features of the watershed. Calibration and verification results show that the model is basically applicable for the high and coarse sediment area of the Yellow River Basin. Due to climate change and human activities, the pad surface of the basin is undergoing profound changes, so the distributed hydrological model in the following aspects is to be further explored and researched: (1) Spatio-temporal homogenization of precipitation data; (2) the integration of the watershed underlying surface change information; (3) sediment transport computations; and (4) the confluence time of water and sediment.

## ACKNOWLEDGMENTS

This work was financially supported by Science and Technology Innovation Foundation of Water Resources Ministry of China (SCX2002-08): Study on Distributed Water and Sedimentation Model in the areas with high and coarse sediment yield of the Loess Plateau.

## REFERENCES

- Jinren Ni, Xiaoyong Liu & Tianhong Li, *et al.* The sediment transport efficiency and its regulation in the lower reaches of the Yellow River [J]. Chinese Science Series E science and technology, 2004, 34 (Suppl.): 144–154.
- Li Li. Research on watershed feature extraction and its application in hydrological model based on DEM [D]. Nanjing: Hohai University, 2003. (in Chinese).
- Maidment David R., Jianyun Zhang & Jisheng Li. Handbook of hydrology [M]. Beijing: Science Press, 2002. (in Chinese).
- Wenyi Yao & Liqun Tang. Process and simulation of hydraulic erosion and sediment yield [M], 2001. (in Chinese).
- Zhonggen Wang, Hongxing Zheng & Changming Liu, *et al.* Distributed hydrological model and its application in the typical river basin of the Yellow River [J]. Chinese Science Series E science and technology, 2004, 34 (Suppl.): 49–59.

# Numerical simulation on the impact of oil spills on a fishing port

RuiJin Zhang, JinMei Zhou & XueZhi Huang

*College of Marine Technology and Environment, Dalian Ocean University, Dalian, China*

**ABSTRACT:** In this paper, the water dynamic model of a fishing port in the east China sea is established by using MIKE 21 which is one of a relatively mature international DHI software series, then a fishing harbour oil spill model which is based on the Lagrangian particle tracking theory was set up to research oil spill pollution problem near an island in the east China sea. Simulating spilled oil under the northeast wind, southerly wind a tide weeks within 12 h diffusion trajectory and the distribution of the different situation are analyzed. Research shows that the direction of the wind and hydrodynamic conditions are the key factors which affect the sea oil spill and the biggest factor is the south wind of this sea area. The research results can be reference for the decision of potential oil spill emergency response.

**Keywords:** hydrodynamic; oil spill; simulation

## 1 INTRODUCTION

As the country's increasing demand for oil and the continuous development of transportation industry, oil spill accidents on ships at sea is also increasing. After the oil flow into the ocean, it can lead to serious pollution to the Marine ecological environment, not only destroys the ecological balance, the impact of tourism development of Marine aquaculture, but also threatens human's health. Recently, the sea oil spill has gradually aroused the concern of the society and people, many marine oil spill event is a sudden one, so after the accident whether we can made a timely and effective manner to emergency response and take corresponding measures to control pollution loss reduction plays a key role. The completion of fishing port engineering of a certain island makes the vessel traffic density increasing, the potential of oil spill risk is also increasing, so it is necessary to conduce the oil spill simulation research of the area for prediction.

In order to improve the forecast accuracy of water spilled oil, extensive research at home and abroad have been carried out. Since the early 1980 s China has carried out oil spill forecasting model research under different conditions, such as ice-free sea, ice sea, shallow sea waters, and so on. Huang Liwen etc use ECOM—si for open boundary islands waters to built sea flow field prediction model for oil spill simulation of the Zhoushan islands; Lou Angang in the tide of harmonic analysis and observation of wind as a force, for plastic chau bay constructs a three-dimensional oil spill at sea transport and the end-result of model; De-qi xiong, such as using HAMSOM three-dimensional ocean model for tidal harmonic

analysis for flow field forecast, to simulate oil spill huhu pearl river mouth waters on the features of the tidal river road extension, drifting of oil spill test; Zhong Deyu on contaminant transport carrying water full transformation rule is simulated. But for the moment for east island fishing port to carry out the oil spill simulation work is relatively lacking.

## 2 THE NUMERICAL SIMULATION OF THE MARINE HYDRODYNAMIC ENVIRONMENT

For the offshore oil spill, the biggest factor is water. So is the hydrodynamic simulation of offshore oil spill simulation work carried out one of the most basic. An island near the water level changes in the East China Sea fishing especially after the completion of the complex hydrological conditions undergone significant changes in recent years in this regard since the technology has been widely studied. Combined with the needs of the project, the project will use water flow field data dimensional hydrodynamic modeling techniques to simulate resolved.

### 2.1 Flow calculation results analysis

Large sea calculate the flow field flow field in front of representatives of the project, where the tide of the field to take the trend analysis. The results show that simulated tidal waters, including two fluctuation process. Observing the trend of changes in tidal C01 as a reference time point, [Figure 1](#) and [Figure 2](#) shows the trend of process on behalf of the two moments of the flow field, respectively, and the ebb

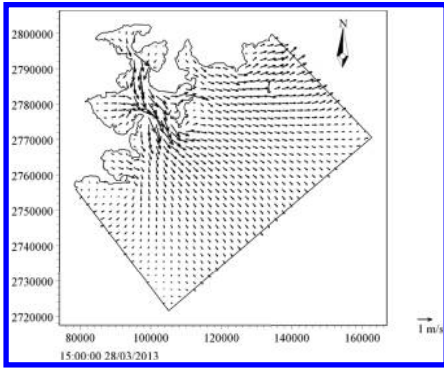


Figure 1. The flow field of ebb middle.

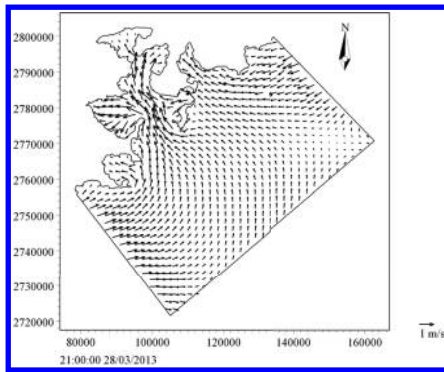


Figure 2. The flow field tide middle.

tide when the middle of the middle. Figure 1 is the first time the ebb tide in the middle field, off the coast of the computational domain tide flowing from the SW to NE, near the project area, the water flowing out from the bay through the island, with the outer flow convergence Sea to the NE flow. Flow field at low tide, and this was the moment bypass, flow decreases. Figure 2 is the first time the tide high tide in the middle field, the basic trend is calculated from the sea outside NE to SW flow, part of the water flowing into the bay through the island, the height of the flow field, and this was the moment bypass flow rate was reduced. From the above chart the flow field can also be seen, mathematical models simulate the flow field of engineering nearby waters to meet the project needs, you can follow the hydrodynamic and oil spill modeling work.

### 3 THE NUMERICAL SIMULATION OF OIL SPILL IN WATERS

#### 3.1 Prediction model

This evaluation uses the oil particle model, and it can correctly predict the spread of the oil spill.

The model of oil particle is based on the tidal current of the wind-driven currents. It use the way of Lagrange particle track method to track the trail of particle. At the same time, it uses the random walk method to simulate the turbulence diffusion of oil particles. This method is based on the behavior selection of the motion object, and use the deterministic model to simulate the conditions of environment dynamic (mainly flow field). It uses the random model to simulate the turbulent diffusion field of the oil spill particle, and Improves the effect of the forecast of oil spill. Regardless of the turbulence diffusion and based on the mathematical simulation of flow field (euler field), it uses the Lagrange to track the drift process of particles. We get the trail of particles which are under the action of tide (including wind current).

#### 3.2 The system of computational condition

The main model simulation NE (7.6 m/s) and S (4.7 m/s) winds ebb tide and high tide period of 100 kg and 10 kg spill occurred when an oil slick drift tide weeks, expansion and scope of pollution caused by the random diffusion and pollution levels. Click on the apron oil spill starting point, shown in Figure 1. Calculation program is divided into eight kinds, detailed in Table 1.

##### 3.2.1 The analysis of spill model simulation results on winds NE

After the data statistical analysis, it is concluded that the direction of prevailing wind of this island is NE in the oil spill waters. The highest frequency of the wind is direction of prevailing wind. So this wind direction is the most likely wind direction of the oil spill accident, and is the most likely to impact on the marine and terrestrial environment. To simulate the direction of prevailing wind in the oil spill sea area, and can produce a positive guiding significance to oil spill emergency action. The following Figure 3 and Figure 4 are respectively oil spill in the early and late diffusion area chart in the direction of prevailing wind (NE).

As can be seen from the above chart, in the initial stages of oil spills, when the tide began to ebb,

Table 1. The calculation scheme.

Condition	Tide	Oil spillage	Climate
1	Spring tide	10 kg	Northeast (7.6 m/s)
2	Spring tide	10 kg	Southerly (4.7 m/s)
3	Spring tide	100 kg	Northeast (7.6 m/s)
4	Spring tide	100 kg	Southerly (4.7 m/s)
5	Neap tide	10 kg	Northeast (7.6 m/s)
6	Neap tide	10 kg	Southerly (4.7 m/s)
7	Neap tide	100 kg	Northeast (7.6 m/s)
8	Neap tide	100 kg	Southerly (4.7 m/s)

sea tide flowing from the SW to NE. After the oil spill from the oil spill point of overflow, the oil spill will drift and diffusion along the direction of the trend. But also by the role of wind direction, facing east and west of the oil spill oil spill points accordingly extended. Its shape to the east is wider, while the west is narrow. When the oil spill occurred about six hours, the trend at low tide, when the bypass time, the film will be in contact with the coast in the joint action of wind and tide. After that, the tide began to rise, the sea tide is dominated by NE to SW flow, then, the trend is consistent with the wind direction, with the accumulation of oil spill on the shore, and by the flow of both the role of coastal waters, the film will spread westward, then, the trend is consistent with the wind direction, will reduce the impact of the oil spill point on the east coast, while the west side continues to spread, thereby increasing the impact area, forming a connection point of a wide strip spill east and west sides of the bay and harbor at other waters less affected by oil spills.

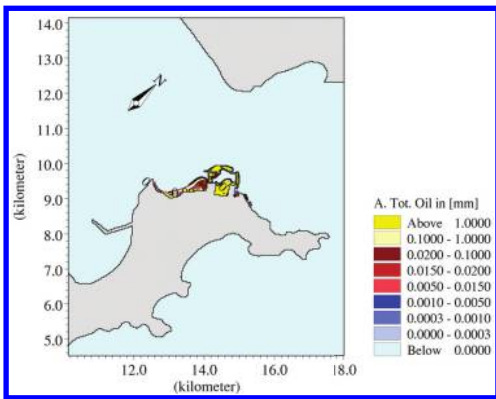


Figure 3. The oil spill area chart of early diffusion on NE.

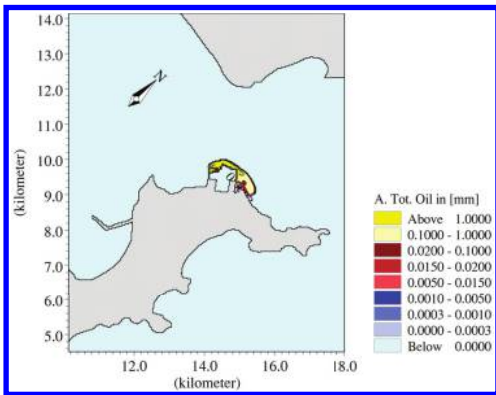


Figure 4. The oil spill area chart of late diffusion on NE.

Area when the spill occurred about 12 hours, the tide was at its height, the joint action of the tide and wind, the point on the eastern side of the oil spill all the basic drift to the west, and with evaporation and emulsification of oil spills, oil spill spread of significantly reduced.

Under constant wind effect, the oil spill will have a serious impact on the marine and terrestrial environments. Due to a wide range of oil pollution in the area, drift-diffusion speed, and a higher likelihood of occurring, oil spill relevant departments need to do this to the appropriate emergency response strategies.

### 3.2.2 The analysis of spill model simulation results on winds S

With the statistical analysis of wind data, the second often wind direction of this island in a sea of oil spills is south, Wind is an important factor affecting the behavior of the oil spill, the simulation results can be seen, the impact of the oil spill behavior is more significant at south, and may cause more severe effects on the marine and terrestrial environments. The oil spill simulation to the greatest impact of the oil spill waters wind, will provide a more clear, effective, and fast guide oil spill response action. The following Figure 5 and Figure 6, respectively, is the initial and late diffusion spill area chart for the wind direction of south.

Early oil spill occurred, the diffusion behavior of the oil spill are mainly affected by the wind and the east China sea tide of two factors. At this time, as can be seen from the initial spill map, the early oil spill drift diffusion direction along the direction of the trend, mainly from SW to NE. Due to southerly wind to function at the same time, the oil spill area has a certain extend in the direction of the gulf. After the oil spill occurred about six hours, the oil film forward continued eastward to, under the action of tide and wind, oil spill things two to spread and form

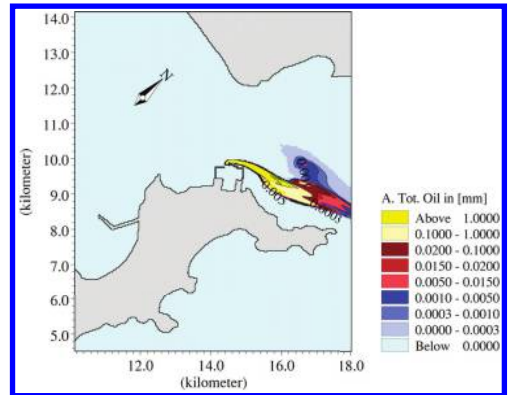


Figure 5. The oil spill area chart of early diffusion on S.

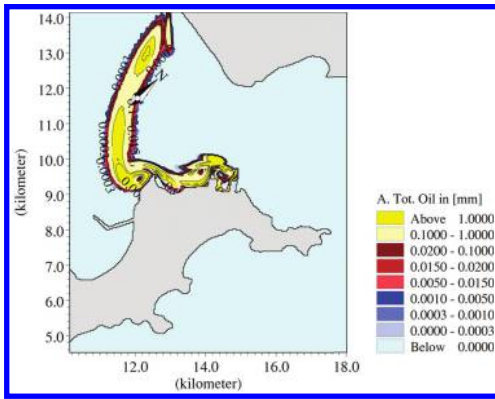


Figure 6. The oil spill area chart of late diffusion on S.

Table 2. List of different tide sweeping Sea area after spill ( $>0.3 \mu\text{m}$ , unit:  $\text{km}^2$ ).

Condition	3 hours	6 hours	9 hours	12 hours
1	0.48	1.37	2.62	2.62
2	4.11	4.73	8.42	14.59
3	0.57	1.75	3.31	3.31
4	4.42	5.51	8.86	16.26
5	0.15	0.24	0.49	1.55
6	1.04	5.20	8.02	1.04
7	0.15	0.29	0.76	1.62
8	1.29	2.35	4.53	12.92

thin strip along the coast. After nine hours, by the terrain and trends together, the amount of spilled oil spill westward drift more. In the latter part of the oil spill, oil spills with the trend to more and more to the west, and southerly winds disturbed the role of the accumulation of oil spill on the coast near the harbor was taken, along with the trend of the movement to drift near the bay the impact of shipping and ports around people's normal life.

In the action of secondary often wind, oil spill will produce a great impact on the marine and terrestrial environment. As a result of oil spill pollution area is wide, the oil spill drift diffusion speed, so need to related department to make emergency countermeasures quickly and accurately.

### 3.3 Calculate result

Different computational scheme and scanning area of spilled oil film at different time of tide is shown in Table 2. We can conclude that the wind direction has a great influence on spilled oil. In case of the south wind, the spring, and the oil spillage of 100 kg, the scanning area reach the maximum of  $16.26 \text{ km}^2$  after a tidal cycle. The current velocity

also affect the scanning area. After a tidal cycle, the area is  $16.26 \text{ km}^2$  during the springs while  $12.92 \text{ km}^2$  during the neaps.

## 4 SUMMARY

1. Using DHI MIKE to build a hydrodynamic model based on an unstructured grid, 2-D's current near a island in the East China Sea. We can find the stimulation results reflect the hydrodynamic character around the Island.
2. Based on the Lagrange and random walk theory, we build a oil spill model near a island on the hydrodynamics basis. Further more, we stimulate the oil spill of the north island during the northeast wind and southerly wind. At last, we analyze the drifting routine and the change of the oil spillage.
3. According the influence on oil spill accident, we can conclude that the wind direction and hydrodynamic condition are the key factors affecting the oil spill at the sea zone, which the south wind has the biggest impact. Futhermore, the scanning area of oil spill during the springs is larger than that during the neaps. At the worst, the scanning area reach  $16.26 \text{ km}^2$  after a tidal cycle.
4. In this paper, we only consider the process of the oil particles' drifting, diffusion, and evaporation under the action of external environment, while we must take the processes of physical, chemical, and biological effects into account during the longer time scale. Thus, we need improve the problem in the future.

## REFERENCES

- [1] Huang Liwen, Wang Xian Fu, Yu Jiqing, Wu Xiuheng, Zou Jian, Wei Min. Hydrodynamical Model for Oilspill Simulation in Archipelagic Waters with Multiple Open Boundary Conditions [J]. Journal of Wuhan transportation university, 2000, 24 (4): 367-371.
- [2] Lou Angang, Wangxue Chang, Sun Chang qing, Xi Pan gen. A Simulation of Oil Spill Trajectory on Sea Surface of Jiaozhou Bay [2] [J]. Journal of Oceanography of Huanghai & bohai Seas, 2001, 19 (1): 1-8.
- [3] Xiong De-qi, Yang Jianli, R&D on oil spill contingency forecast information system for Pearl River Estuary [J]. Marine Environmental Science, 2005, 24 (2):63-66.
- [4] Liu Dong, Lin Weiqing, Characteristic experiment of spread and transport of oil spill in tidal river [J]. Journal of Hydrodynamics (Ser. A). 2006, 21 (6): 744-751.
- [5] Zhong De-yu, Yu Xue-zhong. Simulation of petroleum hydrocarbons transported by sediment flows [J]. Journal of Sediment Research, 2007 (4):24-29.



# Status review and prospect of the research into physical model of the impact force of ice on Yellow River-related buildings

G.Y. Wu, Y.F. Li & C.P. Wu

*Yellow River Institute of Hydraulic Research and Yellow River Institute of Hydraulic Research, MWR Yellow River sediment Lab, Zhengzhou, China*

**ABSTRACT:** In order to study more practical ice force of the Yellow River-related buildings, it is necessary to study practical mode. This study is of great significance to the design of river-related buildings and the standardized management of Yellow River. At present, there are many research results into ice force of the practical model of Yellow River-related buildings and the theory is mature. But there are few research results related to the practical ice force model of Yellow River-related buildings. The research results of many domestic colleges and related units are analyzed in the paper. Their research results all have certain limitations and don't apply to the practical ice force model of Yellow River-related buildings completely. Therefore, it is necessary to do further research into it.

**Keywords:** Yellow River; river-related buildings; ice force; practical model; further research

## 1 INTRODUCTION

Ningxia-Inner Mongolia reach of Yellow River lies at the northernmost tip of Yellow River Valley. Its winter is as long as four to five months. The maximum ice thickness is usually 0.8~1.1 m. It has a serious ice regime. This reach breaks up in early or middle December or at the beginning of next March. The river section is blocked by drift ice, which forms large impact force on river-related buildings. Large areas of ice floes can produce pressure and friction at the same time, which will do great harm to the river-related buildings such as dams and bridges. For example, 11 bridge piers of Guisuihe River Bridge on Beijing-Baotou Railway were broken by the huge ice pressure in the winter of 1957.

With the rapid development of economy, there are more and more Yellow River-related buildings. The river-related buildings are often struck violently by drift ice when Yellow River freezes up or breaks up. At present, the research into the fore against the river-related buildings is not deep enough due to the complexity of the problem. For security's sake, the design department usually adopts large safety coefficients when designing river-related buildings such as bridges, so that the size of piers

is increased and they occupy the valid flooding section and affect the flood safety of river channel. Therefore, it is necessary to conduct physical model tests of ice force on river-related buildings and propose the ice force that is more practical, which will be of great guiding significance to the design of river-related buildings such as bridges and of great reference value to the standard management of Yellow River channel.

## 2 RESEARCH STATUS OF ICE FORCE MODEL TEST

Ice force model test started with the research into ice breakers. The first low temperature ice pool laboratory was set up in the Soviet Union in 1955. At present, most of the existing low temperature ice pool laboratories in the world were founded in the 1980s.

Ice force model test has a long history. Most of the past tests were aimed at static ice force. With the increase of development activities in freezing waters, the requirement for solving the problems caused by the dynamic ice force resulting from ice-structure interaction is more and more urgent. In recent years, dynamic ice force model test has been carried out in some ice force laboratories at home and abroad.

### 2.1 Research status of sea ice force model

1. Low temperature laboratories were founded in Tian Jing University in 198, in which ice force

---

Project supported by Special Fund of Basic research operating expense of Central Public-interest Scientific Institution (No: HKY-JBYW-2013-20).

Project supported by National Natural Science Foundation of China (No: 51409115).

model test on ice-resistant platform in Liaodong Bay of Bohai Sea was carried out for the first time. It was a static ice force model experiment, made in No. 2 low-temperature marine lab of Tianjin University. This lab consists of low temperature chamber, ice pool, trailer, refrigerating machine, buffer chamber and test chamber, and so on. The lowest temperature is up to  $-22^{\circ}\text{C}$  during work. Nanjing University built large ice engineering labs in the Ninth Five-Year Plan period and formed the only ice mechanics and ice engineering experimental base, where many ice mechanics tests have been carried out for years. The material for model ice used in the lab is urea ice that is made up of fresh water and a certain percentage of urea, which can increase the strength and the modulus of elasticity of the ice to make sure the mechanical properties of ice can meet the requirement of the test. Before freezing, spray the mixed urea ice which is the same as the one in the ice pool with the pressure with 20 standard pressure through micropore to the sky above the ice pool. The urea ice freezes in the air and then falls into the pool and forms ice-crystal nuclei so as to avoid too higher ice strength. Stop refrigerating before ice thickness reaches the required value. Make thickness increase naturally to the required value and then make the temperature increase naturally and slowly. The strength and the modulus of elasticity of the ice decrease slowly during temperature returning. Monitor the strength and the modulus of elasticity of the ice when taking these steps and start to conduct the test as soon as the scheduled targets are realized.

In recent years, Song An, Huang Yan, Shi Qingzeng et al. have made related research into dynamic ice model, especially in similarity law. They learned about some similarity criteria applied in dynamic ice model experiment, such as Froude Similarity Criterion, Cauchy Criterion, and ice nuclei equivalence, on the basis of which, they conducted experiments and discussed the applicability of the these laws in static ice model experiment and studied the similarity law of dynamic ice force model by dynamic ice force model experiment. They presented parameter-interaction coefficient resulted from the combined action of elastic control, rate control, and geometric dimensioning. The similarity system based on this coefficient completely adapts to model test of ice-induced vibration on vertical structure.

2. An ice force-related lab, State Key Laboratory of Coastal and Offshore Engineering, was founded in Dalian University of Technology. The first ice force physical model test was conducted at this lab. The monitoring technology

of the area, concentration and movement speed of ice block was developed and the experimental relationship between the impact ice of drift ice on single piles and wharf piles and physical and mechanical parameters of the same models was found. The problem of similarity recovery of the impact force of drift ice from physical simulated results to ice force of the prototype design ice was solved.

The material for model ice was studied in this lab and DUT-1, a kind of non refrigerated model ice, was developed by Wang Xueyong, Li Zhijun and Li Guangwei. It expands range of choice. This kind of model ice was made from the mixture of polypropylene powder, white cement, plastic bead, water and others, which were mixed, stirred, and molded. It needn't be made in a large low temperature lab. Its physical and mechanical properties can keep it stable during a long period of experiment. Li Zhijun et al made systematic experimental research into its physical and mechanical properties and physical simulation and experimental study on the interaction between model ice and wave and the interaction between model and circular pile, conical, and semicircular levee structure. The results of many physical model tests show that this model ice can be used in the 1:10 to 1:30 scale model experiment. All indicators meet the requirement. This model ice is the ideal material for physical simulated experiment on ice and inclined structure and ice and wave, ice accumulation, ice ridge, and ice jam.

## 2.2 *Research status of the impact force of river ice*

River ice research was first made in the former Soviet Union. The calculating formula of ice effect on bridge piers was proposed in bridge and culvert design. Inland river construction standard of USSR was issued in 1959. The research results on ice of the scholar from former Soviet Union were cited in the ice protection and ice resistance design of many cold countries. In addition, much research into river ice was made in Canada and the US and some related rules that were suitable for their situation were made.

According to the domestic research results, the research subject is mostly sea ice and river ice research focuses on a few rivers in Heilongjiang Province. Yu Tianlai et al from Northeast Forestry University made deep research into the physical properties and river ice and the impact force of drift ice on piers. They collected samples of river ice on the spot, carried to the lab in Harbin, machined it in detail, and determined modulus of elasticity by compression test. Then they installed pressure

sensors where drift ice impact piers and vibration pick-ups on the top of piers to measure the value of the impact force of drift ice and the vibration property of the piers under impact, analyzed the collected data, simulated the impact force of drift ice on piers by means of some soft wares, such as ANSYS, and discussed the mechanism of the action of drift ice on structure. Yuan Zhenguo set up a computer simulation analysis model of the impact force of drift ice on piers by explicit dynamical analysis software package LS-DYNA. Through further study, we found research into river ice focuses on mechanical properties of river ice, measured impact force of river ice on piers and numerical simulation analysis of the impact force of river ice on piers and that no research into physical model of the impact force of river ice on piers has been carried out.

According to the analysis, the research into the mechanical properties of river ice is not further enough in our country. In addition, because there are many difference in the nature of river ice in different rivers in different areas, the existing experiment data are not typical. There are some problems in the standard strength value required in the specification. The calculating method of the impact force of drift ice on piers is not on sound experimental basis.

### 2.3 Conclusion

At present, there are few research results on the impact force of ice in Yellow River during ice run. The research results are mostly on field measurement and numerical simulation. No laboratory physical model experiment research has been made. Archetype observation is costly and complicated field conditions add human factors to analysis results. Numerical simulation is less intuitive than physical model research. There are more and more river-related buildings on Yellow River and the problem of the impact force of drift ice on river-related buildings is increasingly prominent. As a result, there is increasing urgent need of physical mode research.

## 3 THE SIMULATION RESEARCH THOUGHTS AND PROSPECT OF THE IMPACT FORCE OF ICE ON RIVER-RELATED BUILDINGS ON YELLOW RIVER

At present, the domestic research into the similarity laws of ice force physical model is mature. By summarizing the existing similarity laws, we can propose model similarity laws that are more suitable for physical model tests of the impact force of ice on Yellow River-related buildings.

Another more important factor in physical model tests is selection of the material for model ice.

At present, refrigerated model ice is usually used for tests in our country. The texture of refrigerated model ice makes great difference to test results. It is hard to control the indicators during the course of the test, which leads to poor comparison of test results. In spite of continuous study at home and abroad, there is no widely accepted material for refrigerated model. In addition, refrigerated model ice must be used in large low temperature laboratories which need huge investment. From all sides, non-refrigerated model ice is more practical during the preliminary stage of physical model research into the impact force of ice on Yellow River-related buildings.

DUT-1, non-refrigerated model ice developed by Dalian University of Technology is only used for sea ice model test at present. Whether it is suitable for the research into the impact force of ice on Yellow River-related buildings is open to question. We look forward to select a material for model ice that is more suitable for Yellow River through continuous study and further research.

The design span of Yellow River-related buildings, especially bridges, is larger and larger. The flexibility of the structure of bridges is higher and higher. The impact of all kinds of ice on structure during ice run is greater and greater. If we can conduct physical model tests on the impact force of ice on Yellow River-related buildings soon, we can provide basis for anti-ice design of river-related buildings and ensure the safety of the structure of buildings. The research will be of great significance to flood control safety of Yellow River.

## REFERENCES

- Cai Z., Sun B., Guo S., Zhou S. Experimental research on ice load and its calculation method [J]. *Earthquake Engineering and Engineering Vibration*, 1997, 17(4): 49-56.
- Huang Y. The Study of Ice Induced Vibration on Marine Platforms by Dynamic Model Test [D]. Doctoral dissertation of Tianjin University, China, 2004.
- Huang Y., Shi Q., Song A. The application of scaling laws to ice force model tests [J] *Journal of Glaciology and Geocryology*, 2003, 25(Suppl. 2): 352-355.
- Huang Y., Shi Q., Song A. The study of the scaling law in dynamic ice force model tests [J]. *China Offshore Oil and Gas*, 2007, 19(6): 419-423.
- Ke S., Wang M., Rao S. Research into Yellow River Ice [M]. Zhengzhou: Yellow River Hydraulic Press, 2002.12.
- Li Z., Li G., Shen Z., Wang Y., Qu Y. Physical properties and modulus of elasticity of model ice DUT-1 [J] *Progress in Natural Science*, 2000, 10(10): 931-935.
- Li Z., Wang Y., Li G. Progress in physical simulated experimental research into the ice force of non-refrigerated model synthetic ice [A], the Proceedings of the Tenth National Coastal Engineering Seminar [C], Beijing: Ocean Press, 2001.

- Li Z., Wang Y., Li G. Experimental analysis of flexural strength and elastic modulus of the DUT-1 model ice. *Advances in Water Science*, 2002, 13(3): 292–297.
- Lu W. Finite Element Simulation and Analysis of the Crushing Failure of ice Sheet that Interact with Structure [D] Doctoral dissertation of Tianjin University, China. 2007.
- Shi Q., Xu J., Song A. The model test of ice forces [J]. *Journal of Glaciology and Geocryology*, 1990, 12(2): 117–123.
- Shi Q., Song A. The characteristics of sea ice static action and ice model test of several typical tests [J]. *Acta Oceanologica Sinica*, 1994, 16(6): 133–141.
- Shi Q., Song A., Xue B. Experimental study of ice force and ice thermal expansive force on semi-circular members [J]. *China Harbour Engineering*, 2002, (3): 7–13.
- Song A., Sun J., Shi Q., Wang Z., Wang Y. Model test for ice fore on the bank-head of the lead navigating bank [J]. *Journal of Tianjin University*, 2006, 39(5): 537–542.
- Song A., Huang Y., Shi Q., Shi Z. Dynamic ice model test and development [J]. *China Offshore Oil and Gas (Engineering)*, 2003, 15(4): 25–31.
- Wang J. Research on Mechanics Characteristic and Its Impinge on Pier of River Ice [D] Harbin: Dissertation for the Degree of Master in Northeast Forestry University, 2007.
- Wang Y., Li Z., Li G. Technique of DUT-1 non-refrigerated breakable ice materials and its applications [J]. *Journal of Dalian University of Technology*, 2001, 41(1): 94–99.
- Xu J. Ice flood disaster and reduction measures in Inner Mongolia section of Yellow River [J]. *Journal of Glaciology and Geocryology*, 1995, 17(1): 1–7.
- Yu T., Wang J., Du F., Zhang L. Experimental research on ice disaster in Huma River. *Journal of Natural Disasters*, 2007, 16(4): 43–48.
- Yuan Z. Research on Inland River Ice Mechanical Property and Ice Impact Force on Bridge Pier [D]. Harbin: HD is sertation for the Degree of Doctor in Northeast Forestry University, 2010.

## Characterization of urban rainwater quality for the reuse purpose

Zheng Li, Weipeng Chen, Jun Li & Siyang Yue

*Suzhou Industrial Park Design and Research Institute Co. Ltd., Suzhou, China*

**ABSTRACT:** In order to provide basic data for the reuse of rainwater to supplement the water resources to alleviate the water stress, rainwater quality was assessed in a typical metropolis in the east of China. Rainwater from seven districts was collected, and chemical oxidation demand, suspended solid,  $\text{SO}_4^{2-}$ ,  $\text{Cl}^-$ ,  $\text{NO}_3^-$ ,  $\text{NO}_2^-$ ,  $\text{NH}_4^+$ , and Fe in rainwater were determined. Possibly because of the release from chemical industry and electronics manufacturer, aromatic compounds such as phenols and toxic heavy metal Hg were also detected. Based on the rainwater quality, several treatment methods and suggestions were thus proposed to guarantee the safety of reusing rainwater for different purposes.

**Keywords:** rainwater; quality; characterization; inorganic ions; organic pollutants

### 1 INTRODUCTION

Most of the surface water distributing on our planet is salt sea water, and can't be used directly currently, or a very high cost is inevitably required (Zimmerman et al. 2008). Various areas on the earth have different geophysics, geochemistry, and climate conditions, leading to the uneven distribution of transpiration and the resulting precipitation (Fischer & Knutti 2015). Arising from the rapid development of agriculture and industry, etc., much more clean water is badly demanded, which has never been seen before on the history, for example, the large usage of water by the agriculture irrigation, livestock products, energy generation (e.g. electric infrastructure) (Bonsch et al. 2015). As a consequence, the world is meeting the problem of water crisis, but this problem is especially further amplified by the increasing water pollution mainly caused by the anthropogenic activity by releasing contaminants from agriculture, industrial, etc. into the environment (Zimmerman et al. 2008, Van Beek et al. 2011, Wada et al. 2011, Schwarzenbach et al. 2010).

In essence, almost all the fresh water on the land, including surface water in rivers and lakes and underground water, is originated from precipitation, with rainwater as the most important source (Jung et al. 2010). Thus, the rainwater harvesting is one of the feasible approach to satisfy the water demand, and has been under intense worldwide study (Vieira et al. 2014, Cheng et al. 2014). More and more technologies including urban planning, infrastructure reconstruction, rainwater harvesting methods, new and optimum building design (green building), and new farming and wetland systems,

have been proposed and developed (Vieira et al. 2014, Cheng et al. 2014, García-Montoya et al. 2015). Actually, rainwater can be used in many fields, such as farm irrigation, toilets, and even for drinking (Naddeo et al. 2013).

However, the anthropogenic activity has caused the global pollution, resulting in various contaminants, e.g. particles, ammonia, aromatic organics, and metals, in the rainwater (Schwarzenbach et al. 2010, Cheng et al. 2014, Kabir et al. 2014). Before reusing, the harvested rainwater should be treated by many methods, for instance, coagulation, precipitation, membrane filtration, and UV or chlorine disinfection. As for the organics, adsorption or even advanced oxidation is usually necessitated. Nonetheless, the treatment methods used depend on the rainwater quality and reuse purpose.

Water stress in China usually occurs, especially in the dry parts and also rapidly developed areas, and thus water use efficiency should be improved, and new sources are indeed required (Zhao et al. 2015). This study dealt with the assessment of urban rainwater quality for the different reuse purposes, and aimed to clarify the district-specific difference in rainwater quality. A typical metropolis, one of the economic and education center located in the east of China, is undergoing rapid development with heavy traffic and extensive infrastructure construction and is also notorious for its lots of chemical industry and bad air quality. The city is facing serious shortage of clean freshwater, so it was selected as the target city. Rainwater quality was assessed in seven different districts having different population and economy style, and the area-specific characteristics were analyzed.

## 2 MATERIALS AND METHODS

### 2.1 Rainwater sampling

Rainwater samples were collected in a rainfall event in June 2013 from seven districts, named XW, QH, GL, JY, PK, JN, and QX, respectively. The rainfall sampling event was defined as the samples collected from the onset until the end of a rainfall period, which lasted for about 70 min. The amount of this rainfall was estimated to be about 54 mm. Rainwater samplers were placed on the rooftop (~1.5 m from the floor of the roof) away from the soil and any specific pollutant sources, and three samples were collected individually at every site. The samples were kept in dark at 4 °C prior to analysis. Precautions were taken in both collection and analysis procedures to minimize the contamination. Average values of three samples with one standard are represent.

### 2.2 Chemical analysis

Solution pH was determined by a pH meter (PB-10, Satorious). The cations ( $\text{Na}^+$ ,  $\text{K}^+$ ,  $\text{NH}_4^+$ ,  $\text{Ca}^{2+}$ , and  $\text{Mg}^{2+}$ ) and anions ( $\text{NO}_3^-$ ,  $\text{NO}_2^-$ ,  $\text{SO}_4^{2-}$ , and  $\text{Cl}^-$ ) were analyzed on a Dionex ICS-3000 ion chromatograph, equipped with a SP gradient pump, an anion self-regenerating suppressor (ASRS 300, 4 mm), a conductive detector, and an AS40 autosampler. For anions, a Dionex AS11-HC column (4 × 250 mm) and a Dionex AG11-HC guard column (4 × 250 mm) were selected for separation using 20 mM KOH as isocratic eluent at 1.5 mL min<sup>-1</sup> with a suppressor current of 75 mA, while an IonPac CS12 A Column (4 × 250 mm), methanesulfonic acid (30 mM at 1.0 mL min<sup>-1</sup>) and suppressor current of 50 mA were used for the analysis of cations. Total Organic Carbon (TOC) and Total Nitrogen (TN) were analyzed using a TOC analyzer (TOCL, Shimadzu). UV absorption at 254 nm was determined on a UV-vis spectrophotometer (Cary 300, Varian). Irons and other metals were analyzed by inductively coupled plasma atomic emission spectrometry (ICP-AES, PerkinElmer). Phenols were determined on LC-MS (Waters). Other analysis was performed according to the EPA standard methods.

## 3 RESULTS AND DISCUSSION

### 3.1 Meteorological data

The city studied is constituted of more than ten districts, of which seven were selected to assess the rainwater quality, and has resident population of more than 8 million. The meteorological and population data are shown in Figure 1. The air was polluted, and the average concentrations of PM<sub>2.5</sub>, SO<sub>2</sub>, and NO<sub>2</sub> were about 105.6 μg/m<sup>3</sup>, 36.3 μg/m<sup>3</sup>,

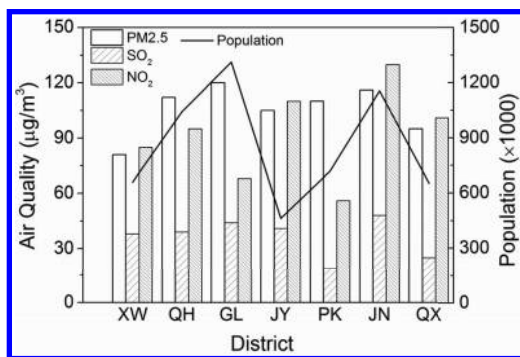


Figure 1. Meteorological and population of the seven districts.

and 92.1 μg/m<sup>3</sup>, respectively. It seems that PM 2.5 partially positively depends on the population. The traffic in QH and JN districts were heavy, and there was an airport in JN district. NO<sub>2</sub> shows a certain relationship with traffic density. It is noted that the data was recorded 7 days after the last rainfall but one day before this one studied here.

### 3.2 COD, SS, and pH

The rainwater was collected and determined as soon as possible. Figure 2 shows the Chemical Oxidation Demand (COD), Suspend Solid (SS) and pH of rainwater. The rainwater in the city had average COD of about 77.6 mg/L and SS of about 11.2 mg/L, suggesting certain pollution. The rainwater pH was all lower than 7.0, indicating some acidity. Especially in QH, JN, and PK districts, pHs were even lower than the threshold of 5.6 for acid rain, indicating the pollution by NO<sub>2</sub> and SO<sub>2</sub>. The results are consistent with that in Figure 1. This can be interpreted by the heavy traffic in QH and JN districts, and many chemical industries in PK district.

### 3.3 Inorganic ions

Typical inorganic ions such as SO<sub>4</sub><sup>2-</sup>, Cl<sup>-</sup>, NO<sub>3</sub><sup>-</sup>, NO<sub>2</sub><sup>-</sup> and F<sup>-</sup> were usually detected in the rainwater (Kabir et al. 2014). Figure 3 shows the SO<sub>4</sub><sup>2-</sup> and Cl<sup>-</sup> in the rainwater in seven districts, with the average concentrations of about 226.3 μM and 25.4 μM, respectively. The rainwater had a similar range of sulfate and chloride with that from many other sites of the world (Kabir et al. 2014). Furthermore, it seems that the two kinds of anions showed no significant dependence on the areas.

### 3.4 Nitrate, nitrite and ammonia

Nitrogen species undergoes complex reactions and transformation in the atmosphere with the assistance of light irradiation (Gruber &

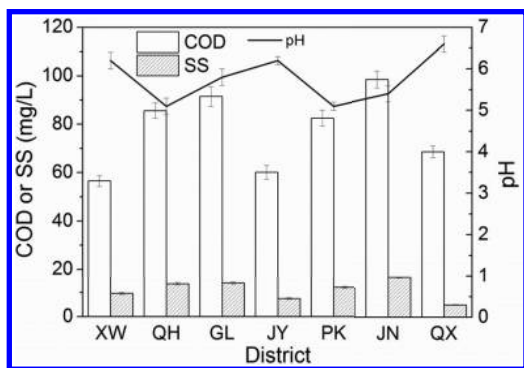


Figure 2. COD, SS and pH of rainwater.

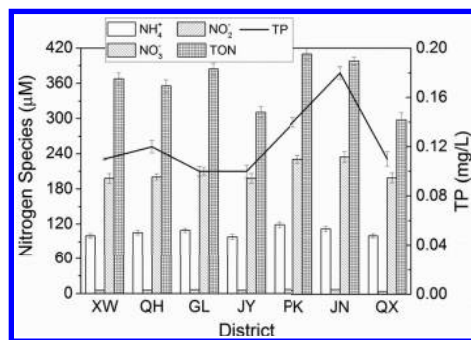


Figure 4. Nitrate, nitrite, ammonia, total organic nitrogen and total phosphorus in the rainwater.

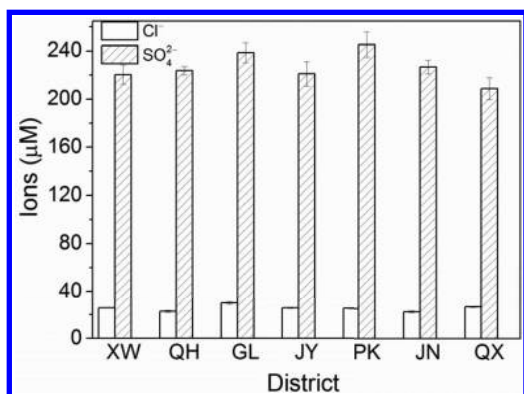


Figure 3. Sulfate and chloride in rainwater.

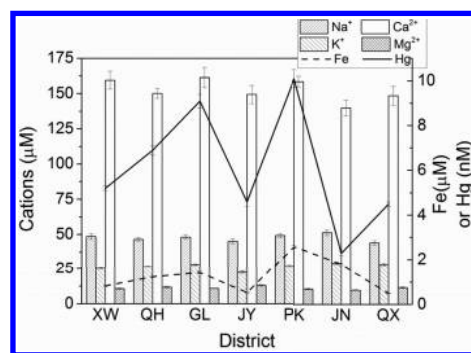


Figure 5. Typical cations and metals in the rainwater.

Galloway 2008). The nitrogen species usually enter the rainwater in terms of  $\text{NO}_3^-$ ,  $\text{NO}_2^-$  and  $\text{NH}_4^+$ . Figure 4 shows the concentrations of  $\text{NO}_3^-$ ,  $\text{NO}_2^-$  and  $\text{NH}_4^+$ , Total Organic Nitrogen (TON) and Total Phosphorus (TP) in the rainwater, with the average concentration of about 210.1  $\mu\text{M}$ , 6.4  $\mu\text{M}$ , 106.5  $\mu\text{M}$ , 360.9  $\mu\text{M}$ , and 0.12 mg/L, respectively. Thus, the rainwater was indeed polluted by the nitrogen species, agreeing with the  $\text{NO}_2^-$  concentration in Figure 1. It seems that the chemical industry in PK district contributed to the nitrogen pollution (e.g. nitrate and TON) in air and rainwater.

### 3.5 Cations and metals

There are usually metal pollutants, such as irons and copper, in the rainwater, depending on the release of ions, metal compounds, etc. (Kabir et al. 2014). Figure 5 shows the typical cations and metals in the rainwater.  $\text{Ca}^{2+}$  showed the highest level among the cations and metals, averaged at about 152.5  $\mu\text{M}$ . Iron in the form of  $\text{Fe}^{2+}/\text{Fe}^{3+}$  was also determined, and had the average concentration of about 1.3  $\mu\text{M}$ .

Note that toxic metal Hg was also detected in the rainwater, with an average concentration of about 6.1 nM. While cations show no significant dependence on districts, Iron and Hg were much higher in rainwater from GL and PK districts. It may be caused by the electronics industry manufacturing screen, electronics board, television, phone, and computer.

### 3.6 Organic pollutants

Arising from the release of volatile organic pollutants, especially aromatic organics such as phenol and benzene, to the air, these organics will be present in the rainwater by participation in the formation of nuclei of rain droplet, adsorption to the interface of droplet, mass transfer to and subsequent dissolution in the rainwater. Figure 6 shows the total volatile phenols in the rainwater and the corresponding UV absorption at 254 nm. An average concentration of about 0.014  $\mu\text{M}$  of phenols were detected, suggesting the pollution of the rainwater. Actually, some aromatics including benzene and derivatives were also detected (data not given). The level of phenols was the highest in PK district, which had many chemical industries as mentioned above. This may

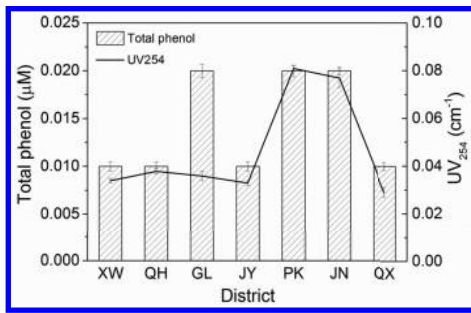


Figure 6. Total volatile phenol in the rainwater and the corresponding UV absorption at 254 nm.

be caused by the industry and the related release of aromatics into air or their volatilization from wastewater or solid wastes from the chemical industry, petrochemical industry, electronics manufacturers, agricultural chemical producers, and traffic exhaust gas (Harrison et al. 2005). The absorbance of UV<sub>254</sub> indicates the presence of unsaturated organics, most of which are aromatics. The result about TON in Figure 4 also supports the organic pollution of rainwater. The results agree with the detection of phenols, both having the similar trend related to different districts. The microbial analysis results were not reported due to the big variance among the three sample (bigger than 30%).

Obviously, the rainwater collected was polluted by the nitrogen species, heavy metals and organics. The quality does not comply with the guidelines of water reuse, especially for the drinking purpose. The nitrogen species are factors that stimulate reproduction and growth of microbe and algae, so biological or chemical denitrification pretreatment is required. Heavy metal like Hg are toxic, and their efficient removal by adsorption or filtration is necessary. Because organic pollutants are volatile and toxic, the rainwater have to be treated to remove them prior to their reuse in irrigation and home use (e.g. toilet). When it is for the purpose of drinking, advanced treatment, such as adsorption, membrane filtration, oxidation and disinfection, is required.

#### 4 CONCLUSIONS

COD, SS, SO<sub>4</sub><sup>2-</sup>, Cl<sup>-</sup>, NO<sub>3</sub><sup>-</sup>, NO<sub>2</sub><sup>-</sup>, NH<sub>4</sub><sup>+</sup>, and Fe in rainwater were about 77.6 mg/L, 11.2 mg/L, 226.3 µM, 25.4 µM, 210.1 µM, 6.4 µM, 106.5 µM, and 1.3 µM, respectively. About 0.014 µM of phenols and 6.1 nM Hg were also determined. The rainwater was mostly acidic, indicating the pollution by SO<sub>2</sub> and NO<sub>2</sub>. The distribution and level of nitrate, ammonia, heavy metals, and aromatic organics in rainwater was possibly partially dependent on the heavy traffic, petrochemical industries, electronics

manufacturers, and agricultural chemical producers, climate conditions in the districts. For various purposes, rainwater should be treated by different methods, to guarantee the safety of water reuse, but also by taking into account the costs.

#### ACKNOWLEDGEMENTS

This work was supported by the Jiangsu provincial science and technology support program (No. SF06).

#### REFERENCES

- Bonsch, M., et al. 2015. Environmental flow provision: Implications for agricultural water and land-use at the global scale. *Global Environmental Change* 30(0): 113–132.
- Cheng, H., et al. 2014. Environmental and Health Impacts of Artificial Turf: A Review. *Environmental Science & Technology* 48(4): 2114–2129.
- Fischer, E.M. & Knutti, R. 2015. Anthropogenic contribution to global occurrence of heavy-precipitation and high-temperature extremes. *Nature Clim. Change* 5(6): 560–564.
- García-Montoya, M., et al. 2015. Simultaneous design of water reusing and rainwater harvesting systems in a residential complex. *Computers & Chemical Engineering* 76(0): 104–116.
- Gruber, N. & Galloway, J.N. 2008. An Earth-system perspective of the global nitrogen cycle. *Nature* 451(7176): 293–296.
- Harrison, M.A.J., et al. 2005. Nitrated phenols in the atmosphere: a review. *Atmospheric Environment* 39(2): 231–248.
- Jung, M., et al. 2010. Recent decline in the global land evapotranspiration trend due to limited moisture supply. *Nature* 467(7318): 951–954.
- Kabir, M.I., et al. 2014. A review of ion and metal pollutants in urban green water infrastructures. *Science of the Total Environment* 470–471(0): 695–706.
- Naddeo, V., et al. 2013. Enhanced drinking water supply through harvested rainwater treatment. *Journal of Hydrology* 498(0): 287–291.
- Schwarzenbach, R.P., et al. 2010. Global Water Pollution and Human Health. *Annual Review of Environment and Resources* 35: 109–136.
- Van Beek, L.P.H., et al. 2011. Global monthly water stress: 1. Water balance and water availability. *Water Resources Research* 47(7): W07517.
- Vieira, A.S., et al. 2014. Energy intensity of rainwater harvesting systems: A review. *Renewable and Sustainable Energy Reviews* 34(0): 225–242.
- Wada, Y., et al. 2011. Global monthly water stress: 2. Water demand and severity of water stress. *Water Resources Research* 47(7): W07518.
- Zhao, X., et al. 2015. Physical and virtual water transfers for regional water stress alleviation in China. *Proceedings of the National Academy of Sciences* 112(4): 1031–1035.
- Zimmerman, J.B., et al. 2008. Global Stressors on Water Quality and Quantity. *Environmental Science & Technology* 42(12): 4247–4254.



# Converse intruding by density current, case study in the Xiao Lang Di Reservoir

Tao Li

*Yellow River Institute of Hydraulic Research, China*

*State Key Laboratory of Water Resources and Hydropower Engineering Science, Wuhan University, China*

Junhua Zhang, Huaibao Ma & Zhihui Ren

*Yellow River Institute of Hydraulic Research, China*

**ABSTRACT:** The river valley of the Xiao Lang Di Reservoir basin is wide upstream and narrow downstream. The width of the upper side of the river valley (above 67 km) is 200 m to 400 m, and the lower sect 800 m to 1400 m. There is a 4-km sect named “Ba li bystreet” 26 km–30 km from the dam whose width is 200 m to 300 m. They are all concentrated in the lower reservoir area which has a rugged topography. This article has researched the modes of density current converse intruding tributary through the prototype and physical model data of Xiao Lang Di Reservoir. Also, the change of the sediment transport character and the silt configuration of tributary density current has been resolved. Formula Han Qiwei and Formula Qin Wenkai on the converse intruding tributary length both have been calculated and validated as an example.

**Keywords:** converse intruding; vertical velocity distribution; Xiao Lang Di Reservoir; sedimentation

## 1 INTRODUCTION

The river valley of the Xiao Lang Di Reservoir basin is wide upstream and narrow downstream. The width of the upper side of the river valley (above 67 km) is 200 m to 400 m, and lower sect is 800 m to 1400 m. There is a 4-km sect named “Ba li bystreet” 30 km near the dam, whose width is 200 m to 300 m. There are more than 10 big branches like Da Yu River, Mei Yao River, Zhen Shui River, Shi Jing River, Dong Yang River, Da Jiao River, Xi Yang River, Yu Li River, Yan Xi River, Bo Qing River and so on, which converge in the reservoir. They are all concentrated in the lower reservoir area which has a rugged topography. Among the inflow and silt load of branches, Dong Yang River has a max annual average inflow of 0.091B m<sup>3</sup> and accounts for 0.22% of the dam; Zhen Shui River has a max annual average silt load of 0.000897B tons and accounts for 0.07% of the dam. So the inflow and silt load of branches could be left out of account when branches’ deposition shape would have been studied.

Since the beginning of water storage in September 1999, with the reservoir water level rising, the inflow and silt load of the stem river have been influencing the deposition of branches greatly. So it is notable to observe the change of branches’

capacity, which account for 35.7% of whole. Since Xiao Lang Di Reservoir has been operated as a higher operating water level, the physical model results and prototype data show [1] that during the early stages, which are demarcated in the sediment retention period, the main deposition mode is deposition induced by the density current converse intruding tributaries.

The branches’ storage capacity of the Xiao Lang Di Reservoir influences the operating mode heavily. Studying typical tributaries can improve understanding of the characteristics of the tributaries flow backward, and clear the changes in the characteristics of tributary storage capacity. It is good for extending the service life of the reservoir and playing a vital role to reservoir sedimentation reserved and reduction effectiveness.

## 2 SEDIMENT TRANSPORT CHARACTER IN RESERVOIR TRIBUTARY

The velocity change process of density current converse intruding tributary varies from the mouth to the climax and from big to small, and it decreases rapidly. Silt concentration decreases along the way. For the coarse particles deposit at the mouth, the fine come into the tributary and its groups settling

velocity is bigger. So the vertical profile of silt concentration is uniformity. But some branches at the mouth have a different convergence regional scale, this cause the vertical profile of velocity and silt concentration being constrained by the main stream. The extent has relations with the mouth width and the convergence angle.

The convergence angle of stem and branches is less than  $90^\circ$  or  $90^\circ$  in the Xiao Lang Di Reservoir. When density current goes through the mouth, it submerged intrudes the tributaries conversely. Its velocity is very small. The muddy interface elevation of the stem near the mouth is close to the mouth. The entrainment sediment have all deposited in branches. The capacity of branches becomes little. Figure 1 and Figure 2 is vertical velocity and silt concentration distribution of individual branch mouth during the Xiao Lang Di Reservoir physical model validated test [1]. Figure 3 is the change process of mainstream average velocity and silt concentration with time during the period of density current converse intruding Yun Xi River mouth, which is one of Xiao Lang Di Reservoir braches [2].

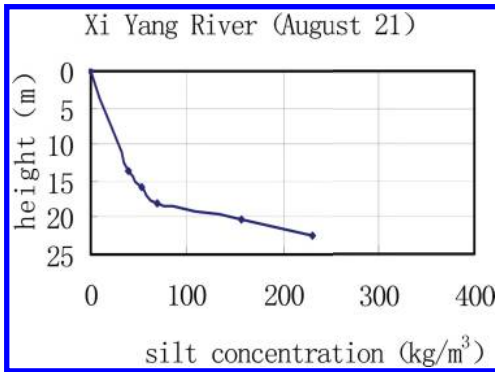


Figure 1. Vertical velocity distribution of branch mouth.

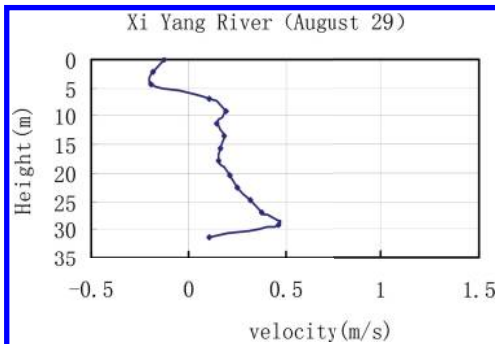


Figure 2. Vertical silt concentration distribution of branch mouth.

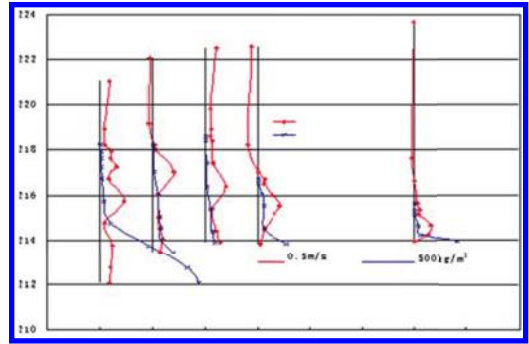


Figure 3. Change process of mainstream average velocity and silt concentration with time during the period of density current converse intruding Yun Xi River mouth, which is one of Xiao Lang Di Reservoir braches in year 2003.

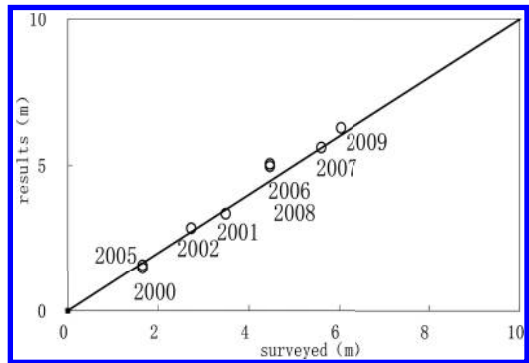


Figure 4.  $L_{han}$  results and measured.

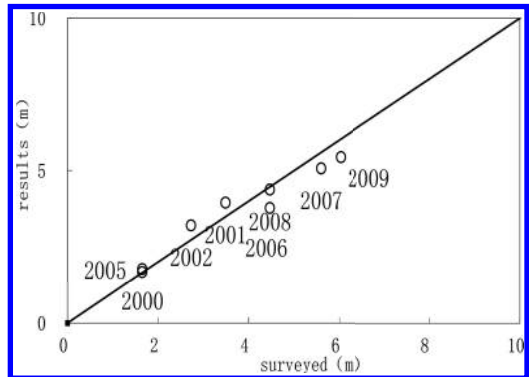


Figure 5.  $L_{Qin}$  results and measured.

Otherwise, when density current moves to the tributary end, along with the processes of silt deposition, the mixing of interface and water coming out of the muddy flow, discharge decreases and its kinetic energy does correspondingly.

### 3 CALCULATION

#### 3.1 Deposition

The river valley of the Xiao Lang Di Reservoir basin is wide upstream and narrow downstream. The width of upper side of the river valley (above 67 km) is 200 m to 400 m, and lower sect is 800 m to 1400 m. There is a 4-km sect named “Ba li bystreet” 30 km near the dam, whose width is 200 m to 300 m. There are more than 10 big branches like Da Yu River, Mei Yao River, Zhen Shui River, Shi Jing River, Dong Yang River, Da Jiao River, Xi Yang River, Yu Li River, Yan Xi River, Bo Qing River and so on, which converge the reservoir. They are all concentrated in the lower reservoir area, which has a rugged topography. Among the inflow and silt load of branches, Dong Yang River has a max annual average inflow of 0.091B m<sup>3</sup>, and accounts for 0.22% of the dam; Zhen Shui River has a max annual average silt load of 0.000897B tons, and accounts for 0.07% of the dam. So the inflow and silt load of branches could be left out of account when branches deposition shape would have been studied.

Since the beginning of water storage in September 1999, with the reservoir water level rising, the inflow and silt load of the stem river have been influencing the deposition of branches greatly. So it is notable to observe the change of branches capacity which account for 35.7% of whole. Since Xiao Lang Di Reservoir has been operated as a higher operating water level. The physical model results and prototype data show: that during the early stages which are demarcated in the sediment retention period, main deposition mode is deposition induced by the density current converse intruding tributaries.

#### 3.2 Formulars

In order to understand the converse intruding tributary length, taking use of the preceding harvest of that for reference, the converse intruding Zhen Shui River lengths have been calculated.

Zhen Shui River is the largest tributary of Xiao Lang Di Reservoir and enters the Yellow River directly. It comes from the second valley in Xin An and into the Yellow River at Xi Wo of Xin An County. Its total length is 51 km, drainage area 84.5 km<sup>2</sup>, and convergence angle of stem and branches 90°. Zhen Shui River has a lot of branches attributed to Luo He Drainage. But Zhen Shui River enters the Yellow River directly.

Han Qiwei [3] has taken use of flow-tube method to build Bernoulli equation for ascertaining the length. He assumes the slope small, flow-tube border and superstratum born shear stress whose

distribution is linear. After a series of derived equations, then:

$$L = \frac{1 + \frac{1}{2} Fr^2}{J_0 + \frac{\lambda_0}{8} Fr^2} h_1 \quad (1)$$

Above:  $Fr^2 = \frac{U^2}{\eta_{eg} h_1}$  is amendments Froude number after intruding.

When  $Fr^2 = 0.247$  and  $\lambda = 0.03$ , then

$$L = \frac{1.13h_1}{J_0 + 0.000926} \quad (2)$$

Qin Wenkai, etc<sup>[4]</sup> has taken use of flow-tube method to build momentum equation for ascertaining the length. After the same thought and different assumption conditions, with they have the length when  $q = 0$  under considerations of the interface resistance.

$$L = \frac{1 + 2Fr^2}{J_0 + \left( \frac{\lambda_0}{4} + \frac{K_1 \lambda_i}{12(1 - K_1)^2} \right) Fr^2} h_1 \quad (3)$$

When  $\zeta = 0.6$ , then  $K_1 = 0.6$ ,  $Fr^2 = \frac{U^2}{\eta_{eg} h_1} = 0.297$ .

When  $\lambda_0 = 0.025$ , then  $\lambda_i = 0.005$ , Formula (3) is briefed for

$$L = \frac{1.594h_1}{J_0 + 0.002135} \quad (4)$$

Formula (1) to Formula (4) have the same form and explain the length decided by amendments Froude number, resistance coefficient and especially muddy flow height and slope. This could be explained from its physical meanings. For muddy flow height represents the discharge of intrusion which functions as the energy magnitude. On the contrary, slope represents resistance along the way which functions as reaction.

#### 3.3 Case study

In the process of calculation, slope takes the data measured before flood, computed separately among the sects and averaged at the end. Muddy flow height is before the mouth. For convenience, Muddy flow height of upstream and downstream sections near braches mouth is borrowed. Distance from the stem to mouth is neglected. So calculation results are smaller than measured.

The results is listed in the [Table 1](#).

Table 1. Results of Zhen Shui River from year 2000 to year 2009 length.

Year	Sect for calculation	Muddy flow height (m)	Length (m)		
			Measured	$L_{Han}$	$L_{Qin}$
2000	–	10.00	1.653	1.640	1.968
2001	HH11	18.40	3.488	3.344	3.949
2002	HH9	11.90	2.728	2.851	3.201
2005	HH9	5.10	1.653	1.570	1.666
2006	HH9	6.2	4.465	4.965	3.772
2007	HH9	10.7	5.600	5.607	5.068
2008	HH9	8.6	4.465	5.046	4.373
2009	HH9	10.7	6.035	6.278	5.440

## 4 DISCUSSION

The deposition process of Zhen Shui is closely related to natural topographic conditions, deposition morphology of confluence areas of mainstream and tributary, process of incoming water and sediment and so on. Field observation data show that there is little incoming water and sediment in Zhen Shui and basically there is no sediment. Therefore, nearly all the deposition comes from flowing backward from mainstream. The sand bar is mainly caused by terrain condition. The Zhen Shui estuary is very narrow and the width is only about 600 m. That is, the width of water and sediment laterally flowing into Zhen Shui from mainstream is narrow, and it means that only a little sediment can flow into Zhen Shui. The Zhen Shui is open internally, for example, the valley width of cross section 3 km apart from estuary is more than 2500 m. It means that the flowing backward width increases suddenly, the flow velocity decreases rapidly, correspondingly, the carrying capacity decreases greatly, and there is a lot of sediment deposition. With the evolution of flow, the distance apart from estuary becomes longer and longer, the sediment carried by the flow becomes less; however, the deposition width becomes large. Therefore, the deposition thickness becomes thinner. In a word, all these are the main causes of less deposition thickness in internal Zhen Shui internal. With the quick uplift of mainstream riverbed, the deposition surface in Zhen Shui internal uplifts slowly, and the height difference of mainstream and tributary internal will increase year by year.

### 4.1 Conclusions

By October 2012, the amount of sediment in Zhen Shui reached 0.224 billion  $m^3$ , and the sand bar was 7.1 m. Until 2010, the converse intruding tributary length by density currents could be predicted

by formula (1). This could be predicted in other lengths in the same condition.

The researches of operational mode of Xiao Lang Di Reservoir for flood control and sedimentation reduction during later sediment retaining periods show that, regardless of the test, the height of Zhen Shui sand bar is more than 25 m. The sand bar can prevent water and sediment exchange between mainstream and tributary, and the internal storage capacity of tributary is not effectively used. The analyses show that because of the particularities of terrain, the formation of sand bar at Zhen Shui estuary has certain inevitabilities.

## ACKNOWLEDGMENTS

This paper is supported by national nature science foundation of China (51309110, 51179072) Non-profit Industry Financial Program of MWR of China (No. 201401023, No. 200901015, No. 200801024) and Yellow River Institute of Hydraulic Research Central level, scientific research institutes for basic R & D operating expenses of special funds of China (compact number: HKY-JBYW-2014-01).

## PHOTOGRAPHS AND FIGURES

Calculation results of the two formulas and measures are compared in the same figure, respectively pointed in Figure 3 and Figure 4. From the figures, calculation results seems to be practical basically, but results of Han's are less than Qin's, and more in line with the measured. For there is no measured data during the flood period. But the flood would have plunged and density current would have come into practice, muddy flow converse intruded tributaries. This makes an excuse for the difference between the results and measured.

## REFERENCES

- Edmonds, D.A. and Slingerland, R.L.: Mechanics of rivermouth bar formation: implications for the morphodynamics of delta distributary networks, (2007) *J. Geophys. Res.*, 112, F02034, doi:10.1029/2006JF000574.
- Paola, C., Twilley, R.R., Edmonds, D.A., Kim, W., Mohrig, D., Parker, G., Viparelli, E., and Voller, V.R.: Natural processes in delta restoration: application to the Mississippi Delta, (2011) *Ann. Rev. Mar. Sci.*, 3, 67–91.
- Han Qiwei. Reservoir sedimentation. (2003). Beijing: science press. 105–108. (in Chinese).

- Zhang J.H., Chen S.K., Ma H.B., Chen X.T., Li T., Wang T., Jiang S.Q., LI K.P., and Wang Y. Report on model test of the second operational mode of Xiaolangdi Reservoir for flood control and sedimentation reduction during later sediment retaining period [R]. (2010) Zhengzhou: Yellow River Institute of Hydraulic Research, YRCC:pp.68–73. (in Chinese).
- Li Tao, Zhang Junhua, Wang Yanping. Study on the common boundary settlement of muddy lake in Xiao Langdi Reservoir [A]. (2006)Conference proceedings on density current problems. Zhengzhou: Yellow River Conservancy Press, pp339–343. (in Chinese).
- Qin Wenkai, Fu Renshou, Han Qiwei. Research of Adverse Slope Density Current [J]; (1995)Journal of Hydrodynamics A part. (6): 637–647.
- Tao Li, Jun Hua Zhang, Guang Ming Tan, Huai Bao Ma, Shu Xia Li. Study on turbidity current head going through the changing width section [J]. (2012) Procedia Environmental Sciences, 13: 214–220.
- Xia JQ, Li XJ, Zhang XL and Li T (2013). Recent variation in reach-scale bankfull discharge in the Lower Yellow River. *Earth Surface Processes and Landforms*. DOI: 10.1002/esp.3474.
- Li Tao, Gao Guoming, Ma Huaibao and Fan Wenling. Calculation on the Settlement of two sands. *Applied Mechanics and Materials*. 2014.9.
- Tao Li, Zhang Junhua, Gao Guoming, Xia Junqiang, Ma Huaibao. Preliminary Prediction on Critical Continuity Duration of Density Current Head in Xiaolangdi Reservoir, Yellow River. (2013) 35th IAHR World Congress, Conference topics.
- Sequeiros, O.E., Cantero, M.I., and Garcia, M.H. (2009). “Sediment management by jets and turbidity currents with application to a reservoir for flood and pollution control in Chicago, Illinois.” *J. Hydraul. Res.*, 47(3),340–348.
- Singh, B., and Shah, C.R. (1971). “Plunging phenomenon of density currents in reservoirs.” *Int. Water J.*, 26(1), 59–64.
- Toro, E.F. (2001). *Shock-capturing methods for free-surface shallow flows*, Wiley, Chichester, U.K.

# Study on the drainage system of the tailing pond by numeric simulation and model test

Q.L. Qi, Q. Li, S.X. Zhang & Z.L. Wang

*School of Civil Engineering, Shijiazhuang Tiedao University, China*

*Key Laboratory of Roads and Railway Engineering Safety Control of Ministry of Education  
Shijiazhuang Tiedao University, China*

**ABSTRACT:** According to the drainage system of the tailing pond in Hebei province, the discharge flux of the drainage system is measured by the normality hydraulic model test. The flow pattern in the drainage system is observed in the condition of the normal water level and flood level. And then the location of instable flow and the possible damage is found. Based on the model test, the three-dimensional numeric model of the drainage system in tailing pond is set up, and then the flow pattern is simulated. Compared with the numeric results and the test result, the numeric results agree well with the test result, and then CFD methods used in the drainage system of the tailing pond is discussed in the paper.

**Keywords:** tailing pond; drainage system; model test; numeric simulation

## 1 INTRODUCTION

Drainage system of the tailing pond is of a special hydraulic structure. Compared with the municipal pipe network and water conveyance pipeline in the hydrographic engineering, its characteristics reflect the difference between the lateral size and axial length. Because of the arrangement along the mountainous terrain, it has a slope gradient. Generally, drainage system of the tailing pond is made from the shaft, drainage pipe, drainage tunnel, and so on. In conditions, such as negative pressure, mixed free-surface-pressure flow, the flow in the drainage system is tangled. For this reason, in the “*Code for design of tailings facilities*” [1], the design of drainage system must abide by the results of the hydrodynamic calculation and flood regulating calculation; in particular, according to the first degree, second degree, and complex drainage system, the hydraulic model test must be used to verify the design.

Hydraulic model test is an important research method in hydraulic structure engineering. The complex flow patterns are observed and predicted by the hydraulic model test designed by the gravity similar theory, through which we can examine the reliability and accuracy of the designing scheme, and then optimize the design of the hydraulic structure engineering.

Wang Shi-xia [2] study the flood carrying capacity of the tower-type inlet silo of the tailing pond by normality hydraulic model test, and the flow

patterns is described. Ma Lin-yuan [3] study the stability of the drainage system of Wai-tou-shan tailing pond by normality hydraulic model test, and verify its discharged capability. Dang Ning [4] studied the flow characteristics of the frame-type drainage well in the Da-xi-gou [5] tailing pond, and analyzed the its discharged capability and flow state. At present, lots of hydraulic model tests have been used in the drainage systems of the tailing ponds, improved the related theory and test technique of the hydraulic model test. However, the numerical simulation, with the development of compute technique, the numerical simulation will be widely used in the design of the drainage system.

In the paper, the drainage system of the tailing pond in Hebei province is selected, and some research works is carried out as the following:

1. The hydraulic model test is designed based on the similarity criterion, which need to abide by gravity similarity criterion strictly.
2. Through the hydraulic model test, the discharge flux of the drainage system is surveyed to judge if the maximum discharge flux meets the design requirements. Meanwhile, the flow pattern in the drainage system is observed, and then determines if the instable flow exists in the drainage system to verify the reasonableness of the design.
3. A three-dimensional numeric model of the drainage system in tailing pond is set up, and then the flow pattern is simulated. By the

numeric simulation, the flow flux, flow velocity, flow pressure, and so on are determined. Then the analysis with the test model is carried out, and some meaningful conclusions are drawn.

## 2 ENGINEERING SITUATION

The drainage system of tailing dam in Hebei province must meet a requirement of the return flow flux 2.01 m<sup>3</sup>/s under the normal condition, and maximum discharge flux 5.69 m<sup>3</sup>/s under the flood condition. The design uses drain well, drain pipe, tunnel, and open channel, which are made from the whole reinforced concrete lining with 300 mm thickness, with the smooth inside edge of the wall, and controlling surface irregularities of height less than 20 mm. Through the drainage calculation the flood drainage structures form and size are determined: the drainage wells are all of frame structure, with the inner diameter 4.0 m, the height 2.0 m, and ring beam height 0.3 m between each layer. Each layer of the frame well has 10 hole-inlets. All the circular pipes' inner diameter is 1.2 m: drainage tunnel are arch-wall type with the width 1.5 m; the clear height of 1.8 m, the straight wall is 1.05 m high, and the arch is 0.75 m. The shafts are connected with the drainage tunnel and drain pipe, and the shaft diameter is 1.5 m.

Through hydraulic model experiment combined with numerical simulation, this paper studies the late drainage system in the accumulation of elevation of 610.0 m (range from the 4th well to the tunnel exit, namely T4-P2-P1-P0 section, the section model total length of 42.71 m, height of 1.85 m). Through the hydraulic model test, the discharge flux of the drainage system is surveyed to judge if the maximum discharge flux meets the design requirements. Meanwhile, the flow pattern in the drainage system is observed, and then determines if the instable flow exists in the drainage system to verify the reasonableness of the design.

## 3 MODEL DESIGN AND CONSTRUCTION

Based on the similarity theory of hydraulic model test, according to the gravity similarity criterion, the hydraulic model is designed. The selected model of geometric scale  $\lambda_L = 24$ . The physical quantities of similar relations are shown in Table 1.

Model materials select organic glass. Roughness of prototypical concrete is  $n_p \approx 0.014$  and the requirements of model roughness is  $n_m \approx n_p / \lambda_n \approx 0.0082$ . The roughness of organic glass is about 0.008~0.010. After testing verification, the selected organic glass meets the similar requirements of resistance.

Table 1. The quantities of the model scale relationship and model scale ratio.

Physical quantity	Scale relations	Physical quantity scale
Velocity	$\lambda_v = \lambda_L^{0.5}$	4.90
Flow	$\lambda_Q = \lambda_L^{2.5}$	2 821.81
Roughness	$\lambda_n = \lambda_L^{1/6}$	1.70
Time	$\lambda_t = \lambda_L^{0.5}$	4.90
Pressure	$\lambda_p = \lambda_L$	24.00



Figure 1. Production, installation and completion of the model.

In order to maintain the water flow similar to the prototype, “Hydraulic (conventional) model testing procedure” (155-2012 SL) regulates that the model Reynolds number should reach the area of resistance. If sometimes there is difficulty reaching the area, at least it should be guaranteed in the turbulent zone. The results show that the Reynolds number of the model and the prototype is far greater than the critical Reynolds number and the flow is in turbulent state.

The model shown in Figure 1 is produced and installed.

## 4 TEST RESULT ANALYSIS

### 4.1 Discharge flow

The discharge of the tailings dam in the accumulation elevation of 610 m under normal condition and flood condition by the model test are shown in Table 2.

Table 2 shows that when tailings pool stacking elevation is 610 m, the discharge flux of the drainage system is 2.57 m<sup>3</sup>/s in normal condition and meet requirement of the return flow flux of

Table 2. Drain system discharge flow at 610 m accumulation height of dam.

Working conditions	Weir head		Discharge flow	
	Model values/m	Prototype values/m	Model values/(L · s <sup>-1</sup> )	Prototype values/(m <sup>3</sup> · s <sup>-1</sup> )
Normal condition	0.013	0.30	0.91	2.57
Flood condition	0.042	1.01	0.60	16.93

2.01 m<sup>3</sup>/s; Under the condition of flood, discharge flux of drainage system is 16.93 m<sup>3</sup>/s, it is greater than the required maximum discharge flux of 5.69 m<sup>3</sup>/s and meets requirement of the design discharge flux.

#### 4.2 Typical flow pattern

Under normal operating condition, the inflow of the 4th drainage well is the overflow of the weir, the flow around the inlet hole of the drainage well is smooth and there is no poor hydraulic phenomenon. The flow at the bottom of the drainage well is rolling violently, the aeration phenomenon in the upper water column is obviously, and it looks cystose. The turbulence is small in the lower water body, without the aeration phenomenon, which is transparent. The free flow is observed in the tunnel from the inlet to the outlet. Under normal condition, the bottom flow pattern of No. 4 drainage well is shown in Figure 2(a). Under flood condition, the inflow flux of the drainage well is larger, the backwater phenomenon occurs in the drainage well. Aeration of drainage wells is obvious and the bubbles enter the downstream tunnel with the water flow. Because the water in the well is very deep, the pressure flow is observed in the tunnel from the inlet to the outlet. The flow pattern at the bottom of No. 4 drainage well under flood condition is shown in Figure 2(b).

Under normal operating conditions, the P1~P2 section of the tunnel is free flow and the depth of the water is about 0.59 m. As with the No. 1 tunnel junction P2 flow steering slightly larger, refracted phenomenon appears in the P1~P2 section of tunnel in the range of 45.60 m, Then the flow pattern is smooth and without aeration phenomenon. Under the condition of flood, because of the large flow rate of the 4 drainage wells, the P1~P2 section tunnel is pressure flow and the maximum pressure head is about 14.5 m. Flow pattern of two operating conditions are shown in Figure 3(a) and Figure 3(b).

Under normal operating conditions, the water flow of No. 1 branch tunnel is free flow and the depth of the water is about 0.59 m in the junction of No. 1 tunnel and main tunnel at P2, because

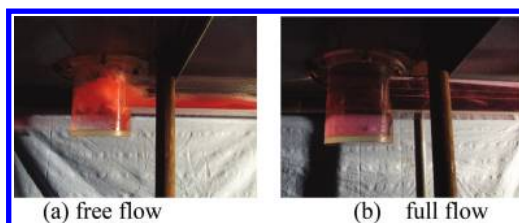


Figure 2. Model test under the normal condition.

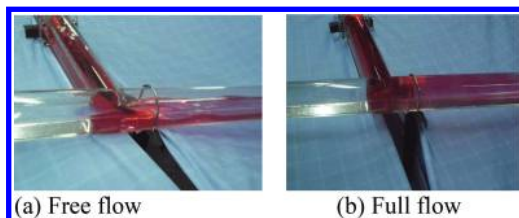


Figure 3. Model test under the flood condition.

flow takes a sudden turn, here the flow pattern is complex and the backwater phenomenon occurs. Far away from the junction of the P2, the flow become stable and water depth grows large, and the maximum hamed water depth is 1.03 m. Under normal operating condition, the flow pattern is shown in Figure 3(a). Under flood condition, because of the large inflow, the 1st tunnel is full of pressure flow and the maximum pressure head is about 19.95 m. Under flood condition, the flow pattern is shown in Figure 3(b).

#### 4.3 Flow velocity

The experimental results show that the flow is approximately uniform flow along the tunnel except the bend section. Under normal operating condition, the velocity of the uniform flow in the drainage system is small, and the flow velocity is 2.90 m/s. Under the condition of flood, the flow velocity of the drainage system is larger, and the flow velocity is 6.81 m/s. Under the two operating



conditions, the flow Reynolds number of each part of the drainage system is much higher than the critical Reynolds number, and the flow is in the turbulent zone.

## 5 NUMERICAL SIMULATION

A numerical simulation is conducted at point P2 where the branch tunnel crosses the main tunnel meeting with the angle of 107 degree. The upstream of main tunnel is blocked, and the water flow direction is changed violently, which flow pattern is complex.

The water pressure distribution and velocity distribution under the two conditions are calculated as shown in Figure 4 and Figure 5.

Figure 4(a) shows normal conditions of the pressure cloud picture, Figure 4(b) is the flow velocity diagram, and Figure 4(c) is the velocity vector diagram. Under normal conditions, from Figure 4(a) we can see that tunnel not only is full of free flow but also has less pressure. Maximum pressure appears at the junction where the branch tunnel crosses the main tunnel, and the maximum pressure is about 9.2 kPa. The pressure cannot

cause damage of the concrete side wall of tunnel. Through Figure 4(b) and Figure 4(c), it is shown that the upstream water flow of branch tunnel is stable; the average velocity of the cross section is 3.16 m/s, which as obtained from tests is 2.90%, the error within 9.0%. As hindering effect by main tunnel side wall, water flow produces backwater area in the branch tunnel. With the flow-cross section increased, flow velocity decreases to 1.48 m/s. The changing flow direction leads to backwater area where velocity is reduced gradually from the outside to the inside. The outside maximum flow velocity is 3.32 m/s and the inner minimum flow velocity is 1.53 m/s.

Figure 5 shows the pressure cloud picture, flow velocity, and velocity vector diagram under the condition of flood. From Figure 5(a), it can be seen that the pressure flow change is larger because discharge flux is greater, and the pressure of the tunnel keeps above 400 kPa. The maximum pressure acted on the tunnel surface caused by the flow of the main tunnel is 502.5 kPa, which will not cause damage of concrete side wall of tunnel. As Figure 5(b) and Figure 5(c) show, branch tunnel velocity distribution is homogeneous, mean velocity in section is 7.11 m/s, which obtained from tests is 6.81 m/s, and comparing error is 4.4%. At the bend location of the tunnel, the flow velocity of the vortex flow is gradually reduced from the outside to the inside of the vortex, and the outside maximum flow velocity is 9.98 m/s, and the inner flow velocity is 0.96 m/s.

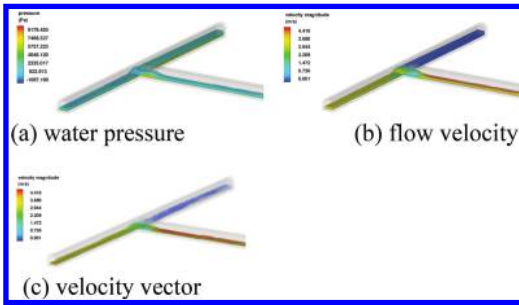


Figure 4. Numerical simulation under the normal condition.

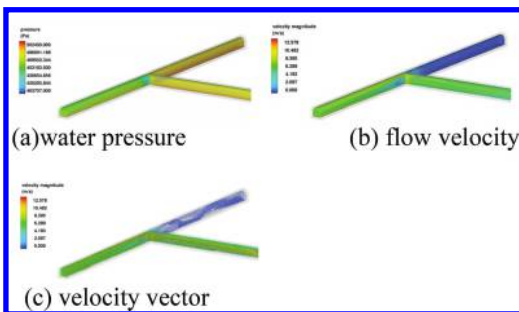


Figure 5. Numerical simulation under the flood condition.

## 6 CONCLUSION

According to the drainage system of a tailing reservoir in Hebei Province, the gravity similarity criterion is used to establish test model, and the following work is accomplished:

1. Through the model test, the discharge flux of the drainage system is obtained. The discharge flux under normal condition is 2.57 m<sup>3</sup>/s, and meets the requirement of the return flow flux 2.01 m<sup>3</sup>/s. The discharge flux under normal condition is 16.93 m<sup>3</sup>/s, and greater than the required maximum flow discharge flux 5.69 m<sup>3</sup>/s, which meet the design discharge flow requirement.
2. A detailed analysis of the flow pattern is carried out, which can supply for next the optimization of the design.
3. The flow velocity of the drainage system is smaller under the normal condition; however, the flow velocity is larger under the flood condition, in which maximum flow velocity is 6.81 m/s. Those will not cause erosion of the drainage system.

4. The three-dimensional numerical model of drainage system is established to analyze the discharge flow characteristic, and the numerical results are in accordance with the model test results, which show Computational Fluid Dynamics (CFD) method can be used in design, optimization and research of drainage system of tailings pond.

## REFERENCES

- [1] China Nonferrous Metals Industry Association. Code for design of tailings facilities [S]. China Planning Press, Beijing, 2013.
- [2] Wang Shixia. Discharge capacity of shaft spillway with framed inlet tower for high tailings dam [J]. Metal mine, 1994(5):36-47.
- [3] Ma Linyuan. Safety and outflow stability of discharge system of Waitoushan tailing reservoir of Benxi Iron Company [D]. Dalian university of technology, Dalian, 2003.
- [4] Dang Ning. Tailing drainage wells experimental study on shape optimization of flood discharge system [D]. Xi'an University of Technology, Xi'an, 2010.
- [5] Zhang Jin, Le Tao, Cao Ji-gang. Experimental research of the hydraulic model for flood discharge structures of Toudishan tailings pond [J]. Metal mine, 2013(1):30-33.

# Analysis on optimizing preloading water head of water distribution ring pipe in hydropower station

Bo Liu

*Changjiang Institute of Survey, Planning, Design and Research, Wuhan, China*

J.T. Lai

*Yalong River Hydropower Development Company, Ltd., Chengdu, China*

**ABSTRACT:** A three-dimensional finite element model of the water distribution ring pipe in hydropower station has been carried out, using the finite element program ANSYS and nonlinear contact theory. With different preloading water head (0.7, 0.8 and 0.9 times of minimum hydrostatic pressure), the stress of surrounding concrete of the water distributing ring pipe has been analyzed, which provide reference for the optimal selection of the preloading water head. The result shows that the surrounding concrete will not crack in the three schemes, because the design tensile strength of the surrounding concrete of the water distributing ring pipe is high (3.27 MPa). Considering the stress of surrounding concrete and the requirements of unit's long-term stable operation comprehensively, the water distribution ring pipe's preloading water head of this project is suggested to be 4.8 MPa, 80% of the minimum head (598.5 m).

**Keywords:** water distribution ring pipe; preloading water head; finite element analysis

## 1 INTRODUCTION

Water distributing ring pipe is an important part of the hydropower station. With the surrounding concrete, it undertakes the water pressure during the operation of the hydropower station<sup>[1]</sup>. Water distributing ring pipe is buried in the concrete and its structure is more complex than the common spiral case structure. It belongs to a part of the joint load-bearing structures, can effectively control and regulate the load-bearing proportion of steel and surrounding concrete, give full play to the advantages of steel to reduce cracking of the surrounding concrete, meet the plant substructure overall stiffness requirement<sup>[2, 3]</sup>. Furthermore, due to gravity of water bodies can effectively prevent water distribution ring pipe floating, eliminating some of the pull anchor when the surrounding concrete pouring, water distribution ring pipe conducive to the stability of unit operation. For large-scale unit and pumped storage unit, water distributing ring pipe has been widely adopted at home and abroad<sup>[4]</sup>.

In this paper, using the software ANSYS and taking into account of the friction of the steel liner with the surrounding concrete<sup>[5]</sup>, a 3-D model is established to calculate the stresses of steel liner and surrounding concrete. Based on one unit of a hydropower station, surrounding concrete stress of

the water distributing ring pipe has been studied, by using a simplified algorithm. The reasonable preloading water head has been proposed. Finally, conclusions were summarized.

## 2 FEM MODEL

In this paper, an actual water distribution ring pipe structure in hydropower station was modeled. The model is built up according to the middle standards unit. The distance in the direction along the longitudinal axis is totally 14.10 m, and the width along the direction from upstream to downstream is 25.26 m, and the vertical distance is 17.5 m. The inlet diameter of cross section of the hydropower station's distributor is 1 meter. The distributor utilizes WDB620 steel plate and the thickness of the section is 25 mm to 50 mm. The distributor is complicated in structure and bears very high internal water pressure, as a result, the design for it is not only a matter of significant techno-economy, but also has a concern in that the power station is or is not able to generate electricity on schedule and realize a long-term safe operation.

Cartesian coordinate system is adopted in the numerical analysis, in which X-axis is assumed as the horizontal direction along the longitudinal axis at the extreme left to plant (facing downstream),

Y-axis is set along the vertical direction and upward is positive. And Z-axis is set along the horizontal direction, whose positive direction is from upstream to downstream. Coordinates origin is set at the intersection of installation elevation and unit axis.

Distributor and its surrounding concrete are all simulated according to their actual size in calculation range. Normal constraints are applied on the sides and bottom of the foundation. Earth pressure is applied on the upstream, downstream and left regions of powerhouse contacted with earth, water pressure is applied on the region contacted with water. The region of right contacted with water is applied water pressure. The else are considered as free surfaces.

The model includes four groups of element, i.e. concrete, distributor, steel liner of motor-pumped well and foundation. Concrete and foundation adopt eight-node hexahedral element, distributor and liner of motor-pumped well adopt four-node plane shell element. The calculation model is of 83821 nodes and 77204 elements among which concrete is 54234 elements, distributor 1690 elements, lining of motor-pumped well 280 elements, and foundation 21000 elements. Parts of the grid are shown in Figure 1~Figure 3.

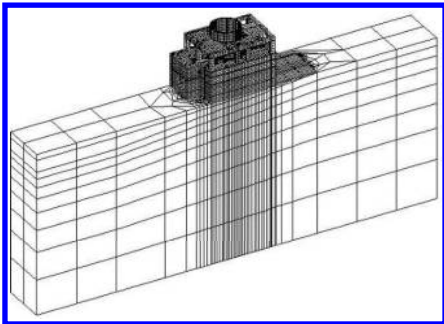


Figure 1. Grids of the whole model.

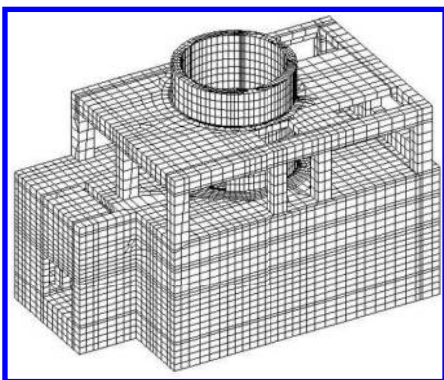


Figure 2. Grids of the powerhouse structure.

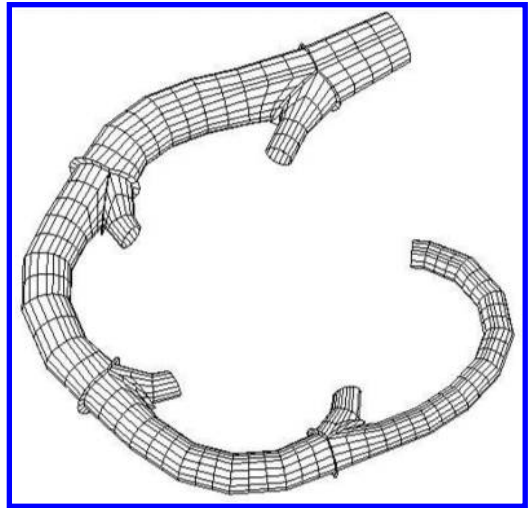


Figure 3. Grids of the distributor.

### 3 CALCULATION SCHEMES

The preloading water head directly determines the value of internal water pressure beared by both distributor and its surrounding concrete under the running operation of a power station, and it has large influence on reinforcement design of the surrounding concrete. Meanwhile the value should ensure no disengaging between distributor and its surrounding concrete in order to guarantee stable operation of units. Based on that, we select 0.7, 0.8 and 0.9 times of minimum hydrostatic pressure (5.985 MPa) as the preloading water head to analyze and compare, in order to choose the preloading water head which is appropriate to the distributor of the hydropower station. Calculation schemes and load combinations are shown as Table 1.

### 4 STRESS OF THE SURROUNDING CONCRETE OF DISTRIBUTOR

According to the above three calculation schemes, circumferential stress of some keypoints are list in Table 2. The numerical value in Table 2 are normal stress of corresponding sections, which is positive for tensile stress and negative for compressive stress. The unit of stress is MPa. The location of sections is shown in Figure 4, and location of keypoints in Figure 5.

1. In the scheme of LC-1, the jointly bearing value shared by both distributor and concrete is larger in this scheme than the other two, so the stress level of concrete is the highest relatively.

From the Table 2, it can be seen that with the interaction of internal water pressure and loads

Table 1. Calculation schemes and load combinations.

Calculation schemes	LC-1	LC-2	LC-3
Preloading water head (MPa)	4.2	4.8	5.4
Structure weight	√	√	√
<i>Stator base plate per each (MN)</i>			
Radial	0.089	0.089	0.089
Tangential	0.145	0.145	0.145
Axial	0.393	0.393	0.393
<i>Under-rack base plate per each (MN)</i>			
Radial	0.066	0.066	0.066
Tangential	0.033	0.033	0.033
Axial	0.025	0.025	0.025
<i>Upper bracket base plate per each (MN)</i>			
Radial	0.031	0.031	0.031
Tangential	0	0	0
Axial	0	0	0
<i>Uniform Live Load on floor (MN/m<sup>2</sup>)</i>			
Generator floor	0.025	0.025	0.025
Turbine floor	0.025	0.025	0.025
Ball valve floor	0.015	0.015	0.015
<i>Vertical load on each upstream and downstream pillar located on generator floor (MN)</i>			
Upstream	0.663	0.663	0.663
Downstream	0.681	0.681	0.681
Tailrace level (m)	1612	1612	1612
Jointly bearing pressure (MPa)	2.62	2.02	1.42

coming from superstructure, the circumferential tensile stress of each section is large and the maximum value is 1.94 MPa. The difference of circumferential tensile stress between top and bottom of the inner edge is a little small. While the medial stress level is higher than the lateral, it is because the thickness of medial concrete is thinner than lateral. The circumferential stress of each keypoint is less than the design tensile strength (3.27 MPa) of the concrete, the concrete will not crack.

2. In the scheme of LC-2, under the jointly bearing internal water pressure of 2.02 MPa, the maximum circumferential stress value of each keypoint is 1.49 MPa. The stress distributions are similar to scheme LC-1. Because of the decrease of the jointly bearing value, the stress level of concrete is less than scheme LC-1, so the surrounding concrete will not crack either.
3. In the scheme of LC-3, under the jointly bearing internal water pressure of 1.42 MPa, the maximum circumferential stress value of each keypoint also appears at the bottom of 2# section and the maximum value is 1.03 MPa.

Overall, since the design tensile strength of the surrounding concrete of distributor is high, the concrete will not crack in above three schemes.

## 5 DETERMINATION OF THE PRELOADING WATER HEAD OF DISTRIBUTOR

From the analysis of previous section, it can be seen that the preloading water head has a significant impact on the stress level of the surrounding concrete. Obviously the higher of the preloading water head, the better to the stress of concrete structure, and the distributor can play a full role when jointly bearing. The preloading filling measurement is essentially making a initial gap between distributor and its surrounding concrete before operation. The gap is not only related to the size of the preloading water head, but also related to the temperature differences between the construction and operation of distributor.

As the impact of hydration heat of concrete, even if the cooling measurement is taken, the temperature of the distributor during construction is generally higher than the minimum temperature during operation, so it will form a gap between distributor and surrounding concrete when the power station is operating. Assuming that the diameter of the distributor inlet is 1 m and maximum thickness is 50 mm, then every 1°C temperature difference will cause a gap of about 0.0078 mm which is equal to increasing the preloading water head of 0.32 MPa.

Table 2. Circumferential stresses of keypoints.

Section	Keypoints	LC-1	LC-2	LC-3
1#	a	1.19	0.94	0.68
	b	1.17	0.91	0.64
	c	0.96	0.7	0.43
	d	0.98	0.72	0.46
	e	—	—	—
2#	a	1.31	1.01	0.7
	b	1.75	1.35	0.96
	c	1.94	1.49	1.03
	d	1.42	1.09	0.76
	e	0.2	0.15	0.1
3#	a	0.75	0.6	0.4
	b	0.74	0.58	0.4
	c	1.18	0.85	0.32
	d	0.86	0.59	0.28
	e	0.43	0.3	0.11
4#	a	1.34	1.03	0.73
	b	1.37	1.06	0.76
	c	1.35	0.98	0.61
	d	0.94	0.68	0.43
	e	0.39	0.27	0.14
5#	a	0.85	0.65	0.46
	b	1.36	1.05	0.73
	c	1.29	0.92	0.54
	d	0.89	0.62	0.36
	e	0.23	0.12	-0.02
6#	a	1.27	0.95	0.65
	b	1.25	0.96	0.67
	c	1.07	0.76	0.45
	d	0.97	0.7	0.43
	e	-0.11	-0.16	-0.2

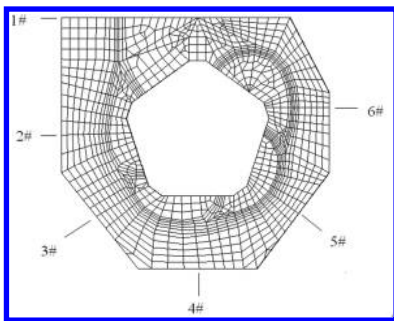


Figure 4. Location of typical sections.

To ensure the stable operation of the units, it needs to guarantee the sum of the actual preloading water head and the increased water head caused by cold gap is less than the minimum hydrostatic pressure, so it will not appear disengaging of distributor at any running water head. Preliminary estimated according to this standard, the allowable maximum temperature differences of scheme LC-1, LC-2, and LC-3 are 5.6°C, 3.7°C and 1.8°C respectively, so the higher of the preloading water pressure, the

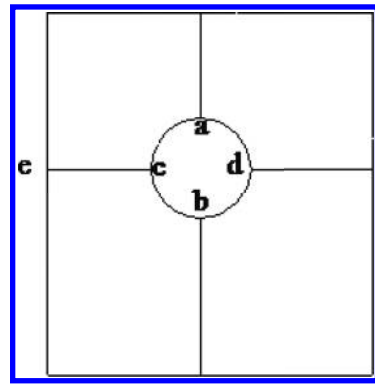


Figure 5. Location of keypoints.

smaller of the allowable temperature difference, and the higher demand of keeping temperature measurements. From this point, the preloading water head can not be too high.

In a word, the determination of the preloading water head of distributor is not only to consider about the impact of the surrounding concrete stress, but also need to take the requirements of stable operation of units into account. Comprehensively considered of the two factors, the preloading water head can be determined as 80% of the minimum hydrostatic pressure, which is 4.83 MPa.

## 6 CONCLUSIONS

As to the preloading water head of water distribution ring pipe, it is necessary to consider the impact of stress of surrounding concrete and also take account of the requirements of unit's long-term stable operation. Considering these two factors comprehensively, the distributor's preloading water head of this project is suggested to be 4.8 MPa, 80% of the minimum head (598.5 m).

## REFERENCES

- [1] Ma Kaibin. Nonlinear analysis and design optimization for distributor structure in hydropower station [D]. Dalian: Dalian University of Technology, 2007.
- [2] Chen Jing, Ma Zhenyue, Zhao Fengyao, et al. Research on structure analysis and design optimum of distributing pipe of impulse turbine in hydropower station [J]. Water power, 2009, 35(4): 64-66.
- [3] Zhao wei. The research on water filling pressurization value for distributors of Yangang hydropower station [J]. Power System and Clean Energy, 2009, 25(6): 65-67.
- [4] He Yemeng. Optimal selection of the pressure value for distributor in CCS hydropower station [D]. Zhenzhou: North China University of Water Resources and Electric Power, 2013.
- [5] ANSYS Theory Manual [J], ANSYS, Inc, 2003.

# Based on the grey GM (1,1) model to predict the total water consumption of Liaoning Province

Jinliang Chen

Liaoning Water Conservancy Vocational College, Shenyang, China

**ABSTRACT:** Based on the theory of grey system, this paper established a GM (1, 1) model for forecasting the amount of water consumed in Liaoning province. The precision of the model was sufficiently high to be used to predict the water demand in Liaoning Province. The results showed that the total water consumption in Liaoning province would grow continuously. The increasing water consumption may eventually lead to a situation where water supply could not keep up with the demand, adversely affecting people's lives and productions. Recommendations were presented for the protection and reasonable use of water resources in Liaoning province.

**Keywords:** GM model; grey system; water consumption; use of water resources

## 1 INTRODUCTION

The grey system is an analysis method proposed by Chinese scholar Deng Julong in the early 80s. The grey nature of a system is the result of its complexity. Grey Model (GM) establishes differential equations from the generating operation of the original data sequence, thus GM is actually generating sequence model. Since the inception of the grey system theory and method in 1982, the breadth and depth of its theoretical research have been constantly expanding. Its application is also popular among engineers and technicians. Because of its less stringent requirements of the quantity and distribution of data, as well as the simplicity of this theory and method, the forecasting method has been widely applied in oil, energy, water conservancy, transport, industrial control and other fields.

## 2 GREY FORECASTING MODEL

### 2.1 Steps of GM (1, 1) model

1. Accumulated generating operation of raw data  
 Perform the first accumulated generation on the measured raw data  $x^{(0)}$  to obtain  $x^{(1)}$ :

$$x^{(0)} = \{x^{(0)}(k) \quad k = 1, 2, \dots, n\} \quad (1)$$

$$x^{(1)} = \{x^{(1)}(k) \quad k = 1, 2, \dots, n\} \quad (2)$$

where  $x^{(1)}(k) = \sum_{i=1}^k x^{(0)}(i) \quad (i = 1, 2, \dots, n)$ .

2. Quasi-smooth test on  $x^{(0)}$

$$\rho(k) = \frac{x^{(0)}(k)}{x^{(1)}(k-1)} \quad (3)$$

If  $\rho(k) < 0.5$ , ( $k = 4, 5, \dots, n$ ) is valid when  $k > 3$ ,  $x^{(0)}$  satisfies the smooth condition.

3. Regularity in index variation test on  $x^{(1)}$

$$\sigma^{(1)}(k) = \frac{x^{(1)}(k)}{x^{(1)}(k-1)} \quad (4)$$

If  $\sigma^{(1)}(k) \in [1, 1.5]$ , ( $k = 4, 5, \dots, n$ ) is valid when  $k > 3$ ,  $x^{(1)}$  has regularity in index variation. Thus, GM (1, 1) can be established for  $x^{(1)}$ .

4. Close to the mean generation on  $x^{(1)}$

$$Z^{(1)}(k) = 0.5(X^{(1)}(k) + X^{(1)}(k-1)) \quad (5)$$

5. Least square estimation of  $\hat{a} = [a, u]^T$  to obtain  $a$  and  $u$

$$\hat{a} = \begin{bmatrix} a \\ u \end{bmatrix} = (B^T B)^{-1} B^T Y_N \quad (6)$$

$$B = \begin{bmatrix} -0.5(X^{(1)}(2) + X^{(1)}(1)) & 1 \\ -0.5(X^{(1)}(3) + X^{(1)}(2)) & 1 \\ \vdots & \vdots \\ -0.5(X^{(1)}(n) + X^{(1)}(n-1)) & 1 \end{bmatrix} \quad (7)$$

$$Y_N = [X^{(0)}(2) \ X^{(0)}(3) \ X^{(0)}(3) \ X^{(0)}(n)]^T \quad (8)$$

6. Establishing model  
 GM (1, 1) model is

$$\frac{dx^{(1)}(t)}{dt} + ax^{(1)}(t) = u \quad (9)$$

whose time response function is

$$x^{(1)}(t+1) = e^{-a}x^{(1)}(t) + \frac{u}{a}(1 - e^{-a}) \quad (10)$$

which gives the differential equation

$$x^{(1)}(t+1) = \left[ x^{(0)}(1) - \frac{u}{a} \right] e^{-at} + \frac{u}{a} \quad (11)$$

### 7. Inverse accumulated generating operation

$$\hat{x}^{(0)}(i) = x^{(1)}(i) - x^{(1)}(i-1), \quad i \geq 2 \quad (12)$$

where  $\hat{x}^{(0)}(1) = x^{(1)}(1) = x^{(0)}(1)$ .

### 2.2 Evaluation of grey system model

Test values are the main criteria to evaluate a model. GM (1, 1) model generally has the following four test values: average relative error, correlation, variance of error to variance of raw data ratio, and small error probability. These four test values together determine the model accuracy grade, that is, the four test values of each grade must be within the required ranges simultaneously. There are four grades of model accuracy, listed in Table 1. The first three grades imply that GM (1, 1) model is a suitable modeling tool. On the other hand, the

Table 1. Reference table of model accuracy grade.

Prediction accuracy grade	<i>P</i>	<i>c</i>
First (Good)	>0.95	<0.35
Second (Pass)	>0.8	<0.5
Third (Barely pass)	>0.7	<0.65
Fourth (Failed)	≤0.7	≥0.65

Table 2. The total water consumption in Liaoning province during 2002–2013.

Year	Total water consumption (× 10 <sup>8</sup> m <sup>3</sup> )	Proportions of different types of water consumption			
		Agricultural	Industrial	Domestic	Ecological
2002	127.1	0.654	0.181	0.165	0.000
2003	128.3	0.651	0.171	0.179	0.000
2004	130.2	0.658	0.153	0.183	0.007
2005	133.3	0.654	0.158	0.179	0.008
2006	141.2	0.648	0.166	0.172	0.014
2007	142.9	0.642	0.171	0.170	0.018
2008	142.8	0.637	0.173	0.172	0.019
2009	142.8	0.638	0.167	0.171	0.023
2010	143.67	0.625	0.174	0.177	0.024
2011	144.56	0.650	0.166	0.154	0.034
2012	142.19	0.644	0.162	0.165	0.031
2013	142.13	0.639	0.160	0.165	0.036

fourth grade means that the raw data cannot be characterized by GM (1, 1) model accurately.

## 3 BASED ON GREY THEORY TO PREDICT WATER AMOUNT IN LIAONING PROVINCE

### 3.1 Raw data

Based on the proportions of water resource usage in Liaoning Province from 2002 to 2013 shown in Table 2, agricultural water was on the decline, industrial water and domestic water remained stable, while ecological water increased year by year. The base value was chosen to be the total water consumption in Liaoning Province from 2002 to 2013. The trend in water demand in Liaoning Province was then predicted by GM (1, 1) model based on the three-year average data.

### 3.2 GM (1,1) model

#### 1. Model parameters

$$a = -0.013447, b = 137.156805$$

#### 2. Time response type

$$\hat{x}^{(1)}(k+1) = 10328.36299 \exp(0.013447k) - 10199.83299$$

### 3.3 The forecasting results

Table 3. The predicted total water demand in Liaoning Province.

Year	2014–2016	2017–2019
Predicted water demand (× 10 <sup>8</sup> m <sup>3</sup> )	145.60	147.55



Table 4. Precision of the model-predicted results.

Index number (k)	Year	Actual value ( $\times 10^8 \text{ m}^3$ )	Predicted value ( $\times 10^8 \text{ m}^3$ )	Absolute error	Relative error (%)
1	2002–2004	128.53			
2	2005–2007	139.13	139.83	0.69	0.50
3	2008–2010	143.09	141.92	-1.37	-0.96
4	2011–2013	142.96	143.63	0.67	0.47
Average					0.3

#### 4 CONCLUSION

In this paper, the grey theory was applied to establish a forecasting model for the total water consumption in Liaoning Province, which was used to predict the water demand of the next 6 years in Liaoning Province. Results showed that this model had a very high precision, suitable for prediction of water demand in Liaoning Province. Predicted results showed that during 2014–2016 and 2017–2019, the total volume of water would reach 14.56 billion  $\text{m}^3$  and 14.755 billion  $\text{m}^3$  respectively. With the continuous growth of water consumption in Liaoning province, demand will definitely exceed supply. Currently, it is crucial to develop and use water resources, so as to achieve the efficient use of water resources. Adopting water conservation measures and enhanced effluent treatment, increasing water recycling and raising residents' awareness of water saving measures are recommended. This paper can provide a reference for optimal and rational allocation of water resources in Liaoning province.

#### REFERENCES

- [1] Deng, J. *Grey forecasting and grey decision*. Huazhong University of Science & Technology Press, 2002.
- [2] Li, X. A study on the forecasting model for summer electricity load based on grey system theory. Beijing Jiaotong University Master's thesis, 2004.
- [3] Wu, X. A study on the forecasting model for the effective irrigation area in Liaoning Province. Shenyang Agricultural University Master's thesis, 2005.
- [4] Men, B. Grey forecasting model for the effective irrigation area of farmland in Sichuan. *Journal of Shenyang Agricultural University*, 2004, 35(2): 1–5.
- [5] Ye, W., Bai, D., Gao, B. Forecast of urban domestic water demand in Xi'an. *Resource Survey & Environment*, 2005, 26(2).
- [6] Qian, X. Application of grey system theory and methods in medical forecasting. Shanxi Medical University Master's thesis, 2000.
- [7] Li, X. Application of GM (1, 1) model in the agricultural water demand prediction based on residual modification. *Water Sciences and Engineering Technology*, 2010(1): 19–21.

# Analysis of research status of the effect of pollutant adsorption on the motion characteristics of sediment

Yanfen Ren, Chao Zhu & Lianjun Zhao

*Yellow River Institute of Hydraulic Research and Yellow River Institute of Hydraulic Research, MWR Yellow River Sediment Laboratory, Zhengzhou, China*

**ABSTRACT:** The inaction between pollutants and sediment is very complicated. On the one hand, sediment has effect on the absorption and desorption of pollutants. On the other hand, the appearance of the sediment changes after absorbing pollutants and the mechanical motion characteristics of sediment also changes. Research trends, such as surface characteristics of the polluted sediment and the effect of pollutants on the behaviors of sediment, are summarized. The direction of further study of environment sediment is proposed: ① research into absorption of organic pollutant on the surface of particles at the micro-scale; ② research into scouring and silting deformation of environmental sediment; ③ the effect of new organic pollutants on the mechanical properties of sediment.

**Keywords:** pollutant; sediment; absorption; motion characteristics

## 1 INTRODUCTION

In recent years, with the geometric growth of the population in China, water discharge from modern industry, municipal waste, pesticide application and so on have led to serious river pollution. The rivers in China have high sediment concentration, so there is a strong interaction between pollutants in the polluted water and sediment. On one hand, sediment has important effect on water quality of rivers, that is to say, sediment has effect on the absorption and desorption of pollutant. And on the other hand, after sediment absorbs pollutants, its physical characteristics (appearance, structure and density and so on) change, which will have effect on its motion characteristics such as start, suspension, transport, and sedimentation.

The research into the law of the start, suspension, transport and sedimentation of the sediment in the river under the action of fluid is the basis of that into the motion characteristics of sediment-laden flow. Many famous scholars at home and abroad have devoted their lives to this research and laid a theoretical foundation for mechanics of sediment transport, which has formed a complete theoretical system. The subject of the traditional sediment research is clean sediment. But water has

been seriously polluted in the past ten years. So the pollutants that act on sediment must be taken into consideration in the study of the characteristics of sediment in water environment system. The study of the effect of pollutant on the physical and chemical characteristics is a necessary part of that of the mechanism of the interaction between pollutants and the sediment in rivers.

## 2 RESEARCH INTO THE EFFECT OF POLLUTANT ABSORPTION ON SURFACE CHARACTERISTICS OF SEDIMENT PARTICLES

### 2.1 *Research into the surface feature of natural sediment*

Sediment surface is the interface of the interaction between sediment and all kinds of pollutants. Correct understanding of the appearance and structure of sediment surface is the basis of the research into the interaction between sediment and pollutants. Surface features are very complicated. Among them, specific surface, pore size distribution, and surface charge are the most basic physical and chemical parameters.

Tang Hongxiao et al. measured the value of specific surface and analyzed the differences between northern and southern distribution. They think the greater the specific surface of sedimentary particles is, the more adsorption sites they have and the stronger their absorbability. As for the research into pore size distribution of particles, the

---

Project supported by National Natural Science Foundation of China (Grant No 51309109), Special Fund of Basic research operating expense of Central Public-interest Scientific Institution (No: HKY-JBYW-2013-08).

scholars at home and abroad discussed the porosity character of different particles, such as modified montmorillonoid, activated carbon, clay. Fang Hongwei et al. studied the pore distribution characteristics of the surface of Guangting bottom sediment through Nitrogen absorption-desorption test and found the fractal dimension of Guangting bottom sediment is 2.6~2.85. The pore volume of the polluted sediment particles whose pore diameter is less than 10 nm changes a lot and their fractal dimension becomes smaller because the surface pore is filled with pollutants.

Aquatic particulates carry a certain amount of charge due to lattice defect, isomorphous replacement and surface chemical reaction. Complex double electrode layer forms on particulates and has strong effect on the stability and interaction in different aspects. Huang Lei et al. made initial research into the distribution of surface charge of sediment particulates and measured the morphology and charge distribution of the surface of particles of silica sand by means of the measuring technical of the Electrostatic Field Microscope (EFM) for Scanning Probe Microscope (SPM) under the mode of phase imaging. They found charge distribution on the surface of sediment particles is uneven. Charge mostly concentrates on the saddle, uplifted parts and sunk parts and few charges distribute at groove, ridge and flat parts.

## 2.2 *Research into the effect on the surface features of environmental sediment particles*

The pollutants in water environment are generally divided into inorganic pollutants and organic pollutants. More attention is paid to heavy metal, nutrients and organics in environmental chemistry. Absorbing different pollutants leads to different changes in the surface features of sediment particles. This part mainly introduces the effect of absorption of heavy metal, nitrogen, and phosphorus nutrients and microbes on the surface features of sediment particles.

### 1. Research into the effect of heavy metal pollutants on the surface characteristics of sediment particles

Heavy metal pollutants mainly results from such human factors, as mining, waste gas discharge, sewage irrigation and use of products with too much heavy metal. Human activities results in the increase of the content of heavy metal in water environment. If the content of heavy metal exceeds the normal range, it will do harm to people's health and leads to water-environmental qualitative deterioration. Heavy metal pollutants exist in water in the form of ions. After sediment absorbs ion pollutants, the

surface characteristics of sediment particles will change. The research into this aspect mainly focuses on copper ions.

Chen Zhihe et al. analyzed pore size distribution and changes in the characteristics of pores through the experiment sand that has absorbed copper ions by means of physical and chemical adsorption instrument. Surface pores of sediment particles are mainly micropores and mesopores. Surface pores of sediment particles have strong copper ion absorption. Copper ions tend to be absorbed in  $r < 5$  nm pores when sediment particles absorb copper ions.  $r > 5$  nm mesopores and macropores are the passage by which copper ions are transported and diffused. The pore volume changes slightly. Specific surface area, total pore volume and average pore size tend to remain constant when copper ions fill the inner space of the pores gradually.

In order to study the morphology change after sediment absorbs pollutants, Chen Zhihe et al. summarized the distribution regularity of copper ions in heavy ions on the surface of sediment particles through copper nitrate absorption experiment and performed a statistical analysis on the micro-morphological characteristics of the particles with copper ions. Copper ions are mainly absorbed on the sides and at the depression of the surface of sediment particles, accounting more than 90% of the absorption number. Curvature reflects the copper ion absorption of complex morphology to a certain extent. The number of absorbed ions is the largest at the areas where Cu is equal to 1.1.

### 2. Research into the effect of nitrogen and phosphorus nutrients on the surface features of sediment particles

Nitrogen and phosphorus nutrients have numerous sources and are large in quantity, including sanitary sewage (organic matter and emergent), agricultural (chemical fertilizer and farmyard manure) and industrial waste water, waste and son on. Nitrogen and phosphorus are important influencing factors in aquatic system and one of the main limiting factors of eutrophication. When phosphorous pollutants come into water, they will spread and transport with water and some of them will be absorbed by the sediment particles in water. The study of the effect of phosphorous pollutants absorption on the surface features of sediment particles mainly focuses on the distribution regularity of phosphorous pollutants on sediment particles.

Chen Minghong et al. studied phosphorous pollutants absorption on the surface of sediment

particles at the micro-scale by means of Scanning Electron Microscope (SEM), and analyzed the distribution regularity of phosphorous on the surface of sediment by picture processing and with differential geometry approaches and expanded the traditional sediment research methods to multidimensional space. The research results show that there are more active chemisorbed sites at the saddle, depression and bulge of sediment particles and they are likely to absorb phosphorous.

Xiao Yang et al. made quantitative research into the surface features of sediment particles and the effect on phosphorous absorption by removing oxide and organic materials. They found that surface feature is one of the important factors that influence pollutant absorption of sediment. The median grain size of sediment has exponent relation to specific surface area. When grain size decreases to cosmid or fine silt, specific surface area increases remarkably. Langmuir isotherm can give a better description of the between liquid phase phosphorus equilibrium concentration and phosphorus equilibrium adsorption quantity in a phosphorus absorption test than Freundlich isotherm. With different initial concentrations of the water phase phosphorus, the phosphorus equilibrium adsorption quantity of sediment decreases with the increase of the grain size of sediment and the equilibrium adsorption quantity in low concentration region increases more quickly than that in high concentration region. When the initial concentration of phosphorus increases to a certain content, equilibrium adsorption quantity doesn't change gradually and increases to the maximum absorption quantity.

### 3. Research into the effect of microorganism adsorption on the surface characteristics of sediment

Microorganism is a kind of living organic matter and beings with the largest number, the widest distribution and the smallest individual. In nature, they live in the growing environment in attached state instead of free state. Sediment can absorb different kinds of nutrient due its unique surface absorption. Therefore, they attract much organic matters to the surface. Fang Hongwei et al. observed the morphology change of sediment particles after biological film grows on them with by means of Scanning Electron Microscopy (SEM). They found that sediment particles with biological film change a lot. The sediment particles in group are connected with each other and form netted texture or flocculent structure, while the surface of single sediment particle

with film is smooth and thus there are fewer changes in morphology.

## 3 RESEARCH INTO THE MOTION CHARACTERISTICS OF ENVIRONMENTAL SEDIMENT

### 3.1 *Research into the effect of ion pollutant absorption on the motion characteristics of sediment*

The effect of ion pollutants on sediment mainly manifest as the effect of positive ions in water on sediment flocculation. Under natural water condition, the surface of sediment usually is negatively charged. The charge on the surface of sediment and ions in water form structure of diffused electric double layer. When reverse ions in water increase, they will neutralize the electric doublet layer on the surface of compressed sediment and make the electrostatic repulsion among particles smaller, which leads to the increase of flocculation degree.

Cation ions in the water mainly refer to  $\text{Na}^+$ ,  $\text{Ca}^{2+}$ ,  $\text{Mg}^{2+}$  and  $\text{Fe}^{2+}$ . Chen Hongsong et al. studied the effect of  $\text{NaCl}$ ,  $\text{CaCl}_2$  and  $\text{AlCl}_3$  on flocculation and sedimentation in static water of fine grained sediment. The results show that during flocculation and sedimentation, the higher the concentration of  $\text{NaCl}$  and  $\text{CaCl}_2$  is, the faster flocculation and settling are. Liu Lin et al from Wuhan University studied the concentration of sediment with different  $\text{Ca}^{2+}$  ion concentrations on the course of flocculation and sedimentation. They found that the flocculating and settling speed increases with the concentration of sediment. It increases at the beginning and decreases gradually when it reaches the maximum. Under different ion conditions, the maximum flocculating and settling speeds and the maximum concentrations are different. The concentration of sediment that has reached the maximum will decrease with the increase of concentration of ion. The maximum speed increases with the concentration of ion.

Jin Ying and Jiang Guojun et al. studied the effect of the number of cation ions and valences on flocculating and settling of fine grained sediment. The sediment with larger number of valences has the larger amount of flocculation. They obtained the relation between flocculation and the number of cation ions in sea water. Wang Jiasheng et al. studied the effect of the common cation ions in the water on the settling of fine grained sediment in river water. The results show that the settling speed of sediment increases with the increase of the concentration of cation ions.

We can see ion pollutants mainly have effect on the flocculating and settling of fine sediment. This phenomenon is remarkable in estuaries. It mainly

influences the deposit of fine grained sediment in estuaries and the evolution of the riverbed in estuaries.

### 3.2 *Research into the effect of microbiological contaminants on the motion characteristics of sediment*

Microbiological contaminants mainly have effect on the biological film of sediment particles. In the polluted water, due to excess nutrients, the biological film resulted from the microbial activity on the surface of sediment has effect on and can change the motion characteristics of sediment.

Fang Hongwei et al. studied the changes in the motion characteristics of the sediment particles with biological film, including start, settling and so on. In the test of analyzing the settling of the sediment particles with biological film, they measured the size of the particles and the changes in settling speed through image analysis and deduced calculation formula of the settling speed of the sediment with biological film. The study shows that biological film has changed the surface characteristics of particles a lot. It increases the resistance to settling of particles. Compared with the sediment particles with the same size without biological film, its settling speed decreases remarkably.

Anderson et al. think the structure and composition of the community in water may have effect on the nature of sediment particles and have an important effect on settling of sediment particles through measured data and studied the effect of microbes' waste on the settling speed of erosion substance on the intertidal riverbed. Stal explored the effect of microbes and their waste on intertidal sediment.

In conclusion, the existing results show that the effect of pollutants on the behavior of sediment in natural water environment, especially in the polluted water isn't allowed to neglect. There is little research into other aspects.

## 4 FUTURE PROSPECT

At present, the research into the effect of pollutants on sediment is still not sufficient and further study need to be made.

1. The research into pollutant absorption on the surface of sediment particles at the micro-scale mainly focuses on heavy metal copper and nutrients such as phosphorus. There is little research into other heavy metal, organic pollutants, especially refractory organics. In the future, we should make more research into the

effect of different kinds of pollutants on the surface characteristics of sediment and set up more perfect interactive mechanism between sediment and pollutants.

2. The research into the effect of pollutants on the motion characteristic of sediment mainly focuses on the effect of pollutants on flocculating, settling, start and flowing speed of sediment. There is no research into scouring and silting deformation of sediment and we should strengthen the research into this aspect.
3. The previous research objects are limited to some common pollutants. But there are various pollutants in water, such as some new organic pollutants, plasticizers, surfactants, antibiotics, spices, cosmetics and so on. These new organic pollutants have complicated compositions, which have complicated effect on the motion characteristics of sediment. For example, different organic pollutants carry different charges. After they are absorbed by sediment, they can increase the flocculating speed of sediment and also may promote the dispersion of sediment, leading to more complicated effect on the motion of sediment.

## REFERENCES

- Chen H.S., Shao M.A. Effect of CaCl<sub>2</sub> on fine sediment flocculation and settling in still water [J]. *Journal of Soil and Water Conservation*, 2000(3):46-49.
- Chen H.S., Shao M.A. Effects of AlCl<sub>3</sub> on fine flocculation and settling [J]. *Advances in Water Science*, 2001(6):445-449.
- Chen M.H., Fang H.W., Chen Z.H. Experiment of phosphorus distribution on sediment surface. *Journal of Sediment Research* 2009, (4):51-57.
- Chen Z.H., Fang H.W., Chen M.H. Experimental research into the change in the surface of pores of fine sediment after absorption, *Journal of Sediment Research* 2010(1):25-29.
- Fang H.W., Chen M.H., Chen Z.H. Analysis of mechanical properties of surface pore of sediment before and after pollution [J]. *Science in China (Series G: Physics, Mechanics & Astronomy)*, 2008, 38(6):714-720.
- Fang H.W., Zhao H.M., He J.G., Chen M.H. Experiment of particles' morphology variation after biofilm growth on sediments. *Journal of hydraulic engineering*, 2011, 42(3).
- Huang L., Fang H.W., Chen M.H., Zhao H. Review of surface charge characteristics of fine sediment [J]. *Journal of tsinghua university (Science & technology)* 2012, 52(6):747-752.
- Jiang G.J., Yao Y.M., Tang Z.W. The analysis for influencing factors of fine sediment flocculation in the Changjiang Estuary [J]. *Acta Oceanologica Sinica*, 2002(7):51-57.
- Jin Y., Wang Y.G., He J. Experimental study on flocculation of cohesive fine grain sediment at Yangze River Estuary [J]. *Journal of Hohai University*, 2002(5):61-63.

- Liu L., Chen L., Wang J.S., He J. Effect on the flocculation sedimentation velocity in different conditions of cation concentration by concentration of sediment particles [J]. *Engineering Journal of Wuhan University (liberal arts ed.)*, 2007, 40(1):29–32.
- Stumm W. *Chemistry of the solid-water interface* [M]. New York: John Wiley and Sons, Inc, 1992.
- Tang H.X., Qian Y., Wen X.H. *Characteristics and control technology principle of aquatic particles and recalcitrant organic matters (Volume I Aquatic particles)* [M] Beijing: China Environmental Science Press, 2000.
- Wang C.C., Juang L.C., Hu T.C., et al. Adsorption of basic dyes onto montmorillonite [J]. *Journal of Colloid and Interface Science*, 2004, 280:27–35.
- Wang J.S., Chen L., Wang Z.G., Huang R.M. Study on the fine sediment settling velocity formula with the parameter of  $\text{Ca}^{2+}$  concentration. *Advances in Water Science*.
- Wang Y.L., Yu F.L., Wang D.S. et al. Fractal-like adsorption kinetic characteristics of dye compounds onto granular activated charcoal [J]. *Acta Scientiae Circumstantiae*, 2005, 25(5):643–649.
- Xiao Y., Lu Q., Cheng H.K., Zhu X.L., Tang H.W. Surface properties of sediments and its effect on phosphorus adsorption. *Journal of Sediment Research*, 2011(6): 64–68.
- Zheng Y.Q., Wang Y.L., Lu J. et al. Fractal characteristics of adsorption of direct dye compounds onto clay particles [J]. *Acta Scientiae Circumstantiae*, 2008, 28(4):634–646.

# Discussion of the quality and safeguard measures of secondary water delivery

Wei Zhang

*College of Municipal and Mapping Engineering, Hunnan City University, Yiyang, China*  
*College of Civil Engineering, Hunan University, Changsha, China*

Yumei Deng & Aihe Wang

*College of Municipal and Mapping Engineering, Hunnan City University, Yiyang, China*

**ABSTRACT:** The secondary water delivery is the important part of the urban water supply and the problem becomes more and more prominent. In this paper, with the factual example of national secondary water supply, the pollution reasons of secondary water supply are analyzed, and the measures for preventing the pollution of secondary water supply are proposed to satisfy the safety of residents drinking water, including improving the pipe network capacity, and regulating the design, construction and management.

**Keywords:** secondary water delivery; water quality pollution; prevention measures

## 1 INTRODUCTION

With the rapid development of China's economy and urbanization, more and more high-rise buildings have appeared, and the level of building water supply, drainage systems and construction equipment will be achieved a higher degree<sup>[1]</sup>. However, many weaknesses in security and stability exposed of the secondary water quality, it attracts more and more public attention. The definition of secondary water supply is that the water from urban public water supply facilities and self-built water facilities is provided for residents by special pipes after storage, compression, advanced treatment and disinfection. Water supply system must ensure adequate water supply to the users and adequate water pressure and also make sure that water meets state drinking water health standards. Now the construction and management of secondary water supply facilities attract more and more attention, and branch end of water distribution system is the truly reflection of the water quality. Therefore the quality assurance system establishment of the secondary water supply is the key mission for the safety of drinking water<sup>[2,3]</sup>.

## 2 EXAMPLE OF THE NATIONAL URBAN SECONDARY WATER SUPPLY AND THE WATER QUALITY EFFECTS

Until the end of 2010, in order to ensure water quality, Shanghai had renovated the secondary water

supply pipe network of residential area before 1997, and the water quality remains improving. However, the quality indexes of water in the secondary, such as sensory color and iron had increased, but the amplitude of residual chlorine tanks was reduced. The water quality deteriorates if it is kept in the tank for a long time. Meanwhile more study and discussion on secondary water supply facilities, capital and property measurement issues needs to be conducted, as well as secondary water supply facilities and management duties.

There were 386 residential areas requiring secondary water supply, 1472 tanks and 344 pools, and the number of users who need secondary water supply was 40% of the total residential users in zhuhai. First, the design of secondary water supply facilities was not rational, with a larger water reservoir, easily to increase the water retention time; second, the pools and water tanks used concrete structure, without appropriate treatment for the inner wall; Finally, operational management was not well, for example pools and water tanks were not cleaned regularly and disinfected, and the inlet holes of pool was damaged or none.

Since 2003, the Wenzhou water company investigated and transformed the secondary water supply facilities, tank construction materials, and the health conditions of water tanks in the urban areas. On the basis of ensuring the water quality, the secondary water disinfection team was established to disinfect the secondary water supply facilities by free. Meanwhile, the secondary water

supply company was also established to manage the received secondary water supply facilities, and combined the reform of “a water meter for one family”. Through these measures, the passing rate of secondary water quality in Wenzhou had become more than 98% by 2006.

### 3 REASONS OF THE SECONDARY WATER POLLUTION

The main problem of secondary water supply is the low pass percent of water quality, and the pass rate without secondary disinfection is only 60% to 70%<sup>[4,5]</sup>. The main pollution sources are ponds and water tanks, and the main pollutants are visible substances, bloodworms, turbidity, microorganisms, organic matter, chlorine and chlorine byproducts<sup>[6,7]</sup>.

The main reasons of pollution are design, construction, pipe materials and management.

#### 3.1 *Design and construction reasons*

##### 3.1.1 *Unreasonable technological design*

Because of improper tank design, the water will be easily “dead”. For example, part of the high water tank volume is too large, which makes water demand greater than domestic consumption. Therefore, the time of the water in the tank is over the theory time. The level of some pool tank is higher than the outlet, as a result that the water cannot be drained. In addition, the inlet pipe and pump suction tube pool are located in the same position, which make the water in the other end of stagnant water fostering a lot of plankton.

##### 3.1.2 *Unreasonable construction and structure*

Now the construction is not standardized, the current urban secondary water supply facilities needn't be required the license of the technical standards, the engineering drawings lack, the health awareness is weak, construction is not satisfied with hygiene requirements, construction are multi-contracting, and engineering quality is difficult to guarantee. According to specification for design of indoor water supply and drainage, life impounding reservoir should be far away from septic tanks of water storage tank, such as kitchen, toilet hygiene (>10 m), to prevent contamination of the drinking water. And the water pump room decorate also have certain requirements. But in the process of construction, real estate developers who want to save costs, are not according to the standard construction, leading to underground cisterns improper site selection, septic tanks and cisterns, mutual penetration, or pump room space is too small, the distance between the equipment

and pipeline cannot meet the specification requirements, and brings to the maintenance of equipment and system are difficult.

#### 3.2 *Unreasonable selection of pipe materials*

Some pipes in water supply system are using eliminated by national compulsory galvanized steel pipe which is easy to oxidizing reaction with water, corrosion fouling, leading the water quality pollution. But there is still a construction unit or develop commercial using cold galvanized steel pipe instead of hot dip galvanized steel pipe, and the leakage of the this tube is easy to burst, making the tap water polluted. Most of the roof water tank uses cement pavement with rough surfaces, providing the survival opportunity for algae and other biological, and lead-based ceramics lining would be harmful to human body.

#### 3.3 *Unreasonable management*

The reasons are as follows: lack of perfect health management system, no personnel management for the maintenance of the facilities, retired worker assumed for this task, a low professional quality, a big liquidity, and poor responsibility binding. Health and safety measures should be taken to ensure if the water tanks are cleaned and disinfected regularly.

According to the basic requirements of drinking water, cleaning the roof of the water tank is necessary atleast once in six months, but most of the water supply facilities are not provided to the secondary water disinfection facilities and equipment<sup>[7]</sup>.

## 4 PREVENTION MEASURES FOR SECONDARY WATER SUPPLY POLLUTION

#### 4.1 *Improve the pipe network and the carrying capacity*

It is needed to make a proper plan for water supply system, innovating the aging pipeline network, increasing the pump station and improving the network carrying capacity to make the pipe network pressure balanced, reducing the secondary water supply facilities. By these measures the problem of secondary water supply, water quality pollution will be solved at the source. Different water supply ways are adopted in building plot or high-rise buildings, and the different water supply pipeline is not with a direct connection to prevent the drinking water pollution by the non-drinking water<sup>[8]</sup>.



#### 4.2 *Regulate the design, construction and management*

Use separate life and fire-fighting pool construction, reasonable pool volume, reduce the stay time in the pool, and the location of the pool and the location of the in and out of the water pipe should be specific in strict accordance with the requirements of design. Use new type of feed water pipe, such as plastic pipe with good corrosion resistance and not easy to scale, keeping good health and long-term water performance. Construction unit must have the corresponding qualifications in strict accordance with the design requirements for construction, and reinforce the management of the construction process. Reform the original unqualified secondary water supply facilities, increasing the necessary disinfection equipment<sup>[9,10]</sup>.

#### 4.3 *Strengthen the facilities maintenance and management of secondary water supply*

Government departments should attach great importance to the management of secondary water supply, and formulate some corresponding regulations and institutions to strengthen the supervision of water supply facilities, regularly cleaning pool, and spottily check water quality. Reinforce the training for the management personnel to help them master the basic knowledge of water supply, preventing water quality pollution again because of improper management.

### 5 CONCLUSIONS

Secondary water supply is an essential part of the urban water supply. Therefore, to solve problems in secondary water supply is related to social stability, peace and contentment for people to live and work. Water quality of secondary water supply problems, whether the construction unit, design, construction and management departments, should be focused seriously, and comply with the relevant state laws and regulations. By these measures, the prevention of the water secondary water supply pollution will be ordering, scientific and legalization.

#### ACKNOWLEDGMENT

This research got the support from industry-university-research cooperation demonstration

base in colleges and universities of human province—the key technology integration for the safety of urban water supply.

#### REFERENCES

- [1] Rygaard M., Godskesen B., Jørgensen C., et al. Holistic assessment of a secondary water supply for a new development in Copenhagen, Denmark [J]. *Science of the Total Environment*, 2014, 497:430–439.
- [2] Yu Haixia, Zhang Deyue, and Chen Hao. Safeguard Measure for Secondary Supply Water Quality [J]. *China Water & Waste Water*, 2009, 25(2):84–86. (in Chinese).
- [3] Wang Jia, Han, Ling, Li Shushu. The collection system for residential recyclables in communities in Haidian District, Beijing: A possible approach for China recycling [J]. *Waste Management*. 2008, 28(9):1672–1680.
- [4] Zhang Kefeng, Liu Jindong and Wang Yonglei. Actualities of water recontamination in secondary watersupply and analysis of measures in prevention and treatment [J]. *Journal of Shandong University of Architecture and Engineering*, 2005, 20(3):49–51. (in Chinese)
- [5] Li M., Qiang Z., Bolton J.R., et al. UV disinfection of secondary water supply: Online monitoring with micro-fluorescent silica detectors [J]. *Chemical Engineering Journal*, 2014, 255:165–170.
- [6] Lixia Wu, Mingsheng Liu. Primary Chilled Water System Control Optimization Integrated with Secondary System Linearization—Part II: Field Investigation [J]. *ASHRAE Transactions*. 2014, 120(1):1–8.
- [7] Mengkai Li, Zhimin Qiang, Bolton, Janmes R et al. UV disinfection of secondary water supply: Online monitoring with micro-fluorescent silica detectors [J]. *Chemical Engineering Journal*, 2014, 255:165–170.
- [8] Yuan Li, Hongxiong Guo, Zhenghui Xu, et al. An outbreak of norovirus gastroenteritis associated with a secondary water supply system in a factory in south China [J]. *BMC Public Health*, 2013, 12(1):1–7.
- [9] Ng G.-H. Crystal, Bekins, Barbara A, Cozzarelli, Isabelle M, et al. A mass balance approach to investigating geochemical controls on secondary water quality impacts at a crude oil spill site near Bemidji, MN [J]. *Journal of Contaminant Hydrology*. 2014, 164:1–15.
- [10] Eisnor, John D, Gagnon, Graham A. Impact of secondary disinfection on Corrosion in a model water distribution system [J]. *Journal of Water Supply: Research & Technology-AQUA*. 2004, 53(7), 441–453.

# Model and application of pressure-dependent leakage detection in water distribution network

J.J. Wang

*School of Civil Engineering, Shandong University, Jinan, Shandong Province, P.R. China*

Z.Z. Tang

*Faculty of Arts and Creative Technologies, Staffordshire University, Stafford, Staffordshire, UK*

Y.W. Gui

*China Machinery International Engineering Design and Research Institute Co. Ltd., Nanjing, Jiangsu Province, P.R. China*

W.Y. Wu

*Faculty of Arts and Creative Technologies, Staffordshire University, Stafford, Staffordshire, UK*

M. Zhao

*School of Municipal and Environment Engineering, Harbin Institute of Technology, Harbin, Heilongjiang Province, P.R. China*

**ABSTRACT:** In order to quickly locate the leakage in urban water distribution network, a model of pressure-dependent leakage detection is developed based on the principle that the leakage is positively correlated with the pressure. Particle Swarm Optimisation (PSO) is applied to solve the model, and the feasibility of pressure-dependent leakage detecting method is verified by using a test function. Finally, the model is applied in the water distribution network of City A to locate leakage. As a result, simulating leakage nodes are located within the range of 125 m to 467 m from actual leakage nodes, which indicates that the developed model can significantly improve the efficiency of leakage detection.

**Keywords:** water distribution network; pressure-dependent leakage location; particle swarm optimisation; leakage node; location deviation

## 1 INTRODUCTION

Water is the life line of cities. Water distribution network is the imperative bridge for connecting the waterworks and end users. However, Leakage occurs frequently along the water pipelines because of inappropriate constructions, pipeline aging and corrosion etc. The 2009 Annual Report of Urban Water Distribution (2010) from the Ministry of Housing and Urban-Rural Development of the People's Republic of China indicated the average leakage rate could be as high as 21.5% in most cities in China, and the leaked water could be as high as 6 billion m<sup>3</sup> every year. Pipe leakage leads to not only treated water resources loss but also the waste of electricity for water treatment, which causes direct economic losses to the water companies. Moreover, the security of drinking water can be threatened by

contaminations on the leak points, and soil losses caused by leakage can make negative impacts on the safety of buildings and traffic and further the related personnel security. Therefore, it is necessary to quickly locate and control the leakage in the complex and belowground water distribution networks.

The core work is to detect the invisible leakage. The conventional leakage detection methods mainly include voice-listening method and district metering method. Both the two methods have considerable disadvantages. The voice-listening method needs plenty of manpower and material resources, which is not efficient. Whilst the district metering method requires the reconstruction of the present water distribution networks to deploy more flowmeters, which is time-consuming and not economically efficient. Wu and Sage (2006) invented a new leakage detection method based

on hydraulic model check in water distribution networks, and applied it to one city in the UK. However, this method requires high accuracy of the input data of the hydraulic model, such as the network topology, pipe property and the real time monitoring data. Dong et al. (2013) built a leakage location inverse problem optimised model for water distribution system, and give a solution based on genetic algorithm. However, this method relies on the accuracy of the real time monitoring data such as water pressure, flow etc. They only used lab simulating platform to verify their model but no further practical verification was made. This paper uses the positive correlation between the leakage and the water pressure to build the leakage location model. PSO is applied to solve the model. After the leakage region is quickly confirmed, traditional leakage detection instruments can be used for further detection around the nodes in the region. This method can significantly reduce the range of detection and enhance the efficiency.

## 2 PRESSURE-DEPENDENT LEAKAGE LOCATION MODEL

The leakage is positively correlated with the pressure. Zhang (2013) indicated leakage can be regarded as a model related to the pressure-dependent water demand. The model can be built by injection flow. The relation between injection flow and pressure is given in Equation (1).

$$Q_i(t) = K_i [P_i(t)]^n \quad (1)$$

where

$Q_i(t)$  is the total leakage of node  $i$  until the time  $t$ ;  
 $P_i(t)$  is the node pressure of node  $i$  at the time  $t$ ;  
 $K_i$  is the injection coefficient at the node  $i$ ;  
 $n$  is the leakage flow index.

The leakage flow index is in a range of 0.5~2.5 based on the different pipe materials. The detectable leakage of the metal pipes refers to the leakage flow index 0.5.

According to Equation (1), every node in the water distribution network has its own injection coefficient. When the injection coefficient at one node is a positive number, there is leakage at this node. When the injection coefficient at one node is zero, no leakage happens at this node. Therefore, it is essential to optimise the injection coefficient to justify whether the leakage happens. When the optimised injection coefficient is above zero at one node, this node is regarded as a leak node (leakage may exist at the pipeline connected with this node).

## 3 APPLICATION OF PSO

In 1995, Kennedy and Barnhart invented the PSO. It suits to solve some problems that cannot be solved by traditional optimisation algorithms.

### 3.1 The fundamental principles of PSO

PSO is introduced by simulating foraging behaviour of the bird flock. Wang et al. (2001) indicated that this process is facilitated by the environmental adaptation of the particles. Wang and Liu (2008) indicated that all the particles in the searching space could be the potential solution of the problem in the entire optimising process. Particles can use their location memorability and share their information to obtain the best location they experienced themselves and the best location they experienced in the flock. Then they can adjust their speed and go to the best solution. PSO is the process that the particles continuously learn from themselves and the neighbours.

### 3.2 The parameter settings of PSO

PSO has relatively fewer parameters and simpler process compared to traditional optimising algorithms. The parameters of standard PSO include the flock scale  $n$ , inertia weight  $w$ , study factors  $c_1$  &  $c_2$ , the maximum speed of the particles  $V_{max}$  and algorithm terminating conditions.

It is important to assign the value of the inertia weight in PSO because the inertia weight can decide the size of the impact of the last speed on the current one and affect the current moving direction of the particle. Chatterjee and Siarry (2006) indicated the introduction of the inertia weight is to balance the local searching capability and the overall searching capability in the algorithm. When  $w = 1$ , the algorithm is the fundamental PSO.

The flock scale is the number of particles in the searching space. There is no unified settings on the flock scale. The empirical flock scale is 20~40 in most situations.

Under normal circumstances, the values of study factors have the relation  $c_1 = c_2$ , and they are in the range 0~4.

The maximum speed of the particles decides the maximum moving distance of the particles at every step of iteration. In the beginning  $V_{max}$  is large, and the overall searching capability is high. Then in the process of iteration, the region of the best solution can be initially confirmed. Finally  $V_{max}$  decreases, and the local searching capability enhances, which lead to the fast converging to the best solution (Fan, 2002).

### 3.3 Test of PSO

#### 3.3.1 Ackley function

Ackley function is used to compare the calculation ability of PSO and Genetic Algorithm (GA) on it. Goldberg (1989) indicated that the most widely used evolutionary algorithm is the GA which is based on the rules of evolution and natural selection.

Ackley function is given in Equation (2).

$$f(x) = -20 \cdot e^{-0.20 \sqrt{\frac{1}{n} \sum_{j=1}^n X_j^2}} - e^{\frac{1}{n} \sum_{j=1}^n \cos(2 \cdot \pi \cdot X_j)} + 20 + e |X_i| \leq 32 \quad (2)$$

The least value of this function is zero at the point of zero.

$$\min(f(x_*)) = f(0, 0, \dots, 0) = 0 \quad (3)$$

There are many local minima on the chamber of Ackley function. If the searching space of traditional algorithms is too small, it is easy to sink into the local minima. However, if the searching space is too large, it is easy to jump over the valley and search the suboptimal solution. Therefore, Ackley function is the problem which is hard to overcome by using traditional optimising algorithms.

#### 3.3.2 Test result

The initial particle number is set to 50, and the study factors are 1.4 and 1.2 respectively for the PSO. Whilst for the GA, the initial population is set to 50, and the mutation probability is 0.2, and selection probability is 0.5, and terminating condition is that the row difference of the best solution is 1e-10, and the maximum iteration times are set 100 and 200 respectively.

Figure 1 and Figure 2 show that the adaptability function value changes with the iteration times by using PSO and GA to solve the Ackley function when the maximum iteration time is 100 and

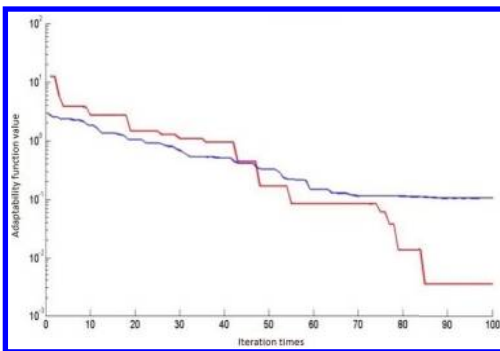


Figure 1. Maximum iteration times: 100.

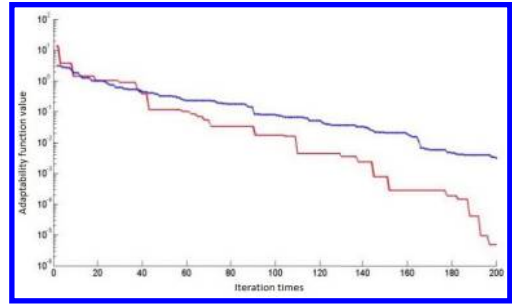


Figure 2. Maximum iteration times: 200.

200 respectively. When the maximum iteration time is set to 100 by using PSO, the best solution converges to 0.00352367. Whilst when the maximum iteration time is set to 100 by using GA, the best solution only converges to 0.10863. When the maximum iteration time is set to 200 by using PSO, the best solution converges to 4.82083e-6. Whilst when the maximum iteration time is set to 200 by using GA, the best solution only converges to 0.0032612.

Set to the same iteration times, the converging speed of PSO is faster than GA, and the optimal solution by using PSO is also nearer to the actual value than by using GA. Therefore, this paper selects PSO to solve the leakage model.

## 4 THE DEVELOPMENT OF PRESSURE-DEPENDENT LEAKAGE LOCATION MODEL

The solution of leakage location model is evaluated by objective function. Objective function is defined by the difference of the actual value and simulating value of node pressure and pipe flow. The smaller value of objective function is, the nearer between the simulating pipe operating condition and the actual pipe operating condition. During the operation of the water distribution network, flow and pressure are the most direct reflection of the pipe operating condition. In order to equally consider the pressure and flow, by using two self-defined transform parameter the pressure and flow can be transformed to no-dimensional values. Then optimisation can be implemented. The objective function is given by Equation (4).

$$F(\bar{X}) = \sum_{t=1}^T \left[ \sum_{nh=1}^{NH} W_{nh} \left[ \frac{H_{S_{nh}}(t) - H_{0_{nh}}(t)}{H_{pnt}} \right]^2 + \sum_{nf=1}^{NF} W_{nf} \left[ \frac{Q_{S_{nf}}(t) - Q_{0_{nf}}(t)}{Q_{pnt}} \right]^2 \right] \quad (4)$$

× NH + NQ

where

$H_{shh}$  is the simulating pressure of node  $nh$  at the time  $t$ ;

$H_{0nh}$  is the actual pressure of node  $nh$  at the time  $t$ ;

$Q_{snf}$  is the simulating flow of pipe  $nf$  at the time  $t$ ;

$Q_{0nf}$  is the actual flow of pipe  $nf$  at the time  $t$ ;

$H_{pnt}$  is the pressure transform factor;

$Q_{pnt}$  is the flow transform factor;

$NH$  is the number of pressure monitoring points;

$NQ$  is the number of flow monitoring points.

Therefore, leakage detection model can be concluded as

$$Mnimize : F(\vec{X})$$

where

$$\vec{X} = (LN_i, K_i), LN_i \in J, i = 1, 2, \dots, N \text{ Leak};$$

The constraint conditions are

$$0 \leq K_i \leq \bar{K}, 1 \leq i \leq n$$

$$P_i > 0, 1 \leq i \leq n$$

$$\sum \pm q_{ij} + Q_i = 0$$

$$\sum h_{ij} - \Delta H_k = 0$$

where

$K_i$  is the injection coefficient of node  $i$ ;

$n$  is the number of nodes;

$\bar{K}$  is the maximum injection coefficient of node  $i$ ;

$P_i$  is the pressure of node  $i$ ;

$Q_i$  is the flow of node  $i$ ;

$q_{ij}$  is the flow of the pipelines connected with node  $i$ , and  $i, j$  are the start and end number of pipelines;

$h_{ij}$  is the head loss of the pipeline in basic ring  $k$ ;

$\Delta H_k$  is the loop closure or the pressure difference caused by pressurizing and decompressing devices in basic ring  $k$ .

## 5 APPLICATION OF PRESSURE-DEPENDENT LEAKAGE LOCATION MODEL IN CITY A

### 5.1 Engineering background of City A

There are one raw water plant, seven waterworks in City A. The capability of daily water distribution is 1.05 million  $m^3$  and the actual output of supplying water is 0.7 million  $m^3$ . The waterworks mainly serve the main city zone, east and west area of the city. The total length of the water distribution network in City A is 3294 km. The maximum height difference of the city is over 100 metres because of the large height difference between north and

south areas. There are 30 pressure stations in the water distribution network, and approximately 500  $km^2$  area and 3.2 million people are served. This paper is proposed to focus on the leakage location model of one certain district in City A.

The sub-model of this district is showed in Figure 3. One water plant in this district includes 1,431 nodes, 2,079 pipelines, 6 pressure monitoring points and 5 flow monitoring points. All the monitoring points are remote communication meters, which can provide real time data. The pressure and flow monitoring points are showed in Figure 4.

### 5.2 Pressure-dependent leakage location

According to the record of pipeline maintenance in City A, leakage occurred on 2nd March 2013 and the leak point is showed Figure 5. Leakage detecting area can be initially confirmed based on the direct pressure and flow data. The whole water

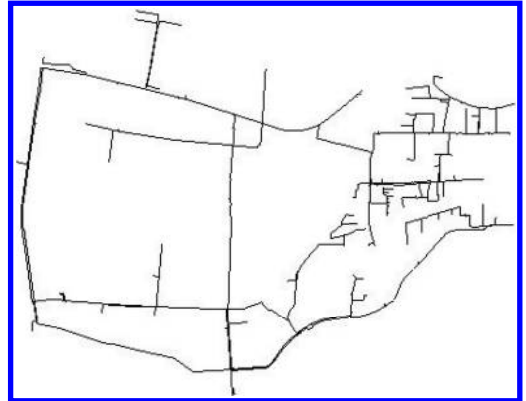


Figure 3. The sub-model of one certain district in City A.

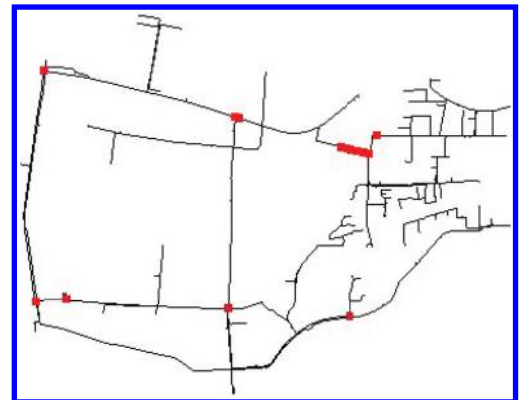


Figure 4. Pressure and flow monitoring points (showed in red colour).

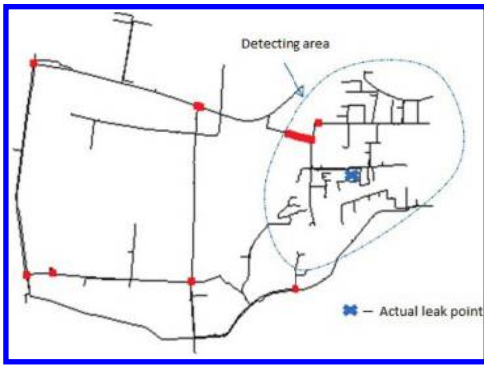


Figure 5. Leakage detecting area in the sub-model.

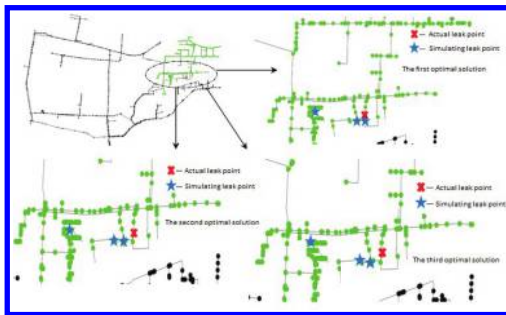


Figure 6. The first, second and third optimal solution.

distribution network can be influenced if leaking water quantity is high, so that it is easy to detect the leakage. This paper uses the monitoring data from the midnight to 4 a.m. for calculation because water consumption is low, pressure and leakage is high during this period. In the process of calculation, optimisation is implemented when the maximum leak points are 4, 2 and 1 respectively. Then the obtained optimal solutions are compared and analysed to accurately locate the leak points. In this area there are 6 pressure monitoring points and 5 flow monitoring points. 44 groups of data were obtained during this period, based on which PSO is implemented. The maximum iteration times are set to 100 and 200 respectively, and the number of particles are 100, and the study factors are set to 1.2 and 1.4 respectively, and the maximum moving speed is set to the 20% of the parameter changing range (that is 0.2).

### 5.2.1 The maximum leak points are 4

Initially the maximum leak points are set to 4, which is the number of the maximum leak points in the optimisation area are 4. The result keeps three optimal solutions showed in Figure 6 and Table 1, 2 and 3.

Table 1. The first optimal solution.

Node	Optimal injection coefficient	Distance to the actual leak point (m)	Value of objective function
Node 17015	0.288	125.299	0.086
Node 17750	0.254	200.96	
Node 13391	0.229	46.606	

Table 2. The second optimal solution.

Node	Optimal injection coefficient	Distance to the actual leak point (m)	Value of objective function
Node 17015	0.290	125.299	0.091
Node 15533	0.239	197.206	
Node 16541	0.238	217.046	

Table 3. The third optimal solution.

Node	Optimal injection coefficient	Distance to the actual leak point (m)	Value of objective function
Node 17015	0.290	125.299	0.103
Node 15533	0.238	197.206	
Node 17057	0.236	467.181	

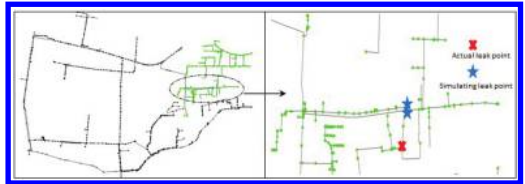


Figure 7. The first, second and third optimal solution.

Table 4. The first optimal solution.

Node	Optimal injection coefficient	Distance to the actual leak point (m)	Value of objective function
Node 12370	0.336	165.06	0.072
Node 12354	0.333	201.851	

### 5.2.2 The maximum leak points are 2

The maximum leak points are set to 2. The result keeps three optimal solutions showed in Figure 7 and Table 4, 5 and 6.

Through the analysis, when the maximum leak points are set to 2, the result of optimisation shows

Table 5. The second optimal solution.

Node	Optimal injection coefficient	Distance to the actual leak point (m)	Value of objective function
Node 12370	0.349	165.06	0.075
Node 12354	0.320	201.851	

Table 6. The third optimal solution.

Node	Optimal injection coefficient	Distance to the actual leak point (m)	Value of objective function
Node 12370	0.349	165.06	0.099
Node 12354	0.324	201.851	

Table 7. The first optimal solution.

Node	Optimal injection coefficient	Distance to the actual leak point (m)	Value of objective function
Node 4744	0.796	323.268	0.007

Table 8. The second optimal solution.

Node	Optimal injection coefficient	Distance to the actual leak point (m)	Value of objective function
Node 4744	0.792	323.268	0.011

Table 9. The third optimal solution.

Node	Optimal injection coefficient	Distance to the actual leak point (m)	Value of objective function
Node 12462	0.790	223.581	0.047

that Node 12370 and Node 12354 are always suspicious leak points.

### 5.2.3 The maximum leak point is 1

The maximum leak points are set to 1. The result keeps three optimal solutions showed in Table 7, 8 and 9 and Figure 8.

Pressure-dependent leakage location cannot exactly accurately locate the leak points, but it can find the district where leakage occurs. The actual leak points need to be confirmed by workers

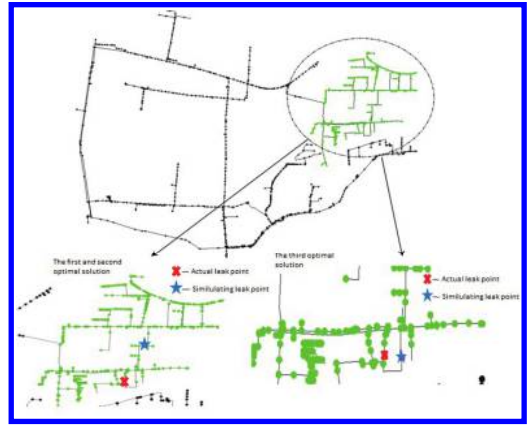


Figure 8. The first, second and third optimal solution.

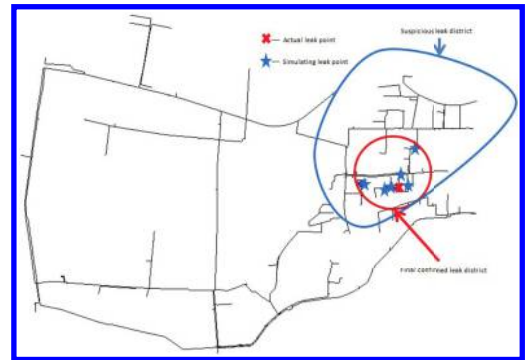


Figure 9. Comparison between the actual and simulating leak district.

using leakage detection devices. According to the result of optimisation, comparing the values of objective function when the maximum leak points are set to 4, 2 and 1 respectively, leak points can be confirmed in the area near Node 17015, 15533, 17750, 16541, 13391, 12462 and 4774. The distance of the nearest simulating leak point to the actual leak point is 125 m, and the farthest is 467 m. Therefore, the leak district can be confirmed as the circle area which the centre is the actual leak point and radius is 467 m, showed in Figure 9.

Shown in Figure 9, the blue district is the detecting area when traditional leakage detection methods are used. All the pipelines in this large area need to be detected if traditional leakage detection methods are used, so that both work and economic efficiency is low and it is a waste of manpower and material resources. The red circle district is the final confirmed leak district by using pressure-dependent leakage location method. Compared to

the blue district it is much smaller. Only the circle area which the centre is the actual leak point and radius is 467 m needs to be detected. Therefore, both detection and repairing efficiency is largely enhanced, and leakage is significantly reduced.

## 6 CONCLUSION

This paper builds pressure-dependent leakage location model based on the sub-model of City A, and PSO is applied to calculate the model. Calculation is based on the actual situation on 2nd March 2013. The maximum leak points are set to 4, 2 and 1 respectively and three optimal solutions are considered. Through analysis, the farthest distance from the actual leak point is 467 m, and the nearest is only 125 m. The leak district can be confirmed in the circle area which the centre is the actual leak point and radius is 467 m. Traditional leakage detection methods need workers to investigate in a large area. However, this method indicated in this paper significantly reduces the suspicious leak district, so that repairing time is reduced and efficiency is enhanced. Pressure-dependent leakage location method is relatively new compared to the conventional methods and the located leak district is relatively accurate. But the exact leak points still needed to be confirmed by using additional detecting devices.

## ACKNOWLEDGEMENT

The authors acknowledge the financial support of the China National Major Science and Technology

Programme for Water Research (2012ZX07404-003-017).

## REFERENCES

- Chatterjee A. and Siarry P. 2006. Nonlinear inertia weight variation for dynamic adaptation in particle swarm optimisation. *Journal of Computers & Operations Research*. Vol. 33(3), pp. 859–871.
- Dong S., Lv M., Sheng Z., Li P. 2013. Reverse question leakage location in water distribution network based on Genetic Algorithm. *Journal of Harbin institute of Technology*.
- Fan H. 2002. A modification to particle swarm optimization algorithm. *Journal of Engineering Computations*, Vol. 19(8), pp. 970–989.
- Goldberg E. 1989. *Genetic Algorithm in Search, Optimization and Machine Learning*, Boston, MA: Wesley Press.
- The 2009 Annual Report of Urban Water Distribution from the Ministry of Housing and Urban-Rural Development of the People's Republic of China. 2010. Beijing: China Architecture and Building Press.
- Wu Z. and Sage P. 2006. Water loss detection via genetic algorithm optimisation-based model calibration. *The 8th Annual International Symposium on Water Distribution Systems Analysis*. pp. 27–30.
- Wang Y., Li B., Weise T. et al. 2011. Self-adaptive learning based particle swarm optimisation. *Journal of Information Sciences*, Vol. 181(20), pp. 4515–4538.
- Wang L. and Liu B. 2008. *Particle swarm optimisation and scheduling algorithm*. Beijing, Tsinghua: University Press.



# Analysis on the status and measures of development and utilization of water resources in Lanling

X. Zhang, J.W. Huang, H.W. Chen & B. Li

*Water Research Institute of Shandong Province, China*

*Shandong Provincial Key Laboratory of Water Resources and Environment, China*

Z.H. Zhang

*Hydrology Bureau of Linyi, China*

**ABSTRACT:** Based on the basic situation of Lanling, water resources, water supply and use, and water utilization level were analyzed. Some engineering and management measures for promoting rational development and utilization of water resources were proposed for water resources development problems. These measures have certain significance for the rational water resources allocation.

**Keywords:** water resources; exploitation and utilization; the most strict water management system; water utilization level; measures

## 1 THE GENERAL SITUATION OF LANLING

Lanling is located in the south of Shandong province, southwest of Linyi. The total area is 1724 km<sup>2</sup>, accounting for 1.1 percent of the province's total area. It is located in the southern edge of the hilly area of Lunan, the north is hilly area, the south is plain area, and the terrain decreases from the northwest to southeast. Northern hilly areas are composed of the Cambrian, middle and lower Ordovician Limestone, shale formations. The formation of southern plain areas is friable rock of quaternary system. The sandstone thickness of quaternary groundwater is thickened from north to south, especially a large sand thickness in the southeastern.

It is warm temperate semi-humid monsoon climate zone in Lanling. It demonstrate typical characteristic of significant continental climate, discernible season, rain in hot season. The rivers belong to middle canal water system of Huaihe Valley. The main rivers are Taoye River, Yunnv River, Xijia River, and other twelve from west to east. The total length is 321.12 km. These rivers are shallow and swift. Most of rivers are seasonal. They import middle canal in Pizhou of Jiangsu Province flowing from north to south.

There are 17 towns (streets), 1024 administrative villages in Lanling. It has favorable natural conditions. The industrial and agricultural production is developing rapidly. It has formed the

industrial system currently. The leading industry is mining, building materials, food, machinery, chemicals, light industry etc. The total population is 127.54 million, county urbanization rate is 7.94%, the GDP is 27.156 billion yuan; industrial added value is 9.652 billion yuan; three industrial structure adjustment is 18:36:46; the per capita GDP is 23,133 yuan, and net income per capita is 10,323 yuan at the end of 2013.

## 2 THE SITUATION OF WATER RESOURCES

### 2.1 *Temporal and spatial distribution of water resources*

According to 55 years (1956–2010) of runoff, annual mean surface water resources is 557.43 million m<sup>3</sup>, and annual mean groundwater resources is 242.83 million m<sup>3</sup>. Apart from overlap counting, the annual total capacity of Lanling is 705.67 million m<sup>3</sup>.

The water resources of Lanling have several important features.

The distribution of precipitation is uneven throughout the year, 72.9% of which is concentrated in June to September, and monthly precipitation has larger difference. The change of precipitation among different years is large, and wet year and dry year are consecutive. Maximum annual precipitation is 40% larger than annual mean, and minimum annual precipitation is 55% of annual mean.

Modulus of surface water resources is 323300 m<sup>3</sup>/km<sup>2</sup>, modulus of groundwater resources is 140900 m<sup>3</sup>/km<sup>2</sup>, and surface water resources are relatively rich in Shandong province. The average person possession of water is only 541 m<sup>3</sup>, slightly higher than the average of Shandong province, just as 25% of our nation's. It belongs to water shortage area.

The time and spatial distribution of water resources is very uneven, which impacted by rainfall, geological structure, topography and geomorphology, and hydrogeology condition. In terms of surface runoff, relatively large difference between water resources formed by wet year and dry year. Shallow groundwater resources are mainly comprise the rain, river and irrigation seepage etc. It has a regulation in the year, annual distribution with small changes.

### 2.2 Water quality of water function area

According to "water function zoning of Shandong province," there are eight first-degree water functional areas and four second-degree water function areas. Water quality regular rate of water function area reach 100%, according to the water quality monitoring data of water function area in 2013.

## 3 PRESENT SITUATION OF EXPLOITATION AND UTILIZATION OF WATER RESOURCES

### 3.1 Water supply project and quantity

It has 135 water storage projects, including a large reservoir, 4 medium-sized reservoirs, 41 small reservoirs, 92 embankments in Lanling. The current supply capacity of water storage project is 53.39 million m<sup>3</sup>. The county has four water diversion projects, diversion size is 1.2 m<sup>3</sup>/s, and the current supply capacity is 12.3 million m<sup>3</sup>. The total amount of surface water development and utilization was 73.04 million m<sup>3</sup>, the utilization ratio was 13.1% in 2013.

There are 2828 shallow groundwater matching electromechanical wells with 59.2 million m<sup>3</sup>/a supply capacity in Lanling, mainly used for industrial production, agricultural irrigation and domestic water supply for urban residents. The total amount of groundwater development and utilization was 59.2 million m<sup>3</sup>, the utilization ratio was 24.4% in 2013.

A sewage treatment plant was built in 2006, with a capacity of treat municipal sewage up to 13.02 million tons, load operation rate of 88%.

The annual average water supply quantity of 5 years (2009~2013) is 136.57 million m<sup>3</sup>. The surface water is 73.87 million m<sup>3</sup>, and groundwater is 62.7 million m<sup>3</sup>. The supply quantity of water storage project

is 52.14 million m<sup>3</sup>, water diversion is 20.21 million m<sup>3</sup>, and mention water is 6.77 million m<sup>3</sup>. The supply quantity of shallow groundwater is 59.91 million m<sup>3</sup>, and deep groundwater is 2.61 million m<sup>3</sup>. The surface water supply is 54.09% of the total water supply, and groundwater is 45.91%.

### 3.2 Water consumption and utilization structure

Water consumption of Lanling includes farmland irrigation, farming, forestry, animal husbandry, and fishery, industry, town public, resident living and ecological environment, etc.

The average water consumption of Lanling from 2009 to 2013 is 135.7 million m<sup>3</sup>. Among them, farmland irrigation is 82.09 million m<sup>3</sup>, farming, forestry, animal husbandry and fishery is 50.6 million m<sup>3</sup>, industry 8.35 million m<sup>3</sup>, town public 5.46 million m<sup>3</sup>, resident living 28.1 million m<sup>3</sup>, ecological environment 9.28 million m<sup>3</sup>, account for total water consumption 60.49%, 3.73%, 6.15%, 4.02%, 20.71%, 6.84%, respectively.

### 3.3 Control targets of the most strict water management system

#### 3.3.1 Control targets of the total water use quantity

The surface water, groundwater index allocated to Linyi by Shandong Province were 1.546 and 0.492 billion m<sup>3</sup> respectively, and the total was 2.605 billion m<sup>3</sup>. The surface water, groundwater index allocated to Lanlin were 0.094 and 0.063 billion m<sup>3</sup> respectively, and the total was 0.157 billion m<sup>3</sup>. (see Table 1).

The total amount of water use is not exceed control targets of the total water use quantity in Lanling in 2013. But groundwater water utilization is 59.2 million m<sup>3</sup>, and it is close to the upper limit of control targets. The local surface water supply is 73.04 million m<sup>3</sup>. There is a certain margin in the total amount control targets of surface water.

#### 3.3.2 Control targets of the water use efficiency

In 2015, the control targets of water consumption of 10,000 Yuan industrial added value decreases 14% compared to 2010. It drops to 14.19 m<sup>3</sup>. The water consumption of 10,000 Yuan industrial added value is 9.14 m<sup>3</sup>, less than control targets.

Table 1. Control targets of the total water use quantity in Lanling in 2013. (billion m<sup>3</sup>).

Administrative area	Surface water	Groundwater	Total
Linyi	1.546	0.492	2.038
Lanling	0.094	0.063	0.157

### 3.3.3 Limit pollutant control targets of water function area

Limit pollutant control targets of water function area COD is 1216.91t/a, and NH<sub>3</sub>-N is 60.38t/a in Lanling. The measured value of COD and NH<sub>3</sub>-N are 230.97t/a and 7.89 t/a respectively in 2013. They meet the limit pollutant control targets of water function area.

## 3.4 Analysis of supply and demand balance

### 3.4.1 National economic indicators

In recent years, economy has developed rapidly in Lanling. The economic development indicators are shown in Table 2.

Table 2. Economic development indicators in Lanling.

Level years	2013
<i>Population (people)</i>	
Urban population	9.85
Rural population	117.69
Total population	127.54
Industrial added value (Yuan)	96.50
<i>Irrigation area (Mu)</i>	
Paddy field	1.60
Irrigated land	16.68
Vegetable fields	23.30
Subtotal	41.58
Fruit irrigated area (Mu)	2.18
<i>Livestock (Ten thousand head)</i>	
Big livestock	2.05
Small livestock	56.05

Table 3. Water requirement in Lanling.

Level years	2013
City Life water requirement (million m <sup>3</sup> )	10.95
Rural life water requirement (million m <sup>3</sup> )	23.80
<i>Livestock (Ten thousand head)</i>	
Big livestock	0.30
Small livestock	4.09
Industrial water requirement (million m <sup>3</sup> )	8.82
<i>Agricultural water requirement (million m<sup>3</sup>)</i>	
50%	109.58
75%	130.37
95%	130.37
Ecological environment water requirement (million m <sup>3</sup> )	14.03
<i>Total water requirement (million m<sup>3</sup>)</i>	
50%	171.57
75%	192.36
95%	192.36

### 3.4.2 Water requirement

Water requirement by various sectors of the national economy is obtained by economic development indicators and water quota in 2013. Agricultural water requirement of 95% guaranteed rate is consistent with guarantee 75%. The total water requirement is the sum of water requirement in various sectors of the national economy and water requirement of ecological environment.

### 3.4.3 Calculation of supply and demand balance

Table 4. Water supply and demand balance analysis and calculation in Lanling in 2013.

Level years	Guaranteed rate	Available water supply (million m <sup>3</sup> )	Water demand (million m <sup>3</sup> )	Deficiency (million m <sup>3</sup> )	Water shortage degree
2013	50%	157.33	17.157	-14.24	-8.30%
	75%	151.76	192.36	-40.60	-21.11%
	95%	142.91	192.36	-49.45	-25.71%

50%, 75%, 95% guaranteed rate, there is a water shortage, mainly for agricultural water.

## 3.5 Water utilization level and efficiency

The total water use quantity is 132.24 million m<sup>3</sup>, water consumption of 10,000 Yuan GDP is 48.7 m<sup>3</sup>, water consumption of 10,000 Yuan industrial added value is 9.14 m<sup>3</sup>, repeated use rate of industrial water is 60%, utilization efficiency of irrigated water is 0.55, water saving irrigation rate is 23%, irrigation consumption of water per mu of farmland is 96.42 m<sup>3</sup>, leakage rate of city's water supply systems is 10%, urban life comprehensive water quota is 150 L per person day, centralized sewage treatment rate is 75%, and water quality double-index regular rate of water function area reach 100%. The total water use quantity, water use efficiency (water consumption of 10,000 Yuan value added, utilization efficiency of irrigated water), limit pollutant indicators of water function area meet the most strict water management system. There is a gap between some indicators and water-saving society control target demands of Shandong province.

## 4 THE MAIN PROBLEMS EXISTING IN THE DEVELOPMENT AND UTILIZATION OF WATER RESOURCES

### 4.1 Water project are not fully unrealized

The supporting construction of water conservancy project has lagged behind in the body and affected

the overall effectiveness for a long time. Most water supply projects built in the 1950s and 1960s is still in disrepair. Much of them are in extended use or ill run. The engineering maintenance costs are inadequate because of the low water price for a long time. Further sedimentation and water pollution are affecting the water supply project benefits seriously.

It should increase investment in water supply project to achieve the desired results.

#### 4.2 *Water utilization is not high*

People's awareness of the water is not clear and water-saving awareness is weak because water resource fee and water fee are persistently low. The utilization efficiency of irrigated water and repeated use rate of industrial water are low. Many residents have not used water-saving appliances. Industry, agriculture and life have a greater life saving potential.

Industrial water save is strengthened by optimizing the industrial structure and layout and speeding up the elimination of backward high-water technology, equipment and product to promote water-saving technology and equipment and other measures. Agricultural water-saving engineering is promoted by speeding up the adjustment of agricultural structure and developing characteristic agriculture. Domestic water is saved by the renewal and transformation of water supply network, reducing the leakage rate, implementing "one family, one table, measuring out the door" reform, trying out ladder water prices, strengthening life water-saving appliances certification, establishing market access system for water-saving products, and enhancing the people's awareness of water saving to achieve the purpose of water saving.

#### 4.3 *There are different levels of water contamination*

With the continuous development of social economy, waste water which is unable to handle and directly into waters is increasing each year. It causes a lot of water pollution and water environment deterioration.

Most rivers are polluted to different degrees currently. Water pollution has infiltrated from the surface to the underground. Control and management of the sewage outfall into the river are strengthened in view of existing situation, in order to reach the standard of water function area, protect, and improve surface water environment.

## 5 MEASURE OF EXPLOITATION AND UTILIZATION OF WATER RESOURCES

### 5.1 *Engineering measures*

On the basis of the existing water conservancy project, as much as possible surface water resources

are remained by strengthening the management of water conservancy projects, optimizing water supply dispatching, carrying out the use of rain floods, improving the utilization of surface water under the premise of meet downstream ecological, strengthening soil and eater conservation in the upper basin, carrying out small watershed management, increasing vegetation and water conservation, constructing reservoirs, ponds, and sluice and dam, in order to store runoff and increase infiltration.

Groundwater supply quantity assumes 45.9 percent of total water supply in Lanling in 2013. It has abundant multi-year regulating characteristic, and plays an important role in the supply pattern. Groundwater is actively protected and rationally explored, accordance with the "overall balance, control overexploitation, regional adjustment, wet season recharge" principle. Groundwater exploitation should be strictly controlled in the range of allowable exploitation by reasonably adjusting groundwater extraction layout and constructing recharge project, in order to gradually achieve rational development, control mining, leave room, and virtuous circle.

Unconventional sources include wastewater reuse, mine water use and rainwater storage and utilization. The sewage treatment and reuse should be increased further, and effluent from sewage treatment plant should be treated profoundly. It is widely used in the less quality demand water such as industrial cooling water, dust, miscellaneous municipal water, irrigation, and other water. The mine is widely distributed in Lanling, with large displacement and use potential. The main pollutants are SS. It can be directly used for industrial production and agricultural irrigation by simple process. Moreover, the construction of rain collection should be carried out according to local conditions, on the base of full using terrain and geological conditions. Rainwater is stored as much as possible by combining small watershed comprehensive management project in the mountainous areas. Rainwater through the housing, space, roads, and other venues are collected in other regions.

### 5.2 *Management measures*

Water resources development or inter-basin water transfer cannot solve fundamentally the increasingly outstanding water shortage problem, in the case of limited total water resources and growing demand for water.

Therefore, we must implement the most stringent water management system, establish, and implement three red lines of water resources management around water resources allocation, conservation and protection, strictly implement

total water control, curb unreasonable demand for water, strengthen water resources unified deployment capability, build a water-saving society, strengthen water demand management, take the content development, strengthen supervision and management of water function area, control the total amount of sewage into the river, promote the protection and restoration of aquatic ecosystems, improve water resources management system, lead the transformation of water resources management approach, and perfect policies and regulations and social supervision mechanism.

The contradiction between water supply and water demand will be effectively alleviated through engineering and management measures in Lanling, with the sustainable use of water resources to support and ensure sustainable economic and social development.

## ACKNOWLEDGMENTS

This work was financially supported by the Ministry of Water Resources' Special Funds for Scientific Research on Public Welfare (201401003) and the Ministry of Water Resources' Technology Extended Plan Projects (TG1407).

## REFERENCES

- [1] Water function zoning of Shandong province. (in Chinese). (2006).
- [2] Water quality monitoring report of water function area in Linyi (in Chinese). (2013).
- [3] Statistical yearbook in Linyi (in Chinese). (2014).
- [4] Water resources bulletin in Linyi (in Chinese). (2013).
- [5] Comprehensive planning of water resources in Shandong Province (in Chinese). (2007).

# Stochastic optimal operation and improved multi-objective particle swarm algorithm for water supply and environment

J. He, S.P. Gu & W.X. Tan  
Hohai University, Nanjing, China

**ABSTRACT:** To alleviate the threat of water shortage and water pollution with economic development, we need to enhance the capacity of the water supply guarantee and environmental protection. Multi-objective optimal operation of Projects is an effective approach. This paper defines indicators and multi-objective functions to coordinate water supply and environment. With stochastic runoff, the method in this paper is to pre-define operation rules of power function and find out optimal parameters. On this basis, the stochastic optimal operation model is established. And the improved multi-objective particle swarm optimization is given. Example of verification gives the satisfactory results. It is proved that the method is reasonable and efficient.

**Keywords:** stochastic optimal operation; multi-objective particle swarm optimization; water supply; environment

## 1 INTRODUCTION

### 1.1 Background

With the acceleration of urbanization, Chinese water resource problems include water shortage and water pollution, etc. In addition to natural conditions and social reasons, reservoirs have not played potential to make the water supply and environment objectives optimal.

### 1.2 Solutions

The first solution in this paper is formulating reasonable water supply indicators and water environment indicators. It is useful to build multi-objective functions. The second difficulty is that hydrological factors are stochastic; it is hard to forecast for a long time. To solve it, optimal rules of power function are designed in this paper. It is more scientific to make stochastic optimal rules instead of assuming that the runoff is certain. At last the improved multi-objective particle swarm optimization algorithm is established. It is more adaptable and effective to solve the model than the traditional dynamic programming.

## 2 DEFINITION OF OPERATION RULES WITH STOCHASTIC RUNOFF

### 2.1 Progress in the field

The long-term optimal operation of reservoirs can be categorized into two: the explicit stochastic

optimization and the implicit stochastic optimization. The former takes Markov Decision Plan as the basic model. There is obstacle for a large number of reservoirs. The implicit stochastic optimization method was proposed by Young first in 1967<sup>[1]</sup>, including two steps<sup>[2]</sup>: a) based on the runoff series measured or generated by Monte Carlo method, apply deterministic operating optimization technology obtain a long-term strategy; b) in the results, using regression analysis to design operating rules.

With development of optimization technology, it also can be pre-defined scope of the rules, and then use simulation and optimization to find the optimal rule. It is consistent with the essence of stochastic optimization operations. In this paper, we are using this method.

### 2.2 Rules pre-defined

Stochastic optimal operation is the optimal rule<sup>[3]</sup> of reservoirs with stochastic runoff. Generally, the decision variables described as a function of the state vector, Assuming, the period is one month, one year is divided into 12 periods. At the beginning of each month, the state variable is the amount of water in the reservoir. Decision variable is the amount of water retained in the reservoir of the end of the month. Now, the monthly runoff is random. So the decision is not definitive, but a rule. Rule is described as a power function defined in [Equation 1](#).

$$X_i = \alpha_i (S_i + Q_i)^{\beta_i} + \varepsilon \quad (1)$$

where  $X_i$  = the amount of water retained in the reservoir at the end of the period  $i$ ;  $S_i$  = the amount of water in the reservoir at the beginning of the period  $i$ ;  $Q_i$  = the inflow to the reservoir in the period  $i$ ;  $\alpha_i$ ,  $\beta_i$  = undetermined parameters;  $\varepsilon$  = random error.

In the long series, the initial water level of the reservoir is uncertain, which can cause errors in the first year benefit assessment. The first solution is to calculate the different strategies under different initial water level, but the solution is not unique. The second is, the first year is not involved in the assessment, but the data is wasted. The third is, the initial water level is optimized, when constraint is that the water level at the end of December last year must equal to the initial level. It can be achieved by penalty function method. See Equation 2.

$$S_0^{(1)} = S_n^{(N)} \quad (2)$$

where  $S_0^{(1)}$  = the initial water level in the first year;  $S_n^{(N)}$  = water level at the end of December last year.

### 3 DEFINE WATER QUALITY INDICATORS AND WATER QUALITY MODEL

#### 3.1 Water quality reaching standard degree

Water quality reaching standard degree is defined as the closeness to the standard (such as Class III water) in this paper. Water quality indicators are too many to be controlled. Key indicators must be controlled. It is better to choose  $COD_{Mn}$  as the representative of the pollution indicator for river water quality. See Equation 3.

$$\varphi = \begin{cases} \frac{\mu_a^*}{x} & x > \mu^* \\ 1 & x \leq \mu^* \end{cases} \quad (3)$$

where  $\varphi$  = the degree of water quality reaching standard;  $x$  =  $COD_{Mn}$  concentration,  $mg/l$ ;  $\mu^*$  =  $COD_{Mn}$  concentration of class III water standard,  $mg/l$ .

This approach allows the flexibility to choose the target water quality standards in accordance with local current situation or water functional area requirements, so as to effectively guide the behavior of water resources management.

#### 3.2 Water quality model

Since the model is designed to optimize strategies statistically to control the average concentration

of pollution, so one-dimension stable river water quality model are adaptable. See Equation 4.

$$C = C_0 e^{-k_1 \frac{x}{u}} \quad (4)$$

where  $C$  = concentration of pollutants downstream section,  $mg/l$ ;  $C_0$  = concentration of pollutants upstream mixing section,  $mg/l$ ;  $u$  = flow rate of the river,  $m/s$ ;  $x$  = distance from the downstream section to the upstream section,  $m$ ;  $k_1$  = pollutant degradation rate constant.

## 4 MULTI-OBJECTIVE OPTIMIZATION OPERATION MODEL

### 4.1 Definitions of water supply objective function

Water supply guarantee degree is defined as indicator. Water supply guarantee degree equals to ratio of water supply and water demand, and equals to 1—water shortage rate. Few if dry months, take the minimum value of the year as an indicator of the year, because the monthly balance is important. Then the objective function is established as the average of the series of water supply guarantee. See Equation 5.

$$\max G = \frac{1}{Y} \sum_{y=1}^Y \min_{t \in 1-T}^{(y)} \frac{\sum_k (u_k^{(t)} + g_k^{(t)})}{R^{(t)}} \quad (5)$$

where  $G$  = multi-year average degree of water supply guarantee;  $Y$  = years of long series runoff;  $y$  = number of year;  $T$  = months of a year;  $t$  = number of month;  $k$  = number of reservoirs;  $R^{(t)}$  = water demand in month  $t$ ,  $10^6 m^3$ ;  $u_k^{(t)}$  = water supply of reservoir  $k$ ,  $10^6 m^3$ ;  $g_k^{(t)}$  = water supply of the others, such as underground water,  $10^6 m^3$ .

### 4.2 Definitions of water environment objective function

The water environment objective function is used as controlling indicators of each river section and each period. See Equation 6. Take the geometric mean to raise the low end value.

$$\max \Phi = \frac{1}{Y} \sum_{y=1}^Y \frac{1}{T} \sum_{t=1}^T \frac{1}{L} \sum_{l=1}^L \varphi_{ytl} \quad (6)$$

where,  $\Phi$  = multi-year average of water quality reaching standard degree.  $\varphi_{ytl}$  = the degree of water quality reaching standard at section  $l$  in month  $t$  of year  $y$ .

### 4.3 Constrains

The main constraints include the water balance of each reservoir, the limit of capacity, the limit of the river flow, the water yield of each sub-basin, groundwater resources, water demand in each district, outfall location and emissions of pollutants, and so on.

## 5 IMPROVED MULTI-OBJECTIVE PARTICLE SWARM ALGORITHM

### 5.1 Improved iteration format

Particle swarm optimization algorithm, PSO, is a computational technique based on swarm intelligence evolution. According to Equation 7, 8, each particle determine itself speed and position of the search space.

$$v_{t+1} = wv_t + c_1 \text{rand}() (p_t - x_t) + c_2 \text{rand}() (g_t - x_t) \quad (7)$$

$$x_{t+1} = x_t + v_{t+1} \quad (8)$$

where  $w$  = the inertia constant;  $c_1$  = learning constant;  $\text{rand}()$  = random numbers on  $[0,1]$  uniformly distributed;  $P_t$  = time  $t$  their own the best position, fitness is  $p_{best}$ ;  $g_t$  = time  $t$  global optimum location, fitness is  $g_{best}$ .

It is found that these parameters need to be debugged. This is because the constraint of operation of reservoir is more complex. After debugging and summary, we found an improved format, more suitable for reservoir optimal (see Equations 9 and 10).

$$v_{t+1} = w[v_t + c_1 \text{rand}() (p_t - x_t) + c_2 \text{rand}() (g_t - x_t)] \quad (9)$$

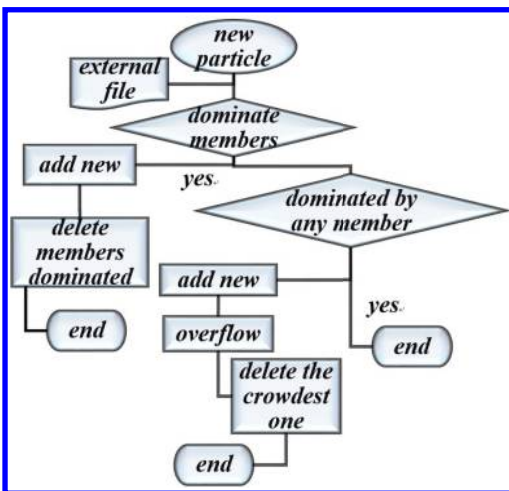


Figure 1. Algorithm for external file manage.

$$w = \begin{cases} 1 & K\%10 < 5 \\ 0.618 & K\%10 \geq 5 \end{cases} \quad (10)$$

where  $K$  = the number of iterations completed; % denotes a remainder operation.

### 5.2 Design of multi-objective particle swarm algorithm for external file

In the multi-objective iteration, the best position is not always with each other without domination. MOPSO of elite strategy is more advanced algorithms. External file update algorithm shown in Figure 1.

## 6 EXAMPLES

### 6.1 Introduce

Shimantan Reservoir and Tiangang Reservoir are located in the Huaihe River basin, upstream of Xiaohonghe River, Huaihe River tributaries. Shimantan reservoir catchment area is  $230 \text{ km}^3$ , total capacity is  $120 \times 10^6 \text{ m}^3$ , and normal capacity is  $63 \times 10^6 \text{ m}^3$ . Tiangang Reservoir at a distance of 5 km from Shimantan Reservoir. The normal capacity is  $8.9 \times 10^6 \text{ m}^3$ . Two reservoirs are connected in series.

Based on hydrology data from 1997 to 2006, upstream basin of Shimantan Reservoir annual average precipitation is 1049 mm. The reservoir annual average inflow is  $84.57 \times 10^6 \text{ m}^3$ . The reservoir's water supply coverage is shown in Figure 2. Reservoirs provide living water, industrial water, agricultural water, and ecological water.

Some companies and factories discharged a large number of untreated wastewater directly. According to the monitoring data, environmental monitoring stations show that in March 1996 at the monitoring section water quality indicators of Chemical Oxygen Demand (COD), permanganate index ( $\text{COD}_{Mn}$ ) exceeded rate is 100%. Main tributaries

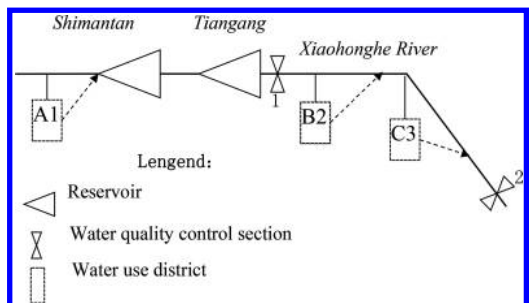


Figure 2. Reservoirs, water use districts, and water quality control sections.



of Huaihe River upstream, the Xiaohonghe water pollution is most serious.

### 6.2 Calculation results analysis

According to MOPSO, improved program was developed with c/c++ language. Data input included monthly runoff, water demand, and emissions information. The Pareto frontier was gained successfully. See Figure 3.

From Pareto front obtained and uniformly select a few typical scenarios, with the base scenario compared in Table 1. From Table 1, optimal scheduling efficiency goals in water supply is not, mainly because the region does not substantially dry, most of the year is a guarantee of 100%. Increased potential is very limited. In terms of water quality improving more obvious, COD<sub>mn</sub> concentration decreased from 25 mg/l to 15 mg/l nearby, and III water standard is close to 10%. This suggests that environmental objectives optimal operation of water is effective. Stochastic optimization rules determined scheduling is credible. On the whole, the solution 3 significantly improved the water quality, but also to ensure water supply guarantee degree, the solution is worth to be recommended. Evaluate

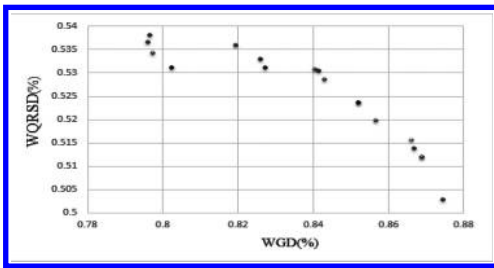


Figure 3. MOPSO Pareto frontier. Where WQRSD is water quality reaching standard; WGD is water guarantee degree.

Table 1. Optimization solutions comparison.

Solutions	Water supply (10 <sup>6</sup> m <sup>3</sup> )	Ave.* GD*	Min GD*	COD <sub>Mn</sub> (mg/l)	RSD*
Basic solution	373	98.6%	83%	25.0	45.4%
Opt. solution 1	363	97.2%	88.9%	19.1	52.8%
Opt. solution 2	362	96.0%	89.4%	17.4	55.6%
Opt. solution 3	362	95.6%	88.6%	14.7	58.4%
Opt. solution 4	360	95.1%	84%	15.2	60%
Opt. solution 5	355	93.7%	82.1%	14.6	60%

\*Ave. = Average; GD = Water Guarantee Degree; RSD = Water Quality Reaching Standard Degree.

## 7 CONCLUSION

This paper established a water supply and environmental objectives stochastic optimal operation model, and improved iteration format and effectiveness of multi-objective particle swarm algorithm. The advantage is that water supply and environmental indicators easy to coordinate, both of which are relative indicators. Flexibility is enough in the choice of Water quality standards according to the actual situation. Second, stochastic optimization operation model concluded realistic, direct search optimization rules, more simple than regression analysis to determine the rules, but also more logical. Third, the improved multi-objective particle swarm algorithm is suitable for solving the problem of reservoir operation. It is proved that good results are achieved in the Examples.

## REFERENCES

Young G.K. 1967. Finding Reservoir Operating Rules. ASCE. HY6.

Dariane A.B, 2009. Momtahn S. Optimization of multi-reservoir systems operation using modified direct search genetically algorithm [J]. Journal of Water Resources Planning and Management. 135(3):141–148.

Wang Jinlong. 2014. Huang Weibin, Ma Guangwen, etc. Derivation of optimal operating rules for cascade hydropower Stations based on projection pursuit regression model [J]. Journal of hydroelectric engineering. 01:50–57.

Huang Cao, Wang Zhong jing, Li Shu-fei, Chen Su-li. 2014. A multi-reservoir operation optimization model and application in the upper Yangtze River Basin (I): Principle and Solution of the Model [J]. Journal of hydraulic engineering. 10:1175–1183.

Liu Xinyuan, Guo Shenglian, Liupan, Guo Fuqiang. 2009. Study on the optimal operating rules for cascade hydropower stations based on output allocation model. Journal of hydroelectric engineering. 03:26–31+51.

Guo Xuning, Hu Tiesong, Huang Bing, Han Yichao. 2011. Joint operation rules for multi-reservoir water supply system based on the model of simulation and optimization. Journal of hydraulic engineering. 06:705–712.

Wang Xingju, Zhao Ranhang. 2003. Theory of optimal reservoir dispatching with multi-objective and its application hydrology [J]. Journal of hydraulic engineering. 03:104–109.

Wang Jinlong, Huang Weibin, Ma Guangwen, Zhao Yunfa, Tan Lei. 2015. Derivation of optimal operating rules for cascade hydropower stations based on projection pursuit regression model [J]. Journal of hydroelectric engineering. 02:37–43+63.

Wang Xingju, Zhao Ranhang, 2003. Theory of optimal reservoir dispatching with multi-objective and its application. Journal of hydraulic engineering. 03:104–109.

# Influence of moisture gradient to concrete strength based on Weibull statistical model

D. Zheng & Q. Chen

*Department of Hydraulic Engineering, Chongqing Jiaotong University, Chongqing, P.R. China*

S.W. Chen

*Guangdong Jindonghai Group Co. Ltd., Shantou, P.R. China*

**ABSTRACT:** The Influence of moisture gradient to concrete strength are investigated in this paper based on Weibull statistical model. The mechanism of how concrete strength is by influence moisture is discussed and the surface energy need to form new microcracks decrease are adopted in this paper. The moisture distribution in concrete is calculated by solving partial different equation. The global elastic modulus and strength reduction of concrete strength element are determined. The relationship between wet concrete strength and the time concrete immersed time is obtained. The comparison between the results by the model proposed in this paper and those by experiments in some available references indicates a good agreement.

**Keywords:** concrete; moisture gradient; strength; Weibull

## 1 INTRODUCTION

Concrete structures such as dams, bridges piers and ship locks, are often working in water environments. Researches have shown that the mechanic properties of concrete were influenced by moisture content. Saturated concrete has higher elastic modulus and lower strength compared with dry concrete. However, the influence of moisture to concrete strength has not been taken into account in structures design nowadays. Hence, it is quite important to make researches on wet concrete and provide more precise parameters for concrete structures design and safety evaluation.

Since the elastic microscopic theory of anisotropic composite material are well developed, elastic modulus of concrete with different porosity and moisture content can be analyzed. However, the mechanism of moisture influence to concrete strength is not very clear and no consensus has yet been reached. There are mainly 2 representative explanation of moisture dependency of concrete strength: (1) incompressible pore water pressure wedged into the cracks, which helps to microcracks propagation, (2) moisture decreases the surface energy need to form new microcracks.

Most research are focused on concrete strength without moisture gradient, i.e. fully dry or fully saturated concrete. However, the moisture gradient will influence concrete strength too. Experiments

of Li have shown that concrete strength when changed with immersed time. Guo attribute the influence of moisture content to different deformation between inner and outer concrete.

In this paper, the moisture distribution in concrete is calculated by solving partial different equation and the global elastic modulus and strength reduction of concrete strength element are determined. The relationship between wet concrete strength and the time concrete immersed time is obtained. The influence of moisture gradient to wet concrete strength is researched in this paper based on Weibull statistical model.

## 2 MECHANISM OF MOISTURE CONTENT INFLUENCE TO CONCRETE STRENGTH

At the base of aforementioned theoretical and experimental research, The mechanism of how concrete strength is influenced by moisture is assumed to be lower surface energy need to form new microcracks.

Firstly, experiments showed that tensile strength of concrete will be influence by moisture content. However, pore water pressure is in proportion to concrete volumetric deformation, which means water content will reduce concrete strength even when pore water pressure cannot be generated.

It also should be mentioned that volume of concrete will increase when the external compressive loading approaching its strength, which is called dilation material. At that moment, pore water pressure cannot be generated either. Therefore, pore water pressure theory cannot explain existed experiments and cannot represent physical mechanism of water influence to concrete strength. Secondly, experiments of cement-based material liquids with different surface tensions showed that strength of mortar decreases linearly with increases in the surface tension of immersion liquid.

Basically, the fracture process of concrete at the macro scale is the generation and propagation of internal microcracks. Strain energy will be stored in concrete when loaded, and parts of strain energy will be released as surface energy in the form of microcracks when the value of the strain energy reaches the limit. According to Griffith (1920), when the value of the released strain energy becomes equal to the surface energy on the new microcracks, the microcracks stop growing. However, further increases in loading result in further accumulation of strain energy. When the value of the strain energy reaches the limit again, microcracks are formed and released again. Through a repetition of these processes, the microcracks accumulated and resulted in the damage in the concrete till final failure. Thus, concrete strength is highly related to microcracks evolution and directly influenced by surface energy of microcracks.

$$\sigma_c = \sqrt{\frac{2E\gamma}{\pi c}} \quad (1)$$

where  $c$  is crack half length,  $E$  is elastic modulus of cracked material and  $\gamma$  is the surface energy of material.

It should be mentioned that Griffith's theory deals with a situation in which tensile force works on an ideal crack. On the other hand, it is thought that the fracture process of concrete under uniaxial compression is the generation and propagation of many microcracks and that several fracture modes are mixed. Thus, the theory cannot be applied directly to the compressive fracture process of concrete. However, it can be applied to research concrete strength variation with different moisture content.

On the other hand, according to Young's equation, solid-liquid interface energy is equal to the difference between solid and liquid surface energies as given by

$$\gamma_{sl} = \gamma_s - \gamma_l \cos \theta \quad (2)$$

where  $\gamma_{sl}$ ,  $\gamma_s$  and  $\gamma_l$  are energy of solid-liquid interface, solid surface and liquid surface respectively,

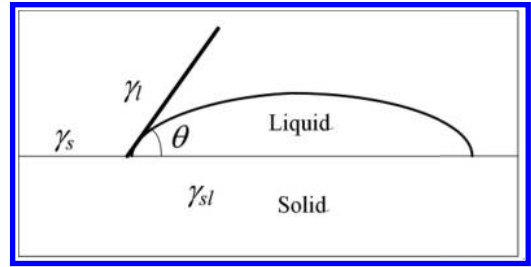


Figure 1. Surface energy of solid-liquid surface schematic diagram.

$\theta$  is contact angle of solid-liquid surface, as shown in Figure 1.

It showed that immersed time will influence wet concrete strength too. For concrete are anisotropic material, it can be assumed that in microscopic level, the element strength are different. Under external loading, concrete failure will happen at the lowest strength. Since the moisture distribution are not uniform in concrete, which makes the surface energy decrease are different too. When concrete are shrinked in water, the outside contact with water and will be saturate very fast, however, the diffusion process will last for a long time, which makes internal keeps dry and the origin strength. Hence, the strength reduction due to water is different in non-saturated concrete, which makes the failure mode differ too.

In this paper, a probability model is establish to analyze the moisture dependent of concrete strength considering the heterogeneity and moisture gradient of concrete.

### 3 MOISTURE DISTRIBUTION IN CONCRETE

#### 3.1 Moisture distribution in concrete

The sorption of pore material like concrete can be theoretically described by Darcy's law. The govern equation of the moisture distribution in concrete can be expressed as:

$$\frac{\partial \theta}{\partial t} = \Delta [D(\theta)\Delta \theta] \quad (3)$$

where  $\theta$  is relative moisture content,  $D$  is diffusion coefficient, which is function of relative moisture content  $\theta$ . For simplification, the problem is ideal as axial symmetries. Then equation can be expressed as:

$$\frac{\partial \theta}{\partial t} = \frac{1}{r} \frac{\partial}{\partial r} \left[ r D(\theta) \frac{\partial \theta}{\partial r} \right] \quad (4)$$

Table 1. Surface energy of cement paste under different humidity.

Moisture content	0	20%	50%	70%	85%	100%
surface energy/ mJ · m <sup>-2</sup>	72.17	41.89	31.35	32.49	29.80	28.2

Since concrete has been completely dried before immersed in liquid, it can be regarded that the initial moisture content is 0 and concrete outer surface are completely contacted with water. Hence, the initial and boundary condition can be showed as:

$$\begin{cases} \theta = 0 & t = 0 \\ \theta = 1 & r = R \end{cases} \quad (5)$$

Researches by Leech showed that can be expressed as exponential function or power function, it can represents water sorption in concrete.

$$D(\theta) = D_0 e^{n\theta} \quad D(\theta) = D_0 \theta^r \quad (6)$$

where  $D_0$  and  $\theta$  are parameters calibrated from experiments. The power function are adopted in this paper. Because the sorption coefficient are not constant, the govern equation are nonlinear partial difference equation, and it is almost impossible to achieve the theoretical solution. Normally, a numerical method in needed to solve the equation.

### 3.2 Influence of moisture to surface energy

The surface energy of concrete is difficult to measure. However, Adolphs (2005) measured the surface energy of cement paste at different moisture content with inverse gas chromatography method, which is shown as Table 1.

Hence, experiments of Adolphs can be utilized to analyze the relationship between moisture content of strength of cement-based material.

## 4 INFLUENCE OF MOISTURE CONTENT TO CONCRETE STRENGTH

### 4.1 Introduction of weibull strength model

As is well known, the Weibull distribution has been found to successfully describe a large body of brittle materials failure process. It is often supposed that a small volume in a brittle material is like a chain of many links, and if any link breaks, then the whole material will fail. Based on this weakest-link principle and an empirical function, the cumulative probability of failure of a brittle material

subjected to a load  $s$ , i.e., the Weibull strength distribution can be represented as:

$$F(u) = 1 - \exp\left[-\left(\frac{u}{\mu_0}\right)^m\right] \quad (7)$$

where  $\mu_0$  and  $m$  are Weibull parameters. Without loss of generality, it is supposed that  $\mu_0 = 1$  and eqa. (7) can be transformed as:

$$F(u) = 1 - \exp(-u^m) \quad (8)$$

Under the acting of stress, the failure probability of a chain with  $N$  links can be expressed as

$$\Phi(y) = 1 - [1 - F(u)]^N \quad (9)$$

The strength expectation is:

$$\sigma_N = \int_{-\infty}^{+\infty} u \, d\Phi(u) = Nm \int_{-\infty}^{+\infty} u^m e^{-Nu^m} \, du \quad (10)$$

Introduce  $Nu^m = x$ , Eqa. (10) can be simplified as:

$$\sigma_N = N^{-1/m} \Gamma\left(1 + \frac{1}{m}\right) \quad (11)$$

where  $\Gamma$  is Gamma Function. When the water gradually diffused into internal concrete, it decrease the surface energy of crack and micro element strength in concrete.

### 4.2 Concrete strength with moisture gradient

During the process of moisture diffusion, the moisture content varied with its location. For simplification, it is assumed a cylindrosymmetry model. Therefore, during the diffusion process, the relative moisture concrete at the same distance to the cylinder centre is the same. The element strength reduction coefficient at radius  $r$  can be expressed as  $0 < f(r) \leq 1$ ,  $0 \leq r \leq R$ , the Weibull strength distribution at radius  $r$  can be represented as:

$$F'(u) = 1 - \exp\left[-\left(\frac{u}{f}\right)^m\right] \quad (12)$$

the failure probability of a chain with  $N$  links can be expressed as:

$$\Phi'(u) = 1 - \prod_{i=1}^N \left[ \exp\left[-\left(\frac{u}{f_i}\right)^m\right] \right] \quad (13)$$

Eq. (13) can be simplified as:

$$\Phi'(u) = 1 - \left[ \exp(-u^m) \right]^{\sum_{i=1}^N f_i^m} \quad (14)$$

Eq. (14) can be transform as when  $N$  is big enough:

$$\Phi'(u) = 1 - \left[ \exp(-u^m) \right]^{N'} \quad (15)$$

where

$$N' = \frac{N}{R} \int_0^R f^{-m}(r) dr \quad (16)$$

Suppose  $r = Rdt$ ,  $g(t) = f(r/R)$ :

$$\frac{\sigma'_N}{\sigma_N} = \left[ \frac{1}{R} \int_0^R f^{-m}(r) dr \right]^{-1/m} = \left[ \int_0^1 g^{-m}(t) dt \right]^{-1/m} \quad (17)$$

Therefore, if the element strength reduction  $f(r)$  is known, the non-saturated concrete strength reduction can be achieved with Eq. (17). For saturated concrete, the relative moisture content is 1,  $g(t) = k$  from Eq. (17),  $\sigma'_N/\sigma_N = k$ .

## 5 NUMERICAL RESULTS AND DISCUSSION

To verify the accurate of difference equation and, the water diffusion in cement pasted is solved and the results are compared with existing experiments. The parameters used are as following:  $n = 4$ ,  $D_0 = 4.5 \text{ mm}^2/\text{s}$ ,  $x = 225 \text{ mm}$ ,  $m = 3$ .

The moisture distribution in cement pasted is showed in Figure 1 along with experiments. The moisture content in the experiments is achieved by NMR test. It can be seen from Figure 2 that the model proposed in this paper can describe moisture content distribution in concrete well.

Figure 3 shows relative moisture distribution in concrete at different time. It can be seen from Figure 3 that, the relative moisture near concrete surface reach saturate rapidly, however, inner concrete still dry, and increasing gradually with moisture diffusion process until it became saturate. If concrete immersed in water for more than 14 days, concrete will be saturated for inner side to outer side.

Figure 4 shows the relation between immersed time and concrete strength reduction along with experiments in reference in Li (2004). It can be seen from Figure 4 that the results correlate well with experiments. The strength of wet concrete

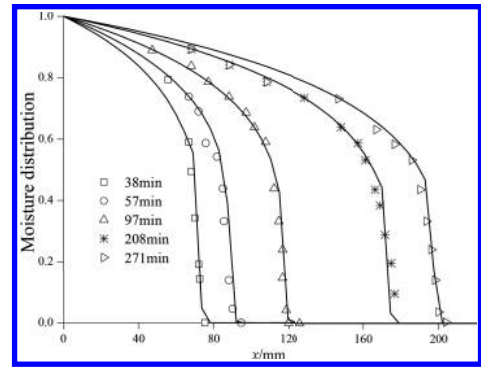


Figure 2. Moisture distribution in concrete.

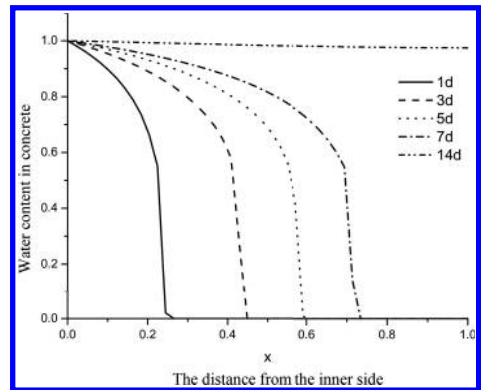


Figure 3. Water content in concrete with different immersed days.

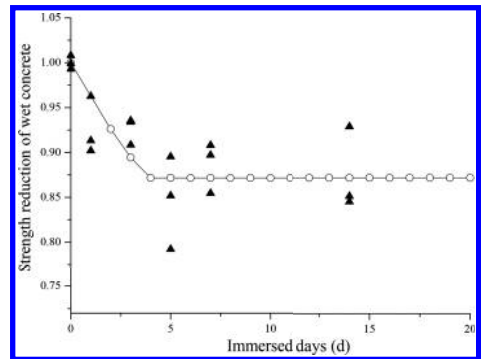


Figure 4. Strength reduction of concrete with different immersed days.

decreased with water diffusion. At the beginning of water contact with concrete, only surface concrete and with water diffused into concrete inner, its moisture content increased and saturated at 8~10 day, concrete strength became stable.

## 6 CONCLUSIONS

Water immersed into concrete can result in decrease of material surface energy, which will decrease concrete strength according to Griffith fracture mechanics.

By analyzing the mechanism of various influence factors to concrete strength, it is considered that immersion liquid reducing concrete surface energy is the main factor causing the wet concrete strength decrease. Based on solid diffusion, fracture mechanics and statistics strength theory, the moisture distribution and compressive strength of concrete under different moisture gradient are analyzed. The influence parameters on concrete strength are also discussed.

## ACKNOWLEDGEMENTS

This work was partly supported by Science Foundation of China Ministry of Transport (grants No. 2012319814210).

## REFERENCES

- [1] Mehta P.K., Nonteiro P.J.M., 1997. Concrete Microstructure Properties and Materials. Indian Concrete Institute.
- [2] Guo J.S., Waldron P. 2001. An elastic model to quantify the effect of moisture on the mechanical properties of concrete at the time of test. Magazine of Concrete Research, 53(3):151–162.
- [3] Li G., 2004. The effect of moisture content on the tensile strength properties of concrete [D]. University of florida.
- [4] Wittmann, F.H., Sun Z. & Zhao T., 2010. Surface energy and fracture energy. The 7th International Conference on Fracture Mechanics of Concrete and Concrete Structures. Jeju (Korea):13–18.
- [5] Matsushita H., Onoue K., 2006. Influence of Surface Energy on Compressive Strength of Concrete under Static and Dynamic Loading. Journal of Advanced Concrete Technology, 4(3):409–421.
- [6] J. Adolphs, 2005. Surface energies of hardened cement paste depending on relative humidity. Materials and Structures, 38:443–448.

*Disaster prevention and mitigation*

# The positioning performance comparison of BeiDou-2 second stage and GPS in some typical regions at home and abroad

Hou-pu Li

*Department of Navigation, Naval University of Engineering, Wuhan, China*

He-peng Cheng

*Chongqing Bureau, Equipment Department of the Navy, Chongqing, China*

Guo-li Feng

*College of Electrical Engineering, Naval University of Engineering, Wuhan, China*

**ABSTRACT:** In order to master the positioning performance of the Beidou-2 second stage, the “5GEO+3IGSO+27MEO” BeiDou global constellation using STK software is simulated. Based on this simulation, the satellite visibility and GDOP (Geometric Dilution of Precision) value in some typical regions such as Beijing, Wuhan, Sanya, Guam, New York and Victoria Island are systematically analyzed. The analysis results are compared with that of GPS, which shows that the numbers of visible satellites and the GDOP values of BeiDou-2 second stage are better than that of GPS in these regions, and the positioning performance of BeiDou-2 second stage needs to be increased in the high latitude and west hemisphere regions.

**Keywords:** BeiDou satellite navigation; typical foreign regions; STK; visibility; GDOP

## 1 INTRODUCTION

The development of Chinese navigation satellite system follows the “three step” strategy, that is, “the demonstration system, the regional system, and the global system” (Yang et al. 2014). The demonstration system is also called BeiDou-1 Satellite Navigation System. The stages of the BeiDou-2 Satellite Navigation System construction are divided into two stages, namely, the BeiDou-2 first stage (the regional navigation system) and the BeiDou-2 second stage (the global navigation system). With the launch of the last GEO satellite on October 25, 2012, BeiDou-2 first stage had been successfully established, which consists of 14 satellites, including 5 GEO (Geostationary Orbit) satellites, 5 IGSO (Inclined Geosynchronous Orbit) satellites, 4 MEO (Medium Orbit) satellites. It is quite important to master the characteristic and positioning performance of the BeiDou-2. Some researchers have done a lot of work about the satellite visibility and GDOP (Geometric Dilution of Precision) of BeiDou-2 first stage, which shows that the performance of BeiDou-2 first stage in Positioning, Navigation, and Timing (PNT) has reached or even exceed the design specification (Yang, 2010; Montenbruck et al. 2013; Li, 2013). But little work has been done about BeiDou-2 second stage. Here we mainly describe the

positioning performance of BeiDou-2 second stage, and give detailed analysis about the comparison of BeiDou-2 second stage and GPS in some typical regions at home and abroad.

## 2 THE SIMULATION OF BEIDOU-2 SECOND STAGE AND GPS CONSTELLATIONS

The BeiDou-2 second stage consists of 30 satellites, including 5 GEO (Geostationary Orbit) satellites, 3 IGSO (Inclined Geosynchronous Orbit) satellites, 27 MEO (Medium Orbit) satellites. GPS

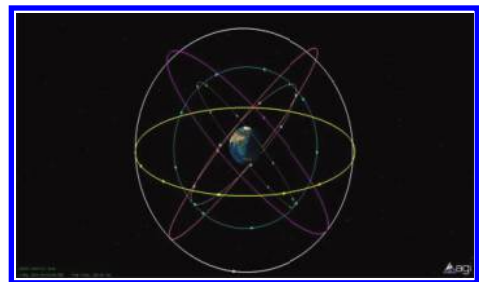


Figure 1. The three-dimensional scene of Beidou-2 second stage constellation.



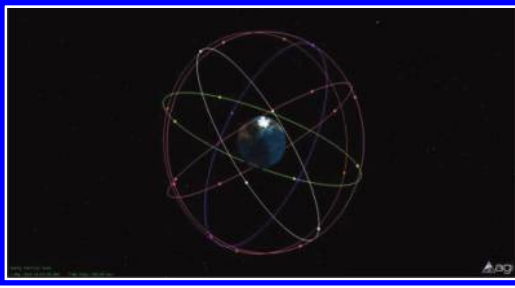


Figure 2. The three-dimensional scene of GPS constellation.

consists of 24 MEO satellites. The Beidou-2 second stage and GPS constellations are constructed with the help of STK (Satellite Tool Kit) software. Their space three-dimensional scenes are shown in Figure 1 and Figure 2 respectively.

### 3 THE POSITIONING PERFORMANCE COMPARISON OF BEIDOU-2 SECOND STAGE AND GPS IN SOME TYPICAL REGIONS AT HOM

Parameters used to indicate the positioning performance mainly include the satellite visibility and GDOP, which could help us master the positioning effect and provide reference for the practical application. These can be obtained using “Coverage Definition” and “Figure of Merit” modules in STK. Assuming the simulation time is from 12 o’clock 1 May 2014 to 12 o’clock 2 May 2014, Beijing (39.55°N, 116.24°E), Wuhan (30.35°N, 114.17°E) and Sanya (18.14°N, 109.31°E) are chosen as the typical regions at home. Taking Beijing as example, the total numbers of visible Beidou-2 second stage and GPS satellites are shown in Figure 3 and Figure 4, while the GDOP values are shown in Figure 5 and Figure 6 respectively. The statistics of visible satellites and GDOP values of Beidou-2 second stage and GPS are listed in Table 1 and Table 2 respectively.

From Table 1 and Figure 2, one could find that the visible satellites of Beidou-2 second stage are much more than that of GPS, while the GDOP value of Beidou-2 second stage is less than that of GPS at home.

### 4 THE POSITIONING PERFORMANCE COMPARISON OF BEIDOU-2 SECOND STAGE AND GPS IN SOME TYPICAL REGIONS AT ABROAD

Assuming the simulation time is from 12 o’clock 1 May 2014 to 12 o’clock 2 May 2014, Guam (14°N,

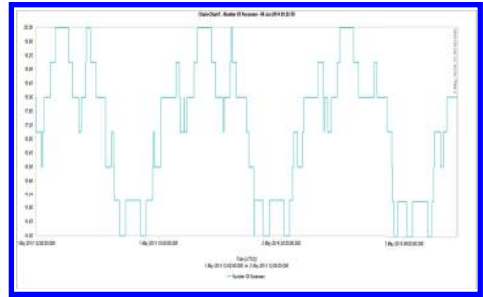


Figure 3. Total numbers of visible Beidou-2 second stage satellites in Beijing.

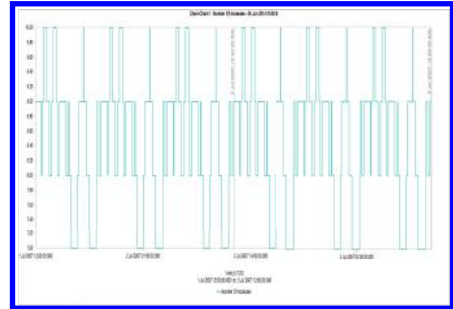


Figure 4. Total numbers of visible GPS satellites in Beijing.

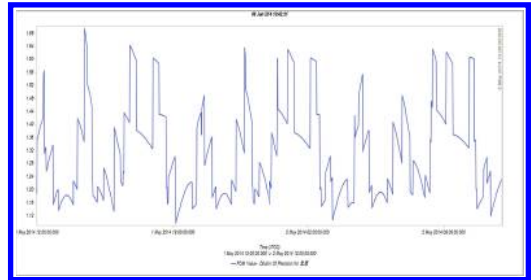


Figure 5. GDOP values of Beidou-2 second stage in Beijing.

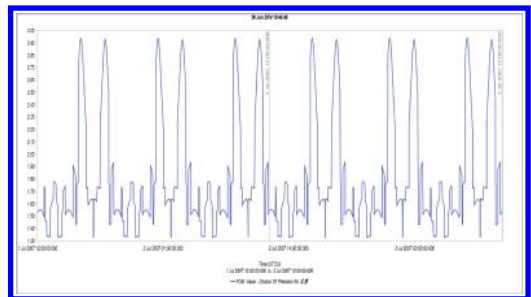


Figure 6. GDOP values of GPS in Beijing.

Table 1. Comparison of total numbers of visible Beidou-2 second stage and GPS satellites at home.

Facilities	Beidou-2 second stage/GPS		
	Min	Max	Mean
Beijing	14/7	20/10	17.5/8.5
Wuhan	13/7	19/11	16.8/9
Sanya	16/7	20/11	18.5/9.4

Table 2. Comparison of GDOP values of Beidou-2 second stage and GPS at home.

Facilities	Beidou-2 second stage/GPS		
	Min	Max	Mean
Beijing	1.09/1.33	1.70/2.94	1.31/1.82
Wuhan	1.25/1.25	2.16/3.00	1.49/1.7
Sanya	1.00/1.32	1.64/2.79	1.25/1.66

in Figure 9 and Figure 10. The statistics of visible satellites and GDOP values of Beidou-2 second stage and GPS are listed in Table 3 and Table 4 respectively.

From Table 1 and Figure 2, one could find that the visible satellites of Beidou-2 second stage are

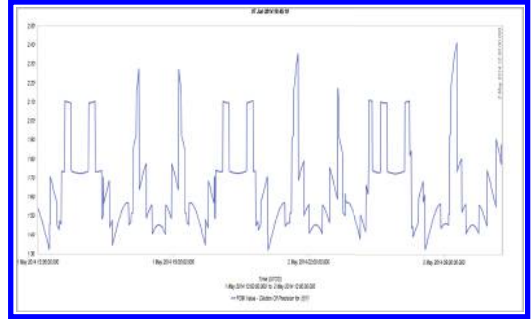


Figure 9. GDOP values of Beidou-2 second stage in New York.

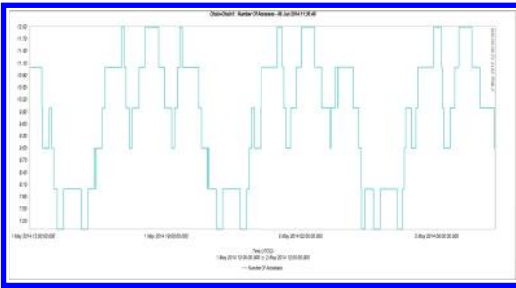


Figure 7. Total numbers of visible Beidou-2 second stage satellites in New York.

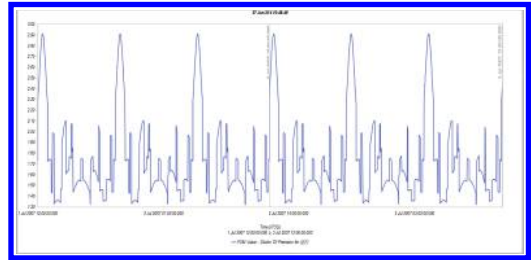


Figure 10. GDOP values of GPS in New York.

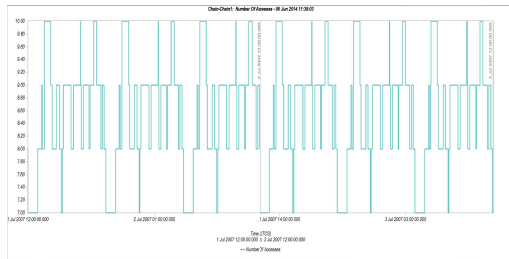


Figure 8. Total numbers of visible GPS satellites in New York.

145°E), New York (30.35°N, 114.17°E) and Victoria Island (71°N, 110°W) are chosen as the typical regions at abroad. Taking New York as example, the total numbers of visible Beidou-2 second stage and GPS satellites are shown in Figure 7 and Figure 8, while the GDOP values are shown

Table 3. Comparison of total numbers of visible Beidou-2 second stage and GPS satellites at abroad.

Facilities	Beidou-2 second stage/GPS		
	Min	Max	Mean
Guam	17/8	19/11	17.7/9.6
New York	7/7	12/10	9.8/8.6
Victoria Island	10/7	14/12	11.8/9.5

Table 4. Comparison of GDOP values of Beidou-2 second stage and GPS at abroad.

Facilities	Beidou-2 second stage/GPS		
	Min	Max	Mean
Guam	1.06/1.31	1.39/2.17	1.21/1.59
New York	1.32/1.33	2.41/2.90	1.66/1.75
Victoria Island	1.35/1.36	2.72/4.70	1.59/2.06

much more than that of GPS at Guam and Victoria Island and the GDOP value of Beidou-2 second stage is a little bigger than that at home.

## 5 SUMMARY

The visibility and GDOP of BeiDou-2 second stage and GPS are analyzed in some important regions, such as Wuhan, Beijing, Sanya, Guam, New York and Victoria Island using STK. The analysis results show that the numbers of visible satellites and the GDOP values of BeiDou-2 second stage are better than that of GPS in these regions, and the positioning performance of BeiDou-2 second stage needs to be increased in the high latitude and west hemisphere regions.

## ACKNOWLEDGEMENT

This research was financially supported by the National Natural Science Foundation of China (41274013, 41471387).

## REFERENCES

- Li J.L, Yang Y.X, Xu J.Y, et al. 2013. Performance analysis of single-epoch dual-frequency RTK by BeiDou navigation satellite system. In: Sun J.D, Jiao W.H, Wu H.T, et al. (eds), *Proceedings of China Satellite Navigation Conference (CSNC) 2013. Lecture Notes in Electrical Engineering*, 245: 133–143.
- Montenbruck O, Hauschild A, Steigenberger P, et al. 2013. Initial assessment of the COMPASS/BeiDou-2 regional navigation satellite system. *GPS Solutions*, 17: 211–222.
- Yang Y.X, Li J.L, Wang A.B, et al. 2014. Preliminary assessment of the navigation and positioning performance of BeiDou regional navigation satellite system. *Science China: Earth Sciences*, 57: 144–152.
- Yang Y.X. 2010. Progress, contribution and challenges of COMPASS/BeiDou satellite navigation system. *Acta Geodaet et Cartograph Sin*, 39: 1–6.

# Analysis of roof water inrush risk and forecast of the outflow rate of 3229 working face in Tianzhu Coal Mine

H. Wang

*Institute of Mine Construction, Tiandi Science and Technology Co. Ltd., Beijing, China*

*Beijing China Coal Mine Engineering Co. Ltd., Beijing, China*

*National Engineering Laboratory for Deep Shaft Construction Technology in Coal Mine, Beijing, China*

**ABSTRACT:** Analyzing water inrush risk and forecasting outflow rate of each workface is one of the important tasks of mine water prevention. 3229 working face in Tianzhu Coal Mine is partial below the Jinsha River. There are four aquifers above the 3229 working face, which are strong pore free aquifer of Quaternary (Q) alluvium, weak pore free aquifer of Early Cretaceous Hekou Group, weak pore-fissured confined aquifer of Late Jurassic Kushuixia Group, and pore-fissured confined aquifer of Middle Jurassic Yaojie Group. Therefore, it will be likely that water inrush will take place during the mining process. On the basis of fully analyzing the geological and hydrogeological data of mine field, adopting “Up Three Zone” Theory of coal seam roof (the caving zone, water flowing fractured zone and bending sinking zone), principles of hydrogeology and theory of ground surface strata movement law, and combining the research results of ground fissure, roof water inrush risk of 3229 working face was analyzed, and outflow rate was forecasted. The results show as follows: (1) Mining 3229 working face will probably lead to the extension of surface subsidence area to Jinsha River valley; (2) The maximum height of water flowing fractured zone is 107.48 m, so the water of Yaojie Formation aquifer will inrush the mined-out area of the working face; (3) The surface crack depth is less than 70 m, so the water of Jinsha River will not rush in the mined-out area of the working face; (4) The ordinary outflow rate of the working face is 13.60 m<sup>3</sup>/h, and the maximum outflow rate is 27.20 m<sup>3</sup>/h. It is proposed that the necessary water prevention and control measures be taken to ensure the safety in mining the working face.

**Keywords:** water inrush risk; outflow rate; water flowing fractured zone; ground fissure; open well calculation method

## 1 INTRODUCTION

Water damage accident, as one of the major coal mine disasters, is prone to cause mass casualty accidents. In extraordinarily serious coal-mine accidents, water damage is second only to the gas outburst/explosion hazard. According to statistics, from 2009 to 2013, 5603 accidents have occurred at the national coal mines in China, causing 9488 deaths, among which 174 water damage accidents occurred, causing 793 deaths, accounting for 3.1% of the total accidents and 8.4% of the total deaths, respectively. 64 large water damage accidents have occurred, causing 313 deaths, accounting for 15.3% of the total large accidents and 15.8% of the total deaths, respectively; 23 serious or extremely serious water damage accidents have occurred, causing 361 deaths, accounting for 24.2% of the total serious or extremely serious accidents and 18.9% of the total deaths respectively; 12 water damage accidents have taken place in working faces, accounting for 18.8% of the total. When the water

damage accident has occurred it will take a long time and is very difficult to rescue, and it is very difficult to carry out the rescue work, causing huge economic losses and extensively negative impact on society, and simultaneously bringing about serious damage to water and environment resources of the mining area [1, 2]. Therefore, before mining working face, accurate and comprehensive analysis of the hydrogeological conditions of the working face, analysis of water inrush risk and forecast of outflow rate, and taking the necessary prevention and measures of controlling water, are of great significance to ensure the safety of mining working face.

## 2 GENERAL OVERVIEW OF TIANZHU COAL MINE AND 3229 WORKING FACE

### 2.1 General overview of tianzhu coal mine

Tianzhu Coal Mine is located in Tanshanling Town, Tianzhu Tibetan Autonomous County,

Table 1. Strata lithologies and aquifers dipartitions of S44 borehole.

Stratigraphic unit											
System	Series	Group	Strata no.	Thickness (m)	Cumulative depth (m)	Lithology	Remark				
Quaternary (Q)			1	6.00	6.00	Loess	Quaternary aquifer				
Creta-ceous (K)	Lower (K <sub>1</sub> )	Hekou (K <sub>1</sub> hk)	2	40.00	46.00	Siltstone	Cretaceous aquifer				
Jurassic (J)	Upper (J <sub>3</sub> )	Kushui-xia (J <sub>3</sub> k)	3	92.97	138.97	Large grained sandstone	Kushuixia group aquifer				
			4	24.91	163.88	Gritstone					
			5	4.82	168.70	Siltstone					
	Middle (J <sub>2</sub> )	Xinhe (J <sub>2</sub> x)	6	8.27	176.97	Gritstone and fine sandstone interbed	Xinhe group aquifuge				
			7	5.83	185.80	Siltstone					
			8	16.71	202.51	Siltstone					
			9	9.74	212.25	Fine sandstone					
			10	41.79	254.04	Siltstone					
			11	2.28	256.32	Fine sandstone					
			12	14.87	271.19	Siltstone and fine sandstone interbed					
			13	2.19	273.38	Fine sandstone					
			14	2.89	276.27	Marl					
			15	5.01	281.28	Gritstone					
			16	3.81	285.09	Siltstone					
			17	2.71	287.30	Fine sandstone					
			18	5.21	292.51	Siltstone and middle sandstone interbed					
			Yaojie (J <sub>2</sub> y)			19		3.55	296.06	Siltstone	Yaojie group aquifer
						20		20.59	316.65	Marl	
						21		5.59	322.24	Mudstone	
						22		13.67	335.91	Marl	
	23	8.21				344.12	Mudstone and marl interbed				
	24	7.56				351.68	Marl				
	25	1.40				353.08	Mudstone				
	26	5.74				358.82	Marl				
	27	6.03				364.85	Oil shale and marl interbed				
	28	8.16				373.01	Oil shale				
	29	5.37				378.38	Upper and middle coal seams				
	30	3.96				382.34	Siltstone				

Gansu Province in Northwest China, about 74 km southwest to the county seat (Huazangsi Town). Its geographical position is 102°41'E, latitude is 36°54'N.

According to the data of drilling engineering and tunnel engineering outcropping, in the coal-field, from old to new the formations are thus distributed: Proterozoic Lower Sinian Maxianshan Group (AnZ<sub>mx</sub>), Proterozoic Middle Sinian (Z<sub>2</sub>), Mesozoic Lower Jurassic Daxigou Group (J<sub>1dx</sub>), Mesozoic Middle Jurassic Yaojie Group (J<sub>2y</sub>) and Xinhe Group (J<sub>2x</sub>), Mesozoic Upper Jurassic Kushuixia Group (J<sub>3k</sub>), Mesozoic Cretaceous (K), Cenozoic Quaternary (Q). Among them, Mesozoic Middle Jurassic Yaojie Group (J<sub>2y</sub>) is main coal-bearing strata (Table 1). Strikes of coal measures strata are generally N10–40°W, of which inclinations are NE, with angles of 9–18; There are four coal seams in coal measures strata, of which the average total thickness is 9.94 m, including two mineable coal seams (Upper and Middle coal seams) and one locally-mineable coal seam (Top coal seam).

It belongs to continental alpine climate in Tanshanling area, with an average annual precipitation of 476.6 mm, annual evaporation of 1548.5 mm. The rainy season is from June to September, and the snowy season is from October to next April. The atmospheric precipitation is main source of water supply for the mining area. Jinsha River and Shajin River are two live streams in the mining area. Jinsha River flows into the area from north, extending in the north-south direction almost threading the entire the mining area.

The strata in mining field is from the top to the bottom divided into six aquifers: strong pore free

aquifer of Quaternary (Q) alluvium, weak pore free aquifer of Early Cretaceous Hekou Group, weak pore-fissured confined aquifer of Late Jurassic Kushuixia Group, pore-fissured confined aquifer of Middle Jurassic Yaojie Group, pore-fissured confined aquifer of Early Jurassic Daxigou Group Lower Member, weak fissured confined aquifer of Early Sinian metamorphic rock. There are two aquifuges, aquifuge of Middle Jurassic Xinhe Group and aquifuge of Early Jurassic Daxigou Group Upper Member.

## 2.2 General overview of 3229 working face

3229 working face is located in No.3 Mining Area, starting from the south spot at the 2060 m general return airway, and extending northward to the 87500 m latitude line. In its west part the 9 m coal pillar is set between it and 3227 working face. In its east part the minimum horizontal projection distance between it and the west boundary Jinsha River is approximately 180 m (Fig. 1). The length of its return airway is 1378 m, transport roadway is 1342 m, with declination width of 140 m, mineable strike length is 1340 m. Upper and middle coal seams will be mined in the working face. In the mining area, the total thickness of upper and middle coal seams is 5.34–8.80 m, the average is 6.42 m; the dip angle is 11–17°, with the average is 14°; between two coal seams there is a rock parting, of which the thickness is 0.19–0.33 m, with the average of 0.26 m. The elevation of middle coal seam floor is 2218.75–2284.92 m, of which the buried depth is 355.89–384.84 m (Fig. 2). The thickness of mantle soil over the working face is 6.00–12.00 m, with the average of 6.21 m. The direct roof of upper coal

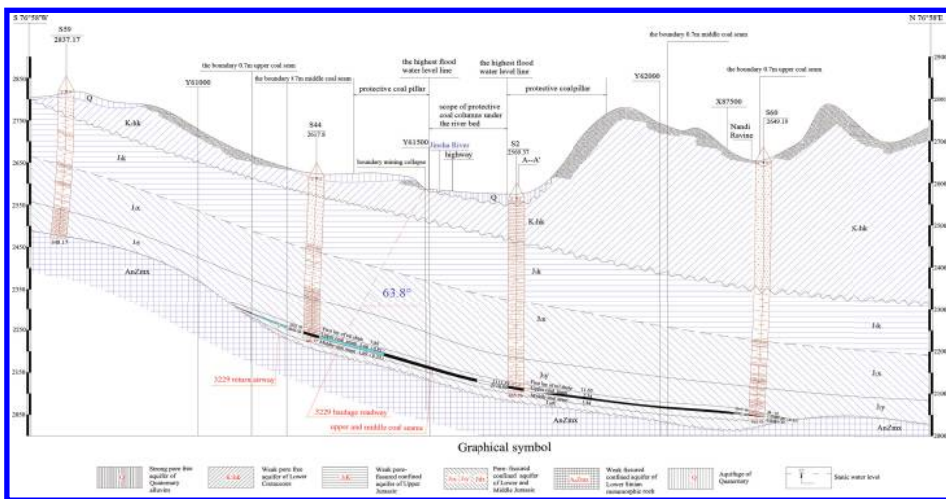


Figure 1. The geological profile of the 16th exploratory line in Tianzhu Coal Mine.

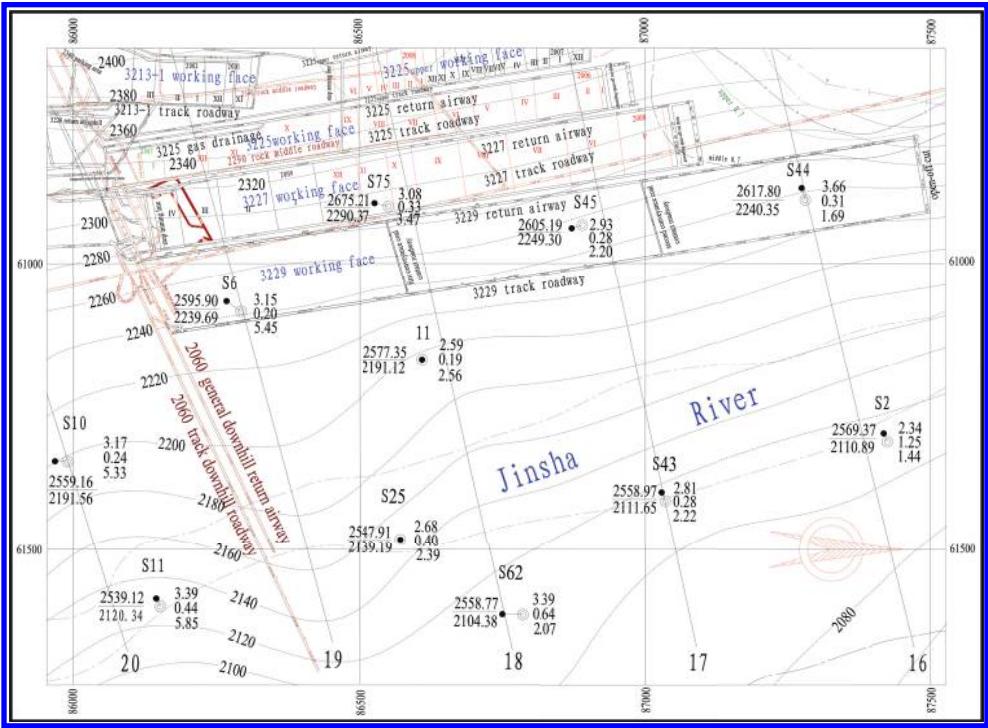


Figure 2. The local excavation engineering chart in Tianzhu Coal Mine.

seam is oil shale, gray-black, with plant fossils fragments and black coal strip, of which the thickness is 5.40–8.54 m, the average is 7.57 m. Direct coal floor is siltstone, partial mudstone, its thickness is 1.07–7.06 m, with the average of 4.34 m. The working face intends to use fully-mechanized top coal caving method. There is no obvious fracture in 3229 working face and its surrounding.

### 3 ANALYSIS OF WATER INRUSH RISK FROM ROOF DURING MINING THE COAL SEAM OF 3229 WORKING FACE

#### 3.1 Forecast of surface subsidence area on the side of transporting roadway

After mining the underground coal seam, overburden and floor rocks of mined-out area will move because the stress balance is destroyed. With the expansion of mined-out area, the scope of rock movement will correspondingly increase. When the mined-out area expands to a certain range, strata movement extends towards ground surface, causing the movement of the strata of ground surface, resulting in the subsidence area. The range of surface subsidence area can be worked out through

some parameters, such as buried depth of working face, dip angle of strata, displacement angles of bedrock and surface soil, shape and dimensions of working face, and etc (Fig. 3). Near the 16th exploratory line, the horizontal distance is the shortest between transport roadway of 3229 working face and Jinsha River (Fig. 2), where the overburden strata are mainly Jurassic strata, of which the coal seams are gently inclined (dip angle  $\theta \leq 35^\circ$ ). According to empirical formula in Fuxin, Jiao River, Jixi and Shuangyashan mining areas of the reference [3], we selected the minimum value as the downhill draw angle of overburden strata of 3229 working face (Table 2).

Therefore, the horizontal distance of geographical coverage positions between the east boundary of ground subsidence area and transport roadway of 3229 working face in 16th exploratory line is calculated as follows:

$$l = h_{jy} \cot \beta + h_{bi} \cot \varphi \quad (1)$$

where,

$l$ —the horizontal distance between mining boundary of working face and boundary of ground subsidence area on the same side, m;

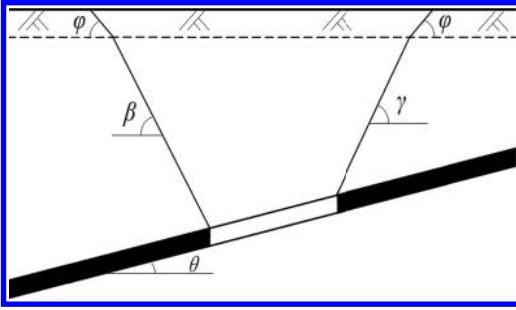


Figure 3. The diagram of surface subsidence area range after mining gently dipping coal seam.

Table 2. Downhill draw angle calculation results of overlying strata of 3229 working face.

Mining area	Downhill draw angle $\beta$ (°)	
	Empirical formula	While dip angle of strata $\theta = 14^\circ$
Fuxin	$\beta = 83 - 0.9\theta$	70.4
Jiaohe	$\beta = 75 - 0.8\theta$	63.8
Jixi	$\beta = 78 - 0.7\theta$	68.2
Shuangyashan	$\beta = 75 - 0.3\theta$	73.8

$h_{jy}$ —the thickness of overburden bedrock of working face, m;

$h_{bt}$ —the thickness of overburden surface soil of working face, m;

$\beta$ —the downhill draw angle of overburden bedrock of working face, (°);

$\varphi$ —the draw angle of overburden surface soil of working face, (°).

On cross section of 16th exploratory line (Fig. 1), we looked on the outside floor of transport roadway of 3229 working face as punch mark, and drew a ray as  $63.8^\circ$  downhill draw angle, the node of the ray and bedrock surface is just below the valley of Jinsha River. On this basis, we could more accurately calculate the east boundary position of ground subsidence area of 3229 working face in the 16th exploratory line. From Figure 1, we could know that the east boundary of ground subsidence area in the 16th exploratory line is close to Jinsha River, and thickness of Quaternary mantle soil near the ground subsidence area boundary is about 6.0 m, where the bedrock surface elevation is about 2590 m, and the bottom elevation of middle coal seam at transport roadway of 3229 working face in the 16th exploratory line is about 2220 m. In addition, according to the reference [3], taking the draw angle of overburden surface soil  $\varphi = 40$ , we calculated as follow:

$$\begin{aligned}
 l &= h_{jy} \cot \beta + h_{bt} \cot \varphi \\
 &= (2590 - 2220) \times \cot 63.8^\circ + 6 \times \cot 40^\circ \\
 &= 189.21 \text{ (m)} \\
 189.21 - 180 &= 9.21 \text{ (m)}
 \end{aligned}$$

This means that the ground subsidence area of 3229 working face entered the Jinsha River valley about 9 m, therefore, we must analyze the risk that Jinsha River water rushes in the 3229 working face.

### 3.2 Calculating the height of water flowing fractured zone

Lithology of overburden strata of 3229 working face is mainly sandstone, secondly marl, on the whole, belongs to hard stratum. According to the reference [4], the height of water flowing fractured zone could be calculated as follow:

$$H_{ii} = \frac{100 \sum M}{1.2 \sum M + 2.0} \pm 8.9 \quad (2)$$

Or

$$H_{ii} = 30 \sqrt{\sum M} + 10 \quad (3)$$

where,

$H_{ii}$ —the height of water flowing fractured zone, m;

$\sum M$ —cumulative mining thickness, m.

The  $\sum M = 8.80$  and  $n = 1$  are substituted into formula (2),(3) respectively, results are as follow:

$$\begin{aligned}
 H_{ii} &= \frac{100 \sum M}{1.2 \sum M + 2.0} + 8.9 \\
 &= \frac{100 \times 8.80}{1.2 \times 8.80 + 2.0} + 8.9 = 78.06 \text{ (m)}
 \end{aligned}$$

(Note: Given safety, the “+” value was selected from formula (2).)

Or

$$H_{ii} = 30 \sqrt{\sum M} + 10 = 30 \sqrt{8.80} + 10 = 98.99 \text{ (m)}$$

In addition, Wu Qiang, a professor of China University of Mining and Technology (Beijing) [1] (2013) combined the measured results of recent scientific research projects and documents, collecting the measured data over 40 working faces by fully-mechanized top coal caving mining technology in “two zones” (caving zone height measured values, water flowing fractured zone), and using the methods of mathematical statistics and regression



analysis, to have obtained the calculation formula for the height of water flowing fractured zone under medium hard overburden strata by fully-mechanized top coal caving mining technology (mining and caving height is 3.5~12.0 m), namely:

$$H_{li} = \frac{100M}{0.26M + 6.88} \pm 11.49 \quad (4)$$

where,  $M$ —thickness of coal seam, m.

The  $M = 8.80$  is substituted into formula (4), and the result is as follows:

$$\begin{aligned} H_{li} &= \frac{100M}{0.26M + 6.88} + 11.49 \\ &= \frac{100 \times 8.80}{0.26 \times 8.80 + 6.88} + 11.49 = 107.48 \text{ (m)} \end{aligned}$$

(Note: Given safety, the “+” value was selected from formula (4).)

Compared with above-mentioned three  $H_{li}$  values, we took the maximum  $H_{li} = 107.48$  m.

In addition, according to the design method of safety waterproof coal rock pillar of mining coal seam around water, the aim of setting safety waterproof coal rock pillar is to keep the water flowing fractured zone from spreading to water body; therefore, its vertical height should be greater than or equal to the sum of the maximum height of water flowing fractured zone( $H_{li}$ ) and the thickness of the protective layer( $H_b$ ) (Fig. 4), namely:

$$H_{sh} \geq H_{li} + H_b \quad (5)$$

where,

$H_{sh}$ —vertical height of safety waterproof coal rock pillar, m;

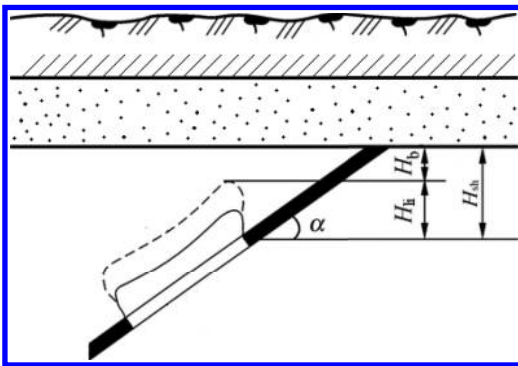


Figure 4. The sketch of setting waterproof coal (rock) pillar while outcrop of gently dipping coal seam contacting with strong watery stratum in loose stratum.

$H_{li}$ —the maximum height of water flowing fractured zone, m;

$H_b$ —the thickness of the protective layer, m.

Currently, there is rarely the study on setting protective layer thickness of the roof bedrock aquifer. Therefore, we referred to the Table 6–4 of reference [4], and selected the maximum value of protective layer under hard overburden rocks, namely:

$$H_b = 7A \quad (6)$$

Thus, we could get:

$$H_{sh} \geq H_{li} + H_b = 107.48 + 7 \times 8.80 = 169.08 \text{ (m)}$$

By the above calculation and referring to Table 1, we could see that after mining the 3229 working face, its water flowing fractured zone will penetrate the roof oil shale stratum, oil shale and marl interbedded strata (the total thickness is 14.19 m), and penetrate the roof Yaojie group aquifer (the thickness between its roof and upper coal seam roof is 80.5 m),  $H_{sh}$  is less than the thickness between the floor of Kushuixia group aquifer and the roof of upper coal seam (196.04 m). Therefore, during mining the 3229 working face, the water of Yaojie group aquifers will flow into the working face, of which the outflow rate should be forecast, and the necessary measures for prevention and control of roof water should be taken; it is very unlikely for the water of Kushuixia group aquifer to flow into the working face.

### 3.3 Forecast of the depth of ground fissure

Mining subsidence causes nonuniform settlement and horizontal movement of the ground surface, leading to ground fissures in part area of the subsidence basin [5]. As one of geological hazards, ground fissure is widespread in many countries all over the world. Its occurrence frequency and disaster scale are aggregating year by year, graduating into a major regional geological hazard. It not only causes direct catastrophic damage to all types of construction engineering, transportation facilities, urban lifeline engineering and land resources, but also may lead to a series of serious eco-environmental problems [6]. In China, ground fissures are also quite serious, especially in Shanxi, Shaanxi, Inner Mongolia, Jilin, Liaoning, Henan, Shandong, Anhui and other coal-producing provinces. In coal mines, the ground fissures even have led to collapse of surface water into the underground mine, causing water inrush accidents, e.g., at 18:00 on August 16 and 23:00 on August 31, 1995, two water inrush accidents took place in No.2 Mining District of Wangjiashan Coal Mine in half a month, the causes of both incidents were attributed to heavy

rainfalls. The rain water affluxed from Shigou Ditch formed debris flow, which flowed into the underground mine through the ground fissures of mined-out area and submerged about 2400 m-long roadway of three levels (i.e. 1600 m level, 1650 m level, 1700 m level) in No.2 Mining District, causing a disastrous accident that claimed eight lives [7]. Based on considering the serious harm of the ground fissure, many experts in China respectively have carried out in-depth studies on the ground fissure disasters in coal mines by the methods of theoretical analysis, numerical simulation, similarity simulation, field measurement, and etc [5, 7–13]. The results showed that: the widths of ground fissures are generally 0.01–2.0 m; depths of ground fissures are generally 1.0–5.0 m, and even up to 30 ~ 70 m in small number of mines.

Quaternary loosen stratum covers the ground surface of 3229 working face, of which the thickness 6.0–12.0 m. Considering 3229 working face belongs to thin loosen stratum and thick bedrock covered working face, the depth of its ground fissure was selected from the maximum value of the above research results (i.e. 70 m). Referring to Table 1, we knew that after mining 3229 working face, ground fissure would only penetrate Cretaceous aquifer, and extend 18 m deeper into the large-grained sandstone stratum of the upper part of Kushuixia group aquifer (thickness 92.97 m), it would not join water flowing fractured zone, in other words, the surface water (including stream water of Jinsha River), and Cretaceous aquifer water will unlikely flow into the 3229 working face.

#### 4 FORECAST OUTFLOW RATE OF 3229 WORKING FACE

There are many methods in forecasting the outflow rate of mine pit, including the analogue method (water content coefficient method, mine specific capacity analogue method, correlation analysis method, etc.),  $Q=f(s)$  curve extrapolation method, analytical method (open well calculation method, horizontal gallery method), water resource balance method, numerical method, and etc [14]. Comprehensively considering the control degree of hydrology geological conditions and the applicable conditions of each forecasting method in reference [14], we used open well (confined water converting unconfined water complete well) calculation method to forecast the outflow rate of 3229 working face.

Under the condition of confined water converting unconfined water complete well:

$$Q = 1.366K \frac{(2H - M)M - h^2}{\lg R_0 - \lg r_0} \quad (7)$$

where,

$Q$ —outflow of water,  $m^3/d$ ;  
 $K$ —coefficient of permeability,  $m/d$ ;  
 $H$ —height of water column,  $m$ ;  
 $h$ —water column height between dynamic level and negative confining bed,  $m$ ;  
 $M$ —height of aquifer,  $m$ ;  
 $r_0$ —radius of the “open well” ( $r_0 = \sqrt{F/\pi}$ ),  $m$ ;  
 $R_0$ —influence radius of the “open well” ( $R_0 = r_0 + 100$ ),  $m$ .

During the course of mining the 3229 working face, the threat of water damage will be mainly from the overlying Yaojie group aquifer ( $J_{2y}$ ). According to the Yaojie Group aquifer ( $J_{2y}$ ) pumping test results of S13 borehole in reference [15], permeability coefficient of Yaojie Group aquifer is  $9.29 \times 10^{-4} m/d$ , confined water level is 322.07 m higher than middle coal seam roof, therefore, normal outflow rate of 3229 working face ( $Q_{nor}$ ) could be calculated as follows:

$$\begin{aligned} Q_{nor} &= 1.366K \frac{(2H - M)M - h^2}{\lg R_0 - \lg r_0} \\ &= 1.366 \times 9.29 \times 10^{-4} \\ &\quad \times \frac{(2 \times 322.07 - 66.31) \times 66.31}{\lg \left( \sqrt{\frac{1340 \times 140}{3.14}} + 100 \right) - \lg \sqrt{\frac{1340 \times 140}{3.14}}} \\ &= 326.43 (m^3/d) = 13.60 (m^3/h) \end{aligned}$$

According to the experience in mining working face of production level (2240 m level), we could calculate the maximum outflow rate of 3229 working face as follows:

$$Q_{max} = \mu Q_{nor}$$

where,  $\mu$  is the spare coefficient maximum outflow rate, generally it is 2.

Thus, there is:

$$Q_{max} = 2Q_{nor} = 2 \times 13.60 = 27.20 (m^3/h)$$

#### 5 CONCLUSIONS

1. The ground subsidence area will extend eastward, to the stream valley of Jinsha River after mining the 3229 working face.
2. The maximum development height of water flowing fractured zone will be 107.48 m; the depth of ground fissure will be less than 70 m. In mining the working face, the threat of water damage will be mainly from the overlying Yaojie group aquifer ( $J_{2y}$ ), while the water of other overlying aquifers and Jinsha River will unlikely flow into the 3229 working face.

3. It is forecasted that the normal outflow rate of 3229 working face is 13.60 m<sup>3</sup>/h in mining process; and the maximum is 27.20 m<sup>3</sup>/h.

## REFERENCES

- [1] Qiang Wu, Suqi Zhao, Shuning Dong, et al. 2013. Manual of water prevention and control coal mines [M]. Beijing: China Coal Industry Publish House.
- [2] Dezhi Zheng. 2014. Type characteristics and developmental status quo of coal mine water disaster in China [J]. China Science and Technology Information, 22: 65–66.
- [3] Rongli Zhang, Guowei He, Duo Li. 2003. Designing manual of mining engineering [M]. Beijing: China Coal Industry Publish House.
- [4] State Coal Industry Bureau. 2000. Regulations of pillar leaving and coal mining under building, water, railway and mail shaft and tunnel [M]. Beijing: China Coal Industry Publishing House.
- [5] Kan Wu, Ming Zhou, Zhenqi Hu. 1997. The prediction of ground fissure depth and width by mining [J]. Journal of Fuxin Mining Institute (Natural Science), 16(6): 549–552.
- [6] Qiang Wu, Peipei Chen. 2003. Research on state of art and prospect of earth fissures [J]. The Chinese Journal of Geology Hazard and Control, 14(1): 22–27.
- [7] Jiancheng Yang. 1996. The formation of geofracture and their hazard in Wangjiashan Coal Mine [J]. ACTA Geological Gansu, 5(2): 91–95.
- [8] Zhanbing Zhang, Changcun Li, Sheng Jiang. 2010. The application of EH4 in probing earth fissures [J]. Science and Technology Innovation Herald, 2: 137–138.
- [9] Mingli Wang. 2014. Analysis on the causes and the impact of ground fissures induced old goaf [J]. Mine Surveying, 4: 63–66.
- [10] Jinli Wang, Yiqing Lu, Hongfu Liu, et al. 2005. Distribution characteristics and genesis of geofracture in Xiqu District [J]. Shanxi Coal, 25 (3): 11–13.
- [11] Liang Li, Kan Wu, Ranli Chen, et al. 2010. Information extraction of surface crack position in mining subsidence area based on wavelet transform [J]. Science of Surveying and Mapping, 35 (1): 165–168.
- [12] Xinjing Wang, Zhenqi Hu, Yaoqi Yang, et al. 2014. Design and application of monitoring device for development characteristic of dynamic ground fissure caused by coal mining [J]. Coal Engineering, 46(3): 131–133.
- [13] Zhenqi Hu, Xinjing Wang, Anmin He. 2014. Distribution characteristic and development rules of ground fissures due to coal mining in windy and sandy region [J]. Journal of China Coal Society, 39 (1): 11–18.
- [14] China State Administration of Work Safety. 2000. Standard for exploration and evaluation of hydrogeology, engineering geology and environment geology in coal bed (MT/T 1091-2008) [S]. Beijing: China Coal Industry Publishing House.
- [15] Tianzhu Coal Mine, Yaojie Coal and Electricity Group Co, Ltd. 2010. Report of the hydrogeological type classification of Tianzhu Coal Mine [R]. Wuwei: Yaojie Coal and Electricity Group Co, Ltd.

# Prediction research on the hazardous extent of volcano secondary debris flow in Changbai Mountains based on simulation of FLOW3D

Xiao Tong, Peihua Xu, Guang Li, Mo Zhang, Pengfei Li & Zhanling Chen  
*College of Construction Engineering, Jilin University, Changchun, Jilin, China*

**ABSTRACT:** The Tianchi Volcano in Changbai Mountains is one of the few extant active volcanoes of our country. Researching on the hazardous extent of volcano secondary debris flow aims at offering scientific references to the prediction and prevention of geologic hazards in Changbai Mountain. Based on the parameters obtained from field geological investigation and indoor simulation experiment, this paper applied FLOW3D, a numerical stimulation software of fluid dynamics, to simulate the developing process of 0.5 trillion cubic meters debris flow of volcanoes in Changbai Mountains. The predicted results show that the maximum packing length of the debris flow is approximately 42 km, with the distance of 8 km from Erdao-baihe town during the 1800s simulated time; however, after the end of the simulation, part of the debris flow still has the velocity, only with the lower velocity and smaller scope, which will not produce much influence on the living and production of the Erdao-baihe area.

**Keywords:** Tianchi volcano in Changbai Mountain; secondary volcano debris flow; FLOW3D; the maximum hazardous extent; numerical simulation

## 1 INTRODUCTION

Locating in the northeastern part of Ji Lin Province of China, and being the frontier between China and North Korea, Changbai Mountains is a renowned active volcano which is likely to erupt<sup>[1]</sup>. As a nature reserve and tourist resort, Changbai Mountains is famous in home and abroad for its unique volcanic landform and entire ecosystem as well as magnificent natural landscape<sup>[2]</sup>. However, debris flow disaster happens frequently in this area because of the special geological environment and weather condition. Among different types of debris flow in this area, secondary debris flow induced by volcanic disaster receives much concern for its prompt destructiveness. Volcano erupts again and produces water in the volcanic lakes spewing or the high temperature, and this melts the ice and snow in the summit of volcano into a large amount of water which mixes the loose deposits previously erupted, then under the effect of gravity they flow fast downward along the ravine or hillside forming a special kind of debris flow, which causes a fatal harm to the buildings and residents in the area of coverage<sup>[3]</sup>.

Foreign scholars gain the understanding and conduct research concerning the secondary debris flow much earlier, such as Yokoyam, Blong who studied and defined the secondary volcano debris flow as a kind of volcano geological hazards as early as in the middle and late periods of the 20th century<sup>[4]</sup>.

During the following 30 years, geologists from different countries made a further research and study towards the material composition, formation, accumulation pattern, scope of influence as well as prevention measures of secondary volcano debris flow<sup>[5]</sup>. Although the domestic research had a late start toward the secondary volcano debris flow, a large number of scholars make joint efforts and made much achievement. For nearly 20 years from the late 20th century, geologists such as Liu Xiang, Wei Haiquan, Sun Ping, and Nie Baofeng made research to the composition characteristics, source reserve, topographic condition, and distribution regularity of volcano debris flow in the Changbai Mountain area<sup>[6-7]</sup>.

It designs and simulates the developing process of secondary volcano debris flow in Tianchi volcano of Changbai Mountain so as to acquire the velocity in the motion process of debris flow and the distribution of section height as well as the influence scope, which could be the scientific references for disaster prevention and reduction.

## 2 MODEL BUILDING BASED ON FLOW3D

### 2.1 Grid partitioning of model area

The model building data derives from topographic map of scale 1:100,000 and imports to FLOW-3D software through Gocad software. After the consideration of computer memory and operational

capability, simulation area is finally confirmed to be integrated with the previous research result (as shown in Fig. 1).

The scope in this model is roughly to the south of 55,000 m and about 34,000 wide of waterfall in the Tianchi Lake area of Changbai Mountains. The simulated area is divided into 13 subregions to make network processing. There are 4,984,048 cells whose scale is 80 m \* 80 m \* 25 m, and the number of the active cells is 2,739,392. We can get the three-dimensional model in Figure 2 after the calculation has been done by FAVOR and VOF numerical method in FLOW3D, and the approximate location of Baishilazi natural reserve and Erdaobaihetown can be seen in the figure. Direction of the X-axis is east, the Y-axis positive direction is north, and the Z-axis is the vertical upward direction.

## 2.2 Setting of boundary condition

There are 10 species of boundary conditions in FLOW3D; the boundary assignment in this simulation will be shown in Table 1.

## 2.3 Debris flow viscous coefficient value

Based on the consulting literature, we learnt that when the proportion of the solid particles in the

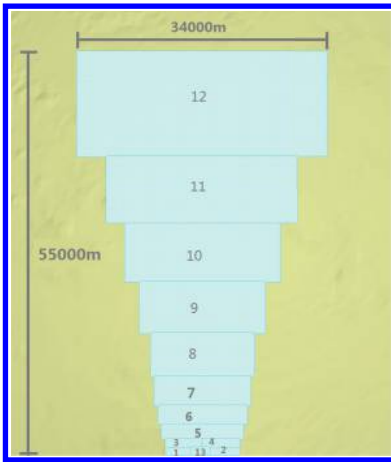


Figure 1. Mesh subdivision of the calculation model.

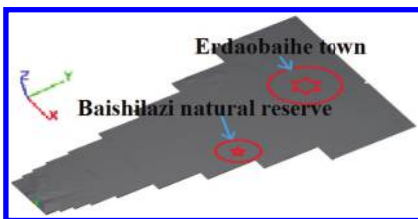


Figure 2. Three-dimensional model based on FAVOR.

Table 1. Boundary conditions at different small zones.

Zone	$X_{\min}$	$X_{\max}$	$Y_{\min}$	$Y_{\max}$	$Z_{\min}$	$Z_{\max}$
1	O	C	S	C	W	S
2	C	O	S	C	W	S
3	O	C	S	C	W	S
4	C	O	S	C	W	S
5	O	O	C	C	W	S
6	O	O	C	C	W	S
7	O	O	C	C	W	S
8	O	O	C	C	W	S
9	O	O	C	C	W	S
10	O	C	C	C	W	S
11	O	O	C	C	W	S
12	O	O	C	O	W	S
13	C	C	P	C	W	S

Notice: C is the continuative boundary, O is the outflow boundary, P is the pressure boundary, S is the symmetry boundary, W is the wall boundary.  $X_{\min}$  is the minimum value in the X direction,  $X_{\max}$  is the maximum value in the X direction.  $Y_{\min}$  is the minimum value in the Y direction,  $Y_{\max}$  is the maximum value in the Y direction.  $Z_{\min}$  is the minimum value in the Z direction,  $Z_{\max}$  is the maximum value in the Z direction.

debris flow is small, the viscous increase in the mixture is not large<sup>[8]</sup>. Assuming that solid particles in debris flow is non-viscous spherical particles, the distance between the particles is large enough and there is no interaction between the particles, the relative viscosity coefficient can be calculated according to equation (1). When there is interaction between the particles, we need to amend equation (1). Based on analyzing and summarizing a lot of literature, Thomas proposed the amendments to the formula, which is now known as equation (2).

$$\mu_r = 1 + 2.5S_v \quad (1)$$

The  $\mu_r$  in equation (1) is the ratio of the viscosity coefficient of viscosity and fluid at the same temperature,  $S_v$  is the volume concentration of solid particles.

$$\mu_r = 1 + 2.5S_v + 10.05S_v^2 + A \exp YBS_v Y \quad (2)$$

Lian Banghui provides that  $A=0.00237$ ,  $B=16.6$ . So, we set the viscous coefficient as 0.00274.

## 2.4 Some assumptions in the simulation

Due to the lack of detailed records of overflow location caused by volcanic eruption, the water head height and the duration of the water spill of Changbai Mountain. So, this article can only combine with the existing domestic and international research and experience and assume that:

1. All water in crater lake comes from the waterfall mouth of Tianchi.
2. The total volume of the water flow from Tianchi and loose accumulational materials on the slope is 5 hundred millions cubic meter.
3. The debris flow is relatively and evenly fluid and it ignores the movement of loose rock.

### 3 SIMULATION RESULTS AND ANALYSIS

#### 3.1 Simulation results

After building the model, analog computation began, producing volume of fluid variable curve, which is shown as following Figure 3.

It can be revealed from the figure that the model total water has increased significantly in the period from 0 to 190 seconds resulting from volcanic eruption, while water level has a dramatic fall and total water decreases after 190 seconds, and the water volume after the curve tending to be steady is water outflow (roughly 0.5 billion  $m^3$ ), which accords with experiment research. After analog computation, 3-dimensional images of section height distribution and velocity of debris flow in 1800 seconds have been acquired, and the author selects the typical timing to analyze.

It can be seen from Figure 4 that debris flow has a down-slope movement within 50 seconds of volcano eruption from waterfall mouth of Tianchi northern slope. Affected by the landform and topography in the vicinity of waterfall mouth, debris flow is not confined to due north, but it is divided into two flow channels: the mainstream flows along the north by east with depth 200 m and flow velocity increasing from 30 m per second to 100 m per second, whereas the tributary volume is smaller with only around ten meter in the first 50 seconds. Due to steep slopes, the early velocity amounts to 50 m per second, increasing rapidly to 100 m per second, and flows along downward north by west.

It can be seen from Figure 5 above, the mainstream flushes downslope in the form of a thin strip within the period from 50 seconds to 300 seconds combined with slower deposit velocity and decreased flow velocity followed by increasing one, which illustrates that this section of slop has experienced some fluctuation. The leading edge of

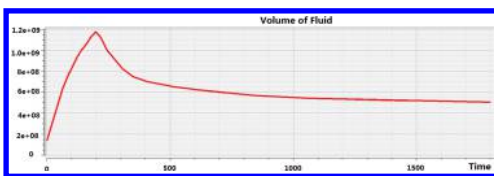


Figure 3. Alternation curve of flow total volume.

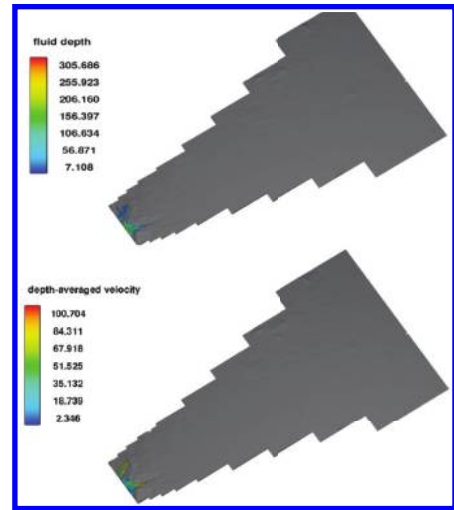


Figure 4. Section depths and section velocity of debris flow at the 50 seconds.

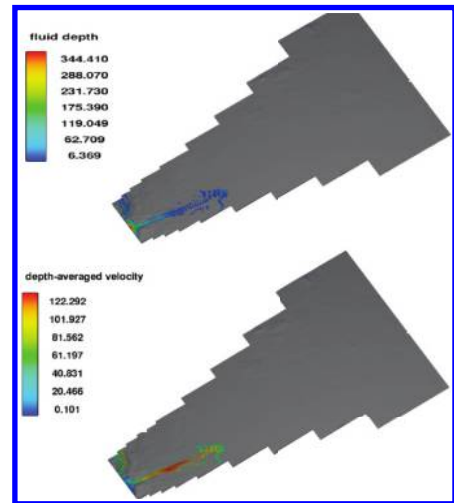


Figure 5. Section depths and section velocity of debris flow at the 300 seconds.

debris flow presents an obvious fan shaped spread, and the flow velocity of debris flow in sections 6 and 7 keep at around 100 m per second accompanied by the relatively small pile thickness of this section, which illustrates that this section is the steepest. After the 100 seconds of the tributary, the fluid runs out of the model with about 10 meters per second deposit velocity. Considering the slower flow velocity compared with the mainstream, the estimated amount of loss is small.

After the time of 1800 seconds, which is shown as Figure 6, the debris flow remains certain flow velocity and continues to run only with pretty

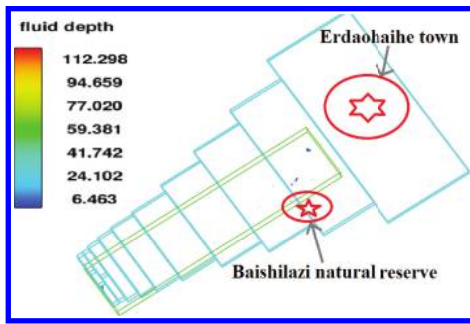


Figure 6. The maximum scope of influence at the end of simulation.

shallow depth and slow flow velocity. Considering the restrictions of computer memory and other objective factors, the simulation has ended. Within the period of 1800 seconds simulation, the maximum deposit length of debris flow is around 42 km with an approximately 8 km to Erdaobaihe town. At the end of simulation, part of debris flow still has certain velocity to flow, which will not exert significant impact on producing and living condition of the Erdaobaihe residents considering the slow velocity and small scale compared with original debris flow condition. The simulation analysis results have guiding influence on the prevention and control as well as study of flow debris.

### 3.2 Result analysis

Throughout the entire process of debris flow in the model from happening to basic static condition, water depth is the deepest in the Tianchi mouth and gradually decreases downward while rebounds when arriving at grid 9, which illustrates that this section is low-lying area with the capacity to store part of the fluid. In terms of the flow velocity, the tributary is generally faster than the mainstream, which demonstrates the steeper terrain of the tributary. The mainstream mean velocity reaches its peak at over 100 m per second at grids 6 and 7, which illustrates big altitude difference and steep slope, and the debris flow velocity increases considerably under the effect of gravity. However, due to the restrictions of computer configuration, memory and computational capabilities, the elaborate model has not been built and current model featured by larger unit size and coarse could not manifest the flow in detail, so there may be some errors.

The purpose of this simulation is to quantitatively estimate the maximum scope of debris flow influence downward Tianchi As is shown in Figure 7, the leading edge of debris flow could reach as far as 4.2 km in the simulation time 1800 seconds with 0.5 billion debris flow. However, at the end

of simulation, the debris flow has still developed to a certain degree. The population of the region is mainly inhabited in Erdaobaihe town, which is 5 km to Tianchi mouth. According to the experience, the scope of debris flow influence under such situation would not reach Erdaobaihe town nor has it any significant influence on it.

## 4 CONCLUSION

According to the conclusion above, we can see that the secondary debris flow in Changbai Mountains has certain threat even in a small volume of fluid; moreover, when the debris flow occurs, the danger is greater than the simulation in this paper. So, we should adopt a comprehensive method to the prevention and treatment of secondary debris flow in Changbai Mountains<sup>[9]</sup>. As long as we all work together, act according to circumstances, make effective defense plans and adopt scientific measures to prevent the debris flow disasters, we will overcome this disaster by all means and protect our lives and property and the ecological environment from more serious violations.

## REFERENCES

- [1] Xu Dong-man. The geological structure of the volcanic activity in Changbai Mountain area [J]. *Northeastern Seismological Research*, 1988, 4(3): 53–63.
- [2] Wang Hui. Research on formation conditions and danger degree of debris flow in the Tianchi Lake area of Changbai Mountains [D]. Jilin University, 2004 K. Elissa, "Title of paper if known," unpublished.
- [3] Wen Zhi-hong, Wan Lu-he, Sheng Jian. Weight analysis of lahar distribution influence factors in Changbai Mountain Area [J]. *Journal of Catastrophology*. 2012, 27(1): 64–72.
- [4] Yokoyama, Tilling R.I., Scarpa R. International mobile early-warning system(s) for volcanic eruptions and related seismic activities [M]. Paris: UNESCOFP, 1984.
- [5] Zhu Jin-lai. Prediction on the hazard extent of volcanic secondary debris flow with LAHARZ [D]. Jilin University, 2004.
- [6] Liu Xiang, Sui Wei-guo, Wang Xi-kui. Lahar deposit of 1000aB. Peruption at Changbaishan volcano and their hazards [J]. *Journal of Changchun University of Science and Technology*, 2000(1).
- [7] Wei Hai-quan, Liu Ruo-xin, Fen Qi-chenget al. Active volcanoes in China and their relevant hazards [J]. *Chinese Journal of Nature*, 1998(4): 196–200.
- [8] Lian Hui-bang. Sediment concentration in debris flow [J]. *Journal of Sediment Research*. 2000, 10(5): 6–15.
- [9] Run Hong-xia, Su-ya-la Ba-ya, Zhang Song-lin et al. Disasters and prevention of debris flow [J]. *Inner Mongolia Forestry Investigation and Design*, 2005, 28(supplement):145–148.

# Research trend on the prediction of coal and gas outburst

Xin Wu

*Institute of Technology, Sichuan Normal University, Chengdu, Sichuan, China*

**ABSTRACT:** This thesis analyzed the development trend of the coal and gas outburst. It introduces some new methods, such as acoustic emission, electromagnetic radiation, microseism technique, dynamic indicators of gas emission, and so on, which predict coal and gas outburst, and meanwhile, this thesis analyzes both the advantages and disadvantages of these methods. Also it sums up the widely used non-linear theories at present in the prediction of the coal and gas outburst, such as, computer simulation, fuzzy mathematics, gray system, neural network technique, expert system, and fractal analysis. Finally based on the analyses above, this thesis foresees the research trend of the field of prediction of coal and gas outburst.

**Keywords:** coal and gas outburst; prediction; acoustic emission

## 1 INTRODUCTION

Coal and gas outburst is one of the most serious natural disasters in mine. It is a complex dynamics phenomenon and badly threatens to the safety of production of coal. The purpose and significance of coal and gas outburst forecast is to provide a scientific basis for taking reasonable and effective measures to reduce outburst, to reduce the anti-outburst engineering and time, to ensure the normal process of mining and production, and to protect underground life and property from danger. For a long time, many scholars both from the domestic and the foreign make a lot of work and achieved in some extent on coal and gas outburst principle and the fatalness of outburst. With the rising of the modern mathematics, physical theory and high technology in other fields, coal and gas outburst forecast also gets its new advancement.

## 2 NEW PREDICTION TECHNIQUES OF COAL AND GAS OUTBURST

### 2.1 *Acoustic emission*

There are a lot of defects such as cracks in internal coal and rock. Coal and rock deformation and damage result in fracture, expansion, and transfixion. Research shows that the production and expansion of cracks will generate energy radiation in the form of elastic waves, which is AE. AE technology can locate the source of rupture. In the early 1940s, the United States was on the use of acoustic emission technology for monitoring the metal mine rock burst. With the application of computer technology, AE technology gets a more extensive

use in the coal mine and it has made some achievements in the rock burst monitoring. In the early 1980s, Australia exploited a dual-channel AE outburst forecasting system; AE outburst forecasting system was tested from 1983 to 1987 in the Cynheidre South Wales Coal Mine in British; however, there were no outburst in the course of the trial. Other countries like the United States, Germany, Japan, and Poland have some study in this area. The former Soviet Union predicts the outburst of coal and gas by recording the number of pulse noise and extends it to Donbas coal field. China's studies begin lately and apply less. Pingdingshan Mining Bureau introduced an AE monitoring system from Russia, and made an application to the study of coal and gas outburst. Chongqing Institute of China Coal Research Institute (CQCCRI) produced acoustic emission monitoring systems and applied it to Pingdingshan mining area during 9th Five-Year Plan. Xi'an Institute of China Coal Research Institute (XACCRI) also developed MJY-1-AE real-time monitoring system, and initiated a local experiment in the 10th Mine of Pingdingshan coal mine<sup>[1]</sup>.

Although the AE technique can assess effectively and continuously the outburst fatalness of coal edge, but there are many shortcomings, mainly because both equipment structure and receive and switch of the signals are complicated, what is more, it requires that piezoelectric sensors and coal wall can be a good coupling, in fact, which is very difficult. However, with the introduction of large capacity, high-speed computer systems and the development of the acoustic receive technological, maybe by using AE technique, outburst forecast will get some breakthrough.



## 2.2 Electromagnetic radiation

Like other materials, coal rock is made of tens of thousands of elementary particles such as atoms of electron. When coal rock suffers from deformation and fracture load, electron and other electronic particles change velocity and release electromagnetic radiation, which is called Electromagnetic radiation. The study of rock electromagnetic radiation starts when chun-worker discovers the electromagnetic anomaly before the earthquake. China and the former Soviet Union launched earlier in this field than other countries, then Japan, Greece, the United States, Sweden, Germany, and other countries also did research in this area. After more than 10-year deep research on electromagnetic radiation, which happens under the circumstances of loaded coal rock and desorption flow of gas, China University of Mining discovers that basically the electromagnetic radiation signal displays the trend of gradually strengthening during the deformation of loaded coal rock (that the coal and rock containing the deformation and fracture process, for a gradual strengthening of trend). The fundamental purpose of electromagnetic radiation technology study is to forecast the earthquakes and other disasters, which satisfactorily succeed in earthquake prediction. The current use of electromagnetic radiation, to forecast Dynamic disaster in coal rock, set off the study upsurge.

Electromagnetic radiation prediction technology is a complete non-contact monitoring method. This method is feasible and will not be influenced by artificial work and the asymmetry and instability of working face, do not drill, and works simply but it requires high level of the testing equipment performance.

## 2.3 Seismic technology

Research shows that there is rupture and shock in the process of destruction of the coal and rock, and shake waves or acoustic waves are emitted from the shake source. Maybe coal will be destructed suddenly, and outburst, when the intensity and frequency of the shock waves or sound waves reach certain values. The shock waves inside coal and rock can be received by the detection equipment (for example, underground sound receiver and shock wave receiver) installed in coal, and can be recorded after enlarging. And then we can predict fatalness of outburst through the analysis on the data.

Research shows that outburst is caused by a series of fracture, and abnormal Seismic radiation produced before fracture 5–45 min, so the Seismic radiation has luciferous prospects as a kind of forecasting methods, but the data monitoring and filtering need to be improved. Since the beginning of the 1970s, the U.S. mining bureau has studied

coal seam structure damage through the standard Seismic technology. At the same time, they adopt ultrasonic monitoring technology to monitor the energy of noise in rock.

## 2.4 Dynamic gas emission targets

V30 is the ratio of gas release quantity and coal drop quantity in 30 minutes after blasting of the excavate working face. The critical value in Germany is 40 percent of the gas content that can be desorption. Fushun Institute of China Coal Research Institute's study on Beipiao bureau shows that the critical value of outburst is  $9 \text{ m}^3/\text{t}$ . Chongqing Institute of China Coal Research Institute's study on Beijiao coal mine of Furong mining Bureau shows that there is outburst risk in front of working face about 2–5 m when the  $V_{30} \geq 9 \text{ m}^3/\text{t}$  or the change coefficient of Gas Emission  $K_V \geq 0.7$ . At present, for casting outburst by  $V_{30}$  or  $\Delta_Q$  has not been promoted to a large area.

In fact, the real forecast technology of gas emission is a kind of technology based on the relation between gas emission situation detected by Environment Monitoring System's continuous monitor and coal and gas outburst, so the real monitoring system is the key to exact forecast.

## 3 NEW METHOD OF COAL AND GAS OUTBURST FORECAST

### 3.1 Computer simulation

Mine is a complex engineering project. Many problems of mining work is very difficult to answer, and it will produce a greater engineering error according to contrast. The application of computer simulation technology in the works of mine gives a new start in mine engineering technology. Computer simulation in the progress of mining, simulation of the roadway stress distribution, simulation of the stability of tailings dam, and other examples show that numerical simulation technology has become an important tool for mining projects. As an advanced productive force to promote the mining engineering technology, computer simulation technology is rising.

### 3.2 Fuzzy math

Fuzzy math theory, first proposed by the U.S. cybernetics expert LAZadeh, is the important means to express and deal with imprecise data and ambiguous information. Many scholars domestic and abroad quantitatively evaluate the mine geological changes, the occurrence of gas and the danger of the gas disaster by using fuzzy evaluation theory combined with statistical methods.

Through analyzing the complexity of the inherent mechanism of coal and gas outburst, and the inaccurate relationship between the outburst factors and the outburst itself, we can give the right express and treatment to the inaccurate information and relation under the help of the fuzzy theory and technique. The treatment means turns from the traditional ones based on the experience and analogy to the practice of mathematics and science<sup>[2-3]</sup>.

### 3.3 Gray system theory

Gray System Theory is a new theory proposed by Professor Deng Julong<sup>[4]</sup>. Coal and gas outburst forecast parameters are fuzzy, randomness, which are the factors of the gray system theory. We can apply gray correlation analysis to quantitatively deal with coal and gas outburst factors in the design of the gray factors. Through the gray correlation analysis, we can analyze the main factors by putting aside the complicated ones, which has some significance to promote the accuracy of the outburst forecast.

Gray cluster method has some advantages, such as dynamic forecasts. This method will consider a number of factors by the numbers, which affect the outburst heavily, it jumps out of the conventional forecasting methods which only rely on a single indicator to predict, so it can improve the forecast accuracy. The result shows that it is a new method to accurately reflect the laws of the coal and gas outburst in the mine.

### 3.4 Neural networks

Neural Networks is another important branch of the science of artificial intelligence, which develops fast in late 1980s of the 20th century. Besides its strong vitality in pattern recognition, treatment and control of nonlinear dynamics, and other areas, it shows a good applicable effect in the forecast, the evaluation and so on. In recent years, fuzzy neural network technology, which is represented by the BP neural network model that is auto-adaptive to outburst intensity forecast gets notable achievements in the coal and gas outburst forecast field.

Coal and gas outburst is a complex phenomenon of nonlinear dynamics, and has a complex non-linear relationship with the factors causing the outburst. The current prediction methods are not effective, because it cannot accurately reflect objective mathematics relationship between the dependent variable and independent variable. To accurately reflect this relationship, we must adopt a more suitable way. Artificial neural network technology can achieve this better: what has been proven is that artificial neural network can

in any precision approach any arbitrary complex functions, if there is a hidden layer. It is a approximation model of common function<sup>[5]</sup>. Therefore, artificial neural network can more accurately reflect the mathematical relations between the coal and gas outburst and its factors, so as to predict the risk of outburst more accurately.

### 3.5 Expert system forecasts the outburst

Expert System is a computer program which simulates a human expert to solve the problem by using knowledge and experience of a human. UPEL expert system in British Coal Company can be used to forecast the danger of coal and gas outburst during the course of underground mining<sup>[6]</sup>. The Chinese Academy of Sciences Institute of Geology is also developing an expert system GASBURST to forecast the outburst. According to its users' information about the mine geological structure, underground water, gas, drilling dust, stress and the information providing the outburst events, this system can mark the the danger area and the danger zone of the outburst, predict the trend of the development of the criticality according to the mining depth. It can also forecast the the location of the outburst, display the location of the danger area of the outburst and the underground location of the outburst, and meanwhile show the relationship among the different outburst on the computer screen.

### 3.6 Fractal theory

Fractal geometry, as a theoretical tool and method for studying the nonlinear problems, has been widely used in the coal industry in recent years. Dr Fu Boxue carried out some fractal research in coal reservoir pores and cracks system, and analyzes the relationship among the fractal dimension, the coal pores, cracks, coal development, and the degree of degeneration, which provides a more precise way to evaluate the coalbed methane adsorption and desorption, the proliferation of seepage, coal and gas outburst prediction and the effective penetration rate estimate. Shao-Lin Lu and other researchers do some research in the outburst coal on the size of fractal, and the result shows that: outburst coal fractal characteristics cannot only give a quantitative description on outburst coal's ability to resist outside devastating forces and recognize the differences between the outburst coal and non-outburst coal from the aspect of media's mechanical behavior, but also comprehensively evaluate coal's ability to absorb and give out the gas. In addition, the fractal geometry is widely applied in analyzing the complexity of the network faults and the distribution characteristics in the region of the coal and gas outburst.

## 4 CONCLUSION

With the development of high technology in various fields, such as acoustic emission technology, electromagnetic radiation monitoring technology, Seismic technology, gas emission dynamic indicators, which all depend on the advanced monitoring technology, develops fast; although these technologies in practice need to be further improved, yet it is promising.

Inherent mechanism of coal and gas outburst is extremely complicated. The relevant laws between the influence factors of outburst and the outburst itself are not accurate and clear. The application of the traditional forecasting technique, which is based on the experience and the statistical forecasting methods based on mathematical modeling, is restrained badly. Presently, some advanced theoretical methods, such as computer simulation, fuzzy math theory, gray system theory, neural network, expert systems, fractal theory, and the theory of nonlinear<sup>[7-10]</sup>, have been applied in the quantitative evaluation and analysis of coal and gas outburst, and get some achievements.

## ACKNOWLEDGMENTS

This project was supported by the Scientific Research Fund of Sichuan Normal University (NO. 14YB01 and ZZYQ2014-05).

## REFERENCES

- [1] Nie Bai-sheng, He Xue-qiu, Wang En-yuan, etc. Present situation and progress trend of prediction technology of coal and gas outburst [J]. China Safety Science Journal, 2003, 13(6): 40-43.
- [2] Zhang Zi-xu, Liu Gao-feng, L. Run-sheng, etc. Regional forecast of coal and gas burst based on fuzzy cluster analysis and fuzzy pattern recognition [J]. Coal Geology & Exploration 2007, 35(3): 22-24.
- [3] Guo De-yong, Li Nian-you, Pei Da-wen, etc. Grey theory-neural network method on Coal and gas outburst [J]. Journal of University of Science and Technology Beijin. 2007, 29(4): 354-357.
- [4] Deng Ju-long. Basic method of Grey Theory [M], WuHan, Huazhong University of Science and Technology Press, 1987.
- [5] You Wei, Liu Ya-xiu, Li Yong, etc. Predicting the coal and gas outburst using artificial neural network [J]. Journal of China Coal Society, 2007, 32(3): 285-287.
- [6] Gao Yan-zhong, Jiang Cheng-lin. Application of Fuzzy Mathematics in Coal and gas outbursts Prediction [J]. Jiangxi Coal Science & Technology, 2002, 2: 6-8.
- [7] Qi Wang-sheng, Ling Biao-can, Cai Si-jin. Developing Trend and Perspective in the Research of Predicting the Coal and Gas Outburst [J]. China Safety Science Journal, 2003, 13(12): 1-4.
- [8] Lu Lian-ning, Zhang Ying-xin, Zhang Bao-yong, Mechanism and region prediction of coaland gas outburs [J], Journal of Heilongjiang Institute of Science & Technolog. 2007, 17(1): 33-36.
- [9] Fan Shuan-Bao. New method on coal and gas outburst prediction at inland and abroad, Ming Safety and Entironment Protection, 2000, 27(5): 258-299.
- [10] Zou Yin-hui, Zhao Xu-sheng, Liu Sheng. Research on sound transmitted continued prediction technology for coal and gas outburs [J]. Coal science and technology, 2005, 33(6): 61-64.

# The research significance of the steel reinforced recycled aggregate concrete's fire resistance

Bing Wang & Xiao Liu

*School of Architectural and Civil Engineering, Shenyang University, Shenyang, China*

Lu Gao

*School of Civil Engineering, Lanzhou University of Technology, Lanzhou, China*

**ABSTRACT:** This paper analyzes the features and significance of steel reinforced recycled aggregate concrete based on reading lots of documents. The analysis shows that steel reinforced recycled aggregate concrete is a new type of structure form can meet the requirements of bearing capacity, but also has significant environmental, economic, and social benefits. Research on the fire resistance of steel reinforced recycled aggregate concrete is the precondition of its wide application. It has important research significance.

**Keywords:** steel reinforced recycled aggregate concrete; recycled aggregate; fire resistance

## 1 INTRODUCTION

In recent years, domestic and foreign scholars on steel have systematically researched the structural performance of recycled concrete composite and made a lot of achievements [1–3]. Along with the research and engineering application, studying the fire resistance performance of concrete structure of recycled steel is becoming more and more urgent. In this paper, on the basis of the reading of vast amount of literature, we deeply analyzed the characteristics and research significance of the steel reinforced recycled aggregate concrete.

## 2 THE CHARACTERISTICS OF STEEL REINFORCED RECYCLED AGGREGATE CONCRETE

### 2.1 *The characteristics of reinforced recycled concrete*

Recycled aggregate is aggregate of the waste concrete after crushing, washing, grading, and resulting from the interaction of aggregate by certain proportion. And the use of recycled aggregates as part or all of the concrete aggregate is known as recycled aggregate concrete, recycled concrete for short. According to the size, the recycled aggregate can be divided into recycled coarse aggregate and recycled fine aggregate; according to the source it can be divided into road construction and recycled aggregate; according to the use, it

can be divided into recycled aggregate concrete, recycled aggregate, and recycled aggregate mortar block. The recycled concrete technology can realize the re-processing of waste concrete, to restore the original performance, and form the new building materials products. Thus, it not only can make the limited resources be reused, but also to solve some environmental problems, and achieve the sustainable development of the construction industry.

Because of the differences between the physical properties of recycled aggregate and natural aggregate, there is a certain difference in mechanical properties between the recycled concrete and normal concrete. The cube, prism compressive strength, and elastic modulus of recycled concrete is lower than that of ordinary concrete. The peak strain is higher than that of ordinary concrete, the ultimate strain lower than that of ordinary concrete [4].

In addition, studies have shown that after heated to 300°C, the residual compressive strength of recycled concrete has increased, and the recycled concrete replacement rate is high, the more obvious upward trend. It has obvious decline to 500°C. The reason for this phenomenon may be that the surface of recycled coarse aggregate is rough, and it makes the interface between recycled coarse aggregate and cement strengthen when they are in contact, so that the high-temperature low-impact compressive strength of recycled aggregate concrete [5].

## 2.2 *The characteristics of steel reinforced recycled aggregate concrete*

Steel reinforced recycled aggregate concrete is an independent structure of steel combined with recycled concrete. Its core part is steel, and its external for recycled concrete and with the right amount of longitudinal are bounded by pushing for reinforcement and the stirrup. The internal steel parts and outsourcing of reinforced concrete formed a whole, namely steel reinforced recycled aggregate concrete. Steel can not only take more load, provide large deformation ability, at the same time it constrains the formation of concrete at the core. The compression of concrete in a three-way state greatly improves the strength and deformation properties of recycled concrete. Steel reinforced recycled aggregate concrete is also used as recycled concrete to reduce construction waste, improve the urban environment, save the characteristics of the economy. So the steel reinforced recycled aggregate concrete structure has become a kind of structure system with ecological significance.

## 3 THE SIGNIFICANCE OF THE RESEARCH

### 3.1 *The significance of the research of recycled concrete*

A large number of construction waste increased due to the increased rate of urban construction and frequent earthquakes and other natural disasters, as shown in Figure 1. According to statistics, the number of building demolition waste and construction waste of most countries in the world accounts for about 30%–40% of the total municipal waste. And the waste concrete containing large aggregates. If they could be reasonably recycling, production of recycled concrete used in the new building, not only can reduce the cost, save natural resources, alleviate the contradiction between supply and demand of aggregate, but also reduce the environmental pollution of waste concrete. And it is an important part of the sustainable development strategy. Therefore, how to make full, efficient, economical utilization of construction waste, especially the waste concrete in many countries has become a topic of common research.

At the same time, China's construction industry is developing vigorously, the thickness of aggregate demand is very big, but will increase along with the development in the future. For such a big consumption, the earth's natural aggregate native thickness will be exhausted, so, seeking to substitute for natural aggregate is very important from the perspective of resources reasonable development use and sustainable development.



Figure 1. A large number of abandoned concrete demolition and earthquake disaster.

The application of recycled concrete, solves the problems of construction waste pollution problem and the lack of natural aggregate, has significant economic benefits, social benefits, and environmental benefits.

### 3.2 *The research significance of the fire*

The fire is the loss of control in time and space the disaster caused by burning. Fire can be divided into building fires, forest fires, traffic fire, and so on. The building fires occur frequently, causing casualties and major property damage because of the number of people and valuables at the scene of the fire; combustible variety; ignition source high frequency; limited space; and prone to secondary disasters. Not only that, but also building fire cause air pollution, destruct the ecological environment, and after fire waste has caused environmental pollution.

In recent years, with the increasing scale and the growing number of buildings, fire frequency increased. Shanghai Yuyao road Jiaozhou road teacher's apartment fire, Hongkong Garden Street in Mong Kok fire, Tianjin Jixian County building fire, Jilin Baoyuanfeng poultry company major fire accident, and Yunnan Shangri-La County dukezong fire, causing casualties and significant property damage.

Recently, our country has undergone several major fire accidents. In January 5, 2015, in Changzhou City, the building of Changzhou Mingtai textile printing and dyeing Co. Ltd. Caught fire killing 3 construction workers; in January 3, 2015, the national key cultural relics protection units Dali Gongcheng saw building fires, Gongcheng floor basically burned; in January 2, 2015, Hal Hama Kuraku fire caused collapse, causing 5 fire fighters' lives to be sacrificed along with 14 people. More than 2000 people were injured, 549 households, and part of the street merchants were affected.

Through the research on fire resistance of structures, we can effectively prevent fire by a local collapse and the overall collapse caused by the fire and personnel evacuation difficult and serious casualties. And it can provide important technical guidance for the repair and reinforcement of structure after fire, reduce the cost of repairing structure after fire, shorten the functional recovery after a disaster, and indirectly reduce economic losses caused by the fire. Therefore, the structure fire resistance design is very necessary.

#### 4 CONCLUSION

In summary, steel reinforced recycled aggregate concrete can not only meet the requirements of bearing capacity, but also has significant environmental, economic, and social benefits. Research on the fire resistance of steel reinforced recycled aggregate concrete is the precondition of its wide application. It has important research significance.

#### ACKNOWLEDGMENTS

It is a project supported by National Science Foundation (51308347); Shenyang Science Plan project (F13-171-9-00), (F14-028-2-00), and (F14-210-6-00); and Liaoning science public research funds (2014004025).

#### REFERENCES

- [1] Huang Yunbiao. Research on the Thermal Properties of Recycled Concrete [D]. Shanghai: Tongji University, 2006.
- [2] Zhou Jinghai, He Haijin, Meng Xianhong, et al. Test of basic mechanical properties of recycled concrete [J]. Journal of Shenyang Jianzhu University (Natural Science), 2010, 26(3):464-468.
- [3] Xiao Jianzhuang, Huang Yunbiao. Residual Compressive Strength of Recycled Concrete after High Temperature [J]. Journal of Building Materials, 2006, 9(3):255-259.
- [4] Xiao Jianzhuang. Experimental Investigation on Complete Stress-Strain Curve of Recycled Concrete under Uniaxial Loading [J]. Journal of Tongji University (Natural Science), 2007, 35(11):1445-1449.
- [5] Xiao Jianzhuang, Li Jiabin, Sun Zhenping, et al. Study on Compressive Strength of Recycled Aggregate Concrete [J]. Journal of Tongji University (Natural Science), 2004, 32(12):1558-156.

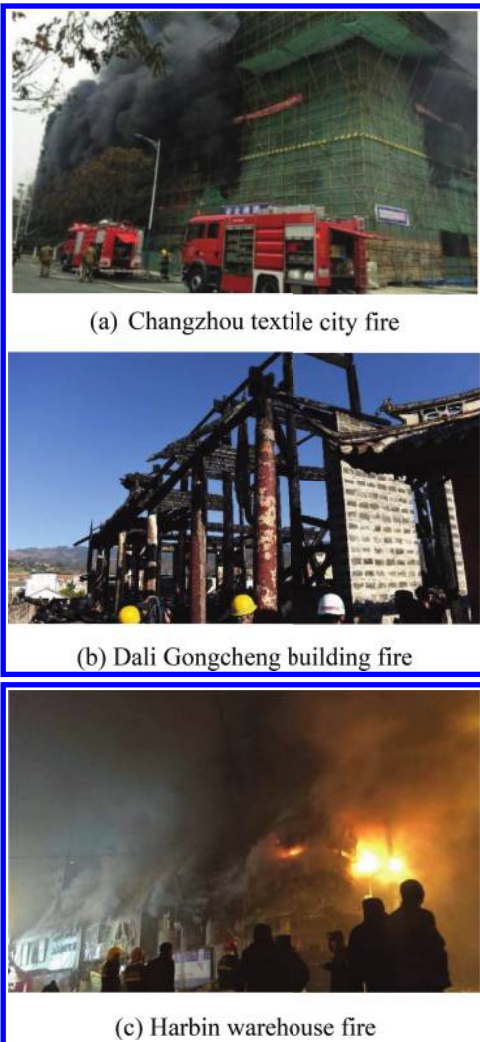


Figure 2. Building fires occur frequently.

# Constitutive model derivation and numerical simulation of iron based Shape Memory Alloy pipe joint

Wei Wang, Bo Wang, JiYuan Liu & Hong Hai

School of Civil Engineering, Shenyang Jianzhu University, Shenyang, China

**ABSTRACT:** Based on the Brinson's constitutive model of Shape Memory Alloys (SMA), and combined with the lame formula of thick wall cylinder, we deduced a simplified constitutive model for SMA pipe coupling. Using MATLAB software to compile executable program, we used this program to carry on the numerical simulation for the SMA coupling structure. The results show that under the condition of the other factors are fixed, firstly, the radial compressive stress between the SMA pipe joint and the connected pipe increases with the increase of wall thickness of SMA pipe joint; secondly, the radial compressive stress decreases with the increase of hole enlargement rate of SMA pipe coupling; lastly, the radial compressive stress decrease with the increase of diameter of connected pipe.

**Keywords:** Shape Memory Alloys; constitutive model; radial compressive stress; pipe joint; wall thickness

## 1 INTRODUCTION

Serious corrosion problems existed in oil and gas pipelines, which lead to huge economic losses. The great part of corrosion existed in the joints of pipeline, which is because the original pipe connected by welding, this method needs high technical requirements, and the welding itself has many defects. NiTi Shape Memory Alloys (NiTi SMA) have excellent shape memory properties, so it was applied earliest in military aircraft hydraulic pipeline connection. Now it has been widely used in aerospace and other fields of pipe connection. Iron base Shape Memory Alloys (Fe SMA) has many advantages, such as high strength, high restored deformation, and good property of corrosion resistance. Its phase transition temperature  $M_s$  is near the room temperature. In addition to the above advantages, the alloy of Fe SMA is easy to process and its price is cheaper than NiTi SMA. Due to the above advantages, this alloy is widely used in pipeline connection in the field of petroleum, chemical industry, and so on.

The Fe SMA pipeline joints are easy to keep at room temperature, due to its inverse phase transition temperature is above room temperature. Because the inner diameter of pipe joint is smaller than the outer diameter of connected pipe, the joint diameter expands in room temperature, then the joint can be set on the outside of the connected pipe. And then to heat the pipe joint, the SMA joint is induced the shape memory effect because

of the increasing temperature, the radius of the joint becomes narrow. At last the joint and pipeline connected together tightly.

This paper, using the Brinson's constitutive model derived previously, and combined with the lame formula of thick wall cylinder, we deduced simplified constitutive model for SMA pipe coupling to simulate the structure of SMA fittings, to study the effect of different factors to the fastening force (radial compressive stress) between SMA joint and pipeline.

## 2 BRINSON'S MODEL FOR SMAS

Brinson [1] divided the martensite fraction into two parts  $\xi_T$  and  $\xi_S$ , where  $\xi_T$  represents the fraction of material that is purely temperature-induced martensite with multiple variants and  $\xi_S$  denotes the fraction of the material that has been transformed, or oriented, by stress into a single martensite variant, the constitutive relation of SMA can be expressed as:

$$\sigma - \sigma_0 = D(\xi)\bar{\epsilon} - D(\xi_0)\bar{\epsilon}_0 + \Omega(\xi)\xi_S - \Omega(\xi_0)\xi_{S0} + \Theta(T - T_0) \quad (1)$$

### 2.1 Conversion to detwinned martensite

For  $T > M_s$  and  $\sigma_s^{er} + C_M(T - M_s) < S < \sigma_f^{er} + C_M(T - M_s)$

$$\xi_s = \frac{1 - \xi_{s0}}{2} \cos \left\{ \frac{\pi}{\sigma_s^{cr} - \sigma_f^{cr}} (S - \sigma_f^{cr} - C_M (T - M_s)) \right\} + \frac{1 + \xi_{s0}}{2} \quad (2)$$

$$\xi_T = \xi_{T0} - \frac{\xi_{T0}}{1 - \xi_{s0}} (\xi_s - \xi_{s0}) \quad (3)$$

For  $T < M_s$  and  $\sigma_s^{cr} < \sigma < \sigma_f^{cr}$

$$\xi_s = \frac{1 - \xi_{s0}}{2} \cos \left\{ \frac{\pi}{\sigma_s^{cr} - \sigma_f^{cr}} (S - \sigma_f^{cr}) \right\} + \frac{1 + \xi_{s0}}{2} \quad (4)$$

$$\xi_T = \xi_{T0} - \frac{\xi_{T0}}{1 - \xi_{s0}} (\xi_s - \xi_{s0}) + \Delta_{T\xi} \quad (5)$$

where, if  $M_f < T < M_s$  and  $T < T_0$

$$\Delta_{T\xi} = \frac{1 - \xi_{T0}}{2} \left[ \cos(a_M (T - M_f)) + 1 \right]$$

else

## 2.2 Conversion to autenite

$$C_A(T - A_f) < \sigma < C_A(T - A_s)$$

For and  $\Delta_{T\xi} = 0$

$$\xi = \frac{\xi_0}{2} \left\{ \cos \left[ a_A \left( T - A_s - \frac{S}{C_A} \right) \right] + 1 \right\} \quad (6)$$

$$\xi_s = \xi_{s0} - \frac{\xi_{s0}}{\xi_0} (\xi_0 - \xi) \quad (7)$$

$$\xi_T = \xi_{T0} - \frac{\xi_{T0}}{\xi_0} (\xi_0 - \xi) \quad (8)$$

$T > A_s$

## 3 STRESS STATE BETWEEN PIPELINE AND SMA PIPE JOINT

By the elastic-plastic theory, the stress state between pipeline and SMA joint meet the thick wall cylinder problem of plane axisymmetric problem [2]. Because of the austenitic phase transformation, the connected pipe limits the shape recovery of SMA joint, so the SMA joint can produce restore stress. The recovery stress provides the hoop stress  $\sigma_\theta$  in the pipe joint system. And then the radial compressive stress  $\sigma_r$  produced in the pipeline and SMA joint P2, the connected pipes thus produced fastening

force P2, and the connected pipelines and SMA joint connected together tightly. The stress analysis of pipe coupling structure is shown in Figure 1.

According to the lame formula, we can get the relationship of hoop stress, radial stress, and fastening force in the connected pipelines just as follows [3]:

$$\sigma_{sr} = -\frac{R_b^2 P_2}{R_b^2 - R_a^2} \left( 1 - \frac{R_a^2}{r^2} \right) \quad (9)$$

$$\sigma_{s\theta} = -\frac{R_b^2 P_2}{R_b^2 - R_a^2} \left( 1 + \frac{R_a^2}{r^2} \right) \quad (10)$$

Can also get the relationship of hoop stress, radial stress, and fastening force in the connected pipelines just as follows:

$$\sigma_r = \frac{R_c^2 P_1}{R_d^2 - R_c^2} \left( 1 - \frac{R_d^2}{r^2} \right) \quad (11)$$

$$\sigma_\theta = \frac{R_c^2 P_1}{R_d^2 - R_c^2} \left( 1 + \frac{R_d^2}{r^2} \right) \quad (12)$$

By above formula can deduce the expressions of radial stress and fastening force using hoop stress:

$$P_1 = \frac{\left( \frac{R_d^2}{R_c^2} - 1 \right)}{1 + \frac{R_d^2}{r^2}} \sigma_\theta \quad (13)$$

$$\sigma_r = \frac{\left( 1 - \frac{R_d^2}{r^2} \right)}{1 + \frac{R_d^2}{r^2}} \sigma_\theta \quad (14)$$

$$p_1 = -p_2 \quad (15)$$

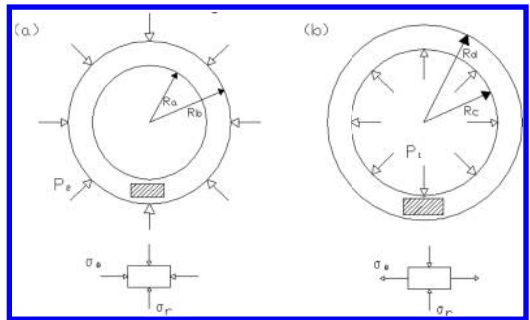


Figure 1. Stress analysis of pipe coupling system.



#### 4 NUMERICAL SIMULATION AND CALCULATION ANALYSIS

The radius of SMA joint in parent phase is smaller than the radius of connected pipes, expanding the diameter under low temperature, in this process, the twin martensite transformation to detwined martensite by the external force, then heating the SMA joint, the joint wants to restore the radius before expanded. But the recovery is limited by the connected pipes, so the SMA joint produce large recovery force. Write the MATLAB program according to the relevant transformation formulas in the reference (1) and formula (13)–(14), to simulate the structure of SMA pipe coupling, analysis the relationships of fastening force and hole enlargement ratio, wall thickness of pipe, and the radius of connected pipe.

The parameter of SMA joint as follows: moduli  $D_a = 67000\text{Mpa}$ ,  $D_m = 26300\text{Mpa}$ , transformation temperature  $M_f = -9\text{ }^\circ\text{C}$ ,  $M_s = 0\text{ }^\circ\text{C}$ ,  $A_s = 80\text{ }^\circ\text{C}$ ,  $A_f = 250\text{ }^\circ\text{C}$ , transformation constants  $C_M = 8\text{ MPa}/^\circ\text{C}$ ,  $C_A = 13.8\text{ MPa}/^\circ\text{C}$ ,  $\sigma_s^{cr} = 100\text{Mpa}$ ,  $\sigma_f^{cr} = 170\text{Mpa}$ . The sizes of connected pipe are  $R_a = 34\text{ mm}$ ,  $R_b = 42\text{ mm}$  respectively. Here assume that the connected pipe is rigid, and the radius is fixed.

Example 1: chose the expanding rate of SMA joint from 0.022 to 0.13, the thickness of SMA joint is 12 mm, and the outer radius of connected pipe is 42 mm. The results are shown in Figure 2, know from the curve that the radial pressure decreases from 108.7 Mpa to 41.3 Mpa. This is mainly because the deformation of SMA joint increases with the increase of hole enlargement ratio, which lowered the recovery stress of SMA pipe joint. So in practical application, while increase the rate of hole enlargement can convenience construction, it will also reduce the recovery stress of SMA pipe joint, and affect the values of fastening force.

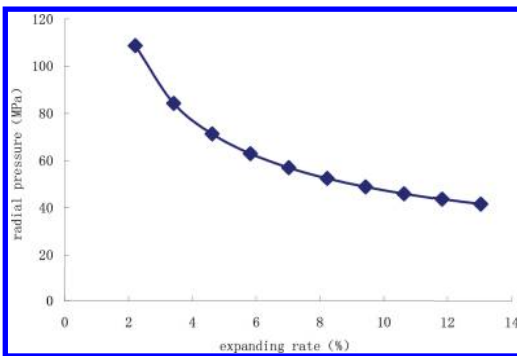


Figure 2. Relationship between radial pressure and expanding rate.

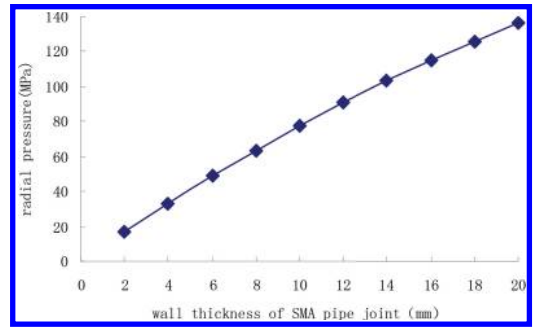


Figure 3. The relationship between radial pressure and wall thickness.

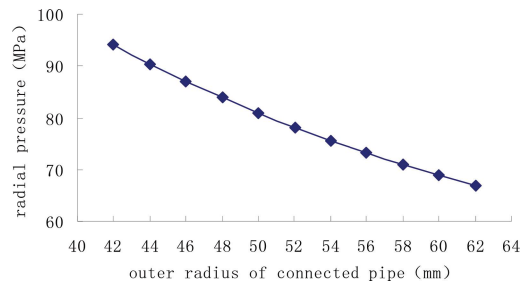


Figure 4. Relationship between radial pressure and outer radius of connected pipe.

Example 2: If the wall thickness of SMA joint is from 2 mm to 20 mm, the expanding rate of SMA joint is 3%, and the outer radius of connected pipe is 42 mm. The results are shown in Figure 3, know from the curve that the radial pressure increases from 17.1 Mpa to 136.7 Mpa. According to the formula (11), when the tangential stress is fixed, the radial compressive stress changed as the change of wall thickness of SMA pipe joint.

Example 3: chose outer radius of connected pipe from 42 mm to 62 mm, the expanding rate is 3%, and wall thickness of SMA joint is 12 mm. The results are shown in Figure 4, know from the curve that the radial pressure decreases from 94.0 Mpa to 66.9 Mpa.

#### 5 CONCLUSIONS

Based on the Brinson's constitutive model of Shape Memory Alloys (SMA), combined with the state of stress distribution between the pipe and pipe joint, get a simplified constitutive model, which fit the SMA pipe coupling structure. Use this constitutive model to simulate the stress distribution during the process of heating up, system discuss the relationship between the radial compressive stress

and various influencing factors. The simulation results show the radial compressive stress increase with the increase of wall thickness of SMA pipe joint, and the radial compressive stress decrease with the increase of hole enlargement ratio of SMA pipe joint and outer radius of connected pipe. Therefore, according to the practical engineering, selecting suitable thickness of SMA pipe wall, hole enlargement ratio, and outer radius of connected pipe, to achieve optimal results.

#### ACKNOWLEDGMENTS

This work was financially supported by the Youth Foundation of National Natural Science (51308357) and the Science and Technology Planning Project

of ministry of housing and urban-rural development (2013-K2-38).

#### REFERENCES

- [1] L.C. Brinson. One-dimensional constitutive behavior of shape memory alloy: thermo-mechanical derivation with non-constant material functions and redefined martensite internal variable [J]. *Journal of Intelligent Material Systems and Structures*, 1993, 4 (2): 229–242.
- [2] Yin X.Q, Gao B.D, Mi X.J. Numerical Simulation of Radial Pressures for TiNiNb Pipe-Couplings [J], *Chinese Journal of Rare Metals*, 2008, 32(5): 579–583.
- [3] Xu B.Y, Liu X.S. *Application of Elastic-plastic mechanics* [M]. Beijing: Tsinghua university Press, 1995, 183.

# Evaluation on thermal stress distribution of a cable-stayed footbridge under temperature loading

X.F. Fan, B. Chen & Y.J. Jiang

*School of Civil Engineering and Architecture, Wuhan University of Technology, Wuhan, China*

Y.Q. Xu

*Key Laboratory of Roadway Bridge and Structural Engineering, Wuhan University of Technology, Wuhan, China*

**ABSTRACT:** The thermal stress distribution of a cable-stayed footbridge is investigated in this study through numerical computation. With appropriate assumption, the temperature field of the footbridge is simplified and divided into several components. Fine finite element models are constructed for the deck plate, bridge section, and bridge tower to calculate the structural thermal stress distribution. The made observations demonstrate that the temperature induced stresses of the footbridge is substantially large, which should be taken in consideration in the maintenance process.

**Keywords:** thermal effect; footbridge; numerical simulation; thermal stress

## 1 INTRODUCTION

To be a kind of important traffic infrastructures, footbridges are widely-constructed and applied across the world for the last hundreds years. Footbridges are in the open air and inevitably subjected to daily, seasonal and yearly environmental thermal effects. Variations of temperature in footbridge components will cause movements due to indeterminacy and non-uniform distribution of temperature, which may induce the non-uniform thermal stress distribution. It is frequently reported that many footbridges across the world are damaged due to the thermal stress effects. The thermal behaviour of bridges has been investigated more than two decades. Zuk investigated the thermal behaviour of several highway bridges and found that the temperature distribution was affected by air temperature, wind, humidity, intensity of solar radiation and material type. Capps measured temperature and longitudinal movements of a steel box bridge in the UK. Early studies in the field include Priesley, and Churchward and Sokai among others.

The thermal stress distribution of a cable-stayed footbridge is investigated in this study through numerical computation. With appropriate assumption, the temperature field of the footbridge is simplified and divided into several components. Fine finite element models are constructed for the deck plate, bridge section, and bridge tower to calculate the structural thermal stress distribution. The made observations demonstrate that the temperature induced stresses of the footbridge is substantially

large, which should be taken in consideration in the maintenance process.

## 2 DESCRIPTION OF THE CABLE-STAYED FOOTBRIDGE

A cable-stayed footbridge constructed in China is taken as the example to examine the thermal stress



Figure 1. Plan view of the footbridge.

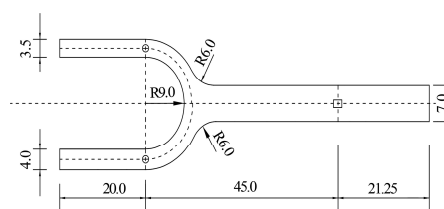


Figure 2. Elevation view of the footbridge.

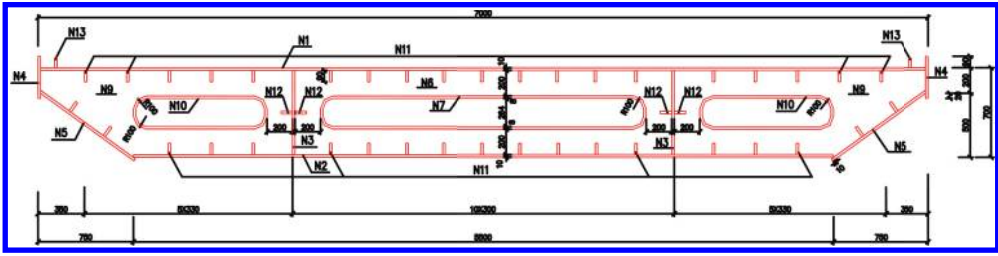


Figure 3. Cross section of the box beam in the main span.

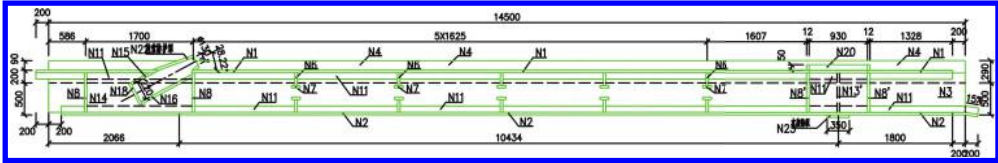


Figure 4. Longitudinal section of the box beam in the main span.

distribution through numerical computation. The elevation view and plane view of the footbridge are displayed in Figures 1 and 2, respectively. It is seen that the footbridge has a single tower and eight stayed cables. The main span is constructed by using steel box girder while the south part of the footbridges is fabricated using concrete piers. The main span is 45 m and the total length of the footbridge is 88.25 m. The height of the tower is 24.5 m above from the ground. Displayed in Figure 3 is the cross section of the box beam in the main span. The width and thickness of the bridge deck are 7.0 m and 0.7 m, respectively.

### 3 THERMAL EFFECT ANALYSIS

#### 3.1 Solar radiation

The flow of heat in a solid is governed by the well-known Fourier partial differential equation. For the footbridge under the solar radiation, it can be assumed that thermal variation in the direction of the longitudinal axis is normally not significant. Consequently, the temperature field  $T$  of a bridge cross section at any time  $t$  can be expressed by a two-dimensional heat flow equation as

$$k \left( \frac{\partial^2 T}{\partial x^2} + \frac{\partial^2 T}{\partial y^2} \right) = \rho c \frac{\partial T}{\partial t} \quad (1)$$

in which  $x$  and  $y$  are Cartesian coordinates,  $k$  is the isotropic thermal conductivity coefficient,  $\rho$  is the density of material, and  $c$  is the specific heat of the material.

For a bridge subjected to solar radiation, the thermal energy transferred between the bridge surface and environment consists of convection  $q_c$ , thermal irradiation  $q_r$ , and solar radiation  $q_s$ . The rate of heat transfer by convection  $q_c$  is associated with the movement of the air particles. It depends on the convection heat transfer coefficient  $h_c$  and difference between the air temperature  $T_a$  and the bridge surface temperature  $T_s$  as

$$q_c = h_c(T_a - T_s) \quad (2)$$

The heat transfer between the bridge surface and the surrounding environment due to thermal irradiation can be expressed in a quasi-linear form as

$$q_r = h_r(T_a - T_s) \quad (3)$$

where  $h_r$  is radiation heat transfer coefficient. The rate of heat absorbed by the bridge surface due to solar radiation  $q_s$  is

$$q_s = \alpha I \quad (4)$$

where  $\alpha$  ( $0 < \alpha < 1$ ) is absorptivity coefficient of the surface material;  $I$  is solar radiation including direct solar radiation, diffuse solar radiation, and reflected solar radiation on a surface, respectively. Then, the temperature variations of the footbridge can be computed with the aids of the finite element method. After that, the temperature variations of the footbridge can be taken as the thermal loading acting on the footbridge to compute the structural thermal effects, such as displacement and stress distribution.

### 3.2 Thermal stress

The displacement of the footbridge can be expressed as

$$\mathbf{u} = \mathbf{N}\mathbf{a} \quad (5)$$

where  $\mathbf{u}$  is the displacement of a certain place;  $\mathbf{a}$  is the displacement vector,  $\mathbf{N}$  is the matrix of the shape function.

The stress vector  $\boldsymbol{\sigma}$  can be expressed as

$$\begin{aligned} \boldsymbol{\sigma} &= [\sigma_x, \sigma_y, \sigma_z, \tau_{xy}, \tau_{yz}, \tau_{zx}]^T \\ &= \mathbf{D}(\boldsymbol{\epsilon} - \boldsymbol{\epsilon}_T) = \mathbf{D}(\mathbf{B}\mathbf{a} - \boldsymbol{\epsilon}_T) \end{aligned} \quad (6)$$

$$\boldsymbol{\epsilon} = [\epsilon_x, \epsilon_y, \epsilon_z, \gamma_{xy}, \gamma_{yz}, \gamma_{zx}]^T \quad (7)$$

$$\boldsymbol{\epsilon}_T = [\alpha_T T, \alpha_T T, \alpha_T T, 0, 0, 0]^T \quad (8)$$

where  $\boldsymbol{\epsilon}$  is the stress vector;  $\boldsymbol{\epsilon}_T$  is the strain induced by temperature variation;  $\mathbf{D}$  is the elastic matrix.  $\nu$  is the passion ratio;  $\alpha_T$  is the thermal expansion coefficient;  $T$  is the temperature change;  $E$  is the Young's modulus.

The force equivalent equation of footbridge under thermal loading can be expressed as

$$\mathbf{K}\mathbf{a} = \mathbf{f}_T \quad (9)$$

where  $\mathbf{K}$  is the entire stiffness matrix of the footbridge;  $\mathbf{f}_T$  is the thermal loading of the footbridge which can be expressed as the sum of thermal loading of each element

$$\mathbf{f}_T = \sum_{i=1}^{ne} \mathbf{f}_T^i \quad (10)$$

$$\mathbf{f}_T^i = \int_v \mathbf{B}_i^T \mathbf{D} \boldsymbol{\epsilon}_T dv \quad (11)$$

where  $\mathbf{B}_i$  is the strain-displacement matrix of the  $i$ th element.

## 4 FINITE ELEMENT MODEL

The finite element model of the cable-stayed footbridge is established by using the commercial package ANSYS as shown in Figure 5. The cables of the footbridge are simulated by using the link elements while the steel box girder is simulated by using shell elements. The two concrete piers are modeled by using three dimensional beam elements. The tower is fabricated using steel plate and is also simulated by using shell63 elements. The deck, tower and cable are constructed by using steel and the

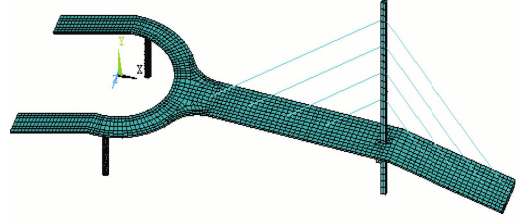


Figure 5. Finite element model of the cable-stayed footbridge.

Table 1. Material properties of the cable-stayed bridge.

	Young's modulus (GPa)	Density (kg/m <sup>3</sup> )
Deck and tower	210	7900
Cable	210	7900
Pier	25	2500

pier is constructed by using concrete. The Young's moduli of the steel and concrete material are 210 and 25 GPa, respectively. The densities of the steel and concrete material are 7900 and 2500 kg/m<sup>3</sup>, respectively. The basic material parameters are listed in Table 1. In the thermal effects analysis, the reference temperature of the footbridge is supposed as the 10°C. Two loading scenarios are taken into consideration, namely the temperature of the bridge increased by 10°C (case No. 1) and 20°C (case No. 2) in the summer, respectively.

It is well-known that there exists some sag for the fixed cable subjected to self-weight. The axial stiffness of the cable may be affected by the sag, which can be modified based on Ernst expression:

$$E_{eq} = \frac{E}{1 + \frac{(wl)^2 AE}{12T^2}} \quad (12)$$

In which:  $E$  is the Young's modulus of the material,  $A$  is the cross-section area of the cable,  $T$  is the tension force of the cable,  $w$  is the weight of the cable per meter;  $l$  is the projected length of the cable on horizontal plane.

## 5 STRESS DISTRIBUTION

Displayed in Figures 6 and 7 are the contours of the footbridge for the 10°C and 20°C temperature increase, respectively. Listed in Table 1 are the stresses of some typical nodes.

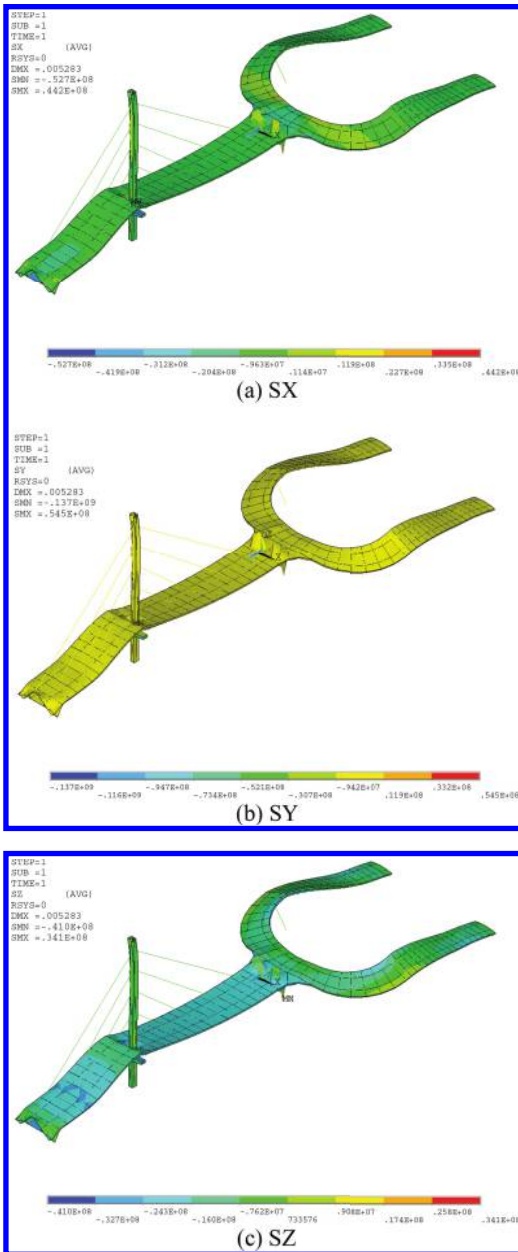


Figure 6. Nodal stress contour of the footbridge (case No. 1).

The made observations demonstrate that the peak tensile stress and pressure stress of the bridge in the  $x$  direction SX are 44.2 MPa and  $-52.7$  MPa, respectively. The made observations demonstrate that the peak tensile stress and pressure stress of the bridge in the  $y$  direction SY are 54.5 MPa

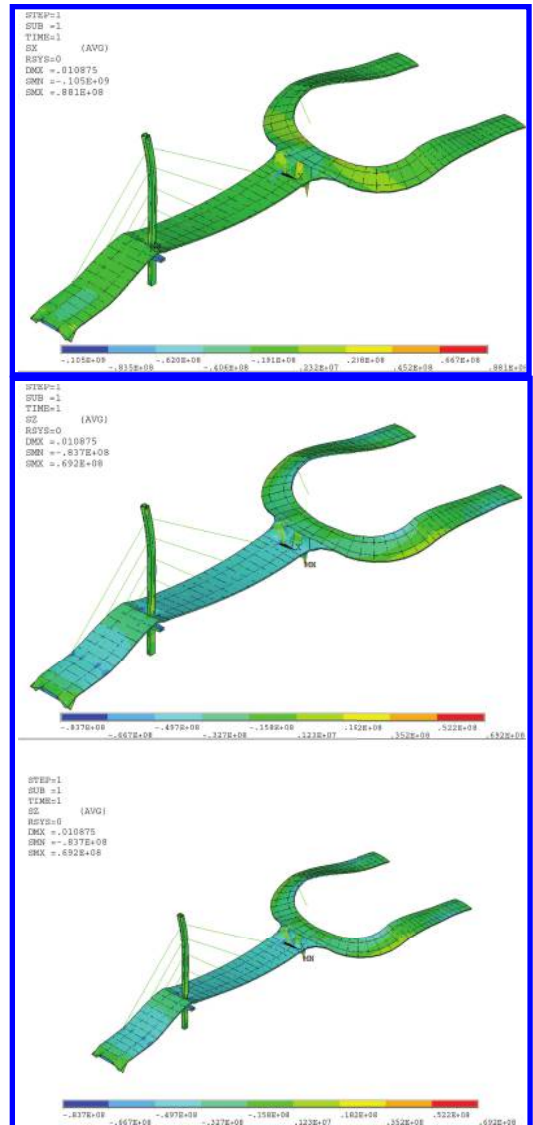


Figure 7. Nodal stress contour of the footbridge (case No. 2).

and  $-137$  MPa, respectively. The made observations demonstrate that the peak tensile stress and pressure stress of the bridge in the  $z$  direction SZ are 34.1 MPa and  $-41.0$  MPa, respectively. It is well know that the  $10^{\circ}\text{C}$  temperature increase in the summer for a single day is very common and even larger. Therefore, it is expected that the thermal stress of the footbridge in a whole day can reach more than 100 MPa and even more. These observations should be taken in consideration in the maintenance process.

Table 2. Nodal stress for scenario No. 1 (case No. 1).

	Node	SX (MPa)	SY (MPa)	SZ (MPa)
Tower	13411	-31.5	-31.4	0.0
	13362	-31.7	-31.3	0.0
	13410	-32.5	-28.2	0.0
	13389	-32.3	-25.9	0.0
Deck	2449	-39.3	-0.033	-28.2
	12569	-40.1	-0.037	-28.7
	12484	-38.5	-0.061	-37.9
	2503	43.9	0.00	-18.9

## 6 CONCLUSIONS

The thermal stress distribution of a cable-stayed footbridge is examined in this study through numerical simulation. The finite element model of the cable-stayed footbridge is established with the aiding of the commercial package. The reference temperature of the footbridge is supposed as the 10°C and the temperature of the bridge is assumed to increase by 10°C to simulate the solar radiation effects in the summer. The made observations demonstrate that the temperature induced stresses of the footbridge is substantially large, which should be taken in consideration in the maintenance process.

## ACKNOWLEDGEMENTS

The writers are grateful for the self-determined and innovative research funds of WUT (Undergraduate project No. 146606002), the financial support from the National Natural Science Foundation of China (51178366), the Natural Science Foundation of Hubei Province (2014CFA026), the open fund of the Engineering Research Center for Bridge Safty Monitoring and Reinforcing of

Hubei Province (QLZX2014013). The correspondence author is B. Chen, cbsteven@163.com.

## REFERENCES

- Chen, B., Xu, Y.L. (2007). A new damage index for detecting sudden change of structural stiffness, *International Journal of Structural Engineering and Mechanics*, 26(3): 315–341.
- Chen, B., Chen, Z.W., Sun, Y.Z., Zhao, S.L. (2013). Condition assessment on thermal effects of a suspension bridge based on SHM oriented model and data, *Mathematical Problems in Engineering*, Vol.2013, Article ID 256816, 1–18.
- Dallard, Y.P. Fitzpatrick, A.J. The London Millennium footbridge. *The Structural Engineer*, 2001, 79(22): 17–33.
- Chen, B., Sun, Y.Z., Wang, G.J., Duan, L.Y. (2014). Assessment on time-varying thermal loading of engineering structures based on a new solar radiation model, *Mathematical Problems in Engineering*, Vol. 2014, Article ID 639867, 1–15.
- Chen, B., Zhao, S.L., Li, P.Y. (2014). Application of Hilbert-Huang transform in structural health monitoring: a state-of-the-art review, *Mathematical Problems in Engineering*, Vol.2014, Article ID 317954, 1–23.
- Farrar, C.R., and James, G.H., III. System identification from ambient vibration measurements on a bridge. *Journal of Sound and Vibration*, 1997, 205(1), 1–18.
- Chen, B., Guo W.H., Li P.Y., Xie W.P. (2014). Dynamic responses and vibration control of the transmission tower-line system: a state-of-the-art-review, *The Scientific World Journal*, Vol.2014, Article ID 538457, 1–20.
- Chen, B., Chen, Z.W., Wang, G.J., Wei, P.X. (2014). Damage detection on sudden stiffness reduction based on discrete wavelet transform, *The Scientific World Journal*, Vol. 2014, Article ID 807620, 1–16.
- Chen, B., Sun, Y.Z., Li, Y.L., Zhao, S.L. (2014). Control of seismic response of a building frame by using hybrid system with magnetorheological dampers and isolators, *Advances in Structural Engineering*, 17(8): 1199–1215.

# Investigation on dynamic properties of a steel-concrete composite cable-stayed footbridge

Xia Fei

CCCC Second Highway Consultants Co. Ltd. (CCSHCC), Wuhan, China

**ABSTRACT:** Footbridges are inevitably subjected to environmental effects, such as wind, traffic induced vibration, human activities and temperature variations. The investigation on the dynamic characteristics of the footbridges is of much importance and is a direct and crucial approach to reflect the structural dynamics responses and assess the structural performance. To this end, a cable-stayed footbridge is taken as a real example to investigate properties of the natural frequency and the mode shapes through finite element analysis in this study. The deck, tower and cable are simulated by using the shell element, beam element and cable element, respectively. The mass matrix of the cable is the lumped mass matrix. The axial stiffness of the cable affected by the sag is modified based on the Ernst expression. The made observation indicate that the dynamic properties of the steel-concrete composite cable-stayed footbridge are different to those of the common long span cable-stayed bridge.

**Keywords:** natural frequency; mode shape; footbridge; dynamic property

## 1 INTRODUCTION

Footbridges are inevitably subjected to environmental effects, such as wind, traffic induced vibration, human activities and temperature variations. The environmental effects may induce the excessive vibration of the footbridges. Vibration of footbridges induced by human activities has been frequently observed across the world. It is well-known that if the lower natural frequencies are close to the frequency of the human activities, resonance of the footbridge can be expected. Therefore, the investigation on the dynamic characteristics of the footbridges is of much importance and is a direct and crucial approach to reflect the structural dynamics responses and assess the structural performance.

To this end, a cable-stayed footbridge is taken as a real example to investigate properties of the natural frequency and the mode shapes through finite element analysis in this study. The deck, tower and cable are simulated by using the shell element, beam element and cable element, respectively. The stiffness and mass matrices of the deck and tower are constructed by using the finite element method. The stiffness matrix of the cable is the combination of the linear stiffness matrix and nonlinear stiffness matrix. The mass matrix of the cable is the lumped mass matrix. The axial stiffness of the cable affected by the sag is modified based on the Ernst expression. The made observation indicate that the first mode shape is the lateral vibration of tower. The second mode shape is the

vertical vibration of the deck. The third one is the first order torsional rotation of the deck. These observations are different to those of the common long span cable-stayed bridge.

## 2 DESCRIPTION OF THE CABLE-STAYED FOOTBRIDGE

A cable-stayed footbridge constructed in China is taken as the example to examine the structural

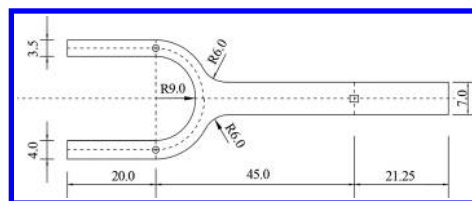


Figure 1. Plan view of the footbridge.

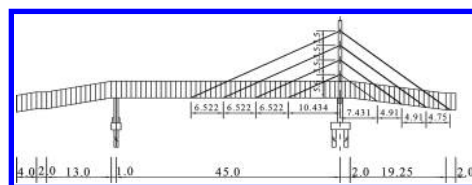


Figure 2. Elevation view of the footbridge.



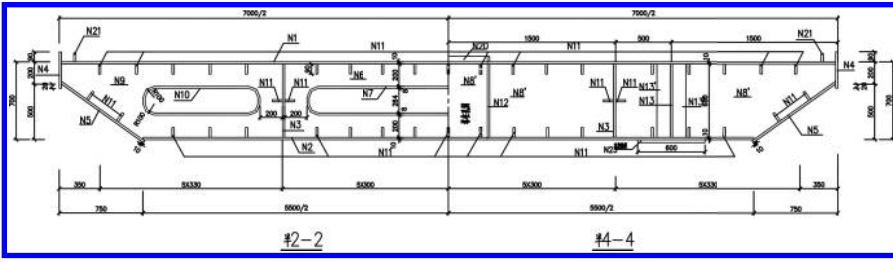


Figure 3. Cross section of the box beam in the main span.

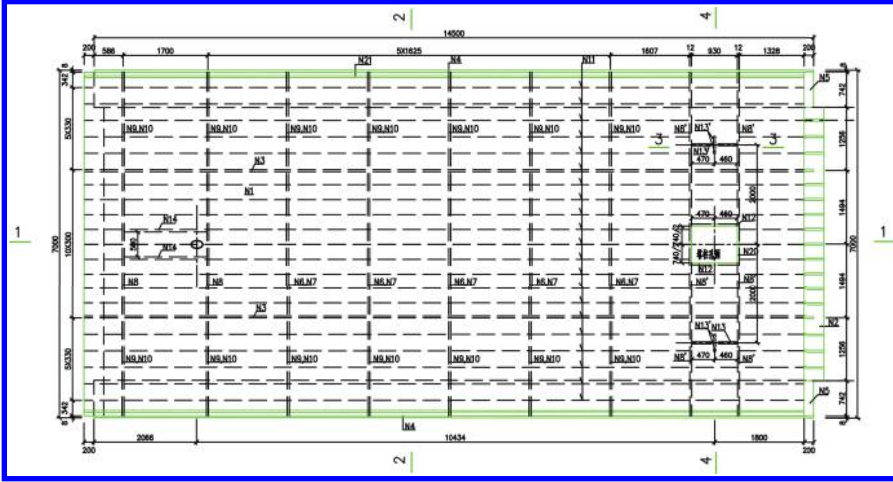


Figure 4. Plane view of the bridge deck in the main span.

dynamic characteristics through the finite element analysis.

The elevation view and plane view of the footbridge are displayed in Figures 1 and 2, respectively. The cross section of the box beam and the plane view of the bridge deck in the main span are displayed in Figures 3 and 4, respectively. It is seen that this is a cable-stayed footbridge with single tower and eight stayed cables. The main span is constructed by using steel box girder while the south part of the footbridges is fabricated using two concrete piers. The main span of the footbridge is 45 m and the total length of the footbridge is 88.25 m. The height of the tower is 24.5 m above from the ground. Displayed in Figure 3 is the cross section of the box beam in the main span, respectively. The width and thickness of the bridge deck are 7.0 m and 0.7 m, respectively.

### 3 FINITE ELEMENT MODEL

As a typical traffic structure, a footbridge can be analyzed based on finite element method by

adopting shell elements, beam elements and cable elements. The element stiffness and mass matrices in the global coordinate system (GCS) are expressed as

$$\bar{\mathbf{K}}_e^{(m)} = \mathbf{T}_a^{(m)T} \mathbf{K}_e^{(m)} \mathbf{T}_a^{(m)} \quad (1)$$

$$\bar{\mathbf{M}}_e^{(m)} = \mathbf{T}_a^{(m)T} \mathbf{M}_e^{(m)} \mathbf{T}_a^{(m)} \quad (2)$$

where  $\mathbf{K}_e^{(m)}$  is the element stiffness matrix in the local coordinate system (LCS);  $\bar{\mathbf{K}}_e^{(m)}$  is the element stiffness matrix in the GCS;  $\mathbf{M}_e^{(m)}$  is the element mass matrix in the LCS;  $\bar{\mathbf{M}}_e^{(m)}$  is the element stiffness matrix in the GCS;  $\mathbf{T}_a^{(m)}$  is the transform matrix.

After determining the element stiffness and mass matrices in the global coordinate system, one can construct the position matrix of elements  $\mathbf{T}_c^{(m)}$  following the FEM connection information of each element under both local and global coordinate systems. Thus, the global stiffness and mass matrices of the footbridge can be formed to establish the three dimensional finite element model

$$\mathbf{K}_T = \sum_{m=1}^{ne} \mathbf{T}_c^{(m)T} \bar{\mathbf{K}}_e^{(m)} \mathbf{T}_c^{(m)} = \sum_{m=1}^{ne} \mathbf{T}^{(m)T} \mathbf{K}_e^{(m)} \mathbf{T}^{(m)} \quad (3)$$

$$\mathbf{M}_T = \sum_{m=1}^{ne} \mathbf{T}_c^{(m)T} \bar{\mathbf{M}}_e^{(m)} \mathbf{T}_c^{(m)} = \sum_{m=1}^{ne} \mathbf{T}^{(m)T} \mathbf{M}_e^{(m)} \mathbf{T}^{(m)} \quad (4)$$

where  $ne$  is the total number of elements of the footbridge model;  $\mathbf{T}^{(m)}$  is the freedom transform matrix from element coordinate system to global coordinate system, which is the product of coordinate transformation matrix  $\mathbf{T}_a^{(m)}$  and position matrix  $\mathbf{T}_c^{(m)}$  of the  $m$ th element

$$\mathbf{T}^{(m)} = \mathbf{T}_a^{(m)} \mathbf{T}_c^{(m)} \quad (5)$$

The stayed cables can be constructed by using steel cable, which can be modelled by using cable elements based on the finite element method. The element stiffness matrix  $\mathbf{K}_{l,e}$  in the LCS is given by

$$\mathbf{K}_{l,e} = \begin{bmatrix} \mathbf{k}_c & -\mathbf{k}_c \\ -\mathbf{k}_c & \mathbf{k}_c \end{bmatrix} \quad (6)$$

In which: the submatrix  $\mathbf{k}_c$  consists of the linear stiffness matrix  $\mathbf{k}_l$  and the nonlinear stiffness matrix  $\mathbf{k}_{nl}$

$$\mathbf{k}_c = \mathbf{k}_l + \mathbf{k}_{nl} \quad (7)$$

The mass matrix of the cable can be expressed by using the lumped mass assumption. To examine the dynamic responses of the footbridge, the finite element model of the cable-stayed footbridge is established with the aiding of commercial package ANSYS as shown in Figure 5.

$$\mathbf{K} = \mathbf{K}_T + \sum_{i=1}^{nl} \mathbf{K}_l^i \quad (8)$$

$$\mathbf{M} = \mathbf{M}_T + \sum_{i=1}^{nl} \mathbf{M}_l^i \quad (9)$$

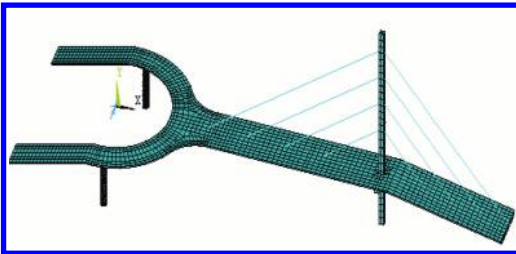


Figure 5. Finite element model of the cable-stayed footbridge.

where  $\mathbf{K}$  and  $\mathbf{M}$  are the stiffness matrix and mass matrix of the footbridge;  $\mathbf{K}_T$  and  $\mathbf{M}_T$  are the stiffness matrix and mass matrix of the deck and tower;  $\mathbf{K}_l$  and  $\mathbf{M}_l$  are the stiffness matrix and mass matrix of the bridge cables in the GCS.

The mass and stiffness matrices for all the cables can be constructed by summarizing the element matrices of each individual cable. In addition, the mass and stiffness matrices of the transmission tower-line system can be established by combining the contribution of towers, deck and cable.

#### 4 DYNAMIC PROPERTY

The finite element model of the cable-stayed footbridge is established with the aiding of the commercial package ANSYS as shown in Figure 5. The cables of the footbridge are simulated by using the link elements while the steel box girder is simulated by using shell elements. The two concrete piers are modeled by using three dimensional beam elements. The tower is fabricated using steel plate and is also simulated by using shell63 elements. The deck, tower and cable are constructed by using steel and the pier is constructed by using concrete. It is well-known that there exists some sag for the fixed cable subjected to self-weight. The axial stiffness of the cable may be affected by the sag, which can be modified based on Ernst expression:

$$E_{eq} = \frac{E}{1 + \frac{(wl)^2 AE}{12T^2}} \quad (10)$$

In which:  $E$  is the Young's modulus of the material,  $A$  is the cross-section area of the cable,  $T$  is the tension force of the cable,  $w$  is the weight of the cable per meter;  $l$  is the projected length of the cable on horizontal plane.

The basic material parameters are listed in Table 1. The natural frequencies and modal shapes are computed by using subspace iteration algorithm.

The first six natural frequencies and modal shapes are listed in Table 2 and Figures 6 to 11, respectively. It is found that the first natural

Table 1. Material properties of the cable-stayed bridge.

	Young's modulus (GPa)	Density (kg/m <sup>3</sup> )
Deck and tower	210	7900
Cable	210	7900
Pier	25	2500

Table 2. Modal properties of the footbridge deck.

No.	Freq. (Hz)	Modal shape
1	1.448	1st Lateral vibration mode of tower
2	2.272	1st Vertical vibration mode of deck
3	2.528	1st Torsional vibration mode of deck
4	3.664	2nd Vertical vibration mode of deck
5	4.205	2nd Torsional vibration mode of deck
6	5.621	3rd Vertical vibration mode of deck

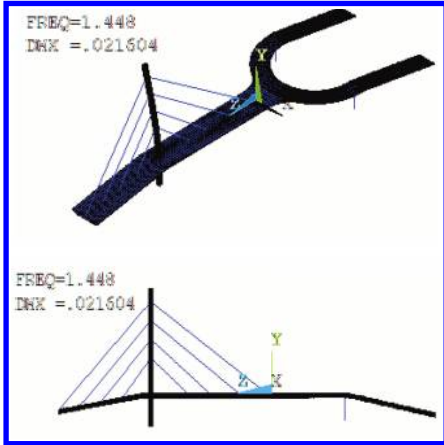


Figure 6. The first modal shape.

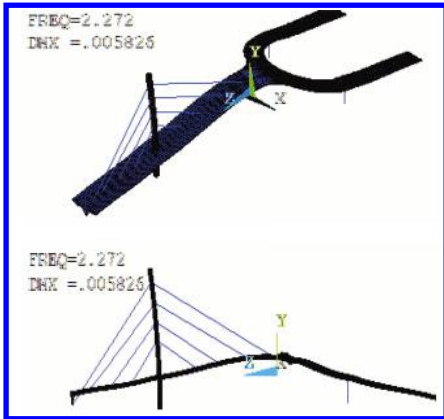


Figure 7. The second modal shape.

frequency of the bridge tower is 1.448 Hz. The made observation indicate that the first mode shape is the lateral vibration of tower. The second mode shape is the vertical vibration of the deck. The third and fifth mode shapes are the



Figure 8. The third modal shape.



Figure 9. The fourth modal shape.

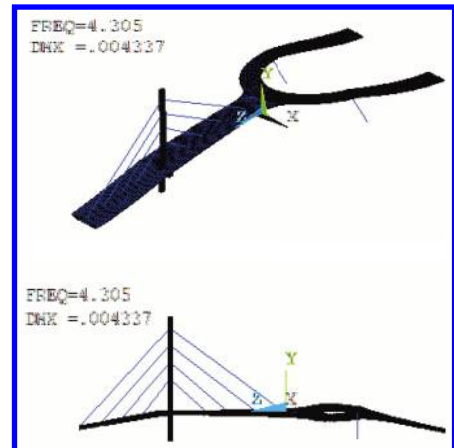


Figure 10. The fifth modal shape.



Figure 11. The sixth modal shape.

first and second order torsional rotation modes of the bridge deck, respectively. The fourth and the sixth mode shapes are the second and third order vertical vibration modes of the bridge deck, respectively. These observations are different to those of the common long span cable-stayed bridge.

## 5 CONCLUSIONS

The natural frequencies and mode shapes of a cable-stayed footbridge is actively investigated in this study. The deck, tower and cable are simulated by using the shell element, beam element and cable element, respectively. The stiffness and mass matrices of the deck and tower are constructed by using the finite element method. The stiffness matrix of the cable is the combination of the linear stiffness matrix and nonlinear stiffness matrix. The mass matrix of the cable is the lumped mass matrix. The axial stiffness of the cable affected by the sag is modified based on the Ernst expression. The made observation indicate that the first mode shape is the lateral vibration of tower. The second mode shape is the vertical vibration of the deck. The third one is the first order torsional rotation of the deck. These observations are different

to those of the common long span cable-stayed bridge.

## ACKNOWLEDGEMENTS

The writers are grateful for the financial support from the National Natural Science Foundation of China (51178366) and the Natural Science Foundation of Hubei Province (2014CFA026).

## REFERENCES

- Chen, B., Xu, Y.L. (2007). A new damage index for detecting sudden change of structural stiffness, *International Journal of Structural Engineering and Mechanics*, 26(3): 315–341.
- Chen, B., Chen, Z.W., Sun, Y.Z., Zhao, S.L. (2013). Condition assessment on thermal effects of a suspension bridge based on SHM oriented model and data, *Mathematical Problems in Engineering*, Vol. 2013, Article ID 256816, 1–18.
- Dallard, Y.P. Fitzpatrick, A.J. The London Millennium footbridge. *The Structural Engineer*, 2001, 79(22): 17–33.
- Chen, B., Sun, Y.Z., Wang, G.J., Duan, L.Y. (2014). Assessment on time-varying thermal loading of engineering structures based on a new solar radiation model, *Mathematical Problems in Engineering*, Vol.2014, Article ID 639867, 1–15.
- Chen, B., Zhao, S.L., Li, P.Y. (2014). Application of Hilbert-Huang transform in structural health monitoring: a state-of-the-art review, *Mathematical Problems in Engineering*, Vol.2014, Article ID 317954, 1–23.
- Chen, B., Guo W.H., Li P.Y., Xie W.P. (2014). Dynamic responses and vibration control of the transmission tower-line system: a state-of-the-art-review, *The Scientific World Journal*, Vol.2014, Article ID 538457, 1–20.
- Chen, B., Chen, Z.W., Wang, G.J., Wei, P.X. (2014). Damage detection on sudden stiffness reduction based on discrete wavelet transform, *The Scientific World Journal*, Vol. 2014, Article ID 807620, 1–16.
- Chen, B., Sun, Y.Z., Li, Y.L., Zhao, S.L. (2014). Control of seismic response of a building frame by using hybrid system with magnetorheological dampers and isolators, *Advances in Structural Engineering*, 17(8): 1199–1215.
- Farrar, C. R., and James, G. H., III. System identification from ambient vibration measurements on a bridge. *Journal of Sound and Vibration*, 1997, 205(1), 1–18.

# Wind-induced dynamic responses of a transmission tower with legs at different height

Y.J. Wu

Zhongshan Power Supply Bureau, Guangdong Power Grid Corporation Co. Ltd., Zhongshan, China

B. Chen, X.X. Song & X.F. Gong

Key Laboratory of Roadway Bridge and Structural Engineering, Wuhan University of Technology, Wuhan, China

**ABSTRACT:** The wind-induced dynamic responses of a transmission tower-line system subjected to strong wind are conducted in this study. A real transmission tower-line system with legs at different height constructed in China is taken as an example to investigate the structural responses subjected to wind loadings. The finite element model of the transmission tower-line system is constructed by using the commercial package. The equation of motion of the transmission tower-line system under wind is established. The wind loading are applied on the tower-line system to study the structural dynamic responses and evaluate the structural performance.

**Keywords:** transmission tower-line system; time history; dynamic responses; wind loading

## 1 INTRODUCTION

To be a typical spatial steel structure, the transmission tower-line system is widely used as electrical power infrastructures throughout the world. The transmission tower is a high-rise structure with small damping and is prone to strong wind loadings [1–3]. It is frequently reported across the world that the excessive vibration of a transmission tower under dynamic excitations may induce the structural damage and even failure [4–6]. Up to now, many wind-induced damages of the transmission tower and lines have been reported and failure of the towers under wind loading has been documented in many literatures. During the past two decades, many theoretical analyses and experiments have been carried out to reveal the performance and responses of transmission tower-line system [7–8]. Therefore, it is necessary to evaluate the performance of transmission tower-line systems subjected to wind loading.

The wind-induced dynamic responses of a transmission tower-line system subjected to strong wind are conducted in this study. A real transmission tower-line system with legs at different height constructed in China is taken as an example to investigate the structural responses subjected to wind loadings. The finite element model of the transmission tower-line system is constructed by using the commercial package. The equation of motion of the transmission tower-line system under wind is

established. The wind loading are applied on the tower-line system to study the structural dynamic responses and evaluate the structural performance.

## 2 ANALYTICAL MODEL OF TRANSMISSION TOWER-LINE SYSTEM

### 2.1 Structural model of transmission tower

The transmission tower and line can be modeled by using the three dimensional spatial beam elements and the cable elements, respectively. The element stiffness matrix  $\mathbf{K}^{(i)}$  and mass matrix  $\mathbf{M}^{(i)}$  of the  $i$ th element in the global coordinate system can be obtained by using the element stiffness matrix  $\mathbf{K}_e^{(i)}$  and mass matrix  $\mathbf{M}_e^{(i)}$  in the local coordinate system through the transforming of the location matrix. The stiffness matrix  $\mathbf{K}_T$  and mass matrix  $\mathbf{M}_T$  of a transmission tower in the global coordinate system can be developed by using the position matrix of element freedom.

$$\mathbf{K}_T = \sum_{i=1}^{nm} \mathbf{T}^{(i)T} \mathbf{K}^{(i)} \mathbf{T}^{(i)} \quad (1)$$

$$\mathbf{M}_T = \sum_{i=1}^{nm} \mathbf{T}^{(i)T} \mathbf{M}^{(i)} \mathbf{T}^{(i)} \quad (2)$$

where  $nm$  is the total element number of the transmission tower;  $\mathbf{T}^{(i)}$  is the freedom transform matrix

from element coordinate system to the global coordinate system.

### 2.2 Model of transmission tower-line system

The transmission tower is a typical spatial structure constructed by using steel members, which can be modelled by using beam and truss elements based on the finite element method. The element stiffness matrix  $\mathbf{K}_{l,e}$  of the transmission line in the local coordinate system can be expressed as

$$\mathbf{K}_l^i = \begin{bmatrix} \mathbf{k}_c & -\mathbf{k}_c \\ -\mathbf{k}_c & \mathbf{k}_c \end{bmatrix} \quad (3)$$

In which: the submatrix  $\mathbf{k}_c$  consists of the linear stiffness matrix  $\mathbf{k}_l$  and the nonlinear stiffness matrix  $\mathbf{k}_{nl}$

$$\mathbf{k}_c = \mathbf{k}_l + \mathbf{k}_{nl} \quad (4)$$

The stiffness matrix and mass matrix of the whole tower-line system in the global coordinate system are given by

$$\mathbf{K} = \mathbf{K}_T + \sum_{i=1}^{nl} \mathbf{K}_l^i \quad (5)$$

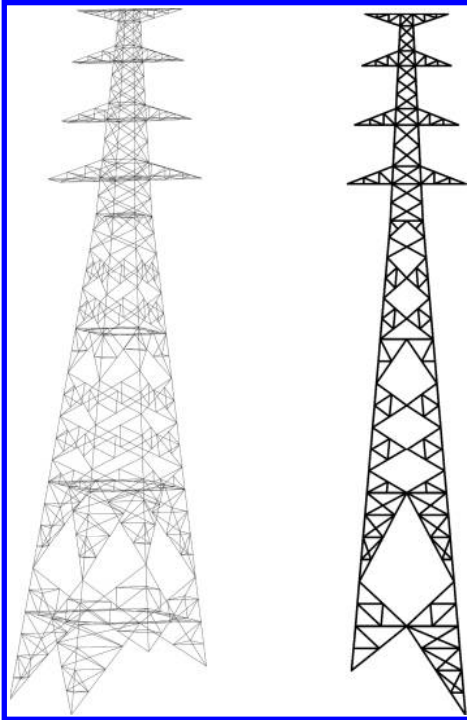


Figure 1. Model of the transmission tower.

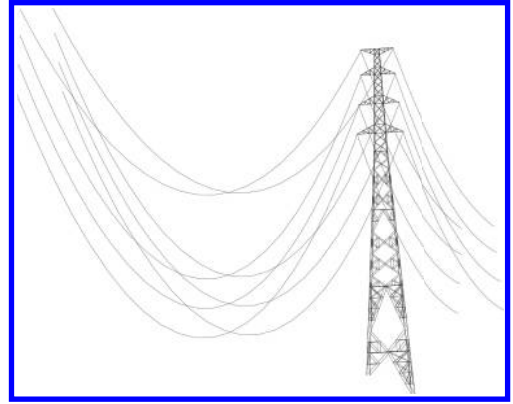


Figure 2. Model of the transmission tower-line system.

$$\mathbf{M} = \mathbf{M}_T + \sum_{i=1}^{nl} \mathbf{M}_l^i \quad (6)$$

where  $nl$  is the total number of the transmission lines;  $\mathbf{K}$  and  $\mathbf{M}$  are the stiffness matrix and mass matrix of the transmission tower-line system;  $\mathbf{K}_T$  and  $\mathbf{M}_T$  are the stiffness matrix and mass matrix of the transmission tower;  $\mathbf{K}_l$  and  $\mathbf{M}_l$  are the stiffness matrix and mass matrix of the transmission line.

To investigate the dynamic responses of the transmission tower-line system subjected to the monsoon wind, the finite element model of the transmission tower can be constructed by using the commercial package ANSYS as shown in Figures 1 and 2.

## 3 EQUATION OF MOTION UNDER WIND LOADING

### 3.1 Wind loading

The wind excitations of transmission tower-line system are simulated by spectral representation approach. The stochastic wind fields  $f_j^0(t)$ ,  $j = 1, 2, \dots, n$ , can be simulated by the following series

$$f_j(t) = 2\sqrt{\frac{\omega_{up}}{N}} \sum_{m=1}^j \sum_{l=1}^N |H_{jm}(\omega_{ml})| \cos(\omega_{ml}t - \theta_{jm}(\omega_{ml}) + \phi_{ml}) \quad (7)$$

where:  $N$  is sufficiently large number;  $\omega_{up}$  is upper cut-off frequency, with the condition that, when  $\omega > \omega_{up}$ , the value of  $\mathbf{S}^0(\omega)$  is trivial;  $\phi_{ml}$  represents a sequence of independent random phase angles, uniformly distributed over the interval  $[0, 2\pi]$ ;  $\omega_{ml}$  is double-indexing frequency;  $H_{jm}(\omega)$  is a typical element of matrix  $\mathbf{H}(\omega)$ , which is defined with Cholesky decomposition of cross-spectral density matrix  $\mathbf{S}^0(\omega)$ ;  $\theta_{jm}(\omega)$

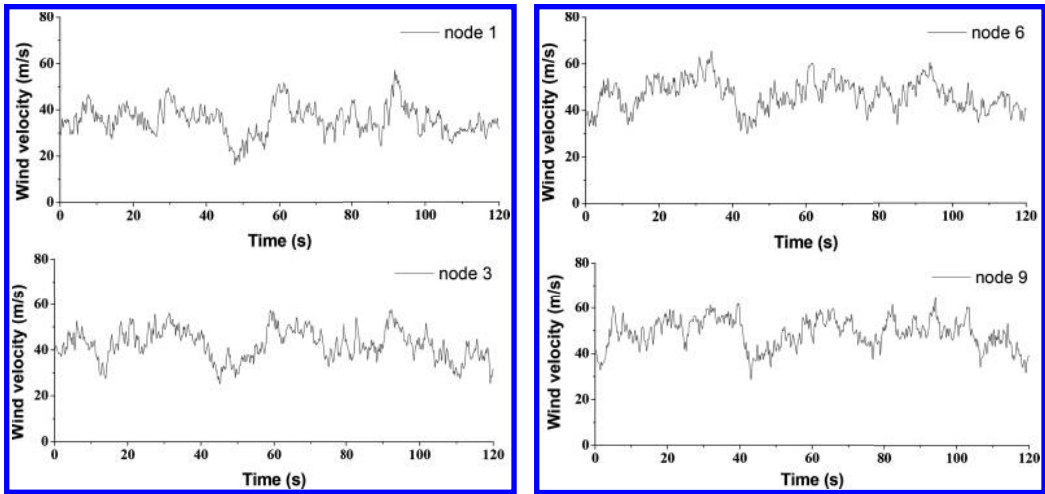


Figure 3. Time histories of wind velocity.

is complex angle of  $H_{jn}(\omega)$ . Figure 3 displays the simulated time histories of wind velocity.

### 3.2 Equation of motion

The equation of motion of the transmission angle tower-line system subjected to wind loading can be expressed as

$$\mathbf{M}\ddot{\mathbf{x}}(t) + \mathbf{C}\dot{\mathbf{x}}(t) + \mathbf{K}\mathbf{x}(t) = \mathbf{W}(t) \quad (8)$$

where  $\mathbf{M}$ ,  $\mathbf{C}$  and  $\mathbf{K}$  are the mass, damping and stiffness matrices of the tower-line system, respectively;  $\ddot{\mathbf{x}}(t)$ ,  $\dot{\mathbf{x}}(t)$  and  $\mathbf{x}(t)$  are the displacement, velocity and acceleration responses of the transmission tower-line system, respectively;  $\mathbf{W}(t)$  is the dynamic wind loading.

## 4 DYNAMIC RESPONSES UNDER WIND LOADING

To examine the structural wind-induced dynamic responses, a real transmission tower-line system with legs at different height constructed in the coastal areas in the southern China is taken as the example structure. The height and the root distance of the tower are 47.5 m and 7.9 m, respectively. The tower is constructed by using Q235 steel. The in-plane and out-of-plane directions are denoted as X and Y directions, respectively. The dynamic responses of the transmission angle tower subjected to strong wind loading are computed. Two loading cases are considered in the study: (1) wind loading in x direction (in-plane direction); (2) wind loading in x direction (out-of-plane direction).

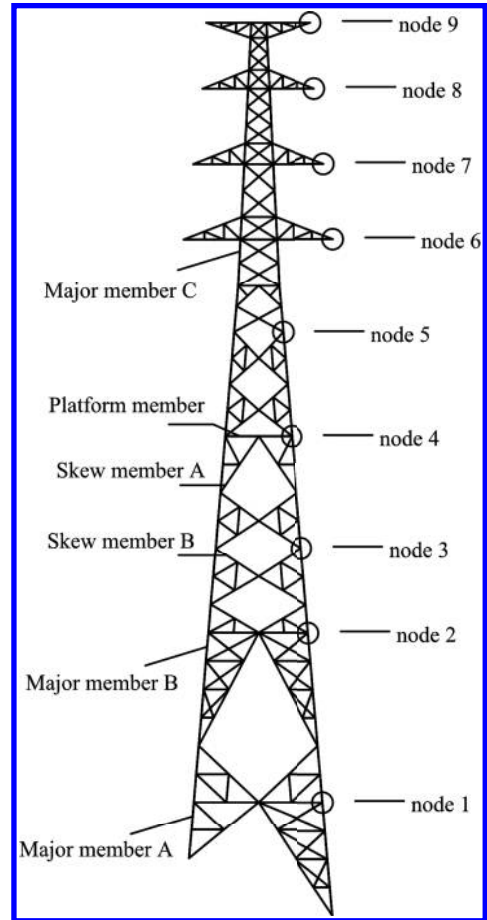


Figure 4. Distribution of crucial nodes and members.

The dynamic responses of the transmission line subjected to strong wind loadings with a speed of 37.94 m/s are investigated. Many crucial nodes and members are selected to examine the structural dynamic responses as shown in Figure 4.

Figures 5 and 6 display the time histories of dynamic responses on top of the tower under different wind direction. The curves in Figures demonstrate that the wind-induced dynamic responses for the out-of-plane vibration are much larger than those of the in-plane vibration. The peak displacements corresponding to the in-plane and out-of-plane vibration are about 0.22 m and 0.58 m, respectively. In addition, the peak velocities corresponding to the in-plane and out-of-plane vibration are about 0.13 m/s and 0.45 m/s, respectively. Similar observations can be made from the peak acceleration responses. It can be seen from Figures 7 and 8 that the time histories of dynamic responses of the lowest cross arm (node 6). It is seen that the responses at the lower part of the tower are much smaller than those on top of the tower. The wind-induced responses in the out-of-plane direction are substantially larger than those of the in-plane vibration, which

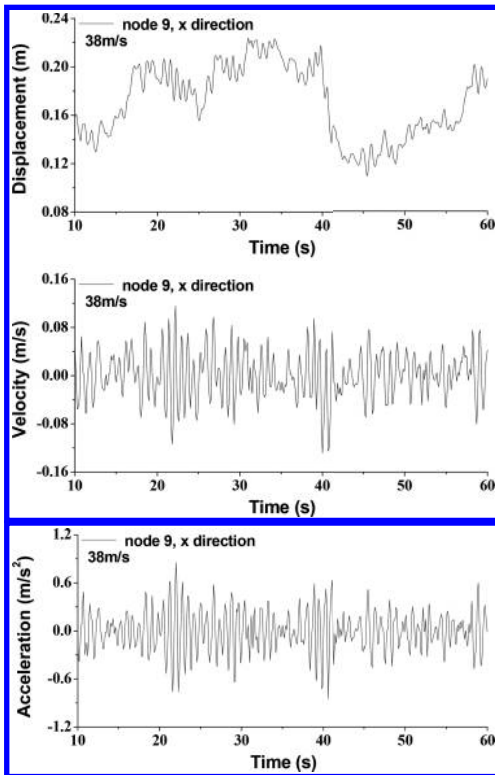


Figure 5. Time histories of dynamic responses on top of the tower (node 9) in x direction.

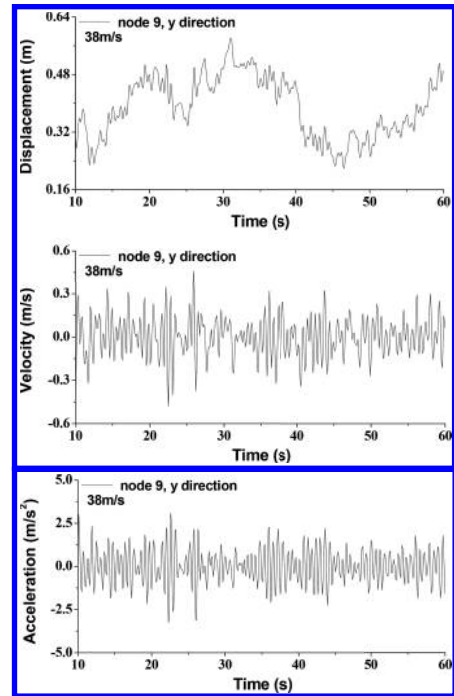


Figure 6. Time histories of dynamic responses on top of the tower (node 9) in y direction.

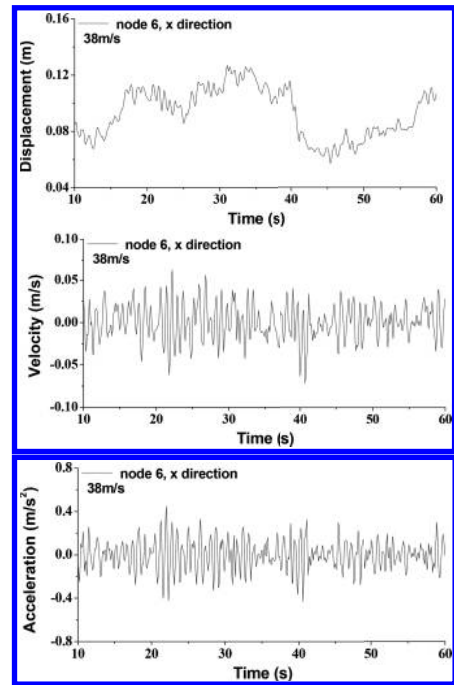


Figure 7. Time histories of dynamic responses of the node 6 in x direction.



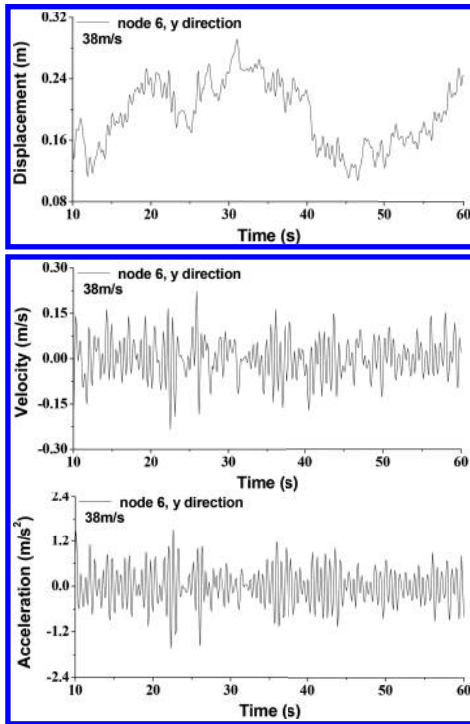


Figure 8. Time histories of dynamic responses of the node 6 in y direction.

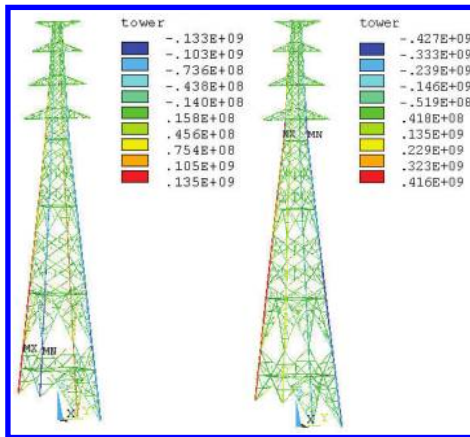


Figure 9. Stress distributions of crucial members.

is similar to the observation of the tower top. The possible reason is that the in-plane stiffness of the tower top is larger than the out-of-plane stiffness due to the contribution of the transmission lines in the longitudinal direction. Figure 9 also indicates the stress distributions of crucial members.

## 5 CONCLUSIONS

The dynamic responses of a transmission tower system with legs at different height subjected to strong wind loading are actively examined in this study. The finite element model of the transmission tower-line system is constructed by using the commercial package. The equation of motion of the transmission tower-line system under wind is established. The wind loading are applied on the tower-line system to study the structural dynamic responses and evaluate the structural performance. The made observations indicate that the wind-induced dynamic responses for the out-of-plane vibration are much larger than those of the in-plane vibration.

## ACKNOWLEDGEMENTS

The writers are grateful for the financial support from the technological project of the Chinese Southern Power Grid Co. Ltd (Grant K-GD2013-0222), the Fok Ying-Tong Education Foundation (Grant 131072) and the natural science foundation of Hubei province (2014CFA026). Correspondence should be addressed to Bo Chen; [cbsteven@163.com](mailto:cbsteven@163.com).

## REFERENCES

- Chen, B., Zheng, J. Qu, W.L. (2009). Control of wind-induced response of transmission tower-line system by using magnetorheological dampers. *International Journal of Structural Stability and Dynamics*. 9(4):661–685.
- Chen, B., Guo W.H., Li P.Y., Xie W.P. (2014). Dynamic responses and vibration control of the transmission tower-line system: a state-of-the-art-review, *The Scientific World Journal*, Vol.2014, Article ID 538457, 1–22.
- Kempner, L.J., Smith, S., and Stroud, R.C. Structural dynamic characterization of an experimental 1200 kilovolt electrical transmission-line system. *Shock and Vibration Bulletin*, 1988, 50:3, 113–123.
- Chen, B., Y. L. Xu, Integrated vibration control and health monitoring of building structures using semi-active friction dampers: Part II-numerical investigation, *Engineering Structures*. 30(3) (2008), 573–587.
- Chen, B., Zheng, J. and Qu, W.L. (2007). Wind-induced vibration control of transmission tower using magnetorheological dampers, *International Conference on Health Monitoring of Structure, Material and Environment*, Nanjing, China, 323–327.
- Kempner L.J. and Smith S. Cross-ropes transmission tower-line dynamic analysis, *Journal of Structural Engineering ASCE*. 110(6) (1984), 1321–1335.
- Irvine, H.M. (1981) *Cable Structures*. The MIT Press, USA.
- Ozono, S., Maeda, J., and Makino, M. Characteristics of in-plane free vibration of transmission line systems. *Engineering Structures*. 1988, 10:4, 272–280.

## The interference effect on aerostatic coefficients of beam in parallel bridge

J. Wang

School of Civil Engineering, Xi'an University of Architecture and Technology, Xi'an, China  
NatHaz Modeling Laboratory, University of Notre Dame, South Bend, IN, USA

J.X. Liu

Wind Tunnel Laboratory, Chang'an University, Xi'an, China

**ABSTRACT:** In order to study the aerodynamic interference effects on aerostatic coefficients of box beam between parallel continuous rigid frame bridges with high pier and long span, sectional model wind tunnel tests of segments of the beam are made by the introduction of factor. The distance between the two beams, height difference and wind attack angles, were changed during the wind tunnel test to study the effects on aerodynamic interferences of aerostatic coefficients of beam. The tests were designed for 12 conditions. The results have shown that the aerodynamic interference effects on aerostatic coefficients of beam in parallel bridges cannot be ignored. The aerodynamic interference effects on parallel bridge beam are shown mainly as follows: The drag coefficient of beam downstream dropped and upstream changed but not changed significantly. There are also the aerodynamic interference effects of lateral force coefficient and torque coefficient between the beams upstream and downstream.

**Keywords:** aerodynamic interference effects; aerostatic coefficients; box beam; parallel bridge

### 1 INTRODUCTION

In recent years, highway network in the western region is extended to loess gully region on a large-scale. When the highway routes pass through the mountains and highland region, the high-pier span continuous rigid frame bridge is often the preferred bridge type. Besides the characteristics of high-pier and large span, the long-span continuous rigid-frame bridge is also arranged with up and down separation arrangement, that is, parallel bridge. For the twin deck continuous rigid frame bridge with high-pier and long-span, the wind load on main beam should obtain aerostatic coefficients by wind tunnel test, in addition, we must also consider the airflow obstruction and interference to study the mutual aerodynamic interference effects of the parallel bridge beams [1–3]. And the aerodynamic interference factor is introduced to define the aerodynamic interference effects of the aerodynamic coefficients of the main beam [4, 5].

### 2 EXPERIMENT RESEARCH

The aerodynamic interference effects on aerostatic coefficients of main beam were investigated by means of section model wind tunnel test in some parallel long-span continuous rigid frame bridge

with high-pier. The wind tunnel test was conducted at Chang'an University wind tunnel laboratory, CA-1 atmospheric boundary layer wind tunnel. Beam model is tested by the vertical end supporting method. Different wind attack angle  $\alpha$  can be obtained by turning the angle turntable. The wind angle range is:  $\alpha = -10^\circ$  to  $+10^\circ$ , the interval is  $1^\circ$ , a total of 21 wind attack changes. Test wind speed  $V = 20$  m/s.

The width of beam model is  $B = 0.314$  m. The average height of beam model is  $H_p = 0.141$  m. The average aspect ratio of beam model is  $\frac{B}{H_p} = 2.227$ . Figure 1 is the section model of the beam model. Figure 2 is the picture of test model of beam. Figure 3 is the diagram of the wind attack angles in the beam

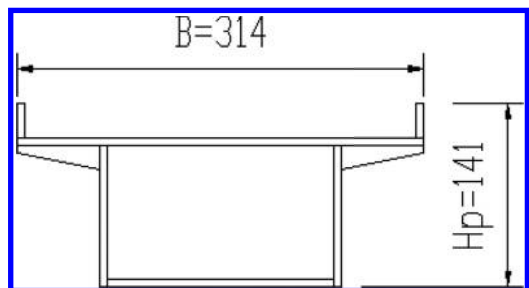


Figure 1. Section model of beam.



Figure 2. Test model of beam.

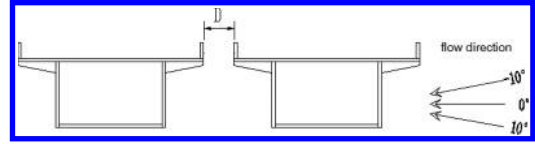


Figure 3. Wind attack angle in beam force test.

Table 1. Beam test conditions table of aerodynamic coefficient effect on beam.

Test conditions	Test model location	Distance D (m)	Bridge deck height $\Delta H$ (m)	Wind attack angle ( $^{\circ}$ )
1	Beam of single bridge	/	/	-10 to 10
2	Upstream	0.5	0	
3		7	0	
4		7	2.45	
5		14	0	
6	Downstream	42	0	
7		0.5	0	
8		7	0	
9		7	2.45	
10		7	-2.45	
11		14	0	
12		42.35	0	

segments model force test. As the main factors affecting aerostatic coefficients of parallel bridge include the spacing between beams and the wind attack angle, test conditions are shown in Table 1. The test results of aerodynamic influence effects on aerostatic coefficient of beam haven't been listed here due to the space.

### 3 THE TEST RESULTS OF AERODYNAMIC INFLUENCE EFFECTS ON AEROSTATIC COEFFICIENT OF BEAM

#### 3.1 The influence of different distances upstream to beam aerostatic coefficient

Figure 4 shows respectively aerostatic coefficient curve under different distance upstream changing with wind attack angle, but also gives the curve of single bridge beam [6, 7].

It can be seen from Figure 4, aerodynamic interference effect of aerostatic coefficient of beam in parallel bridge under different distance upstream is shown as follows: The aerostatic coefficient decreased slightly or changed little compared with the single bridge. The interference effect is not obvious. The change of upstream aerostatic

coefficient with the distance between the beams in the parallel bridge has no obvious regularity. However, overall, the aerostatic coefficient becomes closer and closer to the single bridge, expecting the curve of the distance  $D = 14$  m to have some jumps, so the aerostatic coefficient is the close to that of single bridge. The attack angle and distance are the important factors that impact aerodynamic interference effect in parallel bridges.

#### 3.2 The influence of different distance downstream to beam aerostatic coefficient

Figure 5 gives respectively the result of aerostatic coefficient curve under different distance downstream changing with wind attack angle, but also gives the curve of single bridge beam.

It can be seen from Figure 5, aerodynamic interference effect of aerostatic coefficient of beam in parallel bridge under different distance downstream is shown as follows: When the beam is located downstream, the drag and toque coefficient decreased generally compared with the single bridge, and they tend to close to the case of the single bridge with the distance increases. It shows

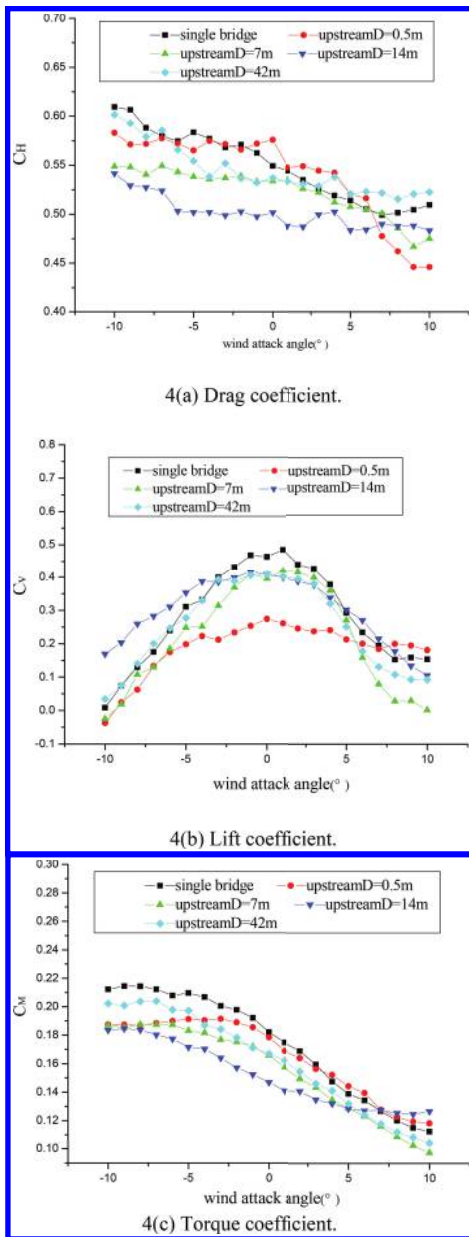


Figure 4. Aerostatic coefficients of beam upstream under different distance changing with wind attack angles.

that the interference effect is weaker and weaker. But even if when the distance  $D = 42.35$  m, the aerodynamic interference effect is still obvious. For the lift coefficient, the regularity of the influence by the distance is not strong. But it is also that the curve of lift coefficient is closest to that of single bridge when the distance is farthest.

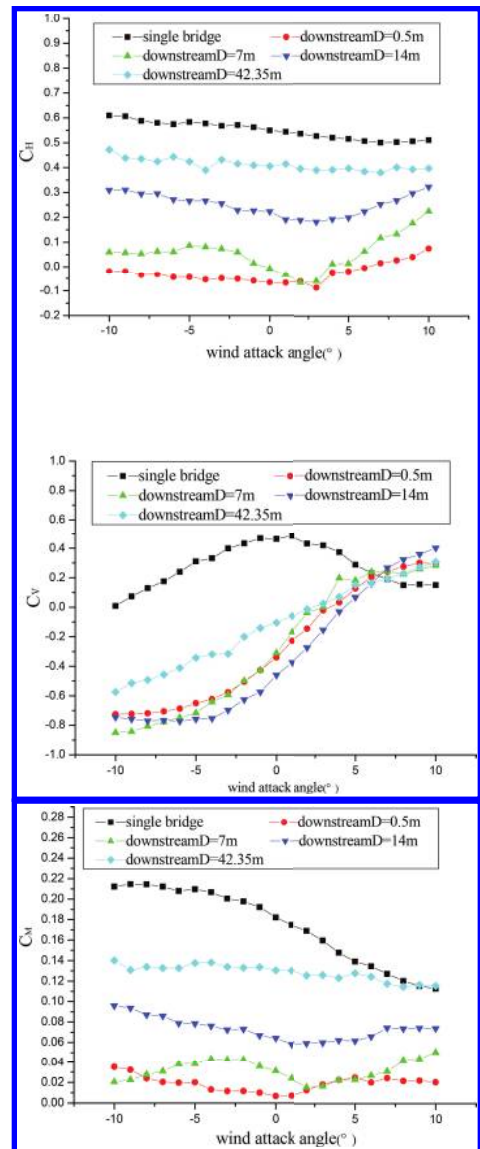
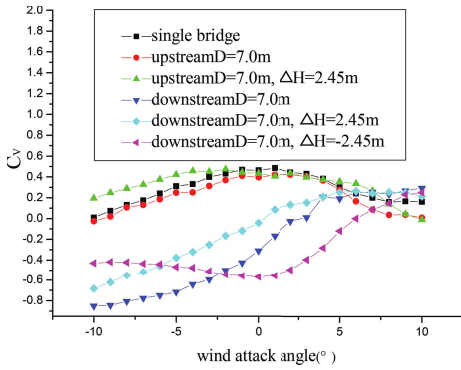


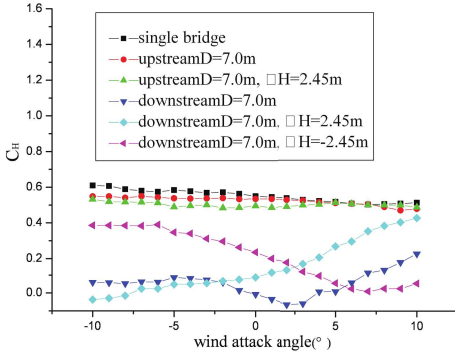
Figure 5. Aerostatic coefficients of beam upstream under. Different distance changing with wind attack angle. (a) Drag coefficient. (b) Lift coefficient. (c) Torque coefficient.

### 3.3 The influence of height difference upstream and downstream to beam aerostatic coefficient

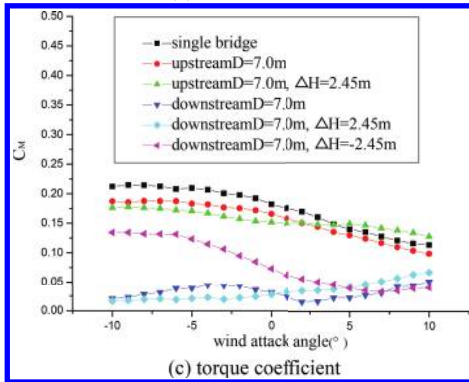
Figure 6 shows respectively aerostatic coefficient curve when the upstream distance  $D = 7$  m, under no height difference and a height difference  $\Delta H = 2.05$  m, and when the downstream distance  $D = 7$  m under no height difference and a height difference  $\Delta H = \pm 2.45$  m changing with wind attack angle, but also gives the curve of single bridge beam.



(a) Drag coefficient.



(b) Lift coefficient.



(c) torque coefficient

Figure 6. Influence of height difference upstream and downstream to aerodynamic interference of beam.

It can be seen from Figure 6, the height difference upstream has influence on beam aerodynamic interference, but the influence is very small and almost negligible. The height difference downstream has obvious influence on beam aerodynamic interference. The details are shown as follows: The aerostatic coefficient under the condition of no height difference is very different compared to that under the condition of positive and negative

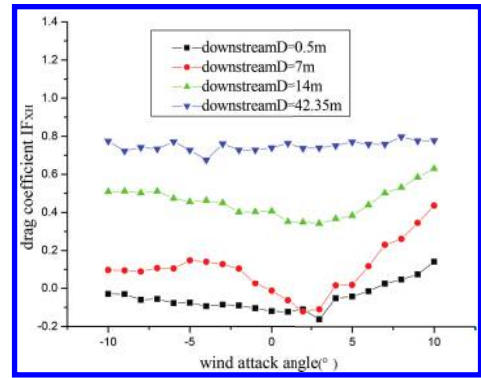


Figure 7. Drag coefficient aerostatic interference factor under different spacing downstream changing with wind attack angle.

height differences. And the two aerostatic coefficient curves with the change of the wind attack angle under positive and negative height differences still showed a symmetrical relationship. The aerostatic coefficient curve with the change of the wind attack when the difference is positive has the same rule with the curve of no height difference. In a word, to the factor of height difference, its impact on downstream is larger than the impact on upstream.

#### 4 INTERFERENCE FACTOR

The aerodynamic interference effects on the beam in parallel bridges show as the impact on aerostatic coefficient upstream and downstream, so the aerodynamic interference factors are defined respectively for the coefficient upstream and downstream:

$$IF_{SH,SV,SM,XH,XV,XM} = \frac{\text{aerostatic coefficient in parallel bridge}}{\text{aerostatic coefficient in single bridge}} \quad (1)$$

where, SH, SV, and SM are the drag, lift, and torque coefficient factor of the beam upstream, respectively. XH, XV, and XM are the drag, lift, and torque coefficient factor of the beam downstream, respectively.

Figure 7 gives the aerodynamic interference factors curve of drag coefficient downstream changing with different spacing and wind attack angle, respectively.

#### 5 CONCLUSIONS

The aerodynamic interference effects on aerostatic coefficients of beam in the parallel continuous

rigid frame bridges were studied by wind tunnel test. The following conclusions are obtained.

The aerodynamic interference effect of aerostatic coefficient of beam in parallel bridge under different distance upstream and downstream is shown as follows: The aerodynamic coefficient upstream and downstream has both been changed compared with the single bridge. And the coefficient downstream changes significantly, showing complex shielding and wake interference effect. The distance between the parallel bridge and the wind attack angle are two main factors that influence the aerostatic coefficients of the beams. However, they have little impact on the upstream, and significantly, affect the downstream.

#### ACKNOWLEDGMENTS

This work was financially supported by the Natural Science Foundation of Shaanxi Province

(2015JM5156) and Fundamental Research Foundation of Xi'an University of Architecture and Technology (JC1302).

#### REFERENCES

- T. Kim & M.R. Flynn. 1995. *Journal of Wind Engineering and Industrial Aerodynamics*. Vol. 56 p.213.
- X.F. Lou, F.C. Cao & Z.X. Lin. 2002. *Journal of Tongji University*. Vol. 30, p.604, in Chinese.
- Khanduriac, Stathopoulost, Bedard C: *Engineering Structures*. Vol. 20(1998), p.617.
- ZH.N. Xie. 2003. *Wind-induced Interference Effects on Typical Tall Buildings [D]*. Shanghai: Tongji University, in Chinese.
- M. Gu & P. Huang. 2003. *Journal of Tongji University*. Vol. 31, p.762, in Chinese.
- ZH.W Liu, ZH.Q. Chen, G. Liu et al. 2008. *Journal of Hunan University*. Vol. 35, p.16–20, in Chinese.
- N. Liu, B. Zhou. 2007. *China Science And Technology Information*. Vol. 11, p.45–46, in Chinese.

*Computer simulation and CAD/CAE*

# Study on the effect of batch piling of coal on silo wall

T.J. Tao, M.S. Zhao & Q. Kang

Guizhou Xinlian Blasting Engineering Group Co. Ltd., Guiyang, Guizhou, China

**ABSTRACT:** Displacement and stress of silo wall influenced by batch piling are studied based on the finite model of the reinforced concrete shallow coal bunker. The results show that asymmetric loading produces larger deformation of the wall compared with symmetric loading. This is because in symmetric loading, the maximum displacement occurs at the top of the wall, the free end, and the maximum stress occurs at the foot of the wall, consistent with a cantilevered arrangement. These distribution patterns are relatively consistent with the mechanical property of the wall. The stress curve exhibits a sharp negative gradient as the stress decreases and then steadily increases to a crest at 10 m, after which it decreases through to the top of the wall.

**Keywords:** numerical analysis; reinforced concrete shallow coal bunker; displacement; stress

## 1 INTRODUCTION

The need to provide space for the diverse and ever increasing needs of mankind has been at the forefront of innovations by designers and engineers alike. These innovations are aimed at satisfying different requirements; of interest to this paper is the requirement of a larger unobstructed space for various usages such as sports arena, conference venue, theaters and general-purpose halls.

In China, reinforced concrete bunkers are in common use in the coal storage systems and are designed in accordance to the Code for Design of Reinforced Concrete Silo, GB 50077-2003. The bunker walls are routinely exposed to both normal pressure and vertical frictional shear or traction produced by the material being stored. Additional loads could include seismic and wind loads, stresses created by temperature differences, potential expansion of the stored material, and differential settlement of the foundation. Failure of a bunker typically results in its total collapse owing to the lack of redundancy in the load path. Adgen et al noted that silo failure is often brittle and sudden, which means no much warning is seen before the collapse.

A research done by Sun Weiwei et al. deduced that differential temperature changes exert a significant influence on the design of reinforcement in silos. The code of design specifies that for silos of diameter >40 m, the atmospheric temperature's influence should be taken as 6–8% of the horizontal circular stress due to the stored material. Most studies, however, focus on the effects of heat transfer through the silo wall, i.e. heat conductivity.

This paper explores the effect of batch piling on the displacements and the stresses of the silo wall.

## 2 FINITE MODEL OF THE SILO WALL

### 2.1 Finite model

A finite element model is built to simulate the pressure exerted by the coal pile on the wall, considering loading different quadrants at a time. The case study for this paper is a reinforced concrete silo being utilized for coal storage. The first phase of the project involved the construction of two super-critical coal-fired thermoelectric generation units,

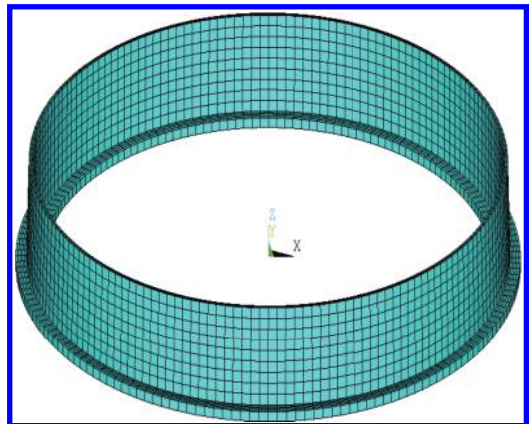


Figure 1. FE model for calculating the effect of batch loading.



and set aside an expansion site for two more coal fired power unit. It is cylindrical with an internal diameter of 55 m and height of 18 m. The wall thickness is tapered from 1.37 m at the bottom to 0.8 m at the top. The silos roof structure is a double-layered latticed shell structure with a net height of 42.3 m.

### 2.2 Load combination and loading pattern





Basically, to simulate batch loading, it is assumed that the storage space is divided into four quadrants and each loading combination is analyzed.

## 3 DISPLACEMENT ANALYSIS

The plot of the displacement vector is shown in the below figures.

As shown in Figure 2, the displacement values change minimally for load cases 1 to 3; however, there is a significant change for load case 4.

Table 1. Load combination and loading patterns.

Load case	Load combination	Load pattern
1	1.2 (load from the roof structure) + 1.3 (load due to coal pressure)	
2	1.2 (load from the roof structure) + 1.3 (load due to coal pressure)	
3	1.2 (load from the roof structure) + 1.3 (load due to coal pressure)	
4	1.2 (load from the roof structure) + 1.3 (load due to coal pressure)	

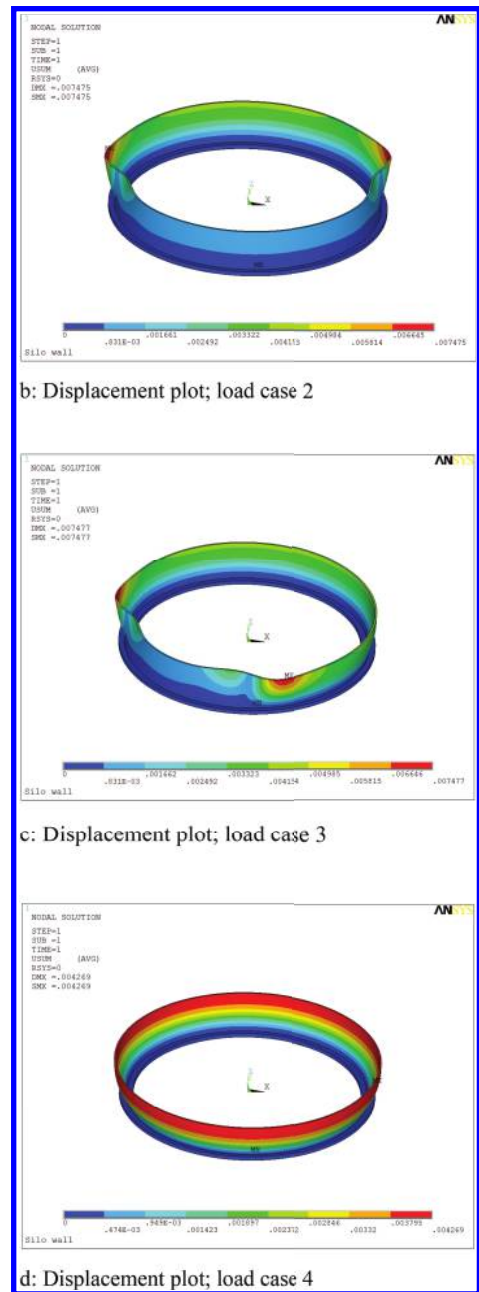
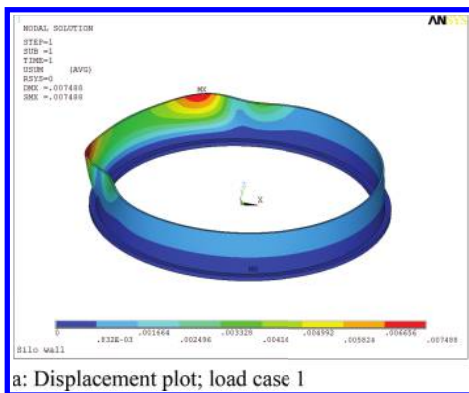


Figure 2. Displacement plot for the four load cases.

This could be attributed to the fact that load cases 1, 2 and 3 are all asymmetric load case, and load case 4 presents a symmetrical loading on the silo wall. As shown in Figure 3, the coal produces a maximum displacement of 0.005 m. The maximum displacement occurs at the top of the wall, the free end.

Figure 2. (Continued).

## 4 STRESS ANALYSIS

The stress values for the four load cases are given in Table 2. The plot of the displacement vector is shown in the below figures.

As shown in Figure 4 and Figure 5, the coal produces a maximum stress of 6.02 N/mm<sup>2</sup>. The maximum stress occurs at the foot of the wall, consistent with a cantilevered arrangement. These distribution

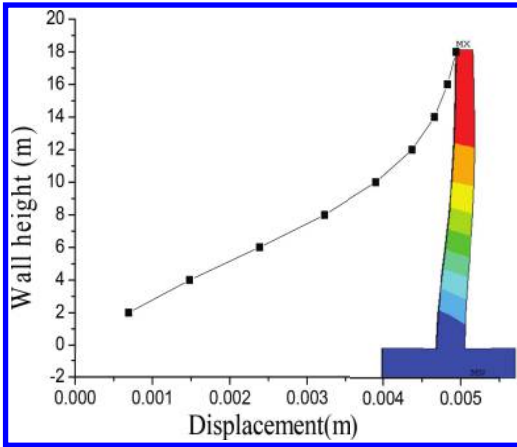


Figure 3. Displacement along the wall height.

Table 2. The stress values for the four load cases.

Load case	Radial stress	Axial stress	1st principal stress	3rd principal stress
1	2.76	-7.71	2.81	-7.78
2	2.76	-7.70	2.81	-7.78
3	2.76	-7.71	2.81	-7.78
4	2.17	-6.39	2.17	-6.43

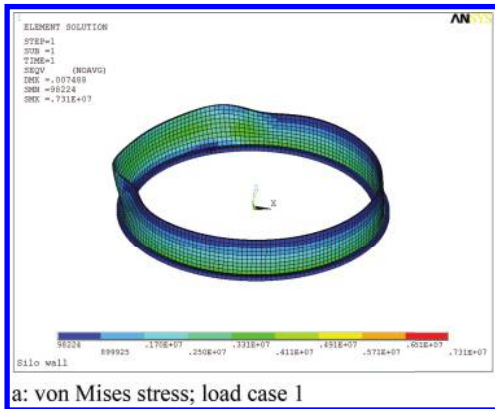


Figure 4. (Continued).



Figure 4. von Mises stress plot for the four load cases.

patterns are relatively consistent with the mechanical property of the wall. On the other hand, the stress curve exhibits a sharp negative gradient as the stress decreases in the range of 0–6 meters. Then, it steadily increases to a crest at 10 m, after which it decreases through to the top of the wall.

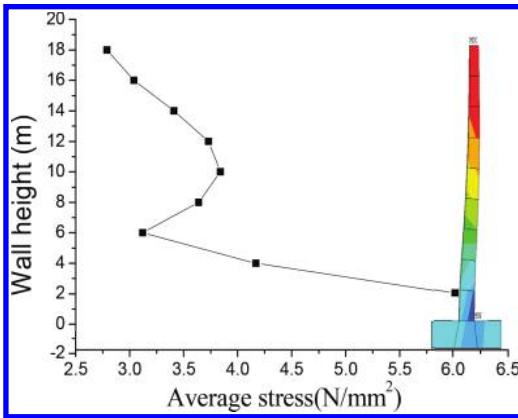


Figure 5. Stress distribution along the wall height.

## 5 CONCLUSIONS

From the analysis results, the following can be deduced:

1. The displacement values change minimally for load cases 1 to 3; however, there is a significant can for load case 4. This could be attributed to the fact that load cases 1, 2 and 3 are all asymmetric load case, and load case 4 presents a symmetrical loading on the silo wall.
2. Asymmetric loading produces larger deformation of the wall compared with symmetric loading. This is because in symmetric loading, the coal produces a maximum displacement of 0.005 m. The maximum displacement occurs at the top of the wall, the free end.
3. The maximum stress occurs at the foot of the wall, consistent with a cantilevered arrangement. These distribution patterns are relatively consistent with the mechanical property of

the wall. The stress curve exhibits a sharp negative gradient as the stress decreases in the range of 0–6 meters. Then, it steadily increases to a crest at 10 m, after which it decreases through to the top of the wall.

## ACKNOWLEDGMENTS

This work was supported by the grants from the Guizhou Science and Technology Plan Project (No. SY2010365), the Key Industrial Research Project Supported by the Science Technology Department of Guizhou Province (No. (2013) 3013) and the Guizhou Province Outstanding Young Scientific Talents Training Program Funded Projects (No. (2013) 30). The authors gratefully acknowledge their support.

## REFERENCES

- Chen C.B., Liang X.P., Shi X.C., Yang B.Y. Application analysis of earth pressure computation formulae in large squat silos. *Chinese Journal of Rock Mechanics and Engineering*. 2007 February; 26(2): 421–426.
- He B. *Ansys Civil Engineering Application Examples*. 3rd ed. Chen T, editor. Beijing: China water conservancy and Hydropower Press; 2011.
- Liu L. Durability design of Reinforced Concrete Coal Bunker. *Research and Application of Building Materials*. 2008 Dec.
- Qiang F.H.M.P. Large Reinforced concrete Silo Temperature Stress Analysis and Calculations. *Special Structures*. 2011 Oct; 28(5).
- Sun Ww, Meng Sp, Luan Wb. Research on Thermal Stress of Large Diameter Concrete Silos. *Engineering Mechanics*. 2011 July; 28(7).
- Sun S.S., Zhao J.H., Zhang C.G., Cui Y. Lateral Pressure of Large Squat Silos based on the unified strength theory. *Engineering Mechanics*. 2013 May; 30(5): 244–249.

# An algorithm for random cave geometry generation in Karst landform

Xue-jiao Cui

*Guizhou Xinlian Blasting Engineering Group Co. Ltd., Guiyang, Guizhou, China*

Chong Shi

*Institute of Geotechnical Engineering, Hohai University, Nanjing, Jiangsu, China*

**ABSTRACT:** A new algorithm, which can randomly generate Karst cave geometry, was developed in this work. Each Karst cave geometry was regarded as a polyhedron. All the suppositional polyhedra, which represent the Karst caves, are cast into the research domain according to the random distribution rule of the Karst caves. Then, the solid polyhedra are transformed into void to model the Karst caves. Thus, the resultant domain is the rock mass that contains Karst caves. Two supernumerary algorithms, the merging neighboring points algorithm and the threshold value interception algorithm, were also employed to obtain caves with random shape and distribution according to the real caves' shapes, area ratios, radius ranges, distributions and smoothness. The method proposed in this work provides a way to numerically simulate Karst caves.

**Keywords:** Karst cave; merging neighboring points algorithm; threshold value interception algorithm; geometrical model

## 1 INTRODUCTION

Karst caves are usually with no fillings or weakly filled. Since the huge difference in mechanical property between the cave surface and the rock mass, there would be a great change during the propagation of the blasting seismic wave. Therefore, a reasonable caves distribution model is the essential base of evaluating the influence of Karst geological conditions on blasting effect. Many scholars home and abroad have generated huge researches on the random cave models and their numerical calculation methods. Yong Ye and Lianguo Dong used High Order Difference Method to numerically simulate a series of caves with different sizes, shapes and fillings, and analyzed the caves' features of change, seismic reflection, etc., on kinematics and dynamics. Huiyan Yang, etc. put forward the modeling principles for the fracture-cave reservoir and primarily studied the 3D geologic modeling method of the fracture-cave carbonate reservoir. Xiangyang Hu, etc. put forward the modeling method of the multi scale Karst facies-controlling fractured-cavity reservoirs. Based on the deterministic modeling, the discrete large cave model and the discrete large fracture model were built. Based on the 3D regular network model, Chenchen Wang, etc. built the networks for Karst caves, big fractures and small fractures with different physical dimensions. Then he put forward a coupling algorithm. Based on the

Karst cave network, the multi-scale network model of carbonate was built by appropriately adding big and small fractures. Xian Xi, etc. put forward two methods for modeling random Karst caves, the merging neighboring points algorithm and the threshold value interception algorithm, and built different models by using different methods. All of these studies did not give a definite description of cast position and intersect estimation during the casting, and just using single method, the merging neighboring points algorithm or the threshold value interception algorithm, has its limit. For example, the merging neighboring points algorithm is not suitable for the case that there are multiple caves with different sizes in each cave distribution area.

In this paper, the local cave radius  $R$  is used to describe the cave's discrete degree on large scale, and the area ratio  $S$  is used to describe local space density in every cave distribution area. By choosing  $R$  and  $S$ , and taking the intersect estimation between polyhedron blocks as the core, different cave models could be built easily and the real complicated caves could be quickly and accurately described.

## 2 KARST CAVE GENERATION

### 2.1 Polygonal cave

There are mainly two ways to generate the polygonal cave in previous researches. One is the method

of using the sequences of random angel increment  $\{1 \dots \theta_i \dots \theta_n\}$  and random side length  $\{1 \dots r_i \dots r_n\}$  in the polar coordinate frame to generate blocks, which was put forward in studying random concrete blocks modeling, the other is to generate rigorous convex polygons by prolongating triangles under a certain principle. The blocks generated by the first method are smoother and their shapes are easier to control by parameters, while long sides and sharp angels are easier to appear by the second method, and there are few parameters for controlling the blocks' shape. Hereby the first method is improved according to the accumulation body's characteristics and applied.

There are two schemes to generate polygons and the generation results are shown in Figure 1(a) and (b). Apparently, blocks generated by the first scheme is smoother and have less concave edges than those by the second. Users can choose different ways to generate blocks based on different circumstances. The introduction of the two schemes is as follow.

Scheme 1. When generating an n-sided polygon, firstly of all generate a sequence of random radiuses  $\{1 \dots r_i \dots r_n\}$ . The range is from  $r_0 - \Delta r$  to  $r_0 + \Delta r$ . So

$$r_i = r_0 + (2 \cdot \xi - 1) \cdot \Delta r \quad (1)$$

in which  $\xi$  is the pseudo-random number within the interval (0, 1) (all the following  $\xi$  are the same),  $r_0$  is the average value of the random radius  $r_i$ , and  $\Delta r$  is the radius amplitude. Then generate a sequence of random angle increments  $\{1 \dots \Delta\theta_i \dots \Delta\theta_n\}$ . The range of  $\Delta\theta_i$  is from  $2\pi/n - \eta \cdot 2\pi/n$  to  $2\pi/n + \eta \cdot 2\pi/n$ . So

$$\Delta\theta_i = \frac{2\pi}{n} + (2 \cdot \xi - 1) \cdot \eta \cdot \frac{2\pi}{n} \quad (2)$$

in which  $\eta$  is a coefficient between 0 and 1. Apparently, the smaller  $\eta$  is, the bigger the amplification of the angle increment is and the more equal the random angel generated is.

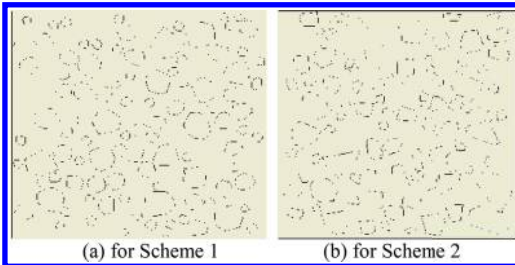


Figure 1. The generated configurations of the two schemes under dissolution ratio 35%.

To make sure the sum of all  $\Delta\theta_i$  is  $360^\circ$ ,  $\Delta\theta_i$  should be processed by the following equation firstly, and then used in the sequence.

$$\Delta\bar{\theta}_i = \Delta\theta_i \cdot \frac{2\pi}{\sum \Delta\theta_i} \quad (3)$$

Generate blocks with Sequence  $\{1 \dots r_i \dots r_n\}$  and Sequence  $\{1 \dots \Delta\theta_i \dots \Delta\theta_n\}$  in the polar coordinate (see Fig. 2). The size of the blocks should be the same, that is  $r_0$  is the same, waiting for the scaling.

Scheme 2. Similar to the way of generating radius sequence in Scheme 1, firstly generate a sequence of random radiuses  $\{1 \dots r_i \dots r_n\}$  according to Formula 1, whose range is from  $r_0 - \Delta r$  to  $r_0 + \Delta r$ .

Then generate a sequence of random angles  $\{1 \dots \theta_i \dots \theta_n\}$ , in which  $\theta_i$  is from 0 to  $2\pi$ .

$$\theta_i = \xi \cdot 2\pi \quad (4)$$

Since  $\theta_i$  is interspersed and the sequence of angles need to be in the ascending order,  $\{1 \dots \theta_i \dots \theta_n\}$  is precessed to make it in an ascending order.

Generate blocks with Sequence  $\{1 \dots r_i \dots r_n\}$  and Sequence  $\{1 \dots \theta_i \dots \theta_n\}$  in the polar coordinate. The size of blocks should be the same.

For Scheme 1 and 2, if strict convex polygons should be generated, concave vertexes could be deleted. Traverse each vertex and make sure each vertex lies on the right side of the counterclockwise vector of its surrounding two vertexes. If not, delete the vertex. What needs to emphasize is that deleting vertexes once cannot make sure the generation of convex polygons. After each deleting, polygons need to be checked until all concave vertexes are deleted.

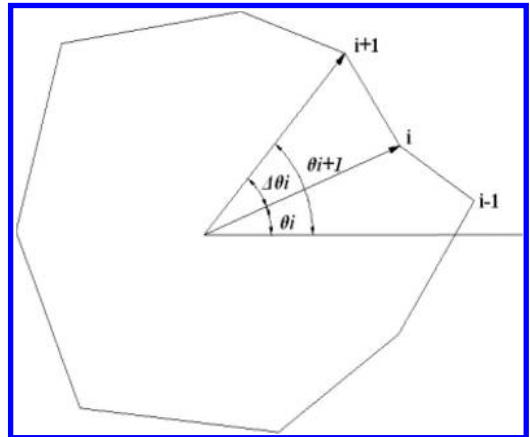


Figure 2. The configuration of the generated polygonal block.

## 2.2 Smooth blocks

Since angles among adjacent points of smooth blocks are the same, the formula of n-sided ( $n > 15$ ) smooth blocks' angle sequence  $\{1 \dots \theta_i \dots \theta_n\}$  is

$$\theta_i = i \cdot \frac{2\pi}{n}. \quad (5)$$

For smooth blocks' radius sequence  $\{1 \dots r_i \dots r_n\}$ , the random number generating method for polygon caves will lead to bumpy surface and disorder. Therefore the radius sequence should be processed by series smoothing, and then generated in polar coordinates. The series processing formula of the radius sequence is

$$r_i = r(\theta_i) = r_0 + \sum_{j=1}^m \alpha_j \cos(j\theta_i + \beta_j) \quad (6)$$

in which  $r_0$  is average radius,  $m$  is number of radius generated in the sequence,  $\beta_j$  is a random number within the interval  $[0, 2\pi]$ , and  $\alpha_j$ 's expression is

$$\log\left(\frac{\alpha_j}{r_0}\right) = -p \cdot \log(j) - b \quad (7)$$

## 3 MEASUREMENT OF THE SIZES OF CAVE BLOCKS

### 3.1 Measurement of cave blocks' width and inclination

The block's width is the length of the shortest line through a block, or it could be considered as the particle size. Take an n-sided polygon for example. The measuring method is as follow: (1) Taking the i-th side as the base, transverse the vertical lines of all the  $n - 2$  vertexes to the side and find the longest vertical line  $l_{\max}(i)$ ; (2) Transverse all the n sides and find the shortest one among all the n sides' longest vertical lines  $\min(l_{\max}(i))$  ( $i = 1 \dots n$ ), like DF in Figure 3. The width of the block Width is  $|DF|$ , and the inclination of the counterclockwise vector  $\overline{AB}$  is the block's inclination  $\alpha$ .

### 3.2 Measurement of cave blocks' length

A cave block's length can be understood as the block's stretch distance along its inclination's direction. Take the block in Figure 3 for example. The calculating method is as follow: (1) Calculate the unit vector  $\vec{e}$  of the vector  $\overline{AB}$ ; (2) The projection distance of the vector  $\overline{AC}$  in the direction of the vector  $\overline{AB}$  is

$$proj(i) = \overline{AC} \cdot \vec{e} \quad (8)$$

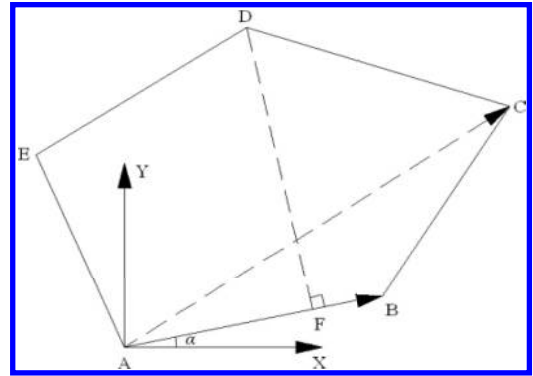


Figure 3. Measurement of the cave block's size.

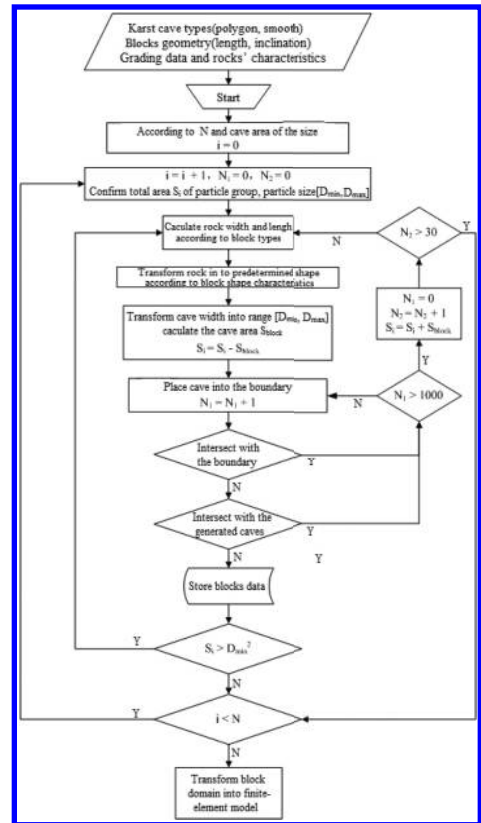


Figure 4. Flowchart for random generation of D-RBM caves.

in which  $proj(i)$  along direction of  $\overline{AB}$  is positive, and that along the opposite direction is negative.

(3) Transverse all the  $n - 2$  vertexes, and find  $\min(proj(i))$  and  $\max(proj(i))$  ( $i = 1 \dots n - 2$ ). The block's length is

$$Length = |\max(proj(i)) - \min(proj(i))|$$

$$(i - 1 \dots n - 2) \quad (9)$$

Based on the principle above, the D-RBM system was composed. Its modeling progress includes 5 parts: (1) generating blocks, (2) scaling and deforming blocks based on the grading data and rocks' characteristics, (3) putting blocks into the area within the boundary and making sure there is no overlapping among blocks, (4) calculating the entity model based on generated data of blocks' profile, (5) deleting generated blocks and the rest is rock with Karst caves. The program flow chart is as shown in Figure 4.

## 4 PLACING OF CAVE BLOCKS

### 4.1 Block placing progress

The block placing progress includes block generation, trail placing, intersection estimation, place adjustment and final defined placing. Details are as follow: (1) Before the placing, choose a random grain size  $D$  from the grain size interval  $[D_p, D_{i+1}]$  of the block's graduation as the block's grain size and scale it to the grain size. If the block has a dip angle, rotate the rock to the certain angle based on its dip angle; (2) Place the block into the boundary and estimate whether it intersects with the boundaries; (3) If not, then estimate whether it intersects with other fixed blocks; (4) If not, the place of the block is defined. If there is intersection in Step 2 or 3, adjust its position and repeat Step 2 and 3 until its place is finally determined.

### 4.2 Intersection estimation between blocks

The study of intersection estimation between blocks is mature in the computational geometry. The computing and estimation of simple polygons cost quite a lot of time and resources of the system, while the estimation of convex polygons is much simpler. Since the number of model blocks generated by the system is huge and the estimation times would grow with the number of fixed blocks, the convexification of all polygons before the estimation is essential.

The intersection estimation of polygons is based on positions of the vertex and the line, and those of lines. It has been solved in the Geometry of Vector.

(1) Estimation of the vertex lying on the right of the line. Suppose there are Vector  $\overline{AB}$  and Vertex  $C$ , their coordinates are  $(x_A, y_A)$ ,  $(x_B, y_B)$ , and  $(x_C, y_C)$ . Make Vector  $\overline{AC}$ , and then  $\overline{AB} = (x_B - x_A, y_B - y_A)$ ,  $\overline{AC} = (x_C - x_A, y_C - y_A)$ . Calculate  $\overline{AB} \times \overline{AC}$ :

$$\overline{AB} \times \overline{AC} = \begin{vmatrix} x_B - x_A & y_B - y_A \\ x_C - x_A & y_C - y_A \end{vmatrix} \quad (10)$$

If  $\overline{AB} \times \overline{AC} > 0$ , then  $C$  is on left of  $\overline{AB}$ . If  $\overline{AB} \times \overline{AC} < 0$ , then  $C$  is on right of  $\overline{AB}$ . Or  $C$  is on  $\overline{AB}$ .

(2) Intersection estimation of two line segments. Put simply, the intersection estimation of two line segments is to estimate whether the two points of one line segment are on the same side of those of the other. Suppose there are  $\overline{AB}$  and  $\overline{CD}$ , in order to estimate whether Point  $C$  and  $D$  are on the different sides of Point  $A$  and  $B$ , make  $\overline{AC}$  and  $\overline{AD}$  (see Fig. 5). According to (1), that Point  $C$  and  $D$  are on the different sides of Point  $A$  and  $B$  means:

$$(\overline{AB} \times \overline{AC}) \cdot (\overline{AB} \times \overline{AD}) < 0 \quad (11)$$

Similarly, that Point  $A$  and  $B$  are on the different sides of Point  $C$  and  $D$  means:

$$(\overline{CD} \times \overline{CA}) \cdot (\overline{CD} \times \overline{CB}) < 0 \quad (12)$$

Apparently, when the above two conditions are established, Line Segment  $AB$  and  $CD$  intersect.

(3) Intersection estimation of two polygons. There are two ways to estimate whether two polygons intersect or not: estimating whether any vertex of one polygon is in the other one and estimating whether there are intersecting lines. When estimating whether Block 1 and 2 (Fig. 6) intersect, transverse all vertexes of Block 1. If there is any vertex in Block 2 (any vertex of Block 1 is on the left of all counterclockwise vectors of Block 2), the two blocks intersect.

It is noteworthy that: when all vertexes of Block 1 are outside of Block 2. There are cases of inclusion and penetration, like Fig. 7 and 8. Conduct

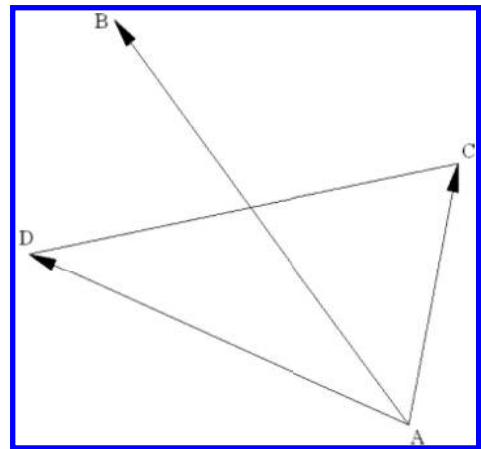


Figure 5. Lines intersection.

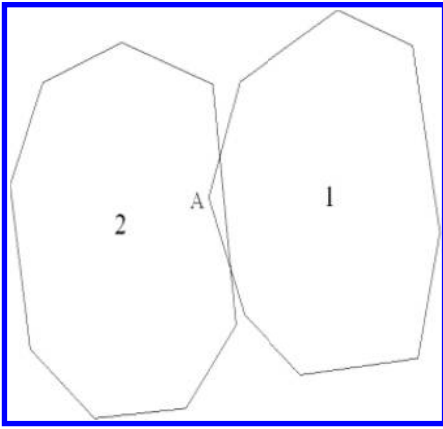


Figure 6. Blocks intersection.

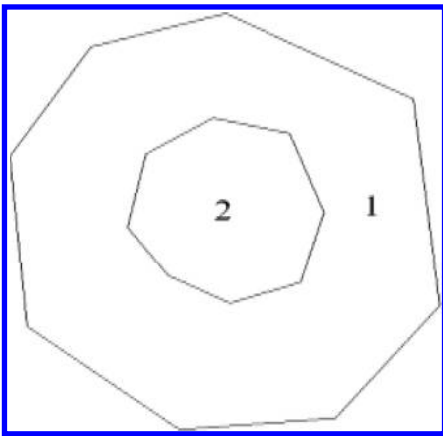


Figure 7. Inclusion of two blocks.

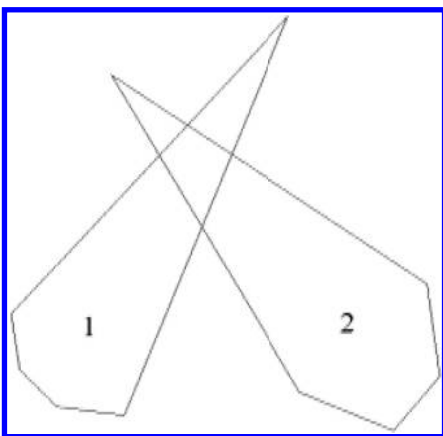


Figure 8. Penetration of two blocks.

the same estimation progress of Block 1 to Block 2. For the case of penetration, the two blocks can be testified non-intersected only when all the sides of Block 1 and 2 are testified non-intersected.

### 5 3D RANDOM CAVE MODEL GENERATED

1. Cave model generated in rectangle area (polygon unit) (Fig. 9 and 10).
2. Cave model generated in rectangle area (circle unit) (Fig. 11 and 12).
3. Cave model generated in circle area (polygon unit) (Fig. 13 and 14).
4. Cave model generated in circle area (circle unit) (Fig. 15 and 16).

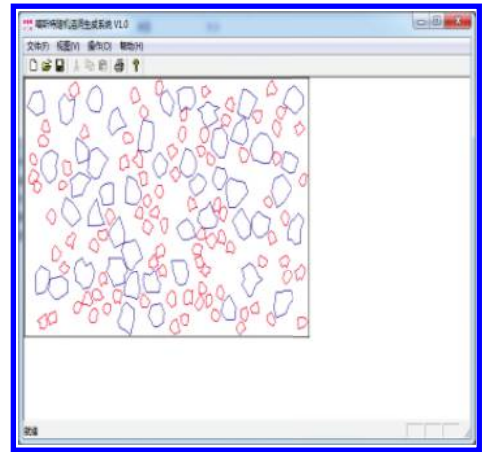


Figure 9. Distribution of Karst cave.

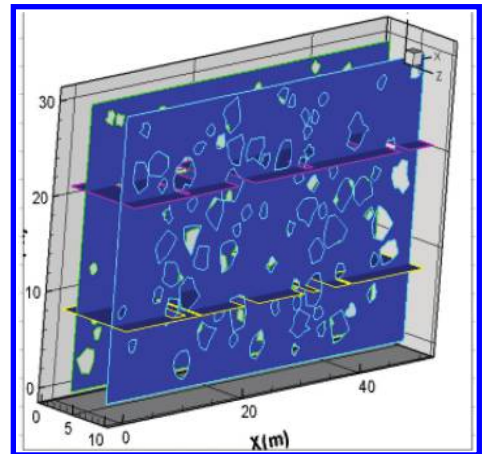


Figure 10. Generated 3D profile.



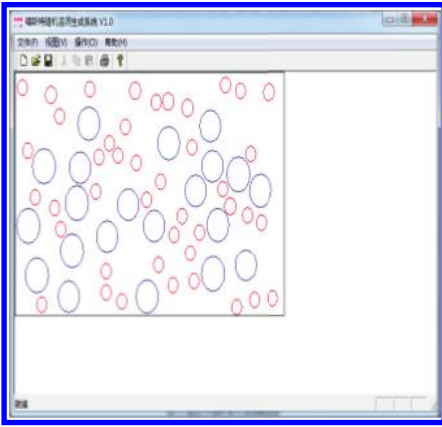


Figure 11. Distribution of Karst cave.

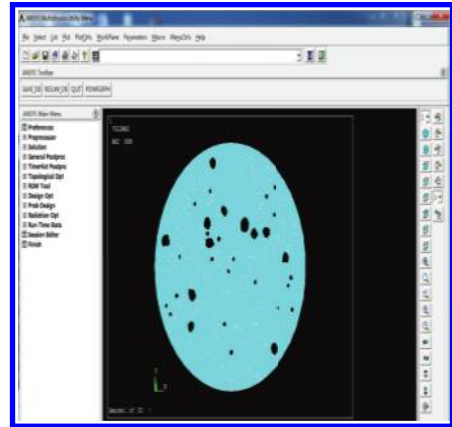


Figure 14. Distribution map of cave model in ansys.

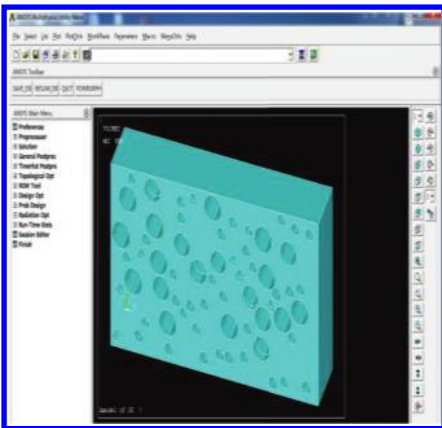


Figure 12. Karst cave model diagram in ansys.

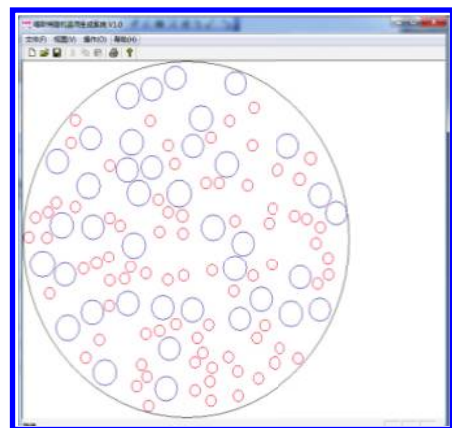


Figure 15. Distribution of Karst cave.

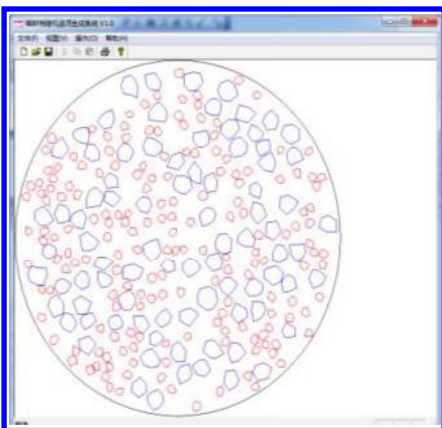


Figure 13. Distribution of Karst cave.

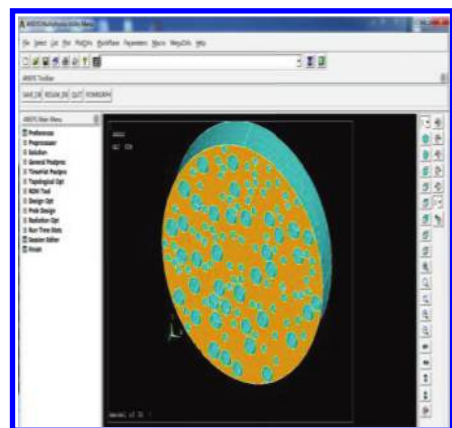


Figure 16. Distribution of cave in ansys.

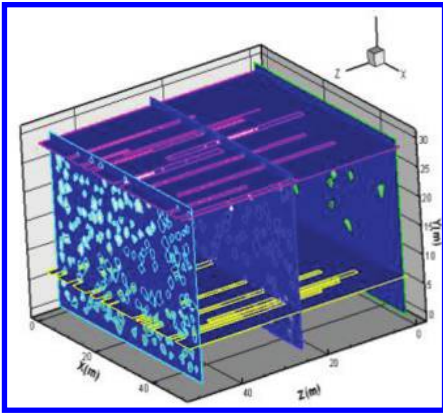


Figure 17. Profile of 3D model (Front side).

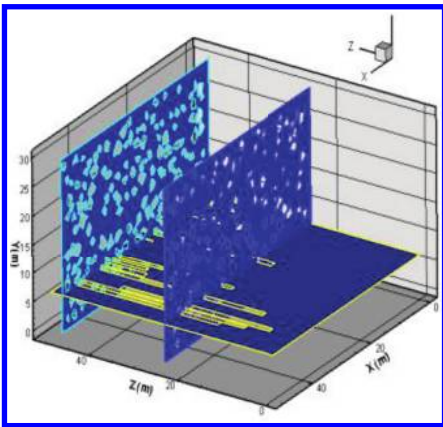


Figure 18. Profile of 3D model (After the side).

## 6 CONCLUSION

1. The Karst cave is a un-uniform discontinuum body, the rock mass of which is complicated and disordered. The non uniformity of its microscope rock mass greatly defines its mechanical property and failure mechanism. So its 3D form is very complicated and un-uniform. If it is simplified as a 2D form, it would be convenient to study the un-uniform cave.
2. By using the local cave radius  $R$  to describe the cave's discrete degree on the large scale, the area ratio  $S$  to describe the local space density in every cave distribution area, and by choosing  $R$  and  $S$ , different cave models could be built easily and the real complicated caves could be quickly and accurately described.

Based on the above, by using the merging neighboring points algorithm and the threshold value

interception algorithm while controlling the element shape, the area ratio, the radius range, the uniformity, the smoothness and the generation area, the generating method of the Karst cave random geometry model was proposed. The generated cave models meet the reality and the randomness of their distribution could be achieved. What's more, the software developed in this study can connect directly with ANSYS and import the generated cave models and their characteristics together into ANSYS. Its convenience of generating cave models provides a good platform for numerical analysis of the Karst cave.

## REFERENCES

- Bailly, D. & Ababou, R. & Quintard, M. 2009. Geometric characterization, hydraulic behavior and upscaling of 3D fissured geologic media. *Mathematics and Computers in Simulation* 79(12): 3385–3396.
- Chen, X.J. & Zhang, J.M. & Wang, S.J. et al. 2010. Computer Simulation about Three Dimensional Random Structure model of Karstic Rock. *2nd International Conference on Information Science and Engineering* 10: 7105–7108.
- Eulogio, P.I. & Juan, J.D.V. & Victor, R.G. 2011. Morphometric analysis of three-dimensional networks of Karst conduits. *Geomorphology* 132(1–2): 17–28.
- Eulogio, P.I. & Peter A.D. & Chaoshui, X. & Juan, J.D.V. 2012. Stochastic simulation of Karst conduit networks. *Advances in Water Resources* 35: 141–150.
- Guillaume, R. & Pauline, C.D. & Marco, F. 2014. Simulation of 3D Karst conduits with an object-distance based method integrating geological knowledge. *Geomorphology* 217(15): 152–164.
- He, L. & An, X.M. & Ma, G.W. & Zhao, Z.Y. 2013. Development of three-dimensional numerical manifold method for jointed rock slope stability analysis. *International Journal of Rock Mechanics and Mining Sciences* 64: 22–35.
- Hu, X.Y. & Yuan, X.C. & Hou, J. et al. 2014. Modeling method of carbonate fractured-cavity reservoirs using multiscale Karst facies-controlling. *Acta Petroli Sinica* 2: 340–346.
- Liu, Y. 2013. Geological Modeling of Paleokarst Cave Reservoir by The Multilevel Facies Conditioning Method. *Xinjiang Geology* 2: 100–106.
- Wang, C.C. & Yao, J. & Yang, Y.F. et al. 2012. The construction of carbonate multiscale network model based on regular network. *Chinese Journal of Computational Mechanics* 30(2): 231–235.
- Xi, X. & Yao Y. & Gu, H.M. 2005. Random cavity medium model and the wave field simulation. *Progress in Geophysics* 33(9): 105–108.
- Yang, H.T. & Jiang, T.W. & Yan, Q.B. et al. 2004. Establishment of 3D Geological Models of Fracture-cavern Carbonate Reservoir. *Petroleum Geology & Oilfield Development in Daqing* 23(4): 11–12,16.
- Ye, Y. & Dong, L.G. & Lee, J.F. 2004. *Numerical Simulation and Testing Technology of Karst cave*. Beijing: Petroleum Industry Press.

## Research on the wind-induced vibration response of adhesive integral-lift scaffold

Weimin Pan, Ningning Kong, Xin Ye & Guohua Li

*School of Mechatronics Engineering, Henan University of Science and Technology, Luoyang, China*

**ABSTRACT:** The adhesive integral-lift scaffold is a kind of new scaffold with economic, safe and convenient that can be applied to the high-rise building construction, especially super high-rise building construction. In this paper, three different kinds of finite element models of the adhesive integral-lift scaffold were established and their dynamic characteristics were analyzed, which were compared to select the scaffold model of conforming to the actual natural frequency of vibration as a calculation model and give the method of the wind vibration coefficient that conforms to the wind vibration response of the studied scaffold. The theoretical results by calculating of the wind vibration coefficient that affects wind load were compared with the results by selecting of actual engineering, which provides the basis to study and optimize the calculation method of wind load on scaffold.

**Keywords:** adhesive integral-lift scaffold; finite element models; wind vibration response; natural frequency

### 1 INTRODUCTION

The adhesive integral-lift scaffold is a new scaffold developed rapidly at the beginning of this century, which has the important influence to the progress of construction technology. It can satisfy the needs of construction technology and safety protection when workers operate on the outside of buildings in the structure, installation and decoration of construction. It has the characteristics of economical, security and convenient because it makes a high and suspended operation to a lower operation and operation in a frame. The adhesive integral-lift scaffold, as shown in Figure 1, refers to the scaffold with roll-over protector and anti-dropping device, which is attached to the



Figure 1. The adhesive integral-lift scaffold during the structure construction.

engineering structure of a certain height. It can climb or decline step by step with the engineering structure by its own lifting equipment and device. It mainly includes the frame structure of scaffold, adhesive bearing, roll-over protector, anti-dropping device, elevator mechanism and control device.

With the increase of structure height, the economy of the adhesive integral-lift scaffold is more obvious. Especially when the height of the building is more than 80 meter, the applicability and economy of the adhesive integral-lift scaffold is particularly prominent. So, it is suitable for high-rise building construction, especially super high-rise building construction. Then, the wind load on scaffold has become the dominant design load, which plays a decisive role in the safety of using the scaffold. If the problem of wind load is solved, the design can be without limiting by height. Therefore, the calculation method of the wind load on scaffold is a primary and urgent task. The wind is formed by air flow from the place where the big pressure to the small pressure. The airflow is formed to the high pressure air curtain by the block of the structure. So, wind load is produced on the structure of different sizes. Wind load is a kind of random dynamic load. In order to analysis conveniently, it can be divided into average wind and fluctuating wind. Fluctuating wind load is the dynamic component of wind, which makes the structure of the random vibration. The correction coefficient that is affected on the fluctuating wind of the wind

effect is called the wind vibration coefficient. Now, the calculation method of Wind load on scaffold most based on *load code for the design of building structures* (GB50009-2001), which provisions the wind load standard values of perpendicular to the surface of buildings. It can be calculated by using Equation (1) as follows:

$$W_k = \beta_z \mu_s \mu_z W_0 \quad (1)$$

where  $W_k$  = wind load;  $\beta_z$  = wind-induced vibration coefficient;  $\mu_s$  = shape coefficient of wind load;  $\mu_z$  = wind pressure height coefficient; and  $W_0$  = fundamental wind pressure. This paper mainly studies on the wind-induced vibration coefficient of the adhesive integral-lift scaffold.

## 2 ESTABLISHMENT OF THE FINITE ELEMENT MODEL

To study the wind load on the adhesive integral-lift scaffold, the first step is the establishment of the finite element model based on a three-dimensional model. The erection height of the scaffold frame in this paper is set as 14.72 m, which includes 7 steps, with each measuring 1.84 m, and the protective structure that is also 1.84 m. The width of the frame is 0.68 m. In addition, the model also has the main frame support at the bottom and reinforced truss rods. According to the three-dimensional model, as shown in Figure 2, three finite element models, namely one truss, two trusses and three trusses, respectively, are established by using ABAQUS, as shown in Figures 3–5. The beam element analysis unit is mainly used for analysis, appoint direction is the default direction of the beam, beam section is consistent with the actual component section, and its each joint is bolt rigid connection. Structural material properties are elasticity modulus  $E = 2.1 \times 10^5 \text{ N/mm}^2$ , Poisson's ratio  $\mu = 0.3$ , and density  $\rho = 7850 \text{ kg/m}^3$ .

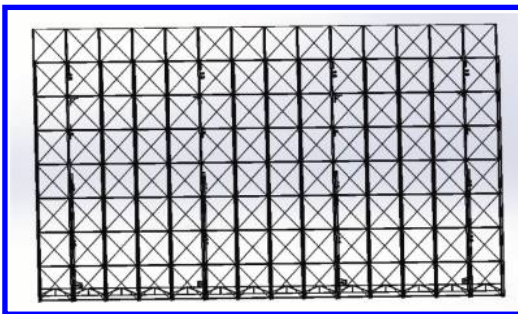


Figure 2. The three-dimensional model of the adhesive integral-lift scaffold.

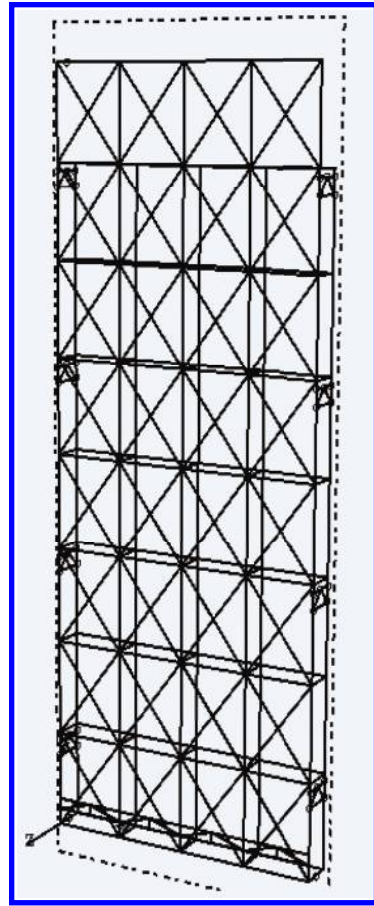


Figure 3. The finite element model of one truss.

## 3 DYNAMIC CHARACTERISTIC ANALYSIS OF THE ADHESIVE INTEGRAL-LIFT SCAFFOLD

The adhesive integral-lift scaffold is strongly influenced by wind load on the study. The effect on the structure of average wind is equivalent static wind, and the effect on the structure of fluctuating wind will cause structural vibration. In order to ensure that the adhesive integral-lift scaffold can work safely and reliably in high-rise, especially super high-rise, building construction, the dynamic characteristic analysis of the wind load on scaffold is very important. In addition, the analysis and cognition dynamic characteristic of structure is the basis of the wind-resistant design and stability analysis of the structure. Considering the computational efficiency and accuracy of the results, by using ABAQUS finite element software to extract the characteristic value of the first five-order natural

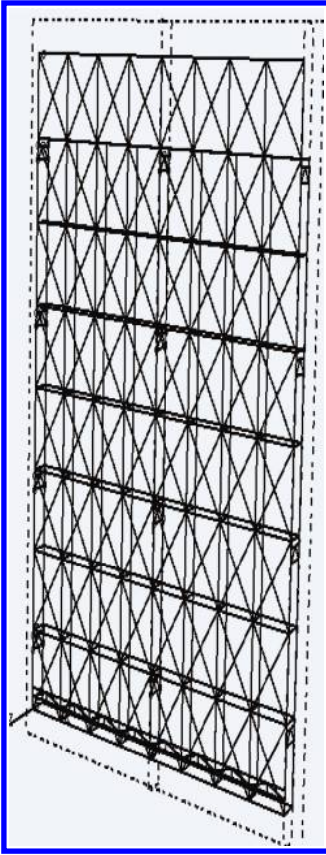


Figure 4. The finite element model of two trusses.

vibration frequency when the scaffold finite element models are one truss, two trusses and three trusses, respectively, as shown in Table 1, and the vibration mode of scaffold is shown in Figures 6–8.

In theory, with the trusses increases of the finite element model, the calculation of dynamic characteristics is more close to the actual situation. However, this will increase the calculation workload. And the frequency of previous order plays a major role in the wind-induced vibration response, as can be seen in Table 1. The calculation results of the first-order vibration frequency when the finite element models are one truss, two trusses, and three trusses that are similar, and their differences were 6.0% and 2.4%. So in order to simplify the calculation, this paper takes the finite element model of one truss as a calculation model. It also takes the first-order vibration frequency  $\omega_1 = 1.0999$  as the representative of the dynamic characteristics of the whole scaffold. Analysis of dynamic characteristics of the scaffold can be used in the following calculation of wind vibration coefficient.

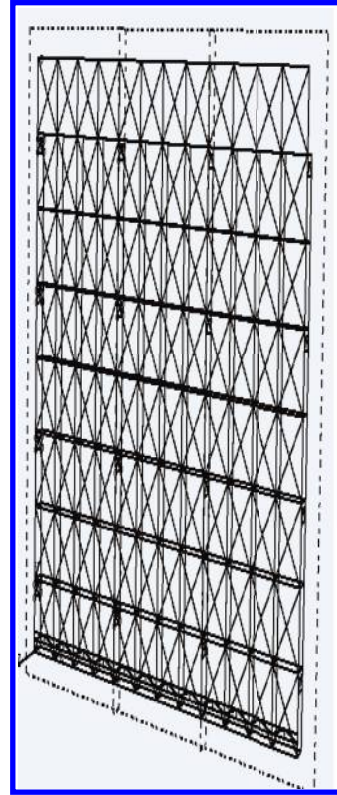


Figure 5. The finite element model of three trusses.

Table 1. The first-five order natural vibration frequency of the scaffold.

	One truss	Two trusses	Three trusses
First order	1.0999	1.0372	1.0132
Second order	1.4539	1.2223	1.1350
Third order	3.2529	3.0945	2.7272
Fourth order	4.3567	3.5287	3.0416
Fifth order	5.3426	3.8659	3.2917

#### 4 CALCULATION AND RESULTS OF THE WIND-INDUCED VIBRATION COEFFICIENT

After organizing references, this paper gives the wind vibration coefficient expressions when the scaffold is at the climbing stage or declining stage. The wind vibration coefficient expression of climbing stage is as follows:

$$\beta_z = 1 + \frac{\sqrt{\eta^2 \cdot \xi_1 \lambda_1 + 2\varphi\eta \cdot \xi_2 \lambda_2 + \varphi^2 \cdot \xi_3 \lambda_3}}{\mu_{z_n}} \quad (2)$$

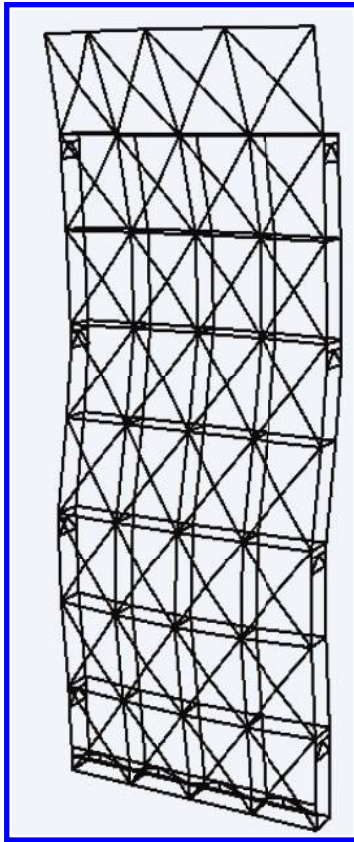


Figure 6. The vibration mode of one truss.

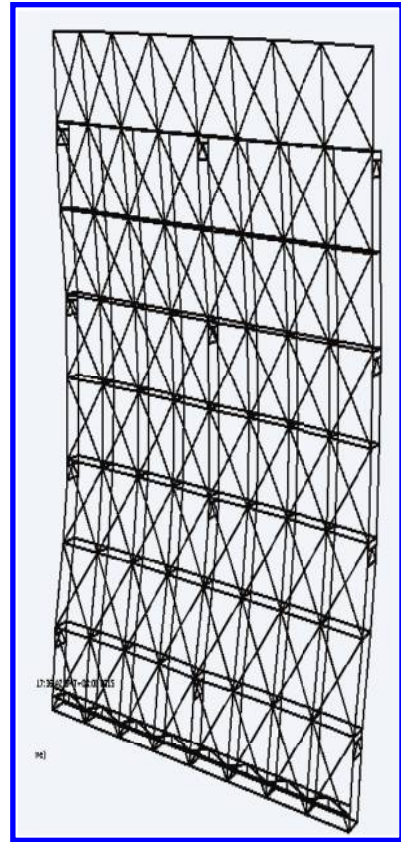


Figure 7. The vibration mode of two trusses.

where  $\xi_1, \xi_2, \xi_3$  = pulse power coefficient under the common action of building structure and scaffold, and the expression is given as follows:

$$\xi_1 = \int_{-\infty}^{+\infty} \omega_s^6 (\omega_s^2 + 4\zeta_s^2 \omega^2) \frac{r}{|D|^2} S_f(\omega) d\omega \quad (3)$$

$$\xi_2 = \int_{-\infty}^{+\infty} \omega_s^5 (\omega_1^2 \omega_s - \omega_s \omega^2 + 4\zeta_1^2 \omega_1 \omega^2) \frac{r}{|D|^2} S_f(\omega) d\omega \quad (4)$$

$$\xi_3 = \int_{-\infty}^{+\infty} \omega_s^2 [(\omega_1^2 - \omega^2)^2 + 4\zeta_1^2 \omega_1^2 \omega^2] \frac{1}{|D|^2} S_f(\omega) d\omega \quad (5)$$

where  $\lambda_1, \lambda_2, \lambda_3$  = pulse influence coefficient when considering pressure fluctuation and spatial correlation, and the expression is as follows:

$$\lambda_1 = \sum_{i=1}^n \sum_{j=1}^n \phi_{i1} \phi_{j1} \rho_{ij} \mu_{fi} \mu_{zi} \mu_{fj} \mu_{zj} \quad (6)$$

$$\lambda_2 = \sum_{i=1}^n \phi_{i1} \rho_{ni} \mu_{fi} \mu_{zi} \mu_{fn} \mu_{zn} \quad (7)$$

$$\lambda_3 = (\mu_{fn} \mu_{zn})^2 \quad (8)$$

where  $\eta$  = ratio of shape coefficient of wind load between building structure and scaffold, and the expression is as follows:

$$\eta = \mu_s / \mu_{ss} \quad (9)$$

where  $\mu_s$  can be used when checking in the relevant formulas and tables of *load code for the design of building structures* (GB50009-2001);  $\mu_{ss}$  can be used at the suggested value of shape coefficient of wind load in practical engineering;  $\varphi$  = wind coefficient of scaffold, 0.8 = suggested value;  $\mu_{zn}$  = wind pressure height coefficient of building structure construction, which can be used when checking in the relevant formulas and tables. The table of calculating values can be selected in the references.

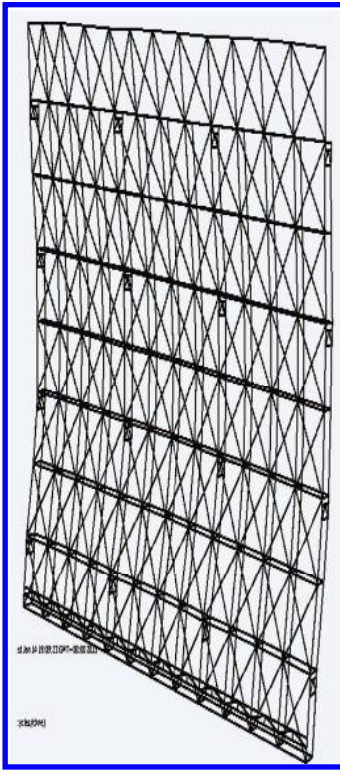


Figure 8. The vibration mode of three trusses.

Table 2. The comparison of the result of two kinds of wind vibration frequency.

	Theory coefficient	Actual coefficient
Climbing stage	1.577	1
Declining stage	1.589	1

The expression of wind-induced vibration coefficient when the scaffold is declining is given as follows:

$$\beta'_z = 1 + \frac{\sqrt{\phi_1^2 \eta^2 \cdot \xi'_1 \lambda'_1 + 2\phi_1 \phi \eta \cdot \xi'_2 \lambda'_2 + \phi^2 z_i^{2\alpha} \cdot \xi'_3 \lambda'_3}}{\mu_{zi}} \quad (10)$$

where  $\xi'_1, \xi'_2, \xi'_3$  = pulse power coefficient under the common action of building structure and scaffold,  $\xi_1 = \xi'_1, \xi_2 = \xi'_2, \xi_3 = \xi'_3$ ;  $\lambda'_1, \lambda'_2, \lambda'_3$  = pulse influence coefficient when considering pressure fluctuation and spatial correlation, and the expression is given as follows:

$$\lambda'_1 = \lambda_1 \quad (11)$$

$$\lambda'_2 = \sum_{j=1}^n \phi_{1j} \rho_{ij} \mu_{fj} \mu_{zj} \mu_{fj} \mu_{zi} \quad (12)$$

$$\lambda'_3 = \frac{(\mu_{fj} \mu_{zi})^2}{z_i^{2\alpha}} = \frac{(\mu_{fj} \mu_{zi})^2}{z_i^{2\alpha} \cdot (\mu_{fj} \mu_{zn})^2} (\mu_{fj} \mu_{zn})^2 = z_n^{2\alpha} \cdot \lambda_3 = H^{-2\alpha} \cdot \lambda_3 \quad (13)$$

where  $\lambda'_2, \lambda'_3$  can be selected in the references.  $\phi_1$  = first vibration mode of building structure in the first particle, the corresponding vibration mode frequency of the adhesive integral-lift scaffold, its calculating method can also be used from the relevant formulas and tables of *load code for the design of building structures* (GB50009-2001);  $z_i$  = height of scaffold;  $\mu_{zj}$  = wind pressure height coefficient in the height of scaffold, it can be used from the relevant formulas and tables;  $\alpha$  = ground roughness index. In this paper, the comparison between calculating theory wind vibration coefficient and the actual coefficient of project with selecting each coefficient is given in Table 2.

## 5 CONCLUSION

In this paper, the dynamic characteristic of the scaffold is analyzed by establishing three different finite element models. We took the scaffold model of one truss as the calculation model, and obtained the scaffold vibration frequency. It was applied to the calculation of wind vibration coefficient, so the theory value of wind vibration coefficient was obtained, which was compared with the actual result of project selected. So, it provides the basis for the research of wind load calculation method of scaffold.

## REFERENCES

- Chen, N.P. 2011. The construction application briefly of the adhesive integral-lift scaffold. *Science and Technology Information* (2):84.
- GB/T 50009. 2001. load code for the design of building structures.
- Li, G.Q. & Yu, F. & Yuan, Y. 2004. Research on wind-induced vibration coefficient of self-climbing scaffold attached to tall buildings in construction. *Earthquake Engineering and Engineering Vibration* 24(5):62–67.
- Yu, F. & Li, G.Q. & Yuan, Y. 2004. Calculation of wind load on self-climbing scaffold in high-rise building construction (part one). *Architecture Technology* 35(8):590–593.
- Yu, F. & Li, G.Q. & Yuan, Y. 2004. Calculation of wind load on self-climbing scaffold in high-rise building construction (part two). *Architecture Technology* 35(9):696–698.
- Zhang, D. 2010. Numerical study of the integral-lifting scaffolds and the ultimate bearing capacity under wind load. *Southwest University of Science and Technology*.
- Zhao, F. & Xu, W. 2008. Construction technology of refuse bin sliding mode at low temperature. *Shan Xi Architecture* 34(13):139–140.

# Finite element analysis for a composite rib floor slab of steel fiber foam concrete

Yabo Wang, Gaofeng Dou, Chuanhao Xi, Lei Qian & Hanting Liu  
*Jilin Jianzhu University, Chanchun, Jinlin, China*

**ABSTRACT:** A new type of fabricated steel fiber foam concrete rib floor slab (henceforth referred to as “composite slab”) and its process flow of manufacture are simply introduced. Based on the finite element analysis with software ABAQUS, the finite element simulations are conducted in one-way “composite slab” and two-way “composite slab”, and their mechanical performance analysis is compared. The fine mechanics behavior of two-way “composite slab” is stated, which can provide a reference for the application of “composite slab”.

**Keywords:** fiber-reinforced concrete; foamed concrete; rib floor slab

## 1 A BRIEF INTRODUCTION OF COMPOSITE SLAB

“Composite slab” is a new type of pre-cast slab, the bottom of which is 2-centimeter steel fiber-reinforced concrete slab with steel mesh in it. The upper portion of the slab is a multi-ribbed structure, which uses ordinary concrete. The width and height of the rib are 6 cm and 8 cm, respectively. There is a reinforcement cage made up of carrying steel and stirrup in the multi-ribbed structure. Since the distance between carrying steel is smaller, the stirrup uses a S-shaped hook. The space between the multi-ribbed structures is filled by the foamed concrete, and then the upper portion of the multi-ribbed structure is casted by the 2-centimeter steel fiber-reinforced concrete slab, which does not have steel mesh in it.

When making “composite slab”, the steel fiber-reinforced concrete slab in the bottom should be poured first, then casting ribbed structure, and curing concrete for a period of time. This is followed by casting the foamed concrete in the space between the multi-ribbed structures and curing it. When it has a definite strength, the surface should be made smooth and clean, and then casting the steel fiber-reinforced concrete in the upper layer. Since the dimensions of all the parts of “composite slab” are small, it is better to use the smaller cobblestone, which is convenient for construction. When mixing the steel fiber-reinforced concrete, the steel fiber and other materials should first be dry-mixed

to make the steel fiber mix well, and then they are mixed with water.

## 2 CHARACTERISTICS OF ONE-WAY SLAB AND TWO-WAY SLAB

According to the theory of elastic thin plate, when the ratio of the long side and short side of the floor exceeds a certain value, the load of the one-way slab can transfer by the bending and shearing action along the “short side direction of the floor”. The load transfer along the long side direction can be ignored. Two-way slab has bending and shearing action in both directions, which can deliver the load along the long side and short side directions at the same time. The stress characteristic of the two-way slab is different from that of the one-way slab [1]. The floor bending in only one direction or mainly in one direction is called the one-way slab, while the floor bending in both directions that cannot be ignored in any direction is called the two-way slab [2]. Mechanical and deformation performance of the two-way slab is much better than that of the one-way slab. Thus, the two-way slab can enhance the bearing capacity and reduce the plate thickness. Meanwhile, it can strengthen the integrity and stiffness of the floor. However, the structure of “composite slab” is comparatively complex. In order to have quantified concepts about its mechanical property, we made a finite element simulation calculation of the one-way “composite slab” and the



two-way “composite slab” to compare the analysis of their mechanical behavior.

### 3 A BRIEF INTRODUCTION OF CALCULATION EXAMPLE AND THE MODELING APPROACH

#### 3.1 Material constructive model

Normal concrete uses the elastic-plastic constitutive relation, because the model uses the monotonous static loading plan. So based on the data of the plastic-damage model of C30 concrete in reference 3, the damage factor is not input, but it uses the elastic-plastic constitutive relation. This is because the constitutive relation of steel fiber-reinforced concrete is relevant to concrete strength and the type of steel fiber. So far, there has not been a unified constitutive relation model of steel fiber-reinforced concrete [4]. So the constitutive relation of steel fiber-reinforced concrete is mainly reflected by the modification of the constitutive relation of normal concrete and its elasticity modulus. The steel uses a double straight line ideal elastoplastic model.

#### 3.2 A brief introduction of the finite element model

The size of the one-way “composite slab” is  $3.6\text{ m} \times 1.2\text{ m}$ ; the size of the two-way “composite slab” is  $3.6\text{ m} \times 3.6\text{ m}$ ; the bottom is steel fiber-reinforced concrete; and its steel fiber content is 1.5%. The strength grade is CF30 and the upper part is a multi-ribbed structure, whose width and height are 6 cm and 8 cm, respectively. Multi-ribbed is ordinary concrete C30. All the concrete elements are an eight-node linear reduced integration entity unit (C3D8R). Multi-ribbed and steel fiber-reinforced concrete at the bottom is divided by the method of partition and gives them different properties, such as one-way slab shown in Figure 1.

The steel mesh in the steel fiber-reinforced concrete slab at the bottom is HPB300, and its

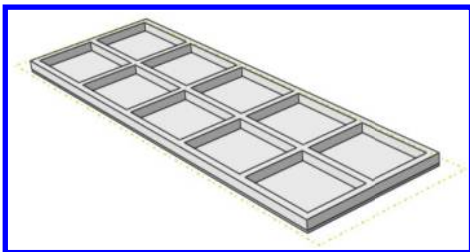


Figure 1. The diagram of the bottom of the one-way “composite slab” and its multi-ribbed structure.

diameter is 6 mm, the steel distance is 190 mm, steel mesh, as shown in Figure 2. The carrying steel in the multi-ribbed structure is HRB400 and its diameter is 8 mm, stirrup in the multi-ribbed is HPB300 and its diameter is 6 mm, the reinforcement cage in the multi-ribbed structure, as shown in Figure 3. All the steel elements are a two-node linear three-dimensional truss element (T3D2), which is applied to the separation-type model with the concrete element, and the steel unit is embedded in the concrete element, proceeding with the degree of freedom coupled to simulate the bond between steel bar and concrete [5].

Because the volume-weight of foamed concrete is  $200\text{ kg/m}^3$ , which is mainly used to fill the gaps, it does not belong to the main stress structure. So in order to simplify the calculation model, there is no simulation of foamed concrete and it directly ties the 2-centimeter steel fiber-reinforced concrete slab to the top surface of the multi-ribbed structure. Mesh generation is very important for finite element calculation. If the mesh is too coarse, the calculation results are not accurate enough; if the mesh is too dense, it will take a lot of computing time. So it needs to ascertain the mesh density reasonably [6]. When defining a tie, it needs to distinguish the master-slave surface, and the slave surface mesh should be denser than the master surface mesh [6]. The upper steel fiber-reinforced concrete slab is as the master surface, as shown in Figure 4, whose element size is 0.07. The top surface of the multi-ribbed surface is as the slave surface, whose element size is 0.05.

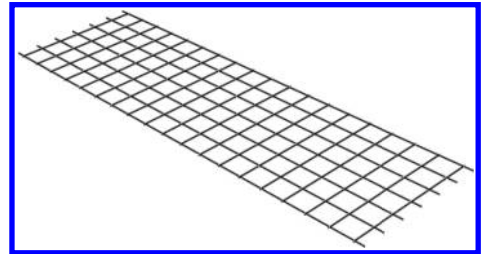


Figure 2. The diagram of the steel mesh at the bottom of the one-way “composite slab”.

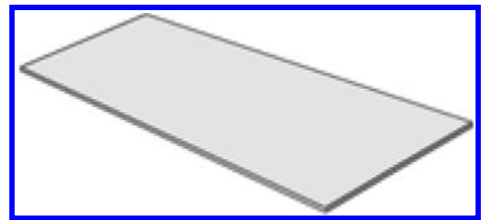


Figure 3. The diagram of the rib frame of the one-way “composite slab”.

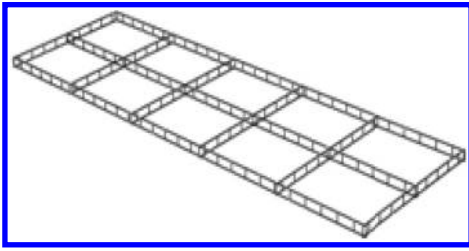


Figure 4. The diagram of the upper steel fiber-reinforced concrete slab of the one-way “composite slab”.

The boundary condition of the one-way “composite slab” is  $U_1 = 0, U_2 = 0, U_3 = 0$ , imposed on the two short sides of the one-way slab. The quadrilateral boundary condition of the two-way “composite slab” is  $U_1 = 0, U_2 = 0, U_3 = 0$ . The area load imposed on the one-way slab is  $40 \text{ KN/m}^2$ , while the area load imposed on the two-way slab is  $60 \text{ KN/m}^2$ .

In the implicit analysis program (e.g. ABAQUS/Standard), the material with softening and rigid-ity weakening traits will make calculation difficult to convergence. In the constitutive equation, it can adopt the viscoplastic regularization to solve the problem partially [7]. When defining the viscosity coefficient of concrete, the greater the viscosity coefficient, the more rigid the structure is, i.e. it is just like a more sticky liquid that is more difficult to flow; the smaller the viscosity coefficient, the lower the computational efficiency [8]. We find that when the viscosity coefficient is less than 0.1, it is difficult to converge through valuing the viscosity coefficient. In order to reduce the calculated quantity, the viscosity coefficient is defined as 0.3 on the premise that it does not affect the result precision.

#### 4 THE FINITE ELEMENT RESULTS OF ABAQUS

von Mises stress of steel mesh at the bottom of the one-way “composite slab” is shown in Figure 5. Its stress of the middle steel element varies with load curve, as shown in Figure 6. When the area load is  $11 \text{ KN/m}^2$ , the curved section appears, which indicates that the lower part concrete of the floor has already cracked. This is mainly by the steel to bear load effect, and when the area load is  $31.6 \text{ KN/m}^2$ , steel yield, the member is already broken.

von Mises stress of steel mesh at the bottom of the two-way “composite slab” is shown in Figure 7. Its stress of the middle steel element varies with load curve, as shown in Figure 6. When the area load is  $18.5 \text{ KN/m}^2$ , the curved section appears,

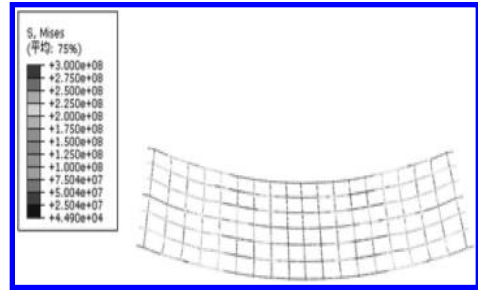


Figure 5. von Mises stress diagram of steel mesh at the bottom of the one-way “composite slab”.

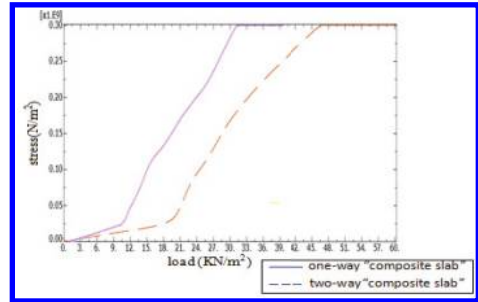


Figure 6. Stress of the middle steel element varied with load curve of the one-way “composite slab” and the two-way “composite slab”.

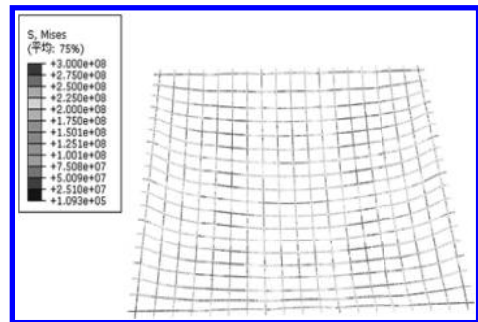


Figure 7. von Mises stress diagram of steel mesh at the bottom of the two-way “composite slab”.

which indicates that the lower part concrete of the floor has already cracked. This is mainly by the steel to bear the load effect, and when the area load is  $46.5 \text{ KN/m}^2$ , steel yield, the member is already broken.

The cracking load of the  $3.6 \text{ m} \times 3.6 \text{ m}$  two-way “composite slab” improves by 68%, compared with the  $3.6 \text{ m} \times 1.2 \text{ m}$  one-way “composite slab”, and the failure load improves by 42%. The deflection limit value of the floor flexural member is

$l_0/200$ , where  $l_0$  is the effective span of the member [1]. The effective span of both the one-way “composite slab” and the two-way “composite slab” is 3.6 m, so their deflection limit value is 0.018 m. The deflection of the one-way “composite slab” is shown in Figure 8. The load-deflection curve of its middle element is shown in Figure 9. As can be seen from the figure, when the deflection of the floor is 0.018 m, its corresponding load is 26.4 KN/m<sup>2</sup>. The deflection of the two-way “composite

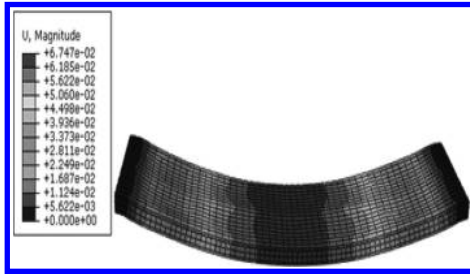


Figure 8. The deflection diagram of one-way “composite slab”.

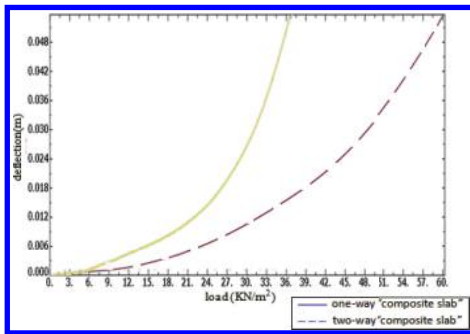


Figure 9. The load-deflection curve of the one-way “composite slab” and the two-way “composite slab”.

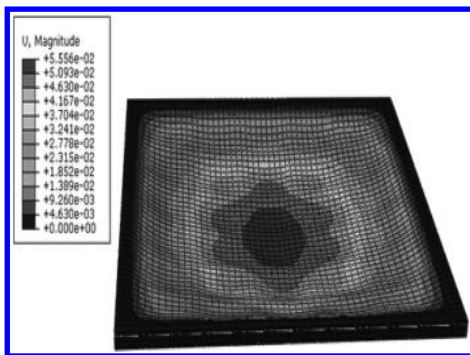


Figure 10. The deflection (m) diagram of the two-way “composite slab”.

slab” is shown in Figure 10. The load-deflection curve of its middle element is shown in Figure 9. As can be seen from the figure, when the deflection of the floor is 0.018 m, its corresponding load is 38.5 KN/m<sup>2</sup>. By comparison, the normal use of the limited load of the two-way “composite slab” is improved by 46%.

So we can see that the mechanical performance of the two-way “composite slab” is much better than that of the one-way “composite slab”. However, restricted by the capacity of hoisting and transportation equipment in the assembled structure, floor is impossible to be made as a whole two-way “composite slab”, but it must be divided into several floor slabs, after hoisted in position, connecting them together to form the two-way slab. So if we can find a safe, reliable and reasonable joint that can make the one-way “composite slab” to deliver the load effect effectively, then it can improve the mechanical performance of the structure.

## 5 CONCLUSIONS

1. “Composite slab” is a new type of pre-cast slab within foamed concrete filling, which can keep warm and sound-insulated well, and the steel fiber-reinforced concrete has a preferable ductility and dissipative capacity. The mechanical performance of its one-way slab and two-way slab can meet the requirements, and they can be applied to the assembled structure and are especially applicable to the north cold area.
2. The mechanical performance of the two-way “composite slab” is much better than that of the one-way “composite slab”, whose cracking load improves by 68%, normal use of limited load improves by 46%, and failure load improves by 42%. If we can find a reasonable joint that can make the one-way “composite slab” to combine with the two-way “composite slab” to deliver the load effect effectively, then it is good to improve the carrying capacity of the structure. Meanwhile, it can also strengthen the integrity and stiffness of the floor.
3. Now the mechanical performance of “composite slab” remains restricted to the finite element simulation analysis, and the bond slip between steel and concrete is shown by the EMBEDDED technology, which is slightly different from the practical engineering. In addition, there is no experiment conducted on the actual construction member, so the corresponding structure test is also needed in order to compare with the finite element model and carry out validation analysis.

## REFERENCES

- [1] Ji Lin. Talking about building two-way slabs stiffened with beams design [J]. Heilongjiang Science and Technology Information. 2012 (24).
- [2] Wenrang Chen, Deheng Yan. Concrete building structures design [M]. Beijing: Chian Building Industry Press, 2003.
- [3] Jin Zhang, Qingyang Wang, Shouying Hu, ChuanJia Wang. Parameters Verification of Concrete Damaged Plastic Model of ABAQUS [J]. Building Structure, 2008. 38(8): 127–130.
- [4] Jisheng Qiu, Study on calculation theory and behavior of steel fiber reinforced concrete Multi-ribbed composite slab [D]. Xi' An University of Architecture and Technology 2011.
- [5] Yuzhuo Wang, Chuanguo Fu. ABAQUS structural engineering analysis example explanation[M]. Beijing: China Architecture and Building Press, 2010.
- [6] Yiping Shi, Yurong Zhou, ABAQUS finite element analysis example explanation [M]. Beijing: Chian Machine Press, 2006. 6.
- [7] Jinchang Wang, Yekai Chen. The application of ABAQUS in civil engineering [M]. Hangzhou: Zhe Jiang University Press, 2006. 11.
- [8] Jinsong Liu, Hongjun Liu. ABAQUS finite analysis of reinforced concrete [J]. Equipment Manufacturing Technology, 2009(6).

# Finite element analysis of steel reinforced recycled aggregate concrete axial compression short column

Bing Wang & Xiao Liu

School of Architectural and Civil Engineering, Shenyang University, Shenyang, China

Lu Gao

School of Civil Engineering, Lanzhou University of Technology, Lanzhou, China

**ABSTRACT:** In this paper, the steel recycled concrete axial compression short column has been analyzed by the finite element analysis using finite element analysis software ABAQUS. We get the ultimate bearing capacity of steel replacement rate under different regeneration concrete stub columns, and give each part temperature peak stress cloud contrast. The results showed that with the increase of recycled coarse aggregate replacement ratio, the concrete stress slightly increased, the ultimate bearing capacity of the component also gradually increased.

**Keywords:** steel reinforced recycled aggregate concrete; axial compression; column; the finite element

## 1 INTRODUCTION

With the rapid development of global economy, the speeding up of urbanization, and the increasing increase in the amount of concrete, natural resources are mined, and a large amount of construction waste are produced. At the same time, with people on the performance of structure and construction waste reuse requirements increase, recycled concrete as a kind of new building materials in the construction field has been researched, popularized, and applied. Research shows that steel reinforced recycled aggregate concrete by steel improves the bearing capacity of components, increases the ductility and durability of the structure, improves the seismic performance of the concrete structure, and it can realize the recycling of construction waste to achieve energy conservation and environmental protection. Steel reinforced recycled aggregate concrete column as the main structural component of construction overcome shortcomings of the simple structure of recycled concrete [1–4]. In this paper, the steel recycled concrete axial compression short column has been analyzed using finite element analysis by finite element analysis software ABAQUS.

## 2 THE CONSTITUTIVE RELATIONS OF STEEL AND RECYCLED CONCRETE

### 2.1 Steel

The steel stress-strain model using bilinear model, as shown in Figure 1.

The elastic modulus of steel is defined  $E_S = 2.06 \times 10^{11} N/mm^2$  Poisson's ratio  $\nu_s = 0.3$ .

### 2.2 Recycled concrete

The constitutive relation of recycled concrete by Xiao Jianzhuang [5] which considers the replacement ratio of recycled coarse aggregate concrete under temperature stress-strain curve

Make  $y = \sigma/f_c, x = \epsilon/\epsilon_0$

$$y = \begin{cases} ax + (3 - 2a)x^2 + (a - 2)x^3 & x < 1 \\ \frac{x}{b(x - 1)^2 + x} & x \geq 1 \end{cases} \quad (1)$$

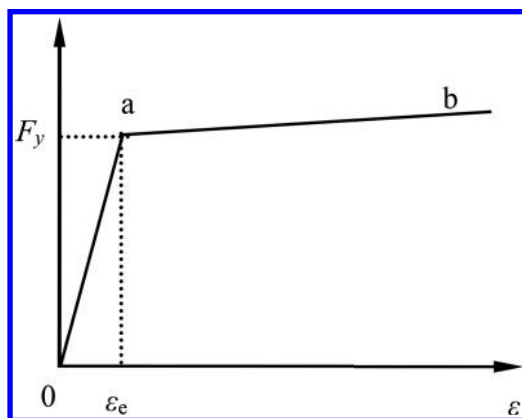


Figure 1. The constitutive relation curves of steel.

$$a = 2.2 (0.748\gamma^2 - 1.231\gamma + 0.975) \quad (2)$$

$$b = 0.8 (7.6483\gamma + 1.142) \quad (3)$$

In the formula:  $\gamma$ —Replace rate of recycled coarse aggregate.

The concrete plastic damage model based on ABAQUS software, the basic parameters of the plastic potential equation and the yield surface equation is similar to the ordinary concrete: the dilation angle is 30, the eccentricity is 0.1, compressive strength of concrete under biaxial and uniaxial compressive strength ratio is 1.16, tension and compression the second invariant meridian stress

ratio (K) is 0.6667, and the viscosity parameter is 0.0001. Concrete tensile softening performance using the energy criterion to describe the damage.

### 3 THE PROCESS OF FINITE ELEMENT MODELING

This paper designed a set of all the fire steel recycled concrete axial compression short column components. Basic parameters are as follows: Component length is  $L = 900$  mm, section size is  $B \times D = 300$  mm  $\times$  300 mm, H-beam section size is  $h \times b \times tw \times t = 150$  mm  $\times$  150 mm  $\times$  9.3 mm  $\times$  9.3 mm, the

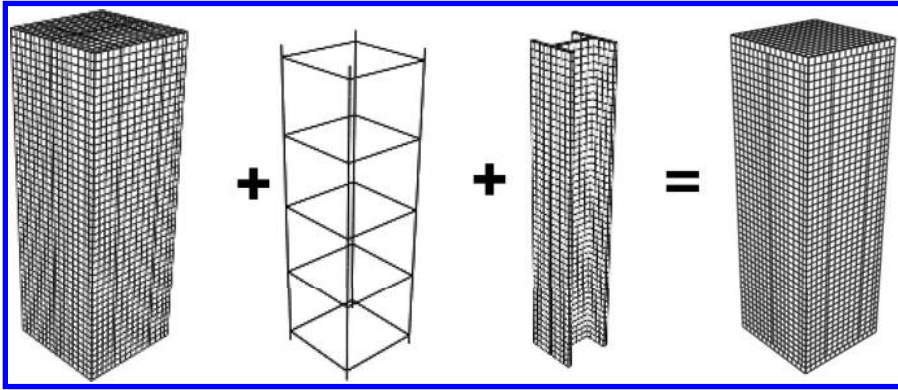


Figure 2. The component model for the finite element analysis.

Table 1. The stress nephogram.

Replace rate of recycled coarse aggregate (%)	Concrete	Steel	Reinforced	Ultimate bearing capacity (KN)
0				5376
50				5504
100				5909

strength of recycled concrete is C60, steel is chosen Q345, longitudinal reinforced is 4B16, stirrup is B8@200, the strength of steel are HRB335, and the protective layer thickness is 30 mm.

Concrete, steel and end plates using an 8-node solid element (C3D8R), reinforced using a 2-node truss element (T3D2). The interface model of steel and recycled concrete (Surface to Surface contact) is composed of bond slip in the normal direction of interface contact and tangential direction. The rebar cage embedded in recycled concrete. Both ends of the column is fixedly connected, and the U3 is released in the direction of loading end displacement. The component form as shown in [Figure 2](#).

#### 4 MODEL ANALYSIS

This paper analyzes the ultimate bearing capacity of the peak stress nephogram of influence of different substitution rate of steel reinforced recycled aggregate concrete.

It can be seen from [Table 1](#), concrete and end plate corner connection undergoes the phenomenon of stress concentration, and the central component concrete high stress value; steel middle stress is larger, both ends gradually decreased; the longitudinal steel basically reached the yield limit, the stirrup with the replacement ratio of recycled coarse aggregate increase stress decreased.

At the same time, with the increase of recycled coarse aggregate replacement ratio, the concrete stress slightly increased; the ultimate bearing capacity of the component also gradually increased. This is because with the increase of recycled coarse aggregate replacement ratio, the bearing capacity of recycled concrete is slightly higher, which makes recycled concrete contribution to the bearing capacity increase.

#### 5 CONCLUSION

With the increase of recycled coarse aggregate replace rate, bearing capacity of recycled concrete

increased under the same concrete strength, the steel reinforced recycled aggregate concrete limit bearing capacity also increases. This shows that steel reinforced recycled aggregate concrete component with reasonable mixture ratio has better mechanical properties.

#### ACKNOWLEDGMENTS

It is a project supported by National Science Foundation (51308347).

It is a project supported by Shenyang Science Plan project (F13-171-9-00).

It is a project supported by Shenyang Science Plan project (F14-028-2-00).

It is a project supported by Shenyang Science Plan project (F14-210-6-00).

It is a project supported by Liaoning science public research funds (2014004025).

#### REFERENCES

- [1] Xiao Jianzhuang, Li Jiabin, Sun Zhenping, et al. Study on Compressive Strength of Recycled Aggregate Concrete [J]. Journal of Tongji University (Natural Science), 2004, 32(12):1558–1561.
- [2] Zhang Weidong, Wang Zhenbo, Zhang Furui. Experimental Study on Axial Compression Behaviors of Steel Reinforced Recycled Aggregate Concrete Columns [J]. Journal of Henan University of Science and Technology (Natural Science), 2011, 32(6): 55–58.
- [3] Xue Jianyang, Cui Weiguang, Chen Zongping, et al. Experimental Study on Axial Compression Behaviors of Steel Reinforced Recycled Aggregate Concrete Composite Columns [J]. Building Structure, 2013, 43(7): 73–76.
- [4] Wang Ni, Chen Zongping, Li Qiliang, et al. Experimental Study on the Behavior of Steel Reinforced Recycled Aggregate Concrete Composite Columns under Axial Compression Loading [J]. Engineering Mechanics, 2013, 30(6): 133–141.
- [5] Xiao Jianzhuang. Experimental Investigation on Complete Stress-Strain Curve of Recycled Concrete under Uniaxial Loading [J]. Journal of Tongji University (Natural Science), 2007, 35(11):1445–1449.

# Research and development of visual monitoring system for prestressed steel structure

Zhancang Li

Tianjin Vocational Institute, Tianjin, China

**ABSTRACT:** Prestressed steel structure is an important measure of the construction level of a nation. For prestressed steel structure construction, both in the construction phase, or in the normal use stage, to monitor their health status is necessary. In order to make the monitoring more vivid, concrete, and humane, we developed the visual monitoring system by using three-dimensional (3D) technology. The system consists of real-time communication subsystem, 3D display subsystem and safety warning subsystem. By observing the 3D model, we can know the monitoring data of the real buildings. At last, the safety warning for the prestressed steel structure was implemented.

**Keywords:** prestressed steel structure, visualization; monitoring

## 1 INTRODUCTION

Nowadays, building a resource-saving society has become a time theme in China. For building construction, it has to be made not only safe and suitable, but also artistic and economic. Benefit by the advantages of high strength, light weight and low cost, the prestressed steel structure has been used more and more in the projects of gymnasiums, warehouses, and so on. As a result of the complexity of prestressed structure, the normal use of structure has been directly affected. To avoid the damage which projects may cause and to extend the life-span, the damage of structure has to be found out in time. For this reason, it is an urgent situation to build a monitoring system of prestressed steel structure<sup>[2]</sup>. By using real-time communication technology and three-dimensional (3D) technology, the visual monitoring system have been designed and developed, this paper introduced the core technology, realization method and application of the system.

## 2 OVERALL DESIGN OF THE MONITORING SYSTEM

Prestressed steel structure 3D visualization real-time monitoring is a system engineering, including the sensor technology, communication technology, 3D modeling technology, software development technology, database technology, and image processing technology etc. According to the functions required by the system, the working model of the system is shown in [Figure 1](#).

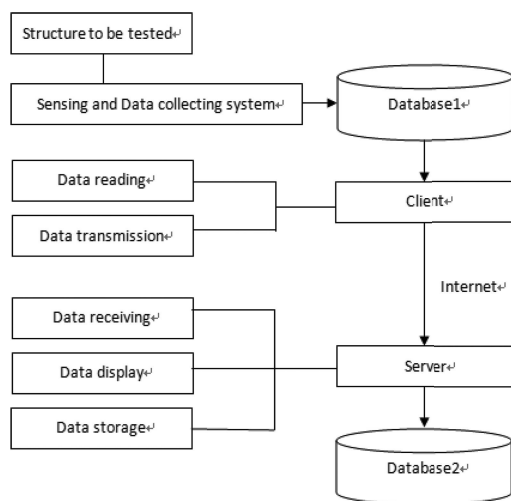


Figure 1. Working model of monitoring system.

The monitoring work is divided into the following parts.

### 2.1 Sensing and data collecting part

According to the prestressed structure to be measured, establish the finite element model of the structure, calculate and analyze stress of the structure, then determine the type, quantity and location of sensor. After that, arrange internet sensors in determining position of the structure. At last, select data collecting devices, read out the



monitoring data from the sensor through the data collecting equipment and store in the database.

### 2.2 Real-time transmission part

The real-time transmission of monitoring data part is realized by “client” and “server” in Figure 1. The client read monitoring data from the database and transmit it to the server by certain frequency; the server implements the receiving, storing, 3D display, and safety warning of monitoring data.

### 2.3 D visualization

After receiving monitoring data real-time from remote client, the server software realizes the 3D display of monitoring data by loading 3D model. When monitoring data exceeds a preset safe range, the warning bell and high light display security early warning will be carried out.

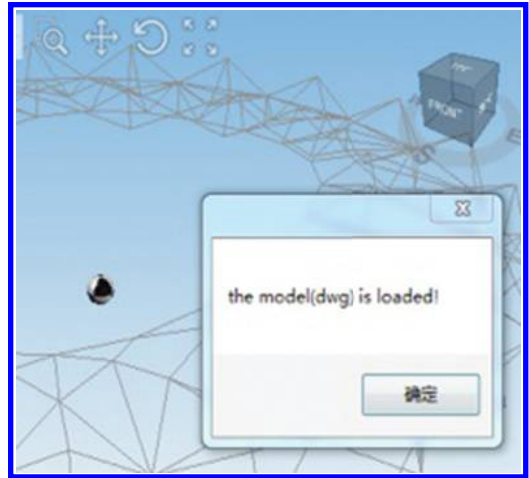


Figure 2. Loading model.

## 3 DEVELOPMENT OF THE MONITORING SYSTEM

The techniques and methods of the realization of each part are introduced, respectively, as follows.

### 3.1 Implementation of sensing and data collecting part

The mature equipment and solutions can be used in the sensing and data collecting part of the system. This project adopts sensing devices and data collecting equipment provided by Data Taker China Limited.

### 3.2 Implementation of real-time transmission part of monitoring data

Monitoring data real-time transmission means to read monitoring data in Figure 1, which is collected in sensing and data collecting system from database and make a real-time transmission to the remote monitoring center, this function will be realized by the monitoring software developed.

As shown in Figure 1, the monitoring adopts C/S system structure, the client realizes the reading and transmission, the server realizes the receiving and storage. Between client and server, socket technology is used for communication.

C/S structure is a structure of software system<sup>[6]</sup>, it can make full use of the advantage of client and server hardware environment at both ends to assign the tasks to the client and server to reduce the communication fee of the system. Socket<sup>[5]</sup> is a basic operation unit which supports TCP/IP protocol of network communication, it can be seen as two-way

communication endpoints among different hosts process, with a correlation function of the socket to complete the communication process. It is like a transport layer interface operated for application layer, application program sends or receives remote data through the interface.

The process of socket communication between client and server is as follows:

1. The server creates a socket and listens at a port and is in a block.
2. The client creates a socket and connects to the server.
3. The server accepts the connection, ready to receive data and is in a block.
4. The client sends data and prepares to receive data.
5. The server receives the data and sends the data.
6. The client exits.
7. The service stops serving.

Considering the target platform and the efficiency of the system, we choose object-oriented programming design language and Studio Visual developing tools.

On the client side, create a connection—oriented network socket, request connection to the server based on the server’s IP address and port: if connection succeeds, create network stream object for data transmission according to the network socket. In a single thread, the monitoring data is read from the scene database and is transmitted to the remote server by the network stream object.

In the server side, create a network socket, and open the monitor. When a client connection requests, create a network socket in the server for communication with the client, when data

arrives, receive the monitoring data and realize the data storage, due to the advantages of the simple deployment and high efficiency of SQLite database, project selects SQLite database.

### 3.3 The realization of 3D visualization display and the safety warning

Visualization technology is methods and techniques, which makes use of computer graphics and image technology to transfer data into graphics or images displayed on the screen or on the software form and makes the interactive processing.

3D visualization is a combination of data and 3D model, which displays the data on the 3D model, monitoring stuff can master the real sensor data on the corresponding position in real-time so as to grasp health status of the structure. The realization of 3D visualization monitoring steps is as follows.

#### 3.3.1 Create the three dimensional model of prestressed steel structure

Using Auto CAD, Revit or other 3D modeling softwares to create the 3D model of the prestressed steel structure, according to the sensor on the structure, mark on the 3D model corresponds to the position.

#### 3.3.2 The loading of the 3D model

For the loading of 3D models, the dynamic connection library EyeShot provided by third party Software dev Dept is used. EyeShot is a good solution for software developers to load 3D graphics into a form application. We can use it to translate, scale and rotate the 3D model on its own application form.

For the realization of loading for 3D model, create a custom control, inherit component SingleViewport Layout provided by EyeShot. The latter provides the functions of loading, operating, and saving 3D model (DWG format). The paper realizes the loading of DWG and MDL (custom) format. After a successful loading, the model can be scaled, rotated, moved and so on. 3D model loading interface is shown in Figure 3.

#### 3.3.3 The addition, setup and deletion of the simulation monitoring points

Simulation monitoring point is a vivid simulation of true monitoring position on the prestressed steel structure, each simulation monitoring point match with an actual monitoring point and its monitoring point sensor, simulation monitoring point carries the coordinate of the point, corresponding sensor identification, and information like monitoring point safety warning limit data. Each simulation monitoring point match with an actual

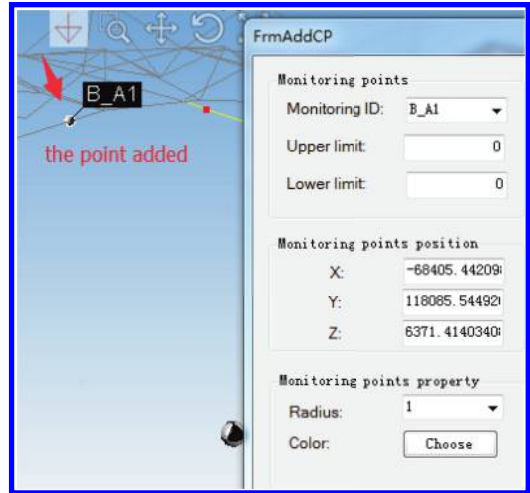


Figure 3. Add monitoring points.

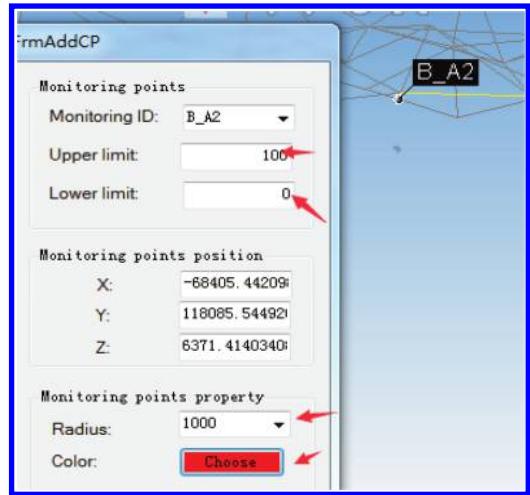


Figure 4. Editing of monitoring points.

monitoring point and its monitoring point sensor, simulation monitoring point carries the coordinate of the point, corresponding sensor identification, and safety warning limit of the point. Each simulation monitoring point is represented by a sphere, as shown in Figure 3, the red arrow in the figure points at the sphere, which is the simulation monitoring point that have been added.

When we need to edit the attributes (color, radius or safety range) of simulation monitoring points for any reasons, we can right-click the sphere, open the “Edit model” dialog to reset the attributes of simulation monitoring points, as shown in Figure 4. When you need to delete the

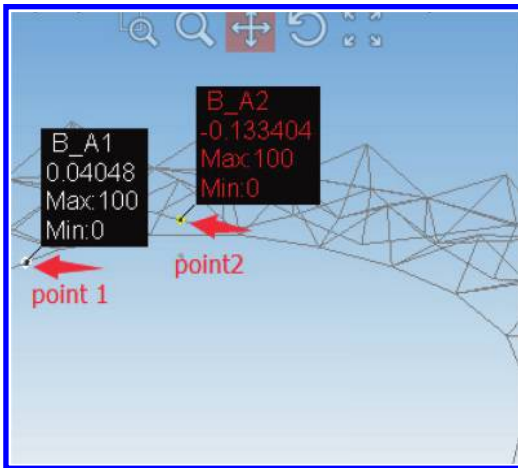


Figure 5. Visualization monitoring.

simulation monitoring point, right—click the ball, select “Delete” menu item from the context menu to delete it.

### 3.3.4 3D visualization display and safety warning

When the model is in a displaying mode, the current value of the actual monitoring sensor will be displayed in real-time at the simulation monitoring point position, when the value received is in the safe range, it will be displayed with white font on the model, when beyond the safe range, the bell sound and a red display will be activated as a security warning, as shown in Figure 5. The monitoring value of “monitoring point 1” is in the safe range, and no alarm; The monitoring value of “monitoring point 2” is beyond the safe range and it will automatically activate alarm and will be displayed in red font with high light so as to realize the safety warning.

## 4 CONCLUSION

According to the content of the whole design, we achieved the collecting of monitoring data real-time transmission of data, 3D visualization display, and the safety warning respectively. The features are the real-time transmission of monitoring data and visualization monitoring, in which real-time transmission part realized self-connection between the client and the server and simplified the configuration and deployment of the software. The visualization monitoring part solved the difficulties of the

loading of 3D model, the additions of simulation monitoring points and safety warning through the dynamic link library by third party to realize the visualization monitoring, and enabled the monitoring stuff mater the status of prestressed steel structure health in real-time through the observation of 3D model.

This system passed a comprehensive test in Guang Zhou university sports venue and Xuzhou stadium project, both designed by Beijing Institute of architectural, and it was put into use, The system improved the way of prestressed steel structure monitoring, the monitoring accuracy and the working efficiency are improved, and it makes the monitoring work more humane.

The deficiency of this paper is the lack of research on the sensor system and the data collecting system. There is no specification for the interface between monitoring software and data acquisition system, data format or structure of the database is not unified, which will bring some inconveniences after replacing the sensing system. The lack of research on the further application of monitoring data, the striving direction in the future is to make full use of the monitoring data, the systematic assessment of prestressed steel structure performance variation so as to scientifically evaluate the health status to provide reference for reinforcement and maintenance of the structure.

## REFERENCES

- [1] Lu Cilin, modern prestressed steel structure [M], Beijing: People's transportation press, 2003.
- [2] Zhong Shantong, prestressed steel structure [M], Harbin: Harbin Institute of Technology press, 1986.
- [3] Lu Cilin, prestressed steel structure development 50 years 2 [J], steel structure, 2002 seventeenth period fifth volume total sixty-first, 45–47.
- [4] Hu Jun. Research and application of the structure health monitoring system of Jing Yue bridge [D]. Wuhan University of Technology, 2012.
- [5] Li Dongsheng, Li Hongnan. Review of the safety assessment of civil engineering structures, the monitoring and diagnosis of [J]. earthquake engineering and Engineering Vibration 2002 (3): 82–90.
- [6] Guo Qi. The theory and method of effective prestress prediction for the beam structure of the complex PC beam [D]. Chang'an University, 2008.
- [7] Zhu Shaomin. Methods and techniques for testing software. Beijing: Tsinghua University press, 58~2005.27.
- [8] Stefan [M]. Boecking. Beijing: Machinery Industry Press, 2000, ISBN 7111080769/TP.

## Ballast particle model and initial packing numerical simulation

W.J. Shao & S.L. Lian

*The Key Laboratory of Road and Traffic Engineering, Ministry of Education, Tongji University, Shanghai, China*

**ABSTRACT:** The shape of ballast particles has an important effect on the settlement and deformation of ballast bed. When the research of the settlement of ballast bed is carried out by using the discrete element method, an accurate shape model of ballast particles needs to be established. However, the application of polyhedral model of ballast particles can handles this problem rather well. In the article, the polyhedral model of ballast particles is first generated by the convex hull generation method. Meanwhile, the approach to bounding sphere packing is used to accelerate the packing process of polyhedral model of ballast particles on basics of packing of ballast particles under gravity. The results show that the initial packing process of polyhedral model of ballast particles can be speeded up through the above mentioned way. And it in turn accelerates the whole packing process of ballast particles.

**Keywords:** discrete element method; ballast particle model; heavy haul railway; sphere packing

### 1 INTRODUCTION

During operations of the heavy haul railway with 30 tons in axle load, the problem of roadbed settlement has grown more important. But traditional research methods rest on the assumption of a continuous medium, which are inadequate to access the effects of shape and crush of ballast particles on the roadbed settlement. Consequently, when considering the effects of the shape of the ballast particles, a model of irregular shaped particles has been adopted to simulate them.

The clusters and clumps are being used to model real ballast particles in the discrete element method, which have been proposed first by the McDowell team (McDowell et al. 2005). And in terms of numerical simulation, the two models are applied to the engineering practices by Indraratna (Indraratna 2013 & Christian 2012). Furthermore, by comparing the experimental results, the validity of these two models are verified by him. However, the number of spheres are bonded together to form a ballast particle in these two models. Because of this way, it will lead to the existence of interspace and overlap in the particles, so the density of the particles is not uniformly distributed.

In order to overcome this shortcoming, a model of irregular polyhedral particles (Tutumluer 2009, Joseph 2013 & Jan 2014) has been adopted to simulate the ballast particles. And the rapid packing algorithm for spherical particles is employed to accomplish the initial packing of polyhedral model of ballast particles.

### 2 THE CONSTRUCTION OF POLYHEDRAL MODEL OF BALLAST PARTICLES

According to Code for Designing Heavy Haul Railway (Ministry of Railways of the People's Republic of China 2011), 1st graded ballast should

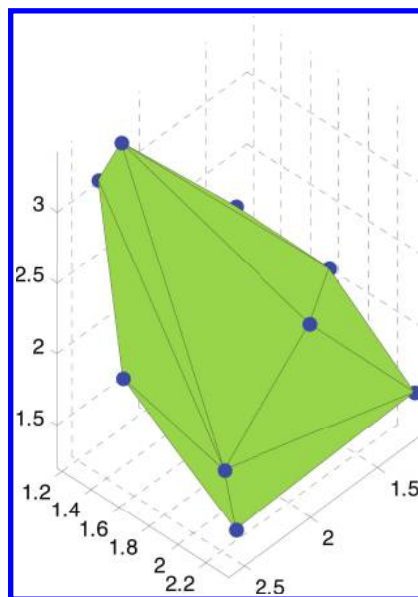


Figure 1. A polyhedral model of ballast particles.

be applied in the heavy haul railway with 30 tons or above in axle load. Thus, a series of cuboids needs to be established in accordance with the size of square whole screen of the 1st graded ballast.

And a certain number of points are randomly inserted into the cuboid in the light of the requirements of slenderness ratios. As shown in Figure 1, a polyhedral model of ballast particles can be generated through computing the convex hull (Barber 1996 & Wang 2011) of these points.

Owing to the randomness of the inserted point, the model might be shaped in needle-like or flake-like. Therefore, the shortest distance and the longest distance of the polyhedral model should be found so as to calculate the slenderness ratios. And the values of slenderness ratios will be used as a criteria for determining whether it meet the requirements of flake index and acicular index.

### 3 THE BOUNDING SPHERE OF POLYHEDRON BALLAST PARTICLE

The benefits of using the spherical model of particles are the simplicity of geometry description. Another advantage of the model can be used to quickly determine whether it is in contact with each other. What's more, the packing process of it is relatively simple and fast to calculate. By using the packing of the spherical model, the packing process of polyhedron model of ballast particles can be speeded up. But it is necessary for the polyhedral model of ballast particles to find the bounding sphere. Then the above mentioned method can be adopted to achieve the initial packing process.

When it comes to computing the bounding sphere, a method of calculation has been proposed by Jack Ritter (Ritter 1990). In the article, a numerical calculation of the bounding sphere is made in the same method. First, it is necessary to find six points which have the maximum and minimum values of  $x$ ,  $y$ , and  $z$  from a vertex set of  $V_i$ . Then the length of the line segment linking any two points chosen from them would be calculated. The longest length of it is named  $d_1$ , which has the corresponding vertices  $A_1$  and  $B_1$ .

1. Find the midpoint  $P_1$  of a line segment joining the vertices  $A_1$  and  $A_2$ . And the sphere  $Q_1$  with center  $P_1$  and diameter  $d_1$  is calculated.
2. Traverse the remaining vertices and determine whether the remaining vertices are in the sphere calculated in the first step. If vertex  $A_i$  is in the sphere  $Q_1$ , the next vertex  $A_{i+1}$  would be tested in the same process. Otherwise, it is necessary to create connection lines between vertex  $A_i$  and center  $P_1$ , which would intersect the sphere  $Q_1$  at the point  $B_i$ . Then the length of the line segment linking the vertices  $A_i$  and  $B_i$  would be

computed and named  $d_i$ . As shown in Figure 2, the sphere  $Q_i$  with center  $P_i$  and diameter  $d_i$  is computed in the same way;

3. Repeat the above mentioned procedure to determine the sphere  $Q_i$  which contains all vertices.

Finally, the bounding sphere of polyhedron ballast particle is calculated and depicted as shown in Figure 3.

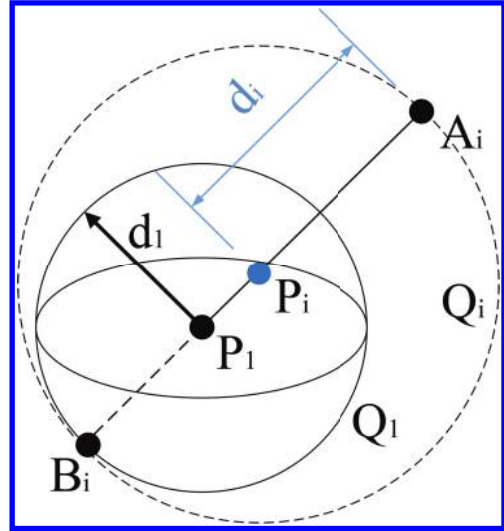


Figure 2. The schematic diagram of the calculation of the bounding sphere.

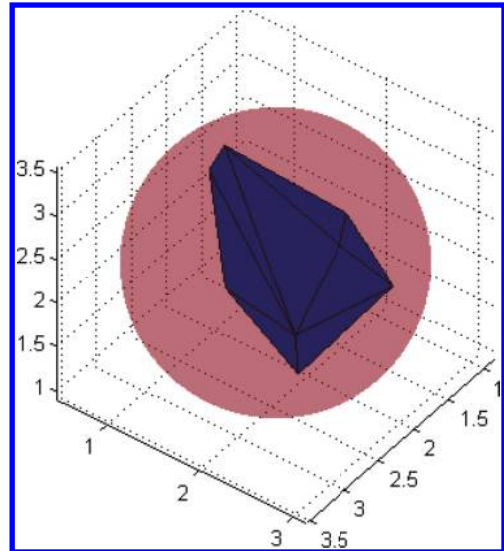


Figure 3. The bounding sphere of polyhedron ballast particle.

#### 4 THE INITIAL PACKING OF POLYHEDRON BALLAST PARTICLE

After the bounding sphere of polyhedron ballast particle model is solved, they can be packed with a geometric based compression algorithm which is proposed by Han (Han 2005). The core idea of the algorithm is described below:

In case of the 2D circle particle, the problem is shown in Figure 5. A is the target circle to be compressed, the remaining circle are A's neighbor. Unit vector of the compression direction is  $n_e(x_n, y_n)$ . The coordinate of A circle center is  $(A_x, A_y)$ , H's center coordinate is  $(H_x, H_y)$ ; as shown in Figure 4, the maximum moving distance of A just touching H is  $l_{max}$  calculated with the equation:

$$l_{max} = l_s - \sqrt{(r_A + r_H)^2 - l_t^2}$$

where:  $l_s = (H_x - A_x)x_n + (H_y - A_y)y_n$   
 $l_t = (H_x - A_x)y_n + (H_y - A_y)x_n$ .

Loop over A's neighbor circle to calculate the minimum of the allowable moving distance in the original paper. The neighbor circle quantity is 7, so solution procedure must be conducted for 7 times. However, if circle A moves along the specified direction, circle C, D, and F are never touching with A. So the judgment condition is used to reduce the neighbor circle quantity. Before calculating the allowable moving distance, the direction vector which A's center to one of circle should be calculated. Then the angle between the direction vector and compression direction are calculated. If the angle is greater than 90 degrees, the circle is removed from the neighbor list. Less than 90 degrees, the distance from the circle to the

compression direction are computed. If the distance is greater than the sum of A's radius and its radius, the circle is removed from the neighbor list. Loop over A's neighbor circle, the neighbor circle quantity can be reduced. For example, A's final neighbor circle are G and H. Finally, the calculation speed of A's minimum allowable moving distance can be increased.

All spheres are looped over and moved, and then a loop global compression is accomplished. Because of the spheres are compressed in the assigned orientation, the local arches are formed. In order to overcome this difficulty, a local compression is performed in which the compression direction is different from the global compression. After the global and local compression is performed, the packing density is significantly increased.

After the packing process of bounding sphere is accomplished, coordinate conversion between polyhedron ballast particle and bounding sphere is carried out. The bounding spheres are replaced by the polyhedron ballast particle. Then the polyhedron ballast particles are initially packed.

#### 5 ILLUSTRATIONS

A box is designed to test the validation of the above method; it is  $70 \times 30 \times 45$ cm. With the method stated above, the packed bounding sphere in the box is shown in Figure 5. Correspondingly, Figure 5 shows the initial packing of polyhedron ballast particle.

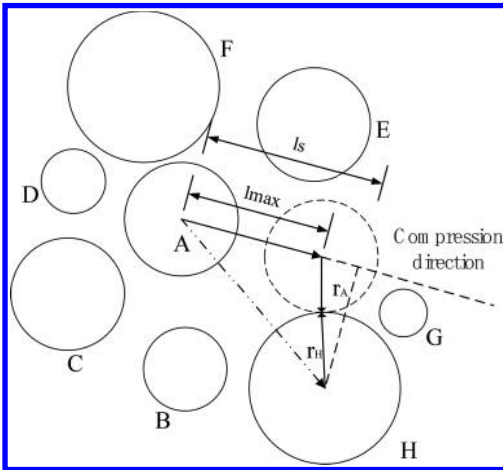


Figure 4. Moving distance of sphere A.

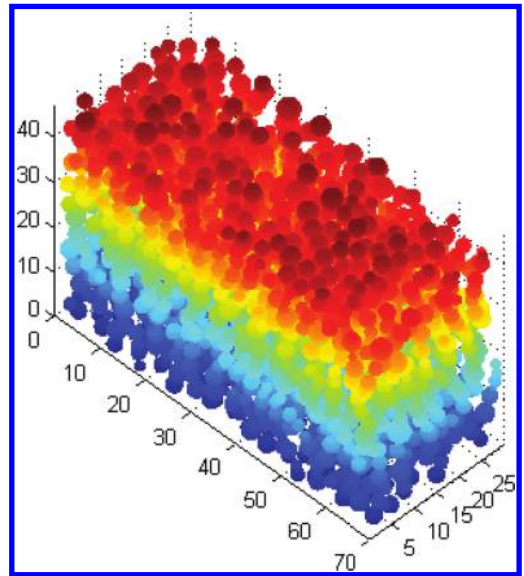


Figure 5. The packed bounding sphere in the box.

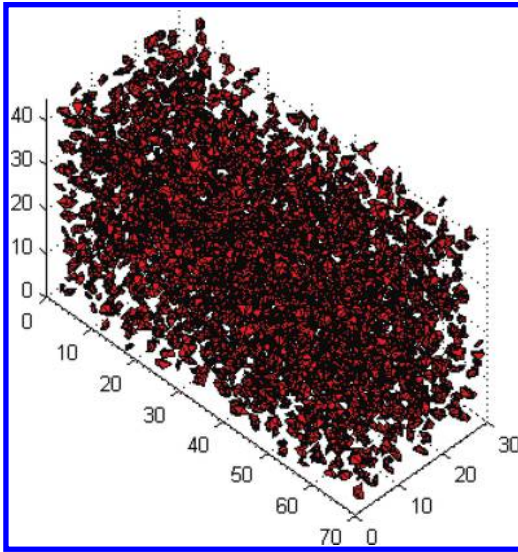


Figure 6. The initial packing of polyhedron ballast particle in the box.

In Figure 6, the number of bounding sphere is 2911, the packing density is 0.323. It takes 336.7 seconds to complete the initial packing of polyhedron ballast particle. Because the volume of polyhedron ballast particle is less than its bounding sphere. As shown in Figure 6, the interspace between the polyhedron ballast particles is bigger. Its packing density is less than 0.323. In order to increase the packing density, random packing under gravity must be performed after the initial packing. The purpose of the paper is to describe a quick initial packing method of polyhedron ballast particles, so random packing under gravity isn't expounded.

## 6 CONCLUSIONS

1. The theory of convex hull can be used to establish the polyhedron ballast particle model of irregular shape; but slenderness ratio must be calculated to determine whether the ballast particle model is needle shaped or flaky particle.
2. Bounding sphere is packed quickly, so the initial packing of polyhedron ballast particle model can be speeded up.

## ACKNOWLEDGMENTS

This research was supported by the National Natural Science Foundation of China (No. 51378395).

## REFERENCES

- Barber, C.B. Dobkin, D.P. & Huhdanpaa, H.T. 1996. The Quickhull Algorithm for Convex Hulls. *ACM Transactions on Mathematical Software* 22(4): 469–483.
- Christian, E. & Robert, S. 2012. A discrete element approach to model breakable railway ballast. *Computers and Structures* 108–109: 3–13.
- Han, K. Feng, Y.T. & Owen, D.R.J. 2005. Sphere packing with a geometric based compression algorithm. *Powder Technology* 155: 33–41.
- Huang, H. & Tutumluer, E. 2009. Discrete element modeling of aggregate behavior in fouled railroad ballast. *Recent Advancement in Soil Behavior, in Situ Test Methods, Pile Foundations, and Tunneling*: 33–41.
- Indraratna, B. & Ngo, N.T. 2013. Deformation of coal fouled ballast stabilized with geogrid under cyclic load. *Journal of Geotechnical and Geoenvironmental Engineering* 139(8): 1275–1289.
- Jan, E. 2014. Simulation of railway ballast using crushable polyhedral particles. *Power Technology* 264: 458–465.
- Joseph, K.A. & Julius, J.K. 2013. Three-dimensional laser scanning technique to quantify aggregate and ballast shape properties. *Construction and Building Materials* 43:389–398.
- Lim, W.L. & McDowell G.R. 2005. Discrete element modeling of railway ballast. *Granular Matter* 7(11): 19–29.
- Laryea, S. & Baghsorkhi, M.S. 2014. Comparison of performance of concrete and steel sleepers using experimental and discrete element methods. *Transportation Geotechnics* 1: 1–16.
- Ministry of Railways of the People's Republic of China. 2011. Code for Designing Heavy Haul Railway. Beijing: China Railway Publishing House.
- Ministry of Railways of the People's Republic of China. 2008. Railway Ballast. Beijing: China Railway Publishing House.
- Ministry of Railways of the People's Republic of China. 2008. Test method for railway ballast. Beijing: China Railway Publishing House.
- Ritter, J. 1990. An efficient bounding sphere. *Graphics Gems*: 301–303.
- Wang, J.Y. 2011. *Computational Geometry and Its Applications*. Beijing: Science Press.

## The comparison of integration methods in cellular material model

Lei Hou & YunQing Feng

Department of Mathematics, Shanghai University, Shanghai, China

**ABSTRACT:** The complex contact problem of cellular composite materials is studied in this paper. The problem is translated into a set of nonlinear fluid-structure coupling partial differential equations. The equations are discretized by the finite element method and finite difference method. Three kinds of integration methods—Gauss, Gauss-Lobatto and Newton-Cotes to compute numerical integration are used in the calculation of numerical solution. Then we can analyze the three numerical integration methods to the influence of numerical solution of nonlinear fluid-structure coupling equations.

**Keywords:** finite element; cellular material

### 1 INTRODUCTION

With the development of economic environment, shortage of energy, timber and other resources is becoming serious, which lead to enormous pressure on the scientific research. Facing with such severe situation, the most important task at present is to minimize resource consumption and environmental damage. Fortunately, the advent of cellular composite materials alleviates these problems. Cellular material is a new material. Its advantages of light texture, strength, stiffness, heat insulation, sound insulation, et al are proposed by [4]. It is recycled and has a high economic value. Currently, cellular materials have been widely used in the construction industry, which has great significance for the conservation of resources and improving the ecological environment. However, its numerical simulation is difficult because of the complexity of material microstructure and the diversity of material properties. International engineering (IEEE, IAENG) think high performance computing technology can be combined with mathematical models to simulate the deformation of the material. An example of such a model has been proposed by Fleck and James [5,6]. Paper [1] attempts to use a set of nonlinear fluid-structure coupling partial differential equations to describe the problem of complex contact surfaces of cellular composite materials.

Now a large number of finite element software can effectively simulate the cellular material deformation and other issues. The problem of complex contact surface of cellular materials are shown in [Figure 1](#) and [Figure 2](#) using Dyna. However, due

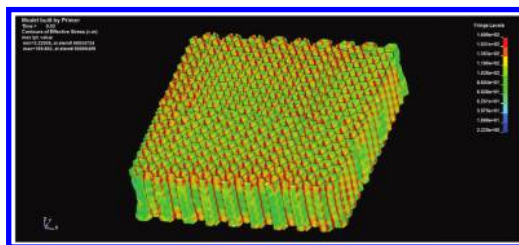


Figure 1. Stress distribution of cellular materials' contact surface.

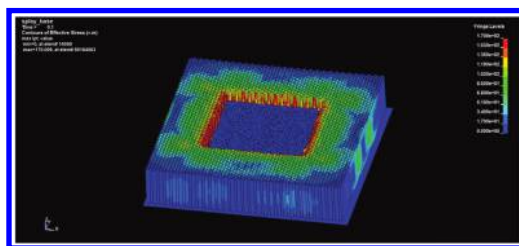


Figure 2. Stress distribution of cellular materials' contact surface in time 0.1.

to too much emphasis on versatility, these software ignore the further analysis to computing formats and results. Due to these considerations, the paper is devoted to study and explore better finite element computing format and numerical integration method for solving nonlinear fluid-structure coupling equations.



$$\begin{cases} \frac{\partial u}{\partial t} = \frac{1}{\rho} \nabla \cdot \tau - (u \cdot \nabla) u \\ \frac{\partial \tau}{\partial t} = \frac{2\eta}{\lambda} D - \frac{1}{\lambda} e^{\frac{\varepsilon \lambda}{\eta_0} (\tau_{11} + \tau_{22})} \tau \\ \quad - (u \cdot \nabla) \tau [\nabla u \cdot \tau + (\nabla u \cdot \tau)^T] \\ \quad - \xi [(D \cdot \tau) + (D \cdot \tau)^T] \\ u|_{(x,y) \in \Gamma} = u_\Gamma, \quad u|_{t=t_0} = u_0 \\ \tau|_{(x,y) \in \Gamma} = \tau_\Gamma, \quad \tau|_{t=t_0} = \tau_0 \end{cases} \quad (1)$$

here  $\rho$  is density,  $\xi$  is the shear factor,  $\eta$  is the viscosity,  $\lambda$  is the relaxation factor,  $u$  is the velocity,  $\tau$  is the stress.

## 2 THE DISCRETION OF COUPLING EQUATIONS

This article use finite element method and finite difference method to solve the coupling equations. The spatial variables are discretized by the finite element method and the time variable is discretized by semi implicit Euler methods. After that, we get large linear equations. For the spatial variables, we use high order shape function—Lagrange three shape function to construct interpolation function. It can avoid the phenomenon of the unit is too rigid and reduce the error caused by finite element discretization.

The first step to construct the finite element interpolation function is to determine the interpolation nodes. This paper uses the zeros of the Lobatto polynomial as the interpolation nodes, constructing Lagrange 16 double three polynomial shape functions. The following problems are considered in the standard element  $-1, 1 \times -1, 1$  square area. The rectangular area divided into four  $2 \times 2$  units, denoted as ① unit, ② unit, ③ unit, ④ unit. Then we use the zeros of the Lobatto polynomial as the interpolation nodes of rectangular mesh and get a  $2 \times 2$  in-equidistant interpolation nodes in each unit.

One-dimensional Lagrange shape functions are as follows:

$$\begin{aligned} L_1(\xi) &= -5/8(\xi^2 - 1/5)(\xi - 1) \\ L_2(\xi) &= 5\sqrt{5}/8(\xi - \sqrt{5}/5)(\xi^2 - 1) \\ L_3(\xi) &= -5\sqrt{5}/8(\xi + \sqrt{5}/5)(\xi^2 - 1) \\ L_4(\xi) &= 5/8(\xi^2 - 1/5)(\xi + 1) \end{aligned}$$

We can get the two-dimensional Lagrange 16 double three shape function, expressed as

$$\varphi_1(\xi, \eta) = L_1(\xi)L_1(\eta), \dots, \varphi_{16}(\xi, \eta) = L_2(\xi)L_3(\eta)$$

here,  $L_i(\eta)$  is one-dimensional Lagrange shape function.

Now, finite element and finite difference methods are used to discrete coupling equations. In equations(1), we set  $u = iu_1(x, y, t) + ju_2(x, y, t)$  as velocity field(Vector). Here,  $u_1(x, y, t)$   $u_2(x, y, t)$  are expressed as x and y components of velocity  $u$ .

$\tau = \begin{pmatrix} \tau_{11}(x, y, t) & \tau_{12}(x, y, t) \\ \tau_{21}(x, y, t) & \tau_{22}(x, y, t) \end{pmatrix}$  is a stress field(Tensor).

Here  $\tau_{11}(x, y, t)$ ,  $\tau_{12}(x, y, t)$ ,  $\tau_{21}(x, y, t)$ , correspond to four component of stress  $\tau$ . We also have  $\tau_{12}(x, y, t)$ ,  $\tau_{21}(x, y, t)$ .

The coupling equations actually contains 5 component equations. The coupling equations(1) expand into five component equations according to the above five components:

$$\frac{\partial u_1}{\partial t} = \frac{1}{\rho} \left( \frac{\partial \tau_{11}}{\partial x} + \frac{\partial \tau_{12}}{\partial y} \right) - \left( u_1 \frac{\partial u_1}{\partial x} + u_2 \frac{\partial u_1}{\partial y} \right) \quad (2)$$

$$\frac{\partial u_2}{\partial t} = \frac{1}{\rho} \left( \frac{\partial \tau_{12}}{\partial x} + \frac{\partial \tau_{22}}{\partial y} \right) - \left( u_1 \frac{\partial u_2}{\partial x} + u_2 \frac{\partial u_2}{\partial y} \right) \quad (3)$$

$$\begin{aligned} \frac{\partial \tau_{11}}{\partial t} &= \frac{2\eta}{\lambda} \frac{\partial u_1}{\partial x} - \frac{1}{\lambda} \tau_{11} - \frac{\varepsilon}{\eta_0} (\tau_{11} + \tau_{22}) \tau_{11} \\ &\quad - \left( u_1 \frac{\partial \tau_{11}}{\partial x} + u_2 \frac{\partial \tau_{11}}{\partial y} \right) + (2 - 2\xi) \frac{\partial u_1}{\partial x} \tau_{11} \\ &\quad + \left[ (2 - \xi) \frac{\partial u_1}{\partial y} - \xi \frac{\partial u_2}{\partial x} \right] \tau_{12} \end{aligned} \quad (4)$$

$$\begin{aligned} \frac{\partial \tau_{22}}{\partial t} &= \frac{2\eta}{\lambda} \frac{\partial u_2}{\partial y} - \frac{1}{\lambda} \tau_{22} - \frac{\varepsilon}{\eta_0} (\tau_{11} + \tau_{22}) \tau_{22} \\ &\quad - \left( u_1 \frac{\partial \tau_{22}}{\partial x} + u_2 \frac{\partial \tau_{22}}{\partial y} \right) + (2 - 2\xi) \frac{\partial u_2}{\partial y} \tau_{22} \\ &\quad + \left[ (2 - \xi) \frac{\partial u_2}{\partial x} - \xi \frac{\partial u_1}{\partial y} \right] \tau_{12} \end{aligned} \quad (5)$$

$$\begin{aligned} \frac{\partial \tau_{12}}{\partial t} &= \frac{\eta}{\lambda} \left( \frac{\partial u_1}{\partial y} + \frac{\partial u_2}{\partial x} \right) - \frac{1}{\lambda} \tau_{12} - \frac{\varepsilon}{\eta_0} (\tau_{11} + \tau_{22}) \tau_{12} \\ &\quad - \left( u_1 \frac{\partial \tau_{12}}{\partial x} + u_2 \frac{\partial \tau_{12}}{\partial y} \right) + \left[ \left( 1 - \frac{\xi}{2} \right) \frac{\partial u_2}{\partial x} - \frac{\xi}{2} \frac{\partial u_1}{\partial y} \right] \tau_{11} \\ &\quad + \left[ \left( 1 - \xi \right) \left( \frac{\partial u_1}{\partial x} \right) + \frac{\partial u_2}{\partial y} \right] \tau_{12} + \left[ \left( 1 - \frac{\xi}{2} \right) \frac{\partial u_1}{\partial y} - \frac{\xi}{2} \frac{\partial u_2}{\partial x} \right] \tau_{22} \end{aligned} \quad (6)$$

We discrete variables of the above five equations (2–6). Only discrete results of the equation (2) are given here. Other equations are similarly available. The discrete results of the equation (2) can be written as:

$$\begin{aligned} & \{A\}_{16 \times 16}^n \{u_i\}_{16 \times 1}^n \\ &= \frac{1}{\rho} \left( \{B_1\}_{16 \times 16}^n \{\tau_{11}\}_{16 \times 1}^n + \{B_2\}_{16 \times 16}^n \{\tau_{12}\}_{16 \times 1}^n \right) \\ & - \left( \sum_{m=1}^{16} u_1(m) \{E_1(m)\}_{16 \times 16}^n \right) \{u_i\}_{16 \times 1}^n \\ & - \left( \sum_{m=1}^{16} u_2(m) \{E_2(m)\}_{16 \times 16}^n \right) \{u_i\}_{16 \times 1}^n \end{aligned} \quad (7)$$

here,  $\{A\}_{16 \times 16}$ ,  $\{B_1\}_{16 \times 16}$ ,  $\{B_2\}_{16 \times 16}$ ,  $\{E_1(m)\}_{16 \times 16}$ ,  $\{E_2(m)\}_{16 \times 16}$  are the corresponding stiffness matrix.

Then, we use the semi implicit Euler method to get discrete time variable of equation (2). First, we rewrite the semi discrete scheme (7) as:

$$\begin{aligned} & \{A\}_{16 \times 16}^n \left\{ \frac{\partial u_i}{\partial t} \right\}_{16 \times 1}^n \\ &= \{F(\tau_{11}, \tau_{12})\}_{16 \times 1}^n - \{G(u_1, u_2)\}_{16 \times 16}^n \{u_i\}_{16 \times 1}^n \end{aligned} \quad (8)$$

Second, we can get the semi implicit Euler scheme:

$$\begin{aligned} & \frac{1}{\Delta t} \{A\}_{16 \times 16}^n \{u_i\}_{16 \times 1}^{n+1} - \frac{1}{\Delta t} \{A\}_{16 \times 16}^n \{u_i\}_{16 \times 1}^n \\ &= \{F(\tau_{11}, \tau_{12})\}_{16 \times 1}^n - \{G(u_1, u_2)\}_{16 \times 16}^n \{u_i\}_{16 \times 1}^n \end{aligned} \quad (9)$$

### 3 THREE KINDS OF NUMERICAL INTEGRATION

Considering the complexity of the integrand, we use three kinds of integral methods—Gauss, Gauss-Lobatto and Newton-Cotes to compute numerical integration in the calculation of stiffness matrices [8,10].

For one-dimensional numerical integral formula of Gauss type, when  $n = 3$ , integral nodes are  $\pm 0.3398810$ ;  $\pm 0.9061793$ , the corresponding coefficients of integral formula are 0.6521452, 0.2369269. For one-dimensional numerical integral formula of Gauss-Lobatto type, when  $n = 3$ , integral nodes are  $\pm 1$ ;  $\pm 0.447214$ , the corresponding coefficients of integral formula are 1/6; 5/6. For one-dimensional numerical integral formula of Newton-Cotes type, when  $n = 3$ , integral nodes are  $\pm 1$ ;  $\pm 1/3$ , the corresponding coefficients of integral formula are 1/8; 3/8.

In two-dimensional case, we take numerical integration approach of choosing the same number of integration points along the x, y direction.

$$I = \int_{-1}^1 \int_{-1}^1 f(x, y) dx dy = \sum_{i=1}^n \sum_{j=1}^n W_i W_j f(x_i, x_j) \quad (10)$$

here,  $W_i, W_j$  are weight coefficients.

Of course, the way of two-dimensional integration is not unique. The stiffness matrix is not the

same obtained by different numerical integration, which lead to the different calculation error.

### 4 NUMERICAL RESULTS

In this section, numerical results obtained by the above numerical integration are presented. The test domain is in  $[0,4] \times [0,4]$  square. We simulated the domain's velocity and stress change under the action of different force. Grid deformation is used to shows the change in the velocity field. In this paper, the space step  $h = 1$  and time step  $\Delta t = 1$  are chosen in the finite element method. The initial position is shown in Figure 3

The following each figure has three mesh deformation diagrams corresponding to three numerical integration methods. In Figure 4, the results are obtained by using Gauss, Gauss-Lobatto and Newton-Cotes integration on  $T = 2$ . The mesh deformation results using three numerical integration on  $T = 3$  are shown in Figure 5.

The following tables show the numerical solution of velocity field  $u$  on mesh node with finite

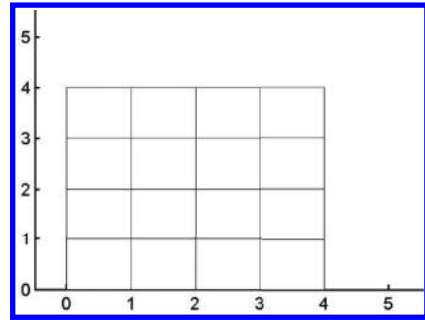


Figure 3. The initial mesh shape.

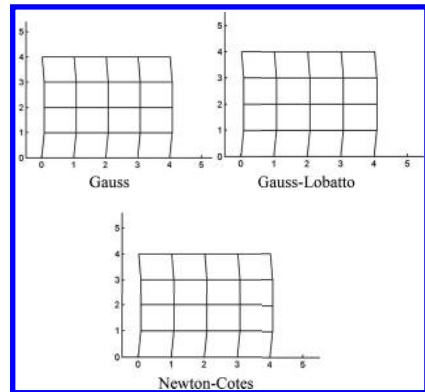


Figure 4. The computation results of mesh deformation using three different numerical integration methods on  $T = 2$ .

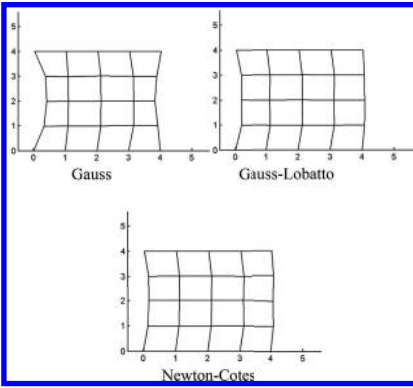


Figure 5. The computation results of mesh deformation using three different numerical integration methods on  $T = 3$ .

Table 1. The numerical solutions of  $u$  using three numerical integration on  $T = 2$ .

Node number	Gauss	Gauss-Lobatto	Newton-cotes
3	0.43	0.12	0.07
6	0.32	0.12	0.07
9	0.28	0.10	0.08
36	0.03	0.05	0.03
39	0.01	0.05	0.03
42	0.03	0.04	0.04
69	0.08	0.05	0.04
72	0.05	0.06	0.03
75	0.06	0.04	0.03
102	0.12	0.06	0.03
105	0.08	0.04	0.04
108	0.08	0.05	0.04
135	0.27	0.01	0.00
138	0.21	0.05	0.01
141	0.15	0.00	0.00

element method, the mesh node number may refer to [3]. Due to external forces acting on the upper and lower bounds, so the numerical solutions of the grid nodes on this boundary are not given. The following formula:

$$u = \sqrt{u_1^2 + u_2^2} \quad (4.1)$$

is used to calculate the effective velocity.

We set initial value are  $u_1 = 0.08$  and  $u_2 = 0$ . It is easy to know  $u = 0.08$  according to (11). Table 1 lists numerical results of the stress on the grid nodes using the three numerical integration methods when  $T = 2$ . The numerical results of the stress using the three numerical integration methods on  $T = 3$  are shown in Table 2.

Table 2. The numerical solutions of  $u$  using three numerical integration on  $T = 3$ .

Node number	Gauss	Gauss-Lobatto	Newton-cotes
3	9.72	3.64	3.59
6	5.14	3.90	3.49
9	3.49	2.93	4.35
36	2.27	1.26	1.73
39	1.38	1.28	1.72
42	1.35	0.91	1.88
69	1.86	1.30	1.99
72	1.18	1.40	1.46
75	0.95	0.99	1.73
102	0.32	1.43	1.58
105	0.40	1.05	1.95
108	0.27	1.37	1.99
135	1.00	0.16	0.17
138	0.73	0.25	0.46
141	1.93	0.07	0.34

## 5 CONCLUSION

We have presented three kinds of numerical integration methods for solving a finite element problem for the coupling equations. Different numerical integration methods lead to the numerical solutions vary widely. Therefore, in order to reduce calculation errors, we should choose the appropriate numerical integration methods. Some other numerical integration methods to improve accuracy of numerical solution will be discussed in the future.

## ACKNOWLEDGMENTS

The authors would like to thank the editor, reviewers and persons who improve the results of this paper. The authors' work was supported by the National Natural Science Foundation of China (No.11271247).

## REFERENCES

- [1] HanL Li. High performance FEM on complex contact interface and its data post processing [D]. Shanghai university, 2014.
- [2] Lin Q, Zhou J. Superconvergence in High Order Galerkin Finite Element Methods [J]. Computer Methods in Applied Mechanics and Engineering, 1999, 196(3):3779–3784.
- [3] YangX Ou, ZhongK Chen. Finite element mesh node number [J]. Journal of Beijing University of Aeronautics and Astronautics, 2002, 28(3):339–342.
- [4] Gibson L J, Ashby M E. Cellular solids: structure and properties [M]. [S.I]: Cambridge university press,1999.
- [5] Fleck N.A. An overview of the mechanical properties of foams and periodic lattice materials [J]. Cell Met Polym, 2004:3–7.
- [6] James Ren X, Silberschmidt V V. Numerical modeling of low-density cellular materials [J]. Computational materials science, 2008, 43(1):65–74.

*Computational mechanics and construction technology*

## Radial temperature field simulation of overhead conductor

K. Xiao & P.Y. Li

*Guangdong Power Grid Corporation Co. Ltd., Guangzhou, China*

L.Y. Mo, Z.W. Chen & Q. Gu

*Department of Civil Engineering, Xiamen University, Xiamen, China*

**ABSTRACT:** It is a meaningful and challenging task to exactly grasp the temperature of conducts in an operational transmission line. A typical uniform temperature distribution of a specific section of overhead conduct is assumed by traditional methods, but several experiments found that this is not true and temperature differences existed in the radial direction. To accurately solve the radial temperature field of conducts, a numerical simulation method is proposed based on 2-D steady-state heat transfer control functions, in which main heat gains and heat loss of conducts are considered. The method has been applied to the type-JL/LB1A-300/50 Aluminum Conductor Steel Reinforced (ACSR) conductor. The results proved the existence of an inappropriate temperature difference in the radial direction of conduct.

**Keywords:** overhead conductor; radial temperature field; numerical simulation

### 1 INTRODUCTION

Along with the rapid economic development, the consumption of electric power has increased significantly over the past few years. Inadequate power supply, especially in peak hours, has become an increasingly critical problem. To resolve this problem, except for upgrading the existing power grids and constructing new transmission lines, another alternative is to dynamically increase the current-carrying capacity of overhead lines in service. Dynamic capacity-increase technology can fully tap the potential of existing lines, and it has the advantages of small investment and quick return. It can provide a higher current-carrying capacity than that determined by formulas in specifications, because it determines the threshold of current-carrying based on the thermal equilibrium theory and using the information of conductor temperature, ambient temperature and wind speed. To ensure the stability and safety of power grid operation when this technology is applied, a critical and difficult task is to exactly determine the temperature of operating lines.

The traditional methods based on the thermal equilibrium theory assume a uniform temperature within the conductor (Peng et al. 2008 & IEEE Std. 2003), but, in fact, it is not the true. Some experimental measurement results indicated that temperature differences within a conductor may reach up to 5–15°C (Douglass et al. 1985). Actually, some radial temperature field analyses of typical

conductors were conducted by introducing several simplifications. For example, conductor models established by Black et al. (1988) and Morgan & Findlay (1993) use assumptions that distances between the neighboring metal wires in the steel core and the aluminum strand are neglected, and that the steel core and the aluminum strand are homogeneous cylinder and cylinder hollow cylinder, respectively, and tightly contact between two layers. Therefore, in a simple way, the effective radial thermal conductivity was adopted to simulate radial thermal transfer within the complicated structure of the conductor. The computational accuracy of this method is largely dependent on whether the effective radial thermal conductivity adopted is reasonable or not, but it is rather difficult to determine precisely. Recently, some FE model-based methods were proposed to simulate the radial temperature field of the conductor (Zhao et al. 2007, He & Li 2010). This method enables us to establish a model fully according to the actual structure of the conductor. Until now, few studies have comprehensively analyzed the effects of the distribution pattern of voids within the conductor, contacts among metal wires, and convention conditions on the temperature field of the conductor.

Therefore, this paper establishes a more delicate conductor model based on 2-D steady-state heat transfer control functions, in which the main heat gain and heat loss of conducts, the void distribution and the contact between metal wires are

considered, and then develops a numerical iterative method for the accurate solution of the radial temperature field of the conductor, and finally applies it to the type-JL/LB1A-300/50 Aluminum Conductor Steel Reinforced (ACSR) conductor.

## 2 RADIAL HEAT TRANSFER WITHIN A CONDUCTOR

Heat within an overhead conductor is generated by electrical ohmic losses. The core is hotter than the surface of the conductor, thus heat radially transfers to the surface, and then dissipated to the surrounding air through heat convections and heat radiations. There are two parallel radial heat transfer paths for concentric-lay-stranded conductors: (1) asperities and air gaps at the contact points between the crossing wires and (2) triangular and rectangular voids between adjacent layers. Morgan & Findlay (1993) studied the radial heat flow in a current-carrying multi-layer stranded conductor, and found that most of the heat transfers through the air gaps at the contacts between strands and through the voids between adjacent layers.

IEEE Standard (2013) concluded the main factors that influence the radial temperature distribution within an aluminum conductor, including the magnitude of the electric current in aluminum layers, electric resistance of aluminum wires, geometric shape of strands (e.g. circular, trapezoidal or "Z"-shaped), number of strand layers, aging situation (e.g. corrosion and bird-caging), contact area and contact forces between layers. Among them, the first two factors mainly affect the magnitude of heat generated within a conductor, and the latter four mainly influence the number and distribution of air gaps and voids in the conductor. The existence of air gaps and voids largely affects the actual radial temperature distribution. Therefore, it must be properly considered in the simulation of radial temperature distribution of the conductor using numerical methods.

## 3 SOLUTION OF THE RADIAL TEMPERATURE FIELD

### 3.1 Two-dimensional steady heat transfer equation

Heat transfer through strands and voids within a conductor accords with the 2-dimensional (2D) steady heat transfer control equation, and thus the heat equilibrium equation in the whole cross-sectional area  $\Omega$  is established as follows (He & Li 2010):

$$k(T_{,xx} + T_{,yy}) + s = 0, (x,y) \in \Omega \quad (1)$$

and the equilibrium equation of heat dissipation at the boundary of the conductor  $\Gamma$  is as follows (He & Li 2010):

$$q_n = -k(T_{,x}n_x + T_{,y}n_y) = \alpha(T_s - T_a), (x,y) \in \Gamma \quad (2)$$

where  $T$  is the two-dimensional temperature field in the conductor;  $T_{,xx}$ ,  $T_{,yy}$ ,  $T_{,x}$  and  $T_{,y}$  are the second and first derivative of coordinates  $x$  and  $y$ , respectively, with materials of the conductor being assumed to be isotropic;  $k$  is the thermal conductivity of the metal or air;  $s$  is the heat gain rate per unit volume and its value varies in different areas of a conductor;  $q_n$  is the heat loss rate in the outward normal direction of the conductor's surface;  $n_x$ ,  $n_y$  are the  $x$  and  $y$  components of the normal direction  $n$ , respectively;  $\alpha$  is the composite coefficient of heat dissipation; and  $T_s$  and  $T_a$  are the surface temperature of the conductor and the ambient temperature, respectively.

Using the principle of virtual work to obtain partial integrations of Equation (1), and then introducing to the boundary conditions of Equation (2), we obtain the following equation as follows:

$$\int_{\Omega} \delta T_{,i} k T_{,i} d\Omega + \int_{\Gamma} \delta T \alpha T d\Gamma = \int_{\Omega} \delta T s d\Omega + \int_{\Gamma} \delta T \alpha T_a d\Gamma \quad (3)$$

### 3.2 Heat gain and loss of transmission conductor

ACSR conductors have been widely used in the existing overhead transmission lines for their large current-carrying capacity and stable performance. Given that the main sources of heat gain and loss for different conductors are different, ACSR conductors are chosen for further discussion. For a typical cross-section of ACSR conductors, it consists of outer-layer aluminum strands and inner-layer steel strands.

Heat sources of a conductor mainly include two parts: current heating (or Joule heating) and solar heating. Since the inner steel core cannot be directly affected by sunshine, current heating is the only heat source considered for it. The heat gain rate of steel core per unit volume is as follows:

$$S_s = \frac{P\lambda(\lambda+1)}{A_s} \quad (5)$$

where  $\lambda$  is the current ratio of steel core  $I_s$  to aluminum strands  $I_a$ ;  $A_s$  is the cross-sectional area of the steel core; and  $P$  is the total heat gain rate. For the

outer-layer aluminum strands, solar heating should be taken into consideration, and thus the heat gain rate per unit volume is as follows:

$$S_a = \frac{P(\lambda + 1)}{A_a} + \frac{\gamma_{sSD}}{A_a} \quad (6)$$

where  $S$  is the solar radiation intensity;  $\gamma_s$  is the solar radiation absorptivity of the conductor, which falls in the range of 0.27–0.95; and  $D$  is the external diameter of the conductor.

Convective cooling  $P_c$  and radiative cooling  $P_r$  are two major ways of heat loss for ACSR conductors. The composite thermal dissipation coefficient of the conductor's surface in Equation (2) can be determined as follows:

$$\alpha = \frac{P_c + P_r}{(T_s - T_a)A} \quad (7)$$

where  $A$  is the side superficial area per length.

### 3.3 Main procedure of the numerical solution

The equation of the radial temperature field indicates that several critical parameters are the function of mean temperature or surface temperature of the conductor, such as thermal conductivity of air, heat gain rate of the steel core and aluminum strands per unit volume, and composite coefficient of heat dissipation. Hence, a series of numerical iterations are used to obtain a stable solution of radial temperature field of the conductor. The main procedure of the numerical iterative solution is concluded as follows:

1. Establish a geometry model for the cross-section of a conductor by the FE method;
2. Set an initial temperature field of the conductor  $T_n^i (n = 0)$ ;
3. Calculate the mean temperature and surface temperature of the section based on the temperature field of the conductor at the  $n$ th step  $T_n^i$ ;
4. Solve the thermal conductivity of air, heat gain rate per unit volume, and composite coefficient of heat dissipation at the  $n$ th step;
5. Solve the temperature field of the conductor at the  $(n + 1)$ th step after introducing the boundary conditions in Equation (2);
6. Repeat steps (3–5) if  $\sum_{i=1}^N |T_{n+1}^i - T_n^i| > tol$ , otherwise output computational result of the temperature field.

Here,  $N$  is the number of Degrees of Freedom (Dof) of the FE model;  $T_n^i$  and  $T_{n+1}^i$  are the temperature of the  $i$ th node at the  $n$ th and  $(n + 1)$ th step; and  $tol$  is the tolerance.

## 4 NUMERICAL SIMULATION OF THE RADIAL TEMPERATURE FIELD

### 4.1 Conductor model for temperature field analysis

As an example, the FE model of the type-JL/LB1A-300/50 ACSR conductor is established according to the geometrical parameters of this conductor. The FE model of the type-JL/LB1A-300/50 ACSR conductor is established and shown in Figure 1b. It is composed of 5804 nodes and 11076 elements.

### 4.2 Radial temperature field of the conductor in the natural convection condition

To determine the radial temperature field of the aforementioned conductor in a typical operational environment, some fundamental computational parameters are input as follows: Alternating Current (AC)  $I_{ac} = 500$  A; Direct Current (DC) resistance  $R_{dc} = 0.0916$   $\Omega/\text{km}$ ; resistivity of the steel core  $\rho_s = 20 \times 10^{-8}$   $\Omega \cdot \text{km}$  and aluminum strand  $\rho_a = 2.8 \times 10^{-8}$   $\Omega \cdot \text{km}$ ; thermal conductivity of the steel core  $k_s = 80$   $\text{W}/(\text{m} \cdot ^\circ\text{C})$  and aluminum strand  $k_a = 237$   $\text{W}/(\text{m} \cdot ^\circ\text{C})$ ; and solar radiation  $S = 900$   $\text{W}/\text{m}^2$ .

First, the radial temperature field of the conductor in the natural convection condition is simulated. The wind speed for the natural convection condition is  $V_w = 0$  m/s. Using the numerical iterative solution in Section 3.3, the results can be obtained. The heating rates of the steel core and the aluminum strand are  $S_a = 1.2 \times 10^5$   $\text{W}/\text{m}^3$  and  $S_s = 1.2 \times 10^4$   $\text{W}/\text{m}^3$ , and the composite coefficient is  $\alpha = 10.5$   $\text{W}/(\text{m}^2 \cdot ^\circ\text{C})$ . Figure 2 shows the radial temperature field of the type-JL/LB1A-300/50 ACSR conductor in the natural convection condition. The results indicate that the highest temperature exists in the aluminum strands of the inner layer, and then in the innermost layer of the steel core, with the lowest one being the outermost layer of aluminum strands. The maximum temperature difference within the conductor is around 4.5°C.

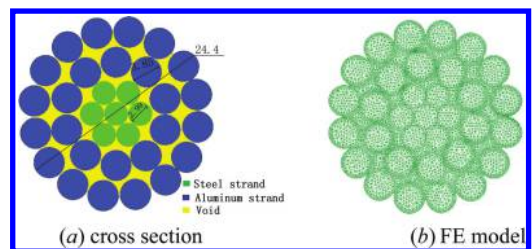


Figure 1. Type-JL/LB1A-300/50 ACSR conductor (unit: mm).

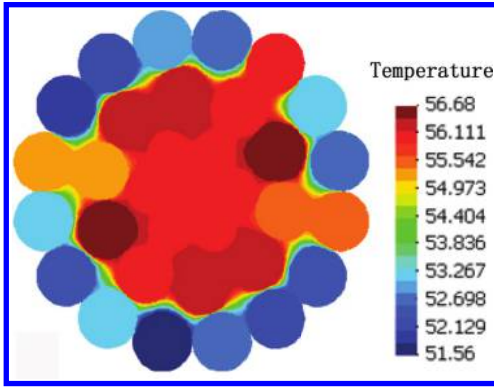


Figure 2. Radial temperature field of the conductor in the natural convection condition (unit: °C).

Some reasons behind the above phenomena are as follows: (1) heat gain rate of aluminum strands is much larger than that of the steel core, and thus the former gains more heat and transfers to the steel core inside; (2) because the steel core of the innermost layer is far from the air convection boundary, the temperature of this layer is relatively high; (3) heat generated in the outermost layer of aluminum strands can be directly dissipated to the surrounding air; therefore, this layer has the highest heat loss rate.

It can also be found that significant differences exist in different strands of the outermost layer. Due to various conditions of contacts between strands, pore distributions and porosities, the actual heat paths and heat transfer efficiencies can be quite different for different local regions of the conductor. The actual contact between strands and contact area does have some effects on the radial temperature field. To study the influence of changing contact locations between strands and the radial temperature field, the contact points between two outermost layers are changed by rotating the outermost aluminum layer in the clockwise direction. Compared with the original temperature field shown in Figure 2, temperature fields for 120° and 240° clockwise rotations are shown in Figure 3. After a comparison, it is found that more heat is transferred from the centre to the surface of a conductor if adjacent aluminum layers closely contact or have less porosity, otherwise heat gathers in the inner layer and causes a local high temperature.

#### 4.3 Radial temperature field of the conductor in the forced convection condition

Furthermore, the radial temperature field of the conductor in the forced convection condition is simulated. In the forced convection condition,

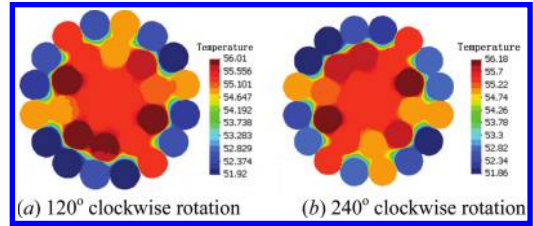


Figure 3. Radial temperature field of the conductor considering different contact positions (unit: °C).

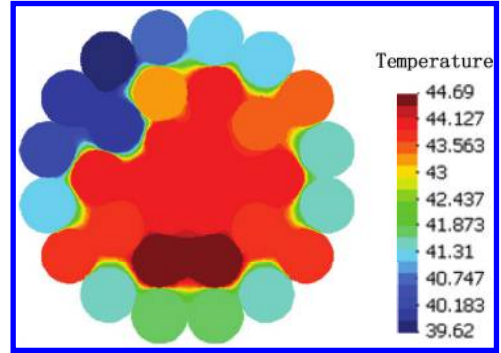


Figure 4. Radial temperature field of the conductor in the forced convection condition (unit: °C).

the wind speed  $V_w$  is assumed to be 0.6 m/s and the wind direction  $d$  is 30°. Using the aforementioned method, the heat gain rates of the steel core and the aluminum strand are determined as  $S_s = 1.1357 \times 10^4 \text{ W/m}^3$  and  $S_a = 1.1736 \times 10^4 \text{ W/m}^3$ , and the composite coefficient of heat dissipation is  $\alpha = 14.4009 \text{ W/(m}^2 \cdot \text{°C)}$ . Figure 4 shows the temperature field of the ACSR conductor in the forced convection condition. Comparing the results in the natural convection condition, we found that: (1) the distribution patterns of the temperature field in different convection conditions are almost the same; (2) the highest temperature of the conductor in the forced convection condition is 12°C lower than that in the natural convection condition; (3) the maximum difference in temperature within a conductor in the forced convection condition is approximately 4°C, and it is very close to that in the natural convection condition. In conclusion, convection conditions have great effects on the average temperature, but a little effect on the radial temperature difference of the conductor.

## 5 CONCLUSIONS

This paper proposes a new computational method for solving the radial temperature field of the



conductor, and then applies it to the type-JL/LB1A-300/50 ACSR conductor. The results proved the existence of an inappropriate temperature difference along the radial direction of conducts, and found that the radial temperature field of the conductor is mainly influenced by the combined effects of the thermal conductivity of metal materials in conductors, contact conditions among strands and external convections.

#### ACKNOWLEDGMENTS

This work was supported by the Technological Project of the Chinese Southern Power Grid Co. Ltd (K-GD2014-0596002-0013-0783).

#### CORRESPONDING AUTHOR

Corresponding author: Dr. Zhi-wei Chen; Email: [cezhiwei@xmu.edu.cn](mailto:cezhiwei@xmu.edu.cn)

#### REFERENCES

Black W.Z. & Collin S.S. 1998. Theoretical Model of ACSR-magnetic and temperature effects. *IEEE Trans on Power Delivery* 3(2), pp:707–715.

Douglass D.A. & Kirkpatrick L.A. & Rathbun L.S. 1985. AC resistance of ACSR-magnetic and temperature effects. *IEEE Trans. On Power Apparatus and System* 5(6), pp:1578–1584.

GB/T 1179-2008. *Round Wire Concentric Lay Overhead Electrical Stranded Conductors*. IEC 61089:1991, MOD, 1991 (in Chinese).

IEEE Power Engineering Society. 2013. *IEEE Standard for calculating the current-temperature relationship of the bare overhead conductor*, New York: The Institute of Electrical and Electronics Engineers, Inc.

Morgan V.T. & Findlay R.D. 1993. Effects of axial tension and reduced air pressure on the radial thermal conductivity of a stranded Conductor. *IEE Trans. on Power Delivery* 8(2), pp:553–558.

Peng X.Y. & Zhou H.M. 2008. Local test research on current carrying and temperature-rise of overhead circulating power transmission line. *Southern Power System Technology* 2(6), pp: 62–83, (in Chinese).

Zhao C.Y. & Zheng L.H. 2007. Numerical study on temperature field of 66 KV overhead transmission line. *Power System Technology* 31(2), (in Chinese).

# Analysis and optimization of the slab transition story support system

S.Y. Xu, S.H. Deng & S.R. Zhu

Beijing University of Civil Engineering and Architecture, Beijing, China

**ABSTRACT:** Research on the construction of the transition story simulation model is proposed. For the first time, the bearing capacity of the concrete story is taken into account. Through a simulation analysis method of a two-story underground and first floor transition story, which are optimized for a multi-story plate frame construction process, the formation of a relatively safe and economical construction technique is ensured, which is verified by a scientific, rational and feasible method. The results showed that the optimization of the transition story support system, which considered the vertical load transfer law, could enable the floor fully to play its role to share the part of the construction load, and make the scaffold template safer, more reliable, economical and reasonable.

**Keywords:** slab transition story; support system; structural design; construction technology

## 1 INTRODUCTION

The transition story system is commonly seen among the high-rise buildings. The transition story has shown a great value and is increasingly well applied. The transition story template support system is one of the key factors in the total construction, and heavily related to the quality and cost of the whole projection.

The load of the members of the support system bearing decreases level by level in the transfer process during the casting construction. This phenomenon shows that each floor could bear its weight and consist the support system in association with the scaffold, exerting the function of support. However at present, the calculation for the transition story template support system is heavily relied on experience, which is excessively safe but leads to wasting. In the current method for designing the support system such as the practical manual for the scaffold of building construction, the transition story concrete casting construction load is applied and the viewpoint that the weight of floors below completely moves down through the support members is adopted. The calculating method corresponding to the viewpoint is adopted without taking the bearing capacity of each floor into consideration. It leads to the common phenomenon that the more support members appear on the lower floors, which increases the difficulty and the cost, and also delays the construction period on its part.

Therefore, the research on the transition story support system is a necessary task. The optimization design of the transition story support system,

which considers the vertical load transfer law, could make the system much more reasonable.

## 2 ESTABLISHMENT MODEL

Simulating the practical process through the FEM analysis software “ANSYS” safely, only single-span slab was taken to analyze the model. The support members were simulated by the unit “PIPE16”, while the beam, slab and the column by the unit “SOLID65”.

On account of simplifying the model, the connection between the support members and the ground was rigid. The connection of the columns and the ground was the same. After dividing the grid and combining the joints, the support

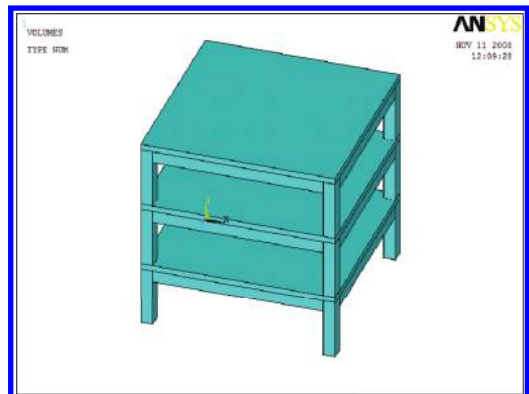


Figure 1. The frame model.

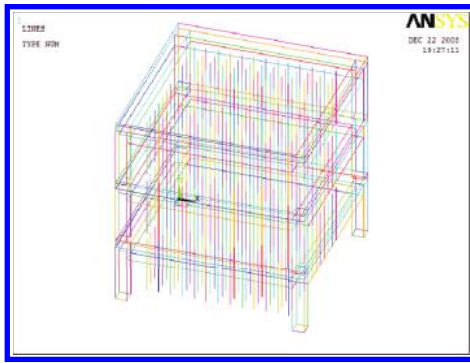


Figure 2. The distribution of the scaffold.

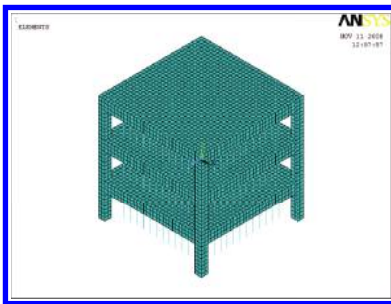


Figure 3. The grid division.

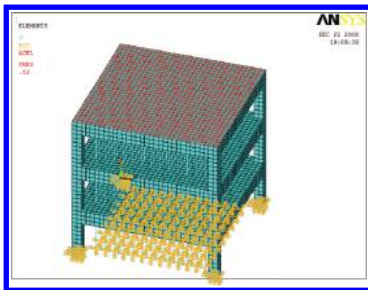


Figure 4. The application of boundary conditions and loads.

members and the slab shared a same joint. They could contact and influence each other.

Figures 1–4 show the analytical model.

### 3 THE OPTIMIZATION OF THE CONSTRUCTION METHOD

#### 3.1 The contraction of solutions

Solution 1: the full load is borne by the template system of each story and moves down to the base.

The materials of the support system need to occupy larger quantities, and take a longer time.

Solution 2: it is designed according to the improved calculation method, when constructing the roof of the first story (the transition story), and the strength of the roof of B2 reaches 100%, while B1 reaches 75%. So, when designing the template support system, it should be considered to remove the roof template and supports of B2 and B1, and place the supports again, so the concrete slab could bear parts of the load. The B2 system bears 100% of the load, and B1 bears 50%.

Solution 2 is much better by contrast. This solution makes the floor fully play its role, in which the scaffold turnover is better and the support system is more secure, reliable, economical and reasonable.

#### 3.2 The improved solution of the constructions

Without considering to bear the load of the transition story transferred, the supports of the roof template of B1 and B2 is placed every  $900 \times 900$  mm to meet the force requirements. Until the construction of the roof of B1, the design strength of B2 reaches 100%. The keel and template of B2 are removed, and the steel tube is re-supported every  $900 \times 900$  mm. The supports of the roof template of B1 are placed every  $900 \times 900$  mm. During transition story pouring, the scaffold members of B1 and B2 are removed and allowed to deform adequately, then the scaffold members of B1 are re-supported after deformation according to every  $450 \times 450$  mm, and then the members of B2 re-supported in the same way. Compared with the former solution, this one could reduce the number of supports and make the scaffold and keel turnover better.

## 4 THE CALCULATION OF THE TEMPLATE SUPPORT SYSTEM AFTER OPTIMIZATION

#### 4.1 The simulation process of construction

When constructing the transition story, the strength of the roof of B2 reaches 100% while B1 reaches 75%. Therefore, we consider B1 and B2, the age and the construction measures of the support system, and then use the concrete slabs to bear load and apply a re-support method. Figure 5 shows the re-support model before construction, and Figure 6 shows the deformation.

During the pouring of the transition story, the scaffold members of B1 and B2 are removed and allowed to deform adequately, and then the scaffold members of B1 are re-supported after deformation, so the load of the scaffold members of B1 bearing is less than that not adopting this method. This can reduce the number of scaffold of B1, and then the

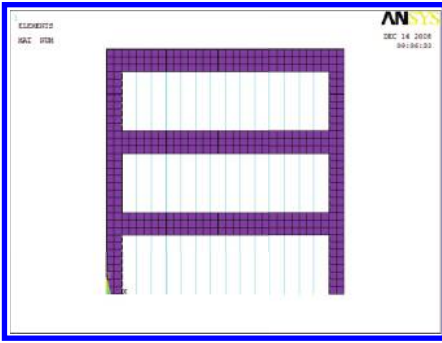


Figure 5. Calculation model.

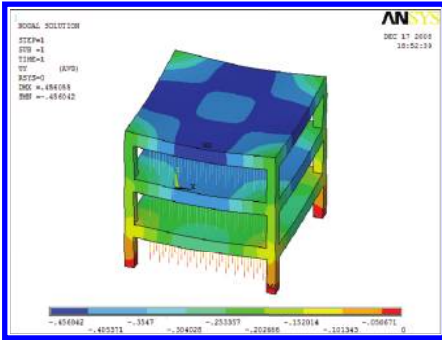


Figure 6. The vertical displacement of the component joint.

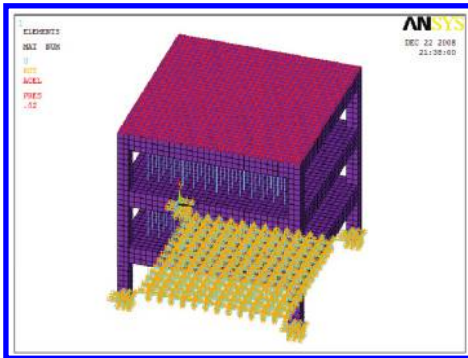


Figure 7. The grid division and the load application.

scaffold members of B2 are re-supported, and the load of the scaffold members of B2 bears is less than that not adopting this method in the same way.

#### 4.2 The construction of the transition story

Pouring concrete of the transition story after re-support, Figure 7 shows the grid division and load application on this model.

## 5 ANALYSIS OF THE CALCULATION RESULT

After modeling and applying the load, we run ANSYS to analyze the model. Simulation results are shown in Figure 8 and Figure 9.

Through the above analysis, we obtain the stress of scaffold supports. The rule between stress and levels is shown in Figure 10.

Through the axial force calculation of supports, we obtain the rule of transition, and then compare the stress of supports on each floor, where the maximum appeared on the first floor while the minimum appeared on B2. So, if we increase the distance of the scaffold and keep the stress of supports uniform, then the number and the expense of scaffold could be saved, and the utilization could be well improved. From the economical comparison of the major material between the solutions before and after optimization, we can conclude that the solution optimized could save reinforcement and concrete, a lot of steel, the labor and the cost.

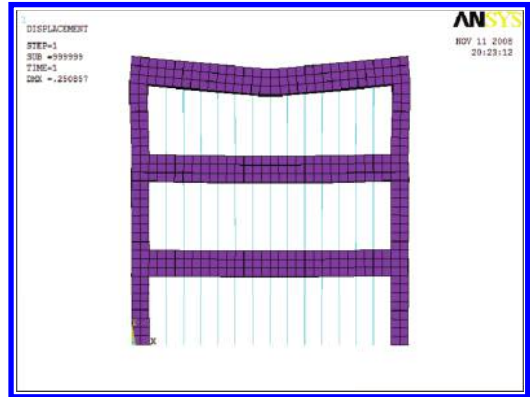


Figure 8. Displacement of the component.

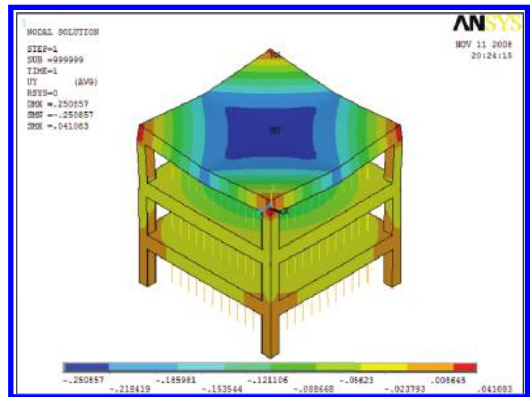


Figure 9. The vertical displacement of the joint.

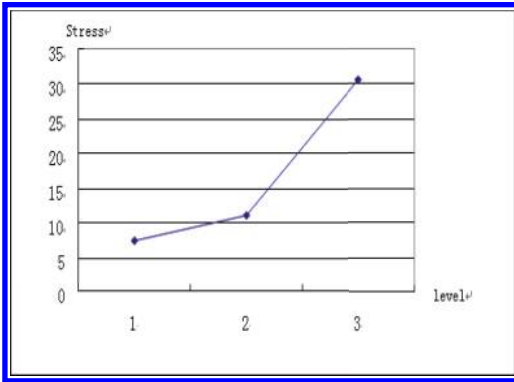


Figure 10. The stress of the supports of the scaffold (MPa).

## 6 CONCLUSION

Through the above discussion, we can conclude that with a reasonable computer-assisted calculation and manual checking, a breakthrough can be achieved in engineering design. Scientific and rational construction organization can be arranged to achieve the most benefit in practical engineering. When meeting template construction projects similar to this one, if the age strength of the lower floor concrete reaches the template removal conditions, the template is first removed and then the support

system is re-supported, which could make the floor redistribution capacity exert best. The construction measures of the supports are strengthened and implementation of quality of design is emphasized, so these actions can make the frame body more practical and economical. This method for the design of the transition story continuous support system has a wide range of adaptability, convenient usability, a wide application prospect and obviously social and economic benefits.

## REFERENCES

- Jiabin, Liu & Zhengxing Guo. 2002. Fastener type steel pipe frame support template. *Construction technology* 31(3): 9–11.
- Sixin, Yang. 2004. *The Manual of Building Template Construction*. Beijing: China Architecture & Building Press.
- Wenhua, Hao. 2004. *The Practical Application of ANSYS on Civil Engineer*. Beijing: China Water & Power Press.
- Xiaofeng Workshop. 2007. *New typical Tutorial of ANSYS and Workbench*. Beijing: Publishing House of Electronics Industry.
- Yongbiao, Lai, Renxi, Hu & Shuzhen, Huang. 2007. *Typical Examples of FEM Analysis on Civil Engineer Based on ANSYS11.0*. Beijing: Publishing House of Electronics Industry.

# Research of roof waterproof technology of steel structure factory building

H. Chen, C.H. Wei & H.L. Li

Chongqing Creation Vocational College, Yongchuan, Chongqing, China

**ABSTRACT:** Due to the high structural strength and a shorter construction cycle before enterprise production, the steel structure factory buildings are now widely applied for current industry. However, under the limitation of construction skills and color steel roof structure, roof leakage is an inevitable problem, which generally exists in steel structure factory buildings. Regarding the defects and limitations in current engineering application as well as deficiency of current engineering skills, this paper proposed the waterproof structure of color steel roof, which can effectively prevent the leakage problem in steel structure factory buildings.

**Keywords:** steel structure; roof; waterproof

## 1 INTRODUCTION

With the increase in construction technology level, during current factory building construction, steel structure is more often adopted. On the one hand, the advanced design theory and high structure strength of steel make less steel usage for today's construction; on the other hand, the standardized and factorization production as well as small machine's lifting work make lower labor intensity and accelerate the construction speed [1] to quickly enter into enterprise production. Current steel structure factory building consists of steel pillar, steel beam and steel purlin. Even though it is very firm in structure, there are big and small gaps existing in the corners of the structure caused by the effect of the large steel structure itself and the unqualified mounting technique of workers. These gaps are the major cause for roof leakage as well as the general problem for current domestic steel structure buildings—"steel roof suffers leakage" [2]—a widespread statement in the engineering construction industry. After completing the construction of steel structure factory building, an additional specialized treatment for roof leakage is often troublesome and costs labor and materials. Therefore, solving the leakage problem is directly related to the normal usage of steel factory buildings during enterprise production. In this paper, waterproof structure of color steel factory building can effectively solve the above problems, and further reinforce the waterproof effects of the factory building, making a simple and quick steel mounting process.

## 2 COMPOSITION AND IMPLEMENTATION OF WATERPROOF STRUCTURE

### 2.1 Roof structure

The waterproof structure of color steel factory building includes steel pillar 1 and steel I-beam 2, and the steel I-beam 2 that is fixed on pillar 1; several evenly laid purlins 3 are fixed on steel I-beam 2. Above purlin 3, there fixed a color steel roof plate 4 parallel to the corresponding purlin 3. Above color steel roof plate 4, there laid roof pressure plate 5; Above roof pressure plate 5, there are several evenly distributed positioning humps 6, and the humps 6 together with roof pressure plate 5 will be produced by a uniform punch forming process. Each positioning hump 6 is equipped with a positioning hole 7.

### 2.2 Steel wall structure

Beside purlin 3, there was fixed a pressure color steel wall plate 8, and in order to enhance the anti-collision ability and avoid deformation due to external force, we adopted the pressure color steel wall plate 8 with a thickness of 15 mm. Between pressure color steel wall plate 8 and purlin 3, we installed an L-type angle steel 9, specifically, the inner side of L-type angle steel 9 was welded on corresponding purlin 3, while the outer side of the angle 9 was riveted to the pressure color steel wall plate 8. Between the pressure color steel wall plate 8 and steel pillar 1, there was installed a U reinforcement connector 12, of which one side was

welded on pillar 1, and the other side was riveted to pressure color steel wall plate 8. Through installing U reinforcement connector 12, the joint strength under pressure color steel wall plate 8 can be effectively enhanced, realizing a more firmly fixing and avoiding shake and looseness.

### 2.3 L-type end bar of the roof

Above roof pressure plate 5, there was mounted L-type end bar 10, and at the upper end of end bar 10, there was set waterproof bevel 13, while the lower end of end bar 10 was in vertical shape, horizontally attaching with the roof pressure plate 5. In addition, the end bar 10 covered some of positioning humps 6 above the roof pressure plate 5, on the positioning holes of covered positioning humps 6, there was mounted self-tapping screws 11, successively penetrating the end bar 10, roof pressure plate 5, and roof plate 4, and locking end bar 10 with roof pressure plate 5. In this process, the focus should be given that the inclination angle of waterproof bevel 13 should be equal to the inclination angle of the side face of positioning hump 6. The waterproof bevel 13 can effectively reduce the probability of rainwater leaking from the gaps of the structure, thus basically avoiding the rainwater leakage problem. In addition, the other end (lower end) of the end bar 10 was vertically attached to the outer side of pressure steel wall plate 8, and the end bar 10 was tightly riveted to the pressure steel wall plate 8. Therefore, the end bar 10, on the one hand, can separate the corners of the structure, realizing the purpose of preventing rainwater leakage, and on the other hand, it enhance the joint strength, improving the tensile capacity of the factory building.

The specific connecting form is shown in Figure 1.

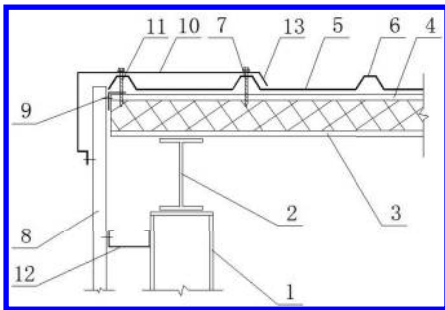


Figure 1. Composition of waterproof structure of color steel factory building.

1-Steel pillar, 2-steel I-beam, 3-Purlin, 4-Color steel roof plate, 5-Roof pressure plate, 6-Positioning hump, 7-Positioning hole, 8-Pressure steel wall plate, 9-Angle steel, 10-End bar, 11-self-tapping screw, 12-U reinforcement connector, 13-Waterproof bevel.

## 3 APPLICATION OF THE WATERPROOF STRUCTURE

The color steel plate, applied in steel factory building construction, plays a major role in waterproofing, wind proofing as well as enhancing the stability of the whole structure; in short, its major function is to keep out wind and rain. Therefore, it entails a higher requirement of waterproofing and anti-leakage ability of color steel itself and the engineering interconnection technique within; especially, the connecting status between steel work pieces to a great degree affects the waterproof performance of the whole structure. At present, normally, flexible waterproof materials [3] are adopted for waterproof roof construction of most steel structure factory building, which solve the leakage problem in most parts of the structure. However, for the intersection portion between the structure wall and the roof, gaps still exist, resulting in deficient waterproof performance by flexible waterproof materials.

This paper proposed a waterproof structure of color steel factory building, which is mainly used in the intersection portion between the structure roof and the wall (area with poor waterproof performance). After completing installation of steel wall and roof, we cover pressure steel roof plates and pressure steel wall plates with the L-type steel end bar, and then using self-tapping screw and rivets to connect pressure steel roof plates and pressure steel wall plates, which can further secure the fixation between them, and cover the gaps between them, greatly enhancing the waterproof ability of the structure. In addition, the proposed waterproof structure can create convenience for factory building construction and later maintenance, and extend the service life of the steel roof plate, which can achieve better performance in solving the leakage problem compared with conventional flexible waterproof materials. Therefore, the structure proposed in this paper can be widely applied in roof waterproofing of color steel structure factory buildings.

## 4 QUALITY CONTROL OF WATERPROOF STRUCTURE CONSTRUCTION

The key point of quality control of the proposed waterproof structure is the lap joint between color steel plates. In the lap joint, we first use rib-plates connecting technique and then fix it by self-tapping screws. In this connecting form, the plate lap joint was fixed with purlin by self-tapping screw, and attention should be paid that between the self-tapping screw and steel, we must add rubber gasket and sealing gum [4], which can prevent

the formation of rigid connection between the end bar and the pressure steel roof plate, getting rid of the occurrence of shakes. In order to prevent rainwater leaking from the gaps between the roof rib-plate and the end bar, we should pay attention during the production that the lap joint between the end bar and the roof plate should contain more than two rib-plates and seal the joint gaps in the lap joint zone. The specific method is to set hidden glue with a width of no less than 2 cm. Moreover, we should strictly control the raw material quality, and conduct specialized treatment to qualified raw materials, for example, rust-proof treatment to self-tapping screws.

## 5 ADVANTAGE AND DISADVANTAGE OF THE WATERPROOF STRUCTURE

Compared with other color steel waterproof structures, the waterproof structure proposed in this paper possesses many advantages. We set reinforcement connector between the pressure steel wall plate and the steel pillar, and one end of the reinforcement connector is welded to the pillar, and the other end of reinforcement connector is riveted to the pressure steel wall plate. Through adjusting the reinforcement connector, we can increase the connecting strength between the pressure steel wall plate and the lower part of the pillar, preventing the shaking movement of the pressure steel wall plate. The pressure steel roof plate and pressure steel wall plate applied in this structure are color steel, wherein, the thickness of the pressure steel roof plate is 5 cm, and the thickness of the pressure steel wall plate is 15 cm. The application of the color steel plate can effectively reduce the weight of the structure, and makes the structure possess a better thermal barrier effect. On one end of the end bar, we set waterproof bevel, for which the inclination angle is the same as that of the positioning hump. Through adjusting the inclination angle of the waterproof bevel, we can further prevent the rainwater leaking from the structure gaps. With the collective function of the waterproof bevel and positioning humps, the rainwater leakage can be fully prevented.

This waterproof structure is designed on the basis of the color steel plate being the roof plate. Through installing the pressure steel roof plate and pressure steel wall plate, a circle can be formed surrounding the steel pillar and roof plate, so as to fundamentally solve the leakage problem and to further enhance the protection effect of the waterproof structure. In addition, possessed with

an excellent thermal barrier performance, good property in bending resistance and pressure resistance, as well as lightweight, the color steel plate can make the installation process more easy and simple, reducing the labor intensity and further extending the service life of factory building.

However, this structure also has some limitations. When combining the roof plate with the cement wall, it is suggested to adopt side retracting connection processing for twice, and while retracting side processing, we should keep a certain angle, and keep fully sealed, and add sealing glue between the retracted sides in advance [5]. The defect is that if the processing is done properly, the waterproof ability will be damped. For example, high tensile strength is necessary to consider for choosing the end bars. When the tensile strength is poor, there may be cracks occurring at the corners of the structure.

## 6 CONCLUSIONS

The promotion and application of steel structure factory buildings can provide convenience for our industrial production. With the emergence of various color steel roofs, the waterproof problem becomes a vital issue in the application of steel structure factory buildings. This paper proposed a waterproof structure, possessing distinguished advantages, which can replace the conventional flexible waterproof materials that have deficient waterproof ability in some particular zones such as gables, gutters and parapets. This new structure has a broader application prospect in the waterproof treatment of color steel roof. In the near future, it will be widely applied.

## REFERENCES

- [1] Q.Y. Wang & Y.J. Shi. 2002. Modern Lightweight Steel Structure and its Application in China [J]. Journal of Building Structures.
- [2] W. Huang & Y.H. Wu. 2013. Application and Analysis of metal roof in China's Engineering [J]. Industrial Architecture.
- [3] Z.Q. Liang. 2013. Anti-seep Technical Control of Steel Structure Containment System [J]. Architecture.
- [4] C.Y. Jiang & Z.D. Liao. 2003. Key Points of Waterproof Design for Pressure Color Steel Roof [J]. China Building Waterproofing.
- [5] R. Su. 2011. Leakage Reason Analysis of Light-steel roof and Related Treatment. [J]. China Oils and Fats.
- [6] H. Chen & J.P. Wei. 2014. Waterproof Structure of Color Steel Factory Building [D]. the People's Republic of China, 201420031671.X.



# Investigation of the effectiveness of vertical load on bending responses for a pile subjected to combined lateral and vertical loads

Fuliang Mei & Guiling Li

*Institute of Mechanics, Jiaxing University, Jiaxing, China*

**ABSTRACT:** Influence of vertical load on bending responses for a partially embedded pile under combined lateral and vertical loads is investigated. The calculated results for a specific pile show that the vertical load can give rise to the additional bending moment and horizontal displacement, and that it has a small influence on maximum horizontal displacement and extreme bending moment when its value is small, but it has a remarkable influence on them when its value is great enough; as its value further increases, the pile may be unstable.

**Keywords:** pile-soil interaction; vertical load; lateral load; bending response; state space method; sub-grade reaction model with three parameters

## 1 INTRODUCTION

In many a circumstance, a number of piles are used to be subjected to combined lateral and vertical loads. In consequence, the prediction of responses for a single pile under lateral and vertical loads simultaneously is urgently an important event in the design, construction and application of pile foundation.

Based on a sub-grade reaction method, a wealth of solutions for a single pile subjected to combined lateral and vertical loads include the following: finite element ones (Karthineyan et al., 2006; Karthigeyan et al., 2007; Zheng et al., 2009), power series ones (Zhao et al., 1987; Wang et al., 2005; Li et al., 2005), and variation principle ones (Han et al., 2000). In the aforementioned solutions, the coefficient of sub-grade reaction is assumed to remain constant or linearly increase with depth (Wang et al., 2005), while it is equal to be zero in the vicinity of ground, so that there is a certain difference between these results and the practical ones. Previously, a three-parameter model, which can authentically represent the distribution of sub-grade reaction with depth and lateral deformation-resisting capability of soil in the vicinity of ground, has been presented for predicting the responses of a pile subjected to a lateral load in the literature (H.L. Wu et al., 2000; B.H. Wang et al., 1999; H. Matlock et al., 1960). Zhang L. et al. (2011) obtained the semi-analytical solution of responses for a pile subjected to oblique loads by using the three-parameter model proposed in H.L. Wu et al. (2000).

In this article, a state space method to solve internal forces and deformations for a partially embedded pile under vertical and lateral loads is given. State space equations for the pile shafts above and below ground are derived according to Euler-Bernoulli's and Winkler' linear elastic beam theory and a sub-grade reaction model with three parameters, and also state space equations for sub-sections above and below ground based on the sub-section approximation approach are presented. The expressions of internal forces and deformations for all the sub-sections are deduced from the matrix theory, boundary conditions and continuity-smooth conditions at the interface between two adjacent sub-sections. Finally, the influence of vertical load on bending responses for a partially embedded pile under combined lateral and vertical loads is investigated.

## 2 STATE SPACE SOLUTION

Consider a uniform cross-section and partially embedded pile subjected to a combined lateral and vertical load, as shown in [Figure 1](#), where  $N_p$ ,  $Q_p$  and  $M_p$  are vertical load, horizontal load and moment load on the pile head, respectively.  $H_0$  and  $H_1$  are the pile lengths above and below ground, respectively.

The force analysis and a local coordinate system for the pile shaft above ground are illustrated in [Figure 2](#), where  $u_g(x)$ ,  $\varphi_g(x)$ ,  $M_g(x)$ ,  $Q_g(x)$  and  $N_g(x)$  are horizontal displacement, declination, moment, shear force and axial force at a depth  $x$ , respectively.

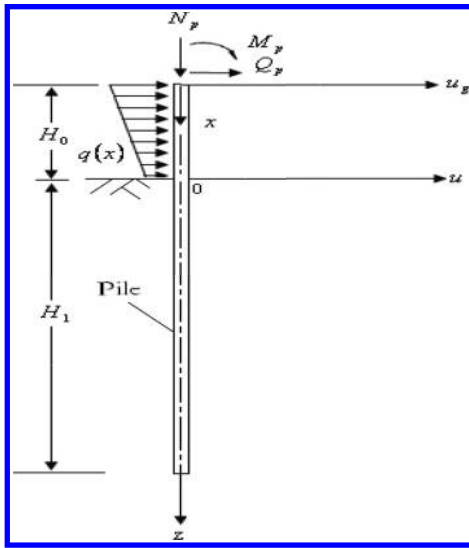


Figure 1. Schematic diagram of a pile under lateral and vertical loads.

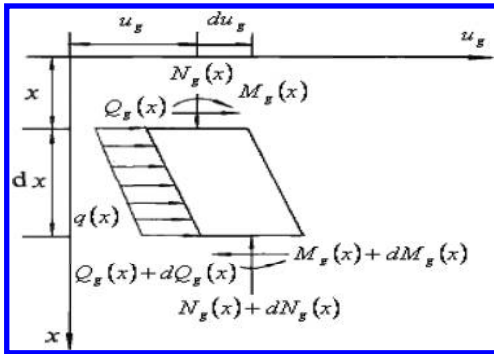


Figure 2. Force analysis of a pile shaft above ground.

We can deduce a set state space equations above ground from Euler-Bernoulli's beam theory as follows:

$$\frac{d}{dx} \begin{Bmatrix} u_g(x) \\ M_g(x) \\ Q_g(x) \\ \phi_g(x) \end{Bmatrix} = \begin{bmatrix} 0 & 0 & 0 & 1 \\ 0 & 0 & 1 & -N_g(x) \\ 0 & 0 & 0 & 0 \\ 0 & 1/EI & 0 & 0 \end{bmatrix} \begin{Bmatrix} u_g(x) \\ M_g(x) \\ Q_g(x) \\ \phi_g(x) \end{Bmatrix} + \begin{Bmatrix} 0 \\ 0 \\ q(x) \\ 0 \end{Bmatrix} \quad (1)$$

where  $EI$  is the pile flexural stiffness,  $N_g(x) = N_p + f_0 x$ , in which  $f_0$  denotes the growth factor of axial force resulting from self-weight, and  $q(x) = q_0 + \Delta q x / H_0$ , in which  $q_0$ ,  $q_0 + \Delta q$  are the distributed loads at the pile head and ground, respectively. It can be noted that Equation (1) is a set of non-homogeneous differential equations of the coordinate  $x$  with variable coefficients.

Similarly, the force analysis and a local coordinate system for the pile shaft below ground are depicted in Figure 3, in which  $u(z)$ ,  $\phi(z)$ ,  $M(z)$ ,  $Q(z)$  and  $N(z)$  are horizontal displacement, rotation angle, moment, shear force and axial force at a depth  $z$ , respectively.

We can obtain another set of state space equations below ground according to Winker's linear elastic foundation beam theory as follows:

$$\frac{d}{dz} \begin{Bmatrix} u(z) \\ M(z) \\ Q(z) \\ \phi(z) \end{Bmatrix} = \begin{bmatrix} 0 & 0 & 0 & 1 \\ 0 & 0 & 1 & -N(z) \\ -k(z)b & 0 & 0 & 0 \\ 0 & 1/EI & 0 & 0 \end{bmatrix} \begin{Bmatrix} u(z) \\ M(z) \\ Q(z) \\ \phi(z) \end{Bmatrix} \quad (2)$$

where  $N(z) = N_p + f_0 H_0 + f_1 z$ , in which  $f_1$  also is the growth factor of axial friction due to combined self-weight and lateral friction of the pile, say,  $f_1 = \gamma_c A_s - \mu \tau / 2$ , here  $\gamma_c$ ,  $A_s$ ,  $\mu$  and  $\tau$  stand for the specific gravity under water, cross-section area, pile perimeter, limit friction [4], respectively; the coefficient of sub-grade reaction  $k(z)$  is calculated, according to H.L.Wu et al. (2000), as  $k(z) = m(z_0 + z)^n$ , in which  $z_0$  is the equivalent depth standing for the lateral deformation-resisting capability of soil at the ground,  $m$  the proportionality coefficient of the soil, and  $n$  the resistance index of the soil. It can also be noted that Equation (2) is a set of homogeneous differential equations of the coordinate  $z$  with variable coefficients.

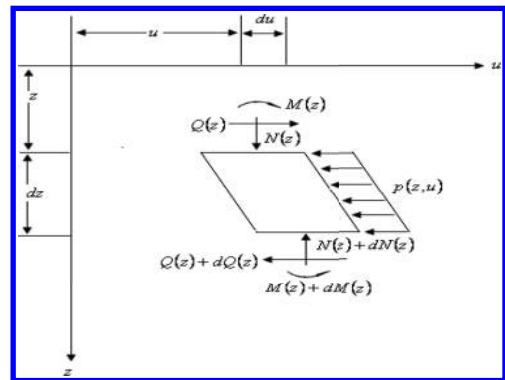


Figure 3. Force analysis of a pile shaft below ground.

When the pile head is free, the state space variables (at  $x = 0$ ) is given by

$$\begin{aligned} & \begin{bmatrix} u_g(0) & M_g(0) & Q_g(0) & \varphi_g(0) \end{bmatrix}^T \\ & = \begin{bmatrix} u_g(0) & M_p & Q_p & \varphi_g(0) \end{bmatrix}^T \end{aligned} \quad (3)$$

where  $u_g(0)$  and  $\varphi_g(0)$  are the horizontal displacement and rotation angle to be determined.

When the pile base is free, the state space variables (at  $z = H_1$ ) is given by

$$\begin{aligned} & \begin{bmatrix} u(H_1) & M(H_1) & Q(H_1) & \varphi(H_1) \end{bmatrix}^T \\ & = \begin{bmatrix} u(H_1) & 0 & 0 & \varphi(H_1) \end{bmatrix}^T \end{aligned} \quad (4)$$

here,  $u(H_1)$  and  $\varphi(H_1)$  are the horizontal displacement and rotation angle to be determined.

When the pile base is fixed, the state space variables (at  $z = H_1$ ) is expressed by

$$\begin{aligned} & \begin{bmatrix} u(H_1) & M(H_1) & Q(H_1) & \varphi(H_1) \end{bmatrix}^T \\ & = \begin{bmatrix} 0 & M(H_1) & Q(H_1) & 0 \end{bmatrix}^T \end{aligned} \quad (5)$$

here,  $M(H_1)$  and  $Q(H_1)$  are the bending moment and shear force to be determined.

Continuity-smooth conditions at the ground can be represented as follows;

$$\begin{aligned} & \begin{bmatrix} u_g(H_0) & M_g(H_0) & Q_g(H_0) & \varphi_g(H_0) \end{bmatrix}^T \\ & = \begin{bmatrix} u(0) & M(0) & Q(0) & \varphi(0) \end{bmatrix}^T \end{aligned} \quad (6)$$

It can be noted that the exact solutions for Equations (1) and (2) are directly difficult to solve. Thus, we have to use a numerical method. To avoid difficulties in directly solving Equations (1) and (2) with variable coefficients, two pile shafts above and below ground are divided into  $N_0$  and  $N_1$  uniform sub-sections according to a sub-section approximation approach. Here, two sub-section lengths above and below the ground are  $\Delta x = H_0/N_0$  and  $\Delta z = H_1/N_1$ , respectively. Then, two local coordinate systems for a sub-section above and below ground are depicted in Figure 4, respectively.

When  $N_0$  is large enough, the axial force  $N_{gi}$  and the horizontally distributed load  $q_i$  for the  $i$ th sub-section above the ground are assumed to be constant, and they are calculated as follows:  $N_{gi} = N_p + f_0(2i-1)\Delta x/2$  and  $q_i = q_0 + \Delta q(2i-1)\Delta x/(2H_0)$  ( $i = 1, 2, \dots, N_0$ ), respectively. And a set of state space equations for the  $i$ th sub-section above ground are as follows:

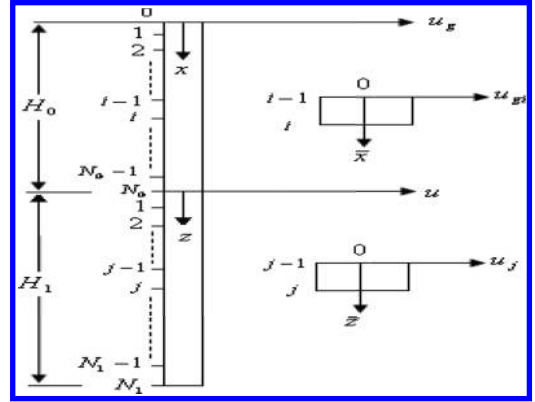


Figure 4. Schematic diagrams of sub-sections and local coordinate systems.

$$\begin{aligned} \frac{d}{d\bar{x}} \begin{Bmatrix} u_{gi}(\bar{x}) \\ M_{gi}(\bar{x}) \\ Q_{gi}(\bar{x}) \\ \phi_{gi}(\bar{x}) \end{Bmatrix} & = \begin{bmatrix} 0 & 0 & 0 & 1 \\ 0 & 0 & 1 & -N_{gi} \\ 0 & 0 & 0 & 0 \\ 0 & 1/EI & 0 & 0 \end{bmatrix} \begin{Bmatrix} u_{gi}(\bar{x}) \\ M_{gi}(\bar{x}) \\ Q_{gi}(\bar{x}) \\ \phi_{gi}(\bar{x}) \end{Bmatrix} \\ & + \begin{Bmatrix} 0 \\ 0 \\ q_i \\ 0 \end{Bmatrix} \quad (i = 1, 2, \dots, N_0) \quad (7) \end{aligned}$$

where  $u_{gi}(\bar{x})$ ,  $M_{gi}(\bar{x})$ ,  $Q_{gi}(\bar{x})$  and  $\phi_{gi}(\bar{x})$  are the horizontal displacement, the bending moment, shear force and rotation angle at a depth  $\bar{x}$ , respectively.

Let

$$\mathbf{H}_{gi} = \begin{bmatrix} 0 & 0 & 0 & 1 \\ 0 & 0 & 1 & -N_{gi} \\ 0 & 0 & 0 & 0 \\ 0 & 1/EI & 0 & 0 \end{bmatrix} \quad \mathbf{B}_{gi} = \begin{Bmatrix} 0 \\ 0 \\ q_i \\ 0 \end{Bmatrix}$$

Based on the matrix theory, we can obtain a set of relationship equations between two state space variables at the top and bottom of the  $i$ th sub-section above ground:

$$\mathbf{U}_{gi}(\Delta x) = \mathbf{T}_{gi} \mathbf{U}_{gi}(0) + \mathbf{A}_{gi} \quad (8)$$

where  $\mathbf{U}_{gi}(\Delta x) = [u_{gi}(\Delta x) \ M_{gi}(\Delta x) \ Q_{gi}(\Delta x) \ \varphi_{gi}(\Delta x)]^T$  and  $\mathbf{U}_{gi}(0) = [u_{gi}(0) \ M_{gi}(0) \ Q_{gi}(0) \ \varphi_{gi}(0)]^T$  are the state space variables at the bottom and top of the  $i$ th sub-section above ground, respectively:

$$\mathbf{T}_{gi} = \exp(\mathbf{H}_{gi} \Delta x), \quad \mathbf{A}_{gi} = (\mathbf{T}_{gi} \mathbf{H}_{gi}^{-1} - \mathbf{H}_{gi}^{-1}) \mathbf{B}_{gi}$$

When  $N_1$  is large enough,  $N_j(z)$  and  $k_j(z)$  for the  $j$ th subsection are also assumed to be constant, and are calculated as follows:  $N_j = N_p + f_0 H_0 + f(2j-1)\Delta z/2$  and  $k_j = m(z_0 + (2j-1)\Delta z/2)^n$  ( $j = 1, 2, \dots, N_1$ ), respectively. And another set of state space equations for the  $j$ th sub-section below ground are given as follows:

$$\frac{d}{d\bar{z}} \begin{Bmatrix} u_j(\bar{z}) \\ M_j(\bar{z}) \\ Q_j(\bar{z}) \\ \phi_j(\bar{z}) \end{Bmatrix} = \begin{bmatrix} 0 & 0 & 0 & 1 \\ 0 & 0 & 1 & -N_j \\ -k_j b & 0 & 0 & 0 \\ 0 & 1/EI & 0 & 0 \end{bmatrix} \begin{Bmatrix} u_j(\bar{z}) \\ M_j(\bar{z}) \\ Q_j(\bar{z}) \\ \phi_j(\bar{z}) \end{Bmatrix} \quad (j=1, 2, \dots, N_1) \quad (9)$$

where  $u_j(\bar{z})$ ,  $M_j(\bar{z})$ ,  $Q_j(\bar{z})$  and  $\phi_j(\bar{z})$  are the horizontal displacement, bending moment, shear force and rotation angle at a depth  $\bar{z}$ , respectively.

Let

$$\mathbf{H}_j = \begin{bmatrix} 0 & 0 & 0 & 1 \\ 0 & 0 & 1 & -N_j \\ -k_j b & 0 & 0 & 0 \\ 0 & 1/EI & 0 & 0 \end{bmatrix}$$

In a similar way, we also can attain another set of relationship equations between two state space variables at the top and bottom of the  $j$ th subsection below ground as follows:

$$\mathbf{U}_j(\Delta z) = \mathbf{T}_j \mathbf{U}_j(0) \quad (j=1, 2, \dots, N_1) \quad (10)$$

where  $\mathbf{U}_j(\Delta z) = [u_j(\Delta z) \ M_j(\Delta z) \ Q_j(\Delta z) \ \phi_j(\Delta z)]^T$  and  $\mathbf{U}_j(0) = [u_j(0) \ M_j(0) \ Q_j(0) \ \phi_j(0)]^T$  stand for the state space variables at the bottom and top of the  $j$ th sub-section below ground, respectively, and  $\mathbf{T}_j = \exp(\mathbf{H}_j \Delta z)$ . From Equations (3)–(6), (8) and (10), a set of relationships between two state space variables at the pile head and base are obtained as follows:

$$\begin{aligned} \mathbf{U}_{N_1}(\Delta z) &= \mathbf{T}_{N_1} \cdots \mathbf{T}_j \cdots \mathbf{T}_1 \mathbf{T}_{gN_0} \cdots \mathbf{T}_{gi} \cdots \mathbf{T}_{g1} \mathbf{U}_{g1}(0) \\ &\quad + \mathbf{T}_{N_1} \cdots \mathbf{T}_j \cdots \mathbf{T}_1 (\mathbf{T}_{gN_0} \cdots \mathbf{T}_{gi} \cdots \mathbf{T}_{g2} \mathbf{A}_{g1}) \\ &\quad + \mathbf{T}_{gN_0} \cdots \mathbf{T}_{gi} \cdots \mathbf{T}_{g2} \mathbf{A}_{g2} + \cdots + \mathbf{A}_{gN_0} \end{aligned} \quad (11)$$

where  $\mathbf{U}_{N_1}(\Delta z) = [u(H_1) \ M(H_1) \ Q(H_1) \ \phi(H_1)]^T$  and  $\mathbf{U}_{g1}(0) = [u_g(0) \ M_g(0) \ Q_g(0) \ \phi_g(0)]^T$  are the state space variables at the pile head and base, respectively. Let  $\mathbf{T}_{N_1} \cdots \mathbf{T}_j \cdots \mathbf{T}_1 \mathbf{T}_{gN_0} \cdots \mathbf{T}_{gi} \cdots \mathbf{T}_{g1} = \mathbf{\Omega}$  and  $\mathbf{T}_{N_1} \cdots \mathbf{T}_j \cdots \mathbf{T}_1 (\mathbf{T}_{gN_0} \cdots \mathbf{T}_{gi} \cdots \mathbf{T}_{g2} \mathbf{A}_{g1} + \mathbf{T}_{gN_0} \cdots \mathbf{T}_{gi} \cdots \mathbf{T}_{g2} \mathbf{A}_{g2} + \cdots + \mathbf{A}_{gN_0}) = \mathbf{\Gamma}$ .

where  $\mathbf{\Omega}$  is a fourth-order matrix and  $\mathbf{\Gamma}$  is a second-order column vector. When both the pile head and base are free, the substitution of boundary conditions Equations (3) and (4) into Equation (11) gives rise to two equations for finding  $u_g(0)$  and  $\phi_g(0)$  at the pile head as follows:

$$\begin{Bmatrix} u_g(0) \\ \phi_g(0) \end{Bmatrix} = - \begin{bmatrix} \Omega_{11} & \Omega_{14} \\ \Omega_{41} & \Omega_{44} \end{bmatrix}^{-1} \times \left( \begin{bmatrix} \Omega_{12} & \Omega_{13} \\ \Omega_{42} & \Omega_{43} \end{bmatrix} \begin{Bmatrix} M_p \\ Q_p \end{Bmatrix} + \begin{Bmatrix} \Gamma_1 \\ \Gamma_4 \end{Bmatrix} \right) \quad (12)$$

When the pile head is free while the pile base is fixed, the substitution of Equations (3) and (5) into Equation (11) yields two equations for finding  $u_g(0)$  and  $\phi_g(0)$  at the pile head:

$$\begin{Bmatrix} u_g(0) \\ \phi_g(0) \end{Bmatrix} = - \begin{bmatrix} \Omega_{21} & \Omega_{24} \\ \Omega_{31} & \Omega_{34} \end{bmatrix}^{-1} \times \left( \begin{bmatrix} \Omega_{22} & \Omega_{23} \\ \Omega_{32} & \Omega_{33} \end{bmatrix} \begin{Bmatrix} M_p \\ Q_p \end{Bmatrix} + \begin{Bmatrix} \Gamma_2 \\ \Gamma_3 \end{Bmatrix} \right) \quad (13)$$

Hitherto, all the internal forces and deformations at the base of the  $i$ th and  $j$ th sub-sections can be calculated step by step by means of Equations (8) and (10) after  $u_g(0)$  and  $\phi_g(0)$  are determined from Equation (12) or Equation (13). Thus, the above solution is called as a state space one.

### 3 EFFECT OF VERTICAL LOAD ON BENDING RESPONSES

In order to investigate the influence of a vertical load on the bending responses, we consider a uniform cross-section and partially embedded pile, in which calculated parameters are taken as follows:  $H_0 = 15$  m,  $H_1 = 30$  m,  $b = 1.8$  m,  $EI = 9.275 \times 10^6$  kN·m<sup>2</sup>,  $q(x) = 0$ ,  $f_0 = 62.345$  kN/m,  $Q_p = 300$  kN,  $M_p = 200$  kN·m,  $N_p = 10000$  kN,  $z_0 = 0.4$  m,  $n = 0.5$  and  $m = 6 \times 10^3$  kN/m<sup>3.5</sup>. We assume that both file head and base are free and the axial force reduces gradually up to zero from the ground to the pile base in a linear fashion. Figures 5–8 show the relationships between bending responses and vertical load for three sets of different lateral loads:  $M_p = 200$  kN·m,  $Q_p = 200$  kN;  $M_p = 600$  kN·m,  $Q_p = 200$  kN;  $M_p = 600$  kN·m,  $Q_p = 400$  kN.

It can be found from Figures 5–7 that the maximum horizontal displacement, maximum bending moment and horizontal displacement at the ground increase slowly with increasing vertical load when the vertical load is small, but they rise rapidly with increasing vertical load when

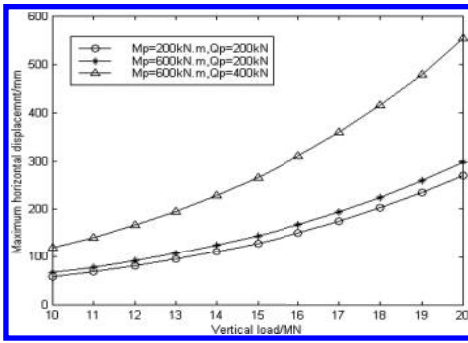


Figure 5. Maximum horizontal displacements versus vertical load.

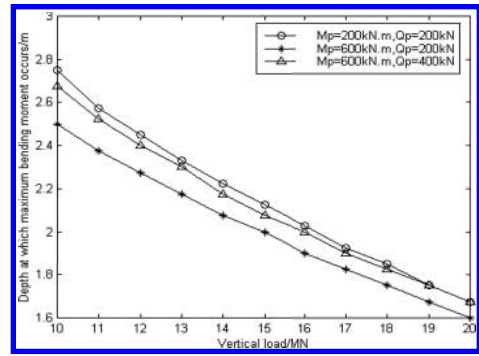


Figure 8. Depth at which maximum moment occurs versus vertical load.

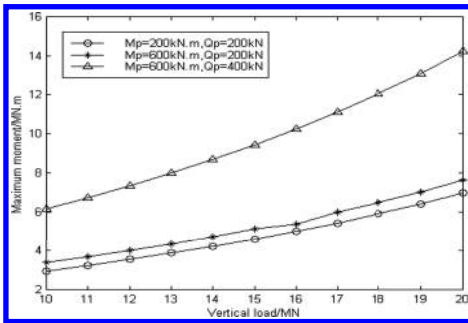


Figure 6. Maximum moment versus vertical load.

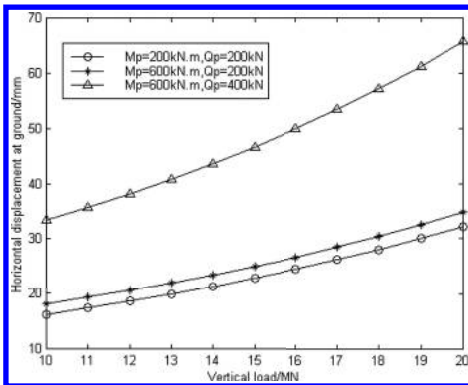


Figure 7. Horizontal displacements versus vertical load.

the vertical load is big. This effectiveness is called as the  $P-\Delta$  one. Therefore,  $P-\Delta$  effectiveness should not be neglected when both vertical load and pile length above ground are great enough. Additionally, the vertical load has a much greater contribution to the bending responses when both

applied horizontal load and bending moment on the pile head are large enough.

In general, the bending responses for the pile subjected to lateral loads and the compressive responses for the pile under vertical loads are separately calculated, and then the above-mentioned bending and compressive responses are superimposed as those for the pile subjected to the above combined lateral and vertical loads. This theory does not take into account the additional bending responses due to axial force. If the horizontal displacement and the axial force are much smaller, the additional bending responses due to the axial force also are considerably small. But if the horizontal displacement and the axial force are large enough, while the pile length above ground is particularly large, neglecting the effect of the additional moment and additional deformation resulting from the axial force on the bending responses can produce a much greater error.

It also can be found from Figure 8 that the depth where the maximum moment occurs decreases with increasing vertical load.

#### 4 CONCLUSIONS

The state space solution for a partially embedded pile under combined lateral and vertical loads is presented. And the influence of vertical load on the bending responses for a specific partially embedded pile is investigated. On this basis, we can draw the following conclusions: the vertical load can give rise to the additional bending moment and horizontal displacement, and it has a little influence on maximum horizontal displacement and extreme bending moment when its value is small, but it has a remarkable influence on them when its value is great enough; as its value further increases, the pile may be unstable.

## REFERENCES

- Han, J. and Frost, J.D. 2000. Load-deflection response of transversely isotropic piles under lateral loads. *International Journal of Numerical and Analytical Methods in Geo-mechanics* 24(5):509–529.
- Karthigeyan, S., Ramakrishna, V.V.G.S.T and Rajagopal, K. 2006. Influence of vertical load on the lateral response of piles in sand. *Computers and Geotechnics* 33(2):121–131.
- Karthigeyan, S., Ramakrishna, V.V.G.S.T and Rajagopal, K. 2007. Numerical investigation of the effect of vertical load on the lateral response of piles. *Journal of Geotechnical and Geo-environmental Engineering*, ASCE, 133(5):512–521.
- Li, W.Z., Zhao, M.H., Shan, Y.M., and Yang, M.H. 2005. Analysis of single pile under eccentric and inclined loading. *Central South Highway Engineering* 30(3):53–57.
- Matlock, H., Reese, L.C. 1960. Generalized solutions for laterally loaded piles. *Journal of the Soil Mechanics and Foundation division*, ASCE, 86 (5):63–91.
- Poulos, H.G. and Davis, E.H. 1980. *Pile foundation analysis and design*. New York:Wiley.
- Wang, Z. and Gong, X.N. 2005. The behavior of single piles under axially and laterally loads. *Journal of University of Science and Technology of Suzhou (Engineering and Technology)* 18(3):32–36.
- Wu, H.L. 2000. Thrust calculation of a pile in the composite stiffness principle and the method of double parameters. Beijing:China Communications Press.
- Wang, B.H., Shang, G.X. 1999. *China's new development of bored piles*. Beijing:China Communications Press.
- Zhang, L., Gong, X.N., Yu, J.L. 2011. Semi-analytical solutions for single piles under lateral loads based on sub-grade reaction method. *Journal of Sichuan University (Engineering Science Edition)* 43(1):37–42.
- Zheng, G. and Wang, L. 2009. Finite element analysis of bearing capacity of pile under inclined load in layered soil. *Rock and Soil Mechanics* 30(3):680–687.
- Zhao, M.H. 1987. Calculation of piles under axial and lateral loads. *Journal of Hunan University* 14(2):68–81.

# Study of integral lifting spots of steel structure for steel truss structures

M. Chen

*Steel Structure and Space Structure Research Institute, Inner Mongolia University of Science and Technology, Baotou, China*

Y.D. Chen

*Inner Mongolia University of Science and Technology, Baotou, China*

**ABSTRACT:** The technique of integral lifting for steel structure acquires rapid development, but the key factor for the hoisting construction safety economy is how to determine the location of lifting. This article takes some integral lifting for steel truss structures as the example, and selected 3 kinds of lifting schemes based on the location and quantity of lifting spots, in accordance with the structural characteristics and forms. This study analyzes and models the 3 kinds of lifting schemes of lifting reaction force, stress ratio, and displacements with MIDAS-Gen, taking economical efficiency and feasibility into account to find out the optimum feasible program. By analyzing and summarizing the location of the lifting spots, the rational collocation principles of the integral lifting of irregular steel structure were found. The conclusions offer references for similar engineering.

**Keywords:** steel roof; integral lifting; lifting spots; contrast of the plan

## 1 INTRODUCTION

In recent years, with the application of steel structure and the development of construction industry, various kinds of the new steel structure systems are springing up constantly. As a consequence, the new technologies, workmanship, and equipment are applied in engineering construction, among which the integral lifting technology develops faster. The integral lifting technology widely applies in the engineering of steel structure, which is developing toward macro-scale and largeness. It has the advantages of less installing height, short period, less scaffold engineering, high security, and so on. The steel structural engineering of National Library Phase, Xiamen West Passenger Station, and Fuzhou International Convention and Exhibition Center adopts the integral lifting technology, with this technology construction costs have been saved, it reduces the time, and has achieved great economic and social efficiency.

The key to a successful integral lifting of irregular steel structure engineering lies in the location of the lifting spots. The influence factors of the project are extensive. This article takes some integral lifting for steel truss structures as the example, makes a detailed analysis on the lifting spots of integral lifting of irregular steel structure engineering.

## 2 GENERAL SITUATION OF THE PROJECT

The project is an integrated super high rise building. It takes a total land area of 932901 m<sup>2</sup> and construction area is 690719 m<sup>2</sup>. The main structure of the project contains 3 parts, they are T1 (58-storey) building, T2 (60-storey) building, and T3 building. They are connected by the skirt building on 11-storeys above ground (2 storeys under ground). The main building is connected by the steel structure at the storey from 43 to 49, the structure form at the storey from 43 to 44 is a space truss structure and it is a frame structure system at the storey from 44 to 49. The elevation of the steel structure is +232.000 m. This project is lifting the space truss structure, the elevation of it is +198.900 m, ranging from 43 to 44 storeys. The space truss structure is 8 m high, the widest span is about 71.6 m, and the weight of steel is about 2729t. The area of the lifting is shown in [Figure 1](#). The model of the space truss structure is shown in [Figure 2](#).

### 2.1 Making sure the location and the number of the lifting points

The lifted structure and the supporting structure for lifting are directly linked to the technology of the integral lifting. Hence, to make sure the location and the number of the lifting spots,

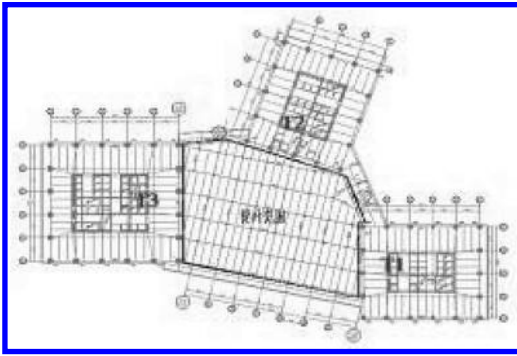


Figure 1. The lifting area.

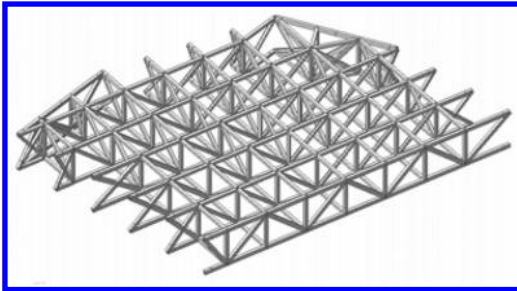


Figure 2. The model of the structure.

we must take the two factors into consideration, based on mechanical characteristics of the structure itself and comprehensive survey of the economics and safety.

### 2.2 Making sure the location of the lifting points

To make sure the location of the lifting spots, the following principles should be considered:

1. No matter the lifted structure symmetry or not. We should take the center of gravity as the center of symmetry to arrange the lifting spots to assure that the lifting force of each lifting appliance is similar. Only in this way can we purchase equipment easily and the whole process works stably.
2. Lifting spots should choose as far as possible in the location that is good for the structural strain, and avoid inducing the additional stress. Hence the lifting spots should be arranged on or near the truss joints or supports.
3. Heavily influenced by the lifting support structure, the lifting spots in the top chord or the down chord of the structure are arranged. If the lifting spots in the top chord are arranged, then the supporting structure for lifting cannot be arranged on the same storey of the

lifted structure. At this time, the spreaders can be directly welded on the top chord as shown in Figure 3. If the lifting spots in the down chord are arranged, then the supporting structure for lifting can be arranged on the same or the top storey of the lifted structure. Such a hole is unfavorable to the structure stress, so in general, decorate the corbel on each side of the down chord to fix the steel strand, as shown in Figure 4.

### 2.3 Making sure the number of the lifting points

For consideration of economic effectiveness and operation, the lesser the number of the lifting spots, the better they are. But taking safety into consideration, the more the number of the lifting spots, the better they are; in this way, we can ensure that there is safety in the lifting process. So, it is important to take the actual requirement in the lifting process into consideration, and make an analysis on different proposals. At last we find out the proposal to be both safe and economical.



Figure 3. The spreaders arranged on the top chord.



Figure 4. The spreaders arranged on the down chord.



### 3 THE SCHEMES TO ARRANGE THE LIFTING POINTS AND THE CONTRAST OF THE PLANS

According to the characteristics of the project, and to bring forward 3 kinds of lifting schemes for consideration, the above all have been combined with the arrangement principles. Plan 1 is based on the structural characteristics, the location of lifting spots being arranged in a symmetrical way; Plan 2 based on the stress form of the structure, the location of lifting spots arranged on the three sides of the up chord; Plan 3 based on Plan 2, but put the lifting spots arranged on the down chord. In addition, Plan 1 and Plan 2 make the comparison on the structure; Plan 2 and Plan 3 make the comparison on the lifting spots which should be arranged on the top or the down chord.

#### 3.1 The schemes to arrange the lifting points

Plan 1 is adopting the scheme of 10-lifting-spots to lifting the steel truss structures. The lifting spots arranged on the steel truss structures, which connected with T1 and T3. Figure 5 shows the scheme of Plan 1.

Plan 2 is adopting the scheme of 15-lifting-spots to lifting the steel truss structures. Based on Plan 1, Plan 2 added five lifting spots on the steel truss structures, which connected with T2. Figure 6 shows the scheme of Plan 2.

Plan 3 is adopting the scheme of 15-lifting-spots to lifting the steel truss structures. Plan 3 arranged the lifting spots on the down chord that is different from Plan 2. Figure 7 shows the scheme of Plan 3.

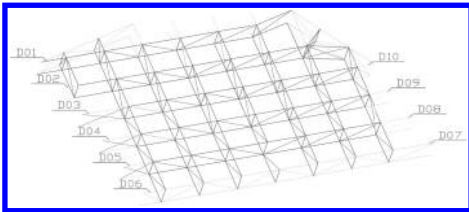


Figure 5. The lifting spots arrangement diagram of Plan1.

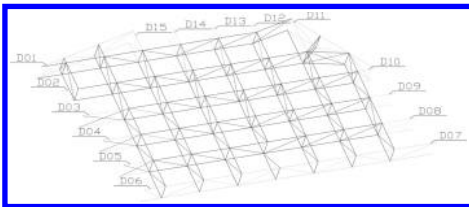


Figure 6. The lifting spots arrangement diagram of Plan 2.

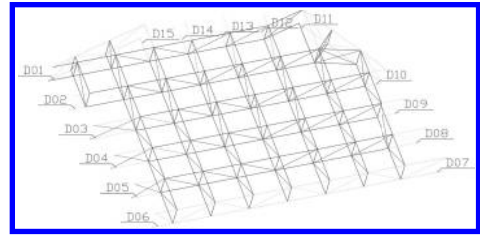


Figure 7. The lifting spots arrangement diagram of Plan 3.

### 4 CONTRAST OF THE PLANS

The structure was analyzed by software MIDAS after that construction the model of the structure in CAD. Taking the weight of the structure joints into consideration, while setting the parameter of the structure, we find that the parameter of gravity coefficient is 1.3 and the parameter of dynamic coefficient is 1.1. Loading the vertical constraint as boundary condition, it is loaded on the horizontal constraint spring bearing to prevent the movement in a horizontal way in the process of lifting. The stiffness of the spring is an infinitesimal amount.

Figures 8–10 show the lifting reaction force of each lifting spot as well as the stresses and displacements of chord member of truss of Plan 1.

Figures 11–13 show the lifting reaction force of each lifting spot as well as the stresses and displacements of chord member of truss of Plan 2.

Figures 14–16 show the lifting reaction force of each lifting spot as well as the stresses and displacements of chord member of truss of Plan 3.

#### 4.1 The comparison of plan 1 and plan 2

The comparison of Plan 1 and Plan 2 are shown in Table 1.

In view of the lifting reaction force, it is seen that in Plan 1, the gap between the lifting force is too big. The maximum lifting force is 11292.6 kN, it means that we need an elevator with an elevating power of 1129t. At present, the maximum lifting force of the commonly used hydraulic elevator is 405t. That is to say, we have to arrange three elevators with the maximum lifting force of 405t on D10 and design a special spreader for the D10. However, the minimum lifting force is 391.07 kN at D07; it is too small to consider. The lifting force of each spot is relatively uniform and meets the requirement of the hydraulic elevator.

In view of the displacements of the member bars, it is seen that in Plan 1, the maximum displacement is 120.25 mm in the member bars connected with T2. Although it is lower than the limit deformation ( $L/200 = 300$  mm), it creates an inconvenience with

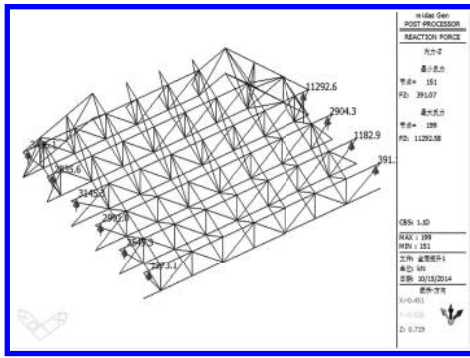


Figure 8. Lifting reaction force of Plan 1.

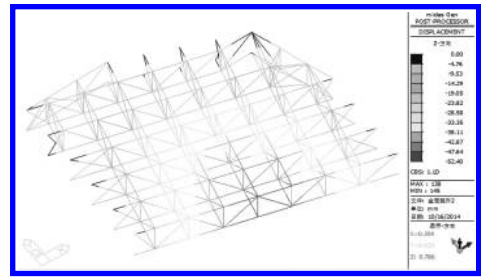


Figure 12. The displacements of the member bars of Plan 2.

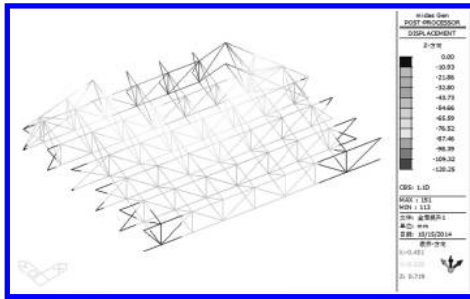


Figure 9. The displacements of the member bars of Plan 1.

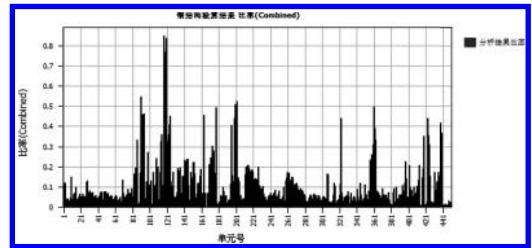


Figure 13. The member bars stress ratio of Plan 2.

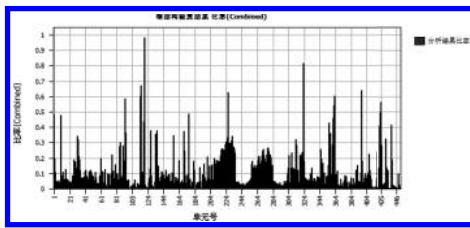


Figure 10. The member bars stress ratio of Plan 1.

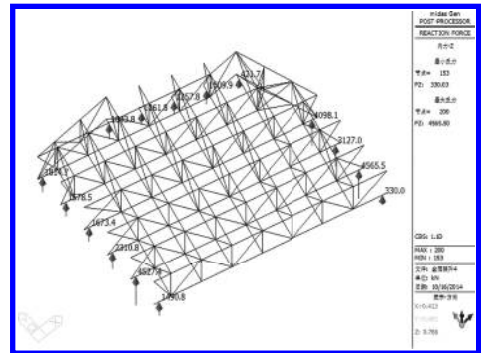


Figure 14. Lifting reaction force of Plan 3.

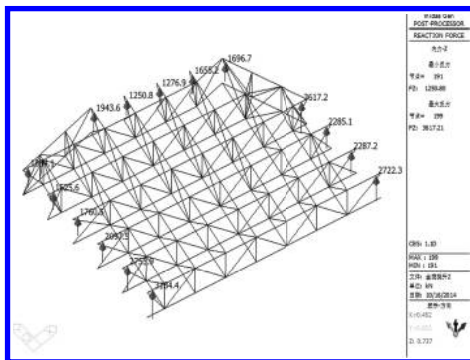


Figure 11. Lifting reaction force of Plan 2.

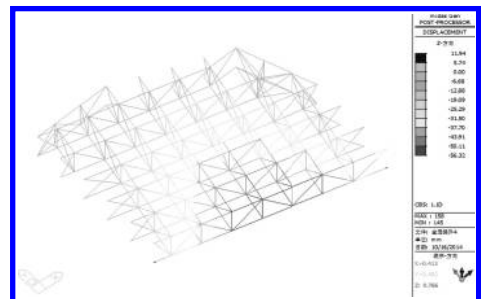


Figure 15. The displacements of the member bars of Plan 3.

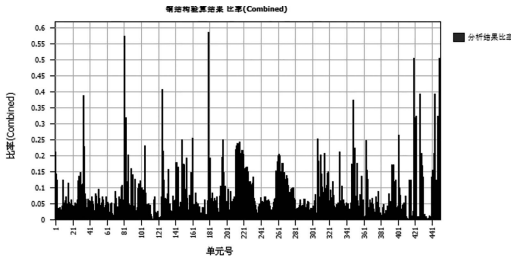


Figure 16. The member bars stress ratio of Plan 3.

Table 1. The comparisons of Plan 1 and Plan 2.

	Maximum lifting force/kN	Minimum lifting force/kN	Maximum displacements /mm	Maximum stress ratio
Plan 1	11292.58	391.07	120.25	0.98
Plan 2	3617.21	1250.80	52.40	0.85

the truss structures closure. In Plan 2 the maximum deformation is in the largest span and meets the requirements of deformation.

In view of the member bars stress ratio it is seen that in Plan 1, the maximum stress ratio is 0.98 (bigger than 0.9), the stress approaches near the yield strength. In Plan 2 the maximum stress ratio is 0.85 (less than 0.9), which has enough safe margin.

Although the number of lifting spots of Plan 1 is less than Plan 2, taking all factors as a whole, Plan 2 is better than Plan 1.

#### 4.2 The Comparison of Plan 2 and Plan 3

The comparison of Plan 2 and Plan 3 are shown in Table 2.

In view of the lifting reaction force, it is seen that the lifting force of D07 and D11 is smaller than the other lifting spots in the part 3. The two spots can be cancelled.

In view of the member bars position it is seen that the maximum displacement in Plan 3 is larger than that in Plan 2, but they meet the requirements of deformation.

In view of the member bars stress ratio, it is seen that in Plan 3, the maximum stress ratio is 0.58 (more or less than 0.9), which has enough safe margin.

Because of the lifting spots arranged on the down chord, each of the lifting spot needs two elevators, the number of the elevators used in Plan 3 is twice as much as it is in Plan 2. It is hard to control the cost and can not be conducive to improve

Table 2. The comparisons of Plan 2 and Plan 3.

	Maximum lifting force/kN	Minimum lifting force/kN	Maximum displacements /mm	Maximum stress ratio
Plan 2	3617.21	1250.80	52.40	0.85
Plan 3	4565.50	330.03	56.32	0.58

synchronization. Taking all factors as a whole, Plan 2 is better than Plan 3.

Through comparison and analysis, take the safety, maneuverability and economy into consideration, Plan 2 is the best scheme.

## 5 CONCLUSION

The way to arrange the integral lifting for irregular steel structure was more complicated than that for regular steel structure.

By analyzing and summarizing the location of the lifting spots, we find out the rational collocation principles of the integral lifting for irregular steel structure. The conclusions offer references for similar engineering.

- Try to balance the Lifting Force of each lifting-spot
- Make the processing and installation technology of the temporary measures on the lifting spots as easy as possible.
- Try to minimize the influence on the original structure.

## REFERENCES

- [1] The People's Republic of China national standard GB 50017-50017 steel structure design specification [S]. Beijing: China building industry press, 2003.
- [2] Shanghai engineering construction standard DG/T J08-2056-2009 heavy structure (equipment) integral lifting technology procedures [S]. Beijing: China building industry press, 2009.
- [3] Wang, Changxing. *Midas/Gen application instance tutorial and troubleshooting* [M]. Beijing: China building industry press, 2010.
- [4] Bao, Jiancong & Qiao, Jufu & LU, Kekuan. *Study and Use of Integral Lifting Spots of Steel Structure for A Large Roof* [J]. Steel Construction, 2005, 20(5): 72–74.
- [5] Bao, Guangjian & Wang, Hong & Sun, Dajun & XU, Zhongliang. *Multi-suspension-centers Asymmetric Integral Lifting Technology for Large Area Steel Roof* [J]. Construction Technology, 2004, 33(5):10–12.
- [6] Gao, Leilei. *The Key Construction of Integral Lifting for Steel Corridor at High Altitude* [J]. Construction Technology, 2014, 43(2):38–41.

# Free vibration analysis on paraboloidal shells of revolution using the Wittrick-Williams algorithm with the consideration of shear deformation and rotary inertia

X.D. Chen

School of Naval Architecture and Civil Engineering, Jiangsu University of Science and Technology, Zhangjiagang, Jiangsu, P.R. China

**ABSTRACT:** This paper analyzed the free vibration of paraboloidal shells of revolution with the consideration of shear deformation and rotary inertia using the Wittrick-Williams algorithm. The vibration of paraboloidal shells of revolution is decomposed into a series of one-dimensional vibration problems. Dynamic stiffnesses of these one-dimensional problems are computed using the ODE solver COLSYS and the Wittrick-Williams algorithm is applied. Numerical examples demonstrated that the present method is applicable and accurate for free vibration analysis of paraboloidal shells of revolution.

**Keywords:** free vibration; paraboloidal shells; Wittrick-Williams algorithm; Hamiltonian governing equations

## 1 INTRODUCTION

Parabolic shells of revolution are widely used in many engineering branches, e.g. civil, mechanical, aeronautical and marine engineering. Investigation on the free vibration of paraboloidal shells of revolution can provide basic parameters for further dynamic analysis, and is of great theoretical and practical significance.

Many researchers investigated the free vibration of paraboloidal shells of revolution<sup>[1][2]</sup>. The above research is based on the traditional thin shell theory. Recently, Kang and Leissa<sup>[3]</sup> conducted three-dimensional analysis on the free vibration of complete paraboloidal shells; Tornabene and Viola<sup>[4]</sup> proposed free vibration analysis of parabolic shells using generalised differential quadrature method based on the first-order shear deformation theory; Al-Khatib and Buchanan<sup>[5]</sup> analyzed the free vibration of a paraboloidal shell of revolution using the three-dimensional finite element method. For moderately thick paraboloidal shells, conventional 2D shell theory with the consideration of transverse shear deformation and rotary inertia is necessary.

In this paper, dynamic stiffness method is employed to obtain the natural frequencies of paraboloidal shells. Governing equations are degraded into a series of one-dimensional vibration problems with respect to different circumferential wave number  $n$ . Ordinary Differential Equations (ODE) solver COLSYS<sup>[6]</sup> is used to solve these

one-dimensional problems and obtain the dynamic stiffnesses. Together with the Wittrick-Williams algorithm<sup>[7]</sup> (refer to W-W algorithm in the context) and bisection, undamped natural frequencies of paraboloidal shells of revolution are found.

## 2 BASIC EQUATIONS

The paraboloidal shell and coordinate system are shown in Figure 1. In  $Oxz$  plane, the meridian equation is

$$z = c \left[ 1 - \left( \frac{x}{a} \right)^2 \right] \quad (1)$$

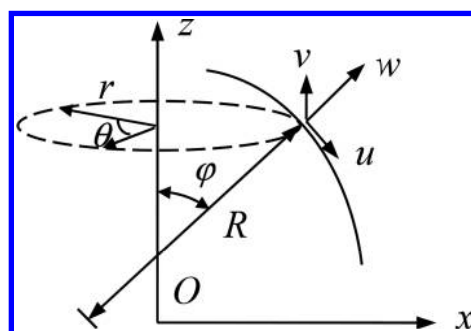


Figure 1. The diagram of a paraboloidal shell of revolution meridian and its coordinates.

Note that  $u$ ,  $v$  and  $w$  are the displacements in the middle surface of the paraboloidal shell along the meridian, circumferential and normal directions.  $\varphi$  is the angle between the radius of curvature and the positive direction of  $z$  axis;  $\theta$  is the circumferential direction. Young's modulus of the paraboloidal shell is  $E$ , Poisson's ratio is  $\nu$ , density is  $\rho$  and thickness is  $h$ .

According to the moderately thick shell theory, the strain-displacement relationship of a paraboloidal shell of revolution is

$$\{\boldsymbol{\varepsilon}\} = [\mathbf{L}]\{\boldsymbol{\Delta}\} \quad (2)$$

where the strain  $\{\boldsymbol{\varepsilon}\} = \{\varepsilon_{\varphi\varphi}, \varepsilon_{\theta\theta}, \varepsilon_{\varphi\theta}, \chi_{\varphi}, \chi_{\theta}, \chi_{\varphi\theta}, \gamma_{\varphi}, \gamma_{\theta}\}^T$ , and  $\{\boldsymbol{\Delta}\} = \{u, v, w, \psi_{\varphi}, \psi_{\theta}\}^T$ .  $\psi_{\varphi}$  and  $\psi_{\theta}$  are angles along the  $\varphi$  and  $\theta$  directions, respectively.

Similarly, the force-strain relationship of a paraboloidal shell of revolution is

$$\{\mathbf{N}\} = [\mathbf{D}]\{\boldsymbol{\varepsilon}\} \quad (3)$$

where  $\{\mathbf{N}\} = \{N_{\varphi}, N_{\theta}, N_{\varphi\theta}, M_{\varphi}, M_{\theta}, M_{\varphi\theta}, Q_{\varphi}, Q_{\theta}\}^T$ , and matrix  $[\mathbf{D}]$  can be found in Ref. [8].

Denote  $dA$  the area of an infinitesimal portion in a shell of revolution,  $dA = rRd\alpha d\beta$ . The total strain energy  $U$  for free vibration of the shell of revolution can be integrated along the whole middle surface  $S$

$$U = \iint_S \frac{1}{2} \{\boldsymbol{\varepsilon}\}^T [\mathbf{D}]\{\boldsymbol{\varepsilon}\} dA \quad (4)$$

The total free vibration kinetic energy is obtained as

$$T = \frac{\rho}{2} \iint_S \left\{ h \left[ \left( \frac{\partial u}{\partial t} \right)^2 + \left( \frac{\partial v}{\partial t} \right)^2 + \left( \frac{\partial w}{\partial t} \right)^2 \right] + \frac{h^3}{12} \left[ \left( \frac{\partial \psi_{\varphi}}{\partial t} \right)^2 + \left( \frac{\partial \psi_{\theta}}{\partial t} \right)^2 \right] \right\} dA \quad (5)$$

The dynamic displacement functions are

$$\{\boldsymbol{\Delta}\} = \begin{cases} u = u_n(\varphi) \cos n\theta \sin \omega t \\ v = v_n(\varphi) \sin n\theta \sin \omega t \\ w = w_n(\varphi) \cos n\theta \sin \omega t \\ \psi_{\varphi} = \psi_{\varphi n}(\varphi) \cos n\theta \sin \omega t \\ \psi_{\theta} = \psi_{\theta n}(\varphi) \sin n\theta \sin \omega t \end{cases} \quad (6)$$

where  $n$  is the circumferential wave number and  $\omega$  is a circular frequency.

According to the Hamilton principle,

$$\delta \int_{t_1}^{t_2} (U - T) dt = 0 \quad (7)$$

Since time interval  $(t_1, t_2)$  is arbitrary, the symplectic components (generalised displacements and forces) can be obtained from equation (7) after displacement substitution and integration manipulation. Also, the vibration governing equations of paraboloidal shells of revolution can be expressed in the Hamilton form

$$[\mathbf{J}]\{\mathbf{z}'\} = [\mathbf{S}]\{\mathbf{z}\} \quad (8)$$

where  $()'$  denotes the derivative with respect to  $\varphi$ .

$$[\mathbf{J}] = \begin{bmatrix} \mathbf{0} & -\mathbf{I} \\ \mathbf{I} & \mathbf{0} \end{bmatrix} \quad (9)$$

$\mathbf{I}$  is a fifth-order identity matrix;  $[\mathbf{S}]$  is a symmetric tenth-order matrix; and  $\{\mathbf{z}\}$  is the combination of both internal forces and displacements

$$\{\mathbf{z}\} = \{q_1, q_2, q_3, q_4, q_5, p_1, p_2, p_3, p_4, p_5\}^T \quad (10)$$

Expression of  $[\mathbf{S}]$  and  $\{\mathbf{z}\}$  can be found in Ref. [9].

According to the definition of stiffnesses, mathematically apply the boundary conditions in Eq. (11) to equation (8) in turns,

$$\{\mathbf{d}\}^e = \{\mathbf{e}_j\}, \quad j = 1, \dots, 10 \quad (11)$$

where  $\{\mathbf{e}_j\}$  is a unit vector with the  $j$ -th element equals to one; and the element-end displacement vector is

$$\{\mathbf{d}\}^e = \{q_1(\varphi_a), q_2(\varphi_a), q_3(\varphi_a), q_4(\varphi_a), q_5(\varphi_a), q_1(\varphi_b), q_2(\varphi_b), q_3(\varphi_b), q_4(\varphi_b), q_5(\varphi_b)\}^T \quad (12)$$

Note that the element-end force vector is

$$\{\mathbf{F}\}^e = \{-p_1(\varphi_a), -p_2(\varphi_a), -p_3(\varphi_a), -p_4(\varphi_a), -p_5(\varphi_a), p_1(\varphi_b), p_2(\varphi_b), p_3(\varphi_b), p_4(\varphi_b), p_5(\varphi_b)\}^T \quad (13)$$

The shell segment element dynamic stiffness matrix  $[\mathbf{k}]^e$  is formulated in Eq. (14).

$$[\mathbf{k}]^e = \{ \{\mathbf{F}\}_{j=1}^e, \{\mathbf{F}\}_{j=2}^e, \{\mathbf{F}\}_{j=3}^e, \{\mathbf{F}\}_{j=4}^e, \{\mathbf{F}\}_{j=5}^e, \{\mathbf{F}\}_{j=6}^e, \{\mathbf{F}\}_{j=7}^e, \{\mathbf{F}\}_{j=8}^e, \{\mathbf{F}\}_{j=9}^e, \{\mathbf{F}\}_{j=10}^e \} \quad (14)$$

Elements of force vector  $\{\mathbf{F}\}^e$  are solved numerically using COLSYS. The global dynamic stiffness matrix  $\mathbf{K}$  of the shell of revolution is assembled in a straightforward way according to regular element location vectors.

### 3 WITTRICK-WILLIAMS ALGORITHM

The W-W algorithm does not solve eigenvalues directly but count the number of frequencies below a given value  $\omega^*$  of interest. The expression of the W-W algorithm is

$$J = J_0 + J_K \quad (15)$$

where  $J$  is the number of frequencies exceeded by a specific trial frequency  $\omega^*$ ;  $J_K = s\{\mathbf{K}(\omega^*)\}$  is the sign count of the global dynamic stiffness matrix  $\mathbf{K}$  and equals to the number of negative elements on the diagonal of an upper triangular matrix obtained from  $\mathbf{K}$  by applying standard Gaussian elimination without row exchange;  $J_0$  is the number of frequencies still exceeded by  $\omega^*$  when segment elements are clamped at both ends and can be guaranteed to be zero should there are enough shell segments along the meridian.

If there are not enough shell segments along the meridian,  $J_0$  can be accumulated from  $J_0^e$  of each shell segment element over the whole meridian

$$J_0 = \sum J_0^e \quad (16)$$

Further discussions on the calculation of  $J_0$  can be found in Ref [9].

### 4 NUMERICAL EXAMPLES

#### 4.1 Example 1: free vibration of a free-fixed paraboloidal dome

Tornabene and Viola<sup>[4]</sup> calculated the lowest five natural frequencies of a free-clamped parabolic dome using the generalized differential quadrature method with the data given in Table 1. The geometric and physical parameters of the paraboloidal dome are: height  $H = 2$  m, thickness  $h = 0.1$  m,  $a = 4$  m,  $c = 2.133$  m,  $\rho = 7800$  kg/m<sup>3</sup>, Young's modulus  $E = 2.1 \times 10^{11}$  N/m<sup>2</sup>, and Poisson's ratio  $\nu = 0.3$ . Results obtained from the present dynamic stiffness method are also tabulated in Table 1 for comparison with corresponding  $(n, m)$  combinations.

Table 1. The lowest five natural frequencies of a free-clamped dome (Hz).

Order	$(n, m)$	Present	Ref. [4]
1	(2, 1)	91.68	91.24
2	(3, 1)	132.33	131.29
3	(4, 1)	154.79	154.91
4	(1, 1)	160.63	157.99
5	(5, 1)	168.19	169.46

Table 2. Frequencies  $\Omega = \omega c \sqrt{\rho/G}$  for a paraboloidal shell cap with  $a = c$ .

$n$	Present	Ref. [5]
0	1.798	1.774
1	1.162	1.159
2	1.180	1.166
3	1.157	1.133
4	1.283	1.240

Table 3. Frequencies  $\Omega = \omega c \sqrt{\rho/G}$  for a paraboloidal shell cap with  $a = 2c$ .

$n$	$m$	Present	Ref. [5]
0	1	0.6998	0.6955
	2	0.8004	0.7896
	3	0.9263	0.9177
1	1	0.6058	0.6043
	2	0.7325	0.7252
	3	0.8793	0.8612

The results obtained from the present method agree very well with data from Ref. [4], showing good convergence and accuracy of the proposed method.

#### 4.2 Example 2: free vibration of a fixed paraboloidal cap

Al-Khatib and Buchanan<sup>[5]</sup> analysed fixed paraboloidal shell caps with  $\nu = 0.3$ ,  $h = 1/20c$ . The apex of paraboloidal shells is closed. To avoid singularity at the apex, a commonly-applied small circular hole<sup>[10]</sup> is employed at the apex so that singularity can be avoided without reducing accuracy. Table 2 listed the lowest natural frequencies when  $a = c$  with  $n$  from 0 to 4; Table 3 gave the first three frequencies when  $a = 2c$  with  $n = 0$  and 1, respectively. Both results from the present method and the Ref. [5] are given for comparison.

The data from the present method reach good agreement with that from Ref. [5], demonstrating that the proposed dynamic stiffness method is capable of analysing the free vibration of apex-completed paraboloidal shells of revolution.

### 5 CONCLUSIONS

The formulation established in this paper is applicable to the free vibration analysis of a variety paraboloidal shell of revolution. Results from the present method are well validated with that from existing literatures. The proposed method can be

straight-forwardly extended to other shape shells of revolution, e.g. spherical, elliptical, hyperbolic shells and etc.

#### ACKNOWLEDGEMENT

The author gratefully appreciate the financial support from the Jiangsu University of Science and Technology (JUST) for this research.

#### REFERENCES

- [1] Lin Y.K., Lee F.A. Vibrations of thin paraboloidal shells of revolution. *Journal of Applied Mechanics*, 1960, 27(4): 743–746.
- [2] Hoppmann W.H., Cohen M.I., Kunukkasseril V.X. Elastic vibrations of paraboloidal shells of revolution. *Journal of Acoustical Society of America*, 1964, 36(2): 349–353.
- [3] Kang J.-H., Leissa A.W., Free vibration analysis of complete paraboloidal shells of revolution with variable thickness and solid paraboloids from a three-dimensional theory. *Computers and Structures*, 2005, 83: 2594–2608.
- [4] Tornabene F., Viola E. 2-D solution for free vibrations of parabolic shells using generalized differential quadrature method. *European Journal of Mechanics A/Solids*, 2008, 27: 1001–1025.
- [5] Al-Khatib O.J., Buchanan G.R., Free vibration of a paraboloidal shell of revolution including shear deformation and rotary inertia. *Thin-walled structures*, 2010, 48: 223–232.
- [6] Ascher U., Christiansen J., Russell R.D., Collocation software for boundary value ODEs. *ACM Transactions on Mathematical Software*, 1981, 7(2): 209–222.
- [7] ittrick W.H., Williams F.W., A general algorithm for computing natural frequencies of elastic structures. *Quarterly Journal of Mechanics and Applied Mathematics*, 1971, 24(3): 263–284.
- [8] Leissa A.W., *Vibration of shells (SP-288)*. Washington D.C., USA: Scientific and Technical Information Office, National Aeronautics and Space Administration, 1973.
- [9] Chen X. Research on dynamic stiffness method for free vibration of shells of revolution. Beijing: THU Master Thesis, 2009.
- [10] de Souza V.C.M., Croll J.G.A. An energy analysis of the free vibrations of isotropic spherical shells. *Journal of Sound and Vibration*, 1980, 73: 379–404.

# R-Function Theory method for free vibration of slip clamped trapezoidal shallow spherical shell

Shanqing Li & Hong Yuan

MOE Key Laboratory of Disaster Forecast and Control in Engineering, Institute of Applied Mechanics, Jinan University, Guangzhou, China

**ABSTRACT:** In this paper, the R-Function Theory (RFT) is applied to solve the free vibration of slip clamped trapezoidal shallow spherical shell. Firstly the fundamental solution of the biharmonic operator, the boundary equation and the R-function are used to construct the quasi-Green's function. Then the model governing differential equation of the problem is reduced to the Fredholm integral equation of the second kind by Green's formula. The singularity of the kernel of the integral equation is overcome by choosing a suitable form of the normalized boundary equation by the R-function. A numerical example shows that this method is an effective numerical method.

**Keywords:** R-function; Green's function; integral equation; free vibration; shallow spherical shell

## 1 INTRODUCTION

In the paper, the R-function theory proposed by Rvachev [1] are utilized. The free vibration of slip clamped trapezoidal shallow spherical shell is studied. A quasi-Green function is established by using the fundamental solution and the boundary equation of the problem. This function satisfies the homogeneous boundary condition of the problem, but it does not satisfy the fundamental differential equation. The key point of establishing the quasi-Green function consists in describing the boundary of the problem by normalized equation  $\omega=0$  and the domain of the problem by inequality  $\omega>0$ . There are multiple choices for the normalized boundary equation. Based on a suitably chosen form of the normalized boundary equation, a new normalized boundary equation can be established such that the singularity of the kernel of the integral equation is overcome. For any complicated area, a normalized boundary equation can always be found according to the R-function theory. Thus, the problem can always be reduced to the Fredholm integral equation of the second kind without singularity. Using the present method, Li and Yuan solved successfully the free vibration of clamped thin plates [2], the simply-supported thin plate [3,4] and shallow spherical shells [5,6]. For the first time, the proposed R-function theory method is applied to study the free vibration problem of slip clamped trapezoidal shallow spherical shell. The numerical example demonstrates the efficiency and the feasibility of the R-function theory method.

## 2 FUNDAMENTAL EQUATIONS

The governing differential equations of the free problem of slip clamped trapezoidal shallow spherical shell [7] can be expressed as follow

$$\nabla^4 \varphi(\mathbf{x}, t) - \frac{Eh}{R} \nabla^2 w(\mathbf{x}, t) = 0, \quad \mathbf{x} \in \Omega, \quad (1)$$

and

$$D \nabla^4 w(\mathbf{x}, t) + \frac{1}{R} \nabla^2 \varphi(\mathbf{x}, t) + \bar{m} \frac{\partial^2 w(\mathbf{x}, t)}{\partial t^2} = 0, \quad \mathbf{x} \in \Omega, \quad (2)$$

where  $\nabla^4 = (\partial^2/\partial x_1^2 + \partial^2/\partial x_2^2)^2$  is the biharmonic operator,  $\varphi$  is the stress function,  $w$  is the radial deflection of the shell,  $R$  is the radius of curvature of the shell,  $\mathbf{x} = (x_1, x_2)$ ,  $\Omega$  is the domain of the trapezoid of shallow spherical shells in Cartesian coordinates,  $t$  is time; and  $D = Eh^3/(12(1-\nu^2))$  is the flexural rigidity of the shell, in which  $h$  is the thickness of the shell, and  $E$  and  $\nu$  are Young's modulus and Poisson's ratio, respectively.

The slip clamped boundary conditions can be written as

$$w|_{\Gamma} = \frac{\partial w}{\partial n}|_{\Gamma} = \varphi|_{\Gamma} = \nabla^2 \varphi|_{\Gamma} = 0, \quad (3)$$

where  $\nabla^2 = \partial^2/\partial x_1^2 + \partial^2/\partial x_2^2$  is the Laplace operator, and  $\Gamma = \partial\Omega$  is the boundary of the domain  $\Omega$ .



Making use of Eqs. (1) and (3), we can easily obtain

$$\nabla^2 \varphi = wEh/R. \quad (4)$$

Substituting Eq. (4) into Eq. (2) yields

$$D\nabla^4 w + \frac{Eh}{R^2} w + \bar{m} \frac{\partial^2 w}{\partial t^2} = 0. \quad (5)$$

The model governing differential equation can be obtained as follow

$$D\nabla^4 W(\mathbf{x}) + \frac{Eh}{R^2} W(\mathbf{x}) - \bar{\omega}^2 \bar{m} W(\mathbf{x}) = 0, \quad \mathbf{x} \in \Omega \quad (7)$$

$$W = 0, \quad \frac{\partial W}{\partial n} = 0, \quad \mathbf{x} \in \Gamma. \quad (8)$$

where  $W$  is the model function.

### 3 INTEGRAL EQUATIONS

Let  $\omega = 0$  be the normalized boundary equation of the first-order on the boundary  $\Gamma$ , i.e.[1]

$$\omega(\mathbf{x}) = 0, \quad |\nabla \omega| = 1, \quad \mathbf{x} \in \Gamma \text{ and } \omega(\mathbf{x}) > 0, \quad \mathbf{x} \in \Omega. \quad (9)$$

The quasi-Green function can be established as follows:

$$G(\mathbf{x}, \xi) = -r^2 \ln r - e(\mathbf{x}, \xi), \quad (10)$$

$$\text{and } e(\mathbf{x}, \xi) = -r^2 \ln R_1 + 2\omega(\mathbf{x})\omega(\xi), \quad (11)$$

where  $r = \|\xi - \mathbf{x}\| = \sqrt{(\xi_1 - x_1)^2 + (\xi_2 - x_2)^2}$  and  $R_1 =$

$$\sqrt{r^2 + 4\omega(\xi)\omega(\mathbf{x})}, \quad (12)$$

in which  $\mathbf{x} = (x_1, x_2)$  and  $\xi = (\xi_1, \xi_2)$ . Obviously, the quasi-Green function  $G(\mathbf{x}, \xi)$  satisfies the following condition

$$G(\mathbf{x}, \xi)|_{\xi \in \partial\Omega} = 0 \quad \text{and} \quad \left. \frac{\partial G(\mathbf{x}, \xi)}{\partial n} \right|_{\xi \in \partial\Omega} = 0. \quad (13)$$

In order to reduce the boundary value problems Eq. (7) and Eq. (8) into an integral equation, the following Green's formula of sets of function  $C^4(\Omega)$ , i.e.,  $U, V \in C^4(\Omega \cup \Gamma)$ , is applied

$$\begin{aligned} & \int_{\Omega} (V\nabla^4 U - U\nabla^4 V) d\xi \Omega \\ &= \int_{\partial\Omega} \left[ V \frac{\partial}{\partial n} (\nabla^2 U) - \frac{\partial V}{\partial n} \nabla^2 U - U \frac{\partial}{\partial n} (\nabla^2 V) \right. \\ & \quad \left. + \frac{\partial U}{\partial n} \nabla^2 V \right] d\xi \Gamma. \end{aligned} \quad (14)$$

Replacing  $U$  and  $V$  in Eq. (10) by  $w$  and Green quasifunction  $G$ , noticing that  $(1/8\pi)r^2 \ln r$  is the fundamental solution [6] of the biharmonic operator, and using Eqs. (7), (8) and (13), we can easily obtain

$$W(\mathbf{x}) = \int_{\Omega} W(\xi) K(\mathbf{x}, \xi) d\xi \Omega, \quad (15)$$

where

$$\begin{aligned} K(\mathbf{x}, \xi) = & -\frac{1}{8\pi} \left( \frac{\partial^4}{\partial \xi_1^4} + 2 \frac{\partial^4}{\partial \xi_1^2 \partial \xi_2^2} + \frac{\partial^4}{\partial \xi_2^4} \right) e(\mathbf{x}, \xi) \\ & + \frac{1}{8\pi} \left( \frac{Eh}{DR^2} - \frac{\bar{\omega}^2 \bar{m}}{D} \right) G(\mathbf{x}, \xi). \end{aligned} \quad (16)$$

Substituting Eq. (11) into Eq. (16), we can obtain the expression of  $K(\mathbf{x}, \xi)$  in detail.

$K(\mathbf{x}, \xi)$  in Eq. (16) appears discontinuous only if  $R_1 = 0$ , i.e., both  $\mathbf{x} = \xi$  and  $\omega = 0$  come into existence. Actually, when  $\mathbf{x} = \xi$ , Eq. (16) can be reduced to

$$\begin{aligned} K(\mathbf{x}, \xi)|_{\mathbf{x}=\xi} = & \frac{1 + \omega \nabla^2 \omega - (\nabla \omega)^2}{\pi \omega^2} - \frac{1}{4\pi} \omega \nabla^4 \omega \\ & - \frac{1}{4\pi} \frac{k - \bar{\omega}^2 \bar{m}}{D} \omega^2. \end{aligned} \quad (17)$$

To make the kernel of the integral equation  $K(\mathbf{x}, \xi) \in C(\Omega \cup \partial\Omega)$ , A normalized boundary equation will be constructed to ensure the continuity of  $K(\mathbf{x}, \xi)$  in the following. It can be easily testified that

$$\omega = \left[ 3\omega_0 + \omega_0^2 \nabla^2 \omega_0 - \omega_0 (\nabla \omega_0)^2 \right] / 2, \quad (18)$$

where  $\omega_0 = 0$  is the normalized equation of the boundary  $\Gamma$ , i.e.,  $\omega_0$  satisfies Eq. (9). Obviously, equation  $\omega$  is also a normalized boundary equation of the first-order.

Based on a suitably chosen normalized boundary equation  $\omega_0 = 0$ , a new normalized boundary equation  $\omega = 0$  can be constructed by using Eq. (18), which ensure the continuity of the integral kernel  $K(\mathbf{x}, \xi)$  everywhere in the integral domain.

In order to obtain numerical results of the boundary problem, the integral equation (15) can be discretized into the homogeneous linear algebraic equation. The determinant of the matrix of coefficients of homogeneous linear algebraic equations Eq. (15) must be equal to zero. So, the natural frequency  $\bar{\omega}$  or  $f = \bar{\omega}/(2\pi)$  can be obtained by solving the equation.

#### 4 NUMERICAL EXAMPLE

A slip clamped trapezoidal shallow spherical shell is shown in Figure 1, and we set  $a = e = 1.2$ ,  $b = d = 1.0$ , and  $c = 1.1$ . The following reference parameters are used: the radius of curvature of the shell  $R = 3$ , the thickness of the shell  $h = 0.1$ , Poisson's ratio  $\nu = 0.3$ , Young's modulus  $E = 3 \times 10^9$ , and mass density per unit area  $\bar{m} = 780$ . According to the theory of R-function [1], a normalized boundary equation of the first rank  $\omega_0 = 0$  can be constructed from the following equation:

$$\omega_0 = \omega_1 + \omega_2 + \omega_3 - \sqrt{\omega_1^2 + \omega_2^2} - \sqrt{\omega_1^2 + \omega_3^2} - \sqrt{\omega_2^2 + \omega_3^2} + \sqrt{\omega_1^2 + \omega_2^2 + \omega_3^2},$$

where

$$\omega_2 = \left( \frac{ac}{a-b} + \frac{c}{a-b} x_1 - x_2 \right) / \sqrt{1 + \left( \frac{c}{a-b} \right)^2} \geq 0,$$

$$\omega_3 = \left( \frac{ac}{a-b} - \frac{c}{a-b} x_1 - x_2 \right) / \sqrt{1 + \left( \frac{c}{a-b} \right)^2} \geq 0,$$

and  $\omega_1 = (c - x_2)x_2/c$ .  $\omega_1 = 0$ ,  $\omega_2 = 0$  and  $\omega_3 = 0$  denote various parts of the boundary of trapezoidal shallow spherical shell, respectively. Numerical results by the R-Function Theory (RFT) and ANSYS Finite-Element Method (FEM) are shown in Table 1 for comparison. Numerical results by

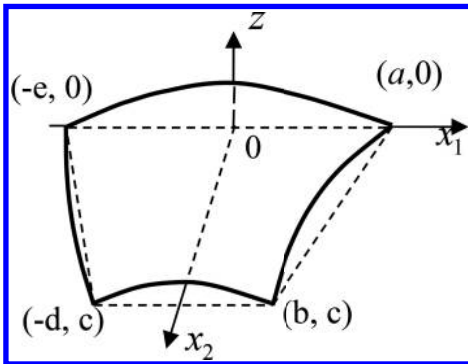


Figure 1. Slip clamped shallow spherical shell.

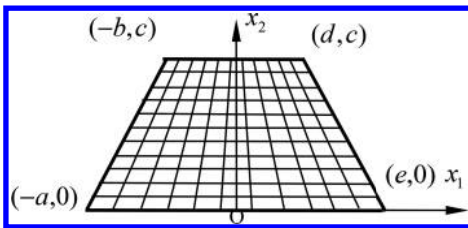


Figure 2. Division of trapezoidal integral domain.

Table 1. Natural frequency  $f$  of slip clamped trapezoidal shallow spherical shell.

R	The mode rank					
	1		2		3	
	RFT	FEM	RFT	FEM	RFT	FEM
3	69.242	69.086	85.020	85.487	114.95	115.92
5	64.046	63.880	80.844	81.339	111.89	112.89
7	62.537	62.370	79.655	80.158	111.04	112.05

$11 \times 11$  trapezoidal integral domain of the R-Function Theory (RFT) show fine agreement with the FEM solution by  $200 \times 200$ . It shows the advantages and efficiency of the present method.

#### 5 CONCLUSIONS

In the present paper, the R-function theory is applied to study the free vibration of slip clamped trapezoidal shallow spherical shell. Compared with ANSYS finite element solution, it shows good agreement. R-function theory can also be used to effectively solve various boundary value problems in engineering by constructing a trial function that satisfies the boundary conditions and by combining with the method of weighted residuals such as the variational method and the spline-approximation [7–8].

#### ACKNOWLEDGEMENTS

The authors gratefully acknowledge the Natural Science Foundation of China (No. 11402099) and the Guangdong Province Natural Science Foundation of China (No. S2013040015146).

#### REFERENCES

- [1] V.L. Rvachev: Theory of R-function and Some of its Application (Nauk Dumka Press, Ukraine 1982) (In Russian).
- [2] S.Q. Li and H. Yuan: Acta Mechanica Solida Sinica, Vol. 25 (2012), p. 37.
- [3] S.Q. Li and H. Yuan: Applied Mathematics and Mechanics (English Edition), Vol. 32 (2011), p. 276.
- [4] H. Yuan, S.Q. Li and R.H. Liu: Applied Mathematics and Mechanics (English Edition), Vol. 28 (2007), p. 847.
- [5] S.Q. Li and H. Yuan: Applied Mathematics and Mechanics (English Edition), Vol. 31 (2010), p. 635.
- [6] S.Q. Li and H. Yuan: Acta Mechanica Solida Sinica, Vol. 23 (2010), p. 370.
- [7] L. Kurpa, T. Shmatko and G. Timchenko: Composite Structures, Vol. 93 (2010), p. 225.
- [8] J. Awrejcewicz, L. Kurpa and A. Osetrov: ZAMM, Vol. 91 (2011), p. 458.

## Reducing blasting vibration technique of the hole-bottom air space charging

M.S. Zhao, Q. Kang & T.J. Tao

*Guizhou Xinlian Blasting Engineering Group Co. Ltd., Guiyang, Guizhou, China*

**ABSTRACT:** The effects of hole-bottom layer air ratio on blasting vibration intensity, blasting vibration frequency as well as vibration lasting time were studied, and the effects of hole-bottom layer air ratio on the band advantage of blasting seismic wave frequency duration and frequency band energy ratio were studied based on the energy theory. And according to the real problems of earth excavation blasting of Zunyi City, Pu District II East Road on the 5th practical still room area, the test of bottom hole air interval charge was done. The test results showed that: the hole-bottom air space charge is an effective means to reduce the blasting vibration, and the optimum air layer ratio in test conditions in fractured rock is recommended as 15%.

**Keywords:** hole-bottom air space charging; air ratio; frequency band; blasting vibration; stress

### 1 INTRODUCTION

The hole-bottom air space charging can improve blasting effect, reduce the blasting vibration effect. So it has been widely used in engineering. Many scholars have studied on the mechanism of the hole-bottom air space charging from many aspects such as the detonation wave theory, numerical simulation, dynamic photoelastic test, dynamic test, model test, and ceiling materials. Lv Shuran thinks that the hole-bottom air space charging is the best through the comparison experiment of different axial spacing. Gu Dazhi carry on many field tests in a mine of Aluminum Group and the results show that if the hole-bottom air gap length is 0.8 m, the vibration reduction rate can reach 10%~15%. Liu Weizhou study on vibration reduction test in mine of Aoshan states that the hole-bottom air space charging can reduce 5.9%~16.1% blasting vibration. Above research provides a reference for reducing vibration control by using the hole-bottom air space charging. However, there is still no study about the effect of the best air space ratio (but no air layer length and the length of the charge ratio) on blasting vibration reduction. Until now, the index of reduction blasting vibration effect is the reduction of the blasting vibration intensity about this research. However, the harmful effect of blasting vibration is the result of three elements interaction. The above studies indicate that the energy of blasting seismic wave can comprehensively effect three elements' interaction of blasting vibration.

So this project is the Zunyi city Sinpo District No. two East Road No. 5 room area earthwork excavation by using the hole-bottom air space charging to study the effect of air space ratio on blasting vibration intensity, vibration frequency, and duration of blasting vibration. Also to explore the use of energy is studied from the point of view of hole-bottom air layer in proportion of blasting seismic wave of dominant frequency continuous time, frequency band energy ratio. In order to conduct a detailed explanation on the vibration reduction effect of the hole-bottom air interval space charging. Our purpose is to provide a new method for determining the best air decking proportion.

### 2 FIELD TEST

Zunyi Road No. 2, Sinpo District No. 5 East District Housing earthwork excavation has complex environment. South, southwest, and southeast of blasting area has residential distribution. The west of blasting area has Dongcheng Avenue viaduct. The distance to the nearest edge to the residents of the blasting area is about 40 m. The nearest distance of the viaduct is about 50 m. Blasting excavation step height is 10 m, the pore size is 140 mm, hole spacing is 5 m, row spacing is 4 m, hole depth is 11.5 m, block length is 4.5 m, continuous loading, use 3 period between holes. Using 5 row detonator by hole detonation and the biggest single charge is no more than 90 kg. There are two aspects of the main problems: one is the effect of

Table 1. Hole-bottom air space charging elements.

Stemming length/m	Charge length/m	Air layer length/m	Air ratio/%
4.5	7	0	0
4.15	7	0.35	5
3.8	7	0.7	10
3.45	7	1.05	15
3.1	7	1.4	20

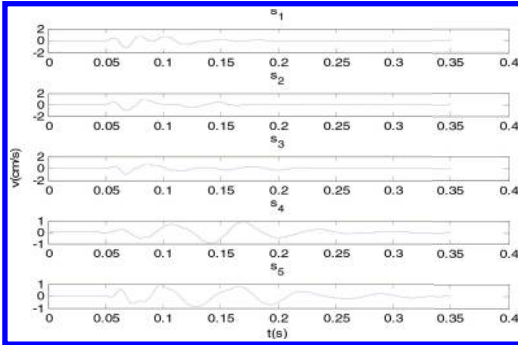


Figure 1. Measuring signal.

blasting vibration. A few houses have wall cracks; another is the size is too big around the hole that increases the operation cost and reduce the production efficiency. So in order to reduce the harm of blasting vibration and reduce the large orifice, hole-bottom air space charging has been used in this project. Under the condition that there is no change in the single dose, improve loading height, reducing orifice blocking scheme. The development of different air layer proportion according to the actual situation of the hole-bottom air interval charge of single hole blasting vibration test. The specific parameters are shown in Table 1. Select the blast center distance is 40 m. Analysis of vertical signal in different working conditions shows the following: Hole-bottom air layer ratio of 0% (i.e. continuous charge) was recorded for S1, hole-bottom air layer ratio is 5% was recorded for S2, and so on. The bottom of the hole air layer to a ratio of 20% was recorded as S5. The measured blasting seismic wave is shown in Figure 1.

### 3 DATA ANALYSIS

In order to compare the influence of air layer proportion on blasting seismic wave peak particle vibration velocity, we use the difference date between the continuous charging particle vibration velocity peak and different air layer ratio of

blasting seismic wave peak particle vibration velocity. The vibration reduction rate.

$$\delta = \frac{V_0 - V}{V_0} \times 100\% \quad (1)$$

$V_0$  is blasting vibration peak velocity of the continuous charge;  $V$  is the peak velocity of blasting seismic wave in different proportion of air layer.

Formula (1) can calculate blasting seismic wave vibration reduction rate of different air decking ratio of Figure 2. Figure 2 shows that if the air layer proportion is between 5% and 20%, the vibration reduction rate is 8.5%–22%. And with the increase of air decking ratio, vibration reduction rate increases.

In order to compare the influence of air layer, the proportion on the total energy of blasting seismic wave and the ratio index of total energy of blasting seismic wave of continuous charge to blasting seismic wave energy of different air proportion layer is analyzed. That is

$$\gamma = \frac{S_i}{S_1} (i = 1, 2, 3, 4, 5) \quad (2)$$

By use AOK time-frequency distribution of blasting vibration signals of different conditions for time-frequency analysis, we get the total energy calculation of the signal. Then calculate the blasting seismic wave energy of different proportion air layer and continuous blasting seismic wave energy ratio. The statistics is in Figure 3. Figure 3 shows: with the increase of the proportion of the air layer, the total energy of blasting seismic wave reduction. This means that with the increase in the proportion of air layer, explosive for rock breaking energy is greater and the energy for blasting earthquake is less.

Because the frequency band energy can directly reflect the vibration intensity of the corresponding frequency band vibration components, to obtain

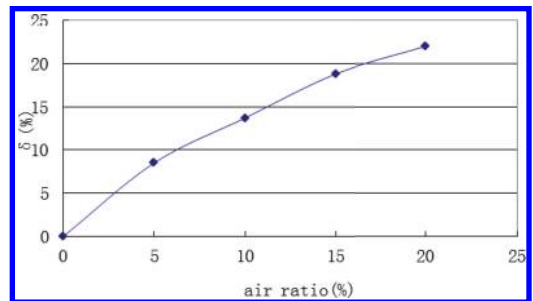


Figure 2. Effect of air ratio on reduction effect.

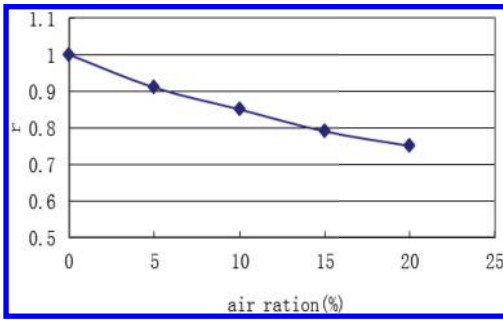


Figure 3. Effect of air ratio on total energy of blasting seismic wave.

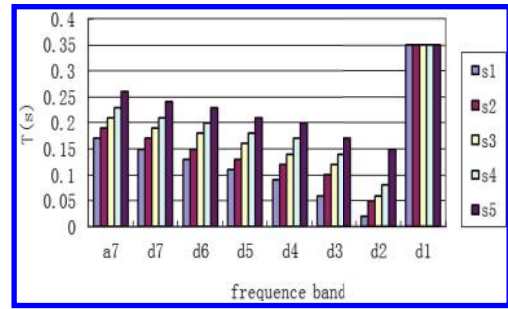


Figure 4. Effect of air ratio on the frequency band energy duration.

the response characteristic of the buildings of different frequency band vibration component, energy sustained time and structure of low cycle fatigue damage accumulation effect, and non elastic structures is related to the destruction. So the ratio of the frequency band energy duration to frequency band energy is regarded as index to study on energy characteristics of blasting vibration wave under different conditions. First, the use of wavelet analysis, to signal under different working conditions of the 7 layer decomposition and reconstruction. Then, the reconstructed signal of different frequency bands for AOK is analyzed. We get the time-frequency contour and 3D spectrum and calculate the energy band frequency band energy ratio. In order to compare the influence of air layer proportion on blasting seismic wave frequency band energy characteristic. The statistics under different frequency band energy duration is shown in Figure 4, the band energy ratio in Figure 5.

Figure 4 shows that: (1) with the increase of the air layer proportion, the duration of different frequency band energy is extending and the accumulation effect of low cycle fatigue damage of the structure is enhanced. It is clearly not conducive to the safety of the building; (2) the duration of the blasting vibration signal energy in different frequency bands is different. The duration of the test conditions from low frequency to high frequency becomes shorter. The frequency of the high frequency part of 500–1000 Hz is longer and its duration time is almost the whole course of blasting vibration. This is mainly due to noise stay in the high frequency part. And along with the whole process of blasting vibration, due to different frequency and duration, the energy ratio is also different.

Figure 5 shows that (1) the advantage of blasting vibration signal energy is mainly concentrated in the low-frequency part of the 0–125 Hz. The maximum energy exists in the main frequency band. High frequency energy accounted for a

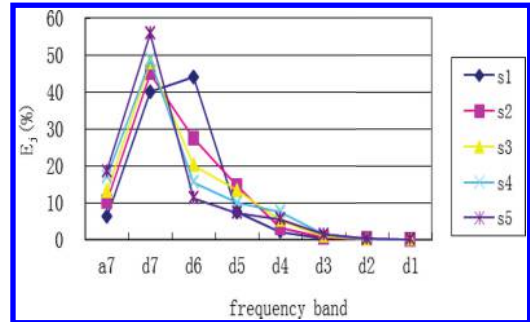


Figure 5. Effect of air ratio on the frequency band energy ratio.

smaller proportion. But there is still a distribution; (2) the air layer ratio has a bigger effect on the frequency band energy ratio of the blasting seismic wave. With the increase in the proportion of the air layer of blasting seismic wave, the structure natural frequency that is close to the D7 frequency band energy ratio gradually increases. This is a hazard for blasting vibration controlling.

From the above analysis, it shows that if the hole-bottom air space charging is used, with the increase of the proportion of the air layer, the total energy of blasting seismic wave and the peak particle vibration velocity is reduced, the duration of main frequency is extended, and main frequency is decreased. The ratio of D7 frequency band energy that is close to the natural frequency of buildings is increased. Therefore, the vibration reduction of the best air layer ratio should be selected according to total blasting seismic wave energy and considering the building response more sensitive D7 frequency band energy ratio. In order to facilitate the comparison of different air layer ratio of D7 band absolute energy, taking the blasting seismic wave D7 frequency band energy ratio of different air layer with the continuous charge ratios for total energy.

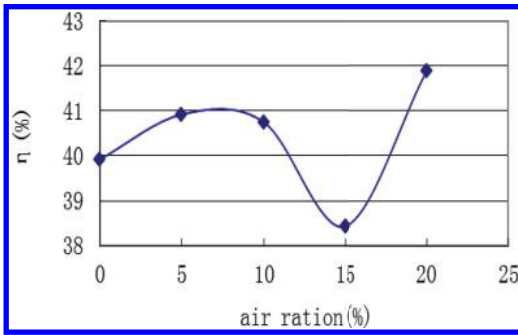


Figure 6. Effect of air ratio on the ratio of D7 band energy to the total energy of continuous charge.

$$\eta = E_2 * r \quad (3)$$

So by Formula (3), the total energy is calculated with different air layers compared to continuous loading ratio. Figure 6 shows when the air layer ratio is 15%, D7 band energy accounts for a minimum proportion of total energy of continuous charging. Therefore, this project selects the air layer ratio as the best ratio to reduce blasting vibration and the proportion of large orifice.

The on-site construction according to the proportion of the best air layer and the usual blasting method under the same conditions are compared. The wall cracks of houses surrounding blasting area were significantly reduced and the orifice blocks are effectively reduces so that it did improve the production efficiency of blasting. It can be considered that the best proportion of air layer by the method to determine the vibration reduction is comprehensive, scientific, and rational.

#### 4 CONCLUSIONS

The effects of hole-bottom layer air ratio on blasting vibration intensity, blasting vibration frequency as well as vibration lasting time were studied, and

the effects of hole-bottom layer air ratio on the band advantage of blasting seismic wave frequency duration and frequency band energy ratio were studied based on the energy theory. And according to the real problems of earth excavation blasting of Zunyi City, Pu District II East Road on the 5th practical still room area, the test of bottom hole air interval charge was done. The test results showed that: the hole-bottom air space charge is an effective means to reduce the blasting vibration, and the optimum air layer ratio in test conditions in fractured rock is recommended as 15%.

#### ACKNOWLEDGMENTS

This work was supported by the grants from the Guizhou Science and Technology Plan Project (No. SY2010365), Key Industrial Research Project supported by Science Technology Department of Guizhou Province (No. (2013) 3013), and Guizhou Province Outstanding Young Scientific Talents Training Program Funded Projects (No. (2013) 30). These grants are gratefully acknowledged.

#### REFERENCES

- Gu Dazhi, Xie Shengquan, Chen Shouru. Study on the hole-bottom space charging's improvement to blasting vibration and effects. *Mining Technology*, 2004, 4(4): 64-67.
- Liu Weizhou. Research on vibration-reduced blasting tests at washan pit, Nanshan iron mine. *Metal Mine*, 2004(6):22-23.
- Lü Shuran. Influence of different interval charge on seism effect of blasting. *Journal of Safety and Environment*, 2006, 6(S1):102-105.
- Ye Haiwang, Shi Wenjie, Wang Ermeng, et al. Research of reasonable delay intervals in Jinduicheng Open-pit Mine. *Blasting*, 2010,27(1):96-99.
- Zhao Mingsheng, Zhang Jianhua, Yi Changping. Time-frequency analysis based on single-stage addition of waveforms of blasting vibration signals. *Journal of China Coal Society*, 2010, 35(8):1279-1282.

# Application of module construction in Beijing elevated subway

X.F. Xu

School of Mechanics and Civil Engineering, China University of Mining and Technology (Beijing), Beijing, China  
School of Architectural and Survey Mapping Engineering, Beijing Polytechnic College, Beijing, China

J.F. Xu

Beijing MTR Construction Management Co. Ltd., Beijing, China

**ABSTRACT:** Based on the 04th section of Beijing Yanfang line subway modular construction, this paper summarizes the shortcomings of the traditional pier column construction and introduces the construction technology of pier column reinforced bar in details; as well as analyzes the economy, construction period, social benefits generated by the application of modular construction. The engineering practice indicates that modular construction can effectively shorten the construction period, reduce project cost and improve the quality of the project, and achieve good results in the practical application, and will be one of the developing directions of construction industrialization in the future.

**Keywords:** modular construction; pier column; viaduct subway

## 1 INTRODUCTION

Compared with the construction of traditional subway, modularization is an advanced idea of construction (Li et al. 2009, Yu et al. 2010, Li et al. 2014). The superiority of that is it could cut down construction period of elevated subway according to reducing construction work on site. Adopting the method of modularization, a large number of processes of construction were accomplished in the factory, which improve the safety of construction, ensure the quality of construction, and save the period of construction and engineering cost meantime. However, while the efficiency of construction was enhanced by using modularization, the difficulty of construction, for instance, the links like process, transport, and hoisting of the module's enlargement of pier's reinforced bars, faced bigger risks and challenges. It is being researched by scholars of engineering that how to organize, plan, and modularize the elevated subway (Xu et al. 2011).

## 2 THE ENGINEERING OVERVIEW

Beijing subway line Yanfang is the west extension of Beijing line Fangshan, the project was started by the end of 2013, and was completed by the end of 2016 according to the plan. The total length of the 04th interval of line Yanfang is 4440.802 m. All of it designed to elevated station and laid down elevated line in interval, it costs

376.8 million according to contract. Scope of construction including: Dazicaowu station~interval of north of Yancun station, north of Yancun station, behind interval of north of Yancun station, in-and-out interval and the west extension elevated interval reserved in line Fangshan, the mileages are: K12 + 137.943 ~ K15 + 090.996, including 118 m of the station, SK0 + 000 ~ SK1 + 605.749, including 118 m of the station, total length is 4440.802 m. All stations and intervals are elevated; all of the pier columns under of all intervals are 169 altogether that constructed on the basis of modularization.

The pier column under of intervals adopt the shape of magnolia that is Y type mainly, individual pier column adopt column type, pier column of intervals contain type of A, B, and C mainly, structure types of those are shown in Table 1.

Table 1. Pier column structure types statistics.

Type	Height (m)	Dimension (m)	Span (m)
A2	$10 < H \leq 12.5$	$2.3 \times 2.0$	$L \leq 40$
A3	$12.5 < H \leq 15$	$2.5 \times 2.3$	$L \leq 40$
B1	$H \leq 11$	$1.6 \times 1.6$	$L \leq 40$
B1'	$H \leq 11$	$1.6 \times 1.6$	$L \leq 40$
B2	$11 < H \leq 16$	$2.0 \times 2.2$	$L \leq 40$
C1	$H \leq 12$	$2.7 \times 1.8$	–
C2	$10 < H \leq 12.5$	$2.5 \times 2.0$	$L \leq 40$
C3	$12 < H \leq 18$	$2.7 \times 2.5$	–

The heaviest pier column reinforcing cage is DY—33, with 15.5 m height and 22.696 t weight.

### 3 THE DISADVANTAGES OF THE TRADITIONAL TECHNOLOGY

Generally, traditional processes of pier column construction are: embedding main bars of pier column before binding reinforced bars of cushion cap, after the strength of concrete at the bottom of cushion cap by more than 70% of the design strength that bear the loads from simulate pouring of upper concrete and other constructions enough, subsequent processes could be started including baiting, binding, and reinforcing stiff reinforcement cage made from reinforced bars of pier, connecting vertical reinforced bars one by one, binding horizontal reinforced bars, installing pier mould, dismantling stiff reinforcement cage, pouring concrete by segment and then dismantling mould, and curing concrete finally. Thus, pouring of whole pier column has been completed.

The disadvantages of traditional process of construction are as follows: 1) stiff reinforcement cage must be installed before binding reinforced bars, then the stiff reinforcement cage should be dismantled, that waste not only period but also labor; 2) when binding reinforced bars, it is difficult to control the verticality of vertical reinforced bars and the quality of concrete cover that lead to a low speed of binding reinforced bars; and 3) the safety of construction facing a large risk because of numerous work of hoisting on site (Yang et al. 2011).

### 4 MODULAR CONSTRUCTION PROCESSES

According to the investigation on site, combining with the project's characteristics of the 04th interval of line Yanfang, the processes of construction are determined as listed below: locating and setting out cushion cap → binding reinforced bars of cushion cap → processing reinforced bars of pier column to integral → locating and setting out reinforced bars of pier columns → binding and hoisting reinforcement cage of pier columns → pouring and roughening surface concrete of cushion cap → locating and setting out mould → reinforcing pier column (pier column's passageway adopt the type of truss) → installing mould and pouring concrete of pier column (pouring once when the concrete's thickness less than 12 m) → pouring the second concrete after roughening (more than 12 m) → dismantling the mould → curing concrete.

## 5 KEY TECHNOLOGIES OF MODULAR CONSTRUCTION

### 5.1 Processing of reinforced bars' modularity

Setting up centralized processing shed for reinforcing bars in steel plant, which equipped NC cutting machine, NC bars bending machine, threading of straight thread machine etc. After the primary material passed the inspection, cutting, welding and bending them in processing shed of reinforced bars, then complete binding reinforced bars on ground manipulator. For individual components which contain plenty of reinforced bars, integral processing first and assembling in advance, transporting to work site separately and assembling finally.

In order to reduce the deformation of reinforcement cage during hoisting, adding crossed reinforced bars, which the same model number as main bars and welding to main bars every 3 m. For the cages which higher than 12 m connected by sleeve of straight thread, controlling index of processing and binding in an allowable deviation strictly and control structure size of reinforcement cage accurately. According to various embedded components in advance settled in manipulator the reinforced bars could through it. Consequently, the integration of reinforcement cage could ensure when hoisting that avert the deformation of reinforcement cage which cause concrete cover thicker or thinner and reduce quantity of reinforced bars' work effectively meanwhile improve efficiency of subsequent procedures of mould, as shown in Figure 1.

### 5.2 Transport of reinforcing cage

The reinforcement cage transported by flat-car, set up temporary pedestal in the car that ensure the stability of reinforcement cage in transportation.



Figure 1. Processing of reinforcing cage.



### 5.3 Hoisting and fixing reinforcement cage

Take C1 type for an instance, welding 4 main reinforced bars and I-steel belong to hanger, on each corner of cage top, welding hanger by I12b-steel, each hanger has six suspension centers, the diameter of lifting steel wire rope is 20 mm, as shown in the Figure 2.

Reinforcement cage of pier inserted into cushion cap by two 80 t auto cranes then reinforced in bottom, when the height of the reinforcement cage of pier columns less than 12 m, hosting once and insert reinforcement cage into cushion cap as shown in the Figure 3.

Reinforcement cage's facade pulled by 20 mm diameter cables, where set 3 cables and set 2 in the

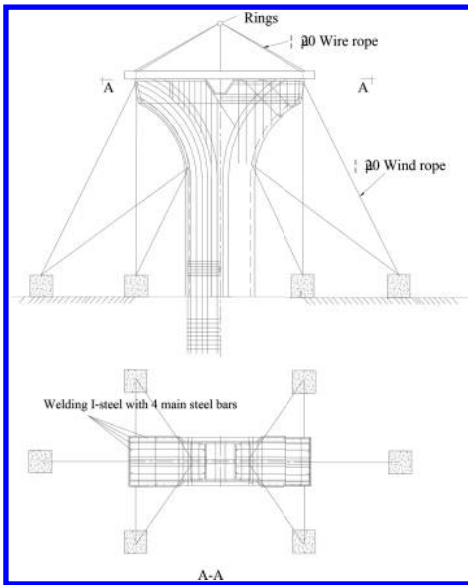


Figure 2. Fixing and reinforcing reinforcement cage.



Figure 3. Lifting of reinforcing cage.

side, amount to 10 cables. It is 1 m \* 1 m \* 2 m prefabricated concrete (each 5.2 t) connect cables into 60° settled in ground and the hooker of prefabricated concrete connect with cables, as shown in Figure 4.

### 5.4 Matched mould of pier column

Mould of pier column adopts standardized design, produced by professional factory, each mould section of the pier column is 2 m high, and each panel is 6 mm thick. The dorsal bars reinforced by U-steel. And fixing the mould by the split bolts which are around 25 mm in diameter.

Column of pier column mould assembled separately on the ground, sealing the edge joint by clamping rubber strip in, and then filling in the gaps and flattening with paint filler. Curve of pier column mould and the beams should be hoisting block by block. Transporting mould separately to site and fixed after inspecting the previous assemblage of mould.

Combine cranes with fixing of formed mould, horizontal position follow control line and verticality controlled by theodolite, next set steel wire ropes around pier column as climb line that one end fixed in cage of mould and another fixed in ground anchors, according to chain block adjust till it is vertical and ground anchors stabilized. Embedded reinforced bars previously in cushion cap for fixing mould of pier column that prevent bottom of mould from shifting as shown in Figure 5.

### 5.5 Pouring and curing concrete of pier column integrally

Confirm all reinforced bars and preembedded piece have been completed, pouring concrete of the cushion cap. Then roughening manually and washing clean that the contact surface of cushion cap with pier column flat, clean and no loose, its better that the leakage of stone is 1/2. Pouring whole flat



Figure 4. Fixed mooring rope and ground anchor.



Figure 5. Installation of pier column formwork.

interval symmetrically and horizontally layer by layer, control the thickness of concrete in 30 cm. Pay attention to correct the deviation of preem-bedded piece meantime to guarantee the density and smooth surface without heel block's mark of concrete. Taking notice of wiping and compaction when pouring to the top of pedestal, especially the reserve of anchor bolt holes. Watering and curing concrete after final set, covering non-woven fabrics on the surface of pier to maintain wetness, dismantling mould and packaging it with plastic membrane, and watering to maintain wetness during the period of curing. Using grass mat package concrete and add plastic membrane inside and outside if the temperature too low. The period of curing must more than 7 days and it is better that the frequency of watering is based on whether the surface of concrete is wet or not.

## 6 THE EFFECT OF APPLICATION

It is beneficial for quality controlled and inspected, improving work efficiency and machine utilization that blanking and integral processing of reinforced bars adopt standardized work in factory. In addition, it could reduce the waste of raw material and cut down the cost of construction. Besides, owing to the decrease in work period, modular construction is advantageous in synthesis cost.

According to the application of modular construction, the pier columns and cushion caps could construct in parallel, transform procedures effectively, improve the continuity and balance of pier construction. Take C1 type as an example again,

C1 in factory processed to integrated, saving the amount of work of build-up and dismantle scaffold platform which should do in traditional construction which cut down the period of construction on site from 21 days to 3 days so that the total period shorten to 18 days to provide guarantee for the project completed on schedule.

Moreover, the construction of line Yanfang elevated subway adopts modular construction technology, which is the first in Beijing region, and rarely applied construction of subway in domestic. The successful application of modular construction obtain high evaluation form the owner and supervision, at the same time, attracted plenty of counterparts come to learning, won the honor for the enterprise and created a good social benefits.

## 7 CONCLUSIONS

The 04th interval of line Yanfang adopted modular construction, realized optimization of the construction technology and avoided the defects of the traditional construction. Furthermore, modular construction is advanced, reliable and applicable, reasonably save construction cost, improve the efficiency of the construction, safety, quality, and overcome the limit time of project. Owing to the benefits of economy, period and society, the modular construction technology could guide the construction of elevated subway actively and the achievements are worthy to be promoted and applied widely.

## REFERENCES

- Li, H.R. & Huang, X.Z. 2009. Modular construction application in engineering practice. *The south of china today* 124: 223–24.
- Li, W. & Chen, G. 2014. Application of Modularization Construction in Metallurgical Construction. *Construction technology* 43: 690–693.
- Xu, L.X. & Tang, B.C. 2009. Modularization Construction Technique of Short-term Overhaul of Big Blast Furnace Structure. *Construction technology* 38: 298–303.
- Yang, Y.W. 2011. Installation Technology of Cast-in-situ Foundation Steel Cage for Qingdao Bay Bridge in Non-sea Route Structure. *Construction technology* 348(40): 5–7.
- Yu, Q.J., Pan, S.M. & Chang, Y.N. 2010. Construction engineering modular construction. *China Hi-Tech Enterprises* 153(18): 129–131.

*Advanced construction materials*

# Effect of metakaolin quantity on the mechanical properties of high-performance concrete

HongBin Liu

State Key Laboratory of Coal Resources and Safe Mining,  
China University of Mining and Technology, Beijing, China

KaiLu Xiao, WeiQi Tang, WeiZhe Ma, ZhengQi Shi & XiGuang Li

School of Mechanics and Civil Engineering, China University of Mining and Technology, Beijing, China

**ABSTRACT:** The effects of five different metakaolin volumetric fractions on the mechanical properties of high-performance concrete were investigated by the cubic compressive, splitting tensile and flexural tensile tests. It is shown that the increasing content of metakaolin can improve the mechanical properties of concrete, and the high-performance concrete can be achieved at the metakaolin volumetric fraction of 15%. In addition, the relationships between the test strengths with the content of metakaolin are empirically formulated.

**Keywords:** high-performance concrete, metakaolin, mechanical properties

## 1 INTRODUCTION

With the development of science and technology, the high-performance concrete has become the development direction of modern concrete technology. Mineral admixture is generally used in high-performance concrete, such as, silica fume, slag, and fly ash. Due to its higher activity, silica fume has been widely used, but it has some disadvantages, such as its low yield, high cost and high energy consumption in China. In order to meet the requirements of sustainable development and environmental protection, it is particularly important to find a suitable active mineral admixture to replace silica fume.

Kaolin ( $\text{Al}_2\text{O}_3 \cdot 2\text{SiO}_2 \cdot 2\text{H}_2\text{O}$ ) is a clay mineral with kaolinite as the main ingredient, rich in silicon, zinc, magnesium, aluminum and other minerals. China is the first country to discover and use kaolin, no coal calcined kaolin reserves rank fifth in the world, accounting for the world's total output of 78%. Calcined at a certain temperature (500–900°C), kaolin can be dehydrated to form a white powder of metakaolin (referred to as MK). The average particle diameter of metakaolin is 1–2  $\mu\text{m}$ . The main components are  $\text{SiO}_2$  and  $\text{Al}_2\text{O}_3$ , and the contents of these two components are more than 90%. Compared with other mineral fume admixtures, the content of  $\text{Al}_2\text{O}_3$  in metakaolin is high, and hydration products of cement hydration reaction with calcium hydroxide are calcium aluminate

and C-S-H cementitious material Metakaolin has a high volcanic ash activity that controls the alkali aggregate reaction effectively, and improves the tensile strength, permeability and corrosion resistance of concrete. Thus, the application prospect of MK is extremely broad<sup>[1–7]</sup>.

Based on the Reactive Powder Concrete (RPC) preparation principle and method<sup>[8]</sup>, we study the effects of different MK volumetric fractions on the mechanical properties of high-performance concrete. This paper aims to provide an experimental basis and reference for promoting the engineering application of metakaolin.

## 2 PHYSICAL PROPERTIES AND VOLCANIC ACTIVITY OF METAKAOLIN

**Physical properties of MK.** The average particle size of metakaolin is 1–2  $\mu\text{m}$ , and the contents of  $\text{SiO}_2$  and  $\text{Al}_2\text{O}_3$  are more than 90%. Table 1 presents the chemical composition of metakaolin.

**Volcanic ash activity.** Murat studied the absorption ability of  $\text{Ca}(\text{OH})_2$  by using metakaolin, and found the main hydration products to be mullite CSH-I, hydration gehlenite  $\text{C}_2\text{AH}_8$  and a small amount of calcium aluminate hydrate<sup>[1]</sup>:

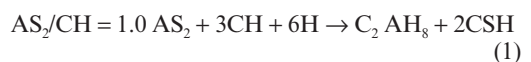


Table 1. Chemical composition of metakaolin.

SiO <sub>2</sub> (%)	Al <sub>2</sub> O <sub>3</sub> (%)	Fe <sub>2</sub> O <sub>3</sub> (%)	TiO <sub>2</sub> (%)	CaO (%)	MgO (%)	K <sub>2</sub> O (%)	Na <sub>2</sub> O (%)	Loss on ignition (%)
55.06	44.12	0.76	0.24	0.17	0.06	0.55	0.06	0.62

Table 2. Ingredients and mix proportion of concrete.

No.	Water-cement (W/B)	Cementing material (B)		Fine sand (S/C)	Plasticizer (%)	Curing method
		Cement (C)	Metakaolin (MK/C)			
S00	0.22	1.00	0.00	1.2	1.5	Room temperature curing for 28 days
S05		0.95	0.05			
S10		0.90	0.10			
S15		0.85	0.15			
S20		0.80	0.20			

### 3 EXPERIMENTAL OVERVIEW

**Mixing ratio and specimen preparation.** Table 2 lists the material ingredients and mixing ratios for the specimens of high-performance concrete. It included P.O42.5 Portland cement and fine quartz sand with grain sizes ranging between 0.15 and 0.63 mm. Metakaolin was supplied by a company in Henan Province, and Sika superplasticizer (water reducing ratio > 30%, solid content 37.2%, and bulk density 1.077 g/cm<sup>3</sup>) was employed.

During specimen preparation, cement, MK, and quartz sand were mixed evenly at the designated mixing ratio. The mixed water and superplasticizer were added and mixed for 3 min. The mixture was poured into a rectangular mold with a size of 100 mm × 100 mm × 100 mm and 40 mm × 40 mm × 160 mm, and vibrated to form on a vibrating table. The specimens were first cured at an ambient temperature for 24 h before demolding, and then cured at room temperature curing for 28 days.

**Testing method and equipment.** According to “the standard for ordinary concrete test” (GB/T 50081-2002), the compression strength and the splitting strength test was carried out by a 3000 kN high rigidity testing machine at the State Key Laboratory of Coal Resources and Safe Mining of China University of Mining and Technology (Beijing). Adopting the load control mode, the test speed values were 0.9 MPa/s and 0.09 MPa/s, until the failure of the specimen, with each ratio being tested for 3–6 samples.

Flexural tensile strength was tested by a 100 kN universal testing machine at China University of Mining and Technology (Beijing). Adopting the displacement mode, the test speed value was 0.05 mm/min, with each ratio being tested for 3–6 samples.

Table 3. Measured strength with different metakaolin volumes.

No.	Cement	MK	Compressive strength (MPa)	Splitting tensile strength (MPa)	Flexure tensile strength (MPa)
S00	1.00	0.00	91.09	4.57	6.38
S05	0.95	0.05	94.01	5.05	7.19
S10	0.90	0.10	97.31	5.20	7.21
S15	0.85	0.15	120.06	6.91	8.59
S20	0.80	0.20	110.85	6.32	7.59

Note: data represent the average values of the 3–6 samples.

**Test results and analyses.** Table 3 lists the compressive strength, splitting test results of the tensile strength and the bending strength at different metakaolin contents. Figures 1–3 show the relationship between the compressive strength, the splitting tensile strength, and the flexure tensile strength at different metakaolin contents.

The experimental results show that: ① the compression strength, the splitting strength and the bending strength increased with the increasing metakaolin content. Compared with MK content of 0%, at the compressive strength of 5%, 10%, 15% and 20%, MK contents in concrete increased to 3.21%, 6.83%, 31.81% and 21.69%, respectively. The splitting strength increased by 10.51%, 13.84%, 51.23% and 38.31%, and the bending strength increased by 12.69%, 12.99%, 34.58% and 18.96%, respectively. ② When the volume of MK was below 10%, each strength parameter increased slowly, and the strength of 5% and 10% volume was closed. When the MK volume

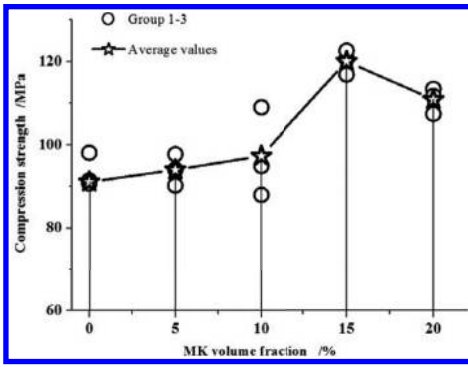


Figure 1. Relationship between compression strength and volumetric contents of MK.

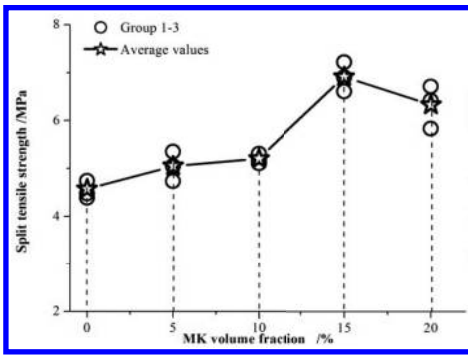


Figure 2. Relationship between the splitting tensile strength and volumetric contents of MK.

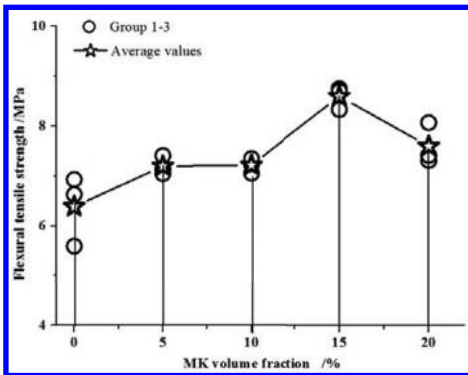


Figure 3. Relationship between flexural tensile strength and volumetric contents of MK.

exceeded 15%, the strength increased significantly, but the strength of concrete decreased when the volume of MK increased to 20%. This shows that it is not beneficial to increase the metakaolin content above 15%.

In summary, metakaolin volume is significantly associated with the mechanical properties of concrete, and there exists an optimal volume. The suitable volume of metakaolin is about 15%.

Figures 4–6 plot the relationships of the normalized compressive strength  $f_{cu}/f_{cu,0}$ , the normalized splitting tensile strength  $f_{t,sp}/f_{t,sp,0}$  and the normalized flexural tensile strength  $f_{t,flx}/f_{t,flx,0}$  with 0% MK content, where the  $f_{cu,0}$  indicates 100 mm cube the compressive strength of 0% MK volumetric fraction;  $f_{cu}$  is the cubic compressive strength;  $f_{t,sp}$  is the splitting tensile strength; and  $f_{t,flx}$  is the flexural strength. Thus, the relationships between the test strengths with the content of MK are formulated.

$$\frac{f_{cu}}{f_{cu,0}} = \begin{cases} 0.99833 + 0.7\rho & 0 \leq \rho \leq 10\% \\ -0.48 + 22.5\rho - 70\rho^2 & 10 < \rho \leq 20\% \end{cases} \quad (2)$$

$$\frac{f_{t,sp}}{f_{t,sp,0}} = \begin{cases} 5.01 \times E^{-2} + 1.41 \times E^{-3}\rho - 7.18 \times E^{-5}\rho^2 & 0 \leq \rho \leq 10\% \\ -5.61 \times E^{-2} + 1.64 \times E^{-2}\rho - 5.04 \times E^{-4}\rho^2 & 10 < \rho \leq 20\% \end{cases} \quad (3)$$

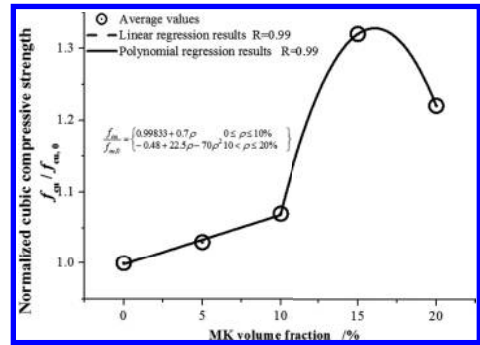


Figure 4. Relationship between the normalized cubic compressive strength and volumetric content of MK.

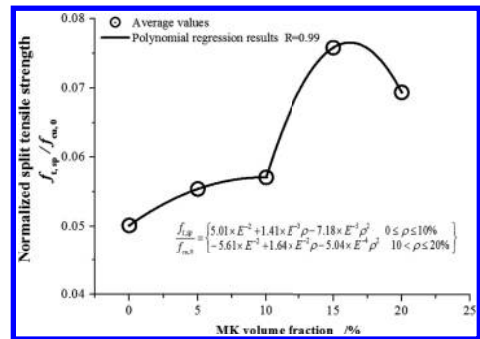


Figure 5. Relationship between normalized splitting tensile strength and volumetric content of MK.

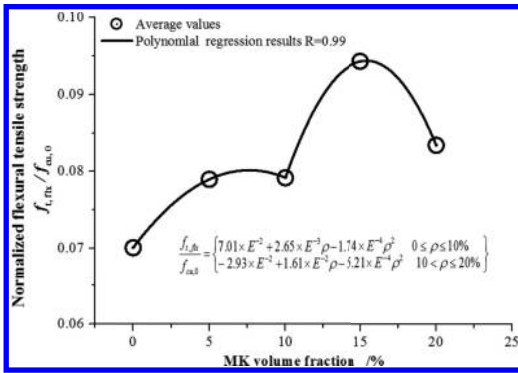


Figure 6. Relationship between normalized flexural tensile strength and volumetric content of MK.

$$\frac{f_{l,fb}}{f_{cu,0}} = \begin{cases} 7.01 \times E^{-2} + 2.65 \times E^{-3} \rho - 1.74 \times E^{-4} \rho^2 \\ 0 \leq \rho \leq 10\% \\ -2.93 \times E^{-2} + 1.61 \times E^{-2} \rho - 5.21 \times E^{-4} \rho^2 \\ 10 < \rho \leq 20\% \end{cases} \quad (4)$$

#### 4 CONCLUSIONS

This paper studies the influence of MK content on the mechanical properties of high-performance concrete, and the following conclusions can be drawn:

1. The metakaolin content can improve the mechanical properties of concrete effectively. The concrete compressive strength, splitting tensile strength, and flexural strength of concrete all appear to increase with the increasing MK volume; however, there exists an optimal volume content. The result of this study shows

that the MK admixture of 15% is the appropriate value.

2. The empirical relationship formulas for concrete's compressive strength, splitting tensile strength, and flexural strength changing with metakaolin admixture are obtained. Thus, they can be used as a reference for engineering application.

#### ACKNOWLEDGMENT

This work was financially supported by the Science and Technology Innovation Program of State Key Laboratory of Coal Resources and Safe Mining of China University of Mining and Technology (SKLCRSM14CXJH07), the National Natural Science Foundation of China (Grant No. 51374211), and the Research Fund for Doctoral Programs of Chinese Ministry of Education (Grant No. 20110023110015).

#### REFERENCES

- [1] M. Murat: Cem. Concr. Res. Vol. 13(2) (1983), p. 259.
- [2] P.S. De Silva, F.P. Glasser: Adv. Cem. Res. Vol. 3(12) (1990), p. 167.
- [3] Z.M. Bai, Y.W. Xiao: J. Chin. Cer. Soc. (in Chinese). Vol. 31(7) (2003), p. 715.
- [4] Z. Ding, D.C. Zhang, X.D. Wang: J. Chin. Cer. Soc. (in Chinese). Vol. 16(4) (1997), p. 57.
- [5] J.Z. Peng, M.M. Gui, C.L. Fu, J.T. Li: J. Build. Mate. (in Chinese). Vol. 14(4) (2011), p. 482.
- [6] C.S. Poon, S.C. Kou, L. Lam: Constr. Build. Mater. Vol. 20(10) (2006), p. 858.
- [7] Y.L. Chen, Y.N. Zhao, J. Li, D.G. Cao: J. Chin. Cer. Soc. (in Chinese). Vol. 32(4) (2004), p. 524.
- [8] H.B. Liu, J. Ch, Y.D. Jia, Y. Ju, G.L. Ye: Ind. Constr. (in Chinese). Vol. 38(6) (2008), p. 74.

# Study on mechanical behavior and thermal properties of recycled brick concrete mixed with cinder insulation

Chunhong Chen, Yongxiang Wu & Yi Lei

Department of Civil Engineering, Changzhou University, Changzhou, Jiangsu, China

Feng Li

School of Mathematics and Physics, Changzhou University, Changzhou, Jiangsu, China

**ABSTRACT:** This paper engaged in the recycled aggregate concrete insulation blocks derived from waste concrete. Based on the method of overall effectiveness, the mix proportion of recycled concrete insulation block with modified cinder and glazed hollow bead was optimized by using the orthogonal experimental principle, contrast test and variance analysis. Mechanical strength and thermal conductivity of blocks were tested. Results showed that the insulation block with optimum mix proportion could meet quality requirements of QGB B (390 mm × 240 mm × 190 mm) 800 Mu5.0 0.30 GB 26538-2011 in terms of Chinese standard.

**Keywords:** recycled aggregate concrete; insulation block; mix proportion; overall efficacy coefficient; mechanical strength; thermal conductivity

## 1 INTRODUCTION

According to statistics, in recent years, average generation of construction waste such as waste concrete and bricks is up to 20 million tons per year in China [1]. Vast majority of construction waste are deposited in the open air or landfill, which not only occupy the land, but also cause serious secondary environmental pollution [2–3]. Recycled coarse and fine aggregate, which were prepared by the machining process of crushing, screening, removing impurities and other processes from construction waste block, have low density, high porosity, high water absorption and heat insulation performance [4–5], can be used to produce thermal insulation energy-saving blocks by replacing partial or all of natural aggregate. Then the blocks are applied to the bearing and enclosure structure of buildings. It can solve the shortage of natural aggregate and some problems such as construction waste dumps, land occupation and environmental pollution, can more solve the problem of wall insulation, which is the effective way to the recycling of construction waste.

In this paper, taking compressive strength, flexural strength and thermal conductivity as assessment indicators, and taking the QGB B (390 mm × 240 mm × 190 mm) 800 Mu5.0 0.30 excellent products in Chinese standard GB26538/2011 as the goal, the mix proportion was optimized by

orthogonal test results with total efficiency coefficient method. Meanwhile, comparative tests were made to study the effects of cinder on the mechanical behavior and thermal conductivity.

## 2 EXPERIMENTAL

### 2.1 Raw material

Grade 42.5 ordinary Portland cement was from Jiangsu Yangzi Plant. Fine grinding slag was from Yangzhou steel Factory, with a specific surface area of 460 m<sup>2</sup>/kg. Fly ash was manufactured by New Materials Company of Yangzhou, with a specific surface area of 458 m<sup>2</sup>/kg. Polypropylene Fiber (PF) namely TB-19 with a length of 12 mm was used. Glazed hollow bead was from Jiangsu Huawei Jia Construction Materials Company, and its physical properties were shown in Table 1. Recycled aggregates were prepared from waste concrete by the machining process of crushing, screening, washing

Table 1. Physical properties of the glazed hollow bead.

Granularity (mm)	Bulk density (kg/m <sup>3</sup> )	Water absorption (%)	Thermal conductivity (W/(m <sup>2</sup> ·K))
0.5–1.5	50–200	20–50	0.028–0.054



and drying. Then recycled aggregates with size of 5–20 mm were chosen as recycled coarse aggregates and with diameter less than 5 mm as recycled fine aggregate. Cinder was prepared by the same process as recycled aggregates, and with diameter of 4.75 mm–9.5 mm was chosen to replace concrete coarse aggregate. Basic properties of recycled aggregates were shown in Table 2 and Table 3.

### 2.2 Mix proportion

Optimize mix proportion by following steps: First, selecting the total amount of cementitious material, mixing amount of cinder ash, mixing amount of recycled fine aggregate and the glazed hollow bead as four influence factors, basic mix proportion was designed referring to the additional water method, whose main purpose was to pick reasonable levels of influence factors. Second, orthogonal experiments were designed, range analysis and variance analysis were made to identify the reasonable matching relationship between each factor. Orthogonal experiment was L9 (3<sup>4</sup>), factor levels were shown in Table 4, in which factors of A, B, C, D respectively represented cementitious materials, cinder content, glazed hollow bead content and recycled fine aggregate content. Finally, the mix proportion with the best overall performance was optimized based on total efficiency coefficient method.

### 2.3 Concrete hollow block type design

In order to meet building energy requirement of 65% in the hot summer and cold winter area, block

Table 2. Physical properties of recycled coarse aggregates.

Coarse aggregates type	Bulk density (kg·m <sup>-3</sup> )	Apparent density (kg·m <sup>-3</sup> )	Crushing value (by mass) (%)	Water absorption at 30 min (by mass) (%)
Natural	–	1727	–	7.29
Cinder	1505	2650	14.9	4.5

Table 3. Physical properties of recycled fine aggregates.

Fine aggregates type	Apparent density (kg/m <sup>3</sup> )	Fineness module (-)	Water demand ratio (-)	Water absorption at 30 min (by mass) (%)
Natural	2616	3.0	1.0	0.20
Recycled	2632	2.73	1.31	6.4

Table 4. Factors and levels.

Level	Factors			
	A	B	C	D
1	330	30	50	10
2	350	50	70	30
3	370	70	100	50

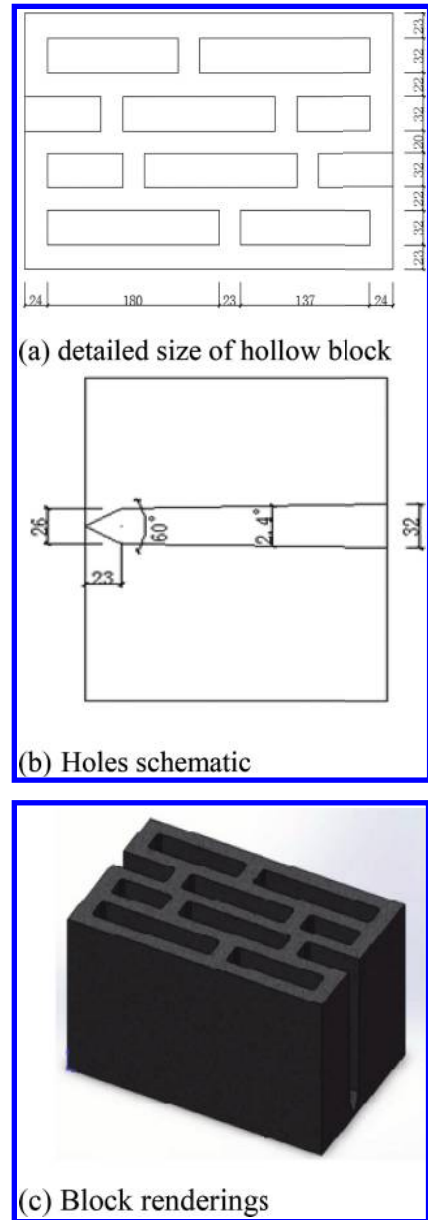


Figure 1. Four rows of hollow block.

needs higher thermal performance. Reasonable considered the number of hole rows, hole arrangement, block wall thickness, air layer thickness and other factors, heat transfer distance can be longer in the block, thereby can reduce the thermal conductivity of the block and increase its thermal insulation performance [6–8]. The block type was shown in Figure 1. Block hole rate was 44%, staggered arrangement of four rows of holes could effectively increase the thermal resistance of the block and improve thermal performance of the walls [9–10]. The bottom of the block was totally enclosed, also most of the surrounding wall, so mechanical properties of the block was better [11], which made blocks hard to be destroyed in links of the manufacture, transportation, masonry and usage.

### 2.4 Test methods

Tests of compressive cube strength and splitting tensile strength were performed due to Chinese Standard GB/T50081-2002. Thermal insulation performance was evaluated by thermal conductivity and the test was due to Chinese Standard GB10294-2008.

## 3 RESULTS AND ANALYSIS

Results of orthogonal test and normalization process were shown in Table 5 and Table 6.

### 3.1 Cube compressive strength

Range and variance analysis of compressive strength of recycled concrete insulation block were shown in Table 7 and Table 8. According to Table 7, the influence degree of various factors on 28d cube compressive strength of the block was: A (cementitious materials content) > B

Table 5. Test results for assessment indicators.

Test number	Cube compressive strength (MPa)	Flexural strength (MPa)	Thermal conductivity (W/(m <sup>2</sup> ·K))
1	7.0	2.6	0.3704
2	5.8	1.4	0.2613
3	5.0	1.0	0.1377
4	7.2	1.6	0.1510
5	6.8	1.1	0.2698
6	6.6	1.9	0.2651
7	8.5	0.9	0.1886
8	8.3	1.3	0.3032
9	7.4	2.5	0.2477

Table 6. Normalization process for assessment indicators.

Test number	Cube compressive strength	Flexural strength	Thermal conductivity	Overall efficacy coefficient
1	0.8235	1.0000	0.3718	0.6740
2	0.7838	0.5385	0.5270	0.6059
3	0.5882	0.3846	1.0000	0.6093
4	0.8471	0.6154	0.9119	0.6758
5	0.8000	0.4231	0.5104	0.6432
6	0.7765	0.7308	0.5194	0.6655
7	1.0000	0.3462	0.7301	0.6323
8	0.9765	0.5000	0.4542	0.6053
9	0.8706	0.9615	0.5559	0.7749

Table 7. Range analysis of compressive strength.

	A	B	C	D
K1	17.799	22.701	21.900	21.201
K2	20.601	20.901	20.400	20.901
K3	24.201	18.999	20.499	20.499
R	2.134	0.833	0.533	0.234

Table 8. Variance analysis of compressive strength.

Variance	Sum of squares	Freedom	Mean square	F	Critical value
A	6.862	2	3.431	83.68	F <sub>0.05</sub> (2,2) = 19.0
B	2.282	2	1.141	27.83	
C	0.536	2	0.268	6.54	
D	0.082	2	0.041	–	
Sum T	9.762	8	–	–	

(cinder content) > C (glazed hollow bead content) > D (recycled fine aggregate content). Table 8 showed that the amount of cementitious materials had more influence on compressive strength and the influence was significant, also the amount of cinder. The compressive strength improved with increasing the amount of cementitious materials, reduced with increasing the amount of cinder. It was because more amount of cementitious materials could make recycled concretes be more dense. Low aggregate strength and high porosity of cinder itself had adversely effect on compressive strengths of recycled concrete.

### 3.2 Flexural strength

Range and variance analysis of flexural strength of recycled concrete insulation block were shown in

Table 9 and Table 10. Table 9 showed that the influence degree of various factors on flexural strength was: C > D > B > A. Flexural strength was lower with increasing the amount of glazed hollow bead and recycled fine aggregates. It was because the powder and mud content of recycled fine aggregate prepared from waste concrete were larger, furthermore many micro cracks produced while crushing, which reduced flexural strength of recycled concrete. Glazed hollow beads had low intensity and certain hydrophobicity, would fill in the cementitious materials and aggregates. Then it weakened caking property between cementitious materials and aggregates, which reduced flexural strength of recycled concrete. From Table 10, the influence of the amount of glazed hollow beads and fine aggregates on flexural strength was significant.

### 3.3 Thermal conductivity

Range and variance analysis of thermal conductivities of recycled concrete block were shown in Table 11 and Table 12. Table 11 showed that the influence degree of various factors on thermal conductivities was: C > B > A > D. The effect of the amount of glazed hollow beads on thermal

Table 9. Range analysis of flexural strength.

	A	B	C	D
K1	5.100	5.199	5.901	6.300
K2	4.599	3.801	5.499	4.200
K3	4.701	5.400	3.000	3.900
R	0.167	0.533	0.967	0.800

Table 10. Variance analysis of flexural strength.

Variance	Sum of squares	Freedom	Mean square	F	Critical value
A	0.047	2	0.0235	–	F <sub>0.05</sub> (2,2) = 19.0
B	0.507	2	0.2535	10.787	
C	1.647	2	0.8235	35.043	
D	1.140	2	0.5700	24.255	
Sum T	3.341	8	–	–	

Table 11. Range analysis of thermal conductivities.

	A	B	C	D
K1	0.785	0.828	0.936	0.768
K2	0.687	0.717	0.780	0.714
K3	0.642	0.551	0.477	0.711
R	0.038	0.095	0.153	0.019

Table 12. Variance analysis of thermal conductivities.

Variance	Sum of squares	Freedom	Mean square	F	Critical value
A	0.002	2	0.0075	1.500	F <sub>0.05</sub> (2,2) = 19.0
B	0.011	2	0.0055	11.000	
C	0.036	2	0.0180	36.000	
D	0.001	2	0.0005	–	
Sum T	0.044	8	–	–	

Table 13. Proportion of contrast test.

Test number	Cementitious materials (kg/m <sup>3</sup> )	Recycled fine aggregate content (%)	Cinder content (%)
1	350	50	0
2	350	50	30
3	350	50	50
4	350	50	70

Table 14. Contrast test results.

Test number	Compressive strength (MPa)	Flexural strength (MPa)	Thermal conductivity (W/(m <sup>2</sup> ·K))
1	15.0	4.1	0.6113
2	10.2	3.2	0.5904
3	8.3	2.6	0.5710
4	5.9	1.8	0.5477

conductivity was largest. Increasing the amount of content, thermal conductivity was less and thermal insulation performance was better. Table 12 also illustrated the effect of the amount of glazed hollow beads on thermal conductivity coefficient was significant, also the amount of cinder. It suggested that thermal insulation properties could increase when cinder replaced a part of recycled coarse aggregates.

Table 5 showed that overall effectiveness of NO. 1, NO. 4 and NO. 9 were larger, while the thermal conductivity of NO. 4 was the lowest and the strength meet the requirements, therefore the optimum mix proportion was NO. 4.

### 3.4 Contrast test

In order to further discuss the influence of cinder on the strengths and insulation performance of recycled concrete blocks, contrast tests were done with optimal mix proportion, which specific mix proportion and results were showed in Table 13 and Table 14. Table 14 showed that, compressive

strength, flexural strength and thermal conductivity of the block obviously reduced with the increase of the amount of cinder, and declined more significantly with the replacement of cinder ash more than 50%. It was because that most cinder had porous block structure and light weight, furthermore some particulate debris produced during crushing cinder, and also damaged the cinder internal, which would further reduce concrete strength. Therefore, the proper amount of cinder should be chosen to meet the strength requirement [12]. Meanwhile, the cinder surface was irregular, relatively loose and had low density, so cinder replacement coarse aggregate had good heat preservation and heat insulation.

#### 4 CONCLUSIONS

Cementitious materials consumption was the main factor affecting compressive strengths of blocks, compressive strength was greater with increasing its amount. The amount of glazed hollow beads and replacement rate of recycled fine aggregate were main factors affecting the flexural strength, with increasing the amount of glazed hollow beads and recycled fine aggregate, flexural strength decreased.

The amount of glazed hollow bead was main factor affecting thermal conductivity, the thermal conductivity was lower with increasing its amount.

Contrast tests showed that with the increase of cinder content, the strength of blocks reduced and insulation performance improved, so the appropriate cinder content should be selected.

With optimal mix proportions, cementitious material  $350 \text{ kg/m}^3$ , cinder content 30%, glazed hollow beads content 70%, and recycled fine aggregate replacement rate of 50%, recycled concrete blocks could meet the quality requirements of QGB B (390 mm × 240 mm × 190 mm) 800 Mu5.0 0.30 GB 26538-2011 in terms of Chinese standard.

#### ACKNOWLEDGEMENTS

This work was financially supported by National Natural Science Fund Project (Grant NO. 51278073)

and Science and Technology Support Program of Changzhou (Grant NO. CE20135043).

#### REFERENCES

- Wenjing Wang, Lin Zhao, Yuanzhen Liu, Zhu Li. 2014. Mix design for recycled aggregate thermal insulation concrete with mineral admixtures. *Magazine of Concrete Research* 66(10):492–504.
- [1] J.Z. Xiao. 2008. *Recycled concrete*. China Building Industry Press.
  - [2] Zhu Ping-hua, Wang Xin, Zhou Jun, et al. 2009. Main research progress and development trend on recycled aggregate concrete. *Concrete* (5):90–94.
  - [3] Chen B.F. 2013. Basic mechanical properties and micro structural analysis of recycled concrete. *Journal of Wuhan University of Technology-Mater. Sci. Ed* 28(1):104–109.
  - [4] Yang Weijun, Li Pengfei, Liang Jianguo. 2011. Experimental study on basic properties of recycled aggregate for the production of concrete perforated brick. *New Building Materials* (3):15–19.
  - [5] HE Jia-peng, Zhang Yuan, Han Li-yan. 2009. Thermal response analysis on blocks hollow rate of building energy conservation. *Journal of PLA University of Science and Technology (Natural Science Edition)* 10(6):623–627.
  - [6] Xu Guo-dong, Yang Xiao-hong, Tang Su-ping. 2012. Study on mechanical and thermal performances analysis of compound insulation concrete blocks. *China Concrete And Cement Product* (9):54–56.
  - [7] B. Lacarriere, B. Lartigue, F. Monchoux. 2003. Numerical study of heat transfer in a wall of vertically perforated bricks: influence of assembly method. *Energy and Buildings* (35):229–237.
  - [8] Farid D., Said K. 2008. The use of coarse and fine crushed bricks as aggregate in concrete. *Construction and Building Materials* 22(2): 886–893.
  - [9] Yang Dingyi, SunWei, Liu Zhiyong, et al. 2003. Research on improving the heat insulation and preservation properties of small-size concrete hollow blocks [J]. *Cement and Concrete Research* (33):1357–1361.
  - [10] Xu Guo-dong, Yang Xiao-hong, Tang Su-ping. 2012. Study on mechanical and thermal performances analysis of compound insulation concrete blocks. *China Concrete and Cement Product* (9):54–56.
  - [11] Zhang Feng, Tian Anguo, Zhang Zhendong. 2010. Mechanical properties optimization analysis of self heat-insulation concrete hollow block catering to thermal performance. *New Building Materials* (3):30–33.

## Calculation of Poisson's ratio of laminate composite

Y.R. Li, H.B. Jiang & W.S. Chen

Logistics College, Naval University of Engineering, Tianjin, China

**ABSTRACT:** Poisson's ratio calculation of laminate is a complex problem, which is usually researched by experimental or numerical methods. This paper attempts to establish a simple calculation model to obtain Poisson's ratio formula by the analytical method. Using equivalent force instead of shear stress, equal strain law of each single plate in laminate was used to establish simultaneous equations, with which Poisson's ratio formulas would be obtained. The results show that the normal direction Poisson's ratio under the action of longitudinal force is equal to the weighted sum of Poisson's ratios of each single plate according to volume fraction, and Poisson's ratio in lateral direction (non-normal direction) is inversely proportional to the lateral elastic modulus of the laminate, and is proportional with the sum of the products of Poisson's ratio, elastic modulus and volume fraction of each single plate.

**Keywords:** laminate composite; Poisson's ratio; analytic calculation; shear stress; equivalent force

### 1 INTRODUCTION

Poisson's ratio calculation of the laminate is a complex problem, which is usually researched by experimental or numerical methods [1–6]. This paper attempts to establish a simple calculation model to obtain Poisson's ratio formula by the analytical method.

### 2 CALCULATION MODEL AND FORCE ANALYSIS

A laminate consisting of two single plates and the coordinate system is shown in [Figure 1](#).

If there is  $x$ ,  $y$ , or  $z$ -axis direction load stress on the laminate, then the junction surface of the

two single plates will produce shear stress because the elastic modulus and Poisson's ratio of each single plate are different, and the two-layer plate would generate the same deformation by the shear stress. If the direction of the load stress is parallel to the  $y$ -axis, two sets of virtual forces  $\pm P_x$  and  $\pm P_z$  in each symmetric end of each single plate could be set instead the shear stress in the junction surface, and the magnitude of the virtual forces could be determined by the law of equivalent strain, i.e., virtual force and shear stresses produce equal strains. By this way, each single plate could be isolated, which makes the calculation easier. This calculation method is called the shear stress equivalent replacement calculation method.

### 3 POISSON'S RATIO CALCULATION UNDER THE ACTION OF LONGITUDINAL FORCE

Referring to [Figure 1](#), we first study the strains produced by the load stress in  $x$ -axis direction (longitudinal direction).

The first layer (lower layer) single plate  $x$ -axis direction strain  $\varepsilon_{1x}$  is equal to the sum of the strain  $\varepsilon_{1\sigma x}$  caused by load stress  $\sigma$ , strain  $\varepsilon_{1P_{xx}}$  caused by virtual force  $P_x$  and strain  $\varepsilon_{1P_{zx}}$  caused by virtual force  $P_z$ :

$$\begin{aligned} \varepsilon_{1x} &= \varepsilon_{1\sigma x} + \varepsilon_{1P_{xx}} + \varepsilon_{1P_{zx}} \\ &= \frac{\sigma}{E_{1x}} + \frac{P_x/A_{1x}}{E_{1x}} - \mu_{1xz} \frac{P_z/A_{1z}}{E_{1z}} \end{aligned} \quad (1)$$

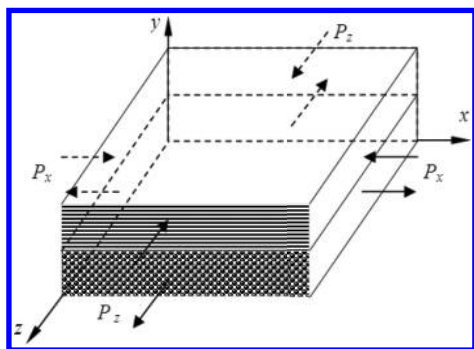


Figure 1. A laminate consisting of two single plates and its coordinate system.

The second layer (upper layer) single plate  $x$ -axis direction strain  $\varepsilon_{2x}$  is equal to the sum of the strain  $\varepsilon_{2\sigma x}$  caused by load stress  $\sigma$ , strain  $\varepsilon_{2P_{xx}}$  caused by virtual force  $P_x$  and strain  $\varepsilon_{2P_{zx}}$  caused by virtual force  $P_z$ :

$$\begin{aligned}\varepsilon_{2x} &= \varepsilon_{2\sigma x} + \varepsilon_{2P_{xx}} + \varepsilon_{2P_{zx}} \\ &= \frac{\sigma}{E_{2x}} - \frac{P_x/A_{2x}}{E_{2x}} + \mu_{2xz} \frac{P_z/A_{2z}}{E_{2z}}\end{aligned}\quad (2)$$

where  $A_{1x}$ ,  $A_{2x}$ , respectively, represent the first and second layer plate cross-sectional areas (perpendicular to the  $x$ -axis);  $E_{1x}$ ,  $E_{2x}$ , respectively, represent the elastic modulus of the first and second layer plates ( $x$ -axis direction); and  $\mu_{1xz}$ ,  $\mu_{2xz}$ , respectively, represent the first and second layer plates in the  $x$ -axis direction and Poisson's ratio under the  $z$ -axis direction force. Laminate longitudinal strain  $\varepsilon_x$  is equal to the first plate longitudinal strain  $\varepsilon_{1x}$ , and also equals the second plate longitudinal strain  $\varepsilon_{2x}$ :

$$\varepsilon_x = \varepsilon_{1x} = \varepsilon_{2x} = \frac{\sigma}{E_x} \quad (3)$$

where  $E_x$  represents the laminate elastic modulus in the  $x$ -axis direction. By formulas (1), (2) and (3), we get the following two equations:

$$\frac{\sigma}{E_x} = \frac{\sigma}{E_{1x}} + \frac{P_x/A_{1x}}{E_{1x}} - \mu_{1xz} \frac{P_z/A_{1z}}{E_{1z}} \quad (4)$$

$$\frac{\sigma}{E_x} = \frac{\sigma}{E_{2x}} - \frac{P_x/A_{2x}}{E_{2x}} + \mu_{2xz} \frac{P_z/A_{2z}}{E_{2z}} \quad (5)$$

where  $A_{1z}$ ,  $A_{2z}$ , respectively, represent the first and second layer plate cross-sectional areas (perpendicular to the  $z$ -axis); and  $E_{1z}$ ,  $E_{2z}$ , respectively, represent the elastic modulus of the first and second layer plates ( $z$ -axis direction).

Similar methods can be used to study the  $z$ -axis direction strain. The first layer plate strain in the  $z$ -axis direction is given by

$$\varepsilon_{1z} = -\frac{\mu_{1zx}\sigma}{E_{1x}} - \frac{\mu_{1zx}P_x/A_{1x}}{E_{1x}} + \frac{P_z/A_{1z}}{E_{1z}} \quad (6)$$

The second layer plate strain in the  $z$ -axis direction is given by

$$\varepsilon_{2z} = -\frac{\mu_{2zx}\sigma}{E_{2x}} + \frac{\mu_{2zx}P_x/A_{1x}}{E_{2x}} - \frac{P_z/A_{2z}}{E_{2z}} \quad (7)$$

where  $\mu_{1zx}$ ,  $\mu_{2zx}$ , respectively, represent the first and second layer plates in the  $z$ -axis direction and Poisson's ratio under the  $x$ -axis direction force.

The first layer plate strain in the  $z$ -axis direction is equal to the second layer plate strain in the same direction, i.e.

$$\begin{aligned}-\frac{\mu_{1zx}\sigma}{E_{1x}} - \frac{\mu_{1zx}P_x/A_{1x}}{E_{1x}} + \frac{P_z/A_{1z}}{E_{1z}} \\ = -\frac{\mu_{2zx}\sigma}{E_{2x}} + \frac{\mu_{2zx}P_x/A_{1x}}{E_{2x}} - \frac{P_z/A_{2z}}{E_{2z}}\end{aligned}\quad (8)$$

By simultaneous equations (4), (5) and (8), we get  $x$ -axis direction equivalent force  $P_x$

$$\begin{aligned}P_x &= \frac{A_{1x}A_{2x} \left\{ \begin{aligned} &A_{1z}E_{1z} [E_{1x}(1 - \mu_{2xz}\mu_{2zx}) \\ &\quad - E_{2x}(1 - \mu_{1xz}\mu_{2xz})] \\ &+ A_{2z}E_{2z} [E_{1x}(1 - \mu_{1xz}\mu_{2zx}) \\ &\quad - E_{2x}(1 - \mu_{1xz}\mu_{1zx})] \end{aligned} \right\} \sigma}{A_{1x}E_{1x} [A_{1z}E_{1z}(1 - \mu_{2xz}\mu_{2zx}) \\ &\quad + A_{2z}E_{2z}(1 - \mu_{1xz}\mu_{2zx})] \\ &\quad + A_{2x}E_{2x} [A_{1z}E_{1z}(1 - \mu_{1xz}\mu_{2zx}) \\ &\quad + A_{2z}E_{2z}(1 - \mu_{1xz}\mu_{1zx})]} \\ &= \frac{V_1V_2A_x \left\{ \begin{aligned} &V_1E_{1z} [E_{1x}(1 - \mu_{2xz}\mu_{2zx}) \\ &\quad - E_{2x}(1 - \mu_{1xz}\mu_{2zx})] \\ &+ V_2E_{2z} [E_{1x}(1 - \mu_{1xz}\mu_{2zx}) \\ &\quad - E_{2x}(1 - \mu_{1xz}\mu_{1zx})] \end{aligned} \right\} \sigma}{V_1E_{1x} [V_1E_{1z}(1 - \mu_{2xz}\mu_{2zx}) \\ &\quad + V_2E_{2z}(1 - \mu_{1xz}\mu_{2zx})] \\ &\quad + V_2E_{2x} [V_1E_{1z}(1 - \mu_{1xz}\mu_{2zx}) \\ &\quad + V_2E_{2z}(1 - \mu_{1xz}\mu_{1zx})]} \quad (9)\end{aligned}$$

where  $V_1$ ,  $V_2$ , respectively represent the volume fraction of the first and second layer plates.

If every single plate is isotropic, formula (9) can be simplified as follows:

$$\begin{aligned}P_x \\ A_x &= \frac{V_1V_2 \left\{ \begin{aligned} &V_1E_1 [E_1(1 - \mu_2^2) - E_2(1 - \mu_1\mu_2)] \\ &\quad + V_2E_2 [E_1(1 - \mu_1\mu_2) - E_2(1 - \mu_1^2)] \end{aligned} \right\} \sigma}{V_1E_1 [V_1E_1(1 - \mu_2^2) + V_2E_2(1 - \mu_2\mu_1)] \\ &\quad + V_2E_2 [V_1E_1(1 - \mu_1\mu_2) + V_2E_2(1 - \mu_1^2)]}\end{aligned}\quad (10)$$

If all products of Poisson's ratio are neglected, then formula (10) can be further simplified to

$$\begin{aligned}
P_x &\approx \frac{V_1 V_2 (E_{1x} - E_{2x})}{V_1 E_{1x} + V_2 E_{2x}} A_x \sigma \\
&= \frac{V_1 V_2 (E_{1x} - E_{2x})}{E_x} A_x \sigma
\end{aligned} \quad (11)$$

By simultaneous Equations (4), (5) and (8), we also can get the  $z$ -axis direction equivalent force  $P_z$

$$\begin{aligned}
P_z &= \frac{E_{1z} E_{2z} A_{1z} A_{2z} (A_{1x} + A_{2x}) (\mu_{2x} - \mu_{1x}) \sigma}{A_{1x} E_{1x} [A_{1z} E_{1z} (1 - \mu_{2xz} \mu_{2zx}) \\
&\quad + A_{2z} E_{2z} (1 - \mu_{1xz} \mu_{2zx})] \\
&\quad + A_{2x} E_{2x} [A_{1z} E_{1z} (1 - \mu_{1xz} \mu_{2zx}) \\
&\quad + A_{2z} E_{2z} (1 - \mu_{1xz} \mu_{2zx})]} \\
&= \frac{E_{1z} E_{2z} V_1 V_2 A_z (\mu_{2x} - \mu_{1x}) \sigma}{V_1 E_{1x} [V_1 E_{1z} (1 - \mu_{2xz} \mu_{2zx}) \\
&\quad + V_2 E_{2z} (1 - \mu_{1xz} \mu_{2zx})] \\
&\quad + V_2 E_{2x} [V_1 E_{1z} (1 - \mu_{1xz} \mu_{2zx}) \\
&\quad + V_2 E_{2z} (1 - \mu_{1xz} \mu_{2zx})]}
\end{aligned} \quad (12)$$

If every single plate is isotropic, formula (12) can be simplified as follows:

$$P_z = \frac{E_1 E_2 V_1 V_2 A_z (\mu_2 - \mu_1) \sigma}{V_1^2 E_1^2 (1 - \mu_2^2) + 2V_1 E_1 V_2 E_2 (1 - \mu_1 \mu_2) + V_2^2 E_2^2 (1 - \mu_1^2)} \quad (13)$$

If all products of Poisson's ratio are neglected, then formula (12) can be simplified to

$$\begin{aligned}
P_z &= \frac{E_{1z} E_{2z} V_1 V_2 A_z (\mu_{2x} - \mu_{1x}) \sigma}{(V_1 E_{1x} + V_2 E_{2x}) (V_1 E_{1z} + V_2 E_{2z})} \\
&= \frac{E_{1z} E_{2z} V_1 V_2 (\mu_{2x} - \mu_{1x}) A_z \sigma}{E_x E_z}
\end{aligned} \quad (14)$$

By Equations (1) and (6), the  $z$ -axis direction Poisson's ratio under the  $x$ -axis direction force is

$$\begin{aligned}
\mu_{zx} &= -\frac{\varepsilon_z}{\varepsilon_x} = -\frac{\varepsilon_{1z}}{\varepsilon_{1x}} \\
&= -\frac{\frac{\mu_{1zx} \sigma}{E_{1x}} - \frac{\mu_{1zx} P_x / A_{1x}}{E_{1x}} + \frac{P_z / A_{1z}}{E_{1z}}}{\frac{\sigma}{E_{1x}} + \frac{P_x / A_{1x}}{E_{1x}} - \mu_{1xz} \frac{P_z / A_{1z}}{E_{1z}}}
\end{aligned} \quad (15)$$

By formulas (11) and (14), formula (15) can be simplified as follows:

$$\begin{aligned}
\mu_{zx} &= \frac{A_{1z} E_{1z} \mu_{1zx} (1 - \mu_{2xz} \mu_{2zx})}{A_{1z} E_{1z} (1 - \mu_{2xz} \mu_{2zx})} \\
&\quad + \frac{A_{2z} E_{2z} \mu_{2zx} (1 - \mu_{1xz} \mu_{1zx})}{A_{1z} E_{1z} (1 - \mu_{2xz} \mu_{2zx})} \\
&\quad + \frac{A_{2z} E_{2z} (1 - \mu_{1xz} \mu_{1zx})}{A_{1z} E_{1z} (1 - \mu_{2xz} \mu_{2zx})} \\
&\quad + \frac{V_1 E_{1z} \mu_{1zx} (1 - \mu_{2xz} \mu_{2zx})}{V_1 E_{1z} (1 - \mu_{2xz} \mu_{2zx})} \\
&\quad + \frac{V_2 E_{2z} \mu_{2zx} (1 - \mu_{1xz} \mu_{1zx})}{V_1 E_{1z} (1 - \mu_{2xz} \mu_{2zx})} \\
&\quad + \frac{V_2 E_{2z} (1 - \mu_{1xz} \mu_{1zx})}{V_1 E_{1z} (1 - \mu_{2xz} \mu_{2zx})}
\end{aligned} \quad (16)$$

If all products of Poisson's ratio are neglected, then formula (16) can be further simplified to

$$\begin{aligned}
\mu_{zx} &= \frac{V_1 E_{1z} \mu_{1zx} + V_2 E_{2z} \mu_{2zx}}{V_1 E_{1z} + V_2 E_{2z}} \\
&= \frac{V_1 E_{1z} \mu_{1zx} + V_2 E_{2z} \mu_{2zx}}{E_z}
\end{aligned} \quad (17)$$

Formula (17) shows that, under the action of longitudinal force, Poisson's ratio in lateral direction (non-normal direction) is inversely proportional to the lateral elastic modulus of the laminate, and is proportional to the sum of the products of Poisson's ratio, elastic modulus and volume fraction of each single plate.

The strains in the  $y$ -axis direction of each single plate are as follows

$$\varepsilon_{1y} = -\mu_{1yx} \frac{\sigma}{E_{1x}} - \mu_{1yx} \frac{P_x / A_{1x}}{E_{1x}} - \mu_{1yz} \frac{P_z / A_{1z}}{E_{1z}} \quad (18)$$

$$\varepsilon_{2y} = -\mu_{2yx} \frac{\sigma}{E_{2x}} + \mu_{2yx} \frac{P_x / A_{2x}}{E_{2x}} + \mu_{2yz} \frac{P_z / A_{2z}}{E_{2z}} \quad (19)$$

The laminate  $y$ -axis direction Poisson's ratio under the  $x$ -axis direction force is given by

$$\begin{aligned}
\mu_{yx} &= -\frac{\varepsilon_y}{\varepsilon_x} = -\frac{(H_1 \varepsilon_{1y} + H_2 \varepsilon_{2y}) / H}{\varepsilon_x} \\
&= -\frac{V_1 \varepsilon_{1y} + V_2 \varepsilon_{2y}}{\varepsilon_x} \approx V_1 \mu_{1yx} + V_2 \mu_{2yx}
\end{aligned} \quad (20)$$

This formula shows that the normal direction Poisson's ratio by the longitudinal force is equal to the weighted sum of Poisson's ratios of each single plate according to the volume fraction.

#### 4 POISSON'S RATIO CALCULATION UNDER THE ACTION OF NORMAL FORCE

Referring to Figure 1, we now study the strains produced by the stress in the  $y$ -axis direction (normal direction).

The first layer (lower layer) single plate  $z$ -axis direction strain is given by

$$\begin{aligned}\varepsilon_{1z} &= \varepsilon_{1\sigma z} + \varepsilon_{1P_{xz}} + \varepsilon_{1P_{zz}} \\ &= -\mu_{1zy} \frac{\sigma}{E_{1y}} - \mu_{1zx} \frac{P_x/A_{1x}}{E_{1x}} + \frac{P_z/A_{1z}}{E_{1z}}\end{aligned}\quad (21)$$

The second layer (upper layer) single plate  $z$ -axis direction strain is given by

$$\begin{aligned}\varepsilon_{2z} &= \varepsilon_{2\sigma z} + \varepsilon_{2P_{xz}} + \varepsilon_{2P_{zz}} \\ &= -\mu_{2zy} \frac{\sigma}{E_{2y}} + \mu_{2zx} \frac{P_x/A_{2x}}{E_{2x}} - \frac{P_z/A_{2z}}{E_{2z}}\end{aligned}\quad (22)$$

The  $x$ -axis direction strains of each layer plate are given by

$$\begin{aligned}\varepsilon_{1x} &= \varepsilon_{1\sigma x} + \varepsilon_{1P_{xx}} + \varepsilon_{1P_{zx}} \\ &= -\mu_{1xy} \frac{\sigma}{E_{1y}} + \frac{P_x/A_{1x}}{E_{1x}} - \mu_{1xz} \frac{P_z/A_{1z}}{E_{1z}}\end{aligned}\quad (23)$$

$$\begin{aligned}\varepsilon_{2x} &= \varepsilon_{2\sigma x} + \varepsilon_{2P_{xx}} + \varepsilon_{2P_{zx}} \\ &= -\mu_{2xy} \frac{\sigma}{E_{2y}} - \frac{P_x/A_{2x}}{E_{2x}} + \mu_{2xz} \frac{P_z/A_{2z}}{E_{2z}}\end{aligned}\quad (24)$$

By  $\varepsilon_{1z} = \varepsilon_{2z}$  and  $\varepsilon_{1x} = \varepsilon_{2x}$ , we get the following equations:

$$\left\{ \begin{aligned} & -\mu_{1zy} \frac{\sigma}{E_{1y}} - \mu_{1zx} \frac{P_x/A_{1x}}{E_{1x}} + \frac{P_z/A_{1z}}{E_{1z}} \\ &= -\mu_{2zy} \frac{\sigma}{E_{2y}} + \mu_{2zx} \frac{P_x/A_{2x}}{E_{2x}} - \frac{P_z/A_{2z}}{E_{2z}} \\ & -\mu_{1xy} \frac{\sigma}{E_{1y}} + \frac{P_x/A_{1x}}{E_{1x}} - \mu_{1xz} \frac{P_z/A_{1z}}{E_{1z}} \\ &= -\mu_{2xy} \frac{\sigma}{E_{2y}} - \frac{P_x/A_{2x}}{E_{2x}} + \mu_{2xz} \frac{P_z/A_{2z}}{E_{2z}} \end{aligned} \right. \quad (25)$$

Ignoring the product form Poisson's ratios, approximate solutions of virtual forces are given as follows:

$$\begin{aligned}P_x &\approx \frac{A_{1x}A_{2x}E_{1x}E_{2x}(E_{2y}\mu_{1xy} - E_{1y}\mu_{2xy})\sigma}{E_{1y}E_{2y}(A_{1x}E_{1x} + A_{2x}E_{2x})} \\ &= \frac{V_1V_2E_{1x}E_{2x}(E_{2y}\mu_{1xy} - E_{1y}\mu_{2xy})}{E_{1y}E_{2y}(V_1E_{1x} + V_2E_{2x})} A_x \sigma\end{aligned}\quad (26)$$

$$\begin{aligned}P_z &\approx \frac{A_{1z}A_{2z}E_{1z}E_{2z}(E_{2y}\mu_{1zy} - E_{1y}\mu_{2zy})\sigma}{E_{1y}E_{2y}(A_{1z}E_{1z} + A_{2z}E_{2z})} \\ &= \frac{V_1V_2E_{1z}E_{2z}(E_{2y}\mu_{1zy} - E_{1y}\mu_{2zy})}{E_{1y}E_{2y}(V_1E_{1z} + V_2E_{2z})} A_z \sigma\end{aligned}\quad (27)$$

The first layer (lower layer) single plate  $y$ -axis direction strain is given by

$$\begin{aligned}\varepsilon_{1y} &= \varepsilon_{1\sigma y} + \varepsilon_{1P_{xy}} + \varepsilon_{1P_{zy}} \\ &= \frac{\sigma}{E_{1y}} - \mu_{1yx} \frac{P_x/A_{1x}}{E_{1x}} + \mu_{1yz} \frac{P_z/A_{1z}}{E_{1z}}\end{aligned}\quad (28)$$

The second layer (upper layer) single plate  $y$ -axis direction strain is given by

$$\begin{aligned}\varepsilon_{2y} &= \varepsilon_{2\sigma y} + \varepsilon_{2P_{xy}} + \varepsilon_{2P_{zy}} \\ &= \frac{\sigma}{E_{2y}} + \mu_{2yx} \frac{P_x/A_{2x}}{E_{2x}} + \mu_{2yz} \frac{P_z/A_{2z}}{E_{2z}}\end{aligned}\quad (29)$$

The  $y$ -axis direction total strain of the laminate is given by

$$\begin{aligned}\varepsilon_y &= \frac{H_1\varepsilon_{1y} + H_2\varepsilon_{2y}}{H} = V_1\varepsilon_{1y} + V_2\varepsilon_{2y} \\ &= V_1 \left( \frac{\sigma}{E_{1y}} - \mu_{1yx} \frac{P_x/A_{1x}}{E_{1x}} + \mu_{1yz} \frac{P_z/A_{1z}}{E_{1z}} \right) \\ &\quad + V_2 \left( \frac{\sigma}{E_{2y}} + \mu_{2yx} \frac{P_x/A_{2x}}{E_{2x}} + \mu_{2yz} \frac{P_z/A_{2z}}{E_{2z}} \right)\end{aligned}\quad (30)$$

The laminate  $x$ -axis direction Poisson's ratio under the  $y$ -axis direction force is given by

$$\begin{aligned}\mu_{xy} &= -\frac{\varepsilon_x}{\varepsilon_y} = -\frac{\varepsilon_{1x}}{\varepsilon_y} \\ &= -\frac{-\mu_{1xy} \frac{\sigma}{E_{1y}} + \frac{P_x/A_{1x}}{E_{1x}} - \mu_{1xz} \frac{P_z/A_{1z}}{E_{1z}}}{V_1 \left( \frac{\sigma}{E_{1y}} - \mu_{1yx} \frac{P_x/A_{1x}}{E_{1x}} + \mu_{1yz} \frac{P_z/A_{1z}}{E_{1z}} \right) + V_2 \left( \frac{\sigma}{E_{2y}} + \mu_{2yx} \frac{P_x/A_{2x}}{E_{2x}} + \mu_{2yz} \frac{P_z/A_{2z}}{E_{2z}} \right)}\end{aligned}\quad (31)$$

The equivalent forces  $P_x$  and  $P_z$  in formula (31) are determined by formulas (26) and (27).

The laminate  $z$ -axis direction Poisson's ratio under the  $y$ -axis direction force could be calculated by a similar method.

## 5 CONCLUSIONS

1. Poisson's ratio of laminate composite could be approximately calculated by the analytical method.
2. The normal direction Poisson's ratio under the action of longitudinal force is equal to the



weighted sum of Poisson's ratios of each single plate according to the volume fraction.

3. Under the action of longitudinal force, Poisson's ratio in the lateral direction (non-normal direction) is inversely proportional to the lateral elastic modulus of the laminate, and is proportional to the sum of the products of Poisson's ratio, elastic modulus and volume fraction of each single plate.

## REFERENCES

- [1] T.P. Philippidis, Pericles S. Theocaris. Transverse Poisson's ratio in fiber reinforced laminate by means of a hybrid experimental approach, *Journal of Composite Materials*, v 28, n 3, p 252–261, 1994.
- [2] Larry D. Peel, Madhuri Lingala. Testing and simulation of stress-stiffening extreme Poisson's ratio twisted fiber-reinforced elastomer composites. *Proceedings of the ASME Conference on Smart Materials, Adaptive Structures and Intelligent Systems, SMASIS2008*, v 1, p 103–111, 2008.
- [3] Ruguang Zhang, Hsien-Liang Yeh, Hsien-Yang Yeh. Preliminary study of negative Poisson's ratio of laminated fiber reinforced composites. *Journal of Reinforced Plastics and Composites*, v 17, n 18, p 1651–1664, 1998.
- [4] Hsien-Liang Yeh, Hsien-Yang Yeh, Ruguang Zhang. Study of negative Poisson's ratio in randomly oriented quasi-isotropic composite laminates. *Journal of Composite Materials*, v 33, n 19, p 1843–1857, 1999.
- [5] P.D. Craig, J. Summerscales. Poisson's Ratios in Glass Fibre Reinforced Plastics. *Composite Structures*, v 9, n 3, p 173–188, 1988.
- [6] Wenqing Liu, Bingyuan Jiang. Calculation of Elastic Modulus and Poisson's Ratio of Symmetrical Composite Laminates, *Aerospace Materials & Technology*, n 3, p 53–56, 2003. (in Chinese).

# The effects of nanophase SiO<sub>2</sub> for the performance of epoxy resin

Y.J. Jin

Jilin Jianzhu University, Changchun, China

SH.J. Wang

The City College of Jilin Jianzhu University, Changchun, China

**ABSTRACT:** This article mainly researches on the uniform dispersion of technology for nanophase SiO<sub>2</sub> in epoxy resin. The tensile test, shock test and scanner electric glass are applied for studying the structure and performance of the compound material. The results indicate that the nanophase SiO<sub>2</sub> are uniformly dispersed in the epoxy resin radical and the mechanical performance of epoxy resin is improved, which will produce the action of increasing strength and increasing toughness for epoxy resin.

**Keywords:** epoxy resin; nanophase SiO<sub>2</sub>; increasing strength; increasing toughness

## 1 INTRODUCTION

Epoxy resin is a thermosetting resin, which has excellent mechanical properties, electrical properties and chemical properties, and it is widely used in fields such as machinery, chemicals, electrical and electronic and aerospace. But the epoxy resin has some disadvantages, such as crosslinking curing crisp poor impact resistance and resistance to stress cracking ability. Introduction of nanoparticles proves to be an effective method in epoxy resin, and it has become a hot research (Shang et al. 2005; Kormmann et al. 2001). Nanomaterials have been shown to have excellent performance because of their unique surface effect, volume effect and the quantum effects that conventional fillers do not have. Nanoparticles have small particle size, surface energy, are easily reunited, and different from the conventional particles that can exist between particles. How to solve the agglomeration problem to achieve a rapid, uniform dispersion of nano-particles in the matrix becomes the key performance of composite material (Liu et al. 2002; Hui et al. 2004).

## 2 EXPERIMENTAL SECTION

### 2.1 The main materials

Epoxy resin takes WSR6101(E-44), which has double A made in Wuxi Resin Industry. Nano silica is provided by Hangzhou Wan Jing New Material Co. Ltd. Its performance is presented in Table 1. It can be seen from Table 1 that nanophase SiO<sub>2</sub> has a surface area of 250 ± 30 m<sup>2</sup>/g and an average particle diam-

eter of 15 ± 5 nm. Curing agent (ethylenediamine) is made by Shanghai Reagent Factory. Acetone is produced by Xi'an Reagent Factory.

### 2.2 Specimen preparation

The powdered nano-SiO<sub>2</sub> is added to a solution of an appropriate amount of acetone, and treated with ultrasonic waves for 30 minutes. The pot in an oil bath is heated to about 130 °C after stirring the solution, and an epoxy resin mixed solvent removed, the epoxy resin and nano-SiO<sub>2</sub> reaction is about 1H. A curing agent (ethylenediamine) stoichiometric is mixed and poured into the vacuum degassing of steel mold coated with a release agent after cooling, the cured completely is cooled after demolding, and the mechanical properties of the test piece are analyzed.

### 2.3 The performance testing and tensile testing

The tensile properties are tested according to the GB1040-79 standard test. The machine used is LJ-500 type.

### 2.4 The impact testing

The impact properties are tested according to the GB1043-79 standard test. The machine used is CHARPY X CJ-40-type.

### 2.5 SEM

The particle morphology of material is observed by the transmission electron microscope and the scanning electron microscope. The machine type

Table 1. The performance parameters of nano-silica.

Name	Performance	Particle size (nm)	Specific surface area (m <sup>2</sup> /g)	Content (%)	Ignition loss (%) 950°C × 2 h
Nano-silica	White powder	15 ± 5	250 ± 30	≥99.5	≤6

is the S-570 scanning electron microscope (Hitachi Ltd, Japan).

### 3 RESULTS AND DISCUSSION

#### 3.1 The mechanical properties of E-44/nm SiO<sub>2</sub> composite material

Nano-SiO<sub>2</sub> with different amounts affects the mechanical properties of E-44/nm SiO<sub>2</sub> composite. It takes the epoxy resin as the base to be incorporated material SiO<sub>2</sub> to find five points dosage of 0%, 2%, 4%, 6%, and 8%, which are measured impact values and the tensile value and the test piece is observed nano-SiO<sub>2</sub> ash on PC impact, tensile impact. Table 2 gives the mechanical properties of nm SiO<sub>2</sub> composite material.

It can be seen that the nm SiO<sub>2</sub> epoxy resin concrete has a toughening effect, within a certain range, as shown in Figure 1 and Figure 2. The impact strength and tensile strength of the composite material obtained are gradually increased with the nm SiO<sub>2</sub> increasing of the content, when nm SiO<sub>2</sub>/E-44 is 2/100 (mass ratio). These two properties reach a maximum value (1.24 J/m, 1.43 MPa), and the material of two kinds of performance declines with the amount of nm SiO<sub>2</sub> increasing.

Nano silica is a light amorphous white powder. It is non-toxic, tasteless, and non-polluting. The microstructure of nano-silica is flocculent and mesh. This special structure makes it to have unique properties, especially its dispersion in the material when combined with polymer chains to form a three-dimensional network structure. So, it can improve the basic properties of the material, such as strength and elastic.

In the study of composite systems by ultrasonic treatment, nm of SiO<sub>2</sub> particles are uniformly dispersed in an epoxy matrix, the matrix impact nm of SiO<sub>2</sub> between the particles, and the matrix can produce a large number of silver streaks (or micro-cracks) between the particles, which is also plastically deformed. Therefore, it absorbs greatly impact energy to achieve toughening effects. Nm SiO<sub>2</sub> is added in an amount within a certain range, if it increases the resulting silver streaks and plastic deformation will increase, the toughening effect will also be better. In addition, its particle diameter is small, has a large surface area, a large

Table 2. The mechanical properties of nm SiO<sub>2</sub> composite material.

SiO <sub>2</sub> contents (%)	0	2	4	6	8
Tensile value (MPa)	0.26	1.43	0.38	0.47	0.36
Impact values (J/m <sup>2</sup> )	0.65	1.24	0.75	0.64	0.60

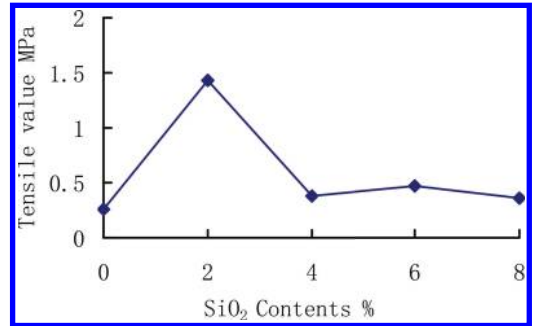


Figure 1. The effects of nanophase SiO<sub>2</sub> to tensile of PC.

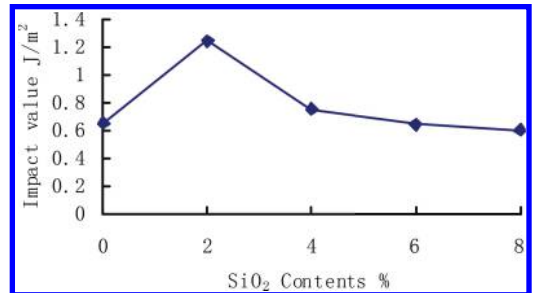


Figure 2. The effects of nanophase SiO<sub>2</sub> to impact of PC.

proportion of atoms within the surface layer with an epoxy resin for the nanoscale particles. It can sufficiently adsorb, bond, couple with the use of silane coupling agent, and enhance the interfacial adhesion of the particles and the matrix, which are conducive to the stress transfer between the particles and the matrix, improving the ability to bear the load. Therefore, the enhancement and toughening of the base body are simultaneous. If nm SiO<sub>2</sub> is added in an amount of more than a critical value, it will result in a short distance between

the nanoparticles, the silver streaks of the material by an external force generated when too much, and very large plastic deformation, thus it will be evolved into a large cracking, leading to the decline in the strength and toughness of the material.

The content of nanophase  $\text{SiO}_2$  effects the tensile of PC is shown in Figure 1, and effects the impact of PC are shown in Figure 2.

### 3.2 Electron microscopic analysis of E-44/nm $\text{SiO}_2$ composite material

Figure 4 shows a SEM image of an epoxy resin nano-composite material. It can be seen from the

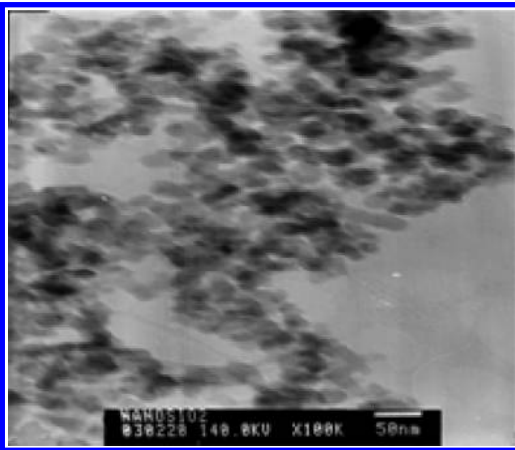


Figure 3. The transmission electron microscope of nano-silica.

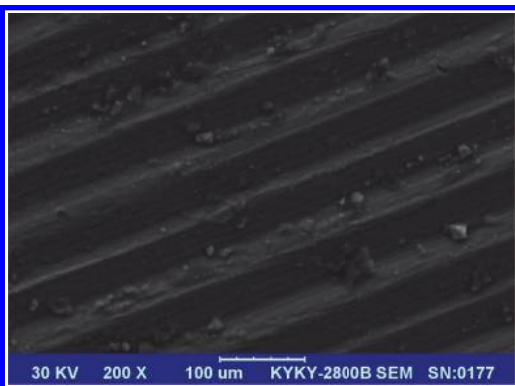


Figure 4. The SEM photo of E-44/nm  $\text{SiO}_2$  composite material.

figure that the nano-composite epoxy system force will produce a lot of crazing. Nano- $\text{SiO}_2$  particles are added to the epoxy resin, the surface of nano- $\text{SiO}_2$  particles has lack of coordination, a large specific surface area characteristics, so that it shows strong activity with the oxygen atoms of the epoxy-like molecules that are prone to key cooperation, and enhance the bond force between the molecules. As part of nano- $\text{SiO}_2$  particles are distributed in the gap of the polymer chain, and a high degree of liquidity, the strength and toughness of epoxy are increased and thus nano- $\text{SiO}_2$  particles are increased greatly.

## 4 SUMMARY

In summary, nano- $\text{SiO}_2$  can enhance toughened epoxy resin (Jin 2010; Xiao & Jin 2009) within a certain range of dosage. In E-44/nm  $\text{SiO}_2$  composites, the ratio of the best use of nano- $\text{SiO}_2$  and epoxy resin is 2/100 in a relatively uniform dispersion.

## ACKNOWLEDGMENT

This work was financially supported by the Jilin Province Science and Technology Development Program (20130206087SF).

## REFERENCES

- Hui, X.M. & Zhang, W. 2004. Research on the dispersion process of the Nano  $\text{SiO}_2$  in the epoxy resin composites. *Thermosetting Resins* 3:21–23.
- Jin, Y.J. 2010. Modified epoxy resin concrete (mortar) and applied research. *Masters Thesis*.
- Kormmann, X., Lindberg, H. & Berglund, L.A. 2001. Synthesis of epoxy-clay nanocomposites: influence of the nature of the clay on structure. *Polymer* 42:1303–1310.
- Liu, J.C. & Zhang, H.L. 2002. The dispersion of particle influences on the epoxy resin/nano  $\text{SiO}_2$  material performance. *Synthetic Resin* 19(1):30–33.
- Shang, H.X., Li, G.S. & Li, W.X. 2005. Research on the performance of Nano  $\text{SiO}_2$ /epoxy resin composites. *New Chemical Material* 1:60–62.
- Xiao, L.G., & Jin, Y.J. 2009. Preparation and properties of a new composite of Epoxy Emulsion (EEM) modified cement. *Journal of Wuhan University of Technology* 10:843–845.

# The study of alkaline-activated magnesium slag cementitious material

Y.J. Jin

Jilin Jianzhu University, Changchun, China

SH.J. Wang

The City College, Jilin Jianzhu University, Changchun, China

L.G. Xiao

Jilin Jianzhu University, Changchun, China

**ABSTRACT:** Magnesium slag cementitious material was prepared successfully using the magnesium slag-furnace slag-clinker system and different activators in this paper. The effect of the activator on the mechanical property of the material was studied. The hydration and microstructure of this composite cement were analyzed by X-ray diffraction and scanning electron microscopy, and the interaction mechanism was researched. The results show that the activity of magnesium slag was enhanced significantly by adding a small amount of the activator. Combined activators have the best effect. The activators have no effect on the species of hydration products of magnesium slag cementitious materials mortar, which are composed of Aft, C-S-H,  $\text{Ca}(\text{OH})_2$ .

**Keywords:** magnesium slag; activators; interaction mechanism; cementitious materials

## 1 INTRODUCTION

Magnesium slag is the sub-product generated in the production of metallic magnesium. Magnesium slag is obtained by the reduction of dolomite by Fe- (Si), resulting in several oxides, being constituted of dicalcium silicate ( $2\text{CaO}\cdot\text{SiO}_2$ ), which is also present in cements and slags (Oliveira et al. 2004). It was nothing more than a latent hydraulic binder and must be activated in practice to react and provide strength. It has been recognized that alkali additions can activate pozzolanic materials to set and harden in their own right (Darko K. et al. 2002). The result showed that cementitious materials composed of magnesium slag and little clinker did not meet the engineering demand in the previous study. By learning from the use of other slags, furnace slag was added to magnesium slag cementitious materials. Magnesium slag cementitious materials consisted of clinker, magnesium slag, furnace slag and activators, consisting of sodium silicate, gypsum and sodium silicate.

## 2 EXPERIMENTAL PROCEDURE

### 2.1 Materials

Magnesium slag was supplied by Dong Feng Colored Metal Industry of Jilin. Furnace slag and clinker were supplied by YaTai Cement Industry.

Details of the chemical composition of the materials used are given in Table 1. Activators were liquid sodium silicate, sodium sulfate, and gypsum. Liquid sodium silicate was bought from the market, and the modulus of sodium silicate was 1.5, with a consistency of 49%. Sodium sulfate was of industrial grade chemical reagent. Gypsum was supplied by YATAI Cement Industry of Jilin, and the content of  $\text{SO}_3$  is 40%.

### 2.2 Specimens and test methods

The original materials were ground in the ball grinding mill according to the proportion fixed in the previous study until the final fineness was 3.6%. Liquid sodium silicate was added by dissolving in water, but gypsum and sodium silicate were added by mixing with the other dry materials. Determination of strength was tested according

Table 1. Chemical composition (by mass) of raw materials (%).

Materials	$\text{SiO}_2$	$\text{Al}_2\text{O}_3$	$\text{Fe}_2\text{O}_3$	CaO	MgO	Others
Clinker	22	5	6	64	1.5	1.5
MS	31.78	2.61	7.73	48.53	8.42	1.65
FS	30.67	17.98	0.73	40.03	8.50	2.09

\*MS refers to magnesium slag, FS refers to furnace slag.

to the GB/T 17671-1999 test. Water requirement of normal consistency, setting time and soundness of the material were tested according to the GB/T1346-2001 test. Fineness of the material was tested according to the GB/T 1345-2005 test. A water-to-binder ratio of 0.5 was used. The type of X-ray machine used was Ultimalv, which operates under the following conditions: 40 kV, 20 mA. The type of SEM machine used was KYKY2800.

### 3 RESULTS AND DISCUSSION

#### 3.1 Determination of minerals of magnesium slag

The minerals phases of magnesium slag were determined by XRD. The result is shown in Figure 1.

It can be seen from Figure 1 that the mineral phases of magnesium slag were  $C_2S$ ,  $MgO$  and  $CF$ . Magnesium slag can harden because there was plenty of  $C_2S$ , which was the mineral of Portland cement.

#### 3.2 Effect of activators on the magnesium slag cementitious material

The experiment was conducted according to the proportion fixed in the previous study (clinker:magnesium slag:furnace slag ratio 35%:32.5%:32.5% by mass). The effects of the single activator and composite activators were studied.

As shown in Table 2, the mechanical properties of magnesium slag cementitious material were enhanced by adding the activator, and the combined activators have the best effect on the material. The hydration process and mechanism can be explained as follows. The hydration of clinker and hydrolyzation of sodium silicate resulted in a high concentration of  $OH^-$ . The structure of magnesium slag and furnace slag is destroyed under the high concentration of  $OH^-$ . It can be described as

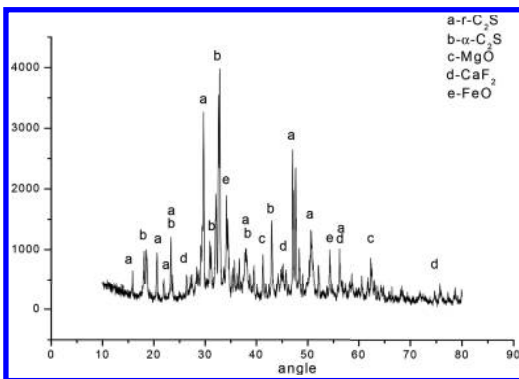


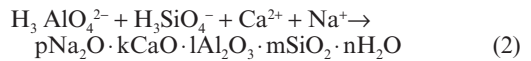
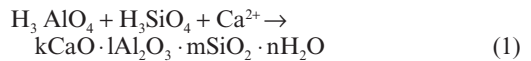
Figure 1. Curves of XRD-ray analysis.

Table 2. Effect of the activators on the mechanical property of magnesium slag cementitious material.

No.	Activator		Compressive strength/MPa		Flexural strength/MPa	
	Kind	Dosage/%	3d	28d	3d	28d
1		0	10.6	25.8	2.45	3.90
2	a	1.5	10.9	28.3	2.60	4.70
3	b	2	15.4	30.3	3.55	5.2
4	c	3	12.9	30.5	2.92	6.2
5	a+ b + c	0.5 + 2 + 2	14.7	42.7	3.52	7.3

\*a indicates sodium silicate, b indicates sodium sulfate, c indicates gypsum.

the breaking of Me-O (Me ≡ Ca, Mg), Si-O-Si, Al-O-Al and Al-O-Si bonds in the slag grains, resulting in high concentrations of ions such as  $H_3SiO_4^-$  and  $H_3AlO_4^{2-}$  in the solution. These ions react with  $Na^+$ , which result in some hydration products of natrolite, The reactions proceed according to the following equations (Xu et al. 2004):



The above reaction absorbed lots of  $Ca^{2+}$  and other ions, which accelerated the rate of the destruction of magnesium slag and furnace slag gradually. At the same time, gypsum and sodium sulfate provided the  $SO_4^{2-}$  ions that reacted with  $C_4AH_{19}$ . Thus, the Aft was produced when gypsum and sodium sulfate were added. The products formed at later times filled in the porous area; furthermore, these products formed a compacted net structure through superposition. The result was that the strength of the material was enhanced finally.

The cementitious material had good mechanical properties, with the compressive strength of 42.7 MPa and the flexural strength of 7.3 MPa. Properties of the material were also tested. The water requirement of normal consistency was 34.4%, the initial time was 116 min, the final time was 175 min, and the soundness of the material corresponded with the standard of cement.

#### 3.3 SEM observations

The microstructure of this composite cement was analyzed by scanning electron microscopy, and as a comparison, two SEM images were

obtained. Figure 2 shows the micrographs of this material.

It can be obviously noted that there exists quite a large difference in the microstructure of the magnesium slag cementitious materials whether the activator was added. The latter generally exhibits compacted and continued integrated morphological characteristics, while the former exhibits some incompact area, i.e., some remaining porous area. We can see this result from the above figure where lots of needle core product exists in the material, and little product linked to each other. It was proved that both magnesium slag and furnace slag hydrated incompletely, with the microstructure of the products showing a compacted structure correspondingly. It proved that the activators accelerate the rate of hydration, and more hydration products were formed.

### 3.4 X-Ray Microanalysis (XRD)

The hydration products have much effect on the properties of cement, such as durability and other mechanical properties. So, the kinds of hydration

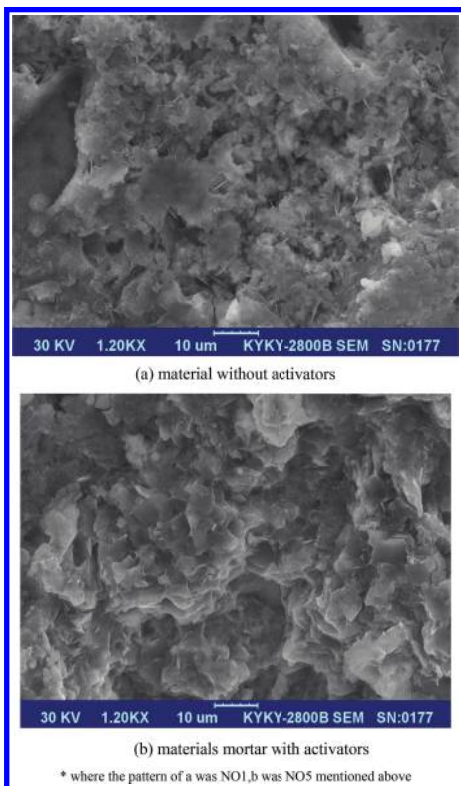


Figure 2. SEM images of magnesium slag cementitious material mortar (28d).

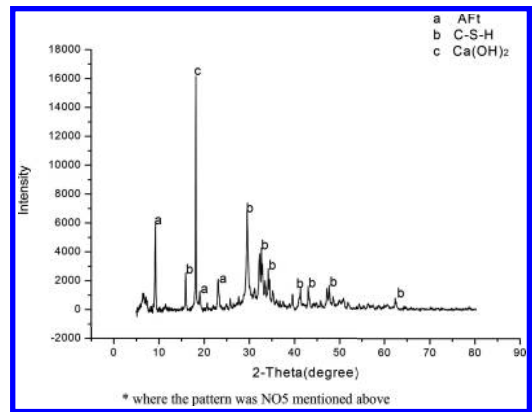


Figure 3. XRD patterns of magnesium slag cementitious materials mortar.

products were analyzed by XRD, and the result is shown in Figure 3.

From Figure 3, we can observe that Aft, C-S-H,  $\text{Ca}(\text{OH})_2$  existed in the hardened cement.

## 4 CONCLUSION

Magnesium slag cementitious material was prepared successfully using the magnesium slag-furnace slag-clinker system and several activators, whose performance was in accordance with the standards of composite cement of 32.5 MPa. The activity of magnesium slag was enhanced significantly by adding a small amount of the activator. The cementitious material performed well mechanically when the activators were combined. The species of hydration products of this material were Aft, C-S-H,  $\text{Ca}(\text{OH})_2$ .

## REFERENCES

- Carlos A.S. Oliveira, Adriana G. Gumieri, Abdias M. Gomes, Wander L. Vasconcelos. Characterization of Magnesium Slag Aiming the Utilization as Mineral Admixture in Mortar [A]. International RILE Conference on the Use of Recycled Materials in Buildings and Structures [C]. Barcelona: [Spain], 2004.
- Darko K, Branislav Z. Effects of dosage and modulus of water glass on early hydration of alkali-slag cements [J], Cement and Concrete Research 32 (2002) 1181-1188.
- Xu Yuanhui, Lu Wenxiong, Wang Xiujuan, Shao Xia. Research and Development in Activation of Steel Slag Activity [J]. Journal of shanghai university (natural science), 2004, 10(1):91-95.

# Effect of lithium on the microstructure and properties of Al-Mg-Si-Li alloys with different Si contents

Z.K. Zhao, Q. Gao, Y. Yao, B.Z. Liu, D. Zhang & G.Q. Wang

Materials Science and Engineering School, Shandong Jianzhu University, Jinan, P.R. China  
Shandong Engineering Research Center for Clean Foundry, Jinan, P.R. China

**ABSTRACT:** The effect of lithium on the microstructure and properties of Al-Mg-Si-Li alloys with different Si contents was investigated. The microstructure was observed by optical microscopy, the phases were determined by X-ray diffractometry, and the mechanical properties were determined by a tensile tester. The result shows that Li reduces the ratio of eutectic in Al-Si-Mg alloys: the alloy containing 20.0 wt.% Si can not obtain the eutectic microstructure completely. The ratio of the eutectic is increased and the constituent of the eutectic is coarsened with the increment of the Si content. Being modified by the Al-P master alloy, the primary Si is refined and granulated, and the ratio of the eutectic is increased. Al-15 wt.% Si-0.3 wt.% Mg-1.1 wt.% Li alloys have excellent mechanical properties: the tensile strength, the yield strength and elongation of the alloys are 265 MPa, 137 MPa and 1.8%, respectively.

**Keywords:** Li; Si content; Al-Mg-Si-Li alloys; microstructure; properties

## 1 INTRODUCTION

Al-Si-Mg alloys have been widely used in the automotive industry due to their good casting characteristics and mechanical properties. Si is the major alloying element, which imparts good castability, high wear resistance and hardness. A small addition of Mg improves solution treatment and age hardening characteristics of these alloys. The mechanical properties of Al-Si-Mg cast alloys depend not only on a chemical composition, but also, more importantly, on microstructural features such as morphologies of dendritic  $\alpha$ -Al, eutectic Si and  $Mg_2Si$  that present in the microstructure.

Lithium is added to Al-Si alloys to decrease the density and improve the specific strength and elastic modulus. Al-Si-Li alloys containing 3.6–8 wt.% Li and 5–14 wt.% Si have been developed by a rapid solidification technique, where the alloys have a low density, high elastic modulus and high ratio modulus [Dubost1987]. The triangle and oval primary Si phases are present in the microstructure of Al-7.0 wt.% Si-0.3 wt.% Mg -xLi alloys, and the precipitation is inhibited to make the alloys have lower elongation and strength [Gröbner 2001]. However, there is no report about the effect of Li on the microstructure and properties of Al-Si-Mg-Li with different Si contents. In the present work, 1.1 wt.% Li was added into Al-Si-Mg-Li alloys containing 7.0%wt.% Si, 12 wt.% Si, 15 wt.% Si or 20 wt.% Si, respectively, to investigate the

microstructure and properties of Al-Mg-Si-Li alloys with different Si contents.

## 2 EXPERIMENTAL SECTION

Composition of the alloys studied is given in Table 1, which were melted in a vacuum furnace and cast in a metal mould under argon. The alloys were modified by the addition of 1.0 wt.% Al-P master alloy provided by Shandong University.

Microstructure of the alloys was observed by using an optical microscope. The different phases of the alloys were analyzed by X-ray diffractometry. The tensile strength was determined by the tensile tester at a constant rate of 1 mm/s using bars of diameter 10 mm and length 50 mm.

Table 1. Chemical composition of the tested alloys.

Item	Si (wt.%)	Li (wt.%)	Mg (wt.%)	Al (wt.%)	Remark
U1	7.0	0.9	0.3	Balance	Unmodified
U2	12.0	0.9	0.3	Balance	Unmodified
M2	12.0	0.9	0.3	Balance	Modified
M3	15.0	0.9	0.3	Balance	Modified
U4	20.0	0.9	0.3	Balance	Unmodified
M4	20.0	0.9	0.3	Balance	Modified



### 3 RESULTS

#### 3.1 Microstructure of as-cast Al-Si-Mg-Li alloys with different Si contents

Figure 1(a)–(c) shows the microstructure of unmodified Al-Si-0.3 Mg-1.1 Li as-cast alloys with different Si contents. Figure 1(a) shows that the microstructure of the alloys containing 7.0 wt.% Si consists of eutectic, granular Si, together with an amount of fine particles in the primary  $\alpha$ -Al matrix. When the Si content in the alloy is 12.0 wt.%, the ratio of the eutectic increases to 50% approximately, and Si becomes coarse block,

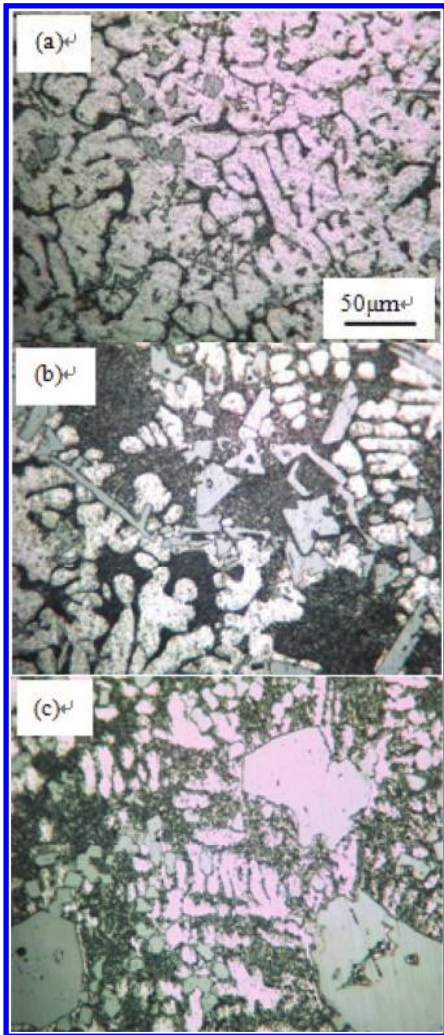


Figure 1. Microstructure of unmodified Al-Si-Mg-Li as-cast alloys with (a) 7.0 wt.% Si, (b) 12.0 wt.% Si, (c) 20.0 wt.% Si.

triangle or needle, and the particles in the  $\alpha$ -Al matrix become coarsened, as shown in Figure 1(b). In the alloy containing 20.0 wt.% Si, the ratio of the eutectic is about 70%, and the primary  $\alpha$ -Al was refined. There are two kinds of Si: granular Si and large block Si, as shown in Figure 1(c). Comparing the eutectic among the three alloys, the ratio of the eutectic increases with the increment of the Si content; however, the ratio of the eutectic is far lower than that of the Li-free alloys. When the Si content is up to 20.0 wt.%, there is still 20% of the primary  $\alpha$ -Al remaining. It should be mentioned that Si in the eutectic is coarsened as the Si content increases.

Figure 2 (a)–(c) shows the microstructure of Al-Si-0.3 Mg-1.1 Li as-cast alloys with different Si contents and the alloys were modified by the 1.0 wt.% Al-P master alloy. The microstructure containing 12.0 wt.% Si shows the oval primary  $\alpha$ -Al phase, eutectic and Si, as shown in Figure 2(a). Figure 2(b) shows the microstructure of the alloy containing 15.0 wt.% Si, the  $\alpha$ -Al is refined, approximately 60% of eutectic occurs, and Si is also refined and granulated. When Si content is 20.0 wt.%, the coarse stick particles are distributed in the  $\alpha$ -Al matrix, which constitutes the eutectic, besides the coarser Si, as shown in Figure 2(c). Comparing the microstructure of the three modified alloys, the ratio of the eutectic increases and the ratio of the primary  $\alpha$ -Al decreases with the increment of the Si content, and the primary  $\alpha$ -Al almost disappears when the Si content increases up to 20.0 wt.%. The constituent of the eutectic is coarsened as the Si content increases. The modified alloys containing 15.0 wt.% Si have the excellent microstructure.

Comparing the microstructure of the unmodified alloys and the alloys modified by the Al-P master alloy, modification of the Al-P master alloy plays an important role for microstructure improvement of Al-Si-Mg-Li alloys, especially for the alloys with the Si content exceeding 12 wt.%. It is the modification of the Al-P master alloy that increases the ratio of the eutectic, and refines and granulates the primary Si, but coarsens the constituent of the eutectic.

#### 3.2 X-ray diffractometry

Figure 3 shows the X-ray diffraction patterns of Al-Si-0.3 Mg-1 Li alloys with 7.0 wt.% Si, 12.0 wt.% Si or 15.0 wt.% Si. Diffraction peaks corresponding to  $\alpha$ -Al, Si and LiAlSi were marked, which shows that the eutectic may be Al-LiAlSi binary eutectic in the as-cast structure [Kadanner1976]. The intensity of the peaks corresponding to Si and LiAlSi is enlarged as the Si content increases, which indicates that the amount of Si and LiAlSi increases with the increment of the Si content.

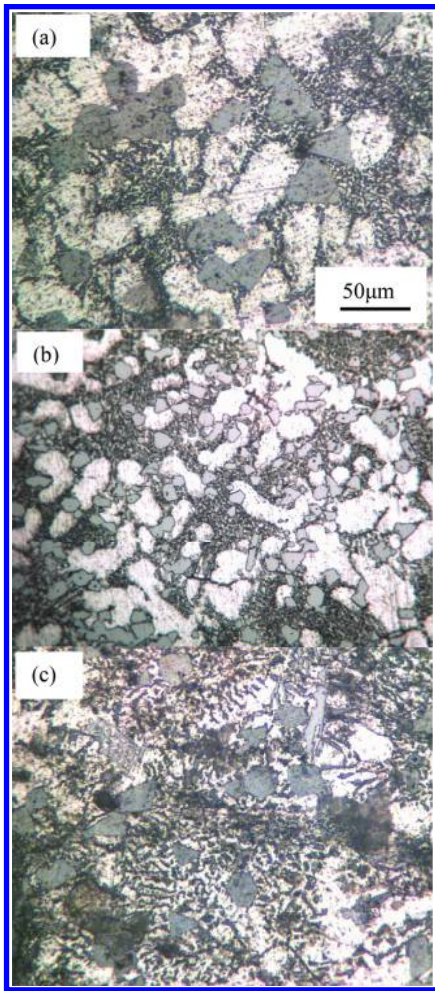


Figure 2. Microstructure of modified Al-Si-Mg-Li as-cast alloys with (a) 12.0 wt.% Si, (b) 15.0 wt.% Si, (c) 20.0 wt.% Si.

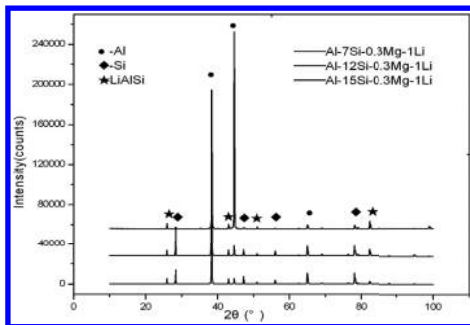


Figure 3. X-ray diffraction patterns of Al-Si-0.3 Mg-1 Li alloys with (a) 7.0 wt.% Si, (b) 12.0 wt.% Si, (c) 15.0 wt.% Si.

Table 2. Mechanical properties of unmodified Al-Si-Mg-Li alloys with different Si contents.

Item	Si content (wt.%)	Tensile strength (MPa)	Yield strength (MPa)	Elongation (%)
U1	7.0	245	89	1.3
U2	12.0	162	78	1.0
U4	20.0	234	85.6	1.2

Table 3. Mechanical properties of modified Al-Si-Mg-Li alloys with different Si contents.

Item	Si content (wt.%)	Tensile strength (MPa)	Yield strength (MPa)	Elongation (%)
M2	12.0	217	84	1.3
M3	15.0	265	137	1.8
M4	20.0	215	82	1.5

### 3.3 Mechanical properties

The mechanical properties of unmodified alloys with different Si contents are listed in Table 2. It can be seen from the table that the unmodified alloys containing 7.0 wt.% alloy have excellent mechanical properties, and the tensile strength is 245 MPa, the yield strength is 89 MPa and the elongation is 1.3%. When the Si content is 12.0 wt.%, the mechanical properties decrease due to the block, triangular or needle primary Si. However, the alloys containing 20.0 wt.% Si have better mechanical properties than those containing 12 wt.% due to the granulation of Si. Table 3 lists the mechanical properties of modified alloys with different Si contents. It can be seen that the alloys containing 15 wt.% Si have excellent mechanical properties, which are superior to those of the alloys containing 12 wt.% Si or 20 wt.% Si.

Comparing the mechanical properties between the unmodified alloys and the modified alloys, it is found that the mechanical properties of the modified alloys are far more excellent than those of the unmodified alloys when the Si content is 12.0 wt.%. When the Si content is 20.0 wt.%, the modification of the Al-P master alloy makes the elongation improve, but the tensile strength is reduced.

## 4 DISCUSSION

Li plays a significant role in the microstructure of Al-Si-Mg alloys. When 1.1 wt.% Li is added into the Al-7.0 wt.% Si-0.3 wt.% Mg alloy, a little of primary Si occurs, which is due to the reduction

of the eutectic. The ratio of the eutectic is just about 50%, which is only a half of the Al-12 wt.% Si alloy. However, the alloy containing 20.0 wt.% Si cannot achieve the eutectic microstructure completely. Given all the above-mentioned factors, the eutectic composition and primary phases are modified by Li.

AlLiSi is a primary phase in Al-Si-Li alloys [Gröbner 2001], and Mg<sub>2</sub>Si is present in the  $\alpha$ -Al matrix when the alloys contain 0.3 wt.% Mg, though Mg<sub>2</sub>Si was not characterized by X-ray diffractometry due to low Mg content. The particles distributed in the  $\alpha$ -Al matrix may be Mg<sub>2</sub>Si, and the eutectic might be the ternary eutectic of Al-Si-AlLiSi. It is the depletion of Si from the primary Si and AlLiSi that causes the reduction of the eutectic.

P and Al form an intermediate phase (AIP) at high temperatures. The crystal structure of the AIP phase is similar to that of Si and is sphalerite type. So, the AIP phase can be used as a heterogeneous nucleation of the primary Si phase, and the final aim is mainly to refine the primary Si phase. But P cannot change the eutectic Si phase. The ratio of the eutectic is improved by the Al-P master alloy due to the reduction of Si depletion during the reaction of P and Li.

## 5 CONCLUSIONS

Li reduces the ratio of the eutectic in Al-Si-Mg alloys, and the alloy containing 20.0 wt.% Si cannot

achieve the eutectic microstructure completely. The ratio of the eutectic is increased and the constituent of the eutectic is coarsened with the increment of the Si content. Being modified by the Al-P alloy, the primary Si is refined and granulated, and the ratio of the eutectic is increased. Al-15 wt.% Si-0.3 wt.% Mg-1.1 wt.% Li alloys have excellent mechanical properties: the tensile strength, the yield strength and elongation of the alloys are 265 MPa, 137 MPa and 1.8%, respectively.

## ACKNOWLEDGMENT

This research was financially supported by the Shandong Provincial Natural Science foundation (ZR2012EMM013 and ZR2012EMM014).

## REFERENCES

- Dubost, B. 1987. Aluminium Alloys With a High Lithium and Silicon Content, and Process for Their Manufacture. *Ausz. Eur. Patentanmeld* 3(3): 93.
- Gröbner, J. et al. 2001. The Al-Li-Si system: 2. Experimental study and thermodynamic calculation of the polythermal equilibria. *Journal of Solid State Chemistry* 156(2): 506–511.
- Kadaner, E.S. et al. 1976. A Constitutional Diagram of the Al-Si-Li System for the Aluminum-Rich Portion. *Izv. Akad. Nauk SSSR, Met.* (1): 181–184.

# Laboratory study on performance of semi-flexible mixture

Lu Zhang

China Agricultural University, Beijing, China

Huoming Wang & Rukai Li

China Merchants Chongqing Communications Research and Design Institute, Chongqing, China

**ABSTRACT:** The semi-flexible pavement refers to matrix asphalt mixture (the void ratio is up to 20%~28%) filled with special mortar in which cement is the major constituent. By laboratory testing of rutting, resistance performance and fatigue characteristics were studied. The results showed that: semi-flexible mixture has excellent high temperature stability, while the test temperature is 70 °C and the tire pressure is 1.0 MPa, the dynamic stability are more than 6000. Compared to the conventional asphalt mixture, the semi-flexible pavement can adapt better to high temperatures and heavy resistance road deformation need. The temperature has a significant effect on the fatigue properties of the semi-flexible mixture: the lower the temperature, the higher the material ultimate tensile strength, however, under such condition, the fatigue life decline faster.

**Keywords:** road engineer; semi-flexible mixture; anti-rutting performance; four-point fatigue bending; fatigue life

## 1 INTRODUCTION

The semi-flexible pavement refers to matrix asphalt mixture (the void ratio is up to 20%~28%) filled with special mortar in which cement<sup>[1,2]</sup> is the major constituent. Researches indicate that semi-flexible pavement with high-temp rutting resistance, low temperature crack resistance and endurance are better than bituminous mixture<sup>[3,4,5]</sup>. Compared with the cement concrete pavement, this pavement has lower modulus and improved traffic comfort and endurance. Additionally, semi-flexible pavement has excellent oil, acid, heat, slippery resistance and water stability, and it is easy to colored up. Based on the above properties, semi-flexible pavement has become a research hot spot in recent years; in some areas experiment have been made by paving semi-flexible pavement to improve the increasingly prominent rutting problem. In this thesis, study of semi-flexible pavement rutting performance and the influence caused by temperature & load have been made through laboratory tests, study of the fatigue characteristics of semi-flexible mixture under different temperature has been made by Four-point bending test, and the logarithm equation of the fatigue life at different temperatures has been concluded by regression analysis.

## 2 SEMI-FLEXIBLE MIXTURE DESIGN

Through the former achievements of this research and many experiments which concentrate on the mix proportion of mother-asphalt mixture, the mix proportion adopted in this thesis can meet the specification of Marshall Stability test and the mother—asphalt mixture and asphalt content adopted in this research is laboratory-made asphalt. And the portion, amount of mixture as well as the Marshall Stability test result are given in [Table 1](#) and [Table 2](#)<sup>[6,7,8]</sup>.

Through many experiments, we get the mortar mix ratio which can meet the need of the mechanical property and mobility. Studies have shown that the admixture of fly ash mortar or polymer helps to improve the performance<sup>[6,8]</sup>. And the physical and mechanical property indices of the mortar

Table 1. Mixture proportion of mother-bituminous mixture in research.

Mesh size (mm)	26.5	19.0	13.2	4.75	2.36	0.6	0.3	0.075
Percent of sifted (%)	100	97	47	18	13	10	8	3

Table 2. Physical-mechanical indices of mother-bituminous mixture.

Bitumen aggregate ratio (%)	Flying shards losses (%)	Drain down losses (%)	Void ratio (%)	Marshall stability (KN)	Flow value (0.1 mm)
2.8	24.7	0.58	23.2	6.8	32.4

Table 3. Mixing proportion of original cement mortar in research.

Cement (%)	Water (%)	Coal ash (%)	River sand (%)	Powder (%)
41.5	31.5	6	12	9

Table 4. Physical-mechanical indices of original cement mortar<sup>[1]</sup>.

Indices	Scope	Remarks
Mobility (s)	10~14	/
Bending strength (MPa)	>2.0	7 days
Compression strength (MPa)	10~30	

mix with fly ash mortar adopted in this research are shown in Table 3 and Table 4.

### 3 RESEARCH ON THE RUTTING RESISTANCE PROPERTIES OF THE SEMI-FLEXIBLE MIXTURE

Rutting test has been adopted to make research on the resistance to deformation of semi-flexible mixture, taking into account the impact of temperature, load, and water to resistance to deformation, the test results are as follows.

#### 3.1 Temperature effects on the rutting test results

Asphalt is a viscoelastic material, to which the temperature has evident effect on its deformation resistance<sup>[4]</sup>. The temperature for the rutting test is 60 °C and 70 °C, while the test wheel ground pressure is 0.7 MPa. The asphalt is SK70 Class A road petroleum asphalt; SBS modified bitumen uses laboratory preparation with 4% of SBS content; and asphalt test results are shown in Table 5. The test results satisfies the Technical Specifications for Construction (JTG F40-2004)<sup>[9]</sup>. The AC-20 mixture has followed the specification, the composition and mixture volume indicators of which are shown in Table 6 and Table 7.

And the results are given in Table 8 and Figure 1, Figure 2.

From the experimental results, the dynamic stability of semi-flexible material is 6000 (times/mm) or more when the temperature is 60 °C or 70 °C. When the temperature increased 10 °C, the dynamic stability declined to 9886 from 11225, with a decrease of 11.9%. In contrast, the dynamic stability of ordinary AC-20 declined from 1890 to 1120 by, with a decrease of 40.7%; and the dynamic stability of SBS modified AC-20 decreased by 31.2%, from 3850 to 2650.

Therefore, it is obvious that the temperature has the greatest impact on ordinary AC rutting dynamic stability; the second greatest on the SBS modified AC and the least on semi-flexible materials.

#### 3.2 Impact of load on rutting test results

In recent years, rutting has occurred to the conventional asphalt pavement because of the increasingly prominent phenomenon of overloading and beyond limitation transportation. Series of measures has been adopted to alleviate the rutting of asphalt pavement, such as high viscosity modified asphalt, low-grade asphalt, high-modulus asphalt concrete, the use of skeleton dense gradation, etc., which have eased to some extent the asphalt pavement rutting, but they are still not effective for the conventional asphalt pavement enough confronting overload and beyond limitation transportation; and rutting still occurs from time to time.

Semi-flexible material is between cement concrete and asphalt mixture; it is the complex of concrete and asphalt, with greater rigidity and better flexibility, integrating the cement and asphalt advantages. From research and practice, semi-flexible material is an effective way to resolve the current rutting problem.

Experimental results show that test wheel ground pressure boasts a good correlation with the weight, for when the weight each increases about 50%, the test wheel ground pressure increases about 0.1 MPa. Thus, rutting test under different load can be made by adjusting the wheel ground pressure to simulate overload. The results are shown in Table 9 and Figure 3.

From the test results, as the test wheel ground pressure increases, all materials' dynamic stability showed reduced trends. When the test wheel ground pressure is from 0.7 MPa to 1.1 MPa (Equivalent to 200% overload simulation), the dynamic stability of ordinary AC-20, SBS modified AC-20 and semi-flexible materials, has decreased 58.5%, 51.2%, 23.5% relatively.

Thus, the use of modified asphalt can provide a more significant improvement in the temperature

Table 5. Test results of asphalt index.

Item	Penetration (25 °C, 0.1 mm)	Softening point (°C)	Ductility (15 °C, cm)	Ductility (5 °C, cm)	Elastic recovery 25 °C (%)	Kinematic viscosity 135 °C (Pa · s)
SK70 asphalt	72	47	>100	/	/	/
4% SBS modified bitumen	65	56	/	42	78	1.7

Table 6. The grading of AC-20 mixture.

Grading	Each sieve (%), mm											
	26.5	19	16	13.2	9.5	4.75	2.36	1.18	0.6	0.3	0.15	0.075
Design grading	100	95.8	84.5	70.2	53.1	31.5	26.8	18.7	15.6	10.2	7.1	5.5

Note: Conventional asphalt AC-20 shares the same grading with SBS modified asphalt AC-20.

Table 7. AC-20 Test results of mixture marshall.

Item	Amount of asphalt (%)	Porosity (%)	VMA (%)	VFA (%)	Stability (KN)	Flow value (0.1 mm)
Conventional asphalt AC-20	4.8	4.7	13.8	65.9	12.8	28.6
SBS modified asphalt AC-20	4.8	4.8	14.2	66.2	14.6	32.4

Table 8. Rutting test results under different temperature conditions.

Test conditions (temp/°C, wheel pressure/MPa)	Test material	Dynamic stability (times/mm)
60°C 0.7 MPa	Ordinary AC-20	1890
	SBS Modified AC-20	3850
	The semi-flexible mixture	11225
70°C 0.7 MPa	Ordinary asphalt AC-20	1120
	SBS modified asphalt AC-20	2650
	The semi-flexible mixture	9886

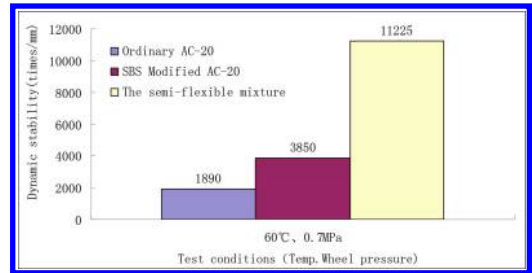


Figure 1. Rutting test results under 60 °C.

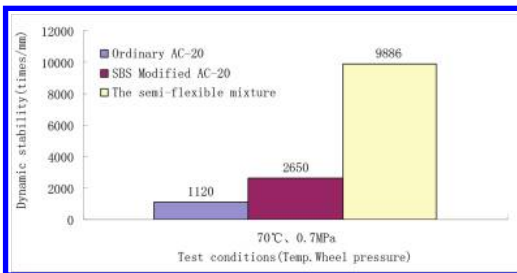


Figure 2. Rutting test results under 70 °C.

Table 9. Rutting test results under different load level.

Test material	The DS test results under different test wheel ground pressure (test temp: 60 °C)			
	0.7 MPa	0.8 MPa	0.9 MPa	1.1 MPa
Ordinary AC-20	1890	1450	1160	785
SBS modified AC-20	3850	3230	2710	1880
The semi-flexible mixture	11225	10800	9650	8585

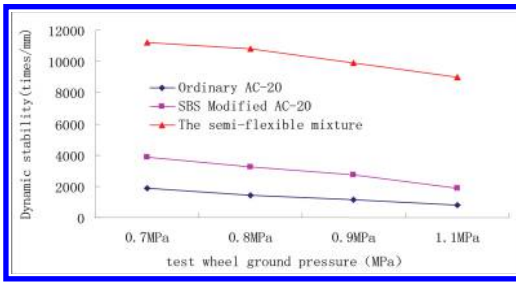


Figure 3. Rutting test results under different wheel ground pressure.

Table 10. Soaking rutting test results.

Test material	Dynamic stability (times/mm)		Residual dynamic stability (%)
	Before soaking	After soaking	
Ordinary AC-20	1850	1365	73.8
SBS modified AC-20	3800	3012	79.3
The semi-flexible mixture	11250	9958	85.2

sensitivity of asphalt, but it is with limited improvement to the load sensitivity. The use of semi-flexible materials can improve both temperature sensitivity and load sensitivity. Even under the road 200% overload conditions, the dynamic stability of semi-flexible materials is also 8000 (times/mm) or more.

### 3.3 Soaking rutting test

In order to test the stability of water of semi-flexible material, soaking rutting test has been conducted. The track plate was saturated in 60 °C water for 5 hours, and then stability test was carried out under conditions of 60 °C for temperature and 0.7 MPa for pressure. The results are shown in Table 10.

From the test results, the soaking rutting residual dynamic stability of ordinary AC-20, SBS modified AC-20 and semi-flexible materials were 73.8%, 79.3%, 85.2%. Based on previous findings, it can meet the requirements of road performance when the residual dynamic stability achieved 70%. It is necessary to adopt high-quality asphalt or other measures to make the residual dynamic stability to achieve more than 80%. The soaking rutting residual dynamic stability of semi-flexible materials was 85.2%, indicating that the water stability is very good.

## 4 RESEARCH ON THE FATIGUE PROPERTY OF THE SEMI-FLEXIBLE MIXTURE

Four-point bending test has been carried out to make research on the fatigue property of the semi-flexible mixture. Taking into account the impact of temperature on the fatigue properties, fatigue performance test has been conducted under three different temperatures (5 °C, 20 °C, 40 °C) and the four stress levels: stress intensity ratios of 0.2, 0.3, 0.4 and 0.5. Corresponding to each intensity ratio, there are 5 items for test and the load frequency is controlled at 10 Hz.

The results are shown in Figure 4 and Table 11. It can be observed in Figure 4 that with increased test temperature, the mixture of semi-flexible pavement breaking strength decreases.

It can be seen from the three temperature fatigue tests results and fatigue curve equation in Figure 5

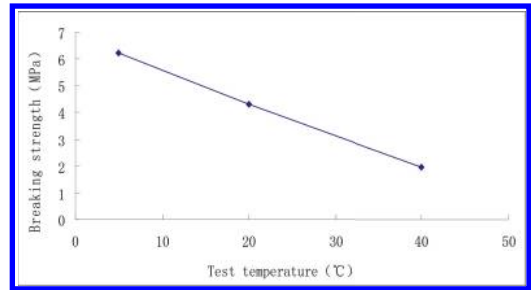


Figure 4. Temperature impact on breaking strength.

Table 11. Fatigue test results under different temperatures and different stress levels.

Temperatures (°C)	Stress-ratio ( $\sigma/\sigma_c$ )	Logarithmic fatigue life $\lg N_f$		Breaking strength (MPa)
		Average	Standard deviation (S)	
5	0.2	5.2254	0.1567	6.21
	0.3	4.4654	0.2458	
	0.4	3.8685	0.1451	
	0.5	3.1451	0.1784	
20	0.2	4.6321	0.0739	4.32
	0.3	3.9218	0.2843	
	0.4	3.4067	0.1781	
	0.5	3.0395	0.2445	
40	0.2	3.5945	0.1475	1.96
	0.3	3.1034	0.0987	
	0.4	2.8811	0.1237	
	0.5	2.3802	0.1179	

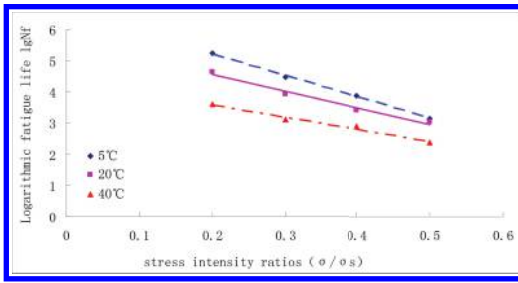


Figure 5. Temperature impact on fatigue life.

Table 12. Fatigue life equation of semi-flexible mixture under three different temperatures.

Temperature (°C)	Fatigue equation	Correlation coefficient
5	$\lg N_f = -6.8378 \sigma/\sigma_s + 6.5693$	0.9981
20	$\lg N_f = -5.2929 \sigma/\sigma_s + 5.6025$	0.9793
40	$\lg N_f = -3.8652 \sigma/\sigma_s + 4.3426$	0.9803

and Table 12, that the fatigue equation slope under 40 °C is significantly less than that is under 5 °C, which demonstrates that semi-flexible mixture has a significant viscoelastic characteristics; although the ultimate tensile strength is low, the rate of decline in fatigue life is more gentle as the stress intensity ratio increases. Semi-flexible mixture will be more brittle under 5 °C, the fatigue life decline faster as the stress intensity °C ratio increases, and lower the temperature, the faster the fatigue life declines.

## 5 CONCLUSION

Through the semi-flexible mixture rutting and four-point bending fatigue test studies, the following conclusions have been obtained:

1. From the experimental results, we can see that the dynamic stability of semi-flexible mixture under 60 °C and 70 °C are above 6000 (times/mm).

The dynamic stability decreases as the temperature increases, for which ordinary AC decreases the fastest, and the SBS modified AC the next, and semi-flexible mixture decreases the slowest.

2. The use of modified asphalt can significantly improve temperature sensitivity, but it is of limited improvement to the load sensitivity. The semi-flexible mixture can improve both temperature sensitivity and load sensitivity. Even with 200% overload, the dynamic stability of semi-flexible mixture is above 8000 (times/mm).
3. With the same stress level, the semi-flexible mixture fatigue life dropped as the temperature increases; and semi-flexible mixture is to some extent brittle at 5 °C, this feature should be considered during actual use.

## REFERENCES

- [1] Japan Association of Roads. Explain for General Code of Asphalt Pavement Engineering [M]. Tokyo: Maruzen Co., Ltd., 1992.
- [2] Yang Yu-liang, Zou Gui-lian, Zhang Xiao-ning. Research on Cement Slurry Filling in Semi-Flexible Asphalt Mixture. Highway. Nov. 2002 No. 11:77–80.
- [3] Pang Chuan-qin, Yang Yu-liang. Research on Properties of Semi-Flexible Mixture. Highway. Apr. 2004 No. 4:108–110.
- [4] Tayebali, A.A., Rowe, G.M., Sousa, J.B. Fatigue Response of Asphalt-Aggregate Mixtures. Journal of the Association of Asphalt Paving Technologists, 1992. Vol. 61:333–360.
- [5] Li Chang-gui. Design method of semiflexible pavement mixture. Journal of Chongqing JiaoTong University. Dec 2003. Vol. 22 Sup:42–48.
- [6] Chenglei, Hao Pei-wen. Mixture of cement slurry with semi-flexible pavement. Journal of Chang'an University(Natural Science Edition). July 2002. Vol. 22 No. 4:1–4.
- [7] Zhou Jie. Study on the composite material of semi-flexible pavement [D]. Master's Thesis of Chongqing Jiao Tong University. 2007.
- [8] Dong Ying-ying. Study on the design parameters and construction technology of high-performance semi-flexible pavement [D]. Master's Thesis of Chongqing Jiaotong University. 2008.
- [9] The industry standard of the People's Republic of China. Highway asphalt pavement construction technical specification (JTG F40-2004) [M] Beijing: China Communications Press, 2004.



## Preparation of $C_3S$ by the sol-gel method

C.L. Zhang, P. Song & Q. Wang

University of Jinan, Jinan, Shandong, China

**ABSTRACT:**  $C_3S$  mineral was synthesized by the sol-gel method, using TEOS as the silicon source,  $Ca(NO_3)_2 \cdot 4H_2O$  as the calcium source, EtOH as the co-solvent and saltpeter solution as the catalyst. XRD was used to analyze the influence of process parameters, such as pre-firing temperature, calcination temperature and heat preservation time, on the  $C_3S$  mineral. It can be concluded that the formation of  $C_3S$  was faster and easier at temperatures ranging from 1350°C to 1400°C.

**Keywords:** sol-gel method;  $C_3S$ ; TEOS

### 1 INTRODUCTION

Portland cement that mainly contains cement clinker, suitable content of gypsum and admixtures is a kind of hydraulic cementing material<sup>[1]</sup>. Cement clinker consists of four kinds of minerals, such as tricalcium silicate ( $C_3S$ ), dicalcium silicate ( $C_2S$ ), tricalcium aluminate, ( $C_3A$ ) and tetracalcium aluminate iron oxide ( $C_4AF$ ). The hydration process of cement that is influenced by many factors is very complicated. In addition to the hydration temperature, additives and admixtures, the key factor is properties of the four main components of cement clinker.

When studying the hydration process of cement, scholars have usually regarded the monomineral as the object of study, in order to avoid the interference of other factors<sup>[2-6]</sup>.  $C_3S$  is doped with  $CaF_2$ . It reduces the hydration degree, chemical combined water, hydration exothermic rate and compressive strength of one day age<sup>[7]</sup>.

When cement clinker minerals are prepared by the traditional high-temperature solid-state sintering method, it is necessary to add a mineralizer and other components in order to decrease the preparation temperature of cement clinker minerals. Consequently, this introduces other ingredients, and thus affects the purity of the single mineral and its properties. Tricalcium silicate ( $C_3S$ ), which is the main mineral of Portland cement, has a faster rate of hydration reaction. Hydration products of  $C_3S$  provide the early strength of cement<sup>[8-9]</sup>. The conventional method of cement clinker minerals with high-temperature sintering furnace has some shortcomings. In this experiment, in order to solve this problem, the sol-gel method, which is new and efficient, was adopted to get  $C_3S$ .

Sol-gel method<sup>[10]</sup> has some advantages including simple manufacture process, high-purity product, good uniformity and low preparation temperature, because it uses liquid reagents as raw materials<sup>[11]</sup>. Through XRD and SEM, samples were analyzed by the microscopic test for increasing the purity of  $C_3S$ .

### 2 EXPERIMENTAL PROCEDURE

#### 2.1 Materials

Tetraethylorthosilicate ( $Si(OC_2H_5)_4$ , TEOS) was selected as the silicon source.

Calcium nitrate tetrahydrate ( $Ca(NO_3)_2 \cdot 4H_2O$ ) was chosen as the calcium source.

Anhydrous ethanol ( $C_2H_5O$ , EtOH) acted as the co-solvent.

Saltpeter solution (4 mol/L) and deionized water were the catalysts.

#### 2.2 Experimental process

##### 2.2.1 Preparation of xerogels

First, the mixture of TEOS, EtOH and deionized water at a certain ratio was added into the saltpeter solution dropwise at a temperature of 30°C. The mixture became a transparent solution by stirring constantly.  $C_3S$  sol was synthesized from the transparent solution and calcium nitrate tetrahydrate solution by stirring frequently. By standing in oven at 60°C,  $C_3S$  gel was obtained, and then converted into xerogels in the oven at 70°C.

##### 2.2.2 Sample preparation

The preliminary heat treatment of xerogels was carried out for removing EtOH, extra deionized water, and structural water of calcium nitrate.

This was beneficial for promoting later solid-phase reactions. The powdered gel that had undergone the heat treatment was pressed into a round slice ( $\Phi 13 \times 2$  mm). The round slice was calcined in a high-temperature furnace heated by  $\text{MoSi}_2$ . The calcination system condition was as follows: warming at a rate of  $4^\circ\text{C}/\text{min}$ , keeping at a constant temperature, quenching in the air.

### 2.3 Test method

Quality change rule and heat flow change caused by chemical reactions during the calcining process of xerogels were determined. The thermal analysis curve was generated by the TGA/DSC1/1600HT Simultaneous Thermal Analysis Instrument (Mettler, Switzerland).

The phase composition of the sample was measured by the D8-ADVANCE X-ray diffractometer (Bruker, Germany).

Micro-structural aspects and micro-constitution were observed by the Guanta FEG 250 field emission scanning electron microscope (FEI, USA), whose resolution was as high as 130 eV.

## 3 RESULTS AND DISCUSSION

### 3.1 Material analysis

#### 3.1.1 The analysis of silicon source

With EtOH as the solvent and saltpeter solution as the catalyst, TEOS and deionized water were adequately hydrolyzed at a temperature of  $30^\circ\text{C}$ . Silicate polymer was obtained through stirring until the appropriate viscosity, aging and drying in the oven. Figure 1 shows the SEM photograph of silicate polymer, and Figure 2 shows the XRD

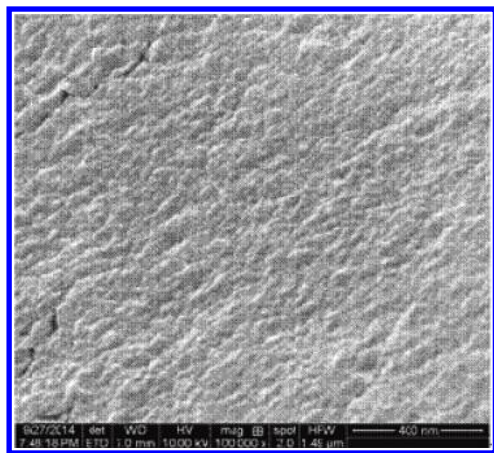


Figure 1. SEM photograph of the silicate polymer.

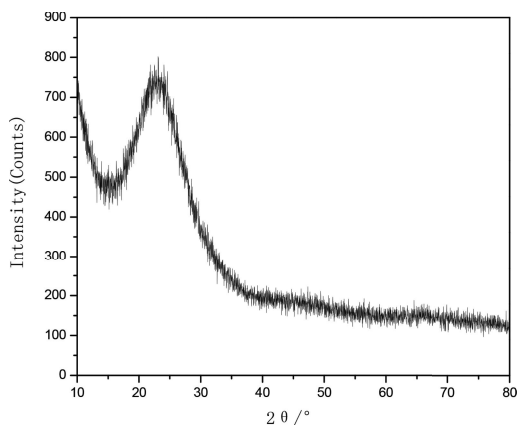


Figure 2. XRD pattern of the silicate polymer.

pattern of silicate polymer. Broad peak from  $20^\circ$  to  $30^\circ$  was found in the XRD pattern of silicate polymer without the characteristic peaks of the crystalline silicon dioxide. The result showed that the hydrolytic product of TEOS was amorphous silicon dioxide.

#### 3.1.2 The analysis of calcium source

Calcium source ( $\text{Ca}(\text{NO}_3)_2 \cdot 4\text{H}_2\text{O}$ ) was dissolved in the co-solvent (EtOH) and dried in the oven at  $70^\circ\text{C}$ . The matter phase of the sample was analyzed by X-Ray Diffraction (XRD).  $\text{Ca}(\text{NO}_3)_2 \cdot 4\text{H}_2\text{O}$  was decomposed at the temperature of  $70^\circ\text{C}$ , yielding  $\text{Ca}(\text{NO}_3)_2 \cdot 2\text{H}_2\text{O}$  and  $\text{Ca}(\text{NO}_3)_2$  (see Fig. 3). Calcium source was heat treated at temperatures of  $520^\circ\text{C}$ ,  $540^\circ\text{C}$  and  $560^\circ\text{C}$ , and then analyzed by X-Ray Diffraction (XRD), as shown in Figure 4. The samples still contained a large amount of  $\text{Ca}(\text{NO}_3)_2$ , a small amount of  $\text{Ca}(\text{NO}_3)_2 \cdot 2\text{H}_2\text{O}$  and a small amount of CaO at  $520^\circ\text{C}$ . When the temperature was up to  $560^\circ\text{C}$ , the samples contained only a large amount of CaO and  $\text{Ca}(\text{NO}_3)_2$ .

Figure 5 shows the DSC-TG curve of the calcium source heated from room temperature to  $800^\circ\text{C}$ . DSC analysis found that there was a decalescence peak at  $100^\circ\text{C}$ , and the TG curve had a smaller drop. This is because the residual solvents and the free water from the calcium source absorbed heat. The another decalescence peak began to appear at about  $162^\circ\text{C}$ , which was caused by the dehydration reaction of  $\text{Ca}(\text{NO}_3)_2 \cdot 2\text{H}_2\text{O}$ .

As shown in Figure 5, there were two obvious decalescence peaks near  $553^\circ\text{C}$  and  $611^\circ\text{C}$ , respectively. Each peak corresponds with one phase transition process. As the same time, the weight loss from  $550^\circ\text{C}$  to  $620^\circ\text{C}$  in the TG curves is attributed to the two-step decomposition of  $\text{Ca}(\text{NO}_3)_2$ : the first step is that  $\text{Ca}(\text{NO}_3)_2$  was decomposed into

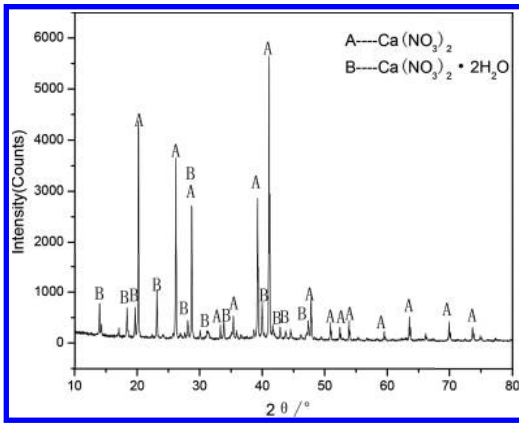


Figure 3. XRD pattern of the calcium source dried at 70°C.

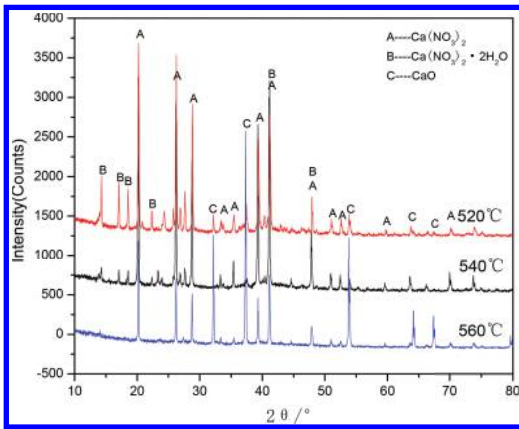


Figure 4. XRD pattern of the calcium source dried at different temperatures.

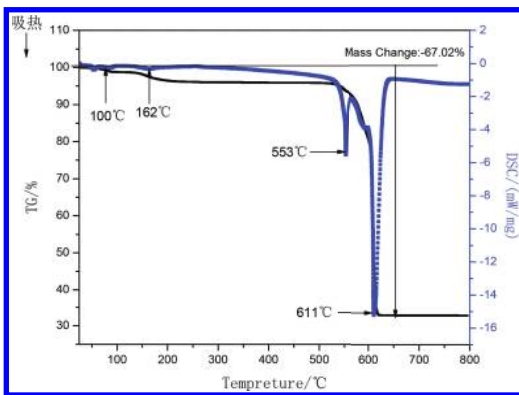


Figure 5. DSC-TG curve of the calcium source.

calcium nitrite ( $\text{Ca}(\text{NO}_2)_2$ ) and oxygen; the second step is that  $\text{Ca}(\text{NO}_2)_2$  was decomposed into  $\text{CaO}$  and nitrous oxide.

### 3.1.3 DSC-TG analysis of the xerogel

Figure 6 shows the SEM photograph of the xerogel granules. As shown in Figure 6, granules were porous. DSC-TG curve of the xerogel is illustrated in Figure 7. As can be seen from the Figure 7, the decalescence peak at 127°, caused by the decalescence of residual solvents from the xerogel granules and structure water from calcium nitrate can led to the weight loss in the TG curve. According to the DSC-TG curve of the calcium source, the main weight loss shown in Figure 7 can be attributed to the two-step decomposition of  $\text{Ca}(\text{NO}_3)_2$ . The decalescence peak at 644°C, with the weight loss in the TG curve, is caused by the silicate polymer formed by the hydrolyzation of TEOS under the

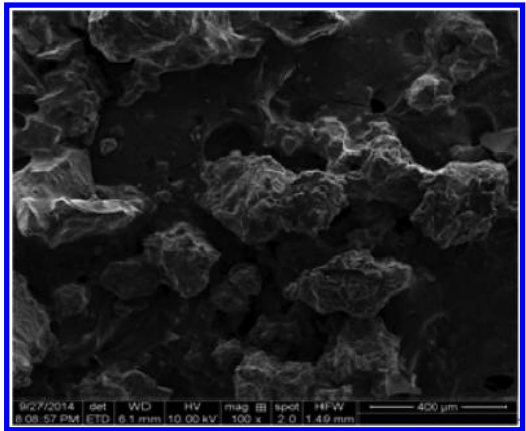


Figure 6. SEM photograph of the xerogel.

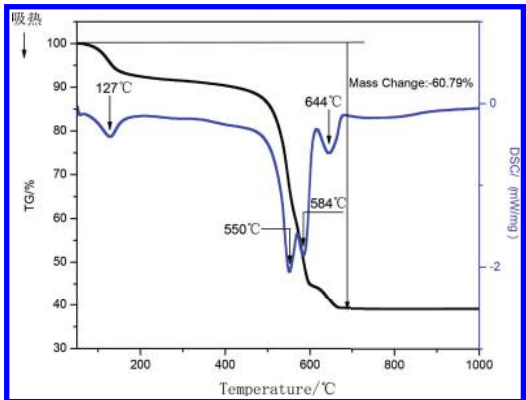


Figure 7. DSC-TG curve of the xerogel.

high-temperature condition resolved into nanometer silica.

### 3.2 The heat treatment of xerogel

#### 3.2.1 Pre-sintering process

Heat treatment of the xerogel included pre-sintering and calcinations. According to the DSC-TG curve of the xerogel, the weight loss ratio reached up to 60 percent. The specimens were pre-sintered, in order to increase the speed of atomic migration in the high-temperature calcination process, and to make the best of activity of the new ecology CaO.

Based on the DSC-TG curve of the xerogel, seven pre-sintering temperatures were set up, namely 510°C, 520°C, 540°C, 560°C, 580°C, 590°C and 600°C. The XRD analysis of the specimens pre-sintered at different temperatures at the heat preservation time of 60 min is shown in Figure 8. As shown in Figure 8, the specimens pre-sintered at 560°C contained CaO and transition phase. While at 580°C, the transition phase of the specimens disappeared, and the diffraction peaks of C<sub>2</sub>S appeared. Meanwhile, one of the great advantages of the sol-gel method, which is the reduction of C<sub>2</sub>S firing temperature (the firing temperature of C<sub>2</sub>S is above 800°C by the traditional high-temperature solid-state sintering method), is illustrated in this experiment.

#### 3.2.2 Calcination process

The XRD analysis of the specimens sintered at different temperatures at the different heat preservation times is shown in Figure 9. The C<sub>3</sub>S mineral diffraction peaks initiated at 1350°C. Compared with the diffraction peaks (0.5957 nm and 0.1777 nm) and the change in the temperature from 1200°C to 1350°C, the C<sub>3</sub>S mineral diffraction

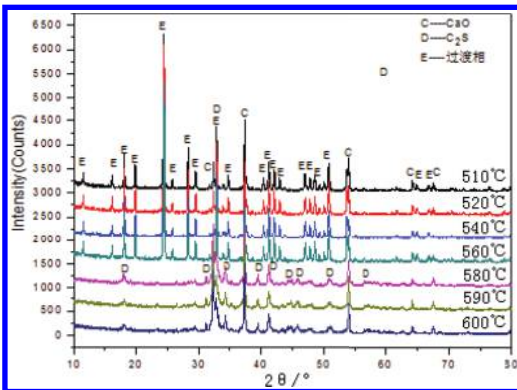


Figure 8. XRD pattern of the specimens pre-sintered at different temperatures at the heat preservation time of 60 min.

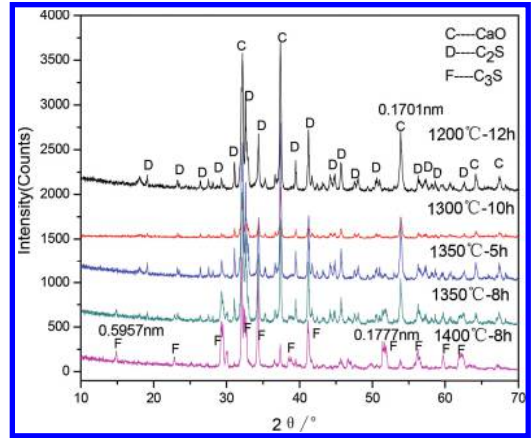


Figure 9. XRD pattern of the specimens at different temperatures at different heat preservation times.

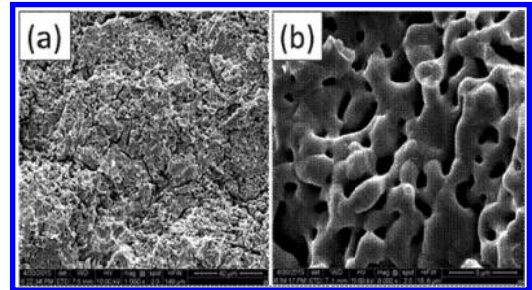


Figure 10. SEM photograph of C<sub>3</sub>S at 1400°C.

peaks increased faster from 1350°C to 1400°C. Compared with the diffraction peak (0.1701 nm) from 1200°C to 1350°C, the CaO diffraction peak at 1400°C was weakest. The diffraction peak intensity indicated the content of the mineral. In consequence, it was concluded that the formation of C<sub>3</sub>S was faster and easier at temperatures ranging from 1350°C to 1400°C.

SEM photos of C<sub>3</sub>S at 1400°C are shown in Figure 10. As can be seen from Figure 10, C<sub>3</sub>S with a uniform particle size has a network structure.

## 4 CONCLUSIONS

The sol-gel method can be used to prepare the C<sub>3</sub>S mineral easily. During the pre-sintering process, the specimens pre-sintered contained the transition phase. In this experiment, the formation temperature of the C<sub>2</sub>S mineral is 580°C, which is lower than the temperature with the traditional high-temperature solid-state sintering method. It can be concluded that the formation of C<sub>3</sub>S is faster

and easier at temperatures ranging from 1350°C to 1400°C.

## FUNDING

This project was supported by the Science and Technology Development Plan of Shandong Province [2013GGB01156].

## REFERENCES

- [1] Double, D.D. Hellowell, A. & Perry, S.J. 1975. The hydration of Portland Cement. *Proc. Roy. Soc. Landon.* 359(1699):435–451.
- [2] Hou, G.H. Shen, X.D. & Xu, Z.Z. 2004. Composition and property of a high tricalcium silicate cement clinker. *Journal of the Chinese Ceramic Society* 32(1): 85–89. [Chinese].
- [3] Gulgun, M.A. Popoola, O.O. & Kriven, W.M. 1994. Chemical synthesis and characterization of calcium aluminate powders. *J. Am. Ceram Soc.* 77(2):531–539.
- [4] Chen, H.X. & Wang, P.M. 2000. Preparation of C<sub>3</sub>S Powders by Sol-gel Method. *Materials Science and Engineering* 18(2):53–56. [Chinese].
- [5] Chen, H.X. Wang, P.M. & Zhao, H. 2003. Research on the Early Hydration Properties of C<sub>3</sub>A Prepared by Sol-gel Method. *Journal of Building Materials.* 6(3):227–230.
- [6] Roy, D.M. & Oyefesobi, S.O. 1977. Preparation of very reactive Ca<sub>2</sub>SiO<sub>4</sub> powder. *J. Am. Ceram. Soc.* 60(34):178–180.
- [7] Wang, S.B. Zhou, Z.H. 1991. Hydration of C<sub>3</sub>S doped with CaF<sub>2</sub>. *Cement and Concrete Comprise.* 19(4): 318–323. [Chinese].
- [8] Tadros, M.E. Skalny, J. & Kalyoncu, R.S. 1976. Early hydration of tricalcium silicate. *Journal of the American Ceramic Society.* 59(7):344–348.
- [9] Gulgun, M.A. Popoola, O.O. & Kriven, W.M. 1994. Chemical synthesis and characterization of calcium aluminate powders. *J. Am. Ceram Soc.* 77(2): 531–539.
- [10] Lu, Z.Y. Xu, X. & Xiao, X.Q. 2007. Effect of grain size of CaCO<sub>3</sub> and SiO<sub>2</sub> on the formation of C<sub>3</sub>S under different conditions. *Journal of Wuhan University of Technology.* 22(3):533–536.
- [11] Page, C.H. Thombare, C.H. & Kamat, R.D. Chatterjee, A.K. 1991. Development of sol-gel technology for cement manufacture. *Advances in Cementitious Materials:* 643–658.

# Study of durability of concrete mixed with cement reducing agent

S.Z. Yue

Department of Architectural Engineering, North China Institute of Science and Technology, Sanhe, China

Y.F. Zuo

Institute of Technical Information for Building Materials Industry of China, Beijing, China

**ABSTRACT:** In this paper, the durability of concrete mixed with cement reducing agent was researched. The results showed that the ability of anti-carbonation, chloride ion penetration resistance and anti-freezing capacity of concrete could be improved obviously after mixing with cement reducing agent in concrete. The three properties of concrete were slightly reduced with the increase of cement reducing rate, but still better than the reference concrete.

**Keywords:** concrete; cement reducing agent; cement reducing rate; durability of concrete

## 1 INTRODUCTION

The cement reducing agent used in concrete, also known as synergistic agent, is a new additive to promote the application of construction market in recent years. The role is to make the cement units of concrete reduced by 8%~15% after mixing with cement reducing agent and ensure comprehensive performance of concrete at the same time (Peng 2011, Sun 2014). With the use of cement reducing agent, it can cut down the dosage of gelatinous material, which is very important in terms of the rapid development of China's construction industry. According to the China Leading Institution of Industry Research database latest data (AskCIData) show that in 2014 China commercial concrete production reached 1,554,127,400 cubic meters, if less per cubic concrete 0.035t gelatinous materials it can be reduced by about 54.4 million tons of gelatinous material. Therefore, promote the use of reducing agent, not only has the technical and economic sense, but also in promoting the sustainable development of China's construction industry, in particular, environmental protection is of great significance.

At present, many research was reported about cement reducing agent of concrete and get consistent affirmation (Chang 2011, Zhang 2012). However, there is rarely study about the mechanism of cement reducing agent and impact on concrete durability and not deep enough. Improve the work in this area will be provide the necessary theoretical guidance and technical support for cement reducing agent promotion (Sun 2014). In this paper, an in-depth research was did to the durability of concrete mixed with cement reducing

agent to look forward to providing the necessary theoretical guidance and technical support for cement reducing agent promotion.

## 2 MATERIALS

### 2.1 Cement

Cement: Jidong P.O. 42.5, Ordinary Portland cement. Its performance was shown in [Table 1](#).

### 2.2 The fly ash

The fly ash: Huaneng Power Plant. Its performance was shown in [Table 2](#).

Table 1. The cement performance.

Standard consistency (%)	Setting time (min)		Strength of cement mortar (MPa)			
	Initial setting time	Final setting time	Flexural strength		Compressive strength	
			3d	28d	3d	28d
27.6	199	273	5.2	8.3	22.8	47.1

Table 2. The fly ash performance.

Fineness (%)	Loss on ignition (%)	Water demand ratio (%)
8.7	1.1	98

### 2.3 Grounded furnace slag

Grounded furnace slag: Specifically for experiments designed. Its performance was shown in Table 3.

### 2.4 Fine aggregate and coarse aggregate

Fine aggregate: fineness modulus 2.4, silt content 0.3%, apparent density 2.65 g/cm<sup>3</sup>, grading qualified.

Coarse aggregate: 5 mm–25 mm continuous gradation, apparent density 2.7 g/cm<sup>3</sup>, packing density 1.55 g/cm<sup>3</sup>.

### 2.5 Admixture

Admixture: naphthalene super plasticizer (liquid, industrial grade, NS, solid content 38%), home-brew AC cement reducing agent (micro dispersant) (yellow, solid content 30%, liquid).

## 3 METHOD

Reference the standard GB/T50082-2009 «Ordinary concrete long-term performance and durability test method»

Table 3. The grounded furnace slag performance.

Specific surface area (m <sup>2</sup> /kg)	Mobility ratio (%)	Activity index (%)	
		7d	28d
324	103	61	89

Table 4. Concrete mix ratio (kg/m<sup>3</sup>).

Number	C (kg/m <sup>3</sup> )	FA (kg/m <sup>3</sup> )	BFS (kg/m <sup>3</sup> )	S (kg/m <sup>3</sup> )	G (kg/m <sup>3</sup> )	W (kg/m <sup>3</sup> )	Naphthalene super plasticizer (%)	AC (%)
A-1	360	0	0	784	1040	173	2	0
A-2	360	0	0	784	1040	173	2	0.06
A-3	330	0	0	797	1057	159	2	0.06
A-4	315	0	0	803	1066	151	2	0.06
B-1	220	60	100	830	1189	185	2	0
B-2	220	60	100	830	1189	185	2	0.06
B-3	202.6	55.3	92.1	842	1207	170.4	2	0.06
B-4	193.9	52.9	88.2	848	1216	163	2	0.06
C-1	300	80	120	686	1014	180	2.8	0
C-2	300	80	120	686	1014	180	2.8	0.06
C-3	282	75.2	112.8	698	1032	169.2	2.8	0.06
C-4	273	72.8	109.2	704	1041	163.8	2.8	0.06

## 4 EXPERIMENTAL DESIGN

Concrete mix ratio was shown Table 4.

In the table, the mix ratio of A-1 was specified in GB8076-2008. The mix ratio of B-1 and C-1 was used the same with C30 and C50 in actual project. A-2, B-2 and C-2 were the same with A-1, B-1 and C-1 respectively except cement reducing agent which admixture were changed to 0.06%. In A-3, B-3 and C-3, the total dosage of gelatinous material were reduced 30 kg compared with A-1, B-1 and C-1. And the total dosage of gelatinous material of A-4, B-4 and C-4 were reduced 45 kg compared with A-1, B-1 and C-1. For all the samples, at the same time with the changing of the mix ratio, the total dosage of gelatinous material were reduced equivalent to the aggregate according to the sand ratio to ensure the volume-weight have no different.

## 5 RESULTS AND DISCUSSIONS

The results were shown in Table 5.

First of all, to group A, the mix ratio of A-1 was specified in GB8076-2008, and other samples were added with cement reducing agent. According to the comparison, the ratio of 200 times freeze-thaw compressive strength was the lowest in A-1 which did not add cement reducing agent only. To A-2, A-3 and A-4, the minimum of A-4 which was 90% and the cement reducing rate was added most, but 200 times freeze-thaw compressive strength still 4.8% higher than A-1 (Fig. 1). For all of the concrete samples mixing with cement reducing agent, A-2, A-3 and A-4, the penetration depth of chloride ion were less than A-1. In the three concrete samples, the maximum was A-4 which was 12.2 mm, but still 2.5% less than A-1 (Fig. 2). To carbonation depth, A-2, A-3 and A-4 were also less

Table 5. Result of durability test.

Number	Ratio of 200 times freeze-thaw compressive strength (%)	Penetration depth of chloride ion (mm)	Carbonation depth (mm)
A-1	84	12.5	1.12
A-2	96	11.6	1.01
A-3	92	12.0	1.07
A-4	90	12.2	1.09
B-1	89	15.6	1.30
B-2	99	14.6	1.24
B-3	95	15	1.25
B-4	94	15.1	1.27
C-1	92	13.2	1.13
C-2	99	12.1	1.02
C-3	95	12.6	1.08
C-4	95	12.7	1.09

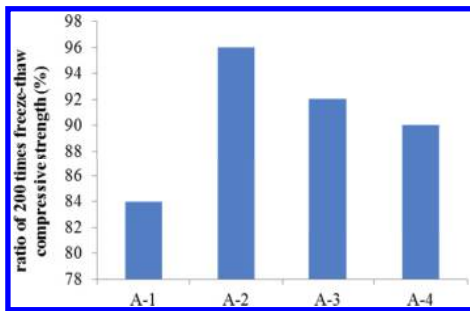


Figure 1. The ratio of 200 times freeze-thaw compressive strength to group A (%).

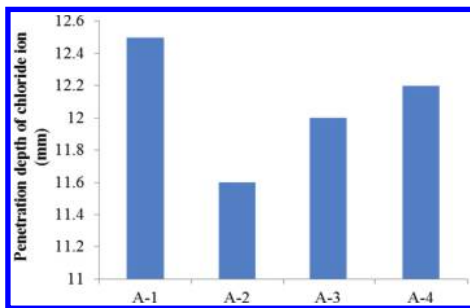


Figure 2. The penetration depth of chloride ion to group A (mm).

than A-1. A-4 was the maximum and the carbonation depth was 1.09 mm, 27.5% less compared with A-1 (Fig. 3). Comparing A-2, A-3 and A-4, with the reduction of the total dosage of gelatinous material, the ratio of 200 times freeze-thaw compressive strength was reduced and the penetration

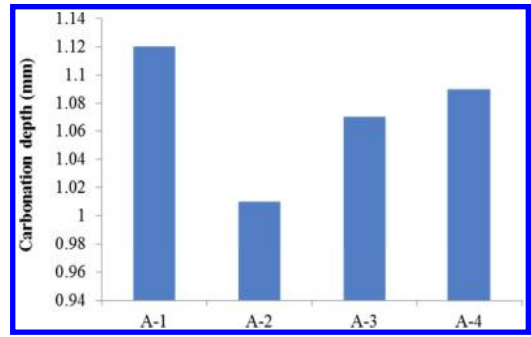


Figure 3. The carbonation depth to group A (mm).

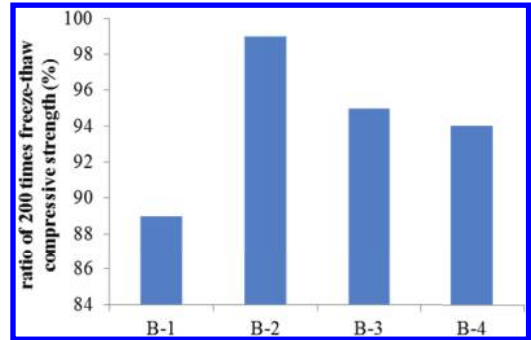


Figure 4. The ratio of 200 times freeze-thaw compressive strength to group B (%).

depth of chloride ion and carbonation depth were increased gradually.

To group B, the mix ratio of B-1 was used the same with C30 in actual project. To B-2, B-3 and B-4, the freeze-thaw compressive strength were higher than B-1. The minimum of B-4 which was 94% and the cement reducing rate was the most, but 200 times freeze-thaw compressive strength still 5% higher than B-1 (Fig. 4). For all of the concrete samples mixing with cement reducing agent, B-2, B-3 and B-4, the penetration depth of chloride ion were less than B-1. B-4 was the maximum and the penetration depth of chloride ion was 15.1 mm, 3.3% less compared with B-1 (Fig. 5). To carbonation depth, B-2, B-3 and B-4 were also less than B-1. B-4 was the maximum and the carbonation depth was 1.27 mm, 2.4% less compared with B-1 (Fig. 6).

To group C, the mix ratio of C-1 was used the same with C50 in actual project. To C-2, C-3 and C-4, the freeze-thaw compressive strength were higher than C-1. The minimum of C-4 which was 95% and the cement reducing rate was the most, but 200 times freeze-thaw compressive strength still 3% higher than C-1 (Fig. 7). For all of the concrete samples mixing with cement reducing agent, C-2, C-3



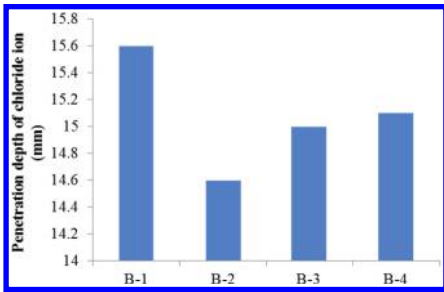


Figure 5. The penetration depth of chloride ion to group B (mm).

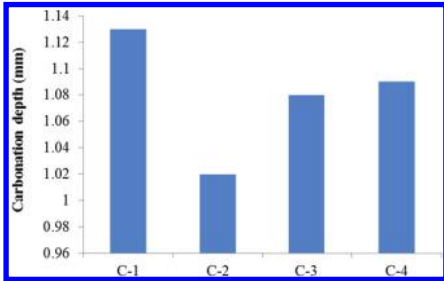


Figure 6. The carbonation depth to group B (mm).

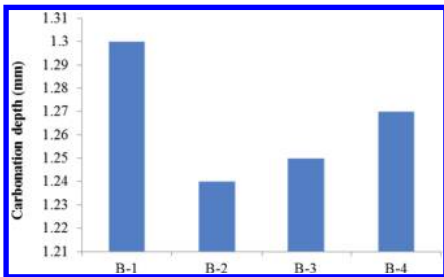


Figure 7. The ratio of 200 times freeze-thaw compressive strength to group B (%).

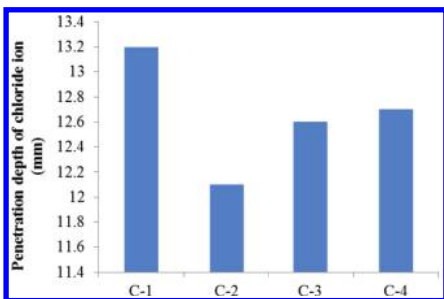


Figure 8. The penetration depth of chloride ion to group C (mm).

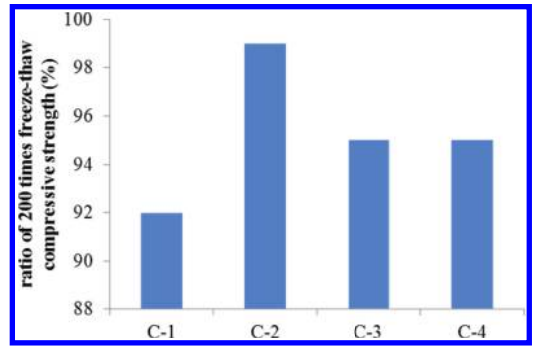


Figure 9. The carbonation depth to group C (mm).

and C-4, the penetration depth of chloride ion were less than C-1. C-4 was the maximum and the penetration depth of chloride ion was 12.7 mm, 3.9% less compared with C-1 (Fig. 8). To carbonation depth, C-2, C-3 and C-4 were also less than C-1. C-4 was the maximum and the carbonation depth was 1.09 mm, 3.7% less compared with C-1 (Fig. 9).

## 6 CONCLUSIONS

The results showed that adding cement reducing agent in concrete could improve the ability of anti-carbonation of concrete, chloride ion penetration resistance, anti-freezing capacity. With the increase of the cement reducing rate, the ability of anti-concrete carbonation and chloride penetration resistance, freeze-thaw slightly lower capacity, but better than the reference concrete. The addition of mineral admixtures can increase the ability of concrete anti-concrete carbonation and chloride penetration resistance, freeze-thaw.

## AUTHOR BIOGRAPHY

\*Author: Yue Su-zhen (1964-), engineer, study in concrete research. Address: Department of Architectural Engineering, North China Institute of Science and Technology, Sanhe, 065201, China. Tel: 13700349332.

## REFERENCES

- Chang, H.Y. 2011. Evaluation of the performance of CTF concrete mixed with concrete synergist. Ready-mixed Concrete (6): 41–43.
- Peng, C.Y. 2011. Effect of synergist on performance above C60 concrete. Concrete (5): 73–41.
- Sun Z.P. 2014. Study of adaptability of cement reducing agent with different type of plasticizers. Ready-mixed Concrete (11): 47–48.
- Zhang, Q. 2012. CTF concrete synergists use technological explanation. Ready-mixed Concrete (1): 49–52.

# Residual stress influence on stability of thin-walled box section column of high-strength steel

Lei Gao, Kebin Jiang, Xiaohui He & Linyue Bai

*College of Field Engineering, PLA University of Science and Technology, Nanjing, Jiangsu, China*

**ABSTRACT:** The residual stress has a significant influence on the stability of column, but experimental data are difficult. So we study the influence on the stability of thin-walled box section column of high-strength steel (the nominal yield stress of 745 MPa to 800 MPa) caused by different residual stresses by using finite element analysis software ANSYS. Based on elastic-plasticity large deflection theory of the thin steel plate and arc length method, the study finite element model was modeled. As to residual stresses, we read it in the element integral point through the preparative initial-stress document. Through the study, we find that residual compressive stress has larger influence on the stability of column than residual tensile stress; the stability of the column is sensitive to the variation of residual stress while slenderness ratio is moderate.

**Keywords:** residual stress; thin-walled box section; high-strength steel; stability coefficient

## 1 INTRODUCTION

Residual stresses always exist in steel structure components as the result of process, transportation, and fabrication<sup>[1]</sup> and welding residual stresses are mainly stress in welding components. The critical stresses of the actual axial compressive column are smaller than the critical stresses of ideal axial compressive column largely due to the existence of the welding residual stress. The residual stresses, especially the welding residual stress, have a great effect on the column stability coefficient, so they have been considered in the design specifications of steel structure<sup>[2]</sup>. The research of the high-strength steel gradually increased with more and more high-strength steel used in skyscraper, bridge, etc.<sup>[3-6]</sup>; however, research about residual stress effects on stability coefficient of high-strength steel components was lacking. High-strength thin-walled box-section steel has been used in movable bridge in china.<sup>[7]</sup> The special fabrication technique was used, first two channel steel components were formed through cold bending method, then the two channel steel components were welded into thin-walled box section. Welding certainly generates welding residual stress for the reason of local high temperature. In this article, based on elastic-plasticity large deflection finite element theory of the thin-walled steel plate, the column's ultimate bearing capacity is achieved by using the arc-length method<sup>[8-9]</sup> to track the column load-displacement curve and the range of decline, in the meantime

the stability coefficient of column is achieved. The different residual tension stress and compressive stress influences on stability of thin-walled box section column of high strength steel were studied. The effects on the stability coefficient of column with different slenderness ratio were also studied, and then some meaningful conclusions were got to supply reference to design.

## 2 RESIDUAL STRESS OUTLINE AND DISTRIBUTION

There are many reasons for creating residual stress, mainly including uneven heating and cooling in welding process, uneven cooling of the steel's different parts in the process of rolling steel, the plastic deformation of components after cooling, the thermal contraction in the edge of plant after thermal cutting, etc<sup>[1]</sup>. We mainly study the effects of welding residual stress generating during the process of welding. Welding residual stress can be divided into transverse residual stress and vertical residual stress. The reason of transverse residual stress is the uneven heating among different parts of the same cross-section, and the uneven heating among different parts along axial leads to the vertical residual stress. As to stability calculation for components, the distribution of vertical residual stress is primary.

Researchers have managed to measure the welding residual stress a long time ago, which has

a great influence on the stability coefficient of construction members<sup>[10]</sup>. The measurement techniques of residual stress consist of mechanical method and physical method. Aimed at studying macroscopic residual stress, mechanical methods, also known as stress releasing method, are classic measurement methods of residual stress and belong to destructive test, mainly include sectioning method, hole-drilling, ring-core method, etc.<sup>[1,11]</sup> Physical methods can test both macroscopic residual stress and microstructural residual stress as a non-destructive testing, mainly including the magnetic testing, X-ray method, Scanning electron microscopy, ultrasonic method, etc.<sup>[1]</sup>

As to the square pipe welded together by two pieces of channel steel, the stress releasing method was used by Zhongquan<sup>[10]</sup> Zhang to confirm the maximum residual stress on cross-section existing  $0.1\sigma_y$  ( $\sigma_y$  is the yield stress of sample steel) of the weldless side wall. Afterwards, the influence of residual stress was considered when Zuyan Shen<sup>[11]</sup> and others studied the ultimate strength of stiffened elements by using curved shell finite element method. In the meantime, they measured the residual stress distribution of the square tube by the stress releasing method, the residual tensile stress was  $\sigma_{rt} = 0.832\sigma_y$  and residual compressive stress was  $\sigma_{rc} = 0.0839\sigma_y$ , as shown in Figure 1.

The welding residual stress of cold-formed thin-walled steel structure has been tested by Feng Zhao, and others<sup>[13,14]</sup>, the study indicates that the residual stress varied along the thickness direction of cross section and the residual stress in the both sides of cross section is equal and opposite. Recently some welding stress of high strength were measured and some distribution rules were put forward.<sup>[12,15]</sup> But the test data was gained with difficulty and

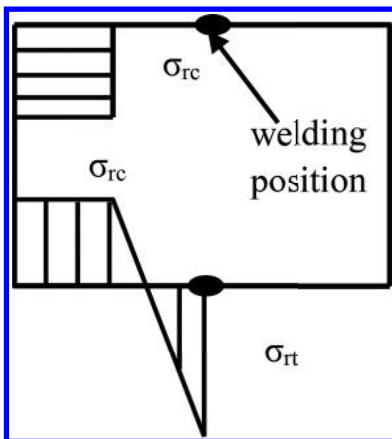


Figure 1. Distribution of residual stress.

discretion, so numerical simulation method is an important method to study residual stress.

Actually, the residual stress in components we used compounded of cold-formed residual stress and welding residual stress, so the distribution is very complex. In addition, different components or welding manner also result in different distributions of residual stress. In order to study the problem conveniently, we adopt the reduced-form residual stress pattern shown in Figure 1. Researchers believe that the stabilizing influence of compressed members caused by residual stress is concerned with the distribution of residual stress. It is worst when the slenderness ratio of bar is around 90, and the impact would reduce either when the value increase or decrease<sup>[13]</sup>. But there is still no search about the influence on stability coefficient of construction members caused by high-tensile steel components residual stress. It is necessary to carry out a study on the influence of the stability coefficient of high-tensile steel components caused by welding residual stress.

### 3 ESTABLISHMENT OF THE FINITE ELEMENT MODEL

The basic finite element model is built by using the finite element analysis software ANSYS12.0 as the working platform<sup>[9]</sup>. For the finite element numerical simulation, the material property was modeled by the multi-linear isotropic hardening model (MISO) according to the material test data<sup>[16]</sup>. In order to consider geometric deformation and residual stress, the shell element 181 was used in model. By adding two pieces of rigid plant (with large elastic modulus) to the ends of the member, we can simulate the rigid surrounding assumption and impose constraints and loads conveniently. The hinged-constraint is used to restrain the central node of both sides of the plate when the constraints are imposed. The flange width is 0.6 times the web width; the web height to thickness ( $h/t$ ) is 30.

Two geometric imperfections were introduced to the FEM model. One was the initial overall imperfection and the other was the local imperfection of the component. The initial overall imperfection was simulated by assuming the beam shape as a half sine wave. For lower grade steel, statistic imperfection amplitude employed in current Chinese code is  $L/1000$ , where  $L$  represents the length of the column<sup>[2]</sup>. Due to lack of statistic data, the amplitude suggested by the Chinese code was adopted in the simulation. The initial local imperfection of the component plate was assumed to be the same as the first order local buckling mode of the beam when only the local buckling of the components come out. The maximum amplitude of the

local imperfection denoted by  $\Delta_0$  takes the expression suggested by Antonio F. M<sup>[17]</sup>as:

$$\frac{\Delta_0}{b} = 0.1 \times \frac{b}{t} \times \frac{\sigma_y}{E} \quad (1)$$

The residual stress is applied in two ways: a) apply the residual stress directly based on the initial data of residual stress provided by the model. B) apply the treated thermal load. We choose way a, although the difference between the two results are very small<sup>[12,15]</sup>. The residual stress is introduced by reading the preparative initial-stress document and is applied on the element integral point, and 5 element integral points are chosen by every shell 181 element.

Using ANSYS Parametric Design Language (APDL), the analysis model was established and solved. The basic program sketch of stability calculation is such as Figure 2. According to the above discussions the FEM model was formed as shown in Figure 3.

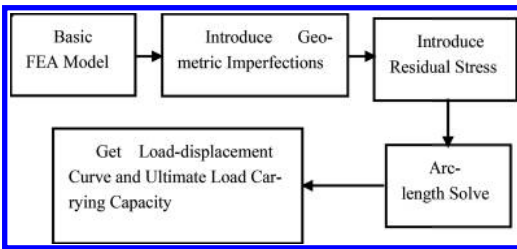


Figure 2. Program sketch of stability calculation.

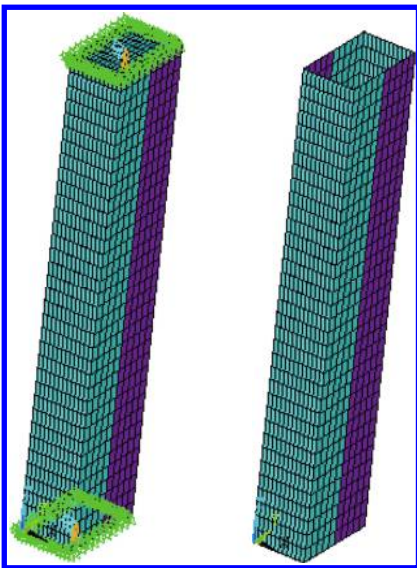


Figure 3. FEA model.

#### 4 THE CALCULATION RESULTS AND ANALYSIS FOR FINITE ELEMENT MODEL

The finite element models are established to analyze different residual stress influences on the thin-walled box section of high-strength steel with different slenderness ratios. The value of residual tensile stress are  $\sigma_{rt} = 0.7\sigma_y, 0.8\sigma_y, 0.9\sigma_y, 1.0\sigma_y, 1.1\sigma_y,$  and  $1.2\sigma_y,$  and residual pressure stress are  $\sigma_{rc} = 0.1\sigma_y, 0.15\sigma_y, 0.2\sigma_y, 0.25\sigma_y, 0.3\sigma_y,$  respectively.

In order to study the different residual stress influence on stability of column, we chose slenderness ratio 70 as study example and the results are shown in Table 1.

It can be seen from the table that the change of the stability coefficient caused by residual compressive stress is larger than that caused by residual tensile stress. Maximum difference of stability coefficient is 7.41% when the range of residual compressive stress changes from  $0.1\sigma_y$  to  $0.3\sigma_y,$  while maximum difference of stability coefficient is just 1.3% when the residual tensile stress change is from  $0.7\sigma_y$  to  $1.2\sigma_y.$  Thus, we can get the conclusion that the effect of residual compressive stress is more significant for the stability coefficient of thin-walled box section of high strength steel column.

In order to study the influence of different compressive stress on stability factor of thin-walled box section of high strength steel column with different slenderness ratios, the value of residual tensile stress is fixed. The value of the residual tensile stress was fixed at  $0.8\sigma_y,$  and the residual compressive stress is set at  $\sigma_{rc} = 0.1\sigma_y, 0.15\sigma_y, 0.2\sigma_y, 0.25\sigma_y, 0.3\sigma_y,$  respectively. The slenderness ratio ranging from 20 to 120 was studied. We achieved the influence on stability coefficient of thin-walled box section made of high-strength steel component caused by different residual compressive stress and different slenderness ratio. (shown in Table 2).

Figure 4 is drawn to indicate the difference in stability coefficient of columns with different slenderness ratio caused by different residual compressive stresses.

The influence of slenderness ratio caused by changes of residual compressive stress can be found from Table 2 and Figure 4 that residual compressive reaches to a maximum with the increase of slenderness ratio stress, and then drops down with the increases of slenderness ratio until it get smoothly. While the slenderness ratio is 60, the stability coefficient of the column is sensitive mostly to residual compressive stress. Influence of stability coefficient caused by changes of residual compressive stress is more than 5% while the slenderness ratio ranges from 30 to 90, it is less than 5% when the slenderness ratio is larger or smaller.

Table 1. Thin-walled column for high-strength steel stability coefficients under different residual stress.

$\sigma_{rt}$	$\sigma_{rc}$						Maximum and minimum difference %
	$0.7\sigma_y$	$0.8\sigma_y$	$0.9\sigma_y$	$1.0\sigma_y$	$1.1\sigma_y$	$1.2\sigma_y$	
$0.1\sigma_y$	0.3050	0.3048	0.3051	0.3052	0.3055	0.3056	0.25
$0.15\sigma_y$	0.3020	0.3019	0.3021	0.3025	0.3026	0.3026	0.22
$0.2\sigma_y$	0.2961	0.2962	0.2986	0.2983	0.2987	0.2989	1.30
$0.25\sigma_y$	0.2903	0.2906	0.2915	0.2912	0.2920	0.2929	0.88
$0.3\sigma_y$	0.2841	0.2838	0.2845	0.2859	0.2863	0.2867	0.97
Maximum and minimum difference %	7.37	7.41	7.21	6.73	6.71	6.58	

Note: The stability coefficient  $\phi = P_u/P_y$ ,  $P_u$  is the load carrying capacity which has got through FEM analysis,  $P_y = A \times \sigma_y$ , where  $A$  is area of column.

Table 2. The stability coefficients of different slenderness ratio column under different residual compressive stress.

$\sigma_{rc}$	$\lambda$										
	20	30	40	50	60	70	80	90	100	110	120
$0.1\sigma_y$	0.933	0.804	0.703	0.624	0.554	0.462	0.375	0.305	0.251	0.209	0.177
$0.15\sigma_y$	0.925	0.784	0.680	0.588	0.530	0.450	0.369	0.302	0.249	0.209	0.177
$0.2\sigma_y$	0.921	0.774	0.664	0.559	0.502	0.434	0.360	0.296	0.245	0.205	0.173
$0.25\sigma_y$	0.91	0.750	0.631	0.533	0.471	0.416	0.351	0.291	0.241	0.202	0.171
$0.3\sigma_y$	0.90	0.739	0.610	0.516	0.439	0.402	0.338	0.286	0.239	0.200	0.169
Maximum and minimum difference %	3.16	8.65	15.19	20.96	26.46	15.08	10.81	6.53	5.23	4.74	4.72

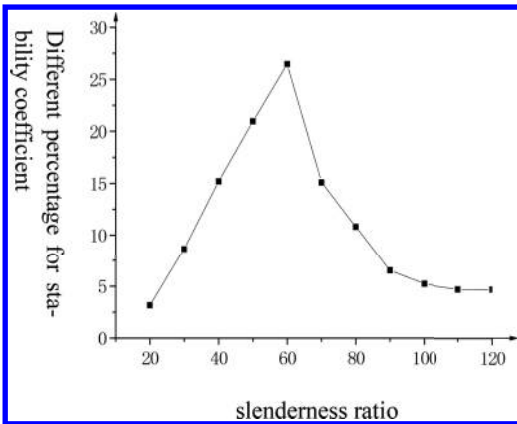


Figure 4. The margin of stability factor under different slenderness ratio.

Thus there is little effect of stability coefficient caused by residual compressive stress on long or short column, however the effect on the moderate-length column is larger which should be considered during design procedure. It is considered that the design for equivalent rigidity (the overall stability

critical stress is equal to the local web critical stress is the optimal design generally.

Take the thin-walled box section column of high strength steel as an example, the local critical pressure of plate is

$$\sigma_{cr} = \frac{k\pi^2 E}{12(1-\nu^2)} \left(\frac{t}{b}\right)^2 \quad (2)$$

$k$  is a buckling coefficient,  $E$  is yang's elastic modulus,  $t$  and  $b$  is thickness and width of plate.

The ideal integral stability critical stress is

$$\sigma = \frac{\pi^2 E}{\lambda^2} \quad (3)$$

If equation (2) is equal to equation (3), then we can get

$$\lambda = \sqrt{\frac{12(1-\nu^2)}{k}} (b/t) \quad (4)$$

In this equation the buckling coefficient is still difficult to confirm. As for the web, one side of web is tensioned and the other side is pressed as a result of the initial imperfection. We study the

press-side only. Actually, the buckling coefficient of press-side web restrained by upper and lower flange ranges from 1.28 (the buckling coefficient of column which is an end fixed and an end simply supported) to 4 (buckling coefficient of column which is simply supported ends). We take that middle value to be  $k$  which is 2.5,  $\nu$  is 0.3,  $b/t$  is 30, then we can get the value of  $\lambda$  as close to 60. It can explain why the stability coefficient of column whose slenderness ratio is 60 is sensitive mostly to residual compressive stress.

## 5 CONCLUSION

Based on the finite element analysis software ANSYS as the working platform, we study the effects on the stability of thin-walled box section column made of high-strength steel caused by residual stress by applying the preparative residual stress documents to the integral point, and we achieved the following conclusion:

1. Adopting finite element SHELL 181, we can simulate the influence on the stability coefficient caused by residual stress through applying the diverse preparative residual stress document to integral point.
2. The influence on stability coefficient of high-strength steel caused by residual tension stress and residual compressive stress are different, and the influence caused by residual compressive stress is larger.
3. The influence on stability of column with different slenderness ratio caused by different residual compressive stress is different. The stability of column is sensitive to the variation of residual stress while slenderness ratio is moderate, especially designed for equivalent rigidity (the overall stability critical stress is equal to the local web critical stress). As for the section we researched, the stability of column is most sensitivity to the variation of residual stress while slenderness ratio is 60.

## ACKNOWLEDGEMENTS

This work was financially supported by the National Key Basic Research Program of China (2014CB046801) and the Project supported by the National Natural Science Foundation of China (KYGJGG1203).

## REFERENCES

[1] Li gengjian. Study on the residual stresses in steel structural members [J]. Journal of Xi'an Highway University, 1999(s0):63–65. (in Chinese).

[2] GB50017-2003. (2003). Code for design of steel structures. China Plan Press.

[3] Pocock, G. High Strength Steel Use in Australia, Japan and the US. The Structural Engineer, 2006(11), 27–30.

[4] Huiyong, Shi Yongjiu, Wang Yuanqing. Overview of Research Progress for High Strength Steel Structures [J]. Engineering Mechanics, 2013, 30(1):1–13. (in Chinese).

[5] Li Guoqiang, Wang Yanbo, Chen Suwen, Sun Feifei. State of the art on research of high strength structural steels and key issues of using high strength steels in seismic structures [J]. Journal of Building Structures, 2013, 34(1):1–13 (in Chinese).

[6] Chen Zhenming, Zhang Yaolin, Peng Mingxiang, Zhang Kun. Application of high-strength steel and thick steel plates to CCTV new site building [J]. Steel Construction, 2009, 24(2):34–38. (in Chinese).

[7] Gou, M.K., and Tao, L. (2002). The application of high strength steel ( $\sigma_s \geq 700$  MPa) to the movable bridge. Steel Structure. 17:5, 6–8. (in Chinese).

[8] Yang D, Hancock G J. Numerical simulation of high-strength steel box-shaped columns failing in local and overall buckling modes [J]. Journal of Structural Engineering, 2006, 132(4): 541–549.

[9] Wang Jinlong. ANSYS12.0 Finite Element Analysis and Example [M]. Beijing: China Machine PRESS, 2010. (in Chinese).

[10] Zhang zhongquan. Experimental study on compressive column of cold-formed steel [A]. The selection thesis on steel structure. Beijing: Country steel structure standard technique committee, 1982 152–191. (in Chinese).

[11] Shen, Z.Y., and Zhang, Q.L. Post-buckling ultimate load-carrying of compressed square-tube steel column [J]. Journal of Civil Engineering, 1991(24)3:15–26.

[12] Li Guoqiang, Wang Yanbo, Chen Suwen. Experimental study on ultimate bearing capacity of axially compression high strength steel columns [J]. Journal of Building Structures, 2012, 33(3):8–14. (in Chinese).

[13] Zhao feng, Guo yaojie. Analysis of cold-formed residual stress field [J]. Industrial Architecture, 2004, 34(6):71–73. (in Chinese).

[14] C.C. Weng, Teoman Pekoz, Compression Tests of Cold-Formed Steel Columns [J]. Journal of Structural Engineering, 1990: 116(5):1230–1246.

[15] Ban Huiyong, Shi Gang, Shi Yongjiu, Wang Yuanqing. Overall buckling behavior of Q460 high strength steel welded box section columns under axial compression [J]. Journal of Building Structures, 2013, 34(1):22–29. (in Chinese).

[16] Lei Gao, Hongcai Sun Fengnian Jin, et al. Load-carrying capacity of high-strength steel box-sections I: Stub columns [J]. Journal of Constructional Steel Research, 2009, 65(4):918–924.

[17] Antonio F. Matens, Joel A Witz, A parameter study of the post-buckling behaviour of steel plate, Engineering Structure, 2001(23), 172–185.

# Laboratory research of hard asphalt applied on bus lane renewal

Long Zhang

*Jinlin Jianzhu University, Jilin, China*

*Changchun Architecture and Civil Engineering College, Jilin, China*

Zhonggen Liu

*Jinlin Jianzhu University, Jilin, China*

**ABSTRACT:** Application of high modulus asphalt (HiMA) concrete can improve not only rutting resistance, but also the bearing capacity of pavement structure. It is consistent with the long-life pavement construction philosophy.

In this paper, combined with bus lane renewal of Chang'an road in Beijing, three technics are applied to resolve significant rutting on the bus lane: coarse aggregate gap-graded mixture, large Nominal Maximum Aggregate Size (NMAS) and hard asphalt.

First, two types of hard asphalt (Pen(20/30) and Pen(40/60)), which are produced by three methods, are compared. It is illustrated that hard asphalt, that produced by the oxidation method, is best at high-temperature performance. For mixture, two kinds of HiMA (HiMA(20-25) and HiMA(40-25)) are selected. These two mixtures have same gradation and NMAS, different asphalt Pen(20/30) and Pen(40/60), respectively. Their volumetric characteristics, high-temperature stability, mechanical characteristics, and fatigue resistant are evaluated. The mechanical characteristics include compressive/flexural strength, compressive resilient modulus and dynamic complex modulus, etc.

The results illustrate that HiMA(20-25) has better rutting resistant, bearing capacity, and durability than HiMA(40-25). So the HiMA(20-25) is applied in engineering of the bus lane renewal in Chang'an road.

**Keywords:** hard asphalt; high modulus asphalt mixes; coarse aggregate gap-grade mixes

## 1 INTRODUCTION

In urban roads, rutting on bus lane is a significant damage. Normally, bus axle load is lower than truck (for example: bus axle load is 8–12 tons; truck axle load is 10–18 tons in China). But the bus lane always has characteristics such as: channelized traffic, high tire contact pressure, frequent stops, and acceleration at bus stations and junctions. All these factors result in more serious rutting. So in German, special criterion has been presented that: The bus traffic area should be designed according to the heavy loaded pavement design criterion.

HiMA has been widely used in Europe and America, but has not been utilized on bus lane renewal on urban main roads in china. The objective of this paper is to introduce the laboratory research.

## 2 LABORATORY SCOPE AND RESEARCH APPROACH

In this research, a coarse aggregate gap-graded mixture is adopted. Its Nominal Maximum

Aggregate Size (NMAS) is 25 mm. This gradation is developed by RIOH. The coarse aggregate content (>4.75 mm) is 70%, and filler (<0.075 mm) content is 5%, so it has close skeleton and small air void(6).

Two hard asphalts, that of penetrations, are 20/30(1/10 mm) (Pen 20/30) and 40/60 (1/10 mm) (Pen 40/60), are selected to investigate the effect of binder. For easy statement in this paper, the HiMA mix with binder pen(20/30) is defined HiMA(20-25) (25 represents NMAS of mix) and the other defined HiMA(40-25).

As the NMAS of mix is 25 mm, the specimens are fabricated by modified Marshall compaction tester. The diameter of specimen is 152.4 mm with 95.3 mm standard height. The weight of compact hammer is 10.21 kg and falling height is 453.2 mm; the number of blows is 112 times on each side (equivalent to standard Marshall compaction 75 times for each side). The compaction temperature for HiMA(20-25) and HiMA(40-25) are 155–165°C and 145–155°C, respectively. The bulk density of test specimen is measured by saturated surface-dry method (AASHTO T166). And

the optimum asphalt–aggregate ratio can be evaluated according to specification in China.

In this paper, for comparing the performance of two types of HiMA, two performance tests are carried out.

### 3 DYNAMIC COMPLEX MODULUS ( $E^*$ ) TEST

Simple Performance Tester (SPT) made in Australia is employed during dynamic complex modulus testing. The test specimen is fabricated by SGC with 15 cm in diameter, and then is cored into a cylinder specimen with 10 cm in diameter, 15 cm in height. For temperature level (5°C, 20°C, 40°C, and 55°C) and 8 frequency level (20 Hz, 10 Hz, 5 Hz, 2 Hz, 1 Hz, 0.5 Hz, 0.2 Hz, and 0.1 Hz) are selected.

Different with the USCRMT and UDCRMT, the specimen dimension of SPT is 1:1.5 (diameter/height), and the deformation measurement is side-aspect method, shown in Figure 1.

Dynamic complex modulus master curve is achieved by sigmoid model (Formula 1).

$$\log |E^*| = A_2 + \frac{A_1 - A_2}{1 + e^{-\frac{\log f - x_0}{d_x}}} \quad (1)$$

where  $E^*$  is the dynamic complex modulus, MPa;  $f$  is the loading frequency, Hz; and  $A_1$ ,  $A_2$ ,  $x_0$  and  $d_x$  are the parameters of curve.

When:  $f \rightarrow +\infty$ ,  $\log f \rightarrow +\infty$ ,  $\log |E^*| \rightarrow A_2$ , i.e. maximum dynamic complex modulus;

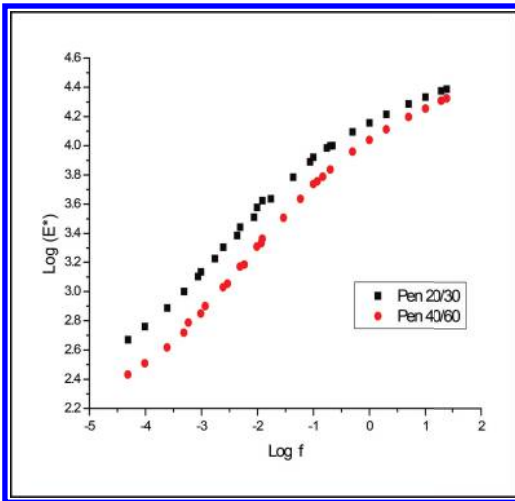


Figure 1. Dynamic complex modulus master curves of HiMA(20-25) and HiMA(40-25).

When:  $f \rightarrow 0$ ,  $\log f \rightarrow -\infty$ ,  $\log |E^*| \rightarrow A_2 + A_1 - A_2 = A_1$ , i.e. minimum dynamic complex modulus.

And phase angle master curve is achieved by GaussAmp regression (Formula 2)

$$\phi = \phi_0 + \frac{A}{w \times \sqrt{\pi/2}} \times e^{-2 \times \left( \frac{\log f - x_c}{w} \right)^2} \quad (2)$$

where  $\phi$  is the phase angle,  $f$  is the loading frequency in Hz,  $\phi_0$ ,  $A$ ,  $w$ , and  $x_c$  are the parameters of curve.

When  $\log f = x_c$ ; phase angle is the maximum,

$$\text{i.e.: } \phi_{\max} = \phi_0 + \frac{A}{w \times \sqrt{\pi/2}}.$$

### 4 FATIGUE TEST

Cooper tester is employed for evaluating the fatigue performance of material. Because HiMA is mainly serving for pavement bearing layer, stress controlled mode is applied in the test, and the stiffness modulus of mix decreasing to 50% initial modulus is defined as the evaluation criterion.

The dimension of specimen and testing temperature are consistent with flexural strength test. The loading wave is Havesine wave, 10 Hz continuously. There are 5 stress levels in testing, such as 1 MPa, 1.5 MPa, 2 MPa, 2.5 MPa, and 3.5 MPa.

The following two fatigue formulas (Formulas 3 and 4) are used to analyze the fatigue performance of HiMA(20-25) and HiMA(40-25).

$$\log N = a_1 \times \ln \sigma + b_1 \quad (3)$$

$$\log N = a_2 \times \ln(\sigma/\sigma_0) + b_2 \quad (4)$$

where  $N$  is the fatigue life,  $\sigma$  is the stress level of fatigue test in MPa,  $\sigma_0$  is the bending strength in MPa, and  $a_1$ ,  $b_1$ ,  $a_2$ , and  $b_2$  are the regression coefficients.

### 5 DATA ANALYSIS

#### 5.1 Analysis of dynamic complex modulus test

Dynamic Complex modulus  $E^*$  of HiMA(20-25) and HiMA(40-25) are measured by SPT testing equipment according to the method recommended by NCHRP 9-29(10), and the results are shown in Table 1.

According to Table 1, the Dynamic modulus  $|E^*|$  of HiMA(20-25) reaches 21528 MPa at 20°C & 10 Hz, and is about 20% higher than that of HiMA(40-25). Based on the  $|E^*|$  at 10 Hz and different temperatures, the  $|E^*|$  of HiMA(20-25) and HiMA(40-25) under 15°C & 10 Hz could



Table 1. Dynamic complex modulus and phase angle of HiMA(20-25) and HiMA(40-25).

Mixes	HiMA(20-25)			HiMA(40-25)		
	20°C	40°C	55°C	20°C	40°C	55°C
Temperature	20°C	40°C	55°C	20°C	40°C	55°C
Frequency (Hz)	Dynamic Modulus $E^*$ (MPa)					
25	24387	10010	4217	21062	6130	2312.5
20	23748	9643	3779	20342.5	5718	2042
10	21528	7768	2772	17996	4331.5	1481.5
5	19310	6098	2024	15742.5	3209	1071.9
2	16419	4334	1362	12935.5	2148.5	706.7
1	14351	3237	1000	10950.5	1529	522.25
0.5	12425	2429	770	9128.5	1133.5	414.45
0.2	9996	1680	577	6877.5	794.2	322.2
0.1	8339	1264	468	5464.5	613.45	270.1
	Phase Angle (Degree)					
25	13.17	27.34	31.47	15.43	31.45	31.97
20	13.82	26.865	30.94	16.26	30.88	31.62
10	15.26	27.9	30.21	18.48	31.42	30.50
5	16.73	28.65	29.25	20.06	31.60	29.16
2	18.7	29.13	27.66	22.17	31.07	27.67
1	20.07	29.32	26.58	23.68	30.87	26.51
0.5	21.44	28.93	25.08	25.00	29.94	24.89
0.2	23.34	27.92	22.66	26.71	28.03	22.44
0.1	24.49	27.11	21.03	27.62	26.72	20.92

be evaluated. They are around 27000 MPa and 22000 MPa, respectively, which are much higher than the recommended value of general HiMA. The facts above are resulting from the application of hard asphalt and coarse aggregate gap-graded mixtures with large size NMAS and reasonable optimum asphalt-aggregate ratio of mixes.

According to the test data, with 20°C as reference temperature, the  $|E^*|$  master curve is constructed, and the master curve model is referred as sigmoid. And the relevant curve parameters are shown in Table 2 and curves shown in Figure 1.

Figure 1 shows that  $|E^*|$  of HiMA(20-25) is obviously higher than that of HiMA(40-25) at identical frequency. Moreover, the  $A_1$  and  $A_2$  of regression curves indicate that the maximum and minimum  $\log|E^*|$ , the  $A_1$  and  $A_2$  of HiMA(20-25) are all higher than that of HiMA(40-25).

With same shifting factor, the phase angle master curve can also be constructed (Fig. 2). Obviously, the phase angle of HiMA(20-25) is smaller than that of HiMA(40-25) at the same frequency. The phase angle determines the elastic (or viscous) properties of asphalt mixes, the higher phase angle leads to prominent viscosity performance; conversely, the smaller of the phase angle represents better elastic performance.

Table 2. Parameters of dynamic complex modulus & phase angle master curve.

Type	parameters	HiMA(20-25)	HiMA(40-25)
dynamic complex modulus master curve	$A_1$	2.0194	1.9771
	$A_2$	4.5487	4.4924
	$x_0$	-2.5020	-2.1597
	$D_1$	1.4722	1.3938
	Mean Square Error	1.49%	1.07%
	40°C→20°C shifting factor	2.0611	2.2318
	55°C→20°C shifting factor	3.3084	3.3122
phase angle master curve	$\gamma_0$	9.5115	10.3472
	$x_c$	-2.1393	-1.8429
	w	3.8916	4.0028
	A	99.5294	105.6655
	$R^2$	0.9648	0.9670
	Maximum $\phi$	29.92	31.41

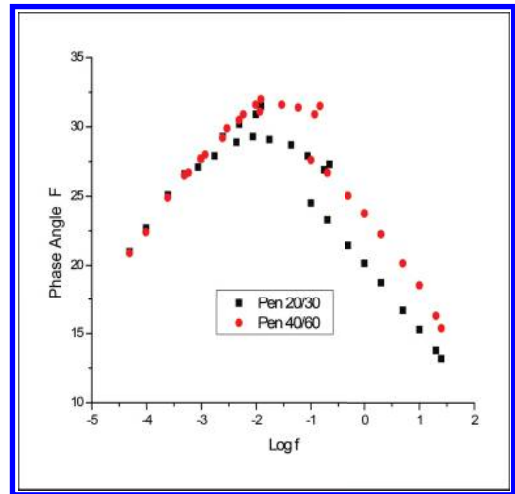


Figure 2. Phase angle master curve of HiMA(20-25) and HiMA(40-25).

Based on the test results, the Gauss curve model is used to construct the phase angle master curve, and the corresponding regression parameters are included in Table 2. The prediction curve of phase angle can be plotted based on regression equations (Fig. 3). The two curves have the same change rule that: with the increasing frequency, the phase angle will reach one peak value (maximum  $\phi$ ), at that point the viscosity reach maximum. But the peak values of the two mixes are different and the frequency corresponding maximum  $\phi$  is not the same, indicated by  $x_c$ . The  $x_c$  of HiMA(20-25) is lower than that of HiMA(40-25). The phase angle increases with the increasing frequency on the left

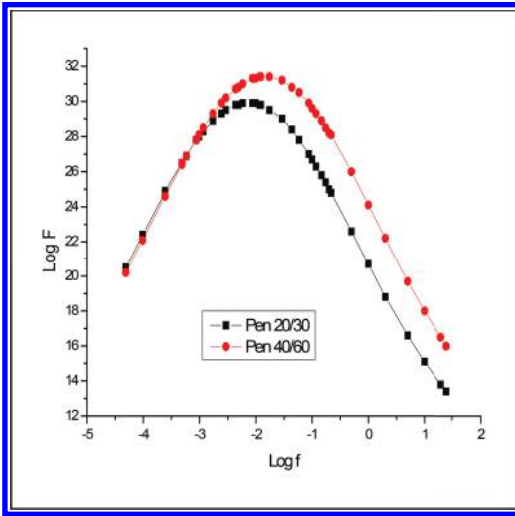


Figure 3. Phase angle master curve of HiMA(20-25) and HiMA(40-25) (prediction curve).

of peak value, and the two curves coincide with each other. On the right of peak value, the phase angle decreases with the increasing frequency; however, the two curves do not get together, and the interval between the two phase angles of the two mixes is maintained consistently at each identical loading frequency.

## 6 FATIGUE TEST ANALYSIS

Table 3 shows the results of three-point bending fatigue test on HiMA(20-25) and HiMA(40-25). Because of the difference between the two mixes of flexural strength, the fatigue life of the mixes appears largely varied under the same stress. The Figure 4 shows the fatigue life versus stress level, it indicates that large difference exists due to variation of asphalt. The fatigue life of HiMA(20-25) is much higher than that of HiMA(40-25) under the same stress level. The Figure 5 shows the fatigue life versus stress/strength ratio. Curves of the two mixes well coincide with each other. According to the changing trend, the curvature of HiMA(20-25) is slightly higher than that of HiMA(40-25), which represents the higher sensitivity of HiMA(20-25) to the change of stress/strain ratio.

Base on the results, the fatigue equation of two mixes are as follows:

To HiMA(20-25):

$$\log N = -2.7465 \times \ln \sigma + 6.9143 \quad r^2 = 0.9997$$

$$\log N = -2.7465 \times \ln \sigma / \sigma_0 + 1.092 \quad r^2 = 0.9997$$

Table 3. Fatigue test results.

Stress level (MPa)	Fatigue life, $N_f$ (times)	
	HiMA(20-25)	HiMA(40-25)
1	>2,000,000	1,020,636
1.5	610,483	95,496
2	105,181	19,268
2.5	26,090	9,262
3.5	2,873	1,239

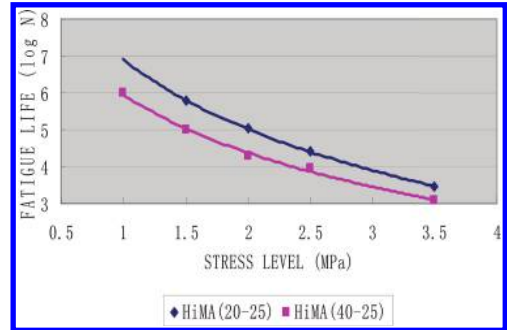


Figure 4. Curves of fatigue life versus stress level.

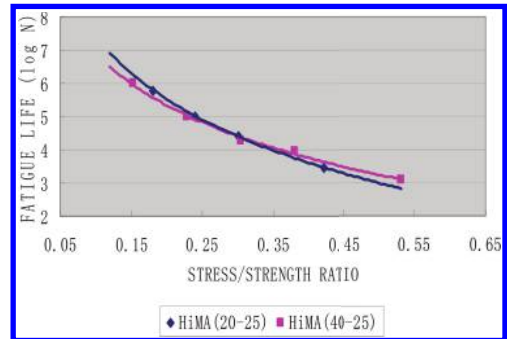


Figure 5. Curves of fatigue life versus stress/strength ratio.

To HiMA(40-25):

$$\log N = -2.2834 \times \ln \sigma + 5.959 \quad r^2 = 0.9951$$

$$\log N = -2.2834 \times \ln \sigma / \sigma_0 + 1.657 \quad r^2 = 0.9951$$

## 7 CONCLUSIONS

For purpose of renewal project of bus lane on Chang'an Road, the corresponding tests on hard

asphalt and HiMA are carried out. The main conclusions are offered.

1. SPT dynamic complex modulus test indicates that the modulus of the two mixes is much higher than that of general HiMAs. It resulted from the use of coarse aggregate gap-graded mixture with large size. Furthermore, based on the analyses of complex modulus master curve and phase angle master curve, it has been discovered that the modulus of HiMA(20-25) is much higher than that of HiMA(40-25); whereas, the phase angle result is converse. HiMA(20-25) performs better on elasticity.
2. During the fatigue test of three-points flexural-tensile by Cooper tester (stress controlled mode), it has been discovered that HiMA(20-25) has better fatigue resistance than HiMA(40-25) at the same stress level, and it is more sensitive to change of stress/strength ratio.

Summarized above, the HiMA(20-25) is applied in engineering of the bus lane renewal in road.

## REFERENCES

- [1] P. Sivapatham, H.J. Beckedahl, S. Janssen. Heavy Loaded Bus Lane Test Sections With High Polymer Modified Asphalt. *The 2009 TRB Annual Meeting CD-ROM*. Transportation Research Board, National Research Council, Washington, D.C., 2009.
- [2] T Distin, L Sampson, H Marais and B Verhaeghe. *High Modulus Asphalt: Assessment of Viability Based on Outcomes of Overseas Fact Finding Mission*.
- [3] J.P. Serfass, A. Bauduin, J.F. Gamier. High Modulus Asphalt Mixes-Laboratory Evaluation, Practical Aspects and Structural Design. *The 1992 ISAP 7th International Conference Proceedings CD-ROM*. International Society for Asphalt Pavements, Nottingham, 1992.

## Self-Compacting Concrete prepared with solid waste

G.X. Han, X.H. An, F. Jin, C.J. Chen & H. Zhou

*State Key Laboratory of Hydrosience and Engineering, Tsinghua University, Beijing, China*

**ABSTRACT:** This study focuses on the development of a novel self-compacting concrete made mainly with Phosphogypsum (PG), Ground Granulated Blast Furnace Slag (GGBFS), steel slag and clinker. The particle size distribution and pH value of PG slurry were tested, and the results showed the properties of PG for hydration of slag was improved. A prolonged setting time of excess-sulfate Phosphogypsum Slag Cement (PSC) was observed, and solved by adding 3% aluminum cement. The PSC showed a slightly higher basic water demand than that of OPC, and more sensitive to water and superplasticizer. Self-compacting concrete using PSC and other mineral fillers showed satisfying fluidity and possessed strength over 40 MPa.

**Keywords:** solid waste; phosphogypsum; self-compacting concrete; excess-sulfate phosphogypsum slag cement

### 1 INTRODUCTION

Phosphogypsum (PG) is a by-product from manufacturing phosphate acid by wet process in fertilizer industry. This powdery waste primarily consists of  $\text{CaSO}_4 \cdot 2\text{H}_2\text{O}$  with soluble impurities such as phosphate, fluoride and residual acid. The annual production of PG is estimated to be 100–280 million tons worldwide, whereas only 15% is utilized as building materials, soil stabilization amendments, and setting controller in Portland cement. In China, more than 22 million tons of PG is generated each year and less than 10% is recycled. (Tayibi et al., 2009, Reijnders, 2007, Yang et al., 2013)

While solid waste is accumulating, the consumption of building materials is increasing with the growing demand for concrete in numerous constructions. The application of solid wastes as building materials in concrete is significant in the conservation and recycling of resources.

Phosphogypsum, fly ash, steel slag, and alkali-activator, such as lime or acetylene sludge, are combined as cementitious materials (Shen et al., 2009, Shen et al., 2007, Qiao et al., 2010, Degirmenci, 2008). The 28 d compressive strength of this material is lower than 15 MPa, which becomes a limitation for their extensive use. Phosphogypsum treated by chemicals can replace natural gypsum and can be used as a conditioning agent in the cement industry (Singh, 2002). Its application range is also limited because of the tiny dosage as a modifier. Calcined PG is used as plaster and composite for masonry (Singh and Garg, 2001) and is also used to produce supersulphate cement (Erdem and

Olmez, 1993). However, the process of calcining consumes a huge amount of energy, which does not make it environment-friendly. Phosphogypsum is also employed as a gypsum to prepare non-autoclaved aerated concrete (Yang et al., 2013), and the use of the product is also limited by its low strength. A non-burnt binder, excess-sulfate Phosphogypsum Slag Cement (PSC), is mainly composed of PG, Ground Granulated Blast Furnace Slag (GGBFS), steel slag and clinker or limestone (Ding et al., 2014, Wan et al., 2013, Huang and Lin, 2011, Huang and Lin, 2010a, Huang and Lin, 2010b). The PG content can exceed 50%, and the 28 d compressive strength can reach 50 MPa. This high PG dosage and the strength equivalent to that of OPC will contribute to the massive utilization of PG as a building material.

Rock-Filled Concrete (RFC) is a novel technology for massive concrete constructions, which was developed in China. This concrete consists of large blocks of rock, usually with a minimum size of 30 cm, and ready-mixed Self-Compacting Concrete (SCC) which has excellent fluidity and segregation resistance. The ready-mixed SCC is poured onto the rock fill body and fills the void between blocks under gravity. RFC mass will be formed after the SCC sets (An et al., 2009, Huang et al., 2008). RFC presents good mechanical properties and impermeability (Mian-song et al., 2008), and has great advantages, such as low heat of hydration, low cost, and low energy consumption (Feng et al., 2008). It has been employed in a number of constructions of hydraulic, transportation, and municipal engineering. As a massive concrete technology, RFC shows potential in recycling solid wastes.

Table 1. Chemical components and basic physical properties of powder materials.

Item	SiO <sub>2</sub> %	Al <sub>2</sub> O <sub>3</sub> %	Tf <sub>e</sub> O <sub>3</sub> %	CaO %	MgO %	SO <sub>3</sub> %	P <sub>2</sub> O <sub>5</sub> %	LOI %	Total %	Density (g/cm <sup>3</sup> )	Blaine's surface area (m <sup>2</sup> /kg)
PG	9.65	0.79	0.37	29.71	0.3	36.62	1.03	20.52	98.99	2.35	282
GGBFS	33.17	16.28	0.26	38.22	8.09	–	0.102	0	96.12	2.91	454
SS	19.48	2.67	16.76	47.55	7.58	–	1.76	0	95.80	3.26	413
Clinker	21.78	5.10	3.40	65.05	2.12	0.64	–	0.13	98.22	3.15	454
FA	52.99	24.51	6.99	5.98	1.41	1.10	2.14	2.19	97.31	2.59	676
LP	2.24	1.07	0.38	52.81	1.28	–	0.01	41.86	99.65	2.80	707
AC	10.36	52.09	1.56	31.35	0.61	0.75	0.12	0.16	97.00	–	–

This study successfully prepared SCC using PSC as cementitious material, and SCC utilizing both PSC and mineral fillers, such as limestone powder and fly ash. This PSC-SCC could be employed in RFC construction and other suitable circumstances, which providing an inspiring prospect for extensive utilization of solid waste.

## 2 MATERIALS

Phosphogypsum was supplied by Tongling Chemical Industry Group Co., Ltd. of China. This powder contains 11.5% of water and granular lumps that require grinding before use in the concrete. The Limestone Powder (LP) and Fly Ash (FA) were used as filler. Aluminate Cement (AC) was used to modify the setting time of this binder. The properties of the powder materials are shown in Table 1. The density of each powder material was tested by Beijing Builder Electronic Technology Co., Ltd. using TD-2200 True Density Analyzer.

The fine aggregate, which was artificially graded, is crushed quartz sand with a density of 2.75 and a fineness modulus of 2.86.

The coarse aggregate is limestone gravel with a density of 2.7 and a maximum particle size of 20 mm. The amounts of gravel with sizes ranging from 5 mm to 10 mm and 10 mm to 20 mm were 40% and 60% of the total, respectively.

The Superplasticizer (SP) is R212 polycarboxylate type obtained from SINOCONFIX Co., Ltd. of China.

## 3 TESTING METHODS

### 3.1 Modification of phosphogypsum

The PSC used in this study is proportioned with PG, GGBFS, SS, and clinker at ratios of 47%, 47%, 2%, and 4% in mass.

Phosphogypsum contains granular lumps that cannot be directly used. Water-soluble impurities

such as phosphate and phosphoric acid are harmful to the hydration of GGBFS, which requires an alkaline environment. Phosphogypsum, GGBFS, steel slag, and water were mixed with a proportion of 63:1:3:33 and milled in a polyurethane jar for two hours. The  $\Phi$  290 mm  $\times$  300 mm sized jar contained corundum balls that rotated at a rate of 70 r/min. The paste was stored for 24 h at  $20 \pm 2$  °C in an airtight container to keep the water content stable. The rest of the powder materials and additional water were mixed with the modified PG slurry to prepare PSC paste.

### 3.2 The basic water demand and setting time of PSC

The initial and final setting times of PSC were tested according to the Chinese standards of GBT1346-2011.

The Slump Flows (SF) of PSC slurries with different water to powder ratios were tested, and the relationship between the water to powder ratio and relative SF ( $\Gamma$ ) was determined using a linear fitting method. The W/P-intercept of the line indicated the actual water content of the PSC slurry at which the slurry began to flow (Kazumasa, 1998). This critical water to powder ratio is the basic water demand of PSC, based on which the water to powder ratio of the PSC slurry for SCC is decided.  $\Gamma$  is calculated using the equation below:

$$\Gamma = \left( \frac{SF}{60 \text{ mm}} \right)^2 - 1$$

### 3.3 The mix design procedure of SCC

The mixing procedure of PSC-SCC is demonstrated in Figure 1. In this study, W/P is the ratio of water to powder by absolute volume, and sand ratio (S%) is the ratio of fine aggregate to mortar by absolute volume. SP% is the percentage of SP by weight in all the powder materials.

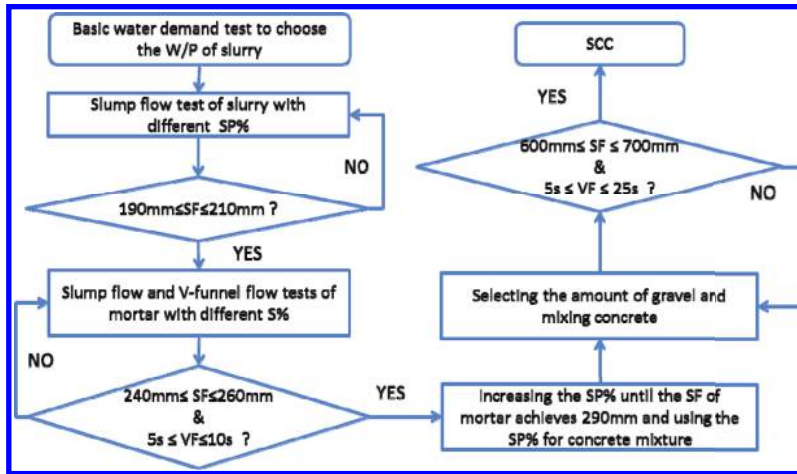


Figure 1. Procedure of PSC-SCC proportioning.

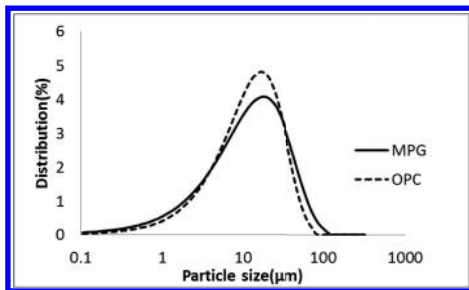


Figure 2. Comparison of the PSD of Modified PG (MPG) and OPC.

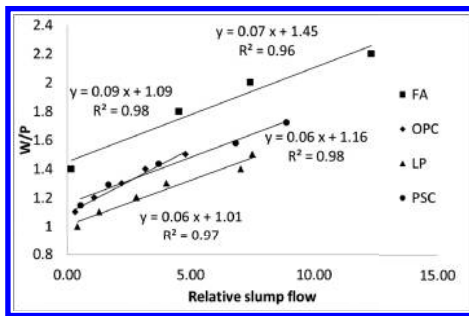


Figure 3. Results of basic W/P test.

Table 2. Setting time of different binders.

No.	Proportion of powder materials %						Ti/h	Tf/h
	PG	G	GGBFS	SS	Clinker	AC		
P1	47	0	47	2	4	0	55.5	76.0
P2	0	47	47	2	4	0	8.9	15.1
P3	0	0	88.7	3.8	7.5	0	5.8	7.5
P4	47	0	47	2	4	3	1.7	2.9



Figure 4. Slump flow of PSC-SCC.

## 4 RESULTS AND DISCUSSION

### 4.1 Properties of modified PG paste and PSC

The Particle Size Distribution (PSD) of Modified PG (MPG) is illustrated in Figure 2. The MPG is slightly coarser than OPC, with a mean particle diameter of 17.37  $\mu\text{m}$  compared to 15.43  $\mu\text{m}$  of OPC.

The pH value of the water separated from the PG slurry increased from 6.5 to 10 after modification, which is favorable to the hydration of GGBFS.

The basic water demand of PSC was 1.16 compared to 1.09 of OPC, as shown in Figure 3. Although the intercept of the former was slightly higher, the latter had a sharper slope, which meant

Table 3. Fluidity and compressive strength of PSC-SCC.

No.	W/P	SP/%	S/%	G/L	AC/%	SF/mm	VF/s	7 d/MPa	28 d/MPa
C1	0.84	1.75	49	325	0	650	130.59	–	–
C2	1.00	0.65	46	325	0	700	18.32	2.7	32.23
C3	1.10	0.50	46	325	3%	625	12.47	28.12	44.70

Table 4. Properties of PSC-SCC with different fillers.

No.	W/P	SP %	Proportion of powder materials %							AC/%	S %	G (L)	SF/mm	VF/s	7 d/MPa	28 d/MPa
			PG	LP	FA	GGBFS	SS	Clinker								
C3	1.1	0.5	47	0	0	47	2	4	3	46	325	625	12.47	28.12	44.7	
C-L	1	0.7	30	25	0	40	2	3	3	46	300	667	14.2	26.85	44.13	
C-F	1.1	1	30	0	30	35	2	3	3	46	300	623	24.97	19.06	40.45	

the relative SF of the slurry changed to the same extent and the change of water to powder ratio of the SSC slurry was smaller than that of the OPC. Thus, the fluidity of the SSC slurry is more sensitive to water than that of the OPC slurry. Furthermore, the SSC slurry is more sensitive to SP dosage in fluidity because the SP effectively disperses powder particles and releases the free water.

As shown in Table 2, both of initial and final setting times are much longer than those of the binder by using pure gypsum (G) instead of PG. Some impurities that cannot be removed by this modifying method still exist and hinder the setting of the binder. Researchers found that washing PG with a milk of lime solution, another alkaline modifying agent, cannot yield a satisfying result in terms of reducing the setting time retardation. (Potgieter et al., 2003). Thus, some uncertain impurities exist in the PG result in the retardation of the binder and cannot be removed using alkaline agents, such as steel slag or lime.

Meanwhile, a binder with pure gypsum has a longer setting time than that without any gypsum. Even though calcium sulphate activates the hydration of GGBFS (Gruskovnjak et al., 2008), the setting time of the binder will be prolonged by the dilution effect when the dosage of gypsum is high enough. Furthermore, the retardation caused by the impurities of PG is more severe than that by the dilution effect, and the use of alumina cement at a dosage of 3% can obviously shorten the setting time of PSC.

#### 4.2 Fluidity and compressive strength of PSC-SCC

Concrete with a water to powder ratio of 0.84 has a satisfying SF value, but it is too viscous to

have a proper VF value. As the W/P value rises, the VF value declines rapidly. The W/P value has a remarkable effect on the viscosity of concrete. Both C2 and C3 meet the qualification of SCC. The mix with a powder ratio of 1.10 has satisfying fluidity and relatively lower cost. Its initial condition is shown in Figure 4.

The 7 d strength of C2 is merely 2.7 MPa. The poor early strength is probably the consequence of the setting retardant caused by the hazardous impurities from phosphogypsum. The addition of aluminum cement obviously improves both the 7 d and 28 d strengths of C3.

#### 4.3 Fluidity and compressive strength of SCC with different fillers

Comparing with C3, the volume of gravel is reduced, but the VF value of C-F rose significantly, reaching the criterion of SCC. This could be attributed to the using of fly ash, which is much finer than the other powder.

C-L and C-F both showed a good performance on fluidity after proper adjustment, and possessing a similar compressive strength with C3.

## 5 CONCLUSIONS

Self-compacting concrete using PSC and other mineral fillers, such as limestone powder and fly ash, are successfully prepared, with good fluidity and compressive strength over 40 MPa at 28 d.

The phosphogypsum slurry becomes alkaline after wet-milled with steel slag, thereby providing a favorable environment for the hydration of GGBFS. Excess-Sulfate phosphogypsum-slag cement has a slightly higher basic water demand

than OPC, and it is more sensitive to water and superplasticizer.

Impurities causing a prolonged setting time still exist after the modification of PG. The retardation of setting caused by these impurities is more severe than that by the dilution effect of gypsum. However, the use of 3% aluminum cement shortens the setting time and improves the early strength.

## ACKNOWLEDGEMENT

The authors gratefully acknowledge the financial support provided by the National 863 Technology Research and Development Program of China (No. 2012AA06A112) and China Postdoctoral Science Foundation (No. 2013M540100).

## REFERENCES

- An, X.H., Huang, M.S., Zhou, H. & Jin, F. 2009. Rock-Filled Concrete in China—Self-Compacting Concrete for Massive Concrete.
- Degirmenci, N. 2008. Utilization of phosphogypsum as raw and calcined material in manufacturing of building products. *Construction And Building Materials*, 22, 1857–1862.
- Ding, S., Shui, Z.H., Chen, W., Lu, J.X. & Tian, S.F. 2014. Properties of supersulphated phosphogypsumslag cement (SSC) concrete. *Journal of Wuhan University of Technology-Materials Science Edition*, 29, 109–113.
- Erdem, E. & Olmez, H. 1993. The Mechanical-Properties of Supersulphated Cement Containing Phosphogypsum. *Cement and Concrete Research*, 23, 115–121.
- Feng, J.I.N., Le, L.I., Hu, Z. & Xuehui, A.N. 2008. Preliminary study on temperature rise property of thermal insulation of rock-fill concrete. *Water Resources and Hydropower Engineering*, 39, 59–63.
- Gruskovnjak, A., Lothenbach, B., Winnefeld, F., Figi, R., Ko, S.C., Adler, M. & Mader, U. 2008. Hydration mechanisms of super sulphated slag cement. *Cement and Concrete Research*, 38, 983–992.
- Huang, M., An, X., Zhou, H. & Jin, F. 2008. *Rock-fill concrete, a new type of concrete*.
- Huang, Y. & Lin, Z.S. 2010a. Effect of Sodium Hydroxide on the Properties of Phosphogypsum based Cement. *Journal of Wuhan University of Technology-Materials Science Edition*, 25, 342–345.
- Huang, Y. & Lin, Z.S. 2010b. Investigation on phosphogypsum-steel slag-granulated blast-furnace slag-limestone cement. *Construction and Building Materials*, 24, 1296–1301.
- Huang, Y. & Lin, Z.S. 2011. A Binder of Phosphogypsum-Ground Granulated Blast Furnace Slag-Ordinary Portland Cement. *Journal of Wuhan University of Technology-Materials Science Edition*, 26, 548–551.
- Kazumasa, O. 1998. *High Fluidity (self-compacting) Concrete Production Manual*, National Concrete Industry Association of Japan.
- Mian-Song, H., Hu, Z., Xue-Hui, A. & Feng, J. 2008. A Pilot Study on Integrated Properties of Rock—Filled Concrete. *Journal of Building Materias*, 206–211.
- Potgieter, J.H., Potgieter, S.S., Mccrindle, R.I. & Strydom, C.A. 2003. An investigation into the effect of various chemical and physical treatments of a South African phosphogypsum to render it suitable as a set retarder for cement. *Cement And Concrete Research*, 33, 1223–1227.
- Qiao, D., Qian, J.S., Wang, Q.Z., Dang, Y.D., Zhang, H. & Zeng, D.Q. 2010. Utilization of sulfate-rich solid wastes in rural road construction in the Three Gorges Reservoir. *Resources Conservation And Recycling*, 54, 1368–1376.
- Reijnders, L. 2007. Cleaner phosphogypsum, coal combustion ashes and waste incineration ashes for application in building materials: A review. *Building And Environment*, 42, 1036–1042.
- Shen, W.G., Zhou, M.K., Ma, W., Hu, J.Q. & Cai, Z. 2009. Investigation on the application of steel slag-fly ash-phosphogypsum solidified material as road base material. *Journal Of Hazardous Materials*, 164, 99–104.
- Shen, W.G., Zhou, M.K. & Zhao, Q.L. 2007. Study on lime-fly ash-phosphogypsum binder. *Construction and Building Materials*, 21, 1480–1485.
- Singh, M. 2002. Treating waste phosphogypsum for cement and plaster manufacture. *Cement and Concrete Research*, 32, 1033–1038.
- Singh, M. & Garg, M. 2001. Phosphogypsum based composite binders. *Journal of Scientific & Industrial Research*, 60, 812–817.
- Tayibi, H., Choura, M., Lopez, F.A., Alguacil, F.J. & Lopez-Delgado, A. 2009. Environmental impact and management of phosphogypsum. *Journal of Environmental Management*, 90, 2377–2386.
- Wan, H.W., Wu, Y.W., Chen, C., Wei, P.L. & Gao, Z.F. 2013. Effects of clinker contents of different C(3) A and C(4)AF on the performance of PSC cement. *Journal Of Wuhan University Of Technology-Materials Science Edition*, 28, 521–526.
- Yang, L., Yan, Y. & Hu, Z.H. 2013. Utilization of phosphogypsum for the preparation of non-autoclaved aerated concrete. *Construction And Building Materials*, 44, 600–606.



# Experimental study on mechanical properties of fiber reinforced lightweight aggregate concrete after freeze-thaw cycle

Jing Huang, Jianmin Wang & Anqing Liu

College of Civil Engineering and Environment, Ningbo University, Ningbo, Zhejiang Province, China

**ABSTRACT:** We use sludge ceramsite as coarse aggregate to make ceramsite concrete without fibers, HPPF and PANF ceramsite concrete. We study the influence of fiber variety and freeze-thaw cycle on characteristics of surface damage, compressive strength, elastic modulus, and splitting tensile strength via the freeze-thaw test. The results indicate that the incorporation of fibers can effectively restrain cracks in concrete from occurring and developing and improve its frost resistance. Freeze-thaw damage would make cement paste layer become brittle and scale, but mass loss isn't obvious. Compressive strength, elastic modulus, deformation, and splitting tensile strength of concrete after freeze-thaw cycle would reduce.

**Keywords:** fiber reinforced lightweight aggregate concrete; freeze-thaw cycle; mechanical properties

Lightweight aggregate concrete has good property of insulation, frost resistance, seismic performance, crack resistance (shrinkage resistance and creep resistance), anti-fatigue performance, and fire resistance<sup>[1]</sup>. Owing to this, lightweight aggregate concrete has been extensively applied to engineering, such as high-rise buildings, marine structures, long-span bridges, and urban overpass, and its application obtains a high technical and economical value<sup>[2,3]</sup>.

The northeast and northwest cold regions in China have a larger temperature difference between day and night. With time, degradation will occur in some buildings and hydraulic structures after frequent repeated action of freeze-thaw cycle. Further, security of concrete will reduce<sup>[4]</sup>. Cracks develop further when influence of environment becomes intensive, which severely affects normal use and durability of structures and causes inadequate concrete for design requirement, and even results in severe engineering accidents<sup>[5]</sup>. Hence, freeze-thaw damage is an important aspect of durability failure of concrete. It has important theoretical significance, practical value, and economic effect.

At present, researches on related mechanical properties of ceramsite concrete with incorporation of High Performance Profiled Fiber (HPPF) and Polyacrylonitrile Fiber (PANF) after freeze-thaw cycle are relatively few.

HPPF and PANF are incorporated after determining the optimal mix proportion via testing, then conduct the freeze-thaw test. Following that, we observe and analyze characteristics of surface damage of fiber reinforced ceramsite concrete and we perform analysis on difference of mechanical

properties such as compressive strength, elastic modulus, splitting tensile strength after freeze-thaw. As a consequence, we obtain the influence of incorporation of fibers on related mechanical properties of ceramsite concrete after freeze-thaw, then analyze and summarize the reasons.

## 1 INTRODUCTION

### 1.1 Testing material

Fine aggregate, coarse aggregate, cement, fly ash, fibers their specific parameters see [Table 1](#).

### 1.2 Testing equipment

Equipment used in freeze-thaw test is CABR-HDK9 automatic rapid freeze-thaw apparatus manufactured by Luda mechanical device limited company. Type WAW-600C 60T hydraulic servo controlled press is used for testing mechanical properties of test specimens.

### 1.3 Specimen making

Mix proportion of test see [Table 2](#). Specimens need 28 days curing at standard conditions in laboratory. Then take them out and place them at room temperature for one month to achieve air-dried state for subsequent freeze-thaw test. Considering that cubes (its dimension is 100 × 100 × 100 mm) and prisms (100 × 100 × 300 mm) need testing for their cubic compressive strength, splitting tensile strength, and elastic modulus and comparing with control concrete, the number of specimens

Table 1. Specification parameters of HPPF and PANF.

Type	Shape	Density (g/cm <sup>3</sup> )	Com. strength (Mpa)	Young's modulus (Gpa)	Elongation at break (%)	Length (mm)	Diameter (μm)	Melting point (°C)
HPPF	Corrugated	0.91	>500	>7	12~40	25~30	≥100	170
PANF	Grain shape monofilament	1.15~1.20	≥450	≥5	10~40	15~20	10~25	235~245

Table 2. Mix proportion.

Fiber (kg/m <sup>3</sup> )	Ceramsite (kg/m <sup>3</sup> )	Sand (kg/m <sup>3</sup> )	Cement (kg/m <sup>3</sup> )	Fly ash (kg/m <sup>3</sup> )	Water (kg/m <sup>3</sup> )
–	780	550	460	80	210
HPPF: 1.8	780	550	460	80	210
PANF: 0.4	780	550	460	80	210

would be  $(3 + 3 + 5 \times 3) \times 3 \times 2 = 126$ . Divide these specimens into six groups based on fiber type and if under freeze-thaw cycle.

#### 1.4 Test scheme

The automatic freeze-thaw apparatus was used to conduct the freeze-thaw test according to “Standard for test methods of long-term performance and durability of normal concrete” (GB/T 50082-2009). Take half of each kind of concrete for test, put specimens in water whose temperature ranges from 15°C to 20°C till they are in full water-saturated state for 4 days before test. Then take them out and dry the surface for weighing. Each freeze-thaw cycle lasts approximately three to four hours. Thawing time should be controlled to take up 1/3 of the total process. The central temperature of specimens was controlled in the range of -17.5°C to 7.5°C when freeze-thaw cycle ends. All specimens went through 25 times of freezing-thawing.

## 2 TEST RESULTS AND DISCUSSION

### 2.1 Analysis of characteristics of surface damage after freeze-thaw cycle

It is obvious that characteristics of surface change after freeze-thaw cycle. Surface which was smooth obviously becomes coarse, and spalling occurs in the cement paste layer on surface of specimens. In some specimens, microcracks occur on surface. Furthermore, some edges start to fall off.

Figure 1 shows that there are obvious pockmark phenomenon in normal concrete (without fiber), whereas prisms with HPPF and PANF respectively almost didn't have spalling.

Temperature difference caused by freeze-thaw process make internal free water repeatedly crystallize and expand, melt, and shrink, thereby resulting in larger temperature stress that destroys mortar matrix. Mortar surface falls off and leads to pockmark phenomenon. With respect to HPPF, its diameter and elastic modulus are larger in, but relative deformation is less. PANF has smaller filament diameter and performs well in ductility. In addition, the bond between it and cement matrix is superior, which makes fewer pockmark phenomenon and spalling.

### 2.2 Cubic compressive strength

Change in cubic compressive strength in three kinds of cubic specimens is seen Table 3. Table 3 shows that freeze-thaw cycle has a negative effect on cubic compressive strength of lightweight aggregate concrete. In addition, in contrast to fiber reinforced lightweight aggregate concrete, strength of normal concrete reduces less. Moreover, time which normal concrete needs to achieve fracture strength is longer than fiber reinforced lightweight aggregate concrete.

By analyzing these data, we conclude that fiber would bear inner tensile stress in concrete occurred in freeze-thaw cycle, thereby significantly improving concrete crack resistance. When under pressure, compression bearing capacity of concrete increases because of horizontal restraint of fiber. However, tensile bearing capacity of fiber decreases dramatically due to frequent loading and unloading; as a consequence, failure in ceramsite concrete occurs in advance.

### 2.3 Cubic splitting tensile strength

Change in cubic splitting tensile strength of three kinds of concrete after 25 freeze-thaw cycles is seen in Table 4.

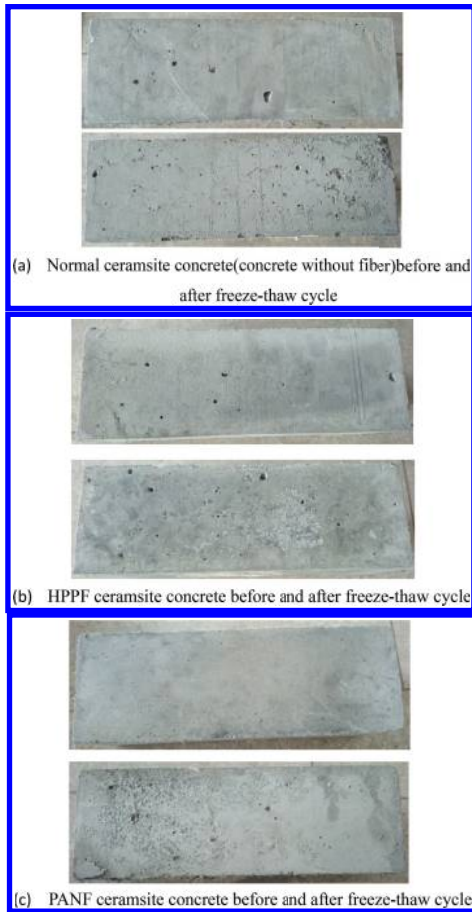


Figure 1. Characteristics of surface damage on prisms among three kinds of specimens before and after freeze-thaw cycle.

Table 3. Change on cubic compressive strength before and after freeze-thaw cycle.

Fiber types	Cubic compressive strength $f_{cu}$ (MPa)		
	Before	After	Reduction rate
Non-fibre	36.2	31.9	11.80%
HPPF	42.7	28.3	33.70%
PANF	40.3	30.3	24.80%

Table 4 shows that splitting tensile strength of ceramsite concrete has an obvious increase before freeze-thaw cycle with fiber incorporated, and enhancement of PANF is superior to HPPF. After freeze-thaw cycle, splitting tensile strength of PANF ceramsite concrete is still higher than the other two. After analysis, these phenomena

Table 4. Change on cubic splitting tensile strength.

Type	Non-fibre		HPPF		PANF	
No.	Before	After	Before	After	Before	After
1	4.77	3.94	4.84	2.83	6.52	4.89
2	5.49	3.16	5.22	2.54	6.19	4.76
3	4.54	3.32	5.56	3.15	6.18	4.79
Average value	4.44	3.14	4.69	2.56	5.67	4.81
Reduction rate	29.28%		45.42%		15.17%	

could be explained by characteristics of PANF such as higher ductility, easy dispersion, acid and alkali resistance, and low temperature resistance. Microfiber disordered distribution lap mutually in concrete restrains air-escape during mixing and molding process, which increases air content and mitigates hydrostatic pressure and seepage pressure during low temperature cycles. Therefore, it has a more obvious enhancement on splitting tensile strength<sup>[6]</sup>. Secondly, crack resistance of PANF is good owing to its small diameter, large quantity in unit volume and short fiber spacing, which increases energy loss during freeze-thaw cycle and effectively restrains cracks because of frost. This is beneficial to the improvement of strength increase and durability of frost thaw resistance in low temperature environment<sup>[7]</sup>. In a word, the improvement in splitting tensile strength of ceramsite concrete of PANF is obvious.

#### 2.4 Prism compressive strength

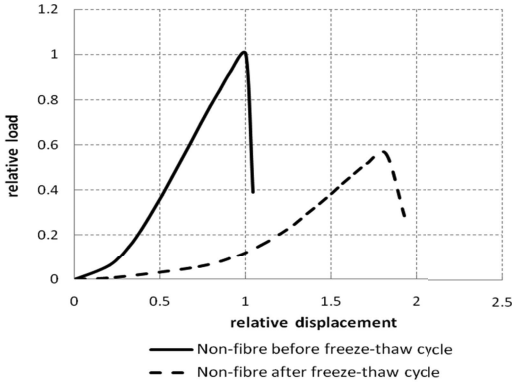
Table 5 shows change on prism compressive strength of three kinds of concrete before and after freeze-thaw cycle. From the data, we see that freeze-thaw cycle has a negative effect on prism compressive strength of lightweight aggregate concrete and prism compressive strength is lower than cubic compressive strength. HPPF and PANF bear tensile stress produced by concrete shrinkage. It restrains development of inner stress in concrete, postpones crack and increases prism compressive strength of ceramsite concrete. Load-displacement curves of the three kinds of concrete before and after freeze-thaw cycle; see Figure 2.

#### 2.5 Elastic modulus

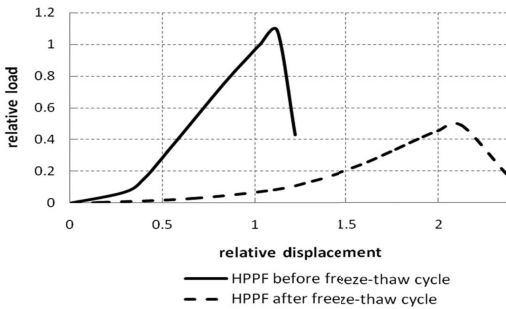
According to test method on non-fiber concrete in ordinary concrete mechanics performance test method standard<sup>[8]</sup>, we continue to conduct the elastic modulus test on ceramsite concrete. We obtain the elastic modulus of three kinds of ceramsite concrete before and after 25 freeze-thaw

Table 5. Change on prism compressive strength before and after freeze-thaw cycle.

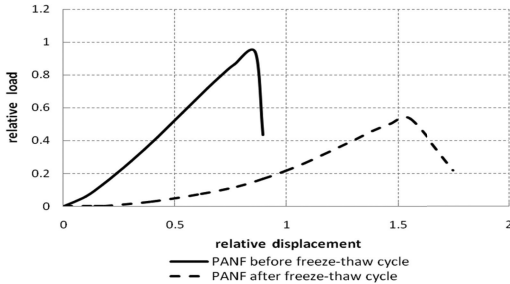
Fiber type	Prism compressive strength $f_{cu}$ (MPa)		
	Before	After	Reduction rate
Non-fibre	36.2	31.9	11.80%
HPPF	42.7	28.3	33.70%
PANF	40.3	30.3	24.80%



(a) normal ceramsite concrete



(b) HPPF ceramsite concrete



(c) PANF ceramsite concrete

Figure 2. Load-displacement curves of prisms of three kinds of ceramsite concrete before and after freeze-thaw cycle.



Figure 3. Elastic modulus measurement and failure mode of three kinds of concrete.

Table 6. Change on elastic modulus before and after freeze-thaw cycle.

Type	Elastic modulus of prism specimens E (MPa)					
	Non-fibre		HPPF		PANF	
No.	Before	After	Before	After	Before	After
1	21356	7256	23011	5795	22028	5735
2	21658	7157	22658	5540	22500	6724
3	20769	7438	21156	5256	21988	5945
Average value	21261	7284	22275	5531	22172	6135

cycles by loading and unloading three times with velocity of 0.5 Mpa/s (apparatus and failure mode of specimens see Fig. 3). Analyzing related data in Table 6, we could conclude that:

1. Elastic modulus of non-fiber ceramsite concrete is lower than HPPF and PANF ceramsite concrete before freeze-thaw cycle;
2. Elastic modulus reduces under freeze-thaw cycle;

3. Change in elastic modulus of non-fiber ceramsite concrete is smaller than HPPF and PANF ceramsite concrete under freeze-thaw cycle.

These phenomena could be explained by following reasons:

1. Non-fiber ceramsite concrete is a brittle material, and has a small deformation, when incorporated fibers, its plasticity enhances, thereby restrains deformation of concrete;
2. The inner structure has been destroyed after freeze-thaw cycle. Consequently, a lot of cracks occur and deformation increase.

### 3 CONCLUSION

1. Degeneration occur in performance of ceramsite concrete after freeze-thaw cycle, mortar, and fine aggregate particles start to spall gradually. Due to effective bonding, some small particles still hang on surface of fiber which has been exposed and form a layer of velvet material, consequently, reduce mass loss.
2. Fibers with uneven surface can form strong mechanical lock effect with hardened cement paste, which increases bonding strength between them, improves plasticity, and tensile strength of ceramsite concrete, simultaneously restrains cracking because of frost, consequently, improves durability and extends the performance life of ceramsite concrete.

### REFERENCES

- [1] Lightweight Aggregate Concrete[M]. William Andrew Publishing, Norwish, NewYork, U.S.A. 2002:5-10.
- [2] Tachibana D., Imai M., Okada T. Qualities of high-strength lightweight concrete used for construction of arctic offshore platform [J]. Journal of Offshore Mechanics and Arctic Engineering, 1990, 112(1):27-34.
- [3] Melby K., Jordet E.A., Hansvold C. Long-span bridges in Norway constructed in high strength LWA concrete [J]. Engineering structures, 1996, 18(11):845-849.
- [4] Feng Naiqian. Durability design and detection on concrete of oceanographic and offshore engineering [J]. Science and technology information in building, 2003, (1):1-6.
- [5] Yao Wu. Research on cryogenic property of PANF concrete [J]. Journal of building materials, 2003, 9. Volume 6, Issue 3.
- [6] Yao Wu, Feng Wei. Research on durability of frost thaw resistance of PANF concrete [J]. Industrial building, 2003, volume 33, issue 11.
- [7] Liu Dapeng, Huo Junfang, Li Jinshuai. Research on frost resistance test of fiber concrete [J]. Journal of Inner Mongol University of Technology (JCR Science Edition), 2009, 02:147-150.
- [8] China Academy of Building Research. Ordinary concrete mechanics performance test method Standard (GB/T50081-2002) [S]. Beijing: China building industry press, 2003.

# Influence of aggregates on coefficient of thermal expansion of concrete

Minjie Gao

*Jiangsu Testing Center for Quality of Construction Engineering Co. Ltd., Nanjing, China*

Guangnan Yuan, Liya Wang & Guibo Gao

*Shandong Provincial Academy of Building Research, Jinan, China*

**ABSTRACT:** The effect of the types, volume percentage and particle size of aggregates on thermal expansion coefficient of concrete was investigated in this research. Experimental results indicated that the type of the aggregates had remarkable effect on concrete thermal expansion coefficient, while particle size of the aggregates had some obvious effect. The thermal expansion coefficient of concrete increased as the volume percentage of the aggregates decreased. It is of crucial importance to select the suitable type and increase properly the volume percentage of the aggregates in order to improve the concrete volume stability.

**Keywords:** concrete; thermal expansion coefficient; aggregates; volume percentage; particle size

## 1 INTRODUCTION

Thermal expansion coefficient of concrete is the change in length/volume per unit in response to a change in temperature (per unit). This change is often characterized by average thermal expansion coefficient in engineering, which is only affected by the properties of concrete itself instead of environmental interference. It is one of the main physical parameters of the materials; also an important parameter to calculate the deformation under heat. In large scale concrete structures, the temperature increase is around 20–50 °C due to cement hydration. If the thermal expansion coefficient of the concrete is  $10 \times 10^{-6}/^{\circ}\text{C}$  with a deformation joint per 50 meters and the yearly temperature difference is 40 °C, the deformation will be 20 mm, which will have great influence on arranging deformation joints in the engineering. Therefore, the heat deformation in large scale concrete structures is extremely important and has to be carefully considered. Heat deformation of concrete can be reduced by in-depth study of the influence factors of the thermal expansion coefficient and taking effective measures to decrease it, which will bring less damage due to temperature decrease, and hence the service life of the structure can be increased.

So far, many developments have been obtained in the research on thermal expansion coefficient of concrete. Neville et al. (Li Q. 2002) found that the thermal expansion coefficient of concrete, mortar and cement stone was  $7.4\text{--}13.1 \times 10^{-6}/^{\circ}\text{C}$ ,  $10.1\text{--}18.5 \times 10^{-6}/^{\circ}\text{C}$ , and  $11\text{--}20 \times 10^{-6}/^{\circ}\text{C}$ , respectively.

However, the thermal expansion coefficient of cement stone was about  $8.8 \pm 1.2 \times 10^{-6}/^{\circ}\text{C}$ , tested by Lars Kraft et al. (Lars K. 2004). Research results from Meyers et al. (Meyers, S.L. 1950) indicated that the thermal expansion coefficient of cement stone was not a fixed value under the temperature  $-10\text{--}100^{\circ}\text{C}$ ; it depended on the water content, water to cement ratio and the age of the cement paste. The thermal expansion coefficient of the cement stone under wet curing for 28 days was  $15\text{--}20 \times 10^{-6}/^{\circ}\text{C}$ . Few studies have been performed on the research on heat deformation of cement based materials in China. Yuan and Yang (Yuan L. 2001 & Yang J. 2000) made use of optical fiber to measure the deformation of the concrete structures, which is a new method to test the thermal expansion coefficient of cement based materials. Xuan and Shui et al. (Xuan 2007) applied workhorse-1 thermal expansion meter to investigate the heat deformation property of the main components of cement based materials, and compared the difference in heat deformation property of the aggregates and the paste.

The obtained achievements provide a sound basis for the research on the thermal expansion property of concrete. However, few studies have been performed on the effect of aggregates on concrete thermal expansion property. Aggregates take up the largest portion in concrete. It is necessary to investigate the influence of aggregates: type, volume percentage, particle size, etc. on thermal expansion coefficient of concrete, which has great significance on the selection of proper aggregates for large scale concrete structures and improvement of concrete durability.

## 2 EXPERIMENTS

### 2.1 Materials

P.O42.5 cement, II grade fly ash and polycarboxylate superplasticizer were used. Fine aggregates were limestone sands and coarse aggregates were sandstone, limestone and marble. The thermal expansion coefficient and elastic modulus of different types of stones were shown in Table 1.

### 2.2 Measurement of thermal expansion coefficient of concrete

Hand-hold portable deflecting meter was used to measure the length of the concrete specimens between two fixed positions at different temperatures, and then the coefficient of thermal expansion was calculated. The details were as follows. Three specimens were cast for each concrete composition. Four bronze heads were embedded in parallel on the surface of the specimen as the endpoints to measure the length. The size of the concrete and the position of the bronze heads were shown in Figure 1 copperhead.

At certain age, concrete specimens were immersed in the water of the temperature  $T_0$ . After 1.5h, the specimens were taken out and the length  $l(T_0)$  between two bronze heads were measured. Subsequently, the specimens were transferred into a thermostatic water tank for

another 1.5h and the length  $l(T)$  was recorded. Valid data were the average values of the several measurements on the copper heads at each temperature. According to the measured length (between two copper heads) of concrete specimens at different temperatures, the coefficient of thermal expansion of concrete can be calculated based on equation (1).

$$\bar{\alpha} = \frac{l(T) - l(T_0)}{l(T_0)(T - T_0)} \quad (1)$$

where  $\alpha$ : the coefficient of thermal expansion of concrete.  $l(T_0)$ : Distance between two copper heads at temperature  $T_0$ .  $l(T)$ : Distance between two copper heads at temperature  $T$ .

The distance between two copper heads should be tested when the temperature in the center of the specimen was the same as that of water. Two free rolling steel bars were placed in parallel at the bottom of the specimen in order to reduce the restraining force of the concrete as temperature increasing. Foam insulation board was used to cover the surface of the specimen during the measurements at different temperatures, which can reduce the heat exchange with the surroundings upon the open and close of the water tank, maintain a constant water temperature in the tank and decrease the temperature variation of the hand-hold portable deflecting meter during the measurements.

Table 1. Thermal expansion coefficient and elastic modulus of different stones.

	Coefficient of thermal expansion ( $\times 10^{-6}/^{\circ}\text{C}$ )	Elastic modulus (GPa)	Density ( $\text{g}/\text{cm}^3$ )
Marble	5.5	26.6	2.7
Limestone	6.8	35.4	2.7
Sandstone	11.5	16.4	2.6
Cement stone	16	12	1.95

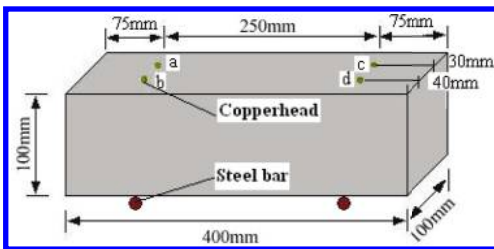


Figure 1. Schematic diagram of the concrete specimen and the embedded bronze heads.



Figure 2. Concrete specimens in water.

### 3 RESULTS AND DISCUSSION

#### 3.1 Effect of the type of aggregates on the coefficient of thermal expansion of concrete

5~25 mm continuous gradation sandstone, marble and limestone were used as coarse aggregates. Limestone sand was used as fine aggregates. The amount of cement and fly ash was  $320 \text{ kg/m}^3$  and  $80 \text{ kg/m}^3$ , respectively. Polycarboxylate superplasticizer was 1% of the total cementitious materials by weight. The water to cement ratio was 0.42 and sand ratio was 40%. The hand-hold portable deflecting meter was used to measure the thermal expansion coefficient of the specimens at certain ages. The results are shown in Figure 3.

The type of the aggregates has remarkable effect on the Coefficient of Thermal Expansion (CTE) of concrete. As shown in Figure 3, the average CTE value of the concrete with sandstone incorporated is 31% higher than that with marble. This is attributed to the difference in the CTE values of the different aggregates. Sandstone has the highest CTE value, followed by limestone. Marble has the lowest CTE value. It can be concluded that the CTE value of the concrete is also high if using the aggregates of a high CTE value, which is consistent with the theory of thermal expansion of composite.

#### 3.2 Effect of the volume percentage of aggregates on the coefficient of thermal expansion of concrete

5~25 mm continuous gradation limestone were used as coarse aggregates. Limestone sand was used as fine aggregates. The weight ratio between cement and fly ash was 4:1. Polycarboxylate superplasticizer was 1% of the total cementitious materials by weight. The water to cement ratio was 0.42 and sand ratio was 40%. The bulk density was  $2400 \text{ kg/m}^3$ . The volume percentage of the

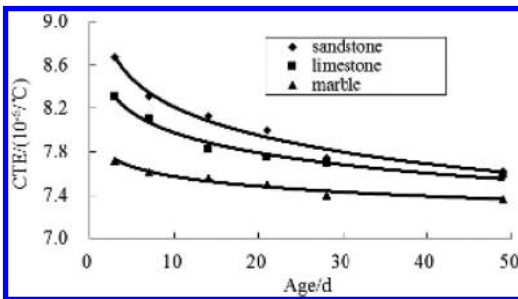


Figure 3. Influence of the type of aggregates on thermal expansion coefficient of concrete.

aggregates was 60%, 70% and 80% of the concrete. The CTE value of the concrete was tested at 3d, 7d, 28d and 49d. The results are shown in Figure 4.

The CTE value of the concrete decreased as the volume percentage of the aggregates increased. As shown in Figure 4, the average CTE value decreased by 9.5% when the volume percentage of the aggregates was increased from 60% to 80%. That is, the CTE value of the concrete decreases by 0.48% when the volume percentage of the aggregates was increased by 1%. This is due to the fact that the CTE value of the aggregates is lower than that of the hardened cement paste. Therefore, the CTE value of the concrete decreases as the volume percentage of the aggregates increases.

#### 3.3 Effect of particle size of the aggregates on the coefficient of thermal expansion of concrete

5~10 mm, 10~20 mm and 20~31.5 mm limestone were used as coarse aggregates. Siliceous river sand was used as fine aggregates. The amount of cement and fly ash was  $320 \text{ kg/m}^3$  and  $80 \text{ kg/m}^3$ , respectively. Polycarboxylate superplasticizer was 1% of the total cementitious materials by weight. The water to cement ratio was 0.42 and sand ratio was 40%. The hand-hold portable deflecting meter was used to measure the thermal expansion coefficient of the specimens at certain ages. The results are shown in Figure 5.

The particle size of the aggregates has obvious effect on CTE values of the concrete. In the aggregate size range of 5~31.5 mm, the CTE value of the concrete increased as the particle size increased. The average CTE value of the concrete with the aggregates of 20~31.5 mm incorporated was about 10% higher than that with the aggregates of 5~10 mm.

The main reason is that different position of the paste has different microstructure. The microstructure of the paste, and the transition zone between aggregates and paste is shown in Figure 6.

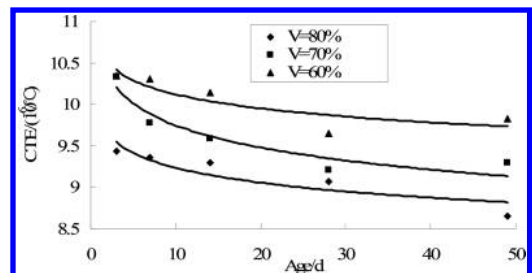


Figure 4. Influence of the volume percentage of the aggregates on CTE values of concrete.



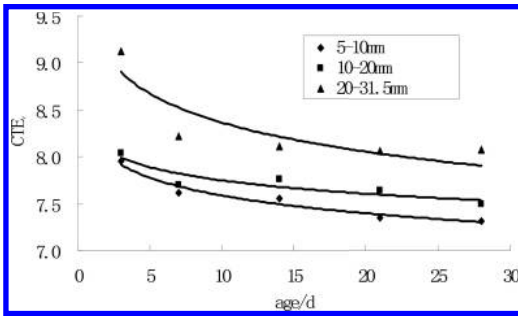


Figure 5. Influence of particle size of the aggregates on CTE values of the concrete.

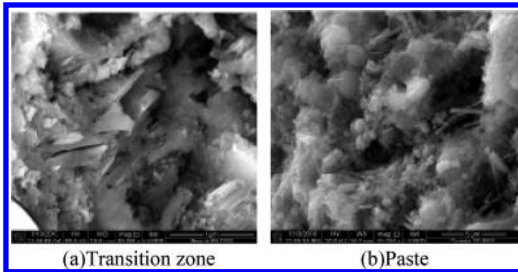


Figure 6. Microstructure of different position of the paste.

It can be seen from Figure 6 that the  $\text{Ca(OH)}_2$  crystal orientation is very obvious. The structure is quite loose and with high porosity. Therefore, the CTE value of this position is a bit lower. No obvious crystal orientation was observed in pure paste, which has a more denser structure with a lower porosity, and hence has a higher CTE value.

The smaller the particle size is, the larger the relative surface area of the aggregates will be. Therefore, the volume percentage of the aggregate-paste transition zone will be also relatively high under the same volume fraction of the aggregates. Thus, the CTE value of the concrete will be relatively low if using the aggregates of small particle size. The aggregates of 20–31.5 mm has a lower surface area compared to small aggregates, leading to less amount of transition zone and higher constraint force from aggregates; and hence the CTE value of this type of concrete is higher.

### 3.4 Theoretical calculation and analysis on the effect of the aggregates on the coefficient of thermal expansion of concrete

Different types of aggregates and hardened cement paste have different thermal expansion property and deformation resistance. Due to this, concrete

with different aggregates incorporated has different CTE values. Therefore, it is necessary to do in-depth calculation and analysis on the thermal deformation property of the concrete with different aggregates incorporated.

Concrete can be regarded as a composite material. The CTE of a composite is determined by its chemical composition, physical structure, and property and content of each component. Thus, the CTE of the concrete is not only directly influenced by the CTE values of the components, but also closed related to the elastic modulus of each component. According to the rule for mixture, the CTE value of the concrete can be approximately expressed by the weighted average of the CTE values of the cement stone and aggregates, when the migration of the water and gas contained in the concrete is not affected by the solid material (Yao W. 2007).

$$\alpha = \frac{\alpha_p E_p V_p + \alpha_s E_s V_s + \alpha_g E_g V_g}{E_p V_p + E_s V_s + E_g V_g} \quad (2)$$

$\alpha, \alpha_p, \alpha_s, \alpha_g$ : CTE values of concrete, cement stone, fine and coarse aggregates, respectively;

$E_p, E_s, E_g$ : elastic modulus of cement paste, fine and coarse aggregates, respectively;

$V_p, V_s, V_g$ : volume percentage of cement paste, fine and coarse aggregates, respectively;

The elastic modulus of the cement stone at 28d was taken as 12GPa and the CTE value was  $16 \times 10^{-6}/^\circ\text{C}$ . Different stones were used as fine and coarse aggregates. The sand ratio was 40%. The volume percentage of the aggregates: limestone, marble and granite, was increased from 60% to 80%. According to equation (2), the theoretical calculation result of the effect of the type and volume percentage of the aggregates on the CTE values of the concrete is shown in Figure 7.

The CTE value of the concrete decreased as the volume percentage of the aggregates increased. As shown in Figure 7, the average CTE value decreased by 10.64% when the volume percentage

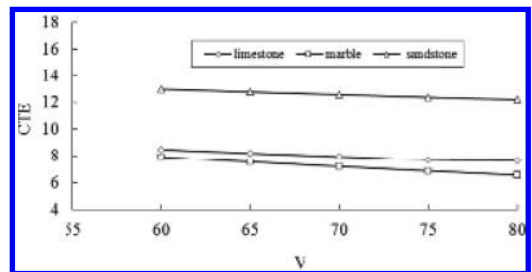


Figure 7. Influence of the type and volume percentage of the aggregates on the CTE values of the concrete.

of the aggregates was increased from 60% to 80%. That is, the CTE value of the concrete decreases by about 0.53% when the volume percentage of the aggregates was increased by 1%. This is consistent with the experimental results shown in Figure 4.

Meanwhile, it can be seen from Figure 7 that the type of the aggregates has remarkable influence on the CTE values of the concrete. When the volume percentage of the aggregates was in the range of 60% to 80%, the average CTE of the concrete with sandstone-aggregates was  $12.58 \times 10^{-6}/^{\circ}\text{C}$ , which is about 1.74 times higher than that of the concrete with marble-aggregates incorporated. This is consistent with the experimental results shown in Figure 3. Therefore, it can be concluded that it is of crucial importance to select proper aggregates to decrease the CTE of the concrete and hence to increase the volume stability of the concrete.

#### 4 SUMMARY

The type of the aggregates has remarkable influence on the CTE values of the concrete. This is due to the difference in the CTE values of the different aggregates. It is extremely important to select proper aggregates to decrease the CTE of the concrete and hence to increase the volume stability of the concrete.

The CTE value of the concrete decreased as the volume percentage of the aggregates increased. The CTE value of the concrete decreased by about 0.5% when the volume percentage of the aggregates increased by 1%. The reason is that the CTE value of the aggregates is lower than that of the hardened cement paste.

The particle size of the aggregates has obvious influence on CTE values of the concrete. In the aggregate size range of 5–31.5 mm, the CTE value of the concrete increased as the particle size increased. This is attributed to the fact that different position of the paste has different microstructure.

#### ACKNOWLEDGEMENTS

Foundation project: National natural science foundation of China (50539040).

#### REFERENCES

- Lars K. 2004. Early-age deformation, drying shrinkage and thermal dilation in a new type of dental restorative material based on calcium aluminate cement. *Cement and Concrete Research*. 34:439–446.
- Li Q. 2002. Model for measurement of thermal expansion coefficient of concrete by fiber optic sensor. *International Journal of Solids and Structures*. 39:2927–2937.
- Meyers, S.L. 1950. Thermal Expansion Characteristics of Hardened Cement Paste and of Concrete. *Proc Highway Res Board*. 30:193–200.
- Xu. 2007. Investigation on Thermal Deformation Divergence Between Components of Cement-basted Materials. *Journal of Wuhan University of Technology*. 29:30–32.
- Yao, W. 2007. Effect of Mix Proportion on Coefficient of Thermal Expansion of Concrete. *Journal of Tongji University Natural Science*. 35:77–82.
- Yuan. L. 2001. Fiber optic 2-D sensor of measuring the strain inside the concrete specimen. *Sensors and Actuators A*. 91:25–31.
- Yang J. 2000. Internal Strain Measuring for Concrete Specimens by Fiber Optical Sensors and Results Analysis. *Journal of Experimental Mechanics*. 15:421–428.

# Analysis of environmental hazard and leaching characteristics of heavy metals in solid waste

S.H. Zhou, H.Q. Yang, J.J. Yan & J. Su

Changjiang River Scientific Research Institute, Collaborative Innovation Center for Geo-Hazards and Eco-Environment in the Three Gorges Area, China

**ABSTRACT:** The experimental results showed that the heavy metal components could be slowly leached from solid waste in the water environment, and the leaching amount was related to the type of heavy metals. Pb, Zn, and As ions were more easily leaching in an acidic environment. The solid waste-dump region for a long time has a greater risk of heavy metal pollution. The Cr ion leaching concentration of blast furnace slag, the Cd and Cu ion leaching concentration of phosphorous slag, and the Cr, Pb, Cd, Cu ion leaching concentration of fly ash and incineration slag exceeded the standard limit of Class V water from GB3838.

**Keywords:** solid waste; heavy metal; leaching; environmental hazard; effective content; total content

## 1 INTRODUCTION

With the rapid development of China's social economy and the emission of industrial liquid effluents, industrial exhaust, and industrial residue, serious environmental problems ensue. Industrial waste may contain heavy metals. The environmental pollution caused by heavy metal wastes and their harm to health are extremely serious. They endanger the nervous and circulatory systems and some of them are carcinogenic. So many countries have established the strict emission standards and dissolution standards of heavy metals.

Appearing with the environmental problems in recent years, the trace element of solid waste has become a research hotspot [Li Cheng, Yu Qijun, Van der Sloot H.A., et al]. It would be a new issue of concern for them that the environmental pollution was caused by the heavy metal ions leaching from the solid waste in certain conditions [Liu Peng, et al]. In this research, we would use several common solid wastes from China, such as blast furnace slag, phosphorus slag, fly ash, incineration slag etc. The NEN7371 tests were applied to study the dissolution characteristics of Cr, Pb, Cd, Zn, As, and Cu ions from solid waste, and discuss the effect of heavy metals on the environment.

## 2 EXPERIMENTS

### 2.1 Experimental materials

In this research, these chemical reagents was used, including nitric acid (analysis purity), acetic acid

(GR), hydrogen peroxide (GR), hydrofluoric acid (GR), anhydrous ethanol (analysis purity), and demineralized water with a maximum conductivity of 150  $\mu$ S/m.

These common solid wastes were used, including Blast Furnace Slag (for short, BFS), Phosphorus Slag (for short, PS), Fly Ash (for short, FA), and incineration slag (for short, GIS). The chemical composition of solid waste was shown in Table 1.

### 2.2 Test methods

**Sample digestion.** The samples were dried and grinded  $5.000 \pm 0.0001$  g then put into 40 mL HF solution, and then placed on the furnace at  $90^{\circ}\text{C}$ – $100^{\circ}\text{C}$ . After the sample was dissolved completely, and been made to stand at room temperature for 30 minutes, it was then taken out and put into 100 mL measuring flask.

**Quick leaching test of trace element.** The NEN7371 tests were applied to study the dissolution characteristics of Cr, Pb, Cd, Zn, As, and Cu elements in solid waste. In this test, the liquid to solid volume ratio was 50:1, and the environmental

Table 1. The chemical composition of solid waste.

Type	CaO %	SiO <sub>2</sub> %	Al <sub>2</sub> O <sub>3</sub> %	Fe <sub>2</sub> O <sub>3</sub> %	MgO %	SO <sub>3</sub> %
BFS	40.6	26.6	12.3	6.6	8.5	0.4
PS	50.3	38.8	4.8	0.1	1.0	–
FA	5.1	59.0	21.6	8.7	1.5	0.7
GIS	20.4	41.7	7.5	13.2	14.3	0.3

temperature was  $20 \pm 2^\circ\text{C}$ . There were two kinds of the leaching liquids, namely acetic acid buffer solution ( $\text{pH} = 7$ ) and nitric-acetic acid buffer solution ( $\text{pH} = 4$ ).  $16.000 \pm 0.0001$  g samples were sieved through  $125 \mu\text{m}$  sieve, and then put into the leaching liquid. The mixtures were stirred to last 6h, and then were filtered with  $0.45 \mu\text{m}$  filter membrane. The clear liquid was shifted into the volumetric flasks after acidification treatment.

Test method of heavy metal ion concentration. With atomic absorption spectrophotometer method, the total content of Cr, Pb, Cd, Zn, and Cu element in fly ash was determined. With atomic fluorescence spectrophotometer method, the total content of As element in fly ash was determined. With atomic absorption spectrometry method, the content of Cr, Pb, Cd, Zn, Cu, and As element among the solution was determined.

### 3 RESULTS AND DISCUSSION

#### 3.1 The total content of heavy metals

The total content of heavy metals in waste shows direct impact on the ecological environment [Shi Huisheng]. The total content of heavy metals in solid waste was calculated and shown in Table 2. From Table 2, it could be found that the contents of heavy metal elements in solid waste could not be ignored. The heavy metal content of BFS content is lower, and that of FA is higher. GIS is extremely high in heavy metal. For example, the Cr content reached to  $433.5 \text{ mg/kg}$ , and the Zn content reached to  $1870 \text{ mg/kg}$ .

Compared to the quality of requirements of Class III soil of GB15618 “environmental quality standard for soils”, all kinds of heavy metal in BFS accorded with the standard requirements, the Cd content in FA and PS exceeded the standard value, and the Cr, Cd, Zn, As, and Cu content in GIS was much more than the standard value except the Pb content.

Table 2. The total content of heavy metals in solid waste.

Type	The total content (mg/kg)					
	Cr	Pb	Cd	Zn	As	Cu
BFS	23.6	12.4	0.1	35.5	0.4	7.5
PS	1.3	2.4	8.7	12.3	26.1	0.3
FA	98.8	82.3	45.5	200.6	18.6	83.9
GIS	433.5	323.1	8.6	1870	18.9	434.7
Class III soil of GB15618	$\leq 300$	$\leq 500$	$\leq 1.0$	$\leq 500$	$\leq 40$	$\leq 400$

#### 3.2 The soluble content of heavy metals

Contents of heavy metal elements in industrial waste can be divided into the total content and soluble content, the latter is often called “the effective content”. The NEN7371 leaching method can be used to test the effective release content of inorganic components in particulate materials or waste under extreme environmental conditions. This method can reflect the possible release amount of heavy metal components in long service concrete, so this method was applied to evaluate the environmental safety of building materials in EU [Kossor D. S., et al].

With NEN 7371 test method, the soluble content of Cr, Pb, Cd, Zn, As, and Cu element was determined and shown in Table 3, and the effective content was shown in Figure 1 and Figure 2.

The test results showed that the soluble content of heavy metals in solid waste was far less than the total content for corresponding. The effective content of heavy metals was in the range of  $8.4\% \sim 66.4\%$ . The effective content of Cu was

Table 3. The soluble content of heavy metal ions from soil waste ( $\text{pH} = 7$ ).

Type	The soluble content (mg/kg)					
	Cr	Pb	Cd	Zn	As	Cu
BFS	10.2	1.5	—	18.4	0.05	4.0
PS	0.4	0.3	5.2	5.0	2.20	0.1
FA	69.3	16.60	25.8	62.6	0.35	58.7
GIS	246.6	120.0	5.0	1017	4.90	288.7
Class III soil of GB15618	$\leq 300$	$\leq 500$	$\leq 1.0$	$\leq 500$	$\leq 40$	$\leq 400$

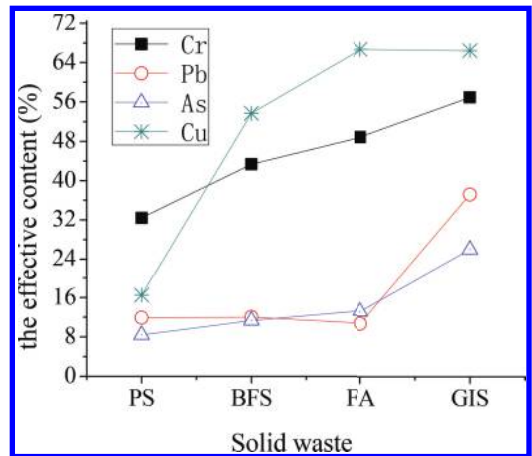


Figure 1. The effective content of Cr, Pb, As, and Cu.

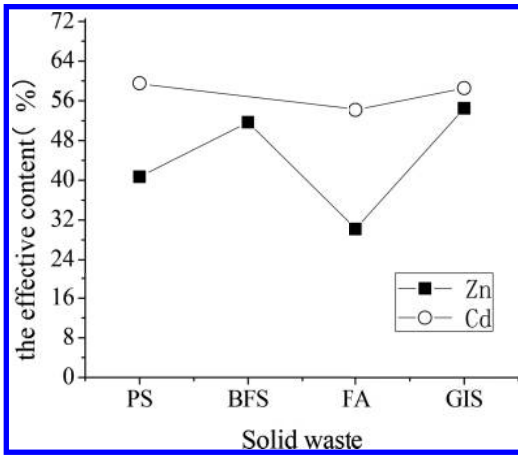


Figure 2. The effective content of Zn and Cd.

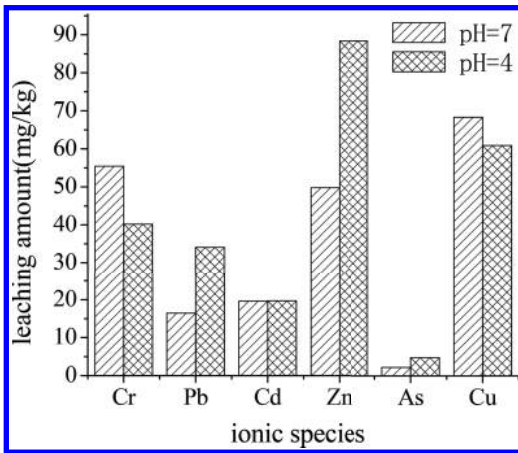


Figure 3. Effect of acid condition on leaching.

highest, and that of As was lowest. From Table 3, the effective content of Cd in FA and PS exceeded the standard value of Class III soil, and the effective content of Cd, Zn in GIS was much more than the standard value.

### 3.3 The effect of acidic condition on the leaching characteristics

It has significant influence of the pH value on the leaching of heavy metal ion. Some researchers [Yu Qijun, Kazuyuki S., Chrysochoou M., et al] had found that some heavy metal ions would decrease the leachability at higher pH solution. The reason may be the decrease of soluble, or the formation of insoluble phase and the re precipitation in solution [Yu Qijun].

In this research, the leaching characteristics of heavy metals from FA in the acid condition (pH = 4) were studied. The experimental results were shown in Figure 3. Compared with the soluble content of heavy metals in pH = 7 leaching liquid, the soluble content of Cr and Cu in pH = 4 leaching liquid was lower, and the soluble content of Pb, Zn, As in pH = 4 leaching liquid was higher. The test results show that acidic solution decreased the leachability of Cr and Cu ions and increased the leachability of Pb, Zn, and As ions. It has less effect of the acidic environment on the leachability of Cd ion. The effect of pH on BFS, PS, GIS was consistent with that on FA.

## 4 ENVIRONMENTAL IMPACT ANALYSIS

How to evaluate the environmental hazards of heavy metals? The researchers adopt various methods, such as the total content method, the simulation test method, the environmental geochemistry method, the chemical speciation method and the indicator plant method etc. [Shi Huisheng].

It is not reasonable to evaluate the influence of solid waste on the ecological environment using the total content method. Obviously, although the total content of heavy metals in solid waste is higher, the solution content possibly is lower. If heavy metal ions in solid waste are inactive, namely not into the recycling ecosystem, these heavy metals are harmless to the environment. In a word, it is reasonable to evaluate the environmental impact analysis using the solution content method. The heavy metal ions concentrations of leaching liquid were detected during the testing process in the soluble content of fly ash. The results were showed in Table 4.

According to the relevant requirements of GB5085.3 “identification standard for hazardous wastes—identification for extraction toxicity”, the

Table 4. The maximum leaching concentration of heavy metals (pH = 7).

Type	The maximum leaching concentration mg/L					
	Cr	Pb	Cd	Zn	As	Cu
BFS	0.20	0.03	—	<0.37	0.01	0.05
PS	0.01	0.01	0.10	0.10	0.04	2.20
FA	1.39	0.33	0.52	1.25	0.01	1.18
GIS	4.93	2.40	0.10	20.34	0.10	4.90
GB5085.3	≤15	≤5	≤1	≤100	≤5	≤100
Class V of GB3838	≤0.1	≤0.1	≤0.01	≤2.0	≤0.1	≤1.0

leaching ion concentrations of Cr, Pb, Cd, Zn, As, and Cu in solid waste were lower than the standard limit. This indicates that BFS, PS, FA and GIS don't belong to hazardous waste. Under certain conditions, the effective contents of heavy metal in solid waste are dissolution. According to the technology requirements of Class V in GB3838 "environment quality standard for surface water", the maximum solution amount of Cr, Pb, Cd, and Cu ions in FA, the maximum solution amount of Cd, Cu ions in PS, the maximum solution amount of Cr ions in BFS, the maximum solution amount of Cr, Pb, Cd, Cu, Zn, and As ions in GIS exceeded the standard limit.

It is reasonable to evaluate the environmental security of heavy metal from the solid waste long-term stacking region by the maximum solution amount of heavy metal [Kossor D.S., et al]. The research results show that the blast furnace slag dumps region for a long time had a greater risk of Cr ions, and the fly ash dumps region for a long time had a greater risk of Cr, Pb, Cd, and Cu ions. The phosphorus slag dumps region for a long time had a greater risk of Cd and Cu ions. The incineration slag dumps region for a long time had a greater risk of Cr, Pb, Cd, and Cu ions.

## 5 CONCLUSIONS

1. The contents of heavy metal elements in solid waste could not be ignored. Compared to the quality requirements of Class III soil of GB15618, the Cd content in FA and PS exceeded the standard value, and the Cr, Cd, Zn, As, and Cu content in GIS was much more than the standard value.
2. The heavy metal components could be slowly leached from solid waste in the water environment. The effective content of Cu was highest, and that of As was lowest. The effective content of heavy metals in GIS was higher than that in BFS, FA, and PS.
3. The acidic solution decreased the leachability of Cr and Cu ions, and increased the leachability of Pb, Zn, and As ions. It has less effect of the acidic environment on the leachability of Cd ion.
4. The blast furnace slag dumps region for a long time had a greater risk of Cr ions, and the fly ash dumps region for a long time had a greater risk of Cr, Pb, Cd, and Cu ions. The phosphorus

slag dumps region for a long time had a greater risk of Cd and Cu ions. The incineration slag dumps region for a long time had a greater risk of Cr, Pb, Cd, and Cu ions.

## ACKNOWLEDGMENTS

It is a project supported by the National Natural Science Foundation of China (51279017, 51139001, and 51209022).

## REFERENCES

- Chrysochoou M., Dermatas D. 2006. Evaluation of ettringite and hydrocalumite formation for heavy metal immobilization: Literature review and experimental study. *Journal of Hazardous Materials*, No. 136: 20–33.
- Huisheng Shi., 2005, Beijing, Utilization technology of eco-cement and waste resources, Chemical Industry Press.
- Kazuyuki S., Yoshiro O. 2008. Leaching characteristics of stabilized/solidified fly ash generated from ash-melting plant. *Chemosphere*, No. 71: 922–932.
- Kossor D.S., van der Sloot H.A., Eighmy T.T. 1996. An approach for estimation of contaminant release during utilization and disposal of municipal waste combustion residues. *Journal of Hazardous Materials*, Vol. 47, No. 1–3: 43–75.
- Li Cheng, Qijun Yu, Jinmei Lin, Nagataki. 2004. Leaching behavior of Cr (VI) from fly ash and hardened fly ash. *Journal of Wuhan University of Technology*, Vol. 26, No. 12: 23–26.
- Peng Liu, Ying Huang, Jianhong Luo. 2009. The simulation study of trace elements from coal fly ash on groundwater pollution, *Journal of Wuhan Polytechnic University*, Vol. 28, No. 3: 82–85.
- Qijun Yu, Li Cheng. 2003 Study on leaching of heavy metals and toxic ions from cement and fly ash. *cement*, No. 1: 8–15.
- Van der Sloot H.A., 2002. Characterization of the leaching behaviour of concrete mortars and of cement-stabilized wastes with different waste loading for long term environmental assessment. *Waste Management*, Vol. 22, No. 2: 181–186.
- Yu Qijun, Nagataki S, Lin Jinmei. 2003. Solidification of municipal solid waste incineration fly ash with cement and its leaching behaviors of heavy metals. *Wuhan University Technology (Mater Science Ed)*, Vol. 18, No. 1: 55–60.
- Yu Qijun, S. Nagataki, Lin Jinmei. 2005. The leachability of heavy metals in hardened fly ash cement and cement—solidified fly ash. *Cement and Concrete Research*, No. 35: 1056–1063.

# Frost resistance of city sludge sintered shale brick

Bei Zhang

Guangxi University of Technology, Liuzhou, Guangxi, China

Bing-Zhang Huang

Shijiazhuang Tiedao University Sifang College, Shijiazhuang, China

Jun Lai

Guangxi University of Technology, Liuzhou, Guangxi, China

**ABSTRACT:** We study the frost resistance about city sludge as a raw material to make city sludge sintered shale brick. City sludge sintered shale brick has contrasts with common sintered shale brick about frost resistance experiment in progress of different cycles (10 times, 20 times, 30 times, and 50 times) and studies the effect on sludge contents. Results show that with the increase in the number of cycles, the loss rate of city sludge sintered shale brick's compressive strength and the appearance of quality are larger than common sintered shale brick. The reason is sludge as an organic to produce contents of energy and pores in the high temperature through burning to have influence on frost resistance; with the increase in sludge content, the loss rate of quality and strength increases.

**Keywords:** city sludge; frost resistance; porosity; sludge content

## 1 INTRODUCTION

At present, due to rapid development of economic and GDP, building consumes too much energy and has a close relationship with environment and resources. China's annual waste of resources is about 15 million tons, so waste utilization by more people is brought to attention to, especially the utilization of sewage sludge. City sludge is a sewage treatment plant in the water purification process of solid waste precipitation, and it contains rich hydrocarbon organic compounds and large numbers of pathogenic bacteria, heavy metals, and other harmful substances. It may become a source of pollution and cause of secondary pollution easily if unreasonably used without any safety. Therefore, the disposal of city waste sludge is a priority, which sludge mixes with shale of preparing sintered shale brick, it is a way to save energy and protect ecological environment. Our research group has laid a solid foundation about city sludge and made achievements to certain properties results. However, the frost resistance of city sludge brick is still inadequate.

Frost resistance refers to materials' resistance in freezing and thawing cycles and free-water, which contains tiny pores that freeze to produce expansion and migrate to the icing area resulting in a great pressure on materials. With the time going by, expand-energy gradually extends from external

to internal to result in cracking and peeling. Therefore, it has reduced the freeze resistance, the material quality, compressive strength<sup>[1-3]</sup>.

## 2 RAW MATERIALS AND TEST METHODS

### 2.1 Raw materials

#### 2.1.1 Shale

We choose shale brick from factory in Liuzhou city of Guangxi where it is taken from near the village place in the ball mill after it dries and breaks to form powder, its components include  $\text{SiO}_2$ ,  $\text{Al}_2\text{O}_3$ ,  $\text{Fe}_2\text{O}_3$ ,  $\text{CaO}$ , and  $\text{MgO}$ . The standard shale particle size distribution are as follows [Table 1](#).

Table 1. Shale particle size distribution.

No.	Particle size (mm)	Quality proportion (%)
1	>2	10
2	1.5~2	12
3	0.5~1.0	38
4	0.25~0.5	15
5	<0.25	25

Table 2. City sludge index.

PH	Color	State	Taste
6.8	Black or brown	Fluid	Stench

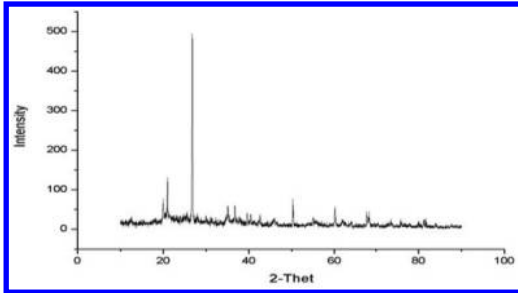


Figure 1. XRD composition of sludge.

### 2.1.2 Sludge

City sludge: sludge from the primary sink of the sewage treatment plant in Liuzhou, Guangxi. The basic properties of city sludge are shown in Table 2, Figure 1 shows that the composition percentages of the sludge are: SiO<sub>2</sub> 83%, KCl 12%, (KAl<sub>2</sub>(AlSi<sub>3</sub>O<sub>10</sub>)(OH)<sub>2</sub> 1.7%, CaNH 1.9%, Mg(OH)<sub>2</sub>0.6%, Li<sub>2</sub>CrF<sub>6</sub> 0.4%, and Mn<sub>1.7</sub>Fe<sub>1.3</sub> 0.3%.

### 2.2 Sintering progress

The brick is making use of sludge and shale as a certain mixture, adding content of water to adjust the mixture of water content and repeatedly mix, it is sealed at 20±1°C and molded after 24 h of aging suppression in relative maintenance of 100% humidity, brick model is made for wood and size is 240 mm × 115 mm × 53 mm. The specific process is that the wet model dries during 1.5 h after sun by drying in oven at 105°C, the second step is to place it in the high-temperature laboratory, programmable to roast according to the setting temperature to fire at temperature of 950°C and it takes 2 h to cool furnace.

### 2.3 Test method

The frost resistance experiment box is a Beijing—Shuzhiyilong instrument. The test is carried out with reference to national standard/T GB 2542–2012 [4], the damage rate of quality and intensity are used as the evaluation frost resistance.

The appearance of test sample (city sludge brick and common sintered shale brick) is better before testing. We divide them into three groups and include 10 bricks per group (1–4 group for city

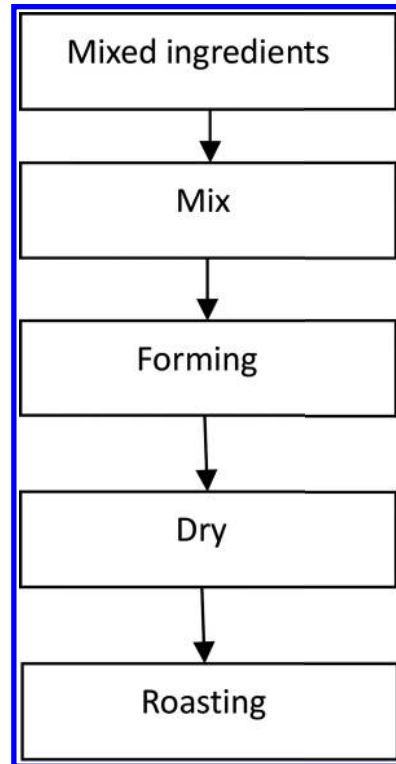


Figure 2. Preparation process of city sludge shale brick.



Figure 3. Freeze-thaw test machine.

sludge sintered shale brick, 5–8 group fired common brick, 9–10 contrast sample), it is tested 10 times, 20 times, 30 times, and 50 times, and the loss rate of quality and strength is measured. According to the laboratory test, the methods and steps are as follows:

1. Samples removing from the place of curing is immersed in water of 10 to 20°C and taken



out after 24 h, comparison samples should be retained in the standard curing room until the completion of the cycles of frost resistance.

2. After the soaking, one should use a damp cloth to wipe the surface moisture then put into the oven at  $105 \pm 5^\circ\text{C}$  for drying (during the dry process, the two difference weighing is less than 0.2%, and the two weighing interval is 2 h) to refer to  $M_1$ .
3. Regulation of freezing and thawing box should be controlled at  $15 \pm 2^\circ\text{C}$ , the specimens should be placed on the bracket at a distance of at least 20 mm spacing, if the temperature rises, until it accurately reaches to  $-15^\circ\text{C}$  to begin freezing (it should be about 4 hours), then the samples should be placed in a higher specimen 20 mm water to keep the temperature at about  $15^\circ\text{C}$ . Water should be used to thaw 4 hours, thaw time must not be less than the entire freeze-thawing cycle of 1/4 of the freeze—thawing cycle.
4. After each freezing and thawing cycle, we should check the appearance whether it has cracking, peeling, and missing angle phenomenon.
5. By freeze-thaw cycle for 10 times, 20 times, 30 times, and 50 times the samples kept the dry-box to weigh dry quality.  $M_2$ . By the ratio of  $M_1$  and  $M_2$  divide the  $M_1$  to get loss rate of quality.
6. Then the dried samples are soaked again in water for 10 to  $20^\circ\text{C}$  during 24 h, after which they will be placed in the center of the plate to be smoothed and loaded until the trial location reads the compressive strength.

### 3 RESULTS AND DISCUSSIONS

#### 3.1 The city sludge about frost resistance test data

Before freezing and thawing of the city sludge sintered shale brick strength has an average value of 15.6. After freezing and thawing strength has an average value of 14.31, loss rate of an average value of  $8.25\% < 25\%$  and loss rate of quality of an average value of  $1.1\% < 2\%$ , F50 after testing strength has an average value of 14.03 and loss rate of average  $10.05\% < 25\%$  and loss rate of quality has an average value of  $1.4\% < 2\%$ , strength grade is MU10 to fit the provisions of the freezing and thawing test.

Based on visual observation, city sludge sintered shale brick is smooth and has no missing angle, cracks and no dregs phenomenon before testing; after 10 times of freezing and thawing, we observe the appearance of the specimen to find that the overall is still good. Thus individual sample is found on the surface in which subtle cracks and no dregs phenomenon exist when we touch them

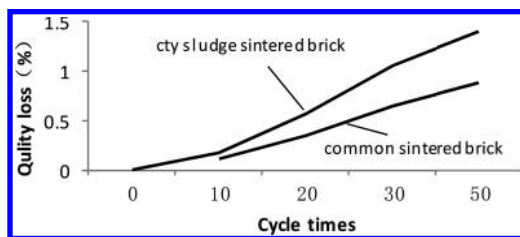


Figure 4. Effect of cycles of quality loss rate.

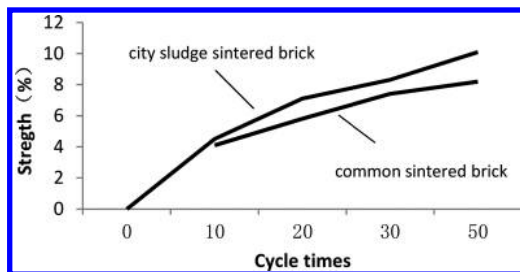


Figure 5. Effect of cycles on the strength loss rate.

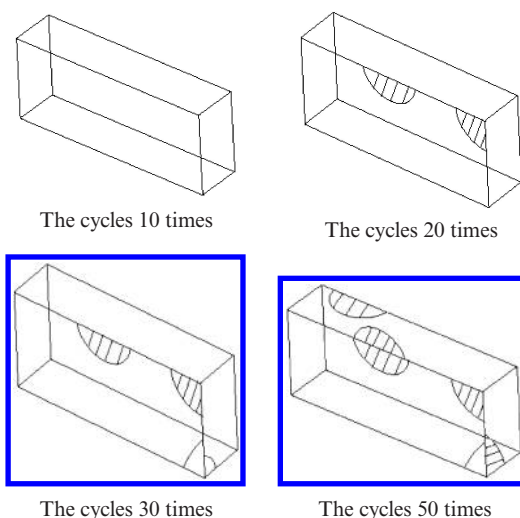


Figure 6. Freeze-thaw phenomenon.

by hand. After 20 times, the appearance of the bricks has an alloy exfoliation phenomenon, and some of samples have a slight missing angle and dregs phenomenon. After 30 times, the appearance is observed at the surface of the crack and spall at different levels. After 50 times of freezing and thawing, the appearance is observed at the surface of the crack and spall, even serious missing angle phenomenon as shown Figure 6.

In Table 3, Table 4, Table 5, and Table 6, with repeated times increase, the loss rate of quality and compressive strength of city sludge sintered shale brick gradually increase. When the freeze-thaw cycle is 50 times, the loss rate of quality reaches 1.4% and average strength loss rate reaches 10.05%, but the frost resistance of city sludge sintered shale brick is poorer than common sintered shale brick, it is a reason that during the process of sintering, city sludge burns and leaves a small content of ash after high temperature as organic, leading to produce a large number of uniform pores which is like capillary hole, it can begin to freeze the water in the low temperature and produce a certain expansion

stress on the surrounding; with the time goes, the bricks gradually generates a minor crack to extend the internal pore and provide favorable conditions for the next time, so that the crack is larger than before resulting in damage such as missing angle.

### 3.2 The influence of sludge amount on the freezing resistance

With contents of sludge increase, the bricks produce the porosity and have missing angle, crack, slag and other phenomenon, and it is true that sludge contains large contents of organic produces. Too much heat leading to the moisture and volatile

Table 3. Freezing-thawing 10 times quality and strength.

No.	1	2	3	4	5	6	7	8
Pre freezing thawing (kg)	2.31	2.35	2.34	2.33	2.38	2.71	2.79	2.80
After freezing thawing (kg)	2.31	2.35	2.34	2.32	2.67	2.71	2.78	2.80
Freeze thaw strength (Mpa)	14.85	14.8	15.53	14.94	26.87	26.92	26.53	26.75
Quality loss rate (%)	0.2	0.14	0.18	0.21	0.1	0.12	0.08	0.13
Strength loss rate (%)	4.8	5.1	4.0	4.2	3.7	3.5	4.9	4.1

Table 4. Freeze-thawing 20 times quality and strength.

No.	1	2	3	4	5	6	7	8
Pre freezing thawing (kg)	2.31	2.35	2.34	2.33	2.38	2.71	2.79	2.80
After freezing thawing (kg)	2.30	2.34	2.33	2.31	2.66	2.71	2.78	2.80
Freeze thaw strength (Mpa)	14.5	14.4	15.53	14.54	26.42	26.28	26.20	26.18
Quality loss rate (%)	0.6	0.7	0.6	0.8	0.5	0.2	0.4	0.3
Strength loss rate (%)	6.4	7.7	6.8	7.4	5.3	5.8	6.1	6.0

Table 5. Freeze-thawing 30 times quality and strength.

No.	1	2	3	4	5	6	7	8
Pre freezing thawing (kg)	2.31	2.35	2.34	2.33	2.38	2.71	2.79	2.80
After freezing thawing (kg)	2.29	2.33	2.31	2.30	2.66	2.70	2.77	2.78
Freeze thaw strength (Mpa)	14.3	14.34	14.37	14.24	25.81	25.83	25.97	25.72
Quality loss rate (%)	1	0.9	1.2	1.1	0.6	0.5	0.7	0.8
Strength loss rate (%)	8.3	8.1	7.9	8.7	7.5	7.4	6.9	7.8

Table 6. Freeze-thawing 50 times quality and strength.

No.	1	2	3	4	5	6	7	8
Pre freezing thawing (kg)	2.31	2.35	2.34	2.33	2.38	2.71	2.79	2.80
After freezing thawing (kg)	2.28	2.15	2.31	2.30	2.65	2.69	2.76	2.79
Freeze thaw strength (Mpa)	14.13	14.26	13.92	13.82	27.68	25.81	25.55	27.65
Quality loss rate (%)	1.4	1.2	1.3	1.6	0.8	0.9	1.0	0.8
Strength loss rate (%)	9.4	8.6	10.8	11.4	8.0	7.5	8.3	9.0

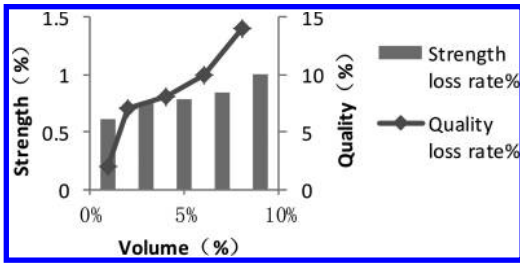


Figure 7. Effect of frost resistance of sludge content.

escaping in the sintering process to form interconnected pores resulting in the increase of porosity and continuing to absorb a lot of water, it is shown in Figure 7 that loss rate of city sludge sintered shale brick quality and strength tend to move to an upward with the content increase [5-7].

#### 4 CONCLUSIONS

1. By utilizing city sludge and agricultural waste sawdust production, it protects ecological system and saves energy to create social benefits, making new contributions to meet the green energy-saving civil engineering.
2. In the article, one designs the city sludge shale sintered brick about frost resistance. The experiment shows that with increasing cycles of freezing and thawing, the quality and intensity of city sludge sintered shale brick and the common sintered shale brick are lost, but it illustrates that city sludge sintered shale brick is much greater, because the city sludge has a higher loss after burning in high temperature and the process of roasting. Organic volatile substances and a small content of ash exist to produce a large number

of homogeneous pores. The water freezes to produce expansion stress at low temperatures resulting in a decline in the frost resistance.

3. With the increase of the contents of sludge, sintering process of burn-out forms a large number of pores leading to loss rate of quality and strength, which tends to rise. Then frost resistance shows to decrease, but having reached the strength of sintered brick loss rate of less than 25%, the loss rate of quality does not exceed 2%.

#### REFERENCES

- [1] Zhang Xianghua. Research and development of municipal sludge sintered shale porous brick and its masonry compression performance analysis [D]. Guangxi University of technology, 2013.
- [2] Huang Bangbiao, Li Xiqiang, Zhu Jizhen, Guan Qiongqiong. The effect of temperature on the basic properties of sewage sludge shale brick [J]. Journal of Guangxi University of technology, 2012, 04: 8-12.
- [3] Huang Bangbiao, Jing Jiahua, Huang and Huang Jianqiang, Ji Zhen Zhu. Temperature of cracks of light shale sintered brick [J]. New building materials, 2011, 03: 37-40.
- [4] Test methods for wall bricks (GB/T 2542-2012).
- [5] Beata Łażniewska-Piekarczyk. The frost resistance versus air voids parameters of high performance self compacting concrete modified by non-air-entrained admixtures [J]. Construction and Building Materials, 2013, 48.
- [6] Yuan Chang, Zhu Jizhen, Huang Bangbiao, Lai Chun, Wu Weifeng. City sludge fired shale perforated brick masonry axial compression tests [J]. Guangxi University Journal (Natural Science Edition), 2014, 01: 32-37.
- [7] Wang Meili, Li Wensheng, Yang Ning. Research on the freeze thaw of recycled aggregate concrete and ordinary concrete [J]. engineering construction, 2010, 03: 1-4.

# The influence of the lithium content on performance to $\text{Li}_x\text{FePO}_4$

Rui He, Zhenfa Liu, Lihui Zhang & Meifang Yan

*Institute of Energy Resources, Hebei Academy of Science, Shijiazhuang, Hebei Province, P.R. China*  
*Hebei Engineer Research Center for Water Saving in Industry, Shijiazhuang, Hebei Province, P.R. China*

Yanliang Zhang

*Institute of Energy Resources, Hebei Academy of Science, Shijiazhuang, Hebei Province, P.R. China*  
*School of Chemical Engineering, Hebei University of Technology, Tianjin, P.R. China*

**ABSTRACT:**  $\text{Li}_x\text{FePO}_4$  ( $x = 1.0, 1.02, 1.04, 1.05$ ) cathode material was prepared by high temperature solid-state method. The structure and morphology of  $\text{Li}_x\text{FePO}_4$  were characterized by Scanning Electron Microscopy (SEM) and X-Ray Diffraction (XRD). Mastersizer 3000 was used to analysis the particle size of the material. Electrochemical performance of the cathode material was researched by Land 2001. The results showed that the samples with different content of Li kept the olivine structure of  $\text{LiFePO}_4$ . And the optimal sample of  $\text{Li}_x\text{FePO}_4$  was the  $x$  equal to 1.02. At 0.2 C, 0.5 C and 1 C rate, the optimal sample ( $\text{Li}_{1.02}\text{FePO}_4$ ) has initial discharge capacities of 151.3 mAh/g, 148.8 mAh/g and 143.8 mAh/g.

**Keywords:** free lithium; lithium iron phosphate; electrochemical properties

## 1 INTRODUCTION

Lithium-ion batteries with high rate performance have attracted considerable interest as cathode material. In recent years, the research and development of the lithium ion battery anode material have attracted much attention in industrial countries<sup>[1-3]</sup>. Zhang Dongyun has studied the “Property and Structure of carbon-coated  $\text{LiFePO}_4$ ”. This paper presented that carbon coated on the surface of  $\text{LiFePO}_4$ , which could inhibit the grain growth and cause the smaller size<sup>[2]</sup>. Hongbo Shu has studied “Effective enhancement of electrochemical properties for  $\text{LiFePO}_4$  materials by Na and Ti co-doping”, this paper showed that the Na and Ti co-doped samples kept the olivine structure of  $\text{LiFePO}_4$ , but Na and Ti could improve the electrochemical performance of the material<sup>[4]</sup>.

The influence of lithium content on the performance of  $\text{LiFePO}_4$  didn't document in the literature. In the synthesis process of  $\text{LiFePO}_4$ , a part of lithium will volatilize in high temperature. Therefore in the process of preparation of  $\text{LiFePO}_4$  the lithium should slightly excess. In the paper, different lithium contents were studied in the process of synthesising  $\text{LiFePO}_4$ .

## 2 EXPERIMENTAL $\text{Li}_x\text{FePO}_4/\text{C}$

### 2.1 Instruments and reagents

Lithium dihydrogen phosphate was produced by Guoli material co., LTD in sichuan province.

Lithium carbonate was produced by Xilong Chemical Co., Ltd. Ferrous oxalate was produced by Hubei hao yuan material technology co., LTD.

Scanning electron microscopy (Inspect S50, FEI Company), Electrothermal blowing dry box (110-0A, Tian jin), X-ray diffraction (U1timal IV, Rigaku), Electronic balance (BSA423S-CW, Sartorius), Laser particle size analyzer (Mastersizer 3000, Malvern Instruments Ltd.), Electric blue test (CT2001A, Wuhan blue electric technology co., LTD) Glovebox (Universal (2440/750) MIKROUNA (CHINA) CO., LTD).

### 2.2 $\text{Li}_x\text{FePO}_4$ preparation and characterization

The  $\text{Li}_x\text{FePO}_4$  composite was prepared via High temperature solid phase method using  $\text{LiH}_2\text{PO}_4$ ,  $\text{FeC}_2\text{O}_4 \cdot 2\text{H}_2\text{O}$ ,  $\text{LiCO}_3$ , Citric acid as raw materials, all the chemicals are analytical grade. The synthesis steps are as follows. The stoichiometric amounts of  $\text{LiH}_2\text{PO}_4$ ,  $\text{LiCO}_3$ ,  $\text{FeC}_2\text{O}_4 \cdot 2\text{H}_2\text{O}$  were mixed in ethanol and ball milled under the speed of nearly 300 revolutions per minute for 4 h. Then, the mixture was dried at 80 °C in the oven for 5 hours. After drying, the mixture was calcined in  $\text{N}_2$  atmosphere at 450 °C for 4 h and 700 °C for 4 h under  $\text{N}_2$  (the purity of 99.99%) atmosphere, the heating rate was 3 °C/min. The vacuum tube furnace (HEFEI KEJING materials technology co. LTD) was used for the preparation of composite electrode material.

The purity and structure of the material were detected with X-Ray Diffraction (XRD) (U1timal IV, Rigaku) using  $\text{Cu K}\alpha$  radiation. Scanning Electron

Microscopy (SEM) (Inspect S50 FEI) was used to observe the particle morphology. Laser particle size analyzer (Mastersizer 3000, Malvern Instruments Ltd.) Electrochemical measurements were carried out using Land CT2001 A (Land., Wuhan blue electric technology co., LTD China).

### 3 RESULTS AND DISCUSSION

#### 3.1 XRD analysis of the cathode material

Figure 1 shows the XRD patterns of the different Li content of  $\text{Li}_x\text{FePO}_4$ . The XRD patterns of the different content of Li samples are similar to the standard of orthorhombic  $\text{LiFePO}_4$ . The XRD patterns shows a pure  $\text{LiFePO}_4$  phase without any obvious evidence of other impurities. This indicates that the content of Li ion does not change the crystal type of  $\text{LiFePO}_4$ .

#### 3.2 Particle size analysis

Figure 2 was the pore size distribution of  $\text{Li}_{1.02}\text{FePO}_4$ . From Figure 2 it can be seen that the median diameter (D50) keeps unchanged in the last tests. It remained at about 2.8  $\mu\text{m}$ .

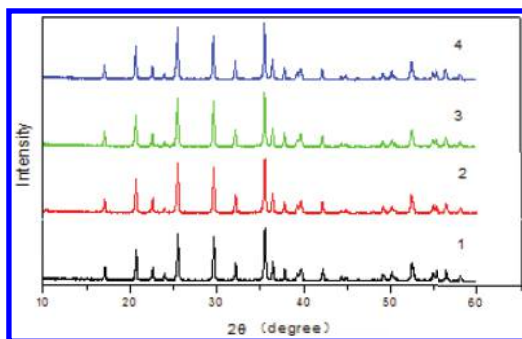


Figure 1. XRD patterns of  $\text{Li}_x\text{FePO}_4$  ((1)  $x = 1.0$ , (2)  $x = 1.02$ , (3)  $x = 1.04$ , (4)  $x = 1.05$ ).

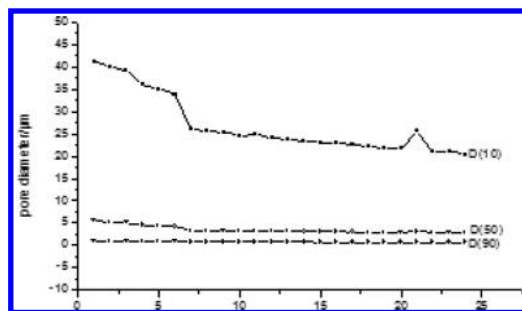


Figure 2. Pore size distribution.

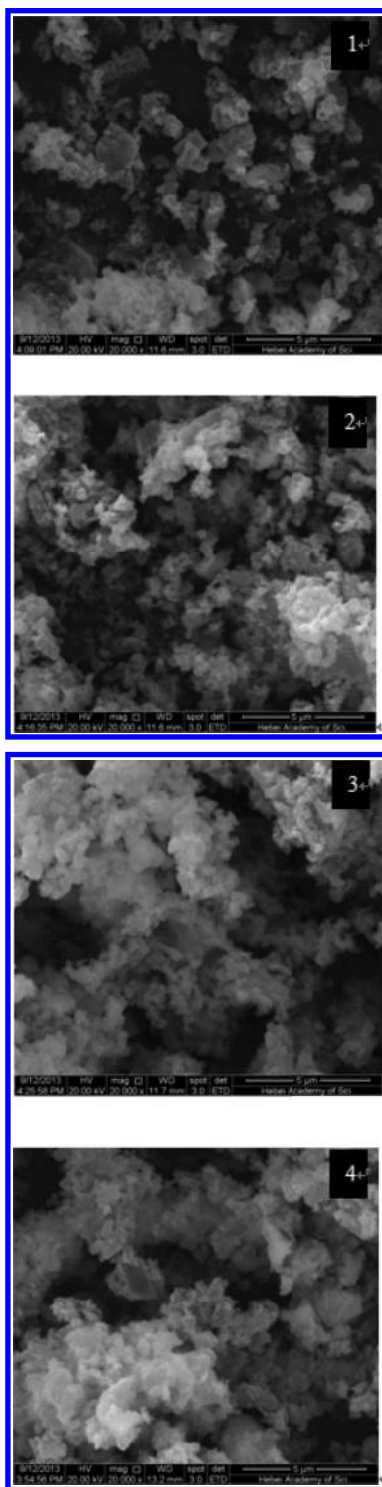


Figure 3. SEM images of  $\text{Li}_x\text{FePO}_4$  ((1)  $x = 1.0$ , (2)  $x = 1.02$ , (3)  $x = 1.04$ , (4)  $x = 1.05$ ).

### 3.3 SEM analysis of the cathode material

Figure 3 was the the morphologies of the material  $\text{Li}_x\text{FePO}_4$  ((1)  $X = 1.0$ , (2)  $X = 1.02$ , (3)  $X = 1.04$ , (4)  $X = 1.05$ ). The  $\text{Li}_x\text{FePO}_4$  is composed of irregular particles. The Figure 3 with different content of lithium didn't change a lot. Only in the Figure 3(2) the particle size distribution looks more homogeneous. The Figure 3(4) with the content of lithium at 1.05 the particles present agglomeration phenomenon.

### 3.4 Electrochemical performance of $\text{Li}_{1.02}\text{FePO}_4$

Figure 4 shows the initial charge and discharge curves of  $\text{Li}_x\text{FePO}_4$  at different lithium content at 0.2 C. From the Figure 4 it can be seen that all samples at 0.2 C have a long flat discharge plateau at around 3.4 V, which indicates that the two-phase redox reaction proceeds via a first-order transition between  $\text{LiFePO}_4$  and  $\text{FePO}_4$ <sup>[5, 6]</sup>. Sample 2 at 0.2 C has a discharge capacity of 151.3 mAh/g. The first discharge capacity of samples 1, 2, 3 and 4 are 145 mAh/g, 151.3 mAh/g, 147.2 mAh/g and 140.1 mAh/g.

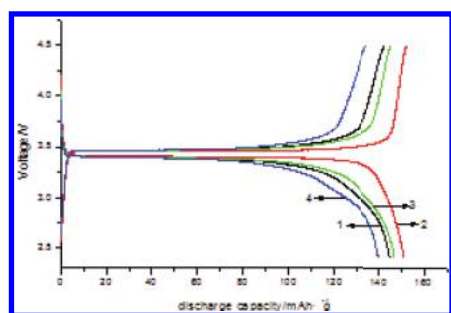


Figure 4. The initial charge and discharge curves of  $\text{Li}_x\text{FePO}_4$  ((1)  $X = 1.0$ , (2)  $X = 1.02$ , (3)  $X = 1.04$ , (4)  $X = 1.05$ ).

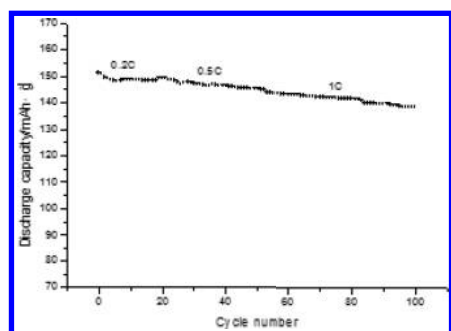


Figure 5. Cycling performance of  $\text{Li}_{1.02}\text{FePO}_4$  at different rates.

These results suggest that the lithium contents of  $\text{Li}_x\text{FePO}_4$  have an influence to electrochemical properties of the materials.

Figure 5 shows the  $\text{Li}_{1.02}\text{FePO}_4$  sample discharge cycle performance at different rates. From the Figure 5, it can be seen that the discharge specific capacity for the first time at 0.2 C, 0.5 C, 1 C respectively are 151.3 mAh/g, 148.8 mAh/g and 143.8 mAh/g. The optimum material with the lithium content at 1.02 the capacity attenuates a little. And after 50-cycle the capacities remain above 99% after 50 cycles at 1 C.

## 4 CONCLUSIONS

$\text{Li}_{1.02}\text{FePO}_4$  cathode material was successfully synthesized by High temperature solid phase method using  $\text{LiH}_2\text{PO}_4$ ,  $\text{LiCO}_3$ ,  $\text{FeC}_2\text{O}_4 \cdot 2\text{H}_2\text{O}$  as raw materials. The impact of different lithium content on the microstructure and electrochemical performance of the material were studied. The XRD results showed that content of lithium did not change the olivine structure. At 1 C rate,  $\text{Li}_{1.02}\text{FePO}_4$  has initial discharge capacities of 143.8 mAh/g, and the discharge capacities remain above 99% after 50 cycles at 1 C.

## ACKNOWLEDGEMENTS

This work was financially supported by the Hebei Science and Technology Support Project (14214404D), Hebei academy of science project (14011016) and Hebei academy of science project (13732, 13003003-2, 13003003-3).

## REFERENCES

- [1] Padhi A.K., Nanjundaswamy K.S., Goodenough J.B. Phospho-olivines as positive-electrode materials for rechargeable lithium batteries. *Journal of the electrochemical Society*, 1997, 144(4):1188–1194.
- [2] Zhang Ddongyun, Zhang Peixin, Lin Muchong, Property and Structure of Carbon-coated  $\text{LiFePO}_4$ . *Journal of Inorganic Materials*, 2011, 26(3):265–270.
- [3] Chen G.Y., Song X.Y., Richardson T.J. Electron microscopy study of the  $\text{LiFePO}_4$  to  $\text{FePO}_4$  phase Transition. *Electrochemical and Solid-State Letters*, 2006,9(6):A295–A298.
- [4] Hongbo Shu, Xianyou Wang, Weicheng Wen, Effective enhancement of electrochemical properties for  $\text{LiFePO}_4/\text{C}$  cathode materials by Na and Ti co-doping. *Electrochimica Acta* 89(2013)479–487.
- [5] A.K Padhi, K.S. Nanjundaswamy, J.B. Goodenough, *Electrochem. Soc.* 144(1997)1188.
- [6] Shuping Wang, Hongxiao Yang, Lijun Feng, A simple and inexpensive synthesis route for  $\text{LiFePO}_4/\text{C}$  nanoparticles by co-precipitation. *Journal of Power Sources*. 233(2013)43–46.

## Research on recycling waste concrete

H.Z. Zhang

*College of Civil Engineering, Shanghai Normal University, Shanghai, China*

W.R. Cao

*Tongzhou Construction General Contracting Group Co. Ltd., Jiangsu, China*

L.Z. Yu, X.H. Zhang & L. Shang

*College of Civil Engineering, Shanghai Normal University, Shanghai, China*

**ABSTRACT:** This article analyzes the significance of recycling waste concrete, comparison of domestic and international research on the utilization of recycled concrete, and finds a solution to the needs of contemporary society on the concrete contradictions, and construction waste and other problems. After sorting the waste concrete crushing aggregate made of different series, then with a certain percentage of natural aggregate concrete made of recycled aggregate. The best ratio of recycled aggregate and natural aggregate has been identified, by the experiment, using compressive strength as the standard, with the slump as the base.

**Keywords:** recycled aggregate concrete; sustainable development; best ratio

### 1 INTRODUCTION

Since twenty-first century, with the process of city urbanization unceasingly rising, demand on concrete, the most extensive application building materials, and the most important material base of city, is also increasing rapidly. Relevant data show that the number of waste concrete from dismantling, being generated by new constructing, and emissions by ready mixed concrete mixing station and precast plant's is enormous in the world every year. The number of waste concrete is  $3 \times 10^7$  t/y in Japan, it is  $6 \times 10^7$  t/y in USA, and it has reached  $1 \times 10^8$  t/y in China, accounted for 50%–60% of construction waste, and it showed an increasing trend year by year<sup>[1]</sup>. This does not include a large number of abandoned concrete caused by natural disaster and the collapse of structures generated by war. If these huge wastes can become resources, its value and meaning is inestimable.

In this paper waste concrete will be made into different series of aggregates after being treated by sorting broken and then into recycled concrete by being mixed with natural aggregates in a certain proportion. Using compressive strength as the standard, with the slump as the base, by the experiment, the best proportion of recycled aggregate and natural aggregate has been identified, and the feasibility of reuse of waste concrete was discussed.

### 2 CONCEPT OF RECYCLED CONCRETE AND SIGNIFICANCE OF REUSE WASTE CONCRETE

Concrete of the old buildings or structures disintegration is crushed and gradated to become coarse aggregates (Fig. 1, Fig. 2), which replace parts of the mixture of sand and gravel to make up concrete, known as recycled concrete, or recycled aggregate concrete. Recycled concrete is a kind of environmental protection concrete using the broken waste concrete as aggregate, and a product under the condition of sustainable development strategy<sup>[2, 3]</sup>.

Dosage the biggest sand in concrete raw materials have been considered to be an inexhaustible,

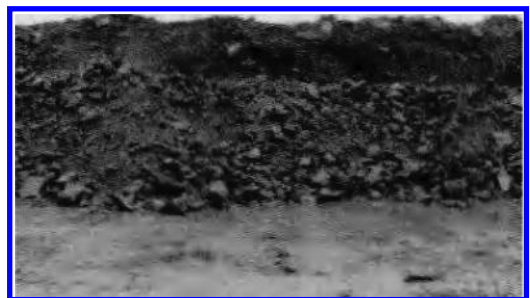


Figure 1. Simple crushing waste concrete.

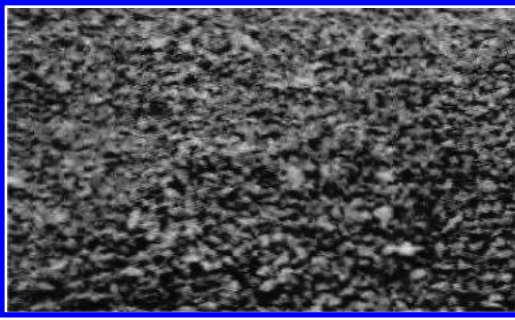


Figure 2. Recycled coarse aggregate.

and the optional mining for a long time, resulting in landslides, river diversions, destroyed the aggregate natively sustainable development of ecological environment. And the formation of natural sand and need after a long geological time, which means we may be about to face the situation of natural aggregate up. Chinese high quality natural aggregate (river sand and pebble) has dried up in some areas. In many areas eligible concrete sand is in short supply, and in some cities, the high performance concrete sand even can't be found. But at present our treatment methods of waste concrete are not much, the traditional processing method is mainly to the suburbs open-air pile up or landfill, which would cause adverse impact on the environment. If a large number of waste concrete can be reused after recycling and disposal, we can not only save the natural aggregate resources, but also reduce waste and environmental pollution in cities. Production process of concrete material recycling is beneficial to advocate the construction of resources saving, environment friendly society now, to adhere to the scientific concept of development, to adhere to sustainable development, to build a harmonious society, and especially beneficial for harmony of man and nature, so it has a great significance [4].

### 3 STATUS OF APPLICATION AND STUDY ON RECYCLED CONCRETE AT HOME AND ABROAD

Europe after the second world war, Japan, the United States and other countries began the research and development of recycled concrete work, held in Brazil in 1992 United Nations conference on environment and development will be the earth environment question was put to a very high position, many countries will be the recycling of the urban construction waste as one of the target of environmental protection and sustainable

development, some countries have worked out the corresponding technical specification [5, 6].

Many abroad studies on recycling process of recycled aggregates are all according to the specific engineering condition of their own, as described below.

#### 3.1 Japan

Type Due to their small size, relatively scarce resources, Japan attaches great importance to the waste concrete as to the development and utilization of renewable resources. As early as in 1977, the Japanese government has made the use of recycled aggregate and recycled concrete, and successively built to handle all the concrete waste regeneration processing plants, production of recycled concrete and recycled aggregate, the production of the largest production of 100 t can be processed per hour. Japanese industry association has formulated the recycled fine aggregate and recycled coarse aggregate quality standards and management methods, and on a large scale of production and application of recycled concrete [7].

#### 3.2 The United States

Super fund law, enacted by the U.S. government, regulates that any production enterprises with industrial waste, must properly handle itself, shall not, without tipping at will. Since 1982, the ASTM C—33—82 “concrete aggregate standard” will be broken hydraulic cement concrete included into the coarse aggregate. Around the same time, the U.S. army Engineers association (Society of American he Engineers, SAME) also in the relevant standards and guidelines encourage the use of recycled concrete aggregate [8].

#### 3.3 Europe and other countries

Netherlands is among the first countries to carry out research and application of the recycled concrete. As early as 1980s, the Netherlands is made about the use of recycled concrete aggregate preparation of plain concrete and reinforced concrete and prestressed reinforced concrete specification. The specification defines the use of recycled aggregates on clarify the technical requirement of the concrete, and pointed out that if the content of recycled aggregates in the aggregate (weight) is less than 20%, the production of concrete is completely according to the design and preparation methods of common and natural aggregate concrete. Germany reinforced concrete committee in 1998, proposed “Application guide of the use of recycled aggregates in the concrete,” which require recycled aggregates concrete must be



completely accords with the national standards of natural aggregate concrete<sup>[9]</sup>.

### 3.4 China

Study on recycled concrete in our country is late, and has become a hot spot in the field of concrete research now. Most of the application of the current domestic construction waste recycled aggregate is in a state of careful test, lack of a system of applied basic research, and perfect technical regulations or standards.<sup>[1]</sup> In practice, the situation of the domestic and foreign also has a certain gap, often lack the relevant identification of waste concrete classification standard, control the quality of the recycled concrete has the certain difficulty. So when use, should be carried out on the performance of the recycled aggregates and recycled concrete test. Large-scale application of recycled concrete also has many problems, some basic indicators and technical parameters is not complete, thus the system study of recycled concrete is necessary<sup>[10]</sup>.

## 4 EXPERIMENTAL STUDY ON COMPRESSIVE PERFORMANCE

### 4.1 Overview on the basic properties of recycled concrete

Recycled aggregate has low intensity, high water absorption, and large surface roughness compared with natural aggregate. Therefore, the basic property of recycled concrete is different from that of natural aggregate concrete. Recycled concrete uses recycled aggregate. Thus, the strength of the recycled concrete are closely linked with that of waste concrete used. In the condition of the same water cement ratio, the higher the strength of recycled aggregate is, the higher the strength of recycled concrete is. In general, the strength of waste concrete by building demolition is about C20. As the Water Cement ratio (W/C) is 0.6 and the recycled aggregates completely replace the natural aggregates, its compressive strength of 28 d can be up to 23.5 MPa, fully meet to the actual application demand. In the same condition of W/C, with the increasing of replacement rate of recycled aggregate, the concrete slump gradually become smaller. Apparently, the workability of fresh concrete is obviously influenced by recycled aggregate because of its surface roughness, high porosity, and high water absorption rate. With the increase of the amount of recycled aggregate replacement, the slump loss of concrete increases gradually. It is closely related with that recycled aggregate surface water absorption needs some time to reach equilibrium<sup>[11, 12]</sup>.

Because various performance of recycled aggregate is different from that of natural aggregate, special study should be conducted on the mixture ratio of recycled concrete, according to the characteristic of recycled aggregate, in order to effectively promote the recycled concrete. Southeast University professor Zhang Yamei<sup>[13]</sup> has studied three series recycled concretes of C20, C30, and C40, and preliminarily discussed the mix proportion design of recycled aggregate concrete. The research results show that when the design strength is C20, the strength of recycled concrete made by the ordinary concrete mix ratio is higher than that of the reference concrete, but its work performance reduced significantly. On the basis of this, she put forward letting recycled aggregate preabsorb water. This method is consistent with that suggested by Shi Wei<sup>[14]</sup>, which based on free water cement ratio, for recycled aggregate's high water absorption ratio. That is, the recycled concrete mixing water consumption is divided into two parts, one part is for aggregate adsorption, known as adsorbed water, it is the water consumption from aggregate starting adsorbing water to saturation state of dry surface; another part is the mixing water consumption, in addition to evaporation, this part water is used to improve the liquidity of mixed complexes and participate the hydration reaction of cement. The amount of adsorbed water is determined according to the tests, mixing water consumption is determined according to the design method of ordinary concrete mixture ratio<sup>[15]</sup>. In practice, the two parts of water are added together.

During the design of mixture ratio, recycled concrete performance can be improved by mixing the recycled concrete aggregate with the natural aggregate and adding admixture or additive etc. In the test of Saroj et al, the performance of recycled concrete has been greatly improved by adding 10% fly ash. The concrete manifestation is that not only the shrinkage strain, permeability and water absorption of recycled concrete is close to that of ordinary concrete but also the acid resistance of recycled concrete is greatly improved. Zhang Yamei<sup>[13]</sup> made up recycled concrete with the strength of 54.6 MPa, by using only recycled aggregate as coarse aggregate, and mixing with high efficiency water reducing agent and fly ash. Xing Zhenxian<sup>[16]</sup> made up recycled concrete with the strength of 40.4 MPa by using waste concrete aggregate with the matrix strength of C20–C25, adding with superplasticizer which makes the water cement ratio decrease to 0.35. Thus, mixture proportion design of recycled concrete is more complex than that of ordinary concrete, however, as long as proper measures were taken, satisfactory mechanical properties of recycled concrete can be obtained.

#### 4.2 Experiment method and data analysis

Experimental conditions and parameters are as follows: test block's design strength is C30, water cement ratio is 0.41, and sand rate is 32%.

Test method: design seven groups of recycled concrete with different replacement ratios (ratio of recycled aggregate and natural aggregate) of: 0, 10%, 30%, 10%, 70%, 90%, 100%; each group employ three blocks. Slump of the first group is used as a benchmark. During the preparation process of the rest six groups, their slumps were adjusted continuously to ensure the consistent of the workability and fluidity, which should be in accordance with the first group. Then draw a graph by comparing ultimate strength values of 7 groups recycled concrete with different proportions, to find out the best proportion. Experiment data are shown in Table 1.

Table 1 shows that the compressive strength of all recycled concretes meet the requirements about strength, and even beyond that of natural aggregate concrete. When the replace rate is 70%, the strength reaches its maximum value, or 34.2 MPa, which is 9.97% higher than that of natural aggregate concrete. Diagram based upon the above data is shown in Figure 3.

Table 1. Ultimate strength values of recycled concretes with different replacement ratios.

No	Replacement ratio %	Measured value KN	Average value KN	Ultimate strength Kpa
1	0	678	707	31.1
2	10	698	671	30.1
3	30	702	763	33.2
4	50	688	713	31.4
5	70	712	789	34.2
6	90	714	743	32.7
7	100	732	749	33.1

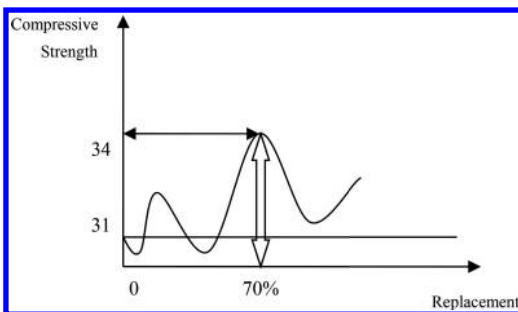


Figure 3. Relationship between the replacement ratio and the compressive strength of recycled concrete.

Through Figure 3, we can find that the compressive strength of recycled concrete fluctuates with the increase of the replacement ratio. When the replace ratio is 70%, it reaches maximum. Therefore, the best proportion of recycled aggregate and natural aggregate is 70%.

## 5 CONCLUSIONS

Experimental results show that the recycled aggregate concrete completely meets the requirements of the strength, and has a strong feasibility. Both from the perspective of optimized distribution of resources and the looming environmental protection point of view, this is a very good method.

The biggest obstacle to promote widely recycled concrete is that there are no protection policies in China. If there is no policy, it is a bit unrealistic to only rely on the consciousness of entrepreneurs. Therefore, the country's policy then became the key factor. There are the related specification and use conditions for a long time in such developed countries as Japan, the United States, Europe, and so on. It also is the important reason for the recycled concrete being widely promoted in those countries. With the support of national policy, related laws and regulations, recycling of waste concrete, which benefits both economic and social, would be popularized in our country.

## ACKNOWLEDGMENTS

The No. 1 author, Hong-zhuan Zhang, female, PhD., a lecturer in College of Civil Engineering, Shanghai Normal University, Shanghai, China.

This research was financially supported by the general scientific research of Shanghai Normal University (SK201342).

## REFERENCES

- Shu J., Chen M. 2010. Recycling waste concrete research in China. *Shanghai building materials* 29(2):37–38.
- Liu X.P., Guo G.L., Yang G. 2014. Experimental research on the physical properties of recycled aggregate concrete. *Low temperature construction technology* 32(6): 1–5.
- Wang B.M., Tu N., Yang Y. 2010. Research progress on disposal and application of construction waste. *Low temperature construction technology* 32(6):7–9.
- Xue W.B., Jin X.O., Wang H.Y. 2009. Sustainable development strategy and development of recycled concrete technology. *Heilongjiang water conservancy technolog*, 37(5):89–90.
- Wang J.C. 2009. Present situation and Prospect of research on recycled concrete. *Shanxi architecture* 35(15):141–142.

- Gun, am Zanker. Miinchen. 1996. Use of Recycled Building Materials in Constructions. Betonwerk fertigteil-Technil 4.
- Xu H.Z. 2004. Solid waste resource technology. Beijing: Chemical Industry Press.
- Liu S.H., Leng F.G. 2007. Recycled concrete technology. Beijing: China Building Materials Industry Press: 11–17.
- Liarbadfiya M.C., Leelawat T., Dhit R.K. Use of recycled aggregate concrete in high strength concrete. Materials and structures [J], 2000, 33:574–580.
- H.Q. Li, T. Du, X.G. Wu, et al. 2002. Research on recycled aggregate concrete by building waste recycling. Journal of Huazhong University of Science and Technology: 125–128.
- Liu C.H., Xing S.H., Zhang J.J. 2009. Feasibility analysis on development and utilization of waste concrete. Construction technology 40(6):542–544.
- Meahah H.A. & Buyle-Bodin F. 1999. Efficiency of polypropylene and metallic fibres on control of shrinkage and cracking of recycled aggregate mortars. Construction and Building Materials 13(8):439–447.
- Zhang Y.M., Qin H.G., Sun W., et al. 2002. Mix design of recycled concrete. Concrete and cement products 20(1):7–9.
- Shi W., Hou J.P. 2001. Technology of recycled concrete and its mix proportion design method. Construction technology development 28(8):18–20.
- Huang Y., Deng Z.H. 2010. Recycled concrete shear performance study. Concrete 32(2):14–17.
- Xing Z.X. 2003 Research on the performance of recycled concrete and ideas of its development. Construction technology development 25(5):28–31.

# Discussion on the cause of concrete floor crack

Zhi Neng Tong

Jiangxi Science and Technology Normal University, Nanchang, China

**ABSTRACT:** The reason for formation of cracks in the concrete is very complex. This paper analyzes the same from the angles of the design, construction, and material properties and explores the reasons and influencing factors, describing the mechanism of crack in order to avoid and reduce concrete slab cracks. It also provides a theoretical basis and references for similar engineering and technical services.

**Keywords:** concrete; floor cracks; factors; performance

## 1 INTRODUCTION

In many engineering quality problems, the concrete crack phenomenon is more outstanding. Therefore one must pay attention to the cause of formation and prevention of concrete crack. The concrete is a heterogeneous brittle material, which is mixed with the aggregate, cement, water, and other materials. Due to the concrete construction and its deformation, a series of problems, such as constraint, hardening, and molding, of concrete exist causing many micropores, cavitation and micro cracks. It is because of the existence of these initial defects that concrete showed some heterogeneous characteristics. But due to load and temperature differences in concrete action, micro cracks will constantly extend and get connected, and ultimately form a visible macro crack.

The shrinkage of concrete is the main reason that causes cracks of cast-in-place plate. The concrete, in the condensation process, will change in volume. When the shrinkage stress exceeds the tensile strength of concrete, the concrete will crack. The crack problem of the concrete is widespread and has become a major problem plagued in the construction engineering and technical personnel, following on from the aspects of design, material, and construction operation to analyze the crack causes of construction for the prevention and control measures.

## 2 PRONE SITE OF CRACKS IN CAST-IN-PLACE FLOOR SLAB

1. The cracks in the room. From the site of the residential project, cast-in-place floor cracks, are the most common and widespread and are the largest in number around the house yang

angle at notch housing (including plane shape mutation Yang corner room) in left yang angle 1 meter, namely, in the floor of the negative bending bars and angle of radial rib terminal or lateral occurred about 45 degrees to the ground floor of the diagonal cracks. This is common in the building of a type of any of cast-in-place floor are widespread.

2. Other cracks of floor slab. Except the floor cracks, there are three more common kinds: one kind is pre embedded pipe and line pipe distribution; second class is when turnover materials used in construction temporary more concentrated and less frequent, lifting unloading stacking area, mainly concentrated in the center of the floor, third class is generated for the effects of concrete material and construction technology of position.

## 3 DESIGN FACTOR

The main reason of the cracks in the cast-in-place floor is that the shrinkage of concrete is caused by the shrinkage of concrete and the temperature difference. And the more the floor crack the closer is the roof. From the design point of view, the current design specification focuses on the intensity of the considerations, not fully according to the temperature difference and the shrinkage of concrete and other factors, such as the amount of reinforcement and thus can not reach the requirements. And around the house yang angle due to the longitudinal and transverse direction shear wall or stiffness relatively large floor beam constraints, limiting the freedom of floor slabs of concrete deformation, so in the temperature and shrinkage of concrete changes, plate in reinforcement weak at first cracking, resulting in about 45 degrees of angle cracks. Although the crack

has no effect on the structural safety of the building, but has the leakage defect in the special case of water source, it is the key of crack prevention. According to the above analysis and consideration on the surrounding angle at the floor panel reinforcement to strengthen, negative reinforcement with no separation type cutting, full-length configuration and appropriate encryption bold.

Over the years, the practice has proved that the design of the concrete floor slab basically no longer occurred 45 degrees diagonal crack, can better solve the problem of floor cracks, the effect is remarkable. For the radial steel bar in the corner, the function is small. The reason is not the length of radial steel (about 1.2 meters), the room in the corner of Danyang by double encryption and still strengthen two-way reinforced by separating tectonic setting negative moment short ribs, 45 degree oblique cracks will still be transferred to the inward radial rib at the end or outside, and when the double encryption to strengthen two-way reinforced, longitudinal, transverse two directions has been reinforced to resist and prevent the occurrence and metastasis of the 45 degree angle of the crack, and radial reinforcement often only the upper layer, above the binding often set aside in the aspect of steel plate, steel lead to overlapping, will negative reinforcement plate under pressure, reducing the effective height of plate negative reinforcement, so that the focus on strengthening the double encryption can be reinforced.

#### 4 MATERIAL PROPERTY FACTOR

Concrete is a kind of non homogeneous brittle material which is mixed with sand aggregate, cement, water, and other materials. The main factor affecting the deformation of concrete is.

##### 4.1 *Influence of cement variety*

Cement selection is the key to the problem of contraction. Different varieties of cement shrinkage depends on calcium aluminate three, three sulfur, gypsum content and fineness of cement. And with the application of high strength concrete, cement grade level requirements has been improved, cement consumption will increase, higher caused by hydration heat, concrete shrinkage deformation is greater.

##### 4.2 *The influence of concrete mix proportion in the raw material certain conditions*

The proportion in certain conditions influences the raw material certain conditions, the water cement ratio of concrete shrinkage has a great influence.

Shrinkage of concrete depends on unit quantity of water and cement, and the effect of water is higher than the cement. In water use in certain conditions, shrinkage of concrete increase with the increase of the amount of cement. In water cement ratio under certain conditions, mixed concrete shrinkage increases with the water cement ratio increased significantly increased; in water cement ratio under the same conditions, concrete shrinkage with increasing sand rate and increase, but increase in amplitude is smaller. The reasons for the shrinkage of concrete are the control parameters such as unit water consumption, cement dosage, water cement ratio, sand ratio and so on.

##### 4.3 *Effect of slump*

Pumping concrete in order to satisfy the pumping conditions: slump, good fluidity, easy to produce less local coarse aggregate, mortar. At this time dehydration concrete stem lapse, it will produce crack surface.

## 5 CONSTRUCTION TECHNOLOGY FACTOR

##### 5.1 *The effective protection measures of the reinforced floor of the upper floors*

Floor panel of the lower layer reinforced bar in the concrete floor plate tensile force plays a dual role of resist external load generated by bending moment and prevent the occurrence of concrete shrinkage and temperature cracks, and the dual role of are required to reinforced in reasonable protection layer under the premise to ensure effective. In the actual construction, the floor and the lower layer of the reinforced net in the concrete block and template based on the protection layer is easier to correct control. But when the pad spacing enlarged to 1.5 meters, the reasonable protection of mesh reinforcement layer thickness can not guarantee, so does the aspect to the pad spacing limit at 1.0 meters.

In contrast, the effective protection of the upper floors has been a big problem in the construction. The reason for this is that the floor panel of the upper reinforcement is generally fine is soft, personnel from the stampede immediately after bending, deformation, straining; reinforced distance template of greater height and are not subjected to template based on the protection; various types of cross operation, resulting in many construction workers, walking is very frequent, no settled at will inevitably be a stampede; the upper layer of the reinforcing steel bar mesh support spacing is too large, or even, resulting in upper mesh reinforcement can not be effectively protected.

### 5.2 *Crack embedded pipe at*

Pre embedded pipe, especially at the center of a plurality of line pipe is concrete section are more weakened, which caused by stress concentration, easily lead to cracks occurring in a weak position. When the pre cut line tube with smaller diameter and the standard width of a room housing width is also smaller, and line pipe laying direction and do not coincide in the vertical to concrete shrinkage and tensile direction, generally not occurred floor cracks. On the contrary, when the pre embedded pipe of larger diameter, width and width is larger, and line pipe laying direction and the coincidence in parallel to concrete shrinkage and tension at the same time, it is prone to cracks in the floor. So for thick pipes or a plurality of line pipe distribution should be according to the technical requirements of additional vertical in line tube short steel mesh strengthening. According to the experience, it is recommended additional crack short reinforced by  $\phi$  6-8 mm, the spacing is less than or equal to 150, at both ends of the anchorage length should be not less than 300 mm.

Using radial distribution is suitable for distribution line tube in installation should avoid stereo crossing, cross wiring can be in accordance with the technical requirements of the line box, at the same time in a plurality of line pipe and avoid closely parallel arranged, to ensure that the line pipe at the bottom of the concrete pouring construction smoothly and vibration compacting. And when the line pipe number, so that the export distribution section of concrete greatly reduces when, should according to leave holes in the structural requirements around added under the 2  $\phi$  12 well shaped anti crack structure is reinforced.

### 5.3 *Strengthening the maintenance of floor concrete*

The moisture curing of the concrete on the strength growth and performance improve is very important, especially early proper maintenance can avoid surface dehydration and reduce the

amount of concrete at early age shrinkage cracks occur. However, in actual construction, due to rush time and watering will affect the missile line and construction personnel, so the floor concrete is often lack of adequate and adequate watering maintenance duration. Therefore, construction must insist on Covering Straw sacks or a week or so proper moisture conservation, and suggest using liquid spray curing, so as to reduce the cost and improve the work efficiency, and can avoid or reduce the impact of construction.

## 6 CONCLUSION

After taking the above comprehensive control measures, there may still be a small amount of floor cracks due to various reasons. According to the experience, the upper part of the ground floor leveling thickness of the paint layer can be strengthened by additional leveling layer with steel wire net, steel nets or crack short reinforced, and the upper part is often floor decorative layer covered. The problem is relatively small.

Now the prevention and control of the cast-in-place reinforced concrete floor cracks which are always worthy of attention, although existing methods can control cracks to a certain degree, but the risk of cracks can be still seen everywhere. Only from the design, materials, construction, use and other aspects continue to explore, and constantly seek better ways to further reduce the cracks in cast-in-place reinforced concrete floor slab.

## REFERENCES

- [1] Yu Shengguang Construction technology [M] Wuhan Industrial University Press.
- [2] Huang Qifa Construction knowledge [M] China Construction Industry Press.
- [3] Jiang jianjing Construction accident and prevention [M] China Building Materials Industry Press.
- [4] Wang Tiemeng The engineering structure crack control [M] China Construction Industry Press.

# Manufactured sand make pumping of high-level concrete mix design and optimization

Xiao Chen

*Key Laboratory of Road Structure and Material Ministry of Transport, Beijing, China*  
*Wuhan University of Technology, Materials Science and Engineering, Wuhan, China*

XiongYi Liang & Zheng Li

*Wuhan University of Technology, Materials Science and Engineering, Wuhan, China*

**ABSTRACT:** This paper compares the Hubei En Lai with En Qian highway zhong jian river bridge main span cable tower concrete engineering, and studies the dosage of gelled material, water-binder ratio, fly ash content and the mechanism of sand fineness modulus and the sand ratio on elevation mechanism sand pumping concrete workability and mechanical properties of the influence law. In addition, it studies selected elevation mechanism sand pumping concrete proportion of optimal theory on its workability, mechanical properties and durability properties.

**Keywords:** mechanism of cable tower; pumping concrete, sand; fineness modulus

## 1 INTRODUCTION

Hubei En Lai highway zhong qian river bridge built with the main span ShuangSuoMian steel truss stiffening girder cable-stayed bridge is a twin tower. Its main cable tower adopts the H form structure, whose main tower height is 245 m, by the high pillar, the middle pillar and lower pillar, high beam, the lower beam and the tower, C50 concrete strength level.

Based on the research of gelled material consumption, water-binder ratio, fly ash content and mechanism sand fineness modulus of sand and sand ratio on mechanism elevation pumping concrete workability, and mechanical properties, the mechanism of sand elevation of theory of pumped concrete mix are optimized for the application of pumped concrete mechanism sand in elevation, in order to provide a technical guidance.

## 2 THE TECHNICAL REQUIREMENTS OF CONCRETE

Integrated cable tower concrete pumping construction, structure, performance, the design of cable tower high-performance concrete indicator are as follows:

1. Work performance: concrete slump and the expansion degree should be increased

with pumping elevation. Initial slump control is  $210 \pm 20$  mm, extension control is  $550 \pm 75$  mm, 1 h after the slump loss value 20 mm or less, extension, degree of loss value 75 mm or less. At the same time, the concrete should have good adhesiveness and water retention, pressure-secrete water  $< 30$  ml, and the exudation rate should be  $< 40\%$ . In order to guarantee the uniformity of the concrete, the appropriate controlling concrete slump into the mould should be  $190 \pm 20$  mm, and the extension degree should be controlled to  $500 \pm 50$  mm.

2. Setting time: initial setting time of concrete general appropriate control is about 12h ~ 14h. The initial setting time and final setting time is short, as far as possible to ensure the concrete 36h ~ 48h stripping strength requirements.
3. Strength: design strength grade of concrete is C50, and for 28d preparation, it should be  $\geq 62$ Mpa compressive strength, but not greater than 70Mpa.
4. Durability: aggregate is used in concrete with alkali activity. The chloride ion diffusion coefficient of concrete 28d age (RCM method) is  $\leq 5.0 \times 10^{-12}$  m<sup>2</sup>/s, age 28d anti-freeze performance achieve F150, and carbide performance fully satisfies the requirement of design service life.

### 3 RAW MATERIALS AND TEST METHODS

#### 3.1 The raw materials

1. Cement: huaxin P.O. 42.5 cement.
2. Fly ash: hunan SangZhi F type of grade I fly ash, with the apparent density of 2.17 g/cm<sup>3</sup>, the ignition loss of 1.56%, and the ratio of 93.2%.
3. Coarse aggregate: limestone rubble, 5–20 mm continuous gradation, two-stage blending. No alkali—aggregate reaction activity.
4. Mechanism of fine aggregate: limestone sand and apparent density of 2.712 g/cm<sup>3</sup>, loose pile density of 1601 kg/m<sup>3</sup>, no alkali—aggregate reaction activity. 1<sup>#</sup> mechanism sand fineness modulus of 3.01, the stone powder content is 6.8%, MB 0.5 value; 2<sup>#</sup> mechanism sand fineness modulus of 3.22, the stone powder content is 6.0%, MB0.8 value; 3<sup>#</sup> mechanism sand fineness modulus of 3.41, stone powder content is 6.5%, MB 0.5 value.
5. Water reducing agent: HD poly-carboxylic acid salt and high-efficient water reducing agent, with the dosage of 0.85 ~ 1.15%.

#### 3.2 Test method

1. The concrete mixture performance test  
Slump/extension, pressure bleeding rate, bulk density, air content, such as setting time test method according to the GB/T50080-2002, JTG E30-2005, CECS 203:2006.
2. The hardened concrete mechanics performance test  
Cubic compressive strength and compressive modulus of elasticity of the test method on the basis of JTG E30-2005.
3. Resistance to the chloride ion penetration test  
The concrete resistance to the chloride ion penetration test according to GB/T 50082-2009.

### 4 THE TEST RESULTS AND ANALYSIS

#### 4.1 Benchmark mixture ratio design

##### 4.1.1 Water-binder ratio optimization

The optimization conditions are as follows: fixed 20% dosage of fly ash, sand ratio 44% and design unit weight of 2450 kg/m<sup>3</sup>. A fixed amount of gelled material 475 kg/m<sup>3</sup> and 490 kg/m<sup>3</sup>, and the water-binder ratio are 0.30, 0.31, 0.32, and 0.30. The process of the test should be fine-tuned, and the dosage of water reducing agent should meet the basic requirements for concrete workability. The results are summarized in Table 1.

From Table 1, we obtain the following results: the water-binder ratio below 0.31 and 28d compressive strength of concrete can satisfy the requirements of mixture strength of 62 MPa. Under the condition of the same water/cement ratio, 490 kg/m<sup>3</sup> gelled material is more suitable for pillar height, upper pillar super elevation in pumping concrete construction needs. Comprehensively considering the workability, strength factor, water-binder ratio optimization is 0.31, the dosage of pillar gelled material is 475 kg/m<sup>3</sup> and pillar gelled material consumption is 490 kg/m<sup>3</sup>.

##### 4.1.2 The choice of the dosage of fly ash

Gelled material was fixed to 475 kg/m<sup>3</sup>, water/cement ratio is 0.31, the design unit weight is 2450 kg/m<sup>3</sup>, sand rate is 44%, with 5% of the dosage of fly ash step growth to 35%. Fine-tuning in testing the water reducing agent dosage should meet the basic requirements for workability. The test results are summarized in Table 2.

Table 2 shows that with the increasing dosage of fly ash, there was a downward trend basically, with bulk density and mixture flowing faster. With the increasing dosage of fly ash, 3d, 7d early age strength reduced, which was more complex, and the intensity at 28d changed. Moreover, 15% and

Table 1. Water-binder ratio on the workability and compressive strength of concrete.

Number	Water/cement ratio	Dosage of gelled material (kg/m <sup>3</sup> )	Slump (mm)	Extension degree (mm)	Bulk density (kg/m <sup>3</sup> )	The compressive strength (MPa)		
						3d	7d	28d
T1	0.30	475	210	520 × 540	2461	44.1	58.9	65.7
T2	0.31		220	540 × 560	2454	43.7	56.4	62.1
T3	0.32		215	560 × 580	2452	41.6	54.9	61.2
T4	0.33		225	590 × 610	2443	40.3	51.9	58.1
T5	0.30	490	220	530 × 510	2465	45.9	60.6	67.2
T6	0.31		230	550 × 540	2459	44.7	59.9	64.8
T7	0.32		240	570 × 590	2457	44.1	57.2	62.1
T8	0.33		230	600 × 610	2450	42.8	54.1	59.3



Table 2. The dosage of fly ash concrete workability and compressive strength of influence.

Number	Dosage of fly ash (%)	Slump (mm)	Extension degree (mm)	Bulk density (kg/m <sup>3</sup> )	The compressive strength (MPa)		
					3d	7d	28d
T9	0	210	540 × 550	2462	51.5	61.7	67.4
T10	15	220	540 × 570	2450	48.2	60.9	64.7
T2	20	220	540 × 560	2454	43.7	56.4	62.1
T11	25	215	580 × 530	2440	42.8	54.9	62.3
T12	30	215	580 × 550	2445	40.9	55.1	63.4
T13	35	230	570 × 600	2440	41.1	54.9	64.8

Table 3. Sand ratio on concrete workability and strength.

Number	Fineness modulus	Sand ratio (%)	Slump (mm)	Extension degree (mm)	The compressive strength (MPa)		Work item description
					7d	28d	
T14	3.01	40	200	560 × 545	56.2	60.7	Slight analysis pulp, harden
T15		42	230	530 × 540	59.0	64.8	Good, soft
T17		44	215	520 × 500	59.4	63.7	Good, high viscosity
T18	3.22	42	220	570 × 530	58.7	64.5	Good, soft
T6		44	230	550 × 540	59.9	64.8	Good
T19		46	210	500 × 520	57.7	65.7	High viscosity, slow expansion
T20	3.41	44	240	570 × 545	52.6	59.9	Segregation
T21		46	230	555 × 530	54.9	63.7	Good
T22		48	210	550 × 540	58.2	63.7	Good

35% of fly ash concrete strength was basically the same, at about 64.7 MPa, and 20 ~ 30% of fly ash content concrete strength of 28d was basically the same, at about 62.3 MPa.

In summary, the cable tower of benchmark of the main parameters of water/cement ratio was 0.31, with 20% of fly ash, the pillar of gelled material of 475 kg/m<sup>3</sup>, and pillar gelled material consumption of 490 kg/m<sup>3</sup>.

#### 4.1.3 Mechanism sand fineness modulus and the best effect of the sand ratio

Gelled material was fixed to 490 kg/m<sup>3</sup>, the water/cement ratio to 0.31, 20% dosage of fly ash, and dosage of water reducing agent to 1.0%. The results are summarized in Table 3.

From Table 3, we can obtain the following test results: fineness modulus of 3.0, the optimal sand at a rate of 43%; sand fineness modulus of 3.2, the optimal rate of 44%; sand fineness modulus of 3.4, and the optimal rate of 46%. With the increase in mechanism sand fineness modulus, the optimal sand ratio increased. When the fineness modulus was larger, the workability of concrete was poor, and there was a significant adhesiveness deterioration of concrete.

#### 4.2 Cable tower elevation mechanism sand pumping concrete nature of basic research

From the above test, we determined the theory of cable tower pumping concrete mixture ratio, as shown in Table 4. In the concrete construction, A0 was used for the lower pillar and A1 for the high and middle pillar.

##### 4.2.1 Fresh concrete workability

As can be seen from the experimental results summarized in Table 5, A0, A1 two mixture workability, slump and extension degree satisfy the requirement of cable tower construction. Pressure bleeding rate is less than 40% and water performance is good. The initial setting time is more than 12 h, which meets the design requirements.

##### 4.2.2 Hardened concrete mechanical properties and durability

For A0, A1 two towers of concrete hardening concrete mechanics performance test, the results are summarized in Table 6.

From Table 6, we obtain the following test results: two theoretical mixture ratios of 28d the chloride ion diffusion coefficient of  $3.2 \times 10^{-12} \text{ m}^2/\text{s}$

Table 4. Cable tower of the pumping concrete mixture theory.

Number	Dosage of rubber material (kg/m <sup>3</sup> )	Water/cement ratio	Sand ratio (%)	Concrete composition (kg/m <sup>3</sup> )					
				Cement	Fly ash	Water	Sand	Gravel	Admixtures/%
A0	475	0.31	45	380	95	147	823	1005	0.9~1.1
A1	490	0.31	45	390	100	152	814	994	

Table 5. Theory mixture workability test results.

Number	Dosage of water reducing agent (%)	Bulk density (kg/m <sup>3</sup> )	New batch slump/extensions (mm)			T <sub>50</sub> (s)	Work item description
			0 min	60 min	90 min		
A0	1.0	2455	225/555 × 540	225/550 × 540	225/550 × 540	11	Good
A1	1.0	2465	230/570 × 560	220/570 × 565	215/545 × 515	10	Good

Number	Air content (%)	Pressure bleeding			Setting time (h:min)	
		V <sub>10</sub> (ml)	V <sub>140</sub> (ml)	S <sub>10</sub> (%)	Initial set	Final set
T0	2.15	9	25	36	12:15	13:10
T1	2.01	6	20	30	13:45	14:30

Table 6. Theory of hardened concrete mechanics performance.

Number	The cube compressive strength (MPa)					Modulus of elasticity (10 <sup>4</sup> MPa)			28d D <sub>RCM</sub> (10 <sup>-12</sup> m <sup>2</sup> /s)
	3d	7d	28d	56d	90d	7d	28d	56d	
T0	44.6	56.7	63.3	69.1	74.9	4.20	4.52	4.77	3.20
T1	47.9	59.5	64.9	72.9	76.9	4.16	4.69	4.81	3.12

and  $3.12 \times 10^{-12} \text{ m}^2/\text{s}$ , are less than  $5 \times 10^{-12} \text{ m}^2/\text{s}$ , which meet the requirements of durability.

## 5 CONCLUSION

1. According to the cable tower structure design, concrete pumping construction, we put forward the cable tower of high performance concrete mix proportion design of technical index requirements.
2. We determined the optimal dosage of the water-binder ratio, fly ash and the dosage of gelled material mix gel system of the main parameters, such as water/cement ratio of 0.31, 20% fly ash, the lower pillar of gelled material of 475 kg/m<sup>3</sup>, high and middle pillar gelled material consumption of 490 kg/m<sup>3</sup>.
3. We conducted comprehensive analysis to determine the optimal sand at a rate of 45%.
4. Dosage of gelled material was studied, and the dosage of the water-binder ratio, fly ash and

sand ratio on the workability, pumping properties and strength of concrete, the influence of the comprehensive analysis of selected workability and physical and mechanical performance meet the requirements of the cable tower design of A0, A1 two directional mixture. And the selection of proportion of the two theories of the research of the system, and the mechanical properties, including the construction performance of concrete and long age law of development, meet the requirement of the corresponding technical indicators, and the surplus coefficient and compressive strength are larger.

## ACKNOWLEDGMENTS

This work was supported by the Opening Funding Supported by the Key Laboratory of Road Structure & Material Ministry of Transport, Beijing (KF201201) and the Fundamental Research Funds for the Central Universities (133237001).

## REFERENCES

- [1] Chen Jiankui, wang dong Ming. The mix proportion design of high performance concrete (HPC) the new law - all calculation method [J]. Journal of Silicate, 2000, 28(2):194–198.
- [2] Ren Shiman. Ready-mixed concrete pumping performance study [J]. Journal of chongqing construction university, 1999, (1):10–13.
- [3] Cai Jiwei Wang Ji good, Ming-kai zhou. The current research status of artificial sand and manufactured sand concrete [J]. Foreign building materials science and technology, 2004, (3):20–24.
- [4] Tong Zhi Yang jian-hui Yang. Using the mechanism of sand preparation self-compacting concrete [J]. The world's bridge, 2003, (1):30–32.
- [5] Mei-li li, Wang Lixia, etc. Mechanism of sand stone powder content on the compressive strength of concrete and the influence of shrinkage [J]. Henan building materials, 2001, 03.

# Experimental research on compounding high-performance pavement concrete by utilizing high titanium heavy slag

Jinkun Sun & Jian Guo

*School of Civil Engineering, Panzhihua University, Panzhihua, Sichuan, China*  
*Sichuan Province Key Laboratory of Higher Education Institution for Comprehensive Development and Utilization of Industrial Solid Waste in Civil Engineering, Panzhihua, Sichuan, China*

HanFeng Duan

*Netherlands Architecture and Civil Engineering College, Xihua University, Chengdu, Sichuan, China*

**ABSTRACT:** We utilize coarse aggregate, fine aggregate, and fine ground admixture made to make high titanium heavy slag to compound the performance of complex high titanium heavy slag pavement concrete. Applying set parameters of bending strength and working property as major examining indexes, we adopt orthogonal experiments and extreme difference analysis method to research the influence of water to binder ratio, sand percentage, and composite powder replacement rate on the performance of high titanium heavy slag, make optimal design for it, seek optimal proportioning, and design a kind of high-performance pavement concrete to popularize in pavement engineering to provide good reference to engineering application.

**Keywords:** complex high titanium heavy slag; high-performance pavement concrete; mixture design; orthogonal experiment; experimental analysis

## 1 INTRODUCTION

High titanium heavy slag is a kind of dense slag that generates from blast furnace slag naturally cooled or hot poured in the air when vanadium-titanium magnetite is smelted in ANSTEEL. Its  $\text{TiO}_2$  content is high up to around 22%; thus, it is called high titanium heavy slag. This project grades and breaks the huge heaps of high titanium heavy slag into coarse aggregate, fine aggregate, and fineground admixture to make compound pavement concrete (hereinafter referred to as “CHTHSPC”). It is a significant measure to apply high titanium heavy slag to the field of engineering construction, as it will help in solving the excessive slag accumulation in ANSTEEL, economizing natural resources, reducing engineering cost, protecting the ecologic environment of the upper reaches of Yangtze River, etc. Following the previous research foundation<sup>[1][2]</sup>, this paper, is also based on the analysis of the technical standards. The aggregates of sand and stone and levigated admixture are used for the road made from high titanium heavy slag. We take the flexural strength index, the most important index for the concrete used for making roads, as the center. Through orthogonal proportion experiment of

the concrete, we select the optimal proportion and design a kind of pavement concrete made from the high-performance high-titanium heavy slag, providing further exploration and verification for the high-titanium heavy slag used to make pavement concrete in Panzhihua.

## 2 ENGINEERING BACKGROUND

The road project of double line of Qingxiangping-Wuguijing belongs to the municipal arterial road project in West District, Panzhihua. The design length, width, and thickness of the road are respectively 6.4 km, 15 m, and 250 mm. The road is mainly used to replace the municipal central prosperous artery to shunt heavy freight locomotives, so the road belongs to the heavy-grade traffic pavement, and its design flexural strength  $R_{28} \geq 5.5$  MPa, and its design grade is secondary road. All the concrete in this section of the road is proposed to adopt high titanium heavy slag thick and thin aggregates to replace ordinary breakstone and sand and mixed with levigated high titanium slag compound micro powder to partly replace cement to confect CHTHSPC 6.4 km.

### 3 EXPERIMENTAL DESIGN

#### 3.1 Selection of raw materials

Thick aggregates. The successive graduation, apparent density 2.72 g/cm<sup>3</sup> and stacking density: 1350 kg/m<sup>3</sup> of the 5–31.5 mm high titanium heavy slag breakstone produced<sup>[3]</sup> by Huanye Co., Ltd.

Thin aggregates. For the high titanium heavy slag produced by Huanye Co., Ltd., the content of its ground-slag: 10%–13%, the modulus of fineness  $M_x = 2.9$ –3.2, the apparent density: 3.14 g/cm<sup>3</sup> and the stacking density: 1680 kg/m<sup>3</sup>.

Composite powder of ground titanium slag<sup>[4]</sup>. See Table 1.

Cement. The selected cement is produced by Huanye Co., Ltd.

#### 3.2 Preliminary mix-proportion calculation

The standard mix-proportion for road concrete is preliminarily calculated as shown in Table 2 through preliminary mix-proportion calculation according to the given design scheme of mix-proportion in Construction Specification for Highway Concrete and Cement<sup>[5]</sup>, and refer to the proportion of plain concrete pavement of the approaches on the south and north of the local Bingcaogang Bridge<sup>[6]</sup>, which has been completed and opened to traffic.

#### 3.3 Optimization design for orthogonal mix-proportion

For further improving mechanical property of CHTHSPC, changes of relevant factors, such as the amount of composite powder, water-binder ratio and sand ratio, should be considered in terms of affecting the mix-proportion of concrete based on the calculation of standard mix-proportion. In this thesis, othogonal design is adopted to learn the

relationship between the property of CHTHSPC and each factor. Then the range of the optimal mix-proportion could be obtained through adjustment.

##### 3.3.1 Parameter determination

Selecting water-binder ratio from 0.46, 0.44, 0.42, 0.40; sand ratio from 33, 34, 35, 36; and composite powder (replacement rate%) from 16, 18, 20, 22 by research. Conducting orthogonal test by orthogonal Table L 9(34) orthogonal Table.

##### 3.3.2 Orthogonal mix-proportion test

Conduct trial concrete mixing based on Property Test Methods for Normal Concrete Mixture and Mechanical Property Test Methods for Normal Concrete. The tested orthogonal mix-proportion and experimental results of concrete under each condition are in Table 3.

## 4 EXPERIMENTAL RESULTS ANALYSIS

#### 4.1 Differential analysis of orthogonal design results

The calculation method of column I factor range  $R_i$  are as follows:

$$R_i = \max(I_i, II_i, III_i, IV_i) - \min(I_i, II_i, III_i, IV_i) \quad (1)$$

The magnitude of range  $R_i$  reflects the magnitude of corresponding factors. The range calculation is as shown in Table 4.

From the Table 4 associated with various factors analysis, conclusions can be drawn:

- The sort order within 7 days of flexural-tensile strength influence for CHTHSPC is: water-binder ratio → the amount of compos-

Table 1. Quality index of ground fine high titania slag composite powder.

Material	Indicators							Screen residue rate (%)	Density (g/cm <sup>3</sup> )	Specific surface area (m <sup>2</sup> /kg)
	MgO	Al <sub>2</sub> O <sub>3</sub>	SiO <sub>2</sub>	CaO	TiO <sub>2</sub>	Fe <sub>2</sub> O <sub>3</sub>				
Ground fine high titania slag	7.67	16.7	24.88	27	21.74	0.34	11.2	2.96	550	

Table 2. Preliminary calculated mixture proportion.

Test content	Sand ratio (%)	Water-binder ratios (%)	Test materials (kg/m <sup>3</sup> )				
			Cement	Slag sand	Slag stone	Water	Composite powder
Standard	31	0.42	380	695	1255	170	Undetermined

Table 3. Mix proportion and test result of orthogonal experiment under the conditions of different levels of factors.

Block	Test materials (kg/m <sup>3</sup> )							7-day flexural-tensile strengths (MPa)	28-day flexural-tensile strengths (MPa)
	Water-binder ratios	Cement	Slag sand	Slag stone	Water	Composite powder	Slumps (mm)		
1	0.46	311	647	1313	170	59	30	4.72	7.41
2	0.46	303	666	1294	170	67	45	4.53	6.65
3	0.46	296	686	1274	170	74	20	4.2	6.78
4	0.46	289	706	1254	170	81	45	4.6	6.8
5	0.44	317	642	1302	170	69	30	5.21	7.76
6	0.44	309	661	1283	170	77	20	5.93	7.15
7	0.44	301	680	1264	170	85	30	6.12	7.46
8	0.44	324	700	1244	170	62	45	6.2	7.5
9	0.42	324	635	1290	170	81	30	6.16	7.65
10	0.42	316	655	1270	170	89	20	6.38	7.58
11	0.42	340	674	1251	170	65	10	6.27	7.68
12	0.42	332	693	1232	170	73	10	6.39	7.8
13	0.4	331	629	1276	170	94	10	6.37	7.45
14	0.4	357	648	1257	170	68	10	6.51	7.86
15	0.4	348	667	1238	170	77	10	6.36	7.87
16	0.4	340	686	1219	170	85	10	6.36	7.5

Table 4. Range analysis of the orthogonal designing result.

Items	Factors	Algebra sum			Average value			Influence order
		Water-binder ratios	Sand ratio (%)	Composite powder replacement rate %	Water-binder ratios	Sand ratio (%)	Ground granulated substance replacement rate (%)	
7-day flexural-tensile strengths (MPa)	K1	18.05	22.46	21.98	4.51	5.62	5.5	Water-binder ratios > composite powder > sand ratio
	K2	23.46	23.35	23.27	5.87	5.84	5.82	
	K3	25.2	22.95	23.23	6.3	5.74	5.81	
	K4	25.6	23.55	23.83	6.4	5.89	5.96	
	R	1.89	0.27	0.46	1.89	0.27	0.46	
28-day flexural-tensile strengths (MPa)	K1	27.64	30.26	29.77	6.91	7.57	7.44	Water-binder ratios > Sand ratio > Composite powder
	K2	29.87	29.24	29.38	7.47	7.31	7.35	
	K3	30.71	29.79	29.71	7.68	7.45	7.43	
	K4	30.68	29.6	30.03	7.67	7.4	7.51	
	R	0.77	0.26	0.16	0.77	0.26	0.16	
Working property	K1	145	100	76	36	25	19	Water-binder ratios > Sand ratio > Composite powder
	K2	130	100	76	32.5	25	19	
	K3	70	70	76	17.5	17.5	19	
	K4	40	115	76	10	28.8	19	
	R	26	11	0	26	11	0	

ite powder → sand ratio; the sort order within 28 days of flexural-tensile strength influence for CHTHSPC is: water-binder ratio → sand ratio → the amount of composite powder.

- The water-binder ratio is the principal factor which has an impact on CHTHSPC's flexural-tensile strength.
- The sizes of the amount of composite powder is the secondary factor that has an impact on

CHTHSPC's flexural-tensile strength, which is getting smaller with the increase of the amount of composite powder; On the 28th day, the sand ratio took place of composite micro powder dosage and became the secondary factor that has an impact on CHTHSPC's flexural-tensile strength. Mainly, because of accompanying with the development of activation effect by composite micro powder dosage, after 7 days,

the impact factors of flexural-tensile strength for the amount of composite powder began to gradually decrease. Associated with the orthogonal experimental results, to select group 9 from test block group numbers as the application of CHTHSPC's optimal ratio in the pavement engineering.

#### 4.2 Experimental result analysis

- The effect of water-binder ratio on CHTHSPC. According to Table 4, the breaking strength of CHTHSPC goes down with the increase of water-binder ratio, especially the early-stage flexural-tensile strength. However, after the age period increased to 28 days, flexural-tensile strengths of CHTHSPC with different water-binder ratios, including 0.46, 0.44, 0.42 and 0.40, tend to approach each other. Except for 0.46, all flexural-tensile strengths with other water-binder ratios are larger than designed flexural-tensile strength, in compare with the ones with the age period of 7 days. When it comes to Day 28, all flexural-tensile strengths with different water-binder ratios in four groups are between 6.65~7.87, which can totally meet the design requirement. Therefore, the water-binder ratio decides the flexural-tensile resistant performance of CHTHSPC.
- The impact of superfine composite powders on CHTHSPC. As the amount of composite powder in CHTHSPC is not that high, ranging from 16% to 22% only, it merely has a positive impact on the working performance of CHTHSPC, and various mixing amounts of superfine composite powders which include 16%, 18%, 20%, and 22% do not have much flexural-tensile strength influence of CHTHSPC, but high amounts can improve the frangibility of concrete.
- The flexural-tensile strength of CHTHSPC of age 28 days is above 7.0.

### 5 CONCLUSION

- Centered on of bending and breaking strength index of CHTHSPC, the optimum mixture ratio of high-performance pavement concrete is obtained through the orthogonal and proportion tests.
- The flexural-tensile strength of CHTHSPC decreases with the growth of water-binder ratio, especially the early-stage flexural-tensile strength. However, with the prolongation of

age period, flexural-tensile strengths of concrete with different water-binder ratios tend to approach each other. The flexural-tensile resistance performance of CHTHSPC is determined by water-binder ratio.

- Every mixing amount of 16%, 18%, 20%, and 22% of grind stiletto titanium slag composite powder has little flexural-tensile strength influence on CHTHSPC, but can improve concrete's workability and fragility.
- CHTHSPC's 28-day flexural-tensile strength can be above 7.0 MPa; in addition, due to its rough surface, good concrete's interface structure, and prolonged wear-resistance, it is suitable for pavement concrete of heavy and extra heavy road.
- Engineering application. Via pavement investigation of Qing-Wu double line project, analyzing from transport rate and pavement's damaged condition, CHTHSPC's quality is good and the qualified rate is 100%; the amount of cement equals to or is below that of concrete formed by naturalgravel of the same level and working performance, possessing excellent tension resistant performance; over half a year of running, no phenomenon of broken slab or founding has occurred.

### REFERENCES

- [1] Jianxiong Chen, Fei Xiao, etc: Study on Comprehensive Utilization of Titanium Slag [J]. *New Building Materials*; Vol. (6) (2004):22-24.
- [2] Jiayun Chen, Bing Li, Ai mei Li, etc: Research on the Application of Fly-ash-cement Concrete with Higher Bending Strength and Higher Antiwear Strength [J] *Panzhuhua Sci-Tech & Information*; Vol. (Suppl.) (2005):85-96.
- [3] Huaibin Wang, Fuzhong Fan, Jianzhang Hao, etc: Action Mechanism of High Titanium Blast Furnace Slag in Concrete[J]. *Steel Vanadium and Titanium*; Vol. 25 (3) (2004):48-53.
- [4] The Studying Team of "High Titanium Bearing BF Slag Concrete and Slag mortar". *Experimental Research in High Titanium Bearing BF Slag Concrete and Slag mortar* [J]. *Panzhuhua Sci-Tech & Information*; Vol. (Suppl.) (2005):14-29.
- [5] Bing Li, Jiageng Chen, Dong Chen: High Performance Concret with Pulverized and Reinforced Mineral Material [J].*Sichuan Architectural*; Vol. 23(5) (2005):82-84.
- [6] Zhi Fu, Hong Li: *Technical Specification Guide for Highway Cement Concrete Pavement Construction (JTGF30-2003)* [M]. China Communications Press. 2003.

## Experimental study on axial compression behavior of recycled aggregate concrete

J.X. Deng

*Guangxi Key Laboratory of Road Structure and Materials, Nanning, China*  
*Guangxi Transportation Research Institute, Nanning, China*

X.G. Zhang

*School of Civil Engineering, Henan Polytechnic University, Jiaozuo, China*

X.J. Qi & X.H. Huang

*Guangxi Key Laboratory of Road Structure and Materials, Nanning, China*  
*Guangxi Transportation Research Institute, Nanning, China*

**ABSTRACT:** Four recycled aggregate concrete of different replacement ratios was prepared using crushed cube block as recycled coarse aggregate. Replacement ratios varied from 0 to 100%, and a total of 12 prismatic block were loaded on the electro-hydraulic servo testing machine. The destruction process and failure mode were observed, the load-displacement curves of the whole process were obtained and analyzed. It is shown that destruction process and failure mode of recycled aggregate concrete and natural aggregate concrete are similar to each other. With the increase of recycled coarse aggregate replacement ratio, peak stress and peak strain of recycled aggregate concrete show no apparent unity law. Replacement ratio of recycled coarse aggregate makes a greater impact on stress-strain curves of recycled aggregate concrete. With the increase of recycled coarse aggregate replacement ratio, elastic modulus of recycled aggregate concrete gradually become larger, ductility and energy performance of recycled aggregate concrete get better.

**Keywords:** recycled aggregate concrete; axial compression; stress-strain curve; peak stress; peak strain

### 1 INTRODUCTION

After crushing, cleaning and grading, the recycled waste concrete blocks and the natural concrete blocks are mixed to form recycled aggregate by a certain percentage and gradation. Then cement and water are added, so Recycled Aggregate Concrete (RAC) can be formulated<sup>[1-3]</sup>. On the one hand, RAC can resolve the process issue of waste concrete; On the other hand, natural aggregate are instead with construction waste, the consumption of natural aggregates, in the construction industry can be reduced, ease the increasingly scarce natural aggregates pressure, the increasingly scarce pressure of natural aggregates will be eased, social, economic and environmental benefits are obvious. So RAC is considered to be green concrete to achieve sustainable development of building resources<sup>[4-6]</sup>.

At present, universities or research institutes have conducted some research about the performance of the RAC. Peng Gaifei<sup>[7]</sup> of Beijing Jiaotong University crushed and processed two ordinary

concrete were for recycled coarse aggregate, after 620°C heat treatment and pulp attached on recycled coarse aggregate was excluded, RAC was prepared to determine strength index. The results showed the mechanical properties of RAC decreased remarkably. Liu Qingtao<sup>[8]</sup> of Air Force Engineering University adopted the double-doped technology with the use of fly ash of high quality and efficient admixture, experimental research on strength and frost resistance of RAC in airport pavement was carried out. It is shown that the performance of the prepared RAC for pavement is more excellent than one of ordinary concrete, and the request of airport pavement can be met. Based on gray clustering evaluation theory, Lanzhou Jiaotong University Bao Xueying<sup>[9]</sup> Proposed the scheme that RAC coarse aggregate quality level can be assessed comprehensively using a number of parameters, and the usefulness of the evaluation scheme was examined through case study. Padmini A.K.<sup>[10]</sup> studied the effects the recycled aggregate of original concrete made on mechanical behavior of RAC. It is shown that RAC strength is related



to the original concrete strength. RAC strength became higher as original concrete strength became higher, but the relationship was not linear.

Since the majority of recycled aggregate of RAC was from the removed old building, the original internal damage will be bring more or less in the crushing process, leading a large number of internal micro-cracks or cracks in aggregate. Accordingly, axial compressive strength and stress—strain curve of RAC prepared by the recycled aggregate will be affected. Therefore, this paper carried out the axial compressive test of RAC, the stress-strain curve of the whole process was measured. Influence different aggregate replacement ratioed made on axial compressive strength was analyzed. So study about RAC will be enriched, reference for further research and application will be provided for RAC structure.

## 2 DESIGN OF EXPERIMENT

### 2.1 Materials of experiment

P.O 42.5R grade cement, ordinary natural river, urban water and natural coarse aggregate and recycled coarse aggregate were adopted as materials of experiment. Continuous graded gravel was selected as natural coarse aggregate, recycled coarse aggregate was obtained from the crushed test cubes through machine. Recycled coarse aggregate and natural coarse aggregate were screened by the same screen. The maximum particle size of coarse aggregate was 20 mm, and are coarse aggregate were all continuously graded gravel. Recycled coarse aggregate was cleaned for number of times to meet the clay content requirement of recycled coarse aggregate, then recycled coarse aggregate will be dried to achieve the required moisture content for the pouring of RAC.

### 2.2 Mixing ratio of RAC

0% was selected as a benchmark of recycled coarse aggregate replacement ratio, there is four kinds of replacement ratios including 0%, 30%, 70% and 100%, Trial strength of RAC was C40. For RAC of different replacement ratios, the composition of

cement and sand were kept unchanged, and the quality composition ratio of natural coarse aggregate and recycled aggregate was changed under the premise of the equal total mass of coarse aggregate. Mixing ratio of RAC was shown at Table 1. For each replacement ratio, three 150 mm × 150 mm × 300 mm prism standard test blocks were made, and curing was carried out under standard conditions.

## 3 LOADING DEVICE AND TEST METHOD

The current national standard “Test method of ordinary concrete mechanical performance” (GB50081-2002) was referred. Loading was carried out on RMT-201 rocks and concrete mechanic test presses. Testing Machine was shown in Figure 1. In order to obtain the curves of load-displacement of the specimens in the load process, displacement control system was adopted. Loading rate was 0.005 mm/s, by the acquisition system of the loading device, load-displacement curves of the whole process of the specimens were obtained.

## 4 TEST RESULTS AND ANALYSIS

### 4.1 Failure process and failure mode

In the early loading, there were no visible cracks in specimens. When the load was closed to the peak point, there were one longitudinal crack or several parallel longitudinal cracks at the specimen central. After peak point, crack of part of the specimens developed rapidly, the test blocks were split into several pieces, then the specimens were destroyed suddenly and bearing capacity became little, at the same time, test machine could not collect the data of descending branch. Based on the destruction process and form, there was no significant difference between the recycled aggregate concrete and natural aggregate concrete.

### 4.2 Stress-strain curve

Based on the measured load-displacement curves, the stress-strain curve of the whole process of all

Table 1. Mixing ratio of RAC.

Replacement ratio	Water-cement ratio	Sand ratio (%)	Clean water (kg)	Cement (kg)	Sand (kg)	Natural coarse aggregate (kg)	Recycled coarse aggregate (kg)
0%	0.45	32.7	186.8	415.2	587.7	1210.3	0.0
30%	0.45	32.7	186.8	415.2	587.7	847.2	363.1
70%	0.45	32.7	186.8	415.2	587.7	363.1	847.2
100%	0.45	32.7	186.8	415.2	587.7	0.0	1210.3



Figure 1. Testing machine of RMT-201.

the specimens were obtained using equation (1) as shown in Figure 2.

$$\sigma = \frac{N}{A}, \varepsilon = \frac{\Delta l}{l} \quad (1)$$

In which:  $N$ —axial compression of specimen,  $A$ —cross-sectional areas of RAC specimens,  $\Delta l$ —specimen displacement during the load Process,  $l$ —Measuring gauge of specimen, taken as 150 mm.

In Figure 2, each curve was taken from the average of three prism curves. It can be seen from Figure 2, replacement ratio of recycled coarse aggregate has a greater impact on stress-strain curves of RAC, but the curves are made up of the ascent and descent segments, and there are the proportional limit point, the critical stress point, peak point, an inflection point and convergence point in these curves. With the increase of recycled coarse aggregate replacement ratio, the slopes of rising section in the stress-strain curve increase gradually, indicating that the elastic modulus of RAC increase gradually. The declined segments of the whole process curve become more relaxed,

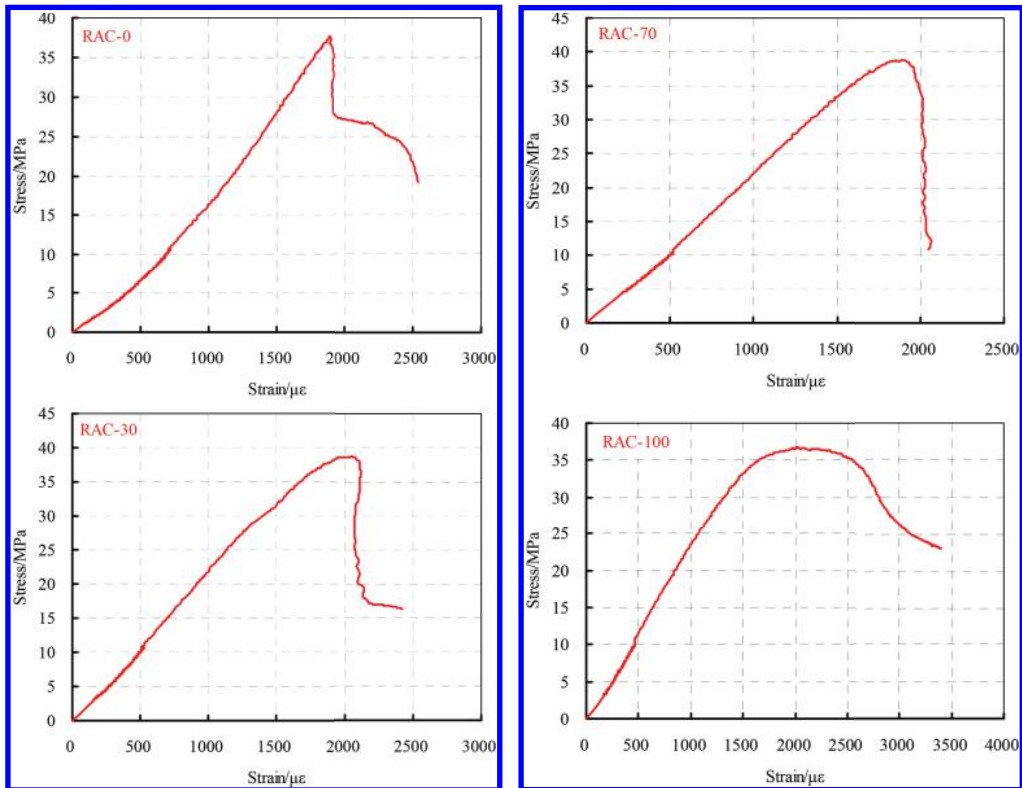


Figure 2. Compressive stress-strain curves of RAC under different replacement ratios.

it is shown ductility of RAC is becoming greater, energy performance is getting better.

### 4.3 Peak stress and peak strain

Peak stress and peak strain of RAC under different replacement ratios were shown in Table 2. It was shown with the increase of replacement ratio, peak stress and peak strain of RAC show no apparent unity law. When the replacement ratio is 70%, the peak stress of RAC is maximum, When the replacement ratio is 30%, the peak strain of RAC is maximum. Figure 3 shows the relationship between the dimensionless peak stress and recycled coarse aggregate replacement ratios, and  $f_c$  represents axial compressive strength of RAC,  $f_{c0}$  represents axial compressive strength when replacement ratio is 0%. Figure 4 shows the relationship between peak strain and recycled coarse aggregate replacement ratios.

It is shown in Figure 3 dimensionless peak stress and recycled coarse aggregate replacement ratio showed a good variation, presenting the basic form of a quadratic function. The fitted relationship is shown as formula (2).

$$y = 0.1954x^2 + 0.1763x + 0.9977 \quad (2)$$

In which,  $y$  represents  $f/f_{c0}$ ,  $x$  represents recycled coarse aggregate replacement ratio, the fitting accuracy is 0.962.

Table 2. Peak stress and peak strain of RAC.

Replacement ratio of recycled coarse aggregate	0%	30%	70%	100%
Peak stress/MPa	37.66	38.69	38.83	36.77
Peak strain/ $\mu\epsilon$	1892	2055	1907	2013

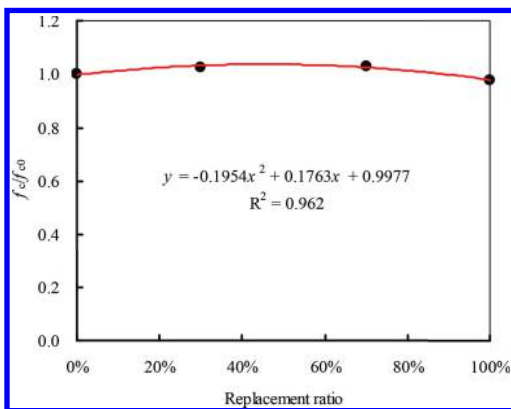


Figure 3. The dimensionless peak stress under different replacement ratios.

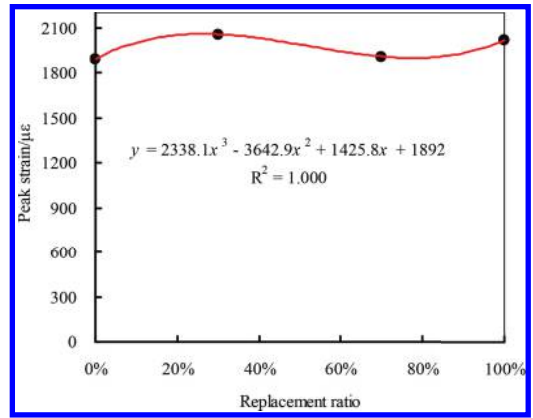


Figure 4. Peak strain under different replacement ratios.

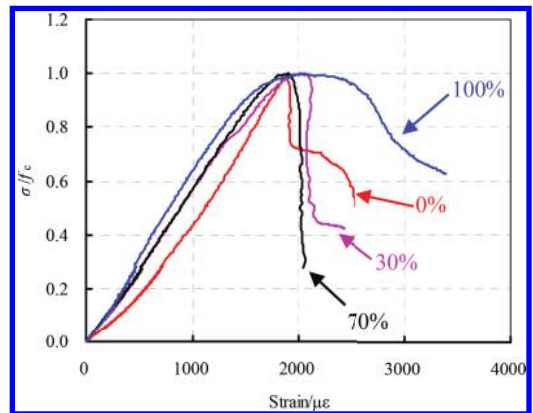


Figure 5. Dimensionless curves of stress-strain.

It is shown in Figure 4 peak strain and recycled coarse aggregate replacement ratio showed a good variation, presenting the basic form of a cubic function. The fitted relationship is shown as formula (3).

$$y = 2338.1x^3 - 3642.9x^2 + 1425.8x + 1892 \quad (3)$$

In which,  $y$  represents peak strain,  $x$  represents recycled coarse aggregate replacement ratio, the fitting accuracy is 1.000.

### 4.4 Dimensionless stress-strain curve

Dimensionless analysis about average curve was carried out based on measured stress-strain curves under different replacement ratios, dimensionless curves were shown in Figure 5.

In Figure 5, it is shown with the increase of recycled coarse aggregate replacement ratio,

dimensional curves of stress-strain become steeper. After peak point, curves come into the falling section. However the falling decline curves become more and more moderate, especially, When replacement ratio of recycled coarse aggregate was 100%, the decline falling curves are very moderate, and the post-deformation properties of the specimens are very favorable.

## 5 CONCLUSION

Based on the destruction process and form, there was no significant difference between the recycled aggregate concrete and natural aggregate concrete. With the increase of replacement ratio, peak stress and peak strain of RAC show no apparent unity law.

Replacement ratio of recycled coarse aggregate has a greater impact on stress-strain curves of RAC, With the increase of recycled coarse aggregate replacement ratio, the elastic modulus of RAC become bigger gradually, ductility of RAC is becoming greater, energy performance is getting better.

In this paper, dimensionless stress-strain curves of RAC are obtained, which establishes foundation for compression constitutive equations and further research of RAC.

## REFERENCES

- [1] Xiao J.Z., Li J.B., Lan Y. Research on recycled aggregate concrete -A review [J]. *Concrete*, 2003, 10: 17-20.
- [2] Zhang X.G., Chen Z.P., Xue J.Y., et al. Experimental study and mechanical behavior analysis of recycled aggregate concrete filled steel tubular long columns under axial compression [J]. *Journal of Building Structures*, 2012, 33(9): 12-20.
- [3] Kiyoshi E., Kohji T., Akira N., et al. Application of recycled coarse aggregate by mixture to concrete construction [J]. *Construction and Building Materials*, 2007, 21(7): 1542-1551.
- [4] Zhou J.H., He H.J., Meng X.H. Basic mechanical properties of recycled concrete experimental study [J]. *Journal of Shenyang Jianzhu University (Natural Science)*, 2010, 26(3): 464-468.
- [5] Xu Y.D., Zhou S.Q. Experimental Study of Recycled Concrete Aggregate [J]. *Journal of Building Materials*, 2004, 7(4): 447-450.
- [6] Vivian W.Y., Tam, Gao X.F., Tam C.M. Microstructural analysis of recycled aggregate concrete produced from two-stage mixing approach [J]. *Cement and Concrete Research*, 2005, 35(6): 1195-1203.
- [7] Peng G.F., Huang Y.Z., Zhang J.F. Influence of defects in recycled aggregate on mechanical properties of recycled aggregate concrete [J]. *Journal of Building Materials*, 2012, 15(1): 80-84.
- [8] Liu Q.T., Cen G.P., Cai L.C. Properties and applications of recycled concrete for airport pavement [J]. *Journal of Central South University (Science and Technology)*, 2012, 43(8): 3263-3269.
- [9] Bao X.Y., Wang Q.C. Application of grey clustering method for quality grade estimate of recycled concrete coarse aggregate [J]. *Journal of Civil, Architectural & Environmental Engineering*, 2014, 36(3): 112-117.
- [10] Padmini A.K., Ramamurthy K., Mathews M.S. Influence of parent concrete on the properties of recycled aggregate concrete [J]. *Construction and Building Materials*, 2009, 23(2): 829-836.
- [11] Sun Y.D., Zhou D.Y. The present study state and problems to be solved on recycled concrete in China [J]. *Concrete*, 2006, 4: 25-28.
- [12] Bairagin K., Ravadne K. Behavior of concrete with different proportions of natural and recycled aggregate [J]. *Resource, Conservation and Recycling*, 2008, 24(4): 109-126.

# Study on mixture ratio design and performance of cement stabilized gravels based on vibratory compaction method

H.Y. Pan

*Guangxi Key Laboratory of Road Structure and Materials, Guangxi, Nanning, China*  
*Guangxi Transportation Research Institute, Guangxi Nanning, China*

L.M. Qin, X.J. Qi & L.L. Xie

*Guangxi Transportation Research Institute, Guangxi, Nanning, China*

M.Q. Jin

*School of Materials Science and Engineering Chang'an University, Xi'an, China*

**ABSTRACT:** With the aim of achieving efficient simulations on the rolling effects in practical engineering and improvement of pavement performance, the mixture ratios of cement stabilized gravels were studied using vibratory compaction method. The maximum dry densities, optimum water contents, unconfined compressive strengths of mixtures obtained by vibratory compaction and static pressure compaction methods were compared, and evaluations on pavement performances were discussed. The experimental results showed that maximum dry density and optimum water content of mixtures by vibratory compaction were as 1.02 and 0.88 times as them by heavy compaction respectively; cement usage could be saved in cement stabilized gravels by vibratory compaction, with the strength requirements guaranteed; and cement stabilized gravels by vibratory compaction exhibited preferable pavement performance than them by traditional methods. The cement stabilized gravels by vibratory compaction could not only save the usage of cements, but also contribute to the improvement of pavement performance.

**Keywords:** cement stabilized gravel; pavement performance; vibratory compaction; mixture ratio design

## 1 INTRODUCTION

China is abundant in natural gravels, especially in the western regions. With the development of expressway constructions, making use of natural gravels from local resources will not only reduce the costs of highway constructions, but also avoid environmental destructions induced by quarrying effectively, which produce remarkable economic and social benefits [1]. As similar to the semi-rigid base materials such as cement stabilized macadam, the improper usage of cement stabilized gravel base will bring about premature damages to pavements, such as cracking, and impair long-term performances of pavements, which may result from the unconformities of methods between design and actual constructions. As is generally known, rolling by vibratory roller is usually adopted in the constructions; however, the compaction and static pressure methods used in the design of materials, cannot simulate the conditions in practical constructions, which gives rise to an invalid field control on the construction quality [2–5].

With the employment of cement stabilized gravel vibro-moulding method, the compaction effect on

the material surface by vibratory roller can be simulated, and steadily dense structure can also be formed in the vibration process [6]. Accordingly, mixture ratio design of cement stabilized gravels and the corresponding pavement performances were studied in present work, with the purpose to solve the problems occurred in the constructions of cement stabilized gravel base, and moreover, to improve the pavement performance and extend the service span.

## 2 EXPERIMENTAL

### 2.1 *Properties of raw materials*

#### 2.1.1 *Cement*

Composite portland cement P.C 32.5 was employed in the experiments, with the technical indexes listed in [Table 1](#), in which three days (3d) compressive strength and flexural strength met the requirements of cement strength grades in Common Composite Portland Cements (GB 175-2007), and the initial and final setting times of cements satisfied the demands in Technical Specifications in the Construction of Highway Pavement Base.

Table 1. Technical indexes of cements.

Technical indexes	Experimental results
Degree of fineness (m <sup>2</sup> /kg)	343
Stability	qualified
3d compressive strength (MPa)	18.3
3d flexural strength (MPa)	3.8
<i>Setting time (min)</i>	
Initial setting time	363
Final setting time	462

Table 2. Technical indexes of aggregates.

Standard of aggregates	Bulk specific gravities
19~31.5 mm	2.660
9.5~19 mm	2.658
4.75~9.5 mm	2.650
0~4.75 mm	0.590

### 2.1.2 Aggregates

By sieving, gravels in the experiment were classified as four standards: 19~31.5 mm, 9.5~19 mm, 4.75~9.5 mm and 0~4.75 mm, in which the crushing value of coarse aggregates was 11.8%, conformed to the claims in Technical Specifications in the Construction of Highway Pavement Base, and the results of bulk specific gravity were presented in Table 2. With reference to gradations in density framework structures, considering a large number of practical experiences and specific conditions in construction sites, aggregate mixtures with dense framework gradation composition were investigated, as shown in Table 3.

### 2.1.3 Water

Underground water was employed in present experiments, in accordance with the standard requirements.

## 2.2 Experimental instruments

Surface vibratory compaction apparatus was adopted, in which vibration frequency could be regulated by the adjustment of rotational speed of electric motor; different magnitudes of exciting force could be obtained with the variations of eccentric mass; and nominal amplitude were varied with the addition or reduction of counterweights. Operational parameters of surface vibratory compaction apparatus were listed as follows, frequency (30 ± 2 Hz), exciting force (7.5 kN), nominal amplitude (1.2 mm) and vibratory compaction time (100 s).

### 2.3 Experimental methods

To overcome the deficiencies in traditional design methods based on heavy compaction and static

Table 3. Gradation compositions of cement stabilized gravels in the experiments.

Sieves sizes (mm)	31.5	19.0	9.5	4.75	2.36	0.6	0.075
Mass percentages (%)	100	67.3	44.8	31.0	20.5	10.6	2.1

pressure moulding, vibratory compaction method and corresponding vibro-moulding method were advanced in view of the summaries of construction experiences at domestic and abroad.

The detailed experiment procedures were illustrated as follows: after bake-drying, 5~6 samples were prepared by the aggregates of different standards, according to predetermined gradation of mineral aggregates, with dry weights being about 5000~6000 g in each samples; preset doses of cement and water were then added, stirred uniformly and put into testing moulds; subsequently, experiments were performed in accordance with the prescriptive vibratory compaction time, in which wet densities and related dry densities were calculated; the experiments were repeated more than 5 times, and the relationship curves between dry density and water were plotted, by which the optimum water contents and maximum dry densities were investigated.

Based on vibratory compaction experiments, the maximum dry density was taken as the standard in the vibro-moulding experiment. Testing models with 98% degree of compaction were obtained, which were taken into standard preservation chamber after weighted and further experiments on mechanical strength and pavement performances would be carried out.

On the basis of the relationship curves of water content and dry density in cement stabilized gravels obtained in vibratory experiments, the optimum water contents and maximum dry densities were determined. Using definitive gradation compositions, experiments were performed on the samples with 3.0%~6.0% cement contents in cement stabilized gravels. The optimum water contents and maximum dry densities of samples with different ratios were discussed extensively using heavy compaction and vibratory compaction methods as introduced in Test Regulations on the Stabilized Materials in Inorganic Binder for Pavement Engineering, and the results were listed in Table 4.

In the current Technical Specifications for the Construction of Highway Pavement Base (JTJ 034-2000), seven days (7 d) unconfined compressive strength under saturated condition was adopted as the index for cement stabilized materials. Concerning the reasonable usage range of the cement stabilized materials were between 3.0% and

Table 4. Optimum water contents and maximum dry densities in mixtures.

Items	Heavy compaction experiment				Vibratory compaction experiment			
	3.0	4.0	5.0	6.0	3.0	4.0	5.0	6.0
Cement contents (%)	3.0	4.0	5.0	6.0	3.0	4.0	5.0	6.0
Optimum water contents (%)	4.9	5.0	5.2	5.3	4.1	4.4	4.7	4.8
Maximum dry densities (g/cm <sup>3</sup> )	2.394	2.402	2.411	2.425	2.431	2.448	2.462	2.473

Table 5. 7 d unconfined compressive strengths of mixtures.

Cement contents	Rs (Mpa)	Rv (Mpa)	Rv/Rs
3.0	3.0	5.2	1.73
4.0	3.8	6.3	1.66
5.0	5.3	8.7	1.64
6.0	6.7	10.5	1.57

6.0%, the cement contents of 3.0%, 4.0%, 5.0% and 6.0% were adopted in the tests, and the cement stabilized gravel models were produced by vibromoulding and static pressure moulding, which were given comparisons herein.

According to Test regulations on the Stabilized Materials in Inorganic Binders for Pavement Engineering (JTG E51-2009), cylindrical specimen were formed on the basis of compaction experimental results, i.e., the maximum dry densities and optimum water contents with different cement contents were used. The specimen were then persevered under the conditions in which the temperature were set within  $20 \pm 2^\circ\text{C}$  and the humidity were set at above 95%, and unconfined compressive strength tests were performed, with the results presented in Table 5.

### 3 RESULTS AND DISCUSSION

#### 3.1 The optimum water content and maximum dry density

As displayed in Table 4, with the variations of the cement contents between 3.0%–6.0%, the optimum water contents of the samples by heavy compaction method were within 4.9%–5.3% while them by vibratory compaction were about 4.1%–4.8%; and moreover, the maximum dry densities by heavy compaction existed between 2.394 g/cm<sup>3</sup>–2.425 g/cm<sup>3</sup>, which were at around 2.431 g/cm<sup>3</sup>–2.473 g/cm<sup>3</sup> when vibratory compaction adopted. To make comparisons between two methods, the average ratio of optimum water content of mixtures by vibratory compaction to it by heavy compaction was 0.88, while the average ratio of maximum dry density between two methods was larger, to be 1.02. Conclusively, among two

methods, larger compactness of mixtures could be obtained by vibratory compaction, in which aggregates were rearranged.

#### 3.2 Unconfined compressive strengths of cement stabilized gravels

It could be easily found from Table 5 that 7 d unconfined compressive strengths of cement stabilized gravels by two moulding methods presented significant differences. 7 d unconfined compressive strengths (Rs) of cement stabilized gravels by static pressure compaction were at around 3.0–6.7 MPa, while 7 d unconfined compressive strengths (Rv) by vibratory compaction were at 5.2–10.5 MPa, i.e., the compressive strengths by vibratory compaction were about 1.65 times than those by heavy compaction. In a word, the mixtures obtained by vibratory compaction provided higher compressive strengths than them by static pressure compaction, with similar material ratios and optimum water contents. Under vibratory compaction, the aggregates became more compact owing to the resonance motion caused by vibration, which led to distinctly larger compressive strengths in the specimens than them by static pressure compaction.

As demonstrated in the experimental results of unconfined compressive strength, the strengths of cement stabilized gravels obtained by static pressure compaction could not satisfied the standard requirements with the cement content being 3.0%, and moreover they were not satisfactory until the cement contents were above 4.0%. However, the mixture obtained by vibratory compaction could meet the standard requirements with the cement content being 3.0%. Illustratively, the strength of materials by vibratory compaction with 3.0%–4.0% cements could be as high as them with 5.0%–6.0% cements by static pressure method. Briefly summarized, the enhancement of material strength could be achieved by vibratory compaction method, and moreover, 20% cement usage could be saved, which presented remarkable economic benefits meanwhile.

#### 3.3 The frost resistance performance of cement stabilized gravels

Freeze-thaw cycle tests of base materials were performed in accordance with Test Regulations

Table 6. Frost resistance performance of cement stabilized gravel mixtures.

Moulding methods	Cement contents (%)	Frost resistance coefficients at different preservation periods (%)		
		14 d	28 d	90 d
Static pressure compaction	3.0	88.4	90.4	92.4
	4.0	90.5	90.7	92.7
	5.0	89.3	91.2	93.6
Vibratory compaction	3.0	94.8	95.7	97.1
	4.0	95.1	96.3	97.8
	5.0	95.5	96.6	98.2

on the Stabilized Materials in Inorganic Binders for Pavement Engineering (JTG E51-2009), in which the specimens were frozen for 16 hours and thawed for 8 hours, repeated for 5 times, and the compressive strength tests were conducted after freeze-thaw cycles finished. Decline of mass after freeze-thaw cycles and frost resistance coefficients K were adopted as the indexes to characterize the frost resistance performance of mixtures.

Experimental results on the frost resistance coefficients of cement stabilized gravels were listed in Table 6, and the relationships of frost resistance with preservation period and cement content were discussed, from which we could observe that frost resistance coefficients increased gradually with the prolong of preservation period. Within the same preservation period, frost resistance coefficients improved steadily with the addition of cement content. It was assumed that, as preservation period or cement content raised, the hydration products of cements increased and then the internal void volume of cement stabilized gravels decreased, which gave rise to better frost resistance performance.

Under similar conditions, the frost resistance coefficients of cement stabilized gravel specimens by vibratory compaction were higher than them by static pressure method, on account of the specimens obtained by vibro-moulding showed more compactness, less internal void volume, and therefore stronger frost resistance.

#### 4 CONCLUSIONS

Vibratory compaction and related vibro-moulding method on cement stabilized gravels were proposed, and mixture ratio design of cement stabilized gravels and their pavement performance were analyzed systematically.

The maximum dry densities and optimum water contents by vibratory and static pressure

compactions were discussed, by which we observed that the optimum water content of cement stabilized gravels by vibratory compaction was as 1.88 times as them by static pressure compaction, and the maximum dry density by vibratory compaction was as 1.02 times as them by static pressure compaction.

By comparisons of the compressive strength in specimens obtained by two methods, the strength of cement stabilized gravels by vibratory compaction was significantly greater than them by static pressure compaction. Obtained by vibratory compaction, cement stabilized gravels with cement contents being 3.0%~4.0% could provide the compressive strength as them by static pressure compaction with 5.0%~6.0% cement content; in other words, the usage of cements could be saved.

Cement stabilized gravel mixtures obtained by vibratory compaction conformed to the rolling mechanisms and effects more reasonably, which could save the usage of cements, enhance the strength and frost-resistance of materials, and reduce the cracks in base, providing remarkable economic and social benefits.

#### ACKNOWLEDGEMENTS

This work was financially supported by the Foundation of Guangxi Key Lab of Road structure and materials (Grant No. 2014 gxjgckf-003), West Light Foundation of The Chinese Academy of Sciences (12KJZRZMY001), and the Special Fund for Basic Scientific Research of Central Colleges (Chang'an University, Grant No. 2014G1311087).

#### REFERENCES

- Sha A.M. 2008. Material Characteristics of Semi-rigid Base. China Journal of Highway and Transport 21(1):1-5.
- Jiang Y.J. et al. 2010. Influence factors of strength properties of cement stabilization of crushed aggregate, Journal of Chang'an University (Natural Science Edition), 30(4):1-7.
- Li L.H. 2013. Construction Quality Control Techniques of Lime-Fly Ash Macadam Base. Transportation Standardization (5):102-104.
- Ministry of Transport of the People's Republic of China 2006, Specifications for Design of Highway Asphalt pavement. Beijing: China Communications Press.
- Ministry of Transport of the People's Republic of China 2009, Test Methods of Materials Stabilized with Inorganic Binders for Highway-Engineering. Beijing: China Communications Press.
- Zhou W.F. et al. 2006. Mix Ratio Optimization Design of Cement Stabilized Macadam Based on Static Pressure Method and Vibration Method. Journal of Chang'an University (Natural Science Edition), 26(1):24-28.



# Contrast on axial compressive strength between FRP and steel reinforced confined concrete

Tuan Wei Bi, Dongsheng Gu & Xuan Zhang

*State Key Laboratory Breeding Base of Mountain Bridge and Tunnel Engineering, Chongqing Jiaotong University, China*

*College of Environmental and Civil Engineering, Jiangnan University, China*

**ABSTRACT:** The research on models of axial compressive strength between FRP confined concrete and reinforced concrete was carried out. Based on typical strength model in the past and the analysis of linear fitting from a large amount of experimental data, a comparative analysis on the coefficient 'k' and the form of compressive strength of models between FRP confined concrete and steel confined concrete was presented. Results indicates that there are quite differences between the coefficient 'k' of two models. However, forms are the same. A conclusion can be drawn that the axial compressive strength model of FRP confined concrete is not safer than the steel confined concrete in contrast.

**Keywords:** FRP cylinder; concrete-filled tubes; axial compressive strength; computational model; fitting analysis

## 1 INTRODUCTION

The bearing capacity and ductility of concrete columns can be improved effectively owing to confined concrete. Massive experimental research of FRP confined concrete columns and reinforced concrete columns have been carried out for many years<sup>[1-2]</sup>. FRP confined concrete and steel tube confined concrete are two of the most common ways of the constraint nowadays. FRP (Fiber Reinforced Polymer) is a high performance material, which is a mixture of fiber material and matrix material (resin) in certain proportion. FRP is light, hard, non-conductive and corrosion resistance. Besides, its mechanical strength is extremely high, but recover ability is highly weaker. Actually, FRP has been aroused widespread interests and heated discussions in recent years. Over the last two decades, a great number of experimental and analytical studies have been conducted to understand and model the compressive behavior of FRP confined concrete. Because it can meet special needs, such as larger span, high-rise, heavier load, lighter weight and so on, for the modern engineering structure thanks to its excellent mechanical properties. Steel tube confined concrete can take advantage of benefits of steel and concrete. And the compressive strength of concrete can be increased in a large scale due to the lateral compression. Moreover, the stiffness of steel will be improved by concrete. Therefore, the bearing capacity can get stronger on

account of the interaction of steel and concrete. In fact, FRP confined concrete and steel tube confined concrete are effective methods to enhance the bearing capacity and ductility of concrete.

## 2 THE PRINCIPLE OF CONFINED CONCRETE

For steel tube confined concrete, concrete supports steel tube and steel tube restrains concrete in the meanwhile. The concrete in tube is in three dimension stress state under pressure so that it can prevent the development of longitudinal crack. As a result, compressive strength and deformation capacity increase relatively. Geometrical stability is enhanced by the support of concrete in tube. In other word, instability and failure of compression gets to be avoided which results in the increase of the bearing capacity. When concrete is stressed in a complex state, its strength, ductility and toughness properties of concrete are all boosted in a certain degree in virtue of the interaction of steel and concrete.

FRP confined concrete is a passive confinement model. Lateral expansion will emerge in concrete columns and hoop tension will appear in FRP. By contrast, FRP in hoop tension will restrain the lateral expansion of concrete columns. So the concrete in tube is in three dimension stress, and the bearing capacity and ductility are both enhanced.

The confinement action exerted by the FRP shell on the concrete core is of the passive type; that is, this pressure arises as a result of the lateral expansion of concrete under axial compression. As the FRP shell is subjected to tension along its hoop direction, the confining pressure ( $f_l$ ) increases proportionally with the lateral expansion until the eventual failure of the system when the FRP shell ruptures. The performances of a large proportion of the existing models were compromised when assessed against a large test database with a parametric range that is much wider than the databases used in the development of these models. At the beginning of loading, the deformation of concrete is larger than FRP outside materials because the difference in stiffness and Poisson ratio between them. Therefore, their circumferential expansion deformation is not the same, and they crush each other resulting in the restraint stress. The early restraint stress delayed the appearance of initial crack of concrete in some degree.

Longitudinal crack turned up gradually with the increase of the axial load. Lateral strain went up rapidly which aggravated the extrusion between the FRP outside materials and core concrete. At the same time, restraint stress got higher preventing the development of longitudinal crack and making the compressive strength of core concrete improved. Finally, FRP will fail to work until maximum of axial load. The entire component will not breakdown until maximum of longitudinal stress. The mechanical model of FRP confined concrete is as shown in Figure 1.

The mechanism of Action and mechanical model between two constraints are similar to each other. The design criterion adopted in ACI 318-991<sup>[3]</sup> for column confinement is based on the premise that confined columns should maintain their concentric capacities after the spalling of cover concrete. This is achieved by providing sufficient confinement to

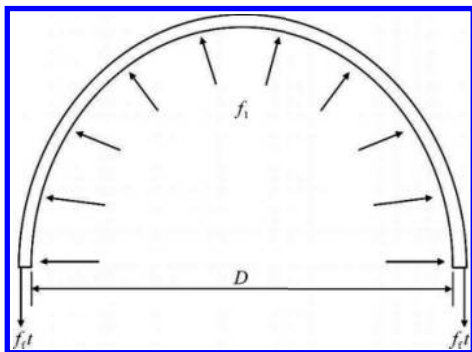


Figure 1. The mechanical model of FRP confined concrete.

the core concrete to attain strength and ductility enhancements. The required volumetric ratio of transverse reinforcement was derived based on the strength gain in core concrete, which was assumed to be  $(f_{cc} - f_{co}) = 4.1f_l$ , where  $f_l$  represents uniform passive confinement pressure.

### 3 INTENSITY MODEL

The model of  $f_{cc}'/f_{co}' = 1 + k f_l/f_{co}'$  is adopted for most existing confined concrete models.  $f_{cc}$  represents axial compressive strength of confined concrete specimen, and  $f_{co}$  represents axial compressive strength of the specimen without lateral pressure constraint.  $f_l$  is defined as lateral restraint force,  $k_1$  is valid coefficient of constraint. The formula first proposed by Richart et al<sup>[4-5]</sup> (1928) in view of active confined concrete.

For compressive strength of concrete filled steel tube, the computational model presented by Richart is as shown below:

$$f_{cc}' = f_{co} + 4.1f_l \quad (1)$$

Domestic and foreign scholars have conducted a lot of research and plenty of computational models concerning compressive strength of FRP confined concrete are proposed.

Intensity calculation model of concrete cylinder confined by stirrup was proposed by Richart<sup>[4-5]</sup> in 1928:

$$f_{cc}' = f_{co} + 4.1f_l \quad (2)$$

Empirical formula raised by Miryachi<sup>[6]</sup> is as shown:

$$\frac{f_{cc}'}{f_{co}} = 1 + 2.98 \left( \frac{f_l}{f_{co}} \right) \quad (3)$$

In 2002, after analyzing a large number of experimental data of FRP confined concrete columns, Lam and Teng<sup>[7]</sup> conclude the model as follows:

$$f_{cc}' = f_{co} + 2.0f_l \quad (4)$$

### 4 EXPERIMENTAL DATA FITTING MODEL

Massive experimental research of FRP confined concrete columns and reinforced concrete columns have been carried out for many years. There are 100 sets of experimental data of the strength of FRP confined concrete columns and 20 sets of experimental data of reinforced concrete columns.

As shown in Figure 2 and Figure 3, the experimental data is made into scatter chart which draws in the ratio of constrain  $f_i/f_{co}'$  as X and the ratio of strength  $f_{cc}'/f_{co}'$  as Y. And then, these scatter are carried on the linear fitting, where  $f_{cc}'$  represents strength of confined concrete,  $f_{co}'$  represents in-place strength of unconfined concrete in column and  $f_i$  represents uniform passive confinement pressure.

After linear fitting of 2 scatter charts, we could conclude the strength models of two different confined concrete:

The strength model of FRP confined concrete columns:

$$\frac{f_{cc}'}{f_{co}'} = 1 + 2.1 \left( \frac{f_i}{f_{co}'} \right) \quad (5)$$

The strength model of reinforced concrete columns:

$$\frac{f_{cc}'}{f_{co}'} = 1 + 5.6 \left( \frac{f_i}{f_{co}'} \right) \quad (6)$$

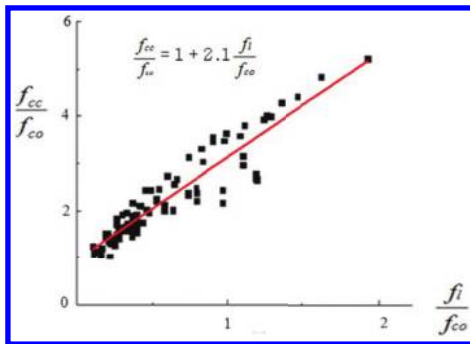


Figure 2. Scatter chart of FRP confined concrete columns.

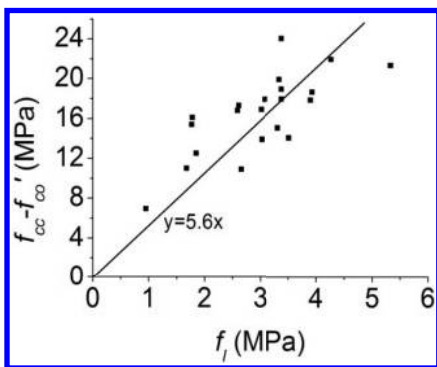


Figure 3. Scatter chart of reinforced concrete columns.

Comparing two strength models, discrete degree of FRP confined concrete columns is smaller than discrete degree of reinforced concrete columns. However, when the same constraint is provided, the strength of FRP confined concrete is lower than that of reinforced concrete columns.

## 5 SUMMARY AND CONCLUSION

According to the research content of this paper, there are 3 conclusions as follows:

1. Both FRP confined concrete and reinforced concrete can attain compressive strength and ductility enhancements.
2. According to the active confined concrete intensity model proposed by Richart et al (1928)<sup>[4-5]</sup>, the same form of intensity model is applicable for both FRP and reinforced concrete:  $f_{cc}'/f_{co}' = 1 + k_1 f_i/f_{co}'$ . In addition, the form of linear fitting model is slightly simple. Furthermore, linear fitting model is a relatively ideal model which agrees well with the experimental data collected.
3. The strength of FRP confined concrete is lower than that of a similarly restrained reinforced concrete by contrast of effective confinement factor  $k$  of them.

## ACKNOWLEDGMENT

The authors would like to acknowledge the financial support from the research fund of key laboratory of bridge-structure engineering, Chongqing Jiaotong University (No. CQSLBF-Y10-1, CQSLBF-Y10-3), and the Natural Science Foundation of Jiangsu province (No. BK20131105).

## REFERENCES

- [1] Balmer, G.G., "Shearing Strength of Concrete under High Triaxial Stress Computation of Mohr's Envelope as a Curve," Structural Research.
- [2] Lab, Report No. SP-23, U.S. Bureau of Reclamation, 1949, 13 pp Scott, B.D.; Park, R.; and Priestley, M.J.N., "Stress-Strain Behavior of Concrete Confined by Overlapping Hoops at High and Low Strain Rates," ACI JOURNAL, Proceedings V. 79, No. 1, Jan.-Feb. 1982, pp. 13-27.
- [3] ACI Committee 318, "Building Code Requirements for Structural Concrete (ACI 318-99) and Commentary (318R-99)," American Concrete Institute, Farmington Hills, Mich., 1999, 391 pp.
- [4] Richart, F.E., Brandtzaeg, A., and Brown, R.L., "A Study of the Failure of Concrete Under Combined Compressive Stresses," Bulletin No. 185, University of Illinois, Engineering Experimental Station, 1928, 104 pp.

- [5] Richart, F.E., Brandtzaeg, A., and Brown, R.L., "The Failure of Plain and Spirally Reinforced Concrete in Compression," Bulletin No. 190, University of Illinois, Engineering Experimental Station, 1929, 74 pp.
- [6] Miryauchi K., Nishibayashi S., Inoue S. Estimation of strengthening effects with carbon fiber sheet for concrete column. In: 3rd Int. Symp of non-metallic reinforcement for concrete structures; 1997.
- [7] L. Lam, J.G. Teng, C.H. Cheung, Y. Xiao. FRP-confined concrete under axial cyclic compression[J]. *Cement & Concrete Composites* 28 (2006) 949–958.

# Research on the fracture toughness of PC/ABS blend

Ming-Hsiung Ho & Jung-Peng Yeh

*Department of Mechanical Engineering, Taoyuan Innovation Institute of Technology, Zhongli, Taiwan, R.O.C.*

Pin-Ning Wang

*Department of Material and Fiber, Taoyuan Innovation Institute of Technology, Zhongli, Taiwan, R.O.C.*

**ABSTRACT:** In this dissertation, fracture toughness of PC/ABS blend was studied. The specimens were prepared under various injections molding conditions, such as filling time, melting temperature, and mold temperature. The fracture mechanisms were examined using a scanning electron microscopy. The following conclusions can be drawn from the tests. The best injection molding conditions of fracture toughness specimen were filling time of 2 seconds, melting temperature of 260°C, and mold temperature of 55°C. The fracture toughness is varied according to skin layer normalized thickness. The stress-whiten, splits, and fibril-like surfaces were typical fracture mechanisms.

**Keywords:** PC/ABS; blend; injection molding condition; fracture toughness; skin layer

## 1 INTRODUCTION

PC/ABS is product of amorphous, thermoplastic polymer blends on the basis of polycarbonate (PC) and Acrylonitrile-Butadiene-Styrene (ABS). PC/ABS combines the excellent properties of the two materials, ABS formability and PC material mechanical, impact strength, heat resistance, and resistance to weather ultraviolet (UV) properties. The material usually used in household, electrical, electronic automotive interior, exterior parts, precision machine parts, food industry, etc. For parts forming methods, the injection molding method has excellent surface accuracy, short processing cycle, low cost, and can be used to molding complex shapes.

The fracture toughness research in plastic is still quite limited, because of the complex structure of the plastic material and the varied fatigue characteristics. To make plastic materials such as metal materials widely used in industry and vehicle industry, the material fatigue properties must have systematic study and discussion.

Lu, M.L. et al. (1996) they studied elastic-plastic fracture toughness of a PC/ABS blend by the conventional J-integral and the Crack Tip Opening Displacement (CTOD) methods. Abuzar E.O. et al. (2014) has been investigated fracture behavior of ABS polymeric material under the full range of in-plane loading conditions using a new loading device to obtain more reliable results. Li H. et al. (2015) experimentally investigated the mixed-mode fracture of PC/ABS alloy. The appearance,

growth, and coalescence of crazes can be observed in the micro-fracture processes, and the macro-crack propagation direction is finally determined by the coalesced direction of crazes. Lee S.K. et al. (2012) they found that addition of PC could have toughened recycled PMMA matrix under impact test conditions.

Because PC/ABS blend is processed and formed by some factors, it needs to find out suitable conditions for its applications.

In this study, the investigative object of PC/ABS material was using the injection molding method for forming a test specimen and following ASTM E399 standard to explore the material properties under different filling times, melt temperatures, and mold temperatures. It was evaluated that the PC/ABS plastic material properties with molding conditions and low cycle fatigue testing conditions. After the experiment, the specimen fracture surfaces were examined with the scanning electron microscope, in order to understand the related fracture mechanism.

## 2 METHODS

### 2.1 Material

The material used in this study is the GE (General Electric) produces granular PC/ABS plastic. The material brand name is Cycloy-C1110HF. The volume percentage of containing the PC and the ABS is 60% and 40%, and the average density is 1.13 g/cm<sup>3</sup>.

## 2.2 Specimen preparation

The injection mold layout is shown in Figure 1. The test specimens used in experiments are melting glue injection from the tail end.

The molding conditions were filling time set to 2/6/12/14 seconds, melt temperature designed for 200/220/240/260/280°C and mold temperature was set to 35/50/65/80°C. The specimen number and the detailed conditions of the molding are listed in Table 1.

During the injection molding, the material was preheated at 110°C for 4–6 hours to get rid of the moisture before it can be used in an injection molding machine. The specimens were cooled to room temperature in atmosphere, after the specimens being ejected out of the mold.

## 2.3 Fracture toughness test

The Experiment planning and methods were followed ASTM E399 standard. Because of the test

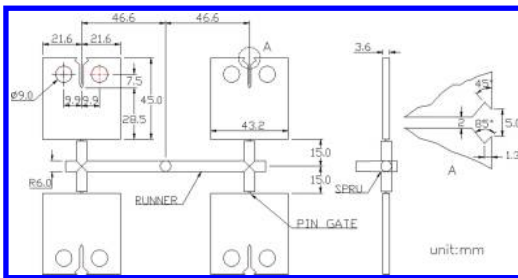


Figure 1. The layout in injection mold.

Table 1. Specimens forming conditions.

Number	Conditions		
	Filling time (s)	Melting temperature (°C)	Mold temperature (°C)
T2	2	260	80
T6	6	260	80
T12	12	260	80
T14	14	260	80
M200	2	200	80
M220	2	220	80
M240	2	240	80
M260	2	260	80
M280	2	280	80
C35	2	260	35
C50	2	260	50
C65	2	260	65
C80	2	260	80

piece initial crack length  $a$ , in accordance with specifications should be between  $0.45 W$  to  $0.55 W$  ( $W = 36$  mm is specimen width). The total length of cracks in this test is to take  $a = 18$  mm, in which the injection molding crack is 7.5 mm. The crack length from 7.5 mm to 16 mm was produced by mechanical processing methods. The last 2 mm is by fatigue pre-crack method.

The specimens were test by MTS 810 100 kN servo-hydraulic testing machine. The PC/ABS specimens with different molding conditions after pre-crack were tensile loading till specimen broke. The load-crack opening displacement data was recording.

The load and displacement data on the slope of the linear range to take five percent deviation obtained material load  $P_Q$ , and calculate the fracture toughness  $K_c$  of the material, the relationship is:

$$K_c = \frac{P_Q}{BW^{1/2}} f\left(\frac{a}{W}\right) \quad (1)$$

and

$$f\left(\frac{a}{W}\right) = \frac{\left[2 + \left(\frac{a}{W}\right)\right] \left[0.886 + 4.64\left(\frac{a}{W}\right) - 13.32\left(\frac{a}{W}\right)^2 + 14.72\left(\frac{a}{W}\right)^3 - 5.6\left(\frac{a}{W}\right)^4\right]}{\left[1 - \left(\frac{a}{W}\right)\right]^{3/2}} \quad (2)$$

After the test, specimen fracture surface was observed by a Scanning Electron Microscope (SEM).

## 3 RESULTS AND DISCUSSIONS

### 3.1 Normalization thickness

As showed in Figure 2, in the pre-crack and pull off surface after the test, the test specimens had whitening phenomenon at fracture surface. This is a stress whiten phenomenon. The phenomenon are also occurs in pure PPO, HIPS, PPO/HIPS blend materials. Moloney (1989) had explained the

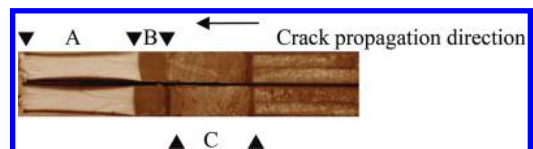


Figure 2. The stress whiten in damage area.

phenomenon: Because skin molecule along a direction perpendicular to the tension direction, when the force to make the epidermis molecular forward direction pull in the same direction, causing whitening phenomenon. The color of layer is changed because the molecule orientation rearrange after external force applied. After force applied process, the surface layer has a lower density and a lower light reflectivity than the original material. A is damage area, B is pre-cark area, C is machining crack area.

The SEM microstructure of Compact Tension (CT) test specimen in thickness direction which is perpendicular to the molecular orientation is showed in Figure 3.

Figure 4-6 are the skin layer normalized thickness distribution under different injection mold conditions in the vertical compact tension specimen thickness direction. The figures show that the material's maximum skin layer normalized thicknesses are in mold temperature of 35 °C, melt temperature of 200 °C and the filling time of 2 seconds. The maximum skin layer normalized thickness decreases downwards as the filling time, melt temperature, and mold temperature increases.

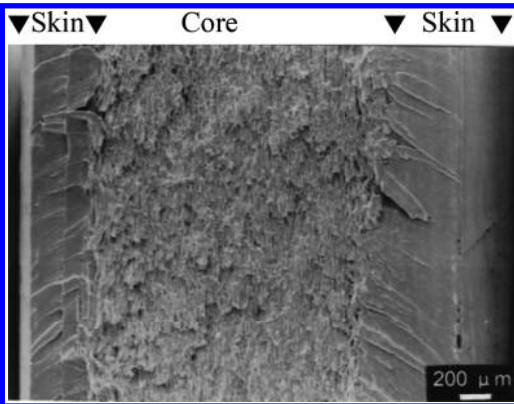


Figure 3. The fracture surface of skin and core layers of M280.

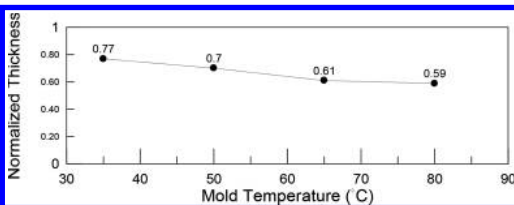


Figure 4. The relationship between mold temperature and skin layer normalized thickness.

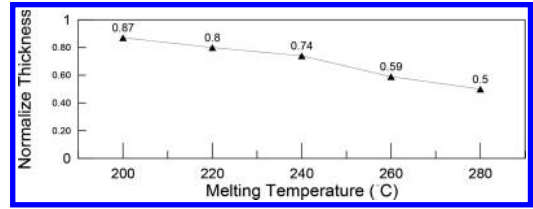


Figure 5. The relationship between melt temperature and skin layer normalized thickness.

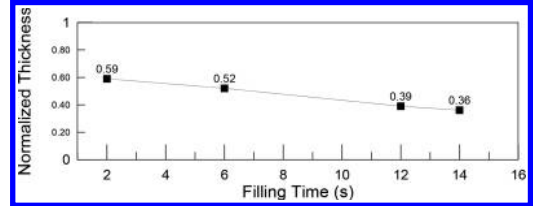


Figure 6. The relationship between filling time and skin layer normalized thickness.

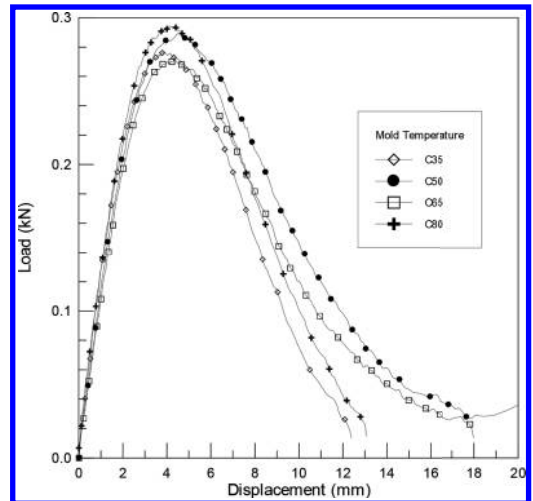


Figure 7. The load—crack open displacement curves under mold temperature conditions.

### 3.2 Fracture toughness

Figures 7-9 show that the load and crack open displacement curves belong to TYPE I as shown in E399, the load that is by 5% deviation slope method to determine  $P_5$  and to locate  $P_{max}$ .

From Figure 10, the mold temperature had little effect on the  $K_{Iq}$ , the difference between the maximum and minimum value is only  $0.84 MPa\sqrt{m}$ , when compared to melt temperature and filling time conditions, the difference value is small.

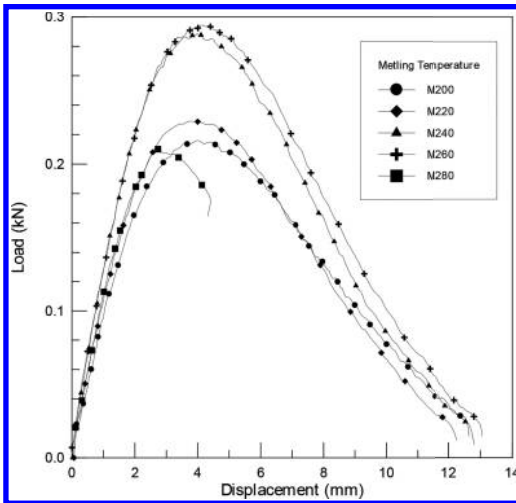


Figure 8. The load–crack open displacement curves under mold temperature conditions.

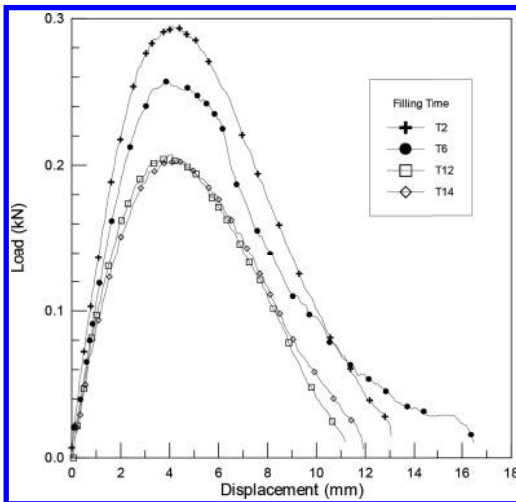


Figure 9. The load–crack open displacement curves under mold temperature conditions.

And overall  $K_q$  values at mold temperature conditions are higher than other molding conditions. Although D80 (M260, T2) in mold temperature conditions is order 3, but in the melt temperature and filling time conditions have maximum  $K_q$  value.

Effect of melting temperature from Figures 8–11 observed, the  $K_q$  gradually increased from M200 to a maximum value M260, but M280 namely drop. In Figure 12, under filling time conditions, the time increases, and the  $K_q$  values decline. The  $K_q$  value of T12 and T14 is the smallest. It is showed

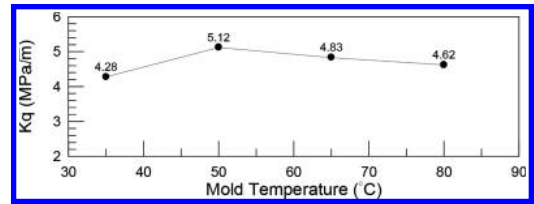


Figure 10. The mold temperature conditions for  $K_q$ .

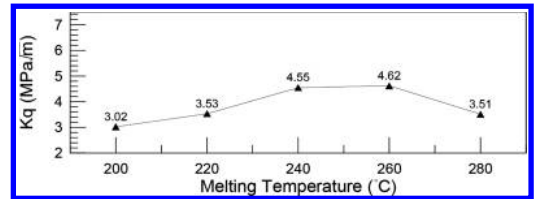


Figure 11. The melt temperature conditions for  $K_q$ .

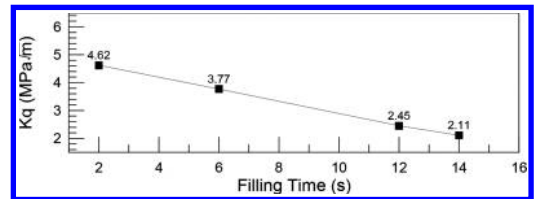


Figure 12. The filling time conditions for  $K_q$ .

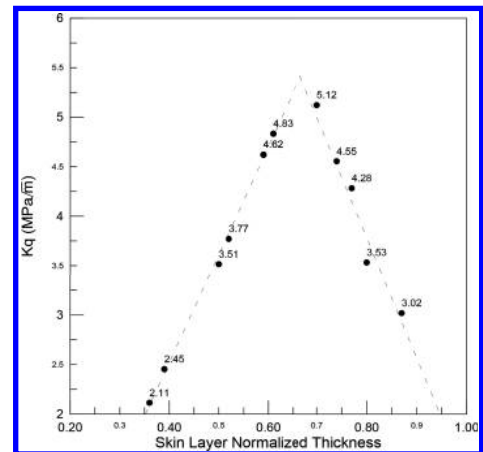


Figure 13. The relation between  $K_q$  and skin layer normalized thickness.

that too long fill time did not help for the fracture toughness. Figure 13 shows the relationship between normalization skin layer thickness and fracture toughness. The data could be divided into two linear regression lines, the two lines intersection



point of the normalized thickness is 0.67 and the value of fracture is  $5.41 \text{ MPa}\sqrt{m}$ . From the point, the optimum injection molding conditions will be filling time 2 seconds, melt temperature  $260^\circ\text{C}$ , mold temperature of  $55^\circ\text{C}$ .

When the skin layer normalized thickness is less than 0.67 and fracture toughness relationship would be  $K_q = -1.83 + (\text{skin layer normalized thickness}) * 10.88$ .

The skin layer normalization thickness greater than 0.67, and the fracture toughness relationship would be  $K_q = 13.51 + (\text{skin layer normalized thickness}) * (-12.16)$ .

### 3.3 Fracture mechanisms

From Figures 2 and 3, the main failure mechanism with a pre-split and pull off during the test, the specimen notched end and crack edges have stress whitening phenomenon. The specimen fatigue pre-crack area with pull-off area of the fracture surface microscopic observations, showing: cracks in the front end of the pre-split region into a laminated sheet-like intermediate core layer of soft material.

Pull off both sides of the zone of hard epidermis tissue, showing the sheet flat section. Intermediate core layer section into hairy pulled fiber, shows the core layer molecular orientation and into a vertical section.

## 4 CONCLUSIONS

The results, process conditions of this chapter for a comprehensive PC/ABS plastic material fracture toughness can be summarized as follows:

1. The destruction of compact tension toughness test specimens from the surface to the center of the fiber orientation can be divided into two regions, the epidermis molecular forward parallel to the direction of flow of melt glue.

The central part of the core layer molecular forward perpendicular to the direction of flow of melt glue.

2. The relation between skin layer normalized thickness and fracture toughness  $K_q$  has a critical value that has a skin layer normalized thickness 0.67 and fracture is  $5.41 \text{ MPa}\sqrt{m}$ .
3. For this optimum value estimates from Figure 13, the injection molding conditions for filling time 2 seconds, melt temperature  $260^\circ\text{C}$ , mold temperature of  $55^\circ\text{C}$ .
4. In skin layer area, the surface is like a sheet of brittle fracturing. The core section has pulled out fiber; it shows the core layer molecular orientation which is perpendicular to the cross section.

## ACKNOWLEDGMENTS

In this paper, the research was sponsored by the Ministry of Science and Technology (Project No. MOST 103-2221-E-253-009).

## REFERENCES

- Abuzar E.O. 2014. Experimental and numerical investigation of fracture of ABS polymeric material for different sample's thickness using a new loading device. *Polymer Engineering & Science* 54(9): 2086–2096.
- Lee S.K. 2012. Mechanical Properties and Fracture Morphology of Blends of PC with PMMA, *International Polymer Processing* 27(5): 626–630.
- Li H. 2015. Experimental investigation on the essential work of mixed-mode fracture of PC/ABS alloy. *Journal of Mechanical Science and Technology* 29(1): 33–38.
- Lu, M.L. 1996. Elastic-plastic fracture toughness of PC/ABS blend based on CTOD and *J*-integral methods. *Polymer* 37(19): 4289–4297.
- Moloney A.C. 1989. *Fractography and Failure mechanisms of Polymers and Composites*. Elsevier Science Publishers Ltd.

# Research on anti-aging performance of high modulus asphalt

Hui Wei

*School of Transportation Engineering, Changsha University of Science and Technology, Changsha, China*

Wei Cao

*Henan Vocational and Technical College of Communications, Zhengzhou, China*

Wei Li & Xi Guo

*State Engineering Laboratory of Highway Maintenance Technology, Changsha University of Science and Technology, Changsha, China*

**ABSTRACT:** In order to study the dynamic mechanical rheological properties of high modulus asphalt after aging, the strain sweep, viscoelasticity cumulative deformation and low-temperature creeping performance of RTFOT asphalt and PAV asphalt are analyzed by Dynamic Shear Rheological (DSR) and Bending Beam Rheometer (BBR). The result shows that (1) storage modulus  $G'$ , loss factor  $\tan\delta$  and delayed elastic recovery index  $\epsilon_p/\epsilon_L$  can accurately evaluate the mechanical properties of different types of asphalt before and after aging, among them, and aging reduces the high modulus asphalt low-temperature performance; (2) the anti-aging performance are different according to the results of different mechanical rheological indicators. The aging resistance of low-temperature, medium, and high temperature indicators are opposite. Above all, for anti-aging performance of high modulus asphalt, it is suggested to select reasonable experimental parameters and combine with the dominant factor indexes for comprehensive evaluation.

**Keywords:** road engineering; high modulus asphalt; dynamic mechanical rheological properties; low-temperature creeping performance

## 1 INTRODUCTION

High Modulus Asphalt Concrete (HMAC), which originated from Germany is mainly used to solve the plastic deformation which is produced by overloading, and improve high temperature rutting resistance by improving the dynamic modulus of asphalt concrete. HMAC properties is studied and put forward the PG grade range, and the high-temperature rut resistance, low-temperature crack resistance, and water stability are evaluated in literatures [1][2]. The corresponding high modulus asphalt modifiers are developed by studying SBS\PE material performance in literatures [3][4]. The climate, traffic conditions and vehicle operating conditions are quite different from foreign country, so the study of high modulus concrete can not completely refer to foreign research. Therefore, it is necessary to independently research and invent high modulus asphalt binder.

However, the high modulus asphalt research is at an early stage in China. There are no standard about performance evaluation and material composition of the high modulus asphalt concrete. The study

is less in long-term mechanical analysis, anti-aging performance (especially long-term aging states), and so on. In this paper, creep recovery testing, low temperature creeping test and other performance tests under different high modulus asphalt states are carried out by using SHRP. The anti-fatigue performance and crack resistance under different aging states are researched. The reasons for difference of high temperature mechanical properties of different high modulus asphalt basing on delayed elastic deformation recovery features are analyzed by Burgers model.

## 2 RAW MATERIALS AND TEST PLAN

Currently, high modulus asphalt concrete using in highways primarily is on-site modification processing, which can reduce costs and keep the excellent properties of modified asphalt. This test is consistent with the real project. High modulus asphalt is laboratory batch processing product. Test instruments are dynamic shear rheometer and asphalt thin-film oven. Test plan is as follows:

In order to analyze conveniently, three different basis bitumen (Shell 70 #, Panjin 70 # and Liaohe 70 #); According to SHRP standard parameters, long-term and short-term aging tests are developed; In repeated creep test, temperature parameters is 60°C, stress is 100 pa, and 20 cycles is under loading 1 s and unloading 9 s. Three parameters are selected in low temperature stiffness creep experiments (BBR), which are temperature parameter (-5°C, -10°C and -24°C).

### 3 EFFECT OF AGING ON THE VISCOELASTIC PERFORMANCE

Under different working conditions, asphalt shows different viscoelastic performance. It needs to further study viscoelastic performance because of the difference of high modulus asphalt, basis bitumen and modified bitumen. Many studies show that mechanical dynamic performance of modified bitumen is closed to the elastic behavior of material in literatures [5][6]. Through proceeding 20 creep recovery of three kinds of asphalt before and after aging under 100 pa (stress) and 60°C (temperature), this paper analyzes the viscoelastic properties by Burgers model parameters.

Figure 1 shows that strain curve of three kinds of asphalt under former three creep recoveries. Because the main component content of asphalt is different, the creep recovery strain appeared differences with the extension of the time. Creep deformation of Shell basis bitumen is much larger than LH and PJ. Accumulated strain is large with the extension of time, while LH and PJ basis bitumen are smaller and show the recovery ability after loading. As  $T = 150$  s, three strains are 115.6%, 0.63%, and 1.77%. The accumulated strains show a significant difference. At the same time, it explains that sticky ingredients of Shell basis bitumen is the main proportion which basically does not change with time except having a small elastic recovery at beginning, and Shell basis bitumen is viciousness creep deformation while LH and PJ are delayed elastic deformation.

It proposed that strain and compliance of the general basis bitumen depends on temperature dependence is totally different from other modified asphalt in literature[6]. Basis bitumen creep cumulative deformation's dependence on temperature is uniform decline and change is relatively simple, while the modified asphalt is more complicated. Permanent deformation of high modulus asphalt increases significantly, after aging, and the anti-aging ability of three kinds of asphalt have significant differences. PJ asphalt is most affected by the factors, the second is LH asphalt, and Shell asphalt which is minimum. Compared with before

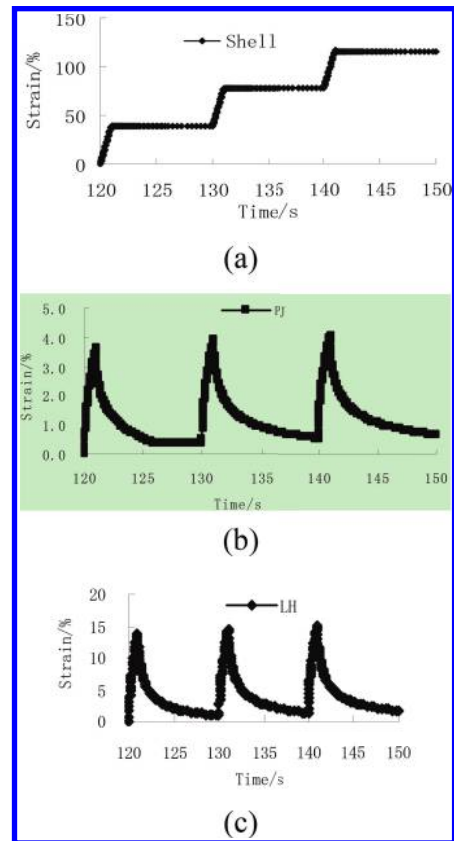


Figure 1. Asphalt before 3 creep state is restored.

aging, PJ asphalt increases 44.871 times, while LH asphalt increases 37.206 times and Shell increases 32.234 times. It shows that accumulative strain of Shell basis bitumen increases in the minimum after aging and PJ improves the sharpest. Four components of asphalt changes after aging, and viscous ingredient ratio increases.

### 4 EFFECT OF AGING ON THE ANTI-FATIGUE PERFORMANCE

Study of fatigue properties of viscoelastic materials contributes to extend the service life of pavement and has important significance to later road maintenance. To test three kinds of asphalt with RTFOT and PAV, fatigue performance is analyzed by using the rheological parameter  $G'$ ,  $\tan(\delta)$  and  $G^*\sin(\delta)$ . The results are shown in Figure 2.

Figure 2 shows:

1.  $G'$  and  $G^*\sin(\delta)$  of three kinds of asphalt further increase with RTFOT and PAV aging, and  $\tan(\delta)$  reduces. Rangeability of the rheological

parameters is different on account of asphalt types. Literature [7] indicates that RTFOT aging can simulate asphalt mixture performance during the construction, and PAV aging can simulate the road running 5–10 years field conditions. It can be used 10 h TFOT to evaluate

its aging-resistant performance on heavy traffic paving asphalt and penetration index to evaluate the fatigue performance before and after aging.

- $G'$  and  $\tan(\delta)$  of Shell asphalt change significantly under different aging states. Sensitivity of  $G'$  reduced with temperature increasing while  $\tan(\delta)$  rising. For PJ and LH asphalt, different aging states influence to  $G'$  is similar to Shell asphalt, while the change of  $\tan(\delta)$  is different.  $\tan(\delta)$  affected by RTFOT aging is weak, and by PAV aging is stronger.  $\tan(\delta)$  of RTFOT and original asphalt decrease with temperature increasing, while  $\tan(\delta)$  of PAV asphalt increases. It shows that PJ\LH high modulus asphalt is different with basis bitumen after aging for a long time. The effect of high modulus composite modifier gradually reduces after a long-term affected on asphalt, which urges the changes of  $G'$  and  $\tan(\delta)$  are similar to basis bitumen. In addition, PAV aging can more accurately reflect anti-aging performance of high modulus modified asphalt for a long time, and found features which are not showed in the short time. It is an important assistance for analyzing and choosing modified asphalt.

## 5 EFFECT OF AGING ON THE LOW TEMPERATURE ANTI-CRACKING PERFORMANCE

In this paper, high modulus asphalt after aging is studied with BBR. Correlation analysis is proceeded by selecting 60 S stiffness modulus (S) and rate of change (m). The data is shown in Table 1.

Table 1 shows:

- Creep stiffness modulus of PAV asphalt increases after aging and creep curve rate reduces. The low temperature rheological properties is reduced by aging, and temperature of asphalt adapt to the low temperature crack resistance improves, which is consistent with the anti-fatigue performance analysis.

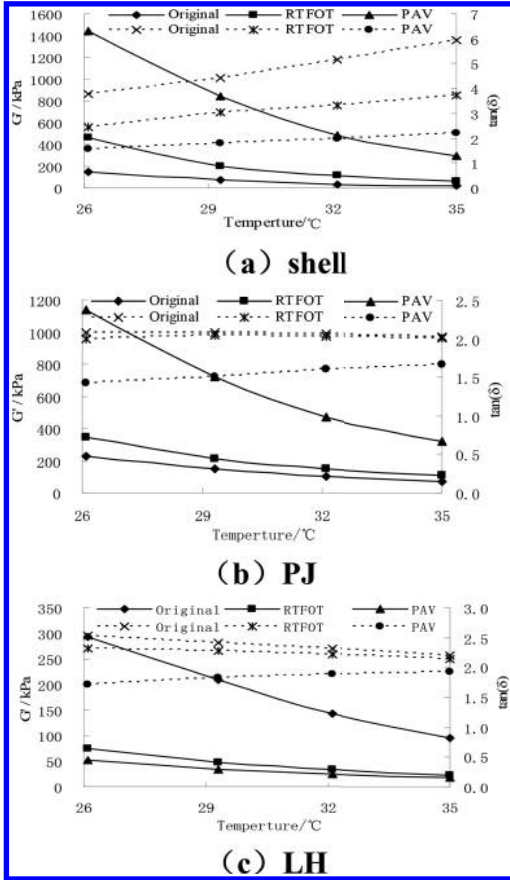


Figure 2. Original asphalt, RTFOT and PAV asphalt  $G'/\tan(\delta)$  along with the change of temperature curve.

Table 1. Three kinds of the original asphalt and PAV asphalt BBR rheological mechanics performance test at different temperatures.

Temperature (°C)	Index	PAV			Original		
		Shell	PJ	LH	Shell	PJ	LH
-5	S/Mpa	65.8	55.6	46.9	45.9	36.6	37.9
	m	0.356	0.413	0.467	0.457	0.484	0.597
-10	S/Mpa	245.5	228.8	189.2	143.3	118.8	123.2
	m	0.296	0.313	0.348	0.369	0.341	0.367
-24	S/Mpa	468.6	368.8	298.5	358.2	278.7	268.9
	m	0.168	0.276	0.307	0.308	0.305	0.317

2. Anti-aging performances of three kinds of asphalt are significantly different. Anti-aging performance of LH asphalt is best and Shell asphalt is the worst. Analysis conclusion about creep stiffness modulus ( $S$ ) and rate of change ( $m$ ) is different with the results of the analysis about high temperature anti-rutting performance and anti-fatigue performance. It mainly exists between PJ asphalt and LH asphalt. Therefore, the analysis of Anti-aging performance about high modulus composite modified asphalt is suggested to be combined with multi-factor index comprehensive evaluation.

## 6 CONCLUSION

1. Aging to high modulus asphalt viscoelastic behavior can have a significant effect. Burgers model analyzes that high modulus asphalt belongs to the delayed elastic recovery deformation, and basis bitumen belongs to viscoelastic rheological deformation.  $\epsilon_L/\epsilon_p$  can evaluate the influence of aging to viscoelastic material delayed elastic deformation which recovers with time increasing.
2. Mechanical rheological parameters  $G'$ ,  $\tan(\delta)$  and  $S$  can accurately reflect the dynamic mechanical rheological properties of different aging states of high modulus asphalt and avoid the problem of conventional index for some defects. But the anti-aging ability evaluation conclusion appears inconsistent phenomenon based on the different mechanical rheological parameters, to evaluate index of medium temperature fatigue performance and high temperature rutting performance.
3. The BBR low temperature susceptibility of high modulus asphalt is reduced after PAV aging. The temperature stability is improved and the low temperature anti-cracking performance is reduced. That is consistent with penetration index (right temperature) of specification evaluating aged asphalt change law. Using BBR low temperature index can further evaluate the low temperature performance of modified asphalt binder. The LH asphalt low temperature anti-cracking performance is better than the PJ asphalt.

## REFERENCES

- [1] Cui Hua-jie, Li Li-han, Liu Dong. Research on Low-temperature Anti-crack Performance of High Modulus Asphalt Mixture [J]. Journal of High way and Transportation Research and Development, 2014, 31(2):37–53.
- [2] Yang Yan-hai, Liu Yun-quan, Zhu Jian-ping. Study and Performance Test of High Module Pavement Asphalt [J]. Journal of High way and Transportation Research and Development, 2008, 25(s):1–4.
- [3] Zhang Xiao-ning, Yang Peng. Finite element analysis of high modulus asphalt pavement [J], International Journal of Advancements in Computing Technology, Vol.4, No. 2, 2012,02,72–79.
- [4] Zhang Xiao-ning, Yang Peng. Study on simplified test method about fatigue performance of cold patch asphalt mixtures [J], Key Engineering Materials, Vol 417–418, 2010, 01, 493–496.
- [5] Yuan Ying-jie, Zhang Zheng-qi. Applicability of Super pave specification to modified asphalt [J]. Journal of Chang'an University (Natural Science Edition), 2004, 24(1):9–11.
- [6] Li Xiao-ming, Zhang Xiao-ning, Nan Xue-li. Research on sticky elastic dynamic behavior of modified asphalt after aging [J]. Journal of China & foreign highway, 2006, 26(3):269–272.
- [7] Gordon D. Airey, Behzad Rahimzadeh, Andrew C. Collop. Linear Rheological Behavior of Bituminous Paving Materials [J]. Journal of Materials in Civil Engineering. 2004, 16(3):212–220.

# Experimental study on low-intensity self-compacting concrete with non-continuous gradation recycled coarse aggregates

J. Ma

*School of Naval Architecture and Civil Engineering, Jiangsu University of Science and Technology (Zhangjiagang), Suzhou, China*

C.Y. Wu & Z.H. Pan

*School of Architecture and Civil Engineering, Jiangsu University of Science and Technology, Zhenjiang, China*

**ABSTRACT:** This paper aims at the feasibility of preparing a low-intensity self-compacting regeneration concrete using non-continuous graded recycled coarse aggregates. Using the variable-control method, the influences of different recycled coarse aggregates replacement rates on its performance and the compressive strength of concrete cubes with different ages are investigated. The results show that non-graded recycled coarse aggregate can be formulated into self-compacting concrete to meet performance and strength requirements. When the recycled coarse aggregate replacement rate is 50%, its performance is best. The replacement rate, greater than 50%, has little influence on the concrete strength development. The early strength of prepared low-intensity self-compacting concrete grows fast, so the molds can be removed early. If the curing time is larger than 7 days, the replacement rate has little influence on the strength development.

**Keywords:** non-continuous coarse aggregates; self-compacting recycled concrete; regeneration coarse aggregate; strength

## 1 INTRODUCTION

The self-compacting regeneration coarse aggregate concrete is a technology based on the theory on self-compacting concrete. It is in accordance with the technical route of self-compacting high-performance concrete. Waste brick recycled aggregates, waste concrete and hybrid-brick waste recycled aggregates are used to prepare the concrete with little vibration. The regeneration concrete solves the transport, storage and disposing of waste building materials, so enormous social and economic benefits are achieved and promising future is expected. Regeneration concrete technology is generally considered the most effective solution to the waste concrete (Xiao 2008).

Available research shows that comparing with natural aggregates, recycled aggregates are of high porosity, liquid absorption and mobility due to the attached large amount of cement mortar on the surface. Therefore whether the mobility, through ability and segregation resistance of the regeneration of self-compacting concrete satisfy the requirements is a key (Jia et al. 2014). Comparing with the high-strength self-compacting concrete, the water-cement ratio of the low intensity self-compacting

concrete is larger, so that the mobility of the concrete blend is guaranteed but the segregation resistance and water retention are difficult to meet the requirements. Therefore, the high mobility, segregation resistance and water retention are mutually contradictory to each other. So the reasonable raw material mixture and reasonable choice of additives are necessary to reach the high mobility, segregation resistance and water retention of the fresh concrete (Zhang et al. 2013).

Current research on the regeneration concrete mainly focuses on the traditional concrete, with little attention paid to the recycled coarse aggregates for the high performance concrete. Most of the aggregates used are consecutive gradation recycled coarse aggregates, and research on the simple and economic single grain degradation coarse aggregates is rare. Based on the existing research (Kou & Poon 2009, Liu 2010, Ramanathan et al. 2013), influences of the replacement rate of recycled coarse aggregate on the regeneration self-compacting concrete are studied in order to find the method for preparing a low-intensity self-compacting regeneration concrete using non-continuous graded recycled coarse aggregates.

## 2 MATERIALS AND TEST METHOD

### 2.1 Materials

1. The P•C 32.5 grade combined Portland cement with the apparent density of 3.1 g/cm<sup>3</sup> is used in the test.
2. The Grade I flyash with the apparent density of 2.04 g/cm<sup>3</sup> is used to make up of 20% of the cementitious material.
3. The medium sand with the fineness modulus of 2.36 is used. Its apparent density is 2.65 g/cm<sup>3</sup>. Its bulk density is 1.45 g/cm<sup>3</sup>. And its sand test rate is 45%. The sieve analysis test of sand is showed in Table 1.
4. The 5–20 mm continuous grain size gravel with the apparent density of 2.75 g/cm<sup>3</sup> is used as natural coarse aggregate. Its bulk density is 1.35 g/cm<sup>3</sup>. The percent passing of natural coarse aggregate is showed in Table 2.
5. The 10–20 mm recycled coarse aggregate with broken brick has the apparent density of 2.35 g/cm<sup>3</sup>, the bulk density of 1.23 g/cm<sup>3</sup>, and the water absorption of 4.76%. The percent passing of recycled coarse aggregate is shown in Table 3.

Table 1. Sieve analysis test of sand.

Sieve size (mm)	Sub meter sieve residue		Cumulative retained percentage (%)	Fineness modulus
	Sieve residue (g)	Rate (%)		
4.75	1.73	0.3	0.3	2.36
2.36	18.94	3.8	4.1	
1.18	38.13	7.62	11.72	
0.6	169.43	33.88	45.60	
0.3	167.40	33.47	79.07	
0.15	86.04	17.20	96.27	
Σ	481.67			
Results	Sand type		Degradation	
	Medium sand		ZoneII	

Table 2. Percent passing of natural coarse aggregate.

Nominal size (mm)	Cumulative retained percentage (%)					
	2.36	4.75	9.5	16	19	26.5
<i>Natural coarse aggregates degradation</i>						
Group 1	98.2	93.2	70.6	24.3	2.5	0
Group 2	98.5	95.6	86.1	31.9	3.1	0
Group 3	98.7	94.3	72.7	22.9	4.7	0
Average	98.5	95.4	76.2	26.4	3.4	0

Table 3. Percent passing of recycled coarse aggregate.

Nominal size (mm)	Cumulative retained percentage (%)					
	2.36	4.75	9.5	16	19	26.5
<i>Natural coarse aggregates degradation</i>						
Group 1	97.3	93.8	90.5	44.2	2.4	0
Group 2	96.5	90.1	86.2	40.5	3.1	0
Group 3	97.2	95.1	88.4	37.2	2.7	0
Average	97	93	88.3	40.6	12.1	0

Table 4. Properties of admixture.

Appearance	Solids content	pH (20 °C)	Total alkali content (%)	Cl <sup>-</sup> (%)
Light yellow powder	98 ± 1%	7–9	<5	<0.1

6. The test uses TOJ800-10 polycarboxylate superplasticizer as admixture. The properties of admixture are given in Table 4.
7. The tap water is used.

### 2.2 Test method

The amount of cement, water, sand and fly ash is fixed, with the replace rate of the regeneration aggregates as 30%, 50% and 70%, respectively. Concrete is designed according to the Chinese codes DG/TJ 08-2018-2007 and JGJT 283-2012. The water is divided into two parts: the net and additional amount of water. The net amount of water is calculated based on DG/TJ 08-2018-2007. The additional amount of water is determined by the water absorption ratio of the regeneration aggregates. The coarse aggregates are divided into the natural and recycled aggregates, the amount of which is calculated based on the mass-volume relations. To investigate the influences of different raw materials on the performance of fresh concrete and the cube compressive strength, only the amount of materials investigated is changed during the test, and the amount of other materials is fixed.

### 2.3 Performance evaluation criteria

The study is based on the replacement ratio of the recycled coarse aggregates, which are 30%, 50%, and 70%, respectively. The additional water consumption is 13.70 kg/m<sup>3</sup>, 22.05 kg/m<sup>3</sup>, and 29.90 kg/m<sup>3</sup>, respectively. A slump flow test, a T<sub>500</sub> test and an L-box test (Rod spacing 60 mm) are conducted to examine the performance of fresh concrete. The slump flow test and the T<sub>500</sub> test are conducted in accordance with

Table 5. Test properties and methods for evaluating self-compacting concrete.

Property	Test method	Performance rate	Technical requirements
Fill ability	Slump flow (mm)	SF1	550–655
		SF2	660–755
		SF3	760–850
	$T_{500}$ (s)	VS1	$\geq 2$
		VS2	$< 2$
Clearance through and segregation resistance	L-box ( $H_2/H_1$ )	I Rod spacing 40 mm	$\geq 0.8$
		II Rod spacing 60 mm	

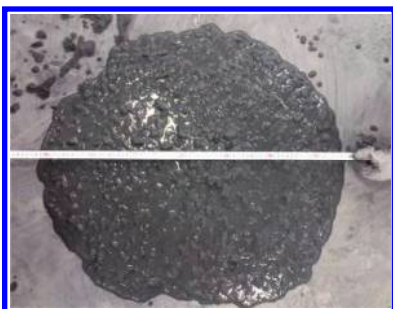


Figure 1. Slump flow test.



Figure 2. L-box test.

the Chinese code JGJT 283-2012, while the L-box test is conducted in accordance with the Chinese code CCES 02-2004. Evaluation details are given in Table 5. Meanwhile, compressive strength values of different concrete cube specimens (150 mm × 150 mm × 150 mm) under 3-days, 7-days and 28-days curing periods are studied in accordance with the Chinese code GB/T 50081-2002. The 60 L compulsory mixer mechanical stirring machine is used for all concrete mixtures, and specimens are placed under standard curing environment. The test procedures are shown in Figures 1–2.

### 3 RESULTS AND ANALYSIS

#### 3.1 Performance of fresh concrete

Firstly, the recycled coarse aggregates are divided into single grains through standard screening procedure, and the gradation adjustment of recycled coarse aggregates is performed in accordance with the Chinese code GB/T 25177-2010. The replacement rates for recycled coarse aggregates are 30%, 50% and 70%, respectively. The test procedure is shown in Figures 1–2, and the results are given in Table 6 and Figures 3–5. According to JGJT 283-2012 and CCES 02-2004, the slump flow rating is SF1 (550–655 mm) when the recycled coarse aggregates replacement rates are 30% and 70%; the slump flow rating is SF2 (660–755 mm) when the replacement rate is 50%;  $T_{500}$  extended time rating is VS1; the L-box test ( $H_2/H_1$ ) rating is grade II.

Figures 3–5 show the fresh concrete slump flow increases along with the recycled coarse aggregates replacement rate. When the replacement rate increases from 30% to 70%, then slump increases first then decreases. It reaches its maximum when the replacement rate is 50% with the slump flow of 700 mm.

The  $T_{500}$  flow time decreases as the recycled coarse aggregates replacement rate increases, and when the replacement rate increases from 30% to 50%, the  $T_{500}$  flow time decreases significantly, and with no further obvious decrease afterwards. When the recycled coarse aggregates replacement rate increases from 30% to 50%,  $H_2/H_1$  obtained by the L-box test increases from 0.80 to 0.85, and the performance of the freshly casted concrete is improved. When the replacement rate increases from 50% to 70%,  $H_2/H_1$  decreases from 0.85 to 0.80, suggesting that the fluidity and filling property of fresh concrete is improved, while the through capacity and segregation resistance decreased. According to the rheology theory, the increase of the recycled coarse aggregates replacement rate in a certain range cause the increase of additional amount of water, which results in the decrease of



Table 6. Results of fresh concrete with different replacements.

Number	Replacement (%)	Slump flow (mm)	$T_{500}$ (s)	L-box		
				$H_1$ (mm)	$H_2$ (mm)	$H_2/H_1$
1	30	640	4.23	90	72	0.80
2	50	700	3.25	100	85	0.85
3	70	650	3.12	100	80	0.80

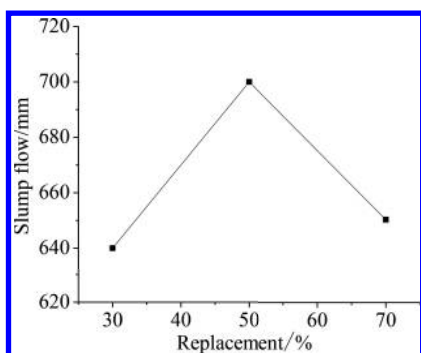


Figure 3. Slump flow with different replacements.

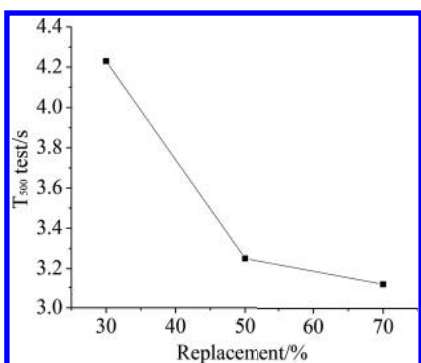


Figure 4.  $T_{500}$  test with different replacements.

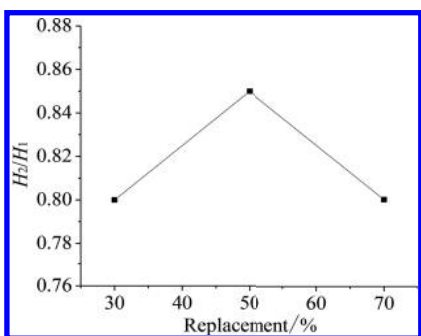


Figure 5. L-box test with different replacements.

the plastic viscosity of concrete mixture, so the fluidity, through capacity and segregation resistance are improved. When the replacement rate is 70%, the additional water amount increases further and the plastic viscosity of the concrete mixture decreases below the critical point at which the performance can be guaranteed, resulting in the decrease of the performance. The test results show that non-continuous gradation of recycled coarse aggregates can be formulated to meet the performance requirements of self-compacting concrete. The best working performance is reached when the recycled coarse aggregates replacement is 50%, with the slump flow of 700 mm,  $T_{500}$  flow time of 3.25 s and  $H_2/H_1$  of 0.85.

### 3.2 Compressive strength of cubes

#### 3.2.1 Failure of specimens

The stresses of self-compacting regeneration concrete specimen increases with the increase of load. Cracks occur in the specimen. Cracks began to appear on the surface in the middle of the test specimen, and then developed gradually along the oblique direction up and down to the corners of the specimen, appearing a V shape in the final. With further increase of stress in the concrete, surface cracks heaved and crushed concrete began to fall, appearing an X-cone shape in the final. From the failure pattern, the destruction of renewable self-compacting concrete is similar to the ordinary concrete, as bonds between aggregates cement are destroyed and no crushing of the recycled coarse aggregates is found. This is in good agreement with Xiao et al. (2004). Figure 6 shows the compressive failure mode of a self-compacting recycled cubic concrete specimen.

#### 3.2.2 Development of cube strengths

The compressive strength values of 3-days, 7-days and 28-days cube concrete specimens under different replacement rates are given in Figure 7.

It can be seen from Figure 7 that for 3 d and 7 d ages, the strengths of concrete with different ages decrease when the replacement rate of recycled coarse aggregate increases from 30% to 50%. However, when the replacement rate increases



Figure 6. Failure mode of cubic specimen.

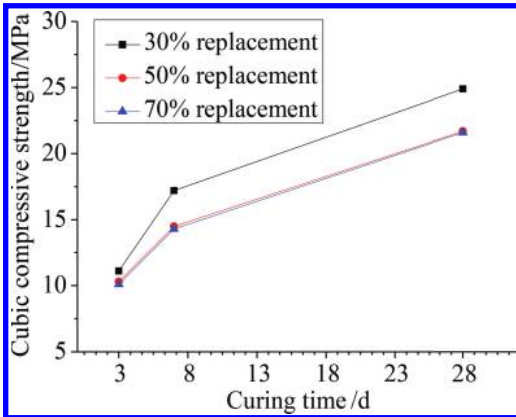


Figure 7. Cubic compressive strength versus curing time.

from 50% to 70%, there is almost no change of the concrete strength, and the strength development rate is basically the same. For 7 d and 28 d ages, the strength values of concrete with different ages decrease when the replacement rate increases from 30% to 50%. When the replacement rate increases from 50% to 70%, the concrete strength is nearly unchanged. The strength development rate is basically the same under three different replacement rates, which indicates that the replacement rate has a minor influence on the strength development. The reason that strength decrease along with the replacement rate is probably that with the increase of the replacement rate, the additional amount of water increases, and hence the water-cement ratio increases indirectly. Meanwhile, it may also be attributed to the decrease of the performance of the interface between recycled

coarse aggregates and both new and old mortars. In addition, the 28 d compressive strengths of regeneration self-compacting concrete cube specimens prepared under different replacement rates all satisfy the strength requirements. And the early strength develops fast as the 3 d strength can reach the 50% of the design strength; the 7 d compressive cube strength can be more than 70% of the design strength, so that molds can be removed early. The strength development in the late stage is obviously slower than that of the early stage, which is mainly due to the incorporation of polycarboxylate superplasticizer as the early hydration of cement is promoted.

#### 4 CONCLUSIONS

1. Non-continuous graded recycled coarse aggregates can be formulated to meet the working performance requirements of low-intensity self-compacting concrete. The best performance is reached when the recycled coarse aggregates replacement rate is 50%.
2. The 28 d compressive strength values of self-compacting regeneration concrete cube specimen under different replacement rates satisfy the strength requirements of C20 concrete. When the recycled coarse aggregates replacement rate is greater than 50%, the replacement rate has little influence on the concrete strength development.
3. The early strength of prepared low-intensity self-compacting regeneration concrete grows fast and molds can be removed early accordingly. The recycled coarse aggregates replacement rate has little influence on the strength development after 7 days.

#### REFERENCES

- Chinese Civil Engineering Society Standard. 2005. *Design and construction guidelines of self-compacting concrete (CCES 02-2004)*. Beijing: China Building Industry Press.
- Jia, Y., Wang, Y. & Sun Z. 2014. Study on the design and the mechanical test of regeneration self-compacting concrete. *Sichuan Building Science* 40(1): 241–244.
- Kou, S.C. & Poon, C.S. 2009. Properties of self-compacting concrete prepared with coarse and fine recycled concrete aggregates. *Cement & Concrete Composites* 31(9): 622–627.
- Liu, M. 2010. Self-Compacting concrete with different levels of pulverized fuel ash. *Construction & Building Materials* 7(24): 1245–1252.
- People's Republic of China Ministry of Housing and Urban-Rural Development. 2011. *Technical regulations of self-compacting concrete applications (JGJT 283-2012)*. Beijing: China Building Industry Press.

- People's Republic of China Ministry of Construction. 2003. *Experimental test methods on ordinary concrete (GB/T 50081-2002)*. Beijing: China Building Industry Press.
- People's Republic of China State Administration of Quality Supervision. 2010. *Recycled concrete aggregates (GB/T 25177-2010)*. Beijing: China Standard Press.
- Ramanathan, P., Baskar, I. & Muthupriya, P. 2013. Performance of self-compacting concrete containing different mineral admixtures. *Journal of Civil Engineering* 17(2): 465–472.
- Shanghai Construction and Transportation Commission. 2007. *Technical specification of regeneration concrete applications (DG/TJ 08-2018-2007)*. Shanghai: Tongji University Press.
- Xiao, J., Li, J. & Sun, Z. 2004. Research on the compressive strength of recycled concrete. *Journal of Tongji University (Natural Science Edition)* 32 (12): 1558–1561.
- Xiao, J.Z. 2008. *Regeneration concrete*. Beijing: China Building Industry Press.
- Zhang, X., Zhao, X. & Zhang, P. 2013. Experimental research on the mix ratio optimization of low-intensity self-compacting concrete. *Concrete* 5: 124–126.

*Engineering management*

# Study on the pre-evaluation of the bench blasting effect based on the uncertainty measurement theory

T.J. Tao, M.S. Zhao & Q. Kang

Guizhou Xinlian Blasting Engineering Group Co. Ltd., Guiyang, Guizhou, China

**ABSTRACT:** In order to resolve the uncertainty problem of influence factors of bench blasting effect pre-evaluation, the pre-evaluation model of the bench blasting effect based on the uncertainty measurement theory was built. Then, this model was used to pre-evaluate the bench blasting effect in Hongshuitai flat engineering. The pre-evaluation results show that the information entropy and confidence identifying criterion were, respectively, used to ascertain the pre-evaluation index weight and identifying criterion. In this way, the pre-evaluation results of this model are found to be more objective, and the pre-evaluation index can be selected flexibly according to the actual situation. The calculation of the evaluation model is found to be simple, so the evaluation results can offer a decision basis for blasting workers to make timely adjustment of the blasting scheme.

**Keywords:** uncertainty measurement theory; bench blasting effect; pre-evaluation; factor index

## 1 INTRODUCTION

With the development of national economic construction, the bench blasting has been increasingly applied in many areas such as mining, cutting shaping of rail and road, and facilities construction of water and hydropower. So, how to achieve an optimum blasting effect has been a topic of concern for the majority of blasting workers. However, in the actual project, as there are many factors that influence the effect of bench blasting, it is difficult to give a reasonable prediction of the blasting effect. Therefore, the study on the pre-evaluation of the bench blasting effect is of important significance for making an optimal blasting scheme to improve the blasting effect and increase the economic efficiency of blasting engineering. For making an accurate prediction of the bench blasting effect and providing a judging decision for improving the blasting scheme, a study on the pre-evaluation of the bench blasting effect is needed. However, current studies on the bench blasting effect are scarce, mainly because there are many influencing factors in evaluating the bench blasting effect, and these factors are often mutually influencing, so it is difficult to make the pre-evaluation of the blasting effect. The current evaluation method for the blasting effect mainly uses AHP, fuzzy mathematics and gray correlation analysis. For example, Ma Li established a comprehensive evaluation model of the blasting effect based on the fuzzy mathematical theory. Hu Xinhua established a comprehensive

evaluation model of the blasting effect based on the AHP and gray correlation analysis. In this model, two layers of gray correlation analysis evaluation mode were used. However, as there is uncertainty in determining the influencing factors of the blasting effect, the model based on fuzzy mathematic, AHP and gray correlation analysis often lost the information, and had defects such as existence of subjective misjudgment in weight distribution and determination. In recent years, the uncertainty measurement theory has been used by many scholars to make a comprehensive evaluation for the multi-factor index, and obtained many achievements. This article uses this theory to establish the pre-evaluation model of the blasting effect and study its practical application.

## 2 UNCERTAINTY MEASUREMENT THEORY

### 2.1 Uncertain measure of a single index

Given  $a_1, a_2, \dots, a_i$  indicates  $n$  factors to be evaluated concerning the object, noting  $A = \{a_1, a_2, \dots, a_i\}$ , which is called the 'domain'; each single-factor pre-evaluation index  $a_i$  has  $j$  evaluation grades  $b_1, b_2, \dots, b_j$ , then  $a_{ij}$  is used to indicate the observed value of single factor  $a_i$  as an object to be pre-evaluated on the  $j$ th evaluation grade  $b_j$ . The single-factor evaluation index  $a_i$ , when it is in the  $j$ th grade of comment, is denoted as  $a_{ij}$ . This paper adopts an expert grading method, providing

that the sum of the value of points on the grade of all the comments about each pre-evaluation factor is 100 points. The related experts will give 0–100, respectively, to each grade  $b_j$  of the comment on each pre-evaluation factor  $a_i$ , marking  $\sum_{j=1}^j a_{ij} = 100$ . The use of  $u_{ij} = a_{ij}/100$  indicates that the observed value  $a_{ij}$  makes  $a_i$  stay at the uncertain measure angle of the grade  $b_j$  of the comment.  $u_{ij}$ , as the result of the measure of ‘degree’, is the possibility measure. From this, we can obtain the measurement matrix of a single pre-evaluation index as the evaluated object:

$$u_{ij} = \begin{bmatrix} u_{i1}, u_{i2}, \dots, u_{ij} \\ u_{21}, u_{22}, \dots, u_{2j} \\ \vdots \quad \vdots \quad \dots \quad \vdots \\ u_{n1}, u_{n2}, \dots, u_{nj} \end{bmatrix} \quad (1)$$

where  $i = 1, 2, \dots, n$ .

### 2.2 Determination of the index weight

What is described about the uncertainty of observed values should be the quantitative measurement of uncertainty as well as the distribution function of observed values, which is called the entropy. Entropy was first brought forward in thermo-dynamics by Clautheus and used to describe the state of a system, and in later years, it was introduced to many domains. For a discrete random variable, its information entropy  $S = -k \sum_{i=1}^k P_i \ln P_i$ , where  $P_i \geq 0$ , where  $\sum_{i=1}^n P_i = 1$ . Entropy has such characteristics as symmetric, non-negative, additive and of extreme value. Given the space of natural state  $X = (x_1, x_2, \dots, x_n)$  is an uncontrollable factor. In the formula,  $x_i$  is the state that has occurred. Given the prior probability distribution of each state that occurred in  $X$  is  $P(X) = \{P(x_1), P(x_2), \dots, P(x_n)\}$ . The uncertain extent of this state is defined as an entropy function:

$$H(x) = -\sum_{i=1}^n p(x_i) \ln p(x_i) \quad (2)$$

where  $0 \leq p(x_i) \leq 1$ ,  $\sum_{i=1}^n p(x_i) = 1$ . The observed value  $x_{ij}$  of the evaluated object of the quality of blasting regarding  $a_i$  makes the uncertain measure of the objects that stay at each grade  $b_i$  of comment become  $u_{i2}, \dots, u_{ij}$ . If the uncertain measure  $u_{ij}$  is regarded as  $p_i$  in  $H(x)$ , then we have

$$H(u) = -\sum_{j=1}^j u_{ij} \ln u_{ij} \quad (3)$$

$$v_i = 1 - \frac{1}{\ln j} H(u) = 1 + \frac{1}{\ln j} \sum_{j=1}^j u_{ij} \cdot \ln u_{ij}$$

$$w_i = \frac{v_i}{\sum_{i=1}^i v_i}$$

where  $W_i$  ( $0 \leq W_i \leq 1$ , and  $\sum_{i=1}^i W_i = 1$ ) is the weight of the pre-evaluation index  $a_i$ .

### 2.3 Comprehensive evaluation system

If the measurement matrix of the single pre-evaluation index concerning the evaluated objects is known, then the classified weights of each index about the evaluated objects are obtained from Formula (3). Let

$$u_j = W \cdot u_{ij} = (w_1, w_2, \dots, w_i) \cdot \begin{bmatrix} u_{11} & u_{12} & \dots & u_{1j} \\ u_{21} & u_{22} & \dots & u_{2j} \\ \dots & \dots & \dots & \dots \\ u_{i1} & u_{i2} & \dots & u_{ij} \end{bmatrix} \quad (4)$$

Then,  $u_i$  is a pre-evaluation vector of the blasting as an evaluated object, describing the classification of uncertainty. In order to obtain the classifications of certainty, the difference in confidence needs to be marked. Because the grade division of comment is in order and because the grade  $b_j$  of the  $j$ th comment is ‘better’ than the grade  $b_{j+1}$  of the  $j+1$  comment, the discrimination criterion for the maximum measure is not suitable to this case. We have to use the discrimination criterion of confidence.

Given the confidence is  $\lambda$ , ( $\lambda > 0.5$ ), then 0.6 or 0.7 is usually adopted. Let

$$j_0 = \min_j \left\{ j : \sum_{j=1}^j u_{ij} \geq \lambda, \quad j = 1, 2, \dots, j \right\} \quad (5)$$

Then, it is judged that the pre-evaluated object of the blasting effect belongs to the  $j_0$ th evaluation grade  $b_{j_0}$ .

## 3 CASE TEST

### 3.1 Establishment of the index evaluation system

The theory and the method of systematic engineering are applied to set up an index system of a complete structure, a substantial content and convenient use for evaluating the quality of blasting, so as to provide a basis for making an accurate prediction of the bench blasting effect and providing a judging decision for improving the blasting scheme. This paper presents bench blasting in Hongshuitai flat engineering, as shown in Figure 1.



Figure 1. Bench blasting in Hongshuitai.

A pre-evaluation index system of the bench blasting effect based on the uncertainty measurement theory was established. The index system for the pre-evaluation of the bench blasting effect is presented in Table 1.

### 3.2 Pre-evaluation of the bench blasting effect

The pre-evaluation grades of each single factor for judging the quality of blasting are classified as follows: fine, good, general, relatively poor and poor, so that the experts give 100 points, respectively, to each evaluation grade of single factors, as given in Table 2.

According to Table 2, the matrix of a single-index uncertain measure is obtained as formula (6):

$$u_{ij} = \begin{bmatrix} 0.21 & 0.43 & 0.25 & 0.09 & 0.02 \\ 0.16 & 0.32 & 0.23 & 0.16 & 0.13 \\ 0.23 & 0.36 & 0.15 & 0.16 & 0.10 \\ 0.18 & 0.33 & 0.14 & 0.21 & 0.14 \\ 0.30 & 0.41 & 0.13 & 0.11 & 0.05 \\ 0.22 & 0.42 & 0.17 & 0.11 & 0.08 \\ 0.31 & 0.41 & 0.13 & 0.11 & 0.04 \\ 0.32 & 0.43 & 0.13 & 0.09 & 0.03 \\ 0.20 & 0.44 & 0.15 & 0.16 & 0.05 \\ 0.35 & 0.41 & 0.15 & 0.6 & 0.03 \\ 0.35 & 0.40 & 0.15 & 0.07 & 0.03 \\ 0.32 & 0.41 & 0.12 & 0.10 & 0.05 \\ 0.23 & 0.47 & 0.17 & 0.08 & 0.05 \\ 0.27 & 0.47 & 0.13 & 0.10 & 0.03 \\ 0.26 & 0.46 & 0.16 & 0.08 & 0.04 \end{bmatrix} \quad (6)$$

By Formula (3) to calculate the index weight of the pre-evaluated factors, we can have  $W = (0.084, 0.017, 0.029, 0.017, 0.068, 0.050, 0.074, 0.089, 0.060, 0.096, 0.090, 0.074, 0.0079, 0.091, 0.084)$ .

Table 1. Index system for the pre-evaluation of the bench blasting system.

First class	Second class
Quality of blasting $A_1$	Drilling cost $a_1$
	Forward and backward strokes $a_2$
	Cost of priming materials $a_3$
	Unit consumption of explosives $a_4$
	Coefficient of bulk increase $a_5$
	Shoveling efficiency $a_6$
	Boulder ratio $a_7$
	Toe $a_8$
Safety of blasting $A_2$	Explosion gas $a_9$
	Explosive shock wave $a_{10}$
	Flying rock $a_{11}$
	Blasting vibration $a_{12}$
	Slope stability $a_{13}$
	Dangerous rock $a_{14}$
	Blind shot $a_{15}$

Table 2. Results of the points that the experts give.

Pre-evaluated factors	Evaluation grade				
	Fine	Good	General	Relatively poor	Poor
$a_1$	21	43	25	9	2
$a_2$	16	32	23	16	13
$a_3$	23	36	15	16	10
$a_4$	18	33	14	21	14
$a_5$	30	41	13	11	5
$a_6$	22	42	17	11	8
$a_7$	31	41	13	11	4
$a_8$	32	43	13	9	3
$a_9$	20	44	15	16	5
$a_{10}$	35	41	15	6	3
$a_{11}$	35	40	15	7	3
$a_{12}$	32	41	12	10	5
$a_{13}$	23	47	17	8	5
$a_{14}$	27	47	13	10	3
$a_{15}$	26	46	16	8	4

By means of Formula (5), we determine the final result of evaluation as follows:  $u = (0.278, 0.425, 0.154, 0.0989, 0.044)$ .

Assuming the confidence  $\lambda = 0.7$ , both the discrimination criterion of confidence and Formula (5) are applied to judge that the grade of pre-evaluation of the blasting effect in this bench blasting is the second, namely 'good'. The way of uncertain measure takes notice of the orderliness of the evaluation space and gives a relatively rational criterion for the discrimination of confidence and the code of points for order, as is just what the fuzzy comprehensive evaluation method does not have at all.

The pre-evaluation of the bench blasting effect in the blasting field in Hongshuitai flat engineering is realized by means of a programmed method, favorable to the improvement at the managerial level on the part of the construction project, promoting the safe, reliable and economical and effective operation of blasting construction.

#### 4 CONCLUSION

1. By applying the theory and method of systematic engineering, it conducts and establishes a pre-evaluation factor index system of the bench blasting effect.
2. A criterion is adopted, respectively, for the discrimination of the information entropy and creditability in determining the weight of each evaluation index and the discrimination criterion, therefore avoiding the defects of the fuzzy comprehensive judgment in these two aspects, making the result of the evaluation more objective.
3. A pre-evaluation of the bench blasting effect in the blasting field is realized by means of a programmed method, favorable to the improvement at the managerial level on the part of the construction project, promoting the safe, reliable and economical and effective operation of blasting construction.

#### ACKNOWLEDGMENTS

This work was supported by the grants from the Guizhou Science and Technology Plan Project

(No. SY2010365), the Key Industrial Research Project Supported by Science Technology Department of Guizhou Province (No. (2013) 3013), and the Guizhou Province Outstanding Young Scientific Talents Training Program Funded Projects (No. (2013) 30). The authors gratefully acknowledge their support.

#### REFERENCES

- Hu Xinhua, Yang Xuesheng. Comprehensive Evaluation of the Blasting Effect Based on Grey Correlation analysis [J]. Journal of the Liaoning Technical University (Natural Science), 2008 (27): 142-144.
- Jia Zheng-yuan, Zhao liang. Comprehensive evaluation of power quality based on the model of entropy weight and unascertained measure [J]. Power System Protection and Control, 2010, 38(15): 33-36.
- Jia Zheng-yuan, Zhao Liang. Comprehensive evaluation of power quality based on the model of entropy weight and unascertained measure [J]. Power System Protection and Control, 2010, 38(15): 33-36.
- Ma Li, Li Kemin, Ding Xiaohua, et al. Fuzzy Synthetic Evaluation On Casting Blast Effect Of Heidaigou Surface Coal Mine [J]. Metal Mine, 2011, 423(9): 58-60.
- Shi Xiuzhi, Zhou Jian. Application of Unascertained Measurement Model to Prediction of Classification of Rockburst Intensity [J]. Chinese Journal of Rock Mechanics and Engineering, 2010, 29(Supp. 1): 2720-2726.



# Dynamic analysis on the ballast track application in urban railway tunnels

Yaqun Wang, Xingchen Zhang & Junhua Chen  
*Beijing Jiaotong University, Beijing, P.R. China*

**ABSTRACT:** Aiming at the ballasted track in urban railway tunnels, based on the coupling dynamics theory, a dynamic analysis model of the vehicle-ballast track-tunnel system is established in this paper. The safety index, vehicle stationarity index, index of track's dynamic response, and vibration index were analyzed dynamically by ABAQUS. Finally, the feasibility of the ballast track in urban railway tunnels can be fully demonstrated from the aspects of track structure, tunnels structure, vehicle safety, and passengers' comfort.

## 1 INTRODUCTION

Urban railway has become a top priority as the public infrastructure in many metropolitans in China; meanwhile, in most of the urban railway lines in China, especially in the tunnel line, the structural form of the ballastless track is usually adopted. However, applications of a large number kinds of ballastless track without independent property rights have led to the increase in the costs in preconstruction. Expense of maintenance and replacement of accessories is also a large expenditure in the late stage.

Elasticity of ballastless track is mainly provided by rail fastenings; therefore, there are more stringent requirements for the fastenings structure design, material selection and technical standards. Beyond that, the adjustment of the track geometric status can only be realized by fastenings [1].

Various levels of vibration damping measures are adopted in order to meet the requirements of environmental protection. Some of them work rather well; nonetheless, the problems of vibration damping cannot be solved in many areas. On the contrary, serious abnormal rail corrugations are caused. These factors have restricted the development of urban railway transit to a certain extent [2].

The concept of building ballast tracks inside tunnels has been adopted in many European cities, namely Paris, London, Helsinki, Moscow, and Berlin, and the tracks have been still in use since the last century. Hence, it is crucial for us to inspire their successful experiences [3].

Coupling dynamics theory is used in this paper [4]. A dynamic analysis model of the vehicle-ballast track-tunnel system is established by procedure software of finite element ABAQUS, analyzing

comprehensively the safety index (wheel-rail force, the derailment coefficient, wheel load reduction rate), vehicle stationarity index (vehicle acceleration), index of track's dynamic response (dynamic stress, dynamic displacement), and vibration index (acceleration of rail, tunnel structure). We can analyze the dynamic characteristics of the ballast track in urban railway tunnels from a structure's point of view, and this includes the track structure, tunnels structure, vehicle safety and passengers' comfort in order to support the argument of ballast track feasibility in railway tunnels.

## 2 DYNAMIC ANALYSIS MODEL

The established dynamic analysis model of the vehicle-ballast track-tunnel system in this paper consists of model for vehicle, model for track, model for tunnel, model for wheel-rail interaction and model for track irregularity.

According to the structure of the vehicle and characteristics of the suspension, we model the vehicle. We regard the train body, two bogies and four wheels as a rigid body. Vehicle model becomes a multi-rigid body system that consists of train body, bogie and wheelset. That is, the whole system can be regarded as the composition of four wheels, two bogies and a body, connected by a two-line spring damper element between each other.

The train body and bogie each has five degrees of freedom, that is, the ups, downs, nod, shifting, roll and yaw. Each wheel has four degrees of freedom, that is, the ups, nod, shifting, roll and yaw. The rotary produced by wheel speed uniformity is not considered. Vehicle model is shown in [Figure 1](#).

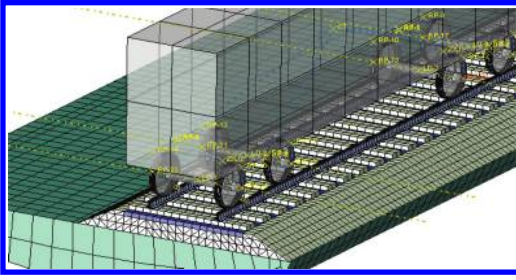


Figure 1. Vehicle model.

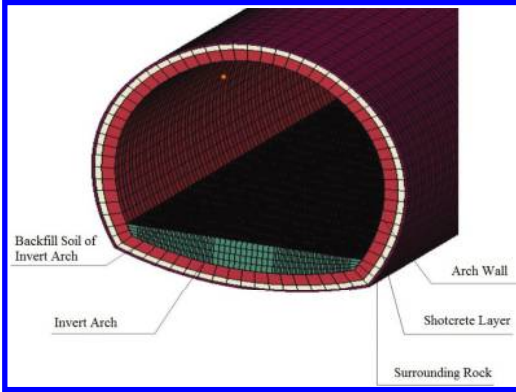


Figure 2. Tunnel model.

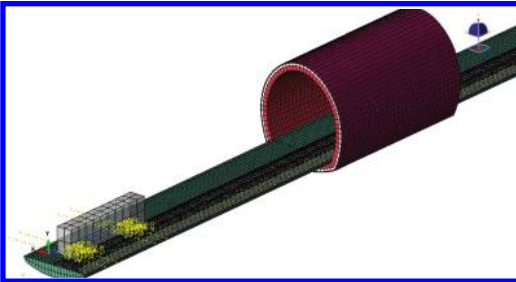


Figure 3. Vehicle-ballast track-tunnel system dynamic analysis model.

When modeling, we simplify the structure of the tunnel, by only considering the inverted arch (using C35 concrete), arch wall (using C35 concrete), invert backfill layer (using C20 concrete), shotcrete layer (using C25 concrete), and part of the wall rock outside of the lining. Tunnel model is shown in Figure 2.

The irregularity of the sample distribution is applied to the left and right rail by the way of

modifying the rail model node coordinates. Vehicle-ballast track-tunnel system dynamic analysis model is shown in Figure 3.

### 3 WHEEL-RAIL COUPLING EFFECT

The coupling action between the wheel and the rail is achieved by the wheel-rail contact. In the system dynamic analysis model, we consider the wheel-rail normal force and tangential force in the following way [4].

#### 3.1 Wheelrail normal force

We calculate the wheel-rail vertical force according to the Hertz nonlinear elastic contact theory:

$$P(t) = \left( \frac{1}{G} \Delta Z(t) \right)^{3/2} \quad (1)$$

where  $G$  is the wheel-rail contact constant ( $m/N^{2/3}$ ); for a cone-shaped tread wheel,  $G = 4.57 R^{-0.149} \times 10^{-8} (m/N^{2/3})$ ; for a worn tread wheel,  $G = 3.86 R^{-0.115} \times 10^{-8} (m/N^{2/3})$ ; and  $\Delta Z(t)$  is the elastic compression between the wheel and the rail at  $T$  moment (m).

Elastic compression between the wheel and the rail includes the wheel loading amount, which can be determined directly by the wheel-rail displacement at wheel-rail contact point:

$$\Delta Z(t) = Z_{wi} - Z_{ri}(t) \quad (i = 1 \sim 4) \quad (2)$$

where  $Z_{wi}$  is the displacement of the  $i$ th wheel at  $T$  moment (m) and  $Z_{ri}(t)$  is the rail displacement under the wheel (m).

When displacement irregularity  $Z_0(t)$  exists in the wheel-rail interface, expressions for the wheel/rail force are given by

$$P(t) = \begin{cases} \left\{ \frac{1}{G} [Z_{wi}(t) - Z_{ri}(t) - Z_0(t)] \right\}^{3/2} \\ 0 \quad (\text{wheel/rail divoced}) \end{cases} \quad (3)$$

#### 3.2 Wheel-rail tangential force

Tangential force will be produced at the contact spot between the wheel and the rail, which is the wheel/rail creep force. Kalker's linear theory is used in this paper. Kalker assumes that the contact area is all adhesion areas and the tangential force distributes symmetrically in his linear theory. Therefore, longitudinal creep force and lateral creep rate are unrelated. The linear relationship between creep

force  $T_x, T_y, M_z$  and the creep rate  $\xi_x, \xi_y, \xi_{sp}$  is as follows:

$$\left. \begin{aligned} T_x &= -f_{11}\xi_x \\ T_y &= -f_{22}\xi_y - f_{23}\xi_{sp} \\ M_z &= f_{32}\xi_y - f_{33}\xi_{sp} \end{aligned} \right\} \quad (4)$$

where  $f_{11}$  is the longitudinal creep coefficient;  $f_{22}$  is the lateral creep coefficient;  $f_{23}, f_{32}$  is the transverse/spin creep coefficient; and  $f_{33} = f_{32}$ ;  $f_{33}$  is the spin creep coefficient.

The creep coefficient can be determined by the following formula:

$$\left. \begin{aligned} f_{11} &= EabC_{11} \\ f_{22} &= EabC_{22} \\ f_{23} &= E(ab)^{2/3}C_{23} \\ f_{33} &= E(ab)^2C_{33} \end{aligned} \right\} \quad (5)$$

where  $a$  is the semi-major axis of the wheel/rail contact ellipse;  $b$  is the semi-minor axis of the wheel/rail contact ellipse;  $E$  is the modulus of elasticity of the wheel and rail material;  $C_{ij}$  is the Kalker coefficient.

Finally, the wheel/rail contact force can be obtained due to creep.

The longitudinal creep force of the left and right wheels is given by

$$\left. \begin{aligned} T_{xl} &= -f_{11} \left( 1 - \frac{l_0}{v} \dot{\psi}_w - \frac{2r_l}{r_r + r_l} \right) \\ T_{xr} &= -f_{11} \left( 1 - \frac{l_0}{v} \dot{\psi}_w - \frac{2r_r}{r_r + r_l} \right) \end{aligned} \right\} \quad (6)$$

The transverse creep force and the spin creep force torque of the left and right wheels are given by

$$\left. \begin{aligned} T_{yl} &= -f_{22} \left( \frac{\dot{y}_w}{v} + \frac{r_l}{l_0} \dot{\theta}_w - \psi_w \right) - f_{23} \left( \frac{\dot{\psi}_w}{v} - \frac{2\delta_l}{r_r + r_l} \right) \\ T_{yr} &= -f_{22} \left( \frac{\dot{y}_w}{v} + \frac{r_l}{l_0} \dot{\theta}_w - \psi_w \right) - f_{23} \left( \frac{\dot{\psi}_w}{v} + \frac{2\delta_r}{r_r + r_l} \right) \\ M_{zl} &= f_{32} \left( \frac{\dot{y}_w}{v} + \frac{r_l}{l_0} \dot{\theta}_w - \psi_w \right) - f_{33} \left( \frac{\dot{\psi}_w}{v} - \frac{2\delta_l}{r_r + r_l} \right) \\ M_{zr} &= f_{23} \left( \frac{\dot{y}_w}{v} + \frac{r_l}{l_0} \dot{\theta}_w - \psi_w \right) - f_{33} \left( \frac{\dot{\psi}_w}{v} + \frac{2\delta_r}{r_r + r_l} \right) \end{aligned} \right\} \quad (7)$$

$$\left. \begin{aligned} M_{zl} &= f_{32} \left( \frac{\dot{y}_w}{v} + \frac{r_l}{l_0} \dot{\theta}_w - \psi_w \right) - f_{33} \left( \frac{\dot{\psi}_w}{v} - \frac{2\delta_l}{r_r + r_l} \right) \\ M_{zr} &= f_{23} \left( \frac{\dot{y}_w}{v} + \frac{r_l}{l_0} \dot{\theta}_w - \psi_w \right) - f_{33} \left( \frac{\dot{\psi}_w}{v} + \frac{2\delta_r}{r_r + r_l} \right) \end{aligned} \right\} \quad (8)$$

where  $r_l, r_r$  are the actual rolling radius of the left and right wheels;  $\delta_l, \delta_r$  is the wheel/rail contact angle; and  $l_0$  is half the track gauge.

In the above formula, the longitudinal creep force of the left and right wheels is in the opposite direction, and the lateral creep force are in same direction.

Kalker linear creep theory is only applicable to situation with small creepages and small spin. For the situation with a large creep rate, high spin or even completely sliding, the linear relationship between the creep forces breaks down. Therefore, we make the following nonlinear correction with Shen theory, in order to adapt to the actual conditions of the simulation calculation of the interaction between the wheel and the rail [5].

Resultant force  $T_r$  of  $T_x$  and  $T_y$  is given by:

$$T_r = \sqrt{T_x^2 + T_y^2}$$

$$T_r' = \begin{cases} \mu N \left[ \frac{T_r}{\mu N} - \frac{1}{3} \left( \frac{T_r}{\mu N} \right)^2 + \frac{1}{27} \left( \frac{T_r}{\mu N} \right)^3 \right], & T_r \leq \mu N \\ \mu N, & T_r > \mu N \end{cases} \quad (9)$$

where  $\mu$  is the maximum static friction coefficient between the wheel and the rail; and  $N$  is the normal force of the wheel/rail contact point [6].

We introduce the correction coefficient  $\varepsilon = T_r'/T_r$ , and then we can obtain the modified creep force (torque) as follows:

$$\begin{cases} T_x' = \varepsilon T_x \\ T_y' = \varepsilon T_y \\ M_z' = \varepsilon M_z \end{cases} \quad (10)$$

### 3.3 Main calculation parameters

Ballast track in urban railway tunnels contains steel, rail fastenings, sleepers, and ballast bed. Among them, the quality of the metro vehicle is 22800 kg, the quality of the bogie is 2550 kg, the quality of the wheel set is 1760 kg, the wheelbase is 2.2 m, and the length of the vehicle is 12.6 m. Using 60 kg/m rail, spacing of rail fastenings is found to be 0.625 m, the vertical stiffness of the fastening system is 75 kN/mm, the lateral stiffness is 40 kN/mm, and the longitudinal resistance is 10 kN/mm. Other related parameters of sleepers and concrete are seen in the relevant standards and related documents.

## 4 RESULTS OF DYNAMIC CALCULATION

The following is part of the typical time history curve of the simulation results after the model calculation. The time history curve is derived from the

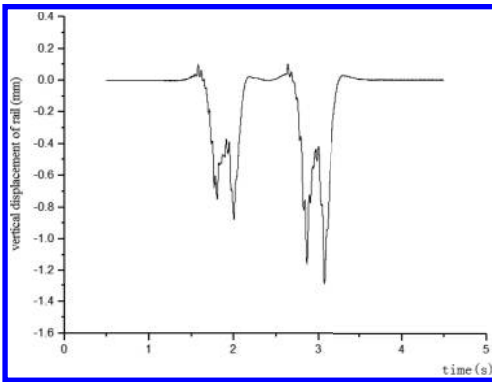


Figure 4. Vertical displacement of the rail.

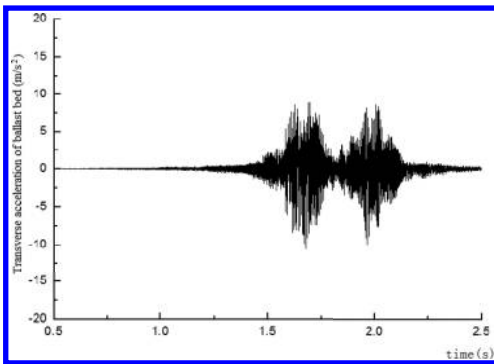


Figure 5. Transverse acceleration of the ballast bed.

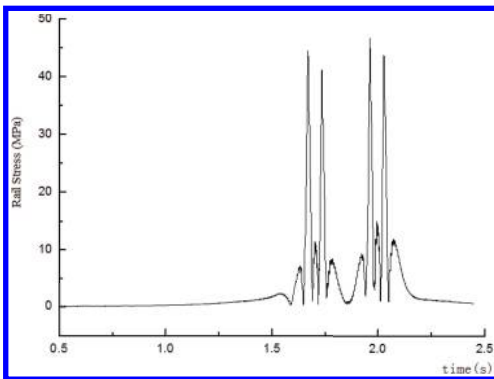


Figure 6. Rail stress.

system dynamic response when the train speed is 60 km/h.

Through the established dynamic analysis model of the vehicle-ballast track-tunnel system, we can get the peak value calculation of the model,

as given. We then analyze the safety index, vehicle stationarity index, index of track's dynamic response, and vibration index. Dynamically, we can analyze the dynamic characteristics of ballast in urban railway tunnels from the aspects of track structure, tunnels structure, vehicle safety, and passengers' comfort.

1. The vehicle safety and comfort: the maximum value of the rate of wheel load reduction is 0.412, the derailment coefficient is 0.041, the maximum of the transverse force is 5.54 kN, and the train safety can be ensured. In addition, the vehicle body acceleration is less than the limit value requirement, and standard of the passenger ride comfort can be satisfied.
2. The dynamic response of track structure: track dynamic stress decreases across the table, and the stress of the rail, sleeper and ballast bed is far less than the allowable stress value of the structure. Vibration acceleration also decreases from the top to the bottom, with the overall volume being small. As for the dynamic displacement, the value of structure displacement is small because the urban rail train axle load is lighter than the train.
3. The dynamic response of tunnel structure: the vertical vibration acceleration of the tunnel structure is 0.194 m/s<sup>2</sup>, the lateral vibration acceleration is 0.048 m/s<sup>2</sup>, and the overall volume of the acceleration is minimum. When the train is in running, the vibration will decrease accordingly because of the materials used on the outer wall of the tunnels.

## 5 CONCLUSIONS

This paper analyzed the safety index, vehicle stationarity index, index of track's dynamic response, vibration index of the ballast track in urban railway tunnels dynamically through establishing the dynamic analysis model of the vehicle-ballast track-tunnel system. It is feasible to use ballast track in urban railway tunnels, no matter from which aspect such as the safety of the structure, dynamic response, passenger's comfort and vibration.

It is important to note that due to the lack of measured data of the ballast track in urban railway tunnels, we are unable to test the calculated data from the vehicle-ballast track-tunnel system's dynamic analysis model established in this paper by practice.

Selection of the typical test is recommended in the new-built urban rail traffic tunnel to fully demonstrate the feasibility of the application of the ballast track in urban railway tunnel lines.

## ACKNOWLEDGMENTS

This work was financially supported by the National High-tech R&D Program of China (863 Program) (Grant No. SS2015AA010504).

## REFERENCES

- [1] Clark M.R., Gillespie R., Kemp T. Electromagnetic properties of railway ballast, *J. NDT & E International*, 34(2001) 305–311.
- [2] Knothe K., Past and future of vehicle/track interaction, *J. Vehicle System Dynamic Supplement*, 45(1995)1–3.
- [3] Vukan R. *Urban Transit: Operations, Planning and Economics*, first ed., New Jersey. Wiley, 2005.
- [4] Grassie S.L. Review of workshop: aims and open questions, *J. Vehicle System Dynamic Supplement*, 45(1995)380–386.
- [5] Saussine G., Cholet C., Gautier P.E., et al. Modelling ballast behaviour under dynamic loading. Part 1: A 2D polygonal discrete element method approach, *J. Computer methods in applied mechanics and engineering*, 195(2006) 2841–2859.
- [6] Selig E.T, Li D. Track modulus: Its meaning and factors influencing it, *J. Transportation Research Record*, 1470 (1994).

# Influence of mixture proportion on bleeding of concrete

Jiwei Yang & Ruiying Bai

*Hebei Provincial Key Laboratory of Inorganic Nonmetallic Materials, College of Materials Science and Engineering, North China University of Science and Technology, Tangshan, China*

Jiwei Cai

*Institute of Materials and Structures, Henan University, Kaifeng, China*

Jixu Wu

*Handan Jinyu Taihang Cement Co. Ltd., Handan, Hebei, China*

Weihua Liu

*Research Center for Materials, Jidong Development Group Co. Ltd., Tangshan, Hebei, China*

**ABSTRACT:** Bleeding is a critical property for successful placement and performance of concrete. In this paper, dormant time and initial bleeding rate were employed to evaluate the effect of different mix design parameters on the bleeding characteristics. The unit water consumption was shown to affect the initial bleeding rate significantly, while the sand-to-aggregate ratio was a key factor in dormant time of bleeding. The water-to-powder ratio can decrease the bleeding in the range of 0.36–0.39.

**Keywords:** fresh concrete, bleeding, mixture proportion

## 1 INTRODUCTION

Bleeding is an important index to measure the workability of fresh concrete. However, the influence factors of concrete bleeding are perplexing. At present, the study on the origin of bleeding and on the performance of concrete is mainly qualitative research, which has not achieved the expected control of bleeding.

The bleeding properties of concrete can be subdivided into the bleeding volume and bleeding rate. According to the dormant time and initial bleeding rate, bleeding of fresh concrete can be divided into four types: early and quickly; early and slowly; lately and quickly; and lately and slowly. Generally, the early and quickly type bleeding occurs in a high water-to-cement ratio (w/b) concrete. The early and slowly bleeding, and lately and quickly bleeding types appear in a medium w/b concrete. The lately and slowly bleeding type occurs in a low w/b concrete.

Concrete mixture proportion has a very important influence on the performance of bleeding. In this paper, the mixture proportion of concrete with different unit water consumption (w/b), fine/total aggregate ratio ( $\beta_s$ ), water-to-powder ratio (w/p) was prepared. The influence of mixture parameters of concrete on dormant time, bleeding rate and bleeding types was investigated.

## 2 EXPERIMENTAL PROCEDURE

### 2.1 Material characterization

The raw materials used in the experiment are listed as follows:

1. Cement: P·O42.5 cement with a compressive strength of 50.2 MPa at 28 curing days.
2. Fly Ash (FA): II grade FA with a Blaine surface area of 411 m<sup>2</sup>/kg, 7% loss on ignition and water requirement ratio of 91%.
3. Ground Granulated Blast Furnace Slag (GGBFS), S75 grade with a Blaine surface area of 411 m<sup>2</sup>/kg.
4. Iron Mill Tailings Powder (IMTP): ground by iron mill tailings with a Blaine surface area of 444 m<sup>2</sup>/kg.
5. Aggregates: sand with a fineness modulus of 2.10 and dust content of 3.3%; coarse aggregate with a continuous gradation of 5–25 mm and crushing index values of 8.2%.

### 2.2 Experimental program and test sequence

**Mix proportion design.** According to the “JGJ55-2000, the specifications for the design of concrete proportion design of ordinary concrete”, concrete mix proportions with the w/b of 0.46, 0.57, 0.78 were designed.

**Specimen prepared and performance test.** Fresh concrete was prepared according to the mixture proportions. The slump and bleeding water content test was conducted in accordance with the Chinese standard GB/T 50080-2002.

The fresh concrete was poured into a mold and cylinder, respectively. Early bleeding concrete would be classified if surface visual bleeding was observed for the test sample in mold after vibration on the vibration table. For the test sample in cylinder, the bleeding rate was measured without vibration, and the dormant time of bleeding ( $t_0$ ) was defined by regression analysis.  $t_0 = 20$  min was considered as the cut-off point of concrete bleeding earlier or later,  $t_0 < 20$  min for the early bleeding type and  $t_0 \geq 20$  min for the late bleeding type.

### 3 RESULTS AND DISCUSSION

#### 3.1 Influence of unit water consumption on bleeding

The mixture proportion of concrete with different w/c (0.78, 0.57, and 0.46) and unit water consumption is given in Table 1. The bleeding rates of concrete samples are tested (see Fig. 1) and the dormant time of bleeding ( $t_0$ ) was calculated. The results are summarized in Table 2.

It can be seen from Figure 1a (w/c = 0.78) that with the increase in unit water consumption for a higher w/c, the concrete bleeding rate is increased and the maximum value of bleeding increases. The variation of the initial bleeding rate is low. But the dormant time of bleeding ( $t_0$ ) of D3 is earlier than that of D1 and D2.

Bleeding can be regarded as free water between the solid particles in fresh concrete floated to the surface. In this process, there is a variety of resistance factors. When the potential energy of the free water is greater than the resistance force, the bleeding occurs.

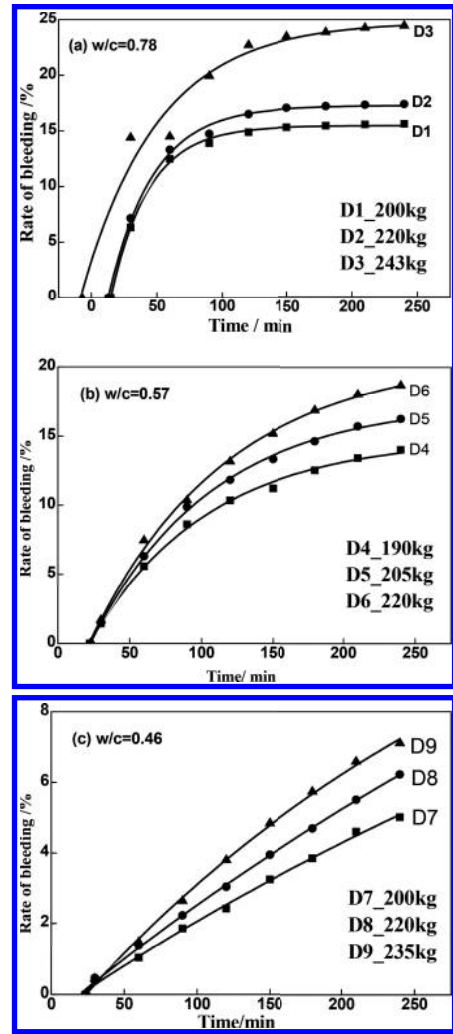


Figure 1. Influence of unit water consumption on the bleeding rate of concrete.

Table 1. Mix proportion of concrete with different water consumption.

Simple no.	w/b/%	$\beta$ /%	w/kg	c/kg	s/kg	g/kg
D1	0.78	40	200	256	720	1174
D2	0.78	40	220	282	740	1109
D3	0.78	40	243	312	718	1077
D4	0.57	38	190	333	713	1165
D5	0.57	38	205	360	696	1138
D6	0.57	38	220	390	682	1113
D7	0.46	39	200	435	688	1077
D8	0.46	39	220	478	664	1042
D9	0.46	39	235	510	645	1009

Table 2. Bleeding of concrete with different water consumption.

Sample no.	w/b/%	w/kg	Slump/mm	Bleeding	$t_0$
D1	0.78	200	55	Slight	14.85
D2	0.78	220	155	Slight	13.09
D3	0.78	243	200	Seriously	-7.11
D4	0.57	190	70	None	22.11
D5	0.57	205	110	Slight	22.92
D6	0.57	220	140	Slight	22.59
D7	0.46	200	110	None	23.6
D8	0.46	220	150	None	23.2
D9	0.46	235	200	None	24.85

Unit water consumption has a close relationship with bleeding, higher unit water consumption, more free water and higher potential energy of bleeding, which resulted in more serious bleeding manifested as earlier dormant time of bleeding ( $t_0$ ) and higher bleeding rate, and larger bleeding volume in concrete.

With the increase in unit water consumption, free water in concrete is also increased and “bleeding potential energy” is greater, the initial bleeding rate and total bleeding water will be improved, as shown in Figure 1b ( $w/c = 0.57$ ) and Figure 1c ( $w/c = 0.46$ ). On the other hand, the increase in unit water consumption means the decrease in the proportion of solid particles. Bleeding resistance can be decreased dramatically with the solid particles, especially the fine cementitious particles and then the bleeding rate increases, and thus the bleeding occurs earlier. So, it can be considered that unit of water consumption is a key factor of concrete bleeding, especially the dormant time of bleeding at a high  $w/c$ .

For the bleeding performance, the  $w/c$  seems also to play a significant role, as shown in Figure 1. Bleeding is much milder for the lower  $w/c$  concrete.

### 3.2 Influence of the fine/total aggregate ratio ( $\beta_s$ ) on bleeding

A series of concrete mixtures were designed at the water/cement ratio of 0.78, 0.57 and 0.46 and the fine/total aggregate ratio ( $\beta_s$ ) for a single variable. Bleeding was measured and dormant time of bleeding ( $t_0$ ) was defined by the regression analysis. Influence of the fine/total aggregate ratio ( $\beta_s$ ) on the bleeding rate of concrete is shown in Figure 2.

The fine/total aggregate ratio ( $\beta_s$ ) play a significant role on the workability of concrete for a given cement paste volume. Too large or too small  $\beta_s$  both make the workability worse and bleeding will occur. As can be seen from Figure 2, with the increase of  $\beta_s$ , dormant time of bleeding ( $t_0$ ) was prolonged, the amount of bleeding was reduced and the bleeding rate decreased slightly. When  $\beta_s$  is the one and only variable in fine/coarse aggregate binary system, with  $\beta_s$  increase, the specific surface area is monotone increasing and porosity decrease first and then increase. Lower porosity will result in increased resistance of bleeding until a minimum porosity reached. Further increased  $\beta_s$  will result in higher porosity and higher specific surface area. Therefore, there is a reasonable gradation exists for bleeding of concrete system.

It can be seen fine/total aggregate ratio ( $\beta_s$ ) is an important factor affected bleeding rate in the range of 32–40%. As the  $\beta_s$  increased, bleeding was much milder. It seems that  $\beta_s = 40\%$  is acceptable for controlling the bleeding of concrete.

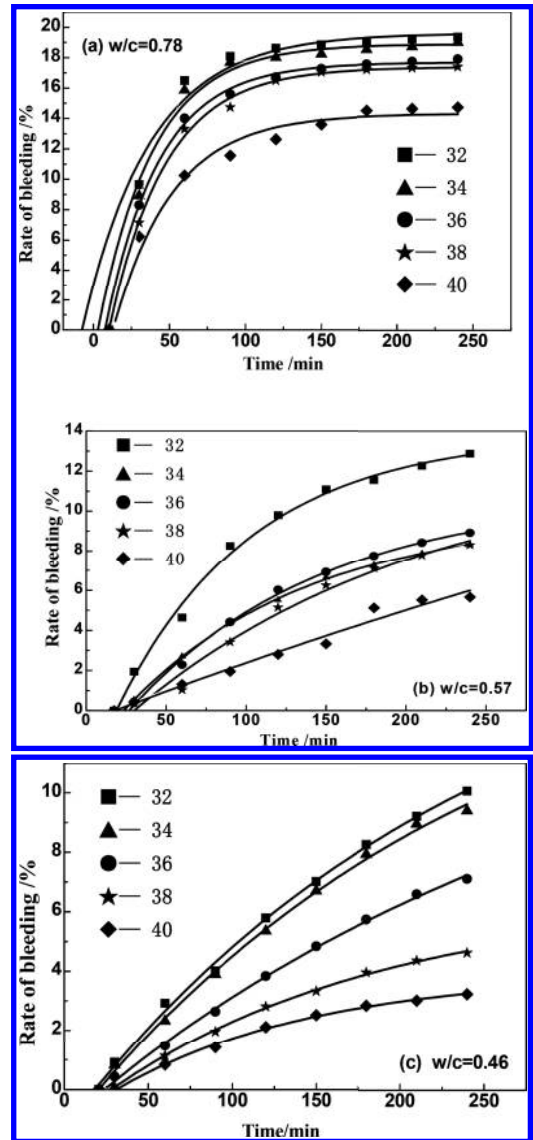


Figure 2. Influence of the fine/total aggregate ratio ( $\beta_s$ ) on the bleeding rate of concrete.

### 3.3 Influence of the water/powder ratio ( $w/p$ ) on bleeding

The influence of the water/powder ratio ( $w/p$ ) on bleeding fixed the fine/total aggregate ratio by 40%, as shown in Figure 3. The relationship between the water/powder ratio ( $w/p$ ) and slump is shown in Figure 4. The composition of powder in concrete samples is listed in Table 3.

At the same water/powder ratio, the powder instead of cement with 15% FA and 15% GGBFS



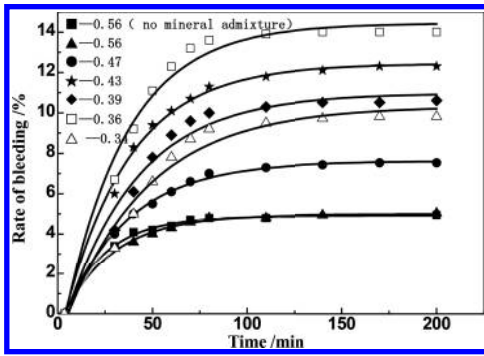


Figure 3. Influence of the water/powder ratio on the bleeding rate of concrete.

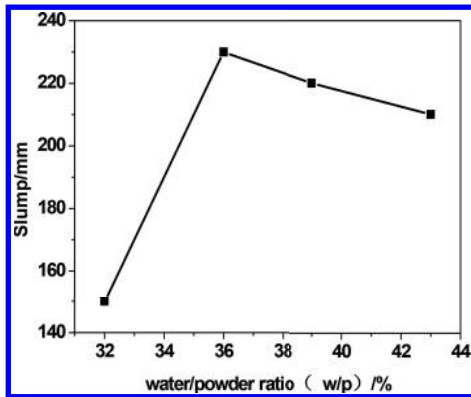


Figure 4. Influence of the water/powder ratio on the slump of concrete.

Table 3. Mix proportion of concrete with different water/powder ratios.

Sample no.	w/p	FA/% <sup>①</sup>	GBFS/% <sup>①</sup>	IMTP % <sup>②</sup>
F1	0.56	0	0	3.3
F2	0.56	15	15	3.3
F3	0.47	15	15	3.3
F4	0.43	15	15	3.3
F5	0.39	15	15	8.3
F6	0.36	15	15	13.3
F7	0.34	15	15	18.3

Note: <sup>①</sup>replacing cement. <sup>②</sup>Iron mill tailings powder, replacing fine aggregate equivalent.

can reduce the bleeding slightly and improve the slump of concrete at the same time. As the IMTP powder replacing fine aggregate mixed into concrete increased, the bleeding rate appeared a peak with w/p = 0.36, corresponding to the slump also

reached the maximum value. When w/p < 0.36 (IMTP > 13.3%), the slump decreased rapidly. It can be seen from Figure 3 and Figure 4 that the bleeding rate and the slump are consistent, i.e. large slump and high bleeding rate is high, and vice versa. Therefore, the w/p in concrete is a major determinant of bleeding and slump factors. It seems that w/p = 39% is acceptable for controlling the bleeding of concrete.

#### 4 CONCLUSIONS

1. The unit water consumption was the key factor of concrete bleeding, especially the dormant time of bleeding at a high w/c.
2. As the fine/total aggregate ratio ( $\beta_s$ ) increased, bleeding was much milder. It seemed that  $\beta_s = 40\%$  was acceptable for controlling the bleeding of concrete.  $\beta_s$  was a key factor of the bleeding rate.
3. Water/powder ratio in concrete was a major determinant factor of bleeding and slump. It seemed that w/p = 39% was acceptable for controlling the bleeding of concrete.

#### ACKNOWLEDGMENTS

This work was financially supported by the Scientific Research Foundation for Colleges and Universities of Hebei Province under grant for Project (ZD2010104) and the College Students' Innovation and Entrepreneurship Training Program of North China University of Science and Technology (X2014088). The authors gratefully appreciate their support.

#### REFERENCES

Ilker B.T. & Veysel B.E. 2004. Influence of concrete properties on bleeding and evaporation. *Cement and Concrete Research*. 34: 275–281.

Jiwei Cai & Xiaoxin Feng. 2008. Bleeding Behavior of Concrete Prepared with Ferrous Mill Tailings as Manufactured Fine Aggregates *Journal of Wuhan University of Technology*. 30(09): 16–19.

Morris P.H. & Dux P.F. 2010. Analytical solutions for bleeding of concrete due to consolidation. *Cement and Concrete Research*. 40: 1531–1540.

Ozcan T.A. & Sahin Z. 2005. Taguchi approach for optimization of the bleeding on cement-based grouts. *Cement and Concrete Research*. 20: 167–173.

Wainwright P.J. & Rey N. 2000. The influence of Ground Granulated Blastfurnace Slag (GGBS) additions and time delay on the bleeding of concrete. *Cement and Concrete Composites*. 22: 253–257.

# The impact of curved track irregularities on dynamical response of rising speed trains

J. Fang

*School of Transportation Engineering, Tongji University, Shanghai, China  
Engineering Research Center of Railway Environment Vibration and Noise of the Ministry of Education,  
East China Jiao Tong University, Nanchang, Jiangxi Province, China*

X.Y. Lei

*Engineering Research Center of Railway Environment Vibration and Noise of the Ministry of Education,  
East China Jiao Tong University, Nanchang, Jiangxi Province, China*

S.L. Lian

*School of Transportation Engineering, Tongji University, Shanghai, China*

L.Y. Liu

*Engineering Research Center of Railway Environment Vibration and Noise of the Ministry of Education,  
East China Jiao Tong University, Nanchang, Jiangxi Province, China*

**ABSTRACT:** Track irregularities are the main excitation sources of vehicle vibration that will produce a direct impact on the vehicle's stability and safe running. Because the curved lines are applied greatly in railway lines, the irregularities of curved lines contribute to more intense interactions between wheels and rails that not only increase the wear of wheels and rails and vibration of vehicles, but also cause great damage to the track structure. Therefore, the main objective of this article is the examination of the effects of curved track irregularities on vehicle dynamics during motion along a curved track. For the track irregularity types with different breadths and wavelengths, the effects of track irregularities on vehicle dynamics are different. Based on the data from the curved track irregularity measurements of the Wu-Jiu line by track inspection car, using coherence function and computer simulation of trains running on the track of different irregularity types, the relationship between curved track irregularity and vehicle vibration was studied. First, based on the result of coherence function analysis and power spectrum analysis, the detrimental wavelengths, which will lead to more intense vibration responses, were defined. Second, by inputting the data from the Wu-Jiu line as the excitation source of the proposed model, the model was implemented via the software ADAMS/rail. On comparison with the simulation results, the defined detrimental wavelengths were proposed. The result of this paper can provide a theoretical and practical guidance for the maintenance of geometrically irregular track and relevant management.

**Keywords:** the curved track; track irregularities power spectrum; coherence functions analysis; detrimental wavelengths

## 1 ANALYSIS OF CURVED LINE TRACK IRREGULARITIES CHARACTERISTICS

### 1.1 Irregular areas

The data of this paper come from the on-site measurements of the Wu-Jiu line by track inspection car. The sampling interval is 0.25 m. The spatial frequency is 4. Thus, for every kilometer, the total number of data point is 4001. The curved radius is 680 m. The curved length is 611 m. The average super elevation is 124.2 mm. The train's average speed is 101 km/h. The irregularity data from

inspection car include: left rail y-displacement, left rail z-displacement, right rail y-displacement and right rail z-displacement.

### 1.2 The curved line track irregularity power spectrum analysis

In order to examine the effects of curved track irregularities on vehicle dynamics, the track irregularity power spectra are calculated and the frequency components are analyzed. [Figure 1](#) and [Figure 2](#) show the power spectrum of track vertical profile irregularities. According to these figures, the

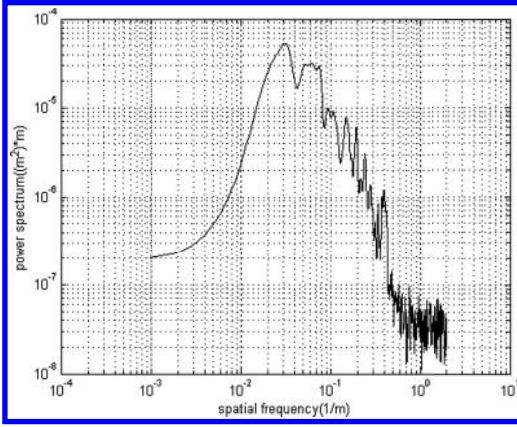


Figure 1. PSD of left-z displacement.

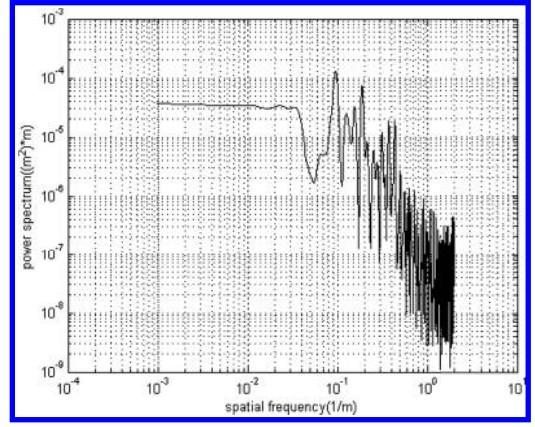


Figure 4. PSD of right-y displacement.

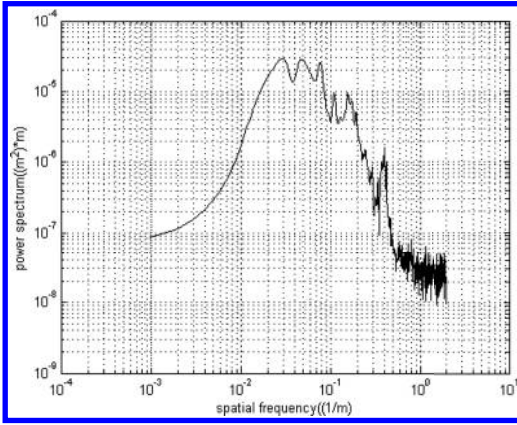


Figure 2. PSD of right-z displacement.

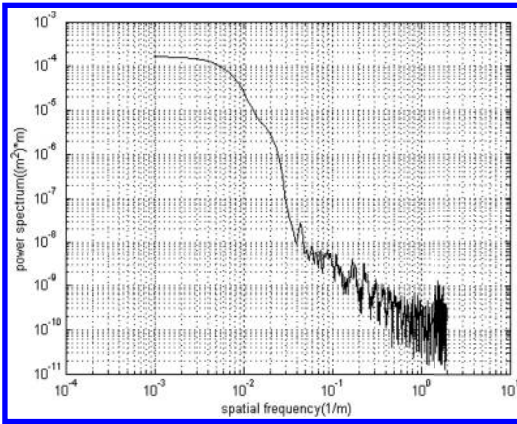


Figure 3. PSD of left-y displacement.

dominant frequencies are  $0.1094 \text{ m}^{-1}$ ,  $0.1564 \text{ m}^{-1}$ ,  $0.194 \text{ m}^{-1}$ ,  $0.2448 \text{ m}^{-1}$ ,  $0.2788 \text{ m}^{-1}$  and  $0.3411 \text{ m}^{-1}$ . Therefore, the corresponding wavelengths are 10 m, 6.5 m, 5 m, 4 m, 3.6 m and 2.8 m.

Figure 3 and Figure 4 show the power spectrum of track direction irregularities. From these figures, the dominant frequencies are  $0.09644 \text{ m}^{-1}$ ,  $0.126 \text{ m}^{-1}$ ,  $0.1553 \text{ m}^{-1}$ ,  $0.1885 \text{ m}^{-1}$  and  $0.3147 \text{ m}^{-1}$ . Thus, the responding wavelengths are 10 m, 7.9 m, 6.4 m, 5.3 m and 3.1 m.

## 2 COHERENCE ANALYSIS OF TRACK IRREGULARITIES AND VEHICLE VIBRATION

Coherence analysis can determine the percentage that shows how much output response is induced by input. Hence, the wavelength, which corresponds to the maximum value of coherence functions, can be regarded as the detrimental wavelength. For a single input and a single output, the coherence function can be described as follows:

$$\gamma_{xy}^2(f) = \frac{|s_{xy}(f)|^2}{s_x(f)s_y(f)}, \quad 0 < \gamma_{xy}^2 < 1 \quad (1)$$

here,  $S_x(f)$  is the auto-power spectrum of the signal  $x(t)$ ;  $S_y(f)$  is the auto-power spectrum of the signal  $y(t)$ ; and  $S_{xy}(f)$  is the cross power-spectrum of  $x(t)$  and  $y(t)$ . For most conditions,  $0 < \gamma_{xy}^2(f) < 1$ , which shows that the two physical quantities are coherent to some extent. If the maximum value of coherent function can be found, then this wavelength will induce the greatest vibration.

The coherence functions are adopted to analyze track irregularities and vehicle vertical or lateral vibration accelerations. By studying the coherent

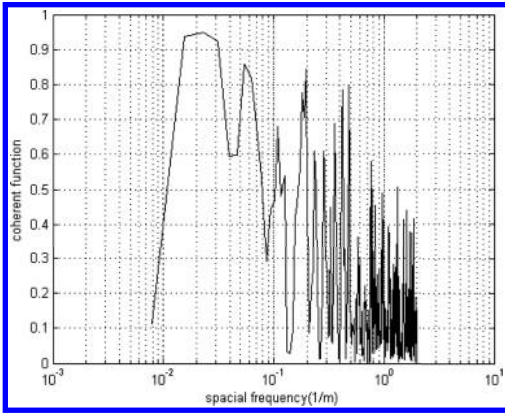


Figure 5. Coherence of left rail vertical irregularities and vertical vibration of vehicles.

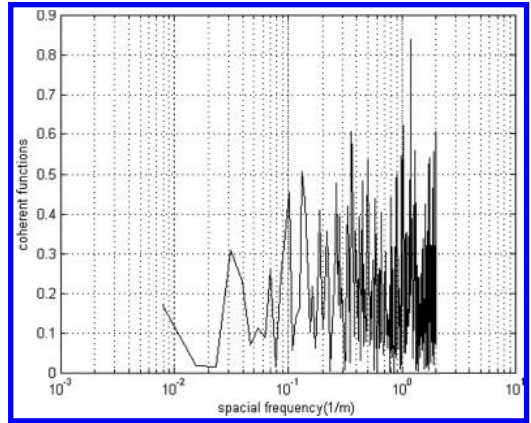


Figure 8. Coherence of right rail direction irregularities and lateral vibration of vehicles.

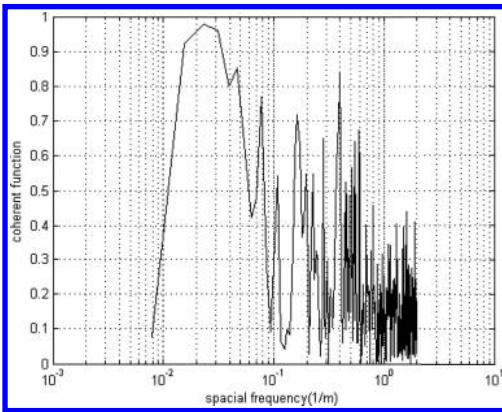


Figure 6. Coherence of right rail vertical irregularities and vertical vibration of vehicles.

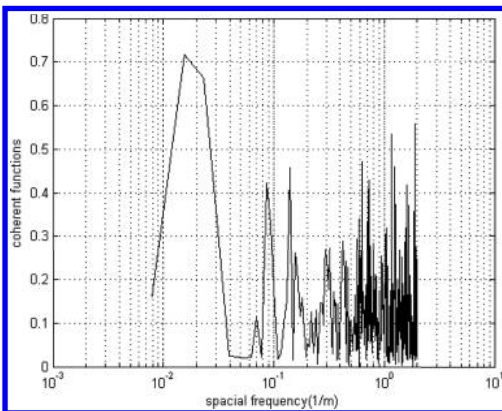


Figure 7. Coherence of left rail direction irregularities and lateral vibration of vehicles.

extent of vehicle vibration and track irregularities, the detrimental wavelength scope can be identified. The power-spectrum analysis can present the distribution of dynamic response of vehicle and track irregularities with wavelengths. Thus, in this paper, the combined method of coherent analysis and power spectrum is adopted to define the detrimental wavelengths.

According to the coherent analysis figures and power spectrum figures, the track vertical irregularities affect the vehicles' vertical vibrations significantly, while the track direction irregularities have significant effects on the vehicles' lateral vibrations. When both the power spectrum of vehicle's acceleration and coherent function curved reach the maximum, the wavelength can be regarded detrimental. For track direction irregularities, the detrimental wavelengths are  $1/0.035 \text{ m}^{-1}$  (28.5 m) and  $1/0.2686 \text{ m}^{-1}$  (3.72 m), and for vertical irregularities, the detrimental wavelengths are  $1/0.05078 \text{ m}^{-1}$  (20 m) and  $1/0.3984 \text{ m}^{-1}$  (2.5 m).

### 3 DYNAMICAL SIMULATION CALCULATION

A vehicle-track system can be considered as a dynamic system whose inputs are track irregularities and whose outputs are vertical force, lateral force and vehicles' accelerations. This study used the rail-wheel dynamic model of ADAMS/Rail. By inputting the irregularity data as excitation functions, the vehicles' dynamical responses under different track irregularities were studied. In order to study the effects of different track irregularity types on the vehicles' vibrations, the model inputs each track irregularity type individually. Figure 9 and Figure 10 show the vehicles' lateral

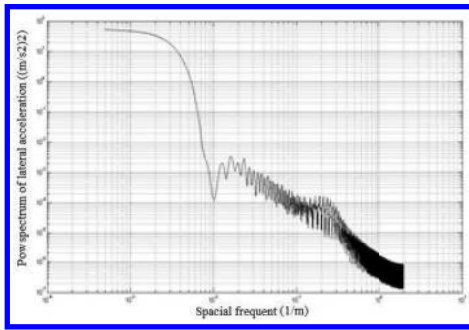


Figure 9. The power spectrum of the vehicles' lateral acceleration induced by left-rail direction irregularities.

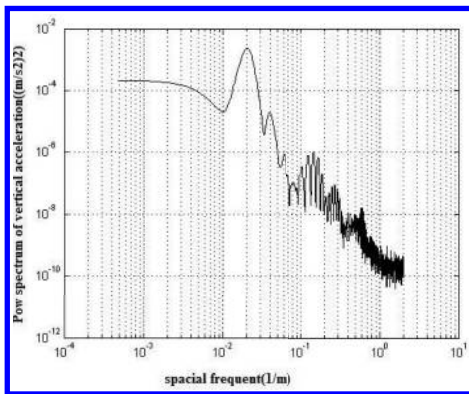


Figure 10. The power spectrum of the vehicles' vertical acceleration induced by left-rail direction irregularities.

and vertical acceleration power spectra induced by left-rail direction irregularities. Figure 11 and Figure 12 show the lateral and vertical acceleration power spectra induced by left-rail vertical level irregularities. Figure 13 and Figure 14 show the lateral and vertical acceleration power spectra induced by right-rail vertical level irregularities. Figure 15 and Figure 16 show the lateral and vertical acceleration power spectra induced by left-rail vertical level irregularities.

By calculation, the main frequency scope of the vehicle lateral acceleration spectrum is found to be  $0.02 \text{ m}^{-1}$ – $0.05 \text{ m}^{-1}$ . According to the coherence analysis, the detrimental wavelengths include  $1/0.035 \text{ m}$ , which belong to  $0.02 \text{ m}^{-1}$ – $0.05 \text{ m}^{-1}$ . Furthermore, from Figure 10, the main frequency scope of the vehicle vertical acceleration spectrum is  $0.4 \text{ m}^{-1}$ – $0.5 \text{ m}^{-1}$ . According to the coherence analysis, the detrimental wavelengths include  $1/0.3984 \text{ m}^{-1}$ , which nearly belong to  $1/0.5 \text{ m}^{-1}$ – $1/0.4 \text{ m}^{-1}$ . The simulation results indicate that the detrimental wavelength obtained from coherence functions and from the simulation model can fit.

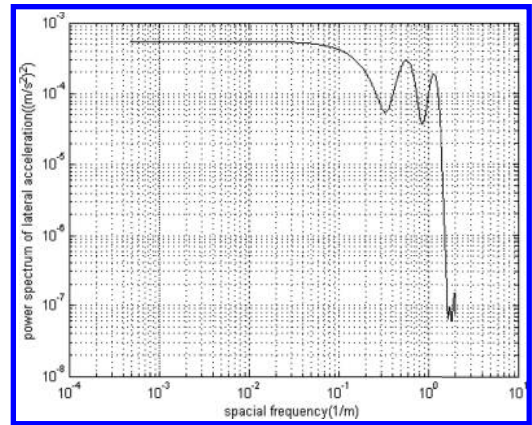


Figure 11. The power spectrum of the vehicles' lateral acceleration induced by left-rail vertical level irregularities.

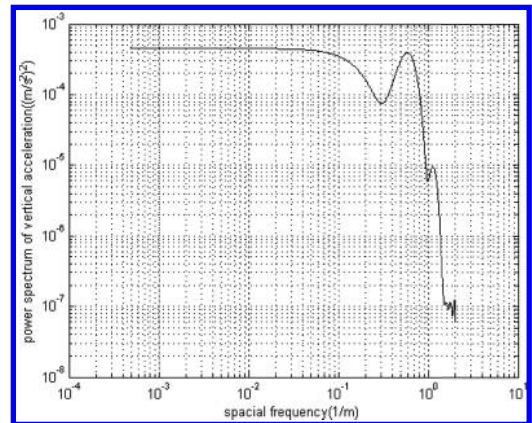


Figure 12. The power spectrum of the vehicles' vertical acceleration induced by left-rail vertical level irregularities.

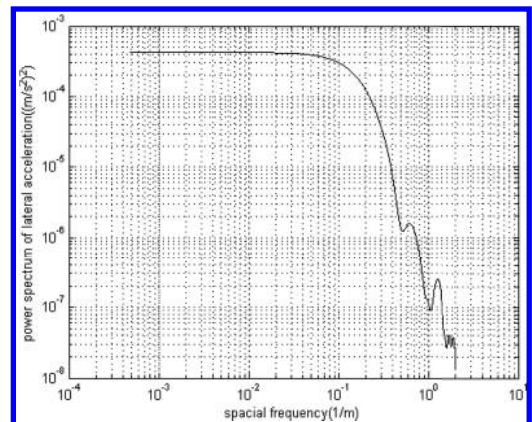


Figure 13. The power spectrum of the vehicles' vertical acceleration induced by right-rail direction irregularities.

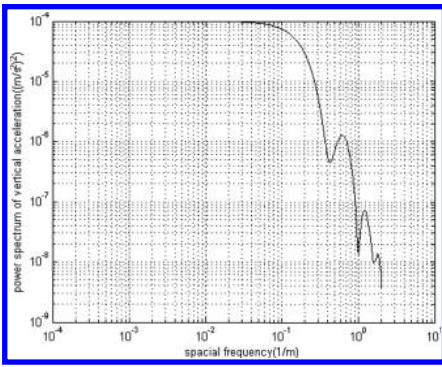


Figure 14. The power spectrum of the vehicles' lateral acceleration induced by right-rail direction irregularities.

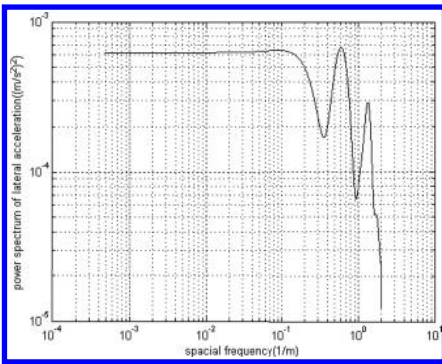


Figure 15. The power spectrum of the vehicles' vertical acceleration induced by right-rail vertical irregularities.

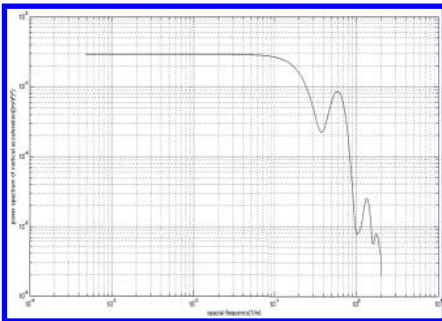


Figure 16. The power spectrum of the vehicles' lateral acceleration induced by right-rail vertical irregularities.

#### 4 CONCLUSION

The irregularities of curved lines will contribute to more intense interactions between wheels and rails. For different track irregularity types, breadths and wavelengths, the effects of track irregularities on

vehicle dynamics are different. Therefore, the effects of different track irregularity types on vehicle dynamics during motion along a curved track were studied. Based on the power spectrum analysis and coherence function theories, compared with the results of dynamic simulations, some conclusions can be drawn as follows:

1. Combining coherence function and power spectrum analysis, the random track irregularities' detrimental wavelengths can be defined.
2. In this paper, the coherent analysis between the acceleration of a vehicle at the speed of 101 km/p and track irregularities is presented. According to the analysis results, the track vertical irregularities affect the vehicle's vertical vibration significantly, and the most detrimental wavelengths are  $1/0.05078 \text{ m}^{-1}$  (20 m), and  $1/0.3984 \text{ m}^{-1}$  (2.5 m). While the track direction irregularities have a significant effect on the vehicle's lateral vibrations, the most detrimental wavelengths are  $1/0.035 \text{ m}^{-1}$  (28 m) and  $1/0.2686 \text{ m}^{-1}$  (3.72 m). The simulation results of ADAMS/Rail indicate that the defined detrimental wavelengths are dependent.
3. In response to the detrimental wavelengths described in this paper, the special track maintenance is suggested to avoid the track irregularities with the most detrimental wavelengths.

#### ACKNOWLEDGMENT

This research was partly supported by grants 20122BAB206005 and 20132BAB206001 from the Jiangxi Natural Science Foundation of China and the Science Foundation of Educational Committee of Jiangxi Province (KJLD14038).

The authors would like to thank the engineers at the respective departments of the project for their assistance during the field measurement of the test.

#### REFERENCES

Katsushi Manabe. Multiple-wheel Induced Vibration of Rail with Surface Irregularities. Chief Research, Research and Development Promotion Div.

Lei Xiaoyan. New methods in railroad track mechanics and technology [M]. Beijing, 2002.

Lian Songliang. Study of the detrimental wavelengths of track irregularities for railway with passengers and freight track [J]. Journal of the China railway society, 2004, (26):112–116.

Wang Chengguo. MSC.ADAMS/Rail basic courses [M]. Beijing, 2005.

Wangji. Matlab in vibration signals application [M]. Beijing, 2007.

## Risk analysis of green building project at the decision-making stage

Wei Xu & Shanshan Liu

*Architectural and Civil Engineering Institute, Inner Mongolia University of Science and Technology,  
Baotou Inner Mongolia, China*

**ABSTRACT:** The decision-making stage is the key to success in a project. From the viewpoint of the contractor, the paper focuses on the analysis of risks before bidding decision-making in the green building project. Based on previous results and past experience, it is at the green construction decision-making stage that the effects of 13 risk factors are identified. The risks are divided into four main aspects such as owner's risk, design risk, policy risk, and management risk. Then the AHP method is used to determine the risk weights and the AHP model is constructed. The relative evaluation criteria are assigned to green buildings. By means of constructing judgment matrix the consistency check is completed. The probability of the 13 risk factors is analyzed. The results show that the risk of the design phase is a key part of influence on project decisions, followed by the owners, management, and policy. It has to be pointed out that the results can help the contractors to identify risk factors, which can be taken measures to avoid. All these provide a theory basis for the further research on risk management of green building during life cycle.

**Keywords:** green building; decision-making stage; risk management; AHP

### 1 INTRODUCTION

In recent years, with the rise of building energy consumption, building energy conservation has become the focus of the construction industry. According to estimates, building energy consumption accounted for about 40% of global energy consumption, so green architecture is the first choice. By 2015, the new green construction area will reach more than 1 billion square meters, in 2020 our country town green building accounted for the proportion of new buildings will rise to 50%<sup>[1]</sup>. Obviously, green building will become the inevitable trend of the future construction. At present, the research of the green building focus on technology evaluation, cost control, and other fields, and understanding of risk is still in the initial stage. Green buildings compared with the ordinary puts forward higher requirements on the construction system, efficient use of resources, reduce the impact on the environment, improve the living comfort, and so on. The risk of green building compared with the ordinary has expanded and changed, concrete manifestations of the expansion of the scope of the risk and the change of risk content<sup>[2]</sup>. Foreign scholars found that, the higher the performance of the building, the higher the safety risk, and the data shown LEED certified project injury rate is 9% higher than the traditional project<sup>[3]</sup>.

In order to ensure the successful promotion of China's green building, this paper based on the perspective of contractor points out the risk of

green building projects to analyze the decision-making stage. This text puts forward the concept of decision-making risk of the green building, based on the existing green building assessment system; the identification of risk factors, using the AHP method to determine the risk in weight and value. These can help the contractors identify the key risk factors of green building, and prepare to effectively cope with the risks of the green building<sup>[4]</sup>.

### 2 THE CONCEPT OF DECISION-MAKING STAGE RISK OF GREEN BUILDING

The risk refers to the uncertainty of loss. Decision-making stage risk refers to the strategic plan of the Target Corp—which is not perfect—lack of understanding of the Target Corp, and choosing the wrong acquisition targets. Green building distinguished from ordinary building is its “green” concept<sup>[5]</sup>. So the concept of decision-making stage risk of green building is: uncertain factors affecting sustainable development of the project in the decision-making stage.

### 3 THE CONCEPT OF DECISION-MAKING STAGE RISK OF GREEN BUILDING

As the green building has its own characteristics and requirements, it is faced with greater risks and higher challenges than traditional architecture,

Table 1. Identification of the decision-making risk.

Goal	Category	Subcategory	Remarks
Decision-making risk $A$	Owner's risk $B_1$	The lack of accurate estimation of the return of long-term investment on green building $b_{11}$	Through the literature
		The funding conditions and management level of owners $b_{12}$	
		Green building investment estimates are inaccurate $b_{13}$	
		The green star target location is not accurate $b_{14}$	
	Design risk $B_2$	The design did not reach the owner's goal about green building $b_{21}$	
		Green design exceeds the level of construction technology $b_{22}$	
	Policy risk $B_3$	Laws and regulations of Green building are not perfect $b_{31}$	
		The change of green building policy $b_{32}$	
		The government bureaucracy and multifarious approval process $b_{33}$	
	Management risk $B_4$	The certification standard of green building is not clear $b_{41}$	
		Without a proper understanding of the market demand for green building $b_{42}$	
		Financial institutions are lack of enthusiasm for green building $b_{43}$	
		The lack of experience in green building consultant $b_{44}$	

thus increasing management difficulty, and making the risk problem more outstanding<sup>[6]</sup>. Risk identification is to find out the possible risk in the project. Recognition method of project decision-making risk is mainly: (1) It can be through the questionnaire survey and consulting experts. (2) According to the previous occurrence of risk events, experience and analysis, statistics, and summary of events, finally obtaining the risk factors that affect the project<sup>[7]</sup>. Qin Xuan by way of a questionnaire survey identified 56 risk factors based on the life cycle of green building in the 'Risk measurement index identification and assessment for green buildings in Haixi region'. It revealed 8 common factors that were extracted to form a risk evaluation function<sup>[8]</sup>. The extracted common factors were classified into three levels: macro, middle, and micro<sup>[9]</sup>. Li Zheng Kun<sup>[10]</sup> points out that the triangle fuzzy analytic hierarchy process and fuzzy comprehensive evaluation method was adopted to calculate the fuzzy comprehensive evaluations of green building project risks, then the key risk factors were identified. This research, based on the basis of previous studies, refers to a large number of literature and carries out the analysis. It is concluded that the risk of project decision-making stage. The decision-making phase of the project risks mainly divided into owner's risk, design risk, policy risk, and risk management. The results are shown in Table 1.

#### 4 TO DETERMINE THE RISK FACTORS OF THE WEIGHTS BY AHP METHOD

##### 4.1 Build the hierarchical analysis model

According to the above results of risk identification, there are mainly 13 risk factors in the decision-making phase of the project. These risk factors are

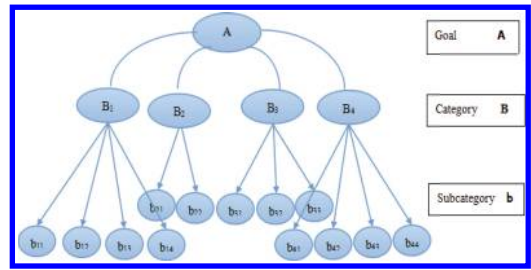


Figure 1. A hierarchical analysis model of risk factors in the decision-making stage.

divided into four classes, so as to form a hierarchical structure. The hierarchical model is divided into three layers: the goal, the risk in the project decision-making stage, and the category. The four main aspects of the risk decision-making phase of the project are, namely, the owner risk, design risk, policy risk, and risk management. The subcategory: the 13 factors of the category, by using AHP method to establish the hierarchical structure of the risk factor analysis model, as shown in the Figure 1.

##### 4.2 Confirming the relative evaluation criteria, constructing judgment matrix

Judgment matrix is expressed in the form of matrix elements in each level relative to the importance of the upper. In order to make the comparison between various factors get quantitative judgment matrix, the introduction of 1-9 scale, as shown in Table 3, the first is the judgment matrix, the comparison matrix, according to the above principles, reference 1-9 scale settings, and according to the expert and the author's experience and references. The judgment matrix is shown in Table 2.



Table 2. Comparison matrix A-B<sub>1-4</sub>.

R	r <sub>1</sub>	r <sub>2</sub>	r <sub>3</sub>	r <sub>4</sub>
r <sub>1</sub>	1	1/3	3	4
r <sub>2</sub>	3	1	4	5
r <sub>3</sub>	1/3	1/4	1	1/2
r <sub>4</sub>	1/4	1/5	2	1

Table 3. 1-9 scale table.

Scale $a_{ij}$	Definition
1	'i' and 'j' are equally important factors
3	'i' is a little important than 'j'
5	'i' is more important than 'j'
7	'i' is very important than 'j'
9	'i' is absolutely important than 'j'
2, 4, 6, 8	The intermediate state standard value If the comparison between I and j, get the value judgment. $a_{ji} = 1/a_{ij}$ , $a_{ii} = 1$

Table 4. 'RI' value.

n	1	2	3	4	5	6	7	8	9	10	11
RI	0	0	0.58	0.90	1.12	1.24	1.32	1.41	1.45	1.49	1.51

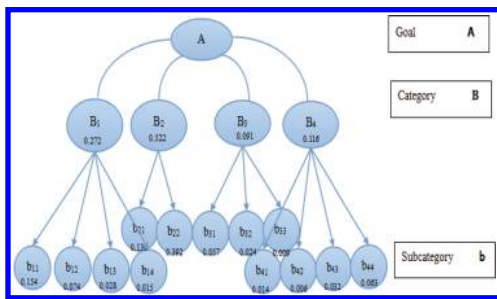


Figure 2. Layers structure calculation results.

4.3 To calculate the maximum characteristic root of judgment matrix and its eigenvector and consistency check

Tested by the consistency index,  $CI = (\lambda_{max} - n) / (n - 1)$   $\lambda_{max}$  it is the biggest characteristic value of comparison matrix 'n' is the matrix order. The value of A is smaller, the closer to the completely consistent judgment matrix. On the contrary, the judgment matrix deviation has a greater degree.

1. For the judgment matrix A,  $\lambda_{max}^{(0)} = 4.21$ ,  $RI = 0.9$  (refer to Table 4)

$$CI = \frac{4.21 - 4}{4 - 1} = 0.07 \quad CR = \frac{CI}{RI} = \frac{0.07}{0.9} = 0.07 < 0.1$$

The extent of the inconsistency of A within the allowable range features vector of A instead of weight vector.

Similarly, through the consistency check on the above principle, the hierarchy drawn from the goal to calculate the factor level is shown in Figure 2.

5 ANALYSIS OF TEST RESULTS

Based on the risk identification and assessment of green building on the decision-making stage, use the AHP to establish the risk quantification model. Based on the comprehensive analysis of the probability of occurrence and harm degree of risk, the importance of risk ranking is realized and the following conclusions are drawn:

1. Project decision stage risk mainly includes the owner's risk, design risk, policy risk, and management risk. Their probability is respectively: 0.272, 0.522, 0.091, and 0.116. That is: design risk > owner's risk > management risk > policy risk. The above shows that in the green building design, there is a key part of the decision-making stage of green building project.
2. The above calculation shows that the owner's risk is mainly the lack of accurate estimation of the return of long-term investment on green building. Design risk is mainly designed to exceed the level of construction technology. Policy risk is mainly green building-related policies and laws are imperfect, risk management is the main financial institutions lack of enthusiasm.
3. The 13 risk factors of green building decision stage, the risk factors affecting the decision-making stage of the occurrence probability and importance: 'Green design exceeds the level of construction technology' > 'The lack of accurate estimation of the return of long-term investment on green building' > 'The design did not reach the owner's goal about green building' > 'The funding conditions and management level of owners' > 'The lack of experience in green building consultant' > 'laws and regulations of Green building are not perfect' > 'Green building investment estimates are inaccurate' > 'The change of green building policy' > 'Financial institutions are lack of enthusiasm for green building' > 'The green star target location is not accurate' > 'The certification standard of green building is not clear' > 'The government bureaucracy and multifarious approval process' > 'Without a proper understanding of the market demand for green building'.

The above results show that: first of all, the owners play an important role in the project decision-making stage, the employer and the contractor of the communication barriers are the root

of the risk, and it will inevitably lead to inconsistent target owners and design target and a series of problems. Second, the policy and the market does not have an accurate grasp, which is a major cause for the green building to cause the error in the decision-making stage. Green buildings, compared to ordinary buildings, have more requirements and market demand, there must be a strict regulation, the policy and the market does not have an accurate grasp, there will be some problems, such as investment estimation is not accurate, cumbersome approval and financing.

## 6 CONCLUSION

Based on the life cycle perspective, green building project's decision-making stage is the key to the success of the project phase, based on the AHP method to analyze the green risk of construction project decision-making stage, which sets up the risk evaluation index system and the risk assessment model of green building. It is concluded that the key risk factors are in the project decision-making stage. The results of the study for the project are to provide a theoretical basis for effective risk management. For the contractor, it is necessary to strengthen the owners understanding, including their funds, credit, and related qualification. So as to reduce the risk of the owners, the contractor should learn from past experience, a correct understanding of the objective demand of the market, grasp the market demand, improve the ability of investment estimation, to reduce the risk of investment, learning green building related laws, regulations, the approval process, etc. Hope that these measures help decision-makers to

identify risk factors for decision-making stage and reduce risk.

## REFERENCES

- [1] China green building network[EB/OL]. (updated 2015-01-17).<http://www.cngbn.com/>.
- [2] Wan Xin & Xuan Qin. Risk Identification and Evaluation of Green Building Projects Based on Empirical Study [J]. *Building Science*, 2013, 29(2):54–61.
- [3] Rajendran S., Gambatese J.A., Behm M.G. Impact of green building and construction on worker safety and health [J]. *Journal of Construction Engineering and Management*, 2009, 135(10):1 058–1 066.
- [4] Jinghu Wang, Qin Xuan & Wan Xin. Risk Factors Identification and Risk Path Analysis on Green Building Project [J]. *Construction Technology*, 2012, 41(11):30–34.
- [5] Fang Zhou, Li Zuo-chen & LiSi-tang. The Management of the Green Risk of Construction Project [J]. *Construction & Design for Project*, 2009, (8):136–138.
- [6] Kibert C.J. *Sustainable construction: Green building design and delivery* [M]. Hoboken: John Wiley & Sons, 2008.
- [7] YunAi Wang. *The Study on Risk Assessment of Green Building Project in Decision Stage* [D]. Zhejiang University, 2014.
- [8] Xuan Qin & Jing Lei. Risk ranking and assessment in the whole life cycle of green building: an empirical investigation from construction industry [J]. *China Civil Engineering Journal*, 2013, 46(8): 123–135.
- [9] Xuan Qin, Yan Ya-qing & Mo Yi-yi. Risk measurement index identification and assessment for green buildings in Haixi region [J]. *China Safety Science Journal*, 2014, 24(9):102–108.
- [10] Li Zheng Kun. Fuzzy Comprehensive Evaluation For Green Building Risk Based On FEAH [J]. *Fujian Construction Science & Technology*, 2014, 87–90.

# Research on collaborative design application based on BIM

Wei Xu & Yuandong Liu

Architectural and Civil Engineering Institute, Inner Mongolia University of Science and Technology,  
Baotou Inner Mongolia, China

**ABSTRACT:** It is difficult to meet the design requirements of large and complex projects by means of the traditional design mode. The design organization makes use of cooperative design based on BIM. In this way, there are many obstacles in the process of implementation. This paper is concerned with the analysis of the main content of obstacle in the process of BIM based collaborative. The emphasis of this study lies in summarizing 3D collaborative design method under the BIM mode. The major object of their further work will be research into the path of collaborative design based on BIM. The procedure they followed can be briefly described as five steps such as specified target, team organizing, execution plan, specified collaborative platform, and the implementation of the collaborative design. As can be seen from the barriers reduced, the accurate and efficient BIM model of collaborative design will gradually replace the single linear traditional model.

**Keywords:** BIM, cooperative work, collaborative design, collaborative work platform

## 1 THE DEFINITION OF BIM AND COLLABORATIVE DESIGN

### 1.1 *The definition and characteristics of BIM*

Building information model also referred as BIM (Building information Modeling) as a concept was first introduced into the building construction industry in the 1970s. So far, there is no concluded definition for BIM regionally or internationally. USA BIM National Committee defines BIM as a digital expression of the physical characteristics and features of facilities. Hong Kong Polytech University and Tsinghua University BIM team defines BIM as a system based on the digital technology and visualization technology, method of information integration and management of construction project life cycle.

Although the above definitions are distinct, it is widely acknowledged that the essence of BIM is an emerging information technology application in the field of construction engineering. BIM (building information model) is based on the most advanced 3D design and engineering software build “visualization” digital building model. It provides collaborative design platform of “simulation and analysis” for construction project staff and uses the 3D model design, construction, and operation management of the project<sup>[1]</sup>. BIM has the following characteristics:

1. Visualization: BIM can achieve real-time visualization in the whole life cycle of the project

construction, each stage includes a project entity by way of three-dimensional modeling. This is the most fundamental characteristics of BIM.

2. Integration: In the integrated information of BIM established model, it not only includes the form of construction project space and related basic information but also other relevant information in the whole life cycle of projects.
3. Coordination: BIM can coordinate collision problem between all the professional designs in the early stage of the project, and generate coordinate data of available submission. This helps the participants of construction project to coordinate the problem of project.

### 1.2 *Collaborative design based on BIM*

Collaborative design is done through the coordination of different individuals and platforms. Collaborative design is a method of design communication to optimize the final design goal. With the raging concept of green energy-saving and sustainability, it requests people to constantly adapt their design to the requirement of construction. Now a project design not only includes planning, building, structure, HVAC, water supply and drainage, electrical, power, also contains rack, steel structure, intelligence, landscape, etc<sup>[2]</sup>. Collaborative design is not only a simple file reference. The traditional collaborative design system which based on two-dimensional plane visualization is no longer flexible to the project running.

Collaborative design based on BIM breaking “information island” of the traditional design mode, sharing project information to all members of the professional design, replacing the traditional single linear working mode, improving the efficiency of design<sup>[3]</sup>. The essence of collaborative design which is based on BIM has various professional work together under the same model. This way is a special concept which is completely different from construction drawing CAD. This way of design not only meets the current architectural design project requirements of professional collaboration, but also helps to coordinate communication among the design units and construction units. Design unit can be combined BIM technology and collaborative design and provides collaborative work platform that does not exist in the traditional design pattern for the professional design. Each professional design uses this platform to share the design results, collision check and crossover design so that the purpose of improving the design precision and optimization design is achieved.

## 2 COLLABORATIVE DESIGN BASED ON BIM SOLVE THE OBSTACLES

### 2.1 *The influence of the traditional thinking model*

In the traditional thinking of the architectural design, various professional designer works are independent: Architectural design ahead, structural design second, mechanical and electrical equipment design at last. The design process and working mode based on the traditional thinking seriously restricted the implementation of collaborative design.

Designers have resentment of the collaborative design based on BIM, mainly because it has been to use their familiar tools to express the design ideas. Compared with the methods of 3D building information and two-dimensional, there are certain shortcomings. For example, there are some blind areas in display<sup>[4]</sup>. Learning BIM will consume part of designer’s energy, which affects the design personnel individual or design unit interest within a certain period.

In addition, the project managers have a certain resentment of the collaborative design based on BIM. Although the long term, the design of enterprises from the traditional design pattern to the collaborative design mode transition is based on BIM which can greatly improve work efficiency, save unnecessary costs, get a lot of money income. But the enterprise will be affected in the short-term interests. What is more worried about using BIM technology is to change design mode and

management mode, which may eventually lead to the failure of the project.

### 2.2 *BIM software support functions less*

Project personnel involved in BIM is common feelings of most of the BIM-related software applications not like the long traditional software meeting the engineering requirements in the process of collaborative design based on BIM. Block collaborative design implementation based on BIM has two main problems:

#### 1. BIM model diagram unable to meet the project specification requirements

Although the mainstream BIM core modeling software is based on the BIM model output 2D drawings, these softwares are all foreign products<sup>[5]</sup>. The expression and the details from the BIM model output of the horizontal and vertical part information section drawings of two dimensions is not consistent with requirements of our country projects, resulting in two-dimensional drawings BIM export cannot be directly applied to the project. So design units in China are often not only with the BIM output of 2D drawings but also to the BIM output of the secondary processing using of traditional software, wasting unnecessary manpower, reducing the efficiency.

#### 2. Information flow between the software

Although associated with BIM software variety, there was no software on the market today that can simultaneously satisfy all the necessary functions of the BIM design projects. Therefore, BIM design project generally needs to be applied to multiple softwares through which the information flow between software transfers becomes the key factor of collaborative design<sup>[6]</sup>. Now, however, almost the import or export of all across software platform model can result in the loss of information. This greatly affected project implementation with collaborative design based on BIM. Many domestic software vendors are used for traditional BIM software and professional software, but it is difficult to completely solve the problem of poor information flow between BIM software in a short period of time. So, BIM design will be mainly used in local projects, local specialty, and the local process in the future transition period<sup>[7]</sup>.

## 3 THE PROMOTION OF COLLABORATIVE DESIGN BASED ON BIM

The promotion of collaborative design based on BIM have different kinds of obstacles. This paper

mainly research on the approach of promoting collaborative design based on BIM, also touches on its application in the design industry.

### 3.1 Specify the BIM object

Specifying the BIM object is to clarify the results of project achieved by using BIM technology, which is the core of project implementation of BIM. According to the project using BIM technology in different stages, the main object is not the same. In the design stage, the main goal of BIM is to realize the collaborative design. The main way of application has demonstration project, design modeling, and 3D coordination.

### 3.2 Headings

The BIM design team constitutes by BIM manager, BIM engineer, BIM coordinator, and BIM modeler according to their role played in the whole process. The responsibilities of these four positions are shown in Figure 1.

BIM manager as the most important role must have a thorough understanding of the entire design process, from concept design to design documentation to contract administration. Certain knowledge of project management is also required in order to specify the plan, management team, the implementation of the monitoring plan, etc. In addition, BIM manager bears the responsibility of communicating with clients and understand their intention, and inform the client if BIM technology can be potentially helpful to achieve their requirements over the proposal.

BIM coordinator is to assist the communication between BIM manager and BIM designers. BIM manager is very scarce talent in BIM project, in general, who will be responsible for multiple projects at the same time. Therefore, the BIM managers do not devote themselves into one single BIM project. The main duty of the BIM coordinator is to assist BIM manager in their work, including the specified implementation plan and supervise the work process. In addition to this work, the BIM coordinator is also responsible for building collaborative work platform and managing coordination model of BIM component library.

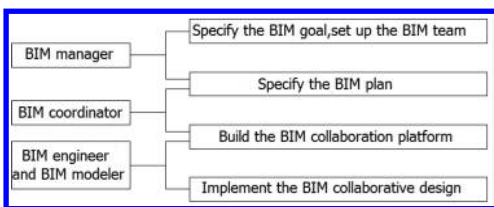


Figure 1. BIM design team responsibilities.

Apart from BIM manager and BIM coordinator, a BIM project team also includes multiple experienced BIM designer and BIM modeler who specialized in using the BIM software. BIM designer or engineer is mainly divided into three professional of construction, structure, electrical, and mechanical. BIM engineers of different professional each lead a BIM modeling team composed of the professional BIM modeler. BIM engineer is responsible for arranging the specific work for the professional staff in BIM modeler and coordinate with problems of the professional team in the process of BIM modeling.

### 3.3 Specify the BIM implementation plan

Compared with the common design approach, the collaborative design based on BIM demands high hardware and more resources. Therefore, design units accept the commission of the BIM projects and determine the BIM target, giving full consideration to the project and the design team, forecast problems may arise in project, forecasting feasible implementation plan. BIM implementation plan of construction project should include the project information, application goal, the specific content of the work mode, and resource requirements.

### 3.4 Building of BIM collaboration platform

Building of BIM collaboration platform is the foundation of collaborative design used in BIM technology in construction projects. First, by combining the design personnel information with the related construction project information. Second, based on the personnel related information, aim to determining the project BIM model split principle, detail and delivery standards. Finally create essential project template and share coordinates and folders in the collaborative work platform. Collaborative work platform to realize the collaborative design based on BIM among different professions, its core is to achieve a smooth information exchange process between different professional deliveries (Fig. 2).

In addition to realize the seamless exchanged transfer process between different professional BIM model information, the collaborative work platform has another function that is to achieve comprehensive and efficient management information which includes information management and personnel management.

Information management includes two aspects of information sharing and information security. A BIM model file storage space is far more than an ordinary CAD file. As a unified platform of collaborative work platform for the professional work together, which meets the characteristics of

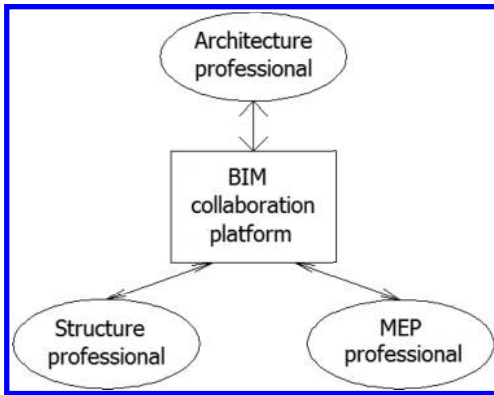


Figure 2. The professional relationship in the BIM collaborative design.

producing a large number of data transmission and improve the design efficiency, realize the sharing of information. Meanwhile, the collaborative work platform as a unified platform to ensure the information security of BIM project. The BIM project contains related information of core technology.

In personnel management, the designers need their own user name, log into collaborative work platform, and have their own working set and corresponding operation permissions. Such a clear division of responsibilities, the responsibility to the people promote the smooth implementation of the plan in accordance with the implementation of BIM project.

### 3.5 Implementation process of the BIM project collaborative design

Collaborative design includes two kinds of collaborative design of the same professional within and different professional. The former is the professional design personnel in the respective model collaborative conflict in place, the latter is the professional person in charge of collaborative models in conflict between the professional.

The structure and mechanical and electrical professional to start drawing at this stage, first the construction of the professional establish their own center files, second the structure and the electrical professional establish the professional file center through building professional established construction center files. Professional internal divided by the working set, professionals with links manner. After major changes from 2D to 3D, eventually reaching a full professional BIM collaborative design stage that is truly collaborative design by the complex transition cooperation.

## 4 CONCLUSION

Along with the social development, the large and complex projects increase gradually. The traditional design methods have been approved gradually losing its capability to meet the design requirements. Collaborative design based on BIM changed the single linear model of the traditional cooperated work, which meets the construction design should achieve the high standard requirements. But there are many obstacles in the implementation process. In this paper, putting forward the paths in the design units through studying the implementation barriers of collaborative design based on BIM. It contains five steps of the choice of target, the work team, execution plan, collaborative work platform construction, and the collaborative design process implement. This allows the designers to be able to working and communicating with contractors on the same platform, thus achieving the cross collaboration design which both sides can have a correct and instant understanding of the division of labor resource. With BIM technology development, the application obstacles of collaborative design based on BIM will reduce gradually. Eventually BIM platform will become a trend in the construction, which will lead to the change of design industry.

## REFERENCES

- [1] Xi Zhao & He Sang. The Effect and Prospect of BIM in the Architectural Design Industry Changes [C]. *The architect branch of China construction institute 2010 academic essays*. Guang Zhou: 2010.
- [2] Dehai Zhang, Jinyu Han, Hainan Zhao, Yunfeng Yao, Li Yin. How to Achieve Efficient Building Collaborative Design Under the Environment of BIM [J]. *Journal of Information Technology in Civil Engineering and Architecture*, 2013, 5(6):43-47.
- [3] Ke Yang, Dengze Kang, Chuanbo Che, Peng Xu. The Research of Collision Detection Based on BIM in Collaborative Design [J]. *Journal of Information Technology in Civil Engineering and Architecture*, 2013, 5(4):71-75.
- [4] Li Li & Xueyuan Deng. Building Information Platform Based on BIM Technology [J]. *Journal of Information Technology in Civil Engineering and Architecture*, 2012, 4(2):25-29.
- [5] Guanpei He. BIM and BIM Software [J]. *Journal of Information Technology in Civil Engineering and Architecture*, 2011, 2(4):110-117.
- [6] Jianxin Zhang. Study on Application of Obstacle of Building Information Modeling in Engineering Design Industry in China [J]. *Journal of Engineering Management*, 2010, 24(4):387-392.
- [7] Jun Qin. The Application of BIM in Architectural Design Stage [J]. *Architecture Technique*, 2011(1): 19-22.

# Experimental study on smoke propagation in titled underground tunnel fires

J.M. Li, Z.H. Huang & C. Chen

*Beijing University of Technology, Beijing, China*

J. Chuang & Y. Li

*Beijing General Municipal Engineering Design and Research Institute Co. Ltd., Beijing, China*

**ABSTRACT:** Fire safety in tunnels is a concern due to the large traffic flow, especially in a tunnel with a great slope. Experimental studies on the smoke spread in a small-scale titled tunnel are carried out. Effects of the titled gradients and longitudinal ventilation speed on the temperature distribution and smoke stratification downstream from the fire along the tunnel will be studied. The results show that the smoke spread upwards much faster with the slope gradient increasing, and a thick smoke layer was formed when smoke moved to the upward part of the tunnel and filled it up. The ventilation speed had a great influence on temperature distribution along the tunnel. Lower ventilation speed should be kept at the start of the fire to ensure the smoke layer not be destroyed downstream of the fire to give the tunnel users more time to escape.

**Keywords:** underground tunnel; reduced-scale model; smoke spread; fire

## 1 INTRODUCTION

In order to mitigate the traffic congestion problems, more and more urban tunnels have been and will be constructed due to the heavy traffic in dense urban areas in China in recent years. Comparing with other kinds of tunnels, traffic in urban tunnels may have larger traffic volumes due to its special site. Fire accidents may occur due to the collision of the cars, the engine overheating, the mechanical or electrical failure, etc. Fire safety in these kinds of tunnels is becoming a major issue following the catastrophic losses experienced in the Mont Blanc tunnel fire in 1999 and the Gotthard tunnel fire in 2001. Consequences of a tunnel fire can be very serious, which might lead to tragic injuries and fatalities, considerable infrastructural damage, loss of income due to the breakdown in operation and loss of public confidence in the use of road tunnels. Due to the confined conditions, such fires can be more severe, in terms of rate of growth and temperature, than that in the open field<sup>[1,2]</sup>.

To assess the hazards arising from tunnel fires and draw some effective mitigation strategies, fully understand the smoke and heat propagation in tunnels is necessary. Knowledge about smoke and fire spread in tunnels has generally been obtained from large scale testing. However, sometimes large scale testing is expensive, time consuming and

logistically complicated to perform. The information obtained is often incomplete due to the limited number of tests and the limited instrumentation. Reduced-scale tests can be used as a complement to large scale testing. They can provide information which is difficult to obtain otherwise as their relatively low cost allows for parameter studies<sup>[3,4]</sup>.

The urban tunnel always having slopes comparing with other kinds of tunnels, and the slope would influence the smoke spread greatly due to the stack effect. Although there were a lot of works having been done on studying the smoke spread in tilted tunnels by experimental or numerical methods<sup>[5-8]</sup>, smoke movement pattern in these kind of tilted tunnels is not fully understood, further studies are needed<sup>[9]</sup>.

## 2 REDUCED-SCALE MODEL EXPERIMENT

A 1/6 scale tunnel model with rectangular cross section was constructed by the fire glasses boards, and the model tunnel itself is 6 m long, 1.5 m wide, and 1.3 m high, as shown in [Figure 1](#). Similarity rules impose a strict conservation of Froude number so that, for a geometrical reduction factor  $\alpha$ , velocities are given in the scale  $\alpha^{1/2}$  and both flow rates and heat release rates are scaled according to  $\alpha^{5/2}$ <sup>[10]</sup>.



Figure 1. Reduced-scale model tunnel.

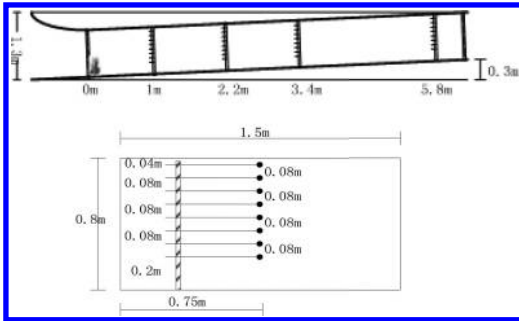


Figure 2. Distribution of the thermocouples.

Different titled gradients of 0, 3% and 5% were built by raising the one end of the model tunnel. Smoke spread in these three tunnels would be studied respectively.

Longitudinal ventilation was achieved by driving inlet air flow by a fan at one end. The rotational speed, and thereby the capacity, could be controlled using an electrical device coupled to the motor. Longitudinal ventilation velocities of 0 m/s, 0.6 m/s, 0.9 m/s and 1.2 m/s are used in the test series.

The fire source was a 0.3 m × 0.3 m (L × W) porous bed burner with its top surface set flush with the tunnel floor, LPG was used as fuel, metered through a rotameter. Fire sizes of 57 kW was produced by changing the flow rate of the LPG respectively in the experiments, these fire sizes correspond to fires of approximately 5 MW when the scaling procedure was applied. They thus represent typical vehicle fire sizes in urban traffic tunnel<sup>[11]</sup>. The burner is located at the center of the tunnel, 0.3 m away from the tunnel entrance.

Thermocouple trees (K-type) distributions in longitudinal direction along the tunnel were shown in Figure 3, and vertical distributions of thermocouples in one thermocouple tree were also shown in Figure 2, measuring the temperatures at the relative positions.

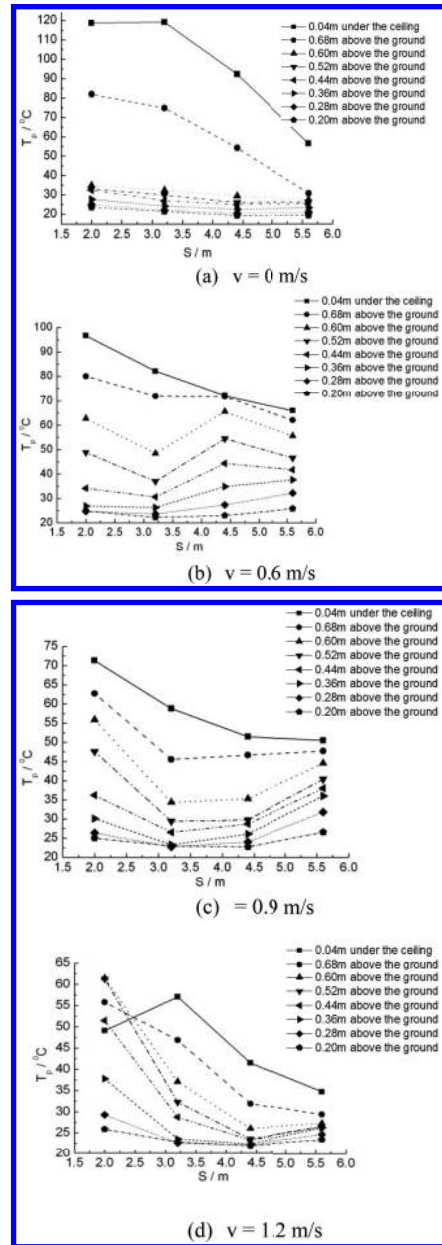


Figure 3. Temperature distributions along the tunnel under different longitudinal ventilation velocities (level tunnel).

### 3 RESULTS AND DISCUSSION

Vertical temperature distributions at different height above the tunnel floor at the center-line of the tunnel and longitudinal temperature distributions along the tunnel under different



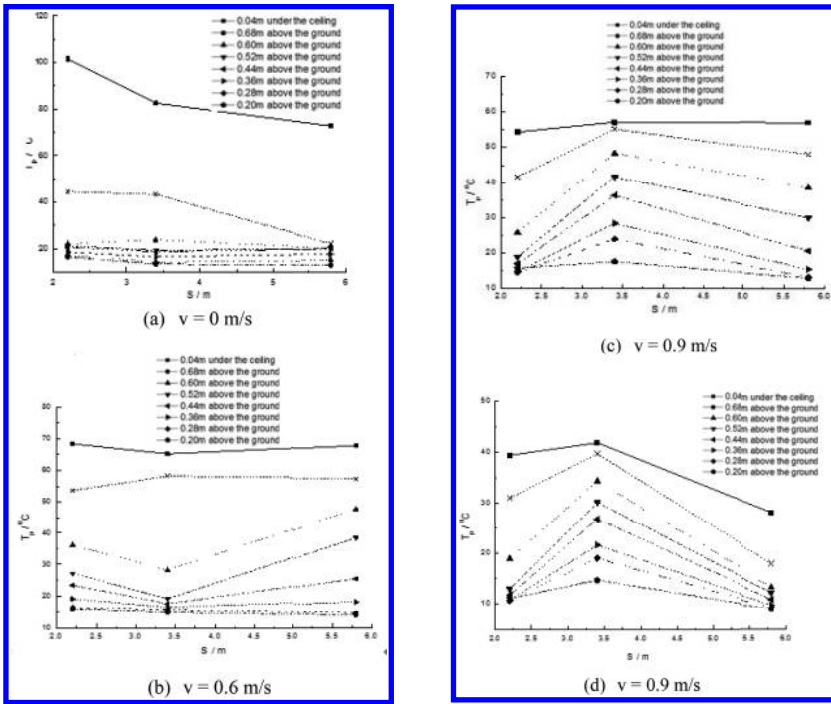


Figure 4. Temperature distributions along the tunnel under different longitudinal ventilation velocities (tunnel slope = 3%).

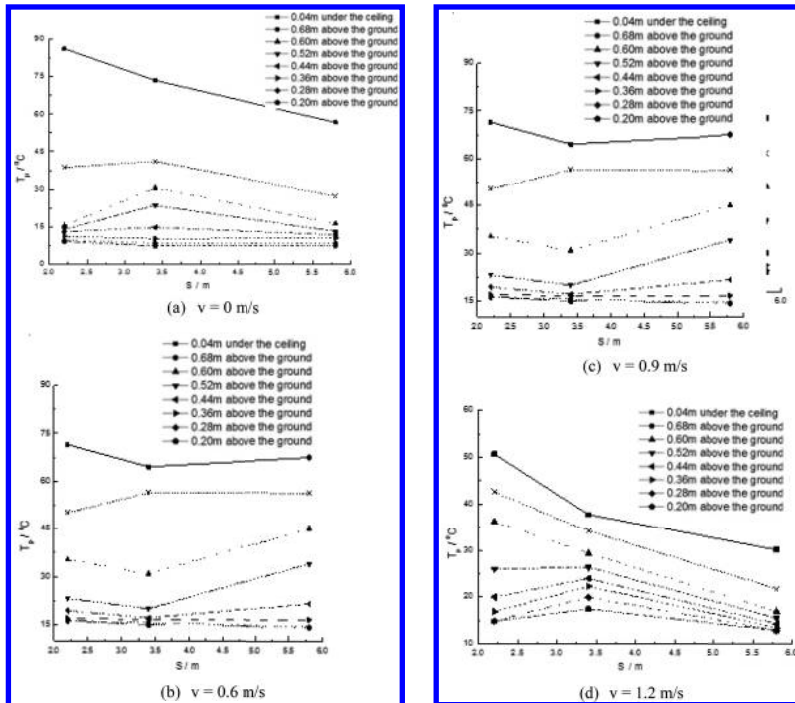


Figure 5. Temperature distributions along the tunnel under different longitudinal ventilation velocities (tunnel slope = 5%).

longitudinal ventilation velocities and different inclined gradient for fire size of 60 kW were shown in Figure 3, 4 and 5 respectively. It can be found that the temperature of the smoke is higher at the zone close to the fire source, and it will be cooling down when it propagates along the tunnel due to the combined effects of the convective heat exchange with walls and mixing between the smoke the fresh air layer. The smoke stratification is found clearly along the tunnel with no ventilation. With the longitudinal ventilation speed increasing, temperature at the higher position above the tunnel floor would decrease due to the flame deflected by the wind, hot smoke will spread at the lower level, this lead to the longitudinal temperature gradients become small, and temperature at the zone far away from the fire source would increase. At the mean time, the vertical temperature gradients were also found to be reduced along the tunnel, and this means that the stratified smoke would be disturbed. This might be dangerous for the tunnel users at downstream of the fire, they need to pass through the hot smoke layer to escape from the tunnel. With the gradient of the slop becoming large, higher temperature would be found at the downstream from the fire, another factor the main factor to hot smoke is found to spread much faster to the top exit than that in the level tunnel. This might be dangerous for the occupant's evacuation.

### 3 CONCLUSION

The smoke spread in a titled tunnel with different titled gradients under different longitudinal velocity is studied by the reduced-scale model test in this paper. The results show that hot smoke spread much faster to the top exit due to the stack effect in a titled tunnel than in the level one, and a thick smoke layer is formed when smoke moved to the upward part of the tunnel and filled it up. This will be dangerous for the occupant's escaping. Some special smoke control measures should be taken when the fire occurs in a tunnel with slope. The ventilation speed is found to have a great influence on temperature distribution along the tunnel, maximum temperature in tunnel due to the fire would be reduced, and the smoke stratification would be distributed when the longitudinal ventilation speed becomes large. Lower ventilation speed should be adopted at the beginning to ensure the smoke

downstream of the fire keep stratified to give the tunnel users more time to escape. The results might be useful for the smoke control design and operation in these kinds of tunnels.

### ACKNOWLEDGEMENTS

This paper was supported by National Key Project of Scientific and Technical Supporting Programs Funded by Ministry of Science & Technology of China (Grant No: 2012BAJ01B03); The National Natural Science Foundation of China (Grant No: 51278018); and Beijing Natural Science Foundation (Grant No: 8132011).

### REFERENCES

- Atkinson G.T. & Wu Y. 1996 Smoke control in sloping tunnels. *Fire Safety Journal* 27(3): 335–341.
- Ballestos T.R., Carlos S.M. & Eduardo B.M. 2006. Influence of the slope in the ventilation semi-transversal system of an urban tunnel. *Tunnelling and Underground Space Technology* 21: 21–28.
- Blanchard E., Boulet P., Desanghere S., Cesmat E et al. 2012. Experimental and numerical study of fire in a midscale test tunnel. *Fire Safety Journal* 47:18–31.
- Chow W.K., Wong K.Y. & Chung W.Y. 2010. Longitudinal ventilation for smoke control in a tilted tunnel by scale modeling. *Tunnelling and Underground Space Technology* 25: 12–28.
- Hwang C.C., Edwards J.C. 2005. The critical ventilation velocity in tunnel fires – a computer simulation. *Fire Safety Journal* 40: 213–244.
- Ingason H. & Li Y.Z. 2010. Model scale tunnel fire tests with longitudinal ventilation. *Fire Safety Journal*, 45: 371–384.
- Li J., Liu X., Fu C. & Li Y. et al. 2010. Numerical Simulation on fire environment in Urban Traffic Tunnel. *Proceedings of the 2010 International Symposium on Safety Science and Technology*, October 26–29, Hangzhou, China, Vol. VIII, Part A, 632–640.
- PIARC. 1999. Fire and smoke control in road tunnels. *PIARC, 05.05B-1999*.
- Quintiere J.G. 1989. Scaling applications in fire research. *Fire Safety Journal* 15: 3–29.
- Lee, S.R. & Ryou, H.S. 2004. A numerical study on smoke movement in longitudinal ventilation tunnel fires for different aspect ratio. *Building and Environment* 41: 719–725.
- Wu Y. & Bakar M.Z.A. 2000. Control of smoke flow in tunnel fires using longitudinal ventilation systems—a study of the critical velocity. *Fire Safety Journal* 35(4): 363–390.

# Joint operation of water quantity and water quality based on dualistic water cycle

J. He, S.P. Gu & L.S. Suo

Hohai University, Nanjing, China

**ABSTRACT:** With the rapid development of China's economy, water shortage and pollution are serious in many river basins. Water storage projects have the potential to simultaneously improve the water supply guarantee and protect the water's environment. In this paper, the degree of water supply guarantee and the degree that standard water quality reaches are defined. Based on dualistic water cycle framework, the hydrological model and the water supply system are integrated. Then multi-objective optimization model for water quantity and quality in River Basin is established. An example proved that water supply indicators and water quality indicators significantly improved. The rationality and validity of the model can be verified. The model provides an effective way to reduce water shortage and water quality deterioration in river basin.

**Keywords:** water quantity and quality; operations optimization; river basin; dualistic water cycle

## 1 INTRODUCTION

With the rapid development of China's economy and urbanization, water shortage and water pollution is becoming more and more serious. Water quality of many rivers is worse than Class III. On one hand, this is due to natural factors, such as the large difference between the space-time distributions. On the other hand, multi-objective optimization of water projects is absent for water quantity and quality. The basic idea of this paper is to integrate precipitation, runoff, water supply, consume, return, and projects operation. Thus, the joint operation optimization model of water quantity and quality is established. The ideas considered are as follows: a) based on dualistic water cycle system on natural and artificial rules, nature, society, economy, and environment factors are combined into an organic system; b) by defining the guarantee degree of water supply and then reaching degree of water quality standard, an optimization model is established. It is more reasonable than ever to avoid results that depart from the actual.

## 2 SYSTEM DESIGN BASED ON DUALISTIC WATER CYCLE

### 2.1 Basic dualistic water cycle framework

Under modern conditions, large-scale human activities cause hydrological cycles showing a significant Natural-Artificial duality (Wang, H. et al. 2006). The first is duality of cyclic nature, which

means the water cycle of human community often involves the natural cycle and artificial cycle to maintain dynamic relations between the two cycles; the second is dual function of water services, which means water, in its conversion process, supports socio-economic system and ecological systems (Wang, H. et al. 2010).

According to the theory of dual water cycle, the basin water resource allocation is based on mutual coupling of natural water production and social water use. Natural water circulation describes the process from slope to the river, social circulation focuses on water regulation, supply, use, and drainage. It means the joint operation optimization models of water quantity and water quality include hydrological model, water quality model, simulation model of project operation, and optimization model.

Hydrological model calculates evapotranspiration and runoff from precipitation in each sub-basin and gets the export flow of each sub-basin. The export water of each sub-basin enters downstream of the river or enters a reservoir if there is a project at sub-basin export. According to water user location, the water is allocated to the right place for human living use, industrial use, agricultural use, and ecological use. The dualistic water cycle system of a river basin is shown in [Figure 1](#).

### 2.2 Basic unit definition and system design

Natural water cycle model calculates runoff from precipitation every 24 hours. So large basins should be divided into several sub-basins according to the

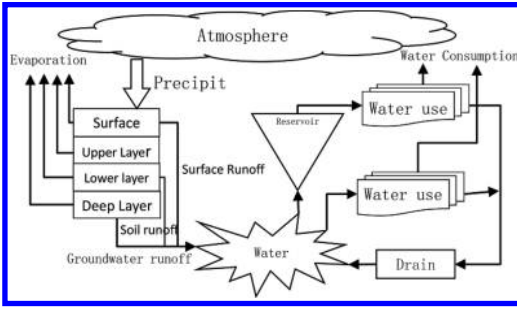


Figure 1. Dualistic water cycle system of a river basin.

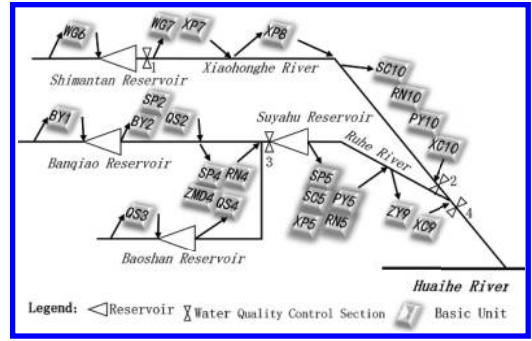


Figure 3. Topological relation of the system.

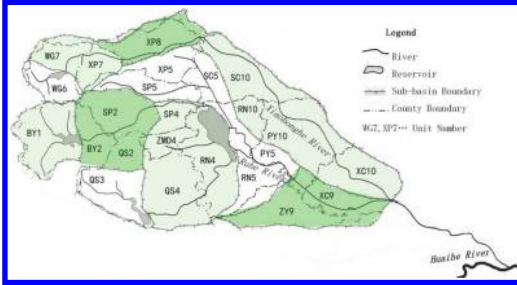


Figure 2. The definition of the basic unit.

hydrological model. Since artificial collateral cycle focuses on water demand and uses each period, the basin is divided into several user partitions according to administrative districts. To solve inconsistent time and space scales of natural cycle and artificial cycle, the basic unit is defined as numbered polygons, made by overlaying administrative region layer on sub-basin layer by GIS software. An example is shown in Figure 2 in section 4.

This method has obvious advantages. Each basic unit can completely belong to a particular sub-basin or user district to facilitate decomposition and polymerization. It is the smallest independent area producing and consuming water inside. It also exports or imports water. It keeps integrity and independence to facilitate description of the relationship between multiple water sources and multiple users. The topological relations between sub-basins for producing water, project for storing water, and user districts for consuming water are convenient to be established. It is the foundation of the joint operation optimization model for water quantity and quality.

### 2.3 Topological relations of the system

Based on the definition of the basic unit, topological relations between water producing, water project operation, water supply, water return, and

sewage discharge can be determined. The example of topological relations can be seen in Figure 3 in section 4. According to Figure 3, the system can be simulated stepwise from upstream to downstream.

## 3 WATER QUANTITY AND QUALITY JOINT OPERATION OPTIMIZATION MODEL

### 3.1 Water quality model determination

Because of too many water quality indicators, the optimization model is impossible to control all indicators. Since concentration of various pollutants generally being associated, so long as key indicators are controlled, other indicators will be synchronized to be improved. According to the characteristics of river water quality, select  $COD_{Mn}$  as the representative of the pollution index (Liu, Y.N. et al. 2009). The purpose of the model is to find out optimization strategy in the statistical sense to control the average annual concentration of pollution, so steady-state one-dimensional river water quality model is appropriate to calculate pollutant concentration along river.

### 3.2 Objective functions

#### 3.2.1 Guarantee degree of water quantity

If guaranteed water amount (Zhang, S.P. et al. 2014) or probability is selected as objective function of the model, maybe water shortage in a number of unit period is too large but not distinguishable. The certain periods sacrifice to save water to benefit other periods. But even small number of period with large water shortage rate is unacceptable in the actual. To overcome these problems, the relative water shortage rate is better for objective function. This paper defines guarantee degree of water quantity as key indicator. The guarantee degree of water quantity equals to ratio

of water supply and water demand, and equals to 1—water shortage rate. It is the basis of the objective function. The objective function of water quantity is average of the minimum guarantee degree each year. See Equation 1.

$$\max_G S(G) = \frac{1}{Y} \sum_{y=1}^Y \left( \min_{t \in [1, T]} \frac{\sum_i \sum_j \sum_k G_{kij}^{(t)}}{\sum_i \sum_j X_{ij}^{(t)}} \right)^{(y)} \quad (1)$$

where,  $y$  = the year number, ranging 1 to  $Y$ ,  $Y$  = the number of years;  $t$  = period number in a year, ranging 1 to  $T$ ,  $T$  = the number of periods;  $k$  = the reservoir number;  $i$  = unit number;  $j$  = the department number of water use, including living use, production use, and ecological use;  $G_{kij}^{(t)}$  = water supply of project  $k$  to department  $j$ , unit  $i$ ;  $G$  = the plan  $\{G_{kij}^{(t)}\}$  constituted by  $G_{kij}^{(t)}$ ;  $X_{ij}^{(t)}$  = water demand of department  $j$ , unit  $i$ ;  $S(G)$  = average of minimum guarantee degree each year.

Equation 1 fits to situation of small water shortage, focusing on controlling the maximum water shortage rate. In situation of big water shortage, it is appropriate to control the average guarantee degree in place of the minimum each year. In addition, arithmetic mean cannot restrict very low guarantee degree appearing because of linear relationship, nonlinear geometric mean is better. The objective function is Equation 2.

$$\max_G S(G) = \frac{1}{Y} \sum_{y=1}^Y \left( \sqrt[T]{\prod_{t=1}^T \frac{\sum_i \sum_j \sum_k G_{kij}^{(t)}}{\sum_i \sum_j X_{ij}^{(t)}}} \right)^{(y)} \quad (2)$$

### 3.2.2 Reaching standard degree of water quality

The water quality optimization means to make use of water storage capacity of projects to improve the water quality along river. If the improvement of water quality level is set as high as possible (Liu, B.J. et al. 2009), or it is only controlled by constrains (Shao, D.G. et al. 2000), will result in depletion of all water supply capacity. It is unacceptable. Relative indicator seems reasonable (Zhang, Y.Y. et al. 2010). Therefore, this paper defines reaching standard degree as the index of how close is water quality indicator to certain standard (such as Class III standard), see Equation 3.

$$\varphi_{il} = \begin{cases} \frac{\mu_l^*}{x_{il}(G)} & x_{il}(G) > \mu_l^* \\ 1 & x_{il}(G) \leq \mu_l^* \end{cases} \quad (3)$$

where,  $G$  = the plan  $\{G_{kij}^{(t)}\}$ , same as Equation 1;  $x_{il}(G)$  = COD<sub>Mn</sub> concentration in period  $t$  at river section  $l$ ;  $\mu_l^*$  = water quality standard, namely,

COD<sub>Mn</sub> concentration of class III water standard at  $l$  river section;  $\varphi_{il}$  = reaching standard degree of water quality in period  $t$  at river section  $l$ .

This definition facilitates the flexibility to choose right target standard in accordance with local requirements or water functional division standard, so as to effectively guide the behavior of water resources management. The objective function is defined to control the closeness to standard in each river section and each period. Take the geometric mean to raise the low end value. Assumed the standard is level of class III water COD<sub>Mn</sub>, water quality objective function see Equation 4.

$$\max \Phi(G) = \frac{1}{Y} \sum_{y=1}^Y \left( \sqrt[T]{\prod_{t=1}^T \left( \frac{1}{L} \sum_{l=1}^L \varphi_{il} \right)} \right)^{(y)} \quad (4)$$

where,  $\Phi(G)$  = multi-year average of reaching standard degree of water quality.

### 3.3 Main constraints

Main constraints of the model are relationship of decomposition and polymerization. The first is the water balance between water projects and their subordinate units, see equation 5; the second is water balance between sub-basin and its subordinate units, see equation 6; the third is the water balance between water user district and its subordinate units, see equation 7.

$$V_{k,t+1} = V_{k,t} + I_{k,t} - \sum_{i \in I_k} G_{i,t} - O_{k,t} - S_{k,t} \quad (5)$$

where,  $I_k$  = members of units controlled by project  $k$ ;  $V_{k,t}$  = project  $k$  beginning storage capacity in period  $t$ ;  $V_{k,t+1}$  = project  $k$  end storage capacity in period  $t$ ;  $I_{k,t}$  = project  $k$  inflow in period  $t$ ;  $O_{k,t}$  = project  $k$  abandon water in period  $t$ ;  $G_{i,t}$  = project  $k$  supply unit  $i$  water including living use, production use, and ecological use in period  $t$ ;  $S_{k,t}$  = project  $k$  loss of water with evaporation and infiltration in period  $t$ .

$$R_{b,t} + U_{b-1,t} - \sum_{i \in I_b} G_{i,t} + D_{b,t} = U_{b,t} \quad (6)$$

where,  $I_b$  = members of units in sub-basin  $b$ ;  $R_{b,t}$  = sub-basin  $b$  production of water in period  $t$ ;  $U_{b-1,t}$  = sub-basin  $b$  import water from upstream sub-basin  $b - 1$  in period  $t$ ;  $G_{i,t}$  = sub-basin  $b$  supply unit  $i$  water in period  $t$ ;  $D_{b,t}$  = sub-basin  $b$  return water from user in period  $t$ ;  $U_{b,t}$  = sub-basin  $b$  export water to downstream in period  $t$ .

$$\sum_{i \in I_c} L_{i,t} + \sum_{i \in I_c} A_{i,t} = \sum_{i \in I_c} D_{i,t} + \sum_{i \in I_c} E_{i,t} \quad (7)$$

Table 1. Optimization solutions comparison.

Solutions	Water supply	Ave* GD**	Min GD**	COD <sub>Mn</sub>	RSD***
	10 <sup>6</sup> m <sup>3</sup>			mg/l	
Basic solution	1215	99%	91%	25.6	44.5%
Opt.Solution 1 (Recommend)	1212	99%	98%	19.6	54.5%
Opt.Solution 2	1211	99%	96%	19.5	54.5%

\*Ave = Average; \*\*GD = Guarantee Degree; \*\*\*RSD = Reaching Standard Degree.

where,  $I_c$  = members of units in district  $c$ ;  $L_{i,t}$  = unit  $i$  receiving water in period  $t$ ;  $A_{i,t}$  = unit  $i$  using water locally in period  $t$ ;  $E_{i,t}$  = unit  $i$  consumption of water in period  $t$ ;  $D_{i,t}$  = unit  $i$  getting return water in period  $t$ .

## 4 EXAMPLE OF THE MODEL

### 4.1 Introduction and definition of basic unit

Hongruhe River is a tributary of Huaihe River in east China. It is composed of Xiaohonghe River and Ruhe River. In this paper, research area is the basin of Bantai watershed, area 11,280 km<sup>2</sup>. There are 4 large reservoirs in the basin, named Shimantan Reservoir, Banqiao Reservoir, Baoshan Reservoir, and Suyahu Reservoir. The area involves a total of 11 county-level administrative regions, and is also made of 10 sub-basins to produce water. The definition of basic unit is shown in Figure 2. Whole area is divided into 24 units, encoded as BY1, BY2, etc. The letters portion represents county-class area. The digital portion represents sub-basin code. For example, the sub-basin numbered as 7 decomposed to WG7 and XP7. The region named as WG can be decomposed to WG6 and WG7.

### 4.2 Topological relationship

Based on dualistic water cycle in the basin, the system topological relationship is shown in Figure 3. The river control sections of water quality numbers 1 to 4, correspond to Shimantan section, Xincui section, Xiatus section, and Bantai section.

### 4.3 Data and calculation

According to the joint optimization model of water quantity and quality, input the precipitation data, runoff data, sewage discharge data (1997–2006), and water demand data of the planning year (2030). The average of annual water demand is 1227 million m<sup>3</sup>. Non-optimization calculations results are basic indicators for comparing. Operation rules of prioritize order is living

water, ecological water, industrial water, agricultural water, and each part have different water consumption rate. Non-optimization results show that water shortage mainly exists in Xiaohong River valley. Due to the lack of reservoir capacity, the minimum Guarantee Degree is low by 65.7%.

### 4.4 Results and solutions

In order to solve the model, multi-objective particle swarm optimizer is designed. The program running results prove that water quantity and quality indicators are better than non-optimization results in each reservoir control areas. Two typical Pareto solutions are compared in Table 1.

Solution 1 greatly enhances the minimum monthly guarantee degree; it increased from 65.7% to 91.6%. The maximum water shortage rate decreased from 34.3% down to 8.4%. In all water quality control sections, average COD<sub>Mn</sub> concentration decreased from 25.6 mg/l to 19.6 mg/l. The reaching standard degree to Class III increased by 10%.

In comparison, solution 1 and solution 2 both ensure average guarantee degree to 99%, meantime COD<sub>Mn</sub> of solution 2 is 19.5 mg/l, little less than solution 1, almost the same. But the minimum monthly guarantee degree is 96%, less than 98% of solution 1. In summary, we recommend solution 1.

### 4.5 Evaluation

The example illustrates that the joint operation optimization model of water quantity and quality can greatly enhance the guarantee degree of water quantity and significantly improve the reaching standard degree of water quality. The rationality and effectivity of the model was verified.

## 5 CONCLUSION

The joint operation optimization model of water quantity and water quality in river basin based on dualistic water cycle, gives a way to reduce the

severe situation on water supply and water environment. The features of the model are as follows:

- a. The definition of guarantee degree for water quantity and reaching standard degree for water quality provides reasonable objective functions.
- b. Since system topology is based on realistic water cycle, the model is convenient to be adjusted. So the model has good applicability.
- c. The model can give fully utilize potential of water storage projects by optimal policy with a long series of runoff.

The model solution is given under various certain runoff conditions. In next research, rule optimization with stochastic runoff will be improved.

## REFERENCES

- Liu, B.J. et al. 2009. Water resources allocation model based on the dual-control of water quantity and quality. [J]. *Advances in water science* 04: 513–517.
- Liu, Y.N. et al. 2009. Union dispatch model for water quality and quantity in the middle reaches in Huaihe River. *Advances in water science*. Vol. 20, No. 2. Mar, 2009.
- Shao, D.G. et al. 2000. Sustainable management model of water quantity and quality for multi-purpose reservoir. *Journal of hydraulic engineering* 08: 10–15.
- Wang, H. et al. 2006. Theory and methodology of water resources assessment based on dualistic water cycle model. *Journal of hydraulic engineering* 17(3): 1496–1502.
- Wang, H. et al. 2010. Subject system of modern hydrology and water resources and research frontiers and hot issues. *Journal of hydraulic engineering* 21(4): 479–489.
- Zhang, S.P. et al. 2014. Basin/region water quality and quantity allocation I theory and method. *Journal of hydraulic engineering* 07: 757–766.
- Zhang, Y.Y. et al. 2010. Study on optimal dam operation of water quantity and quality based on a distributed SWAT model. *Journal of hydroelectric engineering* 05: 159–164+177.

# Design of long-span double-layer steel bracket for the roof of squat silo

JianHua Shao & XiaoFeng Ye

*School of Civil Engineering and Architecture, Jiangsu University of Science and Technology,  
Zhenjiang, Jiangsu, China*

ZaiHui Wang

*Zhenjiang Huahang Engineering Consultation Co. Ltd., Zhenjiang, Jiangsu, China*

XianBin Huang

*Zhenjiang Sijian Construction Co. Ltd., Zhenjiang, Jiangsu, China*

**ABSTRACT:** The long-span double-layer steel bracket for the roof of squat silo is designed and the vertical deflections of structure are calculated by finite element software SAP2000, which is compared with the actual measured results of this structure by loading experiment on site and the rationality of simulated deflections is fully verified. Then, this software is used to analyze the internal force, stress ratio, and overall stability of double-layer steel bracket. It can be seen from the analysis result that all structural members meet the requirements of corresponding design specification. Therefore, the section of steel members can provide a reference for the design of similar engineering project in the future.

**Keywords:** steel structure; bracket; long-span; design

## 1 INTRODUCTION

The concrete dome or single-layer steel reticulated shell is used for the roof of squat silo which is mostly applied in the food industry at present from the need of building function of storage. But for long-span squat silo, the direct use of concrete dome will lead to increasing construction difficulty and construction period of project becomes longer<sup>[1]</sup>. The design of steel bracket for roof of squat silo should take into account the self-weight of steel structure and concrete dome which is supported by the steel bracket, the other vertical loads, wind load, snow load, and various construction live loads and so on<sup>[2-3]</sup>. If the technical scheme at the construction site is unreasonable, there is global or local instability and even overall collapse of structure under the construction condition at the steel bracket. The high strength of steel material cannot be used fully and designed bracket is not economic<sup>[4-5]</sup>. So, the strength and overall stability of steel support on the roof of squat silo should be carefully considered. This problem can better be solved by the use of double-layer steel bracket with the various bracing members inside. A typical kind of design of long-span double-layer steel bracket for roof of squat silo as an actual engineering example is introduced in this paper and its

strength and stability are analyzed, which provides a reference for similar engineering design.

## 2 DESIGN OF STEEL BRACKET

### 2.1 *The selection and arrangement of structure*

The circle or conical structure is the main form for the roof of squat silos, in particular, the conical thin shell has more advantages. As for conical shell, the formwork erection and pouring concrete on the steel bracket at the process of construction are much easier than for spherical shell because the conical shells only have radii in one direction<sup>[6,7]</sup>. The design of double-layer steel bracket for the conical roof of squat silo is mainly discussed in this paper.

The height of this conical steel bracket for roof of squat silo is about 4.14 m, the diameter of conical ring beam at the bottom is about 25.9 m, and the diameter of the upper platform similar to the traditional concrete structure is about 8 m. The 20 radial steel beams connected by 6 ring steel beams are uniformly arranged around the structure. From bottom to top, the vertical steel braces are set down on the fourth ring beam and many other braces are placed inside of structure. The detail design of steel bracket is shown in [Figure 1](#).



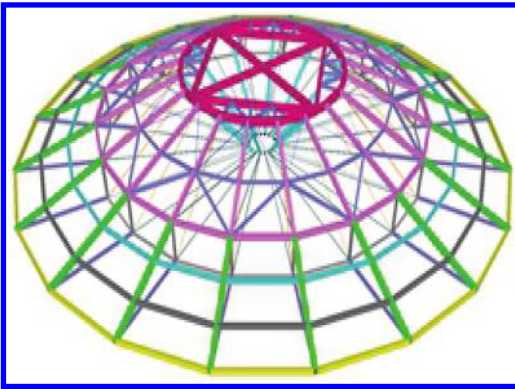


Figure 1. Three-dimensional diagram of steel bracket.

### 2.2 Key point of structural design

The single-layer steel bracket for the roof of squat silo will lead to excessive deflection when the span is large. The maximum deflection usually occurs at the middle of radial beam which needs to be set with vertical braces and diagonal braces<sup>[8]</sup>. Also, a larger deflection value is produced at the center of upper structural platform, and so this location should be also set using diagonal braces, which will increase the vertical stiffness of upper structural platform and improve the whole stiffness of steel bracket. Because steel bracket is a completely symmetrical structure, the internal feature of structure is illustrated by taking a piece of the inner brace. A detailed drawing is shown in Figure 2.

### 2.3 Load distribution

The main bearing loads of steel bracket are dead load and variable load. Dead load includes the weight of steel structure by itself and concrete dome. Variable load includes the live load of roof, construction load, and wind load perpendicular to the structural surface. Specific load calculation is based on the way the surface load is distributed on the surface of the double-layer steel bracket. The design load of region i is  $q = 11.82 \text{ kN/m}^2$ , region ii is  $q = 9.95 \text{ kN/m}^2$ , and region iii is  $q = 9.91 \text{ kN/m}^2$ . The design load at each partition is shown in Figure 3.

### 2.4 Section design of steel members

The structural analysis model used for steel bracket is created by finite element software SAP2000 and the surface loads are applied on the upper surface of the structure. The appropriate sections and materials of designed steel members that can satisfy requirements of the related design specifications

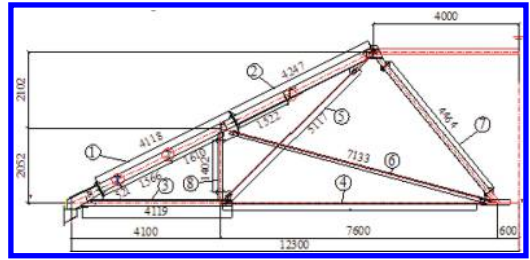


Figure 2. A piece of inside brace.

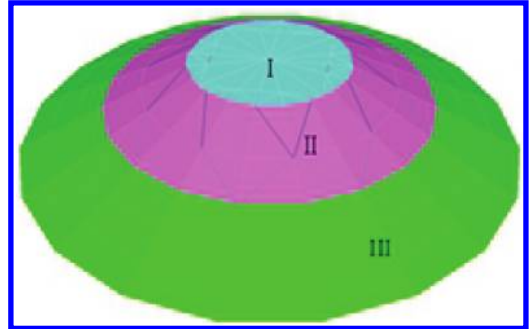


Figure 3. Load distribution.

Table 1. Section and material of each member.

Location	Section	Material
Bar ①	H220 × 125 × 6 × 9	Q345B
Bar ②	H140 × 90 × 5 × 8	Q345B
Bar ③	H100 × 75 × 6 × 8	Q235B
Bar ④	2Φ25	Q235B
Bar ⑤	2Φ20	Q235B
Bar ⑥	2Φ25	Q235B
Bar ⑦	Φ159 × 4.5	Q235B
Bar ⑧	Φ127 × 4.5	Q235B
RB1	GB-128C	Q235B
RB2	H194 × 150 × 6 × 9	Q235B
RB3	H220 × 125 × 6 × 9	Q235B
RB4	H200 × 100 × 5.5 × 8	Q345B
RB5	GB-i16	Q235B
RB6	H300 × 150 × 6.5 × 9	Q345B
CB	H350 × 175 × 7 × 11	Q235B
TB	Φ14	Q235B

are shown in Table 1. RB1 is expressed as the first ring beam, RB2 is the second ring beam counting from bottom to the top, and so on. CB is expressed as the center braces of upper platform and TB is the tie bar between the fifth ring beam and sixth ring beam.

### 3 ANALYSIS OF EXPERIMENT AND THEORY

#### 3.1 Deflection values of loading experiment on site and theoretical analysis

According to the loading experiment on site shown in Figure 4 and Figure 5, the maximum applied load is 500 t and the largest deflection at the center of steel platform is 30.3 mm. The actual measured deflection and calculated deflection are shown in Table 2. Position 1 to 6 in Table 2 is, respectively, the middle point of the first ring beam to the sixth ring beam counting from down to up. The position 7 is the center of upper platform and position 8 is the middle point of radial beam.

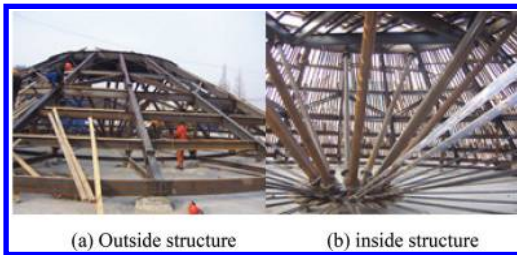


Figure 4. Steel bracket on site.

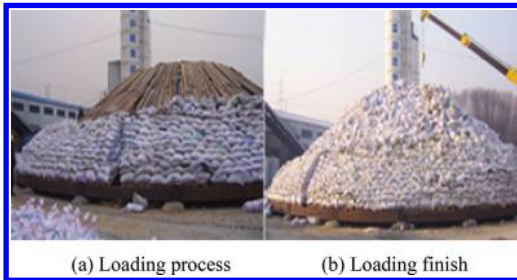


Figure 5. Loading experiment.

Table 2. The contrast of deflection values.

Position	Measured deflection/mm	Calculated deflection/mm	Error /%
1	3.1	3.5	12.9
2	10.5	11.2	6.7
3	14.5	12.8	-11.7
4	8.2	8.0	-2.4
5	12.2	10.8	-11.5
6	4.5	3.7	-17.8
7	30.3	27.2	-10.2
8	11.1	9.7	-12.6

The contour map of overall deflection for the steel bracket is shown in Figure 6.

#### 3.2 Comparison of experimental results and theoretical analysis

It can be seen from the comparison of experimental data and the deflection calculated by software SAP2000 that these simulative deflections are close to the actual measured values obtained from the loading experiment on site. It also shows that this finite element method simulating steel bracket is relatively accurate, and so the numerical calculation method is used to analyze the internal force, stress ratio, and overall stability of double-layer steel bracket. What is more, whatever the experimental result of 1/852 or calculated result of 1/963, the ratio of deflection at the middle of radial beam to the total length is far less than the given allowable ratio of 1/250 which is provided by the design code for the steel structure. Of course, it can also be seen from Table 2 that these deflection values of loading experiment on site are a little different from calculated data of theoretical analysis because there are maybe the following inevitable deviations at the process of actual steel construction:

1. The installation error that exists at the steel members. Connections at the ends of bars do not achieve the ideal rigid joint or hinged joint. Because the different connection types will affect the effective length of bar, the deflection of bar is not the same.
2. There are inevitable initial bending of members, initial eccentricity at the node and the initial stress due to various reasons such as the steel transportation and manufacturing process.

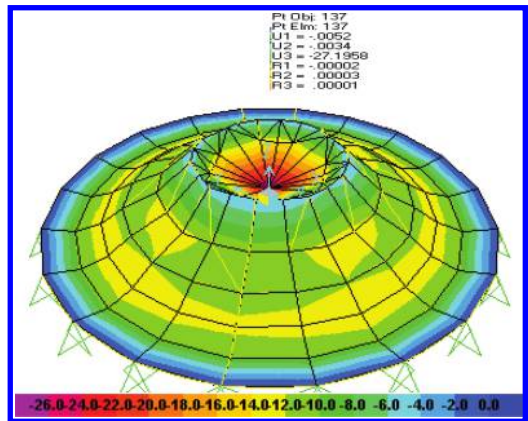


Figure 6. Overall deflection.

## 4 STRESS RATIOS OF MEMBERS

The stress ratio distribution of steel bracket is shown in Figure 7. It can be seen from Figure 7 that the stress ratios of most members are about 0.65 to 0.8 and the stress ratios of very little bars are less than 0.3. So not only can the strength requirement be met, but it can also make full use of the steel strength and does not cause a lot of steel material waste.

## 5 OVERALL STABILITY OF STRUCTURE

Structural stability analysis is different from strength calculation. It is mainly because of the difference between the external applied load and the internal resisting capacity of structure that leads to the sharply increasing structural deformation. The purpose of stability analysis is to determine the buckling modes and buckling loads where the structure becomes unstable.

The function of buckling analysis included in the software SAP2000 is used to calculate overall structural stability for the steel reticulated shell. The eigenvalue  $\lambda$  is sometimes called buckling factor or safety factor. The ultimate buckling load is equal to the product of buckling factor multiplied by the given load. When the buckling factor is greater than 1, the given loads must be increased in multiples of the buckling factor and the structures that cause buckling. If the buckling factor is less than 1, the applied load on the steel structure must be reduced to prevent buckling.

The first-order and second-order buckling modes of double-layer steel bracket for the roof of squat silo are respectively shown in Figure 8 and Figure 9. The first-order buckling factor under the action of vertical load is 4.8. The overall instability of steel structure will occur only when the applied loads are enlarged 4.8 times the standard values of dead load and live load. Because the buckling factor of 4.8 is greater than the buckling safety factor of 4.2 given by technical specifications for space

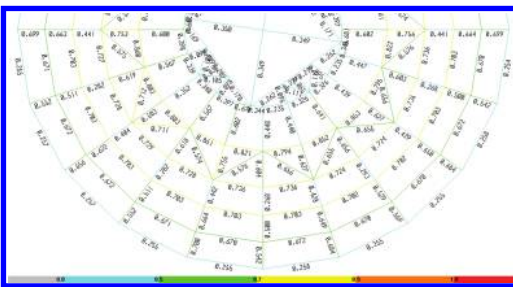


Figure 7. Stress ratio.

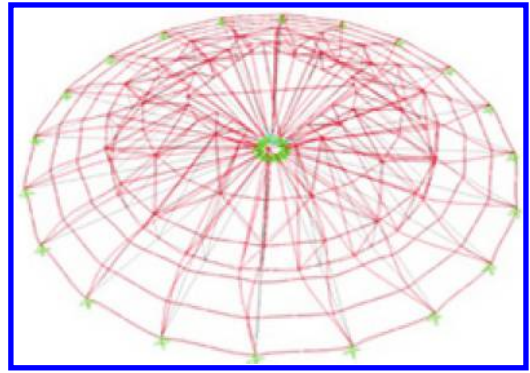


Figure 8. The first-order buckling mode.

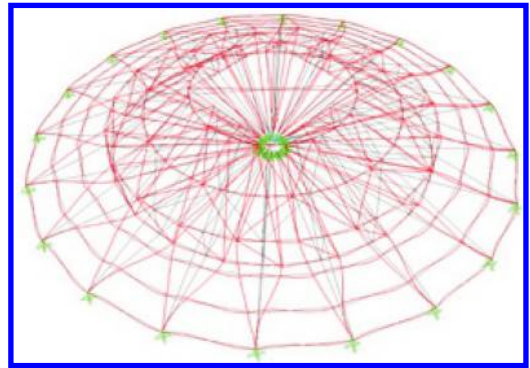


Figure 9. The second-order buckling mode.

frame structures, the overall stability requirement of double-layer steel bracket of the latticed shell will be satisfied.

## 6 CONCLUSIONS

1. The above designed long-span double-layer steel bracket used for the roof of squat silo has good structural strength and overall stability, which can satisfy the technical requirements included in the related design specifications. The section of steel members can provide a reference for the design of similar engineering projects in the future.
2. The simulative deflections through finite element analysis are close to the actual measured values obtained from the loading experiment on site. The experimental deflection of 1/852 and calculated result of 1/963 are far less than the given allowable ratio of 1/250.
3. The first-order buckling factor used for evaluating overall stability of the double-layer steel

bracket under the action of vertical load is 4.8 and is greater than 4.2 given by technical specifications for space frame structures.

#### ACKNOWLEDGMENTS

This work was financially supported by the National Natural Science Foundation (project number: 51308260).

#### REFERENCES

- [1] Huang H.S, Feng Z.J, Lu J.H. 2014. Research on storehouse top design of steel structure of silo [J]. *Cereal and Food industry* 21(2):57–61.
- [2] Tian J.L. 2004. Relation of steel lid incidence of shallow silo to stability of steel structure [J]. *Steel Construction* 19(6):27–33.
- [3] Tian J. 2007. Analysis of brace layout of steel lid of shallow silo [J]. *Steel Construction* 22(12):67–68.
- [4] Lang Y.P, Zhao Z. 2007. The effect for pomb by roof deflection [J]. *Steel Construction* 22(7):63–64.
- [5] Fan J.H, Wang L. Pan J.Y. 1998. Probe into the design of big diameter squat silo [J]. *Journal of Zhengzhou Grain College* 19(2):44–49.
- [6] Wang S.X, Du W.F, Zhao J. 2010. Analysis on design and stability of NanYang jade article supermarket lattice shell structure [J]. *Architecture Technology* 41(7):635–637.
- [7] Du Y.P. 2003. Design and construction method of steel support on the top of big diameter squat silo [J]. *Special Structures* 20(2):69–70.
- [8] Gao B.Q, Liang J.W. 2000. The Design and Construction Techniques of Slipform Used in the Shallow Circular Warehouse with the Diameter of 30 Meters [J]. *Construction Technology* 29(3):41–42.

# An empirical study on the task assignment model building of indemnification for housing construction project—take a case of Guangzhou

Lin Chen, Jian Tan, Jian-hui Tan, Zi-ping Zhang & Tao Tao  
*Business School, Guangzhou University, Guangzhou, China*  
*Real Estate Research Institute, Guangzhou University, Guangzhou, China*

**ABSTRACT:** This paper takes the indemnification house construction project task assignment model as the entry point of the study, with problem-oriented method, and by site visiting, etc., studies the reasonable assignment mechanism of Guangzhou indemnification housing construction tasks shared by the city and by districts, building the weight model with expert evaluation, and on the basis of model analysis, relevant suggestions are raised in the conclusion.

**Keywords:** indemnification housing; task assignment; weight model

## 1 INTRODUCTION

From 2011, Guangzhou has begun the trial of indemnification housing construction tasks shared by the city and the districts. In three years of practice, certain achievements are obtained, and certain obstacles are met. The main problems in the obstacles are the issues of how to effectively establish the assignment model shared by the city and by the districts for the indemnification housing construction tasks with the principles of equal rights and responsibilities. With such background, this study tries to take problem study as the orientation, by site investigations, obtaining relevant information, and on such basis, the indemnification housing construction tasks assignment model is built, to provide foundation and reference for the reasonable assignment of indemnification housing construction tasks in Guangzhou and in cities of same type.

## 2 STATEMENTS IN RELEVANT DOCUMENTS

Construction of indemnification housing is an important measure to realize the policy of the central government “home to live in”. During the period of the 12th 5 Year Plan, the target of construction to build 3.6 million sets in the indemnification housing projects may basically solve the insufficient supply problem of the indemnification housing<sup>[1]</sup>. The research shows that construction of indemnification housing has practically solved

the housing issues of some straitened people. Current large-scale construction of indemnification housing in our country has its reasonability<sup>[2]</sup>. But, behind the completion of the indemnification housing construction many problems are still existing.

In the construction of indemnification housing, insufficient land and shortage of funds are two main problems, which are seriously hindering the progress and effects of the indemnification housing construction tasks<sup>[3]</sup>. Studies and experiences in other countries show that when the funds for indemnification housing construction are not sufficient, the better and effective solution is to use funding leverage, to absorb social capitals or revitalize stock assets<sup>[4-5]</sup>. In China, many experts are of the opinion that<sup>[6-7]</sup> leverage of financing with administrative funding should be sufficiently utilized in the indemnification housing construction, and the assets of indemnification housing construction should be securitized and capitalized, and the model of public-private cooperation should be used in the financing for indemnification housing construction. In other countries, the governments actively provide lands for the indemnification housing construction is the key of solution of such issues<sup>[8]</sup>.

Many studies show that either funding issue or land issue, the sources usually may be summarized as problem of upper-level system. The appraisal mechanism and land finance as the reality have seriously affected the progress and quality of the completion of the indemnification housing tasks<sup>[9]</sup>. Our experts have many researches and studies in this respect.

Mr. Wang Yueping<sup>[10]</sup> has studied the behavior changes of local governments in the indemnification housing construction with the theories of reasonable selections and new institutionalism, etc., and he has found that the behavior changes of local governments are mainly limited by the financial system, the authority structures of different levels of governments, and the relationship of local benefits, etc.

Different hierarchies studies and analysis have been done by the experts in the respects such as the completion situation of the indemnification housing construction tasks, the problems facing, their causes and solutions, etc., providing foundation for the followed studies. The indemnification housing construction practice in other cities are worth learning and reference. In this paper, the intention is to try to build the indemnification housing construction task assigning model as the follow-up study on the basis of the studies and researches of so many experts, and to raise relevant suggestions, as the supplement and verification to the relevant studies.

### 3 INDEMNIFICATION HOUSING CONSTRUCTION TASK ASSIGNING MODEL BUILDING

#### 3.1 *Brief introduction of changes of the sharing situation between the city and the districts for the indemnification housing construction from 2011 to 2014*

In recent years, in the Guangzhou indemnification housing construction, the mode changed

from mainly responsible by the city to the mode of mutually sharing by the city and the districts, it is shown in the transfer of the housing security tasks to the districts step by step. According to the data provided by Guangzhou Housing Management Bureau (see Table 1), the building coefficient  $\Gamma$  the proportion of tasks between the city and the districts is measured:

$$\Gamma = yt/(1 - yt) \tag{1}$$

yt: proportion of indemnification housing construction task assignment of city level itself in year t (of which t = 2011...2014).

The smaller  $\Gamma$  value shows the heavier tasks at the district level layer. Table 2 shows that the  $\Gamma$  value drops from 2.02 to 0.99.

From Drawing 1, we may see that the  $\Gamma$  value changing tendency is like a parabola, dropping together with the time lasting. The decomposition of the indemnification housing tasks is mainly by the mutual sharing between the city and the districts.

#### 3.2 *Building up the task assignment estimated model: weight model*

As the assigned tasks of the districts in the past years are of large occasionality and subjectivity, it is hard to take them for the scientific estimates. For this reason, on the basis of the task volumes of the past years, certain variables are added and the expert evaluation is also added to establish the weight model.

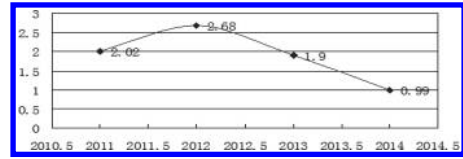
Table 1. 2011–2014 indemnification housing construction tasks quantity and percentage in districts (unit: flats,%).

	2011		2012		2013		2014	
	Quantity	Percentage	Quantity	Percentage	Quantity	Percentage	Quantity	Percentage
Whole city	81457	100	36200	100	16736	100	11682	100
City level	54500	66.91	26370	72.85	10967	65.53	5800	49.65
Yuexiu	500	0.61	200	0.55	100	0.60	100	0.86
Haizhu	1500	1.84	500	1.38	200	1.20	300	2.57
Liwan	3000	3.68	100	0.28	300	1.79	200	1.71
Tianhe	1500	1.84	500	1.38	300	1.79	100	0.86
Baiyun	1300	1.60	200	0.55	100	0.60	200	1.71
Panyu	4000	4.91	1000	2.76	500	2.99	400	3.42
Huadu	1800	2.21	500	1.38	336	2.01	200	1.71
Huangpu	1500	1.84	500	1.38	300	1.79	200	1.71
Luogang	6100	7.49	2000	5.52	1000	5.98	1000	8.56
Nansha	2300	2.82	2100	5.80	1733	10.35	882	7.55
Conghua	1000	1.23	730	2.02	400	2.39	300	2.57
Zengcheng	2457	3.02	1500	4.14	500	2.99	2000	17.12

Source of data: Guangzhou Housing Management Bureau.

Table 2. Shared between city and districts of the tasks 2011–2014.

Time (years)	2011	2012	2013	2014
Proportion between city and districts	2.02	2.68	1.90	0.99



Drawing 1. City-districts proportions of indemnification housing construction tasks in years.

Table 3. District housing security data statistics.

District	District annual financial income (100 million Yuan)	Annual GDP (100 million Yuan)	Annual application volume (new applications)	Regular residents (10 k headcounts)	Annual inspection volume	Clerk quantity
Yuexiu	46.88	2384.71	4500	1157277	15458	9
Haizhu	40.76	871.49	4347	898204	10771	8
Liwan	46.43	1142.75	2926	1558663	9520	11
Tianhe	58.18	2781.61	964	1432431	964	8
Baiyun	17.14	704.03	227	457930	415	2
Panyu	51.95	1329.35	810	2222658	1262	5
Huadu	72.98	1353.23	199	1764869	744	8
Huangpu	52.59	908.03	167	259899	167	4
Luogang	109.18	1892	25	373670	25	1
Nansha	66.43	902.14	70	945053	70	2
Conghua	29.67	284.15	91	593415	91	10
Zengcheng	62.99	989.45	31	1036731	75	11
Total	655.18	15542.94	14354	12700800	39559	79

Notes: ① Data source: District annual financial income and GDP are from Guangzhou City Statistic Yearbook.  
 ② District annual application volumes, inspection volumes and clerk quantities are from the actually reported data from the districts.

Table 4. District housing security relevant index proportion form.

District	District annual finance income (100 million Yuan)	Annual GDP (100 million Yuan)	Annual application volume (new applications)	Regular residents	Annual inspection volume (new applications)	Clerk quantity
Yuexiu	7.16%	15.34%	31.35%	9.11%	39.08%	11.39%
Haizhu	6.22%	5.61%	30.28%	7.07%	27.23%	10.13%
Liwan	7.09%	7.35%	20.38%	12.27%	24.06%	13.92%
Tianhe	8.88%	17.90%	6.71%	11.28%	2.44%	10.13%
Baiyun	2.62%	4.53%	1.58%	3.61%	1.05%	2.53%
Panyu	7.93%	8.55%	5.64%	17.50%	3.19%	6.33%
Huadu	11.14%	8.71%	1.38%	13.90%	1.88%	10.13%
Huangpu	8.03%	5.84%	1.16%	2.05%	0.42%	5.06%
Luogang	16.66%	12.17%	0.17%	2.94%	0.06%	1.27%
Nansha	10.14%	5.80%	0.48%	7.44%	0.18%	2.53%
Conghua	4.53%	1.83%	0.63%	4.67%	0.23%	12.66%
Zengcheng	9.61%	6.37%	0.21%	8.16%	0.19%	13.92%
Total	100.00%	100.00%	100.00%	100.00%	100.00%	100.00%

① *The setting principle and selection variables*  
 Model is based on the actual situations of the districts, with the principles of “construction by demands, shared by the city and the districts, equal rights and responsibilities, balancing

among areas”. Considering the short comings of the deduced model, first it is suggested to take the application volumes of indemnification housing into consideration of indemnification housing construction task assignment indexes, while

Table 5. Indemnification housing assignment weights in districts.

District	Financial income	GDP	Indemnification housing application volume	Regular residents	Clerk quantity	Inspection volume
Weight coefficient	0.45	0.3	0.25	0.05	0.1	-0.15

Table 6. District housing security task volume proportions.

District	Annual financial income	GDP	Annual application volume	Regular residents	Annual inspection volume	Clerk quantity	Total percentage of undertaken task volume
Weight coefficient	0.45	0.3	0.25	0.05	-0.15	0.1	1
Yuexiu	3.22%	4.60%	7.84%	0.46%	-5.86%	1.14%	11.39%
Haizhu	2.80%	1.68%	7.57%	0.35%	-4.08%	1.01%	9.33%
Liwan	3.19%	2.21%	5.10%	0.61%	-3.61%	1.39%	8.89%
Tianhe	4.00%	5.37%	1.68%	0.56%	-0.37%	1.01%	12.25%
Baiyun	1.18%	1.36%	0.39%	0.18%	-0.16%	0.25%	3.21%
Panyu	3.57%	2.57%	1.41%	0.88%	-0.48%	0.63%	8.57%
Huadu	5.01%	2.61%	0.35%	0.69%	-0.28%	1.01%	9.40%
Huangpu	3.61%	1.75%	0.29%	0.10%	-0.06%	0.51%	6.20%
Luogang	7.50%	3.65%	0.04%	0.15%	-0.01%	0.13%	11.46%
Nansha	4.56%	1.74%	0.12%	0.37%	-0.03%	0.25%	7.02%
Conghua	2.04%	0.55%	0.16%	0.23%	-0.03%	1.27%	4.21%
Zengcheng	4.33%	1.91%	0.05%	0.41%	-0.03%	1.39%	8.06%
Total	45.00%	30.00%	25.00%	5.00%	-15.00%	10.00%	100.00%

adding some independent variables are shown in Table 3. In order to assure the objectivity of the model calculation, mainly the average data of 2012 and 2013 of the annual application volume and annual inspection volume are taken.

From 2011 to 2014, the city level itself has undertaken separately 66.91%, 72.85%, 65.53% and 49.65% of the indemnification housing construction tasks, and the remaining parts are assigned among the districts according to their demands and construction abilities. According to above form the proportions of the relevant indexes of the districts are calculated, as shown in Table 4.

#### ② Assignment of weight coefficient

By sufficient demonstration of model A and model B, combining with site visit, we may find that different variables are playing different functions in the assignments of the tasks. Considering the basic principles of the mutual sharing between the city and the districts of "construction by demands, shared by the city and the districts, equal rights and responsibilities, balancing among areas", the weight of financial income is appropriately raised, and the relevant weights evaluations are listed in Table 5.

According to the importance of the relevant factors of the indemnification housing tasks and the actual situations of the districts, the relevant factors are evaluated by expert scoring method. By the evaluations of the indexes, the indemnification housing proportions undertaken by districts are calculated with the results in Table 6.

It has to be emphasized that it is only the proportions of public-rental housing, excluding demolition settlement housing, construction volume of which should be calculated by the actually involved quantity of the large sized or emphasized projects in the cities in all the years.

## 4 MODEL ANALYSIS

Therefore the model is a choice. Surely it is obvious that it is an indemnification housing construction task city and district sharing model among districts based on certain preconditions such as equal rights and responsibilities, right resources distributions, multiple housing security products (including rental allowance), it is feasible only when above conditions are available. At the same



time, it should be realized that there is no unified standard of indemnification housing construction task assignment proportion between the city and the districts. The assignments of indemnification housing construction task between the two level layers of city and district, in its nature, is the transfer of public affairs and responsibilities among different governmental management layers. Different assignment proportions and methods will lead to different results. Combining with practice of other cities, it is sure that when “Funds transferring with projects, rights transferring with responsibilities” is realized, any types of proportions may be admitted and accepted by the parties. In the contrary, huge obstacles and difficulty may appear in the promotion.

## 5 CONCLUSION

The original mode of the indemnification housing construction task shared by the city and the districts in Guangzhou has obtained certain achievements, but there are still many difficulties and obstacles. By document study and empirical study it is confirmed that that the mode of construction task share by the city and the districts is with strong realistic necessity. But if current resources configuration is not making important adjustments, putting the indemnification housing construction task to the district level fully would not get good result. Therefore, the limited resources must be adjusted and the original rules for rights and responsibilities must be refined and regulated. Only above this, the built indemnification housing construction task assignment model may provide important foundation for reference in the refining of the indemnification housing construction task assignment between the city and the district layers.

## ACKNOWLEDGMENT

This work was financially supported by the Guangdong Province Natural Science Fund Project

(S2013010013533) and the Guangdong Province Philosophy Social Science Project (GD13CGL04).

## REFERENCES

- [1] Li Yingsheng: Indemnification housing construction and social management renovation. [J]. Hebei Journal 2013.32(4) 111–117.
- [2] Chen Hongsheng, Li Zhigang: Construction and evaluation of Guangzhou housing and indemnification housing [J]. Tropical Geography 2014, 34(6) 823–830.
- [3] Liao Haiyan: Public-rental housing land supply and financing mode case study [J]. Economic Review 2012 (3):77–80.
- [4] Priemus. Dutch Housing Associations: Current Development and Debates [J]. Housing Studies, 2003, (18):327–351.
- [5] E. Engel, R. Fischer. The basic public finance of Public-Private-Partnerships [J]. Journal of the European economic association, 2012, 11(1):83–111.
- [6] Ba Shusong, Wang Zhifeng: Funding sources, system reform and international experience: From public-rental housing [J]. Reform, 2010 (3) 80–84.
- [7] Guo Mingjie, Wang Yan: Study of modes of financing in the city indemnification housing construction [J]. Financial study, 2011 (11) 36–39.
- [8] Wang Jianqiang: International experience and China’s road—non-profit seeking organization participating construction and management of indemnification housing [J]. Administrative Forum, 2014 (6): 78–83.
- [9] Cheng Datao: Research of motive and mechanism of indemnification housing construction by local government under dual system for housing lands [J]. Zhejiang Journal, 2013 (4): 149–157.
- [10] Wang Yueping: On the system restraint to the changes of local government behaviors—with indemnification housing as the policy behavior observation area [J]. Exploration, 2012(4) 63–65.

*Architecture, landscape planning and design*

# Research on spatial morphology characteristics of traditional “bottom-up” settlements—a case study of Licha Village and Xiangang Village in Gaoyao, Guangdong Province

Yan Lin & Jian-guo Wang

*School of Architecture, Southeast University, Nanjing, China*

**ABSTRACT:** The research of traditional “bottom-up” way of urban development serves as an approach to reflect on the current mainstream “top-down” planning and construction way. Through integration of field research, graphic analysis and theoretical generalization, and by selecting Licha Village and Xiangang Village in Gaoyao, Guangdong Province as case study, the paper probes into characteristics of roads, public spaces and building clustering way in traditional settlement spaces. It concludes that, in traditional “bottom-up” settlements, roads present natural and organic morphological characteristics under the influence of human’s action modes; public spaces are rich in levels, flexible in utilization and concerned about comfort degree of utilization; building clustering way is affected by natural topographic conditions, appropriate residential density and spacing. Also, the paper points out that, the main spatial morphology characteristics of such settlements are to fully reveal characteristics of natural topographic features, to be adaptable by adjusting space according to conducts of daily life, and to be rich both in spatial morphology and geographical features. The paper intends to provide a reference for correction and improvement of urban construction approaches.

**Keywords:** bottom-up; urban design; spatial morphology of traditional settlement; “Eight Trigrams villages” of Gaoyao, Guangdong Province

## 1 INTRODUCTION

In the process of rapid urbanization of China, most domestic cities are planned and constructed by following the “top-down” mode, which leads to poor practicability and lack of local characteristics in terms of urban community. During the same period, numerous vernacular settlements built in the “bottom-up” mode, compared with cities with the “top-down” construction means, have more unique spatial morphology characteristics, the sense of place belonging and practicability in life. Through field research on typical traditional settlements, the paper intends to delve into the morphology characteristics, residents’ behavior characteristics and spatial utilization habits of traditional “bottom-up” settlements, attempting to provide a reference for improving urban construction way by reflecting on and interpreting the spontaneous formation mechanism of traditional settlement spaces.

The paper selects two traditional settlements in the Xijiang River Basin, i.e. Licha Village and Xiangang Village in Gaoyao, Zhaoqing of Guangdong Province as main research objects (Fig. 1).

Built in the Southern Song Dynasty with a history over 700 years, Licha Village, relying on mountains and waters around, presents a circular shape with radius of 90 m in general and gets its name of “Eight Trigrams village” from the eight trigram shape of houses constructed in rows by conforming to the topography. Currently, the well preserved and virtually unpopulated village is already developed into a tourist scenic spot. Xiangang Village, another “Eight Trigrams village”, although similar to Licha Village in spatial morphology, has an area ten times of that of Licha Village with radius being 300 m. with over 600 years history, 8,900 residents and three administrative villages, the village scale falls in between a village and a town.

Since the two villages adopt the traditional “bottom-up” construction way and well preserve spontaneously formed spatial morphology of traditional settlement so far, with the two as research samples, the interpretation of morphology characteristics concerning traditional settlements may bring significant basic research value for analysis of the “bottom-up” development way.

The physical space environment of settlements largely incorporate roads (including streets,

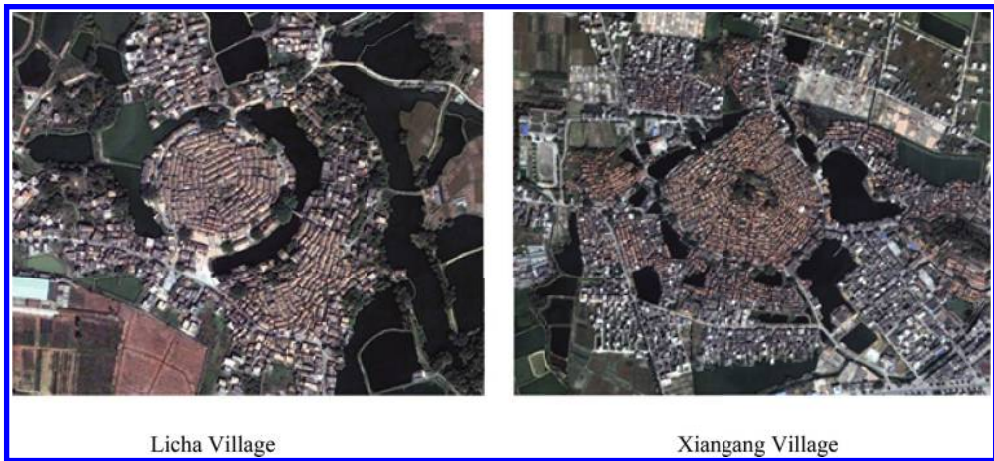


Figure 1. Satellite map of “Eight Trigrams” villages.  
Source: Google map.

sidewalks, steps, alleys, etc.), buildings (including residential and public buildings, etc.), and public spaces (such as squares, natural landscapes, sketch sculptures, etc.). The paper intends to study the spatial morphology of traditional settlements in the perspectives of road, public space and building clustering way.

## 2 SPATIAL FEATURES OF ROADS

In traditional settlements, apart from compliance with the natural topography and catering for facilities (mainly drainage) requirements, the formation of roads is greatly affected by human’s action modes. Characterized by slow speed, physical fatigue limit and strong randomness of path, human action is thus leading to the natural and organic forms of roads.

### 2.1 Spatial composition of roads

Both built on an island surrounded by water, the two villages are similar in overall structure of roads: outside villages is a loop of carriageway, and inside lie alleys arranged in compliance with hills. To the specific, the 5 m wide outer ring cement road serves for vehicles and pedestrians and has roads leading outside every one or two hundred meters; mainly serving for pedestrians, internal roads are changeable since they have to adapt to hills and connect all dwellings. The links between the outer ring roads and internal roads of Licha Village and Xiangang Village are gatehouses and footpaths perpendicular to the outer ring roads respectively (Fig. 2).

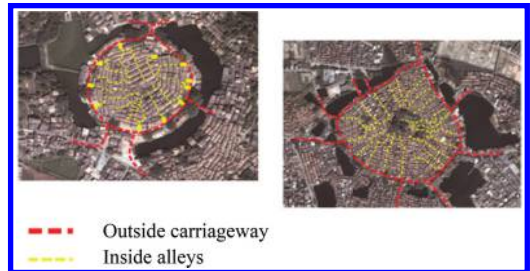


Figure 2. Overall structure of roads of the two villages.  
Source: The author draw.

Internal roads, serving for pedestrians only and being the typical “bottom-up” construction, is the focus of the research. Seen from the internal traffic space composition of the villages, not all spaces have roads, thus the traffic system formed by internal roads might as well be interpreted as accessible space beyond inside for people.

Taking Licha Village as an instance, the internal traffic space can be divided into three forms as below (Fig. 3):

1. The space under eaves such as corridor under gatehouse, freely accessible ancestral hall with side-room opened: unlike general ones in cities, the width of spaces under eaves in Licha Village is about the same as other roads and even superior in terms of identification and road conditions, thus, the guide tempting access shall be an indispensable part of traffic system.
2. Open space such as vacant area in front of and behind gatehouse, small square in front of public building and mountain top square: the space

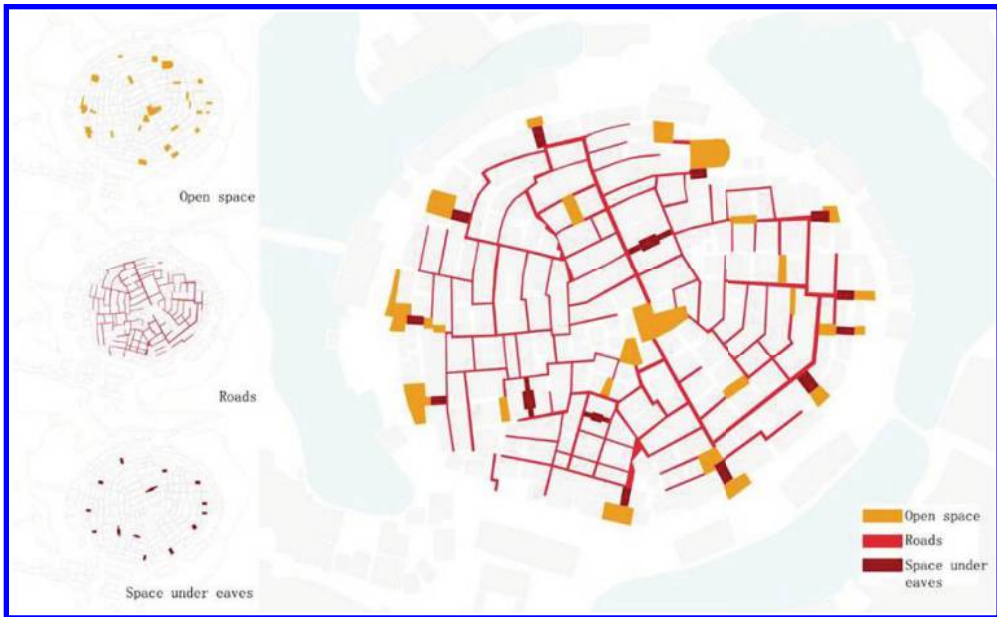


Figure 3. The internal traffic space of Licha Village.  
Source: The author draw.

may accommodate some special behaviors such as worship in ancestral hall and water taking in wellbay. But it is hard to be distinguished from roads due to its limited spatial scale (generally 3–8 m<sup>2</sup>). Incorporated into road system, the space is basically used for passing through.

3. Road space with diverse road forms such as roads serving as main alleys (upward direction along the hill), cross alleys assuming main entry function (along contour line direction) and cracks. Such combination of roads in diverse forms generates complex traffic organization type inside villages.

Yet judged from practical utilization situation, form types with distinct features of roads are still be seen partially (Fig. 4). The local form of roads can be divided into three types as below according to combination relationship among roads (Fig. 5):

1. Fishbone type: in this road type, obvious main alleys are available along building gable and branches perpendicular to main alleys are available to connect building entrance. Most fishbone roads are found along village radius direction and a few long main alleys start from peripheral gatehouse and terminate at mountain top.
2. Cross alley type: in this road form, roads in front and back sides of buildings are much wider than

those along gables, making cross alleys become the main road in this area. Buildings on both sides of the road mostly follow contour line and building entrances can be found on both sides of some cross alleys.

3. Free type: this road type is not definite in spatial logic or can be called residual space beyond buildings. The road presents irregular road network structure or irregular road shape, such as triangle and trapezoid spaces.

## 2.2 Road pavement

As for Licha Village, most road spaces are narrow, but the relationship of paving modes, pavement materials, drainage and plant configuration is complex. Pavement components include the ground near the building generally paved with rubbles or cement, drainage ditch set along building exterior walls or in road centre according to the actual situation and the pavement for pedestrians mainly laid with large stones.

Being about 300–400 mm wide and 1000 mm–1300 mm long, stones for pedestrian roads constitute appropriate road width for one person and for accommodating one's feet exactly if laid horizontally and vertically respectively. Road width is basically determined by stone dimensions and a multiple of single stone dimension. Behavioral momentum is inclined to be transformed into

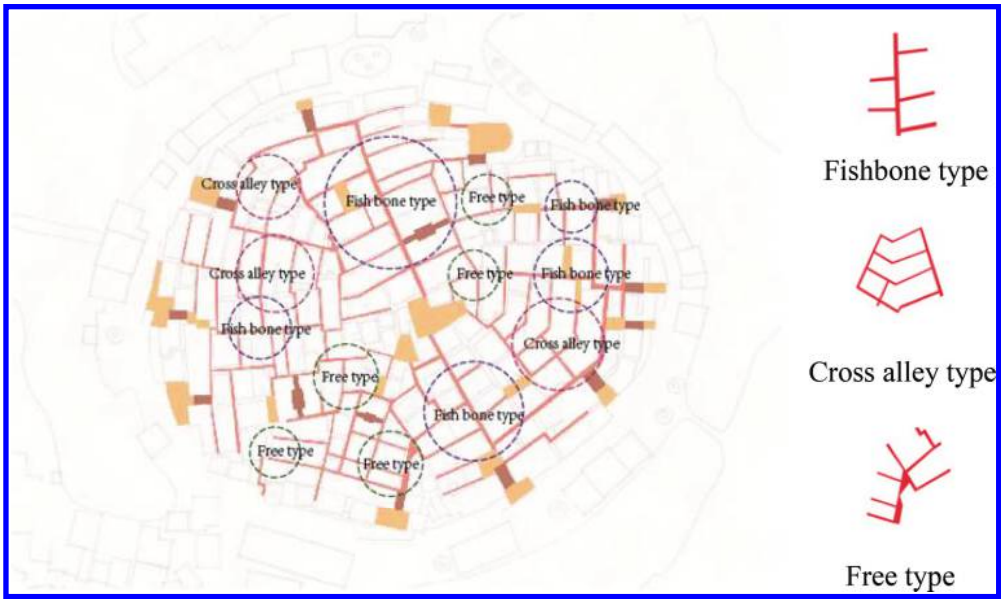


Figure 4. Local form of roads.  
Source: The author draw.



Figure 5. Three types of roads.  
Source: The author draw and shot.

paving mode of materials and especially the paving form, as can be seen in most places. For example, the laying location of stones shall avoid drainage ditch and the laying direction shall give a hint to building entrance; straight roads are rarely seen at

any position, even main alleys; some places may even present abrupt change in width or strange shapes. All these have something to do with human's walking flexibility (Fig. 6).

The importance of roads is more related to elaborate degree of road construction than the road width. Some important roads, although the width is suitable for one pedestrian only, are complex in the stone laying and elaborate in the interface with drainage ditch; some unimportant roads with spacious space leave very limited pavement for pedestrians with other spaces overgrown with weeds to fail passing (Fig. 7).

### 2.3 Impact of bicycles on roads

In terms of bicycles, compared with walking, they just improve the speed and release fatigue and as a daily action relying on body, do not require a lot for road conditions. Therefore, the utilization of bicycles falls into a phenomenon of the "bottom-up" influence on road space.

When it comes to Licha Village, the utilization of bicycles has some impact on its road traffic: although bicycles are basically active on external roads so far, bicycle trace in the village and especially bikeway on several entry steps (bikeways are built late) are still found. Take the step of Suiyuan Village platform, torsion of bikeway and step are formed due to inconsistency between turning radius requirement of bicycles and existing



From left to right:  
The tilted stone relate to the path of the people.  
The drainage is in the centre of the road.  
The direction of stone imply the entrance of building.

Figure 6. Complex pavement.  
Source: The author shot.



From left to right:  
Important road: Narrow space with complex pavement  
Unimportant road: spacious space with limited pavement

Figure 7. The expression of importance of roads.  
Source: The author shot.

step conditions, and bikeways are built in the step center with view to individual handedness (Fig. 8).

Seen from the analysis above, roads deriving from the “bottom-up” settlement mode are paved as per human action needs and vary with objective conditions. Therefore, the actual road information, unlike urban planned road network with the “top-down” construction, cannot be accurately read from site plan as the current situation is much more complex than the drawing with the roads shaded by massive roofs. In most cases, roads are built along with houses and constrained by many other factors, as they have to give way to buildings, plants and even drainage ditches. Human’s free actions make roads become one of the most flexible components of the settlements.



Figure 8. The step of Suiyuan Village platform.  
Source: The author shot.

### 3 CHARACTERISTICS OF PUBLIC SPACE

The abundance of public space is determined by diversification of human community public activities. Therefore, compared with other functional spaces, the public space has the most diverse forms, rich elements and multi-layered types.

#### 3.1 Composition of public space

Taking Licha Village as an example, its public space can be divided into three types according to the spatial scale, composition content and applications (Fig. 9):

1. Wellbay—the space relevant to facilities: the research finds that, the inner and outer diameters of well are 550 mm and 770 mm respectively; the ground around the well is built into a rectangular area (being auxiliary operating space of wellbay) with stones to be distinguished from other areas, with side length being 2,100 mm (about three and half steps) and area being 4 m<sup>2</sup>.
2. Ancestral hall—the space relevant to special activities (worship): the space is hard to define, since externally, the outer spaces of wine course of the village are mixed with other waterfront recreational areas, and internally, they are linked with road system. The actual space for sacrifice rites is limited, ranging from 1–2 m<sup>2</sup> to 4–5 m<sup>2</sup> and requiring incense arranging position. The importance degree of worship space is related to complexity level of altar form. And other auxiliary worship activities such as assembly, communication and leisure activities shall share the space.
3. Leisure space—the space relevant to leisure activities: such space enjoys the most diverse forms and the leisure activity space with intact form basically locates at places with desirable landscape. These spaces have something in

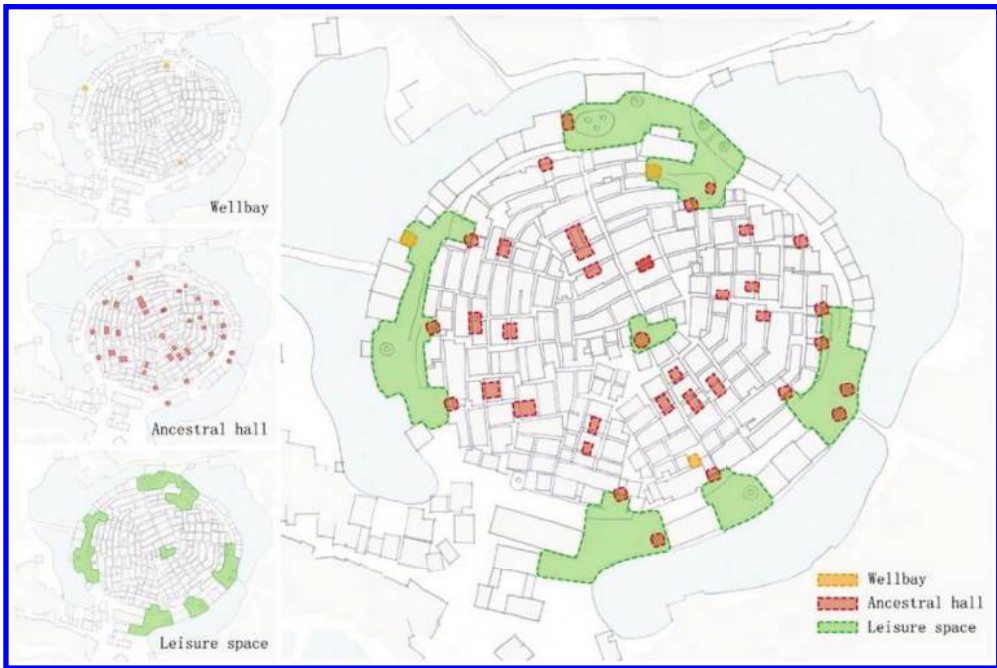


Figure 9. Composition of public space.  
Source: The author draw.

common: for waterfront, it is related to the village terrain and the hilly topography of “Eight Trigrams Village” results in a relatively spacious waterfront space; big tree logo-banyan trees with large volume are common there and comfortable shade space is available under trees; public buildings around-leisure activities are easily associated with public activities; spatial link with all entrance & exits-either exits leading outside or gatehouse leading inside, as leisure activity space prefers places with large flow of people.

Yet in fact, the public space with the intact image is always so interconnected and nested that it is hard to be clearly distinguished from other types, thus together forming public activity nodes, which center on waterfront of outer ring roads in terms of the two villages (Fig. 10–11). This implies that site selection of residential public activity space is closely related to the comfort degree of environment and rich degree of landscape. In total, Licha Village has five public activity nodes and Xiangang Village eleven.

### 3.2 Typical public nodes

To further understand the concrete forms of public nodes, the paper implements pacing research on three typical public nodes (Fig. 12).



Figure 10. Public nodes in Licha Village.  
Source: The author draw.

#### Node 1: “Four in one” public node of Xiangang Village

Being a waterfront leisure space to the south of Xiangang Village, the public node, through pacing, is generally 28-step (about 18 m) long and 16-step (about 9.6 m) wide. In this limited space, four space levels may be seen: a 3.5 m × 6 m slightly lofty worship space, a 2.5 m × 5 m chess





Figure 11. Public nodes in Xiangang Village.  
Source: The author draw.

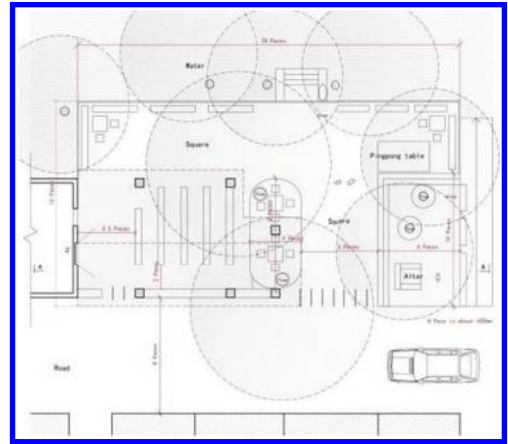


Figure 14. Paving plan of node 1.  
Source: The author draw.



Figure 12. The position of nodes.  
Source: The author draw.

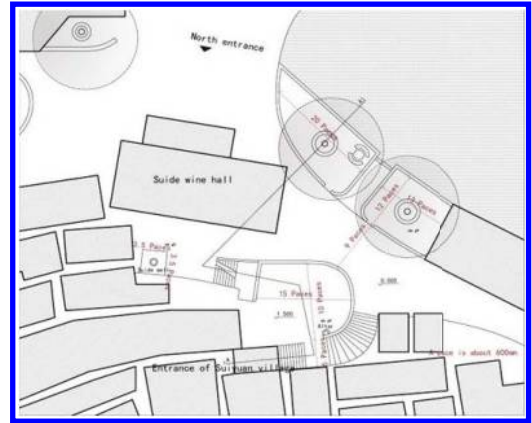


Figure 15. Paving plan of node 2.  
Source: The author draw.

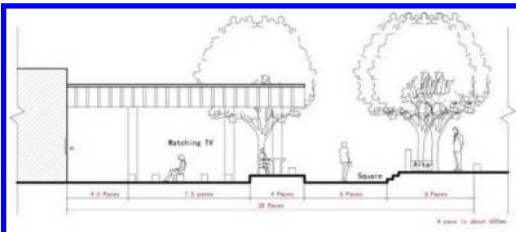


Figure 13. Paving section of node 1.  
Source: The author draw.

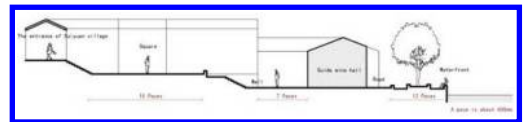


Figure 16. Paving section of node 2.  
Source: The author draw.

space under tree, a 6 m × 6 m TV viewing space under roof and a leisure activity space accommodating seats and sports facilities. Each space is so limited that it is directly related to body dimension (Fig. 13–14).

Node 2: Public node of Suiyuan Village in Licha Village

Located at the north entry of Licha Village and connected with Suiyuan Village platform leading inside, the node's spaces include Suiyuan

Village platform for worship events, outdoor space at entrance of wine hall including Suide Well and worship space and leisure space under tree of waterfront. These spaces are relatively spacious, independent and equipped with special application, yet they have territory feeling of one space and dramatic visual interconnectiveness (Fig. 15–16).

Node 3: Public node at entry of Xiangang Village. Being the entry to the south of Xiangang Village, the node includes a rest platform with long strip stone benches of diverse dimensions to cater for different sitting habits. The different spacing of stones makes single-row or face-to-face sitting available, some longer stones enables lying and the ring-shape stone benches around trees are also popular since they create a dependency feeling by leaning on trees (Fig. 17–18).

Through observation and experience, it is found that these public spaces possess abundant levels, such as the “four in one” node, which realizes multi-level activities via a small-scale space separated from an intact site, and Suiyuan Village, the level of which is divided as per spatial elevation difference. But as for lots of spaces without fixed applications to be served as corridors, squares, gathering spaces and even doors, residents tend to develop their talents and wisdom to make them work interestingly. Since seats constitute the most significant part of public space with leisure function or any sitting space may be called public leisure space, the comfort degree of sitting become one vital factor to judge the vitality of the space.

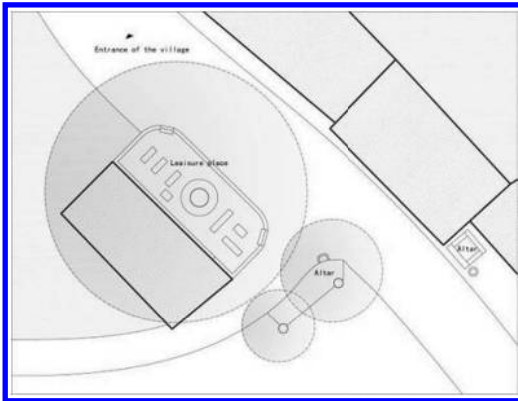


Figure 17. Pacing plan of node 3.  
Source: The author draw.

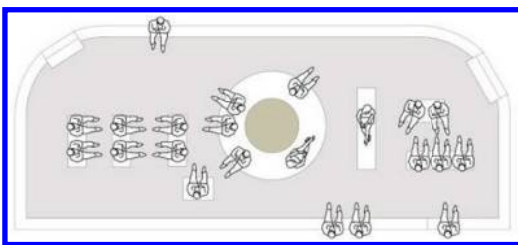


Figure 18. Diverse sitting habits.  
Source: The author draw.

## 4 BUILDING CLUSTERING WAY

As human shelters, buildings arise with inhabitation and are one of the most fundamental constituent substances of settlements. As buildings in traditional settlements are mostly built by residents themselves and the development of building and update of environment are fueled according to the actual life needs and mutual learning of technical skills, the building clustering way is always a reflection of residents’ living habits and conditions.

### 4.1 Integral form of building clustering

The integral form of building clustering of the two villages seems to be specially planned and designed, both presenting irregular shape—the eight trigram shape. This design is related to the topography for one thing: the relatively rounded edges of lonely island make the architecture complex boundary become circular due to land boundary limit; with hills rising toward island center, houses are built against slopes to cater for construction and use habits, so houses are arranged in the direction that follows the contour line, presenting ring shape; the sunlight in Lingnan area is so sufficient that the sunny side and night side of mountain slope can both satisfy residents’ normal life, so houses are evenly distributed in all sides of the hills. On the other hand, with view to flood control and defense needs, most civilian houses are built on higher elevation of hills and the most external buildings are relatively closed to take on “self-defense” gesture. Meanwhile, the eight trigram shape derives from geomancy and faith, as data shows, exquisitely arranged Licha Village has hidden mystery of Hetu Luosliu (the ancient Chinese mythological fiction) and the construction as per eight basic graphics in the *Book of Changes*—the Eight Trigram symbol is to express villagers’ best wishes for being prosperous both in family and purse and keeping life thriving.

But through careful scrutiny on the architectural form of the two villages, it is found that, constrained by actual construction situation, they are somewhat in a mess and quite distinct from the established eight trigram shape. They are composed of several building groups following a few of unified directions other than even and orderly rings, with Licha Village having five directions and Xiangang Village six (Fig. 19). The consistent orientation is formed due to two reasons: first, it is easily be found in adjacent houses since houses are actually constructed one by one; second, it is related to the distribution of extended family, as it is said in the very early period, the Su and Cai families in Licha Village settled in the east or southeast of hills and later the Cai family moved



Figure 19. The directions of clustering.  
Source: The author draw.

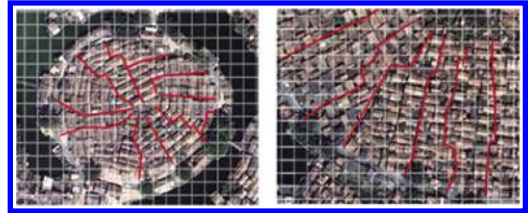


Figure 21. The main roads of the villages.  
Source: The author draw.



Figure 20. The position of ancestral halls.  
Source: The author draw.

to the west. As the most significant building of an extended family, ancestral halls are located in the center of building groups in all directions and have relatively intact exterior space (Fig. 20). The sequence of building construction is thus clear: first to guarantee the favorable position of ancestral hall and other buildings are expanded outward gradually by clinging to the ancestral hall. In contrast, the junction of building groups seems to be very casual, leaving numerous “residual” spaces in irregular shapes.

#### 4.2 Building arrangement rule

Observed separately, the two villages are both arranged evenly with sparse buildings having dramatic contrast in scale. Individual residential building generally has three rooms with depth of 4–6 m. The building spacing is basically 1.2–1.5 m that allows two people passing side by side and wider if building entrances are available on both sides.

Besides the above similarity, compared in the same scale, main mountain roads of the two have similar spacing, mostly being 40–50 m (Fig. 21). It means, in micro environment, actual construction

environment is not affected by the overall structure of villages but by the scale necessary to lives of residents.

In general, the integral form of buildings, although constrained by natural topography, has some randomness on the premise of compliance with natural environment and group needs. But the clustering form of buildings (especially residential buildings) itself is even and rational, since they always present relatively consistent density and spacing and regular repetition, with queer buildings rarely seen.

### 5 MORPHOLOGY CHARACTERISTICS OF THE “BOTTOM-UP” SETTLEMENT SPACE

Through above research on roads, public spaces and building clustering way, the spatial morphology characteristics of Licha Village are listed below:

1. To fully reveal characteristics of natural topography  
Settlement form is directly affected by topography, which is conspicuous in traditional settlements where human tend to adopt corresponding strategies to adapt to environment in most cases due to their limited nature transformation ability. It is found that the life boundary is directly constrained by territory area, the arrangement direction of buildings and road trend are directly affected by topography, and public spaces prefer places with favorable natural landscape. The similarity in form structure of the two villages with diverse scales discloses that, the areas with the same natural topography type are easy to form the settlements similar in form ethics, as the form characteristics of settlements are interconnected with characteristics of natural topography.
2. To adjust space according to conducts of daily life  
During spontaneous construction, human always build the individual space based on daily behavior needs. The construction of residential

buildings, road pavement and living facilities are daily necessity to people and constantly created and altered during use and as time passed by, human tend to adjust the established spaces to make environment reach a balanced state suitable for life. Thus, the space enjoys a progressive development way.

3. To be rich in environment form and regional features

Due to local materials and building technology limitations, the construction way and architecture style in the same region seem to be relatively unified. But the outdoor space of traditional settlements has rich forms, especially the small-scale public spaces, which are full of vigor due to their strong relevance with residential life. Public spaces are abundant in type levels and distinctive in dimension, form and application. It is the unified architecture image and diversified outdoor space that endow the overall environment of traditional settlements with rich forms and regional characteristics.

Thus it can be seen that, the traditional “bottom-up” built settlements are characterized by acting according to local conditions and circumstances and constructing appropriate space according to human needs. Modern cities shall be developed by referring to the “bottom-up” development path, hoping to reserve the desirable nature of cities by revering characteristics of natural environment and giving consideration to lifestyle and occasion needs of natives while digging the development potential of cities.

## 6 CONCLUSIONS

Based on the research above, the paper draws the following conclusions:

1. In traditional settlements, apart from compliance with the natural topography and catering for facilities (mainly drainage) requirements, the formation of roads is greatly affected by human’s action modes, as the combination way of roads and pavement tend to vary with building locations, human’s main path directions and practical applications. Characterized by agility, human action thus endows road forms with the natural and organic features.
2. The rich degree of public space is determined by diversity of human groups’ public activities. As for public space in settlements, its spatial level is achieved through small-scale division

and definition of elevation difference; as for lots of spaces without fixed applications, they tend to be flexibly utilized as per residents’ needs and habits. The utilization frequency of public space depends on its actual comfort degree.

3. As buildings in traditional settlements are mostly built by residents themselves, the development of building and update of environment are fueled according to the actual life needs and mutual learning of technical skills. The integral form of buildings, although constrained by natural topography, has some randomness on the premise of compliance with natural environment and group needs. But buildings themselves always present relatively consistent density and spacing and regular repetition.
4. Main spatial morphology characteristics of “bottom-up” settlements are to fully reveal characteristics of natural topography, to adjust space according to conducts of daily life and to be rich in environment form and regional features. That is to be characterized by acting according to local conditions and circumstances and constructing appropriate space according to human needs.

## REFERENCES

- A Case Study from Settlements in the Form of Eight Trigrams in Gaoyao Region [J]. *Architectural Journal*, 2011 (11): 6–10.
- Kostof, Spiro. *The City Shaped* [M]. Translated by Deng Dong. Beijing: China Architecture & Building Press, 2005.
- Leatherbarrow, David. *The Roots of Architectural Invention: Site, Enclosure, Materials* [M]. Cambridge University Press, 1993.
- Luo Deyin & Sun Na. Li-cha, the Eight Trigrams Village: Living with Flood [J]. *South Architecture*, 2014, (01): 30–33.
- Qi Wenfei. Research of the Forms of Vernacular Houses along Downstream of Xijiang River Basin [D]: South China University of Technology, 2013.
- Wang Jianguo. *Modern Urban Design Theory and Method*. Nanjing: Southeast University Press, 2001.
- Wang Jianguo. On the Large Dimension Spatial morphology of Cities Based on Urban Design [J]. *Science China (Series E-Technological Sciences)*, 2009, (05): 830–839.
- Wang Jianguo. Top-down or bottom-up-exploration on design methods and values of modern cities [J]. *Architect*, 1988, (31): 9–14.
- Yu Benzhe. Research of Bagua Village, Xiangang Town Gaoyao City [D]: South China University of Technology, 2011.

# Bamboo tower—the design exploration of landscape tower in Zunyi Normal College

Zhenyu Song

*Architecture Design Research Institute of SCUT, Guangzhou, Guangdong, China*

Xueqing Liu

*School of Architecture, South China University of Technology, Guangzhou, Guangdong, China*

Xiaoshan Fang

*State Key Laboratory of Subtropical Building Science, School of Architecture, South China University of Technology, Guangzhou, China*

**ABSTRACT:** The landscape tower is an important composition element of view in the regional environment. It plays a significant role in discerning the regional environment, stressing the local culture and controlling the sequence of spaces. This paper probes into the project of landscape tower in Zunyi Normal College with the overall design by several dimensions as the landscape planning design, external space design and the architectural design. This paper also deeply analyzes the sight, the volume, the texture and some other elements in the process of design.

**Keywords:** landscape tower; campus; symbolic; view analysis; volume analysis

## 1 INTRODUCTION

In ancient times, the tower is a symbol of religious belief. While in modern times, it has become a representative landmark of the city and region. The “landmark”, which has been described in detail by Kevin Lynch in *The Image of City*, has a significant meaning for beautifying the environment and figuring the shape of the city [1]. It needs to be unique and with a certain fixed style and format [2]. As a carrier of local culture, the landscape tower fully demonstrates deep cultural details and charms the campus. This paper discusses the design strategies and conception of the landscape tower in Zunyi Normal New College for creating a campus cultural characteristic.

## 2 PROJECT PROFILE

The new school in Xipu belongs to Zunyi Normal College. It contains three campuses namely the northern, the southern and the eastern. The school managers felt it is necessary that the cultural tradition should be protected and continued; therefore, a new landscape tower laden with cultural significance was built in the northern campus. The new landscape tower, which is designed in

steel structure with 42 meters high, is located on the top of the retained mountain, 900 levels above the ground. Judging from the location, the east of the site towards the entrance of the campus, Fine Arts Building and the music-dance Building are on its south and west, respectively, while the reserved forest on its north.

## 3 DESIGN CONCEPT

### 3.1 *Site analysis*

The designing concept of the landscape tower follows the principles of campus landscape planning, which is defined as “according to the mountain topography and rooting in regional culture and indigenous landscape.” As a result, shaping the landscape tower as a node on the northern landscape belt is our starting point. The new tower should be integrated into the framework of the planning of the campus; meanwhile, it should have its own peculiarity. Therefore, we retain the flat area on the top of the mountain as the base of the tower. The tower is kept far away from teaching buildings so that pressure from evacuation can be reduced. Besides, the tension of space, which is formed by the distance and morphological differences, will make it easier to blend the building

structure with landscape organization together. People on the road can easily see the tower because the main entrance of the campus is 866 meters above the ground and 34 meters lower than the tower, which makes the tower look much higher than it was. The location and the master plot plan of the tower are shown in Figure 1 and Figure 2.

### 3.2 The spatial construction

The level on the base of the tower is 38 meters higher than the main entrance. The top of the tower is 80 meters high, which is the highest point of the reserving terrain on the northern campus. The tower changed the flat sky-line of the campus, and has a positive impact on the improvement of the campus' overall planning and carries on the spirit of exploitation and enterprising in Zunyi meeting. Among the various factors determining the richness of space, the details of its interface, that is, the place where the space comes into contact,



Figure 1. The overall plan of the three campuses.



Figure 2. The surroundings of the tower (the red point indicates the location of the tower).

with the outside is particularly important [3]. This place ought to be designed taking into account not only the exigencies of outward appearance but the demands made on the boundary from within. Therefore, the square under the tower is divided into multi-level, fluency garden by the base and the structures around the tower so that the properties of space change from the resting space to the commemorative space. In addition, the square on the mountain gets its genius loci by the memorial of the landscape tower. This is similar to Chinese landscape paintings, which never depict the visual image statically, but rather convey a perception of the experience of traveling amidst the real landscape of natural beauty, accompanied by memories and imagination [4].

### 3.3 The shape design

As a well-known city, Zunyi, which is the turning-point place of China's Revolution, has its specialties like the bamboo shoot and the red sandstone (see Fig. 3 and Fig. 4). In addition, our designing concept comes from their symbol. Growing from ground with the fluency water around it, the tower raises and contracts like a common bamboo shoot in local place, steadily rising towards the sky. Symbolic forms can bring some connotation to space, that is, it can give different meanings to different people to understand [5].

We try to employ symbolic measures to represent the revolutionary tradition in Zunyi city, so the structural form of the tower is given the meaning of "twist". The landscape tower has vivid shapes and neat edges, while its base is triple-tired from inside



Figure 3. The dispositions of the material of the tower.



Figure 4. The conception of the landscape tower.

to outside and clustered around by the structures. The interesting form is fashioned by changing details and small textures. The tower is a triangular prism in shape and topped by indented cutting, the combination of which makes them look like bamboo shoots just breaking out of the earth. Also, the spiraling structural members take concerted with uplifted stairs, creating tortuous climbing experience to visitors. The first-floor plan and the section of the tower are shown in Figure 5 and Figure 6, respectively. The design of the bionic form conveys

the philosophy of “unity of the heaven and human beings” and represents the moral of rising steadily for higher education.

### 3.4 The landscape design

The program emphasizes “person’s participation”: not only it is a work of art to be appreciated from different locations and various angles, but also a landmark in campus students, which can simply recognize their position. The landscape tower is located on the highest point of central landscape belt with a fine extensive view. It is also an important node of the main landscape axis. Two groups of appendages are set around the base to form the layout of radiation so that the surroundings get more harmonious. The design combines original water sources with elevation planning so that the ladder of cascades and the path to the hill top can be integrated together. Also, the vegetation around the tower is set in a well-conceived composition. Meanwhile, the tower can also serve as a sightseeing platform and illuminant.

### 3.5 Continually perfected design

In order to suit for the inner environmental order, some factors such as the axial counterpoint of the tower, harmonious with the surroundings, and landmark of character have to be considered. We keep the balance of the relationship between “see” and “be seen”. Nature observed is immanent: it has an extraordinary allure because it bequeaths the “consciousness” of an immanence in nature—the sense of that man is part of the landscape [6]. So, this paper combines the urban design theory, making a conclusion that the landscape tower should be controlled in 40 meters high for good vision as well as budgetary control.

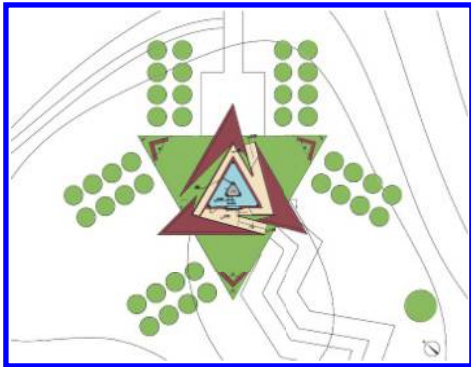


Figure 5. The first-floor plan of the landscape tower.

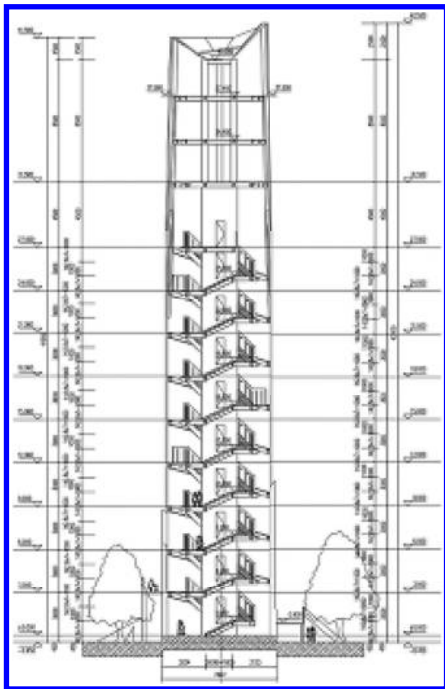


Figure 6. The section of the landscape tower.



Figure 7. The tower of the square plan.

After analyzing the plan shapes in square, circular and triangle, we found that the triangle plan is more practical than the circular plan and more compact than the square plan. It is even closer to our initial designing concept, which represents the moral of rising steadily like a bamboo shoot. With repeated siftings, the triangle plan was chosen instead of the traditional hexagon and octagon. The other two plans are shown in Figure 7 and Figure 8. The sketch of the triangle tower is shown in Figure 9.



Figure 8. The tower of the circular plan.

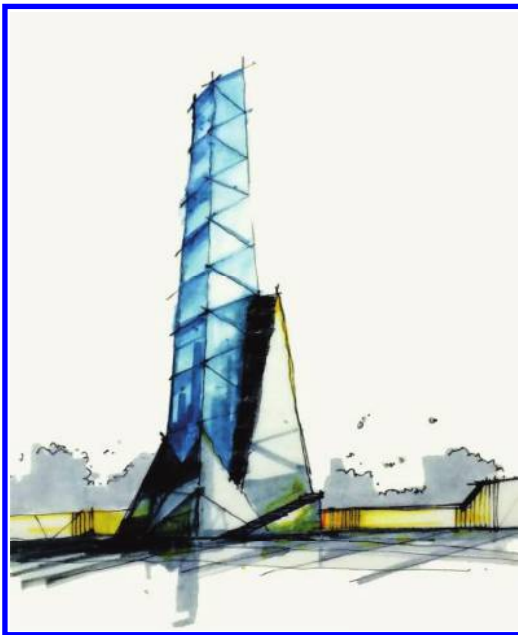


Figure 9. The sketch of the triangle tower.

## 4 HIGH DEGREE OF THE DESIGNING RESULT

### 4.1 High quality of architecture details

Homely but looking at the future, architects' ambition was to create a manifesto for public space design: not just a decoration, but an urban strategy [7]. The above ideas were followed at the stage of designing exploration. By the redefinition of construction and by making it glow in the dark, the steel structure and the local red sandstone were adopted to make a contrast with the penetrating and lightsome glasses. The tower body is barred with LED light to stand out the spiraling steel members. Besides, in order to strengthen the visual impression, the base of the tower is up lightly while the top is hung over the down lightly.

### 4.2 Energy-saving technology

The tower was set up with the solar energy and wind power combined electric device so that the supply of electricity of water pump and automatic mechanism can be ensured. Based on the natural ventilation effect, the wind suction was set at each

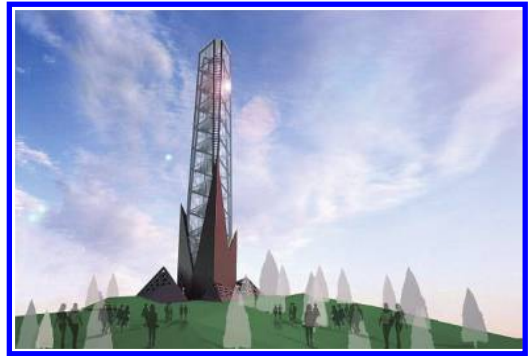


Figure 10. The rendering of the landscape tower.

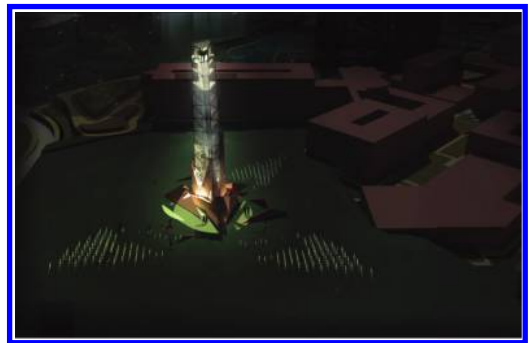


Figure 11. The lighting effects of the landscape tower.



level and the shutter was set on the top to regulate the temperature of the room by organized wind pressure and hot press. As the natural ventilation in summer will predominate in organizing the wind pressure while hot press is in winter, which makes it to control the ventilation quantity with the automatic mechanism on the top of the tower, the greenhouse effect of the glass building can be fully used; therefore, the temperature of the room can meet the demand.

## 5 CONCLUSION

With the development of living standards, people will get a higher aesthetic level in the regional architecture and landscape designing. Meanwhile, the landscape tower gets increasing attention from the general public. This paper mainly probes into the project of the landscape tower in Zunyi Normal New College, which not only is the summary and thinking for the preceding stage, but also the suggestions and ideas for the landscape tower design. When this tower was designed, it was just the 80th anniversary of Zunyi Conference convened. This paper hopes that people can introspect this period of history as well as look into the future when they visit the landscape tower.

(Source: All the above figures were provided by the authors.)

## ACKNOWLEDGMENTS

This work was financially supported by the Fundamental Research Funds for the Central Universities (No. 2014ZZ0013), the Independent Research Project (No. 2014ZC08) from the State Key Lab of Subtropical Building Science, South

China University of Technology, and the National Natural Science Foundation (No: 50908087). The authors specially thank all those who participated in these research projects.

## REFERENCES

- [1] Kevin Lynch: *The Image of City*. (MIT Press publications, USA, 1960).
- [2] Zhang Weiping: *Invisible Logic*. (Publishing House of Southeast University, 2009), p 31 (In Chinese).
- [3] Fumihiko Maki: *Architectural theories and works, 1960–2013*. (Archi Creation publication, China, 2013), p 39.
- [4] Wangshu: *Imagining the house*. (Lars Muller Publishers, Switzerland, 2012), p 2 (In Chinese).
- [5] Grant W. Reid, FASLA: *From Concept to Form in Landscape Design*. (John Wiley & Sons Publications, USA, 2007), p 11.
- [6] Li Xiaodong: *Chinese Conception of Space*. (China Architecture & Building Press, 2007), p 21 (In Chinese).
- [7] AWP, “The Lantern Pavilion”, *Architecture & Detail Journal*, (Dalian University of technology Press, Vol. 9, No. 5, 2011). P 706.
- [8] ZhenYu Song, XiaoShan Fang, *Harmony with site and assimilated into nature*, 2011 International Conference on Multimedia Technology (ICMT), July 26–28, 2011, Hangzhou, China (In Chinese).
- [9] Xiaoshan Fang, Zhenyu Song, *The Climate-adapted Design for the Hot-humid Region—Case Study on the University Library in the Lingnan Region*, IWEEE 2010 Conference Proceedings, Nov. 26–28, 2010, Zibo, China.
- [10] Zhenyu Song, Yongxiang Lin, Debao Qiao, Xiaoshan Fang, *The Exploration of Design Strategies on Regional Characteristics of Southwest Campus Architecture—Case Study on Art Teaching Building Group of Zunyi Normal College in Xinpu New Campus*, Applied Mechanics and Materials, CEABM2014, April. 24–25, 2014, Haikou, China.

# Analysis of building materials transparency effects on building space

H.H. Hu & X.H. Ding

Department of Architectural Engineering, Huaiyin Institute of Technology, Huaian, Jiangsu, P.R. China

**ABSTRACT:** From the perspective of transparency of building materials, building materials of different transparency and performance practices are researched, and the impact of materials transparency on building space is analyzed.

**Keywords:** building materials; transparency; building space

## 1 INTRODUCTION

Architecture is the unification of technology and art. The progress of the construction is mainly in the construction of function and form, construction technology and the development of art and performance on the use of building materials. From a certain perspective, a history of architecture is also the history of materials. It is said that architecture is frozen music, then building materials are the movement of the beat note. A reasonable and effective use of each note alone would compose a wonderful and moving music. The 21st century science and technology changes with each passing day, and new building materials emerge in endlessly. The different material performances lead to the architectural design process in structure and art, and great changes have taken place in all aspects. Architectural art form is also changing. So, the progress of the construction and development and innovation of construction material and use are inseparable. Building materials itself also exist various attributes, including the transparency of materials largely affects the performance of the architectural space.

## 2 THE INFLUENCE OF TRANSPARENCY ON THE MATERIAL

A translucent material and visual penetration to define the transparency of the building can be divided into an opaque, transparent and translucent interposed between transparent and opaque. Therefore, the material may be classified as an opaque material, a transparent material, and a translucent material. The influence of the transparency of the material is generally associated with increasing transparency, decreasing material color saturation, gradually weak texture clarity,

gradually weak roughness, increased weakness in the body taste and sense of weight, and vice versa. These three different transparent materials, having completely different visual effects and lighting effects, form the shape of the space and the atmosphere, and the impact on people's psychological feeling that is completely different.

## 3 BUILDING MATERIALS' TRANSPARENCY EFFECTS ON BUILDING SPACE

### 3.1 *Opaque material*

Opaque and translucent materials do not have the penetrating gaze. Common opaque materials are wood, stone, brick, concrete, and metal, which all have different natural attributes and characteristics, such as their texture and texture, background color and texture, shine and reflection, color and other surface properties and features, shaping space shape and atmosphere.

Wood is a natural organic material, being lightweight, strong and flexible, easy to get and used for simple construction. Its diverse texture, color and texture provide designers with a rich choice. Natural wood has good perception and touch, giving elegant, relaxed, comfortable and warm feeling, can produce other construction materials that are not natural aroma and unique beauty and a comprehensive "environmental" content, in line with modern close to nature, i.e. green concept. Different specifications, timber and construction practices in different varieties of texture formed are different, and the impact on the architectural space is also different (Fig. 1).

Stone is one of the most basic materials. It has a solemn, classical, durable quality. Different types of stone have a different texture and background.



Figure 1. Wood building.



Figure 2. Wright's fallingwater.

Different species, different colors, different textures, different processing methods and different design methods can create a variety of stone walls. Stone size, proportion, shape, and assembled way arrangement patterns also affect the final texture effects of the wall (Fig. 2).

Brick is a clay and cement mixture of long box body, because of the inherent characteristics of the art, classic charm and low cost, dual aesthetic and economic attractiveness and revival. Brickwork in the visual and tactile nature easily gives simple, homely feeling. Constructed with brick masonry building with a rich texture, it will be displayed to the rich local. Brick facade design should primarily consider the overall tone and texture of the walls, tile size and proportion, arrangement, and pointing width.

Concrete is made of cement, sand, water and a mixture of small stones, because in the construction industry in the magical performance as "gray gold." It is not only the basic framework for building materials, but also with durability and distinctive artistic expression, its rough and rustic character ensures that the structural details are fully expressed. It may present shape only by its restrictions template, depending on the flow of concrete, freezing and hardening characteristics template pouring process improvements, will form the concrete and sensory effects of a different nature. Common types of concrete include cast fair-faced concrete, precast concrete and decorative concrete.

A lot of metal materials are used for the development of synthetic polymer industry, aluminum, steel and for civil construction. Sheet metal cover panel consists of a stainless steel plate, color steel plate, aluminum plate, galvanized steel, and plated plastic panels. The common denominator is the ease of installation, superior durability, and good decorative effect. From the visual experience in terms of building soil improvement features using

traditional materials such as wood and stone, there are machines craft gloss, precision and intensity. As the Arab world's cultural center in Paris, France (Fig. 3), using aluminum decorative concrete structure inside the package, as a whole like a skin stretched out to form a highly rhythmic pattern, unique bright shining metal. For example, the Bird's Nest: the main body of revolution by a series of radiation door type steel truss around the bowl seating area, the spatial structure of simple science, architectural and structural integrity and unity design creative, unique for domestic buildings.

### 3.2 Transparent material

Transparent material because of its transparency, and lost the opaque material rich simple sense, but it has yet another warm hide. Glass material is now the most common application of a wide range of transparent materials.

Glass material is now the most common application of a wide range of transparent materials. During the long construction history, the glass is the most landmark building materials; it completely changes the traditional architectural form, as well as the construction of spatial relations with people. Before the 18th-century building, mostly opaque materials such as stone, brick and wood building were used, where the building appeared thick and closed. Until the end of the 19th century, metal and glass were widely used, and modern architecture movement subverts the traditional to the pursuit of transparent quality, with transparent building skin gradually expanding, even as the main body of the construction epidermis, building by the previous close, hard to open and transparent. In the early 20th century, designed by Belem, Germany ge turbine locomotive, and designed by gro skin uz FaGu

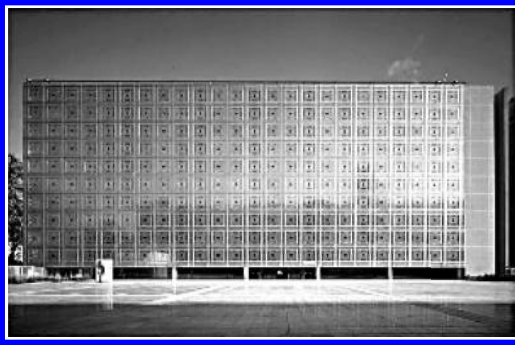


Figure 3. The Arab world's cultural center in Paris.



Figure 4. Fagus factory.

factory (Fig. 4), it may be said that the beginning of Western modernism architecture used a large area of the transparent glass walls, with buildings becoming simple, transparent, and light.

Glass material of transparency, other opaque material is unable to match the material properties and construction performance potential. Completely transparent glass material transparent, connect fully, not only give a person the feeling of pure, crystal clear light, but also convey the pure, psychological feeling of freedom. It is transparent, connects fully, but still has a physical presence. Due to the hard glass, impermeability can satisfy the rain, such as safety containment building functional requirements. At the same time, the glass material unique pervious to light quality can make the outside natural light transmission to the building, make interior space becomes bright, warm and soft, to meet the visual and psychological needs. At the same time, it can create a completely different building from the traditional building in opaque material, and give a person the visual perception and the space effect. Completely transparent glass material can let the line of sight through building inside and outside, people can from the construction of external perspective to the building interior space, structure and decoration can also see from building interior building outside of the natural beauty, life in which people can feel the outside world through transparent glass time, light, weather, and the change of seasons. Therefore, it makes the construction of indoor and outdoor penetrate each other, and in harmony with the surrounding natural environment and perfect together. Application of transparent glass blurred the boundary of the architectural space, the sense of isolation and closed, weakened the architecture and dispelling the architectural dimension sense, and give a person with a transparent, open, visual and psychological feeling of lightness (Fig. 5).

Glass products have good pervious to light, transparent, heat insulation, heat preservation



Figure 5. Farnsworth house.

performance, so widely used in construction. Especially, the emergence of a new type of glass, such as safety glass, thermal insulation glass, laser glass, glass block and expand its application space, and improving the performance of building. In addition to the windows and doors, it can also be used for exterior wall, roof, awning and railings and other parts. Shanghai grand theatre using a novel net printing white glass curtain wall glass from top to bottom with fine white dot from small to large, the architectural appearance during the day there is a fine gauze of hazy transparent texture, reflected light and night translucent. Due to the high strength, heat insulation, sound insulation, glass block and water resistance and good pervious to light the advantages of not through the line of sight, very suitable for quiet, hidden places.

### 3.3 *Translucent material*

Translucent material transparency in a transparent and opaque materials between a fuzzy state, presents a kind of like that does not fully appear, hazy vision effect, with numerous levels and possibility of change. Neither like transparent material perspective and transmit the light completely, nor like opaque material completely blocking the line

of sight and light. “In a transparent and opaque materials some ambiguous condition between the interesting to both the characteristics of the two, present a transparent have qualitative feeling, and this trait changed the architectural space and form, also changed the way architecture and communication”.

Building common translucent materials are paper, poly-carbonate vinegar, ETFE film, and through the study of the processing of the transparent material such as glass and translucent glass material, such as frosted glass, silk screen printing glass, glass block, and u-shaped glass. In addition, through to the opaque material for a variety of processing and translucent material, such as thin and pervious to light stone, perforated metal plate, aluminum louvers, and wire mesh.

Translucent material used in construction can the fuzzy boundaries between opaque and transparent, ever changing space form. While assure indoor illicit close sex, and can provide sufficient

for building internal space and the soft natural light, to avoid the traditional building materials is too depressing to surround close feeling. Natural light through a translucent material happens reflection, refraction, and a large number of diffusion, which is layer upon layer filter, avoids the transparent glass the shortcoming of the light is too strong, play a sunshade. Night, soft and radiant with indoor lamplight, building into a lightsome, pure light, the whole building show a kind of quiet, hazy, implicit beauty. That is like concealed, unreal dim light image, make the building has a subtle dynamics, also conveys a mysterious color, give a person with infinite daydream space (Fig. 6).

#### 4 CONCLUSION

In numerous property characteristics of the material, the influence degree of the transparency of space can be said to be the biggest of all. During the long architectural history, it has experienced from opaque to transparent, and changes to translucent. For transparent materials, opaque, translucent material, the shape of the building space form is completely different visual effect and smooth shadow effect, influence on people’s psychological feelings also completely different.

In addition, three kinds of materials through a certain way of processing, its transparency can be change, also can be mutual transformation, resulting in numerous levels of transparency, enrich the variety of building materials, also provides the new concept of space form and the possibility of more.

As an architect, the use of materials is an important link in building design, choice of materials is one of the important ways to express the design concept of architects, which is a very important means of expression. Reasonable selection of different transparent materials can create a rich variety of architectural space.



Figure 6. Translucent material building.

# SWMM-based evaluation and improvement of drainage infrastructure: A case in Beijing, China

Y. Sun & Q. Chang

*Beijing Key Laboratory of Development and Quality Control of Ornamental Crops, Department of Ornamental Horticulture and Landscape Architecture, China Agricultural University, Beijing, China*

F. Han & H.J. Li

*Department of Rear Service and Construction, China Agricultural University, Beijing, China*

L.J. Zhang

*Grazing Prohibition Office, Bureau of Forestry, Ulanqab, The Inner Mongolia Autonomous Region, China*

**ABSTRACT:** Urbanized hydrological process and its consequent urban waterlogging presents a major challenge to urban planner and civil engineer. This paper aimed to improve urban drainage ability through landscape architectural measures based on Storm Water Management Model (SWMM). The west campus of China Agricultural University is selected as a case of typical build-up regions in Beijing. This optimization process includes to model the infiltration ability of subcatchments, flooding volume of nodes with overload time of conduits in the platform of SWMM, to locate the potential water accumulation area using the spatial information of the above three parameters, and to choose the suitable design method of ecological landscape infrastructures for different water hazard zones. It is hoped to contribute the solid belt between the quantitative evaluation model and parametric landscape planning and design.

**Keywords:** SWMM; storm water; landscape architecture; drainage engineering; Beijing

## 1 INTRODUCTION

Water is the important resource supporting human life and activities. However, in the context of rapid urban development, urban hydrology and process have changed that lead to a series of urban environment problems, such as the shortage and pollution of water, as well as urban waterlogging, etc. There is no doubt that how to prevent urban waterlogging by optimizing the drainage infrastructure has become one hotspot in the field of urban hydrologic infrastructure and civil engineering. The Storm Water Management Model (SWMM) is a comprehensive simulation model developed by USA Environmental Protection Agency. It provides a flexible platform for examining the impacts of drainage network structure on hydrologic response (Meierdiercks et al. 2010).

The aim of this paper is based on SWMM to integrate the quantitative capacity evaluation of current drainage networks into the landscape improvement measures. It is hoped to contribute the solid belt between the quantitative evaluation model and parametric landscape planning and design.

## 2 METHODOLOGY

SWMM can simulate the rainfall and runoff process in the whole city. The steps consist of generalizing subcatchments, preparing the database of sewer, inputting the parameter data and analyzing simulation results.

### 2.1 Generalization of the case area

The case area is a typical built-up area in Beijing. It is located in the west campus of China Agricultural University (Fig. 1), which occupies an area of 33.3 ha, including teaching and dormitory buildings, squares and roads, stadium area and green spaces (Fig. 1). It is calculated that the pervious surface is 6.16 ha, accounted for 18.5% of the total area; alternatively, the impervious surface accounts for 81.5%, about 26.14 ha.

A separate sewer system was built in the case area, and connected with the city's drainage network via three outlet points. The primary sewer is along the east-west direction, while secondary sewer along the north-south direction. The whole system was generalized as 49 subcatchments,

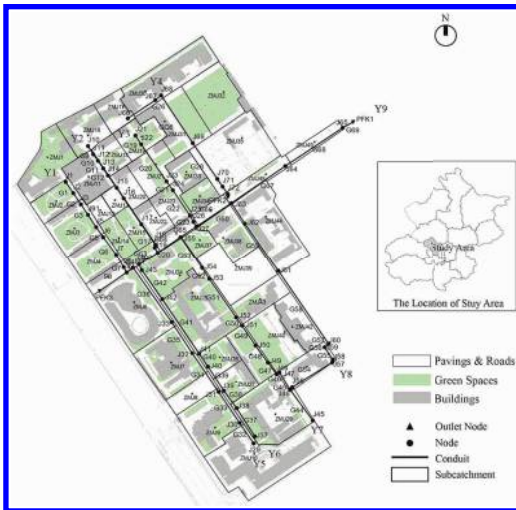


Figure 1. The location and generalized map of case area.

73 nodes (including gutters and inspection wells), 70 conduits and 3 outlet nodes (Fig. 1).

## 2.2 Establishment of the basic database

The parameters were divided into two categories: the measured parameters and the calculated parameters. The measured parameters include the area of subcatchment, the pervious area of subcatchment, the slope of subcatchment, the invert elevation of node, the maximum depth of node, the diameter of conduit and the length of conduit.

The calculated parameters refer to the typical values in the user manual of SWMM model. In this case, for green spaces are the main permeable surfaces, this paper utilized the Horton infiltration model to simulate the process of subcatchment runoff. The required parameter values are as follows: maximum infiltration rate ( $f_0$ ) = 76.2 mm/h, minimum infiltration rate ( $f_\infty$ ) = 38.1 mm/h and attenuation coefficient ( $\alpha$ ) =  $2 \text{ h}^{-1}$  (Zhao, S.Q. et al. 2009). Then we use the nonlinear reservoir to simulate the confluence calculation. Here, the value of depression storage capacity of permeable surfaces is 12 mm (Cong X.Y. et al. 2006) and its manning coefficient is 0.03 (Rossman L.A., 2005); the value of depression storage capacity of impervious surface is 2 mm (Cong X.Y. et al. 2006) and its manning coefficient is 0.011 (Rossman L.A., 2005); the value of sewer's manning coefficient is 0.013 (Rossman L.A., 2005). In the process of simulation, the runoff flow volume is calculated by dynamic wave formula.

According to the statistic rainfall data in the hydrologic handbook of Beijing, three scenarios of rainfall frequency were set as follow: P = 5%, P = 10% and P = 20% (Fig. 2).

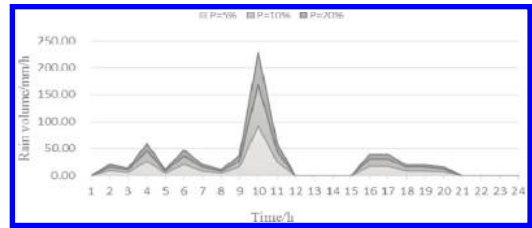


Figure 2. Rain volume data under the different scenarios.

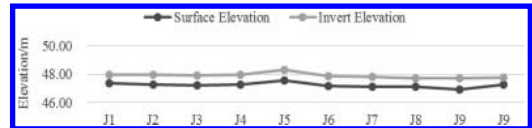


Figure 3. Change of surface elevation and invert elevation from J1 to J9.

## 2.3 Optimization of parameters for higher nodes

On the basis of sewer data, the invert elevation and buried depth have been collected from section Y1 to section Y9. Figure 3 shows the change of surface and invert elevation about section Y1 (node J1 to J9), which depicts that the invert elevation of node J5 is obviously higher than adjacent nodes' invert elevation. The stormwater within the sewer should have flow from J1 to J9, while the raised node (J5) would conduct congestion of J1 to J5. Therefore, these nodes are defined as the potential risk point. Here, it would be much more reasonable to simulate the actual hydrologic process by replacing the “pump” button with the “link” button. Thus, Y1, Y2, Y7 and Y9 have been optimized.

## 3 RESULT

### 3.1 Synthesis of runoff simulation

As Table 1 shows, with different rainfall frequency, runoff volume raises with increasing rainfall frequency. The runoff volume contains two parts: one part flows into the sewer network; the other part is the stagnated runoff at the surface depression as the overland flow converges.

### 3.2 Analysis of the surface infiltration ability

Subcatchment infiltration volumes under three scenarios indicate that the infiltration capacity of ZMJ1, ZMJ3, and other red ones in Figure 4 is higher than black ones. From the generalization map (Fig.1), it is showed that subcatchments with higher infiltration capacity are in the north

Table 1. The runoff summary under three different scenarios.

Scenarios	Total precipitation/mm	Total infiltration/mm	Total runoff/mm	Flood node	Surcharge conduit
P = 5%	276.23	32.74	243.94	41	42
P = 10%	213.02	31.051	182.286	40	40
P = 20%	153.3	27.668	125.842	39	39

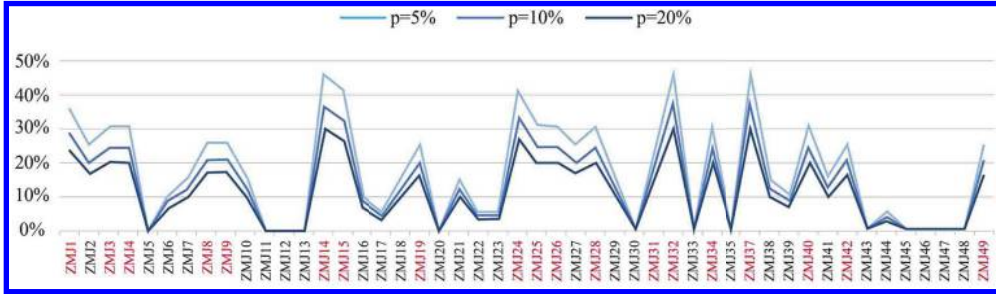


Figure 4. The proportion of rainfall infiltration of total rainfall.

Table 2. The flooding node summary under different scenarios.

Node	Hours flooded (h)			Maximum rate (L/s)			Total flood volume (10 <sup>6</sup> L)		
	P = 5%	P = 15%	P = 20%	P = 5%	P = 15%	P = 20%	P = 5%	P = 15%	P = 20%
J6	10.05	6.72	2.10	167.87	146.37	124	1.815	1.073	0.618
J7	15.23	12.73	8.57	92.88	81.47	69.6	1.720	1.299	0.743
J29	2.10	1.15	1.08	248.94	191.89	132.62	0.917	0.675	0.454
J30	3.60	2.02	1.20	21.11	20.86	19.88	0.142	0.076	0.063
J31	16.17	16.00	15.68	559.06	471.99	381.08	6.309	4.588	2.986
J48	10.13	6.88	2.10	11.38	10.76	11.3	0.258	0.148	0.071
J49	15.60	15.42	15.13	172.99	143.58	113	1.712	1.251	0.799
J50	12.53	11.13	7.00	106.36	87.05	66.97	0.781	0.526	0.320
J51	15.23	14.98	13.13	2.79	2.77	2.79	0.117	0.104	0.073
J27	16.22	15.77	14.63	300.67	265.56	231.66	4.799	3.935	2.782
J63	17.05	16.65	15.93	537.51	449.70	358.5	6.730	5.371	4.031
J64	17.42	16.98	16.22	83.99	69.95	55.37	0.989	0.784	0.589

where many green spaces are located. However, in the south, there are more buildings and pavements to meet the daily needs of teaching and pedestrian commuting. Thus, less surface runoff would infiltrate, and more surface runoff might challenge to the sewer drainage network in the southern area.

### 3.3 Analysis of the node ability

Nodes are the join of sewer drainage network, comprised of rainwater inlet and inspection wells. Based on hours flooded, maximum flow rate and total flood volume, Table 2 records the nodes easy to overflow under the different rain frequency. These nodes are mainly located in the regions with

more impervious surfaces or narrower pipelines. More impervious surface respectively leads to more instantaneous rainwater volume, while narrower pipes only support parts of rainwater. This results in the flooding around these nodes.

### 3.4 Analysis of the conduit ability

Figure 5 displays the conduit sectors which would overload under different rain frequency, particularly G7, G21, G42, G41, G48, G53–50, G64 and G66–69 (with red colors). It results from the limit of pipeline diameters. Most of these overload sectors have pipes with the diameters of 300 mm or 400 mm. But the new canal sections' diameters are 1,000 mm, such as the whole sector of Y6 and



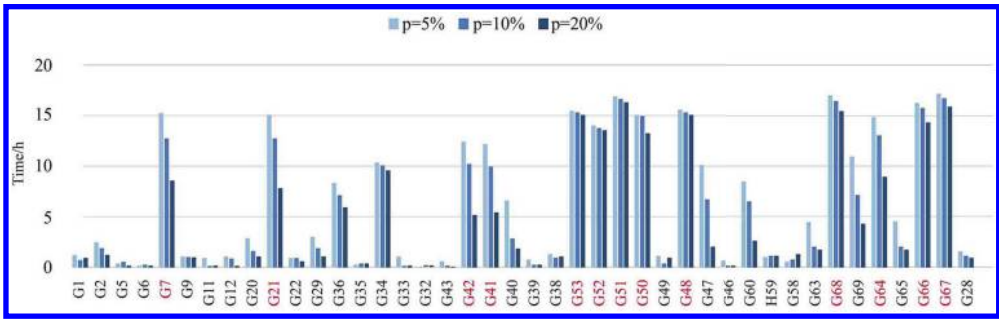


Figure 5. The flooded hours of congested conduits under different scenarios.

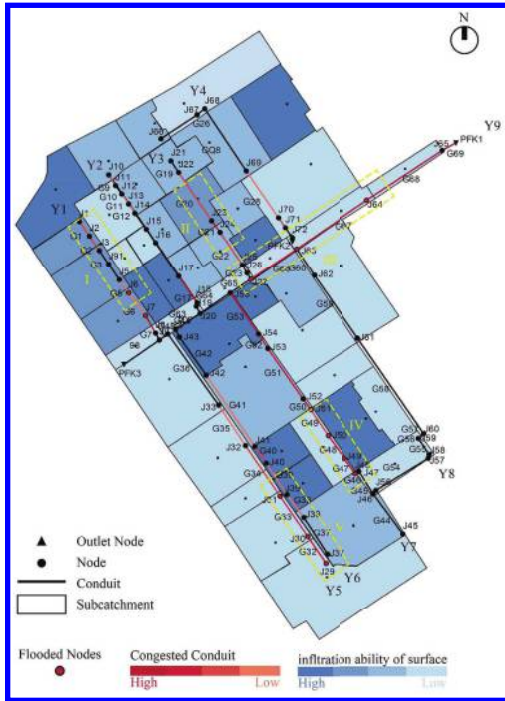


Figure 6. The generalized map of hazard area.

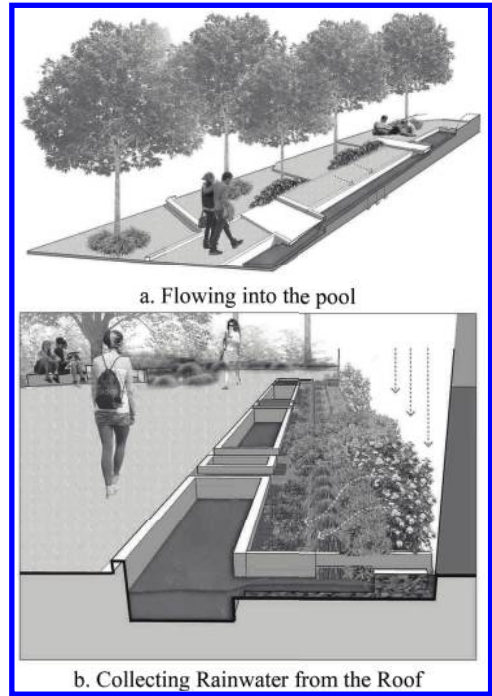


Figure 7. Stormwater facilities.

some sectors of Y5 and Y9. Additionally, the layout pattern of nodes among conduits affects the drainage ability too. Where there is few rainfall gutters, it is easier to accumulate rainwater, such as the downstream of Y7 and Y9.

## 4 DISCUSSION

### 4.1 The potential water hazard zone

Combining the analytical result of surface infiltration, nodes and conduits, this paper concluded five potential water hazard zones, displayed in Figure 6.

These water accumulation zones include three types. The first has the lower nodes and narrower pipelines, such as zone I and zone II. The second has more impervious paving which increases the runoff volume and the overload risk, such as zone IV and V. The last one, as the primary discharge canal, has much more input volumes than output, such as zone III.

### 4.2 The improvement measures

In the north, where the drainage capacity is better than the south, but there still are some sectors

existing waterlogging risk, for instance, the upper part of the Y1 (zone I) and the middle of Y3 (zone II). Aiming at these risk point, the suggestion is relieving the pressure of drainage network and improving the drainage ability by stormwater facilities (Fig. 7a). However, in the southern region with limited spaces (zone IV & V), replacing the impervious pavement by pervious surface and expanding green roofs are recommended (Fig. 7b). As for zone III, it is suggested to distribute the discharge pressure from secondary pipeline via the above methods.

## 5 CONCLUSION

SWMM has a good effect on the simulation and evaluation of rainstorm process in urban typical region. Based on SWMM, this paper have located the potential water hazard zones and provided the corresponding green stromwater infrastructure, which is a more scientific and reasonable method for landscape engineering practices. It provides the technical support for contributing the solid belt between quantitatively evaluating the capacity of existing drainage infrastructures and improving its bug by the low impact method.

## ACKNOWLEDGEMENTS

This paper is financially supported by 2015 Open Funds from Key Laboratory supported of Land Use in the Ministry of Land and Resources of China.

## REFERENCES

- Cong, X.Y., G.H. Ni, S.B. Hui, F.Q. Tian, and T. Zhang. 2006. Simulative analysis on storm flood in typical urban region of Beijing based on SWMM. *Water Resources and Hydropower Engineering* (4):64–67 (in Chinese).
- Meierdiercks, K.L., J.A. Smith, M.L. Baeck, and A.J. Miller, 2010. Analyses of Urban Drainage Network Structure and Its Impact on Hydrologic Response. *Journal of the American Water Resources Association* 46(5):932–943.
- Rossman, L.A. 2005. *Storm Water Management Model, V5, User's Manual*. USA: US Environmental Protection Agency.
- Zhao, S.Q., C.T. Jin, X.L. Li, and Y.W. Zhou. 2009. Application of SWMM model in the system of city rainwater drainage. *Water & Wastewater Engineering* 35(5):198–201 (in Chinese).

# Analysis on the river channel landscape design of Lianjiang River New Town

Yifeng Du

*Zhuhai College of Jilin University, Guangdong, China*

**ABSTRACT:** River channel is an important resource for the existence and development of humans, and the material carrier of cultural inheritance. Well-designed river channel landscape not only dramatically improves the urban outlook, but also may bring good social, environmental and economic benefits. This article carries out a comprehensive analysis to summarize the features and characteristics of Lianjiang River New Town's river channel landscape design in order to provide direction and reference for the future river channel landscape design.

**Keywords:** landscape design, river channel, Lianjiang River New Town

## 1 INTRODUCTION

River channel is an important resource for the existence and development of humans, and the material carrier of cultural inheritance. Well-designed river channel landscape not only dramatically improves the urban outlook, but also may bring good social, environmental and economic benefits. The practices of many cities testify to this. Proper understanding of the urban river channel landscape is the premise of making a good design. The understanding of the urban river channel landscape shall be analyzed from the perspective of landscape ecology. The key point is to make account of the huge ecological function and entertainment value of the urban river channel landscape. Water is the most basic condition for life, and the aquatic ecosystem is considered to be the most important ecosystem. A complete urban river channel landscape consists of riverbed, sandbank and river bank forest belt. Such spatial structure that provides a good living environment and migration corridor for various fishes, birds, insects, small mammals as well as plants is a self-maintainable and self-renewable natural garden in the urban area. Meanwhile, rich historic and cultural traces are retained in the urban river landscape owing to the close relation between urban rivers and urban development. Therefore, the urban river channel landscape can be thought of as a landscape with the most active vitality and changes.

Lianjiang River New Town river channel landscape design project is a quite typical river channel landscape design, located in Guangdong and adjoining to the Haimen Port, only a 10-minute

drive from the Shenzhen-Shantou Highway. It is a key new urban area in governmental planning with convenient transportation and broad land resources as well as a bright future prospect for development entrusted by the government. The design pays great attention in combination with peripheral environment, and simultaneously considers a future development planning on account of the position, particularly in order to carry current functions and reserve a development opportunity for the future. The landscape design shall reflect the harmony between man and nature, pays great attention to connect with surrounding landscape environment around architecture, for example venue, context, transportation, terrain, garden path and planting for greening. In addition to satisfying functions, it provides the condition for tourists to view the scenery, and a growth space for the plants, thus to achieve a harmonious coexistence friendly condition between man and nature.

## 2 INTRODUCTION TO PROJECT BACKGROUND AND BASE

The planning area is located in the north of the Lianjiang River, Chaoyang District, Shantou, Guangdong, adjoining the Chaoyang urban area with a total length of 500 meters and width of 40 meters. The total area of the project is approximately 20,000 square meters. This region is a part and parcel of Lianjiang River New Town. Moreover, it is an important region for the communication between Chaoyang District and Chaonan District. As the Shenzhen-Shantou Highway passes

through Chaoyang District, the base gets a convenient transportation, only a 10-minute drive from the Highway, half hour drive from the Xiamen-Shenzhen Railway Station (Chaoyang Station), 30-min drive from the Shantou urban area, and 40-minut drive from the Chaoshan International Airport. Chaoyang District, in which Lianjiang River New Town is located, has massive outstanding tourist resources, Wenguang Tower, Dongshan Scenic Area, Lingshan Temple, Haimen Lianhua Peak Scenic Area, and Heping Grand Peak Scenic Area, which provide high-quality tourist resources for Chaoyang District and even for Chaoshan.

Chaoyang District has abundant cultural details. Heroes-praising Dance, paper-cut and flute set music are honored as the three treasures in folk art. Traditional art and crafts such as the Chao Opera, woodcarving, stone carving, wood clay as well as folk customs cultural events including Guiyu Color Street Awning Exhibition and Gu Rao Sacrificial Fete enjoy a high reputation at home and abroad.

The base has a smooth geography. At present, it is used for agricultural purpose, and the terrain structure is quite solid, which is quite good for reducing the construction hardness and provides a good platform for landscape design.

### 3 DESIGN THINKING ANALYSIS

With a total length of 500 meters and width of 40 meters, the Lianjiang River new town river channel landscape design project is situated in the north side of the Lianjiang River, Chaoyang District, Shantou, Guangdong, and covers the total area of approximately 20,000 square meters. The landscape planning design includes several aspects as follows: square, water body, green land, building, sculpture, billboard, and lighting fixture. The design is based on the following principles:

1. Sustainable development of natural ecology: the design shall adequately consider diverse plants with long life to sustain and enrich plant diversity. The overall and partial disposal methods shall meet requirements such as ergonomics, rich landscape terrace and material and type variation.
2. Suitability: classify venue function according to different groups and design different function zones to meet the demand of different groups; resort to small functional items to make the landscape zone manifest and serried.
3. Spatial segmentation based on the venue geology: use the uniform and individual plane type matching with landscape elements with varied geometric levels to build the diverse spatial sense of the road environment.

4. Visualization: adequately resort to varied elements of the landscape design, and provide cooperation in terms of design diagram, material application, quality sense, plant shape and color, plane style, and strengthen visual impact and aesthetics of the sidewalk and walkway.

### 4 DESIGN PLAN ANALYSIS

The eco-superior principle is followed throughout the river channel landscape design by involving high-level technologies and high standard landscape design in order to coordinate with the local ecological environment to the maximum extent and to obtain a perfect combination of landscape and environmental protection, thus creating the most resplendent river channel landscape in Lianjiang River New Town, and even in the entire east Guangdong region.

#### 4.1 *Design idea*

As the Chaoshan people have the custom of catching fish since old times, and this project is right along the river channel, fishery is involved in the landscape design elements. Unique modeling of fishing boat and special texture of fishing net are implanted into the design, making people to pay attention to the fishery culture while seeing the view. Meanwhile, along with the increasingly strengthened environmental consciousness, the green environmental friendly scenic areas are increasingly favored by tourists, and a great deal of energy conservation environmental protection science and technologies are adopted in the Lianjiang River New Town river channel landscape design. Besides, with the subject bright design proposal, this project can achieve the combination of science and technology and environmental protection as well as the integration of modern and nature.

#### 4.2 *Design style*

The design style of Lianjiang River New Town river channel landscape is a combination of modern style and new Asian style. Modernistic characteristic is reflected in the simplification on the basis of modernism, stressing the idea of "less is more", with trees embellishing the hard scenery, forming activity spaces for the stream of people, local treatment stressed and intense color contrast to stress the advancing freshness and fashion. The new Asian style is also adopted by using modernism hard scenery combining with Asia's landscape gardening idea, i.e. applying a modern technique to the Asian traditional botanical garden form, retaining the traditional charm in bold innovation

of the local culture element, demonstrating a new kind of Asian style.

## 5 LANDSCAPE PLANNING ANALYSIS

### 5.1 *Design of garden path*

The design of garden path first satisfies the basic function, and coordinates the relationship between path planning and ambient environment, making the path planning manifest the harmonious unification of function beauty and art beauty. In this plan, a long main path connects all nodes to each viewing site with various tracks in-between, providing a convenient channel for tourists, especially the integration of tree shade makes the entire path system closer to the nature. Meanwhile, steps over water embellishes the road system and increases vitality to the Lianjiang River New Town river channel landscape. Fishing net modeling is used as nodes for path distribution, connecting major landscapes, thus forming the overall landscape design. Besides, the nodes scatter like various rare treasures caught by fishing nets in rivers.

### 5.2 *Design of landscape architecture*

Landscape architecture functions as an embellishment and a resting place for tourists during sight-seeing. In this project, the design idea of the main landscape architecture is to use the modeling of fishing boat in the landscape architecture, compared with a person, only one who has experienced enough adventure can be more self-confident on life journey.

### 5.3 *Design of greening*

The all-round urban green landscape considers the plant's ecological habit as well as its ornamental value; we not only understand the plant's own texture, beauty, color and greening effect, but also pay attention to the portfolio group beauty of plant varieties and harmony with the surrounding environment and other geological and environmental conditions. Different plant dispositions in the green space form a diverse botanical garden viewing space, create a different landscape effect, and add splendor to the urban landscape. The selection of reasonable plants is crucial for the success of the green land landscape as well as the main factor for forming urban green land style and creating different feeling.

Different plant dispositions in the green space form a diverse botanical garden viewing space, create a different landscape effect, and add splendor to the urban landscape. This project applies

a large footprint of green plants to manifest the design idea of green space protection. In order to obtain a peaceful and neat leisure environment, the project has planted a great deal of landscape plants in partition of the landscape architecture. The airborne greening over the landscape architecture and plants in part of the landscape nodes mainly are palms that can prevent direct sunlight on the main line and guarantee a broad vision. Other landscape regions are mainly planted with green bushes, forming a level contrast in plant disposition. As Guangdong varies little in seasons, planting of alternative vegetation of different climate manifests the seasonal variation. At the same time, planting divides a relatively peaceful space, which enables the surrounding populace a relatively peaceful leisure environment in the open space away from urban noise.

### 5.4 *Design of water scene*

Water is one of the essential substances for human living as well as the aspiration and source for the artistic creation. Along with the urban development, people demand a higher quality of urban public space environment and urban landscape art. "Water" is introduced into people's life as an important landscape essential factor, using water to make environment space art creation has become one of the important means for architects and landscape designers in creating an urban space landscape environment. In addition, large area of water can also absorb dust in the air and purify air, which is of great help to the health of urban inhabitants.

The water scene design of this project pays great attention to the function of river channel landscape in Lianjiang River New Town, combining with the peripheral development environment, using the height scattered musical fountains and shallow pool to build a overpowering fountain water scene, trying to make a true urban square water scene with current relevance that fits the disparity in ages and humane backgrounds and be loved by the populace.

### 5.5 *Design of square*

The square is a broad and smooth open-air space in the traditional city center, which manifests the richness and complexity of city life. Modern square has many functions including a place for citizens to walk, rest, holding assembly or concert, or starting flea markets. The landscape design of this project considers the peripheral environment for future development quantity, as well as relations between land limit and amount of space occupied. This square covers an area of 0.5 hectare. The square

ground uses buried lamp belt, integrates the element of fishing net, and uses the straight line staggered design. In the meantime, it uses the new tread dynamoelectric floor tiles, which reduces the operation cost besides environmental protection.

## 6 NEW TECHNOLOGY APPLICATION IN LANDSCAPE PLANNING

### 6.1 *Wind electricity complementary street light*

In this project, the designer adopts an innovative street light design that is powered by solar energy and wind energy. It not only uses sustainable energy power for illumination, but also has a fashionable modeling. In virtue of its large capacity accumulator cell and highly effective power technology, this kind of street light hardly needs the urban electrical network's electric power, thus reduces the burden of urban electrical network, and effectively reduces the administration expenditure of Lianjiang River New Town.

### 6.2 *Electricity generation floor tile*

In recent years, with more importance attached to the environment importance, our demand on clean energy also becomes more. Thus, the electricity generation floor tile comes out. Its principle is as follows: once step on it, 5% of the electric energy converted will be collected for lighting one LED in the center of the tile; the remaining 95% electric energy can be directly applied to other purposes or saved in the battery for other purposes.

Electricity generation floor tile is used in this project. It is made by stainless steel and renewable material, its green surface is made of recycling old tires, the internal piezoelectricity part is made by secondary aluminum, and its process of electricity generation is pollution-free. The service life of this floor tile is 20 years. In consideration of the large number of tourists in the future, the electricity generation floor tile will make a significant progress in Lianjiang River New Town. The coordination of large capacity accumulator cell and new technology will greatly reduce the power supply pressure without doubt, i.e. both energy-saving and environmental friendly.

### 6.3 *Water-permeable brick*

Water-permeable brick is a new high-permeable road surface material, while comparing with an ordinary brick, with its biggest feature being the high permeability coefficient. In rainy days, rain water can permeate promptly underground, or be stored in the gap between bricks, thus reducing ponded water on the road. Water-permeable brick can beautify the environment, and can prevent the outflow of precious water resources, which has good social, environmental and ecological effects. The application of water permeable brick in Lianjiang River New Town, on the one hand, adds a pretty color to the landscape, and, on the other hand, makes a contribution to water resources protection.

## 7 CONCLUSION

Rivers have always been the origin of life since the ancient times. River channel is an important resource for the existence and development of humans, and the material carrier of cultural inheritance. At present, the river channel landscape design is the focus of new town construction, whether the waterfront landscape is characteristic, or whether it has the vitality, depends on whether we can fully unearth and inherit the local nature and historical culture. Lianjiang River New Town river channel landscape design is based on Chaoyang District's profound cultural details, in line with natural skin texture, cultural infiltration, and continued design idea. It uses a diverse landscape modeling means to express and strengthen the cultural connotation of landscape, and has given the landscape brand-new vitality.

## REFERENCES

- [1] John O. Simonds. The Spacing of Man's Natural Environment [M]. Beijing: Chinese Architectural Industry Press, 2000.
- [2] Lu Min. Li Yingjie. The construction of city green space system [M]. Beijing: China Forestry Press, 2000.
- [3] HE Jing. Xu Bo. Shaanxi forestry [J]., 2011.5.

# The principles of the spatial layout for the traditional villages in the Northwest Plateau of Sichuan based on the ecological concept

J.W. Hou, Y. Cao & W. Zhu

*Urban and Rural Development College, Sichuan Agricultural University, Dujiangyan, Sichuan Province, China*

P.F. Qiu

*Bazhong Urban Planning Bureau, Bazhong, Sichuan Province, China*

**ABSTRACT:** This paper reviewed the ecological concept and its significances based on its history. The features of ecological concept to integrate in planning were also reviewed. By employing the ecological concept, this paper proposed some principles to solve the environmental problems faced by the Northwest Plateau of Sichuan by integrating the ecological concept with planning. The results showed that equality, respect of history, moderate development, and integrated were important principles, which should be integrated to the village planning in this region.

**Keywords:** the Northwest Plateau of Sichuan; traditional village; the principles of the spatial layout; ecological concept

## 1 INTRODUCTION

Since the ecological planning that was studied from the perspective of a single discipline in 1980, Chinese ecological planning has been framing a set of Chinese characteristic theoretical systems of ecological planning after 30 years of development. Nowadays, ecological planning is classified as the concept category, which should be integrated, guided and constrained in land ecological planning, urban ecological planning, and landscape ecological planning to advance the sustainable development of urban and region (He, X. et al. 2013).

According to the research results of scholars, the ecological status of the Northwest Plateau of Sichuan is not optimistic. The ecological protection situation of the Northwest Plateau of Sichuan is grim with problems, such as wetland shrinkage, wetland degradation (Zhou, H.M. et al. 1999), grassland desertification (Zhang, G.Y. & Zhang, L.X. 2013), vegetation degradation (Chen, L.K. et al. 2013), weakened biodiversity (The Academic Group in Sichuan Academy of Social Science Researching on the Tableland Pastoral Areas' Developing Policies in Upper Reaches of the Yangtze River 2013), and frequent geological disasters.

Under the new urbanization background, how to guide the development of villages by the ecological concept becomes significant, especially for the villages in the Northwest Plateau of Sichuan under the dramatic ecological threat.

## 2 ECOLOGICAL CONCEPT

### 2.1 *Significance of ecological concept*

The evolution of the ecological concept contributes significantly to solve environment problems and sustainable development. First, it pointed out a fundamental solution to the environmental issues (Song, Y.Q. 2005). The starting point of the evolution of ecological connotation is to solve the environmental problems faced by humans, which is the synchronized way for humans to look for a solution to the environmental issues. Second, it is a guideline for current practical works. The continuous development of ecological concept would guide the practical work in a clear direction.

### 2.2 *Features of ecological concept*

In the eye of ecology, the world is regarded as an organism, including human, natural and society. Based on that, ecological implications from the initial 'residence status of creature' extend to the 'existence of the state of the life system', which endowed the ecological concept with four characteristics (Xue, W.C. 2003). The first characteristic is integration. It means the abandonment of the conception that humans occupy *a priori* absolute dominance in the whole world (Xue, W.C. 2003). In other words, on the value orientation, the ecological world view is inclined to 'non-anthropocentrism'. It is impossible to achieve sustainable development

if humanity still adheres to the 'over nature', 'dominate nature' and other concepts.

The second characteristic is organism (Xue, W.C. 2003). In this point, the whole world and everything in the world are taken as an organism. The organic link between them is emphasized. Humans are no exception. Human beings, environment relied by humans, and other living organisms in the same environment all constitute an organic ecosystem. All of them are ecological factors in the world of this ecosystem. The close intrinsic relevance between human beings and other ecological factors also constitutes the human growth and order of life.

The third characteristic is equality. Several ecological factors constitute an ecosystem. They coexist and interact within this ecosystem equally. As one of the ecological factors in earth's ecosystems, humans are equal with other ecological factors. The past values 'anthropocentrism' are inconsistent with the concept of equality of ecological characteristics.

The fourth characteristic is individuality. In the ecological concept, integration, diversity and self-growth are emphasized at the same level. Individuality implies the law and order of a variety of different ecosystems (Xue, W.C. 2003). In a word, to achieve sustainable development, human beings should respect other ecological factors in the ecosystems, identify their value of existence, and are not free to interfere in its development law.

### 3 PRINCIPLES OF SPATIAL LAYOUT OF THE VILLAGE BASED ON THE ECOLOGICAL CONCEPT

#### 3.1 *The features of the Northwest Plateau of Sichuan*

The Northwest Plateau of Sichuan is located in Aba Tibetan and Qiang Autonomous Prefecture in the northwest of Sichuan Province in China. The area of the Northwest Plateau of Sichuan is around 166,000 square kilometers. It is part of the Qinghai-Tibet Plateau, and one of the four pastoral areas in China, and is also the largest animal husbandry based in Sichuan.

In 2008, Aba, Ganzi were included in 'the farming and pasturing transitional areas with a vulnerable ecosystem in the southwest mountain region'. The wavy terrain, the complexity of the geological structure, the visible change of vertical variation of water/thermal conditions, hypoplasia of soil depths, barren soil, and sparse vegetation are the phenomenon of ecological fragility in this region. To some extent, ecological vulnerability limits the development and construction in this region, which causes a great challenge to the sustainable development of this region.

The sparsely populated, the complexion of the ethnic groups, and the fragility of the ecological environment are the three characteristics of the Northwest Plateau of Sichuan.

#### 3.2 *The principle of equality*

In the eye of ecology, any factor in the same organic ecosystem has no priority. The reasonable value of ecological movement would only sustain when there is a symbiotic interaction and self-growth between one factor and the others (Xue, W.C. 2003). Therefore, as a part, every factor is equal within the ecosystem, which is regarded as the whole.

First, equality exists between man and the natural environment. It emphasizes that the equality between man and the natural environment is not just the equality between man and organisms, but also equality between man and other organic life, such as rocks, rivers and soil. There are rich resources, including biological resources, mineral resources and land resources in the Northwest Plateau of Sichuan, which are 'vulnerable groups' compared with humans. According to the ecological concept, other living organisms should be respected fully when designing the planning, such as respecting the wild life habits to ensure its survival growth environment of integrity, using the land resources rationally, and exploiting mineral resources rationally.

Second, equality exists between different ethnic people. The elimination of the ecological crisis is not to achieve the equality relationship between man and nature, but to achieve the equality of human relations (Xiong, Y.B. 2013). In the Northwest Plateau of Sichuan, the ethnic composition is complex with diversity of ethic culture and different levels of development. Integrating the ecological concept, the principle of equality of planning should fully consider the development of the local culture when planning with mutual respect between people, between ethnic groups and between civilizations.

#### 3.3 *The principle of the respect for history*

The principle of the respect for history is shown in the following aspects. First, it is reflected in the respect for the original village's spatial pattern. The vernacular settlement is gradually caused by the specific conditions of nature and geography as well as the development of cultural histories (Meng, H.N. et al. 2008). Besides, the external morphology of the village reflects the local nature and geography as well as the characteristics of cultural histories. Thus, to some extent, the interaction between human activities and the external development of the natural environment has created the



form of the village. Furthermore, those villages that linger to this day are the result from a state of sustainable development. The state takes shape because we humans are frequently in contact with nature. Therefore, the continuation of the spatial pattern of the original heritage village is not only to inherit the historical context, but also to maintain harmonious development between man and nature. What's more, it implements the necessary requirement of 'ecological' concept. Second, it shows the respect for the village's tangible cultural heritages, including traditional architectures and structures. Third, it shows the respect for the village's intangible cultural heritage, including traditional custom, which means planners should consider the specific space for worship, traditional festivals and other needs when planning.

### 3.4 *Moderate development principle*

With a fragile ecological environment, the Northwest Plateau of Sichuan is the water conservation of the Yangtze River and the Yellow River in the upper reaches. Moreover, it is the most important part of the 'Chinese water tower'. Therefore, the natural carrying capacity should be fully considered when designing the planning of the villages in this region. The over-exploitation should be prohibited. On the other hand, since the area is sparsely populated, the development scale of the village should be determined by scientifically forecasting the population in the future. To avoid 'empty village', 'ghost village' and to eliminate unnecessary waste and reduce ecological pressure, blindly expanding a village or building a new village should be prohibited.

### 3.5 *Livable industry principles*

While protecting the environment, a good living environment should be created to villagers. Thus, planning should be based on a clear picture of the local natural ecological background and topography and natural mechanism to maximize the preservation of biodiversity (Song, Y.Q. 2005). Besides, the creation and maintenance of a high level life also needs the scientific industry structure as the economic support. According to the Shenzhen, experience in building low-carbon cities, villages in the Northwest Plateau of Sichuan industrial planning should always adhere to the 'ecology' of development. The development direction and structure of the industrial planning should be based on the village's geographic conditions, resources and other environmental conditions. Furthermore, the infrastructure layout is intimately connected with the industrial distribution (Shen, Q.J. 2000). Therefore, when planning

the infrastructure, not only the local natural and geographical conditions, but all sorts of time outside of the human history should be considered. The infrastructure planning should consider a more long-term effect of human behavior.

### 3.6 *Integrated principles*

On the one hand, integration means the ecological harmony between the historical environment and the natural environment (Song, Y.Q. 2005). The historical environment is full of information resources (Song, Y.Q. 2005). Historical information resources can be converted into energy in certain situations, which helps to save energy and protect the natural environment. Besides, the protection of historical environment means reuse. It is a waste of resources and not conducive to the natural environment protection that demolishes everything to reconstruction. But appropriate reuse will play a catalytic effect for the natural environment. Thus, there is a close relationship between the protection of historical environment and nature conservation. On the other hand, the integration of the environment is reflected in the synchronous development of the artificial and the natural environment. During the production of human life activity, man must absorb the material and energy from nature to meet human survival needs (Shen, Q.J. 2000). To achieve this goal, measures have been taken by humans based on the traditional 'anthropocentrism'. However, to implement the 'ecological' concept, human needs change their conception from the 'anthropocentrism' development model to the 'eco-centrism' paradigm, which lays the ecological basis for human survival and sustainable development (Hu, D. 1996).

## 4 SUMMARY

In this paper, the ecological concept was reviewed from its history. The significances and features of ecological concept to integrate in planning were also reviewed. To explore a way to solve the fragile environment problems that the Northwest Plateau of Sichuan faced, the ecological concept was introduced in planning. Specific to the characteristics of the Northwest Plateau of Sichuan, equality, respect of history, moderate development, and integrated principles were proposed to provide some reference to the village planning in this region.

## ACKNOWLEDGMENTS

This work was financially supported by the Sichuan Center for Rural Development Research Science

Foundation (CR1204), the Sichuan Education Department of Sichuan Province Science Foundation (13ZB0277), the Sichuan Agricultural University of Federation of Social Sciences Circle Social Science Foundation (xck201207), the Sichuan Agricultural University of Research Interest Training Program (2014332) and the Sichuan Agricultural University of Students Innovation Experiment Program (201410626090).

## REFERENCES

- Chen, L.K. et al. 2013. The Degradation and Recovery of the Grassland in Northwest Sichuan Plateau. *Prataculture & Animal Husbandry* 2013, (4): 50–52.
- He, X. et al. 2013. Evolution and discrimination of ecological planning and its related conceptions. *Hn Journal of Ald Ology* 2013, 24(8): 2360–2368.
- Hu, Dan. 1996. The Ecological Connotation of Sustainability Concept and its Implication for Human Development. *Chinese Journal of Ecology* 1996, (2): 31–36.
- Meng, H.N. et al. 2008. From And Meaning Ancient Village—A Case Study of Habitat from of Huang Tan Dong Ancient Village in South Zhejiang Province. *Zhejiang Construction* 2008, 25(5): 1–4.
- Shen, Q.J. 2000. The Ecological Thought of Urban Planning. *Urban Planning Forum* 2000, (6): 7–12.
- Song, Y.Q. 2005. The Analysis about the Evolvement of Ecological Connotation and Ecological Main Body. *Studies in Dialectics of Nature* 2005, (6): 103–106.
- The Academic Group in Sichuan Academy of Social Science Researching on the Tableland Pastoral Areas' Developing Policies in Upper Reaches of the Yangtze River. 2011. Orientation Reconstitution of the Tableland Pastoral Area and Strategic Transforming: Example from the Northwest of Sichuan Province. *Reform* 2011, (11): 76–83.
- Xiong, Y.B. 2013. Study on the Ideology of Eco-concept. *Journal of Jinzhong University* 2013, (1): 23–27.
- Xue, W.C. 2003. On the methodological meaning of the ecological idea. *Journal of Southeast University Philosophy and Social Science Edition* 2003, 5(4): 36–41.
- Zhang, G.Y. & Zhang L.X. 2013. The Investigation and Research on the Ecological Environment of Northwest Sichuan Plateau-The Case of Aba Tibetan Autonomous Prefecture. *Prataculture & Animal Husbandry* 2013, (5): 54–57.
- Zhou, H.M. et al. 1999. Analysis, utilization and protection of wetland resources in the Northwest Plateau of Sichuan Province. *Southwest China Journal of Agricultural Sciences* 1999, 12.

# Study on index system and method of evaluating land suitability for construction in gentle-slope hilly areas at county level in Yunnan Province\*

Shu-qing Zhang

*Institute of Land and Resources and Sustainable Development, Yunnan University of Finance and Economics, Kunming, China*

*Planning and Design Institute of Land and Resources of Yunnan Province, Kunming, China*

Zi-sheng Yang

*Institute of Land and Resources and Sustainable Development, Yunnan University of Finance and Economics, Kunming, China*

Yan Yang & Shi-lin Ma

*Planning and Design Institute of Land and Resources of Yunnan Province, Kunming, China*

Yi-mei He & Ming-jun Xu

*Institute of Land and Resources and Sustainable Development, Yunnan University of Finance and Economics, Kunming, China*

**ABSTRACT:** Carrying out an evaluation of the suitability of gentle-slope hilly lands for urban construction is a precondition and a crucial base for the analysis of development potential thereof, and will provide a firm base for establishing reasonable objectives, and layout as well, for the integrated development thereof. With integrated development and utilization of gentle-slope hilly lands as well as effective ecological protection therein in mind, this paper has established a system of indicators, methods and grading proposal for suitability evaluation to be made at county-level throughout Yunnan Province of its gentle-slope hilly lands. This system of suitability evaluation indicators and methodology have been adopted in “The Technical Guidelines of Yunnan Province for County-Level Preparation of Specialized Planning for Integrated Development and Utilization of Gentle-slope Hilly Lands (Trial)” to be an authentic guide for the preparation of such plans province-wide.

**Keywords:** gentle-slope hilly land; construction land; suitability evaluation; index system; evaluation method; county level

## 1 INTRODUCTION

In recent years, the contradiction between protecting arable land and ensuring construction land is being aggravated by rapid urbanization. As one of typical mountainous provinces in west China, it is very rigorous to protect arable land, especially the quality cultivated land in flatland. For properly dealing with the relationship between urbanization and farmland protection and containing the disorderly expansion of urban construction in flatland, it sets out on a characterized path of urbanization development and promotes the economic and social

sustainable development in Yunnan Province. In 2011 the Government of Yunnan Province devised the important strategy of “Protecting Farmlands in Flatlands and Building Cities & Towns on Mountains”. At the same time, Yunnan Province was listed by the Ministry of Land and Resources of China as one of the pilot provinces for comprehensive exploitation and utilization of unused land and wasteland on the gentle slope of low mountains and hills.

It shall give a priority to the planning for comprehensive development and utilization of gentle-slope hilly land. Therefore, according to the arrangement of the government of Yunnan Province in recent years, it made specialized preparation for comprehensive development and utilization planning of gentle-slope hilly land in county

---

\*Supported by National Natural Science Foundation of China (41261018).

level. For scientifically preparing the rational and feasible specialized planning of comprehensive development and utilization of gentle-slope hilly land in county level, it shall first take the suitability evaluation by adopting scientific and reasonable evaluation indicator system and method. In line with the principle of adjusting measures to local conditions, it evaluates following parts in gentle slopes of low mountains and hills: geological disasters, earthquake fault zone, mineral resources, soil erosion, construction suitability and ecological suitability. Especially, it divides the gentle slopes of low mountains and hills into suitable area and limited area for urban construction and concludes the suitability evaluation on the construction land. It can provide theoretical basis for preparing planning goal and layout of comprehensive development and utilization of gentle-slope hilly land by making construction land suitability evaluation in gentle-slope hilly areas and calculation land resources potential in one county. Therefore, it is of great practical significance in carrying out suitability evaluation for urban construction in gentle-slope hilly areas in a deep-going way.

## 2 INDICATOR SYSTEM OF SUITABILITY EVALUATION FOR URBAN CONSTRUCTION IN GENTLE-SLOPE HILLY AREAS

In Yunnan, the gentle-slope hilly land refer to the low mountainous areas at an inclination between 8 and 25 degrees beyond the range of designated flatland (the intermountain basin, valley bottom and other flatland with the slope  $\leq 8^\circ$  and continuous area  $\geq 1 \text{ km}^2$ ) (Zhang et al., 2007; Yang et al., 2014).

The most essential link in the suitability evaluation is to reasonably select and determine the

evaluation factors (Yang, 2015). Upon the requirement of comprehensive development and utilization planning and ecological protection in gentle-slope hilly areas, it shall screen and determine the evaluation factors according to the significance of mode of land use as well as present situation of land use and the nature of construction. Evaluation factors include general factors and special factors.

Firstly, it shall take qualitative analysis on the special factors. The area involved in following situations shall be determined as unsuitable for construction: any irreversible geological disasters and other natural disasters, 500 meters within the scope of the earthquake fault zone, important minerals below construction, mineral properties, concerning with basic farmland protection areas, constructive expansion prohibited zone, nature reserve core or buffer, important water source, state public welfare forest or provincial public welfare forest.

The general factors mainly include topography and morphology (slope, direction, relief form and relative elevation), geological and earthquake conditions (rock and soil type, foundation bearing capacity and fault distance), natural geological disasters (types of geological disasters, geological hazards and soil erosion), social and economic conditions (traffic conditions and urban crowding effect) and human factors (land use type).

In the suitability evaluation of construction land, it makes analysis the special factors and general factors respectively, and uses “extreme conditions method” (also known as a veto) to directly determine the suitability or unsuitability of evaluation units for urban construction by analyzing the special factors. This method can effectively ensure the accuracy of the evaluation results (Yang et al., 2013).

In conclusion, in this article, the indicator system of land suitability evaluation for construction in gentle-slope hilly areas refers to [Table 1](#).

Table 1. Indicator system of land suitability evaluation for construction in gentle-slope hilly areas.

Aggregative indicator	First grade indexes	Second grade indexes	Evaluation factor	Index type	Remarks
General factors	Natural conditions	Topography and morphology	Gradient	M	
			Relative height difference	M	
			Exposure	O	Alternative
		Morphology	O		
		Seismic geology condition	Lithology type	O	Alternative
			Bearing capacity of foundation soil	O	
			Fault distance	M	
		Natural geologic hazard	Types of geo-hazards	O	Alternative
			Susceptibility of geological hazards	O	
	Soil erosion		M		
	Social and economic condition	Traffic conditions		M	
		Urban agglomeration effect		Influence of main towns	M
	Human factors	Land use		Land-use type	M
Special factors	The area involved in following situations shall be determined as unsuitable for construction: any irreversible geological disasters and other natural disasters, 500 meters within the scope of the earthquake fault zone, important minerals below construction, mineral properties, concerning with basic farmland, constructive expansion prohibited zone, nature reserve core or buffer, important water source, state public welfare forest or provincial public welfare forest.				

Notes: M is required and O, optional.

### 3 METHOD OF SUITABILITY EVALUATION FOR URBAN CONSTRUCTION IN GENTLE-SLOPE HILLY AREAS

In this article, it takes the multifactor weighted summation method to calculate score and determine suitability grades with qualitative analysis results on the basis of special factor analysis. The confirmation of evaluation units will affect the application value and the accuracy of the evaluation results. For accurately reflecting the spatial difference of suitability of construction land in the planning area and reasonably using every inch of land, it takes regular grid (suggested 50 × 50 m) as the basic unit of the construction land suitability evaluation.

Using present land use map as the base map, the evaluation takes the multifactor weighted summation method and grading on the Arc-GIS platform on the basis of field investigation and the topographic map and other relevant information. It determines the weight of indicators by using Analytic Hierarchy Process (AHP) or expert investigation method (Delphi method). The evaluation model is as follows:

$$P = \sum_{i=1}^n Wi \times Ai$$

in which,  $P$  is integrated evaluation value;  $Ai$  is a quantitative score of single index (centesimal system) (refer to Table 2);  $Wi$  is the weight of single index (refer to Table 3).

### 4 GRADING OF LAND SUITABILITY FOR URBAN CONSTRUCTION IN GENTLE-SLOPE HILLY AREAS

According to the evaluation results, the suitability degree of gentle-slope hilly land for construction is divided into four different levels, namely: first class, second class, third class and unsuitable (refer to Table 4). It shall arrange the construction land on the area of high suitability and take corresponding engineering measures to meet the construction requirements for the third class area. For the inappropriate area, it shall be arranged as forestation or farming land rather than urban construction according to land rearrangement planning, forest land use planning and general land use planning in combination with the local agricultural development conditions, natural geographical conditions and the way of life and production.

Table 2. Marking table of evaluation factors of land suitability for construction in gentle-slope hilly areas.

Evaluation Factors	Reference Value			
	80~100	60~80	40~60	0~40
Gradient	≤8°	8°~15°	15°~25°	≥25°
Relative height difference	≤10m	10~25m	25~50m	≥50m
Exposure	S, SE - SW	E, W, W - SW, S - SE	W - NW, E - NE	N, NW - NE
Relief Form	Simple & Complete	Relatively complicated and complete	Complicated and segmented	Serious broken and segmented
Lithology type	Stiff soil or rock	Medium stiff soil	Medium soft soil	Weak soil
Bearing capacity of foundation soil	≥250 KPa	250~180 KPa	180~100 KPa	≤100 KPa
Fault distance	≥3000 m	3000~2000 m	2000~1000 m	1000~500 m
Types of geo-hazards	Single hazard, no harmful	Relatively small and less harmful	Relatively complicated and seriously harmful	Very complicated and seriously harmful
Susceptibility of geological hazards	No susceptible area of hazard	Low susceptible area of hazard	Medium susceptible area of hazard	High susceptible area of hazard
soil erosion	N/A	Low	Medium	Serious
Traffic accessibility	≤1000 m	1000~2000 m	2000~3000 m	≥3000 m

Table 3. Reference weights of evaluation indicators of land suitability for construction in gentle-slope hilly areas.

Aggregate indicator	First grade indicator	Weights	Second grade indicator	Weights	Evaluation factor	Weights
General factors	Natural conditions	0.76	Topography and morphology	0.31	Gradient	0.12
					Relative height difference	0.10
					Exposure	0.09
			Morphology			
			Seismic geology condition	0.24	Lithology type	0.11
					Bearing capacity of foundation soil ;	
	Fault distance	0.13				
	Natural geologic hazard	0.21	Types of geo-hazards	0.12		
			Susceptibility of geological hazards			
			Water and soil erosion		0.09	
	Social and economic condition	0.16	Traffic conditions	0.10	Traffic accessibility	0.10
			Urban agglomeration effect	0.06	Influence of main towns	0.06
Human factor	0.08	Land utilization	0.08	Land-use type	0.08	
Total	1.00		1.00		1.00	

Table 4. Grading of land suitability for construction in gentle-slope hilly areas.

Suitability	Appropriateness	Score	Description
Suitable land	First class	≥80	Very suitable for construction; good natural conditions, social and economic conditions and human factors, little limiting factors
	Second class	80~60	Suitable for construction; good natural conditions, social and economic conditions and human factors, and some limiting factors; to take measures to improve for construction
	Third class	60~40	Having certain natural conditions, limited social and economic conditions and human factors; to take corresponding economic and engineering measures to improve for construction
Unsuitable land	Unqualified	<40	Unsuitable for construction, with adverse and limited factors / special factors

## 5 CONCLUSIONS

To take suitability evaluation of gentle-slope hilly land for construction is the premise and foundation of potential analysis of exploiting gentle-slope land in low mountainous and hilly areas. Furthermore, it shall provide basic information for preparing planning goal and layout scheme of comprehensive development and utilization of slope land. The suggested indicator system and method of suitability evaluation for construction in gentle-slope hilly areas has been absorbed in “*The Technical Guidelines of Yunnan Province for County-Level Preparation of Specialized Planning for Integrated Development and Utilization of Gentle-slope Hilly Lands (Trial)*” as an authentic guide and the direction of the special planning preparing province-wide. As of June 2013, it has completed preparation of special comprehensive development and utilization planning (2012–2016) in 110 counties (cities or districts) except 19 counties (cities or districts) due to location of alpine and cold region or other reasons. According to the special planning, it has 649 suitable construction plots in gentle-slope hilly areas and covers an area of 338,905 hectares, including 159,396 hectares for construction with a budget of RMB584.28 billion Yuan.

## ACKNOWLEDGEMENTS

This article is the result of project (No. 41261018) Supported by the National Natural Sciences

Foundation of China. We thank Department of Land & Resources of Yunnan Province and Planning and Design Institute of Land & Resources of Yunnan Province for their friendly helps.

## REFERENCES

- [1] Zhang Yao-wu, Yu Yun-xiang, Zhao Qiao-gui. *Implementary Detailed Rules of the Second Land Survey of Yunnan Province (Rural Section)*. Kunming: Yunnan People’s Publishing House, 2007: 1–141 (in Chinese).
- [2] Yang Zi-sheng, Zhao Qiao-gui. Study on dividing flatland county, semi-mountainous & semi-flatland county and mountainous county in Yunnan Province based on the Second National Land Survey. *Journal of Natural Resources*, 2014, 29(4): 564–574 (in Chinese).
- [3] Yang Zi-sheng. Analysis on the special factors for evaluating mountainous urban construction land suitability in Yunnan Province. *Research of Soil and Water Conservation*, 2015, 22(4) (in Chinese).
- [4] Yang Zi-sheng, Wr4 Ang Hui, Zhang Bo-sheng. Study on constructive land suitability evaluation in China’s southwestern mountainous areas: a case in Mangshi, Yunnan Province In: Yang Zi-sheng eds. *Research on Land Development & Rearrangement and Building Urban and Industrial Projects on Mountainland in China*. Beijing: Social Sciences Academic Press, 2013: 112–120 (in Chinese).

## A brief discussion about design research on traditional residence renovation as a resort hotel

Ying Shi

*School of Architecture, South China University of Technology, Guangzhou, China*

*State Key Laboratory of Subtropical Building Science, South China University of Technology, Guangzhou, China*

Zhenhua Zhuo

*School of Architecture, South China University of Technology, Guangzhou, China*

**ABSTRACT:** With the strong development of China's social economy, tourism, such as vacation and business, is in high-speed growth as well as the hospitality industry. People begin to pay more attention to vacation tourism, and more traditional villages try to renovate traditional residence into a boutique resort hotel. This article discusses how to replace the function of traditional residence into a resort hotel on the premise of properly keeping its characteristics, and satisfy the function of the resort hotel.

**Keywords:** resort hotel; traditional residence; renovation

### 1 COMBINATION OF TRADITIONAL RESIDENCE AND RESORT HOTEL

With the strong development of China's social economy, tourism, such as vacation and business, is in high-speed growth as well as the hospitality industry. In the meantime, as people are increasingly demanding on the quality and variety of life, the pure ornamental type of tourism can not meet the needs of tourists to tourism product diversity. People tend to prefer a travel in which they can obtain both visual beauty and cultural experience, and scenic spots of strong cultural characteristics such as ancient villages and ancient towns. When the tourist season comes, an endless stream of tourists can be seen everywhere in famous traditional scenic spots in China.

On the other hand, with the development of modern cities, a large number of traditional villages and ancient towns are forgotten, in which exist a large number of traditional residences. Many of these traditional residences are being demolished or abandoned, and only a few with high historical and artistic value ones are properly protected. How to treat this architectural cultural heritage is a challenge that we must face. Making flexible use of these traditional local-style dwelling houses is an important way. In the process of traditional residence switching to other functions, it is a necessary demand to repair and renovate a large number of these residences, which to a certain extent protects them and make them alive.

According to the existing experience abroad, the complete block and houses can be developed again, as a way of protection, while the unique ones usually make the best boutique hotels and stores. In order to protect the old city residential heritage, the European government has a special department for guidance for the renovation of ancient residence, no matter from the law or technology, and they strictly control the style of the buildings. For example, Paris, which has a long history as Beijing, has over 1200 hotels, and most of them are renovated from traditional residence, such as France Perth Hotel, built in the nineteenth Century to twentieth Century, 60 years ago, where the castle was transformed into a hotel (Fig. 1).



Figure 1. France Perth Hotel.

In order to renovate traditional residence into boutique hotels, the elevation, structure, decoration of traditional residence needs to be repaired, and through reasonable management, traditional residence can obtain a good economic benefit. We can use a part of the economic benefit to make persistent protection of traditional residence, and in this way, it may bring sustainable development of the good condition. With more and more tourism development, the ancient villages and towns attract more and more visitors to experience a new way of vacation. Traditional residence becomes boutique hotels through renovation, improving the environment and introducing modern facilities. Thus, in this way, tourist accommodation problems in these traditional villages can be effectively solved and traditional residence obtains good protection and inheritance at the same time. These resort hotels, which are renovated from traditional residences, not only emphasize the traditional hotels' residential function, but also make the regional and cultural experience more valued. On the one hand, there are quaint houses, secluded courtyards and chairs with history and memories; on the other hand, there are leisure time, delicious coffee, fascinating light and elegant furniture. The combination of these diversified elements seems not to be tough but makes the traditional residence shining with glory. This method of renovation brings an impressive holiday experience to visitors. What's more, it promotes the sustainable development of traditional residence and reduces the traditional villages' environmental stress given by the excess population so as to make the Chinese traditional regional heritage well-preserved without being influenced by rapid urban development and numerous old town renewal. This combination not only makes the resort hotels more cultural, but also protects the Chinese traditional residence effectively.

## 2 THE STRATEGY ON THE TRANSFORMATION OF TRADITIONAL RESIDENCE INTO RESORT HOTEL

There are generally two kinds of modes for the transformation of traditional residence into resort hotel: one is the transformation of the ancient village into resort hotel; the other is the transformation of courtyard residence into resort hotel.

### 2.1 *Transformation of the ancient village into resort hotel*

Resort hotels that are transformed from ancient village are located in the beautiful scenery and general scenic suburbs or near the village, with most of the original inhabitants being move out.

This transformation model should be based on the style, quality level and other factors, taking different transformation and protection modes on the abandoned traditional residence. When protecting and renovating traditional residences, we should also take into consideration the settlement pattern and the surrounding environment of traditional village. By analyzing the traditional settlement pattern, especially using the traditional gathering space, such as water, village, pond and trees, Temple Square in front, to create a public space, can be convenient for visitors to leisure activities, and life feel the atmosphere of traditional settlements. In the renovation of the protection of the natural environment, we should pay more attention to the traditional farmland, rivers, streams, forests and other protection landscape geomancy, and should forbid random destruction. For the settlement of the landscape, tree log activities can be made and regional characteristics can be created on the part of the landscape space node, such as Shaoxing Kaiyuan Resort by Da Yu (Fig. 2), Yu Ling Cun transformation, buildings to form a loose river of natural ecological environment, focusing on the overall planning of Yuling Village, without destroying the village stage, every tree and bush, brick, stone, patio, streets, Xiang River Boat Quay, such as scenery of Jiangnan folk customs reflect the gain by contrast.

### 2.2 *Transformation of the courtyard into resort hotel*

These houses are generally located in the old city or tourist resort area, and are generally historic houses into the courtyard. This transformation model should reduce architectural form, general layout, plane, facade, internal structure and decoration of the traditional residence deeply. When we renovate these traditional residences, we should try to retain the original appearance and focus on the protection of the mansion, halls, courtyards



Figure 2. Retaining the traditional settlement pattern and the surrounding environment of Shaoxing Kaiyuan Resort Da Yu.





Figure 3. Suzhou flower hall, third Court Village Landscape.

and natural environment of nodes. For example, Hua jian tang-Tan hua fu (Fig. 3) was the four-courtyard combination of Suzhou Pan's old house, according to the drawings and monograph in 1952 Mr Chen Congzhou painted as an important reference and careful restoration, while retaining the original pan Zhai; according to the needs of modern life and the hotel function was improved, at the same time in the courtyard carefully arranged waterside pavilions, embodies the garden of Suzhou the essence of the landscape.<sup>[1]</sup>

### 3 THE PRINCIPLES ON TRANSFORMATION OF TRADITIONAL RESIDENCE INTO RESORT HOTEL

The transformation of traditional residence to resort hotel would meet many conflicts; at the same time, there are also various standards bound in those processes. For example, the height of the floor to the roof is about 4.5 to 6 meters, which is higher than the modern residential space. In this way, the above room may be too empty and cause visual discomfort, so we can enrich the vertical space by increasing the thermocline in the transformation process. For example, Hua jiang tang Yan yuan (Fig. 4) in Si chuan increases the thermocline in the room to be the tourist activities space. The tourist can see the courtyard through the skylight.

Traditional residence mostly use civil structure, and most of these structures are very old. So, there are some security risks in the traditional residence and cannot meet the needs of modern living. We should renovate the traditional residences by passing on exterior wall renovation, replacing wood component, renovating roof, and strengthening the main structure. In addition, the structure of traditional residence is generally flammable, not conducive to building fire. Therefore, we should



Figure 4. Sunshine courtyard room small thermocline of Hua jiang tang Yan yuan.



Figure 5. Aman fayun resort.

design reasonable evacuation stairs and improve the fire resistance of combustible materials. Fire hydrant, fire extinguishers should be placed in the obvious position, at the same time in the courtyard of the pool can be used as fire water source.

When the transformation of traditional residence, there are two kinds of commonly used methods; one is the "repair old as the old". For example, Hangzhou Amanfayun Resort (Fig. 5) was retained and preserved in the transformation process of village of old houses the original walls, woodwork and famous and ancient trees, in the process of construction of new buildings, and the construction process of the old building, with mud, straw, suiwa compaction, and build a road some were still on the wall, the wall covered with a layer of brown film, even the new public toilets and other mountain houses maintained a unified style, to achieve a "repair old as the old" effect.<sup>[2]</sup>

Another method is to emphasize the "new" and "old" contrast. The transformation will build or transform part of the modern materials and styles, such as glass curtain wall and frame structure. This method can easily damage the body of traditional residence. For example, as part of the Zhou zhuang



Figure 6. The transformation of traditional residence completely dismantled the internal structure.

residential (Fig. 6), in order to transform into the inn, the whole building was demolished, and then rebuilt as antique buildings. This practice has caused great damage to the traditional residence, so attention should be paid to the process of reform. In fact, some new additions should be hidden, such as cabling infrastructure and structure reinforcement, and the old part should be explicit as far as possible to retain the original structure and decoration.

#### 4 CONCLUSION

Nowadays, globalization and localization development has become the mainstream of architecture.

How to treat the valuable traditional residence is a worthwhile topic, which should not be ignored and blindly overthrown. “Fusion and transformation” is an effective method, which not only respects and protects the traditional residence, but also makes use and creates value. Because of their own cultural values, traditional residence fulfills people’s personal and cultural pursuit, and effectively keeps the traditional architectural style and the traditional cultural heritage while they are renovated to resort hotels.

#### REFERENCES

- [1] Liu Su, Zhang Bei. Flowers hall The Inn Boutique design aesthetic humanistic interpretation of [J] era building 20142 49–54.
- [2] From the Amanfayun website <http://www.amanresorts.com/amanfayun/home.aspx>.

# Finite element analysis of confined precast concrete shear wall

Li Jun Dou & Ming Ling Gao

Changchun Institute of Technology, Changchun, China

**ABSTRACT:** This article mainly studies the end of the prefabricated shear wall with steel constraints, the internal distribution of reinforcing welded together with steel. In case of the axial compression ratio unchanged, discuss the different height-to-width ratio on the properties of the shear wall stress research. Design of a total of 1 general whole cast-in-situ shear wall contrast specimen and the constraint of 3 precast prefabricated shear wall specimens, a total of two groups. The results of finite element analysis show that: in general, cast-in-situ monolithic shear wall, the concrete crushing, and exit the work first. With the decrease in the aspect ratio, the bearing of capacity is increasing in precast constraint prefabricated shear wall.

**Keywords:** steel confined; prefabricated; shear wall; finite element analysis

## 1 INTRODUCTION

With the development of the city, the problem of environment is becoming more and more serious; people's awareness of the environmental protection is becoming more and more stronger. The development of housing industrialization can help mankind to protect the environment, improve the environment condition, and realize the sustainable development path.

Housing industrialization is to make the construction of production from extensive to intensive, from the traditional field of large-scale operations to the industrial machinery manufacturing plant. It can save labor, improve labor productivity, save resources, avoid the unnecessary waste of material mass, control the construction production waste effectively, and protect the environment.

Prefabricated shear wall structure is an important one of the components of housing industrialization. Many of them used for high-level and high-rise buildings, bearing horizontal direction and vertical load stress in the main, providing a better overall stability for overall structure, improving stiffness requirements, and superior performance characteristics in the energy dissipation capacity. It is applied widely in high seismic fortification intensity area. At present, although many studies of prefabricated shear wall has a progress, the influence factors of prefabricated shear wall mechanics not only just one or several factors can decide, but also to be connected by multiple factors influence each other. So far, the study of the prefabricated shear wall had a long way to go. There is a lot of research for new prefabricated shear wall structure will also continue to be developed and researched.

With steel reinforced concrete, composite structure can effectively improve the ductility performance of the structure. At the same time, the stress performance and energy consumption have a raise. The structure can help to ensure the reliability. It is used in important structure in prefabricated shear wall structure.

## 2 SPECIMEN DESIGN

### 2.1 Shear wall design

In order to study the influence of different height-to-width ratios on mechanical properties, design of geometry size is 700 mm \* 800 mm \* 800 mm, 1600 mm \* 800 mm \* 800 mm, 2500 mm \* 800 mm \* 800 mm<sup>[1]</sup>, as in the following figure.

Two kinds of section forms are designed, one is with steel reinforced concrete composite structures, the other is general reinforced concrete column structure (Fig. 2).

## 3 THE FINITE ELEMENT ANALYSIS

### 3.1 Summary

ABAQUS is one of the most advanced large-scale general finite element softwares in the world, with a large ability of solving nonlinear mechanics analysis function and is advanced. At present, it has been widely used in some complex and ultra structures of engineering analysis. It also has a lot of different kinds of unit model, material model, such as reinforced concrete and metal, rubber, polymer materials, such as soil rock geological

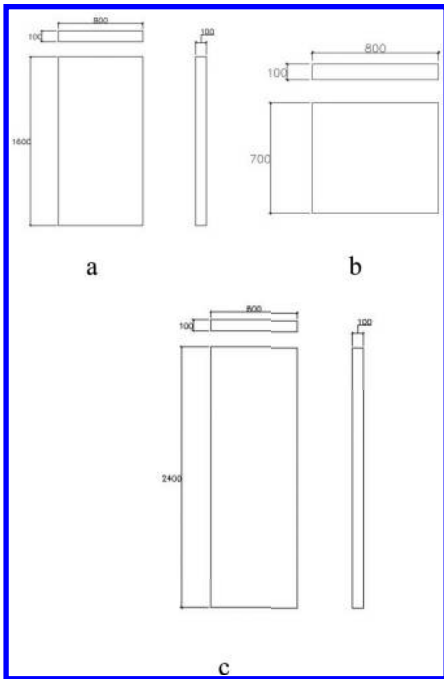


Figure 1. Physical dimension of shear walls (unit: mm).

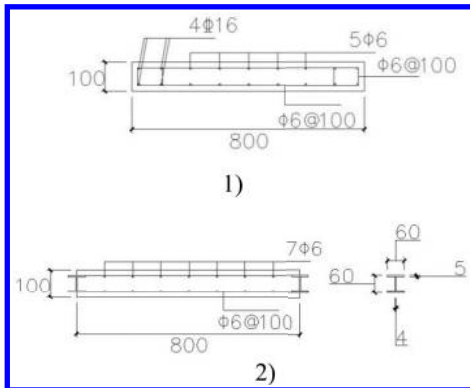


Figure 2. Steel reinforcement of shear walls (unit: mm).

materials, and detailed analysis of the process. Based on the analysis of different materials, under complex loading process and contact condition of complex nonlinear combination problem, it can achieve more satisfactory results. When a nonlinear problem analysis, ABAQUS can automatically select the corresponding load increment and convergence limit, not only can choose the appropriate parameter, but also can adjust the parameters to ensure continuous get accurate solution in the process of analysis.

### 3.2 Modeling

Select the corresponding finite element unit type, steel truss, steel chooses entity model, and wall-board choose solid model. With reference to “Code for design of concrete structures<sup>[1]</sup>” and “Code for design of steel structures<sup>[2]</sup>” input the constitutive relation of concrete, steel bar, and steel. Selected parts of cross-section features, specified cross-section shape, define material, and enter the corresponding reinforcement area. And assembly, creating analysis step, placed inside the steel and concrete in the entire model. Meshing seeding in the first place, and then use rules of hexahedral unit division. Parts of model adopt quadratic integral unit completely. On the bottom of the wall boundary conditions are set to completely fixed with the ground ( $U1 = U2 = U3 = UR1 = UR2 = UR3 = 0$ ), uses the uniform set axial pressure, refer to “technical specification for concrete structures of tall building”, way to control the displacement under horizontal loading, exert<sup>[3]</sup> maximum displacement and the ratio of height to 1/1000, the following figure.

### 3.3 The results of the finite element analysis

1. 100 km on SW-1 shear wall axial force, horizontal displacement of 0.0016 m, the results are as follows:

Results show that at the bottom of concrete sustains the main stress. At the top of the body has much area with a large displacement.

Table 1. The parameters of experimental specimens.

Specimen number	Cross-section type	Wall body geometry size	Horizontal bar	Vertical reinforcing steel bar	H-beam section size (mm)
SW-1	1)	a)	$\phi 6@100$	14 $\phi 6$	
SW-2	2)	b)	$\phi 6@100$	14 $\phi 6$	60 × 60 × 5 × 4
SW-3	2)	a)	$\phi 6@100$	14 $\phi 6$	60 × 60 × 5 × 4
SW-6	2)	c)	$\phi 6@100$	14 $\phi 6$	60 × 60 × 5 × 4

Note: At the end of shear wall at both ends of the SW-1 double limb hoop configuration; SW-6/7 2/3/4 / cross section of steel at a rate of 1.00%; the SW-5/5-5 of section steel at a rate of 1.25%.

Table 2. Parameters and bearing capacity table.

Specimen number	Cut across than	Axial compression ratio	Steel area $A_s$ (mm <sup>2</sup> )	Horizontal bar gap (mm <sup>2</sup> )	Shear capacity V (KN)
SW-1	2	0.13	0	100	51
SW-2	0.875	0.13	800	100	117
SW-3	2	0.13	800	100	86
SW-6	3	0.13	800	100	78

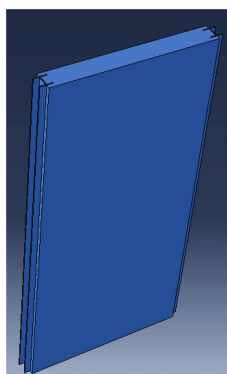


Figure 3. Model of shear wall.

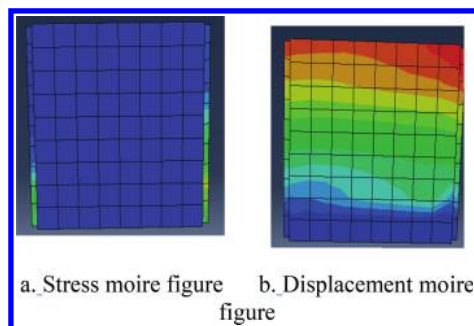


Figure 5. Results of SW-2.

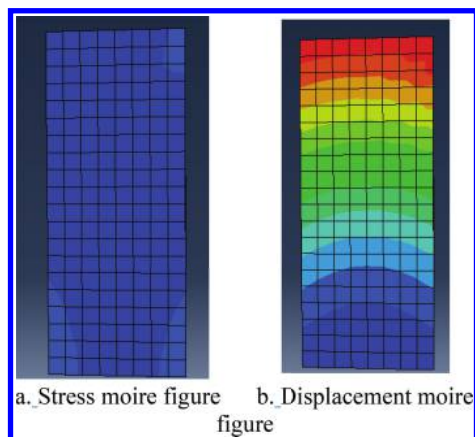


Figure 4. Results of SW-1.

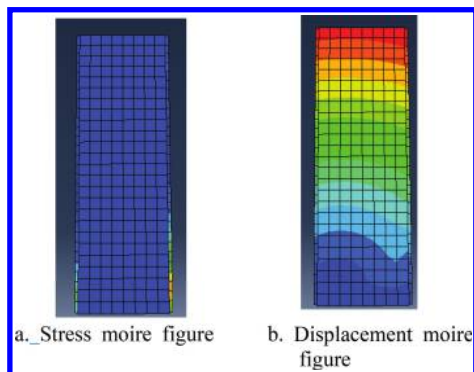


Figure 6. Results of SW-3.

2. Analyze the SW-2 shear wall  
The results showed that at the bottom of H-steel sustains the main stress. At the top of the body has little area with a large displacement.
3. Analyze the SW-3 shear wall  
The results showed that at the bottom of H-steel sustains the main stress. At the top of the body has little area with a large displacement.

4. Analysis of the SW-6 shear wall  
The results showed that at the bottom of H-steel sustains the main stress. At the top of the body has much area with a large displacement.

### 3.4 Comparative analysis

Through comparative analysis of shear wall with H-steel and general shear wall, it show the wall with H-steel than general shear wall has larger capacity reserve. Under the condition of the maximal displacement in a given specification, with the increase of aspect ratio the displacement

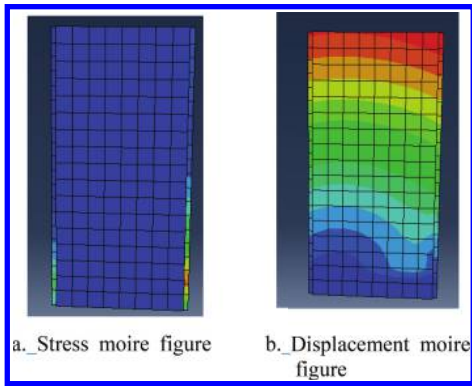


Figure 7. Results of SW-6.

increases obviously, at feet of the steel yield stress also increase. In the bottom of the steel yield failure first. The performance of the concrete characteristics is finer than the general shear wall. It is concluded that the shear wall with steel constraints can be very good to have the first force and energy dissipation effect.

#### 4 CONCLUSION

1. Equipped with steel shear wall play a role in constraining concrete, sustaining load in the previous, protecting concrete, providing higher bearing capacity.
2. With the increase in aspect ratio, displacement scope also increases, larger stress mainly appears at the bottom of H-steel.

#### REFERENCES

- [1] The national standard of the People's Republic of China: Code for design of concrete structures GB 50010-2010 [S], Bei Jing: China building industry press, 2010.
- [2] The national standard of the People's Republic of China: Code for design of steel structures GB 50017-2003 [S], Bei Jing: China building industry press, 2003.
- [3] Industry standard of the People's Republic of China: Technical specification for concrete structures of tall building JGJ 3-2010 [S], Bei Jing: China building industry press, 2010.

# Research on the unification of architecture and art, technology and art in architecture—Take I.M. Pei’s Architectural Design Works for Example

Liqun Guo

Doctor Student in School of Art and Design, Wuhan University of Technology, Jiangxia District, Wuhan, China  
The School of Arts and Design, Wuhan Institute of Technology, Jiangxia District, Wuhan, China

**ABSTRACT:** Building technology and art have the dialectical unifying relationship, and Ieoh Ming Pei’s architectural goal is to seek harmony and unity between them. This article mainly discusses the detail management and design methods in Ieoh Ming Pei’s works, helping to understand the unification of architecture and art, and the combination of technology and art.

**Keywords:** I.M. Pei; architectural; technology; art

## 1 INTRODUCTION

With the development of society, the construction requirement is getting higher and higher. In other words, with the development of social economy, the requirements of architecture will become higher as people’s living standards increase. Although the construction and functions of modern society become more and more complex, the nature of the buildings functionality stays constant, the architecture works with the perfect combination of modern technology and artistic attributes will attract more attention.

Ieoh Ming Pei is one of the most successful world architects of the twentieth century, and he is also the most influential modernist architect in the world as well. Pei has designed many landmark buildings, and gets a lot of symbolization in architecture industry’s highest honor international awards. Through the analysis of his works, it is not difficult to see that Pei’s focus on the unification of architecture and art as well as the combination of technology and art.

## 2 THE UNIFICATION OF ARCHITECTURE AND ART

With the development of society, the construction Ieoh Ming Pei once said: “Architecture and art though somewhat different, but essentially the same, my goal is to seek harmony and unity between the two.” Pei always regards the building as an independent art, and makes full use of the rich architectural space and resources in the sculpture, paintings, and other art forms. These design methods are commonly used in Pei’s architectural

designs to achieve the unification of architecture and art.

### 2.1 *The building as an independent work of art*

Sculpture is a typical feature within many of Ieoh Ming Pei’s works of architecture. When he noticed purification in the morphology of buildings, he specializes at portraying the building using a variety of geometry, the architectural and artistic unity, such as the Des Moines Art Center, East Wing of The National Gallery in Washington, and Iverson Museum of art. These architectural specimens have the appearance of sculptural style. (Figs. 1, 2, and 3).

### 2.2 *The usage of the rich architectural space of modern sculptures and paintings*

Ieoh Ming Pei are of the opinion of that the abstract sculptures can enrich large modern architectural



Figure 1. Des Moines Art Center.



Figure 2. East wing of national gallery.



Figure 3. The Everson Art Museum.

structures, and architecture and art should maintain closeness. Choosing a style or theme of unity within modern sculpture, painting and other works of art can enrich architectural space, to become a part of the whole building's design, processing techniques of architecture and art unity are often used by Ieoh Ming Pei. Such as The National Gallery's famous Calder Henry Moore's sculpture and the tapestry works by Spanish artist Huang Milo [1], Iverson art museum entrance use Henry Moore's sculptures, the French Fragrance Hill Hotel use famous Chinese painter Zhao Wuji's works, well embodying Ieoh Ming Pei's design concept and unification of architecture and art.

### 3 THE COMBINATION OF TECHNOLOGY AND ART

#### 3.1 *The building as an independent work of art*

Ieoh Ming Pei accomplishes geometry as an artistic form for the combination between technology and art. Pei's successful architectural works make a great use of geometry, such as the Louvre Pyramid, the Washington National Gallery's East Pavilion,

the Miho Museum in Japan, and Bank of China in Hong Kong.

Le Louvre Museum in Pyramid is one of the most representative buildings designed by Ieoh Ming Pei, and it is also a very typical architectural work showing the combination of technology and art. From the artistic perspective, the stable triangular Pyramid form is very suitable for the old rear roof form of Le Louvre museum building; Pyramid's glass surface can reflect Le Louvre museum's old palace, and helps people indoor to see the old palaces through it, which skillfully makes the Pyramid to integrate into the surrounding environment; Pyramid's highly transparent glass also injects light to the ancient Le Louvre Museum for a special charm. In addition, the north, south, east sides of this large glass Pyramid all has a five meter high glass Pyramid and seven triangular fountain, it becomes a beautiful geometric scenery complementing each other with the main Pyramid. From a technical perspective, the four sides of Pyramid is from by 673 pieces of diamond glass, and the total weight of Pyramid is 200 tons, of which the glass net weighs 105 tons, the metal stent is only 95 tons [2]. The load of the metal stent is more than its own weight, that fully embodies the unique use of modern science and technology in Pyramid. (Fig. 4).

In the Design of Washington's National Gallery's East Pavilion, Pei's extreme application of this method created the perfect combination of technology and art. First is the layout, the irregular trapezoidal area that combines two large triangles and a small triangle, forming the overall framework of the museum architecture and space form. The internal space is divided in strict accordance with the triangles and the deformation of the form. It carries on the segmentation to the whole space, so that each sub space has a strict correspondence on the whole. The whole sequence of space is filled with change, and is highly unified. On the technical level, the triangular atrium skylight roof structure of triangular, using a slide bearing support, not only solves



Figure 4. Louvre pyramid.



the problem of thermal expansion, but also covers the top of the lighting equipment, in addition to the snow and rain water drainage system. In order to solve the problem of strong ultraviolet sunlight producing damage to the art exhibition, Ieoh Ming Pei is also developing tubular aluminum louvers, this barrier can reduce light and heat projected into the exhibition interior, and transition any remaining room light on the art into soft and stable. In addition, glass skylights placed in addition to the hot-line, melt the snow accumulated on the roof; made of synthetic rubber, small channels discharge rain water into the drains hidden within the walls. The technical treatment of these series creates a triangular atrium space filled with a warm, comfortable and pleasant feeling. (Figs. 5-7).

The use of geometry is also reflected in the design of Ieoh Ming Pei's Japanese Miho Museum. Affected by Japan's Natural Park Act, less than 20% of the Japanese Miho museum is exposed above ground. The top of the triangular structure is made up of many different sizes, intertwined as a geometric painting. From afar, roof peaks and undulating curves are interconnected as if it is one, in the artistic sense. In the waterproof aspect; the basement walls of the library collection are insulated with thermal insulation material to avoid a frosting phenomenon caused by the temperature difference between indoor and outdoor. In order to prevent seepage of mountain soil, the construction site is covered with a cold and corrosive resistant foundation and Swiss waterproof agent and finally a layer of cement. Carefully designed shockproof walls 20 meters high, provide good protection and security to the architecture and the separated ground floor. (Fig. 8).

Ieoh Ming Pei designed the Hong Kong Bank of China Tower, which makes full use of the building structure to create geometric elements, in turn the combination of art and technology has created a classic masterpiece. This work was completed in 1990 and is the tallest skyscraper in Hong Kong, the whole building (70 floors, 315 meters high) uses only the four corners of the giant 12-storey steel columns for support, no internal pillars are



Figure 5. East Wing of National Gallery Aerial View.

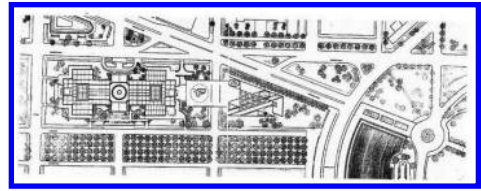


Figure 6. East Wing of National Gallery General.



Figure 7. East Wing of National Gallery's Atrium.



Figure 8. Japanese Miho Museum.

used [3]. In the square construction of the buildings foundation, stands four groups of diagonally placed triangular facades varying in height, like the bamboo trees to give a full vigor, "rising" feeling, and the buildings base is rooted with the granite stones from the Great Wall of China, like the bamboo tree symbolizing a booming future of development for Hong Kong and China, spreading its wings and soaring high. (Fig. 9).

The designs of Le Louvre Museum Pyramid, The National Gallery in Washington East Hall, Japanese Miho Museum and Hongkong Bank of China fully embodies Ieoh Ming Pei's design theories of using triangle geometry to modeling architectural space and the perfect combination of technology and art characteristics.

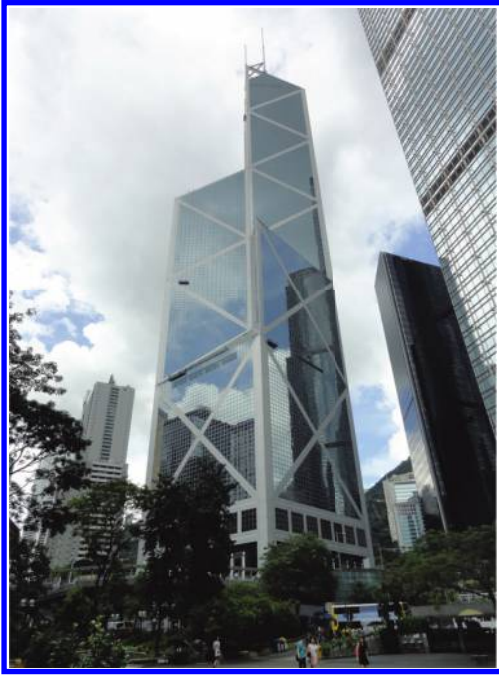


Figure 9. Hong Kong Bank of China Tower building's appearance.

### 3.2 Detail management

Ieoh Ming Pei architectural works pay great attention to detail and technologies, in particular, his designs always regard detail for god. He said: "A good design, not only has a good idea, but also in detail." [4]

As one of Ieoh Ming Pei's beloved works—Iverson Art Museum for example, its shape is created by the use of concrete with a sculptural architecture style. People who understand concrete know that concrete is a kind of rough and easy deformation of building materials, especially in the joint continuous irrigation portion and is easily prone to cracks and crevices, and every little flaw can lead to permanent defects.

Construction of the Iverson museum of art, Ieoh Ming Pei adopted the method in NCAR (American National Center for Atmospheric Research)—all the main outer wall surfaces are smooth and seamless as marble, glowing red granite plaques, the museum and the surrounding red sandstone and brick city buildings all blend seamlessly into one harmonious whole. The architecture benefits from Ieoh Ming Pei's design not only for his good idea, but also by his handling of each architectural detail. Especially in the construction of large concrete surface areas that are chiseled out to form oblique textures, which contrasts to the relationship between

certain and uncertain cut textures, and because it entirely belongs to the same material, the overall effect is unity and coordination.

In the design of East Wing, The National Gallery in Washington, the treatment of the construction details are admirable. In order to save costs, exterior building stone of East Wing, The National Gallery in Washington is very thin, but for the purpose of quality and visual effect, Pei adopted the double wall structure. [5] The wall has paved a layer of ordinary brick wall firstly, and then use the stainless steel strip to fix on the wall, finally the marble is covered on the outstanding wall. For creating solid and perfect effect, each piece of stone is cutting to fit evenly into the preset position. In order to prevent the building stone from experience thermal expansion and contraction, a 1/8 inch gap between the stones has been reserved, and the gap is also filled with an expansion joint, and the gap is filled with neoprene tape which is painted with the same color of the marble stone, so the whole wall looks smooth, neat and beautiful. Especially the corner node (traditional oblique tenon joints) is inlaid with neoprene tape to make up the insufficient and unsightly bevel butt in the marble.

## 4 CONCLUSION

New technology, new materials and new equipment in today's era not only enhance the quality of people's lives, but also improve the level of architectural design. However, the technical skill is still low, and the artistic architecture is few and far between. This article focuses on the outstanding architectural works of Ieoh Ming Pei's success as an example, from the building as an independent work of art and the usage of the rich architectural space of modern sculpture works to analyze the design style of the unification of architectural works and art works; from the usage of geometry and detail management to introduce the combination of art and technology in Pei's works, intended to provide certain inspiration and reference value to the contemporary architects.

## REFERENCES

- [1] Liao Xiaodong. I.M. Pei Biography [M]. Hubei People's Publishing House Press. 2008:295.
- [2] Bohm. Translated by Lin Bin, Conversations with I.M. Pei [M]. Shanghai Wenhui press, 2005:189.
- [3] Philip Jodidio, Janet Adams Strong. I.M. Pei: Complete Works [M]. Rizzoli International Publications, 2008:198.
- [4] (quoted) Chen Juan, Mo Tianwei. Architectural detail design [M]. Tongji University press, 2002:01.
- [5] Mike Kannai. Translated by Xiao Meihui, Ieoh Ming Pei—Master of Modernism [M]. Zhi ku Limited by Share Ltd, 1996:285.

# Research on brickwork dwelling optimization design in Nu-Jiang River drainage basin

Fang Wang

*Center for Post-Doctoral Studies of Urban and Rural Planning in Xi'an University of Architecture and Technology, Shaanxi Province, Xi'an, China*  
*Western Green Architecture Collaborative Innovation Center, Shaanxi Province, Xi'an, China*  
*(West) Key Laboratory of Green Architecture, Xi'an, China*

Jing Chen

*Center for Post-Doctoral Studies of Landscape Architecture in Xi'an University of Architecture and Technology, Shaanxi Province, Xi'an, China*  
*Western Green Architecture Collaborative Innovation Center, Shaanxi Province, Xi'an, China*  
*(West) Key Laboratory of Green Architecture, Xi'an, Xi'an, China*

Qun Zhang & Jiaping Liu

*Architecture College, Xi'an University of Architecture and Technology, Shaanxi Province, Xi'an, China*  
*Western Green Architecture Collaborative Innovation Center, Shaanxi Province, Xi'an, China*  
*(West) Key Laboratory of Green Architecture, Xi'an, China*

**ABSTRACT:** The traditional residence features of our national longitudinal valley areas in Hengduan Mountains in the southwest present a unique style, while, in recent years, the large-scale concrete square-box architecture activities have appeared. Newly built houses lose the aesthetic value of traditional residence and cut off the development venation of dwellings, which suffer a barrage of criticism. This paper selects middle-upper basin of Nu-Jiang River as research area, and makes contrasting analysis about thermal performance of conventional building materials-concrete hollow block and conventional building materials-wooden flute, immature soil with the method of the physical environment test. The test results show that the former is provided with better environmental suitability, which verifies that under the overall background of protecting forest resources, hollow brick is of great significance in promotion. On the basis of this, it analyzes those existing problems in current brickwork houses, and proposes optimization design scheme for residential buildings, referring to more attention to national characteristic decorations and form expression, as well as the structural measures of reinforcing structure and adapting to climatic characteristics.

**Keywords:** concrete hollow block; Nujiang River drainage basin; new-type territorial dwellings

## 1 INTRODUCTION

In the past, our national house cladding material of masonry structure is mainly of agglutination loam brick. To save land resources, our country starts to research a series of new building materials to replace agglutination loam brick step by step. At present, one of the widely used building materials in our national rural areas is concrete hollow block. Research results on this building material mainly are reflected in economic benefits, physical properties (thermal insulation and sound insulation property) of material and several problems to be prevented in the process of construction. Please see literature [1] to [4] for more details about the research results. These researches mainly refer to the aspect of engineering practice application, but to ignore the research on aesthetic values of

material. It is even more so in architectural practice, so that the society throws doubts upon the newly built concrete dwellings.

Longitudinal valley areas of Hengduan Mountains in West China are national nature protection area, multi-ethnic mixed area, and extremely distressed area. The typical vertical three-dimensional climate makes the types of traditional residence in this area diversified, respectively including pile dwelling type of bamboo split house, well-frame house, immature soil house, etc. All these types present bright regional characteristics. However, local civil firewood and dwelling structure lead to a huge consumption of fire wood, which consists of principal factors of local forest resources consumption mode and quantity. According to some statistics, for a 70 m<sup>2</sup> well-frame house, its roof, wall, and floor need total 43.3 m<sup>3</sup> woods with 84.0 m<sup>3</sup>

forest resource consumption; furthermore, a well-framed house is the dwelling type with the largest consumption of forest resources among all traditional residence types [5]. With the sudden increase tendency of national minority population, forests cannot bear the heavy burden, which leads to forest changed into meadow, meadow desertification, and other ecological crisis. To prevent further degeneration of forest resources, local government carries out the policy of closing hillsides to facilitate afforestation, and encourages local people to adopt slag hollow brick as the primary building material for new dwellings. The results cause that “barrack” type of brickwork dwellings appear on a large scale. Relevant researches show that those problems like uncomfortable dwelling and rigid appearance exist in newly built dwellings, which leads to the author’s exploration toward concrete hollow brick application in regional architecture. Researches in this paper are expected to standardize the application mode of new-type building materials in less developed areas, guide brickwork dwellings to actively adapt to local climate, and reflect minority culture traditions, and get newly built brickwork dwellings stepping on development road of regional architecture.

## 2 OVERVIEW

Nu-Jiang River originates from Tanggula Mountains in Qinghai-Tibet Plateau, directing to the south once entering into Yunnan and then directing to Burma renamed as Salween River, and finally flowing into Andaman Sea of the Indian Ocean. The east side of upper-an-middle drainage basin is Biluo Snow Mountain, and west side is Gaoligong Mountain. The flowing areas are from alpine and gorge region of two mountains infibulating a river which is Nujiang Canyon. Nujiang Canyon presents a reverse “V” tendency from north to south, mainly containing Gongshan and Fugong County (northern latitude  $26^{\circ}28' \sim 28^{\circ}23'$ , east longitude  $98^{\circ}08' \sim 99^{\circ}02'$ ). The ridges at both sides of Nujiang Canyon have over 3000 m average elevation, while the average canyon depth is more than 2000 m. The deepest point is Bingzhongluo area in Gongshan County, reaching 3500 m.

Quanzhou is subtropics hilly monsoon climate, and the difference in latitude and elevation leads to difference in air temperature. The latitude has different air temperatures from different elevations, or the same elevation has different air temperatures from different latitudes, which forms a prominent three-dimensional climatic feature. Once the elevation increases above 100 m, the air temperature will decline by  $0.59^{\circ}\text{C}$ ; once latitude directs northward by  $1^{\circ}$ , the air temperature will decline by  $1.2^{\circ}\text{C} \sim 1.7^{\circ}\text{C}$ . Compared with horizontal



Figure 1. Nu-Jiang River region environment.

climate difference, vertical climate difference is more prominent. The diversified landforms and different microclimate characteristics generate diversified microenvironmental habitation.

This paper takes the Baizi District of warm temperate zone in the north of Nujiang Canyon—Bingzhongluo as research area (Fig. 1). Gongshan County has abundant rainfall capacity, and, from February, to October the whole year is a long rainy season with extremely abundant rainfall capacity. Gongshan areas stay in low-temperature climate all year round. It will be winter in rainy days with insufficient heat, and it is a typical clammy climate. The annual mean rainfall capacity in Bingzhongluo is 1657.3 mm; annual average temperature is  $13.1^{\circ}\text{C}$  to  $15.4^{\circ}\text{C}$ ; the average temperature of the coldest month is  $5.9^{\circ}\text{C}$ , while the average temperature of hottest month is above  $20^{\circ}\text{C}$ , and it is warm temperate zone climatic region. The research site is located in Chongding Village, situated in northern latitude  $28^{\circ}01'38''$  and east longitude  $98^{\circ}37'31''$  with 1580 m elevation.

## 3 ADAPTATION OF HOUSE MATERIALS AND ENVIRONMENT

### 3.1 Test object and test result

#### 1. Test object

This time of test is forwarded in winter with research objects (Fig. 2) as representative dwellings R1 (immature soil house), R2 (well-frame house, two floors), and R3 (brickwork house). The three architectural structures locate in a same courtyard, and the difference in outdoor environment can be ignored. R1 is a traditional immature soil—flat pedestal house with an 80-year history and the thickness of wall reaches 0.5 m. And it consists of soil, macadam, and straw by punning. R2 is a newly built family hotel with two floors in the structure of

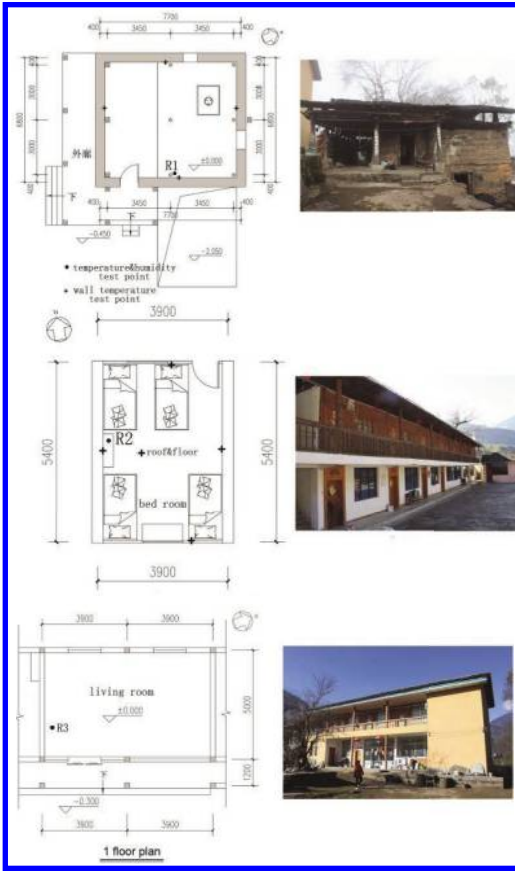


Figure 2. Survey rooms and survey points.

concrete and wooden frame. The wall of first floor is hollow brick masonry, and the second floor is simulated traditional well-frame wall by overlaying half round solid wood with up-and-down two ends chipped off. Its thickness is 5 cm, and the internal surface of wall is stuck with about 3 mm wooden board as facing material. The test object is a room in the middle of second floor. R3 is a newly built brickwork house with two floors. This house is built with concrete frame structure, and masonry wall is from hydraulic-pressure slag hollow block. The block size is 390\*200\*190, and the thickness of wall is about 22 cm (including 10 mm plaster layer of its internal and external surfaces).

The test time is 12:00, December 8, 2010 to 12:00, December 10, and it is rainy from 6:00, December 9 to 6:00, December 10. In Gongshan areas, the amount of precipitation is large, and average relative humidity reaches above 78% all year round. Thus it can be seen that it is of great practical significance to take physical environment test toward houses in rainy days, and to know more

about the indoor temperature and humidity in rainy days in winter.

## 2. Test result

### 1. Indoor and outdoor air temperature

Figure 3 is relative air humidity test result of indoor and outdoor air. This time of test experiences a sunny day and an overcast day. During test period, average outdoor temperature is 11.06°C. In whatever sunny day or rainy day, the appeared time of minimum and maximum air temperatures, respectively, are 5:00~5:30 and 16:00~17:00; daily range in sunny day is 7.6°C, and daily range in rainy day is 3.6°C. The test results of various rooms are shown as below: ① for immature soil house (R1), the indoor average temperature is lower than outdoor air temperature, and both its minimum and maximum air temperatures appearing in sunny days, respectively are 9.5°C and 12.3°C. The daily range is 2.8°C. In rainy days, range ability of indoor temperature is very little, and the daily range is 1.3°C. Therein, 7:00~9:00 is minimum temperature, 10.1°C; Indoor temperature at night rises slowly with opposite variation trend toward outdoor temperature. We can find that for clammy areas, indoor temperature of immature soil house changes a little, and it has favorable heat insulation performance; however, humidity within the house is large (medial humidity reaches 80.4%). Besides, no heat resource is available indoor, which results in lower indoor temperature than outdoor temperature. The earth houses in cold and arid regions of China's northwest are provided with the climate characteristics of hot summer and warm winter. By contrast, earth buildings cannot give play to the thermal insulation properties in clammy regions. ② For the dry-type house (R2), the indoor mean temperature was slightly higher than outdoor temperature, and its minimum value and maximum value, respectively, were 10.3°C and 13.3°C, both happened in fine days. The daily range was 3°C.

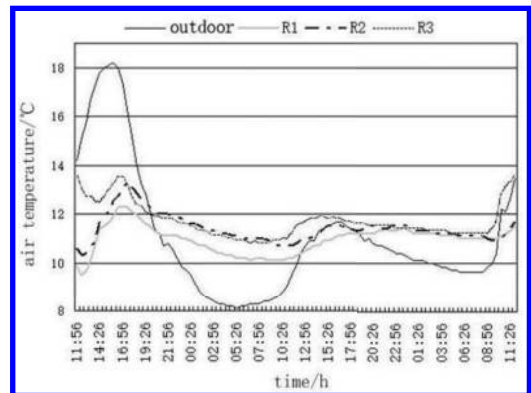


Figure 3. Indoor and outdoor air temperature.

During rainy days, the temperature change was not very little with 0.9°C daily range for the whole day. And the indoor temperature during 10:00 to 11:30 was 10.7°C, which was the lowest in that day; at night, the indoor temperature basically remained unchanged. 3) For the brick house, the indoor mean temperature was the highest; the minimum value happened in cloudy day, which was 10.8°C; while the maximum value happened in fine days, which was 13.6°C. The daily range was 2.8°C. During rainy days, the temperature change was all day long with daily range 1.1°C; At night, indoor temperature gradually dropped.

#### 2. Relative humidity of indoor and outdoor air

Figure 4 is the test result of relative humidity of indoor and outdoor air. It can be seen from the figure that the average value of outdoor relative humidity was 83.8%. At 15:30, of the 8th day, the relative humidity was 41.9%; afterwards, the humidity gradually rose; the 9th day was a rainy day, the average humidity was the highest. For all the tested houses, the low-to-high sequence of indoor mean relative humidity was: R2 (dry-type house), R3 (masonry house), R1 (earth house), which respectively were 75.4%, 77.7%, 80.4%; the tendency of relative humidity change of all houses were as follows: it was fine in the 8th day, and the lowest humidity happened during 14:30 to 16:30. When night fell, and it rained in the 9th day, the humidity gradually rose.

#### 3.2 Environmental adaptability of new and old palisade components

According to test result, the high-to-low sequence of the mean value of base room temperature was

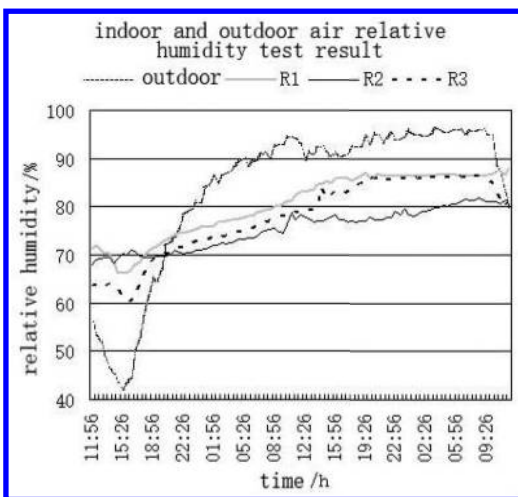


Figure 4. Indoor and outdoor air relative humidity.

R3 (masonry house), R2 (dry-type house) and R1 (earth house); and the high-to-low sequence of the relative humidity was R1 (earth house), R3 (masonry house) and R2 (dry-type house). It can be seen that the thermal performance of brick house and dry-type house is better than earth house, which reflects the adaptability of new materials to the complicated natural environment in Nu-River basin. Although from the perspective of long-term development, concrete material certainly will be replaced by more ecological environmental protection material. However, its current utilization is in line with the reality.

#### 4 PROBLEMS EXISTING IN CURRENT MASONRY DWELLING HOUSES

Cinder bricks are processed and made of industrial waste, which are provided with good performance of energy conservation, soil saving, environmental protection, thermal insulation, heat preservation and sound insulation, so that they are environmental friendly and new type building materials that can replace fired clay bricks. The manufacturing technique of slag hollow bricks is as following: waste slag lime parget, stirring digestion grinding, green brick molding steam curing finished products [4]. Since 1990s, this product has been developed rapidly. Currently, it has been widely applied in eastern coastal regions and western regions in China. Since the implementation of “closing hill-sides to facilitate afforestation” policy in Nu-River basin, the government has funded the promotion of this product in the vast mountainous areas. For its application in house construction in mountainous areas, it is provided with following advantages: ① at present, its replacement of wood reduces the load of forest resources. ② it utilizes industrial waste as the aggregate, which reduces environmental pollution. ③ it can be processed within a small scale nearby, which is free of space limits and reduces energy consumption during transportation process. ④ it is convenient for manual handling. In Nu-River basin, the mountains are high and slopes are abrupt, resulting in inconvenient transportation. Small-scale building blocks can be transported by tractors, handcarts, while it is inconvenient for larger wagons. At present, hollow bricks have the following problems: ① the strength is low due to low material density. ② The level of manufacturing technique is low, resulting in rough surface and broken corners (Fig. 5). Above-mentioned problems can be solved by improving the level of manufacturing technique.

The overall economic level of this region is low, and it is the extreme poverty region in China. Due to limitations of economy and a lack of related



Figure 5. Slag hollow bricks made in Nu-River basin.



Figure 6. Concrete box houses.

technical guidance and masonry dwelling, houses develop fast with the feature of low technology, which results in a large number of problems: the constructional column in the brick-concrete structure lacks steel ties, leading to hidden danger in seismic fortification; the spatial composition is rigid, incomplete, and not in line with the climate; the scene of buildings is stereotyped, and even disgusting. In a word, the newly built dwelling houses fail to improve people's housing quality, and even are far less comfortable than traditional dwelling houses (Fig. 6). In the condition that economy bearing capacity is limited, it is the research objective of this thesis to provide comfortable and pleasant living environment for national minorities.

## 5 OPTIMIZED DESIGN RESEARCH ON MASONRY HOUSES IN NU-RIVER BASIN

In order to facilitate the development of regional architecture and change the architectural image of newly built masonry dwelling houses in less developed areas and the dwelling level, the author explores the approaches to application of this material mainly from the perspective of aesthetic value of concrete hollow bricks and the climatic adaptation of mountainous environment.

### 1. Architectural decoration

Parts of the newly built dwelling houses are constructed on the basis of previous old houses. The traditional Muleng, girders and other components dismantled from the old houses are applicable for reuse for new dwelling houses. The mixed use of new and old material has two construction ways: ① the ground floor utilizes concrete hollow bricks, and the top utilizes traditional materials. In such way, the top room can be used in summer; and the ground room can be used in winter. ② The kitchen and bedrooms utilize concrete hollow bricks, which are fireproof and thermal insulation. Function rooms, such as living room, storeroom and bathroom, utilize the enclosure of traditional woods. On one hand, the mixed use of new and old materials saves building materials, on the other hand, it reflects the regional characteristics of traditional dwelling houses.

Besides, the most common materials are unified gray bricks. Color hollow bricks can be produced so as to satisfy the demands of architectural ornament of multiracial dwelling houses in mixed dwelling regions. Figure 7 shows the ornaments on the eave walls and plinth of the building scheme for new dwelling houses of the Nu nationality in Gongshan area.

### 2. Form expression

In the construction of new dwelling houses, architects should respect the living customs of the minority, and introduce new functional space for living, such as living room, dining room, and bathroom, so that dwelling buildings that combine the



Figure 7. Color concrete used for architectural decoration.



Figure 8. Gongshan area dwelling houses scheme.

traditional and the modern and reflect national features can be designed. In such way, the form expression of new architecture will certainly be enhanced, and the visual performance of new dwelling houses can be strengthened. Figure 8 shows the dwelling houses scheme in Gongshan area, which reflects the humanized design philosophy. (Designed by the author)

### 3. Building construction

The building space of traditional dwelling houses in Nu-River basin, no matter it's dry-type house or bamboo split house, is full of gaps and holes, like ventilating bamboo cages, so that it can adapt to the wet climate. The eave wall top, gable, and the wall body of newly built dwelling houses take advantages of the characteristics of hollow bricks and the wall body with holes in the masonry. Its unique building mechanism reflects the excellent likeness with traditional dwelling houses.

### 4. Structure safety

At present, masonry dwelling houses in Nu-River basin mainly have one or two floors, which mostly utilize brick-concrete structure. The buildings lack technical support, and the constructional column is

not provided with reinforcement. Besides, there are no steel ties between constructional columns and wall body. The consequence cannot be imagined once earthquake happens. The newly built dwelling houses should enhance the brick concrete of reinforcing bars and the composite bearing structure of frame. On one hand, it improves the earthquake resistance of houses, on the other hand, it provides technical guarantee for the scale enlargement of dwelling houses (increase of floors).

## ACKNOWLEDGMENTS

The research described in this paper was supported by science and technology talents fund of Xi'an University Of Architecture And Technology (RC1302) & National Natural Science Foundation of China (No. 51408470, 51221865).

## REFERENCES

- [1] Cinder Brick, 2006, Amendment Team for Industrial Standard. Cinder Brick, Explanation Compilation for Industrial Standard. *Brick and tile*, (06): 59–60.
- [2] Yanqing, H. Haibo, D. Honggang, H et al. 2003. Study on Cracking of Floated Coat of Gas-filled Concrete Block and Slag Concrete Hollow Bricks and Its Treatment Measure. *Project Quality*, (05): 47, 54.
- [3] Qing-guo, Hu. Wei-jun, Y. 2003. Sound Isolation Study of Concrete Hollow Brick Wall. *Chinese and Overseas Architecture*, (04): 83–84.
- [4] Fulian, X. Turn “Slag” into Brick. 2005. *Sichuan Building Materials*, (02): 21–22.
- [5] Wenzhong, Y. Li, J. Weibin, W. 2007. Traditional Dwellings and Sustainable Utility of Forest Resources in Nuijiang Valley of Yunnan Province. *Fujian Forestry Science and Technology*, 34(01): 163–177.



# Landscape pattern dynamic variation for 30 years in Chuanjiang River Basin

Z.L. Yu, T.L. Qin, S.Y. Zhang, C.L. Hao, M.J. Yang & M. He

*State Key Laboratory of Simulation and Regulation of the River Basin Water Cycle, China Institute of Water Resources and Hydropower Research (IWRH), Beijing, P.R. China*

*Water Resources Department, China Institute of Water Resources and Hydropower Research, Beijing, P.R. China*

**ABSTRACT:** Based on the Landsat TM Images in 1985, 1995, 2000, 2005, and 2014, spatial and temporal dynamic variation of landscape pattern for 30 years in Chuanjiang River Basin was analyzed to obtain its characteristics and to transfer features in space and time by software platform of ENVI5.1, ArcGIS10.1 (ArcView) and FRAGSTAT4.2. The results showed that: (1) there were conspicuous differences between characteristics of the landscape components, with the area ratio of grassland and forest landscape lower relatively; (2) as a whole, the landscape structure of the research basin was simple, the diversity was low, the fragmentation degree had an increase trend, and the vulnerability was high; (3) the distribution of different landscape gravity centers reflected the certain zonality in different periods. The movement of the gravity center of the built-up landscape was the most significant in a single landscape type, which was closely related to frequent and intense human activities; and (4) a typical landscape type and the comprehensive landscape dynamic changes shows the significant changes of landscape on different time scales from several angles, and the consistency with the landscape gravity center migration significance.

**Keywords:** landscape analysis; spatio-temporal dynamic variations; transfer model; Chuanjiang basin

## 1 INTRODUCTION

A river basin is a complete natural geographical unit, with its landscape pattern formed by superposition of natural and human's activities, and at the same time, the evolution of watershed landscape pattern restricts the occurrence and development of the natural processes directly, such as hydrological processes, biological processes, and also ensures the ecological safety of river basin as well as guarantees the production and living activities of human-beings (Fu B.J. et al., 2001, Wu J.G., 2000, Xiao D.N. & Li X.Z., 1997). It is the key measure to watershed comprehensive management that analyzing the dynamic changes of landscape pattern and then formulating reasonable landscape control countermeasures, with basins being treated as the research scale, based on the theory of landscape ecology and watershed ecology (Zhao J.Z., 1990, Robert T.W. & William D.S., 1999, Verbrug PH, et al., 1999).

Chuanjiang River Basin refers to the upper reaches of the Yangtze River from Yibin to Chongqing. The basin is the transition zone from mountain area to the low hills in general, with complex geomorphology and topography, severe rocky desertification, sharp contradiction between human and land, and quick urbanization development.

(Da F.Q., 2001, McIntyre, S. & Lavorel, S., 2007). Under the influence of strength human activity and nature, its ecological environment is quite vulnerable. Supported by RS and GIS, together with the software of FRAGSTAT4.1 (grid mode), the variation changes of landscape pattern and composition for 30 years in Chuanjiang River Basin were analyzed. It will provide a scientific reference to adjust landscape structure in the upper Yangtze River, enhance the utilization efficiency of land and natural resources, promote the western economic development, and improve environment quality in the upper Yangtze River. On the other hand, it explores integrated analysis for landscape dynamic changes.

## 2 OVERVIEW OF STUDY AREA

Chuanjiang River Basin, located in the southwest of China, between 102°49'E–109°15'E and 26°15'N–31°41'N, covering a total area of 164,000 km<sup>2</sup>, occupies the border region of four provinces/municipality, including Sichuan, Chongqing, Yunnan and Guizhou. It is also the core economic zone of the upper Yangtze River and an important region of the West China Development Drive. The research area is the southern margin

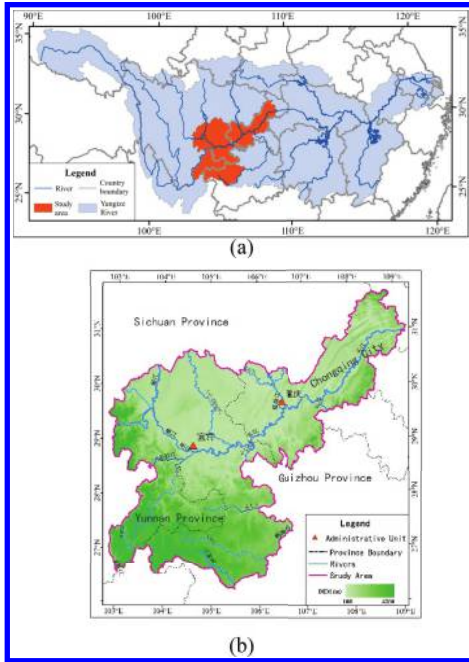


Figure 1. The location of study area in the Yangtze River basin and drainage map with DEM (Digital Elevation Model).

part of the Sichuan Basin, the transition zone from the hilly to the mountainous, with gentle hill terrain along the river sides. The main stream length is 969.6 km, including the main tributaries of Minjiang River, Jialing River, Wujiang River, Tuojiang River, and Jinsha River (as shown in Fig. 1).

It has a moist, subtropical monsoon climate. The annual average temperature is 15.4°C and the maximum and the minimum temperature are 18.9°C and 7.4°C respectively. The annual average rainfall is 1040.1 mm, while the annual maximum and minimum precipitation are 1371 mm and 779 mm, respectively. Soil types and distribution are diverse in the study basin, with the main soil type including paddy soils, purplish soils, yellow earths, limestone soils etc. The main plant types in the river basin are cultivated vegetation, shrubs, brushes, coniferous forest, broadleaf forest, meadows, and coniferous broad-leaved mixed forest.

### 3 DATA AND METHODS

#### 3.1 Data sources

Landscape information source is based on the Landsat TM data in 1985, 1995, 2000, 2005, and 2014 in Chuanjiang River Basin, composed by

4th, 3rd, 2nd (GRB) bands, corresponding to 30 m ground resolution ratio and 6–10 month phase.

#### 3.2 Data processing

##### 3.2.1 Landscape classification

Based on the data processing platform of ENVI5.1 and ArcGIS10.1, according to the *Current land use classification ISBN: GB/T 21010-2007*, promulgated by Ministry of land and resources of the People's Republic of China, combined with the practical situation of river basin, the landscape of research area was divided into 6 landscapes: agriculture landscape, forest landscape, grassland landscape, waterbody landscape, built-up landscape, and desert landscape.

##### 3.2.2 Characteristics evaluation system of landscape pattern

There are many indexes to evaluate the landscape pattern. Considering the specific characteristics of Chuanjiang River Basin, this study selected the indexes as follows to reveal the characteristics of the watershed landscape spatial structure: the number of patches, patch density, landscape shape index, Simpson-landscape diversity index, landscape fractal dimension, and fragmentation (Wu J.G., 2000, Fu B.J., et al., 2001). The combination of ArcView and Fragstat4.2 software platform was used to rasterize the landscape data and to calculate the corresponding parameters.

##### 3.2.3 Spatial variation and landscape types transfer model

In order to quantify the watershed landscape type spatial change trends, a gravity center model (Yan D.H., 2004), a single dynamic model, and a systematic dynamic model were integrated to (Wang X.L. and Bao Y.H., 1998) carry out the analysis study.

#### 1. The gravity center model

$$\left\{ \begin{array}{l} \bar{x}_j = \frac{\sum_{i=1}^n M_i x_i}{\sum_{i=1}^n M_i} \\ \bar{y}_j = \frac{\sum_{i=1}^n M_i y_i}{\sum_{i=1}^n M_i} \end{array} \right. \quad (1)$$

where  $\bar{x}_j$  or  $\bar{y}_j$  = the longitude or latitude coordinates for landscape category “j”;  $M_i$  = the area ( $km^2$ ) for landscape patch “i”;  $x_i$  or  $y_i$  = the longitude or latitude coordinates for landscape patch “i”; and  $n$  = the number of landscape patches in the basin. Latitude and longitude

coordinates of landscape patches mass center are calculated through Arcinfo 9.3 platform.

2. The single dynamic model

$$K_i = \frac{U_b - U_a}{U_a} \times \frac{1}{T} \times 100\% \quad (2)$$

where  $K_i$  = the annual variable rate of landscape category “ $i$ ” in river basin;  $U_a$  or  $U_b$  = the amount of the certain landscape category in early and late periods, separately; and  $T$  = the time length. If  $T$  is set as a year,  $K_i$  would be the annual variable rate of landscape in the river basin.

3. The systematic dynamic model

$$LC = \frac{\sum_{i=1}^n \Delta LU_{i-j}}{2 \sum_{i=1}^n LU_i} \times \frac{1}{T} \times 100\% \quad (3)$$

where  $LC$  = the integrated dynamic;  $LU_{i-j}$  = the area of landscape category “ $i$ ” from the start of monitoring;  $\Delta LU_{i-j}$  = the absolute value of landscape area that landscape category “ $i$ ” transfers to landscape category “ $j$ ” during the period; and  $T$  is the time of monitoring. If  $T$  is set as a year,  $LC$  would be the annual variable rate of landscape in the river basin.

4 RESULTS AND DISCUSSION

4.1 Overview of the landscapes composition in Chuanjiang River Basin

As for the landscape composition in Chuanjiang River Basin, the agricultural landscape occupied the dominant position, accounting for about 53 percent from 1985 to 2014, followed by the forest landscape and grassland landscape, whose distribution ratio are nearly 33 percent and 11 percent, respectively. However, the distribution of water landscape, built-up landscape, and desert landscape are relatively lower (as shown in Table 1). In terms of spatial distribution of landscape, the northern region is dominated by the agricultural landscape, while the southern region and basin boundary are the main areas of the cross landscape of forest and grassland, and the built-up landscape is concentrated in the North-East flat areas near waterbody and is likely to spread outside (as shown in Fig. 2).

4.2 Landscape pattern dynamic change characteristics

It is assumed that there are different structure characteristics of different landscapes and landscape index could be used to describe the landscape

Table 1. Landscapes composition and percentage of the landscape categories in Chuanjiang River Basin from 1985 to 2014.

Landscape Types	Agriculture Landscape	Forest Landscape	Grassland Landscape	Waterbody Landscape	Built-up Landscape	Desert Landscape
In 1985	A 87779.13 P 53.435	53782.18 32.739	19898.21 12.113	1810.02 1.102	946.67 0.576	57.57 0.035
In 1995	A 87143.6 P 53.063	55223.82 33.627	19302.38 11.754	1717.62 1.046	767.75 0.468	70.16 0.043
In 2000	A 87625.74 P 53.352	53962.95 32.856	19507.55 11.877	1820.02 1.108	1261.72 0.768	63.78 0.039
In 2005	A 87691.83 P 53.382	54650.82 33.268	18803.85 11.447	1843.9 1.122	1228.8 0.748	54.58 0.033
In 2014	A 86385 P 52.586	54611.16 33.244	18047.63 10.986	2113.84 1.287	3058.53 1.862	57.66 0.035

\*: A refers to the area of all kinds of landscape type and its unit is km<sup>2</sup>. P presents the percentage of landscape type area and its unit is %.

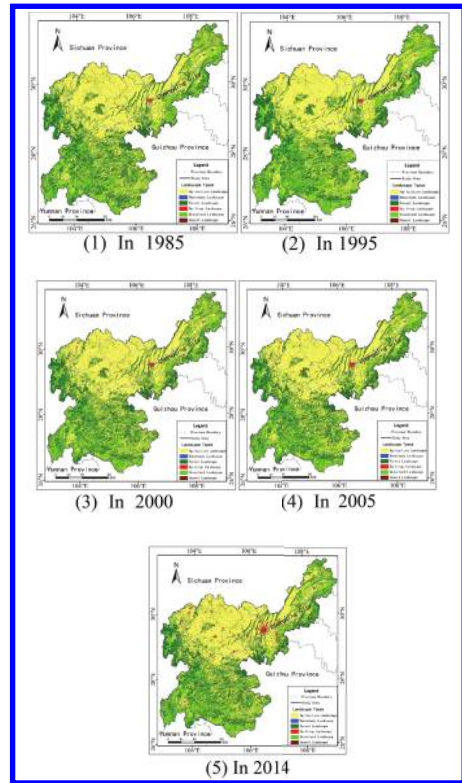


Figure 2. Landscape spatial distribution of the landscape categories in Chuanjiang River Basin from 1985 to 2014.

structure dynamic changes quantitatively, from the perspective of ecology (as shown in Table 2). Overall, the landscape patches number firstly decreased, then increased, then decreased, and then increased during the period of 1985 to 2014, with the number

Table 2. Different landscape index in Chuanjiang River Basin from 1985 to 2014.

Landscape Index	Number of Patches	Patch Density	L-Diversity Index	L-Shape Index	L-Fractal Dimension	Desert Landscape
In 1985	87779.13	53782.18	19898.21	1810.02	946.67	57.57
In 1995	87143.6	55223.82	19302.38	1717.62	767.75	70.16
In 2000	87625.74	53962.95	19507.55	1820.02	1261.72	63.78
In 2005	87691.83	54650.82	18803.85	1843.9	1228.8	54.58
In 2014	86385	54611.16	18047.63	2113.84	3058.53	57.66

\*\* : L-Disversity is the landscape diversity index, L-Shape Index is the landscape shape index, and L-Fractal is landscape fractal dimension.

of landscape patches significantly increasing in 2014. It could be proved that landscape fragmentation degree showed a wave-like curve: down-up-down-up, and the increase trend sustained until 2014. Generally, the patch density became larger; the landscape fragmentation also became larger. So the patch density could reveal the degree of the landscape fragmentation. In addition, the landscape fractal dimension index appeared at a high-low-high-low curve, fluctuating change such that taking landscape edge effect into account, the landscape fractal dimension index reduced. This will negatively affect the stability of the watershed landscape, and, to some extent, it will also increase the fragility of the landscape. Seen from the diversity index, it maintained between 0.5921 and 0.601 showing a weak increasing trend and the landscape complexity and stability were low.

### 4.3 Different landscapes spatial migration and temporal dynamic evolution

#### 4.3.1 Landscape gravity centers and migration

The landscape spatial and temporal change processes in Chuanjiang River Basin could be analyzed by the gravity center migration model: the gravity centers migration of all kinds of landscape types reflects the regional landscape spatial change pattern, and the direction, distance related with regional natural conditions could mirror the trend of the land use/coverage's gravity center migration qualitatively (Wang H. & Wang C.M., 2003).

In the Figure 3 and Table 3, gravity centers spatial characteristics of various landscape types have obvious spatial aggregation and difference, which means that the location of these gravity centers obey a certain zonal distribution pattern. Except gravity center of grassland landscape concentrating in the south of the Yangtze River, gravity centers of other landscape types are scattered in the north valley basin of Yangtze River evenly. From north to south, the landscape gravity centers of waterbody landscape, desert landscape, agriculture landscape, forest landscape, and grassland landscape were

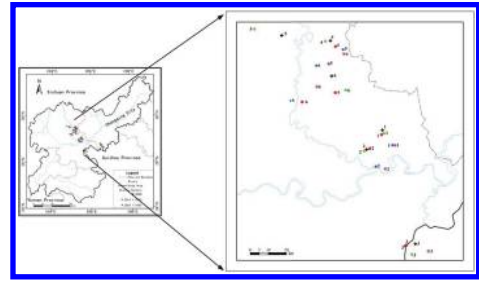


Figure 3. Gravity distribution of different landscape types in the Chuanjiang River Basin.

\*\*\*: The numbers 1, 2, 3, 4, 5, 6 present the gravity center position of the agriculture landscape, forest landscape, grassland landscape, waterbody landscape, built-up landscape and desert landscape, respectively.

Table 3. Gravity centers coordinates of landscape unit: degree.

Landscape Types	Agriculture Landscape	Forest Landscape	Grassland Landscape	Waterbody Landscape	Built-up Landscape	Desert Landscape
In 1985	105.50E, 29.07N	105.39E, 28.98N	105.66E, 28.47N	105.17E, 29.52N	104.76E, 29.58N	105.29E, 29.28N
In 1995	105.57E, 29.01N	105.51E, 28.89N	105.75E, 28.48N	105.28E, 29.46N	105.19E, 29.41N	105.12E, 29.30N
In 2000	105.49E, 29.08N	105.40E, 28.99N	105.68E, 28.52N	105.20E, 29.52N	104.91E, 29.55N	105.21E, 29.35N
In 2005	105.55E, 29.01N	105.46E, 28.90N	105.62E, 28.51N	105.12E, 29.40N	105.27E, 29.48N	104.97E, 29.23N
In 2014	105.49E, 29.06N	105.42E, 28.99N	105.63E, 28.51N	105.23E, 29.49N	105.23E, 29.27N	105.04E, 29.22N

located in order. The grassland landscape gravity center was around the boundary of the basin, while the gravity centers of agriculture and forest landscape mainly distributed in region 1 and 2 and the rest of others concentrated in area 4, 5, and 6.

As shown in Figure 4 and Table 4, in terms of gravity center's migration distance, from 1985 to 2014, was examined to be the most significant for agriculture landscape, followed by desert landscape and grassland landscape. The movement of gravity center of waterbody landscape was slight and that of and forest and agricultural landscape was not remarkable. In terms of orientation of migration of gravity centers, there was no obvious change law about different landscape types gravity centers migration direction in different the research period. The landscape spatial migration pattern could reflect, to a certain extent, the gravity centers migration significance.

The gravitational center of agricultural landscape moved to the northeast by a relatively far distance: moving to northeast from 1985 to 1995 by 39.73 m, to northwest from 1995 to 2000 by 27.47 km, to southeast from 2000 to 2005 by 23.90 km, to southwest from 2005 to 2014 by 23.90 km, and,

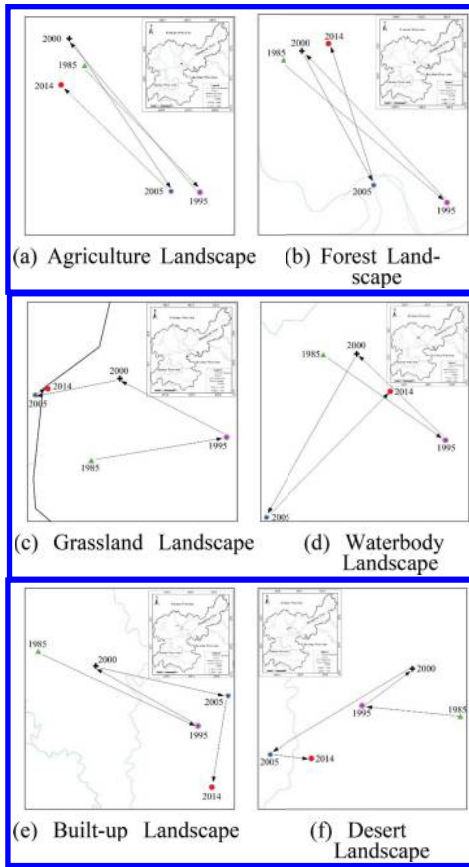


Figure 4. Different landscape types shift variation.

Table 4. Landscape Gravity Centers and Their Migration UNIT: m.

Landscape Types	Agriculture Landscape	Forest Landscape	Grassland Landscape	Waterbody Landscape	Built-up Landscape	Desert Landscape
1985 to 1995	9615.82 ES	16465.18 ES	10157.39 EN	11237.17 ES	39729.84 ES	15521.26 WN
1995 to 2000	11259.31 WN	15676.62 WN	8878.16 WN	9580.9 WN	27466.6 WN	9705.84 EN
2000 to 2005	10141.33 ES	11018.94 ES	6460.95 WS	15211.75 WS	29489.2 ES	26330.83 WS
2005 to 2014	8634.53 WN	10586.61 WN	1051.53 EN	13993.72 EN	23904.62 WS	6963.96 ES
1985 to 2014	1723.45 WN	3803.57 EN	5793.32 WN	5593.32 WN	53083.03 ES	24818.42 WS

\*\*\*\*: The unit of number is meters, and the capital letter monogram is shift directions.

generally, migrating to southeast from 1985 to 2014 by 53.08 km. Compared with other migration orientation, the relatively significant south-eastward migration showed that, in this direction, urbanizing speed is faster. In contrary, the desert landscape gravity center migrated to northwest.

And the range of agricultural and forest landscapes migration were small implying that they were more stable than other landscape types.

In addition, the correlation within the gravity center migration of different landscape types in Chuanjiang River Basin and between the regional economic, population growth, urbanization and other driving factors of migration will be further analyzed in the later research.

#### 4.3.2 Landscape dynamic changes

According to dynamic changes in different periods of all landscapes and integrated landscape dynamic changes (as shown in Table 5), regional landscape pattern changes in Chuanjiang River Basin were analyzed: the proportion of build-up landscape rise up to 44.62%, by 12.87% in period of 1995–2000 and 29.78% from 2000 to 2014, reflecting the significant urbanization speed. Agriculture landscape increased by 0.32% and forest landscape decreased by 0.31% during 1985–2014. Urbanization accelerated, at the same time, forest landscape were construct which influenced the agricultural landscape, like cultivated land, while the grassland landscape and desert landscape both changed in different degree.

The integrated landscape migration rate of Chuanjiang River Basin were 0.45%, 0.39%, 0.23%, 0.39% in 1985–1995, 1995–2000, 2000–2005 and 2005–2014, separately, which means that there were 0.45 km<sup>2</sup>, 0.39 km<sup>2</sup>, 0.23 km<sup>2</sup> and 0.34 km<sup>2</sup> of every 100 km<sup>2</sup> landscape area had changed. With the economic and social development, land use in the Chuanjiang River Basin was affected by various interferences in nearly 30 years, thus the area of each landscape significantly changed. Especially in the early 20th century, the population growth has accelerated, the contradiction between human and land sharpened and land use was faced with great pressure due to the advancement of urbanization (Shu R.Q., He T.R. & Ban B.R., 2013).

Table 5. Dynamic migration of landscape types of Chuanjiang River Basin from 1985 to 2014 UNIT: %.

Types	K <sub>i</sub>				
	1985 to 1995	1995 to 2000	2000 to 2005	2005 to 2014	1985 to 2014
1	-0.14	0.11	0.02	-0.3	-0.32
2	0.54	-0.46	0.25	-0.01	0.31
3	-0.6	0.21	<u>-0.72</u>	-0.8	-1.86
4	-1.02	<u>1.19</u>	0.26	<u>2.93</u>	<u>3.36</u>
5	<u>-3.78</u>	<b>12.87</b>	-0.52	<b>29.78</b>	<b>44.62</b>
6	<b>4.37</b>	-1.82	-2.88	1.13	0.03
LC	<b>0.45</b>	<b>0.39</b>	<b>0.23</b>	<b>0.34</b>	<b>0.99</b>

\*\*\*\*\*: The number of 1, 2, etc. presents the different landscape respectively, namely the agriculture landscape, forest landscape, grassland landscape, waterbody landscape, built-up landscape and desert landscape. The bold is the maximum and underline presents the minimum in the column, and the bold italic is the value of the LC.

## 5 CONCLUSIONS

1. The composition of landscape was obviously different, with the percentages of forest landscape and grassland landscape being relatively lower.
2. The overall landscape pattern is simple, landscape diversity is low, and the increase trend of landscape fragmentation sustained and then aggrandizes the fragility of the landscape. So land use resources utilization should be adjusted to improve the integrity and diversity of watershed landscape and to enhance the anti-interference of landscape itself.
3. Gravity center distribution of different landscape types has particular zonal distribution patterns in different periods. Gravity center migration of a typical landscape type is significant, especially the agriculture and desert landscape, which indicates that the spatial changes of agriculture and desert landscape are largest under the influence of natural force and human activities.
4. A typical landscape type and the comprehensive landscape dynamic changes shows the significant changes of landscape on different time scales from several angles, and the consistency with the landscape gravity center migration significance. The most significant change is built-up landscape for it bears the population and urbanization. The integrated landscape dynamic rate of Chuanjiang River Basin was 0.99% during 1985–2014, which means there are 0.99 km<sup>2</sup> of landscape areas per 100 km<sup>2</sup> have changed.

## ACKNOWLEDGMENTS

This study is financially supported by the Program of the National Natural Science Foundation of China “Research on the Impact that Soil Moisture Change has on Net Carbon Emission in Typical Irrigation District” (51409267) and the Project of the National Technology R&D Plan for “The Impact and Risk Assessment Technique of Climate Changes on Water Resources” (2012BAC19B03).

## REFERENCES

- Da, F.Q. 2001. Reconstruction of ecological barrier: the strategic goal of ecological environment construction of the upper Yangtze. *Chinese Rural Economy* (2): 53–58.
- Fu, B.J. Chen, L.D. & Ma, K.M. et al. 2001. *Principles and Application of Landscape Ecology*. Beijing: Science Press.
- McIntyre, S. & Lavorel, S. 2007. A conceptual model of land use effects on the structure and function of herbaceous vegetation. *Agriculture Ecosystems and Environment* 119(1–2): 11–21.
- Robert, T.W. & William, D.S. 1999. Managing land use and land-cover change: the new jersey pinelands biosphere reserve. *Annals of the Associations of American* 89(2): 220–237.
- Shu, R.Q. He, T.R. Ban, & R.B. 2013. Evaluation of the land resources ecologic security in Chongqing city. *Journal of Chongqing Normal University (Natural Science)* 30(5): 44–49.
- Verbrug, P.H., Koning Ghj de, et al. 1999. A spatial explicit allocation procedure for modeling the pattern of land use change based upon actual land use. *Ecological Modeling* (116): 45–61.
- Wang, H. & Wang, C.M. 2003. Research on the mechanism of hydrological cycle in Yellow River catchment. *Advance in Water Scienc* 14 (Suppl.): 1–9.
- Wang, X.L. & Bao, Y.H. 1998. Study on the methods of land use dynamic change research. *Progress in Geography* 18(1): 81–87.
- Wu, J.G. 2000. *Landscape Ecology: Pattern, Process, Dimension and scale*. Beijing: Higher Education Press.
- Xiao, D.N. & Li, X.Z. 1997. Progress and prospect of modern landscape ecology. *Geographical Science* 17(5): 453–461.
- Yan, D.H. 2004. Landscape Pattern and Its Dynamic Variation in the East Liaohe River Basin. *Resources Science* 26: 31–37.
- Zhao, J.Z. 1990. Index system for dynamic change of spatial structure of landscape ecology. *Journal of Ecology* 10(2): 182–186.

# Effect of motor vehicle emissions on air quality of green urban community

S.M. Zhao

*Tianjin Key Laboratory of Indoor Air Environmental Quality Control, School of Environmental Science and Engineering, Tianjin University, Tianjin, China  
Tianjin Academy of Urban Planning and Design, Tianjin, China*

Q.Q. Li & X.Y. You

*Tianjin Key Laboratory of Indoor Air Environmental Quality Control, School of Environmental Science and Engineering, Tianjin University, Tianjin, China*

**ABSTRACT:** Green building is the core topic of human habitat construction. A comprehensive index of NO<sub>x</sub> pollutant was proposed to evaluate the effect of motor vehicle emissions on green buildings. The evaluation index was extracted from the regulatory requirements of Urban Residential Area Planning Design standard (GB50180-93) and Ambient Air Quality Standard (GB3095-2012). The effect of local meteorological wind field on the comprehensive index was considered. The component transport (species transport) model was adopted to simulate the pollutant distribution of motor vehicle emissions. The air quality of the urban community was evaluated under the condition of typical wind of different seasons. The weight of each season was determined by analytic hierarchy process method. The result showed that the proposed comprehensive index was favorable to evaluate the air quality of green buildings.

**Keywords:** air quality; green buildings; motor vehicle emissions; urban community

## 1 INTRODUCTION

Currently, motor vehicle emissions are considered as a major source of urban ambient air pollution. NO<sub>x</sub> is the main substance near the surface atmospheric which forms photochemical smog. Furthermore, NO<sub>x</sub> delivery leads to regional acid rain, eutrophication and other large-scale pollution.

The study of motor vehicle emissions began in the mid 20th century in Europe and America. (Zhang et al., 2013) estimated on- and near-road NO<sub>2</sub> concentrations and the health risks for freeway and arterial scenarios attributable to traffic for different traffic volumes during rush hour periods. (Madalozzo et al., 2014) investigated numerically the wind flow and pollutant dispersion with a two-dimensional street canyon model by considering three different aspect ratios and four different wall heating configurations. (Tang et al., 2014) investigated the effects of real-time road condition on each vehicle's speed, acceleration, headway, fuel consumption, CO, CH and NO<sub>x</sub> under uniform flow with a car-following model.

The wind effects are not fully considered in the existing evaluation methods to achieve a comprehensive evaluation of motor vehicle emissions of complex buildings, especially in windy areas. In this paper, a comprehensive evaluation index is proposed by considering the frequency of local

wind speed and direction of different seasons. The outdoor motor vehicle emissions diffusion was simulated by CFD and the weight of each season was determined by the analytic hierarchy process (AHP). The results showed that the proposed comprehensive index is favorable to evaluate the quality of atmospheric environment in windy cities.

## 2 MATHEMATICAL MODEL

Air flow around buildings is a low speed incompressible turbulent flow. The widely used RNG  $k-\epsilon$  model was introduced to consider the effects of turbulence and the control equations are the same as those in the reference (Chen et al., 2011). The average inlet air velocity is as following (Liu et al., 2011):

$$\frac{U(z)}{U_0} = \left(\frac{z}{z_0}\right)^{0.25} \quad (1)$$

where  $U(z)$  and  $U_0$  is air velocity at the height of  $z$ ; and the reference height of  $z_0 = 10$  m.

At the outlet boundary, the air velocity is assumed to be fully developed. The non-slip wall boundary is applied to the ground and walls of buildings.

Pollutant convection-diffusion equation:

$$\frac{\partial C}{\partial t} + \frac{\partial(u_i C)}{\partial x_i} = \frac{\partial}{\partial x_i} \left( \frac{V_i}{S_c} \frac{\partial C}{\partial x_i} \right) + S \quad (2)$$

where,  $C$  is concentration of pollutant;  $S_c$  is Schmidt number; and  $S$  is source term of pollutant.

The vehicle pollution was assumed as a line source located in the center of the street and the flow field in the street is not affected by the presence of pollutant. Emission source intensity of motor vehicle was determined by:

$$Q = NE/3600 \quad (3)$$

where  $Q$  = vehicle emission source intensity on the road,  $g/(km \cdot s)$ ;  $N$  = road traffic discharge, vehicle/h; and  $E$  = integrated emission factor of NOx,  $g/km/vehicle$ .

Refer to the literature,  $N$  is 2175 vehicle/h (Ye et al., 2007),  $E$  is 4.4  $g/km/vehicle$  (Liu et al., 2008) in the study area. The emission source was supposed to be at the height of 0.4 m in order to simulate the emission of vehicles.

### 3 MODEL ESTABLISHMENT AND SIMULATION WIND CONDITIONS

The community of the present approach is located in the centre of Tianjin city. The height

Table 1. The selected typical simulated scenes of Tianjin.

Typical season	Typical simulated scenes		
	Winter	Summer	Spring and autumn
Wind velocity (m/s)	4.1	2.2	2.2
Wind direction	Wind frequency (%)		
N	11.5	3.1	4.7
NNE	3.8	4.3	1.4
NE	1.6	3.3	1.9
ENE	11.2	5.1	1.9
E	0.0	0.0	5.6
ESE	9.3	8.4	2.8
SE	4.8	12.0	10.7
SSE	4.8	12.0	3.7
S	4.8	12.0	11.7
SSW	8.3	9.2	11.2
SW	9.3	7.9	13.6
WSW	0.0	0.0	3.7
W	5.4	3.8	7.5
WNW	8.3	7.1	2.3
NW	6.7	5.1	9.8
NNW	9.9	6.6	7.5

\*The wind velocity refers to the wind speed at the height of 10 m.

of computational domain is 5 times of that of the tallest building of the community, which is about 250 meters. Horizontal length and width of the computational domain is taken as the center of the surrounding streets. Since the wind field far above the buildings is affected weakly by them, the computational domain is divided into two zones by the mid-height of the domain. Dense unstructured grids are used in the lower zone, while sparse structured grids are used in the upper zone. After grid independence is checked, two million grids are suitable to the present simulation. The control equations are discretized by finite volume method with second order upwind scheme. Pressure-velocity coupling is realized by the SIMPLEC algorithm.

According to meteorology wind rose of Tianjin (Lu et al., 2013), the selected typical scenes of Tianjin meteorology were shown in Table 1.

### 4 REQUIREMENTS AND EVALUATION INDEX

According to the Urban Residential Area Planning Design standard (GB50180-93) and Ambient Air Quality Standard (GB3095-2012), the air quality of residential area is the secondary level, where the average concentration of NOx is less than 100  $\mu g/m^3$  ( $2.173 \times 10^{-9}$   $kmol/m^3$ ) in 24 hours. Based on the above requirements, one evaluation index called as Standard Area Ratio of Characteristic Pollutant Concentration Limit (SARCL) was proposed. It is the area ratio of the pedestrian area with pollutant concentration above 100  $\mu g/m^3$  to that of outdoor at 1.5 m height.

The outdoor comprehensive index of motor vehicle emissions of a season is calculated as follows:

$$R_K = 100 \sum_{j=1}^M P_j f_j \quad (4)$$

Table 2. Assessment standards of effect of motor vehicle emissions on outdoor air quality.

Outdoor air quality	Assessment standards				
	Poor	General	Good	Better	Very good
R	<60	60-80	80-90	90-95	95-100

Table 3. Weight of typical season.

Typical season	Winter	Summer	Spring and autumn
Weight	0.25	0.25	0.5



where,  $R_k$  is the outdoor comprehensive index of motor vehicle emissions of a season. Large  $R_k$  means good outdoor air quality.  $M$  is the number of typical wind cases.  $f_j$  is the wind frequency of  $j$ th typical wind of the season and  $P_j$  is the value of index (SARCL) at  $j$ th typical wind. For the present case,  $M=16$  is for all seasons.

Considering the season of winter, summer, spring and autumn, the outdoor comprehensive index of motor vehicle emissions for a whole year is calculated as:

$$R = \sum_{k=1}^3 W_k R_k \quad (5)$$

AHP method (Li et al., 2012) was adopted to determine index weight. Assuming the equal weight for all seasons, the weight of typical seasons was shown in Table 3.

## 5 NUMERICAL RESULTS AND DISCUSSION

Figure 1a showed the concentration distribution of NOx on the plane  $z = 1.5$  m under the typical 2.2 m/s

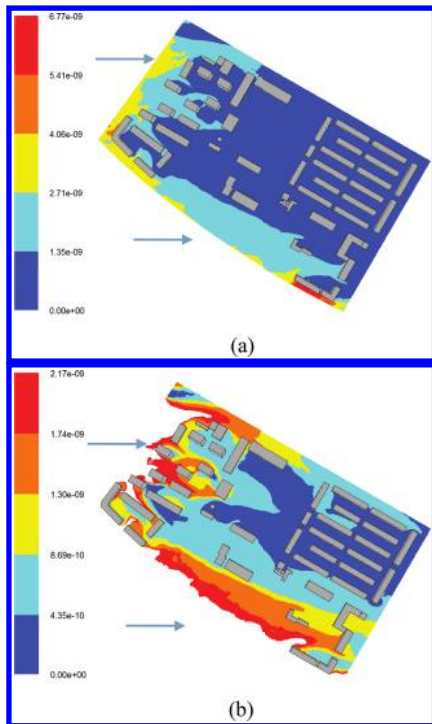


Figure 1. Concentration contours of NOx (kmol/m<sup>3</sup>) at the height  $z = 1.5$  m under the typical 2.2 m/s W wind in summer.

W wind in summer. The maximum concentration is  $6.77 \times e^{-09}$  kmol/m<sup>3</sup>. High concentration of NOx is mainly near the inlets. Figure 1b shows the NOx concentration distribution that meets the requirement of Ambient Air Quality standard. Because the street is the generation place of pollutants, high concentration of pollutants is close to the inlet. At this case, SARCL is 93.8%. The areas not satisfying the standard requirements should be improved by appropriate measures, such as rearranging the buildings to reduce NOx concentration.

Figure 2a showed the NOx concentration distribution on the plane  $z = 1.5$  m under the typical 4.1 m/s S wind in winter. The maximum concentration is  $7.47 \times e^{-09}$  kmol/m<sup>3</sup>. High concentration of NOx is in the region of the inlets mainly. Areas with eddies are poorly ventilated and they are easy to accumulate high pollutant concentration. Figure 2b showed the NOx concentration distribution that meets the requirement of Ambient Air Quality standard. For this case, SARCL is 85.7%.

Similarly, the outdoor NOx diffusion of motor vehicle emissions of different wind directions in all seasons was simulated and the results of SARCL are shown in Table 4.

The outdoor air quality of the studied community of winter, summer and spring and autumn is

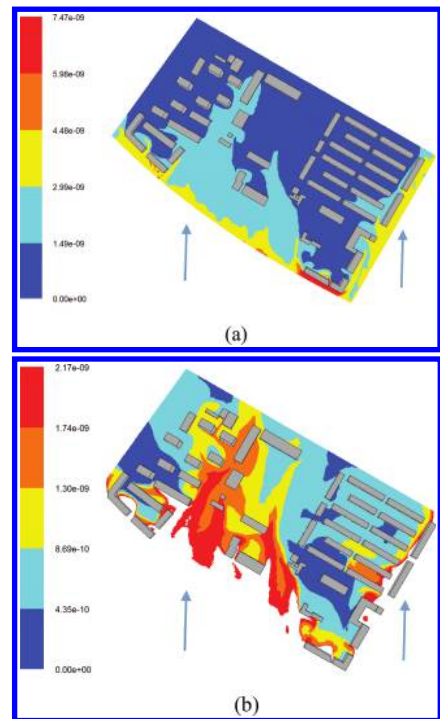


Figure 2. Contours of molar concentration of NOx (kmol/m<sup>3</sup>) at height  $z = 1.5$  m under the typical 4.1 m/s S wind in winter.

Table 4. The value of evaluation index of all seasons.

Typical season	Typical simulated scenes		
	Winter	Summer	Spring and autumn
Wind velocity (m/s)	4.1	2.2	2.2
Wind direction	$P_1$ (%)		
N	82.7	85	83.2
NNE	80.5	82.7	81
NE	84.4	86.6	85.5
ENE	82.1	83.6	82.8
E	84.8	87.5	86.7
ESE	87.4	87	85.9
SE	87.9	89.9	87.9
SSE	87.1	88.5	87.9
S	85.7	89.9	88.1
SSW	89.7	94.2	93.6
SW	92.7	93.1	93
WSW	92.5	93.8	93.1
W	91.9	93.8	93.4
WNW	91.5	93.4	92.8
NW	91	93.8	92.7
NNW	85.7	90.1	88.9

86.96, 89.76 and 89.93, which is all corresponding to the grade of good, respectively. The outdoor air environmental quality of the studied community in the whole year is 89.1, which is also in the grade of good.

## 6 CONCLUSIONS

The outdoor NO<sub>x</sub> concentration of motor vehicle emissions of a community in central Tianjin city were simulated by considering typical local winds. The outdoor comprehensive index of motor vehicle emissions was proposed by considering the standard for Urban Residential Area Planning Design standard (GB50180-93) and Ambient Air Quality Standard (GB3095-2012).

The results indicated that the outdoor air quality of the studied community in all seasons and the whole year is in the grade of good. Obvious eddies and low wind zones were found between the buildings in the seasons of spring, summer and autumn. The windward sides of buildings need to be reduced for small wind obstruction and eddies.

The high concentration of pollutant near the inlet boundary was found to exceed the Ambient Air Quality Standard of China. The areas should be improved through reasonable measures, such as rearrangement buildings.

## ACKNOWLEDGEMENTS

The research is financially supported by the National Key Basic Research and Development Program of China (the 973 Program) through grant No. 2012CB720100, the science and technology project of Tianjin City Planning Bureau and the cooperation innovation project of Tianjin University-Qinghai University for Nationalities.

## REFERENCES

- Chen, W. & Liang, J. 2011. Wind environment simulation of a residential district. *Building Energy Conservation* 39(6): 17–19, 22.
- Li, M. & Cai, J.F. 2012. Comprehensive evaluation research on urban innovation environment based on AHP. *Science and Technology Management Research* (04): 50–53.
- Liu, W. & You, X.Y. 2011. Transportation and risk analysis of influenza indoor and outdoor transportation and exposure risk analysis of influenza aerosol. *Indoor and Built Environment* 21: 614–621.
- Liu, H. & He, K.B. & Wang, Q.D. 2008. Tianjin motor vehicle emission inventory and factors affecting research. *Journal of Tsinghua University (Natural Science Edition)* 03: 370–373.
- Lu, Y. & Li, C.R. & Yu, J.W. 2013. Prevailing wind direction and wind speed determination on outdoor wind environment simulation of Green building. *Construction Technology* 09: 59–61.
- Madalozzo, D.M.S. & Braun, A.L. & Awruch, A.M. & Morsch, I.B. 2014. Numerical simulation of pollutant dispersion in street canyons: geometric and thermal effects. *Applied Mathematical Modelling* 38(24): 5883–5909.
- Tang, T.Q. & Li, J.G. & Huang, H.J. & Yang, X.B. 2014. A car-following model with real-time road conditions and numerical tests. *Measurement* 48: 63–76.
- Ye, S.Bin. & Wang, Q.D. & He, X. 2007. Road vehicle activity level research of Tianjin. *Journal of Beijing Technology and Business University (Natural Science Edition)* 02: 28–31.
- Zhang, K. & Batterman, S. 2013. Air pollution and health risks due to vehicle traffic. *Science of The Total Environment* 450–451: 307–316.

## The old town of Wubu the forgotten stone castle

X. Liang

*College of Architecture and Civil Engineering, Taiyuan University of Technology, China*

**ABSTRACT:** In a class trip, we happened to get acquainted with a centenarian at the west of the Yellow River—the Old Town of Wubu. The Old Town of Wubu awed us greatly with its vigorous and majestic momentum, and profound historical values are embedded in its dilapidated appearance that went through ages. Rammed earth walls, cave dwellings built with bricks as well as streets and roads built under the principle of “adjusting measures to local conditions” all show the wisdom and effort of ancient Chinese people. However, with transportation streamlines moving to the south, the Old Town of Wubu gradually lost its geographic advantages and was abandoned, leaving a “ghost town” standing in the rubble. How should the historical values of Wubu be re-evaluated? In addition, what should be done to protect the Old Town of Wubu?

**Keywords:** old town; current situation; brick and stone masonry structure; protection

### 1 LOCATION ANALYSIS

The Old Town of Wubu, also called the Stone Town of Wubu, is located at the mountain peak on the west bank of the Yellow River. Only 2.5 kilometers to the north of the Town of Songjiachuan, Wubu County, the Old Town of Wubu is the best-remained ancient town with a history of more than a thousand year at northwest China. Located at the east border of Yellow River Plateau and the west side of the mid-stream of the Yellow River, Wubu is an important transportation hub at the road connecting Shanxi and Shaanxi. The Yellow River at its east and the natural moat to its west provide natural covers for defense; meanwhile the town connects with the bank on the south and the mountain to the north by a state road and a strategic passage. Located on

the natural barrier of the Yellow River—the Stone Mountain, the Old Town of Wubu was known as “Bronze Wubu” at ancient times. It is shown in [Figure 1](#) that Wubu is situated on the key gateway of Lvliang Mountain Range. As early as the Spring and Autumn Period, this position was an important checkpoint between the State of Qin and the State of Jin, playing an indispensable role in the aspect of strategic defense. However, nowadays as the important traffic road moving to the new County of Wubu, the Old Town of Wubu lost its geographical advantages and was gradually abandoned.

### 2 A VISIT TO THE OLD TOWN OF WUBU

An accidental occasion brought us to the sleeping old town with a history of more than thousands of years. The destination of our class trip was Lvliang County of Shanxi Province. Originally, we were planning to end our trip at the Town of Qikou, Liulin County, hoping to make the view of the magnificent ferry of the Yellow River the highlight of the whole trip. We did not have the intention of traveling across the Yellow River. However, while passing by the Village of Jundu, we were deeply attracted by the hundreds-meter Yellow River Bridge. Impulsively, we went across the trembling Bridge and arrived at Wubu County across the river.

Exploring the Old Town of Wubu, we found a dilapidated yet exquisite Taoist temple. After traveling along the winding mountain road for dozens of Li, we encountered with fragments of the city wall. The stone town cast a touch of ancient



Figure 1.

style to us. About 300 meters away from the wall, an abandoned building was standing quietly, as if it was a housekeeper welcoming guests from afar. Since it must have been abandoned for a rather long period of time, the building appeared very humble. Entering the only yard of the building, we identified the grand hall in the middle with two blurred stone tablets at the east and west side. The yard was covered with barbed wild grass, and brick rubble and broken tiles scattered around. Picking up a piece randomly, I identified the engraved “dragon scale” on it. It might be a piece from the dragon engraving on the stone pillar. The head of the engraved dragon was missing, maybe it was picked home as a collection. While pitying about the pillar, we also found that the structure of the grand hall was rather completely remained. The outline of the hall was in the shape of a cubic with a flat top, and the inside was a traditional structure of a stone cave. The plaque above the door was engraved with characters “Yu Xu Gong (Temple of Yu Xu)”, from which one can tell that the construction was an abandoned Taoist Temple. The statue of Celestial Yuxu had already disappeared, yet the mark of its base can still be found on the floor. Soft color wall paintings can be seen from the wall and the ceiling, yet they were all blurry under the power of weathering. Thus, contents of the paintings were difficult to tell. Later I also failed to find relevant resources regarding this temple from the internet. We could only tell from the degree of the weathering that the temple was constructed at the same period with the old town of Wubu. Passing this dilapidated yet meaningful Taoist temple, we finally entered the Old Town of Wubu.

Ancient city wall, the weather-beaten stone guardian. The ancient wall of the old town was weathered seriously, standing now with a dilapidated overall structure and grass growing at the crack of stones. The mark of bomb and fire reminded us of the cruel situation during the period of the Anti-Japanese War. It seems that this ancient city had encountered with not only the weather beaten of time, but also the damage brought by the invader. Nowadays it is still sitting quietly and strongly at there, waiting for its visitors. The gate tower above the wall had collapsed yet the gate was still firm. The character “Ying En” can be seen from the stone plaque over the gate. I reckoned that the gate used to be an abustle place, yet with the development of time, it was neglected by people. The two characters presented a feeling of loneliness. Quietly standing under the gate and gazing it, we were overwhelmed with complicated feelings. Climbing onto the wall and walking to the eastern part of it, we looked at the view down from a height. Through the crenel we can see the Yellow River stretching dozens of li with a magnificent momentum. The eastern side of

the wall was better retained. I reckoned the reason was that the eastern part was next to the cliff that was able to prevent the town from the attack of enemies. The advantageous geographical location retained its appearance, leaving valuable materials for researches at later times. At the connection point of southern and eastern wall, there was a three-story masonry-timber structured hexagonal building. An awe-inspiring statue of Kuixing was standing on the top floor. With its red face, bushy beard, red calligraphy brush in his hand and wood bowl on his foot, the statue as if was intimidating enemies from dozens of li to stay away from the town. Walking along the wall to the south gate, we saw a well-structured barbican with a complete and magnificent Temple Of Guan Yu in it. There were three masonry-timber structured grand halls in the Temple, and the statue of Guangong was also remained thus we can identify the function of the temple. Constructing a barbican at this side indicating that the spot was of strategic importance. Although the town does not contain strategic function nowadays, the solid structure and the marks remained from wars still prove its heroic position in people’s mind.

Visiting the dwellings in the old town and feeling the mingling of history and present. Stepping down the city wall and feeling reluctant to leave, we realized that the city wall only contained assistive functions to the old town and cannot represent the folk culture and customs of the town. Thus we decided to enter the town and visit our real destination: the residential area. The roads and streets in the old town were built under the principle of adjusting measures to local conditions. Houses were built alongside the mountain without an obvious axis. Stone cave was the major construction form of the residential building group. Brick caves and wood houses lined alongside the winding and narrow road. Different kinds of constructions echoed each other and formed a harmonious picture, presenting an exquisite beauty that was rarely seen in northern China and bringing pleasant feelings to passersby.

A depiction of major characteristics of the dwellings in the old town—taking an abandoned house as an example. The appearance of the abandoned house is shown as in [Figure 2](#). Just like major construction groups in northern China, the house was a quadrangle dwelling. Unlike usual quadrangle dwellings, houses around the yard were all stone caves. From the decayed window and doorframes as well as knee-high grass, one can tell that this house had been abandoned for years. The time of its construction was also very difficult to tell. The four rooms on the main side were caves built with square stones, the cliffs on two sides supported the outer wall of the caves,



Figure 2.



Figure 3.

bearing side thrusts from the caves and making them stand firmly. Thus after being abandoned for years, the caves can still standing steadily as new. Exquisite decorations made by bricks were placed on the tiles at the top of the cave, telling people that the original host may be a rich and influential family. Other constructions at the old town were similar to this. Most of them were quadrangle dwellings, yet with less structured orders. Thus this house can be analyzed as a typical residential construction in the Old Town of Wubu.

### 3 ANALYSIS ON THE HISTORICAL VALUE OF THE OLD TOWN OF WUBU

Analysis on the geographical location of Wubu: why was the city such a firm fortress? From the geographical location of Wubu as well as relevant documents, one can see that as early as the Spring and Autumn Period and Warring States Period, Wubu was an important strategic point as well as

a business checkpoint. Thus the town had a very high demand for its defensive function. The reason why ancient people built the Town of Wubu as a firm stone fortress was more or less related to its important geographical location. As two important counties at the border of the State of Qin and the State of Jin, Yulin and Lishi, with Jundu and Wubu as their frontier towns, stood opposite to each other on the two banks of the Yellow River. The Old Town of Wubu, located on the hill to the west of the ferry, offered a clear view of dozens of Li. Naturally the view of the town of Jundu can be seen from the gate tower of Wubu. The Yellow River that stretches dozens of Li on the borderline between the State of Jin and the State of Qin played the role of a natural barrier, in addition, Wubu, the stone fortress at the peak of the hill, enhanced the degree of protection. Casting their eyes on each other, the two States never dared to step forward. This kind of strategic confrontation that formed since very long time ago, on the contrary played a decisive role for promoting the “alliance between the State of Qin and the State of Jin”. Hundreds of years later, with the eastward expansion of the State of Qin, China is gradually unified. Yet the strategic significance of Wubu still remained. After being unified, ancient China had experienced long-standing conflicts with nomads from the north, while the middle and lower reaches of the Yellow River became the major area suffered from the conflicts. The County of Yulin thus became the northern gateway of the capital city (near today’s City of Xi’an). If the county of Yulin once was occupied by the invaders, other cities and counties of the ancient China will be easily invaded. Thus the significance of the old town of Wubu in guarding the country became more obvious. With the changes of many dynasties and the expansion of the territory of China, the old town of Wubu, once a border city, gradually became an inland city. With the changing of its geographical meaning, the old town of Wubu entered its transformation period. The major function of it changed from defense to trade, meanwhile the residents moved gradually from the hill to the field by the river. Due to the disadvantage of traffic inconvenience, the stone city of Wubu was neglected by people and was downgraded to a county. During the years of Anti-Japanese War, residents moved back to the stone fortress due to special historical reasons, and Wubu for another time became an important military post of the anti-Japanese revolutionary base area. During this period, the town of Wubu suffered from Japanese Army’s artillery attack. The wall of the town was seriously damaged, yet the town survived from the war and was not occupied by Japanese Army. After liberation, the old town of Wubu was again seriously destroyed in

Cultural Revolution. Residents for another time demolished their houses and moved to the field by the river, leaving only four to five households living at the old town. Thus Wubu became an abandoned town at present. And we could only catch a glimpse of this building group that contains a history of more than thousands of years by accident.

#### 4 SUGGESTIONS ON THE PROTECTION AND PROMOTION OF THE OLD TOWN OF WUBU

What should be done to protect historical living fossils like the Old Town of Wubu? My suggestions are as follows. It is expected that readers of this article can gain certain inspirations from my suggestions and realize the significance of the protection of regional culture.

##### 4.1 *Traffic*

Smooth mountain roads should be paved to connect the Old Town of Wubu with the outside world so that people will not refuse to live there due to traffic inconvenience. This is the most important measure that should be conducted. The biggest disadvantage of Wubu is that rough and rugged roads seriously affect people's daily traveling. Transforming and optimizing traffic conditions as well as setting striking road signs can not only make local people willing to live in the Old Town of Wubu, but also allow more travelers passing by to notice its existence.

##### 4.2 *Reasonable planning*

The original constructions of the Old Town of Wubu should be retained; meanwhile residential areas should be designed and built around the old town. The dilapidated appearance of the Old Town of Wubu can still reflect the style of its historic beauty. Thus rebuilding or repairing ancient constructions should not be the only target of our effort, since only rebuilding or repairing may lead to further damages to historical relics. Building new

residential areas around the original old town cannot only protect the historical and cultural relics to the largest extent; the economy of the old town can also be driven by the development of the new residential area. Indeed the two accomplishments can be achieved by conducting this one measure.

##### 4.3 *Cultural education*

Cultural education to local residents should be further enhanced thus to make people realize the significance of protecting cultural relics. Through holding festival activities at the Old Town of Wubu, the County Government has conducted cultural education and publicity to local residents. Efforts have been made to promote the idea of "Be Proud of Old Town of Wubu" and lead people to spontaneously protect cultural and historical relics. Experts studying local cultural relics were also trained and supported to conduct researches, make surveys and write books on the old town, thus to promote to the largest extent the Old Town of Wubu.

##### 4.4 *Advertising*

More advertising publicity should be conducted to push forward the development of Old Town of Wubu as a tourist spot. Travel routes should be set in the Old Town of Wubu and business commercials should be shot thus to further promote the fame of the old town in Shaanxi Province or even larger area and attract more tourists. These measures can not only drive the business development of the surrounding areas, but also make local residents focus more on the protection and repair of cultural and historical relics.

#### REFERENCES

- Annals of the Prefecture of Yan'an, Volume 8, the reign of Hongzhi (1488-1505), Ming Dynasty.  
Wubu County Annals, the reign of Daoguang (1821-1850), Qing Dynasty.

# Inspiration of evaluation criteria of international historic site to China heritage protection system

X.Y. Zhao & J. Gao

College of Architecture and Civil Engineering, Taiyuan University of Technology, Taiyuan, Shanxi, China

**ABSTRACT:** The essay takes the evaluation criteria of historic sites as the clue to illustrate the means of expressions of historic sites under the different state contexts; makes comparison and analysis on the evaluation criteria of national historic sites of United Nations and China, Japan, Britain, and America; and offers some suggestions to the deficiency of China evaluation criteria.

**Keywords:** historic site; comparative study; historic conservation; evaluation criteria

## 1 THE REFLECTION OF THE DEFINITION OF HISTORIC SITE UNDER DIFFERENT STATE CONTEXTS

With the development of world cultural heritage protection movement, when the historic protection develops from the historic relic protection to the integrality protection of historic and cultural environment protection, an extremely important definition emerges out of demand and opportunity. “Historic District/Historic Site” refers to those the areas with urban historic features, landscape and image which can reflect social life and cultural diversity in the aspects of natural environment, artificial environment, and humanistic environment, and it is the witness of urban history. [1] In China, when publishing the second batches of famous historic cultural cities in 1986, the definition of historic site was officially proposed the definition of historic site—“it refers to the sites with rich relics which can completely and really reflect the traditional scene or national and local features in certain historic period, and it is the area of certain scale existing more cultural relics and historic sites, and modern historic relics and historic building.”

Different countries make use of different means of expression of historic site. The essay makes simple comparison on the names in China, Japan, Britain, and America (Fig. 1).

## 2 EVALUATION CRITERIA OF HISTORIC SITE OF UNITED NATIONS AND BRITAIN, AMERICA, JAPAN, AND CHINA

The protection way for cultural heritage in world-wide scale can be divided into appointment system, listed system, and mixture of appointment system and listed system. [2] Most of countries in Europe and America adopt listed system or mixture of appointment system and listed system. In 1996, Japan also added the heritage listed system in the evaluation criteria while it retained the heritage appointment system by revising the heritage protection law—*Protection Law of Cultural Properties*.

### 2.1 Evaluation criteria of “outstanding universal value” of world cultural heritage

As the only criteria for listing *World Heritage Lists* that was formulated by World Heritage Committee, Outstanding Universal Value (shorten for OUV in the following) mainly emphasizes that the cultural and natural value or some value of heritage is rare. Since the Operational Guidelines of *World Cultural and Natural Heritage Convention* were issued in 1977, it is revised nearly every year. In the current 2005-version *Operational Guidelines*, the OUV definition of world heritage is illustrated as: “OUV means the cultural/historic meaning. It is so special

Historic District/ Historic Area	China	Famous Historic and Cultural City, Historic and Cultural Block, Historic Feature Zone
	Japan	Cultural Properties, Traditional Building Conservation Area
	Britain	Listed Building/conservation Area
	America	Historic Area

Figure 1. Relevant definitions of historic site.

that it exceeds the national boundaries, which is of common significance to all mankind's contemporary and future generations. Therefore, protecting these heritages permanently has the greatest importance for international society which is as a whole."

Assessing 10 criteria of OUV, first six criteria are used to measure cultural heritage, covering all the definitions of historic sites mentioned in the essay: [3]

- i. *represent a masterpiece of human creative genius;*
- ii. *exhibit an important interchange of human values, over a span of time or within a cultural area of the world, on developments in architecture or technology, monumental arts, town-planning or landscape design;*
- iii. *bear a unique or at least exceptional testimony to a cultural tradition or to a civilization which is living or which has disappeared;*
- iv. *be an outstanding example of a type of building, architectural or technological ensemble or landscape which illustrates (a) significant stage(s) in human history;*
- v. *be an outstanding example of a traditional human settlement, land-use, or sea-use which is representative of a culture (or cultures), or human interaction with the environment especially when it irreversible change;*
- vi. *be directly or tangibly associated with events or living traditions, with ideas, or with beliefs, with artistic and literary works of outstanding universal significance. (The Committee considers that this criterion should preferably be used in conjunction with other criteria).*

## 2.2 Criteria of listed heritage in Britain, America, and Japan

I. The conception of listed protection for historic site in Britain appeared in *Law of Urban Planning* in 1944. The definition of listed architecture was given by the law, but the revised *Law of Urban Planning* in 1947 was the law to officially establish the criteria framework. The *Planning (Listed Building and Conservation Areas)* in 1990 gave the definition of listed building and conservation areas: "it refers to the architecture with special architectural art value or historic value whose features and appearance are worth conserving." The listed process of building and listed conservation areas is: first, the experts of architectural history go to the site to investigate the candidate architecture; then the architecture which was assessed to reach the listed criteria should be listed in "tentative list" to

vend; and the suggestions of local government, protection communities, and ordinary citizens should be heard. If there is no objection, the notification will be sent to local government after the official identification of DNH, and then the local government notifies the owner or user of architecture.

The main criteria and objects for selection of Listed Building and Conservation Areas include: [4]

1. *The building which has special value in the aspects of building type, building art, planning and design, or the display of social and economic development history, such as industrial building, train station, school, hospital, theater, city hall, poorhouse, and prison and so on;*
  2. *The master work of technological reform or exquisite workmanship, such as cast iron, pre-cast technology, and the early building with concrete technology;*
  3. *The building which is related to important historic events and important historic figures;*
  4. *The building with the complete architectural complex, especially with the examples of urban regulations, such as square, townhouse, and typical village and so on.*
- II. America formulated *The National Historic Preservation Act* as early as October 1966. The national listed system of Historic Places could be regarded as the footstone of historic and environmental protection system in America, which is one of the important means of The National Historic Preservation Act to protect historic environment. The listed criteria for the national historic places are: it has important meaning in the aspects of American history, building, archeology, engineering technology, and culture; it has the complete area, relic, building, structure, and object in the aspects of site, design, environment, material, craft, emotion, and association; it has a history of over 50 years and complies with the following conditions: [5]
1. *It is associated with important historic events;*
  2. *It has relation to the life of outstanding figures in the history;*
  3. *It should be the work which reflects the unique characteristic of some type, some period, or some construction method, the representative work of masters, the work with high art value, or the ordinary work with group value;*
  4. *The prehistoric or historic important information may be found or has been found in it.*



III. The heritage protection and assessment in Japan is dominated by the appointment system, being assisted by the listed system. Compared with the listed system, the content and procedure of the appointment system is more detailed and strict. While the listed system is more flexible, whose feature is regarding culture as the “resource” to continue to give development space for it and the necessary protection should be done as well. The *Protection Law of Cultural Properties* issued in 1950 is the fundamental law of historic protection in Japan. In June 1996, Japanese Congress passed the new round of revise of *Protection Law of Cultural Properties*. Influenced by similar systems in various countries of West Europe, Japan also introduced the listed system into laws. In Japan, the listed system can be regarded as a report and declaration and record system. If the owner or user wants to be listed, they can apply to the local public group; local public group can also recommend to the state to be listed.

The listed criteria for cultural properties are: it should be the building, which has a history of more than 50 years and it should comply with one of the three following conditions: [6]

1. *It may be the landscape with land historic meaning;*
2. *It should be the example of modeling art;*
3. *It should be the one which is hard to reappear or to be rebuilt.*

### 2.3 Evaluation criteria of Chinese historic site

Conforming to the trend of international protection movement, the historic and cultural heritage protection work in China keeps up with the trend of international protection movement, and experiences the protection process from “point” to “surface”—namely the protection concentrating on cultural building and architectural complex gradually develops into the protection of historic site concentrating on historic area, which gradually establishes the protection system of famous historic and cultural cities and the protection system of scenic spots.

The declaration conditions for the famous historic and cultural cities and towns and villages in China: the cities, town, and villages which comply with the following conditions can be declared as the famous historic and cultural cities, towns, and villages: [7]

1. *It has rich cultural relics;*
2. *There are many concentrated historic buildings;*
3. *It should keep the traditional layout and historic style;*

4. *It was the political center, economic center, cultural center, traffic center, or important military area in the history, or the place where the important historic events happened once; or its traditional industry and important projects in the history had important influence on the development of local area, or the place which could reflect the cultural features and national features of local buildings.*

## 3 THE COMPARISON AND ANALYSIS ON THE EVALUATION CRITERIA OF HISTORIC SITE OF UNITED NATIONS AND BRITAIN, AMERICA, JAPAN, AND CHINA

In summary, by analyzing and comparing the evaluation criteria of historic site of United Nations and Britain, America, Japan, and China, the essay finds that:

- I. In the World Heritage List of the United Nations, the evaluation criteria of OUV are more detailed and comprehensive, which can summarize the evaluation criteria of historic site of China, Japan, Britain, and America from different perspectives without anything uncovered. Moreover, it describes from the more bigger perspective with more flexible description. For example, the content about “building, technology, relic art, urban planning, or landscape design” mentioned in the second criterion of OUV, which cover comprehensive and concrete fields, while other countries only simply describe them by the relevant definitions of “important events”.
- II. In the similar content of criteria of different countries, the value of cultural heritage in historic site is especially emphasized rather than only limited to the definite object of cultural heritage itself in the criteria for the assessment of OUV in the *World Heritage List* of the United Nations. “Spirit” (first criterion), “value” (second criterion), and “witness of civilization or culture” (third criterion) appear multiple times in the criteria. By making comparison, it can be found that the descriptions of the criteria in other countries are static and monotonous, which only focus on the cultural heritage itself and don’t explore the deeper historic value and cultural value.
- III. It is remarkable that it can be found in the comparison that the criteria of Japan, China, Britain, and America are reflected in the first four criteria of OUV, while there is almost no relevant illustration about the fifth and the sixth criteria of OUV in the criteria of

these countries. However, the fifth and the sixth criteria emphasize the relation between “human and environment,” is emphasized in the fifth and the sixth criteria, which is the core of assessment of OUV. The fifth and the sixth criteria take the abstract “culture” and “belief” as the assessment requirement directly. It shows that historic and cultural value is attached more importance, but these content and ways are not mentioned in the criteria of other countries.

#### 4 THE INSPIRATION OF THE EVALUATION CRITERIA OF INTERNATIONAL HISTORIC SITE TO CHINA HERITAGE PROTECTION SYSTEM

By making comparison, there are following inspirations to China heritage protection system:

1. The declaration requirement for famous historic city, town, and village is too closed and static in China.

It can be seen from the comparison from third criterion of OUV in Figure 2 and the similar criterion (1) and criterion (3) of China that now Chinese assessment of historic site only focuses on the description of quality and style of current situation of building, which doesn't consider the historic information, scientific value, art value, and emotional value of building. The assessment only focuses on the stage of horizontal comparison, whose measurement standards only fix on relic quantity, wholeness of building and architectural complex, and relic age. These criteria are too stiff and closed, and the delimitation for protection range and construction control zone can only keep the protection in the state of isolated, static, and negative state. For the protection of historic site, it is not only reflected on the expansion of protected object, but also is reflected on the understanding of material value of historic environmental protection, the understanding and assessment of spiritual value and cultural value of historic environment.

2. China should strengthen the assessment of cultural value of heritage

Except for having precious value in the aspect of material space environment, the deep humanistic value of historic site should also be paid more attention. The real value of historic site and historic environment is not the building or structure itself; it is the outcome of culture and spirit, which creates and carries one or more historic atmosphere(s) with historic value, art

OUV	Country	Content
i. represent a masterpiece of human creative genius;	China	None
	Japan	2. being the model of modeling art
	America	3. It shows the works with unique characteristic in some type, some period, or some construction method, or the works of masters, or the works with high art value, or the ordinary works with group value;
	Britain	None
ii. exhibit an important interchange of human values, over a span of time or within a cultural area of the world, on developments in architecture or technology, monumental arts, town-planning or landscape design;	China	4. It was the political center, economic center, cultural center, traffic center, or important military area in the history, or the place where the important historic events happened once; or its traditional industry and important projects in the history had important influence on the development of local area, or the place which could reflect the cultural features and national features of local buildings.
	Japan	None
	America	1. has association with important historic events; 2. has relation with the life of outstanding figures in the history;
	Britain	1. The building which has special value in the aspects of building type, building art, planning and design, or social and economic development history, such as industrial building, train station, school, hospital, theater, city hall, poorhouse, and prison and so on; The representative buildings of technological reform or exquisite workmanship, such as the building in the early period made of cast iron, precast technology, and concrete technology; 3. The building which has association with important historic events and important historic figures;
iii. bear a unique or at least exceptional testimony to a cultural tradition or to a civilization which is living or which has disappeared;	China	1. With rich relics; 3. It keeps the traditional layout and historic style;
	Japan	1. It is hard to reappear.
	America	1. Prehistoric or historic important information has been found and maybe found.
	Britain	None
iv. be an outstanding example of a type of building, architectural or technological	China	2. There are many concentrative historic buildings;
	Japan	1. It is helpful to shape the historic landscape of land;
	America	None
	Britain	4. The building with the complete architectural complex, especially
ensemble or landscape which illustrates (a) significant stage(s) in human history;		with the examples of urban regulations, such as square, townhouse, and typical village and so on.

Figure 2. Similarities of evaluation criteria of various countries.

value, and cultural value at the same time. They not only witness the environmental change of this region for a long time, but also record the change of culture, thought and concept, and lifestyle in different periods. They reemerge the history and the mutual reform of human and nature at any time. Thus, in the formulation of China heritage protection system the attention to the humanistic value in historic site and historic block must be drawn more..

3. Suggest for bringing in cultural listed system in China

The emergence of new cultural heritage system doesn't mean to deny or replace the original cultural system, but also bring new conception with available value in China protection system to supplement and improve the deficiency. For the current system in China, the formulation of it is mainly from the standing point of state to strictly select and "designate" the one which is important, prominent, and with special value in cultural heritages, and then some necessary limits are added to their owners with the coerciveness more or less. The advantage of listed system lies in that it not only expands the range of heritage relic and protects some modern building and industrial relics, but also the sustainable protection can be deployed on these objects on the purpose of development and a new flexible protection system will be established, which is the trend of world heritage protection.

4. Strengthen the promotion and improvement of laws and regulations

It can be found in Figure 3 that the protection awareness of historic site in Britain, America,

and some European and American countries is formed earlier than that of the United Nations and Asian countries. Britain established the framework of current listed system in *Law of Urban Planning* in 1947, while American enacted *The National Historic Protection Act* issued in October 1966 which became the foot-stone of protection of historic site in America. However, from the perspective of assessment content, the evaluation criteria of OUV of the United Nations are more detailed and comprehensive, because the criteria for the assessment of cultural heritage will be revised every year in United Nations. The revise of the criteria is the constant illustration of the definition of "OUV" in *Convention*. The OUV is endowed by people, which is relative and changeable.

It can be seen that the value of historic site is dynamic and changeable. In the formulation of China heritage protection system, the international vision and acute perspective for international heritage protection trend should be possessed, and the mutual promotion and improvement of laws and regulations should be paid attention.

Item	Name	Starting	Latest Revise
UN	Outstanding Universal Value	1992	2014
Britain	Criteria and Objects of Heritage List	1947	2009
America	National List Criteria of Historic Site	1966	
Japan	Listed Criteria of Tangible Cultural Properties	1996	2005
China	Declaration Conditions of Famous Historic and Cultural City, Town, and Village	2008	2008

Figure 3. Starting time and the latest revise time for evaluation criteria in various countries.

REFERENCES

[1] Zhangsong, *Introduction to Protection Principle of Historic City [M]*, Shanghai: Shanghai Scientific and Technical Publishers, 2003.

[2] Operational Guidelines for the Implementation of the World Heritage Convention, Paris, 2013.

[3] Planning (Listed Buildings and Conservation Areas) Act, UK Statute Law Database, 2009.

[4] National Historic Preservation Act, United States government, 1981.

[5] *Protection Law of Cultural Properties*, Japan State Administration of Cultural Heritage, 2005.

[6] *Protection Act of Famous Historic City, Town, and Village*, The State Council of the People's Republic of China, 2008.

# The application of modular building in post-disaster reconstruction of the countryside

X.S. Wang & Q. Zhao

*College of Architecture and Civil Engineering, Taiyuan University of Technology, Taiyuan, Shanxi, China*

**ABSTRACT:** This paper, contraposes the particularity of post-disaster reconstruction of the countryside and puts forward the application of modular building in the post-disaster reconstruction of country. Then we sort out the concept, summarize the application of modular building, and explore the application of modular building in post-disaster reconstruction of countryside. In the end, we analyze an actual case. This research is expected to reduce the difficulty of post-disaster reconstruction in the vast rural areas of China.

**Keywords:** modular building; post-disaster reconstruction; countryside; application

## 1 INTRODUCTION

Earthquake disasters are very severe in China, with has features of great magnitude, high frequency, wide distribution, and shallow source. In recent years, earthquakes have happened often in China: an earthquake measuring 8.0 on the Richter Scale struck Wenchuan and Beichuan in Sichuan in 2008; another measuring 7.1 occurred in Yushu county of Tibetan Autonomous Prefecture of Yushu in Qinghai in 2010; in 2011, an earthquake measuring 5.8 on struck Yingjiang of Yunnan; another measuring 7.0 happened in Lushan county of Ya'an city in Sichuan in 2013; earthquake quake measuring 6.6 happened in the boundary between Min county and Zhang county of Dingxi city in Gansu in 2013; another measuring 6.5 happened in Ludian county of Shaotong city in Yunnan in 2014; and an earthquake measuring 5.0 Richter Scale happened in Jinkou river area of Leshan city in Sichuan in 2015.

The epicenters of these earthquakes are generally located in rural areas. There was no earthquake resistance measure or fortification measure for the residences in rural areas, so the earthquakes brought a lot of losses to these areas especially. Modular buildings have multiple values, so applying the modular buildings to the post-disaster reconstruction in rural areas is helpful to reduce the difficulties.

## 2 INTRODUCTION TO MODULAR BUILDING

### 2.1 Definition

Modular building is the building which is designed, produced, and constructed modularly

by complying with the module definition and by combining the features of modeling, function, and science and technology. The module feature for the modular building is very obvious. A series of basic modules with relatively independent and standard structures and functions are designed and produced by analyzing the modeling, structure, function, crafts, and technology and so on. These basic modules can be wall unit, door and window unit, stair unit, balcony unit, bathroom unit, kitchen unit, and bedroom unit, which shape the architectural industrial products that meet individual consumer's demand and meet the demand of market by selecting and combining the modules.

### 2.2 The development situation in rural areas

The study on modular building is late in China with slower development. There is less study on modular building in the aspect of residences in rural areas.

As China is increasingly focusing on residences in rural areas, China has also opened up studies on application of modular buildings to rural residences. For example, the 11th Five-Year topic—Modular Technology and Software Development of Design for Residence Building in Rural Areas proposed by Ministry of Science and Technology that Beijing Jintumu Software Technology Co., Ltd has completed the study on Jinzhong area, Lijiang area, and Huizhou area, but there are some rural buildings with national and traditional features to be studied, such as the CHouse CAD three-dimensional software system designed for rural residence building. These research results lay a solid foundation for the application of modular building in rural areas.

### 3 THE APPLICATION VALUE OF MODULAR BUILDING IN THE PROCESS OF POST-DISASTER RECONSTRUCTION IN RURAL AREAS

#### 3.1 *Improve the earthquake-resistance function of rural residence*

Most rural residences are self-built houses, whose earthquake-resistance quality doesn't reach the national or local relevant standards. Rural areas tend to be harder hit by earthquakes. The good earthquake-resistance function of modular building can improve the earthquake-resistance function of the residences in post-disaster reconstruction and reduce the loss that earthquake brings to rural areas.

#### 3.2 *Speed up post-disaster reconstruction and make reasonable reconstruction plan*

The technological level and construction efficiency of rural residence building are lower. Especially under the special situation of post-disaster reconstruction, the traditional construction way and technology cannot meet the urgency of post-disaster reconstruction in rural areas. The efficient way of production and construction modular building can speed up the post-disaster reconstruction in rural areas and play the consoling role of building. Furthermore, as the production efficiency of modular building is fixed, it is beneficial to the post-disaster reconstruction, providing the reliable data support and reference frame for making scientific plan of post-disaster reconstruction work.

#### 3.3 *Raise the usage ration of resources*

The main material for modular building is steel, so the retrievability of whole materials of buildings should be higher than that of ordinary buildings. Only in this, can it save resources. The materials for wall and floor slab are light, which can reduce the column load and therefore reduce the basic construction cost. Under some conditions, the disaster relief funds can be used directly to buy the modular building that is needed in rural areas, so the cycle chain of disaster relief funds will be reduced to raise the usage ratio of funds and to avoid the uncertain factors to some degree.

#### 3.4 *Improve the post-disaster rural environment effectively*

The ecological environment of post-disaster rural areas is destroyed severely, which becomes very weak. Thus, post-disaster reconstruction should be focused on the scientific, environmentally-friendly, and sustainable construction. Compared with the traditional building mode of rural residence, the

production and construction mode of modular building is more environmentally friendly and scientific, which can improve the rural environment after disaster effectively.

#### 3.5 *Motivate people to attend and diversify the building space types*

The functions of modular building are better than that of the residences built by peasants with their limited knowledge and experience. Moreover, due to its special universal system, the non-professional construction staff are able to design and construct residences with some professional knowledge. Local residents can make use of spare time to select the modules that they need and assemble their own residence, which is nearer the individual's special demand than that of the residence designed by professional staff with a shorter time, and exerts the enthusiasm of the people in disaster areas in the post-disaster reconstruction.

#### 3.6 *Raise the energy-conserving and environment-friendly index of residences*

Modular building combines the advanced production technology for low-carbon and energy-saving residences in developed countries. Compared with the traditional building, modular building can save over 47% of energy and reduce 51% of carbon emission, whose energy-saving index has reached 65% of the energy-saving compulsory standard of heating of buildings in the third stage and is developing to the four-step energy-saving requirement.

#### 3.7 *Be helpful to promote residence industrialization*

Residence industrialization began late in China and it is developing slowly. At present, although there are some residence production enterprises, they don't promote residence industrialization remarkably due to the limit of their own technological ability and other factors. Some buildings can be designed and produced like products, if modular building is released.

### 4 THE APPLICATION OF MODULAR BUILDING IN THE PROCESS OF POST-DISASTER RECONSTRUCTION IN RURAL AREAS

#### 4.1 *Special post-disaster situation in rural areas*

Rural residence construction is always a problem that is ignored and needs to be solved. It is very

severe especially in the process of post-disaster reconstruction in rural areas.

#### 4.1.1 Multiple types and strong regional features of rural residence

Rural residences are different features in different regions. For example, the building forms and space structures are different among Hui-style buildings in Huizhou area, quadrangle dwellings in Beijing, and residences in Jinzhong and so on. Thus, it adds the difficulty to the fast, ordered, and scientific post-disaster reconstruction in rural areas. However, modular building can meet the demand of space structure of different residences to the maximum degree due to its flexible and changeable spatial organizational ways.

#### 4.1.2 Complicated and changeable post-disaster environment in rural areas

Rural areas spread all over China, whose environment is different, such as collapsed loess regions with the continental monsoon climate, and saline areas with the temperate continental climate and so on. Due to the complicated and changeable environmental conditions, and the destruction of earthquake, it adds the difficulty of post-disaster reconstruction in rural areas. Owing to the special physical and structural functions, modular buildings can adapt to the complicated environment.

#### 4.2 The application analysis of modular building in post-disaster reconstruction in rural areas

Rural residence building spaces have strong regional features, so the post-disaster reconstruction in rural areas must be combined with local regional environmental conditions. The flexible and changeable spatial assemble forms of modular building are suitable to the regional features of post-disaster rural areas, so the post-disaster reconstruction will be more reasonable and scientific.

According to modular thinking, post-disaster reconstruction work can be divided into the combination of organic space of architectural complex and the spatial structure of single building unit. According to demand, it can be further divided. Finally, various modules can be combined organically. With the help of the effective leading and feedback system of organic space and unit space, both sides can be combined reasonably (Fig. 1). The difficulty in post-disaster reconstruction in rural areas can be reduced by simply facing the complicated situation and stably changing the same.

##### 4.2.1 The combination modes of organic space

The regional feature of organic space is obvious, which emphasizes the organic integration with the

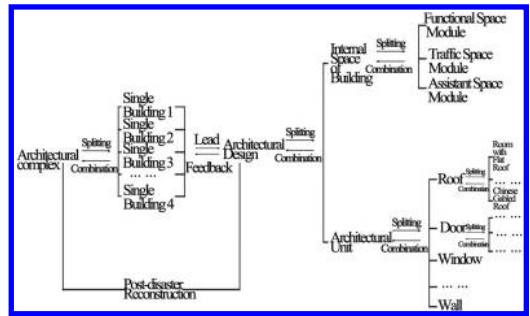


Figure 1. Diagram of construction principle for modular building space.

surrounding environment. It can reflect the modern sense at the same time of keeping the original geomorphic features, thereby improving the quality of environment of post-disaster reconstruction in rural areas. The organic space design of modular architectural complex mainly refers to combine several single building unit modules into a harmonious and complete organic space of architectural complexes, whose forms are as shown in Figure 2. Various single building unit space modules need to respond and connect with each other, so the internal space and external space can be interweaved, harmonious, and uniform, whose basic combination modes are as shown in Figure 3.

The interaction and flexibility of building modules can make architectural complexes combine properly with the special environment to adapt to the complicated and changeable environment in rural areas. For example, the courtyard combination can combine with the forms of “three outsider courtyards and five insider courtyards” and “broking two courtyards with three courtyards” in Jinzhong area of Shanxi; it can also combine with the single courtyard or multiple courtyards in Beijing; it can freely combine with the topographic form of Shanxi to shape the form of architecture complex that is suitable to the local features. This comprehensive combination can combine with the complicated environment to shape the architectural form in harmony with regional culture.

##### 4.2.2 The structural form of unit space

Comparatively speaking any relatively independent single building in the organic space can be called the unit space. The inferior modules of the unit space of single building can be divided into the architectural internal space module and architectural unit module.

###### 4.2.2.1 Architectural internal space module

Architectural internal space module can be divided into functional space module, traffic space module,

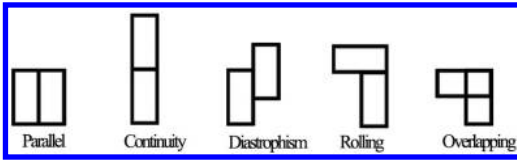


Figure 2. Diagram of combination patterns of building modules.

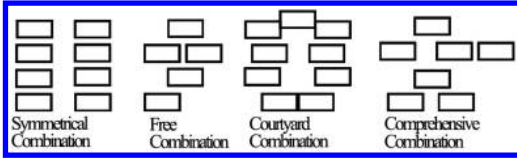


Figure 3. Diagram of combination modes of building modules.

and assistant space module. The distribution of functional module plans divides the reasonable internal space, whose space structure forms are as shown in Figure 4. Its flexible and reasonable space division can meet the different demands of residents in post-disaster rural areas to building internal space.

**Series combination:** Various functional space modules punch through. It is usually suitable for the situation of functional space modules with strong continuity or without independent separation. For example, the series combination can be used in kitchen or dining room.

**Parallel combination:** It is the combination which connects various functional spaces by traffic space module and assistant space module. This combination form makes various space modules relatively independent to reduce the disturbance with each other. For example, the parallel combination can be used between master bedroom and guest bedroom to reduce the disturbance.

**Blended combination:** It flexibly uses series combination and parallel combination so that the architectural internal space can be combined reasonably and scientifically in accordance with the demand of architectural space. It can be used in the complicated space to divide the functional divisions reasonably.

#### 4.2.2.2 Architectural unit module

Architectural unit modules can be divided into wall, door and window, balcony, stair, and some decorative units with local features to divide the inferior modules in accordance with color, material, and scale, such as the grill, suspended ceiling, and doors in different sizes and different qualities. These architectural unit modules can be combined flexibly to shape multiple-form architectural styles

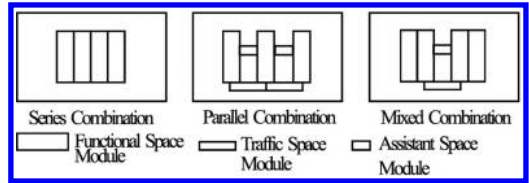


Figure 4. Diagram of structure forms of architectural internal space.

to meet the style demands with different regional features in rural areas.

The division of modules should consider reducing the dependence on each other to make modules have independent functional features, and make modules be divided, combined, and repeated with good interchangeability. For the series standards of the modulus of module size, Chinese Coordinate and Uniform Standard of Architectural Modulus can be referred, whose basic value is 100 mm and whose symbol is M—1 M = 100 mm. The multiple of basic modulus is the modulus size of modular building. For example, the architectural unit module should adopt the horizontal basic modulus number sequence from 1 M to 20 M and adopt the horizontal expansion modulus number sequences of 3 M, 6 M, 12 M, 15 M, 30 M, and 60 M to be the modulus sizes of architectural internal space module.

## 5 MODULAR BUILDING CASES

The demonstration project of the building of vacation room on the mountain developed by Yi De construction consulting (Shanghai) Co., Ltd. is not located in Ba'nán area of Chongqing in Chongqing. The building includes two single houses, whose floor area is 80 square meters and construction area is 160 square meters. The house includes two families which are connected by the stairs. The living room is in the middle of each house. The bedroom with bathroom or the dining room with kitchen is on both sides, which can be allocated flexibly in accordance with user's demand.

The modular system of light steel is used in the project, which has high intensity and good earthquake-resistance function. It can resist earthquakes measuring 8.0 on the Richter Scale. Its deadweight is lighter than that of the traditional buildings, which can reduce 60% of deadweight. The thermal conductivities for outer wall and roof are 0.26–0.45 (W/m<sup>2</sup>·K) and 0.3 (W/m<sup>2</sup>·K), respectively; the fire endurance could reach 1–2 hours; the sound insulation requirement is ≥45 db. Dry process is adopted during the construction without wet operation, which can save 90% of water. There is

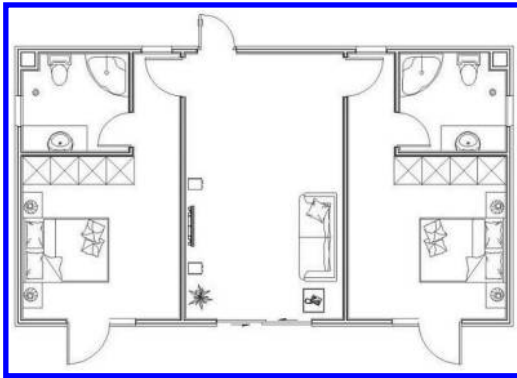


Figure 5. Plane Graph of the Building.



Figure 6. Exterior appearance of the building.

less operation on the construction field, which has less destructive influence on the surrounding environment. Compared with the traditional concrete construction mode on the field, it can reduce 50.9% of carbon emission. The construction is fast with a shorter construction cycle. It only takes 10 days for the whole project. Compared with the traditional construction mode, its construction cycle can reduce 30%–50%. The accurate quantization of industrial production can realize the minimum error of budget and final accounts. The project reaches the centimeter error of construction on the field and the millimeter error of manufacture in plant, whose quality can be improved and the cost can be controlled effectively. The main steel structure can be recycled. Owing to the industrial production and high-accuracy control, the loss of raw materials is less than 3%. It can save 75% of energy in the whole lifecycle from production, construction, to utility.

## 6 CONCLUSION

Now, a complete modular building system that is suitable for rural areas has not been shaped in China, which adds the difficulty of applying modular building in the post-disaster reconstruction in rural areas. However, with the development of standardization, serialization, supporting, and universalization of architectural units in China, the architectural products can be produced in plants with modular construction. Meanwhile, due to the development of information technology, the connection between all industries is more convenient and fast, which is helpful to gradually establish a set of complete and reasonable modular building systems in China which is suitable for different regions, different residents, and different cultural features. When the earthquake disaster happens in rural areas, the reconstruction work can be organized and started rapidly in accordance with the stocked relevant information of building and construction, and residents can return to the original life rapidly. The booming development of modular building will help the post-disaster reconstruction work in China start smoothly, and meanwhile will bring a new industry updating and huge reform in architecture industry, logistics industry, building material industry, and construction industry and so on.

## REFERENCES

- GBJ 2-86 Coordination and Uniform Standard of Architectural Modulus.
- Guo Dali & Li Shuchu. 2011 Systematic Study on Modular Design of Residence Building in Rural Areas. *Civil Engineering Information Technology* (04): 21–26.
- Wu Yun et al. 2011. Study on Processing Distribution and Modular Construction of Architectural Steel Material. *Data Collection of Development Seminar In the Industry of Chinese Rebar Processing and Distribution*: 16–19.
- Zhang Yiyun & Zhu Jie. 2011. Modular Study on Detailed Diagram of Residence Building in Rural Areas. *Civil Engineering Information Technology* (04): 27–31.



# Analysis of development trend of country parks in China

L.N. Li & J. Gao

*College of Architecture and Civil Engineering, Taiyuan University of Technology, Taiyuan, Shanxi, China*

**ABSTRACT:** Based on the need for rapid development of the construction of country parks in China in recent years, as well as 389 research literatures on country parks through retrieval from CNKI (China National Knowledge Infrastructure) in 30 years from 1984 to 2014, this paper has classified statistics of these documents from four aspects, such as the year of publication, sources of database, research point of view, and research methods. It has summarized the progress, results, and trend of related theoretical researches at home and has analyzed the characteristics of the current research in order to provide references for the construction and study of country parks in the future.

**Keywords:** country park; literature; statistical analysis; development trend

## 1 INTRODUCTION

In the rapid process of urbanization, as environmental issues are increasingly projecting, building ecological and livable cities have become widespread concerns. Construction of country parks aim to create ecological and livable cities so as to enhance the quality of urban and rural residents. Country parks belong to a mosaic in the city's overall level or a large plaque, and its mosaic and distribution pattern is repeatable to some degree. Being an important part of an urban green space system, country parks not only protect the fine natural resources at the junction of urban and rural areas, but also can restore the resource conditions that have been destroyed. With important ecological functions, it serves to improve the ecological environment, blocking the city's infinite sprawl. In addition, with the accelerated pace of urban life and magnified work pressure, the demand for pleasure and leisure has been growing. City Park has been unable to meet the needs of residents, and country parks in peri-urban areas have favorable ecological environment and superior geographical advantages, and have become a crucial option of weekend getaways for urban residents. Based on these reasons, there is a rapid development in construction of country parks in various regions of China in recent years. Practice in the development of country park is far ahead of the theoretical development of the construction of country parks, resulting in the great blindness in the construction of country parks. Thus, further improvement and perfection is needed in all aspects.

There is a total of 389 research literatures containing "country park" included in CNKI in 30 years from 1984 to 2014 through retrieval. This paper has conducted statistics of these documents from four aspects, such as the year of publication, sources of database, research point of view, and research methods to make analysis of the progress, results, and trends of current research on country park in the hope of playing a guiding role in research and construction of country parks.

## 2 AN INCREASING TREND OF RESEARCH ON COUNTRY PARKS

By statistical analysis of the year of publishing research literatures on country park, in 1984, Chinese scholars began to conduct research on the country parks, with less number of research papers from 1984 to 2005, for at this time, the research on the country park is still in the initial stage of exploration, developing slowly. From 2006 to 2009, the number of research papers began to increase, the overall showed a rising trend, and the study of country parks became the hot spot. Thus at this time, the study on country parks in our country has begun to develop. From 2010 to 2014, the number of research papers tended to change smoothly, with small differences in research papers each year. Thus at this time, the research on country parks in our country has entered into a relatively stable period of development (See Fig. 1).

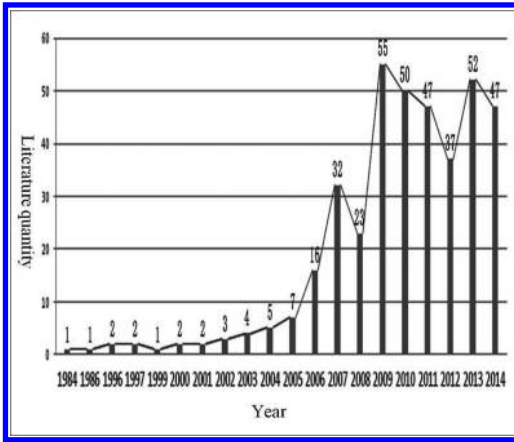


Figure 1. Change in number of research literature on country parks from 1984–2014.

### 3 A RISING TREND OF ACADEMIC DEPTH AND INNOVATION OF RESEARCH ON COUNTRY PARK

By statistical analysis of the source database of research literatures on country parks, the original source database of research literatures on country parks has low academic value, while as research progresses, the academic value of source database has begun to increase, especially in the high academic value in China Doctoral Thesis Full-text Database (See Table 1).

The number of research literatures from China Academic Journals Full-text Database, Proceedings Papers of Chinese Meetings Full-text Database, and China’s Major Newspapers Full-text Database shows an overall upward trend, while the proportion displays an overall downward trend. There is less number of research literatures from Featured Journal and Proceedings Papers of International Conferences Full-text Database, and the proportion is on a declining curve. There is an upward trend in the number of articles from China Outstanding Master’s Thesis Full-text Database as a whole, while the proportion shows the overall upward trend. Research literatures from China Academic Journal Series Full-text Database and China Doctoral Thesis Full-text Database have just appeared in recent years with very few research papers. In 2005, the literature on support of research funds has begun to arise in the study of country parks in our country, and the number of literatures on funds support has shown an overall upward trend (See Fig. 2).

Overall, academic depth and innovation of research literature on country parks in our country has been on the rise, and the type of database

Table 1. Starting year of different sources of databases of research literatures on country parks.

Starting Year	Database source of research literatures on country park
1984	Featured Journal
1996	China Academic Journals Full-text Database Proceedings Papers of Chinese Meetings Full-text Database
1999	Proceedings Papers of International Conferences Full-text Database
2003	China’s Major Newspapers Full-text Database
2006	China Outstanding Master’s Thesis Full-text Database
2010	China Academic Journal Series Full-text Database
2011	China Doctoral Thesis Full-text Database

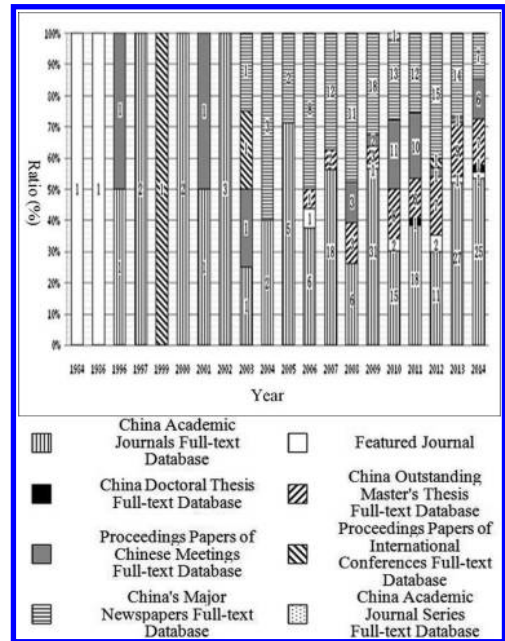


Figure 2. Change in source of database of research literature on country park from 1984–2014.

sources of research literature has gradually increased.

### 4 TRANSFORMATION FROM A SINGLE DISCIPLINE TO INTERDISCIPLINE FROM THE PERSPECTIVE OF RESEARCH ON COUNTRY PARKS

By statistical analysis of the perspective of research literature on country parks, with the

development of the research, the angle of research literature on country parks has begun to increase, gradually involving all aspects of them (See Table 2).

The overall number of articles each year is firstly increased and then decreases from two research perspectives of country park management and description of the construction and development in various regions, and the proportion shows an overall downward trend. The overall number of research papers each year shows a rising trend from two research perspectives of country park planning and design, and vegetation landscape, and the proportion shows a steady rise after decline as a whole. There are less number of research papers each year from two research perspectives of relation between country park and city as well as ecological protection and ecological benefits, and the proportion first decreased and then stabilized. There is a less number of research papers each year from three research perspectives of tourists' behavior and experience in country park, concluding thoughts and review and construction, and the proportion shows a steady trend as a whole. There are a less number of research papers each year from the research perspective of tourism development in country parks, and the proportion shows a declined trend as a whole. The overall number of articles each year first increased

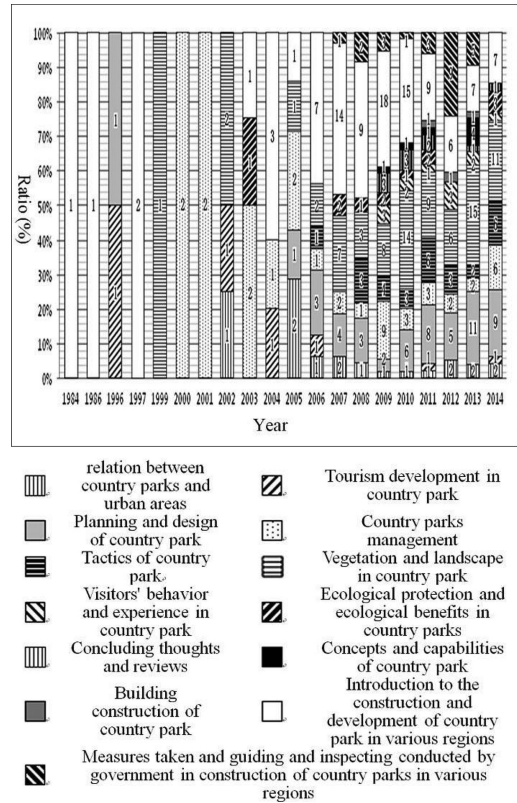


Table 2. Starting year of different research perspectives of research literatures on country parks.

Starting Year	Research perspective of research literature on country park
1984	Introduction to the construction and development of country park in various regions
1996	Tourism development in country park and planning and design of country park
1999	Vegetation and landscape in country park
2000	Country parks management
2002	Relation between country parks and urban areas
2003	Ecological protection and ecological benefits in country parks
2006	Research on tactics of country park
2007	Measures taken and guiding and inspecting conducted by government in construction of country parks in various regions
2009	Concepts and capabilities of country park, concluding thoughts and reviews and visitors' behavior and experience in country park
2011	Building construction of country park

Figure 3. Change in research perspective of research literature on country park from 1984–2014.

and then decreased from the research perspective of measures taken and guiding and inspecting conducted by government in construction of country parks in various regions, and the proportion firstly increased and then decreased. The overall number of research papers each year shows a rising trend from the research perspective of tactics of country park, and the proportion shows a steady trend as a whole. There are a less number of research papers each year from the research perspective of concepts and capabilities of country parks, and the proportion shows a rising trend as a whole (See Fig. 3).

Overall, the research angles are gradually transformed from introduction to construction of country parks in various regions, country parks management, tourism development, vegetation and landscape, and planning and design to research perspective of relation between country parks and urban areas, ecological protection and ecological benefits of country parks, strategy, tourists' behavior and experience, the concept and function and so on.

## 5 STATISTICAL ANALYSIS OF RESEARCH METHODS IN NEARLY 30 YEARS

With the development of the study, the method adopted in research literature on country parks has gradually enriched, and the use of a variety of methods can promote research and development of country parks (See Table 3).

Using frequency of descriptive research and mathematical method first increased and then declined as a whole, and the proportion shows an overall downward trend. Using frequency of case study and qualitative analysis firstly increased

and then declined as a whole, and the proportion firstly increased and then declined as a whole, and gradually stabilized. Using frequency of survey method firstly increased and then declined as a whole, and the proportion shows an overall steady trend after decline. Using frequency of literature research shows an overall upward trend, while the proportion shows an overall downward trend. Using frequency of quantitative analysis method shows an overall upward trend, while the proportion shows a steady trend as a whole. Using frequency of simulation, systematic science, experience summarizing, interdisciplinary research method adopted each year is less, and the proportion shows a steady trend as a whole (See Fig. 4).

Overall, the research methods are transformed from descriptive study, case study, qualitative analysis, mathematical method, investigation method and others gradually to quantitative method, systems research, interdisciplinary research, and simulation and so on.

Table 3. Starting year of different research methods of research literatures on country parks.

Starting Year	Research methods in research literatures on country park
1984	Descriptive research method
1996	Case study, qualitative analysis, literature study
1999	Mathematical method
2000	Investigation method
2006	Quantitative analysis
2007	Experience summarizing
2008	Systematic scientific method
2009	Interdisciplinary research and simulation

## 6 CONCLUSIONS

Since the initial research on country parks in 1980s in China, there has been faster research and development of country parks, and especially in the 21st century, considerable achievements have been made in the related theories and the number of applied research literatures. But currently, the theoretical system of research on country park is imperfect, requiring further development and improvement. The discussion on the above research and summary is as follows.

### 6.1 Future development trend of country parks

Chinese scholars have been increasingly concerned with country parks, the number of research literatures on country park shows a rising trend as a whole, and research on country park has become a hotspot, and it can be predicted that in the next period of time, research on country parks will continue to be the hot issue studied by domestic departments of construction and planning.

### 6.2 The theoretical system of country park research is still not perfect

Although academic depth and innovation of research literature on country parks in our country continues to rise, the theoretical system of domestic research is inadequate. Firstly, the authoritative standard of defining country parks has not formed yet. Secondly, there are still less points of innovation in domestic research. Thus, the theoretical system according with China's reality fails to be formed.

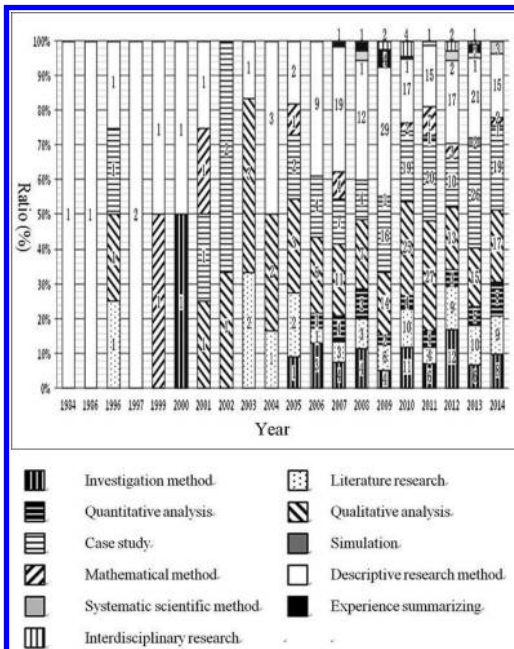


Figure 4. Change in research methods adopted in research literature on country park from 1984–2014.

### 6.3 *Forecast of future country park research perspectives*

Although research on the country parks in our country has already begun to be involved in the relationship between country park and city, ecological protection and ecological benefits of country parks, tourists' behavior, and experience in country parks, it is still in the exploratory stage, with shallow research findings. Nevertheless, the ecological function and recreation function is the most important function of country parks, and in order to give full play to the function, the study on the ecological function of country parks and recreationists' demand is essential, and for country parks as an important part of the urban greening systems, the research on the relationship between country park and city helps to curb unlimited sprawl of urban "overspreading" style so as to achieve the sound development of relationship between country park and urban space. Therefore, the relationship between country park and city, ecological protection and ecological benefits of country park, visitors' behavior and experience in country park should become a crucial perspective of research on country parks in the future.

### 6.4 *Forecast of future country park research methods*

As for research methods of country park, although a number of methods has begun to be adopted, such as quantitative method, systematic

approach, interdisciplinary research, simulation and others, the using frequency is less, and quantitative method and simulation can make more scientific and precise analysis of country parks to forecast the growing trend of country parks. Systematic approach can make the question and conclusion of research on country park become more systematic and clear, and interdisciplinary research method can conduct a comprehensive study of country parks through mutual reference and penetration of a variety of research methods so as to attain the reuse and innovation of knowledge and technology. Therefore, quantitative method, systematic approach, interdisciplinary research, and simulation should become significant methods of research on country parks in the future.

## REFERENCES

- Bian Li. 2014. Accelerate the research on construction of ecological and livable cities. *Economist* (01): 11–12.
- Jiang Bian. 2011. Inspiration from interdisciplinary research method. *Academy* (13): 85–86.
- Ling Shuping. 2009. Characteristics of Urban Landscape Structure. *Chengshi Jianshe yu Shangye Wangdian* (18): 173–174.
- Manuel Baud-Bovy & Fred Lawson. 2004. *Tourism & Recreation Handbook of Planning and Design*. Beijing: China Building Industry Press.
- Qi Tong et al. 2010. Summary of domestic and foreign research on country park. *Urban Problems* (12): 28–33.

# The analysis of urban underground space based on environmental comfort

YanPing Gong

College of Civil and Architecture Engineering, Shandong University of Science and Technology, Qingdao, Shandong, China

**ABSTRACT:** The 21st century has witnessed the constant development of urban underground space. In this paper, combined with the current situation and problems of urban underground space, on the basis of underground works, we discuss the method of environmental design and planning of urban underground space from the points of environmental comfort and artistic views. We discuss the better way to create a comfortable urban underground space environment to improve the level of people's satisfaction in urban underground space.

**Keywords:** environmental comfort; urban underground space; environmental planning; artistic quality; overall planning

## 1 THE STATUS OF URBAN UNDERGROUND SPACE DEVELOPMENT

### 1.1 *The embryonic stage*

Began in the 1960s, China started to construct urban underground projects in large-scale and most of the projects were civil air defense projects. After decades of effort, it has achieved remarkable results in guaranteeing national defense security and become an important part of urban underground space. However, since its function is relatively simple, the civil air defense construction can only be regarded as the initial stage of urban underground space utilization.

### 1.2 *The rapid development stage*

Since the mid of 1980s, with urban redevelopment, the number of underground space projects has continued growing and the type has become increasingly rich. It has built a number of projects, like Shanghai People's Square underground mall, Beijing Xidan underground mall and so on. Meanwhile, underground transportation facilities have also been well developed in many Chinese cities, such as Guangzhou and Tianjin. Qingdao, Harbin, Chongqing. Other cities are also actively being constructed their own underground transportation system.

### 1.3 *Future development stage*

From the air defense projects to underground commercial street, people have accumulated a wealth

of experience on the utilization of urban underground space. With the further development and utilization of urban underground space, people's functional requirements are gradually transformed into the pursuit of "people-oriented" environmental comfort. To achieve the comfortable relationship between people and the environment has become the new trend of underground space development. "Comfort" is the assumption that people will strive to achieve and ultimately reach the "most comfortable environment". Based on the relationship of people's needs, behavior, and environment, people should design underground space from the point of environmental comfort, to realize the coordinated development between urban underground space and over-ground space, to gradually construct three-dimensional integrated future urban space in the future.

## 2 THE PROBLEMS OF URBAN UNDERGROUND SPACE DEVELOPMENT

Throughout the current development of urban underground space in recent years, the main problems are in the following aspects.

### 2.1 *The lacks of coordination and integration on city's 3D space*

Three-dimensional space of the city means the city's upper ground, ground, and underground space. At present, China's comprehensive and multi-functional

urban underground space design is still on embryonic stage. It lacks the coordination between the underground and ground projects. It also lacks the combination of various subsystems and overall planning of the future development. The lacks of 3D space integration effectiveness directly lead to a predicament: the underground space is relatively in a large number, but still can not effectively solve the traffic problems of the city and the city center's ground contradiction is still not eased.

## 2.2 *The lack of advance planning*

Whether it is from the perspective of engineering technology, or from the point of urban space reasonable hierarchical planning and sustainable development, urban underground space hierarchical planning and construction should have been given priority in spatial planning and construction. Because China's underground space development started late, most of urban underground space construction lags behind the over-ground projects. It not only results the waste of underground space resources, but also causes increased construction costs.

In some areas, large-scale underground space development causes a shortage of underground space resources. Municipal pipeline, subways, underpasses and other different facilities emerge contradictions in the underground space occupation. Constructors often meet such situation: When they plan to bury pipelines; they find there are already a completed underground works, so that the pipelines have to change their routes. Some areas even spend a lot of energy to move the completed shallow underground pipelines to utilize deeper space.

## 2.3 *Poor environment and low comfort of underground space*

With the development and utilization of underground space, many shortages of underground space environment have been concerned. Insufficient natural light, inadequate ventilation, humidity, and other physical characteristics are not conducive to people health. At the same time, the poor artistic environment and unclear signpost also cause psychological damage to people. For instance, people will feel anxious, nervous, fear in underground space. From this perspective, underground space environment cannot meet peoples' basic needs and is not suitable for long-term residence.

### 2.3.1 *Factors influencing physical health*

#### 1. Insufficient natural light

Since the underground space is relatively a closed environment, it deeply relies on artificial

lighting. Compared to natural light, artificial light does not have bactericidal function and cannot prevent diseases and other bad effects from human body.

#### 2. Inadequate ventilation

Windowless underground structure is often difficult to achieve natural ventilation resulting in lack of fresh air. It causes people in the underground environment feel shortness of breath.

#### 3. High humidity

In the underground space, when moist air contact with cold wall, it will be cooled and turned into water droplets gathering on the wall. This will lead to high humidity in underground environments, which will cause mold growth and rheumatic diseases.

### 2.3.2 *Factors influencing psychological health*

#### 1. Unclear sign system

Lack of clear indicating information, which fails to provide proper guidance to pedestrian, makes them easy to get lost in underground. Terminology and specifications are not standardized and unified. On some signposts, text, language and symbols do not use national norms, standard and international customary symbols, which are not conducive to people to understand. Labeled small amount of information, some signs only mention in some of the main streets and buildings, but there are still some important places that are not being mentioned. Perhaps, those unmentioned places are the real destinations of pedestrians.

Psychologist has proved that acknowledging and obtaining the environmental information is one of the basic biological needs of human. If you lose this precondition, people will not be able to establish contact with the surrounding environment. To identify their location in the environment is also an indispensable basic condition. A person who has no idea about his location in a chaotic space always tends to feel nervous and produce a sense of emotional instability. Unclear signposts make people easily lose sense of direction in underground space. Thereby it causes nervousness, anxiety, and fear.

#### 2. Low overall culture of art

At present, in China, overall artistic design for underground space is still in its infancy. Underground space usually designed by a single color. Single color in the underground space, where space lacks of natural light, makes people feel tedious. It may cause depression and other psychological disorders over time. Similar underground space artistic design in different place, which lacks of geographical and cultural characteristics, can not improve the city's image.

### 3 URBAN UNDERGROUND SPACE ENVIRONMENTAL PLANNING BASED ON THE ENVIRONMENTAL COMFORT

Through the expansion, urban underground space utilization meets the city's need for space that is essential to city's continued development. Ultimately, it should achieve the goal of "harmonious cities". Development and utilization of urban underground space involve several aspects, and environmental space design is one of the most important parts. Compared with over-ground space, underground space environment has significant differences mainly in the closed space, the lack of natural light, the poor air circulation etc. These will have certain influence on human physiology and psychology. So, for a long time, a social consensus has formed that underground environment is inferior to over-ground environment. Therefore, people's reaction towards underground environment, to some extent, determines the outcome of underground space utilization.

According to the characteristics of underground space and function principles of environmental adaptability, combined with the experience and technology of underground space environment development at home and abroad, the future urban underground space development should include the ventilation system of underground space, moisture-proof system, lighting system, and sign system.

#### 3.1 Ventilation systems of underground space

Ventilation design of urban underground space can be divided into two basic types: decentralized and centralized. Decentralized ventilation system mainly takes small independent ventilation skylights, patio and basement high side windows. Centralized ventilation system usually takes underground central courtyard, atrium, wind tunnel and other methods. Due to the large contact area between underground construction and soil, construction has strong energy storage and high thermal inertia. So, the temperature change is far less severe than over-ground buildings. According to the particularity of underground space, the local regional climate, geographical conditions, considering the use of features such as personnel-intensive, air permeability and equipment fever, we should make full use of ventilation shafts, high side windows, courtyards and light pipes underground, wind tunnel and other methods. Then the design of underground space ventilation system can better meet the ventilation requirements to create a comfortable and energy-efficient space.

#### 3.2 Underground space dehumidification system

Two factors led to the increased humidity in underground space: (1) Leakage: water enters inside through structural layer of underground space and by evaporation into the air, causing increased humidity; (2) Improper Ventilation: people use ventilation in rainy season, the high humidity outside leads air into the underground space, resulting in increased humidity.

To reduce the underground space air humidity, we must prevent two factors mentioned above and design specifically underground space dehumidification system: (1) Build seamless waterproof system: to prevent leak water into the underground space; (2) The reasonable control of ventilation: ventilate in the dry season with low temperatures to purge the humid air out of the underground space; (3) The use of mechanical or chemical dehumidification process: strengthen the underground space dehumidification to further reduce the water vapor in the air content.

#### 3.3 Underground space lighting system

A striking feature of most of today's underground space is the interior space with no natural light and no direct access to outside sight. Humans have depended on natural light to survive for generations. This feature of underground space could make people feel a big difference, psychologically and physiologically, between over-ground and underground. It may even cause adverse physiological consequences due to lack of sunlight. In underground construction, the use of traditional artificial illumination will consume a lot of power. The use of natural lighting can not only meet the requirements of saving energy, but also meets the people's psychological requirements for natural sunlight, sense of direction, sense of diurnal variation, seasonal climate and other perception. The research on directing sunlight into underground construction and forming diffuse natural light, which increases space openness, greatly reduces the negative effects of closed underground space. Therefore, the advanced design of underground space lighting system not only meets the physical needs of people, but also improves the underground construction environment in many ways.

#### 3.4 Underground space sign system

With the increasing size of urban underground space, underground space network becomes increasingly complex. So setting the underground space sign system is especially important. Sign system should be regarded as an important part of the underground space environmental design to design and layout. By accurate and effective sign system,



people, even in a strange underground public environment, can also rely on a sound signpost to their destination.

At present, compared with Japan, Canada and other countries' sound underground space sign system; China's underground system has some shortcomings, such as unclear direction, no-standard sign, less information on sign as well as uneasily recognizable sign. According to these existing problems, when we design underground space sign system: (1) Signs should maintain continuity; (2) Setting proper transition sign between underground and ground; (3) Signs should keep visibility under emergency condition; (4) Setting the map at appropriate place makes pedestrians have a macroscopic realization of underground environment.

#### 4 OVERALL ARTISTIC PLANNING OF UNDERGROUND SPACE ENVIRONMENT

Urban Underground Space Design should meet people's psychological needs, paying attention to environment art design, improving underground physical environment to attract people to use. It should create a good cultural atmosphere to eliminate closed underground space and cold environment, so that users could get spiritual enjoyment.

Combined with the environment art design principles of creating comfort, producing spaciousness, strengthening a sense of direction, and using the knowledge of human factors engineering, we re-create the underground space from color, lighting, decorative graphics, materials and other parts to build a comfortable aesthetically pleasing interior. When we carry out underground space overall artistic planning, we should uphold the people-centered concept in human factors engineering and fully consider the impact of color on mental and physical. Scientific color adjustment and lighting design, let's people work effectively in the comfortable underground space environment.

#### 5 CONCLUSIONS

With the constant urbanization process in China, we are confronted with the acute shortage of land. So, the development and utilization of urban underground space will get more and more attention. With the expansion of the underground space, the number of people living and working in the underground space is also growing rapidly. People requirements for underground environment on environment quality and comfort become increasingly high. Underground space environment

design and planning has become an important point of future underground space development. In modern underground space design, we should combine the traditional design studies with human factors engineering and other emerging cross-disciplinary to promote users experience and comfort. Furthermore, by the design of underground space based on environmental comfort, it can reverse people stereotype about underground space and improve people's production efficiency in underground space.

From the perspective of environmental comfort and artistic design, we research urban underground space in this article. Through analysis of its current situation of the underground space environment, we discuss the method to create a comfortable and attractive urban public space underground, mainly from the physiological factors, like ventilation, moisture, light; and from psychological factors, like sign system and overall artistic planning. In physiological factors, we should take appropriate measures, such as using natural light, improving natural ventilation, promoting dehumidification system, to make underground space as comfortable as over-ground with similar living conditions. To psychological factors, by improving underground sign system, it will enhance the user's sense of security and a sense of direction; By the use of color, lighting, decorative graphics, and other artistic elements, it creates a clever and vivid visual sense, which can ease human adverse feelings in underground space.

Interaction between environmental factors of urban underground space is an organic whole, so that we should consider rational allocation of these factors. Through above new design ideas, from the physical and psychological perspectives, meet the human needs of the urban underground public space, to achieve the comfortable and arts standard, so as to achieve modern urban underground space development goals.

#### REFERENCES

- [1] Wang, B.Y. 2000. Analysis on Factors Affecting Urban Underground Space Environment. *Journal of Tongji University* 06: 656-660.
- [2] Wu, Z.H. 2011. Combination of Natural Ventilation and Lighting in the Northern City Underground Space Ecological Design. *Huazhong Architecture* 10: 67-70.
- [3] Wang, P. 2013. Research and Practice on Urban Underground Space Development and Utilization. China University of Geosciences.
- [4] Chen, H.X. 2012. Planning of Urban Underground Space Development. Shandong University.
- [5] Li, C. 2007. Research on Urban Underground Space Development Stratified Model. Tongji University.

# Post occupancy evaluation of urban public space environment: Take Yingze Park in Taiyuan as an example

X.R. Zhao & Q.F. Shi

*Architecture and Civil Engineering Institute, Taiyuan University of Technology, Taiyuan, Shanxi, China*

**ABSTRACT:** Taking the Yingze Park of Taiyuan as the object of study, the scientific observation and interview is used to plan the layout. Building monomer, facilities, function, and behavior levels are indicative of post occupancy evaluation environment for their research. On the basis of the combination of domestic and foreign outstanding cases, reasonable suggestions for improvement are put forward.

**Keywords:** environmental assessment after use; Yingze Park; index study

## 1 THE RELATIONSHIP BETWEEN ENVIRONMENTAL ASSESSMENT AND POST-EVALUATION

Building Environmental Evaluation is the value of the study built environment, namely, the relationship between the built environment and the subject need. In the development and practice of the discipline of architecture and the built environment evaluation, and it can promote to realize the value of building environment, to reflect the scientific theory of building design and management feedback, making theory to guide practice. The research into the environmental assessment is to make people correct their own behavior, and realize the environmental value of the greater sense. Post-Environmental Evaluation widely spreads. Mainly it includes two aspects, Pre-Design Evaluation and Post-Occupancy Evaluation.

Post-Occupancy Evaluation is the core content of building environmental evaluation. It emphasizes the comprehensive technology research in the building environment. Preiser (1988) in his book “post use evaluation,” the definition of POE is: “after the construction and use of a period of time, the construction of the strict evaluation process.”<sup>1</sup> Focusing on the architectural needs of the user, the success of the architectural design and the performance of the building after the completion of the building POE. All of this will provide the basis and foundation for future architectural design”. The POE intends the purpose of architectural design and the actual use for the construction of the actual benefits and performance standards which are compared, give feedback and for the future improvement of architectural designs that provides reliable basis.

American scholar Jan Jacob believes that the most dynamic place in the city is the city’s public activity space. Public space refers to by the city building, building materials, plant perpendicular to the interface and the road, water and sector level, using combination of elements of urban space. It is the important place for the exchange of material, energy and information between human and nature. It is also the important manifestation of the city image, and it is the “sitting room” and “window” of the city.

## 2 BACKGROUND AND PURPOSE OF THE RESEARCH

City Park is the recreation place for urban residents, and is the urban green infrastructure, but also the main public open space. More caring about users, understanding their needs and interests is the successful design of the park. Which is advocated “people-oriented” ideology today.

The main body of the evaluation of the building environment is the following five factors: users, developers, designers, government, business managers. The main body of the evaluation should be considered in the choice of the city public space after the use of the evaluation of its own characteristics. First, the use of the post-evaluation means that the user is the center of the evaluation of the subject. Second, the characteristics of public space in the city are still the main body of the evaluation. To some extent, the concept of the public is equivalent with the user. But on the other hand, users of the evaluation tend to have tacit, clear and stable, more subjective shortcomings, so this topic choice another evaluation subject, from the point of view

of a more professional designers. In the evaluation of the entire process, such as the construction of the evaluation factor set, beauty of form factors of the evaluation, for measuring, sorting environment physical properties and the user's behavior can give professional advice. Most of the results of the evaluation of data can make more accurate and comprehensive evaluation of the space environment. It also can lay the foundation for the evaluation from the user's angle. Anyway, according to the evaluation goal, the evaluation content, the integrity of the people and the environment of the system from the point of view, we all need to subject and object view of combination of evaluation main body wherein the user is still the core subject.

There are different classification methods for urban public space. The square is characterized by multi-function and comprehensive, which constitutes the public activity center of the public. The park is a pleasant place to enjoy, and relatively square, there is a certain circumference of nature. The street is a pedestrian system, which is closely related to urban public space. Such as the mall, commercial pedestrian street etc. Waterfront space is an important marginal in city, which plays an important role in the connection of city public space, and it is usually the main green space of city.

### 3 CASE INTRODUCTION

Total garden area is 63 hectares. The Yingze Lake area is 20 hectares, lake and Nanhu separated by Qikongqiao. Landscape park to plant landscaping, 39 million lines of the existing landscape plants, 130 varieties, 24 hectares of lawns, built square, decorated archway, the rockery, the peony garden, rose garden and so on. The core of the building is the park celebration, the floor assembly, a variety of cultural activities center.

### 4 OBSERVATION AND INTERVIEW ANALYSIS RESULTS

#### 4.1 *Research on landscape planning and analysis*

Built in the Park rockery in the northwest of the rolling hills, the aim is to reduce the impact of local climate on plant and ecological environment, and to stop the strong wind from northwest during winter. Water park layout is single, only the North Lake, South Lake and lake. Lake should be number one or two human activities and natural ecological integrated design, the park waters system interconnected add radiance and beauty to each other. This will be closer to nature and weaken the interference of artificial factors. The layout of the combination

should be used to increase the river course and flow through a good ecological resource chain. There are no independent green spaces for visitors and sun bathing, just some small forest. It sets a real public open space to visitors. Holiday night is the perfect place to launch a movie. Park within the majority of the elderly and no sports should be added, such as basketball courts, small football field, tennis courts, etc. To attract more young people to increase the vitality, the mini basketball and football field construction reference park along the Fen River Fen river. The lack of open theater or amphitheater Park, research noticed beside the park building at the heart of the Tripitaka floor has many of the elderly in next to rehearse the songs, the apparent lack of suitable for mass of public entertainment buildings. On the south side of the north gate of the musical fountain layout is reasonable, but designers will the north is between the north and the musical fountain increases the rockery, seriously blocked from the north gate to watch the musical fountain sight. (Figs. 1 and 2).



Figure 1. Yingze lake.



Figure 2. Public green space.

## 4.2 *Building environment analysis*

The harmonious charm and the landscape of the public space itself can bring people a wonderful visual to enjoy. Public space makes person produce upward, happy, yearning mood, physical and mental pleasure to achieve the purpose of relaxing, and to realize the beauty of artistic conception creation. An attractive public space belongs to own the special atmosphere, solemn, serene, dynamic and lively. In short, according to their own characteristics, it seems to create a bright spot to attract people.

North Gate imitation can not deeply reflect Taiyuan profound cultural heritage. Because it is not the history of the remains, just a taste of the construction of antique buildings is not the essence of its urban culture. Personally, the design fails, and the construction fee is expensive and can not get the effect. The core building of the park is the relocation of the Taigu County, and there are 800 years of history, which is a non local architecture can not reflect the historical and cultural heritage of Taiyuan. The park of the antique building is similar to more, the Summer Palace garden. However, the Summer Palace is the imperial garden built during the Qing Dynasty, and it is the legacy of the world heritage.

Park design techniques should not be confined to the use of Chinese classical garden gardening practices, combining Chinese and Western design can reflect the inclusive flowing. Artificial factors within the park lose its natural beauty, such as the construction of the large number of antique buildings which doesn't make any sense, and it should be more than the construction of a number of life elements. At the edge of the lake, with artificial stone and marble railing, the structures of human and nature of isolation shall dismantle these structures, and it will narrow the distance between man and nature. Some of the platform design, based on the platform of some arbor below placed some of the tables and chairs; some of the park scattered selling snacks trolley flooding seriously damaging the natural landscape. We should stop and design some small buildings, and checkered shaft uniform network layout, increase convenience; grassland and roads separated by a fence will let man and nature produced the distance. In a word, we should respect all life forms with the basic features, not easily change them, the artificial factors to blend natural factors.

Scale is one of the major elements of the design, the width of public space (D) and the height of adjacent building (H) ratio (D/H) of human psychology and the vitality of the space, which has a great impact. Japanese scholars Yoshinobu ashihara said "when  $D/H > 1$ , with the increase of the

ratio will be formed gradually away from the sense; more than 2 are produced when the broad sense; when  $D/H < 1$ , with the ratio of reduced generated close to the feeling; when the  $D/H = 1$ , height and width between existence with a balanced sense." If the adjacent building height 2 times more than the width of the square, it will produce the empty feeling, a sense of separation, no polymerization; on the contrary, if the width of the square building is less than the height, between buildings interfere too strong and too close, which makes people have a sense of depression.

Therefore, different scales and proportion of space has different atmosphere and vitality, in the design we should adjust measures to local conditions, create a pleasant interesting city public environment space. Urban public space within the facility image compared to "furniture city", and how to make "furniture city" rational and humanized. It will give a person with the cold feeling of material; and people will have the features of local pool depth should not be too deep, lest children stay at the edge of the water, playing accidents.

Entertainment facilities are dilapidated, so it needs to update, a torrent of children's recreational facilities such as a roller coaster. The lack of food and Rest Area, and we should build the lake construction of dining and leisure development and a platform of waterscape construction, such as the introduction of food street restaurants, coffee hall introduction part bars, and other leisure and entertainment. To increase the vitality and popularity of Yingze park, we shall set up a number of irregular and can reflect the nature of the material paving in the park; playground and park should be separated, because of the large Happy Valley old amusement park will be built after the playground should be replaced, so the new children's learning and entertainment facilities, some of the characteristics of the park; small Ferris wheel is not to enhance the landscape effect. We should build a large skyscraper wheel to increase the charm of the city. Such as the eyes of the domestic Tianjin etc. Will park tour bus replacement for European style carriage can be some of the highlights of the artificial factors weakened, better integrated into the natural. Park Lake local can add some landscape corridor rich vertical design. At the edge of the lake, it could be some interesting design plant pieces.

## 5 DEADLINE

The real value of the park is primarily reflected in the pleasure of providing the public with the harmonious coexistence of nature. Then, it is the

important part of the city to increase the vigor of the city, such as the Central Park in New York, Paris La Villette Park. In addition to provide leisure and recreation for the public, these two parks also become a place of exchange visitors everywhere. Tourists come here to rest, enjoy the city characteristics, to talk with local residents, to understand the different customs. They are attractive, parks, and it's still a place for a city in the living room, a city resident in order to display its own features and entertain the guests. So now the Yingze park is not likely to become a landmark and an impor-

tant part of Taiyuan, and it is impossible to make foreign tourists, if the park's planning and architecture can not reflect the Taiyuan historical and cultural heritage as a more vibrant park.

#### REFERENCE

- [1] Wolfgang, F.E. Preiser (University of New Mexico), Harvey. Z. Rabinowitz (University of Wisconsin—Milwaukee), Edward. T. White (Florida A&M University). Post occupancy Evaluation. New York: Van Nostrand Reinhold Company, 1988.

# Influence of the Chinese traditional Feng-shui theory on the layout of contemporary residential space

B. Wang & T. Li

*College of Architecture and Civil Engineering, Taiyuan University of Technology, Taiyuan, Shanxi, China*

**ABSTRACT:** The Oriental attaches importance to feng-shui, feng-shui is the Chinese people's pursuit of an important yardstick of the ideal living environment. But the object of feng-shui research is how people can get along with the environment better, and the core idea and the contemporary design idea have many consistent place. We should study the essence of feng-shui theory, and apply it to the modern design, establish the harmonious coexistence between man and nature of the ecological environment, build and integrate the system of interior design concept.

**Keywords:** chinese traditional culture; feng-shui theory; interior space design

## 1 INTRODUCTION

Feng-shui is an important part of Chinese traditional culture, and it is also a unique cultural manifestation of Chinese millennium culture heritage. The concept of "Feng-shui" first appeared in Guo Pu's "Zang jing" of the Jin Dynasty: "The Tibetan people gathered together to produce" "qi, and the ancients used it to make it effective, so is called feng-shui." The ancient Chinese Feng-shui theory is based on the Chinese traditional philosophy, which has the unique Chinese traditional culture mark. The pursuit of "harmony" realm of thought in western modern space environment of train of thought is such that it coincides with the embodiment.

## 2 THE THOUGHT OF FENG-SHUI IN THE CONTEMPORARY HOUSING SPACE PATTERN

With the rapid development of residential buildings, and the influence of social benefits, the residential buildings may have all kinds of improper places in the design. People tend to be in fixed location based residential choice, and then the choice of residential living space may exist in all kinds of unreasonable places, which requires designers to space transformation to meet the housing needs of the people.

### 2.1 *Physiological and psychological aspects*

In the feng-shui theory, the essence parts are "Jing" "Qi" and "Shen". Qi is a very important concept in

Chinese traditional culture, and it is also the core of Feng-shui theory. As the "Qi" is divided into auspicious and inauspicious. If it can gather "Ji Qi" it is good. While the scattered "Ji Qi" is fierce. When we live in houses, ventilation can product "Ji Qi", but the air circulation can not. It is easy to lead to physical weakness, then it is not belong to the "auspicious gas, and it need to spread out", is commonly known as the "Drafty", the people also do not have good effect. The theory is actually related to the physiological characteristics, discusses how to better to ensure people's health. And feng-shui also discusses some Interior design. Feng-shui is through the "Qi" and "form" of the dialectical relationship between the use of, feng-shui is the essence of the Chinese people for thousands of years are summarized and the survival experience, are based on Chinese people physiological and psychological needs and summed up the rule of thumb.

### 2.2 *The inheritance of context*

As a part of Chinese traditional culture, feng-shui has been deeply rooted in the hearts of every Chinese people, and it is the ancient Chinese context. This is similar to the historical development of the West. Roots of western culture in ancient Egypt, the construction of the pyramid can be seen, the pyramid construction group construction is to ensure that the dead Pharaoh can continue to enjoy the superior environment and rebirth. In fact, this is the ancient Egyptian "Fengshui". The essence and inheritance of Chinese Fengshui is similar. Regardless of the theory of the East and the West are by the ancient life experience accumulated and

inherited the rule of thumb, but Chinese feng-shui theory, theory have its own unique theoretical system, and few people use western scientific methods to test and analyze. “feng-shui theory,” is often cast a mysterious color, mistaken for the superstitious said, in fact, many parts of the feng-shui theory, are based on Chinese ancient and unique cultural heritage of a sense of identity, which is one kind of each country’s unique cultural heritage, and not simply to science two words to explain.

### 3 THE APPLICATION OF FENG-SHUI THEORY IN THE PATTERN OF RESIDENTIAL SPACE

In the traditional architectural composition of China, a large number of balanced symmetry is applied, and the plane and facade of the axis are emphasized. feng-shui believes that the founder of the building plane, the symmetrical symmetry of the trapezoid, the complete lack of environmental patterns are auspicious manifestations. Such as housing of too high to low, building shape of clutter, the door two door width different will is considered unlucky.

Residential space is a whole space, which due to the different functions and separated into different space, every space through different furniture display, decorative furnishings and camp to create a different atmosphere of space and function space. When the Fengshui theory is applied to the study of residential, in fact, is according to feng-shui “Jing, Qi, Shen” concepts to improve residential place that does not accord with people’s living habits and psychological, making it more in line with the requirements of the people living. While the living rooms are closely related with the behavior of the people, bedroom, kitchen, bathroom and other parts, the following is a feng-shui point of view to analysis. (Figs. 1 and 2)

#### 3.1 Living room

In Feng-shui theory, living room as a space point eye “is a key to residential” with the wind to get together “Qi”, we must see the sun, and if hall bright room is dark, parlor, families get together and the main space of living room, the sunshine will give people a psychological comfort.

Doors and windows of the hedge in feng-shui is taboo, by the gate of wealth not through the loop is through the window out, is not conducive to the fortunes of the aggregation. Feng-shui will have this kind of view, because windows and doors hedge causes air to flow without blocking, easily to cause “Drafty”. This is not good for health; therefore need to set up between the living room and the



Figure 1. The case of a feng-shui unfavourable.



Figure 2. The case of a feng-shui unfavourable.

door entrance to change a gas flow path. Second, to meet the privacy requirements to prevent the living room “Porch” is in the traditional local style dwelling houses in “Zhaobi” evolution. It discusses the traditional geom-antic omen contains simple life experience and in real life used, indicating that traditional geom-antic omen in some elaboration is the scientific truth, just need us to use modern ideas to interpret it.

Sofa is the important furniture of the living room, so it has a very important position. The best sofa places against the wall, and feng-shui is known as the “patron”. It will make people have the feeling of stability in psychology. Sofa and tea table is usually a combination, and it should also be unified

and harmonious. In the theory, low for the water, the higher the sofa for the mountain. The tea table is shorter for the water, there are mountains and water to produce a good feng-shui effect and this belongs to the context of the heritage of feng-shui.

### 3.2 *Bedroom*

Bedroom is a very important area of residential space, people have 1/3 of the time in sleep, so the bedroom feng-shui is closely related to the physical health of people.

Master bedroom should be located in the “possession of the wind to get together gas range, in the South or East, and it is the most ideal because of the South and east of the sun can be sufficient irradiation range, people have the sun would” Jing, Qi, Shen, and as a place to rest and sleep, must be placed on a sunny range. While the bedrooms area should not be too large, is not satisfied that the “Qi”, and from the psychological point of view, the bedroom is too crowded to open, it gives a person a kind of insecurity. Yangxin Hall of the Imperial Palace in Beijing is the emperor’s bedroom area only about ten square meters, which also shows the ancient architectural design and feng-shui theory is closely related to, until now still with our lives is closely related to. And feng-shui study said the bedroom door is unfavorable be opposite the bathroom or kitchen door is on the physiological aspects, the fumes from the kitchen and bathroom filthy gas will flow into the bedroom and detrimental to human health.

Placing bed, feng-shui school also has a lot of exposition, “bed to avoid pressure beam” “bed back door” and “straight to avoid door” “bed bogey there after the gap” are the ancients summary of experience living and modern also prove a lot of content and western psychology is consistent. Therefore, when we go to decorate the bedroom space, we can learn from the theory of feng-shui to avoid some inappropriate places.

### 3.3 *Kitchen*

Traditional geom-antic omen that the kitchen is housing the main, like one of the five internal organs of the body organs, it is the key to a healthy family, saying it is “people with food,” said and the location of the kitchen should according to the Yin Yang and the five elements theory to arrange. And Yin Yang and the five elements theory is geom-antic learn important part tradition for thousands of years, rooted in the hearts of the Chinese people, so in the kitchen space arrangement, consider feng-shui theory requirements and taboo, which is the cultural heritage of the embodiment.

From the viewpoint of feng-shui theory, the kitchen is unfavorable to the south, the south is fire, kitchen also belongs to fire is disadvantageous to the home, in the modern scientific point of view. South is not conducive to food preservation. At the same time, the kitchen door is not right is the door to see the stove, it means omen. The kitchen is also not the toilet, bacteria and filth can damage health.

Kitchen stove and water is too close to avoid the two water clip a fire, such as stove caught between the dishes and washing machine, two water grams of a fire, the family will health and harmful. At the same time, the kitchen is very sacred, the kitchen god, this washing dirty clothes, will affect the luck. These claims in the science of place, if the stove and sink and so too close, water easily splashed on the stove, causing rust, dirty water if splashed into the pot, health effects.

### 3.4 *Bathroom*

In feng-shui theory, bathroom is called the “run-off” and “water” is residential to drainage, in relation to a family’s wealth and health. Bathrooms should not be opened in residential center, heart center is like room, and central pollution is not only unsightly and stench easily convection to the other room and health adverse. And the central is soil, toilet placed in the central will occur the soil grams of water, these feng-shui in the taboo are in line with our contemporary scientific truth.

Residential space not only includes the above four parts, but feng-shui theory is broad and profound, and it is not only the part of the point of view, but from the above analysis of the feng-shui in the residential space of several large. The overall core can be attributed to the “Jing, Qi, Shen” connotation, whether from the point of view of human physiological habit the “Qi” of the paper, or from the psychological habit of “Jing, Shen” is discussed, and some inherent in our traditional cultural heritage in cognitive habits, which constitutes a complete residential feng-shui theory. Therefore, there are many traditional geom-antic and modern science with content, only limited to the level of the expression of the ancients, so it will appear to discuss the too profound to be understood, with a sense of mystery, and we need the scientific theory of composition of traditional residential feng-shui inherit and applied into the scientific design method.

## 4 SUMMARY

The essence of Feng-shui theory is the environmental assessment system of ancient China. Although its interpretation system and operating system with ambiguity, coupled with the interpretation of



ancient occult things on the inside, it will give the human one kind of mystical and mysterious feeling, which will lead to being misunderstood as superstition. But the pursuit of “harmony”, the “Jing, Qi, Shen” as the core of the theory of discourse, passing the overall concept and natural humanism thought, it is modern residential environment evaluation system can reference and inspired.

The inheritance of feng-shui has its own rationality and scientific nature, and it inevitably mixed with many superstitious elements during the course of inheritance. This mainly reflects in three aspects: one is the feng-shui of ancient architectural environment of site selection and design experience summary is has certain practical and scientific; second is the ritual of the art of geomancy, assimilated by Confucian metaphysics; three is to theology based superstition thought origins. Feng-shui is

not superstition. On the contrary, “Residential of Feng-shui” is suitable for building practical component, and the essence is a summary of ancient building experience. We should learn to inherit and develop it.

## REFERENCES

- Wang Jinping: Shanxi province Xiaoyi jiajiazhuang conservation planning of historical and cultural blocks, *Taiyuan: Taiyuan University of Technology*, 2013.
- Yu Xuecai. The historical experience of ancient Chinese heritage protection, *the International Symposium on urban tourism in China*, 2006-10-24.
- Yu Xuecai: The traditional research on the protection of architectural heritage in China, *the Department of tourism science, Southeast University*, 2007.

# Research on strategy of ecological security assessment in Beijing urban space

X.Y. Ma, L. Feng & W.L. Zhang

*School of Landscape Architecture, Beijing University of Agriculture, Beijing, China*  
*Beijing Rural Landscape Planning and Design Engineering Technology Center, Beijing, China*  
*Beijing Laboratory of Urban and Rural Ecological Environment, Beijing, China*

**ABSTRACT:** Urban green space provides resources for human and maintains ecological diversity, which plays a major role within the ecological security system. Thus, the ecological security of urban green land is the crucial barrier and foundation of the regional ecological security. Scientific and objective assessment of urban green land ecological security could provide a reference for the establishment, maintenance, management of a guaranteed ecological security system, as well as related laws and regulations. This article in the first place systematically summarized the scope and progress of existing research on ecological security assessment of urban green space. At last it discussed the developmental opportunities of the ecological security of urban green space in Beijing particularly, and put forward its assessment strategy.

**Keywords:** urban green space; ecological security assessment; ecological security of Beijing urban green space

## 1 INTRODUCTION

Ecological security refers to the environment security status which is able to sustain the development of society, economy and nature, as well as safeguarding the social ecological safety, economic safety and natural environment safety. At the beginning of 2000, China announced in its “national ecological environment protection program”, the first clear target of national ecological environmental security. It presents the overall ecology protection strategy called “protection first, prevention first, protection and prevention combined”, which opened the prologue of ecological security research in China. While urban green area able to provide resources for human meanwhile maintains ecological diversity, which acts as the main component within the construction of the entire ecological security, and the important guarantee of regional ecological security.

## 2 RESEARCH SCOPE OF ECOLOGICAL SECURITY OF URBAN GREEN SPACE

Ecological security assessment refers to a series of methods and specifications, which are about: 1. Analyzing, predicting and assessing the regional ecological security values of waters, atmosphere, forest, mineral, animal and plant species; 2. Putting forward the countermeasures and measures to prevent or reduce the ecological risks; 3. Tracing and monitoring the ecological risks. While the research scope of ecological security assessment on urban green land is relatively wider, which mainly researching on urban green land resources as the core of all kinds of green space. Within this research scope, at present scholars at home and abroad has done a lot of research work on “other green space” among the urban green space types (emphasizing on key scenic areas and nature reserves, forest park, wetland, etc.) The study found that with the exception of some well-preserved local area enjoying high-quality natural ecological environment (room use, etc., 2007; Zhang Pin etc., 2013), the overall situation of China’s urban green land ecological security is below average.

According to Urban Green Space Classification Standard, urban green space is divided into five categories, in which the fifth class type of “other green space” refers to the urban ecological environment

---

Sponsored by:

1. Beijing Commission of Education Technical Innovation Platform Project (PXM2015\_014207\_000010).
2. Beijing Laboratory of Urban and Rural Ecological Environment Project (PXM2015\_014207\_000014).

quality, the residents' leisure life, the urban landscape and biodiversity conservation has a direct effect of green space. It includes scenic area, water conservation, country parks, nature reserves, forest park, scenic forest land, urban greening belt, parks, wetlands, green space reclaimed from landfill etc. They mostly have large area and intense influence on the ecological environment of the city. At present, research on urban green land ecological security assessment mainly concentrated in the scenic areas and nature reserves, forest park, wetlands and other green space types.

### 2.1 *Research on ecological security assessment of scenic spot and nature reserves*

Ecological security assessment of scenic spot and nature reserves is an important part of the assessment of overall urban green space. Researches show that, one of world cultural and natural heritage, the Wuyi Mountain has ecological footprint which is 1.503 hm<sup>2</sup>/person, ecological carrying capacity of 4.1476 hm<sup>2</sup>/person, ecological occupying rate being 0.3015, ecological occupying rate of grassland being 11.535 and that of water area being 5.386. These data indicate that Mount Wuyi is in a relatively safe condition as a whole, while its grassland and water area are still in unsecured situation (Tan Dehua etc, 2009). Moreover, from 1986–2009 the ecological security degree of Mount Wuyi Scenery District showed an increasing trend (You Weibin etc, 2011). In year 2004, the tourism ecological footprint per capita of Jiuzhaigou was 0.105190274 hm<sup>2</sup>, with local resident's humanism ecological footprint being 0.994925 hm<sup>2</sup>.

That the coefficient of ecological security was between 1.093158–1.159388, a safe stage for sustainable development. However, there were some main factors influencing the jiuzhaigou ecological security, such as increasing tourist amount and tourism market radius, along with the change of residents' consumption patterns and residents' strong dependence on the natural environment resources (Zhang Jinhe, 2008). When it comes to Mount Qilian Nature Reserve, its ecological security index is 0.5146, which is a very "unsafe" condition (Tang Feifei, 2013).

### 2.2 *Research on ecological security assessment of forest parks*

Research on ecological security assessment of forest parks indicates that the ecological security index of Beijing Jiufeng National Forest Park in 2007 was 0.8421, a relatively high standard (Mi Feng etc., 2010). Wang Chaohui (2012) systematically studied the ecological security assessment of mountain-type forest parks through scoping into 7 mountain-type

forest parks in Wenzhou, among which are 5 national forest parks and 2 provincial ones. His research found that the ecological security condition of these parks was misogynistic, that except the flower rock national forest park being "safe" condition, the other parks suffered various safety risks. Security indexes of humanistic environment of most parks are in unsafe levels. Similar unsafe stage is the indexes environmental pressures such as: water supply and demand balance; prevention and control of forest diseases and insect pests; and the prevention and control of geological disasters. Reversely the conservation levels on water, air, sound and soil environmental quality are considerably high. In particular, study on Zhangjiajie National Forest Park found that its indexes are in "unsafe" stage on the following aspects: visitors receive strength; the strength of local residents growth; water supply and demand balance; meteorology; the prevention and control of geological disasters; surface water environment quality; the protection of animals; the strength of waste-water treatment, development of the education system; development of the legal guarantee system. The threatening factors to its ecological security are mainly made of unreasonable tourism behavior, environmental pollution resulted from weak ecological consciousness of residents and tourism practitioners, environmental capacity pressure of golden tourist line, disturbance to the forest park ecosystem made by adjacent tourism development, imperfection of the ecological education, monitoring and guarantee system.

### 2.3 *Research on ecological security assessment of wetlands*

In recent years, domestic scholars in the area of wetland ecological security assessment have done a lot of work. The study on Guizhou Liupan-shui Ming-Lake National Wetland Park indicated that the parks' connection degree of pressure and response is 0.9315 and 0.6529 respectively, which is unsafe stage. Connection degree of condition elements, a relatively safe stage. Its comprehensive ecological safety connection degree is 0.6726, within the unsafe level (Qin Qu etc., 2014). The study on Zhejiang Leqingwan Wetland showed that 9.66% of the wetland in Leqingwan was at risk, 7.14% being unhealthy, 46.54% being sub-healthy, 27.08% being safe and only 9.58% being healthy. According to the maximum membership principle, the wetland in Leqingwan area could be defined as a specialty (Songguoli etc. 2011). Another study was on China's current highest-elevation paludification meadows wetland—the Dabao Mountain Wetland in Yunnan Province. It shows that at current the ecological security assessment of Dabao Mountain Wetland is in an ordinary, with most of ecological

function not exerted. However, some particular ecological pressure indexes have exceeded the bearing capacity of the ecosystem (Gao Xingguo etc. 2013). More over, a study on wetlands of different phases in tumen river basin of Jilin province indicates that in 1976 and 1990 the value of ecological security was 0.650 and 0.620 respectively, which suggested that the wetland ecosystem was in a safe condition. While in 2000 and 2010 the value was 0.536 and 0.454, which implied that the ecosystem has been an alerting states, that certain arrangements should be made to protect it (Zhu Hongwei etc., 2014).

### 3 MODELS AND SYSTEMS OF ECOLOGICAL SECURITY ASSESSMENT OF URBAN GREEN SPACE

#### 3.1 *The assessment models*

Among the core of the research on urban green space ecological security are the indicator system, evaluation methodology and the evaluation standard (safety criterion). The establishment of the conceptual model could clearly illustrate the relationship between social activities, economic development and ecological process. Therefore the method structuring indicator system through conceptual model is widely applied (Wei Bing etc., 2009).

It is best to first retype the first words manually and then to paste the correct text behind. When the new file contains all the text, the old tags in the text should be replaced by the new Balkema tags (see section 3). Before doing this apply automatic formatting (AutoFormat in Format menu).

##### 3.1.1 *The P-S-R model*

The P-S-R Model is named for the Pressure-State-Response (Allen et al., 1996 Tong, 2000; Wolfslehner et al., 2008) model raised by the United Nations agency for economic cooperation development and the OECD. This model reflects the interactive relationship between human and environment. In this model one particular type of issue can be described by three indicators that are in different but interrelated types.: Pressure refers to the load caused by human activities to the system; the State refers to characterization of environmental quality, natural resources and the status of the ecosystem; the Response refers to humans' corresponding measures when facing humanity environmental problem. This model is widely applied in the ecological security assessment at home and abroad. The R-S-P model has clearer cause-and-effect relationship than other models, that it classifies environmental indicators starting from the interaction of human and environmental systems. Thus having strong systemic

and maneuverability. However, this model singularly regards human activities as pressure without considering natural pressure, resulting from the lack of natural indicators (Liu Zhancai, 2008).

##### 3.1.2 *The D-S-R model*

The D-S-R Model refers to the Driving Force-State-Response Model raised by the UN Department for Policy Coordination and Sustainable Development (DPCSD, 1996). The Driving Force is describing the natural disasters and human activities to ecological system pressure; The State refers to the ecosystem's structure and function, also the reflection that natural ecosystems provides services and resources to human; The Response indicates the operating capability to deal with the ecological environment problem and maintenance/improve the ecosystems' security status.

##### 3.1.3 *The D-P-S-I-R model*

The European Environment Committee combined and improved the former two models, then came up with the Driving Forces-Pressure-State-Influence-Response Model (Smeets et al., 1999; Spangenberg et al., 2009). In another word, it insert into the former P-S-P model with the D (Driving Forces), which describes human economic activities and natural disasters, and the I (influence), which illustrate the impact on human or ecosystem by the change of state. The D-P-S-I-R model can remedy the limitation of the P-S-P model and interpret clear logical relations while offering solutions, as a result preferred by many scholars.

##### 3.1.4 *Other models*

Based on the study on the cons and pros of all the above models, Corvalan and fellows further developed the DPSIR model and raised the Driving Force-Pressure-State-Exposure-Effect-Answer DPSEEA model Waheed et al., 2009. This model introduced the Effect-Answer indicators from risk evaluation and regard pollution exposure as a independent part, emphasizing its pressure on the ecosystem (Zuo An, 2004). Zhang Zhiguang (2013) proposed FES-PSIR model. His model is based on the symbiosis of Ecology and industry, structurally analyzing the compounding system which ecological security (FES) concerns. It also contrastively analyzes the studies on P-S-R, D-S-R, D-P-S-I-R models by domestic and international scholars. Specific to the ecological security issue of urban green space, it establishes the Pressure-State-Influence-Response model.

#### 3.2 *Indicator systems*

The indicator system of ecological security assessment of urban green space requires for

comprehensive evaluation on related issues through multi-layer indicator system, whose contents involve ecological, economic and social factors comprehensively reflecting the compound system of society-economy-ecology. The system usually consists of 3 layers which are the target layer, criterion layer and indicator layer. The target level reflects the comprehensive ecological security situation; the criterion layer is composed of the main factors of ecological security which can be further divided; The indicator layer is on the most basic level of the system which is made up of measurable indicators. The specific measures have clear ecological economic significance there for they are convenient for analyzing the cause of ecological security problems. However, in order to get the synthesizing value, the method mentioned above need the nondimensionalization action to each index, which may result that the synthesized value lost its ecological economic significance and becoming difficult to understand and use. Never the less, when it comes to setting the index weight, the above method suffers the problem of being subjective.

Zhang Zhi-guang (2013) developed the FES-PSIR structured model which is made up of the social and economic pressures (FES-P) subsystem, resources and environment condition (FES-s) subsystem, ecological impact (FES-I) subsystem and human response (FES-R) subsystem. Social and economic pressures (FES-P) subsystem contains the development of social economy and forestry industry demands for forest resources and the ecological environment destruction and so on pressure; Resources and environment condition (FES-s) subsystem, include forest resources, quality, coverage, distribution, type, structure, and the concentration of greenhouse gases, and other state; Ecological impact (FES-I) subsystem, including forest ecosystem health and vitality, ecosystem productivity, ten-fold increase forest, the forest disasters incidence, biological diversity, soil erosion, air quality, climate warming effect; Human response (FES-R) subsystem, improve the ecological status of human input, artificial afforestation, industrial circular economy, science and technology support, integration, legal policy guarantee, ecological civilization consciousness, crisis response mechanism response. Wang Chaohui (2012) type of mountain forest park, population pressure, ecological safety evaluation and study of land and resources pressure, pressure natural disasters, the quality of environmental factors, ecological factors, quality of science and technology input, intellectual support and legal support, community involvement, and visitors safety as the main factors of ecological security, 21 indicators to determine type of mountain forest park, ecological security evaluation index system, including visitor reception, local

residents growth strength, strength, construction land use intensity, water supply and demand balance, forest fire prevention and control, forest diseases and insect pests prevention and control, meteorology, the prevention and control of geological disasters such as, atmospheric environmental quality, surface water environment quality and acoustic environment quality, soil environment quality, plant protection, the protection of animals, landscape resources protection, exhaust gas treatment strength, the strength of wastewater treatment, waste management strength, the perfect degree of the education system, the perfect degree of the legal guarantee system, and community economic development and the management level and visitors safety protection, etc. On the basis of wetland edge soils, plants, aquatic plants and water quality of four features a total of 13 indicators, Spencer (1998) conducted the assessment for the health status of the Murray Darling basin in the southeast Australia permanent floodplain wetland. While Zhao Zhenhe (2005) assessed the health of lake wetland ecosystem, choosing lake ecological structure index (including the biomass of phytoplankton, zooplankton, and the ratio of the two) and lake ecosystem indicators (including quality and structure can quality) as evaluation index.

#### 4 ECOLOGICAL SECURITY OF BEIJING URBAN GREEN SPACE TEXT AND INDENTING

Urban green space is the main part of the regional ecological civilization construction, but also the important guarantee of regional ecological security. Under the background of serious deterioration of Beijing's ecological environment as well as great development of urban ecological civilization, it has been more and more significant to study and conduct urban green space ecological security assessment.

##### 4.1 *Development opportunities of Beijing urban green space for ecological security*

Rapid urbanization and expansion resulted worsening ecological environment in cities, along with the "city disease" such as severe air pollution and water shortages. In his three time's visit of Beijing, our General Secretary emphasized on the strategic positioning to a foothold in the capital city Beijing, accelerate the construction of ecological environment construction, the international first-class harmony and livable city. The "twelfth five-year" is a crucial period for Beijing to develop into a globally recognized livable city. The impression of urban forest is important city, is an important symbol of degree reflect the livable city, and expand the city

livable space, and promote social harmony and stability, enhance people happiness is important carrier and rely on, so the construction of urban forest is Beijing livable environment construction, urban and rural ecological network construction of main job.

Urban forest is capable of dust noise reduction, reduce the concentration of PM<sub>2.5</sub>, emissions increase sinks, conserving soil and water, water conservation, reason fully functional and structural stability directly affect the Beijing urban ecological security. Build reasonable planning and complete functions and benefits of urban forest ecosystem, to ensure ecological security in the capital, improve the ecological environment of the city and meet the demand of residents ecological, world urban construction with Chinese characteristics, the construction of “humanistic Beijing, science and technology Beijing, green Beijing” has important strategic significance. In 2009 Beijing seventh landscaping resources census results show that the city forest area of 658900 hectares, including plain area in the city forest area of 14.41 hectares, the forest coverage of 14.85%. Plain area of forest land accounts for only 15.8% of the city’s forest area. Forest area accounted for 87.14% of forest land area in the plain area. By 2010, the total area of 1.047 million hectares of forest land in the city, 63.8% of the total land area, the forest coverage rate was 37%, 53% green area of forest, mountainous forest, trees afforestation rate reached 50.97%, 71.35% respectively. “Beijing 2013–2017 clean air action plan is put forward, to strengthen the construction of afforestation and beautify, increase forest resources, improve the quality of forest construction, in the plain area, after the end of 2016 millions of acres of afforestation project, by 2017, the city green greening rate of more than 60%. A few days ago, Beijing one million mu of plain afforestation task has been completed ahead of schedule, puts forward nine project of Beijing gardens green bureau points out that in 2020 years ago, the land use is given priority to with horticulture in Beijing, to add 380000 mu of plain afforestation, 100000 mu of high efficient orchard construction, renovation, 100000 mu of inefficient orchard. Beijing, therefore, the existing total forest and gradually perfect the forest network construction for the development of Beijing urban green land ecological security provides a new opportunity and challenge.

#### 4.2 *Strategy of Beijing urban green space ecological security assessment*

##### 4.2.1 *Choose reasonable method for the urban green space ecological security assessment*

Urban green land ecological security assessment makes more use of ecological security evaluation method or its improved version. At present the

study of urban green land ecological security evaluation method is still in its infancy. Beijing urban green land ecological security evaluation methods should be considered the particularity of Beijing urban environment, the characteristics of Beijing forest layout, the structure and function of urban forest in Beijing and Beijing composite factors such as social and economic development needs, choose the suitable Beijing urban green land ecological security evaluation method.

##### 4.2.2 *Construct scientific system for the urban green space ecological security assessment*

The establishment of sustainable management of Beijing urban green land ecological security evaluation system will involve a lot of natural elements such as vegetation, soil, hydrology, and also including forest structure, function such as ecological indicators, as well as social, economic, human pressure, and many other factors. Therefore in the process of the construction of evaluation system should be selected as little as possible, easy to control and operation of indicators to reflect the characteristics of Beijing urban green space ecology system, in order to increase urban green land ecological safety observation index of practicability, avoid too much evaluation index will make the ecological security problem is more complicated, or incomplete information index, the evaluation index system covering the phenomenon of overlap between information or indicators, in order to increase the difficulty of the actual evaluation work.

##### 4.2.3 *Conduct objective and accurate assessment for urban green space ecological security*

The ultimate goal of urban green land ecological security research is the guarantee of urban green land ecological security, maintenance and management research, urban green land ecological security evaluation, prediction and early warning research, is to establish a comprehensive security system, formulate scientific and reasonable ecological security maintenance and management measures, action, and lay the foundation and basis by the relevant laws and regulations. Therefore, should be objective and accurate in Beijing urban green land ecological security evaluation.

## 5 CONCLUSION

As environmental pollution and ecological environment have seriously affected and threatened human survival and social development, ecological environment issues has risen to ecological security issues. Ecological security is the guarantee of the ecological—economic—social system and sustainable development. Ecological security assessment is

of great significance for regional urban green space system. For urban green space ecological security assessment, the main challenge is how to combine various characteristics of the urban environment to build the evaluation index system. There for, ecological security assessment of Beijing urban green space should be combined with the demand of city development and functional needs, should choose the urban green land ecological security evaluation method, should build urban green land ecological security evaluation system on scientific approaches, should conduct accurate and convenient evaluation. It should also provide the basis for the establishment, maintenance and management of the system, as well as related laws and regulations.

## REFERENCES

- [1] Allen H., Albert A. 1995. Environmental indicators: A Systematic Approach to Measuring and Reporting on Environmental Policy Performance in the Context of Sustainable.
- [2] Development. Washington D.C., USA: World Resource Institute.
- [3] DPCSD (United Nations Department for Policy Coordination and Sustainable Development). 1996. Indicators of Sustainable Development: Framework and Methodologies. New York: United Nations.
- [4] Smeets E., Weterings R. 1999. Environmental Indicators: Typology and overview. Technical Report No. 25, European Environmental Agency, Copenhagen.
- [5] Spangenberg J.H., Martinez-Alier J., Omann I., Omann Ines, Monterroso I., Binimelis R. 1998. The DPSIR scheme for analysing biodiversity loss and developing preservation strategies. *Ecological Economics*, 2009, 69(1): 9–11.
- [6] Spencer C., Robertson A.I., Curtis A., et al. Development and testing of a rapid appraisal wetland condition index in southeastern Australia. *Environmental management*, 54(2):143–159.
- [7] Tong C. 2000. Review on environmental indicator research *Research on Environmental Science* 13(4):531.
- [8] Waheed B., Khan F., Veitch B. 2009. Linkage-based frameworks for sustainability assessment: making a case for driving force-pressure-state-exposure-effect-action (DPSEEA) Frameworks. *Sustainability*, 1(3): 441–463.
- [9] Wolfslehner B., Vacik H. 2008. Evaluating sustainable forest management strategies with the analytic network process in a pressure-state-response framework. *Journal of Environmental Management*, 88(1): 1–10.
- [10] Chen Yingting. 2014. Research of the forestry ecological security evaluation were reviewed. *Wireless technology*, (8): 164–166189.
- [11] Room use, shu-jun wang. 2007. The establishment of the ecological security evaluation index system, in order to save forest ecological system as an example. *Journal of northeast forestry university*, 35 (11): 77–82.
- [12] Happy country, wang lei, dai-hua qi, Chen Gude, wang, Zhang Fusheng. 2013. The wetland ecological security assessment based on PSR model—made wetland, for example. *Hunan normal university natural science edition*, 36 (1): 86–90.
- [13] Zhan-cai liu. 2008. Urban ecological security evaluation in arid areas—in lanzhou city as an example. *Anhui agricultural science*, 36 (4): 1523–1525.
- [14] Luo Lou, full wave forever. 2012. The zhoushan islands forestry ecological security construction research. *Rural economy and technology*, 23 (12): 14–16.
- [15] M front, li-li huang, feng-jun sun. 2010. Beijing JiuFeng national forest park ecological security evaluation. *Forestry science*. 46 (11): 52–58.
- [16] Qin, cui xiaoping, generation. 2014. Based on set pair analysis of artificial wetland park, urban ecological security research. *Water ecology*, 35 (3): 42–47.
- [17] Guo-li song, shu-ying zang, xue-yan wang yu-bao li. 2011. Based on the fuzzy comprehensive evaluation method of yueqing bay wetland ecological security evaluation. *Natural disaster*, 20 (5): 24–31.
- [18] QinDeHua, dong-jin he cheng-zhen wu, hong wei, yong-sheng liu, ying-zi wang, Zou Liming. 2009. Based on the ecological footprint analysis of wuyi mountain scenic spot ecological security evaluation. *Journal of north China university (natural science edition)*, 10 (3): 253–257.
- [19] Tang fei fly. 2013. Qilian mountain national nature reserve ecological safety evaluation [d]. Lanzhou: lanzhou university.
- [20] Wang Chaohui. 2012. Type mountain forest park, ecological safety evaluation studies [Ph.D. Thesis]. Changsha: central south forestry university of science and technology.
- [21] Born Wei Bin, Yang school, wu Ming, jiang-hua xiao. 2009. Ecological security evaluation method is reviewed. *Journal of hunan agricultural university (natural science edition)*, 35 (5): 572–579.
- [22] School Wei Bin, Yang, wu Ming, jiang-hua xiao. 2010 b. islands forestry ecological security evaluation. *Journal of nanjing forestry university (natural science edition)*, 34 (4): 161–164.
- [23] Wei Bin. 2010 a. island forestry ecological security evaluation, xiushan island in zhejiang province as an example [d]. Beijing: China academy of forestry science.
- [24] YouWeiBin, dong-jin he WuLiYun, HongWei ZhanShiHua, QinDeHua, hui-ming you. 2011. The degree of spatial and temporal variation of wuyi mountain scenic area landscape ecological security. *Acta ecologica sinica*, 31 (21): 6317–6327.
- [25] Zhang Pin bang-wen zhang, hai-sheng Cai, Jin Surong Han Tianyi. 2013. A matter-element analysis jiangxi forestry ecological security evaluation. *Journal of jiangxi agricultural university*, 35 (4): 791–797.
- [26] Zhi-guang zhang. 2013. Based on the ecological industrial symbiosis of forestry ecological security measure. *Acta ecologica sinica*, 33 (4): 1326–1336.

## Study on types of rural landscape

Yuan Liu

*The school of Landscape Architecture, Beijing University of Agriculture, Beijing, China*  
*Beijing Rural Landscape Planning and Design Engineering Technology Center, Beijing, China*  
*Beijing Laboratory of Urban and Rural Ecological Environment, Beijing, China*

**ABSTRACT:** Rural landscape is different from urban landscape. The purposes of studying on types of rural landscape are to strengthen types of landscape with rural characteristics and highlight unique style of rural landscape in the planning designs of rural landscape in the future. Types of rural landscape can be classified into natural landscape and human landscape, which include material and immaterial attribute, and not one of them can be dispensed with. Starting with material and immaterial attribute, the article makes a further classification.

**Keywords:** rural landscape; material attribute; immaterial attribute; nature; humanity

### 1 SUMMARY OF RURAL LANDSCAPE

#### 1.1 *Landscape*

In China, the word “landscape” is not a vocabulary and concept that has existed from time immemorial. It is a newly rising field in twentieth century, and its concept meaning is different from the Chinese traditional garden and landscape architecture. Landscape is more of a visual vocabulary, which refers to people’s feeling toward the environment’s external characteristics. As a concept in the sense of visual aesthetics, “landscape” is similar to the word “scenery” (Fengjing) and “view” (Jingzhi) in Chinese. From the perspective of subjects, it has more applications and correlations in and with geography, ecology, architecture, etc. In geography, as a scientific terminology, landscape refers to terrain scene within one geographic unit. In ecology, landscape is an ecological system and ecological resource. In architecture, landscape is a design consideration and scenery type.

#### 1.2 *Rural landscape*

The concept “rural landscape” derives from the concept “landscape.” Based on landscape, rural landscape places restriction to the region. It is a type of landscape that taking the countryside as its study objects. With the development of China, people begin to recognize landscape with new requirements, and are in the hope of improving their living environments. More and more people

are involved in the studying and constructing of urban landscapes, hoping to establish perfect homelands. However, in fact, China is a large agricultural country. Agriculture is always the root of the people’s livelihood, since ancient times and farmers are major productive forces in China. Agricultural lands make up the largest portion of the land-use type in China. From the development point of view, agriculture is the root of China’s development. With respect to the industry of landscape planning designs, the key is the development of urban landscapes and the basis is the development of rural landscapes. China put forward the strategy of new rural development, and formulates guidelines of industry re-feeding agriculture, city supporting village and giving more taking less and loosening control, and clarifies the fundamental requirements of simultaneously carrying out modernization of agriculture in the process of developing in-depth industrialization and urbanization, and quickens formation of new pattern of urban-rural integration, which all in all provide with new development and research thoughts for the industry of landscape planning designs.

Rural landscape is a type of regional landscape. However, the defining of region is becoming more and more difficult with the continuous developing in depth of city and countryside integration. For the present, a relatively common approach is to define urban and rural region from the local administrative domination area and land usage. To differ urban from rural region from landscape viewpoint, the differences among types of landscape can basically be made from visual points, which are possibly fixed feelings toward the differences between city and countryside in people’s mind. For example,

---

Foundation item: Beijing Higher Education Young Elite Teacher Project (YETP1719)



one can distinguish one place as city or countryside at a glance from its environment. Now, such distinguishing is becoming more and more difficult due to the continuous integration between city and countryside, and thus, the differences of landscapes between them have narrowed gradually. People in cities have constantly explored methods of naturalization, and in countryside have gradually changed life-style with human landscapes being more and more urbanized. The purposes of studying on types of rural landscape are to strengthen types of landscape with rural characteristics and highlight unique style of rural landscape in the planning designs of rural landscape in the future.

## 2 OVERALL CLASSIFICATION OF RURAL LANDSCAPE

Different subjects have different emphasizes toward rural landscape. Aesthetically, rural landscape conveys pure, clean and rural natural scenery, and unsophisticated cultural customs. Geographically, rural landscape is different from urban landscape from the regional attribute. Ecologically, rural landscape has more abundant natural qualities and biological diversities. I think that those points of view emphasize particularly on the natural qualities of rural landscape. In fact, besides natural scenery, characteristic historic cultures, folk traditions, and folk customs also make up unique style of rural landscape. They cover a wide range of contents, and it is necessary to categorize them, which establish the foundation to certain extent for the planning designs of rural landscape.

### 2.1 Principles of classification

While study on classification of countryside is made, both variety and uniqueness of rural landscapes should be taken into consideration, based on which principles as below should also be mainly considered:

#### 1. Integral principle

Integrity, but not certain individual condition, should be taken into comprehensive consideration in classifying types of rural landscape. For instance, the influences of many factors such as climate, soil, landform, vegetation, hydrology, human activities, etc. toward rural landscapes should be comprehensively considered. Natural and human factors are especially not to be neglected. The classification of rural landscape would be incomplete without taking integral principle into consideration.

#### 2. Characteristic principle

Among the overall factors, each factor has different functions in different landscape types of

different levels. In certain sub classification, the dominant factor that affects the formation transformation of rural landscape should be highlighted and the essence of problem should be taken so as to scientifically and effectively make more precise classification toward rural landscape.

#### 3. Scale principle

In the overall classification of rural landscape, not only the contents should be solved, but also classifying scale should be considered. In fact, it has much relativity with the concept of rural landscape. Due to the lack of unified definition concerning the concept of rural landscape as yet at home and abroad, scholars have different understandings toward it, and thus, there is no unified standard for the scale of landscape studies. Basically, the study of concept of rural landscape determines the grasp of landscape scale. The article simply defines the concept of rural landscape as: the region that outside the urban built-up area with abundant natural and human attributes. Based on the concept, the overall classification of rural landscape is a region type classification of large scale.

#### 4. Level principle

Gradually, progressive level principle of classification should be noticed when region type classification of large scale is made. Scale should be gradually reduced and classification of large scale should be refined to divide types of small scale, so as rich and varied types of rural landscape can be reflected comprehensively and in detail.

### 2.2 Overall classification of rural landscape

In the classification of large scale, rural landscape can generally be classified into natural landscape and human landscape (see Table 1). Natural landscape refers to true type of landscape formed by original material ecology in the nature, which has been affected and reformed by humankind only to a small extent. Human landscape refers to the landscape with regional characteristics in the countryside,

Table 1. Overall classification of rural landscape.

Number	Overall classification of rural landscape	Examples
1	Natural landscape	Such as: woodland, grassland, water area, farmland, etc.
2	Human landscape	Such as: folk traditions and folk customs, religion, garden, architecture and music, etc.

which has been affected and reformed by humankind to a relatively large extent, and based on humanistic background, human landscape has certain atmospheres such as culture, tradition, history, living habit, appreciation of the beauty (includes religious faith), etc. From the meaning of the word "human" we can make out that: (1) the principal part of human landscape is human's creative thought and subjectively transformative capacity; (2) landscape perception created from human's wisdom has historical and cultural attributes, and in contrast to the nature, it has a higher spiritual and cultural meaning.

With respect to the visibility of landscape, overall rural landscape can be classified into material and immaterial attribute. In general division of landscape types, visibility is always taken as standard of division of landscape, and immaterial attributes influencing characteristics of landscape are often neglected. In human landscape, more immaterial attributes are especially included, in which new meanings are given to the human landscape from human's wisdoms and creations. Therefore, the superposition of nature and human landscape with material and immaterial attribute in general classification is stated as in the Figure 1.

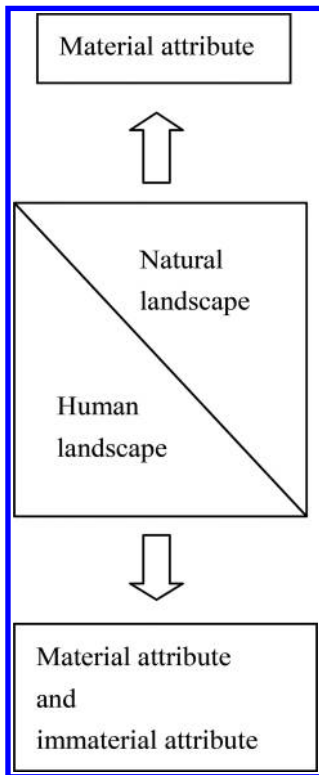


Figure 1. Classification and attribute division of rural landscape.

### 3 CLASSIFICATION OF MATERIAL ATTRIBUTE

#### 3.1 Standard of classification

Taking China's current land use classification (PRC National Standard GB/T21010-2007) as the standard of classification, rural landscape can be further classified into natural landscape, semi-natural landscape, and artificial landscape. In accordance with the standard, with generalizing and improving the classification, the article proposes classification of material attribute concerning rural landscape in Table 2 as below.

#### 3.2 Classification declaration

In the classification of material attribute, natural landscape mainly includes types of landscape in rural region naturally formed such as natural woodland landscape, natural grassland landscape, etc. In semi-natural landscape, artificial woodland landscape, artificial grassland landscape, and artificial water area landscape are the major three landscapes that should be necessarily explained. Though being artificially built, but they are similar to natural landscape so as to be called semi-natural landscape, but not artificial landscape. So are farmland, orchard, tea garden, etc. Semi-natural landscape both has landscape of natural scenery and human landscape. Artificial landscape mainly includes types of landscape influencing human's life to a relatively large

Table 2. Classification of material attribute concerning rural landscape.

Number	Classification of material attribute	Concrete contents
1	Natural landscape	Natural woodland landscape, natural grassland landscape, natural water area landscape, natural mudflat landscape, glacier and snow cover landscape, saline-alkali soil landscape, wetland landscape, sand, bare land, etc.
2	Semi-natural landscape	Artificial woodland landscape, farmland landscape, garden landscape, artificial grassland landscape, artificial water area landscape, etc.
3	Artificial landscape	Settlement landscape, road landscape, engineering facilities landscape, etc.

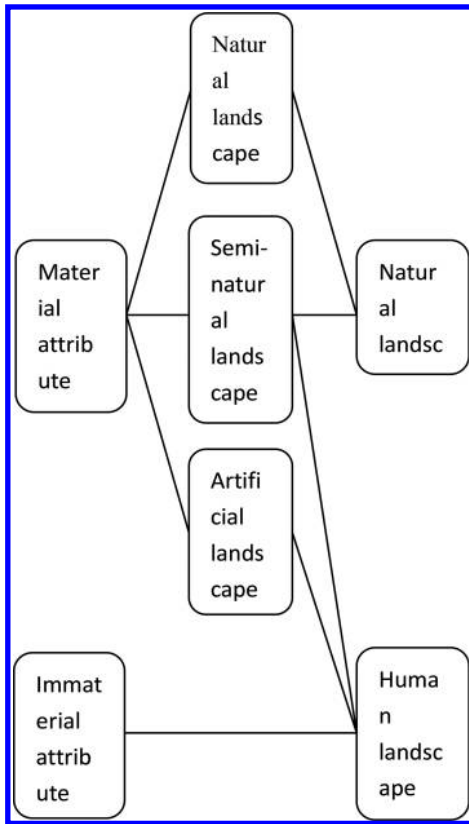


Figure 2. Correlations between each type of rural landscape.

extent, such as rural settlement, road landscape, engineering facilities landscape, etc. The overall classification of natural and human landscape stated in the last section can be seen in Figure 2.

#### 4 CLASSIFICATION OF IMMATERIAL ATTRIBUTE

Immaterial attribute is quite different from material attribute. It refers to the immaterial attribute of cultural and artistic value. It has implicit characteristics of landscape with various forms.

Combined with Chinese cultural characteristics, it includes folk literatures, folk customs, traditional medicines, traditional manual skills, folk arts, acrobatics and athletics, Chinese folk art forms, traditional dramas, folk dances, folk music, etc.

Immaterial cultural landscape is of an indispensable part in rural landscape, which is the display and inheritance of rural historical and cultural characteristics. Its various cultural expressions bring about meanings and features to rural landscapes. It is also an important part that should be necessarily noticed in planning designs of landscape.

#### 5 CONCLUSION

The article has made an explanation toward classification methods and types of rural landscape, and finally reached to some basic classification systems. Diversity and uniqueness of rural landscapes are determined by region. More detailed summarizations and analyses of types of rural landscape would be made in accordance with different regions in the future.

#### ACKNOWLEDGMENTS

This paper is one of the results of Beijing Higher Education Young Elite Teacher Project (YETP1719).

#### REFERENCES

- [1] Li Zhenpeng, Liu Liming, Xie Hualin. Exploration and analysis on classification methods of rural landscape: taking Baijiatuan, Haidian District, Beijing as example [J]. *Beijing: Resource Science*, 2005, 02:167–173.
- [2] Fan Jianhong, Weicheng, Li Songzhi. Study on conceptual meaning of rural landscape and its development [J]. *Guangzhou: Tropical Geography*, 2009, 03:285–289 + 306.
- [3] Liu Lili. Study on immaterial cultural heritage of suburban areas of Beijing and its utilizations in rural tourism. [J]. *Journal of Capital Normal University (Natural Science Edition)*, 2011, 06:56–62.

# Study on the numerical model and design optimization of a green office building in Wuhan, China

Weiyi Liu

*College of Urban Construction, Wuhan University of Science and Technology, China*

Juan Yang

*Hubei Urban Construction Vocational and Technology College, China*

Wei Hu

*College of Computer Science and Technology, Wuhan University of Science and Technology, China*

**ABSTRACT:** With the intensification of the building energy consumption problem and the general sub-health status that the current working group faces, create a low-carbon, efficient and livable working space has become the development goals of the green office buildings. Green technologies as the important way to achieve this goal, how to optimize the integration of active and passive technologies combine with the regional climate characteristics to seek the best balance between the energy use and environmental quality becomes the key point for green office building design. This paper takes the management committee office building in a scenic area of Wuhan city as an example, made a comprehensive analysis of its design objectives, design principles and the specific green design strategies, and in order to provide some useful reference for the future of green building design, in view of the current green building development, puts forward some relevant suggestions from the aspects of architectural design strategy formulation and green technology selection around the essence of green building design.

**Keywords:** numerical model; office building; green design

## 1 INTRODUCTION

As an important place in people's daily work activities, the functional attributes which office building carries should not only provide the necessary space itself, but also to meet the spiritual needs of the office staff. With the intensification of the building energy consumption problem and the general sub-health status that the current working group faces, creates a low-carbon, efficient, and livable working space has become the development goals of the green office buildings. Green technologies as the important way to achieve this goal, how to optimize the integration of active and passive technologies combine with the regional climate characteristics to seek the best balance between the energy use and environmental quality becomes the key point for green office building design.

The main principles that the green office building design should follow include:

### 1. Adjust Measures to Local Conditions

Create a native, low carbon green high quality construction and has the era characteristics that according to the climatic conditions, regional characteristics, resource conditions where the

project locates, eliminate the negative impact brought by the "portability Copy."

### 2. Passive Priority and Active Optimization

Building design should first pay attention to the design itself, allow natural acting by using the rational design means to optimize the layout of the building, interior space and detail design, and give priority to use the passive technology of natural ventilation, natural lighting, high insulation external retaining system, and vertical greening to reduce energy consumption. Then, consider using active technologies as supplement to improve efficiency.

### 3. Optimizing Integration with Ultra Technologies

Avoid focusing on the technology itself, but focus on the suitability, interoperability, economic rationality, and energy efficiency of the technologies when making the choice of technology strategies.

## 2 MATERIALS AND METHODS

The office building located within a well-known scenic spot in Wuhan City, the planned total land area is 10438 m<sup>2</sup>, with a total construction area

of 5760 m<sup>2</sup>. This project site has a very beautiful landscape environment. Its base surface is close to the mountains in the north, Liangzi Lake in the south, and region development plot in the east and west. Based on the need of this study, this paper select the main building orientation and distribution, outside micro-climate, natural lighting, and natural ventilation as the four elements, by use the computer simulation software of Phoenics and Ecotect to make analysis and comparison between the multiple design scenarios, and then take optimize and adjust measures according to the simulation results to get the most ideal design scenario.

According to the Evaluation Standard for Green Office Building, these four elements corresponding to the entry requirements were:

1. Building orientation and distribution  
Wind speed of the pedestrian area around the building at the 1.5 m height should be less than 5 m/s, the site should not appear vortex and dead space, Wind velocity amplification coefficient should be less than 2.
2. Outdoor environment  
Landscape design should choose a suitable local climatic and soil conditions of local, using a complex layer containing shrubs, grasses. etc, and the planting area should have sufficient overburden depth and good drainage.
3. Natural Lighting  
More than 75% of the main function space's daylight factor to meet the requirements of "Standard for Daylighting Design of Building" GB/T 50033-2013.
4. Natural Ventilation  
Architectural design and structural design should have induced flow measures to promote natural ventilation.

### 3 RESULTS AND DISCUSSION

#### 3.1 Building orientation and distribution

Good natural ventilation and sunlight effect are the factors that should be considered in the phase of planning and construction layout. In consideration of there has no affectable surrounding buildings, only take the natural ventilation as the primary factor in this project planning and building layout considerations.

Northeast wind direction perennial dominant wind direction of Wuhan, according to this feature, in order to reduce the impact of cold air infiltration in winter, and get a better natural ventilation effect in summer, the building layout finally select the toward that close to the south. Since the building height and space changes in the organizational relationship will bring a different effect of

indoor and outdoor ventilation, using simulation software of Phoenics to make analysis and comparison between the multiple programs, and take a corresponding adjustment according to the simulation results.

In the optimized layout pattern, the maximum wind speed around the building is less than 5 m/s in both the summer and winter, wind speed amplification factor is less than 2, the wind pressure between the windward and leeward side o is greater than 1.5 Pa, and the site around the construction site has no swirl and dead ends (Figs. 1–4), the overall natural ventilation condition is good, and meet the comfort requirements of pedestrian.

#### 3.2 Outdoor environment

There has an outward Green Square in the south of the main entrance area of the office building, and



Figure 1. Outdoor pressure contours in summer.

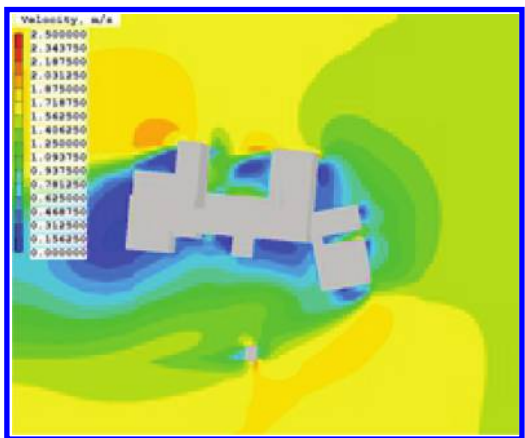


Figure 2. Outdoor wind velocity contours in summer.



Figure 3. Outdoor pressure contours in winter.

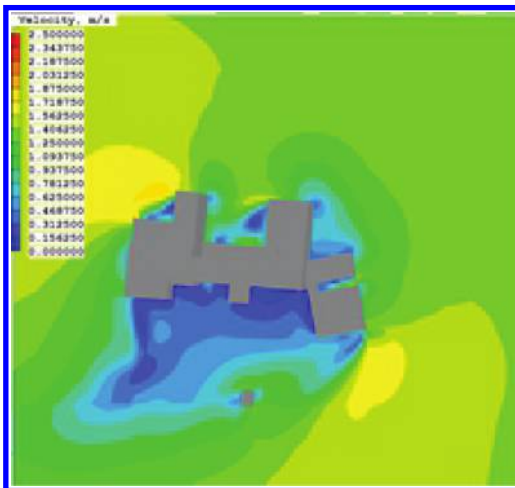


Figure 4. Outdoor wind velocity contours in winter.

with the combination of the space which enclosed by the building body design an inward-looking garden in the north, thereby forming a north-south landscape visual corridor through the building, at the same time, set up a sunken garden green space by using of terrain elevation in the west of the site, thus makes the most functional space have good visual accessibility combined with the design of glass walls and French window design.

In addition to the function of beautify, the more important function of outdoor environment is to improve the micro-climate of the office building. For this reason, the project pays special attention to greening in the aspect of outdoor environment creation. And using the simulation software of Ecotect to simulate the photosynthetic effective

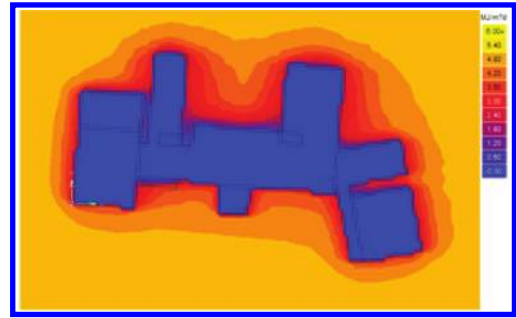


Figure 5. Photosynthetic effective radiation analysis.

radiation of the field around the building prior to the landscape design, which provide the basis for plant configuration. According to the simulation results (Fig. 5), combine with the habits of plants, in the area where the solar radiation is less than 3 MJ/m<sup>2</sup>d planted hi shade plants, in the area where the solar radiation is between the 3 MJ/m<sup>2</sup>d and 6 MJ/m<sup>2</sup>d planted neutral plants, and in the area that larger than 6 MJ/m<sup>2</sup>d planted heliophilous plants. And through the multi-layer green means, by planting local native trees and shrubs to reduce the noise, block cold wind in winter, adjust the solar radiation according to the season change. in addition, by setting the landscape pool, sunken lawn forming organisms climate buffer zone, thus to play the role of water conservation, and regulating outdoor air temperature and humidity.

### 3.3 Natural lighting

Compared with other public buildings, the service time of office buildings is mainly in the daytime, each room of the office has designed the glazed facades to reduce lighting energy consumption. In the south side space of the office blocks, the interior design carries forward the open architecture features, emphasizes open space and clarity skillfully, the continuous glass facade not only can make the interior office staff enjoy the full sun, but also Join together the indoor and outdoor environments effectively, creating a pleasant work environment; In the multi-purpose hall block, through setting an inner courtyard to introduce external light and air into the reception lounge space.

For larger spaces, such as employee dining area, just rely on the limited one-sided lighting cannot fully meet the indoor lighting demand, by extending outwardly 1.5 meters wide of the second floor flat with the stainless steel bottom pane to let outside natural light enter into deeper indoor space throughout reflecting, which greatly improves the effects of indoor lighting. Meanwhile, the overhanging floor settings also played a role in shade.

According to the natural lighting simulation results, interior lighting coefficient of 75% indoor space are above 3.0% (Tables 1–2; Figs. 6–7), meet the requirements of “Standard for daylighting design of building.”

### 3.4 Natural ventilation

Besides setting large windows that can be opened on the exterior walls, the office building also design an inner courtyard to increase natural ventilation. In the layout stage, by using the simulation software of Phoenics to analyze the indoor natural ventilation effect, so as to provide the basis to develop the most reasonable design program.

The indoor air environment simulation results of summer shows that the indoor space has a good

Table 1. Daylight factor of first floor.

Contor Ba (from-to)	Within		Above	
	pts	(%)	pts	(%)
0–2	1696	22.8	7438	100
2–4	3114	41.8	5742	77.2
4–6	1040	13.98	2628	35.33
6–8	513	6.9	1588	21.55
8–10	328	4.41	1075	14.45

Table 2. Daylight factor of fourth floor.

Contor Ba (from-to)	Within		Above	
	pts	(%)	pts	(%)
0–2	1255	35.73	3512	100
2–4	1281	36.47	2257	64.27
4–6	484	13.78	976	27.79
6–8	195	5.55	492	14.01
8–10	133	3.79	297	8.46

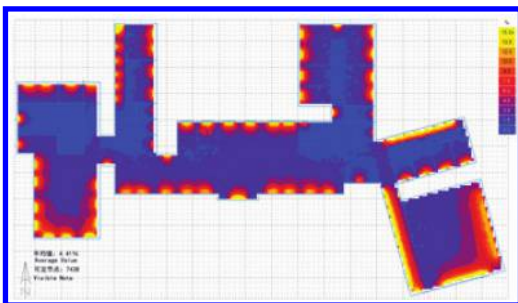


Figure 6. Interior lighting coefficient distribution of first floor.

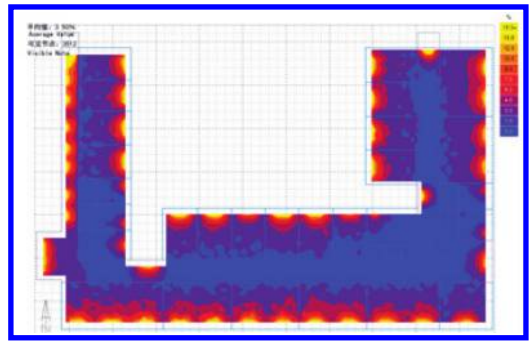


Figure 7. Interior lighting coefficient distribution of fourth floor.

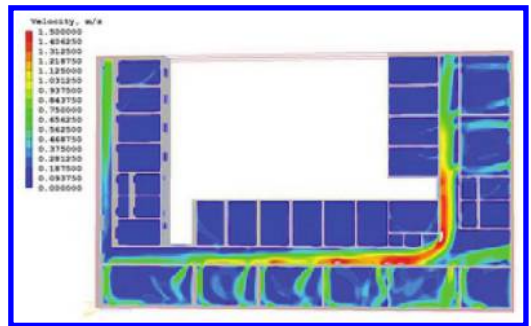


Figure 8. Indoor wind velocity contours in summer.

natural ventilation effect: the wind speed is within 0.2–1.0 m/s range in most indoor areas, the indoor air pressure on both sides is more than 1.5 Pa, and the air age is relatively small (Fig. 8).

## 4 CONCLUSIONS

This study is a useful attempt to the design philosophy of “Optimize Passive and Priority Active” in the green office buildings, by the means of reasonable building orientation and distribution, efficient building envelope design and natural lighting, ventilation, etc, giving full play to the role of passive energy-saving. Meanwhile, use suitable active technologies as supplementary to achieve.

The goal of enhancing the practical performance, energy performance and environmental performance, its investment is not high, but it made a good effect, providing a reference t for future green building design.

In terms of design strategy formulation, nowadays, with the rapid development of green building and under the guidance of energy-saving policy, more and more designers are introducing green

concept in the office building design. However, due to lack the awareness of the essence of green building, there has been emerging some problems that one-sided pursuit of “high input, high-quality,” blindly take the expected energy savings effect in the use of green technology, while ignoring the phenomenon of architectural design itself, which resulting in economic investment of the buildings is much greater than the social and environmental effects it produces, and contrary to the original intention of green buildings. At the beginning green building design, should according to the actual situation of the site conditions and natural resources, excavating the energy-saving potential of architectural detail designs, so as to reduce building energy consumption from the source.

In terms of green technology selection, the key point is to focus on suitability, combine the actual situation of the project with the technology’s practicality and efficiency, avoiding piling up the technologies blindly, and selectively learn and use local traditional technology to achieve implementation technology of human ascension. In addition, the choice making of green technology should consider the economical efficiency, optimize and integrate the active and passive technologies to

improve environmental quality of buildings based on a reasonable cost.

## REFERENCES

- Cha Jinrong, Wu Shuxin. “Localized Green Building Design on Base of Passive Design Priority”, *Journal of Eco-City and Green Building*, No. 8, 2011, pp. 60–71.
- Dai Zhizhong, Yang Zhen, Xiong Wei, “Resolve to Building Creative Ideas—Ecology and Bionic”, Beijing: China Planning Press, 1st Edition, April 2006, pp. 87–90.
- Deng Yong-jie, ‘Application of Green Building Concepts in Office Buildings’, *Journal of Green Architecture*, No. 4, 2013, pp. 52–54.
- Fu Zhaoxiang, ‘Energy-saving Technology in Hot Summer and Cold Winter area’, Beijing: China Architecture & Building Press, 1st Edition, January 2002.
- People’s Republic of China Ministry of housing construction. ‘Evaluation Standard for Green Office Building’, Beijing: China Architecture & Building Press, 1st Edition, September 2013.
- People’s Republic of China Ministry of housing construction. ‘Standard for Daylighting Design of Building’, Beijing: China Architecture & Building Press, 1st Edition, July 2011.



# Research on rural greenway suitable for Beijing

L. Feng & X.Y. Ma

*School of Landscape Architecture, Beijing University of Agriculture, Beijing, China*  
*Beijing Rural Landscape Planning and Design Engineering Technology Center, Beijing, China*  
*Beijing Laboratory of Urban and Rural Ecological Environment, Beijing, China*

**ABSTRACT:** This article first defined Beijing's rural greenway areas, took two successful examples of the Baili Landscape Painting Gallery and the Shen tang yu Landscape Road to draw four main appropriate types of greenways for Beijing countryside, which are riverfront type greenway, valley type greenway, cultural heritage type greenway, and natural ecological type greenway. Then it gives more details on the characteristics of each type of greenway. The authors proposed valley type greenway initially.

**Keywords:** landscape architecture, rural greenway types, beijing, valley type greenway

## 1 INTRODUCTION

The concept of greenway originated in the 19th-century in America. The world's first park system, Boston Park System, was planned by Olmsted, and was the first greenway ever built in its true meaning in America. In the 1950s, the idea of greenway was more about theoretical research and practice. Today, the concept of greenway has developed into a more comprehensive meaning, the *E-way* (environmental way, ecological way, entertainment way, educational way, esthetic way, economic way, exit way, etc.). The *E-way* has various functions such as ecological protection, recreational, popular science education, aesthetic ethic experience, and safety evacuation. (Liu, 2012).

The greenway experienced few courses. It went from park system, to open space, and then to greenway. The study subject also changed, from city to city-and-town combined. (Flink, C.H. Searns, R.M., 1993) (Little, C.E., 1990).

When we see the greenway system of the Pearl River Delta, we know that greenway construction has been developing very quickly in China. (Sun, Pan, 2011) (He, etc., 2010) In 2013, Beijing Municipal Government Executive Council adopted the *Beijing Municipal Greenway Construction Overall Plan* to determine Beijing's municipal greenway, the "three-ring, three-wing, multi-gallery." The plan has an objective to construct 1000-km municipal

greenways within 5 years, connect more than 200 parks, scenic spots, and historical and cultural sites.

The present article divides the greenway into three parts based on different zones: municipal greenway, suburban greenway, and rural greenway. At present, Beijing's construction planning is concentrated in urban and suburban zones and form a chronic-system post. There are few researches on rural greenway. Yet, the rural zone of Beijing is not only the ecological zone of the city, but it also provides natural landscape to the whole city, as well as recreational opportunities and precious historical and cultural heritage. Therefore, conducting a research on rural greenway has a great and important value for the municipal greenway system. In his research about Beijing's suburban greenway, Qin (2014), based on the set-up of the greenway separation between Beijing five ring roads and six ring roads, defined the suburban zone as the zone between the five ring and the six ring. The present article took the above classification method to fix the scope of the research, determined as the zone outside Beijing six ring roads. The article cards about the Baili Landscape Painting Gallery and the Shentangyu Natural Scenic Area to put forward the main Beijing municipal greenways to give a general view on the future planning and construction of rural greenways.

## 2 GREENWAY-RELATED CONCEPTS

There are lots of definitions about greenway. Little defines "greenway" as a kind of linear open space, generally a natural corridor (such as rivers, valleys, and mountains) or a common roadway which has been converted into a recreational way (such as canal, water channel, scenic trail and abandoned

---

Sponsored by:

1. Beijing Commission of Education Technical Innovation Platform Project (PXM2015\_014207\_000010).
2. Beijing Laboratory of Urban and Rural Ecological Environment Project (PXM2015\_014207\_000014).

railway, etc.), or any natural and scenic roads for bicycle and pedestrian. (Little C.E., 1990) But Bertie Ahern is stressing out the comprehensiveness of greenway. He believes that greenway is a land network built through meticulous planning, design and management, and that this network has various functions including ecological, recreational, cultural, aesthetical, as well as many other functions. These functions can all be found in the land network.

The greenway proposed by Bertie Ahern includes 5 meanings: first, greenway has a linear contour; second, greenway must have connectivity; third, greenway has versatility; fourth, greenway has multiple functions; fifth, greenway must satisfy the requirements of the sustainable development, but most important, greenway planning is an important supplement of nonlinear landscape architecture greenway planning. Greenways connect the other non-linear landscape architecture system to form an integral body aiming to protect the landscape ecology. (Ahern J., 1995).

### 3 CASE STUDIES ON BEIJING RURAL GREENWAY

Although the concept of greenways has been heard from abroad only these recent years, Beijing rural zone has already few successful cases about roads complying with the greenway design concept. Let's take the Baili Landscape Painting Gallery of Yanqing and the Shentangyu Natural Scenic Area of Beijing as examples and give more details.

#### 3.1 *Baili landscape painting gallery*

The Beijing Yanqing Baili Landscape Painting Gallery is located in Qianjiadian Town, in the northeast of Yanqing County, and is the core zone of Yanqing Ecological Conservation Development Area. There are 56km main waterfront roads connecting 6 scenic spots, Guihuamuqun, Wulong Canyon, Dishuihu Scenic Area, Chaoyang Temple, Longwang Temple, and Guandi Temple, and numerous geological science and natural landscape such as Kunlun mountains, Shujian peak, marine deposits remains, Caimuguo aleolithic ruins, Wenchang monument, Datan natural reserve, Qianmiao Sunflower Sea, Wanmiao huangqin tea plantation, and Yanshan Painting Academy.

Thanks to the ecological resources, landscape and cultural resources of Baili Landscape Painting Gallery, since their integration, the tourism industry of Qianjiadian Town has boosted and increased the farmers' income. Plus, the recreational activities in the gallery are done in cycles, and the majority of accommodations are farmhouses. This system limits the over-exploitation and development of resorts and lands in the area. Therefore, not only the scenic spot provides to Beijing citizens

a tourism greenway rich in natural and cultural landscapes, but as a waterfront greenway, it also protects the habitat of wildlife, reduces the damages due to flood, and safe keeps water quality and groundwater level.

Having great cycling roadway, Bali Landscape Painting Gallery was named one of the "Ten Best Cycling Route of Beijing" in 2007.

The Bali Landscape Painting Gallery was not meant to be a greenway. But, the site possesses the 5 characteristics given by Ahern: has linear contour, connect many natural scenic spots and cultural landscapes, has various functions (tourism, recreation, education, and protection of historical heritage), contribute to the economic development of surrounding countryside, and satisfy the requirements of the sustainable development.

The waterfront ecological corridor links each part of the valley together to form an ecological network. Bali Landscape Painting Gallery awoke the local tourism resources and its construction is appropriate from the local geographical position point of view, forming a rural green land with strong local characteristic, a very successful rural greenway in Beijing.

#### 3.2 *Shentangyu natural scenic area*

The Shentangyu Natural Scenic Area is located in the Yanqi Valley in Buyegu. The total length from Buyegu Tourism Service Zone to the Shentangyu Natural Scenic Area is 7.558 km; it is Beijing's longest pedestrian plan road alongside cliffs with mountains and waters. The plank road and the roadway in the valley zone are parallel. The natural scenic area crosses fourteen sites, Chuangulanxiu, Taigongchuidiao, Linkongtingquan, Shanyedenghuai, etc., worth seeing, with mountain roads, appropriate for climbing. The place is just simple and natural, near mountains and waters. Shentangyu Natural Scenic Area is at the foot of a hill and beside a stream, a beautiful roadway for sightseeing, recreation, and fitness.

Shentangyu Natural Scenic Area adopts the following measures to reduce the contact between humans coming for recreation in the area and the wild animals living in the site: decrease the width of the greenway so to reduce the interference of wild animals; the greenway must keep distance with the river from vertical and horizontal levels to stay far away from wild animals' habitat; humans' sightseeing, education, experiential activities are all done from far away or from an observation space; reduce the environmental impact by using natural and impermeable materials.

### 4 BUILDING BEIJING RURAL GREENWAY PLANNING SYSTEM

Based on the specific ecological characteristics in Beijing and by combining Beijing's rural

topography, cultural characteristics and road network, the present article divides Beijing's rural greenways mainly into 4 types: riverfront type greenway, valley type greenway, cultural heritage type greenway, and natural ecological greenway.

#### 4.1 *Riverfront type greenway*

For many greenways, the most important landscape is the water landscape. The riverfront type greenway is the most important and the most used greenway. Main rivers in Beijing belong to the Hai River Drainage System, such as Yongding River, Chaobai River and Juma River, and to Ji River Drainage System such as Ju River. Most of the river basins are in the countryside, the source of water of Beijing city, and the lifeline of Beijing ecology and residents' life. The establishment of a waterfront type greenway has a very significant importance to the whole city of Beijing and to its ecological network. The ecological values of waterfront greenways are: provide ecological corridor to migratory species, use vegetation along the river to filter pollutants, reduce stream pollution, mitigate air pollution, regulate local climate. Since the waterfront greenways shall connect the city, the suburbs and the countryside, they run through the northwest of Beijing in the mountain areas, the city in the center and the southwest plain area to form an important ecological corridor. The greenways are the keys to connecting the city's ecological system with the forest ecosystem, garden ecosystem, and wetland eco-systems.

From the point of view of the importance of the ecological use of the waterfront greenways, the author thinks that the primary objective of Beijing's rural waterfront greenway must be ecological protection.

To protect wild animals, numbers of visitors in the site have been limited, and this is one of the important protective measure set. On the other hand, the design of greenway planning shall have close relation with river training work, ecological recovery, the city's drainage management. And when necessary, build a buffer at the appropriate point. The width of the greenway shall be determined based on the status of the area. As well, when needed, give all efforts to recover the natural vegetation, so that humans and cars stay far from the river edges. If there is really a need to approach the water, the plank road must be the first choice in order to avoid the complication of natural terrain and environment impact.

#### 4.2 *Valley type greenway*

Beijing has 7 counties in mountainous areas (Fangshan, Mentougou, Changping, Pingyong, Huaiyi, Miyun County, and Yanqing County), 83 villages and towns in mountainous and half-mountainous areas, a bit more than 1600 villages

committees, a total acreage of 1.04 km<sup>2</sup>, 62% of Beijing total area. Beside Wenyu River, the four drainage systems, the Daqing River, Yongding River, Chaobai River, and Liyun River all are in mountainous areas with large drainage area. The many stream tributaries form lots of valleys. In recent years, Beijing started to develop the valley economy. With valley economy as unit, Beijing began to build greenways to connect each industrial node together, develop the valley with the surrounding areas and plains, set a general plan for city and towns to promote and enrich the industry and provide more functions. (Chen etc., 2012) The boundaries of the valley are not administrative borders; they are mostly connecting most of the villages in the mountainous areas and coincide with main line of communications (Zhang, etc., 2009). At present, Beijing's valleys follow a model of economic development with Beijing mountains areas' local characteristics and a pattern of space network. Based on this pattern, the communication network within the valley economy and the surrounding lands are categorized into the rural greenways. All these contribute to the rational development and use of rural lands, to water protection, to recreational activities and also to increase the income from economic growth.

Since most of the valley greenways disperse the main river streams of Beijing city, valley greenways are mostly for ecological protection, and then for recreational and education of the people. Today, the development of valleys in Beijing has already benefit the city, significantly boosted the development of the rural economy. However, it has also led to some environmental problems. Taking Yebohai in Huairou as an example, it is located on reservoir of the upstream of Huairou river basin, one of the key valley constructions in Huairou district. Following the increase of the number of tourists, rainbow trout farms have been expanding. According to the Environmental Protection Administration test, these farms have already caused a certain degree of contamination on the water quality of the Huairou reservoir. (Shi, 2014) In the meantime, lots of resorts and hotels have been developed and entered the area, causing a great environmental burden. Thus, there is an urgent need to introduce more about the concept of greenways, strictly control the land development and limit the public recreational activities in the valley to protect the rural ecological environment. This has a great significance for the healthy development of Beijing.

#### 4.3 *Cultural heritage type greenway*

Beijing is a world famous historical and cultural city, one of the most ancient capitals. The city has large number cultural resources such as numerous cultural heritage protection units, historical and cultural route, and historical river drainage systems.

Rural greenways that connect historical and cultural heritage can form a green network for heritage protection and let people experience in real the memories of history and tradition, witness history and revisit ancient villages, buildings, ruins, tombs, modern building, historical, and cultural neighborhoods. Besides all, there are lots of historical and cultural routes in Beijing, such as Beijing-Hangzhou Grand Canal, the Royal Road of the Ming and Qing Dynasties, Jingxi Ancient Roads. They often connect with historical and cultural heritage points, have great value. They are important resources for the construction of Cultural Heritage-type Greenway.

#### 4.4 Natural ecological greenway

Beijing's natural ecological greenway is mostly landscape fragmentations due to road construction or mining work combined together and transformed into greenway, a space with greenery connected with wildlife habitats. Natural ecological greenway helps keep alive and healthy the diverse living beings in an area and reduce the facilities destroying the wildlife region within the area; it is a different kind of connecting network ecological corridor.

Beijing's natural ecological corridors are mainly along the western part of Taihang mountains and the northern side of Yanshan mountains, forming a linear space, building connections between natural reserves, forest parks and scenic areas, and provide migration corridors to living being. Simultaneously, implementing greening strategy contributes to reducing the uncertainty of the lands' situation and stopping the exploitation in the western mountainous areas, therefore would achieve the ecological protection, the safety of land and water quality and the survival of living beings in the area. (Wang, 2012).

This kind of natural ecological greenway mainly focuses on the requirements of biodiversity; therefore, the people in charge of the related planning shall have close relationship with wildlife experts to implement the related project. It is necessary to identify the wild animals within the area, the location of the habitats and the breeding-sites, as well as the animal tracks and migratory routes of the animals. The strategic points for wildlife conversation include knowing the animal tracks and migratory routes, the corridor interchanges, the intersection point of the animal biological corridor and the urban road, at least basic information related to the ground and the wildlife in the area. Then based on these key notes, arrange an ecological restoration, set up animal routes. (Yu, 2009).

## 5 CONCLUSION

The construction of rural greenways in Beijing must suit Beijing's geographical position, fully

respect the existing road network, forest network, water network, take into account ecology, landscape science, economy and other field techniques, and reflect multi-functionality and connectivity of the greenway. (Jack Ahern etc., 2011).

Greenways can help protect the countryside's environment since greenways protect natural ridges, rivers and nature, and human and cultural resources, therefore can project the countryside, prevent the countryside to rapidly become a city. Greenways are important supporting planning to protect farmland and open spaces. All the characteristics of greenways combined are protective measures. The whole system forms the rural greenway network, a significant key point for Beijing ecological safety.

## REFERENCES

- [1] Ahern J. Greenways as a planning strategy [J]. *Landscape and Urban Planning*, 1995,33:131–155.
- [2] Chen Junhong, Li Hong, Zhou Liandi. Exploration and Practice of Economic Development in Mountain Area of Beijing City [J]. *Ecological Economy*, 2010,01:57–62.
- [3] Flink, C.H. Searns, R.M. Greenways: Guide to Planning, Design and Development [M]. Washington, DC: Island press, 1993.
- [4] He Fang, etc., An Exploration on the Approaches to the Construction and Planning of Greenways in China\_A Case Study of Pearl River Delta Regional Greenway Planning [J]. *Landscape Architecture*, 2010,02:70–73.
- [5] Jack Ahern, Zhou Xiao. Greenway Planning Theory and Methods [J]. *Landscape Architecture*, 2011,05:104–107.
- [6] Little, C.E. Greenways for America. Johns Hopkins [M]. Baltimore: University Press, 1990.
- [7] Liu Binyi. The Strategic Role of Greenway in the Development of Ecological and Cultural Districts of Chinese Cities and Towns [J]. *China Landscape Architecture*, 2012,06:5–11.
- [8] Qin Fan. Study on Construction Strategy of Greenway System in Beijing Suburb [D]. Beijing Forestry University, 2014.
- [9] Shi Zhongfeng. Some Reflections on Huai'rou Economy Development; Buyugu, Yebohai and Baihe Bay as example [J]. *Beijing Water*, 2014,01:60–62.
- [10] Sun Lei, Pan Yi, Comparative Study of Greenway of Boston Metropolitan Park System and the Pearl River Delta—Shenzhen Case [J]. *China Landscape Architecture*, 2011,01:17–21.
- [11] Wang Xian. Establishing THE Theory of Beijing Greenway Planning and Design [D]. Northwest A&F University, 2012.
- [12] Yu Kongjian, Wang Sisi, Li Dihua, Li Chunbo, The function of ecological security patterns as an urban growth framework in Beijing [J]. *Acta Ecologica Sinica*, 2009,03:1189–1204.
- [13] Zhang Yifeng, Jia Dameng, The Spatial Structure of Valley Economy Development in the Mountainous Areas of Beijing [J]. *Acta Geographica Sinica*, 2009,10:1231–1242.

# Numerical evaluation for climates adaptive capability of traditional alkaline soil dwelling

Tao Zhang

School of Art, Xi'an University of Architecture and Technology, Xi'an, China

Jiaping Liu

School of Architecture, Xi'an University of Architecture and Technology, Xi'an, China

Qiwei Zhang

Construction Management Department, Shaanxi Xixian New Area Development Group, China

**ABSTRACT:** The present study is concentrated on evaluating the climate adaptive capability of alkaline soil dwelling by means of comparing the thermal performances between alkaline soil dwelling and brick house. The analysis results show that, for alkaline soil dwelling, the values of thermal resistance  $R_0$ , thermal inertia index data  $D$ , reduction coefficient of thermal wave transferring  $V_0$ , and thermal transferring delaying time  $\xi_0$  are much bigger than current brick house. Therefore, regarding climate adaptive capability, traditional alkaline soil dwelling is much better than brick house.

**Keywords:** alkaline soil dwelling; thermal resistance; thermal inertia index data; reduction coefficient of thermal wave transferring; thermal transferring delaying time

## 1 INTRODUCTION

Alkaline soil is widely distributed in the western of northeast plain. In west Jilin province, alkaline soil are mainly distributed in the Baicheng, Tongyu, Daan, etc., that most of them are alkaline soil swamp without any plant growth. The local climate belongs semi-arid continental monsoon climate with long and cold winter and short and cool summer. The typical city of this area is Baicheng city with annual average temperature 5 °C, average annual

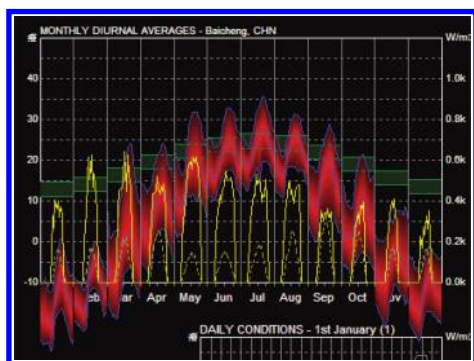


Figure 1. Average daily temperature change curves of Baicheng city.

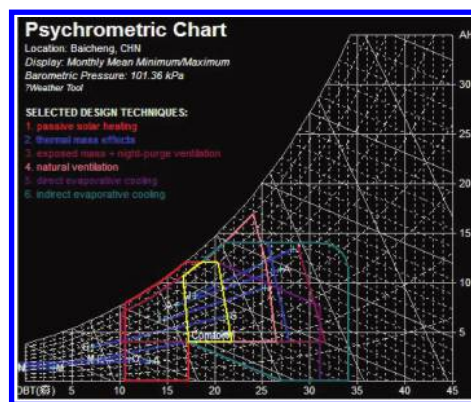


Figure 2. Passive design strategy chart of Baicheng city.

rainfall 398.4 mm, annul sunshine 2919.4 hours and abundant solar energy resources. Average daily temperature change curves and passive design strategy of Baicheng city are shown in Figures 1 and 2.

In order to adapting alkaline land and harsh climate in northeast China, cultivation farmers created a unique residential—alkaline soil dwelling, which is made of local alkaline soil and based on the perspective of nature and aesthetic, adjusting measures to local conditions. There is sparse population in the

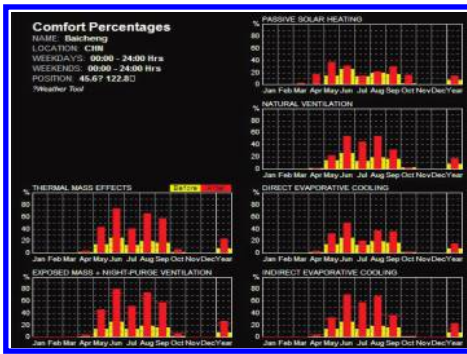


Figure 3. Effect of different passive designs strategies of Baicheng city.

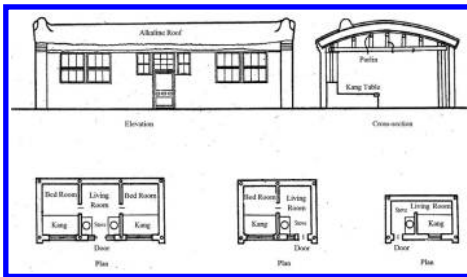


Figure 4. Elevation, cross-section, and plan of typical alkaline soil dwelling.



Figure 5. Typical alkaline soil dwelling.

local area, so local people used to choose shadow embrace sunny area to build houses. Village layouts are usually opening matrix or spread-point distribution. Courtyard layout is usually opening and spacious. Local buildings possess some uniform features—small, compact, sunny exposure, and attached worm room. All of these measures reflect the typical climates adaptability and ecological characteristics. Elevation, cross-section, and plan of typical alkaline soil dwelling are shown in Figure 4 and typical alkaline soil dwelling is shown in Figure 5.

## 2 MATERIAL AND STRUCTURE OF ENVELOPE

Owing to severe natural environment of alkaline soil area such as scarce wood resources, sandy climate, and low temperatures, the envelope and roof of local buildings are usually structured by wood and enclosed by mixture of alkaline soil, sorghum stem, and Chinese wild rye. Alkali soil is grey, very fine particles, no sticky, no hygroscopicity, fine waterproof performance and cheap material. Grasses are widely used for wall, roof, kang mat, and shade curtains because of their properties of wide distribution, diversity species, good flexibility, local materials, and economy.

Rammed soil wall, also known as “cross wall”, is built by ramming alkaline soil incorporation of bits of cathayense. While constructing, well-mixed alkaline soil is filled in the timber formwork. Every 2 meters wall is regarded as one construction segment. Finally, 700 mm bottom width, 500 mm top width, and 600 mm thick wall has been finished. Adobe wall is made of adobe with 440 mm thick gable and 360 mm thick eaves wall. As adobe wall is difficult to avoid the gap space easy to leak wind, rammed soil wall has better thermal protection capability than adobe wall.

There are two types of roof for alkaline dwellings: flat roof and arch roof with slightly curve. Alkaline roof constructing approach is (Fig. 4): first, resting beams on the top of the wall or column and purlins on beams; second, paving 100 mm thick tile baling reed or sorghum stalk; third, paving 100 mm thick chinensis; fourth, and claying 200 mm thick strawed alkaline mud; and finally, compacting 30 mm thick alkaline mud 2 ~ 3 layers. This approach can extend the building life more than one hundred years, even if the beams damaged, roof still will not fall. Exterior wall and roof of typical alkaline soil dwelling are shown in Figure 6.



Figure 6. Exterior wall and roof of typical alkaline soil dwelling.

### 3 THERMAL PERFORMANCE ANALYSIS OF ENVELOPE

#### 3.1 Thermal performance analysis of exterior wall

Two types of exterior wall have been calculated: 600 mm thick rammed earth wall and 440 mm thick adobe wall. Thermal physical properties calculation results are shown in Tables 1 and 2.

Thermal physical properties calculation for two kinds of normal brick wall with 240 mm thick and 370 mm thick have also been carried out. Calculation results are shown in Tables 3 and 4.

Insulation performance: the thermal transfer resistance of rammed earth wall, adobe wall, 240 mm thick normal wall and 370 mm thick normal wall is 1.06 m<sup>2</sup>·K/W, 0.98 m<sup>2</sup>·K/W, 0.57 m<sup>2</sup>·K/W, 0.77 m<sup>2</sup>·K/W respectively. The external walls' thermal insulation performance of alkaline soil dwelling is much better than normal brick wall house. As a result, in winter, the external walls' of alkaline soil dwelling can more effectively reducing heat energy outflow.

Thermal inertia performance: the thermal inertia of rammed earth wall, adobe wall, 240 mm

Table 1. Alkaline soil room rammed earth wall thermal performance calculation table.

	20 mm thick plaster	600 mm thick rammed earth	20 mm thick plaster
$\lambda_i$ (W/m·K)	0.15	0.93	0.15
$R_i$ (m <sup>2</sup> ·K/W)	0.133	0.645	0.133
$S_i$ (m <sup>2</sup> ·K/W)	2.79	11.03	2.79
$D_i$	0.372	7.116	0.372
$R_0$ (m <sup>2</sup> ·K/W)	1.06		
$\Sigma D$	7.86		
$V_0$	585.4		
$\xi_0$ (hour)	23.68		

Table 2. Alkaline soil room adobe wall thermal performance calculation table.

	20 mm thick plaster	440 mm thick adobe	20 mm thick plaster
$\lambda_i$ (W/m·K)	0.15	0.78	0.15
$R_i$ (m <sup>2</sup> ·K/W)	0.133	0.564	0.133
$S_i$ (m <sup>2</sup> ·K/W)	2.79	10.10	2.79
$D_i$	0.372	5.709	0.372
$R_0$ (m <sup>2</sup> ·K/W)	0.98		
$\Sigma D$	6.44		
$V_0$	208.2		
$\xi_0$ (hour)	19.82		

Table 3. Normal 240 mm thick brick wall thermal performance calculation table.

	20 mm thick plaster	240 mm thick brick	20 mm thick plaster
$\lambda_i$ (W/m·K)	0.87	0.64	0.87
$R_i$ (m <sup>2</sup> ·K/W)	0.023	0.375	0.023
$S_i$ (m <sup>2</sup> ·K/W)	10.75	8.49	10.75
$D_i$	0.247	3.184	0.247
$R_0$ (m <sup>2</sup> ·K/W)	0.57		
$\Sigma D$	3.68		
$V_0$	17.68		
$\xi_0$ (hour)	13.31		

Table 4. Normal 370 mm thick brick wall thermal performance calculation table.

	20 mm thick plaster	370 mm thick brick	20 mm thick plaster
$\lambda_i$ (W/m·K)	0.87	0.64	0.87
$R_i$ (m <sup>2</sup> ·K/W)	0.023	0.375	0.023
$S_i$ (m <sup>2</sup> ·K/W)	10.75	8.49	10.75
$D_i$	0.247	4.908	0.247
$R_0$ (m <sup>2</sup> ·K/W)	0.77		
$\Sigma D$	5.40		
$V_0$	59.80		
$\xi_0$ (hour)	17.97		

thick normal wall and 370 mm thick normal wall is 7.86, 6.44, 3.68, 5.40 respectively. The results show that the external walls' of alkaline soil dwelling can more effectively reducing temperature fluctuations.

In summer daytime, the surface temperature of external walls rise by means of absorbing heat from outdoor environment. The peak surface temperature is reached at afternoon. Under the action of thermal inertia, heat storage performance and delay performance, the heat flux, heat flux amplitude and temperature amplitude will reduce greatly, so the peak value of inner surface temperature will be delayed to the early morning. At that time, cooling indoor conditions can be achieved by opening the doors and windows to increase ventilation.

In winter daytime, the external walls absorb and save a large amount of solar heat radiation. When the outside temperature plunge to the lowest at night, under the action of thermal inertia, heat storage performance and delay performance, the heat accumulated in external walls during the daytime radiation from outside can heat the indoor environment at night. Strong thermal inertia of alkaline soil dwelling can keep the wall

Table 5. Thermal performance of roof in alkaline soil room calculation table.

	30 mm thick plaster	200 mm thick clay	100 mm thick chinensis	100 mm thick sorghum stalk
$\lambda_i$ (W/m·K)	0.93	0.349	0.047	0.07
$R_i$ (m <sup>2</sup> ·K/W)	0.032	0.573	2.128	1.429
$S_i$ (m <sup>2</sup> ·K/W)	11.03	6.36	0.83	0.94
$D_i$	0.36	3.64	1.77	1.34
$R_0$ (m <sup>2</sup> ·K/W)	4.32			
$\Sigma D$	7.11			
$V_0$	547			
$\xi_0$ (hour)	21.22			

Table 6. Thermal performance of roof in normal brick house calculation table.

	30 mm thick plaster	100 mm thick RC slab	20 mm thick plaster
$\lambda_i$ (W/m·K)	0.93	0.78	0.87
$R_i$ (m <sup>2</sup> ·K/W)	0.032	0.564	0.023
$S_i$ (m <sup>2</sup> ·K/W)	11.03	10.10	10.75
$D_i$	0.36	5.709	0.247
$R_0$ (m <sup>2</sup> ·K/W)	0.26		
$\Sigma D$	1.60		
$V_0$	4.10		
$\xi_0$ (hour)	8.34		

surface temperature at a higher level whole day in winter.

From the above analysis results, thick heavy envelope of alkaline soil dwelling can effectively reduce indoor outdoor heat transfer, and reduce the indoor temperature fluctuation.

### 3.2 Thermal characteristics analysis of roof

The roof of alkaline soil dwelling is consisted of 200 mm thick clay layer, 100 mm thick chinensis layer and 100 mm sorghum stalk layer. The roof configuration layers of brick house are 30 mm waterproof mortar, 100 mm RC slab, and 20 mm thick plaster. Calculation results are shown in Tables 5 and 6.

To the calculation results, for alkaline soil dwelling, the values of four thermal physical properties are significantly larger than brick house. Therefore, the roof of alkaline soil dwelling can also provide ideal thermal stability and thermal comfort.

In general, by means of its own thermal property of the soil, the thermal transmission speed for wall and roof of alkaline soil dwelling is very slow. As a result, this type of envelope

Table 7. Thermal property comparison of wall between alkaline soil dwelling and energy-saving code.

	Code	Alkaline soil dwellings	Brick house
$R_i$ (m <sup>2</sup> ·K/W)	2.5	4.32	0.26
Percentage	–	172%	10%

Table 8. Thermal property comparison of roof between alkaline soil dwelling and energy-saving code.

	Code	Alkaline soil dwellings	Brick house
$R_i$ (m <sup>2</sup> ·K/W)	1.67	1.06	0.57
Percentage	–	63%	34%

structure can easily adjust the temperature fluctuation and create a pleasant internal thermal environment.

## 4 THERMAL PROPERTY COMPARISON BETWEEN ALKALINE SOIL DWELLING AND ENERGY-SAVING CODE

The comparison results of thermal property between alkaline soil dwelling and energy-saving code are shown in Tables 7 and 8. The results shows that the thermal resistance of envelope of alkaline soil dwelling is very close to the demand of energy-saving code and is much better than brick house. Although thermal resistance of external wall still have to meet the code, it is also better than brick house. In the process of old residential renovation and new residential construction, improvement the thermal property of envelopes will greatly promote indoor comfort property, reduce the cost of renovation and reduce the waste of resource.



## 5 CONCLUSION

In the process of old residential renovation and new residential construction, masses of house in rural area mindlessly aping city building to build brick house. These brick houses look capacious and bright; therefore, their thermal properties are much worse than traditional alkaline soil dwelling. In present study, the climates adaptive capability of traditional alkaline soil dwelling has been evaluated. The comparisons to different thermal physical properties such as thermal resistance  $R_0$ , thermal inertia index data  $D$ , reduction coefficient of thermal wave transferring  $V_0$  and thermal transferring delaying time  $\xi_0$  have been performed between alkaline soil dwelling and brick house. Comparing result shows that the alkaline soil

dwelling has much better thermal properties than brick house. As a result, this type of residential house type can easily adjust the temperature difference and create a pleasant internal thermal environment.

## REFERENCES

- Lin Borong, Wang Peng, Zhao Bin. Traditional courtyard houses the numerical simulation of wind environment research. *Architectural Journal* 393: 47–48.
- Liu Jiaping, Tan Liangbin, He Quan. 2009. *Energy Saving Design in Architectural Design*. Beijing: Architecture & Building Press.
- Zhou Lijun. 2009. *North-East Dwellings-Chinese Tradition Dwelling Research*. Beijing: China Architecture & Building Press.

# Qualitative study of climate adaptability of traditional alkaline dwelling

Tao Zhang

School of Art, Xi'an University of Architecture and Technology, Xi'an, China

Jiaping Liu

School of Architecture, Xi'an University of Architecture and Technology, Xi'an, China

Qiwei Zhang

Construction Management Department, Shaanxi Xixian New Area Development Group, China

**ABSTRACT:** Based on architecture form, construction methods, structure selection, and material application research, this study is concentrated on evaluating the climate adaptive capability of Jilin Alkaline dwelling by means of statistics, calculation and comparison, and the computer simulation method. The analysis results show that Jilin Alkaline dwelling have good climate adaptability and ecological superiority characteristic, which is worth promoting.

**Keywords:** Jilin Alkaline dwelling; climate adaptation; shape coefficient; hybrid wall frame; fork wall

## 1 INTRODUCTION

The production of traditional houses are masses of working people in the long-term production and life practice, according to their own requirements, combining with local climate conditions, geographical environment, customs and habits, with wisdom and skills to create products. Various forms of traditional local-style dwelling houses everywhere reflect the harmony of man and nature, and give us a large number of valuable experience.

Alkali soil in the western of northeast China plain distribute wide, there into Jixi alkaline are

mainly distributed in west Baicheng and Tongyu, Jilin province. In the local, there is alkali swamp land without any plant growth. In order to adapt to the local alkaline land and harsh climate, local people created a unique northeast shape alkaline dwelling, a kind of civil house with soil wall and soil flat.

Baicheng, Tongyu, and Dan'an locate in the sub temperate zone with a sub-humid continental monsoon climate. There are long cold winter and short cool summer. Baicheng is located in the northwest of Jilin Province, altitude of 155.3 m. Average daily temperature change curves and Passive design strategy of Baicheng city are shown in Figure 1.

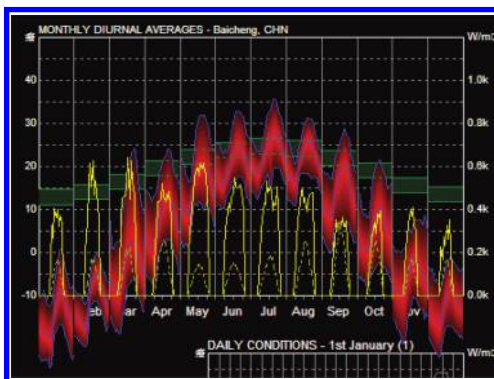


Figure 1. Average daily temperature change curves of Baicheng city.

## 2 CLIMATES ADAPTABILITY AND ECOLOGICAL CHARACTERISTICS OF ARCHITECTURAL FORM

### 2.1 Settlement location—shadow embrace sunny

West Jilin alkali soil area is sparsely populated area. Local people building used to choose shadow embrace sunny area to build houses. Experimental data show that, in the mountain area, the total temperature of sunny side is about 10 °C higher than shadow side due to more sunlight temperature which effectively improve the comprehensive outdoor temperature in winter and create more comfortable indoor thermal environment.

## 2.2 Village layout—opening matrix or spread-point distribution

In sparsely populated northeast area, local people choose open flat field to build independent building whereas forming matrix distribution in city and spread-point distribution in countryside. Both layouts can provide large spacing between each building that winter sunshine can maximum project on the window or outside wall without shade in order to meet the demands of directly winter heat gain for the building. Typical village layout is shown in Figure 2.

## 2.3 Courtyard layout—open and spacious

The courtyard of alkaline dwellings is unique spacious courtyard patten in northeast zone. In each building, foreyard is used for producing and living and backyard is used for food storage. Surrounding 1.5 meters high low alkaline walls are built around the building. Open up channels have been created between houses and walls for the convenience of food conveying; therefore, the separate form between houses and walls have been developed (Fig. 3).

The width-to-depth ratio of Binary compound space is 0.8 ~ 1.9 in northeast zone and 0.3 ~ 1.0 in Shaanxi province, thus courtyard scale is large more than warm temperate region. The reason is that in cold weather northeast zone, the use of open broad courtyard layout to avoid block building by each other, the south walls and windows can get more sunshine in winter, thus more winter sunlight and indoor heat gain be carried out. At the same time, computer CFD compound wind

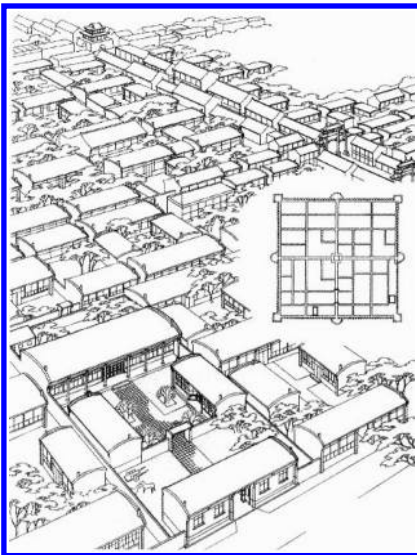


Figure 2. Typical village layout.



Figure 3. Typical courtyard layout.

environment simulation results show that even the opening courtyard will not increase the winter air volume and wind speed.

## 2.4 Building shape features—small, compact, and sunny exposure

The statistical results of 9 representative farmhouse in the Qing Shan Bao Village, Baicheng, Jilin province show, room depth is about 5.46 m, width is about 3.02 m, clear height is about 2.37 m, building shape coefficient average is about 1.04, and window wall area ratio of south direction is about 18%. First, large depth and square layout of Alkaline dwellings can effectively reduce shape coefficient and surface heat dissipation area. Second, large south area can get more winter solar radiation heat gain. The calculation results show that, in alkaline dwellings, south interface absorption of sunlight heat radiant in winter is greater than its heat lost.

## 2.5 Plain layout—compact and attached warm room

Alkaline dwellings usually include three or five rooms. For example, in a three-room dwelling, the kitchen with tanks and stove is located at center of house. (Fig. 4). Heaven is around pass through chamber of fire resistance. The warm room, equipped with small heaven in order to warm cloths in winter is located at back part. Warm room isolated cold air from north wall and gateway together with stove in kitchen. Bed room is located on the right sides and left side of the main room. One straight heatable brick bed with flue directly going through outside is set up in each bed room. Elevation, cross-section and plan of typical alkaline soil dwelling are shown in Figure 3.

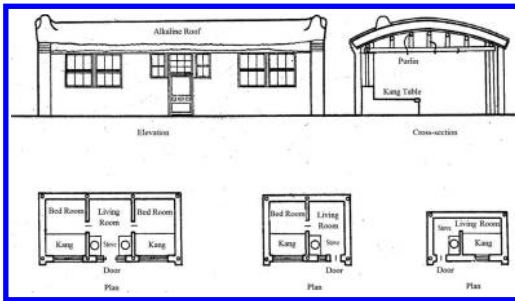


Figure 4. Elevation, cross-section and plan of typical alkaline soil dwelling.

### 3 CLIMATES ADAPTABILITY AND ECOLOGICAL CHARACTERISTICS OF ENVELOPE COMPONENTS

#### 3.1 Wall

There are two types of wall shape: rammed soil wall and adobe wall. Rammed soil wall, also known as “cross wall”, is built by ramming alkaline soil incorporation of bits of cathayense. While constructing, well-mixed alkaline soil is filled in the timber formwork. Every 2 meters wall is regarded as one construction segment. Finally, 700 mm bottom width, 500 mm top width, and 600 mm thick wall has been finished. Adobe wall is made of adobe with 440 mm thick gable and 360 mm thick eaves wall. As adobe wall is difficult to avoid the gap space easy to leak wind, rammed soil wall has better thermal protection capability than adobe wall.

#### 3.2 Roof

There are two types of roof for alkaline dwellings: flat roof and arch roof with slightly curve. Alkaline roof constructing approach is shown in Figure 4: first, resting beams on the top of the wall or column and purlins on beams; second, paving 100 mm thick tile baling reed or sorghum stalk; third, paving 100 mm thick chinensis; fourth, and claying 200 mm thick strawed alkaline mud; and finally, compacting 30 mm thick alkaline mud 2 ~ 3 layers. This approach can extend the building life by more than one hundred years, and even if the beams damaged, the roof will not fall.

Owing to its good thermal inertia property, envelope structure of alkaline dwellings possess slow heat absorption and dissipation characteristics, which can effectively reduce the heat transfer between indoor and outdoor, avoid indoor temperature fluctuation, and adjust the temperature difference between day and night naturally, so as to create a pleasant indoor thermal environment.



Figure 5. Alkaline soil wall.

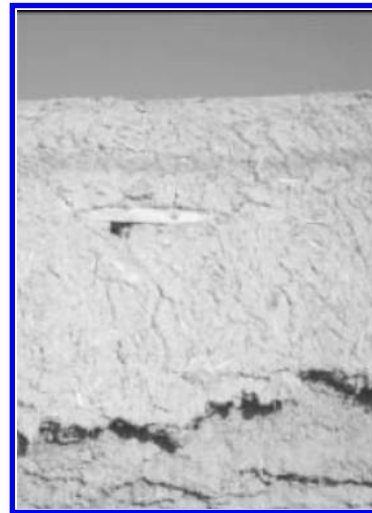


Figure 6. Roof of alkaline soil dwelling.

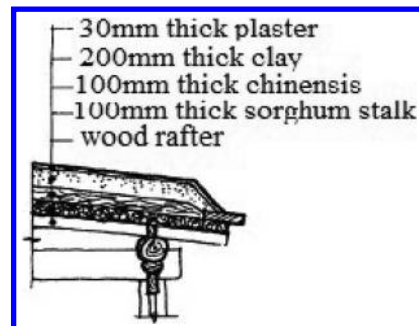


Figure 7. Roof construction detail.

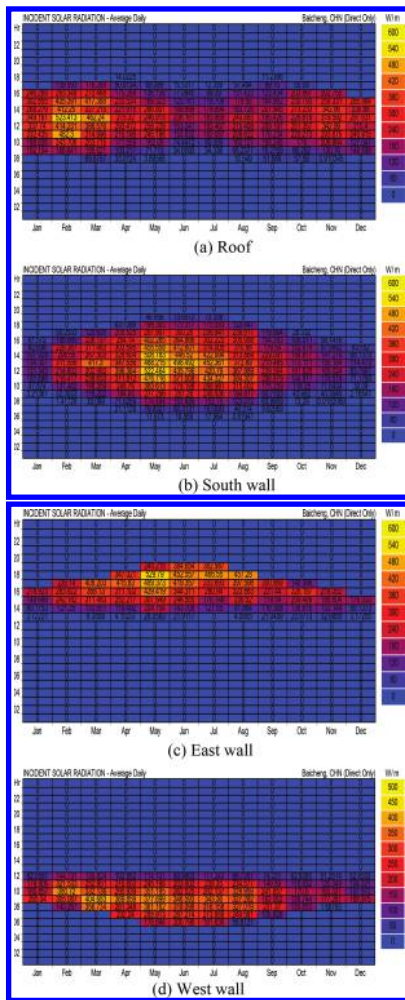


Figure 8. South wall surface of the sun direct radiation.

### 3.3 Window

There are removable window consisting of two fans on the north and south wall of back room. The upper fan can be lifted by the iron hook or with short stick for ventilation. The lower fan can be removed at any time. Outside of the window can be pasted with paper, such as most common Korea paper, a paper tubed oil, or brine-processed special paper in order to effectively prevent the rain and snow wet paper leading to the loss.

Considering the local climate differences, different demands of accepting and rejecting direct solar radiation, almost all traditional dwellings, use overhanging length of eaves to control window shadow. Calculation results of relationship between casting light depth and eave overhanging length are shown in Figure 9.

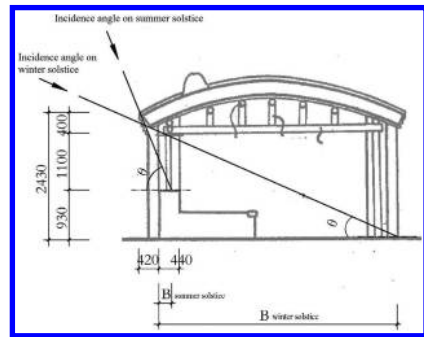


Figure 9. Incidence sunshine analysis.

South eaves are over hanged at 420 mm. The incident angle of the sunlight is low in winter, so the sunlight can completely enter indoor at noon (home invasion depth of 5082.16 mm). The incident angle of the sunlight is high in the summer; the sunlight can only enter on windowsill at noon (home invasion depth of 190.61 mm). At the same time, south roof on the entrance can guide snow away from the foot of the wall, so as to secure and extend the durability of wall. In summer, weather is not so hot, so east-west side of the house need not shade. In winter, maximum sunlight can heat the wall; simultaneously, high heat storage of wall body can also improve indoor comfort level.

## 4 CONCLUSION

Alkaline dwellings have many ecological characteristics such as land resource saving vertical village distribution, functional plain layout, local material use, simple construction method, economic, as well as many climate adaptabilities that modern ordinary residential housing do not possess. Therefore, we should focus on improving the structure node and the construction technology of traditional alkaline dwellings, taking full advantage of local resources, developing built technology, and carrying forward the traditional local-style dwelling houses into modern residential buildings.

## REFERENCES

- [1] Zhou Lijun. 2009. *North-East Dwellings-Chinese Tradition Dwelling Research*. Beijing: China Architecture & Building Press.
- [2] Liu Jiaping, Tan Liangbin, He Quan. 2009. *Energy Saving Design in Architectural Design*. Beijing: Architecture & Building Press.
- [3] Lin Borong, Wang Peng, Zhao Bin. Traditional courtyard houses the numerical simulation of wind environment research. *Architectural Journal* 393: 47-48.

## Plant configuration discussion of urban riparian park in the loess plateau region: Setting Taiyuan Fenhe Park as an example

J.Y. He & J. Gao

*College of Architecture and Civil Engineering, Taiyuan University of Technology, Taiyuan, Shanxi, China*

**ABSTRACT:** Urban riparian park is a characteristic element in urban green space system. It not only assumes the function of urban ecological corridor, but also becomes the bridges in the urban green space network system as its strip shape, waterfront location. Setting Taiyuan Fenhe Park as an example, this paper expounds the concept and characteristics of urban riparian park, explaining the principles of plant configuration. Then, the paper discussed the existing problems of fen river park in Taiyuan, seeking for the ecological plant configuration mode of the urban riparian park of the loess plateau region.

**Keywords:** urban riparian park; the loess plateau region; plant configuration; ecological

### 1 CONCEPT OF RIPARIAN PARK AND SIGNIFICANCE OF PLANT CONFIGURATION

According to the "Urban Green Space Classification Standard" (CJJ/T85-2002), riparian park the park green space in the five urban green space types, at the same time belongs to belt-shaped park, one of the five park green space types. Riparian park is the essence of green space system, usually combined with city water system. And it bears the function of urban ecological corridor. As the land conditions affect the width, the riparian park shape is long and narrow. It is through the landscape node with waterfront greening.

Throughout history, rivers not only provide water to the city and constitute transportation, so that the humans can thrive, creating civilization, but also are closely related to the urban ecological plaque architecture, which has profound significance to the attenuation of the urban heat island and flooding, composition of landscape diversity, and the protection of species diversity. Plants grown thereon, ornamental characteristics, species composition, and community structure have largely determined the quality and its exertion of ecological role in waterfront landscape, affecting the quality and level of urban waterfront landscape and the ecological development of the city. Hence, to create a scientific and rational waterfront plant landscape with urban characteristics is of great significance to conservation of biodiversity in urban waterfront, and to create a harmonious and green living environment. Currently, researches on plant configuration in urban riparian parks are mostly

developed at the macro level using the theory of urban planning, and there are few studies at the micro-level suited to local conditions conducted in the local waterfront plant landscape. Part of them is limited to theory of plant gardening in city park, failed to closely integrated with the specific characteristics of the waterfront environment. Taking Fenhe Park in Taiyuan as an example, this article has made analysis of its plant configuration guidelines and existing problems in order to seek more scientific and suitable way of ecological plant configuration.

### 2 CURRENT SITUATION OF FENHE PARK IN TAIYUAN AND THE FUNCTIONAL CHARACTERISTICS OF URBAN RIPARIAN PARKS

Taiyuan is located in the central of Shanxi. Its east, west, north three sides are surrounded by mountains, besides its middle and southern parts are plains of the valley. Its average elevation is about 800 m. Its average annual rainfall is 442 mm and its annual average temperature is 9.5 °C. The coldest month in Taiyuan is January, the average temperature is 6.8 °C, and the hottest month in Taiyuan is July, the average temperature is 23.5 °C; Frost-free period is 116 d to 165 d. The soil in Taiyuan is slightly alkaline or alkaline, and the brown soil is the main kind [1]. The climate in Taiyuan is north temperate zone continental climate. Taiyuan has rich plant resources, ancient origin, and many single species. Existing greening tree species has 235 species, belonging to 61 families, [2].

Taiyuan Fenhe park laid on both sides of fen river, which place is flat, and with more than 18 kilometers long. The green space of the first issue is 1.3 million square meters, contains 24000 plants and shrubs which belongs to 183 species, and 820000 square meters of lawn, more than 10000 Outdoor perennial root flowers. The park formed an one hundred meters wide, 6 km long green ecological corridor. Launched in 2014, the third phase extends to the north and the south, throughout the city.

In comparison between urban riparian parks and other types of green areas, the two have both general feature and its individual features. General feature includes: recreation, disaster prevention, landscaping, sound ecology, and spiritual culture. Individual features: 1. banding form. 2. Waterfront area. 3. Strong openness. 4. Significant effect of corridor. Role of corridor in urban riparian parks is reflected in the form. First, its linear band is a natural form of corridor; second, in promoting the flow of urban air, it has become airy corridor of the city, while it allows the spread of natural plants more convenient and the ecology more diverse, with quite obvious ecological corridor role. 5. Network connectivity. In the network of urban green space system, the linear and banding urban riparian parks have function of network connection. It can connect green points and green surface distributed in different sections of the city by the extension of linear band, so as to weave the city's green network structure [3].

### 3 THE DESIGN PRINCIPLES OF PLANT CONFIGURATION IN URBAN RIPARIAN PARKS OF LOESS PLATEAU

#### 3.1 *Follow the systematic principle from a macro perspective of the whole region*

Systematic principle refers that in plant configuration of urban riparian parks, the system theory is regarded as the principle, and the urban riparian parks, taken as constituent elements of the entire city green large system, and other forms of urban green spaces are interrelated and interact on each other to form a unified system of urban green space. Plant configuration in urban riparian parks is required to comply with two ways, namely, the coordination with urban master planning and overall urban environment.

Fen River Park runs through the city in belts, and is connected to the city expressway, thus it shall obey the overall urban planning, regulating various types of urban land-use in strict accordance with the overall urban planning, to achieve coordinated and balanced urban development.

#### 3.2 *Follow ecological principle from the micro perspective of city parks*

The natural environment of each region is the most basic guarantee to maintain the city's ecological functions as a whole. During the planting design in urban riparian parks, the ecological environment of the urban riparian parks should be given high priority and strict protection. According to the principles of ecology, natural ecological landscape is simulated in terms of configuration of biological populations and communities, as well as settings of topography, geomorphology and river waters to manually create a living environment adapted to its evolution for biological species and community, so as to make artificial landscape "naturalized, so that the application of the method of ecological greening in "approx-natural" community" can be promoted. The application of the method of ecological greening in "approx-natural" community" refers to regard the potential natural vegetation and community succession in ecology as basic theory to select suitable native plants [4].

Natural plant communities in waterfront of Fenhe Park are located at the boundary of two ecosystems of waters and land, ecologically called ecotone. Its flow and exchange of material and energy is very frequent, with quite high biodiversity and environment productivity, and its natural vegetation is characterized by the community form of abound species and complex structure.

#### 3.3 *Follow humanized principle from perspective of visitors' feelings*

From the view of visitors, the core of the design is to focus on humanized site design. People have the nature to be close to nature and water. Accordingly, in the configuration of plants and on the basis of meeting safety specifications, we shall do our best to imitate nature and increase accessibility. "Design with Nature" is put forward by the designer McHarg, and its essence is to design landscape with the environmental studies and other related disciplines theory as a guide, and its purpose is by introducing natural environment, to ecologically create woods, lawns, streams, etc.[5].

Fenhe Park has open Structure, should be using good color and formation to well-integrated surrounding buildings into the environment, which enables visitors to feel more natural. Waterfront plants have a complex structure, multiple levels and rich types, so that it can take advantage of scale, the degree of enclosure, to combine with the road and architectural pieces. And it can be divided into primary and subordinate fields, public and private spaces, which improves the possibility for people to choose and meet diverse needs.

#### 4 DISCUSSION ON THE EXISTING PROBLEMS IN FENHE PARK AND RECOMMENDATIONS FOR THE PLANT CONFIGURATION IN URBAN RIPARIAN PARKS OF LOESS PLATEAU

Plants have become the main material of landscape planning and design and construction, for they can not only improve the ecological environment which humans rely for existence, but also can create a beautiful space of realm, playing a very important role in construction of garden space [6]. There still exist several aspects that need to be further improved in Fenhe Park in Taiyuan at present, such as the lack of systematicness and stability in plant community structure, landscape heterogeneity to be enhanced, insufficient plant community level, inadequate considerations for storm water management, and the enjoyment of tour. Hence, plant configuration can be improved from the following aspects:

- a. Ecological community structure of natural river shoreline shall be simulated, with emphasis on matching species with the site, and specialized in native trees. Choice of varieties should be in line with various demands of the landscape and ecology, focusing on maintaining structural stability. Final-period management shall be strengthened to avoid ecological imbalance caused by excessive inundation of aquatic and wetland plants. For instance, some floating plants should be planted in a small pool of water, or their growth ranges are delineated with a fence to prevent water eutrophication caused by the large accumulation of plant residues, resulting in secondary pollution of aquatic and wetland plants.
- b. Landscape heterogeneity should be increased to emphasize the landscape character and to promote the circulation of natural objects, thereby framing urban habitat corridor. Elements of natural vegetation should be introduced to ecologically sensitive areas in the waterfront, including the proper construction of ecological protection areas of the waterfront, as well as the establishment of a variety of wildlife habitats, and division of the specific scope of protection.
- c. In addition to focusing on ornamental requirements, also combined with the vertical design of terrain, typical landscape features (such as estuaries, beaches, wetlands, etc.) formed in natural process of forming drainage are simulated to create terrain environment suitable for waterfront plants. With naturalization and diversity of plant as the guiding principle, configuration of aquatic, near-water, terrestrial plants shall be conducted according to the natural distribution and characteristics of the system of waterfront

- waters and land areas, to reflect the characteristics of natural evolution, creating a continuous waterfront green band. In addition to choice of conventional ornamental trees, we must also focus on nurturing water-resistant plants or aquatic plants locally, paying attention to the complex vegetation communities of waterfront.
- d. In allusion to the rainy summer in Loess Plateau, from the angle of urban stormwater management, the urban sponge technology is used to reduce hardening of plant and to increase permeable paving. For the catchment area with serious pollution, vegetation buffer zones are increased for pretreatment of rainwater runoff. In area of water purification in rainwater wetland, according to water depth, different types and levels of aquatic organisms are planted. Vegetation buffer zones should be increased, and the flow velocity of overland runoff is retarded through action of vegetation interception and soil infiltration. Also, part of pollutants in runoff are removed, slope of forest buffers generally being 2% to 6%, the width not less than 2m. The function of waterfront plants absorbing harmful substances can also be fully used, applied to be self-purification of water in the design, so as to improve environmental quality.
  - e. Multifaceted features such as space and appreciation requirements shall be considered focusing on topographical fluctuation and slope and change of bent and straight, so that the plant configuration and the natural environment can be in harmony with ecological environment, with balanced effects of short-term and long-term landscape. It is appropriate to employ the combination of tree, shrub, flower, grass, and rattan, integrated with evergreen and deciduous trees. Spaces are separated by trees, shrubbery mass, and greenbelt, equipped with a certain depth of field, then to reach a large space after passing by several winding small spaces. In configurations with different focuses, one or most multiple ornamental trees are utilized to implement vast clump planting or mass planting, so that each locality can exhibit different characteristics. The effects of landscape construction are taken into account from the many aspects, such as use of color, texture matching, seasonal changes, and so on. For instance, emulational rustic landscape is simulated to introduce the nature by the side of residents, so that the landscape can be more accessible.

#### 5 EXPECTATIONS

The plant configuration of Urban riparian park is a major issue in ecology, behavior psychology,



economics, botany, aesthetics, literature, and other related theories, the issue is difficult to explain clearly, nor can it be realized only by the personal thinking and the subjective desire of landscape architects. This article discusses the plant configuration of Loess Plateau Urban riparian park of China from the perspective of theoretical research, emphasizes the systematic, ecological, humanization three principles, and through the analysis of the current situation of Taiyuan Fenhe Park, proposes some suggestions of the waterfront landscape plant configuration, in order to provide helpful reference to the plant configuration of the Loess Plateau Urban riparian park in the future.

## REFERENCES

- [1] Zhong Shengsheng. 2010. The Analysis of Plant Collocation Mode and the Species Diversity in the Fenhe Wetland Park [J]. Shanxi Forestry Science and Technology. June 2010, Vol 39, 2:21.
- [2] Wang Guozheng, Yan Chenxi, Zhang Hai, Guo Jingpin. 2011. Shanxi Urban Greening Tree Species and its Application [M]. Beijing: China City Press, 261.
- [3] Li Suying. 2005. Network Green Belts in Urban Ecological Construction: Green Ecosystem Planning for Binjiang District, Hangzhou Municipality [J]. Journal of Beijing Forestry University (Social Sciences). 4 (4):18, 19.
- [4] Da Liangjun, Yang Yongchuan, Chen Ming. 2004. The Method of Ecological Greening and its Application in the Construction of the Approaching Nature Plant Community in Shanghai [J]. Chinese Landscape Architecture. (3):38-39.
- [5] (United States) Lan Lennox McHarg. 2006. Design with Nature [M]. Tianjin: Tianjin University Press.
- [6] Su Xuehen. 2012. Landscape Design with Plants [M]. Beijing: China Forestry Press. 105.

# Analysis of traditional architectural heritage protection strategy: Taking Jiajiazhuang historical and cultural district in Xiaoyi as an example

Da Zhang & Yuanping Liu

*Departments of Architecture, Taiyuan University of Technology, Shanxi, China*

**ABSTRACT:** The traditional settlement is the carrier of people's living, and the basic cell of China's social structure and urban development. The vast basin of the Yellow River has a unique and abundant geographical feature, which is a unique and abundant traditional settlement of the protection of many well-preserved villages. This paper takes the protection of the old city dwelling houses in Xiaoyi as an example, and discusses the Protection Countermeasures of the traditional residential buildings.

**Keywords:** historical and cultural county; protection plan; heritage protection

## 1 INTRODUCTION

As the historical remains of the settlement and residential space, the traditional dwelling house is the main building form of the settlement building, and is the main place for people to live and live. With the further development of the society and the continuous improvement of the economic level, the protection of historical buildings is increasingly concerned about the whole society. This paper will address this issue in Xiaoyi, Jiajiazhuang historical and cultural district, as an example and discusses the protection planning countermeasures.

## 2 THE BASIC SITUATION OF JIAJIAZHUANG

Jiajiazhuang is located in the east of Lvliang Mountain in Xiaoyi City, Shanxi Province. It is situated in the northwest corner of West Bank of Fenhe River, in the northwest corner of Jinzhong basin. Traditional block is an important part of Chinese architectural heritage, and its abundant resources are left to state, which is a history and can be called the Chinese cultural treasures.

Jiajiazhuang has a long history, according to "Xiaoyi County Records", in the Neolithic period, the unearthed Lanwenyi red sand pottery in Xiaoyi region belongs to Jiajiazhuang' second level terrace unearthed relics of Yangshao culture. There were two families in Jiajiazhuang whose names are Jia and Li first, gradually formed a settlement, then other families moved in. Because of Jia's large population and earlier immigration,

it is called Jiajiazhuang. The historical district of Jiajiazhuang is composed of two regions of Shangjie and Houjie. In the past, Jiajiazhuang village in Shangjie, largely regarded Sanhuang Temple as its center, and had Dongdao Street, Xitou Street and Miao Street. Miao Street, a total length of less than 500 meters, is the north-south, Dizang Temple to the south, central temple of Sanhuang. The Shangjie is from Jinhuanyi Courtyard in the west, south to Xiao River, east on the Bandao Road, north next to the Houjie Street. With the development of history, Jiajiazhuang's residents continue to expand, people of insight who were from outside gradually moved to settle down, and the formation of Jiajiazhuang, completing Jiajiazhuang historical and cultural blocks from then on.

## 3 HISTORICAL RELICS

Jiajiazhuang historical cultural district has a long history and rich cultural heritage, and its ancient architectural structures are most well preserved. Houjie Street high lies to the west of the village, lower east side, district court seat in southern and in northern built in accordance with the East-West ramp, through hundreds of years, it still retains its original pattern and historical style. These local characteristics of ancient buildings, concentrated reflects the building layout of Ming and Qing dynasties. They are the layout of rigorous, magnificent, exquisite workmanship, full-featured architectural style and level. The history of the settlement building orderly has a strong sense of unity.

### 3.1 *Defensive architecture*

The long-term complex and unstable social environment makes the defense consciousness as a psychological accumulation, directly affecting the settlement pattern of Jiajiazhuang. There is no danger according to the flat land of the village optional site, so the construction of the settlement has a strong sense of Fortress form, which mainly depends on the artificial defense construction. In history, Jiajiazhuang had East gate, West gate, South Gate, and North gate, these four Fort gates combined with high build castle walls, combining linear fortification and defense nodes, and forming a solid defense system. This level of fortification reality defense operation is a typical Jiajiazhuang defense mode.

### 3.2 *Temples and other public buildings*

The typical public buildings in historical and cultural blocks is a temple in Jiajiazhuang. The present temples Sanhuang Temple in the north of Xiao Fen Road, Xiao Fen avenue to the south of the Guanyu Temple, and Dizang Temple. These public buildings are the concentrated reflection of the emotional needs of the villagers' religion and social intercourse.

### 3.3 *Streets*

Road system is contact settlements within and outside the transport hub. It is the basic skeleton of the settlement, and it is divided into different functional areas and the basis of defining the village spatial axis, which plays a pivotal decisive role on the overall layout. Jiajiazhuang village is located in the plain area, the village streets using chessboard layout of traditional. In all, the road system of the village can be divided into three levels, namely main streets, secondary streets, and alleys.

## 4 PROTECTION PLAN

### 4.1 *The strategies of protection plan*

According to the status of Jiajiazhuang historical and cultural blocks of historical and cultural relics, the planning and the "overall protection with emphasis on the protection of the combination, supplemented by the key historical information moderate repair" countermeasures. Jiajiazhuang's protection of historical and cultural blocks planning blocks as a whole and protection of historical and cultural relics of moderate repair is composed of two parts.

A. The historical and cultural protected area of Jiajiazhuang consists of three parts of protected areas, construction control area, and

environmental coordinated area. The protection plan for different protection areas determines the contents of the protection and protection measures.

B. We must moderately repair the parts of the historic block, and analyze the important material and cultural relics that constitute the block, and analyze the status of the material culture remains and the historical form.

### 4.2 *The content of protection plan*

A. On the basis of Jiajiazhuang's natural environment, history and culture, the overall planning, traditional style, space form of in-depth research and analysis, this study summarizes the value characteristics, clear protection, and utilization of some important contents.

B. According to the current situation of distribution of Jiajiazhuang's cultural relics, historic buildings, historic street, in conservation planning regulation protection area, a construction control area, construction of secondary control area, environmental coordination area four degrees of protection and the scope of protection, and then put forward protection requirement, construction control index, environment coordination.

C. According to the present situation of Jiajiazhuang buildings and environment, they will be divided into the protection, the preservation, the renovation, and the renewal of four categories. To protect the classic construction, structures, including mapping, images, text descriptions and protection of the archives and the listing of the public, were proposed for the repair, maintenance, and other measures. The maintenance and improvement of the reserved classic construction are put forward. For the improvement of the construction and structures of the remediation, the improvement and the renovation are proposed; also for the construction of the renewal classic construction, structures, respectively, a targeted renovation, remediation, removal, and other measures.

D. In accordance with the principle of overall protection plan, it concludes Jiajiazhuang's historical and cultural paths and internal historical environment and the surrounding natural environment the protection and remediation requirements.

E. According to the Ming and Qing Dynasties of the office, county annals and witness the oral history, and the textual research of archaeological researchers identified, Jiajiazhuang's historical and cultural blocks for repairing improves Jiajiazhuang's Traditional Pattern and historical style.

F. Under the condition of keeping the traditional pattern and historical style, Jiajiazhuang's historical

and cultural blocks of infrastructure and environmental of comprehensive planning, puts forward the concrete improvement measures.

G. We need to put forward the protection plan implementation measures and suggestion, formulate the protection management method, establish the protection fund raising mechanism, encourage the public participation protection, and so on.

## 5 ANCIENT ARCHITECTURAL HERITAGE PROTECTION MEASURES

In any country or time, architecture cannot exist in isolation. It is hard to understand the ancient architecture without studying the relevant factors. In the same way, the protection of architectural heritage cannot be isolated from other human cultural heritage, even nearly a hundred years of heritage protection movement is no exception. I believe the future of the construction heritage protection, from the following aspects, to expand further.

### 5.1 *The study of the ancient architecture as sociology and cultural anthropology*

The building was built by human. There are different societies, different ethnic groups, in thinking about a problem, although they are common human cognition; but, there are also inevitable differences. Now, the research methods of sociology and cultural anthropology in the world are very mature. We want to study the important living beings of the history of human development—architectural heritage, and can learn from the sociological method. Nowadays, certain primitive tribes of social life phenomenon can also serve as our reference to live fossil. The results of sociological research in the past century are also available for us.

### 5.2 *The relationship between ancient architecture and family, private ownership and state*

For example, documents related to the rites of Ming Dynasty provisions in Nanjing, if you catch the time conflict of visiting Xiaoling Tomb and Confucian Temple, Xiaoling Tomb will visit first. For example, during the reign of Zhu Yuanzhang, Xiaoling engineering has been repeatedly visited. The responsible person must be simple and firm.

### 5.3 *The study on the aesthetic of ancient architectural heritage*

To examine our architectural aesthetics study in addition to the aesthetic vision of our time, we also need to put ourselves from the point of view of the past to examine. For example, Xiao He

created Weiyang Palace for Liu Bang to live, Liu Bang looked with a big temper. Xiao He said a “The non magnificent no heavy prestige” explanation, Liu Bang would no longer say anything. This is the performance of people’s aesthetic in the Qin and Han Dynasties. Sima Guang in Song Dynasty disagreed with this. He thought that Xiao could not say that. Because at that time the world be kept constantly on the run. As the party was responsible for logistics, he was better than anyone who was clear. This is the aesthetic view of the opposition in the background of “Wang Anshi reform” in the Northern Song Dynasty.

### 5.4 *The study on the economic of ancient architectural heritage*

Why did Tang Wuzong want to destroy Buddha? Because his father emperor Wenzong early to he calculated “In ancient times, three people eat need a person cultivated land, now with soldiers and monk is five people dining needs a person farming, which will bring people’s dislike of Buddhism.” The history of China on the rise and fall of Buddhism, not the emperors did not know Buddhism had value, but because in the development of Buddhism in the head, economic forces strongly endanger the national economy and the people’s livelihood situation, had to pain determination.

## 6 CONCLUSION

We protect the historical and cultural heritage of a town, and we are not to limit the involvement of the new towns and the environment. In principle, in addition to the heritage architecture, the other parts can be a new creation, but we must have the idea that people build cities in a city. Its goal is “On the one hand, we should ensure to architectural history and culture heritage protection for the continuity of the basis of urban texture, on the other hand, we should ensure the coordination of the modern urban texture, in consideration of the quality of architecture, urban and landscape.”

## REFERENCES

- [1] Yu Xuecai. The historical experience of ancient Chinese heritage protection, the International Symposium on urban tourism in China, 2006-10-24.
- [2] Wang Jinping: Shanxi province Xiaoyi jiajiazhuang conservation planning of historical and cultural blocks, Taiyuan: Taiyuan University of Technology, 2013.
- [3] Yu Xuecai: The traditional research on the protection of architectural heritage in China, the Department of tourism science, Southeast University, 2007.

*Sustainable development of building energy, traffic and environment*

# Study on the application of iron tailings for the improvement of saline-sodic soil

A.L. Shao

*Mining Company of Anshan Iron and Steel Group Corporation, Anshan, China*

**ABSTRACT:** A new soil amendment was prepared in this study, which was comprised of iron tailings (65%), active slag (20%), acid fertilizer (12%) and other additives (3%). Through comprehensive utilization, the iron tailings can be reused. The pH, salinity, density, porosity and permeability velocity of the soil from the test fields were detected. The results showed that the pH value of the soil decreased from 9.30 to 6.95, and the salinity decreased from 0.42% to 0.25% in one year. The density of the soil was lower by 7.80% than before improvement, while porosity and permeability velocity were higher by 9.35% and 72.73%, respectively. The new soil amendment could effectively resolve the problems of soil secondary salinization and re-alkali. The improvement of the saline-sodic soil by using this soil amendment has not only ecological, environmental and social benefits, but also economic benefits.

**Keywords:** iron tailings; saline-sodic soil; soil amendment; salinity

## 1 INTRODUCTION

With the unprecedented rate of mining and mineral processing over the last decade, there has been an increasing level of concern worldwide about the fate of tailings. An estimated above 10 billion tons of tailings have been discharged in China. The proportion of iron tailings as a solid waste is growing faster. The storage of iron tailings not only covers huge land and pollutes the environment, but also gives rise to security risks. At the same time, iron tailings as secondary resources have been of great importance worldwide. At present, there are several ways of utilization of iron ore tailings, which are as follows: useful metal recycling, producing building materials directly, filling goaf and using as a soil modifier and magnetization fertilizer.

The improvement of saline-sodic soil has a great significance at this stage of China's population growth and reduction of arable land. The traditional methods for improving saline-sodic soil include the physical method, the chemical method and the biological method.

A new high-efficient amendment for improving the saline-sodic soil was studied. The amendment was composed of iron tailings and organic matters. It is a new method to realize the resource utilization. In the laboratory research foundation, the new technique of saline-sodic soil improvement was carried out on industrial tests and obtained success.

## 2 MATERIALS AND METHODS

The iron tailings of magnetic separation were used in this study. Soil amendment was comprised of iron tailings (65%), active slag (20%), acid fertilizer (12%) and other additives (3%), such as starter cultures, precipitants, and humic acid. The saline-sodic soil was taken from Baicheng Town of Jilin Province. The weight of the soil was 150.89 kg and the volume of the water was 60.49 L. The soil was soaked in the water for about 3 days.

Soil amendment was mixed in the saline-sodic soil. The experiment was conducted at 8°C. Various indicators of the soil were tested every 5 days, such as pH value, Cation Exchange Capacity (CEC), Exchangeable Sodium Percentage (ESP), and contents of  $K^+$ ,  $Na^+$ ,  $Ca^{2+}$ , and  $Mg^{2+}$ .

The industrial tests were undertaken on two fields in Jilin Province, named as A and B. The fields A and B were 23 hectares and 3.1 hectares, respectively. The tests were divided into the following several stages: the capital construction of the paddy field, salinity regulation, dynamic test of soil parameters, and result analysis.

## 3 RESULTS AND DISCUSSION

### 3.1 *Iron tailings analysis*

In order to verify the feasibility of magnetic separation iron tailings used as soil amendment, its composition and particle size distribution

were determined. Table 1 presents the chemical composition (%) of the iron tailings. Table 2 presents the particle size distribution of the iron tailings. The results indicated that the iron tailings selected in this study did not contain any substance that was poisonous or noxious to crops. The content of SiO<sub>2</sub> was 76.10% in the chemical composition of the iron tailings. It could be instead of the sand mixed with soil. In addition, the particle size of the iron tailings met the requirements. Therefore, the magnetic separation iron tailings could be used for the improvement of the saline-sodic soil.

### 3.2 Laboratory analysis of the soil

The saline-sodic soil is distributed mainly over the Northeast China, and the soil parent materials were made of clayey or sandy sediments, which have the characteristics of poor permeability and strong capillarity. The improvement of the saline-sodic soil is a problem in the world. How to

Table 1. Chemical composition of the iron tailings.

Element	Fe	Fe <sub>3</sub> O <sub>4</sub>	SiO <sub>2</sub>	CaO
Content (%)	11.31	4.8	76.1	0.28
Element	Al <sub>2</sub> O <sub>3</sub>	MgO	P	MnO <sub>2</sub>
Content (%)	0.43	0.32	0.037	0.12

effectively control soil secondary salinization and re-alkali is the key to solving the problem. According to the survey, the phenomenon of secondary salinization and re-alkali often occurred after planting in paddy for about 2 months, and the pH value returned to the baseline level, i.e. before improvement.

Table 3 presents the variation of the soluble salt contents and the properties of the soil after improving. As can be seen from Table 3, the pH value of the soil decreased from 10.58 to 6.93 within 15 days by adding the composite soil amendment. The concentration of Na<sup>+</sup> decreased from 6511.45 mg/kg to 3566.15 mg/kg, with a decline of 45.23% in 15 days. The concentration of K<sup>+</sup> decreased about 37.25%. Meanwhile, the concentration of Mg<sup>2+</sup> increased from 10.90 mg/kg to 131.65 mg/kg, and the concentration of Ca<sup>2+</sup> increased about 39.09%. With the decreasing pH value, the concentrations of HCO<sub>3</sub><sup>-</sup>, Cl<sup>-</sup>, SO<sub>4</sub><sup>2-</sup>, and CO<sub>3</sub><sup>2-</sup> decreased about 75.69%, 69.67%, 40.67%, and 50.29%, respectively. The Cation Exchange Capacity (CEC) changed from 92.91 mold/100 g to 165.65 mold/100 g. It indicated that the fertilizer preservation ability of the soil is enhanced after improvement. At the same time, the Exchangeable Sodium Percentage (ESP) and salinity of the soil were lower than before improvement. Thus, it can be seen that the soil amendment has a pronounced effect on the improvement of the saline-sodic soil.

Table 2. Particle size distribution of the iron tailings.

Particle size range (mm)	-0.01	0.01-0.02	0.02-0.03	0.03-0.043	0.043-0.06
Particle size (mm)	39.25	5.28	10.83	12.03	11.02
Particle size range (mm)	0.06-0.076	0.076-0.10	0.10-0.0154	+0.154	/
Particle size (mm)	5.00	12.75	3.43	0.41	/

Table 3. The soluble salt contents and the properties of the soil after improving.

No.	S-1	S-2	S-3	S-4
Time (day)	0	5	10	15
pH	10.58	8.43	7.02	6.93
K <sup>+</sup> (mg/kg)	136.12	112.52	95.13	85.41
Na <sup>+</sup> (mg/kg)	6511.45	5859.45	4020.91	3566.15
Ca <sup>2+</sup> (mg/kg)	2217.10	2685.18	2950.18	3083.82
Mg <sup>2+</sup> (mg/kg)	10.90	67.36	112.83	131.65
HCO <sub>3</sub> <sup>-</sup> (mg/kg)	3494.47	3075.96	2401.94	849.60
Cl <sup>-</sup> (mg/kg)	303.46	296.46	286.62	92.03
SO <sub>4</sub> <sup>2-</sup> (mg/kg)	43.20	42.58	41.21	25.63
CO <sub>3</sub> <sup>2-</sup> (mg/kg)	1.75	1.70	1.62	0.87
CEC (mold/100 g)	92.91	117.32	137.58	165.65
ESP (%)	57.81	44.10	46.30	28.60
Salinity (%)	2.13	1.95	1.65	1.12

Because the fine particles in the iron tailings have a porous structure, which could control the concentration of  $\text{Na}_2\text{CO}_3$  and  $\text{NaHCO}_3$ , the iron tailings had a good performance in controlling the soil secondary salinization and re-alkali. In addition, the elements Fe, Si, Mg and S in the iron tailings were essential for crop growth.

In addition, unformed activated carbon was contained in the active slag, which had good adsorption and filtration properties for metal ions. The addition of the acid fertilizer had a clear effect on salt absorbing, and ensured that the crops can be protected from salt damage. The pH value was adjusted to the acidic conditions by adding the other additives, which was beneficial to crops.

The new soil amendment, which was composed of the iron tailings, active slag, acid fertilizer and other additives, could effectively resolve the problems of soil secondary salinization and re-alkali. Through comprehensive utilization, the iron tailings can be reused. This soil amendment used in the saline-sodic soil has not only ecological, environmental and social benefits, but also economic benefits.

### 3.3 Analysis of the test fields

The test fields were leveled first, and then ploughed 20 cm deep. The height difference between the parcels was in the range of 10–15 cm, and the height difference in one parcel was not beyond 2 cm. After leveling, the ditches were constructed.

Iron tailings about 550 t were transported from Anshan tailings ponds to the test fields in May 2013. Active slag, acid fertilizer and livestock manures were also carried to the test fields. After mixing the raw materials at certain proportions, the soil amendments were obtained. According to the plan, the amendments were scattered in the fields and then irrigated. Water was changed every 5 days. After repeating twice, the fields were harrowed, which made the amendments to function.

Table 4 presents the salinity (%) of the test fields. In field A, the salinity of the soil decreased from 2.53% to 0.65% in 2 months. The salinity of the soil in field B decreased from 0.42% to 0.25%. The results show that the soil amendments could significantly reduce the salinity of the fields. It turned the strongly salinized soil into the middle salinized soil, and turned the middle salinized soil into the mild salinized soil. The control of soil secondary salinization and re-alkali was proved to be successful. The improvement of the strongly saline-sodic soil was feasible.

Table 5 presents the pH value of the test fields. Rice could grow normally in this condition. Because of the heavy rains, the data of field A from August to September were missed, but the pH value of field

Table 4. The salinity of the test fields (%).

Data	Test fields	
	A	B
1 Jun	2.53	0.42
16 Jun	1.20	0.25
1 Jul	0.95	0.26
16 Jul	0.75	0.27
31 Jul	0.65	0.25
15 Aug	—*	0.24
31 Aug	—*	0.26
14 Sep	—*	0.26
29 Sep	—*	0.25

\*The field A was flooded because of the heavy rains, and the test was forced to be terminated.

Table 5. The pH value of the test fields.

Data	Test fields	
	A	B
1 Jun	10.27	9.30
16 Jun	8.12	7.52
1 Jul	8.05	7.41
16 Jul	8.06	7.50
31 Jul	8.03	7.31
15 Aug	—*	7.45
31 Aug	—*	7.38
14 Sep	—*	7.10
29 Sep	—*	6.95

\*The field A was flooded because of the heavy rains, and the test was forced to be terminated.

A decreased from 10.27 to 8.03 in about 2 months. The pH value of field B was decreased from 9.30 to 6.95. The change in the pH value was slow, but stable. It indicated that the pH value decreased by adding the soil amendments.

Table 6 presents the properties of the soils before and after using the soil amendment. The addition of the soil amendments played an important role in the improvement of the soils, which decreased the density and significantly increased the porosity and permeability velocity. The density of field B decreased by 7.80%, its porosity increased by 9.35% and its permeability velocity increased by about 72.73%. The trends were beneficial to the growth of rice.

The fields, where the rice cannot grow earlier, became the rice cultivable areas after improvement. In field B, for example, the production of rice was 6800 kg/ha before improvement, and the production reached up to 9300 kg/ha after improvement.



Table 6. The density, porosity and the permeability velocity of the soils.

Test fields	Density (g/cm <sup>3</sup> )	Porosity (%)	Permeability velocity (mm/min)
<i>A</i>			
Before the improvement	1.48	42.19	0.08
After the improvement	1.38	46.10	0.12
<i>B</i>			
Before the improvement	1.41	45.01	0.11
After the improvement	1.30	49.22	0.19

The improvement of the saline-sodic soil by the soil amendment showed a significant effect. It was also technically feasible and economically affordable.

#### 4 CONCLUSIONS

A high-efficient soil amendment was obtained, which comprised iron tailings, active slag, acid fertilizer and other additives. It decreased the pH value of the saline-sodic soil and solved the problem of secondary salinization and re-alkali. The results showed that the pH value of the soil decreased from 9.30 to 6.95, and the salinity decreased from 0.42% to 0.25% in one year. The density of the soil was lower by 7.80% than before improvement, while porosity and permeability velocity were higher by 9.35% and 72.73 than before improvement. The addition of the soil amendment played an important role in the improvement of the soil, which decreased the density and significantly increased the porosity and permeability velocity.

The improvement of the saline-sodic soil by using iron tailings not only restored the soil function, but also reduced the environmental pollution. It has an important significance to the work of ecological environmental protection and mining sustainable development of mining areas.

#### REFERENCES

- Dash, M. & Dwari, R.K. 2011. Studies on the effect of flocculant adsorption on the dewatering of iron ore tailings. *Chemical Engineering Journal* 173(2):318–325.
- Giri, S.K. & Das, N.N. 2011. Magnetite powder and kaolinite derived from waste iron ore tailings for environmental applications. *Powder Technology* 214(3):513–518.
- Li, C. & Sun, H.H. 2010. Innovative methodology for comprehensive utilization of iron ore tailings Part 1. The recovery of iron from iron ore tailings using magnetic separation after magnetizing roasting. *Journal of Hazardous Materials* 174(1–3):71–77.
- Liu, S.H. & Kang, Y.H. 2012. Germination and growth of *Puccinellia tenuiflora* in saline-sodic soil under drip irrigation. *Agricultural Water management* 109:127–134.
- Sakthivel, R. & Vasumathi, N. 2010. Synthesis of magnetite powder from iron ore tailings. *Powder Technology* 201(2):187–190.
- Sanjay, K. & Rakesh, K. 2006. Innovative methodologies for the utilisation of wastes from metallurgical and allied industries. *Resources, Conservation and Recycling* 48(4):301–314.
- Wang, R.S. & Kang, Y.H. 2015. Effects of different drip irrigation regimes on saline-sodic soil nutrients and cotton yield in an arid region of Northwest China. *Agricultural Water management* 153(1):1–8.
- Zeng, L. & Li, X.M. 2004. Adsorptive removal of phosphate from aqueous solutions using iron oxide tailings. *Water Research* 38(5):1318–1326.
- Zhang, Z.S. & Lian, F. 2015. Effects of quick lime and iron tailings as modifier on composition and properties of steel slag. *Journal of Iron and Steel Research, International* 22(1):15–20.

# The general solution of the Sturm–Liouville equation in heat conduction problems

F.B. Lu, Y.Z. Fu & S.Y. Su

*Institute of Urban Construction, Wuhan University of Science and Technology, China*

**ABSTRACT:** In this paper, the method of variable separation is applied to solve the thermal problem, which leads to the Sturm–Liouville problem, also known as the SL problem. Using the solution of Ref. [2] on the SL problem, it then combines own reasoning calculation and gives a more general solution to the SL problem. It considers the orthogonal characteristic functions including weight function, and draws the corresponding coefficient expressions of primary function. Finally, through an example, it shows the solution of the SL equation.

**Keywords:** variable separation; SL problem; orthogonality; primary function

## 1 INTRODUCTION

Unsteady heat conduction and more than one-dimensional partial differential equation of heat conduction problem cannot be solved by the direct integration. Variable separation is one of the methods for solving such partial differential equations. In addition, after the adoption of variable separation, the solution can be written in the form of  $\theta = \sum \theta_n$ , that is, the real variable separation is actually a series expansion of the mathematical problem, which involves the eigenvalue and eigenfunction issue, also known as the Sturm–Liouville problem (SL problems).

## 2 VARIABLE PREPARATION METHOD TO SOLVE THERMAL PROBLEMS

For the one-dimensional unsteady heat conduction problem, suppose there is an endless planumural, then the thickness is  $2\delta$ , the initial temperature is  $t_0$ , the two sides are cooled by the fluid, in which temperature is  $t_f$  and the heat transfer coefficient is  $h$  (see Fig. 1).

The mathematical description is as follows:

$$\begin{cases} \frac{\partial t}{\partial \tau} = a \frac{\partial^2 t}{\partial x^2} \\ \tau = 0 & t = t_0 \\ x = 0 & \frac{\partial t}{\partial x} = 0 \\ x = \delta & -\lambda \frac{\partial t}{\partial x} = h(t - t_f) \end{cases} \quad (1)$$

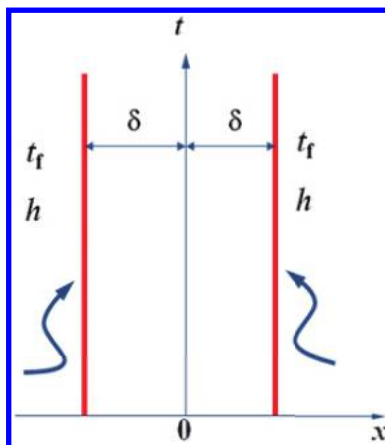


Figure 1. Schematic diagram of heat conduction.

Suppose that  $\theta = t - t_f$ , then (1) can be transformed as follows:

$$\begin{cases} \frac{\partial \theta}{\partial \tau} = a \frac{\partial^2 \theta}{\partial x^2} \\ \tau = 0 & \theta = \theta_0 = t_0 - t_f \\ x = 0 & \frac{\partial \theta}{\partial x} = 0 \\ x = \delta & -\lambda \frac{\partial \theta}{\partial x} = h\theta \end{cases} \quad (2)$$

In order to use the method of integral transform to handle the form of differential equations, suppose that  $\theta(x, \tau) = X(x) \cdot T(\tau)$ , and substitute this

formula into differential equation (2), and then through variable separation<sup>[1]</sup>, we can obtain the following equation:

$$\frac{T'}{aT} = \frac{X''}{X} = \mu \quad (3)$$

From Solution (3), we can obtain the expression of  $X(x)$  and  $T(\tau)$ , respectively, and substitute in the corresponding boundary conditions, and the expression of  $\theta(x, \tau)$  can be obtained. The variable separation method is successful because the solution can be written as follows:

$$\theta = \sum \theta_n = \sum A_n X_n \quad (4)$$

It means that the solution of heat condition equation  $\theta$  can be developed into a series based on  $X_n$ . If it really can, then  $\theta$  already becomes the solution of the problem. Therefore, the essence of variable separation is a series expansion of mathematical problems. The details of this problem include why written series, why can write the series, and the series should take the number of items. This is the famous eigenvalue and eigen function problem.

### 3 SERIES OF ORTHOGONAL FUNCTIONS TO ARBITRARY FUNCTION-BASED SERIES EXPANSION

In mathematics, the eigenvalue and eigenfunction problem were known as the Sturm–Liouville problem, referred to as the SL problem. The following questions deal with the matter of ordinary differential equations:

$$\frac{d}{dx} \left[ p(x) \frac{du}{dx} \right] + [q(x) + \lambda s(x)]u = 0 \quad (5)$$

$$\begin{cases} c_1 u(a) + c_2 u'(a) = 0 \\ d_1 u(b) + d_2 u'(b) = 0 \end{cases} \quad (6)$$

Equation (5) is called the SL equation, Equation (6) corresponds to the boundary conditions of the third boundary condition, also known as the SL boundary condition problem, or SL problems overall.

According to Ref. [2], the orthogonality of the characteristic function series can be proved from the equation and the boundary conditions of the SL problem directly. The solution is as follows:

Suppose that the eigenvalue  $\lambda_m$  and  $\lambda_n$  correspond to the characteristic function of  $u_m(x)$  and  $u_n$ , then:

$$p u_m'' + p' u_m' + (q + \lambda_m s) u_m = 0$$

$$p u_n'' + p' u_n' + (q + \lambda_n s) u_n = 0$$

Multiplying the left-style by  $u_n$  and the right formula by  $u_m$ , the left-style subtracts the right, which is as follows:

$$p(u_m'' u_n - u_n'' u_m) + p'(u_m' u_n - u_n' u_m) + s u_m u_n (\lambda_m - \lambda_n) = 0$$

The type integral between  $[a, b]$  is as follows:

$$\begin{aligned} & \frac{s(\lambda_m - \lambda_n)}{p} \int_a^b u_m u_n dx \\ &= \int_a^b \left[ \frac{d^2 u_m}{dx^2} u_n - \frac{d^2 u_n}{dx^2} u_m \right] dx = \left[ u_n u_m' - u_m u_n' \right]_a^b \\ &= \left[ u_n(b) u_m'(b) - u_m(b) u_n'(b) \right] \\ & \quad - \left[ u_n(a) u_m'(a) - u_m(a) u_n'(a) \right] \end{aligned} \quad (7)$$

Contrast boundary conditions can prove that (7) is equal to 0. For example, the first term, at the boundary conditions of  $x = b$ , is as follows:

$$\lambda u_n'(b) + h u_n(b) = 0$$

$$\lambda u_m'(b) + h u_m(b) = 0$$

Multiplying  $u_m$  by the left-style and  $u_n$  by the right-style, and then subtracting two of them, we obtain

$$\begin{aligned} & \lambda u_n'(b) + u_m(b) + h u_n(b) u_m(b) - \lambda u_m'(b) - h u_m(b) u_n(b) \\ &= \lambda \left[ u_n'(b) u_m(b) - u_m'(b) u_n(b) \right] \\ & \quad + h \left[ u_n(b) u_m(b) - u_m(b) u_n(b) \right] = 0 \end{aligned}$$

As this second term is 0, the first term is also 0. Similarly, we demonstrate that the second term of (7) is also 0.

Therefore, when  $\lambda_m \neq \lambda_n$ ,  $\int_a^b u_m u_n dx = 0$ , i.e. the function  $u_m$  and  $u_n$  are orthogonal.

From the above solution, we can see Ref. [2], the authors regard the function of  $s$  and  $p$ , respectively, as a constant function to solve this SL problem, is one-sided. In fact,  $s$  and  $p$  are the function of  $x$ , namely  $s(x)$  and  $p(x)$ . For  $s(x)$  and  $p(x)$ , at the corresponding different eigenvalue  $\lambda_m$  and  $\lambda_n$  of characteristic function  $u_m(x)$  and  $u_n(x)$  orthogonal under certain conditions, i.e., the general solution. It can be proved as follows.

Suppose that eigenvalues  $\lambda_m$  and  $\lambda_n$  are characteristic function corresponding to  $u_m(x)$  and  $u_n(x)$ , which in turn is satisfied as follows:

$$\frac{d}{dx} \left[ p(x) u_m' \right] + [q(x) + \lambda_m s(x)] u_m(x) = 0 \quad (8)$$

$$\frac{d}{dx} \left[ p(x) u_n' \right] + [q(x) + \lambda_n s(x)] u_n(x) = 0 \quad (9)$$

Multiplying (8) by  $u_n$  and multiplying (9) by  $u_m$ , and subtracting two of them, we obtain

$$u_n \frac{d}{dx} [p(x)u'_m] - u_m \frac{d}{dx} [p(x)u'_n] + (\lambda_m - \lambda_n)s(x)u_m(x)u_n(x) = 0 \quad (10)$$

Substitute (10) integral in  $[a, b]$ :

$$\int_a^b \left\{ u_n(x) \frac{d}{dx} [p(x)u'_m(x)] - u_m(x) \frac{d}{dx} [p(x)u'_n(x)] \right\} dx + (\lambda_m - \lambda_n) \int_a^b s(x)u_m(x)u_n(x) dx = 0 \quad (11)$$

For (11):

$$\begin{aligned} & \int_a^b \left\{ u_n(x) \frac{d}{dx} [p(x)u'_m(x)] - u_m(x) \frac{d}{dx} [p(x)u'_n(x)] \right\} dx \\ &= \int_a^b u_n(x) d[p(x)u'_m(x)] - \int_a^b u_m(x) d[p(x)u'_n(x)] \\ &= [p(x)u_n(x)u'_m(x)]_a^b - \int_a^b p(x)u'_n(x)u'_m(x) dx \\ &\quad - [p(x)u_m(x)u'_n(x)]_a^b + \int_a^b p(x)u'_n(x)u'_m(x) dx \\ &= [p(x)u_n(x)u'_m(x)]_a^b - [p(x)u_m(x)u'_n(x)]_a^b \\ &= [p(x)u_n(x)u'_m(x) - p(x)u_m(x)u'_n(x)]_{x=b} \\ &\quad - [p(x)u_n(x)u'_m(x) - p(x)u_m(x)u'_n(x)]_{x=a} \end{aligned} \quad (12)$$

For formula (12), contrasting the boundary conditions, this term is equal to 0. For the first term, at the boundary conditions of  $x = b$ , it is as follows:

$$\lambda u'_n(b) + hu_n(b) = 0$$

$$\lambda u'_m(b) + hu_m(b) = 0$$

Multiplying  $p(b)u_m(b)$  by the left formula, and  $p(b)u_n(b)$  by the right formula, and then subtracting the two equations, we obtain

$$\begin{aligned} & p(b)u_m(b) [\lambda u'_n(b) + hu_n(b)] \\ & - p(b)u_n(b) [\lambda u'_m(b) + hu_m(b)] \\ &= \lambda p(b) [u_m(b)u'_n(b) - u_n(b)u'_m(b)] \\ &= \lambda [p(x)u_n(x)u'_m(x) - p(x)u_m(x)u'_n(x)]_{x=b} = 0 \end{aligned}$$

Similarly, we prove that the second term of (12) is also equal to 0.

So

$$\int_a^b \left\{ u_n(x) \frac{d}{dx} [p(x)u'_m(x)] - u_m(x) \frac{d}{dx} [p(x)u'_n(x)] \right\} dx = 0$$

Therefore,  $(\lambda_m - \lambda_n) \int_a^b s(x)u_m(x)u_n(x) dx = 0$ .

So, when  $\lambda_m \neq \lambda_n$ , corresponding to different eigenvalues  $\lambda_m$  and  $\lambda_n$  characteristic functions  $u_m(x)$  and  $u_n(x)$  in the interval  $[a, b]$  with weight function on  $s(x)$  orthogonal, i.e.  $\int_a^b s(x)u_m(x)u_n(x) dx = 0$ . Arbitrary function can be expanded based on  $u_n(x)$ :

$$f(x) = \sum_{n=0}^{\infty} A_n u_n(x) \quad (13)$$

where  $A_n$  is the  $n$ th coefficient, which is associated with  $n$ .

Here, we use the nature of the orthogonal function to solve the coefficient  $A_n$ , calculated as follows:

For (13), multiplying both sides by  $s(x)u_m(x)$ , and integrating in  $[a, b]$ , we obtain

$$\begin{aligned} & \int_a^b f(x)s(x)u_m(x) dx \\ &= \int_a^b \sum_{n=0}^{\infty} A_n u_n(x)s(x)u_m(x) dx \end{aligned}$$

When  $m \neq n$ ,  $\int_a^b s(x)u_m(x)u_n(x) dx = 0$

So,  $\int_a^b f(x)s(x)u_n(x) dx = A_n \int_a^b s(x)u_n^2(x) dx$

$$\text{So, } A_n = \frac{\int_a^b f(x)s(x)u_n(x) dx}{\int_a^b s(x)u_n^2(x) dx}$$

That is, arbitrary function can be expanded based on:  $u_n(x)$ :  $f(x) = \sum_{n=0}^{\infty} A_n u_n(x)$ , where

$$A_n = \frac{\int_a^b f(x)s(x)u_n(x) dx}{\int_a^b s(x)u_n^2(x) dx}$$

#### 4 ILLUSTRATION OF THE SL ISSUE

As shown in the example of [Figure 1](#), to solve the  $x$  is a SL problem, variable separation is used in one-dimensional unsteady heat conduction problem of convection boundary conditions, at this point:  $p(x) = 1$ ,  $q(x) = 0$ ,  $s(x) = 1$ ,  $\lambda = -\varepsilon^2$ . So, the SL equation is a differential equation of 2nd-order, linear, homogeneous, constant coefficients. See the concrete solution on Ref. [2].

For (5), take the derivative of the 2nd derivative  $p(x)$  and get the 1st derivative  $p'(x)$ , namely all of them are function of  $x$ , and the SL equation is a differential equation of 2nd-order, linear,

homogeneous, variable coefficients. Although the  $\lambda$  of the SL equation can get its values according to the requirement of the boundary conditions,  $q(x) + \lambda s(x)$  can still express arbitrary functions. This is the reason that  $q(x)$  exists in the SL equation.

For example, the temperature distribution of spherical: to get the solution of harmonic function  $u$  within a radius of 1, which makes it meet the sphere of  $u|_{r=1} = \cos^2 \theta$ . The question boils down to solve the following problem:

$$\begin{cases} \frac{1}{r^2} \frac{\partial}{\partial r} \left( r^2 \frac{\partial u}{\partial r} \right) + \frac{1}{r^2 \sin \theta} \frac{\partial}{\partial \theta} \left( \sin \theta \frac{\partial u}{\partial \theta} \right) = 0, & 0 < r < 1 \\ u|_{r=1} = \cos^2 \theta \end{cases} \quad (14)$$

Using variable separation, suppose  $u(r, \theta) = R(r)\Theta(\theta)$  and substitute it in (14), we get

$$\frac{r^2 R'' + 2rR'}{R} = -\frac{\Theta'' + \cot \theta \Theta'}{\Theta} = \lambda \quad (15)$$

So, (15) can turn into

$$r^2 R'' + 2rR' - \lambda R = 0 \quad (16)$$

$$\Theta''(\theta) + \cot \theta \Theta'(\theta) + \lambda \Theta(\theta) = 0 \quad (17)$$

Solution function (17), in the boundary conditions on  $[0, \pi]$

$$\Theta_n(\theta) = P_n(\cos \theta)$$

However, (16) is the SL equation, namely a differential equation of 2nd-order, linear, homogeneous, variable coefficients. The general solution is:

$$R_n(r) = C_1 r^n + C_2 r^{-(n+1)}$$

To make  $u$  bounded,  $R_n(r)$  must also be in bounded, so  $C_2 = 0$ , namely  $R_n(r) = C_n r^n$ .

So the solution of original problem is

$$u(r, \theta) = \sum_{n=0}^{\infty} C_n r^n P_n(\cos \theta) \quad (18)$$

The solution of the coefficient is (18), thus the problem of the solution is obtained.

## 5 CONCLUSIONS

By inference calculations for the SL problem, when  $\lambda_m \neq \lambda_n$ , different eigenvalues  $\lambda_m$  and  $\lambda_n$  corresponding to the characteristic function  $u_m(x)$  and  $u_n(x)$  in the interval  $[a, b]$  with the weight function  $s(x)$  orthogonal, i.e.,  $\int_a^b s(x) u_m(x) u_n(x) dx = 0$ . Arbitrary function can be expanded based on  $u_n(x)$  as follows:

$$f(x) = \sum_{n=0}^{\infty} A_n u_n(x)$$

where  $A_n$  is the  $n$ th coefficient, which is associated with  $n$ , with

$$A_n = \frac{\int_a^b f(x) s(x) u_n(x) dx}{\int_a^b s(x) u_n^2(x) dx}$$

## REFERENCES

- [1] Wang Yuanming. Mathematical Physics Equations and Special Functions (4th ed.). Higher Education Press, 2012 (In Chinese).
- [2] Sun Dexing. Advanced Heat Transfer—Heat Conduction and Convection of Mathematical Analytical. Beijing: China Building Industry Press, 2005 (In Chinese).
- [3] Lu Quankang. The Eighth Methods of Mathematical Physics Self-counseling Sturm–Liouville Problem Intrinsic. College Physics, 1991, 09 (In Chinese).

## Solar Decathlon—entries of Tongji University

Li Yang & Feng Qian

*Key Laboratory of Ecology and Energy Saving Study of Dense Habitat (Tongji University), College of Architecture and Urban Planning, Ministry of Education, Tongji University, Shanghai, P.R. China*

**ABSTRACT:** International Solar Decathlon (Solar Decathlon, SD) was launched, and hosted by the United States Department of Energy, for universities globally that have an interest in participating in solar building technology competitions. With the technology and originality of the world's top research and design team, goals of the solar energy and energy savings are combined closely with architectural design. This incorporates new methods of design and building to run a fully functional, comfortable, livable, and sustainable solar house. During the competition, solar power alone must provide the energy needed for the solar house. The competition will comprehensively assess each of the entries based on various aspects, including the energy conservation, architectural and environmental physics regulation, and quality of the produced solar energy. The competition determines the final ranking through ten key aspects; therefore it is called a “decathlon” competition.

**Keywords:** Solar Decathlon; building energy consumption; Tongji University works

### 1 SOLAR DECATHLON IN CHINA

#### 1.1 *Solar Decathlon introduced to China*

On January 18, 2011, China National Energy Bureau, Peking University, and The U.S. Department of Energy signed a cooperation agreement called the, “Solar Decathlon Memorandum of Understanding” in Washington, D.C. It introduced the world's highest level of solar application in China. On October 10, 2014, the competition's global launch ceremony in China was held.

The Solar Decathlon in China is the first Sino-US Energy Cooperation Program and included a U.S. visit by Chairman Hu Jintao.

The competition in China was jointly organized by China National Energy Bureau and the United States Department of Energy, contracted by Peking University.

Currently, energy use has become increasingly important and a topic of international affairs. The goal is to reduce and end dependence on high-emission energy resources. It has become an urgent issue of the people, asking the government to provide alternatives to the current unsustainable and contaminating options. The goal of the Solar Decathlon in China is to solidify attention on the promotion of the new energy technology and encourage social responsibility for energy conservation.

#### 1.2 *Influences of the Solar Decathlon in China*

The solar powered building will be an important direction of development for the future in our country, being that the total size of building stock is 44 billion square meters, with two billion new square meters per year. This development is where there exists huge building energy consumption and ecological problems. Participating in the competition not only relates to innovations in domestic construction, but also works to improve public consciousness, both of which are critical for a change in current consumption.

#### 1.3 *Five objective of introduction of Solar Decathlon in China*

**Education:** The application of renewable energy in construction and the important role that new energy plays in future life, college students are motivated to participate in this challenge, in order to put the technological innovations to practical use.

**Public awareness:** as an international competition, the Solar Decathlon has attracted research teams from around the world to participate and is also open to audiences around the world. The entries are lined up for the competition, using realistic living conditions to directly reflect the energy saving technology and the reduction of environmental impact. This method allows for the

public and judges to directly see and understand renewable energy sources, the implementation of the latest energy-saving technology and the individual designs, which encourages awareness of consumption and importance of sustainable development.

**Promote new solar technology market process:** By showing the entry designs for this competition, interest and public understanding of solar energy can be greatly improved. For the entries, the design teams innovatively use industrial construction and solar technologies closely, which integrates the two with architecture design. These innovative technologies include solar photovoltaic technology (independent/micro network technology and network systems), solar thermal cooling, and indoor physical environment of intelligent control.

**Conservation and utilization of water resources:** The application of new technologies and materials, as well as household appliances, solar energy technology research and integration, involve a number of new water-efficient technologies.

**Promotion of solar residential outcomes:** Present a living pattern that contains comfort, appeal and functionality, which satisfies the sustainable development and creates profitable market potential for the future.

## 2 CHINA'S ATTENTION TO THE SOLAR DECATHLON

On January 19, 2011, Chairman Hu Jintao signed the first Sino-US Energy Cooperation Program called, "Solar Decathlon" in China, with the state visit. Hu Jintao met with the U.S. President, Barak Obama, at the White House, specifically to meet regarding the matter. The two leaders showed a high degree of attention and support for the competition. Dozens of Chinese and foreign media such as Economy, China Daily, China Youth Daily, People's Daily, Xinhua, Sina, Sohu, Netease, the White House press, the financial community, HC, Xinmin, Qianlong, the International Energy Network, the China Energy Information Network, reported that "Peking University will host the international Solar Decathlon".

## 3 TEN STANDARD'S OF THE COMPETITION

The competition requirements include the global universities participating to design and construct solar, energy-saving homes that's energy usage can solely be supplied by solar power equipment.

The competition selected 10 aspects of solar power use and efficiency, and through professional

analysis, the final ranking score is determined. The comprehensive assessment is of each entry's energy-saving technology, building physics, environmental regulation and the ability of energy efficiency. This solar power competition is called a "decathlon" competition because of the ten indicators of the assessment. The Solar Decathlon is also called, "solar session of the Olympic Games" due to the introduction of solar technology.

## 4 ENTRY PROCESS

The organizing committee will send the invitation to the universities world-wide. After review, the top 20 University entries are selected for the Solar Decathlon competition finals. Competition requires each participating University to design and construct a 60 square meters to 92 square meters solar energy powered house. The final step of the competition is to move entries to designated locations (successive games were held at the National Mall in Washington America) after assembling construction. After comprehensive evaluations, the entries will be displayed to the public.

Every solar building that participates should meet the daily requirements of a household. This includes use of a complete set of household appliances, furniture and other basic living facilities, such as TV, refrigerator, cooking stove, dishwasher, washing machine and computer. In the competition evaluation period of one week, the organizers will cut off the outside water, and electricity supply. The solar buildings should not only meet the energy consumption, indoor temperature, humidity and comfortable environment that 3 to 6 participating students need to live, but also supply enough energy for dinners for 8, when students invite other international students into the buildings.

## 5 CASE ANALYSIS—TONGJI UNIVERSITY

### 5.1 *China 2010: Solar Bamboo House*

In June 17, 2010, an entry, "Solar Bamboo House", by the team from Tongji University, was submitted for the "Solar Decathlon" for a period of ten days in the Spanish capital Madrid, at the Manzanares River East Bank. The "Solar Bamboo House", with an area of 74 square meters, was a green ecological house. The external facade of the house was composed of bamboo. Indoor flooring, wall decoration, and furniture were also mostly made up with the bamboo as well. A solar photovoltaic system was used in the bamboo house, completing the "solar power" requirement of the competition. The bamboo house used the original ecological architectural style of southern China. The anti-sky

roof structure of classical Chinese architecture was adopted, to maximize power generation efficiency of the photovoltaic panels and ensure ventilation. The Bamboo House integrates a number of energy-saving technologies and systems, including passive and active energy-saving technology in order to achieve an efficient use and management of energy and hydropower required by normal life inside the house. The high-performance vacuum insulation panels, or VIPs, were installed inside the Bamboo House, and phase change materials were applied on the interior wall to maintain the indoor temperature. The wall's interlayer of the phase change material adjusts the room temperature by storing heat and coolness from the day and night. The highest level of vacuum insulation and hollow triple glazing were adopted in the design of the windows, which helps heat insulation performance 4 times that of the ordinary window. The roof of the Bamboo House was covered with solar photovoltaic modules, with cooling and heat recovery equipments set up on the back. These equipments could not only recycle heat, but also ensure the high efficiency of power generation.

### 5.2 2011: Sunshine container house

In the Solar Decathlon held in late September in Washington, the entry from Tongji University was



Figure 1. "Solar Bamboo House"  
(Source: [http://info.bamboo.cn/detail\\_26026\\_1.html](http://info.bamboo.cn/detail_26026_1.html)).



Figure 2. "Y type container"  
(Source: <http://blog.ifeng.com/article/14194380.html>).

a "Y type container". It was composed of 6 shipping containers, from Shanghai's port, that are convenient for movement, economical and comfortable in size. The Sunshine Container House was built to be a Y-shaped structure composed of 3 containers, and the intersection angle of two adjacent containers was 120 degrees, providing a greater perspective. A container was hollowed out as the room, which could be divided into two small rooms by clapboard. In order to connect the indoor and outdoor, the wall can be folded. The terrace is not only useful to have social activities, but it also can collect and store rainwater. The rainwater was then used after filtration. Large windows and glass doors out from the platform allowed light into the house, making it a modern, fully functioning apartment. The "Y type container" was able to become two small bedrooms using clapboard at night, while in the day the bed could be folded up and pushed into the cupboard. A triangle bench was used to be assembled into many different forms of furniture.

### 5.3 2012: Para Eco-House

In 2012, the Solar Decathlon competition was held in Madrid, Spain. Tongji University participated in the competition with a solar house named "Para Eco-House". The entry combined indoor and outdoor architectural spaces with ecological technology. "Para Eco-House" was covered with a diamond mesh that interleaved with the body of the house and stretched across roof supporting the solar photovoltaic power generation tracking system on the roof. The three-dimensional greenery hanging down on the west side of the house was embedded into a thin-film photovoltaic module. It combines solar energy, ventilation and shading as a whole, constituting a gray outdoor space that adjusted the outdoor microclimate. The tacit understanding of construction technology was shown in the use of the solar energy. The parametric method was integrated in the logical language



of architectural design. The integration of passive and active energy saving technology was achieved in the ecological strategy.

This entry made full use of the competition site conditions and many ecological technologies, such as a mono crystal line silicon PV system installed on the roof of Eco-House that could automatically track solar elevation angle, thin film photovoltaic system with good and weak light, high efficient solar flat plate collectors cooperated with the house, PVT system, water source heat pump air-conditioning system that used diurnal temperature to save and release heat, drip irrigation system that recycled water and made wastewater treatment, outdoor spray evaporative cooling system, building shade system, patio hot-pressing ventilation system, VIP high-performance insulation, heat and moisture individually controlled air-conditioning systems, intelligent home energy information system and LED lighting.

## 6 CONCLUSIONS

The Solar Decathlon provides a platform for students to understand the application and impact of sustainability and energy saving technology. It allows them to participate directly against competition from around the world and teaches skills to become global leaders. Through the publicity of the competition and displays of functional living in solar buildings, it provides an opportunity to improve the understanding of solar technology and energy-saving products for the public, and also raises awareness of reducing consumption to allow for environmental protection. Furthermore, the regional development of strategic emerging industries is promoted. Solar Decathlon competitions around the world are a great platform to drive governments, universities, businesses and non-profit organizations to communicate and cooperate to achieve future sustainable goals.

## ACKNOWLEDGMENTS

This work was financially supported by national science foundation of China 51178313/E0801 and 51378365, and by the National “Twelfth Five-Year” Science & Technology Support Plan:

the city high density space efficiency optimization key technology research (Subject Numbers: 2012BAJ15B03).

## REFERENCES

- Li, Z.H. 2011. Solar session of the Olympic Games [J]. China Economy Info.
- Qian, Feng & Zhu, L. 2008. Wenyuan Building in Tongji University Historic Building Protection and Re-use. Architectural Journal, 76–79.
- Qian, Feng. 2010. Research of the Air-conditioning System with CPCP & DOAS via DFD [J]. Residential Technology, 30(12).
- Qian, Feng. 2014. Insulation and Energy-saving Technology for the External Wall of Residential Building, Advanced Materials Research, Vols. 1073–1076, Part 2, 1263–1270.
- Qian, Feng. 2015. Analysis of Energy Saving Design of Solar Building-Take Tongji University solar decathlon works for example, Applied Mechanics and Materials, Vol.737, 139–144.
- Yang, Li. 2010. Computational Fluid Dynamics Technology and Its Application in Wind Environment Analysis [J]. Journal of Urban Technology, Vol. 17, No. 3, 53–67.
- Yang, Li. 2013. Research on Building Wind Environment Based on the Compare of Wind Tunnel Experiments and Numerical Simulations, Nature Environment and Pollution Technology, Vol. 12, No. 3, 375–382.
- Yang, Li. 2013. Research of Urban Thermal Environment Based on Digital Technologies, Nature Environment and Pollution Technology Vol. 12, No. 4, 645–650.
- Yang, X.Q. & Gao, H. 2011 Architectural design idea and technical strategy of zero energy residential solar energy [J]. Journal of Architecture.
- Yang, Li & Song, Y.H. 2011. Brief introduction of “Solar Decathlon” Competition (SD) [J]. Construction techniques.
- Yang, Li & He, B.J. & Ye, M. 2014. Application Research of ECOTECT in Residential Estate Planning, Energy and buildings 72, 195–202.
- Yang, Li, He, B.J. & Ye, M. 2014. CFD Simulation Research on Residential Indoor Air Quality, Science of the Total Environment 472, 1137–1144.
- Yang, Li, He, B.J. & Ye, M. 2014. The application of solar technologies in building energy efficiency: BISE design in solar-powered residential buildings, Technology in Society, 1–8.
- Yu, Z.Q. & Ye, M. 2011. “The bamboo house”-Solar ecological residential practice [J]. Construction techniques.

# The ecological restoration of building landfill and garbage landfill

J.N. Yang, H.Y. Li & L.Y. Lv

*College of Environmental Science and Engineering, Nankai University, Tianjin, China*

**ABSTRACT:** The study on the ecological restoration of landfills has gradually become a hotspot in recent years. The ecological restoration project of garbage landfill in Tangshan South Lake and of building landfill in Tianjin Nancuiping has been proved to be successful. Taking the two successful experiences as examples, we describe the technologies and processes of ecological restoration of the two types of landfills systematically, in order to provide reference for the ecological restoration of other landfills.

**Keywords:** building landfill; garbage landfill; ecological restoration

## 1 INTRODUCTION

A lot of wastes are generated in the process of industrialization and urbanization, which mainly includes industrial waste and city garbage [Yang & Wang 2010]. The three main techniques are landfill, waste incineration, and recycling [Li & Ju 2005]. Landfill is an important component of the solid waste treatment system because of its obvious advantages, such as small investment, high yield and convenient operation [Huang 2003]. However, landfills take up large areas of land in order to meet the capacity and service time. At the same time, landfills affect the surrounding water environment, soil environment, atmospheric environment and ecological system. What's more, landfills can produce acute and chronic damage to surrounding residents, causing a series of diseases. How to control environment pollutions and renovate the ecological environment of landfills is a urgent and outstanding problems in the field of environmental protection [Peng et al. 2002].

Ecological restoration of landfills can bring many benefits. On the one hand, it will reduce the pressure on the ecological environment. On the other hand, it can restore the use value of land. There are three types of land that a landfill site can reform: agricultural land, forest land and land for public entertainment [Yang 2009]. Agricultural land is an ideal landscape that can bring economic benefits and is easily accepted by local residents. However, its restoration project costs are high, and the high management cost is also a problem. Forest land meets the guidelines of urban planning and construction, and it has the potential value of tourism development and business development. Nevertheless, adapting to the use of urban residents is different for forest land. Comparatively, land for

public entertainment meets the requirement of urbanization more than others. It can provide large areas for public activity. It can meet other purposes including nature protection and forestry development at the same time, achieving double harvest of ecological benefits and social benefits. Many practices have been reported abroad. La Vallde'n Joan Park was a typical waste landfill field in valley before ecological engineering [Battle 2006]. Byxbee Park in George Hargreaves built in 1991 was built at a landfill with 18 meters high [Wang & Lin 2002]. Fresh Kills Park, which is about three times the size of Central Park in New York, was the Fresh Kills Landfill before ecological engineering [Yu & Ding 2006]. Korea built golf courses and World Cup Park in the landfill sites [Chen et al. 2013]. Seattle Gasworks Park set up in the landfill site, which was piled with trash and scrap [Chen et al. 2013]. The above examples are successful ecological restoration of landfills.

For garbage landfills, the effects of landfill gas on plant growth should not be neglected, and landfill leachate is good to plant growth because it has higher amounts of organic components [Li & Ju 2005]. However, building landfills are different, kinds of pollutants and concentration of landfill leachate are less, and there is scarcely any landfill gas in a building landfill [Yuan et al. 2006]. Based on the differences between building landfill and garbage landfill, the method of ecological restoration of the two types of landfill is different. In this paper, we take the garbage landfill in Tangshan South Lake and the building landfill in Tianjin Nancuiping as examples, the technologies and processes of ecological restoration of the two types of landfills are described systematically, and thus hope to provide reference for ecological restoration of the two types of landfills.

## 2 GARBAGE LANDFILL IN TANGSHAN SOUTH LAKE

### 2.1 *Background*

Tangshan South Lake landfill was located in the south suburb of Tangshan, covering an area of 9.8 hm<sup>2</sup>. The total landfilled mass was 4.5 million tons, forming a garbage mountain about 50 meters high. The garbage mountain damaged the appearance or environment of Tangshan. What's more, landfills produced acute and chronic damage to the surrounding residents, causing a series of diseases [Zhou 2012]. The ecological recovery project of Tangshan South Lake landfill was completed in April 2009, with 110,400 trees and shrubs planted. The whole mountain greening area achieved 130 thousand square meters after the project [Wang & Li 2009]. The garbage mountain that was once avoided by everyone in the past has now turned into a "phoenix platform", which is the symbol landscape of the South Lake area.

### 2.2 *Recovery process*

#### 2.2.1 *Leachate control system*

Before the recovery, we changed the shape of the garbage mountain with 1:3 slopes. Then, we laid a blind ditch of 2360 meters length along the retaining wall back to collect leachate. Landfill leachate is a kind of liquid containing a high concentration of suspended substances and a high concentration of organic and inorganic compounds. Landfill leachate is produced from soluble substances, rainwater and surface water percolating through the waste. It is formed by the biochemical and chemical degradation processes of the waste [Liu et al. 2006]. The leachate backfilling area was laid 11 double row tubes. Then, leachate was transported to adjust the pool for disposal. There were 35 leachate junction wells in the leachate control system.

#### 2.2.2 *Landfill gas control system*

Organic matter in landfills could be degraded by facultative and specificity of microorganisms, producing landfill gas. Landfill gas contains a lot of CH<sub>4</sub> and CO<sub>2</sub> and other trace elements. If a large amount of landfill gas accumulated within the soil, the growth of vegetation will be affected seriously and even results in an explosion. There were 24 wells for gas collection at the top of the slope and at the 28 meter-elevated platform. We laid blind ditches at other areas to collect horizontal gas. The landfill gas was then funneled to a torch burning furnace for combustion.

#### 2.2.3 *Surface covering*

According to the design, we laid geotechnical cloth, geomembrane, composite geotechnical grid

and geosynthetic at the garbage mountain that shaped according to order from top to bottom and side to bottom. We covered with clay of 30 centimeters thickness, and then with compact clay by a large crawler machine in order to prevent rain-water infiltration. We also covered planting soil of 50 centimeters thickness to provide a good growing environment for the subsequent recovery of vegetation. When the waste rots, it will emit flammable gases and make the soil alkali-affected, leading to difficulty in vegetation survival, so soil amelioration is necessary. We added organic manure and peat soil to the planting soil, resulting in three planting soils for every one organic manure and every one peat soil. Then, we stirred them well and covered them. The soil disposed was rich in N, P, K and other nutrients, and air permeability and water permeability were also good, which are characteristics that are beneficial to the plant growth.

#### 2.2.4 *Vegetation recovery*

A total of 57 kinds of plant species, which were tolerant to drought, poor soil and strong wind, were selected, including 6 species of evergreen trees, 10 species of deciduous trees, 24 species of shrubs and 17 species of ground covers and flowers. We planted these plants with a dense mixture. Considering the land use of landfill after restoration, we planted pioneer plants, constructive plants and auxiliary fertilizer plants with rational coordination to speed up the formation of a stable plant community. Planting trees with grass and shrubs is good to the formation of the plant community. According to the different slopes of the mountain, we selected adaptive species to shape and adjust the slope. The engineering measures can help the formation of the terrain to a certain extent, while the plants planted on the mountain can shape the natural terrain. Plants can guide the mountain runoff in the right direction and form a good microclimate in some part of the area.

## 3 BUILDING LANDFILL IN TIANJIN NANCUIPING

### 3.1 *Background*

Nancuiping Park is located in the south-west of Tianjin, adjacent to the water park. It was a building landfill before the ecological recovery project, which piled up waste including project dregs, mass concrete and harmless industrial waste, totaling 3.2 million cubic meters. Nancuiping Park is the product of ecological restoration of the building landfill. There have been more than 6 thousand tourists per day and about 90 delegates per year who visit the Nancuiping Park since it opened

in 2009. Nancuijing Park has become a bright business card of Tianjin [Chen et al. 2013].

### 3.2 Recovery process

#### 3.2.1 Earthwork

Earthworks included cleaning mud, digging lakes, transporting muck, shaping mountain and covering planting soil. The original topography is fish pond, with the thickness of the mud layer being 7 to 9 meters, which affected the project of piling up hill. So all the silt particles were removed and filled by muck layered to ensure the stability of the mountain.

#### 3.2.2 Covering soil and greening

We covered the planting soil with a thickness of 1.2 to 1.5 meters after the formation of the mountain. The planting soil covered is about 190 thousand cubic meters, and the green area is about 210 thousand square meters. The ground is mainly covered with the ryegrass (*Lolium perenne*), with all slopes covered with the buffalograss (*Buchloedactyloides*) as well as with the wild *Zoysia* (*Zoysia japonica*). Native tree species were mainly planted at the park based on the climate and environment in Tianjin.

#### 3.2.3 Irrigation system

Every plant was equipped with an automatic water-saving irrigation equipment, which was an internationally leading one and adjusted to local conditions. The use of the automatic irrigation equipment compared with artificial water-saving fuel consumed electricity by 60% and water saved by 60%, so labor costs was lowered and irrigation efficiency was improved. Precise irrigation was good to the formation of wet microclimate, which improved the survival rate of plants greatly.

#### 3.2.4 Ecological landscape design

The government of the city of Tianjin carried out a new round of comprehensive environmental control in 2008, and Nancuijing Park was in the list. According to the principle of layout optimization, space connection and function improvement, the park was divided into two parts, which were further subdivided into six landscapes. The six landscapes include the lotus area, big lake area and tortuous channel area in the lake landscape, and grass area, trees area and flowers area in the mountain landscape.

The lake landscape has a changeable waterfront space by making the space open or closed. Both the mirror of water and the twists and turns of the river were included. In a word, the lake landscape's style ranged widely. Accessibility, hydrophilicity, and security were emphasized in the details of the treatment. For example, the revetment of

high straight rubble was replaced by low natural stone and hydrophilic terraced revetment. We set the shallow water in nearshore, and planted a large number of local hygrophilous plants in the shallow water, forming a wetland landscape with distinctive local characteristics. The wetland vegetables played an important role in softening the rigid retaining wall and guaranteeing the safety of tourists. The mountain landscape emphasized the diversity of the plant landscape. The large areas of landscape forest are the main component of the mountain landscape. We planted trees with grass and shrubs. Evergreen trees and deciduous trees were planted in a mixed pattern, which formed a stratified plant community. According to the difference in terrain and orientation at different positions of the mountain, we selected different accent plants, forming a series of characteristic plant landscapes, which included flowering shrubbery, colorized shrubbery, evergreen coniferous forest and gentle slope lawn.

## 4 CONCLUSION

The ecological restoration of a landfill provides a long-term strategy based on the natural evolution and the plant's life cycle. It uses ecological engineering that is mainly based on the interaction between the plant and the soil and the microorganism to deal with waste and to improve the soil. The ultimate aim is to restore and build a virtuous circle ecological environment that is close to the natural environment [Wang & Li 2009]. In this paper, we have taken the garbage landfill in Tangshan South Lake and the building landfill in Tianjin Nancuijing as examples, and the technologies and processes of ecological restoration of the two types of landfills have been described systematically. The following points can be used for reference.

Special attention should be paid to landfill gas control and landfill leachate control. In the process of ecological restoration of garbage landfill in Tangshan South Lake, special research on landfill leachate contamination and landfill gas was carried out. We laid pipelines to collect and transport leachate and landfill gas, and also built leachate equalization basins to treat leachate together. The landfill gas was funneled to a torch-burning furnace for combustion. Measures were also taken to control leachate and gas in the process of ecological restoration of building landfill in Tianjin Nancuijing.

Special attention should also be paid to the land subsidence caused by the degradation of waste, whether in building landfill or in garbage landfill. Some measures were taken to maintain the stability of the mountain for the garbage landfill in Tangshan South Lake, changing the shape of the

garbage mountain with 1:3 slopes and building security platform and retaining wall were included. For the building landfill in Tianjin Nancuiping, all the silt particles were removed and filled by muck layered to ensure the stability of the mountain.

Plants growing in landfills will face many serious environmental stresses, which include landfill gas, landfill leachate and high temperature, drought and poor environment of the final layer. So, it is important to select tolerant species. There were some species selected to be planted in the two types of landfill because of their characteristics of drought resistance, shallow root and stain resistance.

## REFERENCES

- Battle, I.R. 2006. *Fieldwork-Landscape Architecture Europe*. Boston: Birkhauser Publisher for Architecture.
- Chen, X.K. et al. 2013. Study on ecological restoration and landscape construction of industrial wasteland accumulated field. *Modern Landscape Architecture*, 10(11): 19–26.
- Huang, M.H. 2003. *Pollution ecological and ecological restoration*. Science Press.
- Li, Y.Y. & Ju, M.T. 2005. *Principles and practices of ecological restoration*. Chemical Industry Press.
- Liu et al. 2006. Analysis of leachate characteristics of municipal landfill. *Environmental Science and Technology*, 29(6): 55–57.
- Peng, X.Y. & Huang, W.X. & Yu, Y. 2002. Pollution control and ecological reclamation of MSW dumping sites. *Journal of Chongqing Jianzhu University*, 4(1): 206–210.
- Wang, X.R. & Lin, J. 2002. *Theories and practice of modern landscape architecture in the western world*. Beijing: China Building Industry Press.
- Wang, X.Y. & Li, X.Y. 2009. Effective approach for ecological restoration in coal mining collapse area. *The Journal of Hebei Forestry Science and Technology*, (1): 51–52.
- Yang, R. & Wang, H. 2010. Landscape Break through: the ecological restoration and landscape reconstruction of urban landfills. *Sustainable Urban Development*, 17(8): 81–86.
- Yang, R. 2009. Principles and practices of landscape urbanism. *Chinese Landscape Architecture*, (11): 60–63.
- Yu, S.J. & Ding, S.G. 2006. Lifescape from landfills to Fresh Kills landscape. *Landscape Architecture*, (6): 26–31.
- Yuan, Y.Y. et al. 2006. Environmental effects of construction waste landfill site. *Environmental Sanitation Engineering*, 14(1): 25–28.
- Zhou, L. Development situation and thinking of landfill ecological restoration technology. 2012. *Environmental Science and Technology*, 25(4): 71–74.

# The key technologies of ecological restoration of sanitary landfill

J.N. Yang, H.Y. Li & L.Y. Lv

College of Environmental Science and Engineering, Nankai University, Tianjin, China

**ABSTRACT:** With the growing urbanization, the city rubbish is also growing, and consequently its effect on the environment and the ecological restoration of sanitary landfill have become major social problems. There are many different practices at home and abroad. In this paper, with the clue of process, we commented on the key technologies of ecological restoration of sanitary landfill, hoping to provide reference for ecological restoration of sanitary landfill.

**Keywords:** sanitary landfill; ecological restoration; key technologies

## 1 INTRODUCTION

Urban domestic waste is solid waste produced by people's daily life activities, turning out with the city and soaring emissions in the process of urbanization, and currently our cities are facing the predicament of being surrounded by waste [Yang & Wang 2010]. According to information statistics, the annual per-capita output of urban waste extends to 440 kilograms. In 2010, the amount of urban waste was reported to be 3.52 billion tons in China, ranking the first in the world, and is growing 8% to 10% per year. The four main techniques for the disposal of rubbish include landfill, waste incineration, high-temperature composting and recycling. Landfill becomes an important component of the solid waste treatment system because of its obvious advantages, such as small investment, high yield and convenient operation [Li 2005, Liu 2007]. It has been found that nearly 95% of the world's urban domestic waste is buried [Wang 2011]. On the other hand, landfills also lead to many problems. They take up large areas of land in order to meet the capacity and service time. At the same time, landfills affect the surrounding water environment, soil environment, atmospheric environment and ecological system. What's more, landfills will produce acute and chronic damage to the surrounding residents, causing a series of diseases [Zhou 2012]. How to control environment pollutions and recover the ecologic environment of landfills is an urgent and outstanding problems in the field of environmental protection at home and abroad with people's continuous improvement of environmental awareness [Cao 2010, Kwon & Gary 2010, Mutasem et al. 1997, Zhao et al. 2012]. In this paper, with the clue of process, we commented on the key technologies of ecological restoration

of sanitary landfill, hoping to provide future reference for ecological restoration of sanitary landfill.

## 2 POLLUTION CONTROL

### 2.1 Landfill leachate control

Landfill leachate is a kind of liquid containing a high concentration of suspended substances and a high concentration of organic and inorganic compounds. Landfill leachate is produced from soluble substances, rainwater and surface water percolating through the waste. It is formed by the biochemical and chemical degradation processes of the waste [Liu et al. 2006]. In order to prevent the vertical infiltration of leachate, anti-leakage lining is necessary. There are many materials for the impermeable layer. It can be a single clay layer with the permeability coefficient of less than  $10^{-7}$  cm/s and the thickness of at least 1 meter. It also can be a composite liner, which is made by laying an elastic anti-seepage film on the clay layer [Cui 2005]. Generally, we need to lay a blind ditch or a perforated pipe to collect and guide leachate. The pipe's slope to the sump or sewage adjust the pool with more than 40-percent slopes. The main methods to dispose leachate both at home and abroad include dispose leachate and urban wastewater together (outside field), separately *in situ* dispose, and pre-dispose-merged dispose (both inside and outside landfills). It is better to combine the leachate dispose with urban sewage treatment. We can discharge leachate into a sewer system after the *in situ* dispose, and then introduce leachate to municipal sewage treatment plants.

## 2.2 Landfill gas control

Organic matter in landfills could be degraded by facultative and specificity of microorganisms, producing landfill gas. Landfill gas contains a lot of CH<sub>4</sub> and CO<sub>2</sub> and other trace elements. If a large amount of landfill gases accumulated within the soil, the growth of vegetation will be affected seriously and even result in an explosion. So, it is necessary to collect and dispose landfill gas for the safety of landfill and the smooth progress of vegetation restoration. There are two methods to collect landfill gas: sealing method and air-permeable method [Cheng 2009]. Sealing method is the method with no permeability barrier and gas only passes through the top cover, or use the wall to prevent air from flowing. The bottom or the side wall of the landfill with a thickness of 0.5–1.2 meters can be made with compacted clay holding certain moisture, in order to prevent air that escapes from the bottom or side wall. We can also use a thin film made of synthetic materials to cover the bottom or side wall in order to prevent air and protect the groundwater from polluting. Air-permeable method is a method that uses the pebble channel or the groove filling pebble to guide and collect landfill gas. We can set ventilation tubes at the top of the garbage and set branch pipes within the shallow gravel channel, and then connect the branch pipes with vertical ventilation tubes. We can also arrange access shafts evenly in the site, so that the access shafts will both collect vertical landfill leachate and permit a free passage of air. Landfill gas is a kind of precious energy. Only rational utilization can make the landfill gas contribute to humans. The following are the main utilization ways of landfill gas control: electricity generation, used as a civil gas, used for a compressed natural gas and used as a boiler fuel [Gong 2006].

## 2.3 Surface covering

Surface covering for ecological restoration in landfills is a technology that includes both the selection of proper covering materials and the design of effective and reasonable cover thickness and shape. It tends to meet the goals of preventing the escape of landfill gas and decreasing the concentration of landfill leachate. Using surface covering, we can construct an artificial ecosystem, which is mainly vegetation, and make the recovered land for other uses [Peng et al. 2002]. Landfill covering layers can be mainly divided into two parts. One is for ecological restoration, the other is for drainage and seepage control, which is made up of drainage layer, venting layer, seepage control layer (protective layer is included) and base layer. The ecological restoration part includes

nutritive layer and vegetable layer. It can beautify the surroundings and reduce soil erosion, which is good to collect and guide surface runoff. Drainage layer is made up of sand or soil materials with a larger permeability coefficient (generally more than 10<sup>-4</sup> cm/s). It can collect rainwater and avoid the anti-seepage layer in direct contact with the ecological restoration part, which can protect the anti-seepage layer by preventing plant roots from intruding into the anti-seepage layer [Chen 2013]. The anti-seepage layer material usually includes a high-density polyethylene film, geosynthetic clay liner and clay. It can keep rain from penetrating into the rubbish material, and also prevent the landfill gas diffusion through soil porosity. Base layer has the effect of support and stability on the whole cover. Its cover material include soil, gravel, and even some hard solid waste, such as construction waste. The surface covering materials of a city landfill in the ecological restoration project mainly depend on both input costs and output benefits of ecological restoration; at the same time, the surface covering materials vary between the landfill site and the restoration project.

# 3 VEGETATION RESTORATION

## 3.1 Soil amelioration

During the rotting of waste, flammable gases are emitted and make the soil alkali-affected, leading to difficulty in vegetation survival, so soil amelioration is necessary. For soil amelioration, green manure or organic fertilizer is mainly used to increase organic matter content and improve the soil's physical and chemical characteristics. In the place where landfill gas is relatively small, a significant negative correlation was observed between the content of mineral nitrogen and the quality of dry matter of vegetation. It proves that it is necessary to apply nitrogen fertilizer in landfill. Organic substances can stimulate the growth of plants obviously, so some compost is useful [Chang 2008]. Loosening the final soil appropriately improves the soil's physical characteristics because the final soil compressed by the device frequently during construction restricts the growth of plant roots severely. In the process of ecological restoration of garbage landfill in Tangshan South Lake, we added organic manure and peat soil to the planting soil, resulting in three planting soils for every one organic manure and every one peat soil. Then, we stirred them well and covered them. The soil disposed was rich in N, P, K and other nutrients, and air permeability and water permeability were also good, which are the characteristics that are beneficial to the plant growth [Li 2010]. In the

process of ecological restoration of garbage landfill in Wenzhou Yangfushan, nitrogen fertilizer and compost fertilizer were applied to improve soil fertility, and humus soil sieved out from the garbage was also used. At the same time, loosening the final soil appropriately also had a positive effect on the improvement of soil fertility [Han et al. 2008].

### 3.2 *Vegetable selection*

Plants growing in landfill will face many serious environmental stresses, which include landfill gas, landfill leachate and high temperature, drought and poor environment of the final layer. So, it is important to select tolerant species. The basic principle of selecting plants is that the species must be able to endure the stress from landfill gas and landfill leachate and have a stronger tolerance to drought. There are two main different ways of selecting suitable species. One way is to select through the planting experiment. Guo et al carried out a planting experiment at Dongtan Lake landfill, Jiaozhou Bay, Qingdao, Shandong, screening several plants that have good resistance [Guo et al. 1994]. The other way is to select through vegetation investigation in landfill. Ji et al investigated the vegetation of a landfill site in Shenyang closed for 2 years, recommending six plant species that were suitable for ecological restoration of landfill [Ji 2005]. Summarizing different plant species planted in different landfills reported by different researchers is helpful to select suitable plant species for the ecological restoration of landfill. However, the selected species cannot always be employed universally, because there are many differences in the background of landfill. We must combine only with the particular local case.

### 3.3 *Vegetation reconstruction process*

At the beginning of vegetation reconstruction, we can plant some herbs, because herbs have developed roots that can improve the soil and create conditions for the growth of other plants including trees and bushes. After that, we should plant some trees that grow slowly, are small, have shallow roots and are not susceptible to pests to improve the single herb plant landscape. Trees can also accelerate soil improvement. At the same time, trees can create better conditions for the growth of other plants because they can intercept rain water and reduce leachate through absorption and transpiration. In the middle and the development phase, combined with ecological planning and development planning, we need to plant trees with grass and shrubs on a large scale according to the different functional regionalization and green design.

## 4 ENVIRONMENTAL MONITORING

The process of ecological restoration of landfill is long term and dynamic, so environmental monitoring must be done on a continuous basis during the end-to-end process [Han et al. 2013]. The main inspection factors include landfill gas, leachate and plants. In the process of ecological restoration of Shenzhen Guoqiao landfill, we laid many monitoring wells from upstream to downstream. The samples were taken regularly to monitor the migration of landfill gas and leachate, guaranteeing the minimum pollution to the environment after closure [Guo & Zheng 2004]. The vegetation system established at the initial stage is always unstable, so it is necessary to monitor the plant growth. A scientific way of maintenance is very important. We need to adjust the species composition and community structure of green vegetation constantly. At the same time, we should cultivate the plants' power of self-renewal.

## 5 CONCLUSION

In this paper, with the clue of process, we commented on the key technologies of ecological restoration of sanitary landfill systematically from two aspects, namely pollution control and vegetation restoration, hoping to provide reference for ecological restoration of sanitary landfill. At the beginning of ecological restoration, a scientific and reasonable planning and design is necessary, and we need to attach importance to pollution control and utilization of rehabilitation land. It is better to determine the ultimate way of land use in the future before the construction or close of landfill. We should study the critical factors for ecological restoration of sanitary landfill, such as landfill stability, harmful gases and leachate, the nature of the final soil and the selection of plant species. During and after ecological restoration, environmental monitoring must be done on a continuous basis. During ecological restoration, environmental monitoring can help managers and decision-makers to know the degree to which the ecosystem is restored and whether ecological restoration is effective or not. Environmental monitoring after ecological restoration is important for the evaluation of the ecological recovery technique.

## REFERENCES

- Cao, M.H. 2010. Pollution control and ecological restoration of landfill. *China Science and Technology Information*, (13): 21–28.



- Chang, X.F. 2008. A study on techniques of planting and soil improvement at waste sanitary landfill slope—A case study of Liulitun waste sanitary landfill in Beijing. Beijing: Beijing Forestry University.
- Chen, L. 2013. The main influence factor analysis for municipal solid waste landfill closure. Wuhan: Huazhong University of Science and Technology.
- Cheng, X.D. 2009. Urban waste landfill sites ecological restoration technology research. Baoding: North China Electric Power University.
- Cui, S.J. 2005. Research on ecological restoration of municipal landfill. Beijing: China Environmental Sciences Press.
- Gong, S.P. 2006. Research on landfill gas generation rate and selection of treatment methodologies. Wuhan: Huazhong University of Science and Technology.
- Guo et al. 1994. Study on the rehabilitation of an artificial ecosystem of vegetation on a waste landfill site. Chinese Journal of Environmental Science, 15(02): 53–58.
- Guo, J.W. & Zheng, X. 2004. Design introduction of simple landfill closure. Guangdong Chemical Industry, (1): 55–56.
- Han et al. 2008. Closure and ecological restoration design of landfill. Tianjin Science & Technology, (03): 20–23.
- Han et al. 2013. Environmental problems and countermeasures of landfill in Guangzhou. Environment, (S1): 33–36.
- Ji, C.Z. 2005. Investigation on the vegetation restoration in Zhaojiagou landfill site in Shenyang. Environmental Sanitation Engineering, 13(2): 49–54.
- Kwon, R.K. & Gary, O. 2010. Review on potential for enhanced phytoremediation of landfills using biosolids. Journal of Environmental Management, (91): 791–797.
- Li, Y.Y. & Ju, M.T. 2005. Principles and practices of ecological restoration. Beijing: Chemical Industry Press.
- Li, X.Y. 2012. Greening technology of landfill based on ecological restoration. Practical Forestry Technology, (5):45–47.
- Liu et al. 2007. Review on municipal refuse landfills virescence. Research of Soil and Water Conservation, 14(2): 108–111.
- Liu et al. 2006. Analysis of leachate characteristics of municipal landfill. Environmental Science and Technology, 29(6): 55–57.
- Peng et al. 2002. Pollution control and ecological reclamation of MSW dumping sites. Journal of Chongqing Jianzhu University, 4(1): 206–210.
- Wang, X.G. 2011. Study on vegetation and soil characteristics of landfill sites in Shanghai. Shanghai: East China Normal University.
- Yang, R. & Wang, H. 2010. Landscape Break through: the ecological restoration and landscape reconstruction of urban landfills. Sustainable Urban Development, 17(8): 81–86.
- Zhao et al. 2012. Ecological restoration and sustainable landscape design of waste land of landfill. Huazhong Architecture, (4): 114–116.
- Zhou, L. Development situation and thinking of landfill ecological restoration technology. 2012. Environmental Science and Technology, 25(4): 71–74.

# Experimental verification and pair-group analysis study of passive space design strategies

Junjie Li & Yehao Song

*School of Architecture, Tsinghua University, Beijing, P.R. China*

*State Key Laboratory of Subtropical Building Science, South China University of Technology, P.R. China*

Qingguo Wang

*China Design and Research Group, China*

**ABSTRACT:** Passive design has widely been identified as one of the most economical and effective strategies for reducing energy demand. However, the employment of passive design strategies is often based primarily on experience that often lack long-term effective validation data to prove or disprove their effectiveness. This research is based on the physical surveillance, and has adopted physical environment fieldwork test and data analysis methods to evaluate the effectiveness of passive space design strategies and their influence on the main body spaces. The two selected experiment platforms shared various commonalities such as climate environment, layout, structure, designers, construction time, etc., which offered numerous opportunities for parallel comparisons. Therefore, this research adopted a pair-group analysis method to isolate and analyze a single variable through one-year monitoring of one typical passive spaces (a sunlight space) to verify the effectiveness. The experiment tested several physical parameters such as temperature, humidity, wind speed, CO<sub>2</sub> concentration index in winter, summer and trans-seasons, and analyzed the impacts of the passive space on the entire building. This test research also incorporates the results of the quantified data regarding the impact levels of the passive spaces and summarizes its advantages and disadvantages, and provides suggestions regarding possible improvements. The research results indicate that passive space design strategies need to balance the entire year's climate characteristics, and consider matching technologies with technical strategies that approach design problems from both the environment and the human comfort perspectives.

**Keywords:** passive design; building space; pair-group analysis; field work test

## 1 INTRODUCTION

The lack of quantitative research on passive strategies was one of the bottlenecks faced by this present study [1–3]. Current evaluations of sustainable building designs only consider whether or not they are involved in environmental factors, use the regulating function of passive space, or employ new types of thermal insulation materials or construction details. Consequently, the existing body of research is insufficient, and needs to provide answers to questions such as: how might these designs be optimized by the use of technology-based strategies? To what extent might such strategies provide further optimization? And, how should architects go about such optimizations? With the majority of scholarly attention being focused on sustainable concepts and green buildings in recent years, building design needs to proceed beyond the fuzzy qualitative research stage and on to the precise quantitative research stage [4–5].

## 2 EXPERIMENTAL PLATFORM

### 2.1 Platform 1: O-house at Tsinghua University

The O-house is an experimental building designed by a Tsinghua University research team; it took three years to design, construct, and monitor. It is a net-zero house that relies completely on solar energy to supply its energy consumption [6]. To achieve net-zero energy consumption, works on the inflow and outflow of energy were both necessary. A ground floor plan plays an important role in the reduction of a building's energy dissipation. In a building functioning as a house, spaces that are the most often used and user-related should be optimized for physical comfort as much as possible. The O-house is based on a principle of passive priority. The most cardinal and comfort-demanding space is at its very center, and three layers of space encircle this core. The micro-environment transitions from outside layer to inner layer. (as shown in Fig. 1).



Figure 1. Passive strategy for three layers of spaces.

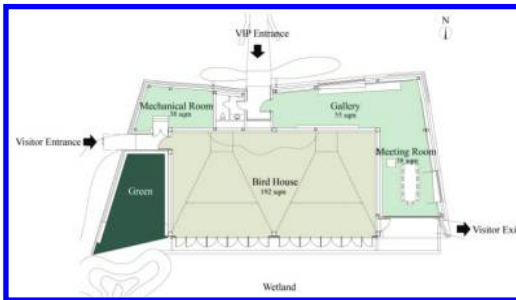


Figure 2. Plan of Waterfowl Pavilion.

## 2.2 Platform 2: Waterfowl Pavilion in Beijing Zoo

The Waterfowl Pavilion is located inside of the Beijing Zoo which has a superior natural environment, and vegetation coverage of more than 90% [7]. On the south side of the site, there is a large wetland area used as a bird habitat. To avoid destroying the building’s ecological status and to provide a natural and livable environment for the birds, this project aims to build a net-zero energy demonstration building that intricately combines green and low carbon concepts. There are two domain spaces in the Waterfowl Pavilion, each based on a different design target. One is an open space used as a bird habitat. To better coordinate with the natural environment and ensure that the birds’ living space allows for sufficient sunshine, the birdhouse is located on the southernmost point of the building. The second domain space is related to people’s needs, rather than birds’ needs. This space includes an exhibition hall, meeting rooms, service rooms, etc. Therefore, after considering the relationship between the building’s shape factors and functional organization, the building envelope was formed into two layers of nested spaces [8] (as shown in Fig. 2).

## 2.3 Platform 1 vs. platform 2

The two experimental platforms’ building information is compared below (as shown in Table 1). The two buildings were built during the same time

Table 1. Building information comparison between the two experimental platforms.

	O-house	Waterfowl Pavilion
Climate zone	Cold climate zone	Cold climate zone
Build time	2013	2013
Surrounding environment	In sculpture park, surrounded by green space	In zoo, surrounded by 90% green space and water
Building area	74.9 m <sup>2</sup>	390.6 m <sup>2</sup>
Building structure	Steel frame	Steel frame
Passive space	Sunshine space	Wind tower, Underground wind tunnel
Details and parameters	Four layers of Low-e insulating glass with a thickness of 5 mm/42 mm and a U-value of 0.48 W/(m <sup>2</sup> ·K), a shading coefficient of 0.443 for the south glazing wall Wall material: 80 mm mineral wool + HIP, a U-value of 0.2 W/(m <sup>2</sup> ·K) Roof material: 130 mm mineral wool & HIP, a U-value of 0.1 W/(m <sup>2</sup> ·K)	Three layers of Low-e insulating glass with a thickness of 5 mm/42 mm and a U-value of 0.7 W/(m <sup>2</sup> ·K), a shading coefficient of 0.443 for the south glazing wall U-value of the wall is 0.3 W/(m <sup>2</sup> ·K); U-value of the roof is 0.3 W/(m <sup>2</sup> ·K); U-value of the ground floor is 0.35 W/(m <sup>2</sup> ·K);
Other strategies	PV system: 70 m <sup>2</sup> PV panels with a capacity of 11.5 kW, thin film photovoltaic panels Solar thermal: solar vacuum tube collectors HVAC: WSHP (cop = 6) & ASHP Water system: membrane bioreactor water treatment	PV system: 110 m <sup>2</sup> PV panels with a capacity of 18 kW, thin film photovoltaic panels Solar thermal: solar vacuum tube GSHP: rated 20 kW cooling capacity, power 3.7 kW HVAC: radiation cooling system

Table 2. Test periods and test contents.

	Dec 2013 –Jan 2014	Apr–May 2014	June–July 2014	Dec 2014 –Jan 2015
	Winter	Trans-season	Summer	Winter
Platform one	Air temperature	PMV, air temperature and humidity, wind speed, black ball radiation temperature	PMV, air temperature and humidity, wind speed, black ball radiation temperature, lighting	PMV, air temperature and humidity, wind speed, black ball radiation temperature, lighting
Platform two	Air temperature	Air temperature	Air temperature and humidity, CO2 concentration, lighting, wind speed	Air temperature and humidity, CO2 concentration, lighting, wind speed

period, designed by the same design group, adopted the same building structures, and are located in the same climate zone and almost identical surrounding environments. Moreover, they have the same topological relationships and spatial layouts that the core spaces are surrounded by functional space to the east, north, and west sides, in response to climate factors. Both of the two core spaces are large and without division. Both buildings' southern sides have large areas of glazing provided by the same manufacturer, and the window-to-wall ratios of the two are 0.6 and 0.52, respectively. One of space design differences between the two buildings is platform one (the O-house) has an extra layer of openable sunspace in the southern façade.

### 3 FIELDWORK TEST SCHEME

The two selected experiment platforms had various commonalities such as climate environment, layout, structure, designers, construction time, etc., which offered the possibility of parallel comparisons. Therefore, this research adopted a pair-group analysis method to make a comparison of the two the topic of this research. In order to test the effectiveness of passive space in different climate conditions over the course of an entire year, the test period had four separate phases. Together, the four phases lasted more than one year, from December of 2013 to January of 2015. (as shown in Table 2). To minimize the interference of other factors, the two buildings were not left open to active system equipment such as the air conditioning system, lighting, and other electrical equipment.

### 4 RESEARCH RESULTS AND ANALYSIS

The test points were located at the east and west doors in the southern façades of the two buildings,

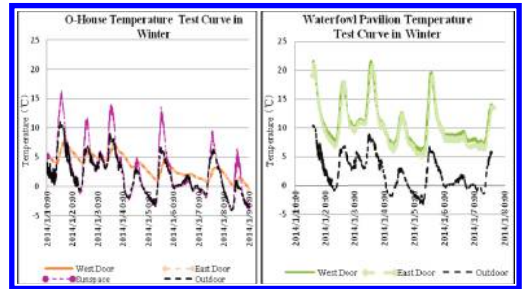


Figure 3. Test temperature curve for platforms 1 and 2 in winter.

the sunspace of the O-house, and outdoors. The outermost layer of sunspace in the O-house was dark thin-film solar PV shutters were closed but not sealed during the test period. It was expected at the design stage that the sunspace would serve as a buffer, preheating the indoor spaces in cold winters and providing shading to reduce the indoor temperature during hot summers.

The test results indicated that there was a substantial gap between the actual test results after the building was constructed and the designer's subjective judgment during the design stage. The curve of the winter test results (as shown in Fig. 3) indicates that the sunspace was greatly influenced by outdoor temperature fluctuations. The mean temperature in the sunspace was just 0.9°C higher than the outdoor temperature during the winter test period, and the indoor temperature was only 1.6°C higher than the outdoor space. Conversely, in the Waterfowl Pavilion, the mean indoor and outdoor temperature differences reached 7.2°C and over 16°C between 12:00 pm and 5:00 pm (as shown in Table 3). The sunspace in the O-house experienced only a slightly greater preheating effect than it would have without the addition of this passive space. The reason for this very different result

Table 3. Average temperature in winter test results (unit: °C).

	Winter				Summer			
	$\bar{T}_{outdoor}$	$\bar{T}_{indoor}$	$\bar{T}_{sunspace}$	$\bar{T}_d$	$\bar{T}_{outdoor}$	$\bar{T}_{indoor}$	$\bar{T}_{sunspace}$	$\bar{T}_d$
P1	1.9	3.5	2.8	1.6	24.7	27.5	25.9	2.8
P2	1.9	9.1	—	7.2	27.9	28.9	—	1

between the built performance and the first design concept is that although the designer had a basic understanding of the sunspace’s preheating function in winter, in practice, due to the vertical layout demands of the photovoltaic panels on the southern facade, the solar spectrum of infrared light was resisted by the dark glazing blinds and generally did not penetrate into the sunspace. Moreover, air leakage and the lack of an up-and-down ventilation device in the PV blind panels were other factors worsening the cold air resistance and pre-heated warm air exchange.

The curve of the summer test results (as shown in Fig. 4) indicate that the temperature in the sunspace fluctuated greatly with the outdoor temperature. Although the highest temperature appeared in the outdoor space, the mean temperature in the sunspace was 1.2 °C higher than that of the outdoor space. The test results indicate that the thermal environment in the sunspace did not benefit from the envelope itself because the unsealed shading blinds on the southern façade offset the heat between the shading’s cooling and the solar radiation’s penetration. With a real-time thermal exchange in and out of the sunspace, the temperature remained almost the same. However, the test data obtained on the 5th of June showed that the sunspace provided a good shading effect to the interior space. The highest temperature occurred at 12:26 pm and reached 38.8°C. The temperature in the sunspace was 36.6°C, while the indoor temperature on both sides of the gate was only 29.2 °C and 29.9 °C, respectively, nearly 10 °C lower than the outside air temperature. The highest indoor temperature occurred at 5:00 pm, thus, the indoor temperature peak obviously lagged behind the outside air temperature. The indoor temperature stayed within a stable range for a long time, and had smaller swings than the outdoor variations.

Comparing these results to the temperature test curve of the Waterfowl Pavilion (as shown in Fig. 4), it can be seen that 90% of the stable temperature in summer conditions was a benefit provided by the passive strategy of the south side sunspace in the O-house. The indoor south side temperature curve in summer was almost synchronous with the outdoor space in the Waterfowl Pavilion, regardless of whether the openings were closed, the indoor and

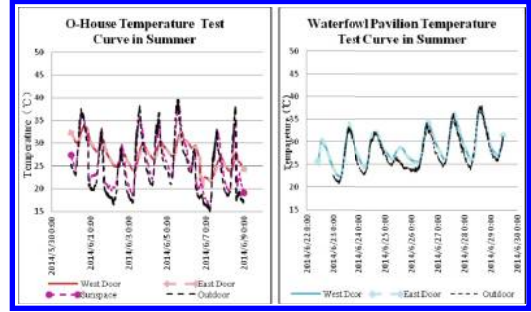


Figure 4. Test temperature curve for platforms 1 and 2 in summer.

outdoor temperature changes were nearly simultaneous. On the one hand, these results demonstrate that with southern façades with similar window-to-wall ratios, the buffer and shading functions of the sunspace had a significant effect, reaching to a 10°C temperature difference between the indoors and outdoors. On the other hand, these results demonstrate that a large glazing area on the southern façade without shading can significantly increase indoor temperatures and cooling loads in summer weather conditions, even in a cold northern climate zone such as in China.

## 5 CONCLUSION

The research results yielded quantified data regarding the impact levels of the passive spaces, and allowed researchers to summarize their advantages and disadvantages and provide some possible improvements. The test results indicated the following conclusions with regards to sunspaces:

1. Don't just “pick up” passive strategies. Different from what was expected from the initial design concept, the passive strategy of using a sunspace in winter may have no effect on the cold air buffer and preheating effect in cases where there are issues of inappropriate glazing color, glazing air tightness, or ventilation measures between the sunspace and the interior space. Therefore, with regards to winter weather

conditions, a sunspace should not only be considered an easy “pick up” of one kind of passive strategy, but rather designers should strive to create cooperation within the design between the sunspace and the main space.

2. Maximize advantages. The O-house is an example of how the solar radiation can be blocked by an unsealed dark blind on the southern façade, in order to maintain better ventilation inside of the sunspace. The indoor temperature benefited from this design that the temperature was 10°C lower than it was in the outside space during the test period. The dual function of shading and providing natural ventilation in the buffer zone maximized these advantages during summer weather conditions.
3. Weigh the pros and cons. considering the climate conditions that occur throughout year, a designer should weigh the pros and cons regarding pursuing a preheating effect in the winter or shading and ventilation effects in the summer. Such decisions do not have to be either/or, but precise research and designs are required to achieve a “win-win” effect.
4. Pay attention to shading in the summer. Even in cold climates such as those experienced in northern China, large areas of south-facing glazed façades without shading devices may result in a sharp increase in the building’s cooling load in summer weather conditions. In addition, a well-designed buffer zone could perform significantly better than simple shading devices with regards to creating a shading effect.

#### ACKNOWLEDGMENTS

This work is supported by the National Natural Science Foundation of China (Grant No. 51278262)

and open project of State Key Laboratory of Sub-tropical Building Science, South China University of Technology (Grant No. 2013KB05).

#### REFERENCES

- [1] Sanja Stevanović. Optimization of passive solar design strategies: A review. *Renewable and Sustainable Energy Reviews* [J]. 2013(9):177–196.
- [2] I. Rajapaksha, H. Nagai, M. Okumiya. A ventilated courtyard as a passive cooling strategy in the warm humid tropics [J]. *Renewable Energy* 2003;28:1755–1778.
- [3] Carlos Ernesto Ochoa, Isaac Guedi Capeluto. Strategic decision-making for intelligent buildings: Comparative impact of passive design strategies and active features in a hot climate [J]. *Build Environ* 2008;11:1829–1839.
- [4] Seoung-Wook Whang, Sangyong Kim. Determining sustainable design management using passive design elements for a zero emission house during the schematic design [J]. *Energy Build* 2014;07: 304–312.
- [5] Yehao Song, Junjie Li, Ning Zhu, Jialiang Wang, Shimeng Hao. Fieldwork Test Research of the Impact on Building Physical Environment on Six Types of Atrium Space in Cold Climates [J]. *Journal of Harbin Institute of Technology*. (EI index). 2014.
- [6] Hong Zhang, Junjie Li, Lei Dong, Huanyu Chen. Integration of sustainability in Net-zero House: Experiences in Solar Decathlon China [J]. *Energy Procedia*, 2014(57):1931–1940.
- [7] Yehao Song, Jingfen Sun, Junjie Li, Dan Xie. Towards Net Zero Energy Building: Collaboration-based Sustainable Design and Practice of the Beijing Waterfowl Pavilion [J]. *Energy Procedia*, 2013(57): 1773–1782.
- [8] Yehao Song, Jingfen Sun. Towards a Net Zero Energy Building [J]. *Time + architecture*, 2014(05):92–99.

# Research into the measurement detection and line optimization of the carbon capture ability of Italian poplars

Zhiguo Wang

*School of Physics and Electronic and Electrical Engineering, Huaiyin Normal University, Huaian, China*

Qing Liu

*School of Liberal Arts, Huaiyin Normal University, Huaian, China*

**ABSTRACT:** Carbon storage can offset more CO<sub>2</sub> emission, creating a broader space for Chinese economic development. By dynamically predicting the carbon sink function of such trees as Italian poplars, we can acquire a reference basis for working out the plan of industrial production and emission reduction. It is one of the important contents and the easiest approaches for China to develop low-carbon economy. This thesis introduces the development process and research tendency for the measurement detection and line optimization of the carbon capture ability of Italian poplars, and explores the measurement detection and line optimization measures and implementation paths of the carbon capture ability of Italian poplars, which can help to boost the construction of ecological civilization, enhance industrial level and achieve the concerted promotion of social and economic benefits.

**Keywords:** carbon capture; forestry carbon sink; measurement detection; line optimization

## 1 INTRODUCTION

Nowadays, people advocate developing low-carbon economy, which means the highly-efficient utilization of energy as well as the development and utilization of clean energy in essence. Low-carbon economy chiefly includes: saving energy, reducing emission; promoting the rate of energy utilization<sup>[1]</sup>; developing clean energy including renewable energy, nuclear energy and hydrogen energy; improving the structure of energy consumption; achieving the control of carbon emission; reducing the emission of CO<sub>2</sub> and its impact by building ecological carbon sink and developing the technology of carbon capture and utilization. Therefore, developing low-carbon economy requires the strong support of the technological innovation of energy-saving and emission reduction, clean energy and carbon capture and utilization.

## 2 RESEARCH BACKGROUND AND ACTUALITY OF THE MEASUREMENT DETECTION AND LINE OPTIMIZATION OF THE CARBON CAPTURE ABILITY OF ITALIAN POLARS

### 2.1 Research background

Carbon sink refers to the process of absorbing CO<sub>2</sub> in the air, chiefly referring to the ability of forests,

wetlands and oceans to absorb and store CO<sub>2</sub><sup>[2]</sup>. Ecological carbon sink refers to the ecological system which can effectively absorb CO<sub>2</sub>. Ecological carbon sink chiefly includes the ecological system of forests, wetlands and oceans. At present, the collection of CO<sub>2</sub> contains two aspects: the construction of ecological carbon sink and the technology of CO<sub>2</sub> capture. Since the global carbon programme was started in 2001, many countries worldwide have been dedicating themselves to relevant researches. With the clean development mechanism of Kyoto Protocol<sup>[3]</sup>, China has already set up several pilot projects, and has signed a contract of carbon emission reduction with a dozen developed countries worldwide. The pilot projects that have been carried out in China include: Inner Mongolian Carbon Sink Pilot Project, Guangxi Pilot Project<sup>[4]</sup>, Sichuan and Yunnan Carbon Sink Project, Zhejiang Carbon Sink Pilot Project and Beijing Carbon Sink Project.

### 2.2 Research actuality

The rapid development of carbon sink trade requires people to put forward the measurement methods of artificial forest carbon sink. So far, scholars worldwide have already carried out intensive research into the measurement methods of forest carbon sink, and have put forward the following two methods: 1) the method of counting

the existing biomass which reflects the cumulative amount of carbon which is closely related to biomass; 2) the method of measuring the CO<sub>2</sub> flux of forests by using microclimate theory and technology, and then converting the amount of CO<sub>2</sub> into the storage of carbon. With the second method, a lot of achievements have been made overseas. So far, over 150 observation stations have already been set up. This method is applied to measure the flux of water vapor, and has been expanded to the research into the flux of CO<sub>2</sub> since the 1980s. Scientists of Euroflux Laboratory have applied the method of eddy correlation to intensively study the change of CO<sub>2</sub> fluxes of European forests at different latitudes. Malhi et al applied the method of eddy correlation to study the seasonal change model of tropical, temperate and northern forests, with the research findings being: tropical forests manifest net carbon sink all the year round, while forests in the high latitude area manifest sink in the growth season and manifest source in winter. China started later in this regard. In 2002, Chinese Academy of Sciences officially started the project of observing the carbon fluxes of Chinese terrestrial ecosystem. So far, 4 CO<sub>2</sub> flux fixed position observation stations of typical forest ecosystems in Changbai Mountain, Qianyan Sandbar, Dinghu Mountain and Xishuangbanna respectively.

### 3 RESEARCH CONTENT OF THE MEASUREMENT DETECTION AND LINE OPTIMIZATION OF THE CARBON CAPTURE ABILITY OF ITALIAN POPLARS

#### 3.1 *The main content of research and development*

The implementation content of this project is the system development of the measurement detection and line optimization of the carbon capture ability of Italian poplar. The system consists of: a central control machine and a large-screen display system; a sound and wind velocity meter, an infrared CO<sub>2</sub> analysis meter, a data recording and data comparison device, a conduit system; wireless sensor nodes and a relay base station, etc.;

The demonstration system of development has the following functions: capable of automatically increasing/decreasing the measurement frequency of each test point according to the external environment and the expert system. When the carbon-absorbing ability of Italian poplars is in a stable state and within a safety scope in spring and summer, the frequency of measurement is reduced. When the weather variation and wind velocity are in an unstable state and at a critical point of safety scope, the frequency of measurement is increased.

Relevant parameters are adjusted dynamically according to the situation of measurements; wireless sensors are networked and relay nodes are set up according to the distribution of monitoring sites, and data transmission free from distance limitation is carried out.

#### 3.2 *Key technological problems to be solved emphatically during project implementation*

3.2.1. The substitution scheme of energy (wind) measurement. The project summarizes empirical data and weather and other factors while combining the fuzzy algorithm method and expert system to substitute the three-dimensional ultrasonic anemoscope, which is the key technological problem to be solved in the project.

3.2.2. The problem of the dynamic networking of wireless sensors. Considering that the woodlands of carbon sink measurement are independent of one another, each woodland of Italian poplars is different from others, and Italian poplars have different carbon capture abilities in different seasons, the dynamic networking of wireless sensors is also one of the key technological problems.

3.2.3. The maintenance-free problem of the monitoring system. For large-sized woodlands, the around-the-clock continuous work of CO<sub>2</sub> concentration analyzer needs to consume a lot of electric energy. The around-the-clock continuous data transmission and receipt of sensor nodes need also to consume a lot of electric energy. The maintenance-free power supply carried by wireless sensor nodes has also become a key problem to be solved.

### 4 MAJOR RESEARCH METHODS

#### 4.1 *The overall technological line of this project*

The design of the overall scheme → the design of various modules → system integrated manufacturing → equipment debugging → system operation.

#### 4.2 *Module design*

##### 4.2.1 *The design of wireless sensor network nodes*

At present, against different applications, the structures of sensor nodes are almost the same, chiefly including the collection unit, the processing unit, the transmission unit and the power supply unit, just as shown in [Figure 1](#).

Against the demand of measurement of CO<sub>2</sub> concentration and the characteristics of wireless sensor network, this project will focus on studying and developing the new-type wireless sensor nodes



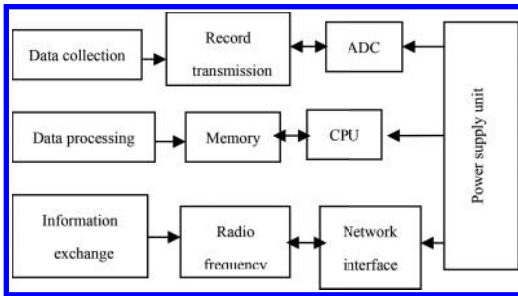


Figure 1. The structure chart of wireless sensor network nodes.

based on ZigBee technology. These nodes shall be designed separately and hierarchically in a modularized way, consisting of the front-end sensor collection module, the signal processing module, the radio frequency transceiver module and the power supply module.

1. The front-end sensor collection unit.

The selection of sensors: The system sensors shall be selected on the principle of high reliability, low cost, simple interface and convenient line connection, and the equipment with a high-cost performance shall be selected according to the situation and the actual project demand.

2. The processor unit: According to the characteristics of wireless sensor nodes: low energy consumption, complete functions, high integration and large memory capacity, embedded microprocessor is adopted. This system is expected to use the MSP430 series processors of TI Company and compile signal processing and corresponding decision-making management software.

3. Communication unit: In the wireless transceiver chips, both the TR1000 of RFM Company and the CC1000 of Chipcon Company are ideal choices of low power consumption. However, considering the conflict-free frequency band, node safety, performance and other factors, the CC2420 wireless transceiver chips of Chipcon Company will be used in the system design because they work on general ISM frequency band, carry their own hardware encryption mechanism and conform to the ZigBee technology designed exclusively for wireless sensor network.

4. Power supply unit: Power supply unit supplies power to various circuits of the system. According to the actual requirement of field monitoring, this project is expected to use storage battery for power supply, and can consider adding a solar panel if necessary.

4.2.2 The design of monitoring system

The monitoring system is used to exert management over nodes, process incoming data, automatically generate database statements, carry out intelligent management according to prepared operation procedures, and deliver the results of system processing to a large screen for display.

4.2.3 The design of relay node communication system

The designed communication system is used to complete the wireless communication between relay nodes and central control machine. Zigbee communication protocol, communication frequency band of 2.4 GHz and band width of 8 MHz will be adopted.

5 INNOVATIVE POINTS OF THE PROJECT

5.1 The wireless monitoring technology and system integration of the carbon capture ability of Italian poplars

In connection with the demand of parameter monitoring of Italian poplar woodlands and the characteristics of wireless sensor network, the wireless monitoring network is used for real-time perception of carbon-capture information and processing of Italian poplar, and transmission of results to the central server. The server uses the method of signal processing and the expert system for integrated decision-making, and commands the processing of relevant data. All the sensors used in the network work intermittently according to requirement, capable of effectively saving limited electric energy resources. The utilization of wireless sensors is characterized by no cable wiring, low expense and no network maintenance.

5.2 Energy (wind) measurement monitoring technology

The high price of three-dimensional ultrasonic wind velocity meter has become a problem for the detection application of Italian poplar carbon sink ability. The project summarizes empirical data and weather and other factors while combining the fuzzy algorithm method and expert system to substitute the three-dimensional ultrasonic anemoscope.

5.3 The dynamic networking of wireless sensors

Considering that the woodlands of carbon sink measurement are independent of one another, each woodland of Italian poplars is different from others, and Italian poplars have different carbon capture abilities in different seasons, the sensors

in the wireless sensor monitoring network work in a state of dynamic changes. The central control machine can issue relevant instructions according to weather and other factors, so as to carry out the optimization of monitoring network.

## 6 CONCLUSION

Since the Forestry Property Exchange was established, China has successively set up carbon sink exchange centers in such cities as Beijing, Shanghai and Tianjin. The measurement detection and line optimization system of carbon capture ability of Italian poplars enjoys a broad development space and a brilliant industrialized prospect. China boasts a huge potential of carbon emission reduction, and the property of forest carbon sink and the compensation and marketing of ecological service have already become a development trend. Carrying out research into carbon sink projects can play a very important role in enabling China to take an active part in international cooperation and become familiar with the trading rules of international carbon market. Developing forestry carbon sink and establishing and perfecting the long-term mechanism of forest ecology compensation can help to save energy, reduce emission,

optimize energy structure and improve ecological environment. Furthermore, it also plays an important role in enriching farmers and boosting the construction of new rural areas.

## ACKNOWLEDGEMENTS

This work was financially supported by the project under the National Spark Program (2011GA690403) and the project of research on the higher educational reform of Huaiyin Normal University (11GJA0020): The Practice and Innovation Projects for university students of Jiangsu (201310323058X).

## REFERENCES

- [1] Energy Saving Office of State Forestry Administration; Carbon Sink Calculation and Detection Guide of Chinese Green Carbon Foundation Afforestation Projects [M]; Beijing: Chinese Forestry Press, Dec. 2008.
- [2] Li Nuyun; Chinese Forestry Carbon Sink [M]; Beijing: Chinese Forestry Press, 2007.
- [3] UNFCCC. Kyoto Protocol [EB/OL]. <http://unfccc.int/resource/docs/convkp/convchi.pdf>, 1997.
- [4] Guangxi Carbon Sink Project [EB/OL]. Chinese Carbon Sink Website, 2006.

# Analysis of current situation after restoration in the Tianjin Lingang ecological wetland park

N. Zhao & H.Y. Li

*College of Environmental Science and Engineering, Nankai University, China*

J. Hu & J.W. Hou & T. Wen

*Tianjin Lingang Industrial Zone Construction Development Co. Ltd., China*

**ABSTRACT:** Ecological restoration and landscape construction of urban wetlands are gradually becoming a research hotspot at home and abroad. In China, urban wetland reconstruction projects have achieved remarkable results. Tianjin Lingang ecological wetland park is a typical urban wetland park, which was constructed on artificial reclamation land. Earlier, the park was deserted salinity tidal flats; however, by the water system design, plant configuration, ecological reconstruction, engineering measures, it became a multifunction park integrating water landscape and ecological restoration. After ecological restoration, the biodiversity level of Tianjin Lingang ecological wetland park increased significantly, reaching up to 149 kinds of plants, belonging to 56 families and 113 genera. Plants were widely distributed in the habitat types of forests, grassland, lawn, flower border, and near water's edge belt. The construction of the vegetation ecosystem was achieved not only through bringing in varieties of cultivated plants, but also by keeping a certain percentage of the wild native species in some sections. The case of Tianjin Lingang ecological wetland park provides an important theoretical guidance and application reference for the similar ecological restoration in the future.

**Keywords:** Lingang ecological wetland park, plant species, habitat types, status analysis

## 1 INTRODUCTION

In 2000, London wetland park nearby the Thames River was opened, which provided a successful model for urban wetland protection and development [1]. With the speeding up of urbanization, urban wetland ecological restoration and landscape construction are gradually becoming a research hotspot at home and abroad [2]. In our country, urban wetland ecological restoration has made a breakthrough. The construction of Xixi wetland park [3], Chongming wetland park [4], Dongying wetland park and Dongtan wetland park has provided a strong reference for the urban wetland park construction.

In the perspective of landscape ecology, urban wetland park is a wetland landscape, which is constructed on the urban artificial landscape matrix and composed of wetland corridor and wetland patches [5]. Wetland park has important roles in adjusting the balance of atmosphere carbon and oxygen as well as reducing the greenhouse effect [6], and it has a very high ecological value. As an ecological park that was constructed on salinity tidal flats, the ecological benefit of Tianjin Lingang

ecological wetland park will directly affect the Tianjin's urban ecological environment. As one of the successful cases in the city wetland ecological restoration, Tianjin Lingang ecological wetland park provides an important theoretical guidance and application reference for similar ecological restoration cases in the future.

## 2 RESTORATION METHOD

### 2.1 Sample area introduction

Tianjin Lingang ecological wetland park is located in the Tianjin Binhai Lingang industrial zone, whose total area is about  $6.3 \times 10^5$  square meters, and it was constructed on artificial reclamation land. The park is located in a typical muddy tidal flat in the Bohai bay. Owing to the long-term development of the coastal zone area, it has accumulated a fair degree of pollution. Through kinds of ecological restoration measures and landscape construction measures, such as water system design, plant configuration measures, salt exclusion engineering design, ecological reconstruction engineering, hard landscape design, and landscape sketch design, it

became a multifunction park integrating water landscape and ecological restoration. Meanwhile, by using the combination of undercurrent wetland technology and surface current wetland technology, its sewage purification treatment function has realized the local wastewater zero discharge in part of the Lingang economic zone. It became a park that possessed the ability of sewage water treatment as well as the landscape effect. The entirety shape of the park is like a butterfly, which mainly includes three big scenic spots, namely undercurrent wetland, regulating lake, the main body of the landscape area.

## 2.2 Field investigation

After the ecological restoration in Lingang ecological wetland park, the vegetation was investigated in this paper in July 2014. The optimal size of samples used for plant community surveys is as follows: the idiomatic sample size of the arbor layer is 10 m × 10 m; the idiomatic sample size of the shrub layer is 5 m × 5 m; and the idiomatic sample size of the herb layer is 1 m × 1 m. According to the different geographical locations, habitats, climate zones, investigation objects (arbor, shrub, herb) and the ecological system types, it has a flexible choice in setting the sample area and samples, but it must abide by the principle of typical sampling, integrity and representative, and the sample area cannot be less than the minimum area of community. For community samples, the longitude, latitude and elevation, and the types, quantity, and height of the dominant species are recorded.

## 2.3 Data analysis

The survey data were analyzed and entered in Excel software.

# 3 RESULTS AND ANALYSIS

## 3.1 Plant species richness

Lingang ecological wetland park has a high level of endemic species: a total of 149 plant species were found in the survey, and these kinds of plants belong to 56 families and 113 genera. As shown in Figure 1, the number of species contained in specific families is as follows: the majority is *Rosaceae*, which contains 24 species (accounting for 16.11% of the total species), the second is *Leguminosae* (13 species, accounting for 8.72% of the total species), *Gramineae* (12 species, accounting for 8.05% of the total species), *Compositae* (8 species, accounting for 5.37% of the total species), *Salicaceae*, *Oleaceae* and *Chenopodiaceae*

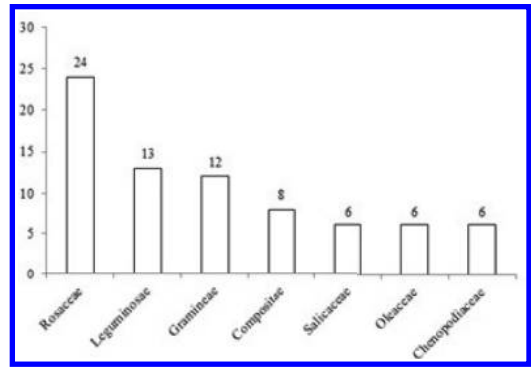


Figure 1. The number of species contained in the families.

(all 6 species, accounting for 4.03% of the total species), respectively. The majority of the above-mentioned families contain the species accounting for 50.34% of the total species, and the rest are less than 6 species.

## 3.2 The habitat types of plants

Tianjin Lingang ecological wetland park has really made lots of efforts in the aspect of building wetland parks, except for bring in lots of aquatic or hydrophilous plants, such as *Schoenoplectus tabernaemontani*, *Pontederia cordata*, *Canna glauca* and *Lythrum salicaria*. Also, the considerable quantity of aquatic, hydrophilous wild herbs in the water area and near water's edge belt, such as *Scirpus planiculmis*, *Rorippa islandica*, *Eclipta prostrata* and *Ceratophyllum demersum* is retained.

After investigation, the habitat types of Lingang ecological wetland park mainly included forest, grassland, lawn, flowers border, water area, or near water's edge belt. According to the survey, the distribution of the plants varies in the habitat types based on their different ecological habits, which is shown in Figure 2. The plants of Lingang ecological wetland park are mostly distributed in forest/grassland: first, the plant species that are mainly distributed in this kind of habitat reach up to 80 species (accounting for 53.69% of the total species); second, the plants that are mainly distributed in water area or near water's edge belt reach up to 30 species (accounting for 20.81% of the total species). The plant species used to create flower border reach up to 30 species (accounting for 20.13% of the total species). The rest of the plant species that are obligatorily distributed in canopy frame, palings and lawn are few, i.e. reaching up to only 8 species (accounting for 5.37% of the total species).

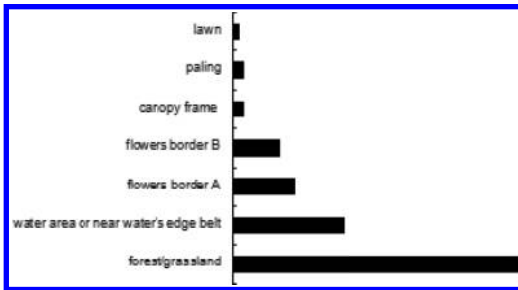


Figure 2. The habitat types of plants.

#### 4 CONCLUSION

After ecological restoration, Tianjin Lingang ecological wetland park was significantly improved in biodiversity level: a total of 149 plant species were found in the survey, and these kinds of plants belonged to 56 families and 113 genera. Lingang ecological wetland park had really made lots of efforts in the aspect of building wetland parks. After investigation, the habitat types of Lingang ecological wetland park mainly included forest, grassland, lawn, flowers border, water area, or near

water's edge belt. The plants in the Lingang ecological wetland park were distributed in the habitat types of forest and grassland.

#### ACKNOWLEDGMENTS

This work was financially supported by the National Natural Science Foundation (41301096).

#### REFERENCES

- [1] Bu Jinghua, Wang Yang: *Huazhong Architecture*, Vol. 23(2) (2005), P. 103–105.
- [2] Cui Baoshan, Liu Xingtuo: *Advances in Earth Science*, Vol. 14(4) (1999), P. 358–364.
- [3] Li Yufeng, Liu Hongyu, Zheng Nan, et al: *Acta Ecologica Sinica*, Vol. 31(4), P. 1021–1028.
- [4] Wang Siyuan, Niu Meng: *Environmental Science and Management*, Vol. 34(7) (2009), P. 137–140.
- [5] Qiao Lifang, Zhang Yichua, Qi Anguo, et al: *Journal of Northeast Agricultural University*, Vol. 19(3) (2011), P. 87–91.
- [6] Lei Kun: *Forest Resources Management*, Vol. 21(2) (2005), P. 23–26.

# The analysis of Lingang Wetland Park's eco-efficiency

Y.Y. Wan & H.Y. Li

*College of Environmental Science and Engineering, Nankai University, Tianjin, China*

J. Hu, J.W. Hou & T. Wen

*Tianjin Lingang Industrial Zone Construction Development Co. Ltd., Tianjin, China*

**ABSTRACT:** Wetland park has a huge environmental adjustment function, eco-efficiency and high ecological value. Earlier, the Tianjin Lingang Ecological Wetland Park was deserted saline-alkali tidal flats, which was built on artificial reclamation land. During the construction of the park, by the methods of ecological reconstruction, and vegetation restoration measures, it has become a multi-function park that is completed integrated with hydrophilic landscape and ecological restoration. Wetland's wastewater treatment capacity has reached the partial zero emissions. After restoration, the Tianjin Lingang Ecological Wetland Park's eco-efficiency improved significantly. After investigation, at the initial stage of the wetland park, its total biomass was 11.61 t/hm<sup>2</sup>, with a relatively small amount of biomass. The post real-time monitoring should be strengthened. Lingang Wetland park plant carbon reserves were 1607.2245 tons with a net carbon reserve calculation. This study will be carried out for the future similar ecological restoration project to provide important theoretical guidance and application of reference.

**Keywords:** Lingang Ecological Wetland Park; carbon fixation; oxygen release; biomass; ecological benefits

## 1 INTRODUCTION

In 2000, the wetland park opened in London on the Bank of the River Thames, for the protection and development of urban wetlands, has provided a successful model. With the accelerated process of urbanization, urban wetland ecological restoration and landscape has gradually become the hot spots at home and abroad. Regulating function of wetland park has huge environmental and ecological benefits, which also had core effects on the protection of biodiversity, the maintenance of fresh water resources, regulating climate, and the degradation of pollutants, providing production as well as living resources.

Utilization of urban wetland resources is under the premise of protecting wetlands, on the rational development and utilization of urban wetland resources. Lingang Wetland Park acts as a ecological park that possesses a high ecological value and was established in saline-alkali tidal flats. It plays a significant role in adjusting the balance of carbon and oxygen in the atmosphere and exerts a big influence on reducing the greenhouse effect. The park's ecological benefits will take a direct impact on the city itself, and will also provide a theoretical guidance and application reference for subsequent ecological restoration cases as a very successful example.

## 2 MATERIALS AND METHODS

### 2.1 *Sample and introduction*

Lingang Wetland Park is located in the Binhai New District of Tianjin, Tianjin Lingang Industrial Zone where is the South of the estuary of the Haihe River shoals area, and built with a total area of about 630,000 square meters on the reclaimed land. The typical park is located in the Bohai Bay muddy tidal flat, which had accumulated a considerable degree of pollution due to the long-term development of the coastal zone. Typical ecological recovery measures, such as water system design, plant configuration measures, salt-removing engineering, ecological reconstruction engineering, hardscaping design, landscape sketches design and the landscape create measures, have been used to build a multi-function park integrated with hydrophilic landscape and ecological restoration. Combined with the undercurrent technology and table flow technology of wetland, its sewage purification processing function achieved partial sewage zero emissions, and the park gives consideration to the function of sewage processing and also brings about landscape effects. The overall shape of the park looks like a butterfly, and there are three main major scenery plots in it, namely Subsurface Flow Constructed Wetlands, Adjusting Lake and Main Landscape.

## 2.2 Field investigation

Vegetation surveys were carried out after the ecological restoration of Lingang Wetland Park July 2014. The optimal quadrat size for community investigations is as follows.

Arbor stratum used the qadrat size of 10 m × 10 m, the fruticose stratum of 5 m × 5 m and the herb layer of 1 m × 1 m. As for community plots, the data of the community's longitude, latitude and elevation, and within the community's species are recorded, especially the dominant species, number and height.

## 3 CALCULATION METHOD

### 3.1 Method of calculating the biomass of arbor

#### 3.1.1 Method of logging

This method includes the clear-cutting method, the average method and size selection.

#### 3.1.2 The biomass

The biomass of the individual tree model is as follows:

$$W = aD^b \quad (1)$$

$$W = a(D^2H)^b \quad (2)$$

where  $W$  is the biomass;  $D$  is the Diameter at Breast Height (DBH); and  $H$  is the height of the tree; and  $a$ ,  $b$  are the estimate parameters.

### 3.2 Fruticose biomass calculation method

Implementing the quantification dispose on each factor effect plant volume, the dependent variable  $y$  relies on the independent variable  $x$ , reading the specific value when  $x$  acts as number indicators (e.g. diameter, tree height, crown diameter and stand age) and qualitative indicators (e.g. growth situation, and stand density), and these quantification indicators of factor and classes are collectively known as category (Ck), which are graded using expectations on its seeking derivatives.

### 3.3 Data analysis

The survey analysis and collation of data were processed and analyzed by Excel software.

### 3.4 Conclusions

Conclusions should state concisely the most important propositions of the paper as well as the author's views of the practical implications of the results.

## 4 RESULTS AND ANALYSIS

### 4.1 Calculated results of Lingang Wetland vegetation biomass

#### 4.1.1 Estimation of arbor biomass

Biomass can be divided into arbor biomass and non-tree biomass two parts, and arbor biomass was calculated according to the formulas of 'lumber timber volume's fast calculation table:

$$V = 5.7468552 \times 10^{-5} D^{1.9155590} H^{0.92659720} \quad (3)$$

where  $V$  is the volume ( $m^3$ );  $D$  is the diameter at breast height (cm); and  $H$  is the height (m).

Single-tree volume calculation was used in 58 species of trees in the Lingang wetland park, resulting in a total volume of 306.40  $m^3$ . This was in accordance with the individual tree biomass model law, by the empirical formula for calculation. Arbor totaled 41382 trees, and total arbor biomass was calculated as 307.61 t. The specific results are summarized in Table 1.

#### 4.1.2 Non-tree biomass estimation

Biomass estimation of non-arbor's part (shrubs, hedges, flower) increased with plant age. Plant parameters (diameter, height and crown width) and biomass changes were very small, so they were calculated with the direct empirical value. The specific results are summarized in Table 2.

#### 4.1.3 Lingang Wetland Park total biomass

①. Biomass:

$$\begin{aligned} B &= B(\text{arbor}) + B(\text{others}) \\ &= 306.40 + 444.05 + 72.02 + 198.29 + 0.78 \\ &= 1021.54 \text{ t} \end{aligned}$$

Table 1. Empirical formula.

Species	Formula
The paulownia	$lgw = 0.8925lgD^2H - 1.2409$
Koelreuteria Paniculata	$lgw = 0.915 + 0.1 D^2H$
Black locust	$lgw = 0.253 (D^2H)^{0.646}$
Acer mono	$lgw = 0.714 + 0.0295 D^2H$
Ginkgo biloba	$lgw = 0.09 D^2H - 0.684$
Poplar	$lgw = 0.13513 (D^2H)^{0.802003}$

Table 2. Biomass estimation of non-tree's part.

Type	Total number	Average individual biomass (Kg)	Total biomass (t)
Deciduous shrub	120994	3.67	444.05
Hedgerow	122063	0.59	72.02
Perennial flowers	271624	0.73	198.29
Chinese rose	7091	0.11	0.78

Table 3. Tianjin Lingang Wetland carbon reserves.

Type	Total number/10 <sup>5</sup>	Average individual biomass/kg	Total biomass/t	Carbon content	Individual carbon reserves/kg	Carbon reserves/t
Aiphyllium	0.072	69.72	50.1984	0.51	35.5572	25.6012
Deciduous trees	3.1297	85.88	2687.786	0.48	41.2224	1290.1373
Deciduous shrub	10.1239	3.67	371.5471	0.49	1.7983	182.0581
Hedgerow	9.4834	0.59	55.9521	0.51	0.3009	28.5356
Perennial flowers	25.1811	0.73	183.8220	0.44	0.3212	80.8817
Chinese rose	0.6748	0.11	0.7423	0.48	0.0528	0.3567

Biomass per unit area:

$$B = [B(\text{arbor}) + B(\text{others})]/S \\ = (306.40 + 444.05 + 72.02 + 198.29 + 0.78)/88 \\ = 11.61 \text{ t/hm}^2$$

Or

② Biomass:

$$B = B(\text{arbor}) + B(\text{others}) \\ = 307.61 + 444.05 + 72.02 + 198.29 + 0.78 \\ = 1022.75 \text{ t}$$

Biomass per unit area:

$$B = [B(\text{arbor}) + B(\text{others})]/S \\ = (37.61 + 444.05 + 72.02 + 198.29 \\ + 0.78)/88 \text{ hm}^2 \\ = 11.62 \text{ t/hm}^2$$

By the two estimate methods of arbor biomass, slight differences were found between the results, which can be ignored basically. The total biomass is small to some extent. The possible reasons for this are as follows. a. Neglect the part from the park's aquatic plant biomass. b. Large errors were caused due to the calculation by using the empirical formula. c. Wetland park itself at the initial period after building and plants at the young stand age so that the biomass was little small to some extent, especially the arbor.

#### 4.1.4 Net carbon reserves calculation

Garden plants biomass and types of plants average carbon content, Tianjin Lingang calculated net carbon storage in wetland park gardens plant taxonomy (Table 3) can be calculated by the following formula:

$$C_i = N_i \times W_i \times C F_i + 10^6 \quad (4)$$

where  $C_i$  ( $10^5$  t) is the type  $i$  of the net carbon reserves;  $N_i$  is the general investigation number of type  $i$  plant;  $W_i$  (g) is the plant individual biomass of type  $i$ ;  $C F_i$  is the average rate of carbon of type  $i$  plant; and  $10^{-6}$  is the unit conversion factor ( $1 \text{ g} = 10^{-6} \text{ t}$ ).

Characteristics of carbon content are given in Table 3. The plant carbon rate ranging between 0.4 and 0.6 is basically stable, with all less than 0.6 and the total average being 0.485; aiphyllium, hedgerow color blocks displays more than 0.50, while the smaller carbon content results from perennial flower.

The reason may be due to evergreen trees' dense material caused by slow growing.

Many studies have proved that little differences in the carbon content of the plant exist and its value is usually between 0.45 and 0.55 in different regions. The IPCC recommends using the average carbon content of 0.5 (2006, National Greenhouse Gas Inventories). The results of this study further validates the conclusions of previous research. Meanwhile, it also supplements the local region parameters with respect to the carbon content of plant communities in Tianjin wetlands.

## 5 CONCLUSION

After investigation, the Lingang ecological wetland park's total biomass was found to be  $11.61 \text{ t/hm}^2$ ; this overall value was a small to some extent. Plant carbon rate ranging between 0.4 and 0.6 is basically stable, and plant carbon reserves were 1607.2245 tons. After restoration, the Tianjin Lingang Ecological Wetland Park's eco-efficiency improved significantly, and subsequent real-time monitoring should be strengthened as well.

## ACKNOWLEDGMENTS

This work was financially supported by the National Natural Science Foundation (41301096).

## REFERENCES

- [1] Y.Q. Man, X.L. Chen, J.W. Mo, et al: Beijing main forest types of constructive species of carbon content analysis. J. Journal of Beijing Forestry University. vol. 24(5/6) (2002), P. 96–100.
- [2] M. Zhao, G.S. Zhou. Mo, et al: Plant carbon of forest ecosystem of China and its impact factor analysis. J. Geographical Science. vol. 24(1) (2004), P. 50–54.
- [3] Fang J.Y., Chen A.P., et al: Changes in forest biomass carbon storage in China between 1949 and 1998. J. Science. vol. P. 262:2320–2323.
- [4] IPCC. Good practice guidance for land use, land-use change and forestry [M]. Hayama: IPCC/IGES, 2003.



# A study on the influence of space expansion in the urban fringe area in megalopolis on urban land used for carbon source and sink: A case of Shanghai

M.L. Qin, J. Zhao, H. Li, J. Ya & Y. Tang

*College of Civil Engineering and Architecture, Guangxi University, Nanning, China*

**ABSTRACT:** Urban fringe area has three characteristics, namely spatial transformation acceleration, urban and rural land boundary fuzziness and carbon sink function sensitivity. To explore the particularity of the urban fringe space expansion on land used for carbon source and sink in megalopolis, the research uses the GIS to have a quantitative analysis of the land used for carbon source and sink fringe areas in Shanghai from the year 1990 to 2013. It is found that the land used for carbon sink in the fringe areas of Shanghai is mainly composed of cultivated land. And in the process of expansion, most cultivated land is transformed into the land used for carbon source, and a part of it is replaced by the garden land; the area of the woodland first falls and then rises. The important ways for megalopolis to realize low carbon include adjusting population distribution, controlling urban development pattern, regulating energy structure, developing sustainable energy sources, protecting carbon sink land, and improving carbon sequestration capacity. In the end, it is found that problems such as land structure confusion and excessively fast erosion of carbon sink land are quite significant in megalopolis.

**Keywords:** megalopolis; fringe area; land used for carbon source and sink; space structure; expansion pattern

## 1 INTRODUCTION

The expansion process in urban fringe areas is a centrifugal and extensional urbanized space process<sup>[1,2]</sup>. In this process, problems such as wasting of land resources, land structure confusion, carbon source land's continuous erosion of carbon sink land and serious ecological damage are becoming increasingly prominent. Such problems are even more remarkable in megalopolis where the rate of urbanization is higher and the transformation of carbon source land is faster. Megalopolis has an early urbanization process, a more complete and complex urban system network, and a wide radiating area in the inner city area, so the transformation process of carbon source land is undoubtedly irreversible. The space expansion in the fringe areas of megalopolis on the land used for carbon source and sink is of its own particularity.

The acceleration of the land transformation process in the fringe areas of megalopolis is one of the most significant features of used land for carbon source and sink. Serious waste of cultivated land resource, low utilization efficiency and unreasonable space structure all lead to the fact that the land used for carbon sink is excessively occupied by land used for carbon source, causing a serious

carbon sequestration capacity<sup>[3]</sup>. In the study of the transformation of fringe areas in megalopolis, overseas scholars have mainly focused on the research of regional land-use and land-cover change (LUCC)<sup>[4-6]</sup>. Because the landscape pattern in the fringe areas of megalopolis has significant features of locality and accumulation<sup>[7]</sup>, the acute change of landscape pattern has accelerated the transformation from traditional agricultural land to industrial land or other non-agricultural land<sup>[6]</sup>. For example, Wu Yanfang<sup>[4]</sup> performed a quantitative analysis of the dynamic change of land utilization in Pinggu District of Beijing from 1993 to 2008, and it was found that within 15 years, the area of the cultivated land in Pinggu District decreased sharply, the area of garden land increased greatly, and urban and rural construction areas increased year by year. Taking Shunyi District of Beijing as an example, Li Can<sup>[8]</sup> carried out an analysis from the perspective of the influence of land utilization and cover on the regional landscape fragmentation pattern and its spatial heterogeneity, and explored the action mechanism of the landscape pattern in the fringe areas of metropolis. The fuzziness of urban and rural land boundaries is another feature. The boundary of the fringe areas in metropolis is more difficult to recognize. The

drastic expansion in urban fringe areas drives the process of urban and regional integration. The urban fringe area breaks the single space expansion scope of suburbanization and becomes the core regional space of urbanization, leading to a fuzzier boundary between urban and rural land utilization. From the research on Fanyu District of Guangzhou, Li Kaiyu<sup>[10]</sup> found that metropolis adopted the method of “withdraw county (city) and set up district” to expand the interior of the city, which leads to the continuous expansion of the urban fringe area. With the top-down expansion in the city and the bottom-up spreading in villages and towns, the dualistic development means is more significant in the fringe areas of metropolis. Fan Lingyun<sup>[9]</sup> found that the fringe area of Guangzhou is influenced by the central city area and the peripheral subcenter, and urban and rural development interweaves with each other and different land plaque intersections within the district are more complex. Land utilization and cover caused by human activities has become the second largest source of the increase in carbon content in the atmosphere, whose effect is only second to the burning of fossil fuels<sup>[11]</sup>. The rapid process of urbanization and industrialization in metropolis leads to the drastic shrink of agricultural land, and the rapid expansion of urban residential land strongly influences regional carbon sink and emission. Shan Fuzheng<sup>[12]</sup> conducted a research on the land utilization and carbon emission of Zhangjiang High-tech Park, and found that the agricultural land similar to the cultivated land decreased dramatically, which brought the negative effect of continuously declining carbon sequestration capacity. In 2009, the carbon sequestration volume reduced by 85.1% compared with that in 2000, while the carbon emission volume is 3037.7 times more than that in 2000. The park is faced with a serious carbon deficit.

The space expansion in urban fringe areas results in drastic changes of land utilization structure as well as a serious unbalance of the carbon cycle, which is more significant in metropolis where transformation of land used for carbon source is quicker. So far, research on the space expansion in fringe areas of metropolis has mainly focused on the change of land utilization and cover from the perspective of regional landscape pattern, while only a few have focused on different space expansion patterns in fringe areas to study the change of land used for carbon source and sink, and there is a lack of quantitative and qualitative studies on land used for carbon source and sink. In this article, taking fringe areas of Shanghai as an example, we study the influence of space expansion in fringe areas on land used for carbon source and sink.

## 2 SPACE EXPANSION PATTERNS

### 2.1 *Finger type*

Finger type usually occurs in the starting stage or initial stage of a city's rapid development period. It relies on the city's traffic lines and expands outwards in a certain axis direction in a linear pattern. Relying on traffic lines, fringe areas' outward development is of rapid driving effect, so the expansion speed of finger type is usually very fast and has a high-efficient driving effect on the regional construction of surrounding areas. That is to say, finger-type expansion can quickly transform the land for carbon sink into land for carbon source. Generally, the transformed land used for carbon sink is cultivated land or garden land, and because of the action of road planning, its invasion of forest is relatively less. The scope of the transformed carbon sink land mainly centers on the surroundings of the traffic line, so relatively, its scope is not quite large but the expansion speed is relatively fast. Meanwhile, the transformation degree in the fringe area is not complete, and there exists a large amount of scattered land for carbon sink, most of which is unconstruction area, having little erosion on land for carbon sink.

### 2.2 *Satellite type*

Satellite-type expansion usually occurs in the middle stage of a city's rapid development period, when the city's development has formed a large scale and the expansion in urban fringe areas chooses to rely on original towns to generate development by leaps and bounds or select a new place to build in order to obtain a better living environment. Not relying on the major city to develop, the city's planning and implementing efficiency is relatively low. Relatively speaking, the satellite-type expansion pattern has a slower speed of transforming carbon sink land, but simultaneously relatively complete. The satellite-type fringe areas relying on original towns present a slow circle-layer shape, and the carbon sink land transformed into carbon source land is mostly the original cultivated land surrounding the villages and towns, whose scale is relatively small. Because of the urban planning and site selection, the newly built satellite town is relatively large, and the carbon skin land within the area has a complex constitution. However, if the two can be better planned and regulated, it will do little damage to the ecological structure of carbon sink land.

### 2.3 *Group type*

Group type occurs in the middle stage or later stage, when the city's development had begun

to take shape and the expansion in fringe areas manifests as the newly planned development area or industrial area. The expansion in urban fringe areas presents a planned and regular form, and the city is able to largely control the scope and function of the expansion in the fringe areas and control the expansion speed and the degree of carbon sink land transformation. However, the group-type expansion will encroach a large area of carbon sink land, whose constitution will be more complex. The transformation speed of cultivated land and garden land into carbon source land is the fastest. Meanwhile, a large area of forest will be transformed into construction land. Without control and planning, the group expansion will do great damage to the ecological structure of fringe areas. At the same time, the group-type expansion pattern has a slower speed of transforming carbon sink land, but simultaneously more complete.

#### 2.4 Spreading type

Spreading type usually occurs in the initial stage or later stage of a city's rapid development, which manifests as the unordered and uncontrolled expansion in fringe areas. The spreading is formed artificially and spontaneously, whose expansion is of significant blindness and randomness. It is formed because of a lack of planning management in the initial stage and because of uncontrolled rapid development in the later stage. The area of a single spreading is relatively small and fast, which has little erosion on carbon sink land. However, because spreading is of highest occurrence probability, its influencing scope is the largest. The carbon sink land eroded by spreading is mainly cultivated land and unconstruction area, and because of a lack of unified planning, its transformation degree is relatively low and it is easy to form repeated demolition and construction.

#### 2.5 Wheel type

Wheel type occurs in the later stage of a city's development, which usually relies on the city's circuits to expand outwards, with a significant circle-layer feature. Because of the construction of urban traffic circle lines as well as its dependency on the development of the main city, the expansion speed in fringe areas of wheel type is generally slow, and at the same time, the surrounding directions present the characteristic of unbalanced transformation degree. The influencing scope of wheel-type expansion is relatively wide, which mainly centers on the surroundings of traffic circuits, whose periphery is generally surrounded by forest and the transformed carbon sink land is usually cultivated land or garden land. Relatively, wheel-type expansion also has

high erosion on carbon sink land, the transformation degree is relatively high and the reserved carbon sink land within the circle is relatively small. Without proper control, it may cause a series of "overspreading" problems in urban development, causing great damage to the ecological structure of carbon sink land.

#### 2.6 Filling type

Filling occurs in any stage of urban development. Filling refers to self-improvement and supplement of infrastructure or complete district in fringe areas or core areas. Filling has a fast speed in transforming carbon sink land into carbon source land, but the area is relatively small and scattered. Generally speaking, the transformed carbon sink land is the unconstruction land or urban green land in the city. The transformation of filling is complete, but its erosion on carbon sink land is small.

### 3 AN EXAMPLE OF THE FRINGE AREA IN SHANGHAI

#### 3.1 Definition method of the fringe areas

The study chooses the remote-sensing image of American Landsat TM in the mid-1990s, covering China as the data source, and has a supervised classification of the land in the fringe area in 1990, 2000, 2006 and 2013 (from September to December). After that, remote-sensing image screen digital technology as well as man-machine interaction numerical analysis is adopted to have a manual visual interpretation, directing the extraction of the inner margin and outer edge of the fringe area of Shanghai from ArcGIS. Based on the interpretation of Shanghai's core district in 1990, at the end of every time period later, a new urban form is formed until the information of urban core districts and fringe areas in different periods is abstracted. The sketched boundary can be directly input into the GIS, and statistics of the area will be done in ArcInfo so as to obtain the area of core area and fringe areas of Shanghai as well as the occupation information of carbon sink land in the expansion process. The spatial form of the fringe area of Shanghai in 1990, 2000, 2006 and 2013 is shown in [Figure 1](#).

#### 3.2 An analysis of the influence of different expansion patterns formed in different stages on land used for carbon source and sinks

Taking the year of 1990, 2000, 2006 and 2013 as the research timings, this paper studies on the change in the features of land used for carbon source and

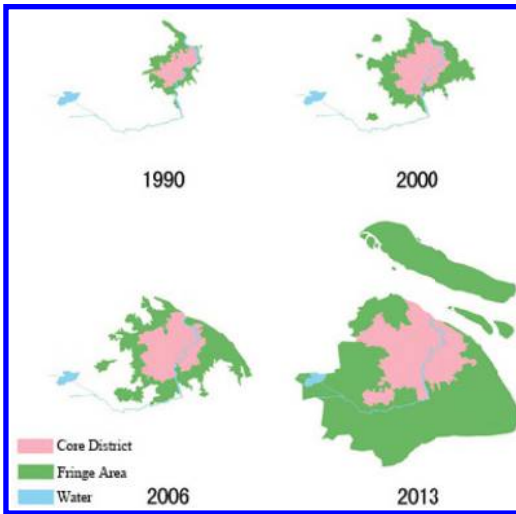


Figure 1. Urban fringe areas form of Shanghai City during the four periods of time from 1990 to 2013.

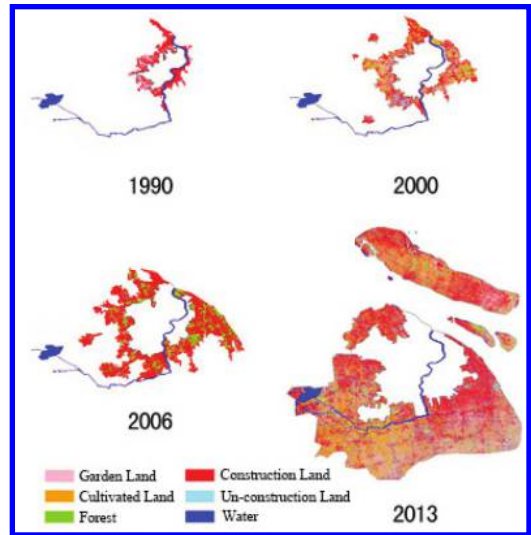


Figure 2. Land used for carbon source and sink distribution in the urban fringe areas of Shanghai City during the four periods of time from 1990 to 2013.

sink in the fringe areas of Shanghai to discuss the changing rules of expansion patterns in different stages. The distribution and data of the land used for carbon source and sink in the urban fringe areas during the four periods of time are shown in Figure 2 and Table 1.

1. **1990–2000: this is a rapid development stage. The expansion pattern in urban areas centers on wheel type and satellite type and the land used for carbon sink is mainly cultivated land.**

In 1990, the urban form of Shanghai was relatively divergent and fragmented, and the expansion pattern in urban fringe areas was mainly spreading type. In the 1990s, Shanghai was already developed well enough, and it was originally one of the Chinese metropolises. At that time, the city needed rapid development, and there was not a proper unified planning and management. As a result, the city was still continuously spreading outwards and it was out of control as a whole. At that time, the total area of the core district was 24663.21 ha, and the total area of the fringe area was 40710.66 ha, in which the carbon source land was 28143.3 ha and the carbon sink land was 12567.36 ha, with the proportion of 2:1. Most of the carbon sink land was cultivated land, which was 7573.67 ha, accounting for 60.26%; unconstruction area was in the second place, which was 3244.22 ha in total, accounting for 25.81%; forest was in the third place, which was 324.77 ha, accounting for 2.59%; the rest was garden land, which was 117.14 ha, accounting for 0.93%.

After the year 1990 and 2000, the city entered a rapid development stage. The major feature

of expansion in urban core district was river-crossing, while the major feature of expansion in fringe areas was the emergence of the satellite town, whose expansion patterns were mainly wheel type and satellite type. At that time, the development of the city was under control, and the city started to use total planning to carry out construction. By 2000, the total area of the core district was 51925.04 ha and the total area of fringe areas was 75029.33 ha. Within the fringe area, the total area of land used for carbon source was 28523.76 ha, and that of land used for carbon sink was 46505.57 ha, with a proportion of 1:1.6. The proportion of land used for carbon sink increased. Among the land used for carbon sink in fringe areas, cultivated land still accounted for the most, which was 20566.51 ha, accounting for 44.22%; garden area was in the second place, which was 10350.54 ha, accounting for 22.27%; unconstruction land was in the third place, which was 8871.85 ha, accounting for 19.08%; forest was in the last place, which was 6414.99 ha, accounting for 13.76%.

Altogether, from 1990 to 2000, the growth rate of carbon source land in the fringe areas of Shanghai City was 1.35%; 270.05% for carbon sink land; 171.55% for cultivated land; 1875.24% for forest, experiencing a large amount of growth; 8736.04% for garden land and 173.47% for un-construction land.

2. **2000–2006: this is a rapid development stage, when the expansion pattern of fringe areas**

Table 1. Situation of constitution of lands used for carbon source and sink in the fringe areas of Nanning City at the four periods of time from 1990 to 2013 (unit: hm<sup>2</sup>).

Land for carbon source and sink	Year			
	1990	2000	2006	2013
<i>Land for carbon sink</i>				
Water	1307.56	301.68	857.56	14466.49
Forest	324.77	6414.99	14967.23	18232.26
Garden land	117.14	10350.54	21579.62	84724.57
Cultivated land	7573.67	20566.51	23232.12	119030.8
Unconstruction land	3244.22	8871.85	5664.02	84541.66
Total	12567.36	46505.57	64611.52	320995.7
<i>Land for carbon source</i>				
Construction land	28143.3	28523.76	41060.93	106805.6
Total	40710.66	75029.33	107361.45	427801.40

**centers on finger type and the land used for carbon sink is mainly cultivated land.**

From 2000 to 2006, the city entered a rapid development stage, the fringe areas expanded continuously and the original fringe area was quickly transformed into the core district, and the urban form became divergent and incomplete. At that time, the major expansion pattern was finger type and the fringe area presented the tendency of connecting to the original satellite town outwards along the road. Until 2006, the total area of the core district of Shanghai was 81943.77 ha, and the total area of fringe area was 107361.48 ha. In the fringe area, land for carbon source was 41060.93 ha and land for carbon sink was 66300.55 ha, maintaining the proportion of 1:1.6. Among the land used for carbon sink, the majority was still cultivated land, accounting for 23232.12 ha, 35.04% of the total; garden land was still in the second place, which was 21579.62 ha in total, accounting for 32.55%; forest was in the third place, which was 14967.23 ha, and accounting for 22.57%; unconstruction area was in the last place, which was 5664.02 ha, accounting for 8.54%.

Altogether, from 2000 to 2006, the growth rate of carbon source land in fringe areas of Shanghai was 43.95%; 42.56% for carbon sink land; 12.96% for cultivated land; 133.32% for forest, 108.49% for garden land and -36.16% for un-construction land, experiencing a fall.

**3. 2006–2013: this is a stage of stable development, when the expansion model of fringe areas centers on wheel type and group type and the land used for carbon sink is mainly cultivated land.**

From 2006 to 2013, Shanghai entered a stage of stable development, and the urban construction was under a unified planning and management with a strong control force. The land of

the city was mostly constructed in the form of group development and the edge of the core district became smooth and square. Until 2013, the core district of the city expanded rapidly, constantly filling the gap with the fringe area, whose total area reached 153655.1 ha. The edge of the fringe area gradually expanded to the city's whole area under administration, the shape tended to be regular, and the inner edge constantly approached the outer edge, whose total area was 427801.37 ha. The expansion models were wheel type and group type. The total area of land for carbon source in fringe areas was 106805.59 ha and the area of land for carbon sink was 320995.78 ha, with a proportion of 1:3, in which the land for carbon sink rose a little. Among the land for carbon sink, cultivated land was the most, which was 119030.8 ha, accounting for 37.08%; garden land was in the second place, which was 84724.57 ha, accounting for 26.93%; unconstruction land was in the third place, which was 84541.66 ha, accounting for 26.33%; forest was in the last place, which was 18232.26 ha, accounting for 5.68%.

Altogether, from 2006 to 2013, the growth rate of carbon source land in fringe areas of Shanghai was 160.11%, experiencing a significant increase in this stage; 384.15% for carbon sink land; 412.35% for cultivated land; 21.81% for forest, experiencing stagnation; 292.61% for garden land and 1392.61% for unconstruction land, experiencing a large increase.

**4 SUGGESTIONS OF FRINGE AREAS IN METROPOLIS BASED ON LOW-CARBON DEVELOPMENT**

The development of metropolis is becoming complete, the urbanization rate is basically up to 70%, and

the transformation from urban sink land to carbon source land has entered a plateau. In going through the process of thrilling and divergence expression as well as large-scale and high-density carbon sink land transformation, the problem of carbon deficit in metropolis is becoming more significant. Therefore, aiming at the characteristic of expansion in the fringe areas of metropolis, it is the only way for metropolis to face low-carbon development by adjusting population distribution, controlling urban development pattern, regulating energy structure and developing sustainable energy sources.

1. Adjusting population arrangement and controlling urban development pattern. The strong radioactivity of the center of metropolis makes the expansion pattern of the fringe area present the significant feature of satellite type, and the peripheral villages, towns and counties become the hinterland for the development of the central city. Because of the complete infrastructure, public facilities and mature function of residence and working, the satellite town in the fringe areas of the metropolis differs from the traditional "dormitory town", which is the major feature distinguishing the development pattern in the fringe areas of metropolis from that in the middle and small cities. In order to relieve the excessively centralized pressure and energy consumption, the metropolis should inevitably carry out population distributing, while the mature satellite towns in the fringe areas thus become the best direction for population distributing of the central city and the gathering of the rural population. Therefore, in the urban development pattern of metropolis, it has become an irresistible trend to establish the development zone for cities and towns, guide urban-rural integration development, control the self-development scale of the central city and lead population and industries in the central city to the satellite town. Therefore, it is necessary to establish a complete "central city-satellite city" system for metropolis, define the industrial orientation of the satellite town, establish ecological industrial parks, promote circular economy and cleaner production, improve energy efficiency, and reduce carbon. Meanwhile, it is also needed to further develop the tertiary industry, transform the industrial city into a metropolis supported by tertiary industry, and reduce its dependence and consumption of energy and industry.
2. Regulating energy structure and developing sustainable energy. There is no doubt that metropolis consumes a large amount of energy. In China, fossil energy accounts for the majority in urban function, and most of it is coal and petrol. In cities, carbon emission

is mostly caused by fossil fuel. Thus, it is unavoidable for metropolis to carry out energy structure adjustment while guaranteeing its development. In future development, the metropolis should try to take natural gas as the main fuel, reduce the consumption of primary energy, develop the research and usage of sustainable energy such as wind energy and solar energy, and increase energy use efficiency, and reduce carbon emission. What's more, the carbon emission caused by a large number of vehicles in metropolis is also difficult to ignore. Therefore, it is essential to control the carbon emission of vehicles, encourage cars, buses and taxis to use hybrid power energy, increase filters of automobile exhaust, and control carbon emission of automobile exhaust. Furthermore, the city should further enhance the coverage and transport capacity of urban mass transit so as to reduce people's dependence on vehicles. In the fringe areas of metropolis, a binary interweaved mixed situation is formed in land used for carbon source, and taking towns and villages as extension, the city constantly permeably encroaches the land for carbon sink surrounding towns and villages. As a result, a large area of land for carbon sink centering on cultivated land is transformed into land for carbon source. In public administration, the metropolis should strengthen its control over towns and villages, strictly plan the development land of towns and villages, strictly designate that cultivated land and garden land do not allow being encroached, change the residential model of residents in towns and villages, advocate centralized residence, and strictly prohibit the encroachment of cultivated land.

3. Protecting land used for carbon sink and increasing carbon sequestration capacity. The metropolis has entered the stage of balance in urban development, when it should start to pay attention to the cultivation and development of land used for carbon sink such as forest. So, it is important to build large-scale forest, water conservation forest and protection forest, strengthen the greening of river banks and roads, and protect the wetland resources. Native trees and subtropical broad-leaf species should be selected. Meanwhile, it is also necessary to promote the community development and expansion of forest, maintain the self-renewal ability of communities, increase tree age, improve the carbon sequestration capacity of forest, increase the carbon sequestration capacity of soil, conserve and fertilize in a scientific and reasonable way, and reduce the carbon wastage rate of soil.

## 5 CONCLUSION

The metropolis is of a large economic aggregate and population scale, so it is still considered as a large carbon source. The metropolis is still in the process of developing continuously, strengthening scale and rapidly developing economy. In the process within a period of time, because of the loss in early development, metropolis is still facing a large carbon deficit. The land for carbon source is still at a level of continuous expansion, but the expansion rate has slowed down to some extent. The change of the land structure for carbon source and sink in the fringe areas of metropolis is a typical process. In the initial stage of urban development, and that is, a slow expansion period, the expansion of land for carbon source and sink in the fringe areas of the city, is basically within the controlled scope, the form is relatively structured and the expansion model mainly centers on the wheel type. Once it enters the stage of rapid expansion, the city turns to the state of uncontrolled exploitation and spreading, whose form is spreading type and the expansion model centers on finger type with a significant feature of divergence. Once it enters the stage of stable and rapid development, with unified planning and construction, the development of the city is again under control, the form tends to completeness and the expansion model centers on spreading type. In the expansion process of the fringe area, although there are lots of construction land within the fringe area, the construction is not perfect and the total construction level is relatively low, so the land for carbon sink has been in the majority. However, with the increasing perfect of land utilization and continuous decrease of land for carbon sink in the core district, the land used for carbon sink in fringe areas is gradually replaced by land for carbon source. The land for carbon sink in fringe areas is mostly cultivated land, garden land is in the second place, and the proportion of forest is inconstant. To reduce the carbon deficit in metropolis, we should first get down to the land used for carbon source and sink. Increasing the carbon sequestration capacity is the development direction for the metropolis in the future.

## ACKNOWLEDGMENTS

This work was financially supported by the National Natural Science Foundation of China (51208119), the Natural Science Foundation of Guangxi (2013GXNSFBA019240), the Foundation

of Guangxi Educational Committee (2013YB010), and the Natural Science Foundation of Guangxi University (XBZ120394).

## REFERENCES

- [1] Y.G. Zong, S.Y. Zhou, Z.S. Zhang, et al. Spatial Characteristics of Suburbanization and Its Developing Strategies in Beijing. *Acta Geografica Sinica*, 2002, 57(2):135–1421.
- [2] N. Zhang, L.N. Fang, J. Zhou, et al. The Study on Spatial Expansion and Its Driving Forces in the Urban Fringe of Beijing. *Geographical Research*, 2008, 27(2):285–294.
- [3] S.F. Li, R.P. Bai. A Strategic Thought about Soil Utilization in Joining Area between City and Suburbs. *Research of Agricultural Modernization*, 2003, 24(4), 248–251.
- [4] Wu Yanfang, Xu Yueqing, Tian Yuan, Guo Hongfeng. Analysis of Land Use Dynamic Change in the Metropolitan Fringe: A Case Study of Pinggu District, Beijing. *Resources Science*, 2011, 33(12):2285–2292.
- [5] Yingui Cao, Wei Zhou, Jing Wang, et al. Spatial-temporal pattern and differences of land use changes in the Three Gorges Reservoir Area of China during 1975–2005 [J]. *Journal of Mountain Science*, 2011, (4):551–563.
- [6] Matthew Luck, Jianguo Wu. A gradient analysis of urbanlandscape pattern: A case study from the Phoenix metropolitan region, Arizona, USA [J]. *Landscape Ecol*, 2002, 17(4):327–329.
- [7] D.N. Xiao, W.B. Chen, F.L. Guo. On the Basic Contents of Ecological Security. *Chinese Journal of Applied Ecology*, 2002, 13( 3): 354–358.
- [8] C. Li, F.R. Zhang, T.F. Zhu, Y.B. Qu. Analysis on Spatial-temporal Heterogeneities of Landscape Fragmentation in Urban Fringe Area: A Case Study in Shunyi District of Beijing. *Acta Ecologica Sinica*, 2013, 33(17):5363–5374.
- [9] Fan Lingyun, Lei Chen. Contradiction and Governance Research in Urban Fringe Area Developing—Based on the Case of Guangzhou City. *Urban Studies*: 2009(12):22–28.
- [10] Li Kaiyu, Cao Tianyan. Research on the Urbanization and Urban Spatial Expansion of the Marginal Area of Metropolitan Cities: A Case Study of Panyu District, Guangzhou. *Journal of Northwest University (Natural Science Edition)*, 2010, 40(3):523–526.
- [11] Hough ton R.A., Hobbles J.E., Mwillillo J.M, et al. Changes in the carbon content of terrestrial biota and soils between 1860 and1980: a net release of CO<sub>2</sub> to the atmosphere [J]. *Ecological Monography*, 1983, 53(3):235–262.
- [12] Shan Fuzheng, Yu Jia, Zhao Jun, Qian Guangren. Land Use Change in the Suburb Area and Its Impacts on Carbon Emissions in the Process of Industrialization: A Case Study of Zhangjiang Hi-Tech Park, Shanghai. *Resources Science*, 2011, 33(8):1600–1607.

# The study on the characteristics of the spatial structure of carbon source and carbon sink in megalopolis: Shanghai as a case

Menglin Qin, Hang Li, Jing Zhao & Jing Ya

*College of Civil Engineering and Architecture, Guangxi University, Nanning, China*

**ABSTRACT:** Compared with other areas, there are highest density and most destructive interruptions in metropolis. With the expansion of the city and the high speed of the urbanization, the metropolitan areas have become the ones where characteristic and varieties of field are changing most dramatically. These changes have directly influenced the carbon fluxes in one area, even the whole world. So, analysis of the spatial characteristics of the carbon source and carbon sink in the metropolis is a crucial premise to reintegrate and plan on the whole area. Based on the orientation that Shanghai is a global metropolis, this paper regards Shanghai as the study area. With the help of the techniques of the RS and GIS, this paper analyzes the distribution of various kinds of lands from 1990 to 2013 in Shanghai, and puts forward some suggestions about the balance between the carbon source and carbon sink, in order to set a foundation for the low-carbon urban planning.

**Keywords:** land-use for carbon source and sink; spatial structure; low-carbonization; Shanghai

## 1 INTRODUCTION

Developing low-carbon city is one of the most important strategies of global climate change, while increasing the carbon sequestration capacity of urban carbon stock is the core of developing low-carbon city. Metropolitan area, the most sensitive area of balancing carbon source and carbon sink in various global habitats, is the concentration with the largest carbon flux gap. So, studies on the spatial structure of carbon source and carbon sink in the metropolitan area and exploration of the core characteristics of its change can provide a theoretical basis for the low-carbon planning and design of carbon source and carbon sink in metropolitan areas, which is realistically significant to the development of low-carbon cities. At present, research on the changes in the spatial structures of city carbon source and carbon sink is focused on land use and the land cover change, especially for the development of “International Geosphere and Biosphere Plan” in 1995 and “International Human Dimension of Global Environmental Change Program (IHDP)”<sup>[1]</sup> as well as the abundant scientific results achieved after “Land Use and Cover Change Plan (LUCC)” was raised jointly<sup>[2]</sup>. Taking advantage of the GIS and RS technologies and the multi-period remote-sensing image and detailed data of land use, characteristics, patterns and impetus of the changes in the spatial structure of land use and land cover have been studied

from the dimensions of urban fringe, city field and districts, which has achieved systematic research results at the urbanization level, cultivated area change, efficiency of farmland conversion and the driving factor of cultivated land conversion<sup>[3-4]</sup>. In terms of ecological environmental influences, relevant studies have shown that the changes in urban land use and land cover could bring relevant environmental changes under the combined action of multiple factors, and urbanization could make the surface runoff of the expanded area increase at various degrees<sup>[5]</sup>, and that the expansion of different administrative units has different influences on the varieties of the soils in the process of urbanization, making the general environmental quality decrease, especially heavy metal pollution<sup>[6]</sup>. Meanwhile, it has also been shown that the changes in land use resulting from urbanization also generate negative effects on vegetation ecological functions and flood discharging capacity.

The aforementioned literature is about the study on the characteristics, patterns and dynamic mechanism of the changes of land use and land cover. However, spatial arrangement in the metropolis is rarely studied from the aspect of land use balance of carbon source and carbon sink in China. This paper attempts to study the land use of carbon source and sink in Shanghai as the entry point with the aim to obtain the core characteristic of spatial change in the land use of carbon source and carbon sink in metropolitan areas.



## 2 DEFINITIONS OF RELEVANT CONCEPTS

### 2.1 Carbon source and carbon sink

United Nations Framework Convention on Climate Change (UNFCCC) gives specific definitions to source and sink. Source refers to the process or activity with the possibilities of discharging greenhouse gases and aerosols to the atmosphere or with the possibilities of discharging greenhouse gases and aerosols to the atmosphere, while sink refers to any process, activity or mechanism of removing greenhouse gases from the atmosphere. Referring to the definitions, carbon source refers to the process or activity of discharging CO<sub>2</sub> to the atmosphere, while carbon sink refers to the process, activity or mechanism of removing CO<sub>2</sub> from the atmosphere.

### 2.2 Land use of carbon source and carbon sink

The defined scope of carbon source and carbon sink corresponds to the town and country land of Urban Land Classifications and Standards for Land Planning for Construction, i.e. various land covers, including carbon source land and carbon sink land. Carbon source land includes urban construction land and regional transportation land, while carbon sink includes water area, cultivated land, garden plot, forest land, grassplot, greenbelt and unused land. Judging whether a land is for carbon source or carbon sink depends mainly on the size of the flux of CO<sub>2</sub> of the land cover and soil

of certain land within a rather long period ( e.g. the time span of this study is from 1990 to 2013). If the flux is positive, the land is carbon source land, whereas if the flux is negative, the land is carbon sink land. Though harvest of crops could make the carbon enter the next cycle, taking the capacity of fixing carbon of soil into consideration, it could be regarded as the carbon sink land, and meanwhile, water region with weak carbon sink capacity is regarded as carbon sink land.

### 2.3 Relevant research index

#### 1. Increasing and decreasing the speed of carbon sink (S, unit: hectare/year)

Increasing and decreasing the speed of carbon sink refers to the land areas increased or decreased within a year, which could be represented by the formula as follows:  $S = (CS_t - CS_0) / \text{year}$ , where CS<sub>0</sub> refers to the area of one type of land in the earlier stage, while CS<sub>t</sub> refers to the area of one type of land in the later stage. When (CS<sub>t</sub> - CS<sub>0</sub>) is a positive value, S is the increasing speed of carbon sink land. When (CS<sub>t</sub> - CS<sub>0</sub>) is a negative value, S refers to the decreasing speed of carbon sink land. The larger the absolute value is, the faster the increasing or decreasing speed is, and the larger the influence on the carbon source and carbon sink land of the city is.

#### 2. Cover intensity of carbon sink land (R, unit:%)

Cover intensity of carbon sink land refers to the percentage of the carbon sink land (CS) in the total carbon source and carbon sink land (CES), the expression of which is given

Table 1. Classification of land types.

Name	Types of land use	CO <sub>2</sub> flux	Carbon source or sink
Forest land	Forest land, shrubland, other forest land	-	Carbon sink land
Garden plot	Garden plot, tea garden, other garden plot	-	Carbon sink land
Cultivated land	Paddy field, irrigable land, dry land	-	Carbon sink land
Grassland garden	Natural grassplot, tame pasture, other grassplot	-	Carbon sink land
Unutilized land	Idle land, saline-alkali soil, wetland, sand, bare land, mud flat, grass land not used for animal husbandry, as well as facility farm-oriented land and ridge of the field	-	Carbon sink land
Water area	Rivers, lakes, reservoirs, ponds, channels, glacier and perpetual snows	-	Carbon sink land
Construction land	Various lands not included greenbelts in urban and rural residents, as well as municipal utilities, including buildings and facilities land	+	Carbon source land
Transportation land	Roads, railroads, airport, ports and lands for inside and outside transportation as well as squares and parking lots	+	Carbon source land

as follows:  $P = CS/CES*100$ . It represents the overall coverage of carbon sink land. The larger it is, the more beneficial it is to the balance of urban carbon source and carbon sink.

### 3. Increasing and decreasing the range of carbon sink land (I, unit:%)

Increasing and decreasing the range of carbon sink land refers to the ratio between the increased or decreased carbon sink land and the area of the carbon source and carbon sink land, the expression of which is given as follows:  $S = (CS_t - CS_0) / CES * 100$ . When  $(CS_t - CS_0)$  is a positive value, it means the carbon sink land is increasing and when the  $(CS_t - CS_0)$  is a negative value, it means the carbon sink land is decreasing. The variable P expresses the relations between the increased or decreased carbon sink land and the overall carbon source and carbon sink land. The larger the absolute value is, the larger the influence of its increasing and decreasing on the balance of the carbon source and carbon sink land of the city.

## 3 ANALYSIS OF SPATIAL STRUCTURE CHANGES OF CARBON SOURCE AND CARBON SINK LAND

### 3.1 Survey region and research method

#### 3.1.1 Survey region

Shanghai is located at N31°14' and E121°29'. It is at the front edge of the Yangtze River, bordering Jiangsu in the west, the Hangzhou Bay in the south and the entrance of the Yangtze River in the north. It is one of the cities with the most developed economy in China and first-tier cities. In 2013, its population in the downtown was about 24,151,500, with per capita GDP of 73,297 yuan and urbanization rate of 89%. It is the center of economic and financial activities in China. Therefore, it is selected as the representative of the megalopolis cities in this study. Based on the requirement of the study and the availability of the data, the survey region is the administrative region of Shanghai City, with the east-west width of 100 km, the south-north length of 120 km and the total area of 6410.03 km<sup>2</sup>.

#### 3.1.2 Research method

This study takes the TM image as the information source to extract the information of carbon source and carbon sink land. The spatial data used in the research region are from Shanghai remote-sensing images of the same season (September to December) of 1990, 2000, 2006 and 2013, the resolution ratio of which is 30 m. Supervised classification is adopted to extract the distributed data of carbon source and carbon sink land at

different times with Erdas. Through interpretation and analysis, the spatial interpretation chart and the structural data of carbon source and carbon sink land at the four periods of time are shown in Figure 1 and Table 2. Since there are few grassplots in Shanghai, they are ignored in this study.

### 3.2 Feature analysis of spatial structure changes

Continuous decrease in carbon sink land is one of the core characteristics of spatial structure changes in rural-urban areas, so the cover intensity of carbon sink land (S), increasing or decreasing speed of carbon sink (R) and change in the ratio of carbon sink land (I) are used to conduct the feature analysis of the spatial structure changes of carbon source and carbon sink land. Their results are summarized in Table 2.

#### 3.2.1 Intensity analysis of carbon sink land increase and decrease (S)

The increasing and decreasing rates during 1990 to 2000, 2001 to 2006 and 2007 to 2013 were, respectively, -4543.14 ha<sup>2</sup>/year, -17549.26 ha<sup>2</sup>/year and -4227.51 ha<sup>2</sup>/year. In other words, the increasing rate of carbon sink land during 1990 to 2000 was retained at about 45 square kilometers; since 2001, the decrease in carbon sink land reached its climax, with an annual decrease of about 175 square kilometers, and from 2006 to 2013,

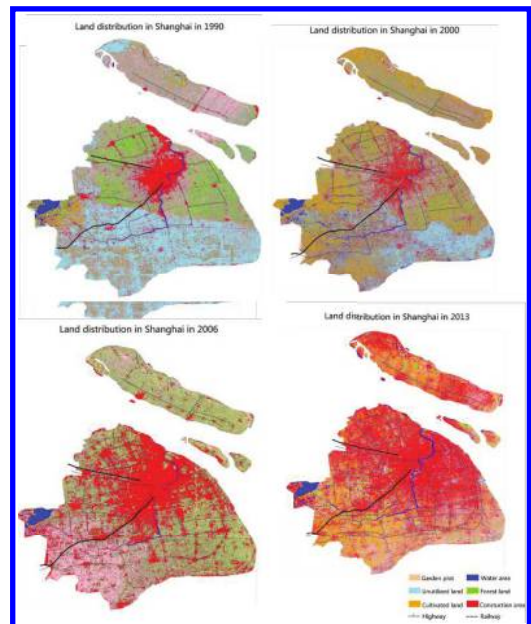


Figure 1. Spatial distribution of lands used for carbon emission and sequestration at the four periods of time from 1990 to 2013.

Table 2. Index analysis of carbon sinks land change.

Analysis index	Periods		
	1990–2000	2001–2006	2006–2013
Increasing and decreasing speed (S, ha <sup>2</sup> /year)	–4543.14	–17549.26	–4227.51
Cover intensity (R, %)	85.44–78.35	78.35–61.92	61.92–57.30
Alternative range index (I, %)	–7.09	–16.43	–4.62

the speed slowed down, with the annual speed decreasing to 42 square kilometers. On the whole, the increase and decrease in carbon sink land were imbalanced, decreasing about 1,053 square kilometers from 2001 to 2006 and about 296 square kilometers from 2007 to 2013.

### 3.2.2 Analysis of carbon sink land cover intensity (R)

With three periods of time, the average carbon sink coverage intensity during 1990 to 2000 (end of the last century) was 81.9%. During 2001 to 2006 (the beginning of this century) was 70.14% and during 2007 to 2013 (the first 10 years of this century), it was 59.1%. The carbon sink land coverage intensity in 1990, 2000, 2006 and 2013 were, respectively, 85.44%, 78.35%, 61.92% and 57.30%.

From the end of the last century until the beginning of this century, as the pioneer of the reform and opening-up, Shanghai was in the period of fast expansion, growth and development, with its carbon sink land decreasing from 85.44% to 78.35%, lowering by 7.09%. During this period, not only Shanghai developed rapidly, but also the towns and villages in the suburbs of Shanghai put into the upsurge of urbanization, especially the city outskirts such as Pudong and Minhang districts<sup>[8]</sup>. Implementing “Pudong reform and opening-up policy”, the Jinqiao development zone, the Lujiazui development zone, the Waigaoqiao development zone and the Pudong international airport were constructed one after another, covering much cultivated lands. Urban construction land including industrial parks of all levels grew continuously like mushrooms after the rain. Pushed by urbanization, traffic construction was also designed and constructed, for example, Luoqing harbor district of Port of Shanghai, metro line 2 at phase I and the road to the Pudong international airport<sup>[9]</sup>.

During 2000 to 2006, urbanization in Shanghai developed dramatically. The downtown, the suburbs and the outskirts advanced urbanization, with the development of Fengxian, Qingpu and Songjiang being the fastest. Meanwhile, the carbon sink land decreased sharply from 78.35% to 61.92%, decreasing by 16.43%, while the carbon

source land cover increased continuously. Limitation of the scope of administrative regions and guarantees of basic farmland also became the bottleneck to further development of the city.

From 2006 to 2013, urbanization of Shanghai transformed from the pattern focused on quantity to the pattern focused on quality, with the changes of various lands becoming steady, which revealed the process of the metropolis growing towards maturity after a certain increase. The spatial structure of the land use in the city tended to be stable, with its average carbon sink land coverage intensity decreasing from 61.92% to 57.30%, lowering altogether by 4.62%.

From 1990 to 2000, the carbon sink land decreased sharply. However, from 2006 to 2013, the change of carbon sink land was small. Because during this period, urbanization of Shanghai changed from quantitative promotion to interior organic renewal. Nevertheless, the carbon sink coverage intensity continued to decrease during the study, dropping from 85.44% in 1990 to 57.30% in 2013, lowering altogether by 28.14%. These 23 years had witnessed the period when Shanghai developed the fastest.

### 3.2.3 Analysis of increasing and decreasing range of carbon sink land (I)

The increasing and decreasing intensities of carbon sink land during the periods from 1990 to 2000, 2001 to 2006 and 2007 to 2013 were, respectively, –7.09%, –16.43% and –4.62%, i.e. The increasing and decreasing intensities of carbon sink land during 1990 to 2000 were small. The increasing and decreasing intensities during 2001 to 2006 were with a large fluctuation, while during 2007 to 2013, they reached their climax. Generally speaking, compared with the total amount of carbon source and carbon sink land, the increasing and decreasing scopes were not large, but from the balance of carbon source and carbon sink, the carbon source had surpassed far the carbon sink. On the one hand, it was because the carbon sink land was decreasing and, on the other hand, urbanization discharged a great amount of greenhouse gases. Therefore, the core reason of carbon imbalance

was the development of urban industry, but not the decrease in carbon sink capacity. Since the existing metropolis is still at the stage of expansion, which means the invaded carbon sink land could not be restored within a short time, it is a problem that must be dealt with for metropolis development to guarantee the quantity of the existing carbon sink land and to increase the carbon reserve of unit area carbon sink land.

## 4 SUGGESTIONS AND LIMITATIONS

### 4.1 *Ensuring the compact growth of Shanghai at different dimensions*

The urban construction land of Shanghai increased from 72843.39 ha in 1990 to 242477.16 ha in 2013, at the speed of 68.80% per year. If it could be said that the previous urbanization of Shanghai used the land development bonus in return for urban development, this kind of development would severely limit the development of the limited lands. Compact development is the most efficient and sustainable way to use limited spatial resources and land resources. The key of the compact growth is to coordinate the relations between growth points and the even aspects at different dimensions, and to guarantee the fast growth of various dimensions within the limited space. Macroscopically, the question is how to coordinate the whole Yangtze River Delta with central Shanghai as well as how to coordinate Shanghai and Hangzhou and Ningbo. In the medium aspect, Shanghai, as the growth point, shall coordinate the relations between the central city and the peripheral clusters and even new towns (including Chengqiao, Lingang New City and Jinshan New City). Microscopically, it is to coordinate the relations between the residential centers and various residential districts.

### 4.2 *Controlling and adjusting to combine Shanghai greenbelts and soil features*

The forest land of Shanghai decreased from 87288.53 ha in 1990 to 21622.58 ha in 2013, at the speed of 6.26% per year, and the cultivated land of Shanghai decreased from 202842.75 ha in 1990 to 126008.44 ha in 2013, at the speed of 6.26% per year. Based on the survey of the actual conditions of Shanghai and analyzing relevant documents, it has been found that the forests of Shanghai were basically man-made forest, with a high cultivation index and young age, which is less than the average national level, so it is with a high carbon sequestration potential. It is suggested to increase the rotation of the woods so as to guarantee full exertion of carbon reserve capacity. Though the quantity of cultivated lands is continuing to decrease, it

is undeniable that it is the indispensable land of Shanghai, and its carbon sequestration capacity could not be ignored. Under the premise of ensuring basic supply of fruits and vegetables, it is suggested to adjust the farming system from the original triple cropping to double cropping per year, to lower the resolving speed of organic carbon and to promote the reservation of soil organic carbon.

### 4.3 *Establishing the joint controlling system*

Keeping the balance of metropolis carbon source and carbon sink is actually a part of constructing a low-carbon city, which could be defined as “the city with low-carbon economy as its development pattern and direction, whose citizens take low-carbon life as the philosophy and characteristic and the governmental management layer regard low-carbon society as their construction specimen and blueprint”. This definition differentiates the traditional management pattern relying purely on the government and stresses on the participation of government organizations, commercial enterprises and non-profit organizations and the public. Its goal is to educate the common people with harmonious and win-win strategies and to guide the enterprise with the market. Joint control of the carbon source and carbon sink balance can be completed through “the government issuing policies, the enterprises investing the capitals and the public participating”.

### 4.4 *Insufficiencies of the study*

There are also some limitations of this study, which are as follows. 1. The resolution of the satellite remote-sensing pictures was low in the supervised classification and limited auxiliary materials, which caused some errors in the supervised classification; 2. To simplify the classification and based on the actual conditions of Shanghai, the areas of grass-plots and greenbelts were not calculated; 3. More years should be calculated as the statistic periods to ensure the accuracy of the conclusion. Based on these shortcomings, the patterns and dynamic mechanism of spatial structures will be researched further so as to obtain a relevant theoretical basis for the low-carbon spatial planning and design.

## ACKNOWLEDGMENT

This work was financially supported by the National Natural Science Foundation of China (Grant No. 51208119), the Natural Science Foundation of the Guangxi Zhuang Autonomous Region of China (Grant No. 2013GXNSFBA019240) and the Foundation of Guangxi Educational Committee (Grant No. 2013YB010).

## REFERENCES

- [1] Turner I BL, Skole D, Sanderson S et al. Land use and land cover change science/research plan, IGBP Report No.35 and HDP Report No.7. Stockholm: IGBP, 1995.
- [2] UNEP —EAPAP. Land cover assessment and monitoring, volume I—A, Overall Methodological Framework and Summary. a Bnkok; UNEP—EAPAP, 1995.
- [3] Qin Meng Lin, Li Hang, Ya Jing, Zhao Jing, Chen Weichu. Study on space structure change of land used for carbon source and carbon sink in urban fringe areas [A]. 3rd International Conference on Civil Engineering and Urban Planning, CEUP 2014[C]. 2014:407–411.
- [4] Xia Li, Anthony Gar-On Yeh. Analyzing spatial restructuring of land use patterns in a fast growing region using remote sensing and GIS. *Landscape and Urban Planning*. 2004.
- [5] Xuelei Zhang, Manzhi Tan, Jie Chen, Yanci Sun. Impact of land use change on soil resources in the peri-urban area of Suzhou city[J]. *Journal of Geographical Sciences*. 2005 (1).
- [6] Ronald Amundson, Y. Guo, P. Gong. Soil Diversity and Land Use in the United States[J]. *Ecosystems*. 2003 (5).

# The environmental factor evaluations on the recycling models of WHA reverse logistics

Yuanyuan Liu & Tianjun Hu

*School of Traffic and Transportation, Beijing Jiaotong University, Beijing, China*

Fangfang Xie

*Beijing Sustainable Development Center, Beijing, China*

**ABSTRACT:** This study first sets forth some basic theory of the WHA (Waste Household Appliances) reverse logistics and three recycling models of the WHA reverse logistics, namely simple recycling mode, individual workshops processing mode and diversified recycling mode. Based on the three modes, we then calculate the environmental impact and resource consumption load for the three recycling models using life cycle assessment from the aspect of environmental load and resource utilization. Finally, we provide some suggestions about building the reverse WHA logistics system in China and promoting diversified recycling modes according to the above analysis.

**Keywords:** WHA reverse logistics; life cycle assessment

## 1 INTRODUCTION

With the development of economy and improvement of technology, the lifecycle of household appliances has been shortening, and the appliances have been upgraded quickly. China is entering the peak period of scrapped appliances. The revolved heavy metals from the WHA could have a large influence on the environment and person's health if the metals cannot be handled correctly, and thus people are paying more attention to the recycling of WHA. WHA reverse logistics is the process of planning, implementing and controlling of logistics activities from the point of consumption to the point of origin. The logistics activities include recycling, detecting, taking apart, abstracting, regeneration and final treatment<sup>[1]</sup>. There are many benefits to build the WHA reverse logistics: it could lower the cost of logistics, the abandoned goods can be recycled and reused effectively, and it also could effectively control the harm caused to the environment<sup>[2]</sup>. This paper analyzes the impact degree of three recycling modes on the resource and environment to explore suitable management methods and recycling technology for reducing energy consumption and environmental pressure. It has an important reference significance for building recycling modes of WHA and WHA reverse logistics system, and regulating the treatment technology of WHA.

## 2 THE RECYCLING MODES OF THE WHA REVERSE LOGISTICS

### 2.1 *Simple recycling mode*

This recycling mode has two characteristics: single method of collection and small number. Generally, it only takes apart the main elements using manual sorting, the residues are usually thrown out directly or buried under the ground, and heavy metals dissolved from the WHA have a large impact on the environment.

### 2.2 *Individual workshops processing mode*

In this recycling mode, individual handicraftsman bought a great deal of WHA from the domestic and abroad to extract the valuable materials through manual workshop, acid leaching and open-burning. However, the final handling method has a great deal of impact on the environment.

### 2.3 *Diversified recycling mode*

In this mode, collected appliances from factories, commodities and individuals are handled through disassembly and metallurgical technology to reclaim valuable units. The recycling residues are handled by burning and burying. Nevertheless, it is not suitable for small factories because of high cost of investment and handling.

### 3 THE EVALUATION OF ENVIRONMENTAL FACTORS ABOUT THE RECYCLING MODES OF THE WHA REVERSE LOGISTICS

#### 3.1 The analysis of environment factor about recycling modes of the WHA reverse logistics

This paper holds that the environmental factors refer to the factors that have an influence on environmental quality and resource consumption in the process of collecting, taking apart, abstracting and final handling. It includes environmental pollution factor and resource consumption factor. The former contains the environmental pollution factor in the WHA recycling process and the electronic wastes environmental pollution factor. The latter contains resource consumption factors in the WHA recycling process and the electronic wastes resource factor<sup>[3]</sup>.

#### 3.2 Life cycle assessment

LCA is defined by the ISO as a tool to evaluate and solve the environmental problems from the whole life cycle of products: the acquirement of materials, producing, using and recycling<sup>[4]</sup>.

It involves four steps. The first phase of LCA is defining goals and scopes to determine the purpose of the study, system boundaries and selection of suitable functional units. The second phase is Life Cycle Inventory (LCI), which is the process of data collection of all relevant inputs and outputs in the life cycle of product. The third phase is the Life Cycle Impact Assessment (LCIA), which evaluates potential environmental impacts and estimates resource consumption. The last phase is the interpretation, which identifies some significant issues, gets conclusions, explains the limitations and provides recommendations<sup>[5]</sup>.

#### 3.3 The LCA of recycling modes of the WHA logistics

##### 3.3.1 The goals and scopes of assessment

The goal is to analyze the resource utility and environmental pollution of the three recycling modes, and evaluate the impacts of the three recycling modes on the environment.

We identify that the scope is from recycling, sorting, dismantling and final disposal. Not including the transportation process. Resource consumption is mainly considered as the non-renewable mineral resources in this paper. Energy consumption is mainly considered as electricity, coal and oil. And pollution emissions are mainly considered as wasted gas, wasted water and wasted solid.

##### 3.3.2 LCI

LCI is the analysis about the energy, material utility and environmental pollution of WHA. It includes three types: data collection, calculating and analyzing of the results.

Data collection includes input of all resources and energy, the output of production and pollution emissions. We suppose that all WHA have the same parameters, and the electricity is all from fire coal in the process of recycling and handling, and the efficiency of energy transferring is 30%<sup>[6]</sup>.

##### 3.3.3 The evaluation of environmental impacts

Impact assessment is the main stage of LCA. It evaluates the index by transferring the data from LCI to comparable index. It includes data classification, characterization and quantification.

From the goal of assessment, we divide the data into two types: resources consumption and environmental pollution. The former includes non-renewable resource consumption and renewable resource consumption. The latter includes global warming, acidification, eutrophication and ecotoxicity. Then, we describe each type of pollutants with the method of reference. CO<sub>2</sub> is the reference of global warming; SO<sub>2</sub> is the reference of acidification. The effect equivalence of reference is 1, and the others can be achieved by comparing with the contribution of reference to the environmental impact, as shown in Table 1.

The environmental impact potential could be obtained by using Equation (1):

$$EP(j) = \sum EP(j)_i = \sum [Q(j)_i \times EF(j)_i] \quad (1)$$

where  $EP(j)$  is the potential value of the product system to type- $j$  of the environment effect;  $EP(j)_i$  is the potential contribution for pollution category  $i$  to impact  $j$ ;  $Q(j)_i$  is the release of emission  $i$ ,  $EF(j)_i$  is the effect equivalent factor for pollution  $i$  to effect  $j$ .

We set the normalization data to compare their contribution to the environment. It can be obtained by using Equation (2):

$$NEP(j) = EP(j) \frac{1}{Te \cdot ER(j)_{90}} = \frac{EP(j)_{pro}}{ER(j)_{90}} \quad (2)$$

where  $NEP(j)$  is the standard value of environment for type  $j$ ;  $Te$  is the time of product service;  $ER(j)_{90}$  is the reference of the environmental effect;  $ER(j)_{pro}$  is the present potential value of environment for type  $j$ .

The standardized resource potential value can be obtained by using Equation (3):

$$NRC(j) = RC(j) \frac{1}{Tr \cdot RR(j)_{90}} = \frac{RC(j)_{pro}}{RR(j)_{90}} \quad (3)$$

Table 1. The effect equivalence of environmental impacts.

Types	Emissions	The equivalent value
Global warming (gCO <sub>2</sub> eq./g)	CO <sub>2</sub>	1
	CH <sub>4</sub>	25
	N <sub>2</sub> O	320
	CO	2
	NMHC	3
	3,4-Benzo pyrene	3
Acidification (gSO <sub>2</sub> eq./g)	Chlor.HC	3300
	SO <sub>2</sub>	1
	NO <sub>x</sub>	0.7
	HF	1.60
	H <sub>2</sub> S	1.88
	HCl	0.88
Photochemical ozone (gC <sub>2</sub> H <sub>4</sub> eq./g)	NH <sub>3</sub>	1.88
	VOC	0.5
	CO	0.03
Eutrophication (gNO <sub>3</sub> eq./g)	CH <sub>4</sub>	0.007
	NO <sub>x</sub>	1.35
	NH <sub>3</sub>	3.64
Eco-toxicity (gEFm <sup>3</sup> soil eq./g)	COD	0.23
	Cadmium	1.8
	Chromium	0.01
	Copper	0.02
	Lead	0.01
	Mercury	5.3
	Nickel	0.05
	Zinc	0.005

where  $NRC(j)$  is the standard value of resource consumption for type  $j$ ;  $Tr$  is the time of using product;  $RR(j)_{90}$  is the reference of resource consumption;  $RC(j)_{pro}$  is the present potential value of resource consumption for type  $j$ .

The resource weighting factors can be obtained by using Equation (4):

$$WR(j) = RR(j)_{90} / RES(PEj)_{90} \quad (4)$$

where  $RES(PEj)_{90}$  is the per capita reserves in 1990.

The environmental weighting factors can be obtained by using Equation (5):

$$WP(j) = ER(j)_{90} / ER(j)_{T2000} \quad (5)$$

where  $ER(j)_{T2000}$  is the per capita level of environmental impact for type  $j$  in 2000.

$WR(j)$  and  $WP(j)$  reflect the amount of occupied average resource and environmental space, which can be compared with different potential values.

Resource depletion factor index can be obtained by using Equation (6), the unit of which is  $PE_{WCnEast90}$ :

$$RDI = \sum WR(j) = \sum \frac{RC(j)_{pro}}{RES(PEj)_{90}} \quad (6)$$

Environmental effect load can be obtained by using Equation (7):

$$EIL = \sum WP(j) = \sum \frac{EP(j)_{pro}}{RE(j)_{T2000}} \sum \frac{\sum [Q(j)_i \times EF(j)_i]}{ER(j)_{T2000}} \quad (7)$$

Resource depletion coefficient reflects the share of product resource consumption in the whole resource, reflecting the scarcity of resources; it also reflects the pressure on the natural environment. Through the data classification, characterization, quantification, we explore environmental factors of a more suitable mode to meet the environmental impact standards.

### 3.4 Case analysis

Guiyu is the largest rubbish processing factory, which is closely monitored because of the severe electronic pollution. This paper evaluates the carrying capacity of resource and environment by taking waste plastic boxes and printed circuit boards in Guiyu as the research object, and explores the suitable recycling technology to give some reference for improving recycling technology in Guiyu.

#### 3.4.1 Simple recycling mode

These modes only dismantle components and bury the wastes, and have no energy consumption, and so the scope of evaluation is resource consumption and pollutant emissions.

The resource input is metals, such as iron, copper and aluminum. Through normalization and weighing, we obtain a potential value of the metal consumption and resource depletion coefficient, as given in Table 2.

From Table 2, we can obtain the resource depletion coefficient as 22345.31. The consumption of copper has the biggest pressure on the resource system.

The pollution emissions are mainly produced by solid waste stacking or release of heavy metals. The results are summarized in Table 3.

From Table 3, we can obtain the carrying capacity of environment as 55.55, which indicates that the heavy metal pollutants that are released directly will cause pressure on the environment.

#### 3.4.2 Individual workshop processing mode

The recycling processes of waste plastic and printed circuit board include four steps: welding,



Table 2. Normalization and weighting of resource consumption.

Type of resource	Iron	Copper	Aluminum
Consumption (kg/a)	$2.05 \times 10^6$	$1.3 \times 10^6$	$0.63 \times 10^6$
The reference of standardization ER [kg/(per capita a)]	103	1.7	3.4
Standardized value	19920.91	764705.88	185294.12
Period (a)	120	36	200
Weighted value	166.01	21241.83	946.47
Resource depletion coefficient	22354.31		

Table 3. The potential value of pollution emission.

Pollution	Emissions (kg/a)	Effect of equivalence factor EF(gw)	Impact potential value EP(gw)
Eco-toxicity		(gEFm <sup>3</sup> soil eq./g)	(kgEFm <sup>3</sup> soil eq./a)
Cadmium	143.66	1.8	258.59
Chromium	293.91	0.01	2.94
Copper	483360	0.02	9667.20
Lead	8481.06	0.01	84.81
Mercury	7.22	5.3	38.27
Nickel	1091.38	0.05	54.57
Zinc	13500.16	0.005	67.50
PE90	—	—	56.55

pickling, burning and mechanical crushing. The scope of evaluation is resource consumption and environmental emission.

We can get the energy consumption list converting the power consumption into coal consumption according to “the Chinese Energy Statistical Year-book” and “People’s Republic of China Environmental Protection Industry Standard”.

The resource input is mainly iron, copper or aluminum. We can obtain the recycling rate of common resource from the “Industrial Pollution and Emission Index Manual”, and then get the results by calculating, as given in Table 4.

From Table 4, we can obtain the resource depletion coefficient as 442.21. The recycling rate of copper is highest; however, consumption of copper has the largest pressure on the resource system. Thus, we should pay more attention to improve the recycling rate of copper and reduce the consumption of copper deposits.

The pollution emissions include waste gas, waste water and heavy metals. Through normalization and weighting, we can obtain the results, as summarized in Table 5.

From Table 5, we can see that the global warming has the largest effect on the environment; the carrying capacity of the environment is 5838005.35.

### 3.4.3 Diversified recycling mode

This mode usually adopts the way of centralized processing, and the scope of the evaluation focuses on the evaluation of energy recovery and discharge of pollutants. Through calculating, we can obtain the results, as given in Table 6.

We can get the results by characterization and normalization and weighting, as given in Table 7.

From Table 7, we can see that the potential value of acidification and eutrophication decreases obviously, and the environmental effect load is 627753.41. The results indicate that this mode realizes the optimization compared with the individual workshop processing mode.

## 3.5 The comparison of resource and environment load for the three modes

To further understand the positive effect on the environment with the centralized processing mode, we compare the resource and environment load of the three modes.

### 3.5.1 The comparison of resource load

From Table 8, we can get the following results: the centralized processing mode can save 98.67% of coal and can slow the shortage condition of supplying electric, and the diversified recycling mode

Table 4. Normalization and weighting of recourse consumption.

Types of resource	Coal	Iron	Copper	Aluminum
Consumption (kg/a)	$5.26 \times 10^6$	$1.94 \times 10^6$	$0.02 \times 10^6$	$0.03 \times 10^6$
Reference [kg/(per capita a)]	574	103	1.7	3.4
Standardized value	91.6	19730.66	7590.13	13282.73
Period (a)	170	120	36	200
Weighted value	0.54	164.42	210.84	66.41
Resource depletion coefficient	442.21			

Table 5. The standardized and weighted analysis of pollution emissions.

Type	Global warming	Acidification	Eutrophication	Eco-toxicity
Potential value EP	$6.58 \times 10^9$	$1.35 \times 10^8$	$2.09 \times 10^8$	961.56
Standardized reference	8700	36	62	358
Standard value	$0.75 \times 10^6$	$3.75 \times 10^6$	$3.38 \times 10^6$	2.69
Weight factor	0.83	0.73	0.73	1.99
Weighted value	$6.28 \times 10^5$	$2.74 \times 10^6$	$2.47 \times 10^6$	5.35
Environmental effects load	5838005.35			

Table 6. The list of resource consumption and reusing.

Energy	Coal (kg/a)	Recycling power (KWh/t)	Coal Consumption (kg/a)
Mechanical grinding	$0.38 \times 10^6$	–	–
Welding components	$0.03 \times 10^6$	–	–
Burning	$0.15 \times 10^6$	6.75	–
Total Consumption	$1.01 \times 10^6$	6.75	$0.07 \times 10^6$

Table 7. The normalization and weighting of environmental impacts.

Type	Global warming	Acidification	Eutrophication	Eco-toxicity
Potential value EP	$6.58 \times 10^9$	245.28	100.33	13.14
Standardized reference	8700	36	62	358
Standard value	$0.75 \times 10^6$	6.81	1.62	0.037
Weight factor	0.83	0.73	0.73	1.99
Weighted value	$6.28 \times 10^5$	1.18	1.18	0.073
Environmental effects load	627753.41			

can recycle resource through the advance technology, equipment and reasonable management.

### 3.5.2 The comparison of carrying capacity of environment

The carrying capacity of the environment of the simple recycling model is from heavy metals. The environmental impact load of individual workshops processing pattern can be divided into the new environment impact load and environmental

impact load caused by heavy metals. The environmental impact load of the heavy metals is lower than the simple recycling mode because of recycling of some heavy metals. However, the air pollutants and water pollutants generated by dismantling account for 89% in the individual workshop processing. Diversified recycling mode adopts advanced technology and uniform management to reduce environment pollution from acid leaching, and it effectively reduces metal emissions.

Table 8. The analysis of resource load.

Resource and energy consumption (kg/a)	Coal	Iron	Copper	Aluminum
Simple recycling mode	–	$2.05 \times 10^6$	$1.03 \times 10^6$	$0.63 \times 10^6$
Individual workshop processing	$5.26 \times 10^6$	$1.94 \times 10^6$	$0.02 \times 10^6$	$0.03 \times 10^6$
Centralized processing mode	$0.07 \times 10^6$	–	–	–

Table 9. The comparison of environment load.

Pollution emission (kg/a)	Simple recycling mode	Individual workshop mode	Centralized processing mode
<i>Atmosphere</i>			
CO <sub>2</sub>	–	$6.58 \times 10^9$	$6.58 \times 10^9$
SO <sub>2</sub>	–	$1.98 \times 10^7$	197.81
HCl	–	$6 \times 10^4$	0
NO <sub>x</sub>	–	$1.55 \times 10^8$	67.82
<i>Water</i>			
COD	–	38.16	38.16
HCl	–	$1.94 \times 10^6$	0
<i>Ecotype</i>			
Cadmium	143.66	143.52	0.4
Chromium	293.91	293.62	89.04
Copper	483360	25440	128.47
Lead	8481.06	8077.2	156.88
Mercury	7.22	7.21	0.51
Nickel	1091.38	606.32	71.11
Zinc	13500.16	8437.6	234.47

The recycling rate of metals can reach up to 70%, and all the indices meet the national standards.

#### 4 CONCLUSION AND ADVICES

From the above analysis, we can draw the following conclusions: in the aspect of resource consumption, the resource depletion coefficient of the simple recycling mode is 22354.31, and it is 442.21 in individual workshop processing; the coal consumption in the centralized processing mode is  $0.07 \times 10^6$ , which saves 98.7% of coal comparing with individual processing. In the aspect of environment factors, the environment load of the simple recycling mode is 56.55, the load of individual mode is 5838005.35, and the load of centralized processing mode is 627753.41. By comprehensively considering the resource consumption and environment load, it can be found that the centralized processing mode is superior to the individual treatment mode and simple mode. Therefore, the diversified recovery and centralized processing mode is the development direction based on building the WHA reverse logistics system. There are some

advices for the building WHA reverse logistics system.

1. Pay attention to the construction of the WHA reverse logistics system. The investment and cost of the diversity recycling mode is high, which is suitable for large-scale manufacturers, so that it should be guided by government, and the special finance funds at all levels of government should promote enterprise and private capital investments in the field as soon as possible, and further promote its industrialization development.
2. Push the concept of green design of home appliances. Instead of passively recycling home appliances, it is better to reduce initiatively its environmental harm, and we can adopt the green design method to solve the problem of environmental pollution and resource recycling WHA reverse logistics.
3. Establish suitable recycling policy regulations of WHA. At present, China is in the home appliances scrapped peak, so it is especially important to reasonably handle the WHA. The regulations clear the responsibility of each side, and enhance operability; the policy can prevent the emergence of improper recycling for the pursuit of economic growth.

#### REFERENCES

- [1] Ying Xu. Game analysis of reverse logistics of waste household appliance based on environment [D]. Beijing: Beijing Jiaotong University, 2006.
- [2] Yazhu Gu. Reverse logistics and sustainable development [J]. Logistics Technology. Harbin: 2004(111): 38–40.
- [3] Ma Yanbin & Cai Liang & Wang Jieyue. Life Cycle Emissions Research of Hybrid-power Gas Engine Heat Pump [J]. Journal of Refrigeration, 2013(34):53.
- [4] Tiezhu Shi. Research about evaluation of waste home appliances recycling process and environmental factors [D]. Gansu: Northwest Normal University, 2012.
- [5] Ahmad Faiz & Abd Rashid. A review of life cycle assessment method for building industry [J]. Renewable and Sustainable Energy Reviews: Volume 45, May 2015: pages 244–248.
- [6] Fei Li. Recycling technology of wasted electronic and life cycle assessment [D]. Guangdong: South China University of Technology, 2004.

# Practice of interprovincial public transport in Beijing–Tianjin–Hebei region

Y.Y. Mai & X.N. Sun

*China Academy of Transportation Sciences, Beijing, China*

**ABSTRACT:** This paper first analyzes the interprovincial public transport demand in Beijing–Tianjin–Hebei region on the basis of studying the development status and problems of road passenger transport in this region, and then summarizes the influencing factors of public transport operation organization, finally puts forward public transport transformation mechanism mode and route operation mode and studies the public transport operation management policies.

**Keywords:** Beijing–Tianjin–Hebei region; interprovincial public transport; practice

## 1 INTRODUCTION

### 1.1 *Research background*

With the acceleration of urban and rural passenger transport integration, the voice of the masses for enjoying equal travel services has been increasingly stronger. To deeply implement the strategic deployment of the Party Central Committee and State Council on Beijing–Tianjin–Hebei synergetic development and adapt to the new situation and requirements of Beijing–Tianjin–Hebei traffic integration development, the Ministry of Transport proposed the implementation of pilot reform of urban and rural passenger transport integration in Beijing, Tianjin, and Hebei in the program of deepening pilot transportation reform comprehensively. Under this background, the exploration on new development mode of public transport in interprovincial adjacent areas will promote the realization of policy coordination, resource sharing, reasonable layout, smooth connection and integrated service of road passenger transport in Beijing, Tianjin, and Hebei and provide powerful support for synergetic development of Beijing, Tianjin, and Hebei and the establishment of interlinked comprehensive transportation network.

### 1.2 *Determination of the study scope*

Areas within the scope of 200 km radius with Beijing and Tianjin as two cores are defined as main adjacent areas, including Beijing, Tianjin, Tangshan, Langfang, Baoding, Zhangjiakou, Chengde, and Cangzhou. Areas within the scope of 200–300 km radius are defined as secondary adjacent areas, including Shijiazhuang, Qinhuangdao, and Xingtai.

## 2 DEVELOPMENT STATUS AND PROBLEMS

### 2.1 *Operation of existing routes*

#### 2.1.1 *Interprovincial passenger transport routes*

According to incomplete statistics, there are over 900 road passenger transport routes and over 2200 operating regular buses among these three provinces. Currently, the public transport of Beijing has covered 14 counties of Hebei Province with 26 operating routes, over 800 operating vehicles and a daily number of passengers originating from 300,000 person-time. It has supported integration development of areas around the capital in Hebei Province with Beijing. However, due to different financial subsidies among administrative divisions, the margin of preference of interprovincial buses is different in Beijing and Hebei. For some buses with sixty percent discount for cardholders in Beijing, the margin of preference is changed or canceled after they drive away from the provincial boundary. Due to the low ticket price of interprovincial buses driven from Beijing, Beijing buses have been resisted by local public transport companies in Hebei for several times.

#### 2.1.2 *Operation of intercity public transport*

The opening of intercity public transport is an inevitable trend of Beijing–Tianjin–Hebei integration development, which will drive the development and utilization of Beijing–Tianjin–Hebei suburbs effectively and can provide powerful support for the circulation of production factors among Beijing, Tianjin, and Hebei.

According to incomplete statistics, there are over 40 bus routes in Beijing leading to various places

in Hebei. Residents in the urban area of Langfang, Dachang, Xianghe, Gu'an, Zhuozhou, Huailai, Xinglong, and Luanping can take the bus to Beijing in the local place. Intercity public transportation plays an important role in the exchange of Beijing, Tianjin, and Hebei.

### 2.1.3 *Operation of intercity rail*

Currently, the process of traffic integration in Beijing, Tianjin, and Hebei is accelerated obviously and an intercity railway network covering Beijing, Tianjin and Hebei is spreading densely. Besides Beijing–Tianjin intercity railway and Tianjin–Qinhuangdao passenger special line built and opened to traffic, Beijing–Chengde passenger special line, Beijing–Zhangjiakou intercity railway, Beijing–Hengshui passenger special line and Beijing–Tangshan intercity railway have entered the stage of planning, exploration or environmental assessment.

## 2.2 *Existing problems*

Currently, road transport in Beijing, Tianjin and Hebei has a good overall development level. However, due to different development strategies and emphases in these three provinces, many uncoordinated phenomena exist. One the one hand, regional policies and legal systems are incomplete. Various regions often start from local interests and intervene in market activities with administrative order, thus influencing the rational allocation of transportation resources. On the other hand, competent authorities go their own way in the planning of transportation system and cross-departmental, trans-regional, and multi-level transportation planning coordination mechanism is lacking. Therefore, problems such as local protection and inadequate resource sharing are caused. It is difficult to meet the development demand of economic integration in Beijing, Tianjin, and Hebei. The following problems exist currently.

### 2.2.1 *Non-smooth transport corridor and interlinked level of infrastructure to be improved*

Currently, many parts of fast highway corridor among provinces (districts and cities) in the area are not interlinked. There are many dead end highways and bottleneck roads between Hebei and Beijing and Tianjin.

### 2.2.2 *Slow overall progress of integration*

The extension of public transport causes conflicts in operation and intergovernment coordination has a great difficulty. The extension of urban public transportation in Langfang and Zhangjiakou around the capital to 14 counties in Beijing is a typical example. It has caused impact on operators of road passenger transport in the same route.

Therefore, they resist it and even stop the traffic and exchange blows, thus seriously influencing traffic safety and the travel of the masses. The government should balance interest subjects and provide public transportation service for the public.

### 2.2.3 *Management mode to be further specified*

The opening of public transport in interprovincial adjacent areas aims at facilitating the travel of the masses and improving the quality of passenger transport service. The operation mode of interprovincial passenger transport route is reformed and adjusted appropriately with the use of operation service pattern of urban public transportation for reference. It belongs to interprovincial road passenger transport and should be managed according to interprovincial passenger transport.

### 2.2.4 *Construction of supporting system to be strengthened*

There are insufficient system, standard and specification with respect to the route length, vehicle standard, safety supervision, site setting, service quality assessment, and management of operation market in the operation of intercity passenger transport route of public transport, which cannot provide basic support for the operation of public transport.

## 3 PUBLIC TRANSPORT DEMAND

### 3.1 *Interprovincial passenger travel demand*

With the acceleration of integration process in Beijing, Tianjin, and Hebei and constant deepening of regional cooperation, an integration pattern of support of regional central city and joint development of hinterland has gradually formed. Transprovincial commuter flow in the region will increase rapidly and passenger travel structure and purpose will change. Therefore, it is imperative to establish a traffic system dominated by public transport.

Traditional long-distance road passenger transport mode is operating in Beijing–Tianjin–Hebei region. Its in adaptation to the increasing commuter flow demand becomes prominent gradually. Therefore, it is necessary to transform the way of route planning, site setting, vehicle disposition, and bus run arrangement for public transport so as to adapt to new features of interprovincial passenger flow in the synergetic development process of Beijing, Tianjin, and Hebei.

### 3.2 *Relevant policies, regulations, and standards demand*

It is an urgent need to issue a unified management method in Beijing, Tianjin, and Hebei and

standardize the opening condition, route selection, site setting, vehicle condition, ticket pricing, and operation subject in the transformation of road passenger transport for public transport so as to provide guarantee for promoting the transformation of road passenger transport of main passages for public transport in Beijing–Tianjin–Hebei interprovincial adjacent areas.

It is an urgent need to discuss and issue a policy of fiscal subsidies for the transformation of road passenger transport for public transport in Beijing, Tianjin, and Hebei. Ticket pricing and the establishment of ticket system in the transformation of road passenger transport for public transport in Beijing, Tianjin, and Hebei involve various interests of different travelers, passenger transport enterprises and government sector. Due to its social publicity, governments of these three regions should discuss and issue appropriate fiscal subsidies to maintain the sustainability of its operation.

It is an urgent need to establish a unified service standard for the transformation of road passenger transport for public transport in Beijing, Tianjin, and Hebei. Currently, there is a great urban-rural gap in these regions and a great gap between Beijing and Tianjin and Hebei in the level of transportation service. To guarantee the consistency of regional transportation service provision after the transformation of road passenger transport for public transport, it is urgent to establish a unified service standard.

## 4 TRANSPORT OPERATION MANAGEMENT

### 4.1 *Influencing factors*

#### 4.1.1 *Passenger flow characteristics*

Interprovincial passenger flow is characterized by large passenger flow volume in the morning and evening, great seasonal variation of passenger flow volume and its great variation in festivals and holidays. It is required to fully consider the unbalance of passenger flow in time and space and the possibility of future rapid increase during the organization of operation.

#### 4.1.2 *Network layout structure*

Net layout structure not only plays a decisive role in organization means of specific routes, but also is the foundation of space organization form of routes. Many route organization forms are available for a net structure with complete layout. Generally, multiple organization forms are combined.

#### 4.1.3 *Urban layout structure and pattern*

Urban layout structure and pattern features directly influence the planning of route and further influence the organization arrangement of route. Different geographic properties have restrictions

on route planning, transport capacity, and vehicle choice. Therefore, geographic features, industrial distribution, and development and resource distribution in the region should be considered in terms of route organization arrangement.

#### 4.1.4 *Transport benefit and cost*

Public transport enterprises of interprovincial road passenger transport should conduct comprehensive analysis and feasibility evaluation on the operation efficiency of the route, reduce transportation costs, and improve the profitability of route and service quality through efficient operation organization management and show coordinated development of fairness and efficiency.

### 4.2 *Mechanism mode*

#### 4.2.1 *Selection standard of passenger transport route for public transportation*

Interprovincial road passenger transport route meeting the following conditions can be transformed for public transportation:

1. A large number of passengers traveling back and forth along the route, large passenger flow volume and daily average passenger capacity more than 1000 person-time in principle;
2. Route operation distance within 100 km in principle;
3. Good road condition. Roads pass the inspection of the police and traffic administration and meet requirements of vehicle meeting and loading and unloading of passengers in public transportation operation.
4. Repetition rate of urban public transportation routes not more than 50%.

#### 4.2.2 *Examination and approval method for passenger transport route for public transport*

It is required to accelerate the improvement of periodical coordination and joint examination and approval mechanism for the operation of interprovincial passenger transport for public transport and implement “one examination and approval for one route” so as to provide convenience for the input of transport capacity and ensure the opening and operation of mature routes as soon as possible.

#### 4.2.3 *Report of passenger transport route for public transport*

It is required to report the opening situation of interprovincial passenger transport routes to the competent department annually and list routes for public transportation separately.

### 4.3 *Route operation mode*

Passenger flow and regional urbanization level are judgment standards for determining the operation

mode of intercity road passenger transport for public transport-complete public transport mode and incomplete public transport mode. Whole-process public transport operation mode should be adopted in urbanized areas with the formation of intercity urban traffic corridor in adjacent areas and connection.

The same passenger transport route should be operated by the same operation subject in corporatization form. Affiliation or contract operation is prohibited. Routes parallel to direct passenger transport route should be operated by the same operation subject or with joint-stock partnership in corporatization form.

#### 4.4 Operation management policies

##### 4.4.1 Establishment of coordinated management mechanism

It is required to establish a daily coordinated management organization composed of Beijing Transport and Communications Committee, Tianjin Transport and Communications Committee and Hebei Department of Transportation, hold coordinated working conference periodically, establish Beijing-Tianjin-Hebei joint conference system, conduct consultative management over the preparation of integration development plan of road passenger transport in Beijing-Tianjin-Hebei region, the establishment of relevant standards, specifications and fiscal guarantee system, examination of interprovincial passenger transport routes for public transport, credit rating of transport enterprises and emergency disposal, and report the opening situation of interprovincial passenger transport routes to the competent department annually.

##### 4.4.2 Connection of regulations, standards and policies

1. Organize the preparation of integration development planning of road passenger transport in Beijing-Tianjin-Hebei adjacent areas positively

It is required to break geographic segmentation according to the principle of “rapid connection and convenience for transfer”, conduct unified planning, construction and management of road passenger transport network and public infrastructure such as station, urban and rural road and bus stop along the route and realize coordinated development of “road, station and transport”; adhere to the dominant role of transformation of existing routes and the helping role of opening of new routes, study and establish the development plan and annual plan of passenger transport routes for public transport in adjacent areas and make them public.

2. Improve relevant service standards on the transformation of road passenger transport route for public transport

It is required to establish and improve passenger transport service quality specification and quality assessment system, strengthen urban-rural passenger transport service quality assessment, use assessment results as the basis of various capital subsidies, link up with tendering and bidding of passenger transport route and enterprise development support policies, supervise and urge enterprises’ standardized management, cooperate with relevant departments to accelerate the improvement of standards and specifications on the route length, vehicle standard, site setting and service quality assessment in the operation of passenger transport route for public transport, and provide basic support for the standardization of public transport service of passenger transport route.

3. Study and establish fiscal guarantee system

The competent department of transportation should cooperate with other departments positively to study and establish low ticket price policies for road passenger transport and propose a preliminary scheme for ticket system and ticket price according to the compensation of public fiscal subsidies so as to improve the attraction of public transport. It is required to determine ticket price management policies according to Road Transport Price Control Regulations and Rules of Freight Rate of Buses jointly issued by the Ministry of Transportation and National Development and Reform Commission and implement cost pricing and the same price for the same route; implement specific ticket price optimization policies according to local fiscal subsidies; establish price evaluation system, strengthen effective supervision on financial management of enterprises engaged in road transport, conduct periodical dynamic monitoring on route cost and benefits and provide basis for scientific pricing of the government.

4. Strengthen integration and informatization management level of public transport regions

It is required to build a road passenger transport information management command center integrating transport management and control decision centers, propose the framework of public transport information system, strengthen information collection, storage, search and transmission functions, guarantee accurate, and rapid transmission of orders and implement “one-card” positively.

5. Attach great importance to safety and green production

It is required to make technical standard examination of vehicles strict. Operating vehicles

should be supplied with satellite positioning vehicle terminal and video surveillance equipment meeting the standard. It is required to further specify safety supervision responsibilities, implement supervision responsibilities of safety source of road transport management organization, supervise and urge relevant operators to strengthen the management over vehicles, drivers, and attendants, implement responsibilities of the subject of safety production in enterprises and improve the ability of emergency disposal in public transport of interprovincial passenger transport.

#### 4.4.3 Resource sharing mechanism

1. Make reasonable use of existing routes, site, and vehicle resources

Make reasonable use of existing routes and site resources; consider the demand for public transport of passenger transport in areas with large passenger flow volume such as important towns and villages, important industrial belt and tourist attractions based on existing routes and sites; form rational division of work and easy transfer with urban public transport, road passenger transport and rail transport in terms of site setting; increase the proportion of nonstop and one transfer in the total amount of travel of the public, reduce the average times of transfer, plan passenger transport, and public transport network structure rationally, and meanwhile select appropriate vehicles based on existing road operating vehicles and buses according to road conditions and passenger source.

2. Establish information sharing platform  
Promote intelligent dispatching system and IC system positively, expand the system module

of public transport service information search of passenger transport positively based on the existing information platform, exert the role of scientific and technological means in the supervision on operation and analysis on the operation of industrial economy, and constantly improve the industrial service quality.

## 5 CONCLUSIONS

In allusion to new situation and new problems of Beijing–Tianjin–Hebei integration development, for the development of Beijing–Tianjin–Hebei road passenger transport, it is required to promote the reform of public transport operation in road passenger transport routes in adjacent areas positively based on the new situation, promote the integration of urban and rural passenger transport into regional traffic integration system, establish a safety and green intercity road passenger transport service system with equal service and efficient information through constant deepening of transformation work and support the integration construction of Beijing, Tianjin, and Hebei comprehensively.

## REFERENCES

- H.L. Ling. 1987. *Study on the public transport of the intercity road passenger transportation in Urban Agglomeration*. A Dissertation Submitted for the Degree of Master.
- LuX, PasET. Socio-den orgraphics, Activity Participation and Travel Behavior. *Transportation Research Part A*, 33(1):1–18.



# Research on adsorption of methyl orange by magnetic activated carbon prepared by Eucalyptuses

Jia Liu, Hua Zhang, Liudan Luo, Haiyi Huang & Wen Chen

*Guangxi Scientific Experiment Center of Mining, Metallurgy and Environment, Guilin University of Technology, Guilin, China*

*College of Environmental Science and Engineering, Guilin University of Technology, Guilin, China*

**ABSTRACT:** Eucalyptuses are the mass agricultural plant in Guangxi province. The sawdust of eucalyptuses were used as the raw materials for the magnetic activated carbon, then analyzed for the adsorption of single factor such as amount of magnetic activated carbon by Eucalyptuses, adsorption time, and initial concentration of methyl orange solution and then gave the fitting and analysis by dynamic model and isothermal model.

**Keywords:** magnetic activated carbon by Eucalyptuses; adsorption removal; Methyl Orange (MO); kinetics model; isotherm

## 1 INTRODUCTION

Eucalyptuses are the mass agricultural plant in Guangxi province. The area of eucalyptuses in the autonomous region has reached to more than 180 million hm<sup>2</sup>, which comprises nearly one-fourth of all planted commercial forest's area in autonomous region. Eucalyptus production accounts for two-thirds of the all region's timber production with the largest area and the highest total output in China. Gross output of eucalyptuses utilized in wood processing, pulping, and paper-making is nearly 64 billion yuan. With the continuous reduction of mineral resource such as oil and coal, more attention is paid to exploitation of biological resource (Zhonglei Meng, Junji Li, Kang Sun, 2012). Activated carbon is a carbon-based adsorption material which has high surface area and abundant pore structures with its preparation technology having been fully developed. Now the major breakthrough of researching and preparation is the selection of new materials. Using the sawdust of eucalyptuses as the raw materials for the activated carbon can effectively reduce environment pollution, and it is an effective way to dispose of agriculture wastes. The sawdust of eucalyptuses are the high-quality raw materials for the activated carbon due to its low mass fraction (Xinping Xie, Zhonglei Meng, Jianchun Jiang, 2013).

## 2 MATERIAL AND METHODS

### 2.1 Materials and reagents

The stock solution (1000 mg/L) of MO was prepared by dissolving 1 g of solid dye in 1 L double ultrapure water and the working concentrations daily were prepared by its suitable dilution. Chemicals were methyl orange, K<sub>2</sub>CO<sub>3</sub>, and FeCl<sub>3</sub> (all were analytical reagent).

### 2.2 Preparation of activated carbon

In this research, the branch of eucalyptuses, popular in Guangxi province, was used. The raw material for the magnetic activated carbon was obtained after it was cleaned, dried and sawed into block. The eucalyptuses were dried at 400°C for 40 min, crushed and passed through a 60-mesh screen. Eucalyptuses carbon was mixed with K<sub>2</sub>CO<sub>3</sub> and FeCl<sub>3</sub> at the mass ratio of 1.5:1:1, then mixed with deionized water, which was shaken for 7 hours using a thermostat shaker bath at 25°C. After having been filtered and dried at 110°C for 8 h–12 h, the samples were placed in a muffle furnace and activated at 800°C for 80 min. The products were cooled to room temperature and washed with deionized water until the pH of the washing solution reached 7. The activated sample were dried in an oven at 110°C for 8–12 h, then passed through a 100 mesh screen, and the magnetic activated

carbon by eucalyptuses were obtained (Xiaolei Liu, 2012).

### 2.3 Methods

Experiments were studied by single factor experiments, Kinetic experiments and Isothermal experiments. Then after filtration with filter paper, the concentrations were analyzed by UV–VIS spectrophotometry whose wavelength of determination was 465 nm, the eucalyptus magnetic adsorbent on adsorption capacity of dye wastewater and the removal rate were calculated as shown in figures.

## 3 RESULTS AND DISCUSSION

### 3.1 Effect of initial concentration

Each 0.1000 g activated carbon was placed into 7 beakers all with 50 ml methyl orange solution whose initial concentrations were 100, 200, 300, 400, 500, 600, and 700 mg/L, respectively. Then stirred for 2 h in a water bath at 25°C. Result is shown in Figure 1.

Figure 1 shows the removal rate at the methyl orange solution of different concentration values. The initial (horizontal) part of the curve represents the methyl orange aqueous solution, which is almost adsorbed completely. Then, the curves gradually fell with increased concentration values of methyl orange solution and finally stabilized just around 58%.

### 3.2 Effect of time

A fixed amount of activated carbon (0.1000 g) and 50 ml of methyl orange solution were placed into a dozen 100 ml centrifuge tubes successively, which were shaken for 3, 6, 9, 12, 18, 30, 45, 60, 75, 90,

120, and 180 min, respectively, using a thermostated shaker bath at 25°C. Result is shown in Figure 2.

Experimental results show that the removal rate of the methyl orange as simulated dye wastewater through activated carbon increased with increased adsorption time. When adsorption lasted over 30 min, the increase in the removal rate has slowed. The removal rate remains unchanged basically after 75 min. It is chiefly because the methyl orange solution was adsorbed completely. So we choose 75 min as the adsorption time in further experiments (Yuanyuan Sun, 2014).

### 3.3 Effect of dosage

Weigh accurately 0.025, 0.5, 0.75, 0.1, 0.125, and 0.15 g of activated carbon in six 100 ml centrifuge tubes with 50 ml of methyl orange solution, respectively, then shake them for 2 h using a thermostated shaker bath at 20°C. Result is shown in Figure 3.

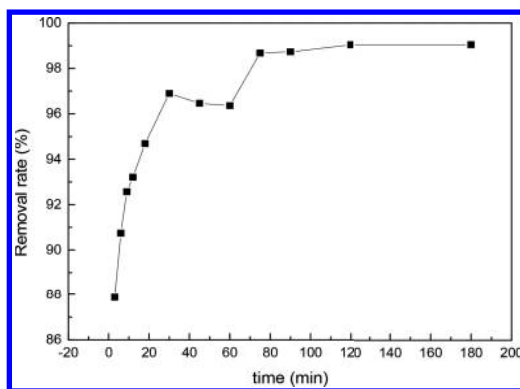


Figure 2. Effect of time on adsorption of MO.

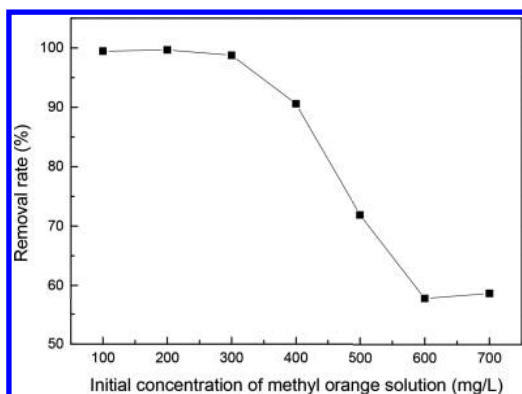


Figure 1. Effect of the initial concentration of MO solution on adsorption of MO.

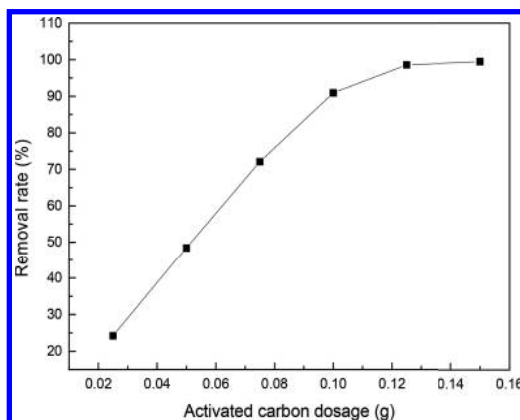


Figure 3. Effect of amount of magnetic activated carbon by Eucalyptuses on adsorption of MO.

Experimental results show that the removal rate of the methyl orange as simulated dye wastewater through activated carbon increased with increased quantity of activated carbon. When its quality has gone over 0.125 g, the increase in the removal rate has slowed and becomes horizontal gradually due to the methyl orange solution being adsorbed completely. So we choose activated carbon quality of 0.125 g in further experiments (Keqi Tian, 2010).

#### 4 KINETIC EXPERIMENTS

Three groups of 50 ml of methyl orange solution with certain concentration whose pH values are 2 were placed into seven 100 ml centrifuge tubes successively, and weighed 0.1 g of activated carbon in each group. Then shake them using a thermostated shaker bath at 25°C. Put them into the colorimetric tube after filtration with filter paper and oscillation by controlling the different oscillation time. The absorbances were analyzed using a UV-visible spectrophotometer at an appropriate wavelength, then compared the dates with a standard curve of dye concentration absorbance to determine the quality of the remaining dye concentration. The amount of adsorption at time t q were calculated by:

$$q = \frac{(C_0 - C_1) V}{m} \quad (1)$$

where  $C_0$  and  $C_1$  are the dye concentration at the beginning and at time t, respectively, and  $m/V$  is the dose of dried carbon ( $1 \text{ gL}^{-1}$ ).

In order to better describe the behavior of activated carbon adsorption kinetics on the methyl orange as simulated dye wastewater, fitting process is conducted on the date in Figure 4 through pseudo-second-order kinetic models.

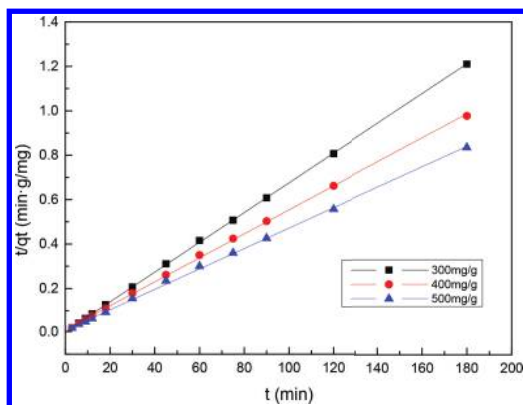


Figure 4. Pseudo-second-order kinetic equation curve fitting.

Pseudo-second-order kinetic equation:

$$\frac{t}{q_t} = \frac{1}{k_2 q_e^2} + \frac{t}{q_e} \quad (2)$$

where  $q_e$  and  $q_t$  are the amount of adsorption at the equilibrium and at time t (mg/g), respectively,  $k_2$  is adsorption rate constants of pseudo-second-order ( $\text{g}/(\text{mg} \cdot \text{min})$ ) (Yude Liu, 2012).

Figure 4. shows that under different concentration conditions, liner correlations are more than 0.99, respectively. Correlation is obvious. Kinetic parameters obtained by calculation are shown in Table 1.

##### 4.1 Isothermal experiments

Three groups of 50 ml of methyl orange solution with 100, 200, 300, 400, 500, 600, and 700 mg/L concentration values, respectively, were placed into seven 100 ml centrifuge tubes successively, and weighed 0.075, 0.1, and 0.125 g of activated carbon in each group, respectively. Then shake them using a thermostated shaker bath for 3 h at 25°C. Put them into the colorimetric tube after filtration with filter paper and oscillation by controlling the same oscillation time. The absorbance is analyzed using a UV-visible spectrophotometer at an appropriate wavelength, then find the corresponding equilibrium concentration. The eucalyptus magnetic adsorbent on adsorption capacity of dye wastewater and the removal rate were calculated.

Fitting process is conducted on the  $C_e - q_e$  date under the different amounts of magnetic activated carbon by Eucalyptuses according to the Langmuir adsorption isotherm (3) and Freundlich adsorption isotherm (4). Fitting results shown in Figures 5 and 6, and adsorption isotherm parameters and correlation coefficient are shown in Table 2.

$$q_e = \frac{q_m K_L C_e}{1 + K_L C_e} \quad (3)$$

where  $K_L$  and  $q_m$  are Langmuir adsorption constants whose name are affinity of adsorbent toward

Table 1. Pseudo-second-order kinetic parameters for the removal of MO.

Pseudo-second-order kinetic parameters				
Concentration (mg/L)	$k_2$ (g/(mg · min))	$q_e$ (mg/g)	$R^2$	$q_e$ (exp) (mg/g)
300 mg/L	0.00581	149.25	0.99992	148.71
400 mg/L	0.01383	185.19	0.99947	184.34
500 mg/L	0.01228	217.86	0.99898	215.79

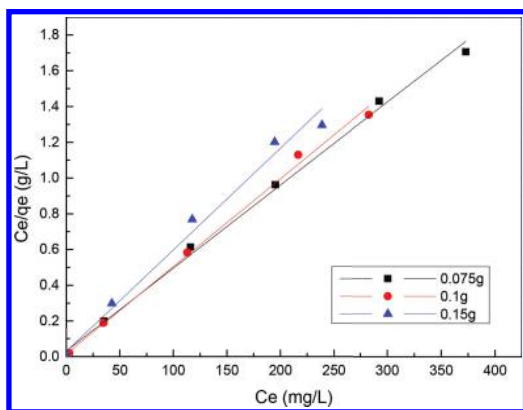


Figure 5. Langmuir plots for adsorption of MO by magnetic activated carbon by Eucalyptuses.

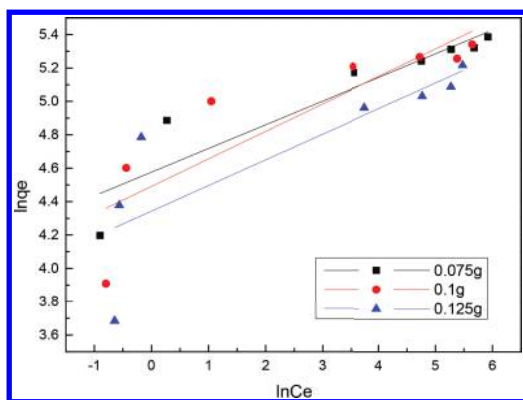


Figure 6. Freundlich adsorption of MO by magnetic activated carbon by Eucalyptuses.

Table 2. Isotherm parameters for MO adsorption onto the magnetic activated carbon by Eucalyptuses.

Langmuir isotherm constants			
Dosage (g)	$K_L/(L/mg)$	$q_m/(mg/g)$	$R^2$
0.075	1.2363	201.2072	0.99628
0.1	0.8409	207.9002	0.99655
0.125	0.8843	176.6784	0.98773
Freundlich isotherm constants			
Dosage (g)	$K_f/(mg/g \cdot (l/mg)^{1/n})$	n	$R^2$
0.075	97.1542	7.0507	0.82966
0.1	89.2436	6.0764	0.71128
0.125	76.9242	6.5129	0.61268

adsorbent and monolayer adsorption capacity, respectively;  $C_e$  is the dye concentration at the equilibrium (mg/L), and  $q_e$  is the adsorption amount.

$$\ln q_e = \ln K_f + \frac{1}{n} \ln C_e \quad (4)$$

where the  $K_f$  is Freundlich adsorption constant; the  $n$  is the constant which is used to judge the degree of difficulty in adsorption. Adsorption is more easily conducted when  $1 < n < 10$  (You Zhou, 2012).

It can be seen from Figure 5 and Table 2 that the dosages of magnetic activated carbon by Eucalyptuses are 0.075, 0.1, and 0.15 g, the correlation coefficients are 0.99628, 0.99655, and 0.98773, respectively, which means the correlation is high. As shown in Figure 6, a plot of  $\ln q_e$  against  $\ln C_e$  gave a fitted curve, and generates Freundlich constants from the plot of sorption date in Table 2 reveals that under different dosages of magnetic activated carbon by Eucalyptuses,  $n \geq 1$ , which means it belongs to the preferential adsorption.

## 5 SUMMARY

In our study, we used magnetic activated carbon by Eucalyptuses as adsorbent and methyl orange simulated wastewater as adsorption object to analyze the potential of this kind of wastewater treatment. We discussed the effect of amount of magnetic activated carbon by Eucalyptuses, adsorption time and initial concentration of methyl orange solution on adsorption of methyl orange and drew the conclusion that the most suitable condition for such adsorption are: initial concentration of methyl orange solution is 100 mg/L, the adsorption time is 75 min, and adsorbent dosage is 0.125 g. Kinetic studies of MO were performed based on pseudo-second-order model. The adsorption experimental result was analyzed through the Langmuir and Freundlich isotherm model. Eucalyptuses are the mass agricultural plant in Guangxi province. It's reasonable and economical that use it to convert into activated carbon to remove of the MO from wastewater instead of commercial activated carbon.

## ACKNOWLEDGEMENTS

The authors especially thank the financial support from the "Guangxi hazardous waste disposal industrialization micro highland of talents" and the experimental center project of mining and metallurgy and Environmental Science of Guangxi, China (Item No. KH2012ZD004), and Guikeneng

1401Z006: the researches on the preparation of magnetic activated carbon and its adsorption of Cr (VI).

## REFERENCES

- [1] K. Tian. 2010. Preparation and adsorption properties of activated carbon-based tea cake, in, Central South University.
- [2] X. Xie, Z. Meng, J. Jiang, K. Sun, X. Lu, Phosphoric acid activation factors and characterization of eucalyptus wood chips preparation of activated carbon, Northeast Forestry University, (2013) 116–119.
- [3] X. Liu, 2012. Activated carbon adsorption of methyl orange and microwave regeneration analytical characteristics, in, Dalian Maritime University.
- [4] Y. Sun, 2014. Preparation of activated carbon *Arundo donax*, Characterization and adsorption properties, in, Shandong University.
- [5] Y. Liu. 2012. Dye Wastewater Treatment coconut shell activated carbon supported metal oxides for the preparation and, in, Nanchang University.
- [6] Y. Zhou. 2012. Macroalgae *Enteromorpha* acidic dyes and basic dyes Adsorption Properties, in, Ocean University of China.
- [7] Z. Meng, J. Li, K. Sun. 2012. Eucalyptus sawdust experimental study prepared by granular activated carbon. *Guangxi Forestry Science*: 356–358.

# Dynamic distribution and balance technique of energy-saving ventilation system

K. Zhang & J.L. Wang

Harbin Engineering University, Harbin, China

**ABSTRACT:** Different from the traditional hydraulic calculation, it constructed the coupled equations of air volume and the pressure through calculating friction factor and operating point of fan and on the basis of various norms. Then it translated the program into machine language using a high level programming language C++. By employing a dynamic relaxation factor  $k$ , it realized the intelligent iterative computation. It also did a dynamic analysis on the ventilation system, including the influence of various parameters on the dynamic distribution and balance of the system. Finally several proposals are offered to improve the independence of the ventilation system. The research method and dynamic technique applied in this paper would help engineers to analyze and solve problems in the design, and optimize the ventilation system.

**Keywords:** ventilation system; air supply; pressure; dynamic distribution and balance

## 1 INTRODUCTION

The chief aim of the traditional hydraulic calculation is twofold. The first issue is to obtain the pipe diameter and resistance according to the request of flow distribution, and find the fan performance curve, finally determine the fan and its power consumption (design calculation). The second is to determine the pipe diameter according to the defined power equipment (checking calculation) (Valiantzas, 1998, Janssens, 2003). While the work in this paper is neither the design calculation nor the checking calculation, it will focus on the dynamic distribution and balance of a given ventilation system which contains four different terminals. As is well known, a complex coupled relationship between the pipe accessory local resistance factor and the air distribution in the hydraulic calculation exists. The local resistance factors will change with the air volume fluctuating, which will again cause the variation of the air distribution, it is a process of dynamic equilibrium. In the circulation, once the relaxation factor is inappropriate, it may lead to a divergence, so a dynamic relaxation factor  $k$  is applied (Otter, 1965, Küttler, 2008). And a high level programming language C++ is applied to translate the program into machine language.

## 2 ORIGINAL CONDITION

As shown in the [Figure 1](#), the ventilation system includes four different terminals: F1, F2, F3, and F4. The computational flow diagram is

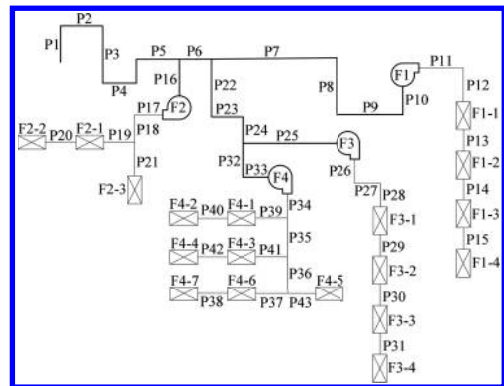


Figure 1. Ventilation system.

shown in [Figure 2](#), in which  $k$  is the dynamic relaxation factor. In the ventilation system, each fan is in charge of the resistance of its own branch. Four fans operate following their own performance curves  $Q = f(P)$ , and simultaneously they exert influence on each other. A new pipe air volume appears with the variation of pressure, and the new air volume will lead to a new pressure. The iterative process will be continued until some criterion for convergence is met.

For the original operational condition in steady-state, four fans run simultaneously, the pressure and air volume as well as the error with normal operating condition for each fan is shown in [Table 1](#). All the errors are less than 5%, which indicates that selection of four fans is appropriate.

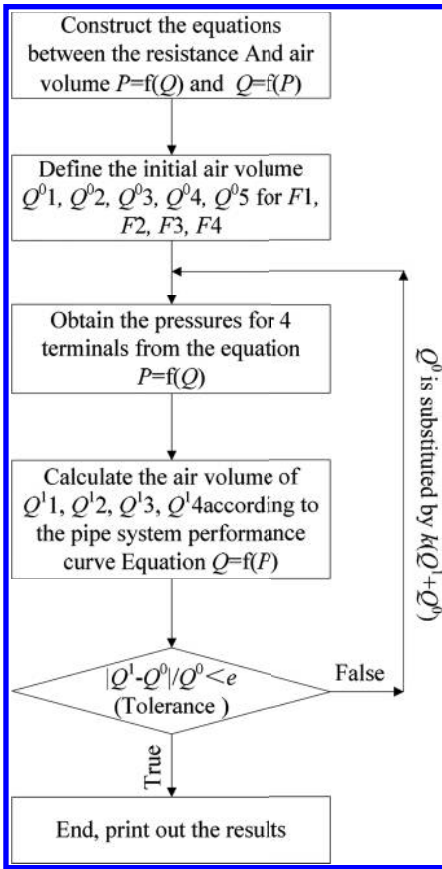


Figure 2. Computational flow diagram.

Table 1. Pressures and air volumes for four fans.

Fans	RP (Pa)	AP (Pa)	Error (%)	RA (m <sup>3</sup> /h)	AA (m <sup>3</sup> /h)	Error (%)
F1	700	697	-0.4	1100	1104	0.0
F2	700	688	-1.7	1100	1131	2.7
F3	4000	3892	-2.7	1000	1016	1.6
F4	1600	1678	4.9	2500	2524	1.0

RP means rated pressure, AP means actual pressure, and RA means rated air volume, AA means actual air volume.

### 3 INTERACTION AMONG DIFFERENT TERMINALS

For the given ventilation system, when parts of the terminals are turned off, the total air volume past the principal pipes will decrease with the reduction of system pressure, which will be bound to produce an effect on the rest terminals. The variation of pressures and air volumes for four fans are

shown in the Figure 3 when turning off different terminals.

It indicates that the pressure for operational user goes on a decrease while other terminals are turned off, while the air volume will increase. And a relative wider fluctuation of air volume is detected than that of pressure. The more terminals are turned off, the greater impact is exerted on the operating user. The result of the fluctuation is that the system operates in off-design performance. The sequence of sensitive degrees for four fans is F1 > F2 > F4 > F3. F1 is the most sensitive while the impact on F3 is minimal, which is due to the resistance of F1 branch,

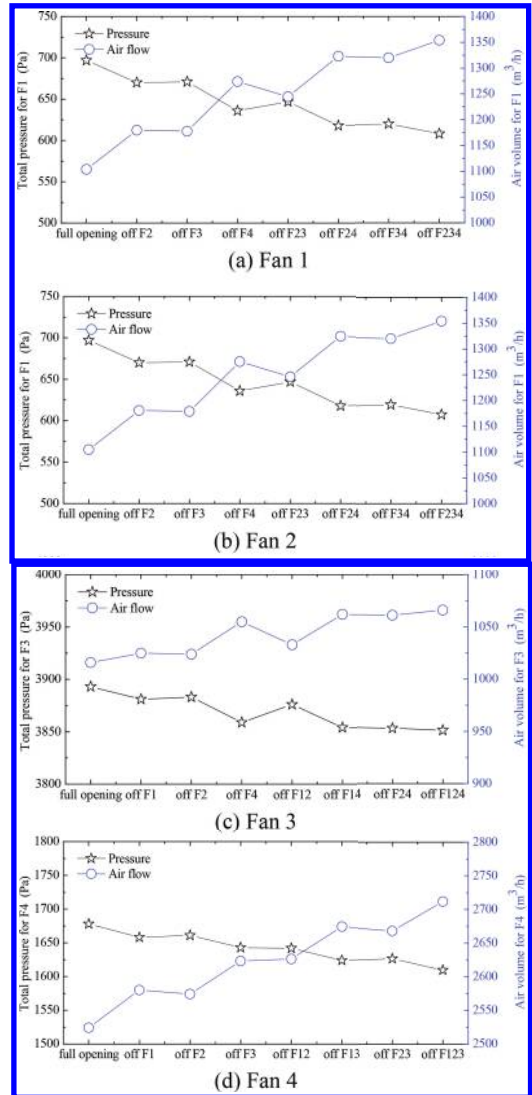


Figure 3. The pressures and air volumes of four fans with turning off different terminals.

which is the least, and it shares the most principal pipes with the other three fans. Relatively speaking, the principal pipes will exert more impacts on it when the other branches experience variations. On the contrary F3 shares the least principal pipes, so it becomes into a high independence of branch. In addition, the variation of four fans also shows that the operational state of F4 exerts the great impact

on the other terminals. For the design air volume of F4 is largest, and its operational state will produce a drastic impact on principal pipes.

#### 4 IMPACT OF PRINCIPAL PIPES ON THE VENTILATION SYSTEM

According to the analysis above, the operational state of terminals will exert impact on the other users, which is mainly because the principal pipes transfer the impact among different terminals. In order to research the impact of principal pipe size on the ventilation system, it compares five groups of different principal pipe sizes. The design case is labeled as Case 0, the diameter for each principal pipe with the increment of 0.1 m is labeled as Case 1 and increment of 0.25 m labeled as Case 2, with the decrement of 0.1 m is labeled as Case 3 and decrement of 0.25 m labeled as Case 4. The air volume fluctuation for four fans with different principal pipe sizes is shown in the Figure 4.

The ventilation system stability of the dynamic performance is degraded with the variation of the principal pipe size, both increment and decrement, namely the impact of the operational state will be enlarged. And the greater the change of the pipe the greater the impact is, which indicates that the original design size has been the optimal condition, so changing the size of the principal pipe can not improve the stability of the ventilation system. Once deviated from the design condition the ventilation system will run in fall-back state. It adequately demonstrates the importance of the jobs in design and model selection.

#### 5 MEASURES OF REDUCING THE MUTUAL EFFECTS AMONG DIFFERENT TERMINALS

In order to improve the independence of the terminals, several measures are recommended. Firstly it should reduce the resistance of the principal pipe, such as reducing the number of elbow and tee reducer-body, or increase the terminal resistance. Reducing the number and the length of the principal pipe is another effective approach. Further more adding an automatic control system to execute real-time monitoring and adjustment will be helpful to improve the independence of the ventilation system and to ensure the ventilation system to work well.

For a series branch like F1, the selection of the pipe diameter is particularly important. If all the pipe diameters are equal to each other, it is bound to cause their air volume to be divided unequally as shown in Figure 5(a). For the constant diameter

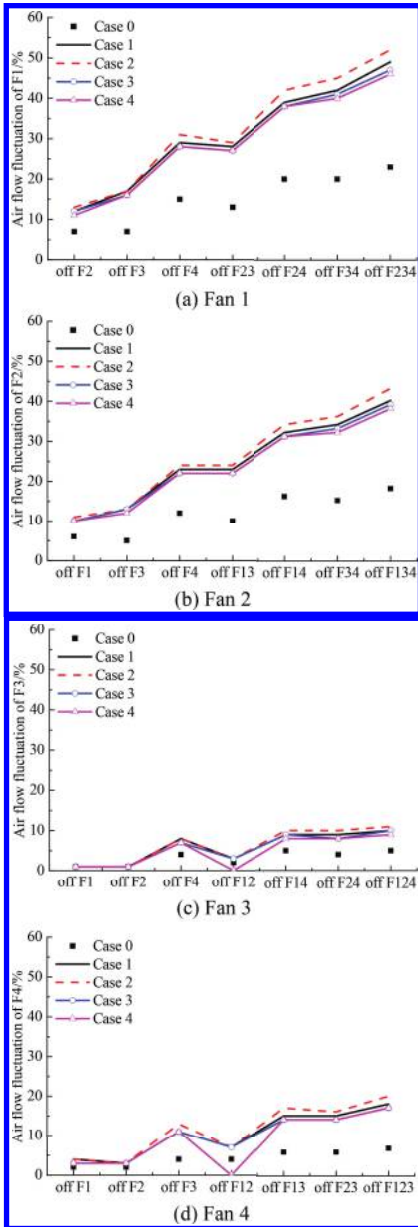


Figure 4. The air volume fluctuations of four fans with different principal pipe sizes.



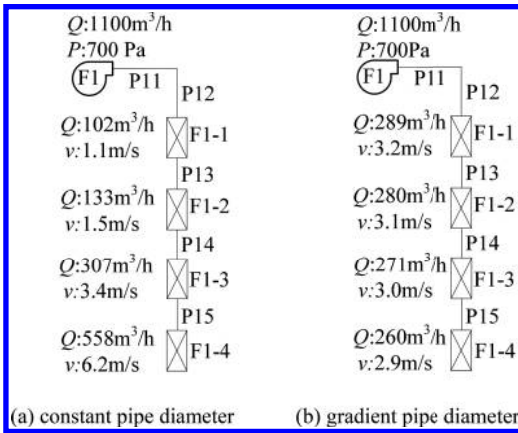


Figure 5. Air volume and velocity for F1 branch.

pipe, the air volume will gradually reduce from the beginning of the branch to the end, coupled with the decrease of dynamic pressure and increase of the static pressure. As a result of the change, the orifice velocity as well as the air volume will increase gradually. In Figure 5(a) the velocity of orifice F1-4 is 6.2 m/s, which is far more than the design value.

In order to improve the uniformity of the air volume, the pipes in the branch are adjusted into convergent pipes. And the modified result of F1 branch is shown in Figure 5(b). In the new state of balance, the air volumes and the velocities of four orifices are more or less the same. Reduction of the velocity will lessen the noise in room and improve the thermal comfort of the human body.

With the help of different measures, the independence of terminal will be improved, and stability of the dynamic performance in ventilation system will be strengthened.

## 6 CONCLUSIONS

For an enormous ventilation system, there will be strong mutual influence among the different terminals. It is important to find the correlation degree and take measures to make sure each fan is working in the optimal state in design stage for the ventilation system designers, which avoids waste of time and money from unreasonable airflow program.

This paper applies C++ to compile the program, and finds out the source of mutual influence. The measures advertized in paper will be helpful and improve the efficiency of each fan with minimum energy consumption.

## REFERENCES

- Janssens, A. 2003. Thermo-Hydraulic Design of Earth-Air Heat Exchangers. *Energy and Buildings* 35(4): 389–397.
- Küttler, U. 2008. Wall W.A. Fixed-point Fluid–structure Interaction Solvers with Dynamic Relaxation. *Computational Mechanics* 43(1): 61–72.
- Otter, J.R.H. 1965. Computations for Prestressed Concrete Reactor Pressure Vessels Ssing Dynamic Relaxation. *Nuclear Structural Engineering* 1(1): 61–75.
- Valiantzas, J.D. 1998. Analytical Approach for Direct Drip Lateral Hydraulic Calculation. *Journal of Irrigation and Drainage Engineering* 124(6): 300–305.

# Application of energy-saving technology of outer wall

Zhi Neng Tong

Jiangxi Science and Technology Normal University, Nanchang, China

**ABSTRACT:** Building energy saving is a hot spot in the construction domain. It is an important sign of the construction technology progress. This paper introduces the wall energy-saving technology application, to speed up the wall thermal insulation energy-saving technology, to create a more comfortable living environment that plays a positive role in promoting energy conservation. The construction of energy-efficient buildings needs to be discussed.

**Keywords:** heat preservation; building energy saving; energy saving technology

## 1 INTRODUCTION

Building energy saving is a new hot spot in the construction field, and it is an important symbol of the technological progress of the construction industry and a key problem of implementing the national sustainable development strategy. Building energy conservation is a big problem concerning the survival of the human environment; its strategic goal is not only to save the limited resources for the benefit of future generations, but also to improve the environment polluted by energy consumption, make human survival space cleaner, more comfortable. The development of building energy efficiency not only can bring great economic benefit and social benefit, but also develop the level of construction technology, effectively promoting the development of the construction industry as a whole.

In the building, the external wall of the structure consumes the most external heat. Therefore, the development of wall energy-saving is the main content of building energy saving technology; the development of exterior insulation technology and energy saving material is the main mode of building energy saving. Wall energy conservation and insulation measures are basically three major categories: external wall insulation, insulation, and exterior insulation.

1. Exterior wall: Internal heat preservation technology, namely in the building space interior wall additional heat preservation material is used in order to achieve the energy conservation goal. But within the external wall insulation exist the following problems: first, thermal efficiency is too low. Some parts of the wall, such as T-shaped wall, and ring beams are difficult to handle. They form a “bridge”, so that the heat preservation performance will be reduced; second thermal insulation layer for the

occupants, decorations adding hanging amenities cause great trouble, with quality issues and their repair and maintenance will cause great distress to tenants; three, insulation occupies indoor space and reduces user area.

2. Sandwich insulation technology, that is, the use of layered treatment measures, the formation of wall—thermal insulation material—wall system, on the external wall to achieve the purpose of energy saving. However, due to the complex production method, the problem of “cold bridge” in the building cannot be solved effectively, and the practice of sandwich insulation is therefore replaced by the practice of wall insulation.
3. Exterior insulation technology, that is, using additional insulation material on the outside of the wall for energy-saving purposes. Exterior insulation technology is currently vigorously promoting a building energy-saving technology. External wall thermal insulation and exterior wall insulation were compared across reasonable structure of energy-saving technology, the use of the same size, the same performance of thermal insulation material. We found that with thermal insulation, the thermal energy-saving effect is better. Exterior insulation technology is not only suitable for the energy saving of the new building, but also for the existing building. External thermal insulation material coated on the outside of the main structure, can effectively protect the construction to the main structure, prolong the service life of the building; can effectively reduce the thermal bridge of building structure, increase the construction of effective use of space; and while the building envelope insulation leads to condensation on the indoor side of the wall producing mildew, external thermal insulation eliminates this phenomenon and improves the indoor living environment of comfort.

## 2 EXTERIOR WALL INSULATION TECHNOLOGY

### 2.1 *Inside wall insulation technology*

Exterior wall internal insulation construction, is inside the outer wall structure of the insulation layer. Internal heat preservation construction is fast, easy in operation and can guarantee the construction progress. The internal heat preservation application time is long, the technology is mature, and the construction technology and the inspection standard are perfect.

The insulation technology: reinforced gypsum composite polystyrene insulation board, polymer mortar composite polystyrene insulation board, reinforced cement composite polystyrene insulation panels, interior wall stickers polystyrene board cast plaster and plastering polyphenyl granule thermal insulation slurry and anti crack mortar is pressed into the mesh. But the heat will be of more use to the area occupied by the “bridge” problem which is difficult to resolve, as it prone to cracking, but it also affects the speed of construction, residents of the second decoration, and wall hanging and fixed objects also easy to damage the insulation structure. The irrationality of internal insulation in the technology decides that it must be replaced by external heat preservation.

### 2.2 *Exterior wall insulation technology*

Exterior insulation is a kind of building heat preservation technology, which is vigorously promoted at present. Thermal insulation compared with the insulation, the technology is reasonable because of its obvious advantages, the use of the same size, the same size and performance of insulation material, thermal insulation than the thermal effect. External insulation technology applies not only to new construction projects, but also applies to the transformation of old buildings, applicable to a wide range, high technology content. External insulation on the outside of the main structure protects the main structure and extends the building's life; effectively reduces the thermal bridge of building structure, does not affect the use of indoor space; and at the same time eliminates condensation and improves living comfort.

There are several main external insulation technologies of the external wall.

#### 2.2.1 *Exterior wall external insulation*

External thermal insulation material rock (ore) cotton, glass cotton blanket, polystyrene foam board (hereinafter referred to as the polystyrene board, EPS, XPS), ceramsite concrete polyphenyl composite imitation stone decoration thermal

insulation board, wire mesh frame sandwich wallboard. The polystyrene board has excellent physical properties and is cheap in cost. It has been widely used in the external wall insulation plug-in technology worldwide. Plug-in technology is the use of adhesive mortar or special fixed pieces which will heat preservation material, hanging on the wall. Then the anticrack mortar is cast along with the pressure glass fiber mesh cloth to form a protective layer. Finally, the decorative surface is added. There is a practice using special fasteners that will not be easily absorbent and the insulation board is fixed on the wall. Then the aluminum, natural stone, and color glass plug in the keel of the pre production direct the formation of surface decoration. This plug-in external insulation installation is time-consuming, construction is difficult, and the construction takes the lead time limit for the construction, the main body after the main acceptance can carry out the construction. In the high-rise construction, it is not easy to get security personnel.

#### 2.2.2 *Insulation polystyrene board and wall once pouring molding*

The technology is in concrete frame—shear wall system with polyphenyl board is built in the architectural template, in the outside of the wall to be cast and pouring concrete, concrete and polystyrene board in a casting for composite wall. This technology solves the main problem of external insulation, for its obvious advantage. Because the main body of the external wall and the insulation layer of a survival, ergonomics, greatly shorten the time limit. In the pouring of concrete to pay attention to uniform, continuous casting, otherwise cause of polystyrene board in after stripping appear deformation and dislocation stubble and effects after construction procedures because of the influence of lateral pressure of concrete.

The built-in polystyrene board can be a double wire mesh or a single wire mesh. Double steel mesh polystyrene board and concrete connection, mainly rely on the medial wire frame and the lateral wall reinforcement phase of banding. Concrete and polystyrene board adhesion and its combination has good performance and a high degree of safety. Single steel mesh polystyrene board and concrete connection, rely mainly on concrete and polyphenyl plate adhesion and oblique in reinforced, L shaped steel and concrete wall anchoring force, combined with the performance is also good. Compared to the double wire mesh, single wire mesh technology saves man hours and material because of the cancellation of the inner steel wire mesh and installing insulation in front of the lateral plate plastering.

### 2.2.3 *Polystyrene particulate insulation mortar external wall insulation*

The waste polystyrene plastic (EPS) was processed into 0.5~4 mm particles, as the lightweight aggregate to prepare the insulation mortar. The technology contains heat preservation layer, anti cracking protective layer and impervious protective layer. This method is currently being widely recognized by the exterior wall insulation technology.

The construction technology is simple, can reduce labor intensity, improve work efficiency; is not affected by differences in the quality of structure, in defective wall construction metope does not need repairing and leveling, and directly using insulation slurry, Zhaobu can avoid other insulation construction technology for fall off phenomenon and leveling plaster that is too thick. And the technology to solve the external wall thermal insulation, engineering conditions by the use of the interface layer is easy for debonding the empty drum, surface layer is easy to crack problems caused by, so as to realize the external wall thermal insulation technology, which is an important breakthrough. Compared to the other external insulation, the cost of the same insulation effect can be reduced, and the construction cost can be reduced.

In addition, energy-saving insulation wall and the wall is made into a sandwich layer, the perlite, sawdust, mineral wool, glass wool, polystyrene foam, polyurethane foam (foam) filled in the inter-layer, the insulating layer is formed.

## 3 HEAT PRESERVATION AND ENERGY SAVING MATERIAL PROPERTIES

Energy saving material belongs to heat preservation and insulation material. Heat insulation material is used in building envelope or thermal equipment, impedance heat transfer of material or material composite material, including heat preservation material, as well as cold material. The significance of the insulation material, on the one hand, is to meet the thermal environment of building space or thermal equipment and on the other hand is to save energy. For residential heating air-conditioning, by using the insulation material, can be based on the existing energy 50%~80%. Therefore, some countries will heat insulation material as the fifth energy after coal, oil, gas, nuclear energy.

Exterior wall heat preservation mainly depends on the insulation material, as the building envelope and the application of the effective insulation material is the effective measure to ensure the building energy conservation.

### 3.1 *Performance of heat insulation material*

Adiabatic is to maximize the impedance of the heat transfer, so the insulation material must

have a large thermal resistance and small thermal conductivity.

From the perspective of the composition of the material, the thermal conductivity of organic polymer is smaller than that of the inorganic materials; non metal thermal conductivity is smaller than that of the metal material; gaseous material coefficient of thermal conductivity is less than that of the liquid substance, liquid matter less than solid. Therefore, in the case of the conditions, should try to use the organic polymer materials or amorphous inorganic materials, which for the insulation is favorable.

From the material structure, when the apparent density of the material is reduced, the porosity is increased, and the porosity of the material is closed. The thermal conductivity of the material is relatively small. For foamed plastics, the best apparent density of the insulation material is 16~40 kg/m<sup>3</sup>.

Due to the presence of porosity, material in the humid environment inevitably to suction. Therefore, when the humidity increases, material balance moisture content increases, and the thermal conductivity of the material also increases. So as heat preservation material, the moisture content of material should be as low as possible, if inevitable, carry on hydrophobic treatment or waterproof material cover with waterproof material.

In addition, heat insulation material must also resist a certain impact load, and has the same mechanical strength as the environment. The bonding performance is good, but also has a small shrinkage rate and the environment to adapt to the durability.

### 3.2 *Commonly used heat insulation material*

For building external insulation energy-saving materials mainly include: polystyrene foam board, rock wool board, glass wool felt, and ultra light polystyrene particles insulation slurry. All of the above materials have a common feature that there are a lot of sealing holes in the material, their apparent density is small, this is also because the heat preservation and heat insulation material are essential.

Rock wool and glass wool is sometimes referred to as mineral wool, which belongs to the field of inorganic materials. Rock wool is not burning, is low in price, has a certain effect on sound insulation, and at the same time it can also meet the insulation performance. But the rock wool quality varies greatly, good in insulation performance and low in density, the tensile strength is low, and the durability is poor.

Polystyrene foamed plastics are made of polystyrene resin as the main raw material and has

many closed microporous materials through foaming agent. Because of its apparent density, small thermal conductivity, low water absorption, good noise, high mechanical strength, and high dimensional accuracy, uniform structure, its occupancy is high in the external wall heat preservation.

Rigid polyurethane foam has a very superior thermal insulation, and its low thermal conductivity is compared with other materials.

Also, its unique obturator structure gives it a more superior water vapor performance because it does not need additional insulation moisture-proof, simplifying the construction procedure, and reducing the project cost. But because of its high price and flammability, its uses are limited.

#### 4 CONCLUSION

Using building energy conservation of building maintenance structure of high levels of insulation, is the main building energy-saving measures, the external wall insulation system with heat preservation function is the key technology of building and energy saving. This technique can effectively solve the temperature difference in summer and winter caused by the loss of energy, indoor and outdoor, in our country.

At present, the development of the external wall insulation technology is very fast, and is the key to energy saving work. The development of exterior insulation technology and energy saving material is inseparable, building energy saving must be based on the premise of developing new energy saving

material, and must have enough heat preservation and heat insulation material for the foundation. The development of energy saving material must be combined with the insulation technology of exterior wall to really play its function. In the field of architecture, if the beginning of the design has a thermal insulation energy-saving ideas, from the perspective of the life cycle of the architecture, heat preservation energy-saving concepts will perforate from the beginning to the end, make the building have good ventilation, vertical integration of sunshade structure, good effect of heat insulation envelope, and reasonable equipment system. These measures of building insulation energy saving will play a positive role, thus truly achieving energy-saving buildings.

#### REFERENCES

- [1] Qi Wenlong. Application of polystyrene board wall insulation technology [M] Building materials—building—decoration, 2000.
- [2] Standard for energy saving design of residential buildings (J10301-2003) [M] China Building Industry Press, 2003.
- [3] Xu Huizhong, Zhou Ming. Production and application of insulation materials. [M] China Building Materials Industry Press, 2001.
- [4] Construction quality acceptance specification (GB50411-2007) [M] China Building Industry Press, 2007.
- [5] Exterior insulation engineering technical specification (JGJ144-2004) [M] China Building Industry Press, 2004.

## Advanced treatment of rainwater by $H_2O_2/UV$ process

Zheng Li, Weipeng Chen, Jun Li & Siyang Yue

Suzhou Industrial Park Design and Research Institute Co. Ltd., Suzhou, China

**ABSTRACT:** Organic pollutants in rainwater is a challenge for rainwater recycling currently. This study investigated efficiency of  $H_2O_2/UV$  process in removing two selected target aromatic compounds, phenol and para-Chlorobenzoic Acid (pCBA), in rainwater collected from a typical eastern metropolis with many chemical industries. The process showed high efficiency on phenol and pCBA removal, which both followed pseudo-first-order kinetics. Higher phenol removal efficiency was observed over pCBA, but effective TOC removal would require higher UV intensity or longer irradiation. The  $H_2O_2/UV$  process was compared with  $S_2O_8^{2-}/UV$  process in terms of pCBA removal efficiency, and thus was assessed for the practical application in rainwater treatment. The  $H_2O_2/UV$  process was advantageous as there was no introduction of secondary pollutants, and therefore, it is recommended to remove aromatic pollutants prior to recycling rainwater to guarantee biological and chemical safety.

**Keywords:** aromatic compounds; advanced oxidation processes; hydrogen peroxide; UV; rainwater

### 1 INTRODUCTION

Arising from the climate change and water pollution caused by anthropogenic activities, less and less fresh water on land and under ground is available, and more and more areas all over the world has been undergoing water crisis (Bohannon 2006, Carpenter et al. 2011, Fischer & Knutti 2015, Schwarzenbach et al. 2010). While it is necessary to treat the wastewater to keep aqueous environment clean, it is indeed an urgent task to explore more or even new water resources, in addition to the rapid development of water treatment technologies for full utilization of wastewater water, alkaline water such as sea water, and even polluted water (Carpenter et al. 2011, Simons et al. 2015). Generally, rainwater or storm water accounts for the most of origins of fresh water in rivers and lakes and under ground. Thus, rainwater harvesting in urban sites such as buildings and artificial turf is one of the feasible approaches, and may serve as a new but important fresh water resource for many cities (Blocken et al. 2013, Naddeo et al. 2013, Vieira et al. 2014, Ward et al. 2012a, Ward et al. 2012b).

One of the formidable problems for rainwater harvesting and reuse lies in its pollution, which is mostly caused by the pollutants in atmosphere released from industrial factories, traffic, etc., depending on the area locations and also type of rainwater reuse. There are many studies reporting the composition of rainwater over the world (Huston et al. 2009, Niu et al. 2014, Xiao et al. 2013). Inorganic ions, such as  $NO_3^-$ ,  $NO_2^-$ ,  $NH_4^+$ ,

sulfate,  $Na^+$ ,  $K^+$ ,  $Ca^{2+}$ ,  $Mg^{2+}$ , and  $Fe^{2+}/Fe^{3+}$  are usually present in the rainwater, besides the micro and macro particles and microbes. However, the occurrence of toxic pollutants, including heavy metals like Hg, and especially organics originating from the chemical industry and exhaust from traffic, inevitably inhibit the direct utilization of rainwater. For example, toxic aromatics like benzene and nitrated phenols, which are generated via the radical oxidation of aromatics followed by attack by and substitution of nitrogen-containing radicals (e.g.  $NO_2\cdot$  and  $NO_3\cdot$ ), exist in rainwater in many areas (Harrison et al. 2005). Most of those toxic organic pollutants are volatile, and their presence in rainwater may thus potentially cause risk during the utilization of rainwater polluted by them. So it is indeed necessary to remove those organic pollutants in the rainwater prior to its effective utilization to guarantee the water safety.

Actually, thanks to the efforts from scientists all over the world, various methods, such as coagulation, membrane filtration, adsorption by activated carbon and other adsorbents, biodegradation, oxidation, and chlorine and UV disinfection have been developed to treat water to comply with different guidelines or standards for water utilization. When these methods are applied in the rainwater treatment specific considerations should be taken individually, according to the chemical compositions of rainwater and the utilization purpose. Membrane filtration seems to be the most feasible method by removing not only particles, but also even the ions by reverse osmosis, and the treated

rainwater should be drinkable. However, high cost of membrane material and process maintenance, the membrane fouling, and intensive energy requirement limit its wide application currently (Elimelech & Phillip 2011). Activated carbon adsorption has been widely used in drinking water treatment plants, though it could only remove hydrophobic organics, leaving the hydrophilic pollutants, ions, and pathogenic virus, and bacterial in the water. Furthermore, the adsorption capacity of activated carbon is limited, and high cost of changing activated carbon indeed hinders its wide application. As for rainwater, it is usually case-specific, such as rain period, intensity, amount, water quality, and the purpose of its utilization.

Advanced Oxidation Processes (AOPs) has raised a great attention for its ability to efficiently remove aromatics and even to totally mineralize organic carbon, attributed to the powerful oxidizing species hydroxyl radical,  $\text{HO}\cdot$  (Heeb et al. 2014). In addition, the pathogenic virus and bacterial are also efficiently killed during the oxidation. Ozone is one of the most used oxidants, but it is restricted by the formation of toxic byproducts in the presence of bromide, and very low efficiency under acidic conditions for the lack of initiators such as  $\text{HO}^-$  (Liu et al. 2013). Most of the rainwater is acidic due to the pollution by  $\text{SO}_2$ ,  $\text{NO}_2$ , etc., so  $\text{H}_2\text{O}_2/\text{UV}$  process, an efficient and clean process, may be a good alternative to the conventional processes (Crittenden et al. 1999). It not only can remove almost all the organic pollutants, but also avoids the formation of toxic byproducts such as bromate. Furthermore, UV can also very efficiently kill the virus and bacterial simultaneously. In addition, this process is feasible in practical application, with simple installation, easy management, safe application, good adaption, and relatively low costs.

Therefore, the aim of this study was to investigate the efficiency of  $\text{H}_2\text{O}_2/\text{UV}$  process in rainwater treatment, and to evaluate the feasibility in practical application. Two typical aromatic compounds, phenol and p-Chlorobenzoic Acid (pCBA), were selected as the target compounds to assess the efficiency of the  $\text{H}_2\text{O}_2/\text{UV}$  process.

## 2 MATERIALS AND METHODS

### 2.1 Materials

Phenol, pCBA, and potassium persulfate were of ACS reagent grade and were purchased from Sigma-Aldrich. Phosphoric acid and methanol of HPLC grade were supplied by Tedia. Hydrogen peroxide and other reagents used were of analytical-reagent grade and purchased from Sinopharm Chemical Reagent Co., Ltd. All the chemicals were used as

received without further purification. All solutions were prepared in  $18.2 \text{ M}\Omega\cdot\text{cm}^{-1}$  Milli-Q-water produced by a Milli-Q Biocel water system.

### 2.2 Procedures

All the photochemical experiments were performed in a cylindrical photoreactor (2.0 L solution, 2.0 cm path length). A low-pressure mercury UV lamp (Heraeus, GPH436T5 L/4, 21 W, 254 nm) was centered in the cylindrical vessel axially along the length of the reactor. Temperature was controlled at  $25 \pm 0.5^\circ\text{C}$ . UV lamp was ignited at least 15 min to reach a stable output prior to the experiments. Reactions started by the addition of  $\text{H}_2\text{O}_2$ . Samples were withdrawn at predetermined time intervals and quenched using excessive sodium thiosulfate. All experiments were repeated independently at least two times, and average values along with a standard deviation are provided. Rainwater samples were collected from a rainfall event in a metropolis located in the east of China, in May, 2014. The samples were filtered using 0.45 mm cellulose membrane filter and were stored at  $4^\circ\text{C}$  prior to use.

### 2.3 Analytical methods

The concentrations of phenol and pCBA were determined by high performance liquid chromatography (Waters 2695 HPLC) equipped with a 2489 UV Detector and an autosampler, using a Waters symmetry C18 column (4.6 mm  $\times$  150 mm, 5  $\mu\text{m}$ ) and C18 guard column for separation. An eluent of phosphate buffer (pH 3) and methanol (40:60, v/v%) was used at a flow rate of 1.0. The concentration of phenol was quantified at 280 nm, while pCBA at 234 nm. The pH value was measured by a pH meter (PB-10, Satorious). The absorption was carried out on a Varian Cary 300 spectrometer. The cations and anions were analyzed on a Dionex ICS-3000 ion chromatograph. Total Organic Carbon (TOC) and Total Nitrogen (TN) were analyzed by a TOC analyzer (TOCL, Shimadzu). Other metals were analyzed by Inductively Coupled Plasma Atomic Emission Spectrometry (ICP-AES, PerkinElmer). Other analysis was carried out according to the standard methods (Association et al. 2012).

## 3 RESULTS AND DISCUSSIONS

The location, where the rainwater was collected, had lots of various chemical industry, including petrochemical industries, agrichemical producers, electronics manufacturers, and electroplating factories. The air was heavily polluted by the release of exhaust and drainage of wastewater. The rainwater quality were as follows: suspend solid  $12.1 \pm 0.1 \text{ mg/L}$ , COD  $82.5 \pm 3.3 \text{ mg/L}$ , pH

5.1 ± 0.1, TOC 12.3 ± 0.2 mg/L, UV254 0.081 ± 0.001 cm<sup>-1</sup>, NH<sub>3</sub>-N 1.67 ± 0.064 mg/L, NO<sub>2</sub>-N 0.100 ± 0.003 mg/L, NO<sub>3</sub>-N 3.23 ± 0.09 mg/L, TP 0.141 ± 0.004 mg/L, Cl<sup>-</sup> 0.89 ± 0.02 mg/L, SO<sub>4</sub><sup>2-</sup> 23.5 ± 1.0 mg/L, Fe 0.152 ± 0.001 mg/L, and Hg 2.0 ± 0.1 μg/L, respectively. It is noted that about 0.02 μM total phenol was also determined, indicating the pollution of aromatics in the rainwater.

### 3.1 Degradation of phenol

Figure 1 shows the phenol degradation in H<sub>2</sub>O<sub>2</sub>/UV process. Phenol underwent significant direct photolysis, because it possesses strong absorption at 254 nm, and after excitation by UV the C–C or H–O bonds break and ring opens in the presence of oxygen (Wu et al. 2001). Compared with the direct photolysis, much rapid indirect photolysis of phenol was observed in the H<sub>2</sub>O<sub>2</sub>/UV process, and complete removal was obtained within 7 min, using 1.0 mM H<sub>2</sub>O<sub>2</sub>.

More quantitative details are shown Figure 2, which indicates the degradation kinetics of phenol in the H<sub>2</sub>O<sub>2</sub>/UV process. Both direct photolysis and indirect photolysis of phenol in H<sub>2</sub>O<sub>2</sub>/UV process followed pseudo-first-order kinetics. The comparison between the two cases shows that 1.0 mM H<sub>2</sub>O<sub>2</sub> could enhance the phenol degradation by at least an order of magnitude, suggesting the very high efficiency of such process in removing phenols.

The mechanism of degradation of phenols in H<sub>2</sub>O<sub>2</sub>/UV processes has been systematically studied and compiled before (Crittenden et al. 1999). Briefly, a powerfully oxidizing species, hydroxyl radical (HO•), is generated during the photolysis of H<sub>2</sub>O<sub>2</sub> in Equation 1, with a quantum yield of about 1.0 at 254 nm (Crittenden et al. 1999). Phenol is attacked by HO• via electron transfer, hydrogen abstraction, and electrophilic substitution pathways, producing organic radicals

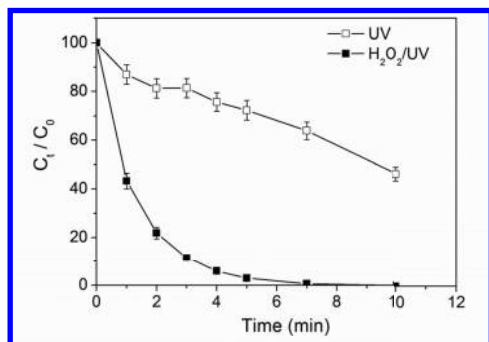


Figure 1. Phenol degradation in UV and H<sub>2</sub>O<sub>2</sub>/UV processes. Conditions: [Phenol]<sub>0</sub> = 10 μM, [H<sub>2</sub>O<sub>2</sub>]<sub>0</sub> = 1.0 mM, pH 5.1 without adjustment by buffer, 25 °C.

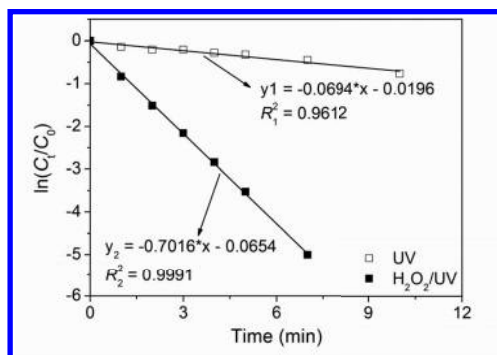
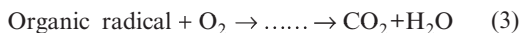


Figure 2. Degradation kinetics of phenol in UV and H<sub>2</sub>O<sub>2</sub>/UV processes. Conditions: [Phenol]<sub>0</sub> = 10 μM, [H<sub>2</sub>O<sub>2</sub>]<sub>0</sub> = 1.0 mM, pH 5.1 without adjustment by buffer, 25 °C.

(Equation 2), which are subsequently oxidized by oxygen and transformed to alcohols, aldehydes, ketones, organic acids, etc. (Equation 3).



### 3.2 Degradation of pCBA

pCBA is much more recalcitrant than phenol studied above, and is usually selected as the HO• probe. The degradation of pCBA in rainwater by H<sub>2</sub>O<sub>2</sub>/UV process was studied in order to evaluate the availability of HO• by target compounds (Rosenfeldt & Linden 2007). Figure 3 shows the degradation of pCBA in H<sub>2</sub>O<sub>2</sub>/UV process. pCBA shows slower direct photolysis than phenol in Figure 1. H<sub>2</sub>O<sub>2</sub> markedly accelerated the degradation of pCBA in the system, and complete removal was observed within 7 min.

Figure 4 shows the degradation kinetics of pCBA in H<sub>2</sub>O<sub>2</sub>/UV process. As degradation of phenol in Figure 2, the direct photolysis and indirect photolysis of pCBA also obeyed well the pseudo-first-order kinetics. The indirect photolysis resulting from the HO• oxidation shows much higher rate than direct photolysis by UV by at least 20 times higher. The degradation kinetics in Figure 2 and Figure 4 indicate the higher efficiency on phenol removal than pCBA removal, possibly attributed to the higher rapid capture of HO• by phenol than that by pCBA and, thus, the less impact of competition of byproducts for HO• (Buxton et al. 1988). Furthermore, the high content of TOC (~12.3 mg/L) in rainwater also competed for HO• significantly, resulting in the less availability of HO• by the target pollutants.



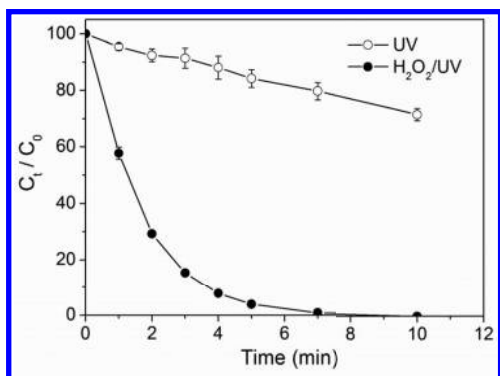


Figure 3. Degradation of pCBA in UV and  $H_2O_2/UV$  processes. Conditions:  $[pCBA]_0 = 10 \mu M$ ,  $[H_2O_2]_0 = 1.0 mM$ , pH 5.1 without adjustment by buffer,  $25^\circ C$ .

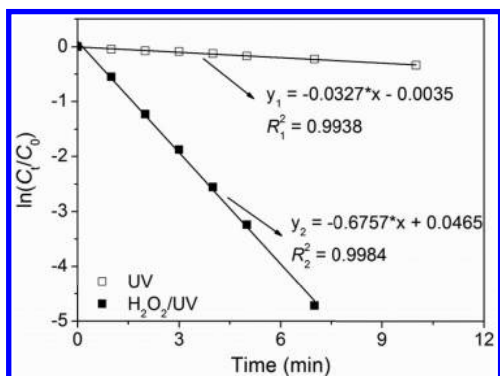


Figure 4. Degradation kinetics of pCBA in UV and  $H_2O_2/UV$  processes. Conditions:  $[pCBA]_0 = 10 \mu M$ ,  $[H_2O_2]_0 = 1.0 mM$ , pH 5.1 without adjustment by buffer,  $25^\circ C$ .

### 3.3 Efficiency comparison

Because of the acidity of the rainwater, ozone should not be feasible in such water matrix. In order to assess the efficiency of  $H_2O_2/UV$  process in removing organic pollutants, comparison with an emerging AOPs, persulfate/UV, was performed. Figure 5 shows the pCBA degradation in the two processes. It seems that  $S_2O_8^{2-}/UV$  process shows higher efficiency than  $H_2O_2/UV$  process, and complete removal of pCBA was obtained within 4 min. According to the degradation kinetics of pCBA in Figure 4 and Figure 5, it is obvious that the  $S_2O_8^{2-}/UV$  process shows about 1.7 times higher efficiency than  $H_2O_2/UV$  process. This may be caused by the higher selectivity of sulfate radical,  $SO_4^{\cdot-}$ , than  $HO^{\cdot}$ . The latter is generally regarded to be non-selective towards organics (Buxton et al. 1988). Nonetheless, the  $S_2O_8^{2-}/UV$  process introduces a high amount

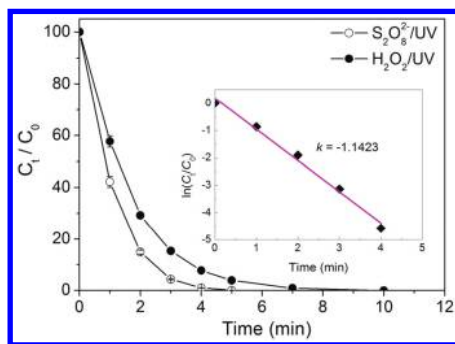


Figure 5. Comparison of pCBA degradation between  $H_2O_2/UV$  and  $S_2O_8^{2-}/UV$  processes. Inset: degradation kinetics of pCBA in  $S_2O_8^{2-}/UV$  process. Conditions:  $[pCBA]_0 = 10 \mu M$ ,  $[H_2O_2]_0 = 1.0 mM$ ,  $[S_2O_8^{2-}]_0 = 1.0 mM$ , pH 5.1 without adjustment by buffer,  $25^\circ C$ .

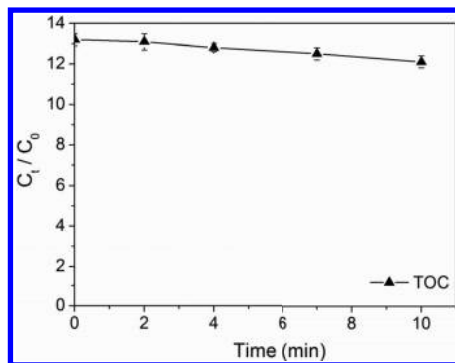


Figure 6. TOC removal in the  $H_2O_2/UV$  process. Conditions:  $[H_2O_2]_0 = 1.0 mM$ , pH 5.1 without adjustment by buffer,  $25^\circ C$ .

of sulfate, and thus, is not recommended to apply in rainwater treatment. In comparison,  $H_2O_2/UV$  process has the advantage that the final product is  $H_2O$ , without introducing secondary pollution such as sulfate in the  $S_2O_8^{2-}/UV$  process.

### 3.4 TOC removal efficiency

The rainwater collected in a district having many chemical industries was polluted by organic chemicals, as indicated by the high TOC content. The TOC in rainwater usually leads to the growth of algae and microbes, resulting in the subsequent biological contamination and thus the limitation of rainwater reuse. Although efficient removal of phenol (Fig. 1) and pCBA (Fig. 3) was obtained by the  $H_2O_2/UV$  process, much lower efficiency was observed on the TOC removal, as shown in Figure 6. Under the given conditions, only about 9% of TOC was removed. It is explained by the low

generation of HO•, which determines the removal of TOC. As reported (Xiao et al. 2015), obvious TOC would be obtained by higher UV dose by improving UV intensity or longer irradiation time.

However, as UV kills almost all the microbes and algae in the rainwater, there will be little proliferation of bacterial, virus, algae, etc. if the treated rainwater is stored correctly. Furthermore, because almost all of the toxic pollutants in rainwater are aromatic, while they can be efficiently removed by the H<sub>2</sub>O<sub>2</sub>/UV process, the safety of rainwater reuse can be consequently guaranteed. For reuse in other stricter fields such as drinking water, further treatment is required.

#### 4 CONCLUSIONS

The H<sub>2</sub>O<sub>2</sub>/UV process showed high efficiency on removal of phenol and even recalcitrant pCBA in the rainwater, which was polluted by organic contaminants and inorganic ions. Both the degradation of phenol and pCBA followed the pseudo-first-order kinetics, while higher efficiency on phenol removal was obtained over pCBA, due to its higher reaction rate constant with HO• than that of pCBA. Efficient TOC removal required higher UV intensity or longer irradiation. The H<sub>2</sub>O<sub>2</sub>/UV process was compared with the S<sub>2</sub>O<sub>8</sub><sup>2-</sup>/UV process in terms of pCBA removal efficiency, and the latter showed about 1.7 times higher efficiency. Nonetheless, the H<sub>2</sub>O<sub>2</sub>/UV process was still advantageous over the S<sub>2</sub>O<sub>8</sub><sup>2-</sup>/UV process on no introduction of secondary pollution. Therefore, the H<sub>2</sub>O<sub>2</sub>/UV could be used to efficiently remove the aromatic pollutants in rainwater to guarantee the safety of the rainwater reuse.

#### ACKNOWLEDGEMENTS

This work was supported by the Jiangsu provincial science and technology support program (No. SF06).

#### REFERENCES

Association, A.P.H., et al. 2012. *Standard Methods for the Examination of Water and Wastewater*, American Water Works Assn, Washington, DC.

Blocken, B., et al. 2013. Rainwater runoff from building facades: A review. *Building and Environment* 60: 339–361.

Bohannon, J. 2006. Running Out of Water- and Time. *Science* 313(5790): 1085–1087.

Buxton, G.V., et al. 1988. Critical review of rate constants for reactions of hydrated electrons, hydrogen atoms and hydroxyl radicals (•OH/•O<sup>-</sup>) in Aqueous Solution. *Phys. Chem. Ref. Data* 17(2): 513–886.

Carpenter, S.R., et al. 2011. State of the World's Freshwater Ecosystems: Physical, Chemical, and Biological Changes. *Annual Review of Environment and Resources* 36(1): 75–99.

Crittenden, J.C., et al. 1999. A kinetic model for H<sub>2</sub>O<sub>2</sub>/UV process in a completely mixed batch reactor. *Water Research* 33(10): 2315–2328.

Elimelech, M. & Phillip, W.A. 2011. The Future of Seawater Desalination: Energy, Technology, and the Environment. *Science* 333(6043): 712–717.

Fischer, E.M. & Knutti, R. 2015. Anthropogenic contribution to global occurrence of heavy-precipitation and high-temperature extremes. *Nature Clim. Change* 5(6): 560–564.

Harrison, M.A.J., et al. 2005. Nitrated phenols in the atmosphere: a review. *Atmospheric Environment* 39(2): 231–248.

Heeb, M.B., et al. 2014. Oxidative treatment of bromide-containing waters: Formation of bromine and its reactions with inorganic and organic compounds—A critical review. *Water Research* 48(0): 15–42.

Huston, R., et al. 2009. Characterisation of atmospheric deposition as a source of contaminants in urban rainwater tanks. *Water Research* 43(6): 1630–1640.

Liu, C., et al. 2013. Chlorination of bromide-containing waters: Enhanced bromate formation in the presence of synthetic metal oxides and deposits formed in drinking water distribution systems. *Water Research* 47(14): 5307–5315.

Naddeo, V., et al. 2013. Enhanced drinking water supply through harvested rainwater treatment. *Journal of Hydrology* 498(0): 287–291.

Niu, H., et al. 2014. Chemical composition of rainwater in the Yulong Snow Mountain region, Southwestern China. *Atmospheric Research* 144(0): 195–206.

Rosenfeldt, E.J. & Linden, K.G. 2007. The R<sub>OH,UV</sub> concept to characterize and the model UV/H<sub>2</sub>O<sub>2</sub> process in natural waters. *Environmental Science & Technology* 41(7): 2548–2553.

Schwarzenbach, R.P., et al. 2010. Global Water Pollution and Human Health. *Annual Review of Environment and Resources* 35: 109–136.

Simons, G.W.H., et al. 2015. Water reuse in river basins with multiple users: A literature review. *Journal of Hydrology* 522(0): 558–571.

Vieira, A.S., et al. 2014. Energy intensity of rainwater harvesting systems: A review. *Renewable and Sustainable Energy Reviews* 34(0): 225–242.

Ward, S., et al. 2012a. Rainwater harvesting in the UK: exploring water-user perceptions. *Urban Water Journal* 10(2): 112–126.

Ward, S., et al. 2012b. Performance of a large building rainwater harvesting system. *Water Research* 46(16): 5127–5134.

Wu, C.D., et al. 2001. Photosonochemical degradation of phenol in water. *Water Research* 35(16): 3927–3933.

Xiao, H.-W., et al. 2013. Chemical composition and source apportionment of rainwater at Guiyang, SW China. *Journal of Atmospheric Chemistry* 70(3): 269–281.

Xiao, Y., et al. 2015. Kinetic modeling and energy efficiency of UV/H<sub>2</sub>O<sub>2</sub> treatment of iodinated trihalomethanes. *Water Research* 75(0): 259–269.

## Effects of ozone and drought on fluorescence physiology of three seedling types in China

Xiaoli Hou & Xue Li

College of Forestry and Landscape Architecture, South China Agricultural University, Guangzhou, China

**ABSTRACT:** Seedlings of *Michelia macclurei*, *Cinnamomum camphora*, and *Rhodolcia championii* were treated with ozone fumigation and drought treatment, and their chlorophyll fluorescence parameters were determined. The results showed that with increasing treatment time, minimal initial fluorescence ( $F_0$ ) of the three seedling types continuously increased or followed by a decrease; *PSII* maximum photochemical efficiency ( $F_v/F_m$ ) of *M. macclurei* under drought stress and *R. championii* under all treatments decreased, whereas it remained stable in *M. macclurei* treated with ozone stress and zone-drought intercross stress, and in *C. camphora* treated with all treatments. Except for *C. camphora* under ozone stress, *PSII* actual quantum efficiency ( $Y(II)$ ) of the three seedling types decreased. Non-photochemical quenching (*NPQ*) of *M. macclurei* under single stress and *R. championii* under all treatments decreased, whereas it remained stable in *M. macclurei* treated with zone-drought intercross stress and in *C. camphora* treated with all treatments. Principal component analysis indicated that resistance abilities of ozone, drought, and ozone-drought intercross stresses for the three seedling types decreased in the order of *C. camphora* seedlings > *M. macclurei* seedlings > *R. championii* seedlings.

**Keywords:** ozone stress; drought stress; chlorophyll fluorescence parameters; seedling

### 1 INTRODUCTION

Ozone is a kind of toxic gaseous pollutant to plants (Zhang et al. 2010). In recent decades, due to the extensive use of fossil fuels, the concentration of nitrogen oxides and volatile organic compounds in the atmosphere increased sharply, resulting in  $O_3$  concentration to rise in the surface layer (Vingarzan et al. 2004). High concentrations of ozone can increase stomatal resistance of plants, change absorbing light energy and structure distribution of *PSII* antenna pigment (Keller et al. 2007), inhibit photosynthetic electron transport (Vandermeiren et al. 2005), reduce photochemical efficiency, and affect the chlorophyll fluorescence parameters (Luo et al. 2012). Ozone can also change the composition of plant thylakoid membrane, resulting in changes in chlorophyll fluorescence yield (Lie et al. 2014). Drought stress is the most common form of plant adversity (Li et al. 2007), which can disrupt the chloroplast photosynthetic mechanism II (*PSII* system) and photosynthetic electron transport of leaves (Zhou et al. 2004, Zhang et al. 2011a), lead to photosynthetic organ damage and chlorophyll content decrease (Li et al. 2008, Yang et al. 2007), and inhibit plant photosynthesis. In the process of photosynthetic response to environmental stress, *PSII* plays an important role (Wei et al. 2012). The

application of chlorophyll fluorescence kinetics to study plant resistance to environmental stress will contribute to screening tree species with strong ozone and drought resistance.

*Michelia macclurei*, *Cinnamomum camphora* and *Rhodolcia championii* are three important tree species for garden greening in south China. Although there were some few studies on photosynthetic physiology of these species (Yu et al. 2011, Zhang et al. 2011b, Guo et al. 2013), we still know little about response of chlorophyll fluorescence parameters of these species to ozone stress or drought stress. This study is aimed at providing the reference for screening tree species with strong ozone and drought resistance.

### 2 MATERIALS AND METHODS

**Experimental material.** One-year-old seedlings of *M. macclurei*, *C. camphora* and *R. championii* were individually planted into nutrition bags (12 cm diameter and 10 cm height). The seedlings growth status was shown in Table 1.

Fumigation test equipment was Open-Top Chamber (OTC) with hexagonal cross-section, glass wall and a diameter of 3 m and a height of 2.4 m, which was located in Yuejinbei Nursery in

Table 1. Growth status of three seedling types.

Tree species	DBH (mm)	Height (cm)	Crown width (cm)
<i>M. macclurei</i>	4.50 ± 0.18	32.97 ± 0.89	14.77 ± 0.64
<i>C. camphora</i>	4.16 ± 0.18	38.96 ± 1.12	13.55 ± 0.97
<i>R. championii</i>	3.15 ± 0.18	32.97 ± 0.95	12.67 ± 0.48

Notice: The data is “average + standard error” in the table.

South China Agricultural University of China. Ozone was provided by CFY5 oxygen manufacture equipment and COM-AD-01 ozone generator (ranges of 0–1 ppm, resolution of 0.001 ppm), and its concentration was detected by GT901-03 portable ozone detector continuously.

**Test method.** Two ozone treatments were designed in two OTCs: E40 (non-filtered air, ozone concentration is about 40 ppb), E150 (elevated ozone at 150 ppb). Each chamber was designed two moisture gradient: control (the relative water content of soil was 75–80%), drought treatment (the relative water content of soil was 40–45%). As a result, three treatments were designed as follows: E40+D (Drought stress), E150 (Ozone stress) and E150 + D (Ozone and drought stress). Ventilation and air system could meet the gas exchange more than one time per min in the chambers, which kept almost consistent in temperature, humidity and CO<sub>2</sub> concentration between the chamber and outside chamber. Aeration time in chambers was 9:00–17:00 every day. The fumigation test lasted for 30 days. At the beginning of experiment, the 15th day and 30th day (the end of experiment), chlorophyll fluorescence parameters were separately measured.

**Determination method for index.** The determination methods of fluorescence parameters were as follows: individuals of three seedling types with similar growth were selected, and three leaves of each seedling were marked among the third to eighth functional leaves. OS-IP pulse modulation fluorometer was used to determine the leaves from 9:00 to 11:00 in the morning. The initial fluorescence yield ( $F_0$ ), maximal fluorescence yield ( $F_m$ ), steady state fluorescence ( $F'$ ), maximum fluorescence in light adapted state ( $F_m'$ ) were measured and variable fluorescence [ $(F_v) = F_m - F_0$ ], the *PSII* maximum photochemical efficiency ( $F_v/F_m$ ), *PSII* actual photosynthetic efficiency [ $Y(II) = (F_m' - F')/F_m'$ ], Non-photochemical quenching ( $NPQ = F_m'/F_m - 1$ ) were calculated.

**Data analysis.** All statistical analyses were used Excel 2010 and the Statistical Analysis System (SAS 9.0). After each index was standardized using range method, principal component analysis was used to analyze the data and the scores of

ozone resistance and drought resistance of each tree species in treatments E40+D, E150, E150 + D were calculated.

### 3 RESULTS

**The changes of minimal initial fluorescence ( $F_0$ ) under ozone and drought stress.** With increasing ozone and drought stress time, the  $F_0$  of *M. macclurei* had a significant increase ( $P < 0.05$ ) followed by a stable status in Treatments E40 + D and E150 + D, while it had an undulation followed by a significant increase ( $P < 0.05$ ) in Treatment E150 (Fig. 1). The  $F_0$  of *C. camphora* had a significant increase followed by a significant decrease in Treatments E40 + D and E150 + D ( $P < 0.05$ ), while it had a continuous increase in Treatment E40. The  $F_0$  of *R. championii* had a continuous increase in Treatments E40 + D and E150, while it had a significant increase followed by a significant decrease in Treatment E150 + D ( $P < 0.05$ ).

**The changes of *PSII* maximum photochemical efficiency ( $F_v/F_m$ ) under ozone and drought stress.** With increasing ozone and drought stress time, the  $F_v/F_m$  of *M. macclurei* had an undulation followed by a significant decrease ( $P < 0.05$ ) in Treatment E40 + D, while it kept stable in Treatments E150 and E150 + D (Fig. 2). The  $F_v/F_m$  of *C. camphora* was stable in each treatment. The  $F_v/F_m$  of *R. championii* decreased significantly ( $P < 0.05$ ) and then stabilized in Treatment E40+D; it had an undulation followed by a significant decrease ( $P < 0.05$ ) in Treatment E150 and a continuous significant decrease in Treatment E150 + D ( $P < 0.05$ ).

**The changes of *PSII* actual quantum efficiency ( $Y(II)$ ) under ozone and drought stress.** With increasing ozone and drought stress time, the  $Y(II)$  of *C. camphora* had a slight decrease followed by a significant increase in Treatment E150 ( $P < 0.05$ ), whereas its other treatments and that of *M. macclurei* and *R. championii* in all treatments tended to decrease (Fig. 3).

**The changes of non-photochemical quenching ( $NPQ$ ) under ozone and drought stress.** With increasing ozone and drought stress time, the  $NPQ$  of *M. macclurei* had an undulation followed by a significant decrease ( $P < 0.05$ ) in Treatment E40 + D, decreased significantly ( $P < 0.05$ ), and then was stable in Treatment E150 and kept stable in Treatment E150 + D (Fig. 4). The  $NPQ$  of *C. camphora* kept stable in all Treatments. The  $NPQ$  of *R. championii* decreased significantly in Treatments E40 + D and E150 ( $P < 0.05$ ), and decreased significantly ( $P < 0.05$ ) and then kept stable in Treatments E150 + D.

**Principal component analysis of the ability to resistance ozone and drought of three seedling types**

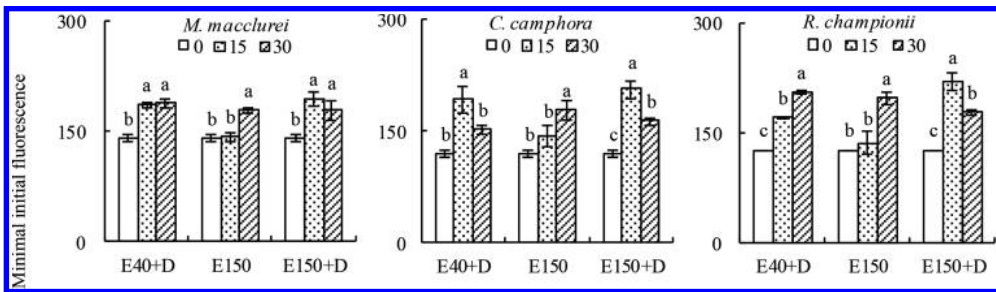


Figure 1. The change of minimal initial fluorescence under O<sub>3</sub> stress and drought stress. Significant differences between treatments were indicated by different letters above bars, P < 0.05.

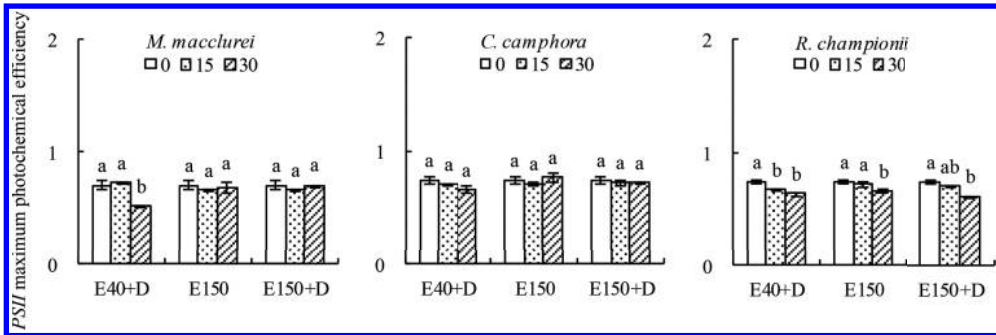


Figure 2. The change of PSII maximum photochemical efficiency ( $F_v/F_m$ ) under O<sub>3</sub> stress and drought stress.

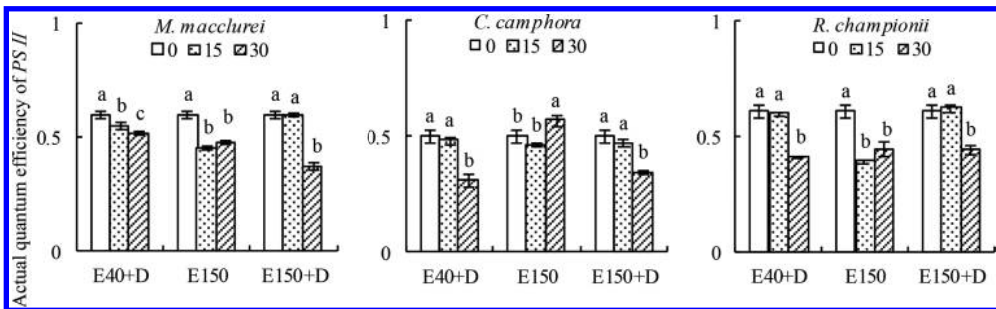


Figure 3. The change of PSII active quantum efficiency under O<sub>3</sub> stress and drought.

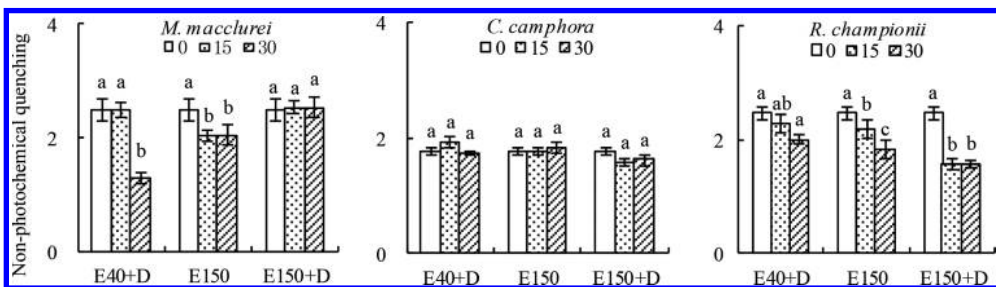


Figure 4. The change of non-photochemical quenching under O<sub>3</sub> stress and drought stress.

Table 2. Comprehensive assessment values and orders of drought resistance of the four seedling types.

Testing indexes	E40 + D		E150		E150 + D	
	Score	Rank	Score	Rank	Score	Rank
<i>C. camphora</i>	1.183	1	0.985	1	1.491	1
<i>M. macclurei</i>	0.665	2	0.864	2	0.549	2
<i>R. championii</i>	0.595	3	0.779	3	0.526	3

by using. In this study, principal component analysis was used to evaluate the resistance ability to ozone and drought of the three seedling types. The calculating score decreased in the order of *C. camphora* seedlings > *M. macclurei* seedlings > *R. championii* seedlings in Treatments E150, E40 + D and E150 + D, indicating that the resistance abilities of the three seedling types to ozone, drought or intercross stresses decreased in the order of *C. camphora* seedlings > *M. macclurei* seedlings > *R. championii* seedlings (Table 2).

#### 4 DISCUSSION AND CONCLUSION

A series of changes of chlorophyll fluorescence parameters will occur under environmental stress, because the initial injured part of photosynthesis is closely related with photosynthetic system II (*PSII*) (Li et al. 2009).  $F_0$  is fluorescence yield when *PSII* reaction center is open, and its size is related to the structure state of *PSII* reaction and the chlorophyll concentration (Chong et al. 2010, Lu et al. 1994). The non-photochemical energy dissipation of *PSII* antenna pigment often leads to the decrease of  $F_0$ , and the destruction or reversible inactivation of *PSII* reaction center causes the increase of  $F_0$  (Yang et al. 2013). With increasing ozone and drought stress time, the  $F_0$  of *M. macclurei* and *R. championii* in Treatment E150 + D, and the  $F_0$  of *C. camphora* in Treatments E40 + D and E150 + D had a significant increase and then a decrease. The reason might be that the reversible inactivation of *PSII* reaction center occurred in the seedling types in ozone stress or drought stress 15 d after the experiment, and the regulating mechanism of photoprotection was launched to reduce the destruction from strong light 30 d after the experiment (Chong et al. 2010, Zhang et al. 2010). However, the  $F_0$  of *M. macclurei* and *R. championii* under single stress, and the  $F_0$  of *C. camphora* under ozone stress increased significantly, indicating that their *PSII* reaction center may not be seriously damaged (Qian et al. 2011).

$F_v/F_m$  is the *PSII* maximum photochemical efficiency under dark adaptation and reflects the efficiency and utilization ability of capturing excitation

energy of *PSII* reaction center, and  $F_v/F_m$  decrease is an important manifestations of photoinhibition (Wang et al. 2009). Most OCT test indicated  $F_v/F_m$  decrease under environment stress was due to  $F_m$  decrease and  $F_0$  increase, the stress can destroy or inhibit the activity of *PSII* reaction center (Flowers et al. 2007). In this study, the  $F_v/F_m$  decrease of *M. macclurei* under drought stress and *R. championii* in each treatment indicated that the activity of *PSII* reaction center was injured or inhibited, but the transfer rate of photosynthetic electron chain recovered in a certain degree through adaptive adjustment, so that it maintained basic physiological functions such as normal dark reaction (Qian et al. 2011). The  $F_v/F_m$  of *M. macclurei* under ozone stress and intercross stress, *C. camphora* in each treatment had no significant change, indicating that the activity of *PSII* reaction center of leaves under ozone stress or drought stress was not damaged (Sun et al. 2009), so that the photoinhibition of seedlings was not obvious.

The actual photosynthetic efficiency ( $Y(II)$ ) reflects actual original light-trapping efficiency when *PSII* reaction center is partly closed, and the consumption ratio of photochemical reaction energy (Park et al. 1995, Govidjee. 2002).  $Y(II)$  decrease indicates that the decrease of actual original light-trapping efficiency and the ability of releasing oxygen, and plant photosynthesis is blocked. Except for *C. camphora* under ozone stress, the  $Y(II)$  of other treatments of all seedlings decreased, indicating that the ability of electron transport of *PSII* decreased, the whole process of photosynthetic electron transport was blocked, as a result, the proportion of converting light energy into chemical energy decreased (Wang et al. 2012). The  $Y(II)$  of *C. camphora* under ozone stress decreased and then increased, indicating that decrease of the actual photosynthetic efficiency was reversible (Liang et al. 2010).

Non-photochemical quenching (*NPQ*) reflects the heat dissipation ability after natural pigment of *PSII* reaction center absorbs excessive light energy and the damage degree of, being a self-protection mechanism of photosynthetic apparatus (Yu et al. 2011). The *NPQ* of *M. macclurei* in Treatments E40 + D and E150 and that of

*C. camphora* in Treatments E40 + D and E150 decreased significantly, and had no significant change in Treatment E150 + D, which might be drought can increase *NPQ* value, namely, relieving ozone stress damage to the efficiency of capturing excitation energy (Showman 1991). The *NPQ* of *C. camphora* in each treatment kept stable, indicating that these species had a steady heat dissipation function. The *NPQ* decrease of *R. championii* in each treatment indicated that heat dissipation was lesser, which is favorable for the absorption light energy entering into electronic transfer system and carbon fixation (Zong et al. 2010).

Principal component analysis indicated that resistance abilities of ozone, drought, and ozone-drought intercross stresses for the three seedling types decreased in the order of *C. camphora* seedlings > *M. macclurei* seedlings > *R. championii* seedlings. The three seedling types have a certain ability to resist ozone or drought by starting adjustment mechanism of photoprotection under ozone stress and drought stress.

#### ACKNOWLEDGEMENTS

This work was financially supported by the Foundation of Guangdong Forestry Department (No. 4400-F11031, 4400-F11055).

#### REFERENCES

Chong P.F., Li Y., & Su S.P., et al. 2010. Diurnal Change in Chlorophyll Fluorescence Parameters of Desert Plant *Reaumuria soongorica* and Its Relationship with Environmental Factors. *Journal of Desert Research*, 30(3), 539–545.

Flowers M.D., Fiscus E.L., & Burkey K.O., et al. 2007. Photosynthesis, chlorophyll fluorescence, and yield of snap bean (*Phaseolus vulgaris* L.) genotypes differing in sensitivity to ozone. *Environmental and Experimental Botany*, 61(2), 190–198.

Govidjee. 2002. A role for a light-harvesting antenna complex of photosystem II in photo protection. *The Plant Cell*, 14, 1663–1667.

Guo S.H., Xue L., & Yang Z.Y., et al. 2013. Effects of waterlogging stress on leaf gas exchange parameters of four kinds of garden greening seedlings. *Journal of South China Agricultural University*, 34(4), 548–552.

Keller F., Bassin S., & Ammann C., et al. 2007. High-resolution modelling of AOT40 and stomatal ozone uptake in wheat and grassland: A comparison between 2000 and the hot summer of 2003 in Switzerland. *Environmental Pollution*, 146(3), 671–677.

Li C.X., & Cao H. 2008. Effects of drought on chlorophyll fluorescence parameters of malus plant. *Journal of Anhui Agricultural Sciences*, 36(31), 13536–13538.

Li Y., Xue L., & Wu M. 2007. Research advances in mechanisms of tree species drought resistance. *Chinese Journal of Ecology*, 26(11), 1857–1866.

Li Z.J., Luo Q.H., & Wu W.M., et al. 2009. The effects of drought stress on photosynthetic and chlorophyll fluorescence characteristics of *Populus euphratica* and *P. pruinosa*. *Arid Zone Research*, 26(1), 45–52.

Liang F., Zheng C.S., & Sun X.Z., et al. 2010. Effects of low temperature- and weak light stress and its recovery on the photosynthesis and chlorophyll fluorescence parameters of cut flower chrysanthemum. *Chinese Journal of Applied Ecology*, 21(1), 29–35.

Lie G.W., Ye L.H., & Xue L. 2014. Effects of ozone stress on major plant physiological functions. *Acta Ecologica Sinica*, 34(2), 294–306.

Lu M.J., Zhang Q.D., & Kuang T.Y. 1994. The effects of water stress on photosystem II in wheat. *Acta Botanica Sinica*, 36(2), 93–98.

Luo K.J., Zhu J.G., & Liu G., et al. 2012. Effects of elevated ozone on leaf photosynthesis of rice (*Oryza sativa* L.) and mitigation with high nitrogen supply. *Ecology and Environmental Sciences*, 21(3), 481–488.

Park Y., Chow W.S., & Anderson J.M. 1995. The quantum yield of photoinactivation of photosystem II in pea leaves is greater at low than at high photon exposure. *Plant and Cell Physiology*, 36(6), 1163–1167.

Qian Y.Q., Zhou X.X., & Han L., et al. 2011. Rapid light response curves of PSII chlorophyll fluorescence parameters in the leaves of *Salix babylonica*, *Salix 'J172'* and *Salix leucopithecia* to Cd<sup>2+</sup> + stress. *Journal of Beijing Forestry University*, 33(6), 8–14.

Showman R.E. 1991. A comparison of ozone injury to vegetation during moist and drought years. *Journal of the Air & Waste Management Association*, 41, 63–64.

Sun J.K., Zhang W.H., & Lu Z.H., et al. 2009. Chlorophyll fluorescence characteristics of *Elaeagnus angustifolia* L. and *Grewia biloba* G. Don var. *parviflora* (Bge.) Hand.—Mazz. seedlings under drought stress. *Bulletin of Botanical Research*, 29(2), 216–223.

Vandermeiren K., Black C., & Pleijel H., et al. 2005. Impact of rising tropospheric ozone on potato: Effects on photosynthesis, growth, productivity and yield quality. *Plant, Cell and Environment*, 28, 982–996.

Vingarzan R. 2004. A review of surface ozone background levels and trends. *Atmospheric Environment*, 38(21), 3431–3442.

Wang L., Long X.H., & Hao L.X., et al. 2012. Effects of nitrogen form on the photochemical efficiency of PSII and antioxidant characteristics of Jerusalem of artichoke seedling under salt stress. *Acta Part Aculturae Science*, 21(1), 133–140.

Wang L., Zeng Q., & Feng Z.Z., et al. 2009. Photosynthetic damage induced by elevated O<sub>3</sub> in two varieties of winter wheat with free air controlled enrichment approach. *Environment Science*, 30(2), 527–534.

Wei X.D., Chen G.X., & Shi D.W., et al. 2012. Effects of drought on fluorescence characteristics of photosystem II in leaves of *Ginkgo biloba*. *Acta Ecologica Sinica*, 32(23), 7492–7500.

Yang W.Q., Gu M.Y., & Kou J.C., et al. 2013. Effects of drought and rewetting on the photosynthesis and chlorophyll fluorescence of *Coronilla varia*. *Acta Agrestia Sinica*, 21(6), 1130–1135.

Yang Y., Liu Q., & Han C., et al. 2007. Influence of water stress and low irradiance on morphological and physiological characteristics of *Picea asperata* seedlings. *Photosynthetica*, 45(4), 613–619.

- Yu X.L., Yi L.T., & Yu S.Q. 2011. Effects of Acid Rain Stress on Chlorophyll Fluorescence Properties of leaves of *Cinnamomum camphora* Seedlings. *Journal of Zhejiang Forestry Science & Technology*, 31(2), 19–24.
- Zhang Q.T., Ai J., & Song R.G., et al. 2010. Comparative research on diurnal changes of the chlorophyll fluorescence parameters of vitisamurens is Rupr. “Zuo you hong” and “beibinghong”. *Journal of Anhui Agricultural Sciences*, 38(18), 9481–9482, 9490.
- Zhang R.H., Zheng Y.J., & Ma G.S., et al. 2011a. Effects of drought stress on photosynthetic traits and protective enzyme activity in maize seedling. *Acta Ecologica Sinica*, 31(5), 1303–1311.
- Zhang W.Q., Zeng L.H., & Wang M.H., et al. 2011b. The photosynthetic physiological characteristics of main tree species in the upper and middle reaches of Dongjiang watershed. *Ecology and Environmental Sciences*, 20(1), 51–57.
- Zheng Y.F., Shi M.H., & Wu R.J., et al. 2013. Effect of elevated O<sub>3</sub> concentration and shading on photosynthesis of winter wheat's leaves. *Journal of Agro-Environment Science*, 32(10), 1925–1933.
- Zhou J., Wei H., & Lv Q., et al. 2012. Effects of soil water regime on leaf photosynthetic characteristics of slash pine (*Pinus elliottii* Engelm) seedlings. *Chinese Journal of Ecology*, 31(1), 30–37.
- Zong M., Tan K., & Wu G.L. 2010. Comparative study on diurnal changes of chlorophyll fluorescence parameters of two types of *Photinia serrulata* Lindl. *Journal of Biology*, 27(1), 27–30.



# Study on Shenyang region PM 2.5 concentration variation characteristic based on GIS

Hua Ding, Lishuang Sun & Xin Wang

*Institute of Transportation, Shenyang Jianzhu University, Liaoning, China*

**ABSTRACT:** PM 2.5 is a kind of fine particulate matter air pollution and the main source of air pollution. In the last decade, PM 2.5 pollution has grown rapidly in major cities of China that seriously damaged the urban economic development and health of residents. This paper has studied temporal and spatial variation characteristics of PM 2.5 concentration and factors of PM 2.5 concentration variation by collecting monitoring data from eleven monitoring stations of Shenyang city for five months, combining electronic map of Shenyang city and adopting GIS techniques and statistical analysis methods. The research findings of this paper would provide great help for Shenyang city's atmospheric fine particulate matter pollution treatment and reliable data support for Shenyang city's air quality improvement and ecological environment preservation.

**Keywords:** PM 2.5; pollution; ArcGIS

## 1 INTRODUCTION

Atmospheric suspended particulate matter was one of the causes of severe air pollution of most Chinese cities and also the primary pollutant of urban air quality that has a strong impact on virtuous cycle of urban climate. Suspended particulate matter referred to solid particles and droplets with diameter of 0–100  $\mu\text{m}$  suspended in air, including PM 10 (particle size range of 0–10  $\mu\text{m}$ ) and PM 2.5 (particle size range of 0–10  $\mu\text{m}$ ). Haze was a general expression of excess level of suspended particulate matter in the atmosphere that has become a new meteorological and environmental disaster phenomenon. Since the beginning of the year 2013, major cities of China have endured persistent haze weather especially cities in surrounding area with Beijing as the center becoming one of the most serious affected area. Due to its regional characteristics and industrial characteristics, Shenyang has experienced serious haze weather repeatedly during recent years, many of which even triggered orange alert. Among toxic substance in haze, PM 2.5 contained the strongest toxicity and the rapid growth of PM 2.5 has been considered to be the “Culprit” of haze weather because its particles were small enough to be directly inhaled into the lungs that may trigger various severe respiratory diseases and may severely impair the health of citizens.

Taking severe haze polluted Shenyang area as research area, collecting 5-month PM 2.5

concentration monitoring data from 11 monitoring stations located in urban and suburbs of Shenyang, and utilizing powerful analysis capabilities of ArcGIS software, our research has studied the temporal and spatial variation characteristic of PM 2.5 concentration in Shenyang area by vertical and horizontal analysis on monitoring data and statistical analysis technique utilization. Combining electronic maps and meteorological data of Shenyang area, our research has analyzed the PM 2.5 concentration variation factors of Shenyang area and provided advice and decision support of great reference value for environmental protection in the region.

## 2 RESEARCH METHOD

### 2.1 Establishment of database

Located in south of the northeast region of China, Shenyang has served as the comprehensive hub connecting northeast China to regions of Yangtze River Delta, Pearl River Delta and Beijing-Tianjin-Hebei. Shenyang covered total area of more than 13,000 square kilometers with 3,495 square kilometers urban area. The urban terrain tilted from northeast to southwest and from both sides to the center, the highest elevation of the city was 65 m and the minimum was 36 m above sea level. Shenyang was densely populated by resident population of 8 million resulting in congested traffic. Within a radius of 150 km of the city, there were

seven large-scale industrial and commercial cities as steel base—Anshan, coal base—Fushun, chemical fiber—Liaoyang, coal and iron base—Benxi, petroleum production base—Panjin, coal and grain base—Tieling, and electric power base—Fuxin. The four-month heating supply period in winter, which consumed large amount of coal has intensified the degradation of air quality in Shenyang. For example, in the beginning of 2014, due to urban heat supplying, air quality degradation was intensified resulting in persistent haze weather and the highest PM 2.5 monitoring index among large-scale cities and also severely affected urban development and health and lives of citizens.

Shenyang, as one of the 113 key environmental protection cities throughout our country, adopted automatic monitoring system in municipal environment air quality monitoring. Currently, there were 11 national environment air quality automatic monitoring spot (National Monitoring Spot), namely, Ermao, Taiyuan Street, Xiaoheyan, Wenyi Road, Beiling, Artillery Academy, Zhangshi, Neusoft, Liaoning University, Hunnan II, and Huishan. These National Monitoring Spots were all certified by Ministry of Environmental Protection and their spot setting and monitoring method were in accordance with national regulations. In this research, we collected PM 2.5 concentration data released by 11 monitoring stations over 5 months from Dec. 1, 2013 to Apr. 26, 2014 on daily basis at four time points of 7:00, 12:00, 17:00, and 20:00 and tabulated the data in form of excel and then imported it into ArcGIS platform and completed the establishment of attribution database.

Establishment of figure database mainly were based on utilization of 1:5000 Shenyang electronic map of the year 2008 and completed by importing grid electronic map into ArcGIS software and then implementing hierarchical vector quantization toward ground features. In addition to 11 monitoring stations scattergram, factors that affecting PM 2.5 concentration, such as map layers of residential areas, factories and mines, vegetation were also included.

## 2.2 Research method

Thematic map is a convenient method for us to achieve various professional study findings. It would highlight one or multiple elements on the basis of normal maps. GIF thematic map function was a product of combination of two powerful functions of GIS platform, namely, charting and analytic statistics which may directly demonstrate and dig out the characteristics of elements making itself an essential tool for data analytic statistics. This paper has analyzed the PM 2.5 variation law of Shenyang city on both daily and monthly basis, pollution level of each monitoring spot, and variation law during the 5 months of each monitoring spot by establishing attributes and graphic database and charting various thematic maps, including pie chart, histogram, line chart assisted by ARCGIS10 comprehensive GIS platform developed by ERSI. The thematic maps in ArCGIS with the features of simple processing and abundant expression forms could directly present the data analytic statistics achievements.

Inverse Distance Weighting was based on the similarity of interpolation area internal sample points to estimate the cell value by calculating weighted average of adjacent area sample points, and then interpolation got a surface. As there were only 11 monitoring stations in Shenyang, in order to do continuous spatial analysis, most regions in Shenyang needed to adopt inverse distance linear interpolation method to do interpolation, PM 2.5 concentration affected weight in the interpolation spot was in inverse proportion with the distance of the monitoring station. In this paper, linear interpolation has been applied to do interpolation of PM 2.5 concentration in each region in accordance with their distance to the 11 monitoring stations, and the calculation results has been demonstrated by rendering, which provide very good guidance in analyzing the pollution situation of the whole Shenyang City.

For better analysis on the influence of temperature, humidity, wind on PM 2.5, SPSS software has been applied in correlation calculation to get relevant parameters of influence factor and PM 2.5. SPSS (Statistical Package for Social Science) is

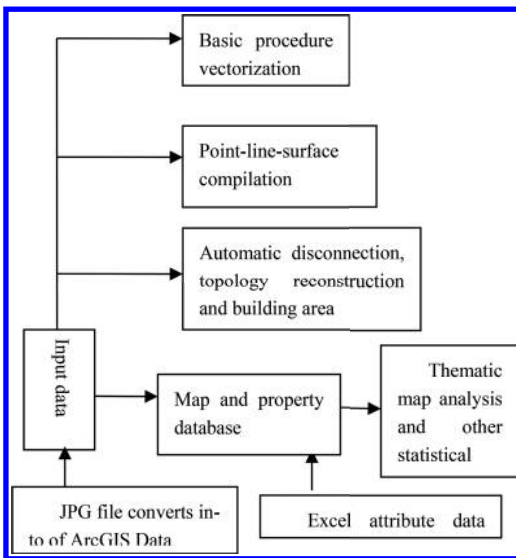


Figure 1. Database establishment procedure diagram.

one of the current popular statistical analysis software with advantages, such as simple to operate, efficient, and accurate in data correlation analysis. SPSS analyzed the closeness between PM 2.5 and factors, such as temperature variation, humidity, and nearby sewage plants, and gave out specific values. By correlation analysis, PM 2.5 pollution could be predicted and prevented to some extent.

### 3 RESULTS AND ANALYSIS

In China, PM 2.5 concentration was classified into 6 grades: excellent (0~35 ug/m<sup>3</sup>), good (35~75 ug/m<sup>3</sup>), mild pollution, (75~115 ug/m<sup>3</sup>), moderate level pollution (115~150 ug/m<sup>3</sup>), heavy pollution, and severe pollution (250~350 ug/m<sup>3</sup>). And PM 2.5 concentration in Shenyang was classified in accordance with aforementioned grades.

#### 3.1 PM 2.5 concentration variation characteristics

PM 2.5 concentration statistics were gathered 4 times during 2013.12~2014.4, 5 months in total, and got excessive rates of each monitoring station by classification (above moderate pollution level): Huishan 40.8%, Hunnan II 50%, Neusoft 52.3%, Zhangshi 56.2%, Artillery Academy 13.1%, Beiling 50%, Wenyi Road 46.9%, Xiaoheyuan 49.9%, Taiyuan Street 57.8%, and Ermao 54.8%, Liaoning University 49.2%. Thus, it can be seen that PM 2.5 in Taiyuan Street was most serious; Zhangshi was second serious; Artillery Academy was the one with lowest pollution. Besides data statistics and analysis of each monitoring station, in order to know rules of PM 2.5 concentration variation with time better, we also analyzed the daily and monthly PM 2.5 variation by gathering PM 2.5 concentration statistics of 7:00, 12:00, 17:00, and 20:00 everyday during the 5 months, and concluded PM 2.5 concentration variation with time in a day by histogram: PM 2.5 concentration kept declining during 7:00~17:00 and after 20:00, had a trend to pick up. This indicated that there was a minimum value during 17:00~20:00 and a maximum value during 20:00~7:00. Therefore, it was better for Shenyang residents to hang out or exercise in the afternoon or evening as during that time PM 2.5 concentration was low. We have formed line chart with monitoring month as independent variable, and PM 2.5 average monthly concentration of the 11 monitoring points as dependent variables, and reached a conclusion that from Dec. 2013 to Apr. 2014, PM 2.5 concentration of each monitoring point has been decreasing every month generally. Thus, it can be seen that PM 2.5 pollution was serious in winter and gradually became better with the arrival of spring.

Inverse distance weighting has been applied to get spatial distribution pattern of PM 2.5 concentration. Taking PM 2.5 concentration of each monitoring point in May as cardinality, reciprocal value of distance between each point and observation station as weight, drawing up the PM 2.5 spatial distribution map of Shenyang by interpolation, Shenyang PM 2.5 concentration distribution could be seen from the map, and PM 2.5 concentration in Zhangshi neighborhood was high and that in Artillery Academy was low.

#### 3.2 Influence factor analysis

PM 2.5 concentration was influenced by temperature and relative humidity, through SPSS software based on weather data and PM 2.5 concentration record during 5 months, we got the conclusion that relative coefficient of temperature and relative humidity to Shenyang PM 2.5 concentration was 0.18 and 0.481 respectively, and the influence of temperature on PM 2.5 concentration was much larger than the relative humidity. In a certain extent, PM 2.5 concentration was also affected by adjacent residential communities, the number and types of factory and traffic conditions, and it was greatly affected by coal-fired pollution for Shenyang residents in winter, winter was high-incidence season for haze in Shenyang.

### 4 PHOTOGRAPHS AND FIGURES

By analyzing PM 2.5 concentration data of 11 monitoring stations in Shenyang, we found that PM 2.5 concentration varied considerably among the monitoring stations, due to lots of traffic pollution and factories in urban district, PM 2.5 concentration of monitoring stations in Taiyuan Street, Beiling and Hunnan II were seriously over-standard, while Artillery Academy, located in rural area close to Arboretum and Qipan Mountain Scenic Zone, its PM 2.5 concentration seldom over-standard. From spatial perspective, PM 2.5 pollution in Tiexi, Yuhong, and Heping were most serious due to high population density, especially Tiexi, who has the largest number of population and factories and the most serious traffic jam, was the most polluted area in December and January to March during the winter heating supply period, while Dadong, Dongling, and Shenbei, who have high greening degree, low population density and scattered factories, were slightly polluted. From an overall perspective, PM 2.5 pollution in Shenyang was very serious, especially, in winter central heating period and it would become better with the arrival of spring. Peak concentration of PM 2.5 was in morning everyday, and then gradually declined,

after 20:00 started to pick up again. Therefore, it was not appropriate to do morning exercise in winter in Shenyang.

## REFERENCES

- [1] Ferhat K., Omar A., Ferruh E. Statistical characterization of atmospheric PM 10 and PM 2.5 concentrations at a non-impacted suburban site of Istanbul, Turkey [J]. 2005, 59:1183–1190.
- [2] Young-Ji Han, Tae-Sik Kim, Hekap Kim. Ionic constituents and source analysis of PM 2.5 in three Korean cities [J]. Atmospheric Environment, 2008, 42(25):4735–4746.
- [3] Querol X., Alastuey A., Ruiz C.R., et al. Speciation and origin of PM 10 and PM 2.5 in selected European cities [J]. Atmospheric Environment, 2004, 38(38): 6547–65.
- [4] Chan L.Y., Kwok W.S., Lee S.C., et al. Spatial Variation of mass concentration of roadside suspended particulate matter in metropolitan Hong Kong [J]. Atmospheric Environment, 2001, 35(18): 3167–3176.
- [5] Tang Huijun, Study on distribution regularity of the air pollution in Guangzhou City [J]. Geographical Research, 2004, 23(4):495–503.

## Studies on the thallium emission standard of industrial wastewater

Huang Yi

*College of Environmental Science and Engineering, Guangzhou University, Guangzhou, China*

Ding-gui Luo, Yong-heng Chen & Qi-hang Wu

*College of Environmental Science and Engineering, Guangzhou University, Guangzhou, China*

*Guangdong Provincial Key Laboratory of Radionuclides Pollution Control and Resources, Guangzhou, China*

*Key Laboratory for Water Quality Security and Protection in Pearl River Delta, Ministry of Education, Guangdong Province, China*

**ABSTRACT:** The main basis for thallium emission standard of industrial wastewater includes factory production technology, wastewater treatment technology, and the characteristics of local water ecological environment. This article discusses the research method of industrial wastewater thallium emission standard by using the thallium wastewater treatment technology and the local ecological environment characteristics. As for thallium wastewater treatment technology, the most practical processing method is precipitation, while biological method is the most prospect method. The local water ecological environment characteristics mainly include the present situation of the water ecological environment, water quality management, the law of water quality change and other aspects. According to the characteristics, ecological environment present situation survey should include the dry season, normal season and wet season. Hydrological survey should focus on the changes in hydrology, sediment, and river channel; Water quality survey focus on conventional, characteristics and the bottom sediment parameters; The objective of water quality management, executes the local “Surface Water Environmental Function Zoning”. As the water environmental health concept study becomes more perfect, the water environment functional zoning will develop to the water ecological environment functional zoning. WASP7 is chosen as the model to study the water quality change laws and the parameter of the model can be confirmed by theoretical method, empirical method, experimental method, and model correction method.

**Keywords:** thallium; emission standard; river basin

### 1 INTRODUCTION

Thallium is a typical toxic element which has lasting harm. Related studies have shown that thallium toxicity for mammals is higher than other heavy metals, much higher for plants. Thallium is a typically rare scattered elements in the earth's crust, coming to the environment with the exploitation of mineral resources. Because of the highly disperse in ore deposit and difficulty in industrial recycling, thallium pollution problem was overlooked all the time before. Along with the rapid population growth, the rapid development of economy and science technology, exploitation of resources is at an unprecedented scale and intensity which makes thallium pollution problem gradually revealed. Thallium contained in sulfide mine water can be dozens of times or even hundreds of times higher than the environmental background value and when it is serious, it can be tens of thousands of times. The thallium contained in tailings of Kellogg' Pb-Zn-Cu-Ag mine

fields which mixed with surface water has a high content up to 110 µg/L; Two rivers near nonferrous metal mineralization zone in New Brunswick contains thallium up to 80 µg/L. In Yunnan province, South China As-Tl Mine contains thallium from 2.91 to 13.0 µg/L in ore pit water. Beijiang river in Guangdong Province has been polluted in 2005, the thallium in Beijiang river is hundreds of times higher than the background value and the pollution accident in 2010, the wastewater from Shaoguan Smelter contains thallium as high as 600 ~ 700 µg/L, thousands of times higher than environmental background. These events also lead downstream to stopping supply water for several days.

The harm of the thallium in water caused the attention of USEPA. It has formulated 0.002 mg/L is the safety valve of thallium in the drinking water in 1993, the long term secure value is 0.0005 mg/L. This standard is more strict than many other harmful element, such as the 0.05 mg/L of As, 0.005 mg/L of Cd and 0.05 mg/L of Pb. Russia has a more

strict safety standards at present, thallium in drinking water must contained less than 0.0001 mg/L. China has begun to focus on thallium toxic materials and the ministry of construction has set up the standard of thallium in urban supply water in 2006, it is 0.0001 mg/L. Hunan Province has published “The Emission Standard Of Thallium In Industrial Wastewater Of Hunan Province”(DB43968-2014) on November 27, 2014 and implemented on January 1, 2015. The standard set 0.005 mg/L as the limit value of thallium emission. However, the study of thallium emission standards is still very weak.

Drinking water sources protection is the most important in the national water environment protection policy. So the establish of river basin’ thallium emission standard and regulate of the factory emission is no time to delay.

According to the basis for emission standard, thallium in wastewater emission standards is related to the factory production technology, wastewater treatment technology and local water environment features. The advanced nature of industrial process is closely related to the characteristics of different businesses. The following study is mainly from thallium wastewater treatment technology and the local ecological environment features to confirm the determination of thallium in wastewater emission standard.

## 2 RESEARCH OF THALLIUM REMOVAL METHOD IN WASTEWATER

At present, thallium pollution control technology mainly include adsorption, ion exchange, membrane separation, chemical precipitation, carrier activated absorption method, biological or composites adsorption method, etc. These methods are shown in Table 1.

According to the Table 1, adsorption and ion exchange methods have a particularly high removal rate, but they cost high; Membrane separation process also has a very high removal rate, but the membranes need to update every few years; Biological or composites adsorption method has a great prospect, but it still needs more tests; Precipitation is low cost and widely used at present, but the removal rate is low, but through the optimization this method also has great prospect.

## 3 ECOLOGICAL ENVIRONMENT CHARACTERISTICS OF LOCAL WATER

Local water ecological environment characteristics mainly include the present situation of the ecological water environment, water quality management and the law of water quality change and other aspects. These aspects are important basis to determine the wastewater emission standard.

### 3.1 Present situation survey of ecological environment

Reference to the “Technical Guidelines For Environment Impact Appraisal—Surface Water Environment”, present situation survey of ecological environment mainly includes hydrology survey and water quality survey. We choose Beijiang in Guangdong Province as an example to decide which parameters should include during the survey.

#### 1. Hydrology survey

The hydrological character of Beijiang river is: an even distribution of rainfall in a year and great seasonal changes in water level, sediment concentration. Sediment transport mainly concentrated in April to August, these five months accounted 84 percent of sediment transport in a year.

Table 1. The main removal method of thallium and its effect analysis.

Current method	Material	Removal rate	Advantages and disadvantages
Adsorption	Activated alumina	Set pH to 4.5, removal rate nearly 100%	High removal rate but the cost is high
	Activated carbon	Removal rate is 96%–99%	High removal rate but high cost
Ion exchange	NaCl solutions	Effluent water quality of Tl <sup>+</sup> is less than 2 μg/L	Less selective of thallium
Membrane separation	Membrane	High effluent water quality	High effluent water quality but high cost
Precipitation	Offscum of pyrite contains Fe <sup>3+</sup> and Mn <sup>2+</sup>	Removal rate is between 69% to 81%,	Medium removal rate but cost free
Biological material	Sawdust	Removal rate is 98%	Fast and low cost
	Nut shell	Removal rate is 96.5%	Low cost
	Tea waste slag	Removal rate is 98.4%	

According to the characteristics of the Beiji-jiang river' hydrology has a great seasonal change, hydrological survey of Beiji-jiang river mainly include: the divide of wet season, normal season, dry season, the change of riverbed shape: the situation of river bend, cross section (flood plain changes, etc.), vertical section (slope), roughness; The change of watercourse' hydrological features: water level, water depth, the river width, flow, velocity, sediment concentration, sediment transport, and water level—flow relations, water—sediment relations.

2. Water quality survey: According to Beiji-jiang river' hydrology features, features of pollution sources (Fankou lead-zinc Mine, Shaoguan Smelter and Dabosan Mine, etc.) all belong to the non-ferrous metal smelting. The water quality survey of Beiji-jiang river mainly include: General parameters: pH, temperature, suspended solids, dissolved oxygen, potassium permanganate index and BOD5, five days kjeldahl nitrogen or non-ionic ammonia, sulfide, fluoride, petroleum, phenol, cyanide, arsenic, mercury, hexavalent chromium, phosphorus, etc.; Characteristic parameters: thallium, copper, zinc, lead, cadmium, etc.; Bottom sediments (including aquatic organisms) parameters: the amount and type of planktonic animals and plants, algae, benthic invertebrates, the consist of aquatic community structure. Bottom materials are accumulative particular pollutants which related to the water quality of drainage. The survey period includes dry, normal, wet seasons. In addition, the water quality of the pollution sources and the particular pollutants should added to the survey.

### 3.2 The object of water quality management—water environment functional zoning

According to the local “Surface Water Environmental Function Zoning”, we can determine the position of the pollution sources. As the water environmental health concept study becomes more

perfect, the water environment functional zoning will develop to the water ecological environment functional zoning.

### 3.3 Research of the law of thallium—water quality

Using the law of water quality change (always express by a mathematical model) is an important method to determine the emission standard, based on the present situation of water quality, water quality management, reflex the water quality of the emission sources by using a model.

1. The choice of model  
Water quality model using mathematical language to describe the mutual transformation relationships, the law of pollutants change in water environment and the influencing factors. At present, the river water quality simulation has two ways, one is to develop a specific water model for a specific river; the other way is use a water quality models which have successfully used before. Among them, the second way is the most commonly used. The water quality simulation models which have successfully used before are: WASP7, MIKE21, CE-QUAL-W2, SMS-SED2D, SMS-RMA4, HEC-RAS, HEC-HMS, QUAL2E, QUAL2K, etc. Table 2 lists the contrast of several main models.

According to Table 2: WASP7 is the most suitable water quality model in type, dimension and computing speed compared to other models. So WASP7 is chosen to be the water quality simulation model.

2. Model parameters and its determination method

WASP7 water quality model parameters include hydrodynamic and water quality (describe pollutant migration). Among them, the hydrodynamic parameters include: the convection velocity and diffusion coefficient in lengthways, crosswise and vertical; roughness coefficient and

Table 2. Contrast of several models.

Model	Dimension	Parameters	Calculation method	Calculation results
WASP7	3	DO, germ, Eutrophication, ss, toxic materials	Difference method	Low accuracy but fast
MIKE21	2	Flow, water level and velocity	Difference method	Low accuracy but fast
SMS-RMA4	2	Diffusion coefficient of pollutants	Finite element method	High accuracy but slow
QUAL2E	1	BOD, DO, T, NH3-N and others	Finite element method	High accuracy but slow
HEC-RAS	1	Flow, water level and velocity	Difference method	High accuracy but slow

hydraulics factors of flow, velocity and water depth. Water quality parameters include: coefficient of heavy metals adsorbed and desorbed by sediments, Coefficient of sediment release, coefficient of absorption and release by aquatic organisms. The parameters of the model can be confirmed by theoretical method, empirical method, experimental method and model correction method.

#### 4 CONCLUSION

Thallium is a typical toxic element which has lasting harm, but the study of thallium emission standards is still very weak. Thallium has severely the rivers in the recent years. So the establish of thallium emission standard is no time to delay.

Thallium in wastewater emission standards is related to the factory production technology, wastewater treatment technology, and local water environment features. This paper mainly discusses from the latter two features to confirm the determination of thallium in wastewater emission standard.

Thallium pollution control technology mainly includes adsorption, ion exchange, membrane separation, chemical precipitation, biological adsorption method. The most practical processing method is precipitation, while biological adsorption method is the most prospect method.

Local water ecological environment characteristics mainly include the present situation of the ecological water environment, water quality management, and the law of water quality change and other aspects. We choose Beijiang in Guangdong Province as an example to decide what parameters should be included during the survey. According to Beijiang river hydrology has a great seasonal change, hydrological survey of Beijiang river include wet season, normal season, and dry season. Hydrological survey focuses on hydrology, sediment and change of river channels; Water quality survey focus on general parameters, characteristic parameters and Bottom sediments parameters; As for the object of water quality management, executes the local "Surface Water Environmental Function Zoning", As the water environmental health concept study become more perfect, the water environment functional zoning will develop to the water ecological environment functional zoning. WASP7 is the most suitable water quality model in type, dimension and computing speed compared to other models. So WASP7 is chosen to be the water quality

simulation model. The parameters of the model can be confirmed by theoretical method, empirical method, experimental method, and model correction method.

#### ACKNOWLEDGMENTS

This work was supported by the projects of National Natural Science Foundation of China (41372248, 41301348) The Synergic innovation key projects of Bureau of Education in Guangzhou City: Drinking water sources protection and pollution control technology of Guangzhou City.

#### REFERENCES

- Chen Mei-dan, Yao Qi, et al. 2006. WASP Water Quality Model and its Advance in Research. *Water Conservancy Science and Technology and Economy* 12(7):420-426.
- Chen Yong-heng, Xie Wen-biao, 2002. Thallium Migration and Diffusion in the Ecological Environment. *Journal of Guangzhou University* 1(3):62-66.
- Eroglua H, Yapici S, Nuhoglu C, et al. An environmentally friendly process: adsorption of radionuclide Tl-201 on fibrous waste tea. *Journal of Hazardous Materials* 163(2/3):607-617.
- He Lan, Chen Wei-yu. et al. 2003. An analysis of water regime in Beijiang's lower reaches. *Journal of Foshan University* 21(2):67-69.
- Li De-xian, Gao Zhen-min, et al. 2002. Distribution of thallium in environmental media and its analytical methods. *Geological bulletin of China* 21(10):682-688.
- Lin Yan-chun, Liu Jing-yong, et al. 2009. Study on the Determination Methods of Thallium in Environmental Media. *Journal of Anhui Agri. Sci.* 37(9):4155-4157, 4174.
- Liu Jing-yong, Chang Xiang-yang. et al. 2007. Thallium Pollution and Its Countermeasures. *Soils* 39(4):528-535.
- Liu Juan, Wang Jin, et al. 2013. Removal of heavy metal in Tl-bearing wastewater by pyrite slag. *Journal of Wuhan University of Science and Technology* 36(4):295-298.
- Lu Shao-ming, Zhao Tian-tian, et al. Study on Removal of Thallium in Drinking Water. *Water Purification Technology* 27(4):25-27.
- Ma Li, Gui He-rong et al. 2011. Study on integration of 2D water quality models and review of RMA4 model. *Journal of Anhui University* 35(1):102-108.
- Qi Jian-ying, Li Xiang-ping, et al. 2008. Advance on The Method Determining Thallium in Environmental Waters. *Bulletin of Mineralogy, Petrology and Geochemistry* 27(1):81-88.
- Rivera-Utrilla J., Ferro-Garcia M. 1984. Studies on the adsorption of cesium, thallium, strontium and cobalt radionuclides on activated carbons from aqueous solutions. *Journal of Chemical Technology and Biotechnology A-Chemical Technology* 34(5):243-250.



- Saima Q.M., Najma M., Amber R.S. Sawdust A green and economical sorbent for thallium removal. *Chemical Engineering Journal* 140(1/3):235–240.
- Wan Shun-li, Ma Ming-hai, et al. 2014. Removal Technologies Of Thallium From Wastewater: A Review. *Technology of water treatment* 40(2):15–19.
- Xu Ting. 2010. Calculation Principle and Application Example of a Two-dimensional Flow Model-MIKE21 HD. *Water Conservancy Science and Technology and Economy* 16(8):867–869.
- Yang Hailin, Yang Shunsheng. 2003. The Application of the QUAL2E Model in the Steam Water Quality Simulation. *Yunnan Environmental Science* 22(6):22–25.
- Zhang L., Huang T., Liu N., et al. Sorption of thallium (III) ions from aqueous solutions using titanium dioxide nanoparticles. *Microchim Acta* 165(1/2):73–78.
- Zhong Yong. 2009. Application of Membrane Technology in Wastewater Treatment System of Shaoguan Smelting Plant. *Nonferrous Metals Engineering & Research* 30(2):13–15, 19.
- Zhou Tao-fa, Fan Yu, et al. 2005. A Review on Progresses and Problems on Environmental Geochemistry Studies of Thallium Element and the Countermeasures to Prevent and Cure the Thallium Pollution. *Geological Review* 51(3):181–188.
- Zolgharnein J., Asanjarani N., Shariatmanesh T. Removal of thallium(I) from aqueous solution using modified sugar beet pulp. *Toxicological and Environmental Chemistry* 93(2):207–214.

# Limit of abandoning wind and sunshine rate research based on wind-photovoltaic-thermal coordinated dispatch model

Ran Li, Lei Dang & Zhe Dong

Department of Electrical Engineering, North China Electric Power University, Baoding, Hebei, China

**ABSTRACT:** Along with the increase of wind and photovoltaic capacity, due to the adverse effect on peak regulation and the probabilistic fluctuation, wind and sunshine power is often abandoned in practice when considering economic or security. However, it is necessary to limit it to avert the seriously abandoning wind and sunshine phenomenon. This paper aims to analyze this problem by establishing the relationship between reliability indices and up-down spinning reserve in order to calculate up-down spinning reserve. At the same time, the start-up and down, output power dispatch model is built and solved by Evolutionary Iteration Particle Swarm Optimization (EIPSO). Meanwhile, thermal power units are start-up and down in order. Second, economic dispatch result when abandoning wind and sunshine is compared with the result when not abandoning wind and sunshine, of which the outage cost is the main change.

**Keywords:** spinning reserve; coordinated dispatch; Evolutionary Iteration Particle Swarm Optimization (EIPSO); abandon wind and sunshine

## 1 INTRODUCTION

With the increase of capacity of wind power and solar power, their anti-peak shaving and fluctuation characteristics bring more difficulty to power dispatching, like more peak-valley differential caused by anti-peak shaving of wind power and more spinning reserve by solar power fluctuation. These will change the schedule of generator's start/stop and power output, which cause more power generation cost [Yang Dongfeng et al. 2014].

Wind/Solar/Thermal power combined scheduling model described in this article need to determine the upper spinning reserve when renewable energy is connected to power grid. Reference [Yuan Bo et al. 2013] correlated the spinning reserve to load-loss forecast. Risk value and conditional risk value are used to define the upper and lower spinning reserve in reference [Zhang Guoqiang et al. 2011]. Upper and lower spinning reserve is determined by upper and lower limit of wind power forecast [Yao Yao et al. 2011]. The error of wind power and solar power forecast is not considered in above literature, so reliability index of LOLP is adopted to define the spinning reserve limit in this article.

The simplified model of selective area includes many same type of generators. To ensure the uniqueness of the start/stop process solution, the start and stop sequence of same type of generators need to be numbered. Coordinate schedule model including wind-discard ratio and solar-discard ratio will be set up by using EIPSO algorithm.

## 2 MODEL ESTABLISHED

### 2.1 Economical and safe wind curtailment and PV curtailment

Economical wind curtailment aims to give up part of wind and PV power to reduce operation costs. Some elements including economical wind curtailment, wind curtailment rate, the biggest limit constraint are added to the scheduling model, after that, the value of economical wind curtailment and PV curtailment will be calculated.

Safe wind curtailment and PV curtailment aims to give up part of beyond planning power and wind power to reduce the demand of down planning reserve when the thermal power is short of cut capacity.

### 2.2 The relationship between up and down planning reserve and reliability index

The forecasting error probability distributions of wind and PV power and load are supposed to be based on normal distribution. And the prediction error percentages are  $\sigma_w$ ,  $\sigma_s$ ,  $\sigma_l$  respectively. The outputs at the moment  $h$  are  $P_{w,h}$ ,  $P_{s,h}$ ,  $P_{l,h}$ , so the total prediction error at the moment  $h$  is  $\sigma_{total,h}$ , and it can be showed as (1).

$$\sigma_{total,h} = \sqrt{(\sigma_w \times P_{w,h})^2 + (\sigma_s \times P_{s,h})^2 + (\sigma_l \times P_{l,h})^2} \quad (1)$$

Up and down planning reserve can be determined according to two parts. One is reserve demand considering prediction error when all units operate normally; the second is same to former but the units are out of service. This paper use LOLP and EENS to determine the value of up and down planning reserve. And the probability of unbalanced power caused by the lack of down planning reserve can be set no more than  $\alpha$ . So, using LOLP, EENS and  $\alpha$ , the value of up and down planning reserve in the model can be calculated [Ronan Doherty et al. 2005].

$$LOLP = \left( 1 - \Phi \left( \frac{P_{L,up,h}}{\sigma_{total,h}} \right) \right) \times \prod_{i=1}^{W,S,T} (1 - FOP_i) + \sum_{j=1}^{W,S,T} FOP_j \times \left( 1 - \Phi \left( \frac{P_{L,up,h} - P_j}{\sigma_{total,h}} \right) \right) \times \prod_{\substack{i=1 \\ i \neq j}}^{W,S,T} (1 - FOP_i) \quad (2)$$

$$EENS_{15} = \left( \int_{P_{E,up,h}}^{P_{w+s}} xP \left( \frac{x}{\sigma_{total,h}} \right) dx \times \prod_{i=1}^{W,S,T} (1 - FOP_i) + \sum_{j=1}^{W,S,T} FOP_j \times \int_{P_{E,up,h} - P_j}^{P_{w+s}} xP \left( \frac{x}{\sigma_{total,h}} \right) dx \times \prod_{\substack{i=1 \\ i \neq j}}^{W,S,T} (1 - FOP_i) \right) \times \frac{1}{4} \quad (3)$$

$$\alpha = \Phi \left( \frac{-P_{\alpha,down,h}}{\sigma_{total,h}} \right) \times \prod_{i=1}^{N_{W,S,T}} (1 - FOP_i) + \sum_{j=1}^{W,S,T} FOP_j \left( \Phi \left( \frac{-P_{\alpha,down,h} - P_j}{\sigma_{total,h}} \right) \times \prod_{\substack{i=1 \\ i \neq j}}^{W,S,T} (1 - FOP_i) \right) \quad (4)$$

where:  $N_{W,S,T}$  is the total number of units according to the rank of wind, PV and fire;  $FOP_i$  is the forced outage rate of the unit  $i$ ;  $P_j$  is the maximum power output of the unit  $j$ ;  $\Phi(x)$  is standard normal distribution function;  $P(x)$  is the probability density function of standard normal distribution.

This area can receive part of power through tie line from other area. So it can be thought that this area just need  $w(w < 1)$  times of up and down planning reserve. And the up and down planning reserve can be defined as following:

$$P_{up,h} = \max(\max(\omega \times (P_{L,up,h}, P_{E,up,h}), P_{maxG})) \quad (5)$$

$$P_{down,h} = \omega \times P_{\alpha,down,h} \quad (6)$$

where:  $P_{maxG}$  is minimum constraint value of up planning reserve in this isolated area, and its value can be set as the maximum output power of the biggest unit.

### 2.3 The determination of the objective function and constraint conditions

Objective function can be set as total generation cost, including unit start-up cost and the cost of fuel. Owing to serious environmental problem, the generation cost of wind and PV is nearing zero. Therefore, in the objective function formula (7),  $SU_{n,d} + SD_{n,d} + F(P_{n,d})$  are starting cost, cost of downtime and generating cost, respectively.

$$C_1 = \sum_{n=1}^{n_r} \sum_{h=1}^{24} (SU_{n,d} + SD_{n,d} + F(P_{n,d})) \quad (7)$$

$$SU_{n,d} = \begin{cases} 0 & U_n^d (1 - U_n^{d-1}) \leq 0 \\ d0_n (1 - e^{-T_{n,d}^{off}/d1_n}) + d2_n & U_n^d (1 - U_n^{d-1}) > 0 \end{cases} \quad (8)$$

$$SD_{n,d} = \begin{cases} 0 & U_n^{d-1} (1 - U_n^d) \leq 0 \\ d3_n & U_n^{d-1} (1 - U_n^d) > 0 \end{cases} \quad (9)$$

$$F(P_{n,d}) = A_n + B_n \times P_{n,d} + C_n \times P_{n,d}^2 \quad (10)$$

where:  $n_r$  is the total number of units;  $d0_n, d1_n, d2_n$  are the parameters of unit start-up cost;  $A_n, B_n, C_n$  are the parameters of fuel;  $U_n^d$  is the unit's state at the moment  $d$ , and 0 stands for closing, 1 stands for starting;  $P_{n,d}$  is the power in practice of unit  $n$  at the moment  $d$ .

Constraint conditions include unit start-up, unit's power, abandon the wind in economy, discard rate limit, climbing constraints power balance constraints and up-down planning reserve constraints.

#### 1. Unit start-up constraints

$$\sum_{s=h}^{h+T_{n,on}-1} U_n^s \geq T_{n,on} (U_n^h - U_n^{h-1}) \quad (11)$$

$$\sum_{s=h}^{h+T_{n,off}-1} (1 - U_n^s) \geq T_{n,off} (U_n^{h-1} - U_n^h) \quad (12)$$

where:  $T_{n,on}, T_{n,off}$  is the minimum time of start-up of unit  $n$ .

#### 2. Constraints of unit's power, efficiency to abandon the wind and discarding rate limit

$$P_n^{\min} \leq P_{n,d} \leq P_n^{\max} \quad (13)$$

$$\begin{aligned} 0 &\leq \omega_{w,d}\% \leq \omega_{eco,w}\% \\ 0 &\leq \omega_{s,d}\% \leq \omega_{eco,s}\% \end{aligned} \quad (14)$$

where:  $P_n^{\min}$ ,  $P_n^{\max}$  are the maximum and minimum power of unit  $n$ ;  $\omega_{w,d}\%$ ,  $\omega_{s,d}\%$  are the rates of abandoning wind and light in practice at the moment  $d$ , respectively.  $\omega_{eco,w}\%$ ,  $\omega_{eco,s}\%$  are the value of abandoning the wind and light in economic, respectively.

### 3. Climbing constraints

$$P_{n,d-1} - 15 \times P_{n,GD} \leq P_{n,d} \leq P_{n,d-1} + 15 \times P_{n,GU} \quad (15)$$

where:  $P_{n,GD}$ ,  $P_{n,GU}$  are the up and down climbing speed respectively.

### 4. Constraints of power balance

$$\begin{aligned} \sum_{n=1}^{n_r} P_{n,d} + (1 - \omega_{w,d}\%)W_{w,d} \\ + (1 - \omega_{s,d}\%)W_{s,d} - P_{lost,d} = L_d \end{aligned} \quad (16)$$

where:  $W_{w,d}$ ,  $W_{s,d}$  are the power of wind and PV at the moment  $d$  respectively;  $L_d$ ,  $P_{lost,d}$  are the load powers and power loss at the moment  $d$ , respectively.

### 5. Constraints of up and down planning reserve

$$\sum_{n=1}^{n_r} \min(P_n^{\max} - P_{n,d}, 15 \times P_{n,GU}) \geq P_{up,h} \quad (17)$$

$$\begin{aligned} \sum_{n=1}^{n_r} \min(P_{n,d} - P_n^{\min}, 15 \times P_{n,GD}) + W_{w,d} \\ \times \omega_{safe,w}\% + W_{s,d} \times \omega_{safe,s}\% \geq P_{down,h} \end{aligned} \quad (18)$$

where:  $\omega_{safe,w}\%$ ,  $\omega_{safe,s}\%$  are the values of safely abandoning wind and light at the moment  $d$ , respectively.

## 3 THE SOLVING PROCESS OF THE MODEL

In order to avoid dimension disaster, model solving process can be divided into two steps. The first step of the outer loop schedules for unit start-up, and the second step of the inner loop schedules for power. The time interval is 1h, and the EIPSO algorithm is used to solve this model. The model solve process is as follows:

1. The first step is to initialize the start up and down sequence of unit particles whose dimension is  $N \times D$ .  $N$  that represents the total units, and  $D$  represents the number of times. Then calculate the start and stop costs according to the formula (6)~(7), and verify the unit particles to meet the constraints of (9)~(10);

2. The second step is to initialize the output power for each unit particles whose dimension is  $N_{up,d} \times D$ .  $N_{up,d}$  and represents the total units for the moment  $d$ , and  $D$  represents the number of times. Then calculate the economic costs according to the formula (5), and verify the unit particles to meet the constraints of (11)~(14);
3. The third step is to add constraints as the form of penalty function to fitness value, and use EIPSO algorithm to solve the inner loop. This step is used to get optimal power corresponding to the start up and down sequence of unit particles;
4. The fourth step uses the EIPSO algorithm to solve the outer loop to obtain the optimal start-up and down sequence of particles;
5. The fifth step use the optimal start up and down sequence of unit particles and optimal output to calculate the thermal output, wind and PV abandon rate scheduling. The method is same as the second step.

## 4 EXAMPLES

This paper establish a mixed integer nonlinear programming model to solve a day-ahead generation scheduling problem and the data of the model selected from some wind-photovoltaic-thermal coordinated area. We assume that there are 10 units whose capacity is 300MW and the capacity of other 10 units 350MW. In addition, the total power of 20 wind farms is 2000MW, the power generated by photovoltaic power generation is 200MW. Characteristics of the units refer IEEE-RTS system and the research. Assuming that the line loss is 5%, the forced outage rate of 300MW, 350MW, wind turbines and photovoltaic panel is separately 7%, 8%, 4% and 4%, Take 2.18%, 9.32% and 19.57% as load, wind power and photovoltaic power's prediction error respectively. Select the data of wind power, photovoltaic power of which anti peak shaving and adulatory property is the most obvious as the research object from scheduling data. The initial state of thermal power units is assumed as unit 9 and 10 in 300MW, unit 5~10 in 350MW are open. Because unit can shut-down quickly,  $T_{on}$  and  $T_{off}$  separately take 1h and 6h.

Shown as Figure 1(a), in 300MW units, unit 3, 4, 7 open and close repeatedly as result of the short of capacity, and 9, 10 unit is always being open. While in 350MW units, unit 9 and 10 is always being open, and unit 5 opens and closes repeatedly because of the short of capacity. Figure 1(b) shows that the output of 350MW units are more than 300MW units, especially 350MW units provide mainly at load peak, that's because the costs of each MW fuel of 350MW unit is less than 300MW units.

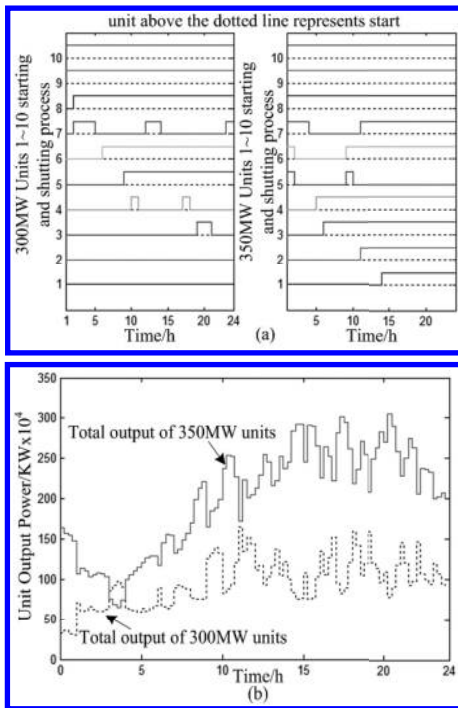


Figure 1. Units dispatch without abandoning wind and photovoltaic ((a) start-up and down, (b) output).

As shown in Figure 2(a), spinning reserve shortage occurred under the cause of the unit start-stop occurred in 1 ~ 10 times, and 18 ~ 21 times, 1 ~ 10 times lead to 7 unit of 300 MW and 350 MW unit 5 to unnecessary start-stop, 18 ~ 21 times the cause of 300 MW generating unit 3, 4 unnecessary start-stop. It's shown in Figure 2(b), the reserve capacity requirements calculated from traditional method are close to the reserve capacity requirements calculated from (1)-(4), when wind power and PV are not considered, therefore the rationality of the alternate calculation method was verified. When wind power and PV are included at the same time, the reason that the limit of spinning reserve rise at time 0~5 times is because wind power is more than PV, in order to prevent the power supply shortage caused by wind power less than its plan, it's necessary to increase the limit of spinning reserve. While, the increase of spinning reserve in 0~5 times is because of the high output of wind power, given the real output may be more than plan output, thermal power should rise the ability of cut to ensure security constraints.

Comparing Figure 1(a) and Figure 3(a), we can find that in Figure 1(a) the units on 300 MW start 9 times and the units on 350 MW start 7 times, and in Figure 3(a) the units on 300 MW start 7 times

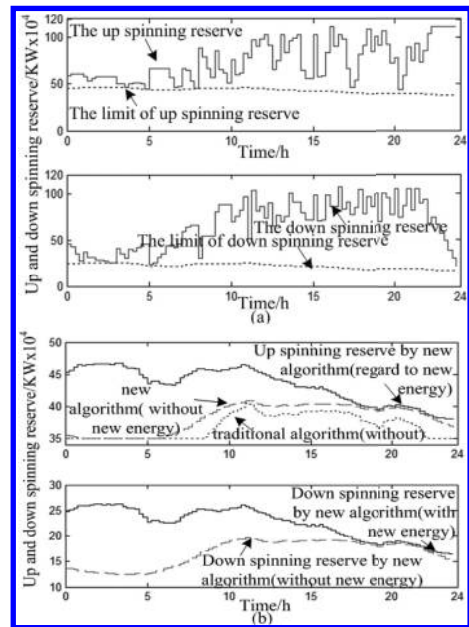


Figure 2. Values of up and down spinning reserve without abandoning wind and photovoltaic.

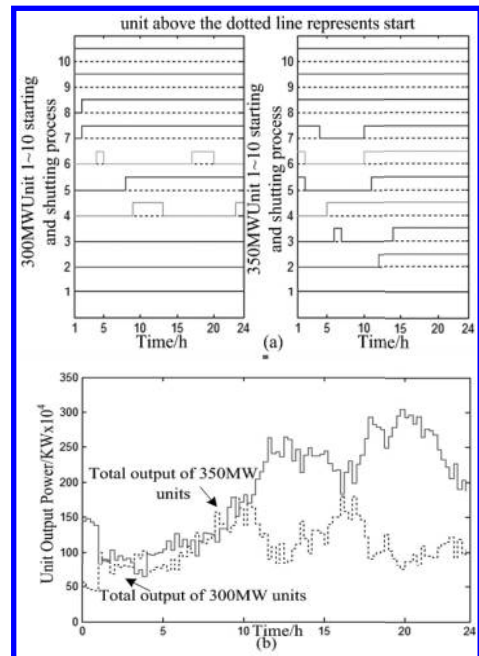


Figure 3. Units dispatch under the limit of abandoning wind and photovoltaic rate is 5% ((a) start-up and down, (b) output).

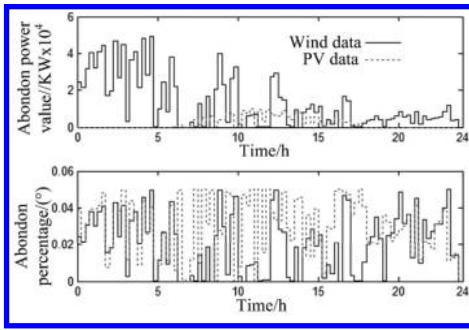


Figure 4. Power and percentage of abandoning wind and photovoltaic rate which is limited within 5%.

and the units on 350 MW start 7 times, that will reduce the start-up costs of two 300MW units. Besides, Figure 3(b) shows that 300 MW units output increase during to the process of an 300 MW unit off and on in the time of 16 to 18.

It's shown in Figure 4, the given-up wind power in used to decrease the influence on economy by the anti-peak shaving of wind power.

## 5 CONCLUSIONS

Comparing the schedule result at economy and safety wind/solar discard ratio, two types of wind/

solar discard ratios can be figured out to reduce the start/stop cost and thermal generation power cost. The limit will be taken into the daily-before schedule to ensure higher economy and restrict the quantity of wind/solar discard. Meanwhile, the calculation effort will be reduced because of setting of lower power of wind/solar power regulation compared with no lower power model.

## REFERENCES

- Ronan Doherty, Mark O'Malley 2005. A New Approach to Quantify Reserve Demand in Systems With Significant Installed Wind Capacity. *IEEE Transactions on Power Systems*, 20:587–595.
- Yang. Dongfeng, Zhou. Suquan, & Bao Feng 2014. Analysis on Peak Load Regulation Capability of Power Grid Integrated With Wind Farms in Valley Load Period. *Power System Technology*, 38:1446–1451.
- Yao Yao, Yu, Jilai 2011. Multi-objective Hybrid Optimal Dispatch of Power Systems Considering Reserve Risk Due to Wind Power. *Automation of Electric Power Systems*, 35:p.118–124.
- Yuan. Bo, Zhou. Ming, Li Gengyin, & Zong Jin 2013. A Coordinated Dispatching Model Considering Generation and Operating Reserve for Wind Power Integrated Power System Based on ELNSR. *Power System Technology*, 37:p.800–807.
- Zhang. Guoqiang, Wu. Wenchuan, Zhang. Boming 2011. Optimization of Operation Reserve Coordination Considering Wind Power Integration. *Automation of Electric Power Systems*, 35:15–19+46.

# A research on intelligent management strategies for municipal solid waste disposal in Wuhan, China

Weiyi Liu

*College of Urban Construction, Wuhan University of Science and Technology, China*

Juan Yang

*Hubei Urban Construction Vocational and Technology College, China*

Wei Hu

*College of Computer Science and Technology, Wuhan University of Science and Technology, China*

**ABSTRACT:** Contradiction between rapid development of economy and technology in deteriorating ecological environment is one of the important challenges in urbanization of China. By learning from foreign experience, this paper aims at the typical problems of the municipal solid waste management, and takes one of China's largest cities Wuhan for example. Using computer data processing technology, this paper explores how to realize intelligent control of the whole process of municipal solid waste, and to promote the sustainable development of urban human settlement environment. This whole process of municipal solid waste management strategies can provide useful references and inspiration for cities in China as well as other developing countries.

**Keywords:** municipal solid waste; intelligent control; management strategies; Wuhan

## 1 INTRODUCTION

With the acceleration of urbanization and the rapid development of economy, municipal solid waste management problems are getting more and more serious. Nowadays, China's strategy for municipal solid waste management and treatment focuses at the end. There are three main ways: composting, landfill, and incineration. However, composting technology can only operate well under microbial environment, and the processing period is too long; Fill method has the advantage of dealing with large capacity and high economic efficiency, but it still has a great negative impact on the groundwater environment; Incineration treatment belongs to the relatively high energy efficiency and resource utilization of the heat produced by the incineration, and occupies an area of small, but easy more pollution to the air environment. Therefore, it is easy to see that the above three ways have their advantages and disadvantages, need for municipal solid waste management problems in the process, then apply the appropriate measures.

## 2 MATERIALS AND METHODS

In this paper, we take Wuhan City, central China's largest city and a center of the city—as the object

of study. According to the statistics, 2010–2013, Wuhan municipal domestic waste output has increased significantly, from 2.2 million tons in 2010, rising to 2.6 million tons in 2013, with an average annual growth rate of 6.1% (Fig. 1). However, the city for waste treatment model and improvements haven't been made. Especially, in the old city and outside the third ring, feel free to dump garbage everywhere. In the course of delivery, garbage truck often sewage leaks, trash overflow, and so on.

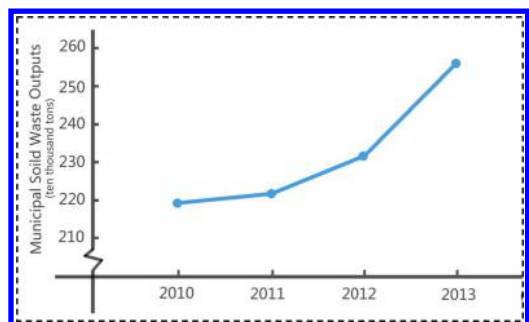


Figure 1. Wuhan municipal solid waste outputs variation in 2010–2013. (data source from Wuhan Environmental Protection Bureau).

Wuhan, have seriously affected the health of cities and also reduce people's quality of life. In this case, information intelligence of the whole process of municipal solid waste is necessary to study. The effective management and monitoring of municipal solid waste not only save existing land resources, highly coordinated transportation, but also can make rational use of existing resources. In February 2011, the city proposed "intelligent city" construction concept. On this basis, promoting urban waste intelligent control strategy can help the whole process of Wuhan municipal solid waste recycling and promoting Wuhan achieved the purpose of building a harmonious and livable city, lead the smart city concept extends to every corner of society and people's livelihood.

The research methods are:

1. Based on current domestic solid waste problems and obstacles faced by the processing system of the whole process, from municipal solid waste processing, transport and processing, and find the optimal solution.
2. Introduction of current urban development promoted by the "intelligent city" concept, using the smart technology, to trash the whole process in real time, linkage, stability, and effectiveness.
3. Waste processing operations connected with the information management system of city, urban data.
4. Use the "3R" concept of municipal solid waste treatment technology and ultimately achieve waste minimization, recycling and harmless requirements.

### 3 WUHAN MUNICIPAL SOLID WASTE MANAGEMENT SYSTEM ANALYSIS

#### 3.1 *Waste separation and recovery system is not perfect*

Because the lack of residents' awareness of environmental protection and waste separation knowledge, the serious problem of the amount of municipal solid waste and miscellaneous. Wuhan construction of waste treatment facilities is still not on the agenda, without waste sorting waste for subsequent recovery of utilization and disposal of inconvenience, not only increases the workload of the operator, and also put forward higher requirements for waste disposal equipment. Eventually, lead to garbage recycling rate is very low, the waste of resources is not reduced.

#### 3.2 *Reduce waste treatment*

Waste reduction is in the waste produced in the process, suppress or avoid the eventual incineration

and land filling of waste, which is source of waste down, reduce the production of waste. As of right now, still follows the end of treatment of domestic waste treatment in Wuhan City pattern, garbage disposal problems piled up on the last incineration or landfill link. Municipal waste reduction, resource recovery, innocent sort of goals also requires long-term efforts to achieve.

#### 3.3 *Inadequate waste collection and transportation system*

Municipal domestic waste collection and transportation work is characterized by traffic, transport level involves more. However, transport of municipal solid waste, and no systematic layout of Wuhan, resulting in waste transportation energy consumption and low efficiency. In addition, part of junk jobs drivers of vehicles not required to route jobs, often reselling halfway through "wild waste" on urban health and environment hazards.

## 4 INTELLIGENT MANAGEMENT STRATEGIES FOR MUNICIPAL SOLID WASTE DISPOSAL

In order to solve the problems above, this paper argues that if municipal solid waste management system wants to achieve the most efficient and optimum condition, there must be a systematical innovation through the whole process of municipal solid waste disposal. Therefore, the municipal solid waste management will be divided into three stages: collection, delivery, and disposal. By combining the intelligent equipment and management system, our paper presents the following optimal solutions.

#### 4.1 *Real-name trash bags*

1. Because that residents' waste classification awareness is not so strong, and current situation of sanitation supervision is inadequate we will trash bags for the new design under the premise of vigorously promoting and popularizing knowledge of waste. The recorded information of urban residents of two-dimensional code combined with the garbage bag, forming a real-name system for garbage bags.
2. Real-name trash bags will be divided into four colors, each color corresponding to a kind of waste categories. It is mainly based on the traditional garbage bag attach the recorded holder of personal information and litter species information the QR code. By scanning the QR code, one of the trash doors can be opened. In addition, when random rubbish is found in garbage



bags, sanitation Inspector can quickly trace spam sources (Fig. 2).

#### 4.2 Solid waste intelligent storage devices

1. Intelligent storage devices for solid waste is a key equipment through the whole management process. For city waste bins sealed enough, often distributing odors and germs a lot of mosquito breeding conditions, we use QR code as rubbish bins open “key.” Once the rubbish is put in the specified bin, the door will shut. When collecting the garbage, our staffs only need to put their own QR code on scanned area, and the door can be opened.
2. To ensure the waste be divided at source, our intelligent waste storage device can be divided into four closed containers according to waste classification category, namely, recycling waste (green), and general waste (yellow), food waste (orange), and hazardous waste (red). Garbage bags are attached to the classified information by scanning the QR code; the door corresponds to the trash will open as quickly as possible.

#### 4.3 Intelligent supervision system

1. Hand out the real-name system garbage bags by the amount and time granted. Quantitative issue with community management institutions each month QR garbage bags, people working at home must do the garbage classification. When garbage processing, such as free classified waste, will be based on the cloud computing system data that can be recorded to the holder’s credit limit cuts. Once the credit falls below a certain value, it will be required for social work. In addition, QR code information will be updated once in every month, updated the original QR codes will not be available. Monthly, the rest of garbage bags are available to users receiving point’s redemption prizes. So that the people can consciously reduce solid waste and achieve the reduction of solid waste.
2. To collect the waste on the amount. Intelligent storage devices can store waste garbage weight monitoring in real time, all data will be input to the database. Once the weight reaches a preset value, it will send hint to the garbage station, and the waste dump position, sending the



Figure 2. Waste information management with real signature.

corresponding vehicle charge. Regularly collecting garbage at this stage of the process is better, so that it can deliver savings greater consumption of energy and improve efficiency.

#### 4.4 Municipal solid waste link

1. The overall handling of hazardous waste box we use, in transport box directly into the waste inside the vehicle. Refuse in the back compartment with two hazardous waste box for the card slot can be fixed for a fixed bin.
2. Installed in the vehicle GPS (Global Positioning System), real-time control of the vehicle location information to stop halfway dump “wild waste” phenomenon. Finally, the information storage systems install in a vehicle, and send information to a Terminal, so that garbage collection agencies keep track of vehicle information.
3. The garbage station, routes will be set in advance for each recycling site, refuse collection vehicles before delivery, vehicle information, operator information, departure time has a record, as judging the rationality of the transportation process basis as well as supervision of the operator (Fig. 3).

#### 4.5 Municipal solid waste processing

When the waste is transported to the landfill successfully, it is then unloaded by unified garbage disposal personnel to deal with. Each staff member’s information will also need to undergo a rigorous monitoring so that waste treatment sessions, determined for each question appear in charge (Fig. 4).

Complement the above procedure is needed innovation and implementing the enterprise

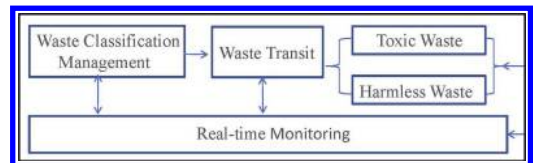


Figure 3. Waste transit information management model.

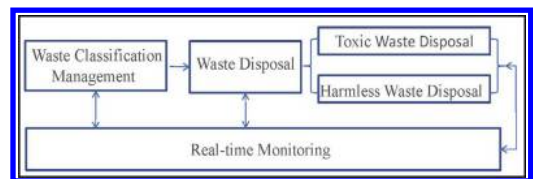


Figure 4. Waste disposal information management model.

system of waste disposal units. Process data via cloud computing meet no harm standards and then focused on the destruction, to achieve the waste harmless. In city life garbage full process management, completely using real networking technology, building dangerous waste regulatory real networking system, on life garbage in the dangerous waste of disposal process and the processing personnel, for real-time monitoring, for solid waste processing process of full of regulatory provides technology guarantees, achieved on dangerous waste from source to fill buried processing of full can tracing of monitoring, prompted solid waste management by traditional artificial management way to modern intelligent management way for change.

## 5 CONCLUSIONS

As the Development and improvement of science and technology information, municipal solid waste management brings out new opportunities and challenges. Through Global perspective on urban development, the paper studies combine the intelligent technology and waste management system, based on the consolidation of the waste management system operation. For whole city garbage disposal process running system, our paper hold wisdom city construction concept, on city life garbage management has optimized strategy: 1) through referencing both at home and abroad city garbage management experience, we proposed that garbage processing can adopt intelligent cloud computing technology. We expect the linkage is what our new management system has. 2) Starting

with whole intelligent management system equipment, we have systematic arrangements on municipal solid waste whole process. Through the garbage disposal and recycling, we expect to achieve stability of solid waste treatment and recycling. In Conclusion, smart city concept-based research on municipal solid waste management strategy is in line with the requirements of the times, The use of intelligent technologies is to address solid waste problems in contemporary cities, and to promote resource-saving and environment-friendly urban development with a positive effect.

## REFERENCES

- Ayhan Demirbas. Waste management, waste resource facilities and waste conversion processes. *Energy Conversion and Management* 2011, (52):1280–1287.
- A. Suna ERSES Yay. Application of Life Cycle Assessment (LCA) for municipal solid waste management case study of Sakarya. *Journal of Cleaner Production*, 2015(94):284–293.
- Binxian Gu. Characterization, quantification and management of household solid waste: A case study in China. *Resources Conversation & Recycling*, 2015, (98):67–75.
- Giovane Lopes Ferri. Reverse logistics network for municipal solid waste management: The inclusion of waste pickers as a Brazilian legal requirement. *Waste Management*, 2015(40):173–191.
- Guerrero L.A., Maas G., Hogland W. Solid waste management challenges forcities in developing countries. *Waste Management*, 2013(33):220–232.
- Rachael E. Marshall, Khosrow Farahbakhsh. Systems approaches to integrated solid waste management in developing countries. *Waste Management*, 2013(33) 988–1003.

# Experimental study of infiltration characteristics of outdoor particulate matter into the indoor

Zhiyong Li, Fan Zhang & Qianqian Shi

*School of Civil Engineering, North China University of Technology, Beijing, China*

**ABSTRACT:** This paper set up an experimental platform and tested the penetration rate of particles of different diameters penetrating the crack. The results show that the particle penetration rate through cracks is mainly influenced by the pressure difference between the ends of the crack and by the diameter of particles. The particle penetration rate through cracks goes bigger as the pressure gets larger, within the scope of the low penetration rate changing with pressure difference is more sensitive. Unlike pressure change, penetration rate turns smaller along with the increase of particle size.

**Keywords:** particulate matter; penetration rate; crack; haze

## 1 RAISE QUESTION

In 2014, haze phenomena occurred frequently in Beijing and other cities in China. The bad influence that haze has on people's lives cannot be sneezed at. In recent years, studies of epidemic diseases and other toxic symptoms indicate that human health is closely related to the degree of body's exposure to fine particulate matter in the air. Firstly, the fine particulate matter in the air can carry bacteria, carcinogens, and virus directly into the lungs, and lungs may get injured and infected. Secondly, outdoor fine particulate matter can carry inorganic composition and heavy metal accumulating toxins, which causes acute or chronic damage to human breathe system, immune system, and cardiovascular system. Studies show that the smaller of the particle size, the acid will be more apparent, namely the acids of PM 2.5 and PM 10 particles will significantly increase. Therefore, the air pollution caused by particulate matter has been closely connected with people's health and environmental quality. For the study of the relationship between the penetration rate and relevant variables, this paper set up an experiment device to test the characteristics of particles penetrating under different experimental conditions.

## 2 EXPERIMENT

### 2.1 *Experiment set-up*

As shown in [Figure 1](#), this experiment device mainly include: 1—entrance, 2—rectifying section, 3—first sampling segment, 4—crack structure,

5—last sampling segment. In the experiment, the air flow entered by the entrance, through the rectifying section, then flowed into the first sampling segment and is tested in it. Under the pressure difference, particulate matter in the first sampling segment flowed arriving in the last sampling segment to be tested. Finally, the air with particles would be exhausted from transition section by the fan. As shown in [Figure 1](#), 4—crack structure was made up of several vertically stacked glass (0.20 m (W) × 0.15 m (L) × 0.004 m (H)) in the test chamber. At the same time, the metal wires were clamped between the two adjacent pieces of glass to make a straight seam, which can connect the first sampling segment and the last sampling segment. This experiment designed two slits in all, as more airflow could pass under the same pressure difference, so as to strengthen the control of the fan and small pressure difference. With different diameters of the wire, the height of the straight crack will also change accordingly. This diameter of wire used in the experiment is 0.3 mm, 0.5 mm, and 1 mm. As the surface of sand paper is inlaid with sand grains uniformly, it can simulate the vast majority of roughness of construction material surface. Therefore, this experiment would use sand papers with different size of grains attaching onto the inner surface of the glass tablet to simulate different roughness of the material surface. The roughness of inner surface of glass tablet in the experiment is 0 μm, and the roughness of the sandpapers also used were 10.3 μm and 20.5 μm. YYT-2000 type micro manometer was used to measure the pressure difference between two sides of the crack structure. The difference of pressure

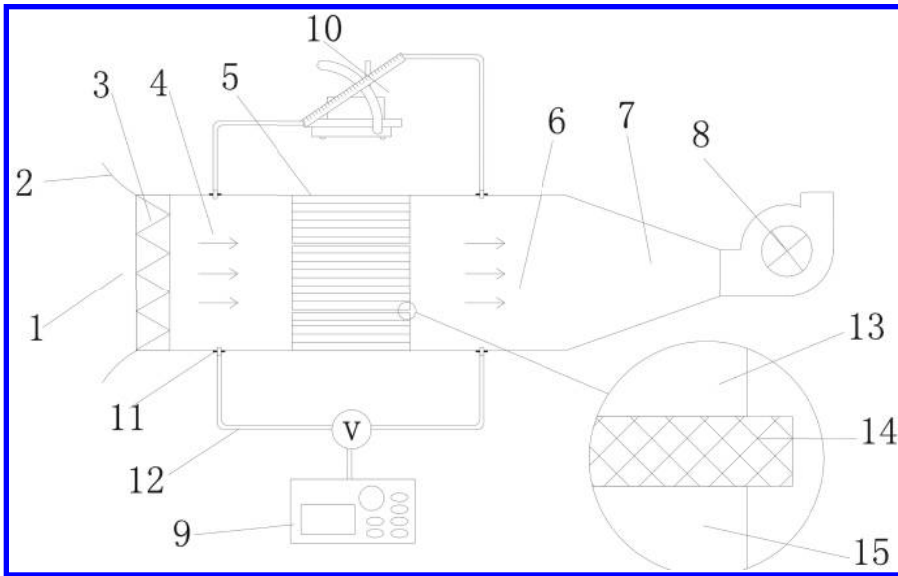


Figure 1. 1-entrance; 2-fence; 3-rectifying section; 4-first sampling segment; 5-crack structure; 6-last sampling segment; 7-transition section; 8-fan; 9-CLJ-03A type laser dust particle counter; 10-micro manometer gauge; 11-copper pipe joint; 12-hose; 13-upper tablet; 14-wire; 15-bottom tablet.

was gained by the fan exhausting the air from last sampling segment to make its pressure down. The positive side of micro manometer connected to the first sampling and negative side was connected to the last sampling segment. The micro manometer was filled with 99%-alcohol solution as the hydraulic fluid. When testing, slope  $K = 0.2$  was chosen to enhance the sensitivity, under which circumstances maximum range can reach 46 pa, and the error can be controlled to 0.5 pa. When the differential pressure changes, we can adjust the fan frequency to control the value of the pressure difference on both sides. CLJ-03A type laser dust particle counter extracts the air from the first sampling segment and the last sampling segment through a hose respectively. The particle counter could be used to measure quantity concentration of the particulate matter with different diameter.

## 2.2 Experiment procedure

Before the experiment was carried out, the glass surface should be cleaned first. The particles attached on the surface of sand papers should also be blown off. When installing crack structure, all other slits (including gaps between the glass plate and the outer wall and other contact gaps between glass tablets) would be sealed except the two cracks made by wire, to ensure that the air can only flow by the specific cracks. After the experiment device was installed, open the fan to make the actual differential pressure

between two ends of the crack is close to the experimental design value. Then open experimental apparatus and rotate the valve V to connect the first sampling segment with the particle counter.

Adjust the fan make the differential pressure between the two ends of the crack stable at the design pressure difference. Then use CLJ-03A laser dust particle counter to test quantity concentration of the particulate matter in the first sampling segment. Rotary valve V to connect the last sampling segment with the particle counter. Again, after the differential pressure between the two ends of the crack was stable, measure the quantity concentration in the last segment with the instrument. The CLJ-03A type laser dust particle counter can measure the concentration of particles in 0.3  $\mu\text{m}$ , 0.5  $\mu\text{m}$ , 1  $\mu\text{m}$ , 3  $\mu\text{m}$ , 5  $\mu\text{m}$ , and 10  $\mu\text{m}$  so on, which has 6 different sizes in all. Though other slits were soft sealed with sludge, there would be still a small amount of gas leak. This part of influence of the gas leak was treated as negligible on penetration ratio. Since the last sampling section is directly connected with the fan, the deposition rate of the particulate matter in the test chamber is negligible as well.

## 3 ANALYSIS

### 3.1 Effect by the height of the crack

As shown in Figures 2–3, the penetration rate has a relationship with the height of the gap, but

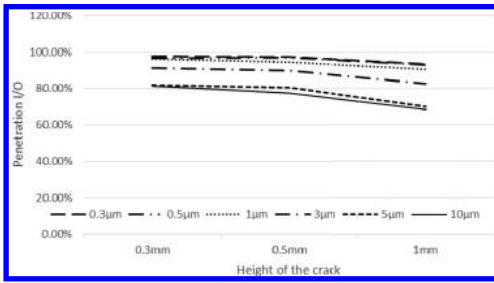


Figure 2. The curve of penetration rate with the change of the crack height; differential pressure is 2 pa and the roughness is 0  $\mu\text{m}$ .

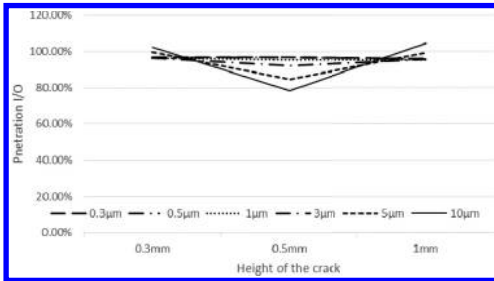


Figure 3. The curve of penetration rate with the change of the crack height; differential pressure is 4 pa and the roughness is 0  $\mu\text{m}$ .

the penetration rate will not always decrease as the height increase and sometimes become more complicated.

### 3.2 Effect by the differential pressure

As shown in Figures 4–6, the value of I/O ratio of different particles becomes increasing with the increase of the differential pressure, and decreases with the pressure difference. Compared with the high pressure difference, the penetration rate is more sensitive in the low pressure difference range, namely the penetration rate within 2–4 pa is increased quickly.

### 3.3 Effect by the diameter of particles

As shown in Figures 7–9, under the same pressure, I/O ratio of particulate matter generally increases as the particle size becomes small. Because of which characteristics the penetration rate curve became scattered as the particle size becomes large at the same differential pressure. When the surface roughness is 0  $\mu\text{m}$ , the permeability of the particles is more regular. When the roughness of the surface is not 0, the infiltration law of the particles is slightly complex.

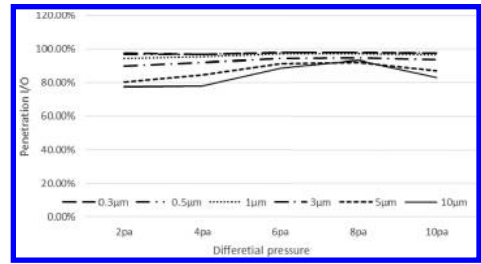


Figure 4. The curve of penetration rate with the change of the differential pressure; crack height is 0.5 mm and the roughness is 0  $\mu\text{m}$ .

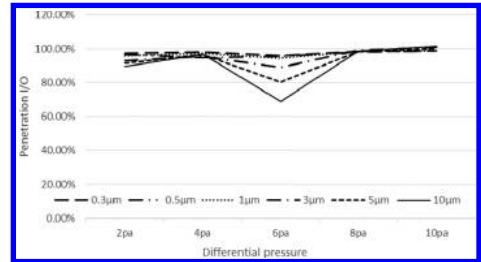


Figure 5. The curve of penetration rate with the change of the differential pressure; crack height is 0.3 mm and the roughness is 10.3  $\mu\text{m}$ .

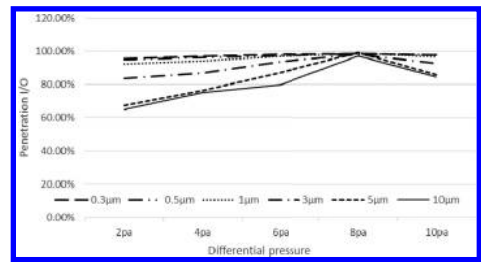


Figure 6. The curve of penetration rate with the change of the differential pressure; crack height is 0.3 mm and the roughness is 20.8  $\mu\text{m}$ .

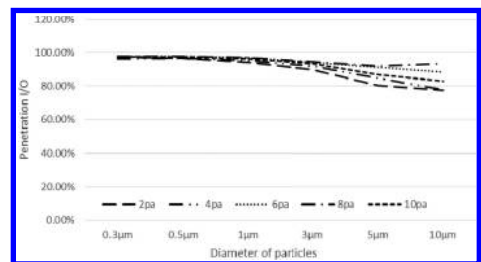


Figure 7. The curve of penetration rate with the change of the particle size; crack height is 0.5 mm and the roughness is 0  $\mu\text{m}$ .

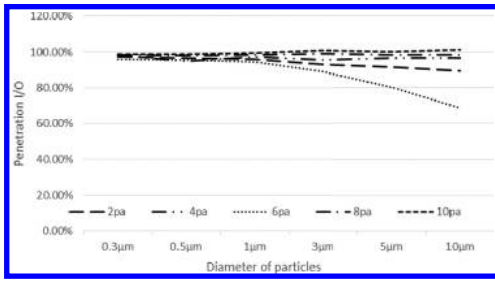


Figure 8. The curve of penetration rate with the change of the particle size; crack height is 0.3 mm and the roughness is 10.3  $\mu\text{m}$ .

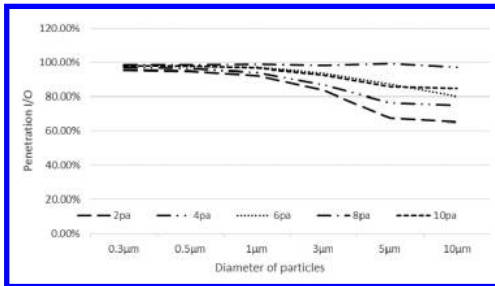


Figure 9. The curve of penetration rate with the change of the particle size; crack height is 0.3 mm and the roughness is 20.8  $\mu\text{m}$ .

#### 4 CONCLUSION

In this paper, an experimental set-up is designed, which is aimed at the main relevant conditions such as the height of the crack, the roughness of the inner surface, the pressure difference between the two ends of the crack, and the diameter of the particle. The experiment cannot fully explain the influence of the roughness and the height of the crack on the penetration rate. But the

results show that even with the minimal pressure difference (such as 2 pa), the penetration rate is also different accordingly. The penetration rate is mainly influenced by the pressure difference and the diameter of the particles. When the pressure difference gets larger, the penetration rate generally goes upward; as the pressure difference decreases, the penetration rate is generally decreased. At the same time, the penetration rate was negatively correlated with the particle size, and as the particles size decreases, the penetration rate decrease as well. In the range of low pressure difference, the permeability of the particles is important for indoor pollutant control. To study the mechanism further of the penetration of particles, we need to study the theory further and get more experimental data.

#### ACKNOWLEDGMENT

This work is supported by the Talent School Action Plan of North China University of Technology.

#### REFERENCES

Chakra, O.R.A. 2007. Genotoxicity of Organic Extracts of Urban Airborne Particulate Matter an Assessment within a Personal Exposure Study. *Chemosphere* 66: 1375–1381.

Chen, Chun et al. 2012. Methodology for Predicting Particle Penetration Factor through Cracks of Windows and Doors for Actual Engineering Application. *Building and Environment* 47: 339–348.

Englert, Norbert. 2004. Fine Particles and Human Health-A Review of Epidemiological Studies. *Toxicology Letters*: 149–235.

Kim, Ki-Hyun. 2015. A Review on the Human Health Impact of Airborne Particulate Matter. *Environment International* 74: 136–143.

Lai, Alvin. 2012. Penetration of Fine Particles through Rough Cracks. *Atmospheric Environment* 60: 436–443.

# The prediction research of underground road pollutant distribution

Zhiyong Li, Qianqian Shi & Hao Zhang

*School of Civil Engineering, North China University of Technology, Beijing, China*

Chao Chen

*School of Civil Engineering, Beijing University of Technology, Beijing, China*

**ABSTRACT:** This paper has established the one-dimensional steady-state diffusion model of underground road pollutant, and applied the finite difference method to solve the model. The source term of equation about pollutant is the measured data, which is obtained by the current national standard motor vehicle emission factor data, combined with the traffic flow, the proportion of vehicles and vehicle speed, etc. Then we verified the model according to the measured data of Shanghai Yan'an east road tunnel. These studies have shown that the established model calculated values tallies with the actual measurement, when the calculated values and measured values of CO concentration within the maximum deviation, the application of the model can realize the prediction of the underground road pollutant concentration distribution.

**Keywords:** heating, ventilation and air conditioning engineering; urban underground roads; pollutants diffusion; intensity of sources

## 1 INTRODUCTION

As the city traffic is increasing, urban underground roads have become an important means to alleviate urban plane transportation. The underground roads with a high pollutant concentration which is difficult to spread, makes the problem of air pollution within road more serious (Gao, 2013). So the analysis and prediction of underground distribution of the pollutant on the road is of great significance to solve the problem of air quality in the underground road (Deng, 2012).

This paper has established the one-dimensional steady-state diffusion model of underground road pollutant. The source term of equation about pollutant is the measured data, which is obtained by the current national standard motor bike emission factor data, combined with the traffic flow, the proportion of vehicles and vehicle speed. The CO concentration is then verified according to the measured data of Shanghai Yan'an east road tunnel. Experimental research shows that the calculation of the CO pollutants concentration field in the tunnel by using model is close to measured values. This model can provide the reference for the safety of urban underground roads ventilation system and the formulation of energy saving operation.

## 2 THE MATHEMATICAL MODEL

In urban underground road, due to the road cross-sectional area scale is far less than the road longitudinal dimension, the pollutants diffusion equation can be considered to one-dimensional processing. Select road longitudinal as the x axis, establish one dimensional convection diffusion equation of underground road pollutant. We solved the problem by applying the finite difference method. The solution ideas as follows: setting up the pollutant diffusion dynamics model, determining the boundary conditions, calculating the pollutant source term S, and finally, inputting model parameters for underground road pollutant concentration field.

### 2.1 Convection diffusion equation

Underground road pollutant diffusion dynamics equation is:

$$u \frac{\partial C_i}{\partial x} = K_x \frac{\partial^2 C_i}{\partial x^2} + S_i(x) \quad (1)$$

This equation consists of three parts, on the left side of the equation is convection item, the first item on the right side is the diffusion item, and the second is the source term. Diffusion item using

central difference scheme and convection item using the first-order difference scheme.

The difference equation of equation (1):

$$u \frac{C_i - C_{i-1}}{\Delta x} = K_x \frac{C_{i+1} - 2C_i + C_{i-1}}{\Delta x^2} + S_i(x) \quad (2)$$

The equation using the first kind of boundary condition:

$$C(x)|_{x=0} = C_1 \quad (3)$$

where

$C_i$ —the  $i$  kind of pollutants mass concentration, mg/m<sup>3</sup>;

$u$ —the piston wind velocity of underground road, m/s;

$x$ —the distance of measuring location and the entrance to the road in underground road, m;

$K$ — $i$  kind of pollutant diffusion coefficient on the  $x$  axis, m<sup>2</sup>/s;

$S_i$ — $i$  kind of pollutant source term in underground road, mg/(m<sup>3</sup>·s);

$L$ —the distance from exit to the entrance in underground road, m; and

$C_1$ —the import pollutants concentration in underground road, mg/m<sup>3</sup>.

## 2.2 The calculation of source term

The source term of equation is mainly composed of motor vehicle exhaust emission in the process of moving parts within the road and pollutants introduced by ventilation shaft. Due to environmental pollutants in the atmosphere have a low pollutant concentration than what in underground road, the pollutants introduced by the ventilation shaft have a low pollutant concentration (Deng, 2004), which can be ignored. Therefore, the source item of equation is mainly caused by motor vehicle pollutants (Han, 2011). Motor vehicle emissions intensity calculated by using line source emission model, according to the type, motor vehicle can be divided into light vehicle, midsize cars, and heavy vehicles. For different kinds of pollutants, it is calculated respectively according to the current vehicle bicycle pollutant discharge factor limit. Line source emission model of intensity of the motor vehicle exhaust pollutant is as follows:

$$S_i = \frac{1}{3600A} \sum_{j=1}^n \alpha \lambda_{ij}(v) E_{ij} A_j \quad (4)$$

where

$S_i$ — $i$  kind of pollutant emission intensity in urban underground roads, mg/(m<sup>3</sup>·s);

$\alpha$ —altitude correction coefficient;

$v$ —motor vehicle average velocity, km/h;

$\lambda_{ij}(v)$ — $j$  kind of vehicle speed correction coefficient in  $i$  kind of pollutant discharge;

$E_{ij}$ — $j$  kind of single vehicle speed emission factor in  $i$  kind of pollutant discharge, mg/(m·veh);

$A$ —underground road cross section area, m<sup>2</sup>;

$A_j$ —underground road motor vehicle traffic capacity per hour, veh/h;

$i = 1, 2, 3$ , respectively, represent the carbon monoxide (CO), hydrocarbons (HC), and nitrogen oxide (NO<sub>x</sub>)

$j = 1, 2, 3$ , respectively, represent the light vehicle, midsize cars, heavy vehicles.

The calculation formula of  $\lambda_{ij}(v)$  for CO, NO<sub>x</sub> is:

$$\lambda_{ij}(v) = a_{ij} + b_{ij}v + c_{ij}v^2 \quad (5)$$

where  $a_{ij}$ ,  $b_{ij}$ , and  $c_{ij}$  as the regression coefficient, the value refers to the following Table 1 (Deng, 2001).

In Table 1, the light vehicle velocity  $v$  (km/h),  $20 \leq v \leq 110$ , when  $110 \leq v$ , for  $v = 110$ , heavy duty vehicle velocity  $v$  (km/h),  $20 \leq v \leq 90$ , when  $90 \leq v$ , for  $v = 90$ .

Because of the enforcement of the national III and IV phase motor vehicle emission standards on July 1, 2008 and November 1, 2009 in Shanghai, the measured date is August 2013, therefore, according to the actual road driving motor vehicle models, single motor vehicle pollutant emission factor  $E_{ij}$  should be determined by the standard of light vehicle emissions limits (GB 18352.3, 2005), light

Table 1. Single vehicle speed correction coefficient in pollutant emission factor.

Pollutant	Vehicle type	a	b	c
CO	Light	3.6169	-0.07394	0.00043
	Mid, Heavy	2.1398	-0.0291	0.00012
NO <sub>x</sub>	Light	1.16875	-0.0896	0.00011
	Mid, Heavy	0.70702	-0.0024	0.000169
HC	Light	2.7392	-0.04655	0.00025
	Mid, Heavy	4.22107	-0.09182	0.00057

Table 2. Value of petrol motor vehicle single vehicle pollutant emission factor mg/(m·veh).

Stage	Vehicle type	CO	HC	NO <sub>x</sub>
III	Light	2.3	0.2	0.15
	Middle	4.17	0.25	0.18
	Heavy	5.22	0.29	0.21
IV	Light	1	0.1	0.08
	Middle	1.81	0.13	0.1
	Heavy	2.27	0.16	0.11



vehicle emissions limits and measurement methods of single motor vehicle pollutant emission factor  $E_{ij}$  values shown in Table 2. Table 2 indicates, the quality of light as a benchmark RM (kg) RM  $\leq 1305$ , mid-size  $1305 \leq RM \leq 1760$ , or less heavy car  $1760 \leq RM$ .

### 3 EXPERIMENTAL VERIFICATION

Measured by Shanghai Yan'an east road tunnel, first, get the distribution data of pollutants along the access road, then validate the one-dimensional pollutants convection diffusion equation established before.

#### 3.1 The experiment method

##### 3.1.1 The underground road case

Yan'an East Road tunnel is at the center area of Shanghai, which is an important hub for east-west trunk road connecting downtown Yan'an Road and Pudong Avenue. This tunnel is a cross-river tunnel established to alleviate traffic problems in the Pudong Lu Jiazui financial district and the city center, which is the second cross-river tunnel in Shanghai. The tunnel start from Fujian Yan'an Road intersection, crossing the Huangpu River to the east to reach Lu Jiazui Road Yang Jiazhai intersection, its municipal environment is relatively complex. The water and land transportation are more complex of Yan'an East Road area, including crowded people, heavy traffic, and the dense buildings. The tunnel parameters are in Table 3.

##### 3.1.2 The experiment data acquisition

On August 21 to August 27, 2013, the project team measured tunnel traffic, CO concentration, the temperature in tunnel, and the piston wind speed of Shanghai Yan'an east road, without mechanical ventilation during measuring. The data acquisition test time is on August 21 to August 27, in morning

Table 3. Yan'an east road tunnel parameters.

Name of parameter	Unit	Parameter values	Remark
Tunnel length	m	2193	
Road	Each	2	Single tunnel
Cross-sectional area of the tunnel	m <sup>2</sup>	40.05	Single tunnel
Tunnel road grade	%	Two-way grade 3.0%	Maximum grade
Number of shaft	Hole	3	
Design of the driving speed	km/h	40–50	
The design flow	veh/h	2400	

and evening peak (early 7:00–9:00, late 17:30 pm—at 19:00) time. The air temperature measuring by using air quality tester in measurement instruments, precision of  $\pm 0.1^\circ\text{C}$ . The tunnel piston wind speed is measured by using hot wire anemometer at the entrance of tunnel, with an accuracy of  $\pm 0.01$  m/s. The CO concentration is measured by using infrared analyzer in each measurement point along the way, the accuracy of  $\pm 0.1$  ppm. Experimental instrument platform probe position is located in the middle bus lateral (leaned out the window of 1 m, 2 m high from ground, away from the tunnel on the right side wall 2 m), inside the bus along the road to road traffic, using radar to measure the average speed. Traffic count calculated by artificial method in the underground road entrance. According to the test data of the underground road motor vehicle model types and conditions, the surveyor could analyze the pollutant emission characteristics of road motor vehicle and selection main CO, NO<sub>x</sub> pollutants to measure distribution of the pollutant along the road of certain city, setting points along the longitudinal spacing and recording road pollutants concentration and traffic environmental data in different time.

#### 3.2 Calculated value compared with the measured values

Applied in this paper, the underground road pollutant diffusion model is established to analyze the pollutant concentration field, and also to compare the numerical results with experimental data. The result is present in Figures 2–5.

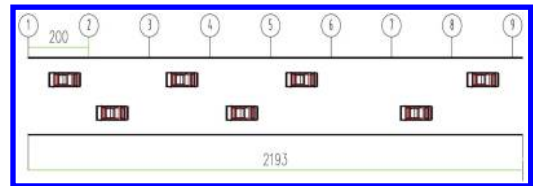


Figure 1. The measurement point position of Yan'an east road tunnel pollutants.

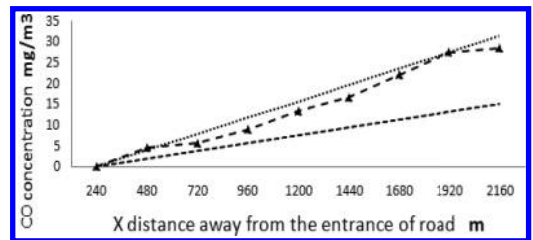


Figure 2. Yan'an east road tunnel in Pudong—Puxi, Aug. 23, 17:12.

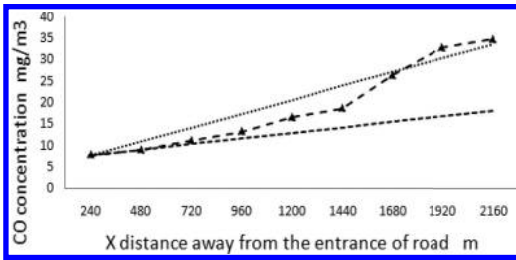


Figure 3. Yan'an east road tunnel in Pudong—Puxi, Aug. 25, 15:34.

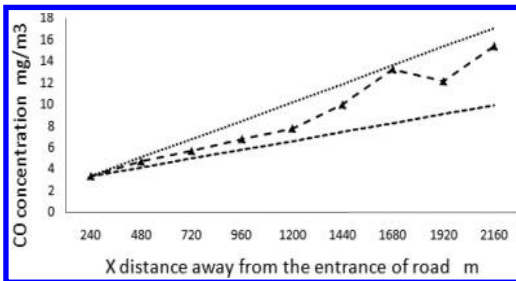


Figure 4. Yan'an east road tunnel in Pudong—Puxi, Aug. 21, 8:59.

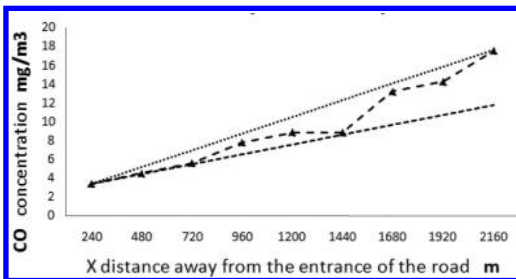


Figure 5. Yan'an east road tunnel in Pudong—Puxi, Aug. 26, 16:53.

Figures 2–5 are the pollutants concentration comparison about calculation and measured values, in the process of model calculation, the convection item select the underground road average wind speed of that period. The figure shows that the pollutants concentration distribution values is a linear model, the reason is that source term of this model, calculated through single emission factor limitation, is a fixed value. The measured concentration is up to the national III and IV standard and conforms to the driving motor vehicle types. The CO concentration value has relative error from 2% to 138% compared with the IV standard calculated value in Figure 2 to Figure 5 mode, has

relative error of 28% with the III standards calculated value. The above data shows that motor vehicle emission characteristics are as per national III standards.

#### 4 CONCLUSION

This article established one dimensional convection diffusion model of underground road pollutants and applied the finite difference method to solve equation. The paper also measured the CO concentration distribution in Shanghai Yan'an east road tunnel and tested CO concentration distribution in different proportion of traffic flow, vehicles size, and motor vehicle speed. The comparison of the measured values and calculated values about CO shows that the model has a relatively high precision, which can be used to analyze the pollutants concentration in underground road. Due to the single vehicle emission factors limited for the fixed value in current national standard, however, the vehicle emissions factors in the process of actual driving is affected by speed, road slope, etc. So the source term in this article calculated by emissions limits, compared with the actual road conditions, has poor adaptability. Subsequent study will be done based on the changing rules of actual road source term.

#### ACKNOWLEDGMENT

This work is supported by the Talent school action plan of the North China University of Technology.

#### REFERENCES

- Chieh Han, et al. 2011. *The measurements of gaseous pollutant concentrations in the Hsuehshan traffic tunnel of northern Taiwan*. The aerosol and air quality research 11 (2): 776–782.
- GB18352.3. 2005. *Light vehicle emission limits and measurement methods*. Beijing: China standard press, 2005.
- Jianping Gao, et al. 2013. The urban tunnel control limitation study of carbon monoxide concentration. *Journal of safety and environment* 13 (5): 190–194.
- Shunxi Deng, et al. 2001. *China's highways source pollutant emissions intensity calculation method* 12 (4): 83–86.
- Shunxi Deng. 2004. *Highway and air pollution in long tunnel effect analysis*. Beijing: science press: 66–68.
- Xin Deng. 2012. Pollution control standards in urban tunnel and the ventilation design research. *Highway traffic technology* 10 (5): 106–111.

# Design and calculation of fluid equilibrium flow in parallel plate-exchangers

Weike Pang

*School of Aeronautic Science and Engineering, Beihang University, Beijing, China  
Institute of Science and Technology, Beihang University, Beijing, China*

Guanghe Li, Meng Liu & Jun Wang

*School of Aeronautic Science and Engineering, Beihang University, Beijing, China*

**ABSTRACT:** It is quite important to flow in equilibrium for fluid in the parallel plates. If there are restriction orifices, the flow characteristic of fluid could be improved obviously; therefore, the fluid flows well-distributed and keeps its flux balanced. While the flux coefficient is measured by the experiment, the optimal orifice is discovered and designed. It shows that the diameter of orifice in experiment is 11.2% smaller than the calculated one in view of flux coefficient. The result could be for reference when the precision is not very high during engineering designs.

**Keywords:** parallel plate-exchanger; restriction orifice; flux coefficient

## 1 INTRODUCTION

At present, as far as known, there are many ways how to get high or low temperature in environment simulation. According to practical application, a temperature-control model that is stable as operating and low in cost is necessary to simulate the surrounding parameters such as its temperature and humidity<sup>[1]</sup>. Heat transferring on the surfaces of solid is not exigent at refrigerant, because its cooling medium is not mixed or contacted with that of the simulation environment. Consequently, the different substance or pollutant is not able to enter into controlled area<sup>[2]</sup>. To plate exchangers in a large space, there are two ways of heat transfer: convection at the boundary between fluid and solid; radiation at the solid surface. These do not only accelerate the cooling rate when temperature is lowering, but also keep the temperature of space balanced during temperature control stage. The way of plate heat-transfer is very popular to some small thermo technical products and some modest engineering projects. The above-mentioned applications are successful and fruitful<sup>[3]</sup>. Further, this study will be on fluid flow and cooling characteristic when many plate exchangers are parallel. It could give some references to apply plate configuration and integration to large scale engineering projects.

## 2 THEORETICAL MODEL ANALYSIS AND DESIGN CALCULATION

Many plates are parallel and made up a plate module; and many modules are parallel to make up a plate unit then. To some extent, the plate unit is basic to lower and control the temperature of environment. The effect of cooling and temperature control is influenced directly by the fluid flow and flux distribution when plates are connected parallel. Consequently, the research on the flow characteristic of medium indoors appears very important<sup>[4]</sup>. As far as engineering studies, it could discover some laws of fluid flow and heat transfer in parallel plates to analyze a sole module of plate. The distance between two plates is short and its loss of resistance could be ignored. So the parallel plates could be simplified as an integral plate that its length is enlarged. The model of whole plate is set up as [Figure 1](#). The fluid in the model is air.

As shown in [Figure 1](#), when the air enters into the whole plate, it need go through each branch way. That is to say, those two series of equations should be solved: one is about that is nearest to the entrance of main way for given air (also the exit of main way for return air); the other is about that is farthest. As to the farthest and nearest branch, there is friction restriction loss along the way, so their kinetic pressure and static pressure (such as  $P_1$  and  $P_n$ ) are different respectively. What is more,

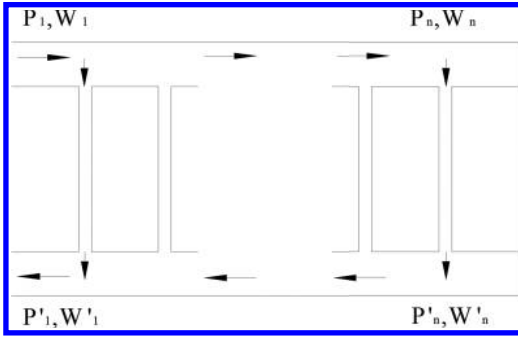


Figure 1. Model of whole plates that are connected in parallel.

their air velocity (such as  $W_1$ , and  $W_n$ ) and flow flux are not equal. If the air flow and heat transfer are also optical in the whole plate, some appropriate restriction orifice should be designed at the entrance of branch ways<sup>[5]</sup>. Meanwhile, the diameter of restriction orifice should be calculated and analyzed to keep the air flow balanced in the whole plate exchanger.

Based on the design of one project, the theory analysis and calculation about plate exchanger are done. The given total of cooling air is 6.4 kg/s in this project, which is called as  $G$ . Around the walls of environment space, there are 4 units of plate, and each unit comprised 3 plate modules. Additionally, six plate exchangers are connected in parallel to make up a whole, and one plate consists of 15 branch tubes with extended surfaces. In summary, the plate modules is called as  $M$  and it is 12; the plates in a module is called as  $P$  and it is 6; the branch tubes is called as  $Z$  and it is 15.

### 2.1 Calculation on flow equations of whole-plate model

The air is distributed equally, then the flow rate at entrance of main tube for given air is:

$$Q_m = \frac{G}{M} = \frac{6.4}{12} = 0.53 \text{ kg/s}$$

The fluid velocity at entrance of main tube for given air

$$\omega_1 = \frac{4Q_m}{\rho\pi d_1^2} = \frac{4 * 0.53}{2.274 * 3.142 * 0.15^2} = 13.19 \text{ m/s}$$

When air goes along the main tube for given air, from its entrance to its end, the flow flux reduces step by step. The velocity of air became low gradually because the diameter of main tube

does not vary. The flow flux of branch tube in whole plate is:

$$q_m = \frac{G}{ZPM} = \frac{6.4}{15 * 6 * 12} = 0.006 \text{ kg/s}$$

The air velocity at entrance of the branch tube that is at the end of main tube for given air is same as that velocity at the end of main tube, and it is

$$\omega_n = \frac{4q_m}{\rho\pi d_1^2} = \frac{4 * 0.006}{2.274 * 3.142 * 0.15^2} = 0.15 \text{ m/s}$$

The stable velocity of air in branch tube is:

$$\omega_2 = \frac{4q_m}{\rho\pi d_2^2} = \frac{4 * 0.006}{2.274 * 3.142 * 0.019^2} = 9.31 \text{ m/s}$$

Additionally,  $d_1$  is the diameter of the main tube; and  $d_2$  is the diameter of the branch tube;  $\rho$  is the density of air.

### 2.2 Calculation on energy equations of whole-plate model

According to these two cross-sections from 1 to  $n$  in main tube for given air, the energy equation is

$$p_1 + \frac{\rho\omega_1^2}{2} = p_n + \frac{\rho\omega_n^2}{2} + p_{l,1-n}$$

The flow loss from cross-section 1 to  $n$  because of friction along the main tube is calculated as following.

The Reynolds number is

$$Re_1 = \frac{\rho_1 \bar{\omega}_{1-n} d_1}{\mu_1}$$

The coefficient of friction restriction is

$$\lambda_1 = \frac{64}{Re_1}$$

The flow loss along the main tube is:

$$\begin{aligned} p_{l,1-n} &= \lambda_1 \frac{l_1}{d_1} \frac{\rho_1}{2} \bar{\omega}_{1-n}^2 = \frac{32\mu_1 l_1}{d_1^2} \bar{\omega}_{1-n} \\ &= \frac{32 * 11.8 * 10^{-6} * 3 * 6 * (13.19 + 0.15)}{2 * 0.15^2} = 2.0 \text{ Pa} \end{aligned}$$

Because the loss is little, it can be ignored. The equation became as

$$p_1 + \frac{\rho\omega_1^2}{2} = p_n + \frac{\rho\omega_n^2}{2}$$

The difference of static pressure from cross-section 1 to  $n$  in main tube is

$$p_n - p_1 = \frac{\rho\omega_1^2}{2} - \frac{\rho\omega_n^2}{2} = \frac{2.274 * (13.19^2 - 0.15^2)}{2} = 198 \text{ Pa}$$

According to these two cross-sections from  $n'$  to  $1'$  in main tube for return air, the energy equation is

$$p'_n + \frac{\rho\omega_n^2}{2} = p'_1 + \frac{\rho\omega_1^2}{2} + p_{l,n'-1'}$$

The flow loss from cross-section  $n'$  to  $1'$  because of friction along the main tube is calculated as following:

$$p_{l,n'-1'} = \lambda_1 \frac{l_1}{d_1} \frac{\rho_1}{2} \omega_{n'-1'}^2 = \frac{32\mu_1 l_1}{d_1^2} \omega_{n'-1'} = \frac{32 * 11.8 * 10^{-6} * 3 * 6 * (13.19 + 9.31)}{2 * 0.15^2} = 3.4 \text{ Pa}$$

Likely, because the loss is little, it can be ignored. The equation became as

$$p'_n + \frac{\rho\omega_n^2}{2} = p'_1 + \frac{\rho\omega_1^2}{2}$$

The difference of static pressure from cross-section  $1'$  to  $n'$  in main tube is

$$p'_n - p'_1 = \frac{\rho\omega_1^2}{2} - \frac{\rho\omega_n^2}{2} = \frac{2.274 * (13.19^2 - 9.31^2)}{2} = 99 \text{ Pa}$$

To calculate the difference of static pressure from cross-section  $n$  to  $n'$  in the farthest branch tube, and that from cross-section 1 to  $1'$  in the nearest branch tube, then compare them:

$$(p_n - p'_n) - (p_1 - p'_1) = (p_n - p_1) - (p'_n - p'_1) = 99 \text{ Pa}$$

If the comparison between the two differences of static pressure is small and could be ignored while the local loss of restriction orifice is large, the whole module of parallel plates is thought ideal. That is to say, in each branch tube, there is same flow loss; so their flow flux is equal similarly. To design their comparison between the two differences is as small as about 5% of the local loss of restriction orifice<sup>[6]</sup>. Hence, the local loss of restriction orifice is

$$\Delta p = 2000 \text{ Pa}$$

According to the relation of flow flux and pressure difference in orifice flow, there is

$$q_m = \rho c_q A \sqrt{\frac{2\Delta p}{\rho}}$$

$c_q$  is defined as flux coefficient, and is measured by experiment.

The area of restriction orifice is

$$A = q_m / (c_q \sqrt{2\rho\Delta p})$$

The diameter of restriction orifice is

$$d = \sqrt{\frac{4A}{\pi}}$$

### 3 MEASURE OF FLUX COEFFICIENT BY EXPERIMENT

#### 3.1 Experiment installation and building

The installation is shown in Figure 2, which is composed of some tubes, one fan, one flow meter and one differential-pressure meter. There are several restriction orifices of different diameter in the main tube. Additionally, one branch tube is linked to one orifice. At entrance of each branch tube where the air is distributed in main tube for given air, there is a measure point for inlet pressure of orifice. After air flows steadily along the branch tube, there is another measure point for outlet pressure of orifice; and the distance (defined as  $L$ ) from orifice is about 5 times as long as the diameter of orifice. Meanwhile, the second point is for inlet pressure of the flow meter. The outlet pressure of flow meter is atmosphere pressure.

The parameter of installations for experiment and measure instruments is shown in Table 1.

#### 3.2 Experiment procedure

When the experiment starts, the differential pressure meter is placed rightly at first. Keep two liquid levels to be same in the tube of U type.



Figure 2. The experiment installation.

Table 1. Parameter of installations and instruments.

Name	Type	Technical parameter
Differential pressure meter	Tube of U	Water column; range: 0~5 kPa
Flow meter	Float	Range: 2.5~25 m <sup>3</sup> /h
Fan	Centrifugal	Range: 0~30 m <sup>3</sup> /h
Tubes for experiment	PV tube	Diameter: 150 mm, 19 mm

Next, link the entrance of flow flux meter and the outlet of branch tube, and keep the gravity center of the meter vertical.

Then, seal the rest restriction orifices and branch tubes; and open the valve at main tube.

At last, start the fan and control the valve to adjust the flow flux of air.

When the state is steady, write down the differential pressure and flow flux of the air going through a restriction orifice.

#### 4 DATA PROCESSING AND ANALYSIS

##### 4.1 Data processing

1. Revise the flow flux of air tested at experiment; revision coefficient  $\varepsilon$  is based on a formula of the flow flux meter.
2. Calculate the theoretical flow flux of air based on a formula following:  $q_{V,t} = A\sqrt{\frac{2\Delta p}{\rho}}$ .
3. Calculate the coefficient of flow flux  $c_q$ :  $c_q = \frac{q_v}{q_{v,t}}$ .

##### 4.2 Data analysis and discussion

1. Relation between pressure drop and orifice diameter

As shown in Figure 3, if the flow-flux of air going through a restriction orifice do not became, the pressure drop will increase while the orifice diameter become small. Take the flow-flux of 7.5 m<sup>3</sup>/h for example, the pressure drop increases from 500 Pa to nearly 7000 Pa when the orifice diameter became from 13.5 mm to 7 mm. On the other hand, keep the orifice diameter constant, the pressure drop rises while the flow-flux grows up. Take an orifice of 10 mm, for example, the pressure drop at the flow flux of 10 m<sup>3</sup>/h is 2000 Pa more than that of 5 m<sup>3</sup>/h. It is indicated that the pressure drop is affected more by the orifice diameter than the flow flux.

2. Relation between flow flux and orifice diameter
- As shown in Figure 4, if the pressure drop of air going through a restriction orifice do not

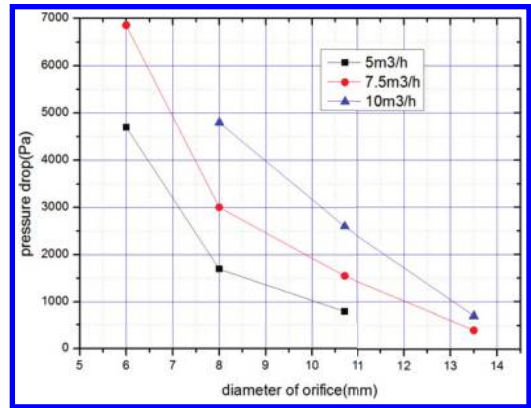


Figure 3. Trend of pressure drop with change of orifice diameter and flow flux.

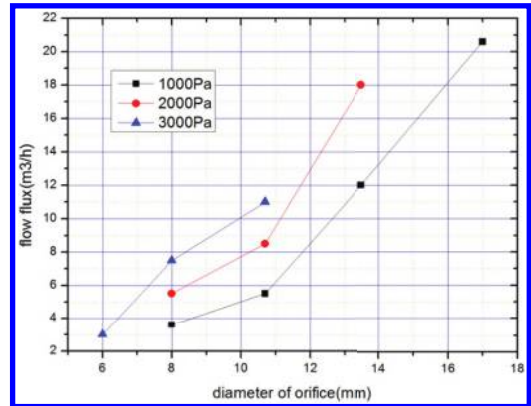


Figure 4. Trend of flow flux with change of orifice diameter and pressure drop.

became, the flow flux will increase while the orifice diameter become big. Take the pressure drop of 2000 Pa for example, the flow-flux increases from 3.8 m<sup>3</sup>/h to nearly 20.8 m<sup>3</sup>/h when the orifice diameter became from 8 mm to 17 mm. It increases about 4.5 times. On the other hand, keep the orifice diameter constant, the flow flux rises while the pressure drop grows up. Take an orifice of 10 mm, for example, the flow flux at the pressure drop of 1000 Pa is 5 m<sup>3</sup>/h more than that of 3000 Pa. It is indicated that the flow flux is affected more by the orifice diameter than the pressure drop.

3. Relation between flux coefficient and orifice diameter

As these two conditions-flow flux and pressure drop are given, a diameter of restriction orifice could be achieved in Figures 3 and 4. Moreover, if the diameter of orifice and pressure drop

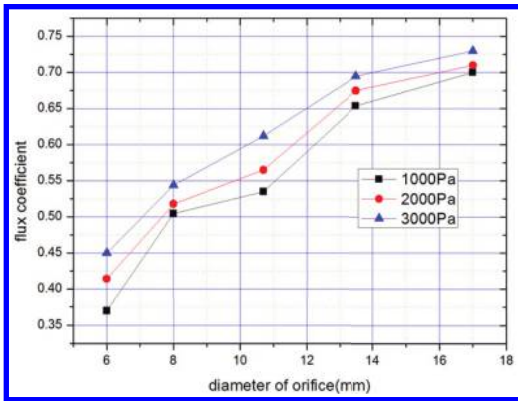


Figure 5. Trend of flux-coefficient with change of orifice diameter and pressure drop.

is given, the flux coefficient could be got from Figure 5.

As shown in Figure 5, if the pressure drop of air going through a restriction orifice do not became, the flux coefficient will also increase while the orifice diameter become big. Take the pressure drop of 2000 Pa, for example, the flux coefficient increases from 0.41 to nearly 0.71 when the orifice diameter became from 6 mm to 17 mm. It increases about 73.2%. On the other hand, keep the orifice diameter constant, the flux coefficient rises while the pressure drop grows up. Take an orifice of 10 mm, for example, the flux coefficient at the pressure drop of 1000 Pa is 0.07 higher than that of 3000 Pa. It is indicated that the flux coefficient is affected by the orifice diameter equally by the pressure drop.

## 5 CONCLUSIONS

The flow characteristic of air in the parallel plates with restriction orifice is analyzed theoretically,

and the optimal diameter is designed by flux coefficient based on experimental measure. The results are:

1. During the application of plate-exchangers configuration and integration, restriction orifices could keep fluid well-distributed and its flux balanced.
2. During the design of restriction orifice, the flux coefficient  $C_q$  is achieved by experiment measure. The optimal diameter of orifice is based on that  $c_q = 0.56$ .
3. Additionally, based on these two conditions-flow flux of air and its pressure drop, the diameter of orifice is 11.9 mm. To compare with that experimental diameter of 10.7 mm, it is 11.2% more. The result could be for reference when the precision is not very high during engineering designs.

## REFERENCES

- [1] Wang Jun. Present status and development of environment simulation technology in China [J]. Aerospace manufacturing technology, 2004.08.
- [2] Song Fangting. Dynamic simulation of atrium thermal environment [D]. Bei Jing. Tsinghua University, 2004.
- [3] Li Xuguan. The reform of a preheater on a pump for catalyzing slurry-oil [J]. Chemical Industry Machinery, 2009.02.
- [4] Ni Xiaohua, Xia qing, Xiao yuan. Calculations of heat transfer and pressure drop in plate heat exchanger [J]. Fluid Machinery, 2002, 30(3).
- [5] Huang Yixiang, Chen Junwen, Chen Qing. Optimizations for the diameter of a restriction orifice [J]. Chemical Industry Administration, 18, 2013.
- [6] Tang Fengjin, Zhang Zhongfei, Wang Guangyou, etc. The diameters calculation and its analysis of a pore plate [J]. Chemical Industry Design, 2014. 04.

# Health risk assessment of heavy metals in PM<sub>2.5</sub> of major and typical cities in China

Lingyue Lv, Hongyuan Li & Jianan Yang

*College of Environmental Science and Engineering, Nankai University, Tianjin, China*

**ABSTRACT:** This study selected typical cities in different regions of China, and based on the experimental results of heavy metal contents in PM<sub>2.5</sub> by different researchers, their health risks were evaluated. The health risk assessment results showed that the risk level of five kinds of heavy metals is Cr > Cd > Pb > Zn > Cu, and the risk through the respiratory route of exposed populations about Cd, Cu, Pb, and Zn is between  $3.10 \times 10^{-7}$ – $1.99 \times 10^{-11}$ , lower than the acceptable risk level  $1 \times 10^{-6}$ . Only the risk index of Cr is higher, and the risk of Cd and Cr was significantly higher than Cu, Pb, and Zn. In addition, five kinds of heavy metal elements had the largest influence on the health risks of adult males, followed by the adult women, and the health risks of the children were minimized.

**Keywords:** PM<sub>2.5</sub>; health risk assessment; heavy metal; exposure parameters

## 1 INTRODUCTION

With the rapid urbanization and industrialization process, the impact of human activities on the natural environment is growing. The environmental impacts of the city continue to gain weight, air dust, smoke, and other harmful gases are gradually increasing, and the atmospheric particulate matter pollution is worsening. In recent years, long-term and high intensity haze has tended to spread with a large range in our country, and PM<sub>2.5</sub> has become the primary pollutant in most cities in China. Therefore, the prevention of PM<sub>2.5</sub> pollution is currently in urgent need.

## 2 OVERVIEW OF PM<sub>2.5</sub> AND HEAVY METAL POLLUTION IN CHINA

In the monitored 74 cities of China in 2013, nearly 92% of the city's PM<sub>2.5</sub> concentration cannot reach the national standard, the PM<sub>2.5</sub> concentration of 32 cities was 2 times above the national standard, and the top 10 cities was nearly 3 times to the national standard. The statistics showed that the average annual concentration of China's northern cities was approximately 89.9 µg/m<sup>3</sup>, the southern cities were about 59.4 µg/m<sup>3</sup>, the eastern cities were about 70.6 µg/m<sup>3</sup>, and the central cities were approximately 76.6 µg/m<sup>3</sup>, west about 59.9 µg/m<sup>3</sup>. Thus, the serious air pollution was not only in developed areas of China, China's central and western provinces also had serious air pollution problem. PM<sub>2.5</sub> concentration of Xi'an, Zhengzhou, Wuhan, Chengdu, Urumqi, Hefei, Taiyuan, and other cities

in 2013 also reached twice more than the national standard. For the majority cities in China, especially Beijing, Tianjin, the Yangtze River Delta and Pearl River Delta, and other key areas, the air PM<sub>2.5</sub> concentration often exceeds the standard, and the haze usually appears (Cheng, 2013).

Monitoring results showed that the frequency of heavy PM<sub>2.5</sub> pollution weather was significantly increased in a number of cities and urban agglomerations in recent years, and the duration of pollution have extended. For example, the haze is of high frequency, long duration, and low visibility in the eastern part of China in January 2013, involving 17 provinces, which is quarter of the land area, and the affected population was about 600 million. Heavy haze pollution process occurred five times in Beijing, Tianjin a Hebei Region, and the most serious haze lasted five days, and PM<sub>2.5</sub> instantaneous concentration of some urban areas was near 1000 µg/m<sup>3</sup>. In December, the air quality index reached six serious pollution level in Jiangsu, Anhui, Henan, Zhejiang, Shanghai and other places. PM<sub>2.5</sub> concentration was seriously overweight in 13 provincial jurisdiction cities of Jiangsu Province, reaching heavy pollution or serious pollution. In February 2014, haze pollution occurred to 1.43 million square kilometers in the eastern part of China, accounting for 1/7 of the land area, lasting longer than 1 week, and heavy or severe pollution attacked Beijing, Tianjin and Hebei area again. The long duration and high concentration of PM<sub>2.5</sub> in this several air pollution had hit a historical record (Wang, 2014; Lu, 2015).

The source and composition of PM<sub>2.5</sub> is very complex. The chemical composition and



Table 1. Comparison of heavy metal contents in PM<sub>2.5</sub> in different cities (μg/m<sup>3</sup>).

Element	Shenzhen	Xi'an	Zhengzhou	Chengdu
Cd	0.0011	0.0300	0.0100	0.0060
Cr	0.0015	0.0100	0.0200	0.0110
Pb	0.0516	0.3500	0.1300	0.1776
Zn	0.2350	2.5100	0.4300	0.3820
Cu	0.0158		0.0200	0.0287
Element	Shanghai	Urumqi	Hangzhou	Tianjin
Cd	0.0030	0.0138	0.0100	0.0006
Cr	0.0473	0.0785	0.0130	0.0207
Pb	0.0590	1.0770	0.1280	0.5924
Zn	0.3060		0.6510	1.0753
Cu	0.0263		0.0760	0.1290
Element	Beijing	Guangzhou		
Cd	0.0040			
Cr	0.0713	0.0090		
Pb	0.2020	0.1920		
Zn	0.2827	0.4200		
Cu	0.0500	0.0360		

composition ratio are not the same due to the natural environment, the economic development and industrial structure in different cities, but most are made from organic carbon, elemental carbon, heavy metal elements, and other organic and inorganic particles. Research results show that many harmful heavy metals and organic carcinogens are enriched in PM<sub>2.5</sub> because of the small particle size, large surface area, long residence time and transmission distance, and the harm to human health is the most prominent. In addition, PM<sub>2.5</sub> can reach the alveoli, damaging the human respiratory system and cardiovascular system, causing heart disease, bronchitis, asthma, lung cancer and a series of diseases, even increasing people's premature death risk (Guo, 2013). Therefore, the health risk evaluation of heavy metal in PM<sub>2.5</sub> has become very important, and the results may provide a scientific basis for the pollution control of PM<sub>2.5</sub>. The heavy metal contents of PM<sub>2.5</sub> in different cities of China are given in Table 1 (Du, 2012; Hu, 2013; Gan, 2011; Bao, 2010; Geng, 2012; Chen, 2013; Wang, 2010; Yalkunjan, 2010).

### 3 HEALTH RISK ASSESSMENT OF HEAVY METALS IN PM<sub>2.5</sub>

#### 3.1 Health risk assessment model

The main way of fine particulate matter PM<sub>2.5</sub> in the atmosphere into the body is breathing intake.

In this paper, the health risk assessment model recommended by the United States Environmental Protection Agency (USEPA) (USEPA, 2011) is adopted, and some parameters in the model have been modified based on the actual situation. This health risk assessment model is applicable to the health risk evaluation of different types of pollutants into the human body through a variety of channels, including the carcinogenic risk and the non-carcinogenic risk. Using the modified evaluation model, the health risk on the human body through the respiratory route of Cd, Cr, Cu, Pb, and Zn in atmosphere PM<sub>2.5</sub> in Chinese major cities (adult males, adult females, children) were evaluated. According to the research results of EPA Integrated Risk Information Database (IRIS) and IARC (IARC), the contaminants can be divided into carcinogenic and non-carcinogenic. In this study, Cd and Cr belong to the carcinogenic substances, Pb, Zn, and Cu is non-carcinogenic, and the health risk assessment model varies.

#### 3.2 Calculation of exposure dose rate

Non-carcinogenic substances usually used commonly daily exposure dose ADD, and carcinogen usually adopted the life-long daily exposure dose LADD.

$$ADD/LADD = (C \times IR \times ED)/(BW \times AT)$$

ADD: daily average exposure dose, mg·kg<sup>-1</sup>·d<sup>-1</sup>; LADD: lifetime average daily exposure dose, mg·kg<sup>-1</sup>·d<sup>-1</sup>; C: pollutant concentration, m<sup>3</sup>·d<sup>-1</sup>; IR: respiratory rate, m<sup>3</sup>·d<sup>-1</sup>; ED: duration of exposure, d; BW: body weight, kg; AT: average exposure time, d. Lack of basic data to support research on exposure parameters, we generally cited the exposure parameters of the United States in health risk assessment. Taking the differences between Chinese people physique (body weight) and Western populations into account, the weight in this article used the national average values in the 2010 National physique monitoring bulletin (State Sports General Administration, 2011): adult males (20–59 years), 69 kg; adult women (20–59 years), 57 kg; children (7–19 years), 44 kg. The exposure parameters into human body through the breath way is in Table 2.

#### 3.3 Carcinogenic risk assessment

The average annual excess risk of carcinogenic pollutant is calculated as:

$$R = [1 - \exp(-LADD \cdot SF)] / \text{Life}$$

R: the average annual excess risk, dimensionless; LADD: daily exposure dose of exposed population, (mg·kg<sup>-1</sup>·d<sup>-1</sup>); SF: cancer potency

Table 2. Exposure parameters into human body through the breath way [3–4].

Population	IR/(m <sup>3</sup> d <sup>-1</sup> )	BW/kg	ED/d
Adult male	15.2	69	30 × 365
Adult women	11.3	57	30 × 365
Children	8.7	44	18 × 365
Population	AT (carcinogenic)/d	AT (non-carcinogenic)/d	
Adult male	70 × 365	30 × 365	
Adult women	70 × 365	30 × 365	
Children	70 × 365	18 × 365	

Table 3. Exposure parameters of toxic heavy metals into the body by the respiratory route [5].

Element	Characteristic	SF (kg · d)/mg	RfD mg/(kg · d)	Source	Foundation
Cd	Carcinogenic	8.4	/	HEA	
Cr	Carcinogenic	56	/	HEA	
Pb	Non-carcinogenic	/	4.3E-4	HEA	NAAQS
Zn	Non-carcinogenic	/	1.0E-2	HEA	TLV
Cu	Non-carcinogenic	/	2.0E-3	HEA	TLV

Table 4. Health risk assessment of 5 heavy metals in PM<sub>2.5</sub> through breathing (adult males).

Element	Shenzhen	Xi'an	Zhengzhou	Chengdu
Cd (×10 <sup>-8</sup> )	1.13	31.0	10.8	6.07
Cr (×10 <sup>-8</sup> )	9.75	67.9	137	72.0
Pb (×10 <sup>-10</sup> )	3.38	23.6	9.12	11.6
Zn (×10 <sup>-11</sup> )	6.61	72.9	13.0	10.8
Cu (×10 <sup>-11</sup> )	2.22	/	3.02	4.04
Element	Shanghai	Urumqi	Hangzhou	Tianjin
Cd (×10 <sup>-8</sup> )	2.88	15.1	9.68	0.586
Cr (×10 <sup>-8</sup> )	268	471	81.4	128
Pb (×10 <sup>-10</sup> )	3.67	76.6	8.04	37.4
Zn (×10 <sup>-11</sup> )	8.17	/	17.6	29.2
Cu (×10 <sup>-11</sup> )	3.51	/	10.3	17.5
Element	Beijing	Guangzhou		
Cd (×10 <sup>-8</sup> )	3.89	/		
Cr (×10 <sup>-8</sup> )	386	588		
Pb (×10 <sup>-10</sup> )	12.7	12.4		
Zn (×10 <sup>-11</sup> )	7.66	11.7		
Cu (×10 <sup>-11</sup> )	6.77	5.02		

factor of carcinogenic chemicals, (kg · d<sup>-1</sup> · mg<sup>-1</sup>); the average life expectancy for each city using the latest average life expectancy, years.

### 3.4 Non-carcinogenic risk assessment

The average annual excess risk of non-carcinogenic pollutant is calculated as:

$$R = (ADD \cdot 10^{-6}) / (RfD \times \text{Life})$$

R: the average annual excess risk, dimensionless; ADD: daily exposure dose of exposed population, mg/(kg · d); RfD: reference dose, mg/(kg · d)<sup>-1</sup>; 10<sup>-6</sup> is the acceptable risk level corresponding to RfD; and the average life expectancy for each city using the latest average life expectancy, years.

Table 5. Health risk assessment of 5 heavy metals in PM<sub>2.5</sub> through breathing (adult women).

Element	Shenzhen	Xi'an	Zhengzhou	Chengdu
Cd ( $\times 10^{-8}$ )	1.02	27.9	9.74	5.47
Cr ( $\times 10^{-8}$ )	8.78	61.2	124	65.0
Pb ( $\times 10^{-10}$ )	3.04	21.3	8.21	10.5
Zn ( $\times 10^{-11}$ )	5.95	65.6	11.7	9.69
Cu ( $\times 10^{-11}$ )	2.00	/	2.72	3.63
Element	Shanghai	Urumqi	Hangzhou	Tianjin
Cd ( $\times 10^{-8}$ )	2.59	13.6	8.71	0.527
Cr ( $\times 10^{-8}$ )	244	433	73.5	116
Pb ( $\times 10^{-10}$ )	3.30	69.0	7.23	33.6
Zn ( $\times 10^{-11}$ )	7.36	/	15.8	26.3
Cu ( $\times 10^{-11}$ )	3.16	/	9.23	15.7
Element	Beijing	Guangzhou		
Cd ( $\times 10^{-8}$ )	3.50	/		
Cr ( $\times 10^{-8}$ )	354	53.0		
Pb ( $\times 10^{-10}$ )	11.4	11.2		
Zn ( $\times 10^{-11}$ )	6.89	10.5		
Cu ( $\times 10^{-11}$ )	6.09	4.51		

Table 6. Health risk assessment of 5 heavy metals in PM<sub>2.5</sub> through breathing (children).

Element	Shenzhen	Xi'an	Zhengzhou	Chengdu
Cd ( $\times 10^{-8}$ )	0.611	16.8	5.84	3.27
Cr ( $\times 10^{-8}$ )	5.26	37.0	75.8	39.3
Pb ( $\times 10^{-10}$ )	3.03	21.2	8.19	10.4
Zn ( $\times 10^{-11}$ )	5.93	65.4	11.6	9.66
Cu ( $\times 10^{-11}$ )	1.99	/	2.71	3.62
Element	Shanghai	Urumqi	Hangzhou	Tianjin
Cd ( $\times 10^{-8}$ )	1.55	8.13	5.22	0.316
Cr ( $\times 10^{-8}$ )	223	278	44.5	70.5
Pb ( $\times 10^{-10}$ )	3.29	68.8	7.21	33.5
Zn ( $\times 10^{-11}$ )	7.34	/	15.8	26.2
Cu ( $\times 10^{-11}$ )	3.15	/	9.21	15.7
Element	Beijing	Guangzhou		
Cd ( $\times 10^{-8}$ )	2.10	/		
Cr ( $\times 10^{-8}$ )	226	32.0		
Pb ( $\times 10^{-10}$ )	11.4	11.2		
Zn ( $\times 10^{-11}$ )	6.87	10.5		
Cu ( $\times 10^{-11}$ )	6.08	4.50		

#### 4 CONCLUSIONS AND OUTLOOK

The health risk assessment results showed that the risk level of five heavy metals is Cr > Cd > Pb > Zn > Cu. The cancer risk Cd and Cr was significantly higher than non-cancer risk of Cu, Pb, Zn, with a difference of 2–5 magnitudes, which has greater harm

to the human health. And the excess risk of Cd, Cu, Pb, and Zn through the respiratory route of exposed population is between  $3.10 \times 10^{-7}$ – $1.99 \times 10^{-11}$ , lower than the acceptable level of risk population  $1 \times 10^{-6}$ , only the risk index of Cr is higher.

The five heavy metal elements in atmospheric PM<sub>2.5</sub> had the largest health risks on the adult males,

followed by the adult women, and the health risks of children are minimized. Under normal circumstances, the elderly and children are more sensitive to  $PM_{2.5}$ , but the results of this study showed that the adult males had the greatest health risk. This may be related to the time length of people outdoors, and the adult males usually have longer outdoor activities, so the  $PM_{2.5}$  exposure is higher than other groups.

In this study, the risk evaluation of toxic heavy metals in the  $PM_{2.5}$  on human health still has many uncertainties. Firstly, a relatively small number of samples were chosen by the researchers subject to the conditions, so the resulting data is still relatively limited, which cannot fully reflect the concentration level of  $PM_{2.5}$  and their heavy metals in urban air environment, and it also indirectly affects the health risk level. In addition, the exposure time, the exposed population and other studies still have some uncertainties, which would have an impact on the assessment results. In addition, due to the current research related to the exposure parameters is still limited in China, lack of the underlying data of exposure parameters, not yet owning the exposure parameter database, although the exposure parameters of life expectancy and weight parameters were modified according to the actual situation in China, the respiratory rate, exposure duration and other parameters referred to the EPA's recommended value. Taking the differences between the different races and regions into account, the risk assessment calculations might have some errors.

## REFERENCES

- Bao Zhen, Feng Yinchang, Jiao Li, et al. 2010. Characterization and Source Apportionment of  $PM_{2.5}$  and  $PM_{10}$  in Hangzhou. *Environmental Monitoring in China*, 26(2):44–48.
- Chang Jing, Liu Min, Li Xianhua, et al. 2009. Primary research on health risk assessment of heavy metals in road dust of Shanghai. *China Environmental Science*, 29(5):548–554.
- Chen Peifei, Zhang Jiaqi, Bi Xiaohui, et al. 2013. Pollution Characteristics and Sources of Heavy Metals in  $PM_{10}$  and  $PM_{2.5}$ : in Tianjin City. *Acta Scientiarum Naturalium Universitatis Nankaiensis*, 46(6):1–7.
- Cheng Nianliang, Li Yunting, Meng Fan, et al. 2014. Analytical Studies of  $PM_{2.5}$  Pollution and Source identification in China in 2013. *Journal of Anhui Agri. Sci.*, 42(15):4721–4724.
- Du Jinhua, Zhang Yisheng, He Lingyan, et al. 2012. The air pollution characteristics and health risk assessment of heavy metals in  $PM_{2.5}$ , Shenzhen. *Journal of Environment and Health*, 29(9):838–840.
- Duan Xiaoli, Nie Jing, Wang Zongshuang, et al. 2009. Human exposure factors in health risk assessment. *Journal of Environment and Health*, 26(4):370–373.
- Duan Xiaoli, Huang Nan, Wang Beibei, et al. 2012. Development of exposure factors research methods in environmental health risk assessment. *Journal of Environment and Health*, 29(2):99–104.
- Gan Xiaofeng, Cao Junyi, Wang Qiyuan, et al. 2011. Concentration Characteristics and Sources of Chemical Elements in Atmospheric Fine Particles ( $PM_{2.5}$ ) in Autumn in Xi'an City. *Journal of Anhui Agri. Sci.*, 39(19):11692–11694, 11697.
- Guo Erguo, Cai Yu, Sai Yin et al. 2013. Advances in abatement Effect by Green Plants on Airborne Particulate Matter in City. *Northern environmental*, 29(3):78–81.
- Hu Zimei, Wang Jun, Tao Zhengkai, et al. 2013. Pollution level and health risk assessment of heavy metals in  $PM_{2.5}$ , Shanghai. *Acta Scientiae Circumstantiae*, 33(12):3399–3406.
- Lu Ju, Xiao Yusheng, Sun Zhe, et al. 2015. The pollution situation, harm and prevention of  $PM_{2.5}$ . *China Construction*, 3:118–119.
- Ningbo Geng. The Analysis and Source Apportionment of trace elements in  $PM_{2.5}$  at Zhengzhou. Zhengzhou: High-Tech Zone Zhengzhou University, 2012.
- Wang Qiyuan, Cao Junji, Gan Xiaofeng, et al. 2010. Characteristics of elements in  $PM_{2.5}$  during normal and haze period in Chengdu. *Environmental Chemistry*, 29(4):644–648.
- Wang Gengchen. 2014. The pollution situation and human health hazards of  $PM_{2.5}$  in China. The 16th annual meeting of the China association—environmental pollution, occupational exposure and human cancers Symposium. Kunming: 1–4.
- Yalkunjan Tursun, Dilnur Talifu, Ablikim Ablizi, et al. Pollution level of heavy metals in  $PM_{2.5}$  and  $PM_{10-2.5}$  during winter in Urumqi. *Journal of Xinjiang University (Natural Science Edition)*, 2010, 27(3):338–342.

## Author index

- An, G. 425  
An, X.H. 1017
- Bai, L. 1005  
Bai, R. 1111  
Bai, Y.Z. 223  
Bao, S.J. 743  
Bi, T.W. 1079  
Bian, W. 233  
Bu, L.-f. 309  
Bu, Z.-Y. 9, 433, 437
- Cai, J. 1111  
Cao, J.X. 383  
Cao, L. 359  
Cao, P. 97  
Cao, S. 79  
Cao, W. 1089  
Cao, W.R. 1049  
Cao, Y. 1183  
Cao, Y.H. 639  
Chai, F.X. 747  
Chai, J.-l. 633  
Chang, Q. 1173  
Chen, B. 351  
Chen, B. 849  
Chen, B. 861  
Chen, C. 3  
Chen, C. 965  
Chen, C. 1129  
Chen, C. 1407  
Chen, C.J. 1017  
Chen, F. 183  
Chen, G.-H. 305  
Chen, H. 85, 927  
Chen, H. 131  
Chen, H. 379  
Chen, H.W. 803  
Chen, J. 199  
Chen, J. 535  
Chen, J. 605  
Chen, J. 781  
Chen, J. 1105  
Chen, J. 1203  
Chen, L. 1145  
Chen, M. 937
- Chen, M.J. 671  
Chen, Q. 813  
Chen, S. 233  
Chen, S.H. 609  
Chen, S.H. 671  
Chen, S.-p. 121  
Chen, S.W. 813  
Chen, T. 117  
Chen, W. 761, 1371  
Chen, W. 1357  
Chen, W.S. 971  
Chen, X. 227  
Chen, X. 1059  
Chen, X.D. 943  
Chen, X.-F. 305, 309  
Chen, X.M. 21  
Chen, Y.D. 937  
Chen, Y.F. 671  
Chen, Y.-h. 1387  
Chen, Z. 833  
Chen, Z.P. 671  
Chen, Z.T. 403  
Chen, Z.W. 917  
Cheng, H.-p. 821  
Cheng, W.-Q. 305  
Cheng, X.Q. 495, 501  
Chuang, J. 1129  
Cui, L.-s. 331  
Cui, T.T. 681  
Cui, X.-j. 879  
Cui, X.M. 269, 275, 281  
Cui, Y. 407, 411, 415
- Dai, J. 707  
Dalvand, A. 187  
Dang, L. 1393  
Deng, C.G. 145  
Deng, H. 51  
Deng, J.X. 1069  
Deng, P.C. 495, 501  
Deng, S.H. 923  
Deng, S.Z. 727  
Deng, Y. 791  
Di, S.-J. 305, 309  
Diao, X.H. 373  
Ding, H. 1383
- Ding, J. 547  
Ding, L. 515  
Ding, X.H. 1169  
Dong, J. 505  
Dong, L. 251  
Dong, P.-H. 505  
Dong, S.J. 583  
Dong, Z. 1393  
Dou, G. 893  
Dou, L. 117  
Dou, L.J. 1195  
Dou, T. 647  
Dou, X. 515, 525  
Du, Y. 1179  
Duan, H.F. 1065  
Duan, J. 21
- Fan, K. 419  
Fan, X.F. 849  
Fan, Z. 103  
Fang, H.Y. 675  
Fang, J. 1115  
Fang, X. 1163  
Fei, X. 855  
Feng, G.-l. 821  
Feng, L. 1253, 1269  
Feng, T. 407  
Feng, Y.Q. 911  
Fu, S.Y. 343  
Fu, Y.Z. 1297
- Gao, G. 1029  
Gao, J. 1223, 1235, 1283  
Gao, J.-h. 555, 559  
Gao, L. 841, 899  
Gao, L. 1005  
Gao, M. 1029  
Gao, M.L. 1195  
Gao, Q. 985  
Gao, W. 109  
Gao, Y.T. 313  
Gao, Y.-T. 319  
Ge, S. 35  
Ge, Y. 613  
Gong, G. 551  
Gong, X.F. 861

Gong, Y.P. 1241  
 Gu, D. 1079  
 Gu, D.-S. 141  
 Gu, Q. 917  
 Gu, S.J. 627  
 Gu, S.P. 809, 1133  
 Gu, Z. 63  
 Gui, Y.W. 795  
 Guo, C. 73, 79, 597  
 Guo, H. 227  
 Guo, J. 9  
 Guo, J. 433, 437  
 Guo, J. 1065  
 Guo, L. 1199  
 Guo, W. 707  
 Guo, X. 59  
 Guo, X. 1089  
  
 Hai, H. 845  
 Han, D. 287  
 Han, F. 1173  
 Han, G.X. 1017  
 Han, X. 295  
 Hao, C.L. 1209  
 Hao, M. 619  
 Hassani, N. 187  
 He, J. 339  
 He, J. 809, 1133  
 He, J.Y. 1283  
 He, J.Z. 665  
 He, M. 1209  
 He, R. 1045  
 He, X. 45  
 He, X. 1005  
 He, Y. 291  
 He, Y.-m. 1187  
 Ho, M.-H. 1083  
 Hou, J.W. 1183  
 Hou, J.W. 1323, 1327  
 Hou, L. 911  
 Hou, X. 1377  
 Hu, H. 301  
 Hu, H.H. 1169  
 Hu, J. 1323, 1327  
 Hu, J.Z. 495, 501  
 Hu, Q.F. 681  
 Hu, T. 1345  
 Hu, W. 1263, 1399  
 Huang, B.-Z. 1039  
 Huang, C. 79  
 Huang, C. 569, 577  
 Huang, H. 1357  
 Huang, J. 727  
 Huang, J. 1023  
 Huang, J.W. 803  
 Huang, L. 51  
 Huang, M. 379  
 Huang, S.Y. 287  
  
 Huang, T. 343  
 Huang, X. 339  
 Huang, X.B. 1139  
 Huang, X.H. 1069  
 Huang, X.-m. 219  
 Huang, X.Z. 717, 753  
 Huang, Y.S. 411  
 Huang, Z.H. 1129  
  
 Ji, S. 551  
 Jia, D.Y. 47  
 Jia, L.g. 453  
 Jiang, H.B. 971  
 Jiang, J. 59  
 Jiang, K. 1005  
 Jiang, L.C. 325  
 Jiang, L.Z. 441, 447  
 Jiang, M.S. 93  
 Jiang, X. 243  
 Jiang, Y. 351, 355  
 Jiang, Y.H. 103  
 Jiang, Y.J. 849  
 Jiang, Z.R. 165  
 Jiao, Z. 515, 525, 531  
 Jin, F. 1017  
 Jin, M.Q. 1075  
 Jin, Y.D. 747  
 Jin, Y.-h. 465  
 Jin, Y.J. 977, 981  
 Jing, F.W. 173  
 Jing, M. 41  
  
 Kang, H.X. 511  
 Kang, Q. 875, 951, 1101  
 Kong, N. 887  
  
 Lai, J. 1039  
 Lai, J.T. 777  
 Lan, J. 149  
 Lei, X.Y. 1115  
 Lei, Y. 965  
 Leng, J. 199  
 Li, B. 97  
 Li, B. 519  
 Li, B. 803  
 Li, C. 73  
 Li, C. 541  
 Li, C. 691  
 Li, C.-x. 731  
 Li, D. 643  
 Li, F. 965  
 Li, F.F. 347, 365  
 Li, G. 833  
 Li, G. 887  
 Li, G. 931  
 Li, G. 1411  
 Li, H. 331  
 Li, H. 565  
  
 Li, H. 1331, 1339  
 Li, H. 1417  
 Li, H.J. 1173  
 Li, H.L. 927  
 Li, H.-p. 821  
 Li, H.Y. 1305, 1309, 1323, 1327  
 Li, J. 45  
 Li, J. 761, 1371  
 Li, J. 1313  
 Li, J.M. 1129  
 Li, L.N. 1235  
 Li, M. 155, 159  
 Li, P. 833  
 Li, P.Y. 917  
 Li, Q. 771  
 Li, Q.Q. 1215  
 Li, R. 989  
 Li, R. 1393  
 Li, S. 155  
 Li, S. 947  
 Li, T. 765  
 Li, T. 1249  
 Li, W. 1089  
 Li, W.W. 325  
 Li, X. 393  
 Li, X. 605  
 Li, X. 1377  
 Li, X.G. 495, 501  
 Li, X.G. 961  
 Li, Y. 59  
 Li, Y. 243, 247  
 Li, Y. 1129  
 Li, Y.F. 757  
 Li, Y.G. 21  
 Li, Y.R. 971  
 Li, Y.Y. 27  
 Li, Z. 761, 1371  
 Li, Z. 903  
 Li, Z. 1059  
 Li, Z. 1403, 1407  
 Li, Z.Y. 3  
 Lian, P. 717  
 Lian, S.L. 623, 627, 907  
 Lian, S.L. 1115  
 Liang, H. 233  
 Liang, H. 425  
 Liang, P.X. 203  
 Liang, W.L. 471  
 Liang, X. 1219  
 Liang, X.Y. 1059  
 Liang, Y. 59  
 Liao, J.H. 609  
 Liao, Y.-x. 555  
 Lin, P. 195  
 Lin, Y. 41  
 Lin, Y. 1153  
 Liu, A. 1023  
 Liu, B. 313

Liu, B. 777  
 Liu, B.Z. 985  
 Liu, C. 701  
 Liu, C.D. 653, 665  
 Liu, H. 511  
 Liu, H. 893  
 Liu, H.B. 137  
 Liu, H.B. 961  
 Liu, J. 1203  
 Liu, J. 1273, 1279  
 Liu, J. 1357  
 Liu, J.-s. 559  
 Liu, J.X. 867  
 Liu, J.Y. 845  
 Liu, L.Y. 1115  
 Liu, M. 419  
 Liu, M. 1411  
 Liu, Q. 1319  
 Liu, S. 1121  
 Liu, T. 73  
 Liu, T. 425  
 Liu, W. 1111  
 Liu, W. 1263, 1399  
 Liu, W.G. 415  
 Liu, X. 69, 841, 899  
 Liu, X. 1163  
 Liu, X.M. 639  
 Liu, Y. 233  
 Liu, Y. 681  
 Liu, Y. 1125  
 Liu, Y. 1259  
 Liu, Y. 1287  
 Liu, Y. 1345  
 Liu, Z. 31  
 Liu, Z. 1011  
 Liu, Z. 1045  
 Long, G.L. 103  
 Long, Y.Q. 681  
 Lu, F.B. 1297  
 Lu, M. 697  
 Lu, Q. 233  
 Lu, Q.X. 339  
 Lu, W. 477  
 Lu, Z. 73, 79  
 Lu, Z.C. 103  
 Lu, Z.-r. 597  
 Luo, D.-g. 1387  
 Luo, L. 1357  
 Lv, L. 1417  
 Lv, L.Y. 1305, 1309  
  
 Ma, H. 765  
 Ma, J. 735, 739  
 Ma, J. 1093  
 Ma, R.Y. 697  
 Ma, S.-l. 1187  
 Ma, W.Z. 961  
 Ma, X.Y. 1253, 1269  
  
 Ma, Y.Y. 547  
 Mai, Y.Y. 1351  
 Mao, Y. 199  
 Mei, F. 931  
 Meng, Q.Y. 541  
 Meng, Y.Y. 583  
 Mo, L.Y. 917  
 Mo, N.-m. 721  
  
 Ning, Q.C. 691  
 Niu, X. 131  
 Niu, Y. 195  
  
 Pan, H.Y. 1075  
 Pan, W. 887  
 Pan, X.D. 127  
 Pan, Y. 199  
 Pan, Y. 515  
 Pan, Z.H. 1093  
 Pang, G.B. 659, 685  
 Pang, W. 1411  
 Peng, X.B. 489  
 Peng, X.W. 397  
 Pu, Q. 31  
  
 Qi, H. 21  
 Qi, Q.L. 771  
 Qi, X.J. 1069, 1075  
 Qian, F. 1301  
 Qian, H.F. 347, 365  
 Qian, L. 893  
 Qin, B. 735, 739  
 Qin, H.R. 347, 365  
 Qin, L.M. 1075  
 Qin, M.L. 1331, 1339  
 Qin, T.L. 1209  
 Qiu, C. 701  
 Qiu, P.F. 1183  
  
 Ran, H.D. 471  
 Ren, J. 713  
 Ren, W. 45  
 Ren, Y. 785  
 Ren, Z. 765  
  
 Shadab Far, M. 187  
 Shan, R. 155, 159  
 Shang, L. 1049  
 Shao, A.L. 1293  
 Shao, J.H. 1139  
 Shao, W.J. 907  
 Shen, H. 351, 355  
 Sheng, T. 643  
 Shi, C. 879  
 Shi, J. 633  
 Shi, K.R. 165  
 Shi, L.J. 287  
 Shi, Q. 1403, 1407  
  
 Shi, Q.F. 1245  
 Shi, Y. 1191  
 Shi, Y.Q. 691  
 Shi, Z. 31  
 Shi, Z.Q. 961  
 Song, P. 995  
 Song, X.G. 541  
 Song, X.X. 861  
 Song, Y. 1313  
 Song, Z. 1163  
 Su, E. 577  
 Su, J. 1035  
 Su, S.Y. 1297  
 Su, Y. 109  
 Sun, H.D. 35  
 Sun, J. 713  
 Sun, J. 1065  
 Sun, J.H. 419  
 Sun, L. 27  
 Sun, L. 1383  
 Sun, L.Z. 27  
 Sun, M.G. 203  
 Sun, M.M. 407, 411  
 Sun, W. 131  
 Sun, X.H. 269, 275, 281  
 Sun, X.N. 1351  
 Sun, Y. 1173  
 Sun, Y.H. 339  
 Sun, Z. 41  
 Sun, Z. 251  
 Suo, L.S. 1133  
  
 Tan, J. 1145  
 Tan, J.-h. 1145  
 Tan, W.X. 809  
 Tang, M. 301  
 Tang, W.Q. 961  
 Tang, Y. 1331  
 Tang, Z. 587  
 Tang, Z.Z. 795  
 Tao, L.J. 295  
 Tao, M. 717  
 Tao, T. 1145  
 Tao, T.J. 875, 951, 1101  
 Tao, W. 155, 159  
 Tao, X.X. 461  
 Tao, Z.R. 461  
 Ten, F. 121  
 Tian, Q.M. 313  
 Tian, X. 731  
 Tong, X. 833  
 Tong, Z.N. 1055, 1367  
 Torquet, I. 477  
  
 Wan, B. 159  
 Wan, Y.Y. 1327  
 Wang, A. 791  
 Wang, B. 41, 45

Wang, B. 69, 841, 899  
 Wang, B. 845  
 Wang, B. 1249  
 Wang, C. 159  
 Wang, C. 291  
 Wang, C. 541  
 Wang, F. 177  
 Wang, F. 1203  
 Wang, G. 495, 501  
 Wang, G.Q. 985  
 Wang, G.-x. 465  
 Wang, H. 825  
 Wang, H. 989  
 Wang, H.D. 339  
 Wang, H.N. 137  
 Wang, H.Y. 149  
 Wang, J. 45  
 Wang, J. 867  
 Wang, J. 1023  
 Wang, J. 1411  
 Wang, J.-g. 1153  
 Wang, J.H. 295  
 Wang, J.J. 795  
 Wang, J.L. 1363  
 Wang, J.-S. 141  
 Wang, K. 373  
 Wang, K. 569  
 Wang, L. 1029  
 Wang, L.-y. 721  
 Wang, P. 177  
 Wang, P. 441, 447  
 Wang, P.-N. 1083  
 Wang, Q. 365  
 Wang, Q. 995  
 Wang, Q. 1313  
 Wang, Q.-f. 593  
 Wang, S. 647  
 Wang, S.N. 109  
 Wang, S.Y. 697  
 Wang, S.Z. 727  
 Wang, SH.J. 977, 981  
 Wang, T. 47  
 Wang, W. 51  
 Wang, W. 73, 79, 845  
 Wang, W. 547  
 Wang, X. 3  
 Wang, X. 309  
 Wang, X. 609  
 Wang, X. 1383  
 Wang, X.Q. 407  
 Wang, X.S. 1229  
 Wang, Y. 155, 159  
 Wang, Y. 893  
 Wang, Y. 1105  
 Wang, Y.T. 681  
 Wang, Z. 319  
 Wang, Z. 1319  
 Wang, Z.H. 1139  
 Wang, Z.J. 653, 665  
 Wang, Z.L. 771  
 Wei, B. 441, 447  
 Wei, C.H. 927  
 Wei, D. 601  
 Wei, G. 63  
 Wei, H. 1089  
 Wei, J.P. 85  
 Wei, Y. 569, 577  
 Wen, T. 1323, 1327  
 Wen, Y. 73, 79  
 Weng, B.S. 743  
 Wu, C.P. 757  
 Wu, C.Y. 1093  
 Wu, G.Y. 757  
 Wu, J. 1111  
 Wu, J.-j. 219  
 Wu, Q.-h. 1387  
 Wu, S.C. 313  
 Wu, W.Y. 795  
 Wu, W.-Y. 9, 433, 437  
 Wu, X. 565  
 Wu, X. 837  
 Wu, Y. 965  
 Wu, Y.J. 149  
 Wu, Y.J. 861  
 Xi, C. 893  
 Xia, J. 351, 355  
 Xia, X.T. 583  
 Xia, Z. 587  
 Xiang, Y. 653  
 Xiao, K. 917  
 Xiao, K.L. 961  
 Xiao, L.G. 981  
 Xiao, S. 313  
 Xie, F. 1345  
 Xie, L.L. 1075  
 Xie, Y. 569, 577  
 Xin, M.M. 359  
 Xing, L. 647  
 Xu, C. 183  
 Xu, C. 183  
 Xu, H.F. 415  
 Xu, J.F. 955  
 Xu, L. 237  
 Xu, L.-Y. 535  
 Xu, M.-j. 1187  
 Xu, P. 833  
 Xu, S.Y. 923  
 Xu, T. 69  
 Xu, T. 97  
 Xu, W. 1121, 1125  
 Xu, W.C. 691  
 Xu, X.E. 675  
 Xu, X.F. 955  
 Xu, X.S. 15  
 Xu, X.-Y. 305, 309  
 Xu, Y.Q. 849  
 Xu, Z.G. 145  
 Xu, Z.H. 659  
 Xue, X.C. 287  
 Ya, J. 1331, 1339  
 Yan, D.H. 743  
 Yan, J.J. 1035  
 Yan, L. 263  
 Yan, M. 1045  
 Yan, Y.X. 227  
 Yang, D.Z. 511  
 Yang, H.Q. 1035  
 Yang, J. 47  
 Yang, J. 1111  
 Yang, J. 1263, 1399  
 Yang, J. 1417  
 Yang, J.N. 1305, 1309  
 Yang, L. 1301  
 Yang, L.Q. 735, 739  
 Yang, M. 547  
 Yang, M.J. 1209  
 Yang, P.B. 287  
 Yang, R. 145  
 Yang, S.F. 85  
 Yang, S.X. 373  
 Yang, T.H. 441, 447  
 Yang, W.L. 489  
 Yang, X.B. 727  
 Yang, X.-m. 219  
 Yang, X.W. 627  
 Yang, Y. 199  
 Yang, Y. 551  
 Yang, Y. 1187  
 Yang, Z. 647  
 Yang, Z.-s. 1187  
 Yao, Y. 985  
 Yao, Z.B. 127  
 Ye, G.B. 255  
 Ye, X. 887  
 Ye, X.F. 639  
 Ye, X.F. 1139  
 Ye, Z.Y. 359  
 Yeh, J.-P. 1083  
 Yi, H. 1387  
 Yin, B.S. 511  
 Yin, Y. 207  
 You, X.Y. 1215  
 Yu, C. 369  
 Yu, L.Z. 1049  
 Yu, X.D. 441, 447  
 Yu, Z.L. 1209  
 Yuan, D.C. 93  
 Yuan, D.C. 397  
 Yuan, G. 1029



Yuan, H. 947  
 Yuan, X. 565  
 Yue, S. 761, 1371  
 Yue, S.Z. 1001  
  
 Zeng, J.J. 325  
 Zeng, Y. 707  
 Zhai, J.-F. 505  
 Zhai, Z.X. 359  
 Zhan, Q. 613  
 Zhang, B. 1039  
 Zhang, C. 301  
 Zhang, C.L. 995  
 Zhang, D. 97  
 Zhang, D. 207  
 Zhang, D. 643  
 Zhang, D. 985  
 Zhang, D. 1287  
 Zhang, F. 1403  
 Zhang, F.L. 383  
 Zhang, H. 203  
 Zhang, H. 219  
 Zhang, H. 1357  
 Zhang, H. 1407  
 Zhang, H.B. 541  
 Zhang, H.F. 623  
 Zhang, H.Z. 1049  
 Zhang, J. 41  
 Zhang, J. 531  
 Zhang, J. 535  
 Zhang, J. 605  
 Zhang, J. 765  
 Zhang, K. 1363  
 Zhang, L. 177  
 Zhang, L. 989  
 Zhang, L. 1011  
 Zhang, L. 1045  
 Zhang, L.J. 1173  
 Zhang, L.-p. 219  
 Zhang, L.Y. 287  
 Zhang, M. 291  
 Zhang, M. 833  
 Zhang, M.-j. 597  
 Zhang, Q. 379  
 Zhang, Q. 1203  
  
 Zhang, Q. 1273, 1279  
 Zhang, Q.W. 255  
 Zhang, R.J. 717, 753  
 Zhang, S. 659, 685  
 Zhang, S.M. 173, 407, 411, 415  
 Zhang, S.-q. 1187  
 Zhang, S.X. 771  
 Zhang, S.Y. 1209  
 Zhang, T. 319  
 Zhang, T. 1273, 1279  
 Zhang, T.W. 213  
 Zhang, W. 791  
 Zhang, W.L. 1253  
 Zhang, X. 247  
 Zhang, X. 515, 525, 531  
 Zhang, X. 803  
 Zhang, X. 1079  
 Zhang, X. 1105  
 Zhang, X.C. 213  
 Zhang, X.G. 1069  
 Zhang, X.H. 1049  
 Zhang, X.L. 213  
 Zhang, Y. 1045  
 Zhang, Y.C. 287  
 Zhang, Y.g. 453  
 Zhang, Y.-S. 319  
 Zhang, Y.Y. 27  
 Zhang, Z. 45  
 Zhang, Z. 177  
 Zhang, Z. 255  
 Zhang, Z. 393  
 Zhang, Z. 519  
 Zhang, Z.B. 145  
 Zhang, Z.H. 803  
 Zhang, Z.-p. 1145  
 Zhao, G. 15  
 Zhao, G.M. 415  
 Zhao, H.J. 747  
 Zhao, J. 251  
 Zhao, J. 465  
 Zhao, J. 1331, 1339  
 Zhao, J.X. 419  
 Zhao, L. 73, 79  
 Zhao, L. 127  
 Zhao, L. 601  
  
 Zhao, L. 785  
 Zhao, M. 155  
 Zhao, M. 795  
 Zhao, M.S. 875, 951, 1101  
 Zhao, N. 1323  
 Zhao, Q. 1229  
 Zhao, S.M. 1215  
 Zhao, W.j. 453  
 Zhao, X.R. 1245  
 Zhao, X.Y. 1223  
 Zhao, Y. 183  
 Zhao, Y.Y. 213  
 Zhao, Z.K. 985  
 Zheng, D. 813  
 Zhong, Q. 453  
 Zhou, H. 1017  
 Zhou, H.L. 295  
 Zhou, J. 647  
 Zhou, J.M. 717, 753  
 Zhou, L. 577  
 Zhou, M.H. 383  
 Zhou, Q. 359  
 Zhou, S.H. 1035  
 Zhou, T.Q. 347, 365  
 Zhou, Y. 31  
 Zhou, Y. 59  
 Zhou, Y. 707  
 Zhou, Y.J. 35  
 Zhou, Y.-p. 535  
 Zhou, Z. 613  
 Zhu, B.H. 461  
 Zhu, C. 785  
 Zhu, G.-l. 369  
 Zhu, L. 369  
 Zhu, S.R. 923  
 Zhu, W. 1183  
 Zhu, W.H. 583  
 Zhu, X. 587  
 Zhu, Z.-X. 505  
 Zhuang, H. 647  
 Zhuang, N. 35  
 Zhuo, Z. 1191  
 Zuo, S.H. 519  
 Zuo, Y.F. 1001